Vol. 76, No. 2 / 2025

e: ISSN 2068 – 2239
p: ISSN 2068 – 4215

INMATEH –

AGRICULTURAL ENGINEERING

MAY - AUGUST

No liability is assumed by the editorial staff for the content of scientific papers and opinions published in this volume. They represent the author's point of view

Managing Editorial Board - INMA Bucharest

Editor in Chief

Lucian-Ionel CIOCA, Professor, PhD.Eng., "Lucian Blaga" University of Sibiu

Executive Editor

Lucreţia POPA
PhD.Eng, SR I

Assistant Editor

Nicolae-Valentin VLADUŢ
PhD.Eng, SR I
Mihai-Gabriel MATACHE
PhD.Eng, SR I

Logistic support, database

Virgil MURARU
PhD.Eng, SR I

Scientific Secretary

Cârdei Petre, math.

Official translator

RADU Daniela-Cristina, English

Editorial Board

- *QUENDLER Elisabeth – Austria, Vienna, Univ. of Natural Resources & Applied Life Sciences;*
- *Ir. HUYGHEBAERT Bruno – Belgia, Walloon Agricultural Research Center CRA-W;*
- *Van IMPE F.M. Jan – Belgia, KU Leuven University*
- *FABBRO Dal Inacio Maria - Brazil, Campinas State University;*
- *ATANASOV Atanas – Bulgaria, "Angel Kanchev" University of Rousse*
- *MOLINOS-SENANTE María – Chile, Pontificia Universidad Católica - Vicedecana, Escuela de Ingeniería UC*
- *BILANDZIJA Nikola – Croatia, Zagreb University, Faculty of Agriculture;*
- *KOSUTIC Silvio – Croatia, Zagreb University, Faculty of Agriculture;*
- *KOVACEV Igor - Croatia, Zagreb University, Faculty of Agriculture;*
- *GONZÁLEZ Omar – Republic of Cuba, Central University "Marta Abreu" de las Villas;*
- *KATHIJOTES Nicholas – Cyprus, University of Nicosia;*
- *HERAK David - Czech Republic, Czech University of Agriculture Prague;*
- *BORCHARD Nils – Finland, Natural Resources Institute Finland (Luke);*
- *SAUER Johannes – Germany, Technical University Munich;*
- *FENYVESI László – Hungary, Hungarian Institute of Agricultural Engineering Godolo;*
- *PEEYUSH Soni - India, Indian Institute of Technology, Kharagpur;*
- *MOHAMMADREZA Alizadeh – Iran, Department of Agricultural Engineering, Rice Research Institute of Iran (RRII);*
- *De WRACHIEN Daniele - Italy, State University of Milan;*
- *BIOCCA Marcello - Italy, Agricultural Research Council, Agricultural Engineering Research Unit;*
- *COLANTONI Andrea – Italy, University Viterbo;*
- *SARAUSSKIS Egidijus – Lithuania, Vytautas Magnus University, Faculty of Agricultural Engineering;*
- *KRIAUCIUNIENE Zita - Lithuania, Vytautas Magnus University;*
- *DUKE Mike – New Zealand, University of Waikato, Faculty of Science and Engineering;*
- *EWEMOJE Temitayo Abayomy – Nigeria, University of Ibadan, Faculty of Technology, Department of Agricultural and Environmental Engineering;*
- *SKIERUCHA Wojciech – Poland, Institute of Agro-physics Polish Academy of Sciences, Lublin;*
- *EKIELSKI Adam - Poland, Warsaw University of Life Sciences;*
- *KOT Sebastian - Poland, Czestochowa University of Technology*
- *SAVIN Lazar– Serbia, University of Novi Sad, Faculty of Agriculture, Department of Agricultural Engineering;*
- *SIMIKIC Mirko– Serbia, University of Novi Sad, Faculty of Agriculture, Department of Agricultural Engineering;*
- *MARTINOV Milan - Serbia, Faculty of Agriculture, Department of Agricultural Engineering,*
- *TURAN Jan – Slovakia, Technical University Kosice, Dept Elect & Multimedia Commun, Kosice;*
- *MADYIRA M. Daniel - South Africa, University of Johannesburg, Mechanical Engineering Science Department*
- *COZ FERNANDEZ Alberto – Spain, University of Cantabria, School of Nautical Studies, Department of Chemistry and Process & Resource Engineering;*
- *ERTEKIN Can - Turkey, Akdeniz University Antalia;*
- *KABAŞ Önder –Turkey, Antalia, Agricultural Scientific Research Institute of Batı Akdeniz;*
- *SELVİ Kemal Çağatay - Turkey, Samsun, University of Ondokuz Mayıs, Faculty of Agriculture, Department of Machines for Agriculture;*
- *ÖTLEŞ Semih - Turkey, Ege University, Engineering Faculty, Food Engineering Department;*
- *MARUSCHAK Pavlo - Ukraine, Ternopil Ivan Pul'uj National Technical University, Department of Technical Mechanics and Agricultural Engineering;*
- *BULGAKOV Volodymyr – Ukraine, National University of Life and Environmental Sciences of Ukraine;*
- *PARASCHIV Gigel - Romania, Politehnica University of Bucharest;*
- *VOICU Gheorghe - Romania, Politehnica University of Bucharest;*
- *BIRIŞ Sorin - Romania, Politehnica University of Bucharest;*
- *MAICAN Edmond - Romania, Politehnica University of Bucharest;*
- *FILIP Nicolae - Romania, Technical University Cluj Napoca;*
- *COZAR Onuc-Romania, „Babes-Bolyai" University of Cluj-Napoca Romania, Faculty of Physics;*
- *VLASE Sorin - Romania, "Transilvania" University of Braşov;*
- *ŢENU Ioan - Romania, USAMV Iaşi;*
- *HERIŞANU Nicolae - Romania, Politehnica University of Timisoara;*
- *MARSAVINA Liviu - Romania, Politehnica University of Timisoara*
- *MARINCA Vasile - Romania, Politehnica University of Timisoara*
- *GERGEN Iosif - Romania, USAMVB Timişoara;*
- *BORDEAN Despina-Maria - Romania, USAMVB Timişoara;*
- *BUNGESCU Sorin - Romania, USAMVB Timişoara;*
- *RODINA Steliana – Romania, ICEADR, Bucharest;*
- *VOICEA Iulian - Romania, INMA Bucharest;*
- *DEAK Gyorgy - Romania, INCDPM Bucharest;;*
- *BELC Nastasia - Romania, IBA Bucharest;*
- *BUŢU Alina - Romania, INCDSB Bucharest;*
- *PAUN Mihaela - Romania, INCDSB, Bucharest*

INMATEH - Agricultural Engineering **journal is indexed in the next international databases:**
ELSEVIER /SciVerse SCOPUS, CLARIVATE - WEB of SCIENCE- Emerging Sources Citation Index (ESCI), ULRICHS Web: Global Serials Directory, CABI, SCIPIO, Index COPERNICUS International, EBSCO Publishing, Elektronische Zeitschriftenbibliothek

INMATEH - Agricultural Engineering
vol. 76, no.2 / 2025
e-ISSN: 2068 – 2239; p: ISSN: 2068 – 4215

https://inmateh.eu/ *E-mail: inmatehjournal@gmail.com*

Edited by: INMA Bucharest
Copyright: INMA Bucharest / Romania
National Institute for Research-Development of Machines and Installations
Designed for Agriculture and Food Industry - INMA Bucharest
6, Ion Ionescu de la Brad Bvd., sector 1, Bucharest, ROMANIA

CONTENT

1.	**DESIGN AND EXPERIMENT OF COTTON STALKS PULLING DEVICE WITH NON-FLAT TOOTHED DISCS /** *仰角齿盘式拔棉秆装置设计与试验* **Weisong ZHAO[1,2,3], MINGJIANG CHEN[1,3], Jianhua XIE[2*], Jia ZHANG[2], Zhenwei WANG[1], Chunsong GUAN[1,3], Yan GONG[1,3]** [1] Nanjing Institute of Agricultural Mechanization, Ministry of Agriculture and Rural Affairs, Nanjing, China; [2] College of Mechanical and Electrical Engineering, Xinjiang Agricultural University, Urumqi, China; [3] Institute of Western Agriculture, the Chinese Academy of Agricultural sciences, Changji, China	15
2.	**DISCRETE ELEMENT MODELING AND PARAMETER CALIBRATION FOR CORYDALIS TUBER /** *延胡索离散元模型构建及参数标定* **Xiangyang LIU[1], Chun WANG[1,2], Yongchao Shao[1], Weiguo ZHANG[1*]** [1]College of Mechanical and Electrical Engineering, Northwest Agriculture and Forestry University, Yangling, China; [2]College of Biological and Agricultural Engineering, Jilin University, Changchun, China	26
3.	**DAMAGE CLASSIFICATION OF CASTOR SEEDS BASED ON MODIFIED AlexNet /** *基于卷积神经网络的蓖麻种子损伤分类* **Junming HOU, Yue MA, Enchao YAO, Zheng LI, Yandong XU** College of Engineering, Shenyang Agricultural University, Shenyang, China	38
4.	**INTELLIGENT OBSTACLE AVOIDANCE CONTROL ALGORITHM FOR AGRICULTURAL DRONES IN COMPLEX FARMLAND ENVIRONMENTS /** *面向复杂农田环境的农业无人机智能避障控制算法研究* **Yuan MEI[1]; Rui ZENG[2]; Wanting XU[1]; Xinyue ZHOU[1]; Zhiwei JIN[1]** [1] Wuhu Institute of Technology, Wuhu, Anhui, China; [2] CETC Wuhu General Aviation Industry Technology Research Institute Co., Ltd., Wuhu, Anhui, China	48
5.	**RESEARCH AND DEVELOPMENT OF AN INTEGRATED HEADER FOR SOYBEAN-CORN COMBINED HARVESTERS ADAPTED TO STRIP INTERCROPPING /** *大豆玉米复合种植一体化联合收获机割台研究与创制* **Jinshan XU[1], Chengqian JIN[1,2*], Qiaomin CHEN[1*], Youliang NI[1], Man CHEN [1], Guangyue ZHANG [1], Tengxiang Yang[1]** [1] Nanjing Institute of Agricultural Mechanization, Ministry of Agriculture and Rural Affairs, Nanjing, Jiangsu / China; [2]College of Agricultural Engineering and Food Science, Shandong University of Technology, Zibo, China	58
6.	**POINT CLOUD GROUND SEGMENTATION ALGORITHM OF VINEYARD AGRICULTURAL ROBOT BASED ON SURFACE FITTING /** *基于曲面拟合的葡萄园农业机器人点云地面分割算法* **Fa SUN, Fanjun MENG, Mengmeng NI, Zhisheng ZHAO, Lili YI** Shandong University of Technology, Collage of Agricultural Engineering and Food Science, ZiBO, China	69
7.	**YOLOv8-STEM: ENHANCED OVERHEAD APPLE STEM DETECTION UNDER OCCLUSIONS /** ***YOLOv8-STEM：俯视视角下的苹果果柄遮挡识别*** **Li WANG[1], Yanqi SUN[1], Tianle ZHANG[1], Panpan YAN[2], Qiangqiang YAO[3], Zhen MA[4], Degui MA[5], Xingdong SUN[1*]** [1]Anhui Agricultural University College of Engineering, Hefei, Anhui, China; [2] Heze Vocational College, Heze,Shandong, China; [3]Qinghai University, China; [4]School of Agricultural Engineering, Jiangsu University, Zhenjiang, Jiangsu, China; [5]Anhui Agricultural University College of Engineering, Hefei, Anhui, China	79
8.	**STRAWBERRY IDENTIFICATION AND KEY POINTS DETECTION FOR PICKING BASED ON IMPROVED YOLOv8-POSE AT RED RIPE STAGE /** ***基于改进YOLOv8-pose的红熟期草莓识别与采摘关键点检测*** **Jinlong WU*[,1,2], Ronghui MIAO[1,2]** [1] College of information science and engineering, Shanxi agricultural university, Taigu / China; [2] College of agricultural engineering, Shanxi agricultural university, Taigu / China	89
9.	**ESTABLISHMENT AND VALIDATION OF A THEORETICAL MODEL FOR SINGLE LONGITUDINAL AXIAL FLOW THRESHING AND SEPARATION OF MILLET /** *谷子单纵轴流脱粒分离理论模型的建立与验证* **Jun-hui ZHANG[1], Lin ZHAO[1], Shu-juan YI[*1]; Dong-ming ZHANG[1]; Xin ZHANG[3]** [1]College of Engineering, Heilongjiang Bayi Agricultural University, Daqing / P.R.China; [2]Beijing Polytechnic, Beijing, China; [3]Engineering Technology Research Institute, Daqing Drilling Engineering Co., Ltd., Daqing, China	100
10.	**LCNET: LIGHTWEIGHT CONVOLUTIONAL NEURAL NETWORK FOR CORN LEAF DISEASE CLASSIFICATION /** एलसीनेट: मकई पत्ती रोग वर्गीकरण के लिए हल्का संवादात्मक तंत्रिका नेटवर्क **Vimal SINGH[*1,2], Anuradha CHUG[1], Amit Prakash SINGH[1]** [1] University School of Information, Communication & Technology Guru Gobind Singh Indraprastha University Dwarka, Sector-16 C, New Delhi, India. [2] School of Computing Science & Engineering Galgotias University, Greater Noida, Uttar Pradesh, India	111
11.	**DESIGN AND PARAMETER OPTIMIZATION OF A SEED STORAGE DEVICE OF A WHEAT PLOT SEEDER /** *小麦小区播种机存种装置的设计与参数优化* **Chen XUE, Liqing CHEN*), Zengbin CAI, Qi WANG** College of Engineering, Anhui Agricultural University, Hefei, Anhui / China	121

12.	**RICE SEED CLASSIFICATION BASED ON SE-ResNet50 /** *基于SE-ResNet50的稻种分类* **Zhen MA[1)], Sa WANG[1)], Hongxiong SU[1)], Juxia LI[*1)], Yanwen LI[1)], Zhifang BI[2)], Xiaojie LI[1)]** [1)] College of Information Science and Engineering, Shanxi Agricultural University, Taigu /China; [2)] Department of Basic Sciences, Shanxi Agricultural University, Taigu / China	131
13.	**SAFF-YOLO-BASED LIGHTWEIGHT DETECTION METHOD FOR THE DIAMONDBACK MOTH /** *基于SAFF-YOLO的白菜小菜蛾轻量化检测方法* **Miao WU [1,2,)], Hang SHI [1,2,)], Changxi LIU [1,2,)], Hui ZHANG [1,2,)], Yufei LI [1,2,)], Derui BAO [1,2,)], Jun HU [*1,2,)]** [1)]College of Engineering, Heilongjiang Bayi Agricultural University, Daqing / China; [2)]Heilongjiang Province Conservation Tillage Engineering Technology Research Center, Daqing / China	142
14.	**DESIGN AND TESTING OF A FULL-DEGREE-OF-FREEDOM CONSTRAINED SEED GUIDING DEVICE FOR ORDERED SEED FLOW /** *有序种子流全自由度约束导种装置设计与试验* **Xin DU*, Qianhao YU, Shufa CHEN, Qixin SUN, Yue JIANG, Jingyi MAO** Jiangsu Ocean University, Lianyungang / China	156
15.	**DESIGN AND EXPERIMENTAL STUDY OF A CRAWLER-TYPE PRECISION PESTICIDE APPLICATOR BASED ON DEM /** *基于DEM的履带式精准施药机设计与试验研究* **ZhiMing SHI[1,2)], Hang ZHAO[1,2)], ShouTai LI[3)], ZiWen CHEN[3)], JunJie CHEN[*1,2)], MingJin YANG [*3)]** Southwest University, College of Artificial Intelligence, Chongqing, China; [2)] National & Local Joint Engineering Research Center of Intelligent Transmission and Control Technology, Chongqing, China; [3)] Southwest University, College of Engineering and Technology, Chongqing, China	167
16.	**DESIGN AND OPTIMISATION OF ROTARY TILLER BLADE FOR ORCHARDS IN HILLY MOUNTAINOUS AREAS BASED ON THE DISCRETE ELEMENT METHOD /** *基于离散元法的丘陵山区果园圆盘式开沟刀具设计与优化* **Jing MI [1)], Huan XIE [*2)] Po NIU[*1)]** [1)]College of Mechanical Engineering, Chongqing Three Gorges University, Chongqing/China. [2)]Chongqing Three Gorges Vocational College, School of Automotive Engineering	177
17.	**DESIGN AND TESTING OF HYDRAULIC DRIVE SYSTEM FOR CRAWLER-TYPE TIGER-NUT HARVESTER /** *履带式油莎豆收获机液压驱动行走系统的设计与试验* **Zhe QU, Jianhao ZHANG, Jintao LE, Xilong WANG, Haihao SHAO, Huihui ZHAO, Zhijun L., Wanzhang WANG*** College of Mechanical and Electrical Engineering, Henan Agricultural University, Zhengzhou, China	187
18.	**DETECTION METHOD OF COTTON COMMON PESTS AND DISEASES BASED ON IMPROVED YOLOv5S /** *基于改进YOLOV5S的棉花常见病虫害检测方法* **Yulong WANG[1,2,3,#], Fengkui ZHANG[1,2,3,#], Rina YANGDAO[1,2,3], Ruohong HE[1,2,3], Jikui ZHU[1,2,3], Ping LI[1,2,3,*]** [1)] College of Mechanical and Electrical Engineering, Tarim University, Alar, Xinjiang, China [2)] Xinjiang Production and Construction Corps (XPCC) Key Laboratory of Utilization and Equipment of Special Agricultural and Forestry Products in Southern Xinjiang, Xinjiang, China [3)] Modern Agricultural Engineering Key Laboratory at Universities of Education Department of Xinjiang Uygur Autonomous Region, Xinjiang, China	199
19.	**DESIGN AND EXPERIMENT OF AN AIR-ASSISTED, GUIDED-GROOVE MAIZE SEED-GUIDING DEVICE BASED ON THE BRACHISTOCHRONE CURVE /** *基于最速降线的气辅-导槽式玉米导种装置设计与试验* **Wen-sheng SUN [1)], Shu-juan YI[*2)], Hai-long QI [2)], Yi-fei LI [1,3)], Yu-peng ZHANG [1)], Jia-sha YUAN [1)], Song WANG [1)]** [1)]College of Engineering, Heilongjiang Bayi Agricultural University, Daqing/P.R.China; [2)]Heilongjiang Beidahuang Modern Agricultural Service Group Zhongrong Agricultural Machinery Co., Ltd, Harbin / P.R.China; [3)]College of Engineering, Northeast Agricultural University, Harbin/P.R.China	210
20.	**DEM-BASED CALIBRATION OF SOIL CONTACT PARAMETERS PRIOR TO GRAPEVINE BURYING /** *基于离散元法的葡萄藤埋前土壤接触参数标定* **Beibei ZHANG[1)], Julaiti MAITIROUZI[*1)], Shixiang XING[1)], Hongcheng DENG[2)], Wenjing BAI[2)], Haileeqguli YASEN[2)]** [1)] College of Mechanical Engineering, Xinjiang University, Urumqi/China; [2)] Turpan Agricultural and Rural Mechanization Development Center, Turpan/China	223
21.	**RESEARCH ON ADVANCED COMPENSATION CONTROL STRATEGY FOR SOYBEAN COMBINE HARVESTER HEADER HEIGHT BASED ON AREA ARRAY LiDAR /** *基于面阵激光雷达的大豆联合收割机割台高度超前补偿控制策略研究* **Qingling LI[1,2)], Chao ZHANG[*1,2)], Shaobo YE [1,2)], Decong ZHENG[1,2)]** [1)] College of Agricultural Engineering, Shanxi Agricultural University, Taigu, China; [2)]Dryland Farm Machinery Key Technology and Equipment Key Laboratory of Shanxi Province, Taigu, China	237
22.	**ASSESSING THE ENVIRONMENTAL ADAPTABILITY BASED ON LASER DETECTION FOR DETERMINING GAS EMISSIONS FROM AGRICULTURAL SOURCES /** *评估使用激光探测确定农业源气体排放的局部环境的适应性* **Xiaofeng LIU[1)], Fuhai ZHANG[1)], Jingjing YU[1)], Jiayuan WANG[1)], Juan LIAO[2)], Qixing TANG[2*)]** [1)]Anhui Eco-Environment Monitoring Center, Hefei, China; [2)]School of Engineering, Anhui Agricultural University, Hefei, China	246

23.	**DETECTION OF EARLY BRUISING IN 'HUANGGUAN' PEAR BASED ON MCC-DeepLabV3+ MODEL / *基于MCC-DeepLabV3+模型的皇冠梨早期瘀伤检测*** **Congkuan YAN, Haonan ZHAO, Dequan ZHU, Yuqing YANG, Ruixing XING, Qixing TANG, Juan LIAO*)** School of Engineering, Anhui Agricultural University, Hefei, China	256
24.	**EFFECT OF MOISTURE CONTENT ON SOME PHYSICAL AND MECHANICAL PROPERTIES OF WHEAT (*Triticum aestivum* L.) SEEDS /** ***ስንዴ (Triticum aestuum L.) ዘሮች የሚያሳው የእርጥበት ይዘት በአንዳንድ የአካላዊ እና መካኒካላዊ ባህሪዎች ላይ ያለው ተጽእኖ*** **Amansis TESHOME[1a*)], Adesoji M. OLANIYAN[2)], Abebe FANTA[1a)], Habtamu ALEMAYEHU[1b)], Meseret ABEBE[3),] Dereje ALEMU[3)], Mubarak MOHAMMED[3)], Tasfaye ASEFFA[3)]** [1a)] Department of Agricultural Engineering, Haramaya Institute of Technology, Haramaya University, Dire Dawa, Ethiopia; [1b)] Department of Mechanical Engineering, Haramaya Institute of Technology, Haramaya University, Dire Dawa, Ethiopia; [2)] Department of Agricultural and Bioresources Engineering, Faculty of Engineering, Federal University Oye-Ekiti, Ikole Ekiti, Nigeria; [3)] Ethiopian Institute of Agricultural Research (EIAR); Melkassa Agricultural Engineering Research, Melkassa Agricultural Research Centre. Adama, Ethiopia	271
25.	**REVIEW OF EXPERIMENTAL RESEARCH INVESTIGATIONS AND THE WORKING PRINCIPLE OF SMALL VERTICAL AXIS WIND TURBINES /** ***REVIZIA INVESTIGAȚILOR DE CERCETARE EXPERIMENTALĂ ȘI PRINCIPIUL DE FUNCȚIONARE AL TURBINELOR EOLIENE MICI CU AX VERTICAL*** **Adrian PANDELE*), Bogdan Ovidiu DURAN, Dragos Mihail PREDA, Gheorghe VOICU*)** National University of Science and Technology POLITEHNICA Bucharest, Romania	282
26.	**RESEARCH ON THE INFLUENCE OF EXTRUSION PARAMETERS ON SOLID-LIQUID SEPARATION PERFORMANCE OF LIVESTOCK MANURE AND OPTIMIZATION OF PARAMETERS** ***畜禽粪污螺旋挤压脱水装置参数优化设计与试验*** **Weisong ZHAO[1,2,3)], Qimin GAO[1)], Chunsong GUAN*[1)], Binxing Xu[1,3)], Biao MA*[1,2)], Yan Gong[1,2)]** [1)]Nanjing Institute of Agricultural Mechanization, Ministry of Agriculture and Rural Affairs, Nanjing, China; [2)]Institute of Western Agriculture, the Chinese Academy of Agricultural sciences, Changji, China [3)]College of Mechanical and Electrical Engineering, Xinjiang Agricultural University, Urumqi, China	308
27.	**LOW-COST IOT-BASED INTELLIGENT SAFFRON MANAGEMENT SYSTEM /** ***低成本物联网智能藏红花管理系统*** **Wai Leong PANG[1)], Jieru WANG[1)], Hui Hwang GOH[1)], Swee King PHANG[1)], Hafisoh AHMAD[1)], Kah Yoong CHAN*[2)]** [1)] School of Engineering, Centre for Sustainable Societies, Taylor's University, Taylor's Lakeside, Subang Jaya, Selangor, Malaysia; [2)] Centre for Advanced Devices and Systems, Faculty of Artificial Intelligence and Engineering, Multimedia University, Persiaran Multimedia, Cyberjaya, Selangor, Malaysia	318
28.	**ANALYSIS AND CALIBRATION OF DISCRETE ELEMENT PARAMETERS FOR *YANHUSUO* BASED ON STACKING TESTS /** ***基于堆积试验的延胡索离散元参数分析与标定*** **Chun WANG[1,2)], Xiangyang LIU[1)], Yongchao SHAO[1)], Weiguo ZHANG*[1)]** [1)]College of Mechanical and Electrical Engineering, Northwest Agriculture and Forestry University, Yangling, China; [2)]College of Biological and Agricultural Engineering, Jilin University, Changchun, China	327
29.	**DESIGN AND EXPERIMENT OF HIGH LEVEL UNLOADING LARGE GRAIN COLLECTION BOX FOR FRESH CORN COMBINED HARVESTER /** ***鲜食玉米联合收获机高位卸粮大型集粮箱设计与试验*** **Xin ZHANG*), Tong YE, Haitao LAN, Jingwen WU, Jianguo CHANG** Heilongjiang Academy of Agricultural Machinery Engineering Sciences, Harbin, China	338
30.	**RESEARCH ON SPEED CONTROL OF AN ELECTRICALLY DRIVEN THRESHING CYLINDER IN A COMBINE HARVESTER BASED ON INERTIA PARAMETER IDENTIFICATION /** ***基于惯量参数辨识的联合收割机电驱动脱粒滚筒转速控制研究*** **Yushuai QIAN*, Li QUAN, Jiapeng DIAO, Lei XU, Zixuan XIANG, Xiaoyong ZHU** School of Electrical and Information Engineering, Jiangsu University, Zhenjiang, Jiangsu, China	353
31.	**STABILITY ANALYSIS OF FLAT-ELLIPTICAL GREENHOUSE SKELETON CONSIDERING INITIAL GEOMETRICAL IMPERFECTIONS / *考虑初始几何缺陷的平椭圆管大棚骨架稳定性分析*** **Hengyan XIE[1,*)], Cunxing WEI[2)], Xin ZHENG[1)], Wenbao XU[1)]** [1)]College of Civil Engineering and Water Conservancy, Heilongjiang Bayi Agricultural University, Daqing, China; [2)] College of Engineering, Heilongjiang Bayi Agricultural University, Daqing, China	369
32.	**OPTIMIZATION DESIGN AND TEST OF BAFFLE STRUCTURE PARAMETERS OF THE HQ-800 STRAW MILL / *HQ-800型秸秆粉碎机隔板结构参数优化设计及试验*** **Kai YONG [1)], Qing TANG [2,3*)], Zhewen SONG [3)], Lan JIANG [2)]** [1)]School of Smart Manufacturing, Wuhu Institute of Technology, Wuhu, China; [2)]Nanjing Institute of Agricultural Meshanization, Ministry of Agriculture and Rural Affairs, Nanjing, China; [3)]Sinomach Changlin Co.Ltd., Changzhou, China.	380

33.	**STUDY ON THE STRAW-SOIL DISTURBANCE CHARACTERISTICS OF A LIFT-TYPE WINGED CHISEL PLOW / *抬土式带翼凿式犁对秸秆-土壤扰动特性的研究*** **Juanjuan WU[1)], Xianliang WANG * [2 3)], Kun CHEN[2 3)]** [1)] School of Intelligent Manufacturing, Zibo Polytechnic University, Zibo, China; [2)] College of Agricultural Engineering and Food Science, Shandong University of Technology, Zibo, China; [3)] Institute of Modern Agricultural Equipment, Shandong University of Technology, Zibo, China	394
34.	**STUDY ON THE IMPACT-BLOCKING EFFECT BETWEEN GRINDING MEDIA AND WHEAT BRAN POWDER DURING THE VIBRATION CRUSHING PROCESS /** ***振动粉碎过程中磨介与小麦麸皮粉体间的冲击阻滞效应研究*** **Min CHENG*[2)], Haocong MENG[1)], Guangbo Xiang*[2)], Shihao ZHOU[1)], Mingxu Wang[1)], Baoguo LIU[1)]** [1)] School of Mechanical and Electrical Engineering, Henan University of Technology, Zhengzhou / China; [2)] School of Mechanical Engineering, Zhengzhou University of Science and Technology, Zhengzhou / China	404
35.	**METHODS AND EXPERIMENTAL STUDY ON THE DETERMINATION OF FRICTION AND MECHANICAL PROPERTY PARAMETERS OF VARIOUS RICE SEED VARIETIES UNDER DIFFERENT CONDITIONS /*不同状态下多种水稻种子摩擦与力学特性参数测定方法及试验研究*** **Hanqing LI[1)], Shengnan LIU*[1)], Guangwei WU[2)], Bingxin YAN[2)], Lin LING[1,2)],** [1)] College of Intelligent Manufacturing, Nanyang Institute of Technology / China [2)] Research Center of Intelligent Equipment Technology, Beijing Academy of Agriculture and Forestry Sciences / China [3)] College of Engineering Technology, Southwest University / China	416
36.	**DESIGN AND EXPERIMENTAL STUDY OF AN ADJUSTABLE WRAPPING MACHINE FOR RICE STRAW BALES OF DIFFERENT SIZES / *可调式秸秆包捆机的设计与试验研究*** **Liyan WU[1)], Huchao TAN[2)], Na ZHANG[1)], Hengyi WEI[1)], Zhenyu WANG[1)], Chunhua BAN[3)], Cuihong LIU*[1)]** [1)]College of Engineering, Shenyang Agricultural University, Shenyang / China [2)]Yantai Taihai Manoir Nuclear Power Equipment Co., Ltd., Yantai / China [3)]Liaoning Provincial Institute of Agricultural Mechanization / China	428
37.	**EFFECTS OF DIFFERENT VENTILATION VELOCITIES ON THE THERMAL ENVIRONMENT OF SOLAR GREENHOUSES / *不同通风速度对日光温室热环境的影响*** **Chuyuan ZHONG, Huiqun ZHOU** Horsh (FUjian) Food Co., Ltd, Fujian / China	441
38.	**EFFECTS OF ELECTRIC VOLTAGE AND WATER VOLUME ON OHMIC HEATING HYDRODISTILLATION (OHHD) OF NUTMEG LEAVES /** ***PENGARUH TEGANGAN LISTRIK DAN VOLUME AIR PADA HIDRODISTILASI OHMIK HEATING DAUN PALA*** **Imam SOFI'I[1)*], WINARTO[1)], Oktaf RINA[1)]** Department of Agricultural Technology, Politeknik Negeri Lampung, Bandar Lampung, Lampung / Indonesia	451
39.	**OPTIMIZATION DESIGN AND TEST OF INTERACTIVE ANTI-STICK GEAR FERTILIZER DISCHARGER FOR PINEAPPLE / *菠萝专用交互式防粘齿轮排肥器的优化与试验*** **Guoqiang DUN*[1)], Chunyu MA[2)], Xinxin JI[2)], Hailiang LI*[3)], Haochun CHENG[2)],** **Haitian SUN[3)], Chaoxia ZHANG[2)]** [1)] Harbin Cambridge University, Intelligent Agricultural Machinery Equipment Engineering Laboratory, Harbin / China; [2)] Northeast Forestry University, College of Mechanical and Electrical Engineering, Harbin/China; [3)] South Subtropical Crop Research Institute, Chinese Academy of Tropical Agricultural Sciences, Key Laboratory of Tropical Fruit Biology, Ministry of Agriculture & Rural Affairs, Key Laboratory of Hainan Province for Postharvest Physiology and Technology of Tropical Horticultural Products, Zhanjiang / China	461
40.	**RESEARCH ON THE VIBRATION AND FRUIT DROP CHARACTERISTICS OF CAMELLIA OLEIFERA BASED ON HIGH-SPEED PHOTOGRAPHY TECHNOLOGY /** ***基于高速摄影技术的油茶振动落果特性研究*** **Zhihao ZHU[1)], Xiaoyu CHAI *[1)], Lizhang XU[2)], Li QUAN[3)], Chaochun YUAN[4)], En LU[1)],** **Shuofeng WENG[3)], Shichao TIAN[1)], Guangqiao CAO[5)]** Chinese Academy of Agricultural Mechanization Science Group Co., Ltd., Beijing / China	475
41.	**RESEARCH ON TORQUE DYNAMIC COORDINATED CONTROL OF A NOVEL DUAL POWER SOURCE THRESHING DRUM OF COMBINE HARVESTER /** ***新型双动力源脱粒滚筒扭矩动态协调控制研究*** **Zhihao ZHU[1)], Xiaoyu CHAI *[1)], Lizhang XU[2)], Li QUAN[3)], Chaochun YUAN[4)], En LU[1)],** **Shuofeng WENG[3)], Shichao TIAN[1)], Guangqiao CAO[5)]** [1)]School of Agriculture Engineering, Jiangsu University, China [2)]Key Laboratory for Theory and Technology of Intelligent Agriculture Machinery and Equipment, Jiangsu University, China; [3)]School of Electrical and Information, Jiangsu University, China [4)]Automotive Engineering Research Institute, Jiangsu University, China [5)]Nanjing Institute of Agricultural Mechanization, Ministry of Agriculture and Rural Affairs, China	483
42.	**SUBSTANTIATION OF EQUIPMENT PARAMETERS FOR COMPACTING PLANT MATERIALS /** ***ОБОСНОВАНИЕ ПАРАМЕТРОВ ОБОРУДОВАНИЯ ДЛЯ УПЛОТНЕНИЯ РАСТИТЕЛЬНЫХ МАТЕРИАЛОВ*** **Dmitry MILKO[*)], Anna PEDCHENKO[1)], Tatyana KLEVTSOVA[1)], Alexander GVOZDEV[1)]** [1)] Melitopol State University / Russia	496

43.	**PREDICTION OF BOESENBERGIA ROTUNDA (L.) DRYING USING HOT AIR AND ULTRASONIC VIBRATION VIA EXTREME GRADIENT BOOSTING /** *การทำนายการอบแห้งของกระชายขาวด้วยลมร้อนและการสั่นสะเทือนความถี่สูงโดยใช้เทคนิคเอ็กซ์ตรีมเกรเดียนต์บูสติง* **Patipat THANOMPONGCHART[1)], Pakamon PINTANA[2)], Tossapon KATONGTUNG[3)], James C. MORAN[3)], Nakorn TIPPAYAWONG[*3)]** [1)] Industrial Energy Management Engineering Program, Faculty of Industrial Technology, Uttaradit Rajabhat University / Thailand; [2)] School of Renewable Energy, Maejo University, Chiang Mai / Thailand; [3)] Department of Mechanical Engineering, Faculty of Engineering, Chiang Mai University, Chiang Mai / Thailand	**506**
44.	**RESEARCH ON THE TRAY CONVEYING AND OUTPUT DEVICE OF AN AUTOMATIC TRAY PLACEMENT MACHINE FOR MULTI-ROW RIGID RICE SEEDLING TRAYS /** *多行水稻硬质育秧盘全自动摆盘机送盘与出盘装置研究* **Cheng-long LIU[1)], Shu-juan YI[*1)], Yi-fei LI[1,2)], Song WANG[1)]** [1)]College of Engineering, Heilongjiang Bayi Agricultural University, Daqing/P. R. China [2)]College of Engineering, Northeast Agricultural University, Harbin/P. R. China	**517**
45.	**RESEARCH ON A DETECTION ALGORITHM FOR DRY-DIRECT SEEDED RICE BASED ON YOLOv11N-DF /** *基于YOLOv11n-DF的旱直播水稻检测算法研究* **Mingyang LI, Bin ZHAO[*)], Song WANG, Di WANG** College of engineering, Heilongjiang Bayi Agricultural University, Daqing/ China	**531**
46.	**DIGITAL TECHNOLOGIES IN AGRICULTURE. SCANFIELD-5S SMART SYSTEM WITH INTEGRATED DIGITAL SOIL CUBE FOR INNOVATIVE SOLUTIONS IN AGRICULTURE /** *ЦИФРОВИ ТЕХНОЛОГИИ В ЗЕМЕДЕЛИЕТО. SCANFIELD-5S СМАРТ СИСТЕМА С ИНТЕГРИРАН ДИГИТАЛЕН ПОЧВЕН КУБ ЗА ИНОВАТИВНИ РЕШЕНИЯ В ЗЕМЕДЕЛИЕТО* **Krasimir BRATOEV[1*)], Ivelin GEORGIEV[2)]** [1)] Department of Agricultural Machinery University of Ruse / Bulgaria; [2)] Scanfield – 5S smart system GmbH, Ruse / Bulgaria	**541**
47.	**OPTIMAL DESIGN AND SIMULATION OF SANDY LOAM SOIL COVERING DEVICE BASED ON BIONIC SAND CRAB PINCERS /** *基于沙蟹螯足仿生的沙壤土覆土装置优化设计与仿真* **Mingtao JIA[1)], Rui ZHANG[*1)], Longze GUO[1)], Yue SUN,[1)] Xin WANG[1)], Haozhe WEI[1)]** College of Mechanical and Electrical Engineering, Qingdao Agricultural University, Qingdao, Shandong/ China	**553**
48.	**DEVELOPMENT AND PERFORMANCE EVALUATION OF AN INTERACTIVE VIRTUAL SIMULATION PLATFORM FOR MECHANIZED PEPPER HARVESTING BASED ON UNITY 3D /** *基于Unity 3D的辣椒机械化收获交互式虚拟仿真平台的开发与性能评估* **Zhiqiang SONG [1, 2)], Xiang DU [1)], Jie YU [1)], Shuyun LIN [3)], Yunxiang YE [*2, 4)]** [1)] School of Agricultural Engineering, Jiangsu University, Zhenjiang, Jiangsu / China; [2)] Key Laboratory of Agricultural Equipment for Hilly and Mountainous Areas in Southeastern China (Co-construction by Ministry and Province), Ministry of Agriculture and Rural Affairs, Hangzhou, Zhejiang / China; [3)] Guizhou Institute of Mountain Agricultural Machinery, Guiyang, Guizhou / China [4)] Zhejiang Academy of Agricultural Sciences Agricultural Equipment Research Institute, Hangzhou, Zhejiang / China	**563**
49.	**DETERMINATION OF OIL PALM FRUIT MATURITY USING A PORTABLE INSTRUMENT BASED ON UV-VIS-NIR SENSOR /** *PENENTUAN KEMATANGAN BUAH KELAPA SAWIT MENGGUNAKAN INSTRUMEN PORTABEL BERBASIS SENSOR UV-VIS-NIR* **Yunisa Tri SUCI [1,2)], I Wayan BUDIASTRA [*1,3], Y Aris PURWANTO[1)], Slamet WIDODO[1)]** [1)] IPB University, Department of Mechanical and Biosystem Engineering / Indonesia; [2)] Jambi Agricultural Training Center, Ministry of Agriculture / Indonesia; [3)] IPB University, Centre for Research on Engineering Application in Tropical Agriculture / Indonesia	**572**
50.	**INVESTIGATION INTO VIBRATION BEHAVIOR OF THE INTEGRATED SHALLOT HARVESTER** *KHẢO SÁT ĐỘNG LỰC HỌC DAO ĐỘNG CỦA LIÊN HIỆP MÁY THU HOẠCH HÀNH TÍM* **Dang NguyenTH[1)], Phi CaoH[2)], Hung TranV[3)], Hau LeT[4)], Giang Pham TT[5)]** [1,2,4)] Faculty of Mechanical Engineering, Vinh Long University of Technology Education / Vietnam [5)] Faculty of Basic Science, Vinh Long University of Technology Education / Vietnam [3)] Faculty of Mechanical Engineering, Phenikaa University / Vietnam	**582**
51.	**LIGHTWEIGHT FRESH JUJUBE TARGET SEGMENTATION ALGORITHM BASED ON IMPROVED YOLOV8: YOLOSEG-JUJUBE /** *基于改进型 YOLOV8 的轻量级鲜枣目标分割算法：YOLOSEG-JUJUBE* **Huamin ZHAO[*1)], Defang XU[*2)]** [1)] College of Agricultural Engineering, Shanxi Agricultural University, Jinzhong / China; [2)] Department of Mathematics and Artificial Intelligence, Lvliang University, Lvliang / China	**592**

52.	**CLAM MEAT DETECTION ALGORITHM BASED ON IMPROVED YOLOv5s /** *基于改进YOLOv5s的蛤肉检测算法* **Xinkai JIAO, Xiangcai ZHANG*), Zhongcai WEI, Xianliang WANG, Xiupei CHENG, Pingchuan MA** Shandong University of Technology, Institute of Modern Agricultural Equipment, ZiBo, China	609
53.	**ANALYSIS OF THE CURRENT STATE OF RESEARCH WORLDWIDE ON SYSTEMS DESIGNED FOR IRRIGATION OF AGRICULTURAL CROPS /** ***ANALIZA STADIULUI ACTUAL DE CERCETARE, PE PLAN MONDIAL, A SISTEMELOR DESTINATE IRIGĂRII CULTURILOR AGRICOLE*** **Dragos Mihail PREDA[1)], Adrian PANDELE*[1)], Bogdan Ovidiu DURAN[1)], Iuliana GAGEANU[2)], Gheorghe VOICU*[1)]** [1)]National University of Science and Technology POLITEHNICA Bucharest, Romania [2)] INMA Bucharest - National Institute for Research and Development for Agricultural Machinery, Romania	621
54.	**DISCRETE ELEMENT PARAMETER CALIBRATION AND OPTIMIZATION OF LAMINARIA JAPONICA BASED ON GP-PSO-XGBOOST MODEL /** *基于 GP-PSO-XGBOOST 模型的海带离散元参数校准与优化* **Xian WANG[1,2,3)], Hua ZHOU[*1,2,3)], Duanyang GENG[1,2,3)], Zehao ZHA[1,2,3)], Zhengzhong LI[1,2.3)]** [1)]School of Agricultural Engineering and Food Science, Shandong University of Technology, Zibo/China. [2)] Institute of Modern Agricultural Equipment, Shandong University of Technology, Zibo/ China. [3)] Key Laboratory of Smart Agriculture Technology and Intelligent Agricultural Machinery Equipment for Field Crops in Shandong Province, Zibo / China	638
55.	**STUDY ON THE INFLUENCE OF VOLUTE WIDTH-DIAMETER RATIO ON THE PERFORMANCE OF MULTI-BLADE CLEANING FANS /** *蜗壳宽径比对多翼清选风机性能的影响研究* **Yichen DONG[1,2,3)], Zheng MA[1,2,3,*)], Jie YU[1,2,3)], Shuai WANG[1,2,3)], Hongyan GAO[1,2,3)], Yaoming LI[1,2,3)]** [1)] School of Agricultural Engineering, Jiangsu University, Zhenjiang, Jiangsu, China [2)] Key Laboratory for Theory and Technology of Intelligent Agricultural Machinery and Equipment, Jiangsu University, Zhenjiang, Jiangsu, China [3)] Faculty of Agricultural Engineering, Jiangsu University, Zhenjiang, Jiangsu, China	652
56.	**APPLICATION OF DEM-BASED ANALYSIS IN THE OPTIMIZATION OF SHOVEL DESIGN FOR THE 1JS-200 ROCK PICKER /** *基于离散元法的1JS-200型捡石机起石铲的优化设计应用* **Yasenjiang BAIKELI *[1,2)], Jiaxi ZHANG [1,2)], Jihuai GAO [3)]; Haodong XU [1,2)]** [1)] College of Mechanical and Electrical Engineering, Xinjiang Agricultural University, Urumqi / China; [2)] Key Laboratory of Xinjiang Intelligent Agricultural Equipment, Urumqi / China; [3)]Xinjiang Dafengge Agricultural Machinery Co., LTD, Bole / China	664
57.	**RESEARCH ON WEED RECOGNITION AND CROP ROW EXTRACTION TECHNOLOGY BASED ON DEEP LEARNING /** *基于深度学习的杂草识别与作物行提取技术研究* **Tengxiang YANG; Chengqian JIN*); Youliang Ni; Man CHEN; Zhen LIU** Nanjing Institute of Agricultural Mechanization, Ministry of Agriculture and Rural Affairs, Nanjing, Jiangsu/China	676
58.	**DISCRETE ELEMENT SIMULATION CALIBRATION OF CONTACT PARAMETERS FOR MILLET SEEDS /** *谷子种子离散元仿真接触参数标定* **Yang HE[1)], Xinxin JI[2)], Guoqiang DUN[2)], Xiaoyi LIU*[1)], Ankang MU[3)], Chunyu MA[1)]** [1)] Northeast Forestry University, College of Mechanical and Electrical Engineering, Harbin / China; [2)]Harbin Cambridge University, Intelligent Agricultural Machinery Equipment Engineering Laboratory, Harbin / China; [3)] Inner Mongolia Chifeng Academy of Agriculture and Animal Husbandry Sciences, Chifeng / China	686
59.	**STRAWBERRY FRUIT DETECTION METHOD BASED ON IMPROVED YOLOv8N /** *基于改进YOLOv8N的草莓果实检测方法* **Zhenwei LI [1)], Suyun LI [1)], Wenting LAN [2)], Shide LI [3)], Yanguan CHEN [1)], Pengcheng LV [4,*)]** [1)] Hezhou University, School of Artificial Intelligence, HeZhou, China [2)] Hezhou University, Academic Affairs Office, HeZhou, China [3)] Guangxi Medical University, School of Information and Management, NanNing, China [4)] Shandong University of Technology, College of Agricultural Engineering and Food Science, ZiBo, China	697
60.	**EFFECT OF MECHANICAL SIDE DEEP FERTILIZATION TECHNOLOGY ON NUTRIENT ABSORPTION AND LOSS IN PADDY FIELDS /** *机械侧深施肥技术对水稻养分吸收及稻田养分损失的影响* **Zhenhua XU [1,2)], Haiying LIU [1,2)], Yanmin YU [1,2)], Changjun DAI [3)], Jing WANG [3)], Ping YAN [1,2*)]** [1)] Biotechnology Institute, Heilongjiang Academy of Agricultural Sciences, Harbin, China [2)] Northeast Branch of National Center of Technology Innovation for Saline-Alkali Tolerant Rice, Harbin, China [3)] Quality and Safety Institute of Agricultural Products, Heilongjiang Academy of Agricultural Sciences, Harbin, China	711
61.	**PADDY RICE POROSITY PREDICTION BASED ON SNAKE ALGORITHM OPTIMIZED SUPPORT VECTOR REGRESSION /** *基于蛇算法优化支持向量回归的稻谷孔隙率预测* **Zhi-Qi ZHANG[1,2)], Lin WAN [*1,2)], Gang CHE [*1,2)], Hong-Chao WANG[1)], Heng PAN[1)], Shuo WANG[1)]** [1)]College of Engineering, Heilongjiang Bayi Agricultural University, Daqing / P.R.China [2)]Key Laboratory of Intelligent Agricultural Machinery Equipment in Heilongjiang Province, Daqing / P.R.China	723
62.	**DEVELOPMENT AND EVALUATION OF AN ENHANCED SMALL-SCALE HYDROPONIC SYSTEM FOR INDOOR SEEDLING PRODUCTION /** ***РАЗРАБОТВАНЕ И ОЦЕНКА НА ПОДОБРЕНА МАЛКА ХИДРОПОННА СИСТЕМА ЗА ПРОИЗВОДСТВО НА РАЗСАД НА ЗАКРИТО***	735

	Neiko V. NIKOLOV[1)], Atanas Z. ATANASOV*[1)] and Boris I. EVSTATIEV[2)] [1)] Department of Agricultural Machinery, Agrarian and Industrial Faculty, University of Ruse "Angel Kanchev", Ruse, / Bulgaria; Department of Automatics and Electronics, Faculty of Electrical Engineering, Electronics and Automation, University of Ruse "Angel Kanchev", Ruse / Bulgaria	
63.	**DESIGN AND EVALUATION OF A NEW DEEP VERTICAL ROTARY TILLER FOR ENHANCED FIELD PERFORMANCE / *新型深松立式旋耕机的设计与试验*** **Chao HE [1,2)], Guiquan HAN[1)], Tie YE[1)], Mingyuan WEI[3)], Chaofan SUN[1)], Yiyuan CHENG[1)]** [1)]School of Intelligent Manufacturing and Electrical Engineering, Nanyang Normal University/China; [2)] Collaborative Innovation Center of Intelligent Explosion-proof Equipment, Henan Province/China; [3)] College of Engineering, China Agricultural University / China	**749**
64.	**EXPERIMENTAL STUDY ON THE INFLUENCE OF STEAM PRESSURE DISTRIBUTION ON WOOD FIBER FEEDING / *蒸汽压力分布对木纤维进给影响实验研究*** **Ao WANG [1)], Guangwei CHEN [1)], FaYi QU *[2)], Yaoning YANG [1)]** [1)]Northeast Forestry University, College of Mechanical and Electrical Engineering, Harbin / China; [2)]Northeast Forestry University, Graduate School, Harbin / China	**757**
65.	**CALIBRATION AND TESTING OF SIMULATION PARAMETERS FOR RAPESEED BLANKET SEEDLING SHEETS BASED ON DISCRETE ELEMENT METHOD / *基于离散元法的油菜毯状苗的苗片仿真参数标定与测试*** **Qing TANG [1,2)], Jing LUO[1)], Minghui HUANG[2)], Jun WU[1)], Lan JIANG[*1)],** **Zhewen SONG[2)], Wei SHI[2)], Yang WU[2)]** [1)] Nanjing Institute of Agricultural Mechanization, Ministry of Agriculture and Rural Affairs of China, Nanjing / China; [2)] Sinomach Changlin Company Limited, Changzhou / China	**765**
66.	**RESEARCH ON CLASSIFICATION METHODS OF BARLEY PLANTS BASED ON TRANSFER LEARNING / *基于迁移学习的大麦植株分类方法研究*** **Wenfeng GUO*[1)], Yanwen LI[2)], Xiaoying ZHANG[3)], Linjuan WANG[1)], Jiahao ZHANG[4)], Guofang XING*[4)]** [1)] Department of Basic Science, Shanxi Agricultural University, Taigu, Shanxi / China; [2)] College of Information Science and Engineering, Shanxi Agricultural University, Taigu, Shanxi / China; [3)] College of Software, Shanxi Agricultural University, Taigu, Shanxi / China; [4)]College of Agriculture, Shanxi Agricultural University, Taigu, Shanxi / China	**776**
67.	**DESIGN AND TESTING OF A SINGLE-ROW FRESH CORN PICKING MECHANISM / *单行鲜食玉米摘穗机构的设计与试验*** **Bang JI [1,3,4)], Yusong XIE [1)], Long PAN [1)], Zhukun WANG [1)], Pu LI [*2)], Xiushan WANG [*1,3)]** [1)] Hunan Agricultural University, College of Mechanical and Electrical Engineering, Changsha/China; [2)] Hunan Mechanical and Electrical Polytechnic, Changsha/China; [3)] State Key Laboratory of Agricultural Equipment Technology, Guangzhou /China [4)] Hunan Key Laboratory of Intelligent Agricultural Machinery and Equipment, Changsha/China	**786**
68.	**DESIGN AND EXPERIMENT OF A NEW TYPE OF SORTING, EVISCERATION, AND CLEANING EQUIPMENT FOR SEA CUCUMBER / *一种新型海参分拣除脏清洗设备的设计与试验*** **Lizheng JIANG*[1)], Zangping GUO[1)], Fangyuan SUN[1)]** [1)]Institute of Intelligent Manufacturing, Zhejiang Polytechnic University of Mechanical and Electrical Engineering, Hangzhou / China	**796**
69.	**DESIGN AND SIMULATION OF SCREW CONVEYOR FOR SESAME COMBINE HARVESTER CUTTING TABLE / *芝麻联合收获机割台螺旋输送装置的设计与仿真*** **Longze GUO[1)], Shuqi SHANG*[1)], Xiaoning HE[1)], Mingtao JIA[1)], Zengcun CHANG[2)], Haipeng YAN[2)],** **Lin GU[1)], Fuwen YAO[1)], Zhentao SONG[1)]** [1)] College of Mechanical and Electrical Engineering, Qingdao Agricultural University, Shandong / China [2)] Dongying Yellow River Delta Intelligent Agricultural Machinery and Equipment Industry Research Institute/ China	**810**
70.	**OPTIMIZATION OF THE STRUCTURE OF THE MILK POWDER CONVEYING DEVICE FOR CALF FEEDING EQUIPMENT BASED ON DISCRETE ELEMENT SIMULATION / *基于离散元仿真的犊牛饲喂装备代乳粉料输送装置结构的优化*** **Yang BAI[1)2)], Yanguo CHEN[3)], Fuxiang XIE*[1)], Yanjun LI[1)], Song JIAN[1)], Wang KAI[1)]** [1)] School of Machinery and Automation, Weifang University, Weifang/China; [2)] Shandong Key Laboratory of Intelligent Manufacturing Technology for Advanced Power Equipment [3)] ShanDong Administration for Market Regulation	**819**
71.	**DEM-BASED MODELING AND CONTACT PARAMETER CALIBRATION OF HAZELNUTS / *基于DEM榛子建模与接触参数标定*** **Chun WANG[1)], Hailin KUI[1)], Xiaoli WU[1)], Yongchao SHAO[2)], Minggang FU[*1)]** [1)]College of Biological and Agricultural Engineering, Jilin University, Changchun, China; [2)]College of Mechanical Electrical Engineering, Northwest A&F University, Yangling, China	**829**
72.	**A STUDY ON THE INFLUENCING FACTORS OF CORN KERNEL COLLISION RESTITUTION COEFFICIENT BASED ON THE OBLIQUE IMPACT COLLISION THEORY / *基于斜撞击碰撞理论的玉米籽粒碰撞恢复系数影响因素研究*** **Zhongqi HE[1)], Mingxu WANG*[1,2)], Ziyan ZHAO[1)], Yingxin XIE[1)], Mengfei LIU[1)]** [1)]College of Mechanical and Electrical Engineering, Henan University of Technology, Zhengzhou, Henan/China [2)]Henan Key Laboratory of Grain & Oil Storage Building and Safety, Henan University of Technology, Henan/China	**840**

73.	**A LIGHTWEIGHT WEED IDENTIFICATION METHOD FOR CHINESE CABBAGE FIELDS BASED ON THE IMPROVED YOLOv11 / *基于改进YOLOv11的轻量化白菜地杂草识别方法*** **Shunshun JI[1)], Jiajun SUN[1)], Chao ZHANG[1,*)]** [1)] College of Information Science and Engineering, Shandong Agricultural University, TaiAn, Shandong/China	851
74.	**EXPERIMENTAL AND DEM-BASED ANALYSIS OF LATERAL STRESS AND SOIL PARTICLE DISPLACEMENT UNDER THE ACTION OF A SUBSOILER /** ***基于试验和离散元仿真模拟方法对深松铲下土壤侧向应力与侧向位移的研究*** **Jun GE, Xu ZHU, Chengmao CAO, Liangfei FANG, Yan SUN, Kuan QIN [*)], Weidong GAO, Junjie LU** School of Engineering, Anhui Agricultural University, Hefei, Anhui/China	862
75.	**ESTABLISHMENT AND PARAMETER CALIBRATION OF QUINOA SEED-SOIL CONTACT MODEL BASED ON DISCRETE ELEMENT METHOD /** ***基于离散元法的藜麦种子-土壤接触模型建立及参数标定*** **Wenxue DONG, Xuan ZHAO, Fei LIU[*)], Hongbin BAI, Dezheng XUAN, Anbin ZHANG, Yuxing REN** College of Mechanical and Electrical Engineering, Inner Mongolia Agricultural University, Hohhot / China	872
76.	**PROFILING DESIGN AND OPTIMIZATION OF END-EFFECTOR FOR PINEAPPLE EYE REMOVAL / *菠萝去眼末端执行机构仿形设计与优化*** **Xingzao MA, Manfeng GONG[*)], Hua LI, Shuai WANG** School of Mechanical and Electrical, Lingnan Normal University, Zhanjiang, China	886
77.	**PREPARATION OF BIOMASS SEEDLING TRAYS USING LIGNIN BONDING PROPERTIES AND DESIGN OF HEATING COMPRESSION FORMING MOLD /** ***基于木质素粘结特性的生物质育苗盘制备及热压成型模具设计*** **Jin-yang LI[1)], Wei ZHANG[*2)], Chun-tao YU[2)], Li-qiang QI[2)], Bo ZHANG[1)]** [1)]College of Information and Electrical Engineering, Heilongjiang Bayi Agricultural University, Daqing/P.R.China [2)]College of Engineering, Heilongjiang Bayi Agricultural University, Daqing/P.R.China	900
78.	**DESIGN AND TESTING OF A WINGED SUBSOILER SHOVEL FOR STRIP MINIMUM-TILLAGE DEEP LOOSENING FERTILISER MACHINE /** ***条带少耕深松施肥机带翼式深松铲设计与试验*** **Shi-cheng XU[1)]; Gui-xiang TAO *[1)]; Shu-juan YI [1)]; Song WANG [1)]; Yu-hang SAN [1)]** College of Engineering, Heilongjiang Bayi Agricultural University, Daqing/P. R. China	910
79.	**RESEARCH ON THE INFLUENCE OF GRINDING TIME ON THE PARTICLE SIZE DISTRIBUTION WHEN OBTAINING ROSEHIPS POWDER /** ***CERCETĂRI PRIVIND INFLUENȚA TIMPULUI DE MĂCINARE ASUPRA DISTRIBUȚIEI DIMENSIUNII PARTICULELOR LA OBȚINEREA PULBERII DE MĂCEȘE*** **Alina-Daiana IONESCU, Gheorghe VOICU[*)], Gabriel-Alexandru CONSTANTIN[*)], George IPATE, Elena Mădălina ȘTEFAN, Mihaela BEGEA, Gabriel MUȘUROI, Mihaela-Florentina DUȚU, Iulian-Claudiu DUȚU, Magdalena-Laura TOMA, Sorin-Dan IORDACHE** National University of Science and Technology POLITEHNICA Bucharest – Faculty of Biotechnical Systems Engineering / Romania	923
80.	**DESIGN AND RESEARCH ON THE TRIGGERING MECHANISM OF ROPE FEEDING IN REED BALING DEVICE / *芦苇打捆装置触发送绳机构的设计和研究*** **Yang BAI [1)], Xiang ZHENG[2)], Kun LU[3)], Yanjun LI[1)], Jian SONG[1)], Fuxiang XIE*[1)]** [1)]School of Machinery and Automation, Weifang University, Weifang/China; [2)]BEIQI FOTON MOTOR CO., LTD [3)]The Affiliated Qingdao Third People's Hospital of Qingdao University	934
81.	**WHEAT HARVESTING QUALITY ONLINE DETECTION SYSTEM AND EXPERIMENTAL VERIFICATION / *小麦收获质量在线检测系统与试验验证*** **Yue QIN [1)], Man CHEN [1,2*)], Tengxiang YANG [1)], Guangyue ZHANG [1)], Chengqian JIN [1*)], Gongwu MO [3)]** [1)] Nanjing Institute of Agricultural Mechanization, Ministry of Agriculture and Rural Affairs, Nanjing, Jiangsu / China; [2)] National Digital Agriculture Equipment (South China Intelligence Agricultural Machine) Innovation Sub-center, Nanjing, Jiangsu / China; [3)] Jiangsu Agricultural Machinery Testing and Appraisal Station, Jiangsu / China	945
82.	**OPTIMIZATION DESIGN AND PERFORMANCE ANALYSIS OF A NOVEL BIONIC ROTARY CUTTER FOR A WEEDING MACHINE /** ***新型除草机仿生旋转刀具的优化设计与性能分析*** **Wenjuan SHUN[2)], Jun GE*[1)], Kuan QIN[1)], Chengmao CAO[1)], Yan SUN[1)], Liangfei FANG[1)], Xu ZHU[1)], Junjie LU[1)], Weidong GAO[1)]** [1)] School of Engineering, Anhui Agricultural University, Hefei, Anhui / China [2)] College of Food and Nutrition, Anhui Agricultural University, Hefei, Anhui / China	954
83.	**RESEARCH ON OPTIMIZATION OF VIBRATION EAR PICKING PARAMETERS BASED ON CORN PLANT VIBRATION RESPONSE CHARACTERISTICS AND FINITE ELEMENT ANALYSIS /** ***基于玉米植株振动响应特性与有限元分析的激振摘穗参数优化研究*** **Pengxuan GUAN[1,2,3)], Yipeng CUI[1,2,3)], Jianning YIN[1,2,3)], Zehao ZHA[1,2,3)], Qiming YU[1,2,3)], Duanyang GENG[1,2,3*)]** [1)] College of Agricultural Engineering and Food Science, Shandong University of Technology, Zibo, China; [2)] Institute of Modern Agricultural Equipment, Shandong University of Technology, Zibo, China [3)] Shandong Provincial Key Laboratory of Smart Agricultural Technology and Intelligent Agricultural Machinery and Equipment for Field Crops, Shandong University of Technology, Zibo, China	964

84.	**CALIBRATION AND OPTIMIZATION OF DISCRETE ELEMENT PARAMETERS FOR TIGER NUTS / *油莎豆种子离散元素参数的标定与优化*** **Yangyang SHI, Xuejun ZHANG, Jinshan YAN*), Xu MA, Huazhi LI** College of Mechanical and Electrical Engineering, Xinjiang Agricultural University, Urumqi, China	**978**
85.	**DESIGN AND EXPERIMENTAL OF A SEED METERING DEVICE FOR SMALL SIZED VEGETABLE SEEDS / *小粒径蔬菜种子排种器的设计与试验*** **Qichao LI*, Guoqin XU, Jinlong FENG** College of Mechanical and Electrical, Lingnan Normal University, Cunjin Street, Zhanjiang, China	**994**
86.	**DETERMINATION AND ANALYSIS OF BIOMECHANICAL PROPERTIES OF POD PEPPERS UNDER DIFFERENT MOISTURE CONTENTS FOR MECHANIZED HARVESTING / *不同含水量下机械化收获朝天椒的生物力学特性的测定与分析*** **Zhiqiang SONG *[1, 2], Yibao CHEN[3], Xiang DU [1], Zhong TANG [1], Shuyun LIN [4], Yunxiang YE *[2]** [1] School of Agricultural Engineering, Jiangsu University, Zhenjiang, Jiangsu / China; [2] Key Laboratory of Agricultural Equipment for Hilly and Mountainous Areas in Southeastern China (Co-construction by Ministry and Province), Ministry of Agriculture and Rural Affairs, Hangzhou, Zhejiang / China; [3] School of Navigation, Xiamen Ocean Vocational College, Xiamen, Fujian / China; [4] Guizhou Institute of Mountain Agricultural Machinery, Guiyang, Guizhou / China	**1006**
87.	**DESIGN AND EXPERIMENTAL RESEARCH ON THE END EFFECTOR OF FRUIT ORCHARD COMB-TYPE FLOWER THINNING / *果园梳齿式疏花末端执行器设计与试验研究*** **Caiqi HU*[1,2], Yechao HAN[1,2], Yichen LI[1,2], Junhao LI[1,2], Pengyu LIU[1,2], Siyuan ZHENG[1,2]** [1] College of Mechanical and Electrical Engineering, Qingdao Agricultural University, Shandong / China [2] Shandong Provincial Key Laboratory of Smart Agricultural Equipment for Protected Horticulture1621	**1019**
88.	**EXPERIMENTAL STUDY ON VARIABLE TEMPERATURE DRYING PROCESS OF PADDY BASED ON GLASS TRANSITION / *基于玻璃化转变的稻谷变温干燥工艺及试验研究*** **Hongchao WANG[1]; Jing WANG[1]; Ziyu WANG *[2]; Lin WAN[1]; Gang CHE*[1]; Shuo WANG[1]; Zhengfa CHEN[1]** [1] College of Engineering, Heilongjiang Bayi Agricultural University, Daqing, China [2] College of Information and Electrical Engineering, Heilongjiang Bayi Agricultural University, Daqing, China	**1030**
89.	**DESIGN AND EXPERIMENT OF TRACTION PERFORMANCE TEST EQUIPMENT FOR AGRICULTURAL TIRES / *农用轮胎牵引性能试验设备的设计与试验*** **Jianguo YAN, Genglong GUO, Jiayao LI, Yaotai LI, Lijuan WANG*)** College of Mechanical and Electrical Engineering, Inner Mongolia Agricultural University, Hohhot, China	**1042**
90.	**A BLOCKCHAIN-BASED PRIVACY-PRESERVING SOLUTION FOR AGRICULTURAL PRODUCT TRACEABILITY BASED ON GROUP SIGNATURES / *基于群签名的区块链农产品溯源隐私保护方案*** **Jiarui ZHANG, Jianyu CHEN, Xuanyu CAO, Shuo LIU, Hao JI, Yongshuai YANG, Lijun CHENG*)** College of Software, Shanxi Agricultural University, Taigu, Shanxi / China	**1058**
91.	**LIGHTWEIGHT RESEARCH OF FORESTRY UNMANNED VEHICLE SWING ARMS BASED ON MULTI-CONDITION TOPOLOGY OPTIMIZATION OF CONTINUUM STRUCTURES / *基于连续体结构多工况拓扑优化的林业无人车辆摆臂轻量化研究*** **Yihan QIN, Yilu ZHAO, Qiang CHEN, Ji WU, Zhongjia CHEN, Qingchun WANG, Xiangyue YUAN*)** The School of Technology, Beijing Forestry University, Beijing / China	**1074**
92.	**DESIGN AND EXPERIMENT OF A BUILT-IN SCREEN-TYPE CYCLONE SEPARATION CLEANING SYSTEM FOR A SMALL-SCALE WHEAT COMBINE HARVESTER / *小型小麦联合收获机内置筛网式旋风分离清选系统设计与试验*** **Yangang LI [1], Xiaoyu CHAI [1], Jinpeng HU [1], Zhiqiang SONG [1], Yuzhe WANG [1], Lizhang XU [1,*)** [1] College of Agricultural Engineering, Jiangsu University, Zhenjiang, China	**1092**
93.	**DESIGN AND EXPERIMENT OF DEEP TOPDRESSING APPLICATOR FOR WINTER WHEAT / *冬小麦深施追肥机的设计与试验*** **Huimin FENG[1], Jianhui NIE[2], Baohui XU[1], Yuming GUO*[3]** [1] Department of Mechanical and Electrical Engineering, Yuncheng University, Yuncheng, China [2]Intelligent Equipment Research Center, Beijing Academy of Agriculture and Forestry Sciences, Beijing, China [3] College of Agricultural Engineering, Shanxi Agriculture University, Taigu, China	**1105**
94.	**STUDY ON THE CHARACTERISTICS OF SAND AND WIND FLOW OF A NEW TYPE OF SAND BARRIER BASED ON NUMERICAL SIMULATION AND EXPERIMENT / *基于数值模拟和实验的新型沙障的风沙流特征研究*** **Sibin ZHANG, Weiqiang ZHENG*), Liping ZHANG** [1]College of Mechanical Engineering, Xinjiang University, Urumqi / China	**1116**
95.	**EFFECTS OF DIFFERENT MICROBIAL FERMENTATION PROCESSES OF RICE STRAW ON ITS QUALITY AS LIVESTOCK FEED / *水稻秸秆发酵特性及饲料化利用*** **Liyan WU[1], Tianyi ZHANG[1], Zheng JIN[1], Fangming CUI[1], Zhicheng ZHANG*[2]** [1] College of Engineering, Shenyang Agricultural University, Shenyang / China; [2] Department of Logistics Support, Jilin Agricultural University, Changchun / China	**1130**

96.	**ELECTRIC RED BEAN PRECISION SEEDING CONTROL SYSTEM BASED ON IHBA-LADRC /** ***基于IHBA-LADRC的电驱动红豆精量播种控制系统*** **Yi-fei LI [1,2], Guang-yu WANG [1]; Lin ZHAO [3], Shu-juan YI *[1]** [1] College of Engineering, Heilongjiang Bayi Agricultural University, Daqing, Heilongjiang/ China [2] College of Engineering, Northeast Agricultural University, Harbin Heilongjiang/ China [3] College of Basic Education, Beijing Polytechnic University, Beijing/ China	1140
97.	**YOLO-LSD: A LIGHTWEIGHT MODEL FOR HIGH-ACCURACY MULTI-BREED SHEEP FACE DETECTION /** ***YOLO-LSD：一种轻量级的高精度多品种羊脸检测模型*** **Xiwen ZHANG[1,2]; Zelin NIU[1]; Yanxin GUO[1,3], Yu CAI[3], Ruiyan SUN[1,3*]** [1] Jiangsu Maritime Institute, College of Marine Electrical and Intelligent Engineering, Nanjing, China [2] Inner Mongolia Agricultural University, College of Mechanical and Electrical Engineering, Inner Mongolia, China; [3] Industrial Center, Nanjing Institute of Technology, Nanjing, China	1155
98.	**DESIGN AND EXPERIMENT OF AN INTEGRATED PRUNING, THRESHING AND BRANCH CHOPPING MACHINE FOR GREEN PRICKLY ASH /** ***青花椒整枝脱粒碎枝一体机设计与试验*** **Hao WANG, Yanjun ZHOU*, Chuanyao LIN, Jian WU, Jia DENG, Xiaobo ZHOU** [1] Sichuan Academy of Agricultural Machinery Science / China	1168
99.	**DESIGN AND EXPERIMENTAL STUDY OF A SHAFTLESS DOUBLE-SCREW FERTILIZER SPREADER FOR RICE /** ***无轴双螺旋式水稻排肥器的设计与试验研究*** **Ziyu WANG[1]; Deyu HONG[1]; Hongchao WANG*[2]; Chengyang LIU[2]; Zanfeng MA[2]; Xingkang LIU[2]; Wentao LI[2]** [1] College of Information and Electrical Engineering, Heilongjiang Bayi Agricultural University, Daqing, China [2] College of Engineering, Heilongjiang Bayi Agricultural University, Daqing, China	1177
100.	**STUDY AND EXPERIMENT ON A CORN FLEXIBLE THRESHING TECHNOLOGY WITH SINGLE-POINT HINGED STRUCTURE BASED ON DEM-MBD COUPLING /** ***基于DEM-MBD耦合的单点铰接玉米柔性脱粒技术研究与试验*** **Qiming YU[1], Jianning YIN[1], Yipeng CUI[1], Zehao ZHA[1], Pengxuan GUAN[1], Yang WANG[1], Xinxin WANG[1], Duanyang GENG[1*)]** [1] School of Agricultural Engineering and Food Science, Shandong University of Technology, Zibo, China	1190
101.	**OPTIMIZATION OF VERTICAL ROTARY TILLAGE BLADE PARAMETERS FOR SALINE-ALKALI LAND IMPROVEMENT /** ***面向盐碱地改良的立式旋耕刀结构参数优化*** **Xuan LUO, He SUN, Haoran BAI*)** College of Mechanical and Electrical Engineering, Qingdao Agricultural University Qingdao /China	1203
102.	**OPTIMIZATION OF ORGANIC FERTILIZER DISTRIBUTION USING EDEM SIMULATION ANALYSIS/** ***OPTIMIZAREA DISTRIBUȚIEI ÎNGRĂȘĂMINTELOR ORGANICE UTILIZÂND ANALIZA PRIN SIMULARE EDEM*** **Vasilica ȘTEFAN[1], Lucreția POPA[1], Alin HARABAGIU *[1], Radu CIUPERCĂ[1], Ana ZAICA[1], Alexandra VIȘAN[1]** [1] National Institute of Research – Development for Machines and Installations Designed for Agriculture and Food Industry – INMA Bucharest / Romania	1217
103.	**PARAMETER OPTIMIZATION AND EXPERIMENT OF A SINGLE LONGITUDINAL AXIAL FLOW FULL-CIRCUMFERENCE SEPARATION THRESHING DEVICE FOR RAPESEED HARVESTER /** ***油菜收割机单纵轴流全周分离脱粒装置参数优化与试验*** **Min ZHANG, Chenke XU, Chengpeng LI, Gang WANG, Yao YANG, Tao JIANG** Nanjing Institute of Agricultural Mechanization, Ministry of Agriculture and Rural Affairs of China, Nanjing	1231
104.	**STRUCTURAL DESIGN AND PERFORMANCE STUDY OF SALT-ALKALI SOIL ROTARY BLADE BASED ON DISCRETE ELEMENTS /** ***基于离散元的盐碱地旋耕刀结构设计与性能研究*** **Shuai ZHENG[1], Ahmed F. El-SHAFIE[2], Jie LIU[1], Abouelnardar SALME[3], Jing ZHANG[4] Haoran BAI*[1]** [1] College of Mechanical and Electrical Engineering, Qingdao Agricultural University, Qingdao / China; [2] National Center of Technology Innovation for Comprehensive Utilization of Saline-Alkali Land, Dongying / China; [3] Yellow River Delta Intelligent Agricultural Machinery Equipment Industry Academy, Dongying / China [4] Academician Workstation of Agricultural High-tech Industrial Area of the Yellow River Delta, [5] Dongying Vocational College School of Ecology and Biology, Dongying / China	1244
105.	**RESEARCH ON GRADING METHOD OF PEPPER PLUG SEEDLINGS BASED ON MACHINE VISION /** ***基于机器视觉的辣椒穴盘苗分级方法研究*** **Fengwei YUAN[1], Shuaiyin CHEN[1], Zhang XIAO*[1], Erjie SUN[1], Guoning MA[1], Gengzhen REN[1], Zhenlong LI[1] Zhenhong ZOU[2], Xiangjiang WANG[1]** [1] College of Mechanical Engineering, University of South China, Hengyang/China. [2] Hengyang Vegetable Seeds Co. Hengyang/ China.	1258

106.	**EXPERIMENTAL AND THEORETICAL STUDY ON STRAIGHTNESS IMPROVEMENT IN AGRICULTURAL MACHINERY MOVEMENT /** ***EKSPERIMENTĀLS UN TEORĒTISKS PĒTĪJUMS PAR LINEARITĀTES UZLABOŠANU LAUKSAIMNIECĪBAS MAŠĪNU KUSTĪBĀ*** **Volodymyr BULGAKOV[1)], Adolfs RUCINS[*2)], Lucretia POPA[3)], Roman ANTOSHCHENKOV[4)], Mykyta KUSKOV[4)], Mariia RUZHYLO[1)], Mykhailo CHERNOVOL[5)], Ivan HOLOVACH[1)], Oleksandra TROKHANIAK[1)]** [1)]National University of Life and Environmental Sciences of Ukraine / Ukraine; [2)]Latvia University of Life Sciences and Technologies / Latvia; [3)]National Institute of Research–Development for Machines and Installations Designed for Agriculture and Food Industry–INMA, Bucharest / Romania [4)]State Biotechnological University / Ukraine	1268
107.	**STUDY ON THE MOVEMENT CHARACTERISTICS OF RAPESEED THRESHING MATERIALS BASED ON DEM SIMULATION AND HIGH-SPEED IMAGING /** ***基于 DEM和高速摄影技术的油菜籽脱粒物料迁移特性研究*** **Guangchao ZHAN[*1)], Wei LIU[2)], Peng ZHANG[1)]** [1)]School of Electromechanical and Intelligent Manufacturing, Huanggang Normal University, Huanggang, Hubei, China [2)] Jiangshan Heavy Industries Research Institute Co., Ltd., Norinco Group, Xiangyang Hubei, China	1279
108.	**DEVELOPMENT OF TRACTOR FRONT MOUNTED CONVEYOR BASED PULSES CROP HARVESTER /** ट्रैक्टर फ्रंट माउंटेड कन्वेयर आधारित दलहन फसल हार्वेस्टर का विकास **Tanmoy DAS[1)], Sanjay KUMAR PATEL[1)], Bibek ISHORE[1)], Jaya SINHA[1)], Sanjay KUMAR[1)]** [1)] Department of Farm Machinery and Power Engineering, College of Agricultural Engineering and Technology, Dr. Rajendra Prasad Central Agricultural University, Pusa, Samastipur, Bihar, India	1289
109.	**FACTORS INFLUENCING THE COMPOSTING PROCESS OF VEGETAL WASTE: A REVIEW /** ***FACTORI CARE INFLUENȚEAZĂ COMPOSTAREA DEȘEURILOR VEGETALE: O ANALIZĂ DE SINTEZĂ*** **Elena-Melania CISMARU[1)], Ana-Maria TĂBĂRAȘU[1*)], Nicolae-Valentin VLĂDUȚ[1)], Gabriel-Valentin GHEORGHE[1)], Ana ZAICA[1)], Dragoș-Nicolae DUMITRU[1)], Alin-Nicolae HARABAGIU[1)], Elena-Mădălina ȘTEFAN[2*)], Mirela Nicoleta DINCĂ[2)]** [1)]National Institute of Research-Development for Machines and Installations Designed to Agriculture and Food Industry, Romania; [2)] National University of Science and Technology POLITEHNICA Bucharest, Romania	1299
110.	**RESEARCH AND EXPERIMENT OF RAPID DISENGAGEMENT SYSTEM FOR KELP SEEDLING ROPES BASED ON A LOCKING DEVICE /** ***基于锁扣结构的海带苗绳快速脱扣技术研究与试验*** **Zehao ZHA[1)], Jianning YIN[1)], Qiming YU[1)], Pengxuan GUAN[1)], Yipeng CUI[1)], Xian WANG[1)], Xinxin WANG[1)], Tongfei SHENG[2)], Duanyang GENG[1*)]** [1)] School of Agricultural Engineering and Food Science, Shandong University of Technology, Zibo, China [2)] Weihai Renhe Electromechanical Co., Ltd., Weihai Shandong, China	1321
111.	**PARAMETER OPTIMIZATION AND EXPERIMENT OF AN INSIDE-FILLING PNEUMATIC HIGH-SPEED PRECISION SEED-METERING DEVICE FOR COTTON /** ***内充气力式棉花高速精量排种器参数优化与试验*** **Meng-jie HU[*1,2)]; Jia-qi ZHANG[1)]; Yao CHEN[1)]; Chu-zhen XU[1)]; Bao-jia LI[1)]** [1)]School of Animal Science and Nutritional Engineering, Wuhan Polytechnic University, Wuhan / P.R.China [2)]Key Laboratory of Agricultural Equipment in Mid-Lower Yangtze River, Ministry of Agriculture and Rural Affairs, Wuhan / P.R.China	1334
112.	**NOVEL SOLUTIONS FOR MITIGATING DROUGHT IMPACT AND RESTORING SOIL FUNCTIONALITY IN AGRICULTURE /** ***SOLUȚII NOI PENTRU ATENUAREA IMPACTULUI SECETEI ȘI RESTABILIREA FUNCȚIONALITĂȚII SOLULUI ÎN AGRICULTURĂ*** **Nicoleta-Alexandra VANGHELE[1), 2)], Nicolae-Valentin VLĂDUȚ[1)], Augustina PRUTEANU[*1)], Andreea MATACHEI[1)], Laurentiu-Constantin VLĂDUȚOIU[1)], Nicoleta-Olimpia VRÂNCEANU[3)]** [1)]The National Institute of Research-Development for Machines and Installations Designed for Agriculture and Food Industry-INMA Bucharest, Romania [2)]Politehnica University of Bucharest, Romania [3)]National Institute for Research and Development for Pedology, Agrochemistry and Environmental Protection – ICPA, Mărăști, Bucharest, Romania	1352
113.	**DESIGN AND EXPERIMENT OF A CLAW-CHAIN GARLIC CLOVE METERING DEVICE /** ***爪链式大蒜播种机取种装置设计与试验*** **Caiqi HU[*1,2)], Peng DENG[1,2)], Junhao LI[1,2)], Pengyu LIU[1,2)], Yichen LI[1,2)], Siyuan ZHENG [1,2)]** [1)]College of Mechanical and Electrical Engineering, Qingdao Agricultural University, Qingdao, China [2)] Shandong Provincial Key Laboratory of Smart Agricultural Equipment for Protected Horticulture, Qingdao, China	1382

DESIGN AND EXPERIMENT OF COTTON STALKS PULLING DEVICE WITH NON-FLAT TOOTHED DISCS
/
仰角齿盘式拔棉秆装置设计与试验

Weisong ZHAO[1,2,3], Jianhua XIE[2*], MINGJIANG CHEN[1,3], Chunsong GUAN[1*], Jia ZHANG[2], Zhenwei WANG[1], Yan GONG[1,3]

[1] Nanjing Institute of Agricultural Mechanization, Ministry of Agriculture and Rural Affairs, Nanjing 210014, China
[2] College of Mechanical and Electrical Engineering, Xinjiang Agricultural University, Urumqi, 830052, China
[3] Institute of Western Agriculture, the Chinese Academy of Agricultural sciences, Changji, 831100, China
Tel: +8609974680383; E-mail: xjh199032@163.com, cs.guan@163.com
***** *Correspondent authors: Jianhua Xie, Chunsong Guan*
DOI: https://doi.org/10.35633/inmateh-76-01

Keywords: *cotton, stalk, uprooting, toothed discs, pulling machine*

ABSTRACT
Efficient cotton stalk recycling is crucial for agricultural sustainability. Traditional manual removal methods suffer from low efficiency and high labor intensity. Existing mechanical harvesters face limitations such as low removal rates, high stalk breakage rates, and significant omission rates. To address these challenges, this study focuses on optimizing a self-developed multi-row disc-type stalk puller. The conventional flat disc was redesigned into an obliquely angled disc with a bending angle. This 3D curved design enhances stalk constraint capability, thereby improving gripping stability and lifting height. A kinematic model was developed using the ADAMS dynamics simulation platform, revealing the relationships between motion trajectories and key structural parameters. Parametric analysis quantified the effects of disc diameter and bending angle on lifting height and working width. A three-factor, three-level orthogonal experimental design was implemented to evaluate the influence of speed ratio, disc diameter, and disc inclination on three performance indicators: removal rate (Y_1), breakage rate (Y_2), and omission rate (Y_3). The results showed that for Y_1 and Y_3, the primary influencing factors, in order of importance, were: disc diameter > bending angle > speed ratio; for Y_2, the order was: speed ratio > bending angle > disc diameter. The optimal parameter combination was determined to be: 600 mm disc diameter, 20° bending angle, and 0.7 speed ratio. Field tests achieved a pull-out rate of 95.7%, a breakage rate of 3.2%, and an omission rate of 1.1%. These findings provide both theoretical and technical support for enhancing the efficiency of mechanized cotton stalk harvesting.

摘要
棉秆高效回收对促进农业可持续发展具有重要意义，然而传统人工拔秆存在作业效率低、劳动强度大等问题，现有机械收获装置普遍存在拔净率低、断秆率高等技术瓶颈。针对现有棉花秸秆机械化收获存在的整株拔除率低、作业效率不高等问题，本研究基于自主研发的多行齿盘式拔秆机开展结构优化。通过将传统平面齿盘创新设计为带有折弯角的仰角齿盘结构，利用三维曲面增强茎秆约束能力，从机构学层面提升夹持稳定性和有效提拔高度。基于 ADAMS 动力学仿真平台，建立仰角齿盘运动学模型，揭示了运动轨迹与结构参数间的映射关系，通过参数化分析明确了齿盘直径、折弯角对提升高度和工作幅宽的量化影响规律。通过构建三因素三水平正交试验平台，系统研究速比、齿盘直径、齿盘倾角等关键参数对拔净率、拔断率和漏拔率的影响规律。试验结果表明：影响拔净率的参数从主到次排序为：齿盘直径 > 折弯角度 > 速比；影响漏拔率的参数从主到次排序为：齿盘直径 > 折弯角度 > 速比；影响拔断率的参数从主到次排序为：速比 > 折弯角度 > 齿盘直径。以拔除率为主要评价指标，得到最优参数组合是：齿盘直径=600mm、折弯角=20°、速比=0.7。验证结果表明，该参数组合下棉秆拔净率为 95.7%、拔断率为 3.2%、漏拔率为 1.1%。研究成果为进一步提高棉秆拔净率提供了理论依据和技术支撑。

INTRODUCTION
China is one of the world's major cotton producing countries, with the third largest cotton planting area in the world and abundant cotton stalk resources. Cotton stalk is a high-quality biomass resource with a wide range of applications such as building boards, chemical product raw materials (such as ethanol and

[1] *Weisong Zhao, Assistant researcher, Ph.D.; Jianhua Xie, Professor, Ph.D.; Mingjiang Chen, Researcher, Ph.D.; Chunsong Guan, Associate researcher, Ph.D.; Jia Zhang, Associate Professor; Zhenwei Wang, Assistant researcher;Yan Gong, Researcher.*

carboxymethyl cellulose), fuel and papermaking *(Agwa et al., 2020; Keshav et al., 2023; Nguyen et al., 2020; Wang Fangzheng et al., 2022)*. The comprehensive utilization of cotton stalks is an important measure to accelerate the green and low-carbon development of agriculture, and mechanized removal of these is the primary link in achieving numerous important uses *(Fernando Correa Da Costa and Cuiaba, 2010; Jiang et al., 2021; Liu Fei et al., 2019).*

The cotton stalk pulling device is a key component of the cotton stalk harvester. Many scholars have carried out work on the design of cotton stalk pulling technology and devices *(Cai Jialin et al., 2020; Chen Mingjiang et al., 2012; He Xiaowei et al., 2020; Tang Zunfeng et al., 2010; Xie Jianhua et al., 2023; Zhao et al., 2023)*. According to the structural form, the pulling devices include toothed discs type *(Ramadan, 2010)*, tire roller type *(Pan, 2014)*, clamping type *(Zhao Weisong et al., 2024)*, flexible belt type *(Cai Jialin et al., 2020)*, toothed roller type *(Zhang Aimin et al., 2016)*, etc. Among them, the toothed discs type stalk puller has a simple structure and affordable price. It is widely welcomed by Chinese farmers and has been applied to a certain extent. However, the operation effect of the toothed discs type stalk puller needs to be further improved, and there are still many cotton stalks that are missed or broken. In order to solve this technical problem, some scholars have carried out mechanism research, structural optimization design and other work. For example, *Wang Xiaoyu et al. (2011)* simulated the motion trajectory of the toothed discs type stalk puller and obtained the trajectory curve under the horizontal working condition of the toothed discs. *Ma Jichun et al., (2010),* further carried out the motion analysis of the toothed discs type stalk puller and explained the influence of different speed ratios on the motion law. *Chen Mingjiang et al. (2019)* used ADAMS to conduct an analysis of the operation process and parameter optimization of a multi-row toothed discs stalk puller. The results showed that the speed ratio was the key factor affecting the removal rate, and the optimal range was 0.55~0.8. *Zhao Weisong et al. (2022),* further conducted a study on the optimization of the toothed discs structure and established the response function of three influencing factors and assessment indicators. However, in the current reported results, the toothed discs are all planar designs, that is, the toothed discs are flat structures. This structure results in unsatisfactory clamping effect and lifting height of cotton stalks. In response to this problem, the goal of this study is to explore the motion law and operation effect of non-planar toothed discs structures, design a non-flat toothed disc, and conduct experimental research on motion trajectory analysis and key influencing factors.

MATERIALS AND METHODS

Overall structure and working principle

The traditional gear-disc type cotton stalk puller is driven by a ground wheel, which relies on the friction between the ground wheel and the ground to achieve power transmission. When operating at high speed, the ground wheel slips and the transmission is unstable, resulting in poor stalk pulling effect and a significantly reduced removal rate. The transmission ratio between the ground wheel and the toothed discs of the traditional toothed discs cotton stalk puller is a constant value, and the working parameters of the mechanism cannot be adjusted according to the changes in the cotton stalk harvesting period, which greatly limits the scope of application of the stalk pulling machinery.

The toothed discs type multi-row cotton stalk pulling device designed in this paper is mainly composed of a parallelogram hanging mechanism, a frame, a hydraulic motor and a speed sensor, a stalk supporter, toothed discs, a folding mechanism and other components, as shown in Figure 1.

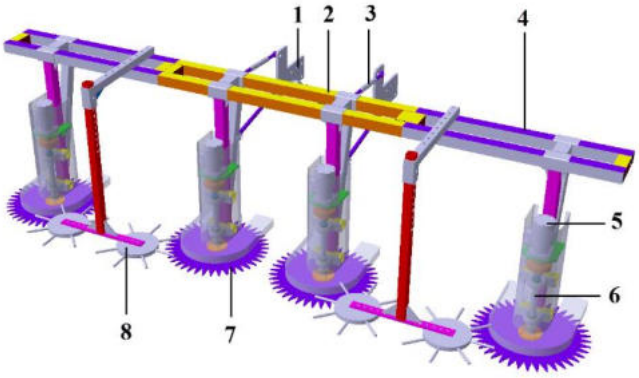


Fig. 1 - Structural diagram of multi-row cotton-stalk uprooting device

1. Hooking mechanism; 2. Fixed frame; 3. Telescopic rod; 4. Foldable frame; 5. Hydraulic motor; 6. Rotating shaft; 7. Non-flat toothed discs; 8. Crop support

The side frames can be folded during transportation, and are easy to assemble and disassemble. They can realize two-row or four-row operations, and the spacing between adjacent toothed discs is adjustable to meet the requirements for harvesting cotton stalks at different row spacings. The electro-hydraulic control technology can realize individual control of each gear disc, and the gear disc rotation direction and speed are adjustable.

Working principle: When working, the stalk pulling tooth plate rotates at a certain speed driven by the hydraulic motor. The tractor moves forward to feed the cotton stalks into the V-shaped tooth grooves on the tooth plate. The stalks are pulled out of the soil.

Key components and hydraulic transmission system design

Overall design of the gear-disc multi-row cotton stalk pulling stand

The overall structure of the gear-disc multi-row cotton stalk pulling stand is shown in Figure 2. It is mainly composed of a load-sensitive pump, an electro-hydraulic proportional valve, a display, a vehicle speed sensor, a cotton stalk pulling device, a tractor, etc. The gear speed and speed ratio are controllable and adjustable, and the gear speed, torque and other key operating parameters are monitored and recorded in real time through sensors, which is convenient for subsequent data mining and analysis.



Fig. 2 - Toothed disc multi-row cotton-stalk uprooting device

1. Hydraulic oil tank; 2. Tractor; 3. Hydraulic proportional valves; 4. Non-flat toothed disc; 5. Hydraulic motor

The cotton stalk pulling device is suspended at the front end of the tractor through a parallelogram mechanism. The pump is driven from the tractor's PTO via a coupling. Each disc is driven by a separate hydraulic motor, for a total of 4 discs, capable of removing 4 rows of cotton stalks per operation. The rack width of the toothed discs type multi-row cotton stalk pulling device is 2400 mm, the toothed discs spacing is adjustable, and it can operate when the cotton stalk row spacing is greater than 500 mm.

Hydraulic transmission system design

In order to achieve adjustable speed ratio during operation, the gear-disc multi-row cotton stalk pulling stand adopts electro-hydraulic control, as shown in Figure 3. The motor drives the stalk pulling gear to rotate, and the tractor moves forward to realize the cotton stalk pulling operation function. The speed sensor can transmit the gear speed signal to the controller. The control system CPU combines the vehicle speed signal and feeds back the control signal to the PVG proportional valve according to the system setting. The PVG proportional valve system controls the motor speed according to the signal.

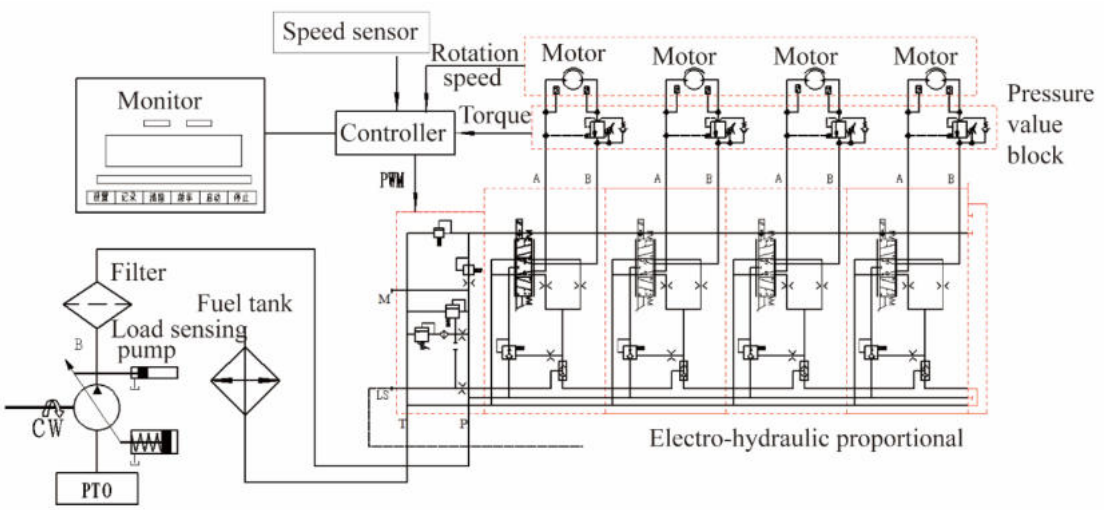


Fig. 3 – Diagram of electro-hydraulic control system

According to the electro-hydraulic control principle in Figure 3, the DANFOSS brand JR-L series load-sensitive pump, PVG16-4 proportional valve, OMP series hydraulic motor and speed sensor, HFBG-NN-0101 pressure measuring valve block, MC024-110 controller, and DP570 display were selected. The numerical range of the hydraulic motor and other modules was determined based on the stalk pulling torque.

According to the cotton stalk uprooting resistance, the stalk pulling torque of a single toothed discs is:

$$M=N\cdot L \tag{1}$$

where:

M is the pulling torque of a single toothed discs, N·m.

N is the pulling resistance of a single cotton stalk, the average value is 500 N, the max. value is 1000N.

L is the pulling arm length, 0.25 m.

The calculation shows that the average stalk pulling torque of a single toothed discs is 125 N·m, and the maximum is 250 N·m. Considering the 20% reserve torque, the maximum torque of a single toothed discs is 300 N·m. When the circumferential speed of the toothed discs ranges from 0 to 6 m/s, the theoretical speed is 0 to 229 r/min. Based on the above calculation results, the OMP 200 hydraulic motor and JR-L-S75C-LS load sensitive pump are selected.

Design and analysis of the elevation gear disc

The gear disc is an important component for clamping and pulling cotton stalks. Its main parameters are the gear disc diameter, tooth shape and tooth angle. The gear disc diameter not only affects its structural strength, but also affects the length of the cotton stalk pulling stroke. The tooth shape is designed as a "V"-shaped tooth groove. The V-shaped tooth groove has strong adaptability to the diameter and thickness of the cotton stalk and good pulling effect. The cotton planting patterns in Shandong Province, China mainly include 760 mm equal row spacing planting and wide and narrow row planting. The narrow row spacing is generally 500-600 mm. Considering the versatility of the test bench, the gear disc radius r is designed to be 250 mm. Too thin gear discs have insufficient strength, and too thick gear discs increase energy consumption and cost. The designed gear disc thickness is 5 mm. The diameter (root) of cotton stalks is mostly between 12 and 15 mm, and some are between 15 and 25 mm. The thinner the root, the easier it is to miss and break, and the thicker the root, the higher the removal rate. According to the geometric relationship in Figure 4, the V-shaped tooth groove must meet the following requirements when it can clamp the cotton stalk:

$$L_{\mathrm{BC}} \geq d_{max} \tag{2}$$

$$L_{\mathrm{AD}} \geq d_{max} \tag{3}$$

$$\angle \mathrm{BAC} = 2\angle \mathrm{BAD} = 2\tan^{-1}\frac{l_{BC}}{l_{AD}} \tag{4}$$

where:

L_{BC} - tooth width, mm; d_{max} - cotton stalk root diameter, taken as 25 mm.

L_{AD} - tooth depth, mm; $\angle$BAC - tooth angle, (°).

Increasing both the tooth width (L_{BC}) and tooth depth (L_{AD}) can enhance the adaptability of the non-flat toothed discs to cotton stalks of varying thicknesses. However, an increase in tooth width reduces the number of teeth, which may raise the probability of omission. Similarly, insufficient tooth depth (L_{AD}) can also increase the likelihood of omission. Based on Equations (2)~(4), when L_{BC} and d_{max} are both set to 25 mm and ∠BAC is set to 35°, the calculated tooth depth L_{AD} is 39.64 mm (>d_{max}), satisfying the required conditions. After rounding, L_{AD} is determined to be 40 mm. As shown in Figure 4, the toothed discs can meet the pulling out of cotton stalks with different root diameters. After the cotton stalks are pulled out, they fall down due to the loss of soil force on the root system. In order to enable the pulled cotton stalks to be smoothly separated from the toothed discs, an auxiliary separation component is designed. It is a curved component that can change the movement path of the cotton stalks so that the cotton stalks can be smoothly separated from the toothed discs.

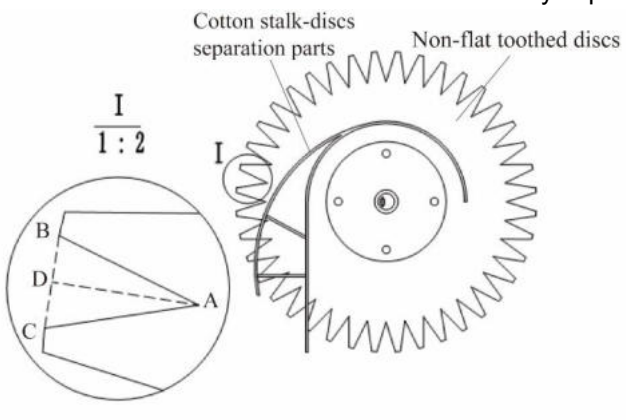


Fig. 4 – Non-flat toothed disc structure diagram

The clamping point (Point *O*, also the contact point) during stalk pulling was analyzed, as shown in Fig. 5. In traditional flat discs, the clamping point follows a trochoidal trajectory *(Chen Mingjiang et al., 2019)*. When discs are horizontally positioned (parallel to the ground), this trajectory becomes two-dimensional (parallel to the ground). Under these conditions, cotton stalks are typically pushed forward by the discs. This occurs because the clamping point lacks upward motion, eliminating vertical pulling forces. In order to optimize the trajectory of the clamping point, non-flat toothed discs were designed in this study. The objective of the design is to make the disc able to hold the cotton stalks firmly and to make the clamping point have an upward motion trajectory. The schematic structure of the non-flat toothed disc and its kinematic sketch are shown in Fig. 5.

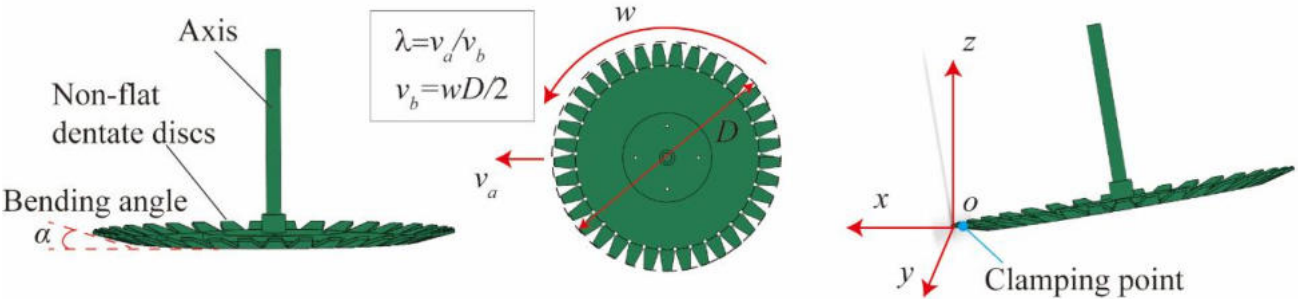


Fig. 5 - Non-flat toothed discs structural diagram and motion diagram

α is bending angle; λ is the ratio of the forward speed of the machine to the speed of the toothed disc, hereinafter referred to as the "speed ratio"; v_D is machine forward speed; w is angular speed of toothed discs; v_b is linear speed at clamping point; D is diameter of toothed discs.

To analyze the motion trajectory of clamping points on non-flat toothed discs and its impact on cotton stalk removal, ADAMS software was used for simulation. Under identical speed ratios, trajectories were simulated with varying disc diameters (D) and bending angles (α), as shown in Figure 6. Four parameter combinations were tested: D =500 mm, α=6°; D =500 mm, α=12°; D =600 mm, α=6°; D=600 mm, α=12°. It can be seen from Figure 6 that the overall movement trends of the trajectory curves of the four parameters are consistent, all of which are spiral lines. However, the curves do not overlap, indicating that both the toothed discs diameter D and the bending angle have an effect on the trajectory. On the whole, under the same bending angle conditions, the larger the diameter of the toothed discs, the larger the value of the curve in the z-axis direction, indicating a higher lifting height. Under the same gear disc diameter conditions, the larger the bending angle, the greater the lifting height.

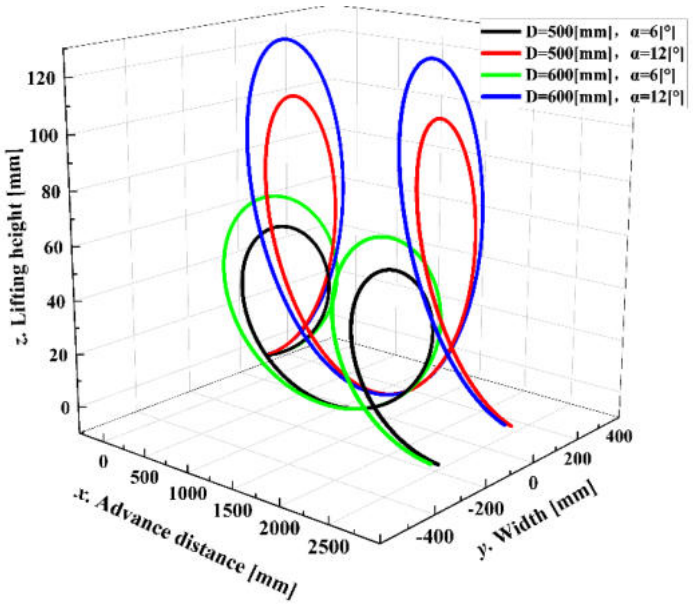


Fig. 6 - Motion trajectory of non-flat toothed discs

In order to further analyze the influence of the gear disc diameter and bending angle on the running trajectory, the x-y curve (Figure 7) and x-z curve (Figure 8) are drawn respectively. The x-y curve is used to analyze the variation of the gear disc working width, and the x-z curve is used to analyze the variation of the lifting height.

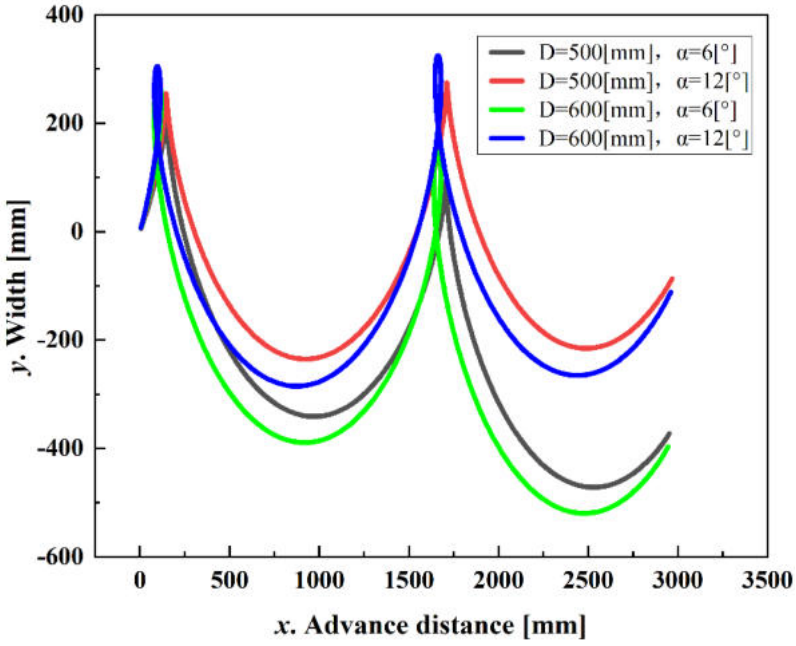


Fig. 7 - x-y curves

As can be seen from Figure 7, when the toothed discs diameters are the same (D=500 mm, D =600 mm), the toothed discs with a large bending angle (α=12°) have a small movement width, while the toothed discs with a small bending angle (α=6°) have a large movement width. The reason is that the large bending angle causes the projection diameter of the toothed discs on the horizontal plane to become smaller, so the movement width is reduced. A small movement width means a small effective working area, which easily increases the probability of missing cotton stalks. When the bending angle is the same, the movement width of the toothed discs with a diameter of 600 mm is greater than that of the toothed discs with a diameter of 500 mm. This shows that increasing the diameter of the toothed discs is an effective way to increase the movement width.

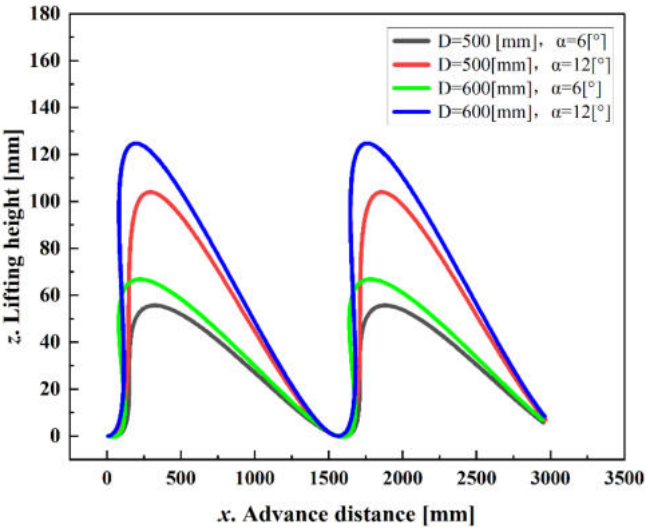


Fig. 8 - x-z curves

As can be seen from Figure 8, when the diameter of the toothed discs is the same, the toothed discs with a large bending angle has a larger lifting distance. This shows that under effective clamping conditions, the cotton stalk can be pulled to a higher height, which is conducive to the successful removal of the cotton stalk. At the same time, it can also be seen that increasing the bending angle (from 6° to 12°) produces a more obvious height increase than increasing the toothed discs diameter (from diameter = 500 mm to diameter = 600 mm).

Through the above research, it can be found that for non-planar toothed discs, the diameter and bending angle of the toothed discs have a greater impact on the movement width and lifting height. Therefore, this study selects three main influencing factors, namely, toothed discs diameter, bending angle and speed ratio, and studies the influence of each factor on the quality of cotton stalk removal through orthogonal experiments.

Experimental conditions

With the help of a self-made toothed discs type cotton stalk pulling test bench (*Chen Mingjiang et al., 2022*), all the tests were completed by replacing different toothed discs. The test site was the Binzhou Cotton Production Full Mechanization Agricultural Machinery and Agronomy Integration Demonstration Base in the National Agricultural Science and Technology Park of Binzhou City, Shandong Province. The test time was November 15-18, 2018, and the weather was cloudy. The cotton variety in the data collection area was Zhongmian 619, cultivated without film, with a planting row spacing of 760 mm, a plant spacing of about 200 mm, and a plant height of 900~1200 mm.

Experimental methods

The test was carried out with reference to GB/T8097-2008 "Test Methods for Harvesting Machinery Combine Harvesters" and DB37/T1856-2011 "General Technical Conditions for Toothed discs Type Cotton Stalk Pullers". Before the test, the toothed discs spacing was adjusted according to the cotton planting row spacing. The effective test length of each test was 30 m, and each group of tests was repeated 3 times. The experimental factors were toothed discs diameter, bending angle and speed ratio. The removal rate is the main test index for cotton stalk removal, and the non-removal rate mainly includes the breakage rate and the omission rate.

The calculation formula for the assessment index is shown below.

$$y_1 = \frac{N_1}{N} \times 100\% \quad (5)$$

$$y_2 = \frac{N_2}{N} \times 100\% \quad (6)$$

$$y_3 = \frac{N_3}{N} \times 100\% \quad (7)$$

$$y_1 + y_2 + y_3 = 100\% \quad (8)$$

In the formula, y_1, y_2 and y_3 are the removal rate, breakage rate and omission rate respectively; N_1, N_2 and N_3 are the number of cotton stalks successfully pulled, the number of cotton stalks broken and the number of cotton stalks missed respectively; N is the total number of cotton stalks, $N = N_1 + N_2 + N_3$.

RESULTS AND ANALYSIS

Based on the single factor test, the tooth disc diameter D, tooth disc inclination angle α and speed ratio λ were selected as influencing factors. The three different levels of factors were arranged according to the $L_9(3^4)$ orthogonal table for orthogonal test. The evaluation indicators were cotton stalk removal rate (y_1), breakage rate (y_2) and omission rate (y_3). Each group of experiments was repeated 3 times, and the experimental factor levels are shown in Table 2.

Table 1

Factors and levels

Levels	Toothed disc diameter, D [m]	Bending angle, α [°]	Speed ratio λ
1	0.5	0	0.5
2	0.6	10	0.7
3	0.7	20	0.9

The three-factor, three-level orthogonal test design scheme and results are shown in Table 2.

Table 2

Tests design scheme and results

No.	Factors			Response indicators		
	D	α	λ	Removal rate y_1 [%]	Breakage rate y_2 [%]	Omission rate y_3 [%]
1	1	1	1	83.31	4.73	11.96
2	1	2	2	90.89	3.95	5.16
3	1	3	3	92.31	6.05	1.64
4	2	1	2	93.69	1.11	5.20
5	2	2	3	95.06	1.43	3.51
6	2	3	1	93.24	5.41	1.35
7	3	1	3	76.74	13.52	9.74
8	3	2	1	82.82	2.30	14.88
9	3	3	2	89.71	2.94	7.35

The experimental results in Table 2 were subjected to range analysis using SPSS software. The range values characterize the relative influence weight of each factor on the evaluation metrics within the selected level ranges. Specifically, factors with larger ranges demonstrate stronger impact weights on the evaluation indicators under their respective level selections, as summarized in Table 3.

Table 3

Orthogonal test range analysis results

Parameters	y_1 [%]			y_2 [%]			y_3 [%]		
	D	α	λ	D	α	λ	D	α	λ
k_1	88.83	84.58	86.45	4.91	6.45	4.15	6.25	8.97	9.40
k_2	94.0	89.59	91.43	2.65	2.56	2.67	3.35	7.85	5.90
k_3	83.09	91.75	88.04	6.25	4.80	7.00	10.66	3.45	4.96
R	10.91	7.17	4.98	3.60	3.89	4.33	7.31	5.52	4.44
Factors of priority	$D>\alpha>\lambda$			$\lambda>\alpha>D$			$D>\alpha>\lambda$		
Optimal parameter combination	$D2\alpha3\lambda2$			$\lambda2\alpha2\ D2$			$D2\alpha3\lambda3$		

Note: k_1~k_3 refer to the mean values of each factor at its respective levels, %; R refers to range, %.

As shown in Table 3, the primary-secondary order of factors influencing cotton stalk removal rate was D > α > λ, while their influence on breakage rate followed the sequence λ > α > D, and the impact order on omission rate was D > α > λ. With removal rate serving as the primary evaluation metric, the optimal parameter combination was determined as $D2\alpha3\lambda2$.

In order to more intuitively show the influence of each factor level on the assessment indicators, Origin 9.0 is used to draw a horizontal indicator relationship diagram with the factor level as the horizontal axis and each assessment indicator as the vertical axis, as shown in Figure 9.

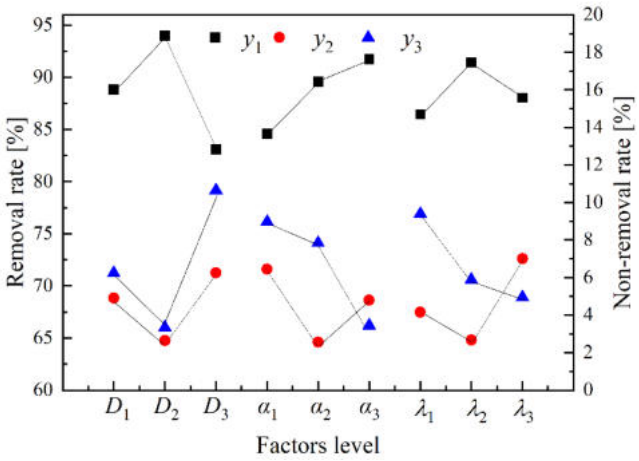


Fig. 9 – Relationship between each factor level and assessment index

An increase in both stalk breakage rate and omission rate directly reduces the removal rate; therefore, the removal rate was selected as the primary evaluation metric. When the removal rate is maximized, the optimal parameter combination is determined as D= 0.6 m, α =20°, and λ= 0.7, as shown in Table 3 and Figure 9. This parameter combination was used for a verification test, and the test was repeated 3 times to calculate the average value of the assessment index. The field environment and the non-flat toothed discs during the test is shown in Fig.10a, and the effect of cotton stalk uprooting is shown in Fig.10b. The test results show that under the $D2\alpha3\lambda2$ parameter combination, the cotton stalk removal rate is 95.7%, the breakage rate is 3.2%, and the omission rate is 1.1%. The test results show that the parameter combination is reasonable and can achieve a good stalk removal effect.



a. Non-flat dentate discs cotton stem uprooting device b. Scene after cotton stalks are removed

Fig. 10 - Cotton stalk removal test

CONCLUSIONS

(1) Based on the requirements and characteristics of cotton stalk uprooting operations, an optimized stalk removal device with non-flat toothed discs was designed. The key advantage of this device is that it imparts a significant upward motion trend to the cotton stalks during the removal process, thereby increasing the lifting height.

(2) ADAMS software was used to simulate and analyze the effects of three factors - disc diameter, bending angle, and speed ratio - on the motion trajectory of the gripping point, lifting height, and working width. The results show that the motion trajectory of the clamping point on the non-flat toothed discs follows a spiral pattern. Increasing the disc diameter helps improve the working width and reduce the omission rate, while increasing the bending angle is more effective than increasing the disc diameter for enhancing the lifting height.

(3) Following the orthogonal experiments carried out, an average cotton stalk removal rate of approx. 96% was obtained, using discs optimized in shape, dimensions and rotation speed. Thus, by using this type of discs, the performance of the cotton stalk removal device can be significantly improved.

ACKNOWLEDGEMENT

This study was supported by the Project category: Autonomous Region Regional Collaborative Innovation Special Project (Science and Technology Aid Xinjiang Program) (2024E02007), and Key R&D Projects in Xinjiang Uygur Autonomous Region (2022293956).

REFERENCES

[1] Agwa, I.S., Omar, O.M., Tayeh, B.A., Abdelsalam, B.A. (2020). Effects of using rice straw and cotton stalk ashes on the properties of lightweight self-compacting concrete. *Constr. Build.* Mater. 235, 117541, https://doi:10.1016/j.conbuildmat.2019.117541.

[2] Chen M., Ping Y., Qu H., Chen Y. (2012). Status and development countermeasures of mechanized cotton-stalk harvesting technologies and equipment (棉秆机械化收获技术与装备现状及发展对策). Chinese *Agricultural Mechanization*, 23–26. Nanjing/China

[3] Chen M., Zhao W., Wang Z., Liu K, Chen Y, Hu Z. (2019). Operation process analysis and parameter optimization of toothed disc cotton-stalk uprooting mechanism (齿盘式多行拔棉秆装置拔秆过程分析与参数优化). *Transactions of the Chinese Society for Agricultural Machinery*, 50, 109–120.Nanjing/China

[4] Chen M. (2022). Research on the key technology of toothed disc cotton-stalk uprooting machine (齿盘式棉秆拔除机具关键技术研究). *Chinese Academy of Agricultural Sciences*, Beijing/China

[5] Cai J., Zhang J., Yeerbolati·T., Gao Z, Rui Z, Liu X. (2020). Design and test of clamping belt cotton straw harvester (夹持带式棉秆收获机设计与试验). *Transactions of the Chinese Society for Agricultural Machinery*, 51, 152–160.Wulumuqi/China

[6] Fernando Correa Da Costa, Av.; Cuiaba, M., (2010) Evaluation of cotton stalks destroyers. J. Soil Sci, Agric, Eng. *Mansoura Univ*, 1, 1061–1073.

[7] He X., Liu J., Xu Y., Wang L, Gao Y, Wang X. (2020). Improvement design of 4mb-6 row-controlled shoveling and drawing placement machine for cotton-stalks in close planting (4MB-6 型密植棉秆对行铲拔铺放机改进设计). *Transactions of the Chinese Society for Agricultural Machinery*, 51, 21–30. Beijing/China

[8] Jiang, P., Li, Y., Li, J., Meng, H., Peng, X., Zhang, B., He, J., Kan, Z. (2021). Experimental Research on the Bending and Fracture Characteristics of Cotton Stalk. *Trans. ASABE*. 64, 1771–1779, https://doi:10.13031/trans.14589.

[9] Keshav, P.K., Banoth, C., Kethavath, S.N., Bhukya, B. (2023). Lignocellulosic ethanol production from cotton stalk: an overview on pretreatment, saccharification and fermentation methods for improved bioconversion process. *Biomass Convers*. Biorefin. 13, 4477–4493, https://doi:10.1007/s13399-021-01468-z.

[10] Liu F., Tian C., Lu X., Han W., Zhang Y., Ye S. (2019). Effect of cotton straw returning planting model on the growth and pest and disease occurrence at the cotton seedling stage along the Yangtze River in Anhui province (安徽省沿江地区棉秆还田种植模式对棉花苗期生长及病虫害发生的影响). *China cotton*. 46, 20–22. Anhui/China.

[11] Ma J., Jian S., Zhou H., (2010). Design of zigzag disk harvester of cotton stem (齿盘式棉花秸秆整株拔取收获机的研究设计). *Agricultural Equipment & Vehicle Engineering*, 3–5, 12. Shandong/China

[12] Nguyen, T.T.; Bailleres, H.; Redman, A.; Leggate, W.; Vandi, L.; Heiztmann, M. (2020). Homogenous particleboard made from whole cotton (*gossypium hirsutum l.*) stalk agricultural waste: optimisation of particle size and influence of cotton residue on performance. *BioResources*, 15, 7730–7748, https://doi:10.15376/biores.15.4.7730-7748.

[13] Pan, Z.G. (2014). Research on cotton stalk harvester based on double roller type. *Adv. Mater. Res.,* 945–949, 286–289, https://doi:10.4028/www.scientific.net/AMR.945-949.286.

[14] Ramadan, Y.Y.R. (2010). Development and evaluation of a cotton stalks puller. *J. Soil Sci. Agric. Eng*., 1, 1061–1073, https://doi:10.21608/jssae.2010.75470.

[15] Tang Z., Han Z., Gan B., Bao C. Hao F. (2010). Design and experiment on cotton stalk pulling head with regardless of row (不对行棉秆拔取收获台设计与试验). *Transactions of the Chinese Society for Agricultural Machinery*, 41, 80–85. Beijing/China

[16] Wang X., Jian S., Ma J., Yu X. (2011). The simulation design and movement analysis of toothed disc cotton stalk pulling machine (齿盘式拔棉秆机的仿真设计与运动分析). *Agricultural Equipment & Vehicle Engineering*, 5–7. Shandong/China

[17] Wang F., Shi Y., Wang W., Ma X., Zhang J., Guo Z., Song R., Li X., Dong D., Wang Y., Ma X. (2022). Analysis of the utilization prospect and technology of cotton straw in feed (棉花秸秆饲料化前景与技术分析). *China cotton*, 49, 37–41, https://doi:org10.11963/cc20220164 Zhengzhou/China

[18] Xie J., Wu S., Cao S., Zhang Y., Zhao W., Zhou J. (2023). Design and test of clamping-roller cotton stalk pulling device (夹持辊式棉秆拔取装置设计与试验). *Transactions of the Chinese Society for Agricultural Machinery*, 54, 101–111. Urumqi /China

[19] Zhao, W., Chen, M., Xie, J., Cao S., Wu A., Wang Z. (2023). Discrete element modeling and physical experiment research on the biomechanical properties of cotton stalk. *Computers and Electronics in Agriculture*, 204, 107502, https://doi:10.1016/j.compag.2022.107502.

[20] Zhao W., Xie J., Chen M., Gao Q., Cao S., Wang Z., Chen Y. (2024). Design and experiments of the clamping and uprooting device with adjustable stiffness for cotton stalk (变刚度夹拔式棉秆整株拔取装置设计与试验). *Transactions of the Chinese Society of Agricultural Engineering,* 40, 35–45. Urumqi/China

[21] Zhang A., Liu K., Wang Z., Liu Y., Wang H. (2016). Design and trial on cotton stalk pulling head with multi- roller (多辊式棉秆收获台的研究与试验). *journal of agricultural mechanization research*, 38, 91–95, https://doi:10.13427/j.cnki.njyi.2016.03.019. Shandong /China

[22] Zhao, W., Xie, J., Wang, Z., Gao Q., Chen M. (2022). Investigation of mechanical properties of cotton stalk based on multi-component analyses. *Int. Agrophys*., 36, 257–267, https://doi:10.31545/intagr/152488.

DISCRETE ELEMENT MODELING AND PARAMETER CALIBRATION FOR CORYDALIS TUBER
/
延胡索离散元模型构建及参数标定

Xiangyang LIU[1)], Chun WANG[1,2)], Yongchao SHAO[1)], Weiguo ZHANG[1*)]
[1)]College of Mechanical and Electrical Engineering, Northwest Agriculture and Forestry University, Yangling 712100, China;
[2)]College of Biological and Agricultural Engineering, Jilin University, Changchun 130000, China
Tel: +86-17391612856; E-mail: cn-lxy@nwafu.edu.cn
DOI: https://doi.org/10.35633/inmateh-76-02

Keywords: *Corydalis tuber, discrete element, parameter calibration, optimal design*

ABSTRACT
To address the lack of contact parameters between Corydalis tuber and mechanical, or soil interfaces during planting, harvesting, and processing stages, this study calibrated discrete element simulation parameters for Corydalis tuber by combination of simulation tests and physical tests. 3D contour model of Corydalis tuber was obtained using 3D scanning technology, and a multi-sphere bonded particle model was constructed by automatic filling method. Simulation tests were conducted with the restitution coefficient, static friction coefficient, and rolling friction coefficient between Corydalis tuber and Q235 steel, as well as between Corydalis tuber and soil, as independent variables. The rebound height, friction angle, and rolling distance were considered as dependent variables. A second-order polynomial fitting method was used to analyze the experimental results. The actual test values were substituted into the polynomial equations to obtain simulation values for the contact parameters of Corydalis tuber with Q235 steel and soil, and these values were then validated against the experimental results. The findings indicate that the restitution coefficients of Corydalis tuber-Q235 steel and Corydalis tuber-soil were 0.728 and 0.44, respectively. The static friction coefficients of Corydalis tuber-Q235 steel and Corydalis tuber-soil were 0.41 and 0.76, respectively, while the rolling friction coefficients were 0.02 and 0.033, respectively. Under these conditions, the relative error between the simulation tests and physical tests was minimized. This study provides calibrated particle models and contact parameters for mechanical processing applications, including sowing, harvesting, and drying of Corydalis tuber.

摘要
针对延胡索在种植、收获、加工等环节中缺乏与机械、土壤接触参数的现状，本研究结合仿真试验与物理试验对延胡索进行离散元仿真参数标定。借用三维扫描技术获得延胡索的三维轮廓模型，采用自动填充法建立延胡索的多球粘结颗粒模型。分别以延胡索与 Q235 钢、土壤的碰撞恢复系数，静摩擦因数及滚动摩擦因数为自变量，以碰撞高度、摩擦倾角及滚动距离为因变量进行仿真试验，并进行二次多项式拟合。将实际试验值带入二次多项式，获得延胡索与 Q235 钢、土壤的接触参数仿真值，并与实际试验值进行校对。试验结果表明：延胡索-Q235 钢，延胡索-土壤的碰撞恢复系数分别为 0.728、0.44；延胡索-Q235 钢，延胡索-土壤的静摩擦因数分别为 0.41、0.76；延胡索-Q235 钢，延胡索-土壤的碰撞恢复系数分别为 0.02、0.033 时，仿真试验与实际试验相对误差最小。本研究可为延胡索播种、收获及烘干等机械加工提供颗粒模型与仿真接触参数。

INTRODUCTION
Corydalis tuber is one of the most widely utilized medicinal herbs in China. It is characterized by a flattened, spherical shape and typically thrives in loose soils, such as sandy or semi-sandy environments. Corydalis tuber contains over 30 types of alkaloids, including tetrahydropalmatine and corydaline (*He et al., 2007; Chen et al., 2008*). It exhibits notable pharmacological effects, such as analgesic, sedative, hypnotic, and anti-arrhythmic properties. In recent years, with the expanding applications of Corydalis tuber in the medical field, its demand has continued to rise, leading to increased profitability in its cultivation. Hanzhong City in Shaanxi Province is the largest Corydalis tuber cultivation area in China, with over 100,000 acres under cultivation, accounting for more than 70% of the nation's total production. Currently, the cultivation and harvesting of Corydalis tuber rely predominantly on manual labor, resulting in high labor intensity and elevated costs, which severely constrain the development of its cultivation industry.

To achieve full mechanization across all stages of Corydalis tuber cultivation, from planting to harvesting, has become an urgent necessity. Objective and accurate collection of the mechanical property parameters of Corydalis tuber is a prerequisite for the development of specialized mechanized equipment (*Han et al., 2017; Liu et al., 2018; Ma et al., 2013; Shi et al., 2014*).

The DEM simulates granular materials discretely, modeling each particle independently and assigning it mass, stiffness, and damping properties. The particles interact with each other through contact, and the dynamic forces and moments at the contact points are calculated using a contact mechanics model (such as the Hertz-Mindlin model), which in turn predicts the motion state of individual particles. This method has unique advantages in studying the plant-soil interaction in mechanized farming: First, it breaks through the continuum assumption and directly characterizes the particle-level stress transfer and displacement processes in the microscopic contact between the agricultural tool and the soil, accurately analyzing the soil fragmentation/compaction mechanism. Second, its multi-physics coupling capability can simultaneously simulate the stress deformation of mechanical components and the dynamic response of the soil, providing a cross-scale analysis basis for the structural optimization of agricultural machinery. This discrete granular dynamics feature makes it an important tool for shortening the research and development cycle of agricultural machinery.

Originally developed to solve geotechnical problems, the discrete element method (DEM) is a numerical method for calculating the mechanical properties of granular materials. It simulates granular materials as individual particles and calculates the forces (such as contact and friction forces) and movements between the particles iteratively over time steps. It is particularly suitable for studying plant-soil interactions in mechanized farming because it can capture the discrete nature of soil particles and irregular shapes of crops (e.g., tubers), enabling precise modeling of dynamic processes such as soil penetration, root-soil adhesion, and mechanical harvesting collisions (*Wang et al., 2024*). In agricultural research, DEM has been widely applied to model interactions between crops (e.g., seeds, roots) and soil or machinery. For example, DEM has been successfully used to optimize soil-tool interactions in potato harvesting by simulating tuber-soil separation processes. (*Zhao et al., 2023*), and to design seed metering devices by analyzing seed motion under dynamic conditions. As a result, the potato tubers obtained by DEM simulation analysis are more stable, and the leakage rate and replay rate (coefficient of variation) are lower under reasonable seeding device structure design and working parameters (forward speed of machine, seeding speed, etc.) (*Chen et al., 2023*). Xu Bing et al., (*2021*) developed a discrete element model for buckwheat seeds using an automatic filling method, followed by parameter calibration. Based on this model, they conducted an optimized design of the three-stage vibration process for buckwheat. The optimized three-stage vibrating screen has higher clearance rate and lower impurity rate. Chen Zeren et al., (*2018*) classified corn seeds by shape and developed discrete element models for corn seeds using varying numbers of spheres in a filling method. This approach aimed to balance computational efficiency and accuracy. The results were validated through a "self-flow screening" experiment, demonstrating close alignment with actual outcomes. Recent studies on root crop mechanization (e.g., sugar beet harvesting) have further validated DEM's accuracy in predicting tuber damage rates under varying soil conditions (*Yang et al., 2023*). These applications demonstrate DEM's capability to capture granular behavior and complex mechanical interactions, which is critical for analyzing Corydalis tuber in soil environments. For example, analyze the uniformity and stability of Corydalis tubers seeding, harvest rate at harvest, loss rate, etc.

Due to the flattened, irregular shape of Corydalis tuber and its dynamic interactions with soil during mechanized harvesting, the discrete element method (DEM) is a preferred approach to capture these complex behaviors. Addressing the lack of particle contact parameters essential for designing key machinery for sowing and harvesting Corydalis tuber, this study employed 3D scanning technology to obtain a three-dimensional model of Corydalis tuber. Using an automatic filling method, a discrete element model for Corydalis tuber was established (*Sun et al., 2022; Wang et al., 2017; Xu et al., 2022; Yu et al., 2020; Xu et al., 2018*). Simulation experiments were conducted with this model to determine the coefficients of restitution, static friction, and rolling friction between Corydalis tuber and both soil and Q235 steel. These simulations were then compared with actual tests to obtain mechanical parameters closest to the true values.

MATERIALS AND METHODS

Determination of fundamental physical parameters

The experimental subject selected was Corydalis tuber, harvested in early May from a designated experimental field in Chenggu County, Hanzhong City, Shaanxi Province, China, cultivated with the "Zhehu

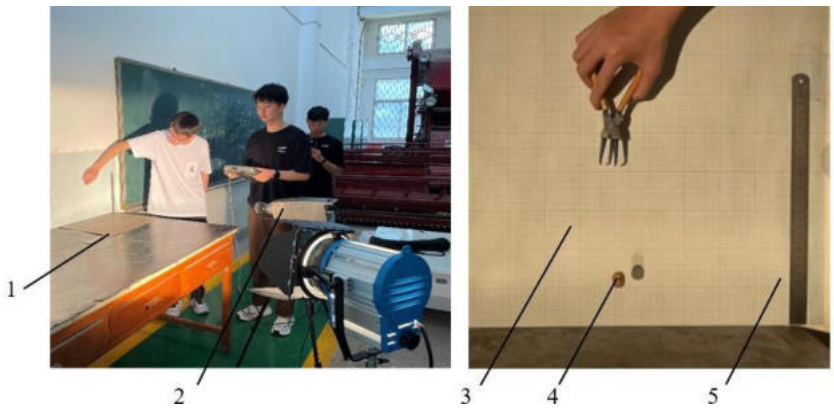
No.1" variety. Sampling was conducted using the five-point sampling method, and subsequent measurements of its physical characteristic parameters were performed. The density of Corydalis tuber was measured using the water displacement method, yielding a density of 1085 kg/m³. The moisture content of Corydalis tuber at harvest was determined using an Ohaus M23 rapid moisture analyzer. The average moisture content obtained was 61.27%.

Determination of contact parameters

During the harvest period, interactions occur between the Corydalis tuber, as well as between the particles and the soil or machinery. In discrete element simulations, the restitution coefficient, static friction coefficient, and rolling friction coefficient play crucial roles in determining the accuracy and reliability of the simulation. The soil selected for the experiment was that typically used for cultivating Corydalis tuber in the local region, while the material chosen for the machinery components was Q235 steel.

Determination of the restitution coefficients of Corydalis tuber - Q235 steel, Corydalis tuber - soil

The restitution coefficient refers to the ratio of the separation velocity to the approach velocity in the normal direction at the point of contact before and after a collision, depending solely on the materials involved. The restitution coefficients for Corydalis tuber colliding with Q235 steel and soil were determined through a free-fall test, as depicted in Figure 1. Corydalis tuber was dropped from a height of 200 mm, and upon collision with the Q235 plate or soil bed, they bounced back. The rebound height *h* was recorded using a high-speed imaging system, with a scale-marked grid paper and steel ruler placed behind the particles. To ensure the reliability of the experimental data, 10 sets of tests were conducted, with each set repeated three times, and the average value was taken.



(a) Free fall test (b) Positive perspective of the free fall test

Fig. 1 - Determination of restitution coefficients of Corydalis tuber – Q235 steel, Corydalis tuber - soil

1. Q235 steel; 2. High-speed camera; 3. Graph paper; 4. Corydalis tuber; 5. Ruler.

The coefficient of restitution can be calculated using the following formula:

$$e = \frac{v_4 - v_3}{v_2 - v_1} \quad (1)$$

$$v_4 = \sqrt{2gh} \quad (2)$$

$$v_2 = \sqrt{2gH} \quad (3)$$

in which:

e – the coefficient of restitution between Corydalis tuber and the colliding material;

v_1 – the velocity of the colliding material before the collision, [m/s];

v_2 – the velocity of Corydalis tuber before the collision, [m/s];

v_3 – the velocity of the colliding material after the collision, [m/s];

v_4 – the velocity of Corydalis tuber after the collision, [m/s];

H – the height from which the object is dropped before free fall, [m];

h – the rebound height, [m];

g – the acceleration due to gravity, [m/s^2].

Both materials underwent 10 sets of experiments, and the results are presented in Table 1.

Table 1

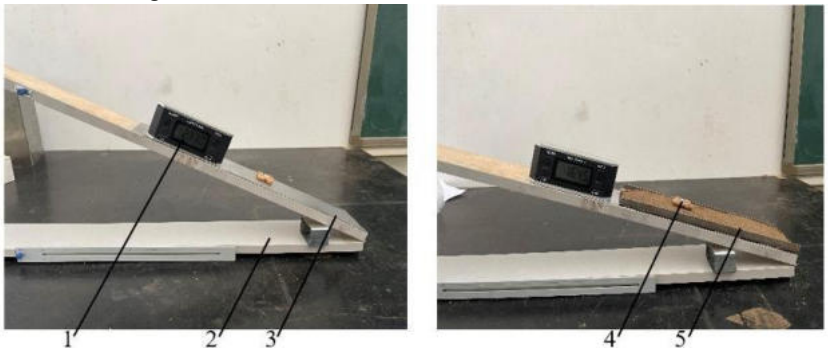
Restitution coefficients of Corydalis tuber – Q235 steel, Corydalis tuber - soil

Number	Corydalis tuber-Q235 rebound height (m)	The coefficient of restitution	Corydalis tuber-soil rebound height (m)	The coefficient of restitution
1	0.0307	0.3916	0.0180	0.3000
2	0.0667	0.5774	0.0110	0.2345
3	0.0443	0.4708	0.0213	0.3266
4	0.0267	0.3651	0.0220	0.3317
5	0.0658	0.5730	0.0170	0.2915
6	0.0773	0.6218	0.0157	0.2799
7	0.0763	0.6178	0.0160	0.2828
8	0.0513	0.5066	0.0270	0.3674
9	0.0760	0.6164	0.0247	0.3512
10	0.0570	0.5339	0.0147	0.2708
The average value	**0.0572**	**0.5274**	**0.0187**	**0.3036**

By substituting the average rebound height of Corydalis tuber on Q235 steel and soil into Equation 2, 3 and 1, the coefficient of restitution of Corydalis tuber-Q235 is obtained as 0.5274, and the coefficient of restitution of Corydalis tuber-soil is 0.3036.

Determination of the static friction coefficients of Corydalis tuber - Q235 steel, Corydalis tuber - soil

The static friction coefficient refers to the ratio of the maximum static friction force to the normal force between two objects. The factors influencing the static friction coefficient mainly include the type of friction materials, the roughness of the contact surfaces, and so on. The static friction coefficients between Corydalis and Q235 steel, as well as between Corydalis and soil, were measured using the inclined plane method, as shown in Figures 2. Since Corydalis tuber have a flattened spherical shape, rolling is likely to occur during the experiment. To ensure accuracy and reduce experimental errors, four Corydalis tubers were bonded into a square shape using a hot glue gun. The inclined plane was equipped with an angle measurement device for easy reading and recording of data. For both materials, 10 sets of experiments were conducted, with each set repeated 3 times, and the average value was taken.



(a) Inclined plane method between Corydalis tuber and Q235 (b) Inclined plane method between Corydalis tuber and Soil

Fig. 2 - Determination of static friction coefficients of Corydalis tuber – Q235 steel, Corydalis tuber - soil

1. Angle measuring device; 2. Friction angle measuring instrument; 3. Q235 steel plate; 4. Corydalis tuber; 5. Soil plate.

The formula for calculating the static friction coefficient is as follows:

$$f = G\sin\theta \tag{4}$$

$$F_N = G\cos\theta \tag{5}$$

$$f = \mu F_N \tag{6}$$

in which: f – the frictional force acting on Corydalis tuber, [N];
G – the gravitational force of Corydalis tuber, [N];
F_N – the support force acting on Corydalis tuber, [N];
μ – the static friction coefficient;
θ – the angle between the inclined plane and the horizontal surface, [°].

Both materials underwent 10 sets of experiments, and the results are presented in Table 2.

Table 2

Static friction coefficients of Corydalis tuber – Q235 steel, Corydalis tuber - soil

Number	Corydalis tuber-Q235 static friction angle (°)	The static friction coefficient	Corydalis tuber-soil static friction angle (°)	The static friction coefficient
1	25.95	0.4867	38.88	0.8064
2	26.12	0.4903	38.88	0.8064
3	26.50	0.4986	41.18	0.8749
4	28.05	0.5328	40.18	0.8632
5	24.42	0.4540	40.97	0.8683
6	25.48	0.4766	39.43	0.8224
7	24.05	0.4463	42.38	0.9126
8	25.25	0.4716	38.83	0.8050
9	28.52	0.5433	40.77	0.8622
10	27.89	0.5292	42.12	0.9041
Average value	26.22	0.4925	40.43	0.8525

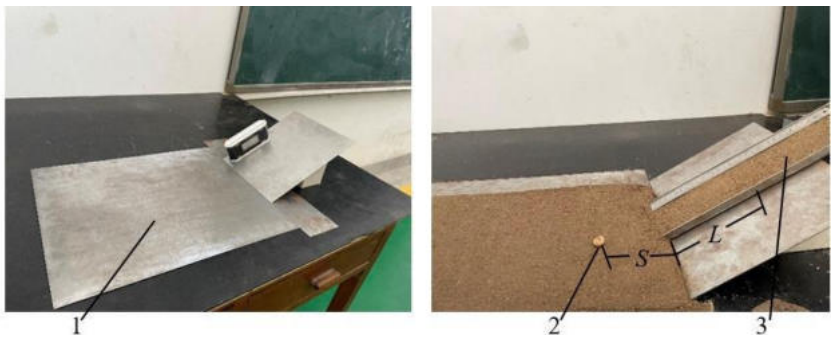
In the ten groups of tests of these two types of materials, the static friction angle between Corydalis tuber and Q235 ranges from 24.05° to 28.52°, and the static friction angle between Corydalis tuber and soil ranges from 38.83° to 42.38°. The surface roughness of the corresponding material plate (Q235 steel plate or soil plate) has been ensured to be continuously consistent before each Corydalis tuber test, and the surface condition of the particles of the Corydalis tuber used for test is unchanged. The friction angle measuring instrument used for the test had an accuracy of $\pm$ 0.2°, and the corresponding angle was displayed during the measurement (two decimal places were retained by default). The experimental environment and the accuracy of the measuring instrument complied with the specifications.

By substituting the average static friction angle of Corydalis tuber on Q235 steel and soil into Equation 4, 5 and 6, the static friction angle of Corydalis tuber-Q235 is obtained as 0.4925, and the static friction angle of Corydalis tuber-soil is 0.8525.

Determination of the rolling friction coefficients of Corydalis tuber – Q235 steel, Corydalis tuber - soil

Rolling friction occurs when an object rolls without slipping or tends to roll on another object's surface, causing deformation at the contact point between the two materials, which generates resistance to rolling. In this study, the rolling friction coefficient between Corydalis and Q235 steel plate, as well as between Corydalis and soil, was measured using the bevel rolling method. The experimental setup is shown in Figure 3.

In the rolling friction factor measurement, the Corydalis tuber roll without sliding on the inclined plane, and the rolling resistance generated by the steel plate on the Corydalis tuber is essentially static friction. According to the results measured in Table 2, the average static friction angle between the Corydalis tuber and Q235 is 26.22°. And in order to facilitate the fixation of the inclined plane and horizontal plate of the steel plate, the angle between the inclined plane and horizontal surface was set to 30°, ensuring the plane interface was as smooth as possible. Corydalis tuber was placed at a distance of L = 35 mm, and with an initial velocity of 0 m/s, they were allowed to roll freely until they stopped. The horizontal rolling distance (S) of the Corydalis tuber was measured. Ten sets of experiments were conducted for each material, with each set repeated three times. The average rolling distance was taken as the final data. The shape of the Corydalis tuber is mostly irregular and flattened spherical, and the size is relatively small and highly variable, air resistance cannot be ruled out during testing, so it may have a slight effect on the test results in actual measurement.



(a) (b)

Fig. 3 - Determination of rolling friction coefficients of Corydalis tuber – Q235 steel, Corydalis tuber – soil

(a) Bevel rolling method between Corydalis tuber and Q235; (b) Bevel rolling method between Corydalis tuber and Soil

1. Q235 steel plate; 2. Corydalis tuber; 3. Soil plate.

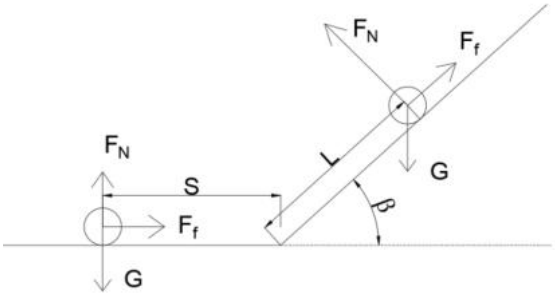


Fig. 4 - Force analysis of the Corydalis tuber rolling process

The force analysis of the rolling process of Corydalis tuber particles is shown in Figure 4. According to the law of conservation of energy during the entire rolling process, the rolling friction coefficient μ' can be calculated as follows:

$$0 - 0 = GL\sin\beta + (-\mu' G\cos\beta\, L) + (-\mu' GS)$$

$$GL\sin\beta = G(L\cos\beta + S)\mu'$$

$$\mu' = \frac{L\sin\beta}{L\cos\beta + S} \tag{7}$$

in which: β – the angle of inclination of the inclined plane, [°];

S – the distance traveled by Corydalis tuber while rolling on a flat surface, [m];

L – the distance traveled by Corydalis tuber while rolling on an inclined plane, [m];

μ' – the rolling friction coefficient of Corydalis tuber and materials.

Both materials underwent 10 sets of experiments, and the results are presented in Table 3.

Table 3

Rolling distances of Corydalis tuber – Q235 steel, Corydalis tuber - soil

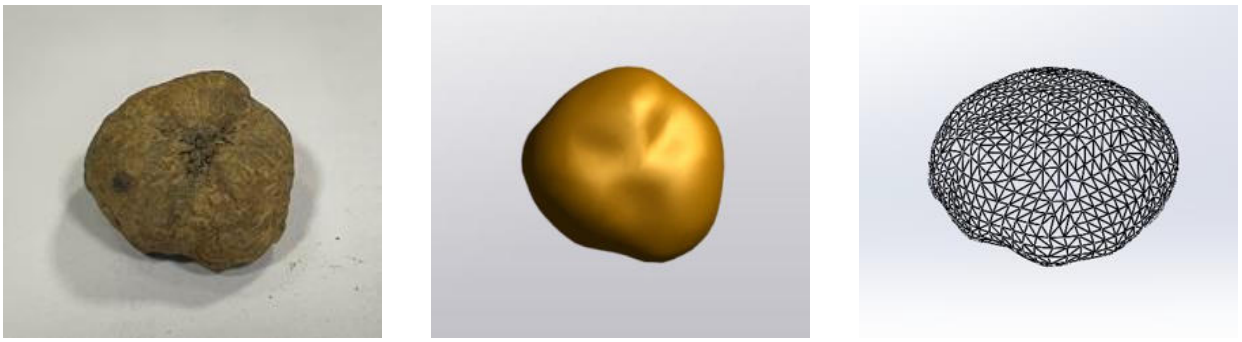
Number	Corydalis tuber-Q235 rolling distance (mm)	Corydalis tuber-soil rolling distance (mm)
1	108.7	65.0
2	109.7	66.3
3	167.0	46.3
4	135.3	40.0
5	114.0	59.7
6	129.3	57.3
7	117.3	35.0
8	109.3	44.3
9	142.3	54.3
10	149.7	44.0
Average value	**122.1**	**49.7**

By substituting the average rolling distances of Corydalis tuber on Q235 steel and soil into Equation 7, the rolling friction coefficient of Corydalis tuber-Q235 is obtained as 0.115, and the rolling friction coefficient of Corydalis tuber-soil is 0.219.

Establishment of the Discrete Element Model for Corydalis tuber

3D model of Corydalis tuber

Given the highly irregular shape of Corydalis tuber, modeling using traditional three-dimensional software proves to be challenging (*Zhang et al., 2024*). In this study, advanced three-dimensional imaging technology was employed, utilizing the HandySCAN3D scanner to capture the three-dimensional morphology of Corydalis tuber (The surface roughness of the Corydalis tuber, deformation of the tuber and slight compression have negligible effects on the accuracy of the model.). The scanner has an accuracy of 0.0025 mm and a measuring rate of 1,300,000 measurements per second， then the contour model was saved in STL file format, as shown in Figure 5.



(a) Corydalis tuber (b) 3D model of Corydalis tuber (c) Corydalis tuber Outline model

Fig. 5 - The 3D model of Corydalis tuber

Discrete element model

In this study, a multi-sphere bonded particle model was employed to establish the discrete element model for Corydalis tuber. The previously scanned contour model of Corydalis tuber was used as the filling space. Spherical particles with diameters of 1 mm, 2 mm, and 4 mm were utilized for the filling, with the respective quantities of spherical particles being 3,439, 426, and 61, as shown in Figure 6. In consideration of both the accuracy of the equilibrium simulation and simulation speed, spherical particles with a diameter of 2 mm were ultimately selected for the particle filling of Corydalis tuber.



(a) 1mm (2) 2mm (3) 4mm

Fig. 6 - Multi ball bonding model

Calibration of contact parameters between Corydalis tuber, Q235 steel and soil

There exists a discrepancy between the parameters used in actual experiments and those in the simulations, making them unsuitable for direct application in subsequent mechanical simulation (*Zhao et al., 2024*). To enhance the accuracy and reliability of the discrete element simulations, calibration of the relevant parameters was performed through simulation experiments.

Calibration of the coefficient of restitution

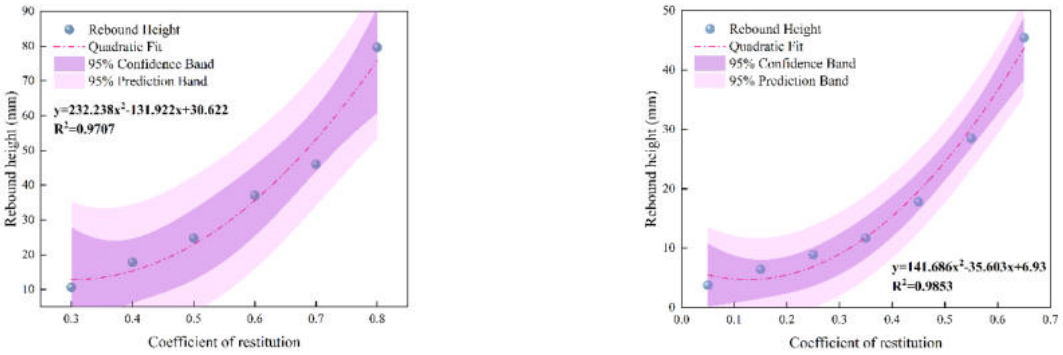
Based on the coefficient of restitution of Corydalis tuber with Q235 steel and soil obtained from previous drop tests, the established discrete element model of Corydalis tuber was utilized to create simulation experiments under actual test conditions, as shown in Figure 7.



Fig. 7 - Drop test simulation

1. Corydalis tuber; 2. Baseplate.

In the simulation experiments, the static friction coefficient and rolling friction coefficient between the Corydalis tuber, Q235 steel, and soil were set to 0. Based on the results of the actual experiments, the coefficient of restitution for collisions between Corydalis tuber and Q235 was selected within the range of 0.3 to 0.8, while the coefficient of restitution for collisions between Corydalis tuber and soil was selected within the range of 0.05 to 0.65. The experimental results and the quadratic curve fitting results are shown in Figure 8.



(a) Corydalis tuber - Q235 steel (b) Corydalis tuber - soil

Fig. 8 - The fitted curves of the coefficient of restitution and rebound height from impact simulation tests of Corydalis tuber with Q235 steel and soil

To establish the functional relationship between the coefficient of restitution and rebound height for collisions between Corydalis tuber and Q235 steel, as well as soil, a quadratic polynomial fitting was performed.

The equation of the fitting curve is as follows:

$$y_1 = 232.238x_1^2 - 131.922x_1 + 30.622 \quad (8)$$

$$y_2 = 141.686x_2^2 - 35.603x_2 + 6.93 \quad (9)$$

in which: y_1 – the rebound height of Corydalis tuber and Q235 steel, [m];

x_1 – the coefficient of restitution between Corydalis tuber and Q235 steel;

y_2 – the rebound height of Corydalis tuber and soil, [m];

x_2 – the coefficient of restitution between Corydalis tuber and soil.

The coefficient of determination for regression equation y_1 was R^2 = 0.9707, and for y_2, it was R^2 = 0.9853. Both models had P << 0.05, indicating that the regression models were highly significant. Substituting the average rebound heights from the actual free-fall experiments, y_1 and y_2, into Equations (8) and (9) yielded the coefficient of restitution between Corydalis tuber and Q235 steel, x_1 = 0.728, and the coefficient of restitution between Corydalis tuber and soil, x_2 = 0.44. By setting x_1 and x_2 as the coefficients of restitution in the simulation experiments and repeating the trials 10 times, the average rebound height for Corydalis tuber and Q235 steel was 58.87 mm, and for Corydalis tuber and soil, it was 18.99 mm. The relative errors compared to the measured results from the actual experiments were 2.02% and 1.55%, respectively. This demonstrates that the calibrated simulation results were consistent with the experimental data. Ultimately, the coefficients of restitution for the discrete element simulation were determined to be 0.728 for Corydalis tuber and Q235 steel, and 0.44 for Corydalis tuber and soil.

Calibration of static friction coefficient

Based on the static friction angles of Corydalis tuber with Q235 steel and soil obtained from previous inclined plane tests (*Zhuang et al., 2023*), the established discrete element model of Corydalis tuber was utilized to create simulation experiments under actual test conditions, as shown in Figure 9.

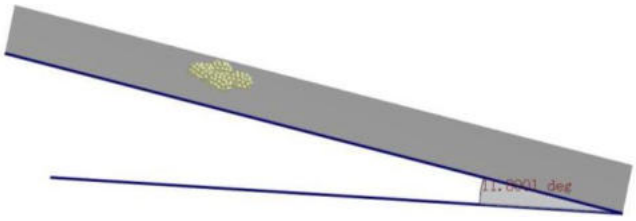


Fig. 9 - Ramp test simulation

In the simulation experiments, the coefficients of restitution between Corydalis tuber and Q235 steel, as well as soil, were predefined. The rolling friction coefficients and inter-particle parameters for Corydalis tuber were set to 0. Based on the actual experimental results, the static friction coefficient ranges for Corydalis tuber with Q235 steel and soil were selected as 0.1~0.7 and 0.3~0.9, respectively, with an increment of 0.1. The experimental results and the quadratic curve fitting results are shown in Figure 10.

The fitted equations for the static friction coefficient curve between Corydalis tuber and Q235 steel, as well as soil, are as follows:

$$y_3 = -20.714x_3^2 + 66.809x_3 + 2.3 \quad (10)$$

$$y_4 = -20.317x_4^2 + 65.666x_4 + 2.336 \quad (11)$$

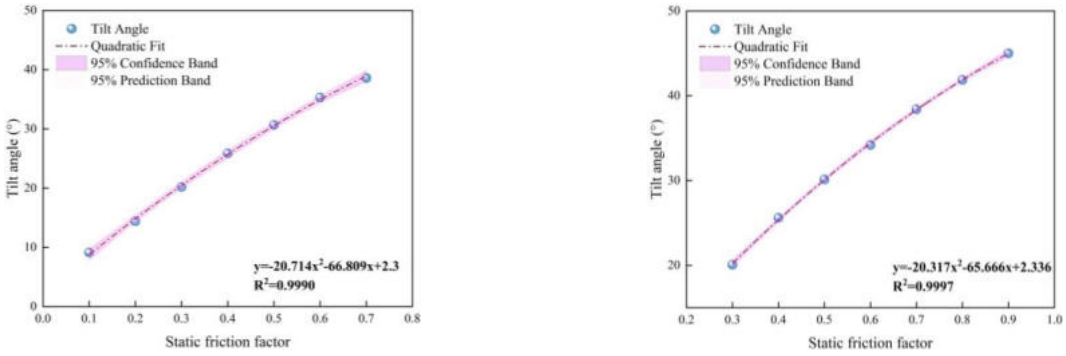
in which:

y_3 – the inclination angle (Corydalis tuber and Q235 steel), [°];

x_3 – the static friction coefficient between Corydalis tuber and Q235 steel;

y_4 – the inclination angle (Corydalis tuber and soil), [°];

x_4 – the static friction coefficient between Corydalis tuber and soil.



(a) Corydalis tuber - Q235 steel (b) Corydalis tuber - soil

Fig. 10 - The fitted curves of the static friction coefficient and inclination angle from simulation tests of Corydalis tuber with Q235 steel and soil

The coefficient of determination for regression equation y_3 was R^2 = 0.9990 with P = 0.0000009 << 0.05, and for y_4, it was R^2 = 0.9997 with P = 0.000000079 << 0.05, indicating that both models were highly significant. Substituting the average inclination angles from the actual inclined plane tests, y_3 = 40.52 and y_4 = 122.1, into Equations (10) and (11), yielded the static friction coefficients x_3 = 0.41 for Corydalis tuber with Q235 steel and x_4 = 0.76 for Corydalis tuber with soil. These static friction coefficients were then set as parameters for the simulation experiments, and 10 trials were conducted for each scenario. The resulting frictional inclination angle between Corydalis tuber and Q235 steel was 26.13°, with a relative error of 0.17% compared to the actual test. The frictional inclination angle between Corydalis tuber and soil was 40.46°, with a relative error of 0.41%. These results demonstrate that the calibrated simulation results closely aligned with the actual experimental data. Therefore, the static friction coefficients determined for the simulation experiments were finalized as 0.41 for Corydalis tuber with Q235 steel and 0.76 for Corydalis tuber with soil.

Calibration of rolling friction coefficient

Similarly, based on the rolling friction distances between Corydalis tuber and Q235 steel, as well as soil, measured in previous experiments, simulation experiments were constructed using the established discrete element model of Corydalis tuber under actual experimental conditions, as shown in Figure 11.

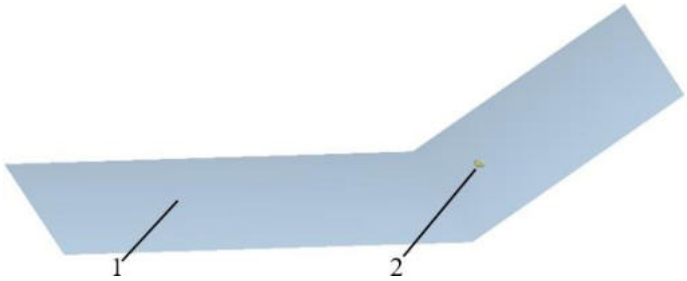
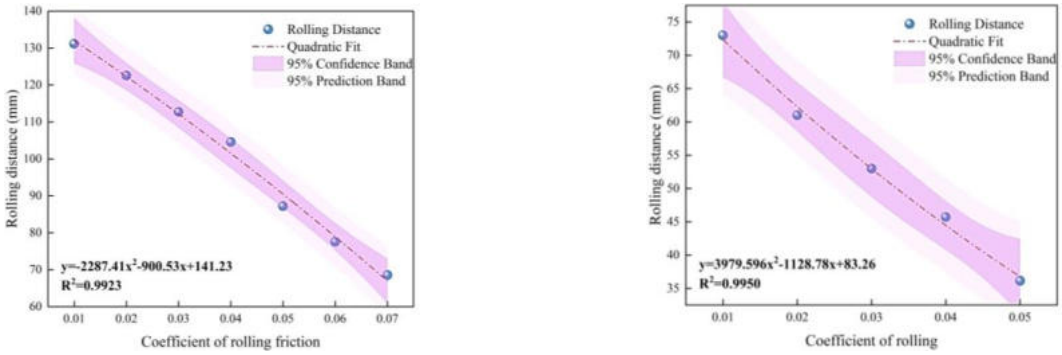


Fig. 11 - Rolling test simulation

1. Material plates; 2. Corydalis tuber.

In the simulation experiments, the coefficients of restitution and static friction coefficients between Corydalis tuber and Q235 steel, as well as soil, were predefined. The inter-particle contact parameters for Corydalis tuber were set to 0. The rolling friction coefficient range for Corydalis tuber and Q235 steel was selected as 0.01~0.07, and for Corydalis tuber and soil, it was 0.01~0.05, both with a step size of 0.01. The results of the simulation experiments and the fitted curves are shown in Figure 12.



(a) Corydalis tuber - Q235 steel (b) Corydalis tuber - soil

Fig. 12 - The fitted curves of the rolling friction coefficient and rolling distance from simulation tests of Corydalis tuber with various Q235 steel and soil.

The fitted equations for the rolling friction coefficient curve between Corydalis tuber and Q235 steel, as well as soil, are as follows:

$$y_5 = -2287.41x_5^2 - 900.53x_5 + 141.23 \quad (12)$$

$$y_6 = 3979.59x_6^2 - 1128.78x_6 + 83.26 \quad (13)$$

in which: y_5 – the rolling distance (Corydalis tuber and Q235 steel), [m];
x_5 – the rolling friction coefficient between Corydalis tuber and Q235 steel;
y_6 – the rolling distance (Corydalis tuber and soil), [m];
x_6 – the rolling friction coefficient between Corydalis tuber and soil.

The coefficient of determination for regression equation y_5 was $R^2 = 0.9923$ with $P = 0.000058 \ll 0.05$, and for y_6, it was $R^2 = 0.9950$ with $P = 0.00495 \ll 0.05$, indicating that both models were highly significant. Substituting the average rolling distances from the actual rolling tests, $y_5 = 122.1$ mm and $y_6 = 49$ mm, into Equations (12) and (13), the rolling friction coefficients were calculated as $x_5 = 0.02$ for Corydalis tuber with Q235 steel and $x_6 = 0.03$ for Corydalis tuber with soil. These rolling friction coefficients were then set as parameters for the simulation experiments, and 10 trials were conducted for each scenario. The resulting rolling distance for Corydalis tuber with Q235 steel was 118.5 mm, with a relative error of 3.04% compared to the actual test. The rolling distance for Corydalis tuber with soil was 48.375 mm, with a relative error of 2.73%. These results demonstrate that the calibrated simulation results were generally consistent with the experimental data. Therefore, the rolling friction coefficients determined for the simulation experiments were finalized as 0.02 for Corydalis tuber with Q235 steel and 0.033 for Corydalis tuber with soil.

CONCLUSIONS

(1) Through experiments measuring the restitution coefficient, static friction coefficient, and rolling friction coefficient between Corydalis tuber and Q235 steel, as well as soil, the actual experimental values for these parameters were obtained. These tests included measurements of the restitution coefficient, static friction coefficient, and rolling friction coefficient for Corydalis tuber under both conditions.

(2) A three-dimensional contour model of Corydalis tuber was obtained using 3D scanning technology. The contour model obtained by scanning cannot be directly used in subsequent discrete element simulation experiments. In order to improve the accuracy of discrete element particle modeling of Corydalis tubers and the simulation accuracy, a multi-sphere bonded particle model of the Corydalis tuber was generated using the automatic filling method in the EDEM software.

(3) The simulation test takes the restitution coefficient, static friction coefficient and rolling friction coefficient between the Corydalis tuber and Q235 steel, and between the Corydalis tuber and soil as independent variables, and the collision height, friction angle and rolling distance as dependent variables. A second-order polynomial fitting was performed based on the simulation results, and the actual experimental values were substituted into the polynomial equation to obtain the simulated contact parameter values of the Corydalis tuber with Q235 steel and soil. The values were then verified based on the actual experimental measurements, and the relative error between the two was less than 5%.

REFERENCES

[1] Chen, Q., Chen, Y., Liu, Y., Huang, B., (2008). High yield cultivation techniques of Yuanhu. *Modern Agricultural Science and Technology*, vol.19, pp.71. (in Chinese), China;

[2] Chen, Z., Yu, J., Xue, D., Wang, Y., Zhang, Q., Ren, L., (2018). An approach to and validation of maize-seed-assembly modelling based on the discrete element method. *Powder Technology*, vol.328, pp.167-183. Switzerland. https://doi.org/10.1016/j.powtec.2017.12.007

[3] Chen, Z., Xue, D., Guan, W., Guo, J., Liu, Z., (2023). Performance Optimization of a Spoon Precision Seed Metering Device Based on a Maize Seed Assembly Model and Discrete Element Method. *Processes*, vol.11(11). pp.1-12. Switzerland. https://doi.org/10.3390/pr11113076

[4] Han, D., Zhang, D., Yang, L., Li, K., Zhang, T., Wang, Y., Cui, T., (2017). EDEM-CFD simulation and experiment of working performance of inside filling air-blowing seed metering device in maize. *Transactions of the Chinese Society of Agricultural Engineering*, vol.33(13), pp.23-31. (in Chinese) China. https://doi.org/10.11975/j.issn.1002-6819.2017.13.004

[5] He, K., Gao, J., Zhao, G., (2007). Advances in studies on chemistry, pharmacology, and quality control of Corydalis tuber. *Chinese Traditional and Herbal Drugs*, vol.12, pp.1909-1912. (in Chinese)

[6] Liu, W., He, J., Li, W., Li, X., Zheng, K., Wei, Z., (2018). Calibration of simulation parameters for potato minituber based on EDEM. *Transactions of the Chinese Society for Agricultural Machinery*, vol.49(5), pp.125-135. (in Chinese) China. https://doi.org/10.6041/j.issn.1000-1298.2018.05.014

[7] Ma, Z., Li, Y., Xu, L., (2013). Summarize of particle movements research in agricultural engineering realm. *Transactions of the Chinese Society for Agricultural Machinery*, vol.44(2), pp.22-29. (in Chinese). China. https://doi.org/10.6041/j.issn.1000-1298.2013.02.005

[8] Shi, L., Wu, J., Sun, W., Zhang, F., Sun, B., Liu, Q., Zhao, W., (2014). Simulation test for metering process of horizontal disc precision metering device based on discrete element method. *Transactions of the Chinese Society of Agricultural Engineering*, vol.30(8), pp.40-48. (in Chinese). China. https://doi.org/10.3969/j.issn.1002-6819.2014.08.005

[9] Sun, J., Liu, Q., Yang, F., Liu, Z., Wang, Z., (2022). Calibration of discrete element simulation paramet ers of sloping soil on loess plateau and its interaction with rotary tillage components. *Transactions of th e Chinese Society for Agricultural Machinery*, vol.53(1), pp.63-73. (in Chinese). China. https://doi.org/1 0.6041/j.issn.1000-1298.2022.01.007

[10] Sun, K., Yu, J., Liang, L., Wang, Y., Yan, D., Zhou, L., Yu, Y., (2022). A DEM-based general modelling method and experimental verification for wheat seeds. *Powder Technology*, Switzerland, vol.401(1173 53), pp.1-22. https://doi.org/10.1016/j.powtec.2022.117353

[11] Wang, H., Ding, K., Xia, J., Zhang, G., Wang, Y., Kang, Q., Tang, N., Liu, W., (2024). Calibration of Dis turbed-Saturated Paddy Soil Discrete Element Parameters Based on Slump Test. *Transactions of the Chinese Society for Agricultural Machinery*, vol.55(S2), pp.222–230. (in Chinese). China. https://doi.or g/10.6041/j.issn.1000-1298.2024.S2.022

[12] Xu, B., Zhang, Y., Cui, Q., Ye, S., Zhao, F., (2021). Construction of a discrete element model of buckwheat seeds and calibration of parameters. *INMATEH-Agricultural Engineering*, vol.64(2), pp.175-185. Romania. https://doi.org/10.356.33/inmateh-64-17

[13] Xu, B., Zheng, D., Cui, Q., (2022). Experimental research on three-level vibrating screening of buckwheat based on discrete element method. *INMATEH-Agricultural Engineering*, vol.68(3), pp.191-200. Romania. https://doi.org/10.35633/inmateh-68-19

[14] Xu, T., Yu, J., Yu, Y., Wang, Y., (2018). A modelling and verification approach for soybean seed particles using the discrete element method. *Advanced Powder Technology*, vol.29(12), pp.3274-3290. Japan. https://doi.org/10.1016/j.apt.2018.09.006

[15] Yang, S., Qiu, T., Ma, C., Li, X., Wang, L., & Liu, Y., (2023). Design and Test of Sugar Beet Combine Harvester Separation and Conveying Device. *Transactions of the Chinese Society for Agricultural Machinery*, vol.54(S1), pp.191–200. (in Chinese). China. https://doi.org/10.6041/j.issn.1000-1298.2023.S1.020

[16] Yu, Q., Liu, Y., Chen, X., Sun, K., Lai, Q., (2020). Calibration and experiment of simulation parameters for Panax notoginseng seeds based on DEM. *Transactions of the Chinese Society for Agricultural Machinery*, vol.51(2), pp.123-132. (in Chinese). China. https://doi.org/10.6041/j.issn.1000-1298.2020.02.014

[17] Zhang, Z., Zeng, C., Xing, Z., Xu, P., Guo, Q., Shi, R., Wang, Y., (2024). Discrete element modeling an d parameter calibration of safflower biomechanical properties. *International Journal of Agricultural and Biological Engineering*, vol.17(2), pp.37-46. China. https://doi.org/10.25165/j.ijabe.20241702.8857

[18] Zhao, P., Yu, T., Xu, G., Guo, R., Li, H., Xu, H., Jin, T., Ji, D., (2023). Design and drag reduction perfor mance analysis of a potato harvest shovel based on the surface texture characteristics of pangolin sca le. *INMATEH - Agricultural Engineering*, vol.70(2), pp.21–36. Romania. https://doi.org/10.35633/inmate h-70-02

[19] Zhao, J., Yu, J., Sun, K., Wang, Y., Liang, L., Sun, Y., Zhou, L., Yu, Y., (2024). A discrete element method model and experimental verification for wheat root systems. *Biosystems Engineering*, England, vol.244, pp.146-165. https://doi.org/10.1016/j.biosystemseng.2024.06.004

[20] Zhuang, H., Wang, X., Zhang, X., Cheng, X., Wei, Z., (2023). Discrete element-based design of key pa rameters for wheel rut tillage devices. *Engenharia Agrícola*, vol.43(3), pp.1-16. Brazil, http://dx.doi.org/10.1590/1809-4430-Eng.Agric.v43n3e20230039/2023

DAMAGE CLASSIFICATION OF CASTOR SEEDS BASED ON MODIFIED AlexNet
/
基于卷积神经网络的蓖麻种子损伤分类

Junming HOU, Yue MA, Enchao YAO, Zheng LI, Yandong XU
College of Engineering, Shenyang Agricultural University, Shenyang 110866, China
DOI: https://doi.org/10.35633/inmateh-76-03

Keywords: *castor seeds, classification of damage, modified AlexNet, damage identification device*

ABSTRACT

The germination of castor seeds was affected by different damage forms after shelling. Traditional methods could not express the change of mechanical damage characteristics on the surface of castor seeds. In the study, an improved migration learning algorithm for castor seed damage classification was adopted. The convolution kernel size of the first convolutional layer of the AlexNet model was modified, part of the convolutional layer was divided into two layers to increase the depth of the convolution model. Then a multi-scale convolution kernel was added to extract the damage characteristics of castor seeds. The results showed that combined with the hyperparameter optimization of convolutional layer stratification and the AlexNet model, the classification effect was improved. The average test accuracy was 98.10%. After the addition of multi-scale convolution, the average test accuracy was improved by 0.57%. The results show that the classification accuracy of cracked castor seeds is 71%, and the classification accuracy of castor seeds with missing shells is 63%. The classification accuracy of whole castor seeds is 67%. The verification of damage identification device for castor seeds was developed to verify the correctness of the algorithm. This study provided a theoretical and convolutional network model supported for the development of an online real-time damage classification detection system for castor seeds.

摘要

蓖麻种子发芽率主要是脱壳后不同形式的损伤引起。传统方法无法表达蓖麻籽表面机械损伤特征的变化。 本研究采用了一种改进的蓖麻种子损伤分类迁移学习算法，修改了 AlexNet 模型第一个卷积层的卷积内核大小。卷积层被分成两层，以增加卷积模型的深度。添加一个多尺度卷积核，以提取蓖麻种子的损伤特征。 结果表明，结合卷积层分层的超参数优化和 AlexNet 模型，分类效果得到了改善。 添加多尺度卷积后，平均测试精度提高了 0.57%。 实验结果显示，开裂蓖麻种子的分类准确率为 71%，缺失壳蓖麻种子的分类准确率为 63%。 整个蓖麻种子的分类准确率为 67%。 本研究为开发蓖麻种子的在线实时损害分类检测系统提供了理论支持。

INTRODUCTION

Castor plant is one of the world's top ten oil crops. Its seeds are rich in oil (35%-55% oil content depending on the species) and are also widely used as raw materials for detergent, cosmetics, medicines and biodiesel *(Acosta-Navarrete et al., 2017; Santos, 2019*). Because of its high viscosity, high ignition point, low freezing point, it is also made into lubricant and widely used in aviation, high-speed lathe and other industrial fields (*Li et al., 2018; Mosquera-Artamonov et al., 2018*). The damage of castor seeds in the process of shelling will directly affect germination and plant growth, and will also affect the yield of castor oil used for oil extraction. Therefore, it is very important to classify and detect damaged castor seeds, which needs to extract the defect features that affect the surface marks of castor seeds. The traditional conventional classification algorithms cannot meet the requirements of damage classification of castor seeds.

At present, convolutional neural network, transfer learning and other deep learning methods are attracting more and more attention. These learning methods have been widely used in image processing (*Kamilaris and Prenafeta-Boldú, 2018*), medical aviation, agriculture and other fields. In the field of agriculture, migration learning is often applied in the identification and classification of plant leaf diseases (*Huang et al., 2019; Rangarajan et al., 2018)*, the identification and location of crop pests (*DeChant et al., 2017; Thenmozhi and Srinivasulu Reddy, 2019)*, the identification and classification of crop fruits (*Liu et al., 2020)*, the location of plant organs and the prediction of growth potential (*Fengle and Zengwei, 2020; Liang et al., 2019; Yang, 2018)*, and so on. Relevant studies show that the pre-training model of migration learning has obvious advantages compared with traditional machine vision technology.

Through the classification of the integrity of different agricultural materials, it can be found that the classification method based on the depth model is more accurate and efficient than the traditional classification algorithms such as support vector machine, linear discriminant model, and artificial neural network (*Xie et al., 2020; Zhiheng et al., 2018; Zhu et al., 2020*). Through the improvement of AlexNet model, relevant studies have improved the accuracy and efficiency of classification, making the improved model more suitable for the objects needing classification (*Lv et al., 2020; Xiaoqing et al., 2019*). The surface stripes of castor seeds affected feature extraction and different damage features extraction required different algorithms, while traditional algorithms could not meet the classification of damage on castor seeds surface.

In this study, the AlexNet model was transferred to the classification of castor seed damage. The AlexNet network model was optimized by modifying the convolution kernel size of the first convolutional layer, layering partial convolution layers, and adding multi-scale convolution. It was optimized from batch size, learning rate to improve the test accuracy of the model. Finally, the modified AlexNet was verified by the damage identification device of castor seeds.

MATERIALS AND METHODS

Dataset construction

The typical variety of ZheBi No.4, widely planted in Tongliao Academy of Agricultural Sciences, Inner Mongolia, was selected as the test sample. The germination experiment showed that the two damaged types of seed shell missing and crack had the most significant effect on the germination of castor seeds. Therefore, castor seeds with these two damage types and whole (no damage) were classified.

In this study, an LT-USB 1080 CMOS industrial camera was used to shoot samples of castor seeds placed on white A4 paper under the indoor environment. The shooting distance was 5~10 cm, then 525 images were obtained. The resolution of the images was 1,920×1,080 pixels, and the images were cropped to 227×227 pixels of samples containing castor seeds. The image of castor seeds with seed shell missing castor seed, crackled castor seed and whole castor seed were flipped to expand the castor seed image data set. The seed shell missing castor seed, cracked castor seed, and the whole castor seed was named with 0_1.jpg, 1_1.jpg, and 2_1.jpg forms, respectively. In the training set, some castor seeds were shown in Fig. 1.



a. Seed shell missing castor seeds; b. Cracked castor seeds; c. Whole castor seeds (no damage)

Fig. 1 – Images of castor seeds of different types

AlexNet Model construction

The AlexNet model consists of five convolution layers, three maximum pooling layers, and three full connection layers, a total of eleven layers. The size of the input image is required to be 227×227×3 (227 pixels high, 227 pixels wide, 3 color channels). After convolution, the output image size is shown in equation (1) while after pooling, the output image size is shown in equation (2).

$$N_{out} = \frac{N_{in} - F + 2P}{S} + 1 \quad (1)$$

$$N_{out} = \frac{N_{in} - F}{S} + 1 \quad (2)$$

where, N_{out} is the image output size; N_{in} is the image input size; F is the size of the convolution kernel; P is the padding; S is the step size.

The image was input into the AlexNet model. Through the convolutional layer, local response normalization layer, and maximum pooling layer, the output image size is 27×27×96. In the second part, the data flow follows the convolutional layer, the maximum pooling layer, and the local response normalization layer successively, and the output image size is 13×13×256. The third part and the fourth part respectively contain a convolutional layer. After the convolution operation of two layers, the output image size is 13×13×384. The fifth part is the convolutional layer and the maximum pooling layer, then the output image size is 6×6×256. The sixth part and the seventh part are the full connection layer, each layer has 4096 neural units. To reduce overfitting, Dropout is added after the full connection layer. The eighth part is the output layer. The structural model is shown in Figure 2.

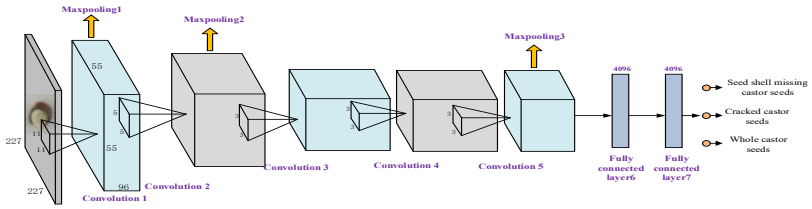


Fig. 2 - AlexNet network model diagram

The convolutional layer extracts the local features of the image through the convolution operation. After the feature map of the upper layer is processed by the convolution kernel, the feature map of the new layer can be obtained by the excitation function. The working process of the convolutional layer is as follows:

$$x_n^l = \sum_{i \in M_n} x_i^{l-1} * k_{in}^l + b_n^l \tag{3}$$

where, x^l_n is the n^{th} feature map of layer l; M_n is a set of feature mappings selected from the input feature mappings; k^l_{in} is the i^{th} element in the n^{th} convolution kernel of the layer l; b^l_n is the n^{th} offset of layer l; '*' is the convolution process.

The pooling layer is also called a downward sampling layer, which produces the sampling results of input feature maps and changes the size of features without changing the number of feature maps. The working process of the pooling layer is shown in equation (4):

$$x_n^l = f_{\text{down}}\left(x_n^{l-1}\right) + b_n^l \tag{4}$$

where, f_{down} (·) is the lower sampling function.

Evaluation Index

The accuracy of the classification algorithm is evaluated by the accuracy index, which is defined as equation (5):

$$a = \frac{N_C}{N_T} \times 100\% \tag{5}$$

where, a is the accuracy rate, %; N_C is the number of correctly classified samples; N_T is the total sample of training.

Operation platform

All the training and testing in this study are carried out on the same computer with the processor is Inter(R) Xeon(R) CPU E5-2643 v3 3.4 GHz, 32 G memory, AMD FirePro W7100 Graphics Adapter, and 8 GB of running memory, running under Windows 10 operation system.

Improvement of the AlexNet model method

Selection of the convolution kernel size

Convolution kernels are referred to as the local receptive field (LRF), which is a kind of filter. In this study, the convolution kernel size of the first convolutional layer in the AlexNet model is selected to learn the key features, to obtain better model performance. In this study, according to the literature(*DeChant et al., 2017; Liu, 2020*) and experimental experience, convolution kernel sizes of 5×5, 7×7, 9×9, 11×11, 13×13, and 15×15 were selected for training.

Convolution layer stratification

In this study, the convolutional layer 2 is divided into two layers, and the LRF size is modified to 3×3. The convolutional layer 3 is divided into two layers, and the LRF size is modified to 2×2. The convolutional layer 5 is divided into 2 layers, and the LRF size is modified to 2×2.

The parameters of each layer are shown in Table 1.

Table 1

Parameters of the convolutional network

CNN layers	Split layers	Output size	LRF size	Strides
Conv 1	Conv 1	55×55×96	11×11	4
Pooling 1	Pooling 1	27×27×96	3×3	2
Conv 2	Conv 2_1	29×29×256	3×3	1

CNN layers	Split layers	Output size	LRF size	Strides
	Conv 2_2	27×27×256	3×3	1
Pooling 2	Pooling 2	13×13×256	3×3	2
Conv 3	Conv 3_1	14×14×384	2×2	1
	Conv 3_2	13×13×384	2×2	1
Conv 4	Conv 4	13×13×256	3×3	1
Conv 5	Conv 5_1	14×14×256	2×2	1
	Conv 5_2	13×13×256	2×2	1
Pooling 3	Pooling 3	6×6×256	3×3	2
FC 6	FC 6	4096×1	\	\
FC 7	FC 7	4096×1	\	\
FC 8 (sorting)	FC 8 (sorting)	3×1	\	\

Adding multi-scale convolution

The structure of multiscale convolution is shown in Fig. 3.

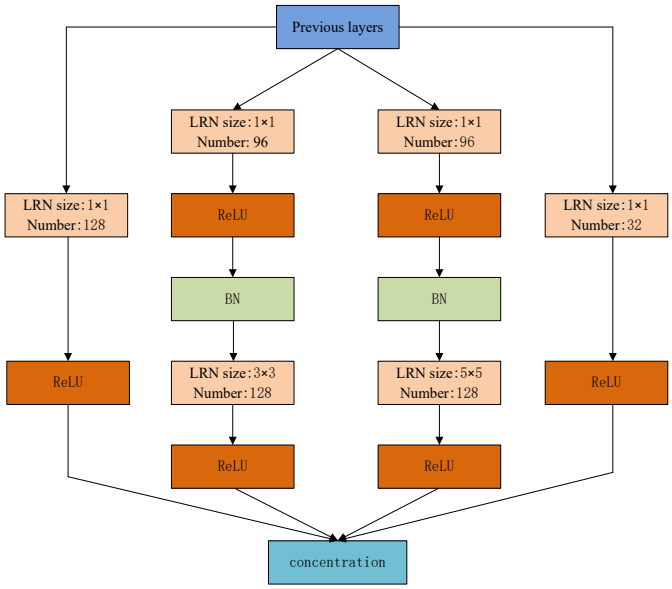


Fig. 3 – Structure of multi-convolution module

Multi-scale convolution has been widely used in VGG-Net, Inception series, GoogLeNet, and ResNet series. These networks have fully verified the superiority of multi-scale convolution in image recognition and target positioning. To learn better damage characteristics of castor seeds, a multi-scale convolution was added between convolutional layer 1 and convolutional layer 2. Three convolution kernels of different scales (1×1), (3×3), and (5×5), with the number of 32, 96, and 128 convolution kernels, were adopted to extract the sample image features in parallel. Then they merged into the same tensor and continue to pass them down.

RESULTS AND DISCUSSION

Influence of parameters on model performance

The influence of convolution layer 1 on the accuracy of model verification

In this study, the convolution kernel size of the first convolution layer of the AlexNet model was changed to learn the key features and obtain better model performance. The influence of the convolution kernel size on the recognition accuracy of the convolutional neural network is shown in Fig. 4.

When the convolution kernel size is 11×11, the average test accuracy is the highest. The results showed that there are significant differences in the shape characteristics among the data sets. So, the model network only needed to learn the shape features of the damage to ensure the fitting ability of the data. Therefore, the convolution kernel of convolutional layer 1 in this paper is selected 11×11.

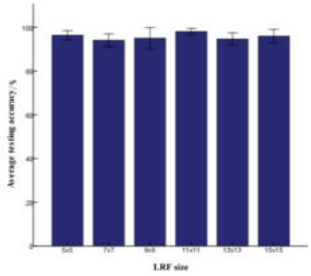


Fig. 4 – Average test accuracy under different convolution kernel sizes

Influence of learning rate on model performance

As an important super parameter in supervised learning and deep learning, learning rate determines whether the objective function converges to the local minimum and when it converges to the minimum. An appropriate learning rate can make the objective function converge to the local minimum in an appropriate time. Fig. 5 shows the curves of training accuracy and loss value. It can be seen that when the learning rate is 0.1, the training accuracy oscillates back and forth around the minimum value, and the loss value fluctuates within a wide range. After convergence, the loss value is relatively large, resulting in the over-fitting phenomenon.

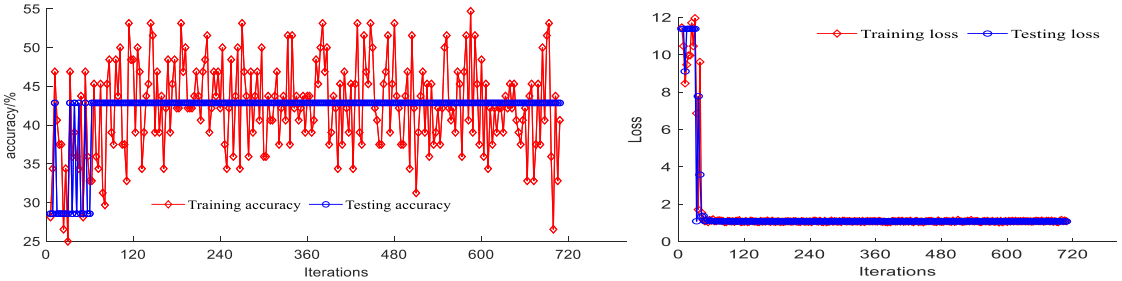
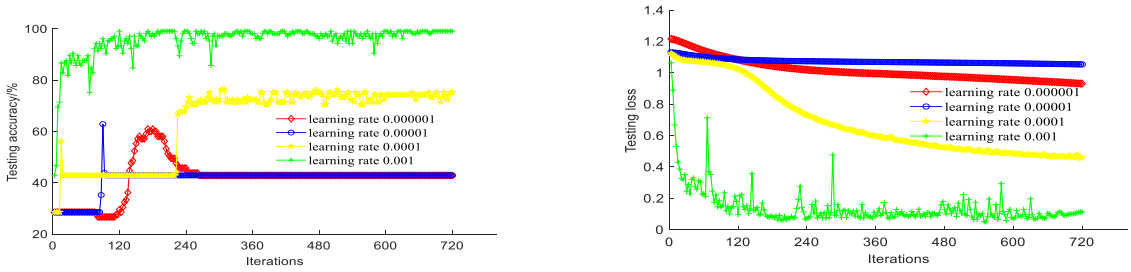


Fig. 5 – The curve of training, testing accuracy, and loss value with excessive learning rate

Fig. 6 is the graph of test accuracy and loss under different learning rates. When the learning rate is 0.00001 and 0.000001, the parameter to be optimized converges very slowly. After 700 iterations, the loss value converges slowly at close to 1. When the learning rate is 0.001, the model test accuracy is better, and the loss value converges near to 0. Therefore, this study chose a learning rate of 0.001 for training.



a) Test accuracy curve under different learning rates b) Test loss curve at different learning rates

Fig. 6 – Test accuracy and loss curves under different learning conditions

Influence of regularization on model accuracy

Regularization is an important means to control model complexity, combat over-fitting, and pursue a better prediction effect. In this study, L2 regularization is adopted to reduce the over-fitting phenomenon by adding a weight loss function. The regularization formula of L2 is shown as equation (6).

$$\Omega(\boldsymbol{\omega}) = \frac{1}{2}\boldsymbol{\omega}^T\boldsymbol{\omega} \tag{6}$$

where, ω is the weight vector.

Influence of stratification of the convolutional layer on the model

The convolutional layer is divided into two layers, which can increase the depth of the network and detect the characteristics of the object to be detected more deeply, then improve the accuracy of the test. After repeated calculations, the average test accuracy of the convolutional layer stratified model is 98.10%, which is 0.48 percentage points higher than the original AlexNet model of 97.62%.

Influence of multi-scale convolution on the model

After adding multi-scale convolution based on the AlexNet model, the average accuracy on the test set is improved by 0.57%, which indicates that the features extracted by the model after introducing multi-scale convolution can more accurately express the features of different damage types.

Comparison of different models

To further verify the recognition effect of the model, the recognition effect of common deep convolutive neural network models such as VggNet-16, GoogLeNet, ResNet-50, and ResNet-101 on damage types of castor seeds is compared in the same experimental conditions.

VggNet-16 model

In the VGG (Visual Geometry Group) network, by using a smaller convolution filter, increasing the depth of the model structure to 16 layers and reducing the number of parameters, which is also known as VggNet-16. The structure model is shown in Fig. 7. The VggNet-16 model is composed of a continuous convolution layer with a convolution kernel of 3×3 and a maximum pooling layer with a convolution kernel of 2×2. Then two full connection layers are added, and the last layer serves as Softmax output. In this study, VggNet-16 was used to classify the damage of castor seeds and compared them with the improved AlexNet model.

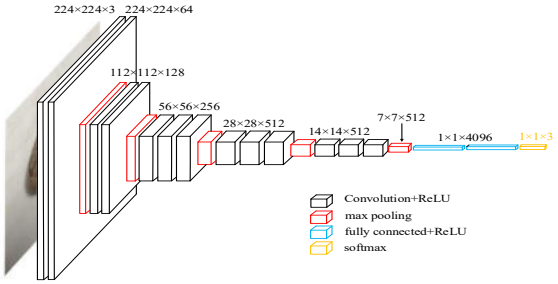


Fig. 7 – VggNet-16 network model diagram

GoogLeNet model

GoogLeNet is a deep convolution network model, which has achieved a good classification effect and improved computational efficiency in many applications. GoogLeNet is also known as the Inception Model. Its architecture consists of twenty-two layers, including 2 convolutional layers, 4 maximum pooling layers, 9 linear stacked Inception modules, and average pooling. Average pooling is applied at the end of the last inception module. Its structural model is shown in Fig. 8. In each initial module, multi-scale convolution such as 1×1, 3×3, and 5×5 are applied for dimension reduction. In this study, GoogLeNet was used to complete the task of castor seed damage classification and was compared with the improved AlexNet model.

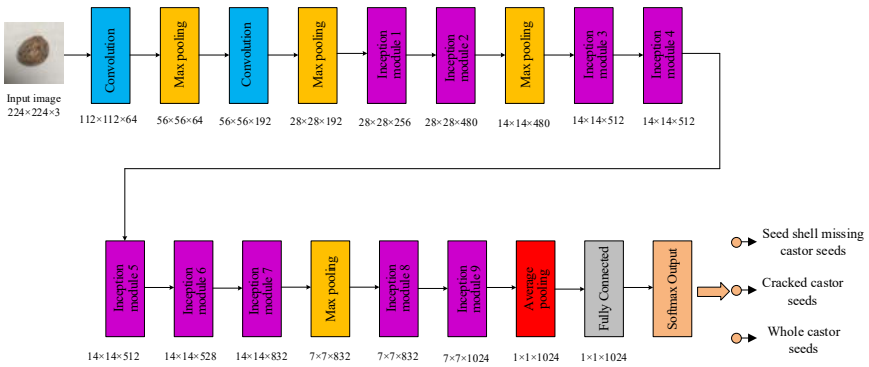


Fig. 8 – GoogLeNet The castor seed has two characteristic arcs, and the mechanical damage characteristics appear randomly on one of the network model diagram

ResNet-50 and ResNet-101 models

ResNet (Deep Residual network) has a good performance, its backpropagation will not encounter the problem of gradient disappearance. In this study, ResNet-50 and ResNet-101 were applied to complete the task of castor seed damage classification and were compared with the improved AlexNet model.

The output results of each model are shown in Table 2. It can be seen that the average test accuracy of the improved AlexNet model is 1.05% higher than that of the AlexNet model. The average test accuracy of the deep learning model based on VggNet-16 and GoogLeNet was slightly higher than the modified AlexNet model in this study. But the training efficiency was much lower than that of the model. VggNet-16 efficiency is 86.26% lower than modified AlexNet, and GoogLeNet efficiency is 56.72% lower than modified AlexNet.

The average test accuracy and training efficiency of ResNet-50 and ResNet-101 pre-training models are lower than modified AlexNet. Therefore, the model used in this study is more suitable for the classification of castor seeds damage types.

Table 2

Test accuracy under different depth models

DCNNS types	Test accuracy/%	Time/h
Modified AlexNet	98.67	1.16
AlexNet	97.62	0.63
VggNet-16	99.10	8.44
GoogLeNet	99.05	2.68
ResNet-50	96.83	4.80
ResNet-101	97.46	8.65

Design and verification of damage identification device for castor seeds

General composition of a damage identification device for castor seeds

The castor seed has two characteristic arcs, and the mechanical damage characteristics appear randomly on one of them. When castor seeds are placed naturally, only one of the character arcs can be picked up by the visual system. Therefore, it is necessary to carry out double-sided identification of castor oil seeds to ensure no damage to castor oil seeds missed detection. According to this requirement, when designing the damage identification device for castor seeds, the turning mechanism of castor seeds must be designed so that the two characteristic surfaces of castor seeds can be collected and recognized. At the same time, the system should include a castor seed conveying and identification mechanism for double characteristic surface detection of castor seeds. The three-dimensional structure diagram of the castor damage identification device is shown in Fig. 9.

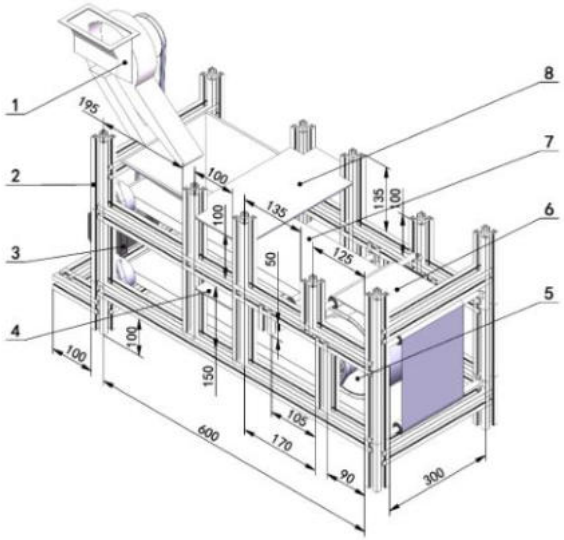


Fig. 9 – Stereo structure diagram of castor damage identification system

1.Castor seed planter; 2. Rack; 3. Electromotor; 4. Camera board Ⅱ; 5. Flipping roller; 6. Conveyor belt Ⅱ; 7. Conveyor belt Ⅰ; 8. Camera board Ⅰ

Experimental verification

In this study, the number of damage identified and classified was applied as the index to verify the rationality of the damage identification device for castor seeds. By comparing the accuracy of device identification with the actual damage accuracy, the superiority of the network model based on improved AlexNet is verified. The damage identification test device of castor seeds was developed. It can change the speed through the frequency modulator to obtain the appropriate speed.

It can verify the feasibility of the combination of the castor seed identification test device and the improved AlexNet model of castor seed damage classification method, it can also measure the stability of the identification performance of the castor seed identification device and verify the robustness of the interface algorithm.

The test equipment in this study is a self-developed damage identification test device for castor seeds. Fig.10 shows the experimental device for damage identification of castor seeds.

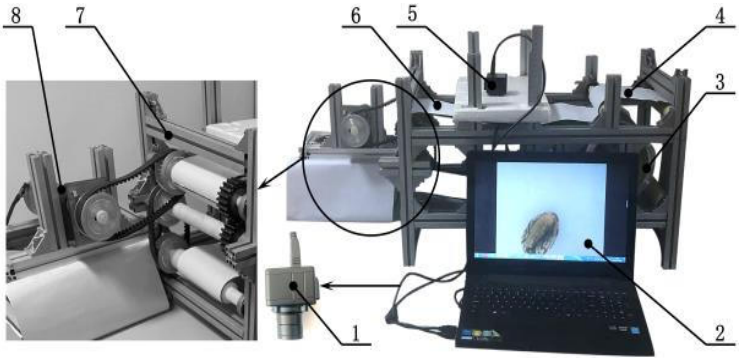


Fig. 10 – Experimental apparatus for damage identification of castor seeds

1. Camera Ⅱ; 2. Computer; 3. Flipping roller; 4. Conveyor belt Ⅱ; 5. Camera Ⅰ;
6. Conveyor belt Ⅰ; 7. Rack; 8. Electromotor

During the test process, castor seeds were placed on the conveyor belt of the castor seed damage device one by one in order through an artificially simulated seed planter. The photos of different types of castor seeds were taken by the camera and saved to the folder of the designated route. The type of castor seeds was verified through the interface of damage classification of castor seeds.

Since the first visual identification system can only verify one characteristic cambered surface of castor seed, three conditions should be taken into account on the process of validating the whole castor seed. When the castor seed is identified as a whole in the first visual system and cracked in the second visual system, the castor seed belongs to cracked castor seed. When the castor seed is identified as a whole in the first visual system and seed shell missing castor seed in the second visual system, it is identified as a seed shell missing castor seed. When the castor seed is identified as the whole in the first visual system and as whole in the second visual recognition system, it is identified as a whole castor seed. The verification results are shown in Fig.11.



a. Whole-Crack verification diagram b. Whole-Seed shell missing verification diagram

Fig. 11 – Verification of non-damaged (whole) castor seeds

Table 3

Repeat tests for each damage type device

Damage category	Predicted damage category			Classification performance			
	Crack	Seed shell missing	Whole	Accuracy / %	Actual damage rate / %	Theoretical damage rate / %	Damage rate difference / %
Crack	71	6	23	71.0	23.7	33.3	9.6
Seed shell missing	9	63	28	63.0	21.0	33.3	12.3
Whole	21	12	67	67.0	0.0	0.0	0.0

In this study, 100 castor seeds with cracks, 100 castor seeds with seed shells missing, and 100 castor seeds without damage (whole) were selected for verification. The verification results are shown in Table 3.

It can be drawn that the device can better identify and classify the three castor seeds. The accuracy of identification of cracked castor seeds was 71%, that of castor seeds with missing seed shell was 63%, and that of castor seeds with the whole shell was 67%. The damage rate of castor seeds was identified by damage. The actual crack damage rate was 23.7% in the process of identification, and the difference in damage rate was 9.6%. The damage rate of seed shell loss was 21.0%, and the difference in damage rate was 12.3%. It can be verified that the identification device and verification algorithm of castor seeds can meet the practical application.

CONCLUSIONS

To eliminate damage of castor seeds, an improved AlexNet model was proposed to classify castor seed damage types. The model was optimized by batch size, learning rate and regularization coefficient. The model was compared with other models and the damage identification device of castor seeds was used to test. The conclusions are as follows:

(1) Compared with other models, the improved AlexNet model has an average test accuracy of 1.05% higher than that of the original model under the same experimental conditions.

(2) The results of experiment show that the identification and classification accuracy of cracked castor oil seeds is 71%, and the identification and classification accuracy of castor seeds with missing shells is 63%. The classification accuracy of complete castor oil seeds is 67%.

(3) The damage rate of castor seeds was identified. The actual crack damage rate is 23.7% in the process of identification, and the difference in damage rate is 9.6%. The loss damage rate of seed shell is 21.0%, and the difference of damage rate is 12.3%, which verified that the identification device and verification algorithm of castor seeds could meet the practical application.

ACKNOWLEDGEMENT

This research was supported by the National Natural Science Foundation of China, China (51457312), the authors thank relevant scholars for their assistance in the literature.

REFERENCES

[1] Altuntaş, Y., Cömert, Z., Kocamaz, A. F. (2019). Identification of haploid and diploid maize seeds using convolutional neural networks and a transfer learning approach. *Computers and Electronics in Agriculture*, 163,104874. https://doi.org/10.1016/j.compag.2019.104874

[2] Chang, L., Deng, X. M., Zhou, M. Q., Wu, Z. K., Yuan, Y, Yang, S., et al. (2016). Convolutional neural networks in image comprehension. *Acta Automatica Sinica*, 42(9), 1300-1312. https://doi.org/10.1145/3065386

[3] DeChant, C., Wiesner-Hanks, T., Chen, S., Stewart, E., Yosinski, J., Gore, M. A, Nelson, R. J., Lipson, H. (2017). Automated Identification of Northern Leaf Blight-Infected Maize Plants from Field Imagery Using Deep Learning. *Phytopathology*, 107(11), 1426-1432. https://doi.org/10.1094/phyto-11-16-0417-r

[4] Guo, X. Q., Fan, T. J., Shu, X. (2019). Tomato leaf diseases recognition based on improved Multi-Scale AlexNet. *Transactions of the Chinese Society for Agricultural Machinery*, 35(13),162-169. https://dx.doi.org/10.11975/j.issn.1002-6819.2019.13.018

[5] Huang, S. P., Sun, C., Qi, L., Ma, X., Wang, W. J. (2017). Rice panicle blast identification method based on deep convolution neural network. *Transactions of the Chinese Society of Agricultural Engineering*, 33(20),169-176. https://dx.doi.org/10.11975/j.issn.1002-6819.2017.20.021

[6] Hang, J., Zhang, D.X., Chen, P., Zhang, J., Wang, J. (2019). Classification of Plant Leaf Diseases Based on Improved Convolutional Neural Network. *Sensors*, 19(19), 4161. https://doi.org/10.3390/s19194161

[7] Kamilaris, A., Prenafeta, F.X. (2018). Deep learning in agriculture: a survey. *Computers and Electronics in Agriculture*, 147(1), 70-90. https://doi.org/10.1016/j.compag.2018.02.016

[8] Li, J.Z., Zhang, B.X., Wang, W.N., Hou, X.Y., Liu, H.G., Yang, Y.F., Tan, D., Wang, G. (2018). Research progress in breeding and cultivation of castor bean in China. *Bulletin of Agricultural Science and Technology*, 10, 198-200. https://doi.org/10.3969/j.issn.1000-6400.2018.10.074.

[9] Ling, Z., Li, Z., Li, C., Jing, W., Yue, J. (2018). High performance vegetable classification from images based on AlexNet deep learning model. *International Journal of Agricultural and Biological Engineering,* 11(4), 190-196. https://doi.org/10.25165/IJABE.V11I4.2690

[10] Liu, F., Liu, Y. K., Lin, S., Guo, W. Z., Xu, F., Zhang, B. (2020). Fast recognition method for tomatoes under complex environments based on improved YOLO. *Transactions of the Chinese Society for Agricultural Machinery*, 51(6), 229-237. http://dx.doi.org/10.6041/j.issn.1000-1298.2020.06.024

[11] Acosta Navarrete M.S., Botello Alvarez J.E., Hernandez Martínez M., Barron Adame J.M., Quintanilla Domínguez J., Gonzalez Alatorre G., Montes Hernandez S., (2017). Variability evaluation of castor seeds (Ricinus communis) by multivariate analysis of local accessions from Mexico. *African Journal of Agricultural Research*,12(29), 2388-2397. DOI:10.5897/AJAR2017.12472

[12] Li, W.L., Chen, P., Wang, B., Xie, C.J. (2019). Automatic localization and count of agricultural crop pests based on an improved deep learning pipeline. *Scientific Reports*, 9(1),7024. https://doi.org/10.1038/s41598-019-43171-0

[13] Liu, Z.H. (2019). Soft-shell Shrimp Recognition Based on an Improved AlexNet for Quality Evaluations. *Journal of Food Engineering*, 266, 109698. https://doi.org/10.1016/j.jfoodeng.2019.109698

[14] Lv, M. J., Zhou, G. X., He, M. F., Chen, A. B., Zhang, W. Z., Hu, Y. H. (2020). Maize leaf disease Identification based on feature enhancement and DMS-Robust Alexnet. *IEEE Access*, 8, pp.(99):57952-57966. http://dx.doi.org/10.1109/ACCESS.2020.2982443

[15] Picon, A., Alvarez, A., Seitz, M., Ortiz, A., Echazarra, J., Johannes, A. (2019). Deep convolutional neural networks for mobile capture device-based crop disease classification in the wild. *Computers and Electronics in Agriculture*, 161,280-290. https://doi.org/10.1016/j.compag.2018.04.002

[16] Rangarajan, A.K., Purushothaman, R., Ramesh, A. (2018). Tomato crop disease classification using pre-trained deep learning algorithm. *Procedia Computer Science*, 133, 1040-1047. https://doi.org/10.1016/j.procs.2018.07.070

[17] Santos, H.O., Carvalho, M.L., Lopes, C.A., Pinho, É.V., & Coelho, S.V. (2019). Physiological and sanitary quality and oil content of castor bean seeds under different storage conditions. *Revista Caatinga,* 32(1), 131-142. http://dx.doi.org/10.1590/1983-21252019v32n114rc

[18] Sun, Z.J., Lv, L.Y., Wu, Y.P. (2012). Development of castor bean industry: from planting to utilization. *Journal of China Agricultural University*, 17(6), 204-214. http://dx.doi.org/10.11841/j.issn.1007-4333.2012.06.026

[19] Thenmozhi, K., Reddy, U.S. (2019). Crop pest classification based on deep convolutional neural network and transfer learning. *Computers and Electronics in Agriculture*, 164, 104906. https://doi.org/10.1016/j.compag.2019.104906

[20] Xie, W.J., Ding, Y.C, Wang, F.H., Wei, S., Yang, D.Y. (2020). Integrity recognition of camellia oleifera seeds based on convolutional neural network. Transactions of the Chinese Society for Agricultural Machinery, 51(7):13-21. http://dx.doi.org/10.6041/j.issn.1000-1298.2020.07.002

[21] Yan, J.W., Zhao, Y., Zhang, L.W., Su, X.D., Liu, Y.H., Zhang, F.G., Fan, W, Ei, L. (2019). Recognition of Rosa roxbunghii in natural environment based on improved Faster-RCNN. *Transactions of the Chinese Society of Agricultural Engineering*, 35(18), 143-150. https://dx.doi.org/10.11975/j.issn.1002-6819.2019.18.018

[22] Yuan, P.S., Li, W., Ren, S.G., Xu, H.L. (2018). Recognition for flower type and variety of chrysanthemum with convolutional neural network. *Transactions of the Chinese Society of Agricultural Engineering*, 34(5), 152-158. https://dx.doi.org/10.11975/j.issn.1002-6819.2018.05.020

[23] Zhao, L.X., Hou, F.D., Lv, Z.C., Zhu, H.C., Ding, X.L. (2020). Image recognition of cotton leaf diseases and pests based on transfer learning. *Transactions of the Chinese Society of Agricultural Engineering*, 36(7), 184-191. https://dx.doi.org/10.11975/j.issn.1002-6819.2020.07.021

[24] Zhou, L., Mu, H. W., Ma, H. J., Chen, G. X. (2019). Remote sensing estimation on yield of winter wheat in north China based on convolutional neural network. *Transactions of the Chinese Society of Agricultural Engineering*; 35(15), 119-128. https://dx.doi.org/10.11975/j.issn.1002-6819.2019.15.016

[25] Zhou, Y.C., Xu, T.Y., Zheng, W., Deng, H.B. (2017). Classification and recognition approaches of tomato main organs based on DCNN. *Transactions of the Chinese Society of Agricultural Engineering*, 33(15), 219-226. https://dx.doi.org/10.11975/j.issn.1002-6819.2017.15.028

[26] Zhu, F.L., Zheng, Z.W. (2020). Image-based assessment of growth vigor for phalaenopsis aphrodite seedlings using convolutional neural network. *Transactions of the Chinese Society of Agricultural Engineering*, 36(9), 185-194. https://dx.doi.org/10.11975/j.issn.1002-6819.2020.09.021

INTELLIGENT OBSTACLE AVOIDANCE CONTROL ALGORITHM FOR AGRICULTURAL DRONES IN COMPLEX FARMLAND ENVIRONMENTS
/
面向复杂农田环境的农业无人机智能避障控制算法研究

Yuan MEI[1)], Rui ZENG[2)], Wanting XU[1)], Xinyue ZHOU[1)], Zhiwei JIN[1)]
[1)] Wuhu Institute of Technology, Wuhu, Anhui, China;
[2)] CETC Wuhu General Aviation Industry Technology Research Institute Co., Ltd., Wuhu, Anhui, China
Tel: 18555350991; E-mail: 18555350991@163.com
Corresponding author: Yuan MEI
DOI: https://doi.org/10.35633/inmateh-76-04

Keywords: *Agricultural drones; Intelligent obstacle avoidance; Improved YOLOv5; Path planning; Adaptive control*

ABSTRACT
To address the challenges of complex farmland environment, an intelligent obstacle avoidance control algorithm for agricultural unmanned aerial vehicles (UAVs) is developed. The objective is to solve the problem of efficient obstacle avoidance in farmland scenarios characterized by dense dynamic obstacles and variable terrain. In this article, a target detection algorithm based on improved YOLOv5 (You Only Look Once v5) is proposed, and an intelligent obstacle avoidance system is constructed by combining reinforcement learning path planning and adaptive motion control strategy. Ghost module is introduced to improve the lightweight of YOLOv5, and the design of CIOU (Complete Intersection Over Union) loss function is optimized, which improves the detection accuracy of the model for small targets and dynamic obstacles. Experiments show that the error of path planning is reduced to less than 2.1 meters, and the time consumption is reduced by about 35%. In addition, fuzzy logic controller is used to realize adaptive PID control, which further enhances the flight stability of UAV in complex environment. The results show that the improved algorithm has excellent performance in many typical farmland scenes. This study provides theoretical and technical support for autonomous flight of agricultural UAV in complex farmland environment.

摘要
面向复杂农田环境，农业无人机智能避障控制算法的研究目的是解决其在动态障碍物密集、地形多变的农田场景中实现高效避障的难题。本文提出一种基于改进 YOLOv5（You Only Look Once v5）的目标检测算法，并融合强化学习路径规划与自适应运动控制策略，构建了一套智能避障系统。研究中引入 Ghost 模块对 YOLOv5 进行轻量化改进，并优化了 CIoU（Complete Intersection over Union）损失函数的设计，从而提高了模型对小目标及动态障碍物的检测精度。实验表明，路径规划误差控制在 2.1 米以内，规划耗时减少了约 35%。此外，通过采用模糊逻辑控制器实现自适应 PID 控制，进一步提升了无人机在复杂环境中的飞行稳定性。研究结果证实，所提出的改进算法在多种典型农田场景下均表现出优异性能。本研究为农业无人机在复杂农田环境中的自主飞行提供了有力的理论支持与技术保障。

INTRODUCTION
Precision agriculture technology has gradually become a key means to improve agricultural production efficiency and reduce resource waste. Under this background, agricultural UAV is widely used in many fields, such as farmland monitoring, crop spraying, sowing and fertilization, with its high efficiency, flexibility and intelligence *(Lu et al., 2023)*. In the complex farmland environment, autonomous flight of agricultural UAV faces many challenges, among which obstacle detection and obstacle avoidance are particularly prominent *(Liu et al., 2021)*. The farmland environment is complex, which is reflected in the diverse terrain, uneven distribution of vegetation and changeable weather conditions. For example, terrain such as slopes and ravines can affect the stability of UAV flight. Trees, shrubs, and other vegetation not only have a variety of species, but also vary in height and density. Changes in external factors such as wind speed and lighting increase the difficulty of perception and decision-making *(Zhao et al., 2020; Seiche et al., 2024; Dorbu et al., 2024)*. When working in the field, UAV will also face the coexistence of static obstacles (such as telephone poles and irrigation equipment) and dynamic obstacles (such as birds and other working machinery) *(Du et al., 2023)*. This puts forward higher requirements for the adaptability and intelligence of obstacle avoidance algorithm.

YOLOv5, as an efficient target detection framework, has attracted much attention because of its fast reasoning ability and high detection accuracy *(Brown et al., 2020)*. However, when it is applied to complex farmland environment, it exposes some problems. First, there are many kinds of obstacles in farmland, and the size difference is large, so the traditional YOLOv5 model has weak small target detection ability [8]. Second, the change of farmland illumination and weather interference will reduce the image quality and affect the model detection performance *(Yang et al., 2020)*. Third, the original architecture of YOLOv5 may not be real-time when it runs on an embedded platform with limited computing resources *(Yang et al., 2021)*. In view of the above challenges, this study proposes an improved YOLOv5 model, combined with intelligent obstacle avoidance control algorithm, to achieve efficient obstacle avoidance of agricultural UAV in complex farmland environment. The research is carried out from the following aspects: first, the Ghost module is introduced to improve the structure of YOLOv5 network, and the running speed of the model is improved on the premise of ensuring the detection accuracy. Secondly, the YOLOv5 loss function is optimized, and the CIoU loss function is used to replace the traditional IoU loss function. CIoU not only considers the overlapping area of the bounding box, but also introduces the constraints of aspect ratio and distance from the center point, which makes the model more accurate in detecting obstacles of different shapes in farmland. Thirdly, combined with binocular vision technology, depth information is used to enhance the three-dimensional perception ability of obstacles and provide more reliable data for path planning.

In the design of intelligent obstacle avoidance control algorithm, this study takes into account the dynamic characteristics of farmland environment and UAV motion constraints. Based on the detection results of the improved YOLOv5 model, the reinforcement learning algorithm is used for path planning, which enables UAV to dynamically adjust its flight path to avoid obstacles in complex farmland scenes. Adaptive control strategy is introduced to improve the robustness of UAV to uncertain environment. In case of strong wind interference or sensor data loss, the system can automatically adjust parameters to ensure flight safety. In addition, the possibility of multi-UAV cooperative obstacle avoidance is explored, and the real-time information sharing and cooperation of multi-UAVs are realized through distributed communication mechanism to improve the overall operation efficiency.

In order to verify the effectiveness of the method, this study built an experimental platform and tested it in a variety of typical farmland scenarios. The results show that the improved YOLOv5 model is superior to the original version in obstacle detection accuracy and speed, especially in small target detection and complex lighting conditions. Combined with intelligent obstacle avoidance control algorithm, UAV has good obstacle avoidance ability in dynamic obstacle dense environment, and the rationality and real-time performance of path planning have been greatly improved.

Theoretical basis

Target detection and deep learning

Target detection is an important way for agricultural UAV to perceive the environment. Its main task is to identify and determine the position of obstacles from the input images or videos *(Yang et al., 2021)*. Traditional target detection methods mostly rely on manual feature extraction (like HOG, SIFT, etc.) and classifiers (such as SVM). In the face of complex farmland environment, such methods usually expose the problem of poor generalization ability. The target detection algorithm based on deep learning has gradually become the mainstream by virtue of its strong feature learning ability and the advantages of end-to-end training *(Dai et al., 2020)*. Among them, YOLO (You Only Look Once) series algorithms emerge with high efficiency and real-time, especially YOLOv5 has great application potential in embedded devices.

However, YOLOv5 has some limitations in practical application, such as unsatisfactory detection effect on small targets and sensitivity to illumination changes, which are more prominent in farmland environment *(Varma et al., 2024)*. Take the telephone pole in the farmland as an example, it may only occupy a few pixels in the long-distance image. It is difficult for traditional YOLOv5 model to accurately capture the characteristics of such small targets. Moreover, the illumination conditions of farmland environment are changeable, especially on cloudy days or in the evening, the image quality will be obviously reduced, leading to the reduction of detection accuracy *(Gao et al., 2024)*. Therefore, this study is based on YOLOv5 to improve the applicability of the model in complex scenes by introducing Ghost module and optimizing the design of loss function.

Path planning and reinforcement learning

The purpose of path planning is to generate an optimal path from the starting point to the end point on the premise of ensuring flight safety. Traditional path planning methods mainly include graph-based algorithm (such as A * algorithm and Dijkstra algorithm) and sampling-based algorithm (such as RRT) *(Saeed et al., 2023)*. These methods perform well in static environment, but they face many problems in dynamic farmland environment. For example, obstacles in farmland may change at any time, and traditional offline planning methods are difficult to adapt to this dynamic change.

Therefore, this study adopts the path planning method based on reinforcement learning to deal with the uncertainty of complex farmland environment. Reinforcement learning is an unsupervised learning method, the core of which is to learn strategies through trial and error, so that agents can optimize decision-making behavior in the process of continuous interaction with the environment *(Zhu et al., 2024)*. In the application scenario of agricultural UAV, reinforcement learning can be used to solve the problem of dynamic obstacle avoidance.

Motion control and adaptive control

Motion control is the last step for agricultural UAV to perform obstacle avoidance task, and the goal is to transform the path planning results into specific flight instructions. Because the external interference in the farmland environment (such as wind speed, terrain fluctuation, etc.) may make the UAV deviate from the predetermined trajectory, it is necessary to design a robust motion control algorithm *(Liu et al., 2020)*. In this study, the method based on adaptive control is adopted to deal with the influence of external disturbance by adjusting the controller parameters online.

The basic principle of adaptive control is to dynamically adjust the control law according to the real-time state of the system to ensure the stability and performance of the system. In the application of agricultural UAV, fuzzy logic controller is introduced to adjust PID parameters adaptively. In addition, in order to further improve the control accuracy, the visual inertial navigation technology is combined to fuse the data of visual sensor and inertial measurement unit (IMU) to achieve higher precision attitude estimation and trajectory tracking.

Multisensor data fusion

In the complex farmland environment, it is often difficult for a single sensor to provide comprehensive environmental information *(Jiao et al., 2020)*. For this reason, multi-sensor data fusion technology has become the key to improve the sensing accuracy. Common sensors include lidar, binocular camera, infrared sensor and ultrasonic sensor, and each sensor has its own advantages and limitations *(Li et al., 2023)*. For example, lidar can provide high-precision distance information, but it is easily disturbed under strong light conditions; Binocular camera can generate three-dimensional depth map through stereo vision, but it requires high computing resources *(Muthanna et al., 2022)*.

In this study, the multi-sensor data fusion method based on Kalman filter is used to integrate the data of different types of sensors, so as to obtain more reliable and comprehensive environmental perception results. Kalman filter is a recursive estimation algorithm, the core of which is to gradually approach the real state of the system through two steps: prediction and update. In the application of agricultural UAV, Kalman filter is used to fuse the depth information of lidar and binocular camera to construct a unified environmental model.

Design of intelligent obstacle avoidance algorithm for agricultural UAV

Improved YOLOv5 target detection algorithm

Target detection is the first step for agricultural UAV to perceive farmland environment. Its core task is to identify and determine the position of obstacles from the input image *(Zhou et al., 2020)*. The traditional deep learning network, like YOLOv5, has excellent performance in the task of target detection, but in the complex farmland environment, there are still some situations, such as large consumption of computing resources and insufficient accuracy of small target detection *(Rienecker et al., 2023; Wenyu et al., 2024)*. In this study, Ghost module is introduced to improve the lightweight of YOLOv5 and optimize the design of loss function.

When traditional deep learning networks extract feature maps, there will be a lot of redundant and similar feature maps. However, these characteristic graphs are indispensable to the accuracy of the model, and they are all obtained by convolution operation and input to the next convolution layer for operation.

This process contains a lot of network parameters and consumes a lot of computing resources. Therefore, an attempt can be made to obtain these redundant feature maps at a lower computational cost. See Figure 1 for the main steps of Ghost module.

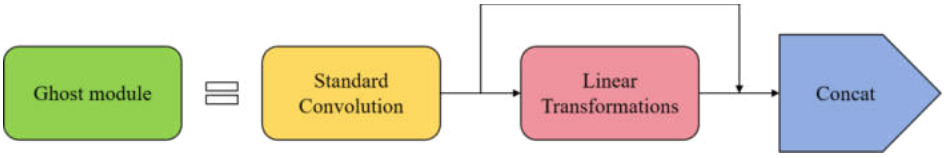


Fig. 1 - Ghost module

The working process of Ghost module is to generate a set of basic feature maps by using standard convolution layer, and then perform linear transformation (such as point-by-point convolution or depth-separable convolution) on these basic feature maps, and then generate a set of "phantom" feature maps *(Just et al., 2020)*.

Suppose the input feature map is $X \in \mathbb{R}^{H\times W\times C}$, where H and W represent the height and width of the feature map respectively, and C represents the number of channels. After the standard convolution layer processing, the basic feature map is as follows:

$$F_{base} = Conv(X) \tag{1}$$

Among them, $Conv(\cdot)$ stands for convolution operation.

Then, F_{base} is linearly transformed to generate a phantom feature map F_{ghost}, and its expression is:

$$F_{ghost} = \Phi(F_{base}) \tag{2}$$

$\Phi(\cdot)$ here stands for linear transformation operation, which generally adopts point-by-point convolution or depth-separable convolution.

The final output characteristic diagram is:

$$F_{out} = Concat(F_{base}, F_{ghost}) \tag{3}$$

$Concat(\cdot)$ refers to the splicing operation of feature graphs. In this way, Ghost module can expand the ability of feature expression without greatly increasing the number of parameters, so as to improve the detection efficiency of the model.

Based on Ghost module and Ghost-BottleNeck module, the CBL module and CSP_X module in YOLOv5s network structure are improved, and GBL(Ghost-Based Layer) and $GCSP_X$ (Ghost-based Cross-stage Partial Network) are obtained respectively. The improved YOLOv5s-Ghost network structure is shown in Figure 2.

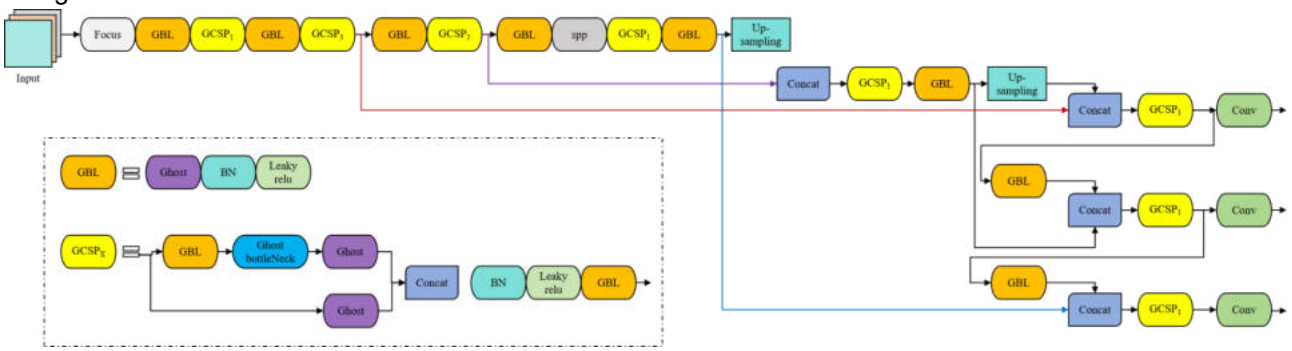


Fig. 2 -YOLOv5s-Ghost network structure

Compared with the original YOLOv5, YOLOv5s-Ghost model only uses a CSP_X structure. This reduces the complexity of the model to some extent and optimizes the feature fusion ability of the network. In addition, the information of gradient change is completely transmitted to the feature map, thus ensuring the accuracy of detection. For example, in the farmland environment, the size of obstacles such as trees and telephone poles is quite different, and the improved model can capture the spatial position of these targets more accurately *(Grau et al., 2020)*.

In order to further improve the bounding box regression performance of the model, CIoU (Complete Intersection Over Union) loss function is used to replace the traditional IOU loss function. CIoU considers the overlapping area between the prediction frame and the real frame, and also introduces the constraints of aspect ratio and the distance from the center point. It is defined as follows:

$$CIoU = 1 - IoU + \frac{\rho^2(b,b^{gt})}{c^2} + \alpha v \tag{4}$$

Where $\rho(b, b^{gt})$ represents the distance between the center point of the prediction frame b and the real frame b^{gt}, c represents the diagonal length of the smallest rectangle surrounding the two frames, and α and v respectively represent the weight and error term of the aspect ratio.
By introducing CIoU loss function, the model can better describe the three-dimensional spatial relationship of obstacles, thus improving the detection accuracy.

Path planning based on ORB feature point extraction

After obstacle detection, the next step is to plan the path based on the detection results. In this study, ORB (Orientated Fast and Rotating Brief) algorithm is used to extract the key feature points in the image, which is used to construct the environment map and guide the path planning. ORB algorithm is an efficient feature point extraction method, and its core steps include FAST corner detection and BRIEF descriptor generation.

Figure 3 shows the feature point extraction results of ORB algorithm in farmland environment. ORB algorithm can effectively capture the key feature points of obstacles, such as the outline of trees and the edge of telephone poles.



Fig. 3 - ORB feature point extraction results

Let the set of extracted feature points be $P = \{p_1, p_2, \ldots, p_n\}$, where each feature point p_i contains its coordinate (x_i, y_i) and descriptor d_i. In order to generate the environment map, the depth information z_i of each feature point is calculated by binocular vision technology, so as to construct a three-dimensional point cloud:

$$Q = \{(x_i, y_i, z_i)\}_{i=1}^{n} \quad (5)$$

Based on 3D point cloud Q, reinforcement learning algorithm is used for path planning, and the environment is modeled as a Markov decision process (MDP). In this framework, the state space AA represents the current position of UAV and the distribution of surrounding obstacles, and the action space represents the moving direction and speed of UAV. The reward function $R(s, a)$ is defined as:

$$R(s, a) = w_1 \cdot \text{Safety}(s, a) + w_2 \cdot \text{Efficiency}(s, a) - w_3 \cdot \text{Energy}(s, a) \quad (6)$$

where $\text{Safety}(s, a)$ represents the safety of the path, $\text{Efficiency}(s, a)$ represents the efficiency of the path, $\text{Energy}(s, a)$ represents the energy consumption, and w_1, w_2, w_3 is the weight coefficient.

Using reinforcement learning algorithm, UAV can quickly adjust its flight trajectory in dynamic environment and avoid collision with obstacles.

Adaptive motion control

The results of path planning need to be transformed into specific flight instructions by motion control algorithm. Because the external interference in the farmland environment (such as wind speed, terrain fluctuation, etc.) may cause UAV to deviate from the predetermined trajectory, it is necessary to design a robust adaptive control algorithm *(Shrestha et al., 2021)*.

An adaptive PID control method based on fuzzy logic controller is adopted in the research. Let the state variable of UAV be:

$$x(t) = [x_p, y_p, z_p, \theta]^T \quad (7)$$

where x_p, y_p, z_p represent the position of UAV and θ represents the yaw angle. The control objective is to minimize the position error:

$$e(t) = x_d(t) - x(t) \quad (8)$$

where $x_d(t)$ is the target position. The output of PID controller is:

$$u(t) = K_p e(t) + K_i \int_0^t e(\tau)d\tau + K_d \frac{de(t)}{dt} \quad (9)$$

where K_p, K_i, K_d are proportional, integral and differential coefficients respectively.

In order to cope with external interference, the fuzzy logic controller is used to adjust K_p, K_i, K_d adaptively. The input of fuzzy logic controller is the current flight state (such as yaw angle, pitch angle, etc.) and external interference intensity, and the output is the adjustment of PID parameters.

In order to further improve the reliability of environmental perception, multi-sensor data fusion technology is adopted in this study. Kalman filter is used to fuse the depth information of lidar and binocular camera, and a unified environmental model is constructed by combining the attitude data of IMU. The state update formula of Kalman filter is:

$$\hat{x}_k = \hat{x}_{k|k-1} + K_k(z_k - H\hat{x}_{k|k-1}) \quad (10)$$

where $\hat{x}_k$ is the estimated state, z_k is the observed value, and K_k is the Kalman gain matrix.

By fusing multi-sensor data, the system can obtain more comprehensive environmental information and provide reliable data support for path planning and motion control.

RESULTS AND DISCUSSIONS

Experimental setup

The hardware platform of this experiment is an agricultural UAV (DJI Matrice 300 RTK). It is equipped with binocular camera, lidar and IMU sensor. These devices are used to collect images and point cloud data in the actual farmland environment. It covers static obstacles (such as trees and telephone poles) and dynamic obstacles (such as birds and moving machinery). In terms of software, the improved YOLOv5s-Ghost model is used to perform the target detection task, and the path planning work is carried out in combination with reinforcement learning algorithm. All algorithms run on the embedded platform of NVIDIA Jetson Xavier NX to simulate the limitation of computing resources under real working conditions. The experimental data are taken from the images and point cloud data collected from the actual farmland environment. All the comparative experiments were carried out on the same hardware platform and the same farmland environment.

Result analysis

Figure 4 shows the time-consuming situation of different algorithms in path planning. When the information of farmland environment is simple and the number of obstacles is small, with the increase of the number of path planning nodes, the time required for the algorithm increases significantly. This is because in the low-complexity scenario, the increase in the number of nodes will cause a waste of computing resources, and the efficiency of path planning algorithm to deal with redundant information will also decrease. However, when the complexity of farmland environment gradually rises (such as more kinds of obstacles or dynamic obstacles), the advantages of multi-node begin to be reflected. This shows that the improved algorithm has stronger adaptability and higher efficiency when dealing with complex farmland environment.

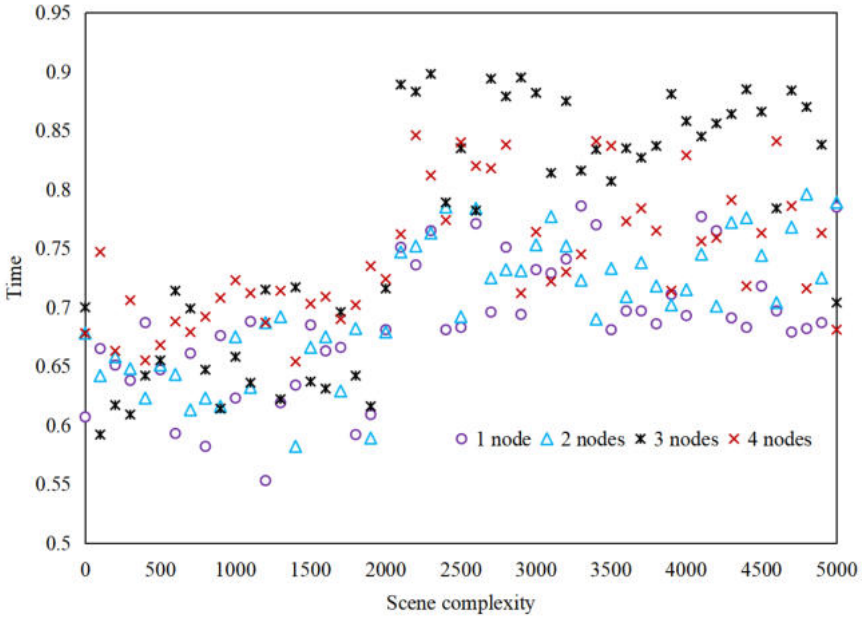


Fig. 4 - Path planning is time consuming

Further analysis shows that the average path planning time of the improved algorithm is about 35% less than that of the traditional Dijkstra algorithm. Compared with the original YOLOv5 model, it is reduced by about 20%. This is mainly due to the improvement of target detection accuracy of the improved YOLOv5 model and the advantages of reinforcement learning algorithm in identifying dynamic obstacles.

Figure 5 compares the errors of different algorithms in path planning. The results show that the traditional Dijkstra algorithm and the unoptimized YOLOv5 model have poor performance in error control. Especially in complex farmland scenes, or when the number of nodes is large, the paths generated by them often deviate from the optimal solution, which leads to failure of obstacle avoidance or low path efficiency. In contrast, the path planning algorithm based on the improved YOLOv5 greatly reduces the path planning error by optimizing the target detection accuracy and improving the dynamic obstacle recognition ability.

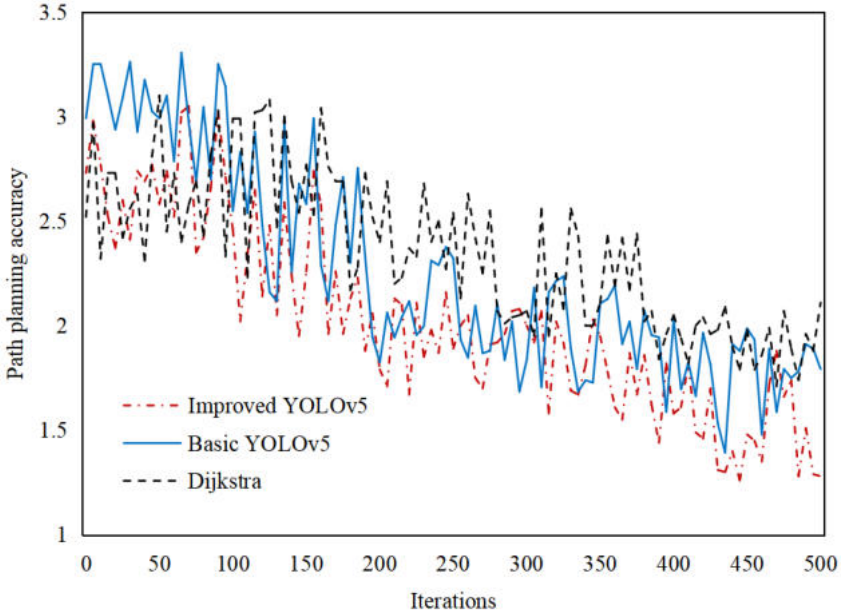


Fig. 5 - Path planning error

Figure 6 shows the comparison results of different algorithms in path planning accuracy. The path planning algorithm based on improved YOLOv5 has the highest accuracy, and its path planning accuracy can reach more than 96%. This result verifies the effectiveness and potential of the improved YOLOv5 in the application of agricultural UAV in complex farmland environment. By introducing Ghost module and CIoU loss function, the improved algorithm obviously improves the detection ability of small target obstacles (such as telephone poles) and dynamic obstacles (such as birds). In addition, the accuracy of the improved algorithm fluctuates little in complex scenes, showing strong robustness.

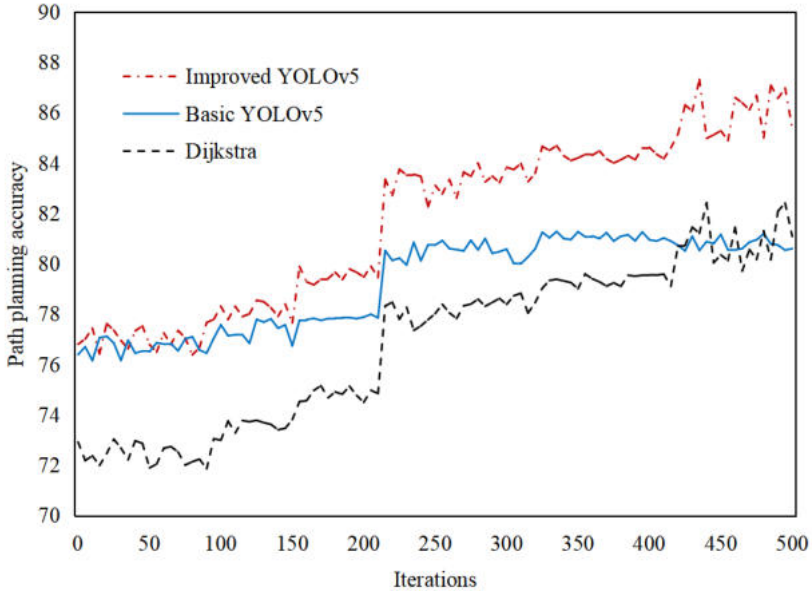


Fig. 6 - Path planning accuracy

It is not difficult to find from Table 1 that with the increase of scene complexity, the time-consuming growth rate of the improved YOLOv5 path planning is the smallest, which shows that it has higher efficiency in high-complexity scenes.

Table 1

Comparison of Path Planning Time Consumption for Different Algorithms

Scene Complexity	Dijkstra Algorithm	A* Algorithm	Unimproved YOLOv5	Improved YOLOv5
Low Complexity	0.85	0.72	0.68	0.58
Medium Complexity	1.23	1.05	0.92	0.75
High Complexity	2.15	1.87	1.54	1.12

Table 2 shows that the path planning error of the improved YOLOv5 in various scenarios is significantly lower than other algorithms. In the dynamic obstacle area, the error is only 2.5 meters, which is about 60% lower than the traditional algorithm.

Table 2

Comparison of Path Planning Errors for Different Algorithms

Scene Type	Dijkstra Algorithm	A* Algorithm	Unimproved YOLOv5	Improved YOLOv5
Dense Tree Areas	6.8	5.4	4.3	2.1
Dynamic Obstacle Areas	7.2	6.1	4.8	2.5
Comprehensive Scenes	6.5	5.7	4.5	2.3

Table 3 shows that the path planning accuracy of the improved YOLOv5 in all kinds of scenarios is over 95%, which is much higher than other algorithms. This result further proves the superiority of the improved algorithm in complex farmland environment.

Table 3

Comparison of Path Planning Accuracy for Different Algorithms

Scene Type	Dijkstra Algorithm	A* Algorithm	Unimproved YOLOv5	Improved YOLOv5
Dense Tree Areas	82	85	89	96
Dynamic Obstacle Areas	78	81	87	95
Comprehensive Scenes	80	83	88	96

Discussion

Based on these results, the improved YOLOv5 model usually has excellent performance in the accuracy of target detection and the efficiency and accuracy of path planning. Especially in the complex farmland environment, the improved algorithm greatly improves the detection ability of small target obstacles and dynamic obstacles by introducing Ghost module and CIoU loss function. In this way, it provides more reliable data support for path planning.

Moreover, the path planning algorithm based on reinforcement learning is particularly outstanding in dynamic scenes. It can quickly adjust the flight path to avoid collision. However, the experiment also revealed some problems. For example, in extreme weather conditions, such as strong wind or heavy rain, the quality of sensor data may decrease.

Future research will further optimize the anti-jamming ability of the algorithm, and also explore the potential application of more emerging technologies in agricultural UAV.

CONCLUSIONS

With the continuous progress of precision agriculture technology, agricultural UAV is more and more widely used in complex farmland environment. According to the characteristics of complex farmland environment, this article proposes a solution that combines the target detection algorithm based on improved YOLOv5 with the intelligent obstacle avoidance control strategy. It is found that the scheme has made significant breakthroughs in target detection accuracy, path planning efficiency and overall system robustness.

In the field of target detection, Ghost module is introduced to improve the lightweight of YOLOv5, and then the regression performance of bounding box is optimized by combining CIoU loss function. This greatly improves the detection ability of the model for small targets and dynamic obstacles. Experiments show that the detection accuracy of the improved YOLOv5 model can reach more than 96% in complex farmland environment, which is about 7% higher than that of the original model. Moreover, the path planning error of the improved algorithm when dealing with dynamic obstacles is only 2.1 meters, which is about 70% lower than the traditional Dijkstra algorithm.

In path planning and motion control, 3D point cloud data generated based on ORB feature point extraction and binocular vision technology provide high-precision input for path planning. Combined with reinforcement learning algorithm, real-time obstacle avoidance decision-making in dynamic environment is realized, and the time-consuming of path planning is reduced by about 35%. At the same time, the adaptive PID control strategy realized by fuzzy logic controller greatly improves the flight stability of UAV when it is disturbed by external interference. The experimental verification shows that the system is particularly outstanding in the comprehensive scene including obstacles such as trees and bushes.

However, there are still some limitations in this study. For example, in extreme weather conditions (such as strong wind or heavy rain), the quality of sensor data may decrease. Future research will further optimize the anti-interference ability of the algorithm, and explore the potential application of emerging technologies such as edge computing and federated learning in agricultural UAV.

REFERENCES

[1] Brown L.A., Sutherland D., Dash J. (2020). Low-Cost Unmanned Aerial Vehicle-Based Digital Hemispherical Photography for Estimating Leaf Area Index: A Feasibility Assessment, *International Journal of Remote Sensing*, Vol. 41, No. 23, pp. 9064 - 9074. https://doi.org/10.1080/2150704X.2020.1802527

[2] Dai X., Mao Y., Huang T., Qin N., Huang D., Li Y. (2020). Automatic Obstacle Avoidance of Quadrotor UAV via CNN-Based Learning[J]. *Neurocomputing*, Vol. 402, pp. 346-358. https://doi.org/10.1016/j.neucom.2020.04.020

[3] Dorbu, F., Hashemi-Beni, L. (2024). Detection of Individual Corn Crop and Canopy Delineation from Unmanned Aerial Vehicle Imagery[J]. *Remote Sensing*, Vol. 16, No. 14, pp. 2679. https://doi.org/10.3390/rs16142679

[4] Du B., Ding X., Ji C., Lin K., Guo J., Lu L., Dong Y., Huang W., Wang N. (2023). Estimating Leymus chinensis Loss Caused by Oedaleus decorus asiaticus Using an Unmanned Aerial Vehicle (UAV)[J]. *Remote Sensing*, Vol. 15, No. 17, pp. 4352. https://doi.org/10.3390/rs15174352

[5] Gao D., Sun Q., Hu B., Zhang S. (2020). A Framework for Agricultural Pest and Disease Monitoring Based on Internet-of-Things and Unmanned Aerial Vehicles[J]. *Sensors*, Vol. 20, No. 5, pp. 1487. https://doi.org/10.3390/s20051487

[6] Grau J., Liang K., Ogilvie J., Arp P., Li S., Robertson B., Meng F. (2021). Improved Accuracy of Riparian Zone Mapping Using Near Ground Unmanned Aerial Vehicle and Photogrammetry Method[J]. *Remote Sensing*, Vol. 13, No. 10, pp. 1997. https://doi.org/10.3390/rs13101997

[7] Gao, M., Zhang Z., Zhang J., Tang S., Zhang H., Pang T. (2024). Web Intelligence-Enhanced Unmanned Aerial Vehicle Target Search Model Based on Reinforcement Learning for Cooperative Tasks [J]. *International Journal of Web Information Systems*, Vol. 20, No. 3, pp. 289-303.

[8] Jiao K., Chen J., Xin B., Li l., Zheng Y., Zhao Z. (2024). Three-Dimensional Path Planning with Enhanced Gravitational Search Algorithm for Unmanned Aerial Vehicle [J]. *Robotica*, Vol. 42, No.7, pp. 2453-2487.

[9] Just, G.E., Pellenz, M.E., Lima, L.A.D.P., Chang, B., Domo-Souza, R., Montejo-Sanchez, S. (2020). UAV Path Optimization for Precision Agriculture Wireless Sensor Networks [J]. *Sensors*, Vol. 20, No.21, pp. 6098. https://doi: 10.3390/s20216098

[10] Lu, Z., Yu, N., Wang, X. (2023). Incentive Mechanism and Path Planning for Unmanned Aerial Vehicle (UAV) Hitching over Traffic Networks[J]. *Future Generation Computer Systems*, Vol. 145, pp. 521-535. https://doi.org/10.1016/j.future.2023.03.048

[11] Liu J., Xiang J., Jin Y., Liu R., Yan J., Wang L. (2021). Boost Precision Agriculture with Unmanned Aerial Vehicle Remote Sensing and Edge Intelligence: A Survey[J]. *Remote Sensing*, Vol. 13, No. 21, pp. 4387. https://doi.org/10.3390/rs13214387

[12] Liu M., Wang X., Zhou A., Fu X., Ma Y., Piao C. (2020). UAV-YOLO: Small Object Detection on Unmanned Aerial Vehicle Perspective[J]. Sensors, Vol. 20, No. 8, pp. 2238. https://doi.org/10.3390/s20082238

[13] Li Y., Gao S., Liu X., Zuo P., Li H. (2023). An Efficient Path Planning Method for the Unmanned Aerial Vehicle in Highway Inspection Scenarios [J]. *Electronics*, Vol. 12, No. 20, pp. 4200. https://doi.org/10.3390/electronics12204200

[14] Muthanna M.S.A., Muthanna A., Nguyen T.N., Alshahrani A. (2022). Towards Optimal Positioning and Energy-Efficient UAV Path Scheduling in IoT Applications[J]. *Comput. Commun*., Vol. 191, pp. 145-160. https://doi.org/10.1016/j.comcom.2022.04.029

[15] Rienecker, H., Hildebrand, V., Pfifer, H. (2023). Energy Optimal 3D Flight Path Planning for Unmanned Aerial Vehicle in Urban Environments[J]. *CEAS Aeronautical Journal*, Vol. 14, No. 3, pp. 621-636.

[16] Saeed, R.A., Ali, E.S., Abdelhaq, M., Alsaqour, R., Ahmed, F.R.A, Saad, A.M.E. (2023). Energy Efficient Path Planning Scheme for Unmanned Aerial Vehicle Using Hybrid Generic Algorithm-Based Q-Learning Optimization [J]. *IEEE Access*, Vol. 12, pp. 13400-13417. https://doi.org/10.1109/ACCESS.2023.3344455

[17] Seiche, A.T., Wittstruck, L., Jarmer, T. (2024). Weed Detection from Unmanned Aerial Vehicle Imagery Using Deep Learning—a Comparison between High-End and Low-Cost Multispectral Sensors [J.] *Sensors*, Vol. 24, No. 5, pp. 1544. https://doi.org/10.3390/s24051544

[18] Shrestha, R., Bajracharya, R., Kim, S. (2021). 6G Enabled Unmanned Aerial Vehicle Traffic Management: A Perspective [J]. *IEEE Access*, Vol. 9, pp. 91119-91136. https://doi: 10.1109/ACCESS.2021.3092039

[19] Varma, K.N.V.S. and Kumari, S.L. (2024). Robotic Vision Based Obstacle Avoidance for Navigation of Unmanned Aerial Vehicle Using Fuzzy Rule Based Optimal Deep Learning Model[J]. *Evolutionary Intelligence*, Vol. 17, No. 4, pp. 2193-2212. https://DOI:10.1007/s12065-023-00881-9

[20] Peng, W., Zhu, J., Huang, M., Lan, Y., Zhao, H., Huang, S., Li, S., Huang, A., Tang, Z. (2024). A bibliometric-based analysis of research progress in unmanned aerial remote sensing of wheat (基于文献计量的小麦无人机遥感研究进展分析). *INMATEH - Agricultural Engineering*, Vol. 74, No. 3, pp. 209-217. DOI: https://doi.org/10.35633/inmateh-74-18 .

[21] Yang Q., Liu M., Zhang Z., Yang S., Ning J., Han W. (2019). Mapping Plastic Mulched Farmland for High Resolution Images of Unmanned Aerial Vehicle Using Deep Semantic Segmentation, *Remote Sensing*, Vol. 11, No. 17, pp. 2008. https://doi.org/10.3390/rs11172008

[22] Yang X., Bao N., Li W., Liu S., Fu Y., Mao Y. (2021). Soil Nutrient Estimation and Mapping in Farmland Based on UAV Imaging Spectrometry, *Sensors*, Vol. 21, No. 11, pp. 3919. https://doi.org/10.3390/s21113919

[23] Zhou Y., Su Y., Xie A., Kong L. (2021). A Newly Bio-Inspired Path Planning Algorithm for Autonomous Obstacle Avoidance of UAV, *Chinese Journal of Aeronautics*, Vol. 34, No. 9, pp. 199-209. https://doi.org/10.1016/j.cja.2020.12.018

[24] Zhao W., Xu T., Wang Y., Du W., Shen A. (2020). Research on Vision Navigation and Position System of Agricultural Unmanned Aerial Vehicle [J]. *International Journal of Computer Integrated Manufacturing*, Vol. 33, No. 10-11, pp. 1185-1196. https://doi.org/10.1080/0951192X.2020.1795925

[25] Zhou F., Hu R.Q., Li Z., Wang Y. (2020). Mobile Edge Computing in Unmanned Aerial Vehicle Networks[J]. *IEEE Wireless Communications*, Vol. 27, No. 1, pp. 140-146. https://doi.org/10.48550/arXiv.1910.10523

[26] Zhu Y., Tan Y., Chen Y., Chen I., Lee K.Y. (2024). UAV Path Planning Based on Random Obstacle Training and Linear Soft Update of DRL in Dense Urban Environment [J]. *Energies*, Vol. 17, No. 11, pp.2762. https://doi.org/10.3390/en17112762

PARAMETER OPTIMIZATION AND EXPERIMENT OF AN INSIDE-FILLING PNEUMATIC HIGH-SPEED PRECISION SEED-METERING DEVICE FOR COTTON
/
内充气力式棉花高速精量排种器参数优化与试验

Meng-jie HU*[1,2]; Jia-qi ZHANG[1]; Yao CHEN[1]; Chu-zhen XU[1]; Bao-jia LI[1]
[1)]School of Animal Science and Nutritional Engineering, Wuhan Polytechnic University, Wuhan / P.R.China
[2)]Key Laboratory of Agricultural Equipment in Mid-Lower Yangtze River, Ministry of Agriculture and Rural Affairs, Wuhan / P.R.China
Tel: +86-027-15527930805; E-mail: humj@whpu.edu.cn
DOI: https://doi.org/10.35633/inmateh-76-111

Keywords: *cotton, inside-filling pneumatic high-speed precision seed-metering device, parameter optimization, CFD, DEM-CFD*

ABSTRACT
To address the poor seeding effect of inside-filling pneumatic high-speed precision seed-metering device for cotton, Computational Fluid Dynamics (CFD) and Discrete Element Method–Computational Fluid Dynamics (DEM-CFD) approaches were employed for simulation and optimization. The CFD technique was applied to analyze the influence of key structural parameters of the negative-pressure air chamber on the adsorption performance of the suction holes, while the DEM-CFD approach was used to investigate the motion of cotton seeds inside the seed-metering device during the seed-throwing stage. Based on these analyses, the optimal combination of structural and performance parameters of the seed-metering device was obtained. The simulation-optimized parameters were then validated through bench tests, which showed that at a suction hole diameter of 3.1 mm, a forward speed of 2.33 m/s (8.4 km/h), and a negative pressure of 3,178 Pa, the evaluation indexes were optimal: 96.25% qualification index, 1.83% multiple sowing index, and 1.92% missed sowing index. Further high-speed adaptability test showed that when the forward speed was 1.67~3.33 m/s (6~12 km/h), the qualification index remained greater than 91%, and both the multiple and missed sowing index were less than 5%, meeting the agronomic requirements of high-speed precision seeding for cotton.

摘要
针对内充气力式棉花高速精量排种器排种效果不佳的问题，采用 CFD 和 DEM-CFD 仿真分析方法对其进行了模拟与优化。利用 CFD 仿真分析了负压气室关键结构参数对吸孔吸附性能的影响，采用 DEM-CFD 气固耦合方法探究了投种环节排种器内部棉花种子运动规律，并获得了排种器关键结构与性能参数最佳组合。仿真优化后的参数经台架排种性能试验表明，当吸孔直径为 3.1 mm、前进速度为 2.33 m/s (8.4 km/h)、负压为 3178 Pa 时，其试验指标最优且为合格指数 96.25%，重播指数 1.83%，漏播指数 1.92%。进一步经高速适应性试验表明，当前进速度为 1.67~3.33 m/s (6~12 km/h) 时，合格指数均大于 91%，重播与漏播指数均小于 5%，满足棉花高速精播农艺要求。

INTRODUCTION
Cotton is an important economic crop in China, with a long history of cultivation *(Bie et al., 2018)*. With the acceleration of agricultural modernization, cotton growers are increasingly demanding high-speed and efficient agricultural machinery *(Dong et al., 2025)*. Sowing represents the first step of planting, the seed-metering device being a seeder key component, its seeding quality directly affecting the operational performance of the machine *(Li et al., 2025; Cortez et al., 2020)*. Cotton seed-metering devices are mainly classified into mechanical and pneumatic types. Mechanical seed-metering devices have simple structures but require high seed shape uniformity, having a tendency to damage seeds and suffer from low seeding accuracy under high-speed operation *(Yang et al., 2024; Li et al., 2025; Li et al., 2024)*. In contrast, pneumatic seed-metering devices, although structurally more complex, exhibit better adaptability to seed shape variations, higher seeding precision, and less seed damage, making them more suitable for high-speed seeding operations *(Zang et al., 2024; Li et al., 2021; Gao et al., 2023; Li et al., 2020; Yatskul & Lemiere, 2018; Pareek et al., 2023)*. At present, existing cotton precision seed-metering devices still suffer from poor seed-filling performance under high-speed conditions, with a typical missed sowing index greater than 10%, a qualification index lower than 75%, and the forward speed generally limited to less than 1.11 m/s (4 km/h) *(Zhang et al., 2021; Zhang et al., 2022; Xu, 2018)*.

Since the seed inside-filling type can make use of gravity, centrifugal force, and inter-seed interaction forces to improve the seed-filling performance, our research group previously designed an inside-filling pneumatic cotton high-speed precision seed-metering device. However, experimental results revealed that although the seed-filling performance was improved, the device still exhibited problems such as unstable seed adsorption and poor seed throwing quality under high-speed operation, leading to poor seeding performance. Therefore, the structural parameters of the seed-metering device still require further investigation and optimization.

In recent years, the Computational Fluid Dynamics (CFD) and Discrete Element Method–Computational Fluid Dynamics (DEM-CFD) techniques have been widely applied in the development of seed-metering devices *(Wang et al., 2025; Sun et al., 2025; Wan et al., 2022; Zhou et al., 2024; Guzman et al., 2020; Bustos-Gaytán et al., 2025)*. Guzman validated the feasibility of using DEM-CFD technique to simulate pneumatic seeder planting green field peas through the combination of simulation and experimentation, and investigated the effects of scaled-down seed tank and fluted roller, single run of a horizontal distributor tube, horizontal-vertical tube transition, and vertical seed manifold on the seed movement *(Guzman, 2024)*. Zha et al. designed a branched air-chamber type pneumatic seed-metering device to meet the varying seed rate requirements for different rice varieties, employing CFD technique to optimize the key structural parameters of the branched air chamber casing *(Zha et al., 2024)*. Cao et al. aimed to improve the operational performance of the mixing component in a horizontal air-assisted centralized wheat metering device. Using CFD and DEM-CFD methods, they investigated the influence of key structural parameters of the mixing component on internal airflow distribution and wheat conveying performance, and determined the optimal parameter combination *(Gao et al., 2024)*. Hussain et al. aimed to optimize the working performance of an air-suction maize seed metering device. CFD was used to investigate the effects of vacuum pressure, suction hole diameter, and seed disk speed on device performance, and the optimal parameter combination was obtained. This was subsequently validated through DEM-CFD coupling simulations and bench tests. At a vacuum pressure of 3.5 kPa, an operating speed of 1.94 m/s (7 km/h), and a suction hole diameter of 4 mm, the qualified index reached 95.98%, while the missed index was 1.5% *(Hussain et al., 2025)*. Zhao et al. combined the DEM-CFD gas-solid coupling method and high-speed camera to investigate the effects of key structural and performance parameters of a novel high-speed precision maize seed-metering device on the seeding performance, determining the optimal combination of operating parameters, and verifying the reliability of the seed-metering device under high-speed operation through bench and field tests *(Zhao et al., 2024)*. In summary, simulation techniques are currently widely applied in the development of seed-metering devices for grain crops such as peas, rice, wheat, and maize, while their application in the research and development of high-speed cotton seed-metering devices is not very developed. Moreover, existing studies have not clarified how the air chamber geometry affect the pressure uniformity at suction hole endface for inside-filling pneumatic seed-metering devices, nor have the DEM-CFD coupling simulation been utilized to define the seed throwing pressure and seed throwing port position angle required for stable seed throwing. Therefore, this study uniquely addresses these gaps by combining CFD and DEM-CFD simulations with experimental research to improve the seeding performance of inside-filling pneumatic cotton high-speed precision seed-metering device.

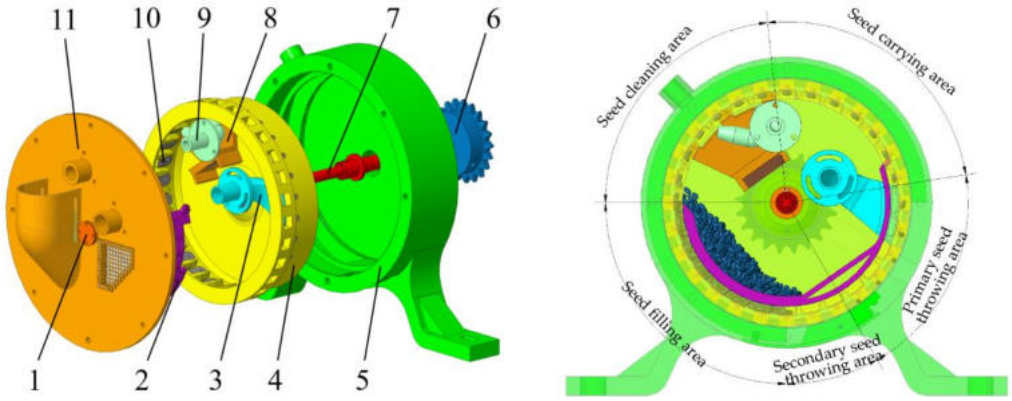
To improve the operational performance of an inside-filling pneumatic high-speed precision cotton seed-metering device, CFD simulations were conducted to analyze the influence of key structural parameters of the negative-pressure air chamber on the pressure at the suction hole end face, and the optimal parameter combination was determined. The DEM-CFD gas–solid coupling technique was then applied to investigate the motion behavior of cotton seeds inside the device during the seed-throwing stage, analyzing the effects of seed-throwing pressure on the initial and stable contact angles between the seeds and the inner wall of the back shell, and determining the optimal seed-throwing pressure and port position. Bench tests of the optimized device were carried out to identify the best combination of performance parameters affecting seeding quality, followed by high-speed adaptability verification. This study provides a reference for the optimization and further improvement of precision seed-metering devices.

MATERIALS AND METHODS

Overall structure and working principle

The inside-filling pneumatic high-speed precision cotton seed-metering device mainly consists of the front shell, seeding plate, suction-hole replacement plate, seed protection board, scraper, seed-cleaning air nozzle, seed-throwing air nozzle, seeding shaft, and back shell, as shown in Fig. 1(a).

As shown in Fig. 1, an arc-shaped groove is arranged on the inner wall of the back shell, which is assembled with the outer wall of the seeding plate to form an air chamber. The back shell is provided with an air outlet hole, which is connected to the air chamber and externally connected to a fan, so that the air chamber can be filled with negative pressure airflow. After cotton seeds enter the inner cavity of the seed-metering device through the seed inlet on the front shell, a seed cluster is formed. The cotton seeds in the lower layer of the seed cluster are adsorbed onto the suction holes under the action of airflow and rotate clockwise with the seeding plate. When the suction hole rotates into the seed cleaning area, excess seeds surrounding the suction hole are removed by the combined action of the scraper and seed cleaning air nozzle, falling back into the seed cluster. The single cotton seed stably adsorbed onto the suction hole is carried by the seeding plate through the seed carrying area and reaches the primary seed throwing area, where it is blown into the collection hole under the action of airflow from the seed throwing air nozzle. As the collection hole continues to move into the secondary seed throwing area, the seed is thrown out through the seed throwing port of back shell, thereby completing the entire seeding process.



(a) (b)

Fig. 1 - Structural schematic diagram of inside-filling pneumatic cotton high-speed precision seed-metering device

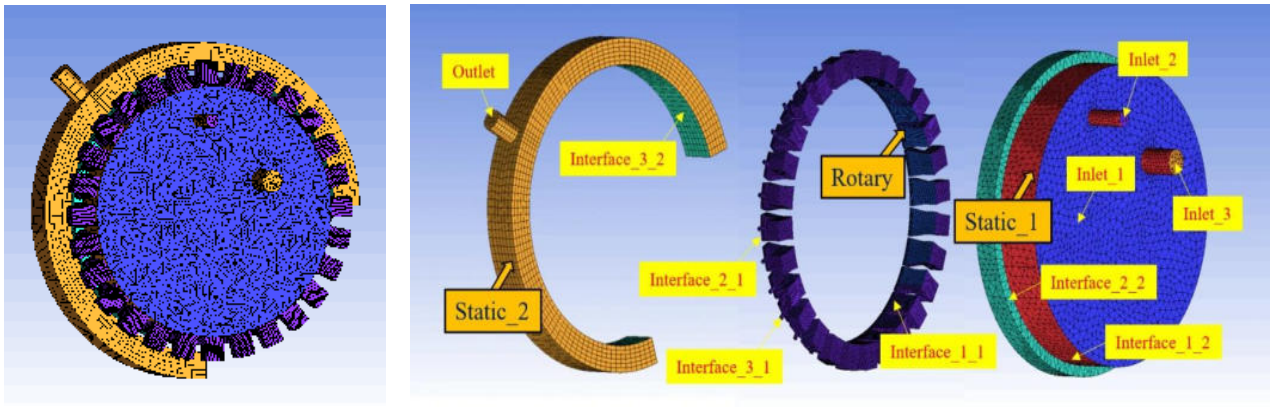
(a) Exploded view diagram of the seed-metering device, (b) Schematic diagram of the working principle of the seed-metering device 1. Bearing end cover; 2. Seed protection board; 3. Seed throwing air nozzle; 4. Seeding plate; 5. Back shell; 6. Sprocket; 7. Seeding shaft; 8. Scraper; 9. Seed cleaning air nozzle; 10. Suction hole replacement plate; 11. Front shell

Simulation analysis method

CFD simulation method for the negative pressure air chamber

Construction and validation of the airflow field model

Using ANSYS Fluent 18.0 software to simulate the airflow field of the negative pressure air chamber, the airflow field model needs to be constructed firstly according to the actual structure and working principle of the seed-metering device, as shown in Fig. 2(a).



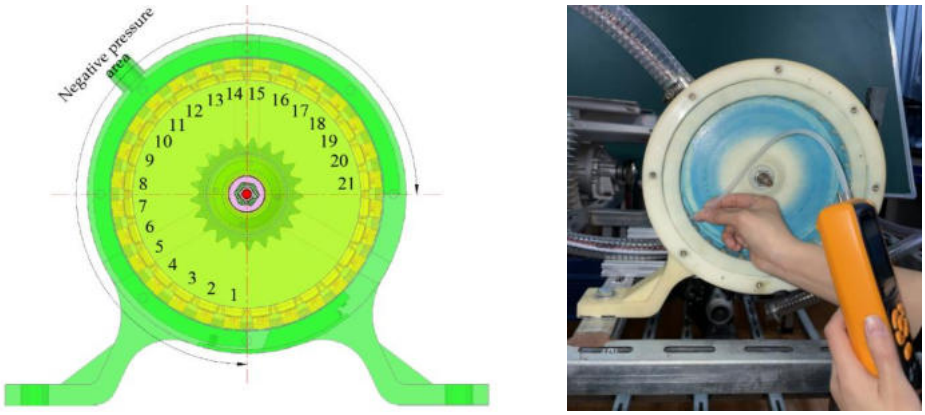
(a) (b)

Fig. 2 - Airflow field mesh model of the seed-metering device

(a) Overall schematic diagram of the mesh model, (b) Exploded schematic diagram of the mesh model

To improve the simulation efficiency, components such as the seeding shaft, seed protection plate, and scraper were omitted to simplify the computational domain. Based on the working principle of the seed-metering device, the airflow field model was divided into one dynamic zone (Rotary) and two static zones (Static_1 and Static_2), as shown in Fig. 2(b). According to the sliding mesh technique, pairs of interfaces were set up between the dynamic and static zones to realize the airflow communication and data exchange across the different regions. Due to the relatively regular geometry of the airflow field in the Rotary and Static_2 zones, structured meshes were applied in these regions. However, the airflow field in the Static_1 zone contains embedded seed cleaning and throwing air nozzles, making it unsuitable for structured meshes, therefore, instead were used unstructured meshes. After meshing the airflow field, the total number of cells was 342356, with the maximum skewness of 0.68. To verify the mesh-independence, two refined meshes with 459749 and 576813 cells were generated for simulation. The pressure differences at the suction hole endface among the three meshes were all less than 5%, indicating that the mesh density had little influence on the pressure at the suction hole endface and that mesh was independent.

In order to test the accuracy of the airflow field model of the seed-metering device, the pressure at the suction hole endface was selected as the evaluation index to carry out the airflow field simulation and physical comparison verification test. Before the test, the central plane of the partition plate between any two adjacent type holes was aligned with the vertical central axis of the seed-metering device, so that the 21 suction holes on the seeding plate were symmetrically and evenly distributed within the negative pressure zone, and sequentially numbered in a clockwise direction, as shown in Fig. 3(a). In the physical test, the pressure at the suction hole endface was measured using a digital differential pressure gauge (Shenzhen Wintact Electronics Co., Ltd., GM520 type, accuracy ±0.3% FSO (factory calibration within 12 months)), and the measurement method was illustrated in Fig. 3(b). The negative pressure at the air outlet was adjusted to –3000 Pa, and after the airflow stabilized, the pressure at suction holes 1–21 was measured and recorded in sequence. The simulation tests were conducted with reference to the physical test, and the boundary conditions were set as follows: the Outlet was set as a pressure outlet with a value of −3000 Pa, the Inlet_1, Inlet_2, and Inlet_3 were set as pressure inlets with the value of 0 Pa, and the rotation speed of dynamic zone was set to 0 r/min. The endface of the suction hole at the measurement points was set as wall. The standard k-ε turbulence model was employed and the pressure-based type solver was selected. The residual convergence criterion was set to 10^{-4}, and the time step was set to 0.003571429, with a total of 500 time steps. After both the physical and simulation tests were completed, the suction holes endface pressure values were compared to verify the accuracy of the airflow field model of the seed-metering device.



(a) **(b)**

Fig. 3 - Measurement of the pressure at the suction hole endface with the negative pressure setpoint of −3000 Pa

(a) Schematic diagram of suction hole numbering (1~21) in the negative pressure area,
(b) Schematic diagram of physical measurement method
Note: 1. Simulation settings: standard k–ε turbulence model, pressure-based solver, Outlet −3000 Pa, Inlet(s) 0 Pa, dynamic zone rotation speed 0 r/min, residual convergence 10^{-4}, time step 0.003571429 s, 500 steps.
2. Test repeats for 3 times.

Simulation method

The negative pressure air chamber is directly connected to the suction holes, providing the required negative pressure to ensure that cotton seeds remain stably adsorbed on the suction hole endface during the normal operation of the seed metering device. The pressure at the suction hole endface can reflect the adsorption performance of suction hole, and investigating the effects of the structural parameters of the

negative pressure air chamber on the pressure at the suction hole endface can provide a basis for optimizing the parameters of the seed-metering device. The key structural parameters of the negative pressure air chamber mainly include the angle and position of the air outlet hole, and the width and thickness of the negative pressure air chamber.

(1) Effect of Air Outlet Hole Angle and Position on Suction Hole Endface Pressure

The air outlet hole serves as the airflow exit of the seed-metering device, with its angle and position parameters directly affecting airflow direction. These include the position angle, vertical inclination angle, and longitudinal (front–rear) inclination angle, which were therefore selected as test factors to investigate their effect on the pressure at the suction hole endface. Because the suction hole endface pressure is the key factor for stable adsorption of cotton seeds, increasing the endface pressure in the seed-filling area improved the filling performance of the seed-metering device, while reducing pressure variation between suction holes in the seed-cleaning and seed-carrying areas helped prevent missed seeding caused by abrupt pressure changes. Therefore, the average endface pressure in the seed-filling area and the standard deviation of endface pressure in the seed-cleaning and seed-carrying areas were selected as evaluation indexes, and a three-factor, three-level orthogonal test was conducted. The levels of each factor are shown in Table 1, and the angle arrangement was illustrated in Fig. 4. In the numerical simulation, the relevant parameters were set as follows: the Outlet was set as a pressure outlet with a value of −3000 Pa, the Inlet_1, Inlet_2, and Inlet_3 were set as pressure inlets with the value of 0 Pa, and the rotation speed of dynamic zone was set to 30 r/min. The standard k-ε turbulence model was employed and the pressure-based type solver was selected. The residual convergence criterion was set to 10^{-4}, the time step was set to 0.003571429, and the number of time steps was 570.

Table 1

The levels of test factors for orthogonal test

Levels	Test factors		
	Position angle θ_a / (°)	Up and down inclination angle θ_b / (°)	Front and rear inclination angle θ_c / (°)
1	45	-45	-45
2	135	0	0
3	225	45	45

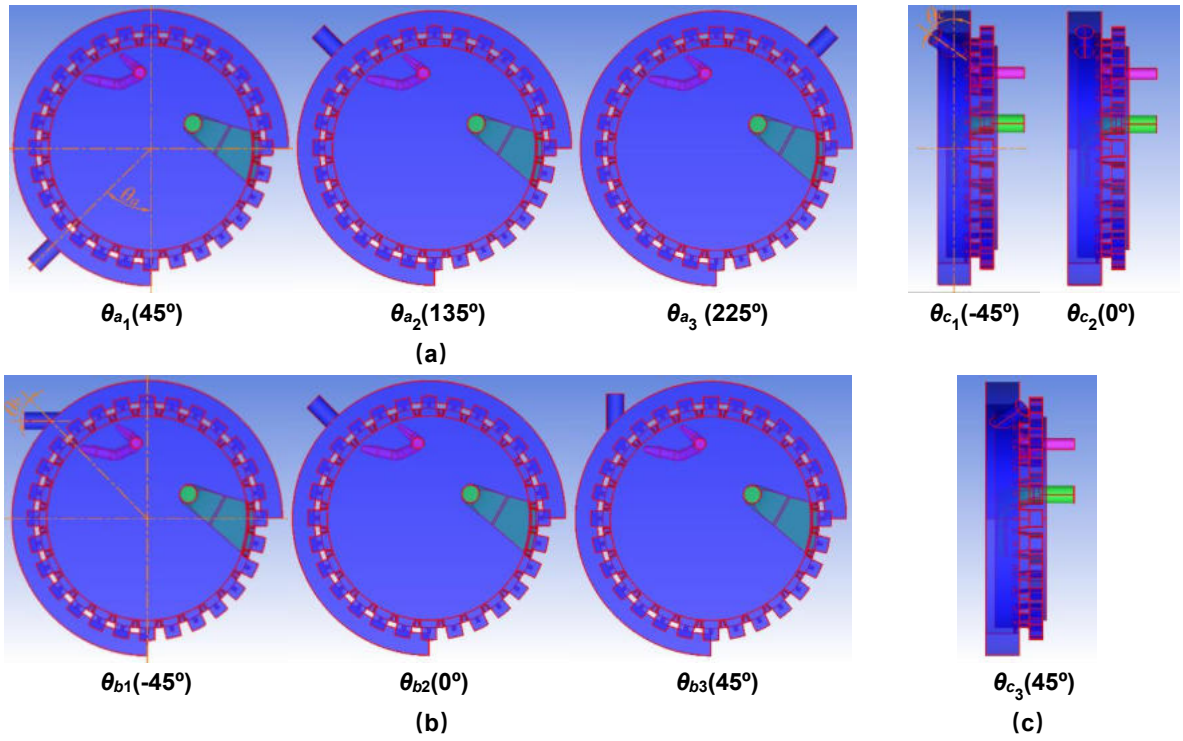


Fig. 4 - Schematic diagram of the angle arrangement of each factor

(a) Position angle, (b) Up and down inclination angle, (c) Front and rear inclination angle

Note: 1. Simulation settings: standard k–ε turbulence model, pressure-based solver, Outlet −3000 Pa, Inlet(s) 0 Pa, dynamic zone rotation speed 30 r/min, residual convergence 10^{-4}, time step 0.003571429 s, 570 steps.

2. Test repeats for 3 times.

(2) Effect of Negative Pressure Air Chamber Width and Thickness on Suction Hole Endface Pressure

The thickness and width of the negative pressure air chamber determine the volume of the air chamber, as shown in Fig. 5, and its influence on the pressure at the suction hole endface can be explored to provide a reference for the optimization of the structural parameters of the seed-metering device. In the simulation test, the air chamber thickness and width were taken as test factors, and the pressure average at the suction hole endface in the seed filling area and pressure standard deviation at the suction hole endface in the seed cleaning and carrying areas were taken as evaluation indexes to carry out a two-factor test.

Based on the actual size of the seed-metering device, the air chamber width b_0 was set at three levels: 22 mm, 26 mm, and 30 mm, while the thickness c_0 was set at 12 mm, 16 mm, and 20 mm. In the flow field model, the position angle, up and down inclination angle, and front and rear inclination angle of the air outlet hole were all set to the optimal levels determined in the previous experiments. All relevant parameters in the Fluent software were kept consistent with the above orthogonal test.

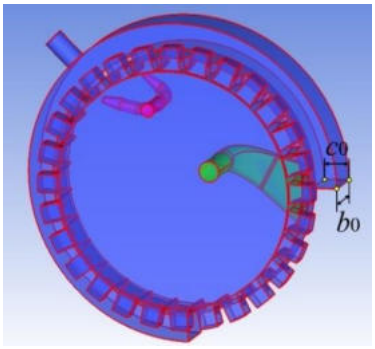


Fig. 5 - Schematic diagram of the width and thickness of the negative pressure air chamber

Note: 1. Simulation settings: standard k–ε turbulence model, pressure-based solver, Outlet −3000 Pa, Inlet(s) 0 Pa, dynamic zone rotation speed 30 r/min, residual convergence 10^{-4}, time step 0.003571429 s, 570 steps. 2. Test repeats for 3 times.

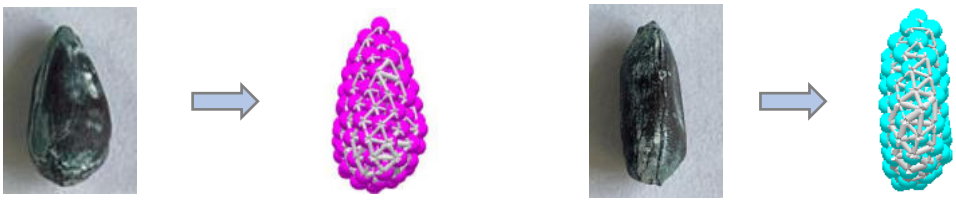
DEM-CFD simulation method for the seed throwing link

In the primary seed throwing area, the cotton seeds adsorbed on the suction hole endface are blown from the filling hole into the collection holes under the airflow action from the seed throwing air nozzle outlet, and then rotated with the seeding plate to the secondary seed throwing area, and finally thrown out through the seed throwing port. The seed throwing air nozzle pressure determines whether cotton seeds can be smoothly blown into the collection hole. To reduce the required air pressure, the seed throwing air nozzle pressure should be selected as low as possible while ensuring the normal operation of the seed-metering device. After cotton seeds fall from the filling hole into the collection hole, collisions between them may cause a certain degree of bouncing. To avoid the impact of bouncing on the seeding performance of seed-metering device, the starting position angle (the angle between the plane formed by the starting edge of the seed throwing port and the center axis of the seeding plate, and the vertical center plane of the seeding plate) of the seed throwing port should be determined to ensure that the seeds have no significant bouncing against the inner wall of the back shell before seed throwing. Since the seeding plate is made of opaque toughness photosensitive resin, and the cotton seeds are coated, the external seed coating agent is easy to adhere to its contact and interfere with the line of sight, so it is not feasible to directly observe the movement of the seeds in the seed throwing area. Therefore, the DEM-CFD gas-solid coupling simulation test method was adopted.

Construction and validation of the cotton seed particle model

EDEM 2018 and ANSYS Fluent 18.0 software were used to perform DEM-CFD gas–solid coupling simulations of the seed-metering device. Bonded particle model (BPM) was adopted to construct cotton seed particles, meaning a single cotton seed consists of several independent fraction particles bonded together. The contact model between fraction particles was set as Hertz-Mindlin with bonding model, and a particle radius of 0.45 mm was chosen. In this study, the E`kangmian-10 cotton seeds (moisture content 11.06% wb, mass of 1000 cotton seeds 94.50 g, length 9.27±0.67 mm, width 5.14±0.37 mm, and thickness 4.50±0.33 mm) were selected as the test material, which can be divided into two categories of ellipsoidal and flat cotton seeds, with the quantity ratio of 22:3, the simulation model being shown in Fig. 6. The ellipsoidal and flat cotton seeds were composed of 146 and 127 fraction particles, respectively. The key components of the seed-metering device were all generated by 3D printing technology with resin materials. Among them, the front shell and seed protection board were made of fully transparent photosensitive resin, while the remaining parts were made of tough photosensitive resin.

Based on previous research and preliminary experiments, the intrinsic material parameters, contact parameters, and main computational parameters used in the coupling simulation are listed in Table 2 *(Hu et al., 2022)*.



(a) **(b)**

Fig. 6 - The physical and simulation particle models of cotton seeds

(a) Ellipsoidal cotton seed, (b) Flat cotton seed

Table 2

DEM-CFD coupling simulation parameters

Program	Parameter	Value
cotton seed	Poisson's ratio	0.14
	Shear modulus/(Pa)	4.01
	Density/(kg/m^3)	917
Tough photosensitive resin	Poisson's ratio	0.42
	Shear modulus/(Pa)	1.04×10^9
	Density/(kg/m^3)	1140
Fully transparent photosensitive resin	Poisson's ratio	0.41
	Shear modulus/(Pa)	9.49×10^8
	Density/(kg/m^3)	1268
cotton seed - cotton seed	Restitution coefficient	0.06
	Static friction coefficient	0.10
	Dynamic friction coefficient	0
cotton seed - Tough photosensitive resin	Restitution coefficient	0.13
	Static friction coefficient	0.33
	Dynamic friction coefficient	0
cotton seed - Fully transparent photosensitive resin	Restitution coefficient	0.12
	Static friction coefficient	0.29
	Dynamic friction coefficient	0
EDEM	Solid time step/(s)	3×10^{-7}
	Gravity acceleration/(m/s^2))	9.81
CFD	Fluid	Air
	Density/(kg/m^3)	1.23
	Fluid time step/(s)	3×10^{-5}

Simulation method

Since the number of particles significantly affects the coupling simulation speed, one ellipsoidal and flat cotton seed was used in the DEM-CFD simulation for calculation, respectively. The seed-throwing pressure was selected as the test factor and set at four levels (500, 1000, 1500, and 2000 Pa) based on pre-tests. The initial contact angle—defined as the angle between the vertical center plane of the seeding plate and the vertical line connecting the center of the bonded particle closest to the vertical center plane with the centerline of the seeding plate at the moment the cotton seed first contacts the inner wall of the back shell—and the stable contact angle—measured when the seed shows no significant rebound after contact—were chosen as evaluation indices. These parameters were then used to conduct the coupling simulation test. Since a higher seeding plate rotational speed reduces the time during which the cotton seed is exposed to the airflow from the seed throwing air nozzle in the primary seed throwing area, making it more difficult for the seed to be smoothly blown into the collection hole, the rotational speed of the seeding plate was set to 35.71 r/min (corresponding to the designed maximum forward speed of 3.33 m/s (12 km/h)) to ensure the normal operation of the seed-metering device.

The remaining parameters were set as follows: the Inlet_1 and Inlet_2 were set as pressure inlets with the value of 0 Pa, the Outlet was set as pressure outlet with the value of -3000 Pa. The number of time steps was 100,000 and the simulation time was 3 s. The structural parameters of the negative pressure air chamber were set to the optimal combinations determined from the previous airflow field simulation tests.

The DEM-CFD coupling frequency was set to 3×10^{-5} s, the turbulence–particle coupling was set to two-way data transfer, and the Freestream model was adopted as the drag model. Each cotton seed type was simulated 10 times, the mean was used as the evaluation index, and the minimum value was used as the diagnostic indicator.

Seeding performance test method of the seed-metering device

To investigate the working effect of the simulation-optimized seed-metering device under high-speed operation, the seeding performance tests were conducted.

Test equipment

The test equipment consisted of a self-built performance test platform for the seed-metering device. The main components of the device were fabricated by 3D printing and installed on the platform, as shown in Fig. 7. The seed-metering device was driven by a DC motor through a speed reducer. The detection system employed a self-developed seed-metering device performance testing device for medium and large seeds, which mainly consisted of an LED photoelectric sensing system and a pulse recognition monitoring system, enabling real time monitoring and display of the seeding operation status *(Liu et al., 2021)*.

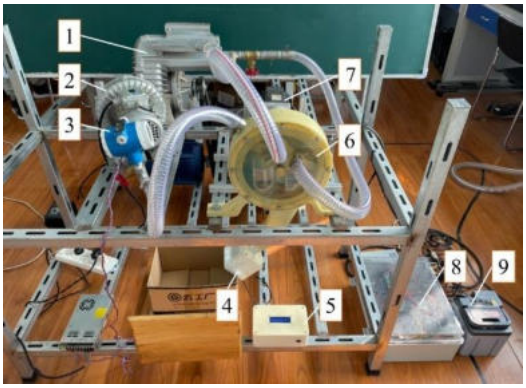


Fig. 7 - Seed-metering device performance test platform

1. Fan Ⅰ; 2. Fan Ⅱ; 3. Pressure gauge; 4. LED photoelectric sensing system; 5. Pulse recognition monitoring system; 6. Seed-metering device; 7. DC motor; 8. Control system; 9. Lithium battery

Test method and evaluation indexes

Referring to GB/T 6973-2005 “Testing Methods of Single Seed Drills (Precision Drills)”, the seed-metering device performance testing device for medium and large seeds continuously detected and recorded the seeding time intervals under stable operation conditions. Every 251 seeds constituted one test group, and each group was repeated 3 times. The qualification index A_1, multiple sowing index D_1 and missed sowing index M_1 were taken as the evaluation indexes, and their calculation formulas were as follows:

$$\begin{cases} A_1 = \dfrac{n_1}{N}\times 100\% \\ D_1 = \dfrac{n_2}{N}\times 100\% \\ M_1 = \dfrac{n_3}{N}\times 100\% \end{cases} \quad (1)$$

where: n_1 is the number of seedings with the seeding time interval between 0.5 and 1.5 times the theoretical value; n_2 is the number of seedings with the seeding time interval less than 0.5 times the theoretical value; n_3 is the number of seedings with the seeding time interval greater than 1.5 times the theoretical value; N is the total number of seedings.

The experimental environmental conditions were a temperature of 25±2℃ and a relative humidity of 50±5%. All experimental runs were randomized.

Test design

Based on previous studies and pre-test, the main factors affecting the seeding performance of the seed-metering device are suction hole diameter, forward speed, and negative pressure. Among them, the conversion formula between forward speed and seeding plate rotational speed was as follows:

$$V_m = \frac{nKI_z}{60} \quad (2)$$

where: V_m is the forward speed, m/s; n is the rotational speed of seeding plate, r/min; K is the number of suction holes, value 28; I_z is the theoretical seed spacing, value 0.2 m.

Therefore, the above three factors were selected as test factors, and the qualification index A_1, multiple sowing index D_1, and missed sowing index M_1 were used as evaluation indexes to conduct the seeding performance tests of the seed-metering device.

(1) A Box-Behnken central combination test was carried out to investigate the effects of each test factor on the evaluation indexes and to determine the optimal parameter combination. According to the pre-test, it was found that the seeding performance was good when the suction hole diameter, forward speed and negative pressure were set to 2.7~3.5 mm, 1.67~3.33 m/s (6.0~12.0 km/h), and 2000~4000 Pa, respectively. Therefore, the levels of each test factor were selected as shown in Table 3. A total of 17 test groups were conducted, with each group repeated 3 times, and the average value was taken as the final evaluation index.

Table 3

The levels of test factors for Box-Behnken test

Levels	Test factors		
	Suction hole diameter X_1 / (mm)	Forward speed X_2 / (m/s)	Negative pressure X_3 / (Pa)
-1	2.7	1.67	2000
0	3.1	2.5	3000
1	3.5	3.33	4000

(2) Based on the optimal parameter combination obtained from the above tests, four levels of 1.67, 2.22, 2.78 and 3.33 m/s (6, 8, 10 and 12 km/h) were selected to carry out the high-speed adaptability test of the seed-metering device with forward speed as the test factor. Each group of tests was repeated 3 times, and the average of the results was taken as the final evaluation index.

RESULTS AND DISCUSSION

Validation of the airflow field model

The pressure registered values at the suction hole endface in both physical and simulation tests are shown in Fig. 8.

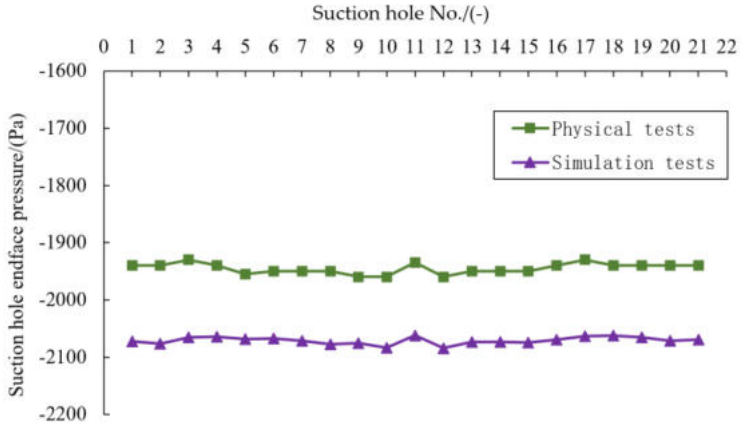


Fig. 8 – Pressure values at the suction hole endface in both physical and simulation tests

Note: 1. Simulation settings: Outlet −3000 Pa, Inlet(s) 0 Pa, dynamic zone rotation speed 0 r/min, residual convergence 10^{-4}, time step 0.003571429 s, 500 steps.
2. Test repeats for 3 times.

As can be seen from Fig. 8, the absolute values of the pressure at the suction hole endface in the physical tests were lower than the simulation values, which was mainly due to the airflow loss caused by the gap between the seeding plate and back shell. Since the seeding plate and the back shell were in axial linear contact, considering the difficulty of ensuring coaxiality due to the limited precision of 3D printing, a clearance of 0.6 mm was reserved between the back shell and the seeding plate to allow the seeding plate smooth rotation. Therefore, the absolute pressure values measured in the physical tests were all lower than those obtained from the simulation tests, but the relative errors between them were all less than 7.04%, indicating that the airflow field model was suitable for the subsequent simulation analysis of the seed-metering device.

Simulation analysis results

CFD simulation results *for the negative pressure air chamber*

Effect of Air Outlet Hole Angle and Position on the Suction Hole Endface Pressure

The design and results of the orthogonal test on the air outlet hole angle and position of the negative pressure air chamber are shown in Table 4, and the results of extreme difference analysis are shown in Table 5. As shown in the table, the factors influencing the pressure average at the suction hole endface in the seed filling area ranked in the following order: front and rear inclination angle θ_c, up and down inclination angle θ_b and position angle θ_a, and for this evaluation index, the optimal combination was $\theta_{c_2}\theta_{b_2}\theta_{a_1}$. The factors influencing the pressure standard deviation at the suction hole endface in the seed cleaning and carrying areas ranked in the following order: position angle θ_a, front and rear inclination angle θ_c and up and down inclination angle θ_b, and for this evaluation index, the optimal combination was $\theta_{a_2}\theta_{c_2}\theta_{b_2}$. Therefore, it can be concluded that the up and down inclination angle should be set to level θ_{b_2}, and the front and rear inclination angle should be set to level θ_{c_2}. However, the optimal value for the position angle remains uncertain and requires further determination through analysis of variance.

Table 4

Orthogonal test design and results

Test serial number	Test factors			Evaluation indexes	
	θ_a	θ_b	θ_c	Pressure average at the suction hole endface in the seed filling area Y_1/(Pa)	Pressure standard deviation at the suction hole endface in the seed cleaning and carrying areas Y_2/(Pa)
1	1	1	1	1207.69	81.11
2	1	2	2	1354.77	70.72
3	1	3	3	1077.77	90.99
4	2	2	3	1145.55	30.06
5	2	3	1	1206.23	31.07
6	2	1	2	1164.85	29.31
7	3	3	2	1190.64	101.31
8	3	1	3	1055.01	113.00
9	3	2	1	1275.71	91.20

Note: 1. Simulation settings: Outlet −3000 Pa, Inlet(s) 0 Pa, dynamic zone rotation speed 30 r/min, time step 0.003571429 s, 570 steps. 2. Test repeats for 3 times.

Table 5

Extreme difference analysis of orthogonal test results

Evaluation indexes	Test factors	Factor levels averages			Maximum difference/(Pa)	Optimal parameter combination
		Level 1/(Pa)	Level 2/(Pa)	Level 3/(Pa)		
Pressure average at the suction hole endface in the seed filling area Y_1/(Pa)	θ_a	1213.41	1172.21	1173.79	41.20	$\theta_{c_2}\theta_{b_2}\theta_{a_1}$
	θ_b	1142.52	1258.68	1158.21	116.16	
	θ_c	1229.88	1236.75	1092.78	143.97	
Pressure standard deviation at the suction hole endface in the seed cleaning and carrying areas Y_2/(Pa)	θ_a	80.94	30.15	101.84	71.69	$\theta_{a_2}\theta_{c_2}\theta_{b_2}$
	θ_b	74.47	63.99	74.46	10.48	
	θ_c	67.79	67.11	78.02	10.91	

Note: 1. Simulation settings: Outlet −3000 Pa, Inlet(s) 0 Pa, dynamic zone rotation speed 30 r/min, time step 0.003571429 s, 570 steps. 2. Test repeats for 3 times.

The results of variance analysis are shown in Table 6. As can be seen from the table, for the pressure average at the suction hole endface in the seed filling area, the front and rear inclination angle had a significant effect on it, and the remaining two factors have no significant effect. For the pressure standard deviation at the suction hole endface in the seed cleaning and carrying areas, all the test factors had a highly significant effect, which was consistent with the results of the extreme difference analysis. Among the three test factors, the position angle had no significant effect on the pressure average at the suction hole endface in the seed filling area, with a contribution rate of 4.78%. However, it had a highly significant effect on the pressure standard deviation at the suction hole endface in the seed cleaning and carrying areas, with a contribution rate as high as 94.83%. Therefore, the selection of the position angle should be primarily based on the pressure standard deviation. Combined with the results of the extreme difference analysis, the optimal level for the air outlet position angle was determined to be θ_{a_2}. Since the factor combination $\theta_{a_2}\theta_{b_2}\theta_{c_2}$ was not included in the orthogonal test design, a simulation verification test was conducted for the airflow field model under this combination using the same method. After the simulation, statistical analysis showed that the pressure average at the suction hole endface in the seed filling area was 1257.64 Pa, which was lower than that of groups 2 and 9 in the orthogonal test, with a maximum pressure difference of 97.13 Pa. The pressure standard deviation at the suction hole endface in the seed cleaning and carrying areas was 8.92 Pa, which was lower than all standard deviations in the orthogonal test. This indicated that when the air outlet was located in the central plane of the negative pressure air chamber, the pressure at the suction hole endface in the seed filling area was not the highest, but the pressure variation in the seed cleaning and seed carrying areas was minimized, resulting in the most stable cotton seed adsorption. Since increasing pressure at the suction hole endface in the seed filling area can be achieved by adjusting the air outlet negative pressure, while reducing the pressure standard deviation at the suction hole endface in the seed cleaning and carrying areas was difficult to accomplish through changing external parameters, the optimal combination of air outlet angle and position was determined to be $\theta_{a_2}\theta_{b_2}\theta_{c_2}$, namely, the position angle of 135°, up and down inclination angle of 0°, front and rear inclination angle of 0°.

Table 6

Variance analysis of orthogonal test results

Source of variation	Pressure average at the suction hole endface in the seed filling area				Pressure standard deviation at the suction hole endface in the seed cleaning and carrying areas			
	Sum of squares	Degree of freedom	*F*-value	Contribution /(%)	Sum of squares	Degree of freedom	*F*-value	Contribution /(%)
θ_a	3269.93	2	1.91	4.78	8156.42	2	4301.73**	94.83
θ_b	23832.41	2	13.93	34.85	219.28	2	115.65**	2.55
θ_c	39572.98	2	23.13*	57.87	223.89	2	118.08**	2.60
Error	1710.77	2		2.50	1.90	2		0.02
Cor total	68386.09	8			8601.49	8		

*Note: 1. Simulation settings: Outlet −3000 Pa, Inlet(s) 0 Pa, dynamic zone rotation speed 30 r/min, time step 0.003571429 s, 570 steps; 2. Test repeats for 3 times; 3. * represents the factor with a significant influence on the index, ** represents factor with a highly significant influence on the index.*

Effect of Negative Pressure Air Chamber Width and Thickness on the Suction Hole Endface Pressure

The results of the two-factor test on the negative pressure air chamber width and thickness are shown in Table 7. As observed, with the increase of thickness, the pressure average at the suction hole endface in the seed filling area gradually increased, while the pressure standard deviation at the suction hole endface in the seed cleaning and carrying areas gradually decreased. This was primarily because an increase in thickness enlarged the airflow circulation area within the air chamber. According to fundamental fluid dynamics theory, a smaller airflow circulation area results in greater resistance losses. Therefore, increasing the thickness of the negative pressure air chamber was conducive to reducing airflow losses and promoting the uniform distribution of suction hole endface pressure. As the width increased, the trend of the average pressure at the suction hole endface in the seed-filling area was not obvious, with only small differences observed, while the pressure standard deviation at the suction hole endface in the seed-cleaning and seed-carrying areas gradually decreased. The main reason is that the suction holes are located along the width of the air chamber, and their diameter is much smaller than the chamber width. Thus, airflow in this direction remained smooth. Consequently, width changes had little effect on the average pressure at the suction hole endface in the seed-filling area, whereas the increased circulation area promoted a more uniform pressure distribution. The results of variance analysis are shown in Table 8.

As can be seen from the table, thickness had a greater influence than width on both the pressure average at the suction hole endface in the seed filling area and the standard deviation in the seed cleaning and carrying areas, which was consistent with the above analysis. In order to obtain a higher pressure average at the suction hole endface in the seed filling area and a lower pressure standard deviation at the suction hole endface in the seed cleaning and carrying areas, the width and thickness of the negative pressure air chamber were selected as 30 mm and 20 mm, respectively.

Table 7

Two-factor test results

Thickness c_0/(mm) / Width b_0/(mm)	Pressure average at the suction hole endface in the seed filling area Y_1/(Pa)			Pressure standard deviation at the suction hole endface in the seed cleaning and carrying areas Y_2/(Pa)		
	12	16	20	12	16	20
22	1229.35	1248.70	1254.92	52.02	22.48	21.16
26	1233.53	1249.32	1257.01	25.22	11.13	10.93
30	1238.97	1246.61	1257.64	23.78	10.65	8.92

Note: 1. Simulation settings: Outlet −3000 Pa, Inlet(s) 0 Pa, dynamic zone rotation speed 30 r/min, time step 0.003571429 s, 570 steps; 2. Test repeats for 3 times.

Table 8

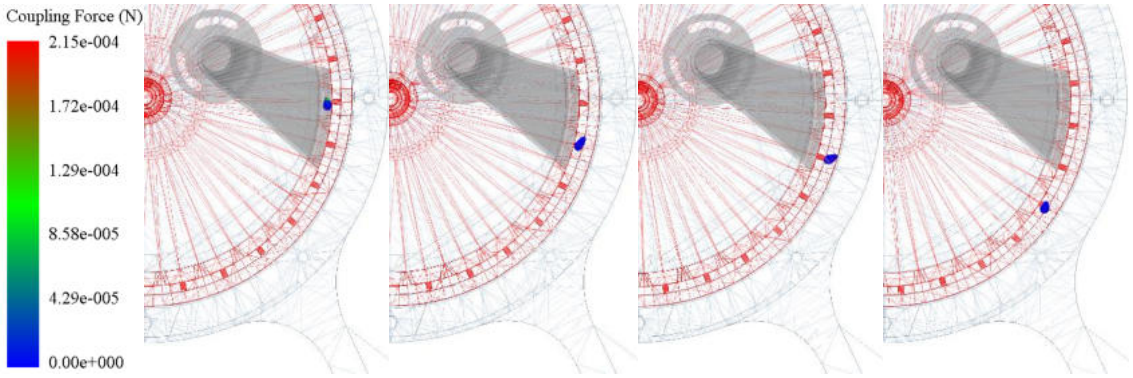
Variance analysis of two-factor test results

Source of variation	Pressure average at the suction hole endface in the seed filling area				Pressure standard deviation at the suction hole endface in the seed cleaning and carrying areas			
	Sum of squares	Degree of freedom	*F*-value	Contribution /(%)	Sum of squares	Degree of freedom	*F*-value	Contribution /(%)
b_0	18.20	2	1.00	2.18	565.82	2	9.76*	39.26
c_0	782.01	2	42.94**	93.47	759.27	2	13.10*	52.69
Error	36.43	4		4.35	115.96	4		8.05
Cor Total	836.64	8			1441.05	8		

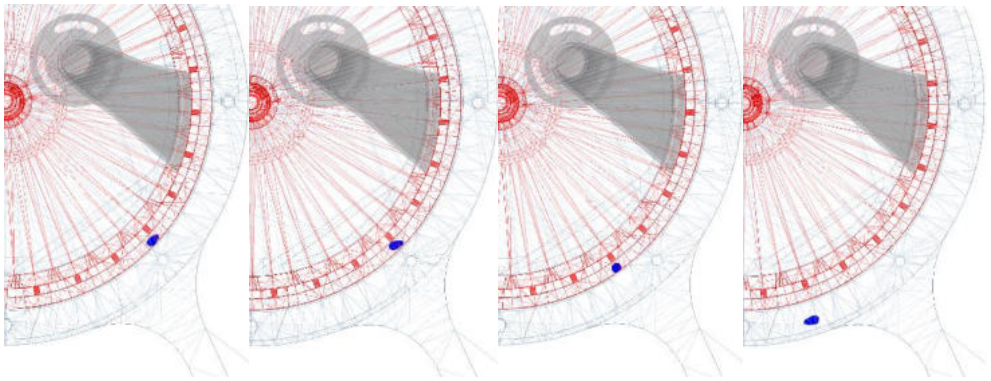
Note: 1. Simulation settings: Outlet −3000 Pa, Inlet(s) 0 Pa, dynamic zone rotation speed 30 r/min, time step 0.003571429 s, 570 steps; 2. Test repeats for 3 times.

DEM-CFD coupling simulation results for the seed throwing link

The single cotton seed throwing process is shown in Fig. 9. As illustrated in the figure, when the positive pressure of the seed throwing air nozzle was 1500 Pa, the cotton seed at the suction hole endface was blown into the collection hole under the drag force of the seed throwing air nozzle. At 1.581 s, the seed makes its first contact and collision with the inner wall of the back shell, and was subsequently bounced upward, followed by a second and third collision with the inner wall at 1.695 s and 1.752 s, respectively. After that, the seed no longer exhibited obvious bouncing behavior but instead moved along the inner wall until it was discharged at the seed-throwing port. This simulation phenomenon indicated that, after entering the collection hole, the cotton seed underwent multiple contacts and collisions with the inner wall of the back shell. Therefore, the starting position angle of the seed-throwing port should be set slightly backward to avoid degraded seeding performance caused by seed bouncing.



(a) (b) (c) (d)



(e) (f) (g) (h)

Fig. 9 - Seed throwing process for single cotton seed

(a) 1.506 s, (b) 1.566 s, (c) 1.581 s, (d) 1.656 s, (e) 1.695 s, (f) 1.707 s, (g) 1.752 s, (h) 1.830 s

Note: 1. Simulation settings: Freestream model, Outlet −3000 Pa, Inlet_1 0 Pa, Inlet_2 0 Pa, Inlet_3 1500 Pa, dynamic zone rotation speed 35.71 r/min, solid time step 3×10^{-7} s, fluid time step 3×10^{-5} s, 100000 steps; 2. Test repeats for 10 times.

The DEM–CFD coupling simulation results for the seed-throwing process are presented in Table 9. As shown, when the seed-throwing pressure was 500 Pa, the outlet velocity of the seed-throwing air nozzle was 19.54 m/s, which was insufficient to blow the cotton seed into the collection hole. When the pressure was ≥1000 Pa, seeds were blown smoothly into the collection hole, and with increasing pressure, the nozzle outlet airflow rate also increased, accelerating seed entry. Consequently, the initial contact angle increased gradually, while the stable contact angles were consistently ≥37.23°, although no clear variation pattern was observed. Simulation and post-processing analyses further revealed no obvious regularity in the bouncing behavior of seeds within the collection hole. Based on this analysis, the seed-throwing pressure should be no less than 1000 Pa to ensure smooth seed delivery. However, considering the gap between the seeding plate and the back shell during actual operation, residual adsorption forces may still act on the seeds at the suction-hole end face after leaving the negative-pressure air chamber. Therefore, the seed-throwing pressure should be appropriately increased, and in this study, a value of 1500 Pa was selected. In addition, to minimize the bouncing of seeds in the collection hole and avoid adverse effects on seeding performance, the starting position angle of the seed-throwing port should be smaller than the minimum stable contact angle of the seeds (37.23°). Accordingly, an angle of 30° was adopted.

Table 9

Simulation test results of seed throwing link

Seed throwing pressure/(Pa)	Outlet velocity of seed throwing air nozzle/(m/s)	Initial contact angle / (°)	Initial contact angle minimum / (°)	Stable contact angle /(°)	Stable contact angle minimum / (°)
500	19.54				
1000	27.85	69.23±1.82	67.1	41.03±1.95	38.03
1500	34.29	75.37±1.43	72.18	39.87±1.46	37.23
2000	39.65	77.84±1.56	75.17	40.26±1.52	37.77

Note: 1. Simulation settings: Freestream model, Outlet −3000 Pa, Inlet_1 0 Pa, Inlet_2 0 Pa, Inlet_3 1500 Pa, dynamic zone rotation speed 35.71 r/min, solid time step 3×10^{-7} s, fluid time step 3×10^{-5} s, 100000 steps; 2. Test repeats for 10 times.

Seeding performance test results of the seed-metering device

Box-Behnken Test

The protocol and results of the Box-Behnken test are shown in Table 10.

Table 10

Box-Behnken test protocol and results

Test serial number	Test factors			Evaluation indexes		
	X_1	X_2	X_3	Qualification index A_1/(%)	Multiple sowing index D_1/(%)	Missed sowing index M_1/(%)
1	-1	-1	0	90.25	3.32	6.43
2	-1	0	-1	81.38	1.06	17.56
3	-1	0	1	91.36	2.78	5.86
4	-1	1	0	88.64	3.69	7.67
5	0	-1	-1	86.78	2.69	10.53
6	0	-1	1	89.46	6.15	4.39

Test serial number	Test factors			Evaluation indexes		
	X_1	X_2	X_3	Qualification index A_1/(%)	Multiple sowing index D_1/(%)	Missed sowing index M_1/(%)
7	0	0	0	97.19	1.19	1.62
8	0	0	0	96.54	1.85	1.61
9	0	0	0	95.93	1.59	2.48
10	0	0	0	94.26	2.53	3.21
11	0	0	0	96.88	1.70	1.42
12	0	1	-1	77.00	4.43	18.57
13	0	1	1	86.98	6.29	6.73
14	1	-1	0	91.13	5.65	3.22
15	1	0	-1	86.92	2.74	10.34
16	1	0	1	88.93	8.52	2.55
17	1	1	0	88.17	6.18	5.65

Note: 1. Air outlet hole position angle 135°, up and down inclination angle 0° and front and rear inclination angle 0°; air chamber thickness 20 mm and width 30 mm; seed throwing pressure 1500 Pa, seed throwing port starting position angle 30°; 2. Test repeats for 3 times.

In order to further analyze the significance of the effect of each test factor and its interaction on the evaluation indexes, Design-Expert 10.0.4 was used to carry out a multiple regression analysis on the test results and establish a quadratic regression model between the test factors and evaluation indexes. The significance analysis results are shown in Table 11. As can be seen from the table, the regression models were all highly significant (P≤0.01) and the lack of fit were all insignificant (P>0.05), so the regression equations were well fitted to the test data. For the qualification index, the linear terms X_2, X_3 and quadratic term X_2^2, X_3^2 had a highly significant effect on it (P≤0.01), interaction term X_1X_3, X_2X_3 and quadratic term X_1^2 had a significant effect on it (0.01<P≤0.05), and the remaining terms had no significant effect on it (P>0.05). For the multiple sowing index, the linear terms X_1, X_3 and quadratic term X_2^2, X_3^2 had a highly significant effect on it (P≤0.01), interaction term X_1X_3 and quadratic term X_1^2 had a significant effect on it (0.01<P≤0.05), and the remaining terms had no significant effect on it (P>0.05). For the missed sowing index, all the linear terms and quadratic term X_2^2, X_3^2 had a highly significant effect on it (P≤0.01) and the remaining terms had no significant effect on it (P>0.05). Moreover, the order of test factors affecting the qualification index was: negative pressure>forward speed>suction hole diameter. And the order of test factors affecting the multiple sowing index and missed sowing index was: negative pressure>suction hole diameter>forward speed. The quadratic regression equations between the test factors and evaluation indexes are as follows:

$$A_1 = 96.16 + 0.44X_1 - 2.10X_2 + 3.08X_3 - 0.34X_1X_2 - 1.99X_1X_3 + 1.83X_2X_3 - 2.26X_1^2 - 4.35X_2^2 - 6.75X_3^2 \quad (3)$$

$$D_1 = 1.77 + 1.53X_1 + 0.35X_2 + 1.6X_3 + 0.04X_1X_2 + 1.01X_1X_3 - 0.4X_2X_3 + 0.91X_1^2 + 2.03X_2^2 + 1.09X_3^2 \quad (4)$$

$$M_1 = 2.07 - 1.97X_1 + 1.76X_2 - 4.68X_3 + 0.3X_1X_2 + 0.98X_1X_3 - 1.42X_2X_3 + 1.35X_1^2 + 2.33X_2^2 + 5.66X_3^2 \quad (5)$$

where:

X_1, X_2 and X_3 represent the coded levels (−1, 0, +1), and the coding of actual factor levels is shown in Table 3.

Table 11

Variance analysis of Box-Behnken test results

Source of variation	Qualification index			Multiple sowing index			Missed sowing index		
	Sum of squares	F-value	P-value	Sum of squares	F-value	P-value	Sum of squares	F-value	P-value
Model	463.19	26.21	0.0001**	73.34	22.66	0.0002**	421.13	27.93	0.0001**
X_1	1.55	0.79	0.4040	18.73	52.09	0.0002**	31.05	18.53	0.0035**
X_2	35.41	18.03	0.0038**	0.97	2.69	0.1452	24.68	14.73	0.0064**
X_3	75.95	38.68	0.0004**	20.54	57.14	0.0001**	175.50	104.74	<0.0001**
X_1X_2	0.46	0.23	0.6447	0.01	0.018	0.8976	0.35	0.21	0.6597
X_1X_3	15.88	8.09	0.0249*	4.12	11.46	0.0117*	3.82	2.28	0.1747
X_2X_3	13.32	6.78	0.0352*	0.64	1.78	0.2239	8.12	4.85	0.0636
X_1^2	21.51	10.95	0.0130*	3.50	9.73	0.0169*	7.66	4.57	0.0699
X_2^2	79.77	40.62	0.0004**	17.29	48.09	0.0002**	22.78	13.60	0.0078**
X_3^2	191.98	97.77	<0.0001**	5.02	13.95	0.0073**	134.93	80.53	<0.0001**
Residual	13.75			2.52			11.73		

Source of variation	Qualification index			Multiple sowing index			Missed sowing index		
	Sum of squares	*F*-value	*P*-value	Sum of squares	*F*-value	*P*-value	Sum of squares	*F*-value	*P*-value
Lack of Fit	8.36	2.07	0.2470	1.56	2.17	0.2341	9.42	5.45	0.0674
Pure Error	5.39			0.96			2.31		
Cor Total	476.93			75.86			432.86		

*Note: 1. Air outlet hole position angle 135°, up and down inclination angle 0° and front and rear inclination angle 0°; air chamber thickness 20 mm and width 30 mm; seed throwing pressure 1500 Pa, seed throwing port starting position angle 30°; 2. Test repeats for 3 times; 3. P ≤ 0.01 (Highly significant, **); 0.01 < P ≤ 0.05 (Significant, *).*

So as to obtain the best combination of test factors, taking the maximum qualification index and the minimum multiple and missed sowing index as the final optimization objective, combined with the boundary conditions of each test factor, the established quadratic regression models were solved by multi-factor optimization.

The objective functions and constraints are as follows:

$$\begin{cases} \max A_1(x_1, x_2, x_3) \\ \min D_1(x_1, x_2, x_3) \\ \min M_1(x_1, x_2, x_3) \\ s.t. \begin{cases} 2.7\ mm \le x_1 \le 3.5\ mm \\ 1.67\ m/s \le x_2 \le 3.33\ m/s \\ 2000\ Pa \le x_3 \le 4000\ Pa \end{cases} \end{cases} \quad (6)$$

Using the optimization module of Design-Expert 10.0.4, the best combination of parameters was determined to be: suction hole diameter of 3.1 mm, forward speed of 2.33 m/s (8.4 km/h), and negative pressure of 3178 Pa. Under these conditions, the seeding performance was optimal, with a qualification index of 96.67%, multiple sowing index of 2.04%, and missed sowing index of 1.29%. To verify the reliability of the optimized parameters, the seeding performance test of seed-metering device was conducted for three repetitions. The average values of the evaluation indexes were as follows: qualification index of 96.25%, multiple sowing index of 1.83%, and missed sowing index of 1.92%, which were generally consistent with the predicted values from the software.

High-speed Adaptability Test

The high-speed adaptability test results of the inside-filling pneumatic cotton high-speed precision seed-metering device are shown in Table 12. As shown in the table, with increasing forward speed, the qualification index first increased and then decreased, the multiple sowing index first decreased and then increased, while the missed sowing index gradually increased, which was consistent with the previous analysis. When the forward speed ranged from 1.67 to 3.33 m/s (6–12 km/h), the qualification index exceeded 91%, and both the multiple sowing index and the missed sowing index remained below 5%. These values were superior to the agronomic requirements specified in JB/T 10293-2013 'Specifications for Single Seed Drills (Precision Drills),' which require a qualification index ≥75%, a multiple sowing index ≤20%, and a missed sowing index ≤10%. This indicates that the optimized seed-metering device meets the high-speed sowing requirements for cotton.

Table 12

High-speed adaptability test results

Forward speed/(m/s)	Qualification index/(%)	Multiple sowing index/(%)	Missed sowing index/(%)
1.67	94.34	3.98	1.68
2.22	95.66	2.61	1.73
2.33	96.25	1.83	1.92
2.78	94.81	2.75	2.44
3.33	91.43	4.55	4.02

Note: 1. Air outlet hole position angle 135°, up and down inclination angle 0° and front and rear inclination angle 0°; air chamber thickness 20 mm and width 30 mm; seed throwing pressure 1500 Pa, seed throwing port starting position angle 30°; 2. Test repeats for 3 times.

CONCLUSIONS

(1) The CFD simulation results of the negative-pressure air chamber showed that, in the orthogonal test of air outlet hole angle and position, the order of influence on the average pressure at the suction hole end face in the seed-filling area was: front–rear inclination angle > vertical inclination angle > position angle. For the pressure standard deviation in the seed-cleaning and seed-carrying areas, the order was: position angle > front–rear inclination angle > vertical inclination angle. The optimal parameter combination was a position angle of 135°, a vertical inclination angle of 0°, and a front–rear inclination angle of 0°. In the two-factor test of chamber thickness and width, thickness had a greater effect than width on both the average pressure in the seed-filling area and the standard deviation in the seed-cleaning and seed-carrying areas, with the optimal combination being a thickness of 20 mm and a width of 30 mm.

(2) The DEM–CFD simulation results of the seed-throwing process showed that, after falling into the collection hole, cotton seeds underwent multiple collisions with the inner wall of the back shell before moving along it. At a seed-throwing pressure of 1500 Pa, the seeds could be smoothly blown into the collection hole. Setting the starting position angle of the seed-throwing port to 30° reduced the adverse effects of seed bouncing within the collection hole on the seed-throwing performance.

(3) The results of the Box–Behnken test indicated that the factors influencing the qualification index ranked in the following order: negative pressure > forward speed > suction hole diameter. For the multiple sowing index and missed sowing index, the order was: negative pressure > suction hole diameter > forward speed. The optimal parameter combination was a suction hole diameter of 3.1 mm, a forward speed of 2.33 m/s (8.4 km/h), and a negative pressure of 3178 Pa. Bench tests verified the corresponding evaluation indexes, yielding a qualification index of 96.25%, a multiple sowing index of 1.83%, and a missed sowing index of 1.92%.

(4) The results of the high-speed adaptability test showed that, as forward speed increased, the qualification index first increased and then decreased, the multiple sowing index first decreased and then increased, and the missed sowing index gradually increased. When the forward speed was 1.67–3.33 m/s (6–12 km/h), the qualification index remained above 91%, while both the multiple and missed sowing indices were below 5%, thereby meeting the agronomic requirements for high-speed precision cotton seeding.

ACKNOWLEDGEMENT

This study was supported by the Research Funding of Wuhan Polytechnic University (2024RZ081; XQ2025006) and Double First Class School Funding - Discipline Building (01003009).

REFERENCES

[1] Bie, S. & Zhang, J.H. (2018). Cotton green light and simple efficient cultivation technology. 1rd ed., *Hubei Science and Technology Press*, Wuhan, China, pp. 1-2.

[2] Bustos-Gaytán, A., Saldaña-Robles, N., Joya-Cárdenas, D.R., Gutiérrez-Vaca, C., Alfaro-Ayala, J.A., Barco-Burgos, J., & Saldaña-Robles, A. (2025). Advancements in pneumatic seed-metering devices: A review of numerical and experimental approaches. *Results in Engineering*, *26*, 105626. https://doi.org/10.1016/j.rineng.2025.105626

[3] Cao, X.Y., Wang, L., Liao, Q.X., & Liao, Y.T. (2024). Simulation of the mixing component of a horizontal air-assisted centralised wheat metering device. *Biosystems Engineering*, *243*, 13-26. https://doi.org/10.1016/j.biosystemseng.2024.05.002

[4] Cortez, J.W., Anghinoni, M., & Arcoverde, S.N. (2020). Seed metering mechanisms and tractor-seeder forward speed on corn agronomic components. *Engenharia Agrícola*, *40(1)*, 61-68. https://doi.org/10.1590/1809-4430-Eng.Agric.v40n1p61-68/2020

[5] Dong, J., Wu, J., Zhu, Y., & Gao, X. (2025). Investigation on Seed-Filling Effect of Quantitative Precision Filling High-Speed Seed-Metering Device for Maize. *Agriculture*, *15*(14), 1517. https://doi.org/10.3390/agriculture15141517

[6] Gao, X.J., Yu, L.Y., Wu, X.P., Huang, Y.X., & Yan, X.L. (2023). Design and Experiment of Intelligent Seed Supply System of Air-assisted High Speed Precision Maize Seed Metering Device. *Transactions of the Chinese Society for Agricultural Machinery*, *54*(s1), 66-75. https://doi.org/10.6041/j.issn.1000-1298.2023.S1.008

[7] Guzman, L. (2024). *Simulation of Agricultural Air Seeding Systems Using the Discrete Element Method and Computational Fluid Dynamics* [Doctoral dissertation, University of Manitoba]. University of Manitoba's Institutional Repository. http://hdl.handle.net/1993/38061

[8] Guzman, L., Chen, Y., & Landry, H. (2020). Coupled CFD-DEM Simulation of Seed Flow in an Air Seeder Distributor Tube. *Processes*, *8(12)*, 1597. https://doi.org/10.3390/pr8121597

[9] Hu, M.J., Xia, J.F., Zhou, Y., Luo, C.M., Zhou, M.K., & Liu, Z.Y. (2022). Measurement and Calibration of the Discrete Element Parameters of Coated Delinted Cotton Seeds. *Agriculture*, *12*(2), 286. https://doi.org/10.3390/agriculture12020286

[10] Hussain, S., Chen, Y., Yu, X., Farid, M.U., Ghafoor, A., Alshamali, S.J., Munir, T., & Hu, J. (2025). Design Optimization and Aerodynamic Investigations of Air Suction Seed Metering Systems through CFD-DEM Approach. *Smart Agricultural Technology*, *12*, 101082. https://doi.org/10.1016/j.atech.2025.101082

[11] Li, C., Zhang, D.X., Yang, L., Cui, T., He, X.T., Zhang, K.L., Li, Z.M., Li, H.S., Xing, S.L., Dong, J.Q., Jiang, Y.Y., Zhang, X.S., Wu W., & Zhang, C.K. (2025). Design of a streamlined structure to minimize seed damage in high-speed centrifugal seed metering devices. *Powder Technology*, *464*, 121251. https://doi.org/10.1016/j.powtec.2025.121251

[12] Li, M.S., Wang, P., Yan, Y.L., Xie, S.Y., Liu, Z.J., Liu, F.Y., & Chen, X.Z. (2025). Design and experiment of chain-spoon type maize precision seed metering device. *Transactions of the Chinese Society of Agricultural Engineering*, 447-459.

[13] Li, Y.H., Yang, L., Zhang, D.X., Cui, T., Zhang, K.L., Xie, C.J., & Yang, R.M. (2020). Analysis and test of linear seeding process of maize high speed precision metering device with air suction. *Transactions of the Chinese Society of Agricultural Engineering*, *36*(9), 26-35. https://doi.org/10.11975/j.issn.1002-6819.2020.09.003

[14] Li, Y.H., Zhao, S., Yang, L., Song, Q., Li, B.G., & Yang, F.Z. (2024). Design and Test of High-speed Precision Seeder of Independent Fractionated Soybean Double-row Brush. *Transactions of the Chinese Society for Agricultural Machinery*, *55*(06), 101-110. https://doi.org/10.6041/j.issn.1000-1298.2024.06.010

[15] Li, Z.D., He, S., Zhong, J.Y., Han, J.F., Chen, Y.X., & Song, Y. (2021). Parameter optimization and experiment of the disturbance pneumatic plate hole metering device for rapeseed. *Transactions of the Chinese Society of Agricultural Engineering*, *37*(17), 1-11. https://doi.org/10.11975/j.issn.1002-6819.2021.17.001

[16] Liu, Z.Y., Xia, J.F., Hu, M.J., Du, J., Luo, C.M., & Zheng, K. (2021). Design and analysis of a performance monitoring system for a seed metering device based on pulse width recognition. *Plos one*, *16*(12), e0261593. https://doi.org/10.1371/journal.pone.0261593

[17] Pareek, C.M., Tewari, V.K., & Machavaram R. (2023). Multi-objective optimization of seeding performance of a pneumatic precision seed metering device using integrated ANN-MOPSO approach. *Engineering Applications of Artificial Intelligence*, *117*, 105559. https://doi.org/10.1016/j.engappai.2022.105559

[18] Sun, W.S., Yi, S.J., Qi, H.L., Li, Y.F., Dai, Z.B., Zhang, Y.P., Yuan, J.S. & Wang, S. (2025). Design and optimization of air-assisted spiral seed-supply device for high-speed dense planting maize seeder. *INMATEH - Agricultural Engineering*, *75*(1), 13-25. https://doi.org/10.35633/inmateh-75-01

[19] Wan, L., Wang, H.C., Che, G., Sun, W.S., & Chen, Z.F. (2022). Design and performance test of spoiler blades of the direct seed-metering device for rice. *INMATEH - Agricultural Engineering*, *68*(3), 60-70. https://doi.org/10.35633/inmateh-68-06

[20] Wang, W.W., Song, L.Z., An, X., Quan, L.Z., Xie, D.B., Chen, Y.X., Li, Z.D., Wu, Z.C., & Chen, L.Q. (2025). Optimizing seed filling performance of the double-filling air suction maize and soybean seed metering device based on DEM-CFD coupling method. *Computers and Electronics in Agriculture*, *237*, 110586. https://doi.org/10.1016/j.compag.2025.110586

[21] Xu, G.J. (2018). *Design and experiment of pneumatic cylinder array precision seed-metering device for cotton*. [Master dissertation, Shihezi University]. Shihezi University Campus Repository.

[22] Yang, L., Li, Z.M., Zhang, D.X., Li, C., Cui, T., & He, X.T. (2024). Design and test of the T-shaped hole of centrifugal high-speed maize precision seed metering device. *Transactions of the Chinese Society of Agricultural Engineering*, *40*(07), 50-60. https://doi.org/10.11975/j.issn.1002-6819.202312208

[23] Yatskul, A., & Lemiere, J.P. (2018). Establishing the conveying parameters required for the air-seeders. *Biosystems Engineering*, *166*, 1-12. https://doi.org/10.1016/j.biosystemseng.2017.11.001

[24] Zang, Y, Huang, Z.S., Qin, W., He, S.Y., Qian, C., Jiang, Y.C., Tao, W.Y., Zhang, M.L., & Wang, Z.M. (2024). Design of hybrid rice air-suction single-seed metering device. *Transactions of the Chinese*

Society of Agricultural Engineering, *40*(6), 181-191. https://doi.org/10.11975/j.issn.1002-6819.202310212

[25] Zha, X.T., Chen, L., Chen, D.Q., He, Y.P., & Yang, R.B. (2024). Design and Testing of a Branched Air-Chamber Type Pneumatic Seed Metering Device for Rice. *Agriculture*, *14*(11), 1934. https://doi.org/10.3390/agriculture14111934

[26] Zhang, C.Y., Kang, J.M., Peng, Q.J., Zhang, N.N., Wang, X.Y., & Jian, S.C. (2021). Design and Test of Secondary Seed Feeding Mechanism of Air-suction Roller Dibbler for Cotton. *Transactions of the Chinese Society for Agricultural Machinery*, *52*(6), 106-116. https://doi.org/10.6041/j.issn.1000-1298.2021.06.011

[27] Zhang, X.J., Zhang, H.T., Shi, Z.L., Jin, W., Chen, Y., & Yu, Y.L. (2022). Design and experiments of seed pickup status monitoring system for cotton precision dibblers. *Transactions of the Chinese Society of Agricultural Engineering*, *38*(5), 9-19. https://doi.org/10.11975/j.issn.1002-6819.2022.05.002

[28] Zhao, P.F., Gao, X.J., Su, Y., Xu, Y., & Huang, Y.X. (2024). Investigation of Seeding Performance of a Novel High-speed Precision Seed Metering Device Based on Numerical Simulation and High-speed Camera. *Computers and Electronics in Agriculture*, *217*, 108563. https://doi.org/10.1016/j.compag.2023.108563

[29] Zhou, H.J., Zhang, C.L., Liu, T., Wang, Y.Z., Fang, J., & Hu, A.T. (2024). Design and experiment of annular air-blowing assisted seed guiding device for corn no-till seeder. *INMATEH - Agricultural Engineering*, *73*(2),50-62. https://doi.org/10.35633/inmateh-73-04

POINT CLOUD GROUND SEGMENTATION ALGORITHM OF VINEYARD AGRICULTURAL ROBOT BASED ON SURFACE FITTING
/
基于曲面拟合的葡萄园农业机器人点云地面分割算法

Fa SUN, Fanjun MENG, Mengmeng NI, Zhisheng ZHAO, Lili YI
Shandong University of Technology, Collage of Agricultural Engineering and Food Science, Zibo, China
Corresponding author: Lili YI; Tel: +86 18553308656; E-mail: yili0001@sdut.edu.cn
DOI: https://doi.org/10.35633/inmateh-76-06

Keywords: *Vineyard robot, Surface fitting, Ground division, Moving least squares*

ABSTRACT
To address the autonomous navigation and operation requirements of agricultural robots in complex terrain environments of vineyards, this report proposes a point cloud Ground segmentation algorithm based on surface fitting, aiming to solve the problems of reduced segmentation accuracy and insufficient adaptability of traditional planar assumption methods in unstructured terrains such as sloped fields and ridge furrows. The core of the algorithm lies in adopting a point cloud representation method based on a non-uniform polar grid, which dynamically allocates face element sizes according to point cloud density and the width between vineyard ridges, effectively addressing the issues of point cloud sparsity and representability. Subsequently, the moving least square method is used to fit surface models. During the fitting process, strategies such as Gaussian weight function, cosine and sine basis functions, and set of orthogonal functions are introduced to shorten the algorithm's running time and reduce computational complexity. The algorithm's performance is evaluated on the public dataset KITTI and in real-world environments, and compared with algorithms such as RANSAC, GPF, R-GPF, and Patchwork. Experimental results show that the proposed algorithm outperforms other algorithms in both Precision and Recall. In practical environments, the algorithm can accurately and effectively segment complex vineyard environments, meeting the operational requirements of agricultural robots and providing technical support for the advancement of smart agriculture.

摘要
针对葡萄园复杂地形环境下农业机器人自主导航与作业的需求，本文提出了一种基于曲面拟合的点云地面分割算法，旨在解决传统平面假设方法在坡地、垄沟等非结构化地形中存在的分割精度下降与适应性不足的问题。算法的核心在于采用一种基于非均匀极坐标网格的点云表示方法，该方法根据点云密度以及葡萄园垄间宽度动态分配面元大小，有效解决了点云稀疏性和可表示性问题；随后用移动最小二乘法拟合曲面模型，在拟合过程引入高斯型权函数、正余弦基函数，正交函数集的策略，缩短算法运行时间，降低计算复杂度。在公开数据集 KITTI、葡萄园环境中评估算法性能，并于 RANSAC、GPF、R-GPF、Patchwork 等算法进行对比。实验结果表明，本文算法在 Precision 和 Recall 均优于其他算法；葡萄园环境中，该算法能准确、有效的分割葡萄园复杂环境，满足农业机器人的作业需求，为推进智慧农业提供了技术支撑。

INTRODUCTION
Agriculture, as the foundational industry underpinning socio-economic development, holds paramount significance in China—a nation with a millennia-old agrarian civilization. The development of agriculture not only determines national food security and social stability, but also serves as a pivotal driver for economic growth and rural revitalization.

In recent years, autonomous driving technology has been developing rapidly, and its research and application have become a core topic in the field of intelligent transportation systems *(Avcı et al., 2024)*. Driven by multiple factors such as algorithm optimization, hardware upgrading, and data-driven, self-driving vehicles have made significant progress in the key technical aspects of perception *(Cong et al., 2024)*, decision-making *(Wang et al., 2024)* and control *(Vidano et al., 2024)*. As the first step of an autonomous driving system, the accuracy of environment sensing is directly related to the performance and safety of the whole system. Among many sensors, LiDAR has become a key component for autonomous driving environment sensing with its advantages of high accuracy *(Wu et al., 2024)* and long-range measurement *(Bayer et al., 2021)*. Light Detection and Ranging (LiDAR for short) is an active remote sensing technology that utilizes laser pulses to measure distances in order to obtain three-dimensional positional information about the target object and

generate high-precision three-dimensional point cloud data. On this basis, the ground segmentation algorithm employs multi-dimensional feature analysis and deep learning framework to achieve accurate recognition of ground and non-ground points in complex terrain.

In a vineyard environment, the ground can have slopes or weeds, etc., that are more rugged than urban transportation surfaces. Weeds, fallen leaves, and highly reflective objects (metal supports, plastic film) can cause noise in LIDAR scans, and fragmented vegetation makes the ground segmentation unclear, as well as surrounding objects, blocking the fit, conventional ground segmentation algorithms selectively exclude it, and this algorithm is optimized for these characteristics. The main contributions are as follows:

1) Dynamic area optimization, improving the traditional fixed-area selection mode and adjusting the scanning focus according to the vineyard environment: the nearest area and the farthest area, it improves the plant recognition accuracy by 7.3%, reduces the leakage rate to 2%, and can detect obstacles as early as possible to provide safe time for the subsequent path planning.

2) Dual noise reduction technology, incorporating multipath reflection suppression and sensor dynamic compensation, the noise false detection rate is reduced by 78.8% and the terrain detection error is optimized by 61.7% under dense foliage and high temperature environments.

3) Design of fast surface fitting algorithms based on orthogonal basis functions: by replacing the traditional planar model with Legendre orthogonal polynomials and combining circular radial weight functions with matrix-free inverse least squares solving, the computational complexity is reduced from $O(n^3)$ to $O(n^2)$, which ensures the accuracy of complex terrain fitting while shortening the computation time of a single frame to 35ms to meet the real-time demand of 10 Hz for agricultural robots.

MATERIALS AND METHODS

Most of the traditional algorithms are adapted to urban traffic surfaces, and the orchard environment is relatively more complex. The ground segmentation algorithm proposed in this paper is based on concentric zone model (CZM), and several key modules are set up to realize the extraction of ground information from radar point cloud. CZM utilizes a uniform polar grid representation to divide the point cloud into multiple fan-ring regions with regularity and orientation, and the density of each region can be set by adjusting the parameters. Key modules include Reflected Noise Removal (S-RNR), Vertical Interference Removal (S-VIE), Sub-Regional Partitioning (SRP), Surface Model Fitting (S-SSF), Adaptive Thresholding (ATS), and Temporal Ground Recovery (TGR).

The overall framework is shown in Figure 1, and the following paragraphs highlight the definitions and rationale for the core modules.

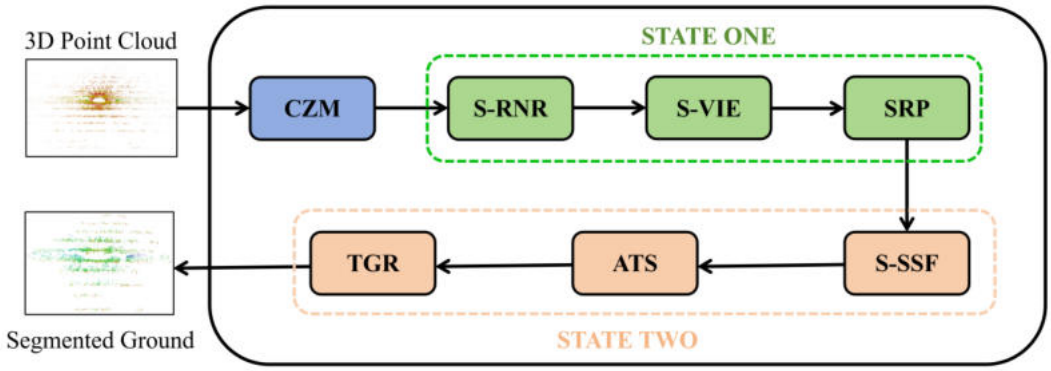


Fig. 1 - Module Flowchart

Concentric Zone Model (CZM)

When dealing with point cloud data of complex terrain, especially vineyard pavements, most of the traditional algorithms designed for flat urban pavements rely on fixed strategies such as adaptive binning and quadratic distributions and assume locally flat ground to simplify the computation. However, the ground is usually not flat and the density of the point cloud data varies with distance, which leads to under- or over-segmentation problems when conventional methods are ineffective in dealing with sparse and under-represented point clouds.

In response to these problems, a uniform polar grid model is proposed, which divides the point cloud collection into multiple sector-ring regions by radial distance and azimuth. However, there are two main problems with this method: the fan ring area near the center is small and has a sparse number of points, while the area away from the center is similarly underpopulated due to a sparse point cloud, both of which affect the accuracy of the ground plane fitting.

To overcome these limitations, the CZM was used. The model parametrically adjusts the density of the sector ring region in each ring band, taking into account the problem of LIDAR being dense in the near and sparse in the far, ensuring that the ring bands have a reasonable number of sector rings regardless of the distance from the center. The model is defined as follows:

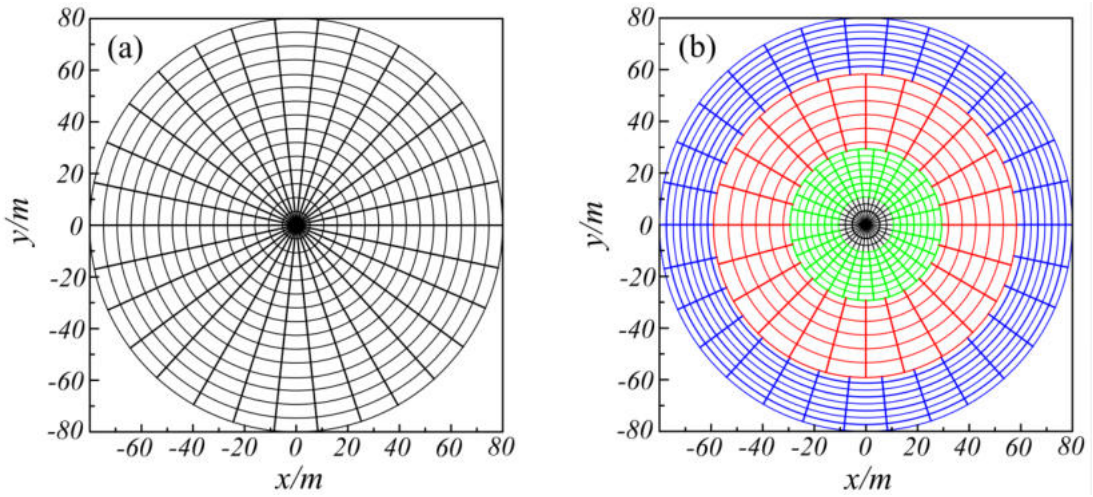


Fig. 2 - (a)Tradition modeling method; (b)concentric zone model

Compared with the traditional model definition Fig. 2(a), Fig. 2(b) is more applicable to the orchard environment by detailing the distant sparse point cloud and the point cloud in the vicinity of the LiDAR, the former confirms that obstacles can be detected in advance for subsequent path planning, while the latter detects obstacles at close range.

Reflected Noise Removal (S-RNR)

The presence of highly reflective objects (metal brackets, plastic films), radius effects (e.g., multiple reflections from plant leaves), and sensor noise in the vineyard point cloud collection can generate noise, these noise points can significantly affect the reliability of the fitted ground plane. Noise points also occur below the ground plane, as shown in Figure 3.

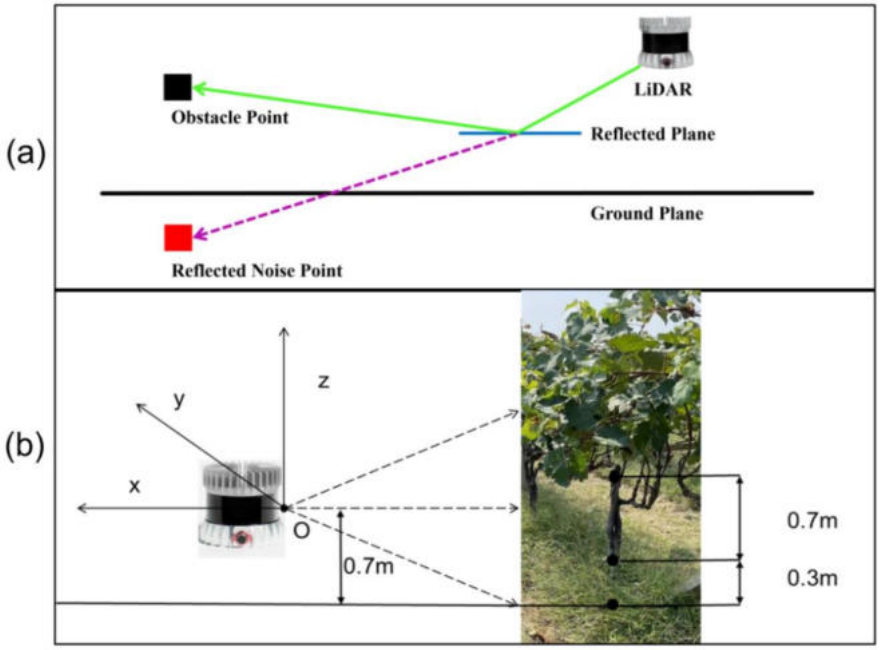


Fig. 3 - (a)Point Cloud Reflection Noise Schematic Diagram; (b)LiDAR Position Schematic Diagram

As shown in the figure, the height of the LIDAR mounted on the wheeled robot is 0.7 m. Let the height threshold be h, with the point O as the origin and the positive direction of the z-axis. Let the height of the point x in the vineyard LiDAR point cloud be z_x, then the equation of the non-ground point will be:

$$z_x > h \tag{1}$$

According to the actual measurement, the weed height of standardized planting vineyard is about 0.3 m, then the threshold is -0.4, then the vineyard LiDAR point cloud can be left when the height is greater than -0.4, otherwise it is separated as a ground point.

In order to solve the noise point problem, the algorithm employs the Regional Reflected Noise Removal (R-RNR) module and introduces the introduction of multipath effect suppression and sensor noise compensation. R-RNR performs reflection noise removal for each sector-ring region separately, searching for all points in the point cloud below a specified height one by one, and identifying points with reflection intensity below a threshold as reflection noise points. Multipath effect suppression establishes a three-frame sliding window that rejects transient points (e.g., vignette points from blade jitter) that persist for <0.3 seconds:

$$\mathrm{P_{valid}} = \{\mathrm{p_i} \mid \sum_{\mathrm{t=1}}^{3} \mathrm{I}\,(\mathrm{p_i} \in \mathrm{F_t}) \geq 2\} \tag{2}$$

Where $\mathrm{F_t}$ denotes the t-th frame point cloud, the suspected multipath point is detected by reverse ray detection, and if there is an occluder (e.g., a leaf point cloud) on the path from the sensor to the point, it is determined as a fictitious point and rejected. Sensor noise compensation, on the other hand, is applied by applying a nonlinear compensation model through a temperature sensor that collects the ambient temperature T in real time:

$$\mathrm{I_{corrected}} = \mathrm{I_{raw}} - \mathrm{k_1 e^{k_2 T}} \tag{3}$$

where $\mathrm{k_1}$=0.03 and $\mathrm{k_2}$=0.12 are the calibration parameters. And the point cloud motion compensation model was constructed by combining the IMU data, and the extended Kalman filter (EKF) was used to estimate the real spatial coordinates of each point:

$$\hat{\mathrm{x}}_\mathrm{t} = \mathrm{x_{meas}} - \int_{\mathrm{t-\Delta t}}^{\mathrm{t}} \mathrm{v}(\tau)\mathrm{d}\tau \tag{4}$$

where $\mathrm{v}(\tau)$ is the instantaneous speed of the agricultural vehicle.

Surface model fitting (S-SSF)

Moving least squares provides an effective polynomial approximation strategy for high-precision surface fitting of scattered point clouds, centered on minimizing the sum of squared node errors. When applied to LiDAR point cloud data, it generates smooth and close fitting surfaces. However, facing the huge amount of point cloud data, the traditional methods have high computational complexity. For this reason, the fast moving least squares method is used to simplify the coefficient matrix solution using weighted orthogonal functions (considering only diagonal elements and avoiding inverse), which significantly improves the computational efficiency and meets the real-time demand of automatic driving while ensuring the accuracy.

The fitting function is expressed as:

$$\boldsymbol{f}(\mathbf{x},\mathbf{y}) = \sum_{\mathbf{i=1}}^{\mathbf{m}} \boldsymbol{\alpha_i}\,(\mathbf{x},\mathbf{y})\mathbf{p_i}(\mathbf{x},\mathbf{y}) = \mathbf{p^T}(\mathbf{x},\mathbf{y})\boldsymbol{\alpha}(\mathbf{x},\mathbf{y}) \tag{5}$$

It can be simplified as follows:

$$f(\mathrm{t}) = \sum_{\mathrm{i=1}}^{\mathrm{m}} \alpha_\mathrm{i}\,(\mathrm{t})\mathrm{p_i}(\mathrm{t}) = \mathrm{p^T}(\mathrm{t})\alpha(\mathrm{t}) \tag{6}$$

where $\mathrm{t}=(\mathrm{x},\mathrm{y})$ and the coordinates t as a function of:

$$\alpha(t) = [\alpha_1(\mathrm{t}), \alpha_2(\mathrm{t}), \ldots\ldots, \alpha_\mathrm{m}(\mathrm{t})]^T \tag{7}$$

The basis function is a complete polynomial of order k and m is the number of terms in the product function:

$$\mathrm{p}(\mathrm{t}) = [\mathrm{p_1}(\mathrm{t}), \mathrm{p_2}(\mathrm{t}), \ldots\ldots, \mathrm{p_m}(\mathrm{t})]^\mathrm{T} \tag{8}$$

For surface fitting, a two-dimensional basis function is required, and the basis function $\mathrm{p}(\mathrm{t})$ takes the form:

Linear base: $\mathrm{p}(\mathrm{t}) = [1, \mathrm{x}, \mathrm{y}]^\mathrm{T}$

Secondary base: $p(t) = [1, x, y, x^2, xy, y^2]^T$

In the moving least squares approximation, the coefficient is determined by minimizing the weighted sum of squares of the errors of the nodes of the approximation function in a neighborhood of point x:

$$J = \sum_{I=1}^{n} w(x)[f(t) - Z_I]^2 = \sum_{I=1}^{n} w(x)[\sum_{i=1}^{m} p(t_I)\alpha(t_I) - Z_I]^2 \quad (9)$$

where n is the number of nodes affected in the neighborhood of x, Z_I is the value of the node at $t = t_I$, and $x = t - t_I$ is the difference between the two points, $t\text{-}t_I = \sqrt{(x - x_I)^2 + (y - y_I)^2}$, $w(x) = w(t\text{-}t_I)$ is the weight function of node t_I.

When the above equation equals zero, J reaches a minimum value and hence the following can be obtained:

$$\sum_{I=1}^{n} w(x)[\sum_{i=1}^{m} p(t_I)\alpha(t_I) - Z_I]^2 = 0 \quad (10)$$

$$\sum_{I=1}^{n} w(x) \sum_{i=1}^{m} p(t_I)\alpha(t_I) = \sum_{I=1}^{n} w(x) * Z_I \quad (11)$$

$h(x)$ and $g(x)$ are introduced to simplify the expression:

$$(h, g) = \sum_{i=1}^{n} w(x - x_i)h(x_i)g(x_i) \quad (12)$$

$$\alpha_1(t)(p_i, p_1) + \alpha_2(t)(p_i, p_2) + \cdots .. + \alpha_n(t)(p_i, p_n) = (p_i, Z), i = 1,2 \ldots, m \quad (13)$$

Organized into a system of linear equations, also known as normal equations:

$$\begin{bmatrix} (p_1, p_1) & (p_1, p_2) & \cdots & (p_1, p_m) \\ (p_2, p_1) & (p_2, p_2) & \cdots & (p_2, p_m) \\ \cdots & \cdots & \cdots & \cdots \\ (p_m, p_1) & (p_m, p_2) & \cdots & (p_m, p_m) \end{bmatrix} \begin{bmatrix} \alpha_1(t) \\ \alpha_2(t) \\ \cdots \\ \alpha_m(t) \end{bmatrix} = \begin{bmatrix} (p_1, Z) \\ (p_2, Z) \\ \cdots \\ (p_m, Z) \end{bmatrix} \quad (14)$$

Solving the above system of linear equations yields the reformation coefficient a(t) at node t. If the basis function $p_i(t)(i = 1,2,3, \ldots, m)$ is taken to be the set of orthogonal functions of the point set $\{x\}$ and the weight $\{w_i(i = 1,2,3, \ldots, m)\}$, we obtain:

$$(p_k, p_j) = \sum_{i=1}^{n} w_i\, p_k(t_i)\, (t_i) = \begin{cases} 0 & , (k = j) \\ A_k & , (k \neq j) \end{cases} (k, j = 1,2 \ldots m) \quad (15)$$

Then the matrix can be obtained:

$$\begin{bmatrix} (p_1, p_1) & 0 & \cdots & 0 \\ 0 & (p_2, p_2) & \cdots & 0 \\ \cdots & \cdots & \cdots & \cdots \\ 0 & 0 & \cdots & (p_m, p_m) \end{bmatrix} \begin{bmatrix} \alpha_1(t) \\ \alpha_2(t) \\ \cdots \\ \alpha_m(t) \end{bmatrix} = \begin{bmatrix} (p_1, Z) \\ (p_2, Z) \\ \cdots \\ (p_m, Z) \end{bmatrix} \quad (16)$$

Then one can solve for $\alpha_i(t)(i = 1,2,3 \ldots, m)$:

$$\alpha_i(t) = \frac{(p_i, Z)}{(p_i, p_i)} \quad (17)$$

Collation is available:

$$f(t) = \sum_{i=1}^{m} p_i(t) \cdot \frac{\sum_{I=1}^{n} w(t - t_I)\, p_i(t_I)}{(p_i, p_i)} = \sum_{I=1}^{n} O_I^k(t) Z \quad (18)$$

where the form function is:

$$O_I^k(t) = w(t - t_i) \sum_{i=1}^{m} \frac{p_i(t) p(t_I)}{(p_i, p_i)} \quad (19)$$

By integrating the set of orthogonal functions, matrix inversion can be avoided, thereby resolving the problem of matrix irreversibility, reducing the computational time of the least squares method, and lowering overall algorithmic complexity.

In the moving least squares method, the choice of the weight function is crucial, and in a complex orchard environment, the appropriate weight function greatly affects the smoothness of the fitted ground. The weight function $w(t\text{-}t_i)$ in the moving least squares method should be tightly supported, that is, the weight

function is not equal to zero in a subdomain of x, and is zero outside of this subdomain, which is called the support domain of the weight function (i.e., the region of influence of x).

Therefore, a circular support domain with radius r was selected for the weight function, where $d = t\text{-}t_i$, $\bar{r} = \frac{d}{r}$.

This choice ensures that the function values at each node are influenced only by data points within the circular support domain, while points outside this region have no impact. Due to the compact support of the weight function, only the data points within the region of influence affect the value at point x. The weight function $w(t\text{-}t_i)$ is required to be non-negative and monotonically decreasing as d^2 increases. In this study, a two-part Gaussian-type weight function is used in place of the traditional three-part moving least squares (MLS) weight function. This modification results in a smoother fit, reduces fitting time, and lowers algorithmic complexity.

The Gaussian-type weight function is shown in equation (20):

$$\bar{w}(\bar{r}) = \begin{cases} \frac{e^{-\beta^2\bar{r}^2} - e^{-\beta^2}}{1 - e^{-\beta^2}}, & \bar{r} \le 1 \\ 0, & \bar{r} > 1 \end{cases} \quad (20)$$

RESULTS

Data set

In this paper, tests are performed using datasets collected by two different devices.

1) KITTI point cloud public dataset, the data acquisition equipment for the U.S. Velodyne company HDL-64 type 3D mechanical rotation Lidar, with 64 lasers, acquisition frequency of 10 Hz, each frame produces about 130,000 scanning points, the effect of the dataset is shown in Figure.

2) The vineyard dataset was collected using the OSI-64 LiDAR, which has a measurement range of 120 meters, a vertical viewing angle of 45°, a horizontal viewing angle of 360°, a rotation angle of 360°, a vertical angular resolution of 0.52°, a horizontal resolution of 1024, and 131072 sampling points per second, with data effects as shown in Fig.4.



(a) (b) (c)

Fig. 4 - (a)Sample Images of the KITTI Dataset; (b)OSI-64 3D LiDAR; (c)Vineyard Dataset Rendering

Algorithm testing

1) Hardware platform

In this study, the KOMODO-03 general-purpose tracked robot mobile chassis developed by Extreme Robotics Technology Co. The chassis is fully electrically powered with a 48V 50Ah Li-ion battery power system with a maximum operating voltage of 54.6 V and a discharge cut-off voltage set at 43 V. The power section consists of two DC brushless motors and two 15:1 gearboxes. The computer is equipped with an AMD R7-4800H processor, 16 GB RAM and a single NVIDIA GeForce GTX1650ti GPU.

The mobile chassis structure is shown in Figure 5.



Fig. 5 - Tracked mobile platform for orchard operation robots

1. External Monitor; 2. Jetson AGX Xavier; 3. Crawler-Type Mobile Chassis; 4. Dual-Antenna GNSS-RTK; 5. 64-Line 3D LiDAR.

2) Measurement indicators

For the evaluation of segmentation accuracy, it is mainly evaluated from Precision, Recall and F1 Score, and the calculation method of each evaluation index is shown below:

$$\mathrm{Precision} = \frac{N_{TP}}{N_{TP} + N_{FP}} \tag{21}$$

$$\mathrm{Recall} = \frac{N_{TP}}{N_{TP} + N_{FN}} \tag{22}$$

$$F1 = 2 * \frac{\mathrm{Precision} * \mathrm{Recall}}{\mathrm{Precision} + \mathrm{Recall}} \tag{23}$$

where: N_{TP} is the number of ground points correctly labelled; N_{FN} is the number of ground points incorrectly labelled as non-ground points; N_{FP} is the number of non-ground points incorrectly labelled as ground points; and N_{TN} is the number of non-ground points correctly labelled.

KITTI dataset testing

The Semantic KITTI dataset is a large-scale dataset designed for autonomous driving scenarios, and in order to validate the accuracy of the algorithms in this paper for ground point cloud segmentation, this dataset was used to evaluate the performance of the proposed algorithms versus existing algorithms for ground segmentation.

In this experiment, the first 100 frames were selected (i.e., numbered 01 to 100) from the KITTI dataset as the test object, and each frame contains about 130,000 cloud data points. In order to make a clear comparison of the point cloud data, the non-ground point cloud was labelled as red and the ground point cloud as green, and the effect of the delineation of the road information was visualized by rviz.

The effect diagram of road information division is shown in Fig. 6, and the algorithm of this paper is compared with four ground segmentation algorithms of RANSAC *(Martin et al., 1981)*, GPF *(Dimitris et al., 2017)*, R-GPF *(Hyungtae et al., 2021)* and Patchwork *(Hyungtae et al., 2021)*. The comparison test is shown in Fig. 7, and the segmentation accuracy is shown in Table 1.

Table 1

Ground segmentation accuracy

Algorithm	Precision	Recall	F1 Score
RANSAC	0.8452	0.8389	0.8417
GPF	0.9256	0.7962	0.8551
R-GPF	0.7678	0.8862	0.8228
Patchwork	0.9279	0.9245	0.9267
Ours	0.9469	0.9458	0.9479

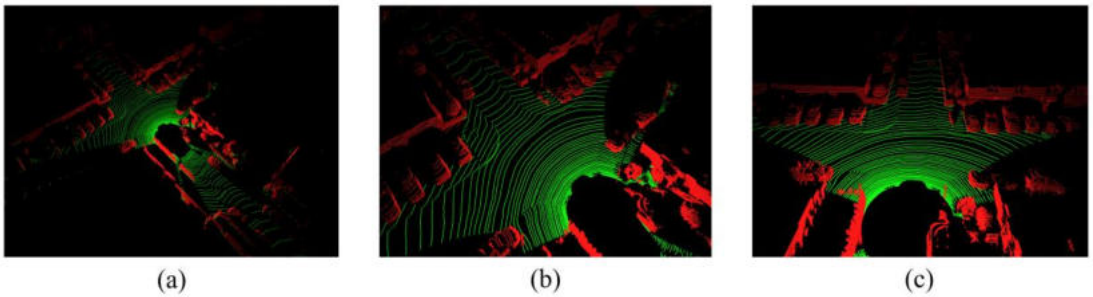


Fig. 6 - (a)Urban environment scene; (b), (c) Local vehicle scene

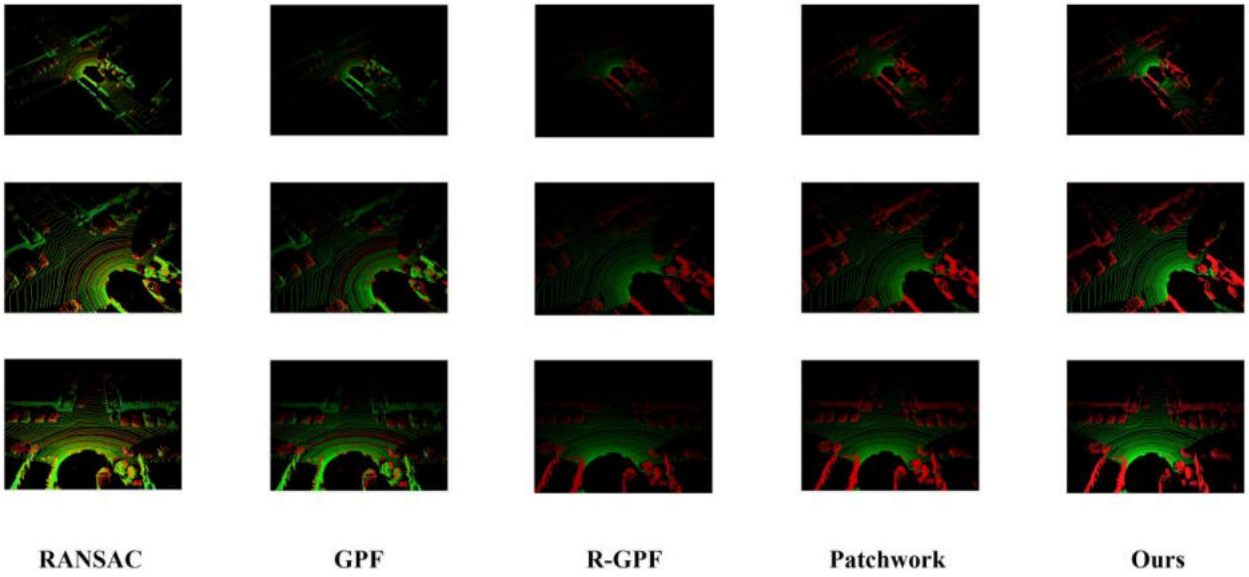


Fig. 7 - KITTI data set comparison test

In Fig. 7, the green point cloud represents the ground point cloud and the red point cloud represents the non-ground point cloud, and it can be seen by the global segmentation information as well as the local segmentation details that the algorithm in this paper is better than the other four algorithms. The ground segmentation accuracy in Table 1 shows that the algorithm in this paper is better than the above four algorithms in terms of segmentation accuracy, precision, recall, and accuracy in road tests in urban environments.

Vineyard Data Testing

The initial design of the algorithm in this paper is applied to the vineyard, using the OSI-64 LiDAR in the actual vineyard scene to collect data, and the original data and the algorithm of this paper to segment the environment comparison, the comparison effect graph is shown in Figure 8.

Figure 8 shows the real environment algorithm test, the test scene is a vineyard road, and 8(a)(d) shows the actual scene, where there is a human-type obstacle in (a), which is used to test the segmentation effect of the algorithm. Figure 8(b)(e) shows the unsegmented point cloud scene of the vineyard. Figure 8(c)(f) shows the scene after segmentation by the algorithm, and it can be seen from the segmentation effect that the algorithm in this paper can segment accurately.



Fig. 8 - Real environment algorithm testing

CONCLUSIONS

Aiming at the problem of insufficient performance of traditional methods for point cloud segmentation in complex scenes in vineyards, this paper proposes a surface-fitting ground segmentation method. By using orthogonal function basis to improve the moving least squares method, the computational complexity is reduced so as to improve the speed of surface fitting, Gaussian-type weight function is introduced to solve the problem of non-smoothness of the fitted surface, and the sine-cosine basis function is introduced, which is more able to restore the original shape of the vineyard ground. By improving the search area range of the radar so that the point cloud focuses on the farthest and nearest regions, obstacles can be detected as early as possible, providing sufficient time for path planning. Dual noise reduction technology is used to integrate multipath reflection suppression and sensor dynamic compensation to reduce the false detection rate of noise and enhance the robustness of ground segmentation in vineyard scenes.

The superiority of this approach is validated through experiments on the KITTI dataset and real vehicles. The results show that the method achieves accurate segmentation of ground point cloud, which is better than RANSAC, GPF, R-GPF and Patchwork algorithms. The segmentation precision can reach 0.9469 and the recall can reach 0.9458.

In future work, multimodal data fusion of LiDAR with visual and inertial measurement unit (IMU) data will be explored to enhance the robustness of the algorithm in complex environments such as rain, fog, and nighttime conditions. Additionally, the algorithm will be extended to other agricultural scenarios, including terraces and orchards, to evaluate its generalization performance.

ACKNOWLEDGEMENT

The project supported by the R&D of low-speed unmanned autonomous navigation controller Project under Grant (No.2022TSGC1175).

REFERENCES

[1] Alherimi N, Saihi A, Ben-Daya M. (2024) A Systematic Review of Optimization Approaches Employed in Digital Warehousing Transformation. *IEEE Access* 12, 145809-145831.

[2] Avcı İ, Koca M. Intelligent Transportation System Technologies, Challenges and Security. In: *Applied Sciences*; 2024.

[3] Bayer MM, Li X, Guentchev GN, Torun R, Velazco JE, Boyraz O. Single-shot ranging and velocimetry with a CW lidar far beyond the coherence length of the CW laser. *Opt Express* 2021; 29(26):42343-42354.

[4] Cong P, Feng H, Li S, Li T, Xu Y, Zhang X. A visual detection algorithm for autonomous driving road environment perception. *Engineering Applications of Artificial Intelligence* 2024; 133:108034.

[5] Deng W, Chen X, Jiang JJE. A Staged Real-Time Ground Segmentation Algorithm of 3D LiDAR Point Cloud. 2024.

[6] Dimitris Z, Izzat I, Nikolaos P. Fast segmentation of 3D point clouds: A paradigm on LiDAR data for autonomous vehicle applications, 2017 *IEEE International Conference on Robotics and Automation* (ICRA), 2017.

[7] Firkat E, An F, Peng B, Zhang J, Mijit T, Ahat A, et al. FGSeg: Field-ground segmentation for agricultural robot based on LiDAR. *Computers and Electronics in Agriculture* 2023; 211:107965.

[8] Huang J, Zheng Z, Zhang Y, Zhou Y. Segmentation Clustering Algorithm for Point Cloud Processing of Targets on The Ground. *Journal of Physics: Conference Series* 2023; 2478.

[9] Hyungtae L, Sungwon H, Hyun M. ERASOR: Egocentric ratio of pseudo occupancy-based dynamic object removal for static 3D point cloud map building. *IEEE Robotics and Automation Letters*, 2021.

[10] Hyungtae L, Minho O, Hyun M. Patchwork: Concentric zone-based region-wise ground segmentation with ground likelihood estimation using a 3D LiDAR sensor. *IEEE Robotics and Automation Letters*, 2021.

[11] Itakura K, Miyatani S, Hosoi F. Estimating Tree Structural Parameters via Automatic Tree Segmentation From LiDAR Point Cloud Data. *IEEE J. Sel. Top. Appl. Earth Obs. Remote Sens*., 2022; 15:555-564.

[12] Jiang X, Xie Y, Na C, Yu W, Meng Y. Algorithm for Point Cloud Dust Filtering of LiDAR for Autonomous Vehicles in Mining Area. *Sustainability* 2024, 16, 2827.

[13] Jin R, Ren M. Background extraction and ground segmentation method based on Roadside LiDAR. *Computer and Digital Engineering* 2023; 51(9):2033-2037+2054.

[14] Martin A, Robert C. Random Sample Consensus: A Paradigm for Model Fitting with Applications to Image Analysis and Automated Cartography. *Communications of the ACM*, 1981.

[15] Petrakis G, Partsinevelos P. Lunar ground segmentation using a modified U-net neural network. *Machine Vision and Applications* 2024; 35(3):50.

[16] Vidano T, Assadian F. Control Performance Requirements for Automated Driving Systems. In: *Electronics*; 2024.

[17] Wang C, Morris JT, Smith EM. A Lidar Biomass Index of Tidal Marshes from Drone Lidar Point Cloud. *Remote Sens.* 2024, 16, 1823. https://doi.org/10.3390/rs16111823

[18] Wang Y, Han Z, Xing Y, Xu S, Wang J. A Survey on Datasets for the Decision Making of Autonomous Vehicles. *IEEE Intelligent Transportation Systems Magazine* 2024; 16(2):23-40.

[19] Wang X, Ma X, Li Z. Research on SLAM and Path Planning Method of Inspection Robot in Complex Scenarios. *Electronics* 2023, 12, 2178. https://doi.org/10.3390/electronics12102178.

[20] Wu L, Chen Y, Le Y, Qian Y, Zhang D, Wang L. A high-precision fusion bathymetry of multi-channel waveform curvature for bathymetric LiDAR systems. *International Journal of Applied Earth Observation and Geoinformation* 2024; 128:103770.

[21] Zhu M, Zhang B, Zhou C, Zou H, Wang X. Target Recognition of Multi Source Machine Vision Pan Tilt Integrated Inspection Robot for Power Inspection. *IEEE Access* 2024; 12:45693-45708.

YOLOv8-STEM: ENHANCED OVERHEAD APPLE STEM DETECTION UNDER OCCLUSIONS

/

YOLOv8-STEM：俯视视角下的苹果果柄遮挡识别

Li WANG[1)], Yanqi SUN[1)], Tianle ZHANG[1)], Panpan YAN[2)], Qiangqiang YAO[3)], Zhen MA[4)], Degui MA[5)], Xingdong SUN[1*)]

[1)]Anhui Agricultural University College of Engineering, Hefei, Anhui, China, 230036
[2)] Heze Vocational College, Heze,Shandong, China, 274002
[3)]Qinghai University, China, 274002, 810016
[4)]School of Agricultural Engineering, Jiangsu University, Zhenjiang, Jiangsu, China, 212000
[5]Anhui Agricultural University College of Engineering，Hefei, Anhui, China, 230036

Corresponding author: Xingdong Sun
Tel: 0551-65786450; E-mail:xdsun@ahau.edu.cn
DOI: https://doi.org/10.35633/inmateh-76-07

Keywords: *stem detection, improved yolov8, occlusion recognition, orchard*

ABSTRACT

Accurate detection of apple stems is crucial for robotic cutting. This study proposed an improved YOLOv8-stem method for apple stem detection in overhead imagery under occlusion conditions. First, several improvements were made to the YOLOv8 neural network: the conventional convolutional process within the intermediate neck layer was substituted with the AK Convolution mechanism, a small object detection head was added, and ResBlock+CBAM attention mechanism was incorporated. Second, stem occlusion was determined by analyzing the positional relationship between the detected bounding boxes of stems and apples. The experimental results showed that compared to the original YOLOv8, this method improved apple stem detection accuracy by 6.0% (from 79.9% to 85.9%) and increased harvesting completeness from 84.2% to 93.2%.

摘要

准确检测苹果茎对于机器人切割至关重要。本研究提出了一种改进的 YOLOv8 茎检测方法，用于遮挡条件下俯视图像中的苹果茎检测。首先，对 YOLOv8 神经网络进行了几项改进：用 AK 卷积机制取代了中间颈层内的传统卷积过程，增加了一个小目标检测头，并引入了 ResBlock+CBAM 注意力机制。其次，通过分析检测到的茎和苹果边界框之间的位置关系来确定茎的遮挡。实验结果表明，与原始 YOLOv8 相比，该方法将苹果茎检测准确率提高了 6.0%（从 79.9%提高到 85.9%），收获完整性从 84.2%提高到 93.2%。

INTRODUCTION

Apples are the third largest fruit in terms of area planted and production globally *(Vasylieva et al., 2021)*. Manual apple harvesting is a time-consuming and labor-intensive task, and improving the competitiveness of the apple market requires addressing this challenge. Leaving apple stem too long during harvesting can cause surface scratches on the apples during transportation and storage, which can affect their freshness and appearance. Fruits stored without their stems exhibited greater weight loss, higher decay rates, and increased vitamin C loss *(Ozturk et al., 2020)*. Small apple stems and complex growing environments, overlapping fruits, branch and leaf shading, and light variations pose challenges to accurate target identification *(Chen et al., 2019)*.

In recent years, a lot of related works had been done by scholars at home and abroad for small target recognition of fruit stems in complex orchard environments. The YOLO family of algorithms had become a leader in target detection due to its rapid development and excellent performance. However, YOLO algorithms were mainly designed to detect and recognize full-size objects, and their performance was not as good when facing special-size objects, especially small targets *(Liu et al., 2023; Liu et al., 2022)*. To address this issue, Wu et al. introduced the YOLO-Banana model for precise identification of bananas and to determine the fruit axis and cutting point. They enhanced the Bottleneck module of YOLOv5 and employed an edge-detection algorithm to segment the fruit axis's contour, allowing them to pinpoint the cut-off location *(Wu et al., 2022; Wu et al., 2021)*. In situations where the fruit stem was covered, *Yu et al.* enhanced Mask R-CNN to address the issues of limited robustness in traditional algorithms when operating in unstructured environments *(Yu et al., 2019)*.

To investigate the method for identifying picking points in cases of partial occlusion, *Xiong et al. (2018)* conducted a study on locating grapes in the presence of disturbances. Other researchers employed stereovision and image processing techniques to detect and determine the locations of grape clusters and picking points, subsequently performing size measurements and enclosure calculations for the grapes *(Luo et al., 2021; Lufeng et al., 2017)*. The analysis of these studies revealed that there were fewer network improvements for short targets such as apple fruit stems, and for the localization of picking points covering the stems, most of them directly segmented the image of the target to be picked, which could produce large errors in the localization of the picking points.

This study concentrated on the detection of apple stems and sought to enhance the conventional YOLOv8 algorithm *(Jocher et al., 2023)*. It presented an enhanced YOLOv8-based method designed specifically for detecting apple stems in overhead imagery. To achieve this, high-quality datasets of apple fruits and stems were collected from a top-down perspective to provide positive samples for network training. In the annotation of training targets, both apples occluded by tree branches and apple stems were annotated as separate categories. When utilizing YOLOv8 for the detection of apples occluded by branches, the presence of an apple stem within the annotated apple bounding box was verified. If a stem was present, it was recognized normally; if not, it was determined that the stem was occluded by branches, necessitating a modification of the camera's position and angle. The YOLOv8 architecture was enhanced by incorporating a detection head specifically designed for small objects, the conventional convolutional process within the intermediate neck layer was substituted with the AK Convolution *(Zhang et al., 2023)* mechanism introducing a 160×160 detection feature map. A ResBlock+CBAM attention mechanism *(Woo et al., 2018)* module was incorporated to enhance the model's feature extraction capabilities for small target objects, thereby adapting to the characteristics of the apple stem dataset. The mean average precision (mAP) value and the harvesting completeness were calculated to evaluate the effectiveness of the stem detection, where the harvesting completeness was determined by applying the detection algorithm to apple stem images and computing the ratio of successfully detected stems to the total number of stems present in the dataset. This study provided a reference for designing a precise cutting vision system for harvesting robots.

MATERIALS AND METHODS

Collection and preprocessing of apple stem data

This study investigated the real orchard environment and the growth of apple stems in Shandong, China, and collected an apple dataset.

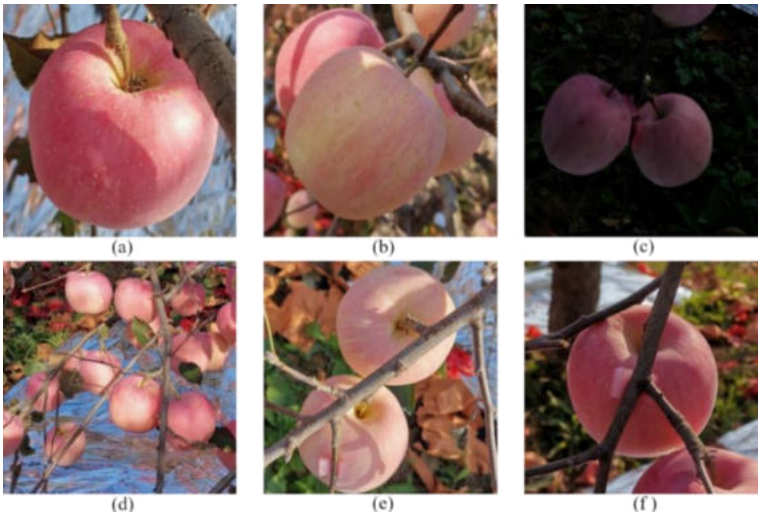


Fig. 1 - Apple images in different conditions

The images of apple stems were collected from apple orchards in Yantai, Shandong, China on October 15th and 16th, 2023. In order to minimize the risk of overfitting the network model, this study collected different distances, including close range (0.3 meters to 1 meter) and long range (1 meter to 3 meters). Images were taken at different times (morning, noon, and evening) to obtain rich and diverse data. Finally, the image dataset was cropped and organized. It was concluded that the apple stem's integrity was highest when viewed from an overhead (top-down) or horizontal perspective. A total of 1671 images of apple stems were collected.

As shown in Figure 1, this was a typical set of apple stem images in a complex environment, this study also collected images of fruit stems completely covered to cope with the special situation of complex orchard environments. All the experimental images were adjusted to a uniform size of 640×640, and then the image transformation module provided by the PyTorch framework was used to enhance the data.

Improved YOLOv8-stem Network Architecture

In order to accurately and quickly identify small objects such as apple stems, this study replaced the original convolutions with AKConv in the 3th and 5th layers of the network, based on the YOLOv8n model. Additionally, it incorporated a 160×160 small object detection head to increase sensitivity to smaller targets. Integrating the CBAM attention mechanism into the P4 and P5 feature maps improved feature representation, suppressed irrelevant information, improved object detection performance, and boosted the network's adaptability to objects of varying scales. The following sections will detail the working principles and technical aspects of each module. The altered network architecture is shown in Figure 2.

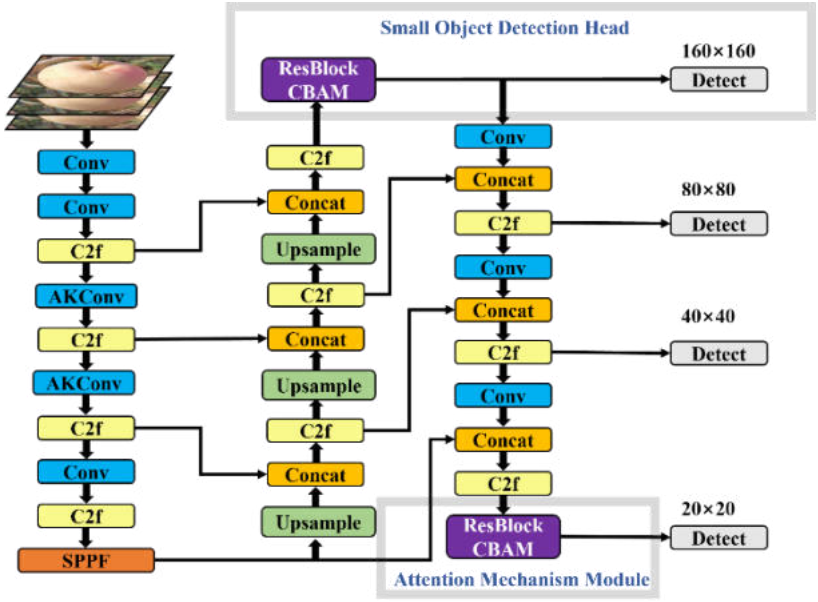


Fig. 2 - YOLOv8-stem Network

Replace the convolution module with AKConv

AKConv assigned initial sampling coordinates to convolutions of varying sizes and modifies the sample shape using learnable offset values. The third and fifth layers typically represent the deep feature extraction stage of the network, with higher resolution and channel numbers. Replacing AKConv in these layers can help the network focus more on extracting high-level and abstract features, thereby enhancing the network's capability to extract features from apple stems and manage occlusion scenarios.

Adding Small Target Detection Head

In the standard YOLOv8 object detection model, the output consists of three layers: P3, P4, and P5, each with three default detection heads. However, the standard model may perform poorly in detecting small objects. Therefore, a new 160x160 detection feature map was introduced for detecting objects larger than 4x4.

ResBlock＋CBAM

When using CBAM in ResNet improved the expressiveness of the feature maps in both the channel and spatial dimensions, thus enhancing the performance of the model. The high-level semantic information and multi-scale information of P4 and P5 made them particularly suitable for detecting small objects. By incorporating the CBAM attention mechanism into the P4 and P5 layers, the model's ability to represent features was enhanced, irrelevant information was suppressed, and target detection performance was improved, thus improving the model's detection and recognition capabilities for apple stems. This weighting mechanism allows the model to be more generalizable, adapting to apple stems of different sizes, shapes, and positions, thereby improving the model's robustness and accuracy.

Experimental Results and Analysis

In experiments to improve various backbone networks, DSConv *(Gennari et al., 2019)* convolution provided better accuracy and continuity in the segmentation of medical tubular structures, but the accuracy of apple stem detection decreased by 31.3%. Replacing the backbone network with ODConv *(Li et al., 2022)* moderately improved accuracy by 0.3% without changing the number of parameters. The results indicated that neither DSConv nor ODConv could effectively extract fruit stem features in highly crowded and complex environments. Bifpn was used to achieve bidirectional fusion of deep and shallow features, but the model parameters and accuracy of identifying fruit stems remained almost unchanged *(Tan et al., 2020)*. The CARAFE *(Wang et al., 2019)* network, which incorporated a kernel prediction module and a content-aware recombination module to generate larger up-sampling kernels, showed a decrease in accuracy of 0.25%. Vanillanet *(Chen et al., 2024)* performed well in terms of parameter and model computation by scaling the neural network model, but its accuracy control was mediocre. On the other hand, the improvement by replacing the backbone network with AKConv showed excellent performance, with a slight decrease in parameters and model computation while increasing detection accuracy (mAP@0.5/% increased by 2.2). This method effectively balanced model parameters and performance. Experimental results are shown in Table 1.

Table 1

Detection accuracy of each model in dataset (%)

Backbone	mAP@0.5/%	mAP@0.5-0.95/%	Params/M	FLOPs/G
Yolov8n(base)	0.799	0.362	3011027	8.2
Yolov8- DSConv	0.486	0.181	2996959	29.6
Yolov8-ODConv	0.802	0.359	2999036	8.1
Yolov8- Bifpn	0.804	0.342	3005852	8.1
Yolov8- CARAFE	0.774	0.332	4053191	8.3
Yolov8-Vanillanet	0.789	0.334	1731635	5.0
Yolov8- AKConv	**0.821**	**0.363**	**2965337**	**8.0**

Among the improvements in various attention mechanisms, LSKA *(Lau et al., 2024)* did not improve accuracy but reduced the model's parameter count. The EMA *(Ouyang et al., 2023)* module focused on retaining feature information on each channel, resulting in a slight increase in accuracy by 2.1%, with no increase in model computation. The parameter-free attention module SE *(Hu et al., 2018)* showed a small improvement in accuracy, while the global attention mechanism GAM *(Liu et al., 2021)* demonstrated a modest rise in the number of parameters while achieving an accuracy improvement of 3.9%. CBAM widely applied in many improvement studies, effectively improved accuracy in this study by combining feature channel and spatial principles to adapt to the complex and multi-feature environment in this scenario. Compared to the base accuracy, mAP@0.5/% improved by 4.6%, and the parameter count and the model's computations were roughly equivalent to those of the original model. Experimental results are shown in Table 2.

Table 2

Various attention mechanisms

Attention mechanism	mAP@0.5/%	mAP@0.5-0.95/%	Params/M	FLOPs/G
Yolov8n(base)	0.799	0.362	3011027	8.2
Yolov8-C2f-LSKA	0.794	0.338	2351555	6.6
Yolov8n+EMA	0.825	0.355	3006515	8.1
Yolov8n+SEAttention	0.808	0.368	3227923	8.4
Yolov8n+GAM	0.838	0.337	3687123	9.5
Yolov8n+CBAM	**0.845**	**0.346**	**3014406**	**8.1**

After testing a variety of attentional mechanisms for detecting small objects, the parts with significant improvements were selected and incorporated. Comparative experiments revealed that the YOLO network algorithm demonstrated strengths with respect to the three improvement modules from current cutting-edge research. However, additional ablation experiments were required to confirm the efficacy of each enhancement module. The findings from these experiments could be found in Table 3.

Table 3

Module ablation experiment

AKConv	CBAM	Head	mAP@0.5/%	mAP@0.5-0.95/%	Params/M	FLOPs/G
✓			0.821	0.362	2965337	8.0
	✓		0.845	0.342	3014406	8.1
		✓	0.826	0.352	2977588	12.5
	✓	✓	0.835	0.347	3239726	8.9
✓	✓	✓	0.859	0.347	3998948	14.6

These three improvements enabled the YOLO model to achieve higher recognition accuracy for small objects with specific apple stem shapes in orchard environments, where occlusion and scene complexity are common. Notably, this enhancement in performance was achieved with only a minimal increase in the number of parameters. Ultimately, compared with the baseline model, the improved YOLO achieved a 6.0% increase in mAP@0.5 on the dataset. The results of the ablation experiments are presented in Table 5. A comparison of detection outcomes before and after the network modifications, as shown in Figure 3, illustrates the effectiveness of the architectural changes. The visual results highlight clear improvements in detection accuracy and robustness achieved through the proposed enhancements.

Evaluation metrics

This study comprehensively evaluates the model's performance using precision (P), recall (R), gigafloating-point operations per second (GFLOPs), and the mean Average Precision (mAP) across all target categories at an IoU threshold of 0.5. The formulas for calculating precision, recall, and average precision (AP) are as follows:

$$P = \frac{TP}{TP + FP} \tag{1}$$

$$R = \frac{TP}{TP + FN} \tag{2}$$

$$AP = \int_0^1 P(R)dr \tag{3}$$

The mean Average Precision (mAP) is calculated as the total of the average precisions for all labels divided by the number of classes.

$$mAP = \frac{\sum_{i=1}^{k} AP_i}{k(classes)} \tag{4}$$

Where n denotes the total number of categories, k is the number of detections, and AP represents the average precision for each category.

RESULTS

Experimental Environment

Experiment setup: The operating system of the experimental platform was Windows 10. The CPU was an Intel(R) Core (TM) i5-12490F, with 16GB of RAM. The GPU was an Nvidia GeForce RTX 4060 Ti with 8GB of VRAM. The CUDA version used by torch vision is 11.7, and the deep learning framework was PyTorch-GPU 2.0.1+cu118. To ensure the fairness and rationality of the experiments, all ablation experiments were conducted in the same experimental environment.

Dataset Preparation

In apple stem images captured from various overhead angles, single-angle camera detection may fail to accurately identify the stem when the field of view is partially obstructed by overlapping branches or fruits. Such occlusions can prevent the camera from capturing the full shape and position of the apple stem, negatively impacting subsequent harvesting or processing tasks. To address this challenge, a specialized labeling strategy was adopted for the dataset used in this study. Apple stems visible from a top-down perspective were labeled as *Apple stem*, while apples obscured by branches were labeled as *Masked apple*. Additionally, apple stems captured from the top-down view were annotated together with apple eyelets to enhance the feature representation of the stem. This custom-labeled dataset formed the basis for training and evaluating the proposed detection algorithm designed to identify apple stems in occluded environments.

This study trained a model to recognize two types of objects: apple stems and apples obscured by tree branches. After detection, it was further determined whether the bounding box of the obscured apple contains the coordinates of the apple stem. If the coordinates of the stem are not within the bounding box of the obscured apple, it could be concluded that the stem is obscured by a branch. Otherwise, it was considered exposed. When tree branches obstruct the apple and cover the stem, the detection angle and position could be adjusted to better observe the stem, thereby more accurately detecting the initially unrecognized stem and providing a technical solution for apple harvesting.

There were a total of 2816 *Apple stem* labeled targets and 1321 *Masked apple* labeled targets in the original 1671 images before data augmentation. It should be noted that because the *Masked apple* was larger and more distinctive in the images, it was not involved in the statistics of the YOLOv8 network structure optimization results. The performance evaluation was conducted only for the target recognition effect of the *Apple stem*. The training of the *Masked apple* category was performed to validate and provide statistics for the specific case when the apple was covered by branches and the fruit stem was also covered. The dataset categorization is shown in Table 4.

Table 4

Classification of data sets

Classification of data sets	Number	Use of data sets
Apple stem	2816	Network Modification Performance Evaluation
Masked apple	1321	Identify and count obscured apples

This study employed K-Fold cross-validation as the evaluation method for the machine learning model. The original dataset was divided into 5 subsets (K=5). In each iteration, one subset was used as the validation set, while the remaining four subsets (K-1) were used as the training set. This process was repeated five times, ensuring that each subset served as the validation set exactly once. After each iteration, the model's performance metrics were calculated on the validation set, and the average of these results was taken as the overall performance evaluation on the entire dataset. The training results presented in the subsequent experiments were obtained using this K-Fold cross-validation approach.

Validate the network model

In order to more intuitively test the apple stem detection performance of the modified network model, this study compared the apple stem detection performance of YOLOv8n and YOLOv8 stalk. The comparison of the detection results is shown in Figure 3.



Fig. 3 - The comparison of detection results

There are a total of three sets of apple stem detection comparisons in the comparison chart. Overall, in terms of detection performance, the improved YOLOv8 stalk has increased the recall rate and overall confidence of apple stem detection.

After comparing the original YOLOv8 model, this study validated the superiority of the improved YOLOv8 stalk model by training and testing it on the same dataset as other detection models such as faster R-CNN, SSD, YOLOv5, YOLOv3, etc. From Table 5, it can be seen that the improved YOLOv8 stalk model has the highest average accuracy compared to other models, with an increase of 5.4 percentage points in average accuracy compared to the original YOLOv8n network.

Table 5

Comparison of the effectiveness of different network models

model	mAP @0.5/%	mAP @0.5-0.95/%	Params/M	FLOPs/G
YOLOv3-tiny	76.2	33.6	4.3	18.9
YOLOv5n	80.1	35.7	1.9	4.5
YOLOv8n	80.3	36.0	3.0	8.2
Faster R-CNN	80.8	35.8	104	268.3
SSD	82.2	35.4	93	195.3
YOLOv8-stalk	85.7	36.7	4.0	14.6

Detection Results and Analysis of Occluded Stems

After modifying the network, the deep learning model achieved higher recognition accuracy for apple stems, but it could not address the issue of incomplete harvesting caused by branches obscuring the apple stems. Therefore, the modified network was used to detect cases where apple stems were obscured by branches to observe the recognition and improvement effects. This study categorized the cases of obscured apple stems into three types: stems inside the corresponding obscured apple box but not recognized, stems inside the corresponding obscured apple box and recognized, and stems inside a non-corresponding apple box. This last category included cases where the stem was recognized or not recognized within the non-corresponding apple box. The number of stems not recognized was the focus for angle adjustment and re-detection to improve the actual harvesting rate. The following images show the detection results for these three different scenarios. Different occlusion scenarios of the stems are shown in Figure 4.



Fig. 4 - Different occlusion scenarios of the stems

This experiment was conducted using the trained inference model on 428 new scene images of apple stems collected from an apple orchard, which were different from the training dataset. Among these new images, 576 apples were annotated as obscured apples (Actual number of occluded apples). After prediction by the model, there were 565 predicted obscured apples (Predicted number of occluded apples). The number of stems recognized within the corresponding obscured apple bounding boxes (Fruit stems not covered by branches) was 485, and the number of stems inside the corresponding obscured apple boxes but not recognized (Fruit stems obstructed by branches) was 52. Other cases included 28 stems inside non-corresponding apple boxes (Other situations).

The statistical results are presented in Table 6.

Table 6

The statistical results

Category	number
Images of apple orchard scenes	428
Actual number of occluded apples	576
Predicted number of occluded apples	565
Fruit stems not covered by branches	485
Fruit stems obstructed by branches	52
Other situations	28

After analyzing the data of predicted obscured apples in the apple orchard scene images, in the case of 576 actually obscured apples, if the stems are also obscured, the deep learning network will not detect the obscured apples from a single camera angle, resulting in 52 stems inside the corresponding obscured apple box but not recognized. When this situation is detected, it can be inferred that the stems are obscured. In this case, changing the position and angle of the single camera to re-recognize the obscured stems can improve the picking efficiency from 576/485=84.2% to 576/ (485+52) =93.2% according to the theoretical statistical data. Moreover, as the apples with recognized stems inside the corresponding obscured apple box are picked, the situation where the stems are recognized inside non-corresponding obscured apple boxes will decrease, further improving the picking efficiency.

CONCLUSIONS

This study presented an enhanced YOLOv8-stem approach for detecting apple stems in overhead imagery under occlusion conditions. First, two datasets comprising apples and apple stems obstructed by tree branches were collected. Second, the YOLOv8 neural network was improved by substituting the conventional convolutional process within the intermediate neck layer with the AK Convolution mechanism. A small object detection head was added, introducing a 160×160 detection feature map, and a ResBlock+CBAM attention mechanism was incorporated. Third, the likelihood of missed detections was decreased by utilizing the coordinates of the apples and apple stems obstructed by tree branches identified by the enhanced YOLOv8-stem model. The experimental results showed that compared to the original YOLOv8 model, this method significantly improved both the detection accuracy of apple stems and the completeness of harvesting. The enhanced stem detection model achieved an average precision of 85.9%, representing a 6.0% improvement over the baseline YOLOv8 model (from 79.9% to 85.9%), and the harvesting completeness increased from 84.2% to 93.2%. This approach demonstrated promising applications in precise apple harvesting and automated fruit picking systems.

ACKNOWLEDGEMENT

This research was funded by the National Natural Science Foundation of China (No.52375228); the National Natural Science Foundation of China (No.52005009); the Post-Master's Enterprise Workstation in Anhui Province (No.2022sshqygzz012); the Key Projects of Natural Science Research Projects of Colleges and Universities in Anhui Province, China (No.KJ2021A0154); High-tech Key Laboratory of Agricultura Equipment and Intelligence of Jiangsu Province (MAET202318), College of Agricultural Engineering, Jiangsu University (MAET202318).

REFERENCES

[1] Akyon F. C., Altinuc S. O., & Temizel A. (2022). October. Slicing aided hyper inference and fine-tuning for small object detection. In 2022 *IEEE International Conference on Image Processing* (ICIP) pp. 966-970. IEEE. DOI:10.1109/ICIP46576.2022.9897990

[2] Chen Y., Lee W. S., Gan H., Peres N., Fraisse C., Zhang Y., & He, Y. (2019). Strawberry yield prediction based on a deep neural network using high-resolution aerial orthoimages (基于深度神经网络的草莓产量预测), *Remote Sensing*, 11(13), 1584. DOI:10.3390/rs11131584

[3] Chen H., Wang Y., Guo J., & Tao, D. (2024). Vanillanet: the power of minimalism in deep learning (Vanillanet：深度学习中极简主义的力量), *Advances in Neural Information Processing Systems*, 36.

[4] Gennari M., Fawcett R., & Prisacariu V.A. (2019). DSConv: Efficient convolution operator, *arxiv preprint* arxiv:1901.01928. DOI: 10.48550/arXiv.1901.01928

[5] Hu J., Shen L., & Sun G. (2018). Squeeze-and-excitation networks (挤压和激励网络), In *Proceedings of the IEEE conference on computer vision and pattern recognition.* pp.7132-7141. DOI: 10.48550/arXiv.1709.01507

[6] Jocher G., Chaurasia A., & Qiu J. (2023). *Ultralytics YOLOv8*. Retrieved from https://github.com/ultralytics/ultralyticsw

[7] Lau K.W., Po L.M., & Rehman Y.A.U. (2024). Large separable kernel attention: Rethinking the large kernel attention design in CNN, *Expert Systems with Applications*, 236, 121352. DOI:10.1016/j.eswa.2023.121352

[8] Li C., Zhou A., & Yao A. (2022). Omni-dimensional dynamic convolution (全维动态卷积), *arxiv preprint* arxiv:2209.07947. DOI:10.48550/arXiv.2209.07947

[9] Liu H., Duan X., Chen H., Lou H., & Deng L. (2023). DBF-YOLO: UAV Small Targets Detection Based on Shallow Feature Fusion (DBF-YOLO：基于浅层特征融合的无人机小目标检测), *IEEJ Transactions on Electrical and Electronic Engineering*, 18(4), 605-612. DOI:10.1002/tee.23758

[10] Liu H., Sun F., Gu J., & Deng L. (2022). Sf-YOLOv5: A lightweight small object detection algorithm based on improved feature fusion mode (Sf-YOLOv5：一种基于改进特征融合模式的轻量级小目标检测算法), *Sensors*, 22(15), 5817. DOI:10.3390/s22155817

[11] Liu Y., Shao Z., & Hoffmann N. (2021). Global attention mechanism: Retain information to enhance channel-spatial interactions (全球注意力机制：保留信息以增强渠道空间互动), *arxiv preprint* arxiv:2112.05561. DOI:10.48550/arXiv.2112.05561

[12] Lu feng L., Xiang jun Z., Cheng lin W., Xiong C., Zi Shang Y., & Weiming S. (2017). Recognition method for two overlapping and adjacent grape clusters based on image contour analysis (基于图像轮廓分析的重叠相邻葡萄簇识别方法), *Nongye Jixie Xuebao/Transactions of the Chinese Society of Agricultural Machinery*. 48(6).

[13] Luo L., Liu W., Lu Q., Wang J., Wen W., Yan D., & Tang Y. (2021). Grape berry detection and size measurement based on edge image processing and geometric morphology (基于边缘图像处理和几何形态学的葡萄果实检测与尺寸测量), *Machines*, 9(10), 233. DOI:10.3390/machines9100233

[14] Ouyang D., He S., Zhang G., Luo M., Guo H., Zhan J., & Huang Z. (2023), June. Efficient multi-scale attention module with cross-spatial learning (具有跨空间学习的高效多尺度注意力模块), In ICASSP 2023-2023 IEEE *International Conference on Acoustics, Speech and Signal Processing* (ICASSP). pp.1-5. IEEE. mDOI:10.1109/ICASSP49357.2023.10096516

[15] Ozturk B., Aglar E., Gun S., & Karakaya O. (2020). Change of fruit quality properties of jujube fruit (Ziziphus jujuba) without stem and with stem during cold storage, *International Journal of Fruit Science*, 20(sup3), S1891-S1903. DOI: 10.1080/15538362.2020.1834901

[16] Tan M., Pang R., & Le Q. V. (2020). Efficientdet: Scalable and efficient object detection (Efficientdet：可扩展且高效的对象检测), *In Proceedings of the IEEE/CVF conference on computer vision and pattern recognition* (pp. 10781-10790). DOI:10.48550/arXiv.1911.09070

[17] Vasylieva N., & Harvey J. (2021). Production and trade patterns in the world apple market, *Innovative Marketing*, 17(1), 16. DOI: 10.21511/im.17(1).2021.02

[18] Wang J., Chen K., Xu R., Liu Z., Loy C. C., & Lin D. (2019). Carafe: Content-aware reassembly of features (Carafe: 功能的内容感知重组), *In Proceedings of the IEEE/CVF international conference on computer vision* (pp. 3007-3016).

[19] Woo S., Park J., Lee J. Y., & Kweon I. S. (2018). Cbam: Convolutional block attention module, *In Proceedings of the European conference on computer vision (ECCV)* (pp. 3-19). DOI: 10.48550/arXiv.1807.06521

[20] Wu F., Duan J., Ai P., Chen Z., Yang Z., & Zou X. (2022). Rachis detection and three-dimensional localization of cut off point for vision-based banana robot (基于视觉的香蕉机器人种族检测和切割点三维定位), *Computers and Electronics in Agriculture*, 198, 107079. DOI: 10.1016/j.compag.2022.107079

[21] Wu F., Duan, J., Chen S., Ye Y., Ai P., & Yang Z. (2021). Multi-target recognition of bananas and automatic positioning for the inflorescence axis cutting point (香蕉多目标识别及花序轴切割点自动定位), *Frontiers in plant science*, 12, 705021. DOI:10.3389/fpls.2021.705021

[22] Xiong J., He Z., Lin R., Liu Z., Bu R., Yang Z., Peng H., & Zou X. (2018). Visual positioning technology of picking robots for dynamic litchi clusters with disturbance (动态荔枝丛采摘机器人的视觉定位技术), *Computers and electronics in agriculture*. 151, 226-237. DOI: 10.1016/j.compag.2018.06.007

[23] Yu Y., Zhang K., Yang L., & Zhang D. (2019). Fruit detection for strawberry harvesting robot in non-structural environment based on Mask-RCNN (基于 Mask RCNN 的非结构化草莓采摘机器人果实检测), *Computers and electronics in agriculture*, 163, 104846. DOI: 10.1016/j.compag.2019.06.001

[24] Zhang X., Song Y., Song T., Yang D., Ye Y., Zhou J., & Zhang L. (2023). AKConv: Convolutional kernel with arbitrary sampled shapes and arbitrary number of parameters (AKConv：具有任意采样形状和任意数量参数的卷积核), *arxiv preprint arxiv:2311.11587*. DOI: 10.48550/arXiv.2311.11587

STRAWBERRY IDENTIFICATION AND KEY POINTS DETECTION FOR PICKING BASED ON IMPROVED YOLOV8-POSE AT RED RIPE STAGE
/
基于改进 YOLOv8-pose 的红熟期草莓识别与采摘关键点检测

Jinlong WU*[,1,2)], Ronghui MIAO [1,2)]

[1)] College of information science and engineering, Shanxi agricultural university, Taigu / China;
[2)] College of agricultural engineering, Shanxi agricultural university, Taigu / China
Tel: +86-18503482797; E-mail: wujinlong8192@163.com
DOI: https://doi.org/10.35633/inmateh-76-08

Keywords: *YOLOv8-pose, strawberry identification, fruit stem, key point detection, red ripe stage*

ABSTRACT

To solve the problems of low precision in locating stem picking points and difficulty in recognizing occluded strawberry during the operation of strawberry picking robots, this paper proposed an improved YOLOv8-pose method for strawberry fruits identification and key points detection at the red ripe stage. Based on the YOLOv8-pose human posture estimation model, three categories (strawberry, stem, and picking points) were annotated. The acquired images were divided into training, validation, and test sets in an 8:1:1 ratio. In order to improve the feature extraction ability of the model for small targets, shuffle attention (SA) mechanism was added into the backbone network of YOLOv8-pose. Additionally, a comparative analysis was conducted to assess the impact of six attention mechanisms of CBAM (Convolutional block attention module), SimAM (Simple attention module), GAM (Global attention module), EMA (Efficient multi-scale attention), SK (Selective kernel attention), and SA on the detection results. Experimental results show that the proposed method can quickly and accurately detect strawberry fruits and key points for picking. The Precision (P), Recall (R), and mean average precision (mAP)50 values for both bounding boxes and key points based on SA mechanism were 99.7%, 100.0%, and 99.5% respectively, which were superior to the other attention mechanisms. Compared with YOLOv5-pose and YOLOv8-pose models, the improved model had the best P, R, and mAP50 values, and its memory usage was 6.4MB, which was also optimal. The improved method can provide crucial technical support for precise robotic strawberry picking.

摘要

为解决草莓采摘机器人作业中果梗采摘点定位精度低和遮挡草莓识别困难等问题，本文以红熟期草莓为研究对象，提出一种改进的 YOLOv8-pose 草莓果实识别及采摘关键点检测方法。以 YOLOv8-pose 人体姿态估计模型为基础，标注了草莓、果梗、采摘点 3 个类别。将采集的图像按 8:1:1 的比例划分成训练集、验证集和测试集。为了提高模型对小目标的特征提取能力，在 YOLOv8-pose 的骨干网络中添加了 shuffle 注意力机制，并对比分析了 CBAM（Convolutional block attention module），SimAM（Simple attention module），GAM（Global attention module），EMA（Efficient multi-scale attention），SK（Selective kernel attention）以及 SA 六种注意力机制对检测结果的影响。实验结果表明，本文提出的方法可以对草莓果实及采摘关键点进行快速准确检测，基于 SA 注意力机制的边界框和关键点的检测精确率（Precison，P），召回率（Recall，R），平均精度均值（Mean average precision，mAP）mAP50 均为 99.7%，100.0%和 99.5%，均优于其他注意力机制；与 YOLOv5-pose、YOLOv8-pose 模型相比，改进模型的 P，R，mAP50 值都是最优的，模型的内存占用量为 6.4MB，也是最优的，该模型可以为机器人精准采摘提供重要的技术支持。

INTRODUCTION

With various nutrients such as amino acids, vitamins, minerals, strawberry is known as the “queen of fruits” *(Hu et al., 2024)*. At present, strawberry picking still rely on manual labor, which is time-consuming and costly *(Wang et al., 2022)*. The implementation of intelligent strawberry picking is of great significance for improving picking efficiency, reducing labor costs, minimizing fruit damage, and enhancing fruit quality. The

[1] *Jinlong Wu, Lect.; Ronghui Miao, Assoc. Prof.*
[2] *Jinlong Wu, Ph.D.Stud.; Ronghui Miao, Ph.D.Stud.*

harvesting of strawberry picking robots is mainly achieved by cutting fruit stems *(Ma et al., 2025)*. However, the diameter of strawberry stem is relatively small, and affected by complex backgrounds such as lighting and obstruction from branches and leaves, making it difficult to identify and locate strawberry. Accurate positioning fruits and stems are of great significance for improving the intelligence and automation of strawberry picking robots.

In recent years, with the development of deep learning technology, researchers at home and abroad applied deep learning algorithms to the recognition and detection of various fruits, and have achieved certain results. *Gai et al.* (*2024*) proposed a blueberry identification algorithm named TL-YOLOv8 based on the YOLOv8 algorithm to improve the detection accuracy, by introducing an improved MPCA (Multiplexed coordinated attention) in the last layer of the backbone network, the feature extraction capability during the training process was enhanced. *Gao et al. (2025)* proposed a novel YOLOv8n-CA method for tomato maturity recognition, which defines four maturity stages: unripe, turning color, turning ripe, and fully ripe, and the experimental results showed that the YOLOv8n-CA model had a computational complexity of 6.9 GFLOPs, and a weight file size of just 4.90 MB. *Chen et al. (2024)* proposed a lightweight target detection method called LFA-YOLO to address the problem of leakage and misdetection in the detection of lychee fruit anthracnose due to the complexity of the agricultural environment, and it achieved a mAP50 of 88.61%, with precision and recall rates of 90.18% and 82.77% respectively. In the application of strawberry recognition and detection, an improved YOLOv5 object detection model was proposed, the ghost module was used to optimize the backbone network, thereby reducing the number of parameters and complexity of the model, and the experimental results indicated that this model can provide a more accurate and efficient detection method for strawberry *(Peng et al., 2025)*. An improved YOLOv5s-based method for rapid detection of strawberry ripeness in greenhouse was proposed, shuffle block was introduced as the feature extraction network in the backbone to lightweight the model, the results showed that the average precision of the improved YOLO-ODM model can reach 97.4%, indicating that this lightweight method can detect the ripeness of strawberry quickly and accurately *(Chen et al., 2023)*. A combination of improved YOLOv4 and traditional image processing technology for strawberry stem recognition in complex picking scenarios was proposed, and this model can accurately locate the picking points and demonstrate better applicability in practical picking scenarios *(Huang et al., 2023)*. However, most of the aforementioned researches mainly focused on object detection of fruits and maturities for strawberry, the detection of key points for picking were relatively few, which cannot be directly applied to strawberry picking operations. Meanwhile, the maturities of strawberry can be divided into four stages: green ripe, white ripe, color change, and red ripe. Among these, the red ripe stage is the complete ripening stage, with uniform red color on the surface, soft texture, and unique aroma. Therefore, identifying the red ripe strawberry and picking points are key steps for strawberry picking robots.

This paper takes red ripe strawberry as research object, refers on the human posture estimation model, and proposes an improved YOLOv8-pose model for detecting key points of fruit and stem. In order to improve the feature extraction ability of the model for small targets (fruit stems, picking points), SA mechanism was added to the backbone network. This study can achieve the prediction of picking point for stems, providing technical support for machine picking of strawberry.

MATERIALS AND METHODS

Data collection

The experimental strawberry images were collected from strawberry planting base in Xianggu village, Taigu District, Jinzhong city, Shanxi province in March 2024. The datasets were carried out using a Huawei P40 Pro camera. The vertical distance between the shooting device and the ground was 150 mm - 250 mm. A total of 158 images were collected, with an image resolution of 3000 pixels × 4000 pixels. The experimental processing platform was configured with Intel Core (TM) i9-9900K @ 3.60GHz, 16GB of memory, and NVIDIA GeForce RTX 2080Ti main graphics card for GPU acceleration. Figure 1 shows the collected strawberry images, which include complex environment such as single fruit, multi fruit, fruit occlusion, and branch and leaf occlusion.



(a) Multi fruit + fruit obstruction (b) Multi fruit + no fruit obstruction (c) Single fruit (d) Single fruit + leaf obstruction

Fig. 1 - Sample images of strawberry

Dataset annotation

This paper used posture estimation model to achieve strawberry identification and key points detection on fruit stems. YOLOv8 is capable of performing complex tasks such as instance segmentation *(Fan et al., 2024)*, object detection *(Kumar and Muhammad, 2023)*, image classification, posture estimation *(Ma et al., 2024)*, and key points detection. Among them, posture estimation can obtain the positions of key points in the images, and the positions are usually represented by two-dimensional coordinates (x, y) or 3D coordinates (x, y, visible), and it is mainly used to recognize various postures of the human body *(Peruzzi et al., 2025)*. In YOLOv8, there are 1 category and 17 key points, the category name is "person", and each key point represents a different part of human body. The mappings of each index to the corresponding body joint are: 0: nose; 1: left eye; 2: right eye; 3: left ear; 4: right ear; 5: left shoulder; 6: right shoulder; 7: left elbow; 8: right elbow; 9: left wrist; 10: right wrist; 11: left hip; 12: right hip; 13: left knee; 14: right knee; 15: left ankle; 16: right ankle. Figure 2 shows the key points of human body.

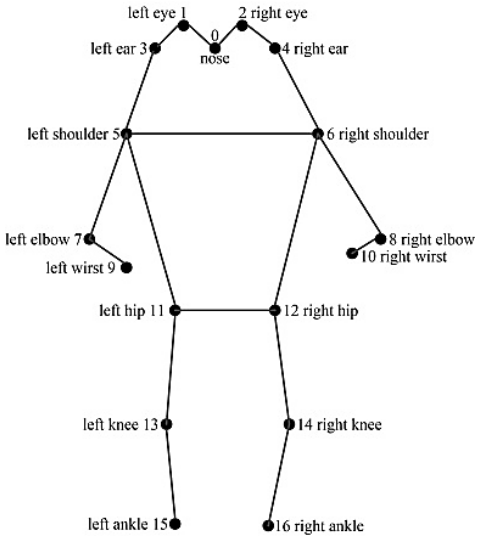


Fig. 2 – Key points of human body

Based on the posture estimation model of human body, a strawberry recognition and stem key points detection model was constructed. In this paper, the annotation tool Labelme was used to annotate the strawberry image datasets, and three types of labels were annotated: strawberry (in rectangle), stem (in point) and pick (in point). The annotation results were shown in Figure 3. The principle of labeling is: only the red ripe strawberry fruits will be labeled, and fruits that are too heavily obscured will not be labeled; the center point of the fruit stem was selected as key point; the picking point is marked at a distance of 1 cm from the stem. The format of the annotation file was JSON, in order to ensure that the datasets required for the experiment meets of COCO format, the annotated files need to be converted to TXT format.

Dataset production

After screening, a total of 98 images were selected for model training, validation, and testing. Then the image datasets were divided in an 8:1:1 ratio. Eighty percent (78 images) were randomly selected as the training sets for model training and parameter optimization. The remaining twenty percent (20 images) were used as validation and testing sets to verify the performance of the model.

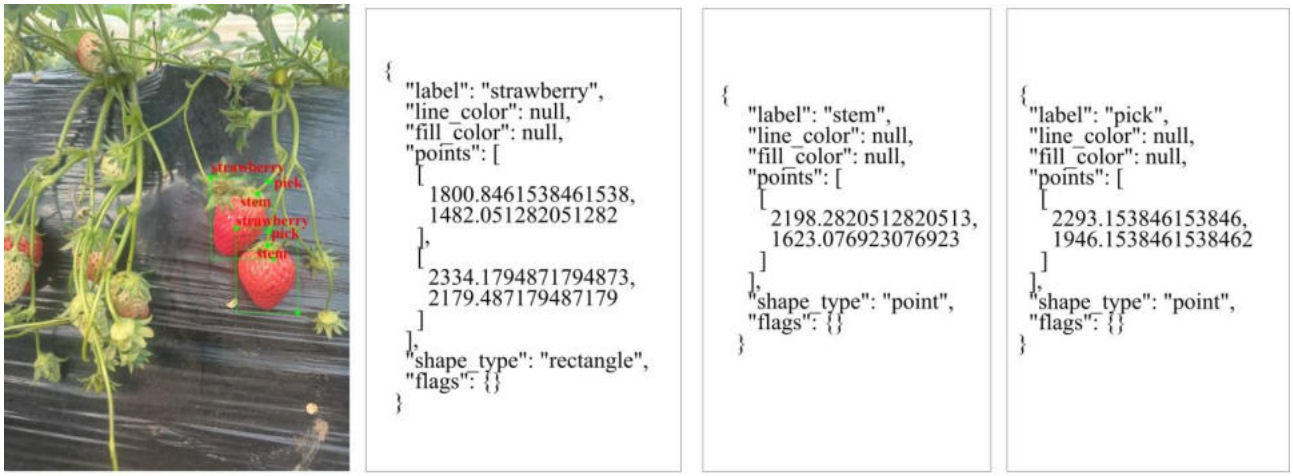


Fig. 3 – Annotation results

Dataset augmentation

YOLOv8 provides some dataset automatic augmentation methods to improve the generalization ability and detection performance of the model, and the main augment strategies include RandAugment, AutoAugment, and AugMix *(Sanat et al., 2023)*. Among them, RandAugment is a commonly used technique that enhances training data by randomly selecting a series of image transformations (such as brightness adjustment, contrast change, rotation, cropping, etc.), thus enabling the model to better learn various features and patterns in the images *(Lee et al., 2023)*. Some of the hyperparameter settings are as follows: the “hsv_h” (proportion of image hue augmentation) is 0.015; the “hsv_s” (proportion of image saturation augmentation) is 0.7; the “hsv_v” (proportion of image value augmentation) is 0.4; the “translate” (proportion of image translation) is 0.1; the “scale” (gain of image scaling) is 0.5; the “fliplr” (probability of image flip left-right) is 0.5, the “mosaic” (probability of image mosaic) is 1.0, etc. Figure 4 shows the data augmentation result, randomly applying image enhancement operations with a certain probability and intensity can generate diverse training samples. And it performs stably on different datasets and model sizes, especially suitable for resource limited scenarios.

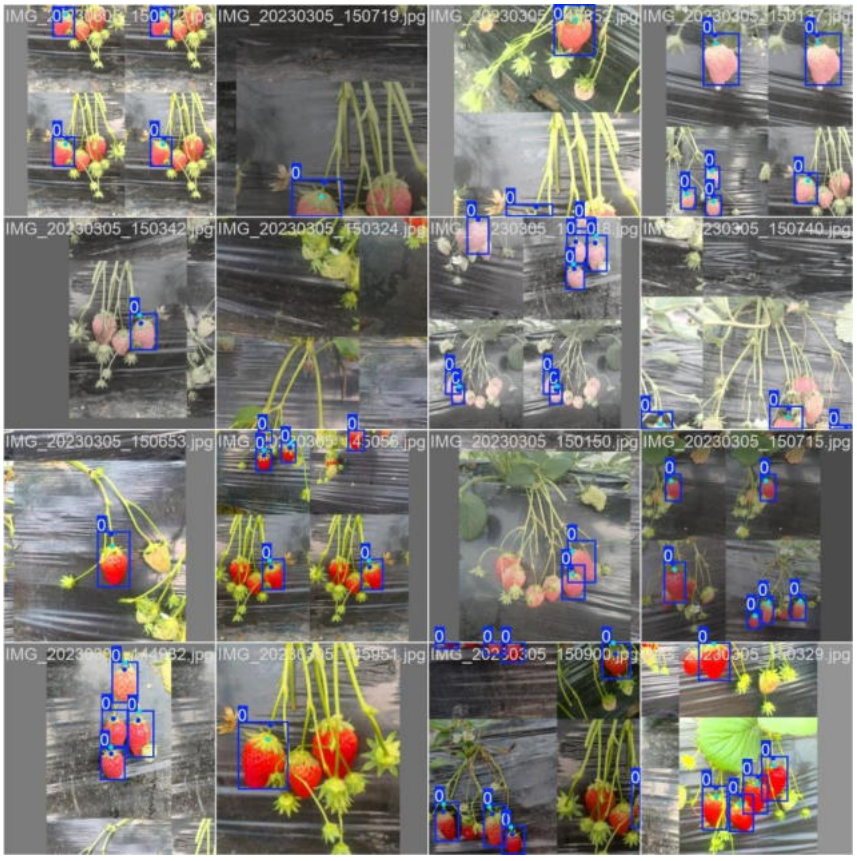


Fig. 4 – Dataset augmentation result

Strawberry identification and picking key points detection model

This paper constructed a model for strawberry identification and fruit stem key points detection based on the improved YOLOv8-pose network. In order to improve the feature expression ability, SA mechanism was added into the backbone network of YOLOv8-pose. Figure 5 shows the network structure of the improved YOLOv8-pose model.

YOLOv8-pose model

With advantages of higher detection accuracy and speed, new backbone network structure, anchor free detection head, and new loss function *(Jo et al, 2024)*, YOLOV8 model can achieve tasks such as object detection, instance segmentation, and key points detection, and it has been widely used in security monitoring, autonomous driving, smart homes and industrial automation. The structure of YOLOv8 mainly consists of three parts: Backbone, Neck, and Head.

a. Backbone: responsible for feature extraction. A series of convolutional and deconvolution layers are adopted to realize deep feature extraction. The introduction of residual connections and bottleneck structures can improve the performance of the network *(Zhai et al., 2024)*. Compared with YOLOv5, C2f module is introduced to replace the original C3 module, which can achieve light weighting with fewer parameters. Moreover, the depth wise separable convolution and dilated convolution techniques can further enhance feature extraction capabilities.

b. Neck: located between the backbone and head parts, responsible for feature fusion enhancement. The spatial pyramid pooling fusion (SPPF) can fuse features maps from different stages of backbone to enhance feature representation capabilities *(Dong et al., 2024)*.

c. Head: responsible for generating the final detect results. This section uses simple convolutional and upsampling layers, combined with the feature maps from the neck part to achieve object detection.

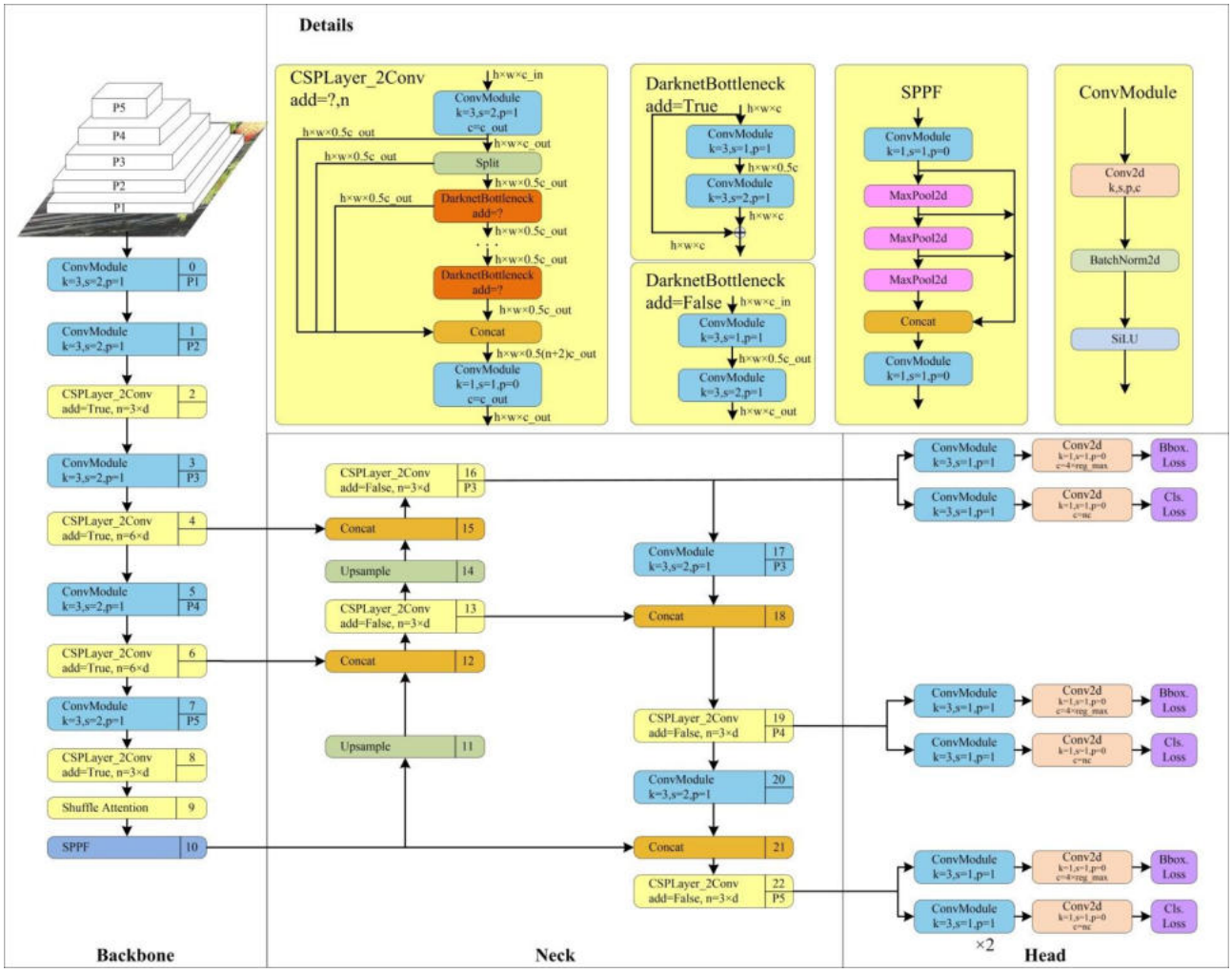


Fig. 5 – The network structure of the improved YOLOv8-pose model

SA mechanism

Attention module can focus on useful feature information and suppress unimportant feature. SA mechanism is capable of selectively weighting the information within the feature maps *(Zhang and Yang, 2021)*. By introducing this mechanism, YOLOv8 model can be made more stable and accurate in finding the position and classifying the tested object. The advantages of SA mechanism are: it efficiently combines spatial and channel attention mechanisms, thus improving the performance of the model; by dividing the channel dimensions of the input feature map into multiple groups, the computational cost is effectively reduced; by using channel rearrangement technique, the expression ability of channel features is enhanced.

The structure of SA is shown in Figure 6. The processing procedure of SA module mainly includes: (1) Making the input feature map into G groups to obtain sub features of each group; (2) Use spatial attention and channel attention to obtain information of the sub features; (3) Channel shuffle operation is used to fuse the features from different groups. The blue parts represent the spatial attention mechanism, and the green ones represent the channel attention mechanism. In Figure 6, X is the feature map; c, h and w represent the number of channels, spatial height and width respectively; the number of channels for each group is c/g; the number of channels for each attention branch is $c/2g$; GN is group normalization.

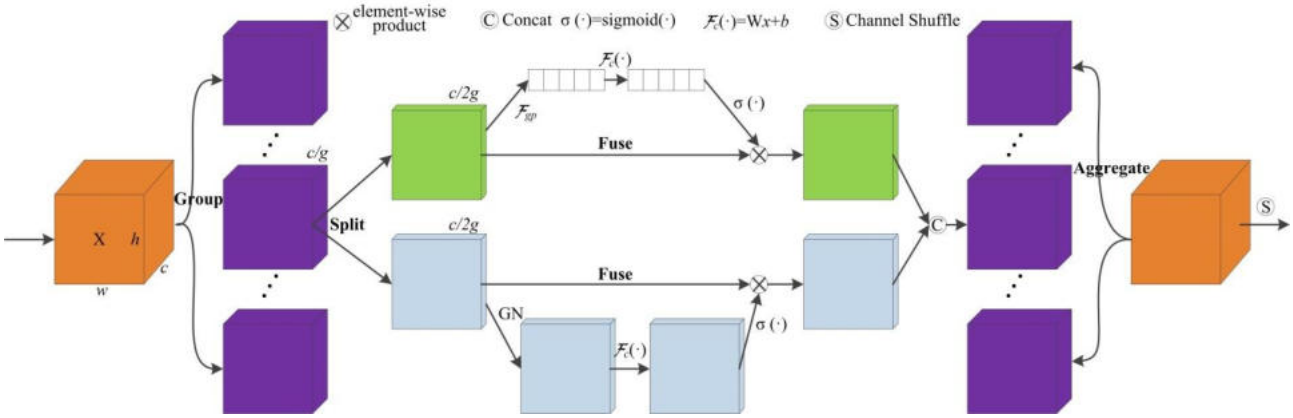


Fig. 6 – SA mechanism structure diagram.

Model evaluation

In order to evaluate the performance of identification and detection, mAP, P and R were selected as evaluation indicators. Among them, mAP refers to the average precision at different recall rates. P represents the proportion of samples predicted as positive cases that are actually positive cases. R represents the proportion of samples correctly identified as positive cases by the model among all actual positive cases. The calculation formulas for evaluation indicators are shown in equations (1) to (3).

$$mAP = \frac{\sum_{i=1}^{C} \int_0^1 P_i dR_i}{C} \quad (1)$$

$$P = \frac{TP}{TP + FP} \quad (2)$$

$$R = \frac{TP}{TP + FN} \quad (3)$$

In which:

C is the number of categories; TP (True positives) is the number of correctly identified positive samples; TN (True negatives) is the number of correctly identified negative samples; FP (False positives) is the number of samples incorrectly identified as positive; FN (False negatives) is the number of incorrectly identified negative samples.

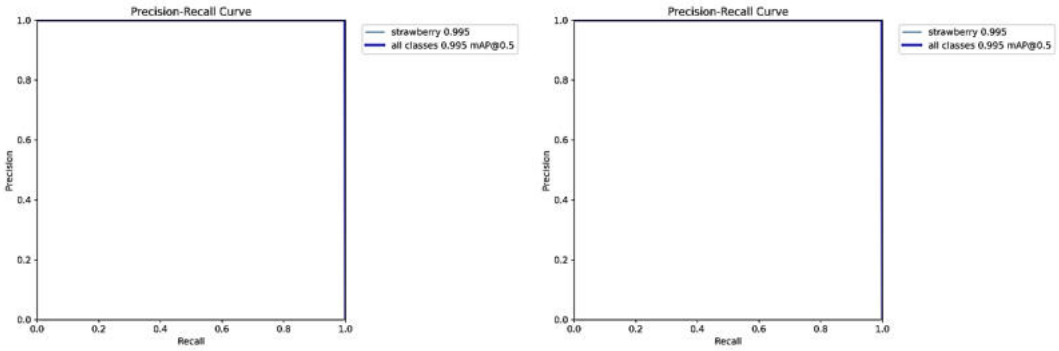
Model parameters

In the improved YOLOv8-pose model, the batch size is 16; the epoch is 200; the initial learning rate is 0.01; the momentum is 0.937. Batch size represents the number of training set images input for each batch; epoch represents the number of iterations of model training; learning rate is a parameter that controls the size of the gradient descent step in each iteration update; momentum can accelerate the update of model parameters.

RESULTS AND DISCUSSION

Identification and detection results of the improved YOLOv8-pose

Figure 7 shows the PR curves of box and pose on the training sets. PR curve is a common method used to evaluate the performance of the classification models. The horizontal axis of the PR curve is precision, and the vertical axis is recall. The closer the PR curve is to the upper right corner, the better the performance of the model. It can be seen that the mAP50 values for both box and pose were 0.995, which were close to 1, indicated that the model had a better balance between precision and recall, and its performance was good.



(a) Box PR curve *(b) Pose PR curve*

Fig. 7 - PR curves on the training sets

Figure 8 shows the loss curves on the training sets. The loss functions of YOLOv8-pose mainly includes five types of losses: bounding box loss (box_loss), key point loss (pose_loss), key point confidence loss (kobj_loss), classification loss (cls_loss), and distribution focal loss (dfl_loss). Bounding box loss represents the deviation between the predicted bounding box and the actual bounding box. Key point loss represents the deviation between the predicted key point positions and the actual positions. Key point confidence loss is used to measure the confidence level of the model in predicting key points, and it is adjusted by comparing it with the true confidence level. Classification loss represents the deviation between the predicted category and the true category. Distribution focal loss is used to optimize the predicted distribution of bounding boxes. As shown in figure 8, with the increase of training epochs, the loss value continuously decreased and tended to stabilize, indicated that the performance of the model was gradually improving in the classification and prediction tasks.

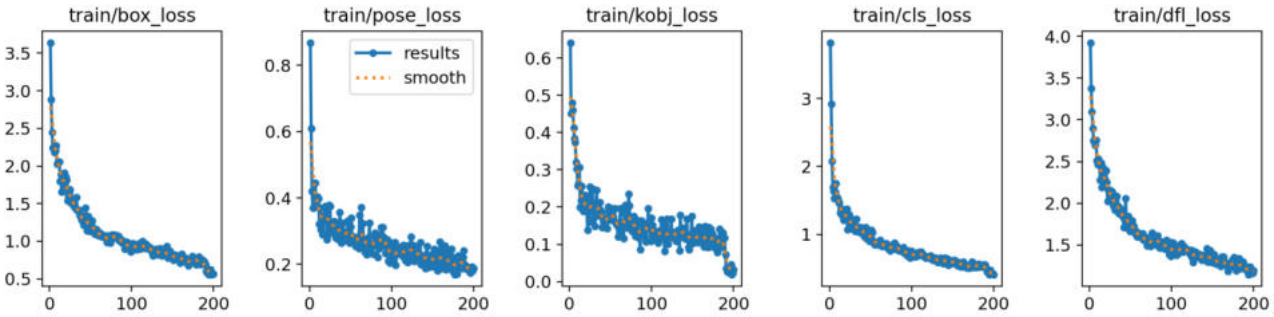


Fig. 8 - Loss curves on the training sets

Figure 9 shows the identification and detection results of strawberry. In the recognition results, the blue rectangle represents the identified results of strawberry at red ripe stage; the red and yellow points present the picking and stem key points. It can be seen that the improved model can accurately identify the strawberry at red ripe stage, because it only has one target in this paper, the detection and recognition rate is relatively high. There is a certain overlap between the stem and picking points, due to the small color difference of key points, the detection results are not ideal.



Fig. 9 – The prediction results of the improved YOLOv8-pose model

Identification and detection results of different attention mechanisms

In order to verify the impact of attention mechanisms on the performance of the model, six attention mechanisms of CBAM *(Woo, et al., 2018)*, SimAM *(Yang, et al., 2021)*, GAM *(Liu et al., 2021)*, EMA *(Zhang et al., 2024)*, SK *(Peng et al., 2020)* and SA were set for comparative experiments.

Table 1 shows the detection results of different attention mechanisms. Here, mAP50 represents the average accuracy of the model when the IoU (Intersection over union) threshold is 0.5, while mAP50-95 represents the average accuracy when the IoU ranging from 0.5 to 0.95. And mAP50-95 provides a more comprehensive evaluation of the performance under different degrees of overlap.

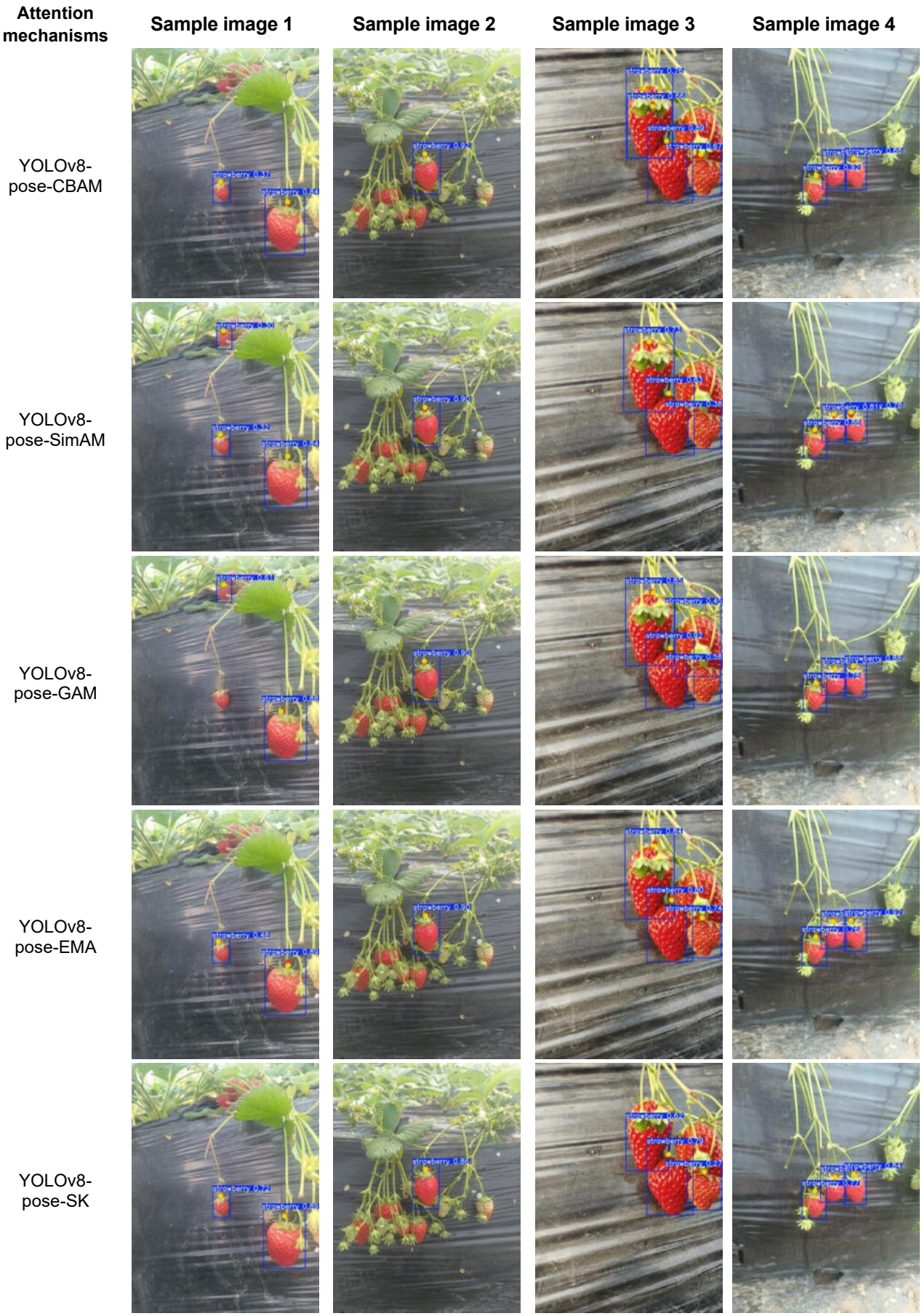
From table 1, it can be seen that the indicators of all the attention mechanisms can reach 81% or above, and the detection results were good; the detection results of YOLOv8-pose-EMA and YOLOv8-pose-SK were relatively poor; the memory usage of YOLOv8-pose-SK was 17.5MB, which was the highest among all the attention mechanisms; the box and pose P, R, mAP50 of SA were all 99.7%, 100.0% and 99.5%, and the memory usage of YOLOv8-pose-SA was 6.4MB, these values were all optimal.

Figure 10 shows the partial identification and detection results of different attention mechanisms. It can be seen that all models were able to identify strawberry fruits and key points of picking with high accuracy; the model of YOLOv8-pose-GAM had a certain of miss detection. Due to the fact that both the stem and picking point are green, there was a certain overlap in the results.

Table 1

Detection results of different attention mechanisms

Attention mechanisms	Box				Pose				Memory usage (MB)
	P (%)	R (%)	mAP50 (%)	mAP50-95 (%)	P (%)	R (%)	mAP50 (%)	mAP50-95 (%)	
YOLOv8-pose-CBAM	99.7	99.9	99.5	82.0	99.7	99.9	99.5	97.5	6.4
YOLOv8-pose-SimAM	99.7	100.0	99.5	82.1	99.7	100.0	99.5	97.3	6.4
YOLOv8-pose-GAM	99.0	96.0	99.1	81.3	100.0	99.5	99.5	97.5	7.3
YOLOv8-pose-EMA	90.9	100.0	98.6	83.7	90.9	100.0	98.6	95.0	7.7
YOLOv8-pose-SK	93.2	96.0	98.7	81.1	100.0	95.1	99.2	96.6	17.5
YOLOv8-pose-SA	**99.7**	**100.0**	**99.5**	**83.5**	**99.7**	**100.0**	**99.5**	**97.3**	**6.4**


Attention mechanisms
Sample image 1
Sample image 2
Sample image 3
Sample image 4
YOLOv8-pose-CBAM
YOLOv8-pose-SimAM
YOLOv8-pose-GAM
YOLOv8-pose-EMA
YOLOv8-pose-SK

YOLOv8-pose-SA



Fig. 10 – The prediction results of different attention mechanisms

Identification and detection results of different models

In order to verify the detection performance of different posture estimation models, this paper compared the results of YOLOv5-pose, YOLOv8-pose, and the improved YOLOv8-pose method. Table 2 shows the detection results of different models. From table 2, it can be seen that the results of our method were optimal, and superior to the other models.

Table 2

Detection results of different models

Models	Box				Pose				Memory usage (MB)
	P (%)	R (%)	mAP50 (%)	mAP50-95 (%)	P (%)	R (%)	mAP50 (%)	mAP50-95 (%)	
YOLOv5-pose	85.6	82.6	83.7	71.2	82.1	83.8	84.1	73.4	7.5
YOLOv8-pose	91.3	83.5	95.7	74.7	81.7	96.0	96.3	93.7	6.4
Improved YOLOv8-pose of our method	**99.7**	**100.0**	**99.5**	**83.5**	**99.7**	**100.0**	**99.5**	**97.3**	**6.4**

CONCLUSIONS

Faced with the characteristics of small stem diameter and easy damage to the flesh of strawberry, in this paper, an improved YOLOv8-pose method was proposed for strawberry fruit identification and key points detection method at red ripe stage. Based on the YOLOv8-pose human posture estimation model, three categories of strawberry, stem, and picking points were annotated. In order to improve the feature extraction ability of the model for small targets, SA mechanism was added into the backbone network of YOLOv8-pose. Experimental results show that the proposed method can quickly and accurately detect strawberry fruits and key points of picking, and can provide crucial technical support for precise robotic strawberry picking.

At present, there are varieties of strawberry, and the method in this paper is only suitable for detecting red strawberry. It may have certain limitations in identifying and locating strawberry in other colors. Subsequent research will introduce white strawberry or pink strawberry to enrich the images, so that improving the generalization ability and adaptability to different strawberry. Generally, intelligent fruit and vegetable picking robots are composed of vision, control, execution and walking systems. Among them, the visual system plays a crucial role in harvesting robots. As the “eyes” of the picking robots, it can accurately identify the position, size, and maturity of the target fruit through image recognition and object detection technology, and provide precise guidance for the execution system. The future research direction is to combine the method proposed in this paper with RGBD depth cameras to further obtain three-dimensional information of fruits, and guide the robotic arm to perform picking operations.

ACKNOWLEDGEMENT

This research was funded by Shanxi Province Applied Basic Research Youth Project, grant number 202203021212428; Shanxi Province Applied Basic Research Youth Project, grant number 202203021212414.

REFERENCES

[1] Chen, J. S., Liu, M., & Li J. C. J. (2024) LFA-YOLO: Detection of lychee fruit anthracnose based on UAV images and deep learning [J]. *Applied Engineering in Agriculture*, *40*(5), 515-523.

[2] Chen, R. F., Xie, Z., & Lin, C. (2023) YOLO-ODM based rapid detection of strawberry[J]. *Journal of Huazhong Agricultural University, 42*(04), 262-269.
[3] Dong, X. H., Li, S. X., Zhang, J. X. (2024) YOLOV5s object detection based on Sim SPPF hybrid pooling[J]. *Optoelectronics Letters, 20*(6), 367-371.
[4] Fan, Y. H., Zhang, L. X., Zheng, C. X., Wang X. Y, Zhu J. H, & W, L. (2024) Instance segmentation of faces and mouth-opening degrees based on improved YOLOv8 method[J]. *Multimedia Systems, 30*(5), 269-278.
[5] Gao, X., Ding, J. Y., Zhang, R. H., & Xi, X. B. (2025) YOLOv8n-CA: Improved YOLOv8n Model for Tomato Fruit Recognition at Different Stages of Ripeness [J]. *Agronomy, 15*(1), 188.
[6] Gai, R., Liu, Y., & Xu, G. (2024) TL-YOLOv8: A Blueberry Fruit Detection Algorithm Based on Improved YOLOv8 and Transfer Learning[J]. *IEEE Access, 12*(000), 13.
[7] Hu, H. P., Chen, M. X., Huang, L. B., & Guo, C. (2024). BHI-YOLO: A Lightweight Instance Segmentation Model for Strawberry Diseases[J]. *Applied Sciences, 14*(21), 9819.
[8] Huang, J. C., Wang, T., & Zhang, D. (2023) Recognition and localization of strawberry stalk leaf based on improve YOLOv4[J]. *Journal of Chinese Agricultural Mechanization, 44*(9), 205-213.
[9] Jo, S., Woo, J., Kang C. H., & Kim, S.Y. (2024) Damage detection and segmentation in disaster environments using combined YOLO and Deeplab [J]. *Remote sensing, 16*(22), 4267.
[10] Kumar, D., & Muhammad, N. (2023) Object Detection in Adverse Weather for Autonomous Driving through Data Merging and YOLOv8 [J]. *Sensors, 23*(20), 8471.
[11] Lee, G., Yonrith, P., Yeo, D., & Hong, A. (2023) Enhancing detection performance for robotic harvesting systems through RandAugment [J]. *Engineering Applications of Artificial Intelligence, 123*(PartC), 11.
[12] Liu, Y., Shao, Z., & Hoffmann, N. (2021) Global Attention Mechanism: Retain Information to Enhance Channel-Spatial Interactions [C]. *arXiv preprint arXiv: 2112.05561*.
[13] Ma, M. X., Ma, H., & Song, H.W. (2024) Pose estimation algorithm for small target pedestrians in urban street view based on YOLO-pose [J]. *Computer engineering, 50*(4), 177-186.
[14] Ma, Z. H., Dong, N. S., Gu J. Y., Cheng H. C., Meng Z. C, & Du X. Q. (2025) STRAW-YOLO: A detection method for strawberry fruits targets and key points [J]. *Computers and Electronics in Agriculture, 230*: 109853.
[15] Peng, Y., Qiao, Y. H., Zhang, C. Y., Yao, J. & Bao, D. L. (2025) Research of strawberry detection method with improved YOLOv5 model [J]. *Journal of Chinese Agricultural Mechanization, 46*(1), 213-219.
[16] Peng, Z. H., Li, Q., & Liang, S. (2020) Multi-Scale Dense Selective Kernel Spatial Attention Network for Single Image De-raining [C]. *2020 IEEE 5th International Conference on Cloud Computing and Big Data Analytics (ICCCBDA), IEEE*, 341-347.
[17] Peruzzi, G., Galli, A., Giorgi G., & Pozzebon, A. (2025) Sleep posture detection via embedded machine learning on reduced set of pressure sensors [J]. *Sensors, 25*(2), 458.
[18] Sanat, R., Diego, D., & Cristians, G. (2023) TRandAugment: temporal random augmentation strategy for surgical activity recognition from videos [J]. *International journal of computer assisted radiology and surgery, 18*(9), 1665-1672.
[19] Wang, Y., Yan, G., Meng, Q. L., Yao, T., Han, J. F., & Zhang, B. (2022) DSE-YOLO: Detail semantics enhancement YOLO for multi-stage strawberry detection [J]. *Computers and Electronics in Agriculture, 198*, 107057.
[20] Woo, S., Park, J. C., Lee J. Y., & Kweon, I. S. (2018) CBAM: Convolutional Block Attention Module[C]. *Proceeding of the European conference on computer vision (ECCV)*, 3-19.
[21] Yang, L., Zhang, R. Y., Li, L., & Xie, X. (2021) SimAM: A Simple, Parameter-Free Attention Module for Convolutional Neural Networks [C]. *International Conference on Machine Learning, Proceedings of Machine Learning Research (PMLR), 11863-11874.*
[22] Zhai, Z. L., Niu N. W. J, Feng B. M., Xu, S. Y., Qu C. Y., & Zong C. (2024) An improved YOLOv8 model enhanced with detail and global features for underwater object detection [J]. *Physica Scripta: An International Journal for Experimental and Theoretical Physics,* (9), 99.
[23] Zhang, Q. L., & Yang, Y. B. (2021) SA-Net: Shuffle Attention for Deep Convolutional Neural Networks [C]. *ICASSP 2021 IEEE International Conference on Acoustics, Speech and Signal Processing (ICASSP), 2235-2239*.
[24] Zhang, X., Li, L. Z., & Han, L. (2024) A cross-spatial network based on efficient multi-scale attention for landslide recognition [J]. *Landslides, 21*(12), 2913-2925.

ESTABLISHMENT AND VALIDATION OF A THEORETICAL MODEL FOR SINGLE LONGITUDINAL AXIAL FLOW THRESHING AND SEPARATION OF MILLET
/
谷子单纵轴流脱粒分离理论模型的建立与验证

Jun-hui ZHANG[1)], Lin ZHAO[2)], Shu-juan YI[*1)], Dong-ming ZHANG[1)], Xin ZHANG[3)]
[1)]College of Engineering, Heilongjiang Bayi Agricultural University, Daqing/P.R.China
[2)]Beijing Polytechnic, Beijing, 100176, China
[3)]Engineering Technology Research Institute, Daqing Drilling Engineering Co., Ltd., Daqing 163319, China
Tel: +86-459-13836961877; E-mail: yishujuan_2005@126.com
Corresponding author: Shu-juan YI
DOI: https://doi.org/10.35633/inmateh-76-09

Keywords: *millet, cumulative threshing rate, cumulative separation rate, fitting, test*

ABSTRACT
The influence of the device's structure and operating parameters, along with the material properties of millet, on threshing and separation performance forms the theoretical basis for designing and researching a single longitudinal axial flow threshing and separation device specifically adapted to millet. Therefore, a theoretical model for grain threshing and separation in a single longitudinal axial flow threshing device was established based on variable mass theory. To validate the theoretical model, single-factor tests were conducted on the feeding rate, rotational speed, and water content of Longgu 31 millet. The error analysis between the experimental and calculated values indicates that within a moisture content range of 17.14% to 32.93%, feeding rates varying from 1 to 3 kg/s, and rotational speeds ranging from 700 to 1000 r/min, the R-squared values consistently exceed 0.97. This indicates an excellent fit of the theoretical model. The theoretical model will serve as a valuable reference for the design and investigation of the single longitudinal axial flow separation device.

摘要
谷子的物料特性和装置的结构参数、工作参数对脱分性能的影响，是适应谷子特性的单纵轴流脱分装置设计和研究的理论依据。因此，应用变质量理论建立了谷子在单纵轴流脱分装置内的脱分理论模型，并构造了脱粒参数和分离参数的表达式。为了验证理论模型，选取龙谷 31 号为试验对象，在搭建的单纵轴流脱粒分离试验台上开展了谷子的喂入量、转速、含水率单因素试验，并将试验数据与模型计算数据进行误差分析，对比结果表明：当含水量为 17.14%-32.93%、喂入量为 1-3kg/s，转速为 700-1000r/min 时，试验数据与模型计算数据的 R-Squared 误差均大于 0.97，理论模型的拟合度好。因此，理论模型将为单纵轴流脱离分离装置的设计和研究提供参考。

INTRODUCTION
Currently, the grain combine harvester has become an indispensable agricultural machine for field operations. As a critical component, the threshing device plays a pivotal role in determining the overall performance of the harvester. Consequently, numerous scholars have devoted significant effort to optimizing this essential mechanism.

The tangential flow threshing device was utilized in early harvesting machinery, and its theoretical model has been well-established. The effects of structural design, operational parameters, and material properties on the threshing and separation efficiencies of the tangential flow threshing device were elucidated (*Wan et al., 1990; Zhang et al., 1994*). Due to its longer threshing time and superior threshing and Separation performance, the axial-flow threshing and Separation device has become predominantly used in grain combine harvesters in recent years. Consequently, scholars have conducted extensive theoretical and experimental research on the threshing and Separation performance of axial-flow devices. The authors investigated the effects of structural and operational parameters of the axial flow threshing device on threshing rate and separation rate through experimental research, and subsequently optimized these parameters (*Liu et al., 2021;*

Jun-hui Zhang, Ph.D.; Lin Zhao, Ph.D.; Shu-juan Yi, Prof. Ph.D.; Dong-ming Zhang, Ph.D.; Xin Zhang, master degree

Wu et al., 2022; Zhang et al., 2025; Liu et al., 2023). Through theoretical analysis, a separation probability model for the vertical axial flow threshing and separation device was developed. The results demonstrate that the structural and motion parameters of the drum significantly influence separation efficiency (*Dong et al., 1988*). In recent years, with millet and other coarse grain crops are more and more recognized by the public, millet harvesting process mechanization requirements are higher and higher. Research on the mechanical properties of millet grains and stems has progressively deepened, providing a solid foundation for the development of threshing devices specifically adapted to the unique characteristics of millet (*Zhang et al., 2018; Zhang et al., 2019; Yang et al., 2015*). Through experimental studies on the threshing process of millet, it was concluded that the rasp bar type axial flow method is most suitable for threshing and separating millet due to its specific characteristics (*Liang et al., 2015; Kang et al., 2017*).

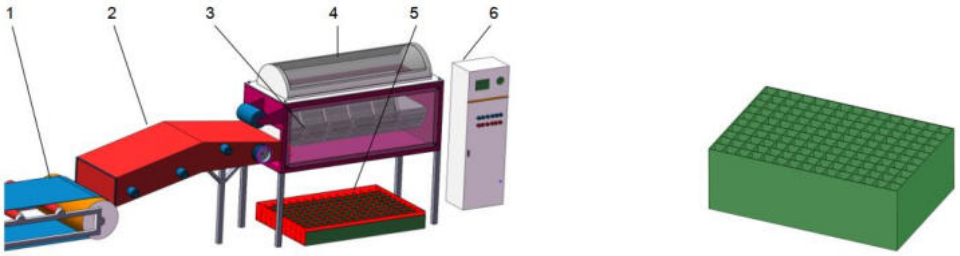
In conclusion, while extensive experimental research has been conducted on the longitudinal axial flow threshing and separation process, there is a notable deficiency in the literature regarding theoretical models of this process. It is imperative to elucidate the impact of grain material characteristics, structural parameters, and operational parameters of the threshing device on the performance of the longitudinal axial flow threshing and separating system. This research will provide a theoretical foundation for designing and developing a longitudinal axial flow threshing and separating device tailored to the specific characteristics of millet.

MATERIALS AND METHODS

Structure and working principles of the single longitudinal axial flow threshing and separation device

The single longitudinal axial flow threshing and separation device is shown in Fig. 1(a). This device primarily comprises the feeding mechanism, threshing cylinder, cover plate, material collection trolley, and control system.

When the device is working, millet is fed into the axial threshing and separation device through the feeding device, and the action process of grain in the single longitudinal axial flow threshing and separation device can be divided into two distinct phases: threshing and separation. The threshing process is completed by rubbing and striking between the rasp bar-nail teeth combined threshing components, the concave plate and the material in the drum. The threshed seeds overcome the resistance of the stalk layer, pass through the grid of the concave plate, and fall into the material collection trolley, thereby completing the separation process.



(a) Primarily comprises of the device *(b) Material collection trolley*

Fig. 1 - Diagram illustrating the single longitudinal axial flow threshing and separation device

1 – Conveyor; 2 – Feeding mechanism; 3 – Threshing cylinder; 4 – Cover plate; 5 – Material collection trolley; 6 – Control system

The material collection trolley (as showed in Fig. 1(b)) consists of a 14×16 matrix of collection buckets, with each bucket measuring 10cm×10cm. During the single longitudinal axial flow threshing and separation device test, this trolley is employed to gather materials threshed from different locations within the device.

Theoretical model for the single longitudinal axial flow threshing and separation device

The cumulative separation rate is a critical metric for evaluating the performance of the axial flow threshing and separation device. This parameter is influenced by the physical properties of the grain, as well as the structural and operational parameters of the threshing and separation device. In the process of investigating their relationship, the following assumptions were made to streamline the calculations.

① The probability of grain being threshed and separated in the single longitudinal axial flow threshing and Separation device varies along the axial position. This variation is influenced by the characteristic parameters of the grain as well as the structural and operational parameters of the device.

② The probability of grains being threshed within an axial differential element is directly proportional to the quantity of unthreshed grains within that infinitesimal segment.

③ The likelihood of threshed grains being separated is directly proportional to the quantity of threshed but unseparated grains contained within the differential elements.

The coordinate system (as show in Fig. 2) was established on the single longitudinal axial flow threshing and separation device.

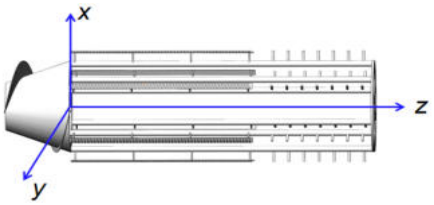


Fig. 2- The coordinate system of the single longitudinal flow threshing and separation device

(1) Threshing and separation model of the rasp bar section

The length of the rasp bar section was expressed as z_1 (as shown in Fig. 3). The total grain mass per unit length in the single longitudinal axial flow threshing and separation device was set as unit 1. The ratio of grain to grass was denoted by γ. And the cumulative threshing rate at the distance z from the feeding inlet was set as *T(z)*. When $0 \le z \le z_1$, the axial micro segment was located in the rasp bar part of the combined threshing and separation component. According to the second assumption, the cumulative threshing rate increment *dT* in differential element *dz* can be expressed as follows.

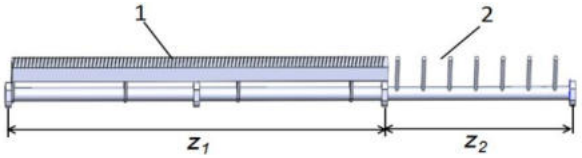


Fig. 3 - The configuration of the rasp bar-nail tooth threshing element
1 – Rasp bar section; 2 – Nail tooth section

$$dT(z) = a_{11}\frac{\gamma}{1+\gamma}\big(1 - T(z)\big)dz \tag{1}$$

where a_{11} is the threshing parameter of the rasp bar section. It is related to the characteristic parameters of millet, the structural parameters and working parameters of the single longitudinal axial flow threshing and separation device.

According to the actual working situation, the cumulative threshing rate of millet is zero when z equals zero. That is $T(z)\big|_{z=0} = 0$. By applying the method of separation of variables and integrating the differential equation in Equation (1), the cumulative threshing rate was obtained as follows:

$$T(z) = 1 - exp\left(-\frac{a_{11}\gamma}{1+\gamma}z\right) \tag{2}$$

The cumulative separation rate at the distance z from the feeding inlet was set as $F(z)$. According to the third assumption, the cumulative separation rate increment dF in axial differential element dz can be expressed as follows:

$$dF(z) = a_{12}\frac{\gamma}{1+\gamma}\big(T(z) - F(z)\big)dz \tag{3}$$

where a_{12} is the separation parameter of the rasp bar section.

According to the actual working situation, the cumulative separation rate of millet is zero when z equals zero. That is $F(z)\big|_{z=0} = 0$. Substituting this into Equation (3), the following expression is obtained:

$$F(z) = 1 + \frac{a_{12}}{a_{11} - a_{12}}exp\left(-\frac{a_{11}\gamma}{1+\gamma}z\right) - \frac{a_{11}}{a_{11} - a_{12}}exp\left(-\frac{a_{12}\gamma}{1+\gamma}z\right) \tag{4}$$

It can be seen from Equation (2) and (4) that both the cumulative threshing rate and the cumulative separation rate of the rasp bar section are an exponential function of the axial coordinate z.

(2) Threshing and separation model of the nail tooth section

The length of the nail tooth section was expressed as z_2 (as shown in Fig. 3). When $z_1 \le z \le z_1+z_2$, the axial micro-segment was located in the nail tooth section of the combined threshing and separation component. According to the second assumption, the cumulative threshing rate increment dT in differential element dz can be expressed as follows.

$$dT(z) = a_{21}\frac{\gamma}{1+\gamma}\big(1 - T(z)\big)dz \tag{5}$$

where a_{21} is the threshing parameter of the nail tooth section.

According to Equation (2), when $z = z_1$, the cumulative threshing rate can be determined and subsequently integrated into Equation (5). Then, by applying the method of separation of variables, the cumulative threshing rate of the nail tooth section can be obtained.

$$T(z) = 1 - exp\left(-\frac{a_{21}\gamma}{1+\gamma}z - \left(\frac{a_{11}\gamma}{1+\gamma} - \frac{a_{21}\gamma}{1+\gamma}\right)z_1\right) \tag{6}$$

According to the third assumption, the cumulative separation rate increment dF in axial differential element dz can be expressed as follows:

$$dF(z) = \frac{a_{22}\gamma}{1+\gamma}\big(T(z) - F(z)\big)dz \tag{7}$$

where a_{22} is the separation parameter of the nail tooth section.

From Equation (4), it can be seen that when $z = z_1$, the cumulative separation rate can be determined and then the expression for the cumulative separation rate can be derived as follows:

$$\begin{aligned} F(z) = 1 + \frac{a_{22}}{a_{21}-a_{22}}exp\left(-\frac{a_{21}\gamma}{1+\gamma}(z-z_1) - \frac{a_{11}\gamma}{1+\gamma}z_1\right) \\ + \left(F(z_1) - 1 - \frac{a_{22}}{a_{21}-a_{22}}exp\left(-\frac{a_{11}\gamma}{1+\gamma}z_1\right)\right)exp\left(-\frac{a_{22}\gamma}{1+\gamma}(z-z_1)\right) \end{aligned} \tag{8}$$

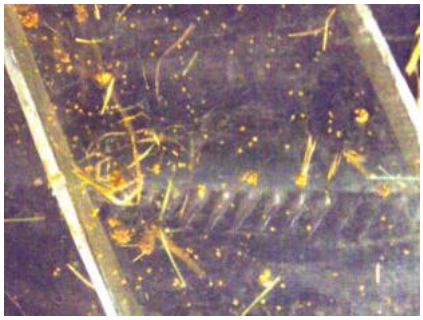
It can be seen from Equations (6) and (8) that both the cumulative threshing rate and the cumulative separation rate of the nail tooth section are an exponential function of the axial coordinate z.

Construction of the threshing parameters and the separation parameters

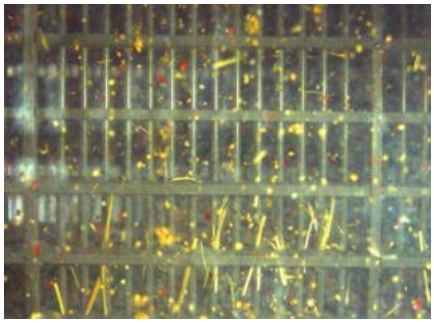
From the derivation of the cumulative threshing rate $T(z)$ and the cumulative separation rate $F(z)$, it is evident that both the threshing parameters a_{11}, a_{21} and the separation parameters a_{12}, a_{22} are dimensionless quantities. In order to determine the threshing parameters and the separation parameters, the threshing process and the separation process of the single longitudinal axial flow threshing and separation device were analyzed.

(1) Construction of the threshing parameters

In the threshing and separation space, there is a periodic impact and rubbing between the rasp bar-nail tooth threshing element and the grain material through the high speed rotation of the threshing component. The grain will be separated from main stem when the acting force between the rasp bar threshing element and the grain material exceeds the connection force of grain and petiole, petiole and branch, branch and main stem. Then the threshing process of the grain will be completed (as Figure 4a).



(a) Threshing process of the grain



(b) Separation process of the grain

Fig. 4 - Threshing and separation process of the grain

The interaction force between the rasp bar section and grain material is mainly determined by the number of rasp bars, the number of transverse lattice on the concave plate and the relative linear velocity between rasps bar and grain material. The connection force of grain and petiole, petiole and branch, branch and main stem is related to the moisture content of millet. According to the analysis of the influencing factors in the threshing process and the theory of dimensional analysis, the following expression of the threshing parameter a_{11} was constructed.

$$a_{11} = c_{10} + c_{11}\frac{n_1 n_2}{h} + c_{12}\frac{n_1 n_2}{hv} \tag{9}$$

where n_1 is the number of rasp bar, n_2 is the number of concave panels, v is the linear velocity of the bar, h is the moisture content of grain, c_{10}, c_{11} and c_{2} are undetermined coefficients.

The interaction force between the nail tooth section and grain material mainly depends on the number of nail teeth, the diameter of nail teeth, the distance between nail teeth and the relative linear speed of the material. According to the theory of dimensional analysis, the following expression of the threshing parameter a_{21} was constructed.

$$a_{21} = c_{20} + c_{21}\frac{n_0 n_1 d_0}{l_0 h} + c_{22}\frac{n_0 n_1 d_0}{l_0 h v} \tag{10}$$

where n_0 is the number of nail teeth in a single combined threshing component, d_0 is the diameter of the nail teeth, l_0 is the distance between nail teeth, c_{20}, c_{21} and c_{22} are undetermined coefficients.

(2) Construction of the separation parameters

The threshed grains need to pass through the stem layer in the single longitudinal axial flow threshing and separation device and then through the grid gap of the concave plate to complete the separation process (as shown in Figure 4b). The resistance of grains passing through the stem layer is proportional to the thickness of the stem layer *(Yi et al., 2008; Vlăduţ et al., 2022)*. The thickness of the stem layer in the threshing separation space mainly depends on the size of the threshing and separation device, the feeding rate of millet, the density of grains and the movement time of grains in the threshing separation space. Therefore, it is assumed that the probability of the grain passing through the stalk layer is inversely proportional to the resistance of the stalk layer. And the resistance of the straw layer is directly proportional to the feeding rate and it is inversely proportional to the roller radius, rotational speed and grain density. The larger the area of grid holes in the concave plate, the easier it is for the seeds to separate through the concave plate. Therefore, it is assumed that the probability of the grain passing through the concave plate is directly proportional to the area of the grid hole of the concave plate. According to the theory of dimensional analysis, the following parameter expressions are constructed.

$$a_{12} = c_{10} + c_{11}\frac{\rho(2R - n_2 l_1)(l - n_3 d_1)}{q} + c_{12}\frac{\rho(2R - n_2 l_1)(l - n_3 d_1)v}{q} \tag{11}$$

where ρ is the density of the grain, n_3 is the number of concave strips, d_1 is the diameter of a concave strip, l_0 is the length of threshing drum, l_1 is the width of the transverse lattice of the concave plate, q is the feed rate, C_{10}, C_{11} and C_{12} are undetermined coefficients.

In the nail tooth section, the stirring effect of nail teeth makes the material in the threshing space loose and increases the probability of grains passing through the stem layer and being separated from the concave plate gap. The separation parameter of the nail teeth is also influenced by the number of nail teeth, their height and the distance between them. According to the theory of dimensional analysis, the following parameter equation is constructed.

$$a_{22} = C_{20} + C_{21}\frac{\rho n_0 n_1 h_0(2R - n_2 l_1)(l - n_3 d_1)}{l_0 q} + C_{22}\frac{\rho n_0 n_1 h_0(2R - n_2 l_1)(l - n_3 d_1)v}{l_0 q} \tag{12}$$

where h_0 is the height of nail teeth, C_{20}, C_{21} and C_{22} are undetermined coefficients.

Fitting test and validation test

Longgu 31 was selected as the test material to carry out the single longitudinal axial flow threshing and separation test in the harvest laboratory of Heilongjiang Bayi Agricultural University (as shown in Fig. 5). The ratio of grain to grass was 1.61. The grain density was 1053 kg/m^3.

(1) Fitting test

There were undetermined coefficients in the threshing parameters a_{11}, a_{21} and the separation parameters a_{12}, a_{22} of the single longitudinal axial flow threshing and separation theoretical model. In order to determine these undetermined coefficients, a single longitudinal axial flow threshing and separation device was built and laboratory tests were carried out. Then the undetermined coefficients in the theoretical model could be determined by fitting equation (4) and (8) with the test data.

The feeding rate was 1.5kg/s. And the grain moisture content was 25% ± 1%. The rotational speed was 800 r/min. All the experiments were repeated 3 times.



(a) Experiment preparation *(b) Experiment in progress*

Fig. 5 - Laboratory testing of threshing and separation performance for Millet

(2) Validation test

To validate the theoretical model, single-factor experiments were conducted on moisture content, feeding rate, and rotational speed. The moisture content of millet was varied between 17% and 32%. The feeding rate was set within the range of 1.5 kg/s to 3.0 kg/s. The rotational speed was tested in the range of 600 to 1000 r/min.

The material receiving trolley was used to collect threshed material from different axial coordinates. The millet in each bucket was separated, weighed, and the weight recorded. At the same time, the mixed millet and unthreshed millet were collected at the straw outlet, weighed, and the weight recorded. Formula (13) was applied to calculate the separation rate of the receiving bucket numbered *i*, and formula (14) was used to calculate the cumulative separation rate at coordinate *z*.

$$F_i = \frac{m_i}{\sum_{i=1}^{14} m_i + m_{mixed} + m_{unthreshed}} \times 100\% \quad (13)$$

$$F(z_i) = \frac{\sum_{j=1}^{i} m_j}{\sum_{i=1}^{14} m_i + m_{mixed} + m_{unthreshed}} \times 100\% \quad (14)$$

RESULTS

The fitting results of undetermined coefficients for threshing parameters and separation parameters

The variation data of the cumulative separation rate along the axis, obtained under the aforementioned test conditions, were presented in Table 1.

Table 1

Single longitudinal axial flow threshing separation laboratory test data of millet

z	Cumulative separation rate			
	Test one	Test two	Test three	Mean value
[m]	[%]	[%]	[%]	[%]
0.00	0.0000	0.0000	0.0000	0.0000
0.01	7.0721	6.8296	6.2932	6.7316
0.02	19.9198	17.7207	18.9419	18.8608
0.03	37.7734	35.6278	41.6141	38.3384
0.04	50.2412	51.9599	56.1289	52.7767
0.05	66.9131	66.4892	71.4036	68.2686

z	Cumulative separation rate			
	Test one	Test two	Test three	Mean value
[m]	[%]	[%]	[%]	[%]
0.06	78.1907	78.2470	80.8602	79.0993
0.07	84.7583	85.2418	86.6465	85.5489
0.08	88.9557	88.4965	90.2538	89.2353
0.09	91.7402	92.3759	93.5216	92.5459
0.10	94.1897	94.7856	95.4434	94.8062
0.11	96.3431	96.6883	97.1033	96.7115
0.12	98.0653	97.6089	98.1360	97.9368
0.13	99.0231	98.5088	98.7495	98.7605
0.14	99.6204	99.3768	99.3977	99.4650

Curve fitted in MATLAB was utilized to fit the data. The fitted process was divided into two segments: the rasp bar section and the nail tooth section, as the cumulative separation rate was a piecewise function. For $0 \le z \le z_1$, the cumulative separation rate of the rasp bar section was fitted using the test data. Consequently, the values of the undetermined coefficients in the threshing and separation parameters were obtained. The equations of a_{11} and a_{12} were then determined as follows:

$$a_{11} = -2.918 + 0.02976\frac{n_1 n_2}{h} - 0.4989\frac{n_1 n_2}{hv} \tag{15}$$

$$a_{12} = 3.867 + 0.01523\frac{\rho(2R - n_2 l_1)(l_0 - n_3 d_1)}{q} + (8.031e - 05)\frac{\rho(2R - n_2 l_1)(l_0 - n_3 d_1)v}{q} \tag{16}$$

Based on the established threshing parameter a_{11} and separation parameter a_{12} in the rasp bar section, parameter fitting for the nail tooth section was carried out. Consequently, the undetermined coefficients a_{21} and a_{22} were obtained. The equations for a_{21} and a_{22} were then determined as follows:

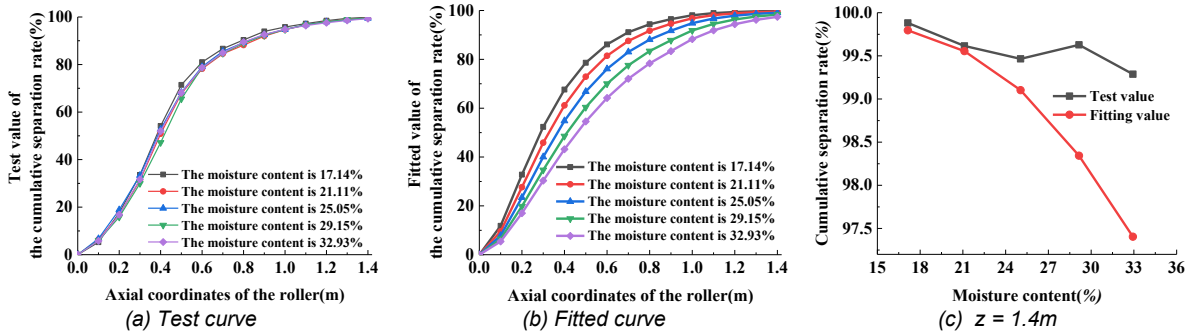
$$a_{21} = 8.165 - 2.464\frac{n_0 n_1 d_0}{l_0 h} + 4.999\frac{n_0 n_1 d_0}{l_0 hv} \tag{17}$$

$$a_{22} = -3.662 + 0.02495\frac{\rho n_0 n_1 h_0(2R - n_2 l_1)(l - n_3 d_1)}{l_0 q} + (5.037e - 04)\frac{\rho n_0 n_1 h_0(2R - n_2 l_1)(l - n_3 d_1)v}{l_0 q} \tag{18}$$

Error Analysis of Calculated Values and Validation Experiments

To validate the accuracy of the theoretical model, a single-factor experiment of millet was conducted using the single longitudinal axial flow threshing and separation device. The factors selected for testing included millet moisture content, feeding rate, and rotational speed. For each varying factor, the separation rate within the buckets was measured, and cumulative separation rate curves as functions of the axial coordinate were plotted. These experimental curves were subsequently compared with the fitted curve obtained from the theoretical model.

(1) Evaluation of the fitting effect of moisture content as a single factor



(a) Test curve (b) Fitted curve (c) z = 1.4m

Fig. 6 - Cumulative separation rate curve under varying moisture content conditions

Table 2

Error analysis table for single factor test of moisture content

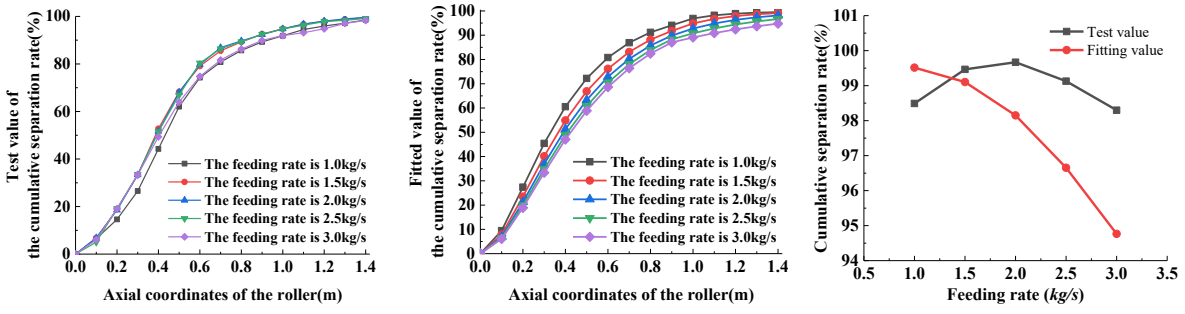
	Error	Moisture content [%]				
		17.14	21.11	25.05	29.15	32.93
Rasp bar section	SSE	0.0926	0.0514	0.0049	0.0245	0.0848
	R-Squared	0.9769	0.9863	0.9987	0.9934	0.9777
Nail tooth section	SSE	0.0015	0.0014	0.0001	0.0039	0.0169
	R-Squared	0.9997	0.9997	0.9999	0.9993	0.9969
Rasp bar-Nail tooth	SSE	0.0934	0.0522	0.0049	0.0264	0.0931
	R-Squared	0.9893	0.9938	0.9994	0.9968	0.9890

The rotational speed was set to 800 r/min, the feeding rate was maintained at 2 kg/s, and the moisture content levels of the millet samples were 17.14%, 21.11%, 25.05%, 29.15%, and 32.93%. The experimental results and fitted values of the cumulative separation rate under different moisture contents were illustrated in Fig. 6. Table 2 presents the SSE and R-Squared values for both the fitted and tested data, specifically detailing the errors for the rasp bar section, the nail tooth section, and the combined rasp bar-nail tooth configuration.

As shown in Fig. 6a) and b), the experimental and fitted values of the cumulative separation rate exhibit exponential distributions with the axial coordinates. On the same axial coordinate, as water content increases, the magnitude of change in the fitting value exceeds that of the test value. As illustrated in Fig. 6c), upon completion of the threshing separation process, both the experimental and fitted values of the cumulative separation rate exceed 97%. As the moisture content increases, both the measured cumulative separation rate and the fitted cumulative separation rate exhibit a downward trend. However, the magnitude of change differs: the measured value decreases by 0.6%, while the fitted value decreases by 2.39%. As shown in Table 2, the SSE values for the rasp bar section, nail tooth section, and the combination of rasp bar - nail tooth components are all less than 1, while the *R-squared* values exceed 0.97. This indicates that the established threshing separation model fits well with changes in moisture content. However, the *R-squared* values for the rasp bar section are consistently lower than those for the nail tooth section, indicating that the model fits the rasp bar section less accurately compared to the nail tooth section.

(2) Evaluation of the fitting effect of feeding rate as a single factor

When the moisture content of millet was 25.0±0.2% and the rotational speed was set to 800 r/min, a single-factor experiment on feeding rate was conducted using the single longitudinal axial flow threshing and separation device. The feeding rate tested were 1.5 kg/s, 2.0 kg/s, 2.5 kg/s, 3.0 kg/s, and 3.5 kg/s. Fig. 7 presents the tested and fitted values of the cumulative separation rate under these different feeding quantities. Table 3 presents the *SSE* and *R-Squared* values for both the fitted data and test data in the single-factor experiment concerning feeding rate.



(a) Test curve *(b) Fitted curve* *(c) z = 1.4m*

Fig. 7 - Cumulative separation rate curve under varying feeding rate conditions

Table 3

Error analysis table for single factor test of feeding rate

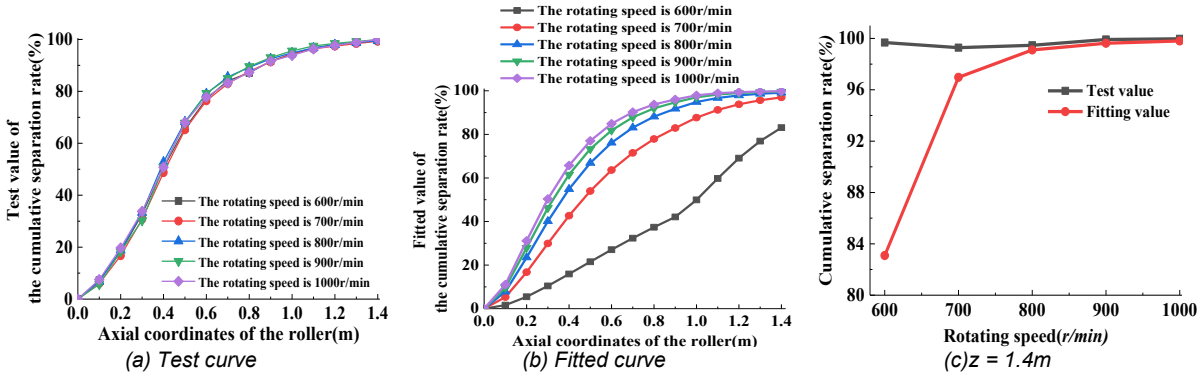
	Error	Feeding rate [kg/s]				
		1.0	1.5	2.0	2.5	3.0
Rasp bar section	SSE	0.1031	0.0049	0.0157	0.0266	0.0120
	R-Squared	0.9704	0.9987	0.9960	0.9931	0.9966

	Error	Feeding rate [kg/s]				
		1.0	1.5	2.0	2.5	3.0
Nail tooth section	SSE	0.0076	0.0001	0.0022	0.0071	0.0052
	R-Squared	0.9986	0.9999	0.9996	0.9987	0.9990
Rasp bar-Nail tooth	SSE	0.1084	0.0049	0.0172	0.0319	0.0163
	R-Squared	0.9862	0.9994	0.9980	0.9963	0.9980

As shown in Fig. 7a) and b), the experimental and fitted values of the cumulative separation rate exhibit exponential distributions with the axial coordinates. As illustrated in Fig. 7c), upon completion of the threshing separation process, the measured cumulative separation rate exceeded 98.30%. The lowest fitted value was 94.76% at a feeding rate of 3.0 kg/s, resulting in a discrepancy of -3.54% between the fitted and measured values. As shown in Table 3, the *R-Squared* values for both the nail tooth section and the rasp bar-nail tooth combination element exceed 0.98. The minimum R-Squared value for the rasp bar section is 0.97, with all fitting values exceeding 0.95. The aforementioned results indicate that the function model exhibits satisfactory fitting performance in response to variations in feeding rate. However, the fitting accuracy for the rasp bar is comparatively lower than that for the nail tooth.

(3) Evaluation of the fitting effect of rotational speed as a single factor

When the moisture content of millet was 25.0 ± 0.20% and the feeding rate was 2.5 kg/s, a single-factor experiment on rotational speed was conducted using the single longitudinal axial flow threshing and separation device. The tested rotational speeds included 600 r/min, 700 r/min, 800 r/min, 900 r/min, and 1000 r/min. Fig. 8 shows the measured and fitted values of cumulative separation efficiency under different rotational speeds. Table 4 shows the *SSE* and *R-Squared* values for both the fitted and test datasets in the single-factor experiment related to rotational speed.



(a) Test curve (b) Fitted curve (c)z = 1.4m

Fig. 8 - Cumulative separation rate curve under varying rotational speed conditions

Table4

Error analysis table for single factor test of rotational speed

	Error	Rotational speed [r/min]				
		600	700	800	900	1000
Rasp bar section	SSE	1.3940	0.0624	0.0049	0.0534	0.0884
	R-Squared	0.6211	0.9827	0.9987	0.9860	0.9763
Nail tooth section	SSE	0.7390	0.0168	0.0001	0.0006	0.0046
	R-Squared	0.8653	0.9969	0.9999	0.9999	0.9992
Rasp bar-Nail tooth	SSE	1.8879	0.0722	0.0049	0.0537	0.0911
	R-Squared	0.7741	0.9913	0.9994	0.9937	0.9891

It can be observed from Fig. 8a) and Fig. 8b) that at the rotational speed of 600 r/min, the fitted curve significantly deviates from the test curve. Furthermore, as shown in Fig. 8(c), when the rotational speed is 600 r/min and z = 1.4, the fitted cumulative separation rate is 83.09%, resulting in a difference of -16.59% compared to the test value. As illustrated in Table 4, when the rotating speed is 600 r/min, the *SSE* values for the rasp bar section and the rasp bar-nail tooth combination exceed 1.

Additionally, the *R-Squared* values for the rasp bar, nail tooth, and rasp bar-nail tooth combination are 0.62, 0.86, and 0.77, all of which are significantly lower than the threshold of 0.95. Consequently, the function model exhibits poor fitting performance at this rotating speed. When the speed is set to 700 r/min, 800 r/min, 900 r/min, and 1000 r/min, the *SSE* values are all below 0.1, while the *R-Squared* values exceed 0.97. Therefore, the function model demonstrates excellent fitting performance.

CONCLUSIONS

(1) Based on the material characteristics of millet, a threshing and separation model utilizing a single longitudinal axial flow threshing separation device was developed. Analysis revealed that both the cumulative threshing rate and the cumulative separation rate of the rasp bar section and the nail tooth section exhibited exponential relationships with the axial coordinate. By examining the threshing and separation processes of millet within the single longitudinal axial flow threshing and separation device, functional expressions for the threshing parameters and separation parameters were formulated.

(2) A single longitudinal axial flow threshing and separation test platform was developed to perform fitting tests. The undetermined coefficients of the threshing and separation parameters were determined through data fitting using Matlab. This process clarified the influence of structural and material parameters on both the cumulative threshing rate and cumulative separation rate of the single longitudinal axial flow threshing and separation device.

(3) A single-factor test was conducted using the longitudinal axial flow threshing and separation device. Through the error analysis of the single-factor test curve and the fitting curve, it was found that when the moisture content ranged from 17.14% to 32.93%, the feed rate was between 1 and 3 kg/s, and the rotational speed was within 700-1000 r/min, the R-Squared values for both the calculated and experimental cumulative separation rate function models exceeded 0.97. This indicates that the model exhibits excellent fit and theoretical capability.

REFERENCES

[1] Dong, C., & Jiang, Y. (1988). Experimental Investigation of the Grain Separation Mechanism and Improvement of Separation Performance in Vertical Axial Flow Separation, Rethreshing, and Cleaning Integrated Devices (籽粒分离机理和提高立置轴流分离、复脱、清选三合一装置分离性能的试验研究) [J]. *Journal of Agricultural Mechanization Research*, (02), 6-16. China.

[2] Kang, D., Wu, C., Liang, S., & Tang, Q. (2017). Design and Test of The Threshing Device of Millet Combine Harvester (谷子联合收获机脱粒装置设计与试验)[J]. *Journal of China Agricultural University*, *22*(02), 135-143. China.

[3] Liang, S., Jin, C., Zhang, F., Kang, D., & Hu, M. (2015). Design and Experiment of 4LZG-3.0 Millet Combine Harvester (4LZG-3.0 型谷子联合收获机的设计与试验) [J]. *Transactions of the Chinese Society of Agricultural Engineering*, *31*(12), 31-38. China.

[4] Liu, J., Wang, D., He, X., Shang, S., Xu, N., Guo, P., Yin, S., & Yang, X. (2021). Design and Experiment of Threshing Device of Sesame Combine Harvester (芝麻联合收获机脱粒装置的设计与试验) [J]. *Journal of Agricultural Mechanization Research*, *12*, 110-114. China.

[5] Liu, W., Ma, L., Zong, W., Liu, J., Li, M., & Lian, G. (2023). Design and Experimentation of a Longitudinal Axial Flow Sunflower Oil Threshing Device [J]. *Agriculture*, *Switzerland, 13*(4), 876. https://doi.org/10.3390/agriculture13040876

[6] Vlăduţ N-V., Biriş S-Ş., Cârdei P., Găgeanu I., Cujbescu D., Ungureanu N., Popa L-D., Perişoară L., Matei G., Teliban G-C. (2022). Contributions to the Mathematical Modeling of the Threshing and Separation Process in an Axial Flow Combine [J]. *Agriculture*, *12*(10), 1520. https://doi.org/10.3390/agriculture12101520

[7] Wan, J., Zhao, X., & Ji, C. (1990). A Mathematical Model for Conventional Grain Thresher and its Application (传统型脱粒装置的数学模型及应用) [J]. *Transactions of the Chinese Society of Agricultural Machinery,* (2), 49-56. China.

[8] Wu, J., Tang, Q., Mu, S., Jiang, L., & Hu, Z. (2022). Test and Optimization of Oilseed Rape (Brassica napus L.) Threshing Device Based on DEM[J]. *Agriculture*, *Switzerland, 12*(10), 1580. https://doi.org/10.3390/agriculture12101580

[9] Yang, Z., Sun, J., & Guo, Y. (2015). Effect of Moisture Content on Compression Mechanical Properties and Frictional Characteristics of Millet Grain (不同含水率对谷子籽粒压缩力学性质与摩擦特性的影响) [J]. *Transactions of the Chinese Society of Agricultural Engineering*, *31*(23), 253-260. China.

[10] Yi, S., Wang, C. Mao, X., & Tao, G. (2008). Observation and Analysis of Motion Rule of Free Kernel in Threshing and Separating Space (轴流滚筒脱粒后自由籽粒空间运动规律的观察与分析) [J]. *Transactions of the Chinese Society of Agricultural Engineering,* (5), 136-139. China.

[11] Zhang, F., & Pang, Q. (2025). Optimization Design of Threshing Device for Dual Longitudinal Flow Combine Harvester (双纵轴流联合收割机脱粒装置优化设计) [J]. *Tractor and Farm Transporter*, *52*(1), 56-60. China.

[12] Zhang, J., & Du, L. (1994). Theoretical Study of Mathematical Model on Threshing and Separating Process (脱粒部件数学模型的建立与模拟)[J]. *Transactions of the Chinese Society of Agricultural Machinery*, (25), 56-60. China.

[13] Zhang, Y., Cui, Q., & Li, H. (2018). Effects of Stem Region, Moisture Content and Blade Oblique Angle on Mechanical Cutting of Millet Stem [J]. *INMATEH-Agricultural Engineering*, *55*(2), 105-112.

[14] Zhang, Y., Cui, Q., & Lin, X. (2019). Variations and Correlations of Shearing Force and Feed Nutritional Characteristics of Millet Straw (谷子秸秆剪切力与其饲料营养特性变化规律及相互关系) [J]. *Transactions of the Chinese Society of Agricultural Engineering*, *35*(5), 41-50. China.

LCNET: LIGHTWEIGHT CONVOLUTIONAL NEURAL NETWORK FOR CORN LEAF DISEASE CLASSIFICATION

एलसीनेट: मकई पत्ती रोग वर्गीकरण के लिए हल्का संवादात्मक तंत्रिका नेटवर्क

Vimal SINGH[*1,2], Anuradha CHUG[1], Amit Prakash SINGH[1]
[1] University School of Information, Communication & Technology Guru Gobind Singh Indraprastha University Dwarka, Sector-16 C, New Delhi 110078 India.
[2] School of Computing Science & Engineering Galgotias University Sector 17-A, Greater Noida, Uttar Pradesh, 203201 India
Tel: +91-9450826954; E-mail: 26.vimal@gmail.com
DOI: https://doi.org/10.35633/inmateh-76-10

Keywords: *LCNet, Convolution Neural Network, Transfer Learning, Corn Leaf Disease, Image Classification*

ABSTRACT
Crop diseases significantly diminish agricultural production, resulting in economic losses. Early detection and species identification remain major challenges. This paper introduces a lightweight Convolutional Neural Network (LCNet) designed for the detection of corn diseases, including blight, common rust, and gray leaf spot, using an efficient, low-latency model. The suggested architecture consists of three convolutional layers, three pooling layers, and one fully linked layer. Experimental findings indicate that LCNet surpasses the pre trained architecture MobileNetV2, DenseNet201, ResNet50, and different past study with an average accuracy of 94.65%. This method enables prompt disease identification, assisting farmers in averting significant crop losses while minimizing human labor in oversight and administration.

ABSTRACT IN HINDI (हिन्दी)
फसल की बीमारियाँ कृषि उत्पादन को काफी कम कर देती हैं, जिसके परिणामस्वरूप आर्थिक नुकसान होता है। इनका शीघ्र पता लगाना और प्रजातियों की पहचान प्रमुख चुनौतियाँ बनी हुई हैं। यह पेपर एक हल्के कन्वोल्यूशनल न्यूरल नेटवर्क (एलसीनेट) का परिचय देता है, जिसे एक कुशल, कम-विलंबता मॉडल का उपयोग करके ब्लाइट, सामान्य जंग और ग्रे लीफ स्पॉट सहित मकई रोगों का पता लगाने के लिए डिज़ाइन किया गया है। सुझाई गई वास्तुकला में तीन संकेंद्रित परतें, तीन पूलिंग परतें और एक पूरी तरह से जुड़ी हुई परत शामिल हैं। प्रायोगिक निष्कर्षों से पता चलता है कि एलसीनेट 94.65% की औसत सटीकता के साथ पूर्व प्रशिक्षित आर्किटेक्चर मोबाइलनेट वी2, डेंसनेट201 रेसनेट50, और विभिन्न पिछले अध्ययनों से आगे निकल जाता है। यह विधि शीघ्र रोग की पहचान करने में सक्षम बनाती है, जिससे किसानों को फसल के महत्वपूर्ण नुकसान को रोकने में सहायता मिलेगी जबकि निरीक्षण और प्रशासन में कम से कम मानव श्रम की आवश्यकता होगी।

INTRODUCTION

The fast proliferation of plant diseases manifests an alarming risk to global crop production, especially for staple crops such as corn, which is a fundamental food supply for millions globally (*Khan et al., 2024*). Traditional disease detection approaches, dependent on human field inspections, are both time-intensive and deficient in the precision required for early-stage diagnosis (*Hossain et al., 2023*). Recent breakthroughs in artificial intelligence and deep learning have enabled the creation of automated, high-precision models for plant disease categorization, therefore markedly improving early detection capabilities (*Hassan et al., 2021*). Convolutional Neural Networks (CNNs) have become the predominant method owing to its capacity to extract hierarchical characteristics from leaf pictures, facilitating the recognition of intricate disease patterns *(Li et al., 2021*). CNNs have emerged as a preeminent method in image-based illness classification, owing to its capacity to acquire hierarchical information, hence enhancing both accuracy and dependability. Several CNN architectures, including MobileNetV2 (*Sandler et al., 2018a*), ConvNet (*Liu et al., 2022*), and EfficientNet (*Howard et al., 2017*) etc. have been applied in previous research to detect and classify plant diseases with high precision. Recent research was used CNN-based deep learning models to improve the categorization of plant leaf diseases. In their study, *Amin et al., (2022*) suggested an end-to-end deep learning system for the detection of corn leaf diseases. Their methodology used two pre-trained convolutional neural networks, EfficientNetB0 and DenseNet121, to derive deep feature representations from corn leaf photos. The retrieved features were concatenated to build a more informative feature set, enhancing model performance. Moreover, data augmentation methods were used to enhance the variety of training samples.

The model was trained and evaluated using the PlantVillage dataset, with an exceptional classification accuracy of 98.56%, surpassing other models such ResNet152 (98.37%) and InceptionV3 (96.26%). Similarly, *Khan et al., (2024*), examined the use of deep transfer learning for the fine-grained categorization of corn leaf diseases. They used four pre-trained deep learning architectures-VGGNet, InceptionV3, ResNet50, and InceptionResNetV2-to identify complex disease patterns in corn leaves. ResNet50 demonstrated exceptional performance, with a validation accuracy of 87.51%, a precision of 90.33%, and a recall of 99.80%, underscoring its proficiency in precise illness detection. This research highlights the capability of deep learning methodologies in enhancing plant disease categorization, facilitating the development of more effective and efficient diagnostic models.

This research presents a LCNet developed for the classification of corn leaf diseases, based on recent advancements. The proposed model improves computational efficiency with a streamlined architecture of three convolutional layers, three pooling layers, and one fully connected layer, therefore significantly reducing the number of trainable parameters while maintaining satisfactory classification accuracy. The key contributions of this study lie in the development of a lightweight CNN-based model specifically designed for the detection of corn leaf diseases, which are summarized as follows:

1. Develop a compact and Lightweight CNN model tailored for the detection of corn diseases such as blight, common rust, and gray leaf spot.
2. The architecture comprising three convolutional layers, three pooling layers, and a fully connected layer to achieve a balance between accuracy and computational efficiency.
3. Achieve superior classification performance with LCNet, outperforming models like MobileNetV2, DenseNet201, and ResNet50, with an average accuracy of 94.65%.
4. Facilitate early and precise identification of crop diseases, aiding farmers in preventing major yield losses while reducing reliance on manual monitoring.
5. Conduct thorough experimental evaluations and comparative studies to validate the proposed model's effectiveness against established deep learning approaches.

The remainder of this paper is organized as follows: The next section provides a review of related studies. The subsequent section details the datasets, methodology, and research framework. Following this, the experimental results are presented and compared with previous works. Lastly, the final section summarizes the conclusions and outlines potential future research directions.

LITERATURE SURVEY

Recent years have seen considerable interest in the early identification and categorization of agricultural diseases with deep learning methods. Conventional techniques for disease diagnosis, including physical examination by agricultural specialists, are often time-consuming, labor intensive, and susceptible to inaccuracies. Researchers have investigated numerous CNN-based algorithms for automated illness diagnosis to tackle these problems. Notable designs, such MobileNetV2 (*Howard et al., 2017*), EfficientNet (*Tan et al., 2019*), and ConvNet *(Liu et al., 2022*) etc. have been widely used owing to their superior accuracy and resilience. Nonetheless, these models sometimes entail substantial computing expenses, rendering them less appropriate for real-time applications in resource-limited agricultural settings.

The article written by *Prasetyo et al., (2023*), focuses on classifying corn plant leaves to distinguish healthy leaves from three disease types: Northern Leaf Blight, Common Rust, and Gray Leaf Spot, using a CNN model based on the ResNet-9 architecture to develop a strong classification system. The dataset included 9,145 photos, allocated into 80% for training and 20% for testing. The researchers performed an epoch comparison to ascertain the ideal model performance across five values: 5, 25, 55, 75, and 100 epochs. The optimal accuracy was attained after 100 epochs, which was then used for the final model training. Furthermore, hyperparameter tweaking experiments were conducted, concentrating on the number of workers (num_workers = 4) and batch size (batch_size = 32), which enhanced the model's performance. The final model had a classification accuracy of 99%. The research study done by *Rachmad et al., (2023*), examined the use of CNN for the early identification and categorization of corn illnesses, with the objective of reducing production losses in Indonesia, a nation heavily reliant on corn. The research used a collection of corn leaf photos gathered from agricultural areas in the Madura Region, focusing on four categorization categories: healthy, gray leaf spot, blight, and common rust. A variety of CNN designs, such as SqueezeNet, AlexNet, ResNet-101, ResNet-50, and ResNet-18, were assessed for their efficacy in illness categorization.

The research used Adam optimization with a learning rate of 0.0001, training models for five epochs with 100 iterations, and implemented a 70:30 division for training and testing. Among the evaluated designs, ResNet-50 exhibited exceptional performance, with an accuracy of 95.59%. These results underscore the capability of CNN-based models in automating corn disease identification, enabling early intervention to reduce agricultural losses.

Ariska et al., (2024), investigated the use of CNN for the automated categorization of corn leaf diseases, using a dataset of 2,145 photos of leaf blight and 1,574 images of leaf spot, capitalizing on the network's capacity to extract and integrate local features for efficient disease detection. The model attained a remarkable classification accuracy of 99%, culminating in a final training accuracy of 99.06% and a validation accuracy of 98.50%. The research proposes further improvements by integrating contemporary architectures like EfficientNet B3 with transfer learning or MobileNet to boost accuracy and processing efficiency. These results highlight the efficacy of CNN-based solutions in precision agriculture, enabling early disease identification and enhanced crop management tactics. *Waheed et al., (2020*), examined the worldwide importance of corn and the adverse effects of diseases such as common rust, gray leaf spot, and northern corn leaf blight, highlighting the need for accurate and prompt disease identification to enhance crop output and quality. The suggested DenseNet model attained an impressive accuracy of 98.06%, surpassing conventional Convolutional Neural Network (CNN) designs like EfficientNet, VGG19Net, NASNet, and Xception Net, while using less parameters. This efficiency indicates the model's applicability for real-time use in agricultural contexts. The research highlights the effectiveness of enhanced deep learning models in diagnosing agricultural diseases, facilitating more sustainable and productive farming methods.

The investigation done by *Ahila Priyadharshini et al., (2019)*, presents a deep learning methodology using a modified LeNet architecture for the categorization of corn leaf diseases. The proposed CNN model is trained on corn leaf images from the PlantVillage dataset, differentiating among four categories: three disease classifications and one healthy category. The experimental findings indicate the model's efficacy, with an accuracy of 97.89%. These results underscore the efficacy of deep learning in agricultural disease diagnosis, providing an economical and precise option for automated crop health monitoring. The work underscores the significance of CNN-based models in precision agriculture, establishing a basis for future research on the optimization and implementation of these systems in practical agricultural contexts. The paper of *Zhang et al., (2021),* presents a CNN model enhanced with a Multi-Activation Function (MAF) module to improve detection accuracy for corn illnesses. Considering the constraints posed by limited illness datasets, the study employs image preprocessing methods to facilitate data augmentation. Furthermore, transfer learning and a warm-up training technique are used to expedite the learning process. The suggested model effectively identifies three corn diseases-maculopathy, rust, and blight-attaining a validation accuracy of 97.41%. To evaluate the efficacy of the MAF module, baseline testing and ablation experiments were performed on many CNN architectures. The findings indicate that the incorporation of the MAF module significantly enhances CNN performance, with optimal results achieved by the amalgamation of Sigmoid, ReLU, and Mish activation functions on ResNet50, resulting in a 2.33% increase in accuracy. The results illustrate the efficacy of optimized CNN models in agricultural contexts, providing a dependable and efficient method for automated corn disease identification.

MATERIALS AND METHODS

The present study adopts a deep learning-based methodology for the automated detection of corn leaf diseases using a lightweight Convolutional Neural Network (LCNet). The proposed framework involves several key stages, including data acquisition, preprocessing, dataset partitioning, model design, training, and performance evaluation (Fig. 1). A diverse set of corn leaf images representing diseases such as blight, common rust, and gray leaf spot was utilized to ensure accurate classification. The LCNet architecture was specifically designed to be computationally efficient, incorporating multiple convolutional and pooling layers to extract relevant features while maintaining low-latency predictions (Fig. 2). The model’s performance was benchmarked against well-known deep learning models such as MobileNetV2, DenseNet201, and ResNet50. Standard evaluation metrics accuracy, precision, recall, and F1-score were employed to assess the model’s effectiveness. Developed using deep learning frameworks, the experimental results demonstrated that LCNet achieved superior classification accuracy with reduced computational overhead, making it a suitable candidate for real-time deployment in agricultural environments.

.

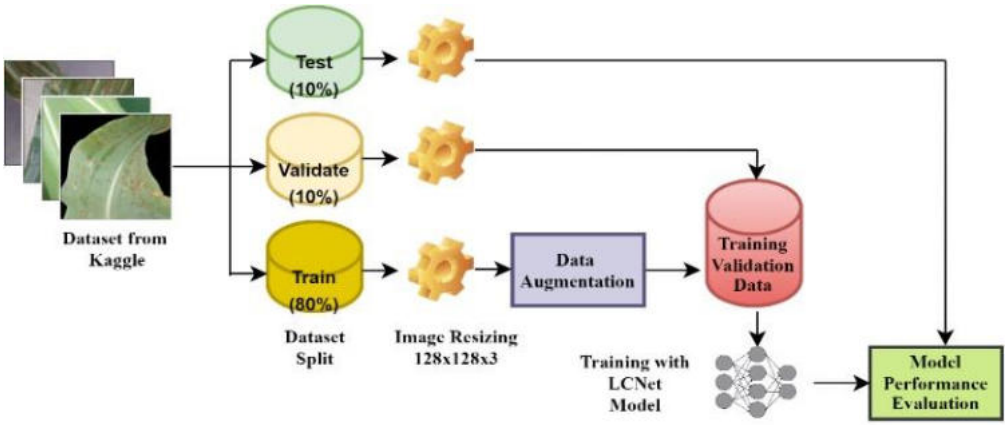


Fig. 1 - Proposed Methodology for CNN based Corn Leaf Disease Classification

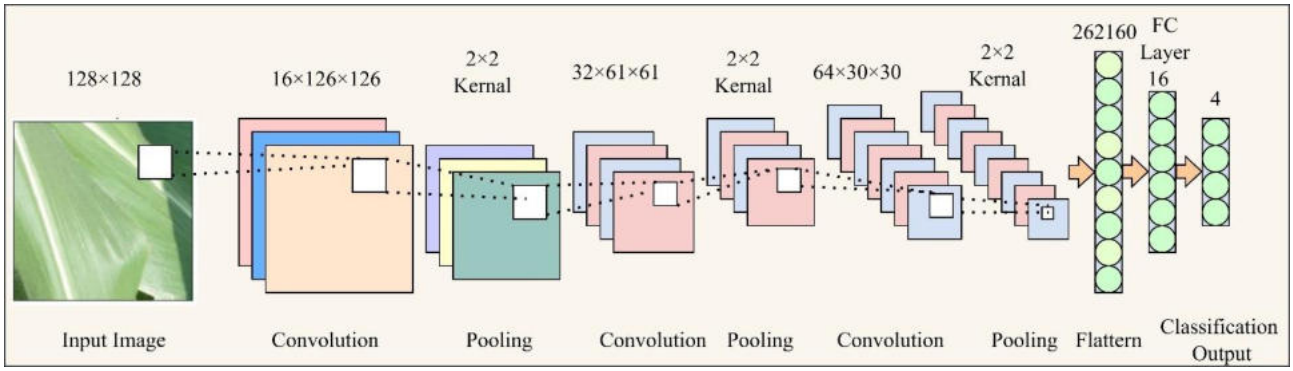


Fig. 2 - Proposed LCNet Model

A. Datasets:

The suggested LCNet model along with existing deep learning architectures, namely MobileNetV2, DenseNet201, and ResNet50, was trained and assessed using a dataset of corn leaf images. These models were employed to classify and identify diseases in previously unseen images. This work used a dataset of 4,188 corn leaf images obtained from Kaggle, classified into four categories: three disease types-common rust, gray leaf spot, and blight-and one healthy category.

To standardize input dimensions, the pictures were scaled to 128×128 pixels for the proposed CNN model. Pixel values were normalized by dividing each by 255, facilitating network weight initialization and enhancing model convergence during training. To facilitate efficient model training and assessment, the dataset was partitioned into training, validation, and testing subsets with an 80:10:10 distribution, a strategy derived from *Sahu et al., (2021*). As a result, 3,348 photos were designated for training, 419 for validation, and 421 for testing. The distribution of the corn dataset is clearly illustrated in (Figs. 3-4). This organized data segmentation enabled effective model training, reducing overfitting and ensuring the model generalizes well to new data. This technique seeks to provide an efficient and precise corn disease detection system with enhanced computing performance.

B. Transfer Learning via popular deep learning pre-trained models:

Training a network from scratch requires a lot of time and resources. Transfer learning is one of the solutions to this problem. It is a set of techniques rather than a single strategy (*Atila et al., 2021*), in which certain pre-trained network weights are employed during training, to handle different problems. According to the requirement of the new problem, the bottom layer of the trained model was replaced by a new layer.

ResNet50: TheResNet50 is a deep convolutional neural network model developed to tackle the difficulties associated with training very deep networks, especially the vanishing gradient issue. It belongs to the Residual Network (ResNet) family, proposed by *He et al., (2016)*, and has 50 layers, making it very efficient for picture classification and identification applications. The fundamental novelty of ResNet50 is its implementation of residual learning via skip connections, enabling

information to circumvent certain levels and directly reach deeper layers. This approach guarantees that deeper networks may be trained effectively without experiencing performance deterioration. The ResNet50 design comprises convolutional layers, batch normalization, ReLU activation, pooling layers, and fully connected layers, with residual blocks crucial for ensuring steady gradient propagation. Each residual block has three convolutional layers (1×1, 3×3, and 1×1), which enhance feature extraction and facilitate dimensionality reduction. ResNet50 utilizes identity mappings to facilitate the learning of intricate patterns while ensuring computational efficiency. One significant feature of ResNet50 is its capacity to attain high accuracy in picture classification tasks while incurring comparatively lower computing expenses than deeper models. It has been extensively used in medical image analysis, object identification, autonomous driving, and transfer learning because of its proficiency in generalizing across diverse domains. ResNet50, pre-trained on extensive datasets such as ImageNet, may be fine-tuned for applications, making it a potent and versatile instrument for diverse computer vision tasks.

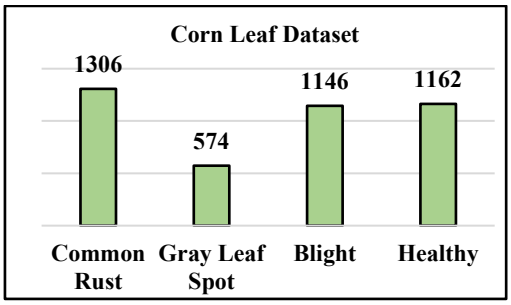


Fig. 3 - Corn Leaf Dataset

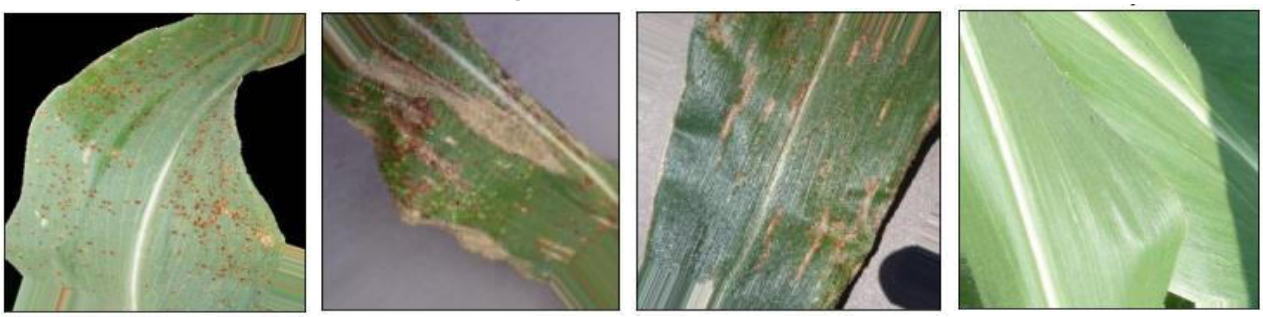


Fig. 4 - Image from Corn Leaf Dataset

(a) Common Rust Disease; (b) Blight Disease; (c) Gray Leaf Spot Disease; (d) Healthy images

DenseNet: This deep learning architecture was designed to enhance feature propagation and address the challenge of vanishing gradients commonly encountered in convolutional neural networks (CNNs). Introduced by *Huang et al., (2017*), DenseNet improves network performance through the implementation of dense connections, where each layer is directly connected to all subsequent layers within a dense block. Unlike traditional CNNs that follow a sequential information flow, DenseNet promotes the reuse of feature maps across layers, thereby improving gradient transmission and supporting efficient feature learning. Its structure comprises densely connected blocks separated by transition layers that incorporate batch normalization, 1×1 convolutions, and average pooling, which help regulate network complexity and reduce the number of parameters. This design leads to higher accuracy with fewer parameters compared to deeper architectures like ResNet. DenseNet is available in various configurations, such as DenseNet-121, DenseNet-169, DenseNet-201, and DenseNet-264, which indicate the number of layers. A significant advantage of DenseNet is its ability to deliver strong performance with reduced computational and memory demands, making it highly suitable for tasks like image classification, medical image processing, and object detection. Additionally, DenseNet models pre-trained on large-scale datasets like ImageNet are widely applied in transfer learning, allowing them to be fine-tuned for domain-specific problems. The model's efficient feature reuse mechanism reduces redundancy and enhances learning capabilities, positioning it as an optimal choice for high-accuracy applications with limited computational resources.

MobileNetV2: MobileNetV2, is a streamlined and effective convolutional neural network architecture tailored for mobile and embedded applications, providing a compromise between precision and computing economy. It was introduced by (Sandler et al., 2018b), with the integration of inverted residuals and linear bottlenecks, therefore markedly enhancing performance and reducing computing complexity. The fundamental innovation of MobileNetV2 is the depth wise separable convolution, which reduces the number of parameters and computations. It preserves a streamlined architecture while attaining competitive accuracy, making it exceptionally appropriate for picture classification, object identification, facial recognition, and AI-driven mobile apps. Its efficacy facilitates implementation on low-power devices, including smartphones, IoT devices, and edge computing systems. MobileNetV2, pre-trained on extensive datasets such as ImageNet, may be fine-tuned for specific applications, enabling significant versatility across several domains. It is extensively used in deep learning applications that need rapid inference and low resource usage, owing to its optimal balance between accuracy and computational economy.

Hyper-Parameters:

Hyperparameters are crucial for enhancing the training process of deep learning models. In this study, all pre-trained models were trained with a learning rate of 0.001 and used the Adam optimizer with a momentum value of 0.999. The ReLU activation function was used in all layers to improve non-linearity, while the softmax function was employed in the output layer to enable multi-class classification. The suggested LCNet model was trained using certain hyperparameters, guaranteeing effective learning and performance. The comprehensive setup of these parameters is shown in Table 1.

Table 1

Different hyper-parameters selected in the proposed CNN model

Hyper-parameter	Description
Learning rate	0.0001
Batch size	32
Number of epochs	250
Dropout	0.3
Optimizer	Adam
Momentum	0.999
Activation function	ReLu

C. Performance Matrices:

The suggested model's performance was assessed using several measures, including accuracy, precision, recall, and F1 score. Where, assessing accuracy and recall is an essential component of machine learning model evaluation, since it quantifies the balance between false positives and false negatives. Precision quantifies the ratio of accurately predicted positive samples to the total expected positives, reflecting the model's dependability in positive classifications. Conversely, recall measures the model's efficacy in identifying true positive samples inside the dataset. Furthermore, the F1 score, denoting the harmonic mean of accuracy and recall, was computed to provide a balanced assessment of model efficacy. An elevated F1 score indicates that the model achieves an effective equilibrium between accuracy and recall, making it a reliable instrument for classification endeavors.

These assessment measures guarantee that the proposed model accurately and reliably differentiates across various classes.

$$Accuracy = \frac{(TP+TN)}{(TP+TN+FP+FN)} \quad (1)$$

$$Precision = \frac{TP}{(TP+FP)} \quad (2)$$

$$Recall = \frac{TP}{(TP+FN)} \quad (3)$$

$$F1 - Score = 2 \times \frac{(TP \times FP)}{(TP+FP)} \quad (4)$$

where: TP is True Positive, TN is True Negative, FP is False Positive, FN is False Negative

D. Hardware and Software Used:

This section presents and examines the outcome of the suggested strategy. The Keras library was employed in this study to create the suggested approach's structure. The Python-based Keras library provides a high-level API for creating deep learning architectures that can be built on top of other numerical computing libraries like TensorFlow. The proposed CNN model was trained with NVIDIA DGX A100 machine. The specification of the system is shown in Table 2:

Table 2

NVIDIA DGX A100 machine specification

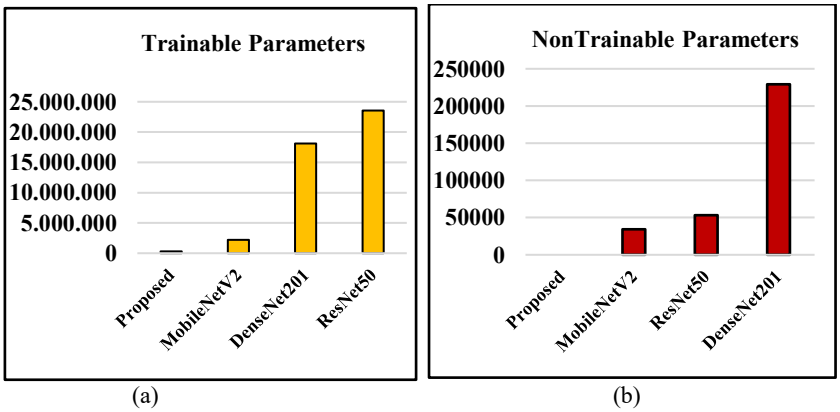
Specification	Description
GPU	8xNVIDIA A100 Tensor core GPUs
GPU Memory	320 GB
Performance	5 peta FLOPS AI 10petaOPS INT8
CPU	Dual AMD Rome 7742, 128 cores, 2.25 GHz(base), 3.4 GHz(max boost)

RESULTS

This research assesses the efficacy of LCNet in identifying corn diseases, comparing its performance with three widely used pre-trained convolutional neural networks: MobileNetV2, ResNet50, and DenseNet201, as illustrated in Fig. 5-6 and Table 3, and compared with previous studies in Table 4. The assessment was grounded on critical performance criteria, including validation accuracy, validation loss, and computing efficiency, quantified by trainable and non-trainable parameters. All models were trained under identical parameter configurations, with a learning rate of 0.001, the Adam optimizer, and a momentum of 0.999, to provide an equitable comparison.

ResNet50 exhibited robust performance, with a validation accuracy of 91.27% and a validation loss of 0.2448. It necessitated 23,542,788 trainable parameters and 229,056 non-trainable parameters, making it computationally demanding. MobileNetV2 attained a validation accuracy of 90.19%, although recorded the greatest validation loss of 0.5175. It surpassed ResNet50 in efficiency, requiring 2,228,996 trainable parameters and 34,112 non-trainable parameters. DenseNet201 had the lowest validation accuracy at 87.88%, accompanied by a validation loss of 0.3413. Notwithstanding its reduced accuracy, it exhibited a markedly elevated computational burden, using 53,120 trainable parameters and 18,100,612 non-trainable parameters. The suggested LCNet model surpassed all pre-trained architectures, with the maximum validation accuracy of 94.65% and the lowest validation loss of 0.1559 as shown in Fig. 7. Moreover, LCNet exhibited exceptional computational efficiency, necessitating just 285,812 trainable parameters, making it an optimal selection for resource-limited settings.

The findings demonstrate that LCNet achieves an optimum equilibrium between precision and computing efficiency, making it suitable for real-time agricultural applications. The substantial decrease in trainable parameters indicates that LCNet can function efficiently on edge devices with constrained processing capabilities, hence guaranteeing its practical applicability for early disease detection in crops. The approach facilitates prompt disease detection, hence promoting proactive strategies to mitigate crop losses and enhance agricultural output.



(a) (b)

Fig. 5 - Comparison of total number of:

(a) trainable and (b) non-trainable parameters for proposed CNN, MobileNetV2, DenseNet201 and ResNet50.

Table 3

Performance of different models used in the study along with the proposed model

Model	Trainable Parameters	Non-trainable Parameters	Validation Accuracy	Validation Loss
MobileNetV2	2,22,89,96	34,112	90.19	0.5175
DenseNet201	1,81,00,612	53,120	87.88	0.3413
ResNet50	2,35,42,788	2,29,056	91.27	0.2448
Proposed Model	2,85,812	0	94.65	0.1559

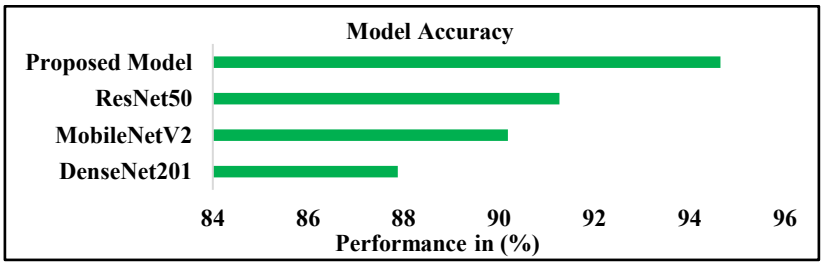
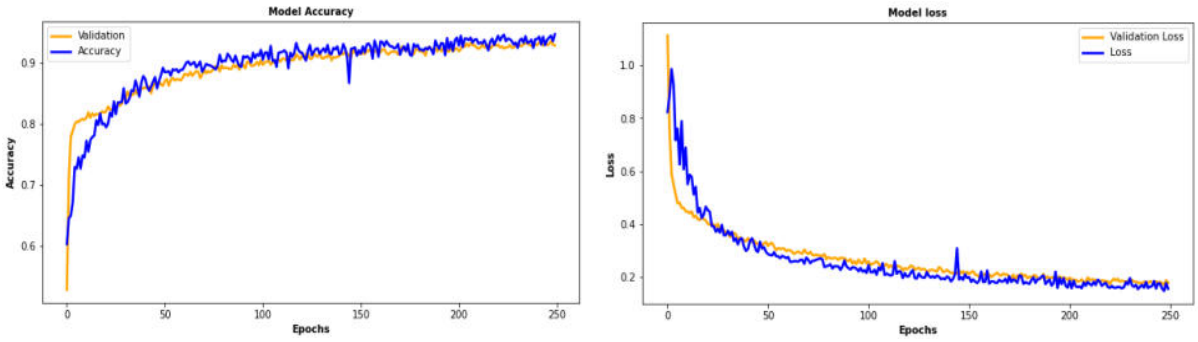


Fig. 6 - Performance of the proposed and pre-trained models in percentage (%)

Table 4

Performance comparison of the proposed model with past study based on corn

Study	Method	Accurcy (%)
Firmansyah et al., (2024)	Proposed CNN training from scratch	84.50
Hang et al., (2019)	CNN with inception module	91.70
Syarief et al., (2020)	AlexNet, VGG16-19, GoogleNet, Inception-V3, ResNet50-101	93.50
Proposed Model	LCNet	94.65



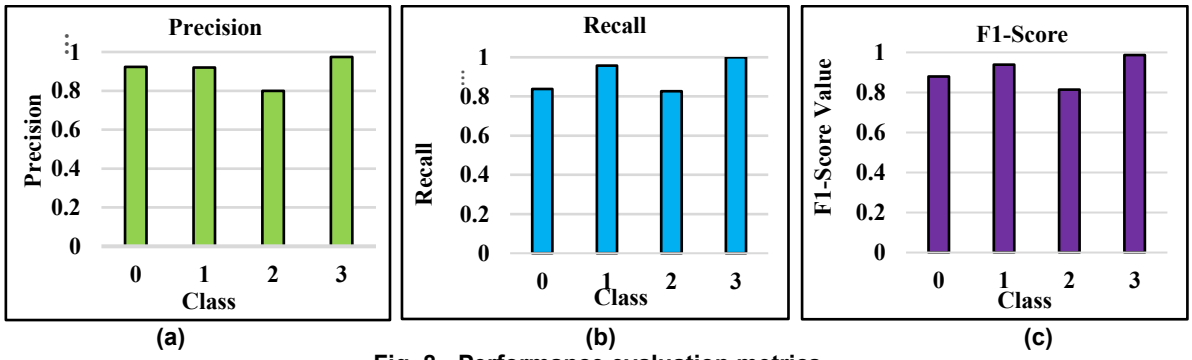
(a) **(b)**

Fig. 7 - (a) Accuracy and (b) Loss plot of the Proposed CNN Model

Table 5

Class-wise performance metrics—precision, recall and F1-score—achieved by the proposed model

Class Name	Class	Precision	Recall	F1-Score
Blight	0	0.9234	0.8391	0.8793
Common Rust	1	0.9194	0.9580	0.9383
Gray Leaf Spot	2	0.8000	0.8276	0.8136
Healthy	3	0.9749	1.0000	0.9873



(a) (b) (c)

Fig. 8 - Performance evaluation metrics

(a) Precision, (b) Recall and (c) F1-Score for the proposed model

CONCLUSIONS

This research presents an effective deep learning-based approach for classifying corn leaf diseases using a dataset of 4,188 images categorized into four groups: Common Rust, Gray Leaf Spot, Blight, and Healthy. A novel model, LCNet, was introduced and its performance was evaluated against established pre-trained architectures-MobileNetV2, DenseNet201, and ResNet50-as well as comparative studies from existing literature. LCNet demonstrated superior performance with a validation accuracy of 94.65% and a validation loss of 0.1559, outperforming MobileNetV2 (90.19%), DenseNet201 (87.88%), and ResNet50 (91.27%). These findings confirm LCNet's effectiveness in achieving high classification accuracy and efficient computation for corn leaf disease recognition. Looking ahead, future work will focus on fine-tuning model parameters through the Optuna optimization framework to further improve predictive accuracy. Additionally, the development of a lightweight mobile application is planned to support real-time, on-field disease detection, offering a practical and cost-effective tool for farmers and agricultural professionals.

ACKNOWLEDGEMENT

This study has been funded by the Department of Science and Technology (DST) under the project bearing reference number "DST/Reference No. T-319/2018-19." The authors sincerely acknowledge the support and financial assistance provided by DST, which played a crucial role in the successful completion of this research.

REFERENCES

[1] Ahila Priyadharshini, R., Arivazhagan, S., Arun, M., & Mirnalini, A. (2019). Maize leaf disease classification using deep convolutional neural networks. *Neural Computing and Applications*, *31*(12), 8887–8895. doi: 10.1007/S00521-019-04228-3

[2] Amin, H., Darwish, A., Hassanien, A. E., & Soliman, M. (2022). End-to-End Deep Learning Model for Corn Leaf Disease Classification. *IEEE Access*, *10*, 31103–31115. doi: 10.1109/ACCESS.2022.3159678

[3] Ariska, R., Sari, C. A., & Rachmawanto, E. H. (2024). Classification of Corn Leaf Disease Using Convolutional Neural Network. *Advance Sustainable Science Engineering and Technology*, *6*(4), 0240408. doi: 10.26877/ASSET.V6I4.772

[4] Atila, Ü., Uçar, M., Akyol, K., & Uçar, E. (2021). Plant leaf disease classification using EfficientNet deep learning model. *Ecological Informatics*, *61*. doi: 10.1016/j.ecoinf.2020.101182

[5] Firmansyah, R., & Nafi'iyah, N. (2024). Identifying Types of Corn Leaf Diseases with Deep Learning. *Journal of Intelligent System and Computation*, *6*(1), 18–23. doi: 10.52985/insyst.v6i1.347

[6] Hang, J., Zhang, D., Chen, P., Zhang, J., & Wang, B. (2019). Classification of Plant Leaf Diseases Based on Improved Convolutional Neural Network. *Sensors*, *19*(19), 4161. doi: 10.3390/s19194161

[7] Hassan, S. M., Jasinski, M., Leonowicz, Z., Jasinska, E., & Maji, A. K. (2021). Plant disease identification using shallow convolutional neural network. *Agronomy*, *11*(12). doi: 10.3390/agronomy11122388

[8] He, K., Zhang, X., Ren, S., & Sun, J. (2016). Deep Residual Learning for Image Recognition. *2016 IEEE Conference on Computer Vision and Pattern Recognition (CVPR)*, 770–778. doi: 10.1109/CVPR.2016.90

[9] Hossain, Md. I., Jahan, S., Al Asif, Md. R., Samsuddoha, Md., & Ahmed, K. (2023). Detecting tomato leaf diseases by image processing through deep convolutional neural networks. *Smart Agricultural Technology*, *5*, 100301. doi: 10.1016/j.atech.2023.100301

[10] Howard, A. G., Zhu, M., Chen, B., Kalenichenko, D., Wang, W., Weyand, T., Andreetto, M., & Adam, H. (2017). *MobileNets: Efficient Convolutional Neural Networks for Mobile Vision Applications*. Retrieved from https://arxiv.org/abs/1704.04861v1

[11] Huang, G., Liu, Z., Van Der Maaten, L., & Weinberger, K. Q. (2017). Densely connected convolutional networks. *Proceedings - 30th IEEE Conference on Computer Vision and Pattern Recognition, CVPR 2017*, *2017-Janua*, 2261–2269. doi: 10.1109/CVPR.2017.243

[12] Khan, I., Sohail, S. S., Madsen, D. Ø., & Khare, B. K. (2024). Deep transfer learning for fine-grained maize leaf disease classification. *Journal of Agriculture and Food Research*, *16*, 101148. doi: 10.1016/J.JAFR.2024.101148

[13] Li, L., Zhang, S., & Wang, B. (2021). Plant Disease Detection and Classification by Deep Learning - A Review. In IEEE Access (Vol. 9, pp. 56683–56698). Institute of Electrical and Electronics Engineers Inc. doi: 10.1109/ACCESS.2021.3069646

[14] Liu, Z., Mao, H., Wu, C. Y., Feichtenhofer, C., Darrell, T., & Xie, S. (2022). A ConvNet for the 2020s. *Proceedings of the IEEE Computer Society Conference on Computer Vision and Pattern Recognition*, *2022-June*, 11966–11976. doi: 10.1109/CVPR52688.2022.01167

[15] Prasetyo, T. A., Desrony, V. L., Panjaitan, H. F., Sianipar, R., & Pratama, Y. (2023). Corn Plant Disease Classification Based on Leaf using Residual Networks-9 Architecture. *International Journal of Electrical and Computer Engineering (IJECE)*, *13*(3), 2908–2920. doi: 10.11591/IJECE.V13I3.PP2908-2920

[16] Rachmad, A., Fuad, M., & Rochman, E. M. S. (2023). Convolutional Neural Network-Based Classification Model of Corn Leaf Disease. *Mathematical Modelling of Engineering Problems*, *10*(2), 530–536. doi: 10.18280/MMEP.100220

[17] Sahu, P., Chug, A., Singh, A. P., Singh, D., & Singh, R. P. (n.d.). Deep Learning Models for Beans Crop Diseases: Classification and Visualization Techniques. *International Journal of Modern Agriculture*, *10*(1), 2021.

[18] Sandler, M., Howard, A., Zhu, M., Zhmoginov, A., & Chen, L. C. (2018a). MobileNetV2: Inverted Residuals and Linear Bottlenecks. *Proceedings of the IEEE Computer Society Conference on Computer Vision and Pattern Recognition*, 4510–4520. doi: 10.1109/CVPR.2018.00474

[19] Sandler, M., Howard, A., Zhu, M., Zhmoginov, A., & Chen, L. C. (2018b). MobileNetV2: Inverted Residuals and Linear Bottlenecks. *Proceedings of the IEEE Computer Society Conference on Computer Vision and Pattern Recognition*, 4510–4520. doi: 10.1109/CVPR.2018.00474

[20] Syarief, M., & Setiawan, W. (2020). Convolutional neural network for maize leaf disease image classification. *TELKOMNIKA (Telecommunication Computing Electronics and Control)*, *18*(3), 1376. doi: 10.12928/telkomnika.v18i3.14840

[21] Tan, M., & Le, Q. V. (2019). EfficientNet: Rethinking Model Scaling for Convolutional Neural Networks. *36th International Conference on Machine Learning, ICML 2019*, *2019-June*, 10691–10700. Retrieved from https://arxiv.org/abs/1905.11946v5

[22] Waheed, A., Goyal, M., Gupta, D., Khanna, A., Hassanien, A. E., & Pandey, H. M. (2020). An optimized dense convolutional neural network model for disease recognition and classification in corn leaf. *Comput. Electron. Agric.*, *175*. doi: 10.1016/J.COMPAG.2020.105456

[23] Zhang, Y., Wa, S., Liu, Y., Zhou, X., Sun, P., & Ma, Q. (2021). High-Accuracy Detection of Maize Leaf Diseases CNN Based on Multi-Pathway Activation Function Module. *Remote. Sens.*, *13*(21). doi: 10.3390/RS13214218

DESIGN AND PARAMETER OPTIMIZATION OF A SEED STORAGE DEVICE OF A WHEAT PLOT SEEDER
/
小麦小区播种机存种装置的设计与参数优化

Chen XUE, Liqing CHEN*), Zengbin CAI and Qi WANG
College of Engineering, Anhui Agricultural University, Hefei, Anhui, 230036 / China
Tel: +86 13966658997; E-mail: lqchen@ahau. edu. cn
DOI: https://doi.org/10.35633/inmateh-76-11

Keywords: *wheat plot seeder; seed storage device; seed separation uniformity; EDEM*

ABSTRACT
To improve the seed separation uniformity in the seed storage device of a wheat plot seeder, this paper investigates the key factors influencing its performance. First, the working principle of the seed storage device and the movement of seeds are analyzed, and the lifting mechanism of the seed storage tube is controlled by an electric pusher. Based on this analysis, the relevant parameter factors are identified. Next, EDEM software is used to simulate the seed storage process and determine the optimal combination of parameters. A three-factor, three-level central composite design experiment is conducted, with the inner diameter of the seed storage tube (D), the lifting height (L), and the lifting speed (V) as the test factors. The coefficient of variation of seed distribution uniformity (m_1) is used as the performance index. The optimal values determined for the parameters are D = 0.06 m, L = 0.015 m, and V = 0.05 m/s. Finally, bench experiments are carried out to verify the results. The experimental findings show that the average coefficient of variation for seed distribution using the traditional lifting lever is 6.46%, while the optimized parameters reduce it to 4.12%, significantly improving seed separation uniformity and meeting the seeding requirements.

摘要
为提高小麦小区播种机存种装置的分种均匀性，对小区播种机存种装置的相关试验因素进行了研究。首先，分析了存种装置的工作原理和种子的运动，通过电动推杆控制存种筒的升降；在此基础上，确定了存种装置的相关参数因素。其次，利用EDEM软件对存种装置进行仿真，以存种筒的内径(D)、上升高度(L)和上升速度(V)为试验因素，以种子分散均匀性变异系数(m_1)为性能指标进行三因素三水平的中心组合设计实验，确定各参数因子的最优组合为 D=0.06m, L=0.015m 和 V=0.05m/s*；最后，通过台架实验对优化参数进行了验证。试验结果表明，传统提升杆的平均种子分散均匀性变异系数为 6.46%，而优化参数下的平均种子分散均匀性变异系数为 4.12%，提高了种子分散均匀性，满足播种要求。*

INTRODUCTION
Seeds are the fundamental core of agriculture, playing a crucial role in agricultural development. Plot seeding is a key step in the breeding process, and its operational quality directly influences seed selection and breeding outcomes, making it highly significant for food security (*Shang et al., 2021; Zhou et al., 2022; Wang et al., 2022; Feng et al., 2024*). In this context, the wheat plot seeder is a specialized machine used in field experiments to breed high-quality crop varieties. The Austrian company WINTERSTEIGER introduced the world's first plot precision seeder in 1980, which employed suction seeding technology to precisely place individual seeds - an innovation that had a revolutionary impact on agricultural production. As a leading model for plot seeding, the wheat plot seeder performs seeding operations through manual feeding, cone filling, grid tray transportation, seed discharge via the outlet, and distribution using a centrifugal seed divider. Both in China and abroad, plot seeding is commonly conducted using such machines, significantly reducing manual labor requirements (*Cheng et al., 2018; Gao et al., 2022; Okeyo et al., 2020*).

In breeding trials or actual production, it is often necessary to sow multiple crop varieties within a single plot, with each variety requiring a relatively independent and appropriately sized area. The quality of seeding is directly linked to the subsequent growth and development of the crops. Uneven seeding can result in irregular plant distribution within the test plot, thereby compromising the accuracy and reliability of experimental results (*Beckman et al., 2022; Kovács et al., 2023*).

To enhance seeding performance, researchers both domestically and internationally have conducted extensive studies (*Karayel et al., 2022; Yatskul et al., 2018; Zhao et al., 2022; Yuan et al., 2024*).

Gong et al., (2011), proposed an electronic control system for plot seeders and identified the optimal distributor speed for sowing different seed types. *Cheng et al., (2019),* analyzed the effects of three key factors - seed distributor speed, seed separation angle, and seed separation distance - on seeding uniformity, and optimized the corresponding parameters. *Yang et al., (2019),* developed a magazine-type seeding device for plant-row drill planters to address issues of excessive manual labor and low operational efficiency. *Chen et al., (2020),* designed a three-leaf automatic cleaning and seed-changing air-suction seeder for soybean breeding, capable of quickly clearing and replacing residual seeds between plots without requiring machine stoppage. *Liu et al., (2023)*, investigated the forces acting on buckwheat seeds, identifying key influencing factors such as seed displacement, rotation rate, and seed gap layout, and determined the optimal parameter combination through experiments. *Yu et al., (2023),* explored the effects of distributor rotational speed, the number of distributor bosses, and boss length on seeding performance, providing a theoretical foundation for further improvements in seed distributor design. These studies have significantly contributed to enhancing the operational performance of plot seeders. However, uneven seed distribution remains an issue in actual sowing operations, which continues to limit overall work efficiency.

The seeding process initiated by the seed storage device is the first and foundational step in the overall operation of a plot seeder. It plays a critical role in ensuring the effectiveness and uniformity of the entire seeding process. In response to the challenges outlined above, this study focuses on the seed storage device of the plot seeder, aiming to enhance seed distribution uniformity. The findings of this research provide a theoretical and practical foundation for improving the uniformity of wheat seeding in plot trials.

MATERIALS AND METHODS

Structure of seed storage device

The XBJ-150 wheat plot seeder is selected as the research subject, with Figure 1 illustrating the overall machine structure and the configuration of its seed storage device. The seed storage system consists primarily of a seed storage tube and an electric pusher. During operation, wheat seeds are loaded into the seed storage device. The seed storage tube is raised via wireless remote control, allowing the seeds to slide evenly along the conical surface into the slots of the conical lattice disc seed-metering device (*Cheng et al., 2021*). Once all the seeds have been dispensed, the seed storage tube is lowered, again via wireless remote control, until it returns to its original position.

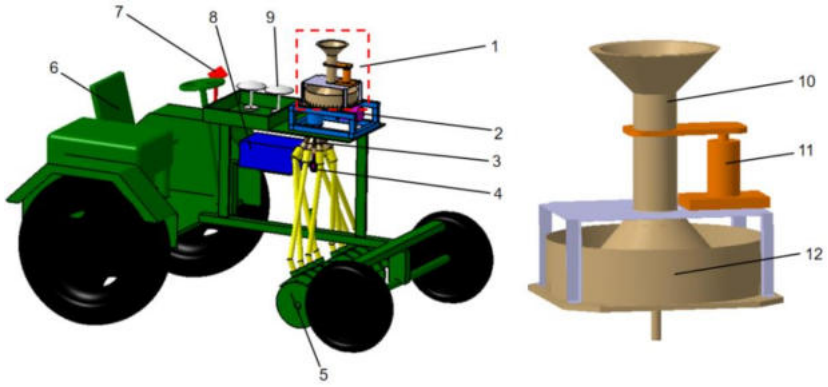


Fig. 1 - Overall structure of the wheat plot seeder and seed storage device structure
1-Seed storage device; 2-Stepper motor; 3-Seed distributor; 4-DC motor; 5-Furrow opener; 6-Operator`s workplace; 7-Human-machine display screen; 8-Controller; 9-BeiDou antenna; 10-Storage tube; 11-Electric pusher; 12-Conical lattice disc seed-metering device

Analysis and determination of experimental factors

As the seed storage tube rises, the wheat seeds slide uniformly into the slots of the conical lattice disc seed-metering device along the cone surface. Figure 2 presents a stress analysis of the forces acting on wheat seeds during their movement along the conical surface. The equations governing this stress analysis are as follows:

$$F_r cos\alpha + \mathrm{mgsin}\alpha - f = \mathrm{m}a_x \quad (1)$$

$$F_r sin\alpha - \mathrm{mgcos}\alpha + F_N = \mathrm{m}a_y \quad (2)$$

where: F_r is the centrifugal force (N); F_N represents the supporting force exerted by the cone on the wheat seeds (N); f is the friction force between the cone surface and the wheat seeds (N); and mg is the gravitational force acting on the seeds (N).

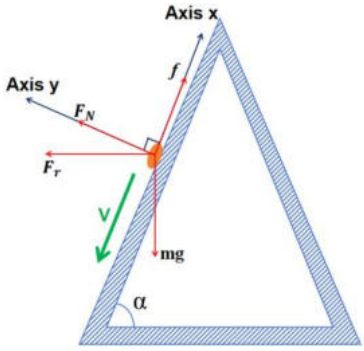


Fig. 2 - Force analysis of wheat seeds moving on the cone

The inner diameter and lifting height of the seed storage tube are key parameters that significantly influence the performance of the seed storage device. The uniform distribution of seeds into the slots of the metering device has a direct impact on seeding quality. The inner diameter of the seed storage tube determines the accumulation height of seeds under a fixed seed quantity. If the diameter is too small, resulting in a high seed accumulation, the vibration-induced adjustment of seed flow is effective. However, excessive seed accumulation can compromise the stability of seed motion when the tube is lifted, thereby negatively affecting distribution uniformity. Conversely, if the diameter is too large and the seed accumulation height is too low, it becomes difficult to generate relative motion within the wedge-shaped slot. This weakens the effect of vibration adjustment, also leading to poor seeding uniformity.

The lifting height of the seed storage tube determines the quantity of seeds that can slide out per unit time once the tube reaches its predetermined height. A smaller lifting height results in reduced seed interference, which can promote stable flow. However, the limited height may also restrict seed movement, increasing the risk of blockage and negatively impacting distribution uniformity. Conversely, when the lifting height is increased, the influence of the seed storage tube on seed flow is reduced, allowing a larger quantity of seeds to be released. However, this also results in a more uniform initial motion state among the seeds, leading to greater mutual interference during descent, which can likewise compromise uniformity.

The lifting speed of the seed storage tube also plays a critical role in maintaining seed distribution uniformity. When the lifting speed is too slow, the seeds remain in contact with the tube for a longer duration, making them more susceptible to interference from the tube wall. This can lead to blockages and uneven seed flow, thereby reducing uniformity. Conversely, if the lifting speed is too fast, the influence of the tube on the seeds is minimized, but the rate at which seeds exit the storage tube increases sharply. This can cause heightened mutual interference among the seeds during their movement, which also negatively affects uniformity.

Therefore, it is necessary to comprehensively consider the influence of the inner diameter, the lifting height, and the lifting speed of the seed storage tube on the uniformity of seed storage to achieve the best seeding effect. The optimal combination of three factors, namely the inner diameter of the seed storage tube (D), the lifting height of the seed storage tube (L) and the lifting speed of the seed storage tube (V), is selected to improve the uniformity of seed dispersion in the slot. According to the structure, working principle and working efficiency of the seed storage device of the wheat plot seeder (*Liu et al., 2010*), it is determined that the diameter of the seed storage tube ranges from 0.04 m to 0.08 m, the lifting height of the seed storage tube ranges from 0.005 m to 0.025 m, and the lifting speed of the seed storage tube ranges from 0.02m/s to 0.08m/s.

Determination of physical characteristics parameters of wheat seeds

The Jimai 22 wheat variety is widely sown in China, especially in northern Anhui. Therefore, the Jimai 22 wheat variety was selected for research. Moreover, 1000 grains are randomly selected and divided into three groups to weigh (W). Then 100 wheat seeds are randomly selected to measure and calculate the average length (l), width (w) and thickness (t), as shown in Table 1.

Table 1

Weight and dimension statistics of 1000 seeds of Jimai 22

Research factor	Group 1	Group 2	Group 3	Average
W/g	44.7	43.8	45.8	44.1
l/mm	6.29	6.39	6.37	6.35
w/mm	3.41	3.38	3.32	3.37
t/mm	3.12	3.16	3.08	3.12

Simulation test

The establishment of simulation model

Based on the results, a three-dimensional model of wheat seeds is established in CATIA software, and the model is imported into EDEM software. Multiple spherical combinations are used to fill the wheat seeds with particles, resulting in the wheat seed model shown in Figure 3.



Fig. 3 - Seed model of grain filling

The establishment of seed storage device model

A three-dimensional model of the seed storage device is built by CATIA software and imported into EDEM software, as shown in Figure 4.



Fig. 4 - Model of seed storage device

The inner wall of the seed storage tube is made of resin, and the surface cone of the conical lattice disc seed-metering device is made of steel. The parameters of seed, resin and steel obtained through literature search and calculation are shown in Table 2 (*Li et al., 2018; Zhu et al., 2019; Diao et al., 2024)*.

Table 2

Relevant parameters of simulation model

Relevant parameters	Seed	Resin	Steel
Poisson's ratio	0.29	0.39	0.3
Shear modulus /Pa	5.01e+8	7.19e+8	7.00e+10
Density /(kg·m^{-3})	1350	1240	7800
Relevant parameters	Seed	Resin	Steel

The parameters of the contact relationship between steel and the wheat seed and between resin and the wheat seed are shown in Table 3.

Table 3

Contact parameters between materials in the simulation model

Contact parameters	Seed-seed	Resin-seed	Steel-seed
Recovery coefficient	0.50	0.50	0.60
Coefficient of static friction	0.58	0.20	0.50
Coefficient of dynamic friction	0.08	0.02	0.01
Contact parameters	Seed-seed	Resin-seed	Steel-seed

Experimental design

According to the three factors obtained in Section 2.2, the optimal parameter combination is obtained using the three-factor and three-level orthogonal test method with the seed scattered uniformity coefficient of variation (m_1) as the evaluation index (*Liu, 2011)*. The seed scattered uniformity coefficient of variation (m_1) can be calculated as:

$$m_1 = \frac{\sqrt{\sum_{i=1}^{n}(M_i - \sum_{i=1}^{n} M_i/n)^2/(n-1)}}{\sum_{i=1}^{n} M_i/n} \quad (3)$$

where i represents the number of the slot of the conical lattice disc seed-metering device; M_i denotes the seed quality in slot number i; n represents the number of slots, n=40.

The relevant parameters of the simulation model are set. Seeds are added into the seed storage tube and an orthogonal experiment is conducted with a designed seed quantity of 0.15 kg.

Table 4 presents the factor level encoding table.

Table 4

Table of factor levels for orthogonal tests

Encoding	D/m	L/m	V/(m/s)
+1	0.04	0.005	0.02
0	0.06	0.015	0.05
-1	0.08	0.025	0.08

After the simulation seeding experiment is completed, the *Analyst Tree* interface is used to generate a grid group in each slot of the conical lattice disc seed-metering device. This allows for the measurement of wheat seed mass in each slot and the calculation of the seed distribution uniformity coefficient of variation, as shown in Figure 5.

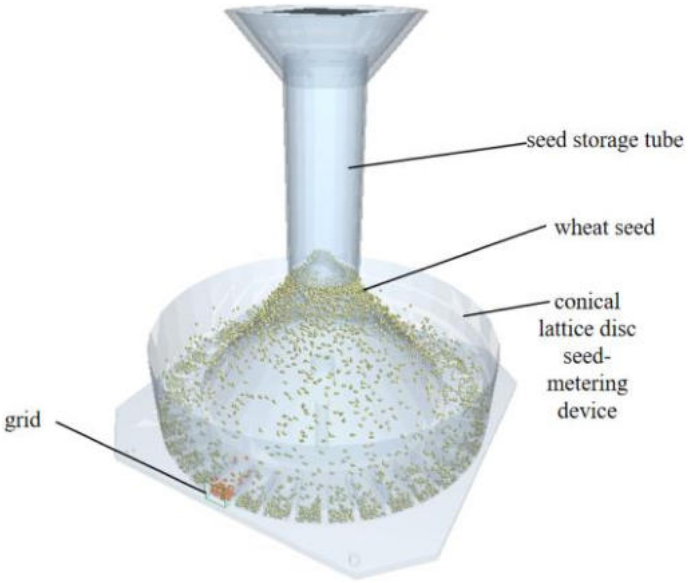


Fig. 5 - The diagram of the simulation experiment

Bench test

To verify the effectiveness of the optimal parameters, the seed storage device is improved according to the optimal parameters analyzed in the previous section. The original lifting lever is replaced with an electric pusher and compared with the traditional lifting lever. Eight sets of tests are conducted on the JPS-12 seed planter performance test bench in the Intelligent Agricultural Machinery Equipment Engineering Laboratory of Anhui Agricultural University, and the seed scattered uniformity coefficient of variation is calculated, as shown in Figure 6.

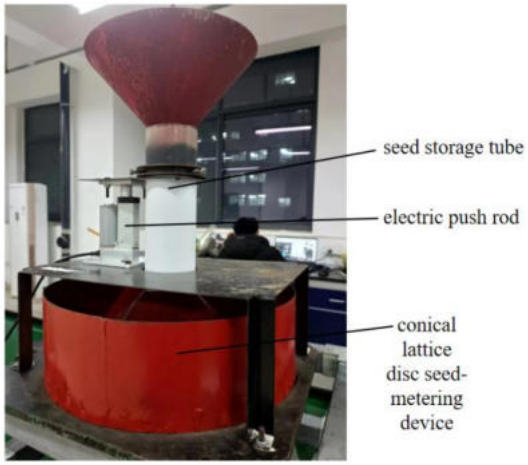


Fig. 6 - The diagram of the bench test

RESULTS

Simulation test results

The seed scattered uniformity coefficient of variation in the orthogonal test is shown in Table 5.

Table 5

Statistics of coefficient of variation of orthogonal test

Number	D/m	L/m	V/(m/s)	m_1/%
1	0.04	0.005	0.05	5.87
2	0.06	0.015	0.05	3.62
3	0.06	0.025	0.02	5.67
4	0.06	0.015	0.05	3.05
5	0.08	0.015	0.08	5.98
6	0.06	0.005	0.02	5.08
7	0.04	0.015	0.08	5.24
8	0.08	0.005	0.05	4.65
9	0.08	0.025	0.05	5.84
10	0.06	0.015	0.05	3.46
11	0.04	0.025	0.05	3.87
12	0.08	0.015	0.02	4.43
13	0.06	0.005	0.08	4.98
14	0.04	0.015	0.02	5.67
15	0.06	0.025	0.08	6.01
16	0.06	0.015	0.05	3.97
17	0.06	0.015	0.05	3.34

According to the simulation results in Table 5, the average of m_1 (μ) is calculated as 4.749%, and the standard deviation (σ) is 0.998%, so the standard deviation ranges, μ±σ, μ±2σ and μ±3σ, are [3.742%, 5.747%], [2.744%, 6.745%] and [1.746%, 7.743%], respectively. That is, when the three factors are orthogonally combined at the three levels, the probabilities of m_1 within the above three intervals are approximately 68%, 95% and 99.7%. Design Expert 13 software (DSP 13) is used to analyze the simulation data, and the dimensionless factor encoding regression equation was obtained as follows:

$$Y_1=3.49-0.2187X-0.0238Y+0.045Z+1.05XY+0.745XZ$$
$$-0.61YZ+0.7323X^2+1.09Y^2+1.36Z^2 \quad (4)$$

where X represents the inner diameter of seed storage tube. Y denotes the lifting height of the seed storage tube. Z represents the lifting speed of the seed storage tube.

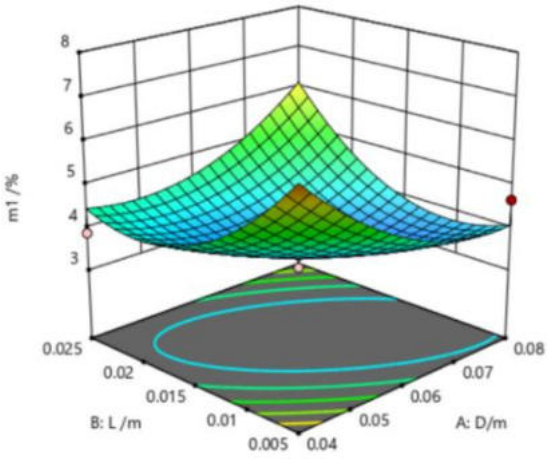
The regression equation analysis is shown in Table 6, and the coefficient of variation model is highly significant (P<0.01), with a mismatch term of P=0.3822>0.05, indicating that the regression equation is well fitted. According to Table 6, the influence of each experimental factor on the coefficient of variation, in descending order, is as follows: the height of the seed storage tube, the inner diameter of the seed storage tube and the speed of the seed storage tube.

Table 6

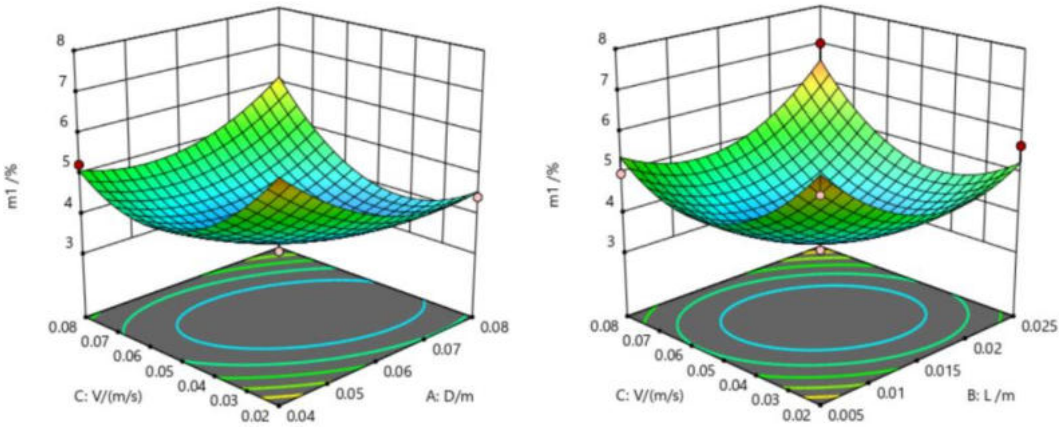
Statistics of coefficient of variation of orthogonal test

Source	Sum of Square	Freedom	Mean Square	F	P
Model	31.23	9	3.98	11.41	0.004
X	3.28	1	3.28	11.13	0.0063
Y	3.85	1	3.85	12.56	0.0054
Z	2.13	1	2.13	6.43	0.0318
XY	1.73	1	1.73	5.13	0.0382
XZ	0.35	1	0.35	1.06	0.3223
YZ	0.23	1	0.23	0.52	0.4747
X^2	11.32	1	11.32	50.45	0.0029
Y^2	6.46	1	6.46	21.55	0.0004
Z^2	3.11	1	3.11	6.34	0.0257
Residuals	3.87	11	0.33		
Lack of Fit	2.22	4	0.42	1.63	0.3822
Pure Error	2.23	7	0.29		
Cor Total	35.1	20			

Figure 7 displays the influence of various factors interacting with each other on the coefficient of variation (m_1). Figure 7a shows the effect of L and D on the coefficient of variation. When L is constant, with the increase of D, m_1 decreases first and then increases. When D is constant, with the increase of L, m_1 decreases first and then increases. Figure 7b shows the effect of V and D on the coefficient of variation. When V remains constant, with the increase of D, m_1 decreases first and then increases. When D remains constant, with the increase of V, m_1 decreases first and then increases. Figure 7c shows the effect of V and L on the coefficient of variation. When V is constant, with the increase of L, m_1 decreases first and then increases. When L is constant, with the increase of V, m_1 decreases first and then increases.



(a) The impact of L and D on m_1



(b) The impact of V and D on m_1 (c) The impact of V and L on m_1

Fig. 7 - The influence of the interaction of various factors on the coefficient of variation

The regression equation for the impact of significant factors on the seed scattered uniformity coefficient of variation is as follows:

$$m_1=26.88-371.28D-744.46L-254.58V+5237.5DL+1241.67DV$$
$$+2033.33LV+1380.625D^2+10872.5L^2+1830.625V^2 \quad (5)$$

Using the objective function m_{1min}, the optimal parameter combination was determined through optimization in MATLAB/Simulink. The resulting optimal values for the three factors are: inner diameter D=0.06 m, lifting height L=0.015 m, and lifting speed V=0.05 m/s.

Bench test results

Table 7 displays the results of the comparative experiment between the traditional lifting lever and the electric pusher, which indicates that the average scattered uniformity coefficient of variation for using traditional lifting levers is 6.46%, and for using the electric pusher, it is 4.12%. Compared to traditional lever lifting, the improved method significantly improves the uniformity of wheat seeds and meets operational requirements, which proves the feasibility of the optimal parameter combination.

Table 7

Result of the bench test

Number	m_1/%	
	Before optimization	After optimization
1	5.61	4.58
2	6.94	3.66
3	6.64	3.89
4	5.71	5.13
5	6.44	3.61
6	6.39	3.16
7	7.17	4.28
8	6.82	3.77
Average	6.46	4.12

CONCLUSIONS

(1) Taking the seed storage device of the wheat plot seeder as the research object, the working principle and experimental factors related to the seed storage device are analyzed. An electric pusher is used instead of a traditional lifting lever to control the lifting of the seed storage tube. And the experimental factors related to the seed storage device are determined, namely the inner diameter of the seed storage tube (D), the lifting height of the seed storage tube (L), and the lifting speed of the seed storage tube (V).

(2) Through analysis, the ranges of the test factors are determined to be [0.04 m, 0.08 m], [0.005 m, 0.025 m] and [0.02 m/s, 0.08 m/s], respectively. A three-factor and three-level simulation experiment is conducted with the seed scattered uniformity coefficient of variation as the performance index. It is determined that the influences of each test factor on the coefficient from large to small are L, D, and V, and the optimal solution of experimental parameters is determined to be D=0.06 m, L=0.015 m, and V=0.05 m/s.

(3) Under the verification test, the range of the seed scattered uniformity coefficient of variation is [3.16%, 5.13%], with an average value of 4.12%. Compared with the traditional lifting lever, its coefficient of variation is reduced by 2.34%. Under the optimized combination of working parameters, the device achieves a relatively high working performance.

ACKNOWLEDGEMENT

The financial supports of the China Agriculture Research System [No. CARS-03] is gratefully acknowledged.

REFERENCES

[1] Beckman, J., Ivanic, M., Jelliffe, J. (2022). Market impacts of Farm to Fork: Reducing agricultural input usage. *Applied Economic Perspectives and Policy*, 44(4): 1995-2013.

[2] Chen, H. T., Wang, H. F., Wang, Y. C., Shi, N. Y., Wei, Z. P., Dou, Y. K. (2020). Design and experiment of three-leaf type air-suction seed meter with automatic clear and replace seeds features for soybean plot test (三叶式自动清换种大豆育种气吸排种器设计与试验). *Transactions of Chinese Society of Agricultural Machinery*, 51(12): 75-85.

[3] Cheng, X. P., Li, H. W., He, J., Wang, Q. J., Lu, C. Y., Wang, Y. B., Wang, C., Wang, C. L., Lou, S. Y. (2021). Optimization of operating parameters of seeding device in plot drill with seeding control system. *International Journal of Agricultural and Biological Engineering*, 14(3): 83-91.

[4] Cheng, X. P., Li, H. W., Lu, C. Y., He, J., Wang, Q. J., Wang, C., Yu, C. C., Wei, Z. C., Wang, C. L. (2019). Parameter optimization and experiment of centrifugal seed dispenser in wheat plot drill (小麦小区条播机离心分种器参数优化与试验). *Transactions of Chinese Society of Agricultural Engineering*, 35(20): 1-9.

[5] Cheng, X. P., Lu, C. Y., Li, H. W., He, J., Wang, Q. J., Mao, Y. J., Wang, C., Niu, Q., Wei, Z. C., Xie, L. J. (2018). Research progress and development trend of plot seeding mechanization, *International Agricultural Engineering Journal*, 27(4): 136-144.

[6] Diao, H. L., Zhang, Y. P., Diao, P. S., Zhao, N. (2017). Design and experiment of a no-tillage and wide band wheat planter with subsoilers based on EDEM (基于 EDEM 的小麦宽苗带深松免耕播种机设计与试验), *Journal of Agricultural Machinery*, 39(01): 58-162.

[7] Feng, Y. B., Zhao, X. S., Li, J. C., Yu, H. L., Zhao, H. P., Yin, B. Z. (2024). Parameter optimization and experiment of the negative pressure precision seed-metering device for wheat, *International Journal of Agricultural and Biological Engineering*, 17(1): 154-162.

[8] Gao, X. J., Cui, T., Zhou, Z. Y., Yu, Y. B., Xu, Y., Zhang, D. X., Song, W. (2022). DEM study of particle motion in novel high-speed seed metering device, *Advanced Powder Technology*, 32(5): 1438-1449.

[9] Gong, L. N., Yuan, Y. L., Shang, S. Q., Jiang, J. L., Zheng, Y. N. (2011). Design and experiment on electronic control system for plot seeder (小区播种机电控系统设计与试验), *Transactions of Chinese Society of Agricultural Engineering*, 27(5): 122-126.

[10] Karayel, D., Güngör, O., Šarauskis, E. (2022) Estimation of optimum vacuum pressure of air-suction seed-metering device of precision seeders using artificial neural network models. *Agronomy*, 12, 1600.

[11] Kovács, P., Casteel, S.N. (2023) Evaluation of a high-speed planter in soybean production. *Agronomy Journal*, 115(3): 1174–1187.

[12] Li, Z. D., Wang, Q. Q., Zhang, Y. L., Wang, W. W., Yang, Y., Chen, L. Q. (2018). Design and experiment of inclined parabolic cell wheel in seed feeding device for wheat (倾斜抛物线型孔轮式小麦供种装置设计与试验), *Transactions of Chinese Society of Agricultural Machinery*, 49(5): 116-124.

[13] Liu, D. Q., Ma, J, W., Qiao, X. D., Xin, P. C., Zhang, X, C., Wang, J. W., Zheng, D. C. (2023). The design of and experiments with a double-row seed-metering device for buckwheat breeding in an experimental area, *Agronomy*. 13(12), 2587.

[14] Liu, S.G. (2011). *Study on design and mechanism analysis of main parts of plot seeder (小区育种播种机关键装置的设计与机理分析)*, Shenyang Agricultural University.

[15] Liu, S. G., Shang, S. Q., Yang, R. B., Zheng, Y. N., Zhao, D. J., Zhao, J. L. (2010). Test and optimization of parameters for the storing device of plot seeder (小区播种机存种装置参数试验及优化), *Transactions of Chinese Society of Agricultural Engineering*, 26(09): 101-108.

[16] Okeyo, S.O., Ndirangu, S.N., Isaboke, H.N., Njeru, L. K. (2020). Determinants of sorghum productivity among small-scale farmers in Siaya County, Kenya. *African Journal of Agricultural Research*, 16(5): 722–731.

[17] Shang, S. Q., Wu, X. F., Yang, R. B., Li, G. Y., Yang, X. L., Chen, D. Q. (2021). Research status and prospect of plot-sowing equipment and technology (小区育种播种装备与技术研究现状与展望), *Transactions of Chinese Society of Agricultural Machinery*, 52(02): 1-20.

[18] Wang, W. W., Wu, K. P., Zhang, Y., Wang, M. X., Zhang, C. L., Chen, L. Q. (2022). The Development of an electric-driven control system for a high-speed precision planter based on the double closed-loop fuzzy PID algorithm. *Agronomy*. 12(4), 12040945.

[19] Yang, W., Fang, X. F., Li, J. D., Li, L. X. (2019). Design and experiment of air-suction precision seed meter with self-clearing seed chamber for corn plot test (种腔自净型气吸式玉米小区精量排种器设计与试验), *Transactions of Chinese Society of Agricultural Machinery*, 50(6): 64-73.

[20] Yatskul, A. & Lemiere, J. P. (2018). Establishing the conveying parameters required for the air-seeders, *Biosystem Engineering*, 166: 1-12.

[21] Yu, C. Y., Chen, Z., Chen, L, Q. (2023). Design and test of electronic control seeding system for wheat plot drill (小麦小区条播机电控排种系统设计与试验), *Transactions of Chinese Society of Agricultural Machinery*, 54(1): 75-83.

[22] Yuan, X. Y., Huang, C. J., Tao, G. X., Yi, S. J., Li, Y. F. (2024). Design and experiment of oil-electric hybrid air-suction sorghum plot seeder, *Agriculture*, 14(3), 432.

[23] Zhao, H. H., Zhang, D. X., Yang, L., Cui, T., Song, W., He, X. T., Wu, H. L., Dong, J. Q. (2022). Optimal design and experiment of critical components of Hand-Pushing corn plot precision planter, *Agriculture*, 12(12), 2103.

[24] Zhou, X. S. & Ma, W. L. (2022). Agricultural mechanization and land productivity in China, International *Journal of Sustainable Development and World Ecology*, 29(6): 530-542.

[25] Zhu, Q. Z., Wu, G. W., Chen, L. P., Zhao, C. J., Meng, Z. J., Shi, J. T. (2019). Structural design and optimization of seed separated plate of wheat wide-boundary sowing device (小麦宽苗带撒播器弹籽板结构设计与优化), *Transactions of Chinese Society of Agricultural Engineering*, 35(01): 1-11.

RICE SEED CLASSIFICATION BASED ON SE-ResNet50
/
基于 SE-ResNet50 的稻种分类

Zhen MA[1)], Sa WANG[1)], Hongxiong SU[1)], Juxia LI*[1)], Yanwen LI[1)], Zhifang BI[2)], Xiaojie LI[1)1]
[1)] College of Information Science and Engineering, Shanxi Agricultural University, Taigu 03080/China;
[2)] Department of Basic Sciences, Shanxi Agricultural University, Taigu 03080/China
Tel: +8615803446486; E-mail: lijxsn@126.com
Corresponding author: Juxia Li
DOI: https://doi.org/10.35633/inmateh-76-12

Keywords: *rice seed classification, SE-ResNet50 network model, deep learning, Image classification*

ABSTRACT
Traditional rice seed classification methods rely on manual observation of morphological features, which are inefficient and limited in accuracy. To improve the efficiency and accuracy of rice seed classification, this paper proposes a deep learning-based rice seed classification method using the SE-ResNet network architecture. This architecture integrates SENet into ResNet50, enabling the model to capture and learn sensitive differential features among rice seeds. Through comparative experiments, the classification accuracies of SE-ResNet50, ResNet, and AlexNet on the rice seed dataset were 89.58%, 72.97%, and 76.35%, respectively. The results demonstrate that SE-ResNet50 significantly outperforms ResNet and AlexNet in classification accuracy, validating its superiority in rice seed classification tasks.

摘要
传统的稻种分类方法依赖人工经验对形态特征的观察，效率低且准确性有限。为提高稻种分类的效率及精度，本文提出了一种基于深度学习的稻种分类方法，采用 SE-ResNet 网络结构，该结构将 SENet 集成到 ResNet 中，使其能够捕捉并学习稻种之间的敏感性差异特征。通过对比实验，SE-ResNet50、ResNet50 和 AlexNet 三种网络结构在稻种数据集上的分类准确率分别为 89.58%、72.97%和 76.35%。结果表明，SE-ResNet50 的分类准确率明显高于 ResNet50 和 AlexNet，验证了其在稻种分类任务中的优越性。

INTRODUCTION
Rice, as one of the most important global food crops, plays a pivotal role in agricultural production and food security. With the growing global population and increasing demand for food, improving rice yield and quality has become a critical goal in agricultural research. Among these efforts, the classification and identification of rice seeds are key to achieving precision agriculture and variety improvement. Accurate rice seed classification not only aids in seed quality control and variety identification but also provides scientific support for rice cultivation, processing, and trade.

In recent years, with the advancement of computer technology and machine vision, deep learning has gradually been applied to the agricultural domain. Significant progress has been made in rice seed classification. Traditional methods primarily rely on manual observation and morphological feature measurements, such as grain length, width, and shape. However, these methods suffer from subjectivity and inefficiency. In contrast, machine learning and deep learning-based approaches can automatically extract features from rice seed images and achieve efficient classification. *Kamilaris et al., (2018),* systematically compared deep learning with traditional methods and found that deep learning significantly outperforms traditional methods in agricultural tasks, establishing its theoretical superiority. *Carneiro et al., (2024)* systematically analyzed 37 recent studies that employed deep learning (DL) and machine learning (ML) models for grape variety identification, aiming to provide a detailed analysis of the classification process and highlight the strengths and limitations of each method. Based on this, researchers have explored various dimensions of convolutional neural networks (CNNs). *Sladojevick et al., (2016)* and *Lu et al., (2017),* employed basic CNN architectures for plant disease recognition, achieving average accuracies of 96.3% and 95.48%, respectively, demonstrating the versatility of CNNs in complex agricultural scenarios.

[1] *Zhen Ma, Lec.; Sa Wang, M.Sc.Stu.; Hongxiong su,, M.Sc.Stu.; Juxia Li, Prof; Yanwen, Li, Prof.; Zhifeng Bi,Lec.; Xiaojie Li, UG.*

Dymann et al., (2016), and *Reyes et al., (2015),* further expanded the application of CNNs, with the former achieving 86.2% accuracy in classifying 22 plant species and the latter focusing on vein pattern recognition in legumes, both overcoming the limitations of traditional manual feature extraction.

To enhance model performance, researchers have proposed various improvement strategies. *Zhang et al., (2019),* designed the GPDCNN model, which optimizes global pooling and dilated convolution to increase the receptive field while maintaining low computational complexity, significantly improving cucumber disease recognition. *Lu et al., (2017),* visualized feature hierarchies using deconvolution networks, enhancing model interpretability and discriminative power. Meanwhile, transfer learning has become an effective approach to address small-sample problems. *Pereira et al., (2019),* achieved efficient grape variety classification using a fine-tuned AlexNet model, while *Too et al., (2019),* systematically evaluated advanced architectures such as VGG, ResNet50, and DenseNet, finding that DenseNet achieved 99.75% accuracy in classifying 38 plant leaf categories with excellent anti-overfitting properties. *Dong et al., (2024),* addressed the challenge of identifying Camellia oleifera varieties caused by genetic diversity and morphological similarities by constructing a dataset of 30,890 leaf images and developing a deep learning model based on the Convolutional Block Attention Module (CBAM) and RegNetY-4.0GF. *Sun et al., (2023),* improved the EfficientNetv2 network model by introducing a transfer learning mechanism, the adaptive moment estimation optimization algorithm, and the MultiMarginLoss function, addressing the issue of low classification efficiency for southern medicinal plant leaves under complex backgrounds. They achieved a recognition accuracy of 99.12%, representing a 1.17% improvement over the initial model. *Zou et al., (2024*), developed a pepper anthracnose fruit classification and recognition model based on MobileNet V2 and created a mobile-based pepper fruit anthracnose recognition system, addressing the challenge of real-time diagnosis of pepper fruit anthracnose in offline field environments. *Peng et al., (2024*), optimized the YOLOV7 model and proposed the WineYOLO-RAFusion model to achieve more comprehensive and accurate recognition of wine grape varieties. Through data augmentation, transfer learning, and parameter fine-tuning, the MobileNet V2 model achieved a precision rate of 97.31% on the test set, with a recognition time of only 75 ms per image. Although these improved models significantly enhance applicability, they are not well-suited for rice seed classification.

To address these limitations, this paper introduces the SE-ResNet50 model, combining deep learning with feature channel recalibration mechanisms to improve the accuracy and efficiency of rice seed classification. Comparative experiments validate the superiority of SE-ResNet50 in rice seed classification tasks, providing new technical support for agricultural intelligence.

MATERIALS AND METHODS

Dataset Construction

For this experiment, a publicly available dataset of rice seed images was employed. The dataset includes four types of rice seeds: AKITAKOMACHI, KOSHIHIKARI, THAI HOM MALI, and YANGDAO-8, as illustrated in Figure 1. To enhance the generalizability of the model and augment the diversity of the dataset, data augmentation techniques, including random rotation and mirroring, were employed. As a result, the dataset was expanded to a total of 5189 images. The collected seed samples were systematically divided into training and validation sets at an 8:2 ratio, as shown in Table 1.



(a) AKITAKOMACHI (b) KOSHIHIKARI (c) THAI HOM MALI (d) YANGDAO-8

Fig. 1 - Examples of images for each category in the dataset
(a) represents the AKITAKOMACHI class, (b) represents the KOSHIHIKARI class, (c) represents the THAI HOM MALI class, (d) represents the YANGDAO-8 class.

Table 1

Dataset Distribution

Category	Training Set	validation Set
AKITAKOMACHI	976	244
KOSHIHIKARI	1056	263
THAI HOM MALI	1150	287
YANGDAO-8	971	242

Dataset Construction

SE-ResNet50-Based Rice Seed Classification Model

The SE-ResNet50 model proposed in this paper integrates the SE module into ResNet50. The SE module dynamically adjusts the weights of feature channels through Squeeze and Excitation operations, enhancing the network's ability to extract important features.

ResNet50 Overview

ResNet50, or Residual Network, is an innovative deep learning model architecture widely used in computer vision *(He et al., 2019; Veit et al., 2016; Rawat et al., 2017)*. ResNet50's deep network structure (over 100 layers) and exceptional performance have demonstrated its broad applicability in various computer vision tasks. The core innovation of ResNet50 is the introduction of residual learning to address the performance degradation problem caused by increasing network depth. This is achieved through the design of residual blocks, which allow direct information transfer between layers. Each residual block consists of multiple residual units, each comprising two convolutional layers and a skip connection that directly passes the input to the output. This skip connection not only helps maintain network stability but also enhances the network's ability to handle more complex data. The structure of the residual block is shown in Figure 2.

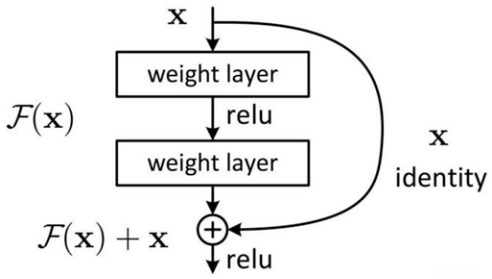


Fig. 2 - Structure of the Residual Block

The diagram summarizes the basic structure of a Residual Network (ResNet50), addressing the vanishing gradient problem in deep neural network training by introducing a skip connection.

The introduction of residual blocks significantly reduces the number of parameters and computational complexity in deep neural networks. Depending on the network depth, residual blocks can take different forms. Typically, ResNet50 employs two main types of residual blocks: the identity mapping module and the downsampling module.

The identity mapping module directly adds the input to the output when the dimensions of the input and output are the same. This process can be mathematically represented as:

$$F_{(x)} = x + H_{(x)} \tag{1}$$

where:

x is the input, $F_{(x)}$ is the output of the residual block, and $H_{(x)}$ is the nonlinear transformation within the residual block. In the identity mapping module, $H_{(x)}$ is typically an identity transformation, that is $H_{(x)} = x$, hence the output $F_{(x)}$ is equal to the input x plus its own value, thus achieving an identity mapping.

The downsampling module is used when the dimensions of the input and output feature maps do not match. This operation reduces the dimensionality of the input feature map to match the output, ensuring the continuity and effectiveness of the network structure. This is typically achieved through convolutional operations. The mathematical representation of the downsampling module is as follows:

$$F_{(x)} = W_{downsample} \cdot x + H_{(x)} \tag{2}$$

where:

x is the input, $F_{(x)}$ is the output of the residual block, $H_{(x)}$ is the nonlinear transformation within the residual block, and $W_{downsample}$ is the weight matrix of the downsampling operation.

These two modules are alternately combined to form the ResNet50 architecture, which is commonly used in constructing deep residual networks. Depending on whether the input and output dimensions are the same, either the identity mapping module or the downsampling module is selected, facilitating the training of deep networks and improving model performance. The structure of ResNet50 is shown in Figure 3.

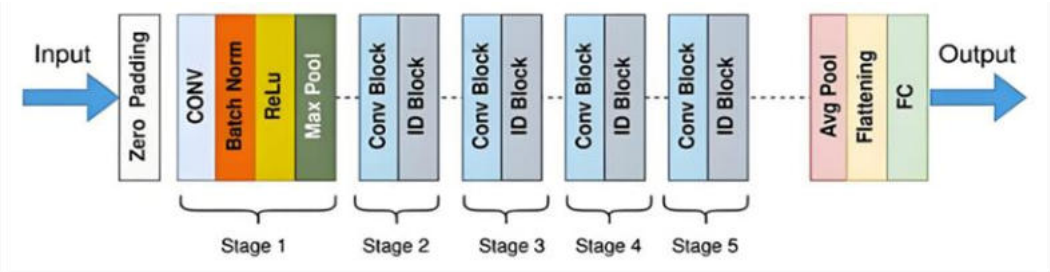


Fig. 3 - Structure of ResNet50

Figure 3 illustrates the overall structure of the ResNet50 model, detailing how data is processed at each stage of the network. The initial stage includes zero padding, a convolutional layer (CONV), batch normalization (Batch Norm), ReLU activation, and a max pooling layer (Max Pool). These layers are used to extract preliminary features from the image and reduce the size of the feature map. In stages 2 to 5, multiple residual blocks, including "Conv Block" and "ID Block," are used to capture deeper features while addressing the vanishing gradient problem through skip connections, thereby improving the network's learning efficiency. Each stage typically begins with a "Conv Block" to adapt to changes in feature map size and reduce computational complexity through bottleneck design. This is followed by several "ID Blocks" for further feature extraction without altering the feature map size. The network ends with a global average pooling layer (Avg Pool) to reduce the feature map to a fixed-size vector. This is followed by a flattening operation to convert the pooled output into a one-dimensional array. Finally, a fully connected layer (FC) maps the extracted features to the probabilities of each class.

Introduction of the SENet-Block Module

The SENet-block module integrates the Squeeze-and-Excitation (SE) module into traditional convolutional neural network blocks *(Hu et al., 2018; Wang et al., 2017; Vaswani et al., 2017)*. This integration enhances the feature representation capability of the network by dynamically adjusting the importance of feature channels, allowing the network to focus more on useful information. Although the SENet-block module may vary across different network architectures, the core idea remains the same: adding the SE module after traditional CNN blocks. The differences between rice seeds are often subtle, and with the development of hybrid rice varieties, these differences have become even more blurred, making the classification of rice seed varieties increasingly challenging. To address this issue, the introduction of the SENet-block module has proven to be an effective solution. The structure of the SENet-block module is shown in Figure 4.

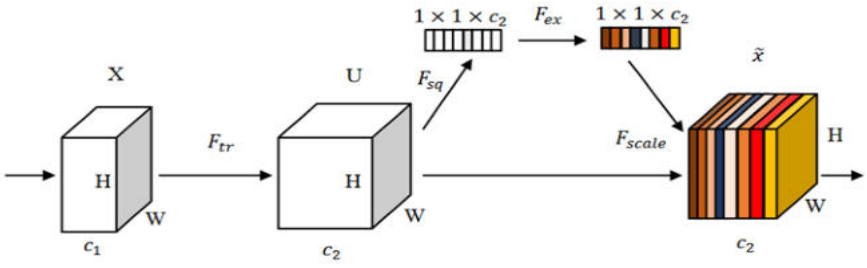


Fig. 4 - Structure of the SENet-Block Module

Figure 4 illustrates the workflow of the SENet (Squeeze-and-Excitation Network) module. First, the input feature map undergoes a Squeeze operation, which compresses the spatial information of each channel through global average pooling. Next, the Excitation operation generates weights for each channel through two fully connected layers. Finally, the Scale operation multiplies these weights with the original feature map to produce the recalibrated output feature map. This process dynamically adjusts the channel weights, enhancing the network's ability to focus on important features and thereby improving model performance.

Squeeze Operation

Through global average pooling, the feature map U is compressed, merging the $H \times W$ spatial information of each channel into a single value, generating a $1 \times 1 \times C_2$ channel descriptor. The purpose of this step is to extract global information from each channel.

The formula for global average pooling is:

$$s_c = \frac{1}{H \times W} \sum_{i=1}^{H} \sum_{j=1}^{W} u_c(i,j) \quad (3)$$

where:

S_c is the output feature of channel C, $H \times W$ is the spatial dimension of the feature map U, $\sum_{i=1}^{H} \sum_{j=1}^{W}$ indicates the summation of all spatial positions (i,j) in the feature map U, $u_c(i,j)$ is the value of the feature map U at channel C and position (i,j).

Excitation Operation

The channel descriptor is first processed by two fully connected layers. The first fully connected layer typically reduces the dimensionality and applies a ReLU activation function. The second fully connected layer maps the dimensionality back to the original number of channels C_2 and uses a sigmoid function to output the weight for each channel. This can be expressed as:

$$z = \sigma(g(s,W)) = \sigma(W_2 \times \delta(W_1 s)) \quad (4)$$

where:

s is the compressed channel descriptor obtained from the Squeeze operation, W_1 and W_2 are the weight matrices of the two fully connected layers, δ represents the ReLU activation function, σ is the sigmoid activation function, and z is the weight for each channel.

Scale Operation

The weights output from the Excitation step x (one weight per channel) are multiplied with the corresponding channels of the original feature map U. This step enhances the channels that the model deems important and suppresses the less important ones. The formula for this step is as follows:

$$\tilde{x}_c = z_c \cdot u_c \quad (5)$$

where:

$\tilde{x}_c$is the recalibrated feature map for channel C, z_c is the weight for channel C, and U_c is the original feature map for channel C.

The above content details the complete structure and operational process of the SENet-block module. By embedding the SENet-block structure into ResNet50, the advantages of deep residual networks addressing the vanishing gradient problem through skip connections—are combined with the feature channel recalibration strategy of SENet-block, significantly enhancing the overall performance of the network. This integration not only preserves the residual learning advantages of ResNet50 but also optimizes the network's ability to process feature information through the feature channel recalibration mechanism, thereby effectively improving network performance.

SE-ResNet50 Network Structure

SE-ResNet50 is a convolutional neural network architecture that integrates the Squeeze-and-Excitation (SE) module into ResNet50. This structure enhances the expressive power and performance of ResNet50 by adding a channel attention mechanism. By introducing the SE module, the network's ability to represent features is improved without significantly increasing computational cost, particularly in image classification and other visual tasks. The SE-ResNet50 model retains the advantages of the original ResNet50, such as using skip connections to train deep networks, while also enhancing the emphasis on channel-level features through the integration of the SE module. This makes the network more effective in handling complex images or other high-dimensional data.

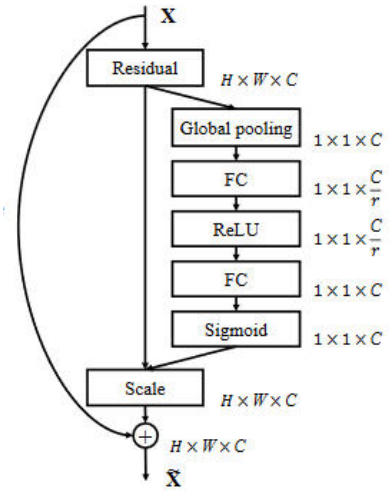


Fig. 5 - Structure of the SE-ResNet50 Residual Block

Figure 5 illustrates the working principle of the SE module combined with skip connections. First, the input feature map X (with dimensions $H \times W \times C$) is compressed through global average pooling into a channel descriptor of size $1 \times 1 \times c$, extracting global information from each channel. Next, the descriptor is processed by two fully connected layers (FC): the first layer reduces the dimensionality to $C \div r$ and applies a ReLU activation function to introduce nonlinearity; the second layer restores the dimensionality to C and generates weights for each channel using a sigmoid activation function. Finally, these weights are multiplied with the original input feature map through a scaling operation, producing the recalibrated feature map x which retains the original dimensions $H \times W \times C$. This process dynamically adjusts the channel weights, enhancing the network's ability to focus on important features and thereby improving model performance without altering the feature map dimensions.

Rice Seed Classification System

To enhance the usability and operational efficiency of the algorithm, this study has developed a rice seed classification application, realized through a dedicated graphical user interface (GUI). Utilizing an object-oriented programming approach, the Qt framework has been employed for the design of this application. The Qt framework facilitates comprehensive interface design by instantiating objects, configuring their properties, and establishing event bindings. This not only achieves separation of the front-end and back-end but also enables real-time target detection. The framework provides an extensive suite of GUI development tools, encompassing over 620 classes and nearly 6,000 functions and methods.

During the operation, users can import the images of seeds that need to be classified into the system by clicking the "Upload Image" button. Subsequently, by clicking the "Start Detection" button, the system will automatically execute the classification process, as illustrated in the figure 6.

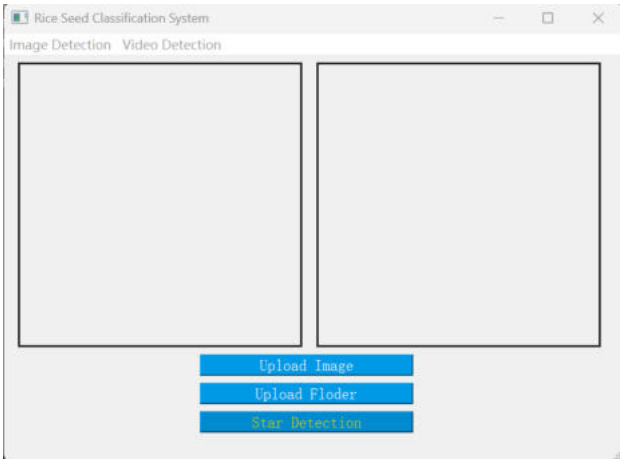


Fig. 7 - Rice seed classification system

Network Model Training

Experimental Platform and Training Parameters

The experimental environment runs on Windows 10 (64-bit) with 16 GB of RAM, an NVIDIA GTX1650Ti GPU, and an Intel(R) Core(TM) i5-10200H CPU @ 2.40GHz processor. The programming platform is Anaconda 4.12.0, with CUDA 10.1, and the development environment is PyTorch, using Python 3.8.

All models in this experiment were trained on the same training set with identical parameters for rice seed classification. The number of epochs was set to 100, the learning rate was 0.0125, and the batch size was 16, ensuring the fairness and comparability of the experimental results.

Model Evaluation Metrics

This method provides four key metrics—True Positives, False Positives, True Negatives, and False Negatives—to reveal the model's performance across different categories, offering a comprehensive understanding of its effectiveness.

Based on these four metrics, more complex evaluation metrics can be derived, such as precision, recall, and F_1 score. $\mathrm{Precision}$ represents the ratio of correctly predicted positive instances to all predicted positive instances. Recall reflects the ratio of correctly predicted positive instances to all actual positive instances. The F_1 score is the harmonic mean of precision and recall, providing a balanced measure between the two. These evaluation metrics collectively form a comprehensive framework for assessing model performance. The formulas for these metrics are as follows:

$$\mathrm{Precision} = \frac{TP}{TP+FP} \tag{6}$$

$$\mathrm{Recall} = \frac{TP}{TP+FN} \tag{7}$$

$$F_1 = \frac{2\times \mathrm{Precision}\times \mathrm{Recall}}{\mathrm{Precision}+\mathrm{Recall}} \tag{8}$$

For multi-class classification, $\mathrm{Precision}$ is calculated as the ratio of true positives for each class to the sum of true positives and false positives for that class. Recall is calculated as the ratio of true positives for each class to the sum of true positives and false negatives for that class. The overall evaluation metrics are as follows:

$$\mathrm{Precision}_{\mathrm{micro}} = \frac{\sum_{i=1}^{n} \mathrm{TP}}{\sum_{i=1}^{n} \mathrm{TP} + \sum_{i=1}^{n} \mathrm{FP}} \tag{9}$$

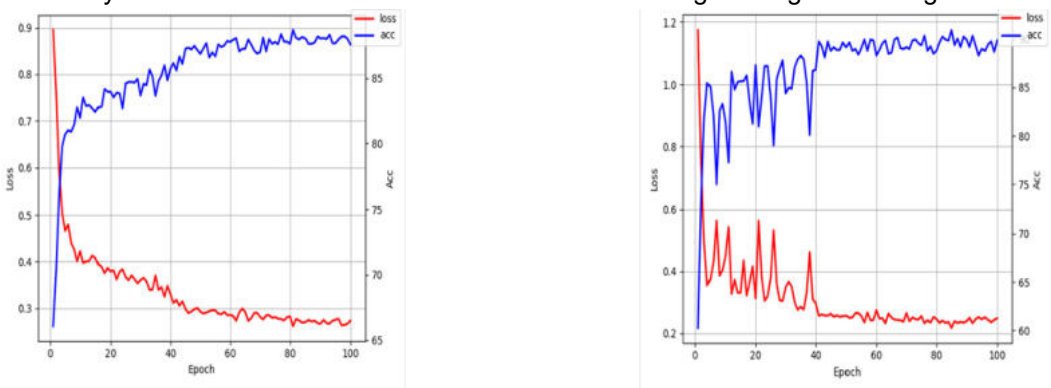
$$\mathrm{Recall}_{\mathrm{micro}} = \frac{\sum_{i=1}^{n} \mathrm{TP}}{\sum_{i=1}^{n} \mathrm{TP} + \sum_{i=1}^{n} \mathrm{FN}} \tag{10}$$

$$\mathrm{F1}_{\mathrm{micro}} = \frac{2\times \mathrm{Precision}_{\mathrm{micro}} \times \mathrm{Recall}_{\mathrm{micro}}}{\mathrm{Precision}_{\mathrm{micro}} + \mathrm{Recall}_{\mathrm{micro}}} \tag{11}$$

RESULTS AND ANALYSIS

SE-ResNet50 Model

The accuracy and loss curves of the SE-ResNet50 model during training and testing are shown in Fig.7.



(a) Training set results (b) Testing set results

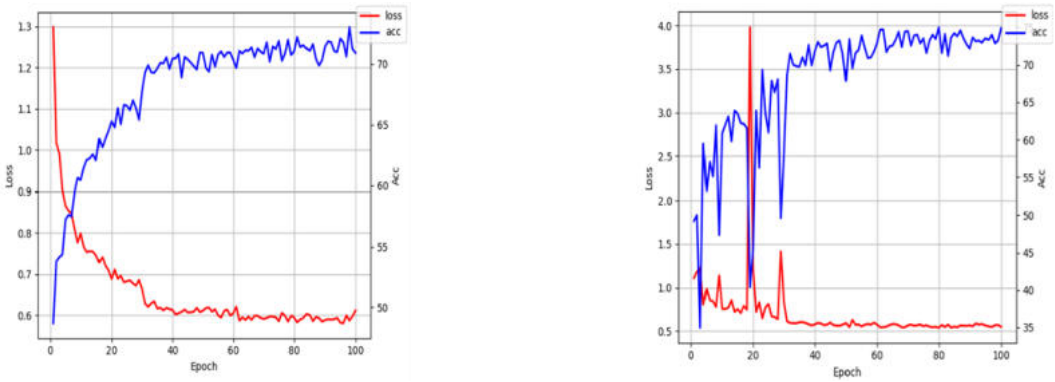
Fig. 7 - Accuracy and Loss Curves of the SE-ResNet50 Model

Figure 6 shows the loss and accuracy curves of the SE-ResNet50 model during training and testing. On the training set, the loss (blue curve) initially decreases rapidly and stabilizes around 0.3 after 100 epochs, while the accuracy (red curve) increases quickly and stabilizes around 95%. On the testing set, the loss (blue curve) also decreases rapidly initially but exhibits more fluctuations, stabilizing around 0.4. The accuracy (red curve) on the testing set increases quickly but fluctuates more, stabilizing around 85%.

From Figure 6, it can be observed that the SE-ResNet50 model exhibits excellent convergence performance during training, with the loss decreasing rapidly and stabilizing. The model shows no signs of overfitting or underfitting, indicating good generalization ability. When applied to the classification task of four types of rice seed images, the model achieves an accuracy of 89.58% on the testing set.

ResNet50 Model

The accuracy and loss curves of the ResNet50 model during training and testing are shown in Fig. 8.



(a) Training set results (b) Testing set results

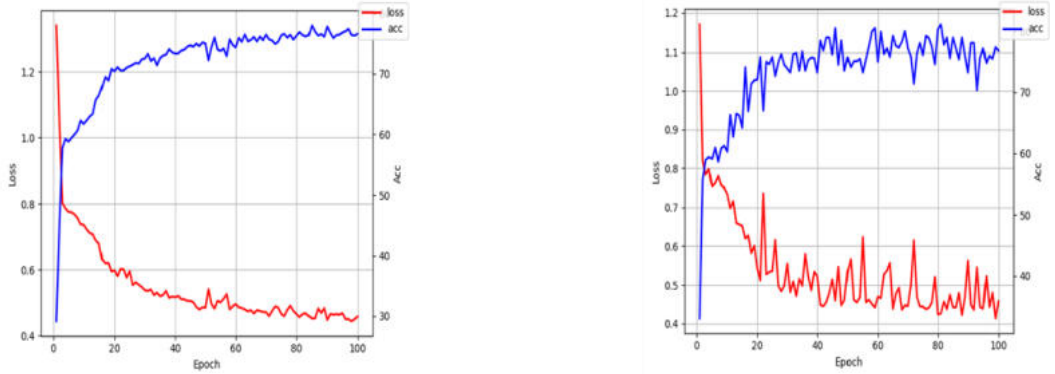
Fig. 8 - Accuracy and Loss Curves of the ResNet50 Model

Figure 7 shows the loss and accuracy curves of the ResNet50 model during training and testing. On the training set, the loss (blue curve) decreases rapidly initially and stabilizes around 0.4 after 100 epochs, while the accuracy (red curve) increases quickly and stabilizes around 70%. On the testing set, the loss (blue curve) decreases rapidly initially but exhibits more fluctuations, stabilizing around 0.5. The accuracy (red curve) on the testing set increases quickly but fluctuates more, stabilizing around 60%.

From Figure 7 it can be observed that the ResNet50 model converges more slowly and fails to achieve the expected performance level. The model's performance on both the training and testing sets is suboptimal. When applied to the classification task of four types of rice seed images, the ResNet50 model achieves an accuracy of only 72.97%.

AlexNet Model

The accuracy and loss curves of the AlexNet model during training and testing are shown in Figure 9.



(a) Training set results (b) Testing set results

Fig. 9 - Accuracy and Loss Curves of the AlexNet Model

Figure 8 shows the loss and accuracy curves of the AlexNet model during training and testing. On the training set, the loss (blue curve) decreases rapidly initially and stabilizes around 0.4 after 100 epochs, while the accuracy (red curve) increases quickly and stabilizes around 70%.

On the testing set, the loss (blue curve) decreases rapidly initially but exhibits more fluctuations, stabilizing around 0.5. The accuracy (red curve) on the testing set increases quickly but fluctuates more, stabilizing around 60%.

From Figure 8, it can be observed that the AlexNet model also converges more slowly and fails to achieve its best performance. The model's performance on both the training and testing sets is suboptimal. When applied to the classification task of four types of rice seed images, the AlexNet model achieves an accuracy of 76.35%.

Comparison of Different Networks

To validate the impact of different networks on model accuracy, this study conducted experiments using SE-ResNet50, ResNet50, and AlexNet. The comparison results are shown in Table 2.

Table 2

Comparison of Experimental Results

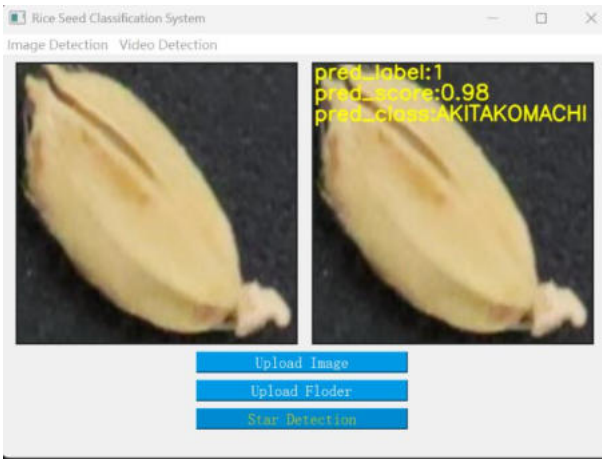
Model	Precision	Recall	F_1 Score
SE-ResNet50	0.8950	0.8922	0.8928
ResNet50	0.7212	0.7202	0.7194
AlexNet	0.7484	0.7582	0.7511

Table 2 shows the performance comparison of SE-ResNet50, ResNet50, and AlexNet in the rice seed image classification task. SE-ResNet50 achieves the best performance in precision (0.8950), recall (0.8922), and F1 score (0.8928), significantly outperforming ResNet50 (precision: 0.7212, recall: 0.7202, F1 score: 0.7194) and AlexNet (precision: 0.7484, recall: 0.7582, F1 score: 0.7511). These results demonstrate that SE-ResNet50 achieves significantly higher accuracy in rice seed image classification compared to the unmodified ResNet50 and AlexNet networks, highlighting the superiority of the selected network model in this task. Specifically, the deeper network layers and feature recalibration strategy (i.e., SENet) of SE-ResNet50 enable it to achieve better classification results in fine-grained image classification tasks such as rice seed classification.

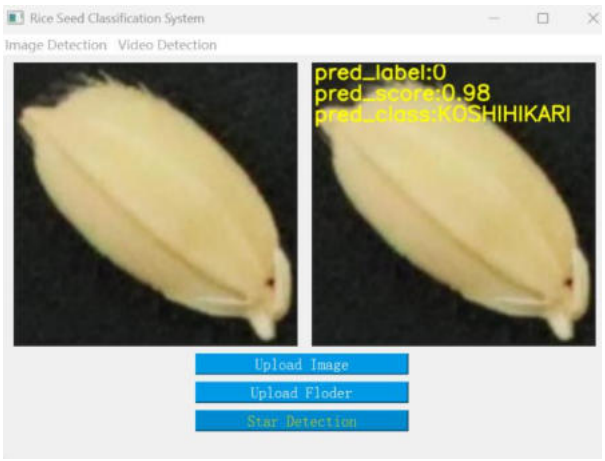
These experimental results comprehensively and convincingly demonstrate that SE-ResNet50 offers higher accuracy and stability in rice seed image classification, validating its significant advantages in classification performance.

Results Presentation of the Rice Seed Classification System

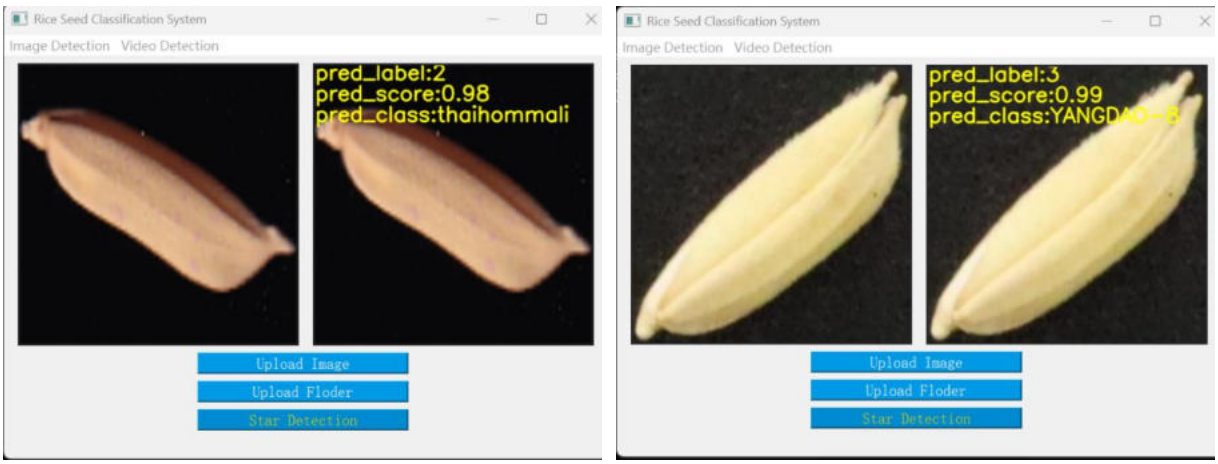
Rice Seed Classification System visually presents the application effectiveness of the constructed intelligent classification model through its user interface (UI), emphasizing the classification process and output results of test set samples. The core interface design focuses on structured output presentation, including (pred_label, pred_class, pred_score), as illustrated in Fig.10. Experimental results demonstrate that the system effectively validates model performance. By visually correlating confidence scores (pred_score) with variety labels (pred_class), it provides an intuitive assessment basis for evaluating the practical applicability and classification accuracy of the model in real-world scenarios. This capability further facilitates subsequent model optimization and system deployment decisions.



(a) Classification results for AKITAKOMACHI variety



(b) Classification results for KOSHIHIKARI variety



(c) Classification results for Thai Hom Mali variety (d) Classification results for YANGDAO-8 variety

Fig. 10 - Test Result Chart

CONCLUSIONS

This study innovatively proposes an SE-ResNet network architecture and develops a rice seed classification system, effectively addressing the technical limitations of traditional methods and existing deep learning models in fine-grained agricultural image recognition. The main contributions include:

(1) The novel integration of Squeeze-and-Excitation (SE) blocks into ResNet50 architecture significantly enhances the model's discriminative feature extraction capability for morphologically similar rice seeds through channel attention mechanisms. The proposed system achieves outstanding performance with precision of 0.8950, recall of 0.8922, and F1-score of 0.8928 on a dataset comprising 5,189 images across four varieties.

(2) A Qt framework-based graphical user interface (GUI) application system was developed, enabling real-time rice seed classification and structured output presentation (including category code pred_label, variety name pred_class, and confidence score pred_score), providing an intelligent tool for seed quality control and breeding decision-making.

These research outcomes offer an effective technical solution for agricultural intelligence development. Future studies will focus on expanding the system's applications in smart agriculture through the incorporation of multimodal sensor data and model lightweight design.

ACKNOWLEDGEMENTS

This work was supported by fundamental research program of Shanxi province) (Project No. 202303021212120).

REFERENCES

[1] Carneiro, G. A., Cunha, A., Aubry, T. J., & Sousa, J. (2024). Advancing Grapevine Variety Identification: A Systematic Review of Deep Learning and Machine Learning Approaches. *AgriEngineering*, 6(4), 4851-4888. https://doi.org/10.3390/agriengineering6040277

[2] Dong Z, Yang F, Du J, et al., (2024), Identification of varieties in Camellia oleifera leaf based on deep learning technology [J]. *Industrial Crops and Products*, 216: 118635.

[3] Dyrmann, M., Karstoft, H., & Midtiby, H. S. (2016). Plant species classification using deep convolutional neural network. *Biosystems Engineering*, 151, 72-80.

[4] He, K., Zhang, X., Ren, S., & Sun, J. (2016). Deep residual learning for image recognition. In *Proceedings of the IEEE Conference on Computer Vision and Pattern Recognition (CVPR)*. pp.770-778. https://doi.org/10.1109/CVPR.2016.90

[5] Hu, J., Shen, L., & Sun, G. (2018). Squeeze-and-excitation networks. In *Proceedings of the IEEE Conference on Computer Vision and Pattern Recognition (CVPR)* pp. 7132-7141. https://doi.org/10.1109/CVPR.2018.00745.

[6] Kamilaris, A., & Prenafeta-Boldú, F. X. (2018). Deep learning in agriculture: A survey. *Computers and Electronics in Agriculture*, *147*, 70-90. https://doi.org/10.1016/j.compag.2018.02.016

[7] Lu, Y., Yi, S., Zeng, N., Liu, Y., & Zhang, Y. (2017). Identification of rice varieties using deep learning. *Journal of Integrative Agriculture*, 16(11), 2516-2525.

[8] Peng J, Ouyang C, Peng H, Hu W, Wang Y, Jiang P. MultiFuseYOLO: Redefining Wine Grape Variety Recognition through Multisource Information Fusion. *Sensors* (Basel). 2024 May 6;24(9):2953.
[9] Pereira, C. S., Morais, R., & Reis, M. J. C. S. (2019). Deep learning techniques for grapevine variety identification. *Computers and Electronics in Agriculture*, *164*, 104918.
[10] Rawat, W., & Wang, Z. (2017). A comprehensive survey of deep learning for image classification. *Neural Computing and Applications*, *28*(10), 3037-3062. https://doi.org/10.1007/s00521-016-2487-1
[11] Reyes, A. K., Caicedo, J. C., & Camargo, J. E. (2015). Fine-tuning deep convolutional networks for plant recognition. *InCLEF* (Working Notes).
[12] Sladojevic, S., Arsenovic, M., Anderla, A., Culibrk, D., & Stefanovic, D. (2016). Deep neural networks based recognition of plant diseases by leaf image classification. *Computational Intelligence and Neuroscience*, *2016*, 3289801. https://doi.org/10.1155/2016/3289801
[13] Sun Daozong, Liu Jinyuan, Ding Zheng, et al., (2023), A Multi-Variety Classification Method for Southern Medicinal Plant Leaves Based on the Improved EfficientNetv2 Model [J] (基于改进 EfficientNetv2 模型的多品种南药叶片分类方法). *Journal of Huazhong Agricultural University*, 42(1): 258-267.
[14] Too, E. C., Yujian, L., Njuki, S., & Yingchun, L. (2019). A comparative study of fine-tuning deep learning models for plant disease identification. *Computers and Electronics in Agriculture*, *161*, 272-279. https://doi.org/10.1016/j.compag.2018.03.032
[15] Vaswani, A., Shazeer, N., Parmar, N., Uszkoreit, J., Jones, L., Gomez, A. N., ... & Polosukhin, I. (2017). Attention is all you need. In *Advances in Neural Information Processing Systems (NeurIPS)*. pp.5998-6008.
[16] Veit, A., Wilber, M. J., & Belongie, S. (2016). Residual networks: A survey. *arXiv preprint arXiv*:1603.05027.
[17] Wang, F., Jiang, M., Qian, C., Yang, S., Li, C., Zhang, H., ... & Tang, X. (2017). Attention mechanisms in computer vision: A survey. *arXiv preprint arXiv:1711.07971*.
[18] Zhang, S., Zhang, S., Zhang, C., Wang, X., & Shi, Y. (2019). Cucumber leaf disease identification with global pooling dilated convolutional neural network. *Computers and Electronics in Agriculture*, *162*, 422-430. https://doi.org/10.1016/j.compag.2019.03.012
[19] Zou Wei, Yue Yanbin, Feng Enying, et al. (2024), Identification of Anthracnose Disease in Chili Fruits Based on MobileNet V2 and Its Application [J] (基于 MobileNet V2 的辣椒果实炭疽病识别及其应用). *Guizhou Agricultural Sciences*, 52(09): 125-132.

SAFF-YOLO-BASED LIGHTWEIGHT DETECTION METHOD FOR THE DIAMONDBACK MOTH

基于 SAFF-YOLO 的白菜小菜蛾轻量化检测方法

Miao WU [1,2,)], Hang SHI [1,2,)], Changxi LIU [1,2,)], Hui ZHANG [1,2,)], Yufei LI [1,2,)], Derui BAO [1,2,)], Jun HU *[1,2,)],
[1)]College of Engineering, Heilongjiang Bayi Agricultural University, Daqing / China;
[2)]Heilongjiang Province Conservation Tillage Engineering Technology Research Center, Daqing / China;
Corresponding author: Jun HU; E-mail: +86 13836962331; E-mail: gcxykj@126.com
DOI: https://doi.org/10.35633/inmateh-76-13

Keywords: *YOLO11; Diamondback moth; Lightweight; Real-time detection*

ABSTRACT

The diamondback moth (Plutella xylostella) is a destructive pest that severely compromises Chinese cabbage production. Infestations caused by this pest significantly reduce both yield and quality, making efficient and accurate detection crucial for cultivation management. To address the challenges of detecting small targets and extracting phenotypic features in complex environments, this study proposes SAFF-YOLO—a YOLO11-based pest detection algorithm specifically designed for diamondback moths in Chinese cabbage fields. First, the loss function was refined to enhance the model's learning capacity for pest samples, optimizing it for precision-driven bounding box regression. Second, Alterable Kernel Convolution (AKConv) was incorporated into the backbone network, strengthening feature extraction capabilities while reducing model parameters. Third, Single-Head Self-Attention (SHSA) was integrated into the C2PSA (Channel and Position Spatial Attention) module, enhancing the backbone network's feature processing efficacy. Fourth, the neck network employed Frequency-aware Feature Fusion (FreqFusion) as the upsampling operator, specifically designed for precise localization of densely distributed targets. Finally, the Feature Auxiliary Fusion Single-Stage Head (FASFFHead) detection module was implemented to boost multi-scale target detection adaptability. Experimental results demonstrate that SAFF-YOLO achieved detection metrics of 90.7% precision, 89.4% recall, and 92.4% mAP50 for diamondback moths in Chinese cabbage, representing improvements of 7.4%, 8.0%, and 8.4% respectively over YOLO11. With only 7.3 million parameters and computational cost of 12.8 GFLOPs, this corresponds to 60.1% and 40.7% reductions compared to the baseline model. These results confirm an optimal balance between model lightweighting and high detection accuracy. Under complex field conditions characterized by small and densely distributed targets, severe background interference, and intense illumination, SAFF-YOLO consistently demonstrates robust detection capabilities, effectively reducing both false negative and false positive rates while maintaining high operational robustness. This research provides a practical solution for real-time diamondback moth detection in field-grown Chinese cabbage.

摘要

小菜蛾是严重危害白菜生产的害虫，其导致的虫害会使白菜产量、质量严重下降，因此高效、准确地检测小菜蛾对白菜栽培至关重要。针对复杂环境下小菜蛾检测存在目标小、表型特征提取困难等问题，本研究提出了基于 YOLO11 的白菜小菜蛾害虫检测算法 SAFF-YOLO。首先，改进损失函数来增强模型对害虫样本的学习能力，使其更适合边界框回归的准确性需求；引入可变核卷积（Alterable Kernel Convolution，AKConv）作为主干网络，增强了特征提取能力，减少了模型参数的数量；将单头自注意力（Single-Head Self-Attention，SHSA）集成至 C2PSA（Channel and Position Spatial Attention）模块中，提高了骨干网络的特征处理能力；颈部网络使用频率感知特征融合（Frequency-aware Feature Fusion，FreqFusion）作为上采样算子，旨在更好的对密集目标识别定位；最后通过 FASFFHead（Feature Auxiliary Fusion Single-Stage Head）检测头增强模型对不同尺度目标的检测能力。试验结果表明，SAFF-YOLO 对白菜小菜蛾的检测准确率、召回率、平均精度均值（mean average precision，mAP50）达到 90.7%、89.4%和 92.4%，对比 YOLO11 各提高了 7.4%、8.0%和 8.4%，且参数量为 7.3M，每秒浮点运算次数（Giga Floating-point Operations Per Second，GFLOPs）为 12.8，相较于基准模型分别降低 60.1%和 40.7%，实现了模型轻量化和较高检测精度的平衡。在小菜蛾小且密集、背景干扰严重、光照强烈等复杂环境下，SAFF-YOLO 均能较好地识别出目标个体，有效地降低漏检率和误检率，具有较好的鲁棒性。本研究可为田间白菜小菜蛾实时检测提供有效技术支持。

INTRODUCTION

Globally cultivated Chinese cabbage (Brassica rapa subsp. pekinensis) serves as a nutritionally essential vegetable crop. However, expanding cultivation and climate change have escalated phytopathological threats (*Ritonga et al., 2024; Li et al., 2016; Zhang et al., 2024; Shi et al., 2025*). The diamondback moth (*Plutella xylostella*), a devastating pest for Chinese cabbage, imposes substantial economic losses on farmers and challenges sustainable agricultural production systems annually (*Ahmed et al., 2022; Shehzad et al., 2023; Li et al., 2016*). Adult diamondback moths exhibit phloem-feeding behavior and rapid reproduction rates, impairing normal plant development and causing yield reduction in Chinese cabbage (*Rahman et al., 2019*). Larval chewing damage during growth stages induces extensive defoliation and leaf perforation, with severe infestations leading to complete leaf skeletonization (*Hussain et al., 2020; Hu et al., 1997*). Morphologically distinct between life stages, adults are flight-capable with predominantly gray-brown to dark brown coloration, while larvae exhibit green or pale yellow pigmentation that enables adaptive concealment within host plants. This phenotypic divergence creates significant detection challenges across developmental phases of diamondback moth (*Chen et al., 2011*). Consequently, developing rapid and accurate detection methods for diamondback moth in Chinese cabbage, coupled with effective monitoring of pest population dynamics, to implement targeted control measures, enables comprehensive pest management across critical growth stages - seedling, rosette, and heading phases - thereby safeguarding crops from significant yield losses. This constitutes an urgent agricultural priority demanding immediate resolution.

The rapid advancement of artificial intelligence has positioned machine learning and deep learning-based object detection algorithms as pivotal technologies in plant disease and pest identification research (*Chakrabarty et al., 2024*). At present, representative two-stage object detection methods such as Faster RCNN (*Ali et al., 2023; Hou et al., 2023; Wang et al., 2017*) and representative single-stage object detection methods such as SSD (*Zhai et al., 2020; Lyu et al., 2021*), YOLO are widely used for the detection and recognition of targets such as crop diseases and pests *(Wang et al., 2024; Dongfang et al., 2024*). To address the challenge of early identification of pests and diseases such as coffee leaf rust and miner pests, *Fragoso et al., (2025)*, proposed a real-time detection solution based on the YOLO series models (versions 8 to 11). The models were trained using the BRACOL dataset. Results demonstrated that YOLOv8s exhibited the optimal inference speed, with its qualitative predictive performance being significantly superior to other versions. While maintaining high accuracy, it meets the requirements for real-time field monitoring, thereby delivering robust technological support for the sustainable management of coffee cultivation. Slim *et al., (2023)*, proposed an intelligent pest detection system based on the YOLOv5 deep learning model by employing transfer learning and data augmentation techniques, the system addressed the challenge of insufficient training data. A companion mobile application was developed to assist farmers in real-time pest identification, localization, and quantification. This system significantly reduced farm inspection costs while also providing efficient, data-driven decision-making support for pest management. Liang et al., (*2024*) proposed an optimized YOLOv8n architecture for corn pest detection, incorporating Deformable Attention (DAttention) and Spatial and Channel Reconstruction Convolution (SCConv) modules. Trained on a dedicated corn pest dataset, this approach maintains high detection accuracy at 71 frames per second (FPS), enabling rapid and precise field-level infestation monitoring.

In field agriculture, micro-dense pests constitute the predominant infestation type. To address small-target detection challenges, optimizing object detection network architectures has emerged as the primary technical approach *(Wen et al., 2022*). *Teixeira et al.,* (*2023*), used the YOLOv5 deep learning model to achieve efficient recognition on the Pest24 dataset in response to the challenge of automatic detection of agricultural pests. Their experiments revealed that the relative scale of insects is a critical factor influencing detection accuracy. This approach provides a novel solution for pest detection in scenarios characterized by dense small objects, while also highlighting that enhancing the detection capability for small-sized insects represents a promising future research direction. Addressing the challenge of citrus disease detection, *Dananjayan et al., (2022),* developed the meticulously annotated CCL'20 dataset, and systematically evaluated the performance of seven state-of-the-art CNN detectors. Experimental results demonstrated that Scaled YOLOv4 P7 achieved the fastest inference speed for early-stage disease prediction, while CenterNet2 with Res2Net-101 DCN-BiFPN significantly outperformed others in detection accuracy for early-stage diseases, leveraging multi-scale feature fusion and attention mechanisms to excel particularly in identifying small-target lesion areas. This framework provides an efficient technical solution for real-time citrus disease diagnosis, effectively balancing the dual demands of inference speed and detection accuracy.

Tian et al., (*2023*), proposed MD-YOLO (Multi-scale Dense YOLO) featuring fused feature extraction/aggregation pathways with DenseNet blocks and adaptive attention modules. Deployed on sticky insect boards, this IoT-embedded system detects three lepidopteran pest species with validated field performance, demonstrating practical applicability.

While object detection algorithms have demonstrated considerable success, significant challenges persist in small-target detection research. When detecting minute pests, inherent complexities include multi-scale targets, dense clustering, and frequent occlusion scenarios. Although algorithmic advances have mitigated feature degradation caused by edge information loss and background interference, such accuracy improvements typically incur increased computational complexity that exceeds the capabilities of edge deployment platforms (*Liu et al., 2020; Lippi et al., 2021; Song et al., 2023*). To address these constraints, SAFF-YOLO is proposed—a lightweight architecture for diamondback moth detection in Chinese cabbage—which maintains high detection accuracy while substantially reducing computational footprint for efficient edge device implementation.

MATERIALS AND METHODS

Data Acquisition and Processing

The primary image acquisition for our diamondback moth dataset was conducted in Anda City, Suihua Municipality, Heilongjiang Province. To ensure data reliability and enhance dataset diversity for robust model generalization, 1,772 raw images were compiled in lossless PNG format, supplemented with carefully selected web-sourced imagery to augment phenotypic variation and ecological representativeness.

To ensure model fidelity, data acquisition employed multiple device platforms including iPhone 15 Pro and Honor 30 Pro, capturing images at dual resolutions (1280×720 and 4096×3072 pixels) thereby enhancing the recognition system's robustness and generalization capabilities across diverse imaging conditions and hardware configurations.

The initial dataset comprises raw images categorized into diamondback moth larvae and adults, supplemented through comprehensive data augmentation techniques including geometric transformations (translation, rotation), photometric adjustments (saturation/exposure modulation), random occlusion, and Gaussian noise injection. As depicted in Figure 1, these augmentations simulate diverse field conditions to enhance dataset variability while improving model sensitivity to phenotypic variations, ensuring sustained high recognition accuracy in complex real-world environments.



Fig. 1 - Data Enhancement

A final dataset of 4,794 images was selected to ensure data quality and diversity, which was then divided into training, validation, and test sets at an 8:1:1 ratio. To ensure annotation accuracy, this study employed the open-source labeling software LabelImg to manually annotate diamondback moth specimens in images, ultimately establishing the Plutella xylostella Dataset.

SAFF-YOLO-based lightweight detection method for the diamondback moth

YOLO11 is an advanced single-stage object detection model whose architecture comprises three core components: a backbone network, a neck network, and a detection head. Building upon its predecessors, YOLO11 incorporates significant optimizations—including a more powerful backbone network to enhance feature extraction efficiency and an innovative neck design featuring an enhanced EfficientDet-inspired FPN architecture to improve multi-scale object detection capabilities. The detection head employs a refined design that achieves precise prediction of object categories and locations, enabling efficient and accurate identification and localization of diverse targets even in complex, dynamic scenarios. The overall architectural layout of the YOLO11 model is illustrated in Figure 2.

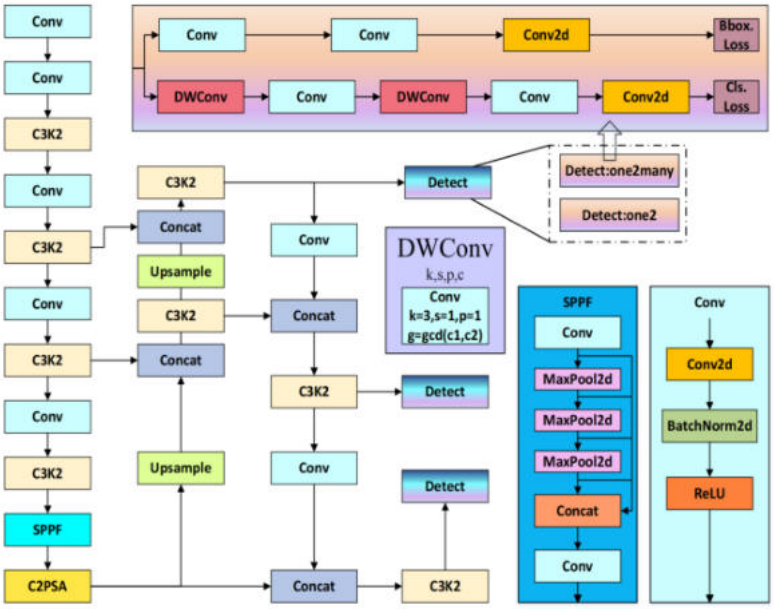


Fig. 2 - YOLO11 network structure

Despite its capability to accurately detect and identify targets, support multi-class object detection, and perform real-time tracking, YOLO11 remains challenged in achieving precise detection of early-stage small-scale pest infestations in field conditions. Specifically for diamondback moth detection, it struggles to extract phenotypic characteristics and accurately identify small targets. To address these limitations, this study proposes SAFF-YOLO (an enhanced YOLO11-based algorithm) for detecting diamondback moth infestations in Chinese cabbage fields, which significantly improves performance in agricultural pest detection tasks. The architecture of the proposed model is illustrated in Figure 3.

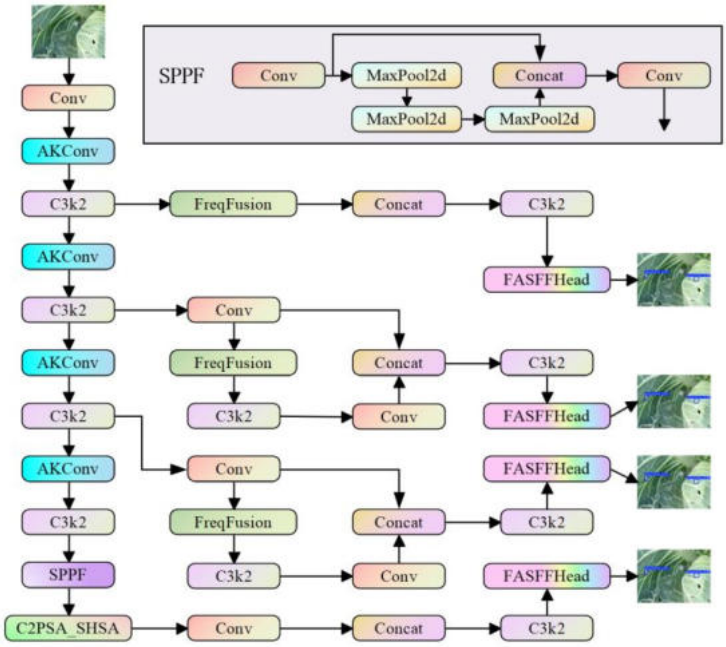


Fig. 3 - Structure of the SAFF-YOLO network

The original loss function was replaced with the Unified-IoU (UIoU) loss function (*Luo et al., 2024*), which dynamically adjusts the model's focus on prediction boxes of varying quality to optimize bounding box regression accuracy in object detection, thereby enabling more precise pest localization. The AKConv lightweight convolutional module was introduced to replace partial network structures *(Zhang et a., 2023*), enhancing feature extraction capability while reducing model parameters. Furthermore, SHSA and C2PSA modules were integrated into a unified SHSA_C2PSA module (*Yun et al., 2024*), which augments the backbone network's feature processing capacity, improves small-target detection performance, and reduces computational redundancy and memory access costs.

The neck network employs FreqFusion as its upsampling operator (*Chen et al., 2024*), enhancing localization in dense object scenarios while reducing computational complexity and improving processing speed. Within the detection head, the adaptive spatial feature fusion (ASFF) method was integrated with the P2 detection layer, evolving into a novel FASFFHead module (*Liu et al., 2019*). This integration mitigates feature loss during cross-scale fusion and implements secondary feature extraction for small targets, thereby enhancing model recognition accuracy.

Improvement of Loss Function

In the context of diamondback moth detection, the YOLO11 model faces challenges due to target density, minute scale, occlusion, and partial body visibility, leading to suboptimal recognition performance. To address this limitation, the original Complete Intersection over Union (CIoU) loss was replaced with the Unified-IoU (UIoU) loss function. This novel approach dynamically reallocates model focus from low-quality to high-quality prediction boxes through adaptive weight assignment, enhancing detection performance on both high-precision and densely clustered datasets while maintaining training efficiency. The mechanism effectively captures spatial relationships and overlapping region information among targets. The UIoU computation is formalized in Equation (1).

$$L_{UIoU} = 1 - IoU + \frac{\rho^2(b,b^{gt})}{c^2} + \alpha v \tag{1}$$

where ρ denotes the Euclidean distance between two points, b represents the center coordinate of the prediction box, b^{gt} indicates the ground truth box center, c is the diagonal length of the smallest enclosing rectangle, α serves as a scaling coefficient for balance, and v incorporates the aspect ratios of both prediction and target boxes into the sigmoid function. This formulation fulfills a dual role: (1) thresholding values to prevent excessive oscillation, and (2) quantifying aspect ratio consistency between boxes. The formal definitions of α and v are given in Equations (2) and (3), respectively.

$$\alpha = \frac{v}{(1-IoU)+v} \tag{2}$$

$$v = \left(\frac{1}{1+e^{-\frac{\omega 1}{h1}}} - \frac{1}{1+e^{-\frac{\omega}{h}}}\right)^2 \tag{3}$$

In the formula, $\omega 1$ and ω represent the lengths of the target box and the predicted box, while h_1 and h represent the widths of the target box and the predicted box.

The derivative calculation of UIoU is shown in equations (4) and (5).

$$\frac{\alpha v}{\alpha \omega} = 2\left(\frac{1}{1+e^{-\frac{\omega^{gt}}{h^{gt}}}} - \frac{1}{1+e^{-\frac{\omega}{h}}}\right)\left[\frac{1}{1+e^{-\frac{\omega}{h}}}\left(1 - \frac{1}{1+e^{-\frac{\omega}{h}}}\right)\right]/h \tag{4}$$

$$\frac{\alpha v}{\alpha h} = 2\left(\frac{1}{1+e^{-\frac{\omega^{gt}}{h^{gt}}}} - \frac{1}{1+e^{-\frac{\omega}{h}}}\right)\left[\frac{1}{1+e^{-\frac{\omega}{h}}}\left(1 - \frac{1}{1+e^{-\frac{\omega}{h}}}\right)\right] \times \frac{\omega}{h^2} \tag{5}$$

UIoU achieves adaptive weight allocation for prediction boxes of varying quality through strategic scaling of both prediction and ground truth boxes. This approach eliminates redundant bounding box computations while maintaining geometric integrity. After acquiring the bounding box dimensions (height, width) and center coordinates, UIoU applies scale factors to proportionally expand or contract these dimensions. This controlled scaling dynamically modulates the model's attention across prediction box qualities—where box contraction intensifies focus on high-quality predictions, thereby enhancing precision detection performance for well-defined targets.

AKConv

Convolutional kernels have achieved remarkable success in deep learning, yet they exhibit two inherent limitations. First, the confinement to local receptive fields restricts their capacity to capture global contextual information, while their fixed sampling patterns further limit adaptability. Second, conventional square-shaped kernels with fixed dimensions cause parameter counts to increase quadratically with kernel size. These rigid sampling geometries and kernel shapes struggle to adapt to the diverse target morphologies and scales across datasets and spatial locations (*Zhang et al., 2023*).

To overcome these limitations, AKConv (Adaptive Kernel Convolution) is introduced, which employs a flexible convolutional mechanism permitting kernels with arbitrary parameter counts. By dynamically adjusting kernel shapes to accommodate diverse image characteristics, this approach enhances model adaptability and computational efficiency. Consequently, AKConv not only improves model performance but also reduces parameter quantities. The architectural configuration of the AKConv module is illustrated in Figure 4.

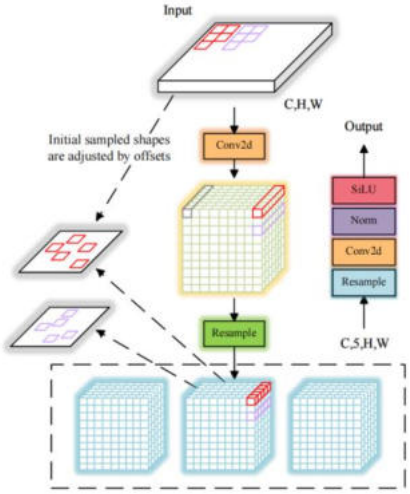


Fig. 4 - AKConv structure diagram

AKConv introduces a novel coordinate generation algorithm that dynamically adapts sampling shapes to varying images and targets. This algorithm generates initial sampling coordinates for kernels of arbitrary sizes and geometries (Fig.5), significantly enhancing flexibility in detecting multi-scale targets. To accommodate target variations, AKConv adjusts sampling positions of non-rectangular kernels through learned offsets, thereby improving feature extraction accuracy.

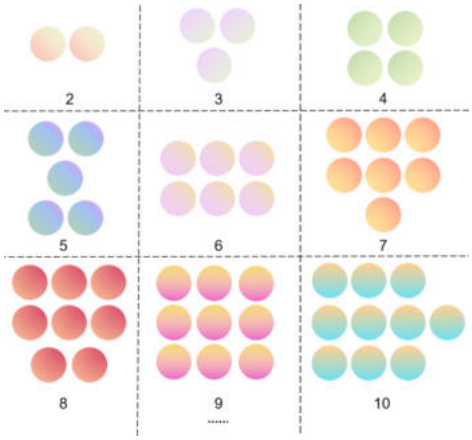


Fig. 5 - Adaptive initial sampling shape

Unlike traditional convolutional kernels that employ regular sampling grids, AKConv targets deformable kernels with irregular geometries. This innovation necessitated the development of an arbitrary-size convolution algorithm that generates initial sampling coordinates P_n for convolutional kernels (*Wu et al., 2024*). The algorithm first generates a regular sampling grid, subsequently constructs an irregular grid for residual sampling points, and finally concatenates both components into a unified sampling structure.

Within this framework, the top-left coordinate (0,0) serves as the sampling origin. Given initial coordinates P_n and kernel parameters ω for irregular convolution, the convolutional operation at position P_0 is formally defined by Equation (6).

$$ConvP_0 = \sum \omega \times (P_n + P_0) \quad (6)$$

AKConv resolves the fundamental mismatch between irregular sampling coordinates and fixed-size convolution operations through its algorithmic innovations.

Traditional convolution suffers from quadratic growth in both parameter count and computational load with increasing kernel size, leading to inefficiency in resource-constrained environments. In contrast, AKConv's unique design reduces model parameters and computational overhead, enabling dynamic complexity adjustment according to task requirements and hardware capabilities. Furthermore, AKConv adapts to spatial feature variations through offset-adjusted kernel positioning, effectively handling non-rigid deformations, occlusions, and complex backgrounds. This capability significantly enhances detection robustness for subsequent diamondback moth identification. The schematic representation of this adaptation process is illustrated in Fig. 6.

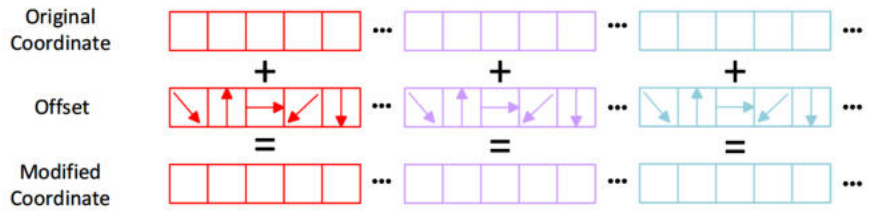


Fig. 6 - Offset adjustment sample shape

Single-Head Self-Attention

Accurate extraction of spatial location information is critical in object detection tasks. In pest-containing images where natural backgrounds dominate, convolutional kernels process non-target regions, introducing substantial redundant information that compromises pest recognition accuracy. The Single-Head Self-Attention (SHSA) mechanism addresses this by applying attention to a subset of input channels (CP=rC), reducing computational redundancy while integrating global and local features to enhance efficiency and precision. As illustrated in Fig. 7, SHSA operates by: (1) applying a single-head attention layer to a channel subset (CP=rC), where r denotes the reduction ratio) for spatial feature aggregation, while (2) preserving original information in remaining channels.

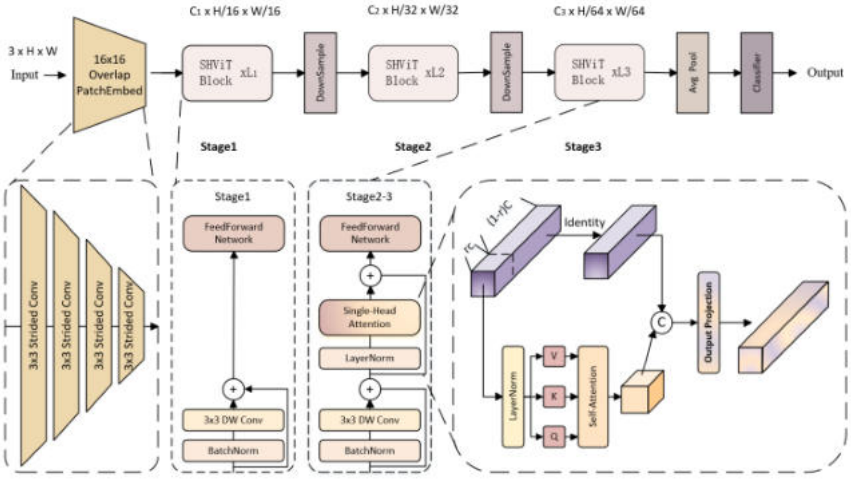


Fig. 7 - Structure of SHSA attention mechanism

The calculation formulas for its operation are shown in equations (7) to (10).

$$SHSA(X) = Concat\left(\widetilde{\mathrm{X}}_{att},\ X_{res}\right)W^{Q} \quad (7)$$

$$\widetilde{\mathrm{X}}_{att} = Attention\left(X_{att}W^{Q},\ X_{att}W^{K},\ X_{att}W^{V}\right) \tag{8}$$

$$Attention\left(Q,\ K,\ V\right) = Softmax\left(QK^{T}/\sqrt{d_{qk}}\right)V \tag{9}$$

$$X_{att},\ X_{res} = Split\left(X,\ \left|C_{p},\ C - C_{p}\right|\right) \tag{10}$$

where W^{Q}, W^{K}, and W^{V} denote projection weight matrices, dqk represents the dimensionality of queries and keys, and Concat signifies the concatenation operation. To maintain memory access consistency, the initial C_p channels serve as representative proxies for the complete feature map. Moreover, SHSA's final projection operates across all channels—not solely the initial C_p subset—ensuring efficient propagation of attention features to residual channels.

Frequency-aware Feature Fusion

Feature extraction of diamondback moths is challenged by small target regions, uneven density distribution, and low image resolution, resulting in insufficient valid information. However, dense image prediction requires high-precision category information and spatial boundaries. Conventional feature fusion methods underperform in maintaining category feature consistency and preserving boundaries, often causing significant intra-class feature variations and boundary ambiguity.

FreqFusion is a frequency-aware feature fusion framework comprising three core modules: an Adaptive Low-Pass Filter Generator (ALPF), an Offset Generator, and an Adaptive High-Pass Filter Generator (AHPF). The ALPF predicts spatially adaptive low-pass filters to mitigate intra-class inconsistency; the Offset Generator predicts feature offsets to refine internal representations and boundary characteristics; while the AHPF extracts high-frequency details for precise boundary delineation. As illustrated in Fig.8, these modules operate synergistically to resolve intra-class inconsistencies and boundary ambiguities in dense image prediction. Through frequency-aware feature refinement, this integrated mechanism enhances model performance.

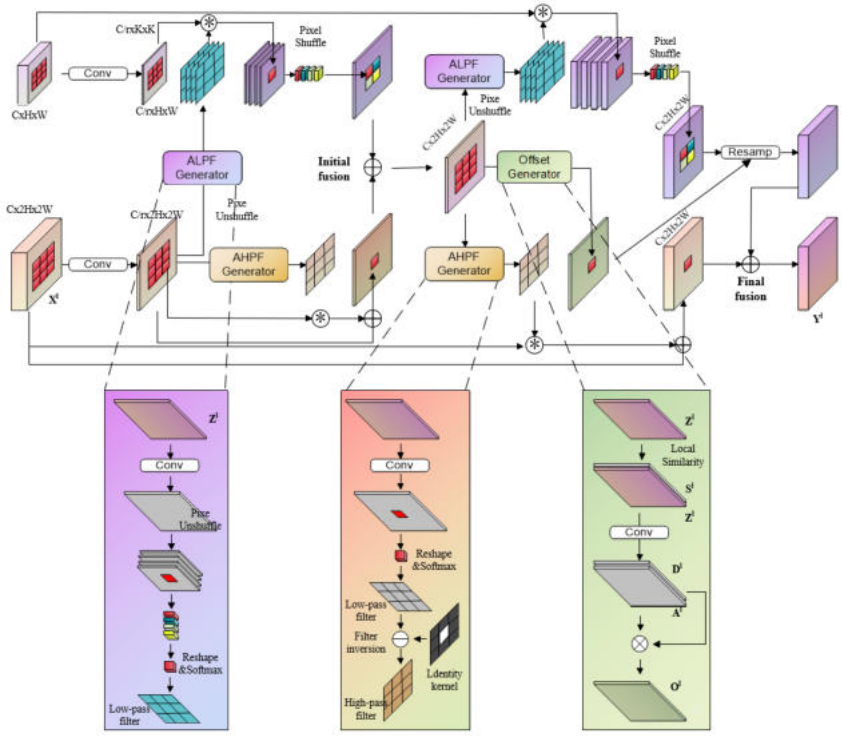


Fig. 8 - FreqFusion structure diagram

The generation calculation formula for FreqFusion is shown in Equations (11) and (12).

$$Y_{i,j}^{l} = \tilde{Y}_{i+u,j+v}^{\ l+1} + \tilde{X}_{i,j}^{\ l} \tag{11}$$

$$\tilde{Y}^{\,l+1} = \mathcal{F}^{UP}\left(\mathcal{F}^{LP}(Y^{l+1})\right),\ \tilde{X}^{l} = \mathcal{F}^{HP}(X^{l}) + X^{l} \tag{12}$$

In this formulation, $\mathcal{F}^{UP}$ denotes the low-pass filter predicted by the ALPF generator, while (u, v) represents the offset values predicted by the Offset Generator for feature coordinates at (i, j), and $\mathcal{F}^{UP}$ signifies the high-pass filter generated by AHPF. These components collectively resolve class inconsistency and boundary displacement by: (1) adaptively smoothing high-level features using spatially adaptive low-pass filtering, (2) replacing inconsistent features through resampling of adjacent class-consistent features, and (3) enhancing high-frequency boundary details in low-level features.

Feature Auxiliary Fusion Single-Stage Head

In object detection, conventional YOLO series achieve efficient detection through multi-scale feature fusion. While the YOLO11 detection head demonstrates advantages, it exhibits limitations in complex scenes or small object detection. The FASFFHead addresses this by: (1) introducing auxiliary feature layers and a feature selection module, (2) fusing multi-level features to enhance network sensitivity towards multi-scale and complex objects, and (3) improving extraction and representation of multi-scale features for superior discriminative feature capture. As illustrated in Fig. 9, the FASFFHead primarily consists of two key components: a Shallow-level Feature Fusion module (SFB) and a High-level Feature Extraction module (HFE), operating through the following mechanism.

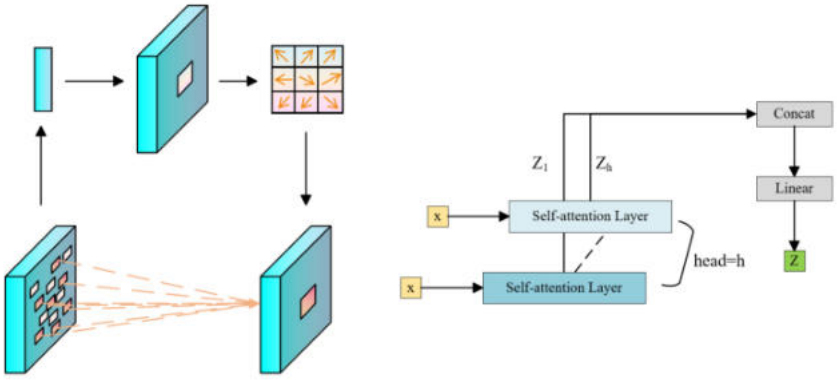


Fig. 9 - FASFFHead structure diagram

Within the SFB module, shallow-level and high-level features are integrated through a cascaded residual network and feature pyramid structure. This fusion preserves detailed spatial information from shallow features while incorporating global semantic context from high-level features, thereby enriching feature maps and enhancing representational capacity. The HFE module subsequently processes these fused features through depthwise convolutional layers to extract deep contextual information, while employing a Spatial Pyramid Pooling (SPP) layer to capture multi-scale representations. This dual mechanism significantly improves detection capability for objects across varying scales.

By synergistically combining SFB and HFE modules, the FASFFHead effectively fuses auxiliary features with high-level representations from the backbone network. This integration substantially boosts detection performance, simultaneously enhancing feature expressiveness while improving model robustness and generalization capability for practical object detection applications.

RESULTS AND ANALYSIS

Test environment and evaluation index

To ensure experimental validity, detailed hardware and software configurations are specified in Table 1.

Table 1

Software and Hardware Environment Configuration Table

Configuration Parameter	Configuration Item
CPU	16 vCPU Intel(R) Xeon(R) Platinum 8352V CPU @ 2.10GHz
RAM	120GB
GPU	NVIDIA GeForce RTX 4090 24GB
Operating system	Ubuntu 18.04
CUDA	12.4
Compiled language	Python 3.9
Deep learning framework	PyTorch3.8.0
Epochs	200
Batch size	32

The evaluation employs three metrics: $mAP@50$, precision (P), and recall (R). Precision quantifies the proportion of true positives among all positive predictions, while recall measures the proportion of actual positives correctly identified. Their computational formulations are given by Equation (13) and Equation (14), respectively.

$$P = \frac{T_P}{T_P + F_P} \tag{13}$$

$$R = \frac{T_P}{T_P + F_N} \tag{14}$$

where F_N denotes the number of false negatives (missed detections), F_P represents false positives (detections with IoU below the threshold), and T_P indicates true positives (detections with IoU ≥ threshold).

For mAP computation, the average precision (A) corresponds to the area under the Precision-Recall (P-R) curve, calculated as specified in Equation (15).

$$A = \int_2^1 P(R)dR \tag{15}$$

Performance comparison test of different models

To evaluate the pest recognition and detection performance of the SAFF-YOLO model, comparative experiments were conducted against prevalent object detection models: Faster R-CNN, SSD, YOLOv8, YOLOv9, YOLOv10, and YOLO11. Identical experimental setups (hardware/software configurations) were maintained across all models to ensure methodological rigor and validity. Model performance was comprehensively assessed using five metrics: precision, recall, mean average precision (mAP), floating-point operations (FLOPs), and parameter count. Comparative results are presented in Table 2.

Table 2

Training effect of different models

Model	Precision(%)	Recall(%)	mAP0.5(%)	GFLOPs	Model Size(MB)
Faster-RCNN	82.1	80.3	83.7	124.2	71.6
SSD	80.1	77.9	80.7	61.1	39.2
YOLOv5	81.3	76.8	81.8	5.9	4.4
YOLOv8	82.0	79.9	84.6	6.9	5.4
YOLOv10	81.7	78.4	82.3	6.6	5.2
YOLO11	83.3	81.4	84.0	21.6	18.3
SAFF-YOLO	90.7	89.4	92.4	12.8	7.3

According to Table 2, the SAFF-YOLO model demonstrates mAP@50 improvements of 8.7%, 11.7%, 10.6%, 7.8%, 10.1%, and 8.4% over Faster R-CNN, SSD, YOLOv5, YOLOv8, YOLOv10, and YOLO11, respectively. These gains indicate superior target localization accuracy, enhanced recognition capability for pests in complex backgrounds and dense populations, and higher confidence scores with improved reliability in detection outcomes.

Ablation Experiments

Targeting diamondback moth infestation detection, this study progressively enhanced the YOLO11 architecture. Each modification underwent statistical analysis to validate efficacy in pest recognition, with quantitative results detailed in Table 3.

Table 3

SAFF-YOLO model ablation experiments

Model	Precision(%)	Recall(%)	mAP0.5(%)	GFLOPs	Model Size(MB)
YOLO11	83.3	81.4	84.0	21.6	18.3
YOLO11-U	85.0	83.5	85.8	21.6	18.3
YOLO11-UA	83.1	82.3	85.1	5.5	4.4
YOLO11-UAB	86.2	83.7	86.7	5.4	4.3
YOLO11-UABC	88.6	87.3	89.6	6.1	4.3
SAFF-YOLO	90.7	89.4	92.4	12.8	7.3

Note: U represents replacing the UIoU loss function; A represents the AKConv improvement; B represents the SHSA improvement; C represents the FreqFusion improvement

Stage 1: UIoU replacement improved precision, recall, and mAP50 of baseline YOLO11 by 1.7%, 2.1%, and 1.8% respectively. Stage 2: AKConv modification reduced parameter count by 76% and computational load by 16.1 GFLOPs versus baseline. Stage 3: Integrating SHSA and FreqFusion modules increased mean average precision by 1.7-2.9 percentage points without computational overhead, enhancing all metrics.

Final integration: Incorporating the FASFFHead module, SAFF-YOLO demonstrated significant improvements over YOLOv11 across all evaluated metrics: a 40.7% reduction in model size, an 8.8 GFLOPs decrease in computational cost, and respective gains of 7.4% in precision, 8.0% in recall, and 8.4% in mAP50. This demonstrates SAFF-YOLO's superior accuracy and robustness when detecting micro-scale pests in dense infestations with scale variations and homogeneous backgrounds.

Model visualization analysis and comparison

Comparative detection results for diamondback moths using YOLOv5, YOLOv8, YOLO11, and SAFF-YOLO are presented in Fig. 10, validating SAFF-YOLO's superior performance in this study. Visual evidence demonstrates SAFF-YOLO's enhanced robustness in complex environments with significant interference, effectively reducing false positives and misclassifications prevalent in baseline YOLO variants. Under challenging conditions featuring small target pests and high identification difficulty, comparator models exhibit frequent false detections, duplicate identifications, and low-confidence predictions. SAFF-YOLO significantly outperforms these models through improved environmental adaptability and superior discriminative feature representation capabilities.

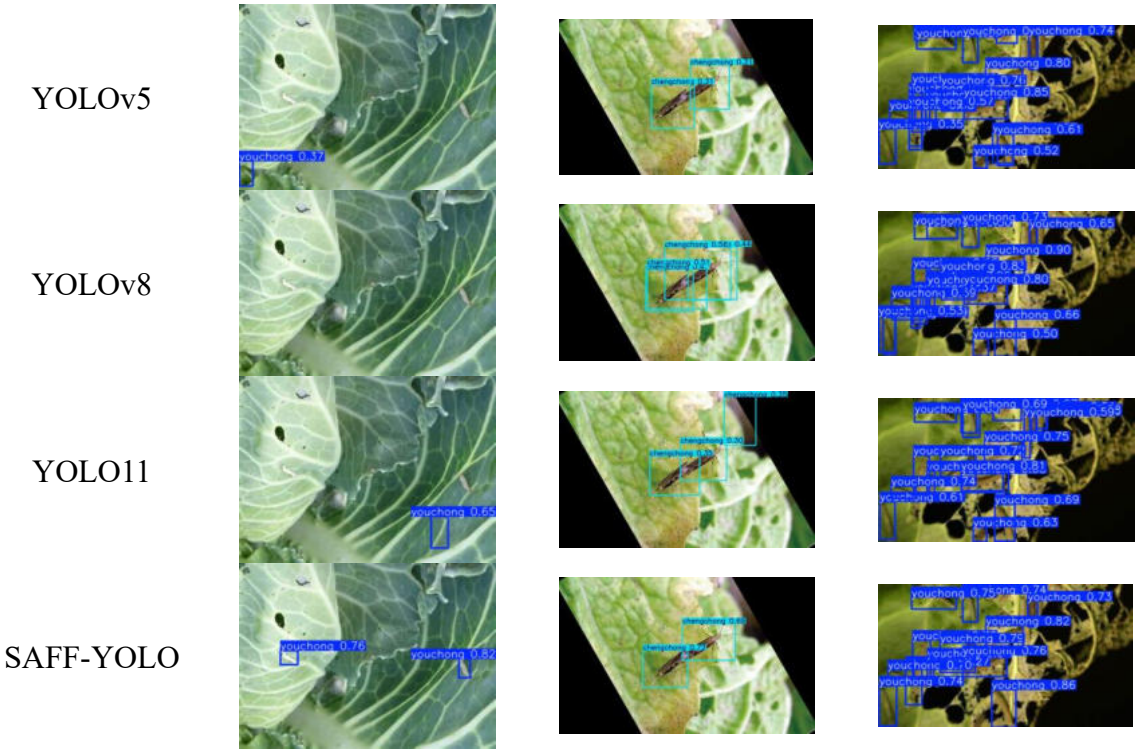


Fig. 10 - Target detection results of different models for the little Chinese cabbage diamondback moth

SAFF-YOLO: Diamondback Moth Pest Detection System

This study designed and implemented a visualization detection system for diamondback moths using the PyQt framework, as illustrated in Fig.11. PyQt integrates Python's concise syntax with Qt's robust functionality, offering comprehensive GUI components, cross-platform compatibility, and efficient signal-slot mechanisms. This architecture ensures consistent and stable user interfaces across diverse operating systems.

The application implements two core functionalities:

1) Pest image import module: Supports four input modalities: single image import, batch directory import, video file processing, and real-time camera-based detection.

2) Detection visualization interface: Presents detection metadata including inference duration, target count, pest classification, confidence scores, and bounding box coordinates. Post-detection, the system generates a comprehensive report listing target serial numbers, file paths, categories, confidence values, and positional coordinates.

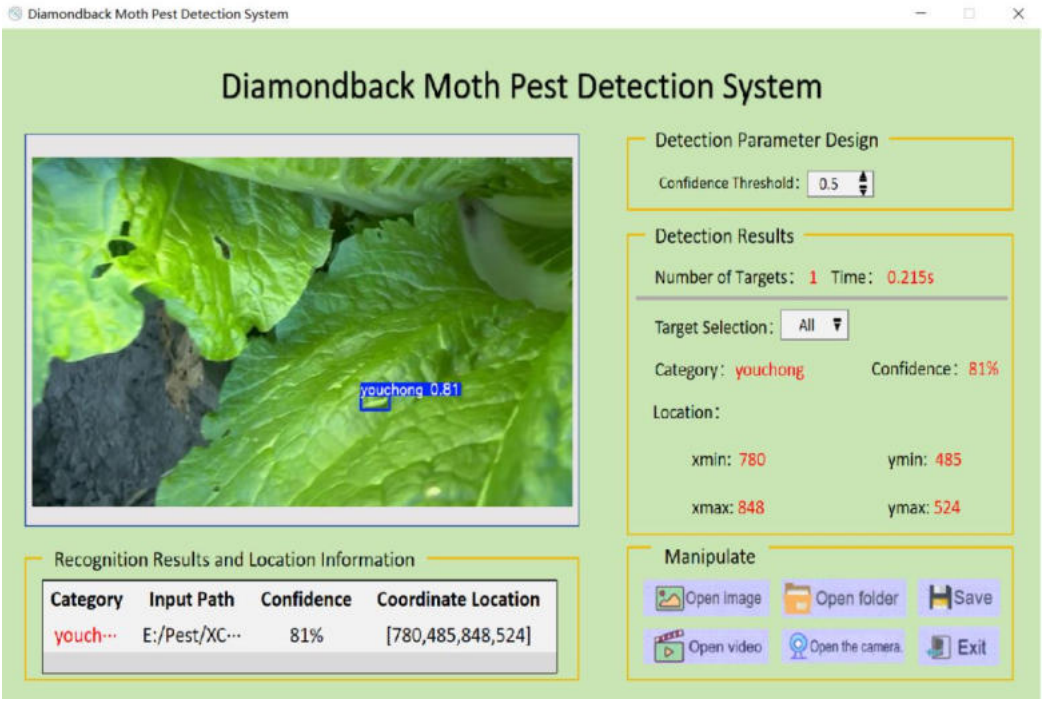


Fig. 11 - Diamondback Moth Pest Detection System

CONCLUSIONS

This study addresses key challenges in Chinese cabbage pest detection—including scale variation, target density, and phenotypic feature extraction difficulties—by proposing SAFF-YOLO: an efficient algorithm for diamondback moth detection on Chinese cabbage plants. The architecture modifies the YOLO11 framework through: (1) replacing the baseline loss function with UIoU to enhance discriminative learning of moth characteristics; (2) integrating AKConv lightweight convolutions and embedding SHSA attention within the C2PSA module to strengthen feature extraction while reducing parameters; (3) implementing FreqFusion as the neck network's upsampling operator for dynamic computation allocation and precise spatial localization; and (4) incorporating the FASFFHead for multi-scale detection capability enhancement. Experimental results demonstrate SAFF-YOLO's 11 MB model size reduction and 8.8 GFLOPs computation decrease versus YOLO11, while achieving 7.4% precision, 8.0% recall, and 8.4% mAP improvements—confirming superior efficiency and accuracy in cabbage moth detection. This approach enables precise localization of infestations for timely intervention in cabbage cultivation, offering valuable references for pest management in related agricultural systems.

ACKNOWLEDGEMENTS

This research was funded by Heilongjiang Province Natural Science Foundation Joint Guidance Project (No. LH2023E106), Heilongjiang Province "Double First-Class" Discipline Collaborative Innovation Achievement Project (No. LJGXCG2023-045), China University Industry-University-Research Innovation Foundation Funded Project (No.2023RY059) and Heilongjiang Province Key Research and Development Program Major Project (No.2023ZX01A06).

REFERENCES

[1] Ahmed, M. A., Cao, H. H., Jaleel, W., Amir, M. B., Ali, M. Y., Smagghe, G., Liu, T. X., (2022). Oviposition preference and two-sex life table of Plutella xylostella and its association with defensive enzymes in three Brassicaceae crops. *Crop Protection*, Vol. 151, pp. 105816, England.

[2] Ali, F., Qayyum, H., Iqbal, M. J., (2023). Faster-PestNet: A Lightweight deep learning framework for crop pest detection and classification. *IEEE Access*, Vol. 11, pp. 104016-104027, United States.

[3] Chakrabarty, S., Shashank, P.R., Deb, C.K., Haque, M.A., Thakur, P., Kamil, D., Marwaha, S., Dhillon, M.K., (2024). Deep learning-based accurate detection of insects and damage in cruciferous crops using YOLOv5. *Smart Agricultural Technology*, Vol. 9, pp. 100663, Netherlands.

[4] Chen, L., Fu, Y., Gu, L., Yan, C., Harada, T., Huang, G., (2024). Frequency-aware feature fusion for dense image prediction. *IEEE Transactions on Pattern Analysis and Machine Intelligence,* pp. 10763-10780, United States.

[5] Chen, Y. X., Tian, H. J., Wei, H., Zhan, Z., Huang, Y., (2011). Morphological Identification of Sexes in Larvae, Pupae, and Adults of the Diamondback Moth (*Plutella xylostella*) (小菜蛾幼虫、蛹和成虫的雌雄形态识别). *Fujian Journal of Agricultural Sciences*, Vol. 26, pp. 4, Fujian/China.

[6] Dananjayan, S., Tang, Y., Zhuang, J., Hou, C. and Luo, S., (2022). Assessment of state-of-the-art deep learning based citrus disease detection techniques using annotated optical leaf images. *Computers and Electronics in Agriculture*, Vol. 193, pp. 106658, England.

[7] Dongfang, Q. I. U., (2024). Research on locust target detection algorithm based on YOLO V7-MOBILENETV3-CA. *INMATEH-Agricultural Engineering*, Vol. 74, pp. 283-292, Romania.

[8] Fragoso, J., Silva, C., Paixão, T., Alvarez, A. B., Júnior, O. C., Florez, R., Palomino-Quispe, F., Savian, L. G., Trazzi, P. A., (2025). Coffee-Leaf Diseases and Pests Detection Based on YOLO Models. *Applied Sciences*, Vol. 15(9), pp. 5040, Romania.

[9] Hou, J., Yang, C., He, Y., Hou, B., (2023). Detecting diseases in apple tree leaves using FPN–ISResNet–Faster RCNN. *European Journal of Remote Sensing*, Vol. 56, pp. 2186955, Italy.

[10] Hu, G. Y., Mitchell, E. R., Okine, J. S., (1997). Diamondback moth (Lepidoptera: Plutellidae) in cabbage: Influence of initial immigration sites on population distribution, density and larval parasitism. *Journal of Entomological Science*, Vol. 32, pp. 56-71, United States.

[11] Hussain, M., Gao, J., Bano, S., Wang, L., Lin, Y., Arthurs, S., Qasim, M., Mao, R., (2020). Diamondback moth larvae trigger host plant volatiles that lure its adult females for oviposition. *Insects*, Vol.11, pp.725, Switzerland.

[12] Li, Z., Feng, X., Liu, S. S., You, M., Furlong, M. J., (2016). Biology, ecology, and management of the diamondback moth in China. *Annual review of entomology*, Vol. 61, pp. 277-296, United States.

[13] Li, Z., Zalucki, M. P., Yonow, T., Kriticos, D. J., Bao, H., Chen, H., Hu, Z., Feng, X., Furlong, M. J., (2016). Population dynamics and management of diamondback moth(Plutella xylostella) in China:the relative contributions of climate, natural enemies and cropping patterns. *Bulletin of Entomological Research*, Vol. 106, pp. 197-214, England.

[14] Liang, Q., Zhao, Z., Sun, J., Jiang, T., Guo, N., Yu, H., Ge, Y., (2024). Multi-target detection method for maize pests based on improved YOLOv8. *INMATEH-Agricultural Engineering*, Vol. 73, pp. 227-238, Romania. DOI: https://doi.org/10.35633/inmateh-73-19

[15] Lippi, M., Bonucci, N., Carpio, R. F., Contarini, M., Speranza, S., Gasparri, A., (2021). A yolo-based pest detection system for precision agriculture. In 2021 29th Mediterranean Conference on Control and Automation (MED), pp. 342-347, Puglia/Italy

[16] Liu, J., Wang, X., (2020). Tomato diseases and pests detection based on improved Yolo V3 convolutional neural network. *Frontiers in plant science*, Vol. 11, pp. 898, Switzerland.

[17] Liu, S., Huang, D., Wang, Y., (2019). Learning spatial fusion for single-shot object detection. arxiv 2019. *arxiv preprint arxiv*:1911.09516.

[18] Luo, X., Cai, Z., Shao, B., Wang, Y., (2024). Unified-IoU: For High-Quality Object Detection. *arxiv preprint arxiv:* 2408.06636, 2024.

[19] Lyu, Z., Jin, H., Zhen, T., Sun, F., Xu, H., (2021). Small object recognition algorithm of grain pests based on SSD feature fusion. *IEEE Access*, Vol. 9, pp. 43202-43213, United States.

[20] Rahman, M. M., Zalucki, M. P., Furlong, M.J., (2019). Diamondback moth egg susceptibility to rainfall: effects of host plant and oviposition behavior. *Entomologia Experimentalis et Applicata*, Vol. 167, pp. 701-712, England.

[21] Ritonga, F. N., Gong, Z., Zhang, Y., Wang, F., Gao, J., Li, C., Li, J., (2024). Exploiting Brassica rapa L. subsp. pekinensis Genome Research. *Plants*, Vol. 13, pp. 2823, Switzerland.

[22] Shehzad, M., Bodlah, I., Siddiqui, J. A., Bodlah, M. A., Fareen, A. G. E., Islam, W, (2023). Recent insights into pesticide resistance mechanisms in Plutella xylostella and possible management strategies. *Environmental Science and Pollution Research*, Vol. 30, pp. 95296-95311, Germany.

[23] Shi, H., Liu, C., Wu, M., Zhang, H., Song, H., Sun, H., Li, Y., Hu, J., (2025). Real-time detection of Chinese cabbage seedlings in the field based on YOLO11-CGB. *Frontiers in Plant Science*, Vol. 16, pp. 1558378, Switzerland.

[24] Slim, S.O., Abdelnaby, I.A., Moustafa, M.S., Zahran, M.B., Dahi, H.F. and Yones, M.S., (2023). Smart insect monitoring based on YOLOV5 case study: Mediterranean fruit fly Ceratitis capitata and Peach fruit fly Bactrocera zonata. *The Egyptian Journal of Remote Sensing and Space Sciences*, Vol. 26, pp. 881-891, Egypt.

[25] Song, L., Liu, M., Liu, S., Wang, H., Luo, J., (2023). Pest species identification algorithm based on improved YOLOv4 network. *Signal, Image and Video Processing*, Vol. 17, pp. 3127-3134, England.

[26] Tian, Y., Wang, S., Li, E., Yang, G., Liang, Z., Tan, M., (2023). MD-YOLO: Multi-scale Dense YOLO for small target pest detection. *Computers and Electronics in Agriculture*, Vol. 213, pp. 108233, England.

[27] Teixeira, A.C., Morais, R., Sousa, J.J., Peres, E. and Cunha, A., (2023). Using deep learning for automatic detection of insects in traps. *Procedia Computer Science*, Vol. 219, pp.153-160, Netherlands.

[28] Wang, R. F., Su, W. H., (2024). The Application of Deep Learning in the Whole Potato Production Chain: A Comprehensive Review. *Agriculture*, Vol. 14, pp. 1225, Switzerland.

[29] Wang, X., Shrivastava, A., Gupta, A., (2017). A-fast-RCNN: Hard positive generation via adversary for object detection. *In Proceedings of the IEEE conference on computer vision and pattern recognition*, pp. 2606-2615, HI/USA

[30] Wen, C., Chen, H., Ma, Z., Zhang, T., Yang, C., ... Chen, H., (2022). Pest-YOLO: A model for large-scale multi-class dense and tiny pest detection and counting. *Frontiers in Plant Science*, Vol. 13, pp. 973985, Switzerland.

[31] Wu, D., Fang, C., Zheng, X., Liu, J., Wang, S., Huang, X., (2024). AMW-YOLOv8n: Road Scene Object Detection Based on an Improved YOLOv8. *Electronics*, Vol. 13, pp. 4121-4121, Switzerland.

[32] Yun, S., Ro, Y., (2024). Shvit: Single-head vision transformer with memory efficient macro design. *In Proceedings of the IEEE/CVF Conference on Computer Vision and Pattern Recognition*, pp. 5756-5767, Seattle/USA

[33] Zhai, S., Shang, D., Wang, S., Dong, S., (2020). DF-SSD: An improved SSD object detection algorithm based on DenseNet and feature fusion. *IEEE Access*, Vol. 8, pp. 24344-24357, United States.

[34] Zhang, H., Hu, J., Shi, H., Liu, C., Wu M., (2024). Precision Target Spraying System Integrated with Remote Deep Learning Recognition Model for Cabbage Plant Centers (融合远端深度学习识别模型的白菜株心精准对靶喷雾系统). *Smart Agriculture,* Vol. 6, pp. 85-95, Heilongjiang/China.

[35] Zhang, X., Song, Y., Song, T., Yang, D., Ye, Y., Zhou, J., Zhang, L., (2023). AKConv:convolutional kernel with arbitrary sampled shapes and arbitrary number of parameters. *arXiv* :2311.11587.

[36] Zhang, S., Liu, Z., Chen, Y., Jin, Y., Bai, G., (2023). Selective kernel convolution deep residual network based on channel-spatial attention mechanism and feature fusion for mechanical fault diagnosis. *ISA transactions*, Vol. 133, pp. 369-383, United States.

DESIGN AND TESTING OF A FULL-DEGREE-OF-FREEDOM CONSTRAINED SEED GUIDING DEVICE FOR ORDERED SEED FLOW
/
有序种子流全自由度约束导种装置设计与试验

Xin DU*, Qianhao YU, Shufa CHEN, Qixin SUN, Yue JIANG, Jingyi MAO
Jiangsu Ocean University, Lianyungang 222005/ China
Tel: 0086-0518-85895322; E-mail: xindu@jou.edu.cn
Corresponding author: Xin Du
DOI: https://doi.org/10.35633/inmateh-76-14

Keywords: *Precision seeding; Seed guiding device; High-speed; Precision agriculture*

ABSTRACT
To improve the uniformity and stability of seed guidance in ordered seed flow and meet the requirements of precision sowing operations, a brush-type seed guiding device capable of constraining all degrees of freedom of the seeds was designed. Bench tests were conducted to optimize the factors affecting performance, namely the nut-bolt head spacing, the brush-to-housing gap, and the brush belt speed. Through single-factor experiments, the influence of each factor on seed guidance performance was clarified, and reasonable value ranges were determined. Combined with a response surface test, a multiple quadratic regression model was established to describe the relationship between these factors and the variation coefficients of pass rate, missed seeding rate, and seed spacing. The results show that optimal seed guidance performance is achieved when the nut-bolt head spacing is 39.15 mm, the brush-to-housing gap is 0.22 mm, and the brush belt linear velocity is 0.644 m/s. This study provides a theoretical foundation and data support for the development of precision sowing technology and its associated seed guiding devices.

摘要
为提高有序种子流导种均匀性与稳定性，满足精量播种作业要求，设计了一种可约束种子全部自由度的毛刷式导种装置，对影响其工作性能的螺母-螺栓头间距、毛刷-外壳间隙和毛刷带线速度等因素进行了台架试验优化。通过单因素实验阐明各因素对导种性能的影响规律，并确定因素的合理取值范围。结合响应面试验，建立了各因素与合格率、漏播率和粒距变异系数间的多元二次回归模型。结果表明，当螺母-螺栓头间距为 39.15 ㎜、毛刷-外壳间隙为 0.22 ㎜、毛刷带线速度为 0.644 m/s 时，导种性能最佳。本研究可为精量播种技术及配套导种装置的研制提供理论基础与数据支撑。

INTRODUCTION
In 2024, the corn planting area and total output in China reached 44.74 million hectares and 294.92 million tons, respectively, consistently securing the top position among the three major grain crops for several years. Nevertheless, China's corn yield remains at only 6.59 tons per hectare, significantly lower than the 11.11–12.04 tons per hectare achieved by the United States and other developed countries (*Awad et al., 2022*). The full mechanization of corn sowing in China has made sowing quality a critical factor influencing corn yield (*Liao et al., 2020*). While significant research has focused on precision seed metering devices within single-seed sowing technology, studies specifically addressing the seed guiding mechanism remain scarce (*Du et al., 2023*). As a result, the seed guiding process has become a limiting factor in improving the quality of high-speed sowing operations. This highlights an urgent need for the development of an efficient seed guiding mechanism tailored to high-speed sowing requirements (*Fanigliulo et al., 2022*).

The seed guiding device is a core component of precision seeders, directly influencing seeding accuracy and efficiency, particularly at high operating speeds. To overcome this bottleneck, recent research has focused on optimizing seed guide designs to improve seed motion stability and placement accuracy.

Xin Du, Lecturer Ph.D. Eng; Qianhao Yu, MA.Eng Stud.; Shufa Chen, Prof. Ph.D. Eng; Qixin Sun, Prof. Ph.D. Eng; Yue Jiang, Lecturer Ph.D. Eng.; Zhanrui Zhang, B.S Stud.*

Key technological strategies include:

Pneumatic-assisted seed guiding: utilizing airflow to guide and constrain seed trajectories. Examples include air-delivery auxiliary seed guides (*Li et al.*, *2025*), guidance restraint-airflow blowing devices (*Liu et al.*, *2025*), and conical spiral airflow high-speed guides (*Zhang et al.*, *2024*). These systems improve seeding uniformity through the optimization of airflow parameters (*Karayel et al.*, *2022*). Internationally, companies like Amazone and Vaderstad employ positive-pressure airflow ejection mechanisms. Air-assisted guidance has also been adapted for specialized applications, such as hill-seeding of sesame (*Wang et al.*, *2023*). Mechanical structure optimization: Researchers have developed novel geometries aimed at minimizing seed bouncing and collisions. These include converging groove-guided seed tubes (*Jia et al.*, *2024*), seed tubes based on the brachistochrone principle (*He et al.*, *2022*; *Li et al.*, *2024*), and belt-type systems. For example, *Chen et al. (2012)* designed a belt-based mechanism to ensure precise seed trajectory and improved spacing uniformity, while *Liu et al. (2017)* developed a sowing synchronous belt device for systematic seed transport to the seedbed. Performance monitoring and simulation: Employing technologies like photoelectric sensors for real-time monitoring of belt-type devices (*Wang et al.*, *2024*) and leveraging DEM-CFD coupling for advanced design and optimization (*Li et al.*, *2024*; *Ma et al.*, *2023*).

Despite being the most prevalent mechanism currently, the reliance of the gravity-based seed guide tube (*Im et al.*, *2023*) on seed descent along the inner wall induces significant bouncing and spacing non-uniformity at high operating speeds. This limitation highlights the urgent need for continued optimization through pneumatic assistance, innovative mechanical designs (including belt-type systems), and simulation-monitored approaches. While scholars domestically and internationally have made progress in mitigating the seed guide's impact on spacing consistency (*Du et al.*, *2024*; *Kumar-Patel et al.*, *2021*; *Ospanova et al.*, *2024*), persistent challenges remain in effectively preventing collisions between seeds and the seeding mechanism's inner wall, particularly under high-speed conditions. These collisions disrupt the initial stable seed flow, leading to uneven spacing, reseeding, or seed loss.

To address this specific bottleneck, this study introduces a seed discharge mechanism engineered for orderliness and smoothness, employing full-degree-of-freedom constraints. The core objective is to minimize spacing deviations induced within the seed guiding process itself, thereby refining precision sowing theory and advancing seeding machinery toward higher speed and precision.

MATERIALS AND METHODS

Overall structure and working principle

This study introduces an advanced mechanism for the high-speed and seamless delivery of maize, employing a fully constrained seed guiding system with a full range of degrees of freedom. This innovative approach is integrated with a high-speed precision seed discharger designed in the preceding phase (*Du et al.*, *2023*). The comprehensive configuration of both the seed discharger and the delivery mechanism is illustrated in Figure 1. The structure primarily consists of the following components: mounting base, housing, seed cleaning brush, air inlet, seed inlet, internal filling plate, brush belt drive motor, inner filling plate drive motor, compression spring, seed pushing wheel, belt-driver wheel, brush belt housing, brush belt, timing belt, belt-driven wheel, tensioning device, and coupling.

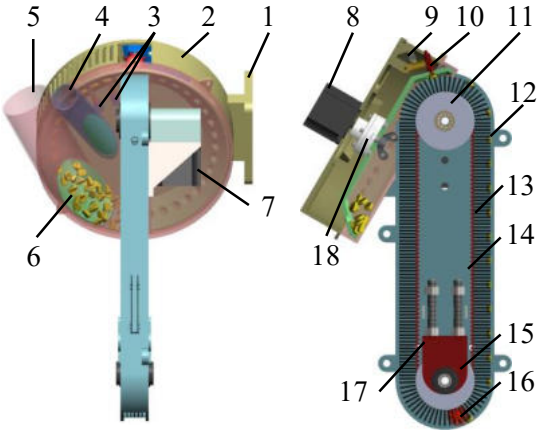


Fig. 1 – Schematic diagram of the structure of the seed-guiding device

1. Mounting base; 2. Housing; 3. Seed cleaning brush; 4. Air inlet; 5. Seed inlet; 6. Inner charging disk; 7. Brush belt drive motor; 8. Inner charging disk drive motor; 9. Pressure spring; 10. Seed pushing wheel; 11. Active belt wheel; 12. Brush belt housing; 13. Brush belt; 14. Synchronous belt; 15. Passive belt wheel; 16. Seed combing rollers; 17. Tensioning device; 18. Coupling

During operation, maize seeds are guided into the seed-filling chamber through the seed inlet by the seed dispenser. The filling process begins with the clockwise rotation of the inner filling disk, driven by a motor via a coupling. Under the combined effects of gravity, centrifugal force, inter-seed interaction, and airflow pressure, seeds are guided into designated holes. Excess seeds are removed by the seed cleaning brush and returned to the filling chamber, ensuring that each hole contains only one seed. Next, the seed tray advances to the seed pushing area, where the air holes at the bottom align with the seed holes to create a sealed path. The seed pushing wheel then rotates, pressing the seeds out of the holes and embedding them into the brush belt. The bristles of the brush constrain the seed's movement, securing it within the guiding system. Driven by a motor, the brush belt transports the seed to the seed outlet. There, the brush housing opens to release the seed, completing the guided delivery process.

Test design

This study utilized "Zhengdan 958" maize seeds as the experimental material to evaluate seed guiding performance, employing the JPS-12 multifunctional seeding test platform. To simulate the relative motion between seeds and the ground during field sowing, the seed guiding device was securely mounted onto the stationary frame of the test platform. The platform's conveyor belt was operated at linear speeds ranging from 3.6 km/h to 14.4 km/h. To minimize seed bounce and displacement upon landing, a 1-2 mm layer of grease was applied to the belt surface. The experimental setup is shown in Figure 2.

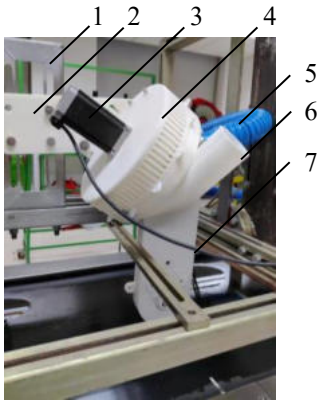


Fig. 2 – Schematic diagram of the bench test of the seed-guiding device

1. seed dispenser fixing frame; 2. seed dispenser fixing plate; 3. seed dispenser drive motor; 4. pneumatic seed dispenser; 5. air inlet pipe; 6. seed inlet; 7. seed guiding device

Test indicators

To assess the operational effectiveness of the seed-guiding device, evaluation criteria based on GB/T 6973-2005 were employed. The evaluation focused on criteria such as qualification, multiplicity, and missed seeding rate. The calculation formulas for each performance index are as follows:

To evaluate the operational performance of the seed-guiding device, assessment criteria were applied in accordance with the national standard GB/T 6973-2005. The evaluation focused on key performance indicators, including qualification rate, multiple seeding rate, and missed seeding rate. The calculation formulas for each performance index are presented below:

$$\begin{cases} Y_1 = \dfrac{n_1}{N} \times 100\% \\ Y_2 = \dfrac{n_0}{N} \times 100\% \\ X_a = \dfrac{\sum_{i=1}^{N-1} X_i}{N-1} \\ C = \dfrac{\sqrt{\dfrac{\sum_{i=1}^{N-1} X_i \left(X_i - X_a\right)^2}{N-1}}}{X_a} \times 100\% \end{cases} \quad (1)$$

Y_1 is the qualified rate, %; Y_2 is the missed seeding rate, %; X_a is the average seed spacing, cm; C is the coefficient of variation of seed spacing, %; n_1 is the number of qualified seed holes (holes); n_0 is the number of empty holes (holes); N is the total number of seed holes tested (251 holes); X_i is the distance between two adjacent seeds, cm.

After conducting three repetitions for each treatment, involving the statistical analysis of 251 holes within corn seed rows, average values were calculated. The data was then organized to derive the qualified rate, missed seeding rate and coefficient of variation of seed spacing (COV).

RESULTS

Influence of synchronous belt tension

The tension of the synchronous belt was adjusted by regulating the distance between two left-handed bolt heads and a nut, as illustrated in Figure 3(a). To evaluate the seeding performance of the synchronous belt under varying tension conditions, a one-factor bench test was conducted at an operating speed of 10 km/h and an air pressure of 1.6 kPa. The experimental variable was the distance between the nut and the bolt head, which was set at five levels: 38.0 mm, 38.5 mm, 39.0 mm, 39.5 mm, and 40.0 mm. The objective was to assess the qualified seeding rate, multiple seeding rate, and missed seeding rate of the seed discharging mechanism. The test results are presented in Figure 3(b).

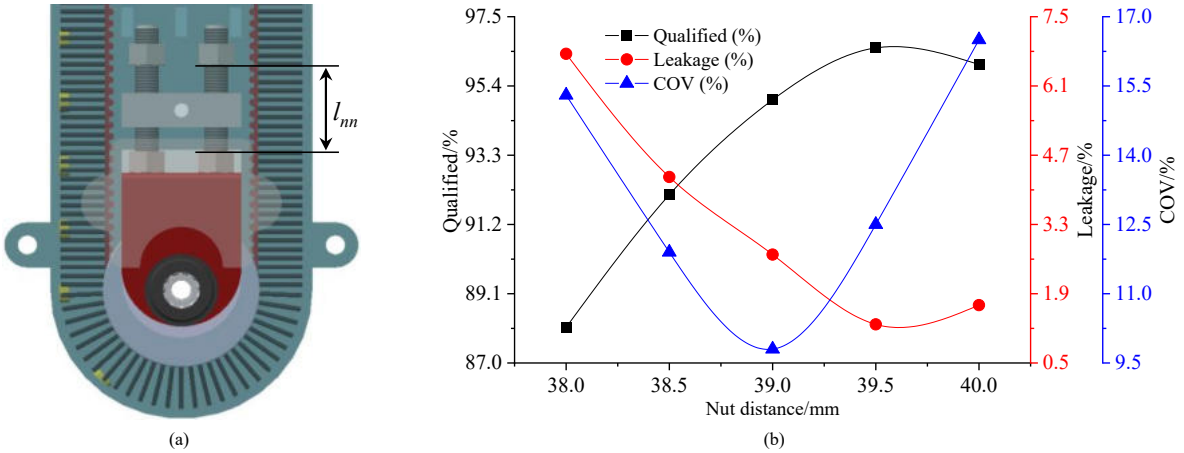


Fig. 3 – Tension adjustment-nut distance and effect of nut spacing on seed displacement performance

As depicted in Figure 3(b), the qualified rate shows a gradual increase with an increment in the distance between the nut and the bolt head. This phenomenon arises because heightened tension prevents the drive belt from easily skipping teeth, facilitating a smoother movement of the bristles carrying the seed. Consequently, this smoother movement reduces the likelihood of seed displacement from the bristles, resulting in decreased missed seeding and reseeding rates. Notably, when the distance between the nut and the bolt head reaches 40.0 mm, the rates of single seed, reseeding, and missed seeding are comparable to those at 39.5 mm, yet the tension force becomes excessively high.

As shown in Figure 3(b), the qualified seeding rate increases progressively with the expansion of the distance between the nut and the bolt head. This trend is attributed to the increased belt tension, which minimizes the risk of tooth-skipping by the drive belt and promotes smoother motion of the bristles that transport the seeds. Improved motion stability reduces the likelihood of seed displacement from the bristles, thereby lowering both missed seeding and multiple seeding rates. However, when the distance reaches 40.0 mm, the qualified, missed, and multiple seeding rates are similar to those observed at 39.5 mm, although the resulting belt tension is excessively high, potentially introducing mechanical strain or inefficiencies.

Influence of brush-housing gap

As shown in Figure 4(a), the clearance between the bristles of the brush belt and the housing plays a critical role in maintaining seed positioning accuracy during transportation. If the gap is too wide, seeds may become dislodged due to vibrations during movement. Conversely, if the gap is too narrow, excessive friction and resistance between the bristles and the inner wall of the housing can hinder the normal operation of the drive belt. To investigate this effect, a one-factor bench test was conducted at an operating speed of 10 km/h and an air pressure of 1.6 kPa. The gap between the bristles and the housing was adjusted to five levels: -2 mm, -1 mm, 0 mm, 1 mm, and 2 mm. The results are presented in Figure 4(b).

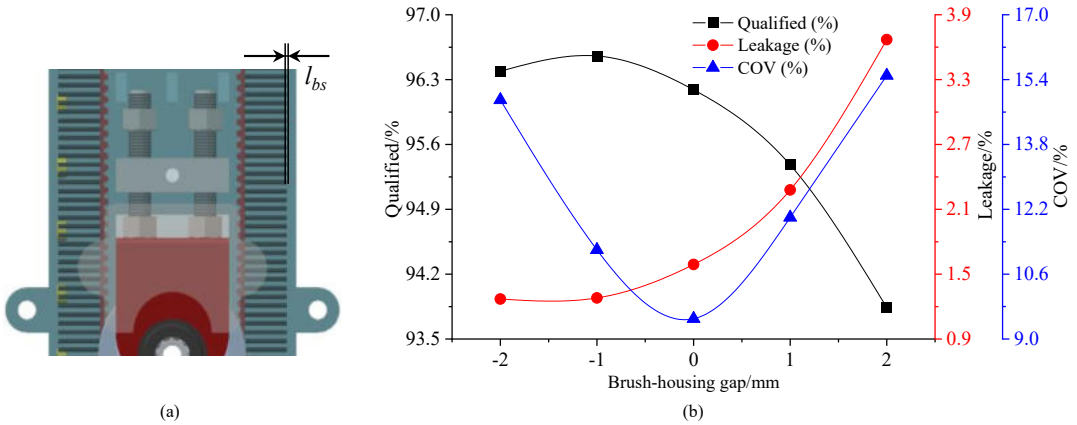


Fig. 4 – Schematic diagram of the clearance between the bristles and the housing, and the effect of the bristle-housing gap on seed discharge performance

As illustrated in Figure 4(b), an excessively large gap results in seed dislodgement during transport, leading to increased missed seeding and multiple seeding rates. Conversely, when the gap is too small, the multiple seeding rate also increases - likely due to the seeds being tightly wrapped by the bristles, which hinders their timely release during the discharge process. Notably, when the gap was set to -1 mm, the qualified seeding rate reached its highest value, while both the multiple and missed seeding rates were at their lowest. Therefore, -1 mm is identified as the optimal bristle-housing gap for ensuring stable and accurate seed discharge performance.

Influence of brush belt linear speed

A single-factor bench test was conducted under the conditions of a 10 km/h operating speed, 1.6 kPa air pressure, and a bristle-to-housing clearance of -1 mm. The test variable was the linear speed of the brush belt, set at five levels: 0.3 m/s, 0.6 m/s, 0.9 m/s, 1.2 m/s, and 1.5 m/s. The results of this test are shown in Figure 5.

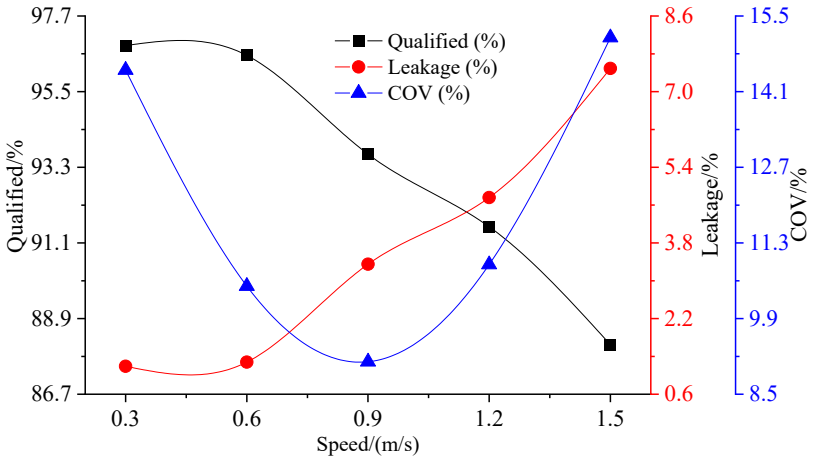


Fig. 5 – Influence of brush belt linear speed on seed displacement performance

As shown in Figure 5, a gradual decline in the qualified seeding rate is observed with increasing brush belt linear speed. This trend is attributed to the increased relative motion between the seed discharge disk and the brush belt, which hampers the ability of the seed pushing wheel to accurately embed seeds into the bristles in a timely manner. As a result, both missed seeding and multiple seeding rates increase. At a brush belt speed of 0.6 m/s, the seed guiding device achieves its highest qualified seeding rate, along with the lowest rates of multiple and missed seedings.

Interactions among the factors

To investigate the interaction effects of nut-bolt head spacing, brush-housing gap, and brush belt linear velocity on seed guiding performance, a Box–Behnken experimental design was employed. The study focused on three performance indicators - qualified seeding rate, missed seeding rate, and seed spacing uniformity - to quantitatively assess the influence of each factor and their interactions on the seed guiding mechanism.

The test scheme and test results are shown in Table 1.

Table 1

Box-Behnken test program and results

No.	l_{nn} (mm)	l_{bs} (mm)	v_m (m/s)	Y_1 (%)	Y_2 (%)	C (%)
1	38	-2	0.9	86.61	6.45	17.6
2	40	-2	0.9	94.01	2.82	17.2
3	38	2	0.9	84.57	5.17	15.6
4	40	2	0.9	92.51	4.78	15.1
5	38	0	0.3	88.36	3.82	14.2
6	40	0	0.3	95.17	2.39	16
7	38	0	1.5	81.61	9.12	19.1
8	40	0	1.5	89.71	6.49	16.4
9	39	-2	0.3	96.58	2.08	15.2
10	39	2	0.3	95.22	2.86	12.5
11	39	-2	1.5	90.66	6.92	17.1
12	39	2	1.5	89.26	7.02	15.8
13	39	0	0.9	94.98	2.69	9.8
14	39	0	0.9	94.74	2.94	9.9
15	39	0	0.9	95.23	2.49	9.6
16	39	0	0.9	94.83	2.43	9.7
17	39	0	0.9	95.13	2.82	9.8

The results of the ANOVA for the qualification rate are shown in Table 2.

Table 2

ANOVA results for qualification rate

Source	Sum of Squares	df	Mean Square	F Value	P value
Model	308.68	9	34.30	864.07	< 0.0001**
A-A	114.38	1	114.38	2881.65	< 0.0001**
B-B	4.96	1	4.96	124.99	< 0.0001**
C-C	72.54	1	72.54	1827.53	< 0.0001**
AB	0.07	1	0.0729	1.84	0.2175
AC	0.42	1	0.4160	10.48	0.0143*
BC	0.0004	1	0.0004	0.01	0.9229
A^2	100.57	1	100.57	2533.60	< 0.0001**
B^2	1.89	1	1.89	47.58	0.0002**
C^2	8.04	1	8.04	202.67	< 0.0001**
Residual	0.28	7	0.0397		
Lack of Fit	0.11	3	0.0376	0.91	0.5110
Pure Error	0.17	4	0.0413		
Cor Total	308.96	16			

*Note: ** indicates highly significant (p<0.01) and * indicates significant (p<0.05).*

A quadratic multiple regression was fitted to the qualified rate to obtain the regression equation:

$$Y_1 = -7465.72 + 384.50 l_{nn} - 3.02 l_{bs} - 19.07 v_m + 0.07 l_{nn} l_{bs} + 0.54 l_{nn} v_m - 0.01 l_{bs} v_m - 4.89 l_{nn}^2 - 0.17 l_{bs}^2 - 3.84 v_m^2 \quad (2)$$

The interaction effects of brush belt speed and nut-bolt head spacing on the qualified seeding rate are illustrated in Figure 6. As the brush belt speed increases, the qualified rate of the seed guide shows a gradual decline. In contrast, with increasing nut-bolt head spacing, the qualified rate initially rises and then falls. Overall, the optimal seed guiding performance is achieved when the brush belt speed is between 0.3 and 0.6 m/s and the nut–bolt head spacing is between 39 mm and 40 mm.

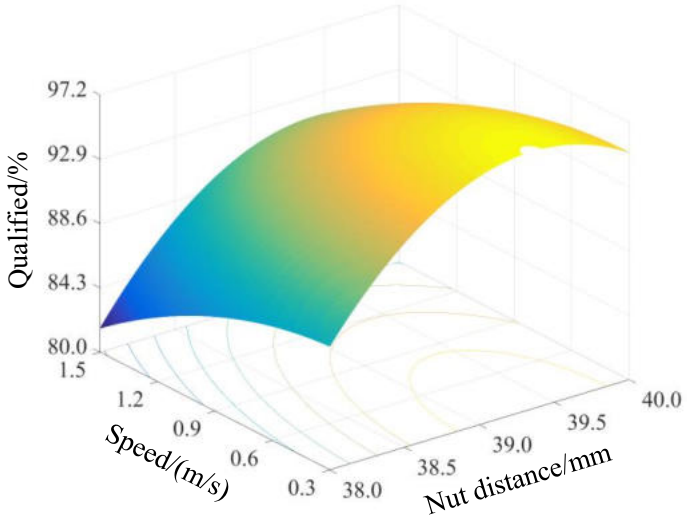


Fig. 6 – Response surface analysis of the interaction effects of factors

The results of the ANOVA for the missed seeding rate are shown in Table 3.

Table 3

ANOVA results for missed seeding rate

Source	Sum of Squares	df	Mean Square	F Value	P value
Model	74.16	9	8.24	273.48	< 0.0001**
A-A	8.16	1	8.16	270.84	< 0.0001**
B-B	0.30	1	0.30	10.10	< 0.0001**
C-C	42.32	1	42.32	1404.51	< 0.0001**
AB	2.62	1	2.62	87.10	< 0.0001**
AC	0.36	1	0.36	11.95	0.01**
BC	0.12	1	0.12	3.84	0.09
A^2	8.65	1	8.65	286.95	< 0.0001**
B^2	2.05	1	2.05	68.08	< 0.0001**
C^2	7.65	1	7.65	253.92	< 0.0001**
Residual	0.21	7	0.03		
Lack of Fit	0.03	3	0.01	0.18	0.9042
Pure Error	0.19	4	0.05		
Cor Total	74.37	16			

*Note: ** indicates highly significant (p<0.01) and * indicates significant (p<0.05).*

A quadratic multiple regression was fitted to the missed seeding rate to obtain the regression equation:

$$Y_2 = 2203.69 - 112.33l_{nn} - 15.57l_{bs} + 16.59v_m + 0.41l_{nn}l_{bs} - 0.50l_{nn}v_m - 0.14l_{bs}v_m + 1.43l_{nn}^2 + 0.17l_{bs}^2 + 3.74v_m^2 \quad (3)$$

The interaction effects of the brush-housing gap and nut-bolt head spacing on the missed seeding rate are shown in Figure 7(a). As the brush-housing gap increases, the missed seeding rate gradually rises. In contrast, with increasing nut-bolt head spacing, the missed seeding rate first decreases and then increases. Overall, the lowest missed seeding rate is observed when the brush-housing gap is between -2 mm and -1 mm, and the nut-bolt head spacing is within the range of 39-40 mm.

The interaction effects of brush belt speed and nut-bolt head spacing on the missed seeding rate are presented in Figure 7(b). The missed seeding rate increases progressively with higher brush belt speeds. Similarly, as the nut-bolt head spacing increases, the missed seeding rate initially decreases and then increases. In general, optimal performance - with the lowest missed seeding rate - is achieved when the brush belt speed is maintained between 0.3 and 0.6 m/s, and the nut-bolt head spacing is in the range of 39-40 mm.

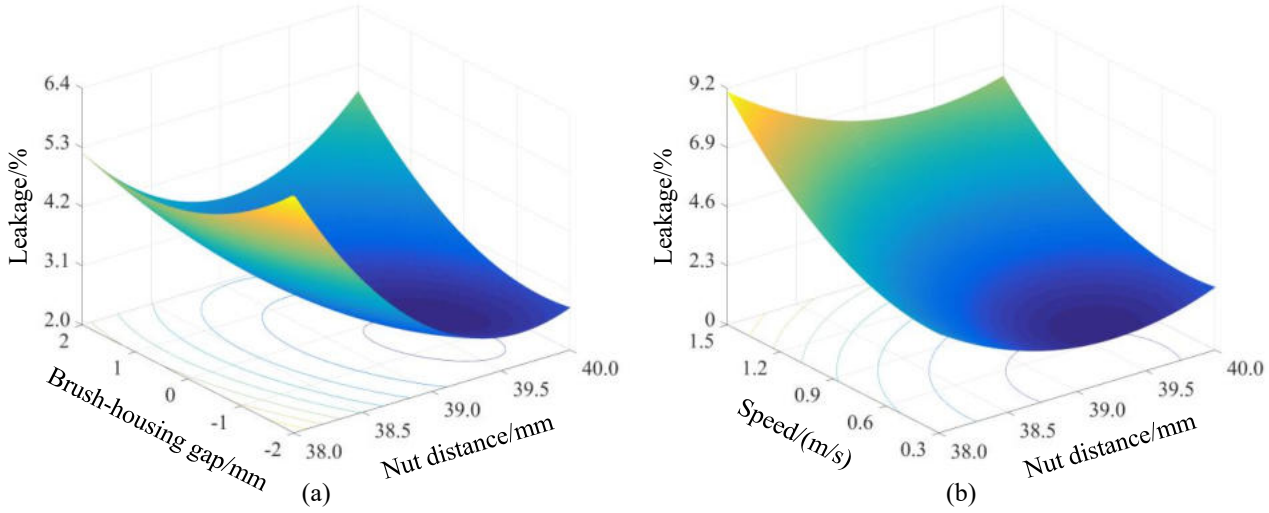


Fig. 7 – Response surface analysis of the interaction effects of factors

The results of the ANOVA for the COV are shown in Table 4.

Table 4

ANOVA results for COV

Source	Sum of Squares	df	Mean Square	F Value	P value
Model	168.81	9	18.76	2409.08	< 0.0001**
A-A	0.41	1	0.41	52.02	0.0002**
B-B	8.20	1	8.20	1053.37	< 0.0001**
C-C	13.78	1	13.78	1770.07	< 0.0001**
AB	0.003	1	0.003	0.32	0.59
AC	5.06	1	5.06	650.23	< 0.0001**
BC	0.49	1	0.49	62.94	< 0.0001**
A^2	65.53	1	65.53	8416.51	< 0.0001**
B^2	30.02	1	30.02	3855.32	< 0.0001**
C^2	31.15	1	31.15	4001.07	< 0.0001**
Residual	0.05	7	0.008		
Lack of Fit	0.003	3	0.0008	0.06	0.9761
Pure Error	0.05	4	0.013		
Cor Total	168.86	16			

*Note: ** indicates highly significant (p<0.01) and * indicates significant (p<0.05).*

A quadratic multiple regression was fitted to the COV to obtain the regression equation:

$$C=5957.22-306.25l_{nn}-0.28l_{bs}+61.71v_m-0.01l_{nn}l_{bs}-1.88l_{nn}v_m+0.29l_{bs}v_m+3.95l_{nn}^2+0.67l_{bs}^2+7.56v_m^2 \quad (4)$$

The interaction effects of brush belt speed and nut-bolt head spacing on the COV of seed spacing are shown in Figure 8(a). The COV initially decreases and then increases with rising brush belt speed and nut-bolt head spacing. The lowest COV values are observed when the speed is between 0.6 and 0.9 m/s and the nut-bolt head spacing ranges from 38.5 to 39.5 mm. Figure 8(b) illustrates the interaction effects of brush belt speed and brush-housing gap on the COV. A similar trend is observed: the COV decreases at first and then increases with increasing values of both variables. The optimal performance - reflected by the lowest COV - is achieved when the brush belt speed is between 0.6 and 0.9 m/s and the brush-housing gap is between -1 mm and 1 mm.

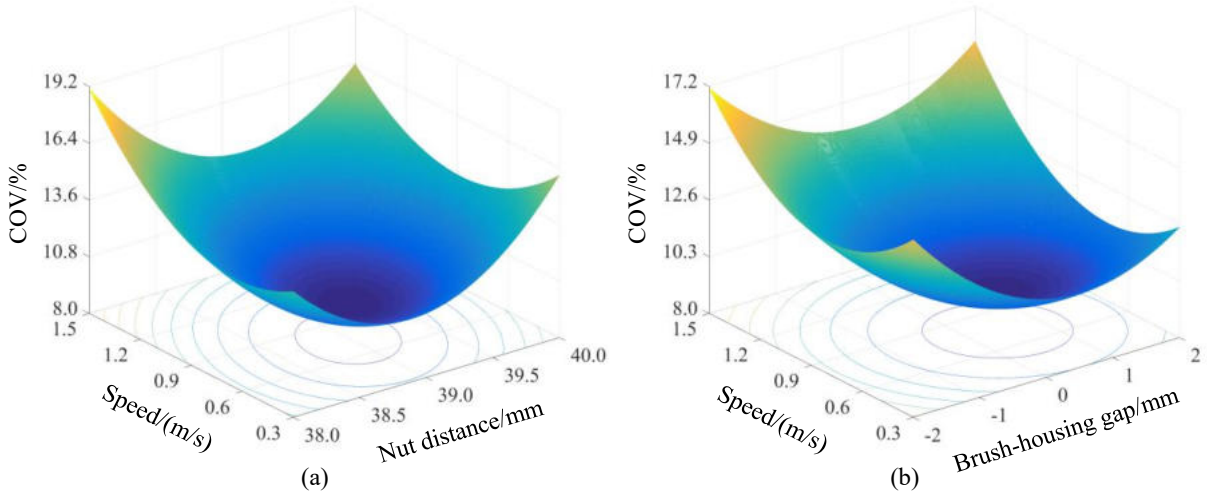


Fig. 8 – Response surface analysis of the interaction effects of factors

To identify the optimal combination of influencing factors within the defined constraint ranges, a multi-objective optimization was performed based on the regression model of seed guiding performance. The evaluation indices included the maximum qualified seeding rate, the minimum missed seeding rate, and the minimum coefficient of variation (COV) of seed spacing.

The optimization problem was formulated with the objective function and corresponding constraints defined as follows:

$$\begin{cases} \max Y_1\left(l_{nn}, l_{bs}, v_m\right) \\ \min Y_2\left(l_{nn}, l_{bs}, v_m\right) \\ \min C\left(l_{nn}, l_{bs}, v_m\right) \\ s.t. \begin{cases} 38 \text{ mm} \le l_{nn} \le 40 \text{ mm} \\ -2 \text{ mm} \le l_{bs} \le 2 \text{ mm} \\ 0.3 \text{ m/s} \le v_m \le 1.5 \text{ m/s} \end{cases} \end{cases} \quad (5)$$

The regression model was optimized and solved using Design-Expert 10 software. The optimal parameter combination was found to be a nut-bolt head spacing of 39.15 mm, a brush-housing gap of 0.22 mm, and a brush belt speed of 0.644 m/s. Under these conditions, the predicted values for the qualified seeding rate, missed seeding rate, and COV were 96.35%, 1.89%, and 9.72%, respectively. To validate the model, the bench test was repeated three times using the optimized parameters. The experimental results yielded a qualified seeding rate of 96.76%, a missed seeding rate of 2.15%, and a COV of 10.09%. The close agreement between the predicted and measured values confirms the high reliability and accuracy of the regression model.

CONCLUSIONS

This study aimed to address the problem of seed bouncing and displacement caused by collisions between corn seeds and the seed guide tube during planting, which disrupts the orderly flow of seeds. To overcome this issue, a seed guiding device was developed to constrain the seeds in all degrees of freedom, utilizing a flexible brush to ensure stable seed transport. A one-factor test was conducted to determine the optimal parameter ranges for nut-bolt head spacing, brush-housing gap, and brush belt speed, and to evaluate their individual effects on seed guiding performance. Subsequently, quadratic regression models were established using response surface test to analyze the effects of these parameters on the qualified seeding rate, missed seeding rate, and COV. Optimization results indicated that the best seed guiding performance was achieved at a nut-bolt head spacing of 39.15 mm, a brush-housing gap of 0.22 mm, and a belt speed of 0.644 m/s, resulting in a qualified seeding rate of 96.35%, a missed seeding rate of 1.89%, and a COV of 9.72%.

ACKNOWLEDGEMENT

This study was supported by Natural Science Foundation of Jiangsu Province (BK20241058), and the Project of Graduate Student Scientific Research and Practical Innovation Program of Jiangsu Ocean University (KYCX2024-41).

REFERENCES

[1] Awad, M., Fouda, O., Abd el-reheem, S., ABD El-reheem, S., Al-gezawe, A., Cottb, M., Okasha, M. (2022). A new seed drill for planting peas on a raised-bed. *INMATEH - Agricultural Engineering,* Vol. 68, pp. 681-692. https://doi.org/10.35633/inmateh-68-67

[2] Chen, X., Zhong, L. (2012). Design and test on belt-type seed delivery of air-suction metering device (气吸式排种器带式导种装置的设计与试验). *Transactions of the Chinese Society of Agricultural Engineering*, Vol. 28, pp. 8-15.

[3] Du, X., Yu, Q., Chen, S., Sun, Q., Zhang, H., Liu, C. (2024). Design and testing of seed push wheel for high-speed precision seed metering device for corn with internal seed filling and positive pressure airflow. *INMATEH - Agricultural Engineering*, Vol. 72, pp. 731-740. https://doi.org/10.35633/inmateh-72-65

[4] Du, X., Liu, C. (2023). Design and testing of the filling-plate of inner-filling positive pressure high-speed seed-metering device for maize. *Biosystems Engineering*, Vol. 228, pp. 1-17.

[5] Fanigiliulo, R., Grilli, R., Benigni, S., Fornaciari, L., Biocca, M., Pochi, D. (2022). Effect of sowing speed and width on spacing uniformity of precision seed drills. *INMATEH - Agricultural Engineering,* Vol. 66, pp. 9-18. https://doi.org/10.35633/inmateh-66-01

[6] He, C., JIN, X., LU, L., Ma, M., Wang, X., Zhang, J. (2022). Design and experiment on seed-guiding tube of T-groove furrowing device based on brachistochrone. *INMATEH - Agricultural Engineering*, Vol. 67, pp. 53-66. https://doi.org/10.35633/inmateh-67-05

[7] Im, D., Lee, H., Kim, J., Moon, D., Moon, T., Yu, S., Park, Y. (2023). Bucket size optimization for metering device in garlic planter using discrete element method. *Agriculture (Basel),* Vol. 6, pp. 1199, Korea.

[8] Jia, X., Zhu, J., Guo, G., Huang, Y., Gao, X., Zhang, C. (2024). Design and test of a novel converging groove-guided seed tube for precision seeding of maize. *Biosystems Engineering*, Vol. 245, pp. 36-55.

[9] Karayel, D., Güngör, O. & Šarauskis, E. (2022). Estimation of optimum vacuum pressure of air-suction seed-metering device of precision seeders using artificial neural network models. *Agronomy (Basel),* Vol. 7, pg. 1600.

[10] Kumar-Patel, S., Bhimani, J. B., Yaduvanshi, B. K., Gupta, P. (2021). Optimization of the design and operational parameters of planter for vegetable pigeon pea (*cajanus cajan l. millsp*.) seed. *INMATEH - Agricultural Engineering,* Vol. 63, pp. 326-334. https://doi.org/10.35633/inmateh-63-33

[11] Li, H., Yang, L., Zhang, D., Cui, T., He, X., Xie, C., Li, C., Du, Z., Xiao, T., Li, Z., Wang, H. (2024). Design and optimization of a high-speed maize seed guiding device based on DEM-CFD coupling method. *Computers and Electronics in Agriculture*, Vol. 227, pp. 109604.

[12] Li, Y., Zhou, W., Ma, C., Feng, Z., Wang, J., Yi, S., Wang, S. (2024). Design and optimization of the seed conveying system for belt-type high-speed corn seed guiding device. *International Journal of Agricultural and Biological Engineering*, Vol. 17, pp. 123-131.

[13] Li, Z., Zhang, H., Huang, J., Lou, C., Chen, Y., Liu, L., Zhang, T., Chen, L. (2025). Design and parameter optimization of air-delivery auxiliary seed guide for pneumatic plate precision rapeseed metering device. *Computers and Electronics in Agriculture*, Vol. 230, pp. 109840.

[14] Liao, Y., Li, C., Liao, Q., Wang, L. (2020). Research progress of seed guiding technology and device of planter (播种机导种技术与装置研究进展分析). *Transactions of the Chinese Society for Agricultural Machinery*, Vol. 51, pp.1-14.

[15] Liu, Q., He, X., Yang, L., Zhang, D., Cui, T., Qu, Z., Yan, B., Wang, M., Zhang, T. (2017). Effect of travel speed on seed spacing uniformity of corn seed meter. *International Journal of Agricultural and Biological Engineering*, Vol. 10, pp. 98-106.

[16] Liu, R., Zhang, G., Xiao, Y., Yan, B., Meng, Z., Dong, J., Wu, G. (2025). DEM-CFD investigation of particle motion characteristic in a guidance restraint-airflow blowing seed guiding device. *Advanced Powder Technology*, Vol. 36, pp. 104747.

[17] Ma, C., Yi, S., Tao, G., Li, Y., Wang, S., Wang, G., Gao, F. (2023). Research on receiving seeds performance of belt-type high-speed corn seed guiding device based on discrete element method. *Agriculture (Basel)*, Vol. 13, pg.1085.

[18] Ospanova, S., Aduov, M., Kapov, S., Orlyansky, A., Volodya, K. (2024). The results of experimental research of a rotor seed-metering unit for sowing non-free-flowing seeds. *Journal of agricultural engineering (Pisa, Italy),* Vol. 55, pg.1556.

[19] Wang, B., Liao, Q., Wang, L., Shu, C., Cao, M., Du, W. (2023). Design and test of air-assisted seed-guiding device of precision hill-seeding centralized seed-metering device for sesame. *Agriculture (Basel)*, Vol. 13, pg. 393.

[20] Wang, S., Yi, S., Zhao, B., Li, Y., Wang, G., Li, S., Sun, W. (2024). Photoelectric sensor-based belt-type high-speed seed guiding device performance monitoring method and system. *Computers and Electronics in Agricultur*e, Vol. 227, pg. 109489.

[21] Zhang, S., Zhu, H., Wang, W., Chen, Y., Zhou, L., Li, M., Wu, J. (2024). Design and optimization test of high-speed seed guide device with conical spiral airflow. *Engenharia Agrícola*, Vol. 44, pg. 20230131

DESIGN AND EXPERIMENTAL STUDY OF A CRAWLER-TYPE PRECISION PESTICIDE APPLICATOR BASED ON DEM

/

基于 DEM 的履带式精准施药机设计与试验研究

ZhiMing SHI[1,2], Hang ZHAO[1,2], ShouTai LI[3], ZiWen CHEN[3] , JunJie CHEN*[1,2], MingJin YANG *[3]

[1] Southwest University, College of Artificial Intelligence, Chongqing 400715, China

[2] National & Local Joint Engineering Research Center of Intelligent Transmission and Control Technology, Chongqing 400715, China

[3] Southwest University, College of Engineering and Technology, Chongqing 400715, China

Tel: +86 13996141140; E-mail: 1031730720@qq.com; ymingjin@swu.edu.cn

DOI: https://doi.org/10.35633/inmateh-76-15

Keywords: *precision quantitative, solid particles, discrete element method, response surface experiment*

ABSTRACT

This study is based on the discrete element method to design a tracked precision solid particle pesticide applicator and establish a coupling model between the pesticide application device and particle swarm EDEM. Simulation shows that particle characteristics significantly affect the uniformity of pesticide application. The coefficients of variation for particles 1, 2, and 3 are 4.25%, 4.63%, and 5.57%, respectively, with relative deviations of 8.51%, 9.28%, and 11.33%. After response surface testing optimization, the measured coefficient of variation of the prototype was 8.25% and the relative deviation was 18.07%, both of which met industry standards.

摘要

本研究基于离散元法设计履带式精准固体颗粒施药机，建立施药装置-颗粒群 EDEM 耦合模型。仿真表明：颗粒特性显著影响施药均匀性，颗粒 1、2、3 的变异系数分别为 4.25%、4.63%、5.57%，相对偏差 8.51%、9.28%、11.33%。响应面试验优化后，样机实测变异系数 8.25%、相对偏差 18.07%，均达行业标准。

INTRODUCTION

Liquid pesticide spraying is the dominant method for pest control in China; however, its effectiveness is limited by issues such as high droplet drift rates, low pesticide utilization efficiency, and environmental pollution (*Nation H.J.*, 1972). As modern agriculture transitions toward precision and intelligent technologies, solid granular pesticides have demonstrated significant potential for applications such as corn borer control and soil disinfection due to their ability to be applied directly to target areas, high resistance to drift, and prolonged efficacy (*Ministry of Agriculture and Rural Affairs, 2022*). However, existing solid granular pesticide application equipment faces technical challenges such as poor quantitative accuracy, uneven discharge, and limited terrain adaptability, restricting its widespread adoption (*Jiang Y.Y. et al., 2021*). Therefore, overcoming these challenges and enhancing the accuracy and adaptability of pesticide applicators are crucial for advancing precision spraying technology.

In recent years, with the rapid development of intelligent agriculture, precision pesticide application technology has been widely adopted. Research in this area primarily focuses on variable pesticide application control, operational parameter optimization, and equipment improvement (*He X.K., 2020*). *Zhai Changyuan et al. (2024)* designed a precision variable spraying monitoring system based on traceability management, which enables real-time detection of pesticide type, ratio, spraying volume, spray pressure, and operating speed, integrating precision pesticide application with traceability management. Gou Yujiang et al. developed a handheld variable fertilizer spreader and constructed a regression model using discrete element simulation experiments to optimize fertilization parameters and improve spreading uniformity. Dong Jiwei et al. designed a crawler-type target-matching pesticide spreader to meet the operational needs of orchards in hilly and mountainous areas. Its lifting and closing mechanism allow flexible adjustment of spraying distance and height, adapting to different fruit tree types. Currently, research on fertilizer and pesticide application equipment with wheeled chassis in plain areas is relatively advanced, with significant progress in variable pesticide application

ZhiMing SHI, M.S. Eng.; Hang ZHAO, M.S. Eng.; ShouTai LI, M.S. Eng.; ZiWen CHEN, A. Prof.; JunJie CHEN, M.S. Eng.; MingJin YANG, Prof.

and operational optimization technologies. However, under the complex terrain conditions of hilly and mountainous areas, research on the coupling mechanism between crawler walking systems and solid granular pesticide discharge mechanisms remains limited (*Hazra D.K. et al., 2019*).

Based on discrete element method (DEM) numerical simulation technology, this study designs a precision quantitative solid granular pesticide applicator suitable for hilly and mountainous areas. By integrating response surface tests, key operational parameters were optimized, and the effects of factors such as operating speed, material port diameter, and application angle on application uniformity were examined. The findings not only provide theoretical support for the development of precision pesticide application equipment in hilly and mountainous areas but also contribute to reducing pesticide use, minimizing environmental pollution, and promoting precision agriculture. This research is of great significance for the intelligent transformation of China's plant protection machinery.

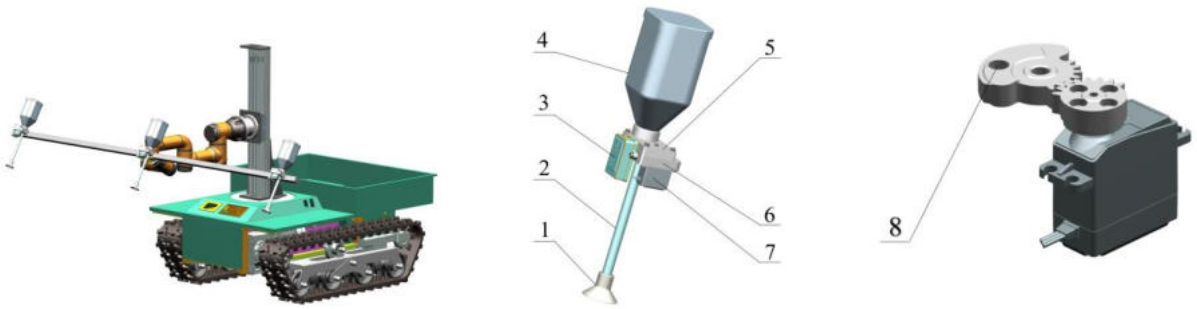
MATERIALS AND METHODS

Machine structure and workflow

Machine structure

To address the complex agricultural environments in hilly and mountainous regions, this study developed a crawler-type precise quantitative solid particle sprayer. The system includes a crawler chassis power platform, a robotic arm, a rotating lifting mechanism, a spraying system, and a control system. The gear transmission component is manufactured by a CNC universal gear grinding machine (YW7232CNC). The power platform uses a self-propelled crawler chassis, known for its superior obstacle-crossing ability and stability, enhancing mobility in challenging terrains (*Qi X.Y. et al., 2015*). The robotic arm features a multi-joint structure for precise control of the spraying device's motion, and combined with the rotating lifting mechanism, it allows for fine-tuned multi-directional adjustments, improving spraying accuracy in diverse crop environments. The spraying system consists of three electronically controlled devices (Fig. 1a), with adjustable spraying spacing for synchronized multi-channel operation, boosting efficiency. The pesticide application device (Fig. 1b) includes a dispensing port, guide pipe, IoT module, material box, loading and unloading module, and servo motor. Solid granular pesticides are evenly dispensed via a rotating material tray (Fig. 1c), ensuring precise coverage and optimal pesticide use. The control system integrates robotic arm motion, pesticide application activation, and operational parameter adjustment. Operators can input commands or use preset programs for precise pesticide application to meet various operational needs.

The concept of targeted pesticide application originated from the manual handheld pesticide application process. In order to improve the utilization rate of granular drugs and reduce the transport and loss in ineffective spaces, the nozzle is aimed at the center of the seedlings during manual pesticide application, and the handheld spray rod is aimed at the seedlings for pesticide application. The tracked precision quantitative solid particle pesticide applicator adopts an automated targeted pesticide application method, and multiple components in the system work together to achieve efficient, precise, and environmentally friendly pesticide application. The pesticide application operation starts from the action of the robotic arm and the pesticide application device. The robotic arm can precisely control the movement of the pesticide application device to ensure that the pesticide is spread in the correct position. Solid particle pesticides are released to the target through the feeding port to ensure precise coverage of the target area. The parameter settings of the pesticide applicator, including the application amount, operating speed, and application angle, are adjusted through the control platform (*Meshram A.T., 2022*).



a) *b)* *c)*

Fig. 1 - Precision quantitative pesticide applicator and pesticide applicator

a) Machine structure b) Application system c) Discharge mechanism; 1. Feeding port 2. Flow guide tube 3. Internet of Things module 4. Material box 5. Feeding port module 6. Discharge port module 7. Servo 8. Feeding port.

Workflow

The crawler-type precision quantitative solid particle applicator developed in this study employs an automated targeted application strategy to ensure efficient, precise, and environmentally friendly pesticide delivery. Targeted application technology originates from the manual handheld precision application method, in which the nozzle remains aimed at the center of the crop throughout the process, enhancing pesticide utilization efficiency and minimizing unnecessary dispersion. The application process is executed by the robotic arm in conjunction with the application device. During operation, the robotic arm precisely adjusts the position of the application device, ensuring the directional release of solid particle pesticides through the drop port for even coverage of the target crop (*Chen Z.W. et al., 2023*). The control system enables intelligent adjustment of application parameters, including dosage, operating speed, and application angle, to accommodate various environmental conditions and agronomic requirements.

Simulation and experiment

Discrete Element Simulation Model

In EDEM software, common particle contact models include the Hertz-Mindlin (no-slip) model, the Hertz-Mindlin with bonding model, the Hertz-Mindlin with JKR (Johnson-Kendall-Roberts) model, and the Linear Cohesion model. These models are suited to different granular materials and conditions. The Hertz-Mindlin with JKR model is preferred for simulating pesticide particle contact due to its ability to characterize particle bonding and agglomeration. Unlike the Linear Cohesion model, which only accounts for normal bonding forces and ignores tangential forces, the JKR model considers both normal and tangential bonding, making it more accurate for complex bonding materials (*Nie C.X. et al., 2022*).

Pesticide particles, with small size, high surface roughness, and moisture content, tend to agglomerate and adhere due to electrostatic and intermolecular forces. The JKR model effectively captures this behavior, which is further intensified in humid climates like those in southwestern regions. Traditional rigid or non-adhesive models are inadequate for such conditions. Thus, this study uses the JKR model to better simulate the flow and application behavior of pesticide particles, providing a solid theoretical foundation for designing and optimizing precision pesticide application equipment (*Wang S. et al., 2024*).

Particle Characterization

To accurately characterize the different physical properties of Imidacloprid pesticide particles and ensure the reliability of the simulation, key parameters such as particle density, moisture content, angle of repose, and particle size distribution were measured (Fig. 2). These parameters are essential for constructing the discrete element simulation model.



a) ***b)*** ***c)***

Fig. 2 - Pesticide particles with different material properties

a) Particles 1; b) Particles 2; c) Particles 3



a) ***b)*** ***c)*** ***d)***

Fig. 3 - Test equipment

a) Repose angle measuring device; b) Electronic balance; c) Halogen Moisture Analyzer; d) Standard test sieve

Particle density was determined using the drainage method, as per GB/T 24528 and GB/T 13477.2-2002 standards. The density was calculated by measuring the particle volume after drainage and combining it with the mass measured by a high-precision electronic balance. Each group was measured three times, and the average value was taken for stability. Moisture content was measured using an FBS-760A halogen moisture analyzer, which heated and dried the samples while automatically recording water evaporation and mass changes. Each group was measured three times, and the average value was used to minimize error. The angle of repose was measured using the natural piling method, where particles fell through a funnel to form a cone, and the angle between the cone and the horizontal plane was recorded. This experiment was repeated 10 times to ensure reliability. Particle size distribution was determined by sieving 1000 g of particles using standard test sieves (GB/T 6003.1-2012). The mass retained on each sieve was recorded to calculate mass percentages. All experiments followed national standards, with multiple repetitions to ensure accuracy and reliability. The measurement tools and results are shown in Fig. 3 and Table 1.

Table 1

Test particle parameter measurement results

Item		Measurements		
		Particles 1	Particles 2	Particles 3
Particle size analysis (mass percentage passing through the sieve/%)	0.25mm	0	0	0
	0.50mm	5.98	12.38	0
	1.00mm	69.33	22.14	13.50
	1.60mm	16.35	47.12	42.47
	2.00mm	8.34	18.36	38.55
	2.50mm	0	0	5.48
Bulk density /（kg/m³）		5.85×103	0.55×103	2.66×103
Moisture content /%		0.170	3.533	0. 54
Angle of repose /（°）		18.6	23.4	32.5
Air humidity during the test /%		68	72	72

Simulation test

Discrete Element Simulation

In this study, the Hertz-Mindlin with JKR model was used to describe the interaction forces between particles and equipment, enabling a more accurate simulation of particle adhesion. Considering the particle size distribution of actual Imidacloprid pesticide particles, the spherical particle modeling method in EDEM software was employed to construct simulation models of particles with various shapes (Fig. 4). The experimental design included single-sphere, double-sphere, three-sphere, four-sphere, and irregular multi-sphere models, based on the actual particle distribution ratio to ensure the simulated morphology closely matched real particle characteristics (*Xie K. et al., 2024*). The simulation model parameters are listed in Table 2. This approach effectively characterizes particle morphology and simulates their motion within the equipment, providing a reliable basis for particle flow analysis and optimization of drug application equipment. Model parameters were set based on experimentally measured data, improving the accuracy and reliability of the simulation results.

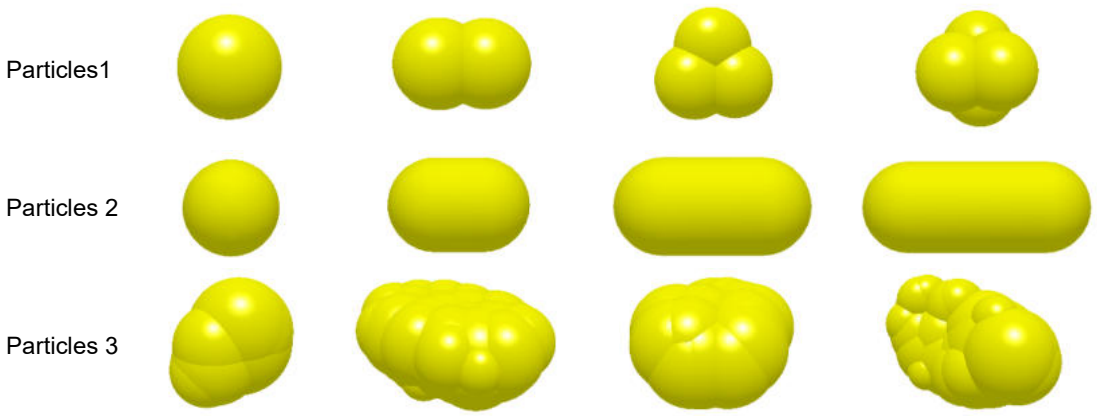


Fig. 4 - Simulation particle model

Table 2

Discrete element simulation model parameters

Item	Parameter	Value		
		Particles 1	Particles 2	Particles 3
Particles	Poisson's ratio	0.35	0.20	0.25
	Shear modulus /Pa	9×10^{10}	5×10^{9}	3×10^{10}
	Number of particles	100000	100000	100000
	Gravity acceleration / $m\cdot s^{-2}$	9.81	9.81	9.81
Steel	Poisson's ratio	0.30		
	Shear modulus /Pa	1.1×10^{11}		
	Density /$kg\cdot m^{3}$	7850		
Particle-Particle	Coefficient of restitution	0.30	0.4	0.30
	JKR surface energy /$J\cdot m^{2}$	13.50	18.55	12.40
	Static friction coefficient	0.30	0.40	0.30
	Dynamic friction coefficient	0.01	0.05	0.01
Granules-Stainless Steel	Coefficient of restitution	0.30	0.50	0.30
	JKR surface energy /$J\cdot m^{2}$	14.50	20.20	15.00
	Static friction coefficient	0.25	0.35	0.30
	Dynamic friction coefficient	0.01	0.05	0.01

Simulation Experiment Design

To verify the design rationality of the spraying mechanism, to further explore the interaction between the spraying mechanism and pesticide particles, and to provide a scientific basis for the design of key parameters of the spraying machine, a simulation experiment was conducted using EDEM software. Based on typical spraying operation conditions in hilly and mountainous areas, the rotation speed of the spraying machine's material plate was set to 60 r/min, the material port diameter was set to 7 mm, and the spraying angle was maintained at 0° to ensure the uniformity of the testing process. Three types of pesticide particles with different material properties were selected for the experiment, covering various particle sizes, densities, and surface morphologies to simulate common pesticide formulations. By keeping the spraying machine's operating parameters constant and adjusting only the particle characteristics, the adaptability and reliability of the spraying machine under different particle types were studied (*Yin Y.S. et al, 2018*).

Field trials

To verify the operational performance of the precision quantitative solid particle sprayer, the experimental design followed industry standards, including the "JB/T 9782-2014 General Test Methods for Plant Protection Machinery" and the "GB/T 21157-2007 Test Methods for Granular Pesticide or Herbicide Spreaders." The focus was on evaluating the performance stability and uniformity of the sprayer. The experiment used the Box-Behnken experimental design method, with operating speed, feed port diameter, and spraying angle as the main influencing factors, and coefficient of variation and relative deviation as response variables.

Design-Expert 13 was used to conduct a three-factor, three-level experimental design, construct a response surface model, and optimize the operating parameters of the precision spraying equipment. Operating speed directly affects the uniformity and efficiency of spraying; feed port diameter determines the unit spraying amount of solid drug particles and is the core parameter of precision spraying; spraying angle, i.e., the vertical angle between the feed port and the crop to be sprayed, affects the distribution range and uniformity of the particles.

This study uses the coefficient of variation and relative deviation as key evaluation indicators to fully reflect the spraying performance of the equipment. By optimizing the combination of various factor levels, data support was provided for the parameter optimization of precision pesticide application equipment, laying a theoretical foundation for reducing pesticide usage, improving pesticide utilization, and promoting the application of precision pesticide technology. The test factors and levels are shown in Table 3, and the field test is shown in Fig. 5.

Table 3

Response surface test factors and levels

Level	Factor		
	Operation speed	Feeding port diameter	Spraying angle
	[km/h]	[mm]	[°]
-1	0.6	5	0
0	1.2	7	30
1	1.8	9	60

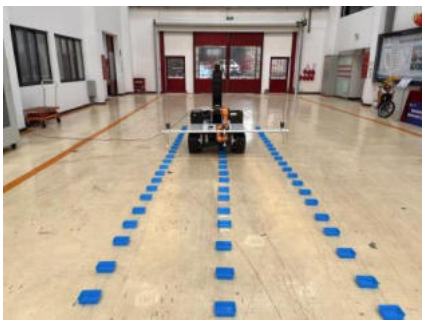


Fig. 5 - Field test of pesticide sprayer

RESULTS

Evaluation indicators

According to the "Test Method for Granular Pesticide or Herbicide Spreader GB/T 21157-2007," this study selected the coefficient of variation (CV) and relative deviation (RD) as evaluation indicators to quantitatively analyze the spreading uniformity and application accuracy of granular spraying equipment. The coefficient of variation (CV) reflects the uniformity of the granule spreading amount in different areas; the smaller the value, the higher the uniformity. The relative deviation (RD) evaluates the degree of deviation between the actual application amount and the target application amount, which is an important indicator for measuring the performance of precision spraying. Through rigorous experimental design and data analysis, this study comprehensively evaluates the performance of equipment spraying and provides a scientific basis for optimizing spraying parameters and improving spraying accuracy.

The average mass $\overline{M_n}$ of a single row of pellet boxes is calculated as follows:

$$\overline{M_n} = \frac{1}{n}\sum M_i \tag{1}$$

where n is the number of particle collecting boxes; M_i is the mass of granules collected by the ith particle collecting box.

The coefficient of variation (CV) calculation formula is:

$$CV_n = \frac{s}{\overline{M_n}} \tag{2}$$

where s is the standard deviation, calculated as follows:

$$s = \sqrt{\frac{1}{n-1}\sum (M_i - \overline{M_n})^2} \tag{3}$$

The relative deviation (RD) of each row is calculated as:

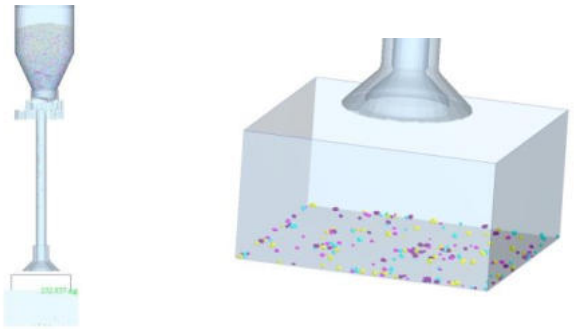
$$RD_n = \frac{M_{i,\max} - M_{i,\min}}{\overline{M_n}} \times 100 \tag{4}$$

Simulation Results Analysis

The simulation test of the pesticide applicator was carried out based on EDEM software, and the results are shown in Figure 6. The simulation analysis shows that the spreading uniformity and stability of the pesticide applicator are greatly affected by the characteristics of the pesticide granule material. The coefficients of variation of granule 1, granule 2, and granule 3 are 4.25%, 4.63%, and 5.57%, respectively, and the relative deviations are 8.51%, 9.28%, and 11.33%, respectively (Fig. 7), all of which meet the industry standard requirements specified in the "Technical Specifications for Quality Evaluation of Fertilizer Machinery NY/T1003-2006." The simulation results show that the increase in particle size, density, surface profile, and friction coefficient will lead to a decrease in spreading uniformity and stability. Among them, the coefficient of variation of particle 3 is relatively high, indicating that its spreading distribution is more discrete, which may be related to the increase in the friction coefficient between particles leading to a decrease in fluidity.

Under fixed operating parameters, the pesticide applicator has the best adaptability to particle 1, and its coefficient of variation and relative deviation are both low, indicating that the pesticide applicator is suitable for particles with small particle size, smooth surface, and low friction coefficient.

In comparison, the simulation results of particle 3 reveal the limitations of the existing design when dealing with high-density, large-size particles. It is difficult to effectively overcome the inertia and friction resistance of the particles by relying solely on the particle gravity and the material inlet diameter, resulting in a decrease in spreading uniformity.



a) *b)*

Fig. 6 - Simulation analysis of pesticide application device

a) Overall sprayer; b) Sprayer drop

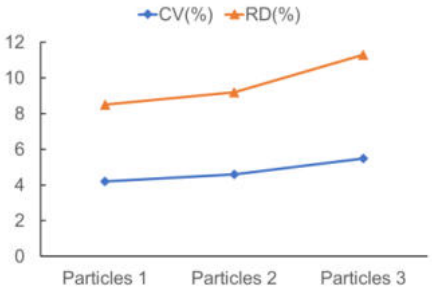


Fig. 7 - Simulation results

Analysis of field test results

According to the Technical Specifications for Quality Evaluation of Fertilizer Machinery (NY/T 1003-2006), the coefficient of variation for granular sprayers should be ≤13% (MARA., 2006). The maximum coefficient of variation was 8.25%, and the average relative deviation was 18.07%, both of which met the industry standard requirements (Table 4). The test data were imported into Design-Expert13 software for variance analysis (Table 5) and response surface analysis (Fig. 8, Fig. 9). From the univariate analysis, operating speed, feed port diameter, and application angle all had a significant effect on the coefficient of variation. Operating speed had the most significant effect, followed by feed port diameter, while the effect of the application angle was relatively small but still statistically significant. This indicates that the variation in the coefficient of variation is primarily affected by operating speed, while feed port diameter and application angle also influence spraying uniformity to some extent. The interaction analysis showed that the interaction effects of operating speed × feed port diameter and feed port diameter × application angle were not significant, while the interaction effect of operating speed × application angle was significant. The response surface analysis showed that at low operating speeds, increasing the feed opening diameter significantly reduced the coefficient of variation, indicating that appropriately increasing the feed opening diameter could improve uniformity. However, at high operating speeds, the effect of increasing the feed opening diameter on the coefficient of variation tended to stabilize. The effect of application angle on the coefficient of variation was more significant at high operating speeds, indicating that optimizing the application angle could improve spreading uniformity at high-speed operation. At low operating speeds, the effect of the application angle was relatively small. Under conditions of extreme application angles and larger feed opening diameters, the coefficient of variation increased slightly, indicating that excessively large application angles may lead to decreased spraying uniformity.

Table 4

Response surface experimental design and results

Test No.	Operation speed	Feeding port diameter	Spraying angle	Evaluation indicators	
				CV	*RD*
	[km/h]	[mm]	[°]		
1	0.6	5	30	6.42	15.61
2	1.8	5	30	8.25	21.32
3	0.6	9	30	6.27	18.59
4	1.8	9	30	7.06	16.64
5	0.6	7	0	4.81	15.38
6	1.8	7	0	6.85	20.26
7	0.6	7	60	5.91	17.45
8	1.8	7	60	5.36	16.96
9	1.2	5	0	7.47	22.28
10	1.2	9	0	6.73	16.67
11	1.2	5	60	7.16	19.24

Test No.	Operation speed	Feeding port diameter	Spraying angle	Evaluation indicators	
				CV	*RD*
	[km/h]	[mm]	[°]		
12	1.2	9	60	6.16	19.51
13	1.2	7	30	5.92	16.58
14	1.2	7	30	5.16	16.65
15	1.2	7	30	5.53	18.48
16	1.2	7	30	6.32	17.19
17	1.2	7	30	6.15	18.38

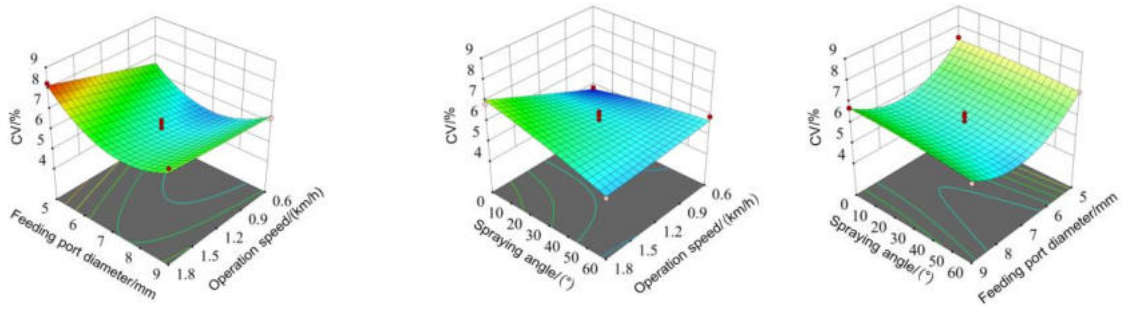
As shown in Table 5 and Fig. 9, the effects of operating speed, orifice diameter, and application angle on relative deviation are statistically significant, with P values of 0.0125, 0.0237, and 0.0342, respectively. From the perspective of the F-value, operating speed has the most significant effect, followed by orifice diameter, while the effect of application angle is relatively small. The two-factor interaction analysis showed that operating speed × orifice diameter and orifice diameter × application angle significantly affected relative deviation (P values of 0.0030 and 0.0114, respectively).

Table 5

Analysis of variance

Sources of variance	*CV*				*RD*			
	sum of squares	DOF	*F-value*	*p-value*	sum of squares	DOF	*F-value*	*p-value*
Model	11.22	9	7.94	0.0061	55.75	9	8.29	0.0054
A	2.11	1	13.46	0.0080	8.30	1	11.12	0.0125
B	1.19	1	7.56	0.0285	6.20	1	8.29	0.0237
C	0.2016	1	1.29	0.2943	0.2556	1	0.3422	0.5769
AB	0.2704	1	1.72	0.2306	14.67	1	19.64	0.0030
AC	1.68	1	10.69	0.0137	7.21	1	9.65	0.0172
BC	0.0169	1	0.1077	0.7523	8.64	1	11.57	0.0114
A^2	0.0014	1	0.0089	0.9273	1.86	1	2.49	0.1588
B^2	5.72	1	36.47	0.0005	6.56	1	8.78	0.0210
C^2	0.0436	1	0.2779	0.6144	2.19	1	2.93	0.1308
Residual	1.10	7			5.23	7		
Lack of Fit	0.2096	3	0.3146	0.8154	1.84	3	0.7231	0.5887
Pure Error	0.8885	4			3.39	4		
Total	12.32	16			60.98	16		
R^2	0.9108				0.9143			
R^2_{adj}	0.7962				0.8040			
Adeq Precision	11.287				9.9928			
Regression Equation	CV=5.82+0.5138A-0.385B-0.1587C-0.26AB-0.6475AC-0.065BC+0.0182A^2+1.17B^2-0.1017C^2				RD=17.46+1.02A-0.88B-0.1788C-1.91AB-1.34AC+1.47BC-0.6643A^2+1.25B^2+0.7208C^2			

Note: p<0.05 shows this term is significant; p<0.01 shows this term is very significant.

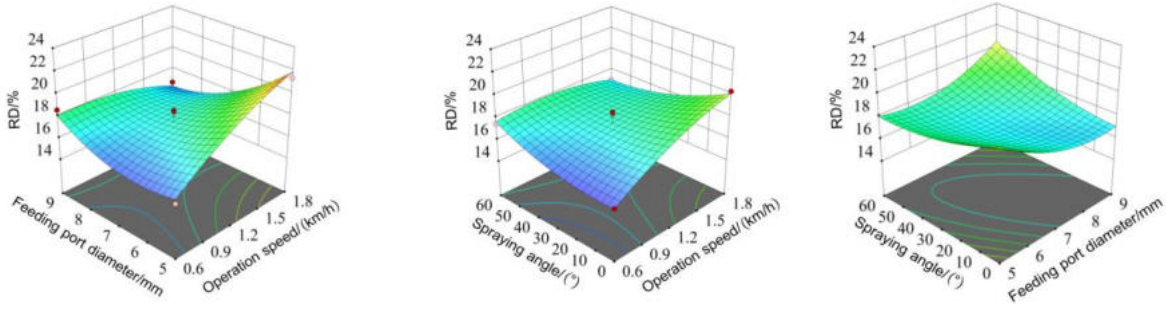


a) *b)* *c)*

Fig. 8 - Response surface plot of the effect of two-factor interaction on the coefficient of variation

a) Feeding port diameter × Operating speed; b) Spraying angle × Operation speed; c) Spraying angle ×Feeding port diameter

The response surface analysis showed that at low operating speeds, increasing orifice diameter had a greater effect on relative deviation, while at high operating speeds, the effect of increasing orifice diameter on relative deviation gradually weakened. This indicates a synergistic effect between the two, but the intensity of the effect is influenced by operating speed. In addition, the interaction between orifice diameter and application angle on relative deviation shows a nonlinear relationship. When the orifice diameter is small, adjusting the application angle has a smaller effect on relative deviation, while when the orifice diameter is large, the effect of changing the application angle on relative deviation becomes more significant. This indicates that when optimizing application parameters, the matching relationship among operating speed, feed port diameter, and application angle should be considered comprehensively to improve application accuracy and reduce deviation.



a) *b)* *c)*

Fig. 9 - Response surface plot of the effect of two-factor interaction on relative deviation

a) Feeding port diameter × Operating speed b) Spraying angle × Operation speed c) Spraying angle ×Feeding port diameter

CONCLUSIONS

This study provides a theoretical basis for the research and development of precision pesticide application equipment in hilly areas, as well as technical support for reducing pesticide use, reducing environmental pollution, and promoting the development of precision agriculture. Discrete element method (DEM) was used to design and optimize a crawler-type precision pesticide applicator. Through simulation and field tests, the effects of pesticide particle characteristics and key operating parameters on application uniformity and accuracy were evaluated. The main findings are:

1. Particle material properties significantly affect application performance. The coefficients of variation for different particles were 4.25% (Particle 1), 4.63% (Particle 2), and 5.57% (Particle 3), with corresponding relative deviations of 8.51%, 9.28%, and 11.33%. Small-size, low-density, and smooth-surfaced particles exhibited good fluidity within the applicator and high spreading uniformity. In contrast, larger and denser particles were more significantly affected by gravity and friction, leading to accumulation at the material port, resulting in uneven spreading and affecting the accuracy of pesticide application.

2. Response surface analysis optimized key parameters such as operating speed, material port diameter, and application angle. Operating speed had the most significant effect on uniformity and accuracy, followed by material port diameter, with application angle having a smaller effect. At low speeds, increasing port diameter improved uniformity, while at higher speeds, optimizing the application angle reduced deviation and improved precision.

3. Field tests showed a maximum coefficient of variation of 8.25% and an average relative deviation of 18.07%, both meeting industry standards. The consistency between simulation and test data confirms the feasibility and stability of the designed applicator for precise pesticide application.

ACKNOWLEDGEMENTS

The study was funded by Chongqing Education Commission Science and Technology Research and Technology Youth Fund Project (KJQN202400208), Chongqing Beibei District Industry-University-Research Cooperation Guidance Program Project (2024cxyhz-04) and Chongqing Beibei District Science and Technology Bureau Science and Technology Talent and Independent Innovation Special Project (2024-30).

REFERENCES

[1] Chen Z.W., Hu Z.R., Xiong Y. F. (2023). Design and experiment of tree crown surrounding type contour target pesticide sprayer (树冠环绕式仿形对靶施药机设计与试验). *Transactions of the Chinese Society of Agricultural Engineering*, 39(03):23-32.

[2] Dong J.W., Pang L., Cao Z.H., (2025). Design and experiment of tracked orchard target-profiling pesticide applicator (履带式果园对靶仿形施药机设计与试验). *Agricultural mechanization research*, 1-10.

[3] Gou Y.J., Li H.Y., Wang D.M., (2022). Design and simulation optimization of small variable fertilizer spreader based on EDEM (基于 EDEM 的小型变量撒肥机设计与仿真优化). *Agricultural mechanization research*, 44(11):65-71+76.

[4] Gou Y.J., He H.B., Li, H. Y., Wang D.M., Zhang M., (2023). Design and experimental study of a vehicle-mounted fertilizing and spraying machine. *INMATEH - Agricultural Engineering*, 55-64.

[5] He X.K., (2020). Research status and development suggestions of precision pesticide application technology and equipment in China (中国精准施药技术和装备研究现状及发展建议). *Smart Agriculture (Chinese and English)*, 2(01):133-146.

[6] Hazra D K., Purkait A., (2019). Role of pesticide formulations for sustainable crop protection and environment management: A review. *AkiNik Publications*.

[7] Jiang Y. Y., Cao D.L., Gao L., Xu X. X., Zhao J., (2021). Design and Experimental Research of Flexible Gripper Based on Fin Ray effect (果园精准施药技术的现状与发展趋势分析). *Southern Agricultural Machinery*, 52(15):44-46.

[8] MARA., (2006). Technical Specification for Quality Evaluation of Fertilization Machinery (施肥机械质量评价技术规范). *NY/T 1003-2006*.

[9] Ministry of Agriculture and Rural Affairs, (2022). The 14th Five-Year Plan for the Development of National Agricultural Mechanization ("十四五"全国农业机械化发展规划). *Livestock Industry*, (05):5-18.

[10] Meshram, A. T., Vanalkar, A. V., Kalambe, K. B., Badar, A. M., (2022). Pesticide spraying robot for precision agriculture: a categorical literature review and future trends. *Journal of Field Robotics*, 39(2), 153-171.

[11] Nation, H. J., (1972). The application of granular pesticides. *Pesticide science*.

[12] Nie C.X., Yang M.J., LI S.T., (2022). Parameter calibration of discrete element model for purple soil in sloping farmland in Southwest China (西南区坡耕地紫色土离散元模型参数标定). *Journal of Shandong Agricultural University (Natural Science Edition)*, 53(03):454-463.

[13] Qi X.Y., Zhou Z.Y., Lin S.Y., Xu L., (2018). Design and experiment of fertilizer sprayer for pneumatic variable fertilizer spreader in paddy field(稻田气力式变量施肥机肥料喷撒器设计与试验). *Transactions of the Chinese Society of Agricultural Machinery*, 49(S1):164-170+180.

[14] Wang S.Y., You Z.Y., Sun D.W., Xiao Q., Luo Q.J., He L., (2024). Performance test of a half-feed peanut-cleaning picker suitable for clay hill areas in southern China. *International Journal of Agricultural & Biological Engineering*, 17(4).

[15] Xie K.T., Zhang Z.G., Wang F.A, Yu X.L., Wang C.L., Jiang S.F., (2024). Calibration and experimental verification of discrete element parameters of Panax notoginseng root. *International Journal of Agricultural & Biological Engineering*, 17(4).

[16] Yin Y. S., Man C., Xiao C. W., (2018). Numerical simulation of spreading performance and distribution pattern of centrifugal variable-rate fertilizer applicator based on DEM software. *Computers & Electronics in Agriculture*, 144:249-259.

[17] Yu Y., Ge R., Li G., (2024). Design and experiment of the pneumatic double disc precision seed metering device for Chinese flowering cabbage. *International Journal of Agricultural & Biological Engineering*, 17(4).

[18] Zhai C. Y., Zhang Y.L., Zhou W., (2024). Design and experiment of precise variable spraying monitoring system based on pesticide spraying traceability (基于农药喷施溯源的精准变量喷药监控系统设计与试验). *Transactions of the Chinese Society of Agricultural Machinery*, 55(02):160-169.

DESIGN AND OPTIMISATION OF ROTARY TILLER BLADE FOR ORCHARDS IN HILLY MOUNTAINOUS AREAS BASED ON THE DISCRETE ELEMENT METHOD / 基于离散元法的丘陵山区果园圆盘式开沟刀具设计与优化

Jing MI [1], Huan XIE *[2] Po NIU*[1]
[1]College of Mechanical Engineering, Chongqing Three Gorges University, Chongqing / China.
[2]Chongqing Three Gorges Vocational College, School of Automotive Engineering / China
Tel: +86 17726251480; E-mail: 1478807149@qq.com
Corresponding author: huan xie, Po Niu
DOI: https://doi.org/10.35633/inmateh-76-16

Keywords: *hilly area, orchard, rotary blade, DEM, RSM, optimization*

ABSTRACT
This study investigates the excessive energy consumption of traditional furrowing cutters used in sticky, heavy soils of orchards located in hilly and mountainous regions. A novel furrowing cutter was designed, taking the wetland rotary bending cutter as a reference. The bending radius, bending angle, and alpha angle were selected as design variables. Quadratic orthogonal regression and discrete element method (DEM) simulations were employed to analyse tool–soil dynamic interactions and assess the influence of key parameters on furrowing power consumption. Response surface analysis revealed that at a bending radius of 30.02 mm, bending angle of 109.97°, and alpha angle of 51.74°, the optimised cutter reduced power consumption by 12.9%, from 0.85 kW to 0.74 kW.

摘要
本研究针对丘陵山区果园粘重土壤条件下传统开沟刀具存在的高能耗问题，以湿地旋耕弯刀为参考，设计了一种适用于丘陵山区果园的开沟刀具。通过选择刀具弯折半径、弯折角度和阿尔法角作为控制变量，结合二次正交回归实验和离散元法（DEM）仿真，分析刀具与土壤的动力学交互特性，探讨关键参数对开沟功耗的影响机制。响应曲面分析结果表明，在弯折半径 30.02 mm、弯折角 109.97°、阿尔法角 51.74°的条件下，优化后的刀具功耗由 0.85 KW 降低至 0.74 KW，减少了 12.9%。

INTRODUCTION
Fertiliser application is crucial to fruit tree management, directly influencing yield and quality. Common fertiliser application methods include water-fertiliser integration, open furrow application, and fertiliser spreading, each with inherent limitations. Water-fertiliser integration can cause soil salinisation, while spreading results in fertiliser wastage and lacks precise depth control. Open furrow fertiliser application meets fruit tree nutrient requirements but remains hindered by high energy consumption and low operational efficiency. In China, premium orchards are primarily found in hilly and mountainous regions, including Sichuan, Guangdong, Guangxi, Shaanxi, and Gansu. These areas have low mechanisation levels, with manual labour remaining predominant due to complex terrain and varying soil properties. Given labour shortages and rising costs, developing mechanised furrowing and fertiliser application technologies tailored to complex terrain is increasingly critical *(Asl and Singh, 2009; Chen P. et al., 2024; Fu et al., 2024; Wang et al., 2015).*

In mechanised furrowing and fertiliser application in orchards, the furrowing tool, as a key component in direct soil contact, plays a crucial role in operational efficiency and power consumption. Extensive research has been conducted globally. *Kang et al., (2017)*, optimised the blade structure, significantly reducing operating power consumption; *QIN et al., (2021)*, proposed a combined cutting and throwing furrowing tool for tea garden mechanisation, effectively enhancing soil-throwing performance; *Barr et al., (2020)*, optimised the tool-soil interaction process using DEM simulation, significantly reducing tool power consumption and providing technical support for optimisation. However, orchard soils in hilly mountainous areas are sticky and heavy, with severe sloughing. The issues of high-power consumption and inefficient furrowing in traditional tools remain unresolved.

Jing Mi, M.S. Stud; huan xie, Assoc. Prof; Po Niu, Assoc. Prof. Ph.D. Eng.

The cutter's structural parameters are critical for enhancing operational efficiency and reducing energy consumption. Inspired by the design of the wetland rotary ploughing curved cutter, this cutter is widely used in wetland and orchard operations due to its superior cutting performance, reduced tangling, and effective soil penetration. Building on these characteristics, this study develops a furrowing cutter tailored for orchard soils in hilly mountainous regions. By optimising the bending radius, bending angle, and alpha angle, soil contact efficiency is improved, and power consumption is reduced.

MATERIALS AND METHODS

Main structure and parameters of furrowing tool

The cutter's structural parameters are essential for enhancing operational efficiency and reducing energy consumption *(Ma et al., 2021; Xiao et al., 2024; Zhang et al., 2022)*. This study adopts the design principles of wetland rotary ploughing curved cutters, which are widely used in wetland and orchard operations for their superior cutting performance, reduced tangling, and effective soil penetration. Building on this concept, a furrowing cutter optimised for orchard soils in hilly mountainous regions was developed. The bending radius, bending angle, and alpha angle were refined to enhance soil contact efficiency and minimise power consumption.

Figure 1 presents a schematic diagram of a furrowing cutter designed based on the wetland rotary ploughing curved cutter concept.

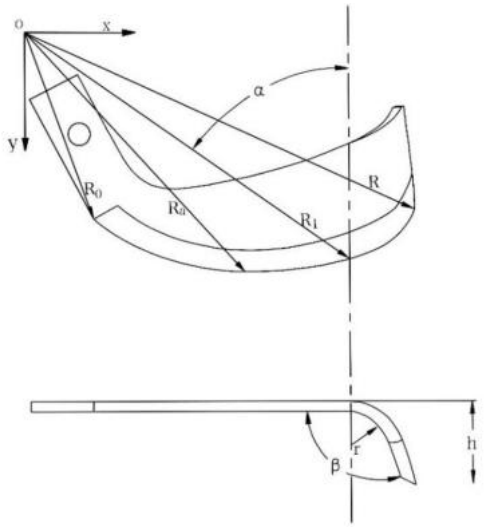


Fig. 1 - Schematic diagram of furrowing tool structure

O - center of rotation, R - radius of rotation, R_0 - radius of the starting point of the side-cutting edge, R_1 - radius of the end point of the side-cutting edge, R_a - radius of any point on the side-cutting edge, α - angle between the radius of the end point of the side-cutting edge and the bend line, r radius of bend, β is the angle of bend, h is the working width.

The main structural parameters of the furrowing tool are shown in Table 1.

Table 1

Main structural parameters of furrowing tool

Parametric	Numerical
Radius of rotation [*R*]	245 [mm]
Radius of the starting point of the side-cutting edge [R_0]	110 [mm]
Radius of the end point of the side-cutting edge [R_a]	220 [mm]
Bending radius [*r*]	45 [mm]
Bending angle [*β*]	135 [°]
Alpha angle [α]	40 [°]
Working width [*h*]	35 [mm]

DEM-based coupled tool-soil modelling

To ensure simulation accuracy, this study selected typical orchard soil from hilly mountainous regions as the simulation environment. The parameters were set based on experimentally measured soil physical properties and supplemented with data from the literature. The soil is primarily compacted clay with fine particles that are difficult to measure directly.

Therefore, reasonable assumptions regarding its physical properties were incorporated into the simulation *(Chen, M. et al., 2024; Chertkiattipol and Niyamapa, 2010; Hao et al., 2023; Wang et al., 2023)*. The Hertz-Mindlin with JKR model was employed to simulate soil particle contact, with a particle size of 5 mm. The simulation parameters for the tool and soil are presented in Table 2.

Table 2

Parameters of the tool-soil coupling model

parametric	numerical	parametric	numerical
Machine forward speed [m/s]	0.3	Soil-soil recovery factor	0.28
Tool speed [rpm]	300	Soil-Fe recovery factor	0.6
Soil density [kg/m³]	2500	Soil-soil static factor	0.5
Poisson's ratio for soil	0.32	Soil-steel static factor	0.5
Soil shear modulus [Pa]	1×10^{6}	Soil-soil rolling factor	0.37
Steel density [kg/m^3]	7850	Soil-steel rolling factor	0.05
Shear modulus of steel [Pa]	7.962×10^{10}	Fe Poisson's ratio	0.3

Lateral cutting-edge curve

During operation, the side-cutting edge vertically cuts the soil, with cutting performance primarily determined by the design of its curve. For furrowing depths of less than 30 cm*(Li et al., 2018)*, the Archimedean spiral is commonly selected as the side-cutting edge curve. Consequently, this study adopts this curve, expressed by the following equation:

$$\rho = \rho_0 + a'\theta \tag{1}$$

ρ_0-polar diameter at the start of the helix, [mm];

a'-increase in polar diameter for every 1 radian increase in the polar angle of the helix, [mm];

θ -arbitrary polar angle on the helix, [°].

To prevent soil compaction by the bladeless section during furrowing, ρ_0 must satisfy the following equation:

$$\rho_0 = \sqrt{R^2 + S^2 - 2S\sqrt{2Ra - a^2}} \tag{2}$$

S - cutting pitch, [mm];

a - furrowing depth, [mm];

R - furrowing knife turning radius, [mm].

The turning radius of the tool is a critical design parameter. Based on the requirements for orchard furrowing in hilly mountainous regions, the maximum gyration radius is set to 245 mm, with a soil-cutting pitch of 30 cm. The pole diameter at the helix's starting point, ρ_0 is calculated as 110 mm.

To ensure a smooth transition between the helix and the tangent edge, the pole diameter at the endpoint, ρ_n is typically 10–20 mm smaller than the gyration radius. Thus, the endpoint pole diameter is designed as 220 mm.

The polar angle θ_n at the helix endpoint is related to the slip shear angle by the following equation:

$$\theta_n = \tan\frac{\rho_n - \rho_0}{\rho_n}\tau_n \tag{3}$$

τ_n-slip angle at the end of the helix, [°].

Considering the requirements of orchards in hilly mountainous regions, the terminal slip cut angle is designed as τ_n=55◦, with a calculated increment of a'=3.14, thereby determining the side-cutting edge helix.

Tangent Curve and Tangent Height

The tangent edge is a spatial curve. To ensure a flat furrow bottom, the curve is positioned on the outer cylindrical surface of the knife stick, where it appears as a circular arc in the side view and transitions smoothly into the side cutting edge *(Fang et al., 2016; Yang et al., 2024)*. In hilly and mountainous orchards, the soil is compacted, requiring the knives to possess soil-breaking capabilities.

Liu et al., (2019), demonstrated that the optimal soil breakage rate and power consumption occurred when the tangent face height was 60 mm. Consequently, in this study, the end face height was set at 60 mm to satisfy the operational requirements of Class I rotary tillage knives. The bending radius, bending angle, and alpha angle influence cutting force and power consumption A smaller bending radius increases efficiency but also friction, whereas a larger radius reduces friction but affects cutting depth. Larger bending angles enhance dispersion efficiency but increase power consumption. The alpha angle influences cutting stability; a smaller angle promotes stable cutting, while a larger angle increases cutting depth but also resistance*(Liu et al., 2024; Zeng et al., 2024)*.

The tool's bending radius r is 30 mm, the alpha angle α is 47°, the bending angle β for the positive cutting part is 120°, the width of the top surface of the side-cutting edge C_1 is 5 mm, and the thickness of the edge C_2 is 1.5 mm.

At this stage, the main dimensional design of the cutter disc-type furrowing tool is essentially complete, and the final three-dimensional representation of the tool is shown in Figure 2.

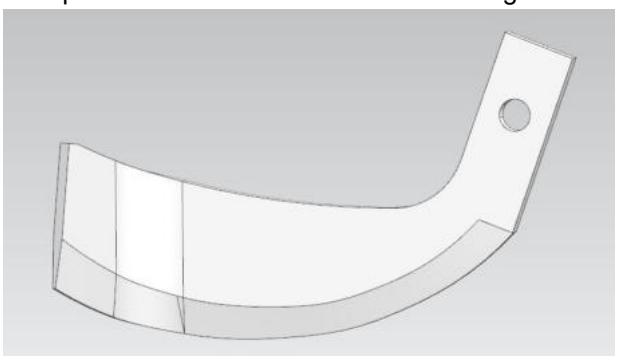


Fig. 2 - Schematic diagram of tool structure

EDEM simulation experiment

The furrowing tool model, based on the tool and soil described in the previous section, is created in UG, saved in STL format, and imported into EDEM. The tool-soil coupling model is then configured according to the physical material properties outlined earlier.

The furrowing tool-soil coupling model, established using the above method and parameters, is shown in Figure 3.

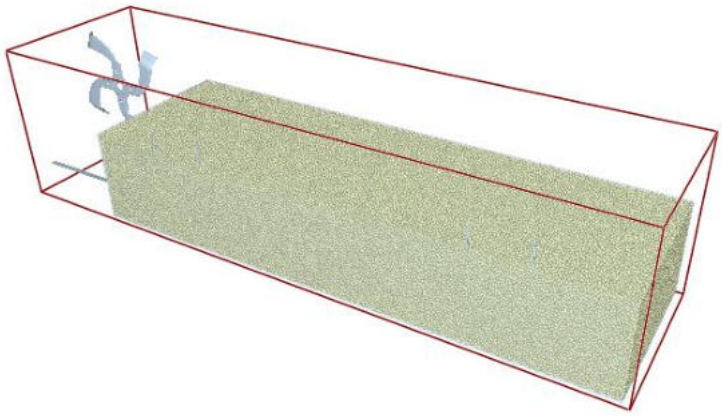


Fig. 3 - Schematic diagram of tool-soil simulation model

As EDEM cannot directly measure the power consumption of the tool, the torque applied to the tool must first be measured and then converted into power consumption using the following formula:

$$P = \frac{T \cdot n}{9549} \tag{4}$$

P - power consumption, [kW];

T - torque, [N·m];

n - tool speed, [rpm].

Quadratic regression orthogonal experimental design

The orthogonal combination design includes a two-level test m_c, asterisk test $2m_\gamma$ and zero-level experiment m_0. The total number of tests, n is calculated using the following equation (*Xiao et al., 2024*):

$$n = m_c + 2m_\gamma + m_0 \quad (5)$$

In accordance with the orthogonality requirement, the arm length parameter, denoted as γ, must satisfy the following relationship:

$$\gamma = \sqrt{\frac{\sqrt{(m_c + 2m + m_0)m_c} - m_c}{2}} \quad (6)$$

The present experiment was a three-factor, two-level full-scale trial, which resulted in $\gamma = 1.353$.

In the context of the given factors, the arithmetic mean is defined as the zero level of factor x_j, denoted x_{j0}, where x_{j2} and x_{j1} represent the upper and lower levels of factor x_j, respectively. Let $x_{j\gamma}$ and $x_{-j\gamma}$ denote the upper and lower asterisk arm levels of factor x_j, respectively. These values correspond to the upper and lower levels of factor x_j.

$$x_{j0} = \frac{x_{j1} + x_{j2}}{2} = \frac{x_{j\gamma} + x_{-j\gamma}}{2} \quad (7)$$

Therefore, the variation in this factor is as follows:

$$\Delta_j = \frac{x_{j\gamma} - x_{j0}}{\gamma} \quad (8)$$

It can be shown that a linear variation in each level of factor x_j leads to the following coding of the levels:

$$z_j = \frac{x_j - x_{j0}}{\Delta j} \quad (9)$$

The factor levels and their corresponding coding results for this experiment are shown in the table 3.

Table 3

Test Factors and Levels

Code	X_1 (Bending radius)	X_2 (Bending angle)	X_3 (Alpha Angle)
γ（1.353）	40	135	52
1	38.6955	131.0864	50.6955
0	35	120	47
-1	31.3045	108.9135	43.3045
$-\gamma$（-1.353）	30	105	42
Δ_j	3.6954	11.0864	3.6954

The test programme and the results obtained from the calculations are presented in the table below.

Table 4

Experimental arrangement and power consumption results

	X_0	X_1 (Bending radius)	X_2 (Bending angle)	X_3 (Alpha Angle)	Y（kW）
1	1	-1	-1	-1	0.837522
2	1	1	-1	-1	0.83587
3	1	-1	1	-1	0.915432
4	1	1	1	-1	0.907356
5	1	-1	-1	1	0.795983
6	1	1	-1	1	0.827545
7	1	-1	1	1	0.832517
8	1	1	1	1	0.883363
9	1	-1.353	0	0	0.850092
10	1	1.353	0	0	0.900149
11	1	0	-1.353	0	0.82978
12	1	0	1.353	0	0.936715

	X_0	X_1 (Bending radius)	X_2 (Bending angle)	X_3 (Alpha Angle)	Y（kW）
13	1	0	0	-1.353	0.891556
14	1	0	0	1.353	0.858958
15	1	0	0	0	0.915705
16	1	0	0	0	0.904034
17	1	0	0	0	0.898701

RESULTS AND DISCUSSION

Analysis of experimental results

Table 5

Analysis of variance

	SS	DF	MS	F-value	P-value	VIF
Model	0.0257	9	0.0029	23.28	0.0002	
A-X_1	0.0017	1	0.0017	13.80	0.0075	1
B-X_2	0.0128	1	0.0128	104.54	＜0.0001	1
C-X_3	0.0035	1	0.0035	28.25	0.0011	1
AB	0.0000	1	0.0000	0.1687	0.6935	1
AC	0.0011	1	0.0011	8.66	0.0216	1
BC	0.0004	1	0.0004	3.32	0.1112	1
A2	0.0024	1	0.0024	19.67	0.0030	1
B2	0.0014	1	0.0014	11.54	0.0115	1
C2	0.0024	1	0.0024	19.52	0.0031	1

Note: P≤0.01 (highly significant), P≤0.05 (significant).

The F-value of the model in the table 5 is 23.28, indicating that the model is significant. The P-value is less than 0.05, further confirming the model's significance. The significant factors include A, B, C, AC, A^2, B^2, and C^2. SS represents the sum of squares, DF is the degrees of freedom, MS is the mean square, and VIF is the Variance Inflation Factor. A VIF value of 1 indicates that the factors are orthogonal. The ANOVA analysis demonstrates that the overall model is significant. The effect of B-X_2 on power consumption is the largest, followed by C-X_3 and A-X_1. Additionally, the interaction between A and C also significantly affects power consumption.

The regression coefficients and goodness of fit can be derived from the ANOVA, and the regression equations are as follows:

$$Y = 0.9069 + 0.0120X_1 + 0.0317X_2 - 0.0178X_3 + 0.0016X_1X_2 + 0.0115X_1X_3 - 0.0093X_2X_3 - 0.0183X_1^2 - 0.0139X_2^2 - 0.0216X_3^2 \quad (10)$$

The results of the significance and confidence analyses for the regression equations are as follows:

Table 6

Confidence analyses of regression equations

Parametric	Numerical
R^2	0.9603
Adjusted R^2	0.9093
P	0.0004

The regression equation had an R^2 of 0.9606 and an adjusted R^2 of 0.9093, with a P-value of 0.0004, indicating that the equation was well-fitted and had a significant effect. The normality of the standardized residuals was verified for the regression model, and these residuals were plotted against the standard distribution, as shown below.

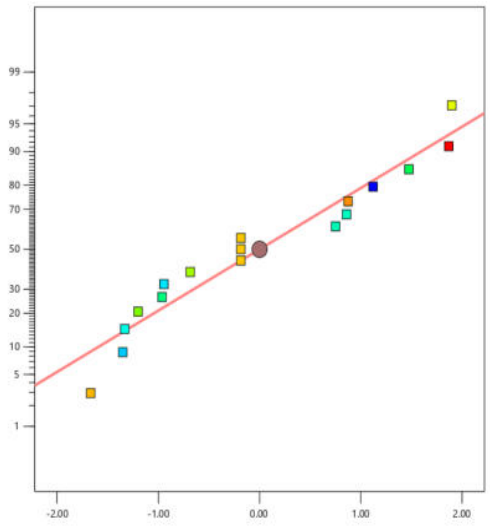


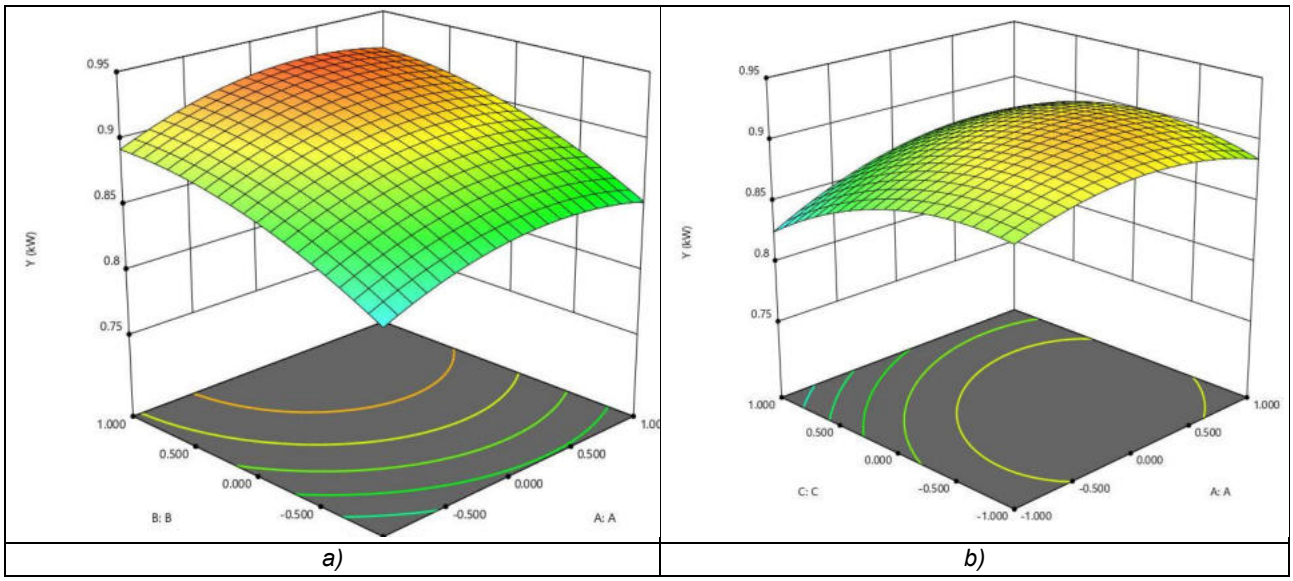
Fig. 4 - Distribution of residual studies

As shown in the Figure 4, the points are distributed along a nearly straight line, indicating that the results are approximately normally distributed. This supports the credibility of the model and aligns with the assumptions of the analysis of variance (ANOVA).

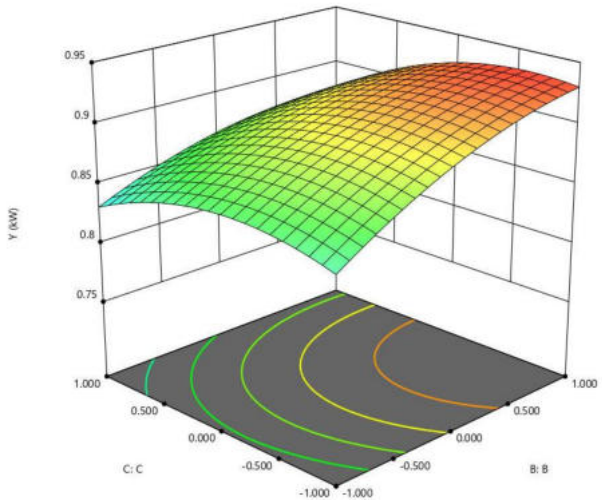
Interaction Effect of Tool Structure Parameters on Power Consumption

In this study, response surface methodology was used to optimise the furrowing tool parameters and analyse the effects of factors and their interactions on power consumption, with the results presented through response surface plots. The response surface of the A (X_1) bending radius and B (X_2) bending angle on power consumption was plotted while keeping the C (X_3) alpha angle at the 0 level. The results show that power consumption increases with the A (X_1) bending radius, with the growth rate slowing at 35 mm and decreasing after reaching a maximum at 36 mm. Power consumption also increases with the B (X_2) bending angle, while it decreases as the C (X_3) alpha angle increases.

The bending radius determines the contact area between the tool and the soil, as well as the force characteristics during the cutting process. A smaller bending radius concentrates the cutting force and reduces the thickness of the soil cutting layer but may result in a larger reaction force. In contrast, a larger bending radius allows the tool to penetrate deeper into the soil, though it may increase power consumption. The bending angle affects both the direction and efficiency of the shear force applied by the tool. Smaller bending angles are suited for shallow cutting but may cause soil build-up and disturbance. Larger bending angles are more suitable for deeper cutting and aid in breaking up compacted layers. The alpha angle influences both the depth of cut and the direction of soil dispersion. Smaller alpha angles enable the tool to cut deeper into the soil but may increase power consumption.



a) *b)*



c)

Fig. 5 - Interaction effects of prop structure parameters on power consumption

a) Interaction of X_1 and X_2 on power consumption. b) Interaction of X_3 and X_2 on power consumption. c) Interaction of X_3 and X_1 on power consumption

Analysis of tool optimisation results

The objective of the optimisation is to minimise the furrowing power through the rational selection of tool structure parameters. Consequently, a regression equation was established with the goal of minimising power, to reflect the relationship between tool structure and power consumption, providing a quantitative basis for optimisation.

The constraints for the optimisation process are as follows:

$$\begin{cases} X_1 = [-1.353, 1.353] \\ X_2 = [-1.353, 1.353] \\ X_3 = [-1.353, 1.353] \end{cases}$$

The optimal solution is obtained by solving the following equation:

$$\begin{cases} X_1 = -1.33373 \\ X_2 = -1.19486 \\ X_3 = \ \ 1.21368 \end{cases}$$

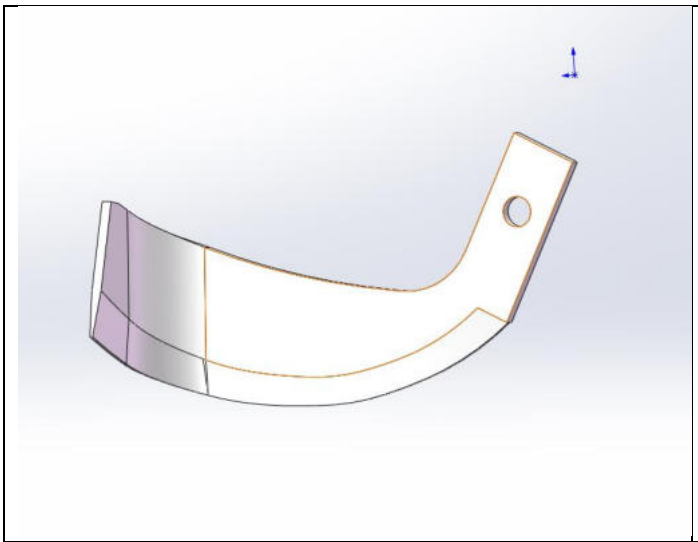


Fig. 6 - Optimised tool model

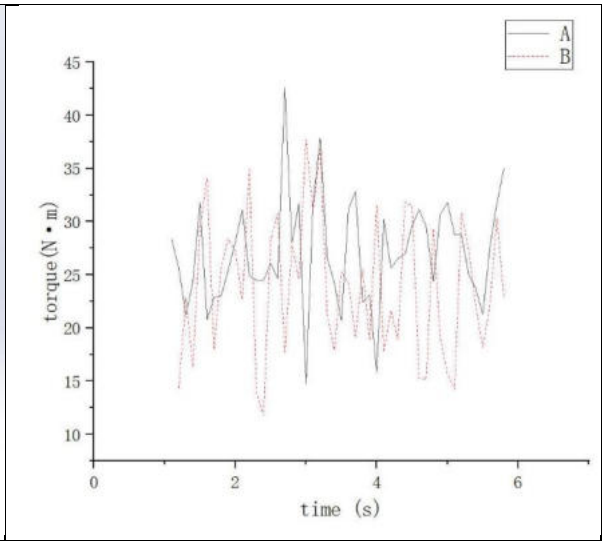


Fig. 7 - Comparison of torque before and after optimization

The optimised furrowing torque graph was generated from EDEM post-processing and plotted using Origin to compare pre-optimisation (torque-A) and post-optimisation (torque-B) values. The results indicate a significant reduction in furrowing torque. After optimisation, the average furrowing torque decreased to 23.90 N·m, while the corresponding furrowing power was 0.75 kW, with a relative error of 1.35%. Compared to the pre-optimisation power of 0.85 kW, furrowing power consumption was reduced by 12.90%.

CONCLUSIONS

This study used a wetland rotary ploughing cutter as a prototype to design a furrowing cutter for orchards in hilly mountainous areas, considering the characteristics of sticky soil. The bending radius, bending angle, and alpha angle of the knives were optimised using quadratic orthogonal regression experiments. The interaction between the knives and soil was analysed through discrete element method (DEM) simulation, with the Hertz-Mindlin with JKR model selected for soil-particle contact modelling. Power consumption during furrowing was used as the evaluation index. Based on the regression analysis and simulation results, the power consumption of the optimised tool is 0.74 kW, 12.9% lower than the pre-optimised value of 0.85 kW. These results demonstrate that by optimally adjusting the tool structure, power consumption can be significantly reduced and working efficiency improved, providing a theoretical basis for the design of orchard furrowing and fertiliser application machinery in hilly mountainous areas.

ACKNOWLEDGEMENT

The work was supported by the Chongqing Municipal Education Commission (KJZD-K202201201), and the Chongqing Wanzhou District Science and Technology Bureau (wzstc20220216), and the Start-up fee for scientific research of high-level talents in Chongqing Three Gorges University (2014/0903341).

REFERENCES

[1] Asl, J. H., & Singh, S. (2009). Optimization and evaluation of rotary tiller blades: Computer solution of mathematical relations. *Soil Tillage Research, 106*(1), 1-7. https://doi.org/10.1016/j.still.2009.09.011

[2] Barr, J., Desbiolles, J., Ucgul, M., Fielke, J. (2020). Bentleg furrow opener performance analysis using the discrete element method. *Biosystems Engineering, 189*, 99-115. https://doi.org/10.1016/j.biosystemseng.2019.11.008

[3] Chen, M., Xu, G., Wei, Y., Zhang, Y., Diao, P., Pang, H (2024). Design and experiment analysis of the small maize harvester with attitude adjustment in the hilly and mountainous areas of China. *International Journal of Agricultural Biological Engineering, 17*(1), 118-127. https://doi.org/10.25165/j.ijabe.20241701.7596

[4] Chen, P., Su, J., Xu, J., Liu, M. (2024). Design and Experiment of Hilly Orchard Vertical Spiral Ditching-fertilizing Machine (丘陵果园立式螺旋开沟施肥机设计与试验). *Transactions of the Chinese Society for Agricultural Machinery, 55*(10), 223-233+274.

[5] Chertkiattipol, S., & Niyamapa, T. (2010). Variations of torque and specific tilling energy for different rotary blades. *International Agricultural Engineering Journal, 19*(3), 1-14.

[6] Fang, H., Ji, C., Zhang, Q., Guo, J. (2016). Force analysis of rotary blade based on distinct element method. (基于离散元法的旋耕刀受力分析). *Transactions of the Chinese Society of Agricultural Engineering, 32*(21), 54-59.

[7] Fu, J., Zhu, J., & Yao, A. I. (2024). The current situation and trend of mechanized ditching and fertilization in hilly and mountainous orchards in China. (我国丘陵山地果园机械化开沟施肥发展现状与趋势). *Agricultural Equipment & Vehicle Engineering, 62*(10), 30-35.

[8] Hao, Z., Zheng, E., Li, X., Yao, H., Wang, X., Qian, S., Li, W., Zhu, M. (2023). Performance analysis of the soil-contacting parts for no-tillage planters and optimization of blade structure. (免耕播种机旋耕刀耕作性能分析与结构优化). *Transactions of the Chinese Society of Agricultural Engineering, 39*(02), 1-13.

[9] Kang, J., Li, S., Yang, X., Liu, L., Wang, C., Liu, X. (2017). Design and Experiment of Ditching Blade Installed in Close Planting Orchard Ditching Machinery. (密植果园开沟施肥机开沟刀片设计与试验). *Transactions of the Chinese Society for Agricultural Machinery, 48*(02), 68-74.

[10] Li, S., Chen, X., Chen, W., Zhu, S., Li, Y., Yang, L., Xie, S., Yang, M. (2018). Soil-cutting simulation and parameter optimization of handheld tiller's rotary blade by Smoothed Particle Hydrodynamics modelling and Taguchi method. *Journal of Cleaner Production*. https://doi.org/10.1016/j.jclepro.2017.12.228

[11] Liu, M., Liu, Y., Ku, H., Chen, L., Wang, J., Xie, B. (2019). Research on the Cutting Performance of Ridger Based on Discrete Element Method. (基于离散元法的筑埂机旋耕切削性能研究). *Journal of Agricultural Mechanization Research, 41*(10), 129-134+140. doi:10.13427/j.cnki.njyi.2019.10.024

[12] Liu, M., Xie, F., Liu, D., Wang, X. (2024). Analysis and experiment of the power of blade roller in reverse-rotary ditching machine based on the granular scale effect. (基于颗粒放尺效应的逆旋开沟机刀辊功耗分析与试验). *Transactions of the Chinese Society of Agricultural Engineering, 40*(07), 83-92.

[13] Ma, C., Qi, J., Kan, Z., Chen, S., Meng, H. (2021). Operation power consumption and verification tests of a trenching device for orchards in Xinjiang based on discrete element. *International Journal of Agricultural Biological Engineering, 14*(1), 133-141.

[14] Qin, K., Liang, X., Cao, C., Ding, W., Wu, Z., Fang, L. (2021). Design and Experiment of Combined Cutting and Throwing Ditching Blade for Tea Garden. (茶园切抛组合式开沟刀设计与试验). *Transactions of the Chinese Society for Agricultural Machinery, 52*(05), 74-82.

[15] Wang, F., Qiu, Z., Pan, Y., Sun, G. (2023). DEM-based parameter optimization and tests of digging green onions. *International Journal of Agricultural Biological Engineering*

[16] Wang, P., Li, G., Li, S., Wu, X., Cao, Z., Chen, J. (2015). The Research Situation and Development Ideas of Orchard Ditcher in China (我国果园开沟机的研究现状与发展思路). *Agricultural Equipment & Vehicle Engineering, 53*(07), 30-33.

[17] Xiao, W., Niu, P., Wang, P., Xie,Y., Xia, F. (2024). Simulation analysis and optimization of soil cutting of rotary blade by ANSYS/LS-DYNA. *INMATEH-Agricultural Engineering, 72*(1), 22-32. DOI: https://doi.org/10.35633/inmateh-72-02

[18] Yang, D., Cai, W., Wu, R., Zhang, X., He, Y. (2024). Optimization design of structural parameters for rotary tiller blade of tea garden micro tiller based on discrete element method. (基于离散元法茶园微耕机旋耕刀结构参数优化设计). *China Southern Agricultural Machinery, 55*(01), 7-10+15.

[19] Zeng, Y., Jiang, X., Wu, M., Tang, L., Li, P. (2024). Development of the layered cut and throw ditching blade groups for oil tea forest based on DEM-MBD. (基于 DEM-MBD 的油茶林分层切抛式开沟刀组研制). *Transactions of the Chinese Society of Agricultural Engineering, 40*(08), 30-42.

[20] Zhang, X., Zhang, L., Hu, X., Wang, H., Shi, X., Ma, X. (2022). Simulation of soil cutting and power consumption optimization of a typical rotary tillage soil blade. *Applied Sciences, 12*(16), 8177.

DESIGN AND TESTING OF HYDRAULIC DRIVE SYSTEM FOR CRAWLER-TYPE TIGER-NUT HARVESTER
/
履带式油莎豆收获机液压驱动行走系统的设计与试验

Zhe QU, Jianhao ZHANG, Jintao LE, Xilong WANG, Haihao SHAO, Huihui ZHAO, Zhijun LV, Wanzhang WANG* [1]
College of Mechanical and Electrical Engineering, Henan Agricultural University, Zhengzhou 450002, China
Tel: 17513301867; E-mail: quzhe071171@henau.edu.cn
Corresponding author: Wanzhang Wang
DOI: https://doi.org/10.35633/inmateh-76-17

Keywords: *tiger-nut harvester, crawler, hydraulic drive, field trial*

ABSTRACT
Tiger-nut is widely cultivated in sandy soils across China, and the mechanization level for harvesting remains low. Harvesters are mainly medium- and small-sized tractor-drawn models, which exhibit weak driving capability, a large turning radius, and poor stability. This paper presents the design of a crawler-type tiger-nut harvester hydraulic-driven travel system, with the required hydraulic motor displacement of 44.65 mL·r^{-1} and hydraulic pump displacement of 44.58 mL·r^{-1}. Experimental results from the harvester showed that the harvester's linear travel deviation rate ranged from 1.19% to 2.10%, with an average travel speed of 1.08 m·s^{-1} and the average value of radius for forward left turn and forward right turn is 2740 mm and 2748 mm. The harvester can achieve bidirectional stepless speed regulation in the field, ensuring stable harvesting performance and meeting the design requirements for the tiger-nut harvester.

摘要
油莎豆多种植于中国的沙土地，目前油莎豆机械化收获水平低，现有收获机以中小型牵引式为主，存在驱动能力弱、转弯半径大和行驶稳定性差等问题。本文设计了一种履带式油莎豆收获机液压驱动行走系统，计算得出所需的液压马达排量为 44.65 mL·r^{-1}，液压泵排量为 44.58 mL·r^{-1}。样机试验结果表明：收获机直线行走偏移率为 1.19%-2.10%，平均行走速度为 1.08 m·s^{-1}，前进左转和前进右转的半径平均值分别为 2740 mm 和 2748 mm。收获机在田间能够实现双向无级调速，收获作业性能稳定，满足油莎豆收获机设计要求。

INTRODUCTION
Tiger-nut, often referred to as the "king of oilseed crops," contains rich nutrients in its underground tubers, which can be used to extract edible oil, sugars, and produce beverages, offering significant economic value *(Roselló-Soto et al., 2018; Edo et al., 2024; Wang et al., 2021; Cantalejo et al., 1997)*. China currently relies on imports for more than 70% of its oilseed crops. In the context of the current international situation, the development of the tiger-nut industry holds great strategic importance in addressing Chinese edible oil security issues *(Zhang et al., 2020; Zhang et al., 2024)*.

Mechanized harvesting is a critical and challenging phase in the full mechanization process of tiger-nut production. To optimize harvesting, tiger-nut is best cultivated in sandy soils. Tiger-nut harvesters are generally classified into two types based on their travel mechanism: towed and self-propelled *(Shang et al., 2004)*. In foreign countries, tiger-nut harvesters are typically towed by high-horsepower tractors to perform digging and transportation tasks. However, these harvesters have large structures with limited functions and require coordination with transport vehicles for synchronized harvesting, making them unsuitable for small-scale farms. Currently, the majority of tiger-nut harvesters in China are small- and medium-sized towed models, which suffer from issues such as weak driving power, large turning radius, and poor stability. These shortcomings negatively impact the digging, cleaning, and screening quality, severely limiting the development of the tiger-nut industry *(Xu et al., 2016; Wei et al., 2023)*.

[1] *Zhe Qu, Associate Professor. Ph.D. Eng.; Jianhao Zhang, M.S. Stud. Eng.; Jintao Le, M.S. Stud. Eng.; Xilong Wang, M.S. Stud. Eng.; Haihao Shao, M.S. Stud. Eng.; Huihui Zhao, Lecturer. Ph.D. Eng.; Zhijun Lv, Lecturer. Ph.D. Eng.; Wanzhang Wang, Professor. Ph.D. Eng.*

The tracked travel system provides low ground pressure, high adhesion, strong load-bearing capacity, and a small turning radius *(Jun et al., 2013; McBride et al., 2000; Leggieri et al., 2022)*. The hydraulic drive system enables stepless speed regulation, offering smooth transmission, ease of operation, and rapid response *(Lv et al., 2024; Guo et al., 2025; Zhao et al., 2025)*. By combining the advantages of both systems, a smooth and efficient harvest of tiger-nut can be achieved. Therefore, this paper presents the design of a crawler-type self-propelled tiger-nut harvester with a hydraulic drive system, to enhance the harvester's adaptability and ensure the stability of the harvesting operation.

MATERIALS AND METHODS

Structure and technical parameters of the machine

The developed tiger-nut harvester comprises an excavating device, cab, lifting device, engine, material box, feeding device, screening device, drive system, crawler travel device, and other components. The overall structure of the machine is shown in Fig. 1, and the main parameters are shown in Table 1.

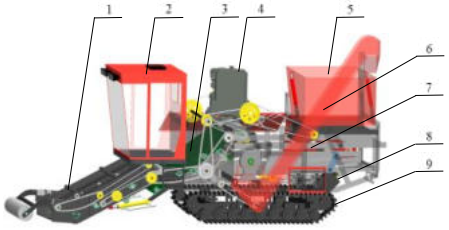


Fig. 1 - The whole structure of tiger-nut harvester

1. Excavating device; 2. Cab; 3. Lifting device; 4. Engine; 5. Material box; 6. Feeding device; 7. Screening device; 8. Drive system; 9. Crawler travel device

Table 1

The main technical parameters of tiger-nut harvester

Parameters	Values
Unladen mass [kg]	7500
Full load mass [kg]	10000
Overall dimensions [mm]	6800×2500×3200
Rated engine power [kW]	103
Rated engine speed [r·min^{-1}]	2300
Working width [mm]	1800
Harvesting speed [m·s^{-1}]	0-0.3
Travel speed [m·s^{-1}]	0-1

The general structure of the hydraulic drive system

The key components of the hydraulic drive system designed in this paper include a hydraulic stepless speed changer, reducer, direction cylinder, and other elements, as shown in Fig. 2.

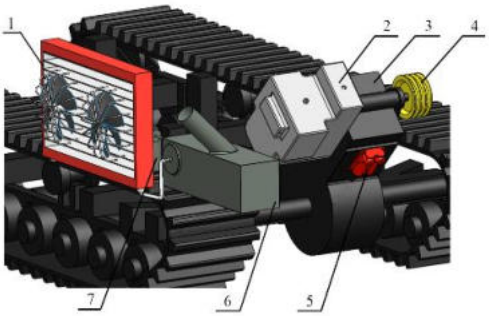


Fig. 2 - The overall structure of the hydraulic drive system

1. Radiator; 2. Stepless speed changer; 3. Reducer; 4. Power input; 5. Direction cylinder; 6. Hydraulic oil tank; 7. Filter

The basic parameters of the hydraulic drive system are shown in Table 2.

Table 2

Basic parameters of hydraulic drive system

Parameters	Values
Transmission mode	stepless gearbox
Steering type	unilateral brake steering
Pump power input method	a leather drive belt
Hydraulic pump displacement [mL·r^{-1}]	46
Maximum system pressure [MPa]	32
Rated system pressure [MPa]	16
Hydraulic motor displacement [mL·r^{-1}]	46
Hydraulic pump input speed [r·min^{-1}]	2300
Low speed reduction ratio	90
High speed reduction ratio	30

Working principle of hydraulic drive system

The working principle of the hydraulic drive system designed in this paper is illustrated in Fig. 3.

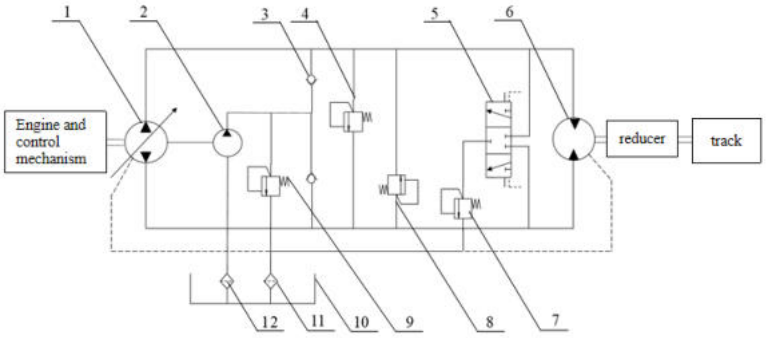


Fig. 3 - Hydraulic schematic of the drive and travel system

1. Variable pump; 2. Charge pump; 3. Check valve; 4. High pressure relief valve; 5. Flush valve; 6. Hydraulic motor; 7. Low pressure relief valve; 8. High pressure relief valve; 9. Charge relief valve; 10. Hydraulic oil tank; 11. Oil return filter; 12. Oil suction filter

The hydraulic pump in the hydraulic drive system is a bidirectional piston variable displacement pump, while the charge pump is a gear pump. The hydraulic pump is connected directly to the power input shaft, supplying hydraulic fluid to the system. The hydraulic motor is a bidirectional piston fixed displacement motor, with its output connected to a reducer, converting hydraulic energy into mechanical output. The charge pump, charge relief valve, and other components form the charge circuit, which replenishes hydraulic fluid in the system and maintains stable system pressure. The flush valve, low pressure relief valve, and oil return filter form the flushing circuit, which aids in reducing system temperature and ensuring proper lubrication. The check valve and high pressure relief valve together make up the protection circuit, maintaining stable system pressure. The system operates as follows: The engine drives the hydraulic pump via a belt, powering the hydraulic system. The hydraulic pump draws fluid from the oil tank, converting the engine's mechanical energy into hydraulic energy. As the oil flows through the circuit, it drives the hydraulic motor, which generates rotational speed and torque, converting hydraulic energy back into mechanical energy. Once the hydraulic motor discharges the oil, the oil flows directly into the intake of the hydraulic pump, starting the next cycle. If the system experiences low pressure or oil leakage, the charge circuit replenishes the oil. To adjust speed or reverse the motion, the operator uses the control handle to adjust the servo control valve. This action moves the servo cylinder, which adjusts the tilt angle of the hydraulic pump's swashplate, changing the pump's displacement and flow rate, enabling continuous variable speed control. When the system is idle, the hydraulic fluid returns to the oil tank through the flushing circuit.

Design of key components of hydraulic drive system

- **Traction Performance Analysis and Calculations**

The traction performance of a travel system is the traction work capacity exerted under specified ground conditions and its efficiency. The force model of the harvester while traveling is shown in Fig. 4.

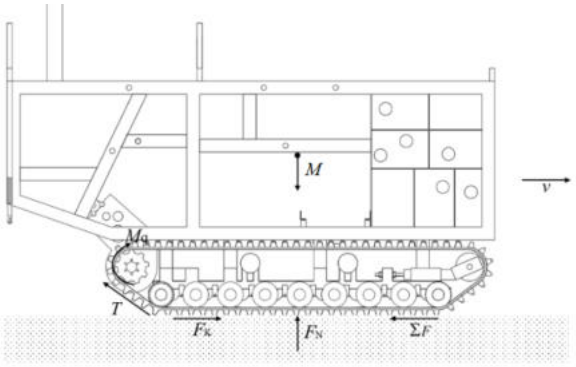


Fig. 4 - Force model of the tracked travel device during operation

From the mechanical model, it can be seen that under the action of the driving moment M_q, the track generates a tension T with the value:

$$T = \frac{M_q}{r_q} = \frac{i_1 \cdot \varphi_e \cdot M_e}{r_q} \quad (1)$$

where:

φ_e is the engine-to-drive-wheel mechanical efficiency, 0.95;

M_q is the drive-wheel torque, [N·m];

r_g is the drive-wheel radius of 0.16 [m] *(Han et al., 2023)*;

Neglecting the friction loss of tension T, the track attachment force F_k is equal to the track tension. The normal operation of the tiger-nut harvester in the field requires overcoming the rolling resistance F_p from the ground, the inertial resistance of the system F_i, the internal resistance of the system F_f, and the ramp resistance F_z and the digging resistance F_c when traveling on a ramp. Rolling resistance is mainly the normal and tangential forces generated by contact with the ground and the deformation of the tracks and the ground under full gravity, which is related to the resistance coefficient and the weight of the whole machine. The main working environment of the tiger-nut harvester is sandy loam soil, and the rolling resistance coefficient is taken as 0.15 *(Pan et al., 2014)*.

$$M = mg \quad (2)$$

$$F_p = f\ M\ \cos\alpha \quad (3)$$

where:

M is the gravity of the harvester, [N];

m is the mass of the harvester when fully loaded, [kg], calculated as 10000 kg;

α is the slope of the ramp, taken as 20°;

g is the acceleration of gravity, [m·s^{-2}];

f is the rolling resistance coefficient;

The rolling resistance F_p = 14095.39 N was calculated.

Inertial resistance is calculated by the following formula:

$$F_i = \frac{2Mv}{gt} \quad (4)$$

where:

v is the travel speed during operation, taken as 0.4 [m·s^{-1}];

t is the acceleration time, taken as 3 s;

The inertial resistance F_i = 2666.67 N was calculated.

The internal resistance of the system is related to the overall lubrication and precision and is calculated from the mass of the whole machine and the internal resistance coefficient:

$$F_f = \partial M \tag{5}$$

where:

∂ is the internal friction drag coefficient, typically 0.05-0.07 *(Ji et al., 2013)*, taken as 0.07;

The internal resistance F_f= 7000 N was calculated.

When the harvester travels uphill or downhill, the component of gravitational force acting along the slope direction generates resistance. This resistance is related to the slope and is calculated using the following formula:

$$F_z = M \sin\alpha \tag{6}$$

The ramp resistance F_z = 34202.01 N was calculated.

When the tiger-nut harvester operates in the field, the travel system is simultaneously subjected to digging resistance. The maximum digging depth of the harvester's digging mechanism is 200 mm, and the digging width corresponds to the full working width of 1800 mm (*Lv et al., 2022; Zhang et al., 2021*). The digging resistance F_c is calculated as follows:

$$F_c = 2\tau h_c W \tag{7}$$

where: τ is the coefficient of integration per unit of transverse area of the soil mound *(Han et al., 2023)*, taken as 5 N·cm^{-2};

h_c is the depth of excavation, [mm];

W is the width of excavation, [mm];

The excavation resistance F_c = 36000 N was calculated.

The maximum traction required by the system is equal to the sum of all resistance forces:

$$F_q = F_p + F_i + F_f + F_z + F_c \tag{8}$$

where:

F_q is the total tractive force, [N];

The total tractive force F_q = 93964.07 N was calculated.

The ground adhesion F_φ was calculated by the following equation:

$$F_\varphi = \varphi M \tag{9}$$

where: φ is the adhesion coefficient factor taken as 1.0 *(Liu et al., 2022)*;

The ground adhesion F_φ = 100000 N was calculated.

A comparative analysis of the calculated data shows that the total traction force F_q is smaller than the ground adhesion force F_φ, indicating that the system meets the calibration requirements and the harvester will not experience slippage during field operation.

The drive wheel speed and driving torque are calculated according to the following formula:

$$n_q = \frac{60v}{2\pi r_q} \times 10^3 \tag{10}$$

$$M_q = \frac{1}{2} \sum F \cdot r_q \times 10^{-3} \tag{11}$$

where:

n_q - maximum speed of the drive wheel, [r·min^{-1}];

r_q - radius of the drive wheel, 160 [mm];

M_q - driving torque, [N·m];

The drive wheel speed n_q = 24 r·min^{-1} and the drive torque M_q = 8000 N·m were calculated.

- **Determination of travel system operating pressure**

The operating environment of the crawler-type tiger-nut harvester consists of sandy loam. The hydraulic system's working pressure is initially set at 14 MPa, with a maximum pressure of 32 MPa *(Dong et al., 2005)*.

- **Parameterization of hydraulic motors**

The hydraulic motor output speed n_m, torque M_m and displacement V_m are as follows.

$$n_m = n_q \cdot i_1 \tag{12}$$

$$M_m = \frac{M_q}{i_1 \cdot \eta_1 \cdot \eta_2} \tag{13}$$

$$V_m = \frac{2\pi M_m}{\Delta P \cdot \eta_3} \tag{14}$$

The synthesized equation yields:

$$V_m = \frac{\pi F_q r_q}{\Delta P \cdot \eta_1 \cdot \eta_2 \cdot \eta_3 \cdot i_1} \tag{15}$$

where:

i_1 is the low-speed reduction ratio (field operation reduction ratio), 90;

η_1 is the hydraulic motor mechanical efficiency, taken as 0.95;

η_2 is the reduction gearbox mechanical efficiency, taken as 0.99;

η_3 is the hydraulic motor volumetric efficiency, taken as 0.95;

ΔP is the system pressure, MPa;

Bringing in the data, it was calculated that the motor speed m_n = 2160 r·min^{-1}, the torque applied to the motor M_m = 94.51 N·m, and the motor displacement V_m = 44.65 mL·r^{-1} during the stable operation of the harvester in the field.

- **Calculation of hydraulic pump parameters**

In the selected hydrostatic (HST) transmission system, the hydraulic pump and hydraulic motor are connected in an integrated closed-loop configuration. By ignoring system flow losses and using the motor displacement along with the desired operating speed, the system flow rate can be calculated. This flow rate is then used to determine the required displacement of the hydraulic pump V_p:

$$Q_m = \frac{n_m \cdot V_m}{1000\eta_3} \tag{16}$$

$$Q_p = Q_m \tag{17}$$

$$V_p = \frac{1000Q_p}{\eta_p \cdot \eta_4} \tag{18}$$

Available:

$$V_p = \frac{n_m \cdot V_m}{\eta_p \cdot \eta_3 \cdot \eta_4} \tag{19}$$

where:

Q_p is the hydraulic pump flow rate, [L·min^{-1}];

n_p is the pump power input speed, [r·min^{-1}];

η_4 is the hydraulic pump volumetric efficiency, 0.99;

The hydraulic pump output flow rate Q_p = 101.52 L·min^{-1} and the hydraulic pump displacement V_p = 44.58 mL·r^{-1} were calculated.

The displacement of the charge pump is 20-25% of the displacement of the variable pump, and the charge pressure is less than 3 MPa.

$$V_p' = (0.2 \sim 0.25) V_p \tag{20}$$

The charge pump displacement V'_p was calculated to be 8.92-11.15 mL·r^{-1} based on the data.

- **Other hydraulic components**

When designing and selecting tubing, fittings, and hydraulic fluid, the process should adhere to relevant national standards *(Standardization Administration of the People's Republic of China, 2021; Standardization Administration of the People's Republic of China, 2022)*, while considering factors such as connection reliability, sealing performance, pressure loss, and overall cost.

The inner diameter of the fuel line is calculated as follows:

$$d = \sqrt{\frac{4q}{\pi v_0}} \times 10^3 \quad (21)$$

where: d is the diameter of the hydraulic pipe, [mm];

q is the flow rate of the hydraulic fluid, [$m^3 \cdot s^{-1}$];

v_0 is the flow rate of the hydraulic fluid, taken as 4 $m \cdot s^{-1}$;

The calculated inner diameter was d = 18.3 mm. According to standard requirements, the hose inner diameter was specified as 20 mm, and appropriate tube fittings were selected accordingly.

- **Selection of hydraulic drives**

Based on the hydraulic principles and component parameters used in the design calculations, a Heckert HT series variable pump with a displacement of 46 $mL \cdot r^{-1}$ and a rated pressure of 16 MPa was selected, along with an integrated hydraulic drive unit consisting of a hydraulic pump and motor. The configuration is shown in Figure 5, and the corresponding parameters are listed in Table 3.



Fig. 5 - Hydraulic drive device

Table 3

Hydraulic drive device parameters

Parameters	Values
System displacement [$mL \cdot r^{-1}$]	46
Charge pump displacement [$mL \cdot r^{-1}$]	10
Rated pressure [bar]	160
Maximum pressure [bar]	320
Control system	mechanical servo
Maximum speed [$r \cdot min^{-1}$]	3300

RESULTS

Performance Tests

- **Site testing**

The field tests focused on evaluating the harvester's straight-line travel performance, response characteristics, and parking brake effectiveness on slopes, as well as measuring its maximum travel speed and operational stability.

- **Travel straightness test**

The straight-line movement test of the harvester is conducted according to the GB/T 15370.4-2012 standard *(Standardization Administration of the People's Republic of China, 2012)*. A 20 m correction zone and a 30 m test zone are defined within the test field. The test factors include the hydraulic pump displacement (maximum and intermediate displacements) and load size (no load, 200 kg load, and 500 kg load). The deviation rate is used as the performance indicator to assess the straightness of the movement process.

The travel offset rate was calculated based on the formula:

$$\Delta C = X_1 - X_2 \quad (22)$$

$$H = \frac{|\Delta C|}{S} \quad (23)$$

where: X_1 is the perpendicular distance between the track and the reference straight line before the test, [m];

X_2 is the perpendicular distance between the track and the reference straight line after the test, [m];

H is the offset rate, [%]; ΔC is the offset, [m]; S is the test distance, [m].

The results of the offset rates obtained for different operating conditions are shown in Table 4.

Table 4

Offset test results

Hydraulic pump displacement	Number of tests	Unladen	200 kg Load	500 kg Load
		Offset rate [%]	Offset rate [%]	Offset rate [%]
Maximum displacement	1	0.14	0.15	0.12
	2	0.09	0.12	0.19
	3	0.15	0.20	0.11
Intermediate displacement	1	0.10	0.15	0.12
	2	0.18	0.13	0.16
	3	0.16	0.12	0.14

The field test results show that the deviation rate of the harvester ranges from 0.09% to 0.20%, significantly lower than the standard requirement of 6%, demonstrating that the harvester exhibits excellent straight-line movement and that the hydraulic drive system fulfills the performance criteria. Additionally, the deviation rate remains relatively consistent across different displacements, indicating that the displacement of the hydraulic pump has a minimal effect on the straight-line movement performance. Furthermore, the deviation rate remains relatively consistent under different loads, suggesting that the hydraulic drive system demonstrates robust adaptability to different load conditions.

- **Travel speed measurement test**

The travel speed measurement test is conducted to verify the speed control stability of the designed hydraulic drive system and to determine the maximum field travel speed. The theoretical maximum travel speed of the designed harvester is calculated using the following formula:

$$n_{qm} = \frac{n_m}{i_2} \tag{24}$$

$$v_m = \frac{2\pi r_q \cdot n_{qm}}{60} \tag{25}$$

where: n_{qm} is the theoretical travel speed of the driving wheel, [r·min^{-1}];

n_m is the output speed of the hydraulic motor, [r·min^{-1}];

i_2 is the high speed reduction ratio, 30;

v_m is the maximum theoretical travel speed, [m·s^{-1}];

The maximum theoretical travel speed of the crawler-type tiger-nut harvester was calculated to be 1.18m·s^{-1}.

In the test field, a 50-meter distance was measured as the travel speed measurement interval. Buffer zones for acceleration and deceleration were marked 10 meters before and after the measurement interval. The central 30-meter section was divided into six equal intervals, each 5 meters in length. The time to traverse each 5-meter interval was recorded, and the speed for each interval, as well as the average speed over the entire section. The harvester was tested in an unloaded state under high gear conditions, with the control lever for speed pushed to its maximum, and the test was repeated three times. The 18 speed measurements obtained from the six segments across the three tests were processed as shown in Fig. 6.

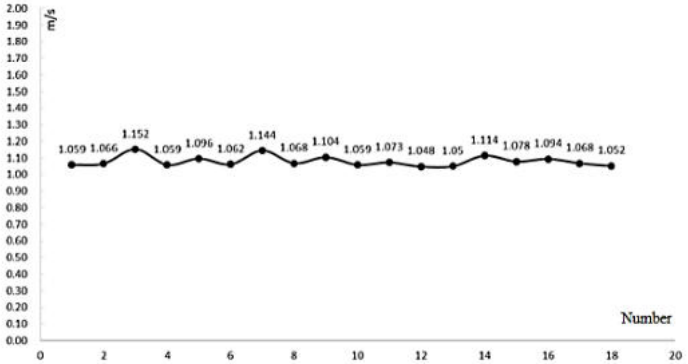


Fig. 6 - Speed stability analysis

As shown in Figure 6, the measured field travel speed ranged from 1.05 to 1.15 m·s^{-1}, with an average speed of 1.08 m·s^{-1} and a standard deviation of 0.03 m·s^{-1}. The overall data exhibited minimal fluctuation, with no significant outliers, indicating good speed stability of the hydraulic drive system. However, due to internal leakage within hydraulic components, track slippage, and other influencing factors, the maximum measured travel speed was slightly lower than the theoretical value of 1.18 m·s^{-1}. Nonetheless, the maximum travel speed of the harvester meets the design requirements, and the travel process remains stable and reliable.

- **Starting and braking performance tests**

The time required for the harvester to accelerate from rest to maximum speed is defined as the startup acceleration time, which reflects the responsiveness of the hydraulic drive system. The time for the harvester to decelerate from maximum speed to a complete stop is termed the braking deceleration time. Three measurements were conducted, and the average value was taken. The average values are shown in Table 5.

The relationship between the drive wheel speed monitored by the tachometer and the travel speed is described by the following equation:

$$n_q = \frac{60}{2\pi r_q} v \tag{26}$$

As can be seen from the speed test results in Fig. 6, the maximum travel speed obtained in the field test was 1.15 m·s^{-1}, which was substituted into the data to calculate the driving wheel speed at the maximum speed of 64.46 r·min^{-1}.

Table 5

Starting and braking performance measurement results

Ordinal number	Start-up acceleration time [s]	Brake deceleration time [s]
1	3.1	1.5
2	3.7	0.8
3	3.3	1.2
Average value	3.4	1.2

As shown in Table 5, the hydraulic drive system of the harvester demonstrates good startup and braking performance. The startup time is close to the simulation response time of 2.8 seconds, which also validates the accuracy of the simulation. The higher measured response time compared to the simulation may be due to the manual stopwatch measurement, which could introduce errors in reaction time.

- **Ramp parking brake test**

The ramp parking brake performance test was conducted in accordance with GB/T 3871.6-2006 *(Standardization Administration of the People's Republic of China, 2006)*. The harvester was driven steadily onto a ramp, and the engine was then shut off to perform parking brake tests in both uphill and downhill conditions. Each test maintained a parking duration of 3 minutes. The test setup is illustrated in Figure 7.



Fig. 7 - Ramp braking test

a. Uphill parking brake test *b. Downhill parking brake test*

The test results showed that the harvester remained stationary during the entire ramp parking duration, demonstrating excellent parking stability. This meets the test requirements and indicates that the hydraulic system provides reliable parking brake performance on slopes.

Field trials

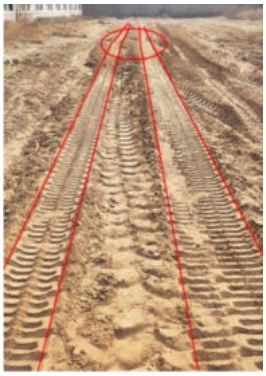
To comprehensively evaluate the performance of the harvester and its hydraulic drive system, field tests on straight-line driving and turning performance were conducted after the simulations and field trials of the hydraulic system.

- **Linear travel test**

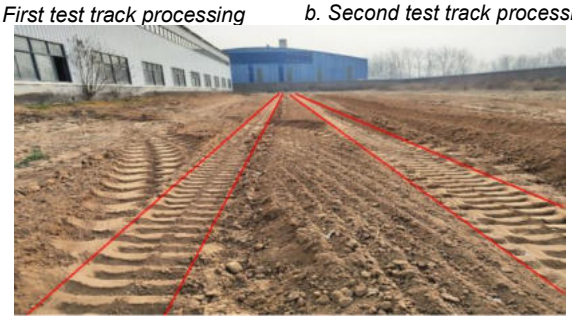
In a test field, the harvester was driven at maximum speed without adjusting the control handle to further assess the straight-line driving performance of the designed drive system. Three sets of tests were conducted, and the track marks were processed to evaluate the straight-line performance. The results are shown in Fig.8.



a. First test track processing



b. Second test track processing



c. Third test track processing

Fig. 8 - Field straight-line travel test

According to the field straight-line driving performance test, the harvester's deviation rate ranges from 1.19% to 2.10%. The sideways slipping of the harvester, caused by soft soil and subsidence, leads to a slightly higher deviation rate compared to the field test, but it still meets the national standard requirements. The test results indicate that the harvester has good straight-line driving performance, meeting the requirements for tiger-nut harvesting.

- **Field steering trials**

In order to verify the steering ability and steering radius of the harvester in the field, three tests were conducted with forward left and right turns respectively, and the steering test and radius measurement process are shown in Fig. 9, and the results are shown in Table 6.



Fig. 9 - Field turning test

Table 6

Field Turning Test Results

Serial number	Left Turning Radius [mm]	Right Turning Radius [mm]
1	2714	2807
2	2763	2726
3	2742	2711
Average value	2740	2748

The theoretical radius R_t is 2720 mm when steering in the field, and the average value of radius for forward left turn and forward right turn is 2740 mm and 2748 mm. There is a track offset within the permissible range when steering, and it can be accomplished by unilateral braking steering in the field as required.

CONCLUSIONS

(1) To improve the adaptability of the tiger-nut harvester and ensure stable harvesting operation, a hydraulic drive system for the crawler-type harvester was designed. The required displacement of the hydraulic motor was calculated to be 44.65 mL·r^{-1}, and the displacement of the hydraulic pump was determined to be 44.58 mL·r^{-1}. A unified hydrostatic drive unit with a displacement of 46 mL·r^{-1} and a system pressure of 16 MPa was selected.

(2) Field evaluations demonstrated that the harvester exhibits a straight-line deviation rate of 1.19–2.10% and an average travel speed of 1.08 m·s^{-1}. The effective implementation of the steering mechanism, which reliably regulates turning performance under various field conditions, confirms the system's capacity to achieve stable and efficient harvesting operations.

(3) Field trials in sandy loam soils show that the hydraulic drive system performs stably under varying loads and speeds, with low deviation and precise turning. These results confirm its reliability for tiger-nut harvesting and support further optimization and industrial application.

ACKNOWLEDGEMENTS

This research was supported by the Key R&D and Demonstration Program of Henan Province (Science and Technology Breakthrough) (Grant Nos. 252102110351 and 242102110378) and the National Key R&D Program of China (Grant No. 2019YFD1002602).

REFERENCES

[1] Cantalejo, J. M. (1997). Analysis of volatile components derived from raw and roasted earth-almond (cyperus esculentus L.). *Journal of Agricultural & Food Chemistry*, Vol.45, No.5, pp.1853-1860. Heidelberg/Germany.

[2] Dong, W. L. (2005). *Hydraulic design handbook*. China Machine Press, Beijing/China.

[3] Edo, G. I., Samuel, P. O., Nwachukwu, S. C., Ikpekoro, V. O., Promise, O., Oghenegueke, O., Ongulu, J., Otunuya, C. F., Rapheal, O. A., Ajokpaoghene, M. O., Okolie, M. C., & Ajakaye, R.S. (2024). A review on the biological and bioactive components of Cyperus esculentus L.: Insight on food, health and nutrition. *Journal of the Science of Food and Agriculture*, Vol.104, No.14, pp.8414–8429. UK.

[4] Guo, T., Zhang, D., Lin, S., Zhang, T., & Lu, M. (2025). Research on hydraulic drive chassis of tobacco harvester in southern hilly area. *INMATEH - Agricultural Engineering*, Vol.75, No.1, pp.819–830. DOI: https://doi.org/10.35633/inmateh-75-70

[5] Han, M. H. (2023). *Design and experiment of traveling device and hydraulic drive system for tiger-nut harvester (油莎豆收获机履带行走装置及其液压驱动系统的设计与试验)*. Master's dissertation, Henan Agricultural University, Zhengzhou/China.

[6] Ji, L. X. (2013). *Design and performance study of the rubber crawler combined with high-range sprayer. Master's dissertation (橡胶履带式喷雾机行走装置的设计及性能研究)*, Nanjing Forestry University, Nanjing/China.

[7] Jun, H.-J., Kang, T.-G., Lee, C.-S., Lee, C.-K., Choi, D.-K., & Choi, C. (2013). Development of a crawler type vehicle to travel in water paddy rice field for water-dropwort harvest. *Journal of Biosystems Engineering*, Vol.38, No.4, pp.240–247. Korea.

[8] Leggieri, S., Canali, C., & Caldwell, D. G. (2022). Design of the crawler units: Toward the development of a novel hybrid platform for infrastructure inspection. *Applied Sciences*, Vol.12, No.11, Article 5579. Switzerland.

[9] Liu, F. S. (2022). *Chassis optimization of crawler self-propelled potato harvester (履带自走式马铃薯收获机的底盘优化)*. Master's dissertation, Huazhong Agricultural University, Wuhan/China.

[10] Lv, X. R., Fu, Y., Cheng, X. P., Zhang, F. G., Len, Y. C., Han, D. D. (2024). Design and performance test of remote driving control system of small agricultural hydraulic chassis. *INMATEH – Agricultural Engineering*, Vol.72, No.1, pp.255–264. DOI: https://doi.org/10.35633/inmateh-72-24

[11] Lv, Y. L. (2022). *Design and experiment of excavating and hoisting device of cyperus esculentus harvester (油莎豆收获机挖掘升运装置设计与试验).* Master's dissertation, *Henan Agricultural University*, Zhengzhou/China.
[12] McBride, R. A., McLaughlin, N. B., & Veenhof, D. W. (2000). Performance of wheel and track running gear on liquid manure spreaders. *Canadian Agricultural Engineering*, Vol.42, No.1, pp.19–25. Canada.
[13] Pan, D. J. (2014). *The design of self-propelled machine integrating the function of fertilization and plant protection for growing grape and Chinese wolfberry (自走式枸杞葡萄施肥植保一体机的设计)*. Master's dissertation, Ningxia University, Yinchuan/China.
[14] Roselló-Soto, E., Poojary, M. M., Barba, F. J., Lorenzo, J. M., Manes, J., & Moltó, J. C. (2018). Tiger nut and its by-products valorization: From extraction of oil and valuable compounds to development of new healthy products. *Innovative Food Science and Emerging Technologies*, Vol.45, pp.306–312. Netherlands.
[15] Shang, S. Q., Wang, F. Y., Liu, S. G., Zhao, Z. H., & Wang, J. C. (2004). Research situation and development trend on peanut harvesting machinery (花生收获机械的研究现状与发展趋势). *Transactions of the CSAE*, Vol.20, No.1, pp.20–25. Shenyang/China.
[16] Standardization Administration of the People's Republic of China. (2006). *Agricultural tractors—Test procedures—Part 6: Determination of braking performance*. Beijing/China.
[17] Standardization Administration of the People's Republic of China. (2012). *General requirement of agricultural tractors—Part 4: Crawler tractors*. Beijing/China.
[18] Standardization Administration of the People's Republic of China. (2021). *Fluid power systems and components—Outside diameters of tubes and inside diameters of hoses*. Beijing/China.
[19] Standardization Administration of the People's Republic of China. (2022). *Rubber hoses and hose assemblies—Rubber-covered spiral-wire-reinforced hydraulic types for oil-based or water-based fluids*. Beijing/China.
[20] Wang, L., Hu, C., Guo, W. S., He, X. W., Wang, X. F., & Jian, J. M., et al. (2021). The effects of moisture content and loading orientation on some physical and mechanical properties of tiger nut. *American Journal of Biochemistry and Biotechnology*, Vol.17, No.1, pp.109–117. Ghana/Africa.
[21] Wei, Z. C., Wang, X. H., Li, X. Q., Wang, F. M., Li, Z. H., & Jin, C. Q. (2023). Design and experiment of crawler self-propelled sorting type potato harvester (履带自走式分拣型马铃薯收获机设计与试验). *Transactions of the Chinese Society for Agricultural Machinery*, Vol.54, No.2, pp.95–106. Zibo/China.
[22] Xu, Y. J. (2016). Design and research of a new type of cyperus esculentus harvesting machine (新型油莎豆收获机的设计与研究). Master's dissertation, *China Agricultural University*, Beijing/China.
[23] Zhang, H. M., Zhou, Z., Lv, Z. J., Wang, W. Z., He, H., & Lv, Y. L. (2021). Kinematic analysis and testing of vibratory sieving mechanism for cyperus esculentus L. harvester (油莎豆收获筛分机构运动学分析与试验). *Journal of Chinese Agricultural Mechanization*, Vol.42, No.10, pp.92–99. Zhengzhou/China.
[24] Zhang, X. M., & Dong, X. R. (2020). The impact of Sino-US trade war on China's soybean market (中美贸易战对我国大豆市场的影响). *Modern Business Trade Industry*, Vol.41, No.14, pp.19–20. Bengbu/China.
[25] Zhang, Z., Jiang, H., He, X., Zhang, F., Wang, J., & Wang, D. (2024). Design and test of threshing and cleaning device for Cyperus esculentus L. combine harvester. *INMATEH - Agricultural Engineering*, Vol.72, No.1, pp.798–808. DOI: https://doi.org/10.35633/inmateh-72-71
[26] Zhao, Y., Liu, W., Song, S., Liu, P., Wang, Y., & Zhang, G. (2025). Design of the leveling system for the wheeled adaptive chassis in hilly and mountainous areas. *INMATEH - Agricultural Engineering*, Vol.75, No.1, pp.253–268. DOI: https://doi.org/10.35633/inmateh-75-22

DETECTION METHOD OF COTTON COMMON PESTS AND DISEASES BASED ON IMPROVED YOLOv5S
/
基于改进 YOLOV5S 的棉花常见病虫害检测方法

Yulong WANG[1,2,3,#], Fengkui ZHANG[1,2,3,#], Rina YANGDAO[1,2,3], Ruohong HE[1,2,3], Jikui ZHU[1,2,3], Ping LI[1,2,3,*]

[1)] College of Mechanical and Electrical Engineering, Tarim University, Alar, Xinjiang, 843300, China

[2)] Xinjiang Production and Construction Corps (XPCC) Key Laboratory of Utilization and Equipment of Special Agricultural and Forestry Products in Southern Xinjiang, Xinjiang, China

[3)] Modern Agricultural Engineering Key Laboratory at Universities of Education Department of Xinjiang Uygur Autonomous Region, Xinjiang, China

[#]These authors contributed equally to this work and should be considered co-first authors.

[*]*Corresponding Author. Email: lpdyy716@163.com*

DOI: https://doi.org/10.35633/inmateh-76-18

Keywords: *Cotton, pest and disease, YOLOv5s, lightweight, target detection*

ABSTRACT

To address the low recognition accuracy and slow detection speed of cotton leaf pests and diseases in natural environments, a detection method based on an improved YOLOv5s model was proposed. The enhanced model integrates the Ghost module and the C3Faster module to increase inference speed and reduce model complexity, achieving lightweight performance without significantly compromising accuracy. To counteract the tendency of common cotton pest and disease features to be lost in complex natural scenes, a Coordinate Attention (CA) mechanism was introduced to improve the network's recognition and localization capabilities. The parameters, FLOPs, and weight file size of the improved model were reduced to 65.5%, 66.2%, and 67.1% of those of the original YOLOv5s model, respectively. On a self-built dataset, the improved YOLOv5s model achieved a mean average precision (mAP) improvement of 10.5%, 0.2%, and 0.4% compared to YOLOv4, YOLOv5s, and YOLOv7, respectively. The model was deployed on a Jetson Orin NX development board with CUDA acceleration, achieving a real-time detection speed of 76.3 frames per second.

中文摘要

针对自然环境中棉花叶片病虫害识别精度低、识别速度慢的问题，提出了一种基于改进YOLOv5s的检测方法。该方法基于YOLOv5s模型，通过结合Ghost模块和C3Faster模块来提高推理速度，实现模型轻量化，而不会显著影响准确性。由于棉花常见病虫害的特征在自然环境中很容易丢失，因此添加了CA注意机制模块，以帮助轻量级网络提高识别和定位能力。改进后的模型参数、FLOP和权重文件大小分别为YOLOv5s的65.5%、66.2%和67.1%。将自建数据集与YOLOv4、YOLOv5s和YOLOv7进行比较，结果表明，改进的YOLOv5模型的平均准确率分别提高了10.5%、0.2%和0.4%。改进后的模型部署在Jetson Orin NX开发板上，并使用CUDA加速。加速模型检测速度为76.3帧/秒。

INTRODUCTION

Cotton is the seed fiber of malvaceous cotton plants in subtropical regions and is one of the most important economic crops in the world. China's cotton planting area and yield account for 9.82% and 23.76% of the world, respectively, with Xinjiang having the largest cotton planting area and yield. In 2024, China's cotton planting area reached 2,838.3 thousand hectares, with a total output of 6.164 million tons. Xinjiang accounted for 2,447.9 thousand hectares of the planting area and 5.686 million tons of the total yield, representing 86.2% and 92.2% of the national totals, respectively. The yield and quality of cotton are affected mainly by pests and diseases. The common pests and diseases of cotton in Xinjiang mainly include yellow wilt disease, aphids, and brown spots *(Chen et al., 2018; Lou et al., 2018; Zhao et al., 2023).* Currently, cotton pests and diseases in Xinjiang mainly rely on the application of plant-protection machinery. During operation, the precision of spraying is poor, making it difficult to accurately and effectively prevent different types of pests and diseases.

Yulong WANG, Master Student; Fengkui ZHANG, lecturer; Rina YANGDAO, Master Student; Ruohong HE, Master Student; Jikui ZHU, lecturer; Ping LI, Professor.

As the computer technology progresses, prevention and control of cotton pests and diseases have evolved from being initially determined by experienced experts to using computer technology and deep learning algorithms to determine pest and disease varieties and control measures. To apply the target detection technology to plant protection machinery, the first step is to solve the problems of a large model, slow recognition speed, and low recognition accuracy.

The YOLO algorithm has been widely used in the detection of crop pests and diseases due to its fast inference speed and high accuracy. YOLO is highly suitable for real-time agricultural applications by directly predicting object classes and positions on feature maps (*Ganesan and Chinnappan, 2022; Amarasingam et al., 2022; Apacionado and Ahamed, 2023; Wang et al., 2023a; Cruz et al., 2022*). In recent years, various YOLO-based models have been applied to crops such as rice, corn, tomato, and cotton (*Masykur et al., 2023; Chen and Yang, 2023; Azath et al., 2021; Susa et al., 2022; Sangaiah et al., 2024*). To improve the detection accuracy in complex field conditions, several enhancements have been proposed. *Shi et al. (2023)* introduced the SimAM attention mechanism into YOLOv5s, improving the accuracy except the model size. *Liu et al. (2023)* upgraded YOLOv7 with deformable convolutions, SENet, and Focal-EIOU loss, enhancing the performance at the cost of increased complexity. *Li and Wang (2020)* used image pyramids in YOLOv3 to boost multi-scale detection without reducing model weight. *Zhang et al. (2023)* applied CBAM to YOLOv7 for cotton disease detection to increase the accuracy without reducing FLOPs. *Wang et al. (2023b)* proposed YOLOv4-G using GhostNet and Ghost modules to improve the accuracy, while the memory usage remained high.

To address the problems of large amounts of calculation and difficult feature extraction in the detection model, an improved model based on YOLOv5s was proposed. The lightweight is convenient for the model to be deployed on mobile devices, and the attention mechanism is added to improve the ability to extract important features of the image, providing a theoretical basis for the automation prevention and control of cotton common pests and diseases.

MATERIALS AND METHODS

Image acquisition

Common pests and diseases, such as cotton yellow wilt disease, aphids, and brown spots were selected as the research objects. The cotton pest and disease image dataset were collected from June to September 2023 at the cotton experimental station of Tarim University, using an iPhone14 camera. To meet the diversity of the natural environment, images of different weather conditions were collected at different times, including sunny days, windy days, morning, noon, etc. A total of 2322 cotton pest and diseases were collected. To improve the robustness of model training and avoid overfitting, the collected pictures were horizontally flipped and randomly cropped to expand the dataset. Finally, 4232 pictures of cotton pests and diseases were obtained. The expanded data were screened and pictures with excessive blur, inconsistent features, and excessive differences in actual shooting were deleted. A total of 4000 pictures were selected as the image dataset for cotton pests and diseases. There were 797 pictures of yellow wilt disease, 1065 pictures of aphids, 1422 pictures of brown spots, and 716 pictures of healthy leaves. Some of the collected images are shown in Fig. 1.

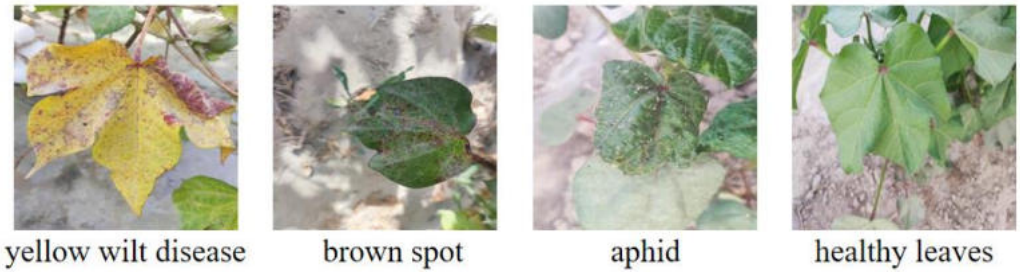


Fig. 1 - Pictures of cotton common pests and diseases

Dataset producing

The cotton pest and disease dataset were labeled with Libeling. Libeling is an open-source data labeling tool that can label tow formats: VOC and YOLO. These 4000 images in the dataset were manually labeled as yellow wilt disease, aphid, brown spot, and healthy leaves. The storage format is a VOC tag format and the file format is an xml file. The code was used to convert the xml format annotation file into a txt format annotation file, which was randomly divided into a training set and a verification set at a proportion of 80%. There were 3203 pictures in the training set and 797 in the verification set.

YOLOv5s algorithm network model

YOLOv5s is a target detection network model in the YOLOv5 series with small model parameters. Because of its small model volume and fast inference speed, it is particularly suitable for real-time target detection tasks deployed on mobile devices or edge computing devices. The model consists of four parts: the input end, Backbone Network, Feature fusion Network Neck and Head Network. In this study, enhancements to the YOLOv5s model are presented, and the architecture of the improved network is illustrated in Fig. 2.

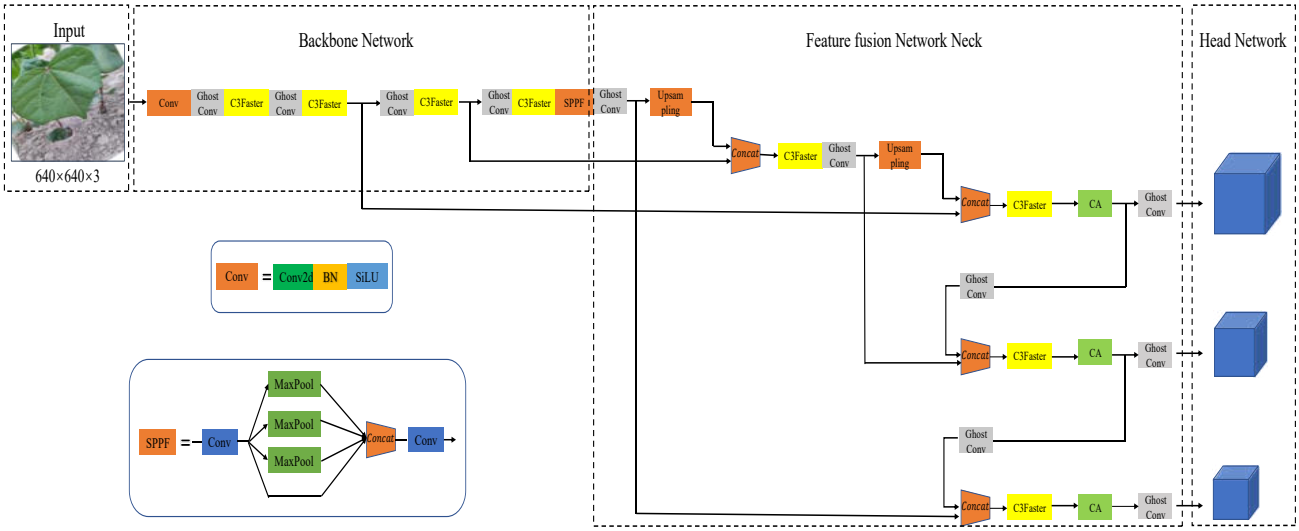


Fig. 2 - Improved YOLOv5s network model structure

Note: The Conv module consists of Conv2d + BN + SiLU, where BN denotes Batch Normalization and SiLU is the activation function. Concat represents tensor concatenation, SPPF stands for Spatial Pyramid Pooling-Fast, and Maxpool denotes the Max Pooling operation. Ghost Conv is the convolution module within the Ghost module used in this study, highlighted with a gray background in the figure. C3Faster refers to the C3Faster module employed in this study, highlighted with a yellow background in the figure. CA represents the CA attention mechanism module used in this study, highlighted with a green background in the figure.

The input end is primarily used for adaptive anchor frame calculation, adaptive image scaling, and mosaic data augmentation *(Passos et al., 2023)*. Mosaic data enhancement is an extension of YOLOv4, which can increase data diversity and model robustness and improve small target detection performance by splicing, flipping, and color gamut changes on four random images. The main structure of the backbone includes Conv, C3, and SPPF modules. After the image enters the neural network through the input end, the backbone network extracts feature and continuously narrows the feature map. The role of the feature fusion Network Neck is to obtain relatively shallow features from the Backbone Network and then stitch them together with deep semantic features. The Head Network contains three prediction branches, which extract feature information to predict targets of different sizes and obtain the category, confidence, and location information of the predicted targets *(Lan et al., 2024).*

Introducing lightweight modules Ghost and C3Faster

In practical applications, it is often necessary to deploy the model on mobile devices to achieve real-time detection. Mobile devices do not possess the computing power of computers. At this point, it is necessary to reduce the calculation time and improve the calculation speed of the model to successfully deploy the model. Based on the YOLOv5s model, all convolutions except the first ordinary convolution are replaced by Ghost Conv, and all C3 modules in the original model are replaced by C3Faster to realize the lightweight of the model and improve the calculation speed while ensuring accuracy.

The Ghost module *(Zeiler and Fergus, 2014)* is a novel plug-and-play component. Since Ghost convolution constitutes the core of the Ghost module, this paper exclusively employs Ghost convolution and refers to the module accordingly. The Ghost module is distinguished by its ability to generate more feature maps using fewer parameters. Initially, intrinsic feature maps are produced through conventional convolution. Subsequently, Ghost feature maps are generated via linear transformation *(Li et al., 2019).* Finally, the intrinsic feature maps and the Ghost feature maps are concatenated to form the final output. The specific structures are shown in Fig. 3.

FasterNet is used to improve the feature expression ability and receptive field coverage while maintaining light weight and high speed *(Shi et al., 2024)*. The network consists of four stages, and its architecture is illustrated in Fig. 4. Based on the YOLOv5s model, the C3Faster module is proposed. It replaces all C3 modules of the original model with C3Faster to reduce the redundancy of calculations and memory

access, thereby improving the efficiency of the neural network. It also improves the efficiency of the floating-point operation per second of the model through partial convolution PConv, thereby achieving high-speed operation on mobile devices while ensuring accuracy.

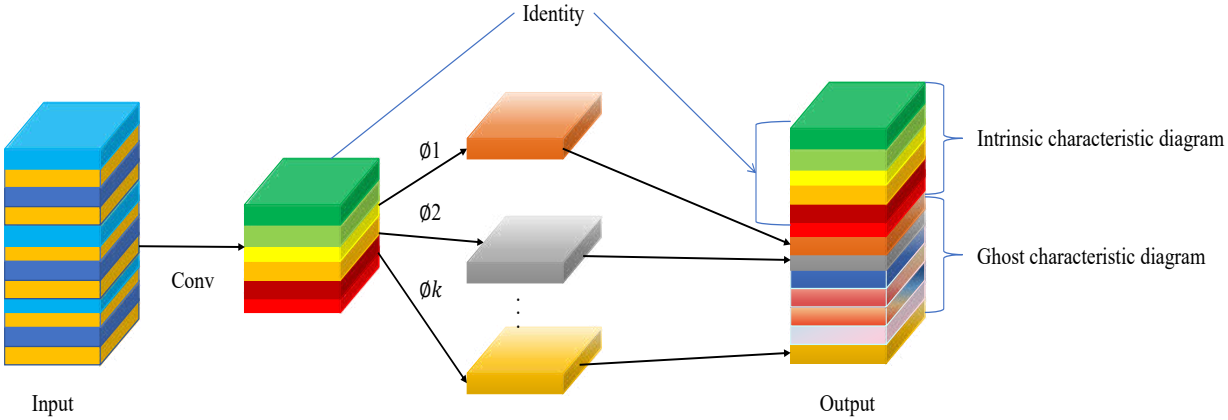


Fig. 3 - Ghost module

Note: Conv represents standard convolution, ∅ denotes linear transformation operations, and Identity signifies the identity mapping.

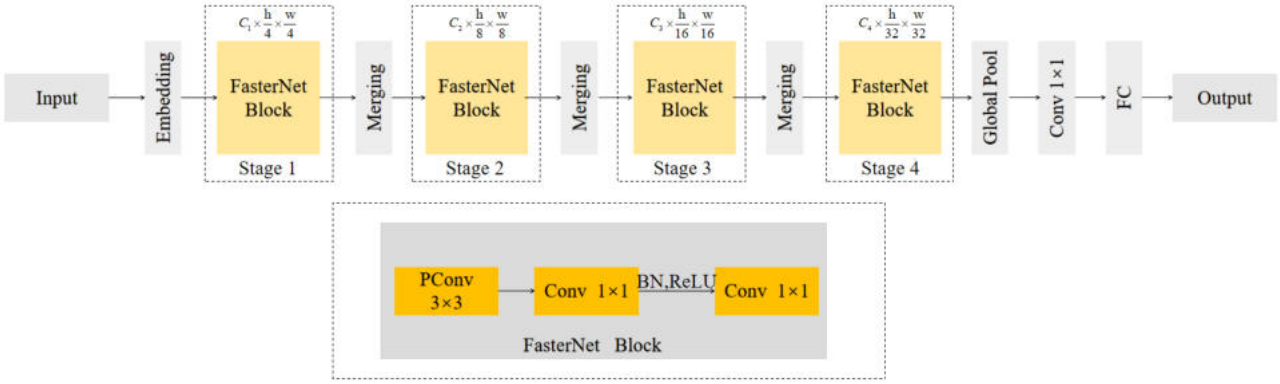


Fig. 4 - FasterNet network architecture

Note: C_x denotes the number of image channels; h represents image height; w represents image width; FasterNet Block refers to a specific module; PConv stands for partial convolution; Conv denotes standard convolution; BN represents Batch Normalization; and ReLU signifies the activation function.

Introducing CA attention mechanism module

In the natural environment, cotton leaves grow densely, and the background is complex. It is difficult for the YOLOv5 model to extract important features of pests and diseases, and the detection results will be misjudged or unrecognized. To improve the extraction effect of the YOLOv5s model on small features, in the neck part of the feature fusion network, a CA (Hou et al., 2021) attention mechanism module was added after other C3 2_1 modules to help the lightweight network rise points. A flowchart of the CA attention mechanism module is shown in Fig. 5(a).

To capture remote spatial interaction with precise location information, global average pooling is decomposed. The specific formula is as follows:

$$z_c^h(h) = \frac{1}{W} = \sum_{0 \le i < W} x_c(h,i) \tag{1}$$

$$z_c^w(w) = \frac{1}{H} = \sum_{0 \le j < H} x_c(j,w) \tag{2}$$

where z_c^h is the height feature diagram representing the output of channel *c*, z_c^w is the width feature diagram representing the output of channel *c*, $x_c(h,i)$ is the input of channel *c* along the *h* direction, and $x_c(j,w)$ is the input of channel *c* along the *w* direction. An input feature diagram with a size of C×H×W is collected in the X- and Y-directions, respectively, and those with a size of C×H×1 and C×1×W are generated, respectively, as shown in Fig. 5(b).

After obtaining the two-feature diagrams, the generated C×H×1 and C×1×W feature diagrams were transformed, spliced, and calculated as follows:

$$f = \delta(F_1([Z^h, Z^w])) \tag{3}$$

where δ is a nonlinear activation function and F_1 is a convolution transformation function. After splicing z^h and z^w, the feature map shown in Fig. 5(b) was generated. F_1 operation (using a 1×1 convolution kernel for dimensionality reduction) and activation operation are performed to generate feature diagram f.

A feature diagram f is generated, and the split operation is performed along the spatial dimension, which is divided into f^h and f^w. A 1×1 convolution was used to increase the dimension, and then the sigmoid activation function was combined to obtain the final attention vectors g^h and g^w. The formula used is as follows:

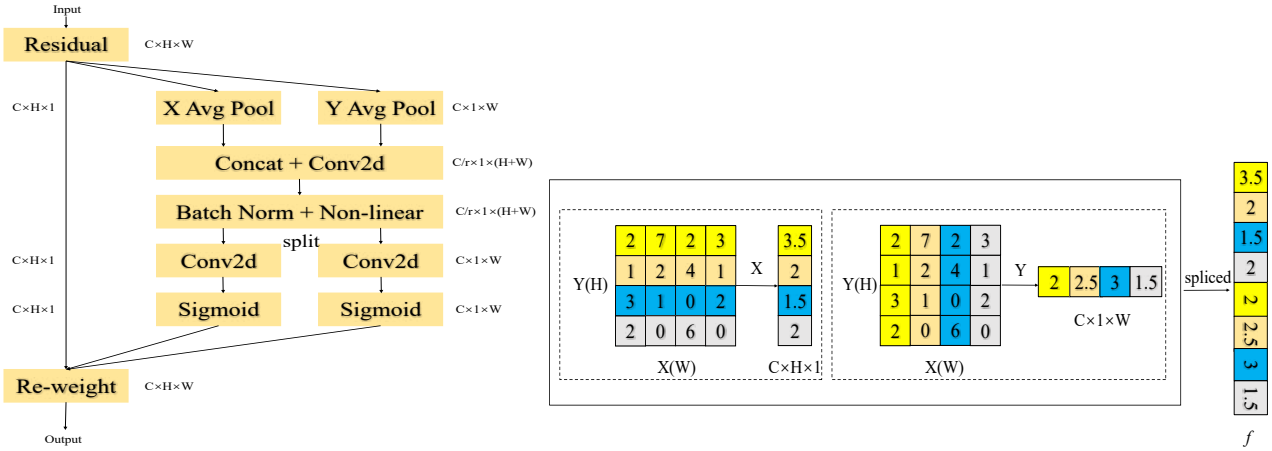
$$g^h = \sigma(F_h(f^h)) \tag{4}$$

$$g^W = \sigma(F_W(f^W)) \tag{5}$$

where σ is the sigmoid activation function, and F_h and F_w are the dimension-up operations. The output formula of the final CA attention mechanism module is as follows:

$$y_c(i,j) = x_c(i,j) \times g_c^h(i) \times g_c^w(j) \tag{6}$$

where $y_c(i,j)$ is the output of channel *c*, $x_c(i,j)$ is the input of channel *c*, $g_c^h(i)$ is the attention vector of channel *c* along the *h* direction, and $g_c^w(j)$ is the attention vector of channel *c* along the *w* direction.



a. CA attention mechanism module flow chart b. C×H×1 and C×1×W characteristic diagram and characteristic diagram *f*

Fig. 5 - CA attention mechanism module

Note: In Figure 5-a, C denotes the number of channels, H represents image height, W represents image width, X Avg Pool refers to horizontal average pooling, Y Avg Pool refers to vertical average pooling, Conv2d denotes the 2D convolution operation, Non-linear represents the non-linear activation function, Sigmoid is the activation function, and Re-weight stands for the weight file. In Figure 5-b, spliced refers to the concatenation operation.

Training environment deployment and parameter adjustment

The hardware environment in this experiment was a CPU 13th Gen Intel (R) Core (TM) i9-13900KF, 3.00GHz, running memory 32.0GB, GPU Nvidia GeForce RTX 4090, operating system Windows 11-64 bit. Deep learning frameworks such as PyCharm2021, Pytorch1.11, and Python3.8, were used to optimize, train, and evaluate the model.

The training parameters of the model were an image input size of 640 × 640, training of 500 rounds, batch size of 16, and maximum working core of 16. The optimizer used was the stochastic gradient descent method, the initial learning rate was 0.001, the learning rate momentum was 0.937, and the weight attenuation coefficient was 0.0005.

Evaluation index

The precision, P, recall rate, R, and mean average precision, mAP, in the training results were used to measure the recognition performance of the model. Parameters, weight file, and FLOPs were used to measure the complexity of the model. Precision P represents the proportion of correctly detected samples to all detected samples. The formula is as follows:

$$P = \frac{TP}{(TP + FP)} \tag{7}$$

The recall rate R denotes the proportion of correctly detected samples to all samples that are expected to be detected and is calculated as follows:

$$R = \frac{TP}{(TP + FN)} \tag{8}$$

The average accuracy mean mAP is the average of the APs of all classes. The average accuracy AP is the area of the P–R curve as a measure of the performance of the multiclass target detection model. The formula is as follows:

$$mAP = \frac{\sum_{i=1}^{N} \int_0^1 P(R)dR}{N} \times 100\% \tag{9}$$

where TPrepresents the number of true positives (samples correctly detected by the model), FP represents the number of false positives (samples incorrectly detected by the model), FN represents the number of false negatives (samples that should have been detected but were missed), and N represents the number of detection categories. The constructed dataset included three types of cotton pests and diseases, along with healthy leaves as a separate category, resulting in a total of four classes ($N = 4$).

RESULTS AND ANALYSIS

Performance comparison of YOLOv5s-FasterCA model ablation test

To clarify the influence of the Ghost, C3Faster, and CA attention mechanism modules on the performance of the YOLOv5s model, ablation tests were conducted using a self-made dataset of common pests and diseases in cotton. The test results are listed in Table 1. It can be seen from Table 1 that in the original network, using the Ghost module and C3Faster module instead of the ordinary convolution module and C3 module can significantly reduce the model parameters, calculation, and weight file, with little reduction in the precision P, recall rate R, and mean average precision mAP. From the experimental results, it can also be seen that only when the CA attention mechanism module is added are the precision P and mean average precision mAP of the original network model increased by 0.7% and 0.4%, respectively. The recall rate R is slightly decreased, and the parameters, floating-point calculation, and weight file are also slightly increased.

Table 1

YOLOv5s model ablation test

Ghost module C3Faster module	CA attention mechanism	Precision *P* / %	Recall rate *R* / %	Mean average precision *mAP* / %	Parameters / ×10⁶M	Weight file size / MB	FLOPs / G
×	×	88.7	92.4	93.4	7.03	13.7	16.0
√	×	88.3	91.8	92.7	4.58	9.14	10.5
×	√	89.4	92.1	93.8	7.06	13.8	16.1
√	√	89.5	91	93.6	4.61	9.20	10.6

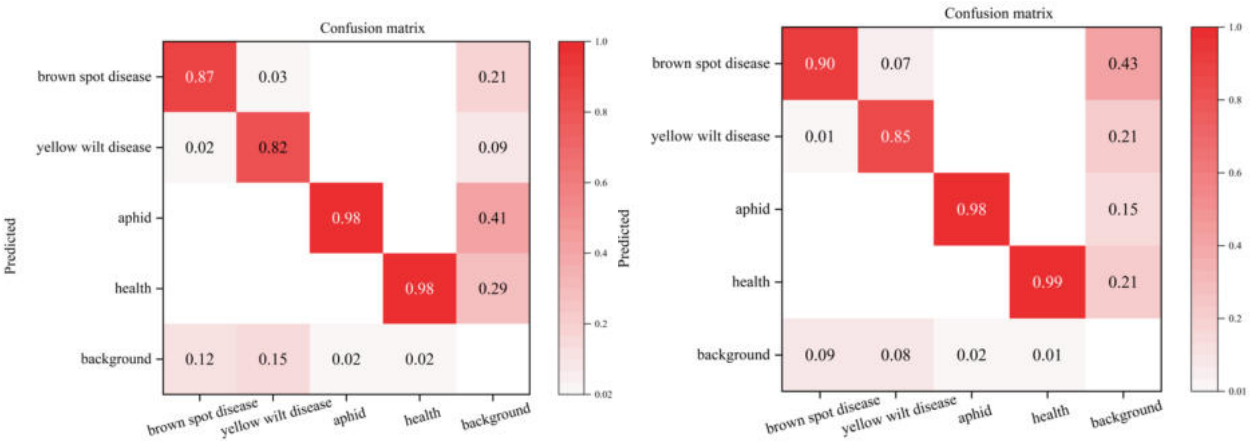
Note: √ indicates the inclusion of the module, while × denotes its exclusion.

Through the ablation test results, under the premise of realizing the lightweight model and ensuring recognition accuracy, the YOLOv5s-FasterCA model is obtained by adding the Ghost, C3Faster, and CA attention mechanism modules to the YOLOv5s model. In the detection and recognition of common cotton pests and diseases, the model parameters were 4.61 × 10^6 M; the FLOPs were 10.6G, and the weight file was 9.20 MB. Compared with the original model, the above parameters were reduced by 34.5%, 33.8%, and 32.9%, respectively, and the accuracy and average accuracy were improved by 0.8% and 0.2%, respectively. This indicates that the YOLOv5s-FasterCA model can improve the recognition accuracy of common cotton pests and diseases while meeting the lightweight requirements.

Performance comparison between YOLOv5s-FasterCA model and original model

To further verify the performance of the improved model, the YOLOv5s original model and YOLOv5s-FasterCA models were used to train and test the dataset of common cotton pests. The model performance was measured by a confusion matrix diagram, P _ curve diagram, R _ curve diagram, and PR _ curve diagram.

From Fig. 6(b), the improved model has a 3% increase in the probability of detecting brown spot disease, a 1% decrease in the probability of misjudging yellow wilt disease, and a 3% increase in the probability of detecting yellow wilt disease compared to Fig. 6(a). There was no change in the probability of aphid detection or a 1% increase in the probability of detecting healthy leaves. It can be seen from the confusion matrix that compared with the original model that the improved model can improve the precision and reduce the probability of misjudgment, indicating that the improved model is better than the original model.

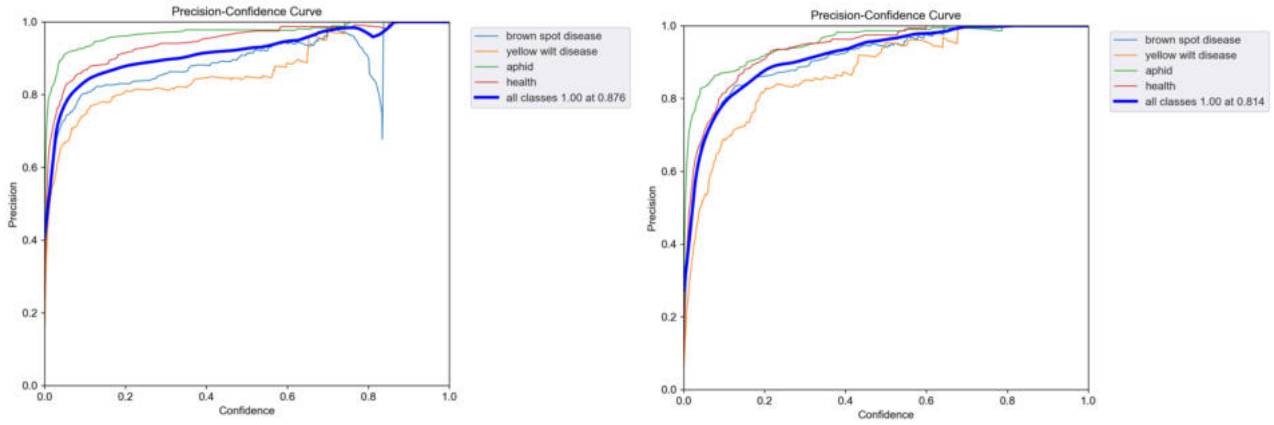


(a) YOLOv5s (b) YOLOv5s-FasterCA

Fig. 6 - Confusion_matrix

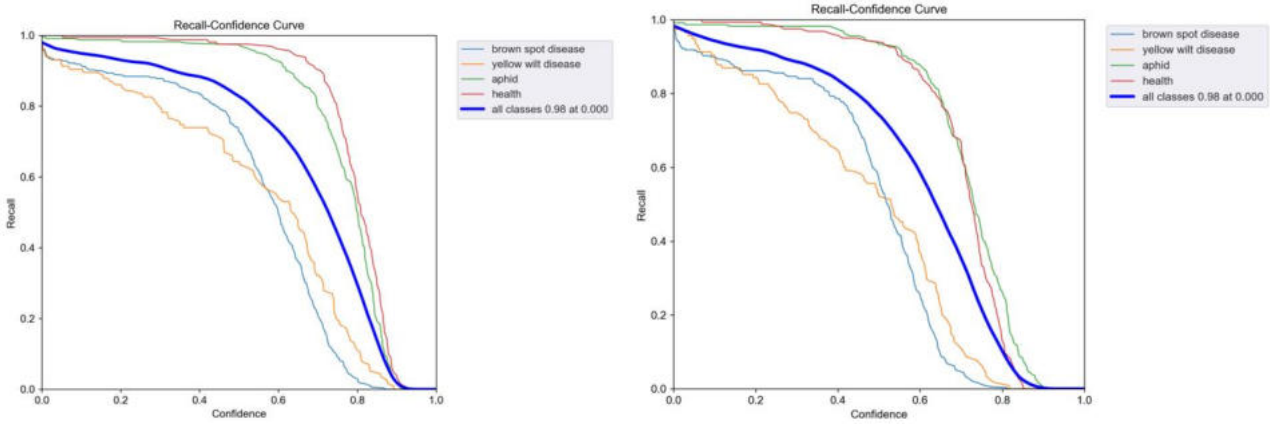
To compare the accuracy and confidence of the improved and original models, the P _ curve graph was used to display the changes in the recognition accuracy of the model for each category under different confidence thresholds.

As shown in Fig. 7(b), the highest confidence of the improved model was 0.814, which was 0.062 lower than that of the original model (Fig. 7(a)). This indicates that the improved model can achieve optimal accuracy when the confidence level is 0.814. Compared with the original model, it can reduce the possibility of missed detection when the confidence threshold is low.



(a) YOLOv5s (b) YOLOv5s-FasterCA

Fig. 7 - P _ curve comparison diagram



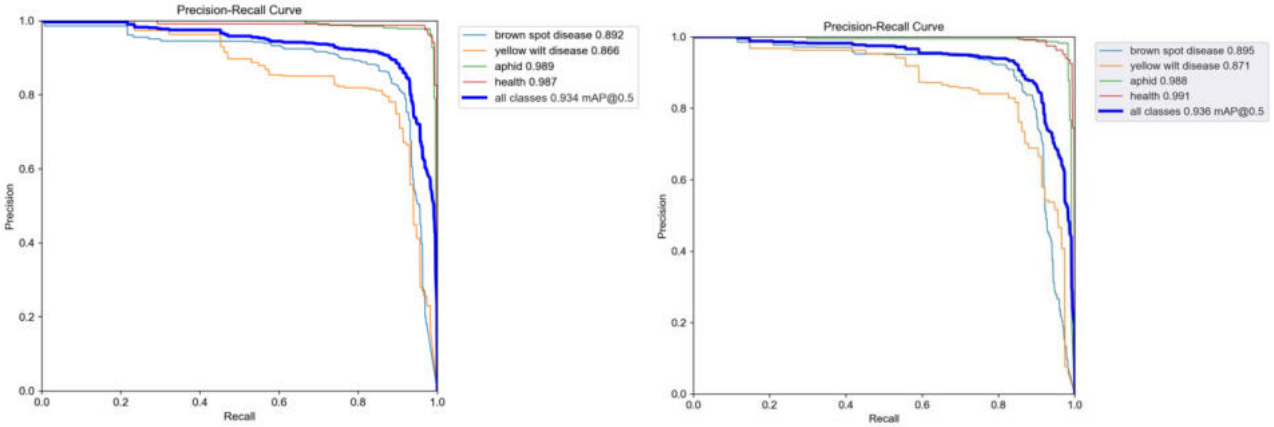
(a) YOLOv5s (b) YOLOv5s-FasterCA

Fig. 8 - R _ curve comparison diagram

To compare the precision and recall rates of the improved model and the original model, the R _ curve diagram was used to display the probability of recall of each category when the confidence was a certain value.

It can be seen from Fig. 8 that when confidence is small, category detection is more comprehensive. Through comparison, it was found that when the confidence level was 0.98, the recall rates of the improved model and the original model were 0.

To compare the accuracy and recall rate of the improved and original models, the PR_curve diagram shows the changes in accuracy with the recall rate. From Fig. 9(b), compared with Fig. 9(a), the improved model has a 0.3% higher accuracy in detecting brown spot disease, a 0.5% lower accuracy in detecting yellow wilt disease, a 0.1% lower accuracy in detecting aphids, a 0.4% higher accuracy in detecting healthy leaves, and a 0.2% improvement in accuracy for all types of mAP.



(a) YOLOv5s (b) YOLOv5s-FasterCA

Fig. 9 - PR _ curve comparison diagram

Performance comparison between YOLOv5s-FasterCA model and different models

The improved YOLOv5s-FasterCA model was compared with YOLOv4, YOLOv5s, and YOLOv7 on a self-built dataset. All models were trained using the same dataset and identical training parameters, and the results are shown in Table 2.

The mean average precision of the YOLOv5s-FasterCA model was 10.5%, 0.2%, and 0.4% higher than that of the other three models. The detection time of a single image was 1ms slower than that of the original model (which can be ignored). This indicates that the detection accuracy and recognition speed of the model meet the requirements for the real-time detection of common cotton pests and diseases.

Table 2

Performance comparison of different models

Modules	Precision P/%	Recall rate R/%	Mean average precision mAP/%	Parameters/×10^{6}M	Weight file size /MB	FLOPs/G	Detect/ms
YOLOv4	78.8	79.42	83.1	64.33	249.7	60.4	37
YOLOv5s	88.7	92.4	93.4	7.03	13.7	16.0	7
YOLOv7	90.2	92.6	93.2	70.83	135	188.9	41
YOLOv5s-FasterCA	89.5	91	93.6	4.61	9.20	10.6	8



Fig. 10 - Comparison of model detection effects in natural environment

Identification of common pests and diseases of cotton in natural environment

It can be seen from Table 2 that the model parameters, weight files, and FLOPs calculations of YOLOv4 and YOLOv7 are too large to meet the lightweight requirements of the model. Only the YOLOv5 and the improved YOLOv5s-FasterCA models were deployed on the Jetson Orin NX development board to detect common cotton pests and diseases under the same natural environment in the test dataset. The results are shown in Fig. 10. The detection results indicate that the YOLOv5s model may fail to identify certain pest and disease types under complex background. In contrast, the improved YOLOv5s-FasterCA model can significantly reduce false detections and missed detections, demonstrating better performance in accurately identifying common cotton pests and diseases, even in challenging environments. Furthermore, after acceleration with CUDA, the YOLOv5s-FasterCA model achieved a detection speed of 76.3 FPS on the Jetson Orin NX development board, meeting the requirements for real-time detection.

CONCLUSIONS

(1) An improved target detection model, YOLOv5s-FasterCA, was proposed by integrating Ghost and C3Faster modules to replace the standard convolution and C3 modules in the original YOLOv5s. The Coordinate Attention (CA) mechanism was introduced. The improved model achieved a precision of 89.5% and a mean average precision (mAP) of 93.6%, 0.8% and 0.5% higher than the original YOLOv5s respectively. In addition, the parameter count, FLOPs, and weight file size of the model were significantly reduced, meeting the requirements for lightweight deployment.

(2) The comparative experiments showed that the mAP of YOLOv5s-FasterCA was 10.5%, 0.2%, and 0.4% higher than those of YOLOv4, YOLOv5s, and YOLOv7, respectively. Although the improvement in single-frame inference time compared to YOLOv5s was minimal (reduced by approximately 1ms), the enhanced model demonstrated excellent detection performance in complex natural environments. It can effectively reduce false and missed detections of common cotton pests and diseases under real field conditions.

(3) The recognition accuracy and robustness of the YOLOv5s-FasterCA model are improved in unstructured field environments. With CUDA acceleration, it achieved a real-time detection speed of 76.3 frames per second on the Jetson Orin NX development board, making it suitable for mobile deployment scenarios with limited computing resources. However, when encountering unseen or unmarked types of pests and diseases, the model may exhibit decreased recognition performance or misclassify them as known categories. Future work will improve generalization ability by expanding datasets and implementing anomaly detection strategies.

ACKNOWLEDGEMENT

This study was financially supported by the Bingtuan Science and Technology Program (Grant No. 2022DB001). The authors are grateful to anonymous reviewers for their comments.

REFERENCES

[1] Amarasingam, N., Gonzalez, F., Salgadoe, A.S.A., Sandino, J., & Powell, K. (2022). Detection of White Leaf Disease in Sugarcane Crops Using UAV-Derived RGB Imagery with Existing Deep Learning Models. *Remote Sensing*. 14(23): 6137. https://doi.org/10.3390/rs14236137

[2] Apacionado, B.V., & Ahamed, T. (2023). Sooty Mold Detection on Citrus Tree Canopy Using Deep Learning Algorithms. *Sensors.* 23(20): 8519. https://doi.org/10.3390/s2320851

[3] Azath, M., Zekiwos, M., & Bruck, A. (2021). Deep Learning-Based Image Processing for Cotton Leaf Disease and Pest Diagnosis. *Journal of Electrical and Computer Engineering.* 2021: 9981437. https://doi.org/10.1155/2021/9981437

[4] Chen, B., Wang, G., Liu, J.D., Ma, Z.H., Wang, J., & Li. T.N. (201)8. Extraction of Photosynthetic Parameters of Cotton Leaves under Disease Stress by Hyperspectral Remote Sensing. *Spectroscopy and Spectral Analysis.* 38(06): 1834-1838. https://doi.org/10.3964/iissn 1000-0593(2018)06-1834-05

[5] Chen, H.L., & Yang, W. (2023). The Technology of Kiwifruit Pest and Disease Identification Based on Deep Learning. *2023 4th International Conference on Intelligent Computing and Human-Computer Interaction (ICHCI), Guangzhou, China, IEEE*. 38-42. Doi:10.1109/ICHCI58871.2023.10277869

[6] Cruz, M., Mafra, S., Teixeira, E., & Figueiredo, F. (2022). Smart Strawberry Farming Using Edge Computing and IoT. *Sensors*. 22(15): 5866. https://doi.org/10.3390/s22155866

[7] Ganesan, G., & Chinnappan. J. (2022). Hybridization of ResNet with YOLO classifier for automated paddy leaf disease recognition: An optimized model. *Journal of Field Robotics*. 39(7): 1085-1109. https://doi.org/10.1002/rob.22089

[8] Hou, Q.B., Zhou, D.H., Feng, J.S. (2021). Coordinate attention for efficient mobile network design. *2021 IEEE/CVF Conference on Computer Vision and Pattern Recognition (CVPR), Nashville, TN, USA, IEEE*. 13713-13722. https://doi.org/10.1109/CVPR46437.2021.01350

[9] Lan, Y.B., Shun, B.S., Zhang, L.C., & Zhao, D.N. (2024). Identifying diseases and pests in ginger leaf under natural scenes using improved YOLOv5s *(基于改进 YOLOv5s 的自然场景下生姜叶片病虫害识别). Transactions of the Chinese Society of Agricultural Engineering*. 40(01): 210-216. Doi:10.11975/j.issn.1002-6819.202310124

[10] Li, G., Yun, I.Y., Kim, J.H., & Kim, J.K. (2019). Dabnet: Depth-wise asymmetric bottleneck for real-time semantic segmentation. arXiv preprint arXiv:1907.11357. https://doi.org/10.48550/arXiv.1907.11357

[11] Li, J., & Wang, X.W. (2020). Tomato Diseases and Pests Detection Based on Improved YoloV3 Convolutional Neural Network. *Frontiers in Plant Science*. 11: 898. https://doi.org/10.3389/fpls.2020.00898

[12] Liu, S.Y., Hu, B., & Zhao, C. (2023). Detection and identification of cucumber leaf diseases based improved YOLOv7*(基于改进 YOLOv7 的黄瓜叶片病虫害检测与识别). Transactions of the Chinese Society of Agricultural Engineering*. 39(15): 163-171. Doi:10.11975/j.issn.1002-6819.202305042 *(In Chinese)*

[13] Lou, Z.X., Xin, F., Han, X.Q., Lan, Y.B., Duan, T.Z., & Fu, W. (2018). Effect of Unmanned Aerial Vehicle Flight Height on Droplet Distribution, Drift and Control of Cotton Aphids and Spider Mites. *Agronomy.* 8(9): 187. https://doi.org/10.3390/agronomy8090187

[14] Masykur, F., Adi, K., & Nurhayati, O.D. (2023). Approach and Analysis of Yolov4 Algorithm for Rice Diseases Detection at Different Drone Image Acquisition Distances. *Tem Journal.* 12(2): 928-935. https://doi.org/10.18421/tem122-39

[15] Passos, W. L., Barreto, C. D. S., Araujo, G. M., Haque, U., Netto, S. L., & da Silva, E. A. (2023). Toward improved surveillance of Aedes aegypti breeding grounds through artificially augmented data. *Engineering Applications of Artificial Intelligence.* 123(Part C): 106488. https://doi.org/10.1016/j.engappai.2023.106488

[16] Sangaiah, A.K., Yu, F.N., Lin, Y.B., Shen, W.C., & Sharma, A. (2024). UAV T-YOLO-Rice: *An Enhanced Tiny Yolo Networks for Rice Leaves Diseases Detection in Paddy Agronomy. IEEE Transactions on Network Science and Engineering.* 11(6): 5201-5216. DIO:10.1109/TNSE.2024.3350640

[17] Shi, J., Lin, S.S., Luo, J.G., Yang, L.L., Zhang, Y.J., & Gu, L.C. (2023). Study on a detection method for crop diseases and insect pests based on YOLO v5s improved model *(基于 YOLO v5s 改进模型的玉米作物病虫害检测方法). Jiangsu Agricultural Sciences.* 51(24): 175-183. DOI:10.15889/j.issn.1002-1302.2023.24.024 *(In Chinese)*

[18] Shi, L., Lei, J.K., Wang, J., Yang, C.K., Liu, Z.H., Xi, L., & Xiong, S.F. (2024). Lightweight Wheat Growth Stage Identification Model Based on Improved FasterNet *(基于改进 FasterNet 的轻量化小麦生育期识别模型)*. Transactions of the Chinese Society for Agricultural Machinery. 55(5): 226-234. *(In Chinese)*

[19] Susa, J.A.B., Nombrefia, W.C., Abustan, A.S., Macalisang, J., & Maaliw, R.R. (2022). Deep Learning Technique Detection for Cotton and Leaf Classification Using the YOLO Algorithm. *2022 International Conference on Smart Information Systems and Technologies (SIST), Sultan, Kazakhstan, IEEE.* 1-6. DIO:10.1109/SIST54437.2022.9945757

[20] Wang, W.X., Liu, Z.Q., Gao, P., Liao. F., Li, Q., & Xie, J.X. (2023b). Detection of Litchi Diseases and Insect Pests Based on Improved YOLOv4 Model *(基于改进 YOLO v4 的荔枝病虫害检测模型). Transactions of the Chinese Society for Agricultural Machinery*. 54(05): 227-235. Doi:10.6041/j.issn.1000-1298.2023.05.023 *(In Chinese)*

[21] Wang, Y.K., Xu, R.J., Bai, D., & Lin H.F. (2023a). Integrated Learning-Based Pest and Disease Detection Method for Tea Leaves. *Forests.* 14(5): 1012. https://doi.org/10.3390/f14051012

[22] Zeiler, M.D., & Fergus, R. (2014). Visualizing and understanding convolutional networks. arXiv:1311.2901. https://doi.org/10.48550/arXiv.1311.2901

[23] Zhang, N.N., Zhang, X., Bai, T.C., Shang, P., Wang, W.H., & Li, L. (2023). Identification Method of Cotton Leaf Pests and Diseases in Natural Environment Based on CBAM-YOLO v7 *(基于 CBAM-YOLO v7 的自然环境下棉叶病虫害识别方法). Transactions of the Chinese Society for Agricultural Machinery*. 54(S1): 239-244. Doi:10.6041/j.issn.1000-1298.2023.S1.025 *(In Chinese)*

[24] Zhao, H.X., Shao, M.Y., Pan, P., Wang, Z.A., Mu, Q., He, Z.K., & Zhang, J.H. (2023). A Training Dataset for Deep Neural Network Model Recognition of Common Cotton Diseases *(一种面向深度神经网络模型的棉花常见病害训练数据集). Journal of Agricultural Big Data*. 5(04): 47-55. DOI: 10.19788/j.issn.2096-6369.230405 *(In Chinese)*

DESIGN AND EXPERIMENT OF AN AIR-ASSISTED, GUIDED-GROOVE MAIZE SEED-GUIDING DEVICE BASED ON THE BRACHISTOCHRONE CURVE

/

基于最速降线的气辅-导槽式玉米导种装置设计与试验

Wen-sheng SUN [1)], Shu-juan YI[*1)], Hai-long QI [2)], Yi-fei LI [1,3)], Yu-peng ZHANG [1)], Jia-sha YUAN [1)], Song WANG [1)]

[1)]College of Engineering, Heilongjiang Bayi Agricultural University, Daqing/P.R.China

[2)]Heilongjiang Beidahuang Modern Agricultural Service Group Zhongrong Agricultural Machinery Co., Ltd, Harbin / P.R.China

[3)]College of Engineering, Northeast Agricultural University, Harbin/P.R.China

Tel: +86-459-13836961877; E-mail: yishujuan_2005@126.com

Corresponding author: Shu-juan Yi

DOI: https://doi.org/10.35633/inmateh-76-19

Keywords: *maize, seed-guiding device, brachistochrone, parameter optimization, CFD*

ABSTRACT

To address the issue that existing seed-guiding devices struggle to meet the high-speed operational requirements of delta-row planters for dense maize planting, a seed-guiding device with air assistance and a guided groove was designed based on the principle of the brachistochrone. The overall structure and working principle of the device are described, and the curved segment of the seed guide tube was optimized using the brachistochrone principle while accounting for frictional effects. Computational fluid dynamics (CFD) simulations were conducted to analyse the flow field characteristics of the seed guide tube at inlet airflow velocities of 63.48, 60.64, 57.73, 54.69, 51.50, and 48.15 m/s. A multi-factor test was performed using chamber pressure and operating speed as test factors, with the qualified index of grain spacing and the coefficient of variation as evaluation metrics. Comparative tests were conducted using a traditional guided-groove seed guide tube and a brachistochrone-based seed guide tube without a guided groove. Results showed that the optimal parameter combination for the newly designed device was a chamber pressure of 3.124 kPa and an operating speed of 12.0 km/h. Under these conditions in the bench test, the qualified index reached 97.04%, and the coefficient of variation was 6.18%, outperforming the other two types of seed-guiding devices. These findings demonstrate that the seed-guiding device based on the brachistochrone principle can significantly improve the seeding quality of delta-row planters for dense maize planting under high-speed operation.

摘要

针对现有导种装置难以满足玉米品字形密植播种机高速作业需求的问题，基于最速降线原理设计了一种气辅-导槽式导种装置。阐述了导种装置的总体结构与工作原理，根据考虑摩擦力下的最速降线原理对导种管曲线段进行了优化设计，得到了曲线段轮廓的解析方程。通过 CFD 仿真试验探究了导种管在入口流速分别为 63.48、60.64、57.73、54.69、51.50、48.15m/s 时的流场特性。以腔室压力与作业速度为试验因素，以粒距合格指数、粒距变异系数为试验指标开展了多因素试验，确定了导种装置最优参数组合并对其进行了试验验证，同时开展了与传统导槽式导种装置、无导槽最速降线式导种装置的对比试验。结果表明：该导种装置的最优工作参数组合为腔室压力 3.124 kPa、作业速度 12.0 km/h，台架验证该参数组合下的粒距合格指数为 97.04%、粒距变异系数为 6.18%，并且较另外两种导种装置表现出了更优的导种性能，说明基于最速降线原理设计的气辅-导槽式导种装置可以进一步提高玉米密植播种机在高速作业条件下的播种质量。

INTRODUCTION

Maize precision planting refers to the process of sowing single maize seeds into a predetermined soil seedbed position with a precision planter according to the sowing density required by local agronomy, in accordance with consistent row spacing, uniform grain spacing and precise depth *(Zhao et al., 2024; Sun et al., 2024)*.

[1]*Wen-sheng Sun, Ph.D.; Shu-juan Yi, Prof. Ph.D.; Hai-long Qi, bachelor degree; Yi-fei Li, Ph.D.; Yu-peng Zhang, master degree; Jia-sha Yuan, master degree; Song Wang, Ph.D.*

The seed-guiding mechanism is one of the final links in the maize precision planting process, ensuring that seeds enter the soil in a uniform and orderly manner. It not only maintains the orderly state of seeds achieved in the preceding steps but also directly influences the uniformity of seed distribution in the field *(Yatskul et al., 2018; Liao et al., 2020)*. However, the random movement of maize seeds from the seed-metering device into the seed-guiding unit, combined with collisions within the guide, disrupts the smooth flow of seeds. This results in deviations from the intended placement in the seedbed, ultimately reducing sowing quality.

Extensive research has been carried out by agricultural machinery companies and researchers to address the issue of maize seed misplacement caused by collisions during the seed-guiding process. The U.S.-based company Precision Planting developed a belt-type seed-guiding device that uses a conveyor belt to transport maize seeds from the seed-metering device to the seed outlet. By matching the conveyor speed with the planter's operating speed, the system ensures consistent seed spacing under varying operating conditions. The Swedish company Vaderstad introduced an airflow-projection seed-guiding device, which utilizes positive pressure airflow to constrain and rapidly project seeds into the soil through a seed guide tube, enabling high-speed maize planting. *Dong Jianxin et al., (2023),* designed a guided seed-casting mechanism that optimizes the seed guide trajectory, enhancing the seed placement accuracy of attitude-controlled drive-guided seed-metering devices under high-speed conditions. *Li Yuhuan et al. (2020)* achieved linear seed-throwing of maize under high-speed conditions by incorporating a seed-pushing mechanism into an air-suction high-speed precision seed-metering device, in coordination with specially shaped holes on the seed-metering plates. *Liu Rui et al. (2023)* designed a seed-guiding device based on the Venturi principle, utilizing positive pressure airflow assistance to effectively address the issue of seeds failing to enter the seedbed in an orderly, single-grain manner due to violent collisions. The brachistochrone theory, which addresses the optimization of velocity and path selection *(Adetifa et al., 2021)*, has also been applied in the optimal design of curved structures in agricultural machinery components. *Tang Han et al. (2023)* applied the brachistochrone theory to the structural design of the curved section of the seed guide tube in an internally-filled, air-blowing seed-metering device. Bench tests showed that, under a working pressure of 4.5 kPa and a working speed of 41 r/min, the seed spacing qualified index and the coefficient of variation reached 96.56% and 9.58%, respectively. Similarly, *Jia Xian et al. (2024)* optimized the seed-guiding curve of a gravity-type seed guide tube based on the brachistochrone principle. Bench test results indicated that the coefficient of variation was reduced by approximately 3% compared to that of a traditional gravity-type seed guide tube within the operating speed range of 9.0 to 14.4 km/h. However, due to the high installation precision and compatibility required between the seed-guiding device and the seed-metering unit, current seed-guiding devices struggle to meet the operational demands of high-speed delta-row planters for dense maize planting.

To improve the seeding quality of high-speed delta-row planters for dense maize planting, a seed-guiding device with air assistance and a guided-groove structure was designed based on the principle of the brachistochrone. The curved segments of the seed guide tube were optimized using the brachistochrone curve while accounting for friction, and were combined with a guided-groove structure to constrain seed movement under high-speed positive pressure airflow. This study provides a technical reference for enhancing the performance of seed-guiding devices in high-speed planters for dense maize planting.

MATERIALS AND METHODS

Overall structure and working principle

As shown in Fig. 1, the seed-guiding device primarily consists of a pressure relief wheel and its connecting frame, a seed-discharge tube, a transition tube, a seed guide tube, and suppression wheels. To coordinate with the seed discharge operation of the seed-metering device *(Sun et al., 2024)*, key components such as the pressure relief wheels, seed-discharge tube, transition tube, seed guide tube, and suppression wheels are symmetrically arranged. Two identical pressure relief wheels are installed inside the corresponding shaped holes at the seed-unloading points of the two seed-metering plates. These wheels serve to block airflow and ensure that seeds are smoothly discharged from the plates into the seed-discharge tube. To maintain the sealing integrity of the air-pressure seed-metering system and to allow smooth transfer of seeds detached from the plates, the seed-discharge tube is integrated into the device shell. The transition tube serves to connect the seed-discharge tube with the seed guide tube.

As the core working part of the whole seed-guiding device, the seed guide tube consists of linear and curved segments, and the upper and lower combined guided-groove structures are set to produce a restraining

effect on the movement of the seeds passing through the seed guide tube. The key structural parameters of the seed guide tube *(Yi et al., 2025)*, such as the outer diameter d_1 of the tube body is 21 mm, the inner diameter d_2 of the tube body is 17 mm, the length L_1 of the seed guide tube is 550 mm, the width H_1 is 100 mm, the length L_2 of the linear section is 310 mm, the length L_3 of the curved section is 240 mm, the guided-groove height L_4 is 355 mm, the width w_1 of the upper guided-groove is 1.3 mm, the width w_2 of the lower guided-groove is 2.2 mm. According to the agronomic requirements of narrow-wide-row delta-row dense planting area of maize in Heilongjiang province, the spacing L of narrow-single-row is 18~20 cm, the spacing L_0 of narrow-double-row is half of the spacing L, and the spacing H of narrow-row is 13 cm. Therefore, the row spacing of the two seed guide tubes is 13 cm.

The seed-guiding device can be divided into three functional zones based on the working process: the seed-delivery zone, the seed-attracting zone, and the seed-attaching zone. After the seed-metering device delivers seeds to the seed-unloading points, the pressure relief wheel blocks the inner side of the corresponding holes at these points, causing the seeds to lose the pressure attachment force. As a result, the seeds enter the seed-delivery zone vertically under the combined action of gravity and airflow. Within the seed-delivery zone, seeds sequentially pass through the seed-discharge tube, the transition tube, and the straight segment of the seed guide tube, accelerating as they fall. When the seeds enter the seed-attracting zone, a pressure difference is generated between the inside and outside of the tube due to the influence of the guided-groove structure. This pressure difference creates an additional pressure field that causes the seeds to move toward the end of the seed guide tube while simultaneously shifting toward the guided groove under the action of this pressure field. Once the seed is stably attached to the guided groove, it enters the seed-attaching zone, where it moves along the inner sidewall of the groove toward the seed-throwing point under the combined forces of gravity, airflow, and friction. Finally, the seed exits the seed guide tube at the seed-throwing point and is pressed into its predetermined position in the seedbed by the suppression wheels, completing the seed-guiding process. Through the staggered discharge timing of the seed-metering device and the orderly regulation provided by the seed-guiding device, maize seeds are accurately placed in the seedbed to form a narrow-row, delta-row sowing pattern.

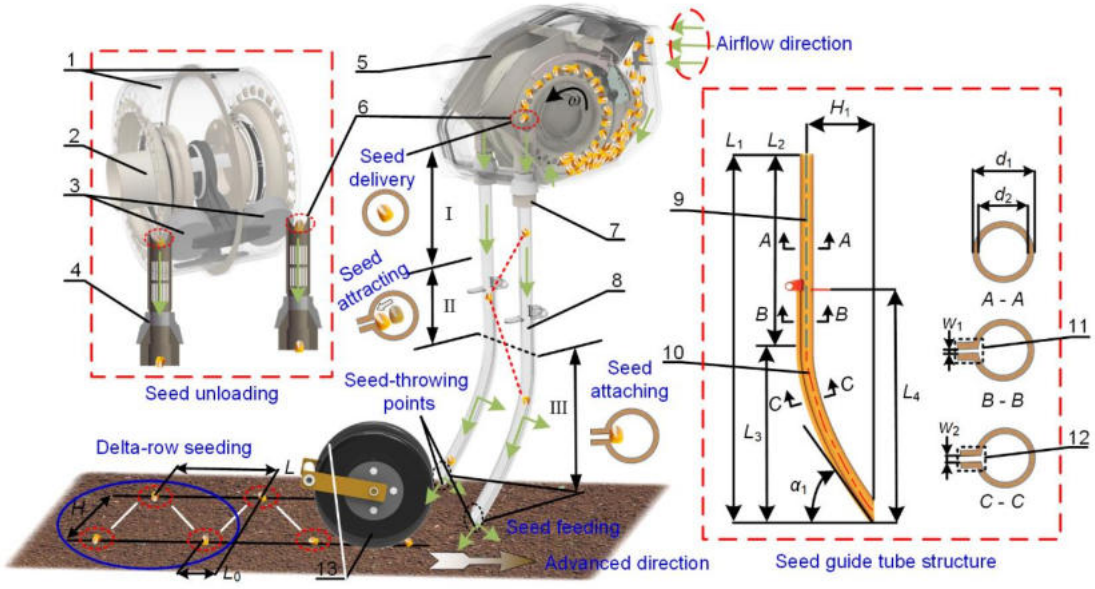


Fig. 1 - Overall structure and working principle

1. seed-metering plates; 2. connecting frame; 3. pressure relief wheel; 4. seed-discharge tube; 5. seed-metering device; 6. seed-unloading point; 7. transition tube; 8. seed guide tube; 9. linear segment; 10. curved segment; 11. upper guided-groove; 12. lower guided-groove; 13. suppression wheels; I. seed-delivery zone; II. seed-attracting zone; III. seed-attaching zone.

Design of curved segments of the seed guide tubes

Under high-speed operating conditions of planters for dense maize planting, the movement of seeds upon detachment from the seed-metering plates becomes highly random. This increased randomness leads to a higher frequency of seed collisions within the seed-guiding device, ultimately reducing seeding uniformity *(Fanigliulo et al., 2022; Ma et al., 2023)*.

Studies have shown *(Li et al., 2023)* that the curve structure designed based on the principle of the brachistochrone is conducive to the improvement of irregular seed mobility and seed-throwing uniformity.

Therefore, in this study, the structural design of the curved segments of the seed guide tubes was carried out based on the principle of the brachistochrone.

As shown in Fig. 2, according to the principle of the brachistochrone, the equation of the curve trajectory (l_1) that takes the shortest time for the maize seed to go from point *A* to point *B* when friction is not considered is:

$$\begin{cases} x = R_1\left(\frac{\pi\theta_1}{180} - \sin\theta_1\right) \\ y = R_1(1-\cos\theta_1) \end{cases} \quad (1)$$

where:

R_1 is the radius of the circle in the *Axy* coordinate system, m; θ_1 is the rolling angle of rotation of the circle in the *Axy* coordinate system, (°).

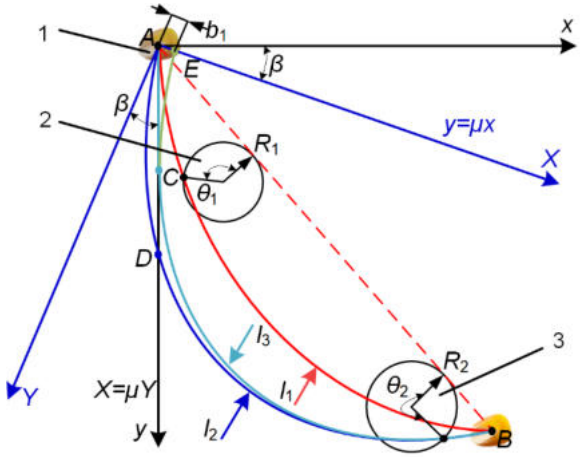


Fig. 2 - Schematic diagram of the combined brachistochrone curve

1. maize; 2. circle in the Axy coordinate system; 3. circle in the AXY coordinate system.

The velocity v_1 at any point during the fall of the seed is:

$$v_1 = \frac{ds}{dt} = \frac{\sqrt{1+y'^2}}{dt}dx \quad (2)$$

where:

s is the length of any curve arc, m; *t* is the time, s; y' is the first-order derivative of the curve trajectory equation.

Assuming that the seed slides tightly against the surface without bouncing, the angle *φ* of the seed during the fall tends to zero. After considering friction, the change ΔE in kinetic energy of the seed during its descent from point *A* according to the kinetic energy theorem is:

$$\Delta E = d\left(\frac{1}{2}mv_1^2\right) = mgdy - \mu mg\cos\varphi ds \Rightarrow v_1 = \sqrt{2g(y-\mu x)} \quad (3)$$

where:

m is the mass of the seed, m; g is the acceleration of gravity, m/s^2; *μ* is the rolling friction coefficient between the maize seed and the seed guide device; *φ* is the angle between the normal direction of the seed's location and the vertical direction, (°); x, y are the coordinates of the seed's position in the *Axy* coordinate system, m.

The time T taken by the seed to travel from point *A* to point *B* can be expressed as:

$$T = \int dt = \int_0^{x_B} \frac{\sqrt{1+y'^2}dx}{\sqrt{2g(y-\mu x)}} \quad (4)$$

Eq. (4) is solved by rotating the *Axy* coordinate system clockwise by an angle *β* to obtain the *AXY* coordinate system under friction, and:

$$\beta = \arctan\mu \quad (5)$$

$$y - \mu x = \frac{Y}{\cos\beta} \quad (6)$$

Eq. (4) is then transformed into:

$$T = \int_0^{x_B} \sqrt{\frac{(1+Y'^2)\cos\beta}{2gY}}\,dX \tag{7}$$

where:

x_B is the horizontal coordinate of point *B*, m.

However, from Fig. 2, it can be seen that the curve *AD* (l_2) enters the *x*<0 region, and the velocity of the seed at point *D* is less than its free fall velocity from point *A*, indicating that the curve *AD* is not the optimal path. When the brachistochrone curve is translated from point *A* to point *E* along the direction of the *X*-axis, the seed falls from point A to point C along the boundary $X = \mu Y$, and then along the curve *CB* to point *B*, the time T used is:

$$T = \sqrt{\frac{2y_C}{g}} + \int_0^{x_B} \frac{\sqrt{1+y'^2}dx}{\sqrt{2g(y-\mu x)}} \tag{8}$$

where:

y_C is the longitudinal coordinate of point *C*, m.

But the position of point C is not fixed, and there may be changes when it occurs:

$$\delta T = \frac{1}{\sqrt{2gy_C}}\left(1 - \frac{y'}{\sqrt{1+y'^2}}\right)\delta y_C \tag{9}$$

When the time T takes the minimum value, the point C needs to satisfy the condition:

$$\begin{cases} \delta T = 0 \\ y' = \infty \end{cases} \tag{10}$$

At this time, the brachistochrone curve *CB* is tangent to the *y*-axis, and its trajectory equation in the *AXY* coordinate system is:

$$\begin{cases} X = R_2\left(\frac{\pi\theta_2}{180} - \sin\theta_2\right) + b_1 \\ Y = R_2(1-\cos\theta_2) \end{cases} \tag{11}$$

where: X, Y is the position coordinate of the *AXY* coordinate system, m; R_2 is the radius of the circle in the *AXY* coordinate system, m; θ_2 is the rolling angle of rotation of the circle in the *AXY* coordinate system, (°); b_1 is the amount of translation of the brachistochrone curve along the *X*-axis direction, m.

Also, the coordinates of point *C* satisfy the following conditions:

$$\begin{cases} X_C = R_2\left(\frac{\pi\theta_C}{180} - \sin\theta_C\right) + b_1 \\ Y_C = R_2(1-\cos\theta_C) \\ X_C = \mu Y_C \\ \left.\frac{dX}{dY}\right|_C = \frac{1-\cos\theta_C}{\sin\theta_C} = \mu \end{cases} \tag{12}$$

where: X_C, Y_C is the positional coordinate of point *C* in the *AXY* coordinate system, m; θ_C is the rolling angle of rotation of the circle in point *C*, (°).

Obtained from Eq. (12):

$$\mu = \tan\frac{\theta_C}{2} = \tan\beta \tag{13}$$

And then there's:

$$b_1 = R_2(2\mu - 2\arctan\mu) \tag{14}$$

The μ is 0.0931 *(Sun et al., 2024)*, and substituting into Eq. (13) yields θ_C of 10.64° and β of 5.32°, and then substituting into Eq. (14) yields $b_1/R_2 = 5\times10^{-4}$. According to the above dimensional parameters of the seed guide tube, the coordinates of the point *A* in the *Axy* coordinate system are (0, 0), and the coordinates of the point *B* are (0.1, 0.24). According to the coordinate transformation formula:

$$\begin{bmatrix} X \\ Y \end{bmatrix} = \begin{bmatrix} \cos\beta & \sin\beta \\ -\sin\beta & \cos\beta \end{bmatrix}\begin{bmatrix} x \\ y \end{bmatrix} \tag{15}$$

the coordinates of point *A* in the *AXY* coordinate system are found to be (0, 0) and the coordinates of point *B* are (0.122, 0.230). Substituting the coordinates of point *B* in the *AXY* coordinate system and $b_1/R_2 = 5\times10^{-4}$ into Eq. (11) yields the rolling angle θ_B at point *B* as 84.45°, R_2 as 0.255, and b_1 as 1.27×10^{-4}. The analytical equation (l_3) for the combined brachistochrone curve AB considering friction is obtained as:

$$\begin{cases} AC: Y = 10.74X \\ CB: \begin{cases} X = 0.255 \times \left(\dfrac{\pi\theta_2}{180} - \sin\theta_2\right) + 1.27 \times 10^{-4} \\ Y = 0.255 \times (1 - \cos\theta_2) \end{cases} \end{cases} \quad (16)$$

By substituting θ_C into Eq. (16), the coordinates of point *C* in the *AXY* coordinate system are calculated as (4×10^{4}, 4×10^{-3}), and the value range of the θ_2 is 10.64~84.45°. Based on the analytical equation (l_3), the curve corresponding to the seed guide tube trajectory was plotted, as shown in Fig. 3. The curved segment of the seed guide tube was then designed in accordance with this trajectory equation.

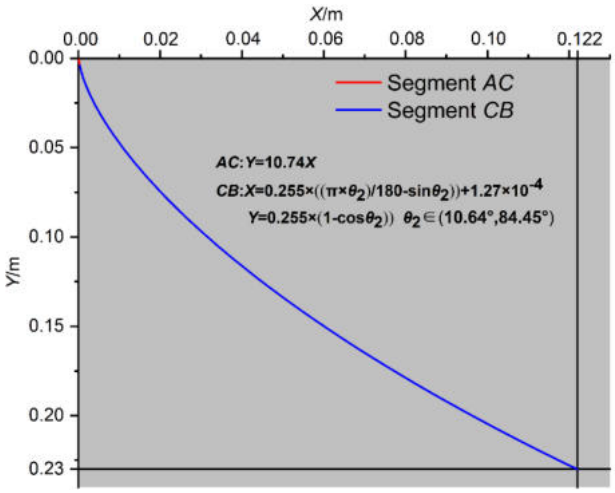


Fig. 3 - Schematic diagram of the outline of the curved section of the seed guide tube

Simulation tests

As shown in Fig. 4, the fluid domain of the seed guide tube is extracted by Space Claim software, and the inlet and outlet of the tube are labelled as "Inlet" and "Outlet", respectively. The labelled model is imported into Fluent Meshing module for meshing. In order to improve the mesh quality of the model, the minimum and maximum values of the surface mesh size were set to 0.5 and 1.5 mm, respectively, and the poly mesh was used for volume mesh-filling. The meshed model is imported into the Fluent solver module, and the widely used standard K-epsilon turbulence model is selected for the simulation. In the Solution Methods, the second-order equations are used for the pressure and momentum equations and the first-order upwind equations are used for the turbulent kinetic energy and turbulent dissipation rate equations. In the Run calculation, the time-step is set to be 1×10^{-2} s, and the total simulation time is set to be 2 s. According to the repeated test results of the actual experiment, the flow velocity v_r of the Inlet was set as 63. 48, 60.64, 57.73, 54.69, 51.50 and 48.15 m/s, respectively, and the pressure of the Outlet was set as 0 Pa to carry out the single-factor simulation experiment, so as to explore the flow field characteristics in the seed guide tube under different inlet velocities.

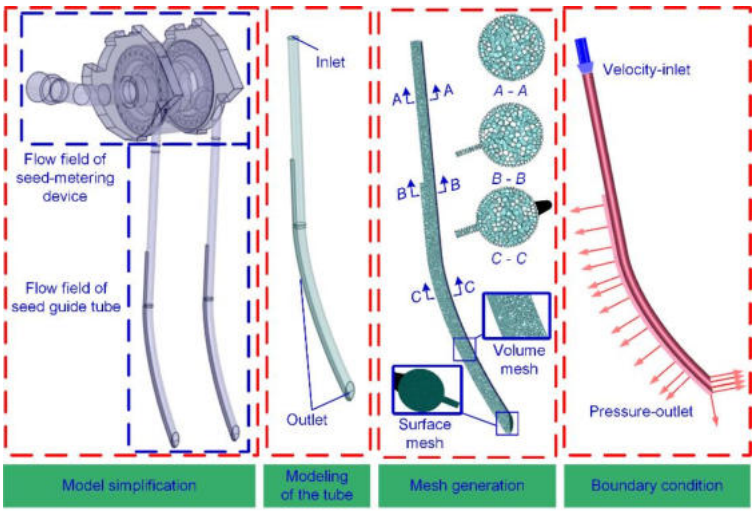


Fig. 4 - Establishment of CFD simulations

Bench tests

In order to determine the optimal working parameter combination of the seed guide device based on the principle of the brachistochrone, and to check its performance improvement effect compared with the traditional seed guide tube with guided-groove and the seed guide tube without guided-groove based on the brachistochrone, the bench performance test was carried out in the High-speed Precision Sowing Lab of the College of Engineering, Heilongjiang Bayi Agricultural University at an ambient temperature of about 20°C and a seed bed oil belt temperature of about 25°C. The test conditions and seeding effect are shown in Fig. 5, and the main devices include seed-supply device, air-pressure seed-metering device, HTB multi-stage blower (Shanghai Liangjin Electromechanical Equipment Co., Ltd, Shanghai), JPS-16 seed-metering device test bench (Heilongjiang Agricultural Machinery Engineering Research Institute, Harbin, Heilongjiang, Mean error of grain spacing measurement ≤2 mm), frequency converter, DP2000 intelligent pressure and wind velocity air volume meter (Shanghai YIOU Instrument Equipment Co., Ltd, Shanghai, resolution 1Pa), as well as three types of seed guide tubes. Among them, the JPS-16 test bench can collect the seed grain spacing falling on the surface of the seed bed oil belt after sowing through computer vision technology, and output the statistical results of the detection indexes using the image acquisition and processing system. The typical maize variety "Dika C2235" planted in Heilongjiang region of China was used for the test seed *(Sun et al., 2024)*, and the related material characteristics are shown in Table 1.

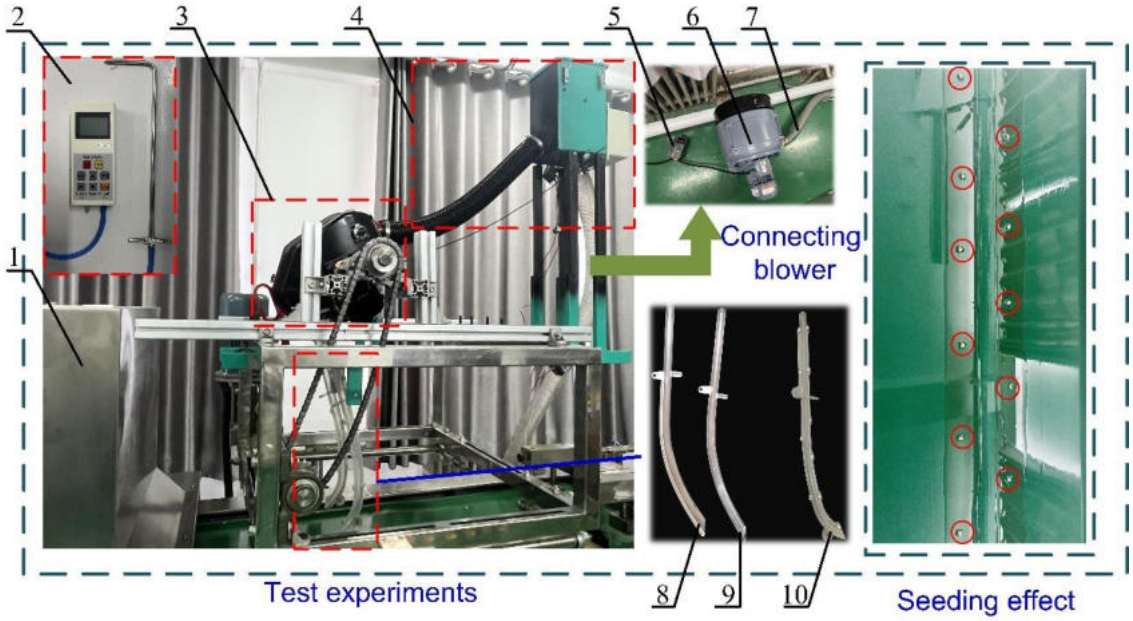


Fig. 5 - Bench test

1. JPS-16 seed-metering device test bench; 2. DP2000 intelligent pressure and wind velocity air volume meter; 3. seed-metering device; 4. seed-supply device; 5. frequency converter; 6. HTB-multi-stage blower; 7. threaded pipe; 8. traditional seed guide tube with guided-groove; 9. seed guide tube without guided-groove based on the brachistochrone; 10. seed guide tube with guided-groove based on the brachistochrone.

Table 1

Basic material characteristics of maize seed

Types	Seed picture	Moisture content / %	Thousand grain weigh / g	Density / g·cm^{-3}	Pile angle/(°)	Length/mm	Width / mm	Thickness / mm
Dika C2235 (big-rounded)		12.4	342.3	1.198	22.42	10.24±0.59	9.74±0.54	7.24±0.61

Based on the actual test conditions, the chamber pressure P_f of the seed-metering device was set in the range of 2.7~4.2kPa, and the operating speed v_p was set in the range of 12.0~16.0 km/h. A two-factor, five-level multi-factor experiment was conducted. The coding of the test factors is shown in Table 2, where *X*1 and *X*2 represent the coded values of chamber pressure P_f and operating speed v_p, respectively.

Table 2

Experimental factors and level codes in multi-factor experiment

Coded values	Experimental factors	
	***X*1/ kPa**	***X*2/ (km/h)**
-1.414	2.70	12.0
-1	2.92	12.6
0	3.45	14.0
1	3.98	15.4
1.414	4.20	16.0

Referring to the international standard ISO 7256/1 (1984) and JB/T10293-2001 "Technical Conditions for Single Grain (Precision) Seeders" *(Tang et al., 2023; Tang et al., 2024)*, the qualified index Q_1 and the coefficient of variation Q_2 were selected as the evaluation indexes of the test, and their calculation formula is as follows:

$$\begin{cases} Q_1 = \dfrac{n_q}{N_1} \times 100\% \\ Q_2 = \sqrt{\dfrac{\sum(x - x_p)^2}{(N_1 - 1)x_p^2}} \times 100\% \end{cases} \quad (17)$$

where:

n_q is the number of qualified grain spacing; N_1 is the total number of intervals; x is the grain spacing measured in the test, m; x_p is the average grain spacing measured in the test, m.

The conversion relationship between the working speed n_p of the seed-metering device and the operating speed v_p of the planter is given by:

$$n_p = \frac{60 v_p}{ZL} \quad (18)$$

where: Z is the number of the holes in the seed-metering plates.

The test was conducted by randomly counting the 250 consecutive seed grain spacings adjacent to the sown homogeneous section, and each set of test was replicated 5 times to calculate the qualified index Q_1 and the coefficient of variation Q_2 under different treatments.

RESULTS AND DISCUSSIONS

Results of the simulation experiments

As shown in Fig. 6 a, in order to investigate the flow field distribution of the seed guide tube at different inlet flow velocities, the pressures and flow velocities of different lengths H_2 in the negative direction of the *y*-axis from the inlet of the seed guide tube at 2 s were extracted, and the cloud diagrams of the pressures and flow velocities of the axial plane of the seed guide tube in the *z*-axis direction as well as the vertical cross sections at distances of 100 mm, 200 mm, and 300 mm from the inlet of the tube were intercepted, respectively. The pressure and velocity curves for different lengths H_2 at each velocity-inlet of the tube are shown in Fig. 6 b. The results of the pressure and velocity cloud diagrams in the axial plane and the vertical cross sections are shown in Fig. 6 c and Fig. 6 d, respectively.

In Fig. 6 b, it can be seen that along with the increase of the length H_2, the trends of pressure and velocity curves at different velocity-inlets are basically the same. The velocity curve shows a slow upward trend within the range of 0~380 mm from the length H_2, and a rapid decrease followed by a gradual increase and then a gradual decrease within the range of 380~550 mm. The velocity ranges for inlet-velocities of 48.15, 51.50, 54.69, 57.73, 60.64 and 63.48 m/s in the *y*-axis direction were 36.87 ~ 56.23 m/s, 39.85 ~ 60.04 m/s, 42.71 ~ 63.66 m/s, 45.47~ 67.11 m/s, 48.13 ~ 70.41 m/s, and 50.72 ~ 73.63 m/s, respectively. When the length H_2 ranges from 0 to 321 mm, the pressure decreases rapidly at first and then decreases slowly. When the length H_2 ranges from 321 to 550 mm, the pressure generally shows a fluctuating upward trend. As the inlet velocity increases, the maximum pressure differential along the y-axis also increases, with values of 484.11, 546.29, 608.66, 670.80, 732.73, and 795.78 Pa corresponding to the respective inlet velocities listed above.

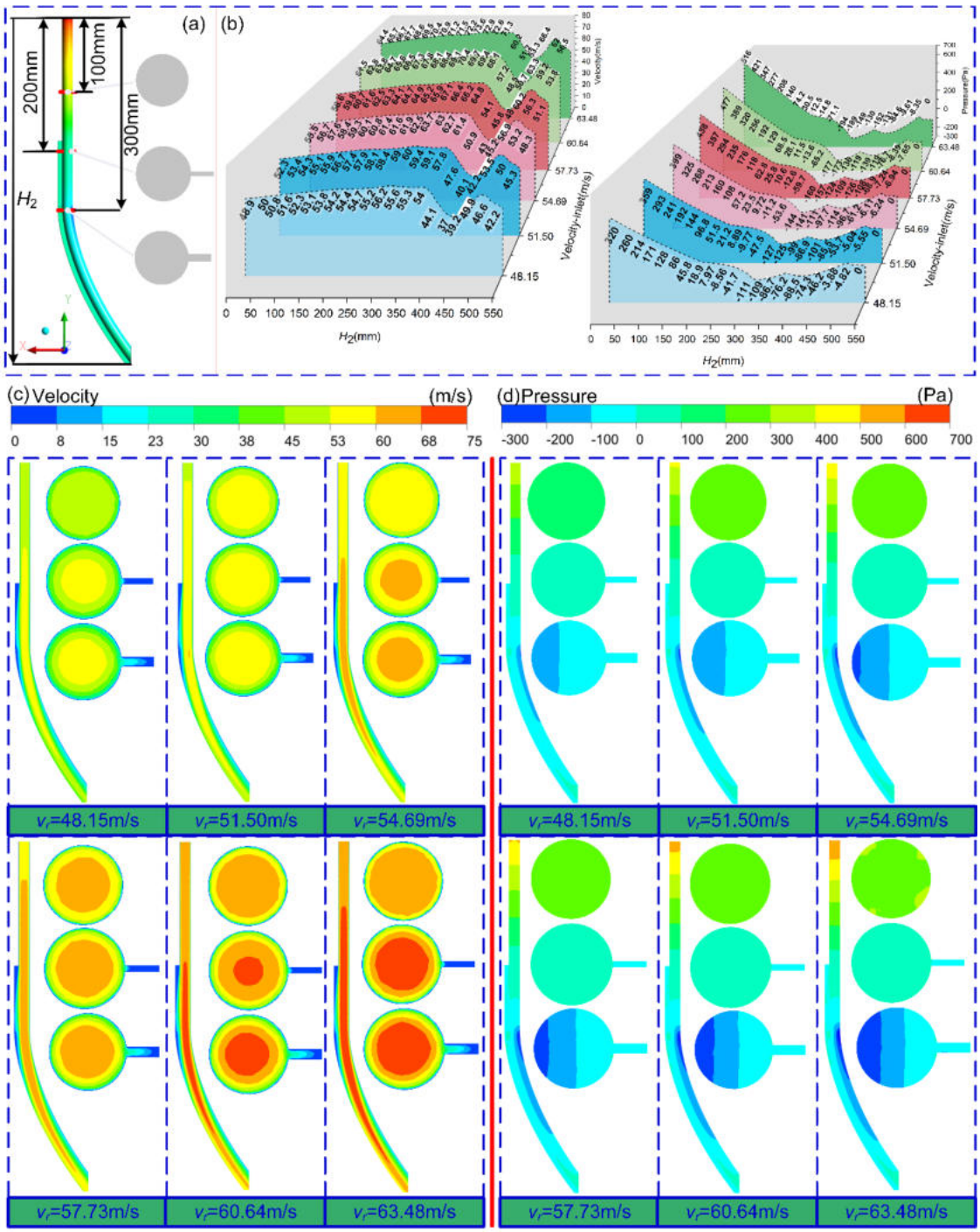


Fig. 6 - Results of CFD simulations

As shown in Fig. 6c, the velocity cloud diagrams in the axial plane reveal that as the inlet velocity increases, the overall flow velocity throughout the flow field also increases. Additionally, the area occupied by the high-velocity zone expands accordingly. However, the increase in flow velocity near the upper guided-groove is less pronounced compared to that observed near the lower guided-groove. Furthermore, the flow velocity near the end of the tube shows a tendency to decrease, which can be attributed to the increase in the vertical cross-sectional area at the tube's outlet. For the velocity cloud diagrams of the vertical cross-sections, the flow velocity is highest near the center of each section. The flow velocity distribution is more uniform in sections without a guided groove, whereas sections with a guided groove exhibit a greater velocity gradient. Notably, the velocity gradient near the lower guided-groove is more pronounced than that near the upper guided-groove, indicating that the curved segment of the lower guided-groove exerts a stronger adsorption effect on the seeds than the linear segment of the upper guided-groove. Furthermore, as the inlet flow velocity increases, the central flow velocity in each vertical cross-section also increases. Specifically, the central flow velocity in sections with a guided-groove trough reaches 68~75 m/s when the inlet velocity ranges from 60.64

to 63.48 m/s. In contrast, the flow velocity at the edge of the guided-groove trough remains largely unaffected by changes in inlet velocity, consistently ranging between 0 and 8 m/s.

It can be seen from Fig. 6 d that for the pressure cloud diagrams in the axial plane, the change of the velocity-inlet has a greater influence on the pressure gradient of the linear segments, and has a smaller influence on the pressure gradient of the curved segments. With the increase of the velocity-inlet, the pressure gradient range of the linear segment increases from 0~400Pa to 0~600Pa, while the area of the cloud of the curved segment, which only has a pressure gradient range of -300~-100Pa, exhibits a trend of gradual expansion. For the pressure maps of each vertical cross section, along with the increase of the velocity-inlet, the pressure distributions of the sections without guided-groove and the sections of upper guided-groove did not show obvious difference, but the sections of lower guided-groove showed an obvious pressure gradient evolution: the area of the maps with the pressure gradient range of -100~0Pa gradually decreased, while the area of the maps with the pressure gradient range of -300~-200Pa continued to increase. This indicates that increasing the velocity-inlet will obviously increase the pressure difference near the lower guided-groove, which will help to improve the stability and reliability of the seed guide tube in the process of seed-attracting and seed-attaching.

Results of the bench experiments

According to the range of factors in Table 2, the bench test was designed and conducted based on the central composite design, and the test results were obtained, as shown in Table 3.

Table 3

Results of the multi-factor experiments

Number.	Experimental factors		Experimental indexes	
	*X*1/ kPa	*X*2/ (km/h)	Q_1/ %	Q_2/ %
1	2.92	12.6	96.23	7.06
2	3.98	12.6	95.54	7.92
3	2.92	15.4	93.42	10.86
4	3.98	15.4	92.83	9.32
5	2.70	14.0	94.82	10.09
6	4.20	14.0	94.08	8.76
7	3.45	12.0	97.07	6.36
8	3.45	16.0	92.01	11.16
9	3.45	14.0	95.93	9.42
10	3.45	14.0	95.62	9.47
11	3.45	14.0	95.91	9.81
12	3.45	14.0	95.88	9.79
13	3.45	14.0	95.69	9.83

The results were processed and analysed using Design Expert 12 software, and the analysis of variance of the quadratic equation was obtained, as shown in Table 4.

Table 4

Analysis of variance of the quadratic equation

Source	Q_1				Q_2			
	Sum of squares	df	*F*-value	*p*-value	Sum of squares	df	*F*-value	*p*-value
Model	26.02	5	86.47	< 0.0001**	22.27	5	37.10	< 0.0001**
*X*1	0.6766	1	11.24	0.0122*	0.8198	1	6.83	0.0348*
*X*2	20.08	1	333.74	< 0.0001**	17.96	1	149.61	< 0.0001**
*X1 X*2	0.0025	1	0.0415	0.8443	1.44	1	11.99	0.0105*
$X1^2$	3.17	1	52.75	0.0002**	0.2649	1	2.21	0.1811
$X2^2$	2.77	1	45.95	0.0003**	1.94	1	16.13	0.0051**
Residual	0.4213	7			0.8405	7		
Lack of fit	0.3415	3	5.71	0.0627	0.6786	3	5.59	0.0649
Pure error	0.0797	4			0.1619	4		
Cor total	26.44	12			23.11	12		

Note: * indicates a significant impact; ** indicates a highly significant impact.

In Table 4, the *p*-value of the regression model of the qualified index Q_1 and the coefficient of variation Q_2 were all less than 0.01, indicating that the regression model was highly significant, and the *p*-value of the lack of fit were all greater than 0.05 as non-significant, indicating that the regression model was well fitted.

In the analysis of variance of the Q_1, the $X2$, secondary terms $X1^2$ and $X2^2$ showed highly significant effects, the $X1$ showed significant effects, and interaction terms $X1X2$ showed insignificant effects. The magnitude of the effect of each factor on the Q_1 was $X2>X1$. After excluding the insignificant factors, the quadratic regression equation of the Q_1 was:

$$Q_1 = 23.00735 + 16.0239X1 + 7.7066X2 - 2.40178X1^2 - 0.31525X2^2 \quad (19)$$

In the analysis of variance of the Q_2, the $X2$ and secondary terms $X2^2$ showed highly significant effects, the $X1$ and interaction term $X1X2$ showed significant effects, and secondary term $X1^2$ showed insignificant effects. The magnitude of the effect of each factor on the Q_2 was $X2>X1$. After excluding the insignificant factors, the quadratic regression equation of the Q_2 was:

$$Q_2 = -91.077 + 10.59639X1 + 10.85005X2 - 0.8X1X2 - 0.251087X2^2 \quad (20)$$

Based on the results of the multi-factor experiment, the highest Q_1 and the lowest Q_2 are used as the optimization objectives, and the optimization equation is established within the factor range:

$$\begin{cases} maxQ_1 \\ minQ_2 \\ s.t. \begin{cases} 2.7\text{kPa} \geq X1 \geq 4.2\text{kPa} \\ 12\text{km/h} \geq X2 \geq 16\text{km/h} \\ 1 \geq Q_1(X1, X2) \geq 0 \\ 1 \geq Q_2(X1, X2) \geq 0 \end{cases} \end{cases} \quad (21)$$

It was calculated that when the chamber pressure was 3.124 kPa and the operating speed was 12.0 km/h, the predicted values of the Q_1 and the Q_2 of the seed-guiding device were 96.709% and 6.08%, respectively. Under this parameter combination, 5 repetitive bench tests were carried out, and the results were shown in Table 5. At the same time, in order to check the performance improvement effect under this parameter combination compared with the traditional seed guide tube with guided-groove (Type B) and the seed guide tube without guided-groove based on the brachistochrone (Type C), five repetitive bench tests were carried out under the same conditions for these two types of seed guide tube, and the comparative results are shown in Table 5.

Table 5

Bench validation and comparative test results

Test number	Type of seed guide tube	Q_1/ %	Q_2/ %	Deviation from the Q_1 predicted value /%	Deviation from the Q_2 predicted value /%
1	A	97.04	6.11	0.33	0.03
	B	94.36	7.22	-2.35	1.14
	C	90.76	7.93	-5.95	1.85
2	A	97.11	6.19	0.40	0.11
	B	94.45	7.37	-2.26	1.29
	C	91.03	8.23	-5.68	2.15
3	A	96.84	6.27	0.13	0.19
	B	93.97	7.13	-2.74	1.05
	C	90.22	8.36	-6.49	2.28
4	A	97.22	6.09	0.51	0.01
	B	94.53	6.93	-2.18	0.85
	C	90.49	7.96	-6.22	1.88
5	A	96.97	6.22	0.26	0.14
	B	93.78	7.24	-2.93	1.16
	C	89.94	8.47	-6.77	2.39
Statistical results	A	97.04±0.13	6.18±0.07	0.33	0.10
	B	94.22±0.29	7.18±0.15	-2.49	1.10
	C	90.49±0.38	8.19±0.21	-6.22	2.11

Note: *A* indicates the seed guide tube with guided-groove based on the brachistochrone, *B* indicates the traditional seed guide tube with guided-groove, and *C* indicates the seed guide tube without guided-groove based on the brachistochrone.

In the table, the Q_1 and the Q_2 of the seed guide tube with guided-groove based on the brachistochrone (Type A) under the optimal parameter combination are 97.04±0.13% and 6.18±0.07%, 95% confidence Interval ≈ [96.88%, 97.20%] and 95% confidence Interval ≈ [6.09%, 6.27%], respectively, and the deviation of the results from the prediction is less than 0.4% with a relatively small error. This parameter combination further improves the seed-guiding performance of the seed-guiding device, which indicates that the results of the parameter optimization have a certain reliability. In addition, the Q_1 of the type A increased by 2.82% and 6.55%

compared with type B and C, and the Q_2 of the type A decreased by 1.00% and 2.01% compared with type B and C, which indicates that the seed guide tube with guided-groove based on the brachistochrone has a better seed-guiding performance. In addition, a high-speed camera was used in the experiment to measure the time for seeds to pass through type A, type B and type C as 0.029s, 0.035s and 0.033s, respectively, and the type A and type C were faster than the type B. This indicates that the seed guide tube designed based on the theory of the brachistochrone is able to shorten the time of the seed-guiding process effectively.

CONCLUSIONS

In order to improve the seeding quality of the planter for maize dense planting when it operates at high speed, a seed-guiding device with air-assisted and guided-groove is designed based on the principle of the brachistochrone. The flow field characteristics of the seed guide tube were investigated using CFD simulation. When the flow velocity at the inlet of the seed guide tube was 63.48, 60.64, 57.73, 54.69, 51.50, and 48.15 m/s, the flow velocity in the *y*-axis direction ranged from 36.87 to 56.23 m/s, 39.85 to 60.04 m/s, 42.71 to 63.66 m/s, 45.47 to 67.11 m/s, 48.13 to 70.41 m/s, and 50.72 to 73.63 m/s, respectively, and the maximum differential pressure was 484.11, 546.29, 608.66, 670.80, 732.73, and 795.78Pa, respectively. The two-factor and five-level central combination test was conducted under the conditions of 2.7~4.2 kPa of chamber pressure and 12~16 km/h of operating speed. The test results showed that the seed-guiding performance of the designed seed-guiding device was optimal under the parameter combinations of 3.124 kPa of chamber pressure and 12.0 km/h of operating speed, and the deviation between the results of the bench validation test and the results of the prediction was less than 0.4%. In addition, under the optimal parameter combination, the device's qualified index increased by 2.82% and 6.55%, and the coefficient of variation decreased by 1.00% and 2.01%, respectively, compared with that of the traditional seed guide tube with guided-groove and the seed guide tube without guided-groove based on the brachistochrone. This study shows that the combination of "airflow assisted + guided-groove structure + the brachistochrone" can effectively control the seed movement in the seed guide tube, and further improve the seeding uniformity and stability of the seed-guiding process of the maize delta-row dense planting planter under high-speed operating conditions.

ACKNOWLEDGEMENT

The study was funded by the Heilongjiang Province Key Research and Development Program Major Projects, China (2022ZX05B02) and Ltd. 2023 Pilot Project on Integration of Agricultural Machinery R&D, Manufacturing, and Promotion and Application.

REFERENCES

[1] Adetifa, B. O., & Aremu, A. K. (2021). Energy and exergy parameters of low-temperature solar thermal energy storage systems: empirical estimation and optimisation. *International Journal of Exergy*, Vol. 35, Issue 3, pp. 374-405. https://doi.org/10.1504/IJEX.2021.115904

[2] Dong, J., Gao, X., Zhang, S., Huang, Y., Zhang, C., & Shi, J. (2023). Design and test of guiding seed throwing mechanism for maize posture control and driving metering device. *Transactions of the Chinese Society of Agricultural Machinery*, Vol. 54, Issue 10, pp. 25-34. https://doi.org/10.6041/j.issn.1000-1298.2023.10.002

[3] Fanigliulo, R., Grilli, R., Benigni, S., Fornaciari, L., Biocca, M., & Pochi, D. (2022). Effect of sowing speed and width on spacing uniformity of precision seed drills. *INMATEH-Agricultural Engineering*, Vol. 66, Issue 1, pp. 9-18. https://doi.org/10.35633/inmateh-66-01

[4] Jia, X., Zhu, J., Guo, G., Huang, Y., Gao, X., & Zhang, C. (2024). Design and test of a novel converging groove-guided seed tube for precision seeding of maize. *Biosystems Engineering*, Vol. 245, pp. 36-55. https://doi.org/10.1016/j.biosystemseng.2024.06.012

[5] Li, X., Liao, Q., Wang, L., Li, M., & Du, W. (2023). Design and experiments of the type-hole wheel with high-speed air-assisted centralized metering device for rice, wheat and rapeseed. *Transactions of the Chinese Society of Agricultural Engineering*, Vol. 39, Issue 14, pp. 35-48. https://doi.org/10.11975/j.issn.1002-6819.202303044

[6] Li, Y., Yang, L., Zhang, D., Cui, T., Zhang, K., Xie, C., & Yang, R. (2020). Analysis and test of linear seeding process of maize high speed precision metering device with air suction. *Transactions of the Chinese Society of Agricultural Engineering*, Vol. 36, Issue 9, pp. 26-35. https://doi.org/10.11975/j.issn.1002-6819.2020.09.003

[7] Liao, Y., Li, C., Liao, Q., & Wang, L. (2020). Research progress of seed guiding technology and device of planter. *Transactions of the Chinese Society of Agricultural Machinery*, Vol. 51, Issue 12, pp. 1-14. https://doi.org/10.6041/j.issn.1000-1298.2020.12. 001

[8] Liu, R., Liu, Y., Liu, Z., & Liu, L. (2023). Research on positive pressure airflow assisted blowing and seed guiding device of corn high-speed precision planter. *Transactions of the Chinese Society of Agricultural Machinery*, Vol. 54, Issue 7, pp. 156-166. https://doi.org/10.6041/j.issn.1000-1298.2023.07.015

[9] Ma, C., Yi, S., Tao, G., Li, Y., Wang, S., Wang, G., & Gao, F. (2023). Research on receiving seeds performance of belt-type high-speed corn seed guiding device based on discrete element method. *Agriculture*, Vol. 13, Issue 5, pp. 1085. https://doi.org/10.3390/agriculture13051085

[10] Sun, W., Yi, S., Qi, H., Dai, Z., Zhang, Y., & Wang, S. (2024). Research progress on narrow row and dense planting delta-row seeding technology and equipment. *Agricultural Engineering*, Vol. 14, Issue 5, pp. 5-9. https://doi.org/10.19998/j.cnki.2095-1795.2024.05.001

[11] Sun, W., Yi, S., Qi, H., Li, Y., Dai, Z., Zhang, Y., & Wang, S. (2024). Design and experiment of progressive seed-cleaning mechanism for air-pressure maize precision seed-metering device. *INMATEH-Agricultural Engineering*, Vol. 73, Issue 2, pp. 473-486. https://doi.org/10.35633/inmateh-73-40

[12] Sun, W., Yi, S., Qi, H., Wang, S., Li, Y., & Dai, Z. (2024). Design and experiment of twin discs intertwined air-pressure high-speed precision seed-metering device for maize delta-row dense plantings. *Transactions of the Chinese Society of Agricultural Machinery*, Vol. 55, Issue 10, pp. 168-179. https://doi.org/10.6041/j.issn.1000-1298.2024.10.016

[13] Tang, H., Guan, T., Xu, F., Xu, C., & Wang, J. (2024). Test on adsorption posture and seeding performance of the high-speed precision dual-chamber maize metering device based on the seed characteristics. *Computers and Electronics in Agriculture*, Vol. 216, pp.108471. https://doi.org/10.1016/j.compag.2023.108471

[14] Tang, H., Xu, F., Guan, T., Xu, C., & Wang, J. (2023). Design and test of a pneumatic type of high-speed maize precision seed metering device. *Computers and Electronics in Agriculture*, Vol. 211, pp.107997. https://doi.org/10.1016/j.compag.2023.107997

[15] Tang, H., Xu, F., Xu, C., Zhao, J., & Wang, Y. J. (2023). The influence of a seed drop tube of the inside-filling air-blowing precision seed-metering device on seeding quality. *Computers and Electronics in Agriculture*, Vol. 204, pp.107555. https://doi.org/10.1016/j.compag.2022.107555

[16] Yatskul, A., & Lemiere, J.P. (2018). Establishing the conveying parameters required for the air-seeders. *Biosystems Engineering*, Vol. 166, pp. 1-12. https://doi.org/10.1016/j.biosystemseng.2017.11.001

[17] Yi, S., Zhang, Y., Dai, Z., Kong, L., Sun, W., & Xu, L. (2025). Design and experiment of positive pressure airflow guide groove seed guiding device for maize delta-row high-speed precision seeder. *Transactions of the Chinese Society of Agricultural Machinery*, Vol.56, Issue 2, pp. 261-274. https://doi.org/10.6041/j.issn.1000-1298.2025.02.025

[18] Zhao, P., Gao, X., Su, Y., Xu, Y., & Huang, Y. (2024). Investigation of seeding performance of a novel high-speed precision seed metering device based on numerical simulation and high-speed camera. *Computers and Electronics in Agriculture*, Vol. 217, pp.108563. https://doi.org/10.1016/j.compag.2023.108563

DEM-BASED CALIBRATION OF SOIL CONTACT PARAMETERS PRIOR TO GRAPEVINE BURYING
/
基于离散元法的葡萄藤埋前土壤接触参数标定

Beibei ZHANG[1)], Julaiti MAITIROUZI*[1)], Shixiang XING[1)], Hongcheng DENG[2)], Wenjing BAI[2)], Haileeqguli YASEN[2)]
[1)] College of Mechanical Engineering, Xinjiang University, Urumqi / China;
[2)] Turpan Agricultural and Rural Mechanization Development Center, Turpan / China
Tel: +86 13986888714; E-mail: 13986888714@163.com
DOI: https://doi.org/10.35633/inmateh-76-20

Keywords: *grapevine, discrete element method, static and dynamic angle of repose, soil, parameter calibration, grapevine burying machine.*

ABSTRACT
To address the lack of simulation parameters when applying discrete element simulations to guide the optimal design of grapevine burying machines, this study focused on the soil conditions in Xinjiang. The soil was divided into three layers, and the static and dynamic angle of repose characteristics of each layer were investigated using the Hertz-Mindlin with Johnson-Kendall-Roberts (JKR) contact model. First, the Plackett-Burman test was used to eliminate parameters that had no significant effect on the static and dynamic angles of repose. Then, the steepest ascent test was applied to narrow the parameter ranges, followed by the Box-Behnken test to develop regression models between the repose angles and the significant parameters. The results showed that the soil-soil restitution coefficient, soil-soil rolling friction coefficient, soil-steel static friction coefficient, and JKR surface energy were the key parameters influencing the static and dynamic repose angles. Experimental validation demonstrated that the average relative errors between the simulated and measured angles of repose using the optimized parameters were 0.92% and 0.32%, respectively, confirming the validity of the selected parameters. This study provides an important reference for the design optimization of grapevine burying machines and for discrete element simulation of other cohesive particulate materials.

摘要
针对应用离散元仿真指导葡萄埋藤机优化设计时仿真参数缺乏的问题。以新疆土壤为研究对象，将土壤分为三层，以 "Hertz-Mindlin with Johnson-Kendall-Roberts"为接触模型，研究了不同土层的静/动态休止角特性。首先利用 Plackett-Burman 检验排除对静/动态休止角影响不显著的参数，利用最陡爬坡检验缩小参数区间范围，利用 Box-Behnken 检验得到静/动态休止角与显著性参数之间的回归模型。结果发现，土-土恢复系数、土-土滚动摩擦系数、土-钢静摩擦系数和 JKR 表面能是影响静/动态休止角的主要参数。通过实验验证，最优离散元模拟参数的静/动态休止角与实测值的平均相对误差分别为 0.92% 和 0.32%，验证了所选参数的有效性，该研究为葡萄埋藤机的优化设计以及其他粘性颗粒物料的离散元模拟提供了重要参考。

INTRODUCTION
In Northwest China, much of the agricultural land in arid irrigated regions is used to cultivate grapes as a specialty crop. In 2021, Xinjiang alone accounted for 1.85 million acres of grape cultivation, producing 3.5 million tons, ranking first in both production and planting area nationwide *(Wang et al., 2024)*. Grapevine burying is a key winter protection technique for grapes in northern China, with its production costs comprising nearly 50% of the annual expenses. Turpan, as the largest grape-growing base in Xinjiang, has seen a rapid increase in mechanized vine-burying, and while the current mechanization level is relatively high, there remain significant shortcomings in terms of efficiency, cost, and adaptability. A major challenge lies in the lack of advanced machinery to further improve productivity (*Shen et al., 2024*). Therefore, the design of suitable agricultural machinery is crucial. In this context, soil modeling plays a vital role in the development and optimization of such equipment, as it contributes to increased production efficiency and reduced operational costs. However, no discrete element simulation models currently exist for soil prior to grapevine mulching and burial. Thus, it is essential to construct a discrete element parameter model of the soil.

To analyse the interaction between soil-engaging components and soil, numerical simulation is commonly used to establish an accurate soil model (*Smith et al., 2014*).

BeiBei Zhang, M.S.Stud. Eng.; Julaiti Maitirouzi, Prof. Ph.D. Eng.; Shixiang Xing, M.S. Stud. Eng.; Honcheng Deng, Senior engineer. M.S. Eng.; Wenjing Bai, Senior engineer. M.S. Eng.; Haileeqguli Yasen, Senior engineer. M.S. Eng.

Xinjiang region is an irrigated area with high evaporation in the surface layer, and there is a large difference in water content between the surface soil and the subsoil, which has a large impact on the contact parameters of the discrete element model (*Li et al., 2019*).

Some scholars have conducted layered sampling of cold-proof soil during grapevine clearing to determine the moisture content of different soil layers. Based on this data, they combined it with simulation tests of the soil's angle of repose to complete discrete element parameter calibration, achieving results with minimal error *(Yang et al., 2023)*. Some scholars have constructed a particle model of mulberry soil under specific moisture conditions based on the soil particle size distribution. Using this model, the discrete element parameters of the soil were calibrated, and the results were found to be reliable (*Song et al., 2022*). The combination of static and dynamic angles of repose for calibrating discrete element particles has been widely applied in fields such as food, pharmaceuticals, industrial materials, and agricultural soils, yielding promising results. The calibrated soil simulation results closely match experimental measurements and meet the intended testing objectives (*Zhang et al., 2024; Luana et al., 2017; Li S. et al., 2024*). In addition, some researchers have applied scaling theory to calibrate the contact parameters in discrete element simulations of wheat flour, using the Plackett-Burman test, steepest ascent test, and Box-Behnken design, with the static angle of repose as the response variable (*Li et al., 2019*).

Most existing soil discrete element simulation parameter calibrations rely on a single static angle of repose as the response variable, without incorporating a combination of static and dynamic angles of repose to evaluate soils with varying moisture content. However, in real-world operations, soil exhibits both static and dynamic behaviours, and using both angles of repose as response variables offers a more accurate representation of the soil's actual mechanical state during field operations (*Zeng et al., 2019*). In Xinjiang, field soil conditions are typically assessed prior to grapevine burying, and in some areas, pre-irrigation is performed to ensure sufficient soil moisture. This results in more cohesive soil, which helps improve the performance and effectiveness of the grapevine burying operation (*Maitadudulili.et al., 2016*).

In this study, the Hertz-Mindlin with Johnson-Kendall-Roberts (JKR) contact model was selected to calibrate the contact parameters of the soil DEM model for different soil layers. The Plackett-Burman (PB) experimental design was first used to screen for significant factors and to analyse their effects on the static and dynamic angles of repose. Subsequently, a Box-Behnken experimental design with multi-objective optimization was applied to determine the candidate discrete element parameter sets for each soil layer. Finally, the calibrated discrete element simulation parameters were experimentally validated. The resulting optimal DEM parameters provide accurate input data for the simulation of grapevine burying operations, and also serve as a reference for discrete element modeling of other cohesive particulate materials.

MATERIALS AND METHODS

Materials and Instruments

The samples of vineyard soil were taken from the planting base of Thompson Seedless in Lianmuqin Township, Shanshan County, Turpan City, Xinjiang Uygur Autonomous Region (42.87°N,89.98°E). Based on the depth of soil disturbance during vineyard operation, the 60 cm soil profile affected by machinery was divided into three layers: the upper layer (0-20 cm), the middle layer (20-40 cm), and the lower layer (40-60 cm). Tests on the soil characterization parameters were conducted in accordance with the Chinese standard GB/T 50123–1999, Standard for Geotechnical Test Methods.

Test apparatus included the following equipment: an FCE-3000 electric constant temperature blast drying oven; a standard ring knife (specifications: diameter 50.46 mm, height 50 mm); a JJ623BF electronic balance (range: 620 g, precision: 1 mg); a standard test sieve set conforming to GB/T 6003–1997, with mesh sizes from top to bottom of 2.0 mm, 1.0 mm, 0.5 mm, 0.25 mm, and 0.075 mm; customized cylinder 1 (inner diameter 40 mm, height 100 mm); customized cylinder 2 (inner diameter 100 mm, height 100 mm); 65Mn iron sheet; 42 stepper motor; flange coupling; metal support; aluminium alloy profiles; a 200-type standard inspection sieve machine; aluminium box; camera; and food preservation bags, among other auxiliary tools.

Intrinsic parameter measurements

The ring knife method was used to measure soil density. In the field, the soil surface was paved and compacted, and the soil was taken with a ring knife, which was placed in an aluminium box and a food preservation bag to preserve the soil sample. After picking out the plant stalks and other impurities in the soil, the total mass of the ring cutter and soil was determined using an electronic balance and recorded as m1, and the mass of the empty ring cutter was determined as m0. Five-point sampling method was used to sample the

soil in three layers, and the average density of soil in the three layers from the top to the bottom was 172.23 kg/m^3, 177.35 kg/m^3, and 177.69 kg/m^3, and the average density of the soil was taken to be 175.76 kg/m^3.

$$\rho = \frac{m1-m0}{v} \quad (1)$$

where: ρ is the soil density (g·cm^{-3}); v is the volume of the ring knife (cm^3); m_1 is the mass of the ring knife and soil *(g);* and m_0 is the mass of the ring knife (g).

The drying method was used to determine soil moisture content. First, the mass m' of the empty aluminium box was measured using an electronic balance. Then, soil was added, and the total mass m' of the box and moist soil was recorded. The box was placed in a preheated oven at (107±2)℃ for 8 hours, cooled to room temperature, and weighed again to obtain the mass after drying.

$$\omega = \frac{m_1 - m_2}{m_1 - m} \quad (2)$$

where:

ω is the moisture content of the soil (%);

m_1 is the mass of the aluminium box and the soil (g);

m_2 is the mass of the aluminium box and the dry soil (g);

m is the mass of the aluminium box (g).

Sieving method was used to measure the particle size distribution of the soil. Soil collected from the field was first dried in a drying oven to remove impurities and pulverized, and then sieved using standard test sieves and oscillating sieves to measure the mass of the soil at different particle sizes and calculate the percentages as shown in Table 1.

Table 1

Soil particle size distribution

Particle radius/mm	Mass/g	Percent/%
≥2	17.48	8.74
2-1	8.34	4.17
1-0.5	11.68	5.84
0.5-0.25	41.50	20.75
0.25-0.075	111.60	55.80
0.075-0	9.40	4.70

According to the soil texture classification standard GB/T 17296, soil with a sand content greater than 50% is classified as clayey soil. Based on this standard, the soil in the study area was identified as clayey sandy loam (*Chen et al., 2017*).

Using the drying method and the addition of pure water, three soil moisture content gradients - 8.39%, 10.74%, and 12.40% - were prepared for the angle of repose tests. A dried soil sample with mass m_3 was measured, and pure water with mass m_1 was added. The mixture was stirred thoroughly and allowed to stand for 24 hours. The actual moisture content ω_x was then determined using the drying method and calculated as follows:

$$\omega_x = \frac{m_s}{m_s+m_3} \quad (3)$$

where*:*

ω_x is the water content of the soil (%);

m_s is the mass of water required to configure the sample (g);

m_3 is the sample mass (g).

Static angle of repose measurement

Common methods for measuring the static angle of repose include the cylinder lifting method and the funnel method (*Han et al., 2020; Zhen et al., 2020*). Given that the soil in this study contains some moisture and exhibits relatively cohesive texture, the hollow cylinder method was considered more suitable for accurately determining the static angle of repose. The test was conducted by placing a 65Mn steel plate horizontally on the test machine platform. The cylinder test apparatus was then connected, and the cylinder was positioned vertically on the steel plate and filled with the test soil.

The test machine was activated to lift the cylinder at a uniform speed of 25 mm/s (*Thomas et al., 2018*). A camera was used to record the formation of the soil pile for each moisture content condition. The test was repeated four times for each condition to ensure repeatability. The actual test setup for measuring the static angle of repose is shown in Fig. 1.

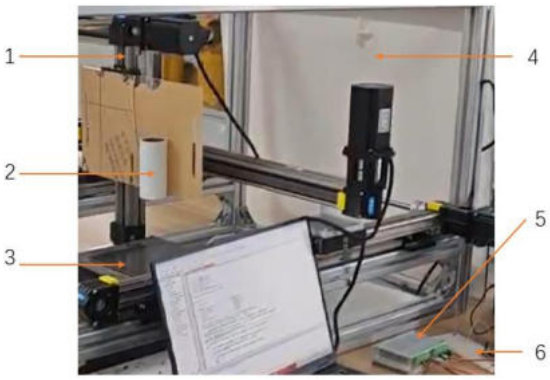
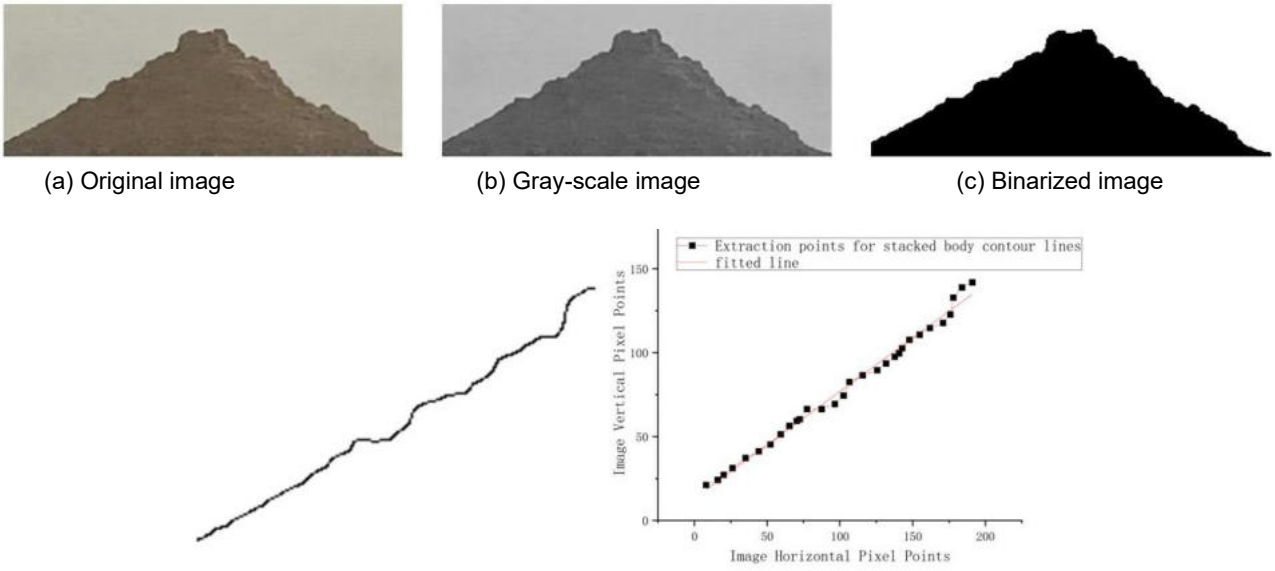


Fig. 1 - Static angle of repose measurement

1. Slipway; 2. Cylinder; 3. Cushion; 4. Background Board; 5. Driver; 6. Controller.

Image processing was used to determine the soil accumulation angle values (*Luo et al., 2018*). First, the original image was cropped to an appropriate size, and then processed through grayscale conversion and binarization. The boundary coordinates of the soil pile were extracted using the image digitizing function in Origin software (Fig. 2d). For each set of coordinates, linear fitting was performed, and the corresponding scatter plots and fitted lines were generated to obtain the fitting equations. The slope of each fitted line was then used to calculate the accumulation (stacking) angle. The arctangent (inverse tangent) of the slope was converted into an angle value (Fig. 2e). The final stacking angle was obtained by averaging the angles from both sides of each image. The image processing procedure and results are illustrated in Fig. 2.



(a) Original image (b) Gray-scale image (c) Binarized image

(d) Contour Extraction Line Image (e) Fitted line

Fig. 2 - Calculation process of static angle of repose of soil

Dynamic angle of repose measurement

The dynamic angle of repose is defined as the maximum angle between the slope of the soil mass and the horizontal plane before collapse occurs, i.e., when the internal forces between soil particles can no longer counteract gravity as the soil ascends with the rotation of the drum. It serves as a key parameter for characterizing the dynamic flow behaviour of soil. A custom-built device was used to measure the dynamic angle of repose, as illustrated in Figure 3.

The apparatus consists of a rotating drum (100 mm in diameter and 100 mm in length, with a steel sheet affixed to the inner wall), a motor, controller, and coupling. The measurement procedure was as follows: a specified amount of soil was loaded into the drum until the fill level reached 25% of the drum volume.

The motor was then activated to rotate the drum at a constant speed of 7 r/min, as recommended in relevant literature (*Zhou et al., 2023*). A video camera positioned directly in front of the drum recorded the rotation process in real time to capture the dynamic angle of repose. After repeating the experiment for five times, the average values of the dynamic angle of repose α of the three layers of soil were obtained as 42.7°, 43.91° and 45.7°, respectively.



Fig. 3 - Dynamic angle of repose measurement

1. Roller; 2. Driver; 3. Controller; 4. Electric Machine; 5. Power Supply.

Contact model

The water content of the soil before burying the vine is not low, and the soil particles will have a certain degree of adhesion between them. The Hertz-Mindlin with JKR model is used as a particle contact model, which is suitable for simulating the particulate materials that are prone to adhesion and agglomeration effects. Therefore, discrete element simulation was carried out using the Hertz-Mindlin contact model with JKR cohesion model, which assumes that the adhesion force acts within the contact area of the particles and contributes to the contact surface manifolds, thus obtaining a larger contact area than predicted by the Hertz-Mindlin theory. In the JKR model, the normal elastic contact force F_{JKR} of the particles is expressed as:

$$F_{JKR} = \frac{4E^*}{3R^*}\alpha^3 - 4\sqrt{\pi\gamma E^*\alpha^3} \tag{3}$$

$$\delta = \frac{\alpha^2}{R^*}\left[1 - \sqrt{\frac{4\pi\gamma R^3}{E^*\alpha^3}}\right] \tag{4}$$

where: E^* is the equivalent elastic modulus; R^* is the equivalent particle radius; α is the normal overlap; γ is the particle surface energy; δ is the tangential overlap.

The first term in Eq. (3) is the normal contact force based on the Hertz-Mindlin theory, and the second term is the particle adhesion force based on the JKR theory; when the particle surface energy $\gamma = 0$, the JKR model will degenerate into the Hertz-Mindlin model.

Principle of particle stiffness reduction

The Rayleigh time step refers to the length of time for 2 collision operations between particles, which is an important factor affecting the computational efficiency of DEM simulation. The formula for the Rayleigh time step is:

$$t_R = \frac{\pi r}{(0.163\upsilon + 0.877)}\sqrt{\frac{\rho}{G}} \tag{5}$$

where: t_R is the Rayleigh time step; r is the particle radius; υ is the particle Poisson's ratio; ρ is the particle density; G is the particle shear modulus.

To ensure the efficiency and accuracy of the simulation, 10% to 30% of the Rayleigh time step is usually chosen as the computational time step. From Eq. (5), it can be seen that the shear modulus of the particles is the main factor affecting the time step, and the reduction of particle stiffness allows the use of a larger time step in the simulation, which reduces the number of computational iterations and thus improves the computational speed. With the introduction of reduced stiffness particles in the JKR model, more overlap of particles occurs during kinematic collisions. If the surface energy of the particles remains constant, the kinetic energy lost in the collision will increase. In order to ensure that the result of the motion of the particles after the collision remains unchanged, so that the separation energy required by the 2 particles in contact remains constant, the reduction of particle stiffness must be balanced by the reduction of the surface energy of the particles, and the conditions to be satisfied are:

$$\gamma_{mod} = \gamma \left(\frac{G_{mod}}{G}\right)^{2/5} \quad (6)$$

where: γ_{mod} and G_{mod} are the surface energy and shear modulus of the modified particles respectively.

With the reduction of particle stiffness and the increase of time step, the calculation speed is improved, but the range of particle stiffness reduction should be limited. In order to prevent the particle stiffness from decreasing too much and causing too much overlap, the particle shear modulus after decreasing the stiffness should be kept above 10^7 Pa (*Lommen et al., 2023*).

Discrete element simulation parameter calibration

According to the theory of particle scaling, the related literature proposes that if the density of the particles corresponding to the scaled model is kept constant, the intrinsic parameters of the particles corresponding to the scaled model are the same as those of the original model, but the contact parameters of the particles with the particles and the particles with the touching soil parts corresponding to the scaled model can't be obtained directly according to the equations, and the related parameters need to be calibrated by simulation tests (*Feng et al., 2009*).

In order to reduce the amount of simulation data and improve the simulation efficiency, the soil particles are simplified into a single sphere model, and then the scaling theory is used to scale the particles of different particle size ranges into appropriate sizes, referring to the relevant literature (*Zhen et al., 2024; Yang et al., 2023; Li et al., 2024*) and the GEMM database, to determine the range of values of intrinsic parameters of the soil and the relevant contact parameters are shown in the following table.

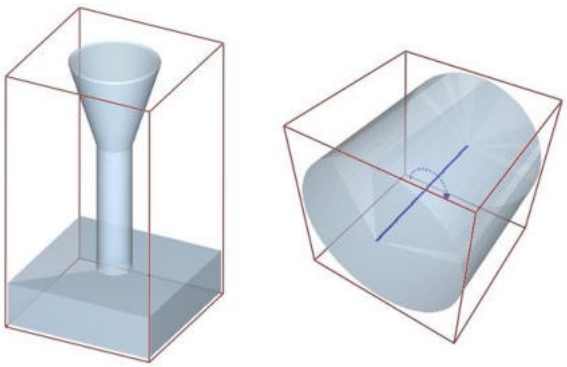
Table 2

Scaling model parameter value range

Parameters	Value	Unit
Soil density	175.7567	**kg·m^{-3}**
Poisson's ratio for soil	0.33	
Soil shear modulus A	10-10 0	**MPa**
Coefficient of restitution between soil particles B	0.15-0.75	
Coefficient of static friction between soil particles C	0.2-1.16	
Coefficient of rolling friction between soil particles D	0.05-0.15	
Steel density	7850	**kg·m^{-3}**
Steel Poisson's ratio	0.3	
Steel shear modulus	7.9×10^4	**MPa**
Coefficient of restitution between soil-steel E	0.25-0.65	
Coefficient of static friction between soil-steel F	0.30-0.80	
Coefficient of rolling friction between soil and steel G	0.20-0.40	
Surface energy (JKR) H	0.1-0.3	**J·m^{-2}**

Discrete element simulation modeling

In SOLIDWORKS software, the 3D geometric model of the static and dynamic angle of repose measurement device was built according to the scale of 1:1 with reference to the dimensions of the measurement device, saved in STL format and imported into EDEM software. The 3D geometric model of the measurement device is shown in Fig. 4.



(a) Static angle of repose model (b) Dynamic angle of repose model

Fig. 4 - Geometric model of the static and dynamic angle of repose determination device

The initial conditions of the simulation were set as follows: the particle sizes of the enlarged spherical particles were set to 2.5 mm, 5 mm and 10 mm, and the generation mode was dynamic. The static angle of repose model establishes a particle factory at the top of the funnel, with a total particle mass of 0.167 kg, and the generation rate is set to 0.5 kg of particles per second. In the dynamic angle of repose simulation model, a particle factory was established inside the cylinder to simulate the soil particles. A total particle mass of 0.209 kg was used, corresponding to a 25% fill rate of the drum volume, consistent with the experimental setup. After the particles settled into a stationary state, a rotational axis was introduced at the centre of the model, and the rotational speed was set to 7 r/min. The computational time step for both the dynamic and static repose angle models was set to 2.5 ms. After the particles stabilized, a rotational axis was added to the centre of the model, and the rotational speed was set to 7 r/min. The computational time step for both models was defined as 20% of the Rayleigh time step, and the mesh size was set to three times the diameter of the smallest spherical particle. Once the simulation reached a stable state, the angle of repose was measured using the EDEMPY measurement tool. The discrete element simulation parameters included the intrinsic properties of the particles, the 3D geometric model, the contact parameters between particles, and the contact parameters between particles and the geometry. The 3D geometry was modeled using 65Mn material, and the range of contact parameter variation was determined through preliminary experiments.

Simulated static/dynamic angle of repose determination

To accurately determine the angle of repose of the simulated particle pile, the simulation result files were analysed using the EDEMPY library, a Python-based post-processing tool for discrete element simulations. Measurement principle: First, a radial array of cylindrical containers is defined. The highest particle in each container is then identified. The centre-of-mass coordinates of these particles are extracted and subjected to least-squares linear fitting. The angle between the resulting fitted line and the horizontal plane is calculated, representing the angle of repose. This measurement principle is illustrated in Fig. 5 and Fig. 6. To improve measurement accuracy, only the stable region of the pile was selected for analysis. In addition, measurements were performed along multiple radial directions (eight directions in this study), and the average angle of repose was calculated. A schematic of the multi-directional measurement method is shown in Fig. 7.

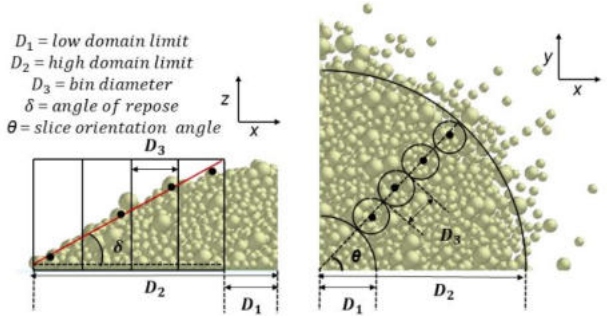


Fig. 5 - Schematic diagram of static angle of repose measurement

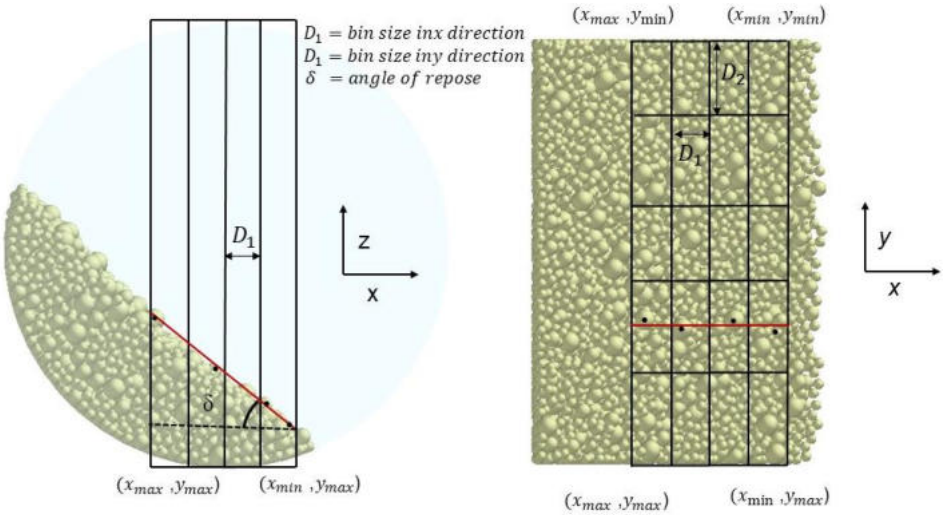


Fig. 6 - Schematic diagram of dynamic angle of repose measurement

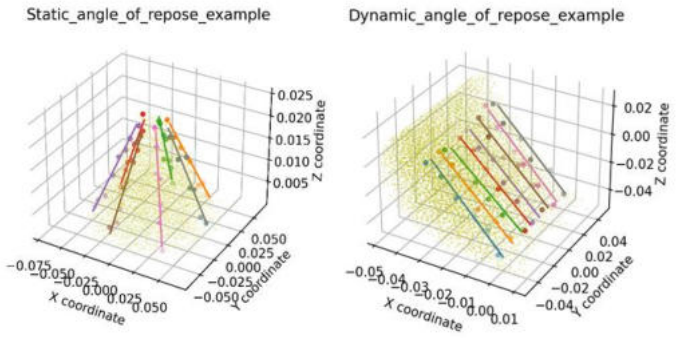


Fig. 7 - Schematic diagram of multiple measurements of angle of repose

RESULTS

Plackett-Burman test for discrete element simulation parameters

Not all parameters set for the discrete element simulation have a significant effect on the angle of repose. To identify the key influencing factors, a parameter screening test was conducted using the Plackett-Burman design in Design-Expert software. The static and dynamic angles of repose were used as response variables, while the eight parameters to be calibrated, along with two dummy variables (as shown in Table 3), were selected as the test factors. This design allowed for the evaluation of each factor's significance on the angle of repose and facilitated the identification of the most impactful parameters for further optimization.

Table 3

Plackett-Burman test scheme and results

Serial number	Experimental factors								Static angle of repose / (°)	Dynamic angle of repose / (°)
	A	B	C	D	E	F	G	H		
1	-1	-1	1	-1	1	1	-1	1	33.33	55.35
2	1	-1	1	1	1	-1	-1	-1	39.44	47.88
3	1	1	1	-1	-1	-1	1	-1	23.57	40.61
4	1	-1	1	1	-1	1	1	1	*45.01*	*61.13*
5	1	-1	-1	-1	1	-1	1	1	31.38	51.45
6	1	1	-1	-1	-1	1	-1	1	27.82	63.35
7	-1	-1	-1	-1	-1	-1	-1	-1	26.82	46.56
8	-1	-1	-1	1	-1	1	1	-1	46.79	50.82
9	-1	1	-1	1	1	-1	1	1	39.27	51.39
10	-1	1	1	1	1	-1	-1	1	32.28	51.25
11	-1	1	1	-1	-1	1	1	-1	27	47.04
12	1	1	-1	1	1	1	-1	-1	36.35	57.19

The test results in Table 3 were analysed by ANOVA, and the significance of each test parameter on the static angle of repose and dynamic angle of repose was obtained as shown in Tables 4 and 5. From Table 4, it can be seen that the rolling friction coefficient of soil-soil D has a $p < 0.01$, which is very significant on the simulation results; soil-soil coefficient of restitution B, soil-steel static friction coefficient F, are significant on the simulation results. The smaller the soil-soil coefficient of restitution, the greater the energy loss during collision of soil particles, which will limit the movement between soil particles and make the static accumulation angle increase. The remaining parameters have p-values greater than 0.05, the effect on the simulation results is extremely small. From Table 5, it can be seen that the soil-steel static friction coefficient F, JKR surface energy H is extremely significant on the dynamic angle of repose with p-value less than 0.01, and p-value of the rest of the parameters is greater than 0.05, the effect on the dynamic angle of repose being extremely small.

Table 4

ANOVA results of the Plackett-Burman test for the static angle of repose

Source	Sum of squares	DF	Mean Square	F-value	P-value	Significance
Model	594.37	8	74.30	20.20	0.0156	*
A	0.3072	1	0.3072	0.0835	0.7914	
B	110.90	1	110.90	30.16	0.0119	*
C	5.07	1	5.07	1.38	0.3251	
D	399.28	1	399.28	108.58	0.0019	**
E	1.67	1	1.67	0.4548	0.5484	
F	46.18	1	46.18	12.56	0.0383	*
G	24.03	1	24.03	6.53	0.0835	
H	6.93	1	6.93	1.88	0.2634	

Table 5

ANOVA results of the Plackett-Burman test for the dynamic angle of repose

Source	Sum of squares	DF	Mean Square	F-value	P-value	Significance
Model	442.08	8	55.26	14.06	0.0262	*
A	30.72	1	30.72	7.82	0.0681	
B	0.4641	1	0.4641	0.1181	0.7538	
C	25.52	1	25.52	6.49	0.0841	
D	19.51	1	19.51	4.96	0.1122	
E	0.9747	1	0.9747	0.2480	0.6527	
F	174.35	1	174.35	44.36	0.0069	**
G	30.53	1	30.53	7.77	0.0686	
H	160.02	1	160.02	40.71	0.0078	**

Note: * indicates a significant difference ($p<0.05$); ** indicates a highly significant difference ($p<0.01$).

Steepest Ascent Test

The steepest ascent test is used to accurately determine the centre point of the test factor levels, enabling the initial response region to quickly approach the optimal response region. Based on the results of the parameter screening tests, the factors with P-values less than 0.05 in Tables 4 and 5 were selected for the steepest ascent test. The selected parameters were gradually increased according to the chosen ascent step size, while the remaining parameters were held constant at intermediate levels: soil shear modulus (1×10^7 Pa), soil-soil static friction coefficient (0.68), soil-steel restitution coefficient (0.45), and soil-steel rolling friction coefficient (0.30). The test results are presented in Table 6. As shown in the table, both the static and dynamic angles of repose increased progressively with higher values of the selected test factors.

Table 6

Steepest Ascent Test Scheme and Results

Serial number	Experimental factors				Static angle of repose / (°)	Dynamic angle of repose / (°)
	B	D	F	H		
1	0.75	0.05	0.5	0.1	25.62	35.61
2	0.63	0.08	0.56	0.14	31.49	47.57
3	0.51	0.11	0.62	0.18	35.6	56.34
4	0.39	0.14	0.68	0.22	38.35	59.95
5	0.27	0.17	0.74	0.26	41.73	62.1
6	0.15	0.2	0.8	0.3	42.05	67.49

Box-Behnken test and regression analysis

In order to obtain the mathematical regression model of the angle of repose with the significant influencing factors (soil-soil restitution coefficient, soil-soil rolling friction coefficient, soil-steel static friction coefficient, and JKR surface energy), a response surface test was conducted using the Box-Behnken method. According to the results of the steepest ascent test, the parameter values of test No. 2 in Table 7 were selected as the intermediate level, and the parameter values of No. 1 and No. 3 were selected as the low level and high level, respectively, for the experimental design. The test scheme and results are shown in Table 7.

Table 7

Box-Behnken test scheme and results

Serial number	Experimental factors				Static angle of repose / (°)	Dynamic angle of repose / (°)
	B	D	F	H		
1	0.51	0.05	0.56	0.14	29.89	48.74
2	0.63	0.05	0.5	0.14	28.94	45.06
3	0.75	0.08	0.56	0.18	30.54	54.77
4	0.63	0.05	0.56	0.18	31.24	53.88
5	0.63	0.08	0.56	0.14	32.92	51.39
6	0.63	0.11	0.5	0.14	34.34	47.28
7	0.75	0.08	0.62	0.14	27.61	53.83
8	0.63	0.11	0.56	0.1	34.93	43.28
9	0.51	0.11	0.56	0.14	35.12	49.71
10	0.75	0.08	0.5	0.14	29.96	44.09
11	0.63	0.05	0.56	0.1	28.52	40.94
12	0.63	0.08	0.56	0.14	32.74	51.94
13	0.63	0.08	0.56	0.14	32.41	51.53
14	0.75	0.08	0.56	0.1	30.51	41.59
15	0.51	0.08	0.56	0.18	33.72	54.53
16	0.63	0.08	0.62	0.1	28.97	46.72
17	0.51	0.08	0.5	0.14	31.43	47.71
18	0.75	0.05	0.56	0.14	27.8	48.9
19	0.63	0.08	0.56	0.14	32.74	51.8
20	0.51	0.08	0.56	0.1	30.79	44.45
21	0.63	0.11	0.62	0.14	31.57	53.67
22	0.63	0.08	0.5	0.1	31.48	36.8
23	0.63	0.08	0.56	0.14	32.66	51.3
24	0.63	0.11	0.56	0.18	34.8	54
25	0.63	0.05	0.62	0.14	28.14	52.58
26	0.63	0.08	0.62	0.18	30.7	55.08
27	0.63	0.08	0.5	0.18	32.23	52.08
28	0.75	0.11	0.56	0.14	32.72	49.83
29	0.51	0.08	0.62	0.14	30.58	52.74

Tables 8 and 9 show the analysis of variance (ANOVA) for the static and dynamic angle of repose in the test, respectively. As can be seen from Tables 8 and 9, the p-values (p-value is the probability of obtaining the observed value of the test statistic and other values that are more unsupportive of the original hypothesis when the original hypothesis is true) of the two fitted models are less than 0.01, indicating that the relationship between the angle of repose and the resulting regression equations is highly significant; the p-values of the out-of-fit terms are all greater than 0.05, indicating that the regression equations are not out-of-fit, and they have a predictive significance; the coefficients of determination for the static angle of repose are 0.9946 for static angle of repose and 0.9926 for dynamic angle of repose, indicating a good fit. For the static angle of repose, the p-values of the soil-soil restitution coefficient B, the soil-soil dynamic friction coefficient D, the soil-steel static friction coefficient F, the JKR surface energy H, and the interaction terms BF, BH, DF, and DH are less than 0.01, which are extremely significant on the static angle of repose; the p-values of each of the quadratic terms, except for H2 and the quadratic term BD are all greater than 0.05, which indicates that these two factors were not significant on the static angle of repose, and all other factors had significant effects on the static angle of repose. For the dynamic angle of repose, the p-values of soil-soil rolling friction factor D, soil-steel rolling friction coefficient F, JKR surface energy, interaction term BF, and secondary terms B2, D2, F2, and H2 are less than 0.01, which are extremely significant on the dynamic angle of repose, and the p-values of soil-soil restitution coefficient B and interaction term BH are less than 0.05, which have a significant effect on the dynamic angle of repose. and the other factors were not significant on the dynamic angle of repose.

Table 8

Analysis of variance of a quadratic regression model for static angle of repose

Source	Sum of squares	DF	Mean Square	F-value	P-value	Significance
Model	127.80	14	9.13	182.58	< 0.0001	**
B- Soil-Soil restitution coefficient	12.79	1	12.79	255.88	0.0290	*
D- Soil-soil rolling friction factor	69.84	1	69.84	1396.96	0.0018	**
F- Soil-steel static friction factor	9.74	1	9.74	194.78	< 0.0001	**
H- JKR surface energy	5.37	1	5.37	107.48	< 0.0001	**

Source	Sum of squares	DF	Mean Square	F-value	P-value	Significance
BD	0.0240	1	0.0240	0.4805	0.9729	
BF	0.5625	1	0.5625	11.25	0.0011	**
BH	2.10	1	2.10	42.05	0.0179	*
DF	0.9702	1	0.9702	19.41	0.3449	
DH	2.03	1	2.03	40.62	0.0754	
FH	0.2401	1	0.2401	4.80	< 0.0001	**
B²	8.12	1	8.12	162.36	0.0040	**
D²	0.2625	1	0.2625	5.25	0.0002	**
F²	18.94	1	18.94	378.79	0.0001	**
H²	0.1434	1	0.1434	2.87	< 0.0001	**
Residual	0.6999	14	0.0500			
Lack of Fit	0.5628	10	0.0563	1.64	0.0501	
Pure Error	0.1371	4	0.0343			
Cor Total	128.50	28				

The quadratic regression equation for the static angle of repose (SAoR) was derived by eliminating the insignificant terms from the model, while ensuring that the remaining terms retained overall model significance and goodness of fit.

$$SRA = 32.69 - 1.03B + 2.41D - 0.9008F + 0.6692H - 0.375BF - 0.725BH + 0.245FH - 1.12B^2 - 0.2012D^2 - 1.71F^2 - 0.1487H^2 \quad (7)$$

Table 9

Analysis of variance for quadratic regression modeling of dynamic angle of repose

Source	Sum of squares	DF	Mean Square	F-value	P-value	significance
Model	630.22	14	45.02	134.73	< 0.0001	**
B- Soil-Soil restitution coefficient	1.98	1	1.98	5.92	0.0290	*
D- Soil-soil rolling friction factor	4.90	1	4.90	14.67	0.0018	**
F- Soil-steel static friction factor	144.21	1	144.21	431.63	< 0.0001	**
H- JKR surface energy	414.89	1	414.89	1241.77	< 0.0001	**
BD	0.0004	1	0.0004	0.0012	0.9729	
BF	5.55	1	5.55	16.60	0.0011	**
BH	2.40	1	2.40	7.19	0.0179	*
DF	0.3192	1	0.3192	0.9554	0.3449	
DH	1.23	1	1.23	3.69	0.0754	
FH	11.97	1	11.97	35.83	< 0.0001	**
B²	3.94	1	3.94	11.78	0.0040	**
D²	8.67	1	8.67	25.96	0.0002	**
F²	9.11	1	9.11	27.27	0.0001	**
H²	36.59	1	36.59	109.52	< 0.0001	**
Residual	4.68	14	0.3341			
Lack of Fit	4.38	10	0.4383	5.96	0.0501	
Pure Error	0.2943	4	0.0736			
Cor Total	634.89	28				

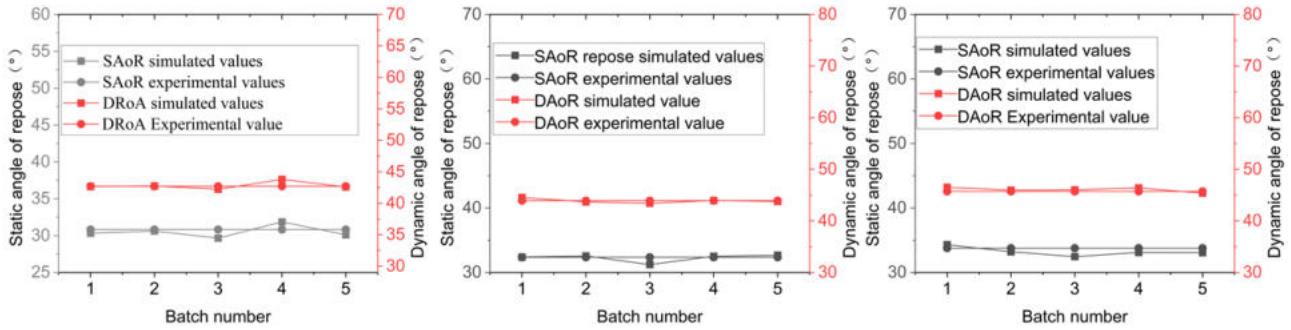
The quadratic regression equation for the dynamic angle of repose (DAoR) was developed by removing the statistically insignificant terms, while ensuring that the model remained significant and exhibited a good fit to the experimental data:

$$DRA = 51.59 - 0.4058B + 0.6392D + 3.47F + 5.88H + 1.18BF + 0.775BH - 0.7789B^2 - 1.16D^2 - 1.19F^2 - 2.38H^2 \quad (8)$$

Determination and validation of discrete element simulation parameters

The experimentally measured soil angles of repose were used as response targets to optimize the regression equations, and the resulting combinations of discrete element simulation parameters were input into EDEM software for validation. Figure 8 presents a comparison between the simulated and experimental values of the optimized parameter sets for each soil layer. The average relative errors for the static angle of repose and dynamic angle of repose were calculated as 1.56% and 0.984%, respectively. These results indicate that the simulated values closely matched the experimental measurements, with no significant differences, thus confirming the accuracy and reliability of the calibrated parameter combinations. Although the angles of repose for each group were relatively similar, different combinations of discrete element simulation parameter values resulted in variations in particle contact interactions and force chain distributions.

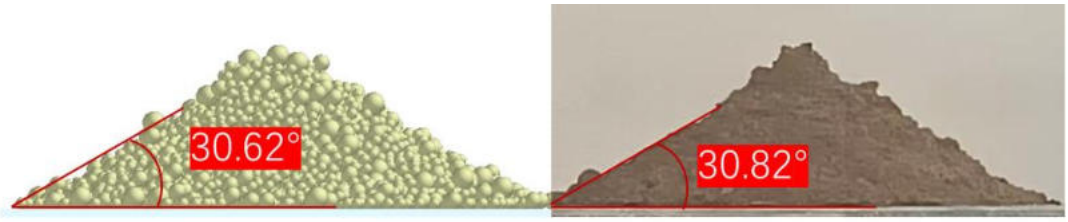
These differences led to distinct stacking morphologies in the simulated particle assemblies. Therefore, among the five DEM parameter combinations tested for each soil layer, the one that produced a stacking morphology most closely resembling the actual experimental observation was selected as the preferred combination. The selected optimal DEM parameter values for each soil layer are as follows: soil-soil restitution coefficient (B) is 0.734, 0.556, 0.643, soil-soil rolling friction coefficient (D) is 0.082, 0.086, 0.095, soil-steel static friction coefficient (F) is 0.564, 0.511, 0.525 and the JKR surface energy (H) is 0.102, 0.117, 0.122.



(a) (b) (c)

Fig. 8 - Comparison between simulated and experimental values using the optimized discrete element simulation parameter combinations

The static and dynamic angles of repose for the upper soil layer are shown in Figures 9 and 10. As illustrated, there is no significant difference between the simulation results and the actual experimental observation. The measured static angle of repose was 30.82°, and the dynamic angle of repose was 42.70°, while the simulated values were 30.62° and 42.75°, respectively. The relative errors for the static and dynamic angles of repose were 0.65% and 0.12%, which are both very low. These results confirm that the optimized discrete element simulation parameter combination is accurate and reliable, and thus suitable for use in subsequent simulation studies.



(a) simulated image (b) actual image

Fig. 9 - Static angle of repose of the soil



(a) simulated image (b) actual image

Fig. 10 - Dynamic angle of repose of the soil

CONCLUSIONS

The computational efficiency of discrete element simulations was significantly improved by scaling particle size and reducing particle stiffness. The results of the Plackett-Burman test indicated that, within a certain value range, factors such as particle shear modulus, particle-steel restitution coefficient, particle-steel kinetic friction coefficient, and particle-particle static friction coefficient did not significantly affect the angle of repose. In the Box-Behnken response surface test, the static and dynamic angles of repose were used as dual response indices to optimize the discrete element simulation parameters. This approach led to more accurate simulation results, with particle behaviour more closely resembling actual soil conditions. In this study, the static and dynamic angles of repose were adopted as macroscopic response indicators for calibrating the discrete element simulation parameters of simplified soil particles. Optimal parameter combinations were determined through the Plackett-Burman and Box-Behnken tests, and subsequently validated through experimental comparison. The main conclusions are as follows:

(1) The average static and dynamic angles of repose of the soil were measured using a custom-built device, yielding values of 30.82°, 32.35°, and 33.77° for the static angle, and 42.7°, 43.91°, and 45.7° for the dynamic angle, corresponding to the upper, middle, and lower soil layers, respectively.

(2) The Plackett-Burman test identified that the soil-soil restitution coefficient, soil-soil rolling friction coefficient, and soil-steel static friction coefficient significantly influenced the static angle of repose, while the soil-steel static friction coefficient and JKR surface energy were significant factors for the dynamic angle of repose.

(3) The Box-Behnken test was employed to establish second-order regression models for both static and dynamic angles of repose. These models were optimized using the experimentally measured angle values as targets. The resulting optimal parameter combinations, validated through experiment, were as follows: soil-soil restitution coefficients were 0.734, 0.556, 0.643, soil-soil rolling friction coefficients were 0.082, 0.086, 0.096, soil-steel static friction coefficients were 0.564, 0.511, 0.525, JKR surface energies were 0.102, 0.117, 0.122.

(4) The simulated static angles of repose for the three soil layers were 30.62°, 32.51°, and 33.2°, and the simulated dynamic angles were 42.75°, 43.95°, and 45.96°, respectively. The corresponding relative errors for the static angle were 0.65%, 0.09%, and 2.03%, and for the dynamic angle were 0.28%, 0.12%, and 0.56%. These small errors confirm that the calibrated discrete element simulation parameters are accurate and reliable, and can be confidently used in subsequent DEM simulations.

REFERENCES

[1] Chen Y., Qi Y., Wang Y. (2017). Spatial Variability and Factors Affecting Soil Available Potassium in the Central Qinling – Daba Mountain Area (秦巴中部山区耕地土壤速效钾空间变异及其影响因素) [J]. *Research of Environmental Sciences*, Vol. 30(2), pp.257-266.

[2] Feng Y.T., Han K., Owen D.R.J., Loughran J. (2009) On upscaling of discrete element models: Similarity principles [J]. *Engineering Computations*, Vol. 26(6), pp.599-609.

[3] Han S., Qi J., Li Y. (2021). Parameters Calibration of Discrete Element for Deep Application of Bulk Manure in Xinjiang Orchard (新疆果园深施散体厩肥离散元参数标定研究) [J]. *Transactions of the Chinese Society for Agricultural Machinery*, Vol. 52(4), pp.101-108.

[4] Li S., Liu Y, Li Y., Hu M. (2024). DEM parameters of slope cultivated purple soil in Southwest China and interaction mechanism between very narrow tine [J]. *Scientific Reports*, Vol. 14(1), pp.18089.

[5] Li J., Tong J., Hu B., Ma Y. (2019). Calibration of parameters of interaction between clayey black soil with different moisture content and soil-engaging component in northeast China (不同含水率黏重黑土与触土部件互作的离散元仿真参数标定) [J]. *Transactions of the Chinese Society of Agricultural Engineering*, Vol. 35(6), pp.130-140.

[6] Luana C., Rodrigo C, Maria D. (2017). Flow properties of coarse and fine sugar powders [J]. *Journal of Food Process Engineering*, Vol. 14(1), pp.1-10.

[7] Li Y., Li F., Xu X. (2019). Parameter calibration of wheat flour for discrete element method simulation based on particle scaling (基于颗粒缩放的小麦粉离散元参数标定) [J]. *Transactions of the Chinese Society of Agricultural Engineering*, Vol. 35(16), pp.320-327.

[8] Luo S., Yuan Q., Gouda S. (2018). Parameters Calibration of Vermicomposting Nursery Substrate with Discrete Element Method Based on JKR Contact Model (基于 JKR 粘结模型的蚯蚓粪基质离散元法参数标定) [J]. *Transactions of the Chinese Society for Agricultural Machinery*, Vol. 49(4), pp.343-350.

[9] Lommen S., Schott D., Lodewijks G. (2014). DEM speedup: Stiffness effects on behavior of bulk material [J]. *Particuology*, Vol. 12(4), pp.107-112.

[10] Maitadudulili A., Litipu Y., Abudureheman K. (2016). Technical Key Points of Grape Trenching and Vine Burying Machine Operation (葡萄开沟埋藤机作业技术要点) [J]. *Agricultural Machinery Technology Extension*, Vol. 16(10), pp.52-53.

[11] Song Z., Li H., Tian F., Li F. (2022). Calibration Method of Contact Characteristic Parameters of Soil in Mulberry Field Based on Unequal-diameter Particles DEM Theory (桑园土壤非等径颗粒离散元仿真模型参数标定与试验) [J]. *Transactions of the Chinese Society for Agricultural Machinery*, Vol. 53(6), pp.21-32.

[12] Shen X., Zhu Z., Yang L., Liu J. (2024). Current situation and development suggestions of wine grape mechanization in Xinjiang (新疆酿酒葡萄生产机械化现状与发展趋势) [J]. *Xinjiang Agricultural Sciences*, Vol.61(SI), pp.147-152.

[13] Smith W., Peng H. (2024). Modeling of wheel-soil interaction over rough terrain using the discrete element method [J]. *Journal of Terramechanics*, Vol. 51(5-6), pp.277-287.

[14] Thomas R., André K. (2018). Scaling of the angle of repose test and its influence on the calibration of DEM parameters using upscaled particles [J]. *Powder Technology*, Vol. 330(2018), pp.58-66.

[15] Wang M., Han S., Liu X. (2024). The current development status of the grape industry in Xinjiang (新疆葡萄产业发展现状分析) [J]. *Xinjiang Agricultural Sciences*, Vol. 61(SI), pp.127-130.

[16] Yang Q., He M., Shi L., Li Z. (2023). Calibration of discrete element simulation parameters for interactions between layered cold soil and contact soil cleaning tools (分层防寒土与接触式清土机具相互作用的离散元仿真参数标定) [J]. *Journal of Jiangsu University*, Vol. 44(1), pp.52-61.

[17] Zhang X., Guo R, Shi Z. (2017). Establishment And Calibration of Discrete Element Model for Coated Wheat Seed Based on Static An [J]. *INMATEH -Agricultural Engineering*, Vol. 74(3), pp.370-379. DOI: https://doi.org/10.35633/inmateh-74-32

[18] Zeng Z., Ma X., Cao X (2021). Critical Review of Applications of Discrete Element Method in Agricultural Engineering (离散元法在农业工程研究中的应用现状和展望) [J]. *Transactions of the Chinese Society for Agricultural Machinery*, Vol. 52(4), pp.1-20.

[19] Zhen W., Liu H., Qian X. (2024). Discrete Element Parameter Calibration for Red Soil with Different Moisture Contents in Fujian Tobacco-growing Areas (福建烟区不同含水率红壤离散元参数标定) [J]. *Journal of Shenyang Agricultural University*, Vol. 55(3), pp.323-333.

[20] Zhou P., He M., Kan Z. (2018). Experiment on the Dynamic Angle of Repose of Soil Particles Based on OpenCV-Python (基于 OpenCV-Python 的土壤颗粒动态休止角试验) [J]. *Journal of Chinese Agricultural Mechanization,* Vol. 44(5), pp.214-222.

RESEARCH ON ADVANCED COMPENSATION CONTROL STRATEGY FOR SOYBEAN COMBINE HARVESTER HEADER HEIGHT BASED ON AREA ARRAY LiDAR
/
基于面阵激光雷达的大豆联合收割机割台高度超前补偿控制策略研究

Qingling LI[1,2], Chao ZHANG[*1,2], Shaobo YE [1,2], Decong ZHENG[1,2]
[1)] College of Agricultural Engineering, Shanxi Agricultural University, Taigu 030801, China;
[2)] Dryland Farm Machinery Key Technology and Equipment Key Laboratory of Shanxi Province, Taigu 030801, China
Corresponding author: Chao Zhang
Tel: +86-152-3541-5968; E-mail: sxndgxyzhangchao@sxau.edu.cn
DOI: https://doi.org/10.35633/inmateh-76-21

Keywords: *Area array LiDAR, soybean combine harvester, header height，Bang-bang control*

ABSTRACT
For the automatic control of soybean harvester header height, this study uses Area array LiDAR for header height detection. An improved quartile range algorithm is used to dynamically remove outliers under crop residue interference. Linear, quadratic, and cubic nonlinear terrain fitting models are established based on the surface undulation characteristics of soybean fields. The Huber loss function is introduced to enhance the robustness of parameter estimation. The balance between model complexity and fitting goodness is quantified using Bayesian information criterion (BIC), and the model intercept term with the smallest BIC value is selected as the terrain reference height. Aiming at the hysteresis characteristics of valve controlled asymmetric hydraulic cylinders, a telescopic dual-mode transfer function model is established, and a Bang-bang switch lead compensation strategy with position threshold is proposed. By predicting the trend of terrain changes, the electromagnetic directional valve is triggered in advance when the height error of the header exceeds the set threshold, effectively reducing the system response delay. Field comparative experiments have shown that at a working speed of 1m/s, the automatic control mode significantly improves the uniformity of cutting compared to the manual mode. When the cutting threshold is set to 20, 25, and 30 mm, the coefficient of variation of cutting height is reduced by 2.13%, 1.71%, and 0.55%, respectively. Moreover, the automatic mode maintains a gentle distribution characteristic within the threshold range of 15-35 mm, verifying the strong robustness and control accuracy advantages of the designed system in complex farmland environments.

摘要
针对大豆收割机割台高度自动控制，本研究采用面阵激光雷达进行割台高度检测，利用改进四分位距算法实现作物残茬干扰下的离群点动态剔除，并依据大豆田地表起伏特征建立线性、二次及三次非线性地形拟合模型，通过引入 Huber 损失函数增强参数估计鲁棒性，结合贝叶斯信息准则（BIC）量化模型复杂度与拟合优度的平衡关系，择优选取 BIC 值最小的模型截距项作为地形基准高度。针对阀控非对称液压缸的迟滞特性，建立伸缩双模态传递函数模型，提出带位置阈值的 Bang-Bang 开关超前补偿策略：通过预判地形突变趋势，在割台高度误差超过设定阈值时提前触发电磁换向阀动作，有效降低了系统响应延迟。田间对比试验表明，在 1m/s 作业速度下，自动控制模式较手动模式显著改善割茬均匀性，当割茬阈值设置为 20、25 及 30mm 时，割茬高度变异系数分别降低了 2.13%、1.71%及 0.55%，且自动模式在 15-35 mm 阈值范围内始终维持平缓分布特征，验证了所设计系统在复杂农田环境中的强鲁棒性与控制精度优势。

INTRODUCTION
The losses during soybean harvesting mainly include header losses, threshing and separation losses, of which header losses account for about 80% of the total losses (*Lian et al., 2024*). Crop cutting and missed cutting are related to the contour and height adjustment of the header. If the position of soybean pods is low, the cutting knife is prone to miss the soybean pods, causing loss of harvest on the cutting platform. If the height of the cutting blade is lowered, it is easy to shovel soil into the cutting table when the blade is in contact with the ground, causing soil to mix with soybean seeds and resulting in "mud flower face" loss, which affects the quality of soybean harvest *(Liu, 2022)*. Therefore, during harvesting, the cutting table should be adjusted in a timely manner according to the height of the soybean bottom pod to achieve cutting table imitation. At present, the detection methods for the height of the cutting table can be basically divided into contact and non-contact methods. For the contact detection method, the Cleodolphi team introduced a position sensor in the height detection of the harvester chassis and used a pressure sensing system to provide real-time feedback on the contact status of the cutter head with the ground (*Cleodolphi et al., 2017*). The combine harvester header

adjustment system developed by Liao Yong achieves dual sensor collaborative detection, capturing crop height information through E18-D80NK infrared diffuse reflection photoelectric sensor, and accurately obtaining header height data with KTC pull rod potentiometer displacement sensor (*Liao et al., 2018*). Li Zerui improved the traditional cutting table system for soybean harvesting characteristics, and designed a floating cutter that achieved adaptive adjustment within a small range through mechanical profiling (*Li et al., 2022*). Zhou developed an intelligent cutting platform system based on angle sensing for the special cultivation mode of soybean under film mulching drip irrigation in Xinjiang. Field test data showed that the relative error of height detection of the device remained stable within 5% (*Zhou et al., 2024*). Non-contact surface parameter detection mainly includes ultrasonic waves, machine vision, infrared sensing, etc. Pasi et al constructed a soil wheel multi ultrasonic sensor fusion measurement system, which controlled the terrain contour detection error within ± 10 mm through multi-source data fusion algorithm (*Pasi et al., 2015*). The ultrasonic dynamic plant measurement system has been validated through orthogonal experiments, and its measurement accuracy is significantly improved compared to traditional floating wheel devices (*Chang et al., 2016*). Huang Yiqi's team proposed a 3D coordinate reconstruction method based on Otsu adaptive thresholding algorithm, which achieved sub centimeter level (MAE<3 mm) terrain detection accuracy through feature point cloud spatial registration (*Huang et al., 2017*). Huang Min proposed a sugarcane ridge height detection scheme based on frequency modulated continuous wave radar. The device can maintain a maximum error level of 3.02 cm under complex working conditions with a vegetation cover thickness of 10 cm and a detection distance of 170 cm (*Huang et al., 2021*). Its penetrating detection mechanism provides an innovative solution for terrain measurement under vegetation cover conditions.

However, the above-mentioned technical systems generally adopt a discrete single point sampling mechanism, which makes the measurement data susceptible to local random noise interference and unable to accurately characterize the macroscopic terrain characteristics of the work area. Based on this, this study proposes a terrain perception system based on area array LiDAR, which uses fusion point cloud feature extraction and introduces a Bang-bang switch advance compensation strategy with position threshold: when the terrain undulation is detected below the preset threshold, the system state remains stable, and only triggers hydraulic actuator adjustment when significant terrain changes are identified.

MATERIALS AND METHODS

Data acquisition and processing of area array LiDAR

This study used Nooploop's TOFSense-MS surface array LiDAR for header height detection, with a ranging range of 1.5c m ~ 4 m and a distance resolution of 1 mm. The data was transmitted through UART interface using NLink protocol, and an 8 × 8 spatial height matrix was constructed in real time to generate a three-dimensional point cloud map. To address the issue of data anomalies caused by crop residues, terrain changes, and sensor noise in the work environment, an improved quartile range algorithm is adopted for outlier detection:

$$Q_1 = P_{25}(h), \quad Q_1 = P_{75}(h), \quad IQR = Q_3 - Q_1 \tag{1}$$

Keep the data range as [Q1-1.5IQR, Q3+1.5IQR], and remove outliers outside the range. Establish three types of terrain fitting models based on the surface topography characteristics of soybean fields:

Linear model:

$$h = \beta_0 + \beta_1 x + \beta_2 y + \varepsilon \tag{2}$$

Quadratic model (including curvature term):

$$h = \beta_0 + \sum_{k=1}^{2}(\beta_k x^k + \gamma_k y^k) + \beta_3 xy + \varepsilon \tag{3}$$

Third order model (high-order nonlinearity):

$$h = \beta_0 + \sum_{k=1}^{3}(\beta_k x^k + \gamma_k y^k) + \beta_4 xy + \beta_5 x^2 y + \beta_6 xy^2 + \varepsilon \tag{4}$$

Among them, (x, y) are the coordinates of the LiDAR array, ε is the residual term, and the model complexity dynamically adjusts with the complexity of the crop field terrain. Huber loss function is used for anti-interference parameter estimation:

$$\min_{\beta}\sum_{i=1}^{n}\rho(\frac{r_i}{\sigma}),\rho(r)=\begin{cases}0.5r^2 & |r|<c\\ c|r|-0.5c^2 & |r|>c\end{cases} \quad (5)$$

The applicability of the model is evaluated based on Bayesian Information Criterion (BIC):

$$BIC = n\ln(\hat{\sigma}^2)+k\ln(n) \quad (6)$$

In the formula, n is the effective data amount, K is the number of model parameters and $\hat{\sigma}^2$ is the robust regression residual variance. The model with the lowest BIC value is selected, and the intercept term of this model is extracted as the fused height value. The left image below displays the original sensor data, which contains four noticeable outlier points. After processing using the method described above, the influence of these anomalies is effectively mitigated.

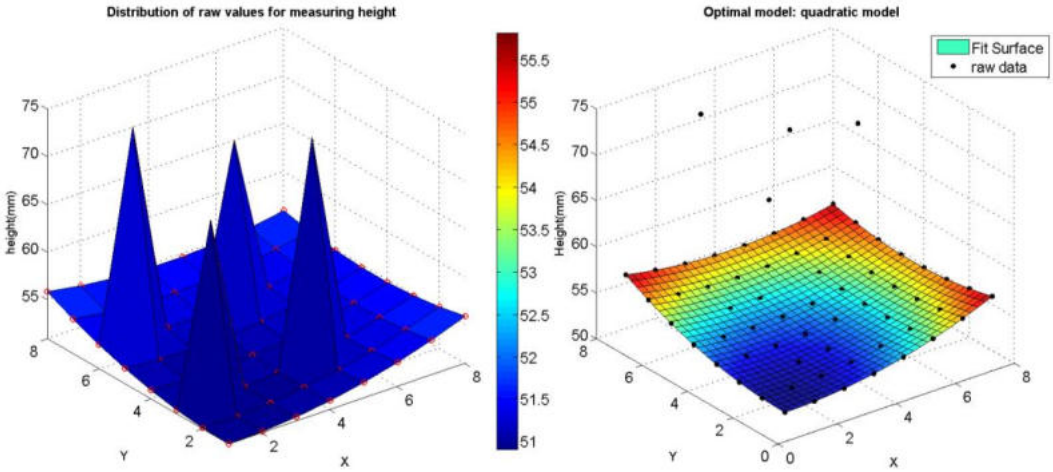


Fig. 1 - Comparison of Front and Rear Processing of Area Array LiDAR Data

Figure 2 illustrates a closed-loop position control system based on the STM32F103ZET6 development board. TOFSense-MS LiDAR data is transmitted to the STM32 master control unit via serial communication. The microcontroller executes control algorithms to drive the H-bridge module, thereby regulating the on/off states and fluid direction of the electromagnetic directional valve, which ultimately achieves header height adjustment. The serial port screen provides a Human-Machine Interface (HMI) supporting parameter configuration, real-time data monitoring, and status display functions.

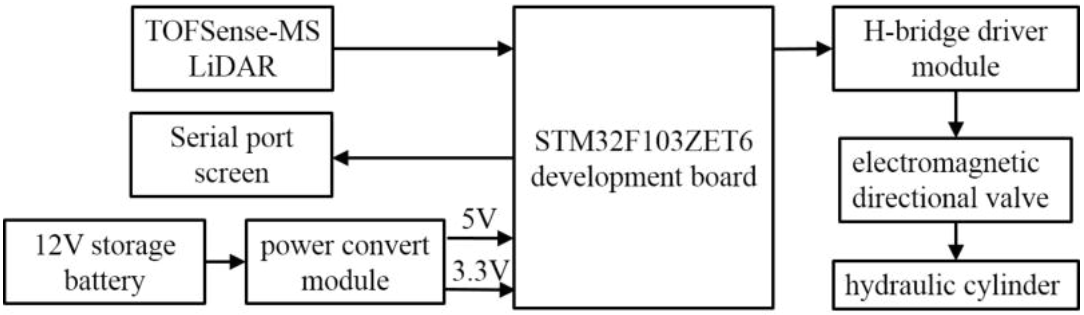


Fig. 2 - Closed-loop position control system

Modeling and analysis of valve controlled asymmetric cylinder system

The height adjustment of the cutting table adopts an asymmetric hydraulic cylinder as the execution unit, and the lifting control is achieved by an electromagnetic directional valve. Compared to proportional valve systems, electromagnetic directional valves have significant engineering applicability in the field of agricultural equipment due to their simple structure, low maintenance costs, and strong resistance to pollution. However, its discrete switch control characteristics result in inherent delay in valve core switching, directly affecting the dynamic response performance of the hydraulic cylinder. To optimize the control accuracy of the system, it is necessary to establish a dynamic model of the valve controlled asymmetric cylinder. The structural diagram is shown in Fig 3.

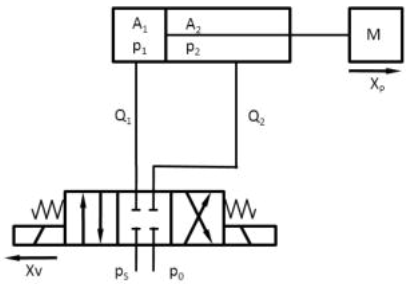


Fig. 3 - Structural diagram of valve controlled asymmetric cylinder system

Assuming the ratio of the two cavity areas is n, that is:

$$n = \frac{A_2}{A_1} \tag{7}$$

Define the load pressure as P_L and the load flow rate as Q_L. When the hydraulic cylinder enters steady state, there are:

$$p_L = \frac{p_1 A_1 - p_2 A_2}{A_1} = p_1 - n p_2 \tag{8}$$

$$Q_L = Q_1 = \frac{Q_1 + n Q_2}{1 + n^2} \tag{9}$$

Due to the different open-loop gains of the extension and retraction of asymmetric hydraulic cylinders, it is necessary to establish basic equations for each case separately. The linear equation for the flow rate of a four-way valve controlled asymmetric cylinder is as follows (*Ye et al., 2015*):

$$Q_L = K_q x_v - K_c p_L \tag{10}$$

$$K_q = \frac{\partial Q_L}{\partial x_v} = \begin{cases} K_{q1} = C_d w \sqrt{\frac{2}{\rho} \frac{(p_s - p_L)}{1 + n^3}}, & x_v > 0 \\ K_{q2} = C_d w \sqrt{\frac{2}{\rho} \frac{n p_s + p_L}{1 + n^3}}, & x_v < 0 \end{cases} \tag{11}$$

$$K_c = -\frac{\partial Q_L}{\partial p_L} = \begin{cases} K_{c1} = C_d w x_v \sqrt{\frac{1}{2\rho} \frac{1}{(1 + n^3)(p_s - p_L)}}, & x_v > 0 \\ K_{c2} = C_d w x_v \sqrt{\frac{1}{2\rho} \frac{1}{(1 + n^3)(n p_s + p_L)}}, & x_v < 0 \end{cases} \tag{12}$$

In the formula: C_d is the valve port flow coefficient; ω is the gradient of the throttle area of the solenoid valve; X_v is the displacement of the reversing valve core; p_1 is the rodless chamber pressure; p_2 is the rodless chamber pressure; P_S represents the fuel supply pressure; ρ represents the density of hydraulic oil.

Assuming that the initial volumes of the two chambers of the piston are the same and the leakage is ignored, the flow continuity equation can be derived:

$$Q_L = A_1 \frac{dx_p}{dt} + \frac{V_t}{2(1 + n^2)\ \beta_e} \frac{dp_L}{dt} \tag{13}$$

$$A_1 P_L = m \frac{d^2 y}{dt^2} + B_c \frac{dy}{dt} + K y + F \tag{14}$$

$$x_p = \frac{A_1 K_q x_v - (K_c + \frac{V_t}{2(1 + n^2)\beta_e} s) F}{(K_c + \frac{V_t}{2(1 + n^2)\beta_e} s)(m s^2 + B_c s + K) + A_1^2 s} \tag{15}$$

Neglecting elastic load, viscous damping, and external load forces, it can be obtained:

$$x_p = \frac{A_1 K_q x_v}{(K_c + \frac{V_t}{2(1+n^2)\beta_e} s)(ms^2) + A_1^2 s} = \frac{\frac{K_q}{A_1} x_v}{s(\frac{V_t m}{2A_1^2(1+n^2)\beta_e} s^2 + \frac{K_c m}{2A_1^2} s + 1)} \quad (16)$$

Table 1

Valve-controlled asymmetric cylinder power structure parameters

Parameter Name	Symbol	Parameter Value	Parameter Name	Symbol	Parameter Value
Effective area of rodless cavity	A_1	1.2566×10^{-3}m^2	Discharge Coefficient	C_d	0.61
Effective area of rod cavity	A_2	0.8765×10^{-3}m^2	Area gradient	ω	0.0047
Area ratio	n	0.6975	Liquid elastic modulus	β_e	6.85×10^{8}Pa
Energy pressure	P_s	8×10^{6}Pa	Oil density	ρ	850kg/m^3
Return oil pressure	P_0	0	Effective volume	V_t	1.2566×10^{-4}m^3

According to the technical manual, the opening time of the 4WE6J61B solenoid valve is 20-45 ms and the closing time is 10-25 ms, both of which are 25 ms. Other parameter settings are shown in Table 1. Therefore, the transfer function when the hydraulic cylinder is extended can be:

$$H_1(S) = \frac{271.0481}{5.8613\times10^{-6}s^3 + 0.001s^2 + s} e^{-0.025s} \quad (17)$$

Similarly, the transfer function when the hydraulic cylinder retracts is:

$$H_2(S) = \frac{226.3698}{5.8613\times10^{-6}s^3 + 0.0012s^2 + s} e^{-0.025s} \quad (18)$$

Analysis of Bang-Bang switch lead compensation strategy with position threshold

The input of an electromagnetic directional valve can be represented as the set $U=\{U+, 0, U-\}$, corresponding to the hydraulic cylinder rising, holding, and falling respectively. Set the height of the header as $h_0(t)$, measure the height value of the sensor as $h(t)$, and the header elevation error e is defined as $h_0(t) - h(t)$. When | e | is less than the position threshold ε, the electromagnetic directional valve does not operate. When e is greater than the position threshold ε, it indicates that the ground elevation increases and the header position is lower, and the header needs to rise. When e is less than the position threshold - ε, it indicates that the ground elevation decreases and the header position is higher, and the header needs to descend. The algorithm flow chart is shown in Fig. 4.

The control algorithm expression is:

$$U = \begin{cases} U_+ & e > \varepsilon \\ 0 & |e| < \varepsilon \\ U_- & e < -\varepsilon \end{cases} \quad (19)$$

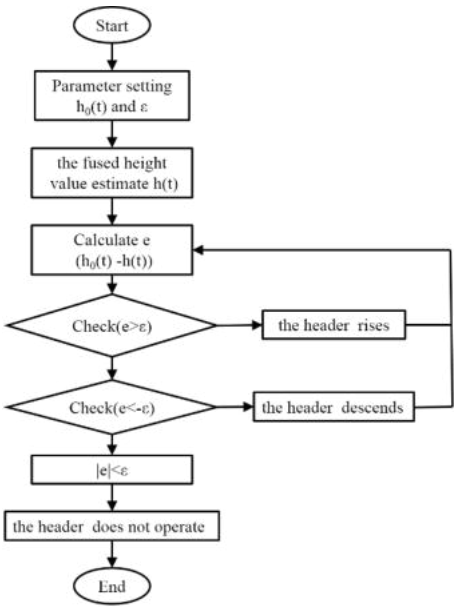


Fig. 4 - Algorithm flow chart

Set the header height to 20 cm and simulate ground height changes using a filtered white noise time-domain road input model, the expression is as follows (*Li et al., 2016*):

$$\dot{q}(t) = -2\pi n_{00} u q(t) + 2\pi n_0 \sqrt{G_q(n_0) u} W(t) \tag{20}$$

In the formula, n_{00} is the lower cut off spatial frequency, taken as 0.011m^{-1}; u is vehicle speed; $q(t)$ is random elevation displacement for road surface; n_0 is reference spatial frequency; $G_q(n_0)$ is the roughness coefficient of the road surface; W(t) is Gaussian white noise with a mean of 0.

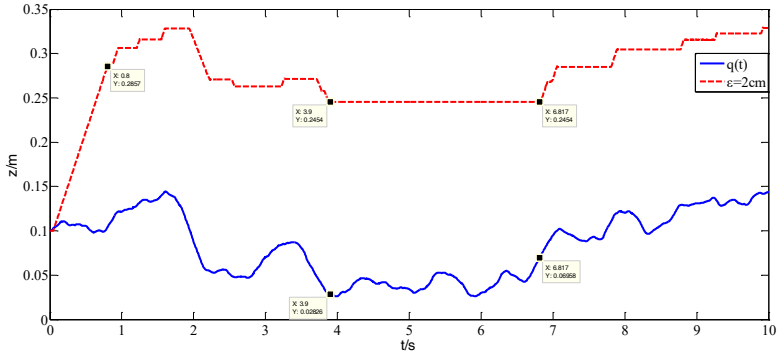


Fig. 5 - Ground elevation (random variation) and cutting height curve

Matlab is used to simulate the variation of the header height and the results are shown in Fig. 5. The position threshold ε is selected as 20 mm. During the time period of 0-0.8 s, due to the fact that the header height is less than 20 cm above the ground, the hydraulic cylinder rises. From 3.9 to 6.817 s, although the ground elevation changes between 2.8 cm and 6.9 cm, the magnitude of the change does not exceed the threshold. At this time, the header height remains at 24.54 cm and does not move. Overall, it shows a control effect of not adjusting the small undulating road surface, and only adjusting it for large undulations.

Field experiment testing

A comparative experiment of soybean harvesting was conducted at the Taigu Shenfeng Experimental Base. The experiment set up a manual and automatic dual-mode control group. The cutting height was used to invert the dynamic changes in the cutting table height, with a constant operating speed of 1 m/s, a preset cutting height of 200 mm, and a working interval length of 30 m. In manual mode, the cutting height will remain at the preset value and will not be adjusted in real-time during the operation process. In automatic mode, the cutting threshold is set to 15 mm, 20 mm, 25 mm, 30 mm, and 35 mm respectively.

Extract 50 sets of cutting height samples continuously from the stable operation section of the harvester, and select the average cutting height and cutting height coefficient of variation (CV). The kurtosis coefficient k is used as a measurement indicator, and its calculation formula is as follows:



(a) Soybean Harvest Experiment (b) Measurement of cutting height

Fig. 6 - Field experiment on height control of soybean sun cutting machine cutting table

$$\bar{L} = \frac{\sum_{i=1}^{n_1} L_i}{n_1} \tag{21}$$

$$C.V = \frac{\sqrt{\frac{\sum_{i=1}^{n_1}(L_i - \bar{L})^2}{n_1 - 1}}}{\bar{L}} \tag{22}$$

$$k = \frac{n(n+1)\sum_{i=1}^{n_1}(L_i - \bar{L})^4 - 3[\sum_{i=1}^{n_1}(L_i - \bar{L})^2]^2(n-1)}{(n-1)(n-2)(n-3)s^4} \tag{23}$$

In the formula: n_1 is the total number of measured cuttings; L_i is the i-th measurement of cutting height, mm; m_i is the i-th weighing mass, kg.

RESULTS

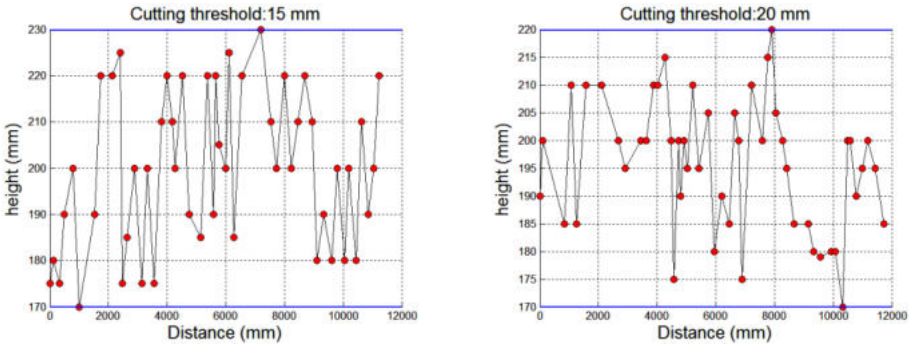
Some measurement data are shown in Table 2, and the distribution of cutting height is shown in Fig. 7.

Table 2

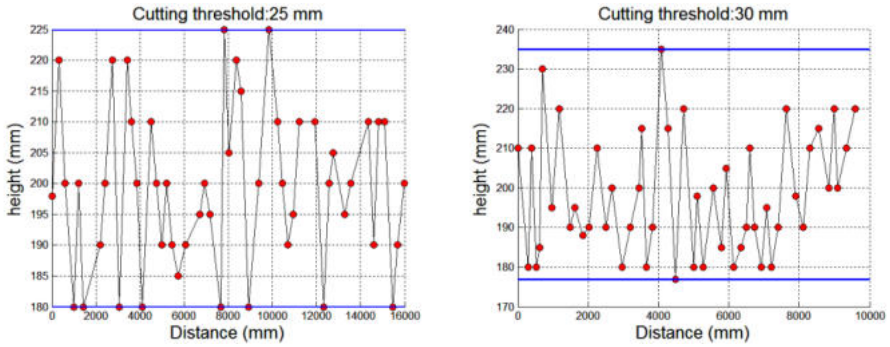
Measurement values of cutting height (top 10 groups)

Cutting threshold / mm	Measurement point cutting height /mm									
	1	2	3	4	5	6	7	8	9	10
15	175	180	175	190	200	170	190	220	220	225
20	190	200	185	210	185	210	210	200	195	200
25	198	220	200	180	200	180	190	200	220	180
30	210	180	210	180	185	230	195	220	190	195
35	200	190	185	190	200	220	180	190	180	210
Manual mode	195	205	200	195	215	185	200	190	195	185

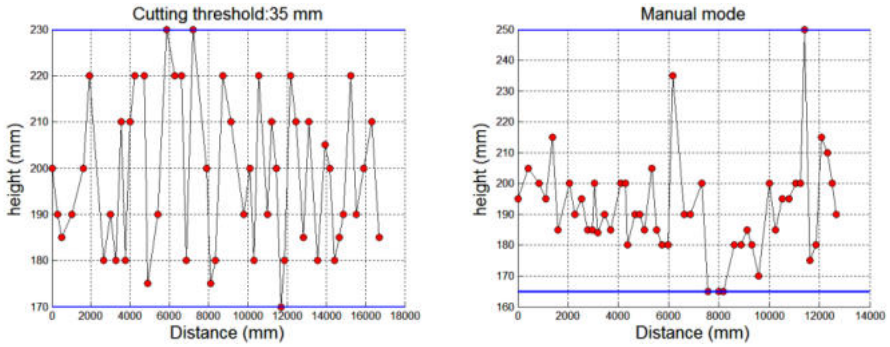
The experimental data processing results are shown in Table 3. In manual mode, the absolute error between the average cutting height and the preset cutting height is less than 8 mm, while in automatic mode it is reduced to 5 mm. Compared with manual mode, when the cutting threshold is set to 20, 25, and 30 mm, the coefficient of variation of cutting height is reduced by 2.13%, 1.71%, and 0.55%, respectively. The kurtosis coefficient analysis further reveals that manual mode presents a peak distribution (kurtosis=3.4635), while automatic mode maintains a gentle distribution feature within the threshold range of 15-35 mm (kurtosis interval: -1.2306 to -0.6541), indicating that the system effectively suppresses the occurrence of extreme deviation values.



（a）The cutting threshold is 15 mm （b）The cutting threshold is 20 mm



（c）The cutting threshold is 25 mm （d）The cutting threshold is 30 mm



（e）The cutting threshold is 35 mm （f）Manual mode

Fig. 7 - Distribution of cutting height

Table 3

Analysis of Experimental Data Processing Results

Cutting threshold / mm	Average cutting height $\bar{L}$	Coefficient of variation of cutting height C.V / %	Kurtosis coefficient
15	199.7	8.49%	-1.2306
20	195.88	6.04%	-0.6541
25	199.36	6.46%	-0.701
30	198.12	7.62%	-0.6658
35	198.3	8.35%	-1.1811
Manual mode	192.08	8.17%	3.4635

CONCLUSIONS

(1) By integrating the high-resolution 3D terrain detection capability of Nooploop TOFSense-MS area array LiDAR, combined with an improved quartile range algorithm, outliers caused by interference sources such as crop residues and sensor noise are dynamically removed. Linear, quadratic, and cubic terrain fitting models are constructed based on Huber robust regression framework. By quantifying the trade-off between model complexity and terrain adaptability using Bayesian Information Criterion (BIC), the intercept term with the smallest BIC value is selected as the reference height to achieve accurate representation of complex farmland terrain.

(2) Aiming at the nonlinear hysteresis characteristics of valve-controlled asymmetric hydraulic cylinder systems, a telescopic dual-mode transfer function model is established, and a Bang-Bang switch lead compensation strategy based on position threshold is proposed. By predicting the trend of terrain changes, the electromagnetic directional valve is triggered to act in advance.

(3) Field comparative experiments show that at a working speed of 1 m/s, the coefficient of variation of cutting height in automatic control mode is significantly reduced compared to manual mode (when ε=20mm, C.) V=6.04%，The automatic mode maintains a gentle distribution feature within the threshold range of 15-35 mm, with a decrease of 26.1%. The research results provide theoretical support and engineering practice paradigm for intelligent control of high-precision agricultural equipment, which can be further extended to the optimization of imitation systems in multi crop harvesting scenarios such as corn and wheat.

ACKNOWLEDGEMENT

This research was funded by the Scientific and Technological Innovation Programs of Higher Education Institutions in Shanxi (No.2022L096) and the Youth Science and Technology Innovation Project of Shanxi Agricultural University (No.2020QC12), the National Key R&D Program of China (2021YFD1600602-09).

REFERENCES

[1] Chang K., Zaman, Q .(2016). An on-the-go ultrasonic plant height measurement system (UPHMS II) in the wild blueberry cropping system. *ASABE Annual International Meeting.* 162460289. DOI:10.13031/aim.20162460289.

[2] Wang Y., Zhang G., Qian X., Dong Q. (2025). Semi-physical simulation research on the control system of combine harvester cutting table [J]. *INMATEH - Agricultural Engineering*, Vol.75, Issue 01, pp.797-808,https://doi.org/10.35633/inmateh-75-68.

[3] Huang M., Li G. (2021). Detection of Ridge Height in Sugarcane Fields Based on Linear Frequency Modulation Continuous Wave Radar (基于线性调频连续波雷达的甘蔗垄高检测). *Journal of Southwest University*, Vol.43, Issue 02, pp. 31-39, https://doi.org/10.13718/j.cnki.xdzk.2021.02.005.

[4] Huang Y., Huang T., Yang R. (2017). Detection and test of sugarcane cutting height based on machine vision.（基于机器视觉的甘蔗切割高度检测与试验）. *Journal of Chinese Agricultural Mechanization*, Vol.38, Issue 09, pp.81-87. https://doi.org/10.13733/j.jcam.issn.2095-5553.2017.09.017.

[5] Li Z., Huang J., Liu Y. (2016). Modeling and simulation on white noise of road roughness in time domain (白噪声路面不平度时域模型的建立与仿真). *Journal of Jiangsu University(Natural Science Edition)*, Vol.37, Issue 05, pp. 503-506+524. https://doi.org/10.3969/j.issn.1671-7775.2016.05.002.

[6] Li Z. (2022). *Design of soybean profiling header and control system for multi-crop crawler combine harvester (多作物兼用型履带式联合收获机大豆仿形割台设计与调控系统研制).* (Master's thesis). Jiangsu University. ZhenJiang/China. https://doi.org/10.27170/d.cnki.gjsuu.2022.000016.

[7] Liao Y., Xiang X., Wu M., Liu D., Chen Y., Li Y. (2018). Design and test of the adaptive height adjustment system for header of the combine–harvester (联合收割机割台高度自适应调节系统的设计与试验). *Journal of Hunan Agricultural University (Natural Sciences)*, Vol. 44, Issue 3, pp. 326-329. https://doi.org/10.13331/j.cnki.jhau.2018.03.017.

[8] Lian X., Wang J., Zhu Y. (2024). Research status analysis of key technology and loss of soybean harvester header.（大豆收获机割台关键技术及损失研究现状分析）. *Journal of Chinese Agricultural Mechanization*, Vol.45, Issue 08, pp.8-13. https://doi.org/10.13733/j.jcam.issn.2095-5553.2024.08.002.

[9] Liu G. (2022). *Research on Profiling Technology of Soybean CombineHarvester Header (大豆联合收获机割台仿形技术研究).* (Master's thesis). Chinese Academy of Agricultural SciencesThesis. Beijing/China. https://doi.org/10.27630/d.cnki.gznky.2022.000712.

[10] Suomi P. (2015). Automatic working depth control for seed drill using ISO 11783 remote control messages. *Comput. Electron. Agric.*, Vol.116, pp. 30-35. https://doi.org/10.1016/j.compag.2015.05.016.

[11] Ye X. (2015). *Research on Modeling and Control Method of Value-controlled Asymmetrical Cylinder System (阀控非对称缸系统的建模与控制方法研究).* (Doctor's thesis). Hefei University of Technology. Hefei/China. https://doi.org/10.7666/d.Y2925638.

[12] Zhang C., Li Q., Ye S., Zhang J., Zheng D. (2024). Header Height Detection and Terrain-Adaptive Control Strategy Using Area Array LiDAR. *Agriculture*. 14(8):1293. https://doi.org/10.3390/agriculture14081293.

ASSESSING THE ENVIRONMENTAL ADAPTABILITY BASED ON LASER DETECTION FOR DETERMINING GAS EMISSIONS FROM AGRICULTURAL SOURCES

/

评估使用激光探测确定农业源气体排放的局部环境的适应性

Xiaofeng LIU[1)], Fuhai ZHANG[1)], Jingjing YU[1)], Jiayuan WANG[1)], Juan LIAO[2)], Qixing TANG[2*)]
[1)]Anhui Eco-Environment Monitoring Center, Hefei 230071, China;
[2)]School of Engineering, Anhui Agricultural University, Hefei 230061, China
E-mail : gxtang@ahau.edu.cn
DOI: https://doi.org/10.35633/inmateh-76-22

Keywords: *laser absorption spectroscopy, measurement, gas emissions, windbreak*

ABSTRACT

In the context of agricultural emissions in China, it is common for fields to be bordered by row windbreaks, which - when located downwind of emission sources - can complicate gas flux measurements. To address this challenge, the environmental adaptability of a laser-based detection system for quantifying gas emissions from agricultural sources was evaluated through a controlled gas emission field simulation experiment. Using methane as a representative gas, a flux measurement system based on open-path laser absorption spectroscopy was developed. The study employed an artificially simulated methane volatilization source and two measurement devices to conduct experiments under three conditions: an ideal environment, a laser path positioned downwind of the source, and a laser path set directly above the source. Results show that the standard deviations of the ratio Q_{bLS}/Q were 0.0277, 0.0283, and 0.0256, respectively. The corresponding maximum fluctuation amplitudes were 7.3%, 7.4%, and 5.9%. These findings suggest that for a row windbreak located downwind of an emission source, selecting an optimal measurement strategy - such as positioning the optical path above, across, or near the vertical downwind axis of the source - can minimize environmental interference and enhance the reliability of methane flux measurements in agricultural settings.

摘要

针对我国农业排放问题，田间地头常常会设置一排防风林。假设防风林位于被测源的下风向，这可能会使测量变得复杂。鉴于这种情况，在气体排放田间模拟实验中，以甲烷为例，对基于激光探测确定农业源气体排放的环境适应性进行了评估。建立了基于开放光路激光吸收光谱技术的甲烷通量测量系统。通过使用人工模拟的甲烷挥发源和两套测量装置，分别开展了理想环境下、源下风向以及源上方环境下的实验。结果表明，理想环境下 QbLS/Q 的标准偏差为 0.0277。源下风向得到的 QbLS/Q 标准偏差为 0.0283。源上方设置得到的 QbLS/Q 标准偏差为 0.0256。QbLS/Q 的最大波动幅度分别为 7.3%、7.4%和 5.9%。由此可见，对于一排防风林，假设其位于被测源的下风向，通过优化测量方法可降低气体通量的估算误差。在测量实际大面积面源时，从源的下风向进行测量，并且可以将光路设置在源垂直下风向的上方，穿过源或靠近源。这种测量方法减少了上风向防风林造成的局部环境干扰，从而实现测量。

INTRODUCTION

The methods for measuring agricultural non-point source emission flux include: vertical radial plume mapping method *(Qian et al., 2023; Obaideen et al., 2022)*, Tracer Correlation method *(Vechi et al., 2023)*, box method, Eddy Correlation method *(Dong et al., 2016)*, Inverse dispersion method *(Flesch et al., 2018)*, and so on *(Flesch et al., 2018; Erland et al., 2022)*. There are big differences in applicability, accuracy, and space-time resolution *(Ghorbani et al., 2017)*. Laser absorption spectroscopy is a widely used technique for large-scale gas sensing applications, including quantitative analysis of gas concentration *(Goldsmith et al., 2012; Harris et al., 2002; Hashmonay et al., 2008; Liu et al., 2015; McBain et al., 2005; Xin et al., 2017)*. The flux detection method combined with tunable diode laser absorption spectroscopy and the backward Lagrangian stochastic (BLS) technology can achieve high time resolution agricultural gas emission, and has high accuracy in agricultural non-point source gas flux monitoring.

However, the precondition is to assume that the measurement conditions are idealized. In the actual agricultural gas emissions measurement process, complex external disturbance conditions, various structures (buildings, trees, etc.) introduce vortices, jets, and sheltered zones *(Viguria et al., 2015; Wilson et al., 2005; Wilson et al., 2003)*.

Comprehensive wind field measurements are generally impractical, and wind modeling is a complex task that may lack accuracy. In an experiment using a 1.25 m-high windbreak fence to enclose the tracer, Flesch concluded that local wind complexity can be neglected when measurements are taken at distances greater than 5h from the fence *(Wilson et al., 2001)*. However, this conclusion may not be applicable to the context of agricultural emissions in China, where windbreaks - often rows of trees - are commonly found along the edges of fields, as illustrated in Fig. 1. It is assumed that the windbreak is located downwind of the emission source, which may introduce additional complexities into the measurement process.

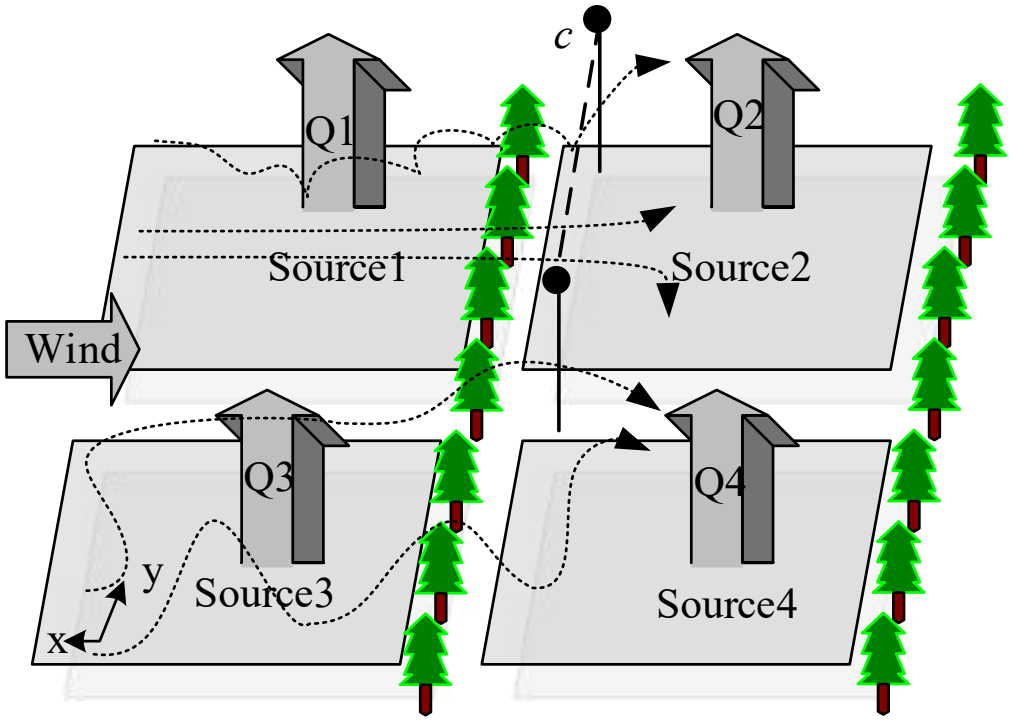


Fig .1 - Windbreaks complicate measurement

In response to this situation, an outdoor field simulation experiment of methane emissions was conducted to evaluate the environmental adaptability of laser-based detection methods for quantifying gas emissions from agricultural sources.

MATERIALS AND METHODS

Measurement principle

According to Beer-Lambert's law, the measured concentration can be expressed as:

$$c = \frac{A}{A_0}\frac{L_0}{L}c_0 \tag{1}$$

Where:

c_0 is the concentration of the standard gas;

L_0 is the optical path length of the standard gas, (cm);

A_0 is the integral absorbance of the standard gas;

L is the actual optical path length of the experimental system, (cm);

A is the fitted integral absorbance.

It is known that the regional source emits gas at a uniform but unknown rate Q (kg/m^2/s). The average gas concentration c is measured at point M within the plume. The emission rate Q can be inferred from the concentration at M and $(c_0/q)_{SIM}$, the ratio of the concentration rise over background at M to the source emission rate [19-20]. As shown in Eq. (2), c_b is the background gas concentration.

$$Q = \frac{c - c_b}{(c/Q)_{SIM}} \tag{2}$$

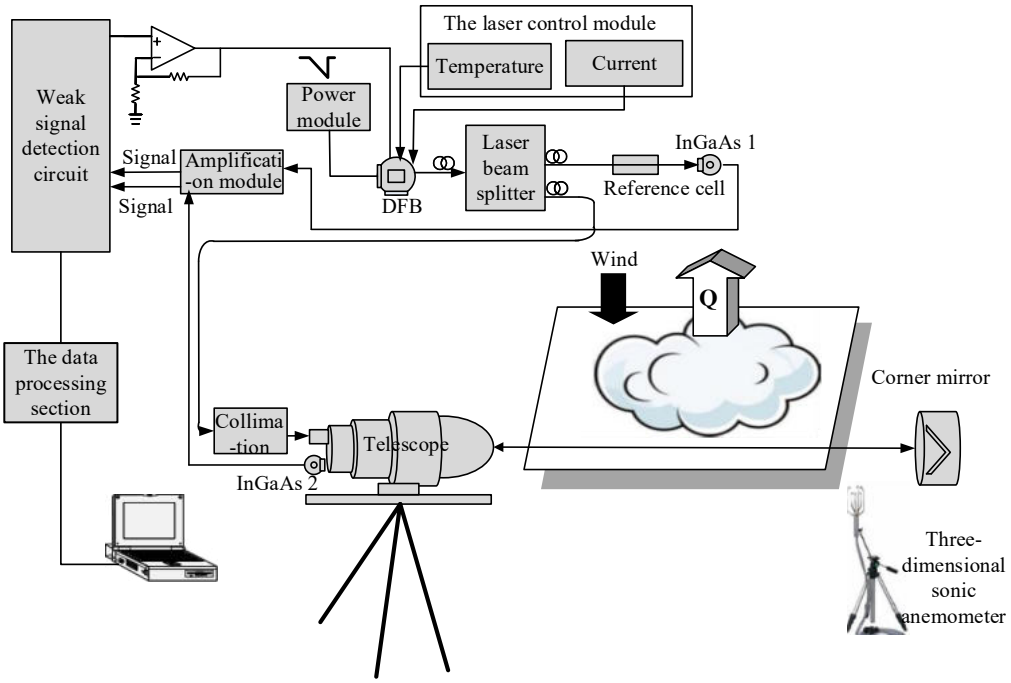


Fig. 2 - Block diagram of the system

The system block diagram is shown in Fig 2, which mainly includes a laser absorption spectrum detection device and a three-dimensional sonic anemometer. The laser absorption spectrum detection device is used to detect the methane gas concentration *(Wang et al., 2022)*. The three-dimensional sonic anemometer is used to measure three-phase orthogonal wind speed components (Ux, Uy, Uz).

The laser absorption spectrum detection device consists of a laser and its control module, an optical structure section, a reference optical cell, a calibration section, a weak signal detection circuit, and a data processing unit. A DFB laser with a center wavelength of 1653 nm - corresponding to a near-infrared single absorption line of CH_4 - is used as the detection light source. The laser control module (LDC3724B) is employed to adjust the laser's output wavelength. Driven by the scanning signal, the output wavelength of the laser is rapidly scanned around the target absorption line. The single-mode laser beam is evenly split into reference and probing optical paths. The reference beam is directed into the reference optical gas cell via the optical structure section to calibrate the standard gas. The probing beam is transmitted to the transceiver telescope of the optical structure, then reflected by a corner mirror and focused onto InGaAs photodetector 2. After passing through the weak signal detection circuit and the data processing section, the concentration of CH_4 gas is retrieved through spectral inversion.

By combining the integrated line concentration with meteorological data, the BLS model is employed to estimate gas emissions.

The height of the laser detection optical path is taken as the laser path height. A gas simulation volatilization device is used to simulate uniform methane emission.

The methane volatilization source consists of a weight sensor, a gas flow meter, high-purity sample gas, and an artificial simulated source, as illustrated in Fig. 3.

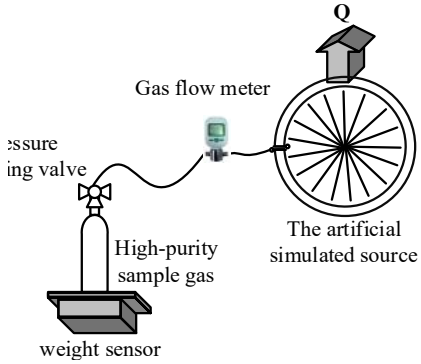


Fig. 3 - Gas simulation volatility device diagram

The weight sensor has a measuring range of 30 kg, and the measurement accuracy is 1 g, which meets the measurement needs of gas weight changes. High-purity sample gas is controlled by the gas flow meter to ensure uniform gas discharge at a uniform speed. It is sent to two connected 3x1.5 m artificial simulated sources, which are made of polyvinyl chloride with an inner diameter of 18 mm. The simulated source is provided with a diameter of 1 mm diffusion holes at every 0.3 m above it to simulate methane gas emission.

The high-purity sample gas used is methane gas (99.9% purity), which is released from the high-pressure gas cylinder at a rate of 5-40 L/min. In order to avoid the marginal effect of methane volatilization, the flux measurement is started after 5 minutes of gas release, and the duration of each release is not less than 30 minutes.

Evaluative experiment

The experiment is conducted on the experimental base adjacent to Science Island, Hefei, China. The monitoring area can be regarded as a uniform underlying surface.

Building the experimental environment

To eliminate the influence of environmental factors on the measurement results, and in alignment with the prevailing wind direction, two sets of methane flux measurement instruments - based on open-path laser absorption spectroscopy and constructed as described in Section 2 - are positioned according to the geometric layout shown in Fig. 4. Device 1 is located in an area affected by a tree, while Device 2 is placed in an assumed ideal environment, free from obstruction. Prior to the measurement experiments, a consistency analysis is conducted between the two instruments to ensure they operate under equivalent conditions. The BLS model is used to estimate the emission rate, with simulations performed using WindTrax software. A three-dimensional sonic anemometer is installed at a height of 1.35 m above the ground to record wind data.

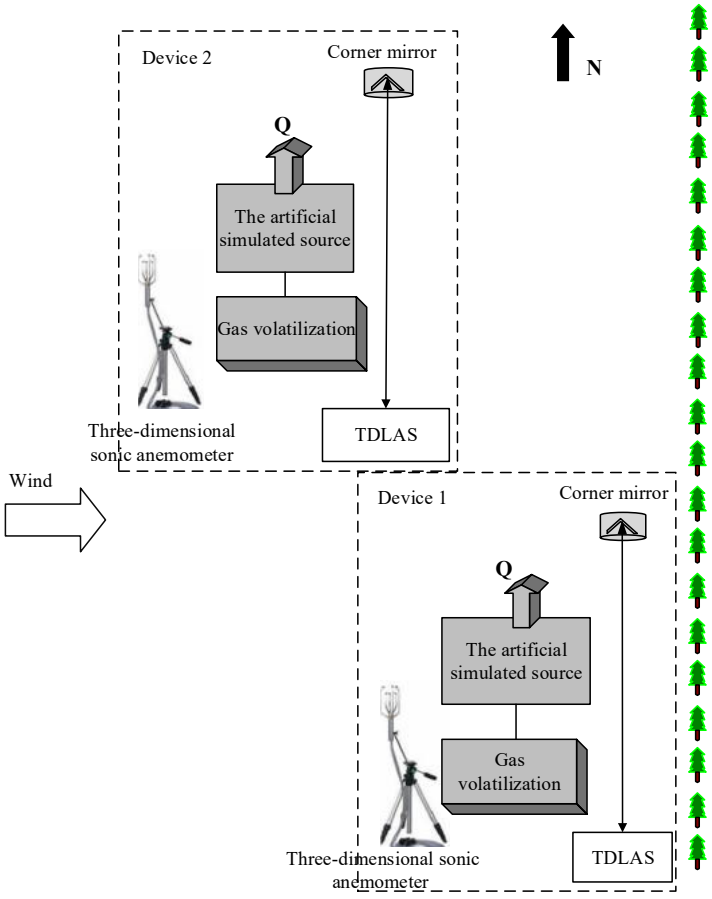


Fig. 4 - Instrument environment diagram

The experimental site is shown in Fig. 5. Both sets of instruments began data collection simultaneously. The artificial simulated sources used in the experiment have identical areas and shapes, and the distance between each laser path and the edge of the emission source is the same. However, due to slight positional deviations, the measurement locations are not identical, and weather conditions may differ slightly between the two setups.

Experiments are conducted under varying environmental conditions. The ratio of Q_{bLS} to the actual release rate Q is calculated and compared to 1 to evaluate the influence of environmental complexity.



Fig. 5 - The experimental site

Experimental design scheme

Considering the feasibility of actual measurement processes, Device 1 in the experiment is tested using two different configurations for setting up the laser path. In the first configuration, the laser path is placed at a distance of at least 0.5×x from the downwind direction, where *x* is the distance between the emission sources. In the second configuration, the laser path is positioned directly above the source and passes over it. All other construction conditions are assumed to remain unchanged.

During the first setup experiment, the measurement results from both devices are recorded simultaneously. After completing the measurement, the gas simulation volatilization device is turned off, and the system is left undisturbed for 30 minutes to minimize the residual effects of methane volatilization. The background methane concentration is then measured and assessed. Once the measurement conditions are confirmed to be stable, the second setup experiment is initiated.

In the second setup experiment, only the measurement laser path of Device 1 is altered, while the conditions for Device 2 remain unchanged and continue to represent an ideal environment. During this phase, gas emission is again simulated using the gas simulation volatilization device.

RESULTS

Methane concentration measurement consistency between two instruments

Before the measurement experiments, a consistency analysis was conducted to verify that the two instruments operate under equivalent conditions. In the laboratory, a 20 m multi-reflection gas cell was placed in the detection optical path to measure a fixed CH_4 concentration of 40 ppm. During the measurement process, after the gas was injected into the chamber, the inlet and outlet of the multi-reflection cell were sealed, ensuring that the gas concentration remained constant throughout the experiment. Both instruments continuously measured the fixed concentration for 240 minutes. The recorded signals were processed using 50-point averaging to retrieve the concentration values. The correlation coefficient for consistency between the two instruments was 0.991, while the relative errors compared to the standard gas concentration were 0.023 and 0.017, respectively. A follow-up consistency analysis was conducted in a simulated environment. Under the same experimental conditions, a rotatable thin phase screen plate was used to simulate atmospheric turbulence, incorporating a pseudo-random phase distribution that follows Kolmogorov spectrum statistics. The CH_4 concentration was maintained at 40 ppm throughout the experiment. Both instruments continuously measured the fixed concentration for 200 minutes. As in the previous test, the recorded signals were processed using 50-point averaging to retrieve the concentration values. The consistency correlation coefficient between the two instruments was 0.982, and the relative errors compared with the standard gas concentration were 0.059 and 0.067, respectively. These results indicate that both instruments demonstrate good consistency. Although the correlation decreased and the relative errors increased in the simulated turbulent environment, this degradation is attributed to environmental noise. Nonetheless, both instruments are capable of accurately and consistently measuring line concentration.

Analysis of experimental results from two instrument setups with different laser paths

Experiments were conducted under different environmental conditions using two distinct laser path configurations. The two instruments were tested simultaneously. The ratio of Q_{bLS} to the actual release rate Q was calculated and compared to 1. The results obtained from the two laser path configurations are presented in Tables 1, 2, and 3.

Table 1

Measurement results of Device 2 under ideal environmental conditions

Time (min)	15	30	45	60	75	90
Wind speed ($m \cdot s^{-1}$)	1.260	1.302	1.334	1.323	1.361	1.371
Temperature T (℃)	24.188	24.179	24.175	24.170	24.157	24.137
Wind direction θ (°)	60.815	61.785	62.100	63.190	62.914	62.550
Frictional velocity u^* ($m \cdot s^{-1}$)	0.187	0.195	0.197	0.195	0.191	0.197
Obukhov stability length L (m)	-42.108	-50.457	-55.565	-59.413	-65.040	-70.939
Surface roughness length z_0 (m)	0.037	0.039	0.038	0.038	0.033	0.036
σ_u/u^*	2.818	2.786	2.773	2.694	2.770	2.708
σ_v/u^*	2.113	1.973	2.030	2.075	2.194	2.097
σ_w/u^*	1.420	1.401	1.418	1.418	1.477	1.440
Q ($g. m^{-2} \cdot s^{-1}$)	0.012	0.012	0.012	0.012	0.012	0.012
Concentration c (ppm)	7.349	7.348	7.189	7.045	7.007	6.994
Q_{bLS} ($g. m^{-2} \cdot s^{-1}$)	0.011	0.013	0.012	0.011	0.012	0.012
S (m^{-2})	14.37	14.37	14.37	14.37	14.37	14.37
Q_{bLS}/Q	0.974	1.045	1.018	0.971	1.006	0.100

Table 2

Measurement results of Device 1 during the first setup

Time (min)	15	30	45	60	75	90
Wind speed ($m \cdot s^{-1}$)	1.365	1.335	1.314	1.316	1.322	1.359
Temperature T (℃)	25.274	25.256	25.231	25.172	25.140	25.102
Wind direction θ (°)	57.389	56.727	54.285	53.275	53.155	53.484
Frictional velocity u^* (m·s-1)	0.217	0.217	0.212	0.215	0.217	0.218
Obukhov stability length L(m)	-12.509	-12.303	-11.666	-12.199	-12.421	-12.801
Surface roughness length z_0 (m)	0.039	0.041	0.040	0.042	0.042	0.040
σ_u/u^*	2.541	2.518	2.525	2.504	2.476	2.440
σ_v/u^*	2.497	2.469	2.637	2.634	2.639	2.668
σ_w/u^*	1.258	1.209	1.219	1.194	1.200	1.225
Q ($g. m^{-2} \cdot s^{-1}$)	0.011	0.011	0.011	0.011	0.011	0.011
Concentration c (ppm)	7.025	7.104	7.202	7.272	7.281	7.309
Q_{bLS} ($g. m^{-2} \cdot s^{-1}$)	0.011	0.011	0.011	0.011	0.012	0.012

S (m^{-2})	14.37	14.37	14.37	14.37	14.37	14.37
Q_{bLS}/Q	0.995	0.992	1.003	1.022	1.028	1.068

Table 3

Measurement results of device 1 by Second erection

Time (min)	15	30	45	60	75	90
Wind speed ($m \cdot s^{-1}$)	1.169	1.166	1.182	1.240	1.278	1.335
Temperature T (℃)	25.045	25.060	25.061	25.032	25.041	25.042
Wind direction θ (°)	56.847	56.427	58.126	59.967	61.541	62.963
Frictional velocity u^* ($m \cdot s^{-1}$)	0.196	0.190	0.188	0.196	0.199	0.207
Obukhov stability length L (m)	-9.683	-9.058	-9.245	-10.734	-11.193	-12.854
Surface roughness length z_0 (m)	0.043	0.039	0.037	0.038	0.036	0.037
σ_u/u^*	2.662	2.742	2.828	2.980	3.098	3.152
σ_v/u^*	2.721	2.820	2.771	2.682	2.700	2.582
σ_w/u^*	1.453	1.494	1.509	1.487	1.502	1.457
Q (g. $m^{-2} \cdot s^{-1}$)	0.007	0.007	0.007	0.007	0.007	0.007
Concentration c (ppm)	7.897	7.863	7.815	7.825	7.745	7.777
Q_{bLS} ($g. m^{-2} \cdot s^{-1}$)	0.007	0.007	0.007	0.007	0.007	0.007
S (m^{-2})	14.37	14.37	14.37	14.37	14.37	14.37
Q_{bLS}/Q	0.903	0.906	0.938	0.954	0.958	0.959

It can be seen from the measurement results in Fig. 6 and Fig.7.

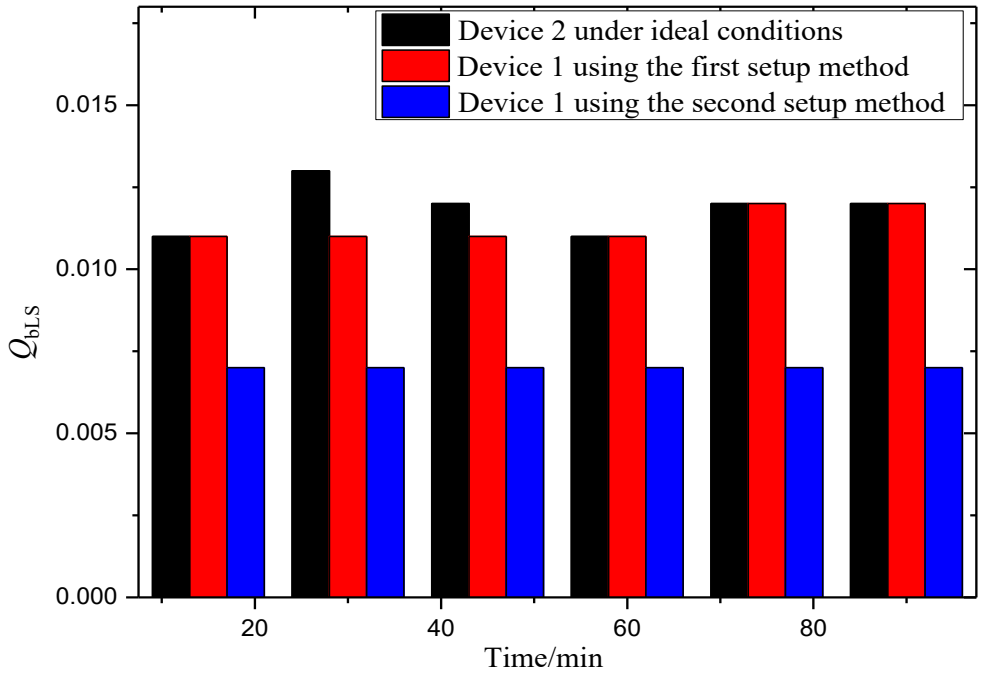


Fig. 6 - Measurement results Q_{bLS} for the two devices

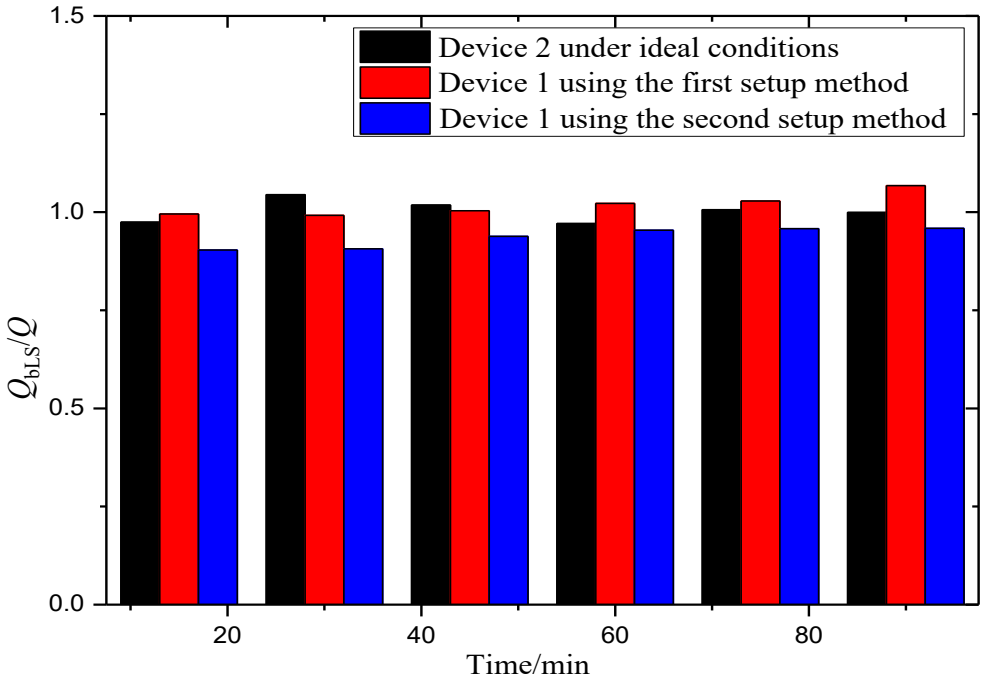


Fig. 7 - Measurement results Q_{bLS}/Q for the two devices

The results indicate that the standard deviation of Q_{bLS}/Q in the ideal environment is 0.0277. For Device 1, the standard deviation is 0.0283 when the laser path is placed downwind of the source, and 0.0256 when the laser path is placed directly above the source. The maximum fluctuation amplitudes of Q_{bLS}/Q are 7.3%, 7.4%, and 5.9%, respectively. Although Device 2, operating under ideal conditions, yields a Q_{bLS}/Q ratio closest to 1 - indicating the highest accuracy - both setup methods used with Device 1 remain within an acceptable error range. Among them, the second setup (with the laser path above the source) performs better. These results suggest that in the presence of a row windbreak assumed to be located downwind of the emission source, the estimation error in gas flux can be effectively reduced by selecting an optimal measurement configuration.

When measuring an actual large-scale surface source, measurements are taken from the downwind direction of the source. The optical path can be set directly above, across, or near the vertical downwind direction of the source.

CONCLUSIONS

In the process of measuring agricultural gas flux emissions, the presence of windbreaks can introduce environmental interference and complicate measurements. To address this issue, a methane flux measurement system based on open-path laser absorption spectroscopy was developed. Experiments were conducted under three conditions: an ideal environment, a setup with the laser path downwind of the source, and a setup with the laser path directly above the source. The results show that the standard deviation of Q_{bLS}/Q in the ideal environment is 0.0277, compared to 0.0283 when measured from the downwind direction of the source, and 0.0256 when measured directly above the source. The corresponding maximum fluctuation amplitudes of Q_{bLS}/Q are 7.3%, 7.4%, and 5.9%, respectively. These results indicate that for a row windbreak located downwind of the emission source, measurement accuracy can be improved by selecting an optimal measurement configuration.

When measuring emissions from a large-scale surface source, the recommended approach is to position the optical path in the downwind direction - either above, across, or near the vertical axis of the source. This configuration reduces local environmental interference from windbreaks located upwind and enables accurate measurement of farmland gas emissions.

ACKNOWLEDGEMENT

Thank you to all the participating authors. The research was funded by Anhui Province science and technology major projects (No.202203a07020004). Project of National Natural Science Foundation of China (52105539).

REFERENCES

[1] Dong, L., Tittel, F. K., Li, C., Sanchez, N. P., Wu, H., Zheng, C., ... & Griffin, R. J. (2016). Compact TDLAS based sensor design using interband cascade lasers for mid-IR trace gas sensing. *Optics express*, 24 (6), A528-A535.

[2] Erland, B. M., Thorpe, A. K., & Gamon, J. A. (2022). Recent advances toward transparent methane emissions monitoring: a review. *Environmental Science & Technology*, 56(23), 16567-16581.

[3] Flesch, T. K., Baron, V. S., Wilson, J. D., Basarab, J. A., Desjardins, R. L., Worth, D., & Lemke, R. L. (2018). Micrometeorological measurements reveal large nitrous oxide losses during spring thaw in Alberta. *Atmosphere*, 9(4), 128.

[4] Flesch, T. K., Basarab, J. A., Baron, V. S., Wilson, J. D., Hu, N., Tomkins, N. W., & Ohama, A. J. (2018). Methane emissions from cattle grazing under diverse conditions: An examination of field configurations appropriate for line-averaging sensors. *Agricultural and Forest Meteorology*, 258, 8-17.

[5] Ghorbani, R., & Schmidt, F. M. (2017). ICL-based TDLAS sensor for real-time breath gas analysis of carbon monoxide isotopes. *Optics express*, 25(11), 12743-12752.

[6] Goldsmith Jr, C. D., Chanton, J., Abichou, T., Swan, N., Green, R., & Hater, G. (2012). Methane emissions from 20 landfills across the United States using vertical radial plume mapping. *Journal of the Air & Waste Management Association*, 62(2), 183-197.

[7] Harris, M.R., Pajooman, G. H., & Sharkh, S.A. (2002). The problem of power factor in VRPM (transverse-flux) machines. *Eighth International Conference on Electric Machines and Drives*.

[8] Hashmonay, R. A., Varma, R. M., Modrak, M. T., Kagann, R. H., Segall, R. R., & Sullivan, P. D. (2008). Radial plume mapping: a US EPA test method for area and fugitive source emission monitoring using optical remote sensing. In *Advanced environmental monitoring*. pp. 21-36. Dordrecht: Springer Netherlands.

[9] Liu, C., Xu, L., Chen, J., Cao, Z., Lin, Y., & Cai, W. (2015). Development of a fan-beam TDLAS-based tomographic sensor for rapid imaging of temperature and gas concentration. *Optics Express*, 23(17), 22494-22511.

[10] McBain, M. C., & Desjardins, R. L. (2005). The evaluation of a backward Lagrangian stochastic (bLS) model to estimate greenhouse gas emissions from agricultural sources using a synthetic tracer source. *Agricultural and forest meteorology*, 135(1-4), 61-72.

[11] Obaideen, K., Abdelkareem, M. A., Wilberforce, T., Elsaid, K., Sayed, E. T., Maghrabie, H. M., & Olabi, A. G. (2022). Biogas role in achievement of the sustainable development goals: Evaluation, Challenges, and Guidelines. *Journal of the Taiwan Institute of Chemical Engineers*, 131, 104207.

[12] Qian, H., Zhu, X., Huang, S., Linquist, B., Kuzyakov, Y., Wassmann, R., ... & Jiang, Y. (2023). Greenhouse gas emissions and mitigation in rice agriculture. *Nature Reviews Earth & Environment*, 4(10), 716-732.

[13] Xin, F., Guo, J., Sun, J., Li, J., Zhao, C., & Liu, Z. (2017). Research on atmospheric CO2 remote sensing with open-path tunable diode laser absorption spectroscopy and comparison methods. *Optical Engineering*, 56(6), 066113-066113.

[14] Viguria, M., Ro, K. S., Stone, K.C., & Johnson, M. H. (2015). Accuracy of vertical radial plume mapping technique in measuring lagoon gas emissions. *Journal of the Air & Waste Management Association*, 65(4), 395-403.

[15] Vechi, N. T., & Scheutz, C. (2023). Measurements of methane emissions from manure tanks, using a stationary tracer gas dispersion method. *Biosystems Engineering*, 233, 21-34.

[16] Wilson, J. D. (2005). Deposition of particles to a thin windbreak: The effect of a gap. *Atmospheric environment*, 39(30), 5525-5531.

[17] Wilson, J. D., & Flesch, T. K. (2003). Wind measurements in a square plot enclosed by a shelter fence. *Boundary-layer meteorology*, 109, 191-224.

[18] Wilson, J. D., Flesch, T. K., & Harper, L. A. (2001). Micro-meteorological methods for estimating surface exchange with a disturbed windflow. *Agricultural and Forest Meteorology*, 107(3), 207-225.

[19] Witzel, O., Klein, A., Meffert, C., Wagner, S., Kaiser, S., Schulz, C., & Ebert, V. (2013). VCSEL-based, high-speed, in situ TDLAS for in-cylinder water vapor measurements in IC engines. *Optics express*, 21(17), 19951-19965.

[20] Wang, Q., Sun, P., Zhang, Z., Zhang, L., Pang, T., Wu, B., ... & Culshaw, B. (2022). Multi-component gas measurement aliasing spectral demodulation method for interference separation in laser absorption spectroscopy. *Sensors and Actuators B: Chemical*, 369, 132292.

[21] Ye, W., Li, C., Zheng, C., Sanchez, N. P., Gluszek, A. K., Hudzikowski, A. J., ... & Tittel, F. K. (2016). Mid-infrared dual-gas sensor for simultaneous detection of methane and ethane using a single continuous-wave interband cascade laser. *Optics express*, 24(15), 16973-16985.

DETECTION OF EARLY BRUISING IN 'HUANGGUAN' PEAR BASED ON MCC-DeepLabV3+ MODEL
/
基于 MCC-DeepLabV3+模型的皇冠梨早期瘀伤检测

Congkuan YAN, Haonan ZHAO, Dequan ZHU, Yuqing YANG, Ruixing XING, Qixing TANG, Juan LIAO*)
School of Engineering, Anhui Agricultural University, Hefei 230036, China
Tel: +8617755108602; Email: liaojuan@ahau.edu.cn
Corresponding author: Juan Liao
DOI: https://doi.org/10.35633/inmateh-76-23

Keywords: *early bruise detection, MCC-DeepLabV3+, near infrared imaging, semantic segmentation, 'Huangguan' pear*

ABSTRACT
Due to their delicate and thin skin, 'Huangguan' pears are very vulnerable to pressure and impact during picking, packing and transportation, which can cause bruising. Early detection of bruises allows for timely identification of affected fruits to reduce potential food safety risks. However, early bruises in 'Huangguan' pears, particularly those that occur within the 30 minutes, often show no visible differences in external features compared to healthy tissue, making conventional techniques such as manual and machine vision sorting ineffective. Accordingly, a near-infrared (NIR) camera imaging technique combined with deep learning segmentation algorithm for early bruise 'Huangguan' pears detection is proposed in this study. Firstly, a near-infrared camera imaging system is applied to collect early bruise images of 'Huangguan' pears, and then a lightweight segmentation model based on the DeepLabV3+ architecture, referred to as MCC-DeepLabV3+ is presented. In the MCC-DeepLabV3+ model, MobileNetV2 is used as the backbone network, reducing the parameter size and enhancing deployment efficiency. Additionally, the coordinate attention (CA) mechanism is integrated into the shallow feature extraction and ASPP modules to improve the extraction of positional information across various features, minimizing the discrepancy between segmented areas and the actual bruised regions. Furthermore, a cascade feature fusion (CFF) strategy is incorporated into the encoder to reduce segmentation edge discontinuities and ensure effective multi-level semantic fusion, improving segmentation accuracy. The experimental results show that the proposed model has achieved a mIoU of 95.68%, and mPrecision of 97.58% on the self-built dataset of early bruising in 'Huangguan' pears. Compared to benchmark models such as U-Net, SegNet, PSPNet and HRNet, the proposed model demonstrates superior segmentation performance, offering promising support for the development of nondestructive detection techniques for agricultural product quality.

摘要
由于黄冠梨的表皮细腻而娇嫩，在采摘、包装和运输过程中非常容易受到压力和冲击，这可能导致瘀伤。早期发现瘀伤可以及时识别受影响的水果，有助于减少潜在的食品安全风险。然而，皇冠梨的早期瘀伤，特别是那些在 30 分钟内发生的瘀伤，与健康组织相比，通常在外部特征上没有明显的差异，这使得人工和机器视觉分类等传统技术的效果不佳。因此，本研究提出了一种结合深度学习分割算法的近红外(NIR)相机成像技术用于早期皇冠梨瘀伤检测。首先，采用近红外相机成像系统采集黄冠梨的早期瘀伤图像，然后，提出了一种基于 DeepLabV3+架构的轻量级分割模型，称为 MCC-DeepLabV3+。该模型采用 MobileNetV2 作为骨干网络，减少了参数大小，提高了部署效率。此外，将坐标注意（CA）机制集成到浅层特征提取和 ASPP 模块中，提高了不同特征之间的位置信息提取，最大限度地减少了分割区域与实际损伤区域之间的差异。在编码器中引入级联特征融合（CFF）策略，减少了分割边缘不连续，保证了有效的多级语义融合，提高了分割精度。实验结果表明，在自建的黄冠梨早期瘀伤数据集上，该模型的 mIoU 和 mPrecision 分别达到了 95.68%和 97.58%。与 U-Net、SegNet、PSPNet 和 HRNet 等基准模型相比，该模型显示出优越的分割性能，为水果早期无损检测技术的发展提供了有力的支持。

INTRODUCTION

"Huangguan" pear is a high-quality pear variety widely grown in China, which has become an important cash crop in many areas because of its attractive appearance, delicate texture and high yield. However, the soft structure and high water content of 'Huangguan' pears make them susceptible to physical trauma or impact damage during harvesting, packing and transport, resulting in early tissue bruising. Bruising is usually defined as damage to the subcutaneous tissue of fresh produce that does not result in rupture of the epidermis *(Al-Dairi et al., 2024*). Early bruises in 'Huangguan' pears are cosmetically indistinguishable from healthy tissue and are difficult to detect with the naked eye, but they provide an ideal environment for microbial colonisation. If early damage is not detected and treated in a timely manner, the resulting microorganisms may spread and infect other healthy fruits, thus seriously affecting product quality and economic value *(Opara et al., 2014)*. Traditionally, testing the quality of 'Huangguan' pears in packinghouses has relied on manual inspection by trained professionals *(Patel et al., 2024)*, but this method is highly subjective and suffers from limitations such as time-consuming, labour-intensive and the possibility of secondary damage to the fruit *(Li et al., 2024)*. To cope with these shortcomings, machine vision technology based on RGB images is widely used *(Manavalan, 2020; Arumuga et al., 2023; Tian et al., 2024)*. The technology achieves a reduction in labour costs and the rate of misjudgement as well as an increase in detection speed during the inspection process by capturing RGB images of fruits and combining them with image processing algorithms *(Du et al., 2020)*. However, since the RGB image inspection method relies on surface visible light information, its detection effect is mainly limited to surface defects visible to the naked eye and restricted to early bruises or internal damage hidden under the fruit skin *(Li et al., 2021)*. Therefore, this method still has significant shortcomings in meeting the needs of early bruise detection.

It is well known that when fruit undergoes physical trauma, the pulp tissue is damaged and a series of complex physiological and biochemical reactions occur at the site of injury, altering the density and vibrational strength of the molecular bonds *(Li et al., 2018)*. These changes affect the sugar and water content, which leads to alterations in optical properties, making it possible to utilize optical properties for early identification of internal damage. Several studies have used hyperspectral imaging to extract spectral information to evaluate the intrinsic and extrinsic qualities of fruit. *Zhu et al., (2016)* applied hyperspectral imaging and chemo-metrics to predict the integrated quality of tomato non-destructively and determine the optimal harvesting period. *Wu et al., (2023)* used HSI combined with spectral and texture features to detect and classify early damage of Lingwu longdate based on 1D convolutional neural network (1D-CNN). *Liu et al., (2023)* used hyperspectral imaging, transfer learning and convolutional neural network modelling techniques to detect early mechanical damage in pears, and the resulting model achieved an accuracy of 96.61% on the test set, which was 3.64% higher than the pre-fine-tuning network. The above studies show that HSI performs well in fruit damage detection, but it faces challenges in practical applications such as high equipment cost, complex data processing and high computational resource requirements *(Mei et al., 2023)*. Compared with hyperspectral imaging and processing, NIR imaging offers simpler data processing, eliminating the need to analyse large amounts of spectral band information, which significantly simplifies data processing and reduces inspection costs. Due to the higher absorption of NIR light by bruised tissue, NIR cameras are able to acutely capture subcutaneous damage that cannot be identified by the naked eye and visible light, and visualise healthy tissue and damaged areas by combining spectral information with spatial information *(Ünal et al., 2024)*. In addition, the high sensitivity of NIR cameras to changes in key components such as moisture and sugar, as well as their small size and light weight, make them ideal for early bruise detection in fruit.

Based on near infrared imaging, traditional machine learning techniques are combined for fruit damage detection. *Nandi et al., (2016),* proposed an automatic mango ripeness grading method based on support vector machines (SVM) and fuzzy learning, achieving a grading accuracy of 87%. *Hu et al., (2018)* developed an algorithm for bruised apple identification using 3-D infrared imaging, featuring a vertex-based local binary pattern (vmLBP) for feature extraction and SVM for classification. The algorithm achieved a 91.83 ± 0.46% accuracy, outperforming traditional methods. However, the performance of machine learning models is highly dependent on feature selection, requiring manual elimination of redundant features or identification of the most representative information to minimize the effect of irrelevant input variables *(Li et al., 2022)*, which is not only time-consuming but also depends on expert knowledge. In contrast, due to its powerful feature learning capabilities, deep learning has become an alternative technology in several areas of agriculture *(Attri et al., 2023)*, such as pest and disease detection *(Shafik et al., 2024)*, crop yield estimation *(Barbosa et al., 2021)*, water management *(Chen et al., 2021)*, and soil analysis *(Zhong et al., 2021)*.

Deep learning automatically learns important features from images through multi-layer neural networks, significantly simplifying the feature extraction process, thereby eliminating the reliance on experts to manually select features *(Wu et al., 2020)*.This process not only improves classification accuracy but also reduces human intervention. In recent years, deep learning has demonstrated notable advantages in computer vision and agricultural applications. *Yuan et al., (2022),* developed an early bruise detection system for apples by combining near-infrared imaging with deep learning, achieving an accuracy rate exceeding 99%. The powerful learning and inference capabilities of deep learning give it a clear edge in fruit damage detection tasks, enabling more accurate and efficient automated detection.

Based on the analysis of the aforementioned detection methods and deep learning techniques, this paper proposes a method for early bruise detection in 'Huangguan' pears that integrates near-infrared imaging technology with deep learning algorithms. DeepLabV3+ *(Chen et al., 2018),* as a basic framework for segmentation model is employed for detecting damaged regions in near-infrared images of 'Huangguan' pears, with MobileNetV2 *(Sandler et al., 2018)* chosen as the backbone network to reduce the model's parameter size. Additionally, the coordinate attention (CA) *(Hou et al., 2021)* mechanism is introduced at both shallow and deep feature levels within the encoder to enhance the model's ability to detect bruise regions and improve segmentation accuracy. Furthermore, the cascade feature fusion (CFF) *(Zhao et al., 2018)* strategy is incorporated to better integrate shallow and deep semantic features, thereby enhancing the continuity of edge detection. Experimental results demonstrate that the improved model achieves early bruise detection in 'Huangguan' pears with a model size of only 6.103MB, while key metrics, such as mIoU and mPrecision, reach 95.68% and 97.58%, respectively, significantly improving both detection efficiency and accuracy.

MATERIALS AND METHODS

Experimental samples and damage device

The skin colour of 'Huangguan' pears closely resembles the colour of bruising in its early stages, making bruise identification particularly challenging. Bruise samples of 'Huangguan' pear were prepared as shown in Figure 1.

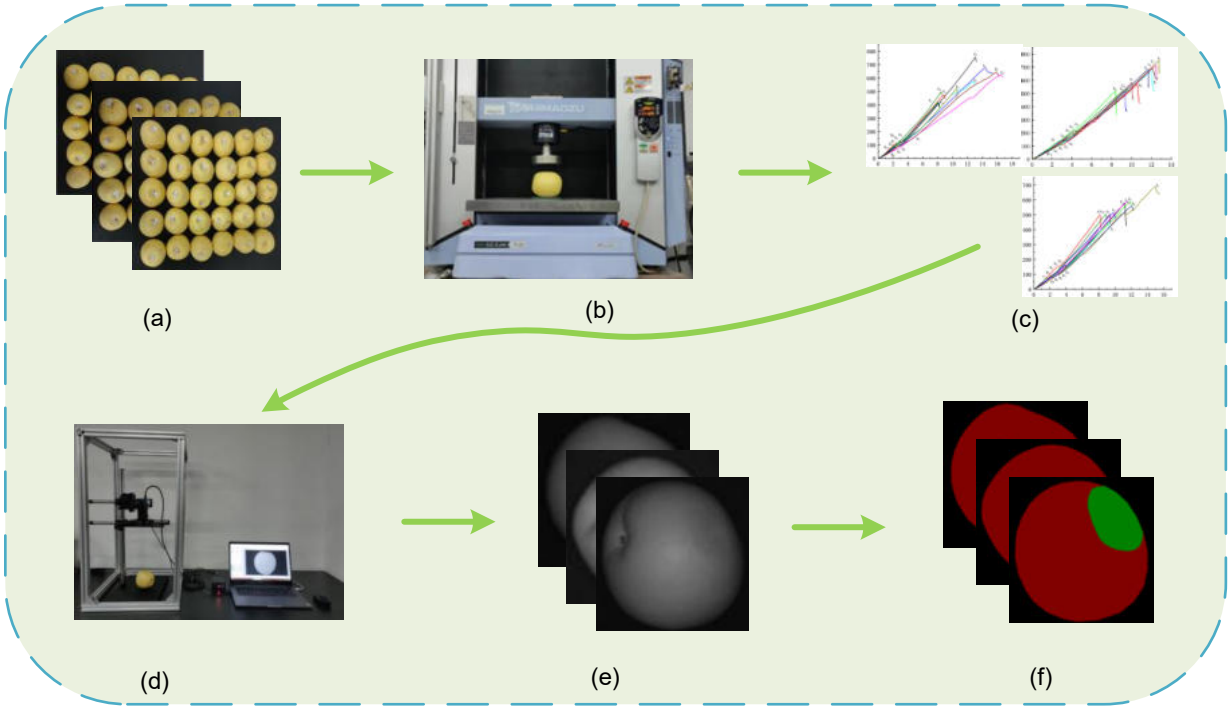


Fig. 1 - Process of bruise sample and data preparation

A total of 120 'Huangguan' pears, free of damage and disease, were purchased from a supermarket and stored at room temperature. These pears were categorized into three groups based on size: large, medium, and small, as shown in Figure 1(a). The diameters of the large pears ranged from 90 to 100 mm, medium pears from 80 to 90 mm, and small pears from 70 to 80 mm.

Since early-stage bruises on 'Huangguan' pears are not visible to the naked eye, it is difficult to obtain naturally bruised pears. Therefore, the bruised pear samples were artificially created. To simulate various levels of compressive bruising, a universal testing machine was used to perform mechanical compression tests, as shown in Figure 1(b). First, ten pears from each size group were randomly selected for preliminary compression tests to determine their biological yield and rupture points, providing a reference for pressure control during the bruise sampling process. The results, shown in Figure 1(c), indicated that the rupture force range for large pears was between 515.73 N and 749.91 N, for medium pears between 457.87 N and 755.73 N, and for small pears between 414.91 N and 689.29 N. Then, it was determined that the maximum lower bound of the rupture force range was 515.73 N, and the minimum upper bound was 689.29 N. For the subsequent bruise sampling, 90 pears were subjected to forces ranging from 520 to 680 N. To simulate varying degrees of internal bruising that 'Huangguan' pears may experience during harvesting and transport, a universal material testing machine applied pressure to the equatorial region of the pears. The pressure was initially set at 520 N and incrementally increased by 10 N until it reached 680 N.

Near infrared camera imaging system and image acquisition process

A NIR camera employed as the imaging device in this experiment is the IUA4100KPA model, manufactured by Hangzhou Jiecheng Instrument Co., Ltd., which features a Sony sensor with a resolution of 2688 × 1520 pixels and a maximum frame rate of 90 frames per second. The lens used is a C-M0418IR (3MP) high-definition industrial lens produced by FordTech, ensuring high-resolution, high-quality image capture suitable for precise detection of surface bruises on 'Huangguan' pears. The imaging system, shown in Figure 1(d), comprises a ring light source, a dark box, and a stand, providing stable and uniform illumination. The camera and lens are positioned at the centre of the ring light source, with the samples placed on a black background plate. The height and aperture of the lens were adjusted for optimal imaging conditions, and the camera's aperture and focal length were fine-tuned to ensure clarity and high resolution. This imaging system minimizes environmental interference and provides consistent, accurate image acquisition, laying a robust foundation for subsequent image processing and analysis.

Immediately after pressure application and bruise induction, NIR images were captured and subsequently collected at 10 min, 20 min, and 0.5 hour intervals to enrich the sample set. To ensure the diversity and comprehensiveness of the dataset, images were taken from multiple angles and positions. After removing unclear or substandard images, a final dataset consisting of 2700 high-quality NIR images of bruised 'Huangguan' pears was obtained, as shown in Figure 1(e). These images were annotated using LabelImg software, where the intact regions of the pears were marked in red, and the bruised regions were highlighted in green. A visualization of the labelled images is shown in Figure 1(f). The dataset was ultimately divided into training, validation, and test sets in an 8:1:1 ratio, comprising 2160, 270, and 270 images, respectively.

DESIGN OF BRUISE SEGMENTATION MODEL

DeepLabV3+ is a state-of-the-art deep learning-based semantic segmentation model designed to address the challenges of spatial information loss and low-resolution outputs commonly encountered in traditional convolutional neural networks for segmentation tasks. Its key innovations include the incorporation of atrous convolution and encoder-decoder architecture, which significantly enhance feature extraction capabilities and improve the resolution of segmentation results. In the model architecture, the input image is first processed by the backbone network, Xception, which extracts hierarchical features: shallow features that retain spatial details and deep features that encode rich contextual semantics. The deep features are then refined through the atrous spatial pyramid pooling (ASPP) module, which employs atrous convolutions with varying dilation rates and global pooling to effectively capture multi-scale contextual information and enrich feature representation. During the decoding stage, low-resolution deep feature maps are upsampled and fused with high-resolution shallow feature maps. This fusion process, followed by additional convolutional operations, restores the spatial resolution of the feature maps to match that of the input image, ultimately producing precise and high-quality segmentation outputs.

Although DeepLabV3+ demonstrates strong performance in multi-scale feature processing and output resolution enhancement, it exhibits certain limitations when applied to the segmentation of early bruise regions in near-infrared images of 'Huangguan' pear. The early bruise regions have minimal visual differences compared to healthy areas, particularly at the boundaries, making them challenging to distinguish, which leads to segmentation discontinuities and missed detections around these boundaries.

Furthermore, the high computational complexity of Xception as the backbone network restricts the model's scalability and efficiency in processing large-scale mass near-infrared datasets. To address these challenges, this paper proposes an improved model, MCC-DeepLabV3+. First, the original Xception backbone is replaced with MobileNetV2, which significantly reduces both the parameter count and computational complexity while retaining robust feature extraction capabilities. Second, a coordinate attention (CA) mechanism is integrated into the shallow features and ASPP modules of the backbone network. This enhancement improves the model's ability to capture spatial information at multiple feature levels, thereby increasing segmentation accuracy and mitigating missed detections. Finally, a cascaded feature fusion (CFF) strategy is introduced during the fusion of shallow and deep features. This strategy ensures a more effective integration of multi-level semantic information, addressing edge discontinuities and further improving the overall segmentation quality. The architecture of the improved model is illustrated in Figure 2.

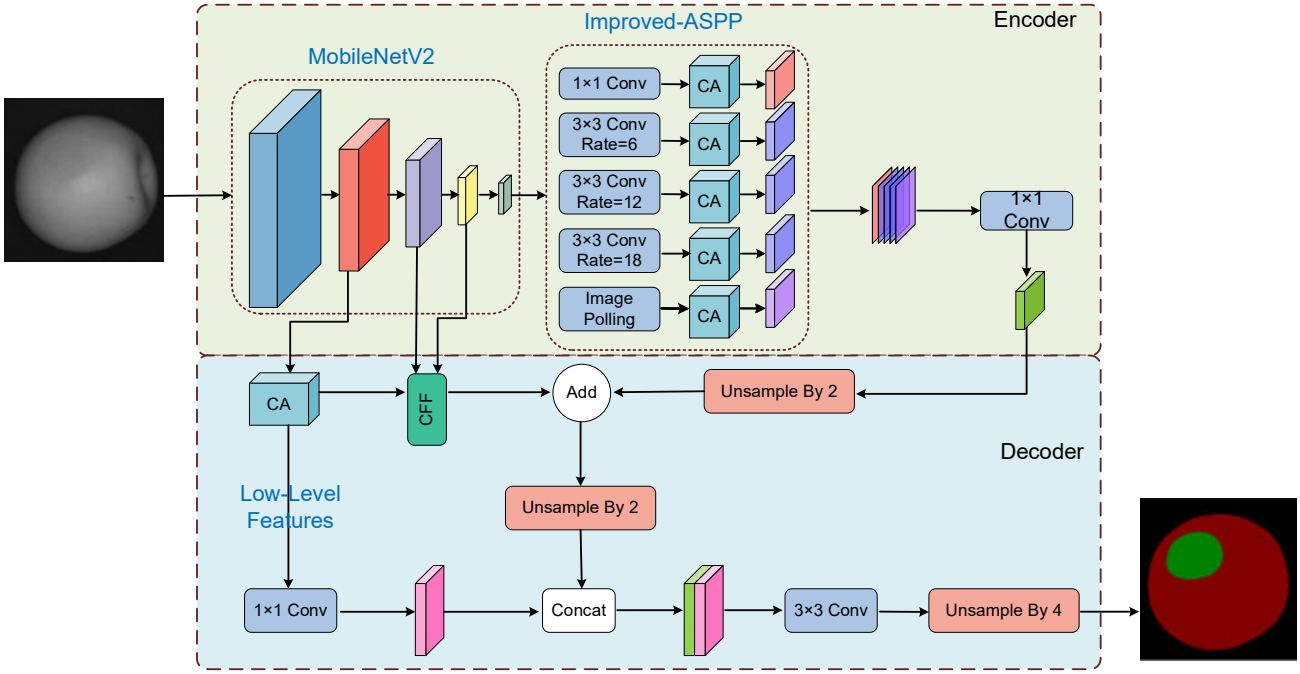
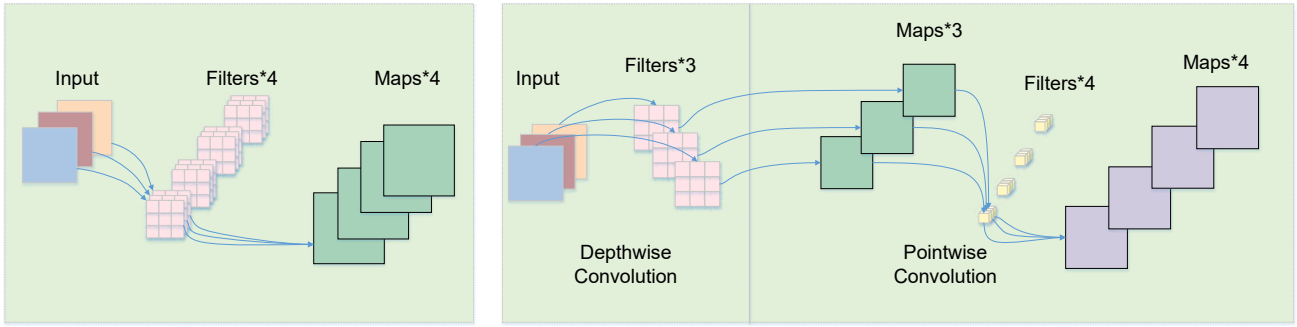


Fig. 2 - The structure of the improved DeepLabV3+ model for bruise 'Huangguan' pear detection

Lightweight backbone network

The Xception network, employed in DeepLabV3+, possesses robust feature extraction capabilities. However, its architecture, composed of numerous stacked convolutional layers, involves extensive multi-level computations, leading to a high parameter count and significant computational complexity. This computational burden presents a bottleneck for the early bruise segmentation task of 'Huangguan' pears, where rapid processing of large-scale near-infrared images is required. To address this issue, the MCC-DeepLabV3+ model replaces Xception with MobileNetV2. MobileNetV2 is a lightweight network architecture that leverages depthwise separable convolutions instead of standard convolutions, significantly reducing the parameter count and computational complexity. Additionally, its inverted residual structure minimizes feature redundancy while maintaining high representational power, enabling efficient feature extraction with a low computational cost.



(a) standard convolution *(b) depth separable convolution*

Fig. 3 - Structures of standard convolution and depth-separable convolution

Depthwise separable convolution is the core operation in MobileNetV2 for achieving model lightweighting. It decomposes the standard convolution operation into two independent steps: depthwise convolution (DW) and pointwise convolution (PW), effectively reducing the computational load of the model. As shown in Figure 3, compared with standard convolution, depthwise separable convolution is divided into two parts: first, depthwise convolution performs convolution independently on each input channel to extract spatial features; then, pointwise convolution applies 1×1 convolutions to perform point-by-point operations, linearly combining features from different channels and fusing spatial and channel information. This decomposition significantly reduces the computational complexity.

Specifically, as shown in Figure 3, depthwise convolution (DW) extracts spatial features by independently processing each input channel, while pointwise convolution (PW) fuses spatial and channel information through 1×1 convolutions. The computational complexity of depthwise separable convolution can be represented by the following two formulas:

$$C_{DW} = M \times D_F \times D_F \times D_K \times D_K \quad (1)$$

$$C_{PW} = M \times N \times D_F \times D_F \quad (2)$$

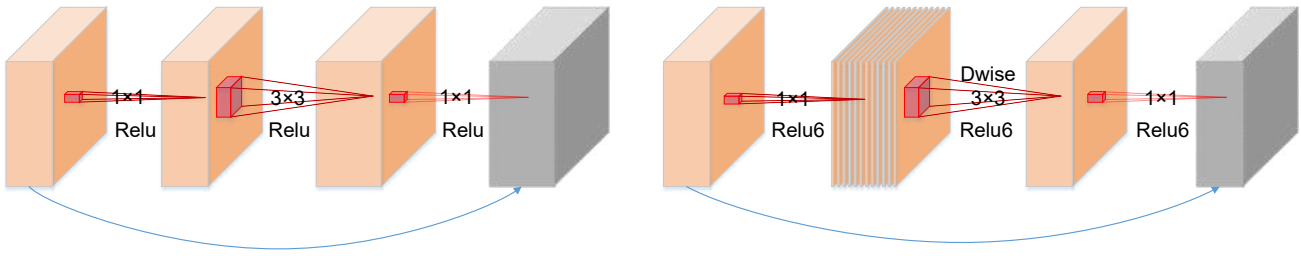
where D_F is the dimension of the feature map, D_K represents the size of the convolution kernel, M is the number of input channels, and N is the number of output channels.

Under equations (1) and (2), the total computation of the depth separable convolution can be expressed as Eq.(3). In contrast, the standard convolution is computationally intensive, which is calculated as Eq.(4). Comparing Eq. 3 and Eq. 4, it can be seen that the computational complexity of the depth-separable convolution is reduced to $\frac{1}{N}+\frac{1}{D_K^2}$ of the standard convolution, which allows MobileNetV2 to maintain a high feature extraction capability while reducing the computational effort.

$$C_{DS} = C_{DW} + C_{PW} = M \times D_F \times D_F \times D_K \times D_K + M \times N \times D_F \times D_F \quad (3)$$

$$C_{SC} = M \times N \times D_F \times D_F \times D_K \times D_K \quad (4)$$

In addition, MobileNetV2 introduces a novel inverted residual block, optimized based on traditional residual networks. While traditional residual networks mitigate the vanishing gradient problem through skip connections, the inverted residual block enhances computational efficiency and feature representation through a “dimensionality enhancement-extraction-dimensionality reduction” design, as illustrated in Figure 4. Specifically, the 1×1 convolution is used to reduce dimensions initially, followed by 3×3 depthwise separable convolution for feature extraction, and finally, another 1×1 convolution to restore the feature dimensions. The use of a linear activation function Relu6 helps to minimize feature loss during dimensionality reduction and improves the efficiency of information flow. Thus, by introducing deeply separable convolutions and inverted residual structures, MobileNetV2 reduces the model’s parameter count while maintaining strong feature extraction capabilities.



(a) Residual network **(b) Inverted residual network**

Fig. 4 - The structure of inverted residual network

Introduction of CA attention mechanism

In semantic segmentation tasks, the traditional DeepLabV3+ model relies on shallow features to provide spatial information and utilizes the ASPP module to extract multi-scale contextual information. However, this architecture exhibits certain limitations. Firstly, shallow features are different to capture the global positional information of bruise regions due to their small receptive fields. Secondly, the ASPP module demonstrates relatively weak capability in capturing spatial location information, although it focuses on aggregating cross-scale semantic features.

These challenges are exacerbated in the segmentation of early bruises in 'Huangguan' pears, where the subtle visual differences between healthy and bruised regions, combined with blurred boundaries, significantly increase the segmentation difficulty. To address these issues, this paper introduces the coordinate attention (CA) mechanism into the shallow feature and ASPP modules of the MCC-DeepLabV3+ model to enhance their spatial localization capabilities. In the shallow feature extraction stage, the CA mechanism strengthens the representation of local spatial details in bruise regions by leveraging cross-channel information modeling and orientation-awareness properties. In the ASPP module, the CA mechanism compensates for its inherent limitations in capturing spatial location information, enabling the model to more accurately perceive the boundary positions of bruise regions. This enhancement effectively improves the spatial localization capability of the model, thereby increasing the accuracy and continuity of boundary segmentation for early bruise regions in 'Huangguan' pears. Therefore, the introduction of the coordinate attention (CA) mechanism enables the encoding of channel relationships and remote dependencies based on precise location information, and the structure is shown in Figure 5.

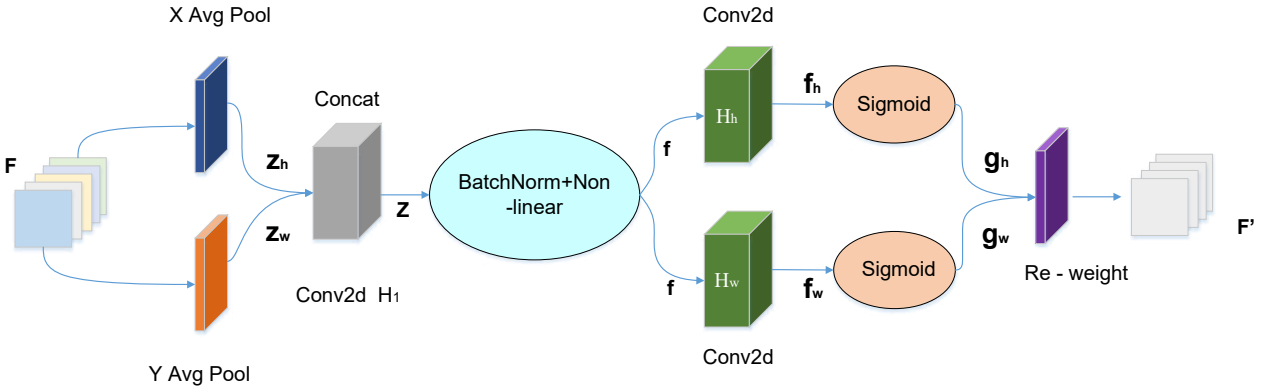


Fig. 5 - Structure of the coordinate attention mechanism module

From Figure 5, to globally encode the height H and width W directions of the input feature map **F**, the CA mechanism implements a global average pooling operation along the H and W directions, respectively, which generates the corresponding two 1D feature maps $\mathbf{z_h}$ and $\mathbf{z_w}$, as follows:

$$\mathbf{z_h}(h)=\frac{1}{W}\sum_{i=0}^{W}x_c(h,i)\ ,\ \mathbf{z_w}(w)=\frac{1}{H}\sum_{j=0}^{H}x_c(j,w) \tag{5}$$

where $\mathbf{z_h}$ and $\mathbf{z_w}$ denote the aggregation results of the feature map in the H and W directions, respectively. The $\mathbf{z_h}$ and $\mathbf{z_w}$ obtained above are spliced and downscaled by a 1×1 Conv H_1 operation to generate an intermediate feature map **Z** of size $C/r\times1\times(W+H)$, where r is the channel reduction ratio. Next, batch normalization and nonlinear activation operations are applied to **Z** to obtain the processed feature map **f**, where δ denotes the nonlinear activation operation.

$$\mathbf{Z}=\mathrm{H}_1\left[\mathbf{z_h},\mathbf{z_w}\right] \tag{6}$$

$$\mathbf{f}=\delta\left[\mathrm{BN}(\mathbf{Z})\right] \tag{7}$$

Then, **f** is split into $\mathbf{f_h}$ and $\mathbf{f_w}$ in both H and W directions and the attention weights $\mathbf{g_h}$ and $\mathbf{g_w}$ are computed by 1×1 Conv H_h, H_w operations and Sigmoid activation function, respectively:

$$\mathbf{g_h}=\sigma\left[\mathrm{H_h}\left(\mathbf{f}_h\right)\right]\ ,\ \mathbf{g_w}=\sigma\left[\mathrm{H_w}\left(\mathbf{f_w}\right)\right] \tag{8}$$

where σ denotes the Sigmoid function.

Finally, the input feature maps are multiplied with the generated attention weights $\mathbf{g_h}$ and $\mathbf{g_w}$ in the X and Y directions, respectively, to obtain the final feature maps after fusing the attentional information:

$$\mathbf{F}^{'}=\mathbf{F}\otimes\mathbf{g_h}\otimes\mathbf{g_w} \tag{9}$$

Integration of CFF module

In DeepLabV3+, the backbone network generates features at varying levels of abstraction during feature extraction. Shallow features are particularly effective for pixel-level localization tasks and ability to excel at capturing edge details and local information due to their high resolution. In contrast, deep features are progressively abstracted and aggregated through a multi-layer network, encapsulating rich global semantic information, which helps in understanding overall image context and category differentiation. Effective fusion of shallow and deep features is the key to achieving a more comprehensive and robust feature representation. However, the traditional DeepLabV3+ decoder employs a simple concatenation method for feature fusion, which inadequately addresses the distinct characteristics and synergistic relationships between shallow and deep features. This limitation can result in the loss of critical detail information, particularly in challenging scenarios such as segmenting bruised areas with blurred boundaries. Consequently, issues such as edge discontinuities and breaks may arise, significantly compromising segmentation accuracy.

To address these challenges, this study introduces the cascaded feature fusion (CFF) module to more effectively integrate shallow and deep features. The core processes of the CFF module are illustrated in Figure 6. First, the shallow feature map $\mathbf{F_1}$ undergoes a 3×3 dilated convolution with a dilation rate of 2 to adjust the channel dimensions. Simultaneously, the deep feature map $\mathbf{F_2}$ is upsampled by a factor of two using bilinear interpolation, followed by the same dilated convolution operation to align its dimensions and receptive field with $\mathbf{F_1}$. This approach not only ensures feature resolution consistency but also expands the receptive field, enabling the capture of richer contextual information while reducing computational overhead. Next, batch normalization is applied to both feature maps to standardize data distribution, which accelerates network training and enhances model convergence. Finally, the normalized $\mathbf{F_1}$ and $\mathbf{F_2}$ are element-wise added, and the result is processed through a ReLU activation function to produce the fused feature map, denoted as $\mathbf{F_{12}}$.

The integration of the CFF module enables a more effective combination of the edge detail information from shallow features and the global semantic information from deep features. This enhancement significantly improves segmentation accuracy for bruised areas while ensuring smoother and more continuous boundary delineation. Moreover, the optimized design of the CFF module reduces computational costs, thereby improving overall segmentation efficiency.

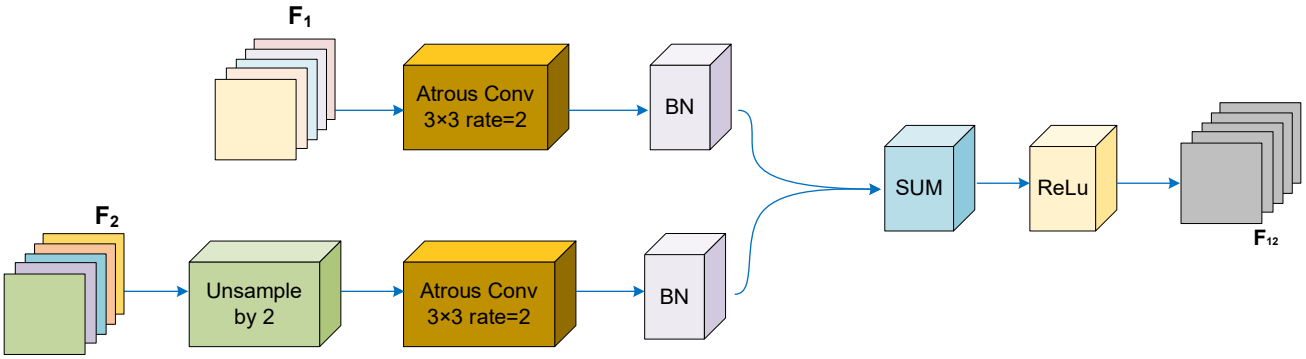


Fig. 6 - Structure of the cascaded feature fusion module

RESULTS AND ANALYSIS

Experimental setup and evaluation metrics

The experiment uses Windows11 operating system. The hardware platform employs Intel I7-11700K CPU and NVIDIA GeForce RTX 4080 GPU with 32G video memory. Network construction, debugging, training and testing are carried out under the Pytorch framework based on the Python language, in which the torch version is 1.13 and the CUDA version is 12.1. The size of the input image is set to 512×512, and the batch size and the number of iterations are set to 2 and 300, respectively, for the training process. In the experiment, the initial learning rate is set to 0.01, and the model is optimized by using SGD. The network is initialized by loading pre-training weights.

For quantitatively comparing the performance of semantic segmentation network models in detecting bruises on 'Huangguan' pears, four evaluation metrics were used: mean Intersection over Union (mIoU), mean Pixel Accuracy (mPA), mean Precison (mPrecision) and mean Recall (mRecall). mIoU is the ratio of the intersection to the union of the ground truth and predicted labels, averaged over all classes. mPA represents

the proportion of correctly classified samples, providing an intuitive measure of overall performance. mPrecision refers to the proportion of true position samples among those predicted as positive by the model, which serves as an evaluation of the model's accuracy in predicting positive cases. mRecall measures the model's ability to correctly identify positive samples, indicating the proportion of true positive samples correctly predicted from all actual positive samples. The four evaluation metrics are defined as follows:

$$mIoU = \frac{1}{k+1}\sum_{i=0}^{k}\frac{TP}{TP+FP+FN} \tag{10}$$

$$mPA = \frac{1}{k+1}\sum_{i=0}^{k}\frac{TP+TN}{TP+TN+FP+FN} \tag{11}$$

$$mPecision = \frac{1}{k+1}\sum_{i=0}^{k}\frac{TP}{TP+FP} \tag{12}$$

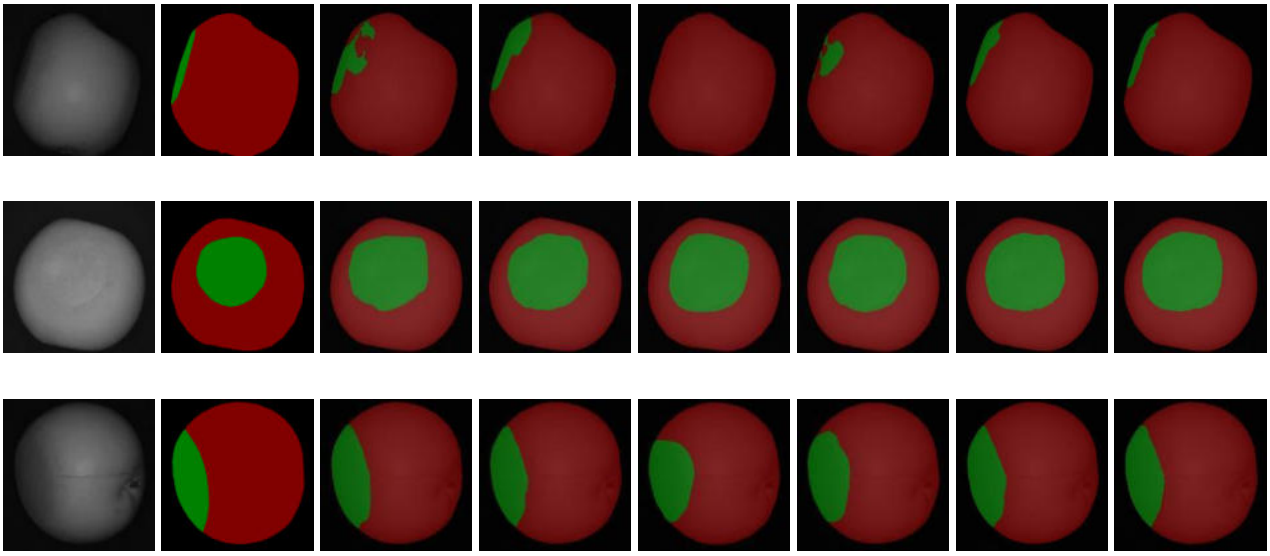
$$mRecall = \frac{1}{k+1}\sum_{i=0}^{k}\frac{TP}{TP+FN} \tag{13}$$

In the above formulas, TP (True Positive) refers to cases where the prediction is positive and the ground truth is also positive. FP (False Positive) denotes situations where the prediction is positive but the ground truth is negative. FN (False Negative) refers to instances where the prediction is negative but the ground truth is positive. TN (True Negative) indicates cases where both the prediction and the ground truth are negative.

Comparison experiment of different models

To verify the effectiveness of the proposed MCC-DeepLabV3+ model in early bruise segmentation of 'Huangguan' pears, it is compared with five classical segmentation models: UNet (*Ronneberger et al., 2015*), SegNet (*Badrinarayanan et al., 2016*), PSPNet (*Zhao et al., 2017*), HrNet (*Sun et al., 2019*), and DeepLabV3+. The experiments were conducted using the same parameter settings and test conditions, and the performance of each model in detecting bruises was visualized through segmentation results.

Figure 7 illustrates the segmentation performance of different models on randomly selected test data.



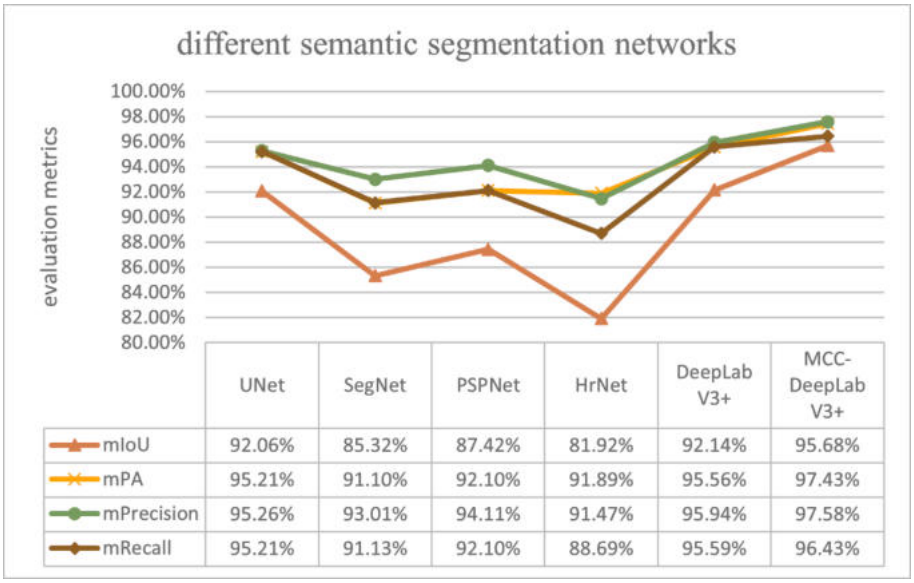
(a) Input *(b) Groud-truth* *(c) UNet* *(d) SegNet* *(e) PSPNet* *(f) HrNnet* *(g)DeepLab V3+* *(h) Ours*

Fig. 7 - Comparison of segmentation results of different networks

UNet performs poorly in locating bruise regions. In UNet, the upsampling process often introduces noise and skip connections that tend to mix high-level features leads to frequent misclassification of healthy tissue as bruise regions. SegNet suffers from significant loss of spatial information due to multiple pooling operations during the decoding stage, especially when precisely segmenting boundary regions. PSPNet is prone to missing bruise features, indicating insufficient sensitivity to the characteristics of bruise regions. HrNet retains high-resolution feature maps through its multi-resolution parallel network branches, capturing global context information.

However, this design may overlook local details, especially when the contrast between the background and bruise areas is low, leading to misclassification of the background as bruise regions. Among the five models, DeepLabV3+ achieves relatively better performance. However, its spatial convolutions have limited capacity to preserve spatial location information, leading to some healthy regions being misclassified as bruise areas. In Figure 7(h), the proposed MCC-DeepLabV3+ model demonstrates more precise bruise segmentation compared to the other five models, significantly reducing misclassification and omission errors. It closely aligns with the ground truth shown in Figure 7(b), delivering more reliable and accurate segmentation results.

To further validate the performance of the proposed MCC-DeepLabV3+ model, mIoU, mPrecision, and mRecall metrics were evaluated on the 'Huangguan' pear bruise dataset, with results summarized in Figure 8. MCC-DeepLabV3+ achieved superior performance across all metrics, with mIoU, mPA, mPrecision, and mRecall reaching 95.68%, 97.43%, 97.58%, and 96.43%, respectively, outperforming all comparison models. For instance, in terms of mIoU, the proposed model demonstrated improvements of 3.93%, 12.14%, 9.45%, 16.80%, and 3.84% over UNet, SegNet, PSPNet, HrNet, and DeepLabV3+, respectively. These results show that the proposed model's robustness and effectiveness in achieving high segmentation accuracy and accurately detecting bruise regions. The above qualitative and quantitative comparison results show that MCC-DeepLabV3+ performs excellently in the task of early bruise segmentation in 'Huangguan' and pear. It effectively addresses the limitations of classical segmentation models, such as inaccurate bruise localization, insufficient boundary smoothing and incorrect segmentation. With higher segmentation accuracy and enhanced robustness, the model provides a practical and efficient solution for bruise detection in industrial applications.



	UNet	SegNet	PSPNet	HrNet	DeepLab V3+	MCC-DeepLab V3+
mIoU	92.06%	85.32%	87.42%	81.92%	92.14%	95.68%
mPA	95.21%	91.10%	92.10%	91.89%	95.56%	97.43%
mPrecision	95.26%	93.01%	94.11%	91.47%	95.94%	97.58%
mRecall	95.21%	91.13%	92.10%	88.69%	95.59%	96.43%

Fig. 6 - Comparison of segmentation performance of different semantic segmentation networks

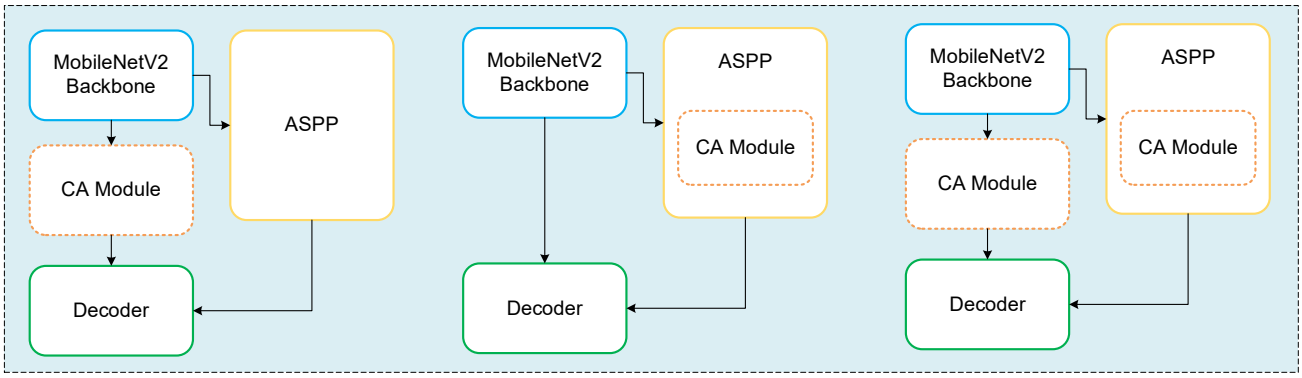


Fig. 7 - The structure of CA attention mechanisms in different positions

To determine the optimal application of the attention mechanism in DeepLabV3+, three different encoder architectures shown in Figure 9 were designed and evaluated on the custom 'Huangguan' Pear dataset. These architectures include: incorporating the attention mechanism only after the shallow feature output from MobileNetV2 (referred to as "CA after MobileNetV2"), integrating it solely within the ASPP module ("CA in ASPP"), and applying it to both MobileNetV2 output and the ASPP module ("CA after MobileNetV2 and in ASPP"). Figure 10 illustrates the segmentation results of the three structures, while Table 1 presents their performance metrics.

As shown in Table 1, Structure 3 achieved the highest performance across all metrics, with mIoU, mPA, mPrecision, and mRecall reaching 95.22%, 96.93%, 96.41%, and 95.57%, respectively. Specifically, as depicted in Figure 10, structure 1 enhances the extraction of local features but lacks reinforcement of deep semantic features, leading to inadequate global information capture. This limitation reduces segmentation accuracy, particularly for irregular bruise morphologies, which are prone to misclassification. Structure 2 (in ASPP) improves global contextual perception and optimizes the receptive field across multi-level features, enabling more accurate contour detection. However, it struggles with fine boundary delineation. In contrast, structure 3 combines the strengths of both approaches. The attention mechanism applied after MobileNetV2 refines edge features and improves detail segmentation, while the mechanism in the ASPP module strengthens global semantic feature representation and ensures effective spatial information capture. This dual-attention mechanism achieves a balanced integration of global and local features, significantly enhancing overall segmentation performance and edge detail accuracy. By combining subjective visual evaluations with objective performance metrics, it is evident that the dual-attention mechanism substantially improves the performance of DeepLabV3+ in 'Huangguan' pear bruise segmentation. This approach not only preserves the integrity of global semantic features but also restores fine edge details, thereby enhancing both segmentation accuracy and model robustness. Therefore, it was selected as the final design in this study.

Table 1

Comparison of network segmentation performance after adding attention mechanism at different locations

Network type	mIoU	mPA	mPrecision	mRecall
Structure 1	92.06%	95.21%	95.26%	93.21%
Structure 2	92.14%	95.56%	95.94%	94.59%
Structure 3	95.22%	96.93%	96.41%	95.57%

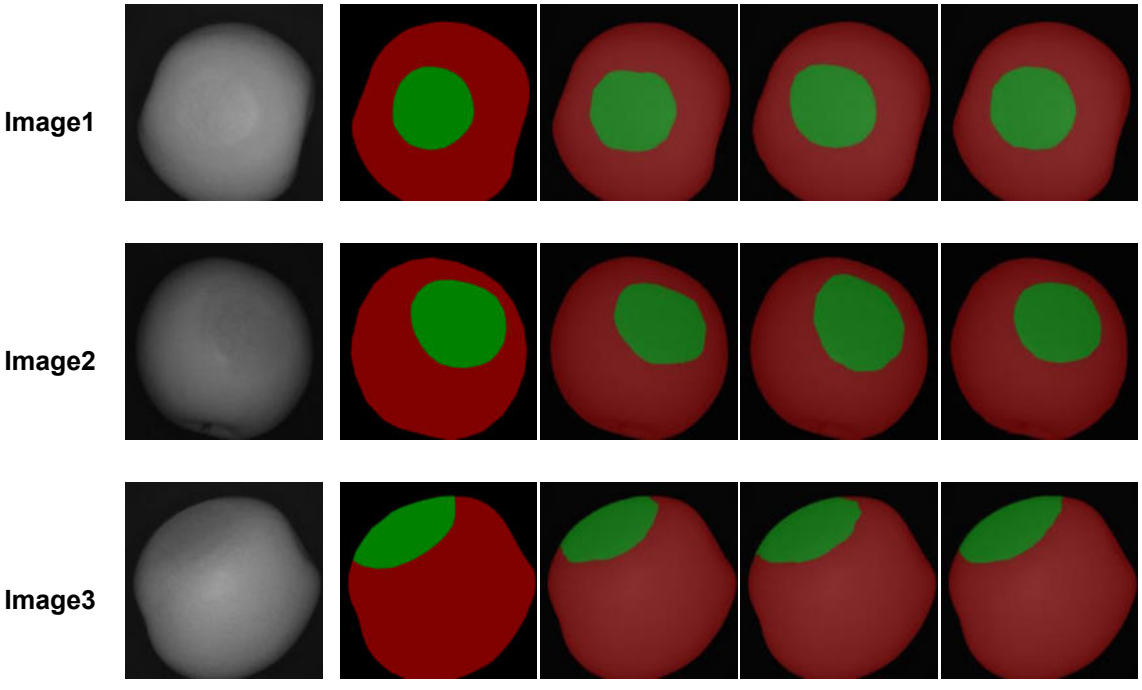


Fig. 8 - Comparison of segmentation results after adding attention mechanism at different locations

Ablation experiment

To verify the contribution of each module in 'Huangguan' pear bruise detection, this study conducts ablation experiments using a self-constructed dataset, with DeepLabV3+ as the base framework. By comparing the effects of embedding the MobileNetV2 backbone network, the Coordinate Attention (CA) mechanism, and the Cascaded Feature Fusion (CFF) module, the effectiveness and individual contributions of these modules are thoroughly evaluated. The test effect graphs and performance metrics for different module combinations are shown in Figure 11and Table 2, respectively.

Firstly, the backbone of DeepLabV3+ was replaced from Xception to MobileNetV2, reducing the model parameters from 54.71M to 5.82M, nearly a tenfold decrease. This number of parameters has decreased, but the mIoU, mPA, mPrecision, and mRecall metrics improved from 91.24% to 93.52%, 95.56% to 96.55%, 95.94% to 96.56%, and 95.59% to 96.55%, respectively, demonstrating the effectiveness of the lightweight design. The efficient depthwise separable convolutions and inverted residual structure of MobileNetV2 significantly reduce the parameter count while maintaining robust feature extraction capabilities, offering a practical solution for resource-constrained industrial applications. Next, the CA mechanism was embedded in both the output of MobileNetV2 and the ASPP module, keeping the model parameters unchanged at 5.82M. However, the performance improved further, with mIoU, mPA, mPrecision, and mRecall reaching 93.54%, 96.59%, 96.64%, and 96.57%, respectively. The CA mechanism effectively enhances the model's ability to capture global spatial information by combining spatial coordinates with channel attention. Specifically, it strengthens long-range dependencies through global average pooling in the horizontal and vertical directions, improving the model's capability to handle complex bruise shapes while significantly reducing omissions and misclassifications. This demonstrates the critical role of the CA mechanism in enhancing the spatial feature representation of the model. Finally, the introduction of the CFF module slightly increased the model parameters to 5.87M but improved performance. Compared to the initial network with Xception as the backbone, the mIoU, mPA, mPrecision, and mRecall improved by 1.65%, 1.10%, 0.77%, and 1.07%, respectively. The CFF module employs a cascaded feature fusion strategy, combining fine-grained details from shallow features with global semantics from deep features, enhancing the model's ability to capture multi-level features, improving segmentation accuracy.

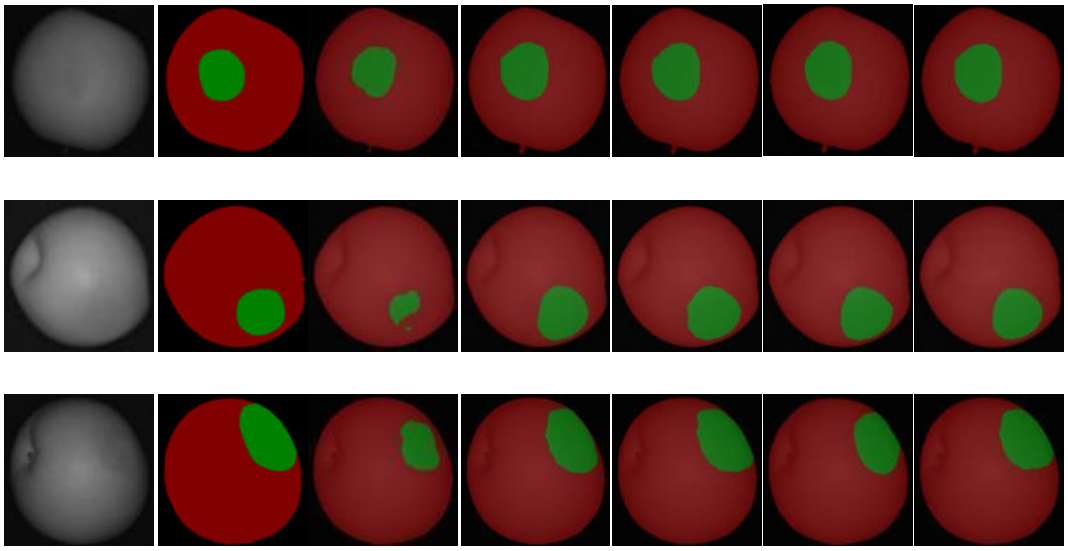
Table 2

The segmentation performance comparison of different modules

DeepLabV3+	Backbone		CA	CFF	Params (M)	mIoU (%)	mPA (%)	mPrecision (%)	mRecall (%)
	Xception	MobileNetV2							
√	√				54.71	92.14	95.56	95.94	95.59
√		√			5.82	93.52	96.55	96.56	96.55
√		√	√		5.82	93.54	96.59	96.64	96.57
√		√		√	5.87	93.66	96.61	96.68	96.61
√		√	√	√	6.10	95.68	97.43	97.58	97.43

Figure 11 illustrates the segmentation performance of the model on the test set after the progressive addition of different modules. Comparing Figure 11(c) and Figure 11(d), it can be observed that replacing the backbone network with MobileNetV2 resulted in clearer segmentation of bruise regions, enhancing the model's initial segmentation capability. Further comparison between Figure 11(d) and Figure 11(e) shows that the introduction of the CA attention mechanism significantly improved the model's feature extraction capability, leading to more precise segmentation and clearer delineation of bruise contours. Comparing Figure 11(e) and Figure 11(f), the inclusion of the CFF module enhanced the handling of edge details in early bruise region segmentation, effectively avoiding issues such as edge blurring or irregularities. Overall, the segmentation results of the proposed model (Figure 11(g)) are more closely aligned with the ground truth (Figure 11(b)), demonstrating the effectiveness of the combined modules in improving segmentation accuracy and detail preservation.

The above objective metrics and subjective segmentation results from the ablation experiments demonstrate that the MobileNetV2 backbone significantly reduced the model's parameters, improving segmentation efficiency. The CA mechanism enhanced the model's ability to represent spatial positional information, resulting in more accurate segmentation. Meanwhile, the CFF module, by integrating multi-level features, further improved the localization accuracy and detail preservation in bruise regions. Together, these three modules achieve a balance between lightweight design and high performance.



(a)Input	(b) Groud-truth	(c)Xception	(d) MobileNet V2	(e)MobileNetV2+CA	(f) MobileNet V2+CFF	(g) Ours

Fig. 9 - Comparison of segmentation results of different modules

CONCLUSIONS

This paper introduces a lightweight semantic segmentation network, MCC-DeepLabV3+, designed for early bruise detection in ‘Huangguan’ pears using near-infrared (NIR) imaging technology and deep learning techniques. A universal testing machine was employed to generate real early bruises, and a corresponding dataset of early bruising in ‘Huangguan’ pears was prepared. The proposed network adopts MobileNetV2 as the backbone, which effectively reduces the parameter size of the original Xception model, thereby addressing the issue of model complexity. Furthermore, a Coordinate Attention (CA) mechanism is integrated into both the shallow feature extraction stage and the Atrous Spatial Pyramid Pooling (ASPP) module, significantly enhancing the model’s segmentation performance and improving its ability to process edge details. The introduction of the Cascaded Feature Fusion (CFF) module further optimizes the integration of shallow detail features with deep semantic information, which is crucial for improving accuracy in detecting early bruises.

To assess the performance of the proposed model, a series of comparative experiments with classical segmentation networks such as UNet, SegNet, PSPNet, HrNet, and DeepLabV3+ was conducted. The evaluation focused on key metrics, including mIoU, mPA, mPrecision, and mRecall, as well as a detailed analysis of the segmentation results on the test set. Our findings reveal that MCC-DeepLabV3+ consistently outperforms the other models across all evaluated indices, demonstrating superior segmentation reliability and performance in detecting early bruises in ‘Huangguan’ pears.

In terms of attention mechanisms, the impact of adding CA attention mechanisms at various stages of the network, specifically at the shallow input of the MobileNetV2 backbone and within the ASPP module, was explored. Our results indicate that incorporating CA attention mechanisms at both locations simultaneously significantly improves model performance, compared to models with either individual or no attention mechanisms. This reinforces the importance of integrating attention mechanisms at multiple stages of the network to enhance segmentation results.

To further validate the effectiveness of the proposed enhancements, ablation experiments were conducted, which confirmed that MCC-DeepLabV3+ outperforms various combinations of individual improvements.

The model's segmentation results closely align with the ground truth labels, showcasing its ability to accurately detect early bruises in 'Huangguan' pears. This advancement provides a new, efficient, and precise approach for early bruise detection, which can be effectively applied in automated fruit quality detection and precision agriculture.

In conclusion, the enhanced MCC-DeepLabV3+ network introduced in this paper offers significant improvements in the accuracy and efficiency of early bruise detection in 'Huangguan' pears. While the proposed model demonstrates impressive performance, there remains potential for further optimization. Future research will focus on refining both the accuracy and speed of detection to further enhance the practicality and effectiveness of this approach for real-world applications in agriculture. Additionally, addressing challenges such as the detection of complete overlap between bruises in densely packed pears will be a key area for future improvement.

CREDIT AUTHOR STATEMENT

Congkuan Yan: Conceptualization, Methodology, Formal analysis, Writing – original draft. **Haonan Zhao**: Formal Analysis, Data curation. **Dequan Zhu:** Supervision, Writing – review & editing. **Yuqing Yang**: Formal Analysis. **Ruixing Xing**: Data curation. **Qixing Tang**: Investigation, Validation. **Juan Liao**: Project administration, Funding acquisition, Writing – review & editing.

DECLARATION OF COMPETING INTEREST

The authors declare that they have no known competing financial interests or personal relationships that could have appeared to influence the work reported in this paper.

ACKNOWLEDGEMENT

The research was funded by the National Natural Science Foundation of China (No.32201665) and the National Key Research and Development Program (2022YFD2001801-3).

REFERENCES

[1] Al-Dairi, M., Pathare, P. B., Al-Yahyai, R., Jayasuriya, H., & Al-Attabi, Z. (2024). Banana fruit bruise detection using fractal dimension based image processing. *Food chemistry*, *455*, 139812.

[2] Opara, U. L., & Pathare, P. B. (2014). Bruise damage measurement and analysis of fresh horticultural produce—A review. *Postharvest Biology and Technology*, *91*, 9-24.

[3] Patel, K. K., & Pathare, P. B. (2024). Principle and applications of near-infrared imaging for fruit quality assessment—An overview. *International Journal of Food Science and Technology*, *59*(5), 3436-3450.

[4] Li, Y., You, S., Wu, S., Wang, M., Song, J., Lan, W., ... & Pan, L. (2024). Exploring the limit of detection on early implicit bruised 'Korla' fragrant pears using hyperspectral imaging features and spectral variables. *Postharvest Biology and Technology*, *208*, 112668.

[5] Manavalan, R. (2020). Automatic identification of diseases in grains crops through computational approaches: A review. *Computers and Electronics in Agriculture*, *178*, 105802.

[6] Arun, R. A., & Umamaheswari, S. (2023). Effective multi-crop disease detection using pruned complete concatenated deep learning model. *Expert Systems with Applications*, *213*, 118905.

[7] Tian, M., Zhang, J., Yang, Z., Li, M., Li, J., & Zhao, L. (2024). Detection of early bruises on apples using near-infrared camera imaging technology combined with adaptive threshold segmentation algorithm. *Journal of Food Process Engineering*, *47*(1), e14500.

[8] Du, Z., Zeng, X., Li, X., Ding, X., Cao, J., & Jiang, W. (2020). Recent advances in imaging techniques for bruise detection in fruits and vegetables. *Trends in Food Science & Technology*, *99*, 133-141.

[9] Li, X., Liu, Y., Jiang, X., & Wang, G. (2021). Supervised classification of slightly bruised peaches with respect to the time after bruising by using hyperspectral imaging technology. *Infrared Physics & Technology*, *113*, 103557.

[10] Li, C., Li, L., Wu, Y., Lu, M., Yang, Y., & Li, L. (2018). Apple variety identification using near-infrared spectroscopy. *Journal of Spectroscopy*, *2018*(1), 6935197.

[11] Zhu, Q., Guan, J., Huang, M., Lu, R., & Mendoza, F. (2016). Predicting bruise susceptibility of 'Golden Delicious' apples using hyperspectral scattering technique. *Postharvest Biology and Technology*, *114*, 86-94.

[12] Wu, D., Wan, G., Jing, Y., Liu, G., He, J., Li, X., Shihu, Y., Ma, P., & Sun, Y. (2023). Hyperspectral imaging combined with deep learning for discrimination of Lingwu long jujube in terms of the time after bruising. *Microchemical Journal*, *194*, 109238.

[13] Liu, D., Lv, F., Wang, C., Wang, G., Zhang, H., & Guo, J. (2023). Classification of early mechanical damage over time in pears based on hyperspectral imaging and transfer learning. *Journal of Food Science*, *88*(7), 3022-3035.
[14] Mei, M., & Li, J. (2023). An overview on optical non-destructive detection of bruises in fruit: Technology, method, application, challenge and trend. *Computers and Electronics in Agriculture*, *213*, 108195.
[15] Ünal, Z., Kızıldeniz, T., Özden, M., Aktaş, H., & Karagöz, Ö. (2024). Detection of bruises on red apples using deep learning models. *Scientia Horticulturae*, *329*, 113021.
[16] Nandi, C. S., Tudu, B., & Koley, C. (2016). A machine vision technique for grading of harvested mangoes based on maturity and quality. *IEEE sensors Journal*, *16*(16), 6387-6396.
[17] Hu, Z., Tang, J., Zhang, P., & Patlolla, B. P. (2018). Identification of bruised apples using a 3-D multi-order local binary patterns based feature extraction algorithm. *IEEE Access*, *6*, 34846-34862.
[18] Li, X., Cai, C., Zheng, H., & Zhu, H. (2022). Recognizing strawberry appearance quality using different combinations of deep feature and classifiers. *Journal of Food Process Engineering*, *45*(3), e13982.
[19] Attri, I., Awasthi, L. K., Sharma, T. P., & Rathee, P. (2023). A review of deep learning techniques used in agriculture. *Ecological Informatics*, *77*, 102217.
[20] Shafik, W., Tufail, A., De Silva Liyanage, C., & Apong, R. A. A. H. M. (2024). Using transfer learning-based plant disease classification and detection for sustainable agriculture. *BMC Plant Biology*, *24*(1), 136. https://doi.org/10.1186/s12870-024-04825-y
[21] Barbosa, B. D. S., Costa, L., Ampatzidis, Y., Vijayakumar, V., & dos Santos, L. M. (2021). UAV-based coffee yield prediction utilizing feature selection and deep learning. *Smart Agricultural Technology*, *1*, 100010.
[22] Chen, M., Cui, Y., Wang, X., Xie, H., Liu, F., Luo, T., Zheng, S., Yufeng Luo, Y. (2021). A reinforcement learning approach to irrigation decision-making for rice using weather forecasts. *Agricultural Water Management*, 250: 106838.
[23] Zhong, L., Guo, X., Xu, Z., & Ding, M. (2021). Soil properties: Their prediction and feature extraction from the LUCAS spectral library using deep convolutional neural networks. *Geoderma*, *402*, 115366.
[24] Wu, S. L., Tung, H. Y., & Hsu, Y. L. (2020, December). Deep learning for automatic quality grading of mangoes: methods and insights. In *2020 19th IEEE International Conference on Machine Learning and Applications (ICMLA)*. pp.446-453. IEEE.
[25] Yuan, Y., Yang, Z., Liu, H., Wang, H., Li, J., & Zhao, L. (2022). Detection of early bruise in apple using near-infrared camera imaging technology combined with deep learning. *Infrared Physics & Technology*, *127*, 104442.
[26] Chen, L. C., Zhu, Y., Papandreou, G., Schroff, F., & Adam, H. (2018). Encoder-decoder with atrous separable convolution for semantic image segmentation. In *Proceedings of the European conference on computer vision (ECCV)*. pp. 801-818.
[27] Sandler, M., Howard, A., Zhu, M., Zhmoginov, A., & Chen, L.C. (2018). Mobilenetv2: Inverted residuals and linear bottlenecks. In *Proceedings of the IEEE conference on computer vision and pattern recognition*. pp. 4510-4520.
[28] Hou, Q., Zhou, D., & Feng, J. (2021). Coordinate attention for efficient mobile network design. In *Proceedings of the IEEE/CVF conference on computer vision and pattern recognition*. pp.13713-13722.
[29] Zhao, H., Qi, X., Shen, X., Shi, J., & Jia, J. (2018). Icnet for real-time semantic segmentation on high-resolution images. In *Proceedings of the European conference on computer vision (ECCV)*. 405-420.
[30] Ronneberger, O., Fischer, P., & Brox, T. (2015). U-net: Convolutional networks for biomedical image segmentation. In *Medical image computing and computer-assisted intervention–MICCAI 2015: 18th international conference, Munich, Germany, October 5-9, 2015, proceedings, part III 18*. pp. 234-241. Springer international publishing.
[31] Badrinarayanan V., Kendall A., Cipolla R. (2016) SegNet: A deep convolutional encoder-decoder architecture for image segmentation. *IEEE Transactions on Pattern Analysis and Machine Intelligence 卷 2017 卷 39 (12)*, 2481-2495.
[32] Zhao, H., Shi, J., Qi, X., Wang, X., & Jia, J. (2017). Pyramid scene parsing network. In *Proceedings of the IEEE conference on computer vision and pattern recognition.* pp. 2881-2890.
[33] Sun, K., Xiao, B., Liu, D., & Wang, J. (2019). Deep high-resolution representation learning for human pose estimation. In *Proceedings of the IEEE/CVF conference on computer vision and pattern recognition.* pp. 5693-5703.

EFFECT OF MOISTURE CONTENT ON SOME PHYSICAL AND MECHANICAL PROPERTIES OF WHEAT (*Triticum aestivum* L.) SEEDS

/

በስንዴ (Triticum aestuum L.) ዘሮች የሚገኘው የእርጥበት ይዘት በአንዳንድ የአካላዊ እና መካኒካላዊ ባህሪቶች ላይ ያለው ተጽእኖ

Amansis TESHOME[1a*)], Adesoji M. OLANIYAN[2)], Abebe FANTA[1a)], Habtamu ALEMAYEHU[1b)], Meseret ABEBE[3)], Dereje ALEMU[3)], Mubarak MOHAMMED[3)], Tasfaye ASEFFA[3)]

[1a)] Department of Agricultural Engineering, Haramaya Institute of Technology, Haramaya University, P.O.Box 138, Dire Dawa, Ethiopia
[1b)] Department of Mechanical Engineering, Haramaya Institute of Technology, Haramaya University, P.O.Box 138, Dire Dawa, Ethiopia
[2)] Department of Agricultural and Bioresources Engineering, Faculty of Engineering, Federal University Oye-Ekiti, Post Code 370001, Ikole Ekiti, Nigeria
[3)] Ethiopian Institute of Agricultural Research (EIAR); Melkassa Agricultural Engineering Research, Melkassa Agricultural Research Centre. P.O.Box 436, Adama, Ethiopia
** Corresponding author; Amansis Teshome Gemmechu*
Phone number: +251951321198; E-mail: teshomea4@gmail.com
DOI: https://doi.org/10.35633/inmateh-76-24

Keywords: *engineering properties, equipment design, moisture level, Triticum aestivum grain*

ABSTRACT

The selection of design, improvement, and utilization of seed planting, harvesting, and postharvest implements depends on the grain physical and mechanical property information of the specific crop type and variety. However, this information is lacking for wheat varieties produced in different regions of Ethiopia. The objective of the study was to generate data on the physical and mechanical properties of grains from selected wheat varieties. Three wheat varieties (Danda'a, Jalanne, and Kakaba) were selected. A factorial combination of 3 × 5 treatment levels was adapted with three replications. The variables studied were the grain size, shape, weight, bulk density, angle of repose, and coefficient of friction. The data were subjected to analysis of variance (ANOVA), and the Dunnett multiple range test was used to separate the means. Significance was accepted at a 95% confidence interval ($p < 0.05$). As moisture increased, the grain's dimensions, shape, thousand kernel weight, coefficient of friction, and angle of repose all increased while bulk density decreased. The bulk density decreased from 0.73 to 0.54 g/cm³ as moisture increased from 8.50% to 28.50%. The study indicated large variations in the treatments used. The mean values for grain length, surface area, and volume increased from 5.786 ± 0.253 to 6.525 ± 0.361 mm, 38.514 ± 2.997 to 49.627 ± 3.201 mm², and 22.531 ± 2.644 to 32.933 ± 3.201 mm³, respectively. Similarly, thousand kernel weight, repose angle, and friction coefficient increased from 26.70 to 42.00 g, 23.20 to 34.70°, and 0.4142 to 0.8391, respectively. Variations in grain properties indicate the necessity for diverse design and calibration criteria for seed planting, harvesting, and postharvest equipment tailored to different wheat varieties at different moisture levels.

አጎፅሮተ-ጥናት

የዘር መዝራት፣ አዝመራ እና ድህረ ምርት መሳሪያዎች የንድፍ፣ የማሻሻያ እና አጠቃቀም የሚወሰነው በሚመለከታቸው የሰብል አይነት እና የእህል አካላዊ እና ሜካኒካል ባህረት መረጃ ነው። ነገር ግን ይህ መረጃ በኢትዮጵያ የተለያዩ ክልሎች ለሚመረቱ የስንዴ ዝርያዎች እጥረት ነው። የጥናቱ አላማ ከተመረጡ የስንዴ ዝርያዎች የዘርን አካላዊ እና ሜካኒካል ባህሪያት መረጃ ማመንጨት ነው። ሶስት የስንዴ ዝርያዎች (ዳንዳአ, ጃላኔ እና ቀቀባ) ተመርጠዋል. የ 35 የትርትመንት ደረጃዎች የፊክቶርያል ጥምር ከሶስት ድግግሞሽ ጋር ተወስዷል. የእህል መጠን፣ ቅርፅ፣ ክብደት፣ የጅምላ እፍጋት፣ የርፖስ አንግል እና የሰበቀ ጥምርታ ከተጠኑት ተለዋዋጮች መካከል ናቸው። ውሂቡ የልዩነት ትንተና (ANOVA) ተደርገዋል፣ እና የዱኔት ባለብዙ ክልል ሙከራ ዘዴዎቹን ለመለየት ጥቅም ላይ ውሏል። ትርጉሙ በ95% የመተማመን ልዩነት ($p < 0.05$) ተቀባይነት አግኝቷል። እርጥበቱ እየጨመረ ሲሄድ የእህሉ ስፋት፣ ቅርፅ፣ ሺህ የዘር ክብደት፣ የሰበቀ መጠን እና የርፖስ አንግል ሁሉም ጨምረዋል፣ የጅምላ እፍጋት ግን ቀንሷል። እርጥበት ከ 8.50% እስከ 28.50% በማደጉ የጅምላ መጠኑ ከ0.73 ወደ 0.54 ግ/ሴሜ³ ቀንሷል። ጥናቱ ጥቅም ላይ በሚውሉት ትርትመንት ውስጥ ትልቅ ልዩነቶችን አመልክቷል. የእህል ርዝመት፣ የገጽታ ስፋት እና የዘር መጠን ከ 5.786 ± 0.253 ወደ 6.525 ± 0.361 ሚሜ፣ 38.514 ± 2.997 ወደ 49.627 ± 3.201 ሚሜ2, እና 22.531 ± 2.644 to 32.933 ± 3.201 በቅደም ተከተል ጨምሯል። በተመሳሳይ የሺህ የከርነል ክብደት፣ የርፖስ አንግል እና የሰበቀ ቅንጅት ከ26.70 ወደ 42.00 ግ፣ ከ23.20 ወደ 34.70° እና 0.4142 ወደ 0.8391 በቅደም ተከተል ጨምሯል። የእህል ባራቶች ልዩነት በተለያዩ የእርጥበት ደረጃ ላይ ለሚገኙ የተለያዩ የስንዴ ዝርያዎች የተዘጋጁ ዘርን ለመትከል፣ ለመሰብሰብ እና ለድህረ ምርት የሚውሉ መሳሪያዎች የተለያዩ የንድፍ እና የካሊብሬሽን መስፈርቶች እንደሚያስፈልግ ያመለክታሉ።

INTRODUCTION

Wheat (*Triticum aestivum L.*) is among the most important staple food crops and a major diet that is consumed by more than 2.5 billion people globally (*Bentley et al., 2022*). It is a staple food in all parts of the world, supplying 35% of food and providing 20% of the calories (Statista, 2022). In Ethiopia, wheat is one of the most important food grain crops. The grain is used for food utilization in different forms such as bread, porridge, soup, *injera, nifro, tella, arki,* and other industrially processed products like pasta and macaroni *(Nigussie et al., 2015*). Furthermore, farmers use wheat grain for marketing to generate income, and the straw is used as animal feed and bedding. Ethiopia's annual wheat production is about 5.80 million tons, with mean productivity of three tons per hectare (ton ha^{-1}) (CSA, 2021), which is relatively lower than the attainable yield of five tons ha^{-1} (*Zegeye et al., 2020*). Wheat accounts for about 17.00% of the total cereal grain produced in Ethiopia, making it the third most important cereal crop after teff and maize (CSA, 2021).

Certain physical attributes and engineering properties of the materials should be considered significant and crucial engineering data when designing machinery, structures, processing systems, and controls that will be used in the production, handling, and processing of food and agricultural products (*Mohsenin, 1986*). The engineering characteristics of wheat with various moisture contents must be understood to develop a machine for handling, transporting, and planting (*Tabatabaeefar, 2003*). Knowledge of the mechanical and physical characteristics of grains is necessary for the design, operation, adaptation, modification, and enhancement of any equipment. In general, the physical and mechanical characteristics of the grains from particular crop types and varieties determine and influence these processes (*Krishnakumar, 2019*). Depending on the crop type and variety, the grains of any food crop differ in terms of size, shape, mass, volume, surface area, density, porosity, angle of repose, coefficient of friction, hardness, resistance to compressive and shear forces, and force-deformation relationship (*Adinoyi et al., 2017; Surpam et al., 2019*). Variations in the location of the production environment, such as climate, soil, and cultural techniques, also impact the mechanical and physical properties of grains (*Mohite et al., 2019*). Furthermore, the grain moisture content has a major impact on how these characteristics vary, suggesting that the physical and mechanical properties are characterized as a function of the grain moisture levels (*Masane et al., 2016*).

For seed planting, threshing, cleaning, and grading, the grain's size and shape, defined by its three-dimensional (3D) parameters, are essential (*Kenghe et al., 2015; Surpam et al., 2019*). The design, selection, and proper functioning of equipment used for handling, storing, and processing grains of certain crop kinds and varieties are influenced by the mechanical characteristics of the grain, such as its coefficient of friction and angle of repose (*Fayed et al., 2020*). The significance of physical and mechanical properties, along with the characteristic variability of the grains, cannot be undermined for the widely diverse wheat cultivars adapted to different agro-ecological zones of Ethiopia and produced under varying cultural practices of the farming communities across various regions of the country.

Therefore, a comprehensive understanding and knowledge of the physical and mechanical properties of wheat grains from particular cultivars or varieties are necessary for the proper selection, design, fabrication, testing, improvement, evaluation, and operation of the machinery required for wheat harvesting, threshing, cleaning, grading, storage, conveying, milling, seed planting, and other tasks. Although it is crucial for the selection, design, improvement, and operation of seed planting, harvesting, and postharvest tools, there have been very few studies on the mechanical and physical characteristics of grains, and there is generally insufficient information on the mechanical and physical characteristics of wheat grains produced in Ethiopia.

Since the physical and mechanical characteristics of wheat grains are essential for the selection, design, development, and use of seed planting, harvesting, and postharvest tools, this study was conducted to generate data that can fill the gaps in this knowledge. The current study aimed to determine the mechanical and physical characteristics of wheat seeds at various moisture content.

MATERIALS AND METHODS

Location of the Study

The study was conducted at the Melkassa Agricultural Research Centre (MARC) in the East Shoa Zone, Oromia Regional State, Ethiopia, in 2024.

Materials and Sample Preparation

In this study, the three most important varieties of wheat - Danda'a, Jalanne, and Kakaba, were used. The Danda'a and Jalanne varieties were obtained from Kulumsa Agricultural Research Center and the Kakaba variety was sourced from a farm at Haramaya University, Ethiopia. The samples were manually cleaned to remove foreign matter, dust, dirt, and broken and immature grains. A digital oven drying machine (Universal

Oven Model of Memert Brand, Germany) was used for testing. The initial moisture content of the samples was determined by oven drying at 104 ±2ºC for 24 hours (*AOAC, 2005*). Samples at desired moisture levels were prepared by adding calculated amounts of distilled water, thoroughly mixing, and then sealing in separate polyethylene buckets. The quantity of distilled water was calculated using the following equation:

$$W_2=W_1\left(\frac{M_1-M_2}{100-M_1}\right) \quad (1)$$

where: W_2 – mass of water added (g), W_1 – total seeds mass (g), M_1 –initial moisture content (%), and M_2 – final moisture content (%).

The samples were stored in a refrigerator at 4ºC for 12 days to allow the moisture to distribute uniformly throughout the samples. Before starting a test, the required quantities of the sample were allowed to warm up to room temperature (*Tabatabaeefar, 2003*). All physical and mechanical properties of wheat seed were measured at moisture levels of 8.50%, 13.50%, 18.50%, 23.50%, and 28.50% (w.b) for all seed varieties, with three replications at each moisture level.

Methods

Treatment variables

Wheat varieties and grain moisture levels were the independent variables. The physical and mechanical properties of the grains were determined at five different wet-based (w.b) grain moisture levels ranging from 8.50% to 28.50% with the levels selected at 5.00% intervals. The moisture range was chosen based on the recommended optimum moisture levels at harvesting, threshing, marketing, and safe storage (*John, 2021*). The 3 × 5 factorial combinations of treatments (3 varieties and 5 moisture levels) were arranged in a Completely Randomized Design, with the appropriate number of replications for each specific parameter.

Determination of physical properties

Grain size

The length, width, and thickness in the three dimensions (3D), designated by L, W, and T, were measured by randomly sampling 100-grain kernels at each selected grain moisture level using a digital vernier caliper with a resolution of 0.01 mm. The mass of each sampled grain was also recorded using an analytical balance, and this measurement was repeated for all the involved varieties. The representative geometric mean diameter, surface area, and degree of sphericity were calculated from basic dimensions using the following Equations 2 to 6 (*Mohsenin, 1986; Adinoyi et al., 2017; Krishnakumar, 2019*).

$$\text{Geometric mean diameter: } D_g=(L\times W\times T)^{\frac{1}{3}} \text{ [mm]} \quad (2)$$

$$\text{Surface area: } A_s=\pi D_g{}^2 \text{ [mm}^2\text{]} \quad (3)$$

$$\text{Volume: } V=\frac{\pi\times L\times W\times T}{6} \text{ [mm}^3\text{]} \quad (4)$$

$$\text{Aspect ratio: } R_a=\frac{W}{L} \quad (5)$$

$$\text{Sphericity: } S=\frac{(L\times W\times T)^{\frac{1}{3}}}{L}\times 100 \text{ [\%]} \quad (6)$$

Thousand kernel weight (TKW)

The grains were counted using a digital counter and placed into a cylinder container of known weight. Thousand kernel weight (TKW) was measured by counting 1,000 seeds with a seed counter and weighing them on an electronic balance to an accuracy of 0.001 g. The cylinder with grain was weighed using a digital balance. This procedure was repeated three times at each moisture level.

Bulk density (ρ_b): Bulk density was calculated from the mass and volume of a circular container with a known volume, which was filled with the wheat samples. After filling the container, excess seeds were removed by passing a flat metal across the top surface with five zigzag motions. The grain was then carefully filled from a height of 150 mm into a 500 mL graduated cylinder of known weight. It was repeated three times. The cylinder was weighed with its content, and the difference above the cylinder weight was used to calculate the bulk density using Equation 10 (*Khanahmadzadeh et al., 2021*):

$$\text{Bulk density: } \rho_b=\frac{M_b}{V_b} \text{ [g cm}^{-3}\text{]} \quad (7)$$

where: M_b = mass of bulk grains (g); V_b - the container volume (cm^3).

Determination of mechanical properties

Angle of repose

The flow characteristics of solids is the angle of repose, which is associated with inter-particulate friction or the resistance to movement between particles. It is also related to the density, surface area, shape of the

particles, and the coefficient of friction of the materials (*Sen et al., 2020*). Two cylindrical containers: one hollow and placed on top of a closed side, were used in the setup for the experiment for measurements of the repose angle. The measurements of the repose angle were taken using equation (8), as provided by *Baryeh (2002)*, *Mohsenin (1986)*, and *Saparita et al. (2019).*

$$\text{Angle of repose: } \theta = tan^{-1}\left(\frac{H}{R}\right) \quad (8)$$

where: H - depth of the slope (mm) and R - the bottom horizontal span of the slope (mm).

Coefficient of friction

The coefficient of static friction was determined using a plywood box with 350 mm in length, 190 mm in width, and 35 mm in height, featuring an open base and top faces. The box was placed on a graduated angular tilting table, on which the test surface plate was fixed. Friction was measured against aluminum, galvanized iron sheets, glass, mild steel, painted surfaces, plastic, plywood, and rubber. A hollow metal cylinder, 50 mm in diameter and 50 mm in height, open at both ends, was filled with seeds at the desired moisture content and placed on an adjustable tilting surface, ensuring that the cylinder did not come into contact with the surface. The surface was then raised gradually until the filled cylinder began to slide down (*Razavi and Milani, 2006; Khanahmadzadeh et al., 2021*). The tilt angle (α) was read from an angular scale when the box began to slide down on the test surfaces and was replicated three times at each moisture level. The coefficient of static friction was calculated using Equation (9).

$$\text{Coefficient of friction: } \mu = tan\,\alpha \quad (9)$$

Data Analysis

The data collected were organized into the required forms for every parameter and subjected to statistical analysis. Minitab 18th edition software was used for statistical analysis. Both descriptive statistics and Analysis of Variance (ANOVA) models were employed as needed, depending on the specific behavior of each parameter. The descriptive method was used to analyze the grain mean dimensions with standard deviations. Analysis of variance was applied to the bulk grain properties, using the Dunnett multiple comparison test with the least significance difference (LSD) at a 5% probability level. Mean line graphs, trend line equations, and coefficients of determination (R^2) were generated for some of the property variables.

RESULTS AND DISCUSSION

Physical Properties

Table 1 summarizes the measured and determined dimensions of 100 kernels from each wheat variety with a moisture content ranging from 8.50 to 28.50%. For the three wheat seed (*Triticum aestivum L*) varieties: Danda'a, Jalanne, and Kakaba, the physical parameters and ANOVA values are shown. The evaluated physical parameters include length, width, thickness, geometric mean diameter, surface area, volume, aspect ratio, and sphericity. The table presents the mean ± standard deviation for each parameter.

Table 1

Descriptive Statistics Wheat varieties dimension, geometric mean diameter, surface area, volume, aspect ratio, and sphericity at Moisture Content Levels from 8.50% to 28.50%.

Wheat Variety	Variable	Moisture Content Level (%)				
		8.50	13.50	18.50	23.50	28.50
Danda'a	Length, mm	5.975±0.39	6.1789±0.392	6.227±0.400	6.349±0.314	6.362±0.307
	Width, mm	2.969±0.194	3.031±0.254	3.176±0.306	3.288±0.377	3.311±0.306
	Thickness, mm	2.453±0.184	2.483±0.225	2.512±0.302	2.646±0.287	2.814±0.230
	Geometric diam., mm	3.512±0.156	3.591±0.213	3.668±0.256	3.800±0.271	3.894±0.222
	Surface area, mm^2	38.805±3.457	40.627±4.689	42.444±5.901	45.577±6.564	47.761±5.346
	Volume,mm^3	22.803±3.054	24.479±4.136	26.194±5.455	29.161±6.354	31.191±5.140
	Aspect ratio	0.492±0.044	0.499±0.044	0.512±0.057	0.518±0.055	0.521±0.046
	Sphericity, %	58.208±3.049	58.917±2.813	59.032±4.276	59.880±3.554	61.232±2.626
Jalanne	Length, mm	6.050±0.399	6.192±0.426	6.266±0.411	6.358±0.480	6.525±0.361
	Width, mm	2.958±0.242	3.030±0.303	3.156±0.230	3.238±0.246	3.321±0.211
	Thickness, mm	2.579±0.198	2.641±0.173	2.761±0.213	2.867±0.316	2.907±0.186

Wheat Variety	Variable	Moisture Content Level (%)				
		8.50	13.50	18.50	23.50	28.50
	Geometric diam., mm	3.581±0.172	3.668±0.230	3.789±0.199	3.885±0.243	3.974±0.128
	Surface area, mm^2	40.352±3.879	42.416±5.234	45.196±4.668	47.585±5.910	49.627±3.201
	Volume, mm^3	24.192±3.484	26.131±4.765	28.693±4.375	31.051±5.763	32.933±3.201
	Aspect ratio	0.490±0.049	0.491±0.050	0.505±0.046	0.510±0.056	0.511±0.048
	Sphericity, %	59.351±3.225	59.375±3.792	60.614±3.618	61.335±4.622	61.026±2.906
Kakaba	Length, mm	5.786±0.253	5.988±0.332	6.157±0.382	6.198±0.295	6.315±0.289
	Width, mm	2.954±0.187	2.972±0.214	3.056±0.252	3.105±0.250	3.218±0.266
	Thickness, mm	2.514±0.150	2.583±0.172	2.784±0.235	2.851±0.197	2.965±0.194
	Geometric diam., mm	3.499±0.136	3.577±0.148	3.736±0.210	3.796±0.185	3.916±0.185
	Surface area, mm^2	38.514±2.997	40.254±3.317	43.968±4.982	45.343±4.371	48.264±4.502
	Volume, mm^3	22.531±2.644	24.083±2.956	27.551±4.733	28.818±4.122	31.639±4.386
	Aspect ratio	0.512±0.040	0.498±0.046	0.498±0.044	0.501±0.037	0.511±0.040
	Sphericity, %	59.856±2.870	60.537±2.081	60.769±2.725	61.297±2.687	62.064±2.685

Principal Dimension - Significant differences were observed among the measured parameters as moisture content increased. As moisture content rose, the size of the wheat kernels also grew. The dimensions (length, width, and thickness) of all varieties increased with rising moisture content. This growth was probably caused by small air voids on the kernels, which may have formed from the swelling effect of the added water. Similar findings were reported for barley grain by *Tavakoli et al., (2009),* sorghum grain by *Mwithiga and Sifuna (2006)*, and *Birehanu et al., (2024)*.

The findings confirm that the principal dimensions of wheat grains from the three varieties increased with an increase in moisture content (Table 1). The average seed length for Danda'a, Jalanne, and Kakaba increased from 5.975±0.39 to 6.362±0.307 mm, 6.050±0.399 to 6.525±0.361 mm, and 5.786±0.253 to 6.315±0.289 mm, respectively, as moisture content increased from 8.50% to 28.50%. Similarly, the average seed width for Danda'a, Jalanne, and Kakaba increased from 2.969±0.194 to 3.311±0.306 mm, 2.958±0.242 to 3.321±0.211 mm, and 2.954±0.187 to 3.218±0.266 mm, respectively, at the same moisture level. The average seed thickness for Danda'a, Jalanne, and Kakaba increased from 2.453±0.184 to 2.814±0.230 mm, 2.579±0.198 to 2.907±0.186 mm, and 2.514±0.150 to 2.965±0.194 mm, respectively, as the moisture content increased from 8.50% to 28.50%. These results align with the findings of *Majdi and Taha (2007)*, who reported that axial dimensions and mean diameter increase with the moisture content of green wheat. Changes in seed dimensions with increasing moisture are important to consider when designing equipment. As indicated in the literature, the physical properties of seeds change with the moisture content. Parameters such as moisture content, external friction, and material density are key factors influencing technological processes (*Kaliniewicz et al., 2018*). Variations in seed dimensions may also result from differences in the seeds' ability to absorb water, as well as variations in chemical composition, morphological structure, and endosperm structure. The water absorption capacity of cereal seeds is crucial not only during storage but also during conditioning before sowing.

Mean diameter. The geometric mean diameters varied among the different wheat varieties at similar moisture levels, with all test varieties showing a linear increase in diameter as moisture content increased (Table 1). The average geometric mean diameter for Danda'a, Jalanne, and Kakaba increased from 3.512±0.156 to 3.894±0.222 mm, 3.581±0.172 to 3.974±0.128 mm, and 3.499±0.136 to 3.916±0.185 mm, respectively, as moisture content increased from 8.50% to 28.50%. The geometric mean diameter is a useful parameter in the design of the metering cells. The metering cells for wheat planters should be designed based on the geometric mean diameter of 3.974±0.128 mm. The increase in the grain's geometric mean diameter may have been due to an overall increase in grain size resulting from the rise in moisture content. This diameter is primarily used in equipment designing, while the equivalent mean diameter represents the average size of bulk grain in a package (*Simonyan et al., 2007*).

Seed surface area and volume. Both surface area and volume for a seed showed significant increases with rising moisture content, with a notable variation among the varieties at similar moisture levels (Table 1). The mean seed surface area for Danda'a, Jalanne, and Kakaba increased from 38.805±3.457 to 47.761±5.346 mm^2, 40.352±3.879 to 49.627±3.201 mm^2, and 38.514±2.997 to 48.264±4.502 mm^2, respectively, the moisture content increased from 8.50% t0 28.50%. Similarly, the mean seed volume for Danda'a, Jalanne, and Kakaba increased from 22.803±3.054 to 31.191±5.140 mm^3, 24.192±3.484 to 32.933±3.201 mm^3 and 22.531±2.644 to 31.639±4.386 mm^3, respectively, at the same moisture levels. A similar linear increase in sorghum grain volume, from 29 to 38 mm^3, was reported by *Kenghe et al., (2015)* for a grain moisture increase from 10.94 to 24.22% (db.). Additionally, *Birehanu et al., (2024),* also observed a linear increase in grain volume with rising moisture levels.

Aspect ratio and Sphericity. The mean aspect ratio and sphericity of wheat seed showed a linear relationship with seed moisture content (Table 1). The seed aspect ratio showed non-significant increases for the Kakaba variety but slightly significant (P = 0.05) increases for Danda'a and Jalanne. The mean aspect ratio of Danda'a and Jalanne increased from 0.492±0.044 to 0.521±0.046, and 0.490±0.049 to 0.511±0.048, respectively, as moisture content increased from 8.50 to 28.50. Similarly, the mean seed sphericity for Danda'a, Jalanne, and Kakaba increased from 58.208±3.049 to 61.232±2.626%, 59.351±3.225 to 61.026±2.906%, and 59.856±2.870 to 62.064±2.685%, respectively, at the same moisture content levels. The shape of the Kakaba seed was the most spherical compared to the Danda'a and Jalanne. The increase in sphericity was attributed to the swelling of the grain kernels with additional water intake, where the thickness (minor diameter) increased more than the major and intermediate diameters (*Birahenu et al., 2024*).

Bulk Density. The experimental results showing the relationship between bulk density and moisture content are presented in Figure 1. A linear decrease in bulk density was observed with increasing moisture content, and this trend was statistically significant at the 5% significance level. The bulk density of Danda'a, Jalanne, and Kakaba varieties decreased from 0.71 to 0.61 g cm^{-3}, 0.73 to 0.64 g cm^{-3}, and 0.70 to 0.54 g cm^{-3}, respectively, as the moisture content increased from 8.50 to 28.50%. This decline in bulk density suggests that the mass increase due to moisture absorption was less than the corresponding volumetric expansion of the bulk, as previously noted in soybean samples (*Tabatabaeefar, 2003*). An inverse relationship between bulk density and moisture content has also been reported by various other studies (*Garnayak et al., 2008; Shahbazi, 2015; Birahenu et al., 2024*). The models fitted to the data using regression analysis showed that the bulk density decreased linearly with increases in the moisture content for all cultivars. Therefore, the following equations were derived for the relationship between bulk density (ρ, g cm^{-3}) and moisture content (M, %), for each variety.

Danda'a variety: $\rho_D = 0.7597 - 0.005780M$, $R^2=0.927$

Jalanne variety: $\rho_J = 0.7461 - 0.004189\ M$, $R^2=0.769$

Kakaba variety: $\rho_K = 0.7857 - 0.00963\ M$, $R^2=0.739$

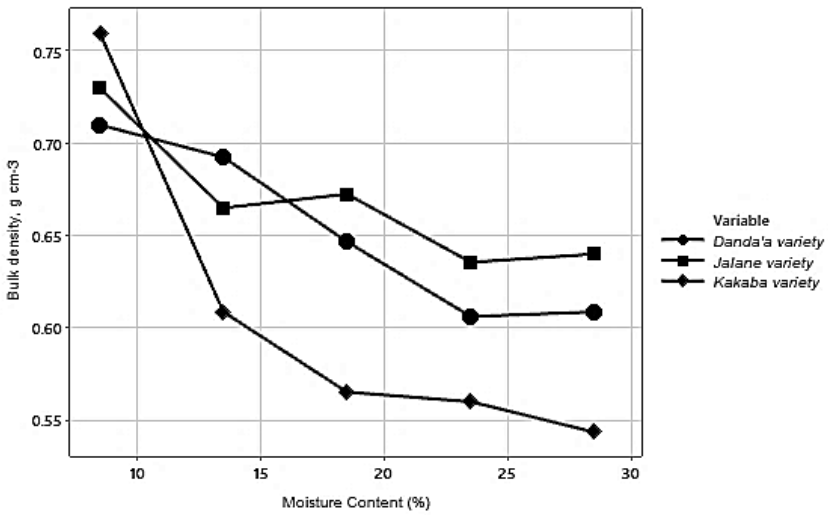


Fig. 1- Effect of moisture content on bulk density of wheat seed varieties

Thousand Kernel Weight. The results obtained for the thousand-kernel weight of wheat with an increase in moisture content are shown graphically in Figure 2. It was observed that the thousand-kernel weight increased linearly with an increase in moisture content, and this change was significant at the 5% significance level. The figure reveals that, for all the wheat seed varieties considered, the thousand-kernel seed mass increases as the moisture content increases. The thousand-kernel weight of the Danda'a, Jalanne, and Kakaba varieties increased from 28.70 to 35.00 g, 31.30 to 42.00 g, and 26.70 to 38.00 g, respectively, as the moisture content increased from 8.50 to 28.50%. The thousand-kernel weight means showed a significant variation among the test varieties, and it also increased linearly with an increase in grain moisture content. The thousand-kernel weight of Jalanne exceeded that of the Danda'a and Kakaba varieties by about 13.11% and 11.73%, respectively. The means of thousand-kernel weight at 13.50% (wb) were 36.30 g, 32.30 g, and 30.00 g for Jalanne, Kakaba, and Danda'a, respectively. The 13.50% moisture is the standard level recommended for wheat grain marketing (*John, 2021*). A mean increase in thousand-kernel weight from 20.67 g to 22.01 g was also reported for sorghum, with a corresponding moisture increase from 8.70% to 21.80% (wb) (*Sabar et al., 2020*). Regression analysis was used to find and fit the best general models to the data. The results showed that as the moisture content of the seeds increased, the thousand-grain weight of wheat increased linearly. Thus, the dependence of the thousand-kernel mass of wheat seeds (TKW, g) on the seed moisture content (M, %) was expressed by the following best-fit equations for each variety:

Danda'a variety: $TKW_D = 26.11 + 0.2720M$, $R^2=0.834$

Jalanne variety: $TKW_J = 28.18 + 0.4680M$, $R^2=0.912$

Kakaba variety: $TKW_K = 23.47 + 0.5260M$, $R^2=0.935$

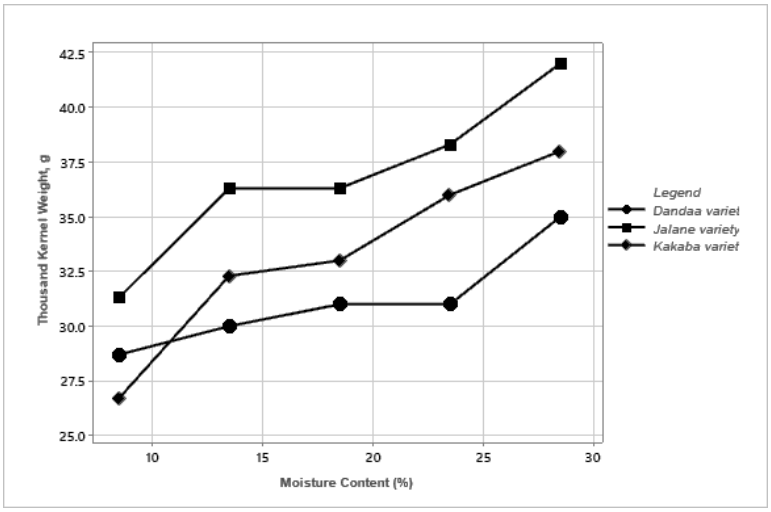


Fig. 2 - Effect of moisture content on thousand kernel weight of wheat seed varieties

Mechanical Properties

Repose Angle. The variation observed in the angle of repose of wheat seeds with increasing moisture content is shown graphically in Figure 3. It was observed that the angle of repose increased linearly with an increase in moisture content, and this change was found to be significant at the 5% level. The angle of repose exhibited a linear increase with significant differences at higher moisture content levels, regardless of the wheat variety tested. The mean repose angle increased for Danda'a from 23.20 to 34.70°, for Jalanne from 24.10 to 32.30°, and for Kakaba from 24.50 to 32.31°, as the moisture content increased from 8.50% to 28.50% (Figure 3). Overall, the angle of repose ranged from 23.20° to 34.70°, indicating flow characteristics classified as good to fair. Angles of repose between 25° to 30°, and 31° to 40°, have been reported to correspond to good and fair, flow properties, respectively (*Sen et al., 2020; Birhanu et al., 2024*). Therefore, the observed values in this study suggest that all wheat varieties demonstrated flowability ranging from good to fair under varying moisture conditions.

At higher moisture content within the experimental range, the grains tended to clump together, resulting in increased pile stability and reduced flowability, which in turn led to higher angles of repose. The observed increase in the angle of repose for the wheat seed varieties was primarily attributed to the expansion in seed size and mass at elevated moisture levels. Additionally, higher moisture content made the seed surfaces stickier, reducing their ability to roll over one another - an effect also reported by *Razavi et al. (2007)*.

Regression models fitted to the experimental data indicated a linear increase in the angle of repose with moisture content for all wheat varieties. The following equations describe the relationship between the angle of repose (θ, °) and moisture content (M, %) for each variety:

Danda'a variety: $\theta_D = 17.85 + 0.5780\ M$, $R^2=0.993$

Jalanne variety: $\theta_J = 21.39 + 0.3940\ M$, $R^2=0.971$

Kakaba variety: $\theta_K = 22.19 + 0.3680\ M$, $R^2=0.951$

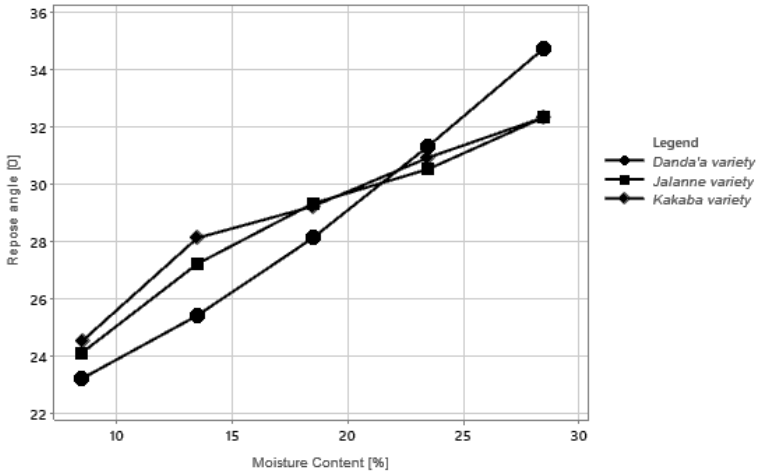


Fig. 3 - Effect of moisture content on the repose angle of wheat seed varieties

Static coefficient of friction

The static coefficient of friction for wheat seed was determined for eight different structural surfaces, as presented in Table 2. It was observed that the static coefficient of friction increased with an increase in moisture content across all surfaces. The values of the static coefficient of friction ranged from 0.4142 to 0.8391 on various surfaces for all wheat seed varieties tested at the specified moisture content levels.

Moisture content played a significant role in influencing μ, with higher moisture levels typically increasing friction due to enhanced adhesive forces between grains and surfaces. However, at the upper moisture range (near 28.50%), some smoother surfaces exhibited slight reductions in μ, possibly due to a lubricating effect from excess moisture. Varietal differences were also notable: Danda'a displayed broad friction ranges, suggesting high sensitivity to surface type, while Jalanne unexpectedly showed high friction on plywood, possibly due to grain morphology. Kakaba, unlike the other varieties, had plastics as the second-highest friction surface, indicating unique grain-surface interactions. These findings have practical implications for grain handling and storage systems, where rubber linings could be used to prevent slippage, while smoother surfaces like aluminum or painted materials might be preferred for applications requiring reduced friction. Further research could explore dynamic friction under movement or the effects of surface wear over time to optimize post-harvest processing and machinery design.

Across all moisture contents, the highest static coefficient of friction was observed on the compressed rubber surface. This could be attributed to the more unpolished surface of the compressed rubber compared to the other materials used. It was also noted that moisture had a greater effect on the static coefficient of friction than the material surface itself. This is likely due to increased adhesion between the grain and the material surface at higher moisture content. Similar results were reported by *Sahoo and Srivastava (2002)*, *Ozarslan (2002), Tabatabaeefar (2003), Bulent Coskun et al. (2005)*, and *Shepherd and Bhardwaj (1986)* for okra, cotton, lentil, wheat, sweet corn, and pigeon pea seeds, respectively. *Parde et al., (2003),* reported that the friction coefficient against the plywood, galvanized steel, and concrete surfaces for the Koto buckwheat cultivar increased significantly from 0.26 to 0.31, 0.25 to 0.29 and 0.38 to 0.43, respectively, with increases in moisture content from 14.8% to 17.9%, which were lower values than compared to the current findings.

The variation between the current findings and previously reported studies could be attributed to differences in seed variety, study location, and other related factors. The increase in grain moisture content likely caused an increase in the grain's surface roughness, which reduced its slipping characteristics and led to higher friction between the grains and the surfaces. These differences could provide important insights for the design of postharvest equipment, such as hoppers, storage structures, and auger conveyors (*Mohite et al., 2019*).

Table 2

Descriptive Statistics of Wheat varieties of static coefficient of friction

Static coefficient of friction, μs						
Surface	**Variety**	**Moisture Level (%)**				
		8.5	**13.5**	**18.5**	**23.5**	**28.5**
Aluminum	Danda'a	0.4627	0.4877	0.4986	0.5317	0.7399
	Jalanne	0.4663	0.4877	0.4986	0.5774	0.7002
	Kakaba	0.4452	0.4877	0.4986	0.5317	0.6249
Galvanized iron	Danda'a	0.4699	0.5317	0.5774	0.6619	0.7673
	Jalanne	0.4521	0.4877	0.5658	0.6249	0.6619
	Kakaba	0.4452	0.5317	0.5774	0.6619	0.7002
Glass	Danda'a	0.4949	0.5429	0.5774	0.6128	0.7002
	Jalanne	0.4593	0.4986	0.5206	0.5317	0.5774
	Kakaba	0.4699	0.5429	0.5774	0.6128	0.6494
Mild steel iron	Danda'a	0.5206	0.5774	0.6249	0.6745	0.7265
	Jalanne	0.5168	0.5317	0.5429	0.6009	0.6619
	Kakaba	0.4557	0.5774	0.6249	0.6745	0.7133
Painted	Danda'a	0.4142	0.4877	0.5658	0.6249	0.7536
	Jalanne	0.4663	0.5317	0.5429	0.5658	0.6249
	Kakaba	0.4699	0.4877	0.5658	0.6249	0.6745
Plastic	Danda'a	0.4733	0.5774	0.589	0.6249	0.7002
	Jalanne	0.4663	0.5095	0.5317	0.6009	0.6745
	Kakaba	0.4699	0.5774	0.589	0.6249	0.7002
Plywood	Danda'a	0.5023	0.5095	0.5543	0.6128	0.6873
	Jalanne	0.5774	0.6128	0.6249	0.6494	0.7133
	Kakaba	0.4521	0.5095	0.5543	0.6128	0.6494
Rubber;	Danda'a	0.6452	0.4452	0.6873	0.7002	0.8243
	Jalanne	0.6536	0.7002	0.6873	0.7536	0.8391
	Kakaba	0.6452	0.6552	0.6745	0.7002	0.7133

The relationships between the static coefficient of friction and moisture content for compressed aluminum, galvanized, glass, mild steel iron, painted, plastic, plywood, and rubber are represented by the following equations:

Aluminum
Danda'a: $CoF_a = 0.3227 + 0.01197M$, $R^2 = 0.721$
Jalanne: $CoF_a = 0.3398 + 0.01115M$, $R^2 = 0.846$
Kakaba: $CoF_a = 0.3684 + 0.008068M$, $R^2 = 0.894$

Galvanized steel
Danda'a: $CoF_g = 0.3334 + 0.01450M$, $R^2 = 0.975$
Jalanne: $CoF_g = 0.3525 + 0.01114M$, $R^2 = 0.985$
Kakaba: $CoF_g = 0.3464 + 0.01280M$, $R^2 = 0.985$

Glass
Danda'a: $CoF_{gl} = 0.4079 + 0.009610M$, $R^2 = 0.962$
Jalanne: $CoF_{gl} = 0.4179 + 0.005386M$, $R^2 = 0.961$
Kakaba: $CoF_{gl} = 0.4118 + 0.008578M$, $R^2 = 0.971$

Mild steel iron
Danda'a: $CoF_{ms} = 0.4365 + 0.01018M$, $R^2 = 0.999$
Jalanne: $CoF_{ms} = 0.4379 + 0.007188M$, $R^2 = 0.895$
Kakaba: $CoF_{ms} = 0.3826 + 0.01225M$, $R^2 = 0.939$

Painted
Danda'a: $CoF_p = 0.2673 + 0.01632M$, $R^2 = 0.98$
Jalanne: $CoF_p = 0.4163 + 0.007026M$, $R^2 = 0.93$
Kakaba: $CoF_p = 0.3624 + 0.0109\ M$, $R^2 = 0.976$

Plastic (Mica)
Danda'a: $CoF_pl = 0.4075 + 0.01003M$, $R^2 = 0.927$

Jalanne: $CoF_{pl} = 0.3687 + 0.01016M$, $R^2 = 0.960$
Kakaba: $CoF_{pl} = 0.4043 + 0.01016M$, $R^2 = 0.925$

Plywood (MDF)
Danda'a: $CoF_{pw} = 0.3981 + 0.009466M$, $R^2 = 0.932$
Jalanne: $CoF_{pw} = 0.5215 + 0.006168M$, $R^2 = 0.928$
Kakaba: $CoF_{pw} = 0.3714 + 0.009958M$, $R^2 = 0.995$

Rubber
Danda'a: $CoF_{ru} = 0.4336 + 0.01226M$, $R^2 = 0.497$

Jalanne: $CoF_{ru} = 0.5697 + 0.008488M$, $R^2 = 0.859$
Kakaba: $CoF_{ru} = 0.6106 + 0.003624M$, $R^2 = 0.981$

where: CoF - coefficient of friction a - aluminum, g - galvanized, gl - glass, ms - mild steel iron, p - painted, pl - plastic, pw - plywood, ru - rubber, and M - moisture content.

CONCLUSIONS

The study investigated the physical and mechanical properties of different wheat varieties at varying moisture levels, aiming to enhance process and equipment design for improved wheat grain yield and quality. Significant differences were observed among the test wheat varieties in terms of grain properties, and these properties varied with changes in moisture content.

Key findings include:

- All test varieties showed an increase in grain size as moisture content increased, with the Jalanne variety exhibiting the largest mean values for grain size and all other studied properties.
- As moisture content increased, grain dimensions, shape, thousand kernel weight, coefficient of friction, and angle of repose also increased, while bulk density decreased. Specifically, bulk density decreased from 0.73 to 0.54 g/cm³ as moisture content increased from 8.50% to 28.50%.
- Grain length, surface area, and volume increased significantly, with mean values rising from 5.786±0.253 mm to 6.525±0.361 mm, 38.514±2.997 mm² to 49.627±3.201 mm², and 22.531±2.644 mm³ to 32.933±3.201 mm³, respectively.
- Thousand kernel weight, repose angle, and friction coefficient also showed increases, highlighting the impact of moisture on these parameters.

In conclusion, the study emphasizes the need for varied design and calibration criteria for equipment used in seed planting, harvesting, and postharvest handling, based on the different physical and mechanical properties of wheat at various moisture levels. These findings suggest that to minimize seed damage and losses during operation, it is essential to tailor equipment design and operation to account for the grain's physical and mechanical properties at different moisture contents. This approach will optimize the efficiency and effectiveness of machinery used in wheat production.

ACKNOWLEDGEMENT

The author expresses gratitude to the Department of Agricultural Engineering and Food Process Engineering from Awash Melkassa Agricultural Research Centre for the provision of laboratory facilities and technical support, Haramaya University, and Kulumsa Agricultural Research Centre for the provision of certified wheat seed varieties, and Haramaya University for financing this study through grant number HURG_2023_03_05_12.

REFERENCES

[1] Adinoyi, H., Ajeigbe, I., Angarawai, I., and Kunihya, A. (2017). Effect of grain moisture content on the physical properties of some selected sorghum varieties. *International Journal of Scientific and Engineering Research*, 8(6): 1796–805.

[2] AOAC. (2005). *Official Methods of Analysis. Association of Official Analytical Chemists*, Washington DC, USA.

[3] Baryeh E.A. (2002) - Some physical properties of millet. *Journal of Food Engineering*, 51: pp 39-46.

[4] A.R. Bentley, J. Donovan, K. Sonder, F. Baudron, J.M. Lewis, et al. (2022). Near-to long-term measures to stabilize global wheat supplies and food security, *Nature Food*, 3 (7): 483–486

[5] Birhanu Atomsa, Yetenayet Bekele, Abebe Fanta, Solomon Abera and Sirawdink Fikireyesus. (2024). Assessment of on-farm sorghum grain loss under farmers' traditional postharvest practices in the East Hararghe Lowlands of Ethiopia. *International Journal of Postharvest Technology and Innovation*, 9(2): pp; 167–188.

[6] Bulent Coskun, M., I. Yalcin and C. Ozarslan (2005). Physical properties of sweet corn seed (Zea mays saccharata Sturt.). *J. Food Eng*., 74: pp; 523-528.

[7] Central Statistics Agency (CSA), (2021). *Agricultural sample survey: Report on area and production of major crops (Private peasant holdings, Meher Season)*. Addis Ababa, Ethiopia.

[8] Fayed, M.I., El-Shal, M.S. and Omar, O.A. (2020). Determination of some apricot seed and kernel physical and mechanical properties. *Agricultural Engineering International*, 22(4): pp; 229–237.

[9] Garnayak D.K., Pradhan R.C., Naik S.N., Bhatnagar N. (2008). Moisture dependent physical properties of jatropha seed (Jatropha curcas L.). *Industrial Crops and Products*, 27: 123-129.

[10] John, W. (2021). *Grain sorghum: harvesting, drying, and storing. Cooperative Extension Service Bulletin*, Department of Agriculture, the University of Georgia, USA. Pp. 27.

[11] Kaliniewicz, Z.; Zuk, Z.; Krzysiak, Z. (2018). Influence of Steel Plate Roughness on the Frictional Properties of Cereal Kernels. *Sustainability*, 10, 1003.

[12] Kenghe, R.N., Jadhav, M.S. and Nimbalkar, C.A. (2015). Physical properties of sorghum (Sorghum bicolour L.) grains as a function of moisture content. *International Journal of Engineering Sciences and Research Technology*, 4(10): 496–504.
[13] Khanahmadzadeh K., Goli, H. and Ghamari, S. (2021). Moisture-dependent physical properties of wild safflower (Carthamus oxyacanthus) seeds. *Agricultural Engineering International*, 23 (3): 201–210.
[14] Krishnakumar, T. (2019). *Engineering properties of agricultural materials*, pp; 1–13 DOI: 10.13140/RG.2.2.20324.83842.
[15] Majdi, A. and M. Taha. (2007). Effect of moisture content on some physical properties of green wheat. *J. Food Eng*., 79(4):1467-1473.
[16] Masane, P.K., Mate, V.N., Borkar, P.A., Murumkar, R.P., Rajput, M.R. and Rathod. P.K. (2016). Physical properties of tender sorghum (Sorghum bicolour L.) grains. *Journal of Ready to Eat Food*, 3(4): 51–54.
[17] Mohite, A.M., Sharma, N. and Mishra, A. (2019). Influence of different moisture content on engineering properties of tamarind seeds. *Agricultural Engineering International*, 21(1): 220–224.
[18] Mohsenin, N. (1986). *Physical properties of plant and animal materials*. Gordon and Breach Science Publishers, New York.
[19] Mwithiga, G., Sifuna, M.M. (2006). Effect of moisture content on the physical properties of three varieties of sorghum seeds. *J. Food Eng*., 75, 480–486
[20] Nigussie Aklilu., Kedir Adem, Adisu Abiy, Belay Geatnet, Gebrie Desta, and Kidane Desalegn. (2015). Bread wheat production in small-scale irrigation user's agro-pastoral households in Ethiopia: Case of Afar and Oromia regional states. *Journal of Development and Agricultural Economics*, 7(4), pp; 123-130
[21] Ozarslan, C. (2002). Physical properties of cotton seed. Bio-systems. Eng., 83: 169-174.
[22] Parde, S. R., Johal, A., Jayas, D. S., and White, N. D. G. (2003). Physical properties of buckwheat cultivars. *Canadian Bio-systems Engineering*, Technical Note.
[23] Razavi, S., & Milani, E. (2006). Some physical properties of the watermelon seeds. *African Journal of Agricultural Research*, 13: 65–69.
[24] Sabar, S.S., Swain, S.K., Behera, D., Rayaguru, K., Mohapatra, A.K., and. Dash, A.K. (2020). Moisture-dependent physical and engineering properties of sorghum. *International Journal of Current Microbiology and Applied Science*, 9(8): 2365–2375.
[25] Sahoo, P.K. and A.P. Srivastava, (2002). Physical properties of Okra seed. *Bio-systems. Eng*., 83: 441 448.
[26] Saparita R., Hidajat D.D., Kuala S.I. (2019). Statistical analysis on the geometric, physical and mechanical properties of dried robusta coffee cherry resulting from natural system processing. *In IOP Conference Series: Earth and Environmental Science*. Vol. 251, No. 1, p. 012041.
[27] Sen, D.J., Nandi, K., Patra, F., Nandy, B., Bera, K. and Mahanti, B. (2020). Angle of repose walks on its two legs: Carr's index and Hausner's ratio. *World Journal of Pharmacy and Pharmaceutical Sciences*, 9(5): 1565 1579.
[28] Shahbazi F. (2013). Evaluation and modelling some engineering properties of three safflower varieties. *Agronomic Research in Moldavia*, 157(4): pp; 23-40
[29] Simonyan, K.J., El-Okene, A.M. and Yiljep, Y.D. (2007). Some physical properties of Samaru sorghum 17. *Agricultural Engineering International*, 9: 1–15.
[30] *Statista*, (2022). www.statista.com/news/global-industry-reports-2022/en
[31] Surpam, T.B., Pardeshi. I.L. and Rokade, H.N. (2019). Engineering properties of sorghum. *International Journal of Chemical Studies*, 7(5): 108–110.
[32] Tabatabaeefar, A. (2003). Moisture-dependent physical properties of wheat. *Int. Agrophysics*, 17: 207-211.
[33] Tavakoli, M., Tavakoli, H., Rajabipour, A., Ahmadi, H. and Gharib-Zahedi, S. M. T. (2009). Moisture-Dependent Physical Properties of Barley Grains. *Int. J. Agric. Biol. Eng*., 2(4): 84-91.
[34] Zegeye, F., Alamirew, B., and Tolossa, D. (2020). Analysis of wheat yield gap and variability in Ethiopia. *International Journal of Agriculture Extension*, 5(4), 89–98.

REVIEW OF EXPERIMENTAL RESEARCH INVESTIGATIONS AND THE WORKING PRINCIPLE OF SMALL VERTICAL AXIS WIND TURBINES
/
REVIZIA INVESTIGAȚILOR DE CERCETARE EXPERIMENTALĂ ȘI PRINCIPIUL DE FUNCȚIONARE AL TURBINELOR EOLIENE MICI CU AX VERTICAL

Adrian PANDELE*), Bogdan Ovidiu DURAN, Dragos Mihail PREDA, Gheorghe VOICU*) [1]
National University of Science and Technology POLITEHNICA Bucharest, Romania;
Tel: +40 722655056, E-mail: adrian.pandele@arrows.ro, Tel: +40274715585; E-mail: ghvoicu_2005@yahoo.com;
DOI: https://doi.org/10.35633/inmateh-76-25

Keywords: *small vertical axis wind turbine, working principle, experimental testing wind turbines evaluation,*

ABSTRACT
This review paper provides a comprehensive analysis of the working principles of wind turbines, with a specific focus on experimental research studies for Vertical Axis Wind Turbines (VAWTs). Wind turbines are essential in harnessing renewable energy, and understanding their operational mechanisms is crucial for optimizing efficiency and performance. The paper outlines the basic working principles of both Horizontal Axis Wind Turbines (HAWTs) and VAWTs, with a deeper exploration of the latter due to its unique advantages in urban and low-wind conditions used in agriculture. The review critically examines recent experimental research on VAWTs, including various design modifications, aerodynamic performance studies, and energy efficiency improvements. Key parameters such as blade shape, turbine configuration, and site-specific factors are discussed, drawing on findings from experimental setups in laboratory and field conditions. The paper also highlights challenges in scaling VAWTs, including structural integrity, noise reduction, and cost-efficiency. Future trends and advancements in VAWT technology are considered, aiming to enhance their viability as a competitive solution for renewable energy generation in households, companies and agricultural farms. Cost-effectiveness, noise reduction, and structural durability remain significant barriers to the widespread adoption of VAWTs, despite promising advancements. This underscores the need for additional research into scalable designs, advanced materials, and optimal configurations for a variety of environmental conditions.

ABSTRACT
Această lucrare de oferă o analiză cuprinzătoare a principiului de funcționare ale turbinelor eoliene, cu un accent special pe studiile experimentale de cercetare pentru turbinele eoliene cu ax vertical (VAWT). Turbinele eoliene sunt esențiale în valorificarea energiei regenerabile, iar înțelegerea mecanismelor lor operaționare este crucială pentru optimizarea performanțelor. Lucrarea conturează principiul de bază de lucru atât ale turbinelor eoliene cu ax orizontal (HAWT) cât și al clor cu ax vertical (VAWT), cu o explorare mai profundă a acestora din urmă datorită avantajelor unice în condiții urbane și de vânt scăzut ce pot fi utilizate in agricultura. Studiul examinează critic cercetările experimentale recente privind VAWT, inclusiv diverse modificări de proiectare, studii de performanță aerodinamică și îmbunătățiri ale eficienței energetice. Sunt discutați parametri cheie, cum ar fi forma palei, configurația turbinei și factorii specifici locului, bazându-se pe constatările din configurații experimentale în condiții de laborator și de teren. Lucrarea evidențiază, de asemenea, provocările în scalarea VAWT, inclusiv integritatea structurală, reducerea zgomotului și eficiența costurilor. Sunt luate în considerare tendințele și progresele viitoare în tehnologia VAWT, cu scopul de a spori viabilitatea acestora ca soluție competitivă pentru generarea de energie regenerabilă în gospodarii, companii si ferme agricole. Eficiența din punct de vedere al costurilor, reducerea zgomotului și durabilitatea structurală rămân bariere semnificative în calea adoptării pe scară largă a VAWT-urilor, în ciuda progreselor promițătoare. Acest lucru subliniază necesitatea unor cercetări suplimentare privind designurile scalabile, materialele avansate și configurațiile optime pentru o varietate de condiții de mediu.

[1] *Adrian PANDELE, PhD Student; Bogdan Ovidiu DURAN, PhD Student; Dragos Mihail PREDA, PhD Student; Gheorghe VOICU, Prof. PhD. Eng*

INTRODUCTION

Wind energy is a key pillar in the global transition toward renewable and sustainable energy systems, offering a clean and inexhaustible alternative to fossil fuels (*Arutyunov et al., 2017*). With increasing concerns over climate change, energy security, and environmental sustainability, wind turbines have gained widespread adoption as reliable sources of electricity generation. Advances in turbine technology continue to improve efficiency and reduce costs, thereby accelerating their integration into both large-scale power grids and small, decentralized energy systems (*Franković et al., 2001*).

Wind turbines function by converting the kinetic energy of moving air into mechanical energy, which is subsequently transformed into electrical energy (*Hau et al., 2006*). This process involves several key stages:

- *Wind capture*: The turbine blades, designed with aerodynamic profiles, intercept wind flow and convert it into rotational motion. The efficiency of this process depends on wind speed, blade geometry, and orientation (*Kusiak et al., 2010*).
- *Mechanical energy conversion*: The rotational energy of the blades is transferred through the rotor hub and main shaft to a generator, where it is transformed into electrical energy via electromagnetic induction (*Cheng et al., 2014*).
- *Electricity generation*: Within the generator, a system of magnets and copper coils produces an electric current as the rotor turns, which is directed to the grid for consumption (*Kan et al., 2021*).
- *Energy conversion and control*: Most turbines produce alternating current (AC), which is conditioned—typically through transformers or inverters—to match grid requirements. Advanced control systems adjust rotor orientation and blade pitch to optimize performance under varying wind conditions (*Yaramasu et al., 2015*).
- *Transmission and distribution*: Generated electricity is routed through substations and delivered to end users via the electrical grid. In larger wind farms, this process may involve energy storage systems and voltage regulation to maintain grid stability (*Hossain, 2021*).

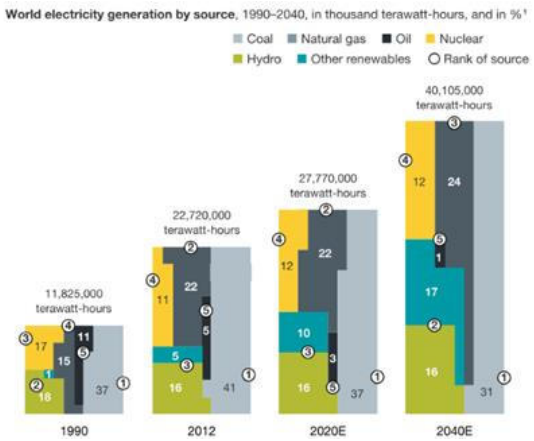


Fig. 1 - Evolution of electricity generation sources
(*www.mckinsey.com*)

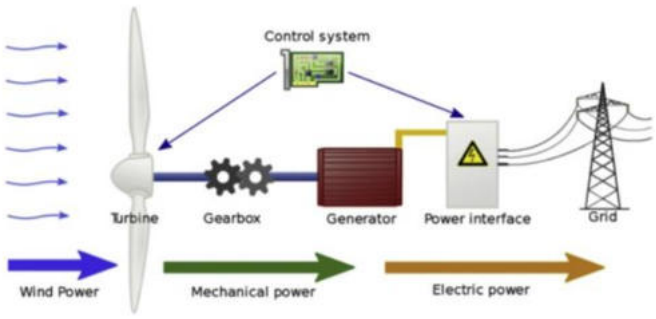


Fig. 2 - The operating principle of wind turbines
(*Gupta et al., 2021*)

While the basic principle remains consistent across all wind turbines, their configurations vary significantly, influencing their efficiency, cost, and suitability for different environments. The two primary types are horizontal-axis wind turbines (HAWTs) and vertical-axis wind turbines (VAWTs).

HAWTs are the most prevalent, particularly in utility-scale wind farms. In these systems, the rotor shaft is aligned horizontally, and the blades rotate in a vertical plane (*Mohammadi et al., 2016*). The blade design, often modeled after aircraft wings, optimizes lift-to-drag ratio for maximum energy capture at high altitudes (*Dal Monte et al., 2013*). These turbines are known for their high efficiency and scalability, though they can be challenging to maintain due to their large size and offshore or remote locations.

Table 1

Advantages and disadvantages of Horizontal Axis Wind Turbines (*Eftekhari et al., 2022*)

Advantages	Disadvantages
- *High efficiency*: HAWTs are generally more efficient than other types of wind turbines. - *Proven technology*: They have been in operation for decades, and their performance is well known. - *Large-scale production*: HAWTs can be scaled up for large wind farms, making them ideal for commercial energy production.	- *Complicated maintenance*: HAWTs are often located in remote or offshore locations, requiring significant maintenance and repair costs. - *Noise and visual impact*: These turbines can be noisy and are sometimes criticised for their visual impact on landscapes.

In contrast, VAWTs feature vertically oriented blades that rotate around a shaft perpendicular to the ground. Common designs include the Savonius and Darrieus models. A key advantage of VAWTs is their ability to capture wind from any direction, eliminating the need for yaw mechanisms. Their compact and accessible design makes them well-suited for turbulent, low-wind urban environments (*Kragten, 2004*).

Table 2

Advantages and disadvantages of Vertical Axis Wind Turbines (*Kragten, 2004*)

Advantages	Disadvantages
- *Omnidirectional*: VAWTs can capture wind from any direction, eliminating the need for the turbine to be constantly adjusted. - *Lower maintenance expenses*: Because the mechanical components of VAWTs are located closer to the ground, they are easier to maintain than HAWTs. - *Suitability for urban areas*: Their compact design and ability to operate in turbulent and low-speed winds make them more suitable for urban environments.	- *Lower efficiency*: VAWTs are generally less efficient than HAWTs, especially in large-scale power generation. - *Mechanical complexity*: VAWT designs can be more complex, leading to potential reliability issues and higher production costs.

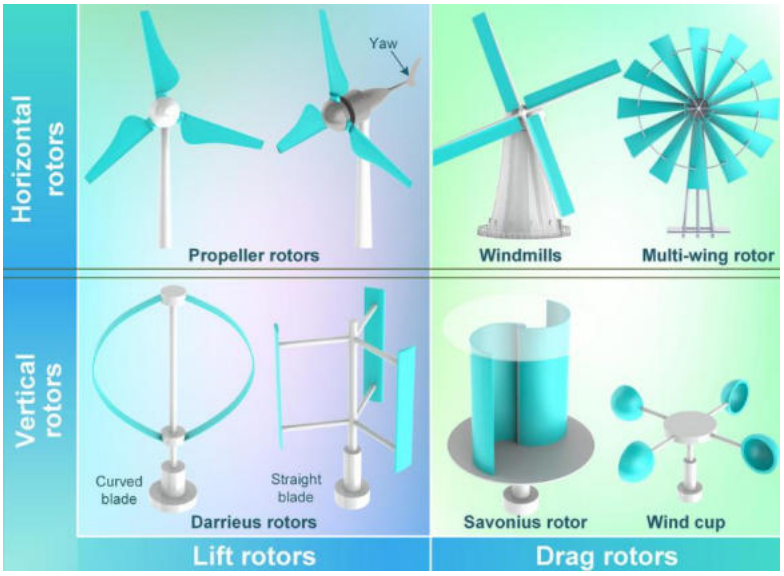


Fig. 3 – Wind turbines types (*Wang et al., 2023*)

A distinct subcategory within wind energy systems is small wind turbines, typically intended for domestic or small commercial applications. These systems are often horizontal-axis designs, though vertical-axis models are also used where spatial or wind conditions favor them. Small turbines are installed on rooftops or in open areas to provide localized power generation.

Table 3

Advantages and disadvantages of Small Wind Turbines (*Probst et al., 2011*)

Advantages	Disadvantages
- *Energy independence*: They allow homeowners or small businesses to generate their electricity and reduce grid dependency.	- *Limited power generation*: small turbines may not generate enough electricity to meet the power needs of larger buildings or multiple homes.
- *Cost-effective for small installations*: For smaller energy needs, these turbines are more cost-effective than large-scale installations.	- *Wind dependence*: These turbines are highly dependent on local wind conditions, which can be variable.

This introduction provides an overview of the principles, configurations, and applications of wind turbines, setting the stage for deeper exploration into their design optimization. In particular, as interest grows in sustainable urban energy systems, vertical-axis wind turbines are attracting renewed attention due to their adaptability and compact footprint. The following sections will focus on modeling and enhancing the performance of such turbines, with a particular emphasis on computational approaches and design refinement.

SPECIFICITY OF WIND TURBINES. WIND TURBINE TECHNOLOGIES

Wind energy has emerged as one of the most popular and rapidly growing renewable energy sources worldwide. Concerns about climate change and the environmental impact of fossil fuels have fueled the need for sustainable alternative resources. Wind turbines stand out from other renewable energy sources due to their efficiency, scalability, and environmental reasons (*Savino et al., 2017*). This section investigates wind turbine technology, focusing on their many varieties, the concepts behind their operation, their advantages, and current technical developments. Wind turbines are divided into two categories: horizontal axis wind turbines (HAWTs) and vertical axis wind turbines (VAWTs) (*Paraschivoiu et al., 2018*). Both types convert the kinetic energy of the wind into mechanical energy that is then used to create electricity. However, their design, application, and efficiency vary greatly.

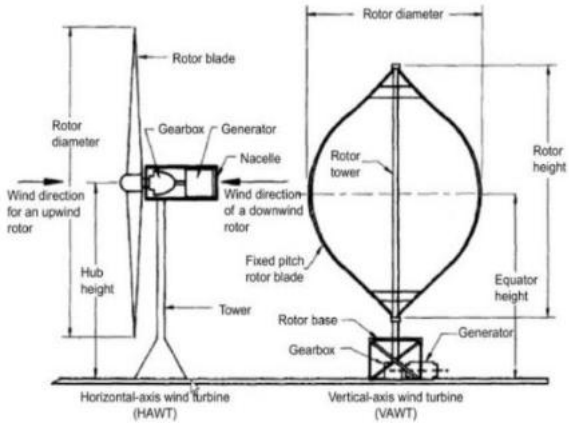


Fig. 4 - The Basics of HAWT and VAWT Configurations (*Ismail et al., 2021*)

Horizontal axis wind turbines are the most common and commonly used in large-scale commercial wind farms. These turbines have their blades attached to a horizontal shaft, and the entire turbine is aligned with the direction of the wind. HAWTs are often considered the most efficient form of wind turbine due to their aerodynamic design (*Sedaghat et al., 2014*). They generally have three blades that are designed to capture the most wind energy. HAWT blades rotate along a horizontal axis and can generate huge amounts of power, making them suitable for use in areas with regular wind speeds, such as coastal or offshore areas. On the other hand, vertical axis wind turbine blades rotate around a vertical axis that is perpendicular to the ground (*Chaudhary et al., 2014*). VAWTs are suitable for areas with irregular or turbulent wind patterns because, unlike HAWTs, they do not require orientation into the wind. Because they can be positioned closer to the ground, VAWTs offer advantages in terms of maintenance, although they are often smaller and less efficient than horizontal ones (*Xisto et al., 2016*). In addition, VAWTs are often quieter and have a smaller aesthetic impact, which may increase their acceptability in residential and urban environments (*Kumar et al., 2018*).

The essential concept behind wind turbines is the transfer of kinetic energy from the wind into mechanical energy, which is then converted into electrical energy by the generator (*Wang et al., 2018*). The operation of a wind turbine can be divided into several parts (*Li et al., 2011*). The first is wind capture, in which wind turbines use enormous blades to capture the kinetic energy of the wind. When wind blows over the blades, it generates lift and drag forces, causing them to rotate (*Schaffarczyk et al., 2017*). This rotational motion powers the turbine generator. The rotating blades are attached to a shaft, which is connected to a gearbox. The gearbox increases the rotational speed of the shaft to reach the speed required by the generator. The mechanical energy is transmitted to the generator and converted into electrical energy (*Keung et al., 2008*).

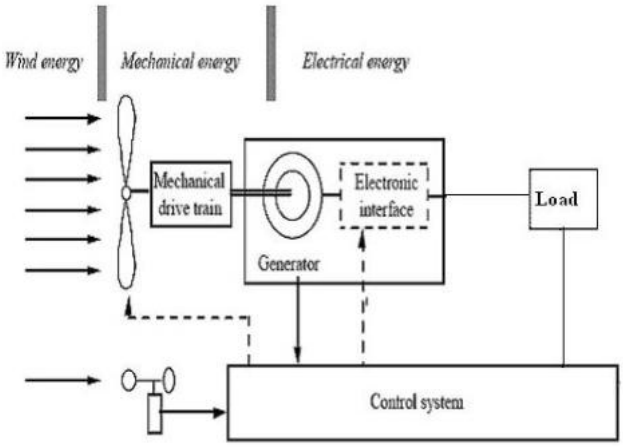


Fig. 5 - Wind energy conversion scheme (*Rambabu et al., 2012*)

The generator, which normally consists of a rotor and a stator, works on the concept of electromagnetic induction. The shaft rotates, causing the rotor to rotate inside the stator, generating energy. The electricity produced is then sent through wires to the grid or to a local power system. Modern wind turbines are equipped with advanced control systems that improve their performance (*Balat et al., 2009*). These systems use wind speed, direction, and other environmental parameters to determine the turbine's orientation, blade pitch, and energy output. This increases efficiency and reduces damage in adverse weather conditions. Due to their many advantages, wind turbines are becoming an increasingly important part of the world's transition to renewable energy. Unlike fossil fuels, wind energy does not emit greenhouse gases or air pollutants while it is operating. Since wind turbines have a low environmental impact, they are a crucial tool in the fight against climate change and reducing the carbon footprint (*Pryor et al., 2010*). In addition, wind energy has become one of the most affordable sources of renewable energy in recent decades due to the huge reduction in costs. The design, materials, and manufacturing methods of wind turbines have improved, making wind energy more competitive with traditional sources such as nuclear, coal, and gas (*Abbasi et al., 2017*).

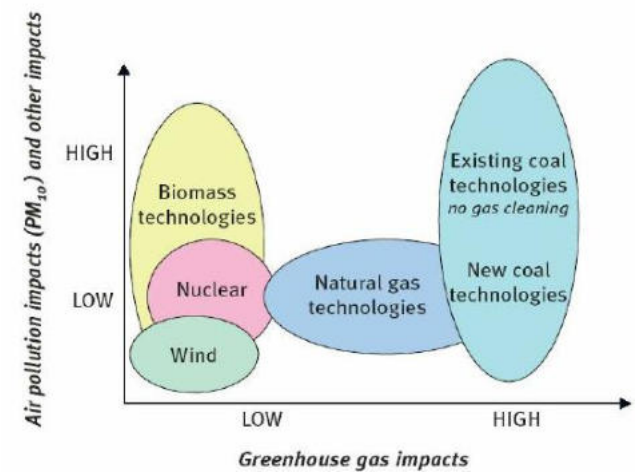


Fig.6 - Comparison of energy sources
(Van Kuik et al., 2008)



Fig.7 - Decreasing the cost of renewable energy
(*https://www.statista.com/chart/26085/price-per-megawatt-hour-of-electricity-by-source/*)

By investing in wind energy, nations can reduce their dependence on imported fossil fuels, improving their economic stability and energy security.

Producing wind energy locally can help the renewable energy industry create jobs and reduce dependence on international energy markets. Around the world, the wind energy sector has generated millions of jobs in production, installation, operation, and maintenance (*Aldieri et al., 2017*). The need for skilled personnel in a variety of disciplines, including engineering, logistics, and research, is growing with the demand for wind turbines.

In recent years, significant technological developments have taken place in the operation and design of wind turbines. Thanks to these advances, wind energy is now more economical, reliable, and efficient (*Kaldellis et al., 2011*). Some contemporary wind turbines have rotor diameters of over 200 meters, demonstrating the significant increase in wind turbine size. Since offshore wind farms have a lot of space and wind resources, these larger turbines are of great help there (*Bilgili et al., 2022*).

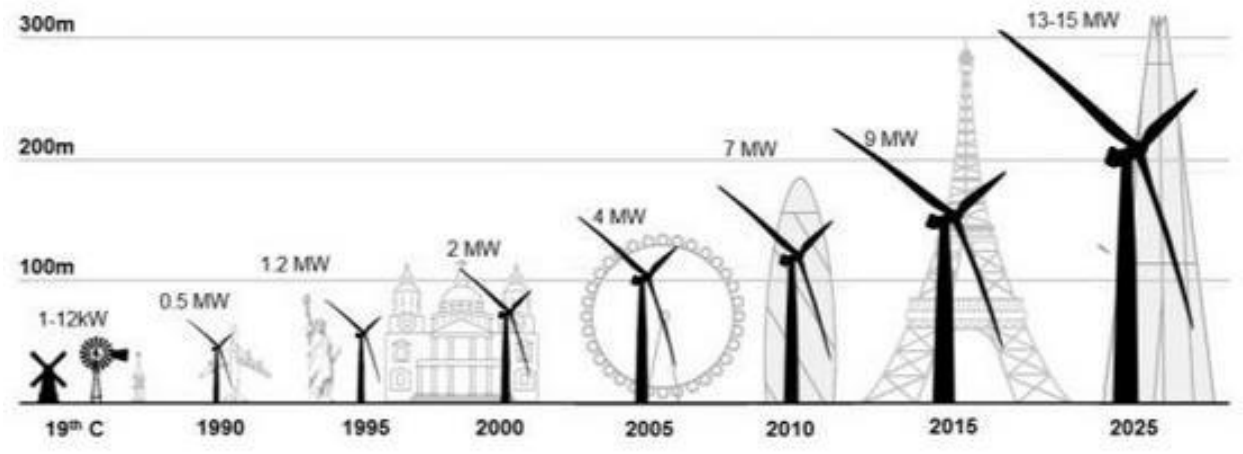


Fig. 8 - Evolution of wind turbine size (*Pisanò et al., 2019*)

Floating wind turbines are an innovative technology that allows wind turbines to be installed in deeper oceans, where conventional fixed-bottom turbines are impractical. These turbines are fixed to the seabed by floating platforms and can be erected in places with strong and persistent winds, far from shore. Floating wind technology has the potential to open up vast new areas for wind energy generation.

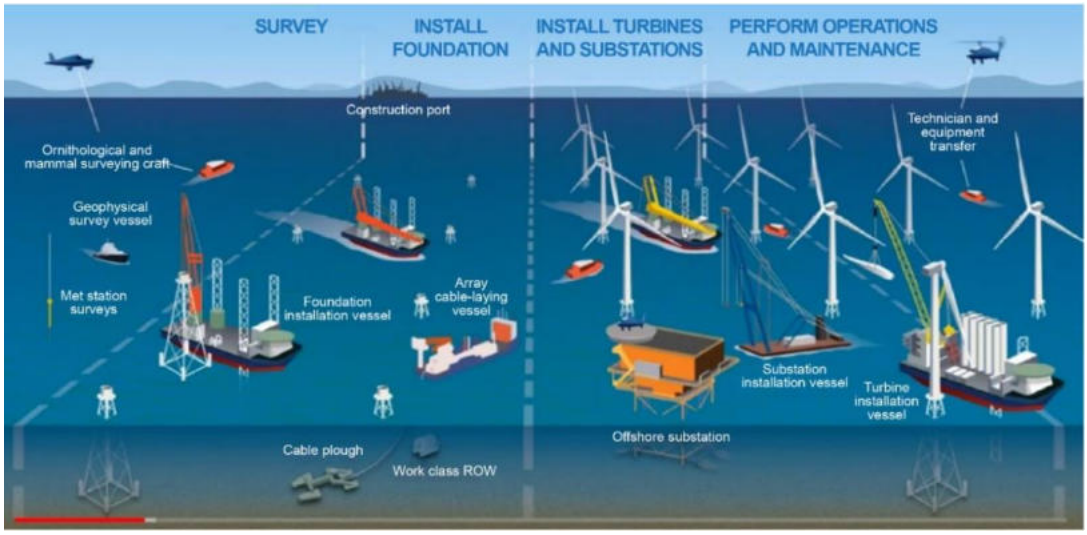


Fig. 9 - Offshore wind turbine installation (*Ryu et al., 2022*)

Because wind power is intermittent, its production is dependent on the availability of wind. However, more efficient integration of wind power into the electricity grid is possible with the development of smart grid technology. Energy storage devices, sophisticated forecasting methods, and wind power can all be used by smart grids to control the fluctuation of wind power and provide a constant and reliable source of energy (*Abbey et al., 2008*).

To increase efficiency, the design of turbine blades has changed dramatically. More wind energy can be captured at lower speeds due to the aerodynamic efficiency, reduced length, and weight of modern blades. Innovative features such as fins, which reduce drag and improve performance, are also included in some blades (*Chehouri et al., 2015*).

In addition to size increases and floating offshore installations, recent breakthroughs in materials science have had a substantial impact on wind turbine performance. The adoption of carbon fiber-reinforced polymers (CFRPs) and other advanced composites has led to lighter yet stronger blades, improving aerodynamic efficiency and durability while reducing maintenance needs (*Sun et al., 2025*). These materials also contribute to the feasibility of longer blades without compromising structural integrity.

Additive manufacturing (3D printing) is beginning to revolutionize turbine component production. It allows for complex, custom geometries that were previously unfeasible and enables localized manufacturing, reducing costs and transportation emissions (*Sivamani et al., 2020*).

Another major breakthrough is the integration of artificial intelligence (AI) and machine learning algorithms in wind turbine control systems. These smart controllers optimize blade pitch, yaw, and even predict maintenance needs based on real-time environmental data and turbine health metrics (*Al Noman et al., 2022*). Predictive maintenance, enabled by AI-driven condition monitoring, significantly reduces downtime and increases turbine lifespan.

Modular turbine designs are also emerging as a way to reduce installation complexity and allow for easier transportation, especially in remote or urban environments (*GU et al., 2021*). In offshore installations, autonomous robotic systems are being developed for turbine inspection, repair, and cleaning, reducing the need for human intervention in harsh marine conditions.

Looking ahead, several trends are poised to define the next generation of wind energy technology:

- *hybrid renewable systems*: Future wind turbines will increasingly be integrated into hybrid energy systems, combining wind with solar, hydrogen production, or battery storage. These systems enhance grid stability and ensure continuous energy supply during low-wind periods (*Mohamed*, 2023).

- *vertical axis wind turbine farm optimization*: As urban and distributed generation grows, VAWTs may see renewed attention. New research into aerodynamic interaction in VAWT arrays is improving their efficiency when placed in close proximity, enabling more compact and urban-friendly wind farms (*Barnes et al., 2019*).

- *bio-inspired blade design*: Nature-inspired designs—like humpback whale tubercles or bird wings—are being mimicked to reduce drag, increase lift, and enhance performance in turbulent wind conditions (*Hassan et al., 2023*).

- *dynamic blade morphing*: Research into smart materials such as shape-memory alloys and piezoelectrics is paving the way for turbine blades that adapt in real time to changing wind conditions, optimizing power capture (*Baghdadi et al., 2020*).

- *end-of-life and recycling innovations*: With sustainability at the forefront, the development of fully recyclable turbine blades and circular economy strategies for decommissioned components will become increasingly important (*Kouloumpis et al., 2020*).

- *high-altitude wind energy* (HAWE): Technologies such as airborne wind turbines (e.g., tethered drones or kites) are being explored to capture stronger, steadier winds at higher altitudes, potentially revolutionizing onshore energy production (*Breban et al., 2020*).

In a short period of time, wind turbine technology has advanced significantly, becoming a major force in the global energy transition due to advances in design, operation, and efficiency. With increasing accessibility and scalability, wind energy could contribute significantly to global energy supply.

Even so, ongoing developments in infrastructure and technology are helping to eliminate obstacles such as intermittency and grid integration. Wind turbines will be essential for reducing dependence on fossil fuels, preventing climate change, and building a sustainable energy future as the globe continues to embrace renewable energy.

WORKING PROCESS OF VERTICAL AXIS WIND TURBINES - COMPARATIVE ANALYSIS OF SAVONIUS AND DARIEUS TURBINES

Wind energy has become one of the most promising renewable energy sources in the modern world as sustainable ways are sought to meet energy demands. The vertical axis wind turbine (VAWT) is a special and often overlooked option among the different types of wind turbines. The VAWT is much more versatile than the horizontal axis wind turbine, which is more popular due to its design, which allows it to harness wind energy from any direction, especially in regions with irregular wind patterns (*Ashwill et al., 2012*).

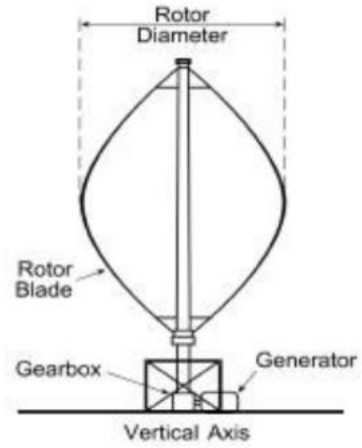


Fig. 10 - VAWT (*Salem, 2016*)

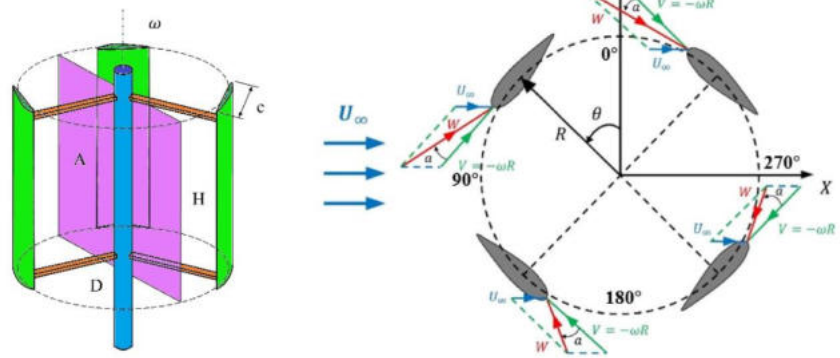


Fig. 11 - Force distribution on a VAWT (*Abbasi et al., 2024*)

The moment the wind hits the blades of a VAWT is when the action begins. The design of a VAWT ensures that it can capture wind energy regardless of the direction of the wind, unlike conventional turbines that must be pointed into the wind. This feature makes a VAWT an excellent option for urban settings where airflow can be disrupted by buildings or other obstacles, and wind flows are erratic.

VAWTs differ fundamentally in their construction in that their blades rotate along a vertical axis instead of a horizontal one. The shape of these blades varies depending on the type of turbine. Similar to the wings of an airplane, the blades in some designs are designed as curved sails that provide lift. In others, the blades are designed to produce drag, much like a cup or spoon that catches the wind. These two types are called Darrieus and Savonius turbines, respectively.

The entire process from wind to electricity is a smooth, uninterrupted cycle. An environmentally friendly alternative to conventional energy sources such as coal or natural gas, the energy produced by VAWTs is clean and renewable. One benefit of this system is that VAWTs are more suitable for residential and urban environments, as they are quieter and less invasive than their horizontal equivalents. Furthermore, compared to traditional turbines, which often have parts located at high altitudes, the VAWT design ensures that its mechanical components are easily accessible, making maintenance simpler and less expensive (*Abdolahifar et al., 2024*).

VAWTs have many disadvantages, despite their benefits. Their lower efficiency compared to HAWTs is one of their main disadvantages, especially in regions with regular wind patterns. In addition, the durability of the blades can occasionally be affected by mechanical stresses caused by the rotational forces acting on them. To increase the turbine's performance and longevity, experts are still working to improve the design by using stronger materials and improving the aerodynamics of the blades (*Kragten, 2024*).

An important feature that makes the VAWT unique among turbine designs is its ability to capture wind from all directions. A rotating mechanism, which orients the turbine towards the wind, is not required for VAWTs, unlike HAWTs, which must be orientated towards the wind. This ensures that the turbine will continue to operate efficiently in settings where wind direction changes frequently (*Lee et al., 2018*).

The small size of the VAWT offers an additional benefit. The turbine is an excellent option for cities with limited space, as it can be located in smaller areas and can operate well in stormy or low-wind conditions. Whether installed on a rooftop or incorporated into the architecture of a building, the VAWT is a discreet yet efficient source of renewable energy. Furthermore, by reducing dependence on fossil fuels, VAWTs contribute to a sustainable future (*Bashir et al., 2021*). Finding sustainable, reliable, and scalable

energy solutions is more crucial than ever as cities expand and populations grow. With its practical and environmentally beneficial energy solution, VAWTs have great potential in this field. Although still in development, VAWTs have already shown promise in small-scale applications, and research is still ongoing to increase their effectiveness and design. VAWTs could become increasingly widespread in urban energy networks as engineers strive to maximize turbine performance, providing a creative response to the problems associated with contemporary energy use (*Aresti et al., 2013*).

The vertical axis wind turbine is an interesting and efficient way to capture wind energy. VAWTs have enormous potential for the future of renewable energy due to their small size, ease of maintenance, and ability to capture wind from any direction. Although there are still issues, mainly with sustainability and efficiency, these are being addressed by ongoing technological developments. With the introduction of clean, renewable energy in cities and small-scale applications around the globe, VAWTs may become increasingly significant in the coming years as we move towards a more sustainable energy future (*Kavade et al., 2017*).



Fig. 12 - Applications of VAWT in urban environments (*Tasneem et al., 2020*)

The type of wind turbine known as vertical axis wind turbines (VAWTs) has attracted interest in both research and real-world applications. Two well-known types of VAWTs, among the many designs, are the Savonius and Darrieus turbines. The efficiency, adaptability for specific applications, operating processes, and design complexity of these two categories vary greatly. Based on their operating principles, benefits, disadvantages, and applicability to different applications and climatic situations, they can be compared (*Abid et al., 2015*).

Among the vertical axis wind turbines, the Savonius turbine is one of the most basic designs. Two or more semi-cylindrical blades arranged in an “S” shape and fixed on a vertical axis usually make up its rotor. For strength and longevity, these blades are often composed of metal or composite materials. A Savonius turbine operates on the basis of drag forces. The curved blades rotate when the wind hits them due to wind pressure. Due to the configuration of the blades, the turbine always rotates because one side of the rotor experiences a greater drag force than the other (*Akwa et al., 2012*).

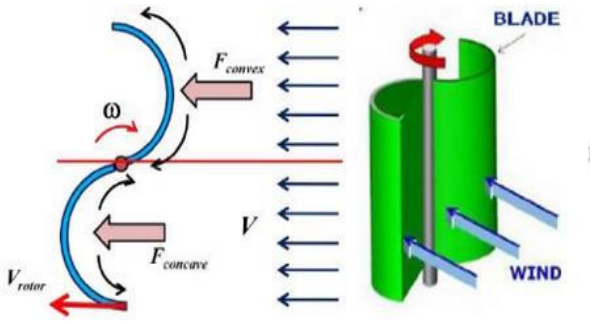


Fig. 13 - Diagram of a Savonius VAWT (*Khandagale et al., 2017*)

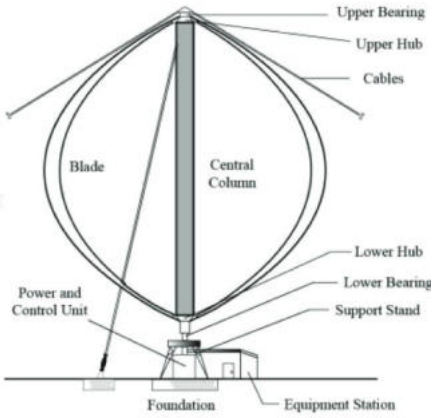


Fig. 14 - Diagram of a Darrieus VAWT *(Li, 2019)*

Often called an “egg beater” because of its unusual design, the Darrieus turbine has vertical blades that are usually curved and mounted on a vertical shaft. Like an airplane wing, the blades are often shaped with aerodynamic profiles to increase lift forces. The Darrieus turbine works on the basis of aerodynamic lift, which produces rotational motion by varying the air pressure on the opposing surfaces of each blade (*Tjiu et*

al., 2015). The lift force works in a direction that causes the turbine to rotate when the wind blows over the blades. Since the Darrieus turbine cannot start rotating at low wind speeds without external help, it often requires a starting mechanism. It is well known that the Savonius turbine is not as efficient as other types of wind turbines. The main reason for this is that it uses drag forces, which are less efficient than lift-based methods. The efficiency of the Savonius turbine is typically between 10% and 20%, depending on environmental conditions and design differences. However, it has the particular benefit of being able to start rotating at low wind speeds, making it suitable for locations with frequent low wind speeds (*Menet et al., 2004*). The Savonius turbine is also frequently used in settings such as cities or smaller wind farms, where reliability and robustness are more important than efficiency. Compared to the Savonius turbine, the Darrieus turbine often offers higher efficiency. Unlike the Savonius design, which uses drag forces, it uses lift forces, which are more efficient. Depending on the system configuration, wind speed, and blade design, the efficiency of the Darrieus turbine can range from 25% to 45% (*Zereg et al., 2024*). However, in low-wind areas, the Darrieus turbine is less successful because it requires higher wind speeds to start spinning. Large-scale wind power generation is feasible due to its high efficiency and ability to generate more electricity in steady wind.

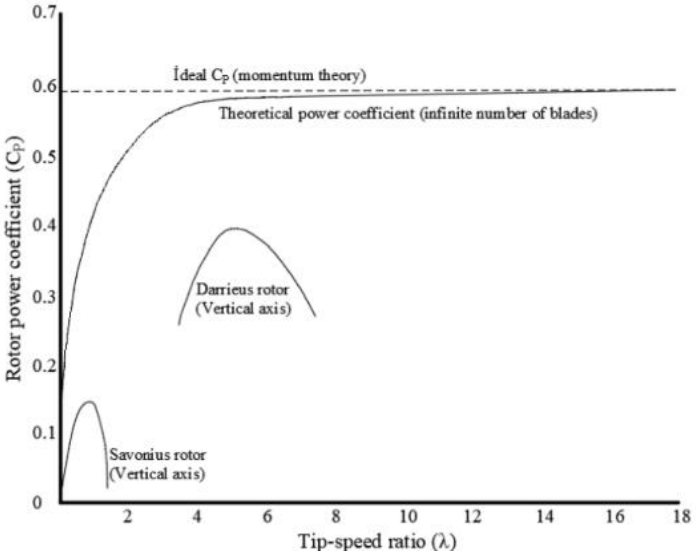


Fig. 15 - Efficiency comparison between Savonius and Darrieus VAWTs (*Muratoğlu et al. , 2019*)

Table 4

Advantages and disadvantages of the Savonius turbine(*Shende et al., 2022*)

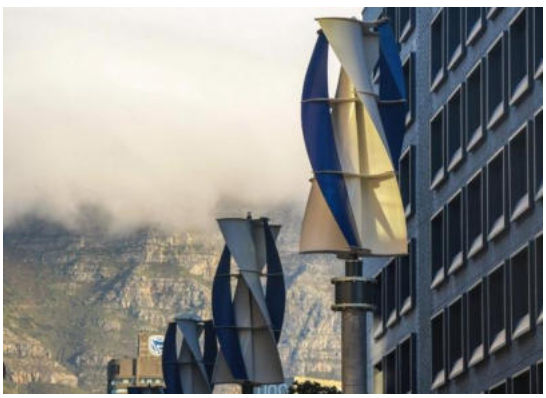
Advantages	Disadvantages
- *Low wind speed*: One of the most significant advantages of the Savonius turbine is its ability to start operating at low wind speeds. This makes it ideal for areas where wind conditions are inconsistent or low. - *Simple design*: The Savonius turbine has a relatively simple design and is easy to manufacture, making it cost-effective. This simplicity also leads to easier maintenance and repairs. - *Durability*: Savonius turbines are known for their durability and can withstand high winds and turbulent conditions, making them suitable for harsh environments. - *Vertical axis*: The vertical axis design allows the turbine to operate regardless of wind direction, making it more versatile in environments where wind direction is variable.	- *Low efficiency*: Due to its dependence on drag forces, the Savonius turbine has a relatively low efficiency compared to lift-based designs. This limits its power generation capacity. - *Limited power output*: The design of the Savonius turbine typically results in a lower power output compared to other wind turbines, making it unsuitable for large-scale power generation. - *Noise*: Savonius turbines tend to produce more noise compared to Darrieus turbines, which can be a negative factor in residential or urban areas.

Table 5

Advantages and disadvantages of the Darrieus turbine (*Paraschivoiu et al., 2002*)

Advantages	Disadvantages
- *High efficiency*: the Darrieus turbine operates on aerodynamic lift, which is more efficient than the drag-based operation of the Savonius turbine. This leads to a higher power generation potential. - *Higher power output*: Due to its more efficient operation, the Darrieus turbine can generate much more power than the Savonius turbine, making it more suitable for large-scale applications. - *Compact design*: Although larger than the Savonius turbine, the Darrieus turbine can still be compact in terms of footprint, making it suitable for urban and offshore installations where space is limited. - *Less noise*: the Darrieus turbine typically produces less noise than Savonius turbines, making it more suitable for residential or urban environments.	- *High wind speed*: One of the main disadvantages of the Darrieus turbine is that it requires higher wind speeds to start rotating, making it less efficient in low-wind regions. - *Complex design*: The Darrieus turbine is more complex to manufacture and often requires additional components, such as a starting mechanism, making it more expensive to install. - *Structural challenges*: Darrieus turbines can suffer mechanical stresses due to high loads on the blades, which can lead to fatigue over time, leading to maintenance challenges.

In low-power, small-scale applications where efficiency is not the main concern, the Savonius turbine is frequently used. In cities with irregular wind conditions, the Savonius turbine is frequently used due to its low wind speed. Due to its design, it can work well in places with complicated wind patterns. For off-grid installations or as additional energy sources for homes, farms (*Glasberg et al., 2024*), or industrial sites, the Savonius turbine is perfect. The Savonius turbine is suitable for applications such as water pumping, where constant rotation at low speed is required, due to its robustness and simplicity.



(*www.engineeringnews.co.za*)



(*https://greenoteka.eu*)

Fig. 16 - Savonius in an urban environment

The higher efficiency and power output of the Darrieus turbine make it more suitable for large-scale applications. In utility-scale wind farms that require a lot of power, the Darrieus turbine is frequently used. When wind conditions are consistent, it can produce more electricity and is more efficient than smaller turbines. For offshore sites, where wind speeds are often higher and more reliable, the Darrieus turbine is perfect due to its robust design and increased power output. To summarize, both Savonius and Darrieus wind turbines have various benefits and uses due to their design, efficiency, and operating circumstances. The Savonius turbine works well in low-wind environments, providing a low-cost and long-lasting solution for small-scale applications, while the Darrieus turbine has higher efficiency and power, making it more suitable for large-scale wind power generation in areas with more consistent wind conditions. Each turbine has a place in the renewable energy landscape, and the decision to choose between them is largely determined by individual energy requirements, environmental circumstances, and available space.

Hybrid vertical axis wind turbines (VAWTs), which integrate Savonius and Darrieus rotor designs, aim to capitalize on the advantages of both configurations—namely, the high starting torque of the drag-based Savonius turbine and the superior aerodynamic efficiency of the lift-based Darrieus rotor (*Hosseini et al., 2019*). This combination enhances self-starting capabilities while maintaining favorable power output at higher wind speeds, making hybrid models particularly attractive for small-scale and urban wind energy applications. The synergy between the two mechanisms contributes to improved rotational stability, smoother power generation across varying wind conditions, and better overall performance compared to standalone designs. Researchers have explored a variety of geometric configurations—such as blade overlap, angular positioning, and rotor placement—to optimize the interaction between the components. Numerical and experimental investigations have demonstrated that these hybrid systems offer a balanced compromise between torque generation and power coefficient, addressing key limitations inherent to each individual turbine type.

SYNTHESIS OF EXPERIMENTAL RESEARCH ON WIND TURBINES AND THEIR WORKING PROCESS

As a clean and sustainable alternative to fossil fuels, wind energy has emerged as a key source of renewable energy in the fight against climate change (Barthelmie et al., 2021). Wind turbines have emerged as a key component of this energy shift, transforming wind energy from kinetic to mechanical and ultimately electrical forms. However, extensive experimental research is needed to ensure that these turbines are efficient, reliable, and capable of operating in a variety of situations. Testing a turbine involves more than just determining how efficiently it produces energy; it also involves evaluating its performance, robustness, and safety in a range of real-world scenarios (He et al., 2022).

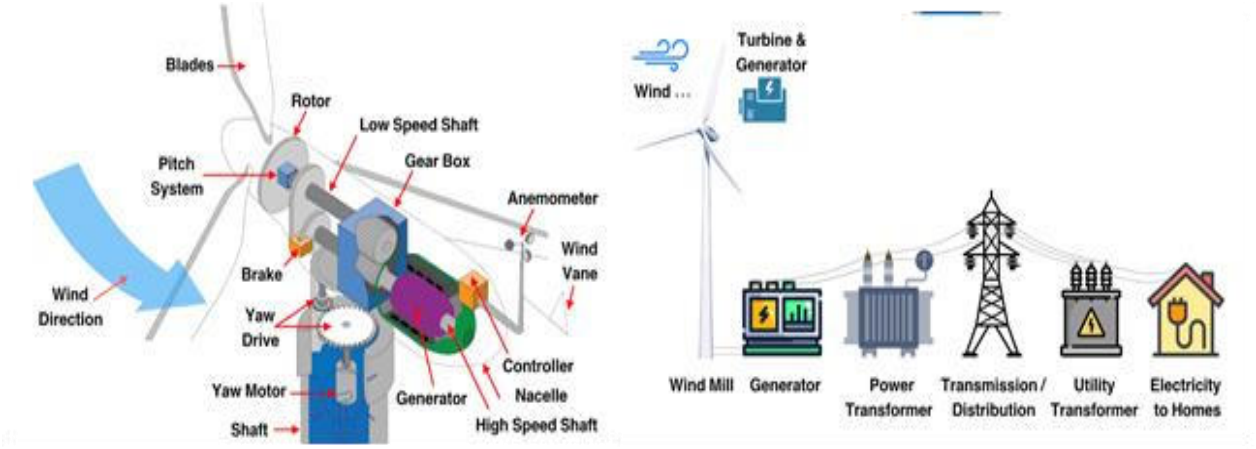


Fig. 17 - Wind turbine diagram
(*https://www.electricaltechnology.org/2021/08/wind-power-plant.html.*)

The fundamentals of wind turbine mechanics need to be understood before getting into the finer points of experimental testing. The parts of a conventional wind turbine include a tower, nacelle, generator, rotor, and blades. The blades rotate as the wind passes over them. A generator is turned by this rotational motion, and the mechanical energy is converted into electrical energy. Wind speed, the turbine operating under different conditions, and the design of the blades are some of the variables that affect the efficiency of this energy conversion (*Elizondo et al., 2009*). Testing these turbines in controlled, real-world settings is necessary to maximize performance and reliability.

To ensure that wind turbines meet the required performance and safety criteria, experimental testing is essential. These tests are primarily designed to evaluate the turbine's ability to generate electricity under a range of wind conditions (*Gaunt et al., 2012*). By monitoring the turbine's response to mechanical loads and severe weather conditions, engineers also aim to assess the structural integrity of the machine. This facilitates the identification of potential defects, predicts the turbine's durability, and ensures its safe operation. In addition, experimental testing helps improve turbine designs by improving overall efficiency and reliability through refinement of materials, control systems, and aerodynamic characteristics (*Bottasso et al., 2014*).

Key elements, including energy production, efficiency, and reliability under varying wind speed and climate conditions, can be measured by engineers through testing. Testing can identify a turbine's power curve, for example, which shows the relationship between wind speed and energy production. This curve helps optimize the turbine design and provides insights into its operating limits (*Carrillo et al., 2013*).

Laboratory testing, field testing, and accelerated life testing are the three main testing approaches that can be used to analyze the complex process of wind turbine testing (*Bastankhah et al., 2017*). Each of them contributes in a different way to the evaluation of different turbine performance factors. Laboratory tests usually focus on specific parts of the wind turbine, such as the generator, nacelle, and blades. The aerodynamic characteristics of the blades are investigated in wind tunnels, and additional tests are conducted to evaluate mechanical performance, stress resistance, and material durability in simulated environments. Before the turbine is assembled and placed in the field, the intention is to understand how each component functions.

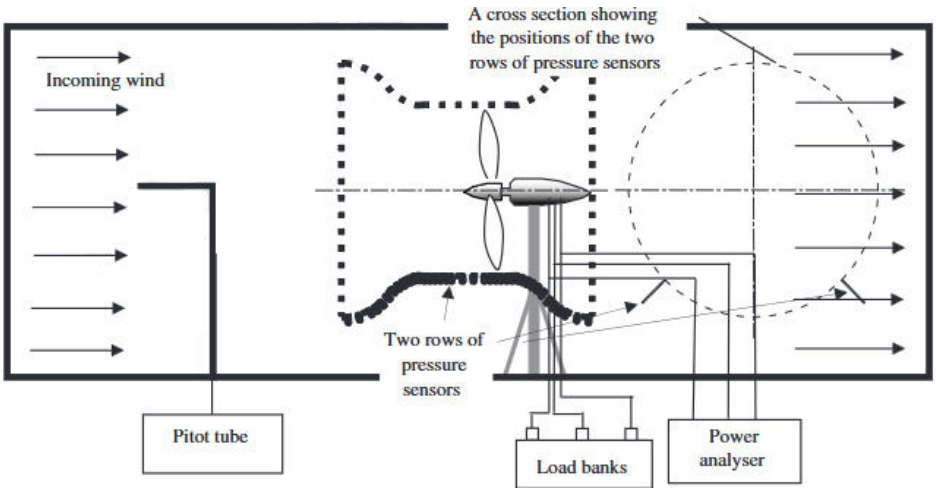


Fig. 18 - Wind turbine testing diagram in wind tunnel (*Agha et al., 2018*)

As an alternative to laboratory testing, field testing involves putting turbines in realistic settings to evaluate how well they perform in wind conditions. Measuring energy production at different wind speeds, evaluating turbine performance under varying wind load conditions, and monitoring long-term performance are common examples of such tests. Field testing allows engineers to see how turbines respond to variables that are difficult to replicate in a laboratory, including turbulence, humidity, and temperature changes.

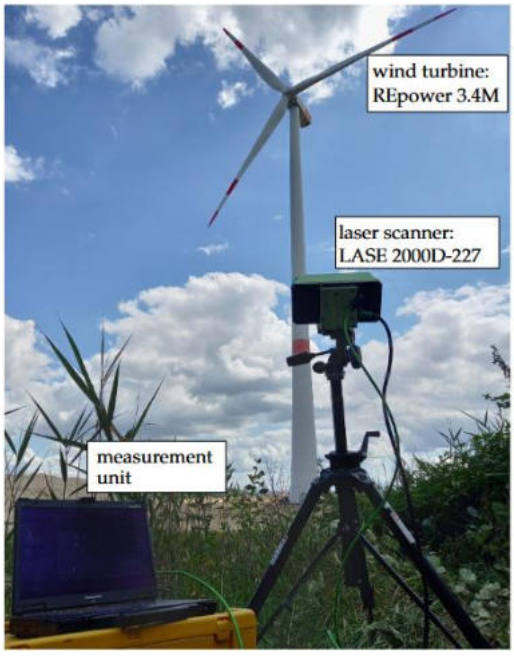


Fig. 19 - Field testing setup (*Helming et al., 2021*)

The data must be examined thoroughly after it has been collected. Key performance parameters such as the power curve, efficiency, and capacity factor are of particular interest to engineers. While efficiency shows how much of the wind energy is converted into electricity, the power curve allows engineers to see how much power a turbine produces at different wind speeds. Engineers can assess the overall performance of the turbine by analyzing the capacity factor, which shows how efficiently the turbine generates energy relative to its maximum potential.

It is also essential to test for noise and vibration. The structural integrity of the turbine can be compromised by excessive vibration or noise, which could lead to mechanical failure or environmental problems in populated areas. Engineers can improve turbine designs to minimize noise and wear by monitoring these variables during experimental testing (*Shinagam et al., 2020*).

Wind turbine testing presents certain challenges. The instability of the wind itself is the main challenge. Because wind direction, speed, and turbulence are so variable, it is difficult to reproduce constant conditions in both laboratory and field experiments. Wind is rarely as predictable as one would like, and conditions in the field can vary rapidly, even though wind tunnels provide controlled environments for some studies. Although engineers frequently use sophisticated forecasting models to predict wind patterns, unpredictability is still a persistent problem.

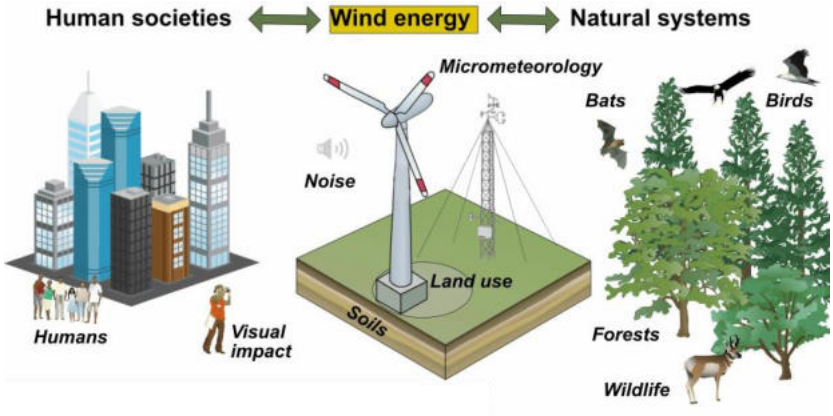


Fig. 20 - Testing challenges and environmental factors (*Sander et al., 2024*)

There are also logistical issues, especially with outdoor tests. Turbines are often located in remote areas, far from maintenance teams or test facilities. The testing procedure could be further complicated by the high cost of installation, maintenance, and transportation. In addition, wind turbines are heavy and bulky, making them difficult to move and install, especially in hilly or offshore wind farms (*Vis et al., 2016*). Another important factor is safety. Field tests can be dangerous for personnel, especially when carried out in adverse weather. Therefore, strict safety procedures must be followed to ensure that people are protected during the testing procedure (*Jin et al., 2016*). Potential risks such as strong winds, electrical failures, or even structural failure of a turbine component during testing must be considered by engineers.

The results of experimental tests have significant ramifications for the future of wind energy and turbine design. Engineers have gained important knowledge through testing, which has led to notable increases in turbine cost-effectiveness, efficiency, and reliability. Modern turbines now have higher energy conversion efficiencies, for example, due to advances in materials science, control systems, and blade design. In addition, superior testing techniques have produced turbines that are more resilient to harsh weather conditions (*Sun et al., 2022*), such as the hot, dry climate of desert regions or the icy winds of the North Sea.

SYNTHESIS OF EXPERIMENTAL RESEARCH ON THE WORKING PROCESS OF SAVONIUS TURBINES

The interest in wind energy has increased significantly due to the search for renewable and sustainable energy sources. Among the types of wind turbines, the Savonius wind turbine (SWT), a vertical axis wind turbine (VAWT), stands out for its ease of use, efficiency in low wind conditions, and low production costs (*Zemamou et al., 2017*). Aerodynamic drag forces drive the turbine, making it perfect for small-scale energy production. However, a large number of experimental tests are required to exploit its potential fully and maximize its performance (*Akwa et al., 2012*).

The original form of the Savonius wind turbine, created in the 1920s by the Finnish engineer Sigurd Savonius, consists of two or more vertically positioned curved blades (*Zoucha et al., 2023*). The drag force generated by the wind hitting the blades of a Savonius turbine allows it to harness wind energy, unlike horizontal-axis wind turbines. The blades are typically spoon-shaped, with one side facing the wind to "catch" it and the other side acting as a drag force to rotate the turbine (*Gall et al., 2023*). Wind energy is converted into mechanical energy as the blades rotate about a vertical axis as a result of the wind interacting with them. Because the Savonius turbine relies on drag forces rather than lift, it is often less efficient than horizontal-axis turbines, while still being successful at low wind speeds (*Dewan et al., 2021*). However, the turbine's simple design and ability to operate in irregular and fluctuating wind conditions make it a desirable choice for small-scale energy applications, especially in off-grid, domestic, or urban environments.

To better understand and improve the performance of Savonius wind turbines, experimental testing is essential. The complexity of real-world wind conditions and turbine performance cannot be fully captured by theoretical models and simulations, although they can provide some insight (*Wenehenubun et al., 2015*). Researchers can evaluate elements such as power output, efficiency, and the impact of environmental conditions through physical tests, which improve design and operation methods. Real-world information about the turbine's power output, efficiency under different wind conditions, and the impact of turbulence and mechanical wear are all provided through testing. Engineers can improve turbine performance and make it more reliable and efficient for specific applications by adjusting important design parameters through experimental testing, such as rotor height, number of blades, and blade curvature (*Zhou et al., 2013*). To determine whether the turbine is suitable for practical use, researchers conduct long-term experiments in a variety of climatic situations to evaluate its longevity and mechanical durability. The best economical and efficient design for a given situation can be found by comparing several turbine designs, combinations, and materials through experimental testing (*Shamsuddin et al., 2022*).

Savonius wind turbines can be experimentally tested in several ways, each designed to evaluate a specific facet of the turbine's performance. Wind tunnel testing, field testing, and computational fluid dynamics (CFD) simulations are the most commonly used techniques (*Ferrari et al., 2017*).

By carefully adjusting wind direction, speed, and turbulence in a controlled wind tunnel, researchers can evaluate how a turbine responds to particular circumstances. Wind tunnel testing is useful for determining power coefficients, evaluating aerodynamic forces acting on blades, and fine-tuning turbine shape (*Ross et al., 2011*). Although wind tunnel testing provides controlled settings and repeatability, it cannot accurately capture the complexity of environmental circumstances seen in the real world.

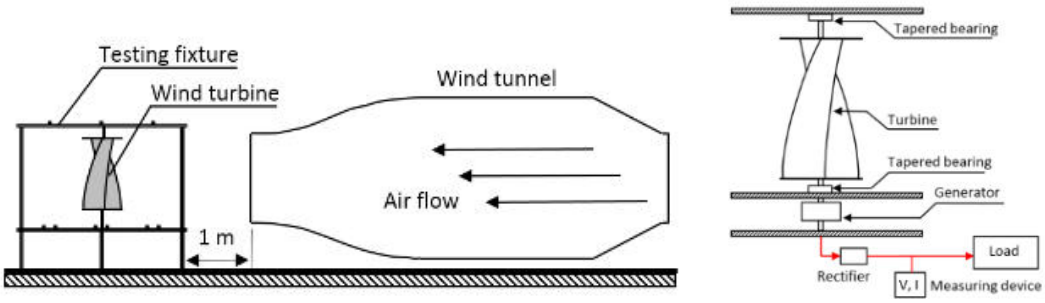


Fig. 21 - Wind tunnel setup for testing Savonius wind turbine
(*Zakaria et al., 2019*)

To track the performance of Savonius turbines over time, field testing involves placing them in real-world outdoor environments. Field tests provide information about the turbine's performance in a variety of wind conditions, including turbulence, gusts, and changing wind directions, unlike wind tunnel experiments. The turbine's behavior in different climates, reliability, and long-term performance are all evaluated through field tests.

A useful technique for simulating wind flow around turbine blades and predicting aerodynamic performance is computational fluid dynamics simulations. In addition to helping researchers refine design features, including blade shape, size, and length, these models provide information about the distribution of aerodynamic forces, drag, and lift (*Dobrev et al., 2011*). Although CFD can help improve the design before physical testing, it may not be able to account for all environmental factors that influence turbine performance.

Turbine output and mechanical load must be measured during field and wind tunnel testing to determine efficiency. Researchers can measure the turbine's rotational speed and torque using instruments such as dynamometers and torque sensors. In addition to providing information to evaluate the turbine's overall performance and energy production, these measurements allow the calculation of the power coefficient (Cp) (*Kadam et al., 2013*).

Several experimental investigations have provided useful information on the performance of Savonius wind turbines. Key findings from these investigations include blade configuration, blade curvature, rotor height, power coefficient, and efficiency.

The number of blades in a Savonius turbine has a large influence on its performance. While two-blade variants are popular due to their simplicity, three- or four-blade turbines offer better torque and stability at low wind speeds. However, this may increase drag and decrease the turbine's efficiency. According to experimental results, the appropriate number of blades is determined by the intended use, with fewer blades being more efficient in higher wind speeds and more blades providing greater efficiency at lower speeds (*Chaichana et al., 2019*).

The curvature of the turbine blades is another crucial component that affects its aerodynamic performance. Blades with steeper curvatures create more drag, which can increase the rotational speed but can also cause mechanical stress, leading to increased wear rates. Blades with shallower curvatures, on the other hand, generate less drag but may be less efficient in transferring wind energy into rotational motion (*Chan et al., 2018*). Experimental investigations suggest that moderate curvature is usually the most effective for balancing drag and performance; however, modifications may be necessary depending on the circumstances and turbine size.

The height of the turbine rotor, or the distance between the center of rotation and the tip of the blades, is also important in influencing performance. Taller rotors can gather wind from a wider region, increasing the power generation capacity. However, increasing the rotor height can increase the complexity and expense of the turbine, with performance gains decreasing beyond a certain point. The rotor height should be adjusted based on the anticipated wind conditions and the unique power requirements of the application, according to tests (*Tahani et al., 2017*).

The power coefficient (C_p) is a useful indicator of the efficiency of a wind turbine. Experimental tests have indicated that the C_p of Savonius turbines typically ranges between 0.2 and 0.3, which is lower than that of horizontal axis wind turbines. However, experimental investigations have shown that by carefully optimizing the design, including changes in blade shape, spacing, and rotor height, it is feasible to increase the power coefficient and improve overall efficiency (*Gad et al., 2014*).

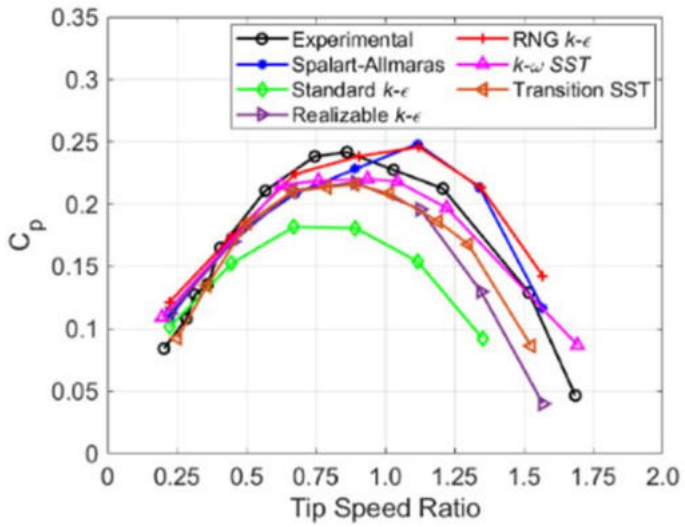


Fig. 22 - Power coefficient (Cp) vs. tip speed ratio (TSR) (*Dewan et al., 2023*)

The Savonius wind turbine is a viable alternative for sustainable energy generation, especially in low to very high wind conditions, where conventional wind turbines have great difficulty operating. Experimentation has provided vital information on its performance characteristics, including blade geometry, rotor height, and energy efficiency. This information can be applied to improve turbine designs, making them more efficient and reliable for real-world applications (*Roy et al., 2017).*

SYNTHESIS OF EXPERIMENTAL RESEARCH ON THE WORKING PROCESS OF DARRIEUS TURBINES

Wind energy, previously considered an alternative energy source, is rapidly becoming a cornerstone of global efforts to reduce dependence on fossil fuels. Wind turbines have played a major role in the renewable energy revolution, and among the various designs investigated, the Darrieus wind turbine stands out for its novel approach to capturing wind energy. Unlike standard horizontal-axis wind turbines (HAWTs), which operate on a horizontal axis, the Darrieus turbine has a vertical axis that allows it to capture wind from any direction (*Du et al., 2019*). While offering fascinating benefits in some situations, the Darrieus turbine faces a number of obstacles that have required substantial experimental study to increase its performance, efficiency, and practicality.

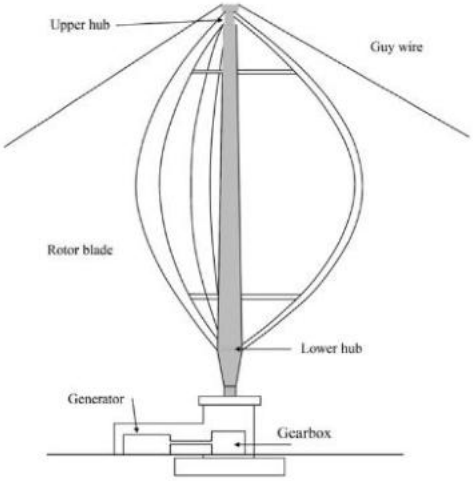


Fig. 23 - Power coefficient (Cp) vs. tip speed ratio (TSR) (*Tasneem et al., 2020*)

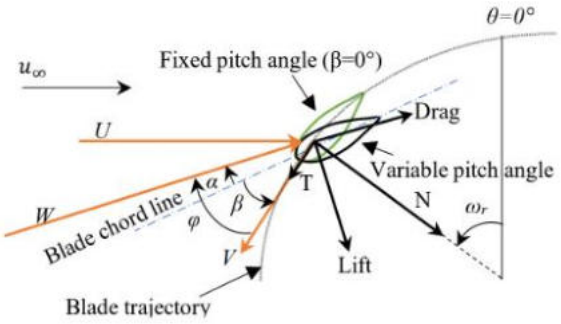


Fig. 24 - Aerodynamic forces on the blade of a Darrieus turbine (*Abdalrahman et al., 2021*)

The Darrieus wind turbine, invented by French engineer Georges Darrieus in the 1920s, is notable for its characteristic curved blades connected to a central vertical shaft. This design sets it apart from conventional turbines. One of the main benefits of the Darrieus turbine is its ability to collect wind from any direction, avoiding the need for a turning mechanism, which is necessary for horizontal-axis turbines to cope with wind (*Malael et al., 2021; Castelli et al., 2011*). While this may seem like a significant benefit, the turbine has long struggled with efficiency, starting torque, stability in varying wind conditions, and structural durability. Experimental research has become critical in an attempt to optimize its design and overcome these obstacles. Much of the initial research on Darrieus turbines has focused on understanding their aerodynamic characteristics. Scaled-down versions of Darrieus turbines are being tested in wind tunnels under controlled wind conditions, and the results provide valuable insight into how many aspects influence turbine performance (*Bedon et al., 2015*). One of the most important findings from these studies is the link between blade shape and efficiency. Curvature, aspect ratio (the ratio of blade length to blade width), and number of blades all play an important role in determining how much energy a wind turbine can generate. Researchers have found that blades with a higher aspect ratio are more efficient at converting wind energy into mechanical power, but their design must be balanced with concerns about structural integrity. The blade profile, whether flat or curved, also influences the lift-to-drag ratio, which is a significant component of turbine efficiency (*Mohamed et al., 2019*).

However, one of the major problems faced by Darrieus turbines is the difficulty of starting. Unlike horizontal-axis turbines, which can start rotating with a light breeze, the Darrieus turbine frequently fails to overcome its inertia when wind speed is low. Early experiments identified this “starting problem” as a significant drawback (*Asr et al., 2016*). In response, various solutions have been sought, some of which have been tested both in the laboratory and in the real world. One way is to include a small starter motor or Savonius rotor in the base of the Darrieus turbine. The Savonius rotor works as a traction-based device, providing the initial torque needed to start the system. In initial experiments, this hybrid technique has produced encouraging results, with the Savonius rotor providing enough torque to start the Darrieus turbine even in low wind conditions (*Chegini et al., 2023*).

The design of Darrieus turbines is further complicated by a phenomenon known as “stall.”. When the wind exceeds the ideal range for turbine operation, lift decreases. Due to the enormous working forces,

turbine efficiency can drop drastically, and in the worst cases, the blades can be damaged (*Fujisawa et al., 2001*). One of the main objectives of experimental research has been to overcome this obstacle. To maximize performance, several experimental setups have investigated the possibilities of active control systems, such as variable pitch blades, which change the angle of attack in real time. Dynamic stall control, which uses sophisticated control algorithms to modify the torque or blade angles in response to changing wind conditions, has been the subject of several investigations. Research into the use of these technologies on a large scale is still ongoing, despite their enormous potential.

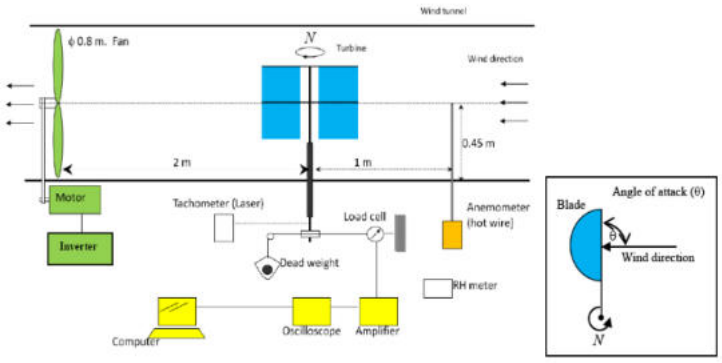


Fig. 25 - Darrieus type wind turbine test setup in the wind tunnel (*Chaitep et al., 2011*)

A crucial method for assessing the practicality of Darrieus turbines has been field testing, despite these difficulties. Turbines are exposed to the unpredictability of real wind conditions during field tests, unlike wind tunnel tests, which provide a controlled environment. In particular, the behavior of the turbine in turbulent wind conditions is one of the performance patterns that is often revealed by the results of these tests (Ferroudji et al., 2016). The vertical axis design of Darrieus turbines makes them particularly vulnerable to vibrations, which over time can cause structural damage. These vibrations can lead to fatigue, reduced efficiency, and, in some cases, failure. They are created by the oscillations of the blades as they move through the wind. Consequently, much of the experimental research in this field has focused on reducing these vibrations through the use of damping devices, including tuned mass dampers, which reduce the oscillations of the turbine blade. The use of materials with better mechanical properties and lighter weight for turbine blades has improved mechanical stability and provided pertinent information on materials science (Olivera et al., 2024).



Fig. 26 - Combination of Darrieus and Savonius wind turbines
(*https://www.windsystemsmag.com/news/first-vertical-axis-wind-turbine-awarded-certification/*)

Along with these experimental methods, computational fluid dynamics (CFD) simulations have emerged as a powerful tool for understanding Darrieus turbine airflow (*Malael et al., 2024*). To reproduce how air moves over the turbine blades, CFD simulations require complex mathematical models. These models provide researchers with a deep understanding of the aerodynamic forces acting on the turbine, allowing them to identify inefficient or turbulent airflow regions. In a wind farm configuration, CFD has been particularly useful in understanding the dynamics of Darrieus turbines, or the turbulent air left behind the

moving blades, and how these flows can affect the operation of neighboring turbines (*Dumitrescu et al., 2015*). CFD has played a key role in guiding experimental research and optimizing turbine configurations by modeling various design changes, such as changing the geometry of the blades or changing the distance between the blades. Increasing the turbine's power coefficient, which measures how well the turbine can convert wind energy into mechanical energy, is one of the main goals of all this research. A wind turbine can only capture 59.3% of the wind's kinetic energy, according to a theoretical restriction called the Betz limit (*Huleihil et al., 2012*). Experimental studies have shown that improvements in blade design and the mitigation of energy losses from friction and turbulence can bring the efficiency of Darrieus turbines closer to their potential limits, even though they frequently operate below this theoretical maximum. According to some research, the power coefficient of the Darrieus turbine could significantly outperform conventional designs and reach values Cp of up to 0.4 or 0.5 with an ideal design. The figure below illustrates turbine efficiency and ideal operating range using a power coefficient versus tip speed ratio (TSR) graph.

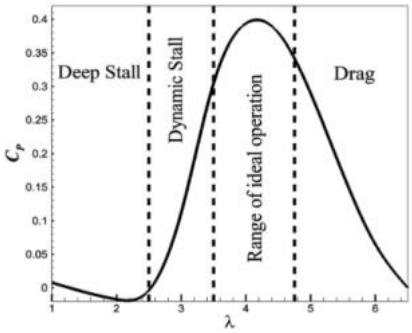


Fig. 27 - Darrieus rotor performance CP versus blade tip speed ratio (*Sagharichi et al., 2016*)

Despite the progress, many obstacles still need to be overcome before Darrieus turbines can be considered a viable alternative for large-scale wind power generation. Field testing, for example, is an expensive and time-consuming operation, with findings often affected by local wind conditions, which are difficult to recreate in controlled environments. Furthermore, while the use of modern materials such as carbon fiber composites holds great potential to increase turbine strength and reduce weight, these materials come at a high cost that must be justified by the long-term performance and longevity of the turbine.

CONCLUSIONS

Vertical Axis Wind Turbines (VAWTs) have been thoroughly examined in this review, with a focus on experimental studies and current developments in their efficiency, performance, and design. Although large-scale wind energy generation is dominated by Horizontal Axis Wind Turbines (HAWTs), VAWTs offer a special opportunity due to their space efficiency and versatility, especially in urban, low-wind, and agricultural areas.

Numerous important areas where VAWT technology is developing, including turbine configuration, blade design, and aerodynamic performance enhancements, have been brought to light by the examination of experimental investigations. Despite their potential, these developments are frequently hampered by issues with cost-effectiveness, noise reduction, and structural integrity—all of which are crucial for the broad use of VAWTs.

Addressing these challenges through innovative engineering solutions and advancements in materials science could significantly enhance the viability of VAWTs. As the demand for renewable energy sources continues to grow, ongoing research and development will be essential in overcoming these obstacles and unlocking the full potential of vertical axis wind turbines.

These issues must be resolved in future advancements, with an emphasis on scalability and integration into various contexts. To ensure that VAWTs can compete with conventional wind turbines and make a significant contribution to the generation of renewable energy, it will be essential to optimize their designs for durability, reduce operating costs, and increase their energy efficiency.

To sum up, VAWTs have a lot of promise as an alternative energy source, especially in areas where conventional wind turbine designs might not be as successful. Unlocking their full potential requires ongoing experimental study in addition to technological and material advancements. VAWTs

may become more important in the shift to decentralized and sustainable energy systems for homes, companies, and the agricultural sector if current constraints are addressed.

This could lead to greater adoption and integration of VAWTs into various environments, ultimately contributing to a more resilient and sustainable energy landscape. As research continues to evolve, innovative designs and applications may emerge that further enhance the viability of vertical axis wind turbines in the renewable energy market.

REFERENCES

[1] Abbasi, K. R., Shahbaz, M., Zhang, J., Irfan, M., & Alvarado, R. (2022). Analyze the environmental sustainability factors of China: The role of fossil fuel energy and renewable energy. *Renewable Energy*, 187, 390-402. https://doi.org/10.1016/j.renene.2022.01.066

[2] Abbasi, S., & Daraee, M. A. (2024). Ameliorating a vertical axis wind turbine performance utilizing a time-varying force plasma actuator. *Scientific Reports*, 14(1), 18425. https://doi.org/10.1038/s41598-024-69455-8

[3] Abbey, C., Chahwan, J., & Joos, G. (2008). Energy storage and management in wind turbine. *EPE Journal*, 17(4), 6-12. https://doi.org/10.1080/09398368.2008.11463660

[4] Abdalrahman, G., Daoud, M. A., Melek, W.W., Lien, F.S., & Yee, E. (2021). Design and implementation of an intelligent blade pitch control system and stability analysis for a small Darrieus vertical-axis wind turbine. *Energies*, 15(1), 235. https://doi.org/10.3390/en15010235

[5] Abdolahifar, A., & Zanj, A. (2024). Addressing VAWT Aerodynamic Challenges as the Key to Unlocking Their Potential in the Wind Energy Sector. *Energies*, 17(20), 5052. https://doi.org/10.3390/en17205052

[6] Abid, M., S Karimov, K., A Wajid, H., Farooq, F., Ahmed, H., & H Khan, O. (2015). Design, development and testing of a combined Savonius and Darrieus vertical axis wind turbine. Iranica *Journal of Energy & Environment*, 6(1). https://doi: 10.5829/idosi.ijee.2015.06.01.02

[7] Agha, A., Chaudhry, H. N., & Wang, F. (2018). Diffuser augmented wind turbine (DAWT) technologies: A review. *International Journal of Renewable Energy Research*, 8(3), 1369-1385.

[8] Akwa, J.V., Vielmo, H.A., & Petry, A.P. (2012). A review on the performance of Savonius wind turbines. *Renewable and sustainable energy reviews*, 16(5), 3054-3064. https://doi.org/10.1016/j.rser.2012.02.056

[9] Aldieri, L., Grafström, J., Sundström, K., & Vinci, C. P. (2019). Wind power and job creation. *Sustainability*, 12(1), 45. https://doi.org/10.3390/su12010045

[10] Al Noman, A., Tasneem, Z., Sahed, M. F., Muyeen, S. M., Das, S. K., & Alam, F. (2022). Towards next generation Savonius wind turbine: Artificial intelligence in blade design trends and framework. *Renewable and Sustainable Energy Reviews*, 168, 112531. https://doi.org/10.1016/j.rser.2022.112531

[11] Aresti, L., Tutar, M., Chen, Y., & Calay, R. K. (2013). Computational study of a small scale vertical axis wind turbine (VAWT): comparative performance of various turbulence models. *Wind and Structures*, 17(6), 647-670. DOI:10.12989/was.2013.17.6.647

[12] Arutyunov, V. S., & Lisichkin, G. V. (2017). Energy resources of the 21st century: problems and forecasts. Can renewable energy sources replace fossil fuels. *Russian Chemical Reviews*, 86(8), 777. DOI**:** 10.1070/RCR4723

[13] Ashwill, T.D., Sutherland, H.J., & Berg, D.E. (2012). A retrospective of VAWT technology. Sandia National Laboratories, 1-64. DOI: 10.2172/1035336

[14] Asr, M. T., Nezhad, E. Z., Mustapha, F., & Wiriadidjaja, S. (2016). Study on start-up characteristics of H-Darrieus vertical axis wind turbines comprising NACA 4-digit series blade airfoils. *Energy*, 112, 528-537. https://doi.org/10.1016/j.energy.2016.06.059

[15] Baghdadi, M., Elkoush, S., Akle, B., & Elkhoury, M. (2020). Dynamic shape optimization of a vertical-axis wind turbine via blade morphing technique. *Renewable Energy*, 154, 239-251. https://doi.org/10.1016/j.renene.2020.03.015

[16] Balat, M. (2009). A review of modern wind turbine technology. *Energy Sources*, Part A, 31(17), 1561-1572. DOI:10.1080/15567030802094045

[17] Barnes, A., & Hughes, B. (2019). Determining the impact of VAWT farm configurations on power output. *Renewable energy*, 143, 1111-1120. https://doi.org/10.1016/j.renene.2019.05.084

[18] Barthelmie, R. J., & Pryor, S. C. (2021). Climate change mitigation potential of wind energy. *Climate*, 9(9), 136. https://doi.org/10.3390/cli9090136

[19] Bashir, A., & Khan, S. (2021, June). Renewable energy sources: A study focused on wind energy. In *Turbulence & Energy Laboratory Annual Conference*. pp. 99-118. Cham: Springer International Publishing. https://doi.org/10.1007/978-3-030-92148-4_5

[20] Bastankhah, M., & Porté-Agel, F. (2017). A new miniature wind turbine for wind tunnel experiments. Part I: Design and performance. *Energies*, 10(7), 908. https://doi.org/10.3390/en10070908

[21] Bedon, G., De Betta, S., & Benini, E. (2015). A computational assessment of the aerodynamic performance of a tilted Darrieus wind turbine. *Journal of Wind Engineering and Industrial Aerodynamics*, 145, 263-269. https://doi.org/10.1016/j.jweia.2015.07.005

[22] Bilgili, M., & Alphan, H. (2022). Global growth in offshore wind turbine technology. *Clean Technologies and Environmental Policy*, 24(7), 2215-2227. https://doi.org/10.1007/s10098-022-02314-0

[23] Bottasso, C. L., Campagnolo, F., & Petrović, V. (2014). Wind tunnel testing of scaled wind turbine models: Beyond aerodynamics. *Journal of wind engineering and industrial aerodynamics*, 127, 11-28. https://doi.org/10.1016/j.jweia.2014.01.009

[24] Breban Ş., Drancă M.A., Mălăel I. (2019) *Airborne wind-motor system for producing electric energy*, Priority number(s): RO20190000673 20191023. https://worldwide.espacenet.com/publicationDetails/biblio?II=2&ND=3&adjacent=true&locale=en_EP&FT=D&date=20200228&CC=RO&NR=133886A0&KC=A0#

[25] Carrillo, C., Montaño, A. O., Cidrás, J., & Díaz-Dorado, E. (2013). Review of power curve modelling for wind turbines. *Renewable and Sustainable Energy Reviews*, 21, 572-581. https://doi.org/10.1016/j.rser.2013.01.012

[26] Castelli, M. R., Englaro, A., & Benini, E. (2011). The Darrieus wind turbine: Proposal for a new performance prediction model based on CFD. *Energy*, 36(8), 4919-4934. https://doi.org/10.1016/j.energy.2011.05.036

[27] Chaichana, T., & Thongdee, S. (2019, November). Effect of blade number and angle on the characteristics of the Savonius type wind turbine. In *Journal of Physics: Conference Series*. Vol. 1380, No. 1, p. 012110. IOP Publishing. doi:10.1088/1742-6596/1380/1/012110

[28] Chaitep, S., Chaichana, T., Watanawanyoo, P., & Hirahara, H. (2011). Performance evaluation of curved blades vertical axis wind turbine. *European Journal of Scientific Research*, 57(3), 435-446.

[29] Chan, C. M., Bai, H. L., & He, D. Q. (2018). Blade shape optimization of the Savonius wind turbine using a genetic algorithm. *Applied energy*, 213, 148-157. https://doi.org/10.1016/j.apenergy.2018.01.029

[30] Chaudhary, U., Mondal, P., Tripathy, P., Nayak, S.K., & Saha, U.K. (2014). Modeling and optimal design of small HAWT blades for analyzing the starting torque behavior. In *2014 Eighteenth National Power Systems Conference (NPSC)*. pp. 1-6. IEEE. DOI:10.1109/NPSC.2014.7103886

[31] Chegini, S., Asadbeigi, M., Ghafoorian, F., & Mehrpooya, M. (2023). An investigation into the self-starting of Darrieus-Savonius hybrid wind turbine and performance enhancement through innovative deflectors: A CFD approach. *Ocean Engineering*, 287, 115910. https://doi.org/10.1016/j.oceaneng.2023.115910

[32] Chehouri, A., Younes, R., Ilinca, A., & Perron, J. (2015). Review of performance optimization techniques applied to wind turbines. *Applied Energy*, 142, 361-388. https://doi.org/10.1016/j.apenergy.2014.12.043

[33] Cheng, M., & Zhu, Y. (2014). The state of the art of wind energy conversion systems and technologies: A review. *Energy conversion and management*, 88, 332-347. https://doi.org/10.1016/j.enconman.2014.08.037

[34] Dal Monte, A., Castelli, M. R., & Benini, E. (2013). Multi-objective structural optimization of a HAWT composite blade. *Composite structures*, 106, 362-373. DOI:10.1016/j.compstruct.2013.05.038

[35] Dewan, A., Gautam, A., & Goyal, R. (2021). Savonius wind turbines: A review of recent advances in design and performance enhancements. *Materials Today: Proceedings*, 47, 2976-2983. https://doi.org/10.1016/j.matpr.2021.05.205

[36] Dewan, A., Tomar, S. S., Bishnoi, A. K., & Singh, T. P. (2023). Computational fluid dynamics and turbulence modelling in various blades of Savonius turbines for wind and hydro energy: Progress and perspectives. *Ocean Engineering*, 283, 115168 https://doi.org/10.1016/j.oceaneng.2023.115168

[37] Dobrev, I., & Massouh, F. (2011). CFD and PIV investigation of unsteady flow through Savonius wind turbine. *Energy Procedia*, 6, 711-720. https://doi.org/10.1016/j.egypro.2011.05.081

[38] Dong, L., Liao, M., Li, Y., Song, X., & Xu, K. (2009, October). Study on aerodynamic design of horizontal axis wind turbine generator system. In *2009 International Conference on Energy and Environment Technology*. Vol. 1, pp. 841-844. IEEE. DOI: 10.1109/ICEET.2009.208

[39] Du, L., Ingram, G., & Dominy, R. G. (2019). A review of H-Darrieus wind turbine aerodynamic research. Proceedings of the Institution of Mechanical Engineers, Part C: *Journal of Mechanical Engineering Science*, 233(23-24), 7590-7616. https://doi.org/10.1177/0954406219885962

[40] Dumitrescu, H., Cardoş, V., & Mălăel, I. (2015). The physics of starting process for vertical axis wind turbines. *CFD for wind and tidal offshore turbines*, 69-81. DOI:10.1007/978-3-319-16202-7_7

[41] Eftekhari, H., Al-Obaidi, A.S.M., & Eftekhari, S. (2022). Aerodynamic performance of vertical and horizontal axis wind turbines: A comparison review. *Indonesian Journal of Science and Technology*, 7(1), 65-88. DOI:10.17509/ijost.v7i1.43161

[42] Elizondo, J., Martínez, J., & Probst, O. (2009). Experimental study of a small wind turbine for low-and medium-wind regimes. *International Journal of Energy Research*, 33(3), 309-326. https://doi.org/10.1002/er.1482

[43] Ferrari, G., Federici, D., Schito, P., Inzoli, F., & Mereu, R. (2017). CFD study of Savonius wind turbine: 3D model validation and parametric analysis. *Renewable energy*, 105, 722-734. https://doi.org/10.1016/j.renene.2016.12.077

[44] Ferroudji, F., Khelifi, C., & Meguellati, F. (2016). Modal analysis of a small H-Darrieus wind turbine based on 3D CAD, FEA. *International Journal of Renewable Energy Research (IJRER)*. 6(2), 637-643.

[45] Franković, B., & Vrsalović, I. (2001). New high profitable wind turbines. *Renewable energy*, 24(3-4), 491-499. https://doi.org/10.1016/S0960-1481(01)00033-7

[46] Fujisawa, N., & Shibuya, S. (2001). Observations of dynamic stall on Darrieus wind turbine blades. *Journal of Wind Engineering and Industrial Aerodynamics*, 89(2), 201-214. https://doi.org/10.1016/S0167-6105(00)00062-3

[47] Gad, H. E., Abd El-Hamid, A. A., El-Askary, W. A., & Nasef, M. H. (2014). A new design of Savonius wind turbine: numerical study. *CFD letters*, 6(4), 144-158.

[48] Gall, M., Mălăel, I., & Preda, D. (2023). Numerical Analysis of the Interaction of Savonius Vertical Axis Wind Turbines in Tree-type Cluster Configuration. In 2023 *27th International Conference on Circuits, Systems, Communications and Computers (CSCC).* pp.272-276. IEEE. DOI: 10.1109/CSCC58962.2023.00051

[49] Gaunt, B., & Johnson, D. A. (2012). Wind turbine performance in controlled conditions: Experimental results. *International Journal of Green Energy*, DOI: 10.1155/2016/5460823

[50] Glasberg, D., Stratila, S., & Malael, I. (2024). A Numerical Analysis on the Performance and Optimization of the Savonius Wind Turbine for Agricultural Use. Engineering, *Technology & Applied Science Research*, 14(1), 12621-12627. https://doi.org/10.48084/etasr.6543

[51] Gu, Y., Kamel, E., Tsitron, I., & Aginskiy, M. (2021). Design and performance study of a unique modular vertical axis wind turbine. *WIT Transactions on Ecology and the Environment*, 254, 93-100. DOI: 10.2495/ESUS210091

[52] Gupta, N., Kaur, N., Jain, S. K., & Joshal, K. S. (2021). Smart grid power system. *Advances in Smart Grid Power System.* pp. 47-71. Academic Press DOI: 10.1016/B978-0-12-824337-4.00003-5

[53] Hassan S.S., Javaid, M.T., Rauf, U., Nasir, S., Shahzad, A., & Salamat, S. (2023). Systematic investigation of power enhancement of Vertical Axis Wind Turbines using bio-inspired leading edge tubercles. *Energy*, 270, 126978. DOI: 10.1016/j.energy.2023.126978

[54] Hau, E., & Renouard, H. (2006). *Wind turbines: fundamentals, technologies, application, economics*. Vol. 2. Berlin: springer. https://doi.org/10.1007/3-540-29284-5

[55] He, R., Sun, H., Gao, X., & Yang, H. (2022). Wind tunnel tests for wind turbines: A state-of-the-art review. *Renewable and Sustainable Energy Reviews*, 166, 112675. DOI: https://doi.org/10.1016/j.rser.2022.112675

[56] Helming, P., von Freyberg, A., Sorg, M., & Fischer, A. (2021). Wind turbine tower deformation measurement using terrestrial laser scanning on a 3.4 MW wind turbine. *Energies*, 14(11), 3255. https://doi.org/10.3390/en14113255

[57] Hosseini, A., & Goudarzi, N. (2019). Design and CFD study of a hybrid vertical-axis wind turbine by employing a combined Bach-type and H-Darrieus rotor systems. *Energy conversion and management*, *189*, 49-59. https://doi.org/10.1016/j.enconman.2019.03.068

[58] Hossain, M. F. (2021). Application of wind energy into the transportation sector. *International Journal of Precision Engineering and Manufacturing-Green Technology*, 8, 1225-1237. https://doi.org/10.1007/s40684-020-00235-1
[59] Huleihil, M., & Mazor, G. (2012). Wind turbine power: The Betz limit and beyond. In Advances in wind power. *IntechOpen*. DOI: 10.5772/52580
[60] Ismail, A. M. M., Ali, Z. M., Isa, K. M., Abdullah, M., & Zawawi, F. M. (2021). Study on the potentiality of power generation from exhaust air energy recovery wind turbine: a review. *Journal of Advanced Research in Fluid Mechanics and Thermal Sciences*, 87(3), 148-171 https://doi.org/10.37934/arfmts.87.3.148171
[61] Jin, X., Ju, W., Zhang, Z., Guo, L., & Yang, X. (2016). System safety analysis of large wind turbines. *Renewable and Sustainable Energy Reviews*, 56, 1293-1307. https://doi.org/10.1016/j.rser.2015.12.016
[62] Johari, M. K., Jalil, M., & Shariff, M. F. M. (2018). Comparison of horizontal axis wind turbine (HAWT) and vertical axis wind turbine (VAWT). *International Journal of Engineering and Technology*, 7(4.13), 74-80. DOI: 10.14419/ijet.v7i4.13.21333
[63] Kadam, A. A., & Patil, S. S. (2013). A review study on Savonius wind rotors for accessing the power performance. *IOSR Journal of Mechanical and Civil Engineering*, 5, 18-24.
[64] Kaldellis, J. K., & Zafirakis, D. (2011). The wind energy (r) evolution: A short review of a long history. *Renewable energy*, 36(7), 1887-1901. https://doi.org/10.1016/j.renene.2011.01.002
[65] Kan, J., Liao, W., Wang, S., Chen, S., Huang, X., & Zhang, Z. (2021). A piezoelectric wind energy harvester excited indirectly by a coupler via magnetic-field coupling. *Energy Conversion and Management*, 240, 114250. https://doi.org/10.1016/j.enconman.2021.114250
[66] Kavade, R. K., & Ghanegaonkar, P. M. (2017). Design and analysis of vertical axis wind turbine for household application. *Journal of Clean Energy Technologies*, 5(5), 353-358. DOI: 10.18178/JOCET.2017.5.5.397
[67] Keung, P. K., Li, P., Banakar, H., & Ooi, B. T. (2008). Kinetic energy of wind-turbine generators for system frequency support. *IEEE Transactions on power systems*, 24(1), 279-287. DOI**:** 10.1109/TPWRS.2008.2004827
[68] Khandagale, M. R., & Marlapalle, M. B. (2017). Design & Analysis of Savonius VAWT for 50W Rated Power output. *Int J Eng Res Gen Sci*, 5, 189-200
[69] Kouloumpis, V., Sobolewski, R. A., & Yan, X. (2020). Performance and life cycle assessment of a small scale vertical axis wind turbine. *Journal of Cleaner Production*, 247, 119520. DOI: 10.1016/j.jclepro.2019.119520
[70] Kragten, A. (2004). *The Darrieus rotor, a vertical axis wind turbine (VAWT) with only a few advantages and many disadvantages. Report KD215*. Engineering Office Kragten Design, Populierenlaan, 51, 5492
[71] Kumar, R., Raahemifar, K., & Fung, A. S. (2018). A critical review of vertical axis wind turbines for urban applications. *Renewable and Sustainable Energy Reviews*, 89, 281-291. https://doi.org/10.1016/j.rser.2018.03.033
[72] Kusiak, A., & Song, Z. (2010). Design of wind farm layout for maximum wind energy capture. *Renewable energy*, 35(3), 685-694. https://doi.org/10.1016/j.renene.2009.08.019
[73] Lee, K. Y., Tsao, S. H., Tzeng, C. W., & Lin, H. J. (2018). Influence of the vertical wind and wind direction on the power output of a small vertical-axis wind turbine installed on the rooftop of a building. *Applied Energy*, 209, 383-391. DOI: 10.1016/j.apenergy.2017.08.185
[74] Li, Y. (2011). Discussion on the principles of wind turbine condition monitoring system. In 2011 *International Conference on Materials for Renewable Energy & Environment*. Vol.1, pp. 621-624. IEEE. DOI: 10.1109/ICMREE.2011.5930888
[75] Li, Y. (2019). Straight-bladed vertical axis wind turbines: history, performance, and applications. *Rotating machinery*, 1. DOI: 10.5772/intechopen.84761
[76] Malael, I., & Bucur, I. O. (2021). Numerical Evaluation of the Flow around a New Vertical Axis Wind Turbine Concept. *Sustainability*, 13(16), 9012. https://doi.org/10.3390/su13169012
[77] Mălăel, I., & Strătilă, S. (2024). High-precision numerical investigation of a VAWT starting process. *Processes*, 12(10), 2263. https://doi.org/10.3390/pr12102263
[78] Menet, J. L., & Bourabaa, N. (2004). Increase in the Savonius rotors efficiency via a parametric investigation. In *European Wind Energy conference & exhibition*. pp. 22-25.

[79] Mohamed, M. H. (2013). Impacts of solidity and hybrid system in small wind turbines performance. *Energy*, 57, 495-504. https://doi.org/10.1016/j.energy.2013.06.004

[80] Mohamed, M. H., Dessoky, A., & Alqurashi, F. (2019). Blade shape effect on the behavior of the H-rotor Darrieus wind turbine: Performance investigation and force analysis. *Energy*, 179, 1217-1234. https://doi.org/10.1016/j.energy.2019.05.069

[81] Mohammadi, M., Mohammadi, A., & Farahat, S. (2016). A new method for horizontal axis wind turbine (HAWT) blade optimization. *International Journal of Renewable Energy Development*, 5(1), 1-8. DOI: 10.14710/ijred.5.1.1-8

[82] Muratoğlu, A., & Demir, M. S. (2019). Numerical analyses of a straight bladed vertical axis Darrieus wind turbine: Verification of DMS algorithm and Qblade code. *European Journal of Technique (EJT)*, 9(2), 195-208. DOI:10.36222/ejt.643483

[83] Olivera, A. F., Chica, E., & Colorado, H. A. (2024). Design and manufacturing with 3D printing and life cycle analysis of a recyclable polymer-based H-Darrieus wind turbine. *Engineered Science*, 31, 1156. DOI: 10.30919/es1156

[84] Paraschivoiu, I. (2002). Wind turbine design: with emphasis on Darrieus concept. *Presses inter Polytechnique*. https://doi.org/10.1260/030952403321833789

[85] Paraschivoiu, I., Ammar, S., & Saeed, F. (2018). VAWT versus HAWT: a comparative performance study of 2–6 MW rated capacity turbines. *Transactions of the Canadian Society for Mechanical Engineering*, 42(4), 393-403. DOI: 10.1139/tcsme-2017-0137

[86] Pisanò, F. (2019). Input of advanced geotechnical modelling to the design of offshore wind turbine foundations. *Proceedings of the XVII ECSMGE-2019: Geotechnical Engineering foundation of the future*, 1-6 DOI: 10.32075/17ECSMGE-2019-1109

[87] Probst, O., Martínez, J., Elizondo, J., & Monroy, O. (2011). Small wind turbine technology. *Wind turbines*, pp. 107-136. DOI: 10.5772/15861

[88] Pryor, S.C., & Barthelmie, R.J. (2010). Climate change impacts on wind energy: A review. *Renewable and sustainable energy reviews*, 14(1), pp. 430-437. https://doi.org/10.1016/j.rser.2009.07.028

[89] Rambabu, C., Kumar, M. S., & Harish, N. S. (2012). Design Of MPPT Based Hybrid Wind and Fuel-Cell Energy System. *International Journal of Computer Science & Communication Networks*, 1(3), 297-304

[90] Ross, I., & Altman, A. (2011). Wind tunnel blockage corrections: Review and application to Savonius vertical-axis wind turbines. *Journal of Wind Engineering and Industrial Aerodynamics*, 99(5), 523-538. https://doi.org/10.1016/j.jweia.2011.02.002

[91] Roy, S., Das, R., & Saha, U. K. (2017, December). Identification of geographical locations to operate Savonius wind turbine rotor for meeting a desired performance. In *Gas Turbine India Conference.* Vol. 58516, p. V002T06A003. American Society of Mechanical Engineers. DOI: 10.1115/GTINDIA2017-4566

[92] Ryu, M. S., Kim, S. R., Cho, D. H., & Kang, J. G. (2022). Innovative single-day installation vessel for offshore wind turbines. *Energies*, 15(11), 3914. https://doi.org/10.3390/en15113914

[93] Sagharichi, A., Maghrebi, M. J., & Arab Golarcheh, A. (2016). Variable pitch blades: An approach for improving performance of Darrieus wind turbine. *Journal of renewable and sustainable energy*, 8(5). DOI: 10.1063/1.4964310

[94] Salem, M. E. M. (2016). *Design of a pitch angle control system for a horizontal axis small wind turbine*. DOI: 10.13140/RG.2.2.27324.36487

[95] Sander, L., Jung, C., & Schindler, D. (2024). Global Review on Environmental Impacts of Onshore Wind Energy in the Field of Tension between Human Societies and Natural Systems. *Energies*, 17(13), 3098. https://doi.org/10.3390/en17133098

[96] Savino, M. M., Manzini, R., Della Selva, V., & Accorsi, R. (2017). A new model for environmental and economic evaluation of renewable energy systems: The case of wind turbines. *Applied energy*, 189, 739-752. https://doi.org/10.1016/j.apenergy.2016.11.124

[97] Schaffarczyk, A. (2024). Introduction to wind turbine aerodynamics. *Springer Nature*. https://doi.org/10.1007/978-3-031-56924-1

[98] Sedaghat, A., Mirhosseini, M., & Moghimi Zand, M. (2014). Aerodynamic design and economical evaluation of site-specific horizontal axis wind turbine (HAWT). *Energy Equipment and Systems*, 2(1), 43-56. 10.22059/ees.2014.5009

[99] Sivamani, S., Nadarajan, M., Kameshwaran, R., Bhatt, C. D., Premkumar, M. T., & Hariram, V. (2020). Analysis of cross axis wind turbine blades designed and manufactured by FDM based additive manufacturing. *Materials Today: Proceedings*, 33, 3504-3509. DOI:10.1016/j.matpr.2020.05.438

[100] Shamsuddin, M. S. M., Kamaruddin, N. M., & Mohamed-Kassim, Z. (2022). The influence of material on the power performance of Savonius turbines in wind and water applications. *Ocean Engineering*, 266, 112638. https://doi.org/10.1016/j.oceaneng.2022.112638

[101] Shende, V., Patidar, H., Baredar, P., & Agrawal, M. (2022). A review on comparative study of Savonius wind turbine rotor performance parameters. *Environmental Science and Pollution Research*, 29(46), 69176-69196.

[102] Shinagam, R., Ajay, G., Patta, L., & Gandam, A. S. (2020). Vibration and noise studies on wind turbine generator for reduction of vibrations and noise. *World Journal of Engineering*, 17(1), 134-143. https://doi.org/10.1108/WJE-09-2019-0275

[103] Sun, S., Wang, T., & Chu, F. (2022). In-situ condition monitoring of wind turbine blades: A critical and systematic review of techniques, challenges, and futures. *Renewable and Sustainable Energy Reviews*, 160, 112326. https://doi.org/10.1016/j.rser.2022.112326

[104] Sun, M., Peng, L., Lei, H., Zhang, J., Zhang, Z., Chen, Q., Zhang, G., & Li, J. (2025). A novel small-scale H-type Darrieus vertical axis wind turbine manufactured of carbon fiber reinforced composites. *Renewable Energy*, 238, 121923. https://doi.org/10.1016/j.renene.2024.121923

[105] Tahani, M., Rabbani, A., Kasaeian, A., Mehrpooya, M., & Mirhosseini, M. (2017). Design and numerical investigation of Savonius wind turbine with discharge flow directing capability. *Energy*, 130, 327-338. https://doi.org/10.1016/j.energy.2017.04.125

[106] Tasneem, Z., Al Noman, A., Das, S. K., Saha, D. K., Islam, M. R., Ali, M. F., ... & Alam, F. (2020). An analytical review on the evaluation of wind resource and wind turbine for urban application: Prospect and challenges. *Developments in the Built Environment*, 4, 100033. https://doi.org/10.1016/j.dibe.2020.100033

[107] Tjiu, W., Marnoto, T., Mat, S., Ruslan, M. H., & Sopian, K. (2015). Darrieus vertical axis wind turbine for power generation I: Assessment of Darrieus VAWT configurations. *Renewable energy*, 75, 50-67. https://doi.org/10.1016/j.renene.2014.09.038

[108] Van Kuik, G., Ummels, B., & Hendriks, R. (2008). Perspectives on wind energy. *Sustainable Energy Technologies: Options and Prospects*, 75-97. https://doi.org/10.1007/978-1-4020-6724-2_4

[109] Vis, I. F., & Ursavas, E. (2016). Assessment approaches to logistics for offshore wind energy installation. *Sustainable energy technologies and assessments*, 14, 80-91. https://doi.org/10.1016/j.seta.2016.02.001

[110] Wang, D., Gao, X., Meng, K., Qiu, J., Lai, L. L., & Gao, S. (2018). Utilisation of kinetic energy from wind turbine for grid connections: a review paper. *IET Renewable Power Generation*, 12(6), 615-624. 10.1049/iet-rpg.2017.0590

[111] Wang, H., Xiong, B., Zhang, Z., Zhang, H., & Azam, A. (2023). Small wind turbines and their potential for internet of things applications. *iScience*, 26(9). https://doi.org/10.1016/j.isci.2023.107674

[112] Wenehenubun, F., Saputra, A., & Sutanto, H. (2015). An experimental study on the performance of Savonius wind turbines related with the number of blades. *Energy Procedia*, 68, 297-304. https://doi.org/10.1016/j.egypro.2015.03.259

[113] Xisto, C. M., Páscoa, J. C., & Trancossi, M. (2016). Geometrical parameters influencing the aerodynamic efficiency of a small-scale self-pitch high-solidity VAWT. *Journal of Solar Energy Engineering*, 138(3), 031006. https://doi.org/10.1115/1.4032794

[114] Yaramasu, V., Wu, B., Sen, P. C., Kouro, S., & Narimani, M. (2015). High-power wind energy conversion systems: State-of-the-art and emerging technologies. *Proceedings of the IEEE*, 103(5), 740-788. 10.1109/JPROC.2014.2378692

[115] Zakaria, A., & Ibrahim, M. S. N. (2019). Experimental evaluation of multiple Savonius turbines in oblique and cluster configurations. *Int. J. Emerg. Trends Eng. Res.*, 7, 790-793. DOI: 10.30534/ijeter/2019/10712201

[116] Zemamou, M., Aggour, M., & Toumi, A. (2017). Review of Savonius wind turbine design and performance. *Energy Procedia*, 141, 383-388. https://doi.org/10.1016/j.egypro.2017.11.047

[117] Zereg, A., Aksas, M., Bouzaher, M. T., Laghrouche, S., & Lebaal, N. (2024). Efficiency improvement of Darrieus wind turbine using oscillating gurney flap. *Fluids*, 9(7), 150. https://doi.org/10.3390/fluids9070150

[118] Zhou, T., & Rempfer, D. (2013). Numerical study of detailed flow field and performance of Savonius wind turbines. *Renewable energy*, 51, 373-381. https://doi.org/10.1016/j.renene.2012.09.046
[119] Zoucha, J., Crespo, C., Wolf, H., & Aboy, M. (2023). Review of Recent Patents on Vertical-Axis Wind Turbines (VAWTs). *Recent Patents on Engineering*, 17(4), 3-15. https://doi.org/10.2174/1872212117666220829143132
[120] *** https://greenoteka.eu
[121] *** https://www.electricaltechnology.org/2021/08/wind-power-plant.html
[122] *** https://www.statista.com/chart/26085/price-per-megawatt-hour-of-electricity-by-source/
[123] *** https://www.windsystemsmag.com/news/first-vertical-axis-wind-turbine-awarded-certification/
[124] *** www.engineeringnews.co.za
[125] *** www.mckinsey.com

RESEARCH ON THE INFLUENCE OF EXTRUSION PARAMETERS ON SOLID-LIQUID SEPARATION PERFORMANCE OF LIVESTOCK MANURE AND OPTIMIZATION OF PARAMETERS

/

畜禽粪污螺旋挤压脱水装置参数优化设计与试验

Weisong ZHAO[1,2,3)], Qimin GAO[1)], Chunsong GUAN[*1)], Binxing XU[1,3)], Biao MA[*1,2)], Yan GONG[1,2)]

[1)]Nanjing Institute of Agricultural Mechanization, Ministry of Agriculture and Rural Affairs, Nanjing 210014, China;
[2)]Institute of Western Agriculture, the Chinese Academy of Agricultural sciences, Changji 831100, China
[3)]College of Mechanical and Electrical Engineering, Xinjiang Agricultural University, Urumqi，830052, China

Tel: +8602584346161; E-mail: cs.guan@163.com; mabiao@caas.cn
** Correspondent authors: Chunsong GUAN; Biao MA*
DOI: https://doi.org/10.35633/inmateh-76-26

Keywords: *livestock manure, screw extrusion, solid-liquid separation, parameter optimization*

ABSTRACT

Solid-liquid separation is essential for utilizing livestock and poultry manure, impacting greenhouse gas emissions and pollution control. This study aimed to address the high water content and low efficiency issues in screw extrusion solid-liquid separation technology. A screw separator was designed, and a Box-Behnken test scheme was used to optimize parameters with dairy manure as the test object. The study identified extender length, screw rotation speed, and counterweight mass as the influencing factors, with extrudate water content and solids extraction rate as evaluation indices. A quadratic regression model was established to describe the relationships between the influencing factors and evaluation indices. Optimal parameters were determined as: extender length=10 cm, screw rotation speed=55 r/min, and counterweight mass=34.73 kg. The predicted extrudate water content was 65.44 %, and solids extraction rate was 2.39 m³/h. Validation tests showed an average extrudate water content of 67.71 % and solids extraction rate of 2.10 m³/h, with relative errors of 3.3 % and 9.6 % respectively. The model's reliability was confirmed, providing a reference for designing livestock and poultry manure screw extrusion separators.

摘要

固液分离是畜禽粪便资源化利用的关键共性环节，对控制温室气体排放和环境污染治理具有重要意义。针对螺旋挤压固液分离技术存在的挤出物含水率偏高、处理效率较低的问题，本研究设计了一种螺旋挤压脱水装置，以奶牛粪为试验对象，采用 Box-Benhnken 试验方案开展了参数优化研究。以延长器长度、螺杆转速、配重重量为影响因素，以挤出物含水率和固形物提取率为考核指标，建立了影响因素与考核指标之间的二次回归模型。通过多目标优化函数，确定一组最佳参数组合为：延长器长度=10cm，螺杆转速=55r/min，配重重量=34.73kg，此时挤出物含水率预测值为 65.44%，固形物提取效率预测值为 2.39m³/h。验证试验结果表明，在最优参数组合下，挤出物含水率均值为 67.71%，与预测值相对误差为 3.3%。固形物提取效率均值为 2.10 m³/h，与预测值的相对误差为 9.6%。两个考核指标的实测值与理论预测值均＜10%，表明建立的二次回归模型可靠，可用于参数优化。研究结果可为畜禽粪污螺旋挤压分离机的设计提供参考。

INTRODUCTION

Livestock and poultry manure is one of the most important factors leading to ecological damage and environmental pollution, and is also the second largest source of greenhouse gas emissions from farms *(Aguirre-Villegas et al., 2017)*. For several consecutive years, the Chinese government has been introducing new policies with the aim of increasing the resource utilization of livestock and poultry manure. Solid-liquid separation (compression dewatering) machines are among the core equipment for livestock and poultry manure management and resource utilization, representing a current research hotspot and priority area *(Camilleri-Rumbau et al., 2021; Wu et al., 2021; Zhang et al., 2022)*.

[1] *Weisong Zhao, Ph. D. Assistant Researcher; Qimin Gao, Assistant Researcher; Binxing Xu, Assistant Researcher; Chunsong Guan, Ph. D. Associate Researcher; Biao MA, Associate Researcher; Yan GONG, Researcher.*

After dewatering, dry solids and low impurity filtrate are obtained, which facilitates subsequent management, disposal and field utilization, and reduces the cost of manure treatment *(Husfeldt et al., 2012; Zhang et al., 2009; Zhou et al., 2023)*. In addition, solid-liquid separation has great potential to contribute to the realization of the "two-carbon" goal. Studies have shown that the use of solid-liquid separation can reduce greenhouse gas emissions from farms by up to 38% *(Aguirre-Villegas et al., 2014; Aguirre-Villegas et al., 2019)*. However, the solid-liquid separation technology for livestock and poultry manure in China is relatively weak. The inability to achieve high quality and high efficiency solid-liquid separation seriously restricts the subsequent links to carry out, and is the bottleneck of livestock and poultry manure resource utilization *(Hjorth et al., 2011)*.

Currently, livestock and poultry manure solid–liquid separation technologies mainly include three types: centrifugal, filter-press, and screening. Among them, screw extrusion separation technology, which features low energy consumption and lower investment costs, is the most widely used *(Anlauf, 2007)*. However, there is a trade-off between processing efficiency and the water content of the extrudate, improving one performance indicator often leads to a decline in the other. Therefore, the screw extrusion solid-liquid separator still requires optimization, with the goal of achieving the best possible balance between these two performance parameters.

Currently, the separation technology of solid-liquid mixtures of livestock and poultry manure is receiving attention and research applications from many scholars both in China and abroad *(Jiang et al., 2016; Luo et al., 2020)*. The study done by *Burton et al. (*2007*)* emphasized the key role of solid-liquid separation in livestock and poultry manure treatment, pointing out that the mechanical separation means can effectively remove about 80% of the dry matter components of manure. *Moller et al (2000)*, on the other hand, revealed that the dry matter concentration (TS) of raw materials has a significant effect on the treatment capacity of screw solid-liquid separation equipment. Concentration (TS) has a significant effect on the processing capacity of screw solid-liquid separation equipment. *Shi Huixian et al. (2014)* explored the relationship between TS and apparent viscosity of swine manure and found that swine manure exhibited pseudoplastic fluid properties and followed a power rate equation.

Popovic et al., (2014) investigated the effect of additives, such as biochar, on the separation performance of a screw extruder, and the results showed that the addition of biochar to swine manure could improve the separation efficiency by 2% to 3%. *Apachanov et al*. *(2016)* modeled the material movement inside the screw extruder, and pointed out that the "dead zone" of the material inside the screw and the rotation around the center of the axis are the main factors leading to the decrease of separation efficiency and the increase of energy consumption.

Guan Zhengjun et al. (2011) optimized the process parameters of a screw press separator by taking the TS of separated solids as the main evaluation index. *Shen Jiangtao et al. (2014)* designed a broken screw extrusion separator. *Zhao Weisong et al. (2017)* and *Zhu et al., (2017)* optimized the design of a broken-tooth screw extrusion separator and carried out structural optimization and simulation studies to achieve better progress.

The influence of many factors on separator performance has been explored in previous studies *(Hjorth et al., 2011; Husfeldt et al., 2012).* Examples include material properties of the manure, structural parameters of the screw (e.g., pitch, screw length, interrupted distance, etc.), and kinematic parameters (e.g., screw rotation speed) *(Zhao et al., 2017)*. However, there are more influencing factors on the operation of screw extrusion separator, and the influence law of the factors and the interaction of the factors on the performance of solid-liquid separation still needs to be studied in depth. In particular, the structural parameters at the solid outlet, the lack of research on the effects of extrudate water content and solid extraction rate, restricts the further optimization of the design of the screw extrusion separator.

For this reason, this study designs a screw separator and investigates the effects of extender length, screw rotation speed, and counterweight mass on the device's dewatering performance. It analyzes the influence of each factor on the evaluation indices and determines the optimal parameter combination. The goal is to provide theoretical support for the design and optimization of screw extrusion dewatering machines.

MATERIALS AND METHODS

Test materials

The cow manure used in the experiment was from a dairy farm in Haimen City, Jiangsu Province, and the TS of the cow manure was 10.11% at the time of the experiment. The experiment was conducted in August 2022.

Test equipment

Self-developed livestock and poultry manure screw extrusion dewatering device (Nanjing Agricultural Mechanization Research Institute of the Ministry of Agriculture and Rural Development), SKFG-01 dryer electric constant temperature blower drying box (Shanghai Jiecheng Experimental Instrument Co., Ltd.), SAMPO DT2234A tachymeter (Shenzhen Xinbao Science and Technology Instrument Research and Development Center), NL50-8 sewage slurry pump (Shanghai Sunshine Pump Manufacturing Co., Ltd.), QJB3 /8 sludge mixer (Jiangsu Ru Ke Environmental Protection Equipment Co., Ltd.), SECURA612-1CN electronic balance (Suzhou Sainz Instruments Co., Ltd.).

Machine structure and working principle

Livestock and poultry manure screw separator mainly consists of three-phase motor, reducer, screen, screw, extender, head and other parts, of which the screw is one of the key components of the extrusion separator, used to complete the process of conveying materials, extrusion dewatering and discharging, etc. Self-designed screw is divided into the feeding section, extruding section, discharging section, and adopts a double-screw design. The outer diameter of the screw is 260 mm and the diameter of the screw shaft is 120 mm.

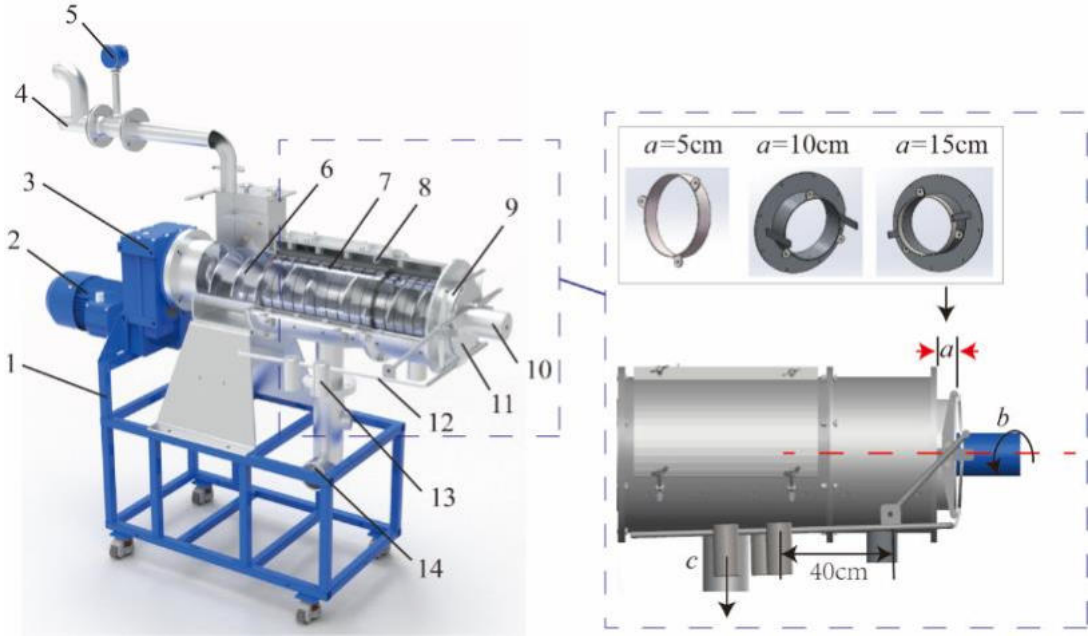


Fig. 1 Structural sketch and parameter adjustment method of screw separator

1. Frame; 2. Motor; 3. Reducer; 4. Inlet; 5. Flow meter; 6. Screw; 7. Screen; 8. Screen retainer; 9. Extender; 10. Rotating shaft; 11. Solid outlet baffle; 12. Pressure plate; 13. Counterweight; 14. Liquid outlet

Test method

The water content of extrudate characterizes the wet and dry separation effect of manure, which has a significant impact on the subsequent utilization, and is an index of the performance of wet and dry separator. Separation efficiency reflects the volume of manure that can be processed by the machine per unit of time, and is the main basis for the matching relationship between the scale of farming and the number of machines. Therefore, the water content of the extrudate and the processing efficiency were selected as the objective function. The results of existing studies have shown that the rotational speed of the screw and the outlet resistance are important factors affecting the water content of the extrudate and the separation efficiency. The previous pre-test study shows that the extender length has a greater impact on the wet and dry separation performance: when the extender is shorter, the discharge speed is faster, but the water content is high. When the extender is longer, the discharge speed is slower, but the water content is lower. Therefore, based on the existing results and pre-test results, the initial ranges of the three influencing factors, screw rotation speed, outlet resistance and extender length, were determined, where the outlet resistance is usually measured by the counterweight mass. A three-factor, three-level response surface test design methodology was used with 17 sets of tests, which included five zeros. Based on the Box-Behnken design principle, the response surface test was carried out on the three factors of screw rotation speed, counterweight mass and extender length with extrudate water content and separation efficiency as the evaluation indices, and the test factors and levels are shown in Table 1.

Table 1

Factors and levels of response surface test

Level	Extender Length *a* [mm]	Screw rotation speed *b* [r·min^{-1}]	Counterweight mass *c* [kg]
-1	5	25	20
0	10	40	30
1	15	55	40

The indices were determined by the following methods: separation efficiency was calculated by the volume of cow dung treated per unit time, and water content was calculated by the standard drying method. Before the test, the cow dung was placed in the liquid storage tank, the stirring pump worked continuously to ensure good uniformity of the material in the tank, the timing started when the machine was running stably, and stopped after 30 min of operation, and the separated solids and liquids were collected to be weighed and measured, and the test was repeated three times. Design-Expert 8.0.6 software was used to perform quadratic polynomial regression analysis on the test data for separation efficiency and water content of the extrudate, and response surface analysis was used to study the correlation and interaction effects of the factors.

RESULTS AND ANALYSIS

Test results

The test results and 2 response values are shown in Table 2. In the test, the livestock and poultry manure screw extrusion dewatering device can successfully complete the extrusion dewatering operation, and within the range of the selected parameters, the solids extraction rate varies from 1.78 to 2.63 m³/h, and the water content of extrudate varies from 53.54% to 74.49%.

Table 2

Experiment design and response values

std	run	Extender length *a*	Screw rotation speed *b*	Counter weight mass *c*	Moisture content of dried fecal solids after separation y_1 [%]	Efficiency of dried manure extraction y_2 [m³·h^{-1}]
4	1	1	1	0	53.54	2.10
3	2	-1	1	0	72.05	2.60
17	3	0	0	0	68.88	2.40
1	4	-1	-1	0	74.49	2.58
11	5	0	-1	1	67.47	2.11
6	6	1	0	-1	57.27	1.97
5	7	-1	0	-1	73.85	2.30
12	8	0	1	1	63.87	2.34
15	9	0	0	0	68.64	2.30
10	10	0	1	-1	69.01	2.22
8	11	1	0	1	55.09	1.97
13	12	0	0	0	69.72	2.30
9	13	0	-1	-1	69.86	2.11
14	14	0	0	0	65.39	2.32
16	15	0	0	0	68.23	2.33
2	16	1	-1	0	56.57	1.78
7	17	-1	0	1	70.74	2.63

Regression modeling and significance test

According to the sample data in Table 2, multiple regression fitting analysis was carried out using Design-Expert software to establish the quadratic polynomial response surface regression models of y_1 and y_2 on extender length *a*, screw rotation speed *b* and counterweight mass *c* as shown in Eqs. (1) and (2), and the regression equations were subjected to analysis of variance (ANOVA), and the results are shown in Table 3.

$$y_1=68.17-8.58a-1.24b-1.60c-0.15ab+0.23ac-0.69bc-3.66a^2-0.35b^2-0.27c^2 \quad (1)$$

$$y_2=2.33-0.29a+0.09b+0.06c+0.08ab-0.08ac+0.03bc-0.02a^2-0.04b^2-0.09c^2 \quad (2)$$

where, y_1 is moisture content of dried fecal solids after separation, %; y_2 is efficiency of dried manure extraction, m³·h^{-1}; *a* is extender length; *b* is screw rotation speed; *c* is efficiency of dried manure extraction.

Table 3

Variance analysis

Index	Source	Sum of Squares	df	Mean Square	*F*-value	*P*-value
y_1 [%]	Model	683.05	9	75.89	38.44	< 0.0001**
	a	589.27	1	589.27	298.44	< 0.0001**
	b	12.30	1	12.30	6.23	0.04*
	c	20.54	1	20.54	10.40	0.01*
	ab	0.087	1	0.087	0.04	0.84
	ac	0.22	1	0.216	0.11	0.75
	bc	1.89	1	1.89	0.96	0.36
	a^2	56.47	1	56.47	28.60	0.001**
	b^2	0.51	1	0.51	0.26	0.628
	c^2	0.31	1	0.31	0.16	0.70
	Residual	13.82	7	1.97		
	Lack of Fit	2.96	3	0.99	0.36	0.78
	Pure Error	10.86	4	2.71		
	Cor Total	696.88	16			
y_2 [$m^3 \cdot h^{-1}$]	Model	0.84	9	0.09	26.87	0.0001**
	a	0.66	1	0.66	188.64	2.56E-06**
	b	0.06	1	0.06	16.63	0.005**
	c	0.03	1	0.03	7.28	0.030*
	ab	0.02	1	0.02	6.47	0.038*
	ac	0.03	1	0.03	7.83	0.027*
	bc	0.003	1	0.004	1.04	0.343
	a^2	0.002	1	0.002	0.55	0.484
	b^2	0.008	1	0.008	2.32	0.172
	c^2	0.035	1	0.035	10.09	0.016*
	Residual	0.024	7	0.003		
	Lack of Fit	0.018	3	0.006	3.44	0.132
	Pure Error	0.007	4	0.002		
	Cor Total	0.865	16			

*Note: P＜0.01 (highly significant,**); P＜0.05 (significant, *).*

Based on the results of the analysis in Table 3, it can be seen that the *P*-values of the regression equations y_1 and y_2 are less than 0.01, which indicates that the response surface model is highly significant. The *P*-value of the misfit term of the model is greater than 0.05 (y_1=0.784, y_2=0.132), and the non-significant misfit term indicates that the model matches the data to a high degree. y_1 and y_2's coefficient of determination, R^2, are 0.98 and 0.97, respectively, which indicates that the two models can explain more than 97% of the evaluation indices. Based on the above results, it can be seen that the model can adequately describe the 2 response variables of extrudate water content and treatment efficiency, and the prediction of the response surface model is accurate and can be used to optimize the parameters of the screw.

In order to optimize the regression equation, the independent variables that have less influence on the response variables need to be eliminated, and the influence of each parameter on the regression model equation can be reflected by the *P* value.

In the extrudate water content model y_1, the effects of 2 items, a and a^2, were highly significant (P < 0.01); the effects of 2 items, b and c, were significant (P < 0.05); and the effects of the remaining 5 items, ab, ac, bc, b^2 and c^2, were not significant (P > 0.05).

In the dry matter extraction rate model y_2, the effects of a and b^2 terms were highly significant (P < 0.01); c, ab, ac, and c^2, 4 terms were significant (P < 0.05); and the remaining bc, a^2, and b^2 3 terms were insignificant (P > 0.05).

The optimized model was obtained after removing the insignificant terms, as shown in Eq.(3) and Eq.(4).

The significance test *P*-values of the optimized models y_1 and y_2 are both less than 0.01 respectively, indicating that the models are highly significant. None of the misfit terms are significant, indicating a good match between the data and the model. The optimized model is more concise and precise, and can be used for prediction and analysis of actual production.

$$y_1=67.9-8.58a-1.24b-1.60c-3.7a^2 \quad (3)$$

$$y_2=2.3-0.2862a+0.085b+0.0562c+0.075ab-0.0825ac-0.0949c^2 \quad (4)$$

Effect analysis of the influence of each factor on the response value

The influence magnitude of each factor on the evaluation index was determined through the analysis of variance (ANOVA) results in Table 3. The influence of each factor on the water content of the extrudate is in the following order from the largest to the smallest: $a > c > b$. It indicates that among the three factors, the extender length (a) has the greatest influence on the water content of the extrudate, the counterweight mass are the second largest (c), and the screw rotational speed (b) has the smallest influence. This finding is in line with the previous findings that the effects of b and c on y_1 are consistent with the findings of literature (*Zhao et al., 2017*). It was also found that the effect of extender length (a) on y_1 was highly significant over the effect of factors b and c. This finding was missing in the previous study.

The effect of each factor on solids extraction rate was ranked in descending order: $a > b > c$. This indicates that among the three factors, extender length (a) had the greatest effect on solids extraction rate, followed by screw rotational speed (b), and counterweight mass (c) had the least effect. This conclusion indicates that the extender length is an important factor affecting the operational performance of the screw extruder separator, and is the key influence factor of the two evaluation indices of extrudate water content and solids extraction rate. The length of the extender can be adjusted to seek a balance between the two indices of extrudate water content and solids extraction rate to maximize the performance of the separator design.

Interaction analysis of influence factors

Response surface analysis was utilized to examine the effects of factors a, b, and c on the 2 response values of extrudate water content and solids extraction rate, with the goal of determining whether there is an optimal combination of factors when extrudate water content is minimized and solids extraction rate is maximized.

The response surface curves of the interacting factors on extrudate water content are shown in Figure 2, with each response surface plot representing the interaction between the other 2 independent variables when one factor is at the center level.

As can be seen in Fig. 2a, y_1 increases with decreasing a, exhibiting a more pronounced change, and y_1 decreases with increasing b, showing a smaller effect.

The shape of the response surface in Fig. 2b is basically the same as that in Fig. 2a, i.e., c decreases and y_1 increases by a small amount.

From Fig. 2c, it can be seen that y_1 increases as either b or c decreases, and the surface change trend is overall flatter.

From Figure 2d, it can be seen that y_2 increases as a decreases, with a larger change, and y_2 increases as b increases.

From Fig.2e, it can be seen that y_2 increases with the decrease of a, and y_2 shows *a* trend of first increase and then decrease with the increase of *c*, and there is a maximum value.

Similarly, in Fig. 2f, y_2 shows *a* trend of change with the increase of c, and there is a maximum value. The change rule of the response surface is consistent with the analysis results in Table 3.

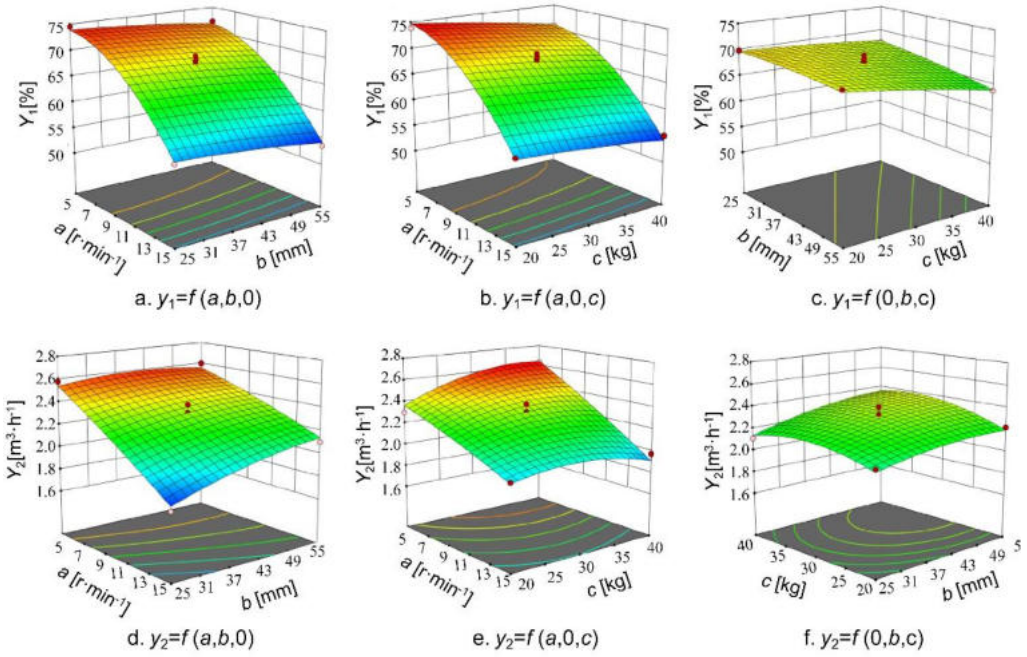


Fig. 2 - Effect of interaction factors on response indicators

Parameter optimization and validation tests

Parameter optimization

In order to realize the optimal operating effect, the solids extraction rate is maximized by ensuring that the water content of the extrudate meets the process requirements for fermentation and other procedures (≤70%). According to the response surface analysis, it can be seen that: to improve the solids extraction rate, it is necessary to reduce the extender length and increase the screw rotation speed. To reduce the water content of extrudate, it is necessary to increase the extender length, increase the screw rotation speed and increase the counterweight mass. The influence of each factor on the water content of the extrudate and the solid extraction rate is more complex, therefore, multi-objective optimization is used to seek the optimal combination of parameters to meet the objectives.

In the livestock and poultry manure fermentation and composting process, the water content of extrudate <70% is more appropriate. In the actual operational requirements, the larger the solids extraction rate is, the higher the efficiency is. Therefore, with y_1 <70% and at the same time y_1 maximum as the objective, Design-Expert software was used to optimize the solution of each parameter. Establish the parameter optimization mathematical model, set the solution objective and constraints as shown in equation (5).

$$\begin{cases} max y_2(a,b,c) \\ 60\% \le y_1(a,b,c) \le 70\% \\ s.t. \begin{cases} 5 \le a \le 15 \\ 25 \le b \le 55 \\ 20 \le c \le 40 \end{cases} \end{cases} \quad (5)$$

According to the solution results, one of the optimal parameter combinations is selected: a=10 cm, b=55 r/min, c=34.73 kg, at this time, the theoretical value of extrudate water content y_1=65.44%, and the theoretical value of solids extraction rate y_2=2.39 m³/h.

Experimental verification

In order to verify the accuracy of the obtained model prediction results, a validation test was carried out. Five replicate tests were conducted with parameter combinations (*a*=10 cm, *b*=55 r/min, *c*=34.73 kg) and the results are shown in Table 4.

Table 4

Validation test results

No.	y_1 [%]	y_2 [$m^3 \cdot h^{-1}$]
1	69.72	1.89
2	68.26	2.51
3	67.78	2.36
4	62.93	1.99
5	69.88	2.06
Average	67.71	2.16
Relative error/%	2.82	0.34

In the validation test, the mean value of water content of the extrudate was 67.71% with a relative error of 3.3% from the theoretical prediction (65.44%). The mean value of solids extraction rate was 2.10 m³/h, and the relative error to the theoretical prediction (2.39 m³/h) was 9.6%. The measured and theoretically predicted values of the two evaluation indices are <10%, indicating that the model is reliable and can be used for parameter optimization. The test site is shown in Figure 3.



Fig. 3 - Tests Scenarios

CONCLUSION AND DISCUSSION

The Box-Behnken central combination test method was used to study the influence law of three factors (extender length, screw rotation speed, counterweight mass) on two evaluation indices (water content of extrudate, solids extraction rate), and the optimization model of the influence factors and evaluation indices was established. The model and optimization results were verified through tests, and the results showed that the model and optimization results were accurate and reliable.

The test results show that the order of significance of the influence of each factor on the water content of extrudate is extender length (*a*), counterweight mass (*c*), screw rotation speed (*b*) in descending order of significance. The order of significance of the effect of each factor on solids extraction rate was in descending order of significance: extender length (*a*), screw rotation speed (*b*), counterweight mass (*c*). In this study, extender length was found to be one of the most critical factors affecting the working performance of the screw extruder separator. This factor has a highly significant effect on both extrudate water content and solids extraction rate. As the extender length increases, the water content of the extrudate decreases, but the solids extraction efficiency also declines. In order to obtain the optimal parameter combinations, a multi-objective optimization function was established, and one of the optimal parameter combinations was obtained as: *a*=10 cm, *b*=55 r/min, *c*=34.73 kg. Under the optimal parameter combinations, the mean value of extrudate water content was 67.71% and the mean value of solids extraction rate was 2.10 m³/h in the validation test.

ACKNOWLEDGEMENTS

We thank all colleagues for their advice and support during this study. This work was supported by the Jiangsu Province Agricultural Science and Technology Independent Innovation Fund Project (project number: CX(22)3093), and the Key Research and Development program of Hebei Province (Grant No.20327313D).

REFERENCES

[1] Aguirre-Villegas, H. A., Larson, R. A. (2017). Evaluating greenhouse gas emissions from dairy manure management practices using survey data and lifecycle tools. *Journal of cleaner production,* Vol 143, pp.169-179.

[2] Aguirre-Villegas, H.A., Larson, R.A., Reinemann, D.J. (2014). From waste-to-worth: Energy, emissions, and nutrient implications of manure processing pathways. *Biofuels Bioprod. Biorefining*. 8: 770–793.

[3] Aguirre-Villegas, H. A., Larson, R. A., Sharara, M. A. (2019). Anaerobic digestion, solid-liquid separation, and drying of dairy manure: Measuring constituents and modeling emission. *Science of the total environment,* Vol. 696, p.134059.

[4] Anlauf, H. (2007). Recent developments in centrifuge technology. *Separation and Purification Technology,* Vol.58, pp. 242-246.

[5] Apachanov, A.S., Rud, A.V., Belousov, K.Y. (2016). Modeling of the motion clay mass in the screw channel of the screw press. *Procedia Engineering,* Vol 150, pp. 906-910.

[6] Burton, C.H. (2007). The potential contribution of separation technologies to the management of livestock manure. *Livestock Science,* Vol.112, pp. 208-216.

[7] Camilleri-Rumbau, M.S., Briceño, K., Fjerbæk Søtoft, L., Christensen, K. V., Roda-Serrat, M. C., Errico, M., Norddahl, B. (2021). Treatment of manure and digestate liquid fractions using membranes: opportunities and challenges. *International Journal of Environmental Research and Public Health,* Vol.18, p. 3107.

[8] Guan, Z., Li, W., Zheng, G., Bi, L. (2011). Effect of solid-liquid separation on utilization of dairy manure (固液分离对牛粪利用效果的影响). *Transactions of the Chinese Society of Agricultural Engineering,* Vol 27, pp.259-263. Beijing/China.

[9] Hjorth, M., Christensen, K.V., Christensen, M.L., Sommer, S.G. (2011). Solid–liquid separation of animal slurry in theory and practice. *Sustainable Agriculture Volume 2,* pp. 953-986.

[10] Husfeldt, A.W., Endres, M.I., Salfer, J.A., Janni, K.A. (2012). Management and characteristics of recycled manure solids used for bedding in Midwest free stall dairy herds. *Journal of dairy science,* Vol.95, pp. 2195-2203.

[11] Jiang, T., Ma, X., Yang, J., Chen, M., Frank, S., Li, G. (2016). Characteristics and efficiency evaluation of livestock slurry separation technologies (畜禽粪便固液分离技术特点及效率评估). *Transactions of the Chinese Society of Agricultural Engineering,* Vol 32, pp. 218-225. Beijing/China.

[12] Luo, J., Zhao, L., Yao, Z., Feng, J., Yu, J., Yuan, Y. (2020). Construction and application of comprehensive evaluation index system for waste treatment on intensive livestock farms (规模化养殖场畜禽粪污处理综合评价指标体系构建与应用). *Trans. Chin. Soc. Agric. Eng,* Vol 36, pp.182-189. Beijing/China.

[13] Møller, H. B., Lund, I., Sommer, S. G. (2000). Solid–liquid separation of livestock slurry: efficiency and cost. *Bioresource technology,* Vol 74, pp. 223-229.

[14] Popovic, O., Gioelli, F., Dinuccio, E., Balsari, P. (2014). Improved pig slurry mechanical separation using chitosan and biochar. *Biosystems engineering,* Vol.127, pp. 115-124.

[15] Shen, J., Wu, D., Mingjie, Zhao, M., Jiang, Q. Ma, X., Guo, N. (2014). Design and experiment of KP-250 screw separator (KP-250 螺旋挤压式固液分离机的设计及试验). *Journal of Agricultural Mechanization Research,* Vol.36, pp. 210-213, Heilongjiang /China.

[16] Shi H., Lü, T., Zhu H., Xu, K., Wang, Y. (2014). Rheological properties and apparent viscosity model of pig manure (猪粪流变特性与表观粘度模型研究). *Transactions of the Chinese Society for Agricultural Machinery*, Vol. 45, pp.188-193.

[17] Wu, J., Zhong, X., Liu, F. (2021). Study on the preparation of composite flocculant for solid-liquid separation of livestock manure. Paper presented at the *IOP Conference Series: Earth and Environmental Science*.

[18] Zhang, P., Yanli, Yang, Y., Tian, Y., Yang X., Zhang, Y., Zheng, Y., Wang, L. (2009). Bioenergy industries development in China: Dilemma and solution. *Renewable and sustainable energy reviews,* Vol.13, pp. 2571-2579.

[19] Zhang, X., Liu, C., Liao, W., Wang, S., Zhang, W., Xie, J., Gao, Z. (2022). Separation efficiency of different solid-liquid separation technologies for slurry and gas emissions of liquid and solid fractions: A meta-analysis. *Journal of Environmental Management,* Vol. 310, p. 114777.

[20] Zhao, W., Zhu, D., Zong, W., Xie, H., Cao, J., Han, B., Li, R., Qu, H., (2017). Operation parameter optimization of interrupted-whorl screw dewatering device of solid-liquid separator for livestock and poultry manure (畜禽粪污固液分离机断齿螺旋脱水装置运行参数优化). *Transactions of the Chinese Society of Agricultural Engineering*, Vol. 33, pp. 25–31. Beijing /China.

[21] Zhao, W., Zhu, D., Qu, H., Xie, H., Wang, D., Ha, I. B., Cao, J. (2017). Design and experiment of interrupted-whorl screw extrusion device, （断齿式螺旋挤压装置设计与试验）. *Journal of Agricultural Mechanization Research,* Vol.39, pp.86-91, Heilongjiang /China.

[22] Zhou, T., Wang, S., Zhang, W., Yin, F., Cao, Q., Lian, T., Dong, H. (2023). Comparison of different aerobic sludge on enriching polyhydroxyalkanoate mixed microbial culture using lactic acid fermentation broth of agricultural wastes. *Chemical Engineering Journal,* Vol.475, p. 146000.

[23] Zhu, D., Zhao, W., Zong, W., Qu, H., Xie, H., Cao, J. (2017). Numerical Simulation Analysis of Flow Field in Flow Channel of Internal Interrupted-whorl Screw Separator（断齿式挤压脱水流道内流场数值模拟）. *Transactions of the Chinese Society for Agricultural Machinery,* Vol. 48, pp. 92-100, Beijing/China.

LOW-COST IOT-BASED INTELLIGENT SAFFRON MANAGEMENT SYSTEM

低成本物联网智能藏红花管理系统

Wai Leong PANG[1)], Jieru WANG[1)], Hui Hwang GOH[1)], Swee King PHANG[1)], Hafisoh AHMAD[1)], Kah Yoong CHAN[*2)]
[1)] School of Engineering, Centre for Sustainable Societies, Taylor's University, Taylor's Lakeside, 47500 Subang Jaya, Selangor, Malaysia;
[2)] Centre for Advanced Devices and Systems, Faculty of Artificial Intelligence and Engineering, Multimedia University, Persiaran Multimedia, 63100 Cyberjaya, Selangor, Malaysia.
Tel: +603 8312 5438.; E-mail: kychan@mmu.edu.my
DOI: https://doi.org/10.35633/inmateh-76-27

Keywords: *Internet of Things, Low-cost, Saffron, Smart Agriculture*

ABSTRACT

Saffron is a high-value crop that requires low growing temperatures and cannot be cultivated in equatorial climates. To address this limitation, an IoT-based Intelligent Saffron Management System (IISMS) is proposed to simulate suitable growing conditions for saffron cultivation in equatorial regions. The IISMS remotely monitors key environmental parameters, and the collected data is displayed via a mobile APP over a Wi-Fi network. The cooling system is automatically activated when the temperature exceeds 10 °C, which is the critical threshold required during the flowering phase. Similarly, the irrigation system is triggered when soil moisture drops below 70%. By providing responsive and automated crop management, the IISMS optimizes growth conditions and improves yield quality. Experimental results showed that saffron cultivated under the IISMS was healthier, taller, exhibited more green shoots, and was generally stronger compared to saffron grown under standard room conditions in Malaysia.

摘要

藏红花是一种高价值作物，需要较低的生长温度，而赤道气候无法种植。本文提出了一种基于物联网的智能藏红花管理系统(IISMS)，用于模拟赤道国家适宜藏红花的生长条件。IISMS远程监控生长条件，并通过Wi-Fi 网络将数据显示在移动应用程序中。如果温度高于10°C，则会启动冷却系统。10°C 被设定为阈值，藏红花在开花期间需要10°C的低温。当土壤湿度低于规定的70% 阈值时开始灌溉。IISMS提供响应式藏红花作物管理，优化生长条件并提高产量质量。与马来西亚室温下未采用 IISMS种植的藏红花相比，在 IISMS下种植的藏红花更健康、更高大、绿芽更多、更强壮。

INTRODUCTION

Saffron is one of the world's most expensive crops due to its rarity, labor-intensive harvesting process, and nutritional and medicinal benefits. It is native to Southwest Asia and is primarily cultivated in the Mediterranean region, including countries such as Iran, Greece, and Turkey (*Cardone et al., 2020*). Successful saffron cultivation depends on mild weather and moderate rainfall, with optimal temperatures of 23–25°C in September. Flowering of the bulbs requires mild conditions as well, with daytime temperatures around 17°C and nighttime temperatures near 10°C (*Mehmeti et al., 2024*). Saffron is a high-value crop with notable nutritional and medicinal properties. It is highly favored in the market due to its broad applications in healthcare products, pharmaceuticals, and the food industry (*Dalir et al., 2025*). The primary active compound in saffron is crocin, which is responsible for its distinctive color and aroma. Crocin also exhibits significant pharmacological effects (*Malik et al., 2024*). As a result, saffron has increasingly become a key player in the global market for premium agricultural products, with demand rising steadily each year. However, the growing demand and high market value of saffron are placing pressure on production, and current efficiency levels have not kept pace with the rapid increase in demand.

A key challenge for saffron cultivation expansion is the need for more information about optimal growing conditions. Factors like temperature, humidity, light intensity, and pH are essential for saffron growth and development. It is important to monitor these critical parameters such as moisture level, pH value, light intensity, and environmental humidity *(Narayana et al., 2024)*. Continuous observation and accurate monitoring of these variables are essential to growing saffron in the best possible conditions.

Nevertheless, the growth and production features of saffron have very high demands on such environmental conditions as temperature, humidity, light, soil moisture and so forth. This slight negligence might harm the saffron growth cycle and yield quality. Conventional planting methods still depend on manual monitoring and adjustment of the environmental conditions. These methods are costly and time-consuming, whilst becoming obsolete with climate change and environmental fluctuations. Such suboptimal approaches of management not only hamper the increase in yields but also raise the cost of production, making it hard to achieve complete economic returns for saffron production.

Temperature is one of the essential factors of the entire growing cycle of saffron. A low temperature of around 10°C is needed for saffron to start the flowering process *(Pirasteh-Anosheh et al., 2023)*. The temperature for flower formation is between 23°C to 27°C. However, the yield of the saffron will drop when the temperature is more than 30°C. It can be concluded that maintaining a suitable temperature is the key to achieving high yields in saffron cultivation.

The second important factor for saffron cultivation is humidity, particularly during the flowering and bulb stages. A study suggested that maintaining humidity at around 65.7% can significantly enhance flower production *(Iqbal et al., 2024)*. However, humidity levels become difficult to manage when rainfall is unpredictable. Controlling humidity is essential for optimizing both the quality and yield of saffron. Uncontrolled humidity levels can negatively affect plant health and reduce overall yield.

The growth and development of saffron are significantly influenced by light. According to research, the yield and quality of saffron can be significantly influenced by properly adjusting the lighting. The red-to-blue light ratio of 3:2 with a photosynthetic photon flux density of 200 $\mu molm^{-2}s^{-1}$ has been found to enhance stigma yield and improve nutritional content *(Kang et al., 2022)*. However, while high light intensity can promote photosynthesis and leaf growth, it may also reduce both the quantity and quality of saffron stigmas (*Zhou et al., 2022*). These findings suggest that optimizing both the light spectrum and intensity is essential for improving saffron output and quality.

Saffron is highly sensitive to soil pH, which significantly affects microbial activity, nutrient availability, and overall plant health. Soil pH, which ranges from 0 to 14, indicates the acidity or alkalinity of the soil. Values below 7.0 signify acidic conditions, while those above 7.0 indicate alkalinity. Most crops thrive in a pH range of 6.0 to 7.5, which supports optimal root development and nutrient absorption. Saffron performs best in neutral to slightly acidic soils, with an ideal pH range of 6.0 to 8.0 *(Kumar et al., 2022)*. This pH range ensures the availability of essential nutrients such as nitrogen, phosphorus, potassium, and various micronutrients, supporting the healthy development of saffron bulbs and sprouts.

Numerous projects were carried out to collect and analyze environmental data in order to enhance agricultural yield and productivity. One such initiative proposed a portable system that monitors air humidity, temperature, and soil moisture using sensors, with the collected data used to control irrigation for vegetable crops *(Penchalaiah et al., 2021)*. Sensor networks have also been employed in precision agriculture to optimize crop yields and resource efficiency *(Sanjeevi et al., 2020)*. A real-time remote management and monitoring system was introduced for greenhouses, utilizing wireless networks to track plant conditions *(Bersani et al., 2022)*. The Internet of Things (IoT) was used to monitor 14 environmental parameters in order to increase the crop yield *(Aditya et al., 2024)*. Another IoT-based system was designed to capture and analyze environmental variables such as humidity, indoor and outdoor temperature, soil moisture, and carbon dioxide concentration in tomato plantations *(Ge et al., 2022)*. Additionally, a prototype equipped with Bayesian predictive networks was proposed to respond to sensor feedback on plant growth metrics, water levels, pH, light intensity, and humidity *(Kocian et al., 2020)*. All collected data and prototype operations were stored in the cloud, highlighting the potential of IoT technologies in advancing sustainable agriculture.

Intelligent and automated planting management strategies are urgently needed to enhance the yield of saffron plantations. IoT technology presents promising opportunities to address this challenge. The integration of IoT with agriculture has greatly advanced precision farming practices by improving crop monitoring and resource management *(Dhanaraju et al., 2022; Haziq et al., 2022; Leao, 2024; Lokman et al., 2024)*. Furthermore, IoT has demonstrated strong potential in regulating microclimate conditions to enhance crop yield and quality *(Pangave et al., 2023)*. An intelligent planting system equipped with IoT sensors and automated control mechanisms can continuously collect environmental data such as temperature and humidity. This enables real-time monitoring and precise regulation of the saffron growing environment, optimizing conditions for plant development. As a result, such systems not only improve crop yield and quality with high efficiency but also provide a scientific foundation for data-driven saffron cultivation.

Existing research has yet to propose a smart and reliable IoT system specifically tailored for saffron cultivation. Due to the unique environmental requirements of saffron, conditions that are particularly difficult to achieve in equatorial regions, there is an urgent need for a dedicated IoT-based intelligent management system. To address this gap, the IoT-Enabled Smart Saffron Management System (IISMS) is proposed. This system is designed to monitor and control four critical environmental parameters essential for saffron growth: temperature, humidity, light intensity, and soil pH.

MATERIALS AND METHODS

The proposed IISMS provided a real-time monitoring and intelligent control of the saffron planting environment to meet the strict requirements of saffron for temperature, humidity, light and soil moisture. The architecture of the IISMS system is shown in Figure 1. IISMS consists of four main systems, i.e., 1) a lighting system, 2) an irrigation system, 3) a cooling system, and 4) a soil monitoring system. The lighting system supplies the artificial light source through LED. A water pump is equipped in the automatic irrigation system. A semiconductor cooling module is installed to control the temperature. A monitoring system is used to monitor the soil's parameters. The IISMS provides real-time monitoring and automated management of saffron growth environments.

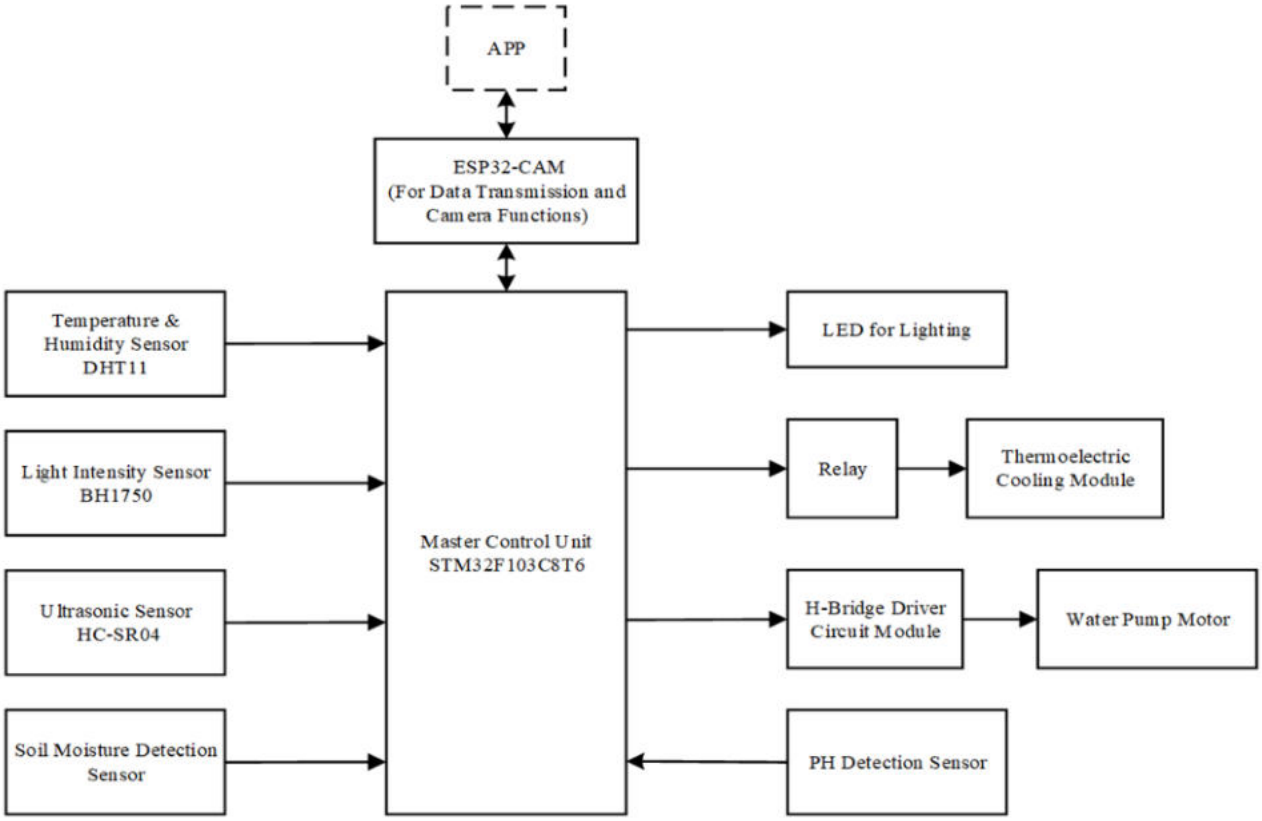


Fig. 1 – The System Architecture of IISMS

The STM32 (STM32F103C8T6) microcontroller is the core controller of IISMS. The STM32 microcontroller is used to control and process the data collected. It is responsible for reading different sensors and controlling the actuators based on a pre-configured threshold so that saffron in its growing environment finds a suitable environment. The STM32 microcontroller offers a wide range of input/output (I/O) interfaces, enabling efficient integration and operation of various sensors and actuator modules. It serves as the central controller of the system, coordinating all sensors and actuators to perform data acquisition, logical processing, and control output. With its high performance, low power consumption, and rich peripheral interfaces, the STM32 is well-suited to meet the system's requirements for handling multiple sensor inputs and controlling multiple actuators simultaneously.

IISMS used a BH1750 light sensor (Figure 2) to measure the light intensity of the environment and provide the system with reliable light data, thereby assisting in automated light control. BH1750 is a light sensor that has I2C communication to output the digital value of ambient light intensity and this will reduce the

overhead in data processing. It has high sensitivity and stability. It can give accurate measurement results under different light conditions, which is very suitable for monitoring the saffron growth environment. When the system detects that ambient light intensity drops below the predefined threshold, the IISMS sends a high-level signal to the General Purpose Input/Output (GPIO) to activate the LED fill light. This ensures that saffron plants receive adequate illumination under low-light conditions, supporting healthy growth. Once the light conditions return to normal, the system deactivates the LED light. The LED light operates at a voltage of 3.3 V. The design of the lighting system is simple and the power consumption is low. The LED has a long service life and low power consumption, which is suitable for long-term continuous operation to meet the needs of plant growth.

The soil moisture sensor was used to track the soil moisture level instantly (Figure 3). The sensor is used to measure the moisture content in the soil where saffron is cultivated. It detects the level of dryness or wetness, allowing the system to automatically regulate irrigation based on real-time soil moisture data. The output of the sensor is an analog signal, which is connected to the analog-to-digital interface of the STM32 to achieve real-time measurement of soil moisture. The sensor module was equipped with a potentiometer, and the user can configure the threshold by adjusting the potentiometer to adapt to different soil moisture requirements. The system automatically starts the water pump for irrigation when soil moisture is less than the threshold value to keep humidity conditions in the range.

The pH detection sensor (Figure 4) was used to measure the pH value of the soil. Accurate monitoring of the pH value is essential for the healthy growth of saffron, so this sensor module is used to measure the pH value of the soil in real time. The sensor transmits data to the main control unit through serial communication. The pH sensor will measure the pH of the soil and give the user the health status of the soil to ensure that the soil is well-suited for saffron growing.

The DHT11 temperature and humidity sensor (Figure 5) was used to obtain the current environmental temperature and humidity data, which provides the basic information for temperature–humidity control. The DHT11 sensor can provide relatively stable temperature and humidity data. The sensor uses a single bus protocol for data transmission and can read data by occupying a GPIO pin of the microcontroller.

The IISMS automatically activates the semiconductor cooling system, LED lights, and water pumps based on predefined thresholds to regulate temperature, supplement light, and provide irrigation. The ESP32-CAM module collects and transmits real-time images and environmental data to a mobile. The APP (Figure 6) provided users with a data display to monitor the saffron growth. Users can remotely view the key parameters such as temperature and humidity, light intensity, soil moisture and pH value of the environment through the APP.



Fig. 2 – BH1750 light sensor

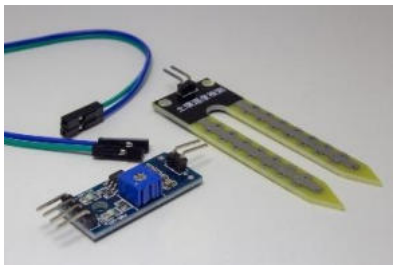


Fig. 3 – Soil moisture sensor



Fig. 4 – PH sensor

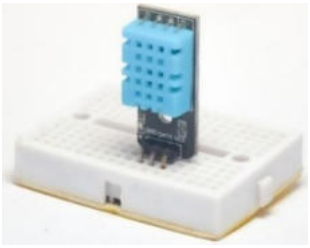


Fig. 5 – DHT11 temperature and humidity sensor



Fig. 6 – The mobile APP of the IISMS

A relay was used to control the semiconductor cooling module shown in Figure 7. It began to cool down the temperature as soon as the thermostat detected that the temperature was above the threshold value. A HC-SR04 ultrasonic sensor was used to measure saffron growth height and provide data support for crop growth monitoring. The system can monitor the height changes from time to time to record and indicate saffron growth for subsequent planting management and data analysis.

The system used the AMS1117-3.3 voltage regulator chip to step down the input voltage to a stable 3.3V ensuring reliable operation of the STM32 microcontroller. To minimize power supply noise and stabilize the output voltage, decoupling capacitors of 100 µF and 10 µF were connected at the input of the voltage regulator circuit. These capacitors effectively filtered out voltage fluctuations and contributed to a smooth and consistent power supply.

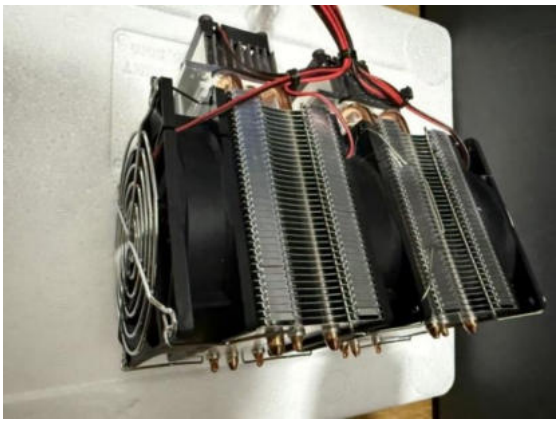


Fig. 7 – The cooling module used in IISMS

The proposed IISMS provides a customized solution designed to simulate optimal environmental conditions for saffron cultivation. Threshold values for key parameters were carefully selected based on the physiological requirements of the saffron plant. The soil moisture threshold was set at 70%, representing the ideal hydration level to support bulb development and flowering while avoiding waterlogging. The temperature threshold was set at 10°C, a critical value for initiating the flowering phase of saffron.

An extensive experiment was carried out to evaluate the performance of IISMS. The experiment was conducted indoors using two pots of saffron plants. Saffron was planted in both pots under identical initial conditions and cultivated in parallel. One pot was cultivated using the IISMS inside a styrofoam box, which actively monitored and regulated environmental parameters. The other pot served as a control and was grown under standard indoor, air-conditioned room conditions with an artificial light source in Malaysia. A general-purpose fertilizer was used in this experiment. IISMS was exposed to varying environmental conditions to test its responsiveness and accuracy. The LED fill light was triggered when ambient light intensity dropped below the predefined threshold, and deactivated once normal lighting conditions were restored. Similarly, the cooling module was activated when the temperature exceeded 10°C. The irrigation system was programmed to initiate when soil moisture fell below 70%, which is the optimal level for saffron bulb development without risking overwatering. The experiment was carried out with the styrofoam box closed to control a low temperature, and the LED light was turned on to provide a light source. The experiment was conducted over a one-week period, during which environmental data and plant responses were continuously recorded. The results were presented in the next section.

RESULTS

The extensive experimental test was carried out through the testbed shown in Figure 8.

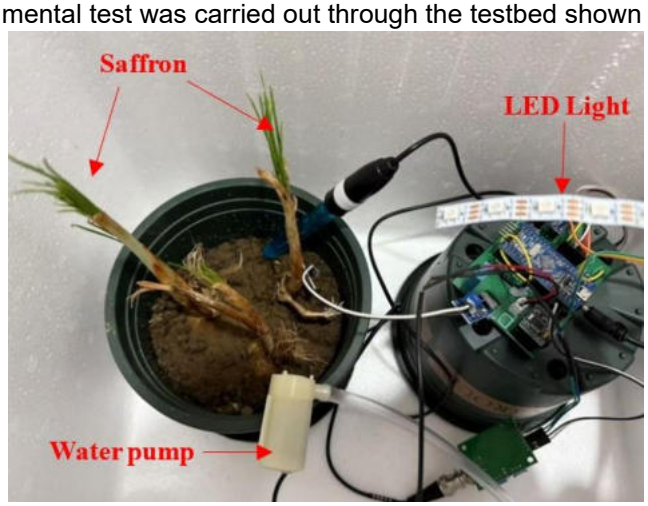


Fig. 8 - The System Architecture of IISMS

The testbed was designed for small-scale saffron cultivation. The saffron plant was cultivated in a pot filled with soil. An automated water pump was connected to the pot to ensure consistent irrigation, while an LED light strip was installed above the plant to provide artificial lighting, simulating optimal sunlight conditions. The LED light was turned on for 8 hours daily, since the experiment was conducted inside a closed Styrofoam box. The IISMS was activated at the beginning of the experiment to monitor and regulate environmental parameters.

Figure 9 illustrates the soil moisture level of the testbed. Initially, the moisture level started at around 60%. The IISMS detected a drop in soil moisture, and the irrigation system was activated, maintaining the moisture level at approximately 70% over the following hour. The moisture level reached around 100% by day 2 due to the excess water that was supplied to the saffron plant, resulting in a high moisture percentage. After this peak, the moisture level dropped and stabilized around the 70% reference line. The result showed that IISMS effectively maintained the target soil moisture level throughout the remainder of the observation period.

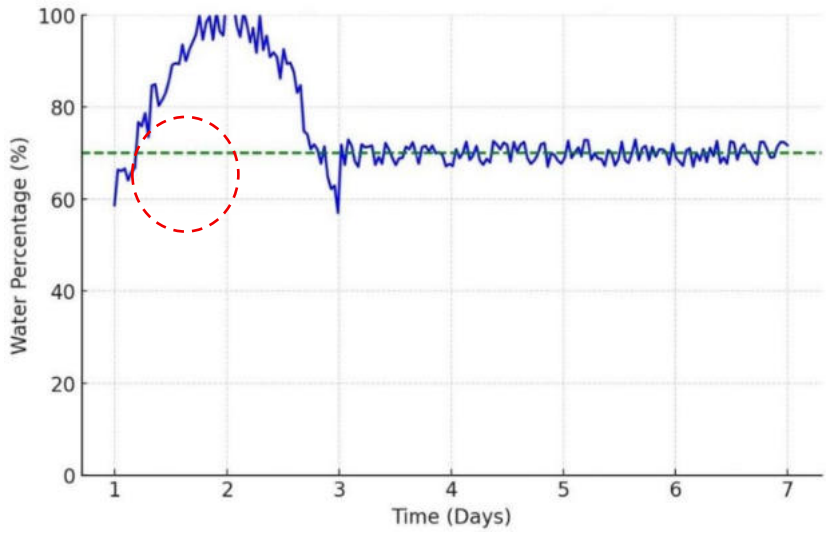


Fig. 9 – The soil moisture levels measured over a week

Figure 10 illustrates the variation in temperature over 7 hours. The temperature initially remained high at around 35°C but dropped sharply to approximately 10°C after 2.5 hours, as a result of the IISMS activating the cooling system. The temperature stabilized with minor fluctuations for the remainder of the 7-hour observation period. The IISMS was designed to automatically activate the cooling module when the temperature exceeded the preset threshold of 10°C and to deactivate it once the temperature returned to the threshold. The temperature remained stable at 10°C over a period of 7 days. However, the graph was presented over a 7-hour timespan to highlight the initial temperature changes during the early stage of the experiment. This shows the effectiveness of the IISMS in regulating temperature and provides the desired temperature level for saffron cultivation.

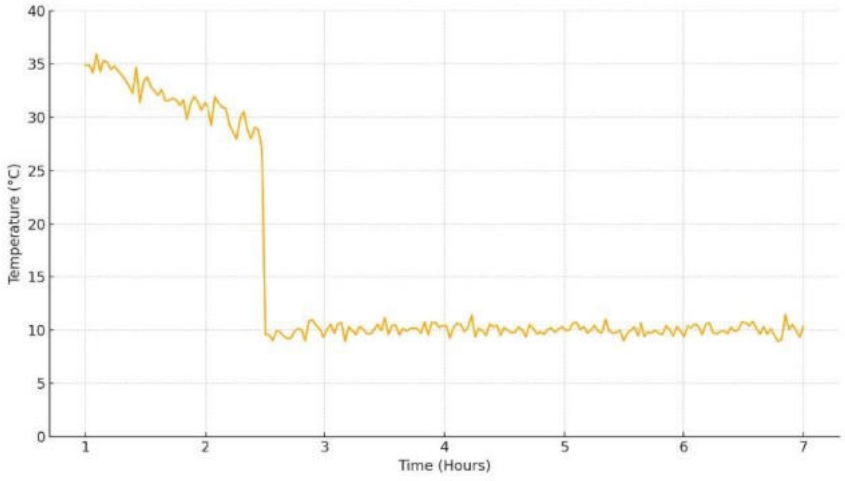


Fig. 10 – The temperature values measured over a week

Figure 11 illustrates the change in pH value over 7 days. The pH level started at approximately 7.2 and gradually declined to around 6.6 by Day 7. An annotation on the graph noted that the pH value dropped by 0.6 over the week. The pH dropped from 7.05 to 6.6 over the week, and several peaks were observed in the collected data. These fluctuations were primarily caused by the uneven distribution of fertilizers through the irrigation system's water flow. This pattern demonstrated that soil pH was directly influenced by soil fertility and irrigation practices, highlighting the importance of consistent monitoring and controlled nutrient delivery to maintain optimal growing conditions.

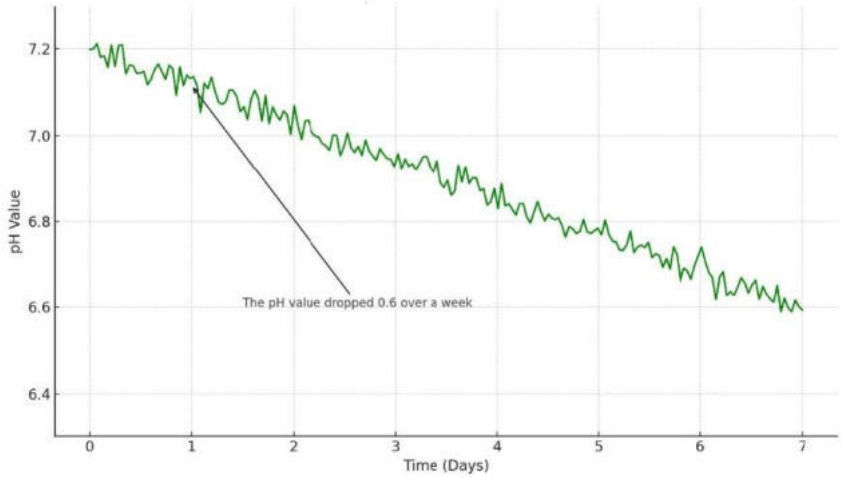


Fig. 11 – The pH values obtained over a week

Figure 12 shows two pots of saffron planted in parallel, one pot was planted with the IISMS, and the other was grown under standard indoor conditions. As shown in Figure 12, the saffron grown with the IISMS appeared healthier, taller, with more green shoots and stronger compared to the saffron cultivated without IISMS under room conditions, with fewer and less vigorous shoots. This indicated that the IISMS successfully simulated suitable growing conditions for saffron in Malaysia.



Fig. 12 – The growing conditions of saffron plants with and without IISMS

CONCLUSIONS

The proposed IISMS successfully simulates optimal growing conditions for saffron, demonstrating high accuracy and stability in environmental monitoring. All sensors performed reliably under varying environmental conditions, delivering accurate data that supports the system's automatic control functions. The IISMS effectively monitors key environmental parameters, such as temperature, humidity, light intensity, and soil pH,

in real time and automatically adjusts these conditions to promote healthy saffron development. Additionally, it enables users to remotely access environmental data and respond promptly to abnormal conditions. However, some areas for improvement were identified. The DHT11 temperature and humidity sensor exhibited a delayed response during rapid environmental changes, which affected the real-time accuracy of the readings. Despite this limitation, the IISMS performed well across environmental monitoring, automatic adjustment, and remote control functionalities, validating its feasibility and potential for agricultural applications. Future improvements could include integrating solar energy to offset the high power consumption of the cooling system. Moreover, deploying the IISMS in greenhouse environments would allow assessment of its performance in managing larger-scale cultivation. The system's adaptability also suggests potential for application in other crop management scenarios, enhancing its flexibility and scalability for broader agricultural use.

ACKNOWLEDGEMENT

This research was supported by Taylor's University, Malaysia through Taylor's Internal Research Grant Scheme - Impact Lab Grant (TIRGS-ILG/1/2024/SOE/001).

REFERENCES

[1] Aditya, B. R., Hernawati, E., Gunawan, T., & Aji, P. (2024). Design an Agricultural Soil and Environment Monitoring System Based on IoT. *Pertanika Journal of Science and Technology*, *32*(6), 2575–2589. https://doi.org/10.47836/pjst.32.6.09

[2] Bersani, C., Ruggiero, C., Sacile, R., Soussi, A., & Zero, E. (2022). Internet of Things Approaches for Monitoring and Control of Smart Greenhouses in Industry 4.0. *Energies*, *15*(10), 3834. https://doi.org/10.3390/en15103834

[3] Cardone, L., Castronuovo, D., Perniola, M., Cicco, N., & Candido, V. (2020). Saffron (Crocus sativus L.), the king of spices: An overview. *Scientia Horticulturae*, *272*, 109560. https://doi.org/10.1016/j.scienta.2020.109560

[4] Dalir, M., Choobchian, S., & Abbasi, E. (2025). Identifying the relative importance of cultivating medicinal plants in improving rural livelihoods. *Environmental Development*, *54*, 101159. https://doi.org/10.1016/j.envdev.2025.101159

[5] Dhanaraju, M., Chenniappan, P., Ramalingam, K., Pazhanivelan, S., & Kaliaperumal, R. (2022). Smart Farming: Internet of Things (IoT)-Based Sustainable Agriculture. *Agriculture*, *12*(10), 1745. https://doi.org/10.3390/agriculture12101745

[6] Ge, Y., Lin, S., Zhang, Y., Li, Z., Cheng, H., Dong, J., Shao, S., Zhang, J., Qi, X., & Wu, Z. (2022). Tracking and Counting of Tomato at Different Growth Period Using an Improving YOLO-Deepsort Network for Inspection Robot. *Machines*, *10*(6), 489. https://doi.org/10.3390/machines10060489

[7] Haziq, M., Pang, W. L., Chan, K. Y., Lee, I. E., Chung, G. C., & Wong, S. K. (2022). High-efficiency Low-cost Smart IoT Agriculture Irrigation, Soil's Fertility and Moisture Controlling System. *Universal Journal of Agricultural Research*, *10*(6), 785–793. https://doi.org/10.13189/ujar.2022.100616

[8] Iqbal, A., Taqvi, S. A. A., Asim, J., Muneeb, Q., Mahajan, G., Sambyal, R., & Anand, S. (2024). Design of an IOT-based saffron crop irrigation system. *Industrial Crops and Products*, *212*, 118350. https://doi.org/10.1016/j.indcrop.2024.118350

[9] Kang, Y., Wu, Q., Qin, J., Zhong, M., Yang, X., & Chai, X. (2022). High relative humidity improves leaf burn resistance in flowering Chinese cabbage seedlings cultured in a closed plant factory. *PeerJ*, *10*, e14325. https://doi.org/10.7717/peerj.14325

[10] Kocian, A., Massa, D., Cannazzaro, S., Incrocci, L., Di Lonardo, S., Milazzo, P., & Chessa, S. (2020). Dynamic Bayesian network for crop growth prediction in greenhouses. *Computers and Electronics in Agriculture*, *169*, 105167. https://doi.org/10.1016/j.compag.2019.105167

[11] Kumar, A., Devi, M., Kumar, R., & Kumar, S. (2022). Introduction of high-value Crocus sativus (saffron) cultivation in non-traditional regions of India through ecological modelling. *Scientific Reports*, *12*(1), 11925. https://doi.org/10.1038/s41598-022-15907-y

[12] Leao, H.R., Lee C.L.., Thien G.S.H., Lee I.E., Chung G.C., Pang. W.L., Ng Z.N., Tan K.B., & Chan K.Y. (2024). Artificial Intelligence-Powered IoT-Based Irrigation System for Precision Farming. *International Journal of Intelligent Systems and Applications in Engineering*, *12*(19s), 329–335.

[13] Lokman, M. L., Chan, K. Y., Ting, Y. T., Lee, C. L., Chung, G. C., & Pang, W. L. (2024). LoRa Based IoT Enabled Sensor Networks for Plantations. *Journal of Engineering Technology and Applied Physics*, *6*(1), 16–24. https://doi.org/10.33093/jetap.2024.6.1.3

[14] Malik, S., Akhtar, N., Shadab, M., Amir, M., & Siddiqui, M. B. (2024). Medicinal and Nutritional Importance of Crocus sativus L. in Human Health. In *Medicinal Plants and their Bioactive Compounds in Human Health: Volume 1* (pp. 315–335). Springer Nature Singapore. https://doi.org/10.1007/978-981-97-6895-0_16

[15] Mehmeti, A., Candido, V., Canaj, K., Castronuovo, D., Perniola, M., D'Antonio, P., & Cardone, L. (2024). Energy, Environmental, and Economic Sustainability of Saffron Cultivation: Insights from the First European (Italian) Case Study. *Sustainability*, *16*(3), 1179. https://doi.org/10.3390/su16031179

[16] Narayana, T. L., Venkatesh, C., Kiran, A., J, C. B., Kumar, A., Khan, S. B., Almusharraf, A., & Quasim, M. T. (2024). Advances in real time smart monitoring of environmental parameters using IoT and sensors. *Heliyon*, *10*(7), e28195. https://doi.org/10.1016/j.heliyon.2024.e28195

[17] Pangave, V., Khandekar, P., Joshi, M., & Naik, S. (2023). IoT based smart saffron cultivation system. *AIP Conference Proceedings*, 020071. https://doi.org/10.1063/5.0154421

[18] Penchalaiah, N., Nelson Emmanuel, J., Suraj Kamal, S., & Ramana, K. (2021). IoT Based Automatic Irrigation System Using Wireless Sensor Networks. In *Lecture Notes in Electrical Engineering* (pp. 1255–1272). https://doi.org/10.1007/978-981-15-7961-5_116

[19] Pirasteh-Anosheh, H., Babaie-Zarch, M. J., Nasrabadi, M., Parnian, A., Alavi-Siney, S. M., Beyrami, H., Kaveh, H., Hashemi, S. E., Durrer, U., McDonald, K., & Race, M. (2023). Climate and management factors influence saffron yield in different environments. *Agrosystems, Geosciences & Environment*, *6*(3). https://doi.org/10.1002/agg2.20418

[20] Sanjeevi, P., Prasanna, S., Siva Kumar, B., Gunasekaran, G., Alagiri, I., & Vijay Anand, R. (2020). Precision agriculture and farming using Internet of Things based on wireless sensor network. *Transactions on Emerging Telecommunications Technologies*, *31*(12). https://doi.org/10.1002/ett.3978

[21] Zhou, T., Qiu, X., Zhao, L., Yang, W., Wen, F., Wu, Q., Yan, J., Xu, B., Chen, J., Ma, Y., & Pei, J. (2022). Optimal light intensity and quality increased the saffron daughter corm yield by inhibiting the degradation of reserves in mother corms during the reproductive stage. *Industrial Crops and Products*, *176*, 114396. https://doi.org/10.1016/j.indcrop.2021.114396

ANALYSIS AND CALIBRATION OF DISCRETE ELEMENT PARAMETERS FOR *YANHUSUO* BASED ON STACKING TESTS

I

基于堆积试验的延胡索离散元参数分析与标定

Chun WANG[1,2], Xiangyang LIU[1], Yongchao SHAO[1], Weiguo ZHANG[*1]

[1]College of Mechanical and Electrical Engineering, Northwest Agriculture and Forestry University, Yangling 712100, China;
[2]College of Biological and Agricultural Engineering, Jilin University, Changchun 130000, China

Tel: +86-18291918130; E-mail: Wangchun11@nwafu.edu.cn

DOI: https://doi.org/10.35633/inmateh-76-28

Keywords: *Yanhusuo, discrete element, simulation parameter, calibration, stacking angle.*

ABSTRACT

To address the lack of contact parameters for yanhusuo during the mechanization process, its basic physical and contact parameters were derived through both theoretical calculations and practical measurements. Utilizing 3D scanning technology, a 3D model of yanhusuo was obtained. A discrete element model was then established using an automatic filling method. The key factors influencing the stacking angle of yanhusuo were identified using Plackett-Burman tests. The optimal ranges for these factors were determined through the steepest ascent experiment, and a quadratic regression model for the stacking angle was developed using response surface methodology (RSM) based on a rotational orthogonal experimental design. The optimized parameters - a restitution coefficient of 0.481, static friction coefficient of 0.508, and rolling friction coefficient of 0.029 - yielded a stacking angle of 21.23°. Experimental validation showed a relative error of just 0.86% between the simulation and physical tests. These results demonstrate that the discrete element model and calibrated parameters closely replicate real-world conditions, providing valuable insights for the mechanical design of yanhusuo planting and harvesting equipment.

摘要

针对延胡索机械化过程中延胡索接触参数缺乏的问题，通过理论计算和实际测量，推导了延胡索的基本物理参数和接触参数。利用 3D 扫描技术，获得延胡索的 3D 模型。采用自动填充法建立延胡索离散元模型。通过 Plackett-Burman 试验确定了影响延胡索堆积角的重要因素。通过最陡上升试验确定了这些重要因素的最佳范围，并通过旋转正交实验设计的响应面法（RSM）建立了与这些因素相关的堆积角的二次回归模型。优化后的参数—恢复系数为 0.481、静摩擦系数为 0.508、滚动摩擦系数为 0.029——产生的堆叠角为 21.23°。实验验证显示模拟与实际测试之间的相对误差为 0.86%。这些结果表明，离散元模型和校准参数密切复制了现实条件，为延胡索种植和收获的机械设计提供了宝贵的见解。

INTRODUCTION

Corydalis yanhusuo, a plant belonging to the Papaveraceae family and the Corydalis genus, is a traditional Chinese medicinal herb *(Chen et al., 2013; Ping et al., 2019*) that grows in loose, moist soils such as sandy or semi-sandy land. It typically has a flattened spherical shape, with a diameter ranging from 6 to 25 mm. *The yanhusuo* contains over 30 alkaloids, including tetrahydropalmatine and protopine, and exhibits significant pharmacological effects such as pain relief, sedation, and antiarrhythmic properties. As a result, *yanhusuo* hold considerable medicinal value *(Gu et al., 2020; Zhang et al., 2018*). In recent years, the increasing demand for *yanhusuo* due to its expanding applications in the pharmaceutical industry has led to a rise in its cultivation benefits. However, the seeding and harvesting of *yanhusuo* largely depend on manual labor, which presents challenges such as low efficiency and high costs. As an emerging economic crop, *yanhusuo* suffers from underdeveloped mechanization, and the lack of research in this field severely restricts the growth of the *yanhusuo* industry. Therefore, the mechanization of *yanhusuo* cultivation, from sowing to harvesting, is an urgent need. The accurate and objective collection of the mechanical parameters of *yanhusuo* is a prerequisite for developing specialized mechanized equipment.

Discrete Element Method (DEM) model and parameter calibration (*Ahmad et al., 2020; Horabik and Molenda, 2016; Mousaviraad and Tekeste, 2024; Ur Rehman et al., 2022*) are pivotal components in the simulation research of agricultural machinery. *Zhang et al., (2024),* developed a DEM model for red flowers, employing the Hertz-Mindlin (no slip) contact model to conduct packing angle tests and determine the optimal parameter set through orthogonal testing.

Chen et al., (2018), introduced a model approach for individual corn seeds and seed combinations, based on a classification of seed shapes, and validated their method through piling tests and "self-flow screening" tests. *Sun et al., (2022),* utilized the multi-sphere method to create wheat seed models consisting of 13, 17, 25, and 33 spheres. The accuracy and applicability of these models were verified through stacking angle simulations and physical tests. However, the *yanhusuo* exhibits a complex shape, and no DEM studies related to the *yanhusuo* have been reported, resulting in a lack of reference material. Therefore, the DEM model and parameters calibration for *yanhusuo* are critical for advancing simulation studies on this plant.

This study presents the determination of the fundamental physical and contact parameters for *yanhusuo* through theoretical analysis and empirical measurement tests. A multi-sphere bonded DEM model (*Guo et al., 2020; Ucgul et al., 2014, 2018; Wang et al., 2022; Xu B. et al., 2021; Xu T. et al., 2018*) for *yanhusuo* was established using the auto-filling method. The Plackett-Burman design and steepest ascent tests were employed to identify the significant factors affecting the packing angle of *yanhusuo* and their respective ranges. The optimal parameter combination was determined through an orthogonal rotation combination test. The reliability of the DEM model and contact parameters *(Katinas et al., 2019; Li et al., 2024; Poppa et al., 2024; Zhuang et al., 2023*) for the *yanhusuo* was further validated through test verification. The results provide fundamental parameters for simulating the mechanized seeding and harvesting of *yanhusuo*, offering a reference for the calibration of similar crops.

MATERIALS AND METHODS

Determination of basic physical parameters

The y*anhusuo* variety examined in this study is ZheHu No.1. The five-point sampling method was employed to collect a sample of *yanhusuo*, and its fundamental physical parameters were measured. A total of 50 *yanhusuo* were randomly selected and divided into five groups. Using an electronic balance with a precision of 0.01 g, the total mass of each group was measured and recorded. A graduated cylinder with a precision of 0.1 mL was filled with 98% ethanol to ensure complete submersion of the y*anhusuo* samples. The volume of each group was calculated by determining the difference between the initial and final readings of the graduated cylinder. Subsequently, the density of the *yanhusuo* was determined using the density formula, yielding a value of 1.085 g/cm³.

The moisture content of the *yanhusuo* is one of its fundamental parameters. In this study, an OHAUS MB23 rapid moisture analyzer was used to measure the moisture content of *yanhusuo*. The samples were divided into five groups for individual measurements, resulting in an average moisture content of 61.27%.

Poisson's ratio is the ratio of lateral strain to axial strain when a material is subjected to uniaxial compression (*Zhao et al., 2024*). It is a crucial mechanical characteristic parameter of *yanhusuo*. In this test, the compression deformation of *yanhusuo* was tested by Texture Analyzer. The Poisson's ratio of *yanhusuo* was calculated by measuring the deformation in the lateral (horizontal) and vertical (height) directions before and after loading, as shown in Figure 1.



Fig. 1- Compression test of *yanhusuo*

Before the test, the length and height of the *yanhusuo* were measured. At the start of tests, the *yanhusuo* was placed on the platform of Texture Analyzer. The compression head was manually adjusted to ensure its plane made contact with the upper surface of the *yanhusuo*. The experimental parameters were set with a loading rate of 0.5 mm/s and a loading duration of 3 seconds. After the test, the length and thickness of the

yanhusuo were measured again. The tests were repeated five times, and the average value was taken. The Poisson's ratio of the *yanhusuo* was calculated to be 0.49 using Eq.(1).

$$\lambda = \frac{\Delta L / L}{\Delta H / H} \quad (1)$$

where:

λ – Poisson's ratio;

ΔL – the absolute deformation in the direction of the length of the *yanhusuo*, mm;

L – the original length of the *yanhusuo*, mm;

ΔT – the absolute deformation in the direction of the height of the *yanhusuo*, mm;

T – the original length in the direction of the height of the *yanhusuo*, mm.

Young's modulus (*Khatchatourian et al., 2014; Shi et al., 2024*) is one of the mechanical characteristic parameters of the *yanhusuo*. In this study, Young's modulus of the *yanhusuo* was determined through compression testing by Texture Analyzer. The resulting compression force-displacement curve was obtained using the post-processing module of the computer software, as depicted in Figure 2.

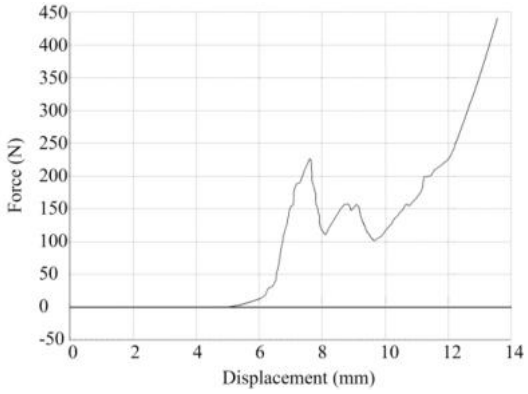


Fig. 2 - Load-displacement curve

The tests were repeated 5 times, the average value was calculated, and the Young's modulus of *yanhusuo* was calculated from Eq. (2) as *E* = 5.93 MPa

$$E = \left(\frac{\sigma}{A}\right) / v \quad (2)$$

where: E is the Young's modulus of the *yanhusuo*, [Pa]; σ is the maximum compressive stress, [kN]; A is the contact area of the compression head with the *yanhusuo* is 1.58 mm^2; v is the line strain.

Determination of contact parameters

Determination of the restitution coefficient

The restitution coefficient between the *yanhusuo* and steel plate was determined using a free-fall test (*Xu Bing et al., 2022)*. Before testing, the grid paper was positioned vertically on a horizontal surface, as illustrated in Figure 3. The *yanhusuo* sample was clamped at a height of H = 200 mm and released to fall freely. Upon impact with the steel plate, the rebound motion was captured using a high-speed camera system. The rebound height (h) was measured with the aid of graph paper and a ruler. This procedure was repeated ten times, and the average value was calculated.

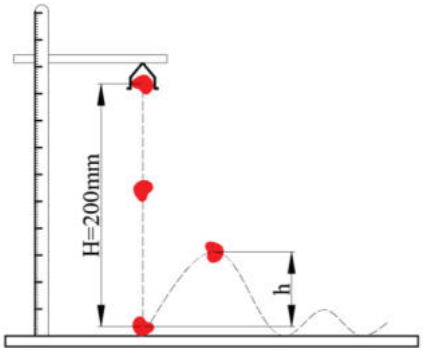


Fig. 3 - Schematic diagram of the test used to measure the restitution coefficient

The restitution coefficient can be calculated using the following formula:

$$e = \frac{v_4 - v_3}{v_2 - v_1} \quad (3)$$

$$v_4 = \sqrt{2gh} \quad (4)$$

$$v_2 = \sqrt{2gH} \quad (5)$$

where: e is the restitution coefficient between the *yanhusuo* and the colliding material; v_1 is the velocity of the colliding material before the collision, [mm·s^{-1}]; v_2 is the velocity of the y*anhusuo* before the collision, [mm·s^{-1}]; v_3 is the velocity of the colliding material after the collision, [mm·s^{-1}], v_4 is the velocity of the *yanhusuo* after the collision, [mm·s^{-1}]; H is the height from which the object is dropped before free fall, [mm]; h is the rebound height, [mm]; g is the gravity acceleration, [m·s^{-2}].

The measured restitution coefficient between *the yanhusuo* and the steel plate was 0.531.

Determination of the static friction coefficient

In this study, the inclined plane method was employed to measure the static friction coefficient between the *yanhusuo* and steel plate, as shown in Figure 4. By the hand-cranked mechanism, the angle of the inclined plane was gradually increased at a constant rate. The angle at which the tuber began to slide downward was recorded.

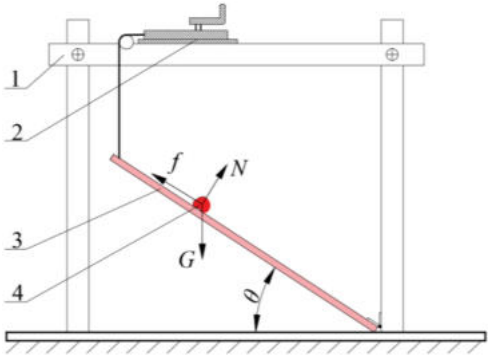


Fig. 4 - Static friction coefficient measurement test schematic

1. Rack; 2. Adjusting screws; 3. Inclined plane; 4. Yanhusuo.

Ten sets of tests were conducted for *yanhusuo* with steel plates, and the average values were calculated.

The formula for calculating the static friction coefficient is as follows:

$$f = G\sin\theta \quad (6)$$

$$F_N = G\cos\theta \quad (7)$$

$$\mu = \frac{F_N}{f} \quad (8)$$

where: f is the frictional force acting on *the yanhusuo*, [N]; G is the gravitational force on the *yanhusuo*, [N]; F_N is the support force acting on the *yanhusuo*, [N]; μ is the static friction coefficient; θ is the angle between the inclined plane and the horizontal surface, [°].

The average inclination angles for the *yanhusuo* tests with steel plate were substituted into Eq. (8) to calculate the static friction coefficients. The resulting static friction coefficient between *the yanhusuo* and the steel plate was 0.493.

Determination of rolling friction coefficient

The rolling friction refers to the resistance encountered when one object rolls on the surface of another without slipping, or when there is a tendency for rolling. It occurs as the contact surfaces of the two objects are compressed, resulting in deformation, which in turn generates a hindrance to the rolling motion. This study employs the bevel rolling method to measure the rolling friction coefficients between *the yanhusuo* and steel plate. As shown in Figure 5, where the angle between the inclined and horizontal planes is 30°. *The yanhusuo* was placed at a distance of L = 35 mm and allowed to roll freely with an initial velocity of 0 m/s until it came to a stop. The horizontal rolling distance(S) was subsequently measured. A total of 10 trials were conducted for each material.

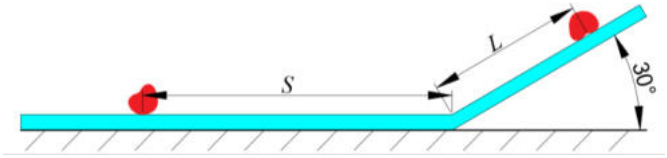


Fig. 5 - Schematic diagram of the method used to measure the rolling friction

The formula for calculating the rolling friction coefficient is as follows:

$$\mu' = \frac{GL\sin\beta}{G(L\cos\beta + S)} \tag{9}$$

where: G is the gravitational force on the *yanhusuo*, [N]; β is the angle of inclination of the inclined plane, [°]; S is the distance by the *yanhusuo* while rolling on a flat surface, [mm]; L is the distance by *the yanhusuo* while rolling on an inclined plane, [mm]; μ' is the rolling friction coefficient of *the yanhusuo* and the steel plate.

The rolling distance between *the yanhusuo* and the steel plate is 122.1 mm. Substituting these values into Eq. (9), the rolling friction coefficient between *the yanhusuo* and the steel plate is calculated to be 0.115.

The test for determining the stacking angle of *Yanhusuo*

In this study, data was initially obtained using the funnel method, followed by verification through the draw plate method. In the funnel method stacking test, the funnel, the base plate, and the baffle plate are all made of steel. The funnel has a height of 260 mm, a bottom diameter of 80 mm, and a top diameter of 240 mm. The funnel is positioned 150 mm above the base plate, with its discharge opening covered by the baffle plate. A total of 1000 *yanhusuo* are placed inside the funnel. The baffle plate is quickly removed, allowing *yanhusuo* to fall freely onto the base plate and accumulate. The test is shown in Figure 6.



Fig. 6 - Funnel method stacking test

1. Funnel; 2. Baffle plate; 3. Base plate; 4. Yanhusuo.

After photographing stacked *yanhusuo*, MATLAB image processing techniques are applied. Through binarization, edge detection is performed to extract the edge contour curve. A linear fit is then conducted to obtain the equation of the line, from which the stacking angle is calculated, as shown in Figure 7.



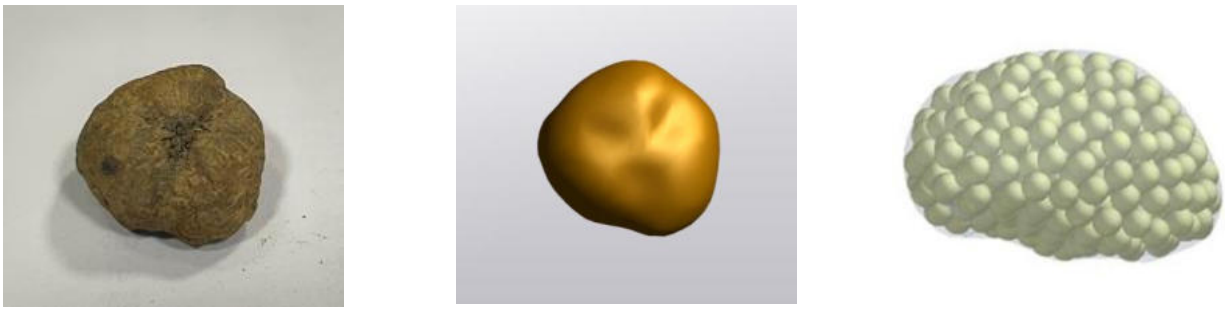
(a) Original image (b) Edge extraction and fitted image

Fig. 7 – *Yanhusuo* stacking angle

A total of 10 tests were conducted, with the slope values taken from both the left and right sides for each group. The final average value obtained was 21.05°.

Discrete element method modeling and simulation

The complex shape of *the yanhusuo* was addressed in this study by using 3D scanning imaging technology to capture their external contour models. The 3D contour models of *the yanhusuo* were exported in STL format. These files were imported into EDEM software, where a multi-sphere bonded particle model was applied, and the particle auto-fill method was used to construct the discrete element model of the *yanhusuo*, as illustrated in Figure 8.



(a) *Yanhusuo* (b) Physical model © Discrete Element Model

Fig. 8 – *Yanhusuo* and discrete element model

The contact model between *the yanhusuo*, as well as between *the yanhusuo* and equipment components, was based on the Hertz-Mindlin contact theory. The material in contact with the *yanhusuo* is stainless steel, with the relevant parameters presented in Table 1.

Table 1

Simulation test parameters

Parameters	Numerical value
The Poisson's ratio of the y*anhusuo*	0.49
The density of the y*anhusuo,* [kg·m^{-3}]	1085
The Young's modulus of the *yanhusuo*, [Pa]	5.93×10^{6}
The Poisson's ratio of the steel	0.289
The density of the steel, [kg·m^{-3}]	7850
The Young's modulus of the steel, [Pa]	2.1×10^{11}

Parameter optimization for discrete element simulation

Plackett – Burman test

Plackett-Burman design was employed to screen for parameters that have a significant effect on the stacking angle. In the DEM simulation of y*anhusuo*, 8 parameters were selected as variable factors. The Plackett-Burman tested design was conducted using Design-Expert 13.0 software. A Plackett-Burman table with *N* = 12 was employed, with the stacking angle of *yanhusuo* as the response value. Each variable was set at two levels: high (+1) and low (-1). Table 2. provides an overview of the factors and levels used in the simulation.

Table 2

Plackett-Burman test measurement range table

Symbols	Test parameters	Low level (-1)	Hight level (+1)
A	Poisson's ratio of *the yanhusuo*	0.29	0.69
B	Young's modulus of the yanhusuo, [Mpa]	3.0×10^{6}	3.0×10^{7}
C	The collision recovery factor of *yanhusuo*	0.25	0.65
D	The coefficient of static friction of *yanhusuo*	0.35	0.75
E	The rolling friction coefficient of *yanhusuo*	0.005	0.045
F	*Yanhusuo*–steel plate collision recovery factor	0.3	0.8
G	*Yanhusuo*–steel plate coefficient of static friction	0.1	0.7
H	*Yanhusuo*–steel plate rolling friction coefficient	0.01	0.07

The steepest climb test

Based on the results of the Plackett-Burman test, significant factors were identified. Subsequently, the steepest ascent method was employed to quickly approach the optimal range of these significant factors.

Central composite design with quadratic orthogonal rotations

Based on the optimal factor level ranges identified through the steepest climb test, significant factors were selected for a central composite design with quadratic orthogonal rotations. Using the test results, a response surface model was fitted to derive the regression equation, which was then used to predict the optimal combination of simulation parameters for the *yanhusuo* that closely matches the actual stacking angle.

RESULTS AND DISCUSSION

Results of Plackett – Burman test

The results and analysis of variance for the Plackett-Burman test are presented in Tables 3 and 4. The results indicate that the restitution coefficient of *yanhusuo*, the static friction coefficient of *yanhusuo*, and the rolling friction coefficient of *yanhusuo* significantly influence the stacking angle, while other factors exhibit no significant effect. Therefore, the three significant factors identified above were selected for the steepest ascent tests.

Table 3

Design and results of the Plackett-Burman test

No.	*A*	*B*	*C*	*D*	*E*	*F*	*H*	*G*	Stacking angle
1	1	1	-1	1	1	1	-1	-1	22.72
2	-1	1	1	-1	1	1	1	-1	28.26
3	1	-1	1	1	-1	1	1	1	22.45
4	-1	1	-1	1	1	-1	1	1	20.35
5	-1	-1	1	-1	1	1	-1	1	27.14
6	-1	-1	-1	1	-1	1	1	-1	16.61
7	1	-1	-1	-1	1	-1	1	1	27.53
8	1	1	-1	-1	-1	1	-1	1	15.79
9	1	1	1	-1	-1	-1	1	-1	25.36
10	-1	1	1	1	-1	-1	-1	1	17.52
11	1	-1	1	1	1	-1	-1	-1	26.77
12	-1	-1	-1	-1	-1	-1	-1	-1	20.87

Table 4

Significance analysis of Plackett-Burman test parameters

Parameters	Degree of freedom	Sum of squares	F value	P value
A	1	8.12	2.91	0.1867
B	1	10.77	3.86	0.1443
C	1	46.53	16.66	0.0266*
D	1	28.61	10.25	0.0493*
E	1	97.30	34.84	0.0097**
F	1	2.46	0.8799	0.4174
G	1	7.92	2.84	0.1907
H	1	8.02	2.87	0.1887

*Note: *indicates that the impact was significant (P<0.05), and **indicates that the impact was extremely significant (P<0.01).*

Results of the steepest climb test

The design and results of the steepest climb test are shown in Table 5. The combination from group 3 yielded the smallest relative error in the stacking angle, with a value of only 1.08%. Therefore, Group 3 is selected as the zero level, and the optimal range of factor levels lies between group 2 and group 4.

Table 5

Scheme and results of the steepest climbing test

No.	Test factors			Result
	C	*D*	*E*	Relative Error (*Y*)
1	0.25	0.35	0.005	11.2206
2	0.35	0.45	0.015	6.8525
3	0.45	0.55	0.025	1.0847
4	0.55	0.65	0.035	4.1025
5	0.65	0.75	0.045	5.3476

The results of the second-order orthogonal rotating combination test

The results and analysis of variance for the three-factor, five-level orthogonal rotating combination test are presented in Tables 6 and 7.

Table 6

Test plan and results

No.	Test factors			Relative Error (Y)
	C	*D*	*E*	
1	-1	-1	-1	5.7982
2	1	-1	-1	8.6674
3	-1	1	-1	6.3763
4	1	1	-1	15.6287
5	-1	-1	1	8.4399
6	1	-1	1	1.5175
7	-1	1	1	4.5945
8	1	1	1	3.7030
9	-1.682	0	0	5.5840
10	1.682	0	0	7.9052
11	0	-1.682	0	2.7370
12	0	1.682	0	5.9228
13	0	0	-1.682	13.3637
14	0	0	1.682	6.2699
15	0	0	0	1.0018
16	0	0	0	2.1952
17	0	0	0	2.5026
18	0	0	0	1.3268
19	0	0	0	0.1075
20	0	0	0	0.9398

Using Design-Expert 13.0, the data in Table 6. was subjected to fitting analysis. The resulting regression equation for the relative error of the stacking angle, considering the collision restitution coefficient between *yanhusuo* (C), the static friction coefficient between *yanhusuo* (D), and the rolling friction coefficient between *yanhusuo* (E), is as follows:

$$Y = 1.36 + 0.6013C + 0.8228D - 3.31E + 1.55CD - 2.94CE - 1.15DE + 1.81C^2 + 0.9572D^2 + 2.90E^2 \quad (10)$$

The analysis of variance (ANOVA) for the regression equation is shown in Table 7. The coefficient of determination R^2 of the regression equation is 0.9713, indicating a high reliability of the model. The factors influencing the relative error of the stacking angle, in descending order of impact, are the rolling friction coefficient E, the static friction coefficient D, and the collision restitution coefficient C.

Table 7

ANOVA for quadratic equation models

Parameters	Sum of Squares	Degree of freedom	Mean square	F value	P value
Modal	319.13	9	35.46	72.39	<0.0001**
C	4.94	1	4.96	10.08	0.0099**
D	9.25	1	9.25	18.88	0.0015**
E	66.54	1	66.54	135.85	<0.0001**
CD	19.26	1	19.26	39.33	<0.0001**
CE	49.68	1	49.68	101.42	<0.0001**
DE	10.58	1	10.58	21.60	0.0009**
C^2	47.26	1	47.26	96.49	<0.0001**
D^2	13.20	1	13.20	26.96	0.0004**
E^2	120.96	1	120.96	246.95	<0.0001**
Residual	4.90	10	0.4898		
Lack of Fit	1.02	5	0.2043	0.2636	0.9152
Pure Error	3.88	5	0.7753		
Cor Total	324.03	19			

*Note: * indicates that the impact was significant (P<0.05), and **indicates that the impact was extremely significant (P<0.01).*

Parameter optimization

Based on the test results and the derived regression equation, the optimization function in Design-Expert 13.0 was used to minimize the relative error. The software was employed to search for the optimal combination of significant factors that yields the smallest relative error.

The objective function and constraints are as follows:

$$\begin{cases} \min Y(C,D,E) \\ \begin{cases} 0.282 \le C \le 0.618 \\ 0.382 \le D \le 0.718 \\ 0.008 \le E \le 0.042 \end{cases} \end{cases} \quad (11)$$

The optimized collision restitution coefficient between *yanhusuo* is 0.481, the static friction coefficient is 0.508, and the rolling friction coefficient is 0.029, with a relative error of the stacking angle of 0.804%. These parameters were input into the EDEM software, where 10 accumulation simulation trials were conducted. The average stacking angle obtained was 21.23°, with a relative error of only 0.86%. This indicates that the optimized parameter combination is highly reliable and can be used for subsequent DEM simulation tests.

Experimental validation

To further validate the authenticity of the *yanhusuo* discrete element simulation parameters, the board removal method was used for verification. A cuboid made of stainless steel was selected for the test. The dimensions of the cuboid are 150 mm in length, 150 mm in width, and 300 mm in height. A total of 1000 *yanhusuo* were placed inside. The baffle plate was quickly removed, allowing the *yanhusuo* to freely accumulate. The stacking angle was obtained using MATLAB image processing. Simultaneously, the corresponding DEM simulation was conducted. The test setup is shown in Figure 9.

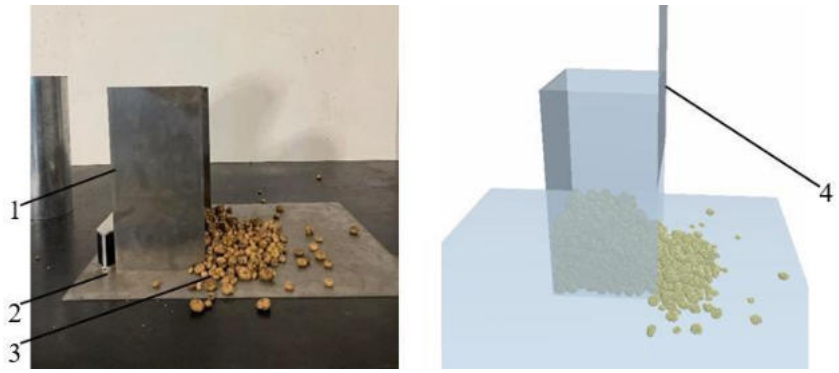


Fig. 9 - Measurement of *Yanhusuo* stacking angle by extraction plate method

1. Empty box of cuboids; 2. Base plate; 3. Yanhusuo; 4. Baffle plate.

Both types of tests were conducted for 10 trials each, and the average values were taken. The results are shown in Table 8.

Table 8

Actual and simulation test results of stacking angle by *Yanhusuo* draw plate method

No.	Actual test slope	Actual stacking angle / °	Simulation test slope	Simulation stacking angle / °
1	0.382	20.92	0.428	23.17
2	0.397	21.65	0.321	17.80
3	0.474	25.36	0.472	25.27
4	0.418	22.70	0.410	22.29
5	0.373	20.46	0.392	21.41
6	0.369	20.26	0.369	20.26
7	0.403	21.95	0.415	22.54
8	0.422	22.90	0.431	23.32
9	0.425	23.00	0.398	21.70
10	0.511	27.06	0.422	22.88
Average	**0.410**	**22.25**	**0.399**	**22.06**

The relative error between the actual measured stacking angle and the simulated value is 0.96%, indicating that the calibrated and optimized *yanhusuo* discrete element parameters can be reliably used for subsequent DEM simulations.

CONCLUSIONS

1. This study focuses on "Zhehu No. 1" as the research subject and conducts physical testing to determine the basic physical parameters of *yanhusuo*, including its density, moisture content, Young's modulus, and Poisson's ratio. Furthermore, the contact parameters between *yanhusuo* and steel plate were determined, including the restitution coefficient, static friction coefficient, and rolling friction coefficient.

2. The physical parameters of *yanhusuo* were selected as the simulation test parameters. Significant factors affecting the stacking angle were identified through the Plackett-Burman test, and the optimal range for these significant factors was further determined through the steepest ascent tests. Subsequently, a second-order orthogonal rotating combination test was conducted, with the minimization of the relative error in the stacking angle as the optimization objective, resulting in the optimal combination of simulation parameters.

3. The optimal parameter combination for *yanhusuo* was determined through calibration: a restitution coefficient of 0.481, a static friction coefficient of 0.508, and a rolling friction coefficient of 0.029. Verification tests showed that the relative error between the simulation and test tests was only 0.86%.

REFERENCES

[1] Ahmad, F., Qiu, B., Ding, Q., Ding, W., Khan, Z. M., Shoaib, M., Chandio, F.A., Rehim, A., Khaliq, A. (2020). Discrete element method simulation of disc type furrow openers in paddy soil. *International Journal of Agricultural and Biological Engineering*, *13*(4), 103–110.

[2] Chen, Y., Cao, Y., Xie, Y., Zhang, X., Yang, Q., Li, X., … Wang, S. (2013). Traditional Chinese medicine for the treatment of primary dysmenorrhea: how do *yuanhu* painkillers effectively treat dysmenorrhea? *Phytomedicine*, *20*(12), 1095–1104. https://doi.org/10.1016/j.phymed.2013.05.003

[3] Gu, Y., Huang, J., Guo, H., Song, X., Li, J., Shi, Y., Xie, X. (2020). A randomized controlled study for yuanhu zhitong dropping pills in the treatment of knee osteoarthritis. *Medicine*, *99*(24), e20666. https://doi.org/10.1097/MD.0000000000020666

[4] Guo, Y., Chen, Q., Xia, Y., Westover, T., Eksioglu, S., Roni, M. (2020). Discrete element modeling of switchgrass particles under compression and rotational shear. *Biomass and Bioenergy*, *141*, 105649. https://doi.org/10.1016/j.biombioe.2020.105649

[5] Horabik, J., Molenda, M. (2016). Parameters and contact models for DEM simulations of agricultural granular materials: a review. *Biosystems Engineering*, *147*, 206–225. https://doi.org/10.1016/j.biosystemseng.2016.02.017

[6] Katinas, E., Chotěborskỳ, R., Linda, M., Jankauskas, V. (2019). Wear modelling of soil ripper tine in sand and sandy clay by discrete element method. *Biosystems Engineering*, *188*, 305–319. https://doi.org/10.1016/j.biosystemseng.2019.10.022

[7] Khatchatourian, O. A., Binelo, M. O., de Lima, R. F. (2014). Simulation of soya bean flow in mixed-flow dryers using DEM. *Biosystems Engineering*, *123*, 68–76. https://doi.org/10.1016/j.biosystemseng.2014.05.003

[8] Li, Y., Zhou, W., Ma, C., Feng, Z., Wang, J., Yi, S., Wang, S. (2024). Design and optimization of the seed conveying system for belt-type high-speed corn seed guiding device. *International Journal of Agricultural and Biological Engineering*, *17*(2), 123–131. https://doi.org/10.25165/j.ijabe.20241702.8427

[9] Mousaviraad, M., Tekeste, M. Z. (2024). Systematic calibration and validation approach for discrete element method (DEM) modeling of corn under varying moisture contents (MC). https://doi.org/10.13031/ja.14763

[10] Ping, W., Tinglan, Z., Guohua, Y., Mengjie, L., Jin, S., Jiaqi, Z., … Hongjun, Y. (2019). Poly-pharmacokinetic strategy-delineated metabolic fate of bioactive compounds in a traditional Chinese medicine formula, yuanhu zhitong tablets, using parallel reaction monitoring mode. *Phytomedicine*, *53*, 53–61. https://doi.org/10.1016/j.phymed.2018.09.026

[11] Poppa, L., Frerichs, L., Liu, J., Böl, M. (2024). Development and implementation of a damage model for potato tuber blackspot in discrete element method to analyze harvesting and handling processes. *Journal of the ASABE*, 0. https://doi.org/10.13031/ja.15825

[12] Shi, Z., Wang, M., Zhang, X., Cheng, J., Lu, D. (2024). Calibration and optimization of discrete element parameters for coated cotton seeds. *Engenharia Agrícola*, *44*, e20230085. https://doi.org/10.1590/1809-4430-eng.agric.v44e20230085/2024

[13] Ucgul, M., Fielke, J. M., Saunders, C. (2014). Three-dimensional discrete element modelling of tillage: determination of a suitable contact model and parameters for a cohesionless soil. *Biosystems Engineering*, *121*, 105–117. https://doi.org/10.1016/j.biosystemseng.2014.02.005

[14] Ucgul, M., Saunders, C., Fielke, J. M. (2018). Comparison of the discrete element and finite element methods to model the interaction of soil and tool cutting edge. *Biosystems Engineering*, *169*, 199–208. https://doi.org/10.1016/j.biosystemseng.2018.03.003

[15] Ur Rehman, A., Awuah-Offei, K., Sherizadeh, T., Guner, D. (2022). Use of scaled discrete element model of rubber tire loader buckets for draft prediction. *Biosystems Engineering*, *214*, 1–10. https://doi.org/10.1016/j.biosystemseng.2021.12.003

[16] Wang, S., Yu, Z., Zhang, W. (2022). Study on the modeling method of sunflower seed particles based on the discrete element method. *Computers and Electronics in Agriculture*, *198*, 107012. https://doi.org/10.1016/j.compag.2022.107012

[17] Xu, B., Zhang, Y., Cui, Q., Ye, S., Zhao, F. (2021). Construction of a discrete element model of buckwheat seeds and calibration of parameters. *INMATEH-Agricultural Engineering*, *64*(2). https://doi.org/10.356.33/inmateh-64-17

[18] Xu, T., Yu, J., Yu, Y., Wang, Y. (2018). A modelling and verification approach for soybean seed particles using the discrete element method. *Advanced Powder Technology*, *29*(12), 3274–3290. https://doi.org/10.1016/j.apt.2018.09.006

[19] Xu, B., Zheng, D., Cui, Q. (2022). Experimental research on three-level vibrating screening of buckwheat based on discrete element method. *INMATEH-Agricultural Engineering*, *68*(3), pp.191-200. https://doi.org/10.35633/inmateh-68-19

[20] Zhang, H., Wu, X., Xu, J., Gong, S., Han, Y., Zhang, T., Liu, C. (2018). The comparative pharmacokinetic study of yuanhu zhitong prescription based on five quality-markers. *Phytomedicine*, *44*, 148–154. https://doi.org/10.1016/j.phymed.2018.02.005

[21] Zhao, J., Yu, J., Sun, K., Wang, Y., Liang, L., Sun, Y., … Yu, Y. (2024). A discrete element method model and experimental verification for wheat root systems. *Biosystems Engineering*, *244*, 146–165. https://doi.org/10.1016/j.biosystemseng.2024.06.004

[22] Zhuang, H., Wang, X., Zhang, X., Cheng, X., Wei, Z. (2023). Discrete element-based design of key parameters for wheel rut tillage devices. *Engenharia Agrícola*, *43*(3), e20230039. https://doi.org/10.1590/1809-4430-eng.agric.v43n3e20230039/2023

DESIGN AND EXPERIMENT OF HIGH LEVEL UNLOADING LARGE GRAIN COLLECTION BOX FOR FRESH CORN COMBINED HARVESTER
/
鲜食玉米联合收获机高位卸粮大型集粮箱设计与试验

Xin ZHANG*), Tong YE, Haitao LAN, Jingwen WU, Jianguo CHANG
Heilongjiang Academy of Agricultural Machinery Engineering Sciences, Harbin 150081, China
Tel: +86-18249059533; E-mail: xinzhang135689@163.com
DOI: https://doi.org/10.35633/inmateh-76-29

Keywords: *fresh corn harvester, grain collection box, high-level unloading of grain, electro hydraulic control, low loss*

ABSTRACT
In response to the problems of low unloading height, small collection box capacity, and high ear damage rate during grain collection in the fresh corn combine harvester, a large collection box with buffering and shock absorption mechanism and high unloading height was designed based on the 4YX-6 fresh corn combine harvester, which is a fully hydraulic driven fresh corn combine harvester. The device mainly consists of a box body, a buffering and shock-absorbing mechanism, a grain unloading extension mechanism, an electro-hydraulic system, etc. According to the agronomic requirements for fresh corn cultivation, the volume of the grain collection box is designed to be 10 m³. According to the height range of the grain receiving truck during the harvest of fresh corn, the unloading stroke height of the grain collection box is designed to be 2.9 m~4.4 m. To achieve synchronization of lifting and flipping actions during high-level unloading, a synchronous series hydraulic system is designed. Conduct force analysis on the drop of fruit ears to the bottom of the grain collection box and design a buffering and shock-absorbing mechanism. The designed grain collection box was installed on the 4YX-6 fresh corn combine harvester for field experiments, with ear damage rate and unloading time as performance indicators. The results showed that the ear damage rate ranged from 0.5% to 0.8%, the unloading time was from74 s to 126 s, and there were no safety issues such as deformation or tilting of the device during operation. The ear damage rate met the standards, and the working performance was stable, meeting the operational requirements.

摘要
针对鲜食玉米联合收获机卸粮高度低、集粮箱容积小、集粮时果穗损伤率高的问题，基于4YX-6型鲜食玉米联合收获机设计了具备缓冲减震机构、可高位卸粮的全液压驱动鲜食玉米联合收获机大型集粮箱。该装置主要由箱体、缓冲减震机构、卸粮延长机构、电液系统等组成。根据鲜食玉米种植的农艺技术要求，将集粮箱容积设计为10 m³。根据鲜食玉米收获期间接粮车的厢体高度范围，将集粮箱卸粮行程高度设计为2.9 m ~ 4.4 m，为实现高位卸粮时升举、翻转动作的同步性，设计了同步串联式液压系统。对果穗掉落到集粮箱底部时进行受力分析，设计缓冲减震机构。将设计的集粮箱安装在4YX-6型鲜食玉米联合收获机上进行田间试验，以果穗破损率和卸粮时间为性能指标，结果表明：果穗损伤率范围在0.5% ~ 0.8%，卸粮时间在74 s~126 s，作业过程中装置未出现形变、倾斜等安全性问题，果穗损伤率符合标准，工作性能稳定，满足作业要求。

INTRODUCTION
Fresh corn, including sweet corn and glutinous corn, refers to a type of corn that can be processed and consumed after harvesting or directly harvested for consumption (*Zhou et al., 2020; Zhao et al., 2011; Li et al., 2019*). Due to its delicious taste, sweet and glutinous texture, and high nutritional value that are beneficial to the human body, it has attracted increasing attention, and therefore its planting area has been increasing year by year (*Chen et al., 2023; Zhu et al., 2012; Zhang et al., 2023*). At present, the annual planting area of fresh corn in China has reached 1.67 million hectares, and the annual market consumption has reached 75 billion ears. China has become the world's largest producer and consumer of fresh corn. Against the backdrop of the current promotion of green and high-quality development strategies, the Ministry of Agriculture and Rural Affairs has also issued a notice stating that the area of fresh corn should remain stable at over 20 million acres (*Islam et al., 2021; Geng et al., 2023*).

For fresh corn, its harvest period is relatively short. After reaching the picking conditions, it should be picked and sent to the production line for processing as soon as possible. If the optimal picking time is exceeded, it will cause the aging of fresh corn, which not only affects the quality and taste of fresh corn, but also leads to nutrient loss, affects the processing flow, and ultimately affects sales, causing property losses and a series of other problems.

At present, technical personnel have conducted extensive research on the issue of grain collection boxes in combine harvesters. Scholar analyzed and summarized various structures of ear boxes, such as side flip and back flip, and analyzed the structural characteristics and operational advantages and disadvantages of different styles of ear boxes (*Zhou, 2013*). Scholars from Heilongjiang academy of agricultural machinery engineering sciences analyzed a loss reduction and diversion device was designed for the problem of ear damage caused by impact of fresh corn entering the grain collection box, effectively reducing the ear damage rate (*Zhang et al., 2025*). Scholars from Modern Agricultural Equipment Co. Ltd. analyzed optimization of the support structure for the ear box of the corn harvester for seed production has been carried out, improving the stress strength of the ear box (*Liu et al., 2017*). Foreign scholars often use DEM methods to design grain tanks and study the motion and mechanical characteristics of grains in the silo, providing assistance for the design of harvesting machinery grain tanks (*González-Montellano et al., 2012; Ma et al., 2022; Balevičius et al., 2011*). In response to issues such as large capacity grain tanks and high position unloading, major foreign companies have designed corresponding products to reduce the number of unloading times and improve operational efficiency (*Fu, 2020; Yan, 2016*). Existing research has mainly focused on the design of grain collection boxes for ordinary grain corn. Although the volume and unloading height have been improved, the effect of the improvement is not significant for fresh corn combine harvesters, and the damage caused by the collision between fresh corn ears and the box body has not been considered.

In response to the above challenges, this article presents the design of a large grain collection box for a fully hydraulic-driven fresh corn combine harvester, based on the 4YX-6 model. The collection box features a buffering and shock-absorbing mechanism and is capable of high-position unloading. The design includes the external structure, functional components, and dimensional specifications of the grain collection box, tailored to meet the unloading method and operational requirements. Field performance tests were conducted to evaluate the effectiveness and reliability of the proposed design.

MATERIALS AND METHODS

Whole machine structure and working principle

This article focuses on the design of a large grain collection box for the 4YX-6 fresh corn combine harvester, with a side flip unloading method. The main external structure of the host of the 4YX-6 fresh corn combine harvester is shown in Fig. 1.

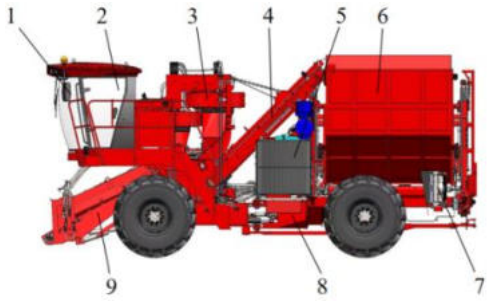


Fig. 1 – 4YX-6 Fresh corn harvester

1. Electrical system; 2. Driving cab; 3. Fan; 4. Elevator; 5. Powertrain; 6. Grain collection box; 7. Hydraulic system; 8. Chassis; 9. Bridge elevator

The main technical parameters are shown in Table 1.

Table 1

Main Technical Parameters

Technical parameter	Numerical value
Overall dimensions (length x width x height) / (mm×mm×mm)	11280×3390×3840
Number of working rows	6
Row spacing/mm	700/400
Working width/mm	3300
Fuel tank capacity/L	460

Technical parameter	Numerical value
Hydraulic oil tank capacity/L	205
Wheelbase/mm	4180
Track width/mm	2920
Rated power/kW	194
Grain collection box capacity/m^3	10

Structure and working principle of grain collection box

The grain collection box is mainly composed of a box body, a box body bracket, a buffering and shock-absorbing mechanism, a grain unloading extension mechanism, a hydraulic system, etc. Fresh corn ears are transported via an elevator and enter the bottom of the grain collection box. When the grain collection reaches a certain level, it can be unloaded at a high position either at the center or head of the cornfield. The box body is connected to the bracket through a hydraulic cylinder. The bracket itself is securely fixed to the chassis of the harvester. The overall structure of the grain collection box is illustrated in Fig. 2.

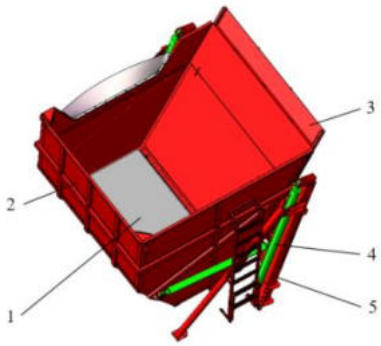


Fig. 2 – Structure of grain container

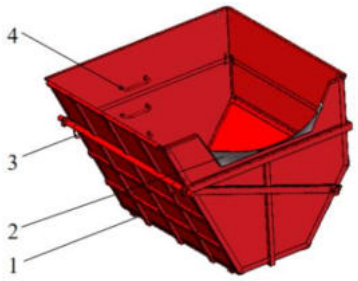
1. Buffer and shock absorber mechanism; 2. Box; 3. Unloading extension mechanism; 4. Hydraulic cylinder; 5. Anti-nose-dive leg

Fresh corn has a higher moisture content at harvest and is more prone to damage compared to grain corn. Therefore, a buffer and shock absorber mechanism is installed on the bottom plate of the grain collection box to reduce the probability of damage caused by rigid collision between fresh corn and the bottom plate. To increase the unloading distance between the harvester and the grain receiving truck, an unloading extension mechanism is designed. To achieve stable and fast lifting and flipping of the grain collection box when unloading to the high-level grain receiving truck, a hydraulic compensation directional valve is developed, and a synchronous series hydraulic system with adjustable lifting and flipping speeds is designed.

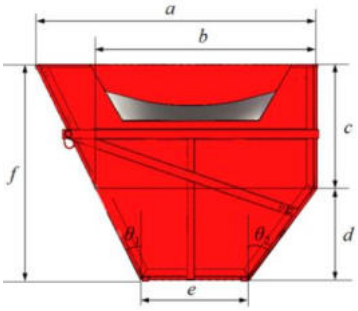
Box design

Due to the short optimal harvesting period of 2-3 days for fresh corn after maturity, the harvesting efficiency should be improved. If the volume of the grain collection box is small, it will increase the number of grain unloading times and reduce the harvesting efficiency. To reduce the frequency of unloading grain and lower transportation costs, large trailers are often parked on the ground and directly loaded onto the trailers from the harvester. According to the agricultural technology requirements for fresh corn cultivation, the planting method in Northeast China is mostly large ridges and double rows, with a ridge width of 1100 mm and a plant spacing of 250 mm to 280 mm (*Cui et al., 2024*). The length of a single ridge is usually around 500 meters. Taking a 6-row fresh corn harvester as an example, one round trip of the grain collection box can store about 24000 ears of fresh corn.

Using the variety Wannuo 2000 fresh corn as the research object, the drainage method was used to measure the volume of a single ear (*Tang, 2024*). Taking the average of multiple experiments, the volume of a single ear was found to be 0.0003 m^3. After calculation, it was found that the volume of an ear harvested in one round trip was 7.2 m^3. Due to the irregular arrangement of fruit clusters in the grain box and the large gaps between them, the total volume needs to exceed 7.2 m^3. In actual harvesting operations, the grain collection box cannot be filled to the brim, otherwise it will fall and lose. Therefore, in order to leave sufficient space, the volume of the grain collection box is set to 10 m^3. The box structure is shown in Fig.3 (a).



(a) Axonometric drawing



(b) Front view of the box

1-Reinforcement board; 2-Rubber baffle; 3-Unloading and flipping axis; 4-ladder

Fig. 3 – Box structure

Figure 3(b) shows the structural dimensions from the front view of the grain collection box. The left slope in the figure represents the unloading side. To prevent tipping or sliding of fresh corn after the box is lifted to its highest position, the slope angle should exceed the natural rolling angle of fresh corn. Therefore, θ1 is designed at 25°. Additionally, due to the installation of a cooling fan at the lower right section of the box, the opposite slope angle (θ2) is set at 35°, and the distance d is designed at 0.93 mm to accommodate and avoid interference with the fan's position. The chassis of the 4YX-6 fresh corn combine harvester is designed with a 1.0 m distance and a 2.5 m length between the two support beams that hold the grain collection box. Accordingly, the width (e) of the grain collection box is set to 1.1 m, and the length in the front–rear direction (l) is set to 2.5 m to match the chassis structure. In field operations, grain is often unloaded into small trucks with guardrails typically around 2.5 meters high. To improve unloading efficiency, the design adopts a method that allows unloading without lifting. Considering the chassis height, the box height (f) is designed to be 2.2 meters. Based on geometric and structural calculations, the value of c is determined to be 1.27 meters. The remaining dimensions, a and b, can be calculated using Equations (1) and (2):

$$a = f\tan\theta_1 + dan\theta_2 + e \quad (1)$$

$$b = d\tan\theta_1 + dan\theta_2 + e \quad (2)$$

The calculation shows that a is 2.77 m and b is 1.8 m. The volume of the box is:

$$V = \left[\frac{(b+e)d}{2} + \frac{(a+b)c}{2}\right]l \quad (3)$$

By inputting the relevant data into the above equation, the volume can be obtained as 10.625 m^3. To increase the ability of the box to resist deformation, all steel plate materials are selected as Q345B, and reinforcing ribs are used around the ear box for reinforcement.

Design of Unloading Extension Mechanism

During the unloading process, the distance between the harvester and the grain receiving truck needs to be maintained within the range of 0.3 m to 0.4 m, which requires accurate control of their relative positions to achieve the goal of unloading all grain into the grain receiving truck. However, when the two are very close, it is easy to cause scratches and safety hazards during unloading. When the two are far apart, it is easy to cause the grain to not be accurately dumped onto the receiving truck during unloading, resulting in waste. Therefore, it takes a long time to adjust the relative position of the two, greatly reducing the efficiency of the operation. Therefore, a retractable unloading extension mechanism is installed on the unloading outlet side of the grain collection box through a connecting plate. During harvesting, the opening of the box is facing upwards, and the moving extension plate slides in a fixed slide through a pulley under the action of gravity, naturally contracting to an unexpanded state without blocking the opening of the box or exceeding its own height. When it is necessary to dump grain, the box flips over, and the moving extension plate slides out naturally under the action of gravity. The moving extension plate can be limited in travel by a locking slider. A limit plate can be optionally installed in the fixed slide, which is divided into two gears and can be selectively installed according to different operating conditions to adjust the travel of the slide. The unloading extension mechanism is shown in Fig.4.

The dimensions of the mobile extension plate designed here are 2500 mm in length and 600 mm in width. Due to the locking slider, the actual extendable stroke is 400 mm, which can achieve unloading of grain within a distance of 0.7 m between the harvester and the grain receiving vehicle. The unloading distance is greatly increased, avoiding repeated adjustment of vehicle distance, accelerating unloading efficiency, and reducing safety hazards.

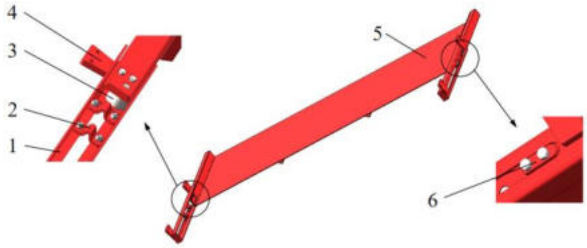


Fig. 4 – Unloading extension mechanism

1. Fixed slide; 2. Limit plate; 3. Pulley; 4. Connecting plate; 5. Mobile extension board; 6. Lock slider

Dynamic analysis of fruit ear

The harvest period of fresh corn is during the milk or wax ripening stage, when the grain moisture content is very high at around 65%, which can easily cause serious damage during rigid impact (*Zhang et al., 2019; Gao et al., 2024*). The corn ears are thrown out by the elevator and then dropped into the box in an inclined manner, resulting in a height difference between the ears and the bottom plate of the box. Due to the steel plate material of the box, the fruit clusters that enter the box at the beginning of harvesting will directly fall onto the bottom plate of the box, causing severe collision between the clusters and the steel plate, resulting in significant damage and loss. When the bottom plate is covered with a layer of fruit clusters, elastic collisions between clusters will occur inside the box, reducing or eliminating damage. To solve this problem, a buffering and shock-absorbing mechanism is installed on the bottom plate of the box, so that the initially entering fruit clusters come into elastic contact with the box to reduce damage.

Study on the mechanical properties of fresh corn

Fresh corn has a high moisture content and crisp grain texture. To provide reference for the design of buffering and shock-absorbing mechanisms, the mechanical properties of fresh corn ears during harvesting were studied. The variety Wannuo 2000 was used for the experiment of fresh corn ears, and 10 ears of fresh corn were randomly picked from the experimental field for measurement. The compressive strength and elastic modulus of the ear during harvest are important parameter indicators. This article used the RGT series desktop universal testing machine (speed accuracy ± 0.5%, load accuracy ± 0.5%) to measure 10 fruit ears (*Zhao et al., 2022*). Compression tests were conducted on the front, middle, and tail sections of the fruit ears, and the results were averaged. When the grain underwent significant deformation to the point of bleeding, it was considered damaged. The experimental process is shown in Fig.5.

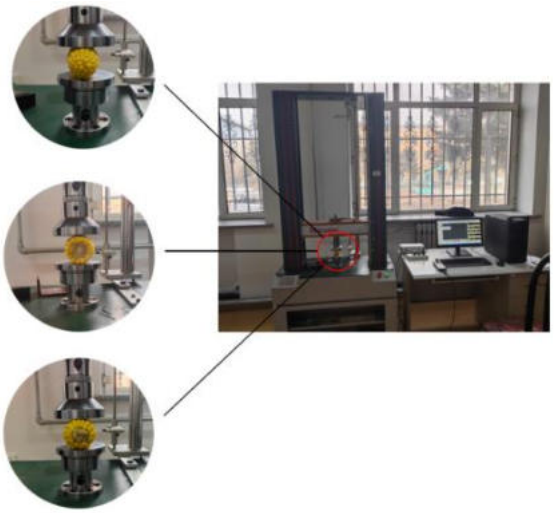


Fig. 5 – Mechanical measurement test

Statistical analysis was conducted on 10 fruit ears, with an average compressive strength of 8.16×10^4Pa, an average elastic modulus of 0.82 MPa, and a Poisson's ratio of 0.35.

Dynamics analysis of corn ear

Fresh corn was thrown out of the conveyor belt and entered the grain collection box in a diagonal motion. The dynamic analysis of the movement process of the ear is shown in Fig.6.

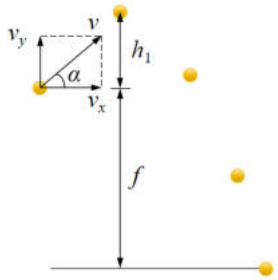


Fig. 6 – Movement process of the fruit ear

The movement of fruit ears in the air is divided into two stages: ascending and descending. Analyzing the movement stages of fruit ears includes:

$$\begin{cases} v_x = v\cos\alpha \\ v_y = v\sin\alpha \\ h_1 = v_y^2/(2g) \\ h = h_1 + f \end{cases} \quad (4)$$

where:

v—represents the initial velocity at which the ear leaves the conveyor belt, m/s;

V_x—horizontal velocity of the fruit ear, m/s;

V_y—vertical velocity of the fruit ear, m/s;

α—the angle between the initial velocity of the fruit ear and the horizontal direction, (°);

H_1—the distance at which the ear rises to the highest point, m;

G—gravitational acceleration, taken as 9.8 m/s^2;

H—the distance between the fruit ear being thrown to the highest point and falling onto the bottom plate of the grain collection box, m;

The speed range of the conveyor belt was 300-350 r/min, and the installation angle between the conveyor belt and the horizontal ground α was 45°. This article takes the middle value of the speed as calculate based on 325 r/min, with an initial velocity v of 3.4 m/s. By substituting the data into the above equation, h can be obtained as 2.5 m.

When the corn ear came into collision contact with the bottom plate, its contact stress was calculated to evaluate the impact force (*Wei, 2023*).

$$\begin{cases} \sigma_c = \dfrac{F_j}{A_c} \\ A_c = 0.8973h + 112.2 \end{cases} \quad (5)$$

where:

σ_c —represents the contact stress between the ear and the bottom plate during collision, Pa;

F_j—the contact force between the ear and the bottom plate during collision, N;

A_c—contact area at the time of collision, mm^2;

The previous analysis showed that h was 2.5 m, and the calculated contact area at the time of collision was 2355.45 mm^2.

According to the contact mechanics calculation formula, the load and compressive deformation at the point of contact between the corn ear and the steel plate were analyzed to evaluate the mechanical response during impact.

$$\begin{cases} F_j = \dfrac{4}{3} E^* \sqrt{R^*}\, \delta^{\frac{3}{2}} \\ \dfrac{1}{E^*} = \dfrac{1-\mu_1^2}{E_1} + \dfrac{1-\mu_2^2}{E_2} \\ R^* = \dfrac{1}{R_1} + \dfrac{1}{R_2} \\ \delta = \left(C\sigma \dfrac{\pi\sqrt{R^*}}{2E^*} \right)^2 \\ C = \min\left(1.295e^{0.763\mu_1}, 1.295e^{0.763\mu 2}\right) \end{cases} \quad (6)$$

According to the above formula:

$$F_j = \frac{(\pi C\sigma)^3}{6} \left(\frac{E^*}{R^*} \right)^2 \quad (7)$$

where: E^*—Comprehensive modulus of elasticity, MPa;

R^*—Compressing equivalent radius, m;

δ—The compression deformation amount when the ear undergoes deformation, mm;

μ_1—Poisson's ratio of fruit ear;

μ_2—Poisson's ratio of steel plate;

E_1—Elastic modulus of fruit ear, MPa;

E_2—Elastic modulus of steel plate, MPa;

R_1—Vertical radius of collision between fruit clusters and steel plates, mm;

R_2—The radius of the steel plate when in contact, mm;

C—Stress coefficient, take the smaller value;

σ—Yield stress of fruit ear, taken as 0.27 MPa.

The previous experiment has measured the elastic modulus of the fruit ear to be 0.82 MPa and the Poisson's ratio to be 0.35. According to the Mechanical Design Manual, the elastic modulus of the steel plate is 2.1 × 10^5 MPa and the Poisson's ratio is 0.3. By measuring the external dimensions of the ear, the diameters of the top, middle, and tail of the ear were measured separately, and the average diameter was 40 mm, which was used as the vertical radius when the ear collided with the steel plate. Since the steel plate is located at the bottom of the grain collection box as a plane, its radius can be considered infinite.

By substituting the relevant data into equations (6) and (7), the contact force between the ear and the bottom plate during collision was 294.95 N. As mentioned earlier, the contact area between the ear and the bottom plate during collision was 2355.45 mm^2. Combining equation (5), the contact stress between the ear and the bottom plate was 12.8 × 10^4 Pa. In the section on mechanical properties of the ear, the average compressive strength of the ear was measured to be 8.16 × 10^4 Pa, which means that the contact stress between the ear and the bottom plate was greater than the compressive strength of the ear. Therefore, when the ear was thrown out of the conveyor belt and came into contact with the steel plate, it was damaged.

Design of buffer and shock absorption mechanism

The buffering and shock-absorbing mechanism is installed on the bottom plate of the grain collection box and is required to bear the majority of the load from the accumulated corn ears. When the box is full, the mechanism must remain structurally intact and capable of restoring to its original state after unloading. To ensure its reliability, it is essential to calculate the maximum pressure the buffering and shock-absorbing mechanism can withstand. For this purpose, the front view of the grain collection box was simplified, as shown in Figure 7, and a force analysis was conducted based on this model.

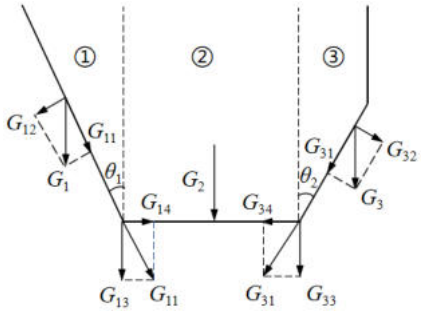


Fig. 7 – Force analysis of the box body

According to the structure of the box, the box is divided into three areas ①, ②, and ③ for separate force analysis. The first regional analysis is:

$$\begin{cases} G_{11} = G_1 \cos\theta_1 \\ G_{12} = G_1 \sin\theta_1 \\ G_{13} = G_{11} \cos\theta_1 \\ G_{14} = G_{11} \sin\theta_1 \end{cases} \quad (8)$$

where: G_1—total gravity of fruit ears in the first region, N;

G_{11}— component of G_1 along the inclined plane, N;

G_{12}— component of G_1 perpendicular to the inclined plane, N;

G_{13}—G_{11} vertical bottom plate force, N;

G_{14}—G_{11} component force along the bottom plate, N.

For Region ②, the entire gravitational force G_2 of the fruit ears acts directly and vertically on the bottom plate.

The third regional analysis is:

$$\begin{cases} G_{31} = G_3 \cos\theta_2 \\ G_{32} = G_3 \sin\theta_2 \\ G_{33} = G_{31} \cos\theta_2 \\ G_{34} = G_{31} \sin\theta_2 \end{cases} \quad (9)$$

where: G_3—total gravity of fruit clusters in the third region, N;

G_{31}—G_3 component force along the inclined plane, N;

G_{32}—the force component of G_3 vertical inclined plane, N;

G_{33}—G_{31} vertical bottom plate force, N;

G_{34}—G_{31} component force along the bottom plate, N.

From the above analysis, it can be seen that the total gravity of the fruit clusters inside the box does not act entirely on the bottom plate, but is partially shared by the inclined surfaces on both sides, reducing the pressure that the air cushion needs to bear. In section 2.1, it was calculated that a 6-row fresh corn combine harvester can harvest 24000 ears of fresh corn in one round trip. The average weight of a single ear was 290 g measured in the field, and the total weight was 6960 kg with a total gravity of 68208 N. The cross-sectional area ratio of the three regions is the ear gravity ratio, and the area of the three regions is calculated as:

$$\begin{cases} S_1 = \dfrac{f^2 \tan\theta_1}{2} \\ S_2 = ef \\ S_3 = \dfrac{(c+f)d \tan\theta_2}{2} \end{cases} \quad (10)$$

where: S_1 - the cross-sectional area of the region ①, m²;

S_2 - the cross-sectional area of the region ②, m²;

S_3 - the cross-sectional area of the region ③, m²;

Enter data to obtain S_1: S_2: S_3 =G_1: G_2: G_3 =1.13:2.42:1.13. Calculate G_1, G_2, and G_3 as 16469N, 35270N, and 16469N, respectively. The total pressure on the bottom plate of the box, G_z, is:

$$G_Z = G_{13} + G_2 + G_{33} \quad (11)$$

Combining equations (8), (9), and (11), the total pressure exerted on the bottom plate is 59684 N.

The area S_d of the bottom plate of the box is:

$$S_d = el \quad (12)$$

The calculated area of the bottom plate is 2.75 m^2.

Combining equations (11) and (12), it can be concluded that the pressure exerted on the bottom plate is 21.7 kPa. Therefore, the designed shock absorber pad should have a compressive strength greater than 21.7 kPa and a load capacity greater than 6.9 t. There are very few products that can achieve such a large load capacity and restore elasticity after compression in this area, and the price is expensive. The actual production and application costs are high. Therefore, this article designs a buffering and shock-absorbing mechanism with a simple structure and low cost. The schematic diagram of the buffer and shock absorber mechanism is shown in Fig.8.

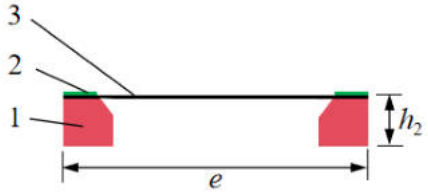


Fig. 8 – Schematic diagram of buffer and shock absorber mechanism

1.Heel; 2.Splint; 3.High elasticity rubber

High elasticity rubber is fixed by pads and clamps, with the pads fixed to the bottom plate of the box. To reduce stress concentration caused by downward bending of the rubber, a 20 mm chamfer is designed on the inside of the pads. Due to the thin thickness of the rubber sheet, which is much smaller than its length and width, and the linear elastic deformation of the rubber, a certain horizontal pre tension T is applied to the rubber sheet during clamping to ensure sufficient buffering deformation space between the rubber and the bottom plate of the box. The pre tension taken in this article is 500 N.

When the ear falls onto the rubber plate, the calculation condition is based on the ear falling into the middle of the rubber plate. The deformation of the rubber sheet can be regarded as the result of the combined action of pre tension and intermediate pressure. To calculate the deformation of the rubber sheet:

$$\begin{cases} \delta_1 = \dfrac{PL^3}{192D} \cdot \dfrac{1}{1+\dfrac{TL^2}{12D}} \\ D = \dfrac{E_3 H^3}{12\left(1-\gamma^2\right)} \end{cases} \quad (13)$$

Where: δ_1—Rubber deformation amount, mm;

P—Contact force between fruit ear and bottom plate collision, N;

L—Rubber sheet length, taken as 2.5 m;

D—Rubber sheet bending stiffness;

E_3—Rubber elastic modulus, 4×10^6 Pa;

H—Rubber sheet thickness, m;

γ—Rubber Poisson's ratio, taken as 0.47.

This article takes a rubber sheet thickness of 10 mm. The deformation obtained by inputting the data into the above equation is 0.09 m. In order to provide sufficient buffer space when the ear comes into contact with the rubber, the height h_2 of the cushion block is designed to be 100 mm. As the number of fruit clusters in the box gradually increases, the high elasticity rubber deforms and comes into contact with the bottom plate. After unloading the grain, the rubber rebounds and continues to play a buffering role.

Design of hydraulic system

The grain collection box is connected to the plunger pump oil supply system through hydraulic fittings and joints. The hydraulic system circuit is shown in Fig.9, mainly including hydraulic compensating directional valves, hydraulic cylinders, overflow valves, and other auxiliary components. When the system is in operation, the inlet P and outlet T are respectively connected to the oil supply system and oil tank of the pump body. When solenoid valves 3 and 4 are powered on, they can respectively achieve the lifting function of the grain collection box, and when solenoid valves 1 and 2 are powered on, they can respectively achieve the flipping function of the grain collection box. The overflow valve regulates the system pressure and protects the hydraulic circuit from overpressure conditions.

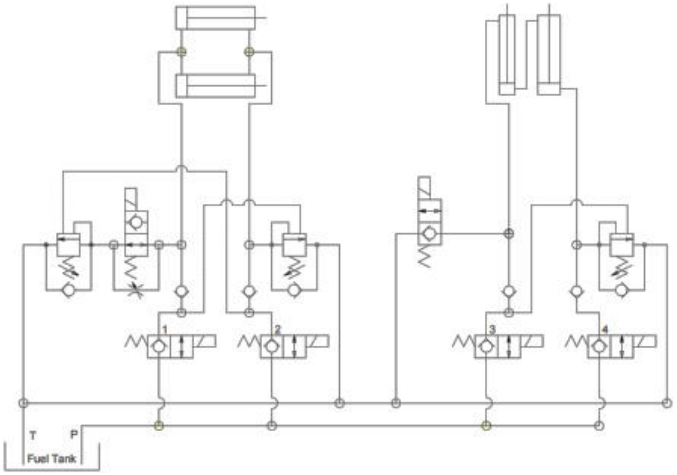


Fig. 9 – Hydraulic circuit of grain collection box

The grain box bracket for installing the lifting oil cylinder moves through a slide. Due to the uneven distribution of the weight of the fruit clusters in the grain box, the load on the grain box is the highest during lifting. If the lifting speed of the two oil cylinders is not the same, it will cause the grain box to tilt. In mild cases, the grain box will be stuck and unable to move, and in severe cases, the grain box frame will deform, causing safety issues. To ensure stable lifting, the two hydraulic cylinders must operate in synchronization. Therefore, the lifting oil cylinder design uses synchronous series oil cylinders, which should ensure that the effective working area of the two series oil cylinders is equal. Due to leakage in the series circuit during actual operation, a hydraulic compensation type reversing valve is designed in the circuit to replenish oil to the system. When the oil cylinder is in a constant power state during the lifting process, it can stop at any position within the stroke range at any time. When the oil cylinder is in a stationary state, the system is in a constant pressure state. The maximum working pressure of the oil source system is 16 MPa, and the maximum load-bearing ear weight calculated earlier is 68208 N. The theoretical thrust of the hydraulic cylinder can be calculated using the following formula:

$$F_u = \eta \frac{\pi}{4} D_0^{\,2} P_1 \qquad (15)$$

where: F_u—Theoretical thrust of the hydraulic cylinder, N;

η— Mechanical efficiency, taken as 0.85;

D_0— Diameter of the main piston in the synchronized hydraulic cylinder, mm;

P_1— Working oil pressure, Pa.

Select the hydraulic cylinder based on the above analysis. Refer to the product manual and select the HSG type hydraulic cylinder for engineering use. The synchronous main oil cylinder uses a hydraulic cylinder with a piston diameter of 140 mm and a piston rod diameter of 70 mm. Based on the above formula, the maximum pressure can reach 209249 N, which is greater than the total weight of the ears and grain collection box when fully loaded, meeting the lifting requirements. Due to the fact that the effective working area of the two series connected oil cylinders should be equal, that is, the cross-sectional area of the main cylinder with a rod chamber is equal to the cross-sectional area of the auxiliary cylinder without a rod chamber, when selecting, the piston rod diameter of the auxiliary cylinder and the main cylinder should be kept consistent. After calculation, the piston diameter of the auxiliary cylinder is 121.2 mm.

The flipping cylinder has relatively low synchronization requirements during flipping operations, so parallel cylinders are selected for flipping cylinders. During the operation, the box rotates around the flipping axis under the extension of the reverse oil cylinder. The force analysis of the reverse oil cylinder operation process is shown in Fig.10. In the figure, O_1 is the support point of the flipping cylinder, simplifying the fruit clusters inside the box into particle O_2, O_3 is the hinge point of the flipping axis when the box is flipped, and O_4 is the hinge point of the flipping cylinder. O_1O_3 is the direction of the connection between the support point of the flipping cylinder and the hinge point of the flipping shaft, O_1O_4 is the length direction of the flipping cylinder, O_2O_3 is the direction of the connection between the grain particle and the hinge point of the flipping shaft, and O_3O_4 is the direction of the connection between the hinge point of the flipping cylinder and the hinge point of the flipping shaft.

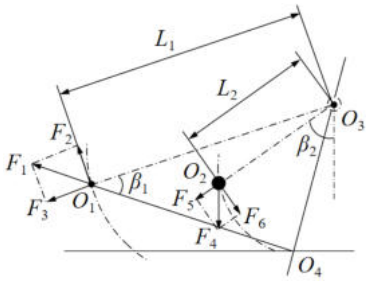


Fig. 10 – Force analysis of flipping cylinder operation

To achieve the flipping of the box, it is necessary to meet the following requirements:

$$\begin{cases} F_2 L_1 > F_6 L_2 \\ F_2 = F_1 \sin \beta_1 \\ F_6 = F_4 \sin \beta_2 \end{cases} \quad (16)$$

where: F_1—The force exerted by the flipping cylinder, N;

F_3—The force component of F_1 in the O_1O_4 direction, N;

F_2—F_1 component perpendicular to O_1O_4 direction, N;

F_4—Total gravity of box and ear, N;

F_5—Force component of F_4 in the direction of O_2O_3, N;

F_6—F_4 component perpendicular to O_2O_3 direction, N;

β_1—Angle between O_1O_3 and O_1O_4, (°);

B_2—The angle between O_2O_3 and the vertical direction, (°);

During the unloading reversal process, the maximum hydraulic cylinder pressure is required when the box is about to flip, so this state is analyzed. According to the installation structure of the grain collection box, the length of L_1 is 2381 mm and β_1 is 25 °. To obtain the length of L_2, the position of the center of mass needs to be obtained. In the 3D software SolidWorks 2020, 6960 kg of mass is added to the inside of the box according to the shape of the box, and material properties are added to each component of the grain collection box. After calculation, the box mass is 800 kg, β_2 is 81 °, and the length of L_2 is 1412 mm. Combining equation (16), it can be concluded that F_1 should meet the minimum requirement of 60686 N. Therefore, the HSG type hydraulic cylinder with a piston diameter of 80 mm and a piston rod diameter of 40 mm is selected for the flipping cylinder.

Design of electronic control system

All functions of the grain collection box are operated inside the cab, and the buttons use a reset switch. The control system mainly includes power supply, handle, controller, solenoid valve, etc. To streamline the system structure, a hydraulic compensating directional valve has been developed, with all solenoid valves concentrated on top. The lifting and flipping functions are controlled by solenoid valves to control the oil cylinder. To achieve rapid unloading of grain, a speed regulating valve is added to the flipping circuit of the grain collection box. Fast flipping can be selected according to the actual harvest situation. When the grain collection box is not fully loaded and the load is close to half, fast flipping unloading can be selected to reduce unloading time and improve operational efficiency. The control logic is shown in Fig.11.

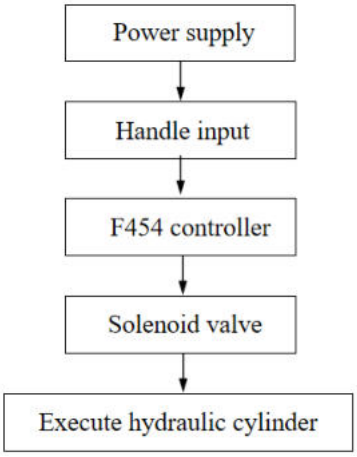


Fig. 11– Logic schematic diagram

Draw the grain collection box in the 3D software SolidWorks 2020 and configure its lifting and flipping operation modes, as shown in Fig.12.



(a) Ascending status *(b) Flip state*

Fig. 12 – Operating status of grain collection box

RESULTS

Field performance test

The experiment was conducted in September 2024 at the 47th parallel farm in Yi'an County, Qiqihar City, using the 4YX-6 fresh corn combine harvester. The fresh corn variety planted on the experimental plot was Wannuo 2000. At the time of the experiment, the fresh corn was in the milk ripening stage, which met the harvesting conditions for fresh corn. The planting mode adopted a large ridge double row, with a ridge length of 500 m, a ridge spacing of 1.1 m, and a plant spacing of 0.25 m.

The basic parameters of the fruit ear were measured using random sampling method, and the results are shown in Table 2.

Table 2

Determination of Basic Parameters of Ears

Parameter	Average value
Ear length/mm	173
Large end diameter of fruit ear/mm	46
Grain quality/g	291
Moisture content/%	69

The measurement was conducted based on the ear damage rate and unloading time as experimental indicators, and the GB/T 21961-2008 Corn Harvesting Machinery Test Method (*Wang, 2023*) was used as the ear damage evaluation standard. The field experiment site is shown in Fig.12.



(a) Small grain truck unloading grain



(b) Large grain trucks unloading grain

Fig. 12 – Field unloading experiment

When conducting ear damage statistics, the main consideration is the ears in direct contact with the bottom of the box. Therefore, during the experiment, the harvester advances ten meters each time and stops immediately after harvesting ten meters to conduct damage statistics on the ears in the grain collection box. The experiment is repeated five times, and the damage rate ranges from 0.5% to 0.8%, which meets the operational requirements.

There are two main types of grain receiving vehicles used in field operations, namely small grain receiving vehicles pulled by high-powered tractors (low-level unloading) and large heavy-duty trucks (high-level unloading). During the experiment, unloading tests were conducted on both types of grain receiving vehicles. The experiment is conducted when the grain collection box is empty (without fruit ears) and full (harvested by the harvester back and forth once), and the entire process time from the start of lifting the grain collection box to the end of unloading and returning to its original position is taken as the unloading time. To obtain an accurate range of unloading time, various situations were used to calculate the unloading time, and the unloading time was found to be between 74 s and 126 s. The correspondence between operating status and unloading time is shown in Table 3.

Table 3

Operating Status and Unloading Time

Work status	Time/s
Empty load low position quick flipping unloading of grain	74
Empty high position quick flipping unloading of grain	113
Fully load low position normal flipping unloading of grain	86
Full load high position normal flipping unloading of grain	126

The whole machine did not experience any safety issues such as tilting, overturning, or cracking of the frame during operation, and both the harvester and the grain receiving truck can unload grain within a range of 0.7 meters, with an unloading height of 2.9 meters to 4.4 meters. The operation is stable and safe.

CONCLUSIONS

(1) A large grain collection box suitable for fresh corn harvesting was developed to address key issues in existing combine harvesters, including low unloading height, limited grain box capacity, and a high damage rate to corn ears during collection. The box volume was designed to be 10 m³, based on agronomic requirements and harvesting operation needs. To extend the unloading reach between the harvester and grain-receiving trucks, a grain unloading extension mechanism was incorporated. Additionally, dynamic analysis of the unloading process was performed, leading to the design of a buffering and shock-absorbing mechanism to reduce ear damage during impact.

(2) To improve the convenience of unloading grain, an electro-hydraulic control system was designed. It can achieve synchronization of hydraulic mechanism operation and has fast flipping function, reducing unloading time.

(3) Field experiments revealed that the damage rate of corn ears resulting from direct contact with the bottom of the grain collection box ranged between 0.5% and 0.8%. Statistical analysis of unloading time under various working conditions showed that the unloading height ranged from 2.9 m to 4.4 m, while the unloading time ranged from 74 s to 126 s. The test results meet relevant standards and satisfy operational requirements, demonstrating the effectiveness and reliability of the proposed design.

ACKNOWLEDGEMENT

This study was supported by the National Corn Industry Technology System Special Project (CARS-02-28); Heilongjiang province key research and development plan project major project (2022ZX05B01); Heilongjiang province key research and development plan project major project (2024ZX07B02) funding.

REFERENCES

[1] Balevičius R., Sielamowicz I., Mróz Z., Kačianauskas R., (2011). Investigation of wall stress and outflow rate in a flat-bottomed bin: A comparison of the DEM model results with the experimental measurements. *Powder Technology, Vol.214*, pp.322-336. Lithuania.

[2] Chen, S., Yi, K., Zhang, X., Jiang, C., Wang, Q., Huang, X., (2023). Design and test of longitudinal axial flow high and low roller type fresh corn flexible peeling device (高低辊组合式鲜食玉米柔性剥皮装置设计与试验). *Transactions of the Chinese society for agricultural machinery*, Vol. 54(S2), pp. 30-42. China.

[3] Cui, J., Xiao, Q., Xing, Q., Wu, M., Mu, J., Mei, Z., Bo, T., (2024). High yield cultivation techniques for fresh corn (鲜食玉米高产栽培技术). *Rural science and technology*, Vol. (06), pp. 7-11. China

[4] Gao, P., Zhang, X., Jiang, C., Yi, K., Zhang, X., Ma, Z., (2024). Optimized design and test of axial roller fresh corn threshing device (轴向滚筒式鲜食玉米脱粒装置优化设计与试验). *Transactions of the Chinese society for agricultural machinery*, Vol. 55(S2), pp. 145-156. China.

[5] Geng, N., Li, Y., Zhang, Y., (2023). Effects of modified dietary fiber from fresh corn bracts on obesity and intestinal microbiotain high-fat-diet mice. *Molecules,* Vol. 28(13), pp. 4949. China.

[6] González-Montellano C.., Ramírez A., Fuentes J.M., Ayuga F., (2012). Numerical effects derived from *en masse* filling of agricultural silos in DEM simulations. *Computers and Electronics in Agriculture*, Vol.81, pp.113-123. Spain.

[7] Guan, X., (2023). Design and mechanism of low loss debris removal device for fresh corn ears harvesting (鲜食玉米果穗收获低损除杂装置的设计及机理研究). Harbin: Northeast Agricultural University. China.

[8] Islam M.S., Liu, J., Jiang, L., (2021). Folate content in fresh corn: effects of harvest time, storage and cooking methods. *Journal of Food Composition and Analysis*, Vol. 103, pp. 104-123. Islam.

[9] Li, T., Zhou, F., Guan, X., Wu, H., (2019). Design and experiment on flexible low-loss fresh corn picking device. *International Agricultural Engineering Journal*, Vol.28(2), pp. 233-247. China.

[10] Liu, S., Tang, Z., (2017). Structure optimization of ear box bracket of 4YZS-4 type corn for seed harvester (4YZS-4型制种玉米收获机果穗箱支架结构优化). *Agricultural Engineering*, Vol. 7(01), pp. 64-67+71. China.

[11] Ma, Z., Souleymane, N., Zhu, Y., Li, Y., Xu, L., Lu, E., Li, Y., (2022). DEM simulations and experiments investigating of grain tank discharge of a rice combine harvester. *Computers and Electronics in Agriculture*, Vol.198,107060. China.

[12] Tang H. (2018). *Design and mechanism analysis of ripple surface pickup finger maize precision seed metering device (波纹曲面指夹式玉米精量排种器设计及其机理研究).* Harbin: Northeast Agricultural University. China.

[13] Wang L., Zhang, Z., Liu, T., Wang, Y., Jia, F., Jiang, J., (2020). Design and experiment of device for chopping stalk of header of maize harvester (玉米收获机割台砍劈式茎秆粉碎装置设计与试验). *Transactions of the Chinese society for agricultural machinery*, Vol. 51(07), pp. 109-117. China.

[14] Wei Z., Wang, Y., Li, X., Wang, J., Su, G., Meng, P., Han, M., Jing, C., Li, Z., (2023). Design and experiments of the potato combine harvester with elastic rubbing technology (弹性揉搓式马铃薯联合收获机设计与试验). *Transactions of the CSAE*, Vol.39(14), pp. 60-69. China.

[15] Yan K. (2016). John Deere S660 combine harvester (约翰迪尔S660型联合收获机). *Modernizing Agriculture*, Vol. (05), pp. 44. China.

[16] Zhang X., Yuan, Y., Nie, M., Li, Z., Ye, T., (2023). Design and testing of a double fan high-pressure impurity removal and cleaning device for fresh corn harvesters. *Engenharia Agrícola*, Vol.43(n4), pp. e20230069. China.

[17] Zhang X., Zhao, W., Nie, M., Li, Z., Liu, X., Lan, H., Chang, J., Yang, J., Ye, T., (2025). Design and test of diversion device for reducing the loss of fresh corn harvester ear box (鲜食玉米收获机果穗箱减损导流装置设计与试验). *Journal of Agricultural Mechanization Research*, Vol.47(03), pp. 41-47. China.

[18] Zhang X., Wu, H., Wang, K., Li, A., Shang, S., Zhang, X., (2019). Design and experiment of 4YZT-2 type self-propelled fresh corn double ridges harvester (4YZT-2型自走式鲜食玉米对行收获机设计与试验). *Transactions of the CSAE*, Vol.35(13), pp.1-9. China.

[19] Zhao S., Zhang, X., Yuan, Y., Hou, L., Yang, Y., (2022). Design and Experiment of powder organic fertilizer drilling fertilizer distributor (粉末状有机肥条施排肥器设计与试验). *Transactions of the Chinese society for agricultural machinery*, Vol.53(10), pp.98-107. China.

[20] Zhao Y., He, X., Shi, J., Liu, Q., Shao, G., Xie, Q., (2011). Design and experiment of sweet and waxy corn husker (鲜食玉米剥皮机的设计与试验). *Transactions of the CSAE*, Vol.27(02), pp.114-118. China.

[21] Zhou F., Guan X., Tang Z., et al. (2020). Parameter optimization and experiment of negative pressure impurity removal device for fresh corn ear harvest (鲜食玉米果穗收获负压除杂装置参数优化与试验). *Transactions of the Chinese society for agricultural machinery*, Vol.51(11), pp.138-147. China.

[22] Zhou H. (2013). A brief discussion on the ear box structure of corn harvester (浅议玉米收获机的果穗箱结构). *Hebei Agricultural Machinery*, Vol.No.185(05), pp.46-47. China.

[23] Zhu G., Li T., Zhou F. (2022). Design and experiment of flexible clamping and conveying device for bionic ear picking of fresh corn (鲜食玉米仿生摘穗柔性夹持输送装置设计与试验). Journal of Jilin University (Engineering Edition), Vol. (10), pp. 2486-2500. China.

RESEARCH ON SPEED CONTROL OF AN ELECTRICALLY DRIVEN THRESHING CYLINDER IN A COMBINE HARVESTER BASED ON INERTIA PARAMETER IDENTIFICATION
/
基于惯量参数辨识的联合收割机电驱动脱粒滚筒转速控制研究

Yushuai QIAN*, Li QUAN, Jiapeng DIAO, Lei XU, Zixuan XIANG, Xiaoyong ZHU
School of Electrical and Information Engineering, Jiangsu University, Zhenjiang, 212000, Jiangsu, China
E-mail: 2112107010@stmail.ujs.edu.cn
DOI: https://doi.org/10.35633/inmateh-76-30

Keywords: *combine harvester, threshing cylinder, motor drive, dynamic parameter identification, real time speed adjustment, adaptive control*

ABSTRACT

In response to the speed control requirements of the threshing cylinder in combine harvesters, this paper analyzes the working condition characteristics of the threshing cylinder and establishes a dynamic model. A mathematical model for the electrically driven threshing cylinder is established, and an adaptive speed control strategy is proposed based on the identification of moment of inertia. Experimental results indicate that, the control accuracy and robustness of the system are enhanced. During the start-up process, the overshoot in speed and convergence time are reduced by 11.1% and 31.3%, respectively; when fluctuations occur in the feed rate of the threshing cylinder, the maximum speed fluctuation and adjustment time are reduced by 55% and 33.3%, respectively; when the moisture content of crops changes, the shortest convergence time and maximum fluctuation amplitude of the threshing cylinder's speed are reduced by 57.7% and 18.8%, respectively. This research provides theoretical support and practical foundation for the intelligent control of electrically driven combine harvesters, demonstrating considerable application value.

摘要

针对联合收割机中脱粒滚筒的转速控制需求，本文分析了脱粒滚筒的工况特征并建立了动力学模型，构建了电驱动脱粒滚筒的数学模型，提出了一种基于转动惯量辨识的电驱动脱粒滚筒转速自适应控制策略。实验结果表明，系统的控制精度和鲁棒性得到增强。启动过程中的转速超调量和收敛时间分别减少了11.1%和31.3%；作物喂入量发生波动时，最大转速波动和调整时间分别减少了55%和33.3%；当作物的含水率变化时，脱粒滚筒的转速最短收敛时间和最大波动幅度分别减少了57.7%和18.8%。本研究为电驱动联合收割机的智能化控制提供了理论支持和实践基础，具备良好的应用价值。

INTRODUCTION

Under the dual challenges of skyrocketing global food demand and climate change, combine harvesters hold a central position in modern agricultural systems. Due to the seasonal nature and high labor intensity of the crop harvesting process, there is an urgent demand for combine harvesters that are efficient in production, provide good operational quality, are easy and comfortable to control, and possess intelligent features *(Liu et al., 2024; Ou et al., 2024)*.

The main working components of the combine harvester include header, threshing cylinder, separation and cleaning device and grain unloading auger. Among them, the threshing cylinder is one of the core components, with the main function of separating the grains from the rice heads. Threshing cylinder not only largely determines the threshing quality and production efficiency but also significantly impacts the subsequent processes of separation and cleaning in the combined harvester *(Wang et al., 2023; Tang et al., 2022; Yang et al., 2018; Miu et al., 2007)*. Traditional combine harvesters rely on mechanical transmission systems to transfer engine power to various working components, which limits the speed adjustment range and overload capacity. As a result, it is challenging for the speed of these working components to be adjusted in real-time according to fluctuations in the feed rate of the harvester. This can lead to issues such as significant crop losses due to carryover and clogging of the threshing cylinder, which in turn reduces the crop cleaning rate and overall production efficiency. Therefore, enhancing the dynamic responsiveness and overload capacity of the threshing cylinder's speed adjustment is crucial for improving the harvesting quality and efficiency of combine harvesters.

In response to issues such as the narrow adjustment range of the threshing cylinder speed of the combine harvester, high threshing loss rate, and frequent clogging, some scholars have conducted related research. The research on the operation quality and efficiency of the threshing cylinder of the combine harvester primarily focuses on improving the quality and efficiency of the threshing process through mechanical structural design and the collaborative optimization of operational parameters *(Ivan et al., 2015; Cristea et al., 2023; Vlădut et al., 2023)*. *Vlădut et al., (2022),* proposed a mathematical model describing the axial flow characteristics during the threshing and separation processes of the threshing cylinder. *Wang et al., (2022),* addressed the issue of clogging in the threshing cylinder by designing a telescopic rod tooth-ribbed rod roller type threshing device. This design improves the flow of crops through the synergistic operation of the internal structures. *Zewdie et al., (2024),* explored the performance of bean threshers, using different cylinder speeds, concave apertures, feed rates, and moisture levels as variables. They obtained relatively ideal operating parameters for the threshing cylinder, which improved threshing efficiency and reduced grain loss rates. In addition, research on the threshing cylinder mainly focuses on exploring the interactions between threshing quality, operating parameters, and mechanical structure, aiming for structural optimization design *(Wang et al., 2021; Song et al., 2022; Li et al., 2023; Gong et al., 2024; Tang et al., 2024)*. *Abdeen et al., (2025),* improved the operational parameters and structure of the rice threshing device, reducing costs and power consumption, and significantly enhancing the overall efficiency of the threshing cylinder. *Gou et al., (2025),* introduced the structural design and advancements in intelligent technology applications of the combine harvester's threshing device. However, the drawbacks of multi-stage mechanical transmission systems still exist, such as long transmission routes and low transmission efficiency, which restrict the independent control capacity for adjusting the speed of various operating components as needed. Additionally, the working environment of combine harvesters is complex, with issues such as crop lodging and uneven moisture content, leading to high harvesting loss rates and poor cleanliness.

With the global climate change and the increasing awareness of environmental protection, the rapid development of new energy technologies has become a key driver for the green transformation and upgrading of industries. This provides impetus and ideas for promoting the intelligent development of new energy agricultural equipment. The integration of smart technologies with new energy sources can enhance operational efficiency, reduce emissions, and optimize resource use in agricultural practices, ultimately contributing to sustainable farming and improved productivity *(Liu et al., 2024)*. However, research on electrically driven combine harvesters is still in the preliminary exploration stage *(Jiang, 2015; Han, 2017; Hou, 2020)*, and there is a notable lack of information regarding the electric drive research of core components like the threshing cylinder. This gap indicates a significant opportunity for further study and innovation in this area. Developing electric drive systems for the threshing cylinder could enhance efficiency, reduce fuel consumption, and support the overall shift toward sustainable agricultural practices. Addressing this research gap could lead to advancements in the performance and adaptability of electric combine harvesters in various working conditions.

In summary, this paper addresses the speed requirements of the threshing cylinder during the operation of combine harvesters and aims to improve the system's control accuracy and responsiveness, thereby enhancing harvesting quality and efficiency. Considering that the threshing cylinder is a special component with large inertia affected by its shape, size, and structure, a self-disturbance control method for the threshing cylinder's speed in rice and wheat combine harvesters based on moment of inertia identification is proposed. This research analyzes the working principle and operational needs of the threshing cylinder, develops a dynamic model for it, and establishes a torque equation. By directly driving the threshing cylinder with a Permanent Magnet Synchronous Motor (PMSM), the advantages of quick dynamic response, superior speed control, and strong overload capacity of the motor are utilized. This approach resolves issues related to fixed transmission ratios and the inability to individually control the threshing cylinder's speed. Furthermore, by combining the PMSM's motion model, the operational characteristics of the electrically driven threshing cylinder is analyzed. This allows the combine harvester to maintain the threshing cylinder's speed within optimal ranges under different working conditions, ultimately reducing threshing losses and improving operational efficiency and quality. The study supports the advancement of combine harvesters from automation to intelligent operation.

MATERIALS AND METHODS

Analysis of operating requirements for electrically driven threshing cylinder

This paper is based on the 4LZ-6.0ME tracked combine harvester from World Agricultural Machinery Co., Ltd. (Zhenjiang, Jiangsu Province, China). A schematic diagram of the motor-driven threshing cylinder is shown in Figure 1. In the diagram, T_e represents the electromagnetic torque of the PMSM, while $T_L+B\omega_m$ denotes the load torque on the threshing cylinder and external friction resistance. The PMSM drives the threshing cylinder to generate the rotational angular velocity ω_m. This setup illustrates the relationship between the motor's output and the load conditions on the threshing cylinder, emphasizing the importance of effectively managing these parameters to enhance operational performance.

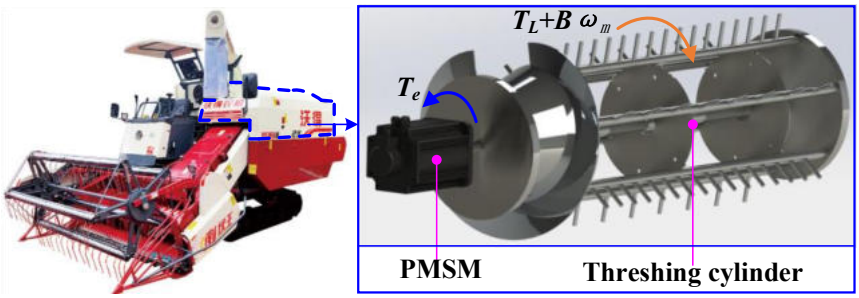


Fig. 1 - Schematic diagram of electrically driven threshing cylinder

The PMSM structure of this paper is shown in Figure 2 and its structural parameters are shown in Table 1 *(Xiang et al., 2024; Xiang et al., 2024)*:

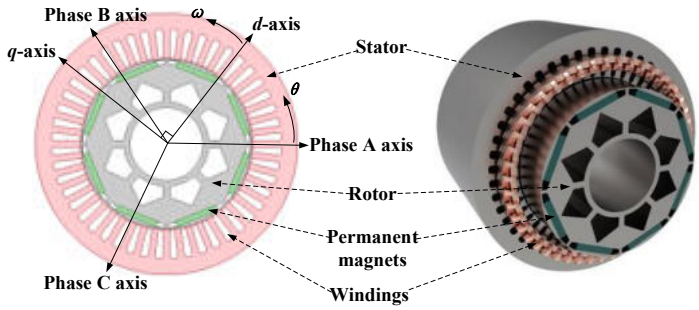


Fig. 2 - Structure diagram of PMSM (Permanent Magnet Synchronous Motor)

Table 1

Parameters of PMSM

Parameter	Value	Unit
Rated voltage	600	V
Rated power	11	kW
Rated speed	1500	rpm
Rated torque	70	Nm
Stator outer diameter	248	mm
Rotor outer diameter	160	mm
Rotor axial length	131	mm
Number of rotor poles	8	/

Relationship between threshing cylinder speed and threshing performance

There are many factors that influence the threshing quality of combine harvesters, including cylinder speed, feed rate, concave clearance, crop properties, field conditions, and the structural design of the cylinder. Among these, the rotational speed of the threshing cylinder is one of the key parameters affecting threshing performance, as the strength of the impact, brushing, and rubbing actions on the crops primarily depends on this speed *(Da, 2021)*. As shown in Figure 3, the relationship between the threshing cylinder speed and various performance indicators indicates that at lower speeds, the impact force is weakened, leading to reduced cleaning and separation rates, which in turn lowers production efficiency. Conversely, as the threshing speed increases, the brushing and rubbing actions become more pronounced, improving both the cleaning rate and

operational efficiency *(Han, 2017)*. However, excessively high speeds can lead to increased damage to the grains and straw, as well as higher power consumption *(Qu et al., 2018)*. Additionally, the timing of crop harvesting and the moisture content of the crops impose certain requirements on the cylinder speed. When threshing wetter crops, it is advisable to increase the cylinder speed to enhance separation rates. Conversely, for drier crops, the cylinder speed should be reduced to ensure the integrity of the grains and minimize breakage *(Jiang, 2015)*.

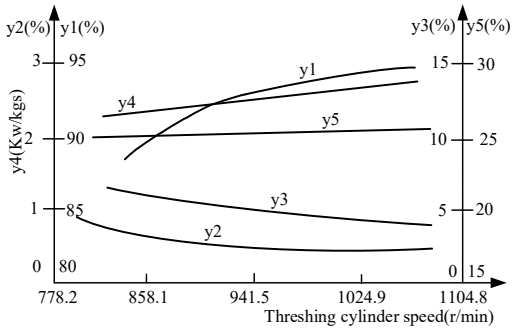


Fig. 3 - Relationship curves between threshing cylinder speed and various performance indicators
y1 – separation rate; y2– unthreshed rate; y3 – entrainment loss rate; y4 – unit power consumption; y5 – trash content

In summary, it is essential to determine the most suitable threshing speed range for the threshing cylinder based on its real-time operational conditions. Additionally, the threshing speed should be adjustable according to factors such as the crop feed rate and growth status. By maintaining the cylinder speed within this optimal range, the harvesting quality and efficiency of the combine harvester can be significantly improved. This adaptive control approach not only enhances overall performance but also ensures better handling of varying crop conditions during operation.

Performance requirements of permanent magnet driven motors for threshing operations

For the electrically driven threshing cylinder, the performance requirements of the drive motor are shown in Figure 4. The performance requirements that the motor must meet include: (1) The motor should have a robust overload capability, able to output 2-3 times the peak torque for short durations. This is essential for overcoming the large inertia loads of the threshing cylinder, enabling acceleration and stable operation while maintaining the required rubbing intensity to reduce crop impurity and loss rates. (2) A higher torque-to-inertia ratio enhances the acceleration performance of the threshing cylinder. This ratio is critical for achieving quick response times during operation. (3) The motor should offer a broad range of speed adjustments to meet the threshing speed requirements for various crop types and operating conditions, thereby further reducing production costs. (4) The driving motor should operate efficiently across a wide range to accommodate random fluctuations in operational load, which helps increase the duration of effective operation for the electric drive system.

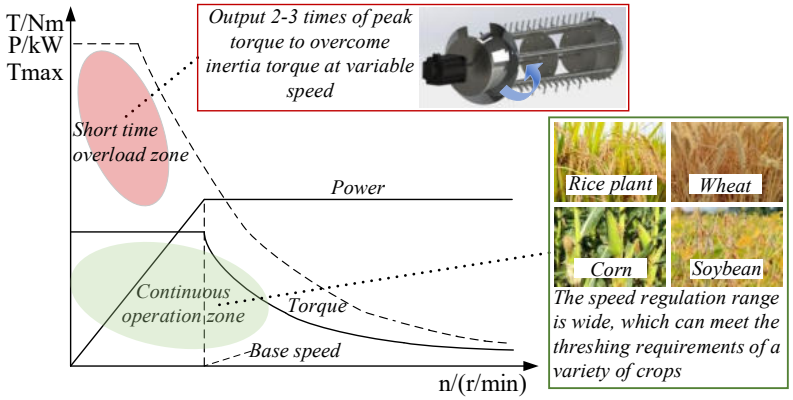


Fig. 4 - Performance output requirements of driving motor

By meeting these performance criteria, the electric motor can significantly enhance the operational efficiency and effectiveness of the electrically driven threshing cylinder in combine harvesters.

Mathematical model of electrically driven threshing cylinder

Mathematical model of PMSM

According to Figure 2, the mathematical model of PMSM in d-q axis system is established. The stator voltage equation for PMSM in the d-q coordinate system is as follows (eq. 1) *(Fu et al., 2024; Zhang et al., 2025)*:

$$\begin{cases} u_d = R_s i_d + L_d \frac{di_d}{dt} - \omega_e L_q i_q \\ u_q = R_s i_q + L_q \frac{di_q}{dt} + \omega_e (L_d i_d + \psi_f) \end{cases} \quad (1)$$

The electromagnetic torque equation is as follows (eq. 2) *(Fu et al., 2024; Zhang et al., 2025)*:

$$T_e = \frac{3}{2} P_n [\psi_f + (L_d - L_q) i_d] i_q \quad (2)$$

The mechanical motion equation is as follows (eq. 3) *(Fu et al., 2024; Zhang et al., 2025)*:

$$T_e = J \frac{d\omega_m}{dt} + B\omega_m + T_L \quad (3)$$

where: u_d, u_q = the stator voltage direct and cross-axis components [V]; i_d, i_q = the stator current direct and cross-axis components [A]; R = the stator winding resistance [Ω]; P = the number of pole pairs; ω_m = the mechanical angular velocity [rad/s]; L_d, L_q = the stator d, q axis inductance [H]; L_s = the stator inductance [H]; ψ_f = the magnetic chain of permanent magnets [Wb]; J = the rotational moment of inertia [kg·m²]; T_e = the electromagnetic torque [N·m]; T_L = the load torque [N·m]; B = the viscous friction factor.

Mathematical model of threshing cylinder

When the combine harvester starts operation, the active torque required to drive the threshing cylinder rotor shaft mainly includes the torque M_k required to overcome its own idle running, the torque M_g to overcome its own moment of inertia to generate angular acceleration, and the torque M_w (working torque) that pushes the crop to overcome the resistance movement and make it gain acceleration *(Zhang et al., 2001)*. The force analysis is shown in Figure 5.

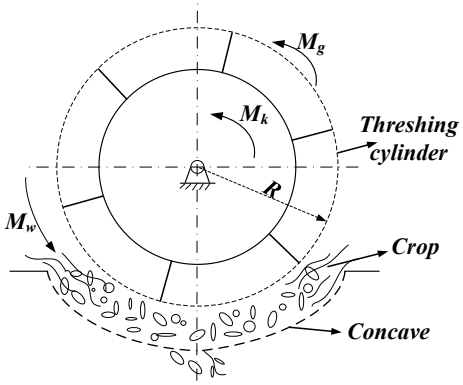


Fig. 5 - Force analysis diagram of threshing cylinder

M_k –idle running load torque of threshing cylinder, [N·m]; M_g – the inertia moment of threshing cylinder, [N·m]; M_w –the working torque of threshing cylinder, [N·m]

(1) Idle running load torque

The threshing cylinder has to overcome mechanical friction resistance and wind resistance during idle running, and according to Golikovich's cylinder theory *(Zhao,1984)*, the total idle running resistance torque is:

$$M_k = A + B\omega^2 \quad (4)$$

where: ω = the angular velocity of the cylinder[rad/s]; A = the torque generated by mechanical friction, taken as 0.004; B = the cylinder wind force torque coefficient, taken as 0.64 × 10-6.

(2) Moment of inertia of threshing cylinder

$$M_g = J \frac{d\omega}{dt} \quad (5)$$

where: J = moment of inertia of the threshing cylinder [kg·m²].

(3) Working torque of threshing cylinder

The working torque of the threshing cylinder includes the torque required to accelerate the movement of the crops and the torque needed to overcome the friction between the crops and the cover plate, concave plate, and spike teeth during the movement. The research shows that *(Zhang et al., 2000)*, the tangential speed of crops at the threshing cylinder outlet is 1/2~1/5 of the linear speed of the cylinder rotation. The crop outlet speed ratio λ is introduced, which is defined as the ratio of the velocity of the stalks being ejected at the discharge opening to the rotational linear velocity, helps to analyze the process. The crop movement speed at the feeding inlet of the threshing cylinder is significantly lower than the average movement speed within the cylinder, so it can be neglected. Assuming that the crop flows continuously through the threshing cylinder without crop breakage or clogging, the amount of crop fed in at time Δt is essentially equal to the amount of crop flowing out. Neglecting the axial speed of motion of the stem draft output, the amount of change in the kinetic energy of crop in the threshing cylinder in time Δt is given as follows *(Zhang et al.,1999)*:

$$E_v = \frac{1}{2} q \Delta t \frac{\lambda+\Delta}{1+\Delta} R^2 \omega^2 \tag{6}$$

where: q = feed rate [kg/s]; λ = crop outlet speed ratio; Δ = grass-to-grain ratio; R = the effective radius of the spike teeth on cylinder [m].

Therefore, the torque required by the threshing cylinder to propel the crop in accelerated motion is:

$$M_v = \frac{1}{2} q \frac{\lambda+\Delta}{1+\Delta} R^2 \omega \tag{7}$$

Research has shown that the torque required to accelerate the crop always accounts for a certain proportion of the total working torque. Therefore, Golikovich introduced the friction coefficient f to represent the proportional relationship between the working resistance and the total working torque *(Kanavetsky,1983)*, as shown in equation (8):

$$M_w = \frac{M_v}{1-f} \tag{8}$$

where: f = the friction coefficient of threshing cylinder.

Combining equations (4), (5) and (8), the torque equation for the threshing cylinder can be obtained as shown in equation (9):

$$M_T = M_g + M_k + M_w = J \frac{d\omega}{dt} + (A + B\omega^2) + \frac{qR^2\omega(\Delta+\lambda)}{2(1-f)(\Delta+1)} \tag{9}$$

Combining equations (2), (3) and (9), the mathematical model of motor-driven threshing cylinder can be obtained as shown in equation (10):

$$\frac{3}{2} P_n i_q \left[\psi_f + (L_d - L_q) i_d\right] = J \frac{d\omega}{dt} + (A + B\omega^2) + \frac{qR^2\omega(\Delta+\lambda)}{2(1-f)(\Delta+1)} \tag{10}$$

Control strategy for electrically driven threshing cylinder

When the rotating shaft of the PMSM is coupled to the threshing cylinder, the moment of inertia of the motor consists of the moment of inertia of the motor rotor and the moment of inertia of the threshing cylinder. The fluctuation of crop feed rate makes the load of threshing cylinder produce random disturbances, which causes the change of moment of inertia, and the required torque of threshing cylinder is positively correlated with its own moment of inertia, when the moment of inertia of the threshing cylinder increases, the required torque of the cylinder increases accordingly, and vice versa *(Liu, 2013; Li, 2023)*. Therefore, the online identification strategy of moment of inertia is introduced to enhance the control accuracy and stability of the system.

The control system block diagram of the electrically driven threshing cylinder is shown in Figure 6, including speed control loop, current control loop, coordinate transformation and moment of inertia identification module.

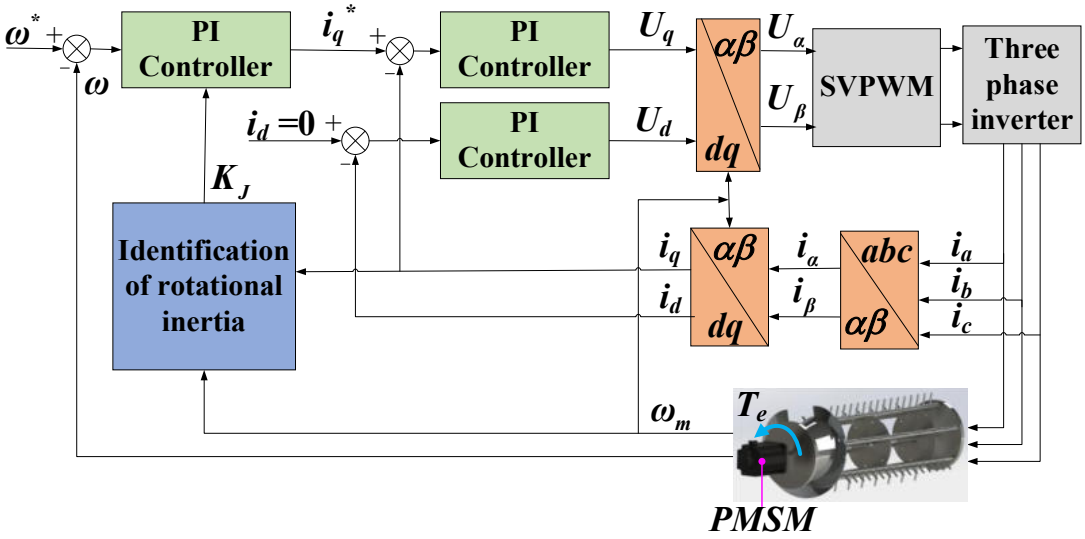


Fig. 6 - Control block diagram of electrically driven threshing cylinder

Identification of moment of inertia of electrically driven threshing cylinder system

Identification of moment of inertia of motor rotor

When the motor is undergoing acceleration or deceleration, the direction of the electromagnetic torque and the load is not fixed. Ignoring the motor's damping coefficient, let $\alpha=d\omega_m/dt$, then the mechanical motion equation of the motor can be expressed as:

(a) Acceleration process:

$$J\alpha_1 = T_e - T_L = K_T I_q - T_L \tag{11}$$

(b) Deceleration process:

$$J\alpha_2 = T_e + T_L = -(K_T I_q + T_L) \tag{12}$$

where: K_T = torque coefficient; I_q = q-axis current of motor(A).

In order to accurately identify the moment of inertia, it is necessary to take into account the effect of the load torque, and the load is equated as follows:

(a) Equation of motion for acceleration process:

$$K_T I_q = J\alpha_1 + T_L \triangleq J_{Acc}\alpha_1 \tag{13}$$

Then the equivalent moment of inertia during acceleration process is shown in equation (14):

$$J_{Acc} \triangleq J + \frac{T_L}{\alpha_1} \tag{14}$$

(b) Equation of motion for deceleration process:

$$K_T I_q = J\alpha_2 - T_L \triangleq J_{Dec}\alpha_2 \tag{15}$$

Then the equivalent moment of inertia during deceleration process is shown in equation (16):

$$J_{Dec} \triangleq J - \frac{T_L}{\alpha_2} \tag{16}$$

This leads to the estimation equation for the moment of inertia of the motor rotor as shown in equation (17):

$$\hat{J} = \frac{J_{Acc}+J_{Dec}}{2} = J + \frac{1}{2}\left(\frac{T_L}{\alpha_1} - \frac{T_L}{\alpha_2}\right) \approx J \tag{17}$$

The identification process of motor rotor moment of inertia is shown in Figure 7:

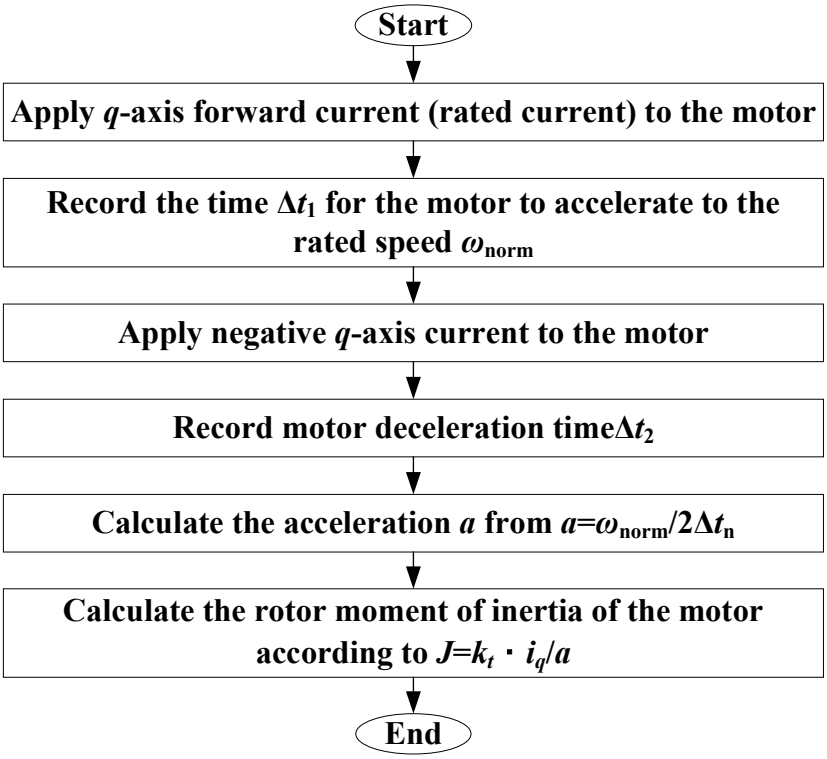


Fig. 7 - Flowchart for identification of motor rotor moment of inertia

Identification of moment of inertia of threshing cylinder

The moment of inertia identification of the threshing cylinder is implemented using the recursive least squares method with a forgetting factor *(He, 2020)*. The dynamic equations of the servo system are shown in equations (18) - (20):

$$T_m = JA_m \tag{18}$$

$$T_m = T_e - T_d - T_f \tag{19}$$

$$A_m = \frac{d\omega_m}{dt} \tag{20}$$

The performance index function equation (21) is constructed using T_m and A_m as input observations and the threshing cylinder moment of inertia J as the estimated quantity:

$$y = [T_m - JA_m]^2 \tag{21}$$

The criterion function is shown in equation (22):

$$V_N(k) = \frac{1}{N}\sum_{i=1}^{N}\left[T_m(k) - \hat{J}(k)A_m\right]^2 \tag{22}$$

The moment of inertia identification algorithm of the threshing cylinder is constructed based on the recursive least squares theory *(Song, 2019)*, as shown in equation (23):

$$\begin{cases} \hat{J}(k) = \hat{J}(k-1) + L(k)\left[T_m(k) - \hat{J}(k-1)A_m(k)\right] \\ L(k) = \frac{P(k-1)A_m(k)}{1+A_m^2(k)P(k-1)} \\ P(k) = [1 - L(k)A_m(k)]P(k-1) \end{cases} \tag{23}$$

Based on equation (23), the least squares identification algorithm with the addition of a forgetting factor λ is shown in equation (24):

$$\begin{cases} \hat{J}(k) = \hat{J}(k-1) + L(k)\left[T_m(k) - \hat{J}(k-1)A_m(k)\right] \\ L(k) = \frac{P(k-1)A_m(k)}{\lambda+A_m^2(k)P(k-1)} \\ P(k) = [1 - L(k)A_m(k)]P(k-1)\lambda^{-1} \end{cases} \tag{24}$$

where: T_m = the torque for accelerating or decelerating the rotational inertia of the threshing cylinder [N·m]; T_e = the motor output torque [N·m]; T_d = the disturbance torque of threshing cylinder [N·m]; T_f = friction torque [N·m]; A_m = the motor acceleration [r/s^2]; J = the moment of inertia of threshing cylinder [kg·m^2].

The moment of inertia identification process for the threshing cylinder is illustrated in Figure 8.

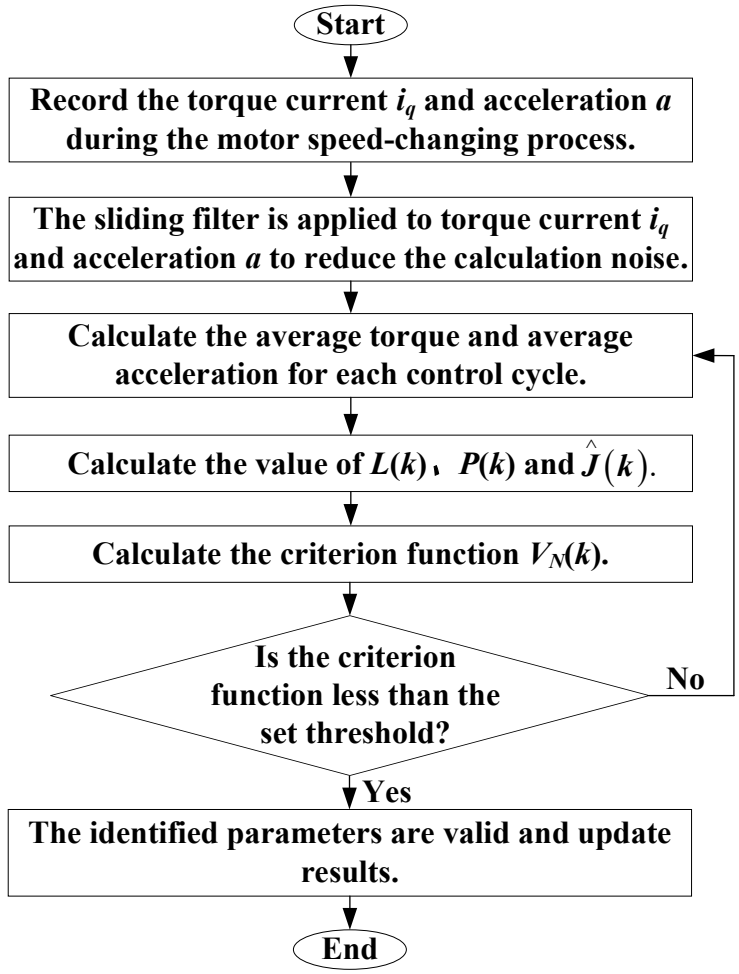


Fig. 8 - Flowchart for the identification of the moment of inertia of the threshing cylinder

Self-tuning of speed loop parameters in electrically driven threshing cylinder control system

The purpose of moment of inertia identification is to make real-time adjustments to the speed loop parameters based on changes in inertia, optimizing the conversion structure of the speed loop, and improving the responsiveness of speed conversion. The speed loop control block diagram is shown in Figure 9.

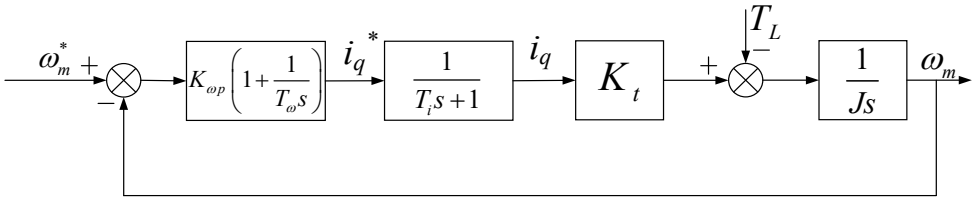


Fig. 9 - Speed loop control block diagram

In Figure 9, ω^*_m is the given speed; $K_{\omega p}$ is the proportional coefficient of the speed loop; T_ω is the integral time constant of the speed loop; T_i is the equivalent time constant of the current loop.

Based on the control block diagram in Figure 9, the open-loop transfer function of the system is derived as Equation (25):

$$G(s) = K_{\omega p}\left(1+\frac{1}{T_\omega s}\right)\left(\frac{1}{T_i s+1}\right)\frac{K_t}{Js} \tag{25}$$

The speed loop is a typical type II system *(Zhu et al., 2023)*, and the relationships of the system parameters are shown in equations (26) and (27):

$$T_\omega = hT_i \tag{26}$$

$$K = \frac{h+1}{2h}\cdot\frac{J}{T_i K_t} \tag{27}$$

where: K = the open-loop gain; h = the intermediate frequency bandwidth, according to the performance index of the system, take h = 5.

The calculation process of the PI parameters in the speed loop is shown in equations (28) and (29):

$$K_{\omega p} = \frac{J(h+1)}{2hT_i K_t} = \frac{J(h+1)R_s}{3hLp_n\psi_f} \tag{28}$$

$$K_{\omega i} = \frac{J(h+1)}{2h^2T_i^2 K_t} = \frac{J(h+1)R_s^2}{3h^2L^2p_n\psi_f} \tag{29}$$

where: $K_{\omega i}$ = Integral coefficient of speed loop.

When the motor drives the threshing cylinder, the total moment of inertia J is shown in equation (30):

$$J = J_0 + J_L \tag{30}$$

where: J_0 = the moment of inertia of motor rotor [kg·m²]; J_L = the moment of inertia of threshing cylinder [kg·m²].

The ratio of the moment of inertia of the threshing cylinder to the motor rotor is defined as the load inertia ratio K_J, the expression of which is shown in equation (31):

$$K_J = \frac{J_L}{J_0} \tag{31}$$

According to equations (28), (29) and (31), the PI parameters can be transformed as shown in equations (32) and (33):

$$K_{\omega p} = \frac{(K_J+1)J_0(h+1)}{2hT_i K_t} = \frac{(K_J+1)J_0}{3hLp} \tag{32}$$

$$K_{\omega i} = \frac{(K_J+1)J_0(h+1)}{2h^2T_i^2 K_t} = \frac{(K_J+1)J_0(h+1)R_s^2}{3h^2L^2p_n\psi_f} \tag{33}$$

By substituting the identified inertia ratio K_J into equations (32) and (33), the PI parameters of the speed loop are continuously revised, achieving the self-tuning capability of the PI parameters for the electrically driven threshing cylinder control system.

Experimental equipment

In this paper, based on the $dSPACE1007$ platform, a control system equivalent simulation test bench for an electrically driven threshing cylinder is constructed, as shown in Figure 10.

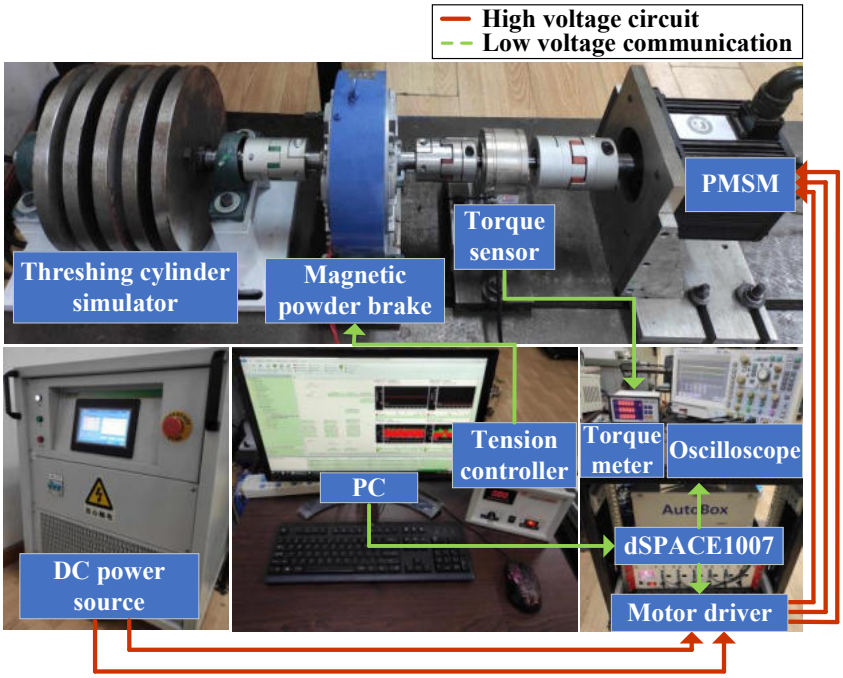


Fig. 10 - Equivalent simulation test bench for electrically driven threshing cylinder

Among them, the threshing cylinder simulator is used to simulate the threshing cylinder of the combine harvester, and the magnetic powder brake is used to simulate the load disturbance of the threshing cylinder caused by the crop feed rate of the combine harvester during the field operation. According to the field operation environment and operational requirements of combine harvester, three experimental conditions are designed to compare control effects and verify the superiority of the proposed algorithm.

RESULTS ANALYSIS AND DISCUSSION

Condition 1:

As shown in Figure 11, the threshing cylinder is considered a large inertia component due to its size, shape, structure and other factors, and the required torque is positively correlated with its own moment of inertia. Therefore, at the beginning of the harvesting operation the resistance of the threshing cylinder is larger, resulting in a higher starting current, which can lead to overshoot in the speed and a slower response time of the control system. Thus, it is necessary to enhance the responsiveness and robustness of the control system.

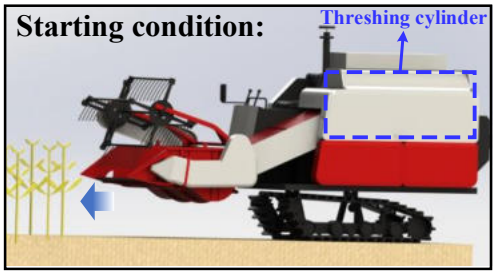
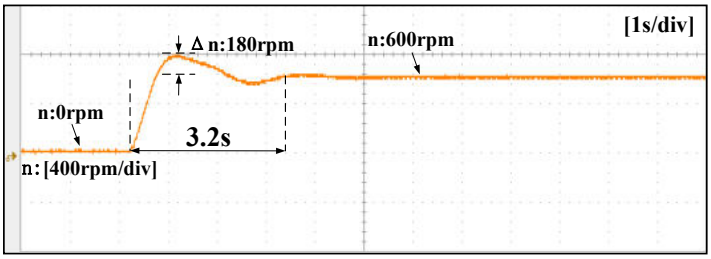


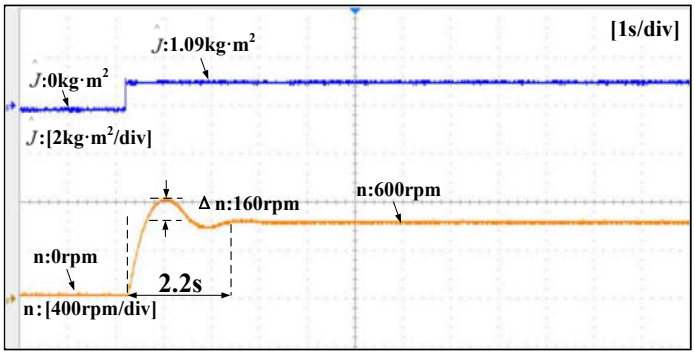
Fig. 11 - Starting condition of the threshing cylinder in the combine harvester

As shown in Figure 12, the start-up performance of the electrically driven threshing cylinder is compared with that of the traditional PI control method and the moment of inertia identification control method based on this paper, in which the sum of the moment of inertia of the motor and the threshing cylinder simulator is J=1.09 kg·m^2, and the target speed is 600 r/min.

It can be found that, in the start-up process of the electrically driven threshing cylinder, when the speed reaches the target speed, the value of the moment of inertia identified by the system in Figure 12(b) reaches the actual moment of inertia value, demonstrating high accuracy and good steady-state performance. After adaptive adjustment of the parameters of the speed loop, the start-up speed overshoot is 160 r/min, and the convergence time of speed oscillation is 2.2 s, which is 11.1% and 31.3% shorter than that of the speed overshoot amount of 180 r/min and the convergence time of 3.2 s in Figure 12(a), respectively.



(a) Traditional PI control method



(b) Control method based on moment of inertia identification

Fig. 12 - Comparison of start-up performance of electric drive system

The electrically driven threshing cylinder control method based on moment of inertia identification can effectively reduce the speed inertial shock and oscillation of the system during start-up process, which can effectively mitigate wear and tear on combine harvester.

Condition 2:

As shown in Figure 13, during harvesting operations, the combine harvester may encounter adverse weather conditions such as strong winds and heavy rain, which can cause crops to lodge. Additionally, the natural growth density of the crops may fluctuate, and the forward speed of the combine harvester can also vary due to factors like ground conditions and driver operating habits. These various external factors can lead to fluctuations in the feed rate of the combine harvester. Therefore, it is essential to enhance the stability of the threshing cylinder's speed to ensure a smooth operation process and improve the quality of threshing.

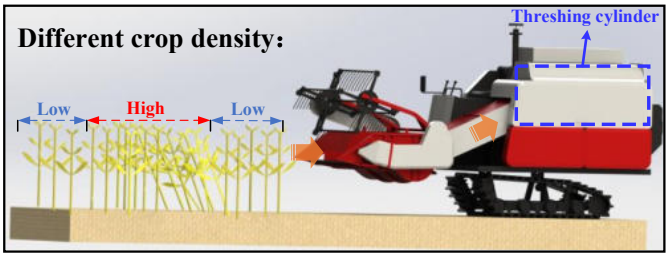
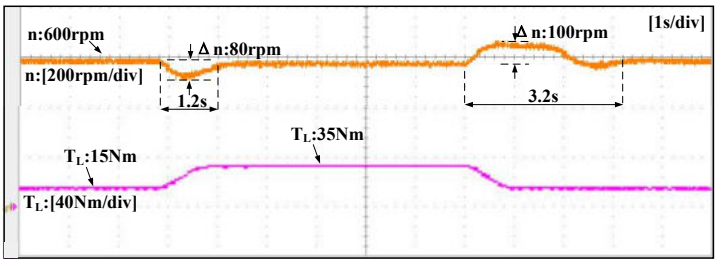
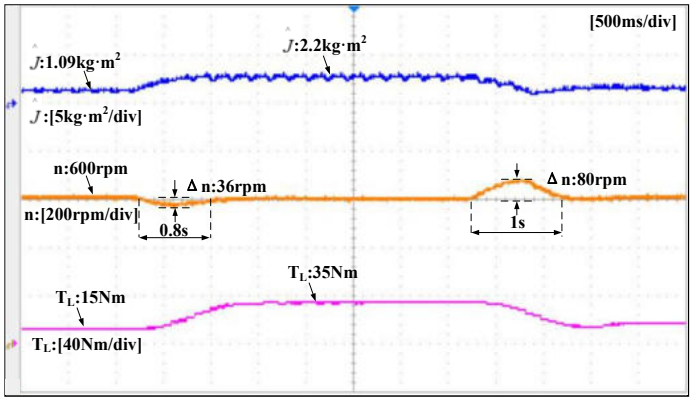


Fig. 13 - Fluctuation condition of feed rate to the threshing cylinder in combine harvester

The experimental results of the feed rate fluctuation tests for the two control strategies are given in Figure 14. In the feed rate fluctuation test, the electrically driven threshing cylinder runs at the rated speed of 600 r/min, the feed rate load changes abruptly from 15 Nm to 35 Nm, and then the load changes abruptly to 15 Nm after the speed stabilizes. As can be seen in Figure 14(b), when the feed rate load changes abruptly, the system can identify the actual value of moment of inertia and track the actual value, which has a better dynamic performance. The value of moment of inertia is fed back to the controller for real-time updating, and after self-tuning of the PI values of the speed loop, the maximum drop in speed and the maximum overshoot are 36 r/min and 80 r/min respectively, which are 55% and 20% less than those of 80 r/min and 100 r/min in Figure 14(a), and the dynamic adjustment time in Figure 14(b) during the process of abrupt increase and decrease of feed load are shortened by 33.3% and 68.8% respectively, indicating an enhanced disturbance rejection capability of the control system for the electrically driven threshing cylinder.



(a) Traditional PI control method



(b) Control method based on moment of inertia identification

Fig. 14 - Comparison of load sudden change experiment

The moment of inertia identification-based speed control method significantly enhances the load disturbance rejection performance of the electrically driven threshing cylinder, improving the system's robustness. This results in a smoother and more seamless threshing process for the crops, thereby further increasing the processing efficiency and the quality of threshing.

Condition 3:

As shown in Figure 15, during harvesting operations, the moisture content of crops in the same field can fluctuate due to external environmental influences. Therefore, the speed of the threshing cylinder needs to be adjusted in real-time. When the moisture content of the crops increases, the speed of the threshing cylinder should be appropriately increased; conversely, when the moisture content decreases, the speed should be appropriately reduced.

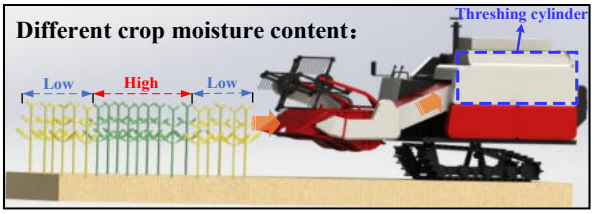
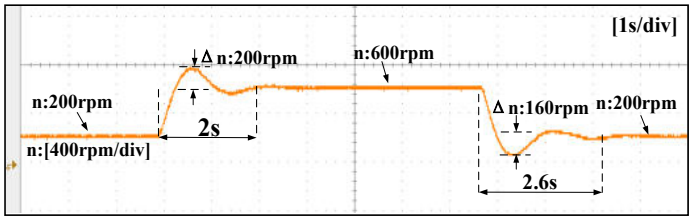


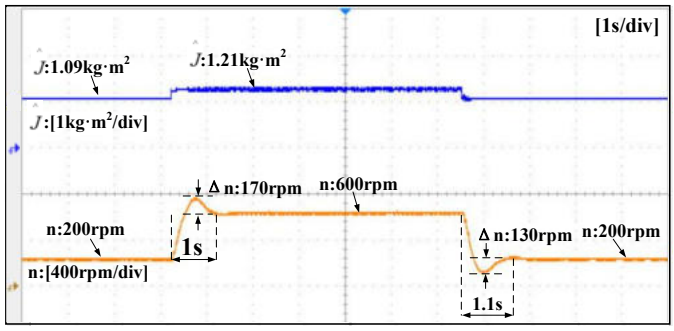
Fig. 15 - Fluctuating condition of crop moisture content

In order to verify the dynamic performance of the strategy proposed in this paper in the speed regulation process, the results of the comparison of the variable speed performance of the two control methods are given in Figure 16. In the experiment, the speed of the electrically driven threshing cylinder is increased from 200 r/min to 600 r/min, and then decreased back to 200 r/min after the speed stabilizes.

It can be seen that the system in Figure 16(b) can identify the actual value of moment of inertia during the speed change process and can track the actual value faster; the speed adjustment time during acceleration is 1 s, and the overshoot of the speed of the threshing cylinder is 170 r/min, which is 50% shorter and 15% smaller than the 2 s convergence time and 200 r/min speed overshoot of the traditional PI control strategy in Figure 16(a); the speed convergence time and the overshoot of the speed in Figure 16(b) are 57.7% shorter and 18.8% smaller, respectively, compared to Figure 16(a) during the speed deceleration process.



(a) Traditional PI control method



(b) Control method based on moment of inertia identification

Fig. 16 - Comparison of speed variation experiment

The speed control method based on moment of inertia identification effectively improves the speed regulation responsiveness and stability of the threshing cylinder in the combine harvester. For different types of crops or varying growth stages of the same crop, the adaptability of the threshing cylinder's speed is enhanced, which helps reduce harvesting losses and improve the crop's cleaning rate, further enhancing the quality of the harvest.

CONCLUSIONS

This paper studies the electrically driven speed control system for the threshing cylinder of a combine harvester during field operation, based on the working condition requirements. A dynamic model of the threshing cylinder is established, and a mathematical model of the electrically driven for the threshing cylinder is constructed by combining the motor motion model and characteristics of a permanent magnet synchronous motor. A load variation control strategy based on rotational inertia identification is proposed to meet the demands of multiple working points at different speeds under various operating conditions.

The experimental results indicate that during the startup process of the threshing cylinder, the control method based on rotational inertia identification reduces the overshoot and convergence time of the rotational speed by 11.1% and 31.3% respectively, compared to the traditional PI control method, effectively lowering the system's inertial impact and oscillation.

When there are fluctuations in the crop feed rate of the combine harvester, the control method based on rotational inertia identification decreases the speed drop and overshoot by 55% and 20%, respectively, while the dynamic adjustment time is shortened by 33.3% and 68.8%, enhancing the system’s disturbance resistance. Additionally, under varying crop moisture content conditions, the convergence times of acceleration and deceleration during speed adjustments are reduced by 50% and 57.7%, while the overshoot of the rotational speed decreases by 15% and 18.8%. These improvements enhance the responsiveness and stability of the threshing cylinder speed regulation. This system can effectively adapt to the dynamic power demands of modern agriculture, providing a theoretical basis for the development of intelligent agricultural equipment.

Based on this study, follow-up research will focus on conducting collaborative research between the threshing cylinder and other working modules to explore the optimal speed matching ratios between the modules, thereby improving the overall operational efficiency of combine harvester. In addition, the research will also aim to further reduce energy consumption through advanced energy management strategies, achieving greater economic efficiency and environmental friendliness. Furthermore, the research will involve manufacturing a prototype for field experiments to further verify the superiority of the electric drive operating system.

ACKNOWLEDGEMENT

This work was supported by the Jiangsu Agricultural Science and Technology Innovation Fund (CX(22)1005).

REFERENCES

[1] Abdeen, M. A., Wu, W., Salem, A. E., Elbeltagi, A., Salem, A., Metwally, K.A., Zhang, G., Elwakeel, A.E. (2025). The impact of threshing unit structure and parameters on enhancing rice threshing performance. *Scientific Reports*, 15(1), 6250. DOI: https://doi.org/10.1038/s41598-025-91118-5.

[2] Cristea O-D., Niţu M., Constantin G., Munteanu M., Milea O-E., Zaharia R., Grădilă M. (2023). Research on the testing of axial flow threshing apparatus for improving their qualitative working indices, *INMATEH-Agricultural Engineering,* 70(2), pp.607-614, DOI: https://doi.org/10.35633/inmateh-70-58.

[3] Da, Q. (2021). *Analysis and optimization design of threshing device of combine harvester (联合收割机脱粒装置分析及优化设计)* (Master's thesis). Xi'an University of Technology) master https://link.cnki.net/doi/10.27398/d.cnki.gxalu.2021.000349 DOI: 10.27398/d.cnki.gxalu.2021.000349.

[4] Fu, X. H., Gu, S. D. &Xiong, J. X. (2024). Overview of decoupling control methods for AC and DC axis currents of permanent magnet synchronous motors (永磁同步电机交直轴电流解耦控制方法综述). *Proceedings of the CSEE* (01), 314-332. DOI: 10.13334/j.0258-8013.pcsee.222266

[5] Gong, J.L., Luo, Z.J., & Zhang, Y.F. (2024). Optimised design and simulation analysis of longitudinal flow corn cone threshing device. *INMATEH - Agricultural Engineering*, Vol. 73(2), pp. 63-72. https://doi.org/10.35633/inmateh-73-05

[6] Gou F., Wang J., Ni Y., Qian Z., Yang T., Jin C. (2025). A review of innovative design and intelligent technology applications of threshing devices in combine harvesters for staple crops, *INMATEH - Agricultural Engineering,* 75(1), pp. 706-725, DOI: https://doi.org/10.35633/inmateh-75-61.

[7] Han, S.Q. (2017). *Research on electro hydraulic proportional control technology of hydraulic drive for threshing cylinder of combine harvester (联合收割机脱粒滚筒液压驱动电液比例控制技术研究)* (Master's thesis). Chinese Academy of Agricultural Sciences. https://kns.cnki.net/kcms2/article/abstract

[8] Hou, A. K. (2020). Design of Control System for Fully Feeding Combine Harvester (全喂入式联合收割机控制系统设计) (Master's Thesis, Shanghai Jiao Tong University). DOI: 10.27307/d.cnki.gsjtu.2020.000906.

[9] He, X.H. (2020). *Research on active disturbance rejection control strategy of permanent magnet synchronous motor based on inertia identification (基于惯量辨识的永磁同步电机自抗扰控制策略研究)* (Master's thesis). Harbin Institute of Technology. DOI: 10.27061/d.cnki.ghgdu.2020.002991.

[10] Ivan Gh., Vlăduţ V. (2015). The intensification of shaking process to the conventional cereal harvesting combines, *Proceedings of the 43 International Symposium on Agricultural Engineering "Actual Tasks on Agricultural Engineering",* pp. 417-430, Opatija –Croatia.

[11] Jiang, R.F. (2015). Research on Intelligent Control System of Electric Driven Combine Harvester (电驱动联合收割机智能控制系统的研究) (Master's Thesis)., Northwest A&F University https://kns.cnki.net/kcms2/article/abstract

[12] Kanavetsky (1983). *Harvesting machinery China Agricultural machinery press*.

[13] Liu, H.L., Shen, C., Hu, L.L., Chang, C.& Cao, G.Q. (2024). Research progress and development trend of electric agricultural equipment (电动农业装备研究进展与发展趋势). *Transactions of the Chinese Society of Agricultural Engineering* (23), 39-51

[14] Li, H.B., Wang, Q.H., Ma, J., Wang, Y.N., Yue, D. & Geng, D.Y. (2023). Design and Experiment of Transverse Axial Flow Corn Flexible Threshing Device. *INMATEH - Agricultural Engineering,* 69(1), 461–470. https://doi.org/10.35633/inmateh-69-43

[15] Liu, X.F., Chen, T.K., Song, H., Duan, G.C., Wei, Z.S.& Wang, S.Q. (2024). Development history and trend of domestic wheat combine harvesters (国内小麦联合收割机发展历程及趋势). *Tractor & Farm Transporter* (03), 15-17+32

[16] Liu, Z. (2013). Design and implementation of permanent magnet synchronous motor servo system with PI parameter self-tuning (带 PI 参数自整定的永磁同步电机伺服系统的设计与实现) (Master thesis). Hunan University. https://kns.cnki.net/kcms2/article/abstract

[17] Li, Y. (2023). *Research on sliding mode control system of permanent magnet synchronous motor based on moment of inertia identification (基于转动惯量辨识的永磁同步电机滑模控制系统研究)* (Master's thesis). Jiangsu University. master DOI: 10.27170/d.cnki.gjsuu.2023.001030.

[18] Miu, P. I., & Kutzbach, H. D. (2007). Modeling and simulation of grain threshing and separation in threshing units—part I. *Computers & Electronics in Agriculture*, 60(1), 96-104. DOI: 10.1016/j.compag.2007.07.003.

[19] Ou, Y.A., Wang, M.L., Cui, T.& Wang, C. (2024). Application status and development trend of grain crop production equipment(粮食作物生产装备应用现状与发展趋势). *Journal of Chinese Agricultural Mechanization* (10), 298-304. Doi: 10.13733/j.jcam.issn.2095-5553.2024.10.043

[20] Qu, Z., Zhang, D. X., Yang, L., Zhang, T. L., Wang, Z. D. &Cui, T. (2018). Longitudinal flow corn threshing and separation device feeding rate and cylinder speed test (纵轴流玉米脱粒分离装置喂入量与滚筒转速试验) . *Transactions of the Chinese Society for Agricultural Machinery* (02), 58-65

[21] Song, Z.C., Diao, P.S., Cui, P.D., Wei, M.J., Miao, H.Q. & Yao. W.Y. (2022). Design and Experimental Study of Flexible Threshing Device for Longitudinal Axial Flow Corn. *INMATEH - Agricultural Engineering*, 67(2), 155–165. https://doi.org/10.35633/inmateh-67-15

[22] Song, H.S. (2019). *Research on identification method of moment of inertia of permanent magnet synchronous motor (永磁同步电机转动惯量的辨识方法研究)* (Master's thesis). Qilu University of Technology https://kns.cnki.net/kcms2/article/abstract

[23] Tang, Q., Jiang, L., Yu, W.Y., Wu, J. & Wang, G. (2024). Design and Experiment of High Moisture Corn Threshing Device with Low Damage. *INMATEH - Agricultural Engineering*, 74(3), 172–183. https://doi.org/10.35633/inmateh-74-15

[24] Tang, X.H., Jin, C.Q., Zhang, G.H., Guo, Z., Zhao, N. &Xu, B. (2022). Research status of threshing and separating device of combine harvester in China(我国联合收获机脱粒分离装置的研究现状). *Journal of Agricultural Mechanization Research* (03), 1-9+15. DOI: 10.13427/j.cnki.njyi.2022.03.001

[25] Vlădut N.-V., Biris S.St., Cârdei P., Găgeanu I., Cujbescu D., Ungureanu N., Popa L.-D., Perişoară L., Matei G., Teliban G.-C. (2022). Contributions to the Mathematical Modeling of the Threshing and

Separation Process in An Axial Flow Combine, *Agriculture*, 12(10),1520, https://doi.org/10.3390/agriculture12101520.

[26] Vlădut N.-V., Ungureanu N., Biris S.St., Voicea I., Nenciu F., Găgeanu I., Cujbescu D., Popa L.-D., Boruz S., Matei G., Ekielski A., Teliban G.C. (2023). Research on the identification of some optimal threshing şi separation regimes in the axial flow apparatus, *Agriculture,* 13(4): 838, DOI: 10.3390/agriculture13040838, agriculture-2301663.

[27] Wang, Z.D., Cui, T., Zhang, D.X., Yang, L., He, X.T.& Zhang, Z.P. (2021). Design and experiment of striped threshing element of corn combine harvester (玉米联合收获机纹杆式脱粒元件设计与试验). *Transactions of the Chinese Society for Agricultural Machinery* (09), 115-123

[28] Wang, J.W., Wang, X.G., Yu, X.H., Zheng D.C., Li, Z.W. & Song, H.Y. (2022). Design and Experiment of Telescopic Rod Tooth-Ribbed Rod Roller Type Buckwheat Threshing Device. *INMATEH - Agricultural Engineering*, 67(2), 434–444. https://doi.org/10.35633/inmateh-67-44

[29] Wang, P., Jin, C.Q., Wang, C., Li, P.P.& Zhao, Z.H. (2023). Research status of threshing system of grain combine harvester (谷物联合收获机脱粒系统研究现状). *Journal of Chinese Agricultural Mechanization* (05), 48-57. DOI:10.13733/j.jcam.issn.2095-5553.2023.05.007

[30] Xiang, Z.X., Wei, J.Q., & Zhu, X.Y. (2024). Torque Ripple Suppression of a PM Vernier Machine From Perspective of Time and Space Harmonic Magnetic Field. *In IEEE Transactions on Industrial Electronics*, vol. 71, no. 9, pp. 10150-10161, Sept. 2024. DOI: 10.1109/TIE.2023.3333052.

[31] Xiang, Z.X., Zhou, Y.T., Zhu, X.Y., Quan, L., Fan, D.Y., & Liu, Q. (2024). Research on Characteristic Airgap Harmonics of a Double-Rotor Flux-Modulated PM Motor Based on Harmonic Dimensionality Reduction. *In IEEE Transactions on Transportation Electrification*, vol. 10, no. 3, pp. 5750-5761, Sept. 2024.Doi: 10.1109/TTE.2023.3318648.

[32] Yang, L.Q., Wang, W.Z., Zhang, H.M., Li, L.H., Wang, M.M.& Hou, M.T. (2018). Improved design and bench test of tangential axial flow corn threshing system (切流-横轴流玉米脱粒系统改进设计及台架试验). *Transactions of the Chinese Society of Agricultural Engineering* (01), 35-43

[33] Zewdie, B., Olaniyan, A. M., Wako, A., Alemu, D., & Lema, T. (2024). Optimization of Melkassa Agricultural Research Center (Marc) Bean Thresher Parameters Using Response Surface Method (Rsm). *INMATEH - Agricultural Engineering*, 74(3), 335–344. https://doi.org/10.35633/inmateh-74-29

[34] Zhang, K., Ma, J. E., Lu, J. Y., Liu, Y. Q., Qiu, L., Liu, X., &Fang, Y. T. (2025) Nonlinear flux observer for Sensorless control of IPMSM based on a novel regression model. *IEEE Transactions on Power Electronics*, 40. DOI: 10.1109/TPEL.2024.3498001.

[35] Zhang, R.C., Sang, Z.Z. (2001). Dynamic simulation of axial threshing process (轴流脱粒过程的动力学仿真研究). *Research of Agricultural Modernization* (02), 111-114+125

[36] Zhao, Y. (1984). On the dynamic balance of threshing cylinder of combine harvester (试论联合收获机的脱粒滚筒的动力平衡问题). *Transactions of the Chinese Society for Agricultural Machinery* (04), 34-45

[37] Zhang, R.C., Sang, Z.Z. (2000). Grain dynamics simulation in axial threshing space (轴流脱粒空间谷物动力学仿真). *Journal of Agricultural Mechanization Research* (04), 36-40. DOI: 10.13427/j.cnki.njyi.2000.04.012

[38] Zhang, R.C., Sang, Z.Z. (1999). Study on power consumption model of axial threshing cylinder (轴流脱粒滚筒功耗模型的研究). *Transactions of the Chinese Society of Agricultural Engineering* (04), 121-125

[39] Zhu, L.T.& Jiang, Q. (2023). A novel load torque and moment of inertia identification strategy for PMSM (一种新型 PMSM 负载转矩和转动惯量辨识策略). *Electronic Science and Technology* (06), 80-86. DOI: 10.16180/j.cnki.issn1007-7820.2023.06.012

STABILITY ANALYSIS OF FLAT-ELLIPTICAL GREENHOUSE SKELETON CONSIDERING INITIAL GEOMETRICAL IMPERFECTIONS
/
考虑初始几何缺陷的平椭圆管大棚骨架稳定性分析

Hengyan XIE[1,*], Cunxing WEI[2], Xin ZHENG[1], Wenbao XU[1]
[1] College of Civil Engineering and Water Conservancy, Heilongjiang Bayi Agricultural University, Daqing 163319, China;
[2] College of Engineering, Heilongjiang Bayi Agricultural University, Daqing 163319, China
Tel: +86-459-13766785587; E-mail: xiehy555@byau.cn
Corresponding author: Hengyan Xie
DOI: https://doi.org/10.35633/inmateh-76-31

Keywords: *flat-elliptical pipe greenhouse; initial imperfections; nonlinear buckling; full dynamic wind load; finite element analysis; structural stability*

ABSTRACT
This study investigates the nonlinear stability of flat-elliptical greenhouse skeletons under wind loads, accounting for initial imperfections. A finite element model was developed in ABAQUS, with nonlinear buckling analysis conducted via the arc-length method. Eigenvalue buckling analysis identified imperfection modes, and the impact of imperfection amplitudes on bearing capacity was assessed. Results showed that increasing imperfection amplitude decreased the ultimate bearing capacity, with a 461.2 N·m² capacity at L/300, and 520.26 N·m² at L/800. Initial imperfections notably influenced yield stages. This study demonstrates that considering initial imperfections provides a more accurate assessment of the skeleton's stability under extreme loads.

摘要
本研究研究探讨了在风荷载作用下，考虑初始缺陷的平面椭圆形温室骨架的非线性稳定性。通过 ABAQUS 建立了有限元模型，并采用弧长法进行非线性屈曲分析。特征值屈曲分析用于识别缺陷模式，并评估缺陷幅度对承载力的影响。研究结果表明，随着缺陷幅度的增加，最终承载力下降，在 L/300 情况下承载力为 461.2 N·m²，而在 L/800 情况下为 520.26 N·m²。初始缺陷显著影响了屈服阶段。研究表明，考虑初始缺陷能够更准确地评估骨架在极端荷载下的稳定性。

INTRODUCTION
In modern agriculture, greenhouses are essential for maintaining stable crop growth, particularly in regions with harsh or fluctuating climates. They offer controlled environments that improve yield and quality. The structural skeleton, as the main load-bearing system, is critical to a greenhouse's longevity, stability, and safety. Thus, investigating its mechanical behavior under complex loads holds significant theoretical and practical value.

Historically, bamboo served as the primary structural material until the 1950s, but its susceptibility to corrosion and degradation limited its durability. In the 1980s, hybrid structures combining bamboo and steel emerged to improve strength, yet corrosion at the interface remained problematic. With advancements in steel production and reduced costs in the 21st century, steel—particularly galvanized steel pipes with high corrosion resistance and load-bearing capacity—became the dominant material, markedly enhancing greenhouse performance and lifespan. Plastic greenhouses with different skeleton types as shown in Fig. 1.



a) Bamboo skeleton ***b) Bamboo-steel skeleton*** ***c) Steel skeleton***

Fig. 1 – Plastic greenhouses with different skeleton types

Hengyan Xie, Prof. Ph.D. Eng.; Cunxing Wei, Ph.D. Eng. Xin Zheng, Prof. Ph.D. Eng.; Wenbao Xu, Ph.D. Eng.

Steel structures, favored for their high strength and stiffness, resist external loads like wind and snow effectively while minimizing deformation. However, initial imperfections in steel components can compromise stability, often causing local or global buckling prior to reaching ultimate strength. These imperfections—defined by their location, shape, and evolution—are critical factors influencing failure modes. Nonlinear buckling analysis offers a more accurate evaluation of these effects, especially under complex or extreme load conditions. Cylindrical lattice shells, akin to greenhouse frames, have been extensively studied. For instance, Liu (2016) and Gu (2019) analyzed stochastic initial imperfections and their impact on buckling under various loads. Their findings underscore the necessity of including imperfections in structural analyses to ensure safety and performance reliability. Traditional analyses often assume ideal, defect-free models. Studies by *Ren (2019), Jiang (2021)*, and others employed finite element and time-domain methods to analyze stress and vibration responses in idealized skeletons. However, such simplifications may underestimate structural vulnerability under severe loads like heavy snow or strong winds, leading to significant instability and deformation.

Given the nonlinear nature of the loads acting on greenhouses, initial imperfections can exacerbate the risk of buckling and instability, affecting the long-term performance of the structure. Therefore, nonlinear buckling analysis of greenhouse skeletons, considering initial imperfections, is essential for a more accurate assessment of structural behavior under real-world loading conditions. Moreover, such analysis can reveal the impact of initial imperfection on the stability of the structure under extreme loads or adverse environmental conditions *(Cai, 2015; Zeng, 2024)*. While several studies have incorporated initial imperfections in the stability analysis of greenhouse skeletons, including the work by *Yu (2007) and Bao (2023)*, who performed nonlinear buckling analysis of arch-roof and Venlo-type greenhouses, there remains a gap in the research on the nonlinear buckling behavior of greenhouse skeletons under full dynamic wind loads. The specific mechanisms of structural instability in these conditions are not yet fully understood.

This study aims to fill this gap by assessing the stability of greenhouse structures under full dynamic wind load, highlighting potential instability risks induced by local buckling, and ultimately improving structural safety margins. The findings of this research will provide valuable theoretical support for the design, construction, and long-term operation of greenhouse structures, ensuring their safety and performance under extreme loading conditions.

MATERIALS AND METHODS

Analysis process

According to the code for design of steel structures *(GB50017-2017)* and the technical specification for space skeleton structures *(JGJ 7—2010)*, the impact of initial geometric imperfections, specifically the installation deviations from the intended curved surface shape, must be considered in the full-process analysis of lattice shell structures (skeletons). The distribution of initial geometric imperfections is typically represented by the lowest-order buckling mode of the structure, with the maximum value of the imperfection taken as 1/300 of the span of the lattice shell.

Based on these specifications, the following steps were taken to perform the nonlinear buckling analysis of the greenhouse skeleton structure:

(1) Finite Element Model Creation and Verification: A detailed finite element model of the greenhouse skeleton was established and verified to ensure its accuracy in simulating the structural behavior.

(2) Eigenvalue Buckling Analysis: A characteristic eigenvalue buckling analysis was conducted on the skeleton structure to determine the lowest-order buckling mode of the system.

(3) Simulation of Initial Geometric Imperfections: The distribution pattern of the initial geometric imperfections was simulated using the lowest-order eigenmode. The maximum value of the imperfections was set as 1/300 of the span of the greenhouse skeleton, as per the relevant design codes.

(4) Nonlinear Stability Analysis: A nonlinear stability analysis was performed using the arc-length method. The load-displacement curves and stability coefficients of the structure under different initial imperfections were compared to explore the influence of these imperfections on the stability of the structure.

Finite element model

In this study, a finite element model of a plastic greenhouse skeleton with 50 elliptical pipes was established using ABAQUS. The dimensional schematic of the skeleton is shown in Fig. 2.

As shown in Fig. 2, the structural span $L=10$ m; the structural height $H=3.6$ m; the rafter spacing $d=1$m.

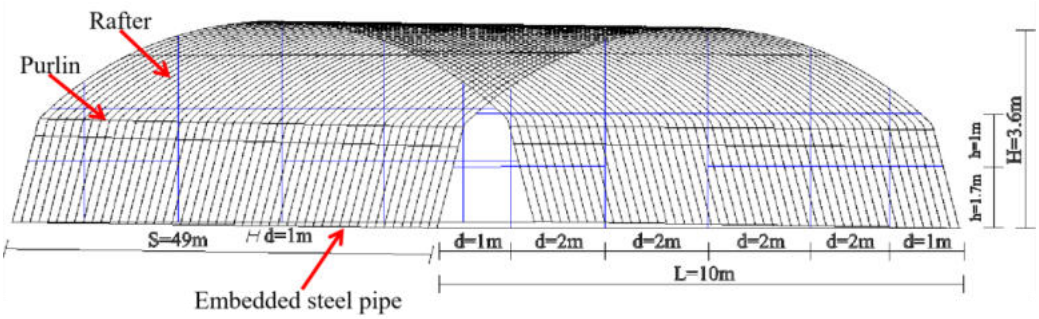


Fig. 2 – The dimensional schematic of the flat-elliptical pipe plastic greenhouse's skeleton

The material property parameters of the rafter, embedded steel pipe, and purlin are shown in Table 1.

Table 1

Material parameter of steel pipe

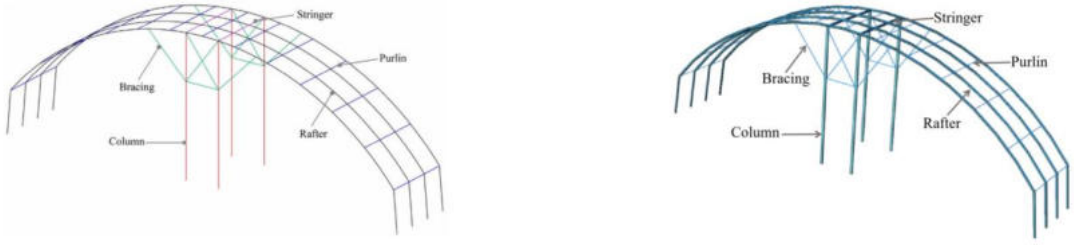
Material	*b*×*h* or *R* (mm)	*t* (mm)	ρ (kg/m³)	f_y (MPa)	λ	E (MPa)
Rafter	30×60	2	7.85	235	0.28	2.1×10^5
Embedded steel pipe	30×80	2	7.85	235	0.28	2.1×10^5
Purlin	ϕ 20	2	7.85	235	0.28	2.1×10^5

where: *b* is the width of section; *h* is the depth of section; *t* is thickness of section; *ρ* is density; f_y is the yield strength of steel; *λ* is Poisson ratio of steel; *E* is elasticity modulus of steel.

The C3D8R eight-node linear hexahedral element was selected to simulate the elliptical pipe greenhouse skeleton. The rafter was meshed according to its dimensions, with an approximate overall size set to 0.2, and each rafter was discretized into 2,380 elements. In actual engineering, the rafters and purlins are connected by clips, while the connections between the skeleton and the embedded steel pipe are welded. To improve computational efficiency, the connections between the rafters, purlins, and the embedded steel pipe were simplified to binding connections. This study applies full constraints between the two ends of the skeleton and the embedded steel pipe, restricting translational and rotational movements in all directions. For the other skeletons, hinged connections are used between the rafter and the embedded steel pipe.

Validation of the accuracy of the modeling method

Wang (2023) conducted a numerical analysis of a large-span pipe skeleton structure plastic greenhouse under the combined effects of dead load, wind load, live load, and crop load. Figure 3(a) shows the schematic diagram of the greenhouse skeleton model from the literature, while Figure 3(b) shows the finite element model established using the ABAQUS software in this study.



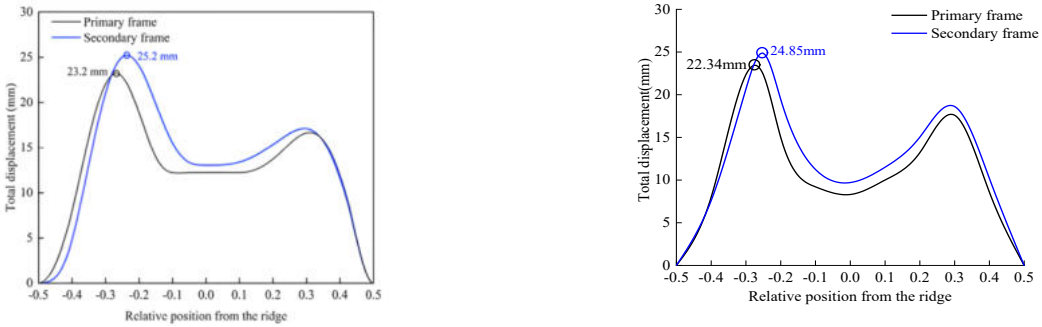
a) Literature ***b) Present***

Fig. 3 – Comparison of the structural diagrams of the greenhouse

To verify the accuracy of the modeling method, the validation model established in this study has the same material properties, skeleton dimensions, and boundary conditions as those in the original literature. All components are made of Q235 steel, with a yield strength of 235 MPa, Young's modulus of 206 GPa, Poisson's ratio of 0.3, and a density of 7850 kg/m³. The material is modeled using an ideal elastic-plastic constitutive relation. The rafter has a cross-section of a flat elliptical hollow pipe ($w\times h\times t=90\text{mm}\times40\text{mm}\times3\text{mm}$), while the columns have a rectangular hollow pipe cross-section ($w\times h\times t=90\text{mm}\times40\text{mm}\times3\text{mm}$).

The stringer also has a rectangular hollow pipe cross-section, with the same dimensions as the columns. The bracing has a circular hollow pipe cross-section ($d \times t = 32\text{mm} \times 2\text{mm}$), and the purlins have a circular hollow pipe cross-section as well ($d \times t = 25\text{mm} \times 1.5\text{mm}$). The bottom of the rafters and columns are set as fixed ends, restricting all degrees of freedom in all directions. The rafters and columns are connected with binding connections, and the connections between the bracing and the columns, rafters, and purlins are modeled as hinged.

In the literature, the greenhouse skeleton was modeled and analyzed using ANSYS software. In this study, the greenhouse skeleton was modeled and analyzed using the C3D8R solid element in ABAQUS finite element software. To verify the accuracy of the modeling method, displacement data at various points of the 1st and 2nd skeletons were extracted. The displacement data for the 1st and 2nd skeletons at each point are shown in Fig. 4.



a) Literature result *b) Present result*

Fig. 4 – Comparison of the total displacement distribution curves

As shown in Fig. 10, the displacement variation trend calculated using the modeling method in this study is in good agreement with the displacement variation trend from the literature. In the literature, the maximum displacement of the 1st skeleton is 23.2 mm, while the modeling method in this study yields a maximum displacement of 22.34 MPa, with a relative error of 3.7%. For the 2nd skeleton, the maximum displacement in the literature is 25.2 mm, while the maximum displacement calculated in this study is 24.85 MPa, with a relative error of 1.38%. The results fall within a reasonable error range, indicating that the finite element modeling method used in this study is reliable.

Wind loads calculation

This study primarily investigates the nonlinear behavior of the steel skeleton under wind loads. Therefore, the structural load combination mainly consists of dead loads and wind loads. For simplicity, in the subsequent eigenvalue buckling analysis, the critical buckling load of the structure is determined by applying the dead and wind loads in the form of concentrated forces at each point of the skeleton, as shown in Fig. 5.

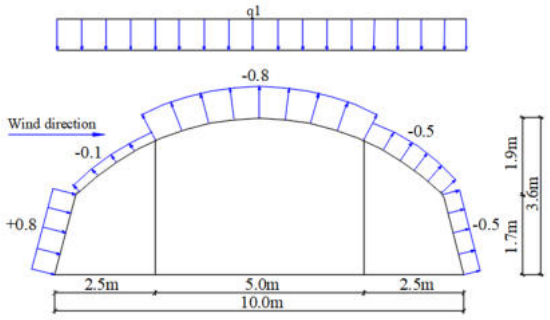


Fig. 5 – Shape coefficient on the flat-elliptical pipe skeleton plastic greenhouse

The plastic greenhouse studied in this study is located in Jiamusi City, Heilongjiang Province, China. According to the Chinese standard *GB/T51183-2016 (MOHUED, 2016),* the design service life of a plastic greenhouse is 10 years. Based on this code, the basic wind pressure in Jiamusi is 0.38 kN/m², which corresponds to the instantaneous wind speed with a duration of 3 seconds. On the other hand, according to the *Chinese standard GB/T50009-2012 (MOHUED, 2012),* the basic wind pressure in Jiamusi is 0.65 kN/m², which is based on the 10-minute average wind speed for a 50-year return period. The ratio of the 10-year return period wind pressure to the 50-year return period wind pressure is 0.734, thus the basic wind pressure for a 10-year return period with a 10-minute duration is 0.65 × 0.734 = 0.477 kN/m². After comparing the results from both codes, the basic wind pressure of 0.477 kN/m² was adopted in this study.

RESULTS AND DISCUSSION

Eigenvalue buckling analysis

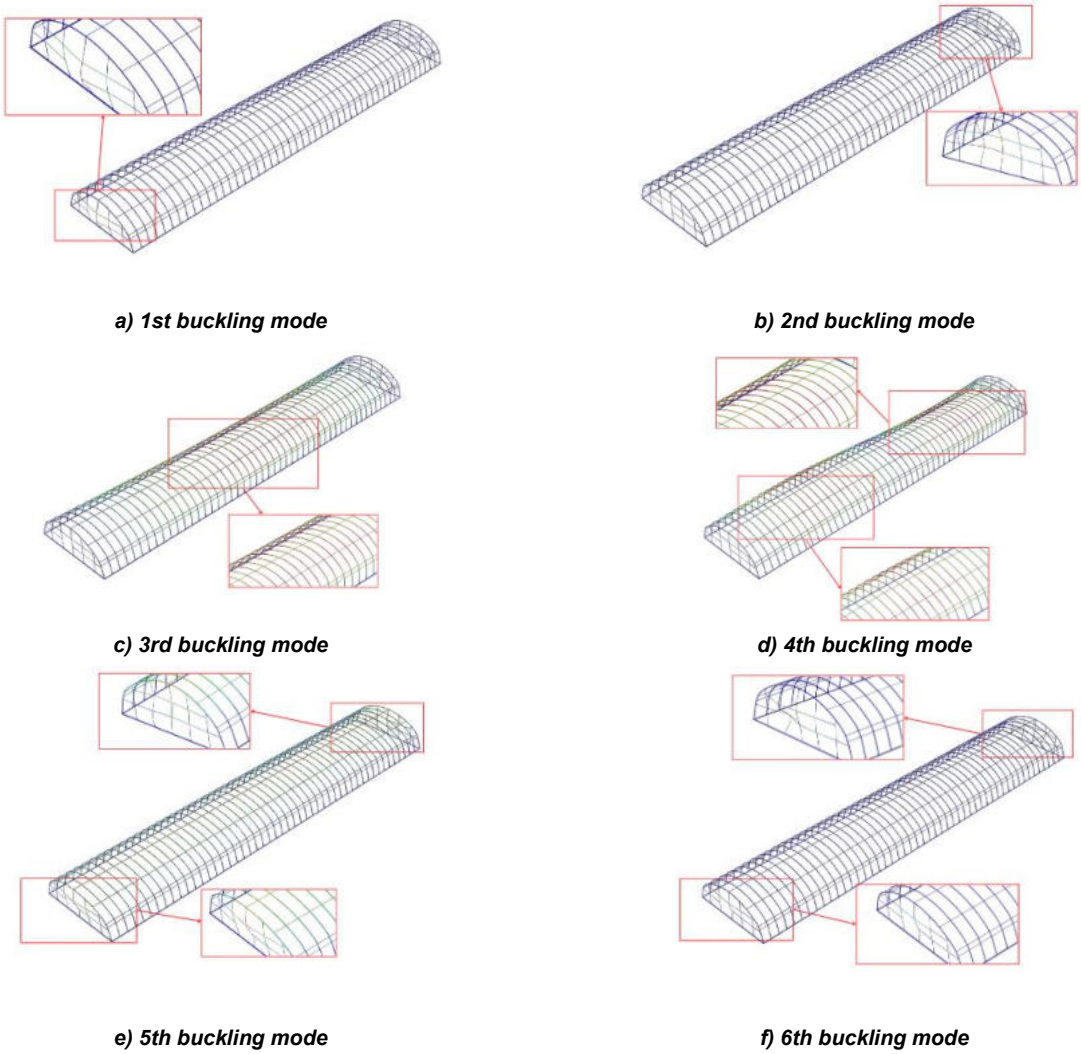
First, the linear buckling analysis of the greenhouse skeleton structure was conducted using the finite element software ABAQUS, yielding the buckling modes and eigenvalues of the structure. Since initial imperfections are inevitably present in real structures, eigenvalue buckling analysis often overestimates the stability and load-bearing capacity of the structure. However, the linear buckling analysis provides an upper limit load value and initial imperfection distribution, serving as a basis for nonlinear buckling analysis.

The governing equation for eigenvalue buckling analysis is:

$$\left(\left[K_E\right]+\lambda\left[K_\sigma\right]\right)U=0 \tag{1}$$

where: $[K_E]$ is the elastic stiffness matrix of the structure; $[K_\sigma]$ is the geometric stiffness matrix of the structure; λ is the buckling factor, which is the eigenvalue, and U is the eigenvector matrix corresponding to each buckling factor, representing the buckling mode.

The eigenvalue buckling analysis of the greenhouse skeleton was conducted using ABAQUS finite element software under the action of dead load and wind load. The first 6 buckling modes and corresponding eigenvalues of the greenhouse skeleton are shown in Figure 6 and Table 2. To better visualize the buckling modes of the skeleton, the displacement has been amplified by a factor of 500 for easier observation.



a) 1st buckling mode *b) 2nd buckling mode*

c) 3rd buckling mode *d) 4th buckling mode*

e) 5th buckling mode *f) 6th buckling mode*

Fig. 6 – The first 6 buckling modes of the skeleton structure

As shown in Figure 6, the first 2 modes of instability of the greenhouse skeleton structure occur in the sidewall areas. This is because, when the skeleton is considered as a whole, the skeletons on the sidewalls are weaker regions, causing the sidewall skeletons to experience instability first. The 3rd mode of instability exhibits an overall wave-like buckling, with the largest displacement observed near the central skeleton, where the structure bulges outward toward one side. The 4th mode of instability also shows wave-like buckling, but

the overall instability manifests as the skeletons near the two ends bulging outward in opposite directions. The 5th mode of instability is characterized by strip-like buckling, with localized instability occurring in the sidewall areas. The 6th mode, compared to the 5th, lacks the overall strip-like instability, and the instability is concentrated in the skeletons at both ends of the sidewalls.

Table 2

First 6 eigenvalues of the structure

Mode order	1st	2nd	3rd	4th	5th	6th
Eigenvalue	-25.1	-33.31	-35.43	-39.6	-41	-48.48

Nonlinear buckling analysis

According to the Technical specification for space frame structures *(JGJ 7—2010)*, the stability of the grid shell can be calculated using the finite element method considering geometric nonlinearity (i.e., load-displacement full process analysis). In the analysis, material behavior can be assumed to be elastic or elastic-plastic. In this study, both geometric and material nonlinearities are considered in the nonlinear buckling analysis of the structure. The first-order buckling mode of the skeleton structure is introduced as an initial imperfection into the greenhouse skeleton model, and a load-displacement full process analysis is performed. The iteration equation is as follows:

$$\left[K_t\right]\Delta U^{(i)} = F_{t+\Delta t} - N_{t+\Delta t}^{(i-1)} \tag{2}$$

where, $[K_t]$ is the tangent stiffness matrix of the structure at the current time step, $\Delta U^{(i)}$ is the iterative increment of the displacement at the current time step; $F_{t+\Delta t}$ and $N_{t+\Delta t}^{(i-1)}$ represent the external nodal load vector and the corresponding internal force vector of the structural members at the current time step, respectively.

For solving the above equation, various equilibrium path tracking methods can be used, such as the displacement increment method, load increment method, work increment method, residual energy method, and arc-length method. In this study, the Modified Riks method, commonly used for nonlinear buckling analysis in ABAQUS, is employed for solving. The constraint equation for the Modified Riks method is as follows:

$$(\Delta\bar{u})^T(\Delta\bar{u}) + \psi(\Delta\lambda)^2 = (\Delta l)^2 \tag{3}$$

where, ψ=1 represents the arc length increment for each iteration. An initial arc length must be specified, and during the calculation process, the arc length Δl is adjusted according to the specific problem to ensure both computational efficiency and accuracy.

In addition, during the loading process, the original geometry and shape of the structure will change due to the applied loads, causing the overall stiffness matrix to vary. Therefore, the linear equilibrium equation cannot effectively represent the behavior of the structure in the nonlinear process.

The linear equilibrium equation of the structure can be expressed as:

$$\left[K\right]u = F \tag{4}$$

where, $[K]$ is the overall stiffness matrix of the structure; u is the displacement vector of the structure; and F represents the external loads, which, for buckling problems, are typically the loads modified by the buckling load factor.

The updated overall stiffness matrix $[K]$ is commonly represented by the tangent stiffness matrix $[K_t]$, which is equivalent to the slope of the load-displacement curve. This type of nonlinear situation falls under the category of geometric nonlinearity. The tangent stiffness matrix is often used in the calculation of the equilibrium path to achieve rapid convergence. Its calculation is given by the following equation:

$$\left[K_t\right] = \left[K\right] + \left[K_\sigma\right] + \left[K_L\right] \tag{5}$$

where, $[K_t]$ is the tangent stiffness matrix of the structure at the current time step; $[K_L]$ is the initial displacement matrix.

In the absence of initial imperfections, the critical buckling load P_{cr} can be calculated using the Euler's buckling formula:

$$P_{cr} = \frac{\pi^2 EI}{L^2} \tag{6}$$

where, P_{cr} is the critical buckling load in the absence of imperfections; E is the Young's modulus; I is the moment of inertia of the cross-section; and L is the span of the structure.

The modified formula after introducing initial imperfections is as follows:

$$P_{cr}(\delta) = P_{cr}(1-\frac{\delta}{L}) \tag{7}$$

where, $P_{cr}(\delta)$ is the critical buckling load after introducing imperfections; δ is the initial imperfection amplitude.

The buckling analysis formula considering initial displacement imperfections, geometric nonlinearity, material nonlinearity, and the modified critical buckling load can be written as follows:

$$\left[K + K_{\sigma} + K_{L}\right]u + P_{cr}(1-\frac{\delta}{L})u = F \tag{8}$$

Nonlinear buckling analysis with initial imperfections was performed on the flat elliptical pipe greenhouse skeleton using the Riks method in ABAQUS finite element software. The load-displacement curves at the top of the middle rafter under different initial imperfections are shown in Fig.7.

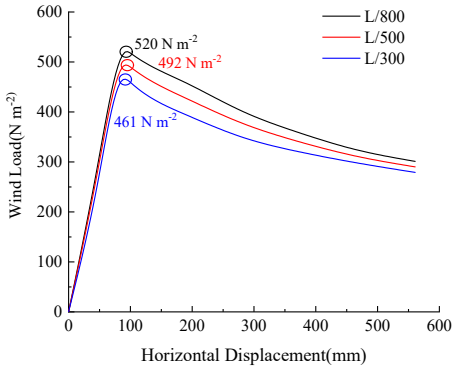


Fig. 7 – Load-displacement curves at the top of the middle rafter

As shown in Figure 7, when the load is small, the displacement increases in a linear trend. According to the technical specification for space frame structures *(JGJ 7—2010)* the first critical load value obtained from the full process analysis of the structure is taken as the ultimate load-bearing capacity of the structure. Therefore, when the maximum initial geometric imperfection amplitude is L/300, the ultimate bearing capacity is 461.2 N·m²; when the maximum initial geometric imperfection amplitude is L/500, the ultimate bearing capacity is 492.22 N·m²; and when the maximum initial geometric imperfection amplitude is L/800, the ultimate bearing capacity is 520.26 N·m². This shows that the ultimate bearing capacity of the structure decreases with the increase in the maximum initial geometric imperfection amplitude. This result is consistent with the conclusions previously drawn by *Xie and Chen (2015)*.

Comparison analysis of overall and local buckling of the skeleton

To investigate whether the post-buckling behavior of the structure meets the safety design requirements for steel structures, stress–displacement curves at various positions of the deformed skeleton were extracted. This analysis aims to clarify the impact of structural buckling on the stress distribution of individual members and to identify the most vulnerable positions within the skeleton. The displacement diagram of the skeleton structure, obtained through nonlinear buckling analysis, is presented in Fig. 8.

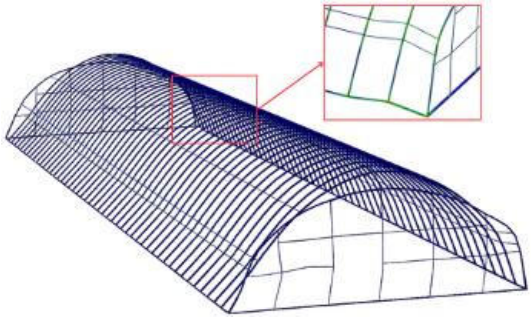
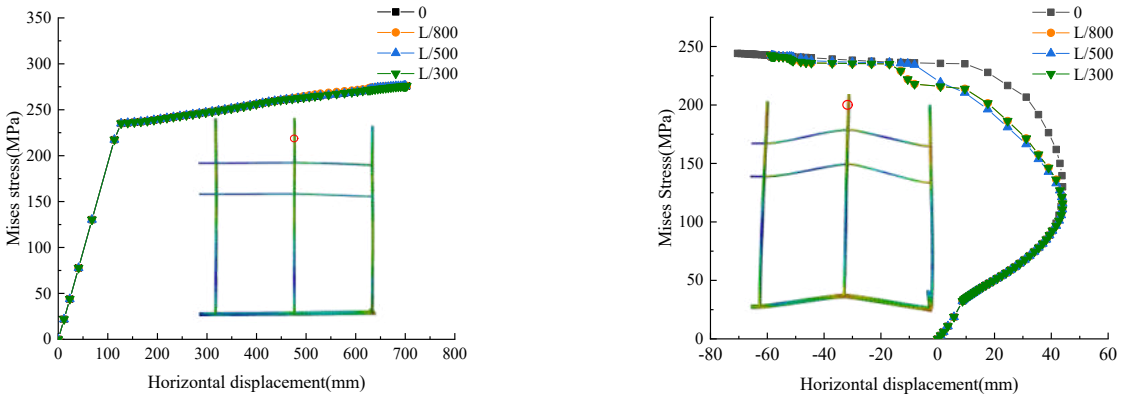


Fig. 8 – Displacement diagram of the skeleton structure

As shown in Fig. 8, the structure experiences significant overall buckling on the windward side, primarily manifesting as an overall strip-like instability. Meanwhile, on the leeward side, localized buckling deformation occurs at the end regions, primarily characterized by the arching of the steel pipes at the base, which induces deformation in both the skeleton and purlins. Therefore, this study will focus on analyzing the stress–displacement behavior of the components at both the localized buckling and overall buckling regions.

Stress analysis of rafter

The rafter, as the primary load-bearing components of the greenhouse skeleton, play a crucial role in supporting the structure under wind loads. Since wind loads primarily induce horizontal displacement in the structure, this study focuses on the variation of stress and horizontal displacement during the stress analysis. The Mises stress–horizontal displacement curves for the most unfavorable position of the rafter during the overall buckling and the local buckling of the structure were extracted and are shown in Fig. 9.



a) overall buckling *b) local buckling*

Fig. 9 – Most unfavorable position of Mises stress–horizontal displacement curves for rafter

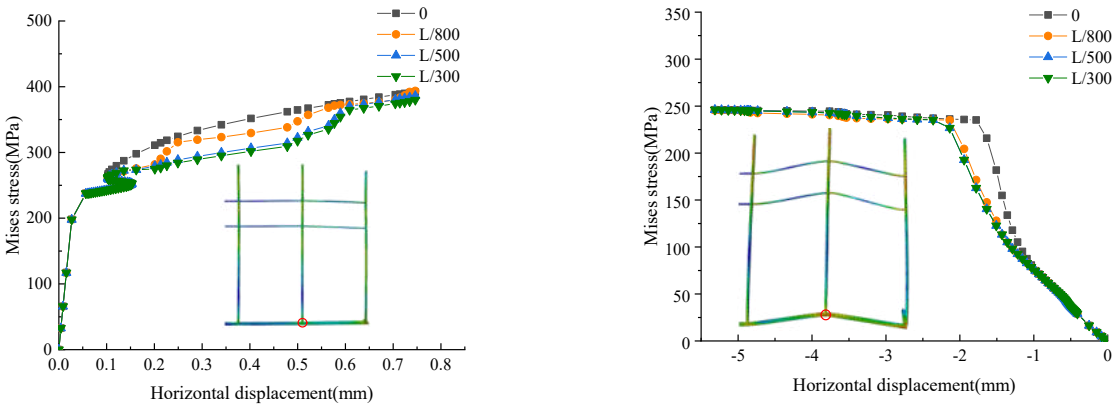
As shown in Figure 9(a), when the horizontal displacement ranges from 0 mm to 150 mm, all curves exhibit a similar linear trend, indicating that initial imperfections have minimal impact on the structure's linear elastic behavior. During this stage, stress increases steadily, with a near-linear relationship between displacement and stress. As the displacement increases further, the structure enters the yielding stage, where the rate of stress growth slows. No significant differences are observed between curves with varying initial imperfections during this stage. From 200 mm to 700 mm horizontal displacement, the curves under different initial imperfection conditions stabilize, with minimal difference observed between the curves with and without initial imperfections (L/800, L/500, L/300). This suggests that, during overall buckling, initial imperfections have a relatively limited effect on the yield strength of the rafters, particularly in the linear-elastic stage.

In contrast, Figure 9(b) illustrates that the impact of initial imperfections becomes significant after local buckling. In the 0 mm to 40 mm displacement range, all curves show a near-linear increase, but as displacement reaches 40 mm, the curves diverge sharply. Samples with no initial imperfections show the highest yield stress, while increasing initial imperfections (L/800, L/500, L/300) cause the yield point to occur earlier and the yield strength to decrease. This indicates that initial imperfections considerably weaken the structure's resistance to yielding.

From 10 mm to -10 mm displacement, the gap between the curves narrows after reaching the yield point. In the range from -10 mm to -70 mm, the stress increase becomes more gradual, and the curve for the structure without initial imperfections exhibits a longer plateau, indicating greater plastic deformation capacity and higher ultimate load-bearing capacity.

Stress analysis of embedded steel pipe

The Mises stress–horizontal displacement curves at the most unfavorable position of the embedded steel pipe during the overall buckling and the local buckling of the structure were extracted and are shown in Fig. 10.



a) overall buckling *b) local buckling*

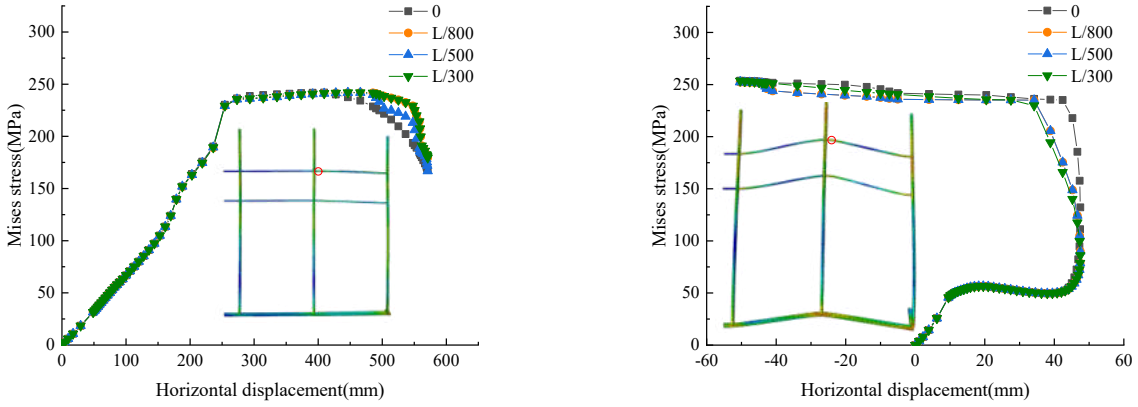
Fig. 10 – Most unfavorable position of Mises stress–horizontal displacement curves for embedded steel pipe

Figure 10(a) illustrates that within 0 mm to 0.06 mm of horizontal displacement, the curves exhibit a nearly identical linear trend, suggesting minimal impact of initial imperfections on the linear elastic behavior of the embedded steel pipe. Stress increases linearly, indicating stable elastic deformation. However, as the displacement progresses beyond 0.06 mm, the curves enter the yielding stage, where stress growth slows down. Between 0.1 mm and 0.6 mm displacement, the curves deviate from the linear relationship, displaying non-linearity. Notably, as initial imperfections increase, the curve flattens, reflecting a decrease in plastic deformation capacity and overall bearing capacity. This indicates that initial imperfections significantly weaken the yield strength and stability during overall buckling.

As shown in Fig. 10(b), from 0 mm to -1 mm displacement, the curves show a similar linear trend, again suggesting minimal impact of initial imperfections in the early stage. As displacement increases from -1 mm to -2 mm, the curves exhibit a nonlinear increase. The yield point varies significantly depending on initial imperfections, with structures without imperfections showing the steepest slope. From -2 mm to -5 mm displacement, the curves deviate further, entering the yield stage. The rate of stress increase slows, and significant differences emerge: without initial imperfections, the structure maintains higher yield strength and bearing capacity. However, with increasing initial imperfections (L/800, L/500, L/300), the yield point shifts earlier, and yield strength decreases, particularly under L/300 imperfections, highlighting the substantial reduction in load-bearing capacity.

Stress analysis of purlin

The Mises stress-horizontal displacement curves at the most unfavorable position of the purlin during the overall buckling and the local buckling of the structure were extracted and are shown in Fig. 11



a) overall buckling *b) local buckling*

Fig. 11 – Most unfavorable position of Mises stress–horizontal displacement curves for purlin

As shown in Fig. 11(a), within the 0 mm to 100 mm horizontal displacement range, stress increases linearly, reflecting elastic deformation of the purlin. Initial imperfections have minimal impact during this phase. From 100 mm to 250 mm displacement, the curves show slight nonlinearity, with negligible differences between initial imperfection conditions, suggesting limited influence on the elastic behavior. As displacement reaches 250 mm to 450 mm, the purlin enters the yielding stage, characterized by a deceleration in stress increase. Curves for different initial imperfections level off, indicating stable plastic deformation. From 450 mm to 575 mm, stress sharply decreases as the purlin enters the necking stage. Notably, the curve without initial imperfections has a steeper slope, reflecting a weaker load-bearing capacity during the necking phase compared to those with initial imperfections (L/800, L/500, L/300).

Figure 11(b) reveals that the impact of initial imperfections becomes more significant after local buckling. In the 0 mm to 10 mm range, stress increases linearly, with minimal variation across curves. From 10 mm to 20 mm, the slope of the curves decreases, and from 20 mm to 50 mm, stress initially decreases before rising again. At 50 mm displacement, the curve without initial imperfections exhibits the steepest slope, indicating higher stiffness. The slope decreases with increasing imperfection size (L/800, L/500, L/300), highlighting a more pronounced effect of initial imperfections during the elastic stage of the purlin.

In summary, initial imperfections have a significantly different impact on the overall buckling and local buckling of the structure. In the case of overall buckling, initial imperfections have a relatively small effect on the rafters, embedded steel pipes, and purlins, especially during the elastic deformation stages, where the change in yield strength is minimal. However, as the horizontal displacement increases, the negative effects of the initial imperfections become more pronounced, primarily as the structure enters the yield and plastic stages. The yield point occurs earlier, and the yield strength significantly decreases, indicating a weakened ability to resist yielding.

CONCLUSIONS

In this study, an FEM model of the elliptical pipe greenhouse skeleton was established using ABAQUS software. The consistent imperfection method was employed to simulate the initial imperfections of the greenhouse skeleton, and the arc-length method was used to conduct nonlinear buckling analysis of the skeleton. The ultimate bearing capacity of the skeleton under different initial imperfection conditions was obtained. Stress analysis of various structural components at both overall and local buckling regions was performed. The following conclusions were drawn:

(1) The impact of initial imperfections on the rafters, embedded steel pipes, and purlins at the overall buckling positions is primarily concentrated in the yielding and plastic deformation stages. In contrast, the influence of initial imperfections at the local buckling positons on the rafters, embedded steel pipes, and purlins is not limited to the yielding and plastic stages; it also manifests significantly during the elastic stage. This results in a reduction in the structural stiffness and a decrease in the bearing capacity of the skeleton.

(2) When considering only the impact of initial imperfections, with the initial imperfection amplitude being L/300, the maximum displacement of the skeleton is approximately 1.33 times that of the skeleton without initial imperfections. Similarly, the maximum stress of the skeleton is approximately 1.11 times that of the skeleton without initial imperfections.

From the results of this study, it is evident that initial imperfections have a significant impact on the loading behavior of the greenhouse skeleton. After considering the effects of initial imperfections, both the displacement and stress of the skeleton increase significantly. Therefore, it is recommended that the design of such structures take into account the adverse effects of initial imperfections in order to enhance the structure's ability to resist wind loads.

ACKNOWLEDGEMENT

This study is supported by Natural Science Foundation of Heilongjiang Province of China (LH2019E072). All authors are grateful for this support.

REFERENCES

[1] Bao Z. (2023). Study on stability and seismic performance of Venlo greenhouse considering skin effect (考虑蒙皮效应的 Venlo 型温室稳定性及抗震性能研究). Master dissertation, *Sichuan Agricultural University*.

[2] Cai, J., He S., Jiang Z., Zhang Y., Liu Q. (2015). Investigation on maximum value of initial geometric imperfection in stability analysis of single layer reticulated shells (单层网壳结构稳定分析中初始几何缺陷最大值的研究). *Journal of Building Structures*. 36(06):86-92.

[3] Jiang Y., Bai Y., Wang C., Wang Y., Pang X. (2021). Dynamic response analyses of plastic greenhouse structure considering fluctuating wind Load. *Advances in Civil Engineering*. Vol. 2021, pp.1-13.

[4] Gu L., Gong J., Lu B. (2019). Influence of initial geometrical imperfections on overall stability of long-span truss string structure (初始几何缺陷对大跨张弦桁架结构整体稳定的影响研究). *Steel Construction*. Vol. 3, Issue 34, pp. 64-68.

[5] Liu Y., Cui X., Li Y., Hong H. (2021) Reliability analysis of stability of latticed shell structure considering initial geometric imperfections (考虑初始几何缺陷的网壳结构整体稳定性可靠度分析). *China civil engineering journal*. Vol. 54, Issue 7, pp. 12-23.

[6] Li, X., Wang C., Jiang Y., Bai, Y. (2022). Dynamic response analysis of a whole steel frame solar greenhouse under wind loads. *Scientific reports*. Vol. 12, Issue 5200, pp. 1-12.

[7] MOHURD (2017). *GB 50017-2017 Code for design of steel structures* (钢结构设计标准). Beijing, China: China Architecture & Building Press.

[8] MOHURD. (2016). *GB/T 51183-2016 Code for the design load of horticultural greenhouse structures*. (农业温室结构荷载规范) Beijing, China: China Planning Press. https://www.mohurd.gov.cn/gongkai/zhengce/zhengcefilelib/201702/20170214_230578.html

[9] MOHURD. (2010). JGJ7—2010 Technical specihcation for space frame structures (空间网格结构技术规程). Beijing, China.

[10] Ren, J., Wang, J., Guo, S., Li, X., Zheng, K., & Zhao, Z. (2019). Finite element analysis of the static properties and stability of a large-span plastic greenhouse. *Computers and Electronics in Agriculture*, Vol. 165, Issue 104957, pp.1-9.

[11] Wang C., Jiang Y., Xu Z., (2022). Ultimate bearing capacity of the solar greenhouse with hat-shaped steel under snow loads. *Transactions of the Chinese Society of Agricultural Engineering*, Vol. 38, Issue 19, pp. 172-179.

[12] Wang, C., Jiang, Y., Wang, T., Xu Z., Bai, Y. (2022). Analysis of wind-induced responses of landing assembled Chinese solar greenhouses. *Biosystems Engineering*, Vol. 220, Issue 6, pp. 214-232.

[13] Wang, C., Xu Z., Jiang, Y., Bai, Y., & Wang, T., (2023). Numerical analysis of static and dynamic characteristics of large-span pipe-framed plastic greenhouses. *Biosystems Engineering*, Vol. 232, Issue 6, pp. 67-80.

[14] Xie, H., Chen, B., & Chai, D. (2015). Ultimate load carrying capacity analysis of single-span arched plastic greenhouse frame (钢拱单栋塑料大棚平面内极限承载力分析). *Low Temperature Architecture Technology*, Vol. 37, Issue 8, pp. 46-49. https://doi.org/10.13905/j.cnki.dwjz.2015.08.018

[15] Yu Y., Wang J., Ying Y., (2007). Nonlinear finite element analysis of the bearing capacity of arch structure in plastic greenhouse on snow load working condition (塑料温室拱结构雪载工况下极限承载力的非线性有限元分析) *Transactions of the CSAE*, Vol. 23, Issue 3, pp. 158—162.

[16] Zeng Q., Zhu S., Yang X., Wu C., (2024). Research progress on simulation methods of initial geometric imperfection fields of single-layer gridshells (单层网壳结构初始几何缺陷场模拟方法研究进展). *Progress in Steel Building Structures*. Vol. 26, Issue 5, pp. 12-21.

OPTIMIZATION DESIGN AND TEST OF BAFFLE STRUCTURE PARAMETERS OF THE HQ-800 STRAW MILL

/

HQ-800 型秸秆粉碎机隔板结构参数优化设计及试验

Kai YONG [1], Qing TANG [2,3*], Zhewen SONG [3], Lan JIANG [2]

[1]School of Smart Manufacturing, Wuhu Institute of Technology, Wuhu 241006, China;
[2]Nanjing Institute of Agricultural Meshanization, Ministry of Agriculture and Rural Affairs, Nanjing 210014, China;
[3]Sinomach Changlin Co.Ltd., Changzhou 213000, China.
Tel: +86.15366092914; E-mail: tangqing01@caas.cn
DOI: https://doi.org/10.35633/inmateh-76-32

Keywords: *straw mill, baffle, curved optimization, field test*

ABSTRACT

Crop straw is a key feed raw material processed by straw mills, but traditional mills have been hindered bulky structures, high power consumption, and low productivity. Previous research has primarily focused on optimizing the hammer structure, often overlooking the baffle, despite its considerable weight and lack of specific design applications. This study addresses that gap by optimizing the baffle design of the HQ-800 straw mill, simplifying it using a double-baffle framework. The force analysis considered gravity, hammer centrifugal force, shaft centrifugal force, main shaft torque, and material impact. Deformation and stress nephograms revealed that the area between the hammer shaft holes required structural improvement. Two optimization schemes - flat and curved - were compared. The curved design reduced maximum deformation to 29.007 μm, compared to 52.009 μm for the flat design, making it the preferred approach. Key parameters, including cutting circle diameter, center distance, and baffle thickness, were optimized using a three-factor, three-level orthogonal test, resulting in preliminary values of 200 mm, 250 mm, and 12.5 mm, respectively. Subsequent Box–Behnken testing refined these parameters to optimal values: 209 mm, 256 mm, and 12 mm. Under these conditions, the straw mill achieved a productivity of 1673 kg/h and a power consumption of 10.42 kWh/t. Compared to the unoptimized design, the optimized mill reduced volume by 44.46%, increased productivity by 5.89%, and lowered power consumption by 14.10%, fully meeting the design objectives.

摘要

农作物秸秆经粉碎机加工是饲料重要来源，传统粉碎机隔板结构不合理致能耗高、效率低。本文以 HQ-800 型粉碎机隔板为对象，简化模型后进行受力与有限元分析，确定锤轴孔间区域为优化位置，对比方案选弧面优化。通过三因素三水平正交试验得初步参数：切割圆直径 200 mm、圆心距 250 mm、隔板厚度 12.5 mm。Box-Benhnken 试验验证最佳参数为 209 mm、256 mm、12 mm 时，生产率 1673 kg/h，吨料电耗 10.42 kW·h/t，体积减 44.46%，效率提 5.89%，能耗降 14.10%，试验结果满足设计要求，为粉碎机结构优化提供理论支撑。

INTRODUCTION

Feed is the material basis for the development of animal husbandry, providing essential nutrition for herbivorous livestock such as cattle and sheep, and ensuring the high-quality, high-yield and efficient development of animal husbandry. However, the supply of feed raw materials is insufficient, and there has been a long-term reliance on imports *(Zhang et al., 2021; Zartha et al., 2021)*. Crop straw, as one of the feed raw materials, can alleviate the shortage of feed supply if utilized efficiently. Crop straw can be processed into feed through the straw mill, but traditional straw mills have several issues, including a bulky structure, high power consumption and low productivity *(Cao et al., 2021; Cotabarren et al., 2020; Thomas et al., 2018)*. The baffle is the key component in the crushing mechanism of the straw mill, responsible for guiding the straw through the straw mill and ensuring it is effectively crushed and processed. The weight of the baffle typically accounts for more than 50% of the total weight of the crushing mechanism. Therefore, it is necessary to optimize the baffle structure to reduce weight, reduce power consumption and improve productivity.

In recent years, both domestic and international scholars have conducted extensive research on the structural optimization and performance enhancement of crushing-related machinery. *Li et al., (2024),* optimized the process parameters of feed crushing using a back-propagation neural network combined with particle swarm optimization, identifying optimal parameters that significantly improved pulverizer performance.

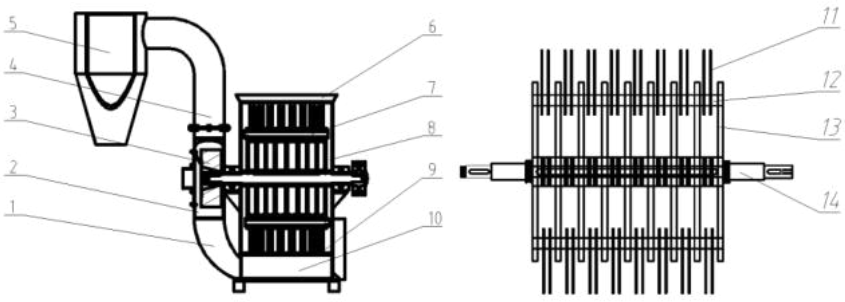
Ismail et al., (2022), analyzed the synergistic effects of classifier blade lengths and opening angles in coal pulverizers using CFD technology, revealing the classification mechanism by examining the coupling between flow field characteristics and particle movement trajectories. *Kshirsagar et al., (2014),* used finite element analysis software to analyze the stress and deformation of the main components of an automation can/plastic bottle crusher machine, ensuring the stability of the machine. These studies mainly used simulation and machine tests to optimize the structure, and their approaches are worth learning from. However, due to different objects of study, the relevant results cannot be directly applied to straw mill. *Wang et al., (2023),* designed a new type of biomimetic hammer with beaver incisors as biomimetic prototype, and used response surface method to optimize the structural parameters of biomimetic hammer, which showed improved performance compared to conventional hammers. *Zhang et al., (2024),* designed a field returning machine with a biomimetic serrated grinding knife with good straw crushing performance, and when used in combination with traditional crushing knife, it significantly increased the crushing efficiency of the entire machine. *Yancey et al., (2013),* optimized the shape parameters of the mill's hammer, enhancing the crushing performance of the machine. The straw mill is mainly hammer-type, the current optimization focus is mostly on hammers. However, the baffle in the crushing mechanism has a larger weight proportion and is in greater need of optimization. *Ruan et al., (2014),* analyzed the baffle force under both no-material and material conditions of the hammer mill, and verified its strength using simulation software, with results meeting the requirements. *Zhang et al., (2019),* performed topological optimization on the baffle structure with a 50% material removal rate, and used finite element analysis software to conduct static and modal analysis on the optimized structure, obtaining a lightweight baffle that meets strength and stiffness requirements. Overall, research on baffle structural parameter optimization is currently limited, and the few existing studies mainly focus on simulation and verification of specified dimensions, without combining gradual optimization and machine tests in actual working scenarios, lacking a systematic optimization scheme.

In this study, the HQ-800 straw mill was selected as the research subject, with a specific focus on baffle design. Aiming to achieve weight reduction, energy efficiency, and productivity enhancement, the model was simplified, and a comprehensive force analysis was conducted. The structural parameters of the baffle were optimized using finite element simulation, and the proposed improvements were rigorously validated through experimental testing. This research not only provides a strong theoretical foundation but also offers practical guidance for the optimized design of straw mills, contributing to the advancement of agricultural machinery engineering.

MATERIALS AND METHODS

Machine structure

The HQ-800 straw mill is composed of a motor, an air conveying system, a crushing system, and other components (see Figure 1a). The air conveying system includes a lower conveying pipeline, an upper conveying pipeline, an air pump, and a pump chamber. The crushing system, which is central to the machine's operation, consists of a crushing chamber, an advanced crushing mechanism, and a screen. The crushing mechanism comprises a main shaft, 9 baffles, 32 hammer shafts, and 64 hammers (see Figure 1b). The baffles are fixed to the main shaft at specific intervals, providing essential structural support. Each baffle is securely connected to four hammer shafts, and each hammer shaft supports two hammers, which are hinged to allow swinging at a certain angle. This configuration enables efficient impact and pulverization of straw into finer particles.



(a) *(b)*

Fig. 1 - Schematic of straw mill

1. lower conveying pipeline; 2. pump chamber; 3. air pump; 4. upper conveying pipeline; 5. discharge port; 6. feed port; 7. crushing mechanism; 8. crushing chamber; 9. screen; 10. material bin; 11. hammer; 12. hammer shaft; 13. baffle; 14. main shaft (a)Straw mill; (b)Crushing mechanism

Working principle

The crushing system is equipped with a feed port, through which crop straws are introduced into the crushing chamber. When the motor is activated, it drives the main shaft via belt transmission. The main shaft then rotates the baffle, which in turn sets the hammers on the hammer shaft into motion. These rotating hammers work in conjunction with the screen to crush the crop straws into feed particles, which subsequently fall into the material bin. Simultaneously, the motor also drives the air pump through the main shaft of the crushing mechanism. The air pump generates air pressure that transports the feed particles from the material bin through both the lower and upper conveying pipelines, ultimately delivering them to the discharge port for packaging. The main technical parameters of the HQ-800 straw mill are listed in Table 1.

Table 1

Main technical parameters

Parameter	Unit	Value
Power	kW	55
Voltage	V	380
Machine size (length×width×heigh)	mm×mm×mm	1800×1500×2000
Maximum speed of main shaft	rpm	2800
Diameter of main shaft	mm	80
Number of hammers	/	64
Feed particle size	mm	2

Design of baffle model

Although the crushing mechanism consists of numerous components, many along the main shaft are highly repetitive. Therefore, two adjacent baffles were selected as the focus of the research and analysis. This section includes four hammer shafts and eight hammers. The simplified baffle model is illustrated in Figure 2.

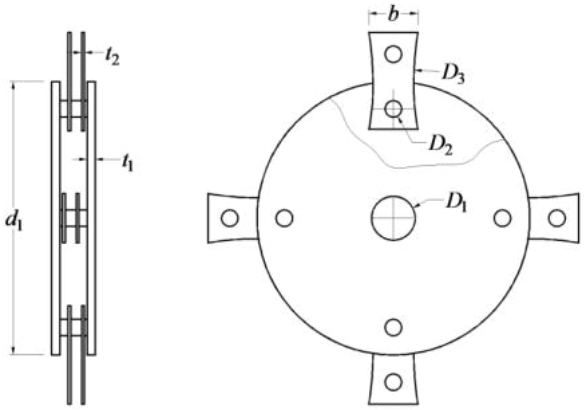


Fig. 2 - Schematic of baffle model

The baffle parameters are as follows: baffle diameter d_1=500 mm, baffle thickness t_1=15 mm, diameter of the main shaft hole D_1=80 mm, and diameter of the hammer shaft hole D_2=30 mm. The hammer features a cambered structure with the following specifications: cambered surface diameter D_3=550 mm, hammer width b=90 mm, and hammer thickness t_2=5 mm.

Force analysis of baffle model

The force analysis of baffle model can be categorized into two types: operation without material and operation with material. In the absence of material, the forces acting on the baffle model primarily consist of the gravity of the baffle model, the friction between the hammer and the hammer shaft, the centrifugal force of the hammer on the hammer shaft, and the torque transmitted by the main shaft *(Liu et al., 2011; Li et al., 2012; Ruan et al., 2014)*. However, when material is present, the impact force of the material on the hammer is added, and the torque transmitted by the main shaft will also change due to the altered load. This results in a more complex force situation for the baffle model, which more accurately reflects the actual operating conditions of the machine. Therefore, the force analysis of the baffle model in the presence of material will be detailed below.

The force analysis diagram of the baffle model is depicted in Figure 3.

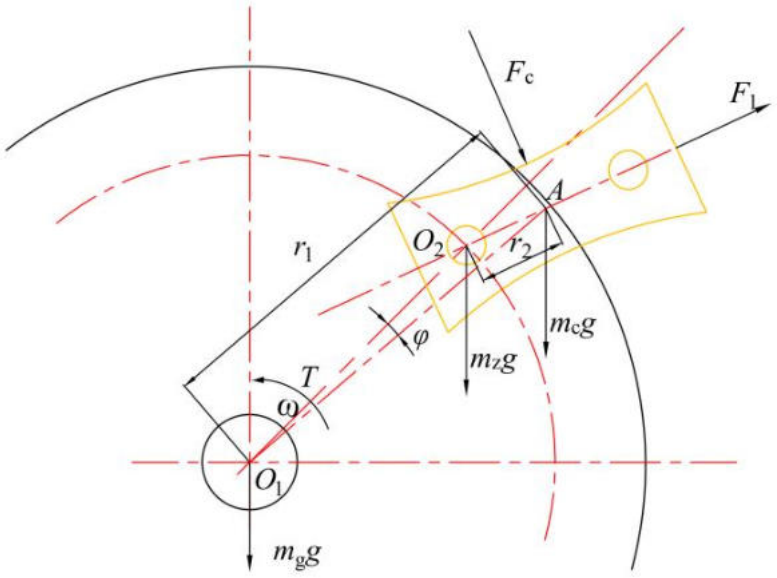


Fig. 3 - Force analysis diagram of baffle model

During the operation of the straw mill, the hammers experience a critical deflection angle $\varphi \approx 3^{\circ}$ relative to the center of the hammer holes *(Ruan et al., 2014)*.

The total weight of the baffle model is the sum of the weights of all its components, and is calculated using Equation (1).

$$G_z = 2m_g g + 4m_z g + 8m_c g \quad (1)$$

where: G_z - total weight of baffle model, [N]; m_g - baffle mass, [kg]; m_z - hammer shaft mass, [kg]; m_c - hammer mass, [kg].

The torque on each baffle is calculated using the following Equations (2) and (3).

$$T_1 = T/9 \quad (2)$$

$$T = 9550 \times \frac{P}{n} \quad (3)$$

where: T_1 - torque on each baffle, [N·m]; T - main shaft torque, [N·m]; n - main shaft rotation speed, [rpm]; P - crushing system power, [kW].

The crushing system power P=20 kW, the main shaft rotation speed n=2000 rpm. It is calculated that the main shaft torque T=95.5 N·m, and the torque on each baffle T_1=10.6 N·m.

Each hammer shaft experiences centrifugal force generated by a hammer, which can be calculated using Equation (4).

$$F_l = m_c \omega^2 r_2 \quad (4)$$

where: F_l - centrifugal force generated by each hammer, [N]; ω - angular velocity of the main shaft, [rad/s]; r_2 - distance from O_2 (the center of the hammer shaft hole) to A (the center of mass of the hammer), [mm].

Under operating conditions with material loaded, the main shaft rotation speed is n=2000 rpm, the hammer mass is m_c =0.16 kg, and the distance from O_2 to A is r_2=50 mm. Based on these values, the angular velocity of the main shaft is calculated as ω=209.33 rad/s, and the centrifugal force generated by each hammer is F_l=350.55 N. Since each hammer shaft is hinged to two hammers, the total centrifugal force acting in one direction of the baffle model is 701.10N.

The hammer experiences the maximum impact force from the material *(Wang et al., 2009)*, and this force is calculated using Equations (5) and (6).

$$F_c = \frac{m_w}{t}(v_c - v_1) \quad (5)$$

$$v_c = \omega r_1 \quad (6)$$

where F_c - maximum impact force exerted by the material on the hammer, [N]; m_w - maximum mass of material carried by a hammer, [kg]; v_c - peripheral velocity of the hammer during impact, [m/s]; v_l - minimum peripheral velocity of the material during impact, [m/s]; t - minimum collision time [s]; r_1 - distance from O_1 (the center of the main shaft hole) to A (the center of mass of the hammer), [mm].

Under maximum feed conditions, the maximum mass of the material carried by a hammer is m_w=0.1 kg, the distance from O_1 to A is r_1=247 mm, and the peripheral velocity of the hammer is v_c=51.70 m/s. During the feeding process, the material accelerates from an initial state of rest to match the hammer's motion, with its peripheral velocity gradually increasing. Therefore, the minimum peripheral velocity of the material is v_1=0m/s. The collision time typically ranges from 1×10^{-3} to 4×10^{-3} seconds; for this analysis, the minimum collision time is taken as t=1×10^{-3} s. It is calculated that the maximum impact force is F_c=5170 N.

Model settings of simulation test

Simulation testing is a widely used method in structural optimization design, employing techniques such as static analysis, dynamic analysis, and fluid mechanics to evaluate the physical behavior of the designed structure *(Wu et al., 2023; Wang et al., 2024)*. In this study, the 3D model was imported into ANSYS Workbench. The materials were assigned as follows: Q235 for the baffle and hammer shafts, and 65Mn for the hammers. A Body-Ground Revolute constraint was applied to the virtual main shaft, while a Body-Body Revolute constraint was used between the hammer and hammer shaft. The mesh size was set to 5 mm. The resulting mesh, shown in Figure 4, consists of 488,740 nodes and 99,252 elements, with an average mesh quality of 91.87%.

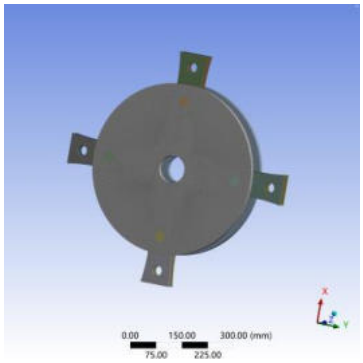
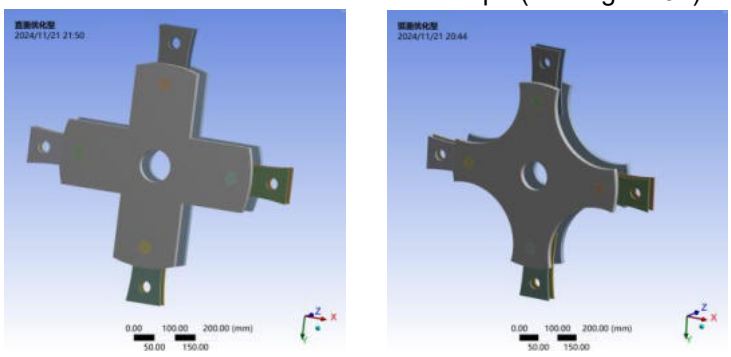


Fig. 4 - Schematic of grid model

Optimization method of baffle structure

As shown in Figure 5, the baffle structure can be optimized using either flat-surface removal or curved-surface removal. Two models are proposed, each removing the same volume of material, while maintaining the original installation configuration of the baffle, hammer shaft, and hammers. In the first model, the baffle corners are removed in a sector shape, resulting in a "cross"-shaped remaining structure (see Figure 5a). In the second model, the baffle corners are removed in an oval shape (see Figure 5b).



(a) *(b)*

Fig. 5 - Schematics of optimized contrastive baffle model

(a)Flat-optimized baffle model; (b)Curved-optimized baffle model

Simulation parameter optimization of baffle structure

During the operation of the straw mill, the maximum deformation of the components in the crushing mechanism affects the efficiency of the machine. *Xu et al., (2021),* conducted a study on the maximum deformation of key components in the crushing mechanism. Combining this with the team's prior analysis and tests, it was found that when the maximum deformation of the baffle reaches 35 μm, the efficiency of the machine significantly decreases, and malfunctions are more likely to occur. Referring to the unoptimized baffle model, the maximum deformation is 27.803 μm. It is recommended that the simulation analysis reference index should not exceed 5% of this value, and the smaller the maximum deformation, the better.

Combining the topological optimization study of the baffle by *Zhang et al., (2019),* the curved-optimized scheme can cut the four corners of the baffle along a curve, but it is necessary to avoid the hammer shaft hole and maintain a certain distance from the main shaft hole. Considering that the parameters of a variable-curvature curve are numerous and have minimal impact on the optimization results, four equal-diameter circular arcs are used to trim the edges of the baffle. The optimization parameters of the curved-optimized baffle are shown in Figure 6, where the main shaft hole is located at the center of the baffle, and the four hammer shaft holes are located at the edges of the baffle, the center distance *L* between the center of the baffle and the center of the cutting circle, and the cutting circle diameter *D*, together affect the amount of baffle removal. In addition, the baffle thickness *t* also has a significant impact. Therefore, the main optimization parameters of the baffle include the cutting circle diameter, the center distance, the baffle thickness, the diameter of the main shaft hole, and the diameter of the hammer shaft hole.

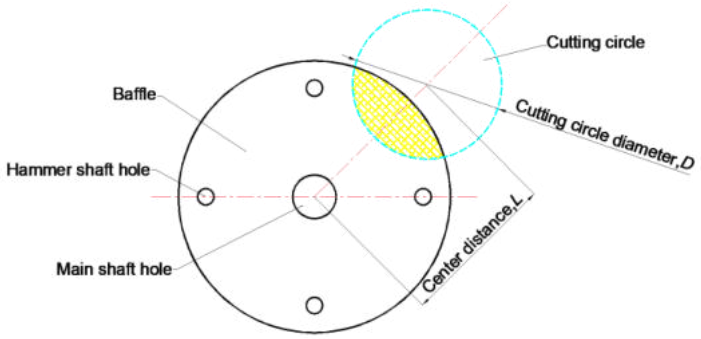


Fig. 6 - Optimization parameters of curved-optimized baffle

In accordance with the assembly requirements of the crushing mechanism, the baffle's main shaft hole and hammer shaft holes are precisely fitted with the main shaft and hammer shafts, respectively. In the early lightweight design of the main shaft and hammer shafts, their dimensions have already been optimized to the minimum. Increasing the diameters of the main shaft hole and hammer shaft holes could reduce the mass of the baffle but would also increase the mass of the main shaft and hammer shafts, thereby negatively impacting the overall performance of the crushing mechanism. Therefore, the optimization analysis of the baffle only considers three factors: the cutting circle diameter, the center distance, and the baffle thickness. The evaluation indexes are selected as the maximum deformation and the volume reduction ratio. The maximum deformation is the greatest deformation of the baffle caused by the force when it is in operation with material, while the volume reduction ratio is calculated as (The volume of the unoptimized baffle - The volume of the optimized baffle for each test group) / The volume of the unoptimized baffle. The volume reduction ratio reflects the optimization rate of the baffle structure for each test group. Considering the structural characteristics of the baffle, the table of test factors is presented in Table 2. The orthogonal test method with three factors and three levels is adopted *(Wang et al., 2017; Li et al., 2024)*, and the simulation results are shown in Figure 9.

Table 2

Table of test factors

Number	Factors		
	Cutting circle diameter A, (mm)	**Center distance B,(mm)**	**Baffle thickness C,(mm)**
1	150	200	10
2	200	250	12.5
3	250	300	15

Field test standard

The tests are conducted in accordance with the standards GB/T 6971-2007 "Test Method for Feed Mills" and NY/T 1554-2007 "Technical Specification of Quality Evaluation for Feed Grinder"

These standards clearly specify the evaluation indexes for the performance of straw mill, which include productivity, power consumption, feed particle size, feed temperature rise, motor load, noise, and dust concentration. Based on the results of the previous tests, it was found that the optimized baffle structure primarily affects the first two performance evaluation indexes.

The feed production per unit time of the straw mill is termed the productivity, and is calculated using Equation (7).

$$E = \frac{M}{t_1} \tag{7}$$

where: E - productivity, [kg/h]; M - feed production during test time, [kg]; t_1 - test time, [h].

The energy consumption required for the straw mill to produce each ton of feed is termed the power consumption, and is calculated using Equation (8).

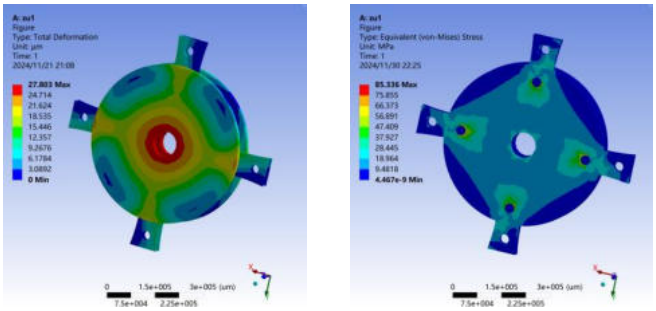
$$W = \frac{W_n}{M/1000} \tag{8}$$

where: W- power consumption, [kWh/t]; W_n - energy consumption during test time, [kW·h].

RESULTS

Simulation results

As shown in Figure 7a, the maximum deformation was mainly concentrated around the main shaft hole and the hammer shaft holes, with the maximum deformation being 27.803 μm. There were some positions between the hammer shaft holes of the baffle where the deformation was relatively low, which could be considered for optimization and removal. Figure 7b showed that the positions of the stress concentration were consistent with the positions of the deformation. Therefore, the positions between the hammer shaft holes of the baffle could be optimized and removed.

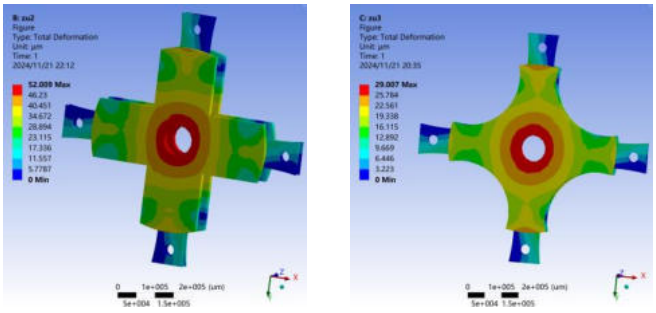


(a) (b)

Fig. 7 - Total deformation and stress nephogram of baffle model

(a)Total deformation nephogram; (b)Stress nephogram

As shown in Figure 8a, the flat-optimized scheme reduced the baffle volume, but the contour transition was poor, leading to stress concentrations close to the main shaft center. The maximum deformation was concentrated at the main shaft hole and the hammer shaft holes, with the maximum deformation reaching 52.009 μm. In Figure 8b, the curved-optimized scheme offered a more coordinated contour, also significantly reduced the baffle volume, and was less likely to produce noticeable stress concentrations. The maximum deformation was 29.007 μm, with a small increase in deformation. Therefore, the curved-optimized scheme could ensure a significant reduction in baffle volume while maintaining a small increase in deformation.

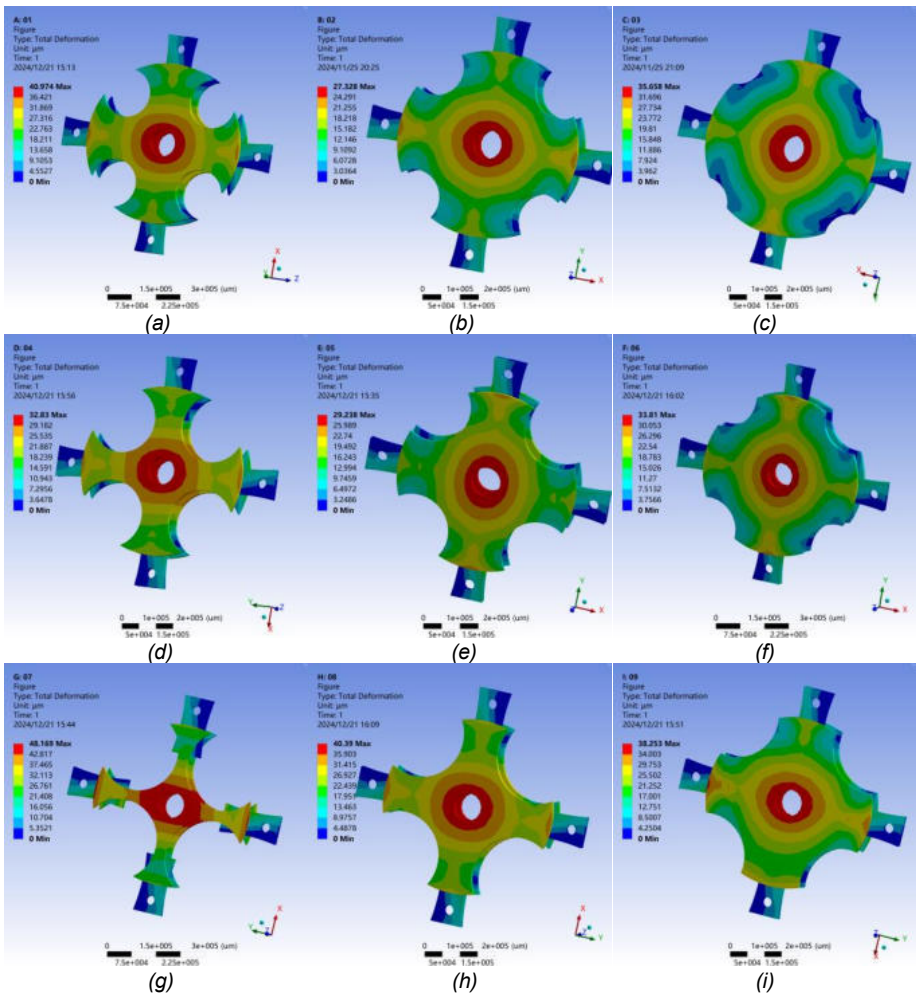


(a) (b)

Fig. 8 - Contrastive nephogram of total deformation

(a) Flat-optimized baffle model; (b) Curved-optimized baffle model

As shown in Figure 9, the distribution trend of the maximum deformation across the nine sets of curved-optimized baffles aligned well with the structural optimization logic. The highest deformation was concentrated around the main shaft hole and hammer shaft holes, while smaller deformations appeared near the material removal regions. The simulation results were consistent with the force analysis outcomes. Although the amount of material removed increased, the maximum deformation did not exhibit a strictly linear growth. This indicates that the relationship among the three influencing factors and the maximum deformation is complex and requires further analysis.



(a) (b) (c) (d) (e) (f) (g) (h) (i)

Fig. 9 - Contrastive nephogram of total deformation of curved-optimized type

(a) test 1; (b) test 2; (c) test 3; (d) test 4; (e) test 5; (f) test 6; (g) test 7; (h) test 8; (i) test 9

Analysis of simulation results

The test scheme and results are presented in Table 3. Through range analysis, the factors influencing the maximum deformation of the baffle were identified as the cutting circle diameter, the center distance, and the baffle thickness. The optimal combination of these factors was found to be $A_2B_2C_2$, corresponding to a cutting circle diameter of 200 mm, a center distance of 250 mm, and a baffle thickness of 12.5 mm. Comparison of the volume reduction ratios revealed that the maximum deformation was not directly proportional to the volume reduction, indicating that the volume reduction ratio should be used as a secondary evaluation index. Variance analysis was conducted to test the significance of the impact of each factor on the maximum deformation, as shown in Table 4. The results confirmed that the cutting circle diameter, the center distance, and the baffle thickness have a significant effect on the maximum deformation, validating the rationality of the orthogonal test.

Table 3

Test scheme and results of simulation analysis

Test number	Factors			Baffle volume (mm^3)	Volume reduction ratio (%)	Maximum deformation (μm)
	Cutting circle diameter A, (mm)	Center distance B, (mm)	Baffle thickness C, (mm)			
1	150	200	15	1899824	32.8	40.974
2	150	250	12.5	1942597	31.3	27.328
3	150	300	10	1815645	35.8	35.658
4	200	200	12.5	1143800	59.5	32.830
5	200	250	10	1310187	53.7	29.238

Test number	Factors			Baffle volume (mm^3)	Volume reduction ratio (%)	Maximum deformation (μm)
	Cutting circle diameter A, (mm)	Center distance B, (mm)	Baffle thickness C, (mm)			
6	200	300	15	2504307	11.4	33.810
7	250	200	10	512190	81.9	48.169
8	250	250	15	1512059	46.5	40.390
9	250	300	12.5	1824638	35.5	38.253
Maximum deformation			K_1	34.65	40.66	38.39
			K_2	31.96	32.32	32.80
			K_3	42.27	35.91	37.69
			R	10.31	8.34	5.59
			Better level	A_2	B_2	C_2
			Effects of various factors		$A > B > C$	

Table 4

Analysis of variance of maximum deformation

Source of variance	Sum of variance	Degree of freedom	F value	P value	Significance
A	171.60	2	1452.13	0.001	***
B	104.98	2	888.38	0.001	***
C	55.58	2	470.29	0.002	**
Pure Error	0.12	2			

*Note: *** indicates an extremely significant effect (P < 0.01); ** indicates a significant effect (P < 0.05). The same applies below.*

Field test scheme and results

The test site was a corn planting test field, and the test machine was the HQ-800 straw mill. The test material was corn straw, with a length of approximately 400 mm and a moisture content controlled between 12% and 18%. The material contained no other impurities. The main shaft speed of the test machine was set at 2000 rpm, and each test lasted 20 minutes. The test was repeated three times, and the average value was taken.

Based on the simulation analysis results, further verification of the effects of cutting circle diameter, center distance, and baffle thickness on the performance of the straw mill was conducted through machine tests. The coding of test factors is presented in Table 5. The performance evaluation indicators for the straw mill are productivity and power consumption.

Table 5

Coding of test factors

Level	Factors		
	Cutting circle diameter A, (mm)	Center distance B,(mm)	Baffle thickness C,(mm)
-1	150	200	10
0	200	250	12.5
1	250	300	15

The completely randomized test design was developed by coding the cutting circle diameter, center distance and baffle thickness as test factors *(Wen et al., 2023; Zhang et al., 2022).* The test scheme and results are presented in Table 6.

Table 6

Test scheme and results

Test number	Factors			Productivity E, (kg·h^{-1})	Power consumption W, (kWh·t^{-1})
	Cutting circle diameter A, (mm)	Center distance B, (mm)	Baffle thickness C, (mm)		
1	-1	-1	0	1546	11.64
2	1	-1	0	1583	11.05
3	-1	1	0	1572	11.25
4	1	1	0	1603	11.12
5	-1	0	-1	1585	11.25
6	1	0	-1	1628	10.98
7	-1	0	1	1558	11.45
8	1	0	1	1594	11.08
9	0	-1	-1	1604	11.11
10	0	1	-1	1623	11.02
11	0	-1	1	1578	11.22
12	0	1	1	1602	10.68
13	0	0	0	1675	10.38
14	0	0	0	1677	10.28
15	0	0	0	1676	10.25
16	0	0	0	1665	10.44
17	0	0	0	1673	10.41

The Box-Behnken Design (BBD) module in Design-Expert software was utilized to analyze the test data. The outcomes of this analysis are detailed in Tables 7 and 8. The regression model expressing the relationship between the productivity, the power consumption, and the encoded values is provided below:

$$E=1673.20+18.38A+11.13B-13.50C-1.5AB-1.75AC+1.25BC-53.85A^2-43.35B^2-28.10C^2 \quad (8)$$

$$W=10.35-0.089A-0.026B-0.060C+0.140AB+0.313AC+0.053BC+0.554A^2+0.384B^2+0.322C^2 \quad (9)$$

The regression models for productivity and power consumption were found to be extremely significant ($P < 0.01$). The P values for the lack of fit were 0.6558 and 0.2163, respectively, both of which were non-significant ($P > 0.1$), indicating a high degree of model fit. As shown in Table 7, the cutting circle diameter, center distance, and baffle thickness had extremely significant effects on productivity, with the cutting circle diameter having the greatest impact, followed by baffle thickness and then center distance. Table 8 indicates that the cutting circle diameter had an extremely significant effect on power consumption, while the center distance had a significant effect and the baffle thickness had a non-significant effect. The order of influence was cutting circle diameter, center distance, and baffle thickness. The determination coefficients (R^2) for the regression models of productivity and power consumption were 0.9957 and 0.9743, respectively, indicating excellent model fit. The adjusted determination coefficients (Adjusted R^2) were 0.9902 and 0.9413, respectively, which are close to the R^2 values, suggesting strong correlations. These results confirm the validity and reliability of the test design and analysis.

Table 7

Analysis of variance of productivity

Source of variance	Sum of variance	Degree of freedom	Mean square deviation	F value	P value	Significance
Model	31145.51	9	3460.61	181.39	< 0.0001	***
A	2701.13	1	2701.13	141.58	< 0.0001	***
B	990.13	1	990.13	51.90	0.0002	***
C	1458.00	1	1458.00	76.42	< 0.0001	***
AB	9.00	1	9.00	0.4717	0.5143	
AC	12.25	1	12.25	0.6421	0.4493	
BC	6.25	1	6.25	0.3276	0.5850	
A^2	12209.78	1	12209.78	639.97	< 0.0001	***
B^2	7912.52	1	7912.52	414.73	< 0.0001	***
C^2	3324.67	1	3324.67	174.26	< 0.0001	***
Residual	133.55	7	19.08			
Lack of Fit	40.75	3	13.58	0.5855	0.6558	
Pure Error	92.80	4	23.20			
Cor Total	31279.06	16				

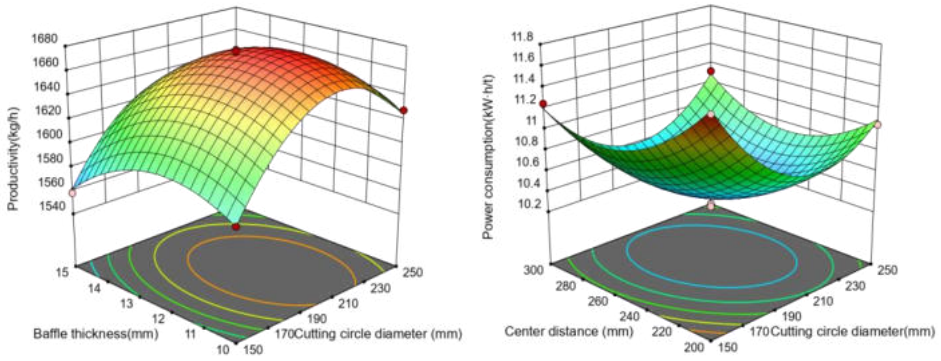
Table 8

Analysis of variance of power consumption

Source of variance	Sum of variance	Degree of freedom	Mean square deviation	F value	P value	Significance
Model	2.86	9	0.3180	29.52	< 0.0001	***
A	0.2312	1	0.2312	21.46	0.0024	***
B	0.1128	1	0.1128	10.47	0.0143	**
C	0.0006	1	0.0006	0.0569	0.8184	
AB	0.0529	1	0.0529	4.91	0.0622	
AC	0.0025	1	0.0025	0.2321	0.6447	
BC	0.0506	1	0.0506	4.70	0.0668	
A^2	1.26	1	1.26	117.27	< 0.0001	***
B^2	0.5617	1	0.5617	52.15	0.0002	***
C^2	0.3547	1	0.3547	32.93	0.0007	***
Residual	0.0754	7	0.0108			
Lack of Fit	0.0479	3	0.0160	2.33	0.2163	
Pure Error	0.0275	4	0.0069			
Cor Total	2.94	16				

Analysis of field test results

To further analyze the effects of each factor on productivity and power consumption, two-factor response surfaces were generated using Design-Expert software. The response surface for productivity of baffle thickness and cutting circle diameter is shown in Figure 10a. As the cutting circle diameter increases from 150 mm to 250 mm, the baffle volume decreases, and productivity first increases steadily and then gradually decreases. This is because, when the cutting circle diameter is small, increasing its size results in more material being removed from the baffle, reducing the mass of the crushing mechanism. With constant input power, the straw mill can then allocate more energy to the actual crushing of straw, thereby increasing productivity. However, once the cutting circle diameter reaches a certain value, further increases in size lead to a decrease in the baffle's stiffness and other mechanical properties, which reduces the straw mill performance and thus productivity. As the baffle thickness increases from 10 mm to 15 mm, the baffle volume increases, and productivity first increases and then decreases. Response surface for power consumption of center distance and cutting circle diameter is shown in Figure 10b. As the cutting circle diameter increases from 150 mm to 250 mm, the baffle volume decreases, and power consumption first decreases and then increases. Similarly, as the center distance increases from 200 mm to 300 mm, the baffle volume increases, and power consumption first decreases and then increases.



(a) *(b)*

Fig. 10 - Response surface for productivity and power consumption

(a) Response surface for productivity of baffle thickness and cutting circle diameter;
(b) Response surface for power consumption of center distance and cutting circle diameter

Based on the test data and as shown in Figure 10, the optimal productivity of 1677.105 kg/h and power consumption of 10.352 kW·h/t were achieved when the cutting circle diameter was 208.638 mm, the center distance was 256.123 mm, and the baffle thickness was 11.892 mm. These values closely aligned with the simulation results. Considering the manufacturing characteristics for the baffle, the dimensions were rounded to the nearest whole numbers, resulting in a final optimized cutting circle diameter of 209 mm, a center distance of 256 mm, and a baffle thickness of 12 mm. The baffle with the final optimized dimensions was tested on the machine, with each test repeated three times to obtain the average values. The test results were then compared to those of the unoptimized baffle, as shown in Table 9.

Table 9

Contrastive analysis of before and after optimization

Baffle Structure	Baffle volume (mm^3)	Maximum deformation (μm)	Productivity ($kg \cdot h^{-1}$)	Power consumption ($kWh \cdot t^{-1}$)
Unoptimized	2827433	27.803	1580	12.13
Finally optimized	1570436	28.525	1673	10.42
Rate of change(%)	-44.46	+2.60	+5.89	-14.10

As shown in Table 9, the finally optimized baffle volume was significantly reduced, while the maximum deformation slightly increased but remained within the allowable range. Productivity slightly improved, and power consumption was notably reduced. These results indicate that the optimization logic for the baffle structure is rational and the optimization effect is satisfactory.

CONCLUSIONS

Based on the domestic and international status quo analysis of straw mill, the baffle was identified as the target for optimization. A simplified double-baffle model was established. Through force analysis of the baffle model under material conditions, the force parameters of the baffle model were obtained, including the gravity of the baffle model, the impact force of the material on the hammer, the centrifugal force of the hammer, and the torque transmitted by the main shaft.

Finite element analysis software was used to simulate the baffle model. Based on the total deformation and equivalent stress nephogram, it was determined that the positions between the hammer shaft holes on the baffle could be optimized. Comparing the flat-optimized and curved-optimized schemes, it was found that under the same volume removal conditions, the curved-optimized baffle resulted in a smaller increase in maximum deformation and allowed for greater volume optimization.

Further finite element analysis tests were conducted, with the cutting circle diameter, center distance, and baffle thickness as the three factors in an orthogonal test design, and the maximum deformation as the evaluation index. The preliminary optimized dimensions of the baffle were determined to be a cutting circle diameter of 200 mm, a center distance of 250 mm, and a baffle thickness of 12.5 mm.

The machine tests were conducted using the Box-Behnken test design method. Productivity and power consumption were used as evaluation indexes. Considering the manufacturing characteristics of the baffle structure, the optimal combination was found to be a cutting circle diameter of 209 mm, a center distance of 256 mm, and a baffle thickness of 12 mm. The finally optimized baffle achieved a productivity of 1673 kg/h and a power consumption of 10.42 kWh/t. Compared to the unoptimized baffle, the finally optimized baffle volume was reduced by 44.46%, productivity increased by 5.89%, and power consumption decreased by 14.10%, demonstrating a significant improvement in overall performance.

ACKNOWLEDGEMENT

This research was supported by Anhui provincial quality engineering project, 2024jyxm0909; Anhui provincial college and university scientific research project, 2024AH052010; Wuhu institute of technology innovation team project, wzykytd202403; Wuhu institute of technology scientific research project, wzyzrzd202507.

REFERENCES

[1] Cao L.Y., Li S.B., Li C.D., Wang Y., Wang F. (2021). The research and development status of hammer feed mill (锤片式饲料粉碎机的研究发展现状). *Feed Industry*. Vol. 42, no. 3, pp. 31-36, Liaoning/China.

[2] Cotabarren I., Fernandez M.P., Di Battista A., Piña J. (2020). Modeling of maize breakage in hammer mills of different scales through a population balance approach. *Powder Technology*. Vol. 375, pp. 433-444, Switzerland.

[3] Ismail F.B., Al-muhsen N.F.O., Hasini H. (2022). Computational Fluid Dynamics (CFD) investigation on associated effect of classifier blades lengths and opening angles on coal classification efficiency in coal pulverizer. *Case Studies in Chemical and Environmental Engineering*. Vol. 6, pp. 100266, Britain.

[4] Kshirsagar V.N., Choudary D.S.K., Misname A.P. (2014). Experimentation and analysis of an automation can/plastic bottle crusher machine. *International journal for innovation research in science & technology*. Vol. 1, no.2, pp. 1-5, India

[5] Li C.D., Zhou Y., Cao L.Y., Bai Y.Q., Wang Y. (2024). Multi-objective optimization design of feed crushing process parameters (饲料粉碎过程工艺参数多目标优化设计). *Feed Research*. Vol. 47, no.5, pp.127-132, Beijing/China.

[6] Liu B., Zong L., Zhang D.X. (2011). Force and motion states of hammer mill at unloaded running (锤片式粉碎机空载运行中锤片的受力及运动状态). *Transactions of the Chinese Society of Agricultural Engineering*. Vol. 27, no.7, pp. 123-128, Beijing/China.

[7] Li G.Q., Guo X.R. (2012). Design and research on hammer of hammer mill (锤片式粉碎机锤片的设计与研究). *Agricultural Technology & Equipment*. no.5, pp. 38-40, Shanxi/China.

[8] Li C.D., Liu Y., Cao L.Y., Bai Y.Q., Wang F., Zhang S.W. (2024). Experimental research on optimization of working parameters of hammer mill (锤片式粉碎机工作参数优化试验研究). *Journal of Chinese Agricultural Mechanization*. Vol. 45, no.2, pp. 122-129, Jiangsu/China.

[9] Ruan J.L., Zhang L. (2014). Intensity analysis of the hammer framework of hammer mill (锤片式粉碎机锤架板强度分析). *Food & Machinery*. Vol. 30, no.6, pp. 82-84, 237, Hunan/China.

[10] Ruan J.L., Zhang L., Zeng G.L. (2014). The dynamic analysis on the closed rotor of hammer mill (锤片粉碎机封闭式转子结构的动力学分析). *Cereal & Feed Industry*. no.10, pp. 43-45, 54, Hubei/China.

[11] Thomas M., Hendriks W.H., van der Poel A.F.B. (2018). Size distribution analysis of wheat, maize and soybeans and energy efficiency using different methods for coarse grinding. *Animal Feed Science and Technology*. Vol. 240, pp. 11-21, Netherlands

[12] Wang J.D., Xie Y.H., Chen Y., Wu Z.Y. (2023). Biomimetic design of hammer pieces for hammer mill based on beaver incisors (基于河狸门齿的锤片式粉碎机锤片仿生设计). *Chinese Journal of Engineering Design*. Vol. 30, no.4, pp. 476-484, Zhejiang/China.

[13] Wang Y.C., Yu X.G. (2009). Main methods to improve crushing efficiency of sieve hammer mill (提高有筛锤片粉碎机粉碎效率的主要途径). *Feed Industry*. Vol. 30, no.17, pp. 1-4, Liaoning/China.

[14] Wu W.X., Yu X.L., Zhang Z.C., Li Q., Sun Q.Y., Zhao F., Jia Z.C. (2023). Improved design of the classification structure of vertical mechanical impact superfine grinder (立式机械冲击式超微粉碎机分级结构的改进设计). *Transactions of the Chinese Society of Agricultural Engineering*. Vol. 39, no.12, pp. 245-253, Beijing/China.

[15] Wang P.F., Xu S., Yang X., Li S.K. (2024). Optimization design and test of air delivery system for tower sprayer (塔形喷雾机风送系统优化设计与试验). *Transactions of the Chinese Society for Agricultural Machinery*. Vol. 55, no.11, pp. 342-351, 390, Beijing/China.

[16] Wang D.F., Wang M., Li L.Q. (2017). Mechanism analysis and parameter optimization of hammer mill for corn stalk (锤片式粉碎机粉碎玉米秸秆机理分析与参数优化). *Transactions of the Chinese Society for Agricultural Machinery*. Vol. 48, no.11, pp. 165-171, Beijing/China.

[17] Wen X.Y., Hong Y.M., Xiong J.M., Yu Y.G., Tan J.H., Meng X.B. (2023). Design and experiment of fixed automatic natural rubber tapping machine (固定式天然橡胶自动割胶机设计与试验). *Transactions of the Chinese Society for Agricultural Machinery*. Vol. 54, no.z2, pp. 128-135, Beijing/China.

[18] Xu W., Cao C.P., Sun Yu. (2021). Optimization design of hammer structure parameters of hammer mill (锤片式粉碎机锤片结构参数优化设计). *Journal of Agricultural Mechanization Research*. Vol. 43, no.1, pp. 27-33, Heilongjiang/China

[19] Yancey N., Wright C.T., Westover T.L. (2013). Optimizing hammer mill performance through screen selection and hammer design. *Biofuels*. Vol. 4, no.1, pp. 85-94, Britain

[20] Zhang X.R., Cao C., Zhang L.N., Xing J.J., Liu J.X., Dong X.H. (2022). Design and test of profiling progressive natural rubber automatic tapping machine (仿形进阶式天然橡胶自动割胶机设计与试验). *Transactions of the Chinese Society for Agricultural Machinery*. Vol. 53, no.4, pp. 99-108, Beijing/China.

[21] Zhang Y.X., Wang G.G., Tao S., Xu W.P. (2021). Development status, future trend and countermeasures of feed industry in 2020 (2020 年饲料产业发展状况、未来趋势及对策建议). *Chinese Journal of Animal Science*. Vol. 57, no.6, pp. 265-268, Beijing/China.

[22] Zhang X.R., Ni S.L., Liu J.X., Hu X.H., Zhang Z.F., Fu S.H. (2024). Design and flow field analysis of bionic blade of banana straw crushing and throwing machine (香蕉秸秆粉碎抛撒还田机仿生刀片设计与试验). *Transactions of the Chinese Society for Agricultural Machinery*. Vol. 55, no.8, pp. 138-151, 160, Beijing/China.

[23] Zhang Y.J., Xu H.M., Jay H.K., Liu S., Wang C.L., Jiang W. (2019). Finite element analyses and topology optimization of hammer feed grinder frame plate (锤片式饲料粉碎机架板的有限元分析及拓扑优化). *Journal of Huazhong Agricultural University*. Vol. 38, no.05, pp. 159-167, Hubei/China.

[24] Zartha J.W., Pinto P.J., Palaclo J.C., Rios A.F. (2021). Trends in grinding of agroindustrial products - a literature review. *Recent Patents on Food*, *Nutrition & Agriculture*. Vol. 12, no. 1, pp. 19-28, United Arab Emirates.

STUDY ON THE STRAW-SOIL DISTURBANCE CHARACTERISTICS OF A LIFT-TYPE WINGED CHISEL PLOW
/
抬土式带翼凿式犁对秸秆-土壤扰动特性的研究

Juanjuan WU[1)], Xianliang WANG * [2 3)], Kun CHEN[2 3) 1]
[1)] School of Intelligent Manufacturing, Zibo Polytechnic University, Zibo 255300, China;
[2)] College of Agricultural Engineering and Food Science, Shandong University of Technology, Zibo 255000, China;
[3)] Institute of Modern Agricultural Equipment, Shandong University of Technology, Zibo 255000, China;
Tel: +8615264311735; E-mail: wxl1990@sdut.edu.cn
Corresponding author: Xianliang Wang
DOI: https://doi.org/10.35633/inmateh-76-33

Keywords: *DEM, Soil-lifting plate, Straw buried, Mixed*

ABSTRACT
This study developed a lift-type winged chisel plow-straw-soil interaction model, and its validity was confirmed through multiple experimental indicators obtained from both soil bin tests and simulation experiments. The Discrete Element Method (DEM) was employed to analyze soil disturbance behavior and straw incorporation performance. Results showed that the plow tip of the lift-type winged chisel plow effectively sheared, loosened, and fractured the plow pan soil, while the soil-lifting plate pushed and turned the soil, promoting thorough mixing of straw and soil. Compared to traditional designs, the addition of wings increased the working width, and the soil-lifting plate significantly enhanced the frequency of straw–soil disturbance and soil fragmentation - resulting in a mixing rate of 42.98% and a uniformity rate of 92%.

摘要
本研究建立了抬土式带翼凿式犁-秸秆-土壤相互作用模型，通过土槽实验和仿真实验中的多试验指标（秸秆的正向和侧向位移、牵引力、秸-土混埋率）证明了模型的合理性。采用 DEM 研究其对土壤的扰动行为和秸秆的混埋行为。结果表明：抬土式带翼凿式犁的铲尖剪切、松动、破碎犁底层土壤；抬土板推移、翻动、混合秸秆-土壤。相比于传统的凿式犁相比，铲翼提升了作业宽度，同时抬土板增加了其对秸秆-土壤的扰动次数和土壤的破碎程度，混埋率提高到 42.98%，秸-土混合均匀度提高到 92%。

INTRODUCTION
Surface residue cover helps retain soil moisture and enhance soil fertility (*Reicosky & Saxton, 2007; Jacobs et al., 2022*). However, excessive residue density can negatively affect seeding quality and hinder seedling growth, becoming a key limiting factor for crop yield (*Wu & Chen, 2024; Li et al., 2022*). Therefore, evaluating the effectiveness of residue displacement and incorporation is essential for assessing the operational performance of tillage tools (*Hobbs et al., 2008*). Traditional tillage methods, such as rotary tillage for full straw incorporation (*Zhou et al., 2020; Zhu et al., 2023*), bury most of the straw in the soil. While effective in incorporation, these methods disturb the original soil profile, expose moist soil to the surface, and leave minimal residue cover - leading to increased soil erosion and runoff (*Wu & Chen, 2024*). In contrast, the winged chisel plow used for partial straw incorporation has proven effective in both straw incorporation and soil loosening (*Salar et al., 2021*). This implement mixes a portion of the straw residue into the soil to improve soil organic matter content while retaining some surface residue to minimize moisture loss. However, its performance can be limited by uneven soil aggregate fragmentation and inconsistent straw-soil mixing.

The winged chisel plow not only breaks through the limitations of the soil tillage layer system but also incorporates part of the straw into the soil, achieving straw incorporation and surface coverage operations (*Zhang et al., 2022*). *Xia, (2018),* demonstrated that the winged chisel plow could break through the constraints of the tillage layer and plow pan, achieving more uniform soil fragmentation and improving soil permeability. However, this study did not explore the effectiveness of straw incorporation (straw-soil mixing mechanism) in conjunction with its operation.

[1] *Juanjuan Wu, Lecturer Ph.D. Eng; Xianliang Wang, Assoc. Prof. Ph.D. Eng; Kun Chen, M.S. Stud. Eng.*

Wang, (2018), investigated the effects of the winged chisel plow on soil disturbance behavior, suggesting that soil fragmentation at different depths, real-time displacement, and velocity changes of particles at key positions are important indicators for evaluating its operational performance. *Zeng et al., (2020),* studied the effects of different types of chisel plows on straw-soil disturbance and straw burial rate. However, they did not examine the degree of soil aggregate fragmentation after disturbance, nor did they relate this to the degree of straw-soil mixing. These studies primarily focused on soil fragmentation, soil disturbance, and straw-soil mixing rates, without considering the uniformity of straw-soil mixing after incorporation. In contrast, the straw-soil mixing mechanism during the operation of the winged chisel plow is more complex. Investigating the mechanism of incorporation and mixing is a prerequisite for designing and optimizing high-performance winged chisel plows. Building on the foundation of incorporation and return-to-field technology, this study proposes adding a soil-lifting plate to the rear of the winged chisel plow (*Wang., 2021*). This addition aims to improve soil loosening and fragmentation effects and enhance the uniformity of straw-soil mixing during partial straw incorporation.

This incorporation mechanism involves mixing a portion of the straw into the soil while leaving the rest on the surface to improve soil structure, reduce soil erosion, and lower runoff risks (*Salar et al., 2021*). However, accurately and intuitively representing the operational mechanism of the lift-type winged chisel plow remains a challenge.

The discrete element method (DEM) offers unique advantages in analyzing the interactions between agricultural machinery components, straw, and soil. It provides data on the forces and motions of soil and straw under specific machinery structures and operational conditions from a microscopic perspective (*Barr et al., 2018; Sadek et al., 2021*). By building precise models, DEM overcomes the limitations of two-dimensional measurements. During the simulation of straw-soil operations, it reveals the complex coupled mechanisms of factors such as straw morphology distribution and soil aggregate interactions. Additionally, it enables precise capture and quantification of the dynamic changes in the uniformity of straw-soil mixing (*Liu et al., 2023a&b*), addressing the limitations of single-point practical observations that fail to present the mixing effects. DEM also comprehensively represents the three-dimensional spatial characteristics of the straw-soil mixing process (*Zeng et al., 2020*), providing theoretical support and technical guidance for the study of the lift-type winged chisel plow.

In summary, the objectives of this study are to establish a discrete element model of the interaction among the lift-type winged chisel plow - straw - soil, reveal the mechanisms of straw-soil disturbance and incorporation by the soil-lifting plate from a microscopic perspective during the incorporation operation, and quantify the changes in straw burial rate and the uniformity of straw-soil mixing under the influence of the soil-lifting plate, so as to provide a theoretical basis for the research and evaluation of straw incorporation tools and operational performance.

MATERIALS AND METHODS

Measurement of Straw and Soil Basic Parameters

(1) Measurement of Straw and Soil Properties

Soil samples were taken from a no-tillage seeding experimental field in Xilu Village, Zhangdian District, Zibo City, Shandong Province (36°87′~36°88′ N, 117°98′~119°99′ E). The soil samples were weighed on an electronic balance (model FA2104B), and the average soil sample density was calculated to be 241 kg/m³. The soil moisture content was determined using the drying method according to the "Standard for the Determination of Soil Dry Matter and Moisture by Weight" (Standard No.: HJ 613-2011), yielding a moisture content of 21.37% (on a dry weight basis).

Prior to selecting straw samples, corn plants (Zhongbang 1088 corn, commonly grown in northern China) were screened to ensure they were disease-free. Using a sampling knife, whole corn stalks were cut at a height of 50 mm above the ground. According to the methods outlined in GB/T 14699.1-2005 (Feed Sampling) and GB/T 6435-2014 (Determination of Moisture and Other Volatile Substances in Feed), the straw moisture content and density were measured to be 16.59% and 1450 kg/m³, respectively.

The soil shear strength was measured using the ZJ-type strain-controlled direct shear apparatus from Nanjing Soil Instrument Factory, under a vertical load pressure of 50 kPa. The shear force was obtained by combining the mechanical dial readings with the stress ring correction coefficient (C = 1.531 kPa/0.01 mm). Shear tests were conducted on soil samples from three different depths, and the values collected from each point were averaged. The measured internal friction angle of the test soil was 21.93°, and the Poisson's ratio was calculated as 0.38 using Equation 1.

$$\tau = c + p\,tan\,\varphi \quad (1)$$

where: τ is Stress (N); c is Soil cohesion (N); p is Vertical pressure (N); φ is Internal friction angle of the soil (°).

(2) Measurement of the straw-soil mixture repose angle

The repose angle of the soil and straw mixture was measured physically. Since this study does not involve radial and axial damage to the straw, only the physical parameters related to the straw skin were calibrated. The repose angle of the straw-soil mixture was measured as 38.415° using an intelligent powder characteristics tester (model BT-1001).

(3) Measurement of Material Friction Between Agricultural Machinery Components, Straw, and Soil Using an Inclined Plane Test

The static and dynamic friction coefficients between the straw-soil-steel plate are determined using the inclined plane method. The static and dynamic friction coefficients between the two materials are calculated using Equations 2 and 3, respectively.

$$f_s = \tan\theta \quad (2)$$

where:

f_s is the static friction coefficient; θ is the angle between the wooden board and the horizontal plane (°).

$$f_d = \frac{L_1 \sin\theta + L_2}{L_1 \cos\theta} \quad (3)$$

where:

f_d is the rolling friction coefficient; θ is the angle between the wooden board and the horizontal plane (°); L_1 is the sliding distance along the inclined plane (cm); L_2 is the horizontal sliding distance (cm).

The experiment was repeated 10 times, and the average values were calculated. The static and dynamic friction coefficients were measured for the following material pairs: soil-soil, straw-soil, soil-steel plate, straw-straw, and straw-steel plate.

Establishment of the Straw-Soil Simulation Model

The soil particles were defined as uniform spherical particles with a radius of 5 mm, and the Hertz-Mindlin with Bonding contact model was selected. During the operation of the lift-type winged chisel plow, the effect on the straw was primarily spatial displacement, with negligible deformation of the straw. Therefore, the straw was treated as a rigid body. The corn straw was modelled as an assembly of uniform particles with a radius of 10 mm. The mechanical interaction model between the straw, soil, and the lift-type winged chisel plow was set to the Hertz-Mindlin (no-slip) contact model to facilitate the analysis of the interactions between the implement, straw, and soil.

Establishment and Validation of the Lift-Type Winged Chisel Plow-Straw-Soil Model

The soil and straw model parameters were defined based on the calibrated values. Particle positions were randomly generated, resulting in a total of 234,250 soil particles and 709,181 bonding keys used to simulate cohesive interactions among the soil particles. The soil bin dimensions were set to 2000 × 1000 × 300 mm. Considering the actual working depth of the implement and the variation between the cultivated layer and the plow pan, the soil profile was divided into two layers: a cultivated layer and a plow bottom layer. To simulate field straw coverage, 1,200 straw pieces were randomly distributed on the soil surface, corresponding to a surface coverage density of 0.5 kg/m². The geometric model of the lift-type winged chisel plow was created using SolidWorks 2022, exported in STEP format, and imported into EDEM 2022 for simulation. The material used was 65Mn steel.

Simulation experiment of the motion state measurement of the lift-type winged chisel plow-straw-soil interaction

In the simulation experiments, the motion states of the soil and straw are monitored by tracking the positions of 12 soil tracers and 5 straw tracers. The soil cutting force (traction force, vertical force, and lateral force) is the sum of the contact forces between the soil particles and the machine in the corresponding directions.

In the center direction of the chisel plow operation, starting from the surface, four particles are sequentially marked at intervals of 50 mm downwards, labeled as J12, J22, J32, and J42. Then, 8 additional particles are marked 100 mm to the left and right of these four particles, labeled as J11, J21, J31, J41, J13, J23, J33, and J43, as shown in Figure 1.

At the same time, straw tracer 3 is placed at the center of the chisel plow's working area, with tracers 1, 2, 4, and 5 placed in parallel on either side of straw tracer 3 at a 40 mm interval. The soil displacement in the forward, lateral, and vertical directions is calculated by the changes in the coordinates of the soil tracers, while the forward and lateral shifts of the straw are calculated by the changes in the coordinates of the straw tracers in the forward direction.

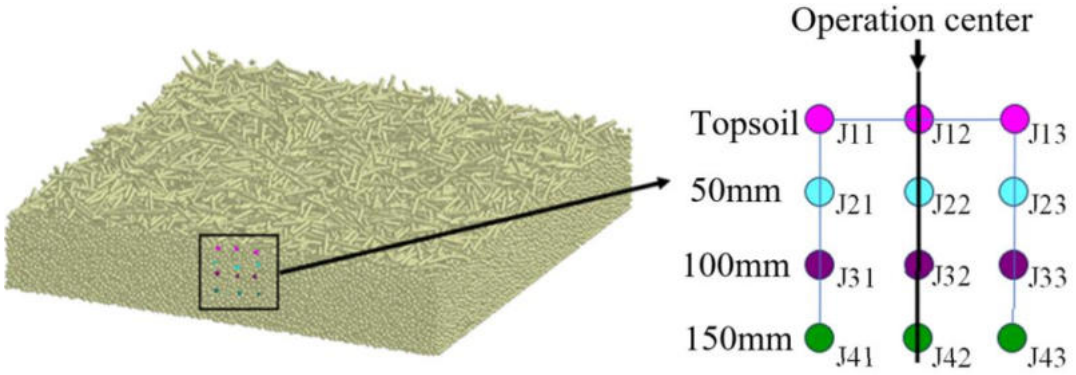


Fig. 1 - Marking the Position of Particles

Comparison of working performance between the lift-type winged chisel plow and the standard chisel plow

The experiment was conducted in the digital soil bin at the Agricultural Machinery Equipment Greenhouse of Shandong University of Technology. The soil in the bin was loam (72% sand, 15% silt, and 13% clay). Before each test, the soil was tilled using a 1 GKN-125 rotary tiller (tillage depth 120-160 mm), and then compacted using the soil bin vehicle. Soil samples were randomly taken from 10 different locations in the soil bin using a ring knife, with sampling depths of 5 mm, 10 mm, and 15 mm. The soil samples were dried in an oven at 105°C for 24 hours to measure soil moisture content. The average moisture content and average bulk density of the soil were measured as 17.6% (dry basis) and 1.36 g/cm³, respectively, according to ASABE Standards (2015).

RESULTS

Contact Model Parameter Results and Validation

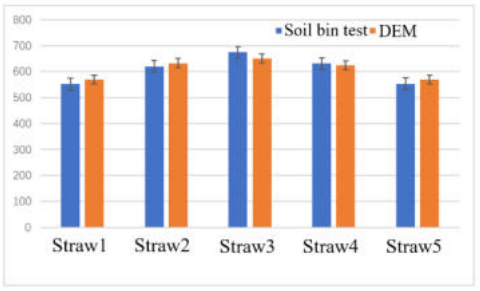
Within the parameter range set for the simulation test, the optimization module in Design Expert 12 software was used to optimize the regression equation for the repose angle, with the measured repose angle of 38.415° from the actual experiment as the target value. Several solutions obtained were validated through discrete element simulations to find the solution that most closely matched the actual repose angle. The optimal solution was chosen based on the simulation results.

The optimized parameters are as follows: soil-soil static friction coefficient of 0.57, soil-soil rolling friction coefficient of 0.18, and straw-soil dynamic friction coefficient of 0.12. The model parameters were set to these optimal values in EDEM 2022 software, while other parameters were taken as the average values measured in the actual experiment. The simulation was repeated five times, with the average measured repose angle being 39.49°, resulting in a relative error of 3.29% when compared to the actual experimental repose angle, thus validating the accuracy of the discrete element model.

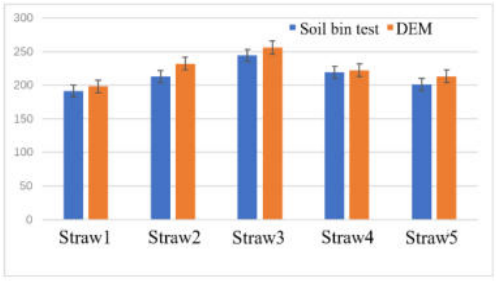
Validation Results of the Lift-Type Winged Chisel Plow-Straw-Soil Interaction Model

The forward and lateral displacements of straw, traction force, and straw burial rate from both the soil bin experiment and the simulation experiment were compared, with relative error used to assess consistency.

The forward and lateral displacements of the five marked straw pieces from both the soil bin experiment and the simulation experiment were plotted as bar charts, as shown in Figure 2. From the figure, it can be observed that straw 3, located at the center of the machine's operation, has the largest displacement. The further the straw is from the center position, the smaller its displacement. The overall trend of straw displacement is consistent with the simulation results. The forward displacement error of the straw ranges from 1.67% to 5.45%, and the lateral displacement error ranges from 0.52% to 6.84%.



(a)



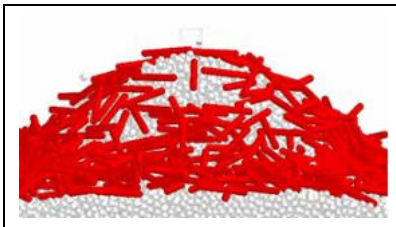
(b)

Fig. 2 - Comparison between simulation and actual experiment. (a) Horizontal displacement (b) Positive displacement

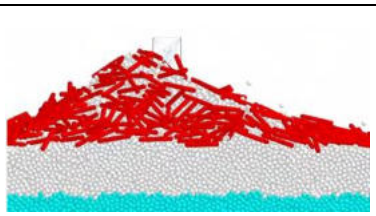
The average straw burial rates in the soil bin experiment and the simulation experiment were 84.37% and 78.3%, respectively, with a straw burial rate error ranging from 2.54% to 6.37%. The average traction force of the machine during stable operation in the soil bin experiment and the simulation experiment were 1603.24 N and 1498.77 N, respectively, with a machine traction resistance error ranging from 5.29% to 12.60%. All indicator errors are within the permissible range of model errors (*Ucgul et al., 2017*), and the variation trends in the experimental data are consistent with the simulation results. The soil bin experiment verified the accuracy of the discrete element simulation and the feasibility of discrete element modeling for field trials.

Analysis of the Performance of the Lift-Type Winged Chisel Plow in Simulation Experiments

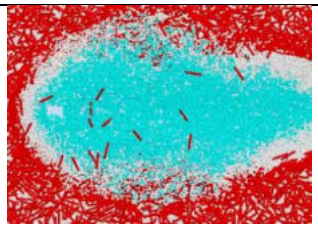
The lift-type winged chisel plow is equipped with a soil-lifting plate on the winged part of the chisel plow. By comparing the working performance of the two plows, the role of the soil-lifting plate in the operation of the machine can be analyzed more intuitively. Figures 3 and 4 show the disturbance trajectories of soil and straw in the X (horizontal), Y (longitudinal), and Z (vertical) directions at the same moment, with color processing applied to the straw and soil (red for straw, white for tilled soil, green for plow bottom soil), enhancing the contrast. Compared to the Winged Chisel Plow with less burial effect, the lift-type winged chisel plow has a wider working width and less straw residue on the soil surface (Figures 3c and 4c). It also demonstrates better soil turnover (Plow bottom soil eversion, Figure 3b and 4b), surface straw burial, and straw-soil mixing effects. In summary, the soil-lifting plate can increase the working width of the winged chisel plow (51.5%) and improve the efficiency of straw mixing (69.3%).



(a)

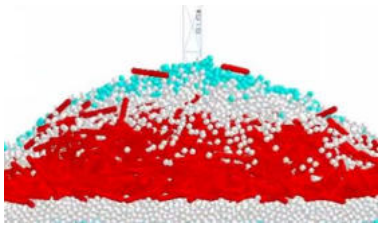


(b)

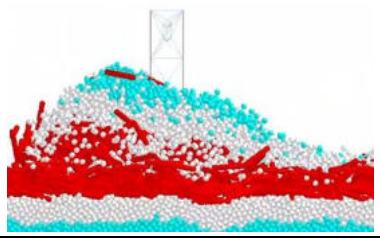


(C)

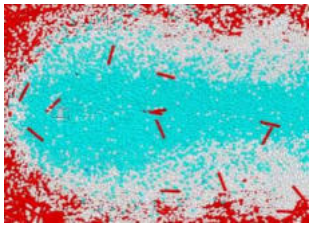
Fig. 3 - Analysis of the Winged Chisel Plow Operation Process
(a) X-direction, (b) Y-direction, (c) Z-direction



(a)



(b)



(C)

Fig. 4 - Analysis of the Lift-Type Winged Chisel Plow Operation Process
(a) X-direction, (b) Y-direction, (c) Z-direction

Analysis of Straw-Soil Micro-Disturbance Process at Different Moments

To understand the disturbance state of soil at different positions below the surface as the lift-type winged chisel plow moves forward, the Clipping function in the post-processing module of EDEM software is used to create a cross-sectional view of the soil model along the longitudinal centerline of the lift-type winged chisel

plow. Four moments are selected for the cross-section: when the plow has not yet entered the soil (0.02 s), when it has fully entered the soil (0.22 s), during the deep loosening process (0.42 s), and during the soil ejection process (0.62 s), as shown in Figure 5.

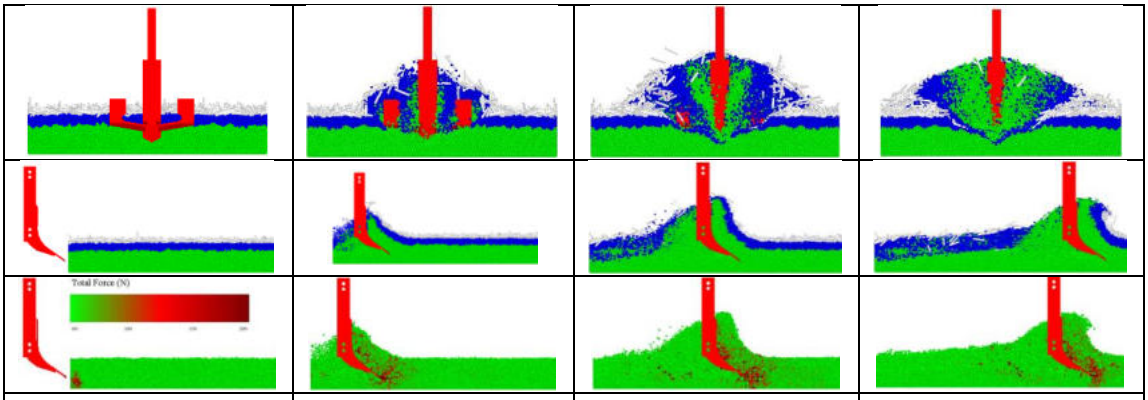


Fig. 5 - Disturbance of soil-lifting plow with wing chisel at different times
(a) 0.02 s (b) 0.22 s (c) 0.42 s (d) 0.62 s

Micro-disturbance Analysis of Straw-Soil at Different Positions

In order to explore the working range of the lift-type winged chisel plow and understand the soil disturbance state at different positions and depths, the role of each component in mixing and burying the straw was clarified. The longitudinal and transverse cross-sections of the soil at intermediate moments during the stable working process of the lift-type winged chisel plow were obtained. Based on the width of the chisel wing and the horizontal distance from the chisel tip to the chisel wing, the distances between the longitudinal and transverse cross-sections were set to 80 mm and 50 mm, respectively. Figure 6 shows the cross-sections in each direction at intermediate moments.

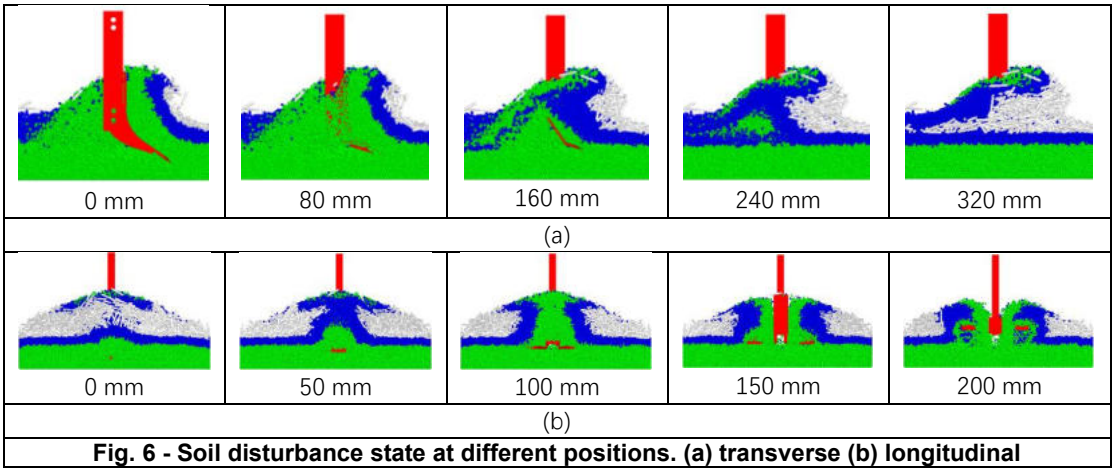


Fig. 6 - Soil disturbance state at different positions. (a) transverse (b) longitudinal

As shown in Figure 6(a), the disturbance of the plow bottom layer by the lift-type winged chisel plow gradually decreases as the horizontal longitudinal distance increases. Comparing the positions at 0 mm and 160 mm, the disturbance of the plow bottom layer by the chisel wing is relatively small. Due to the effect of the lifting plate, the straw-soil mixture in front of the chisel wing undergoes a turning action, and secondary disturbance is caused to the straw-soil mixture overturned by the lifting plate. From the changes in the number of straws before and after the positions at 240 mm and 320 mm in Figure 6(a), it can be seen that the working width on one side of the tool is about 300 mm, with the total working width of the tool being 600 mm. Within the horizontal width range of 300 mm from the center, there is very little straw.

Figure 6(b) illustrates that the lift-type winged chisel plow effectively turns and displaces the soil in the plow bottom layer, loosening the compacted soil by pushing it to both sides. The chisel tip initially cuts through the bottom layer soil, while the lifting plate lifts it through a turning motion. At transverse positions of 150 mm and 200 mm, the chisel wings notably expand the working width of the implement. Additionally, the lifting plate introduces secondary disturbances to both soil and straw particles (Figure 6a & 6b), thereby enhancing soil loosening, increasing fragmentation, and improving the uniformity of the straw-soil mixture following incorporation.

Straw-soil motion state analysis

To analyze the effect of the lift-type winged chisel plow on the overall motion behavior of the straw-soil mixture during operation, longitudinal cross-sections were taken at three key positions: the longitudinal center of the chisel plow (0 mm), the midpoint of the winged blade (160 mm), and the edge of the winged blade (320 mm). Three time points were selected for analysis: the moment the chisel tip enters the soil (0.02 s), the point at which the entire lift-type winged chisel plow is fully engaged in the soil (0.152 s), and the midpoint of the working stroke (0.302 s). A comparative analysis of the straw-soil motion velocity and distribution patterns at different times and cross-sectional positions was conducted, as shown in Figure 7.

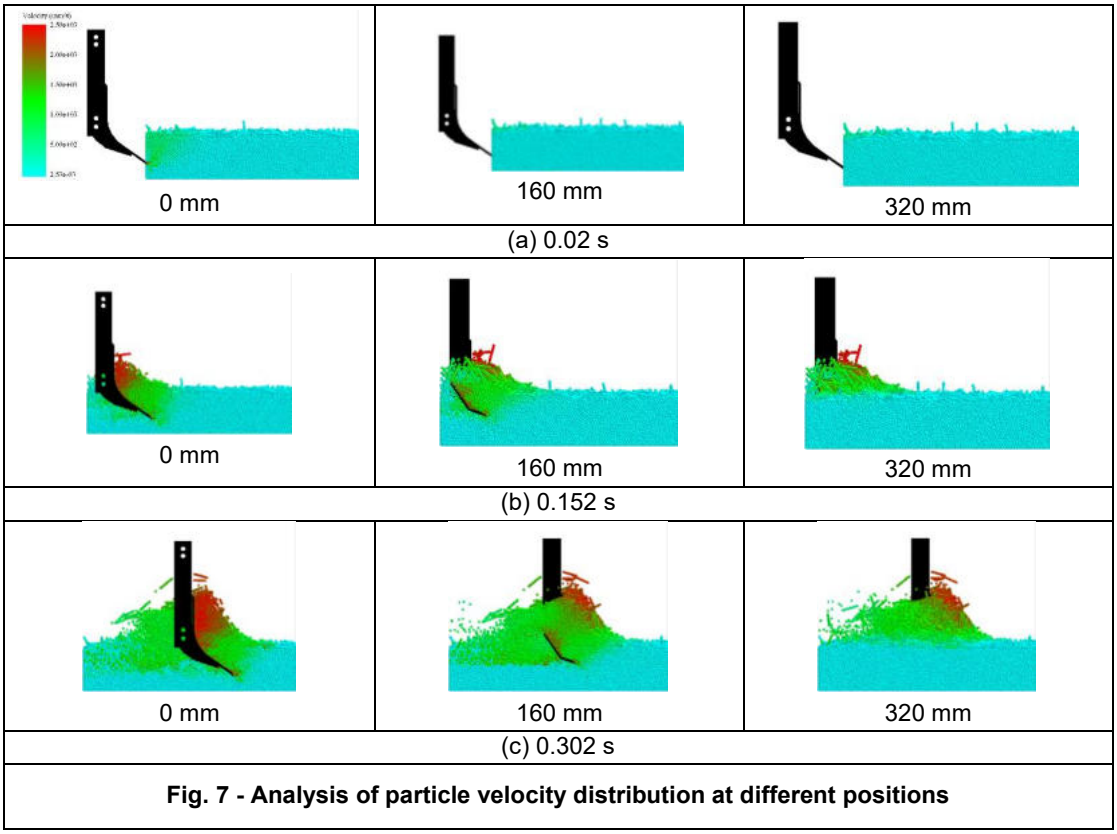


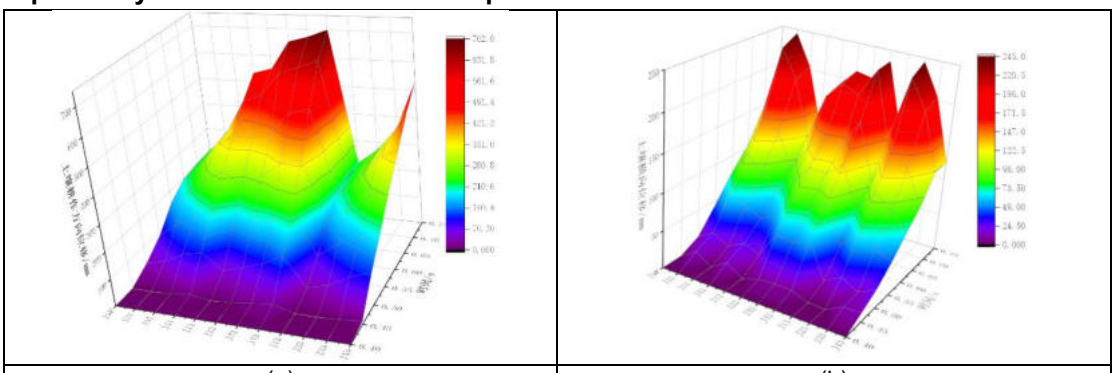
Fig. 7 - Analysis of particle velocity distribution at different positions

After the chisel tip enters the soil (Figure 7a), the subsoil begins to move upward due to the extrusion effect generated by the chisel tip. Simultaneously, the straw on the soil surface above the chisel tip begins to shift. However, because the pushing force of the chisel tip is limited, it produces minimal disturbance in the soil at the wing and wing-edge positions. When the wing enters the soil (Figure 7b), significant surface soil movement is observed at the horizontal center position (0 mm). This is attributed to the combined action of the lifting plate's pushing force and the extrusion pressure from the underlying soil. The highest movement velocities of both straw and soil occur in the region near the lifting plate of the lift-type winged chisel plow.

At the wing position, 160 mm from the horizontal center, the soil adjacent to the wing exhibits higher velocity. The maximum soil velocity curve closely aligns with the contour of the wing's lifting plate, indicating that this region is directly influenced by the wing structure. At this stage, the surface straw located above also begins to move under the combined action of the wing and lifting plate. By 0.302 s, the lifting plate actively flips the straw and soil through its plowing action. The highest movement velocities of both soil and straw are observed in front of the lifting plate. In these regions, particularly around the wing and lifting plate, the surface straw also gains significant velocity due to tool-induced disturbance. Meanwhile, the ridged soil lifted above the surface gradually collapses and backfills into the furrow under the influence of gravity.

Analysis of the velocity distribution across different positions reveals that the region in front of the lifting plate experiences the most intense disturbance. The maximum velocity contours of the soil particles correspond closely with the shape of the lifting plate and wing of the lift-type winged chisel plow. This demonstrates that the wing notably enhances disturbance in the cultivated soil layer and surface straw, contributing to improved mixing and loosening performance.

Microscopic Analysis of Soil Disturbance Displacement



(a) (b)

Fig. 8 - Soil displacement analysis Soil tillage.
(a) vertical displacement; (b) horizontal displacement

In the working direction (Figure 8a), the soil particles located beneath the lift-type winged chisel plow's lifting plate (J12, J22, J32, J42) exhibit relatively larger displacements. Among them, the bottommost soil particle at the center of the tool (J42) shows the greatest displacement in the working direction, while the soil particles near the wing blades and the lifting plate exhibit relatively smaller displacements. The soil particle directly beneath the lifting plate (J41) displays the smallest displacement. In the horizontal direction (Figure 8b), the soil particles directly beneath the lifting plate (J41, J43) exhibit minimal horizontal movement. In comparison, the remaining soil particles show relatively consistent horizontal displacement magnitudes. The soil particles located at the center of the lifting plate and the chisel tip (J21, J42, J23) experience the largest displacements. Considering the combined horizontal and working-direction displacements of soil particles, it can be observed that J41 and J43 are not directly influenced by the tool. Instead, the movement of particles in their vicinity is indirectly caused by the compressive forces among soil particles. At this point, the wing blades are positioned above a soil depth of 150 mm, and the lifting plate exhibits a greater disturbance effect on the cultivated soil layer. For soil particles located at the center of the lifting plate and chisel tip, the displacement increases with depth. This is due to the overturning action of the lifting plate, which flips the bottom-layer soil to a higher position, resulting in a longer forward movement duration. Conversely, the soil particles near the wing blades and the lifting plate are flipped to a lower height due to the height limitations imposed by the lifting plate. As a result, these particles experience a shorter forward movement duration and smaller displacements in the working direction.

In summary, the lift-type winged chisel plow exhibits the greatest disturbance within the cultivated soil layer. The addition of wing blades and the lifting plate effectively expands the disturbance range within this layer, although the direct force exerted by the wing blades on the plow pan is relatively limited. The chisel tip is capable of disturbing deeper soil layers, and a lower installation height of the wing blades increases the effectiveness of disturbance at depth. However, this also results in greater resistance, leading to increased energy consumption and reduced soil-loosening efficiency. The lifting plate of the lift-type winged chisel plow plays a critical role in achieving effective straw-soil mixing. However, its height significantly influences the displacement of the soil in front of it. During tillage operations, an insufficient lifting height may limit the upward movement of the soil above the lifting plate, impairing the burial of surface straw. This can ultimately reduce the effectiveness of straw-soil mixing achieved by the implement.

Performance Comparison of Soil Bin Tests

To investigate the effects of the winged blade and lifting plate on implement performance, soil bin tests were conducted to compare the straw burial rate (R), working width (W), straw burial depth (H), and straw-soil mixing uniformity (E) between the conventional chisel plow and the lift-type winged chisel plow. The lift-type winged chisel plow, with its wing blades and soil-lifting plate, demonstrated superior straw burial performance.

As shown in Table 1, compared to the conventional chisel plow, the lift-type winged chisel plow increased the burial rate to 42.98%, working width to 81.33 cm, and straw-soil mixing uniformity to 92%. The experimental results indicate that the lift-type winged chisel plow meets the quality standards for straw burial treatment as specified in DB21/T 3590-2022: Technical Specifications for Mechanized Operations of Corn Straw Incorporation into Soil. Comparing the actual working performance of the two implements, the lift-type winged chisel plow demonstrated superior loosening and crushing of the soil, as well as better uniformity of straw-soil mixing after incorporation.

Table 1

Soil bin test results

Category	R / %	W / cm	H / cm	E / %
Lift-type winged chisel plow	42.98	81.33	16.1	92
Ordinary chisel plow	13.2	39.47	17.2	61

CONCLUSIONS

This study investigated the motion characteristics of straw and soil during the operation of the lift-type winged chisel plow, as well as its effect on the micro-disturbance of the straw-soil mixture. A discrete element interaction model of the lift-type winged chisel plow, straw, and soil was established to explore the mechanism of straw-soil disturbance caused by the implement. The accuracy of this interaction model was validated through soil bin tests, and the working performance of the conventional chisel plow and the lift-type winged chisel plow was compared. The main conclusions are as follows:

1. The optimal combination of contact parameters for the straw-soil mixture was determined to be: a soil-soil static friction coefficient of 0.57, a soil-soil rolling friction coefficient of 0.18, and a soil-straw dynamic friction coefficient of 0.12. Under this parameter combination, the relative error between the simulated and experimental repose angles was 3.29%.

2. From a micro-scale perspective, the motion states of straw and soil at different time intervals and locations, as well as their influence on straw-soil micro-disturbance, were analyzed. The height of the soil-lifting plate was identified as the primary factor affecting soil fragmentation and straw burial efficiency.

3. The lift-type winged chisel plow shears and loosens the subsoil with its chisel tip, while the soil-lifting plate pushes, overturns, and mixes the straw and soil. Compared to the conventional chisel plow, the wing blades increased the working width, while the soil-lifting plate enhanced the frequency of straw-soil disturbance. The burial rate was improved to 42.98%, and the straw-soil mixing uniformity increased to 92%.

ACKNOWLEDGEMENT

This work was supported financially by the National Natural Science Foundation of China (Grant No. 32101631); Science and Technology Program of Guizhou Province (QKHZDZX [2024]004); Science and Technology Project of Guizhou Company of China National Tobacco Corporation (2024XM20).

REFERENCES

[1] Aluko, O. B., & Seig, D. A. (2000). An experimental investigation of the characteristics of and conditions for brittle fracture in two-dimensional soil cutting. *Soil and Tillage Research*, 57(3), 143-157.

[2] Barr, J. B., Ucgul, M., Desbiolles, J. M., & Fielke, J. M. (2018). Simulating the effect of rake angle on narrow opener performance with the discrete element method. *Biosystems Engineering*, 171, 1-15.

[3] Hobbs, P. R., Sayre, K., & Gupta, R. (2008). The role of conservation agriculture in sustainable agriculture. *Philosophical Transactions of the Royal Society B: Biological Sciences*, 363(1491), 543-555.

[4] Jacobs, A. A., Evans, R. S., Allison, J. K., Garner, E. R., Kingery, W. L., & McCulley, R. L. (2022). Cover crops and no-tillage reduce crop production costs and soil loss, compensating for lack of short-term soil quality improvement in a maize and soybean production system [J]. *Soil and Tillage Research*, 218: 105310.

[5] Li, R., Zheng, J., Xie, R., Ming, B., Peng, X., Luo, Y., Zheng, H., Sui, P., Wang, K., Hou, P., Hou, L., Zhang, G., Bai, S., Wang, H., Liu, W., & Li, S. (2022). Potential mechanisms of maize yield reduction under short-term no-tillage combined with residue coverage in the semi-humid region of Northeast China. *Soil and Tillage Research*, 217, 105289.

[6] Liu, L., Wang, X. L., Zhang, X. C., Cheng, X. P., Wei, Z. C., Zhou, H., & Zhao, K. L. (2023a). The Impact of 'T'-Shaped Furrow Opener of No-Tillage Seeder on Straw and Soil Based on Discrete Element Method. *Computers and Electronics in Agriculture*, 213, 108278.

[7] Liu, L., Wang, X. L., Zhang, X. C., Zhong, X. K., Wei, Z. C., Geng, Y. L., Cheng, X. P., Zhao, K. L., Bai, M. Y. (2023b). Determination and verification of parameters for the discrete element modelling of single disc covering of flexible straw with soil. *Biosystems Engineering*, 233, 151-167.

[8] *National Feed Quality Inspection Center, Feed Quality Inspection Center of the Ministry of Agriculture. GB /T14699.1-2005, Feed Sampling* [S]. Beijing: China Standards Press, 2005.

[9] Reicosky D. C., Saxton K E. (2007). The benefits of no-tillage [J]. *No-tillage seeding in conservation agriculture*, 2: 11-20.
[10] Sadek, M. A., Chen, Y., & Zeng, Z. (2021). Draft force prediction for a high-speed disc implement using discrete element modelling. *Biosystems engineering*, 202, 133-141.
[11] Salar, M. R., Karparvarfard, S. H., Askari, M., & Kargarpour, H. (2021). Forces and loosening characteristics of a new winged chisel plough. *Research in Agricultural Engineering*, 67(1).
[12] Spoor, G., & Godwin, R. J. (1978). An experimental investigation into the deep loosening of soil by rigid tines. *Journal of agricultural engineering research*, 23(3), 243-258.
[13] Wang, X. Z. (2021). *Soil-Winged Subsoiler Interactions and Their Effects* (Doctoral Dissertation, Northwest A&F University).
[14] Wang, X. Z., Yue, B., Gao, X. J., Zheng, Z. Q., Zhu, R.X., & Huang, Y.X. (2018). Discrete Element Simulations and Experiments of Disturbance Behavior as Affected by Mounting Height of Subsoiler's Wing. *Transactions of the Chinese Society of Agricultural Machinery* (10),124-136.
[15] Wu, P., & Chen, Y. (2024). Discrete element modelling of the effect of disc angle and tilt angle on residue incorporation resulting from a concave disc. *Computers and Electronics in Agriculture*, 224, 109222.
[16] Wu, P., & Chen, Y. (2024). Discrete element modelling of the effect of disc angle and tilt angle on residue incorporation resulting from a concave disc. *Computers and Electronics in Agriculture*, 224, 109222.
[17] Xia, L. (2018). *Optimum parameter and experimental study of shovel wing based on discrete element method.* Master dissertation.
[18] Zeng, Z., Ma, X., Chen, Y., & Qi, L. (2020). Modelling residue incorporation of selected chisel ploughing tools using the discrete element method (DEM). *Soil and Tillage Research*, 197, 104505.
[19] Zhang, L., Zhai, Y., Chen, J., Zhang, Z., & Huang, S. (2022). Optimization design and performance study of a subsoiler underlying the tea garden subsoiling mechanism based on bionics and EDEM. *Soil and Tillage Research*, 220, 105375.
[20] Zhou, H., Zhang, C., Zhang, W., Yang, Q., Li, D., Liu, Z., & Xia, J. (2020). Evaluation of straw spatial distribution after straw incorporation into soil for different tillage tools. *Soil and Tillage Research*, 196, 104440.
[21] Zhu, D., Shi, M., Yu, C., Yu, Z., Kuang, F., Xiong, W., & Xue, K. (2023). Tool-straw-paddy soil coupling model of mechanical rotary-tillage process based on DEM-FEM. *Computers and Electronics in Agriculture*, 215, 108410.
[22] *** *Feed Quality Supervision and Testing Center of the Ministry of Agriculture, Institute of Agricultural Quality Standards and Testing Technology of the Chinese Academy of Agricultural Sciences, China Feed Industry Association. GB /T6435-2014, Determination of Moisture in Feed* [S]. China Standards Press, Beijing, 2014.

STUDY ON THE IMPACT-BLOCKING EFFECT BETWEEN GRINDING MEDIA AND WHEAT BRAN POWDER DURING THE VIBRATION CRUSHING PROCESS
/
振动粉碎过程中磨介与小麦麸皮粉体间的冲击阻滞效应研究

Min CHENG*[1)], Haocong MENG[1)], Guangbo XIANG*[2)], Shihao ZHOU[1)], Mingxu WANG[1)], Baoguo LIU[1)]
[1)] School of Mechanical and Electrical Engineering, Henan University of Technology, Zhengzhou / China;
[2)] School of Mechanical Engineering, Zhengzhou University of Science and Technology, Zhengzhou / China
Corresponding author: Min Cheng, Tel: +86-18623710936; E-mail: chengminhappy2006@163.com,
Guangbo Xiang, Tel: +86-18625520309; E-mail: xianggpo@163.com
DOI: https://doi.org/10.35633/inmateh-76-34

Keywords: *wheat bran, vibration mill, impact-blocking effect, powder particle size, grinding media diameter, damping coefficient*

ABSTRACT
During the vibration crushing of wheat bran, an impact-blocking effect occurred between the grinding media and wheat bran powder. Experimental results showed that the impact depth exhibited quadratic relationship with respect to particle size, while the acceleration and damping coefficients followed the order: fine powder > coarse powder > uncrushed bran > micro powder. Increasing the diameter of the grinding media enhanced the impact depth by 81.10% for uncrushed bran and by 40.41% for coarse powder, but reduced acceleration by 45.35% and 29.56%, respectively. Damping coefficients positively correlated with grinding media diameter but negatively with cylinder diameter. Material layer thickness demonstrated threshold-dependent bidirectional regulation, peaking at 40 mm, with maximum damping difference rates of 20.40% for uncrushed bran and 17.67% for coarse powder. Drop height linearly influenced the impact depth, while showing cubic relationships with both acceleration and damping. Both parameters were minimized at 500 mm. Sensitivity analysis identified grinding media diameter as the primary factor affecting damping coefficients, revealing the sensitivity hierarchy: grinding media diameter > drop height > material layer thickness > cylinder diameter. This study provided a theoretical foundation and experimental support for optimizing the vibration superfine crushing efficiency of wheat bran.

摘要
在振动粉碎小麦麸皮时，磨介与粉体间存在冲击阻滞效应。实验表明，冲击深度与粉体粒度呈二次非线性关系，加速度、阻尼系数大小顺序为：细粉 > 粗粉 > 未粉碎麸皮 > 微粉。增加磨介直径可使未粉碎麸皮和粗粉的冲击深度分别增加 81.10% 和 40.41%，加速度降低 45.35% 和 29.56%。阻尼系数与磨介直径正相关，与圆筒直径负相关。料层厚度对各参数有双向调控作用，临界厚度为 40mm。下落高度与冲击深度线性相关，与加速度、阻尼呈三次非线性关系，500mm 时二者取极小值。灵敏度分析显示，磨介直径是影响阻尼系数的主因，灵敏度顺序为：磨介直径 > 落差高度 > 料层厚度 > 筒体直径。该研究为优化小麦麸皮振动超微粉碎效能提供依据。

INTRODUCTION
Wheat bran is rich in essential nutrients such as protein, dietary fiber, vitamins, and minerals. Its superfine powder has shown significant application potential in the development of functional foods, pharmaceutical excipients, and biochemical research (*Praveenet et al., 2023; Zheng et al., 2022; Ying et al., 2022*). However, the high lignocellulose content in its structural layers poses a major challenge for conventional grain crushing equipment, which often fails to achieve the required superfine particle size (<25 μm) (*Hemery et al., 2011*). Vibration mills, leveraging comprehensive crushing actions including impact, shearing, extrusion, and friction, have emerged as a promising solution for wheat bran superfine crushing (*He et al., 2018; Rajaonarivony et al., 2021*). During the vibration process, wheat bran particles in the grinding cylinder are subjected to continuous crushing forces from grinding media, while imposing a blocking effect that hinders media movement, reduces collision velocity, and consumes energy (*Bulgakov et al., 2018*).

[1]Min Cheng, Lecturer Ph.D.Eng.; [1]Haocong Meng, M.Stud.Eng.; [1]Guangbo Xiang, Lecturer M.S.Eng.; [2]Shihao Zhou, M.Stud.Eng.; [1]Mingxu Wang, Prof. Ph. D. Eng; [1]Baoguo Liu, Prof. Ph. D. Eng.

This bidirectional impact-blocking interaction directly influences grinding media dynamics and energy transmission, thus determining the overall crushing efficiency.

Current research on vibration mills focuses on grinding media dynamics, crushing process optimization, and media-material interaction mechanisms. High-speed cameras and the discrete element method (DEM) have been applied to analyze media dynamics. The former confirmed three motion forms of spherical media: impact, total rotation, and self-rotation, while DEM studies on non-spherical media remain limited. *Yokoyama et al. (1996)* simulated 2D media motion, analyzing collision characteristics and grinding rate. *Lee et al. (2010)* established an impact model for media-material grinding, and *Yang et al. (2015, 2016)* studied media flow dynamics under different vibration conditions.

In the optimization of vibration crushing process efficiency, DEM and experimental research methods are typically employed to investigate the effects of vibration characteristics, grinding media properties, filling rate, crushing time, and other factors on the crushing efficiency mechanism of vibration mills. *Li et al. (2015)* discovered that grinding media size correlates with power density, achieving a 42% increase in griseofulvin dissolution through process optimization. *Yang et al. (2016)* demonstrated that medium-frequency and large-amplitude operation of double-mass vibration mills optimizes super hard particle crushing, refining diamond to a median particle size (D_{50}) of 0.26 μm. *Bogdanov et al. (2019)* proposed a poly-harmonic vibration mill with adjustable multi-parameters to enhance crushing efficiency. *Qian et al. (2023)* revealed that amplitude-frequency coupling dominates particle crushing, developing a model that reduced calcium carbonate crushing energy consumption by 29.2%. *Haddad (2020)* identified rotating mass as a key factor, determining optimal conditions (1500 rpm, 16 mm media, 222 g rotating mass) for minimal grinding time. *Yildirim et al. (2025)* recently achieved the multi-objective optimization of the dry grinding of hydrated lime in a vertical vibratory mill, producing powders with a D_{50} of 6.26 μm and a specific surface area of 2.71 m²/g.

Concerning the interaction between grinding media and materials and the grinding mechanism, it primarily reveals the formation process of impact, compression, shear, friction, and other mechanisms through which grinding media in the grinding cylinder act on the crushed material, as well as their influence on the crushing effect. *Frolov et al. (2017)* found ceramic media had 30-50% lower wear than steel, with cylindrical shapes reducing contamination. *Cheng et al. (2019, 2021)* showed particle size affects crushing mechanisms (impact extrusion for large particles, impact shearing for small) and media properties (density, size, shape) influence yield by up to 70.07%. *Tomach (2024)* reported a grinding time that was 22.5% shorter with 15 mm media than with 12 mm media. Notably, research on materials' reverse influence on media dynamics remains scarce, with most studies relying on indirect evidence via particle size or moisture comparisons.

To investigate the impact-blocking effect between the grinding media and wheat bran in the vibration crushing process, this study constructed a grinding media-wheat bran powder impact test platform. Wheat bran powder with different particle sizes was used to simulate various stages of wheat bran crushing, material layer thickness simulated the bran filling amount, drop height simulated the impact velocity of the grinding media, and grinding media diameter and cylinder diameter directly represented the geometrical dimensions of the grinding media and the cylinder. Using impact depth, average acceleration, and damping coefficient as key indicators, this study systematically investigated the effects of wheat bran particle size, grinding media diameter (8–16 mm), cylinder diameter (60–180 mm), layer thickness (20–60 mm), and drop height (400–800 mm) on the impact-blocking effect. On this basis, a sensitivity analysis was conducted to rank the influence of factors on damping coefficients. The study aims to provide both theoretical foundations and practical guidance for optimizing vibration mill efficiency in wheat bran superfine crushing.

MATERIALS AND METHODS

Preparation of wheat bran powder samples

The raw material of wheat bran was Zhengmai 379, produced in 2024 and purchased from Zhengzhou Jinyuan Flour Mill. During the experiment, materials passing through a 5 mesh sieve and retained by a 20 mesh sieve were taken as wheat bran samples, with an adjusted moisture content of approximately 10.65%. To simulate the different crushing stages of wheat bran in a vibration mill, the samples were pre-crushed in a vibration mill prior to the experiment. The crushed samples were then sieved and classified, yielding four types of powder: uncrushed bran (d_A > 900 μm), coarse powder (280 μm < d_A < 900 μm), fine powder (74 μm < d_A < 280 μm) and micro powder (d_A < 74 μm). Their morphologies are shown in Fig. 1.



a. Uncrushed bran b. Coarse powder c. Fine powder d. Micro powder

Fig. 1 - Wheat bran powder samples

Experimental principle and platform

To investigate the impact-blocking effect between grinding media balls and wheat bran powder during vibration crushing, a test platform for the impact mechanical properties of wheat bran powder was constructed based on the free–fall principle, as shown in Fig. 2. This experimental platform mainly consists of a height-adjustable support, an electromagnet capable of adsorbing the grinding media balls, and a plexiglass cylinder filled with wheat bran powder (*Seguin et al., 2008*).

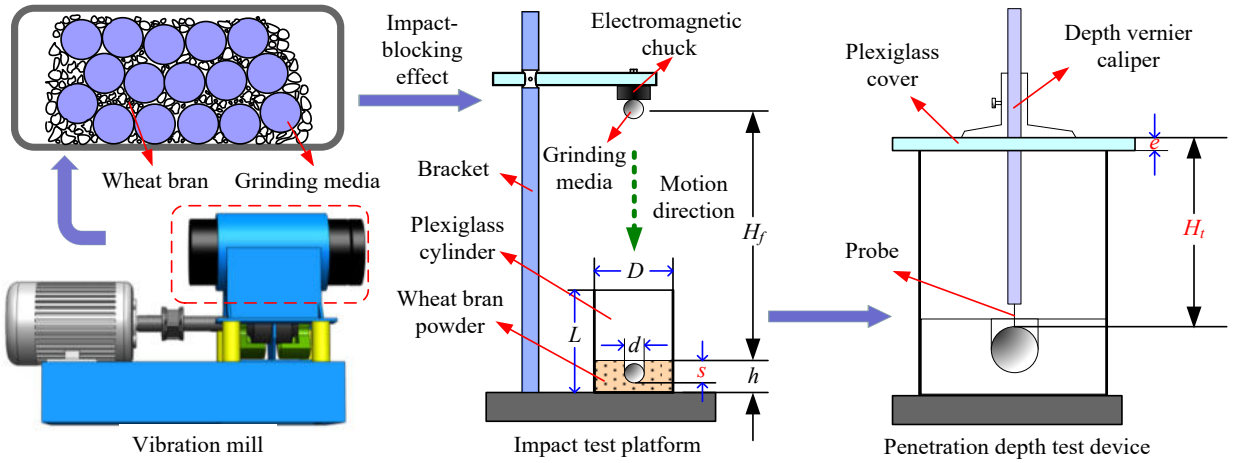


Fig. 2 - Grinding media-wheat bran powder impact test platform

d - grinding ball diameter; D - cylinder diameter; e - plexiglass cover plate thickness; h - material layer thickness; H_f - grinding ball height from material surface; H_t - distance between depth gauge base and probe; L - cylinder height; s - grinding ball impact depth in bran powder

During the experiment, the height of the grinding media is first adjusted, then the grinding media is aligned with the center of the cylinder and the power supply to the electromagnet is disconnected. At this point, the grinding media will continuously accelerate under the effect of gravity until it contacts the surface of the bran powder and starts to decelerate, and finally stops at a certain depth due to the resistance of the bran powder. To measure the impact depth of the grinding media, a probe is installed at the bottom of the depth gauge, and a glass cover plate is installed at the top, forming a gauge that allows direct read of the impact depth of the grinding media ball. After the experiment, first gently brush away the bran powder above the grinding media; then, touch the probe of the depth gauge to the upper surface of the grinding ball and read the distance H_t between the depth gauge's measuring base and the probe. Finally, the impact depth of the grinding ball s as it penetrates into the bran powder can be calculated using the mathematical relationship among the cylinder height L, grinding ball diameter d, and plexiglass cover plate thickness e.

Experimental scheme

Numerous impact test studies on powder or granular materials have shown that factors such as the particle size of the powder or granules, the size of the impacting object, the cylinder diameter, the material layer thickness, and the drop height (or impact velocity) can all affect the impact mechanical properties (*Ji et al., 2012, 2016; Wang and Ji, 2018*). To explore the impact-blocking effect between the grinding media balls and the wheat bran powder, the bran powder particle size, grinding media ball diameter, cylinder diameter, material layer thickness, and drop height were selected as experimental conditions. A series of tests were conducted to investigate the effect of grinding media balls on wheat bran powder.

The objectives were to simulate different crushing stages of wheat bran by using powders with different particle sizes, to simulate the boundary effect of the grinding cylinder by using cylinders with different diameters, to simulate the filling rate of bran by using material layers with different thicknesses, and to simulate the impact velocity of the grinding media balls by using different drop heights.

During the experiment, one experimental condition was selected as the variable, while the other four were kept constant. The specific experimental design is shown in Table 1. To improve the reliability of the results, each group of experiments was repeated at least 10 times. To reduce experimental errors, unreasonable test data such as extreme values were excluded. To eliminate the impact of the cylinder's boundary effect, the cylinder diameter was required to be more than 5 times the grinding media ball diameter (*Ji et al., 2012*). As shown in Table 1, the diameters of the media balls and cylinders meet this requirement. The masses of the grinding media balls with different diameters listed in Table 1 were 2.14 g, 4.17 g, 7.23 g, 11.45 g, and 17.06 g, respectively.

Table 1

Experimental scheme

Experimental factors	Variable experimental conditions					Constant experimental conditions			
	NO.1	NO.2	NO.3	NO.4	NO.5	Grinding media diameter [mm]	Cylinder diameter [mm]	Material layer thickness [mm]	Drop height [mm]
Powder particle size [μm]	5-20	20-60	60-200	<200	—	10	90	30	500
Grinding media diameter [mm]	8	10	12	14	16	—	90	30	500
Cylinder diameter [mm]	60	90	120	150	180	12	—	30	500
Material layer thickness [mm]	20	30	40	50	60	10	90	—	500
Drop height [mm]	400	500	600	700	800	10	90	40	—

Experimental evaluation indicators

To simulate and analyze the impact-blocking effect between the grinding media ball and the bran powder in the grinding cylinder of the vibration mill, the impact depth of the grinding media ball in the bran powder, the average acceleration of the grinding media ball after being blocked by the bran powder, and the average damping coefficient were selected as evaluation indicators.

According to Fig. 2, the impact depth of the grinding media ball can be obtained as:

$$s = H_t + h + d - e - L \tag{1}$$

Assuming that the grinding media ball undergoes uniform deceleration while impacting through the wheat bran powder, its average acceleration can be calculated from Fig. 2 as:

$$a = \frac{gH_f}{H_t + h + d - e - L} \tag{2}$$

Where: a is the average acceleration, m/s^2; g is the gravitational acceleration, 9.8 m/s^2.

By neglecting the elastic compression effect of the grinding media ball on the wheat bran powder during the impact process and the frictional energy consumption between the powder particles, the average damping coefficient of the bran powder acting on the grinding media ball is derived as:

$$c = m\sqrt{2gH_f}\left(\frac{1}{H_f} + \frac{1}{H_t + h + d - e - L}\right) \tag{3}$$

Where: c is the average damping coefficient, Ns/m. During the experiment, H_f, h, d, e, and L are known parameters. By measuring H_t with a depth gauge and substituting it into Eqs. (1), (2), and (3) respectively, the specific values of evaluation indicators s, a, and c can be determined.

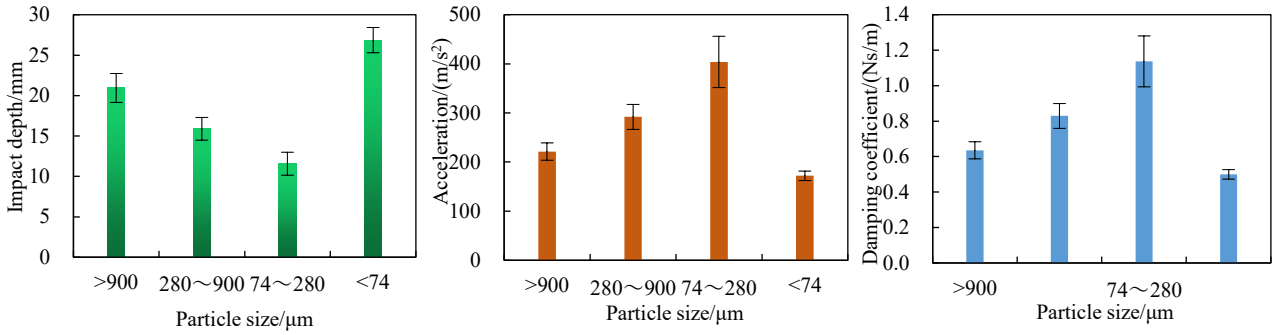
RESULTS

Influence of powder particle size on the blocking effect of wheat bran powder

Fig. 3 shows the variations in the impact depth, acceleration, and damping coefficient when grinding media balls impact four types of wheat bran powders respectively. Under the same impact conditions, as depicted in Fig. 3 (a), the impact depth exhibits a quadratic nonlinear trend of first decreasing and then increasing with decreasing powder particle size.

The average acceleration of the grinding media balls and the damping coefficient of the wheat bran powder both demonstrate a quadratic nonlinear pattern: they first increase and then decrease. This pattern is exactly opposite to the trend of the impact depth, as shown in Fig. 3 (b) and Fig. 3 (c).

When the bran powder particle size is relatively large, the inter-particle voids are large, and the powder fluidity is good. When the grinding media balls penetrate, the resistance mainly originates from the frictional force between the particles and the grinding media surface. At this point, the resistance is relatively small, leading to a large impact depth. When the powder particle size is moderate, the inter-particle voids decrease, and powder fluidity diminishes. During media ball penetration, the particle collision frequency increases, as does the resistance to particle rearrangement. Here, the resistance reaches a maximum, and the impact depth attains a minimum. When the powder particle size is relatively small, the inter-particle voids further decrease, and the powder fluidity significantly declines. During grinding media ball penetration, the inter-particle collision resistance decreases, and the particles become more flowable. The resistance instead decreases, causing the impact depth to increase. In the field of particle damping and vibration reduction, studies have shown that for a specific type of damping particles, an optimal particle size typically exists, at which the particle-generated damping is the maximized (*Shinde and Pathak, 2016*; *Kumbhar, 2021*).



a. Impact depth b. Average acceleration c. Damping coefficient

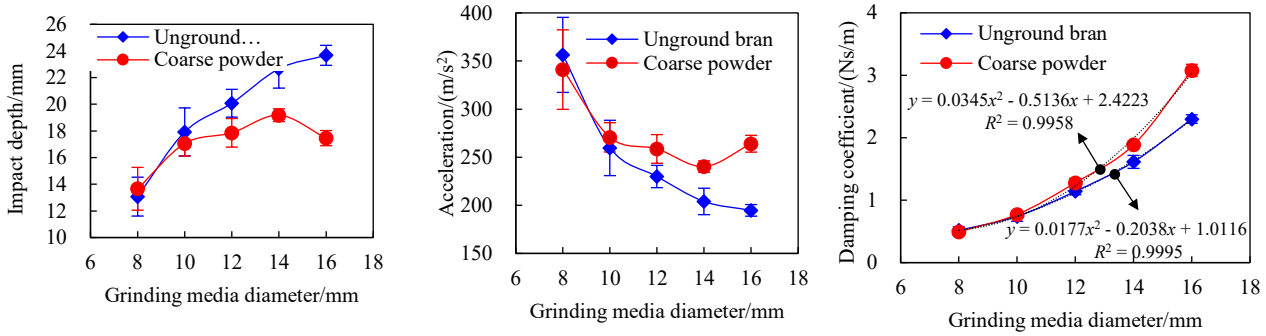
Fig. 3 - Impact mechanical property parameters of wheat bran powders with different particle sizes

As shown in Fig. 3, the impact depth of the grinding media ball in the fine powder is the smallest, measuring 11.57 mm, and that in the micro powder is the largest, reaching 26.86 mm. The difference rate between the maximum and minimum impact depths is 132.15%, while the difference rates for the acceleration and damping coefficient are 134.79% and 127.53% respectively. This indicates that the bran powder particle size significantly influences the blocking effect on the grinding media ball. Given that the impact depth in the fine powder is minimal and the damping coefficient is maximal, the grinding media ball encounters the greatest resistance when penetrating the fine powder, whereas penetration into the micro powder is the easiest. This implies that crushing the fine powder into micro powder is relatively difficult. It further reveals that during different stages of vibration crushing, the crushing difficulty of wheat bran particles varies, as do the required crushing force and energy consumption. To avoid the mutation region between fine powder and micro powder and ensure test result reliability, this study selects uncrushed bran and coarse powder as the impacted materials to further investigate the effects of grinding media diameter, drop height, material layer thickness, and cylinder diameter on their blocking effect.

Influence of grinding media diameter on the blocking effect of wheat bran powder

According to Fig. 4(a), as the impact depth of the grinding media ball generally increases as its diameter increases. This is because, at the same drop height, a larger media ball diameter corresponds to higher gravitational potential energy, thereby increasing its impact kinetic energy gradually. It is also observed that the impact depth in uncrushed bran is typically greater than that in coarse powder, consistent with the results in Section 3.1. Notably, when the grinding media ball diameter is 8 mm, its impact depth in coarse powder exceeds that in uncrushed bran. This can be explained by the better fluidity of coarse powder, which facilitates the penetration of the small grinding media ball. Conversely, when the grinding media ball diameter is 16 mm, the impact depth in coarse powder decreases. This may be due to the larger grinding media ball encountering changes in structural support or inter-particle friction within the coarse powder, leading to reduced impact depth (*Ye et al., 2015*).

As shown in Fig. 4(b), the variation trend of acceleration during the grinding media ball impacts and penetration into the two types of bran powder is completely opposite to that of the impact depth. According to Fig. 4(c), the damping coefficients for the two types of wheat bran powder increase with the grinding media ball diameter, and the damping from the coarse powder exceeds that from the uncrushed bran. This is because a larger grinding media ball diameter increases the contact area between the grinding media surface and the bran powder, thereby enhancing the frictional force between the wheat bran powder particles and the grinding media surface. As the grinding media ball diameter increases, the damping coefficient of the coarse powder rises more rapidly, widening the gap between the damping coefficients of the two types of bran powder. This can be attributed to the voids and mobility of the coarse powder particles. Based on the fitted expressions in Fig. 4(c), when the grinding media diameter exceeds 9.25 mm, the coarse powder exhibits higher sensitivity than the uncrushed bran, meaning its damping coefficient is more susceptible to changes in the grinding media diameter. Therefore, to optimize the vibration crushing efficiency of wheat bran, the grinding media diameter should be rationally selected based on the results of wheat bran vibration crushing tests (*Cheng et al., 2021*).

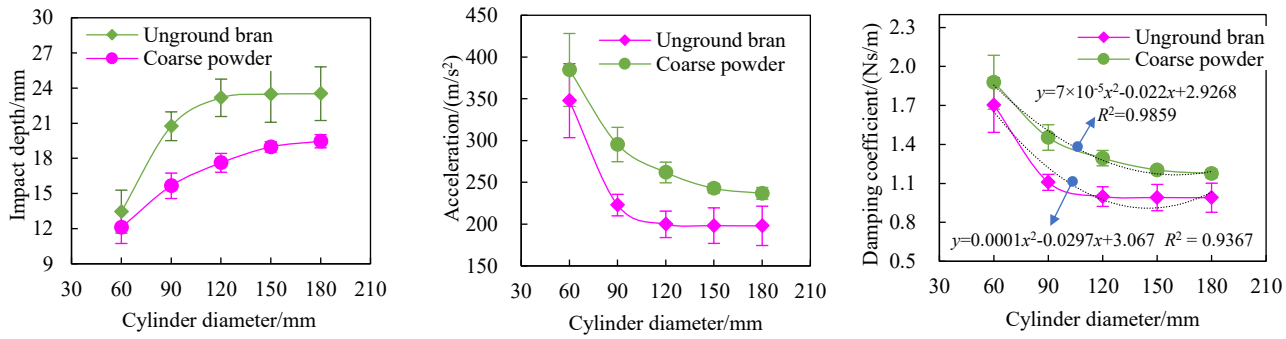


a. Impact depth b. Average acceleration c. Damping coefficient

Fig. 4 - Influence of grinding media diameter on the blocking effect of wheat bran powder

Influence of cylinder diameter on the blocking effect of wheat bran powder

As shown in Fig. 5(a), the impact depth of the grinding media in uncrushed bran is consistently greater than that in coarse powder, in line with the results in Section 3.1. As the cylinder diameter increases, the impact depth of the grinding media in the two types of bran powders increases and gradually stabilizes, following an approximate quadratic nonlinear trend. In other words, the boundary effect of the grinding cylinder on the impact depth of the grinding media diminishes as the cylinder diameter increases. This is because a small cylinder diameter imposes higher resistance to bran diffusion in all directions, leading to a larger proportion of frictional energy consumption between bran powder particles and the cylinder wall during impact (*Seguin, 2023*). Conversely, a larger cylinder diameter results in lower diffusion resistance, and the proportion of frictional energy consumption between particles and the cylinder wall is small and tends to be stabilize. As shown in Fig. 5(b) and Fig. 5(c), the average acceleration and damping coefficient exhibit identical variation trends, which are opposite to that of the impact depth of the grinding media. Both parameters decrease with increasing cylinder diameter and eventually reach a stable state.



a. Impact depth b. Average acceleration c. Damping coefficient

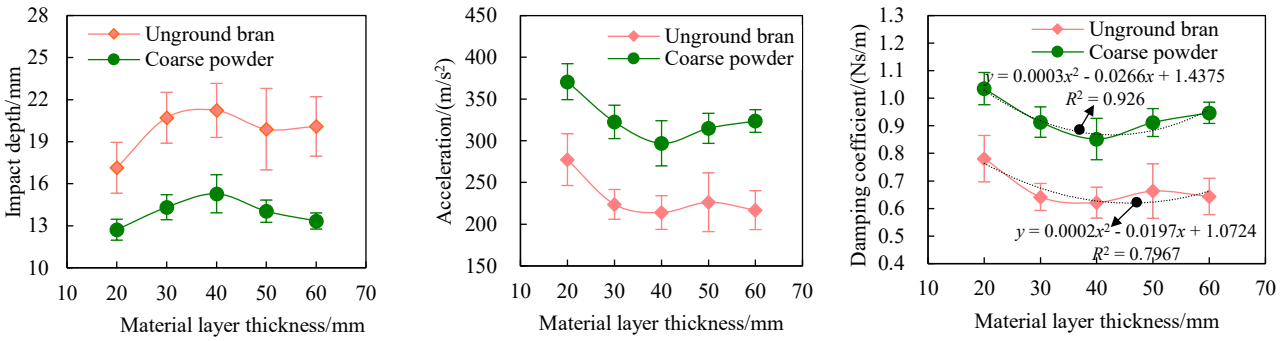
Fig. 5 - Influence of cylinder diameter on the blocking effect of wheat bran powder

As shown in Fig. 5(c), when the cylinder diameter exceeds 114.46 mm, the uncrushed bran exhibits higher sensitivity than the coarse powder. When the cylinder diameter surpasses 145.12 mm and 160.35 mm respectively, the slopes of the functional relationships for the damping coefficients of uncrushed bran and coarse powder become zero, and the damping coefficients stabilize, indicating the disappearance of the cylinder's boundary effect. In conclusion, the critical cylinder diameters for the two types of bran differ, with the coarse powder having a larger critical diameter than the uncrushed bran. This discrepancy may primarily arise because the coarse powder has a higher density than the uncrushed bran, enabling a more stable energy transfer path that allows the impact wave from the grinding media ball to propagate further. As demonstrated above, the ratios of cylinder diameter to grinding media diameter for the two types of bran powders are 9.54 and 12.09 respectively. This indicates that the cylinder's boundary effect is influenced by both the powder type and its particle size (*Ji et al., 2012*).

Influence of material layer thickness on the blocking effect of wheat bran powder

As depicted in Fig. 6(a), with the increase in thickness of the two types of wheat bran powder layers in the cylinder, the impact depths of the grinding media both display a trend of first increasing, then decreasing, and finally stabilizing. This can be attributed to the fact that when the material layer thickness exceeds an optimal threshold, its elastic effect intensifies, absorbing the impact energy of the grinding media. *Tomach (2024)* and *Seguin (2023)* have also pointed out that for particles with different shapes, the critical material layer thickness varies, and the damping rate exhibits a pattern of increasing first, then decreasing, and eventually stabilizing with increasing thickness—findings that align well with the results of this study. When the material layer thickness reaches a critical value of 40 mm, the impact depths of the grinding media in both bran powders attain their maxima. The ratio of material layer thickness to the grinding media diameter at this point is 4:1. Additionally, it is observed that the impact depth of the grinding media in uncrushed bran is consistently greater than that in coarse powder, in line with the results presented in Section 3.1. The difference rates between the maximum and minimum impact depths for uncrushed bran and coarse powder are 23.86% and 20.13%, respectively. This indicates that material layer thickness has a significant effect on the impact depths of the two types of wheat bran powders. The maximum difference rate in impact depth between the two types of bran powders is 33.60%, with the minimum rate at 25.79%, further highlighting the substantial influence of powder particle size on the blocking effect of wheat bran powder.

As shown in Fig. 6(b) and Fig. 6(c), the variation trends of the average acceleration and damping coefficient of the grinding media are consistent and opposite to that of the impact depth. The average acceleration and damping coefficient for the coarse powder are consistently higher than those for the uncrushed bran. When the ratio of material layer thickness to grinding media diameter is 4:1, the damping coefficient reaches its minimum. The difference rates between the maximum and minimum damping coefficients of uncrushed bran and coarse powder are 25.63% and 21.47%, respectively.



a. Impact depth b. Average acceleration c. Damping coefficient

Fig. 6 - Influence of material layer thickness on the blocking effect of wheat bran powder

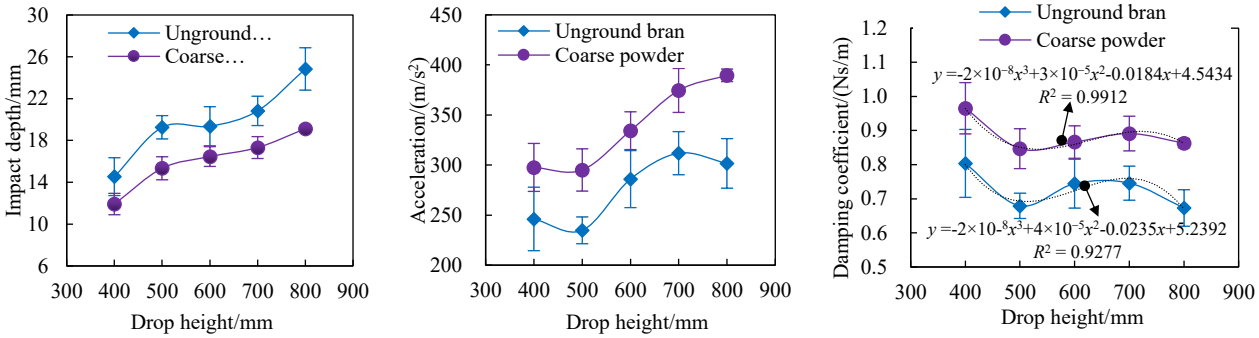
As shown in Fig. 6(c), when the material layer thickness is between 26.1 mm to 45.8 mm, the uncrushed bran demonstrates higher sensitivity than the coarse powder. During this range, variations in material layer thickness more significantly influence the damping coefficient of the uncrushed bran. For thicknesses of 20–26.1 mm and 45.8–60 mm, the coarse powder exhibits greater sensitivity, indicating it is more responsive to thickness changes. In wheat bran vibration crushing, the material layer thickness correlates positively with the bran filling amount. The higher the filling, the thicker the material layer that the grinding media need to penetrate.

When the thickness reaches the critical value, the damping coefficient of the bran powder is minimized, optimally facilitating the penetration of the grinding media. Thus, to improve wheat bran crushing efficiency, the bran powder filling amount should be rationally determined through experimental analysis.

Influence of drop height on the blocking effect of wheat bran powder

As shown in Fig. 7(a), the impact depth increases overall with the drop height of the grinding media (*Seguin et al., 2008*). Within a certain error margin, the relationship between drop height and initial impact velocity can be considered approximately linear. Thus, drop height can be regarded as equivalent to the initial impact velocity of the grinding media. This is consistent with the conclusion that "under identical conditions, the greater the initial impact velocity of an object, the deeper its impact depth"(*Ye et al., 2016*). The impact depth of the grinding media in uncrushed bran exceeds that in coarse powder, in line with the results in Section 3.1.

As shown in Fig. 7(b), owing to varying initial impact velocities, the average acceleration of the grinding media during their impact and penetration into wheat bran powder shows a cubic nonlinear trend: decreasing first, then increasing, and then decreasing again. The average acceleration of the coarse powder remains higher than that of the uncrushed bran. According to Fig. 7(c), the damping coefficient reaches a local minimum at a grinding media drop height of 500 mm. From the impact velocity perspective, it is not that the higher the impact velocity, the more favorable the penetration of grinding media into bran powder; instead, there exists a locally optimal impact velocity. The difference rates between the maximum and minimum damping coefficients of the uncrushed bran and the coarse powder are 19.41% and 13.98%, respectively; those for impact depths are 70.84% and 60.40%, respectively; and the coefficients of variation for accelerations are 32.83% and 32.04%, respectively. As shown above, the uncrushed bran exhibits higher difference rates in impact depth, acceleration, and damping coefficient than the coarse powder. The order of influence of drop height on the three parameters is: impact depth > acceleration > damping coefficient.



a. Impact depth b. Average acceleration c. Damping coefficient

Fig. 7 - Influence of drop height of the grinding media ball on the blocking effect of wheat bran powder

As shown in Fig. 7(c), when the drop height is between 429 mm and 656 mm, the uncrushed bran demonstrates higher sensitivity than the coarse powder. Within this range, variations in drop height more significantly influence the damping coefficient of the uncrushed bran. For drop heights of 400–429 mm and 656–800 mm, the coarse powder exhibits greater sensitivity, indicating it is more responsive to drop height changes. In conclusion, the performance parameters of the vibration mill, such as rotational speed and amplitude, should be rationally selected within a defined range to bring the grinding media's impact velocity close to the optimal state. This approach reduces the damping coefficient between the grinding media and bran powder, enabling more energy to be converted into crushing energy.

Sensitivity analysis of the damping coefficient of wheat bran powder

Given that the dimensions and value intervals of the experimental factors (e.g., the grinding media diameter, material layer thickness, drop height, and cylinder diameter) vary, the sensitivities of the damping coefficients for uncrushed bran and coarse powder with respect to these influencing factors are not comparable. Thus, dimensionless normalization of these factors is necessary.

Considering the non-negativity of the factors' value intervals, the following equation for dimensionless normalization can be used.

$$X_i = (x_i - \min\ x_i)/(\max\ x_i - \min\ x_i) \quad (4)$$

where:

X_i is the i-th dimensionless value, with $X_i \in (0, 1)$; x_i is the i-th dimensional value.

By using Eq. (4) to perform dimensionless normalization on the above influencing factors, the dimensionless fitting expressions for the damping coefficients of uncrushed bran and coarse powder with respect to these factors can be derived, as shown in Table 2.

According to Table 2, the dimensionless sensitivity distribution curves for the damping coefficients of the two types of wheat bran powders can be derived, as illustrated in Fig. 8.

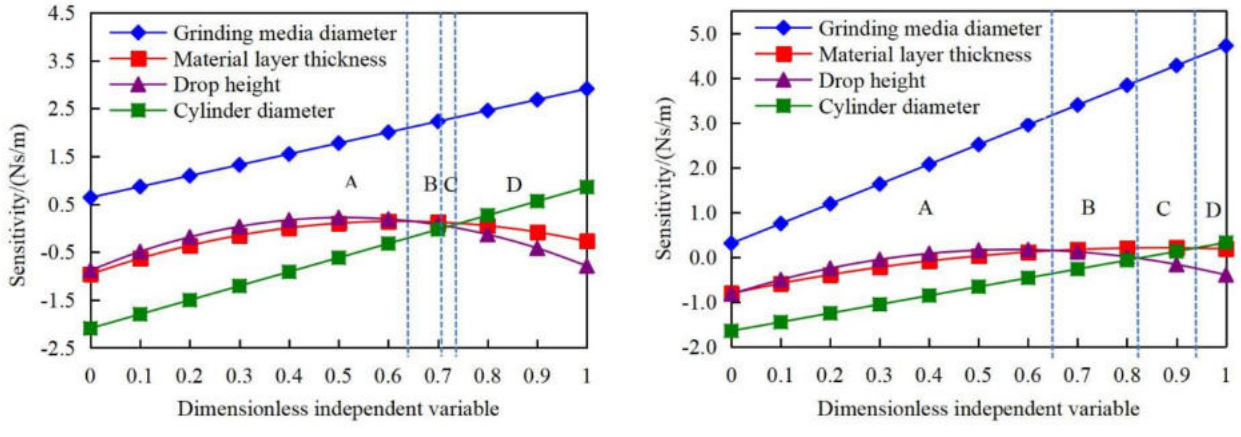
Fig. 8 shows that the sensitivity distribution laws of the damping coefficients of the two types of bran powders are very similar. This indicates that the test results have relatively high reliability. For both types of wheat bran powders, the grinding media diameter is consistently the most sensitive factor for changes in the damping coefficient, exceeding the drop height, material layer thickness, and grinding cylinder diameter.

Table 2

Dimensionless fitting expressions of damping coefficients of two types of wheat bran powders

Powder type	Uncrushed bran	Coarse powder
Grinding media diameter	Y=1.1354X^2+0.6402X+0.5164 (R^2=0.9995)	Y=2.2072X^2+0.306X+0.5211 (R^2=0.9958)
Cylinder diameter	Y=1.4754X^2-2.0933X+1.6515 (R^2=0.9367)	Y=0.986X^2-1.6491X+1.8558 (R^2=0.9859)
Drop height	Y=-1.4062X^3+2.1542X^2-0.8787X+0.8002 (R^2=0.9277)	Y=-1.0171X^3+1.7386X^2-0.8236X+0.9641 (R^2=0.9912)
Material layer thickness	Y=-0.9577X^3+1.7805X^2-0.96X+0.7818 (R^2=0.9962)	Y=-0.451X^3+1733X^2-0.8101X+1.0379 (R^2=0.9658)

For uncrushed bran and coarse powder, when 0 < X < 0.65 or 0 < X < 0.68 (Region A), the sensitivity ranking is: grinding media diameter > drop height > material layer thickness > cylinder diameter; when 0.65 < X < 0.72 or 0.68 < X < 0.82 (Region B), the sensitivity ranking is: grinding media diameter > material layer thickness > drop height > cylinder diameter; when 0.72 < X < 0.74 or 0.82 < X < 0.94 (Region C), the sensitivity ranking is: grinding media diameter > material layer thickness > cylinder diameter > drop height; when X > 0.74 or X > 0.94 (Region D), the sensitivity ranking is: grinding media diameter > cylinder diameter > material layer thickness > drop height.



a. Uncrushed bran b. Coarse powder

Fig. 8 - Dimensionless sensitivity of damping coefficient of wheat bran powder

Thus, when regulating the vibration crushing effect of wheat bran, the grinding media diameter should be adjusted preferentially. Subsequently, the performance parameters of the vibration mill and powder filling amount can be optimized. In practice, the size or capacity of the grinding cylinder is typically non-adjustable, which aligns with previous research conclusions (*Haddad, 2020; Cheng et al., 2021*).

CONCLUSIONS

This paper constructed an impact test platform for grinding media-wheat bran powder to simulate the impact-blocking effect, with impact depth, average acceleration, and damping coefficient serving as evaluation indicators. The effects of powder particle size, grinding media diameter, cylinder diameter, material layer thickness, and drop height were investigated, leading to the following conclusions:

(1) Under identical impact conditions, as wheat bran powder particle size decreases, impact depth demonstrates a quadratic nonlinear trend of decreasing first and then increasing, whereas average acceleration and damping coefficient change in the opposite direction. Particle size exerts a significant influence on the impact-blocking effect, with maximum-minimum difference rates of the three indicators reaching 132.15%, 134.79%, and 127.53%, respectively. The order of acceleration and damping coefficient is: fine powder > coarse powder > uncrushed bran > micro powder.

(2) An increase in media or cylinder diameter results in an increase in impact depth, but a decrease in acceleration. The damping coefficient exhibits a quadratic nonlinear relationship with both diameters: it increases with grinding media diameter (accompanied by growing differences) and decreases with cylinder diameter, stabilizing at critical diameters of 145.12 mm (uncrushed bran) and 160.35 mm (coarse powder). This finding helps to select the grinding media diameter and cylinder diameter based on the powder type or crushing stage.

(3) With the increase in material layer thickness, impact depth first increases then decreases, while acceleration and damping coefficients first decrease and then increase, stabilizing at a critical thickness of 40 mm (4:1 ratio to grinding media diameter). Impact depth increases monotonically with drop height, whereas acceleration and damping coefficients follow a cubic nonlinear pattern, reaching minima at 500 mm. Drop height has the most significant influence on impact depth, followed by average acceleration and damping coefficient. This finding facilitates the determination of the cylinder's material filling amount based on the critical warning value of layer thickness.

(4) Uncrushed bran and coarse powder show consistent dimensionless sensitivity distributions for damping coefficients, with grinding media diameter being the most sensitive factor, outperforming drop height, material layer thickness, and cylinder diameter. This finding contributes to the development of sensitivity weight-based control algorithms for multi-parameter coupled control of vibration crushing.

This study revealed the impact-blocking mechanism in wheat bran vibration crushing by simulating different stages and parameters of the crushing process. The results contribute to the understanding of the vibration mill's crushing mechanism and provide insights for optimizing its efficiency.

ACKNOWLEDGEMENT

This research was supported by the Joint Fund Project of Henan Province Science and Technology R&D Plan (232103810087), Scientific Research Project with R&D Special Fund Subsidy in Zhengzhou (22ZZRDZX14) and Scientific Research Fund for Senior Talents of Henan University of Technology (2020BS020).

REFERENCES

[1] Bogdanov V.S., Bogdanov N.E., Bogdanov D.V., & Samsonova P.S. (2019). Intensification of the grinding process in vibration mills. *Journal of Physics: Conference Series*, 1353(1), 012041.

[2] Bulgakov V., Pascuzzi S., Ivanovs S., Kaletnik G., & Yanovich V. (2018). Angular oscillation model to predict the performance of a vibratory ball mill for the fine grinding of grain. *Biosystems engineering*, 171, 155-164.

[3] Cheng M., Liu B.G., Cao X.Z., & Wang M.X. (2021). Effect of grinding medium characteristics of vibration mill on superfine grinding of wheat bran (振动磨机磨介特征对小麦麸皮超微粉碎效果的影响). *Transaction of the Chinese Society of Agricultural Engineering*, 37(23), 256-263.

[4] Cheng M., Liu B.G., & Liu Y.X. (2019). The influence of grinding ball on the vibration-impact crushing properties of wheat bran (磨介球对小麦麸皮振动冲击破碎性能的影响). *Journal of Vibration and Shock*, 38(24), 261-268.

[5] Frolov V., Blinichev V., Bogorodsky A., & Vetyugov A. (2017). Research of the influence of abrasive wear of grinding bodies in the rotational vibration mill. *Technical Transactions*, 10(4), 179-187.

[6] Gock E., & Kurrer K.E. (1999). Eccentric vibratory mills — theory and practice. *Powder Technology*, 105(1), 302-310.

[7] Haddad J. (2020). Experimental study of the effect of ball diameter, rotating mass and input grain size of silica sand on the efficiency of milling in vertical vibrating mill. *International Journal of Mechanical and Production Engineering Research and Development*, 10(1), 355-368.
[8] He S., Li J., He Q., Jian H.F., Zhang Y., Wang J.L., & Sun H.J. (2018) . Physicochemical and antioxidant properties of hard white winter wheat (Triticum aestivm L.) bran superfine powder produced by eccentric vibratory milling. *Powder Technology*, 325, 126-133.
[9] Hemery Y., Chaurand M., Holopainen U., Lampi A.M., Lehtinen P., Piironen V., Sadoudi A., & Rouau X. (2011). Potential of dry fractionation of wheat bran for the development of food ingredients, Part I: Influence of ultra-fine grinding. *Journal of Cereal Science*, 53(1), 1-8.
[10] Ji S.Y., Li P.F., & Chen X.D. (2012). Experiments on shock-absorbing capacity of granular matter under impact load. *Acta Physica Sinica*, 61(17), 184703.
[11] Ji S.Y., Fan L.F., & Liang S.M. (2016). Buffer capacity of granular materials and its influencing factors based on discrete element method. *Acta Physica Sinica*, 65(10), 104501.
[12] Kumbhar S.R. (2021). Effect of particle material, size and filling Percentage on particle damping phenomenon for gear transmission system. *International Journal for Research in Applied Science and Engineering Technology*, 9(6), 3740-3753.
[13] Lee H., Cho H., & Kwon J. (2010). Using the discrete element method to analyze the breakage rate in a centrifugal/vibration mill. *Powder Technology*, 198(3), 364-372.
[14] Li M., Zhang L., Dave R.N., & Bilgili E. (2015). An intensified vibratory milling process for enhancing the breakage kinetics during the preparation of drug nanosuspensions. *AAPS PharmSciTech*, 17(2), 389–399.
[15] Qian H., Dong Z.H., Zhuang H.J, Zheng M.Q., & Wang K. (2023). Numerical study on particle movement and crushing characteristics in vibromill. *Journal of Physics: Conference Series*, 2610(1), 2050.
[16] Rajaonarivony K.R., Mayer-Laigle C., Piriou B., & Rouau X. (2021). Comparative comminution efficiencies of rotary, stirred and vibrating ball-mills for the production of superfine biomass powders. *Energy*, 227(3): 120508.
[17] Saini P., Islam M., Das R., Shekhar S., Sinha A.S.K., & Prasad K. (2023). Wheat bran as potential source of dietary fiber: Prospects and challenges. *Journal of Food Composition and Analysis*, 116, 105030.
[18] Seguin A., Bertho Y., & Gondret P. (2008). Influence of confinement on granular penetration by impact. *Physical Review E*, 78(1), 010301.
[19] Seguin A. (2023). Force model in the penetration by impact into confined granular media. *Europhysics Letters*, 144(6), 670001.
[20] Shinde V.L., & Pathak A.K. (2016). Review on particle damping technique for vibration suppression. *International Journal of Innovative Research in Science, Engineering and Technology*, 5(3), 2890-2895.
[21] Tomach P. (2024). The Influence of the grinding media diameter on grinding efficiency in a vibratory ball mill. *Materials*, 17(12), 2924.
[22] Wang S.Q., & Ji S.Y. (2018). Discrete element analysis of buffering capacity of non-spherical granular materials based on super-quadric method. *Acta Physica Sinica*, 67(9): 094501.
[23] Yang X.L., Liu J.F., Zhang X., & Cheng S.W. (2015). Dynamic numerical simulation on grinding medium flow field for vibration mill under various vibrating amplitude–frequency combination conditions. *International Journal of Modeling, Simulation, and Scientific Computing*, 6(01), 1550004.
[24] Yang X.L., Zhang N., Liu J.F., Wang Z.J., & Zhou Y.J. (2016). Simulation analysis and experimental demonstration of velocity vector field of medium flow in double mass vibration mill. *International Journal of Modelling and Simulation*, 36(1-2), 34-43.
[25] Yang X.L., Wang Y.T., Xia Z.Q., Zhang T., & Liu J.F. (2018). Numerical simulation and experiment of medium flow energy field in vibrating mill. *International Journal of Modeling, Simulation, and Scientific Computing*,9(2), 1850011.
[26] Ye X.Y., Wang D.M., & Zheng X.J. (2015). Effects of density ratio and diameter ratio on penetration of rotation projectile obliquely impacting a granular medium. *Engineering Computations*, 32 (4), 1025 - 1040.
[27] Ye X.Y., Wang D.M., & Zheng X.J. (2016). Criticality of post-impact motions of a projectile obliquely impacting a granular medium. *Powder Technology*, 301, 1044-1053.

[28] Yildırım O., Ariol H., & Sabah E. (2025). Multiobjective optimization of dry batch micronized grinding of slaked lime in a vibrating mill via TOPSIS and ANOVA. *Separation Science and Technology*,60(7), 873-886.

[29] Ying W., Li X., Lian Z., Xu Y., & Zhang J.H. (2022). An integrated process using acetic acid hydrolysis and deep eutectic solvent pretreatment for Xylo oligosaccharides and monosaccharides production from wheat bran. *Bioresource Technology*, 363, 127966.

[30] Yokoyama T., Tamura K., Usui H., & Jimbo G. (1993). Numerical analysis of movement of balls in a vibration mill in relation with its grinding rate. *KONA Powder and Particle*, 11, 179-190.

[31] Yokoyama T., Tamura K., Usui H., & Jimbo G. (1996). Simulation of ball behavior in a vibration mill in relation with its grinding rate: effects of fractional ball filling and liquid viscosity. *International Journal of Mineral Processing*, 44: 413-424.

[32] Zheng Y, Wang X, Sun Y, Cheng C.X., Li J.R., Ding P., & Xu B.F. (2022). Effects of ultrafine grinding and cellulase hydrolysis separately combined with hydroxypropylation, carboxymethylation and phosphate crosslinking on the in vitro hypoglycaemic and hypolipidaemic properties of millet bran dietary fibres. *LWT-Food Science and Technology*, 172, 114210.

METHODS AND EXPERIMENTAL STUDY ON THE DETERMINATION OF FRICTION AND MECHANICAL PROPERTY PARAMETERS OF VARIOUS RICE SEED VARIETIES UNDER DIFFERENT CONDITIONS
/
不同状态下多种水稻种子摩擦与力学特性参数测定方法及试验研究

Hanqing LI[1)], Shengnan LIU*[1)], Guangwei WU[2)], Bingxin YAN[2)], Lin LING[1,2)],
[1)] College of Intelligent Manufacturing, Nanyang Institute of Technology / China
[2)] Research Center of Intelligent Equipment Technology, Beijing Academy of Agriculture and Forestry Sciences / China
[3)] College of Engineering Technology, Southwest University / China
TeL: 0377-62232522; E-mail: LShengnan1210@163.com
**Corresponding author: Shengnan LIU*
DOI: https://doi.org/10.35633/inmateh-76-35

Keywords: *Rice, Multidimensional, Friction Characteristics, Mechanical Properties, Sowing Device*

ABSTRACT
Precision rice broadcasting technology plays a significant role in the mechanization of planting and yield enhancement, with seed friction and mechanical properties being critical factors in seeder design. In this study, experiments were conducted to evaluate the frictional and mechanical properties of different rice seed varieties. The results showed that higher seed moisture content led to reduced flowability and lower mechanical strength. When rice seeds underwent chitting treatment, their viability remained above 90% under external loads not exceeding 20 N or cutting lengths within 1.5 mm. This study provides a theoretical foundation and data support for the design and optimization of direct-seeding machinery, contributing to the advancement of rice direct-seeding technology and equipment.

摘要
水稻精准直播技术对种植机械化和产量提升意义重大，种子摩擦与力学特性是排种器设计的关键。因此，本研究对不同稻种的摩擦与力学特性进行实验。结果表明，种子含水率越高，流动性越差，力学强度越低。当种子处于露白处理后，外部载荷不超过 20 N 或切除长度不超过 1.5 mm 时，种子存活率均在 90%以上。本研究为水稻直播排种器设计优化提供了理论依据和数据支持，推动了水稻直播技术及装备发展。

INTRODUCTION
Rice, the staple food for over half of the global population, is critical for global food security *(Liberatore et al., 2025; Shang et al., 2024; Zhang et al., 2018*). However, traditional rice transplanting methods have become increasingly impractical due to rising labor costs and shifting rural demographics *(He et al., 2024; Qian et al., 2024*). In response, rice direct seeding technology has gained widespread adoption valued for its labor-saving, cost-effective, and high-efficiency characteristics (*Li et al., 2023a; Li et al., 2023b*). This approach involves mechanized direct seeding, eliminating the labor-intensive and resource-consuming aspects of traditional transplanting. Nevertheless, the precision of direct seeding remains constrained by the performance of seeders, which directly impacts seeding uniformity, seedling establishment rates, and overall field management costs *(Li et al., 2022; Liu et al., 2023*).

Accurate determination of seed mechanical and frictional characteristics is essential for developing theoretical models and defining simulation boundary conditions in seeder design *(Gao et al., 2022; He et al., 2022; Xing et al., 2018*). While traditional empirical trial-and-error approaches have been largely replaced by numerical simulations - such as those based on the Discrete Element Method (DEM) and Computational Fluid Dynamics (CFD) - the accuracy and completeness of material property parameters remain critical to simulation reliability. Previous studies have primarily focused on specific rice seed varieties or single physical states *(Dun et al., 2022; Wang et al., 2022a)*. Domestic researchers have conducted a series of studies on the characteristic parameters of rice seeds. The results indicated significant differences in the frictional and mechanical characteristic parameters among rice seeds of different varieties and types.

Currently, research methods are primarily focused on parameter calibration within EDEM software or rely on referencing and extending previous findings. However, existing studies still face limitations in both the scope of research objects and methodological innovation. Most research has concentrated on single rice varieties or seeds in the dry state *(Dong et al., 2022; Wang et al., 2022b)*. However, China's vast rice-growing regions span multiple climatic zones and involve diverse direct seeding practices - such as dry seeding, wet seeding, and film mulching - alongside a wide variety of rice types (including conventional, hybrid, and water-saving drought-resistant varieties). This complexity poses significant challenges to the applicability of existing parameter systems. In particular, the contact model parameters used in DEM simulations for rice seeds vary considerably depending on the seed's physical state. Relying on empirical or generalized parameters may result in design deviations in critical seeder components, ultimately reducing seeding efficiency and performance. Current methods for determining the mechanical and frictional properties of rice seeds are often limited to single varieties or seed states, and there is a lack of systematic studies encompassing multiple varieties and treatment conditions. Furthermore, the standardization of parameter acquisition methods remains inadequate, leading to poor data comparability across studies *(Li et al., 2021; Xing et al., 2021; Xing et al., 2020*).

To address these challenges, this study innovatively developed a multidimensional parameter determination system. The system encompassed seven conventional and three hybrid rice varieties, representing the primary direct-seeded rice types cultivated across China's major rice-growing regions *(Baral et al., 2021; Shun et al., 2020; Tang et al., 2021*). It simultaneously evaluated seeds in dry, soaked, and chitted states, and analyzed the effects of moisture content gradients on the mechanical and frictional properties of the seeds. This comprehensive approach enabled the establishment of accurate methods for determining the physical properties of rice seeds, offering strong theoretical and data support for the design and optimization of rice direct-seeding machinery. The findings lay a solid foundation for future theoretical modeling and virtual simulation studies, and ultimately contribute to the advancement of rice direct-seeding technology, improved mechanization, and enhanced national food security.

MATERIALS AND METHODS

Experimental Materials

This study selected 7 conventional rice varieties (Suigeng 27, Longjing 31, Nangeng 9108, Huanghuazhan, Xiangzaoxian 45, Longken 2021, Nongken 58) and 3 hybrid rice varieties (Jingliangyouhuazhan, Jingliangyou 534, Longliangyouhuazhan) as experimental materials based on dimensions such as planting areas, promotion areas, and farmer preferences. For ease of data compilation, the 10 different rice varieties were represented as M_i, where M_1 represented Suigeng 27, M_2 represented Longjing 31, M_3 represented Nangeng 9108, M_4 represented Huanghuazhan, M_5 represented Xiangzaoxian 45, $M6$ represented Longken 2021, M_7 represented Nongken 58, M_8 represented Jingliangyouhuazhan, M_9 represented Jingliangyou 534, and M_{10} represented Longliangyouhuazhan. Different states of rice varieties were represented as G_i, where G_1 represented untreated and G_2 represented treated with exposure.

Experimental Methods

The friction and mechanical properties of rice seeds could serve as a basis for analyzing the complex motion mechanisms such as friction and rolling between the seed population inside the seeder and between seeds and working components. This effectively revealed the operational mechanisms for precise seeding in rice precision hole direct seeding seeders.

Static Friction Coefficient

The static friction coefficient was crucial for assessing a material's scattering performance. In this study, the inclined plane method was utilized to measure the static friction coefficient of rice seeds. The procedure involved placing the material on an inclined plane in contact with the rice seeds and gradually tilting it until sliding occurred. High-speed photography captured the angle between the inclined and horizontal planes at the onset of sliding. The tangent of this angle represented the static friction coefficient. Measurements were conducted using a custom-built device, depicted in Figure 1.

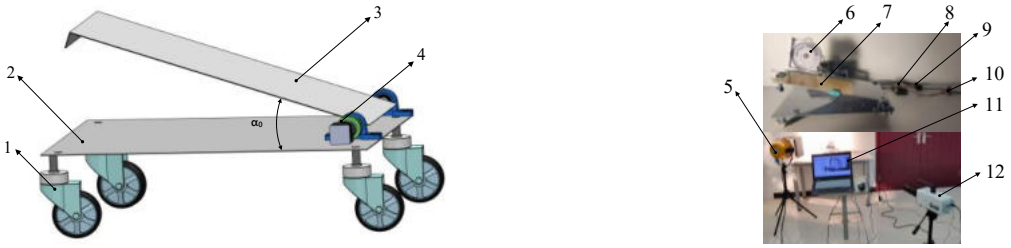


Fig.1 - Static friction coefficient measuring device

(1) Supporting Wheel; (2) Base Plate; (3) Inclined Plane; (4) Drive Motor; (5) Supplementary Lighting Device; (6) Angle Measurement Instrument; (7) Contact Material; (8) Microcontroller; (9) Start-Stop Button; (10) Speed Controller; (11) Computer Terminal; (12) High-Speed Photography Device

Different contact materials could be installed on the inclined plane, and when rice seeds came into contact with different materials, simply placing the respective material on the inclined plane was sufficient. During measurement, 100 grains of each of 10 randomly selected rice varieties in different states were placed on different contact materials on the inclined plane. The start-stop button was then activated to slowly raise the inclined plane. The computer terminal recorded the angles between different rice varieties in different states and different contact materials, providing a theoretical basis for subsequent simulation and theoretical analysis studies. The formula for calculating the static friction coefficient was shown in Equation 1.

$$\mu_1 = \tan \alpha_0 \tag{1}$$

where: μ_1 is the static friction coefficient, and α_0 is the angle between the contact surface and the horizontal plane (°).

Coefficient of Dynamic Friction

When the rice seeds moved on the inclined plane at different angles of inclination α_0, the experiment involved capturing the coordinates (x_{n-1}, y_{n-1}), (x_n, y_n), and (x_{n+1}, y_{n+1}) corresponding to frames $n-1$, n, and $n+1$ using a high-speed photography device, with each frame interval was t_0, as illustrated in Figure 2.

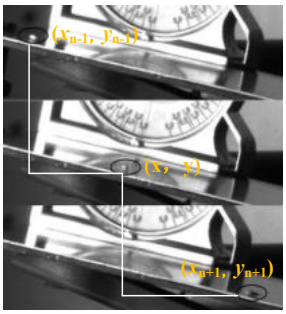


Fig. Error! No text of specified style in document. **- Rice seed coordinate point measurement**

Based on the coordinates measured for the rice seeds, the instantaneous velocity v_0 of the rice seeds at frame n could be calculated. The formula for calculating the instantaneous velocity v_0 was shown in Equation 2.

$$v_0 = \frac{\sqrt{(x_n - x_{n-1})^2 + (y_n - y_{n-1})^2} + \sqrt{(x_{n+1} - x_n)^2 + (y_{n+1} - y_n)^2}}{2t_0} \tag{2}$$

By measuring the instantaneous velocity of the rice seeds at time point n, it was possible to further calculate the rice seeds' instantaneous kinetic energy at that moment. Simultaneously, by using the specific coordinates of the rice seeds at time point n, the total distance traveled by the rice seeds along the inclined plane since the release could be determined. Based on this distance, it was then possible to estimate the proportion of energy loss due to frictional forces during the movement of the rice seeds on the inclined plane to the total energy. The formula for calculating this proportion was shown in Equation 3.

$$C_0 = \frac{W_f}{U_0} = \frac{k_0 mg \cos \alpha_0 \cdot L_0}{mgL_0 \sin \alpha_0} = k_0 \cot \alpha_0 \tag{3}$$

where:

C_0 represents the proportion of lost energy to total energy; W_f denotes the work done by frictional force, (J); U_0 stands for gravitational potential energy, (J); k_0 represents the coefficient of dynamic friction; m is the mass of the grains, (g); g is the acceleration due to gravity, (m/s²); L_0 is the travel distance of the rice seeds on the inclined plane, (m).

From Equation 3, it could be observed that the proportion of lost energy to total energy was linearly related to the cotangent of the angle, with the coefficient of dynamic friction as the correlation factor. Therefore, by varying the angle α_0 between the inclined plane and the horizontal plane, it was possible to calculate the proportion of different lost energy to total energy. Subsequently, by performing a linear regression, the relationship between C_0 and $\cot\alpha_0$ could be fitted, with the slope of the fitted line represented the coefficient of dynamic friction.

Elastic Modulus

The experiment utilized a TMS food physical performance analyzer from FTC, as shown in Figure 3, to evaluate the elastic modulus, shear modulus, and Poisson's ratio of rice seeds. The sensor had a measurement range of 0–2000 N, with an accuracy of 0.015% and a data acquisition frequency of 10 Hz. To reduce the risk of cracking in white rice seeds during testing, the samples were prepared by trimming their axial ends. The height, width, and thickness of each sample were measured to calculate the cross-sectional area. The elastic modulus is a critical parameter that reflects the seeds' resistance to deformation under external forces. This mechanical property is essential for evaluating seed stability within seeders and their capacity to withstand pressure and impact during handling and movement in direct-seeding equipment.

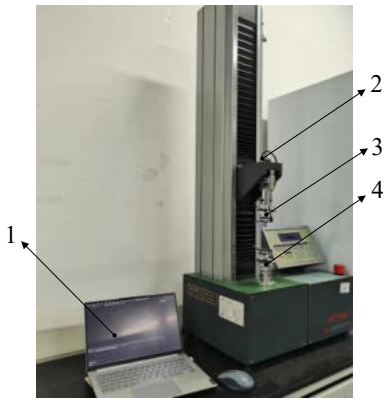


Fig. 3 - Mechanical properties test instrument

(1) Data Acquisition Device; (2) Sensor; (3) Compression Probe; (4) Baseplate

In the compression experiments, the elastic modulus of rice seeds was determined as the ratio of stress to strain. When a force was applied to a sample with a known cross-sectional area and initial length, the sample underwent deformation. Within the elastic range, stress was defined as the applied force per unit area, while strain was defined as the deformation per unit length. By measuring these two parameters, the elastic modulus was calculated according to Equation (4).

$$\begin{cases} E_1 = \frac{\sigma_0}{\varepsilon_0} \\ \sigma_0 = \frac{F_0}{A_0} \\ \varepsilon_0 = \frac{\Delta L_1}{L_1} \end{cases} \quad (4)$$

where:

E_1 is the elastic modulus of the rice seed, (MPa); σ_0 is the stress acting on the rice seed, (MPa); ε_0 is the strain of the rice seed; F_0 is the force applied axially to the rice seed, (N); A_0 is the cross-sectional area of the rice seed, in square meters (m^2); $\triangle L_1$ is the length of the cross-section, (m); and L_1 is the deformation of the cross-section, (m).

To measure the elastic modulus of rice seeds, 10 grains were randomly selected from various samples and the moisture content for the white rice treatment group was adjusted. During the compression test, the compression probe was configured to move at 20 mm/min, with a test speed of 1 mm/min and a return speed of 50 mm/min. The maximum testing distance was set to 60% of the specimen's length.

Shear Modulus

The preparation of test samples and the experimental procedure followed the same methodology used for measuring the elastic modulus, with calculations provided in Equation (5). Prior to the experiment, the following parameters were configured: the probe's moving speed was set to 20 mm/min, the test speed to 1 mm/min, and the initial pressure to 0.1 N. The maximum testing distance was set to 120% of the specimen's original length, and during the return phase, the return speed was adjusted to 50 mm/min.

$$\begin{cases} E_2 = \frac{\tau_0}{\zeta_0} \\ \tau_0 = \frac{F_1}{A_1} \\ \zeta_0 = \frac{\Delta L_2}{L_2} \end{cases} \quad (5)$$

where:

E_2 is the shear modulus of the rice seed, (MPa); τ_0 is the shear stress acting on the rice seed, (MPa); ζ_0 is the shear strain of the rice seed; F_1 is the force applied to the cross-section of the rice seed, (N); A_1 is the area on which the force is applied on the upper surface of the rice seed, (m²); $\triangle L_2$ is the distance moved on the upper surface, (m); and L_2 is the deformation of the upper surface, (m).

Coefficient of Restitution

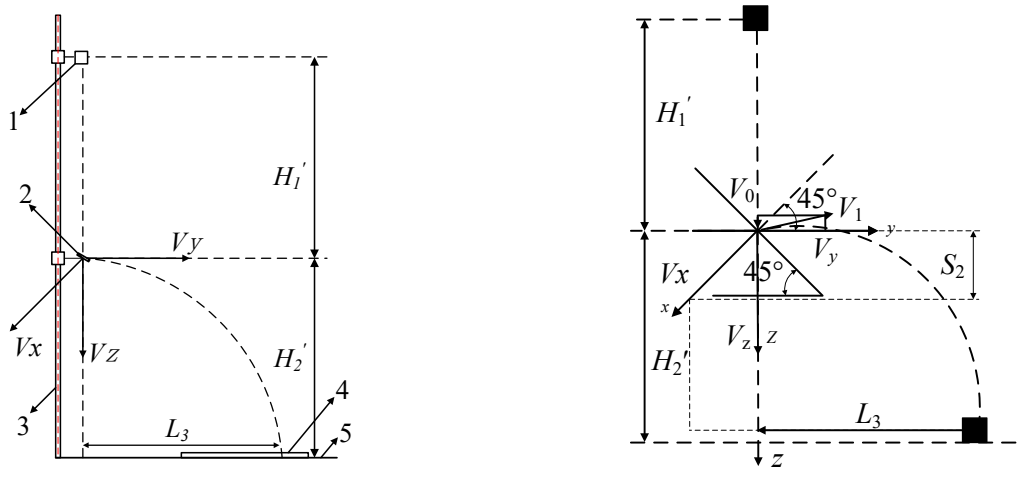
A coefficient of restitution of 1, 0, and less than 1 respectively indicated that the collision of particles was perfectly elastic, perfectly inelastic, and partially inelastic. This signifies that particles could fully recover to their original state, particles could not recover to their original state, and there was energy loss in particles after collision. The calculation formula for the coefficient of restitution is shown in Equation 6.

$$e^2 = \frac{E_3}{E_4} \quad (6)$$

where:

e is the coefficient of restitution; E_3 is the energy after the collision, measured in joules, (J); and E_4 is the energy before the collision, (J).

Using the energy physics definition of the coefficient of restitution, a measurement model was established as depicted in Figure 4.



(a) **(b)**

Fig. 4 - Measurement principle of collision recovery coefficient

(1) Seed Drop Point; (2) Inclined Plane (45°); (3) Support Stand; (4) Coordinate Collection Plate; (5) Support Plate; (a) Measurement Principle; (b) Velocity Decomposition

In this model, a seed underwent free fall from a fixed height with an initial velocity of zero. Upon colliding with the contact material, the seed's velocity was decomposed into the x, y, and z axes. The collision height was set to a constant value. Due to the seed's geometric shape and instantaneous friction during the collision, it experienced displacement along the x and y axes post-collision. High-speed photography captured the entire sequence from collision to landing on the collection plate. By varying the contact test plate, the coefficient of restitution between the rice seed and different contact materials under various conditions could be determined.

One hundred rice seeds were individually dropped from the seeding point with zero initial velocity. During the descent, the seeds first encountered a 45° inclined plate, and then followed a projectile motion to land on the coordinate collection plate. To prevent the seeds from sliding on the coordinate collection plate, a layer of oil was applied to its surface. When the test rice seeds fell onto the coordinate collection plate at the bottom, the coordinate points of each experimental sample were statistically analyzed. Based on this, IBM SPSS software was used to post-process the data of each variety to determine the center coordinates of the seeds and calculate the distance from the center point to the origin. The distance from the center point to the origin satisfies the Pythagorean theorem with the horizontal and tangential deviations of the seeds. During the experiment, a high-speed camera was used to measure the average time taken for the seeds to collide and fall. The formula for calculating the coefficient of restitution is shown in Equation 7.

$$e = \sqrt{\frac{E_3}{E_4}} = \sqrt{\frac{V_x^2+V_y^2+V_z^2}{2gH_1}} = \sqrt{\frac{S_2^2+L_3^2+\left(H_2-\frac{1}{2}gT_1{}^2\right)^2}{2gH_1T_1{}^2}} = \sqrt{\frac{D_1^2+\left(H_2-\frac{1}{2}gT_1{}^2\right)^2}{2gH_1T_1{}^2}} \quad (7)$$

where:

V_x is the velocity component along the x-axis of the rice seed after collision, (m/s); V_y is the velocity component along the y-axis of the rice seed after collision, (m/s); V_z is the velocity component along the z-axis of the rice seed after collision, (m/s); g is the acceleration due to gravity for the rice seed, (9.8 m/s²); S_2 is the tangential deviation distance of the rice seed's motion after collision, (m); L_3 is the horizontal deviation distance of the rice seed's motion after collision, (m); D_1 is the distance from the center to the origin, (m); and T_1 is the average time taken for the rice seed to fall after collision, (s).

External Load and Survival Characteristics

Initially, 10 rice seed varieties under different conditions were selected, with each variety divided into 3 groups of 50 seeds. The moisture content for the white exposure treatment group was adjusted accordingly. Seeds that met sowing criteria were secured in a prone position on the base of a mechanical testing instrument. A rigid probe head served as the flat probe, descended at 2 mm/min and applied a load started from 0 N, increased by 5 N per test group along the seed embryo's thickness. Afterwards, samples were placed in planting pots within a controlled environment at 20°C to 25°C with appropriate lighting, as shown in Figure 5.

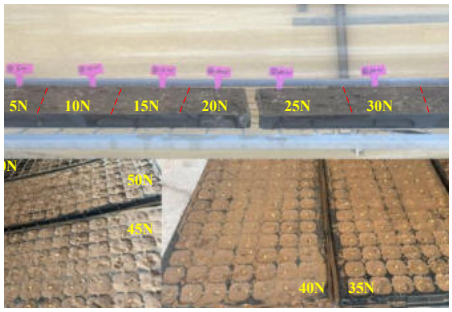


Fig. 5 - External static load and survival test

The non-white exposure group was watered twice daily to ensure thorough soil saturation. After germination and stabilization, the growth continuation percentage post-load was calculated for each sample group, based on consistent data over three consecutive days.

Cutting and Seedling Characteristics

Ten different varieties of rice seeds in different conditions were selected for this study. Specifically, three groups of each variety, with 50 rice seeds in each group, were chosen as experimental samples. The moisture content of the rice seeds in the white exposure treatment group was adjusted accordingly. Each group of experimental samples has the rice seeds cut along the embryonic axis, with the embryo length being approximately 3 mm. Therefore, the difference in embryo length cut each time is 0.5 mm. The rice seeds after cutting were then used for sowing experiments to evaluate their ability to continue surviving based on their germination status. The experimental process and methods were the same as those in the External Load and Survival Characteristics test. By analyzing the experimental data, the relationship between cutting length and survival rate was determined.

RESULTS AND ANALYSIS

Experiment Results and Analysis of Static Friction Coefficient

ABS resin was chosen as a contact material and various materials were affixed to an inclined surface on a custom static friction coefficient measurement device. Seed boards were created by attaching rice seeds to resin boards, simulating seed-to-seed contact. A brush board was made by attaching brush material to resin boards to simulate seed-to-brush contact, reflecting common seeding device configurations. This setup enabled separate measurement of static friction coefficients between rice seeds, and between seeds and ABS plastic or brush materials. High-speed photography captured the angle at which the inclined surface was gradually raised. These angle values were substituted into a formula to calculate the static friction coefficients. The experimental results were detailed in Table 1.

Table 1

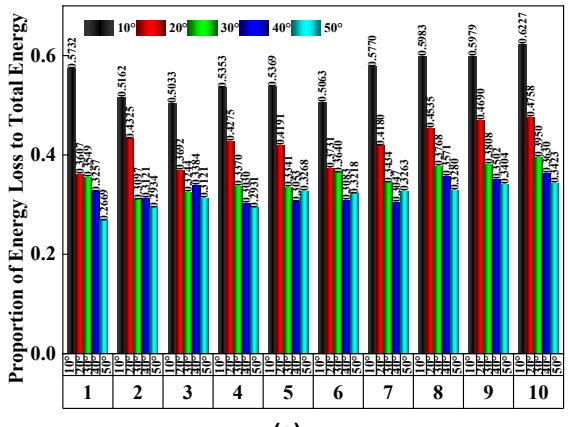
Static friction coefficient test results

Experiment Rice Seeds	Contact Materials			Experiment Rice Seeds	Contact Materials		
	Rice Seeds	ABS	Brushes		Rice Seeds	ABS	Brushes
G_1-M_1	0.36	0.28	0.32	G_2-M_1	0.54	0.42	0.46
G_1-M_2	0.39	0.30	0.34	G_2-M_2	0.64	0.48	0.52
G_1-M_3	0.41	0.29	0.33	G_2-M_3	0.61	0.46	0.50
G_1-M_4	0.36	0.23	0.26	G_2-M_4	0.52	0.37	0.41
G_1-M_5	0.31	0.20	0.24	G_2-M_5	0.54	0.39	0.42
G_1-M_6	0.34	0.23	0.26	G_2-M_6	0.59	0.45	0.49
G_1-M_7	0.37	0.25	0.29	G_2-M_7	0.55	0.40	0.44
G_1-M_8	0.33	0.22	0.25	G_2-M_8	0.59	0.43	0.48
G_1-M_9	0.37	0.23	0.27	G_2-M_9	0.63	0.47	0.51
G_1-M_{10}	0.35	0.21	0.25	G_2-M_{10}	0.61	0.44	0.48

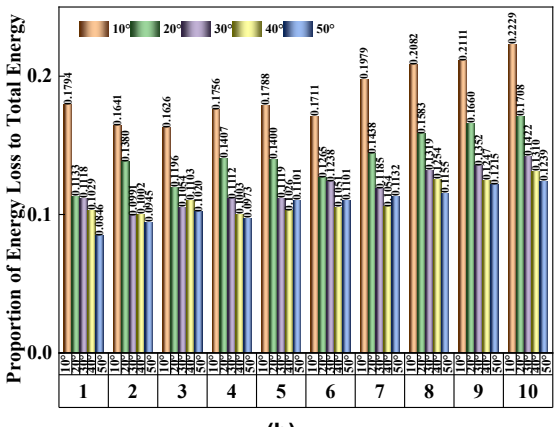
The analysis indicated that the rice seed variety had minimal impact on the static friction coefficient, while the moisture content had a significant effect. For dry seeds, the static friction coefficients between seeds, between seeds and ABS plastic, and between seeds and a brush were in the ranges of 0.31 to 0.41, 0.20 to 0.30, and 0.24 to 0.34, respectively. After chitting treatment, these values increased to 0.52–0.64, 0.37–0.48, and 0.41–0.52, respectively. This is because the increased moisture enhanced the adhesion forces, thereby raised the static friction coefficient and reduced the flowability. Further analysis reveals that at the same moisture level, the friction between rice seeds was higher than that between seeds and ABS plastic, suggesting that the surface of rice seeds was rougher and that the flowability on the ABS plastic surface was better.

Experiment Results and Analysis of Dynamic Friction Coefficient

Rice seeds were placed at a certain height on an inclined plane with a certain angle to the horizontal plane and were initially at rest before sliding along the incline. By analyzing high-speed photography videos, the coordinates of the seeds in each frame could be obtained, with the experimental data extracted a time interval of 0.001 s between two frames. The experiment involved selecting five incline angles ranged from 10° to 50°, with 10 seeds of each variety tested for each angle and the average value taken. The experimental results were shown in Figure 6.



(a)



(b)

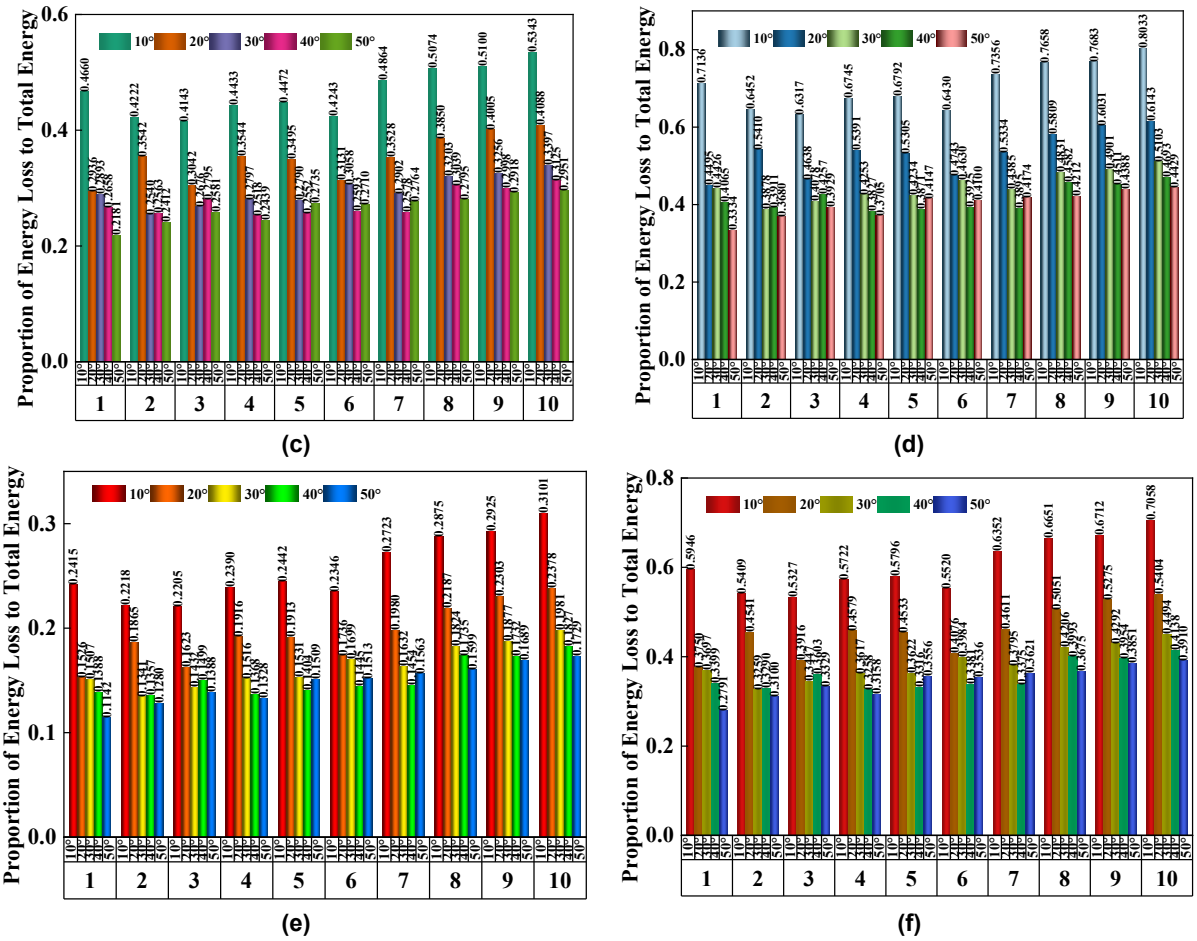


Fig. 6 - Dynamic friction coefficient test results

(a) G_1 Rice Variety - G_1 Rice Variety (b) G_1 Rice Variety - ABS Material (c) G_1 Rice Variety - Bristle Brush
(d) G_2 Rice Variety - G_2 Rice Variety (e) G_2 Rice Variety - ABS Material (f) G_2 Rice Variety - Bristle Brush

The results indicated that whitening treatment increased the energy loss proportion in rice varieties, suggested greater energy dissipation on the contact surface and a higher friction coefficient. As the angle increased, energy loss proportion decreased due to the conversion of gravitational potential energy into kinetic energy and frictional heat, with shorter incline travel time reducing energy loss. Among different conditions, energy loss was greatest between rice varieties, followed by rice varieties with bristle brushes, and lowest with ABS materials, highlighting better flowability on ABS. Linear fitting of the energy loss proportion (C_0) against cot α_0 for each contact material yielded the dynamic friction coefficients k_0, as shown in Table 2.

Table 2

Coefficient of dynamic friction between different kinds of rice and different materials

Experiment Rice Seeds	Materials			Experiment Rice Seeds	Materials		
	Rice Seeds	ABS	Brushes		Rice Seeds	ABS	Brushes
G_1-M_1	0.0601	0.0181	0.0427	G_2-M_1	0.0724	0.0242	0.0601
G_1-M_2	0.0494	0.0151	0.0391	G_2-M_2	0.0599	0.0203	0.0499
G_1-M_3	0.0411	0.0124	0.0321	G_2-M_3	0.0490	0.0168	0.0411
G_1-M_4	0.0547	0.0167	0.0472	G_2-M_4	0.0648	0.0227	0.0547
G_1-M_5	0.0515	0.0158	0.0398	G_2-M_5	0.0607	0.0215	0.0515
G_1-M_6	0.0426	0.0131	0.0329	G_2-M_6	0.0501	0.0179	0.0426
G_1-M_7	0.0615	0.0191	0.0472	G_2-M_7	0.0716	0.0262	0.0615
G_1-M_8	0.0613	0.0193	0.0496	G_2-M_8	0.0709	0.0263	0.0612
G_1-M_9	0.0611	0.0192	0.0466	G_2-M_9	0.0703	0.0264	0.0611
G_1-M_{10}	0.0657	0.0207	0.0499	G_2-M_{10}	0.0751	0.0286	0.0657

The results showed that in dry conditions, the average dynamic friction coefficients were 0.0411 to 0.0657 between rice varieties, 0.0124 to 0.0207 with ABS, and 0.0321 to 0.0499 with bristle brushes. After whitening treatment, these coefficients increased to 0.0490 to 0.0751, 0.0168 to 0.0286, and 0.0411 to 0.0657, respectively. Higher moisture content elevates these coefficients, reducing flowability. The order of dynamic friction coefficients, from highest to lowest, was: rice seeds, bristle brushes, and ABS material. This indicates that rice seeds flow most easily over ABS surfaces, but exhibit greater resistance when interacting with other seeds. These findings provide important insights for future structural design considerations.

Elastic Modulus

After each sample test, the pressure versus displacement curve was exported using software compatible with the testing machine. Stable data before the yield point was selected, and stress and strain values were calculated to determine the elastic modulus, as shown in Table 3. Differences in the elastic modulus were observed at varying moisture contents. As moisture content increased, the elastic modulus decreased, as higher moisture reduced cohesion between seeds, leading to decreased stiffness. In dry conditions, the elastic modulus ranged from 365.27 to 418.19 MPa, while chitting treatment reduced it to 180.92 to 209.15 MPa.

Table 3

Elastic modulus test results

Experiment Rice Seeds	Elastic Modulus/MPa	Experiment Rice Seeds	Elastic Modulus/MPa
G_1-M_1	365.27	G_2-M_1	206.37
G_1-M_2	371.96	G_2-M_2	194.12
G_1-M_3	379.60	G_2-M_3	200.35
G_1-M_4	377.72	G_2-M_4	209.15
G_1-M_5	388.63	G_2-M_5	192.56
G_1-M_6	398.74	G_2-M_6	183.01
G_1-M_7	376.26	G_2-M_7	204.54
G_1-M_8	410.45	G_2-M_8	184.49
G_1-M_9	407.03	G_2-M_9	180.92
G_1-M_{10}	418.19	G_2-M_{10}	184.70

Shear Modulus

During the shear modulus testing process, the same experimental method as the elastic modulus was used to process the data of the samples to obtain the shear modulus of the samples, and the test results were shown in Table 4. The analysis of the results revealed that there were differences in the shear modulus of rice seeds at different moisture contents. With an increase in moisture content of each rice seed, the shear modulus of the test sample showed a decreasing trend. When rice seeds are in dry condition, the shear modulus ranged from 137.38 to 151.88 MPa. When rice seeds underwent chitting treatment, the shear modulus ranged from 74.08 to 82.45 MPa.

Table 4

Shear modulus test results

Experiment Rice Seeds	Shear Modulus/MPa	Experiment Rice Seeds	Shear Modulus/MPa
G_1-M_1	137.38	G_2-M_1	81.58
G_1-M_2	139.27	G_2-M_2	77.69
G_1-M_3	141.51	G_2-M_3	79.76
G_1-M_4	140.89	G_2-M_4	82.45
G_1-M_5	144.00	G_2-M_5	77.19
G_1-M_6	146.77	G_2-M_6	74.08
G_1-M_7	140.48	G_2-M_7	80.85
G_1-M_8	149.83	G_2-M_8	74.49
G_1-M_9	148.91	G_2-M_9	73.46
G_1-M_{10}	151.88	G_2-M_{10}	74.63

Impact Restitution Coefficient Test Results and Analysis

The test results for the impact restitution coefficient, as outlined in Table 5, indicated a positive correlation between the moisture content of rice seeds and their deformation upon collision.

Higher moisture content resulted in increased deformation, led to greater energy loss during impact, thus reduced the normal separation velocity and subsequently the impact restitution coefficient. In dry conditions, the impact restitution coefficient ranged from 0.412 to 0.471 between rice seeds, 0.438 to 0.501 between rice seeds and ABS material, and 0.454 to 0.519 between rice seeds and brush. After chitting treatment, these values decreased to 0.351 to 0.408, 0.357 to 0.414, and 0.396 to 0.460, respectively. The coefficients were ranked from highest to lowest as follows: rice seeds and brush, rice seeds and rice seeds, and rice seeds and ABS material, across both states of the rice seeds.

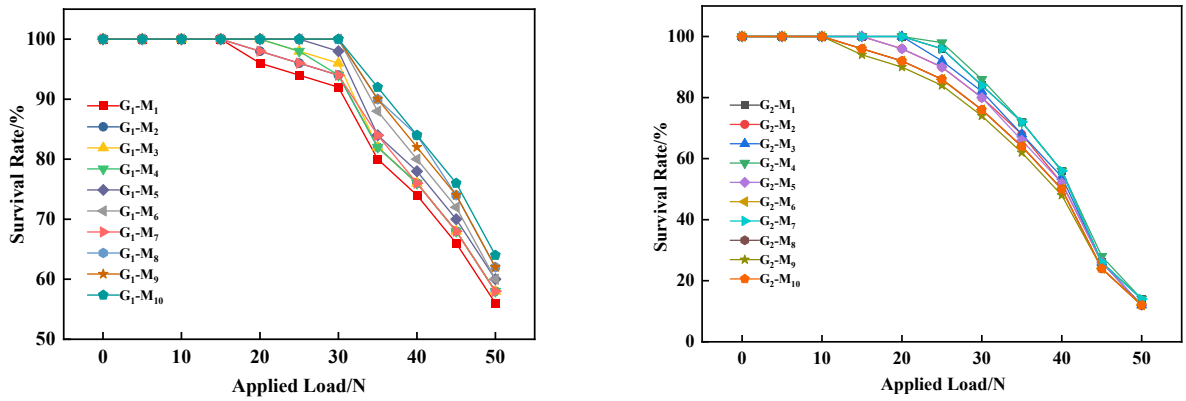
Table 5

Experimental results of collision recovery coefficient

Experiment Rice Seeds	Impact Contact Materials			Experiment Rice Seeds	Impact Contact Materials		
	Rice Seeds	ABS	Brushes		Rice Seeds	ABS	Brushes
G_1-M_1	0.412	0.438	0.454	G_2-M_1	0.402	0.362	0.454
G_1-M_2	0.419	0.446	0.462	G_2-M_2	0.379	0.384	0.427
G_1-M_3	0.427	0.454	0.470	G_2-M_3	0.389	0.374	0.438
G_1-M_4	0.426	0.453	0.469	G_2-M_4	0.408	0.357	0.460
G_1-M_5	0.437	0.465	0.481	G_2-M_5	0.376	0.387	0.424
G_1-M_6	0.448	0.477	0.494	G_2-M_6	0.357	0.407	0.403
G_1-M_7	0.424	0.452	0.467	G_2-M_7	0.403	0.361	0.454
G_1-M_8	0.462	0.492	0.509	G_2-M_8	0.362	0.402	0.408
G_1-M_9	0.459	0.488	0.505	G_2-M_9	0.351	0.414	0.396
G_1-M_{10}	0.471	0.501	0.519	G_2-M_{10}	0.361	0.403	0.407

External Load and Survival Characteristics Test Results and Analysis

After the external load and survival characteristics test method, static loads ranged from 0N to 50N were applied to the test samples. The resulting data was used to plot a load-survival rate curve, as shown in Fig. 7.



(a) (b)

Fig. 7 - Survival rate and applied load curve of rice seeds

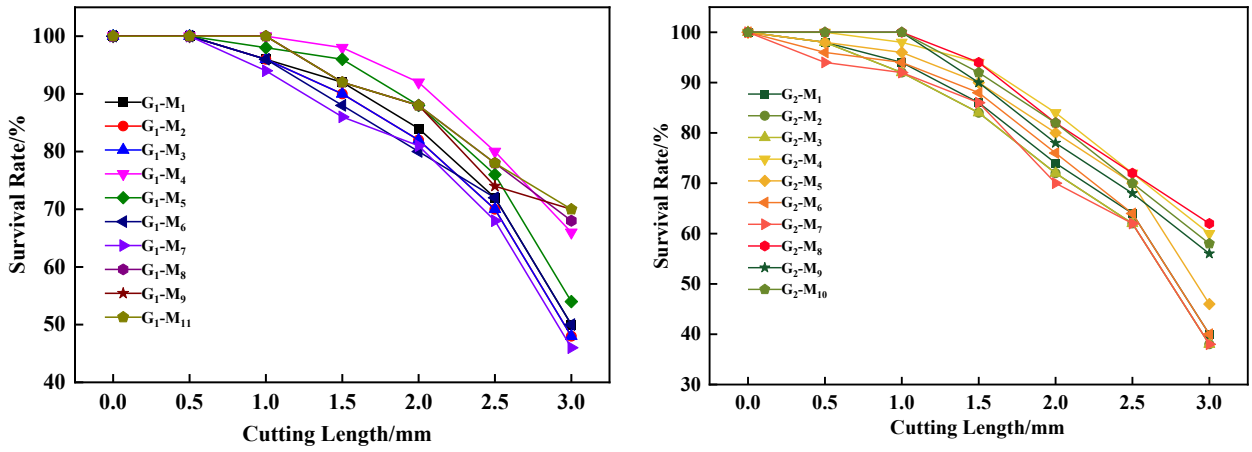
(a) Dry Rice Seeds (b) Chitting Treatment

Analysis revealed a decline in the survival rate of rice seeds with increased static load. For the same type of seeds, higher moisture content correlated with a reduced ability to withstand static loads, making them more susceptible to breakage. In dry conditions, survival rates ranged from 62% to 100%, but rapidly dropped below 90% when loads exceeded 35N. For seeds undergoing chitting treatment, survival rates ranged from 12% to 100%, with a noticeable declined when loads exceeded 20N, and a rapid dropped below 90% beyond 25N. Further analysis indicated that excessive static loads compromised seed survival by rupturing the surface membrane, disrupting moisture regulation, and impairing germination and growth. The data showed that external loads up to 20N did not significantly impact germination, with survival rates remaining above 92%. These findings suggest that, during direct seeding, rice seeds can withstand certain levels of external load without compromising viability.

Cutting and Seedling Characteristics

Using the experimental method for cutting and seedling characteristics, cuts were made along the embryo axis of rice seeds at lengths from 0 mm to 3 mm. A relationship curve between cutting length and survival rate was plotted, as shown in Figure 8.

The results indicated that survival rates decreased with increased cutting length, underscored the critical impact of embryo damage on seed survival. In dry conditions, survival rates ranged from 48% to 100%, with a rapid decline beyond 1.5 mm. For seeds undergoing chitting treatment, survival rates ranged from 38% to 100%, with a noticeable drop below 90% when the cutting depth exceeded 1.0 mm. Further analysis showed that seeds with larger three-axis dimensions exhibited slightly higher survival rates under the same cutting length. Additionally, higher moisture content enabled seeds to maintain survival rates above 90% when cutting lengths did not exceed 1.5 mm. These findings suggest that during direct seeding, minor damage to seeds does not significantly impact survival, provided that the cutting depth remains within these thresholds.



(a) (b)

Fig. 8 - Survival rate and cut length curve of rice seeds

(a) Dry Rice Seeds; (b) Chitting Treatment

CONCLUSIONS

The study's methodology and results offered a robust theoretical foundation and data support for optimizing planter design, constructing theoretical models for various processes, and conducting virtual simulations. The main conclusions were as follows.

For untreated rice seeds, static friction coefficients with seeds, ABS plastic, and bristle plates ranged from 0.31-0.41, 0.20-0.30, and 0.24-0.34, respectively, with dynamic coefficients at 0.0411-0.0657, 0.0124-0.0207, and 0.0321-0.0499. Post-chitting, static coefficients increased to 0.52-0.64, 0.37-0.48, and 0.41-0.52, with dynamic coefficients at 0.0490-0.0751, 0.0168-0.0286, and 0.0411-0.0657.

For untreated seeds, the restitution coefficients with seeds, ABS plastic, and bristle plates were 0.412-0.471, 0.438-0.501, and 0.454-0.519. After chitting, these stabilized at 0.351-0.408, 0.357-0.414, and 0.396-0.460, respectively. Untreated seeds showed an elastic modulus of 365.27-418.19 MPa, shear modulus of 137.38-151.88 MPa. Chitting reduced these values to 180.92-209.15 MPa, 74.08-82.45 MPa.

Under dry conditions, maintaining an external load below 20 N and a cutting length under 1.5 mm ensured seed survival rates above 90%. While this study provided a comprehensive analysis of the frictional and mechanical properties of rice seeds, it did not include calibration experiments for key parameters, which represents a noted limitation of the research.

ACKNOWLEDGEMENT

We are grateful to the Henan Provincial Science and Technology Attack Project/Henan Nanyang Municipal Science and Technology Attack Project for its financial support under grant number 252102111175/2024KJGG0102. We also extend special thanks to the National Engineering Research Center for Agricultural Intelligent Equipment for its contributions to this research.

REFERENCES

[1] Baral, B.R., Pande, K.R., Gaihre, Y.K., Baral, K.R., Sah, S.K., Thapa, Y.B., and Singh, U. (2021). Real-time nitrogen management using decision support-tools increases nitrogen use efficiency of rice. *Nutrient Cycling in Agroecosystems,* 119, 355-368.

[2] Dong, H., Zhang, B., Jiang, T., Zhang, Y., Qu, J., Chen, C., Xiao, Y., Ding, Y., Xi, X. (2022). Design and Optimization of Rice Grain Screening System Based on DEM–CFD Coupled Rice Seed Testing Platform. *Agronomy-Basel,* 12(12), 3069.

[3] Dun, G., Mao, N., Gao, Z., Wu, X., Liu, W., Zhou, C. (2022). Model construction of soybean average

diameter and hole parameters of seed-metering wheel based on DEM. *International Journal of Agricultural and Biological Engineering*, 15, 101-110.

[4] Gao, X., Zhao, P., Li, J., Xu, Y., Huang, Y., Wang, L. (2022). Design and Experiment of Quantitative Seed Feeding Wheel of Air-Assisted High-Speed Precision Seed Metering Device. *Agriculture-Basel,* 12(11), 1951.

[5] He, S., Qian, C., Jiang, Y., Qin, W., Huang, Z., Huang, D., Wang, Z., Zang, Y. (2024). Design and optimization of the seed feeding device with DEM-CFD coupling approach for rice and wheat. *Computers and Electronics in Agriculture,* 219, 108814.

[6] He, S., Zang, Y., Huang, Z., Tao, W., Xing, H., Qin, W., Jiang, Y., Wang, Z. (2022). Design of and Experiment on a Cleaning Mechanism of the Pneumatic Single Seed Metering Device for Coated Hybrid Rice. *Agriculture-Basel*, 12(8), 1239.

[7] Li, H., Ling, L., Wen, C., Liu, H., Wu, G., An, X., Meng, Z., Yan, B. (2023a). Structural optimization method of rice precision direct seed-metering device based on multi-index orthogonal experimental. *Frontiers in Plant Science,* 14, 1183624.

[8] Li, H., Yan, B., Meng, Z., Ling, L., Yin, Y., Zhang, A., Zhao, C., Wu, G. (2023b). Study on influencing factors of hole-filling performance of rice precision direct seed-metering device with hole ejection. *Biosystems Engineering,* 233, 76-92.

[9] Li, H., Zhao, C., Yan, B., Ling, L., Meng, Z. (2022). Design and Verification of the Variable Capacity Roller-Wheel Precision Rice Direct Seed-Metering Device. *Agronomy-Basel*, 12(8), 1798.

[10] Li, J., Lai, Q., Zhang, H., Zhang, Z., Zhao, J., Wang, T. (2021). Suction force on high-sphericity seeds in an air-suction seed-metering device. *Biosystems Engineering*, 211, 125-140.

[11] Liberatore, C.M., Biancucci, M., Ezquer, I., Gregis, V., Di Marzo, M. (2025). Investigating how reproductive traits in rice respond to abiotic stress. Journal of Experimental Botany. https://doi.org/10.1093/jxb/eraf031

[12] Liu, W., Zhou, Z., Xu, X., Gu, Q., Zou, S., He, W., Luo, X., Huang, J., Lin, J., Jiang, R. (2023). Evaluation method of rowing performance and its optimization for UAV-based shot seeding device on rice sowing. *Computers and Electronics in Agriculture,* 207, 107718.

[13] Qian, C., He, S., Qin, W., Jiang, Y., Huang, Z., Zhang, M., Zhang, M., Yang, W., Zang, Y. (2024). Influence of Shaped Hole and Seed Disturbance on the Precision of Bunch Planting with the Double-Hole Rice Vacuum Seed Meter. *Agronomy-Basel*, 14(4), 768.

[14] Shang, Y., Zhou, B., Yang, J., Zhang, S. (2024). Design and experiment of impeller seed guide device for rice internal suction hole direct seeding device. *Scientific Reports*, 14, 63-71.

[15] Shun, Z., Yong, L., Haoyu, W., Juan, L., Zhaodong, L., Dequan, Z. (2020). Design and Experiment of U-shaped Cavity Type Precision Hill-drop Seed-metering Device for Rice. Nongye Jixie Xuebao. *Transactions of the Chinese Society of Agricultural Machinery*, 51(10), 98-108.

[16] Tang, H., Jiang, Y., Xu, C., Zhou, W., Wang, Q., Wang, Y. (2021). Experimental study on the correlation between hill direct seeding rate and field seedling rate of typical rice varieties in cold areas. *International Journal of Agricultural and Biological Engineering,* 14, 63-71.

[17] Wang, B., Na, Y., Pan, Y., Ge, Z., Liu, J., Luo, X. (2022a). CFD Simulation and Experiments of Pneumatic Centralized Cylinder Metering Device Cavity and Airflow Distributor. *Agronomy-Basel*, 12(8), 1775.

[18] Wang, J., Xu, C., Qi, X., Zhou, W., Tang, H. (2022b). Discrete Element Simulation Study of the Accumulation Characteristics for Rice Seeds with Different Moisture Content. *Foods*, 11(3),295.

[19] Xing, H., Wang, Z., Luo, X., Zang, Y., He, S., Xu, P., Liu, S. (2021). Design and experimental analysis of rice pneumatic seeder with adjustable seeding rate. *International Journal of Agricultural and Biological Engineering*, 14, 113-122.

[20] Xing, H., Wang, Z., Luo, X., Zang, Y., Yang, W., Zhang, M., Ma, Y. (2018). Design of an active seed throwing and cleaning unit for pneumatic rice seed metering device. *International Journal of Agricultural and Biological Engineering*, 11, 62-69.

[21] Xing, H., Zang, Y., Wang, M.Z., Luo, W.X., Zhang, H.M., Fang, Y.L. (2020). Design and experimental analysis of a stirring device for a pneumatic precision rice seed metering device. *Transactions of the Asabe*, 63, 799-808.

[22] Zhang, M., Wang, Z., Luo, X., Zang, Y., Yang, W., Xing, H., Wang, B., and Dai, Y. (2018). Review of precision rice hill-drop drilling technology and machine for paddy. *International Journal of Agricultural and Biological Engineering*, 11, 1-11.

DESIGN AND EXPERIMENTAL STUDY OF AN ADJUSTABLE WRAPPING MACHINE FOR RICE STRAW BALES OF DIFFERENT SIZES
/
可调式秸秆包捆机的设计与试验研究

Liyan WU[1)], Huchao TAN[2)], Na ZHANG[1)], Hengyi WEI[1)], Zhenyu WANG[1)], Chunhua BAN[3)], Cuihong LIU[*1)]

[1)]College of Engineering, Shenyang Agricultural University, Shenyang / China
[2)]Yantai Taihai Manoir Nuclear Power Equipment Co., Ltd., Yantai / China
[3)]Liaoning Provincial Institute of Agricultural Mechanization / China
Tel: +8615942060166; E-mail: cuihongliu77@syau.edu.cn
Corresponding author: Liu Cuihong
DOI: https://doi.org/10.35633/inmateh-76-36

Keywords: *rice straw; adjustable wrapping machine; straw bale; tensile film*

ABSTRACT

China annually produces over 210 million tons of rice straw; however, its utilization as feed remains low due to the scarcity of supporting equipment. In feed production, wrapping straw bales with plastic film is crucial for accelerating degradation. Given the diverse types of straw balers, a variety of wrapping machines are required. This study presents the design of an adjustable wrapping machine capable of handling straw bales with diameters ranging from 400 to 1200 mm and lengths between 500 - 1000 mm. Wrapping time, coefficient of variation, and elongation rate were selected as key evaluation indicators. Experimental results demonstrate that all performance metrics comply with industry standards for straw bale machinery, indicating the machine's practical feasibility and reliability in agricultural applications.

摘要

中国水稻秸秆年产量在 2.1 亿吨以上，但饲料化利用率仍然很低，其原因是缺少配套的装备，饲料化生产需要利用塑料膜包裹稻草捆以加速降解。由于秸秆打包机类型较多，故此需要不同型号的包膜机与之相匹配。本工作设计了一种可调包装机，可实现直径 400~1200mm、长度 500~1000mm 的稻草捆进包膜处理。选取缠绕时间、变异系数和伸长率作为评价指标，通过包膜检验包膜效果。结果表明，各项指标均达到了秸秆包捆机械的行业标准。

INTRODUCTION

China boasts a colossal crop straw yield, with annual production reaching 800 million tons—equivalent to 30% of the global total, ranking first worldwide (*Tian, 2020; Cong et al., 2021; Zhang et al., 2021*). Among this, rice straw contributes 210 million tons yearly, accounting for approximately one - fourth of China's total crop straw resources *(Li et al., 2020; Lu et al., 2021; Liu, 2024*). However, current utilization methods (Fig. 1) remain inefficient. Burning straw for heat or char production results in low calorific value and causes environmental pollution. Returning straw to the soil offers limited economic benefits and increases the risk of pests. Industrial applications, such as the production of low-quality paper and rope, are hindered by high costs associated with collection, transportation, and labor (*Wang et al., 2017; Huo et al., 2019; Feng et al., 2021; Cong et al., 2019*). In contrast, feed utilization has emerged as a promising solution, offering economic benefits without causing environmental harm.

Nevertheless, raw rice straw is unpalatable and nutritionally inadequate for livestock, necessitating degradation and fermentation before being used as feed. Transforming rice straw into feed not only optimizes resource utilization (*Liu, 2021; Huo et al., 2022; Gu et al., 2017*) but also alleviates forage shortages, thereby benefiting animal husbandry.

In the rice straw feed production process, key steps include bundling, spraying decay agents, wrapping bales with plastic film, and fermenting. These treatments reduce crude fiber content while increasing protein and soluble sugar levels, thus boosting livestock feeding rates.

Liyan Wu, Prof. Ph.D. Eng.; Huchao Tan, Na Zhang, Hengyi Wei, Zhenyu Wang, M.S. Stud. Eng.; Chunhua Ban, engineer; Cuihong Liu Prof. Ph.D. Eng.

Commercially available wrapping machines struggle to accommodate straw bales of diverse sizes (with diameters ranging from 500 to 1200 mm and lengths from 500 to 1000 mm). In response, this study developed an adjustable wrapping machine compatible with various balers. Following tests and analysis of the mechanical properties of wrapping plastic films, the machine's structure was designed, and subsequent wrapping tests were conducted. Key parameters—including wrapping time, variation coefficient, and film elongation rate—were evaluated. These findings not only significantly enhance rice straw feed production efficiency but also provide valuable insights for the design of wrapping machinery for other crops and grasses.

MATERIALS AND METHODS

Prior to designing the adjustable rice straw wrapping machine, a study on the mechanical characteristics of the tensile film was conducted. The test results will provide basic data for the subsequent determination of motion parameters, rotational speed, and the overall structural design of the machine.

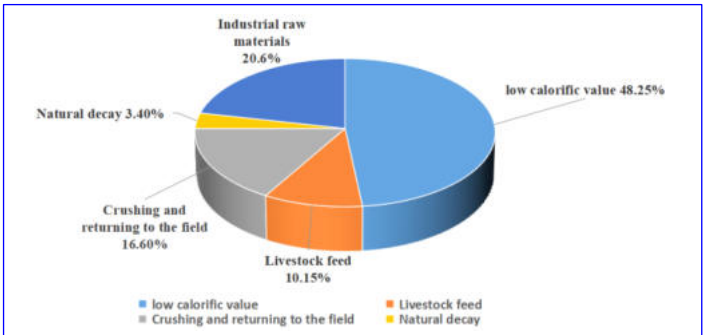


Fig. 1 - Different utilization of rice straw

Materials and Instruments

Tensile film: Antioxidant silage tensile film (thickness: 0.025 mm; width: 250 mm; material: linear low-density polyethylene (LLDPE)), produced by Shandong Xinlian Heavy Industry Agriculture and Animal Husbandry Machinery Company.

Test instrument: Universal material tensile testing machine. The sensor has a measuring range of 2 mN–2 kN with an accuracy of ±1% or better. The loading speed is adjustable within the range of 0.01–500 mm/min.

Methods

The operation process includes 5 steps: sample preparation, length and width determination, calibration, testing, and data processing. A quadratic orthogonal rotation combination test scheme was adopted, with tensile film length (X_1), width (X_2), and loading speed (X_3) set as the test factors. According to the test requirements, the levels of the test factors are represented by the coded values -1.628, -1, 0, 1, and 1.628. The corresponding relationship between the coded values and actual values of the test scheme is shown in Table 1.

Table 1

Factor level coding

Levels	Factors		
	Length X_1/(mm)	Stretch film width X_2/(mm)	Loading speed X_3/ (mm/min)
-1.682	70	18	60
-1	100	23	75
0	150	30	100
1	200	37	125
1.682	230	42	140

In accordance with the national standards "Determination of Tensile Properties of Plastic Films" (GB/T 13022-91) and "Test Conditions for Films and Sheets in the Determination of Plastic Tensile Properties" (GB/T 1040-2006), the maximum tensile force (Y1) and elongation at break (Y2) were designated as the test indicators. Tensile film samples were cut neatly, as illustrated in Fig. 2.

Y1, the maximum force at which the film breaks.

ε_t, elongation rate calculated by Equation (1).

$$\varepsilon_t = \frac{L - L_0}{L_0} \times 100\% \quad (1)$$

where:

L_0—original length of the tensile film, [mm];

L—length after breaking, [mm].

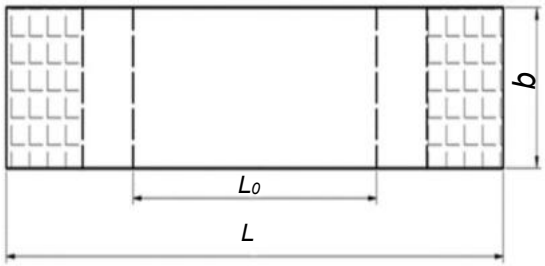


Fig. 2 - Tensile test device

RESULTS AND ANALYSIS

Establishment of tensile film model

Using Design-Expert 12.0 software, an analysis of the test factors and indicators was conducted to determine the influence of each factor. The test scheme and corresponding results are presented in Table 2.

Table 2

Test scheme and results

Test number	Test factors			Test indicators	
	Mold length X1 / (mm)	Film width X2 / (mm)	Loading speed X3 / (mm/s)	Maximum breaking force Y1 / (N)	Elongation rate Y2 / (%)
1	-1	-1	-1	16.2	262.7
2	1	-1	-1	12.6	212.1
3	-1	1	-1	21.1	283.4
4	1	1	-1	16.4	253.7
5	-1	-1	1	10.8	257.1
6	1	-1	1	9.3	214.8
7	-1	1	1	18.3	239.8
8	1	1	1	16.8	232.1
9	-1.682	0	0	18.5	286.4
10	1.682	0	0	12.8	205.4
11	0	-1.682	0	10.1	209.1
12	0	1.682	0	21.4	265.2
13	0	0	1.682	11.8	276.5
14	0	0	-1.682	10.5	230.1
15	0	0	0	11.3	242.3
16	0	0	0	10.7	236.1
17	0	0	0	10.6	246.4
18	0	0	0	11.7	239.6
19	0	0	0	10.9	232.1
20	0	0	0	10.3	231.6
21	0	0	0	11.5	234.1
22	0	0	0	10.3	235.9
23	0	0	0	9.9	227.4

Establishment of regression model of the maximum breaking force

The regression equation composed of primary, quadratic and interaction terms are obtained, equation (2). This regression equation expressed the relationship of the maximum breaking force Y1 and the three factors, the film length X1, width X2, and the loading speed of X3.

$$\hat{Y_1} = 10.78 - 1.53X_1 + 3.13X_2 - 0.97X_3 + 0.66X_1X_3 + 0.79X_2X_3 = 1.88{X_1}^2 + 1.92{X_2}^2 \quad (2)$$

The significance of the regression equation was tested using ANOVA, and the results are presented in Table 3.

Table 3

Variance analysis of experiment results Y_1

Variance source	Square sum	Degrees of freedom	Mean square	F-value	P-value
Mold	301.84	9	33.54	47.30	< 0.0001**
X_1	31.94	1	31.94	50.45	< 0.0001**
X_2	133.53	1	133.53	188.33	< 0.0001**
X^3	12.93	1	12.93	18.23	0.0009**
X_1X_2	0.15	1	0.15	0.21	0.6518
X_1X_3	3.51	1	3.51	4.95	0.0444*
X_2X_3	4.96	1	4.96	7.00	0.0202*
X_1^2	56.18	1	56.18	79.24	< 0.0001**
X_2^2	58.32	1	58.32	82.25	< 0.0001**
X_3^2	1.33	1	1.33	1.68	0.1939
Residual	9.22	13	0.71		
Lost proposal	6.30	5	1.26	3.45	0.0869
Error term	2.92	8	0.36		
Aggregate	311.06	22			

Note: * * Most significant level (p <0.01); * significant level (p <0.05).

As showed in Table 3, the established model is highly significant ($P < 0.0001$), the P-values of the three factors X_1, X_2, X_3 are less than 0.05, indicate that each factor exerts a significant effect on the maximum breaking force. The lack-of-fit term (P=0.0869)>0.05) is non-significant, demonstrating that the model has a high degree of reliability. The order of influence of the three factors on the maximum breaking force is $X_2>X_1>X_3$. i.e., tensile film width> tensile film length > loading speed. Specifically:

The linear terms X_1, X_2 and X_3 have highly significant effects on the results ($P < 0.01$).

The interaction terms X_1X_3 and X_2X_3 exert significant effects ($p < 0.05$), while the interaction term X_1X_2 has a non-significant effect ($p > 0.05$).

The quadratic terms X_1^2 and X_2^2 show highly significant effects ($p < 0.01$), whereas the quadratic term X_3^2 has a non-significant effect ($p > 0.05$).

Establishment of regression model of the elongation rate

Through fitting the test results using Design-Expert 12.0 software, a regression equation incorporating linear terms, quadratic terms, and interaction terms was derived, as shown in Equation (3). This regression equation characterizes the relationship between the elongation (Y_2) and the three factors: tensile film length (X_1), width (X_2), and loading speed (X_3).

$$\hat{Y_2} = 238.08 - 19.52X_1 + 11.47X_2 - 10.70X_3 + 6.94X_1X_2 + 7.79X_2X_3 + 5.71{X_3}^2 \quad (3)$$

This regression equation is tested with ANOVA, and the results are shown in Table 4.

Table 4

Variance analysis of Y_2

Variance source	Square sum	Degrees of freedom	Mean square	F-value	P-Value
Mold	10121.78	9	1124.64	18.93	< 0.0001**
X_1	5201.47	1	5201.47	78.67	< 0.0001**
X_2	1796.81	1	1796.81	27.17	0.0010**
X_3	1563.72	1	1563.72	23.65	0.0003**
X_1X_2	385.03	1	385.03	5.82	0.0313*
X_1X_3	114.76	1	114.76	1.74	0.2104
X_2X_3	485.16	1	485.16	7.34	0.0179*
X_1^2	154.65	1	154.65	2.34	0.1501
X_2^2	110.11	1	110.11	1.64	0.8900
X_3^2	522.79	1	522.79	7.91	0.0147*
Residual	859.58	13	66.12		
Lost proposal	586.66	5	117.37	3.44	0.0590
Error term	272.72	8	34.09		
Aggregate	11080.08	22			

Note: * * Most significant level (p <0.01); * significant level (p <0.05).

As can be seen from Table 4, the established model is significant ($P < 0.0001$), the P-value of the three factors X1, X2, X3 are all less than 0.05, indicating that the three factors have a significant impact on the elongation. The lack of fit term (P(0.059)>0.05) is not significant, which suggests that the model has a high degree of reliability. The order of influence of the three factors on the elongation Y2 is X1 > X2 > X3, i.e., the film length X1 > width X2 > loading speed X3. Specifically:

The linear terms (primary terms) X1, X2, and X3 all have a highly significant effect on the results (P < 0.01).

The interaction terms X1X2 and X2X3 have a significant effect (P < 0.05), while the interaction term X1X3 has no significant effect (P > 0.05).

The quadratic term (secondary term) X3 has a significant effect on the results (P < 0.05), whereas the quadratic terms X1 and X2 have no significant effect (P > 0.05).

Overall structure of the machine

The adjustable wrapping machine is designed for wrapping rice straw bales of varying sizes, consisting primarily of a frame, an adjustable roller mechanism, a rocker mechanism, a film-supplying mechanism, a lifting mechanism, and a transmission system. The adjustable roller, rocker mechanism, and transmission system are all motor-driven.

The adjustable roller mechanism is mainly composed of two rollers and a circulating reciprocating drive device, where the latter consists of a stepper motor, left- and right-hand screws, rails, and sliding blocks. This mechanism is capable of lifting straw bales with diameters ranging from 500 to 1200 mm. The transmission system drives the rollers to rotate the straw bale.

The rocker mechanism comprises a rocker arm, a frame, and a gear motor. The overall structure of the adjustable straw bale wrapping machine is illustrated in Fig. 3.

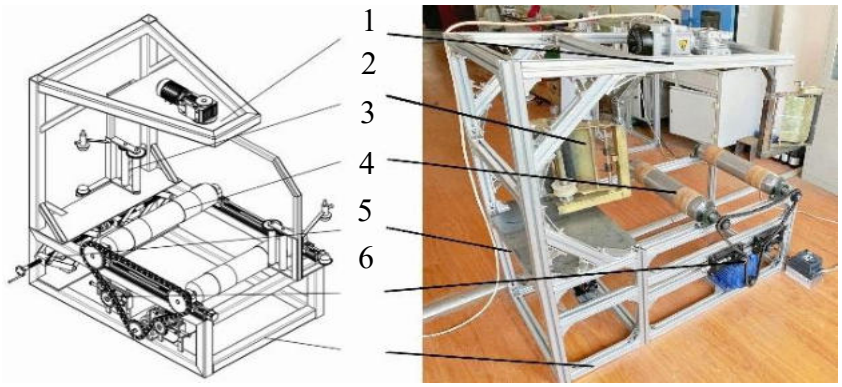


Fig. 3 - The overall structure of the machine

1- Rocker mechanism; 2-Film supplying mechanism; 3-Adjustable roller mechanism; 4-Lifting mechanism; 5-Chain tensioning mechanism; 6-Frame

Working principle

Before operation, the distance between the two rollers is adjusted to an appropriate position by moving the sliding blocks according to the size of the straw bale. The straw bale is then placed on the supporting rollers. Via the lifting mechanism, the symmetrical center plane of the film-feeding mechanism is aligned with the center plane of the straw bale. Subsequently, the tensile film is threaded through the film-feeding rollers, preparing for the wrapping process.

During operation, the sprocket motor is activated to rotate the rollers, which in turn drives the straw bale to rotate around its axis. Simultaneously, the rocker mechanism is initiated, carrying the film-supplying mechanism to revolve around the straw bale. The tensile film is fed through the film-supplying rollers and exits with a certain degree of tension and elongation. Through the combined rotation of the straw bale and the rocker arm, the plastic film is wrapped around the bale.

In the wrapping process, the film-supplying mechanism and the straw bale rotate simultaneously, with their respective rotation planes perpendicular to each other. For each full rotation of the film, the straw bale rotates by a corresponding angle. When the tensile film completes its second rotation, it overlaps with the first rotation by a certain extent; this rotation continues until the wrapping process is finished.

For each batch of straw bales of the same size, the roller spacing and height only need to be adjusted once to meet operational requirements. The overall design of the machine complies with the standard DB21/T 3527-2021, featuring simple operation, a compact structure, and low noise. Relevant parameters of the machine are listed in Table 5.

Table 5

Main parameters of the whole machine

Name	Parametric
Mass / kg	380
Sizes / mm	1580×1140×1780
Drive method	Electric powered
Round bale size (Diameter×Length)	Φ500×500~Φ1200×1000
Number of film layers/layer	≧2
Operating efficiency/(pack/h)	50
Bunching rate /%	≧99

Theoretical analysis of the wrapping process

Force analysis of the wrapping process

During the wrapping process, the straw bale is subjected to several forces: its own gravity G, the tension from the tensile film F_{pull}, the normal support forces from the two rollers $F1$, $F2$, and the frictional forces between the rollers and the bale surface f_1, f_2 (*Li et al.,2018*), as illustrated in Fig.4.

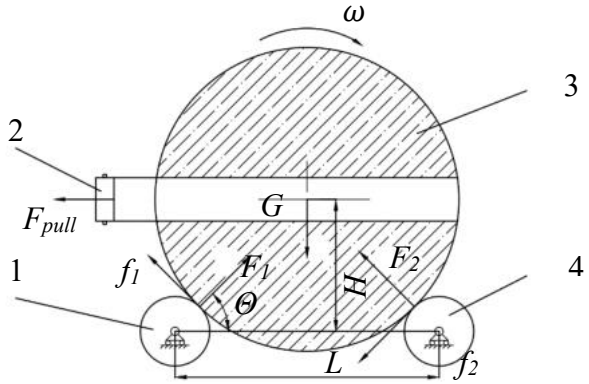


Fig. 4 - Stress analysis diagram of straw bale

1-Left roller; 2-Film roller; 3-Straw bale; 4-Right roller

The tensile force of the film significantly affects the quality and stability of the wrapping effect. Excessive tensile force can easily cause the straw bale to become unbalanced and roll. In such cases, the normal support force of the right roller becomes zero, and the frictional force between the right roller and the straw bale also vanishes. It is therefore necessary to analyze the forces acting on the bale in this critical state, as expressed in Equation (4) below:

$$F_{pull}L_1 = F_1\frac{L_1}{2}cos\,\theta - f_1\frac{L_1}{2}sin\,\theta \tag{4}$$

In Fig.4:

$$G = F_1\,sin\,\theta \tag{5}$$

$$f_1 = \mu F_1 \tag{6}$$

where:

F_{pull}— The pulling force exerted by the film on the straw bale, [N];

G— Gravity, [N];

F_1—The normal support force of the left roller, [N];

f_1—The friction between the left roller and the straw bale, [N];

L_1—The length of the straw bale, [mm];

μ—The coefficient of friction between the left roller and the straw bale;

θ—The angle between F_1 and the horizontal direction, [°].

From the above equation, it can be seen that in the process of wrapping, the F_{pull} should satisfy the following equation (7):

$$F_{pull} \le \frac{G}{2}(cot\theta - \mu) \tag{7}$$

Furthermore, based on equations from (4) to (6), the F_{pull} is related to the gravity of the bale, the friction coefficient between the bale and the rollers, and the angle between the support force and the horizontal line. For the maximum bale size is selected, its weight is approximately 72 kg. When the angle is 45°, the straw bale rotates most smoothly on the roller. With a friction coefficient of 0.78, the calculated F_{pull} value is 79.2N. Therefore, to ensure the smooth rotation of the straw bale during the wrapping process, the tensile force exerted by the film on the bale should be less than 79.2 N.

Determination of the speed ratio (i)

The overlap rate directly affects the quality of wrapping, fermentation efficiency, storage duration, and compactness of straw bales. Theoretically, more wrapping layers improve fermentation outcomes (*Zhang et al., 2017*), but in practical production, 2 layers of tensile film are sufficient to ensure effective fermentation. In this experiment, wrapping tests with 2, 4, and 6 layers of film were conducted to analyze film elongation performance and wrapping efficiency.

The overlap rate must be set reasonably: an excessively low rate results in poor sealing, which can easily lead to fermentation failure; while an excessively high rate, although ensuring good sealing, may cause film waste and significantly reduce efficiency. In this study, the film overlap rate was set at 50%, meaning each cycle of film covers half of the area wrapped in the previous cycle (*Zhang et al., 2019; Wang et al., 2024*). A schematic diagram of the overlap effect is shown in Fig. 5.

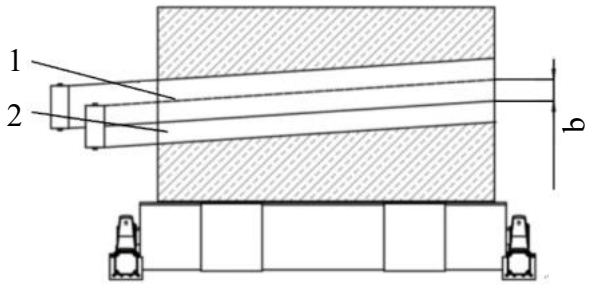


Fig. 5 - Overlapping diagram of straw bale

1 - First film; 2 - Second film

The overlap coefficient M of the tensile film can be calculated by Equation (8):

$$M = \left(\frac{b_1 - b}{b_1}\right) \times 100\% \tag{8}$$

And the following equations:

$$b = \omega r t \tag{9}$$

$$\omega = \frac{2\pi n_1}{60} \tag{10}$$

$$t = \frac{60}{n_2} \tag{11}$$

where:

M—Overlap coefficient of the tensile film, 50 %;

b_1—Width of the tensile film, 250 mm;

b—Staggered distance between two adjacent films, [mm];

ω—Angular speed of the roller, [rad/s];

r—Roller radius, 80 mm;

t—Time for the rocker to rotate around the bale, [s];

n_1—Roller speed, [r/min];

n_2—Rotational speed of the rocker, [r/min].

By substituting Equations (9) ~ (11) into Equation (8), M can be calculated using Equation (12).

$$M = \left(1 - \frac{2n_1}{n_2}\right) \times 100\% \tag{12}$$

Wrapping efficiency is determined by the roller speed and rocker speed. When the overlap rate (M) is 50%, the calculated speed ratio between the roller and the rocker arm (n_1/n_2) is approximately 0.25, which provides a basis for the design of the transmission mechanism.

DESIGN OF THE KEY COMPONENTS OF THE WHOLE MACHINE

Design of the adjustable roller mechanism

The adjustable roller mechanism, as illustrated in Fig. 6, mainly consists of two rollers, a stepper motor, a guideway, a sliding plate, a coupling, left- and right-hand threaded rods, and a limit block. During the wrapping process, the straw bale is placed on the two rollers, and the adjustable roller mechanism allows for the placement of straw bales with different diameters. In this study, the distance between the two rollers can be adjusted within the range of 466 mm to 960 mm to accommodate straw bales of varying sizes.

The two rollers are fixed to the ends of the sliding plates via bearing blocks. While the rollers drive the straw bale to rotate, the stepper motor drives the threaded rods to rotate, enabling the symmetrical movement of the sliding blocks.

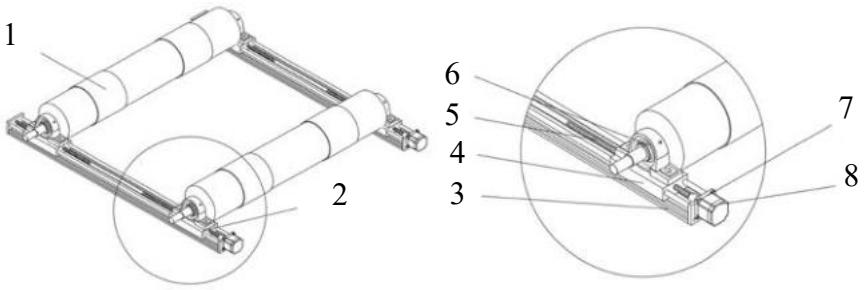


Fig. 6 - Structure diagram of adjustable rice straw bale wrapping machine
1 - Roller; 2 - Reciprocating drive; 3 - Guideway 4 - Slider; 5 - Left and right rotating screws; 6 - Rolling bearing; 7 - Limit switch; 8 - Stepper motor

Design of the film supply mechanism

The film supply mechanism is mounted on the rocker arm (*Yang et al., 2020; Zhao et al., 2024*), consisting of upper and lower support rollers, two film supply rollers, a supply frame, a torsion spring, a film baffle, a sprocket, and a film roll. Its structure is illustrated in Fig. 7. The film is secured between the upper and lower support rollers, with the two film supply rollers positioned on the supply frame. The two film supply rollers are driven by a sprocket, which pulls the tensile film from the film roll.

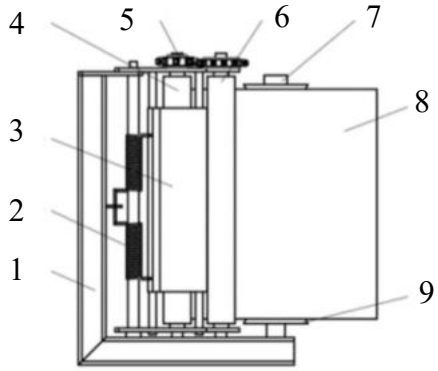


Fig. 7 - Schematic diagram of the film supplying mechanism
1 - Frame; 2 - Torsion spring; 3 - Baffle 4 - Supply rollers 5 - Sprocket; 6 - Supply rollers; 7 - Upper supporting roller; 8 - Film; 9 - Lower supporting roller

Rocker arm mechanism design

The rocker mechanism is primarily responsible for supporting the rocker arm and motor, while driving the rocker arm and film-supplying mechanism to rotate around the straw bale. Composed of a rocker arm, support frame, motor, and fixing plate (as shown in Fig. 8), the mechanism features a rocker motor connected to the middle of the rocker arm. The lower part of the rocker arm is positioned facing the adjustable roller mechanism, with its rotation center aligned with the symmetric central plane of the adjustable roller mechanism. This design prevents eccentricity.

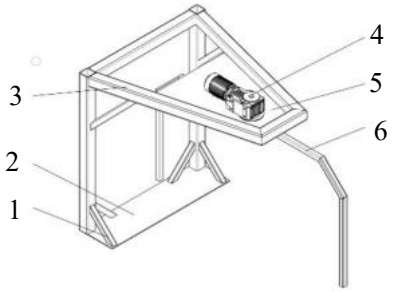


Fig. 8 - Schematic diagram of rocker arm mechanism

1 - Stiffener; 2 - Fixed base plate; 3 - Rocker racks; 4 - Rocker motor; 5 - Motor fixing plate; 6. Rocker

PERFORMANCE TEST OF ADJUSTABLE RICE STRAW ROUND BALE WRAPPING MACHINE

Materials: Three sizes of rice straw bundles (400×400 mm, 500×500 mm, 600×600 mm) with good compaction were used in the test. All bundles were well compacted, free from protrusions or sharp edges, and had an average moisture content of 55%. Tensile film: The wrapping film used was linear low-density polyethylene (LLDPE) with a thickness of 0.025 mm and a width of 250 mm. It was supplied by Shandong Xinlian Heavy Industry Agriculture and Animal Husbandry Machinery Co., Ltd.

Methods: In accordance with the standards DB21/T 3527–2021 and NY/T 3121–2017, straw bales were divided into three groups by size (400×400 mm, 500×500 mm, 600×600 mm). Wrapping tests with 2, 4, and 6 layers of film were conducted for each group, with the following evaluation indicators:

Wrapping time

Defined as the time required to wrap a single straw bale. Five replicate tests were performed, and the average value was calculated.

Coefficient of variation of layers

For each bale size, 5 bales were randomly selected. At 5 randomly chosen positions on each bale, the tensile film was cut along the circumferential direction, and the average number of film layers at these 5 positions was recorded.

Elongation rate

Marker holes were punched in the middle of the film roll, with tracers inserted into the holes as reference marks. After wrapping, the positions of these marker holes were identified on the bale surface, and the distance between two adjacent holes was measured as L. The elongation rate (ε_t) was then calculated using Equation (13):

$$\varepsilon_t = \frac{L - L_0}{L_0} \times 100\% \quad (13)$$

where:

L is the distance between two marking holes after wrapping operation, and L_0 is actually the circumference of the film roll.

The rocking arm mechanism speed was set to 35 r/min, as referenced by *Yang, (2016)*. Based on the transmission ratio between the roller and the rocker arm (i = 0.25), the corresponding roller speed was calculated to be 8.75 r/min. The spacing between the two rollers was adjusted according to the size of the straw bale: 353 mm for 400×400 mm bales, 424 mm for 500×500 mm bales, and 495 mm for 600×600 mm bales.

RESULTS AND ANALYSIS

Wrapping time

The test results are presented in Table 6. Wrapping time varies depending on the specifications of the straw bales:

For 400×400 mm bales, the average wrapping times for 2, 4, and 6 layers were 18.6 s, 32.4 s, and 44.8 s, respectively.

For 500×500 mm bales, the average wrapping times for 2, 4, and 6 layers were 20.4 s, 33.6 s, and 45.2 s, respectively.

For 600×600 mm bales, the average wrapping times for 2, 4, and 6 layers were 21.4 s, 34.4 s, and 46.4 s, respectively.

All results meet the industry standards for straw bale wrapping machinery.

Table 6

Wrapping time of straw bales with different sizes

Number of wrapping layer	400×400 mm wrapping time /s					
	1	2	3	4	5	Average value
2	18	19	18	19	19	18.6
4	33	32	33	32	32	32.4
6	44	44	46	45	45	44.8
Number of wrapping layer	**500×500 mm wrapping time /s**					
	1	2	3	4	5	Average value
2	19	21	20	21	21	20.4
4	33	33	34	33	35	33.6
6	45	45	46	45	45	45.2
Number of wrapping layer	**600×600 mm wrapping time /s**					
	1	2	3	4	5	Average value
2	21	21	21	22	22	21.4
4	34	35	34	34	35	34.4
6	46	47	47	46	46	46.4

Coefficient of variation of layers

Fifteen groups of tests were conducted, with forty-five points randomly selected to record the number of film layers. The results are presented in Table 7. All 15 groups showed a film overlap rate exceeding 50%, and the number of layers at each point was calculated using Equation (14).

$$C = \frac{C_1 + C_2 + C_3 + \cdots C_{45}}{45} = \sum_{i}^{45} C_i/45 \tag{14}$$

where:

C—Average value of layers.

C_i—$C_1 \cdots C_{45}$ Number of layers at each point.

The coefficient of variation is calculated using Equation (15).

$$X = \frac{S}{C} \times 100\% \tag{15}$$

where: S is the standard deviation calculated by Equation (16).

$$S = \sqrt{\frac{\sum_i^{45}(C_i - C)^2}{45 - 1}} \tag{16}$$

After calculation, the coefficients of variation for the uniformity of the wrapping film were found to be 8.70% (400×400 mm), 11.20% (500×500 mm), and 10.70% (600×600 mm), respectively. All these values are below the 15% threshold specified in the industry standards for straw bale wrapping machinery.

Table 7

Number of wrapping film pickup points for different straw bale sizes and layer counts

Straw bale specifications	Straw bale number	2-layer film pickup point number					4-layer film pickup point number					6-layer film pickup point number				
		1	2	3	4	5	1	2	3	4	5	1	2	3	4	5
400×400mm Straw bale	1	2	2	2	2	2	4	4	4	4	4	6	6	6	6	6
	2	2	2	2	2	2	4	3	4	4	4	7	6	6	6	6
	3	2	3	2	2	2	4	4	4	5	4	6	6	6	5	6
	4	2	2	2	2	2	4	5	4	4	4	6	6	6	6	6
	5	2	2	2	2	3	4	4	4	4	4	6	6	6	6	6
500×500mm Straw bale	1	2	2	2	2	2	4	4	4	4	4	6	6	6	6	6
	2	2	2	3	2	2	4	4	5	4	4	6	5	6	6	6
	3	2	2	2	2	2	4	4	4	4	4	6	6	6	6	6
	4	2	2	2	2	2	4	4	4	5	4	6	6	5	6	6
	5	2	2	2	2	2	4	4	4	4	4	6	6	6	6	6

Straw bale specifications	Straw bale number	2-layer film pickup point number					4-layer film pickup point number					6-layer film pickup point number				
		1	2	3	4	5	1	2	3	4	5	1	2	3	4	5
600×600mm Straw bale	1	2	2	2	2	2	4	4	5	4	4	6	6	7	6	6
	2	2	2	3	2	2	4	4	4	4	4	6	6	6	6	6
	3	2	2	2	2	2	4	4	5	4	4	6	6	6	7	6
	4	2	2	3	2	2	4	4	4	4	4	6	6	6	6	6
	5	2	2	2	2	2	4	4	4	4	4	6	6	6	6	6

Elongation rate ε_t

Five wrapped bales of each size were randomly selected, and the elongation rate (ε_t) was calculated using Equation (13). The final result was approximately 59%, with a 2.4% deviation from the design requirements. This elongation rate meets the industry standard, and detailed results are presented in Table 8.

Table 8

Elongation rate

Measured parameter	Elongation of 5 tested wrapping bales - 400×400mm					
	1	2	3	4	5	Average value
L_0(mm）	315.8	312.6	310.1	307.4	304.3	310.04
L_1(mm)	496.1	491.7	498.6	487.5	484.7	491.72
ε_t	(491.72-310.04)/310.14×100%=59%					
Measured parameter	**Elongation of 5 tested wrapping bales - 500×500mm**					
	1	2	3	4	5	Average value
L_0(mm）	329.1	326.9	323.7	320.9	318.6	323.84
L_1(mm)	519.6	525.0	511.7	504.8	507.2	513.66
ε_t	(513.66-323.84)/323.84×100%=59%					
Measured parameter	**Elongation of 5 tested wrapping bales - 600×600mm**					
	1	2	3	4	5	Average value
L_0(mm）	341.3	338.9	336.2	333.4	331.7	336.3
L_1(mm)	539.3	539.5	544.6	529.4	528.1	536.18
ε_t	(536.18-336.3)/336.3×100%=59%					

CONCLUSIONS

In the entire process of rice straw forage production, straw bales require wrapping, but the supporting machinery cannot adapt to bales of different sizes. To address this issue, this study designed a rice straw bale wrapping machine with adjustable rollers to accommodate various bale sizes, laying a foundation for improving the production efficiency of straw forage. The main conclusions are as follows:

(1) The mechanical properties of stretch films were studied. Film length, width, and loading speed were selected as test factors, with maximum tensile force and elongation rate as evaluation indicators. The results indicate that in actual wrapping operations, using shorter film lengths, lower loading speeds, and wider film widths can not only enhance the tensile strength of the film but also increase its elongation, thereby improving wrapping effectiveness.

(2) The overall structural scheme of the adjustable straw bale wrapping machine was designed. Based on theoretical analysis of the wrapping process, the tension applied to straw bales should be less than 79.2 N. A speed ratio of 0.25 between the roller and the rocker arm ensures a 50% wrapping overlap rate, achieving optimal wrapping results.

(3) Key components including the adjustable roller mechanism, film feeding mechanism, and rocker mechanism were designed. The spacing between the two rollers can be adjusted within the range of 466–960 mm, enabling the wrapping of bales with sizes ranging from 400 to 1200 mm.

(4) Performance testing of the adjustable straw bale wrapping machine was completed, with the rocker speed set at 35 r/min. The average wrapping times for 2, 4, and 6 layers of different-sized bales were measured. The film overlap rate reached 50%, with coefficients of variation for film uniformity at 8.70%, 11.20%, and 10.70% respectively, and the total average elongation rate of the stretch film was 59%. All indicators meet the design standards.

ACKNOWLEDGEMENT

This research was supported by the National Key Research and Development Program of China (2023YFD2301605). Key Research and Development Program of Liaoning province, China (2024JH2/102500004).

REFERENCES

[1] Cong, H., Meng, H., Yu, J., Ye, B., Yao, Z., Feng, J., Yu, B., Qin, C., Huo, L., Yuan, Y., Dai, M., Li, L., Shen, Y., Zhao, L., (2021). Analysis of the long-term mechanism of straw industry development in Northeast China under the guidance of "green" ("绿色"引领下东北地区秸秆产业发展长效机制解析). *Journal of Agricultural Engineering*, Vol. 37, pp. 314-321, Beijing/China.

[2] Cong, H., Yao, Z., Zhao, L., Meng, H., Wang, J., Huo, L., Yuan, Y., Jia, J., Xie, T., Wu, Y., (2019), The distribution of crop straw resources and their industrial system and utilization path in China (中国农作物秸秆资源分布及其产业体系与利用路径). *Journal of Agricultural Engineering*, Vol. 35, pp. 132-40, Beijing/China.

[3] Feng, P., Wu, H., Meng, F., Zheng, H., Yang, Z., Wang, J., Shen, Z., (2021). Effect of different compatible biological agents on the silage quality and feeding value of rice straw (不同配伍生物制剂对水稻秸秆青贮品质及饲喂价值的影响). *China Feed*, Vol. 17, pp. 122-128, Beijing/China.

[4] Gu, Y., Zhan, J., Ding, C., Sha, W., (2017). Effect of different treatments on the fermentation quality of fermented rice straw (不同处理对发酵稻秸秆发酵品质的影响). *China Feed*, Vol. 12, pp. 18-20 + 23, Beijing/China.

[5] Huo, L., Yao, Z., Zhao, L., Luo, J., Zhang P., (2022), Research on the contribution and potential of emission reduction and carbon sequestration in the comprehensive utilization of straw (秸秆综合利用减排固碳贡献与潜力研究). *Journal of Agricultural Machinery*, Vol. 53, pp. 349-359, Beijing/China.

[6] Huo, L., Zhao, L., Meng, H., Yao, Z., (2019). Study on the comprehensive utilization potential of crop straw in China (中国农作物秸秆综合利用潜力研究). *Journal of Agricultural Engineering*, Vol. 35, pp. 218-224, Beijing/China.

[7] Li, L., Wang, D., Yang, X., (2018). Study on round rice straw bale wrapping silage technology and facilities [J]. *Int J Agric & Biol Eng*, Vol. 11, pp. 88-95, Beijing/China.

[8] Li, S., Ji, X., Deng, K., Zhu, J., Li, C., Jian, Y., Peng, H., (2020). Analysis of regional straw resources distribution and full quantitative utilization potential (区域秸秆资源分布及全量化利用潜力分析). *Journal of Agricultural Engineering*, Vol. 36, pp. 221-228, Beijing/China.

[9] Liu, M., (2021). Application of Aspergillus Niger in the resourcable utilization of straw. *IOP Conference Series: Earth and Environmental Science*, Vol. 859, pp. 012092, England.

[10] Liu, Y., (2024). Research status and development trend of large square baler (大方捆打捆机的研究现状与发展趋势). *Xinjiang Agricultural Mechanization*, Vol. 06, pp. 54-57, Xinjiang/China.

[11] Lu, H., Chen, Y., Zhang, P., Huan, H., Xie, H, Hu, H., (2021). Impacts of farmland size and benefit expectations on the utilization of straw resources: Evidence from crop straw incorporation in China. *Soil Use and Management*, Vol. 38, pp. 929-939, England.

[12] Tian, Y., (2020). Research on the industry promotion policy of the comprehensive utilization of crop straw in China (我国农作物秸秆综合利用产业促进政策研究). *Agricultural Resources and regionalization*, Vol.41, pp. 28-36, Beijing/China.

[13] Wang, J., Li, X., Huang, W., Wu, L., Cui, J., Bai, H., Zeng, F. (2024). Mathematical model for bale-density prediction in large steel roller-type round balers during bale rolling. *Bioresource technology*. Vol. 396, England.

[14] Wang, J., Tang, H., Wang, J. (2017). Analysis on the comprehensive utilization status and development of crop straw resources in Northeast China (东北地区作物秸秆资源综合利用现状与发展分析). *Journal of Agricultural Machinery*, Vol.48, pp. 1-21, Beijing/China.

[15] Yang, R., Wang, Z., Shang, S., (2020). Experiment on Removing Soil Device with Spring Tooth of Peanut Combine Harvester (花生联合收获机弹齿式去土装置设计与性能试验). *Journal of Agricultural Machinery*, Vol.51, pp. 109-117, Beijing/China.

[16] Zhang, H., Liu, X., Wu, H., Xu, X., Xu., D., (2019). Suspended silage round bundle machine (悬挂式青贮圆捆包膜机的研究). *Agricultural mechanization research*, Vol.41, pp. 159-164, Heilongjiang/China.

[17] Zhang, X., Wang, Z., Shen, M., Bai, H., Ta, N., (2021). Analysis of the yield and comprehensive utilization of crop straw in China (中国农作物秸秆产量及综合利用现状分析). *Journal of China Agricultural University*, Vol.26, pp. 30-41, Beijing/China.

[18] Zhang, Y.I, Li, X., Wang, J., Li, X., An, T., (2017). The effect of the coating number on the quality of sweet sorghum silage (裹包层数对甜高粱青贮饲料品质的影响). *Acta Agrestia Sinica*, Vol. 25, pp. 670-674, Beijing/China.

[19] Zhao, G., Liu, X., Wu, H., Chen, A., Zhang, Q., Song, Q., Xing, W., Zhang, H., (2024). Design and Test of Key Components of Corn Straw Baler Conveyor (玉米秸秆打捆机输送装置关键部件的设计与试验). *Journal of Agricultural Mechanization Research*, Vol. 47, pp. 82-87, Heilongjiang/China.

EFFECTS OF DIFFERENT VENTILATION SPEEDS ON THE THERMAL ENVIRONMENT OF SOLAR GREENHOUSES

/

不同通风速度对日光温室热环境的影响

Chuyuan ZHONG, Huiqun ZHOU
Horsh (FUjian) Food Co., Ltd, FUjian, 363000, China
E-mail: z2019052798@163.com (Chuyuan Zhong)
Corresponding author: Huiqun Zhou
DOI: https://doi.org/10.35633/inmateh-76-37

Keywords: *Computational fluid dynamics, Solar greenhouse, Temperature, Ventilation rate*

ABSTRACT

The solar greenhouse is the main agricultural facility in northern China, providing a suitable environment for cultivating vegetables and flowers during the winter season. However, during the months of March and April, adjustments to the indoor temperature in northern Chinese solar greenhouses are necessary through the manipulation of upper and lower air vents. To investigate the impact of varying ventilation speeds on the thermal conditions within a solar greenhouse, Computational Fluid Dynamics (CFD) simulations were employed. The study assessed four different ventilation speeds on the air, soil, and wall temperatures within the greenhouse, assuming the absence of crops and disregarding humidity levels. The results showed that a wind speed of 0.5 m/s effectively reduced air temperature but had little effect on soil and wall temperatures; at wind speeds of 1.0 m/s and 1.5 m/s, the differences in air, soil, and wall temperatures inside the greenhouse were small. Considering economic benefits and crop growth conditions comprehensively, a wind speed of 1.0 m/s was identified as the optimal choice. This study provides data support and a theoretical basis for ventilation design in solar greenhouses.

摘要

日光温室是中国北方主要的农业设施，可为越冬期的蔬菜和花卉种植提供适宜环境。但是在中国北方 3 月和 4 月份需要通过开启上下风口调控室内温度。为研究不同通风风速对日光温室内热环境变化影响，本文通过 CFD 模拟，在假定温室内无作物和忽略湿度工况下，设置 0 m/s、0.5 m/s、1.0 m/s、1.5 m/s 四种风速，研究其对温室内空气、土壤和墙体温度的影响。结果表明，0.5 m/s 风速可有效降低空气温度，但对土壤和墙体温度影响较小；1.0 m/s 和 1.5 m/s 风速下，温室内空气、土壤和墙体温度差异较小。综合考虑经济效益与作物生长环境等因素，1.0 m/s 风速为最佳选择。该研究为日光温室通风设计提供了数据支撑和理论依据。

INTRODUCTION

Solar energy, as the best green and renewable energy source, is one of the effective ways to address energy shortages and environmental pollution through its maximum utilization (*Liu W. et al., 2018*). Agriculture, the most traditional industry utilizing solar energy, includes the Chinese solar greenhouse (CSG), a unique horticultural facility in northern China with thermal insulation walls on three sides and a plastic film on the south side, enabling off-season cultivation during the northern winter (*Liu X. A. et al., 2022*). However, current CSGs still suffer from excessively high daytime temperatures, leading to pest and disease outbreaks and reduced crop yields. Therefore, it is urgent to study the temperature and humidity in the crop area of CSGs to control the temperature within the range suitable for crop growth (*Zhang Q. Y. et al., 2023*).

Given the issue of high daytime temperatures in solar greenhouses causing pest damage and crop yield reduction, domestic scholars have made notable achievements in researching the thermal environment and optimizing ventilation in these greenhouses.

Lu L., (2022), designed and developed a ventilation control system for solar greenhouses, achieving automated regulation combined with sensor data and enhancing the intelligent level of the greenhouse environment. *Yang Y. Q. et al., (2024),* investigated the impact of different natural ventilation methods on the performance of solar greenhouses in desert areas, pointing out that rational ventilation design can effectively improve the greenhouse microclimate and promote crop growth.

Zhao G. M., (2024), focused on the impact of different natural ventilation methods on the environment of solar greenhouses and tomato growth. The experimental results indicated that the ventilation method directly affects the distribution of temperature and humidity in the greenhouse and the physiological state of crops.

With the development of Computational Fluid Dynamics (CFD) technology, many scholars have used CFD numerical simulation to study greenhouse ventilation. Several studies have investigated the indoor thermal conditions of solar greenhouses using Computational Fluid Dynamics (CFD) (*Baglivo et al., 2020; Dhiman et al., 2019; Kim et al., 2021; Wei et al., 2022*). The outcomes of these simulations offer valuable insights for optimizing the thermal regulation within solar greenhouse environments.

Wei D.D., (2022), systematically studied the numerical simulation of the thermal environment and ventilation characteristics of solar greenhouses, emphasizing the impact of wind speed and ventilation methods on the temperature field in the greenhouse.

Wu X.Y., (2022), conducted research on the structural optimization of energy-saving solar greenhouses based on CFD thermal environment simulation, proposing several structural improvement measures. *Zhao Z., (2022)*, studied the summer cooling effect of a new type of connected solar greenhouses, verifying the practical value of CFD simulation in greenhouse design. *Jing W. T., (2023)*, studied the ventilation simulation and optimization of active heat storage solar greenhouses, proposing ventilation control strategies based on heat storage characteristics. *Zheng R.L., (2023),* analyzed the impact of ventilation methods on greenhouse environment regulation through numerical simulation. *Qiu Y., (2023),* focused on the optimization and thermal environment analysis of pipeline ventilation in plant factories. *Ding Y.Y., (2023),* explored the experimental and numerical simulation methods of greenhouse thermal environment. *Bo G.K., (2023),* studied the growth response of greenhouse tomatoes under different ventilation modes and CFD environmental simulation. *Zhou C.F., (2023),* combined CFD simulation with fuzzy control system design to achieve intelligent control of the environment in edible fungus greenhouses, enhancing the stability of the greenhouse environment. *Qu M.H., (2024),* analyzed the temperature distribution characteristics in solar greenhouses through CFD numerical simulation. *Mao C., (2024),* focused on the heat transfer characteristics, combined with CFD simulation, to establish a greenhouse microclimate model and proposed model-based greenhouse environment control strategies. *Qian C.H., (2024),* combined CFD simulation with control system research to achieve precise control of the environmental temperature in agricultural greenhouses. *Wan M. et al., (2024),* simulated the microclimate of solar greenhouses under different ventilation methods and analyzed the impact of crop transpiration on the humidity field in the greenhouse, emphasizing the coupling effect of ventilation and crop transpiration.

In summary, foreign scholars mainly focus on Venlo-type glass greenhouses and plastic greenhouses. This paper simulates the changes in indoor temperature and humidity fields in solar greenhouses under different ventilation types and speeds. The simulation provides references for natural ventilation control, making the greenhouse environment more suitable for crop growth, reducing pests and diseases, and improving economic benefits.

MATERIALS AND METHODS

The construction and meshing of the solar greenhouse geometric model

Computational Fluid Dynamics (CFD) integrates mathematical models, fluid mechanics, and computer science to numerically simulate fluid flow, efficiently and intuitively solving complex fluid problems. It allows in-depth analysis of air flow and heat transfer in greenhouses. By simulating the impact of different wind speeds on the thermal environment of solar greenhouses, it reveals air flow patterns and temperature distribution changes. This provides a scientific basis for greenhouse ventilation design, energy-saving control, and crop growth environment optimization, holding significant theoretical and practical value.

A three-dimensional geometric model of a common solar greenhouse in Hulun Buir City, Inner Mongolia was constructed. The greenhouse faces south, with a span of 12 meters, a ridge height of 5 meters, a north wall height of 4.8 meters, and an east-west length of 100 meters. The north wall and the east-west gable are trapezoidal, with a base width of 8 meters and a top width of 2 meters. Solid Works software was used for 1:1 three-dimensional modeling, as shown in Figure 1.

In Computational Fluid Dynamics (CFD) simulation, fluent meshing aims to construct an accurate mathematical model. Mesh size and quality directly affect computational accuracy. For the solar greenhouse model, only the wall surface involving heat transfer needs to be refined. The 3D model uses structured, unstructured, and hybrid meshes.

Considering boundary refinement and accuracy, a hybrid mesh was chosen. The mesh size was set to 500 mm, with a total of 156,775 cells. Grid quality was determined using the grid metric, with values closer to 1 indicating better quality. The meshing and corresponding quality are illustrated in Figures 2 and 3.

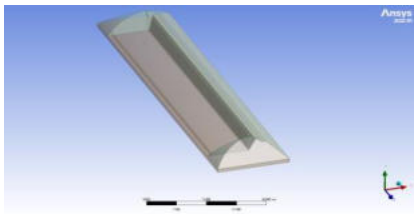


Fig. 1 - 3D model of solar greenhouse

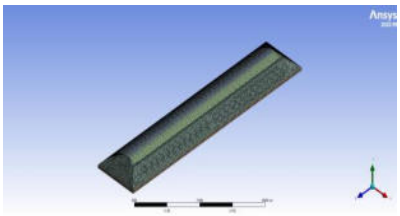


Fig. 2 - Mesh Division

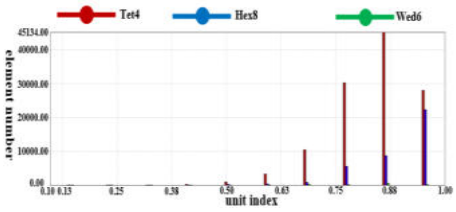


Fig. 3 - Grid Quality

The establishment of CFD numerical model

Model assumptions

The temperature change in a solar greenhouse is a dynamic and complex process, influenced by various factors including greenhouse structure, outdoor climate, crop growth, and ventilation. To reduce analysis time and enhance accuracy, the CFD numerical model of greenhouse temperature was simplified as follows:

(1) The solar greenhouse is in a completely closed state except for the upper and lower vents;

(2) The influence of humidity on the temperature of the solar greenhouse was not considered;

(3) The material parameters of each part did not change with the change of temperature.

The basic control equation of CFD

CFD is based on the conservation laws of mass, momentum, and energy for heat and mass transfer in fluids. The mass conservation equation describes the relationship between fluid motion and mass distribution. The momentum conservation equation links the rate of change of fluid momentum to external forces. The energy conservation equation is crucial in solar greenhouses, embodying the first law of thermodynamics and describing the conservation of total energy during fluid flow. Temperature changes and fluid motion interact to maintain energy balance.

Turbulence model and Radiation model

To better simulate the complex fluid flow and illumination environment inside the solar greenhouse and handle radiation heat transfer, this study selected the standard k-ε model, the DO radiation model, and the solar radiation model.

The solar radiation calculator sets the solar orientation, radiation intensity, and material thermal radiation parameters. The solar greenhouse is at 49°21′N, 119°25′E in the East 8 time zone. Solar radiation data from March 1, 2025 (sunny day) was used for simulation. Starting at 8:00, the coordinate axis was set with the X-axis positive to the north, the Z-axis positive to the east, the sunshine coefficient at 1, and illumination parameters configured using the solar calculator.

Setting of material parameters

Solar greenhouse experience temperature differences due to solar radiation during the day, causing minor changes in air density. The Boussinesq approximation, which treats air density as constant, simplifies the solution of fluid mechanics equations. The thermal properties of the greenhouse enclosure materials are shown in table 1.

Boundary conditions and initial conditions

The setting of boundary condition parameters has a great influence on the numerical simulation. According to the experimental data, the boundary conditions and initial conditions are determined as follows:

(1) Setting of boundary conditions. The boundary conditions mainly include the setting of the boundary of the front and rear roofs, the east and west gables, the north wall and the soil of the solar greenhouse. The interface between the various parts is set to the coupling wall. From 8:00 a.m. to 15:00 p.m., the south roof was provided with a transparent plastic film.

(2) The setting of initial conditions. The exterior surface of the wall was set as a convective boundary condition with a heat transfer coefficient of 10; the south roof was set as a mixed (convective + radiative) boundary condition with a heat transfer coefficient of 15; the back roof was set as a convective boundary condition with a heat transfer coefficient of 5; the soil around was set as adiabatic. The experimental measurement data on March 6, 2025 were selected for model construction. The initial temperatures near the south, middle and wall of the greenhouse were 15.2°C, 16.8°C and 18°C, respectively. The outdoor temperature was applied to the outer surface of the greenhouse envelope. In addition, the initial values of the inner surface temperature of the north wall, soil and rear roof were 19°C, 20°C and 15°C, respectively.

(3) The upper and lower tuyeres were opened at the same time. The lower tuyere, measuring 100 m in length and 1 m in width, was located at the base of the southern shed film. In contrast, the upper tuyere, also 100 m long and 1 m wide, was positioned at the top of the shed film, approximately 1 m horizontally from the north wall and 5 m above the ground. The upper tuyere was set as the pressure outlet condition. The wind speed of the lower tuyere was set to 0m/s, 0.5m/s, 1m/s, and 1.5m/s. The effects of different wind speeds on air temperature, soil temperature, and wall temperature at different positions in the solar greenhouse were explored.

Solve the setting of control parameters

In this simulation, the relaxation factors were set as follows: pressure at 0.3, density, body force, turbulent viscosity, and energy at 1, k and ε at 0.8, and momentum at 0.7. The convergence criteria were set at 1×10^{-3} for continuity, momentum, k, and ε equations, and at 1×10^{-6} for energy and radiation equations. These settings ensured high-precision results suitable for engineering applications.

Table 1

Material thermal property parameters of the solar greenhouse envelope

Parameters	PE	Wall	Soil	backward slope
Densities [kg/m³]	950	2000	1600	70
Specific heat capacity [J/[kg·K]]	1600	1050	1050	1880
Thermal conductivity[W/[m·K]]	0.34	0.8	0.75	0.04
Absorption coefficient	0.15	0.88	0.88	0.1
Scattering coefficient	0	0.12	0.12	0
Index of refraction	1.72	1.92	1.92	1.72

RESULTS AND DISCUSSION

In this research, CFD simulation was used to analyze the effects of four different wind speeds on the temperatures of air, soil, and walls inside a solar greenhouse across horizontal, vertical, and longitudinal dimensions. The coordinate origin was at the greenhouse's south bottom corner, with the y-axis extending upward and the x-axis pointing north.

Influence of different ventilation rates on indoor air temperature

Influence of different ventilation rates on indoor air temperature along the horizontal direction

To investigate the impact of different wind speeds at the ventilation openings on air temperature at various horizontal positions in a solar greenhouse, a cross-sectional analysis along the north-south direction at the midspan in the east-west direction was conducted. Temperature variation curves at four different locations (Y=1200 mm, X=3000 mm, X=5000 mm, X=7000 mm, X=9000 mm) were selected for data analysis.

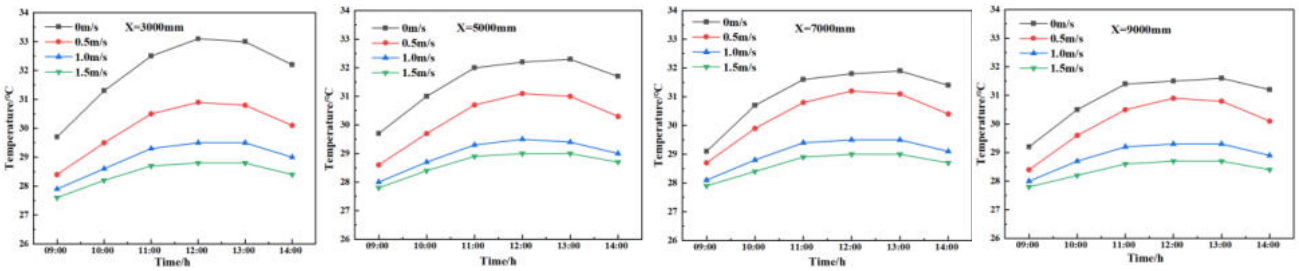


Fig. 4 - Influence of different wind speeds on indoor air temperature at various horizontal locations

As shown in Figure 4, under different wind speeds, the temperature at all horizontal measurement points increased rapidly from 9:00 to 11:00, stabilized from 11:00 to 13:00, and then decreased. Higher wind speeds led to lower temperatures, with the most evident differences at 13:00. At X=3000 mm, X=5000 mm, X=7000 mm, and X=9000 mm, the temperature differences between 0.5 m/s and 0 m/s wind speeds were 2.2°C, 1.3°C, 0.8°C, and 0.8°C, respectively. The differences between 1.0 m/s and 0.5 m/s were 1.4°C, 1.6°C, 1.6°C, and 1.5°C, respectively. The differences between 1.5 m/s and 1.0 m/s were 0.7°C, 0.4°C, 0.5°C, and 0.6°C, respectively.

It was concluded that Ventilation significantly reduces air temperature, with greater cooling effects at locations farther from the north wall. At 0.5 m/s, the cooling effect was more significant at X=3000 mm; at 1.0 m/s, it was more pronounced at X=5000 mm, X=7000 mm, and X=9000 mm.

Influence of various ventilation rates on indoor air temperature in the vertical direction

To investigate the influence of different wind speeds at the ventilation openings on air temperature at various vertical locations in a solar greenhouse, a cross-sectional analysis along the north-south direction at the midspan in the east-west direction was conducted. Temperature variation curves at four different locations (X=6000 mm, Y=1000 mm, Y=2000 mm, Y=3000 mm, Y=4000 mm) were selected for data analysis.

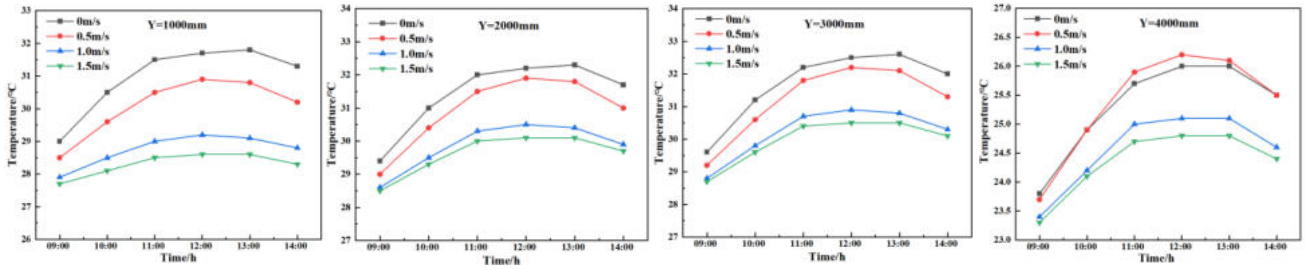


Fig. 5 - Influence of different wind speeds on air temperature at various vertical locations

As shown in Figure 5, under different wind speeds, the temperature trends at all vertical measurement points were consistent: rapid increase from 9:00 to 12:00, stabilization from 12:00 to 13:00, and gradual decrease after 13:00. Higher wind speeds led to lower temperatures. The temperature data at 0.5 m/s for the measurement point at Y=4000 mm, located directly beneath the greenhouse film and influenced by unique convective effects, were excluded from the analysis. At 13:00, when temperature differences were most pronounced, the differences at Y=1000 mm, Y=2000 mm, and Y=3000 mm were 1.0°C, 0.5°C, and 0.5°C between 0.5 m/s and 0 m/s; 1.7°C, 1.4°C, and 1.3°C between 1.0 m/s and 0.5 m/s; and 0.6°C, 0.3°C, and 0.3°C between 1.5 m/s and 1.0 m/s.

It was concluded that ventilation significantly reduced air temperature at different vertical locations, with the effect diminishing as the Y value increased. A wind speed of 0.5 m/s had a more pronounced impact on the measurement point at Y=1000 mm.

Influence of different ventilation rates on indoor air temperature along the longitudinal direction

To investigate the influence of different wind speeds at the ventilation openings on air temperature at various longitudinal locations in a solar greenhouse, temperature variation curves at four different locations (X=7000 mm, Y=1200 mm, Z=20440 mm, Z=32940 mm, Z=45440 mm, and Z=70440 mm) were analyzed.

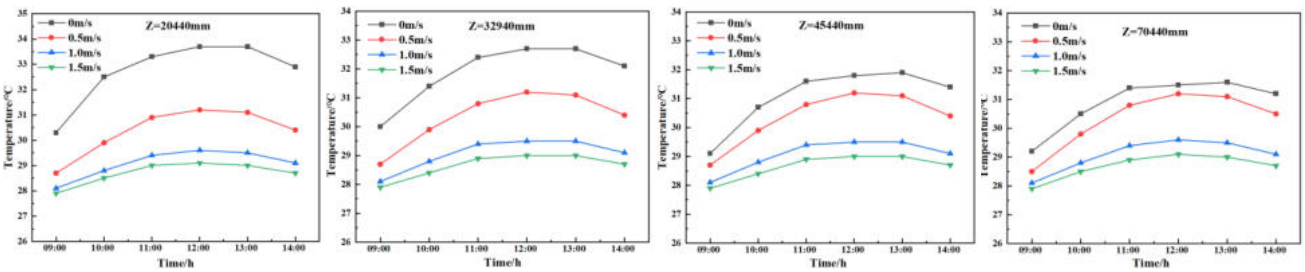


Fig. 6 - Influence of different wind speeds on air temperature at various longitudinal locations

As shown in Figure 6, under different wind speeds, the temperature trends at all longitudinal measurement points were consistent: rapid increase from 9:00 to 12:00, stabilization from 12:00 to 13:00, and gradual decrease after 13:00. The maximum temperature increases at the same measurement point varied significantly under different wind speeds: 3.5°C at 0 m/s, 2.7°C at 0.5 m/s, 1.4°C at 1.0 m/s, and 1.2°C at 1.5 m/s. This indicates that higher wind speeds result in smaller temperature increases and overall lower temperatures. At 13:00, temperature differences were most pronounced. At measurement points Z=20440 mm, Z=32940 mm, Z=45440 mm, and Z=70440 mm, the temperature differences between 0.5 m/s and 0 m/s were 2.6°C, 1.6°C, 0.8°C, and 0.5°C, respectively. The differences between 1.0 m/s and 0.5 m/s were all 1.6°C, and between 1.5 m/s and 1.0 m/s were all 0.5°C.

It was concluded that Ventilation significantly reduced air temperature at different longitudinal locations, with the effect diminishing from west to east. A wind speed of 0.5 m/s had a more pronounced impact at Z=20440 mm. Overall, ventilation effectively reduced air temperature, with 0.5 m/s and 1.0 m/s wind speeds having more pronounced cooling effects. However, considering the smaller influence range of 0.5 m/s compared to 1.0 m/s, and taking into account multiple factors such as economic benefits and crop growth environment, a wind speed of 1.0 m/s was determined to be a more optimal choice for ventilation.

Influence of different ventilation rates on soil temperature

Influence of different ventilation rates on soil temperature along the horizontal direction

To investigate the influence of different wind speeds at the ventilation openings on soil temperature at various horizontal locations in a solar greenhouse, a cross-sectional analysis along the north-south direction at the midspan in the east-west direction was carried out. As documented in reference (*Cheng W. W. et al., 2024*), soil temperature at a depth of 50 mm from the ground surface is considerably influenced by air temperature. Thus, soil temperatures at a depth of 50 mm at locations X=3000 mm, X=5000 mm, X=7000 mm, and X=9000 mm were analyzed.

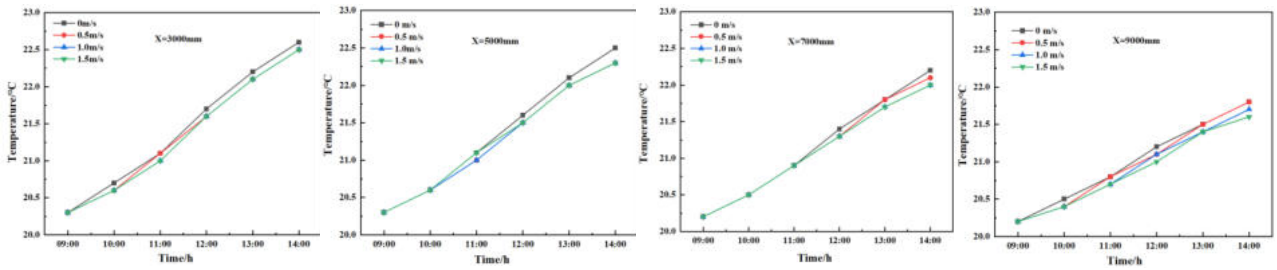


Fig. 7 - Influence of different wind speeds on soil temperature at various horizontal locations

As shown in Figure 7, from 9:00 to 14:00, the soil temperature at each location increased. Ventilation significantly affected soil temperature at different horizontal positions. After the ventilation openings were opened at 9:00, the soil temperatures at X=3000 mm and X=9000 mm changed rapidly, with clear temperature differences appearing soon after; the soil temperatures at X=5000 mm and X=7000 mm changed more slowly. Under various wind speeds, the soil temperature differences at each location grew over time, with maximum differences of 0.1°C, 0.2°C, 0.2°C, and 0.2°C, respectively.

At X=3000 mm and X=5000 mm, soil temperatures showed no significant variation under wind speeds of 0.5 m/s, 1.0 m/s, and 1.5 m/s, and were significantly lower than those at 0 m/s. At X=7000 mm and X=9000 mm, soil temperature decreased with increasing wind speed. The differences in soil temperature under wind speeds of 1.0 m/s and 1.5 m/s were minor, with maximum differences of 0°C and 0.1°C, respectively.

Influence of different ventilation rates on soil temperature along the vertical direction

To investigate the impact of different wind speeds at the ventilation openings on soil temperature at various vertical locations in a solar greenhouse, a cross-sectional analysis along the north-south direction at the midspan in the east-west direction was conducted. Soil temperature variation curves at four different depths (50 mm, 200 mm, 350 mm, and 500 mm) at X=7000 mm were analyzed.

As shown in Figure 8, from 9:00 to 14:00, the soil temperature at each location increased progressively over time. Specifically, the rate of increase was faster from 9:00 to 11:00 and slower from 13:00 to 14:00.

After the ventilation openings were activated at 9:00, noticeable temperature differences at all locations under different wind speeds emerged by 11:00. The response rate was slower under a wind speed of 0.5 m/s compared to those under 1.0 m/s and 1.5 m/s.

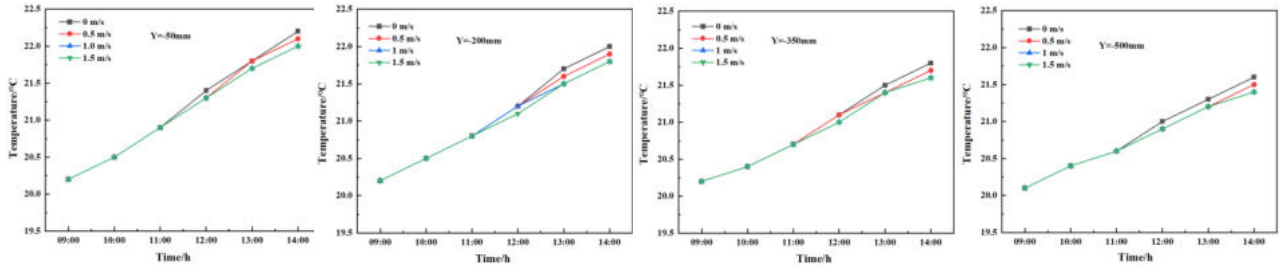


Fig. 8 - Influence of different wind speeds on soil temperature at various vertical locations

At depths of 50 mm, 200 mm, 350 mm, and 500 mm from the ground surface, opening the ventilation openings effectively reduced soil temperature. Under wind speeds of 1.0 m/s and 1.5 m/s, soil temperatures were similar and lower than at 0.5 m/s, with a maximum difference of 0.2°C.

Influence of different ventilation rates on soil temperature along the longitudinal direction

To investigate the impact of different wind speeds at the ventilation openings on soil temperature at various longitudinal locations in a solar greenhouse, temperature variation curves at four different locations (X=7000 mm, depth of 50 mm, Z=20440 mm, Z=32940 mm, Z=45440 mm, and Z=57940 mm) were analyzed.

As shown in Figure 9, from 9:00 to 14:00, the soil temperature at each location increased over time. Ventilation had a significant impact on soil temperature at different longitudinal positions. After the ventilation openings were activated, noticeable temperature differences emerged at Z=20440 mm and Z=32940 mm. For Z=45440 mm and Z=57940 mm, significant temperature differences appeared after 11:00. The soil temperature differences at each location under various wind speeds gradually widened over time, with the maximum differences reaching 0.3°C, 0.3°C, 0.2°C, and 0.1°C, respectively.

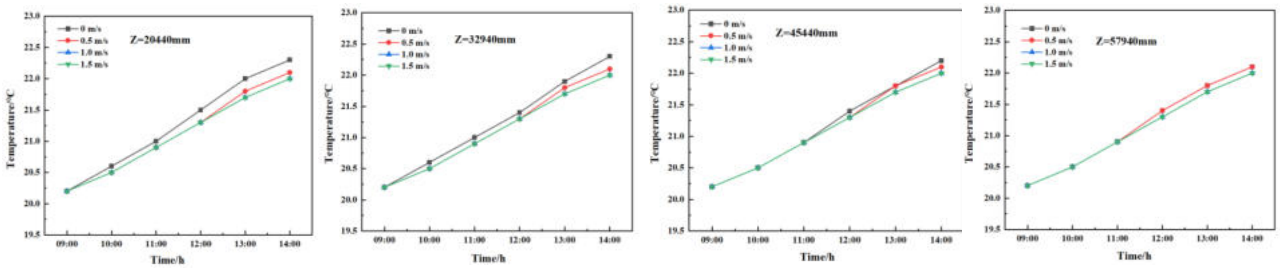


Fig. 9 - Influence of different wind speeds on soil temperature at various longitudinal locations

At locations Z=20440 mm, Z=45440 mm, and Z=32940 mm, At Z=20440 mm, Z=45440 mm, and Z=32940 mm, soil temperature was not affected by wind speeds of 0.5 m/s, 1.0 m/s, and 1.5 m/s during 9:00-12:00. From 12:00 to 14:00, soil temperatures under 1.0 m/s and 1.5 m/s were the same but significantly higher than those under 0.5 m/s, with a maximum difference of 0.1°C. At Z=57940 mm, during 9:00-14:00, 0.5 m/s had no effect on soil temperature, matching that under 0 m/s. Soil temperatures under 1.0 m/s and 1.5 m/s were the same and significantly lower than that under 0.5 m/s, with a maximum difference of 0.1°C.

In summary, ventilation effectively reduced soil temperature. Wind speeds of 1.0 m/s and 1.5 m/s achieved more pronounced cooling effects on soil temperature. However, given that the impact of these two wind speeds on soil temperature was relatively close, and considering economic benefits and the crop growth environment, a wind speed of 1.0 m/s was selected for ventilation.

Influence of different ventilation rates on wall temperature

Influence of different ventilation rates on wall temperature along the horizontal direction

To investigate the impact of different wind speeds on the horizontal variation of wall temperature in the greenhouse, a cross-sectional analysis along the north-south direction at the midspan of the east-west direction of the north wall was conducted. Temperature variation curves at four locations (L=300 mm, L=600 mm, L=900 mm, and L=1200 mm) from the inner side of the north wall were analyzed.

As shown in Figure 10, from 9:00 to 14:00, the wall temperature at locations L=300 mm, L=600 mm, L=900 mm, and L=1200 mm increased progressively over time. Different wind speeds had an impact on wall temperature at different horizontal positions. Specifically, at locations L=300 mm and L=600 mm, noticeable temperature differences emerged after 11:00. At locations L=900 mm and L=1200 mm, the temperature differences were consistent from 9:00 to 12:00 but began to change after 12:00. The wall temperature differences at each location under various wind speeds gradually widened over time, with the maximum differences reaching 0.2°C, 0.1°C, 0.1°C, and 0.1°C, respectively.

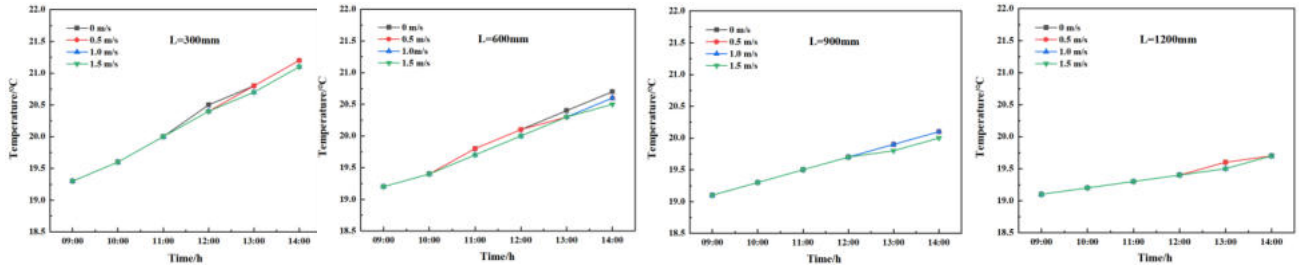


Fig. 10 - Influence of different wind speeds on wall temperature at various horizontal locations

At L=300 mm and L=600 mm, a 0.5 m/s wind speed had little impact on wall temperature, while 1.0 m/s and 1.5 m/s wind speeds effectively reduced it, with minimal differences (max 0°C and 0.1°C, respectively). At L=900 mm, 0.5 m/s and 1.0 m/s had no effect, but 1.5 m/s significantly lowered wall temperature. At L=1200 mm, all wind speeds had almost no impact.

Influence of different ventilation rates on wall temperature along the vertical direction

To study the impact of different wind speeds on the vertical variation of wall temperature in the greenhouse, a cross-sectional analysis along the north-south direction at the midspan of the north wall was conducted, analyzing temperature variation curves at four locations (Y=1000 mm, Y=1500 mm, Y=2000 mm, and Y=2500 mm) 200 mm from the inner side of the north wall.

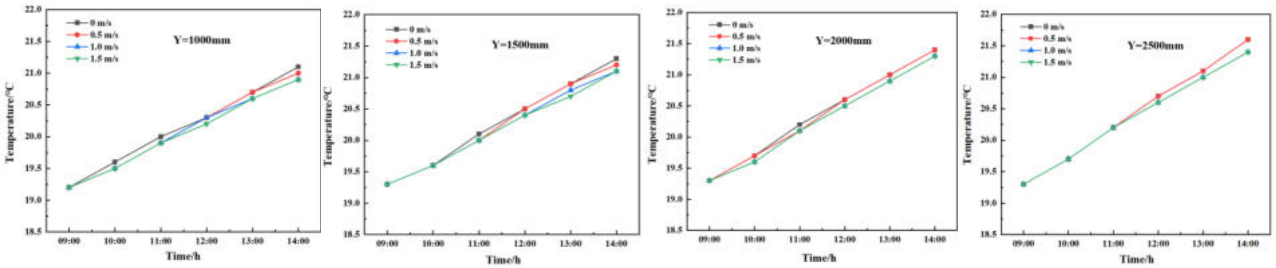


Fig. 11 - Influence of different wind speeds on wall temperature at various vertical locations

As shown in Figure 11, from 9:00 to 14:00, the wall temperature at various vertical locations increased over time. Different wind speeds had varying impacts on wall temperature. At Y=1000 mm and Y=1500 mm, the impact of wind speed showed synchronicity, with temperature differences gradually increasing over time. Differences were minimal from 9:00 to 11:00 but became more pronounced after 11:00. At Y=2000 mm, the impact was slower, with stable differences from 9:00 to 11:00 and changes beginning after 12:00. At Y=2500 mm, the impact was most delayed, with minimal differences from 9:00 to 12:00 and increasing differences after 12:00. The maximum temperature differences at each location under various wind speeds were 0.2°C, 0.2°C, 0.2°C, and 0.2°C, respectively.

At Y=1000 mm, Y=1500 mm, Y=2000 mm, and Y=2500 mm, wind speeds of 1.0 m/s and 1.5 m/s effectively reduced wall temperature with minimal differences between them. At Y=1000 mm and Y=1500 mm, 0.5 m/s had a smaller impact, while at Y=2000 mm and Y=2500 mm, 0.5 m/s had almost no effect.

Influence of different ventilation rates on wall temperature along the longitudinal direction

To investigate the impact of different wind speeds on the longitudinal variation of wall temperature in the greenhouse, temperature variation curves at four different locations (X=10900 mm, Y=1875 mm, Z=20440 mm, Z=32940 mm, Z=45440 mm, and Z=70440 mm) were analyzed.

As shown in Figure 12, from 9:00 to 14:00, the wall temperature at Z=20440 mm, Z=32940 mm, Z=45440 mm, and Z=70440 mm increased. The impact of different wind speeds varied. At Z=20440 mm, the wind speed effect was delayed, with differences increasing after 11:00. At Z=32940 mm, wind speeds of 0.5 m/s, 1.0 m/s, and 1.5 m/s reduced wall temperature after 11:00. At Z=45440 mm and Z=70440 mm, the wind speed impact was synchronized, with differences increasing after 11:00, and wind speeds of 1.0 m/s and 1.5 m/s having a pronounced cooling effect. The wall temperature differences at each location gradually increased over time, with maximum differences of 0.4°C, 0.2°C, 0.2°C, and 0.1°C, respectively.

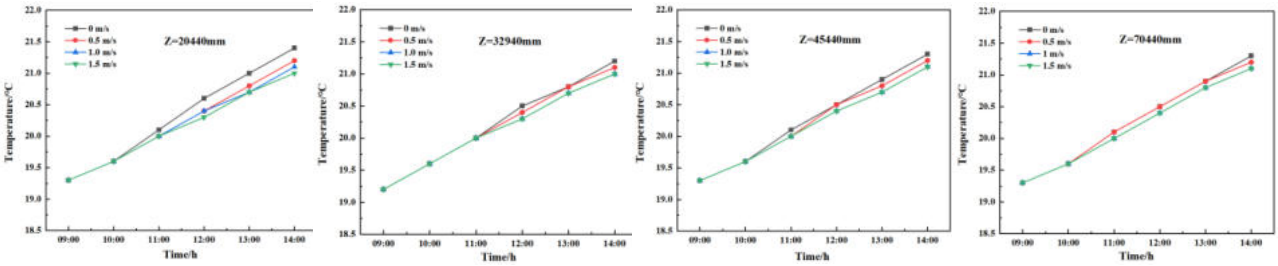


Fig. 12 - Influence of different wind speeds on wall temperature at various longitudinal locations

At a wind speed of 0.5 m/s, the impact on wall temperature was greatest at location Z=20440 mm and smaller at locations Z=32940 mm, Z=45440 mm, and Z=70440 mm. At location Z=20440 mm, the difference in wall temperature between wind speeds of 1.0 m/s and 1.5 m/s was minimal, at 0.1°C. At locations Z=32940 mm, Z=45440 mm, and Z=70440 mm, there were no significant differences in wall temperature between wind speeds of 1.0 m/s and 1.5 m/s.

The study found that greenhouse wall temperature rose over time, with varying impacts of wind speed by location. Horizontally, impact decreased with distance from the north wall. Vertically, higher positions showed more lag. Longitudinally, greater distance from the midspan increased lag. Wind speeds of 1.0 m/s and 1.5 m/s had stronger cooling effects than 0.5 m/s, with 1.5 m/s being more effective later on.

CONCLUSIONS

Through CFD simulation of the solar greenhouse, the impact of different ventilation rates on the indoor air, soil, and wall temperatures within the solar greenhouse was investigated. The conclusions are as follows:

(1) Between 9:00 and 14:00, indoor air temperature initially increased rapidly, stabilized, and eventually decreased. Concurrently, soil and wall temperatures gradually increased over time. Additionally, wind speed inversely correlated with temperature, with higher speeds corresponding to lower temperatures.

(2) A wind speed of 0.5 m/s exerts minimal influence on indoor air temperature, soil temperature, and the temperature of the north wall. In contrast, wind speeds of 1.0 m/s and 1.5 m/s have a pronounced impact on these parameters. The magnitude of variation in indoor temperature, soil temperature, and north wall temperature was greater with an increase in wind speed from 0.5 m/s to 1.0 m/s compared to an increase from 1. m/s to 1.5 m/s.

In summary, a wind speed of 0.5 m/s effectively reduced indoor air temperature but had a minimal impact on soil and wall temperatures. The differences in temperature for indoor air, soil, and walls were relatively small under wind speeds of 1.0 m/s and 1.5 m/s.

REFERENCES

[1] Baglivo C., Mazzeo D., Panico S., Bonuso S., Matera N., Congedo P.M., Oliveti G. (2020). Complete greenhouse dynamic simulation tool to assess the crop thermal well-being and energy needs, *Appl. Therm. Eng.* 179.

[2] Bo G.K. (2023). *Response of greenhouse tomatoes to different ventilation modes and CFD environment simulation research (温室番茄对不同通风模式的响应及 CFD 环境模拟研究).* North China University of Water Resources and Electric Power.

[3] Cheng W. W., Wang C. C., Wang Y., Hao L. R., Liu Z. H., & Cui Q. L. (2024). Soil Marginal Effect and LSTM Model in Chinese Solar Greenhouse [J]. *Sensors*, 24(14):4730-4730.

[4] Dhiman M., Sethi V.P., Singh B., Sharma A. (2019). CFD analysis of greenhouse heating using flue gas and hot water heat sink pipe networks, *Comput. Electron. Agric.*, 163.

[5] Ding Y. Y. (2023). *Experimental and numerical simulation methods of greenhouse thermal environment (日光温室热环境优化及相似模拟研究)*. North China Electric Power University (Beijing).

[6] Jing W.T. (2023). *CFD simulation and optimization of active heat storage solar greenhouse ventilation (基于 CFD 的主动蓄热日光温室通风模拟与优化)*. Northwest A&F University.

[7] Kim R.W., Kim J.G., Lee I.B., Yeo U.H., Lee S.Y., Decano Valentin C. (2021) Development of three-dimensional visualisation technology of the aerodynamic environment in a greenhouse using CFD and VR technology, part 1: development of VR a database using CFD, *Biosyst. Eng.,* 207, 33–58.

[8] Liu W., Liu L. Q., Guan C. G., Zhang F. X., Li M., Lv H., Yao P. J., & Ingenhoff J. (2018). A novel agricultural photovoltaic system based on solar spectrum separation [J]. *Sol Energy*, 162:84–94.

[9] Liu X. A., Wu X. Y., Xia T. Y., Fan Z. L., Shi W. B., Li Y. M., & Li T. L. (2022). New insights of designing thermal insulation and heat storage of Chinese solar greenhouse in high latitudes and cold regions [J]. *Energy*, 242:122593.

[10] Lu L. (2022). *Design and development of ventilation control system for solar greenhouses (日光温室通风控制系统的设计与开发)*. Shenyang Agricultural University.

[11] Mao C. (2024). *Analysis of heat transfer characteristics of greenhouse and modeling and control of greenhouse microclimate based on CFD (基于 CFD 的温室传热特性分析及温室小气候建模与控制研究)*. Jiangxi University of Science and Technology.

[12] Qiu Y. (2023). *Optimization and thermal environment analysis of pipeline ventilation in plant factories based on CFD (基于 CFD 的植物工厂管道通风优化与热环境分析)*. Anhui Agricultural University.

[13] Qu M. H. (2024). *Numerical simulation research on temperature environment of solar greenhouse based on CFD (基于 CFD 的日光温室温度环境数值模拟研究)*. Shenyang Agricultural University.

[14] Qian C. H. (2024). *CFD simulation and control system research of agricultural greenhouse environment temperature field (农业大棚环境温度场 CFD 模拟及测控系统研究)*. Yancheng Institute of Technology.

[15] Wei D.D. (2022). *Numerical simulation of thermal environment and ventilation characteristics of solar greenhouses (日光温室热环境数值模拟与通风特性研究)*. Henan Agricultural University.

[16] Wan M., Yang W., Liu Z. Q., Xu C. X., & Liu D. (2024). Simulation of microenvironment of solar greenhouse under different ventilation methods and research on crop transpiration (不同通风方式日光温室微环境模拟与作物蒸腾研究). *Transactions of the Chinese Society for Agricultural Machinery*, 55(01):328-338+349.

[17] Wei D., Zhang Y., Liu S., Lv Y. (2022). Simulation study of ventilation characteristics of solar greenhouse under natural ventilation[J]. Proceedings of the SPIE, Volume 12160.

[18] Wu X. Y. (2022). *Structural optimization of energy-saving solar greenhouses based on CFD thermal environment simulation (基于 CFD 热环境仿真的节能日光温室结构优化研究)*. Shenyang Agricultural University.

[19] Yang Y. Q., & Liu Y. F. (2024). The impact of different natural ventilation methods on the performance of solar greenhouses in desert areas (不同自然通风方式对沙漠日光温室性能的影响). *Agricultural and Technology*, 44(10):18-23.

[20] Zhao G. M. (2024). The impact of different natural ventilation methods on the environment of solar greenhouses and tomato growth (不同自然通风方式对日光温室环境及番茄生长的影响). *China Agricultural Machinery Equipment*, (05):59-61.

[21] Zheng R. L., Yang W., & Liu Z. Q. (2023). Numerical simulation of humidity and heat characteristics of solar greenhouses under different ventilation forms (不同通风形式日光温室湿热特性的数值模拟). *Journal of China Agricultural University*, 28(03):140-150.

[22] Zhang Q. Y., & Du Z. Y. (2023). Numerical simulation of springtime temperature and humidity fields in the solar greenhouse based on soil evaporation and crop transpiration (基于土壤蒸发与作物蒸腾的春季日光温室内温湿度场数值模拟). *Journal of Taiyuan University of Technology*, 1-14.

[23] Zhou C. F. (2023). *CFD simulation and fuzzy control system design of edible fungus greenhouse environment (食用菌温室环境 CFD 模拟与模糊控制系统设计)*. Huazhong Agricultural University.

[24] Zhao Z. (2022). *Study on summer cooling effect of a new type of connected solar greenhouses based on CFD (基于 CFD 的新型连栋日光能温室夏季降温效果研究)*. Nanjing Agricultural University.

EFFECTS OF ELECTRIC VOLTAGE AND WATER VOLUME ON OHMIC HEATING HYDRODISTILLATION (OHHD) OF NUTMEG LEAVES
/
PENGARUH TEGANGAN LISTRIK DAN VOLUME AIR PADA HIDRODISTILASI OHMIK HEATING DAUN PALA

Imam SOFI'I[1*)], Winarto[1)], Oktaf RINA[1)]
Department of Agricultural Technology, Politeknik Negeri Lampung, Bandar Lampung, Lampung 35144, Indonesia.
E-mail: imam.sofii@polinela.ac.id
Corresponding author: Imam Sofi'i
DOI: https://doi.org/10.35633/inmateh-76-38

Keywords: *energy, hydrodistillation, nutmeg leaves, ohmic heating*

ABSTRACT
The objectives of the study were: to determine the ratio of electrical voltage and volume to the hydrodistillation rate, conductivity, energy, and yield. The method used is hydrodistillation of nutmeg leaves according to the treatment. The treatment of voltage and water volume were 3 levels each. Observations included voltage, current, temperature, and yield. The results showed that the hydrodistillation rate, electrical conductivity, energy, and oil nutmeg leaves yield were influenced by electrical voltage and solvent volume. The maximum oil yield was 1.07% at a voltage of 50 Vac and 750 ml of water.

ABSTRAK
Tujuan penelitian adalah: mengetahui rasio tegangan listrik dan volume terhadap laju hidrodistilasi, konduktivitas, energi, dan rendemen. Metode yang digunakan adalah melakukan hidrodistilasi daun pala sesuai perlakuan. Perlakuan tegangan dan volume air masing-masing 3 level. Pengamatan meliputi tegangan, arus, suhu, dan rendemen. Hasil penelitian menunjukkan bahwa laju hidrodistilasi, konduktivitas listrik, energi, dan rendemen minyak daun pala dipengaruhi oleh tegangan listrik dan volume pelarut. Rendemen minyak maksimum sebesar 1,07% pada tegangan 50 Vac dan air 750 ml.

INTRODUCTION
Distillation is one of the methods used to extract distillates in the form of oil or other materials contained in certain materials. Distillation is the process of heating a liquid or solid until it turns into steam, which is channeled into a separate vessel, then condensed with a cooler. In distillation, a mixture of substances is boiled so that it evaporates, and this steam is cooled back into liquid form. Substances that have a lower boiling point will evaporate first.

The distillation method includes physical operations that involve heat transfer and mass transfer. There are 2 types of distillation methods, i.e., the dry distillation method and the wet distillation method. The dry distillation method is carried out without using water, while wet distillation uses water. There are 3 types of water distillation methods, i.e., the material is boiled in water in one vessel, the material is steamed using water vapor in one vessel, and the material is steamed with water vapor in a separate vessel. Each of the three methods has advantages and disadvantages for the results and quality of the distillate produced. These three methods are commonly used to extract materials from plants containing essential oils.

Plants that produce essential oils include cloves, nutmeg, patchouli, and so on. Essential oils have a selling value and are among Indonesia's leading export commodities. According to the latest report from the Ministry of Industry, Indonesia's essential oil production in 2020 reached around 8,500 tons. From 2017 to 2020, an increase in the value of essential oil exports was recorded, with a total value of essential oil exports from January to September 2021 reaching USD 185 million (*Mukhtarom*, *2024*). Nutmeg is a plant that produces essential oils. Indonesia is the largest producer of nutmeg in the world, i.e., between 70% and 75% *(Balai Komoditi Industry, Deptan, 2009*). Essential oil from nutmeg plants can be obtained from fruit, mace, and nutmeg leaves. The highest oil content is obtained from fruit and mace, while nutmeg leaves have a low content. The yield of essential oil from 1 kg of fresh nutmeg leaves is 0.4% (*Damayanti, 2017*). Although the content of nutmeg leaf oil is small, if the amount is large, it will still provide economic value.

The extraction of nutmeg leaf essential oil by craftsmen/farmers is done by distilling a mixture of steam and water. Steaming the leaves in a closed vessel produces a mixture of water vapor, which is then routed into a cooling pipe for condensation. The condensation results in a liquid consisting of water and nutmeg leaf oil. The energy used for steaming nutmeg leaves comes from firewood. The use of firewood for the distillation process is not environmentally friendly because it can pollute the environment due to the smoke from burning firewood.

Currently, many researchers are developing environmentally friendly distillation and extraction methods. One distillation method is using ohmic heating. Ohmic heating is a heating process that occurs due to alternating electric current in a liquid that has conductivity. Ohmic heating (OH) is a volumetric heating technique that emerged as an alternative to conventional heating by utilizing alternating electric current to heat the product (*Sain et al., 2024; Talha et al., 2024*). Heat will be generated in the liquid due to the collision of particles in the liquid. Heating in this way is environmentally friendly because it does not produce smoke and other hazardous materials. Research utilizing ohmic heating for extraction includes the extraction of phytochemical component products from potatoes (*Pereira et al., 2016*), the extraction of essential oils of aromatic plants (*Gavahian et al., 2020*), the extraction of olive leaves (*Safarzadeh et al., 2022*), the effectiveness of ohmic heating technology for the extraction of phenolic compounds from red beet roots (*Cabas and Icier, 2021*), grape pomace (*Ferreira-Santos et al., 2024*), the extraction of phenolic content and antioxidant activity of cocoa bean skin (*Sánchez et al., 2023*), and the phenolic extraction of avocado leaves (*Gumustepe et al., 2023*).

The conditions for heating in ohmic heating are the presence of electrical voltage and liquid materials that have conductivity values. The mixture of water and nutmeg leaves has a conductivity value, so if given an electric voltage, it will be able to flow an electric current. The electric current flowing in the mixture of water and nutmeg leaves will generate heat. The heat will increase the temperature of the mixture of water and nutmeg leaves until it reaches boiling point (100°C). The water vapor formed contains a mixture of water and oil; if condensed, it will produce separate water and oil. The use of ohmic heating for nutmeg leaf extraction can be done using the water distillation or hydrodistillation method. Hydrodistillation is done by boiling essential plant materials and water in one vessel. The success of ohmic heating is influenced by many factors such as electrical conductivity, field strength, particle size, concentration, ionic concentration, and electrodes (*Kaur & Singh, 2016*).

The electrode in ohmic heating is a connection between a solid-state conductor (i.e., the current feeder) and a liquid-state conductor (i.e., the heating medium) (*Samaranayake & Sastry, 2005*). There are several types of electrodes used for heating using ohmic heating, i.e., aluminum (*Uemura et al., 1994*), carbon (*Getchell, 1935*), glassy carbon, titanium (*Amatore et al., 1998*), platinum (*Tzedakis et al., 1999*), rhodium (*Palaniappan & Sastry, 1991*), stainless steel (*Assiry et al., 2003*), and platinized titanium (*Stirling, 1987*). Based on the description above, the author is interested in knowing the amount of electrical energy needed in the process of hydrodistillation of nutmeg leaves using ohmic heating. The use of different electrical voltages and electrode areas will affect the energy and also the time for the distillation process of nutmeg leaves. The objectives of this study are (a) to determine the effect of voltage and water volume on the hydrodistillation rate, (b) to determine the effect of voltage and water volume on electrical conductivity, (c) to determine the effect of voltage and water volume on hydrodistillation energy consumption, and (d) to determine the effect of voltage and water volume on the yield of nutmeg leaf oil.

MATERIALS AND METHODS

Materials

The ohmic heating hydrodistillation equipment used consists of an outer pan made of aluminum and an inner pan made of stainless steel. The outer pan functions as a protector. The inner pan is a treatment room as a heating place. There are 2 inner pans, i.e., the one located on the edge with an open position with a height of 106 mm and a diameter of 182 mm. This pan functions as a place for materials and water for the boiling process as well as a neutral electrode. The second pan with an open position with a diameter of 88 mm and a height of 82 mm is located in the middle and functions as a phase electrode (fig. 1). Other equipment needed is a 1000 W step-up/down transformer, ampere meter, volt meter, measuring cup, analytical balance, camera, and stopwatch. The material used is dried nutmeg leaves. The treatments carried out were 3 voltage levels, i.e., 50 Vac, 75 Vac, and 100 Vac, and 3 levels of water volume treatment, i.e., 750 ml, 1000 ml, and 1250 ml.

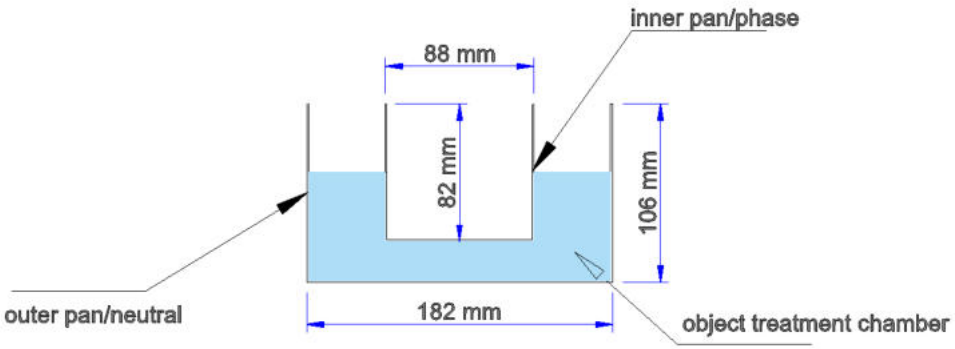


Fig. 1 - Treatment chamber scheme

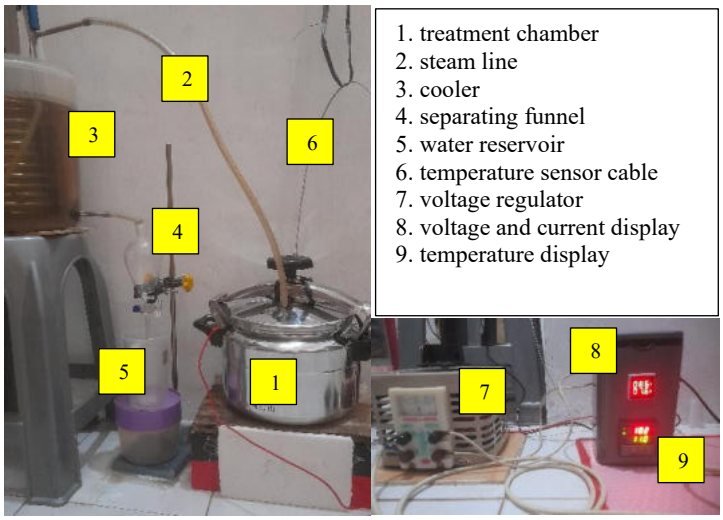


Fig. 2 - Ohmic heating device

Research stages

1. Designing and assembling the 1.3 liter ohmic heating hydrodistillation device (fig. 2)

2. Testing the ohmic heating hydrodistillation device by (a) Weighing 100 g of dried nutmeg leaves and cutting them into several parts. (b) Inserting the cut dried leaves into the treatment chamber and adding distilled water according to the treatment. (c) Closing the treatment chamber and flowing alternating current with the voltage according to the treatment. (d) Turning on the switch so that the hydrodistillation process takes place. (e) Recording the temperature, voltage, and electric current during ohmic heating hydrodistillation. (f) Collecting oil and water from the hydrodistillation process. (g) Separating the water and nutmeg leaf oil using a separating funnel. (h) Weighing the nutmeg leaf oil. (i) Conducting ohmic heating hydrodistillation of nutmeg leaves with different voltages and ratios of water and nutmeg leaves. (j) Repeating the steps above according to the treatment, and each is repeated 3 times.

3. Conduct observations on changes in voltage, changes in electric current, changes in temperature, oil yield, and oil characteristics according to SNI.

4. Process data and present it in the form of tables and graphs.

5. Electrical conductivity (σ) is calculated using the following equation (*Assiry et al., 2003; Zell et al., 2009; Salengke et al., 2007*).

$$\sigma = \frac{L}{A} x \frac{I}{V}$$

where:

σ = Electrical conductivity (S/m);
L = distance between electrodes (m);
A = area of the material to be heated (m^2);
I = electric current (Amperes);
V = Electric voltage (Volts).

RESULTS

Voltage

The requirement for heating in ohmic heating hydrodistillation is the presence of electric voltage flowing in the liquid to be heated. The liquid must have a conductivity value; if the conductivity approaches zero, then the electric current does not flow and will not generate heat. The mixture of water and nutmeg leaves has a conductivity value, so if given an electric voltage, it will be able to flow an electric current. The electric current flowing in the mixture of water and nutmeg leaves will generate heat. One of the factors that affects the success of the hydrodistillation process is electric voltage. In this study, 3 voltage levels were used, i.e., 50 Vac, 75 Vac, and 100 Vac. The volume of water used was 3 levels, i.e., 750 ml, 1000 ml, and 1250 ml. The results of the study on the treatment of electric voltage and water volume are presented in Fig. 3 and Fig 4.

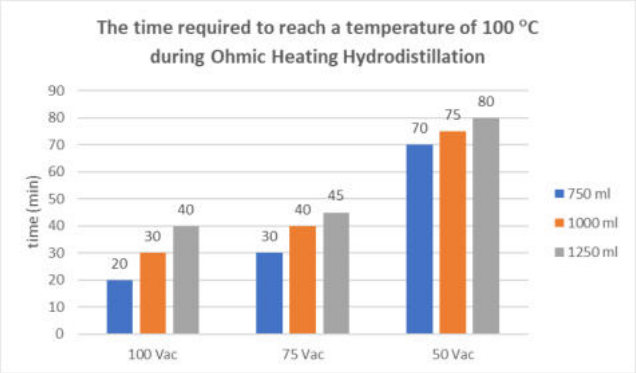


Fig. 3 - Time required to reach a temperature of 100°C

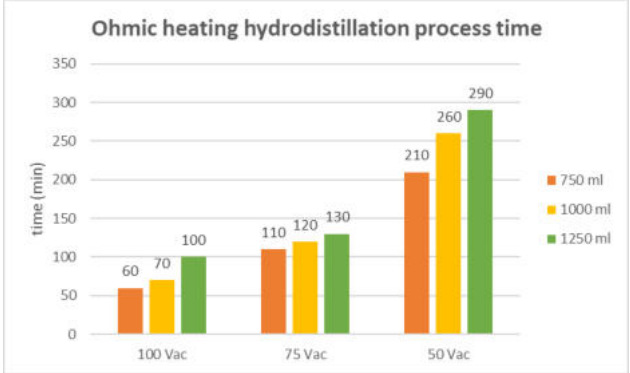


Fig. 4 - Time required for ohmic heating Hydro distillation process

Based on Fig. 3, it can be seen that the magnitude of the voltage affects the heating of the mixture of nutmeg leaves and water. At a voltage of 100 Vac, the heating time to reach a temperature of 100°C requires a shorter time compared to a voltage of 75 Vac and a voltage of 50 Vac. At the same water volume of 750 ml, the time required to reach a temperature of 100°C at a voltage of 100 Vac is 20 minutes; at a voltage of 75 Vac, it takes 30 minutes; and at a voltage of 50 Vac, it takes 70 minutes. At a water volume of 1000 ml, with a voltage of 100 Vac, it takes 30 minutes to reach a temperature of 100°C, while at a voltage of 75 Vac, it takes 40 minutes, and at a voltage of 50 Vac, it takes 75 minutes. At a larger water volume of 1250 ml, the time to reach a temperature of 100°C at a voltage of 100 Vac is 40 minutes, while at a voltage of 75 Vac it is 45 minutes, and at a voltage of 50 Vac it is 80 minutes. The higher the voltage, the faster the time to reach the boiling point of the liquid.

From Fig. 3, it can be seen that at the same voltage, the time required for ohmic heating hydrodistillation process is influenced by the volume of water used. The greater the volume of water used, the longer the time to reach the boiling point. The fastest time to boil a mixture of water and nutmeg leaves is at a volume of 750 ml, followed by 1000 ml, and the longest is 1250 ml. The higher the volume of water, the heating rate will decrease. The heating process using ohmic heating is influenced by many factors such as electrical conductivity, field strength, particle size, concentration, ionic concentration, and electrodes (*Kaur & Singh, 2016*).

Based on Figure 4, it can be seen that at the same voltage, the hydrodistillation process is influenced by the voltage and water used. The higher the voltage and the less volume of water used, the shorter the hydrodistillation process will be. This is like using a voltage of 100 Vac with 750 Watts; the hydrodistillation process takes 60 minutes. At a low voltage of 50 Vac with a water volume of 1250 ml, the longest time is required during the hydrodistillation process, which is 290 minutes. At a higher voltage of 100 Vac, the heat generation process is faster, while at a lower voltage of 50 Vac, the heating process is slow.

Electrical conductivity

Electrical conductivity (σ) is a measure of a material in accommodating the movement of an electric charge, i.e., the ratio of current density to electric field strength. The unit of electrical conductivity is Siemens per meter (S/m) (*Assiry et al., 2003; Salengke & Sastry, 2007; Zell et al., 2009*). Electrical conductivity is the ability of a material to conduct heat and electricity. Electrical conductivity works based on the physical

movement of electrons and the transfer of energy between electrons. The existence of electrical conductivity is very necessary in ohmic heating. The requirement for the heating process in ohmic heating, in addition to the presence of electric voltage, is that the liquid must have a conductivity value. The electrical conductivity value is influenced by the content of conductive materials in the liquid, such as acid, base, salt, or materials containing electrolytes such as silver, copper, gold, aluminum, zinc, nickel, and brass.

The measurement of the initial electrical conductivity value of a mixture of distilled water and nutmeg leaves before the hydrodistillation process using ohmic heating averaged 34 µS/cm. Pure water has a conductivity close to zero because it contains little electrolyte (*Asgarpanah & Kazemivash, 2012*). The addition of nutmeg leaves to pure water can increase the conductivity value even though the value is relatively small. The electrical conductivity value of the mixture of water and nutmeg leaves during the hydrodistillation process varies depending on the volume of water, voltage, and temperature. The results of the calculation of the electrical conductivity value during the hydrodistillation process of nutmeg leaves using ohmic heating on the same water volume are presented in Fig. 5–Fig. 7.

In general, at the start of heating, the electrical conductivity of the same volume of water is low, but it increases with process time. Each voltage's electrical conductivity has a maximum value, which decreases over time. The higher the voltage, the faster it reaches its maximum conductivity value. The magnitude of conductivity during the ohmic heating hydrodistillation process at the same volume of water is affected by the magnitude of voltage.

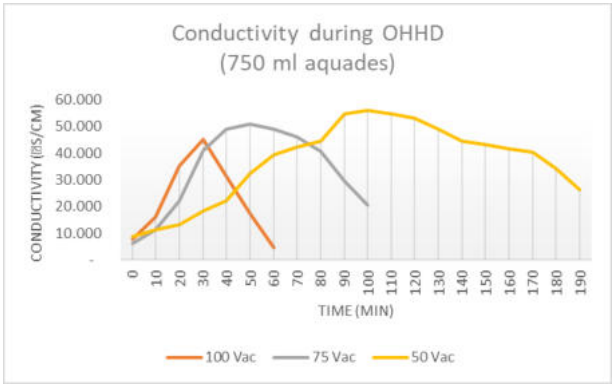


Fig. 5 - Conductivity during OHHD (750 ml of distilled water)

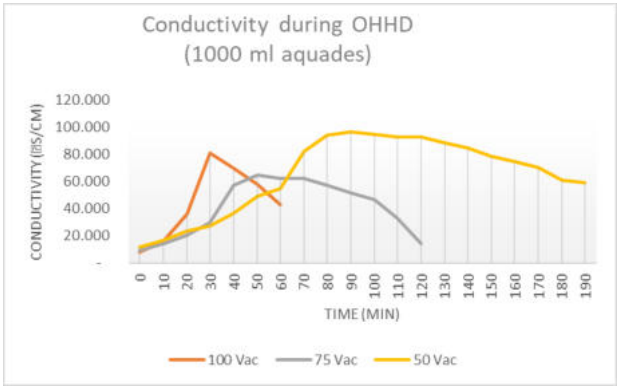


Fig. 6 - Conductivity during OHHD (1000 ml of distilled water)

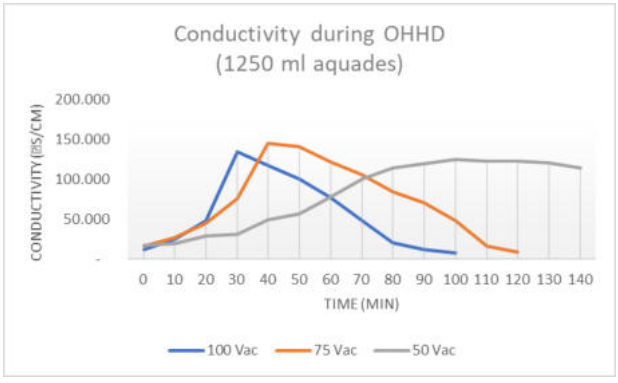


Fig. 7 - Conductivity during OHHD (1250 ml of distilled water)

Electrode area

Electrode area in ohmic heating are important components for heat to occur. Without electrodes, there will be no heating. The electrodes used in ohmic heating are selected from materials that do not change properties (corrosive) due to electricity flowing and do not dissolve in the heated solution. In this study, stainless steel was used as the electrode because it has corrosion-resistant properties (*Assiry et al., 2003*).

The electrodes used are a pair of parallel plates in the form of a cylinder/tube. The inner and outer electrodes have different areas. The cavity between the two electrodes functions as a place for agricultural materials that are given heating treatment or a hydrodistillation chamber. The outer electrode (neutral) has a tube cover area of 592.2 cm² with a tube base area of 253.2 cm², while the inner electrode (phase) has a tube

cover area of 227.1 cm² and a base area of 61.1 cm². The area of the outer electrode (blanket and base) is 845.4 cm², and the area of the inner electrode (blanket and base) is 288.2 cm². When given different treatments of adding water and nutmeg leaves, the electrode plates immersed in water are also different. The difference in the water that is immersed causes a difference in the contact area of the electrode or a difference in the electrode area. Table 1 presents the relationship between water volume and electrode surface area.

Table 1

Electrode area

water volume (ml)	water level (cm)	outer electrode area (cm^2)	inner electrode area (cm^2)	average electrode area (cm^2)
750	*3,9*	*473,1*	*105,4*	*289,3*
1000	*5,1*	*540,8*	*138,6*	*339,7*
1250	*6,7*	*631,0*	*182,9*	*407,0*
full	*10,5*	*845,4*	*288,2*	*566,8*

The electrode area, or the area of contact between the object and the electrode, also affects the success of ohmic heating hydrodistillation. The electrode area will affect the value of electrical conductivity. The results of the calculation of the electrical conductivity value during the nutmeg leaf hydrodistillation process using ohmic heating at the same electrical voltage are presented in figures 8, 9, and 10. Based on the figure, in general, at the same voltage, the conductivity value is influenced by the volume of water used. The greater the volume of water used, the greater the conductivity value.

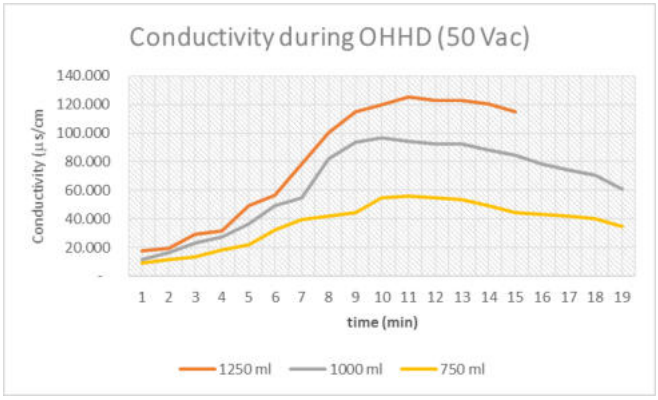


Fig. 8 - Conductivity during OHHD (Voltage 50 Vac)

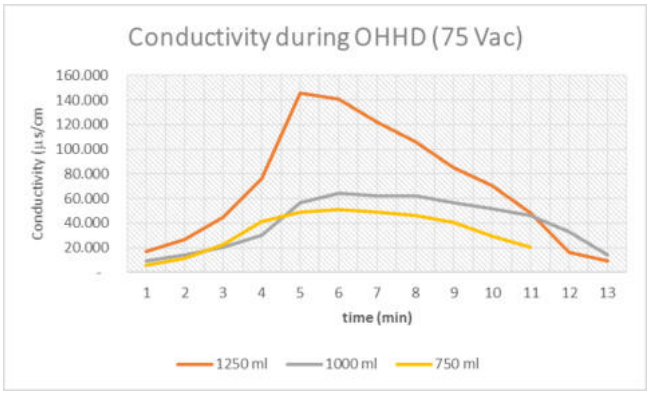


Fig. 9 - Conductivity during OHHD (Voltage 75 Vac)

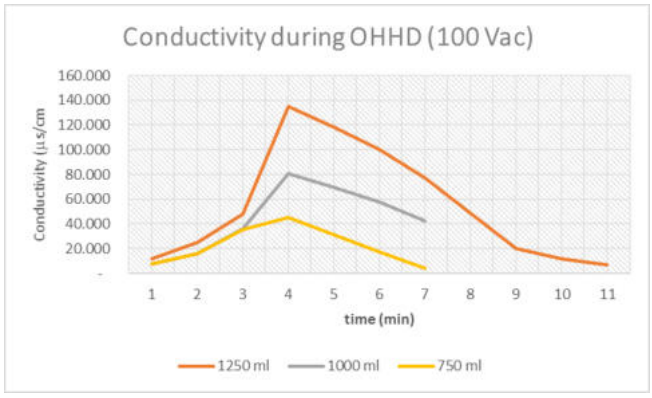


Fig. 10 - Conductivity during OHHD (Voltage 100 Vac)

The greater the volume of water used, the higher the water level in the treatment chamber. The higher the water level in the treatment chamber, the greater the surface area of the electrode. So, at the same voltage, the wider the electrode surface, the greater the electrical conductivity value. Electrical conductivity in the ohmic heating hydrodistillation process is influenced by the distance between electrodes, surface area, electric current, and electric voltage (*Zell et al., 2009*).

During the ohmic heating hydrodistillation process, energy is required from electricity. The electric current is converted into heat energy to boil the mixture of water and nutmeg leaves. In ohmic heating hydrodistillation, heating occurs due to the electric current in the mixture of water and nutmeg leaves. The heating rate is influenced by the amount of voltage and the volume of water used. In this study, 3 different voltage levels were used, i.e., 50 Vac, 75 Vac, and 100 Vac, and 3 levels of water volume that affect the duration of the heating process. Both factors will affect the amount of energy required during the ohmic heating hydrodistillation process. The amount of energy during ohmic heating hydrodistillation is as shown in Fig. 11 and Fig. 12.

The amount of hydrodistillation energy varies from each water volume treatment and voltage treatment. Figure 11 shows that the energy consumption pattern for a water volume of 1250 ml and a water volume of 1000 ml gives the same results. At the same water volume, the higher the voltage, the greater the energy required during the process.

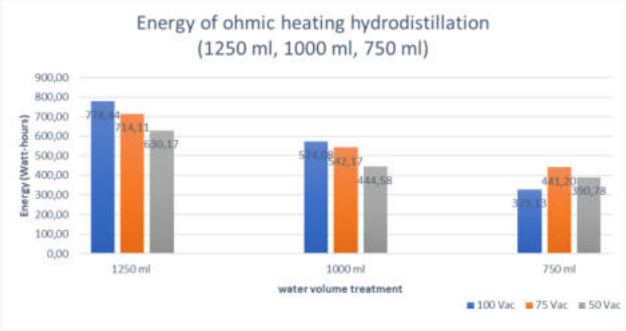


Fig. 11 – Energy of OHHD at 1250 ml, 1000 ml, and 750 ml

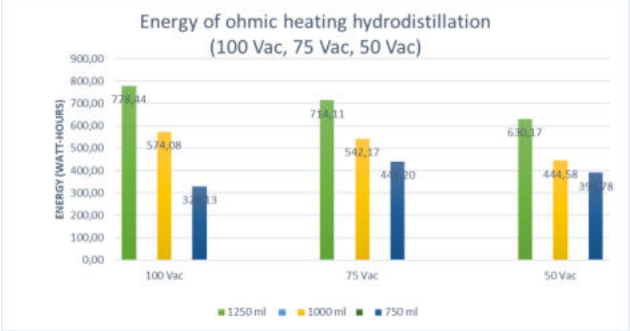


Fig. 12 – Energy of OHHD at 100 Vac, 75 Vac, and 50 Vac

A different pattern occurs in a water volume of 750 ml, i.e., at a voltage of 100 Vac, the energy produced during the process is smaller than the energy at a voltage of 75 Vac and 50 Vac. This is influenced by the duration of the hydrodistillation process. At a voltage of 100 Vac, the time required for the ohmic heating hydrodistillation process is only 50 minutes, while for voltages of 75 Vac and 50 Vac, it is greater, i.e., 100 minutes and 190 minutes. In the combination of 100 Vac voltage and 750 Vac water, the water evaporates faster so that the electric current stops because there is no water.

Ohmic heating hydrodistillation energy at the same voltage is shown in Fig. 12. Based on the figure, it can be seen that the energy required from each voltage has the same pattern. At a voltage of 100 Vac, the energy required for a water volume of 1250 ml is greater than for a water volume of 100 ml and a water volume of 750 ml. At voltages of 75 Vac and 50 Vac, the pattern is the same as at a voltage of 100 Vac. At the same voltage, energy consumption is influenced by the amount of water. The greater the volume of water, the greater the energy required to boil the mixture of water and nutmeg leaves.

Oil yield

The results of laboratory analysis indicated that the resulting oil had a refractive index of 1.4776 and an optical rotation of -4.834. The results of GC (gas chromatography) analysis indicated that nutmeg leaf oil had 25 compounds (Fig. 13). The content of nutmeg leaf oil includes main compounds such as Sabinene compounds (19.07%), α-pinene (18.04%), 4-terpineol (11.83%), limonene (8.32%), and β-pinene (7.92%) (*Asgarpanah & Kazemivash, 2012*). According to the measurement of mass spectrometry (MS), the myristicin concentration was 4.80% (SNI min 10%). SNI 06-2388-2006, pertaining to nutmeg oil derived from nutmeg seed distillation, serves as the standard reference for nutmeg oil. Since there is no SNI for nutmeg leaf oil used as a reference, some test results, like optical rotation and myristicin content, do not meet the SNI.

Oil yield is an extract of nutmeg leaves oil produced from the hydrodistillation process using ohmic heating. The resulting nutmeg leaves oil has a pale yellow color (Fig.14). The highest oil yield that could be extracted in this research was 1.07% when 50 Vac voltage and 750 ml of water or a nutmeg leaf to water ratio of 1:0.75 was combined, while the lowest yield of 0.38% was obtained when 75 Vac voltage and 1250 ml of water were combined (Fig. 15). The production of nutmeg leaf oil in ohmic heating hydrodistillation is influenced by the electric voltage and water volume. Ohmic heating not only produces a heating effect but also causes the cell walls of the leaves to permeate. The rate of diffusion through the cell wall, the extraction yield, and the reaction process can all be accelerated by increasing cell wall permeabilization (*Sofi'i & Arifin, 2022*).

Results of laboratory tests on the content of nutmeg leaf oil using the Soxhlet method chemical solvent gave a yield of 1.49%, while according to *BSN (2006)*, the oil content of nutmeg leaves is no more than 1.7%. If the hydrodistillation method using ohmic heating with a water solvent is compared to the Soxhlet method with an n-hexane solvent, it shows that the ohmic heating hydrodistillation method has an oil extraction efficiency of 1.07% divided by 1.49% or 71.8%.

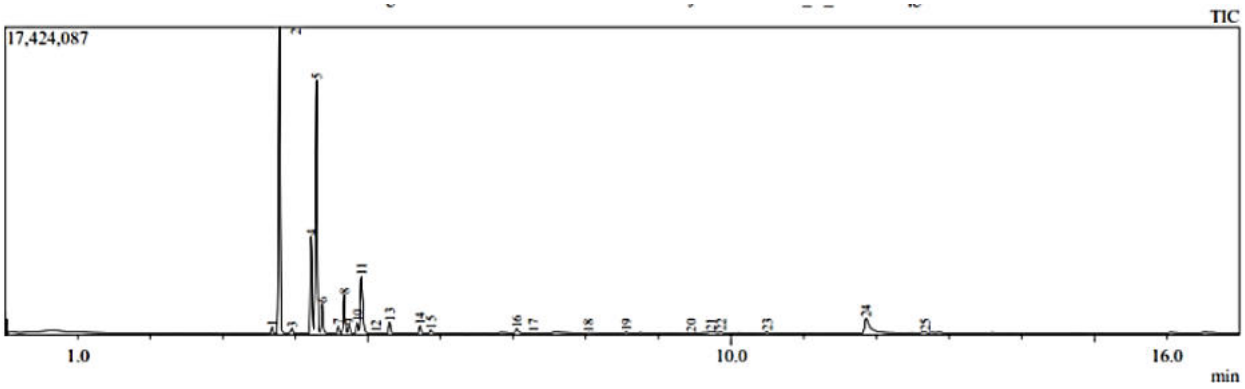


Fig. 13 – Chromatogram of nutmeg leaves oil



Fig. 14 – Nutmeg leaves oil

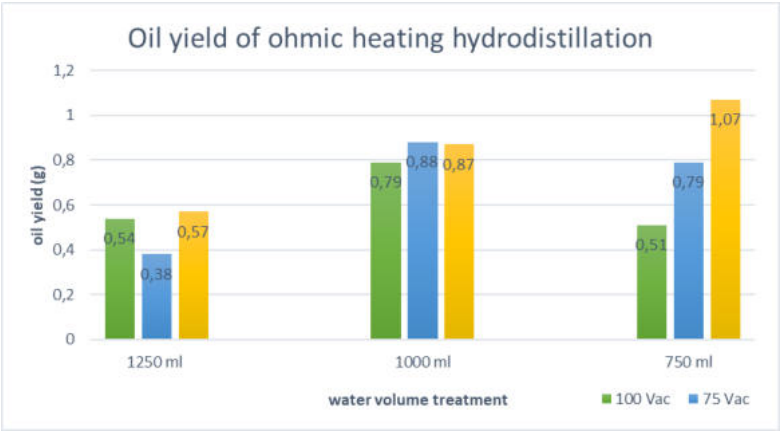


Fig. 15 - Nutmeg leaves oil yield

CONCLUSIONS

The higher the voltage, the faster the time to reach the boiling point of the liquid. The higher the volume of water, the lower the heating rate. The duration of the hydrodistillation process is influenced by the voltage and water used. The electrical conductivity value of the mixture of water and nutmeg leaves during the hydrodistillation process varies depending on the volume of water, voltage, electrode surface area, and temperature. At the same volume of water, the higher the voltage, the greater the energy required during the process. The greater the volume of water, the greater the energy required to boiling the mixture of water and nutmeg leaves. In ohmic heating hydrodistillation, the magnitude of the electric voltage and the volume of water used affect the yield of nutmeg leaf oil. The maximum oil yield that can be extracted is 1.07% at a combination of 50 Vac voltage and 750 ml of water, while the lowest yield is 0.38% at a combination of 75 Vac voltage and 1250 ml of water.

ACKNOWLEDGEMENT

The author would like to thank the Lampung State Polytechnic and the Ministry of Education, Culture, Research, and Technology, Directorate General of Vocational Education for financial assistance through the Research and Community Service Program Batch III in 2024.

REFERENCES

[1] Amatore, C., Berthou, M., & Hebert, S. (1998). Fundamental principles of electrochemical ohmic heating of solutions. *Journal of Electroanalytical Chemistry*, 457(1-2), 191-203.

[2] Asgarpanah, J., & Kazemivash, N. (2012). Phytochemistry and pharmacologic properties of Myristica fragrans Hoyutt.: A review. *African Journal of Biotechnology,* 11(65), 12787-12793.
[3] Assiry, A., Sastry, S. K., & Samaranayake, C. (2003). Degradation kinetics of ascorbic acid during ohmic heating with stainless steel electrodes. *Journal of Applied Electrochemistry*, 33, 187-196.
[4] Balai Komodity Industry, Deptan. (2009). Nutmeg Plant Cultivation. http://balitri.litbang.deptan.go.id/database/BUDIDAYA%20PALA.pdf.
[5] BSN (National Standardization Agency). (2006). SNI Numeg Oil (SNI 06-2388-2006). BSN Jakarta.
[6] Cabas, B.M. & Icier, F. (2021). Ohmic Heating–Assisted Extraction of Natural Color Matters from Red Beetroot. *Food Bioprocess Technol,* 14, 2062–2077. https://doi.org/10.1007/s11947-021-02698-9
[7] Damayanti, R dan Ervilita, R. (2017). The potential of nutmeg leaf essential oil as an antioxidant. National Seminar II USM 2017 Exploration of Aceh's Maritime Wealth in the Era of Globalization in Realizing Indonesia as the World's Maritime Axis. Vol. 1, Oktober 2017, 554-556.
[8] Ferreira-Santos, P., Nobre, C., Rodrigues, R. M., Genisheva, Z., Botelho, C., & Teixeira, J. A. (2024). Extraction of phenolic compounds from grape pomace using ohmic heating: Chemical composition, bioactivity and bioaccessibility. *Food Chemistry*, 436, 137780. https://doi.org/10.1016/j.foodchem.2023.137780.
[9] Gavahian, M., Sastry, S., Farhoosh, R., & Farahnaky, A. (2020). Ohmic heating as a promising technique for extraction of herbal essential oils: Understanding mechanisms, recent findings, and associated challenges. *Advances in food and nutrition research*, 91, 227-273. https://doi.org/10.1016/bs.afnr.2019.09.001
[10] Getchell, B.E. (1935). Electric pasteurization of milk. *Agric. Eng*, 16(10), pp.408-410.
[11] Gumustepe, L., Kurt, N., Aydın, E., & Ozkan, G. (2023). Comparison of ohmic heating-and microwave-assisted extraction techniques for avocado leaves valorization: Optimization and impact on the phenolic compounds and bioactivities. *Food Science & Nutrition*, 11(9), 5609-5620. https://doi.org/10.1002/fsn3.3556
[12] Kaur, N., & Singh, A. K. (2016). Ohmic Heating: Concept and Applications—A Review. Critical Reviews in *Food Science and Nutrition*, 56(14), 2338–2351. https://doi.org/10.1080/10408398.2013.835303
[13] Mukhtarom, A.D. (2024). Potensi Ekspor Minyak Atsiri Indonesia ke Luar Negeri. https://asiacommerce.id/blog/potensi-ekspor-minyak-atsiri/ diakses 1 Januari 2025.
[14] Palaniappan, S. and Sastry, S.K., (1991). Electrical conductivity of selected juices: influences of temperature, solids content, applied voltage, and particle size 1. *Journal of Food Process Engineering*, 14(4), pp.247-260.
[15] Pereira, R. N., Rodrigues, R. M., Genisheva, Z., Oliveira, H., de Freitas, V., Teixeira, J. A., & Vicente, A. A. (2016). Effects of ohmic heating on extraction of food-grade phytochemicals from colored potato. *Lwt*, 74, 493-503. https://doi.org/10.1016/j.lwt.2016.07.074.
[16] Safarzadeh Markhali, F., Teixeira, J. A., & Rocha, C. M. (2022). Effect of ohmic heating on the extraction yield, polyphenol content and antioxidant activity of olive mill leaves. *Clean Technologies*, 4(2), 512-528.
[17] Sánchez, M., Ferreira-Santos, P., Gomes-Dias, J. S., Botelho, C., Laca, A., & Rocha, C. M. (2023). Ohmic heating-based extraction of biocompounds from cocoa bean shell. *Food Bioscience*, 54, 102886. https://doi.org/10.1016/j.fbio.2023.102886
[18] Sain, M., Minz, P. S., John, H., & Singh, A. (2024). Effect of Ohmic Heating on Food Products: An In-Depth Review Approach Associated with Quality Attributes. *Journal of Food Processing and Preservation*, 2024(1), 2025937. https://doi.org/10.1155/2024/2025937
[19] Salengke, S., & Sastry, S. K. (2007). Experimental investigation of ohmic heating of solid–liquid mixtures under worst-case heating scenarios. *Journal of Food Engineering*, 83(3), 324-336.
[20] Samaranayake, C.P. and Sastry, S.K. (2005). Electrode and pH effects on electrochemical reactions during ohmic heating. *Journal of Electroanalytical Chemistry*, 577(1), pp.125-135.
[21] Sofi'i, I., & Arifin, Z. (2022). Energy consumption for patchouli oil extraction using ohmic heating. In IOP Conference Series: Earth and Environmental Science (Vol. 1012, No. 1, p. 012062). *IOP Publishing*.
[22] Stirling, R. (1987). Ohmic heating-a new process for the food industry. *Power Engineering Journal*, 1(6), 365-371.
[23] Talha, M., Khalid, S., Maan, A. A., Tanveer, N., Khan, M. K. I., Asif, M., Sarwar, A. (2024). Ohmic assisted extraction: a sustainable and environment friendly approach to substitute conventional extraction methods. *Food Reviews International,* 40(10), 3508–3529. https://doi.org/10.1080/87559129.2024.2366841

[24] Tzedakis, T., Basseguy, R. and Comtat, M. (1999). Voltammetric and coulometric techniques to estimate the electrochemical reaction rate during ohmic sterilization. *Journal of Applied Electrochemistry*, 29, pp.819-826.
[25] Uemura, K., Noguchi, A., Park, S.J. And Kim, D.U. (1994). Ohmic heating of food materials; effects of frequency on the heating rate of fish protein. Development in Food Engineering. In *Proceedings of the Sixth International Congress on Engineering and Food*. (Chiba, Japan), (R. Matsuno and K. Nakamura, eds.) pp. 310–312, Blackie Academic and Professional Press. London.
[26] Zell, M., Lyng, J. G., Morgan, D. J., & Cronin, D. A. (2009). Development of rapid response thermocouple probes for use in a batch ohmic heating system. *Journal of food engineering*, 93(3), 344-347.

OPTIMIZATION DESIGN AND TEST OF INTERACTIVE ANTI-STICK GEAR FERTILIZER DISCHARGER FOR PINEAPPLE
/
菠萝专用交互式防粘齿轮排肥器的优化与试验

Guoqiang DUN*[1)], Chunyu MA[2)], Xinxin JI[2)], Hailiang LI*[3)], Haochun CHENG[2)], Haitian SUN[3)], Chaoxia ZHANG[2)]

[1)] Harbin Cambridge University, Intelligent Agricultural Machinery Equipment Engineering Laboratory, Harbin / China;
[2)] Northeast Forestry University, College of Mechanical and Electrical Engineering, Harbin / China;
[3)] South Subtropical Crop Research Institute, Chinese Academy of Tropical Agricultural Sciences, Key Laboratory of Tropical Fruit Biology, Ministry of Agriculture & Rural Affairs, Key Laboratory of Hainan Province for Postharvest Physiology and Technology of Tropical Horticultural Products, Zhanjiang / China;
Tel: +86 13836027042; E-mail: dunguoqiangpaper@163.com; lihailiang@126.com
DOI: https://doi.org/10.35633/inmateh-76-39

Keywords: *Gear fertilizer; EDEM simulation; Fertilization uniformity; Response surface test; Precision fertilization*

ABSTRACT
Based on the agronomic characteristics of pineapple fertilization and the challenges posed by moist fertilizer particle adhesion, an interactive gear fertilizer discharger was developed. This device utilizes a pair of continuously meshing, counter-rotating gears to achieve centralized and interactive mixing of fertilizer. Through theoretical analysis, the fertilizer discharge volume and maximum operating speed of the discharger were determined. In the experimental design, the pressure angle and helix angle of the fertilizer wheel were selected as test factors, while the coefficient of fluctuation in fertilizer uniformity served as the test index. A single-factor test was conducted to analyze the influence of each factor on the index and to determine the appropriate range of values. Subsequently, a quadratic general rotary combination design was used to optimize the fertilizer wheel parameters. The results indicated that both the pressure angle and helix angle had a significant effect on the coefficient of fluctuation of fertilizer uniformity (P<0.01). The lowest fluctuation coefficient, 11.82%, was achieved when both angles were set to 30°. A simulation verification test yielded a result of 11.92%, with a relative error of 0.85% compared to the theoretical value. Bench tests conducted under optimal parameters showed a relative error of 2.77% between the experimental and simulated values. Furthermore, the average error between the measured fertilizer discharge flow rate and the theoretical value under varying speeds was 3.75%. No fertilizer adhesion was observed on the surface of the discharge wheel, demonstrating that the system enables fine regulation of fertilizer output while effectively mitigating fertilizer adhesion.

摘要
根据菠萝施肥的农艺特性以及潮湿肥料颗粒粘连问题，设计了一种交互式防粘齿轮排肥器，其采用一对持续啮合反向挤压旋转的齿轮实现肥料的对中交互混排。通过理论分析确定交互式齿轮排肥器的理论排肥量与最大转速，利用 EDEM 软件对排肥过程进行仿真模拟。以排肥轮的压力角和螺旋角为试验因素，以排肥均匀性波动系数为试验指标，通过单因素试验分析试验因素对试验指标的影响，并确定试验因素的范围。通过二次通用旋转组合设计试验优化出排肥轮的最优参数。试验结果表明：排肥轮压力角和螺旋角对排肥均匀性变异系数均有极显著影响（P＜0.01），当排肥轮压力角和螺旋角均为 30°时，排肥均匀性变异系数最小为 11.82%。仿真验证试验结果为 11.92%，相对误差为 0.85%，最优参数下台架试验结果表明：试验值与仿真值的相对误差为 2.77%，排肥流量可通过排肥轮转速线性调节。其结果表明：在排肥转速流量曲线下排肥流量与理论值平均误差为 3.75%，排肥轮表面并无粘结肥料，实现对排肥量的精量调控且有效降低其肥料对排肥轮的粘连作用。

INTRODUCTION
The proper use of fertilizers plays a crucial role in the growth of pineapples in terms of fruit quality and yield. Unreasonable fertilization methods will not only damage crops and reduce their production but also cause some problems, such as the waste of resources, environmental pollution, and land degradation. Studies have shown that compared with unreasonable fertilization methods, precision fertilization can better alleviate the above problems under the premise of meeting the needs of crop growth, which is of great significance for the sustainable development of agriculture *(Chen et al., 2015; Li et al., 2008; Du et al., 2020)*.

At present, the widely used fertilizer discharger in the market is the external grooved wheel type fertilizer discharger, which has high requirements for the physical properties of fertilizers. Still, the effect is good when discharging and applying dry granular fertilizers, and poor when discharging and applying moist granular fertilizers and powdered fertilizers *(Lv et al., 2013; Liu et al., 2021)*. Mechanical fertilizer application can effectively reduce the labor intensity of fruit farmers, improve the efficiency and quality of fertilizer application, and reduce the cost of agricultural production.

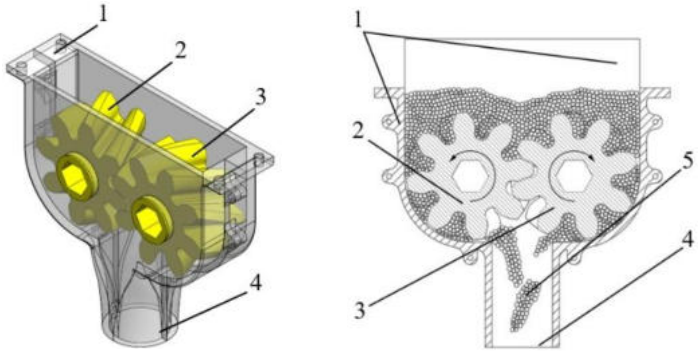
The fertilizer discharger is the key component of the fertilization device, and its performance will directly affect the fertilization effect. If the uniformity of the fertilizer discharger is very low, it will not only reduce the fertilizer utilization rate, and affect the quality and yield of crops, but also make it difficult to achieve precision fertilization *(Tai et al., 2020; Su et al., 2015)*. Relevant experts and scholars have done a lot of research on improving the uniformity of fertilizer discharge and realizing precision fertilization. *Wang et al., (2017),* analyzed the effects of the working length of the outer groove wheel, the rotational speed of the fertilizer shaft, and the opening angle of the fertilizer tongue on the amount of fertilizer and the uniformity of fertilizer discharge. *Dun et al., (2018),* analyzed the influence of the structural parameters of the fertilizer tongue of the outer groove wheel fertilizer discharger on the uniformity of fertilizer discharge by discrete element method. *Zhu et al., (2018),* analyzed the influence of the groove wheel radius, the number of grooves, the effective working length and the shape of the groove section on the uniformity of fertilizer discharge. *Yao et al., (2020),* realized precision fertilization by adjusting the motor speed to control the amount of fertilizer. *Zuo et al., (2016),* developed a precise fertilizer control system, which can adjust the amount of fertilizer in real time according to the operation speed of the machine. *Yu et al., (2020),* designed a double-gear type fertilizer discharger, whose tooth ridge and tooth groove continuously alternating operation even fertilizer effect has been significantly improved, but its uniformity still has room for improvement. The research of experts and scholars in discrete element simulation and precision fertilization has played an important supporting role in this study.

In this study, an interactive gear fertilizer distributor was designed based on the principle of fertilizer alignment and interactive mixing. Through theoretical analysis, the theoretical fertilizer discharge amount and maximum speed of the fertilizer discharger are determined, and the fertilizer discharge process is simulated by discrete element simulation technology. The test range was determined by single factor test, and the influence of different factors on the coefficient of variation of fertilizer uniformity was analyzed by quadratic general rotary combination design test, and the structural parameters of the interactive gear fertilizer distributor were optimized when the coefficient of variation of fertilizer uniformity was the lowest. The interactive gear fertilizer distributor prototype with optimal parameters was made by 3D printing technology. The simulation value and theoretical value were verified by bench test, and the relationship between fertilizer discharge flow and fertilizer discharge wheel speed was analyzed by controlling the rotational speed of fertilizer discharge wheel through motor controller. Based on the speed-flow relationship curve of the fertilizer wheel, an electronically controlled fertilizer discharge controller was developed and its working performance was tested in order to improve the uniformity of fertilizer discharge and achieve precise control of fertilizer discharge.

MATERIALS AND METHODS

The Structure and Working Principle of The Whole Machine

The three-dimensional model and sectional working diagram of the interactive gear fertilizer discharger are shown in Fig.1. The device consists of a left-handed fertilizer discharge gear, a right-handed fertilizer discharge gear, a fertilizer discharge box, and a fertilizer outlet.



a) *b)*

Fig. 1 - Interactive gear fertilizer apparatus schematic diagram

a) Three-dimensional model diagram; b) The schematic diagram of section work

1. Fertilizer box; 2. Left-handed fertilizer gear; 3. Right-handed fertilizer gear; 4. Outlet; 5. Fertilize

When working, the drive motor drives the left-handed fertilizer gear to rotate counterclockwise. The right-handed fertilizer gear rotates clockwise through the gear meshing, and the rotation of the fertilizer gear drives the fertilizer movement. The fertilizer is confined in the fertilizer space formed by the tooth grooves and the fertilizer box. It moves downward along the contour of the fertilizer box until the tooth grooves rotate to the top of the fertilizer outlet. The fertilizer is discharged alternately to fall into the fertilizer outlet by gravity, which ensures the continuity of fertilizer discharge and realizes the uniformity of fertilizer discharge.

Fig. 2 illustrates the anti-sticking mechanism during the fertilizer discharge process. Moisture in the fertilizer can cause particles to stick to the gear surface. As the gears rotate and mesh in the interaction zone, the clinging material is subjected to rolling and squeezing forces between adjacent teeth. This mechanical contact helps dislodge the adhered fertilizer, causing it to fall into the discharge area. The use of diagonally arranged gear teeth increases the meshing duration and overlap, improving the cleaning effect and enhancing anti-adhesion performance.

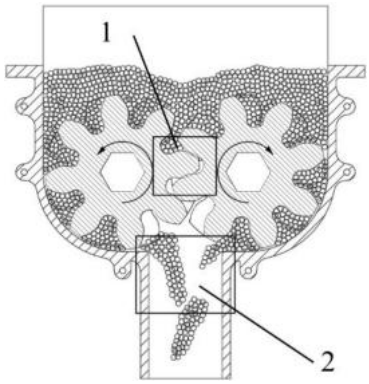


Fig. 2 - Interactive gear fertilizer apparatus schematic diagram

1. Interaction zone; 2. Fertilizer discharge zone.

Theoretical Fertilizer Discharge and Maximum Speed

The interactive gear fertilizer discharger alternately discharges fertilizer through continuous meshing and reverse rotation of a pair of gears. The volume of a single discharge fertilizer is determined by the size of the fertilizer space formed by the tooth groove and the fertilizer discharge box. Therefore, calculating the volume of the tooth groove of the fertilizer discharge gear is of great significance for studying the theoretical fertilizer discharge and maximum speed of the fertilizer discharger. The fertilizer discharge gear model is shown in Fig. 3.

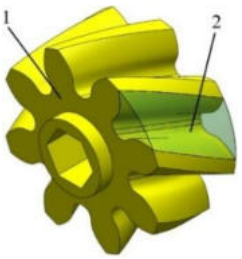


Fig. 3 - Fertilization gear model

1.Fertilizer gear; 2. Fertilizer space.

According to the existing research *(Hu et al., 2016)*, the area of a single tooth groove of the fertilizer gear is calculated using the following equations:

$$s_c = \frac{s_a - s}{z} \tag{1}$$

$$s_a = \frac{\pi d_a^2}{4} \tag{2}$$

$$da = mz + 2h_a^* m \tag{3}$$

$$s = \frac{\pi d^2}{4} \tag{4}$$

$$d = mz \tag{5}$$

where: s_c is the area of the single tooth groove of the fertilizer gear, [mm^2]; s_a is the top circle area of fertilizer gear, [mm^2]; s is the pitch circle area of the fertilizer gear, [mm^2]; d_a is the top circle diameter of fertilizer gear, [mm]; d is the pitch circle diameter of the fertilizer gear, [mm]; h_a* is the top height coefficient of fertilizer gear; z is the number of teeth; m is the modulus, [mm].

The total mass of the fertilizer discharged by the fertilizer discharger is calculated as follows:

$$M = \rho\gamma V \tag{6}$$

where:

$$V = \frac{s_c bntz \times 10^{-4}}{3} \tag{7}$$

where: M is total mass of discharged fertilizer, [g]; P is the bulk density of fertilizer, [g/cm^3]; γ is fertilizer filling coefficient; V is total volume of discharged fertilizer, [cm^3]; b is tooth width of fertilizer gear, [mm]; n is the rotational speed of the fertilizer gear, [r/min]; t is the operating time of the fertilizer discharger.

According to the combined formula (5) ~ (7), the total mass of the fertilizer discharged by the fertilizer discharger is:

$$M = \frac{\rho\gamma bnt\pi\left[m^2\left(z+2h_a^*\right)^2-\left(mz\right)^2\right]\times 10^{-4}}{12} \tag{8}$$

The fertilizer gear is a standard cylindrical gear. The tooth width is set to 30 mm, the number of teeth is 8, the modulus is 6 mm, the addendum height coefficient is 1, the fertilizer bulk density is 0.9 g/cm^3, and the filling coefficient is 0.7. The maximum moving speed of the fertilizer applicator is 7 km/h. Based on the design of the crop ridge spacing of 65 cm, it can be calculated that in order to meet the fertilization requirements of 750 kg/hm^2, the maximum theoretical speed required for the fertilizer distributor is 147.484 r/min *(Dun et al., 2019; Liang et al., 2023; Sun et al., 2019)*.

Discrete Element Simulation Test

Establish Fertilizer Particle Model

The water content of urea particles on the market is usually less than 0.5%, the surface adhesion is small, more than 0.5% will significantly increase the inter-particle hydrogen bonding, so that the adhesion increases, and most of them are spherical. Therefore, urea is selected as the test material for discrete element simulation *(Wen et al., 2020; Yuan et al., 2018; Michele et al., 2015)*. 80 urea particles produced by Anhui Red Sifang Fertilizer Co. Ltd. were randomly selected to measure the triaxial length and mass. The average radius of urea particles was 1.11 mm and the density was 1158 kg/m^3. Therefore, the spherical particles with a particle radius of 1.11 mm are selected as the particle model of discrete element simulation.

Setting Simulation Parameters

Hertz-Mindlin (no slip) in EDEM software was selected as the contact model between fertilizer and fertilizer, fertilizer and fertilizer wheel, shell *(Marcinkiewicz et al., 2019)*, and the parameters were set as shown in Table 1 by consulting literature *(Dun et al., 2020)*.

Table 1

Discrete element simulation parameters

Item	Particle Property	Numerical Value
Fertilizers	Poisson's Ratio	0.25
	Shear modulus/Pa	2.8×10^7
	Density/kg·m^{-3}	1158
Fertilizers unit	Poisson's Ratio	0.43
	Shear modulus/Pa	1.3×10^7
	Density/kg·m^{-3}	1240
Fertilizers - Fertilizers	Restitution coefficient	0.11
	Static friction coefficient	0.30
	Rolling friction coefficient	0.10
Fertilizers - Fertilizers wheel shell	Restitution coefficient	0.41
	Static friction coefficient	0.32
	Rolling friction coefficient	0.18

Discrete Element Model of Fertilizer Distributor

SolidWorks 2020 is used to design the structure of the interactive gear fertilizer discharger and establish the three-dimensional model. The specific steps are as follows: The Maidi three-dimensional design tool set is used to generate the fertilizer wheel model with different pressure angles and helix angles, and the model of the fertilizer discharger is completed according to the fertilizer wheel model. Simplify the fertilizer model, save it as a .stl file, and import it into the discrete element simulation software EDEM, and set the fertilizer and model parameters according to Table 1.

Independent particle factories were created above the two rows of fertilizer wheels, separated by a diaphragm in the middle, and the same fertilizer parameters were used to generate particles. The total number of particles generated in both factories was 10,000, and the generation rate was 10,000/s. Then, a fertilizer collection plate will be set up below the fertilizer discharger. To facilitate the observation of the interaction of fertilizer particles and their distribution on the fertilizer collection plate, the rotational speed of the fertilizer wheel was set to 60 r/min, and the movement speed of the fertilizer collection plate was 1 m/s. The simulation step size was 4.89×10^{-6} s, the data recording time interval was 0.01 s, and the total simulation time was 2.6 s. The simulation process is shown in Fig. 4.

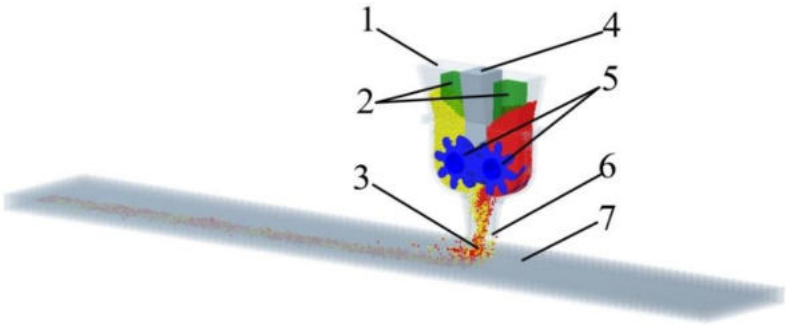


Fig. 4 - Simulation process

1. Fertilizer discharge zone; 2. Particle factory; 3. Fertilizer; 4. Diaphragm; 5. Fertilizer wheel; 6. Fertilizer outlet; 7. Fertilizer collection plate.

Evaluation of Fertilizer Performance

The timing diagram is used to show the process of fertilizer discharge in order to observe the mixing process of fertilizer particles, as shown in Fig. 4. The fertilizer quality monitoring area was established, and the quality data of yellow particles, red particles and total particles in the monitoring area were collected and the particle quality change curve was made by Origin software. The change process of two kinds of fertilizer particles and total particle quality can be seen more intuitively, as shown in Fig. 5.

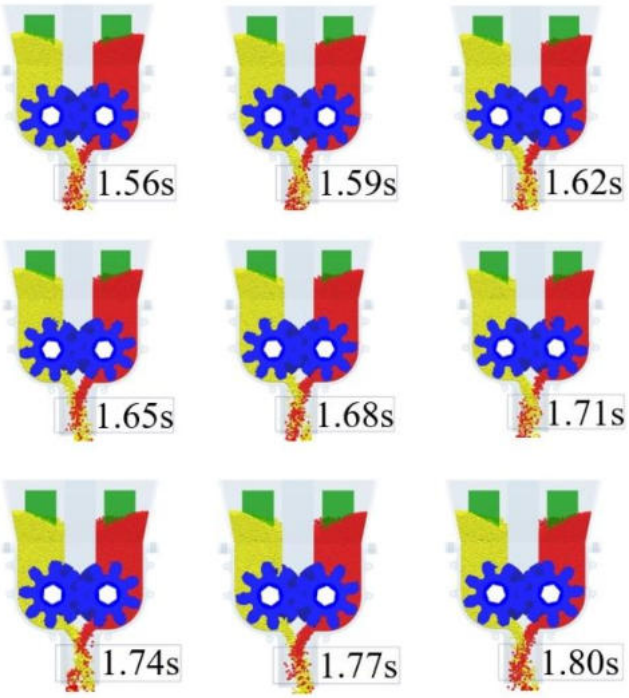


Fig. 5 - Time sequence diagram of fertilizer discharge process

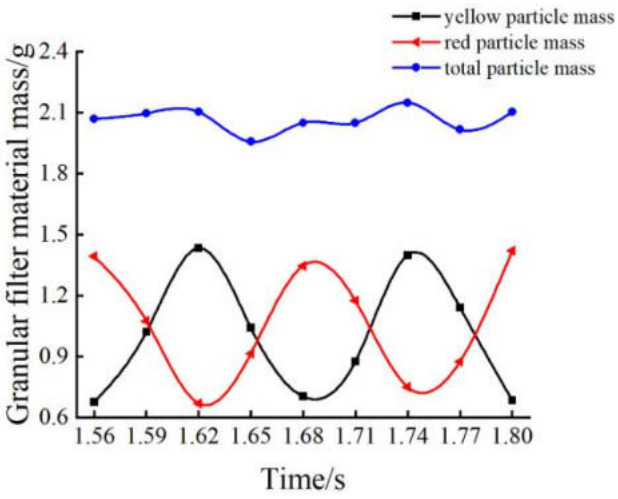


Fig. 6 - Particle mass change diagram

It can be seen from Fig. 5 and Fig. 6 that yellow particles and red particles are alternately discharged and mixed with each other under the action of the fertilizer wheel. The mass of yellow particles and red particles fluctuates with time. When the mass of yellow particles is the most, the mass of red particles is the least. When the mass of yellow particles increases, the mass of red particles decreases, and vice versa. This way of fertilizer discharge can ensure the uninterrupted discharge of fertilizer and ensure the uniformity of fertilizer discharge.

In order to accurately evaluate the uniformity of the interactive gear fertilizer distributor, the grid method was used to count the fertilizer quality on the fertilizer collection plate *(Yang et al., 2020)*, as shown in Fig.7.

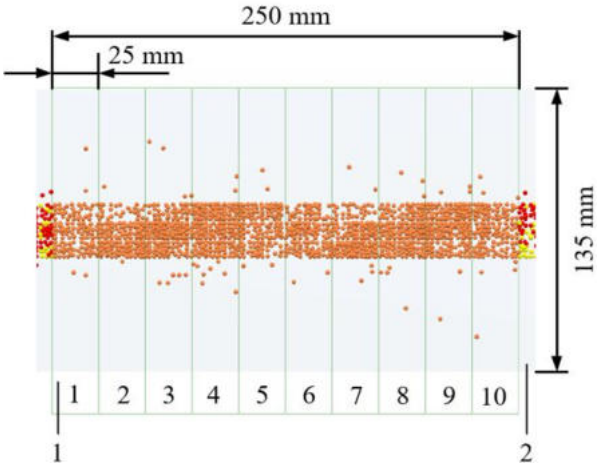


Fig. 7 - Grid division diagram

1. Uniformity test area; 2. Fertilizer collection plate.

The fertilizer is alternately discharged by the left-handed fertilizer gear and the right-handed fertilizer gear, and presents a periodic distribution on the fertilizer collection plate. According to the rotational speed of the fertilizer wheel and the moving speed of the fertilizer collection plate, the moving distance of the fertilizer collection plate is 125 mm for each cycle of fertilizer discharge. Therefore, the length of the monitoring area is set to 250 mm, and the monitoring area is divided into 10 parts by grid and numbered from 1 to 10, and the fertilizer quality in each grid is counted respectively. The smaller the coefficient of variation of the uniformity of the fertilizer is, the better the uniformity of the fertilizer is. Therefore, the coefficient of variation of the uniformity of the fertilizer is used as the evaluation index of the fertilizer performance of the fertilizer discharger. The average value, standard deviation and coefficient of variation of fertilizer quality in the monitoring area were calculated by formulas (9) ~ (11).

$$\overline{m} = \frac{\sum_{i=1}^{10} m_i}{n} (i = 1,2,\ldots,10) \tag{9}$$

$$s = \sqrt{\frac{\sum^{10}(m_i - \overline{m})^2}{n-1}} (i = 1,2,\ldots,10) \quad (10)$$

$$\sigma = \frac{s}{m} \times 100\% \quad (11)$$

where: $\overline{m}$ is Average quality of fertilizers in the monitoring area, [g]; m_i is the total mass of fertilizer in the i grid, [g]; n is the number of grids, n = 10; s is the standard deviation of fertilizer quality in monitoring area, [g]; σ is Coefficient of variation of fertilizer uniformity in monitoring area.

Relationship Between Pressure Angle of Fertilizer Discharge Wheel and Uniformity of Fertilizer Discharge

The size of the pressure angle of the fertilizer discharge wheel will affect the size and shape of the fertilizer space *(Liu et al., 2020)*, which in turn will affect the time interval between two adjacent slots discharging fertilizer, the falling speed of fertilizer and other factors during the fertilizer discharge process.

According to the design principle of the involute gear, the pressure angle of the fertilizer discharge wheel is selected as 5°, 10°, 15°, 20°, 25°, 30° *(Chen et al., 2008; Song et al., 2016)*. During the single-factor comparative test of the pressure angle of the fertilizer discharge wheel and the uniformity of fertilizer discharge, the helix angle of the fertilizer discharge wheel was uniformly 0°. The variation coefficient of fertilizer discharge uniformity of fertilizer discharge wheels with different pressure angles is shown in Fig. 8 below.

The variation coefficient of fertilizer discharge uniformity decreases with the increase of pressure angle of fertilizer discharge wheels. When the pressure angle of the fertilizer discharge wheel is 30°, the coefficient of variation of the uniformity of fertilizer discharge is the smallest, indicating that when the pressure angle of the fertilizer discharge wheel is 30°, the distribution of fertilizer on the collecting plate is the most uniform, and the fertilizer discharge performance is the best.

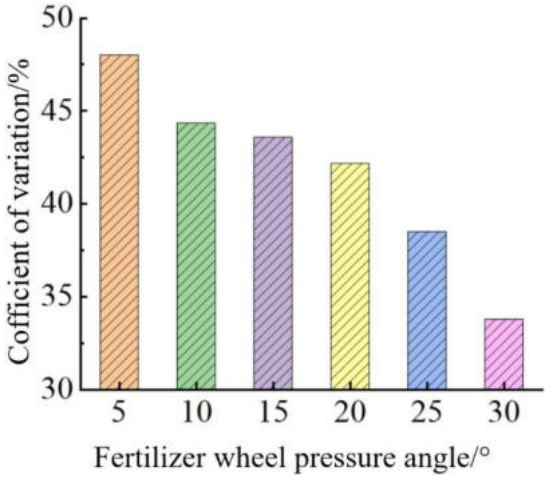


Fig. 8 - The relationship between the pressure angle of fertilizer wheel and the coefficient of variation of fertilizer uniformity

The Relationship Between the Helix Angle of The Fertilizer Discharge Wheel and The Uniformity of Fertilizer Discharge

The size of the helix angle will also affect the size and shape of the fertilizer space. Compared with the spur gear, the helical gear with the same tooth groove has a longer longitudinal length during the falling process, and the fertilizer is more evenly distributed on the collecting plate. When two adjacent tooth slots of the helical fertilizer discharge gear overlap in the axial direction, the fertilizer in the previous slot may not be fully discharged before the next slot begins releasing fertilizer. This overlapping discharge process ensures a continuous and uninterrupted flow, thereby improving the uniformity and effectiveness of fertilizer application.

According to the design principles of helical gears, the helix angle of the fertilizer discharge wheel was selected as 0°, 5°, 10°, 15°, 20°, 25°, and 30°. In the single-factor comparative experiment evaluating the effect of helix angle on the uniformity of fertilizer discharge, the pressure angle was fixed at 20°. The coefficient of variation in fertilizer discharge uniformity for wheels with different helix angles is presented in Figure 9.

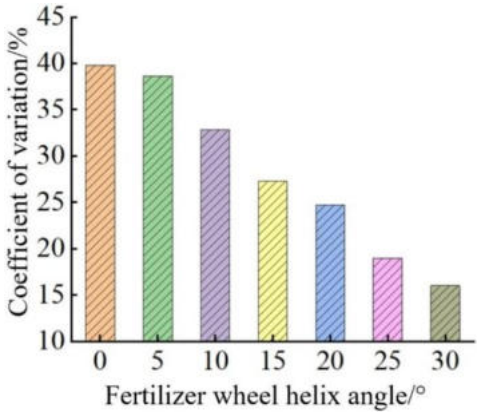


Fig. 9 - Relationship between the helix angle of the fertilizer discharge wheel and the coefficient of variation of fertilizer discharge uniformity

The coefficient of variation in fertilizer discharge uniformity decreased with increasing helix angle of the fertilizer discharge wheels. When the helix angle reached 30°, the variation coefficient was at its lowest, indicating the most uniform distribution of fertilizer on the collecting plate. This suggests that a 30° helix angle provides the optimal discharge performance and the highest uniformity in fertilizer application.

RESULTS

RESPONSE SURFACE EXPERIMENT

Test Design

Based on the results of the single-factor experiments, it was observed that the coefficient of variation in fertilizer discharge uniformity decreases with increasing pressure angle and helix angle of the fertilizer discharge wheel. By analyzing the effects of different pressure angles and helix angles of the fertilizer discharge wheel on the fertilizer distribution performance of interactive anti-adhesion gears, the structural parameters of the fertilizer discharge wheel are optimized. A secondary general rotational combination test method was selected to analyze the effects of the pressure angle and helix angle of the fertilizer discharge wheel on fertilizer uniformity. The coefficient of variation of fertilizer uniformity was used as the evaluation criterion. Based on the results of single-factor simulation tests, the pressure angle range of the fertilizer discharge wheel was selected as 5° ~ 30°, and the helix angle range was selected as 0° ~ 30°. The coded levels of the experimental factors are shown in Table 2, where X_1 and X_2 are the factor code values for the pressure angle and helix angle, respectively.

Table 2

Test factor coding table

Coding	Test Factor	
	Fertilizer Wheel Pressure Angle X_1 / [°]	Fertilizer Wheel Helix Angle X_2 / [°]
1.414	30.00	30.00
1	26.34	25.61
0	17.50	15.00
-1	8.66	4.39
-1.414	5.00	0.00

Test Results and Analysis of Variance

Taking the pressure angle X_1 and the helix angle X_2 of the fertilizer discharge wheel were selected as test factors, and the coefficient of variation σ of the fertilizer discharge uniformity was used as the evaluation index. Using Design-Expert software a regression analysis was conducted on the experimental data to determine the relationship between discharge uniformity and the two factors. In addition, an analysis of variance (ANOVA) was performed to assess the statistical significance of the regression model (*Dun et al., 2024*). The test scheme and corresponding results are presented in Table 3, while the ANOVA results are shown in Table 4.

Table 3

Test scheme and results table

Serial number	Test Factor		σ [%]
	Pressure Angle X_1 / [°]	Helix Angle X_2 / [°]	
1	17.50	0.00	41.47
2	8.66	4.39	41.74
3	17.50	15.00	27.75
4	30.00	15.00	25.17
5	17.50	15.00	31.13
6	17.50	30.00	13.40
7	17.50	15.00	28.41
8	17.50	15.00	30.72
9	5.00	15.00	32.61
10	8.66	25.61	19.65
11	17.50	15.00	27.40
12	26.34	4.39	35.46
13	26.34	25.61	17.08

Table 4

Significance analysis of test parameters

Source	Sum of squares	Degree of freedom	Mean square	F number	P value
Model	857.58	5	171.52	95.58	0.0001**
X_1	46.91	1	46.91	26.14	0.0014*
X_2	803.34	1	803.34	447.68	0.0001**
X_1X_2	3.44	1	3.44	1.92	0.2087
X_1^2	1.781×10^{-3}	1	1.781×10^{-3}	9.924×10^{-4}	0.9757
X_2^2	3.85	1	3.85	2.14	0.1866
Residual	12.56	7	1.79		
Lack of fit	0.63	3	0.21	0.070	0.9728
Pure error	11.93	4	2.98		
Sum	870.15	12			

*Note: ** indicates highly significant effect (p<0.01), * indicates significant effect (0.01<p<0.05).*

From the analysis of variance in Table 4, it can be seen that the significance test of the model is F=95.58, P<0.0001, and the coefficient of determination R^2=0.9856. This indicates that the regression model is extremely significant, and the test result of the lack of fit item is not significant (P>0.05). This also indicates that the regression model fit well within the experimental range. At the same time, X_1 and X_2 have a very significant effect on the variation coefficient of fertilizer uniformity (P<0.01), and the remaining items have no significant effect (P>0.05). Remove the coefficients of insignificant factors from the regression equation. The finally regression equation of the fertilizer uniformity coefficient model is:

$$\sigma = 49.1 - 0.42X_1 - 0.92X_2 \quad (12)$$

Influence of Experimental Factors on Indicators

The influence of the pressure angle and helix angle of the fertilizer discharge wheel on the uniformity of fertilizer discharge is shown in Fig. 10. It can be seen from the response surface plot in Figure 9 that when the helix angle is 0° and 30°, the coefficient of variation decreases with the increase of the pressure angle, and when the helix angle is 30°, the coefficient of variation is generally lower. When the pressure angle is 5° and 30°, the coefficient of variation decreases with the increase of the helix angle, and when the pressure angle is 30°, the coefficient of variation is generally lower. At the same time, it can be seen that the variation trend of the coefficient of variation with the change of pressure angle is relatively gentle, this is because the influence of pressure angle on the coefficient of variation is smaller than that of the helix angle. Overall, the trend of change is consistent with the results of the single-factor test and analysis of variance. After optimization, it can be obtained that the pressure angle and helix angle of the fertilizer discharge wheel corresponding to the minimum coefficient of variation are both 30°, and the minimum coefficient of variation is 11.82%.

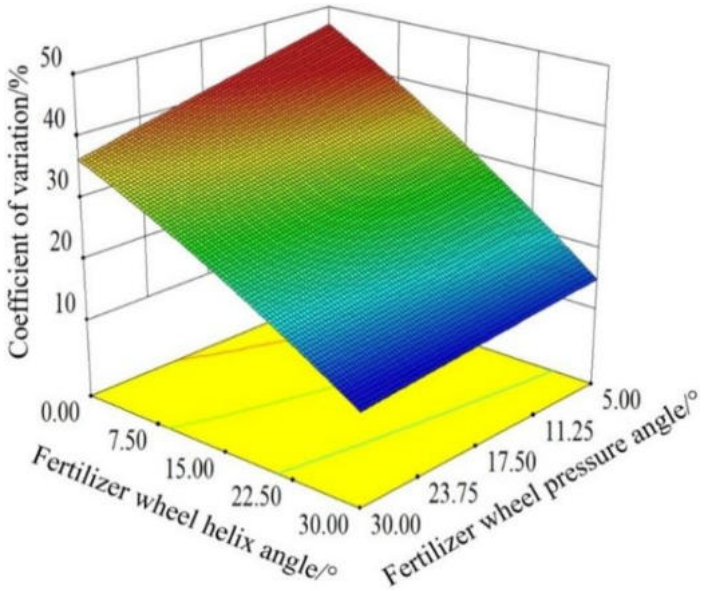


Fig. 10 - Response Surface Plot

In the discrete element simulation software EDEM, a discrete element simulation test was carried out on the model of the optimized interactive gear fertilizer discharger. The test measured that the coefficient of variation of the fertilizer uniformity of the optimized interactive gear fertilizer discharger was 11.92%, The relative error with the theoretical value is 0.85%, which proves the accuracy and validity of the theoretical value.

Bench Experiment and Results

In order to verify the correctness of the simulated value and the theoretical value, the uniformity of the fertilizer discharge of the interactive gear fertilizer was tested through a bench test, and the relationship between the speed of the fertilizer discharge wheel and the flow rate was analyzed by controlling the speed of the fertilizer discharge wheel. D printing technology was used to make an interactive gear fertilizer prototype with optimal parameters, and urea produced by China Salt Anhui Hongsifang Fertilizer Co. Ltd. was selected as the test material.

Verification Test

The width of each fertilizer collection box used in the bench test was 20 mm. To facilitate the calculation of the coefficient of variation for fertilizer discharge uniformity, the monitoring area was divided using 10 fertilizer collection boxes. The conveyor belt speed was set to 0.5 m/s, and the rotational speed of the fertilizer discharge wheel was set to 60 r/min. The test was repeated three times, and the average value was taken as the final result, as shown in Figure 11. The test results showed that the coefficient of variation for fertilizer discharge uniformity of the interactive gear fertilizer discharger was 12.25%, with a relative error of 2.77% compared to the simulation value. The discrepancy is attributed to the fact that the urea particles used in the test were not perfect spheres. However, since the relative error was less than 5%, it is considered within an acceptable range, thus validating the accuracy of the simulation model.

Fertilizer Discharge Flow Rate Test

According to the theoretical calculation of the limit speed of the fertilizer discharge wheel, the rotational speed was set to 30 r/min, 60 r/min, 90 r/min, 120 r/min, and 150 r/min, and five groups of experiments were conducted. During testing, the conveyor belt was turned on and maintained at a constant speed of 0.5 m/s. The motor controller was used to adjust the fertilizer discharge wheel to each specified speed. Once the system reached stable operation at each speed, 10 fertilizer collection boxes were used to collect fertilizer discharged from the outlet. The fertilizer discharge flow rate was then calculated based on the time required for all 10 boxes to fill. Each experiment was repeated three times, and the average value was recorded as the final result. The relationship between fertilizer discharge flow rate and the rotational speed of the fertilizer discharge wheel was analyzed using linear fitting in Origin software. The fitting results showed a strong linear correlation, with the regression equation $y=0.74x+1.39$. This indicates that the fertilizer flow rate can be linearly adjusted by controlling the rotational speed of the fertilizer discharge wheel.

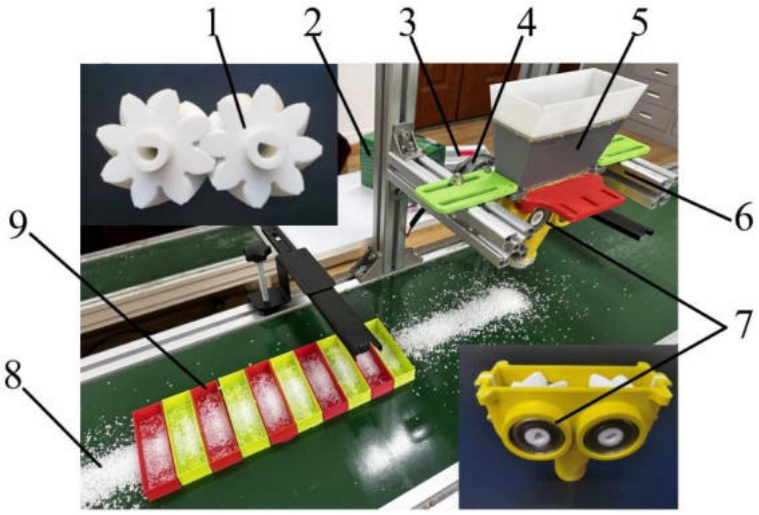


Fig. 11 - Fertilizer flow and fertilizer wheel speed test

1. Fertilizer wheel; 2. Lithium battery; 3. Motor controller; 4. Drive motor; 5. Fertilizer box; 6. Test frame; 7. Interactive gear fertilizer; 8. Urea granules; 9. Fertilizer collection box.

Five speeds were randomly selected within the range of 30 r/min to 140 r/min, and the fertilizer discharge controller was used to set the fertilizer discharger to the corresponding speeds for testing. The fertilizer discharge flow rate test was conducted at each speed, repeated three times, and the average value was taken as the final result. The measured values were then compared with the corresponding preset target values. The test results are shown in Figure 12. From the results, it can be seen that the mean deviation between the measured discharge flow rate and the preset value is 3.75%, indicating that the system is capable of achieving precise control of the fertilizer discharge amount.

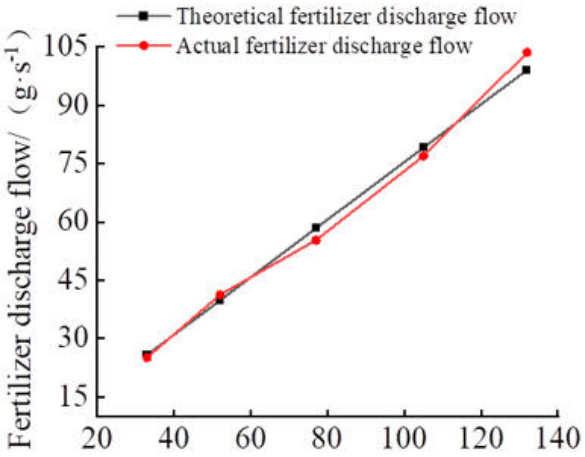


Fig. 12 - Test result diagram

Anti-Adhesion Verification Test

To simulate real working conditions, urea particles were moistened with water to increase adhesion. The Double-Gear Fertilizer Discharger *(Dun et al., 2019)* was used as a reference. Both the reference discharger and the Interactive Anti-Stick Fertilizer Discharger were tested at a fertilizer discharge wheel speed of 30 r/min. Each test was repeated five times, and the surfaces of the fertilizer discharge wheels were inspected after operation. The results showed that in the Double-Gear Fertilizer Discharger, fertilizer adhesion was clearly observed on the surface and in the grooves of the discharge wheel. Sticking traces were particularly evident at the bottom of the gear grooves, as shown in Figure 13a. In contrast, the Interactive Anti-Stick Fertilizer Discharger exhibited no obvious fertilizer adhesion during or after operation. Upon removal, the gear surfaces showed no significant sticking traces, as seen in Figure 13b. These results suggest that the Interactive Anti-Stick design effectively reduces fertilizer adhesion. Its mechanism allows residual fertilizer on the wheel to be dislodged during gear meshing, where compression between meshing teeth helps detach moist fertilizer particles. Compared to the conventional double-gear design, the anti-sticking performance is significantly improved.

The 3D model was saved in IGS format and imported into EDEM software. Hertz-Mindlin (no slip) in EDEM was selected as the contact model between granular fertilizer and granular fertilizer, caking fertilizer and caking fertilizer, granular fertilizer and caking fertilizer, granular fertilizer and fertilizer discharge device, and caking fertilizer and fertilizer discharge device. The fertilizer discharge device was modeled using PLA (polylactic acid) as the material. The detailed material and contact parameters used in the simulation are provided in Table 2.



a) ***b)***

Fig. 13 - Comparison of Fertilizer Wheel Surfaces

a) Double-gear Type Fertilizer Discharger; b) Interactive Anti-Stick Fertilizer Wheel

CONCLUSIONS

（1）Based on the agronomic fertilization requirements of pineapple orchards, an interactive gear fertilizer discharger was designed using the principle of fertilizer centering and interactive mixed discharge. The system utilizes a pair of continuously meshing, counter-rotating gears to alternately discharge fertilizer. A single-factor experiment and a response surface experiment were conducted using the pressure angle and helix angle as experimental factors, with the coefficient of variation of fertilizer discharge uniformity as the evaluation index. The structural parameters of the fertilizer discharger were optimized, and bench tests were performed to verify the results and analyze the relationship between the fertilizer discharge wheel speed and the fertilizer discharge flow rate.

（2）The results of the single-factor and response surface experiments indicate that both the pressure angle and helix angle of the fertilizer discharge wheel have a highly significant effect on the coefficient of variation of fertilizer discharge uniformity. The coefficient of variation decreases as the pressure angle and helix angle increase. When both angles are set to 30°, the minimum variation coefficient of fertilizer discharge uniformity is achieved at 11.82%.

（3）The bench test results show that the relative error between the theoretical, simulated, and experimental values is 2.77%, confirming the model's accuracy. Additionally, the fertilizer discharge flow rate can be linearly adjusted by changing the rotation speed of the fertilizer discharge wheel. The fitted linear relationship is described by the equation y=0.74x+1.39. Under the optimal parameter combination, the average deviation between the actual and preset fertilizer discharge flow rates is 3.75%, indicating a high level of precision and stable performance.

（4）A comparison of fertilizer adhesion on the gear surfaces under identical working conditions demonstrated that the interactive anti-adhesive fertilizer discharge wheel significantly reduces adhesion compared to the conventional double gear-type fertilizer discharger. This verifies the feasibility and effectiveness of the anti-adhesion design, effectively enhancing the anti-stick performance of the fertilizer discharge wheel surface.

（5）Therefore, the interactive anti-stick gear fertilizer discharger developed in this study is well-suited for fertilizer application in pineapple orchards. It effectively enhances the accuracy of fertilizer application, improves the stability of fertilizer discharge, and increases the utilization efficiency of fertilizer, ultimately contributing to higher yield and improved fruit quality. Additionally, the system offers environmental benefits by reducing fertilizer waste. These findings provide a valuable reference for the design and development of fertilizer application machinery for pineapple orchards and other orchard-based fertilization systems.

ACKNOWLEDGEMENT

This study was funded by the Heilongjiang Province Natural Science Foundation of China (No. LH2023E025). Central Public-interest Scientific Institution Basal Research Fund (No.1630062025018). Harbin Cambridge University Key Scientific Research Application Research Project (No. JQZKY2022021).

REFERENCES

[1] Chen, X., Luo, X., Wang, Z. (2015). Design and experiment of fertilizer distribution apparatus with double-level screws (两级螺旋排肥装置的设计与试验). *Transactions of the Chinese Society of Agricultural Engineering (Transactions of the CSAE)*, vol.31(3), pp.10-16. DOI: 10.3969/j.issn.1002-6819.2015.03.002.

[2] Chen, X., Chen, W. (2008). New Involute Clock Gear with Double Pressure Angles (新型双压力角渐开线钟表齿轮). Journal of Mechanical Transmission, vol. 26(1), pp. 28-30.

[3] Dun, G., Sheng, Q. (2024). Optimal Design and Experiment of Electronically Controlled Inclined Spiral Precision Fertilizer Discharger. *Agriculture*, vol. 14, pp. 1131. DOI: https://doi.org/10.3390/agriculture14071131.

[4] Du, J., Yang, Q., Xia J. (2020). Discrete Element Modeling and Verification of an Outer Groove Wheel Fertilizer Applicator with Helical Teeth. *Transactions of the ASABE*, vol, 63(3), pp. 659-665. DOI: 10.13031/trans.13289.

[5] Dun, G., Yu, C., Yang, Y. (2018). Discharging characteristic test of outer-groove wheel fertilizer and parameter optimization of fertilizer tongue by discrete element simulation (外槽轮排肥器排肥离散元仿真及排肥舌参数优化). *Journal of Hunan Agricultural University (Natural Sciences)*, vol. 44(06), pp. 661-665. DOI: 10.13331/j.cnki.jhau.2018.06.015.

[6] Dun, G., Yu, C., Guo, Y. (2020). Design and experiment of double-gear type fertilizer apparatus (双齿轮式排肥器设计与试验). *Transactions of the Chinese Society for Agricultural Machinery*, vol. 51(03), pp. 87-96. DOI: 10.6041/j.issn.1000-1298.2020.03.010.

[7] Dun, G., Ye, J., Xia, W. (2019). Simulation design and test of reverse rotation meshing gear fertilizer apparatus based on EDEM (基于 EDEM 的反转啮合齿轮式排肥器的仿真设计与试验). *Journal of Shenyang Agricultural University*, vol. 50(02), pp. 231-237. DOI: 10.3969/j.issn.1000-1700.2019.02.015.

[8] Dun, G., Gao, Z., Guo, Y. (2020). Simulation test and optimization for structural parameters of circular arc gear discharging fertilizer apparatus (圆弧齿轮排肥器圆弧结构参数仿真试验及优化). *Journal of Zhejiang University (Agriculture and Life Sciences)*, vol. 46(05), pp. 625-636. https://doi.org/10.3785/j.issn.1008-9209.2019.11.101.

[9] Hu, Y., Yang, Y., Xiao, H. (2016). Simulation and parameter optimization of centrifugal fertilizer spreader for tea plants (茶园施肥机离心撒肥过程仿真与参数优化). *Transactions of the Chinese Society for Agricultural Machinery*, vol. 47(05), pp. 77-82. DOI: 10.6041/j.issn.1000-1298.2016.05.011.

[10] Liang, Y., Tang, Z., Ji, C. (2023). Optimization and experiment of structural parameters of outer groove wheel fertilizer drainer (外槽轮排肥器结构参数优化与试验). *Journal of Agricultural Mechanization Research*, vol. 45(12), pp. 7-14. DOI: 10.13427/j.cnki.njyi.2023.12.002.

[11] Liu, C., Zhang, F., Du, X. (2020). Design and experiment of precision fertilizer distribution mechanism with horizontal turbine blades (水平涡轮叶片式精量排肥器设计与试验). *Transactions of the Chinese Society for Agricultural Machinery*, vol. 51(S1), pp. 165-174. DOI: 10.6041/j.issn.1000-1298.2020.S1.019.

[12] Li, C. (2008). Study on precision fertilization system of farmland based on GPS technique (基于 GPS 技术环境下的农田精量施肥系统研究). MSc Thesis, *Henan Agricultural University*.

[13] Lv, H., Yu, J. (2013). Simulation of the operation of a fertilizer spreader based on an outer groove wheel using a discrete element method. *Mathematical & Computer Modelling*, vol. 58(3-4), pp. 836-845. DOI: 10.1016/j.mcm.2012.12.017.

[14] Liu, X., Wang, X., Chen, L. (2021). Design and experiments of layered and quantitative fertilization device for rapeseed seeder (油菜直播机分层定量施肥装置设计与试验). *Transactions of the Chinese Society of Agricultural Engineering*, vol. 37(05), pp. 1-10. DOI: 10.11975/j.issn.1002-6819.2021.05.001.

[15] Michele, M., Hugh, S. (2015). Discrete Element Method (DEM) for Industrial Applications: Comments on Calibration and Validation for the Modelling of Cylindrical Pellets. *Kona Powder and Particle Journal*, vol. 32, pp. 236-252. DOI: 10.14356/kona.2015016.

[16] Marcinkiewicz, J., Selech, J. (2019). DEM simulation research of selected sowing unit elements used in a mechanical seeding drill. *MATEC Web of Conferences*, vol. 254. DOI: 10.1051/matecconf/201925402021.

[17] Su, N., Xu, T. (2015). Variable rate fertilization system with adjustable active feed-roll length. *International Journal of Agricultural and Biological Engineering*, vol. 8(4), pp. 19-26. DOI: 10.3965/j.ijabe.20150804.1644.

[18] Sun, C., Cao, L., Shi, Z. (2019). Analysis on fertilizer performance of fertilizer machine based on discrete element method (基于离散元法的施肥机排肥性能分析). *Journal of Chinese Agricultural Mechanization*, vol. 40(03), pp. 44-50+127. DOI: 10.13733/j.jcam.issn.2095-5553.2019.03.08.

[19] Song, B. (2016). Research of the Effects of Pressure Angle on Mesh Characteristic of Involute Cylindrical Gear (渐开线圆柱齿轮压力角对啮合性能影响研究). *Journal of Mechanical Transmission*, vol. 40(12), pp. 48-51. DOI: 10.16578/j.issn.1004.2539.2016.12.010.

[20] Tai, Q. (2020). Design and experiment of adjustable socket-eye precision fertilizer feeder (可调窝眼轮式精量排肥器设计与试验). MSc Thesis, *Anhui Agricultural University*.

[21] Wang, B., Bai, L, Ding, S. (2017). Simulation and experimental study on impact of fluted-roller fertilizer key parameters on fertilizer amount (外槽轮排肥器关键工作参数对排肥量影响的仿真与试验研究). *Journal of Chinese Agricultural Mechanization*, vol. 38(10), pp. 1-6,23. DOI: 10.13733/j.jcam.issn.2095-5553.2017.10.001.

[22] Wen, X., Yuan, H., Wang, G. (2020). Calibration method of friction coefficient of granular fertilizer by discrete element simulation (颗粒肥料离散元仿真摩擦因数标定方法研究). *Transactions of the Chinese Society for Agricultural Machinery*, vol. 51(02), pp. 115-122, 142. DOI: 10.6041/j.issn.1000-1298.2020.02.013.

[23] Yao, L., Cao, X., Song, S. (2020). Design of synchronous precision fertilizer machine for rice transplanting (水稻插秧同步精量施肥机的设计). *Journal of Agricultural Mechanization Research*, vol. 42(10), pp. 75-80. DOI: 10.13427/j.cnki.njyi.2020.10.014.

[24] Yuan, W., Li, K., Jin, C. (2018). Design and experiment of hill placement fertilizer applicator (穴施肥排肥器设计与试验). *Journal of Agricultural Mechanization Research*, vol, 40(01), pp.145-149, 165.

[25] Zhu, Q., Wu, G., Chen, L. (2018). Influences of structure parameters of straight flute wheel on fertilizing performance of fertilizer apparatus (槽轮结构参数对直槽轮式排肥器排肥性能的影响). *Transactions of the Chinese Society of Agricultural Engineering (Transactions of the CSAE)*, vol. 34(18), pp. 12-20. DOI: 10.11975/j.issn.1002-6819.2018.18.002.

[26] Zuo, X., Wu, G., Fu, W. (2016). Design and experiment on air-blast rice side deep precision fertilization device (风送式水稻侧深精准施肥装置的设计与试验). *Transactions of the Chinese Society of Agricultural Engineering (Transactions of the CSAE)*, vol. 32(03), pp. 14-21. DOI: 10.11975/j.issn.1002-6819.2016.03.003.

RESEARCH ON THE VIBRATION AND FRUIT DROP CHARACTERISTICS OF CAMELLIA OLEIFERA BASED ON HIGH-SPEED PHOTOGRAPHY TECHNOLOGY
/
基于高速摄影技术的油茶振动落果特性研究

Enlong ZHAO, Jinhui ZHAO*), Tengfei ZHUANG, Lijing LIU, HaiHua WU, Yanwei YUAN*)
Chinese Academy of Agricultural Mechanization Science Group Co., Ltd., Beijing (100083), China
Corresponding author: Yanwei YUAN; Tel: +86 13522326652; E-mail: yyw215@163.com
JinHui ZHAO, Tel: +86 18810569281; E-mail: zhaojh281@163.com
DOI: https://doi.org/10.35633/inmateh-76-40

Keywords: *Camellia oleifera, vibration harvest, High-speed photography, Mechanical vibration*

ABSTRACT
This study employed high-speed photography to reproduce the vibration behavior of Camellia oleifera fruit and flower buds. Vibration energy was transmitted through the branches to break the balance of the Camellia oleifera branch system, causing the fruit and flower buds to exhibit anisotropic chaotic swings. Post-processing of images showed that the fruit detachment force ranged from 4.57 to 11.85 N, and the flower bud detachment force ranged from 0.68 to 3.24 N. At a vibration frequency of 12.98 Hz, the vibration amplitude did not have a significant effect on the detachment force of fruit and flower buds. The detachment time of Camellia oleifera fruit and flower buds decreased with the increase of vibration amplitude or excitation frequency. Through fitting and analysis of the collected data, the Fourier fitting curves and functions of the motion acceleration of oil-tea fruit and flower buds were obtained, with R^2 values of 0.83996 and 0.73718, respectively.

摘要
通过高速摄影还原了油茶果实与花苞振动行为，振动能量经枝干传递打破枝条系统平衡，使其呈各向异性混沌摆动。后处理影像显示，果实脱落力4.57~11.85N、花苞0.68~3.24N，12.98Hz振动下幅值对脱落力影响不明显，脱落时间随幅值或频率增加而减少。经数据拟合得果实、花苞运动加速度傅里叶拟合曲线及函数，R^2分别为0.83996、0.73718。

INTRODUCTION
Camellia oleifera, a tree species lacking a distinct main trunk, is well-suited for mechanical harvesting of its fruits using canopy vibrators *(Du et al., 2024; Wu et al., 2022; Zhang et al., 2020)*. Compared to manual picking, mechanical harvesting equipment significantly reduces production costs. Mechanical vibration devices apply excitatory forces to fruit trees, inducing synchronized vibration of fruits through branch movement. When the inertial force of a fruit exceeds the binding force between the fruit and its stalk, the fruit detaches *(Freitas Grupioni et al., 2020; Juan et al., 2020; Zhou et al., 2022)*.

Current research on fruit abscission faces a key limitation: most studies rely on physical experiments and theoretical models *(Tombesi et al., 2017; Wu et al., 2020a; Brondino et al., 2021)*, primarily measuring static detachment forces between fruits and stalks. Dynamic analysis of real-time abscission forces under forced vibration remains scarce. While some researchers use physical sensors (e.g., accelerometers) to monitor target motion during tree vibration—requiring sensor placement on fruits or branches to measure acceleration responses under excitation *(Castro-Garcia et al., 2017; Niu et al., 2022; Yuan, 2022; Wu et al., 2020b)*—others have detected through trunk/fruit sensors that fruit drop frequency correlates with vibrator frequency, with resultant acceleration values dependent on fruit-vibrator system interactions *(Torregrosa et al., 2014; Juan et al., 2020; Sargent et al., 2020)*. Though these sensor-based methods efficiently capture motion response patterns, they inherently alter the physical properties of the original branch-fruit system. The added mass and mechanical interference from sensors introduce uncertainties into experimental results.

Enlong Zhao, Ph.D. Stud. Eng; JinHui Zhao, Engineer, M.S. Eng; Tengfei Zhuang, engineer Ph.D. Eng.;
Lijing Liu, Researcher, Ph.D. Eng.; HaiHua Wu, Researcher, Ph.D. Eng.; Yanwei Yuan, Researcher, Ph.D. Eng.

Non-contact measurement technologies offer a solution to these limitations. High-speed photography (HSP) and image processing *(Torregrosa et al., 2014; Xu et al., 2019)* enable precise, contact-free reconstruction of fruit motion during forced vibration. By recording the instantaneous process of fruit-stalk separation with HSP and analyzing key parameters (displacement, velocity, acceleration) via post-processing software, researchers can characterize dynamic behaviors of fruits under vibration and deepen mechanistic understanding of abscission.

This study employs high-speed photography to capture dynamic changes in Camellia oleifera fruits and flower buds during vibration, documenting their abscission timing and modes. Through video data processing, movement trajectories are quantified and vibration-responsive characteristics are analyzed, providing a theoretical basis for optimizing vibrator-based harvesting equipment parameters.

MATERIALS AND METHODS

This study utilized dwarf *Camellia oleifera* trees cultivated in Hunan Province, China, with "Xianglin" fruit varieties as the experimental material. The experiments were conducted in November 2024, corresponding to the mature and optimal harvest period of the "Xianglin 210" cultivar. Branches bearing both fruits and flower buds were excised from the trees and transported to the laboratory for vibration testing.

Excitation device

In the mechanical picking process, regardless of the excitation method employed, vibration energy is transmitted from the branches to the fruits. When the inertial force of the fruits reaches the binding force, the Camellia oleifera fruits will fall off. The experimental test uses a crank - connecting rod - slider mechanism as the vibration energy source (as shown in Figure 1). The vibration frequency of the excitation device can be continuously adjusted within the range of 0 – 30 Hz, and the excitation amplitude values are available in size specifications of 10 mm, 20 mm, 50 mm, and 100 mm. The excitation device is fixed on the small lifting platform to adjust the height of the excitation position. At the same time, a specific clamping mechanism is designed at the end of the slider. Theoretically, the acceleration of the excitation device can be obtained through the following formula:

$$a = \frac{dv}{dt} = -\omega^2 R \sin\left(\omega t + \varphi\right) \tag{1}$$

The maximum absolute value in this case:

$$Abs\left(a_{\max}\right) = \omega^2 R = \left(2\pi f\right)^2 R \tag{2}$$

where: t — time, [s];
R — the length of the crank, [m];
ω — the angular velocity, [rad/s];
f — the frequency, [Hz];
φ — the phase, [rad];
v — the linear velocity, [m/s];
a — the acceleration, [m/s^2].

The theoretical values of the parameters at different amplitudes and frequencies are compared with the results of video analysis.

Image acquisition and analysis

The images were captured using a high-speed industrial camera (resolution: 1920(H)×1080(V); 2.0 megapixels; Model: L-PRI 1000; Exposure time: 2 μs/frame rate; AOS Technologies AG), along with a computer, Phantom control software, and data analysis and processing software.

Data analysis and processing software was employed to analyze the motion states of Camellia oleifera fruits and buds. Using the center of the target fruit or bud as the origin, the position of the tracked fruit or bud was collected every 0.02 seconds. The acceleration of fruits and buds during the forced vibration of Camellia oleifera branches was calculated using the following acceleration formula:

$$a = \frac{v}{t} = \frac{x}{t^2} \tag{3}$$

where:

a — the acceleration, [m/s^2];

v — the velocity, [m/s];

t — the interval between two adjacent photos, which is 0.02 s;

x — the relative displacement of the fruit in the two pictures, [m].

By measuring the quality of the fruit and bud, you can know the size of the inertia force when the fruit and bud fall off. The inertia force when falling off is:

$$\begin{cases} F_g = m_g a_g \\ F_h = m_h a_h \end{cases} \tag{4}$$

where: F_g — the inertial force when the fruit falls off, [N];

F_h — the inertial force when the bud falls off, [N];

m_g — fruit mass, [kg];

m_h — bud mass, [kg];

a_g — the acceleration of fruit shedding, [m/s^2];

a_h — the acceleration when the bud falls off, [m/s^2].

Test

The slider's end is fixed to the Camellia oleifera stem, with the fixed point located 100 mm away from the fixture (Fig. 1).



Fig. 1 - Vibration test device

During the test, the excitation amplitude is regulated by altering the connecting rod's position on the crank, while the excitation frequency is adjusted by using a frequency modulator to control the motor speed. In each test run, after setting the excitation frequency and amplitude, the clamp is used to secure Camellia oleifera branches under laboratory conditions. Specifically, the branch samples are clamped onto the fixture to ensure they form a specific angle with the vibration platform, simulating the natural growth posture of branches on the tree. Subsequently, the motor is activated, and a high-speed camera records the motion response of Camellia oleifera fruits under forced vibration.

RESULTS AND DISCUSSION

Vibration exciter movement analysis

According to the method given, the video in high-speed photography is analyzed frame by frame and the actual acceleration is calculated. Comparing these accelerations with the theoretical calculations results in very close values (Tab.1). The maximum relative error between the theoretical value and the actual value of the output acceleration of the exciter is 1.84%, and the parameter combination at this time is the excitation frequency of 2.05 Hz and the amplitude of 10 mm. It shows that the moving image acquired by high-speed photography base is reliable after post-processing.

Table 1

Vibration transfer efficiency with different parameters

Amplitude [mm]	Frequency [Hz]	Vibration exciter output acceleration [m/s^2]		error [%]
		Theoretical value	Actual value	
10	2.05	1.66	1.63	1.84
20	7.52	44.61	44.35	0.59
50	12.98	332.23	333.52	0.39

Impact analysis of vibration parameters

Through analysis of the high-speed video, the shedding force of Camellia oleifera fruit was found to range from 4.57N to 11.85N, while that of buds ranged from 0.68N to 3.24N. These values are significantly lower than the binding force measured via static testing of Camellia oleifera fruit *(Wang et al., 2024)*. This phenomenon can be attributed to the following: during static measurement of the fruit-stalk binding force, the fruit was pulled vertically along the stalk. In contrast, high-speed photography revealed that during vibration, the fruit-stalk exhibited a certain swing angle relative to the branch — indicating that the shedding force of the fruit-stalk varies with different angles of application.

Table 2

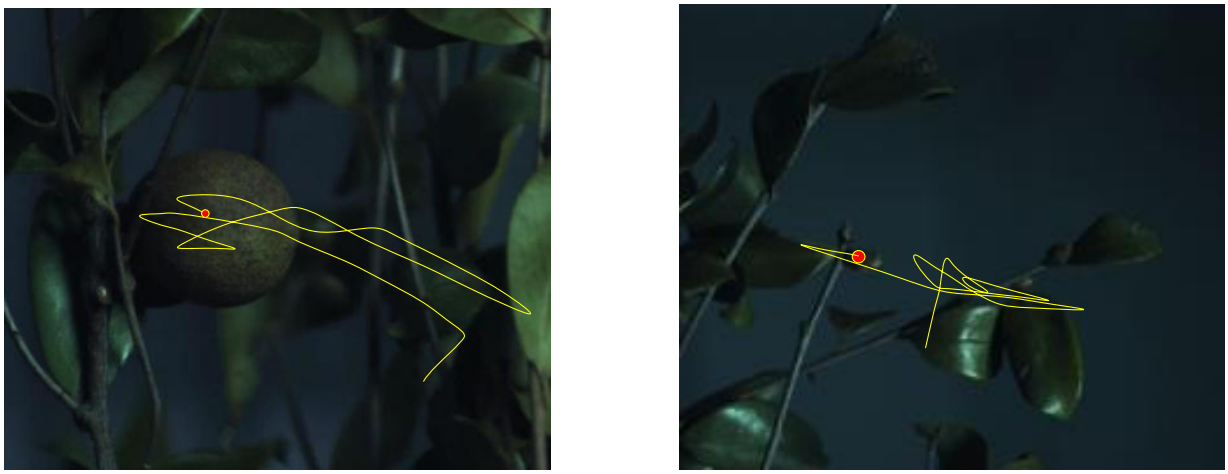
Effects of vibration parameters on fruit and bud shedding of *Camellia oleifera*

Amplitude [mm]	Frequency [Hz]	Fruit			Bud		
		Mean shedding force [N]	Mean shedding time [s]	Swing period	Mean shedding force [N]	Mean shedding time [s]	Swing period
20	2.05	6.78	3.38	5	2.37	5.97	4
20	7.51	4.57	2.96	6	3.24	5.25	4
20	12.98	7.34	1.54	4	1.98	4.76	5
50	2.05	6.58	2.47	4	2.26	4.58	6
50	7.51	11.51	1.98	6	2.54	3.42	6
50	12.98	7.38	1.27	5	1.92	2.54	4
100	2.05	11.85	1.24	5	0.93	2.57	5
100	7.51	8.54	1.08	4	0.75	1.78	4
100	12.98	7.64	0.69	5	1.88	0.83	4

The table also indicates that at low frequency (2.05 Hz), increasing the vibration amplitude from 20 mm to 50 mm results in only a 0.2 N difference in fruit shedding force and a 0.11 N difference in bud shedding force, whereas increasing the amplitude from 50 mm to 100 mm causes fruit shedding force to rise from 6.58 N to 11.85 N and bud shedding force to decrease from 2.26 N to 0.93 N; at high frequency (12.98 Hz), the effect of vibration amplitude on the shedding force of both fruits and buds is negligible.

The shedding time of Camellia oleifera fruits and buds is inversely related to excitation parameters, decreasing as either vibration amplitude or frequency increases, with the rate of change in fruit vibration shedding time being lower when increasing from low frequency (2.05 Hz) to medium frequency (7.52 Hz) than when transitioning from medium frequency (7.52 Hz) to high frequency (12.98 Hz), while the opposite pattern is observed for buds, where the change rate is higher during the low-to-medium frequency increase than during the medium-to-high frequency increase.

Movement rules of Camellia oleifera fruit and bud



(a) Fruit movement path *(b) Locus of bud movement*

Fig. 2 - Motion state of *Camellia oleifera* fruit under forced vibration

Under the condition that Camellia oleifera fruits and buds move within the same plane, high-speed video was used to capture the approximate trajectories of fruits (Fig. 3a) and buds (Fig. 3b) under vibration excitation with a vibration amplitude of 50 mm and a frequency of 7.52 Hz. Vibrational energy is transferred to the fruits and buds through the branches, disrupting the overall system balance and causing the fruits and buds to exhibit anisotropic random and disordered mixed oscillation behavior *(Hoshyarmanesh et al., 2017; San et al., 2018)*.

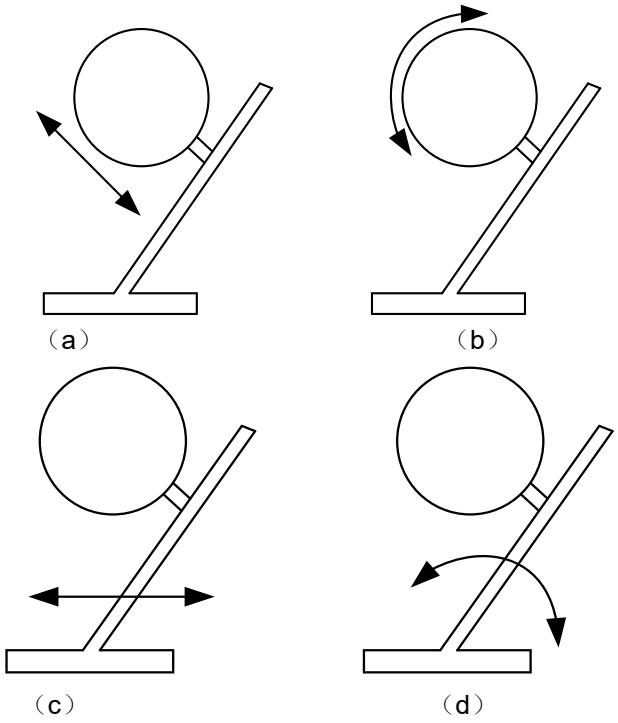


Fig. 3 - Motion decomposition

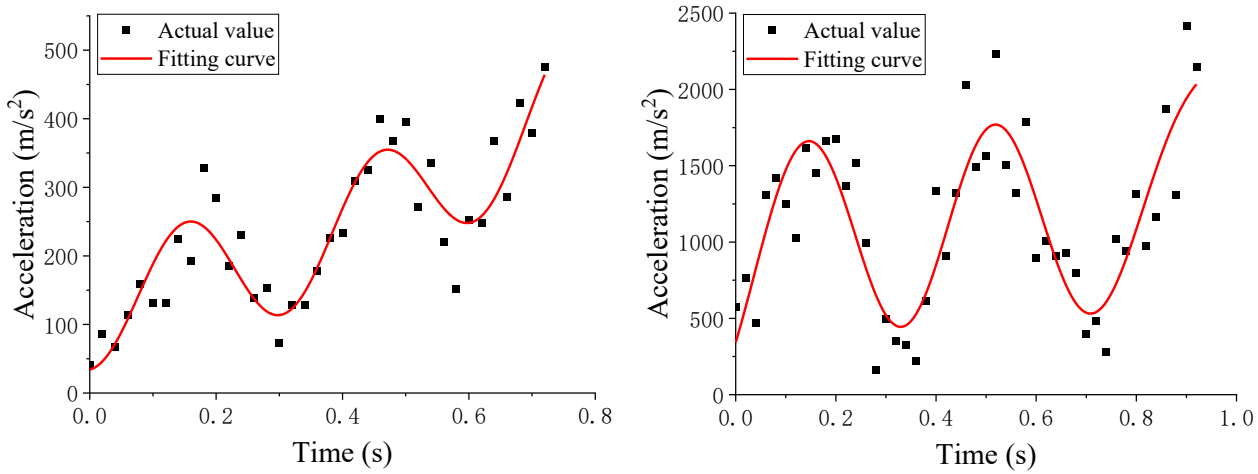
(a) Parallel stalk movement of fruit; (b) The fruit moves around the stalk; (c) The fruit and the branch move together; (d) The fruit and the branch move together around the excitation point.

Trajectories of Camellia oleifera Fruit and Buds Under 7.52 Hz Excitation (Fig. 2). Under 7.52 Hz excitation, Camellia oleifera fruits and buds exhibit dynamic oscillatory behavior: they first accelerate and swing in the direction of the applied force, then rapidly reverse direction. The entire branch-fruit and branch-bud system undergoes periodic oscillations around the excitation origin. Notably, the fruit and its supporting branch show significant positional displacement, characterized by wobbling of the fruit and torsional movement of the branch. Observation points on the structures demonstrate altered relative positions, with marked fruits displaying obvious deflection. This complex motion can be attributed to the combined behaviors illustrated in Figure 3, consistent with similar findings in prior studies *(Cao et al., 2023; Hoshyarmanesh et al., 2017; San et al., 2018; Wang et al., 2024)*.

As shown in Figure 4, the movement trajectories of fruits and buds do not reciprocate along a straight line within the same period, indicating relative motion (e.g., swinging or twisting) between fruits and branches during vibration. Under identical vibration conditions, fruits exhibit significantly greater motion responses (i.e., displacement) than buds. The movement of fruits and buds is also influenced by neighboring fruits and branches in an unpredictable manner, leading to frequent changes in their trajectories due to potential collisions. Quantitative analysis of these trajectories represents a promising direction for future research.

Motion curve fitting

When the camellia fruit and flower bud acquire sufficient inertial force, that is, when the critical value of the binding force between the fruit stem and the branch is exceeded, the camellia fruit or flower bud will fall off. Through the analysis of the movement images and data of the target camellia fruit and flower bud captured by the high-speed camera, the sample will be taken every 0.02 s, as shown in Figure 4 of the acceleration and time relative to the origin point.



(a) fruit (b) bud

Fig. 4 - Vibration shedding process

From the beginning of vibration to the shedding acceleration, *Camellia oleifera* fruit experienced three stages: 0 to 0.3 s, 0.3 to 0.58 s and 0.58 to 0.72 s. The first stage period of *Camellia oleifera* fruit was 0.3 s, and the peak acceleration occurred at 0.18 s (328.24 m/s^2). The period of the second stage is 0.28 s, and the peak acceleration occurs at 0.46 s and is 400.18 m/s^2. The fruit of *Camellia oleifera* fell off before reaching the complete cycle in the third stage. The vibration shedding time was 0.72 s and the shedding acceleration was 475.38 m/s^2. Fourier fitting was performed on the acceleration of *Camellia oleifera* fruit. The R2 of the fitting curve was 0.83996, and the equation of the fitting curve was as follows:

$$a_g = 208.52 + 1612.57\sin(0.59t) - 85.14\cos(0.002t) - 383.53\sin(1.87t) - 89.25\cos(20.52t) \quad (5)$$

There were 3 stages from the initial vibration to the shedding acceleration: 0 to 0.36 s, 0.36 to 0.74 s and 0.74 to 0.92 s. In the first stage, the movement period was 0.36 s, and the peak acceleration occurred at 0.2 s (1676.63 m/s^2). The period of the second stage is 0.38 s, and the peak acceleration occurs at 0.52 s, which is 2232.17 m/s^2. The buds of *Camellia oleifera* fell off before reaching the complete cycle in the third stage.

The vibration shedding time was 0.92 s, and the shedding acceleration was 2147.4 m/s^2. Fourier fitting was performed on the acceleration of *Camellia oleifera* bud. The R2 of the fitting curve was 0.73718, and the equation of the fitting curve was as follows:

$$a_h = -780.29 + 39212.57\sin(0.11t) + 1375.24\cos(3.45t) + 471.89\sin(14.61t) - 252.91\cos(18.72t) \quad (6)$$

CONCLUSIONS

In this paper, the motion of *Camellia oleifera* fruit and bud was observed by image acquisition technology, and the motion behavior of *Camellia oleifera* fruit and bud under different vibration parameters was analyzed in detail. By using mathematical model to study the characteristics of *Camellia oleifera* branches, and using high-speed photography technology to measure and analyze the dynamic characteristics of *Camellia oleifera* fruits and buds, the following conclusions are drawn:

- The maximum relative error between the theoretical value and the actual value of the output acceleration of the exciter is 1.84%; The fruit shedding force of *Camellia oleifera* ranged from 4.57 N to 11.85 N, and the bud shedding force ranged from 0.68 to 3.24 N.
- Under high frequency (12.98 Hz) vibration, the change of vibration amplitude has no obvious effect on the shedding force of fruit and bud. The shedding time of *Camellia oleifera* fruit and bud decreased with the increase of vibration amplitude or excitation frequency.
- The vibrational energy is transferred to the fruit and bud through the branches, the balance of the whole system is broken, and the fruit and bud show anisotropic random and disorderly chaotic oscillation behavior;
- Using the collected data for fitting analysis, the Fourier fitting curve and your sum function of the motion acceleration of *Camellia oleifera* fruit and the bud were obtained, with R2 of 0.83996 and 0.73718, respectively.

ACKNOWLEDGEMENT

The project was supported by the National Key Research and Development Program of China (No. 2022YFD2202100).

REFERENCES

[1] Brondino, L., Borra, D., Giuggioli, N.R., Massaglia, S. (2021). Mechanized Blueberry Harvesting: Preliminary Results in the Italian Context. *Agriculture*, 11, 1197. United States. DOI: https://doi.org/10.3390/agriculture11121197

[2] Cao J., Bai X., Xu D., Li W., Chen C., (2023). Experiment and analysis on walnut (Juglans regia L.) shedding force based on low-frequency vibration response. *Industrial Crops and Products.* Volume 204, 117242. Holland. DOI: https://doi.org/10.1016/j.indcrop.2023.117242.

[3] Castro-Garcia S., Blanco-Roldán G.L., Ferguson L., González-Sánchez E.J., Gil-Ribes J.A., (2017). Frequency response of late-season 'Valencia' orange to selective harvesting by vibration for juice industry. *Biosystems Engineering*, 155, 77-83. United States. DOI: https://doi.org/10.1016/j.biosystemseng.2016.11.012

[4] Du X., Han X., Shen T., Meng Z., Chen K., Yao X., Cao Y., Castro-García S., (2024). Natural frequency identification model based on BP neural network for Camellia oleifera fruit harvesting, *Biosystems Engineering*, 38-49, United States. DOI: https://doi.org/10.1016/j.biosystemseng.2023.11.012.

[5] Freitas Grupioni C.M., Santos F.L., Velloso N.S., Magalhães Valente D.S., Carvalho Pinto F.A., (2020). Macaw palm supply chain: Evaluation of a semi-mechanized fruit harvesting system. *Industrial Crops and Products*, 151, 112444. DOI: https://doi. org/10.1016/j.indcrop.2020.112444.

[6] Hoshyarmanesh H., Dastgerdi H.R., Ghodsi M., Khandan R., Zareinia K., (2017). Numerical and experimental vibration analysis of olive tree for optimal mechanized harvesting efficiency and productivity. *Computers and Electronics in Agriculture,* 132, 34–48, United States. DOI: https://doi.org/10.1016/j.compag.2016.11.014.

[7] Niu Z., Xu Z., Deng J., Zhang J., Pan S., Mu H., (2022). Optimal vibration parameters for olive harvesting from finite element analysis and vibration tests. *Biosystems Engineering*. 215, 228–238. United States. DOI: https://doi.org/10.1016/j.biosystemseng.2022.01.002

[8] San Y., Yang H., Wang X., Guo W., Hou S., (2018). Dynamic response analysis of apricot fruit dropping during vibration harvesting (振动收获过程中杏果实脱落的动态响应). *Transactions of the Chinese Society of Agricultural Engineering*, 34(18): 68 - 75, Beijing/China, DOI: 10.11975/j.issn.1002-6819.2018.18.009

[9] Sargent, S.A., Takeda, F., Williamson, J.G., Berry, A.D. (2020). Harvest of Southern Highbush Blueberry with a Modified, Over-The-Row Mechanical Harvester: Use of Handheld Shakers and Soft Catch Surfaces. *Agriculture*, 10, 4. United States. DOI: https://doi.org/10.3390/agriculture10010004

[10] Tombesi S., Poni S., Palliotti A., Farinelli D., (2017). Mechanical vibration transmission and harvesting effectiveness is affected by the presence of branch suckers in olive trees, *Biosystems Engineering*, 158, 1-9. United States. DOI: https://doi.org/10.1016/j. biosystemseng.2017.03.010

[11] Torregrosa A., Albert F., Aleixos N., Ortiz C., Blasco J., (2014). Analysis of the detachment of citrus fruits by vibration using artificial vision. *Biosystems Engineering*, 119, 1-12. United States. DOI: https://doi.org/10.1016/j.biosystemseng.2013.12.010

[12] Wang R., Fang D., Wu C., Wang B., Zhu H., Hu T., Wu D., (2024). Dynamic response of Camellia oleifera fruit-branch based on mathematical model and high-speed photography, *Biosystems Engineering*, 237, 232-241, United States. DOI: https://doi.org/10.1016/j.biosystemseng.2023.12.010

[13] Wu Delin, Li Chao, Cao Chengmao, Fan Erbo, Wang Qi. (2020). Analysis and experiment of the operation process of branch-shaking type camellia oleifera fruit picking device. (摇枝式油茶果采摘装置作业过程分析与试验). *Transactions of the Chinese Society of Agricultural Engineering*, 36(10):56-62. Beijing/China, DOI: 10.11975/j.issn.1002-6819.2020.10.007

[14] Wu Delin, Fu Liqiang, Cao Chengmao, Li Chao, Xu Yanping, Ding Da. (2020). Design and Experiment of Shaking-branch Fruit Picking Machine for Camellia Fruit. (摇枝式油茶果采摘机设计与试验). *Transactions of the Chinese Society for Agricultural Machinery*, 51(11):176-182,195. Beijing/China, DOI: 10.6041/j.issn.1000-1298.2020.11.019

[15] Juan W., Yang G., Yan H., Jing B., Yu Y., (2020). Rigid-flexible coupling simulation and experimental vibration analysis of pistachio tree for optimal mechanized harvesting efficiency. *Mechanics of Advanced Materials and Structures*, 28 (22), 2360–2369. DOI: https://doi.org/10.1080/15376494.2020.1734889

[16] Wu, D., Zhao, E., Fang, D., Jiang, S., Wu, C., Wang, W., Wang, R. (2022). Determination of vibration picking parameters of Camellia oleifera fruit based on acceleration and strain response of branches. *Agriculture-Basel*, 12(8), 1222. United States. DOI: https:// doi.org/10.3390/agriculture12081222

[17] Xu L., Liu G., Xuan Y., Zhou J., (2019). Mathematical model of fruit's aerial movement in vibration response (果实振动响应时的空中运动数学模型). *Transactions of the Chinese Society of Agricultural Engineering*, 35, 206-213, Beijing/China, DOI: https://doi.org/10.11975/j.issn.1002- 6819.2019.16.023

[18] Yuan, J., (2022). *Optimization and experiment of canopy vibration parameters of Camellia oleifera on energy transfer and tree response,* (油茶树冠振动参数对能量传递和树体响应的优化与试验,硕士论文). MSc Thesis, *Anhui Agricultural University*. Hefei/China, DOI: https: //doi:10.26919/d.cnki.gannu.2022.000742

[19] Zhou J., Xu L., Zhao J., Hang X., Zhou H., (2022). Effective excitation conditions for the intense motion of the ginkgo seed-stem system during mechanical vibration harvesting. *Biosystems Engineering*, 215, 239-248. United States. DOI: https://doi.org/10.1016/j. biosystemseng.2022.01.014

[20] Zhang, Z., Igathinathane, C., Li, J., Cen, H., Lu, Y., Flores, P. (2020). Technology progress in mechanical harvest of fresh market apples. *Computers and Electronics in Agriculture*, 175, 105606. United States. DOI:https://doi.org/10.1016/j.compag.2020.105606

RESEARCH ON TORQUE DYNAMIC COORDINATED CONTROL OF A NOVEL DUAL POWER SOURCE THRESHING DRUM OF COMBINE HARVESTER

/

新型双动力源脱粒滚筒扭矩动态协调控制研究

Zhihao ZHU[1)], Xiaoyu CHAI *[1)], Lizhang XU[2)], Li QUAN[3)], Chaochun YUAN[4)], En LU[1)], Shuofeng WENG[3)], Shichao TIAN[1)], Guangqiao CAO[5)]

[1)]School of Agriculture Engineering, Jiangsu University, 212013, China
[2)]Key Laboratory for Theory and Technology of Intelligent Agriculture Machinery and Equipment, Jiangsu University, 212013, China
[3)]School of Electrical and Information, Jiangsu University, 212013, China
[4)]Automotive Engineering Research Institute, Jiangsu University, 212013, China
[5)]Nanjing Institute of Agricultural Mechanization, Ministry of Agriculture and Rural Affairs, 211200, China
Tel: 18852832940; E-mail: xfpaxy521123@163.com
DOI: https://doi.org/10.35633/inmateh-76-41

***Keywords**: Combine harvester, threshing drum, electric drive, torque compensation*

ABSTRACT

In response to the issues faced by conventional combine harvesters' threshing drums, such as the difficulty in maintaining stable speed due to load fluctuations and torque disturbances, as well as the limited speed adjustment range to adapt to changes in crop varieties and properties, this study proposes a novel dual power source threshing drum (DPSTD). By incorporating a power coupling device and a motor into the existing mechanical structure, the DPSTD utilizes the flexible speed and torque output capabilities of the motor to achieve a wide speed adjustment range and enhance its resistance to interference. A robust model predictive control strategy is designed based on finite time disturbance observer (FTDO) to compensate for torque under load fluctuations. Simulation results demonstrate that the DPSTD can achieve rapid and accurate speed regulation. Moreover, under torque disturbances and load mutations, the DPSTD with the torque compensation control strategy, can reduce the speed error by 73.90%. This significantly improves the speed tracking performance of the threshing drum, exhibiting good anti-interference capabilities. Finally, the superiority of the DPSTD is validated through bench tests, confirming its effectiveness and feasibility and providing new insights for control research on threshing drums.

摘要

针对传统联合收获机脱粒滚筒面对负载波动和扭矩干扰时难以稳速影响作业效果，以及调速范围小难以适应作物品种和属性的变化等问题，本文基于并联式混合动力技术提出了一种新型双动力源脱粒滚筒 (DPSTD)，通过在原有的机械驱动结构上加入动力耦合装置和电机，利用电机灵活的转速和转矩输出功能实现脱粒滚筒的大范围调速并提高抗干扰能力。本文对 DPSTD 各部件进行数学建模，并设计了基于有限时间干扰观测器 (FTDO) 的电机鲁棒模型预测控制策略，以实现 DPSTD 在负载波动和干扰下的扭矩补偿，进一步对 DPSTD 的调速和稳速性能进行研究，仿真结果表明，DPSTD 可以快速精准地进行转速调节，并且在存在扭矩干扰和负载突变的情况下，采用扭矩补偿的控制策略的 DPSTD 可以将脱粒滚筒的转速误差均方根值降低 73.90%，最大转速误差降低 76.18%，冲击度均方根值降低 33.51%，最大冲击度降低 73.18%。可明显改善模式切换平顺性和脱粒滚筒转速跟踪效果，具备较好的抗干扰能力。最后台架试验进一步验证了 DPSTD 的调速和稳速性能，证明了其有效性和可行性，为联合收获机脱粒滚筒控制研究提供了新思路。

INTRODUCTION

The combine harvester is one of the widely used core agricultural machinery in agricultural production *(Sun et al., 2018)*. With the development of agricultural automation technology, there is an increasing demand for automatic control of combine harvesters *(Chen et al., 2017; Shojaei, 2021)*. The threshing drum has always been considered a core component of the combine harvester and has been extensively studied *(Vlădut et al., 2022; Zhang et al., 2024; Hou et al., 2023; Li et al., 2023)*.

Zhihao Zhu, Student; Xiaoyu Chai, Lecture; Lizhang Xu, Research fellow; Li Quan, Professor; Chaochun Yuan, Professor; En Lu, Associate professor; Shuofeng Weng, Student; Shichao Tian, Student; Guangqiao Cao, Research fellow

Resistance to interference and speed control are important research directions in the control of threshing drums, and they are of significant importance for enhancing the overall functionality and operational performance of the machine *(Olaye et al., 2016; Sudajan et al., 2002; Alizadeh and Khodabakhshipour 2010). Zhang et al (2011)* designed a robust control method for the threshing drum speed in a combine harvester, with the travel speed and feeding rate of the harvester as control variables and the drum speed as the controlled variable. The effectiveness of this method was verified through simulations and experiments. *Qin et al (2009)* proposed a mathematical model for the walking, harvesting, and threshing system of a combine harvester, which can effectively simulate the actual working process of the harvester. *Zhang et al (2023)* designed a control system based on active disturbance rejection and dynamic matrix modeling. This approach achieved real-time control of the drum speed and compensation of the control delay.

However, due to the limitations of the mechanical structure in conventional combine harvesters, the control of the threshing drum speed is typically achieved indirectly through the vehicle speed and feeding rate. This approach suffers from drawbacks such as low speed control accuracy, time delays, reduced operational efficiency, and the inability to adjust the speed according to changes in crop varieties and properties. In recent years, the research and application of electrification technology in agricultural machinery are becoming increasingly widespread *(Khatawkar et al., 2019; Scolaro et al., 2021; Mocera, & Somà, 2022; Zhu et al., 2023)*. Electric motors offer advantages such as fast response, high driving efficiency, and a wide range of speed and torque outputs. These advantages can effectively enhance the flexibility and efficiency of agricultural equipment. *Yang et al (2022)* conducted an electrification transformation of the reaping and threshing components of a combine harvester and designed a control system for the motors. Furthermore, they tested the system's speed tracking and anti-clogging functionalities in wheat harvesting experiments, and the results indicated that the system exhibited favorable practicality. *Sahoo & Raheman (2020)* developed a pure electric small rice harvester driven by two DC motors. Field test results showed that the product has high operational efficiency and endurance, and can effectively reduce environmental pollution and harvesting costs. *Wang et al (2020)* electrified the reaping part of a combine harvester, conducted finite element simulation on its mechanical structure, and designed a control method for the motor. Field test results showed that the modified harvester can automatically adjust its reaping speed according to the travelling speed, thereby improving the operational performance.

The purpose of this article is to improve the anti-interference capability of the threshing drum and broaden its speed range to adapt to the harvesting requirements of various crops using electric drive technology. However, considering that the threshing drum is the most power-demanding component in a combine harvester, relying solely on electric motor drive would require the installation of high-power motors and a high-power supply system, resulting in higher costs. Therefore, this article retains the original mechanical transmission components and proposes a novel dual power source threshing drum that combines an electric motor with a power coupling device. The power coupling device diverts power from both the motor and the engine, allowing the threshing drum to achieve a wide speed range. By incorporating an additional smaller electric motor. Additionally, the torque compensation provided by the electric motor enhances the threshing drum's anti-interference capability, enabling stable and high-quality operation.

In this study, a dual power source threshing drum (DPSTD) is proposed and an electric motor robust model predictive control system based on disturbance observer is designed. Furthermore, the speed control and torque compensation functions of the DPSTD are validated through simulation and bench test.

MATERIALS AND METHODS

Architecture of the DPSTD

The specific structure of the newly designed DPSTD for a combine harvester, as depicted in Fig.1, incorporates a power coupling device with a planetary gear set to distribute the power from both the engine and the motor. The power coupling device comprises a reducer, a sun gear, an outer planetary carrier, and an inner planetary carrier. The central shaft of the primary gear of the reducer serves as Input 1 of the power coupling device (connected to the motor), while the secondary gear of the reducer is coaxially integrated with the sun gear. The inner planetary carrier has an outer gear ring and an inner gear ring, the outer gear ring meshes with the outer planetary carrier, the inner gear ring meshes with the sun gear, the central axis is the input 2 of the power coupling device (connected to the engine source power output shaft), and the central axis of the outer planetary carrier is the output end of the power coupling device (connected to the threshing drum). The motor power is transmitted through the reduction set, resulting in torque amplification, and then delivered to the sun gear. Simultaneously, the engine power is transmitted to the inner planetary carrier.

As the inner planetary carrier engages with both the sun gear and the outer planetary carrier, the engine power and the motor power are combined and transmitted through the outer planetary carrier to drive the threshing drum. The speed of the engine source power output shaft remains relatively stable during operation. By adjusting the motor speed, the speed regulation function of the threshing drum is achieved to adapt to different harvesting conditions.

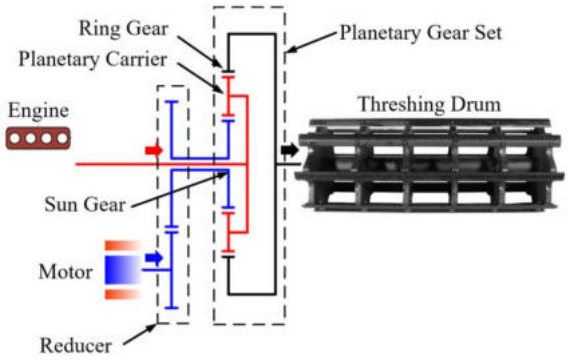


Fig. 1 - Structure of the DPSTD

The DPSTD has three power modes: hybrid mode, conventional mode, charging mode, and reversal mode, as shown in Fig. 2. In the hybrid mode, the threshing drum is driven by the engine and the motor. This mode is used when the engine's allocated power to the threshing drum during the harvesting process is lower than the instantaneous power required for threshing or when the preset mechanical speed of the threshing drum does not match the actual required speed. In the conventional mode, the threshing drum is solely driven by the engine. This mode is used when the power provided by the engine to the threshing drum meets the operational load requirements, and the preset speed of the threshing drum satisfies the harvesting needs of the current crop. In reversal mode, the threshing drum is driven by the motor to rotate in the opposite direction. This mode is used for special working conditions where the drum is overloaded and causes blockage.

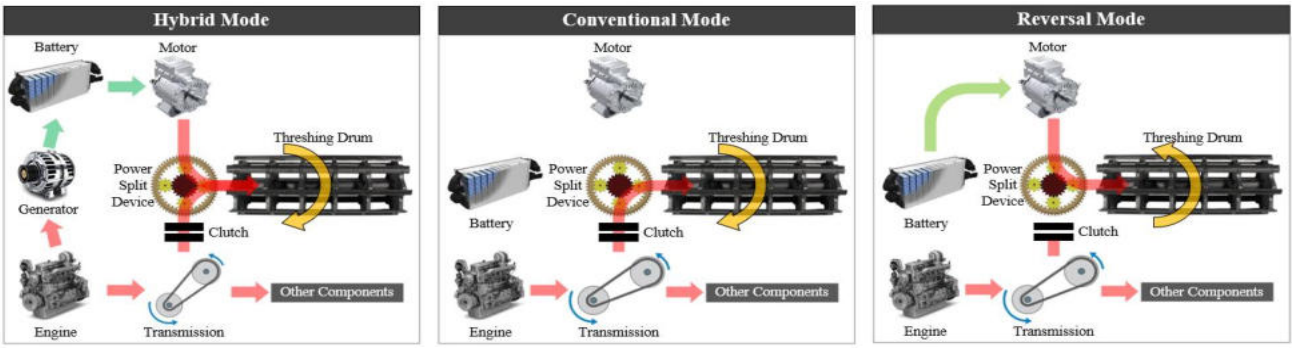


Fig. 2 - Three power mode of the DPSTD

DPSTD model

Dynamic model of the threshing drum

The active torque required by the threshing drum mainly includes the torque required for the idling of the drum itself, the torque to push the grain to overcome the resistance movement, the torque to overcome the angular acceleration generated by the rotational inertia of the drum itself, and the torque to push the grain to obtain acceleration. The total driving torque of threshing drum is

$$T_{TD} = A + B\omega_{TD}^{\ 2} + \frac{qR_{TD}^{\ 2}\omega_{TD}}{2(1-f_r)}\frac{\lambda+\Delta}{1+\Delta} + J_{TD}\dot{\omega}_{TD}$$

$$q = \rho v H \tag{1}$$

where ω_{TD} is the angular velocity of the drum, A is the torque to overcome mechanical friction, B is the air friction coefficient, q is the harvest quantity, ρ is the crop density, v is the travelling speed of the harvester, H is the cutting range, R_{TD} is the operating radius of threshing drum, Δ is the grass-grain ratio, f_r is the friction coefficient, J_{TD} is the rotational inertia of the threshing drum.

Model of the power coupling device

According to Fig.1, the power coupling device in the DPSTD consists of a reducer and a single-row planetary gear mechanism. The corresponding components are connected to the power output shaft of the engine, the motor, and the threshing drum, respectively, which closely relate the system's power transmission to the speed-torque characteristics of the power coupling device.

The output speed of the power coupling device can be expressed as:

$$\omega_{out} = \frac{(1+k)\omega_e - \omega_m / i_r}{k} \tag{2}$$

The output torque of the power coupling device can be expressed as:

$$T_{out} = -(\frac{T_m}{i_r \eta_r} + T_e) \tag{3}$$

where ω_e and ω_m are the speed of engine power output shaft and motor, T_e and T_m are the torque of engine power output shaft and motor, i_r is the gear ratio of the reducer, η_r is the efficiency of the reducer, and k is the ratio of the number of teeth on the outer planetary gear to the number of teeth on the sun gear.

It can be seen that the speed and torque of the threshing drum can be adjusted by adjusting the output speed and torque of the motor.

Torque coordination control of the DPSTD

As described previously regarding the DPSTD's three modes, its hybrid mode offers speed control and stability—features not found in conventional threshing drums—effectively enhancing the combine harvester's performance and versatility. Therefore, the torque coordination control of the DPSTD motor in hybrid mode is a key issue addressed in this study. During the operation of the harvester, complex and varying terrains, as well as uncertainties in crop attributes, will generate random and time-varying disturbances. These disturbances are transmitted through the powertrain, resulting in torque impacts and interferences on the threshing drum, which in turn affect the operational performance. Therefore, it is crucial to pay special attention to disturbance estimation and compensation under such conditions during the operation of DPSTD. Designing reliable control strategies is necessary to mitigate the performance fluctuations caused by torque disturbances. The key issues of torque coordination control in DPSTD operation in hybrid mode can be summarized in the following two aspects:

(1) A high-performance controller needs to be designed to accurately regulate the motor speed during the drum speed adjustment process, ensuring that the threshing drum operates at the desired speed and improving operational performance.

(2) To address unpredictable disturbances caused by varying terrains and crop attributes, it is necessary to design corresponding disturbance observers to estimate the disturbances and uncertainties, and then perform compensation control.

Based on the analysis of the hybrid mode of DPSTD mentioned above, a torque coordination control strategy for dual power sources is proposed. The strategy structure is illustrated in Fig. 3.

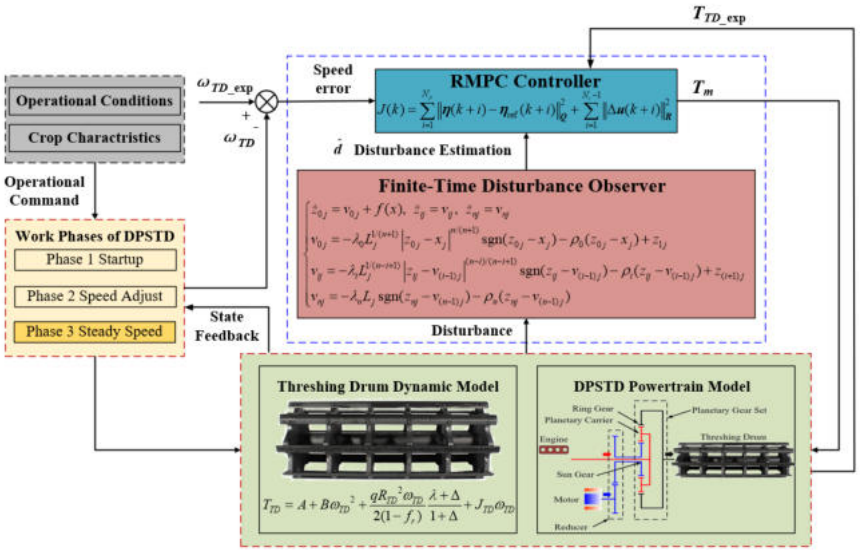


Fig. 3 - Control strategy structure of DPSTD

During the harvesting operation, the operator first sends instructions to the system according to the operating conditions and crop properties to determine the working stage and expected rotation speed of the threshing drum. The expected rotation speed of the threshing drum can be expressed as *(Li et al., 2009):*

$$\omega_{TD_\exp} = \frac{60\sqrt{\frac{2R_{\max}}{m}}}{\pi D(1+\varepsilon)\cos\beta} \tag{4}$$

where $R_{\max}$ is the maximum work required to detach the grains from the spike, m is the mass of the grain, β is the angle between the axial direction of the grain and the direction of the axial movement of the threshing teeth, ε is the restitution coefficient during the impact between the grain and the threshing teeth, and D is the diameter of the threshing drum.

During harvesting operations, the engine power is generally kept relatively constant. Therefore, at the desired speed of the threshing drum, the target output speed of the motor is:

$$\omega_{m_\text{tgt}} = i_r[(1+k)\omega_e - k\omega_{TD_\exp}] \tag{5}$$

The preliminary target output torque of motor without considering disturbances is:

$$T_{m_\text{tgt}} = -(T_e + T_{TD_\exp})i_r\eta_r \tag{6}$$

where $T_{TD_\exp}$ is the theoretical torque required by the threshing drum at the desired speed.

Based on this, in order to further achieve precise torque coordination control of the motor, a Robust Model Predictive Control (RMPC) controller is designed to regulate the motor torque. Furthermore, a Finite-Time Disturbance Observer (FTDO) is introduced to estimate the torque disturbances that exist during the harvesting process.

Design of the RMPC controller

Defining the speed of threshing drum and the speed of engine power output shaft as the state variables, motor output torque as the control variables, and the load fluctuation of threshing drum and the resistance torque of engine source as the disturbance variables, the dynamics equation of the threshing system can be written as the following state space equation:

$$\begin{cases} \dot{\boldsymbol{x}} = \boldsymbol{A}\boldsymbol{x} + \boldsymbol{B}\boldsymbol{u} + \boldsymbol{C} + \boldsymbol{\Gamma}\boldsymbol{d} \\ \boldsymbol{y} = \boldsymbol{D}\boldsymbol{x} \end{cases} \tag{7}$$

where the state variables $\boldsymbol{x} = \left[\omega_{TD}, \omega_{TD}^{\ 2}, \omega_e\right]^T$, $\boldsymbol{u}$ is the control variables, the disturbance variables $\boldsymbol{d} = \left[d_1, d_2\right]^T$,

$$\boldsymbol{A} = \begin{bmatrix} -\frac{qR_{TD}^{\ 2}}{2J_{TD}(1-f_r)}\frac{\lambda+\Delta}{1+\Delta} & -\frac{B}{J_{TD}} & 0 \\ 2 & 0 & 0 \\ 0 & 0 & -\frac{c_e}{J_e} \end{bmatrix}, \boldsymbol{B} = \left[\frac{1}{J_{TD}i_r\eta_r}, 0, 0\right]^T, \boldsymbol{C} = \left[\frac{T_{TD}-A}{J_{TD}}, 0, \frac{T_e}{J_e}\right]^T, \boldsymbol{\Gamma} = \begin{bmatrix} \frac{1}{J_{TD}} & 0 \\ 0 & \frac{1}{J_e} \end{bmatrix}, \boldsymbol{D} = \left[1, 0, 0\right]^T,$$

c_e is the damping of the engine power output shaft, J_e is the rotational inertia of the engine power output shaft.

The forward Euler method is used to discretize the above state space equation, and the corresponding discretization form can be expressed as:

$$\begin{cases} \boldsymbol{x}(k+1) = \boldsymbol{A}_k\boldsymbol{x}(k) + \boldsymbol{B}_k\boldsymbol{u}(k) + \boldsymbol{C} + \boldsymbol{\Gamma}_k\boldsymbol{d}(k) \\ \boldsymbol{y}(k+1) = \boldsymbol{D}\boldsymbol{x}(k) \end{cases} \tag{8}$$

where $\boldsymbol{A}_k(T_s) = \boldsymbol{I} + T_s\boldsymbol{A}$, $\boldsymbol{B}_k(T_s) = T_s\boldsymbol{B}$, $\boldsymbol{\Gamma}_k(T_s) = T_s\boldsymbol{\Gamma}$.

A new model prediction equation is established according to the above formula, which is expressed as:

$$\xi(k) = \left[\boldsymbol{x}(k),\ \boldsymbol{u}(k-1)\right]^T \tag{9}$$

Then the system state space equation in incremental form can be written as:

$$\begin{cases} \xi(k+1) = \tilde{\boldsymbol{A}}_k\xi(k) + \tilde{\boldsymbol{B}}_k\boldsymbol{u}(k) + \tilde{\boldsymbol{\Gamma}}_k\boldsymbol{d}(k) + \boldsymbol{C} \\ \boldsymbol{\eta}(k) = \tilde{\boldsymbol{D}}\xi(k) \end{cases} \tag{10}$$

where $\tilde{\boldsymbol{A}}_k = \begin{bmatrix} \boldsymbol{A}_k & \boldsymbol{B}_k \\ 0_{m\times n} & \boldsymbol{I}_{m\times n} \end{bmatrix}$, $\tilde{\boldsymbol{B}}_k = \begin{bmatrix} \boldsymbol{B}_k \\ \boldsymbol{I}_{m\times n} \end{bmatrix}$, $\tilde{\boldsymbol{\Gamma}}_k = \begin{bmatrix} \boldsymbol{\Gamma}_k \\ \boldsymbol{I}_{m\times m} \end{bmatrix}$, $\tilde{\boldsymbol{D}} = [\boldsymbol{D} \quad 0 \quad 0]$, $\boldsymbol{\eta}(k)$ is the output variable, m is the dimension of the control variable, and n is the dimension of the state variable.

If the current time of the system is k, the prediction time domain is N_p, and the control time domain is N_c, and $N_c \le N_p$, then the system output vector at N_p step and the control increment vector at N_c step can be expressed as:

$$\begin{aligned} \boldsymbol{Y}(k) &= [\boldsymbol{\eta}(k+1\,|\,k), \boldsymbol{\eta}(k+2\,|\,k), \cdots, \boldsymbol{\eta}(k+N_p\,|\,k)] \\ \Delta\boldsymbol{u}(k) &= [\Delta\boldsymbol{u}(k), \Delta\boldsymbol{u}(k+1), \cdots, \Delta\boldsymbol{u}(k+N_c)-1] \end{aligned} \tag{11}$$

The output of the system at step N_p can be calculated by the prediction equation in the following form:

$$\boldsymbol{Y}(k) = \boldsymbol{S}_{\xi}\boldsymbol{\xi}(k) + \boldsymbol{S}_u\Delta\boldsymbol{u}(k) + \boldsymbol{S}_{\omega}\Delta\boldsymbol{d}(k) \tag{12}$$

where $\boldsymbol{S}_{\xi} = \begin{bmatrix} \tilde{C}_{dk}\tilde{A}_{dk} \\ \tilde{C}_{dk}\tilde{A}_{dk}^2 \\ \vdots \\ \tilde{C}_{dk}\tilde{A}_{dk}^{N_c} \\ \vdots \\ \tilde{C}_{dk}\tilde{A}_{dk}^{N_p} \end{bmatrix}$, $\boldsymbol{S}_{\omega} = \begin{bmatrix} \tilde{C}_{dk}\tilde{\Gamma}_{dk} \\ \tilde{C}_{dk}\tilde{\Gamma}_{dk}^2 \\ \vdots \\ \tilde{C}_{dk}\tilde{\Gamma}_{dk}^{N_c} \\ \vdots \\ \tilde{C}_{dk}\tilde{\Gamma}_{dk}^{N_p} \end{bmatrix}$, $\boldsymbol{S}_u = \begin{bmatrix} \tilde{C}_{dk}\tilde{B}_{dk} & 0 & 0 & \cdots & 0 \\ \tilde{C}_{dk}\tilde{A}_{dk}\tilde{B}_{dk} & \tilde{C}_{dk}\tilde{B}_{dk} & 0 & \cdots & 0 \\ \cdots & \cdots & \vdots & \ddots & \vdots \\ \tilde{C}_{dk}\tilde{A}_{dk}^{N_c-1}\tilde{B}_{dk} & \tilde{C}_{dk}\tilde{A}_{dk}^{N_c-2}\tilde{B}_{dk} & \cdots & \cdots & \tilde{C}_{dk}\tilde{B}_{dk} \\ \tilde{C}_{dk}\tilde{A}_{dk}^{N_c}\tilde{B}_{dk} & \tilde{C}_{dk}\tilde{A}_{dk}^{N_c-1}\tilde{B}_{dk} & \cdots & \cdots & \tilde{C}_{dk}\tilde{A}_{dk}\tilde{B}_{dk} \\ \vdots & \vdots & \vdots & \ddots & \vdots \\ \tilde{C}_{dk}\tilde{A}_{dk}^{N_p-1}\tilde{B}_{dk} & \tilde{C}_{dk}\tilde{A}_{dk}^{N_p-2}\tilde{B}_{dk} & \cdots & \cdots & \tilde{C}_{dk}\tilde{A}_{dk}^{N_p-N_c-1}\tilde{B}_{dk} \end{bmatrix}$

According to the prediction equation, the reference vector of the system can be expressed as:

$$\boldsymbol{\eta}_{\text{ref}}(k) = [\boldsymbol{\eta}_{\text{ref}}(k+1\,|\,k), \boldsymbol{\eta}_{\text{ref}}(k+2\,|\,k), \cdots, \boldsymbol{\eta}_{\text{ref}}(k+N_p\,|\,k)] \tag{13}$$

Therefore, the system objective function with quadratic form corresponding to the RMPC controller can be expressed as:

$$J(k) = \sum_{i=1}^{N_p} \|\boldsymbol{\eta}(k+i) - \boldsymbol{\eta}_{\text{ref}}(k+i)\|_{\boldsymbol{Q}}^2 + \sum_{i=1}^{N_c-1} \|\Delta\boldsymbol{u}(k+i)\|_{\boldsymbol{R}}^2 \tag{14}$$

where $\boldsymbol{\eta}_{\text{ref}}$ is the reference vector of system, $\boldsymbol{Q}$ and $\boldsymbol{R}$ are the weight coefficient matrix of output and control of system respectively.

The objective function reflects the tracking error and control quantity. It can be transformed into a standard quadratic form, which is easy to solve, so as to minimize the tracking error and control increment.

According to the output of system, the reference vector of system can be written as:

$$\boldsymbol{\eta}_{\text{ref}} = [\omega_{TD_\text{ref}}] \tag{15}$$

The weight coefficient matrix of output and control quantity of system is:

$$\begin{cases} \boldsymbol{Q} = diag([w_{\omega_{TD}}]) \\ \boldsymbol{R} = diag([w_{T_m}]) \end{cases} \tag{16}$$

The deviation within the prediction range is defined as:

$$\boldsymbol{E}(k) = \boldsymbol{S}_{\xi}\boldsymbol{\xi}(k) - \boldsymbol{\eta}_{\text{ref}}(k+1) \tag{17}$$

The objective function of the system can be transformed into a standard quadratic form and expressed as:

$$J(\Delta\boldsymbol{U}(k)) = \begin{bmatrix} \Delta\boldsymbol{U}(k) \\ \varepsilon \end{bmatrix}^{\text{T}} \boldsymbol{H} \begin{bmatrix} \Delta\boldsymbol{U}(k) \\ \varepsilon \end{bmatrix} + \boldsymbol{G} \begin{bmatrix} \Delta\boldsymbol{U}(k) \\ \varepsilon \end{bmatrix} \tag{18}$$

where $\boldsymbol{H} = \begin{bmatrix} \boldsymbol{S}_u^{\text{T}}\boldsymbol{Q}'\boldsymbol{S}_u + \boldsymbol{R} & 0 \\ 0 & \rho \end{bmatrix}$, $\boldsymbol{G} = [2\boldsymbol{E}(k)^{\text{T}}\boldsymbol{Q}'\boldsymbol{S}_u \quad 0]$.

The constraints of system state, control quantity and output variable are respectively defined as:

$$\begin{cases} \Delta\boldsymbol{U}_{\min} \le \Delta\boldsymbol{U} \le \Delta\boldsymbol{U}_{\max} \\ \boldsymbol{U}_{\min} \le A\Delta\boldsymbol{U} + \boldsymbol{U} \le \boldsymbol{U}_{\max} \\ \boldsymbol{Y}_{\min} - \varepsilon \le \boldsymbol{S}_{\xi}\boldsymbol{\xi}(k) + \boldsymbol{S}_u\Delta\boldsymbol{U}(k) \le \boldsymbol{Y}_{\max} + \varepsilon \end{cases} \tag{19}$$

where $\Delta\boldsymbol{U}$ is the increment of control quantity.

By solving the quadratic programming problem in each control domain, a series of increments of control input in the control domain can be calculated:

$$\Delta \boldsymbol{U}^* = \left[\Delta \boldsymbol{u}^*(k), \Delta \boldsymbol{u}^*(k+1), \Delta \boldsymbol{u}^*(k+2), \cdots, \Delta \boldsymbol{u}^*(k+N_c-1)\right]^{\mathrm{T}} \tag{20}$$

Therefore, the control input of motor torque can be calculated by the following formula:

$$\boldsymbol{u}(k) = \boldsymbol{u}(k-1) + \Delta \boldsymbol{U}^* \tag{21}$$

Design of the FTDO

The FTDO is further introduced to estimate the disturbance variables. For the system with the form of Eq. (7), the system disturbance satisfies the following conditions: the disturbance term d_i is *n*-order continuously differentiable (where *n* represents the system order), and its *j*-order derivative is bounded and satisfies $\left|d_i^{(j)}\right| \le L_i$, where $L_i > 0$, $i = 1, \cdots, n$, and $j = 0, 1, \cdots, n$.

The FTDO to be designed has the following standard forms:

$$\begin{cases} \dot{z}_{0j} = v_{0j} + f(x) \\ \dot{z}_{ij} = v_{ij} \\ \dot{z}_{nj} = v_{nj} \\ v_{0j} = -\lambda_0 L_j^{1/(n+1)} \left|z_{0j} - x_j\right|^{n/(n+1)} \operatorname{sgn}(z_{0j} - x_j) - \rho_0 (z_{0j} - x_j) + z_{1j} \\ v_{ij} = -\lambda_i L_j^{1/(n-i+1)} \left|z_{ij} - v_{(i-1)j}\right|^{(n-i)/(n-i+1)} \operatorname{sgn}(z_{ij} - v_{(i-1)j}) - \rho_i (z_{ij} - v_{(i-1)j}) + z_{(i+1)j} \\ v_{nj} = -\lambda_n L_j \operatorname{sgn}(z_{nj} - v_{(n-1)j}) - \rho_n (z_{nj} - v_{(n-1)j}) \end{cases} \tag{22}$$

where $\lambda_0, \cdots, \lambda_n$ and $\rho_0, \cdots, \rho_n$ are the pending coefficients of the FTDO respectively. z_{0j} is the estimated value of the state variable. $z_{1j}, \cdots, z_{nj}$ are the estimated values of the disturbance quantity $d_j^{(0)}, \cdots, d_j^{(n-1)}$ respectively. $i = 1, \cdots, n-1$, $j = 1, \cdots, n$, and $f(x)$ corresponds to the equation of state shown in Eq. (7).

When $j = 1$ and $j = 2$ respectively, the torque disturbance can be estimated by the following FTDO equation respectively:

$$\begin{cases} \dot{z}_{01} = v_{01} + f(x_1) \\ \dot{z}_{11} = v_{11} \\ \dot{z}_{21} = v_{21} \\ v_{01} = -\lambda_0 L_1^{1/3} \left|z_{01} - x_1\right|^{2/3} \operatorname{sgn}(z_{01} - x_1) - \rho_0 (z_{01} - x_1) + z_{11} \\ v_{11} = -\lambda_1 L_1^{1/2} \left|z_{11} - v_{01}\right|^{1/2} \operatorname{sgn}(z_{11} - v_{01}) - \rho_1 (z_{11} - v_{01}) + z_{21} \\ v_{21} = -\lambda_2 L_1 \operatorname{sgn}(z_{21} - v_{11}) - \rho_2 (z_{21} - v_{11}) \end{cases} \quad \begin{cases} \dot{z}_{02} = v_{02} + f(x_3) \\ \dot{z}_{12} = v_{12} \\ \dot{z}_{22} = v_{22} \\ v_{02} = -\lambda_0 L_2^{1/3} \left|z_{02} - x_2\right|^{2/3} \operatorname{sgn}(z_{02} - x_2) - \rho_0 (z_{02} - x_2) + z_{12} \\ v_{12} = -\lambda_1 L_2^{1/2} \left|z_{12} - v_{02}\right|^{1/2} \operatorname{sgn}(z_{12} - v_{02}) - \rho_1 (z_{12} - v_{02}) + z_{22} \\ v_{22} = -\lambda_2 L_2 \operatorname{sgn}(z_{22} - v_{12}) - \rho_2 (z_{22} - v_{12}) \end{cases} \tag{23}$$

where: z_{01} and z_{02} are the estimated values of the state quantity ω_{TD} and ω_e respectively. z_{11} and z_{12} are the estimated values of disturbance d_1 and d_2 respectively. z_{21} and z_{22} are the estimated values of $\dot{d}_1$ and $\dot{d}_2$ respectively.

To further analyze the stability and convergence of the proposed FTDO, the above estimation errors are defined as:

$$\sigma_{0j} = \frac{z_{0j} - x_j}{L_j}, \sigma_{1j} = \frac{z_{1j} - d_j}{L_j}, \cdots, \sigma_{nj} = \frac{z_{nj} - d_j^{(n-1)}}{L_j} \tag{24}$$

From Eq. (9), the differential form of Eq. (24) can be obtained as follows:

$$\dot{\sigma}_{0j} = -\lambda_0 \left|L_j \sigma_{0j}\right|^{n/(n+1)} \operatorname{sgn}(\sigma_{0j}) - \rho_0 \sigma_{0j} + \sigma_{1j} \tag{25}$$

Similarly:

$$\dot{\sigma}_{1j} = \frac{1}{L_j}\left(-\lambda_1 L_j^{1/(n+1)} \left|z_{1j} - v_{0j}\right|^{(n-1)/n} \operatorname{sgn}(z_{1j} - v_{0j}) - \rho_1 (z_{1j} - v_{0j})\right) + \sigma_{2j} \tag{26}$$

It can be seen that:

$$z_{1j} - v_{0j} = \lambda_0 L_j \left|\sigma_{0j}\right|^{n/(n+1)} \operatorname{sgn}(\sigma_{0j}) + \rho_0 (L_j \sigma_{0j}) = L_j (\sigma_{1j} - \dot{\sigma}_{0j}) \tag{27}$$

Then, substituting Eq. (27) into Eq. (26) yields:

$$\dot{\sigma}_{1j} = -\lambda_1 \left|\sigma_{1j} - \dot{\sigma}_{0j}\right|^{(n-1)/n} \operatorname{sgn}(\sigma_{1j} - \dot{\sigma}_{0j}) - \rho_1 (\sigma_{1j} - \dot{\sigma}_{0j}) + \sigma_{2j} \tag{28}$$

Similarly, for i = 2, …, n-1, it follows that:

$$\dot{\sigma}_{ij} = -\lambda_i \left|\sigma_{ij} - \dot{\sigma}_{(i-1)j}\right|^{(n-i)/(n-i+1)} \operatorname{sgn}(\sigma_{ij} - \dot{\sigma}_{(i-1)j}) - \rho_i (\sigma_{ij} - \dot{\sigma}_{(i-1)j}) + \sigma_{(i+1)j} \tag{29}$$

$$\dot{\sigma}_{nj} = -\lambda_n \operatorname{sgn}(\sigma_{nj} - \dot{\sigma}_{(n-1)j}) - \rho_n (\sigma_{nj} - \dot{\sigma}_{(n-1)j}) + \frac{1}{L_j} d_j^n \tag{30}$$

Therefore, the estimation error of the FTDO can be expressed as follows:

$$\begin{aligned}
&\dot{\sigma}_{0j} = -\lambda_0 \left|\sigma_{0j}\right|^{n/(n+1)} \operatorname{sgn}(\sigma_{0j}) - \rho_0 (\sigma_{0j}) + \sigma_{1j} \\
&\vdots \\
&\dot{\sigma}_{(n-1)j} = -\lambda_{n-1} \left|\sigma_{(n-1)j} - \dot{\sigma}_{(n-2)j}\right|^{1/2} \operatorname{sgn}(\sigma_{(n-1)j} - \dot{\sigma}_{(n-2)j}) - \rho_{n-1} (\sigma_{(n-1)j} - \dot{\sigma}_{(n-2)j}) + \sigma_{nj} \\
&\dot{\sigma}_{nj} = -\lambda_n \operatorname{sgn}(\sigma_{nj} - \dot{\sigma}_{(n-1)j}) - \rho_n (\sigma_{nj} - \dot{\sigma}_{(n-1)j}) + \frac{1}{L_j} d_j^n
\end{aligned} \tag{31}$$

According to the relevant research conclusions *(Nguyen et al, 2021)*, it can be seen that the system (31) is stable in finite time, indicating that the estimation error of the FTDO can converge to zero in finite time.

Then the compensation torque of motor is:

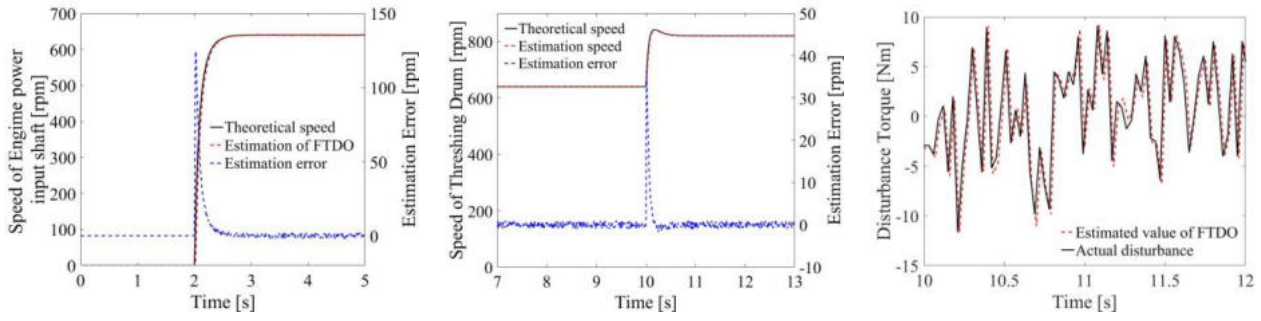
$$\boldsymbol{u} = T_{m_\mathrm{com}} = -i_r \eta_r (z_{21} + z_{22}) \tag{32}$$

RESULTS AND DISCUSSION

The previous section focused on the control methods of the designed DPSTD in hybrid mode, specifically addressing the regulation of drum speed for combined harvester operation, as well as its resistance to disturbance and overload. To explore the effectiveness of the DPSTD's structure and control methods proposed in this paper, a simulation model of the DPSTD was further developed using the MATLAB/Simulink platform. The simulation includes the performance evaluation of the designed FTDO, speed control functions of the DPSTD, as well as a comparison of the proposed control method's effectiveness in suppressing disturbances and load fluctuations with and without disturbance compensation.

Verification of the FTDO performance

Assuming that the combine harvester experiences a random disturbance torque from the engine power source during the harvesting process, characterized by Gaussian white noise with a sampling time of 0.01, a variance of 30, and a mean of 0. This disturbance torque is applied to the actual output torque of the DPSTD engine power input shaft. The results of the state estimation and the disturbance estimation of the FTDO during the operation of the DPSTD are shown in Fig. 4.



(a) (b) (c)

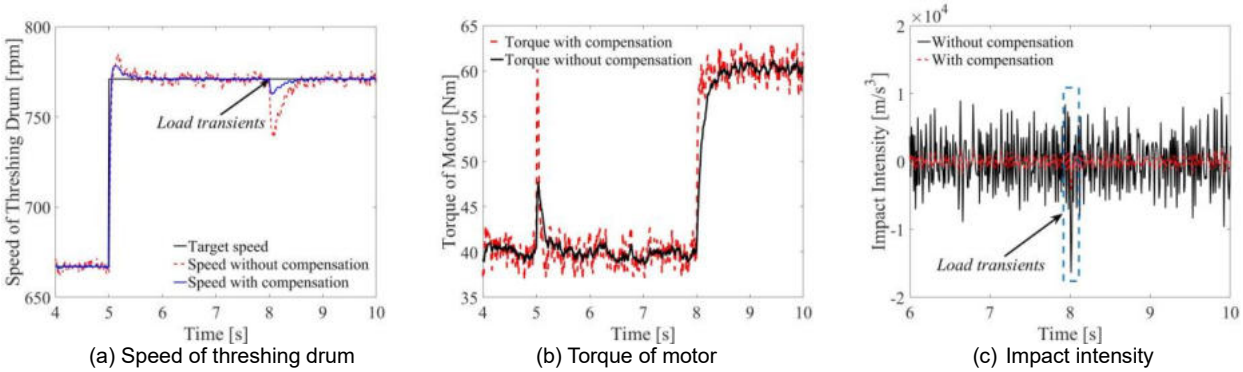
Fig. 4 -The result of the FDTO estimation

(a) State estimation (speed of engine power input shaft); (b) State estimation (speed of threshing drum); (c) disturbance estimation

Fig. 4(a) and Fig. 4(b) show the variations of the two state variables of the speed of engine power input shaft and threshing drum obtained by the FTDO during the estimation of random disturbance. The engine startup process begins at approximately 2.0 s, while the speed adjustment process of the threshing drum starts at 10.0 s. It can be observed that the FTDO accurately estimates the speed of engine power input shaft and the threshing drum with small estimation errors and convergence stability within a finite time. Fig. 4(c) represents the estimated disturbance torque obtained by the FTDO, which exhibits the same trend with the actual values and demonstrates good estimation accuracy.

Simulation of torque dynamic compensation control of the DPSTD

A control simulation analysis of the DPSTD torque compensation control was performed to test its anti-interference and overload resistance capabilities. Assume that the target speed of the DPSTD is from 660 rpm to 770 rpm, and there is a random disturbance torque during the operation. Additionally, a step change in load of 20 Nm occurs at the 8th second. Fig. 5 compares the effects of the DPSTD with torque compensation control based on FTDO and without compensation control under the influence of torque disturbances and load transients.



(a) Speed of threshing drum (b) Torque of motor (c) Impact intensity

Fig. 5 - Comparison of torque compensation control

From Fig. 5(a) and Fig. 5(b), it can be observed that when the DPSTD does not employ any interference compensation control strategy, the torque disturbances significantly deteriorate the smoothness of the threshing drum speed tracking. Additionally, these disturbances are not detected by the upper-level controller, and the torque command to the motor continues to be issued by the basic torque controller. However, when employing the FTDO interference compensation control strategy, the current disturbance signal value can be estimated, and subsequently, the output torque of the motor is recalculated, which greatly reduces the impact of the DPSTD, improves the stability of speed tracking, and enhances the quality of mode switching.

Furthermore, according to the simulation results of load transients starting at the 8th seconds in Fig. 5(c), when there is no torque compensation control, the output load transients greatly deteriorate the operation quality of the DPSTD, causing an impact with an amplitude of $1.64 \cdot 10^4$ m/s^3, and the speed tracking shows obvious oscillation. However, the torque compensation control based on FTDO accurately estimates the load changes and coordinates the output torque of the motor, effectively limiting the impact within the range of [$-0.45 \cdot 10^4$ m/s^3, $0.45 \cdot 10^4$ m/s^3]. It also reduces the speed oscillations, achieving a smoother speed tracking. Table 1 presents a comparison of the effects with and without torque compensation control. It can be observed that the control strategy with compensation significantly reduces the impact and speed errors of DPSTD. The root mean square (RMS) value of speed errors is decreased by 73.90%, the maximum speed error id decreased by 76.18%, the RMS value of impact is decreased by 33.51%, and the maximum impact is reduced by 73.18%. In conclusion, the designed torque compensation control strategy based on FTDO can significantly improve the smoothness of mode switching and the speed tracking of the threshing drum, making the DPSTD has a strong anti-interference capability.

Table 1

Comparison of control effects based on two strategies

Control strategy	RMS of speed error (rpm)	Maximum speed error (rpm)	RMS of impact intensity (m/s^3)	Maximum impact intensity (m/s^3)
Without compensation	32.64	31.32	1.94×10^3	1.64×10^4
With compensation	8.52	7.46	1.29×10^3	0.43×10^4

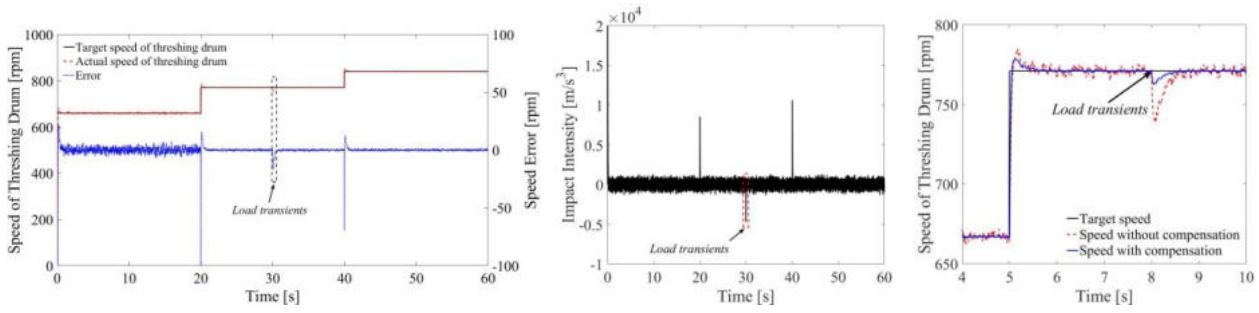
Bench test

In order to verify the feasibility of the structure and control strategy of the DPSTD, a bench test is carried out based on a testing platform. It should be noted that due to the limitations of the experimental equipment, the engine test cannot be realized but considering that the purpose of the test is to verify the effectiveness of the control strategy in the presence of torque disturbances from the engine source, the motor can be used to simulate this part of the torque disturbance. Fig. 6 is the schematic diagram of testing platform for the DPSTD, which is mainly composed of a multi-functional power coupling device (with two built-in motors), two electric dynamometers (corresponding to the left and right driving semi-axis respectively), a testing platform controller and related auxiliary equipment. The functionality of reading the status parameters of the power coupling device, load simulation of the electric dynamometers, and parameter settings and status monitoring of the upper computer can be achieved through CAN bus communication. The multi-functional power coupling device can be used to simulate the power coupling device in the DPSTD, while one of its built-in motors emulating the engine source power, while the other one acts as the driving motor in the DPSTD. Additionally, the electric dynamometers are used to simulate the load input.



Fig. 6 - The testing platform

The designed observer and controller are integrated into the motor controller application layer of the testing platform, enabling the application of the designed control strategy. Fig.7 presents the bench test results of the DPSTD applying the torque compensation control strategy during mode switching, speed regulation, and when subjected to load transients.



(a) (b) (c)

Fig. 7 - The results of bench test

(a) Speed of threshing drum; (b) Impact intensity; (c) Torque of motor and engine power input shaft

It can be observed from Fig. 7(a) that in the bench test, the actual speed of the threshing drum is closely aligned with the target speed, with only significant errors occurring during demand speed transients. This is attributed to the controller response and communication delays in the experiment. However, the error duration is short and will not significantly affect the performance. Hence, the errors generated in this case can be disregarded. Additionally, in the conventional mode where the motor is not engaged, the speed error is noticeably higher compared to the hybrid mode. This observation demonstrates that the DPSTD employing motor disturbance compensation control can effectively improve speed tracking accuracy. Fig. 7(b) shows that compared to the simulation results with compensation control, the bench test exhibits higher impact intensity but remains within 1.1×10^4 m/s^3. During load transients, the impact intensity is slightly higher than the simulation results, but the overall effect is still satisfactory.

It can be seen from Fig. 7(c) that the driving motor can promptly start and engage during mode switching, accomplishing the speed regulation function of the DPSTD. Simultaneously, effective torque compensation can be achieved to mitigate disturbances and load transients, reducing speed oscillations and minimizing torque shocks in the transmission system.

To sum up, compared with the closed simulation environment, the bench test results are different from the simulation results due to the differences in equipment parameters, motor performance, communication and control time delay and other factors, but still achieved satisfactory outcomes. The test verifies that the designed DPSTD possesses sensitive and versatile speed regulation capabilities, enhancing the versatility of the combine harvester. Additionally, the proposed motor control method realizes disturbance identification and compensation control, improving the DPSTD's anti-interference ability during operation, thereby ensuring stable operational performance. Consequently, the superiority of the DPSTD's threshing system over that of conventional combine harvesters is demonstrated.

CONCLUSIONS

Based on a parallel hybrid system, this study proposes a dual power source threshing drum that can be driven by both an engine and an electric motor. A RMPC controller is designed for the motor control, and FTDO are incorporated to enhance the control performance. The study further explores the performance of the DPSTD, including its speed regulation capability and disturbance rejection ability. Finally, a bench test is conducted to validate the effectiveness and superiority of the DPSTD. According to the findings above, the following conclusions were reached:

(1) Compared to conventional threshing drums, the DPSTD driven by engine and motor can use the large-scale speed regulation function of motor to realize the adjustable speed of threshing drum in hybrid mode, and has fast dynamic response, allowing for quick parameter adjustments according to the harvesting requirements of different crops, enabling versatile applications.

(2) The RMPC controller for motor based on the FTDO can accurately estimate the disturbance torque and operating load during operation, enabling fast and precise torque compensation. Simulation results show that, in the presence of torque disturbances and load transients, the control strategy with torque compensation reduces the RMPC value of speed error by 73.90%, the maximum speed error by 76.18%, the RMPC value of impact intensity by 33.51%, and the maximum impact intensity by 73.18% compared to the control strategy without compensation. This approach significantly improves smoothness of mode switching and speed tracking performance of the threshing drum, demonstrating excellent anti-interference ability.

(3) The bench test demonstrates that the designed DPSTD with torque compensation can effectively perform speed adjustment and exhibits anti-interference ability. The test results are similar to the simulation results, which proves the rationality and effectiveness of the designed DPSTD in terms of its structure and control strategy, and provides a novel and valuable reference for the research on the speed control of threshing drum of combine harvester.

ACKNOWLEDGMENTS

The authors gratefully acknowledge the Jiangsu Agricultural Science and Technology Innovation Fund (CX[22]1005), the Project of Faculty of Agricultural Equipment of Jiangsu University (NZXB20210103), the Postgraduate Research & Practice Innovation Program of Jiangsu Province (KYCX23_3668), the Major Scientific and Technological Special Project of Anhui Province (202203a06020025) and the National Natural Science Foundation of China (52405271) for the financial support.

REFERENCES

[1] Alizadeh, M. R., Khodabakhshipour, M. (2010). Effect of threshing drum speed and crop moisture content on the paddy grain damage in axial-flow thresher. *Agronomical Research in Moldavia (Cercetări Agronomice în Moldova)*, *4*(144), 5-11. https://repository.iuls.ro/xmlui/handle/20.500.12811/2571

[2] Chen, J., Ning, X., Li, Y., Yang, G., Wu, P., Chen, S. (2017). A fuzzy control strategy for the forward speed of a combine harvester based on KDD. *Applied engineering in agriculture*, *33*(1), 15-22. https://doi.org/10.13031/aea.11299

[3] Hou, Y., Shang, S., Li, X., He, X.N., Zheng, H., Dong, T., Li, X., Liu, Z., Yang, S., Wang, D.W. (2023). Discrete element method (EDEM) simulation and parameter optimization design and testing of a low-loss and high-efficiency corn threshing device. *INMATEH – Agricultural Engineering 71*(3), 194-204. https://doi.org/10.35633/inmateh-71-16

[4] Khatawkar, D.S. James, P. S., Dhalin, D. (2019). Modern trends in farm machinery-electric drives: A Review. *International Journal of Current Microbiology and Applied Sciences*, (8), 83-98. https://doi.org/10.20546/ijcmas.2019.801.011.

[5] Li, B. (2009). *Agricultural Mechanics (农业机械)*. Beijing, China Agriculture Press. (in Chinese)

[6] Li, H., Wang, Q., Wang, Y., Ma, J., Yue, D., Geng, D. (2023). Design and experiment of transverse axial flow corn flexible threshing device. *INMATEH – Agricultural Engineering, 69*(1), 461-470. https://doi.org/10.35633/inmateh-69-43

[7] Mocera, F., Somà, A. (2022). A Review of Hybrid Electric Architectures in Construction, Handling and Agriculture Machines. *New Perspectives on Electric Vehicles*, *49.* https://doi.org/10.5772/intechopen.99132

[8] Nguyen, N. P., Oh, H., Kim, Y., Moon, J., Yang, J., Chen, W. H. (2021). Finite-time disturbance observer-based modified super-twisting algorithm for systems with mismatched disturbances: Application to fixed-wing UAVs under wind disturbances. *International Journal of Robust and Nonlinear Control*, *31*(15), 7317-7343. https://doi.org/10.1002/rnc.5678

[9] Olaye, A. R. I. B., Moreira, J., Hounhouigan, J., Amponsah, S. K., Hounhouigan, D. J. (2016). Effect of threshing drum speed and crop weight on paddy grain quality in axial-flow thresher (ASI). *Journal of Multidisciplinary Engineering Science and Technology*, *3*(1), 3716-3721. https://www.researchgate.net/publication/305618996

[10] Qin, Y., Zhao, D., Li, Z., & Ji, W. (2009). Constant speed control of threshing drum of combine harvester based on RBF network (基于 RBF 网络的联合收获机脱粒滚筒恒速控制). *Transactions of the Chinese Society for Agricultural Machinery*, *40*(11), 59-63. *(in Chinese)*

[11] Sahoo, A. U., & Raheman, H. (2020). Development of an electric reaper: a clean harvesting machine for cereal crops. *Clean Technologies and Environmental Policy*, *22*, 955-964. https://doi.org/10.1007/s10098-020-01838-7

[12] Scolaro, E. Beligoj, M., & Estevez, M, P. (2021). Electrification of Agricultural Machinery: A Review. *IEEE Access*, (9), 164520-164541. https://doi.org/10.1109/ACCESS.2021.3135037.

[13] Shojaei, K. (2021). Intelligent coordinated control of an autonomous tractor-trailer and a combine harvester. *European Journal of Control*, *59*, 82-98. https://doi.org/10.1016/j.ejcon.2021.02.005.

[14] Sudajan, S., Salokhe, V. M., & Triratanasirichai, K. (2002). PM—Power and machinery: effect of type of drum, drum speed and feed rate on sunflower threshing. *Biosystems engineering*, *83*(4), 413-421. https://doi.org/10.1006/bioe.2002.0133.

[15] Sun, D. Chen, D., & Wang, S, M. (2018). Development on electrical system performance test stand for combine harvester. *Proceedings of the 6th International-Federation-of-Automatic-Control (IFAC) Conference on Bio-Robotics*, 2(7), 13-15. https://doi.org/10.1016/j.ifacol.2018.08.195.

[16] Vlădut, N.-V., Biris, S.St., Cârdei, P., Găgeanu, I., Cujbescu, D., Ungureanu, N., Popa, L.-D., Perişoară, L., Matei, G., Teliban, G.-C. (2022). Contributions to the Mathematical Modeling of the Threshing and Separation Process in an Axial Flow Combine. *Agriculture, 12*(10), 1520. https://doi.org/10.3390/agriculture12101520

[17] Vlădut, N.-V., Ungureanu, N., Biris, S.St., Voicea, I., Nenciu, F., Găgeanu, I., Cujbescu, D., Popa, L.-D., Boruz, S., Matei, G., Ekielski, A., Teliban, G.C. (2023). Research on the identification of some optimal threshing şi separation regimes in the axial flow apparatus. *Agriculture, 13*(4), 838. 10.3390/agriculture13040838, agriculture-2301663

[18] Wang, P., Tian, M., Wang, H., Jiang, W., Cao, Q. (2020). Electrical Modification and Experimental Study of Combine Harvester Reaping Unit. In *IOP Conference Series: Materials Science and Engineering*, *790*(1), 012168. https://doi.org/10.1088/1757-899X/790/1/012168.

[19] Yang, Z., Wang, H., Sun, H., Wang, P., Cao, Q. (2022). Experimental Study on Electric Harvesting of Combine Harvester. In *Journal of Physics: Conference Series*, *2218*(1), 012064. https://doi.org/10.1088/1742-6596/2218/1/012064.

[20] Zhang, J., Zhao, B., Yan, X., Liu, M., Xu, L., & Shang, C. (2023). Design and optimization of dual-motor electric tractor drive system based on driving cycles. *Plos one*, *18*(6), e0286378. https://doi.org/10.1371/journal.pone.0286378.

[21] Zhang, J., Zhao, D., Shen, H. (2011). Robust predictive control of threshing drum speed of combine harvester. *Control engineering of China*, *18*(4), 568-571.

[22] Zhang, Z., Jiang, H., He, X., Zhang, F., Wang, J., Wang, D. (2024). Design and test of threshing and cleaning device for Cyperus Esculentus L. combine harvester. *INMATEH – Agricultural Engineering 72*(1), 798-808. https://doi.org/10.35633/inmateh-72-71

[23] Zhu, Z., Chai, X., Xu, L., Quan, L., Yuan, C., & Tian, S. (2023). Design and performance of a distributed electric drive system for a series hybrid electric combine harvester. *Biosystems Engineering*, *236*, 160-174. https://doi.org/10.1016/j.biosystemseng.2023.10.015.

SUBSTANTIATION OF EQUIPMENT PARAMETERS FOR COMPACTING PLANT MATERIALS

ОБОСНОВАНИЕ ПАРАМЕТРОВ ОБОРУДОВАНИЯ ДЛЯ УПЛОТНЕНИЯ РАСТИТЕЛЬНЫХ МАТЕРИАЛОВ

Dmitry MILKO*[)], Anna PEDCHENKO[1)], Tatyana KLEVTSOVA[1)], Alexander GVOZDEV[1)]
[1)] Melitopol State University / Russia
*E-mail: milkodmitry@gmail.com
DOI: https://doi.org/10.35633/inmateh-76-42

Keywords: *compacting process, physical and mechanical properties, adding of preservatives, dosage, mathematical modelling, non-uniformity, quality indicators, storage, structuring.*

ABSTRACT
The article addresses the development of foundational principles for improving the quality of plant product preservation. The application of the proposed technologies enables a reduction in nutrient losses in raw plant materials during storage. This assertion is supported by the results of both theoretical and experimental studies on the physical and mechanical properties of plant materials, as well as on the energy, operational, and technological performance of the equipment, including its structural design parameters and modes of operation. The use of the proposed technology enhances nutrient preservation by preventing cell structure damage and preserving plant juices, while also minimizing internal voids and reducing the amount of free air within the compacted monolith. Consequently, this leads to a decrease in the cost of dietary components. The implementation of the proposed technological process in haylage production significantly reduces nutrient losses during storage. Furthermore, using plant raw materials stored with this method results in lower milk production costs compared to traditional storage techniques.

АННОТАЦИЯ
Статья посвящена разработке основ повышения качества хранения растительной продукции. Применение предложенных технологий позволит снизить потери питательных веществ в растительном сырье в процессе его хранения. Достоверность такого утверждения подтверждаются результатами теоретических и экспериментальных исследований физико-механических свойств растительного сырья, энергетических, эксплуатационных и технологических показателей агрегата, его схемы, конструктивных параметров и режимов работы. Использование предложенной технологии улучшает сохранность питательных веществ, благодаря отсутствию повреждений клеточной структуры и сохранности внутриклеточного сока, снижением свободного пространства между стеблями, что соответственно уменьшает объем воздушной массы в уплотненном монолите. Предложенная технология обеспечивает снижение стоимости компонентов рациона. Применение предложенной технологической линии при заготовке сенажа обеспечивает снижение потерь питательных веществ в процессе консервирования растительного сырья. При использовании растительного сырья, заложенного по предложенной технологии, себестоимость молока снижается в сравнении с существующими вариантами.

INTRODUCTION
Much attention has been paid to plant raw materials research since ancient times. Compaction of straw materials as an alternative fuel can be considered as the first attempts. The devices for stem materials compaction have been used since the end of the 9th century. Approximately the same time, there were the first attempts to provide a scientific substantiation for this process. Yet more detailed studies of stem materials compaction were started in the early twentieth century.

The first mechanisms for fuel briquettes production were peat briquette presses of the stamp type. But they were not adapted to the pressing of plant raw materials. Therefore, it was necessary to conduct physical and mechanical research as well as technological properties of materials to be pressed. All of the above was necessary for defining the design and technological parameters and modes of operation of the press equipment.

Great contribution to the study of vegetable raw materials compaction problems was made by the scientists *Goryachkin,(1965), Gutyar, (1936), Pustigin, (1948)* and others and no plant materials (*Olaleye et. al., 2020; Vanhoorne et al., 2020; Orisaleye and Ojolo, 2019 and others*).

Special press briquetting machines for stem materials were the results of their work for stem materials. As the result of stem materials compaction research, having been conducted by many authors, various dependences of the material density *ρ* and the degree of its compression on the applied force *P* were set. However, despite all the efforts, researchers did not come a single opinion as for the regularities of the process of hay and straw materials pressing.

On the bases of data obtained, many equations have been proposed that relate the pressure to the deformation or density of the pressed material. Some scientists believe that the relationship between the pressing pressure and the density of the material in the chamber can be expressed by a power function, in the form $P = C\rho S$, while other researchers (*Pustigin M., 1948, Osobov V., 1963, Dolgov I., 1971*) consider that the dependence should have an exponential dependence in the form $P = AeB\rho$. Whereas *Dolgov I. (1971)* was certain that the relationship between pressing pressure and density will change its physical meaning when the humidity of the pressing materials changes, namely at humidity up to 15.6%, the dependence will be gradual, while with increasing humidity more than 18% the dependence will already be exponential. We should also not forget about the supporters of Hooke's law, such as *Goryachkin V., (1965)* and *Gutyar* E., *(1936).*

For example, *Goryachkin V., (1965),* proposed the dependence of the axial pressure on the movement of the piston.

$$p = p_{max}(1 - \frac{x^2}{S^2}) \quad (1)$$

where:

p, p_{max} - respectively, the current and maximum pressure on the piston, [Pa];

x, S - respectively, the path and stroke of the piston, [m].

Pustygin M., (1948), noticed that in the presence of nodes availability, leaves and stems with different orientation there is no direct fracture of the stems, and the process takes place along with the flattening. As a result, the compaction process proceeds smoothly and evenly. The materials to be pressed have only physical, mechanical and technological properties that affect the compaction process. That is why many researchers have sought to identify these properties and identify their impact on the process. For example, *Gutyar E., (1936),* in the proposed dependences took into account the modulus of elasticity of the first kind and the Poisson's ratio. Such researchers as *Perezhogin M., (1963),* and *Khrapach E., (1956),* took into account the moisture content of the fodder as well as the rate material of deformation.

THEORETICAL BACKGROUND

At the present stage, it is no longer a secret that the preservation of feed should first avoid contact of the feed mass with the air. It is achieved in a various way, such as filling storage containers with inert gases, compacting the feed mass, compacting near the shelter storage or containers with airtight films or laying in polymer sleeves, and so on. But the most widespread ones are the processes of compaction of the feed mass, where due to the direct compression of freely placed particles there is the displacement of air from the feed mass. *Khvorostyanov, (1980), Semenikhin, (1998),* and others have already dealt with these issues. However, these issues could not be finally resolved. Theories of fodder mass compaction as well as theories of porosity, stacking, etc. were offered. However, the issue remains topical due to excessive nutrient losses (about 15%) during storage. Therefore, the relevance of this topic remains and needs further development. *Khvorostyanov, (1980),* was engaged in the processes of self-compaction of fodder masses in small storages. He most systematically considered the physical and mechanical properties of silage. Academician Muller R., (*Muller, 1963*) put forward some empirical formulas for soils of normal humidity, which, with certain assumptions, can be applied to silage monoliths. According to them, the normal vertical pressure p_z will be equal:

For containers with rectangular cross section:

$$p_z = 9.81\rho_{cp}\frac{1}{2}\sqrt{\frac{\pi si}{2\Psi(i+1)}}\cos\left(\sqrt{\frac{1}{s}}\cdot\frac{2x}{a}\right)\cos\left(\sqrt{\frac{1}{s}}\cdot\frac{2y}{b}\right)\Phi\left[\frac{2z}{a}\sqrt{\frac{\Psi(i+1)}{si}}\right] \quad (2)$$

For containers with round section:

$$p_z = 9.81\rho_{cp}\frac{1}{2}\sqrt{\frac{\pi si}{2\Psi(i+1)}}\cos\left(\sqrt{\frac{2}{s}}\cdot\frac{r}{R}\right)\Phi\left[\frac{2}{R}\sqrt{\frac{2\Psi}{s}}\right] \quad (3)$$

where:

ρ_{cp} - average mass density, [kg/m^3];

a, b - length and width of a rectangular container, [m];

i - the ratio b/a;

R - the radius of the round container, [m];

s - the coefficient that characterizes the smoothness of the tank walls;

Ψ - coefficient of lateral pressure;

Φ (a) - is the Laplace function;

$$u = \frac{r}{R}\sqrt{\frac{2\Psi}{s}}$$

x, y, z, r - coordinates of the point for which the pressure is being determined, [m].

The optimal from the positions of providing the highest normal vertical pressure p_z are containers with a round cross section, which are already followed by containers with a square cross section because they have a smaller perimeter with the same cross-sectional area. Moreover, in all cases, containers with large cross-sectional areas have advantages over containers with small cross-sections, and containers with large heights have advantages over smaller ones.

Many authors in making their hypotheses use the provisions of Hooke's law on the deformation of elastic-plastic materials, namely:

$$Hn\frac{d\varepsilon}{dt} + E\varepsilon - \sigma - n\frac{d\sigma}{dt} = 0 \quad (4)$$

where:

E, H - long and instantaneous modulus of elasticity, [Pa];

σ, ε - stress and relative deformation, [Pa];

$n = \mu / E$ - relaxation time, [s];

μ - viscosity, [Pa*s].

Semenikhin A., (1998), studied the compaction processes of forage material by tractors, specifically how the forage mass is compacted in the track or inter-track area of the tractor. He derived the following equation, which expresses the magnitude of the relative deformation in the horizontal plane: (5), where L is the track width or wheelbase of the traction vehicle, and l_0 is a parameter of the laying body.

$$\varepsilon_H = \frac{2l_0}{(L-2l_0)} \quad (5)$$

where:

ε_H is the amount of relative deformation in the horizontal plane;

L is the width or wheelbase of the energy source;

l_0 – is a parameter of the laying body.

In the work of *Semenikhin, (1998)*, it was proposed to continue the above theory through the use of echelon loading of the feed mass when stacked in storage. As a result, they offer optimal conditions for the implementation of the proposed method of compaction, which requires maintaining the required level of the monolith surface, and setting the required geometric size of the deformation. To maintain a zero balance of voids and compaction along the stroke of the rammer, and to ensure that the monolith remains in a position aligned with the path of the support element, it is necessary to implement a combined scheme with geodetic levels placed along the direction of movement. Additionally, several studies have examined the effects of periodic loading in similar contexts.

For example, *Gurinenko, (2007)*, in her work, in addition to examining the impact of heavy mobile equipment, also addresses the problem of particle placement within the feed mass monolith during compaction and proposes three placement schemes.

The process of distributing silage mass within the storage volume is accompanied by periodic loading from caterpillars or wheels over a gradually increasing layer. This layer consists of particles with finite size, geometric shape, and varying orientations. At the points of loading, specifically under the tracks of the rammer, these particles form discrete aggregates that respond differently to the rammer's deformation. These include both relaxing and non-relaxing deformation centers, which are not structurally connected. In such conditions, the feed mass does not form a unified structure; its mechanical strength is governed by frictional interactions, which are influenced by the height and size of the particles. As the layer's height increases, the number of elementary aggregates also increases, while the distances between them decrease only slightly. This results in the silage mass simulating imperfections of the original discrete particles and gradually integrating the mechanical behavior of these disconnected aggregates. Eventually, the mass transitions to a new boundary condition level, where elementary structures begin to interconnect.

At this stage, the structure becomes dominated by horizontally oriented particles. When the layer height reaches approximately 0.8 m to more than 1 m, its surface begins to exhibit load-bearing capacity, characterized by shear strength (τ) and compressive strength (σ) due to cross-dense packing, while retaining the elastic-viscous behavior of its constituent components. Thus, it can be concluded that before compaction, the feed mass behaves as an elastic-viscous body composed of numerous aggregates distributed throughout its volume.

The particles possess defined dimensions and can migrate toward areas of lower density and between layers. Under the influence of periodic loading, the feed mass undergoes changes in both its physical-mechanical and rheological properties, gradually approaching the upper density limit and minimum porosity characteristic of a compacted monolith. This study is based on the dynamic behavior of multicomponent media, considering variations in their damping properties and their capacity to absorb mechanical energy during compaction.

The mechanics of elastic-viscous media of plant origin are characterized by properties such as stress relaxation, viscosity, and creep, which are not functionally dependent on porosity and density. This distinction highlights the relevance of the present work. Considering all the above, it can be concluded that significant efforts have been made to reduce porosity - an important factor in minimizing feed contact with air. However, there is still a lack of sufficient technological solutions to effectively eliminate voids and prevent the formation of empty layers within the feed mass. Therefore, it is deemed necessary to enhance the theoretical foundations of the feed mass compaction process and to continue research in this critical area.

MATERIALS AND METHODS

Based on the results of laboratory research having been conducted by *Milko, (2020, 2019), Maraldi et al., (2016), Lisowski et al., (2020), Kaliyan et al, (2013), Cabrales et al, (2020), Siyal et al., (2021)*, an experimental and production prototype of equipment for plant material compaction was developed (Fig. 1).

The system consists of a frame *1* equipped with a feeder *2* and a twin-screw compactor *3*, all integrated into a single technological unit. All actuators are powered by adjustable electric drives, which are automatically controlled and can also be manually operated via a centralized control panel. The technological process for compacting vegetable raw materials is as follows: the material is first delivered by the feeder *2* into the twin-screw compactor *3*, where the screws - arranged in layers - separate and structure the incoming particles. The mass is then directed toward the diffuser, where it undergoes a twisting motion. This twisted mass is subsequently fed through the diffuser, where it is compacted (Fig. 2).

In the present research, the following equipment was used: RN-50SHVP-1 scale, electronic scales, laboratory quadrant scales VLK-500-M, sampling bags, a box for volume determination, caliper, engineering ruler, and a type S 0.2 stopwatch. Scales for measurements up to 500 kg. Additional measuring instruments included: dial scales РН–10Ц13У (TU 25.06.575–70), laboratory technical quadrant scales VLTK-500, pointer tachometer PM-10R (GOST 21339), mechanical stopwatch SOPpr-2a-3-000 "Agate" 4282 (GOST 5072-79), metal ruler 0–500 mm (GOST 427-75), tape measure P2 (GOST 7502-80), vernier caliper ShTs 0–150 (GOST 166-80), camera, metal container (V = 0.15 m^3), and a measured set K-50 (GOST 8711 and GOST 8476).



Fig. 1 - Equipment for plant raw materials compaction

1 – frame; 2 – feeder; 3 - twin-screw compactor.



Fig. 2 - Compaction of the twisted mass as it passes through the diffuser

The measuring stand was equipped with a Danfoss VLT Micro FC51 frequency converter integrated with the MCT-10 software suite (Fig. 3). Using the mathematical theory of experimental design, the dependencies of quantitative, qualitative, and energy performance of the preservative dispenser and the twin-screw compactor on the studied factors were also determined. The corresponding regression equations were based on three factors.



a) b)

Fig. 3 – General view of the measuring stand

a) Danfoss VLT Micro FC51 frequency converter; b) MCT-10 software package;
1 - Danfoss FC-51 frequency converter; 2 - personal computer.

The research on a twin-screw compactor for vegetable raw materials was conducted by analyzing the influence of design parameters, operating conditions, and material properties. Specifically, the study focused on the ratio of the inlet height to the screw diameter, screw rotation speed, and the initial mass density of the material. Both active and passive experimentation methods were employed - active variation of selected factors was combined with passive observation of others. The screw speed and the inlet height-to-screw diameter ratio were varied according to a three-level, three-factor experimental design matrix. The initial mass density was based on values obtained during previous compaction cycles. The variation range for the inlet height-to-screw diameter ratio was 1.27 to 1.95, with an average value of 1.6, representing a 20.6% variation. Screw rotation speeds ranged from 21 to 125 rpm, giving a variation interval of 72 rpm or 71.2%, indicating a wide experimental scope for both parameters. The initial mass density of haylage varied from 150 to 555 kg/m³. To optimize the design and operational parameters of the twin-screw compactor, a full second-order factorial design matrix with three levels and three factors was applied.

RESULTS AND DISCUSSION

During the experiment, screws with the required pitch and diameter were installed on the twin-screw compactor for vegetable raw materials, and the screw rotation speed was adjusted accordingly. The pre-compaction press parameters were then set, including the loading window height coefficient and the piston speed, to achieve the desired density at the entrance of the twin-screw compactor. Next, the hopper of the pre-compaction press was loaded with vegetable raw materials. The electric motor reducers of both the twin-screw compactor and the pre-compaction press were activated, and the compaction cycle was initiated. Throughout the process, energy consumption and the productivity of filling the polymer storage unit were recorded. These values reflect all stages of the material handling process: loading, compaction, and storage. To prevent air infiltration during storage, it is necessary to hermetically seal or tightly pack the polymer storage unit after filling. The variation levels of the independent factors - screw speed n (1/s), window height coefficient k (the ratio of the feed window height to the screw diameter), and the pre-compacted mass density ρ (kg/m³) - along with their combinations, were organized according to a three-level, full-factorial second-order experimental design and are presented in Table 1.

Table 1

Variation levels of factors for investigating the twin-screw compactor for plant raw materials

№	Factor level					
	Coded			Decoded		
	X_1	X_2	X_3	Screw speed	Window height coefficient	Pre-compacted mass density
				[1/s]	-	[kg/m³]
1	-1	-1	-1	25	1.25	320
2	1	-1	-1	125	1.25	320
3	-1	1	-1	25	1.95	320
4	1	1	-1	125	1.95	320
5	-1	-1	1	25	1.25	720
6	1	-1	1	125	1.25	720
7	-1	1	1	25	1.95	720
8	1	1	1	125	1.95	720
9	-1	0	0	25	1.6	520
10	1	0	0	125	1.6	520
11	0	-1	0	75	1.25	520
12	0	1	0	75	1.95	520
13	0	0	-1	75	1.6	320
14	0	0	1	75	1.6	720

Experimental data and studies for performance (Q), power consumption (N), energy consumption (E), and output density (R), based on the factor combinations presented in Table 1, are summarized in Table 2.

Table 2

Results of hay compaction studies

№	Screw speed	Window height ratio	Input density	Productivity	Power	Energy consumption	Output density
	[s^{-1}]	-	[kg/m³]	[kg/h]	[kW]	[kJ/kg]	[kg/m³]
1	25	1.25	320	173	4.17	88.23	803
2	125	1.25	320	526	7.17	54.10	630
3	25	1.95	320	232	4.15	63.69	813
4	125	1.95	320	404	6.15	52.64	676
5	25	1.25	720	198	5.82	113.58	761
6	125	1.25	720	342	8.16	88.84	619
7	25	1.95	720	681	5.38	25.69	851
8	125	1.95	720	589	6.73	33.56	745
9	25	1.6	520	237	4.77	77.53	803
10	125	1.6	520	393	6.95	61.80	664
11	75	1.25	520	136	6.55	149.04	377
12	75	1.95	520	300	5.82	90.60	444
13	75	1.6	320	156	5.77	112.65	416
14	75	1.6	720	253	6.88	111.92	430
15	25	1.25	320	178	4.39	87.39	841
16	125	1.25	320	535	7.60	53.92	666
17	25	1.95	320	236	4.42	63.64	847
18	125	1.95	320	416	6.48	51.92	706
19	25	1.25	720	202	6.17	112.92	802
20	125	1.25	720	351	8.63	88.05	644
21	25	1.95	720	707	5.66	25.11	894
22	125	1.95	720	603	7.03	33.07	780
23	25	1.6	520	242	5.04	76.79	845
24	125	1.6	520	386	6.64	62.32	637
25	75	1.25	520	134	6.24	150.44	364
26	75	1.95	520	294	5.55	91.20	427
27	75	1.6	320	152	5.53	114.27	400
28	75	1.6	720	250	6.52	111.85	413
29	25	1.25	320	169	4.00	89.05	779
30	125	1.25	320	519	6.83	54.28	603
31	25	1.95	320	230	3.96	63.76	785
32	125	1.95	320	395	5.89	53.27	651
33	25	1.25	720	195	5.55	114.14	730
34	125	1.25	720	335	7.79	89.66	598
35	25	1.95	720	663	5.13	26.09	819
36	125	1.95	720	579	6.48	33.98	720
37	25	1.6	520	232	4.55	78.21	770
38	125	1.6	520	403	7.34	61.26	698
39	75	1.25	520	140	6.96	147.63	393
40	75	1.95	520	308	6.18	89.92	467
41	75	1.6	320	161	6.06	111.11	436
42	75	1.6	720	257	7.43	112.19	448

According to the data presented in correlation Table 3, which is based on the experimental results in Table 2, a statistically significant ($p < \alpha$) moderate correlation (as per Chaddock's scale) is observed between productivity, power, and output mass density with the screw rotation speed during the compaction of haylage and heap material. Notably, the correlations for output mass density are negative.

Productivity, energy consumption, and power also show statistically significant correlations with the window height coefficient, but only when considering the input density. Among these, power demonstrates a correlation strength ranging from moderate to relatively high across all analyzed indicators.

Table 3

Correlation table for haylage compaction estimation

Indicator	Productivity	Power	Energy consumption	Output density R
Haylage				
Screw speed	.3780	.8020	-.1982	-.3654
	p=.014	p=.000	p=.208	p=.017
Window height ratio	.4299	-.2706	-.5806	.1763
	p=.004	p=.083	p=.000	p=.264
Input density	.2962	.4118	.0057	.0348
	p=.057	p=.007	p=.971	p=.827

The results of the preliminary evaluation of the experimental data for determining the values of productivity, power, and energy consumption - using Student's *t*-test, the range of the truncated sample, and Cochran's test at a significance level of α = 0.05 - are presented in Table 4.

Table 4

Preliminary evaluation results of experimental data using statistical criteria

Name of the criterion	The value of the criterion	Criterion			
		Productivity	Power	Energy consumption	Output density
Haylage					
Student's *t*-test	Maximum value	1.061	1.061	1.135	1.066
	Critical value	4.303			
Truncated sample range k	Maximum value	0.602	0.602	0.805	0.612
	Critical value	3.157			
Cochran's test G	Estimated value	0.438	0.146	0.298	0.124
	Critical value	0.570			

Table 4 shows the preliminary evaluation of experimental data for productivity, power, energy consumption, and output density. Statistical assessments were carried out using Student's *t*-test, the range of the truncated sample (*k*), and Cochran's *G* test at a significance level of α = 0.05 are given in Table 4.

Table 5

Regression equation indicators for the dependent variable – performance of the two-screw compactor

Indicator	Decoded regression coefficient	Standard error of the regression coefficient	Student's actual criterion	Significance Level
Haylage				
Free term	1634.059	171.534	9.526	0.001
Screw speed	0.738	0.688	1.072	0.344
Window height ratio	-1487.907	217.063	-6.855	0.002
Input density	-2.382	0.239	-9.950	0.001
Speed of rotation × Window ratio	-2.984	0.259	-11.533	$3.228 \cdot 10^{-4}$
Speed of rotation × Input density	-0.006	$4.528 \cdot 10^{-4}$	-13.096	$1.963 \cdot 10^{-4}$
Window ratio × Input density	1.420	0.065	21.957	$2.546 \cdot 10^{-5}$
Square of screw speed	0.057	0.003	17.533	$6.214 \cdot 10^{-5}$
Square of window height ratio	378.571	66.640	5.681	0.005
Square of input density	0.001	0.000	3.966	0.017

As a result of processing the extended matrix of experimental data - including pairwise interactions of independent factors and their squared terms, based on Table 1 - Table 5 presents the decoded regression coefficients and their statistical evaluation for haylage compaction. The regression model was established using Statistica software.

CONCLUSIONS

Analyzing the response surface of energy consumption during plant material compaction - based on the screw speed of the two-screw compactor, the window height coefficient, and the input density - it is observed that optimizing compaction parameters for maximum productivity also allows achieving the desired output density. Specifically, when the screw rotational speed is set at 40-45 rpm, the window height coefficient is around 1.8, and the input density is approximately 350–370 kg/m^3, the output density of the compacted heap reaches 600 - 700 kg/m^3 under the same equipment settings.

Based on the conducted research, the following compaction parameters for vegetable raw materials are recommended. For haylage compaction: window height coefficient: k = 1.6; input density ρ = 620 kg/m^3; screw rotation speed n = 100 rpm. For heap compaction: window height coefficient k = 1.8; input density: ρ = 420 kg/m^3; screw rotation speed: n = 100 rpm

ACKNOWLEDGEMENT

The research was carried out within the framework of the scientific topic: "FRRS-2023-0019 Improving the efficiency of grain production through the introduction of modern processing methods in the conditions of the MSU Food Safety Research and Production Center."

REFERENCES

[1] Cabrales H., Arzola N., Araque O. (2020). The effects of moisture content, fiber length and compaction time on African oil palm empty fruit bunches briquette quality parameters. *Helion,* Vol.6, Iss.12.

[2] Dolgov I. (1971). *Scientific foundations of the methodology for calculating the working bodies of pressing, briquetting and rolling hay harvesters (Научные основы методики расчета рабочих органов прессующих, брикетирующих и прокатывающих сеноуборочных машин)*, (Doctoral thesis). Moscow / USSR.

[3] Goryachkin V. (1965). *Collection of repairs (Собрание починений),* Kolos. Moscow. Vol.3.

[4] Gutyar E. (1936). *Experience in the theory of haymaking. Theory, design and production of agricultural machinery (Опыт теории сенопрессования. Теория, конструкция и производство сельскохозяйственных машин),* Selchozhiz. Moscow. Vol.4.

[5] Gurinenko L. (2007). *Improving the process of compaction of silage in horizontal storage*. *(Совершенствование процесса уплотнения силосной массы в горизонтальных хранилищах)*, (PhD thesis). Azov-Black Sea State Agro-Engineering Academy. Zernograd / Russia.

[6] Kaliyan N., Morey R., Schmidt D. (2013). Roll press compaction of corn stover and perennial grasses to increase bulk density. *Biomass and Bioenergy.* Vol. 55. pp. 322 -330.

[7] Khvorostyanov L. (1980). *Research and substantiation of parameters of the separator of the stationary unloader of canned fodder from trenches (Исследование и обоснование параметров отделителя стационарного выгрузчика консервированных кормов из траншей),* (PhD thesis). Volgogradsk. Agricultural Institute. Volgograd / USSR.

[8] Khrapach E. (1956). *Theoretical and experimental research of a straw press for the combine (Теоретическое и экспериментальное исследование соломо-пресса для комбайна),* (PhD thesis). Kharkiv / USSR.

[9] Lisowski A., Wojcik J., Klonowski J., Sypuła M., Chlebowski J., Kostyra K., Nowakowski T., Struzyk A., Swiętochowski A., Dąbrowska M., Mieszkalski L., Piątek M. (2020), Compaction of chopped material in a mini silo. *Biomass and Bioenergy.* Vol. 139.

[10] Maraldi M., Molari L., Regazzi N., Molari G. (2016), Method for the characterization of the mechanical behaviour of straw bales. *Bio systems engineering,* Vol. 151, pp. 141 -151.

[11] Milko D., Bratishko V., Kuzmenko V., Kholodiuk O. (2019). Theoretical aspects of plant material sealing in a wedge-shaped canal. *Modern Development Paths of Agricultural Production: Trends and Innovations.* pp. 139–144.

[12] Milko D., Sclyar O., Sclyar R., Pedchenko G., Zhuravel D., Bratishko V. (2020). Results of the nutritional preservation research of the alfalfa laying on storage with two-phase compaction. *INMATEH - Agricultural Engineering*, 60(1), pp. 269–274.

[13] Muller R. (1963). *Some problems of static soil mechanics (Некоторые задачи статической механики грунтов) "*Mathematical methods in mining", (Conference thesis). Novosibirsk / USSR.

[14] Osobov V. (1971). *Technological bases of calculation of working bodies for consolidation of hay-straw materials (Технологические основы расчета рабочих органов для уплотнения сено-соломистых материалов)* (Doctoral thesis). Leningrad-Pushkin / USSR.
[15] Olaleye B., Wu Ch., Liu L. (2020). The effects of screw-to-roll speed ratio on ribbon porosity during roll compaction. *International Journal of Pharmaceutics.* Vol. 558.
[16] Orisaleye J., Ojolo S. (2019). Parametric analysis and design of straight screw extruder for solids compaction. *Journal of King Saud University - Engineering Sciences.* Vol. 31, Iss. 1, pp. 86-96.
[17] Perezhogin M. (1963). *Investigation of roughage briquetting processes (Исследование процессов брикетирования грубых кормов),* (PhD thesis). Chelyabinsk / USSR.
[18] Pustigin M. (1948). *Theory and technological calculation of threshing devices (Теория и технологический расчет молотильных устройств),* Selchozhiz. Moscow / USSR.
[19] Semenikhin A. (1998). *Mechanical and theoretical bases of processes and technological means of silage production in horizontal storages (Механико-теоретические основы процессов и технологических средств производства силоса в горизонтальных хранилищах)* (Doctoral thesis). Zernograd / Russia.
[20] Siyal A., Mao X., Liu Y., Ao W., Jiang Zh., Wahab N., Ran Ch., Zhang R., Liu G., Dai J. (2021). Pellet production from furfural residue and sawdust: Evaluating the characteristics and quality of pellets and their dependency on process parameters. *Biomass and Bioenergy.* Vol. 149.
[21] Vanhoorne V., Almey R., De Beer T., Vervaet C. (2020). Delta-mannitol to enable continuous twin-screw granulation of a highly dosed, poorly compactable formulation. *International Journal of Pharmaceutics.* Vol. 583.

PREDICTION OF BOESENBERGIA ROTUNDA (L.) DRYING USING HOT AIR AND ULTRASONIC VIBRATION VIA EXTREME GRADIENT BOOSTING
/
การทำนายการอบแห้งของกระชายขาวด้วยลมร้อนและการสั่นสะเทือนความถี่สูงโดยใช้เทคนิคเอ็กซ์ตรีมเกรเดียนต์บูสติง

Patipat THANOMPONGCHART[1)], Pakamon PINTANA[2)], Tossapon KATONGTUNG[3)], James C. MORAN[3)], Nakorn TIPPAYAWONG*[3)]

[1)] Industrial Energy Management Engineering Program, Faculty of Industrial Technology, Uttaradit Rajabhat University / Thailand;
[2)] School of Renewable Energy, Maejo University, Chiang Mai / Thailand;
[3)] Department of Mechanical Engineering, Faculty of Engineering, Chiang Mai University, Chiang Mai / Thailand
Tel: +6653944146; E-mail: n.tippayawong@yahoo.com
DOI: https://doi.org/10.35633/inmateh-76-43

Keywords: *dehydration, food preservation, machine learning, postharvest technology*

ABSTRACT
This study used eXtreme Gradient Boosting (XGBoost) to predict the drying behavior of Boesenbergia rotunda (L.) under hot air and ultrasonic vibration. A dataset of 73 samples with temperature, time, and vibration as inputs was used. The model achieved high accuracy with R^2 = 0.99 and RMSE = 8.71 on test data. SHAP analysis revealed that ultrasonic vibration improved moisture reduction, especially during longer drying times. These results demonstrate the effectiveness of combining XGBoost and SHAP for understanding and optimizing complex drying processes in food and agricultural engineering.

บทคัดย่อ
งานวิจัยนี้ใช้เทคนิค XGBoost เพื่อพยากรณ์พฤติกรรมการอบแห้งของกระชายขาว (Boesenbergia rotunda (L.)) ด้วยลมร้อนร่วมกับคลื่นการสั่นสะเทือนความถี่สูง โดยใช้ชุดข้อมูลจำนวน 73 ตัวอย่างที่มีอุณหภูมิ เวลา และการสั่นสะเทือนเป็นตัวแปรนำเข้า โมเดลสามารถทำนายได้อย่างแม่นยำ โดยมีค่า R^2 เท่ากับ 0.99 และ RMSE เท่ากับ 8.71 จากข้อมูลทดสอบ การวิเคราะห์ด้วย SHAP แสดงให้เห็นว่าคลื่นเสียงช่วยลดความชื้นได้ดีขึ้นเมื่อใช้กับเวลาการอบแห้งที่นาน ผลลัพธ์นี้ชี้ให้เห็นถึงศักยภาพของการผสาน XGBoost กับ SHAP ในการเพิ่มประสิทธิภาพกระบวนการอบแห้งสำหรับงานด้านวิศวกรรมอาหารและเกษตร

INTRODUCTION
White fingerroot, also known as Chinese ginger, is an important medicinal herb primarily found in Southeast Asia (*Larsen, 1996; Taheri et al., 2022*). Its significance stems from both its culinary uses and its medicinal properties, making it highly valued in traditional medicine and modern pharmaceutical research. White fingerroot contains important nutrients, including vitamins, minerals, and antioxidants (*Trakoontivakorn et al., 2001; San et al., 2022*). Drying is an important step in processing herbs to enable them to be stored for a longer period and effectively retain their medicinal value (*Orphanides et al., 2016; Thamkaew et al., 2021*).

Ultrasonic vibration drying is an innovative drying technique that uses high-frequency sound waves to enhance the removal of moisture from various materials, including food, herbs, and industrial products (*Musielak et al., 2016*). This method leverages mechanical vibrations, typically at frequencies between 20 kHz-1 GHz, to break the bonds between water molecules and the material, allowing for faster and more efficient evaporation compared to conventional drying methods (*Yao, 2016; Cheeke, 2012*). In ultrasonic vibration drying, a transducer generates high-frequency sound waves that are transmitted into the material being dried. These waves cause rapid, microscopic vibrations in the material and the surrounding moisture. These vibrations break up water droplets and reduce the surface tension, enabling moisture to evaporate more easily. The process is highly efficient because the mechanical energy from the vibrations increases the rate of moisture transfer without requiring high heat (*Kahraman et al, 2021; García-Pérez et al., 2023; Thanompongchart et al., 2022*).

Patipat Thanompongchart, Asst. Prof.; Pakamon Pintana, Lecturer; Tossapon Katongtung, PhD student; James C. Moran, Assoc. Prof.; Nakorn Tippayawong, Prof.

The use of ultrasonic vibration for drying offers several significant advantages. Firstly, it enables faster drying times as the ultrasonic waves substantially accelerate the evaporation process. This method also consumes less energy because it operates at lower temperature compared to traditional drying techniques. Additionally, minimal temperature exposure is a key benefit, making it ideal for preserving sensitive materials such as herbs and food, which can otherwise lose essential nutrients, flavor, or texture due to excessive heat. Furthermore, ultrasonic vibrations promote uniform moisture evaporation, ensuring improved quality and consistency by preventing issues like over-drying or uneven results. Lastly, this drying method is environmentally friendly, as it is non-invasive and sustainable, relying neither on chemicals nor high temperatures, which makes it an eco-friendlier option *(Musielak et al., 2016; Gallego-Juarez et al., 1999).* However, ultrasonic vibration still poses a problem of high heat accumulation at the vibrator, resulting in a short lifespan. This technology is especially beneficial in industries where preserving the quality of sensitive materials is essential, such as food, herbs, and pharmaceuticals. Its ability to enhance moisture removal without high heat positions ultrasonic vibration drying as a modern, sustainable solution to traditional drying challenges (*Mujumdar, 2004; 2006*).

Machine learning (ML) can improve the industry by enabling more accurate predictions of drying behavior, thus optimizing efficiency, quality, and resource management. By analyzing large datasets generated during the drying process, ML models can uncover patterns and relationships between key variables like temperature, humidity, airflow, and material properties. These models, including regression models, neural networks, and support vector machines are trained to predict drying kinetics and outcomes (*Martynenko and Misra, 2020; Taur et al., 2019; Đaković et al., 2023*). ML models identify how these factors interact to influence the drying rate and moisture ratio (*Çetin, 2022*). Once trained, the model can accurately predict the behavior of agricultural products under given drying conditions (*Tagnamas et al., 2023*), offering insights into optimizing the process for better energy efficiency, faster drying, and improved product quality (*Soares et al., 2013*). Moreover, ML algorithms estimate product yields, optimal conditions, and variables or affect operational efficiency in others applications (*Katongtung et al., 2022; 2024a; 2024b; Kittichotsatsawat et al., 2023*).

The novelty of this work lies in the fact that an ML algorithm is applied to estimate the drying of white fingerroot with conventional hot air dryer combined with an ultrasonic vibration system. The objective of this study is to develop a predictive model for the drying behavior of *Boesenbergia rotunda* (L.) using hot air combined with ultrasonic vibration. The eXtreme Gradient Boosting (XGBoost) algorithm was employed to optimize and analyze the drying process with the goals of minimizing material waste, enhancing product consistency, and increasing overall processing efficiency. The findings emphasize the importance of dataset expansion in mitigating overfitting and improving the model's generalization capability, in line with prior studies (*Chamorro et al., 2026*). A larger and more diverse dataset enables the model to capture fundamental patterns more effectively, thereby increasing the accuracy and robustness of predictions in both experimental validation and practical applications.

MATERIALS AND METHODS

Experimental setup and procedure

The experimental dryer is a modified hot air oven integrated with an ultrasonic vibration system, as illustrated in Fig. 1(a). Positioned centrally beneath the product trays inside the dryer is an ultrasonic vibration unit operating at a frequency of 40 kHz, 60 W (Piezoelectric) with 1 unit set per tray. The dryer accommodates two tiers of product trays. To prolong the operational life and durability of the ultrasonic system, an air-cooling system is installed via ducts beneath the trays in Fig. 1(b). The system is programmed to operate in cycles of 1 min on and 5 min off.

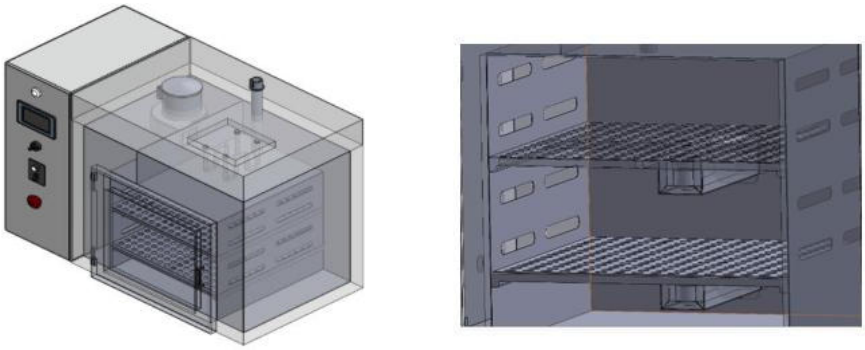


Fig. 1 – (a) Hot air dryer integrated with an ultrasonic vibration system and (b) installation of the ultrasonic vibration system underneath product trays

The dryer's heating system uses electric heaters and a fan to ensure uniform airflow and efficient moisture extraction through the top vent. White fingerroot (*Boesenbergia rotunda* (L.)) was prepared for drying by washing and cutting it longitudinally into pieces generally less than 1 cm thick and approximately 10 cm long. The pieces were arranged on mesh trays at 1.5 kg per tray, with a maximum spacing of 8 ± 1 cm. Two trays were used for each drying run. Each condition was tested in triplicate. Drying experiments were conducted at temperatures of 50 °C, 60 °C, and 70 °C using a combined method involving hot air and ultrasonic vibration. The dried white fingerroot was weighed every hour during the drying process. Afterward, samples were further dried in a hot air oven at 103 °C for 72 hours to determine dry matter content based on AOAC (1995) standards. The final moisture content was then calculated. According to *Rungsardthong, (2002),* the moisture content of dried white fingerroot suitable for storage should not exceed 7% on a wet basis.

Data analysis

In physics-based modeling, the drying process is analyzed through theoretical models derived from mathematical reasoning. This section establishes a boundary value problem by incorporating the governing equations of transport phenomena, along with relevant assumptions, initial conditions, and boundary conditions (*Akter et al., 2022*). The moisture content of the drying material decreases as it absorbs thermal energy, along with the sensible heat present in the surrounding air. During the drying process, the amount of thermal energy absorbed by the material corresponds to the latent heat required for the evaporation of its moisture (*Wengang et al., 2024*).

Determination of humidity on a wet basis is the ratio of the weight of water in a material to the material weight, calculated as:

$$M_w = \frac{(w - d)}{w} \times 100 \quad (1)$$

where:

M_w is moisture content wet basis (%), w is initial weight of the material (kg) and d is weight of dry material (kg). The initial moisture content of the white fingerroot was 93 ± 1.5% wb and the final value was lower than 7% wb.

The drying water evaporation rate is the amount of water that evaporates during the drying process per unit of time. It can be calculated by:

$$\dot{M}_w = \frac{M_w}{t} \quad (2)$$

where:

$\dot{M}_w$ is water evaporation rate ($kg_{(water)}$/h), M_w is evaporated water mass ($kg_{(water)}$) and *t* is time (h).

Machine learning model and evaluation

In this study, an ML model was developed to predict average moisture content using XGBoost, a widely used and highly efficient algorithm (*Katongtung et al., 2022; 2024a; 2024b*). XGBoost is a machine learning algorithm that builds multiple decision trees in an iterative fashion to solve both regression and classification problems. It is an implementation of gradient boosting that is optimized for performance and speed. Gradient boosting is a technique where weak learners, typically decision trees, are trained sequentially with each new tree attempting to correct the errors made by the previous ones. XGBoost has become widely used because of its ability to handle large datasets and its robustness across a variety of tasks, including structured/tabular data problems, where it often outperforms other models. It is also popular in many Kaggle competitions due to its competitive accuracy.

The high efficiency of XGBoost is derived from several key factors. One of the most important is regularization, as it incorporates both L1 (Lasso) and L2 (Ridge) techniques to prevent overfitting, allowing the model to generalize well on unseen data. XGBoost also benefits from parallel processing, enabling parallel tree construction, which reduces computational time and significantly improves training efficiency. Additionally, XGBoost is equipped with built-in mechanisms to handle missing data, a critical feature when working with real-world datasets. Its sparsity-aware learning optimizes performance when dealing with high-dimensional datasets that often contain many zero-valued features. Moreover, the algorithm includes automatic pruning of trees, helping to avoid unnecessary complexity, reduce model size, and enhance interpretability.

XGBoost is an ensemble learning method that implements gradient boosting using decision trees. The algorithm builds the model in an additive, stage-wise manner by iteratively fitting new trees to the residuals (errors) of previous predictions. The goal is to minimize a regularized objective function, which is composed of two main components (*Noh et al., 2024*):

(a) Loss function (L): This measures the difference between the predicted values and the actual values. For a given dataset with n examples, the loss is typically represented as:

$$L(\theta) = \sum_{i=1}^{n} l(y_i, \hat{y}_i) \quad (3)$$

where:

l is a differentiable loss function, y_i are the true values, and $\hat{y}_i$ are the predicted values.

(b) Regularization term (Ω): This term penalizes the complexity of the model to prevent overfitting. For decision trees, complexity might be measured in terms of the number of leaves and the magnitude of leaf weights. The regularization term for a tree model *f* can be written as:

$$\Omega(\boldsymbol{f}) = \boldsymbol{\gamma}\mathbf{T} + \frac{1}{2}\boldsymbol{\lambda}\sum_{j=1}^{T}\boldsymbol{w_j^2} \quad (4)$$

where:

$\mathbf{T}$ is the number of leaves in the tree, w_j is the weight of the j leaf, γ is a parameter controlling the penalty for additional leaves, and λ is the L2 regularization term on leaf weights.

The combined objective function that XGBoost aims to minimize is:

$$obj = \sum_{i=1}^{n} l(y_i, \hat{y}_i^{(t)}) + \sum_{k=1}^{t} \Omega(f_k) \quad (5)$$

where:

$\hat{y}_i^{(t)}$ is the prediction for the i^{th} instance at the t iteration, and f_k represents the k decision tree. At each iteration, the model updates its prediction by adding the output of a new tree f_t

$$\hat{y}_i^{(t)} = \hat{y}_i^{(t-1)} + f_t(x_i) \quad (6)$$

The new tree f_t is chosen by approximating the loss function using a second-order Taylor expansion and then optimizing the objective with respect to the structure and leaf weights of the tree. This results in an efficient, scalable algorithm that is capable of handling large datasets and complex models. XGBoost's effectiveness lies in its ability to balance model complexity with predictive accuracy through this rigorous mathematical framework, making it a popular choice for various machine learning tasks.

The dataset comprised 73 data points, with three input features (temperature, time and vibration), and one target output (average moisture), presenting a significant challenge in ML model development due to the limited number of data points and features. Despite these limitations, the model's performance was assessed using the coefficient of determination (R^2) and root mean square error (RMSE). Furthermore, the relationship between the input features and the target output was analyzed using Shapley values, providing a detailed explanation of the contribution of each variable to the model's predictions. Shapley values are used in machine learning to analyze the relationship between input features and the target output by quantifying each feature's contribution to the model's predictions. They provide a fair and consistent method to attribute the influence of each variable, offering detailed explanations of how each feature affects the prediction. Shapley values enable both local interpretability for individual predictions and global insights into overall model behavior. This approach ensures transparency in understanding the model's decision-making, helping to identify which variables drive outcomes and to what extent. The distribution of data used in this study is shown in Fig. 2. Shapley values originate from cooperative game theory and provide a fair distribution of a total payoff among players based on their individual contributions. Mathematically, consider a set *N* of players (or features) and a value function $v: 2^N \rightarrow \mathbb{R}$ that assigns a real number to every subset S⊆ N.

The Shapley value $\emptyset_i$ for player ii is defined as:

$$\emptyset_i(v) = \sum_{S \subseteq N \setminus \{i\}} \frac{|S|!(|N|-|S|-1)!}{|N|!} [v(S \cup \{i\}) - v(s)] \quad (7)$$

where:

N is the set of all players (or features), S is any subset of players not including ii, |S| is the number of players in S, |N| is the total number of players, $v(s)$ is the value (or payoff) of the subset S, and $v(S \cup \{i\}) - v(s)$ represents the marginal contribution of player ii to the subset S.

The fraction:

$$\frac{|S|!\,(|N|-|S|-1)!}{|N|!}$$

represents the probability of S occurring as the set of players preceding ii in a random ordering of N. In machine learning, Shapley values are used to attribute the contribution of each feature to the prediction made by a model, offering a robust and theoretically justified method for model interpretation.

The trained models were assessed using various performance metrics, such as the R^2 score and RMSE. These metrics were defined as follows: Eqs. (8)-(9) (*Katongtung et al., 2022; 2024a; 2024b*).

$$R^2 = 1 - \frac{\sum(y_i - \hat{y}_i)^2}{\sum(y_i - \bar{y}_i)^2} \tag{8}$$

$$RMSE = \sqrt{\frac{\sum_{i=1}^{N}(y_i - \hat{y}_i)^2}{N}} \tag{9}$$

where:

y_i is represents the actual value, $\hat{y}_i$ is represents the predicted value, $\bar{y}_i$ is represents the mean value of the *i-th* data point, and *N* is the total number of data points.

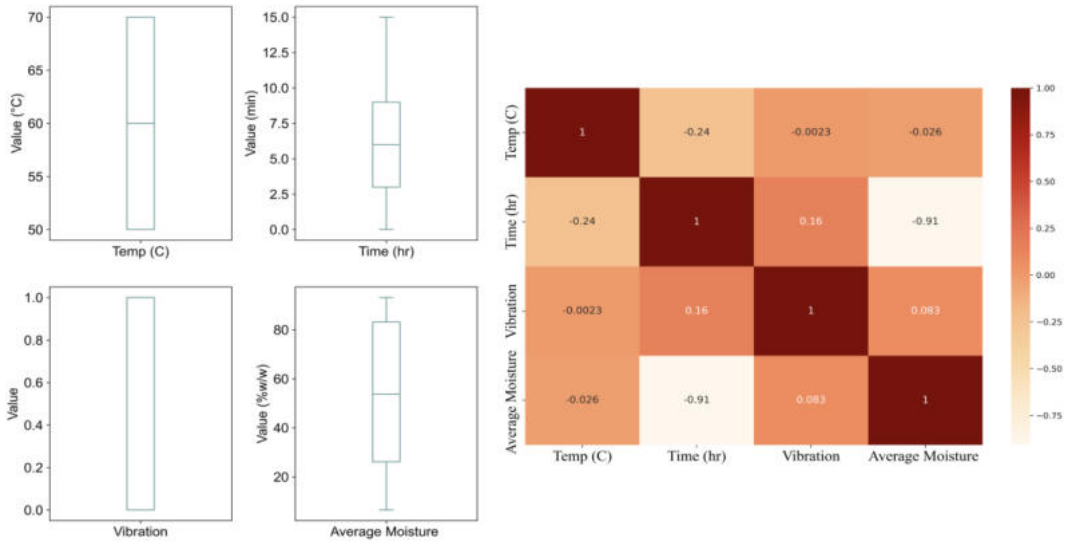


Fig. 2 – Box plot and heat map of the data set

In this study, cross-validation was not employed due to the limited size of the dataset, which comprised only 73 data points. Applying cross-validation under such conditions may lead to excessively fragmented training and validation subsets, potentially resulting in unstable performance estimates and diminished model generalizability. Therefore, a simple train–test split (75% training, 25% testing) was adopted to retain enough data for both model training and performance evaluation. To address potential overfitting, multiple regularization strategies were implemented during model development. These included early stopping, which halts training once performance on a validation set ceases to improve, as well as the tuning of regularization parameters such as lambda (L2 regularization), alpha (L1 regularization), and gamma (minimum loss reduction required to make a further partition). These techniques effectively constrained model complexity and contributed to enhanced generalization on unseen data. The incorporation of these regularization and validation strategies strengthens the reliability and transparency of the predictive modeling approach, particularly when working with limited datasets.

RESULTS AND DISCUSSION

Water evaporation rate

From the experiment, the water evaporation rate when using hot air drying combined with an ultrasonic vibration system is higher than conventional drying methods under all conditions. The maximum value was achieved at a drying temperature of 70°C, reaching 0.313±0.016 $kg_{(water)}$/h.

A 25% increase in performance was observed compared to the conventional hot air drying process. Additionally, a linear regression analysis was conducted based on experimental data, as illustrated in Fig. 3.

The results of this study showed that increasing ultrasonic vibration for drying significantly reduced drying time, which is consistent with previous research on pineapple drying (*Thanompongchart et al., 2022*). The dried white fingerroot exhibited superior quality in terms of its physical properties and active compound content, particularly when dried at a temperature of 60°C.

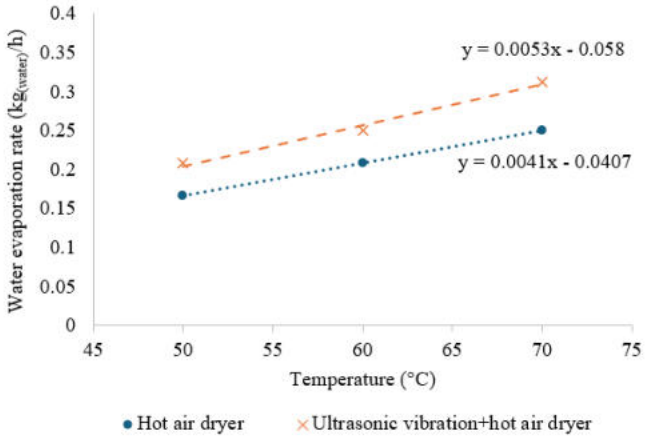


Fig. 3 – Water evaporation rate during drying of white fingerroot

ML model accuracy

In machine learning, a dataset is often split into two key sections: one for training and another for testing. The training portion is used to help the model recognize patterns and relationships in the data. As the model learns, it fine-tunes its internal parameters to improve its predictions or classifications. After training, the test set, which remains unseen by the model during training, is used to assess how well the model performs. This helps provide a fair evaluation of its ability to generalize to new data, offering insights into its overall accuracy and effectiveness. In this study, the dataset was divided into 75% training data and 25% test data to evaluate the performance of the ML model.

Fig. 4 presents the accuracy graph for the average moisture content prediction of the ML model, using both training and test data.

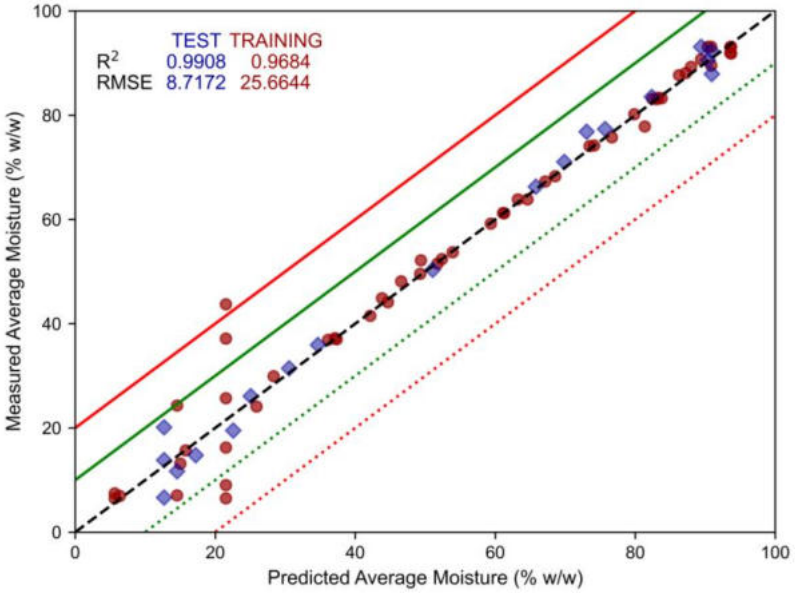


Fig. 4 – Distribution and accuracy of training and test data

The red line indicates the 20% error range, while the green line marks the 10% error range. The model demonstrated high prediction accuracy, with an R^2 value of 0.9908 and an RMSE of 8.7171. However, due to the relatively small dataset, the training data yielded an R^2 value of 0.9684 and an RMSE of 25.6644, which was a bit lower than the test prediction accuracy. This suggests that increasing the dataset size would reduce overfitting and enhance the reliability of the ML model.

In ML, overfitting occurs when a model learns not only the underlying patterns in the training data but also noise and random fluctuations that do not generalize to new, unseen data. As a result, the model performs well on the training dataset but fails to generalize, leading to poor performance on test or real-world data providing more examples for the machine learning model to learn from. When the dataset is small, the model is more likely to memorize specific details rather than learning general patterns, which leads to overfitting. With a larger dataset, the model is exposed to a wider variety of examples and variations, making it harder for the model to memorize individual points, encouraging it to generalize instead.

Increasing the size of a dataset offers several important advantages. Firstly, it helps reduce overfitting by providing more diversity in the data, allowing the model to distinguish between noise and true patterns. With a larger and more representative dataset, the model can capture generalizable trends instead of focusing on anomalies specific to the training set. Secondly, it improves generalization, meaning the model becomes better at making accurate predictions on unseen data. This ensures that the model performs well not just on the training data but also in real-world scenarios. Thirdly, increasing the dataset size enhances the reliability of the model, making it more robust and dependable by learning from a broader and more diverse set of examples. As a result, the model is less likely to make erroneous predictions, leading to more trustworthy and consistent outcomes. Lastly, a larger dataset helps reduce the variance in predictions, making the model less sensitive to small changes in the training data and resulting in more stable and reliable predictions.

Fig. 5 illustrates the use of Shapley values to explain the impact of individual variables on the model's predictions. The analysis reveals that drying time is the most significant factor, followed by vibration and temperature. The color of the SHAP summary plot further indicates whether the effect is positive or negative. In this study, it was found that longer drying times negatively affect average moisture content, whereas shorter drying times have a positive effect. Longer drying times can negatively affect the average moisture content of a material due to uneven moisture removal, with some areas drying too much while others retain moisture. This unevenness, combined with the potential for moisture reabsorption over time, increases the overall average moisture content. In contrast, shorter drying times promote more efficient and uniform moisture removal, reducing the chances of reabsorption and preventing over-drying in certain sections. Reduced drying time without raising temperature effectively minimizes color changes, decreases undesirable texture attributes (hardness, cohesiveness, gumminess, chewiness), and preserves bioactive compounds (*Yitayew and Fenta, 2021*).

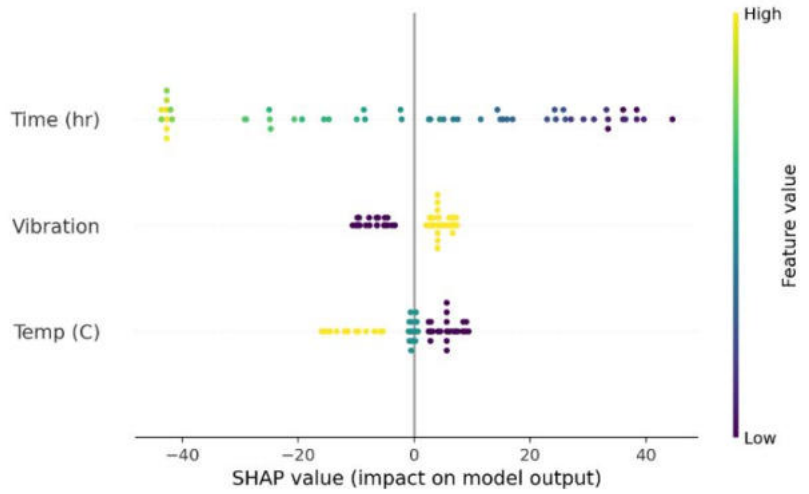


Fig. 5 – SHAP summary plot

Similarly, the vibration variable positively affects average moisture content during the drying process by enhancing moisture movement within the material, allowing water molecules to migrate more easily to the surface for evaporation. It improves airflow around the material, facilitating better interaction between the moist material and the drying medium, which helps carry away evaporated moisture more effectively. Additionally, vibration promotes uniform drying, ensuring no parts of the material dry excessively while others remain wet. It also reduces surface tension, making it easier for moisture to escape, and minimizes heat stress by distributing heat evenly. Together, these factors contribute to a more efficient and effective drying process, leading to a lower average moisture content (*Yang et al., 2024*).

The temperature variable influences average moisture content similarly to drying time, with higher temperatures negatively impacting moisture levels while lower temperatures have a positive effect. High temperatures can lead to rapid surface evaporation, causing the outer layers of a material to dry too quickly and potentially trapping moisture in the inner layers, a phenomenon known as "case hardening." This uneven drying not only increases average moisture content but can also degrade the quality of sensitive materials, such as food, by stripping away essential nutrients and flavors. In contrast, lower temperatures promote gradual and even moisture removal, reducing the likelihood of trapping moisture and preventing reabsorption from the environment. This controlled drying process helps maintain the quality of the material while effectively lowering average moisture content, leading to better overall results (*Mougang et al., 2024*).

Moreover, Fig. 6 showcases SHAP dependence plots, which help visualize how specific variables influence the average moisture content of a material. Fig. 6(a) focuses on the relationship between temperature and drying time. At a low temperature of 50°C, extending the drying time tends to have a positive effect on reducing average moisture content, meaning that longer drying periods at this temperature help remove more moisture. When the temperature is raised to a medium level of 60°C, the effect of drying time becomes minimal; in this range, increasing the drying time does not significantly change the average moisture content. Finally, at a high temperature of 70°C, shorter drying times become more beneficial for reducing average moisture content, suggesting that quick drying at this temperature effectively removes moisture without causing detrimental effects. Fig. 6(b) examines how vibration interacts with drying time. It shows that introducing vibration during the drying process has a more pronounced positive effect on average moisture content when the drying times are longer. This means that the benefits of using vibration in the drying process are more noticeable over extended periods, helping to enhance moisture removal compared to shorter drying times, where the effect is less significant.

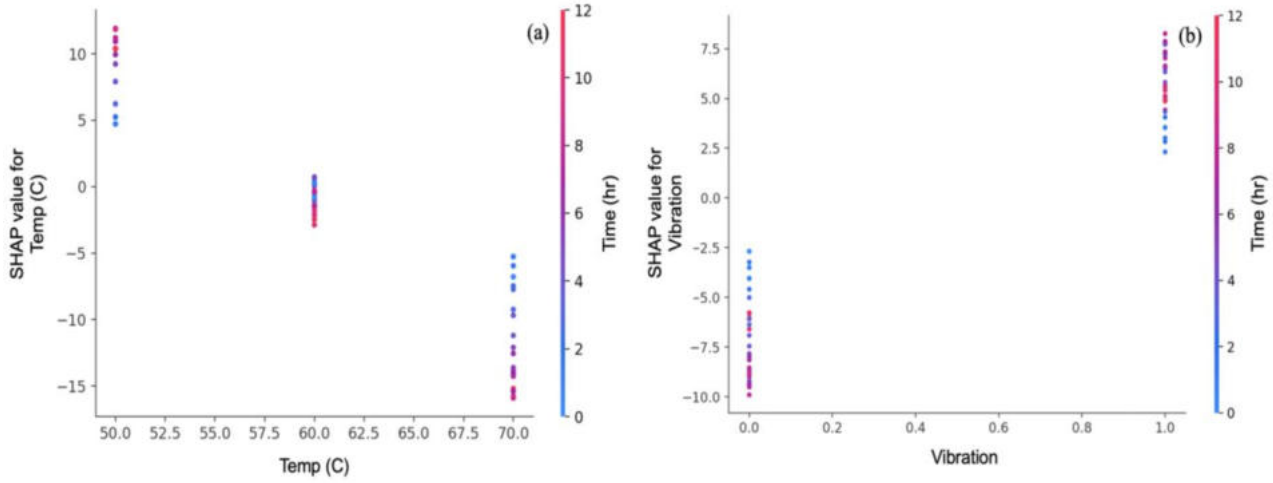


Fig. 6 – SHAP independence plot: (a) temperature and time; (b) vibration and time

Table 1 shows the prediction results from the ML model compared to experimental data at 50, 60, and 70°C, using combined hot air and ultrasonic vibration methods, based on a random selection of 10 runs. The results indicate that the ML model predictions closely align with the experimental values, with the smallest difference being 0.09 and the largest difference being 1.15. Overall, the predicted values demonstrate strong agreement with the experimental data, suggesting that the ML model is well-suited for predicting the average moisture content in the drying process. However, this ML approach may be effective under hot air drying combined with an ultrasonic vibration system. Further research may be required to develop and validate its applicability for other drying methods.

Table 1

ML average moisture content prediction results compared with experimental results

Run	ML (average moisture content)	Experimental (average moisture content)	Difference
1	79.87	80.19	0.32
2	5.62	6.48	0.86
3	63.22	63.85	0.63
4	90.36	90.59	0.23
5	12.67	13.82	1.15
6	43.80	44.89	1.09
7	73.47	74.09	0.62

Run	ML (average moisture content)	Experimental (average moisture content)	Difference
8	44.65	44.12	0.53
9	82.44	83.14	0.7
10	15.77	15.68	0.09

CONCLUSIONS

This study developed a predictive machine learning model based on the XGBoost algorithm to estimate the average moisture content during the drying of *Boesenbergia rotunda* (L.). The drying process employed a hybrid technique combining hot air and ultrasonic vibration. A dataset comprising 73 samples with three input features, temperature, drying time, and vibration amplitude was utilized. The dataset was divided into training and testing sets at a 75:25 ratio, yielding a high predictive performance with an R^2 of 0.9908 and RMSE of 8.7171 on the test set.

SHAP analysis was conducted to interpret model behavior, revealing that drying time was the most influential variable, followed by vibration amplitude and temperature. The findings indicate that shorter drying durations and moderate temperatures contribute to more uniform and efficient moisture removal, while ultrasonic vibration enhances internal moisture migration and airflow dynamics. Comparison between model predictions and experimental results at 50, 60, and 70 °C demonstrated strong agreement, confirming the model's robustness. However, the relatively small dataset may introduce limitations such as overfitting. Therefore, future work should focus on expanding the dataset to improve generalization capability and reliability. While the model has shown promising results under the hot air–ultrasound drying system, further investigations are recommended to assess its applicability across different drying techniques and material types.

ACKNOWLEDGEMENT

This project is partially funded by National Research Council of Thailand (NRCT) contract no. N42A671047, and Chiang Mai University. The first author also wishes to thank Thailand Science Research and Innovation for research funding and Uttaradit Rajabhat University for technical assistance.

REFERENCES

[1] Akter F., Muhury R., Sultana A., Deb U.K. (2022). A comprehensive review of mathematical modeling for drying processes of fruits and vegetables. *International Journal of Food Science*, 2022, 6195257. https://doi.org/10.1155/2022/6195257

[2] AOAC. (1995). *Official Method of Analysis*, 16th ed., The Association of Official Analytical Chemists. Inc. Arlington, Verginia, USA

[3] Cheeke, JDM. (2012). *Fundamentals and Applications of Ultrasonic Waves*, 2nd ed. Boca Raton (USA): CRC Press.

[4] Chamorro M., Gallego F.A., Rojas J.C. (2026). Reducing overfitting in ResNet with Adaptive Lipschitz regularization. *Journal of Computational and Applied Mathematics*, 471. https://doi.org/10.1016/j.cam.2025.116747

[5] Çetin, N. (2022). Machine learning based estimation of drying characteristics of apple slices. *Current Trends in Natural Sciences*, 11(22), 44-52. https://doi.org/10.47068/ctns.2022.v11i22.006

[6] Đaković D., Kljajić M., Milivojević N., Doder Đ., Anđelković A.S. (2023). Review of energy-related machine learning applications in drying processes. *Energies*, 17(1). https://doi.org/10.3390/en17010224

[7] Gallego-Juarez J.A., Rodriguez-Corral G., Moraleda J.C.G, Yang T.S. (1999), A new high-intensity ultrasonic technology for food dehydration, *Drying Technology*, 17(3), 597–608. https://doi.org/10.1080/07373939908917555

[8] García-Pérez J.V., Carcel J.A., Mulet A., Riera E., Andrés R.R., Gallego-Juarez J. (2023). Ultrasonic drying for food preservation. In: *Power Ultrasonics*, 743-771, Woodhead Publishing

[9] Kahraman O., Malvandi A., Vargas L., Feng H. (2021). Drying characteristics and quality attributes of apple slices dried by a non-thermal ultrasonic contact drying method. *Ultrasonics Sonochemistry*, 73. https://doi.org/10.1016/j.ultsonch.2021.105510

[10] Katongtung T., Onsree T., Tippayawong N. (2022). Machine learning prediction of biocrude yields and higher heating values from hydrothermal liquefaction of wet biomass and wastes, *Bioresource Technology*, 344. https://doi.org/10.1016/j.biortech.2021.126278

[11] Katongtung T., Prasertpong P., Sukpancharoen S., Sinthupinyo S., Tippayawong N. (2024a). Predictive modeling for multifaceted hydrothermal carbonization of biomass. *Journal of Environmental Chemical Engineering*, 12(5). https://doi.org/10.1016/j.jece.2024.114071

[12] Katongtung T., Phromphithak S., Onsree T., Tippayawong N. (2024b). Machine learning approach for predicting hydrothermal liquefaction of lignocellulosic biomass, *BioEnergy Research.* https://doi.org/10.1007/s12155-024-10773-0

[13] Kittichotsatsawat Y., Boonprasope A., Rauch E., Tippayawong N., Tippayawong K.Y. (2023). Forecasting arabica coffee yields by auto regressive integrated moving average and machine learning approaches, *AIMS Agriculture and Food*, 8(4). https://doi.org/1052-1070. 10.3934/agrfood.202305 7

[14] Larsen K. (1996). A preliminary checklist of the Zingiberaceae of Thailand. *Thai Forest Bulletin (Botany)*, 24, 35-49.

[15] Martynenko A., Misra N.N. (2020). Machine learning in drying. *Drying Technology*, 38(5), 596-609. https://doi.org/10.1080/07373937.2019.1690502

[16] Mougang N.N., Tene S.T., Zokou R., et al. (2024). Influence of fermentation time, drying time and temperature on cocoa pods (Theobroma cacao L.) marketability. *Applied Food Research*, 4(2). https://doi.org/10.1016/j.afres.2024.100460

[17] Mujumdar A.S. (2004). Research and development in drying: Recent trends and future prospects. *Drying Technology*, 22(1), 1-26. https://doi.org/10.1081/DRT-120028201

[18] Mujumdar A.S. (2006). An overview of innovation in industrial drying: Status and R&D needs. *Transport Porous Media*, 66, 3-18. https://doi.org/10.1007/s11242-006-9018-y

[19] Musielak G., Mierzwa D,, Kroehnke J. (2016). Food drying enhancement by ultrasound-A review. *Trends in Food Science & Technology*, 56, 126-141. http://dx.doi.org/10.1016/j.tifs.2016.08.003

[20] Noh H., Lee S., Kim S., Mudawar I. (2024). Utilization of XGBoost algorithm to predict dryout incipience quality for saturated flow boiling in mini/micro-channels. *International Journal of Heat and Mass Transfer*, 231. https://doi.org/10.1016/j.ijheatmasstransfer.2024.125827

[21] Orphanides A., Goulas V., Gekas V. (2016). Drying technologies: Vehicle to high-quality herbs. *Food Engineering Reviews*, 8, 164-180. https://doi.org/10.1007/s12393-015-9128-9.

[22] Rungsardthong V., (2002). *Food Processing Technology*, 2nd ed. Bangkok, King Mongkut's University of Technology North Bangkok. (In Thai)

[23] San H.T, Khine H.E.E, Sritularak B., Prompetchara E., Chaotham C., Che C.T., Likhitwitayawuid K. (2022). Pinostrobin: An adipogenic suppressor from fingerroot (Boesenbergia rotunda) and its possible mechanisms. *Foods*, 11(19). https://doi.org/10.3390/foods11193024

[24] Soares J.D.R., Pasqual M., Lacerda W.S., Silva S.O., Donato S.L.R. (2013). Utilization of artificial neural networks in the prediction of the bunches' weight in banana plants. *Scientia Horticulturae*, 155, 24-29. http://dx.doi.org/10.1016/j.scienta.2013.01.026

[25] Tagnamas Z., Idlimam A., Lamharrar A. (2023). Predictive models of beetroot solar drying process through machine learning algorithms. *Renewable Energy*, 219. https://doi.org/10.1016/j.renene.2023.119522

[26] Taheri S., Teo C.H., Heslop-Harrison J.S., Schwarzacher T., Tan, Y.S., Wee, WY, Harikrishna, J.A. (2022). Genome assembly and analysis of the flavonoid and phenylpropanoid biosynthetic pathways in fingerroot ginger (Boesenbergia rotunda). *International Journal of Molecular Sciences*, 23 (13). https://doi.org/10.3390/foods11193024

[27] Taur K.H., Deng X.Y., Chou M.H., Chen J.W., Lee Y.H., Wang W.J. (2019). A study on machine learning approaches for predicting and analyzing the drying process in the textile industry. *The International Automatic Control Conference,* 13-16 November, IEEE. https://doi.org/10.1109/CACS47674.2019.9024364

[28] Thamkaew G., Sjöholm I., Galindo F.G. (2021). A review of drying methods for improving the quality of dried herbs. *Critical Reviews in Food Science and Nutrition*, 61(11), 1763-1786. https://doi.org/10.1080/10408398.2020.1765309.

[29] Thanompongchart P., Pintana P., Tippayawong N. (2022). Thermal performance enhancement in hot air and solar drying of pineapple slices with ultrasonic vibration. *Case Studies in Thermal Engineering*, 37. https://doi.org/10.1016/j.csite.2022.102296

[30] Trakoontivakorn G., Nakahara K., Shinmoto H., Takenaka M., Onishi-Kameyama M., Ono H., Tsushida T. (2001) Structural analysis of a novel antimutagenic compound, 4-hydroxypanduratin A, and the antimutagenic activity of flavonoids in a Thai spice, fingerroot (Boesenbergia pandurata Schult.) against

mutagenic heterocyclic amines. *Journal of Agricultural and Food Chemistry*, 49(6), 3046-3050. https://doi.org/10.1021/jf0100160

[31] Wengang H., Xiyu W., Jiajie M., Ping G., Lei W. (2024). Operation prediction of open sun drying based on mathematical-physical model, drying kinetics and machine learning. *Innovative Food Science and Emerging Technologies*, 97. https://doi.org/10.1016/j.ifset.2024.103836

[32] Yang X., Niu M., Wang S. (2024). Effects of vibration parameters on the drying kinetics of lignite in a vibrated fluidized bed. *Fuel,* 375. https://doi.org/10.1016/j.fuel.2024.132655

[33] Yao Y. (2016). Enhancement of mass transfer by ultrasound: Application to adsorbent regeneration and food drying/dehydration. *Ultrasonic Sonochemistry*, 31, 512-531. http://dx.doi.org/10.1016/j.ultsonch.2016.01.039

[34] Yitayew, T., Fenta, T. (2021). The effect of drying method on the texture, color, vitamin C and β-carotene content of dried mango slices (*Cv. Apple and Kent*). *Proceedings of 8th EAI International Conference part1*, 97-109. https://doi.org/10.1007/978-3-030-80621-7_7

RESEARCH ON THE TRAY CONVEYING AND OUTPUT DEVICE OF AN AUTOMATIC TRAY PLACEMENT MACHINE FOR MULTI-ROW RIGID RICE SEEDLING TRAYS
/
多行水稻硬质育秧盘全自动摆盘机送盘与出盘装置研究

Cheng-long LIU[1)], Shu-juan YI*[1)], Yi-fei LI[1,2)], Song WANG[1)]
[1)]College of Engineering, Heilongjiang Bayi Agricultural University, Daqing/P. R. China
[2)]College of Engineering, Northeast Agricultural University, Harbin/P. R. China
Tel: +86-459-13836961877; E-mail: yishujuan_2005@126.com;
Corresponding author: Shu-juan Yi
DOI: https://doi.org/10.35633/inmateh-76-44

Keywords: *enclosed seedling cultivation; seedling tray; seedling tray placement machine; output device; simulation analysis*

ABSTRACT
To address the issue of height disparity between the output device of the tray placement machine and the seedbed in stacked-tray germination under enclosed conditions - which can lead to vibration and displacement when trays are placed - a slide-type output device with a buffering function equal to the height difference was designed to ensure gentle placement of seedling trays. A three-factor, five-level quadratic orthogonal rotational combination test was conducted using Adams software for simulation analysis. The test factors included the horizontal inclination angle of the tilting frame, the horizontal inclination angle of the sliding plate, and the speed of the seedling tray pusher. Evaluation indices included the qualification rate of tray spacing, the qualification rate of alignment, and the efficiency of tray placement. Test results were analyzed using Design Expert 13 software, and multi-objective parameter optimization was performed. The optimal parameter combination was determined as follows: a tilting frame inclination angle of 15°, a sliding plate inclination angle of 18°, and a tray pusher speed of 0.16 m/s. Field trials conducted to validate these parameters resulted in a 96.11% qualification rate for tray spacing, a 95.89% alignment qualification rate, and a tray placement efficiency of 714 trays per hour - within 1% of the theoretical optimal value. These findings provide a theoretical foundation for the smooth and efficient operation of automatic seedling tray placement machines.

摘要
针对叠盘暗室育秧模式下摆盘机因出盘装置与苗床之间存在高度落差，导致秧盘着床时易产生震动位移的问题，设计了一种具有落差缓冲能力的滑板式出盘装置，实现秧盘的平稳摆放。通过 Adams 软件仿真分析，以倾斜架水平倾角、出盘滑板水平倾角、推盘推杆速度为试验因素，秧盘间距合格率、排齐率、摆盘效率为试验指标，进行三因素五水平二次正交旋转组合试验。应用 Design Expert 13 软件对试验结果进行分析并进行多目标参数组合优化，确定仿真最佳参数组合为：倾斜架水平倾角 15°，出盘滑板水平倾角 18°、推盘推杆速度 0.16m/s，并通过田间试验验证得到秧盘间距合格率 96.11%，排齐率 95.89%，摆盘效率 714 盘/h，与理论优化值误差小于 1%。研究结果为摆盘机平稳摆盘提供理论基础。

INTRODUCTION
Rice is one of the most important grain crops in China, with total output ranking first in the world. Heilongjiang Province is the main rice-growing region in China, with an annual rice output that continues to rank first in the country (*Yan et al., 2023; Li et al., 2024*). As Heilongjiang Province (*Xue et al., 2024*) is a high latitude cold region prone to cold damage at low temperatures when sowing in spring, relying on constant temperature stacked seedling tray darkroom rice seedling cultivation can improve the quality of rice seedlings and shorten the rice-planting cycle (*Li et al., 2021*). However, manual seedling tray placement is labor-intensive, so using a seedling tray placement machine reduces labor requirements and intensity (*Cheng et al., 2025; Li et al., 2020*).

The existing seedling tray placement devices can be divided into two types according to the seedling tray-out mode *(Pan et al., 2024; Li et al., 2018; Yang et al., 2023)*. One type uses a seedling tray placement machine with a fixed truss to move to the designated position. The storage frame servo controls the seedling tray's movement status. When the servo opens, the lowest seedling tray falls into the seedling bed under its own gravity to achieve orderly seedling tray placement. The other type uses a seedling tray placement machine with a conveyor to transport the seedling tray to the seedling tray-out device. Finally, a pushing device throws the seedling tray into the seedbed. In the latter case, the seedling tray is transported to the discharge device by a tractor via a conveyor belt, and is then thrown into the seedbed by a pushing device. Regardless of how the seedling tray is discharged, due to the height difference between the seedling tray device and the seedbed, the seedling tray will vibrate and displace when landing on the bed. This results in the seedling tray not being placed neatly and can even cause the phenomenon of 'overlap'. This not only wastes the seedbed, but also makes it easy for weeds to grow in the cracks of the seedling tray. This makes it difficult for the subsequent disking operation (*Yan et al., 2024*).

Currently, many scholars at home and abroad have conducted research on rice seedling devices. For example, the precision automated production line from Dutch company *Visser (2016)* is equipped with a special device for rice seedling cultivation that can accommodate seedling trays of various sizes and has a production efficiency of 1250 trays per hour. However, such equipment is relatively expensive to purchase, and the automated production lines developed in Europe and the United States are mainly aimed at vegetable and flower cultivation, so they have not yet been widely used in China (*Luo et al., 2019*). For example, indoor rice seedling cultivation equipment developed by companies such as *Kubota (2024)* and *Yanmar (2024)* is highly integrated, achieving a high degree of automation in factory-based seedling cultivation. Its precision tray feeding mechanism has a complex structure and an operating efficiency of over 1000 trays per hour *(Iseki et al., 2024)*. The degree of automation is higher and it can realize the automatic placement of seedling trays. However, these models are expensive and have high installation and commissioning requirements, making them difficult to implement in China's agricultural production. In China, an earlier hand-pushed, trackless seedling tray placement device has a lower degree of automation and needs to be controlled manually, but because of its simple structure and ease of operation, it is widely used for small-scale household seedling tray placement operations (*Lv et al., 2018*).

Zhang Xiuhua et al., (*2018*), developed an articulated automatic placement machine for vegetable seedling hole trays, featuring a high degree of automation. However, the robotic program costs were too high for large-scale rice seedling tray placement. *Xie Lianshuang et al.,* (*2015*), developed a machine for potting rice seedlings, which uses a motorized rod propulsion device on a conveyor belt to place seedling trays in greenhouses. *Xia Xudong et al.,* (*2021*), designed a double cam-controlled seedling tray placement trolley, which moves along a truss to the designated area and automatically arranges the trays by separating them using a dual-cam mechanism.

This paper aims to address the above challenges by investigating an automatic seedling tray placement machine for multi-row rigid rice seedling trays. To ensure smooth tray placement without vibration or spacing gaps, the machine is equipped with a slide-type tray output mechanism featuring a fall-buffering design. One end of the slide naturally aligns with the seedbed under its own weight, enabling stable and gap-free placement of seedling trays.

MATERIALS AND METHODS

Overall structure and working principle

The automatic seedling tray placement machine for multi-row rigid rice seedling trays primarily consists of a conveyor belt, a transverse conveying device, a frame, a tray discharge mechanism, a mobility system, a height adjustment unit, a battery, and a PLC control system, as shown in Fig. 1. The frame serves as the core structural support of the entire machine and mainly includes a tilting frame, tray positioning guides, and other components. The transverse conveying device comprises a transverse pushing mechanism, a longitudinal pushing mechanism, an overturning frame, a linear push rod mechanism, and other parts. The machine is operated via a PLC control system, which coordinates the working sequence of each mechanism to achieve efficient tray conveying and placement. It moves along a fixed track to ensure stable transportation of trays, while the frame height is adjustable to accommodate different operational environments. The performance indicators of the automatic seedling tray placement machine for multi-row rigid rice seedling trays are presented in Table 1.

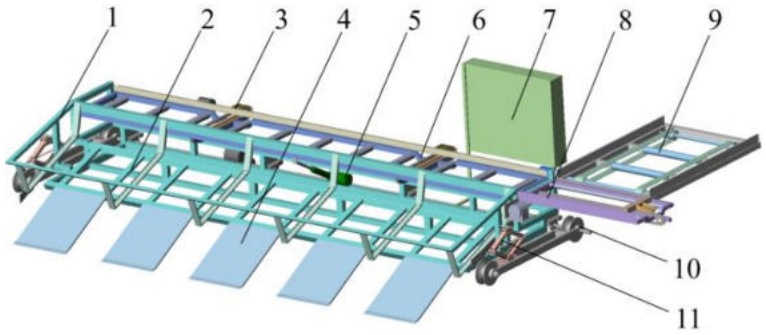


Fig. 1 – Automatic seedling tray placement machine for multi-row rigid rice seedling trays

1. Frame; 2. Tilting frame; 3. Longitudinal pushing mechanism; 4. Output device; 5. Linear pusher mechanism; 6. Flip frame; 7. PLC control box; 8. Transverse pushing mechanism; 9. Conveyor belt; 10. Mobility device; 11. Height adjustment device.

Table 1

Main technical parameters

Parameter	Number
Machine size / (length x width x height) / (mm×mm×mm)	4000×2100×950
Supporting power / W	1200
The working width is wide / mm	3000
Overall machine quality / kg	350
Number of cycles in operation / unit	5
Seedling tray size / (length x width x height) / (mm×mm×mm)	600×300×30

The working process of the automatic seedling tray placement machine for multi-row rigid rice seedling trays is illustrated in Fig. 2. First, the conveyor belt delivers seedling trays to the placement machine. The transverse pushing mechanism then transfers the trays to the flip frame. When five seedling trays are in position, the conveyor belt halts, and the linear pusher mechanism contracts, causing the flip frame to rotate to a specific angle and dock with the tilting frame. Next, the linear pusher mechanism stops, and the longitudinal pushing mechanism gently pushes the five trays down onto the seedbed. Simultaneously, the entire tray placement machine moves forward along the working direction, completing one placement cycle. Afterward, each mechanism returns to its initial position, and the process is ready to repeat.

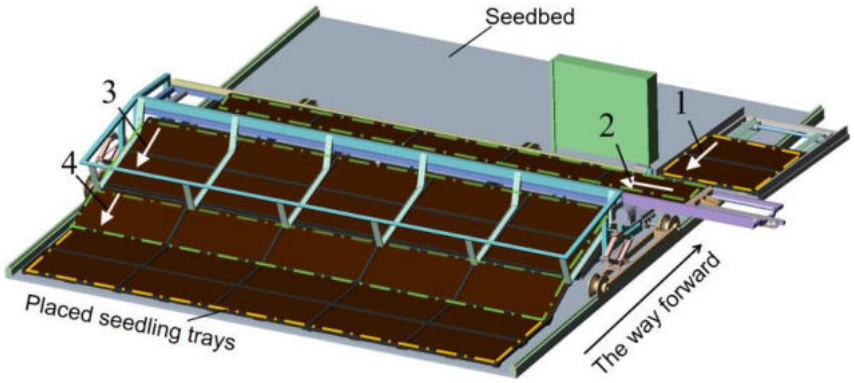


Fig. 2 – Workflow diagram of the seedling tray placement machine

1. Tray supply process; 2. Transverse conveying process; 3. Longitudinal conveying process; 4. Tray placement process.

Transverse conveying device

The transverse conveying device is an important component that affects the working efficiency of the tray placement machine and ensures the smooth transfer of seedling trays. It is primarily composed of a transverse pusher, transmission chain, push-type seedling tray pusher, flip frame, conveyor rollers, longitudinal push motor, linear pusher, and other auxiliary components. The structural diagram of the transverse conveying device is shown in Fig. 3.

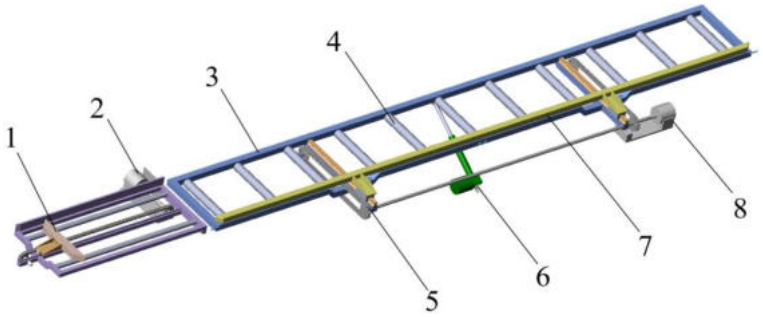


Fig. 3 – Transverse conveying device

1. Transverse pusher; 2. Transverse pusher motor; 3. Flip frame; 4. Conveyor roller; 5. Transmission chain; 6. Linear pusher motor; 7. Seedling tray pusher; 8. Longitudinal pusher motor.

The transverse pusher motor drives the transverse pusher in a continuous reciprocating motion. Once five seedling trays are pushed onto the flip frame, the linear pusher motor begins to contract, causing the flip frame to rotate around its axis to a predetermined angle. The linear pusher mechanism stops contracting once the flip frame is fully docked with the tilting frame. Subsequently, the seedling tray pusher pushes out a row of five trays simultaneously. The operating speeds of both the transverse pusher and the seedling tray pusher can be adjusted by regulating their respective motor speeds to accommodate different working requirements.

Tilting frame structure design

The horizontal inclination angle of the tilting frame directly influences the smooth movement of rice seedling trays during the discharge process. If the inclination angle is too small, the trays experience greater frictional resistance, which can lead to discharge blockages. Conversely, if the inclination angle is too large, the trays may slide uncontrollably due to gravity acting along the surface of the tilting frame, negatively affecting the placement accuracy. To analyze the forces acting on the rice seedling tray during its movement along the tilting frame, a right-angle coordinate system is established: the direction along the tilting frame is defined as the positive x-axis, and the direction perpendicular and upward from the tilting frame is defined as the positive y-axis. The force analysis of the seedling tray under these conditions is illustrated in Fig. 4.

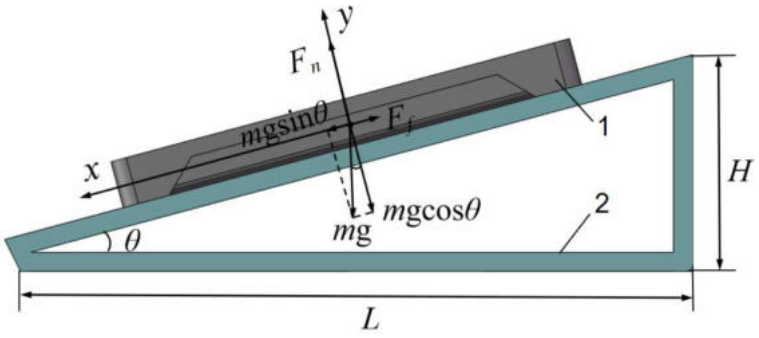


Fig. 4 – Force analysis diagram of the seedling tray

1. Rice seedling tray; 2. Tilting frame.

As can be seen from the Fig. 4, the conditions for the seedling tray to remain smooth on the tilting frame without producing the relative sliding phenomenon are as follows:

$$F_f - mg\sin\theta \geq 0 \tag{1}$$

The following equation is derived from the friction formula:

$$F_f = \mu_1 F_n = \mu_1 mg\cos\theta \tag{2}$$

where: μ_1 is friction coefficient between the seedling tray and the inclined frame; m is quality of seedling tray, (kg); F_n is the support force of the inclined frame on the seedling tray, (N); F_f is the friction between the seedling tray and the inclined frame, (N); θ is horizontal inclination of the tilting frame, (°).

Substituting formula (1) into formula (2) results in:

$$\theta \leq \arctan \mu_1 \tag{3}$$

The coefficient of friction between the seedling tray and the tilting frame was determined to be approximately 0.4 based on the material properties (*Yi et al., 2023*). The maximum horizontal inclination angle θ of the tilting frame was calculated to be 21.8° using the following formula:

$$\tan \theta = \frac{H}{L} \tag{4}$$

where:

H - height of the tilting frame, (m); L - horizontal distance between the inclined supports, (m).

Due to the low height of the edge of the rice-planting shed, the overall height of the machine must be reduced. To accommodate this constraint and to make the structure of the tray placement machine more compact, the horizontal inclination angle of the tilting frame is set between 10° and 20°, and the height H is set to 0.2 m. Once the inclination angle is determined, the horizontal distance L can be calculated using formula (4).

Design of the output device

(1) Overall structure

One of the key performance indicators of the seedling tray placement machine is whether the trays are arranged neatly on the seedbed. To address the issue of vibration and displacement of seedling trays caused by the height difference between the output device and the seedbed - which often results in misaligned trays - a slide-type output device with buffering capability was developed. The device is composed of five sliding plates, each connected to the tilting frame via bolts. Under the action of gravity, the sliding plates naturally conform to the surface of the seedbed, ensuring stable and accurate tray placement without vibration or gaps. The structural diagram of the seedling tray output device is shown in Fig. 5.

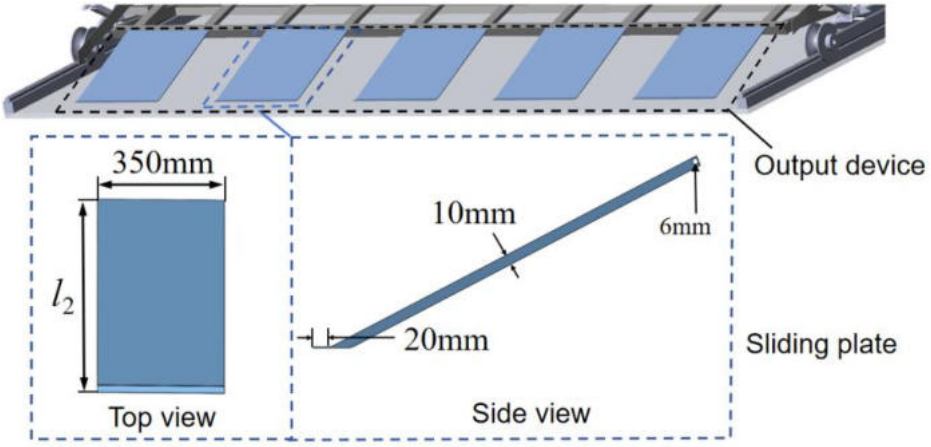


Fig. 5 – Structure of the seedling tray output device

(2) Mechanical analysis of the seedling tray placement process

During the placement of seedling trays, the angular difference between the tilting frame and the discharge sliding plate is considered in the theoretical analysis to prevent tray jamming. A right-angle coordinate system is established, where the downward direction along the tilting frame is defined as the positive x-axis, and the upward direction perpendicular to the tilting frame is defined as the positive y-axis, as illustrated in Fig. 6.

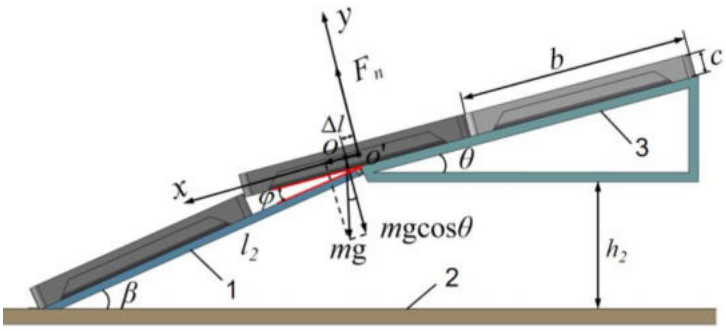


Fig. 6 – Mechanical analysis of the seedling tray placement process

1. Sliding plate; 2. Seedbed; 3. Titling frame.

As illustrated in Fig. 6, the angular difference between the tilting frame and the sliding plate is clearly shown, along with its relationship to the horizontal inclination angle of the sliding plate and the inclination angle of the tilting frame. This angular difference is expressed as:

$$\varphi = \beta - \theta \tag{5}$$

When the angular difference is large, the rear edge of the seedling tray may ride up over the front edge of the tray in front of it, causing a "hitching" phenomenon. This interference negatively impacts the proper arrangement of trays and can hinder subsequent seedling growth. In the theoretical analysis, counterclockwise rotation of the seedling tray around its center of mass is defined as positive, while clockwise rotation is defined as negative.

Define the center of mass of the seedling tray as point O, and the point of applied force as O`. Let $e$ represent the distance between the center of mass O and the force point O`. Before reaching the critical state, the force point O` coincides with the center of mass O, thus e=0. The moment equation under this condition is given by:

$$M = -mg\cos\theta \times \Delta l = 0 \tag{6}$$

After reaching the critical state, e>o. At this time:

$$M = -mg\cos\theta \times \Delta l + F_n \times 0 < 0 \tag{7}$$

where: M is torque on the seedling tray, (N·m).

In this state, the seedling tray will begin to rotate counterclockwise under the action of gravity. Simultaneously, the angle difference between the sliding plate and the tilting frame will gradually decrease. When e = 0, φ reaches its maximum value. To prevent the occurrence of the interference phenomenon at the tray outlet stage, the angle difference between the sliding plate and the tilting frame must satisfy the following condition:

$$\varphi \leq \arcsin\frac{2c}{b} \tag{8}$$

where: b is the width of the seedling tray, (mm); c is height of the seedling tray, (mm).

Based on the dimensions of the seedling tray, the width b is 300 mm, and the height c is 30 mm. When these values are substituted into formulas (7) and (8), the horizontal inclination angle β of the seedling tray sliding plate is calculated to be less than 21.53°.

Furthermore, as illustrated in Fig. 8, a direct correlation is evident between the height of the tilting frame above the ground and the length of the sliding plate.

$$h_2 = l_2\sin\beta \tag{9}$$

where: h_2 is the height of the tilting frame above the ground, (mm); l_2 is the length of sliding plate, (mm).

To avoid interference between the seedling tray machine and the seedbed, the tilting frame is set 100 mm above the ground. Once the sliding plate's horizontal inclination has been determined, its length can be calculated using formula (9).

(3) Speed analysis of seedling tray placement process

The placement of seedling trays is influenced not only by the angle at which they land on the seedbed, but also by their relative speed at the moment of landing. To ensure smooth discharge and neat placement of the trays, it is necessary to analyze the discharge speed of the seedling tray. This speed primarily depends on two factors: the traveling speed of the tray placement machine and the pushing speed of the seedling tray pusher.

To investigate this relationship, a right-angle coordinate system is established, as shown in Fig.7, where the positive x-axis corresponds to the forward motion of the machine (locomotive direction), and the positive y-axis is defined as the direction perpendicular and upward relative to the seedbed. A theoretical analysis of the placement process is then performed based on this coordinate system.

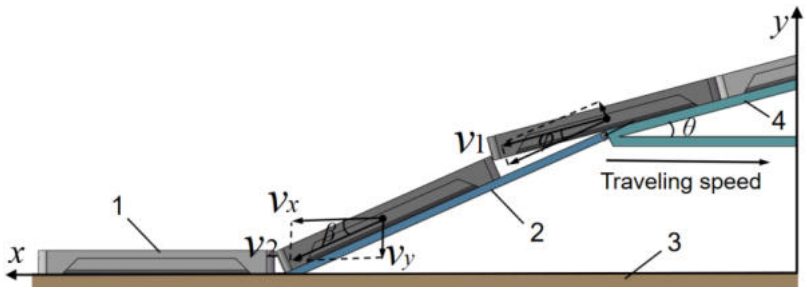


Fig. 7 – Speed analysis of seedling tray placement process
1. Placed seedling trays; 2. Sliding plate; 3. Seedbed; 4. Titling frame.

In this study, the focus is on the relationship between the pusher speed (which corresponds to the motion of the seedling trays along the tilting frame), the tray movement speed, and the relative speed of the trays along the X-axis on the sliding plate. The relationship among these three velocities is given by the following system:

$$\begin{cases} v_1 \cos\varphi = v_2 \\ v_2 \cos\beta = v_x \end{cases} \quad (10)$$

By combining these two equations, it results:

$$v_x = v_1 \cos\varphi \cos\beta \quad (11)$$

The speed of the seedling tray relative to the ground is then given by:

$$v_3 = v_0 + v_x \quad (12)$$

where:

v_0 - machine travel speed, (m/s); v_1 - speed of the pusher, (m/s); v_2 - speed of the seedling tray along the tilting frame, (m/s); v_x - relative velocity of the seedling tray along the x-axis, (m/s); v_3 - velocity of the seedling tray relative to the ground, (m/s).

When the velocity of the rice seedling tray relative to the ground $v_3 > 0$, the pusher speed exceeds the traveling speed of the tray placement machine. In this case, the seedling tray will land with excess forward motion and may overlap or press against the previously placed tray, causing tray displacement and compromising the placement quality. Conversely, when $v_3 < 0$, the pusher speed is less than the machine's travel speed. As a result, the seedling tray lands more slowly, leading to an increased gap between trays, which also affects the overall placement uniformity. Therefore, the most stable and precise placement occurs when $v_3 = 0$, meaning the seedling tray's velocity relative to the ground is zero at the moment of landing. Under this condition, the relationship between the travel speed of the tray placement machine and the pusher speed satisfies the following equation:

$$v_0 = -v_1 \cos\varphi \cos\beta \quad (13)$$

Simulation test

To evaluate the performance of the seedling tray placement machine and determine the optimal parameter values for each influencing factor, the tray discharge process was simulated and analyzed using ADAMS kinematic simulation software.

(1) Simulation parameter determination

During the simulation, the seedling tray comes into contact with other trays, the tray placement mechanism, and the seedbed. Therefore, the contact and material parameters - including those related to seedbed soil and tray materials - were determined with reference to relevant literature (*Che et al., 2023; Yi et al., 2024; Ma et al., 2025*), as summarized in Table 2.

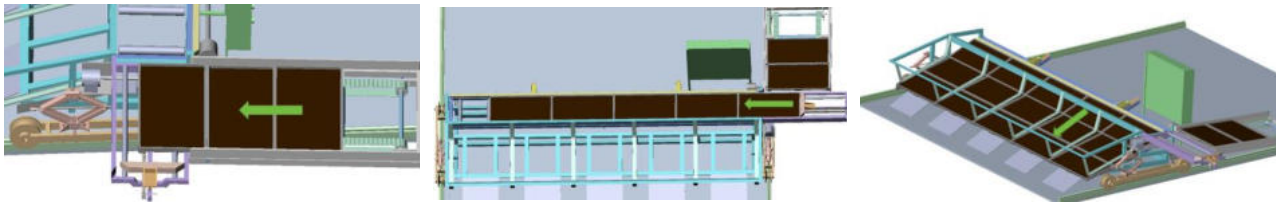
Table 2

Soil parameters of the seedling bed and the contact parameters of each material

Type of interacting material	Parameter	Numerical value
Seedling tray - Seedling tray	Coefficient of restitution	0.3
	Static friction coefficient	0.114
	Kinetic friction coefficient	0.1
Seedling tray - Tray placement machine	Coefficient of restitution	0.5
	Static friction coefficient	0.4
	Kinetic friction coefficient	0.03
Seedling tray - Seedbed	Coefficient of restitution	0.4
	Static friction coefficient	0.8
	Kinetic friction coefficient	0.2
Tray placement machine - Seedbed	Coefficient of restitution	0.6
	Static friction coefficient	0.6
	Kinetic friction coefficient	0.05
Nursery soil	Density（kg/m^3）	1189
	Poisson ratio	0.4
	Shear modulus (Pa)	1e+08

(2) Simulation modelling

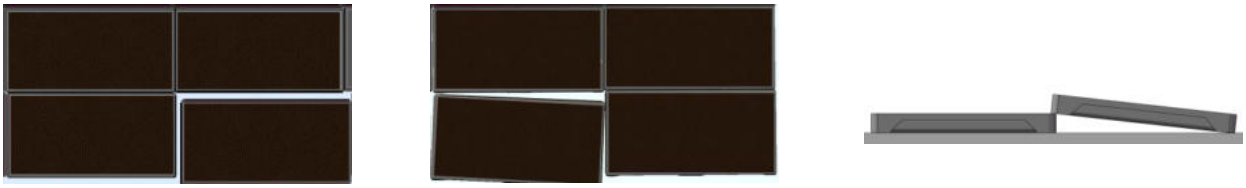
To facilitate simulation and computation, the 3D model of the seedling tray placement machine was simplified using SolidWorks and imported into ADAMS simulation software. The material properties of each component and the contact parameters between interacting parts were defined prior to assigning the driving conditions for the simulation. Although the soil inside the seedling trays is relatively viscous, it does not significantly impact the simulation results. Therefore, only the weight of the seedling tray was considered in the model. The simulation process is illustrated in Fig. 8.



(a) Seedling tray supply process (b) Transverse conveying process (c) Seedling tray placement process

Fig. 8 – Simulation process of seedling tray placement machine

To improve the accuracy and convenience of identifying unqualified seedling tray placements, visual observations can be made during the simulation to detect trays exhibiting clear signs of 'slip' (Fig. 9(a)), 'deflection' (Fig. 9(b)), or 'overlap' (Fig. 9(c)). These phenomena indicate improper placement. Following this, the post-processing module is used to plot the velocity-displacement curves of the center of mass of the seedling trays at different time points. By analyzing these curves, the placement quality of each tray can be evaluated to determine whether it meets the qualification criteria.



（a）The "slip" phenomenon （b）The "deflection" phenomenon （c）The "overlap" phenomenon

Fig. 9 – Unqualified rice seedling tray placement

(3) Evaluation indicators

According to the standardized rice planting operation regulations of Heilongjiang Province, the agronomic requirements for rice seedling tray placement are as follows: seedling trays must be placed horizontally and vertically aligned, starting from the end of the preparatory area. The first row of seedling trays serves as the reference benchmark. For subsequent trays, the horizontal misalignment with respect to the corresponding tray in the first row must not exceed 10 mm (±0.5 mm). The spacing between two adjacent seedling trays must be ≤ 5 mm (±0.5 mm). In addition, there must be no visible overlap between trays. The agronomic placement requirements for rice seedling trays are illustrated in Fig. 10.

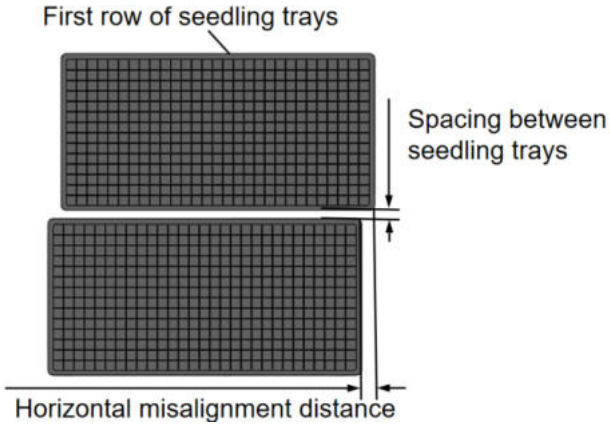


Fig. 10 – Rice seedling tray placement requirements

The qualification rate of seedling tray spacing refers to the percentage of seedling trays for which the spacing between two adjacent seedling trays is ≤5 mm (±0.5mm) and for which the 'overlap seedling trays' phenomenon (i.e. where the spacing between seedling trays is≥0) does not occur.

$$Y_1 = \frac{N_1}{N} \times 100\% \tag{14}$$

where:

Y_1 is the qualification rate of seedling tray spacing, (%); N is the total number of seedling trays placed, (unit); N_1 is number of eligible seedling trays in stock, (unit).

The qualification rate of alignment is defined as the percentage of seedling trays with a lateral misalignment distance of ≤10 mm (±0.5mm) from the corresponding seedling trays in the first row. This is calculated by using the first row of seedling trays as the reference and then determining the percentage of seedling trays with this misalignment.

$$Y_2 = \frac{N_2}{N} \times 100\% \tag{15}$$

where: Y_2 is the qualification rate of alignment, (%); N_2 is the number of seedling trays with qualifying lateral misalignment distance, (unit).

The efficiency of seedling tray placement is calculated by timing and counting the time taken to place 60 seedling trays. This time is then converted and rounded up using the following formula:

$$Y_3 = \frac{60}{t} \times 3600 \tag{16}$$

where: Y_3 is seedling tray efficiency, (trays/h); t is the time taken to successfully place 60 seedling trays, (s).

(4) Experimental method design

In order to further investigate the influence of each working parameter on the effect of seedling tray placement, the following three-factor, five-level quadratic regression orthogonal rotational combination test was carried out. According to the theoretical analysis in the early stage, the tilting frame horizontal inclination angle was set at 10~18°, the horizontal inclination angle of sliding plate at 14~22°, and the pushing speed of the seedling tray pusher at 0.10~0.22m/s. As a result, regression equations and optimization models between the test factors and the evaluation indexes were established. The coded values of the experimental factors are presented in Table 3, where X1, X2 and X3 represent the coded forms of each factor.

Table 3

Test factors coding

Coding	Factor		
	Horizontal inclination angle of tilting frame. X_1 (°)	Horizontal inclination angle of sliding tray X_2 / (°)	Pushing speed of the seedling tray pusher X_3 / (m/s)
1.682	18	22	0.22
1	16.38(16)	20.38(20)	0.1957(0.20)
0	14	18	0.16
-1	11.62(12)	15.622(16)	0.1243(0.12)
-1.682	10	14	0.10

Field validation test

To verify the optimal working parameters of the seedling tray placement machine, a field experiment was conducted at the '895 Farms' Rice Ecological Planting Base in Heilongjiang Province. The primary instruments used in the test included electronic scales, a 5-meter tape measure, and vernier calipers. The experimental trays were rigid rice seedling trays. Before the test, the pusher speed was calibrated by adjusting the motor speed, while the horizontal inclination angles of both the tilting frame and the sliding plate were adjusted to their target values using the height adjustment device. All three parameters - the horizontal inclination of the tilting frame, the horizontal inclination of the sliding plate, and the pusher speed - were set to their optimized values. To minimize experimental error, the five-point sampling method was adopted. Five positions were selected for group testing, with three repeated trials conducted at each position. The average of each group was calculated to validate the results. The experimental site is shown in Fig. 11.



Fig. 11 – Field test of the seedling tray placement machine

RESULTS AND ANALYSIS

Analysis of simulation test results

A number of simulation experiments were carried out, and the experimental results are shown in Table 4.

Table 4

Test results

Number	Factor			Performance indicators		
	X_1	X_2	X_3	Qualification rate of seedling tray spacing Y_1/(%)	Qualification rate of alignment Y_2/(%)	Efficiency of seedling tray placement Y_3/(trays/h)
1	1	1	1	88.33	90	760
2	1	1	-1	91.67	91.11	646
3	1	-1	1	93.33	90	732
4	1	-1	-1	93.33	92.78	620
5	-1	1	1	86.67	86.67	742
6	-1	1	-1	92.78	90	604
7	-1	-1	1	90	88.33	724
8	-1	-1	-1	94.44	92.22	596
9	1.682	0	0	88.89	87.78	632
10	-1.682	0	0	91.11	90	706

Number	Factor			Performance indicators		
	X_1	X_2	X_3	Qualification rate of seedling tray spacing Y_1/(%)	Qualification rate of alignment Y_2/(%)	Efficiency of seedling tray placement Y_3/(trays/h)
11	0	1.682	0	95.56	93.33	659
12	0	-1.682	0	91.67	90.56	710
13	0	0	1.682	95	93.89	782
14	0	0	-1.682	90	89.44	586
15	0	0	0	96.11	96.67	720
16	0	0	0	96.11	96.11	710
17	0	0	0	96.67	96.67	714
18	0	0	0	96.11	96.11	724
19	0	0	0	96.67	96.11	714
20	0	0	0	95	95.56	724
21	0	0	0	96.67	96.11	706
22	0	0	0	96.11	96.67	720
23	0	0	0	96.11	96.11	724

ANOVA was used to analyze the data in Table 4 and obtain the regression models for the rice seedling tray spacing qualification rate, alignment rate, and seedling tray placement efficiency. The results are shown in Table 5.

Table 5

ANOVA results

Sources of variance	Qualification rate of seedling tray spacing		Qualification rate of alignment		Efficiency of the seedling tray placement	
	Sum of squares	P-value	Sum of squares	P-value	Sum of squares	P-value
Model	205.06	<0.0001**	234.16	<0.0001**	62380.79	<0.0001**
X_1	2.28	0.0122*	12.78	<0.0001**	2358.04	<0.0001**
X_2	24.23	<0.0001**	4.03	0.0005**	1736.54	<0.0001**
X_3	36.41	<0.0001**	25.32	<0.0001**	49431.45	<0.0001**
X_1X_2	0.3486	0.2761	0.6105	0.0974*	98.00	0.1133
X_1X_3	6.50	<0.0003**	1.39	0.0185*	200.00	0.0306*
X_2X_3	3.14	0.0046**	0.6216	0.0947	18.00	0.4797
X_1^2	88.26	<0.0001**	89.87	<0.0001**	5222.33	<0.0001**
X_2^2	15.31	<0.0001**	56.57	<0.0001**	1477.79	<0.0001**
X_3^2	30.07	<0.0001**	45.51	<0.0001**	1942.99	<0.0001**
Residual error	3.51		2.49		441.82	
Lack of fit	1.37	0.4631	1.39	0.1808	134.26	0.6399
Error	2.14		1.10		307.56	
Sum total	208.56		236.65		62822.61	

Note: '*' denotes a significant difference (P < 0.05), while '**' denotes a highly significant difference (P < 0.01). The same applies below.

The experimental data were analyzed using Design Expert 13 software to perform analysis of variance (ANOVA), allowing identification of the factors with the most significant influence. Based on this, regression equations between the performance indicators and the coded factor values were established.

$$\begin{cases} Y_1 = 96.18 + 0.41X_1 - 1.33X_2 - 1.63X_3 + 0.90X_1X_3 - 0.63X_2X_3 - 2.36X_1^2 - 0.98X_2^2 - 1.38X_3^2 \\ Y_2 = 96.24 + 0.97X_1 - 0.54X_2 - 1.36X_3 + 0.42X_1X_3 - 2.38X_1^2 - 1.89X_2^2 - 1.69X_3^2 \\ Y_3 = 716.19 + 13.14X_1 + 11.28X_2 + 60.16X_3 - 5.00X_1X_3 - 18.13X_1^2 - 9.64X_2^2 - 11.06X_3^2 \end{cases} \quad (17)$$

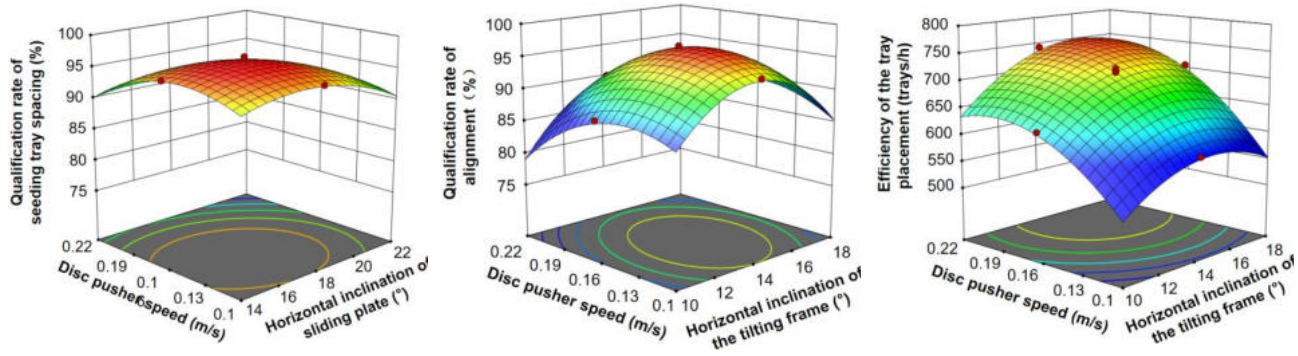
Response surface analysis

To analyze the relationship between the test indexes and the factors more intuitively, the response surface of the factors' interaction with the test indexes was obtained using Design-Expert 13 software, as shown in Fig. 12.

Fig. 12(a) illustrates the effects of the horizontal inclination angle of the sliding plate and the pusher speed on the passing rate of rice seedling tray spacing. Overall, the passing rate remains relatively stable and consistently high. However, as both the horizontal inclination angle and the pusher speed increase, the passing rate gradually declines. This trend can be attributed to the influence of the tilt angle on the tray's orientation during landing and the pusher speed on its vertical velocity. Both factors affect the placement accuracy and alignment of the seedling trays, leading to decreased spacing uniformity and thus a lower passing rate.

Fig. 12(b) shows the influence of the horizontal inclination angle of the tilting frame and the pusher speed on the alignment qualification rate of the seedling trays. When the pusher speed is held constant, increasing the tilting frame inclination angle initially improves the alignment qualification rate, but further increases lead to a decline. In contrast, when the tilting frame inclination is fixed, increasing the pusher speed results in a continuous decrease in the alignment qualification rate. This indicates that pusher speed has a more significant effect on alignment accuracy compared to the tilting frame angle.

Fig. 12(c) illustrates the effects of the horizontal inclination angle of the tilting frame and the pusher speed on the tray placement efficiency. As both the inclination angle and pusher speed increase, the efficiency of the tray placement process also improves. Among the two factors, the pusher speed has a more pronounced influence on overall efficiency. In general, high placement efficiency is observed when the pusher speed is within the range of 0.16~0.22 m/s and the horizontal inclination angle is between 12° and 18°.



（a）X_1=0 （b）X_2=0 （c）X_2=0

Fig. 12 – Response surface of the interaction effect of test factors on the qualified rate of seedling tray spacing

Optimization of parameter combinations

To obtain the optimal parameter combination of the tray placement machine, the multi-objective parameter optimization algorithm in Design Expert 13 software was used to optimize the experimental design, establish a parametric mathematical model, and combine the boundary conditions of the experimental factors, thereby improving the overall operational quality of the machine. The objective function is:

$$\begin{cases} \max y_1(X_1,\ X_2,\ X_3) \\ \max y_2(X_1,\ X_2,\ X_3) \\ \max y_3(X_1,\ X_2,\ X_3) \\ \text{s.t.} \begin{cases} -1.682 \le X_1 \le 1.682 \\ -1.682 \le X_2 \le 1.682 \\ -1.682 \le X_3 \le 1.682 \end{cases} \end{cases} \tag{18}$$

Using the multi-objective parameter optimization module in Design-Expert 13 software to analyze and solve the objective function, the optimal operating parameters for the seedling tray placement machine were determined. Optimal performance is achieved when the horizontal inclination angle of the tilting frame is 15°, the horizontal inclination angle of the sliding plate is 18°, and the pushing speed of the seedling tray pusher is 0.16 m/s. Under these conditions, the qualification rate for tray spacing reaches 96.25%, the qualification rate for alignment is 96.16%, and the tray placement efficiency is 722 seedling trays per hour.

Field test results

To verify the optimal parameter combination of the seedling tray placement machine, multiple field validation tests were conducted, and the results were processed and analyzed. The machine was tested under the optimized conditions: a horizontal inclination angle of the tilting frame set to 15°, a horizontal inclination angle of the sliding plate set to 18°, and a pusher speed of 0.16 m/s. Under these conditions, the average qualification rate for tray spacing was 96.11%, the alignment qualification rate was 95.89%, and the tray placement efficiency reached 714 trays per hour. The mean error between the simulation and field results was less than 1%, indicating that the optimization model is reliable. A comparison of the simulation results and field test results is provided in Table 6.

Table 6

Comparison test results

Type	Qualification rate of seedling tray spacing Y_1/(%)	Qualification rate of alignment Y_2/(%)	Efficiency of seedling tray placement Y_3/(trays/h)
simulation test	96.25	96.16	722
field test	96.11	95.89	714

CONCLUSIONS

1) To address the problem of height disparity between the output device of the tray placement machine and the seedbed in the enclosed stacked-tray seedling cultivation mode, which leads to vibration and displacement of the seedling trays during landing, an output device with buffering capability was designed. This structure ensures that the seedling trays are placed smoothly and accurately, improving overall placement quality.

2) Field validation tests showed that under the optimized operating parameters - 15° horizontal inclination angle of the tilting frame, 18° horizontal inclination angle of the sliding plate, and 0.16 m/s pusher speed - the qualification rate for tray spacing was 96.11%, the alignment qualification rate was 95.89%, and the tray placement efficiency reached 714 trays per hour. These results are largely consistent with the simulation predictions, confirming the reliability of the optimization model.

3) The developed automatic seedling tray placement machine for multi-row rigid rice seedling trays is controlled via a PLC system, which enables fully automated tray conveying and placement. The system ensures high efficiency and standardized operation, while the precise alignment of trays minimizes greenhouse space waste and reduces production costs for farmers.

ACKNOWLEDGEMENT

This study was supported by the National Key Research and Development Plan Project of Heilongjiang Province, China (2023YFD2301604-2).

REFERENCES

[1] Che G., Liu W., Wan L., Yi S., Liu H., Wang Q., Lu B. (2023). Design and experiment of the automatic leveling system for the seedbed precision leveler in rice seedling nursery (水稻秧棚苗床精平机自动调平系统设计与试验) [J]. *Transactions of the Chinese Society of Agricultural Engineering (Transactions of the CSAE)*, 39(22): 9-17.

[2] Cheng J., Li Y., Jin C., Li F., Liu Y., Ji K., Wang H., Yu Z., Pei Z. (2025). Design and testing of dual-station high efficiency whole tray air-suction seeding assembly line for rice seedling cultivation. *INMATEH Agricultural Engineering,* Vol.75, pp.309-322, Romania. DOI: https://doi.org/10.35633/inmateh-75-26

[3] Iseki (2015). *Iseki rice planting equipment* [EB/OL]. (accessed on 27 December 2015). http://www.iseki.co.jp/products/nougyou/noug-02/#rice.

[4] Kubota (2015) *Automatic Supply Device for Seedling Box* [EB/OL]. (accessed on 27 December 2015). http://www.jnouki.kubota.co.jp /sisetu/ikubyou/ autobox/index.

[5] Li M., Xue M., Sha Y., Li H., Chen Y. (2024). Synergistic and optimal allocation of water, land and fertilizer resources of rice in Heilongjiang province based on Meta-analysis (基于 Meta 分析的黑龙江省水稻水土肥资源协同优化调配) [J]. *Transactions of the Chinese Society for Agricultural Machinery*, 55(5): 302-311.

[6] Li Y. (2021) Application of seedling cultivation technology in dark room with stacked trays (叠盘暗室出苗育秧技术应用) [J]. *Northern Rice*, 51 (06): 42-43.

[7] Li D., & Li Z. (2020). System analysis and development prospect of unmanned farming (无人农场系统分析与发展展望) [J]. *Transactions of the Chinese Society for Agricultural Machinery*, 51(7): 1-12.

[8] Li Z., Ma X., Li X., Chen L., Li H., Yuan Z. (2018). Research progress of rice transplanting mechanization (水稻栽植机械化技术研究进展) [J]. *Transactions of the Chinese Society for Agricultural Machinery*, 49(5): 1-20.

[9] Luo X., Wang Z., Zeng S., Zang Y., Yang W., & Zhang M. (2019). Recent advances in mechanized direct seeding technology for rice (水稻机械化直播技术研究进展) [J]. *Journal of South China Agricultural University*, 40(5): 1-13.

[10] Lv X., Yang B., Yao J., Chen Y., Yang M., Wang H., Xue C. (2018). Research on trackless rice seedling tray covering machine (无轨道铺垫式水稻育秧摆盘覆土机研究) [J]. *Plant Maintenance Engineering*, 2018, (08): 171-173.

[11] Ma Q., Li T., Xu D., & Wang Q. (2025). Determination of physical parameters of pelleted rice seeds and calibration of discrete element simulation parameters. *INMATEH Agricultural Engineering,* Vol.75, pp.490-500, Romania. DOI: https://doi.org/10.35633/inmateh-75-42

[12] Pan J., Yang M., Li X., & Lin J. (2024). Full-process rice mechanization production models and equipment configuration in Jiangxi province (江西省水稻全程机械化生产模式与装备配置研究) [J]. *Transactions of the Chinese Society for Agricultural Machinery*, 55(s2): 231-239, 245.

[13] Visser, M.-L.B. (2016). *Tray Destacker and Pot Dispenser* [EB/OL]. (accessed on 23 February 2016). http://www.visser.eu/products/all-products/ MHD-LB/

[14] Xue L., Zhang Z., Qi Z., Han Y., Zhang Z., Li T., & Du S. (2024). Effects of biochar and organic fertilizer addition on net carbon emission of paddy field in black soil area under water-saving irrigation (节水灌溉下生物炭与有机肥添加对黑土区稻田净碳排放的影响) [J]. *Transactions of the Chinese Society for Agricultural Machinery,* 55(9): 382-390, 441.

[15] Xie L., Wang C., Zhang X., Li Y. (2015). Design and motion simulation for rice yangpan machine using Pro/E (基于 Pro/E 的水稻秧盘摆放机的设计与模拟仿真分析) [J]. *Journal of Agricultural Mechanization Research*, 37(11): 46-50.

[16] Xia X., Wang J., Zhou Q., Zhou Y., Zhou B., & Chen J. (2021). Design and experiment of sequential seedling trays laying mechanism controlled by double cams (双凸轮控制的水稻工厂化育秧有序铺盘机构设计与试验) [J]. *Transactions of the Chinese Society for Agricultural Machinery*, 52(5):44-51.

[17] Yan R., Gan G., Zhao X., Yin D., Li Y., Jin H., Zhu H., & Li J. (2023). Study on the production pattern and fertilization status of rice dominant production areas in China (我国水稻优势产区生产格局及施肥现状研究) [J]. *China Rice*, 29(3): 1-8.

[18] Yang J., Fang X., Ma L., Zhou C., Shao C. (2023). Research and development of rice seedling raising machinery (水稻育秧机械研究和进展) [J]. *Journal of Agricultural Mechanization Research*, 45 (06): 264-268.

[19] Yan Y., Yi S., Li B., Li Y., & Tian Y. (2024). Design and test of toggle gear type electric drive rice transplanting tray starter (拨齿式电驱动水稻育秧盘起盘机设计与试验) [J]. *Journal of Agricultural Mechanization Research*, 46(5):210-215.

[20] Yanmar (2015). *Fully automatic seedling box automatic supply device for rice seedling facilities* [EB/OL]. https://www.yanmar.com/jp/agri/implement/agri_implement/flooded_rice.(accessed on 27 December 2015).

[21] Yi S, Zhang G., Li Y., Li B., Luo L., & Wang P. (2023). Design and experiment of a fully automatic tray lifting machine for rice hard disk seedling cultivation [J]. *Agriculture*, 13(10):1-19.

[22] Yi S., Wang P., Li Y., Li B., & Cao Z. (2024). Lifting and stacking device of automatic tray lifting machine for rice hard tray seedling (水稻硬质育秧盘全自动起盘机提升与叠盘装置研究) [J]. *Transactions of the Chinese Society for Agricultural Machinery*, 55(7):168-178.

[23] Zhang X., Xie X., Yi J., Yang S., Kong D., Yuan Y. (2018). Design of joint-style automatic machine for placing planted vegetable seeding tray (关节式蔬菜育苗穴盘播后自动摆放机设计) [J]. *Transactions of the Chinese Society of Agricultural Engineering* (*Transactions of the CSAE*), 34(21): 27-36.

RESEARCH ON A DETECTION ALGORITHM FOR DRY-DIRECT SEEDED RICE BASED ON YOLOv11N-DF

/

基于 YOLOv11n-DF 的旱直播水稻检测算法研究

Mingyang LI, Bin ZHAO*), Song WANG, Di WANG
College of engineering, Heilongjiang Bayi Agricultural University, Daqing/ China
Tel: +86-13589180106; E-mail: limingyangwf@126.com
DOI: https://doi.org/10.35633/inmateh-76-45

Keywords: *YOLOv11n, Automatic detection, Dry direct-seeded rice, DSConv, FASFFHead*

ABSTRACT

Identifying dry-direct seeded rice seedlings provides valuable information for field management. To address the challenges of seedling detection in cold-region dry-direct seeded rice fields, this study proposes an enhanced YOLOv11n-DF model. Key innovations include: 1) integrating DSConv into the C3k2 module to optimize phenotypic feature extraction, and 2) employing the FASFF strategy to improve scale invariance in the convolutional head. Experimental results show that the improved model achieves an mAP50 of 96%, with high recall, precision, and a processing speed of 251.5 FPS, outperforming the original YOLOv11n by 5 percentage points in mAP50, and surpassing YOLOv7–YOLOv10 in detection accuracy. The proposed algorithm effectively addresses challenges such as seedling occlusion and non-uniform distribution, offering a robust solution for automated seedling monitoring in precision agriculture.

摘要

识别旱直播秧苗，可为田间管理提供一定苗情信息。本研究为应对寒地旱直播稻田的幼苗检测难度大的问题，提出改进 YOLOv11n-DF 方法。该方法引入了两个关键创新：1）DSConv 引入 C3k2 模块以优化水稻表型特征提取，2）利用 FASFF 策略优化卷积头增强模型特征尺度不变性。实验结果表明，改进后模型的 mAP50、召回率（R）、检测精度（P）分别为 87.12%、77.07%和 84.11%，处理速度为 49.5 FPS，mAP50 较改进前 YOLOv11n 提高 4.28 个百分点，在检测精度方面超过了同类目标检测网络（YOLOv7~10）。该算法有效地处理了旱直播秧苗相互遮挡和非均匀分布挑战，为精准农业应用中的自动秧苗监测提供了新的解决方案。

INTRODUCTION

Dry-direct seeding is a rice cultivation method that replaces traditional transplanting with direct mechanical seeding. This planting approach - often referred to as dry-direct seeding - offers advantages such as water conservation, labor savings, and greater planting efficiency (*Li et al., 2023*). As a major production area for high-quality rice, Heilongjiang Province adopted dry-direct seeding technology in response to labor shortages and the development of drought-tolerant rice varieties (*Liu et al., 2022*). However, the emergence rate of dry-direct seeded rice is highly sensitive to climatic conditions, particularly in the cold regions of Northeast China, often resulting in uneven or unstable seedling emergence, which impairs rational dense planting (*Li et al., 2024*). Accurate identification and counting of seedlings provides a scientific basis for evaluating planting density, which reflects both sowing quality and varietal performance. Notably, the accuracy of seedling identification directly impacts the reliability of seedling counting (*Liu et al., 2024*).

The traditional rice seedling emergence number counting is determined manually, which is time-consuming, costly and difficult to implement (*Zhu et al., 2024*). In the past decade of research, machine vision technology has been gradually applied to the field of agricultural engineering, which greatly improves the reliability of agricultural information acquisition and provides a new solution idea for the detection of dry-direct seeded rice seedlings. For example, *Lu et al. (2021)* proposed the use of the TasselNetv3 segmentation network to achieve accurate rice plant counting. Similarly, *Takaho et al. (2022)* employed the Super Green Index (SGI) algorithm to predict seedling growth.

Interference from occlusion and background noise can affect image segmentation techniques. In addition, target detection is an important method of acquiring agricultural information. *Yi et al.* (*2022*) used a peak detection-based algorithm to count sunflower and soybean seedlings. *Rojas et al.* (*2022*) used a principal component analysis combined with an SVM detection algorithm to detect weeds. This type of hand-designed algorithm has strong specificity for target detection and better performance on tidy crops with obvious characteristics. Along with the introduction of deep learning methods for target detection, the way of agricultural information acquisition has become more diversified. Velumani et al. proposed the density statistics of maize seedlings by Faster R-CNN. *Shen et al.* (*2024*) utilized the improved YOLOv8 algorithm to achieve the detection of pod pepper. *Qiu D.F.* (*2024*) realized the detection of locust targets by improving the YOLOv7. improvement to achieve locust target detection. The single-stage target detection algorithm in deep learning networks directly realizes the simultaneous regression of target localization and classification through the end-to-end network architecture, and compared with the two-stage target detection algorithm, it discards the candidate region generation, reduces the computational redundancy and maintains a better detection accuracy at the same time.

Currently, there is limited research on target detection in complex scenarios such as dry-direct seeded rice seedlings, which are characterized by high planting density, complex backgrounds, and severe mutual occlusion. For instance, *Huang et al. (2024)* and *Li et al. (2023)* optimized YOLOv5 for the plant counting of oilseed rape seedlings, achieving improved detection accuracy. Although studies targeting this specific type of context-aware object detection remain scarce, such research is crucial for advancing precision agriculture.

In summary, while deep learning-based target detection algorithms demonstrate strong adaptability in agricultural applications, their detection accuracy remains limited when applied to dry-direct seeded seedlings, which often exhibit multi-scale morphological features and densely distributed, non-uniform row patterns. To address this issue, this paper proposes an improved YOLOv11n-based method tailored for the dry strip sowing environment. The approach enhances the feature extraction capabilities of the backbone network and improves the model's ability to capture deep, multi-scale features of densely distributed seedlings, thereby achieving more accurate detection of dry-direct seeded rice plants.

MATERIALS AND METHODS

Data Acquisition and Pre-processing

Image data was acquired on 18 June 2024 at the Jian Sanjiang Qixing Farm in Jiamusi City, Heilongjiang Province, China. Acquisition took place between 08:00 and 11:00 under clear weather conditions. Figure 1 shows the image acquisition device and the acquisition route diagram. The DJI Mavic 3T UAV was used at a height of 3 m and a speed of 1 m/s, in accordance with the planned route, to acquire images at an orthographic angle. The original image was filtered to remove some of the edges of the paddy field images and 640×640 pixel images were randomly extracted from different areas of the image, totaling 1489.



Fig. 1- Image acquisition equipment and range

The rice variety under study is "Magic Rice 119", which was planted according to the pattern of alternating wide and narrow row spacing (300 mm/200 mm). Field management followed the "dry sowing and water pipe" cultivation technique, in which the paddy field is irrigated after the four-leaf stage of rice growth. To accurately capture the morphological characteristics of dry-direct seeded rice seedlings and avoid the influence of water reflections on plant feature extraction, images were collected during the pre-irrigation stage. This standardized image acquisition process provides a reliable data foundation for subsequent rice phenotyping.



(a) Rice field environment (b) Background Straw (c) Post-irrigation environment

Fig. 2- Live streaming of dry rice paddy environment

Data set construction

Adobe Lightroom was used to preprocess 1489 of the images: adjusting contrast, exposure and saturation to enhance the distinction between straw and seedlings, and combining sharpening and noise reduction to highlight the details of the plants and reduce background noise, resulting in a darker background and more distinctive morphological features of the seedlings, which facilitated the algorithm's extraction of plant features. Mixed preprocessing and original images are used to enhance the adaptability of the model, and 90504 “rice” target frames are labeled by Labelimg. Finally, the independent training set, validation set and test set are divided according to the ratio of 8:1:1, which ensures the reliability of model training and testing while guaranteeing the richness of data.

Model selection and construction

The heterogeneity of plant morphology, the narrow, linear structure of rice leaves, and the low contrast between dark green moss and light green leaves on wet soil surfaces make classical target detection algorithms highly susceptible to lighting and background interference, hindering the effective capture of seedling features. Furthermore, due to the nature of strip sowing and variable soil moisture, seedling distribution is often non-uniform, exhibiting both aggregated bands and random sparsity. This complexity requires the detection model to possess both robust feature extraction capabilities and the ability to adapt to irregular spatial distributions.

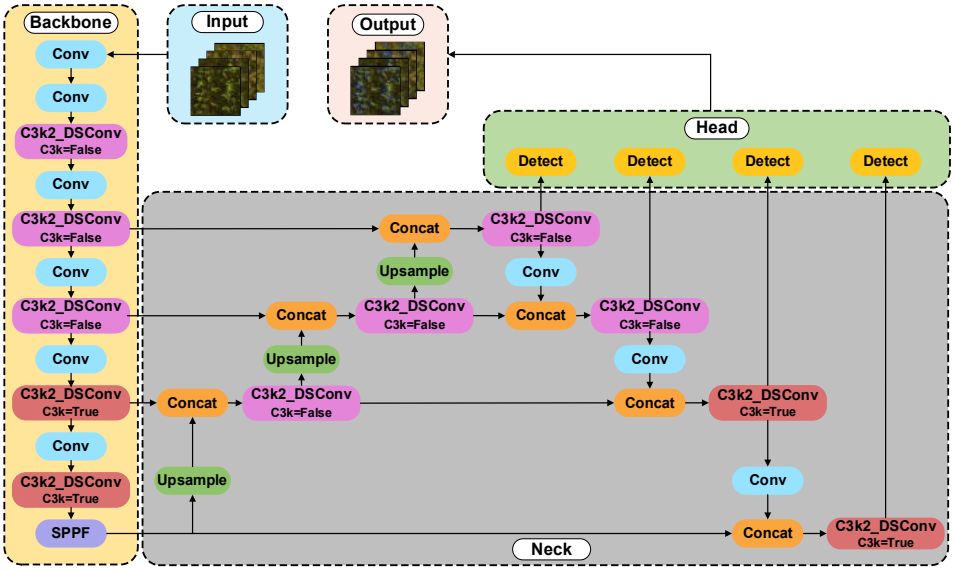


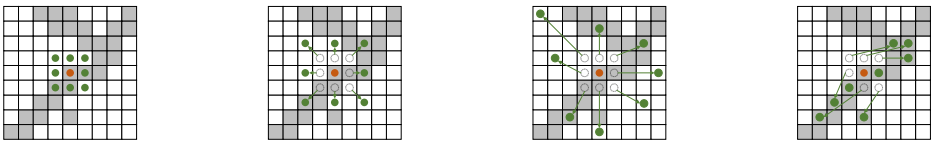
Fig. 3- YOLOv11n-DF model structure diagram

The YOLO model, with the advantage of single-phase detection architecture, exhibits excellent detection performance in the complex environment. Among them, YOLOv11 embeds multi-attention through the C2PSA mechanism, which strengthens the feature fusion ability and can cope with the scale changes and background interference in the large field environment (*He et al., 2025*). The YOLOv11 algorithm provides five different depth models, YOLOv11n, YOLOv11s, YOLOv11m, YOLOv11l, and YOLOv11x, in order to cope with different detection scenarios. It is important to note that the number of floating-point computations and parameters increases with the increase of the model depth. Among them, the model depth of YOLOv11n is the shallowest, which requires the least number of floating-point computational parameters to maintain better accuracy, while the training cycle is shorter than other models (*Wang et al.,2025*). This is consistent with the application scenario of high-efficiency real-time dry-direct seeded rice detection. Therefore, this paper selects the YOLOv11n algorithm for optimizing the detection algorithm for dry-direct seeded rice.

In this study, the C3k2 module in the YOLOv11n network was optimized by integrating DSConv convolution, and the original Detect head was replaced with the FASFFHead to improve the model's consistency in handling seedling phenotypic feature scales. The structure of the improved YOLOv11n-DF algorithm is shown in Fig. 3.

DSConv convolution

The leaves of the dry-direct seeded rice seedlings sown in strips, exhibit distinct narrow and slender morphological characteristics at the four-leaf stage, forming interlocking bands that provide mutual shading. The convolutional layer, a critical component in shallow phenotypic feature extraction, has a direct impact on the model's ability to assess target features. As illustrated in Fig. 4, which compares different convolution strategies, the standard convolutional kernel extracts local features with spatial invariance using a fixed receptive field, based on local connections, weight sharing, and hierarchical abstraction. However, the stacked structure with globally shared weights struggles to adapt to the irregular morphology of seedlings. Therefore, employing structure-adaptive convolution is essential for achieving accurate detection.



(a) Conv (b) Dilated Conv (c) Deformable Conv (d) DSConv

Fig. 4 - Comparison of different convolution strategies

Dynamic serpentine convolution focuses on slender and meandering local structures by adaptively adjusting the offsets of sampling paths, which enhances the model's ability to capture features of elongated structures (*Qi et al., 2023*). These characteristics make DSConv significantly more effective than the rigid grid sampling used in traditional convolutional kernels for extracting features from non-rigid and non-linear structures in complex scenes (*Zhang et al., 2024*). To address the challenge of capturing the narrow, elongated structures of dry-direct seeded rice seedlings, this study introduces DSConv into the C3k2 module. This integration takes into account the distributional characteristics of dry-direct seeded seedlings and enhances the geometric perception of convolutions by dynamically adjusting the sampling paths of convolution kernels, allowing them to continuously extend along thin, curved leaf structures. A lightweight subnetwork is used to predict incremental offsets at each sampling point, with each point's position determined by the cumulative offset from the previous point. This design ensures a smooth and continuous sampling path and prevents perceptual drift - a common issue in traditional deformable convolution caused by independent offset predictions.

The incremental offset of each sampling point is calculated as follows:

$$\delta \mathrm{p}_k = f_{\mathrm{offset}}(\mathrm{X};\mathrm{p}_0,\mathrm{p}_k) \tag{1}$$

where f_{offset} is the offset prediction network; X is the input feature map; p_0 denotes the coordinates of the center position of the current convolution kernel; p_k represents the coordinates of the kth sampling point; along the x-axis.

Since the offset values may be floating-point numbers, sampling at non-integer coordinates becomes necessary. To address this, bilinear interpolation is employed to compute the pixel values at these non-integer positions, ensuring smooth and continuous feature extraction. The interpolation is performed using the following formula:

$$\mathrm{X}(\mathrm{p}_0+\mathrm{p}_k+\Delta\mathrm{p}_k)=\sum B(q,\mathrm{p}_0+\mathrm{p}_k+\Delta\mathrm{p}_k)\cdot \mathrm{X}(q) \tag{2}$$

where B is a bilinear interpolation kernel decomposed into one-dimensional interpolations along the x and y directions; $\mathrm{p}_k+\Delta\mathrm{p}_k$ is the dynamically adjusted coordinate of the kth sampling point; q refers to the four surrounding integer-coordinate neighbors.

During the image acquisition process, the morphology of field-grown seedlings exhibits significant heterogeneity. To enhance the model's generalization capability for seedling detection, a multi-feature fusion approach is proposed. This involves extracting feature maps $f^l(K_x)$, $f^l(K_y)$ along the x-axis and y-axis, respectively, at the lth layer, using multi-morphology convolutional kernel templates generated by DSConv. The goal is to capture the shallow morphological features of the seedlings and to efficiently cluster key features, thereby improving detection robustness across varying seedling shapes.

During the target detection process, the model often fails to capture the shallow structural features of seedlings due to mutual occlusion among the leaves of dry-direct seeded rice. To reduce detection inaccuracies caused by disrupted seedling targets and to preserve the overall linear structure of the seedlings as much as possible, a topological continuity constraint loss is introduced into DSConv. This is achieved by calculating the bi-directional Hausdorff distance between the persistence maps of the predicted and ground truth labels, as defined by the following equation:

$$d_H^*(P_O, P_L) = \max(\max_{u \in P_O} \min_{v \in P_L} \|u - v\|, \max_{v \in P_L} \min_{u \in P_O} \|v - u\| \quad (3)$$

where P_O is the persistence map of the prediction, recording the birth and death times of topological features; P_L is the persistence map of the ground truth labels used for comparison with P_O; d^*_H represents the bi-directional Hausdorff distance, which quantitatively measures the topological discrepancy between P_O and P_L.

Serpentine convolution has been proven effective in extracting fine and narrow structural features of seedling leaves. Additionally, the C3k2 module has been optimized to enhance the model's perception of seedling features through four key mechanisms: chained accumulation of dynamic offsets, bilinear interpolation of fractional coordinates, a multi-view feature fusion strategy and a topological continuity constraint loss.

Multi-scale detection head

Seedling scale diversity in field environments leads to inconsistent seedling features in feature maps, affecting single-stage target detectors. The paper proposes a FASFFHead for the head network as a four-head detection mechanism based on an adaptive spatial feature fusion design to maintain feature scale consistency in the seedling detection model (*Liu et al., 2019*).

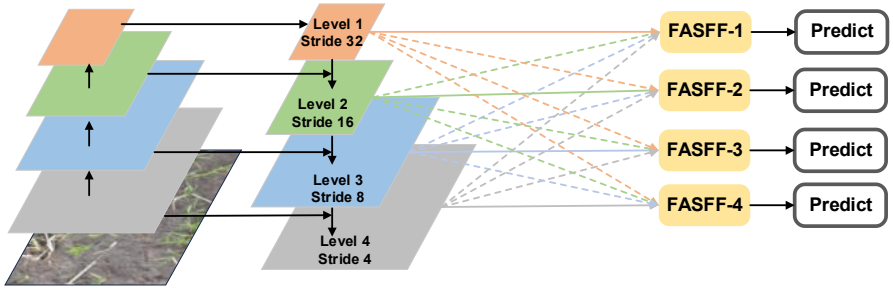


Fig. 5 - Schematic diagram of FASFF

The FASFFHead model adopts an improved feature fusion mechanism based on ASFF and introduces an additional small-scale target detection layer to the original 3-layer ASFF architecture, resulting in a 4-layer FASFF feature fusion framework (*Li et al., 2023*). This enhancement improves the algorithm's ability to capture and integrate features of small seedlings, enabling cross-scale information fusion through dynamic optimization of multi-layer feature strategies. As shown in Fig. 5, the working principle diagram of the FASFF mechanism illustrates how Level 1 through Level 4 (represented by different colors) correspond to varying spatial resolutions in the feature pyramid, each encoding seedling features at different scales. The labels FASFF-1, FASFF-2, FASFF-3, and FASFF-4 denote the fusion operations applied at each respective level, enabling layer-wise feature fusion across different resolutions.

To balance seedling feature representation, information retention, and computational efficiency, the FASFF method introduces a unified hierarchical structure for feature fusion. The core mechanism, Feature Aggregation and Selection (FAS), aims to standardize the resolution of feature maps from different hierarchical levels. For low-resolution seedling features, the number of channels is first compressed to match the target hierarchy using 1×1 convolution, followed by bilinear interpolation for up-sampling, thereby enhancing spatial resolution. In contrast, for high-resolution features, the resolution is first reduced via max pooling, and then 3×3 convolution is applied to achieve effective down-sampling.

Building on this foundation, a learnable spatial attention weight matrix is constructed. Through a parameterized weight learning module, the model dynamically learns the spatial contribution of features at each level, enabling adaptive aggregation of shallow features across multiple layers in the spatial dimension. This mechanism also preserves the local responses of features sensitive to different target scales, while effectively suppressing cross-level semantic conflicts and filtering out interfering information during feature fusion.

To address the scale inconsistency inherent in single-stage detection algorithms, FASFF enhances scale invariance by introducing an adaptive spatial feature fusion strategy. This approach improves the consistency across different feature scales by learning to suppress conflicting features. As a result, the model can flexibly determine which feature layers contribute most significantly to final predictions, depending on the contextual information at each specific location and scale.

RESULTS

Experimental Environment

The hardware equipment platform in this experiment includes: CPU Intel Core I7-13700KF, RAM 32GB, GPU Nvidia GeForce RTX 4070TI Super 16G; the software platform includes: 64-bit Windows 10 operating system and deployed Cuda11.8, Cudnn11.x with Python 3.11, using Pytorch 2.0.1 depth learning framework, PyCharm2023.3.5 editor for network model training. The relevant hyper-parameters were set: the number of epochs was 400, the batch size was 16, the optimizer was selected as SGD, and the initial learning rate was set to 0.02 in order to improve the convergence rate.

Evaluation index

In order to verify the applicability of the improved model for dry-direct seeded rice seedling detection, this study selects key performance indicators for multi-dimensional evaluation: in terms of detection accuracy, Precision - *P,* Recall - *R* and mAP50 are used as the core indicators; for the model complexity and model volume, the floating point operations (GFLOPs) and model Size are selected for quantitative analysis, and the detection speed of the model is evaluated using the detection speed (FPS). By comparing the experiments with mainstream target detection algorithms, the proposed method is comprehensively verified to see if the enhancement effect of the proposed method in model accuracy meets the expectation.

Model Performance Analysis

The training set of dry-direct seeded rice seedlings was used to train the improved model. The results showed that the YOLOv11n-DF model achieved an mAP50 of 87.12%, precision (*P*) of 84.11%, and recall (*R*) of 77.07%. Compared with the pre-improvement baseline, the mean average precision (mAP50) increased by 4.28 percentage points. Additionally, the model size remained compact at 12.7 MB, supporting efficient deployment.

The loss function curve, shown in Fig. 6, illustrates that both training loss and validation loss decrease rapidly and in synchronization during the first 50 epochs. After approximately 300 epochs, both curves converge in parallel, indicating that the model has reached a Pareto optimal state. Throughout the training process, the two models exhibit similar trends, and no significant fluctuations are observed in the validation loss. The final convergence difference between training and validation loss remains below 2%. The YOLOv11n-DF model, designed specifically for dry-direct seeding detection, does not exhibit overfitting or underfitting. Furthermore, it demonstrates strong memory retention and excellent generalization performance.

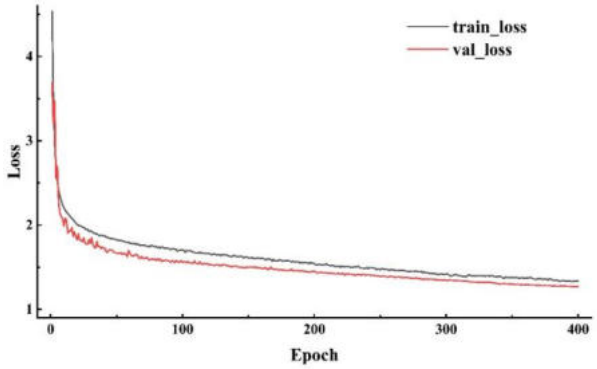


Fig. 6 - Loss function curve

As shown in Fig. 7, the detection results for both pre-processed and unpreprocessed images across different scenes are compared before and after the model improvement. The improved YOLOv11n-DF algorithm demonstrates a significantly enhanced ability to accurately detect dry-direct seeded rice seedlings in both types of images. Compared to the pre-improvement version, the improved model can more effectively identify individual seedlings, reduce redundant detections, and accurately focus on small targets - particularly in sparsely populated regions. These results highlight the enhanced robustness and adaptability of the improved algorithm under various image conditions.

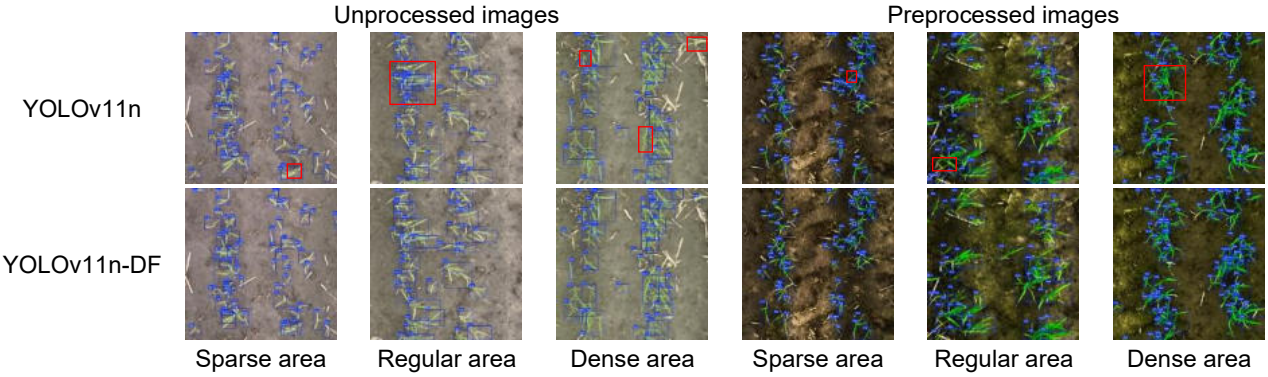


Fig. 7 - Sample images for image detection in different scenarios

Ablation experiments

To evaluate the effectiveness of the model improvements, ablation experiments were conducted based on the YOLOv11n baseline. The results demonstrated that both incorporating the DSConv mechanism into the C3k2 module and replacing the original detection head with the FASFFHead independently enhanced the model's ability to detect dry-direct seeded rice seedlings. In particular, the FASFFHead yielded a notable improvement in mAP50, although the addition of multiple detection heads also led to a corresponding increase in GFLOPs. Further module combination experiments confirmed the good compatibility of the improved components. Integrating both DSConv and FASFFHead significantly increased GFLOPs due to the multi-head structure, but this trade-off was justified by the sustained accuracy gains. The experimental findings indicate that the proposed improvements form a two-tier optimization architecture: DSConv enhances the backbone's ability to extract linear structural and distributional features of seedlings, while the four-head FASFFHead improves multi-scale detection performance. The final YOLOv11n-DF model achieves an mAP50 of 87.12%, representing a 4.28% increase over the baseline, with only a 13% increase in computational cost, thus meeting the expected performance improvements.

Table 1

Results of ablation experiment

YOLOv11n	DSConv	FASFFHead	mAP	Precious	Recall	FPS	GFLOPs	Size (M)
√	-	-	82.84%	80.62%	74.35%	**273.4**	**6.3**	**5.3**
√	√	-	84.62%	82.55%	74.63%	168.7	6.5	5.6
√	-	√	85.13%	83.20%	75.10%	154.7	7.1	11.8
√	√	√	**87.12%**	**84.11%**	**77.07%**	49.5	7.3	12.7

Note: The bolded data in the table represents the maximum value of the same group

Comparison of detection results across models

To more clearly highlight the performance differences in dry-direct seeded rice seedling detection, a comparative experiment was conducted between the improved YOLOv11n-DF model and several mainstream YOLO-based architectures. These comparisons provide a comprehensive evaluation of the model's effectiveness in handling the challenges of dry-direct seeded rice seedling detection. The detailed performance metrics and detection results are presented in Table 2.

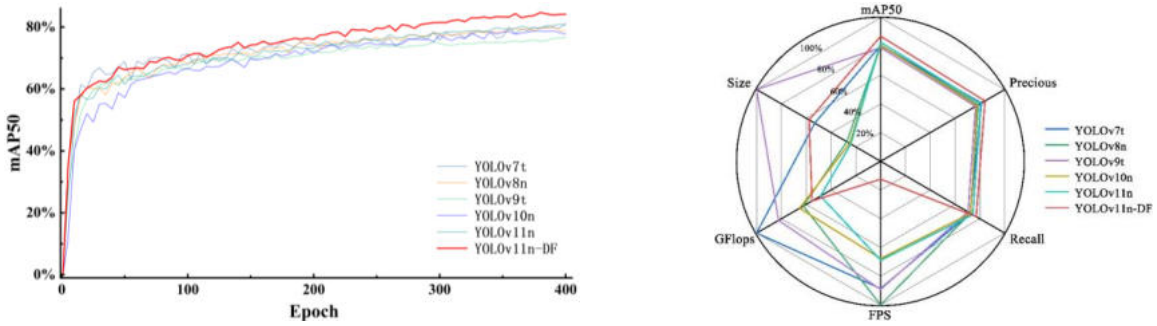
Table 2

Comparison of detection results by model

Models	mAP	Precious	Recall	FPS	GFLOPs	Size (M)
YOLOv7t	80.70%	81.25%	72.13%	351.6	13	11.7
YOLOv8n	80.91%	78.61%	72.22%	**396.8**	8.1	6
YOLOv9t	79.17%	76.49%	70.42%	354.3	10.7	22
YOLOv10n	80.83%	77.68%	72.53%	268.6	8.5	5.5
YOLOv11n	82.84%	80.62%	74.35%	273.4	**6.3**	**5.3**
YOLOv11n-DF	**87.12%**	**84.11%**	**77.07%**	49.5	7.2	12.7

Note: The bolded data in the table represents the maximum value of the same group

Fig. 8(a) shows the change curves of the mAP50 of different models with the number of training rounds. As the number of training rounds increases, the mAP50 of each model shows a general growth trend, and all models achieve basic convergence after about 300 epochs, with only small fluctuations. Among them, the pre-improved YOLOv11n model has a slower curve growth after 200 epochs, but still has some growth, and shows better learning ability in the detection of dry-direct seeding of rice seedlings. The improved YOLOv11n-DF grows second after the YOLOv7t model in the first 100 epochs, and the mAP does not fluctuate significantly in the training epoch, and still maintains a steady growth after 100 epochs, compared with the YOLOv11t model. After 300 epochs, the mAP50 stabilizes without significant growth, reaching a basic convergence.



(a) mAP50 comparison curve chart (b) Model performance radar chart

Fig. 8 - Comparative experimental results

To visually compare the performance differences among the models, radar charts based on normalized results were generated, as shown in Fig. 8(b). The improved YOLOv11n-DS network demonstrates clear advantages in terms of mAP50, *P*, and *R*, aligning with the intended improvement objectives. These results confirm that the YOLOv11n-DS network, which integrates enhanced feature extraction in the backbone and a multi-head detection strategy, outperforms similar object detection models in the task of dry-direct seeded rice seedling detection.

Visual Analysis

The visual analysis of the model can break through the limitations of the “black-box” model in the deep network. Heat map localization analysis can quantify the intensity with which the model focuses on the target region, verify whether the improved model suppresses noise and strengthens the target region of seedling plants, and assess the interpretability of the improved YOLOv11-DF model for seedling detection.

As shown in Fig. 9, Grad-CAM was used to visualize and analyze six detection scenarios. After integrating DSConv into the C3k2 module of the backbone network, the model exhibited a stronger focus on the banded distribution of dry-direct seeded rice seedlings, particularly in denser regions, compared to more sparse or scattered areas. The visualization shows that the model can effectively identify target regions in both preprocessed and original images, demonstrating enhanced generalization ability. Furthermore, the model’s attention is more concentrated on the seedling distribution in preprocessed images, suggesting that image preprocessing aids in the extraction of phenotypic features. Overall, the improved C3k2 module with DSConv significantly enhances the network’s ability to capture the structural and morphological characteristics of dry-direct seeded rice seedlings, especially those arranged in regular banded patterns.

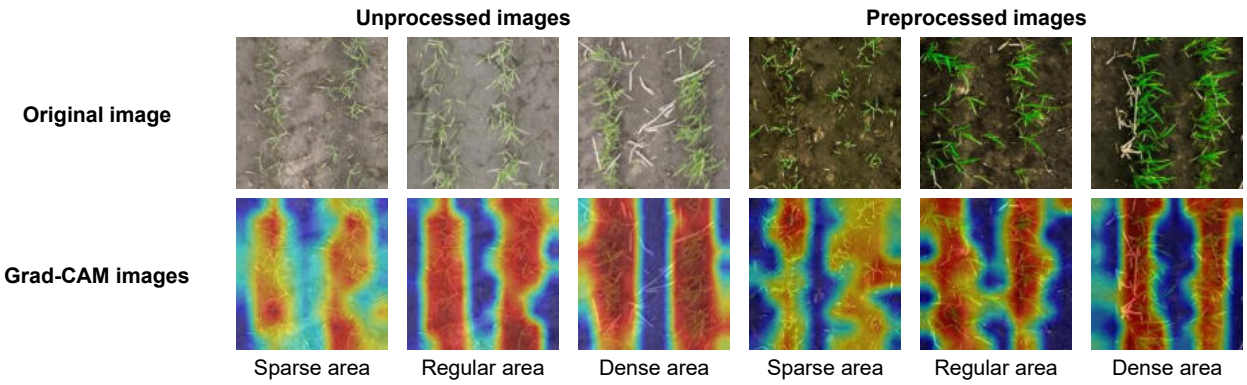


Fig. 9 - Grad-CAM visualization of detection scenarios

CONCLUSIONS

This study proposes an individual seedling detection algorithm based on an enhanced YOLOv11n network, aimed at addressing the challenges posed by the heterogeneous morphology and uneven distribution of dry-direct seeded rice. The following section outlines the results of this method:

(1) Use YOLOv11n to create a target algorithm that captures the visual traits of dry-direct seeded rice. The DSConv depthwise separable convolutional optimization C3k2 module strengthens the linear extraction of seedlings' traits, while a FASFF-based adaptive feature fusion mechanism improves the detection head's structure to better capture the multi-scale traits of seedlings.

(2) Use comparison and ablation experiments to verify the effectiveness of model improvement. The YOLOv11n-DF model's accuracy and recall reached 84.11% and 77.07%, respectively. Its mAP50 was 87.12%, showing better detection performance than the original model and mainstream algorithms. This model accurately detected multiscale seedlings in complex field environments.

(3) The interpretability of the model improvement is analyzed using visualization tools. DSConv improves the detection of linear phenotypic features of seedlings by the C3k2 module and focuses on seedlings with banded distributions. The four-detector-head architecture of FASFFHead mitigates the inconsistency in the scale of the fused multiscale features through dynamic weight allocation. The model improvement meets the design expectation, and YOLOv11n-DF has better generalization and interpretation.

(4) In summary, the improved model can accurately detect dry-direct seeded rice seedlings. Subsequent research could reduce the model's complexity using a pruning technique to meet video detection requirements in field management.

ACKNOWLEDGEMENT

This research, entitled "Research on a detection algorithm for dry-direct seeded rice based on YOLOv11n-DF", was funded by the National Natural Science Foundation of China Youth Fund Program (32201655).

REFERENCES

[1] He, L. H., Zhou, Y. Z., Liu, L., Cao, W., Ma, J. H. (2025). Research on object detection and recognition in remote sensing images based on YOLOv11. *Scientific Reports*, Vol. 15, pp. 14032, London/UK

[2] Huang, X., Zhang, W., Qiu, T., Zhu, Y., Xu, S., & Li, W. (2024). Rapeseed seedling detection and counting based on UAV videos (基于无人机视频影像的油菜苗检测与计数). *Transactions of the Chinese Society of Agricultural Engineering*, Vol. 40, pp. 147-156, Beijing/China.

[3] Li, C.P. (2025). *Research on Seedling Rape Plant Counting Algorithm Based on Improved Neural Network (基于改进卷积神经网络的苗期油菜植株计数算法研究)*, MSc dissertation, Anhui Agricultural University, Hefei/China.

[4] Li, M., Xue, M., Sha, Y., Li, H., Chen, Y., (2024). Synergistic and Optimal Allocation of Water, Land and Fertilizer Resources of Rice in Heilongjiang Province Based on Meta-analysis (基于 Meta 分析的黑龙江省水稻水土肥资源协同优化调配). *Transactions of the Chinese Society for Agricultural Machinery*, Vol. 55, pp. 302-311, Beijing/China.

[5] Li, Y., Xue, J., Zhang, M., Yin, J., Liu, Y., Qiao, X., Li, Z. (2023). YOLOv5-ASFF: a multistage strawberry detection algorithm based on improved YOLOv5. *Agronomy*, Vol. 13, pp. 1901. Basel/Switzerland

[6] Liang, C., Li, Y., Zhang, K., Wu, Z., Liu, J., Liu, J., Zhou, C. Wang, S., Li, F., Sui, G. (2023). Selection and yield formation characteristics of dry direct seeding rice in Northeast China. *Plants*, Vol. 12, pp.3496, Basel/Switzerland.

[7] Liu, S., Huang, D., Wang, Y. (2019). Learning spatial fusion for single-shot object detection. *arxiv preprint* arxiv:1911.09516, USA.

[8] Liu, Y., He, C., Gai, D., Geng, Y., Guo, L., Shao, X. (2022). Morphological and physiological traits of roots and their relationships with shoot growth and grain yield in direct-seeded rice in northeastern China. *Crop and Pasture Science*, Vol. 73, pp. 1229-1244. Australian.

[9] Lu, H., Liu, L., Li, Y. N., Zhao, X. M., Wang, X. Q., & Cao, Z. G. (2021). TasselNetV3: Explainable plant counting with guided upsampling and background suppression. *IEEE Transactions on Geoscience and Remote Sensing*, Vol. 60, pp.1-15, USA.

[10] Qiu, D. (2024). Research on locust target detection algorithm based on YOLO v7-Mobilenetv3-CA. *INMATEH-Agricultural Engineering*, Vol. 74, pp.283-292, Bucharest/Romania.

[11] Lu, H., Liu, L., Li, Y. N., Zhao, X. M., Wang, X. Q., & Cao, Z. G. (2021). TasselNetV3: Explainable plant counting with guided upsampling and background suppression. *IEEE Transactions on Geoscience and Remote Sensing*, Vol. 60, pp. 1-15, USA.

[12] Qi, Y., He, Y., Qi, X., Zhang, Y., & Yang, G. (2023). Dynamic snake convolution based on topological geometric constraints for tubular structure segmentation. *In Proceedings of the IEEE/CVF international conference on computer vision*, pp. 6070-6079, USA.

[13] Rojas, C. P., Guzmán, L. S., Toledo, N. V. (2017). Weed recognition by SVM texture feature classification in outdoor vegetable crops images. *Ingeniería e Investigación*, Vol. 37, pp. 68-74, Bogota/Spain.

[14] Shen, J., Jiang, Q., Liu, Y., Ma, N., (2024). Pod pepper target detection based on improved YOLOv8. *INMATEH-Agricultural Engineering*, Vol. 74, pp. 273-282, Bucharest/Romania.

[15] Ueno, T., Nagano, S., Moriyuki, S., Hayashi, T., Fukuda, H. (2022). Optimized Excess-Green Image Binarization for Accurate Estimation of Lettuce Seedling Leaf-Area in a Plant Factory. *Environmental Control in Biology*, Vol. 60, pp. 153-159, Japan.

[16] Velumani, K., Lopez-Lozano, R., Madec, S., Guo, W., Gillet, J., Comar, A., Baret, F. (2021). Estimates of maize plant density from UAV RGB images using faster-RCNN detection model: Impact of the spatial resolution. *Plant Phenomics*, pp. 9824843, USA.

[17] Wang, C., Song, X., Wang, J., Yan, X. (2025). An improved YOLOv11 algorithm for small object detection in UAV images. *Signal, Image and Video Processing*, Vol. 19, pp. 1-12, Germany.

[18] Bai, Y., Nie, C., Wang, H., Cheng, M., Liu, S., Yu, X., Shao, M., Wang, Z., Wang, S., Tuohuti, N., Shi, L., Ming, B., Jin, X. (2022). A fast and robust method for plant count in sunflower and maize at different seedling stages using high-resolution UAV RGB imagery. *Precision Agriculture*, Vol. 23, pp. 1720-1742, Germany.

[19] Zhang, J., Zhang, D., Liu, J., Zhou, Y., Cui, X., Fan, X. (2024). DSCONV-GAN: a UAV-BASED model for Verticillium Wilt disease detection in Chinese cabbage in complex growing environments. *Plant Methods*, Vol. 20, pp. 186, UK.

[20] Zhu, W., Dai, S., Feng Z., Duan, K., Shao, C. Wei, X. (2024). Estimation of Rice Basic Seedling Number Based on Mixed Pixel (基于混合像元分解的分蘖期水稻基本苗数量估测方法研究) *Transactions of the Chinese Society of Agricultural Machinery*, Vol. 55, pp. 202-209, China.

DIGITAL TECHNOLOGIES IN AGRICULTURE. SCANFIELD-5S SMART SYSTEM WITH INTEGRATED DIGITAL SOIL CUBE FOR INNOVATIVE SOLUTIONS IN AGRICULTURE [1]

/

ЦИФРОВИ ТЕХНОЛОГИИ В ЗЕМЕДЕЛИЕТО. SCANFIELD-5S СМАРТ СИСТЕМА С ИНТЕГРИРАН ДИГИТАЛЕН ПОЧВЕН КУБ ЗА ИНОВАТИВНИ РЕШЕНИЯ В ЗЕМЕДЕЛИЕТО

Krasimir BRATOEV[1*)], Ivelin GEORGIEV[2)]
[1)] Department of Agricultural Machinery University of Ruse / Bulgaria;
[2)] Scanfield – 5S smart system GmbH, Ruse / Bulgaria
Tel: +359 082 888 324; E-mail: kbratoev@uni-ruse.bg
DOI: https://doi.org/10.35633/inmateh-76-46

Keywords: *ECa, soil spatial heterogeneity, soil sampling design, soil quality*

ABSTRACT

In the conditions of intensively developing digital technologies, agriculture is also an active environment for their application. The article demonstrates some of the capabilities of the intelligent Scanfield-5S system and the integrated DSC - "Digital Soil Cube" for assessing the condition of the soil. The DSC method uses non-contact measurement of electrical conductivity (ECa) up to 0.4m depth in the soil. The study was usually conducted after harvest and before agricultural operations for the next crop. All collected ECa data are georeferenced. An adaptive soil sampling scheme was applied, which is specific for a given field. The number of sampling sites was determined after applying a graph-analytical method. A high confidence probability (over 80%) was obtained from the ECa data, which is a confirmation of the suitability of the method. Analyses were performed for bulk density (BD), relative humidity (dW), clay content (Clay), organic matter (OM) and activated carbon (C_(act.)) in the soil. The presented results characterize the soil as homogeneous with relatively good biological indicators (OM and C_(act.)). The adaptive soil sampling scheme and the obtained regression models for the soil parameters are specific to the studied field. The regression models for the observed parameters are linear and are presented through spatial resolution maps. The Scanfield-5S system provides solutions such as variable rate maps (VRA), soil carbon prediction, and overall soil health assessment. The digital soil model created using the DSC method is specific to the field under study, but has the potential for universality.

РЕЗЮМЕ

В условията на интензивно развиващи се цифрови технологии селското стопанство също е активна среда за тяхното приложение. Статията демонстрира част от възможностите на интелигентната система Scanfield-5S и интегрирания DSC – „Digital Soil Cube" за оценка на състоянието на почвата. DSC методът използва безконтактно измерване на електрическата проводимост (ECa) до 0,4 m дълбочина в почвата. Проучването обикновено се провежда след прибиране на реколтата и преди земеделските операции за следващата реколта. Всички събрани данни от ECa са георeферирани. Приложена е адаптивна схема за вземане на почвени проби, която е специфична за дадено поле. Броят на пробовземните места е определен след прилагане на графо-аналитичен метод. От данните на ECa е получена висока степен на доверие (над 80%), което е потвърждение за пригодността на метода. Извършени са анализи за обемна плътност (BD), относителна влажност (dW), съдържание на глина (Clay), органична материя (OM) и активен въглен (C_(act.)) в почвата. Представените резултати характеризират почвата като хомогенна със сравнително добри биологични показатели (OM и C_(акт.)). Адаптивната схема за вземане на почвени проби и получените регресионни модели за почвените параметри са специфични за изследваното поле. Регресионните модели за наблюдаваните параметри са линейни и са представени чрез карти с пространствена разделителна способност. Системата Scanfield-5S предоставя решения като карти с променлива скорост (VRA), прогнозиране на въглерода в почвата и цялостна оценка на здравето на почвата. Цифровият модел на почвата, създаден по метода DSC, е специфичен за изследваното поле, но има потенциал за универсалност.

[1] *NOTE: This article was initially published as a pre-print. The current version represents an improved and expanded manuscript that has not been published in any other peer-reviewed journal.*

INTRODUCTION

With the rapid development of digital technologies, agriculture has become a key area for their application. These technologies provide solutions that enable agriculture to strike a balance between protecting natural resources and meeting the growing demand for high-quality food and industrial raw materials, all while ensuring sound management decisions at various levels of government.

The basis of the predominant part of digital technologies in agriculture is the use of mathematical models proven by science and practice, describing separately or in combination various physical, mechanical, biological and other processes occurring during the cultivation of agricultural crops. In this way, technologies in agriculture can acquire adaptive, can become adaptive and even proactive - capable of responding promptly to changing conditions and adjusting the expected outcomes accordingly. The sustainability of such technologies largely depends on maintaining a constant connection with the environment in which they are implemented. By developing adequate mathematical models, it is possible to predict and adapt processes and phenomena manifested at a later stage as a result of changes in the factors influencing the object of impact.

Advances in understanding plant growth and development, as well as improvements in instrumentation, lead to better analysis and interpretation methods.

In the past and even today, many farms treat the entire cultivated area as a uniform unit—irrigating the whole field when it's time to water, or applying the same fertilizer rate across the entire area when needed. In reality, however, the needs of different parts of the field vary due to soil heterogeneity.

Acquiring, analyzing and applying accurate information through analytics is essential for making the right decisions. Soil testing is an important tool related to the application of technologies for growing crop plants. The adequacy of soil analysis largely depends on the methodology's ability to determine the non-uniform nature of the soil in a given field.

The basis of the existing methods for soil analysis is the classical methodology with its three main stages, which include:

Stage 1. Building the soil sampling – the surveyed field is divided into modular units (plots) of certain sizes, with the number and locations for drilling marked along a pre-defined trajectory. Generally, the "W-scheme" is suitable for most plot shapes and sizes, but "Z-scheme" or "X-scheme" also apply. Thus, one soil sample should be formed from each modular unit, obtained after mixing the samples from the drilling sites. The goal in drawing up a drilling scheme is to capture the soil diversity in the surveyed field. The number of drilling sites in a modular unit varies from 10 to 40, and the size of a modular unit from 0.5 ha to 10-12 ha (*FAO soil bulletin 18; https://sites.google.com/site/poushkarov/home/vzemane-na-pocveni-probi; The LaMotte soil handbook*);

Stage 2. Soil sampling – it is done either manually or mechanically using special tools that extract samples from soil layers with a depth of 0-30 cm; 30-60 cm and 60-90 cm, according to the purpose of the surveyed field and the goals of the analysis;

Stage 3. Laboratory analysis – soil samples collected from the field are subjected to laboratory tests according to established procedures and standards (*Benton, 2001*). The analysis of the results compares the reported with the reference values of the observed indicators and on this basis a generalized assessment of the soil condition is formed and relevant recommendations can be prepared.

A mandatory requirement for the classic method is soil sampling, and the reliability of the results depends on the sampling density (*https://bds-bg.org/bg/project/show/bds:proj:109684*). This determines the representativeness of the soil material collected. Due to the complexity of ensuring the representativeness of soil samples in Stage 1 of the conventional method, modern specific developments such as global navigation satellite system (GNSS), global positioning system (GPS), geographic information systems (GIS) are being used. According to a set algorithm, these systems can divide the field into modular units of a certain shape and size, which forms a network of drilling points on the field. The network density, resp. the density of sounding points is set by the size of the modular unit.

Conventional soil analysis methods typically rely on a set of samples to ensure representativeness and reliability of the analysis results. These samples are often combined into a composite sample, the analyses of which are assigned to the soil in the entire field. This makes their application difficult in modern digital technologies.

In the sense of the digital transformation in agriculture, classical soil analysis cannot provide a high enough degree of precision. It also takes a lot of time and resources, which is why farmers often neglect it.

The idea of the DSC method is related to digitalization of soil analysis. A key point in it is the replacement of the soil sample from the so-called "Digital soil cube" which, by means of mathematical models, provides timely information on the condition of the soil.

To develop the method, a cybernetic approach known from science is applied. The approach is based on the principle of the black box, according to which any object can be studied and managed only by its reactions caused by one or other external influences, without knowing the processes and phenomena that take place inside the object (*Mitkov, 2011; Mitkov and Bratoev, 2023*). The application of this approach is also related to the use of probabilistic statistical methods (*Kardashevski and Mitkov, 1977; Mitkov, 2011; Mitkov and Minkov, 1989, 1993; Mitkov and Bratoev, 2023*), in which the reactions shown by the object are viewed as a random event, a random variable or a random process. At the so-called poorly organized systems (objects) including soil, these methods are a means of obtaining objective information. The DSC methodology uses the elements of mathematical statistics, correlation analysis, dispersion analysis and regression analysis (*Kardashevski and Mitkov, 1977; Mitkov, 2011; Mitkov and Bratoev, 2023*).

The reactions of the object (the soil) and the external influences are considered as random quantities that describe a given feature (property) of the general population (the soil in the entire field). A given property of the soil is seen as a reaction of the soil, and the soil itself as an object with an external influence. The entire soil survey process is passive in terms of the statistical data collected (*Kardashevski and Mitkov, 1977; Mitkov, 2011; Mitkov and Bratoev, 2023*). The methodology for implementing the DSC is distinguished by a dynamic functional scheme. In its entirety, this functional scheme consists of five stages that must be followed to obtain the final digital soil model. Once created, the digital soil model allows the functional scheme to be reduced to two stages - the first and the last, and the soil analysis itself takes on a proactive nature.

Stage 1. Measurement of the electrical conductivity of the soil - one of the significant measurements that can be used as an indicator of soil fertility and digitized is its electrical conductivity (*Corwin et al.,1996, 2005; Drommerhausen et al. 1995; Greenhouse et al.,1983; Hanson et al., 1997; Kitchen et al., 1999*). Soil electrical conductivity (ECa) is a measurement that correlates with soil properties that affect crop productivity. Such properties include soil texture, cation exchange capacity (CEC), organic matter, salinity, nutrient availability, etc. The nature of the current flow in soil has been described in detail in numerous studies (*Corwin et al.,1999; Ellsbury et al., 1999; Fitterman et al., 1986; Halvorson et al., 1976; Rhoades et al., 1990, 1991, 1992, 1999*). Some studies have reported the effects of soil salinity, CEC, water content, and bulk density on ECa (*Bohn et al.,1979; Bratoev et al., 2020; Corwin et al.,2005; Hanson et al., 1997; Slavich et al., 1990*). Others have analyzed the effects of clay, organic matter, soil temperature, texture, and cation availability (*Brevik et al., 2002; Cook et al., 1992; Corwin, 1996; Corwin et al.,1999; Drommerhausen et al., 1995; Stroh et al., 2001; Triantafilis et al., 2001*). ECa measurements should be interpreted with these factors in mind. Studies have shown that the optimal ECa values for fertile soils should be in the range of 110 – 570 mS/m (*Cook et al., 1992; Triantafilis et al., 2001*). The level of soil moisture and the nutrients dissolved in it play a decisive role in the measured ECa in the soil. In order to use it as an indicator of soil health and therefore to make informed decisions, it is necessary to understand the relationship of ECa with soil properties. The complex nature of the relationships between individual soil parameters is also transferred to their relationship with ECa (*Bohn et al., 1979; Brevik et al., 2002; McDaniel et al., 2014*). Such complex relationships are difficult to describe with traditional functional mathematical relationships. By measuring the ECa, the information contained in the soil about its main characteristics is recorded as a numerical series that provides an opportunity to describe the complex interrelationships. In the DSC method, non-contact measurement of ECa is used, based on the principle of electromagnetic induction. Soil ECa screening is performed for 100% of the surveyed field area, with the location of each record being marked with geographic coordinates.

Stage 2. Building the soil sampling - the collected data on ECa of the soil in the surveyed field are subjected to statistical processing. The aim is to identify areas of the field in which the ECa can be assumed to be the same from a statistical point of view. In general, zones with strong, medium and weak electrical conductivity of the soil are formed, but in detail the number of zones depends on the observed soil diversity in the field. Statistical processing consists of determining the estimates of numerical characteristics and testing statistical hypotheses. The information from the received assessments is used to find the so-called the maximum relative error, which is accepted in the DSC method, should not exceed 10%. Such an error value determines the number of soil samples that must be taken from an area in order to guarantee the results obtained at a 95% confidence level. By performing a statistical hypothesis test for equality of a series of means it can be

determined at how many zones within the field the hypothesis will be rejected. Thus, zones will be formed on the field, which will be significantly different from each other by the measured ECa of the soil in them.
The outlines of each of the zones are determined by the geographic coordinates of the individual records during the scan. The field locations where soil samples will be taken are also set with their geographic coordinates, their location being adjusted to avoid autocorrelation with respect to ECa.

Stage 3. Soil sampling - it is carried out either manually or mechanically using special tools that extract samples from four soil layers with a depth of 0.2 m; 0.4 m; 0.7 m and 1.0 m, according to the purpose of the surveyed field and the goals of the analysis. Each soil sample is marked with its geographic coordinates and recorded ECa value.

Stage 4. Laboratory analyses - the soil samples collected from the field are subjected to laboratory tests according to established procedures and standards (*Benton, 2001*). The obtained results of the laboratory analyses are used in the next stage to compile mathematical models.

Stage 5. Creating digital soil models - a digital soil model is a collection of separate regression models expressing the relationship between a given soil parameter and the measured soil ECa. To obtain a specific regression model, the ECa data at the drilling (sampling) site and the results obtained from the laboratory analysis for the selected soil indicator are used. With these data, a regression analysis is carried out to quantitatively describe the relationship between the soil parameter and ECa. The statistical analysis of the obtained regression models shows that the change of the soil index can be described by ECa and the obtained regression model. Another aspect of the statistical analysis is determining the adequacy of the model, which in the case of individual digital models is confirmed by Fisher's criterion (*Kardashevski and Mitkov, 1977; Mitkov, 2011; Mitkov and Minkov, 1989; ; Mitkov and Minkov, 1993; Mitkov and Bratoev, 2023*). This gives reason to assume that the error of the model does not exceed the error of the experimental data. By including a given regression model to the coordinates of the field, georeferenced data is obtained, with which the values of the observed soil indicator in the given field can be presented visually (through spatial resolution maps) or digitally.

MATERIALS AND METHODS

The digital nature of the DSC method allows it to be integrated with other modern digital technologies. Such a digital technology is the Scanfield-5S system, which offers innovative services and solutions for agriculture. The Scanfield-5S system platform is built on several main pillars of a digital nature: 3D scanner, Data processing and analyses.

3D scanner – a patented scanner is used for non-contact measurement of soil electrical conductivity (*https://geoprospectors.com/en/*). Raw data from the ECa scanner is converted into information on several baseline metrics: soil zones, depth to compaction, relative soil moisture and tillage maps. The scanner mounts directly on a vehicle, which can be a tractor, ATV, pickup truck, or similar field vehicle. The sensor can be used on any soil, even when it is covered with vegetation. There is also no restriction on minimum or maximum soil moisture content. The scanner works on the principle of electromagnetic induction. A magnetic field is induced through a transmission coil (Fig. 1). Four receiving coils then measure electrical conductivity at four cumulative depths, up to 1.0 m. The device also permanently records spatial information. No contact with the ground is required to obtain soil electrical conductivity data, making it suitable for scanning dry soils. The data is collected and can be processed in real time to be immediately used on the tractor (for example for managing agricultural equipment).

Data processing - raw data is processed with filters and sophisticated algorithms to produce a series of files. Some of these files can be used directly from the agricultural machine's ISOBUS terminal for further use. With the filtered data, spatial resolution maps of the observed indicators are prepared. From the spatial resolution maps for the soil zones, the locations of the soil sampling sites are determined.

Analysis – physical soil samples are sent to a soil analysis laboratory. The obtained results are processed and analyzed using specialized software and the DSC method, after which the data are transformed into soil maps. The soil maps are spatial resolution maps for each soil parameter for which a digital model was obtained using the DSC method. Each map is made by specialized software. The data from the maps can also be transformed into a tabular form. The detail in the soil map can be changed according to the needs of the user.

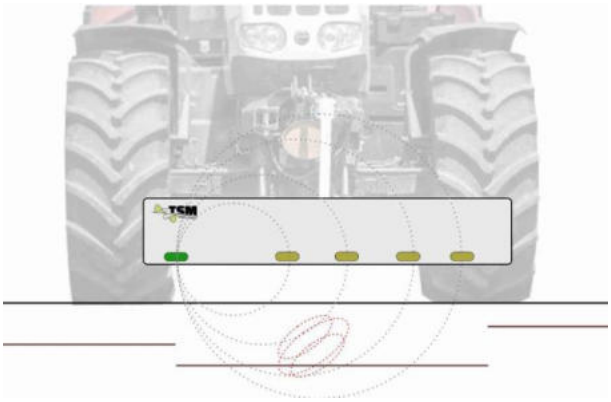


Fig. 1 - Top Soil Mapper (Geoprospectors GmbH)

1) Description of the study site

The studied field is located in the territory of the village of Boychinovtsi, Montana region in Bulgaria. The soil in this field is loam (*Gyurov and Artinova, 2001*). The field has an area of 207.7 ha, on which cereals and cereal crops are grown. The research was conducted after the wheat harvest. Up to the time of the study, no soil treatments were carried out.

2) Soil condition

In order to assess the soil condition, the following steps were taken: (a) ECa measurement across the field, (b) formation of markers for soil sampling, (c) analysis of soil properties, and (d) compilation of georeferenced spatial resolution maps for visual presentation of results.

a) ECa measurement across the field

The measurement of the ECa was carried out on 01.09.2023 with a mobile electromagnetic scanner TSM (Top Soil Mapper) of Geoprospectors GmbH. Successively, the measurements were taken about 1 m apart, collecting almost 20000 soil ECa data in four layers at the depth of 0.2 m; 0.4 m; 0.7 m and 1.0 m. All collected data are georeferenced with a GLONASS system (GNSS) receiver.

b) Formation of markers for soil sampling

Using the ECa data and the methodology of the Scanfield-5S system, six characteristic zones were formed within the field (Fig. 2). The resulting zones are distinguished by the average ECa in them, covering a different proportion of the field area, and in general characterize the spatial variability in ECa of the whole field. The marker in a given zone provides a statistical representation of the most frequently measured ECa in the zone. The location of the marker is georeferenced and a soil sample should be taken from it.

The soil samples were taken on the ECa measurement day (September 1, 2023). Soil cores were taken consecutively from the top two soil layers with a depth of 0.2 m to a depth of 0.4 m. Extraction of soil cores from the soil was carried out with a Royal Eijkelkamp hand probe. Duplicate soil samples were taken within each zone to ascertain variability at the zonal level. A total of 12 markers (stars on Fig. 4) were formed, from which a total of 24 soil samples were taken (12 from both soil layers).

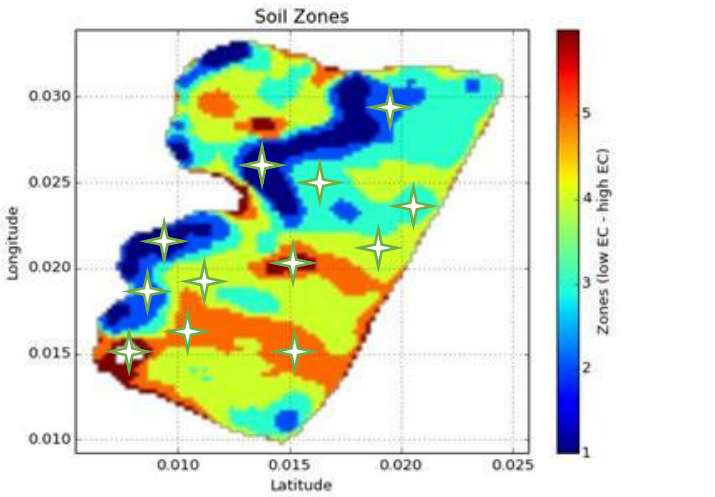


Fig. 2 - Zones and field markers (from TSM Client Cloud & Scanfield-5S) *

*Note: * full field coordinates not presented*

c) Analysis of soil properties

Relative humidity dW, bulk density BD and clay content were analyzed for the 24 soil samples from soil physical properties, and organic matter OM and active carbon $C_{act.}$ in the soil were analyzed as biological indicators. The choice on these indicators is dictated by the fact that the physical and biological properties of the soil are often not a focus when performing soil analyses. Validated methods were used to analyze these indicators (*Trendafilov and Popova, 2007; Moebius-Clune et al., 2017*). The relative humidity is expressed as a percentage of the maximum field moisture content of the soil, the value of which is 31.5%. Statistical processing was performed with TIBCO's "Statistica" software product.

d) Compilation of georeferenced spatial resolution maps for visual presentation of results

All spatial data for the ECa, as well as those from soil analyses, are entered into the Scanfield-5S system. Georeferenced spatial resolution maps are created for each of the observed soil indicators, for which a digital model was obtained using the DSC method. The data from the maps can also be transformed into a tabular form. The detail in the soil map can be changed according to the needs of the user.

RESULTS

After statistical processing of the ECa values measured by TSM for the soil layer with a depth of 0.2 m, an overall average value $\overline{ECa}_{20cm} = 27.95\ mS/m$ and a coefficient of variation $V_{20cm} = 14.9\ \%$ are obtained. For the layer with a depth of 0.4 m, these estimates are respectively $\overline{ECa}_{40cm} = 34.71\ mS/m$ and $V_{40cm} = 15.4\ \%$.

All data for ECa_{20cm} and ECa_{40cm} are divided into six groups (classes), which are a prerequisite for the formation of georeferenced areas in the field. The number of classes was determined after applying a graph-analytical method (*Mitkov and Bratoev, 2023*). Its result shows that over 80 % is the confidence probability that the average value obtained from the six groups does not differ by more than 10 % from the ECa average for the corresponding layer, i.e., $\overline{ECa}_{20cm}$ and $\overline{ECa}_{40cm}$. The high confidence probability justifies the spatial variation of the ECa to be represented by six georeferenced zones along the field.

After grouping the data for ECa_{20cm}, the average coefficient of variation in individual groups is $\bar{V}_{20cm} = 5.3\%$. For the groups of data referring to ECa_{40cm}, the average coefficient of variation is obtained $\bar{V}_{40cm} = 5.4\%$. The nearly identical values of the two coefficients of variation, along with the previously mentioned graph-analytical method, indicate that two measurements within a group or field zone are sufficient to guarantee 90% accuracy of the ECa group average. This confirms the necessity of collecting duplicate soil samples in each zone.

This is how the 12 markers for this field are formed, and their locations are determined by the georeferenced data associated with the most common ECa in a given group. The number and locations of markers, i.e., the soil sampling scheme depends on the spatial variability of soil ECa in the field being studied. Therefore, such a soil sampling scheme is adaptive in nature. The need to change existing soil sampling schemes when using the ECa is noted in research by D.L. Corwin and S.M. Lesch (*Corwin et al., 2005*).

From the correlation matrix (Table 1) it can be seen that ECa_{20cm} stands out as the most influential and most powerful indicator. As expected, this indicator has the strongest linear correlation with ECa_{40cm} ($\hat{r} = 0.94$), which is positive. The correlation of ECa_{20cm} are significant and with the other indicators, such as with BD_{20cm}, it is negative - $\hat{r} = -0.74$. A negative correlation is also observed between ECa_{40cm} and BD_{40cm} - $\hat{r} = -0.61$. Therefore, in areas of the field where the observed ECa decreases, the bulk density BD of the soil in these areas is expected to increase. An increase in soil stiffness is likely to occur as BD increases, but this was not included in this study.

A similar but positive correlation of ECa_{20cm} is observed with $Clay_{20cm}$ and the included biological indicators - OM_{20cm} and $C_{act.20cm}$, respectively $\hat{r} = 0.7$; $\hat{r} = 0.77$ and $\hat{r} = 0.74$. The correlation of the indicators OM_{40cm} and $C_{act.40cm}$ with ECa_{40cm} is also significant ($\hat{r} = 0.6$; $\hat{r} = 0.74$). The absence of a significant correlation of ECa_{40cm} with $Clay_{40cm}$ ($\hat{r} = 0.4$) as well as with dW_{40cm} ($\hat{r} = 0.51$) may be due to unforeseen circumstances, since sees that they are highly correlated with the conductivity ECa_{20cm}.

The significant correlation of ECa_{20cm} and ECa_{40cm} with biological indicators (OM_{20cm}, $C_{act.20cm}$, OM_{40cm} and $C_{act.40cm}$) makes the measurement of soil ECa a suitable tool for determining the amounts of organic carbon (OC) in the soil.

Table 1

Correlation matrix- Marked correlations are significant at p <0.05. N=12

Variable	Means	Std.Dev.	ECa_{20cm} (mS/m)	ECa_{40cm} (mS/m)
ECa_{20cm} (mS/m)	26.49	8.21	1.00	0.94
ECa_{40cm} (mS/m)	29.40	8.19	0.94	1.00
BD_{20cm} (t/m^3)	1.30	0.39	-0.74	-0.66
BD_{40cm} (t/m^3)	1.17	0.33	-0.62	-0.61
dW_{20cm} (%)	38.30	10.79	0.58	0.59
dW_{40cm} (%)	50.70	14.67	0.58	0.51
$Clay_{20cm}$ (%)	28.28	4.03	0.70	0.68
$Clay_{40cm}$ (%)	29.03	4.34	0.62	0.40
OM_{20cm} (%)	3.39	0.28	0.77	0.89
OM_{40cm} (%)	2.66	0.83	0.76	0.60
$C_{act.20cm}$ (mg/kg)	527.23	110.00	0.74	0.65
$C_{act.40cm}$ (mg/kg)	430.11	124.15	0.72	0.74

Tables 2 and 3 show the basic statistics characterizing the observed soil properties in the 0.2 m and 0.4 m depth layers, respectively. The average values of the properties show that the soil in the studied field has good levels of the observed indicators. The higher values of the coefficient of variation (Coef. Var.) for ECa_{20cm} and ECa_{40cm} compared to $V_{20cm} = 14.9\%$ and$V_{40cm} = 15.4\,\%$ is the result of the 12 measurements being counted as individual rather than group data. Taking into account the grouping of the data for the measured ECa_{20cm} and ECa_{40cm} in the entire field, the obtained values of the corresponding coefficient of variation differ by less than 5% from the total V_{20cm} and V_{40cm} (*Kardashevski and Mitkov, 1977*). A similar result can be expected regarding the variation in the other indicators in the tables. At values of coefficient of variation around and below 30 %, it can be assumed that the spatial variability of the given indicator obeys the normal distribution (*Kardashevski and Mitkov, 1977*). The higher BD values in the upper soil layer (0.2 m) are probably the result of the movement of agricultural machines during the harvest and the lower relative humidity in it.

Table 2

Mean and range statistics for 0.2 m sample depth

Variable	Mean	Confidence -95,000%	Confidence 95,000%	Std.Dev.	Coef.Var.
ECa_{20cm} (mS/m)	26.49	21.27	31.70	8.21	31.00
BD_{20cm} (t/m$^{3)}$	1.30	1.05	1.55	0.39	30.20
dW_{20cm} (%)	38.30	31.44	45.16	10.79	28.18
$Clay_{20cm}$ (%)	28.28	25.72	30.84	4.03	14,25
OM_{20cm} (%)	3.39	3.21	3.57	0.28	8.15
$C_{act.20cm}$ (mg/kg)	527.23	457.34	597.13	110.00	20.86

Table 3

Mean and range statistics for 0.4 m sample depth

Variable	Mean	Confidence -95,000%	Confidence 95,000%	Std.Dev.	Coef.Var.
ECa_{40cm} (mS/m)	29.40	24.19	34.60	8.19	27.86
BD_{40cm} (t/m$^{3)}$	1.17	0.96	1.38	0.33	28.38
dW_{40cm} (%)	50.70	41.38	60.02	14.67	28.93
$Clay_{40cm}$ (%)	29.03	26.27	31.79	4.34	14.96
OM_{40cm} (%)	2.66	2.13	3.19	0.83	31.21
$C_{act.40cm}$ (mg/kg)	430.11	351.24	508.99	124.15	28.86

The spatial variation of the observed soil indicators is represented by spatial resolution maps shown in Figures 3 and 4. Each of the maps was obtained using the Scanfield-5S system methodology. The maps combine information on the values of the observed parameter and the georeferencing of this information within the studied field. The different color representation of the field sections is integrated into a legend explaining what notional mean values are expected from the presented metric in the respective sections.

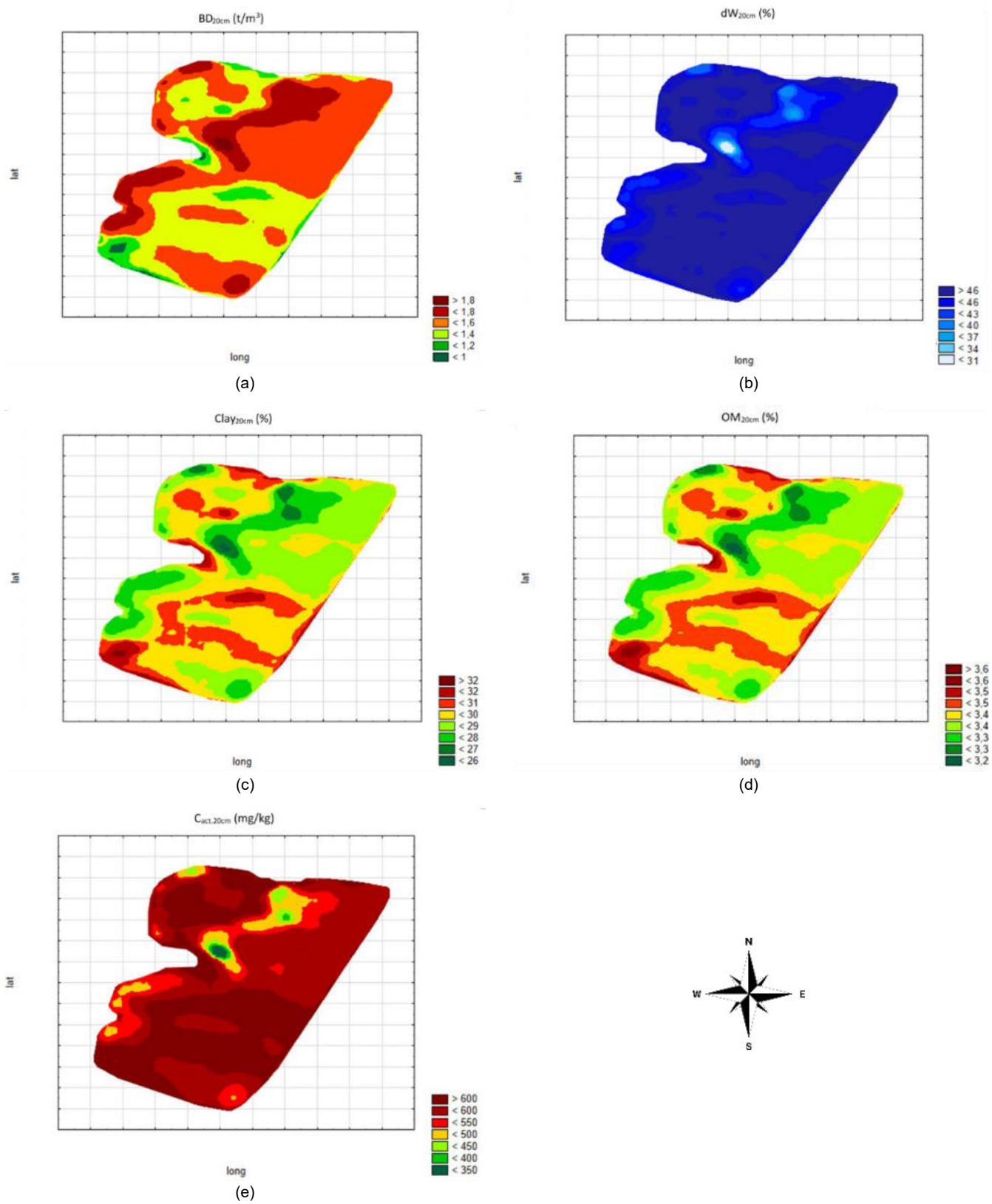


Fig. 3 - Spatial resolution maps of soil properties in the layer with a depth of 0.2 m:
(a) - bulk density (BD); (b) - relative humidity (dW); (c) - clay content (Clay);
.(d) - organic matter (OM); (e) - activated carbon ($C_{act.}$)

The presented spatial models of the observed properties of the soil are quantitatively related to the spatial variation of its ECa in the two layers - ECa_{20cm} and ECa_{40cm}. The analysis of the spatial resolution maps from Fig. 3 shows that 72 % of the field area is occupied by sections in which the volume density of the soil (BD_{20cm}) has a value falling within the confidence interval for the general average value. Similar results are also observed for the other indicators of this soil layer, and for active carbon ($C_{act.20cm}$) the relative share of

these areas reaches 90 %. These results mean that the soil in the topsoil is consolidated around some good levels of its indicators. Slightly lower relative humidity values (dW_{20cm}) are an expected result around the harvest period. The obtained levels of the biological indicators (OM_{20cm} and $C_{act.20cm}$) testify to a fairly good activity of microorganisms in the soil.

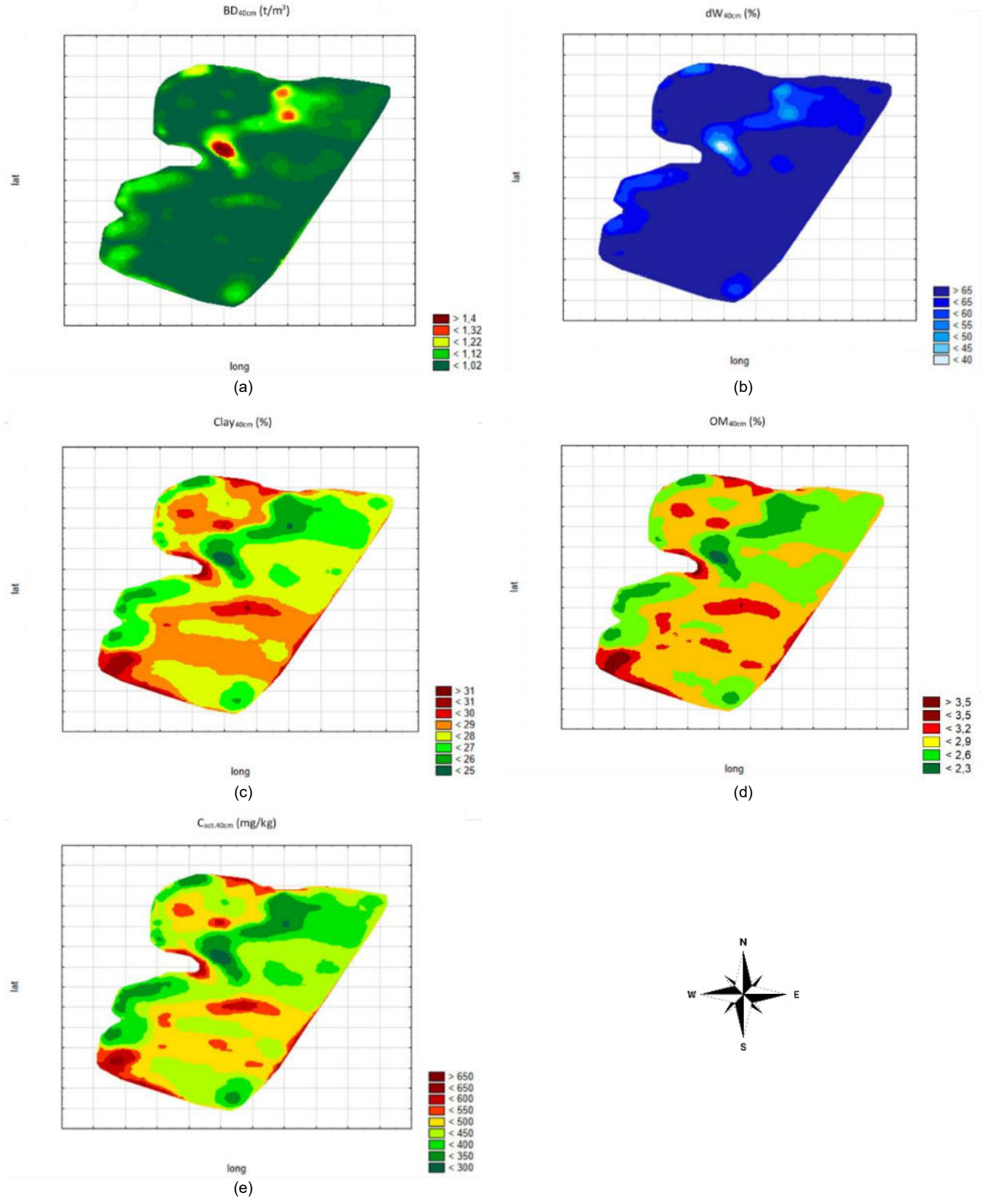


Fig. 4 - Spatial resolution maps of soil properties in the layer with a depth of 0.4 m
(a) - bulk density (BD); (b) - relative humidity (dW); (c) - clay content (Clay);
(d) - organic matter (OM); (e) - activated carbon ($C_{act.}$)

A similar analysis can be made for the spatial resolution maps from the deeper soil layer - 0.4 m (fig. 4). Here, the predominant part (81 %) of the soil has a bulk density $BD_{40cm} < 1.02\ t/m^3$, which suggests the appearance of a positive (left) asymmetry in the normal and distribution. An asymmetry in the normal distribution is also assumed for the relative humidity, but here it should be negative (right), since for 83 % of the layer area, the relative humidity is $dW_{40cm} > 60$ %. The average levels of biological indicators (OM_{40cm} and $C_{act.40cm}$) in this layer are lower than the previous layer (0.2 m), but still remain good.

Together, the two sets of spatial resolution maps outline that the soil in the surveyed field has a deep (up to 0.4 m) and thick humus horizon and has good levels of bulk density ($\sim 1.3\ t/m^3$). This implies that such technologies are applied in the cultivation of crops that ensure sustainability of the resources in the soil of that field.

CONCLUSIONS

The presented DSC method offers the possibility of digitalization of soil analysis, the key point of which is the use of information on soil electrical conductivity (ECa) and its relationship with soil properties through mathematical models. The DSC application methodology is distinguished by a dynamic functional scheme that provides timely information on the state of the soil. The creation of a digital soil model allows traditional soil analysis to become proactive. The adaptive soil sampling scheme used can be designed only after the spatial variability of ECa in the soil of the entire field has been measured. As the spatial variation of ECa increases, the number of places from which soil samples need to be taken also increases. It can be said that soil heterogeneity is a leading factor in the preparation of the sampling scheme. In conventional soil analysis methods, its heterogeneity is based on external signs in the field and a large number of samples, which vary depending on the standard used.

The five observed indicators: bulk density (BD_{20cm}, BD_{40cm}), relative humidity (dW_{20cm}, dW_{40cm}), clay content ($Clay_{20cm}, Clay_{40cm}$), organic matter (OM_{20cm}, OM_{40cm}) and active carbon ($C_{act.20cm}, C_{act.40cm}$) have a significant correlation with ECa, which is confirmed by the results in Table 2. The application of the DSC method is an opportunity for a reliable and adequate presentation of the change in these indicators for 100% of the field area.

The created spatial resolution maps are a convenient tool for visualizing and evaluating the condition of the soil in a given field. It was found that the spatial variability of ECa in the upper two layers of the soil is about 15 %, which is sufficient reason to consider this soil as sufficiently homogeneous. This is also confirmed by the results in the spatial resolution maps, where from 72-90 % of the field area is occupied by soil, whose indicators have values close to the average for the entire field. The levels of biological indicators are quite good for a soil that is engaged in agricultural production and the soil can be considered healthy and the applied agricultural practices sustainable.

The integrated solution of the intelligent Scanfield-5S system provides a practical tool for soil assessment when soil properties are related to ECa. The application of mathematical models requires the use of both precise measuring instruments and methods that determine individual soil parameters with the smallest possible error. The presented soil analysis solution demonstrates a way to digitally transform the most important resource in agriculture - soil. The Scanfield-5S system can provide farmers with reliable solutions tailored to their needs and applicable to modern technologies. One such solution is the creation of a variable rate application (VRA) maps. Such a map can be used for sowing, fertilizing with liquid or solid fertilizers, watering and other agricultural operations that are advisable to be carried out with a high degree of precision. Another potential option is the issuance of carbon certificates that would allow farmers to declare the amount of carbon accumulated in their fields. In addition to the direct benefits of carbon certificates, farmers will have information on how much their farming practices contribute to improving soil health.

Another proven option for determining soil health is to compare its experimental indicators with its corresponding reference indicators using the Harrington function. The minimum difference between the obtained functions is an indicator of soil health, i.e. it tends to its natural state.

The digital soil model created by the DSC method is specific to the studied field, but has the potential for universality.

ACKNOWLEDGEMENT

The research was conducted within the European Union-Next Generation EU through the National Recovery and Resilience Plan of the Republic of Bulgaria, project No. BG-RRP-2.013–0001.

REFERENCES

[1] Benton Jones, Jr., (2001). *Laboratory guide for conducting soil test and plant analysis*. CRC Press.

[2] Bohn, H.L., McNeal, B.L., O'Connor, G.A., (1979). *Soil Chemistry*. Wiley, New York, USA.

[3] Brevik, E.C., Fenton, T.E., (2002). The relative influence of soil water, clay, temperature, and carbonate minerals on soil electrical conductivity readings taken with an EM-38 along a Mollisol catena in central Iowa. *Soil Survey*, Horizons 43, 9–13.

[4] Bratoev K, H. Beloev, A. Mitkov, G. Mitev, (2020). On the possibility of conducting fast and reliable soil tests, *Agricultural machinery*, 1, 75-80

[5] Cook, P.G., Walker, G.R., (1992). Depth profiles of electrical conductivity from linear combinations of electromagnetic induction measurements. *Soil Sci. Soc. Am. J.* 56, 1015–1022.

[6] Corwin, D.L., (1996). GIS applications of deterministic solute transport models for regional-scale assessment of non-point source pollutants in the vadose zone. In: Corwin, D.L., Loague, K. (Eds.), Applications of GIS to the Modeling of Non-point Source Pollutants in the Vadose Zone. *SSSA Special Publication No. 48. SSSA*, Madison, WI, USA, pp. 69–100.

[7] Corwin, D.L., Loague, K., Ellsworth, T.R., (1999). Assessing non-point source pollution in the vadose zone with advanced information technologies. In: Corwin, D.L., Loague, K., Ellsworth, T.R. (Eds.), Assessment of Nonpoint Source Pollution in the Vadose Zone. *Geophysical Monogr.*, 108. AGU, Washington, DC, USA, pp. 1–20.

[8] Corwin D.L., S.M. Lesch., (2005). Characterizing soil spatial variability with apparent soil electrical conductivity Part II. Case study. *Computers and Electronics in Agriculture* 46 135–152

[9] Corwin, D.L., Lesch, S.M., (2005). Characterizing soil spatial variability with apparent soil electrical conductivity: I. survey protocols. *Comp. Electron. Agric.* 46, 103–133.

[10] Corwin D.L., S.M. Lesch, (2005) Apparent soil electrical conductivity measurements in agriculture. *Computers and Electronics in Agriculture* 46, 11–43.

[11] Drommerhausen, D.J., Radcliffe, D.E., Brune, D.E., Gunter, H.D., (1995). Electromagnetic conductivity surveys of dairies for groundwater nitrate. *J. Environ. Qual*. 24, 1083–1091.

[12] Ellsbury, M.M., Woodson, W.D., Malo, D.D., Clay D.E., Carlson, C.G., Clay S.A., (1999). Spatial variability in corn rootworm distribution in relation to spatially variable soil factors and crop condition. In: Robert, P.C., Rust, R.H., Larson, W.E. (Eds.), *Proceedings of the Fourth International Conference on Precision Agriculture*,

[13] Fitterman, D.V., Stewart, M.T., (1986). Transient electromagnetic sounding for groundwater. *Geophysics 51*, 995–1005.

[14] Gyurov G., N. Artinova., (2001), *Soil Science (Почвознание)*. ISBN: 954-702-064-1.

[15] Greenhouse, J.P., Slaine, D.D., (1983). The use of reconnaissance electromagnetic methods to map contaminant migration. *Ground Water Monit*. Rev. 3 (2), 47–59.

[16] Guide to the calibration of soil tests for fertilizer recommendations. *FAO soil bulletin* 18. FOOD AND AGRICULTURE ORGANIZATION OF THE UNITED NATIONS

[17] Halvorson, A.D., Rhoades, J.D., (1976). Field mapping soil conductivity to delineate dryland seeps with four electrode techniques. *Soil Sci. Soc. Am. J*. 44, 571–575.

[18] Hanson, B.R., Kaita, K., (1997). Response of electromagnetic conductivity meter to soil salinity and soil-water content. *J. Irrig. Drain. Eng*. 123, 141–143.

[19] Kardashevski S., A. Mitkov. (1977), *Statistical Methods in Agricultural Engineering (Статистически методи в селскостопанската техника)*, Zemizdat, Sofia.

[20] Koinov V., I. Kabakchiev, K. Boneva, (1998), *Atlas of Soils in Bulgaria (Атлас на почвите в България)*, ISBN: 954-05-0116-4.

[21] Kitchen, N.R., Sudduth, K.A., Drummond, S.T., (1999). Soil electrical conductivity as a crop productivity measure for claypan soils. *J. Prod. Agric*. 12, 607–617.

[22] McDaniel, M. D., Tiemann, L. K., & Grandy, A. S. , (2014). Does agricultural crop diversity enhance soil microbial biomass and organic matter dynamics? A meta-analysis. *Ecological Applications*, 24(3), 560-570.

[23] Mitkov A., D. Minkov. (1989), *Statistical Methods for Research and Optimization in Agricultural Engineering – Part II (Статистически методи за изследване и оптимизиране на селскостопанската техника – II част),* Zemizdat, Sofia.

[24] Mitkov, A.L., D.P. Minkov, (1993), *Mathematical Methods in Engineering Research (Математични методи на инженерните изследвания),* Ruse.

[25] Mitkov A., (2011), *Theory of Experiment (Теория на експеримента)*, Dunav Press, Ruse.
[26] Mitkov A., K. Bratoev., (2023*), Statistical Methods in Agriculture and Agricultural Engineering (Статистически методи в земеделието и земеделската техника)*, ISBN: 978-954-712-901-6, Ruse.
[27] Moebius-Clune B.N., D.J. Moebius-Clune, B.K. Gugino, O.J. Idowu, R.R. Schindelbeck, A.J. Ristow, H.M. van Es, J.E. Thies, H.A. Shayler, M.B. McBride, K.S.M. Kurtz, D.W. Wolfe, and G.S. Abawi., (2017). *Comprehensive Assessment of Soil Health*, The Cornell Framework, Third Edition, ISBN 0-967-6507-6-3.
[28] Rhoades, J.D., (1992). Instrumental field methods of salinity appraisal. In: Topp, G.C., Reynolds, W.D., Green, R.E. (Eds.), Advances in Measurement of Soil Physical Properties: Bring Theory into Practice. SSSA Special Publication No. 30. *Soil Science Society of America, Madison*, WI, USA, pp. 231– 248.
[29] Rhoades, J.D., Corwin, D.L., (1990). Soil electrical conductivity: effects of soil properties and application to soil salinity appraisal. Commun. *Soil Sci. Plant Anal*. 21, 837–860.
[30] Rhoades, J.D., Corwin, D.L., Lesch, S.M., (1991). Effect of soil ECa – depth profile pattern on electromagnetic induction measurements. *Research Report #125. U.S. Salinity Laboratory,* Riverside, CA, USA, 108 pp.
[31] Rhoades, J.D., Corwin, D.L., Lesch, S.M., (1999). Geospatial measurements of soil electrical conductivity to assess soil salinity and diffuse salt loading from irrigation. In: Corwin, D.L., Loague, K., Ellsworth, T.R. (Eds.), Assessment of Non-point Source Pollution in theVadose Zone. *Geophysical Monograph* 108. American Geophysical Union, Washington, DC, USA, pp. 197–215.
[32] Slavich, P.G., Yang, J., (1990). Estimation of field-scale leaching rates from chloride mass balance and electromagnetic induction measurements. *Irrig. Sci.* 11, 7–14.
[33] Stroh, J.C., Archer, S.R., Doolittle, J.A., Wilding, L.P., (2001). Detection of edaphic discontinuities with groundpenetrating radar and electromagnetic induction*. Landscape Ecol.* 16 (5), 377–390.
[34] The LaMotte soil handbook. La Motte chemical products company. Box 329. Chestertown. Maryland, USA.
[35] Trendafilov K., R. Popova., (2007), *Manual for Practical Exercises in Soil Science (Ръководство за упражнения по почвознание)*, ISBN 10: 954-517-016-6, 2007.
[36] Triantafilis, J., Huckel, A.I., Odeh, I.O.A., (2001). Comparison of statistical prediction methods for estimating field-scale clay content using different combinations of ancillary variables. *Soil Sci*. 166 (6), 415– 427.
[37] https://sites.google.com/site/poushkarov/home/vzemane-na-pocveni-probi
[38] https://bds-bg.org/bg/project/show/bds:proj:109684
[39] https://geoprospectors.com/en/
[40] https://eea.government.bg/bg/legislation/soil

OPTIMAL DESIGN AND SIMULATION OF SANDY LOAM SOIL COVERING DEVICE BASED ON BIONIC SAND CRAB PINCERS
/
基于沙蟹螯足仿生的沙壤土覆土装置优化设计与仿真

Mingtao JIA[1)], Rui ZHANG*[1)], Longze GUO[1)], Yue SUN,[1)] Xin WANG[1)], Haozhe WEI[1)]
College of Mechanical and Electrical Engineering, Qingdao Agricultural University, Qingdao, Shandong/ China
Tel: +8617853840106; E-mail: 2849956020@qq.com
Corresponding author: Rui Zhang
DOI: https://doi.org/10.35633/inmateh-76-47

Keywords: *Sandy loam soil, Tooth shape bionics, Soil covering device, EDEM Simulation*

ABSTRACT

Aiming at the problems that corn planters are prone to in sandy loam soil conditions, such as uneven soil covering thickness and seed position deviation, which affect the sowing quality, an innovative disk-type soil covering device based on the bionic shape of the claw legs of sand crabs has been optimized and designed. In this study, the contour features of the pincers of sand crabs were extracted using MATLAB software and applied to the tooth profile design of the soil cover plate, aiming to improve their operational performance in sandy loam soil. This study analyzed the operation mechanism of the bionic soil covering device based on the characteristics of sandy loam soil and determined the key parameters affecting the soil covering effect, including the installation deflection angle, installation inclination angle and the distance between the openings at the back of the soil covering tray. Taking the qualified rate of soil cover thickness and the standard deviation of seed lateral displacement as evaluation indicators, and with the help of EDEM discrete element simulation technology, the interaction model of sandy loam - seed - bionic soil cover device was constructed, and the single-factor and Box-Behnken response surface experimental designs were systematically carried out. Through simulation analysis and optimization, the optimal parameter combination of the soil covering device suitable for sandy loam soil was determined as follows: installation deflection angle 21.3°, installation inclination angle 20.1°, and the opening spacing behind the soil covering tray 100.0 mm. It has laid a foundation for the research on improving the uniformity of soil covering and the straightness of seed rows in the soil covering device of sandy loam soil seeders.

摘要

针对沙壤土条件下玉米播种机覆土易出现覆土厚度不均、种子位置偏移等影响播种质量的问题，创新性地优化设计了一种基于沙蟹螯足齿形仿生的盘式覆土装置。本研究利用 MATLAB 软件提取了沙蟹螯足的轮廓特征，将其应用于覆土盘齿形设计，旨在提升其在沙壤土中的作业性能。本研究基于沙壤土特性分析了仿生覆土装置的作业机理，确定了影响覆土效果的关键参数，包括安装偏角、安装倾角和覆土盘后方开口间距。以覆土厚度合格率和种子横向位移标准差作为评价指标，借助 EDEM 离散元仿真技术，构建了沙壤土-种子-仿生覆土装置的互作模型，系统开展了单因素与 Box-Behnken 响应面试验设计。通过仿真分析与优化，确定了适用于沙壤土的覆土装置最优参数组合为：安装偏角 21.3°、安装倾角 20.1°、覆土盘后方开口间距 100.0mm。为研究改善沙壤土播种机覆土装置的覆土均匀性与种行直线度奠定了基础。

INTRODUCTION

Sandy loam is an important type of agricultural soil due to its good air and water permeability *(Wang et al., 2025; Deng et al., 2025).* However, its loose texture and low cohesion characteristics can easily cause problems such as uneven soil cover thickness and seed positioning deviation in mechanical sowing and soil covering operations, seriously affecting the germination rate of sowing and the uniformity of crop growth *(Wang et al., 2025; Luo et al., 2025).* Traditional soil covering devices often face challenges such as difficult soil flow control, large disturbance and poor soil covering stability in sandy loam soil, making it difficult to meet the requirements of high-quality sowing. Therefore, optimizing the soil covering device plays a significant role in improving the uniformity of seed soil covering under sandy loam conditions.

In recent years, researchers at home and abroad have conducted extensive studies on soil covering devices on various seeders. The basic structural forms of the soil covering device mainly include three types:

the eight-shaped plate soil covering device, the double disc soil covering device and the extrusion type soil covering and pressing wheel *(Feng et al., 2025; Wu et al., 2024; Liu et al., 2023; Geng et al., 2022; Zhang et al., 2024., Guo, 2019).* Researchers have also conducted research and analysis on the soil covering performance. Lu Qi et al. first constructed a discrete element model of the interaction among soil, seeds and soil covering devices, breaking through the limitations of the traditional "soil-machine" binary simulation and laying the foundation for the parameter optimization of soil covering devices *(Lu et al., 2024).* Liu Fang et al. designed an arc-shaped double-toothed disc soil covering device in response to the fact that traditional scraper or disc soil covering devices are prone to causing fluctuations in soil covering thickness, resulting in exposed seeds or overly deep soil covering, which improved the uniformity of sowing *(Liu et al., 2024).* Inspired by the digging feet of the Oriental mole cricket, Zhang *Zhijun et al. (2018)* designed a bionic soil-breaking disc soil-covering device by measuring key parameters of the insect's toe claws to enhance the soil-breaking performance of a soybean planter. In order to improve the uniformity of seed distribution and the consistency of soil covering thickness, Li Liyan designed a new type of soil covering device with separate discs placed at the front and back. This enables the soil covering volume of two sets of discs to be the same as that of a traditional set of discs, avoiding the drawback of excessive soil covering volume at one time causing significant displacement of seeds *(Li et al., 2017).*

Inspired by the efficient ability of sand crab claws to manipulate sandy soil, this study designed a disc-type soil covering device based on the bionic shape of its teeth. The contour features of the claw legs of sand crabs were digitally extracted using MATLAB and applied to the tooth shape design to enhance the adaptability to sandy loam soil and operational performance. By analyzing the operation mechanism of the device, it was determined that the installation inclination angle, deflection angle and the distance between the rear openings were the key adjustable parameters. To optimize performance, taking the qualified rate of soil cover thickness and the difference in seed lateral displacement as indicators, an interaction model of sandy loam - seed - device was established using EDEM *(Lu et al., 2023)*, and based on this, single-factor and Box-Behnken response surface tests were carried out to seek the optimal parameter combination to improve the uniformity of soil cover and the accuracy of seed positioning.

MATERIALS AND METHODS

The working principle of the soil covering device

The operation process of the soil covering device (Fig.1) consists of three stages: soil insertion, stabilization operation and soil removal. The device is inserted into the soil at an angle, and its deflection angle drives the toothed cutting edge to push the soil laterally, guiding the soil to converge towards the center line to evenly cover the seed furrows. The thickness of the soil cover is dynamically controlled based on the principle of volume conservation through the deflection angle (to regulate the amount of soil pushed) and the spacing of the rear openings (to regulate the concentration of the soil cover). This process of "tangential soil insertion - directional soil transportation - precise soil covering" adapts to the fluidity of sandy loam soil and builds a stable seed bed for seeds.

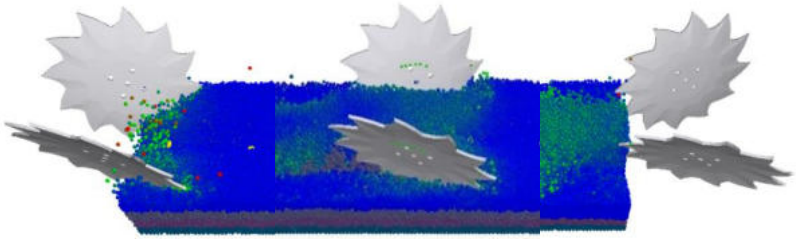


Fig. 1 - Working process of the soil covering device

a) Soil insertion stage; b) Stable operation stage; c) Excavation stage

Tooth profile design of the soil covering device

When the soil covering device is in operation, it mainly achieves soil covering by pushing the soil laterally. However, while its tooth shape pushes away the soil, it is prone to exert lateral forces on the soil and seeds, causing the seeds to shift and thereby disrupting the uniformity of soil coverage and the straightness of the seed rows. To effectively inhibit the lateral sliding of seeds, this study adopted bionics principles and drew on the tooth shape of the claw legs of sand crabs to optimize the design of the soil covering device.

The contour curve of the claw teeth of the sand crab was extracted using MATLAB software, as shown in Fig. 2a. Some of the curves were fitted through MATLAB software, and the fitting process is shown in Fig.2b.

The extracted data coordinates of the outer contour points are imported into the MATLAB curve fitting machine, with the X-axis and Y-axis representing the horizontal and vertical coordinates of the contour points respectively, with the unit being mm. The outer contour curve was fitted using an eighth-degree polynomial function, as shown in Equation (1):

$$y = -1.714x^8 + 2.659x^7 + 8.724x^6 - 13.98x^5 - 12.96x^4 + 25.88x^3 - 6.283x^2 - 17.39x + 756.8 (R^2 = 0.9957) \quad (1)$$

The coefficient of determination $R^2 > 0.99$, indicates that the fitted curve closely matches the actual biometric contour, demonstrating a high level of fitting accuracy.

Studies have shown that the number of notches on the grass-pulling wheel and the notch disc typically ranges from 8 to 15 *(Liu et al., 2024).* Although the uniformity of soil cover is high when the number of teeth is greater than 15, it also leads to increased forward resistance and wear. If the number of teeth is less than 10, uneven soil covering will cause the seed furrows to collapse. Therefore, 12 teeth were selected, and the spacing between the teeth can effectively inhibit the flow of sandy loam soil.



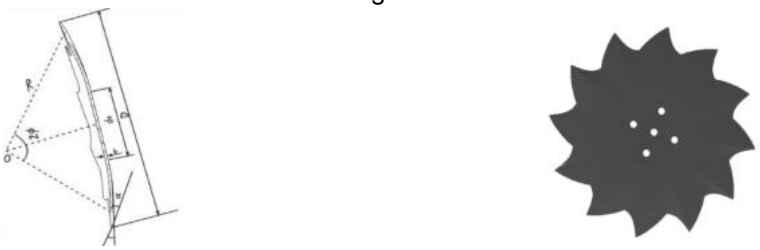
a) ***b)***

Fig. 2 - Tooth profile and fitting process diagram

a) Outline of the claw leg teeth of sand crabs; b) Curve fitting process

Diameter design of the soil covering device

Using the fitted equation as a reference, a bionic soil covering device was modeled in SolidWorks 3D software. As the device falls under the category of disc rakes, its key design parameters were calculated based on empirical formulas commonly used for shallow tillage disc rakes *(Lu et al., 2024; Liu et al., 2024)*. The structural schematic of the device is shown in Figure 3.



a) ***b)***

Fig. 3 - Schematic diagram of the soil covering device structure

a) Structural parameters of the soil covering device; b) Three-dimensional modeling of the soil covering device

$$D = kH \quad (2)$$

where: D is the diameter of the bionic soil covering device, [mm]; k is diameter to depth ratio coefficient; H is maximum designed depth of penetration into the ground, [mm].

The sowing depth of corn is generally 30 to 50 mm. The soil in this study is sandy loam with poor water retention. Therefore, the sowing depth was taken as 50 mm, and the maximum depth of penetration was 60 mm. The k value of the disc is generally taken as 4 to 6 *(Liu., 2025)*. Thus, the diameter of the bionic soil covering device is ≤ 360 mm.

Considering that sandy loam soil has loose particles, low viscosity and is prone to being scattered during soil covering operations, the diameter should be designed to avoid splashing of sandy loam soil. The formula is:

$$D \geq \frac{v^2}{g tan\varphi} \quad (3)$$

where: v is the operating speed of the seeder, taken as 0.8 to 1.4 m/s; g is acceleration due to gravity, taken as 9.8 m/s; φ is the angle of repose in sandy loam soil, taken as 28° to 32°.

After calculation, it can be found that the critical diameter of the bionic soil covering device for avoiding sandy loam soil splashing is ≥ 346 mm, and the final selected diameter is 360 mm.

Thickness design of the soil covering device

The selection of the thickness of the bionic soil covering device is related to the depth of the device's penetration into the soil and the size of the working load *(Bai., 2019)*. It was calculated by the empirical formula: $b = (0.008 \sim 0.012)D$

The thickness b of the bionic soil covering device was calculated to range between 2.88 and 4.32 mm. Given that sandy loam contains a high proportion of hard, abrasive sand particles, excessive wear at the device's edge can lead to failure. Additionally, a thinner and lighter disc lacks sufficient rigidity, which may increase vibration and negatively impact soil covering uniformity. Therefore, a thickness of b=4 mm was selected for this study.

Design of other structural parameters of the soil covering device

In sandy loam soil, the spherical radius R is the key to regulating the stability and resistance of flow diversion. Reducing the spherical radius R can enhance the directional restraint of the soil, but the frictional resistance increases significantly. Although increasing the spherical radius R reduces resistance, it weakens the accuracy of flow guidance. The design experience formula is:

$$R = \frac{D}{2\sin\phi} \tag{4}$$

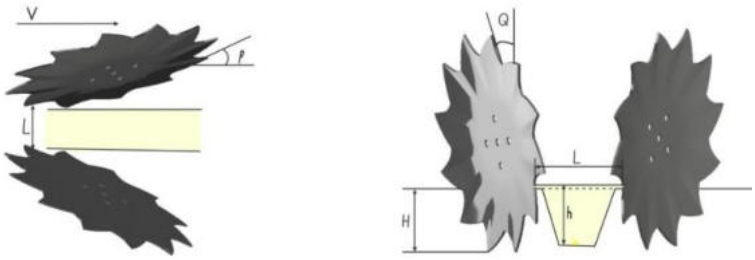
where: ϕ is spherical center angle, taken as 21 to 27 degrees, [°].

After calculation, 396≤R≤502, and finally R=450 mm was selected.

Under the condition of ensuring the strength of the cutting edge and allowing the manufacturing process, the cutting edge angle should be taken as small as possible to reduce the resistance of cutting soil. The common range of cutting edge angles is 14°30' to 22° *(Chinese Academy of Agricultural Mechanization Sciences., 2007)*, so α is taken as 15°.

Analysis of the Relationship between Installation Parameters and Soil Cover Volume

Based on the principle of volume conservation per unit time, the volume of soil pushed by the soil covering device ≈ the volume of soil covering. The parameter ranges of the installation deflection angle *P*, installation inclination angle *Q* and the distance *L* of the rear opening of the bionic soil covering device were calculated, as shown in Fig. 4



a) ***b)***

Fig. 4 - Schematic diagram of the relationship between the bionic soil covering device and the soil in the seed furrow

$$h \times L \times v = A_d v$$

$$A_d = k \times D \times H \times \sin P \times \cos Q$$

$$h = \frac{25920 \times \sin P \times \cos Q}{L} \geq 50 \tag{5}$$

where: h is requirements for soil cover thickness, h≥50 mm; v is the forward speed of the seeder, v =1.4 m/s; k is soil displacement efficiency coefficient of the soil covering device, k=1.2; A_d is the cross-sectional area of the soil pushed by the soil covering device; L is rear opening spacing, [mm]; D is diameter of the soil covering device, D=360 mm; H is the depth of the soil covering device's penetration into the soil, H=60 mm; Q is installation inclination angle, [°]; P is installation bias angle, [°].

After calculation, it can be determined that the rear opening spacing of the bionic soil covering device is 90 mm <L< 125 mm, the installation inclination angle is 15°< Q < 30°, and the installation deflection angle is 17°< P <30°. Due to the high fluidity of sandy loam soil, to avoid uneven soil cover caused by excessive soil dumping, the lower limit of the deflection angle was extended to 10°.

Establishment based on the EDEM simulation model

Based on the research on the qualified rate of soil covering thickness and the standard deviation of lateral displacement of the bionic soil covering device, solid modeling was carried out using SolidWorks 3D software and imported into EDEM in step format to establish a corn seed model and a soil trough model with a length, width and height of 1500×300×180 mm. Considering the soil characteristics of sandy loam, the Hertz-Mindlin (no slip) model in EDEM software was adopted as the contact model *(Hao et al., 2020)*. The simulation model of the sandy loam - seed - bionic soil covering device established is shown in Fig. 5.

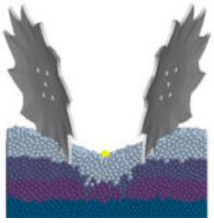
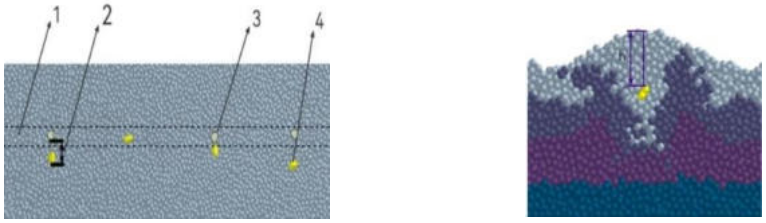


Fig. 5 - Simulation model establishment of soil-seed-soil covering device

The corn seeds are located in the middle of the seed trench, evenly distributed with a total of 8 seeds. Given the small sample size and relatively large error, the number of seeds per replicate was increased to eight. Seeds were sown in the same row for ten consecutive replicates, resulting in a total of eighty seeds. As shown in Fig. 6a, the horizontal offset of the actual position of a single seed after soil covering operation relative to its position before soil covering in the direction perpendicular to the sowing advance is called the lateral displacement S. By statistically analyzing the lateral displacement of the seeds, the standard deviation of the lateral displacement of the seeds was calculated to represent the straightness of the seed rows. The thickness of the soil cover above 80 seeds was measured using the Ruler tool in the post-processing of EDEM, as shown in Figure 6b. A thickness of 40 mm < soil cover thickness h<60 mm is considered qualified, Pass rate $\eta = \frac{\sum_{i=1}^{N} I(h_i)}{N} \times 100\%$ .The basic parameters of discrete element simulation obtained through literature are shown in Table 1 *(Lin et al., 2022; Wang et al., 2017)*.



a) ***b)***

Fig. 6 - Simulation test diagram of soil cover

a) The lateral movement of seeds within the seed furrows; b) Measurement of simulation values of soil cover thickness
1. Seed furrow soil; 2. Lateral displacement of seeds; 3. Seed position before lateral movement;
4. Seeds that move laterally away from the seed furrows

Table 1

Basic parameters of discrete element simulation model

Parameters	Numerical value
Soil density [kg·m^{-3}]	1.39
Soil Poisson's ratio	0.4
Soil shear modulus [Pa]	1.09e+07
Steel density [kg·m^{-3}]	7.85
Steel Poisson's ratio	0.26
Steel shear modulus [Pa]	8.0e+10
Soil - soil recovery coefficient	0.15
Soil-soil static friction coefficient	0.27
Soil-soil kinetic friction coefficient	0.70
Soil-steel plate recovery coefficient	0.50
Soil-steel plate static friction coefficient	0.75
Soil-steel plate kinetic friction coefficient	0.15

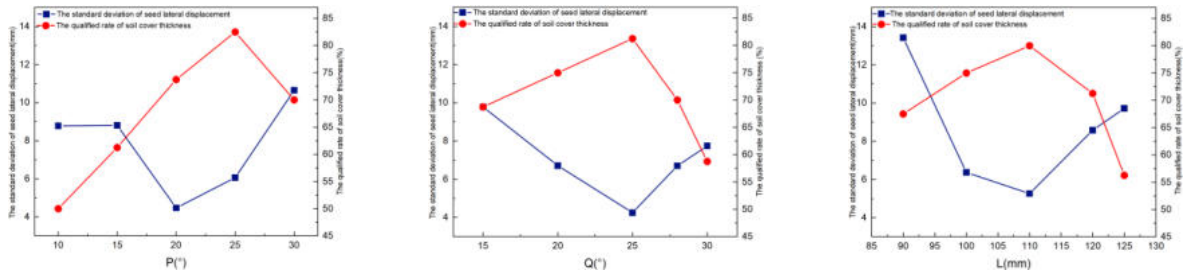
Single-factor trial

Based on the structural design and working principle analysis of the bionic soil covering device, the structural parameters that affect the performance of soil covering operations, namely the installation deflection angle P, installation inclination angle Q, and rear opening spacing L, were selected as the test factors. The influence of each factor on the soil covering thickness and the standard deviation of the seed lateral displacement was analyzed. According to the actual operation of the seeder, the forward speed of the equipment was set at 1.4 m/s. The levels of the single-factor test are shown in Table 2, and the test results are presented in Fig. 7.

Table 2

Single-factor test factor levels for the operation effect of the soil covering device

level	installation deflection angle [°]	installation inclination angle [°]	opening spacing behind the soil covering tray [mm]
1	10	15	90
2	15	20	100
3	20	25	110
4	25	28	120
5	30	30	125



a) *b)* *c)*

Fig. 7 - Results of the single-factor simulation test

To ensure the uniformity of soil covering and the straightness of seed rows, a larger amount of soil covering and a smaller standard deviation of seed lateral displacement are required. As shown in Fig. 7a, the pass rate of soil cover thickness is the highest when the deflection angle is 25°. When the deflection angle is less than 15°, the pass rate is low due to insufficient soil throwing. If the deflection angle is greater than 25°, it will decrease due to excessive scattering and insufficient soil covering at the center. The standard deviation of the lateral displacement of the seeds is the lowest when it is 20°, because the soil reflux path is the optimal. If the deviation angle is too large or too small, the seeds will shift sideways due to the imbalance of soil flow direction. After comprehensive consideration, the recommended installation deflection angle ranges from 15° to 25°.

As shown in Fig. 7b, the qualified rate of soil cover thickness increases slowly with the increase of inclination angle, reaching the peak at 25°. When the inclination angle is less than 20°, the qualified rate is low due to the formation of soil ridges on both sides of the seed furrows and insufficient soil covering in the center. The inclination angle greater than 28° drops due to soil being flung out of the seed furrows and insufficient backfilling. The standard deviation of the lateral displacement of the seeds changes gently between 15° and 25°, and increases significantly between 25° and 30° (if the inclination angle is too high, the soil cover is roughly insufficient, and the seeds exposed on the surface are affected by vibration, resulting in a sudden increase in displacement). To ensure the qualified rate of soil covering and the straightness of the seed rows, the installation inclination angle should be selected between 20° and 28°.

As shown in Fig. 7c, the qualified rate of soil cover thickness increases with the subsequent opening spacing, reaching a maximum at 110 mm. When the spacing is less than 100 mm, the narrow and congested passage leads to discontinuous soil coverage, resulting in a low pass rate. Conversely, if the spacing exceeds 120 mm, the qualified rate decreases due to poor soil concentration and insufficient coverage on both sides of the seed trench. The standard deviation of the lateral displacement of the seeds is the lowest when it is 110 mm (uniform soil coverage ensures balanced force on the seeds). To ensure the stability and continuous uniform soil coverage of the seeds, the spacing of the rear openings should be selected as 100 mm to 110 mm.

RESULTS

Box-Behnken Design Simulation Tests

Based on the single-factor test, taking the installation deflection angle P, inclination angle Q, and rear opening spacing L as factors, and the qualified rate of soil cover thickness and the standard deviation of seed lateral displacement as indicators, a three-factor and three-level Box-Behnken test was conducted to explore the relationship between the key factors and the indicators. The codes of the experimental factors are shown in Table 3, and the protocols and results are presented in Table 4.

Table 3

Factor coding for multi-factor test on the operation effect of the soil covering device

Encodings	Factors		
	P [°]	Q【°】	L【mm】
-1	15	20	100
0	20	25	110
1	25	28	120

Table 4

Experimental Scheme and Results

Serial Number	Factors			Standard deviation of seed lateral displacement [mm]	The qualification rate of soil cover thickness [%]
	P[°]	Q[°]	L[mm]		
1	15	20	110	6.71	68.75
2	25	20	110	2.63	85.00
3	15	28	110	3.61	80.00
4	25	28	110	5.06	75.00
5	15	24	100	3.98	76.25
6	25	24	100	2.13	86.00
7	15	24	120	4.39	80.00
8	25	24	120	4.68	85.00
9	20	20	100	3.87	82.50
10	20	28	100	4.73	78.75
11	20	20	120	7.21	82.50
12	20	28	120	4.78	85.00
13	20	24	110	4.21	77.50
14	20	24	110	3.85	78.75
15	20	24	110	3.91	78.75
16	20	24	110	4.05	77.50
17	20	24	110	3.45	75.00

Table 5

Analysis of variance in the simulation test of standard deviation of seed lateral displacement

Source	Sum of Squares	df	Mean Square	F-value	P-value
Model	24.24	9	2.69	31.90	＜0.0001
P	2.19	1	2.19	25.99	0.0014
Q	0.6272	1	0.6272	7.43	0.0295
L	5.04	1	5.04	59.70	0.0001
PQ	7.65	1	7.65	90.55	＜0.0001
PL	1.14	1	1.14	13.56	0.0078
QL	2.71	1	2.71	32.05	0.0008
P^2	0.5827	1	0.5827	6.90	0.0341
Q^2	4.05	1	4.05	47.95	0.0002
L^2	0.3138	1	0.3138	3.72	0.0952

Source	Sum of Squares	df	Mean Square	F-value	P-value
Residual	0.5910	7	0.0844	-	-
Lack of Fit	0.2675	3	0.0892	1.10	0.4455
Pure Error	0.3235	4	0.0809	-	-
Cor Total	24.83	16	-	-	-

Table 6

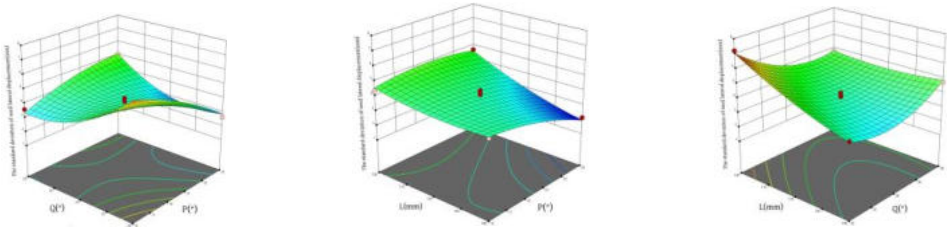
Analysis of variance in the simulation test of the qualified rate of soil cover thickness

Source	Sum of Squares	df	Mean Square	F-value	P-value
Model	314.56	9	34.95	18.51	0.0004
P	84.50	1	84.50	44.75	0.0003
Q	0.00	1	0.00	0.00	1.00
L	10.13	1	10.13	5.36	0.0537
PQ	112.89	1	112.89	59.78	0.0001
PL	5.64	1	5.64	2.99	0.1276
QL	9.77	1	9.77	5.17	0.0571
P^2	0.4975	1	0.4975	0.2635	0.6235
Q^2	0.0041	1	0.0041	0.0022	0.9641
L^2	91.29	1	91.29	48.34	0.0002
Residual	13.22	7	1.89	-	-
Lack of Fit	3.84	3	1.28	0.5467	0.6764
Pure Error	9.37	4	2.34	-	-
Cor Total	327.78	16	-	-	-

As can be seen from Table 4, when the installation deflection angle P=25°, the installation inclination angle Q=24°, and the rear opening spacing L=100 mm, the minimum standard deviation of the seed lateral displacement is 2.13 mm, and the maximum qualified rate of the soil cover thickness is 86%.The results of the analysis of variance (see Tables 5 and 6) indicate that the installation deflection angle P, inclination angle Q, and rear opening spacing L have extremely significant effects on the standard deviation *(Z)* of the seed lateral displacement and the qualification rate *(F)* of the soil cover thickness, and the regression equations of Z, F with P, Q, and L have been established. Based on the analysis of the influence of the interaction of P, Q and on Z and F by Design-Expert, the response surfaces are shown in Fig. 8 and 9.

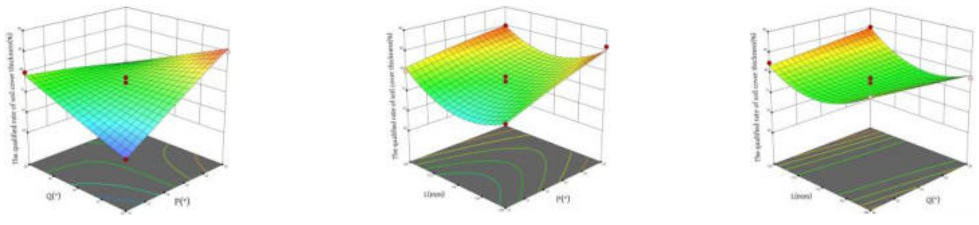
$$Z = +3.89 - 0.5237P - 0.2800Q + 0.7938L + 1.38PQ + 0.5350PL - 0.8225QL - 0.3720P^2 + 0.9805Q^2 + 0.2730L^2 \quad (6)$$

$$F = +77.50 + 3.25P + 1.12L - 5.31PQ - 1.19PL + 1.56QL - 0.3438P^2 + 0.0313Q^2 + 4.66L^2 \quad (7)$$



a) *b)* *c)*

Fig. 8 - Response surface illustrating the interaction effects of various factors on the standard deviation of seed lateral displacement



a) *b)* *c)*

Fig. 9 - Response surface illustrating the interaction effects of various factors on the qualification rate of soil cover thickness

Experiments show that P, Q and L all affect Z and F. To obtain the optimal parameters of the device, the Design-Expert optimization module was utilized for optimization.

The objective function and constraint conditions are: $\begin{cases} min\, Z\,(P,Q,L) \\ max\, F\,(P,Q,L) \\ 20^\circ \le P \le 25^\circ \\ 20^\circ \le Q \le 28^\circ \\ 100\text{mm} \le L \le 120\text{mm} \end{cases}$

The optimal parameter combination that satisfies the constraint conditions was obtained as follows: when the installation deflection angle is 21.3°, the installation inclination angle is 20.1°, and the installation spacing is 100.0 mm, the standard deviation of the seed lateral displacement is 3.1 mm, and the qualified rate of the soil cover thickness is 85.0%.

CONCLUSIONS

1. Considering the characteristics of sandy loam soil and soil covering requirements, a bionic soil covering device was optimized. Using MATLAB, the claw profile of the sand crab was fitted ($R^2 > 0.99$) to realize continuous operations of "tangential soil entry–directional transport–precise covering," which enhanced soil adaptability while ensuring uniform covering thickness and the straightness of the seed rows.

2. Theoretical analysis defined the test factor ranges, and single-factor simulations via the discrete element method were conducted. Installation deflection angle *(P)*, inclination angle *(Q)*, and rear opening spacing *(L)* were selected as variables, while the standard deviation of seed lateral displacement *(Z)* and soil covering qualification rate *(F)* served as evaluation indices. A regression model between *(P, Q, L)* and *(Z, F)* was developed using Box-Behnken design. The optimal parameter set was determined as P = 21.3°, Q = 20.1°, and L = 100.0 mm.

ACKNOWLEDGEMENT

This research was supported by the National Key Research and Development Program of China (No. 2023YFD2000402-2), the Open Project of the Collaborative Innovation Center for Mechanized Production Equipment of Major Crops in Shandong Province, and the Doctoral Start-up Fund Project of Qingdao Agricultural University.

REFERENCES

[1] Bai L. (2019). Design and Experiment of Seed Fertilizer Distribution Device Based on Active Soil Covering (基于主动覆土的种肥分施装置设计与试验). *Northwest A&F University,* Shanxi/China.

[2] Chinese Academy of Agricultural Mechanization Sciences. (2007). Agricultural Machinery Design (Volume 1) (农业机械设计(上册)). *China Agricultural Science and Technology Press,* Beijing/China.

[3] Deng C., Feng J., Wang J., Li H., Qiao H. (2025). Effects of Soil Factors on emergence and emergence of Goji berry red gall Mosquito (土壤因子对枸杞红瘿蚊出土羽化的影响). *Journal of Environmental Entomology,* Vol. 47, no. 2, pp. 483-490, Guangdong/China.

[4] Feng B., Sun W., Xin S., Wang G., Lv W. (2025). Optimization Design and Experiment of Soil-Covering Device for Astragalus Mulching Transplanting Machine. *Agriculture,* Vol. 15, no. 7, pp. 769-769, US.

[5] Geng Y., Wang X., Zhong X., Zhang X., Chen K., Wei Z., Lu X., Cheng X., Wei M. (2022). Design and Optimization of a Soil-Covering Device for a Corn No-Till Planter. *Agriculture,* Vol. 12, no. 8, pp. 1218-1218, USA.

[6] Guo H. (2019). Research on Evaluation of Corn Sowing Quality and Soil Covering and Pressing Device (玉米播种质量评价与覆土镇压装置研究). *Jilin University,* Jilin/China.

[7] Hao J., Long S., Li J., Ma Z., Zhao X. (2020). Particle scale effect of discrete element model for fluidity of sandy loam soil in Yam Planting field(麻山药种植田沙壤土流动性离散元模型颗粒放尺效应). *Transactions of the Chinese Society of Agricultural Engineering,* Vol.36, no. 21, pp. 56-64, Beijing/China.

[8] Li L. (2017). Experimental Study and Simulation Analysis of Front and Rear Disc-type Soil Cover (前后分置圆盘式覆土器的试验研究与仿真分析). *Jilin Agricultural University,* Jilin/China.

[9] Lin H., Wang Q., Liao P., Zheng W., He J. (2022). Calibration of discrete element simulation parameters for the interaction between tobacco-planted sandy loam and soil contact components (植烟沙壤土与触土部件相互作用的离散元仿真参数标定). Journal of Chinese Agricultural Mechanization, Vol. 43, no. 5, pp. 196-203, Jiangsu/China.

[10] Liu F., Gao X., Jia X., Huang Y., Zhang C. (2024). Design and Experiment of Archimedean Helical Arc-shaped Double-Toothed Disc Soil Covering Device for High-Speed Precision Seeder (高速精量播种机阿基米德螺线型弧面双齿盘覆土装置设计与试验). *Transactions of the Chinese Society for Agricultural Machinery,* Vol. 55, no. 6, pp. 91-100+120, Beijing/China.

[11] Liu G. (2025). Corn Conservation Tillage and Full-process Mechanized Planting Technology (玉米保护性耕作及全程机械化种植技术). *Seed Science and Technology,* Vol. 43, no. 11, pp. 87-89, Shanxi/China.

[12] Liu Q., Sun W., Wang H., Meng Y. (2023). Design and Field Test of a Leaping Type Soil-Covering Device on Plastic Film. *Agriculture,* Vol. 13, no.9, US.

[13] Lu Q., Liu F., Liu L., Liu Z., Liu Y. (2023). Establishment and Verification of Discrete Element Model of soil-seed-soil Covering Device Interaction in Seed furrows (种沟土壤-种子-覆土装置互作离散元模型建立与验证). *Transactions of the Chinese Society for Agricultural Machinery,* Vol. 54, no. 10, pp. 46-57, Beijing/China.

[14] Lu Q., Liu L., Liu Z., Jin W. (2024). Design and Experiment of Star-toothed Spherical Disc Soil Covering Device for Seeder (播种机星齿球面盘式覆土装置设计与试验). *Transactions of the Chinese Society for Agricultural Machinery,* Vol. 55, no. 4, pp. 23-31+73, Beijing/China.

[15] Luo M., Guan Z., Yan Y., Chai Y., Liu J. (2025). Analysis of the Differences in Growth and Quality of Qinggan Leek in Simulated Rhizosphere Habitat(模拟根际生境下青甘韭生长与品质的差异分析). *Plateau Agriculture,* Vol. 9, no. 1, pp. 65-72+132, Xizang/China.

[16] Wang J., Liu R., Guo Z., Wang S., Gao W. (2025). Root Morphology and tensile characteristics of different varieties of quinoa in the northern foot of Yinshan Mountain, Inner Mongolia (内蒙古阴山北麓地区不同品系藜麦根系形态和抗拉特性). *Jiangsu Agricultural Sciences,* Vol. 53, no.2, pp. 61-67, Jiangsu/China.

[17] Wang T., Shang Z., Zhang G., Tao C., Guo R. (2025). Effects of Soil pH of Different Types of Tobacco Planting on Soil Nutrient Availability (不同类型植烟土壤酸碱度对土壤养分有效性的影响). *Central South Agricultural Science and Technology,* Vol., 46, no. 4, pp. 29-32+51, Hubei/China.

[18] Wang X., Hu H., Wang Q., Li H., He J. (2017). Parameter Calibration Method for Soil Model Based on Discrete Elements (基于离散元的土壤模型参数标定方法). *Transactions of the Chinese Society for Agricultural Machinery,* Vol., 48, no. 12, pp. 78-85, Beijing/China.

[19] Wu X., Jiang Z., Zhang L., Hu X., Li W. (2024). Optimization Design and Experimentation of a Soil Covering Device for a Tree Planting Machine. *Agriculture,* Vol. 14, no.3, US.

[20] Zhang F., Wu M., Li A., Wei Q., Zheng Z. (2024). Design and Experiment of Transverse Interlaced Transplanting Device for Polygonatum odoratum Root Seedlings (黄精块根苗横向交错移栽装置设计与试验). *Transactions of the Chinese Society for Agricultural Machinery,* Vol. 55, no. S1, pp. 186-196, Beijing/China.

[21] Zhang Z., Sun X., Jin Z., Bing Z., Sun J. (2018). Design and Experiment of Bionic Soil Covering Device for Soybean Planter Crushing (大豆播种机破碎式仿生覆土装置设计与试验). *Transactions of the Chinese Society for Agricultural Machinery,* Vol. 49, no. 2, pp. 34-40+73, Beijing/China.

DEVELOPMENT AND PERFORMANCE EVALUATION OF AN INTERACTIVE VIRTUAL SIMULATION PLATFORM FOR MECHANIZED PEPPER HARVESTING BASED ON UNITY 3D

/

基于 Unity 3D 的辣椒机械化收获交互式虚拟仿真平台的开发与性能评估

Zhiqiang SONG [1, 2], Xiang DU [1], Jie YU [1], Shuyun LIN [3], Yunxiang YE *[2, 4]

[1] School of Agricultural Engineering, Jiangsu University, Zhenjiang, Jiangsu / China;
[2] Key Laboratory of Agricultural Equipment for Hilly and Mountainous Areas in Southeastern China (Co-construction by Ministry and Province), Ministry of Agriculture and Rural Affairs, Hangzhou, Zhejiang / China;
[3] Guizhou Institute of Mountain Agricultural Machinery, Guiyang, Guizhou / China
[4] Zhejiang Academy of Agricultural Sciences Agricultural Equipment Research Institute, Hangzhou, Zhejiang / China

Tel: +8619741702769; E-mail: yeyx@zaas.ac.cn; Corresponding author: Ye Yunxiang

DOI: https://doi.org/10.35633/inmateh-76-48

Keywords: *virtual reality, Unity 3D, pepper harvesting, 3D modelling, simulation training*

ABSTRACT

This study used SolidWorks to create a chili harvester model, 3ds Max to create planting terrain and chili plant models, and developed a virtual simulation platform for chili harvesting experiments based on Unity 3D. Finally, the feasibility of the virtual simulation platform was confirmed through human-machinery interaction effects and virtual simulation harvest experiments, which can provide reliable training and research data, solve the drawbacks of on-site training and testing, and contribute to the sustainable development of China's chili industry.

摘要

本研究应用 SolidWorks 创建辣椒收获机模型，应用 3ds Max 创建种植地形和辣椒植物模型，以及基于 Unity 3D 开发了一款的辣椒收获实验虚拟仿真平台。最后，通过人机交互效果和虚拟仿真收获实验证实了该虚拟仿真平台的可行性，能够提供可靠的训练和研究数据，解决了场地培训、试验的弊端，有助于中国辣椒产业的可持续化发展。

INTRODUCTION

China has been an agrarian society since ancient times, with a continuous history of farming and animal husbandry spanning over ten millennia. Throughout the extended period of traditional agricultural economy, ancestors created a splendid farming civilization through their diligence and wisdom *(Peng et al., 2011)*. Against the backdrop of China's comprehensive rural revitalization and accelerated modernization of agriculture and rural areas, it is of significant practical importance to provide mechanical harvesting training for agricultural engineering students and new-era professional farmers. By conducting harvest training experiments on crops, it can cultivate students' passion for agriculture, enhance the skills of new-era professional farmers, and accelerate the translation of agricultural machinery R&D achievements into field applications *(Liu et al., 2023)*.

However, field experiments for pepper harvesting face limitations such as seasonal constraints, farming cycles, and weather dependencies, resulting in prolonged timelines and high costs. To address these challenges, this study developed a virtual simulation platform for pepper harvesting experiments based on Virtual Reality (VR) technology.

In recent years, with the rapid advancement of computer and information technologies, virtual reality (VR) technology has emerged as a powerful tool grounded in computational systems. Leveraging its immersion, interactivity, and simulation capabilities, VR has been successfully implemented across diverse domains such as industry, agriculture, medicine, military, and education. The progress in VR has further facilitated the digitization and visualization of operational processes, offering innovative solutions to challenges in experimental training and practical applications *(Seth et al., 2011)*.

Both domestic and international researchers have conducted numerous explorations in utilizing VR technology to showcase cultural heritage and disseminate traditional culture.

For instance: *Zhang et al. (2011)* from Beijing Forestry University employed VR technology to design and implement a virtual landscape of the Northern Song Dynasty imperial gardens; *Liu et al.(2010)* from Northwest University reconstructed a 3D digital model of the Small Wild Goose Pagoda from the Tang Dynasty by acquiring point cloud data; *Chen Yan et al. (2019)*, *Wang Jianxiang et al. (2022)* developed a virtual simulation platform for mechanized corn harvesting based on Unity 3D respectively, conducting harvest simulation experiments under various conditions such as different operating speeds and plant densities. *Liu et al. (2014)* established a virtual testing platform for sprinkler irrigation vehicles using Unity 3D and *Li et al. (2017)* created a virtual demonstration platform for ancient Chinese farming scenes based on Unity 3D. Other similar research has been conducted by *Cheng et al. (2018),* who studied the performance of combined forest harvesters through a Unity 3D-based virtual training system; *Lü et al. (2015)* developed a virtual fruit tree pruning platform using Unity 3D and *Cheng et al. (2018)* designed a virtual exhibition platform for agricultural culture based on Unity 3D.

The aforementioned studies demonstrate that numerous scholars and experts in China have conducted extensive research on virtual reality technology. Developing virtual simulation platforms based on virtual reality technology can effectively demonstrate operational processes, showcase cultural and product features, and exhibit market potential. Among these, Unity 3D, as an engine for virtual reality system development, can create high-quality 3D virtual simulation environments with immersive experiences. By using the C# scripting language to develop control programs, it enables interactive behaviors between objects, revealing the principles of their interactions *(Yan et al., 2013; Liu et al., 2014).* This provides valuable references for the related research in this paper.

Although numerous researchers have developed virtual simulation platforms using VR technology, no existing studies have specifically addressed interactive virtual simulation for pepper harvesting operations. As the world's leading producer and consumer of peppers, with cultivation widespread across China's agricultural regions, peppers represent both a nutritionally valuable vegetable containing unique bioactive compounds and a significant cash crop for natural pigment extraction *(Zhang et al., 2021; Du et al., 2023)*. Given this agricultural importance, the present study establishes pepper as the target crop for developing an interactive virtual simulation platform of mechanized harvesting processes using Unity 3D. This innovative platform will not only simulate the complete mechanized harvesting workflow but also enable comprehensive performance evaluation of pepper harvesting machinery *(Wang et al., 2024)*.

MATERIALS AND METHODS

Structure of pepper harvesters

The pepper harvester consists of several key components: a picking device, conveying mechanism, cleaning and separation mechanism, collection bin, chassis, power transmission system, and hydraulic control system. Fig. 1 illustrates the schematic diagram of a typical pepper harvester structure. The key components are numerically labeled as follows: *1*. spring-tooth drum picking device, *2*. operator control cabin, *3*. primary conveying system, *4*. operator seat, *5*. engine and power transmission assembly, *6*. cleaning and re-picking device, *7*. secondary conveying system, *8*. auto-discharging collection bin, *9*. crawler-type traveling mechanism, *10*. belt pulley assembly, *11*. sprocket-chain transmission set.

Among these components, the picking device serves as the most critical part of the pepper harvester, as shown in Fig. 2. The key components are numerically labeled as follows: *1.* steel frame, *2.* upper cover plate; *3.* shield cover plate; *4.* left side plate; *5.* driving shaft; *6.* imitate terrain roller; *.7* left divider; *8.* spring finger cylinder; *9*. roller for bending branches; *10*. right divider. It performs dual functions of combing and conveying peppers, directly determining the machine's overall harvesting efficiency and quality *(Song et al., 2024)*.

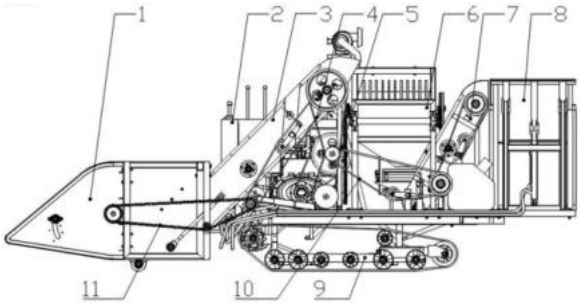


Fig. 1 - Schematic diagram of pepper harvester structure

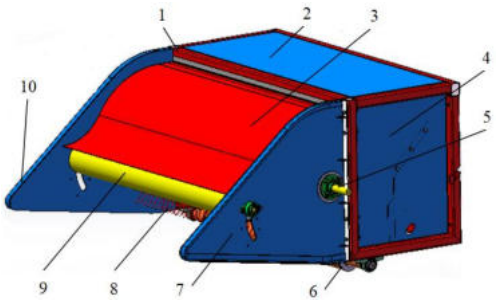


Fig. 2 - Structure model of pepper picking device

Working principle of pepper harvesting

During field harvesting operation, the pepper harvester advances forward with its picking device. The terrain-following wheels maintain continuous ground contact, providing stable support for the picking assembly. The pressure roller first bends the taller pepper plants to an optimal harvesting angle for spring-tooth drum picking. The spring-tooth drum rotates clockwise at 180-220 rpm, with the flexible teeth executing a combined action of impact detachment, frictional removal, and combing collection. Then, the peppers picked attain an initial velocity, and the subsequent trajectory controlled by its gravity acceleration, aerodynamic resistance, and the guide baffle's surface geometry. Then, the chili peppers enter the primary conveyor along the rotating path of the drum for next process under the interaction of multiple factors *(Du et al., 2024; Zhou et al., 2024)*. Fig. 3 schematically illustrates this dynamic harvesting process.

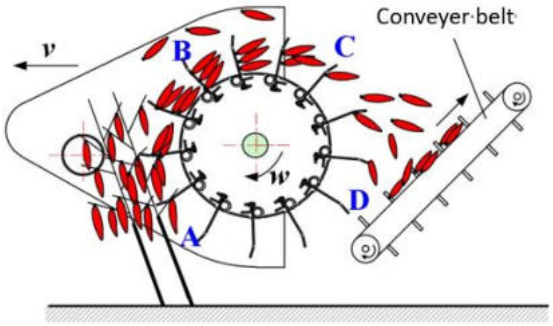


Fig. 3 - Schematic diagram of spring-tooth drum pepper picking mechanism

Development logic of virtual simulation platform

The virtual simulation platform for mechanized pepper harvesting was developed using Unity 3D within a Client-Server (C/S) architectural framework. As shown in Fig. 4, the system implements a structured five-layer architecture consisting of model layer, data layer, service layer, development layer, application layer. This hierarchical architecture offers several technical advantages: modular system design enabling component-based development, clear functional decoupling between layers, scalable infrastructure for future capability expansion, distributed computing support through C/S architecture.

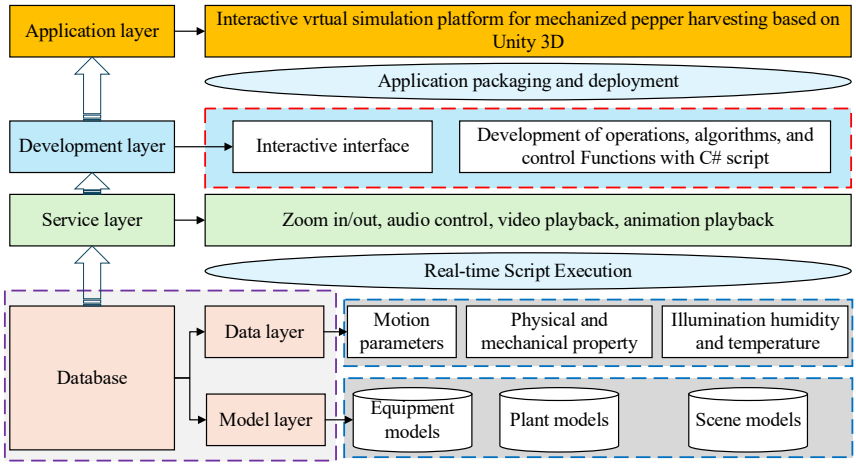


Fig. 4 - Hierarchical structure diagram for development of the virtual harvest simulation platform

The model layer provides basic resources for the virtual harvest simulation system, including virtual models of chili harvesters, chili plant models and environment models designed by 3D modeling software such as SolidWorks and 3D Max *(Xiang et al., 2014)*. Data layer is used to manage agricultural datasets and operational parameters. The service layer is used to make real-time calls to the model library and database, enhancing the performance of the simulation system, such as configuring animation playback, interface zooming in and out, background sound, etc.

The development layer is located between the service layer and the application layer, and is the central hub of the system, including control programs edited in C # language, statistical algorithms for harvesting chili peppers, view stitching algorithms, and other script files, as well as human-machinery interaction interfaces. The data collected by the application layer can be sent to the service layer, and the data feedback from the service layer can be sent to the application layer for display.

The application layer is located at the outermost layer of the entire system, which packages the various modules of the system logically and hierarchically before publishing the application program, thus forming a set of application programs with functions such as interface display, human-machinery interaction, and data input.

Structural framework of the virtual simulation platform

Based on the working principles of pepper harvesters and the development logic of virtual simulation platforms, the structural framework of the mechanized pepper harvesting virtual simulation platform is shown in Fig. 5. The virtual simulation platform consists of six core modules, which are interface & perspective observer, pepper harvester model manager, pepper plant models manager, environment observer, models base, and database.

Interface & perspective observer is used to provide user interaction and multi-angle visualization by setting the camera follows mode. Pepper harvester model manager is used to provide configurable component models for harvesters, such as picking device model, material conveying mechanism model, walking mechanism model, and steering system model. Pepper plant model manager is used to provide chili plant virtual model and planting patterns. The harvesting operation environment model includes sunlight, sky, fields, trees, buildings, etc. Model base stores 3D component models. The database is used to store various characteristics and motion parameters of chili harvesters, harvest data, as well as various parameters of chili plants.

In addition, to achieve an interactive virtual simulation platform for mechanized harvesting of chili peppers, rigid body properties and physical collision functions should be added to the virtual models, and script files should be edited using C # language in the Unity 3D development environment.

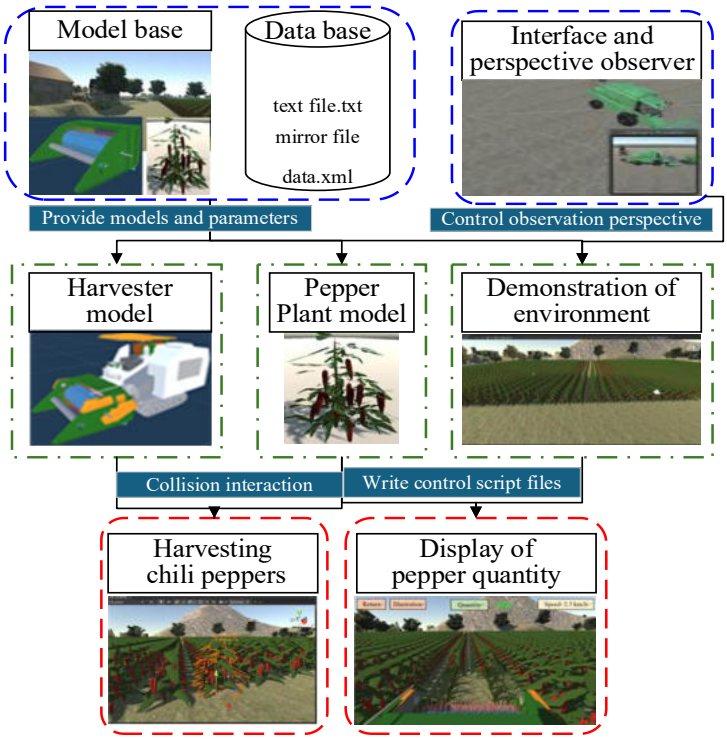


Fig. 5 - System architecture diagram of chili harvesting virtual simulation platform

Technical process of virtual simulation platform development

Development of the virtual simulation platform follows the relevant technical development flowchart, as illustrated in Fig. 6. Firstly, collect relevant data of the pepper harvester, pepper plants, and virtual harvesting scene, create 3D models using SolidWorks and 3D Max, followed by optimization, rendering, and unit/size format conversion; Secondly, import the constructed models into Unity 3D software for editing, and create a virtual farm scene using the Terrain component in Unity 3D software. Once again, design rigid body components and collider components for the constructed models to enable physical interactions, and add sound and animation playback, write application programs, and implement the relevant functions and harvesting tasks of the virtual harvester. Finally, generate the application software and conduct relevant virtual simulation experiments.

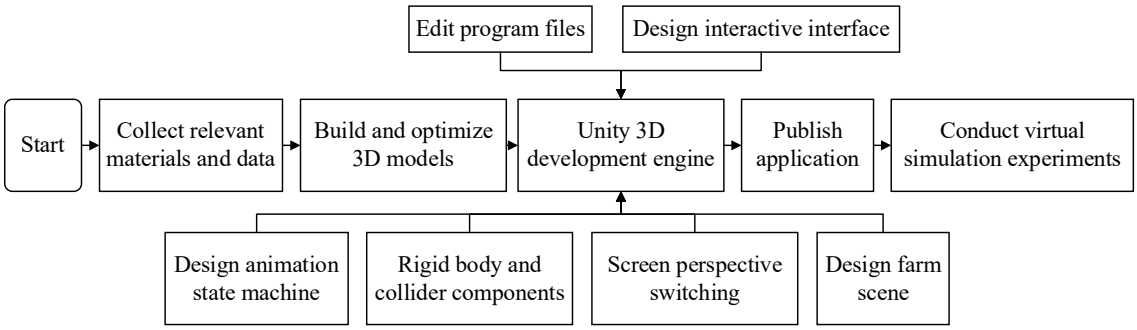


Fig. 6 - Relevant technical development flowchart

Development of virtual simulation platform

Under the structural framework of the interactive virtual simulation platform, adhere to the technical workflow for virtual simulation platform development to develop 3D virtual models for each component, design the UI interactive interface, integrate attribute components, and design control strategies and corresponding programs, thereby realizing the interactive functions of the virtual simulation platform and achieving the simulation effect of chili pepper mechanized harvesting.

Virtual model of chili harvester

Taking a certain chili pepper harvester as a reference, a three-dimensional model of the pepper harvester was established using SolidWorks, the key components include picking device, material conveying mechanism, cleaning and separation mechanism, aggregate box, walking mechanism, and hydraulic control system, as illustrated in Fig. 7. Among them, the picking device is the core harvesting component for pepper, consisting of spring teeth and roller. The 3D model was then imported into 3D Max for texture rendering and optimization before being exported in .fbx format for compatibility with the simulation platform.

Virtual model of pepper plants

A three-dimensional model of peppers and pepper plant was established based on relevant parameters of chili peppers, as shown in Fig. 8. To optimize performance and reduce computational load, the model underwent texture mapping and rendering in 3D Max, then exported as an .fbx file for importing into Unity 3D.

Construction of terrain model

The virtual farm terrain was constructed using Unity 3D's built-in Terrain Toolkit, enabling realistic topographical features such as elevation variations, soil textures, and crop row layouts. Key parameters (e.g., field size, slope gradient) were calibrated to match real-world harvesting conditions, as shown in Fig. 9.

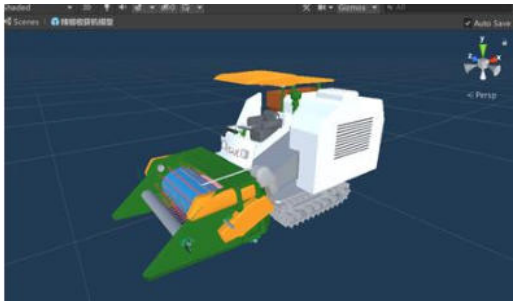


Fig. 7 - Virtual model of pepper harvester



Fig. 8 - Pepper plant model

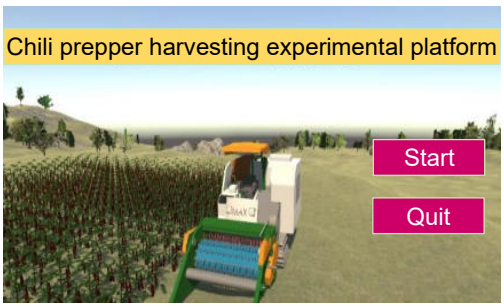


Fig. 9 - Terrain model

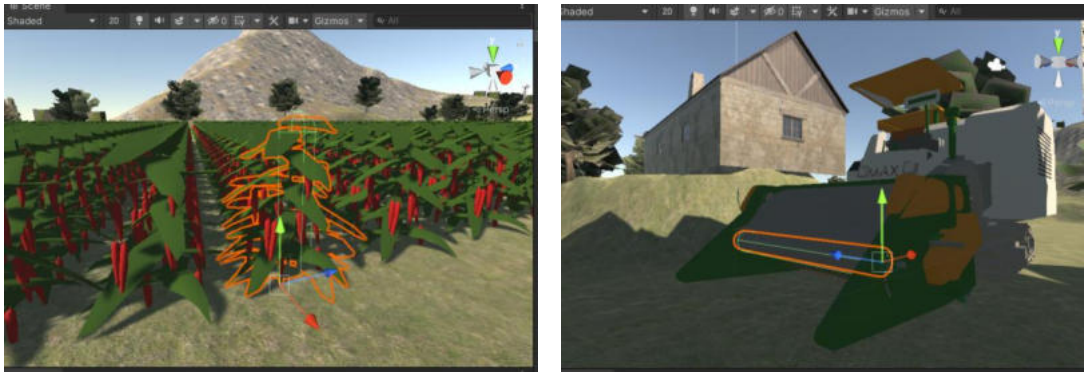
Configuration of rigid body and collider properties

To accurately simulate the physical interactions between the chili pepper harvester and pepper plants within the virtual environment, rigid body and collider components were assigned to both models. This implementation ensures the pepper harvester and pepper plant models adhere to Newtonian motion laws, enabling authentic collision responses (e.g., plant displacement during harvesting), *(Wu et al., 2018)*.

There are six types of colliders provided by Unity 3D software to simulate physical interactions: Box Collider, Sphere Collider, Capsule Collider, Wheel Collider, Terrain Collider, and Mesh Collider. Each type of collider is strategically implemented based on its unique characteristics. Box Collider is applied to the harvester body for optimal performance due to its simple geometry, low computational overhead, and fast processing speed. Mesh Collider is utilized for high-precision collision detection, matching the complex geometry of the cutting surface with accurate mesh representation.

Wheel Collider is implemented for realistic wheel physics, featuring integrated collision detection, physical parameters, and a slip-based tire friction model. Terrain Collider is assigned to the field plot to provide ground physical properties and support all 3D models within the scene, to avoid model penetration (e.g., harvester falling through terrain) *(Wang et al., 2022)*. Capsule Collider is custom-fitted to both the chili pepper plant model and toothed roller model to enable accurate collision detection during harvesting operations, as shown in Figures 10 (a) and 10 (b).

This script executes the picking action when the toothed roller interacts with chili peppers, ensuring realistic harvesting behavior.



a) b)

Fig. 10 - Configuration of collider components

a) Collider configuration for the chili plant model; b) Collider configuration for the toothed roller

Animation state machine

An animation state machine is a control system designed to manage the sequential or conditional transitions between discrete animation states of a character or object. By partitioning complex animation sequences into modular, action-specific segments (e.g., "idle," "walk," "attack"), it enables dynamic state transitions triggered by in-timeline events, user inputs, or programmatic logic. Widely adopted in game development and interactive applications, this system streamlines animation control by defining states (distinct animation phases) and transition rules (conditions for switching between states), ensuring efficient, scalable, and maintainable animation pipelines.

The process of mechanized harvesting of chili peppers includes multiple animation states such as users getting on a harvester, starting the engine, adjusting the height of the cutting table, adjusting the operating speed, controlling the movement of the harvester, and picking chili peppers. Therefore, the animation can be controlled and serialized using the functions of the animation state machine, achieving modular editing and improving the maintainability and reusability of the control code.

The design process of an animation state machine is as follows: Firstly, complete the entire animation process of operating the chili harvester using 3D Max software, and focus on the start and end frames of each animation segment for each operating state. Then, group the "*.fbx*" format files according to their animation states and divide them into animation segments. Drag and drop the divided animation clips to the already created state machine to assign attributes and create animation transition lines. Write relevant code programs to drive trigger functions on the timeline, so as to enable an animation to be called at a certain time node and complete the transformation of the animation.

First-person navigation and view control

To enhance user immersion and experience, a first-person navigation system has been applied in the virtual environment. The first-person navigation system enables users to freely explore the scene and control their viewing perspective through intuitive keyboard and mouse inputs. Create script files within the character controller to manage movement and viewpoint rotation. Implementation details include configuring appropriate motion parameters (such as speed, gravity, etc.), using the W/S keys to control forward and backward movement, A/D keys to control left and right steering, and Q/E keys to control vertical movement (up/down). Right-click and drag to activate 'View Control' for adjusting the camera's rotation and orientation.

This implementation provides users with an intuitive and immersive navigation experience while maintaining optimal performance within the virtual environment. The system can be easily modified to accommodate different movement styles or control schemes as needed.

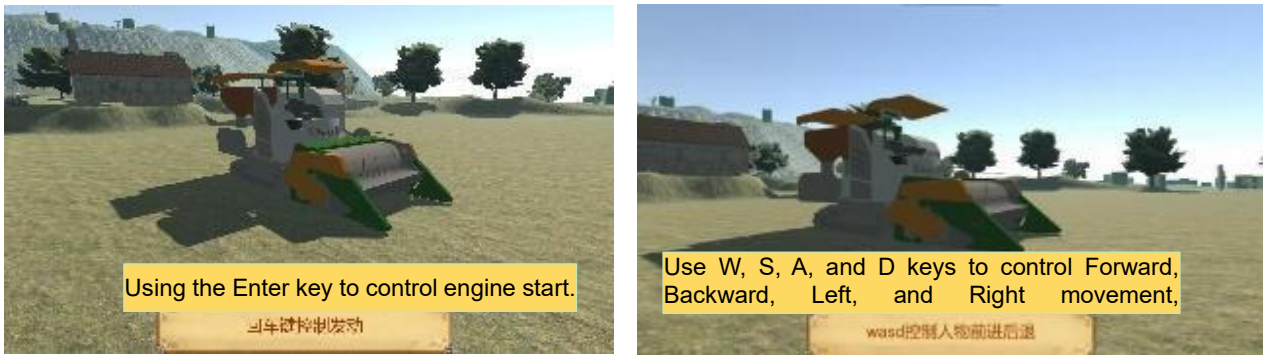
Design and implementation of UI Interface

A human-computer interaction system was designed through the graphical user interface (GUI) in Unity3D, utilizing the built-in UI system for optimal functionality and user experience. In order to ensure the user experience of the UI interface, the creation of UI components, button configuration, visual design parameters, interactive functions, and other aspects need to be carefully designed. The implementation process included the creation of a hierarchical UI structure consisting of a main control panel, function-specific submenus, and a status display area. Each button was configured with multi-state visual settings, event listeners for click actions, associated sound effects, and tooltip information for hover events. Interaction handling was implemented using Unity's EventTrigger component, custom C# scripts for complex interactions, and animation controllers to provide smooth transitions.

RESULTS

Human- harvester interaction operation effect

Upon logging into the PC-based virtual simulation platform, users can engage in practical simulation operation training. When a user is outside the chili pepper harvester, the W, S, A, and D keys on the keyboard enable control of the user's movements, supporting forward, backward, left, and right turns. Upon reaching the proximity of the virtual chili pepper harvester model and pressing the F key (designated as the "boarding" action), the user enters the harvester's cab. At this point, the control target shifts to the harvester itself, transitioning to a first-person perspective for direct operation of the pepper harvester model. Then, the engine can be started by pressing the "Enter" key on the keyboard, accompanied by a realistic "rumbling" startup sound (Fig.11 a). Following engine ignition, movement control - forward, backward, left, and right-is enabled via the W, S, A, and D keys, delivering an immersive operational experience that closely mimics real-world harvester work (Fig.11 b).



a) b)

Fig. 11 - Control of the motion state of the virtual pepper harvester

a) Engine start; b) Harvester movement: forward, backward, left/right steering

The virtual simulation results demonstrate that the mechanized pepper harvesting simulation platform effectively supports human-machine interaction, confirming the feasibility of the proposed design.

Demonstration and analysis of the effect of pepper harvest experiment

Within the UI interactive interface, clicking the "Experiment" button activates the chili harvesting experiment module. From a first-person perspective, users perform pre-operation preparations such as adjusting the picking device height above the ground and shifting gears. Once the harvester is started, users can switch to a third-person perspective to observe the machine's working process in the field. Movement control (forward/backward/left/right) is managed via the W, S, A, and D keys on the keyboard. When the spring teeth on the picking device make contact with chili plants, the fruits are harvested while the plant stems remain intact on the ground. Meanwhile, the graphical user interface (GUI) dynamically displays real-time statistics of harvested chili fruits. Figure 12 illustrates the pre- and post-harvest scenarios of chili plants, visually demonstrating the efficiency of the picking process.



a) b) c)

Fig. 12 - The state before and after harvesting chili peppers

a) Before harvest; b) Choose walking speed; c) After harvest

A comprehensive series of virtual harvesting simulation experiments were conducted to evaluate system functionality and operational validity under varying operating speeds and drum rotation speeds. These virtual harvesting simulation experiments validated that the virtual simulation platform for mechanized pepper harvesting can execute harvesting experiments according to preset parameters and align with actual harvesting principles. These results confirm the platform's effectiveness as both a training tool and a research platform for optimization pepper harvesting.

CONCLUSIONS

This study successfully developed a virtual simulation platform for mechanized chili pepper harvesting based on Unity 3D. During the simulation platform development phase, detailed 3D models of chili harvesters, chili plants, and their operational environments were constructed. Functional control script files were programmed using C# to enable human-machine interaction simulations and virtual harvesting experiments under diverse conditions.

Experimental results validated the rationality of the design of virtual simulation platform and the correctness of the code governing overall machine movement. In addition, trainees provided feedback that the platform helps them carefully observe the harvesting process, understand the working principle of the harvester, and gain an immersive operating experience, thus confirming that the platform authentically simulates real-world field harvesting operations.

Although this research has achieved phased milestones, several limitations require further improvement. For instance, future work will focus on developing a flexible stem model with elastic properties to better simulate the stress dynamics during the picking process. Additionally, enhancing interaction rules through behavioral reasoning will improve the realism of virtual harvester-chili plant interactions, enabling more lifelike simulations of plant and fruit motion. Furthermore, conducting multi-factor, multi-level orthogonal experiments under varied conditions will help analyze the impacts of key parameters (e.g., operational speed, drum rotation) on harvest loss rate, net harvest rate, and damage rate. These advancements will provide critical references for optimizing harvester design and manufacturing processes.

ACKNOWLEDGEMENT

This research was funded by the project from Key Laboratory of Agricultural Equipment for Hilly and Mountainous Areas in Southeastern China (Co-construction by Ministry and Province), Ministry of Agriculture and Rural Affairs (KFKT2024005), the Jiangsu Province Education Science Planning Project (B/2023/01/60), the National Natural Science Foundation of China (No.32401690), and Guizhou Pepper Industry Technology System (GZLJCYJSTX-05), and Qiankehe Platform ZSYS (2025) 013 Guizhou Province Key Laboratory of Mountain Intelligent Agricultural Machinery.

REFERENCES

[1] Chen, Y., Zeng, Z., Wang, J., Zou Xi., Jia C., Zhang P. (2019). Virtual environment construction and simulation platform of harvesting machinery (收获机虚拟环境模型与仿真平台构建). *Transactions of the Chinese Society for Agricultural Machinery*, 50(7): 159-166, Beijing/China.

[2] Cheng B., Zheng Y., Huang Q., Liu J. (2018). Forestry felling & cultivation machine virtual training system based on Unity 3D (基于 Unity3D 的林木联合采育机虚拟训练系统研究). *Journal of System Simulation*, 30(4): 1310-1318, Beijing/China.

[3] Cheng C., Kang L., Cai S., Li J. , Sun R. (2018). Virtual display and interactive experience platform of farming culture based on Unity3D. IFAC Papers On Line, 51(17): 637-642, Netherlands.
[4] Du C., Han D. Song Z., Chen Y., Chen X., Wang X. (2023). Calibration of contact parameters for complex shaped fruits based on discrete element method: The case of pod pepper (Capsicum annuum). *Biosystems Engineering*, 226:43-54, United Kingdom.
[5] Du C., Fang W., Han D., Chen X., Wang X. (2024). Design and Experimental Study of a Biomimetic Pod-Pepper-Picking Drum Based on Multi-Finger Collaboration. *Agriculture-Basel*, 14 (2), Switzerland.
[6] Li C., Sun R., Dai Y., Cai S., Li Q., Li J. (2017). Intelligent exhibition platform of Chinese ancient farming virtual scene based on Unity3D (基于 Unity 3D 的中国古代农耕虚拟场景智能展示平台). *Transactions of the Chinese Society for Agricultural Engineering,* 33(Supp.1): 308-314, Beijing/China.
[7] Liu J, Geng G. (2010) Research on 3D reality-based modeling and virtual exhibition for cultural sites: Taking the small wild goose Pagoda in Tang-Dynasty as the case. //2010 *International Conference on Computer Application and System Modeling (ICCASM 2010)*. 15: 307-313, Taiyuan/China.
[8] Liu G., Li S. (2014). Virtual Simulation Design for Agricultural Spraying Machinery (农田喷灌车虚拟仿真设计). *Journal of Agricultural Mechanization Research*. 36(12):24-29, Harbin/China.
[9] Liu J., Liang J., Zhao S., Jiang, Y., Wang, J., Jin, Y. (2023) Design of a Virtual Multi-Interaction Operation System for Hand–Eye Coordination of Grape Harvesting Robots. *Agronomy*, 13(3), Switzerland.
[10] Liu, J., Ma, T. (2014). Design of the electric motor virtual simulation display platform based on Unity3D (基于 Unity3D 的电动机虚拟仿真展示平台设计). *Journal of Heilongjiang Bayi Agricultural University*, 26(3): 66-68,78, Daqing/China.
[11] Lv M., Guo X., Lu S., Wu J. (2015). Virtual interactive pruning operation on fruit tree based on Unity3D (基于 Unity 3D 果树交互虚拟修剪技术及其实现). *Journal of Agricultural Mechanization Research,* 37(4): 7-11, 35. Harbin/China
[12] Peng J. (2011). The connotation of farming culture and its inspirations to modern agriculture (农耕文化的内涵及对现代农业之意义). *Northwestern Journal of Ethnology*, 1(68): 145-150, Lanzhou / China.
[13] Seth A., Vance J M., Oliver J H. (2011). Virtual reality for assembly methods prototyping: a review. *Virtual Reality*, 15(1): 5-20, United Kingdom.
[14] Song Z., Du C., Chen Y., Han D., Wang X. (2024). Development and test of a spring-finger roller-type hot pepper picking header. *Journal of Agricultural Engineering*, 55(2), Italy.
[15] Wang G., He B., Han D., Zhang H., Wang X., Chen Y., Chen X., Zhao R., Li G., (2024). Investigation of Collision Damage Mechanisms and Reduction Methods for Pod Pepper. *Agriculture-Basel*, 14 (1), Switzerland.
[16] Wu T., & Wang X. (2018). Research on collision detection in Unity 3D (Unity3D 中碰撞检测问题的研究). *Electronic Test*, (1): 83-84, Beijing/China.
[17] Zhang Y., Yang G. (2011). Design and implementation of virtual royal garden in northern Song dynasty with stereoscopic display. *Advanced Materials Research*, 291-294: 2388-2392, Switzerland.
[18] Zhou M., Sun H., Xu X., Yang J., Wang G., Wei Z., Xu T., Yin J. (2024). Study on the Method and Mechanism of Seedling Picking for Pepper (Capsicum annuum L.) Plug Seedlings. *Agriculture-Basel*, 14(1), Switzerland.
[19] Wang J., Ci C., Liu X., Zhang K. (2022). Virtual harvest design and simulation test of corn ear harvester (玉米果穗收获机虚拟收获设计与仿真试验). *Journal of Chinese Agricultural Mechanization*, 43(5): 07-13, Nanjing/China.
[20] Xiang, M., Ma, C., & Han, Y. (2014). Research on chemical equipment virtual training system based on Unity 3D (基于 Unity3D 的化工设备虚拟培训系统研究). *Computer Technology and Development*, 24(7): 196-200, Xi'an/China.
[21] Yan, H., Gao, S., & Hong, Y. (2013). Application of Virtual Reality Technology in Underground Simulation Based on Unity (基于 Unity 的虚拟现实技术在井下仿真中的应用). Safety in Coal Mines, 44(8): 99-101, Fushun/China.
[22] Zhang D., Sun X., Battino M., Wei X., Zou X. (2021). A comparative overview on chili pepper (capsicum genus) and Sichuan pepper (zanthoxylum genus): From pungent spices to pharma-foods. *Trends in Food Science & Technology*, 117 (16):148-162, United Kingdom.

DETERMINATION OF OIL PALM FRUIT MATURITY USING A PORTABLE INSTRUMENT BASED ON UV-VIS-NIR SENSOR
/
PENENTUAN KEMATANGAN BUAH KELAPA SAWIT MENGGUNAKAN INSTRUMEN PORTABEL BERBASIS SENSOR UV-VIS-NIR

Yunisa Tri SUCI [1,2], I Wayan BUDIASTRA *[1,3], Y Aris PURWANTO[1], Slamet WIDODO[1]
[1] IPB University, Department of Mechanical and Biosystem Engineering / Indonesia;
[2] Jambi Agricultural Training Center, Ministry of Agriculture / Indonesia;
[3] IPB University, Centre for Research on Engineering Application in Tropical Agriculture / Indonesia ;
Tel: +622518623026; E-mail: wbudiastra@apps.ipb.ac.id

DOI: https://doi.org/10.35633/inmateh-76-49

Keywords: *k-NN, multispectral sensor, oil palm fruit, precision agriculture, UV–Vis–NIR*

ABSTRACT
An accurate method for determining palm fruit maturity is needed by the palm oil industry to increase productivity and quality of crude palm oil. This study developed a portable instrument based on the AS7265x sensor (410–940 nm) to determine oil palm maturity accurately. Reflectance from 270 oil palm fruits at various maturity were measured, pre-processed, and classified into three maturity levels using PCA. PCA with SNV pre-treatment explained 97% of the variance. Classification was validated using SVM, RF, and KNN, with KNN achieving 100% accuracy. The instrument with SNV-PCA-KNN method has the potential to be used for oil palm fruit maturity classification.

ABSTRAK
Metode penentuan tingkat kematangan buah kelapa sawit dibutuhkan oleh industri sawit untuk meningkatkan produktivitas dan mutu minyak sawit kasar. Penelitian ini mengembangkan sebuah instrumen portabel berdasarkan sensor AS7265x (410-940 nm) untuk menentukan kematangan kelapa sawit. Reflektansi dari 270 buah kelapa sawit dengan beragam kematangan diukur, dilakukan pra-pengolahan, dan diklasifikasikan ke dalam tiga tingkat kematangan dengan menggunakan analisis komponen utama (PCA). PCA dengan pra-perlakuan SNV menjelaskan 97% dari varians. Klasifikasi divalidasi menggunakan SVM, RF, dan KNN, dengan KNN mencapai akurasi 100%. Instrumen dengan metoda SNV-PCA-KNN berpotensi diterapkan untuk klasifikasi kematangan buah kelapa sawit.

.

INTRODUCTION

Palm oil (*Elaeis guineensis*) is a major commodity crop, with global demand for palm oil continuing to increase due to its versatility and economic value. Timely and accurate harvesting is essential to maximize oil yield and quality *(Junior & Suharjito, 2023)*. Conventionally, harvesting is based on the maturity level of the fruit, which is determined by changes in fruit color and the detachment of fruit from the bunch. Manual classification is greatly affected by environmental factors like inconsistent lighting, rain, and shading, leading to misjudgments (*Mansour et al., 2022*). This time-consuming process relies on manual labor, limiting scalability and consistency in large plantations. Consequently, operational efficiency declines, which can negatively impact oil extraction rates (OER), resulting in lower yields, higher free fatty acid (FFA) content, reduced oil quality, and increased waste from suboptimal fruit (*Malyala, 2024*). These challenges highlight the limitations of manual methods for precise and large-scale harvesting especially in large plantations where variability in fruit maturity is high.

Recent studies have explored non-destructive to tackle the shortcomings of visual maturity assessment approaches such as image processing *(Saifullah et al., 2023),* electrical properties (Chin-Hashim et al., 2022), and near infrared (NIR)(Suci et al., 2024) *Budiastra et al., 2024*). Spectroscopy technologies have attracted growing interest due to their rapid detection capabilities and ability to simultaneously measure multiple constituents of oil palm fruit. Although these methods are promising, many rely on complex instrumentation and are limited in portability and field applicability, primarily due to the high costs of the necessary hardware and software.

Yunisa Tri SUCI, PhD.Stud.Agr. Eng; I Wayan Budiastra, Prof. Dr.Agr.Eng; Y Aris Purwanto,Prof.Dr.Agr.Eng; Slamet Widodo Assoc. Prof. Dr.Agr.Eng

Multichannel spectral sensors, particularly the AS7265x which covers the visible to near-infrared range (410–940 nm), offer a compact and cost-effective alternative for real-time spectral data acquisition. Despite its potential, the application of the AS7265x sensor in oil palm maturity classification remains underexplored. This sensor measures the absorption and reflection of light at particular wavelengths using various materials, including oil palm fruits. This sensor can provide precise information on the oil palm fruit's maturity by recognizing its spectral "fingerprints".

Researchers have used machine learning techniques and spectroscopic sensors to classify various agricultural products. A portable and low-cost spectrometric system using an AS7265x sensor and custom microcontroller was successfully used to classify coffee roasting levels using the Random Forest model *(Sagita et al., 2024)*, and to accurately determine the maturity of 'Ataulfo' mangoes *(Cano et al., 2024)*. Moreover, the integration of multichannel spectral sensors with machine learning models especially for on-site classification tasks has not been fully investigated in oil palm research. Prior work has focused on lab-based data acquisition or single-wavelength approaches, which do not reflect the complexities of dynamic outdoor environments. This study proposes an innovative solution by developing a portable, non-destructive instrument based on the AS7265x sensor, capable of real-time spectral acquisition, and coupling it with dimensionality reduction (PCA) and machine learning classifiers (SVM, RF, KNN) has the potential to be used for accurate maturity classification of oil palm fruitlets. The integration of spectral sensing and data-driven classification supports the advancement of precision agriculture, where timely and site-specific harvesting decisions are crucial for optimizing productivity and quality of crude palm oil. This approach not only addresses the limitations of existing manual and laboratory methods, but also contributes a novel, field-deployable solution that integrates multispectral sensing. This study aims to develop a portable instrument based on an AS7265X multichannel sensor and test its performance equipped with several machine learning algorithms for classifying the maturity level of oil palm fruits non-destructively.

MATERIALS AND METHODS

Portable instrument design based on multichannel spectral sensors

A portable instrument using multichannel sensors was developed to classify palm fruit maturity. The multichannel sensor used to build the palm oil detection system is the AS7265x sensor (9) of Austria Micro System, Styria, Austria. The sensor is explicitly composed of three TRIAD AS726x sensors, AS72651 (visible), AS72652 (UV) and AS72653 (IR) that detect absorbance at 18 wavelengths (410, 435, 460, 485, 510, 535, 560, 585, 610, 645, 680, 705, 730, 760, 810, 860, 900 and 940 nm). By default, UV LED emissions are recorded at six wavelengths from 410 to 535 nm, visible LED reflectance from 560 to 705 nm, and IR reflectance from 730 to 940 nm. This sensor allows for customizable LED configurations and data collection, enabling additional spectral data features. In this study, UV LED reflectance was also measured at 560 to 705 nm, known as fluorescence. This multispectral data acquisition sensor operates based on the principle of an optical reflective sensor. It features a light-emitting diode (LED) that emits light towards the palm kernel, which acts as the illuminated object. The light reflects off the palm oil fruit and is captured by a photodetector as the receiving sensor. The chemical composition of the oil palm influences the reflected light signal, resulting in a light wavelength signal that contains information about the chemical content of the palm fruit. The optoelectronic sensor then processes this information.

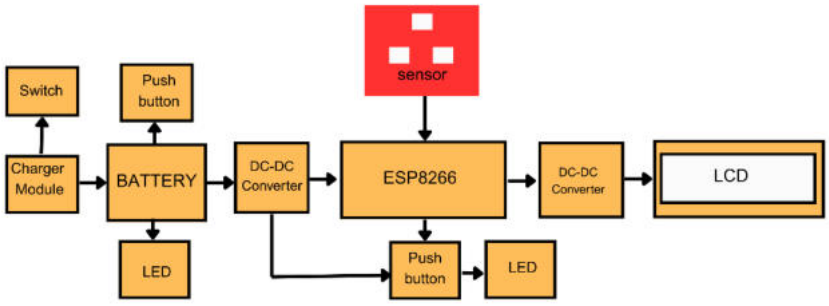


Fig. 1 - Component schematic of UV VIS NIR multichannel sensor acquisition equipment

The AS7265x multichannel sensor is connected to the ESP8266 via a jumper cable with resistors and integrated with a power supply (battery) for stable power supply. The electronic circuits are designed to be embedded in the PCB so that the connection of each component is stable. The data acquisition results will be sent to the cloud via Wi-Fi on the ESP8266 connected to a Wi-Fi router.

Data recorded in the form of date, time, and 24 channel spectrum data with symbols A, B, C, D, E, F, G, H, I, J, K, L, F1, F2, F3, F4, F5, and F6 sequentially.

The software used to control the microcontroller during data acquisition from the AS7265x sensor is Arduino IDE. The measurement results will be transferred in Microsoft Excel format, processed and analyzed using Unscrambler X for Principal component analysis (PCA), and classified using a machine learning algorithm. The component schematic of the portable instrument is summarized in Figure 1.

Sample preparation and spectra acquisition

The palm fruits used in the study were Tenera variety palm fruits from Cikabayan Plantation at IPB University, Bogor, Indonesia. The fruits were classified into 10 levels of harvesting age from young to old, starting at week 12 to 24 weeks of age, where at the age of 12 to 16 weeks, fruit collection was carried out once a week. The fruitless samples were taken from fresh fruit bunches from 3 different trees. A total of 9 fruits were taken from the center and apical parts of the FFBs, so the total number of loose fruit samples used was 270.

Spectra acquisition procedure is shown in Figure 2. The fruitlet was placed on a sample holder. A light beam from an LED exposed the fruitlet sample. Light reflected from the sample was captured by a photodetector with a 410-940 nm wavelength. The reflectance of the sample was measured by an instrument three times with different positions. The data acquisition results were sent to the cloud via Wi-Fi on the ESP8266 connected to a Wi-Fi router. The data spectral is recorded and stored in the cloud as date, time, and 24-channel spectrum data, which is then downloaded for further analysis.

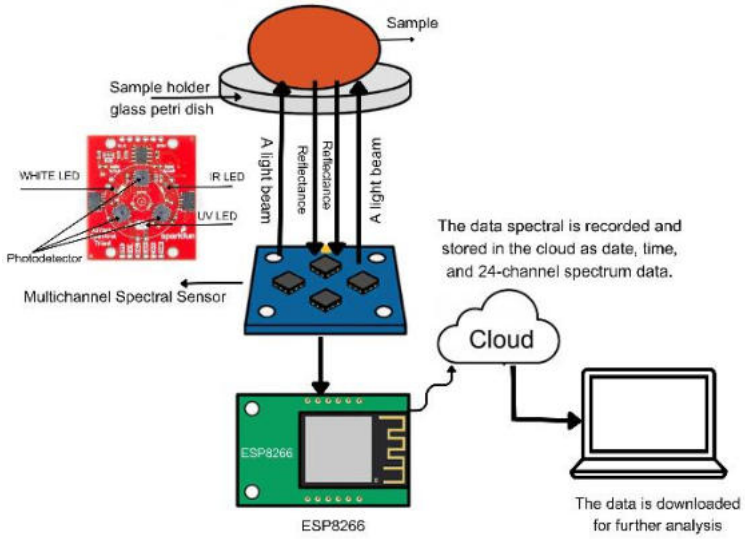


Fig. 2 - Spectra acquisition procedure

Classification of palm fruit maturity with machine learning

In this research, data from the AS7262X sensor is evaluated using PCA and machine-learning algorithms to classify oil palms according to their maturity level. This research utilizes three widely recognized machine-learning algorithms. RF, SVM, and KNN. The classification of oil palm fruit maturity, which includes 10 maturity levels, involves several stages: pre-treatment of spectroscopic data, dimensionality reduction using PCA, classification with machine learning models, and performance evaluation.

Pre-treatment of spectroscopic data

Raw reflectance data were pre-processed using three techniques: normalization, Standard Normal Variate (SNV), and Savitzky–Golay derivative filtering. These methods were applied to enhance signal quality, reduce noise, and correct for baseline shifts and light scattering effects, which are common in spectral data collected under field conditions. Spectral measurements obtained from multichannel sensors often exhibit variations caused by illumination changes, surface reflections, and environmental noise. The selected preprocessing techniques mitigate these issues by leveling the baseline, reducing scattering effects, and emphasizing subtle spectral features associated with chemical changes during fruit ripening. This preprocessing step is essential to improve feature differentiation and enhance the performance of subsequent classification models.

Principal component analysis (PCA)

After pre-processing, PCA was performed to reduce high-dimensional spectral data into uncorrelated variables (principal components) that capture significant variance related to fruit maturity. It aids in data compression and reveals clustering patterns among the 10 ripeness levels. Typically, the principal components explain 80% to 95% of the dataset's variability (*Michael et al., 2025*). PCA is effective for dimensionality reduction and identifying natural patterns in maturity data, serving as a foundation for advanced classification.

Classification using Machine Learning

To evaluate the effectiveness of the reduced features from PCA, three supervised machine learning algorithms SVM, RF, and KNN were implemented. These models were trained on the PCA-transformed data to classify the fruitlets into three consolidated maturity levels, which were derived from the original ten stages based on their PCA groupings. Based on the cluster pattern from PCA and referring to previous studies *(Eya'a et al., 2023)* the classification was consolidated into three maturity levels: unripe, ripe, and overripe. These categories are not only more physiologically representative but also more industrially relevant and applicable to support harvesting decisions. With this approach, the classification becomes more stable and accurate for application in portable sensor based non-destructive systems in the field. The machine learning classification process was conducted using Google Colab with Python 3.11.13 and the Scikit-learn package version 1.3.0. A total of 270 spectral samples from oil palm fruitlets were used, initially processed through group labelling into three maturity classes (unripe, ripe, overripe), followed by standardization to ensure uniform feature contribution, significant for distance-based algorithms such as KNN and SVM and class balancing to prevent bias toward dominant classes. The dataset was split into 70% training and 30% testing using stratified sampling to maintain class proportions and improve generalizability. Three classification models (SVM, RF, KNN) were trained on the training data, with hyperparameter optimization performed using GridSearchCV. This method conducts an exhaustive search over specified parameter grids via cross-validation to prevent overfitting and ensure optimal model configuration. Each model was then calibrated and validated on the test set and evaluated based on accuracy, precision, recall, and F1-score using both classification reports and confusion matrices. The final performance evaluation enabled the selection of the best-performing model by comparing all metrics, with the optimal model and its tuned parameters retained for potential deployment and future analysis.

Performance metric

Classification metrics are crucial for evaluating the efficacy of models and directing advancements. They offer a way to assess how well a classification algorithm performs and give insight into how effectively a model is differentiating between classes. Metrics for evaluating classification models include accuracy, precision, recall, and F1 score *(Arifuddin et al., 2024).*

RESULTS

Characteristics of UV-VIS-NIR Spectra

The original spectra of oil palm fruit at various harvesting maturities within the UV-VIS-NIR wavelength range, obtained using a multichannel sensor, are illustrated in Figure 3.

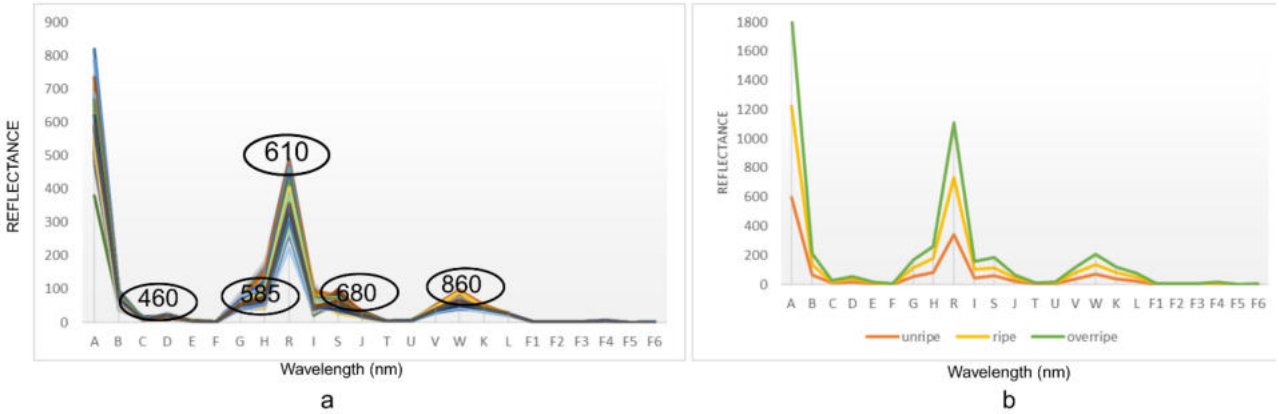


Fig. 3 - Spectrum of oil palm fruits at different harvesting ages

a. Original spectrum b. averaged spectrum

The resulting spectra exhibit peaks and waveforms indicative of the absorption of chemical bonds by UV-VIS-NIR wavelengths. Prominent peaks are observed at wavelengths such as 460, 585, 610, 680, and 860 nm. Peaks within the UV-VIS region correspond to pigments in the fruit, including chlorophyll, carotenoids, xanthophylls, anthocyanins, and other phenolic compounds. As reflected in these pigments, fruit color is a critical quality attribute closely associated with the fruit's functional properties and developmental stages.

The spectra were averaged to discern the variations in peaks and wavelengths at every harvesting age of oil palm fruit (Fig. 3b). Although the peaks and wavelengths often lie within the same range, younger and older fruits can differ in values and peak positions. Carotenoids are present in the wavelength range of 430 nm to 510 nm, where these changes and variations are visible. Furthermore, alterations in the 535-560 nm range point to a fluctuation in the anthocyanin content, especially in the green color region. Spectral value variations are also seen in chlorophyll, which is detected in 680 and 720 nm regions. Changes in the NIR region occur in the 810-900 nm range, suggesting modifications in the O-H bond absorption.

Figures 3a and 3b show that classification based on the ten picking ages faces significant challenges due to overlapping spectra between groups, despite each age exhibiting variations in spectral values. This overlap causes the boundaries between groups to become less distinct, making the classification process more challenging. However, when the spectra were averaged and consolidated into three main age groups, unripe, ripe, and overripe, a more consistent and discrete shift in the spectra was observed. Classifying the data into three age groups for selection provides better separation and has the potential to enhance accuracy in the subsequent classification stage.

Classification of the sample using PCA

Separation and clustering were carried out to examine the differences in the characteristics of each picking age. Principal Component Analysis (PCA) was used to visualize palm fruits based on their characteristics. PCA is used to analyze VIS/NIR spectral data qualitatively. It synthesizes the data into principal components (PCs) with the highest spectral data variance.

PCA (Principal Component Analysis) can effectively represent the overall wavelength as input data for further processing and identify potential outliers. The original spectra of oil palm fruit are shown in Figure 4, which illustrates that three principal components (PCs) account for a total variance of 88%. Specifically, PC1 explains 54% of the variance, and PC2 contributes 34%. As for the classification based on the overall age of the input data, data processing still needs to be done so that it can be separated. Clustering with original data has formed clusters, but there is still visible overlap between PCs of each picking age. The original spectrum still contains background and noise in addition to information on the spectrum content for which pre-treatment is necessary.

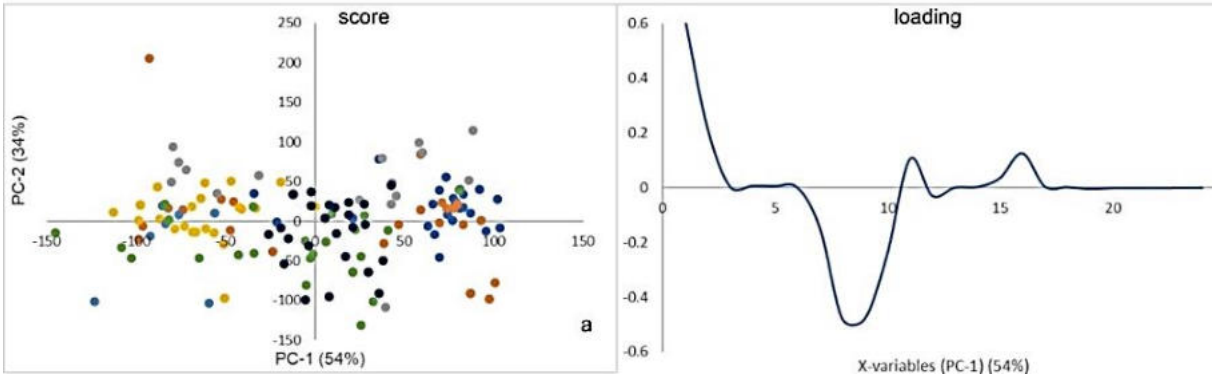


Fig. 4 - PCA spectra and loading plot

Figure 5 explains the difference in classification in the spectra averaged over several pre-treatments, while the total variance of each PC can be seen in Table 1. After the sample spectra data were averaged, it can be seen that the spectra data formed clusters at each picking age. The total variance explained by 2 PCs has exceeded 90% in both the original and pre-treatment data, but they still appear to overlap in the original spectra. PCA was performed on the processed spectral data, which had been subjected to various pre-treatment methods, including the original data, normalization, Standard Normal Variate (SNV), and Savitzky-Golay. The results show that the total variance explained by the two principal components (PC1 and PC2) varies depending on the pre-treatment method used. In the original data without pre-treatment, PC1 explained 71% of the variance, and PC2 20%, so the total variance captured by the two principal components was 91%.

However, when the data was processed using normalization and SNV methods, the value of PC1 increased significantly to 85%, while PC2 decreased to 11-12%, resulting in a total variance of 96-97%. This increase indicates that the data, which has been normalized or transformed with SNV, becomes more structured and exhibits a more dominant direction of the main variance in the first component. This indicates that the pre-treatment helps simplify the structure of the spectral data and improves the ability of PCA to separate important information.

Meanwhile, the Savitzky-Golay method yielded PC1 of 73% and PC2 of 17%, with a total variance of 90%. Although these results are promising, the explained variance value is still lower than that of normalization and SNV. Based on these results, it can be inferred that SNV is the most effective pre-treatment for improving PCA's representation ability of palm oil spectral data, so it is recommended for use in the subsequent classification stage.

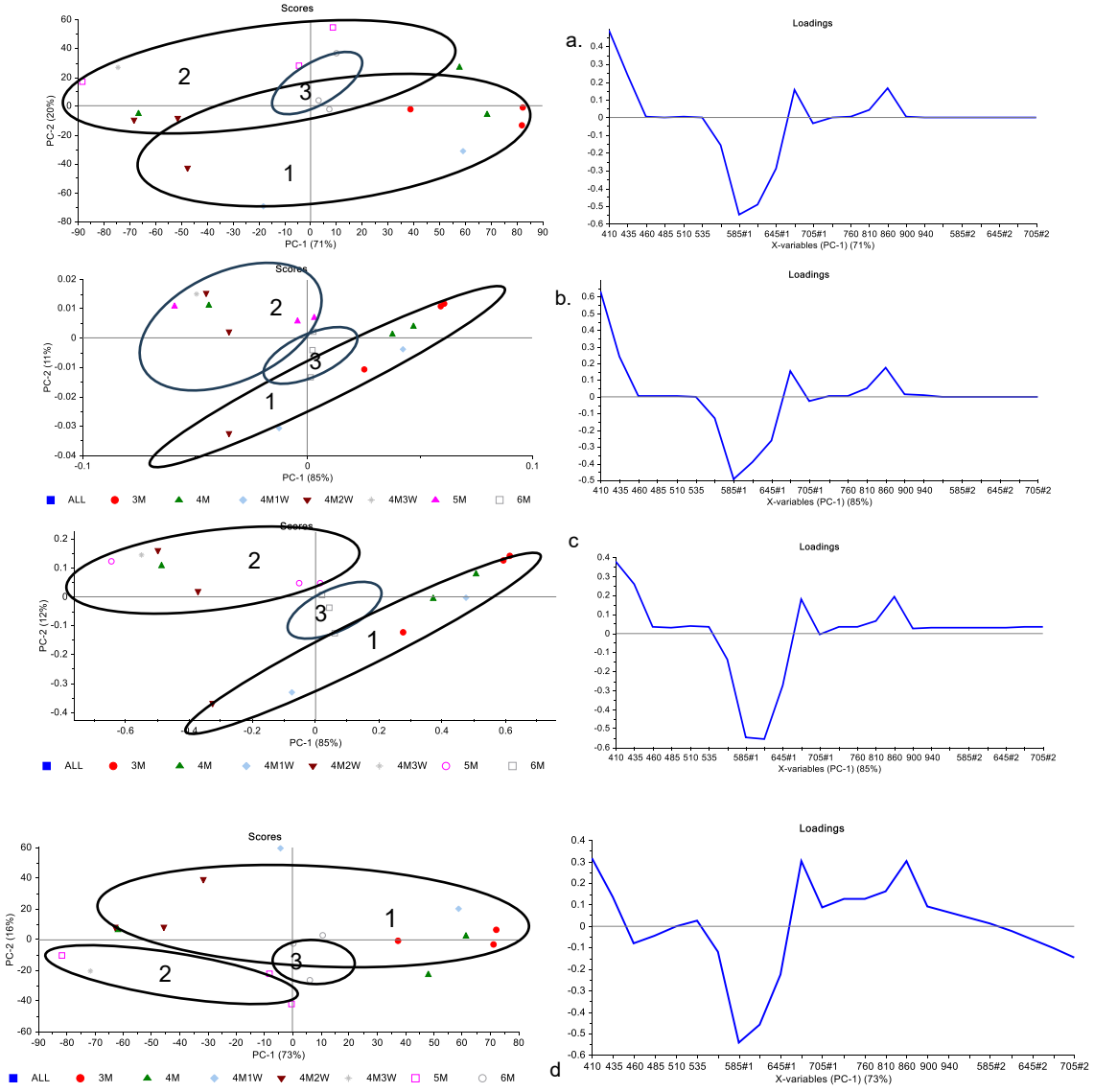


Fig. 5 - Sample average PCA spectrum and loading plot Sample average PCA spectrum and loading plot
(a) original (b) normalization (c) SNV (d) Savitzky Golay

Palm oil reflectance spectra frequently exhibit intensity changes due to sample surface, size, or thickness variances. SNV standardizes each spectrum independently by subtracting the mean and dividing it by the spectrum's standard deviation. This process removes the effects of baseline shift and scattering without altering spectrum's shape, maintaining the primary spectral information. As a result, variability unrelated to chemical components decreases, allowing PCA to capture more meaningful information in PC1. SNV enhances the dominance of Principal Component 1 (PC1) to 85% by making the differences in palm maturity more apparent than other disturbances, like measurement variation or noise. Unlike the Savitzky-Golay method, which reduces noise but ignores scattering, SNV effectively highlights fundamental inter-sample differences. Additionally, while normalization only scales data without addressing baseline disparities, SNV reveals actual inter-sample *(Rinnan et al., 2009; Zhu et al., 2025).*

Table 1

PC1 and PC2 values for each pre-treatment

No	Pre-treatment	PC1 (%)	PC2 (%)
1	Original	71	20
2	Normalization	85	11
3	SNV	85	12
4	Savitzky Golay	73	17

Classification of the sample using machine learning

To evaluate the accuracy of the clustering that has been formed from the PC classification using PCA and SNV, the oil palm spectra data is divided into unripe (spectra of 3 months, 4 months, 4 months 1 week and 4 months 2 week), ripe (4 months 3 weeks, 5 months, 5 months 1 week, 5 months 2 week), and overripe (5 months 3 week and 6 months) groups using SVM, RF, and KNN algorithms using phyton with the parameters used can be seen in Table 2. This classification is also based on standard harvesting practices in the field and refers to previous research *(Eya'a et al., 2023)*.

Table 2

Optimization parameters

Classification Method	Parameter	Range
SVM	Kernel Gamma C	Linear 0.7 10
KNN	n_neighbors weights metric p (distance)	5 uniform Minkowski 2
RF	n_estimators random_state	200 42

The selection of hyperparameters for each classification model (SVM, KNN, and RF) was carried out using GridSearchCV, a method that systematically explores combinations of predefined hyperparameter values through cross-validation. This approach ensures that the selected parameters yield optimal model performance on unseen data while minimizing the risk of overfitting. For SVM, a linear kernel was selected after comparing it with other kernels, as it yielded the most stable results while maintaining low computational complexity. The gamma parameter was set to 0.7, controlling the influence of individual data points, and the C value was set to 10, indicating a relatively substantial penalty for misclassification, which helps the model create a more accurate separating hyperplane.

In the case of KNN, the number of neighbors (n_neighbors) was optimized to 5, which balances bias and variance. The weights parameter was set to uniform, meaning that each neighbor has equal influence. The distance metric used was Minkowski with a p-value of 2, equivalent to the Euclidean distance, which is commonly used and effective for continuous data, such as spectra. For RF, the number of decision trees (n_estimators) was set to 200, providing a good balance between performance and computation time. The random_state was set to 42 to ensure the reproducibility of results. These parameters were selected based on their ability to reduce overfitting while capturing enough decision boundaries for accurate classification. GridSearchCV optimized model performance for classifying palm oil maturity levels using PCA-reduced spectral features.

SVM is well-suited for high-dimensional data, where the choice of kernel function plays a critical role in determining classification performance (*Pathak et al., 2022*). To enhance accuracy, spectral and spatial features were integrated using a joint kernel-based approach. In this study, meta-parameter optimization was performed using the regularization parameter C and the RBF kernel parameter G, with values set to C = 10, G = 0.7, and a linear kernel. This configuration yielded an accuracy of 0.80. The resulting confusion matrix presented in Figure 6.

Figure 7 shows one of the decision trees of a random forest. Random forests can reduce the impact of noise and outliers, resulting in more accurate and stable predictions. The random forest's ensemble nature allows it to average the predictions of each tree. Noise-containing predictions from individual trees can be mitigated when combined across the ensemble, resulting in more robust and stable predictions *(Raposo-neto et al., 2024)*.

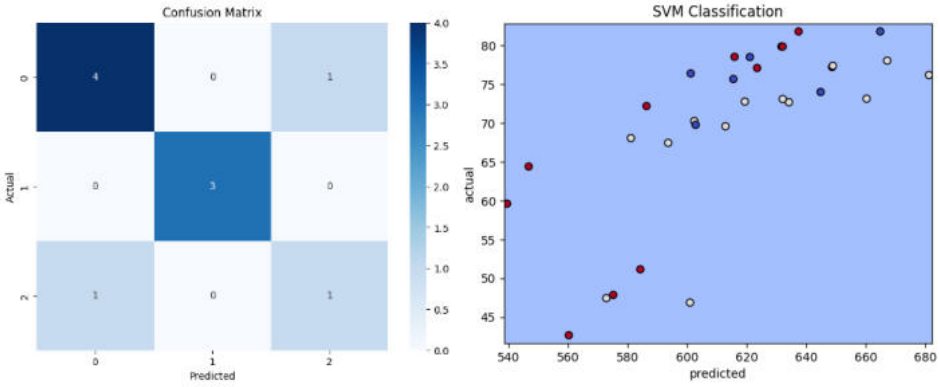


Fig. 6 - Confusion Matrix and decision boundary algorithm SVM classifier

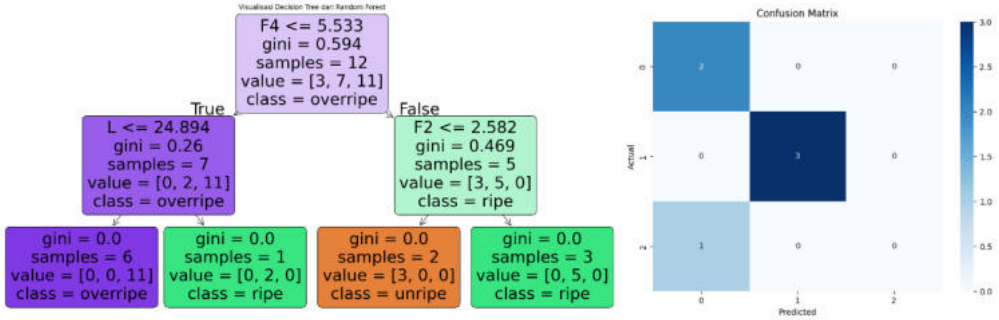


Fig. 7 - Decision tree of oil palm classification using random forest

Figure 8 shows the classification results using KNN. The KNN classification algorithm is one of the simplest machine learning algorithms with mature theory and wide application. The principle is to judge attributes based on the category of the k nearest points when predicting new values, which is simple and fast.

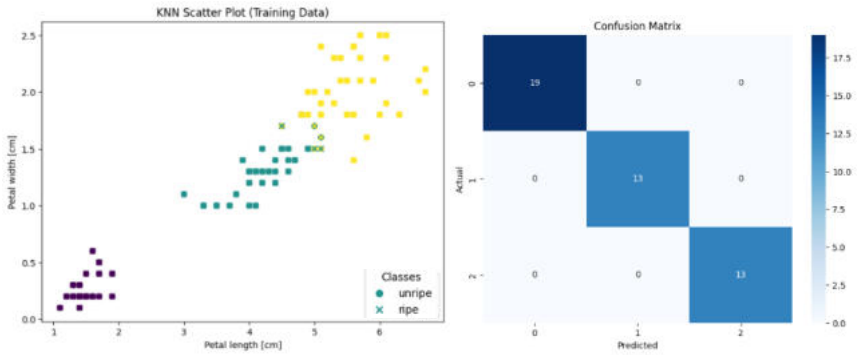


Fig. 8 - Scatter plot and confusion matrix of KNN classifier algorithm

Table 3 shows the classification results of the three models. The three algorithms used can classify well, but only KNN can classify with 100% accuracy, while SVM and Random Forest can only classify with 80% and 60% accuracy. KNN algorithm demonstrated 100% accuracy, indicating its effectiveness in distinguishing among the three classes. Several key factors contribute to KNN's superiority in this study. First, the relatively small number of features (18 wavelengths) and the limited sample size (270 spectra) enhance KNN's ability to learn data distribution efficiently, minimizing the risk of high computational costs. Second, the initial clustering performed using Principal Component Analysis (PCA) likely led to clear class separations in the feature space. This clarity allows distance-based algorithms like KNN to classify samples based on their nearest neighbors. In this study, a value of k=5 was utilized employing the Minkowski metric (p=2, which is equivalent to Euclidean distance) and applied uniform weighting. This approach ensures that classification is determined by averaging the five closest samples without giving additional weight to nearer neighbors. When the class distribution in the feature space is well-separated, the KNN model tends to achieve very high accuracy. KNN is known for its high computational complexity. It requires calculating the Euclidean distance between the input feature and every feature in the database.

While it does not involve a training phase, it is computationally intensive during the classification phase (*Eya'a et al., 2023*), *Saifullah et al., (2023*) utilized K-Nearest Neighbors (KNN) with RGB and Lab color extraction for automatic oil palm maturity classification, achieving 95.4% and 97.4% accuracy, respectively.

Table 3

Classification results

Parameter	SVM	RF	KNN
Accuracy	0.80	0.60	1.00
Recall	0.77	0.60	1.00
Precision	0.77	0.69	1.00
F_1 score	0.77	0.58	1.00

The Support Vector Machine (SVM) model achieved an accuracy of 80%, which is lower than the K-nearest neighbors (KNN) model but still better than the Random Forest (RF) model. SVM operates by constructing an optimal hyperplane to separate different classes in the feature space. This study used a linear kernel with parameters of gamma = 0.7 and C = 10. Linear kernels separate classes using straight lines, which can be a limitation when the data distribution is not linear. SVM is limited in speed and size during both the training and testing phases of the algorithm, and it is also limited in speed concerning the selection of the kernel function parameters *(Kumar et al., 2024)*. It is likely that the results from Principal Component Analysis (PCA) still exhibit non-linear patterns that cannot be fully captured by a linear-based model, leading to some misclassification near the edges of class separations.

Meanwhile, with its 60% accuracy, Random Forest demonstrated the lowest performance in capturing data distribution patterns after PCA. This study configured RF with 200 decision trees (n_ estimators = 200) and random_ state = 42. Despite RF's theoretical ability to handle complex data, the low results suggest that the PCA data structure may be too simple for a decision tree-based approach. The complexity of the data is a challenge that needs to be addressed, as it could be a contributing factor to the model's performance. Another possibility is overfitting on some subsets of the data, so RF fails to generalize well to the entire dataset. Random Forest (RF) can be overly sensitive to minor variations in the training set, sometimes leading to instability and a tendency to overfit. In contrast, Support Vector Machines (SVM) and RF are generally resilient to noise and excessive training, indicating their effectiveness in handling unbalanced data *(Kausik et al., 2025)*.

CONCLUSIONS

A portable instrument based on the AS7265x multichannel spectral sensor integrated with machine learning algorithms was developed and tested for oil palm fruit maturity classification. PCA analysis of SNV-pre-treated reflectance spectra revealed that the first two principal components accounted for 97% of the variance, resulting in a clear separation among the three maturity levels. Among the evaluated models, KNN achieved the highest classification accuracy of 100%. The system has the potential to be used for oil palm fruit maturity classification and to reduce human error in visual maturity assessment. However, the system has also some limitations such as classification is still processed out of the instrument, and the number of samples used is relatively limited. Further research is needed to ensure this system can be used as an accurate and real-time method for oil palm fruits classification to support precision agriculture such as integration of the trained model into the instrument as well as system validation in large number of oil palm fruit samples.

ACKNOWLEDGEMENT

The authors are grateful to Directorate General of Higher Education Research, and Technology under Ministry of Education, Culture, Research, and Technology of the Republic of Indonesia for the Research Grant (PDD) of Program Implementation Contract for the Year 2024: 027/E5/PG.02.00.PL/2024 and the Agency of Agricultural Extension and Human Resources Development, Ministry of Agriculture, Indonesia for supporting this research.

REFERENCES

[1] Arifuddin, A., Buana, G. S., Vinarti, R. A., & Djunaidy, A. (2024). Performance Comparison of Decision Tree and Support Vector Machine Algorithms for Heart Failure Prediction. *Procedia Computer Science*, *234*, 628–636. https://doi.org/10.1016/j.procs.2024.03.048

[2] Budiastra, W., Marjan, S., Adiarifia, N., Novianty, I., & Suci, Y. T. (2024). Non-Destructive Prediction of Oil and Free Fatty Acid of Oil Palm Fruitlets Using Near-Infrared Spectroscopy and Hybrid Calibration Method. *INMATEH - Agricultural Engineering*, *73*(2), 461–472. https://doi.org/10.35633/inmateh-73-39

[3] Chin-Hashim, N. F., Khaled, A. Y., Jamaludin, D., & Abd Aziz, S. (2022). Electrical Impedance Spectroscopy for Moisture and Oil Content Prediction in Oil Palm (Elaeis guineensis Jacq.) Fruitlets. *Plants*, *11*(23). https://doi.org/10.3390/plants11233373

[4] Eya'a, N. C., Nsimi, M. A., Ndele, P. H., Ngalle, B. H., Molo, T., Mbo, N. L. F., Fouman, A., Likeng, L.-G. B., Ngando, E. G. F., & Bell, J. M. (2023). A Review of Main Factors Involved in the Maturation of Oil Palm (Elaeis guineensis Jacq.) Fruit Bunches. *American Journal of Plant Sciences*, *14*(07), 727–740. https://doi.org/10.4236/ajps.2023.147049

[5] Guido, R., Ferrisi, S., Lofaro, D., & Conforti, D. (2024). An Overview on the Advancements of Support Vector Machine Models in Healthcare Applications: A Review. *Information (Switzerland)*, *15*(4), 235. https://doi.org/10.3390/info15040235

[6] Junior, F. A., & Suharjito. (2023). Video based oil palm ripeness detection model using deep learning. *Heliyon*, *9*(1), e13036. https://doi.org/10.1016/j.heliyon.2023.e13036

[7] Kausik, A. K., Rashid, A. Bin, Baki, R. F., & Jannat Maktum, M. M. (2025). Machine learning algorithms for manufacturing quality assurance: A systematic review of performance metrics and applications. *Array*, *26*(2025), 100393 Contents. https://doi.org/10.1016/j.array.2025.100393

[8] Kumar, A., Gaur, N., & Nanthaamornphong, A. (2024). Machine learning RNNs, SVM and NN Algorithm for Massive-MIMO-OTFS 6G Waveform with Rician and Rayleigh channel. *Egyptian Informatics Journal*, *27*(March), 100531. https://doi.org/10.1016/j.eij.2024.100531

[9] Malyala, R. (2024). Development of a Convolutional Neural Network Model for Automated Ripeness Classification of Palm Oil Fresh Fruit Bunches. *International Journal of Innovative Science and Research Technology (IJISRT)*, *9*(11), 1040–1046. https://doi.org/10.38124/ijisrt/ijisrt24nov762

[10] Mansour, M. Y. M. A., Dambul, K. D., & Choo, K. Y. (2022). Object Detection Algorithms for Ripeness Classification of Oil Palm Fresh Fruit Bunch. *International Journal of Technology*, *13*(6), 1326–1335. https://doi.org/10.14716/ijtech.v13i6.5932

[11] Michael, N. A., Ibrahim, M. A. Al, Scheibe, C., & Craigie, N. (2025). Best practices of utilizing Principal Component Analysis (PCA) in chemostratigraphic studies Data ro o f. *Applied Geochemistry*, 1–12. https://doi.org/10.1016/j.apgeochem.2025.106355

[12] Raposo-neto, J. J., Kowalski-neto, E., Luiz, W. B., Fonseca, E. A., Karla, A., Lograd o, C., Singh, M. N., Martin, F. L., Vassallo, P. F., Cristina, L., Campos, G., & Barauna, V. G. (2024). Near-Infrared Spectroscopy with Supervised Machine Learning as a Screening Tool for Neutropenia. *Personalized Medicine*, *14*(9), 1–13. https://doi.org/https:// doi.org/10.3390/jpm14010009 Academic

[13] Rinnan, Å., Berg, F. van den, & Engelsen, S. B. (2009). Review of the most common pre-processing techniques for near-infrared spectra. *TrAC - Trends in Analytical Chemistry*, *28*(10), 1201–1222. https://doi.org/10.1016/j.trac.2009.07.007

[14] Saifullah, S., Prasetyo, D. B., Indahyani, Drezewski, R., & Dwiyanto, F. A. (2023). Palm Oil Maturity Classification Using K-Nearest Neighbors Based on RGB and L*a*b Color Extraction. *Procedia Computer Science*, *225*, 3011–3020. https://doi.org/10.1016/j.procs.2023.10.294

[15] Suci, Y. T., Budiastra, I. W., Purwanto, Y. A., Widodo, S., & Novianty, I. (2024). Wavelengths Selection Method in Near Infrared Spectra Using Multivariate Analysis for Nondestructive Determination of Oil Content in Palm Oil Fruits. *IOP Conference Series: Earth and Environmental Science*, *1386*(1). https://doi.org/10.1088/1755-1315/1386/1/012009

[16] Zhu, J., Zhu, X., Yan, B., Ren, F., Chen, B., Han, Z., Yao, X., He, S., & Liu, H. (2025). Evaluation and categorization of various pea cultivars utilizing near-infrared spectroscopy in conjunction with multivariate statistical techniques. *Food Chemistry*, *474*(January), 1–15. https://doi.org/10.1016/j.foodchem.2025.143268

INVESTIGATION INTO VIBRATION BEHAVIOR OF THE INTEGRATED SHALLOT HARVESTER
/
KHẢO SÁT ĐỘNG LỰC HỌC DAO ĐỘNG CỦA LIÊN HIỆP MÁY THU HOẠCH HÀNH TÍM

Dang NguyenTH[1)], Phi CaoH[2)], Hung TranV[3)], Hau LeT[4)], Giang Pham TT[5)]
[1,2,4)] Faculty of Mechanical Engineering, Vinh Long University of Technology Education/ Vietnam
[5)] Faculty of Basic Science, Vinh Long University of Technology Education/ Vietnam
[3)] Faculty of Mechanical Engineering, Phenikaa University/ Vietnam
Corresponding author: Dang NguyenTH
Tel: 0917499199; E-mail: dangnth@vlute.edu.vn

DOI: https://doi.org/10.35633/inmateh-76-50

Keywords: *Integrated shallot harvester, 17-dof model, vibration dynamics, harvesting depth, Bekker soil sinkage*

ABSTRACT
The study investigates the vibration dynamics of the integrated shallot harvesting machine to support design refinement, aiming to improve operational efficiency, harvesting performance, and packaging for transportation. The investigation is based on an existing integrated machine developed under a Vietnamese State-Level Scientific Research Project. A dynamic model with 17 degrees of freedom was developed to comprehensively represent the system's motion, including the tractor, harvester, harvesting head, coupling joint, and eight wheels. Nonlinear soil characteristics were modeled using the Bekker terrain model, with specific soil parameters measured in Vietnam fields. Simulation results show notable vibrations in the integrated shallot harvesting machine and the harvesting head. At the beginning of the harvesting phase, the head experiences large amplitudes and high accelerations, which may damage shallot bulbs. The study proposes technical solutions such as optimizing damping coefficients, adjusting system stiffness, or incorporating active control systems to maintain stable harvesting depth and improve harvesting quality. The results provide a foundation for further refinement of integrated shallot harvesting machine design.

TÓM TẮT
Nghiên cứu động lực học liên hiệp máy thu hoạch hành tím thông qua khảo sát các thông số dao động sẽ góp phần hoàn thiện thêm thiết kế nhằm tăng thêm hiệu quả hoạt động và tăng năng suất thu hoạch cũng như đóng gói và vận chuyển. Phương pháp khảo sát dựa trên liên hiệp máy hiện có là sản phẩm của đề tài nghiên cứu khoa học cấp Nhà nước Việt Nam. Một mô hình động lực học được phát triển với 17 bậc tự do mô tả đầy đủ chuyển động của hệ thống gồm máy kéo, máy thu hoạch, mũi thu hoạch, khớp nối và 8 bánh xe. Các tính chất phi tuyến của đất ruộng theo mô hình Bekker đã được áp dụng với các hệ số đặc trưng trên đồng ruộng Việt Nam. Kết quả mô phỏng cho thấy dao động của liên hiệp máy và mũi thu hoạch. Ban đầu mũi thu hoạch có biên độ lớn và gia tốc cao sẽ gây hư hỏng củ hành. Nghiên cứu này đề xuất các giải pháp kỹ thuật bao gồm tối ưu hóa hệ số giảm chấn, điều chỉnh độ cứng của hệ thống hoặc bổ sung bộ điều khiển chủ động để duy trì ổn định độ sâu thu hoạch nhằm nâng cao chất lượng thu hoạch hành tím. Các kết quả thu được có thể dùng tham khảo cho hoàn thiện thiết kế liên hiệp máy thu hoạch hành tím.

INTRODUCTION
Shallots (*Allium cepa var. aggregatum*) are a high-value crop from the Allium family, cultivated extensively in many countries worldwide. In Vietnam, shallots are considered a specialty seasoning crop with significant economic importance.

In the context of agricultural mechanization, using an integrated shallot harvesting machine (ISHM) during harvesting and transportation phases can enhance labor productivity, reduce manual effort, lower production costs, and contribute to the modernization of agriculture. Developing a dynamic model for this system aims to define its real-world operational characteristics based on an existing ISHM design, thereby assessing the current design and providing essential data for further optimization.

International studies on shallot harvesters have shown that while these machines share general design principles, their specific configurations differ to suit local field conditions and soil properties in each country.

In the study by *Massah & Arabhosseini (2012)*, a design calculation and experimental validation were conducted using the cutting blade angle as the input parameter. The results indicated that setting the blade at an inclination angle of 20° yielded the best performance, as evidenced by the lowest damage rate to shallot bulbs among the tested configurations. An optimized design of the working mechanism in the integrated harvesting machine, combining digging, gathering, and sieving into a single operational unit with sequential automation and no manual intervention, helps reduce overall machine dimensions. It also enhances component modularity, allowing for easy assembly/disassembly, on-field maintenance, and compatibility with small tractors or walk-behind machines. The tip angle of the digging blade and the operating speed of the ISHM directly affect the quality of the harvested shallots. The use of a vibrating V-shaped digging blade with an adjustable angle of 18–21°, controlled via a hand screw mechanism, allows for easy operation and adaptability to various soil types.

In the harvesting study by *Kumawat & Raheman (2023)*, an analysis was conducted based on a dataset of shallot bulb dimensions. It was reported that bulbs with diameters ranging from *44* to 58 mm and weights between 47 and 66 g required an extraction force of 20–25 N. Regarding field conditions, the study found that a soil moisture content of 12% was optimal for harvesting. However, achieving such conditions is often challenging in practice due to unstable weather patterns, particularly the frequent alternation of sun and rain during the period when shallots have fully matured and are ready for harvest.

After being uprooted from the soil, shallot bulbs are transported via conveyors integrated within the machine body to the discharge point above the storage bin. Synchronizing the speed of the uprooting mechanism with the storage bin filling process helps reduce clogging and enhances harvesting efficiency. The synchronization is influenced by the travel speed of the chain and belt conveyors within the harvester. A study by *Erokhin et al. (2022)* addressed the issue and proposed an optimal conveyor speed of 1.7 m/s, which achieved a soil separation efficiency of 98.4%.

In the design process, the structure and shape of the digging blade are also carefully considered, as the forces acting on the blade tip resemble those experienced by a plowshare during soil penetration. The study by *Mehta & Yadav (2015)* demonstrated that a V-shaped digging blade with appropriately designed tip angles provides the lowest draft force, measured at approximately 625.6 N. The study by *Khura & Mani (2011)* reported that an optimal operating speed of approximately *2–4 km/h* effectively reduces vibration and prevents mechanical damage to shallot bulbs during harvesting.

In practice, vibration is a major concern during the operation of integrated shallot harvesting machines (ISHM) due to its direct impact on bulb damage, operator health, and machine durability. Vibrations originate from components such as the digging blade, chassis, and rotating or oscillating parts, and are often transmitted through the seat and frame to the operator. The intensity of vibration varies depending on machine design, soil characteristics, and terrain conditions. If not properly controlled, vibration can lead to fatigue and long-term musculoskeletal disorders *(Vlăduţ et al., 2023; Vlăduţ et al., 2013)*. A recent study by *Marin et al. (2024)* applied methods such as acceleration spectrum analysis, RMS calculation, and fatigue prediction models to assess risks and define safe exposure durations in accordance with ISO 2631-1 and 2631-5 standards. Experimental research conducted by *Cârdei et al. (2023)* on soil tillage machines such as the MCLS revealed that vibrations at the working components are random and nonlinear, requiring analysis through statistical tools like spectral density and autocorrelation to identify critical stress zones and propose improvements to the damping system.

Although *Bekker (1969)* foundational work remains the seminal reference on soil behavior and is considered the cornerstone of terramechanics, further studies have pointed out limitations in its practical applications. In particular, *Rashidi et al. (2012)* raised concerns regarding the limitations of the Bekker model in accurately predicting pressure–sinkage responses of soil under real-world conditions, especially when applied directly to wheel–soil interaction in agricultural field studies.

Their research referenced the classic Bekker equation:

$$p = \left(\frac{k_c}{b} + k_\phi\right) z^n \quad (1)$$

where: p: the contact pressure; z: the sinkage; k_c and k_ϕ: soil stiffness coefficients; b: the contact width; n: the sinkage exponent.

To improve the accuracy of dynamic analysis, *Múčka (2018)* combined Bekker's soil sinkage model with ISO 8608 road surface classifications, selecting the appropriate surface type to realistically simulate agricultural field terrain.

MATERIALS AND METHODS

The Integrated Shallot Harvesting Machine

The demand for shallot production in the Mekong Delta region of Vietnam has been supported through a scientific research project under code KHCN-TNB.ĐT/14-19/C29. The authors conducted the design and fabrication of a prototype, followed by field testing. The machine is powered by a KUBOTA L4508VN tractor, operating under stable working conditions. Initial evaluations have demonstrated the design's suitability for shallot fields in the Mekong Delta. An image of the machine is shown in Fig. 1 *(Phi et al. 2021).*



Fig. 1 - Research Prototype of the Designed and Fabricated Machine

The specifications of the ISHM, as cited by the project leader and the research team, are presented in Table 1 (*Phi et al., 2022; Phi et al., 2020).*

Table 1

Basic Specifications of the Integrated Shallot Harvester

No.	Parameter	Value
1	Width of shallot-contacting component	*897.6* cm
2	Distance between shallot-lifting tines	*3* mm
3	Width of transport conveyor belt	*45* cm
4	Number of transport buckets	*16*
5	Transport bucket dimensions	*(27 × 1.5 × 0.7)* cm
6	Soil sieve dimensions	*(85 × 95)* cm

Modeling of the Integrated Shallot Harvester (ISH)

The ISHM is modeled as a mechanical system consisting of the tractor, harvesting unit, harvesting head, the coupling joint between the tractor and the working machine, and eight wheels. The model has 17 degrees of freedom (DOF) to describe the full motion of the system. Excitation forces from the ground are considered with nonlinear factors, including soil sinkage behavior and wheel–soil interaction modeled using the Bekker theory. A schematic of the dynamic model of the ISH is shown in Fig. 2.

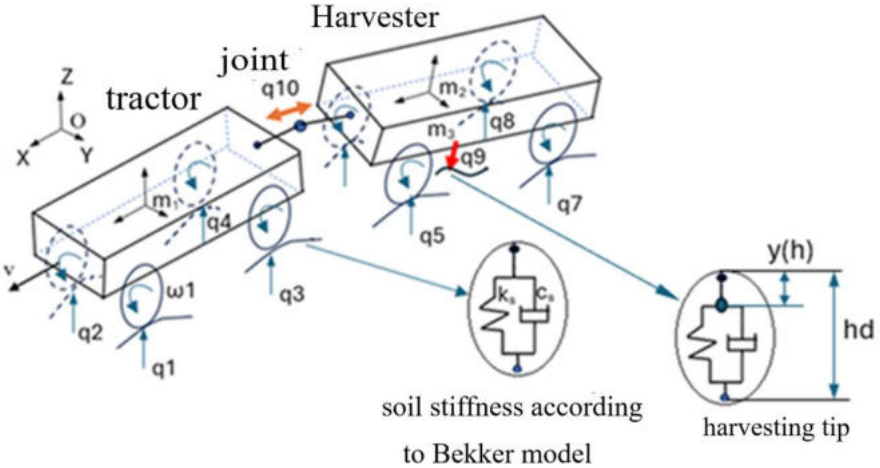


Fig. 2 - Dynamic Model of the Integrated Shallot Harvester

The DOF correspond to the generalized coordinates of the system as follows:

- Tractor: 4 DOF - x_1, z_1, φ_1, θ_1 (translation in the x and z-directions, pitch angle, and roll angle)
- Harvester: 4 DOF - x_2, z_2, φ_2, θ_2 (translation in the x and z-directions, pitch angle, and roll angle)
- Harvesting head: 1 DOF - z_3 (vertical motion corresponding to digging depth h_d)
- Wheels: 8 DOF (rotational motion around the wheel axis)

The forces acting on the system, based on the Bekker soil interaction model, include:

- Forces from the field surface on the 4 tractor wheels: q_1, q_2, q_3, q_4
- Forces from the field surface on the 4 harvester wheels: q_5, q_6, q_7, q_8
- Force from the field surface on the harvesting head: q_9
- Coupling force at the joint between tractor and harvester: q_{10}

Formulation of the System's Dynamic Equations

Based on the Newton–Euler dynamics principle, the system of differential equations corresponding to the 17 degrees of freedom is presented in Equations (2) to (11).

Equations of Motion for the tractor:

$$m_1\ddot{z}_1 = q_1 + q_2 + q_3 + q_4 - m_1 g - q_{10-z} \quad (2)$$

$$m_1\ddot{x}_1 = -q_{9-x} - q_{10-x} \quad (3)$$

$$I_{1-y}\ddot{\varphi}_1 = q_3\frac{c_1}{2} + q_4\frac{c_1}{2} - q_1\frac{c_1}{2} - q_2\frac{c_1}{2} - q_{10-z}(L_1 - L_{kn}) - q_{10-x}h_1 \quad (4)$$

$$I_{1-x}\ddot{\theta}_1 = q_2\frac{b_1}{2} + q_4\frac{b_1}{2} - q_1\frac{b_1}{2} - q_3\frac{b_1}{2} \quad (5)$$

where:

z_1: vertical displacement of the tractor;
I_{1-y}: moment of inertia of the tractor about the y-axis;
I_{1-x}: moment of inertia of the tractor about the x-axis;
L_{kn}: distance from the coupling joint to the front of the tractor.

Equations of motion for the harvester:

$$m_2\ddot{z}_2 = q_5 + q_6 + q_7 + q_8 - m_2 g + q_{10-z} - q_{9-z} \quad (6)$$

$$m_2\ddot{x}_2 = q_{9-x} + q_{10-x} \quad (7)$$

$$I_{2-y}\ddot{\varphi}_2 = q_7\frac{c_2}{2} + q_8\frac{c_2}{2} - q_5\frac{c_2}{2} - q_6\frac{c_2}{2} + q_{10-z}(L_{kn2}) - q_{9-z}(L_2 - st_x) - q_{9-x}h_2 \quad (8)$$

$$I_{2-x}\ddot{\theta}_2 = q_6\frac{b_2}{2} + q_8\frac{b_2}{2} - q_5\frac{b_2}{2} - q_7\frac{b_2}{2} - q_{9-z}st_y \quad (9)$$

where:

z_2: vertical displacement of the harvester;
I_{2-y}: moment of inertia of the harvester about the y-axis;
I_{2-x}: moment of inertia of the harvester about the x-axis;
L_{kn2}: distance from the coupling joint to the front of the harvester;
st_x, st_y: coordinates of the harvesting mechanism.

Equation of motion for the harvesting head:

$$m_3\ddot{z}_3 = q_{9-z} - m_3 g \quad (10)$$

where:

z_3: vertical displacement of the harvesting mechanism

Equations of motion for the eight wheels:

$$I_{bx}\dot{\omega}_i = r_{bx}q_i \qquad (i = 1, 2, ..., 8) \quad (11)$$

where:

I_{bx}: moment of inertia of the wheels;
$\dot{\omega}_i$: angular acceleration of the i^{th} wheel;
r_{bx}: wheel radius.

Excitation Forces Acting on ISHM Components

Soil Sinkage:

The Bekker mechanical model is used to calculate the soil stiffness (sinkage resistance) under the load of the ISH, as expressed in Equation (12) *(Gerhart, 1990)*.

The authors introduced Bekker's Derived Terramechanics Model (BDTM) to evaluate the mobility performance of ground vehicles, including the ISHM. This approach utilizes seven soil parameters rather than a single index with traditional coefficients, allowing for more detailed comparisons of vehicle mobility performance across various operating conditions.

$$p = k_c \left(\frac{z}{b}\right)^n \quad (12)$$

where:

p: contact pressure (kN/m²);

k_c: soil modulus of deformation (kN/m$^{(n)}$), consisting of two components: k_1 is horizontal modulus, representing the cohesive properties of the soil - its ability to resist sinkage under loading, which reflects soil stiffness; k_2 is vertical modulus, representing the frictional properties of the soil—its resistance to vertical deformation under load;

z: sinkage depth (m);

b: contact width (approximated by the wheel width - m);

n: the soil deformation exponent, which characterizes the nonlinear relationship between stress and strain under loading; it defines the degree of nonlinearity in the soil's response to pressure.

Typical values for loose soil conditions in shallot harvesting fields:

k_1 = 0.9-2.5 kN/m$^{(n+1)}$, assumed value: 1.5;

k_2 = 1.5-3.0 kN/m$^{(n+2)}$, assumed value: 2.25;

n = 0.9-1.2, assumed value: 1.

Wheel-Soil Interaction Forces:

Based on the Bekker model, the vertical reaction forces q_i (i = 1, 2, ...,8) acting on the wheels of the ISHM are calculated using Equation (13).

$$q_i = A.p = A.k_c \left(\frac{z}{b}\right)^n \quad (13)$$

where:

A: effective contact area between the wheel and the ground;

z: sinkage depth of the wheel;

b: wheel width;

k_c, n: soil parameters characterizing stiffness and nonlinearity.

Forces Acting on the Harvesting Head:

Similarly, the forces acting on the harvesting head in the *x* and *z*-directions, corresponding to longitudinal and vertical soil stiffness, are calculated using Equation (14).

$$\begin{aligned} q_{9-z} &= k_9(h_d.y(h) - z_3 + z_2 + st_y.\theta_2 - st_x.\varphi_2 \\ q_{9-x} &= c_9.v \end{aligned} \quad (14)$$

where:

k_9: soil stiffness at the harvesting head;

c_9: soil damping coefficient;

h_d: field depth (0.3 m);

$y(h)$: relative depth of the harvesting head;

v: travel speed (5 km/h).

Forces Acting on the Coupling Joint:

Similarly, the forces acting on the coupling joint in the x and z-directions are calculated using Equation (15):

$$\begin{aligned} q_{10-z} &= k_{10}(z_2 - z_1 - L_1\varphi_1 + L_3\varphi_2) \\ q_{10-x} &= k_{10}(x_2 - x_1 - h_1\varphi_1 + h_3\varphi_2) \end{aligned} \quad (15)$$

where:

k_{10}: stiffness of the coupling joint;

L_1, L_3: distance from the center of mass to the coupling joint;

h_1, h_3: height of the center of mass.

RESULTS

Nonlinear Analysis and Selection of Solution Method

The ISHM model is a nonlinear dynamic system. The degree of nonlinearity in the model is influenced by multiple factors that affect the vibration behavior of the system *(Wong, 2001)*. This work provides a comprehensive description of vehicle dynamics and road interaction for mechanical systems. It synthesizes and extends models developed by Bekker and other researchers, forming the theoretical foundation for multi-degree-of-freedom dynamic modeling in this study.

Specifically, the nonlinear factors affecting the ISHM model include:

- The soil reaction force is modeled by the Bekker equation, which is nonlinear to z^n.
- Soil resistance at the harvesting head, which exhibits nonlinear behavior.
- Coupling joint force, modeled with elastic stiffness, introduces dynamic response due to relative motion between components.
- Road-induced excitation modeled according to ISO 8608 (random vibration) *(ISO 8608, 1995)*. This international standard classifies and quantifies road surface roughness into eight categories (A–H). It is applied in the study to simulate Category D agricultural terrain with representative surface irregularities.
- Wheels encountering sudden terrain irregularities, introducing impact-like excitation *(Pacejka, 2006)*. The Magic Formula tire model is used to describe tire–terrain interaction, accounting for tires' slip behavior on soft soil.

Model Parameter Identification

The parameters of the model were determined based on the pilot-scale prototype of the ISH, and are as follows:

- Mass of the tractor: m_1 = 1600 kg (excluding the four wheels);
- Mass of the harvester unit: m_2 = 600 kg (including its four wheels);
- Mass of the harvesting head: m_3 = 80 kg (fixed to the harvester frame, operating similarly to a plow blade);
- Mass of each wheel: m_{bx} = 10 kg;
- Mass of the coupling joint: m_k = 30 kg;
- Tractor dimensions: *Length* × *Width* × *Height* ($L_1 \times B_1 \times H_1$) = *2.0m* × *1.2m* × *1.6 m.*
- Wheel track (front/rear): $b_1 \times c_1$ = 1.2m × 1.4 m;
- Wheel radius (front/rear): r_{bx11}/r_{bx12} = 0.3/0.5 m;
- Center of mass height (symmetrical along the longitudinal plane): h_1 = 0.9 m;
- Harvester unit dimensions: *Length* × *Width* × *Height* ($L_2 \times B_2 \times H_2$) = 1.6m × 1.0m × 1.4 m;
- Wheel track (front/rear): $b_2 \times c_2$ = 1.1m × 1.1 m;
- Wheel radius (front/rear): r_{bx21}/r_{bx22} = 0.6/0.15 m;
- Center of mass height (symmetrical along the longitudinal plane): h_2= 0.6 m;
- Harvesting head coordinates: $st_x = b_2/2$; $st_y = c_2/2$;
- Penetration depth of the harvesting head into the soil: $h_t = h_d$. $y(h)$, where h_d = *0.3 m* is the nominal field depth, and $y(h)$ is a variable penetration factor depending on real-time field interaction during operation.

Model Assumptions

The following assumptions were applied in the model:

- At the initial moment of system operation, the relative penetration factor is set to $y(h)$=0.1 m, so that the initial digging depth h_t is fixed and subsequently varies with $y(h)$.
- The harvesting head is assumed to be perfectly rigid, with no deformation.
- Dimensions of the towing joint: *Length* × *Height* ($L_3 \times H_3$) = 0.6m × 0.1 m;
- Center of mass height of the towing joint (symmetrical along the longitudinal plane): h_3 = 0.6m;
- The tractor and the harvesting unit are connected by a rotational joint (revolute coupling);
- The system operates over a soil surface path length of L_d = 30 m;
- Soil parameters: Soil stiffness: k_s = 3000; Soil damping coefficient: c_s = 100000;
- In addition to Bekker sinkage behavior, road excitations include surface irregularities modeled using ISO 8608, Category D, with varying conditions for each wheel throughout the travel path; sinusoidal bumps: Amplitude h_{x1} = 0.12 m over length L_{d1} = 8 m; Amplitude h_{x2} = 0.2 m over length L_{d2} =15 m;
- Maximum longitudinal velocity along the x-direction: v = 5 km/h.

Result Analysis

Dynamic Vibration of the System:

Modern numerical simulation tools were used to solve the system of dynamic differential equations governing the harvester model. The Runge–Kutta method was selected due to its computational efficiency and ease of implementation in MATLAB. The basis for selecting the Runge–Kutta method for solving nonlinear differential equations is supported by *Chauhan & Srivastava (2019)*, who provided theoretical justification for its suitability in complex dynamic system simulations.

The simulation results of the system's dynamic behavior are illustrated in Fig. 3.

The graphs show that large-amplitude oscillations occur during the initial time frame (0-0.5 seconds), then gradually diminish toward zero, indicating that the system stabilizes. This implies that the damping in the system is sufficiently high to suppress oscillations. Frequency analysis reveals *3-4* oscillations within the first second, suggesting a natural frequency of approximately 3-4 Hz. The oscillations are almost entirely damped out within 2.5 seconds, indicating that the damping coefficient c_s = 300 Ns/m for the wheels is appropriate for suppressing vibrations.

The tractor unit exhibits minimal vibration, primarily due to elastic excitation from the ground via the soil stiffness, k_s. The large mass of the tractor (1200 kg) leads to high inertia, resulting in low-frequency, small-amplitude, phase-lagged responses relative to the excitation. The harvester unit shows larger vibration amplitudes than the tractor due to its lower mass (500 kg). The coupling joint stiffness contributes to the overall system stiffness, causing resonant-like behavior in the harvester's response (q_2). The harvesting head experiences forced vibrations induced solely by the soil. Due to its small mass, it exhibits relatively strong vibrations. Initially, the head shows large displacement amplitudes (about 0.1 m), which may negatively affect the harvesting process-causing mechanical damage to the machine or bruising the shallots due to excessive impact with the soil.

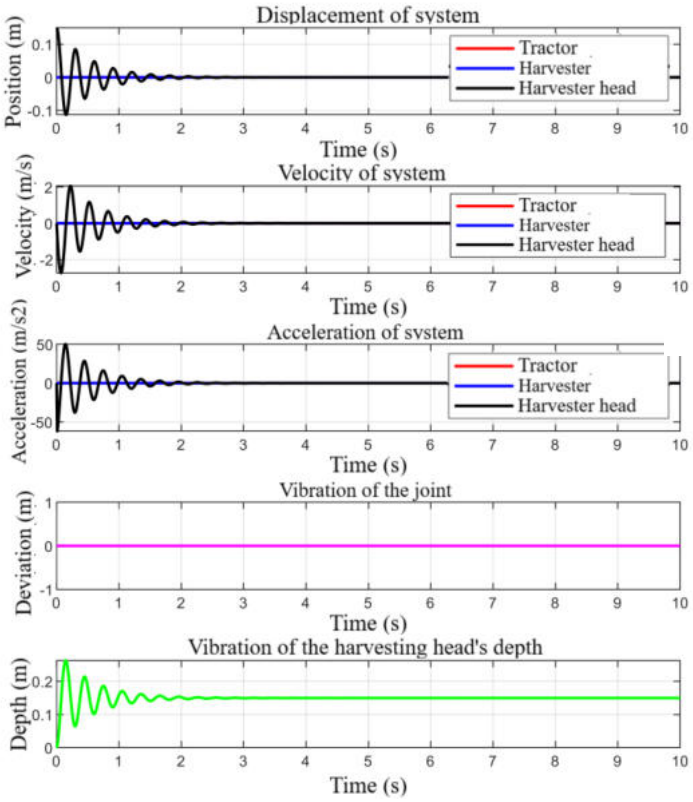


Fig. 3 - Simulated Dynamic Response of the System

The vibration velocity follows a similar trend to the displacement response, with an initially high amplitude of approximately 2 m/s for the harvesting head. Frequency analysis again reveals 3-4 oscillations within the first second, confirming a natural frequency of approximately 3-4 Hz. The velocity decreases rapidly after each oscillation cycle, reaching near-zero levels within approximately 2.5 seconds. The tractor exhibits low vibration velocity, characterized by a slow and smooth response due to its high mass and relatively low velocity frequency. The harvester unit shows relatively larger vibration velocities, reflecting its greater sensitivity to excitation.

Notably, certain segments show clearly defined velocity ripples, which correspond to impulsive excitations caused by surface irregularities. The harvesting head exhibits strong velocity oscillations with large amplitude, especially when directly encountering sinusoidal or pulse-shaped bumps.

The initial vibration acceleration of the harvesting head reaches up to ±50 m/s², then gradually diminishes and approaches a quasi-steady state. The peak acceleration amplitude of 50 m/s² is considered relatively high compared to typical operational thresholds for mechanical systems used in agriculture. Based on the presence of 3-4 oscillation cycles within the first second, the estimated natural frequency remains around 3-4 Hz. Each oscillation cycle shows a rapid reduction in amplitude-approximately 50% per cycle, indicating effective damping behavior. This raises a critical need to implement design improvements, including: evaluating the fatigue strength of the harvesting structure, introducing an active damping system or impact absorption unit, reducing initial excitation levels or increasing the damping coefficient c_s. These measures are essential to minimize excessive accelerations, enhance system durability, and protect the shallot bulbs from damage during the harvesting process.

The vibration graph of the coupling joint shows that its oscillation amplitude remains close to zero throughout the entire simulation period (0 to 10s), with no significant variation or large fluctuations. This indicates that the connection between the tractor and the harvester operates stably, with no significant phase difference, and no abnormal elongation or compression that could lead to fatigue or mechanical failure of the joint. The rigid coupling ensures structural integrity, and based on this observation, the influence of the coupling joint can be neglected in the analysis. The simulation focus can thus be directed primarily toward the vibrations of the harvester body and the harvesting head.

Harvesting Depth of the Digging Head:

The harvesting depth of the digging head is a critical parameter, reflecting the operational capability of the ISHM. It is directly related to the design of the machine and strongly affects both the quality and efficiency of the harvesting process. Ideally, the digging depth h_d should remain stable, but in practice, it varies along the *z-axis* due to system vibrations. This variation is referred to as the depth error, denoted by $h(y)$. When the harvesting mechanism undergoes significant vibration, $h(y)$ also fluctuates strongly, resulting in unstable harvesting depth, which can cause premature cutting (if too shallow) or bulb breakage (if too deep). If the vibration-induced variation in depth exceeds ±0.05 m, mechanical interventions are required, such as increasing system stiffness, adding damping mechanisms, and implementing active control strategies. To reduce the initial vibration amplitude and improve harvest quality, the system should be optimized in terms of the damping coefficient (c_s), soil stiffness (k_s), or by deploying real-time active depth control using depth sensors and actuator-based mechanisms for continuous adjustment. An illustration of this behavior is shown in Fig. 4.

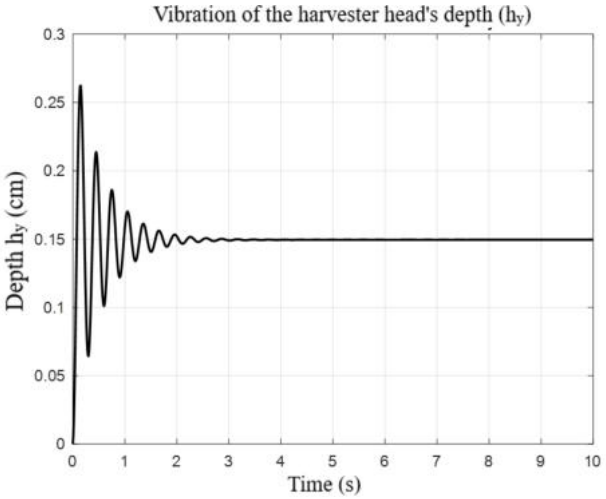


Fig. 4 - Vibration Response of the Harvesting Head

The graph shows that during the initial harvesting phase (0 to 2.5 s), the variation in digging depth is clearly noticeable. The vibration amplitude increases rapidly from 0 to over 0.25cm, before stabilizing as the tractor and harvester reach steady-state operation. If such behavior were to occur in real-world field conditions, it could pose a risk of damaging the shallot bulbs, particularly during the initial moments of harvesting operations when the ISHM first engages with the soil.

Fig. 5 illustrates the relationship between the mass of each component of the ISHM and the vehicle's travel speed, and how these factors affect the digging depth of the harvesting head.

It is evident that the digging depth is significantly influenced by the mass distribution of the system and its operating velocity.

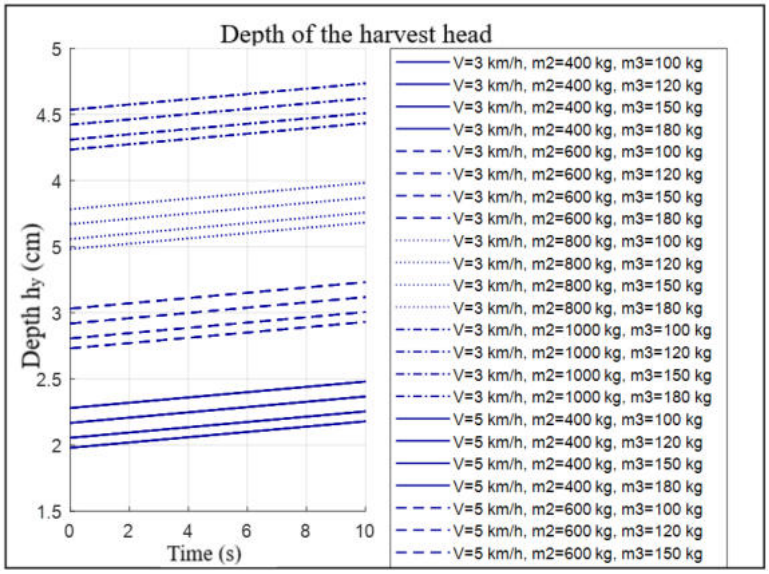


Fig. 5 - Graph of the Influence of Speed and Mass on the Digging Depth of the Harvesting Head

CONCLUSIONS

By developing a 17 DOFs dynamic model for the ISHM, in combination with the Bekker soil sinkage model and surface irregularities including sinusoidal, pulse-shaped, and ISO 8608-based terrain profiles, this study successfully captured the nonlinear interactions between the wheels and the soil, as well as the resistive forces acting on the wheels and the harvesting head.

The main parameters influencing the vibration dynamics and the harvesting quality include the mass of the tractor, harvester, and harvesting head, the travel velocity, the soil stiffness, and the damping coefficient of the system. The overall system exhibits a natural frequency of approximately 3-4 Hz, with vibrations effectively damped within about 2.5s due to the selected damping coefficient of c_s = 300 Ns/m, indicating that the current damping design is reasonably effective for suppressing oscillations.

When the ISHM begins operation, the harvesting head exhibits vibration amplitudes up to 0.1 m, with a peak acceleration reaching 50 m/s². The digging depth h_d fluctuates along the *z-axis*, with an initial variation amplitude of up to 0.25 cm, which exceeds the acceptable depth error threshold of ±0.05 m. This level of vibration may damage shallot bulbs or even cause structural failure of the digging head, especially during the initial phase of harvesting. Therefore, this period represents a critical window in designing and evaluating real-world operating conditions.

The coupling joint between the tractor and the harvester unit operates stably, showing no significant vibration or variation, confirming that the current joint design is structurally sound.

Recommendations for improving harvesting performance: increase the structural stiffness of the harvesting head mechanism; integrate an active damping system to reduce initial vibration effects; design a depth control system that uses sensors and actuators to maintain a stable digging depth h_d dynamically; optimize the operating speed to within the range of 2–4 km/h, which has been shown to reduce vibration and improve harvesting quality.

ACKNOWLEDGEMENT

The authors would like to express their sincere gratitude to Vinh Long University of Technology Education for providing support and favorable conditions for this study.

REFERENCES

[1] Bekker M. G., (1969). *Introduction to Terrain-Vehicle Systems*. The University of Michigan Press.

[2] Cardei P., Constantin N., Muraru V., Persu C., Sfiru R., Vladut N., Ungureanu N., Matache M., Muraru-Ionel C., Cristea O., Laza E., (2023). The random vibrations of the active body of the cultivators,

Agriculture, vol.13, no.8, article 1565, MDPI / Switzerland. DOI: https://doi.org/10.3390/agriculture13081565

[3] Chauhan V., Srivastava P. K., (2019). Computational techniques based on Runge-Kutta method of various order and type for solving differential equations, *International Journal of Mathematical, Engineering and Management Sciences*, vol. 4, no. 2, pp. 375–386. doi: https://doi.org/10.33889/IJMEMS.2019.4.2-030

[4] Erokhin M., Dorokhov A., Sibirev A., Aksenov A., Mosyakov M., Sazonov N., Godyaeva M., (2022). Development and Modeling of an Onion Harvester with an Automated Separation System, *AgriEngineering*, vol. 4, no. 2, pp. 380–399, Jun. DOI: https://doi.org/10.3390/agriengineering4020026

[5] Gerhart G., (1990). Bekker's Terramechanics Model for Off-Road Vehicle Research, *US Army TARDEC*. Available: https://www.researchgate.net/publication/235069513

[6] ISO 8608:1995, (1995). Mechanical vibration-Road surface profiles - reporting of measured data, *The International Organization for Standardization*.

[7] Khura T., Mani I., Srivastava A. P., (2011). Design and development of tractor-drawn onion (Allium cepa) harvester, *The Indian Journal of Agricultural Sciences*, vol. 81, no. 6, pp. 44–48, Jun. Available: https://www.researchgate.net/publication/267251851

[8] Kumawat L., Raheman H., (2023). Determination of engineering properties of onion crop required for designing an onion harvester, *Cogent Engineering*, vol. 10, no. 1. DOI: https://doi.org/10.1080/23311916.2023.2191404

[9] Marin E., Cârdei P., Vlăduţ V., Biriş S., Ungureanu N., Bungescu S., Voicea I., Cujbescu D., Găgeanu I., Popa L., Isticioaia S., Matei G., Boruz S., Teliban G., Radu C., Kabas O., Caba I., Maciej J., (2024). Research on the influence of the main vibration-generating components in grain harvesters on the operator's comfort, *INMATEH Agricultural Engineering*, vol.74, no.3, pp.808–823, Bucharest/Romania. DOI: https://doi.org/10.35633/inmateh-74-71

[10] Massah J., Arabhosseini A., (2012). Effect of Blade Angle and Speed of Onion Harvester on Mechanical Damage of Onion Bulbs, *Agricultural Mechanization in Asia, Africa & Latin America*, vol. 43, pp. 60–63. Available: https://www.researchgate.net/publication/287778155

[11] Mehta T. D., Yadav R., (2015). Development and Performance Evaluation of Tractor Operated Onion Harvester, *Agricultural Mechanization in Asia, Africa & Latin America*, vol. 46, no. 4, pp. 7–13, Dec. Available: https://www.researchgate.net/publication/296259068

[12] Múčka P., (2018). Simulated road profiles according to ISO 8608 in vibration analysis, *Journal of Testing and Evaluation*, vol. 46, no. 1, pp. 405–418. DOI: https://doi.org/10.1520/JTE20160265

[13] Pacejka Han B., (2006). *Tyre and Vehicle Dynamics*, 2nd ed. Butterworth-Heinemann.

[14] Phi C. H., (2021). Research on technology and equipment for high-tech vegetable and fruit production towards automation and compatibility with growing conditions in the Southwest, *Ministry of Science and Technology*.

[15] Phi C. H., Hau L. T., Long C. D., (2022). Design and dynamics calculations of shallot seed feeding mechanism, *Engineering Solid Mechanics*, vol. 10, no. 1, pp. 71–78. DOI: https://doi.org/10.5267/j.esm.2021.10.001

[16] Phi C. H., Van N. T., Ky L. H., (2020). Design and Manufacturing of a Non-Standard Chain Parts for a Chain Conveyor for a Harvest Shallot: A Case Study, *Applied Mechanics and Materials*, vol. 902, pp. 91–96. DOI: https://doi.org/10.4028/www.scientific.net/AMM.902.91

[17] Rashidi M. et al., (2012). Evaluation of Bekker model in predicting soil pressure-sinkage behaviour under field conditions, *Middle East Journal of Scientific Research*, vol. 12, no. 10, pp. 1364–1369. DOI: https://www.idosi.org/mejsr/mejsr12%2810%2912/9.pdf

[18] Vlăduţ N.-V. et al., (2023). Considerations regarding the effects of shocks and vibrations on operators of self-propelled agricultural equipment, *INMATEH Agricultural Engineering*, vol.71, no.3, pp.843–856, Bucharest/Romania. DOI: https://doi.org/10.35633/inmateh-71-74

[19] Vlăduţ V., Biris S.-Ş., Bungescu S.T., Herişanu N., (2013). Influence of vibrations on the operator in the grain harvesters, *Applied Mechanics and Materials*, vol.430, pp.290–296, Switzerland. DOI: https://doi.org/10.4028/www.scientific.net/AMM.430.290

[20] Wong J. Y., (2001). *Theory of ground vehicles*, 3rd ed. John Wiley.

LIGHTWEIGHT FRESH JUJUBE TARGET SEGMENTATION ALGORITHM BASED ON IMPROVED YOLOV8: YOLOSEG-JUJUBE

/

基于改进型 YOLOV8 的轻量级鲜枣目标分割算法：YOLOSEG-JUJUBE

Huamin ZHAO*[1)], Defang XU*[2)]

[1)] College of Agricultural Engineering, Shanxi Agricultural University, Jinzhong /China;

[2)] Department of Mathematics and Artificial Intelligence, Lvliang University, Lvliang /China

Corresponding authors: Huamin Zhao; Tel: +86-18001093228; E-mail: zhaohuamin@sxau.edu.cn

Defang Xu, Tel: +86-18935460012; E-mail: xudefang0012@163.com

DOI: https://doi.org/10.35633/inmateh-76-51

Keywords: *YOLOseg-Jujube；YOLOv8n； Fruit detection； Area estimation*

ABSTRACT

Fruit instance segmentation algorithms are critical for target localization in fruit-picking robots, enabling accurate area estimation of fruits within images. However, existing methods often face limitations such as high computational cost, poor adaptability to low-power devices, and reduced detection performance in complex environments. To address these challenges, YOLOSeg-Jujube was proposed - an improved instance segmentation algorithm based on YOLOv8 - validated on a jujube image dataset annotated with bounding polygons. The architecture of YOLOSeg-Jujube was optimized through ablation studies to identify the most effective structure. The final network design includes Focus, CBS, Conv4cat, SPD, and SPPFr modules as the backbone, and a YOLOv8 head incorporating the SIoU loss function. Compared to YOLOv4-tiny, YOLOv5n, YOLOv7-tiny, and YOLOv8n, YOLOSeg-Jujube achieves reductions in parameter size of 62.8%, 9.8%, 73.9%, and 23.6%, respectively. The model achieves 83.5% B_mAP and 83.2% S_mAP, outperforming mainstream YOLO variants in both segmentation accuracy and area estimation of target objects. YOLOSeg-Jujube is robust, fast, and computationally efficient, making it suitable for deployment on resource-constrained platforms. Furthermore, it demonstrates strong potential for recognizing ripeness stages of fresh jujubes, providing technical support for intelligent harvesting systems in the field.

摘要

水果实例分割算法是水果采摘机器人目标定位的重要方法。能够确保对图像中的目标进行正确的区域估算。与此同时，模型在复杂农业环境下计算成本高、不便于在低功耗计算设备上部署等都对水果采摘机器人用实例分割造成限制。因此，为了解决这些问题，本研究在 YOLOv8 的基础上设计了 YOLOseg-Jujube，并在自然光照环境下的红枣图像数据集上进行了验证。YOLOseg-Jujube 网络由 Focus、CBS、Conv4cat、SPD 和 SPPFr 组成骨干网络，YOLOv8 head 和 SIoU loss 组成头部网络。通过对比，YOLOseg-Jujube 的参数分别比 YOLOv4-tiny、YOLOv5n、YOLOv7-tiny 和 YOLOv8n 低 62.8%、9.8%、73.9% 和 23.6%。YOLOseg-Jujube 的 B_mAP 为 83.5%，S_mAP 为 83.2%，YOLOseg-Jujube 在分割目标的面积估计方面性能优于 YOLO 主流变体的算法。YOLOseg-Jujube 算法稳健、快速、准确，计算成本低，并且能够识别枣果的成熟阶段，可为田间鲜枣采摘机器人的研究提供技术支撑。

INTRODUCTION

Jujube (*Ziziphus jujuba*) is a fruit that is known around the world for its high in vitamins and minerals and low calories. The fruit comes with a host of several health benefits to humans. Nevertheless, it is a difficult task to sort and harvest, including hand-picking the fruit, since their maturity stages, for example, change from green to dark red. Meanwhile, jujube fruit can be divided into white, crisp, or fully mature depending on its color, flesh firmness, and composition. A fruit detection method using deep learning offers the best solution to recognize and locate the jujube fruit targets in an image or video according to *Yichen et al., (2022)* and *Defang et al., (2023).* This method allows for proper monitoring, quick sorting, and accurate harvesting of fruit. Notwithstanding, an extensive investigation on jujube fruit instance segmentation is needed to consolidate fruit detection.

Furthermore, it is essential to develop an algorithm with fewer parameters, greater robustness, and better compatibility with low-power computing devices such as the Nvidia Jetson Nano and Raspberry Pi, which will help extend the packing robot's battery life and enhance picking efficiency.

The ability to detect fruit targets using computer vision with deep learning has been widely investigated by researchers over the years, providing a groundbreaking outcome in fruit-quality detection and estimation *(Wang Z., Walsh, & Koirala, 2019)*, fruit counting *(Yanchao et al., 2022)*, yield prediction *(Koirala, Walsh, Wang, & McCarthy, 2019)*, harvesting/picking robot applications *(Lawal, 2021)*, and so on. However, the complex environment, such as occlusion, illumination, background, and nonstructural field, where fruits are grown, is still a difficult factor for fruit detection. Additionally, it is limited to rectangular bounding boxes, which in turn led to the introduction of fruit instance segmentation. Fruit instance segmentation is more granular with target shape deterministic through pixel characterization compared to fruit detection.

The application of the You Only Look Once object detector has demonstrated remarkable performance for fruit detection. Using YOLOv3, *Redmon & Farhadi, (2018*), *Wendong, Yakun, Jing, & Gang, (2021)* improved the method, and reported an average precision (AP) of 95.56% and speed of 35.5 frames per second (fps) for real-time object detection revealed AP of 90.05% and speed of 29.4 fps for kiwifruits detection in orchard. *Fu et al., (2021*), *Yang-Yang et al., (2019),* reported AP of 88.8% and speed of 40 fps for muskmelon fruit detection, *Peichao, Hao, Kunfeng, Jiachao, & Shanda, (2023*), designed MYOLO to achieved mean AP of 97.03% and speed of 50.6 fps for mushrooms detection, and *Liu G., Nouaze, Mbouembe, & Kim, (2020)* proposed YOLO-Tomato to reached 94.58% of AP and revealed that the factors of fruit detection are solvable. Next, *Yunchao, et al., (2023)*, reported 92.07% of AP and speed of 32.3 fps based on YOLOv4 *(Bochkovskiy, Wang, & Liao, 2020)* to detect each camellia oleifera fruit targets in orchard. The modification of YOLOv4-tiny by *Borja & Tofael, (2021),* revealed a speed of more than 50 fps and AP of 94.19% for real-time pear fruit detection and counting. *Huang & Wu, (2023),* designed GCS-YOLOv4-tiny and reported AP of 93.42% to detect different growth stages of fruits. Owning to YOLOv5 *Defang et al., (2023),* proposed YOLO-Jujube and achieved AP of 88.8% and a speed of 245 fps to detect jujube fruit, and the counting method of red jujube by *Yichen et al., (2022)* recorded AP of 94% and speed of 35.5 fps. *Bin Y et al.(2021)* reported AP of 86.75% and a speed of 66.7 fps to detect apple fruit targets, and *Bin Z. et al., (2022)* realized AP of 97.4% to detect a dragon fruit using modified YOLOv5. The proposed YOLOv5s-cherry by *Gai et al., (2021)* for cherry detection revealed F_1-score of 0.08 and 0.03 more than the YOLOv4 and YOLOv5, respectively. The YOLOv7 by *Wang, Bochkovskiy, & Liao, (2023),* was declared to have outperformed YOLOv4 and YOLOv5 in object detection performance. *Bin et al., (2022),* revealed AP of 95.6% and 96.0% respectively using YOLOv7 and YOLOv7-tiny for dragon fruit detection, and *Junyang et al., (2022),* modified the YOLOv7 to achieved AP of 97.29% and a speed of 14.4 fps for citrus detection. In quest for improvement, YOLOv8 by *Jocher et al, (2023),* was introduced, having a new feature with anchor free that can directly predict the center of the target, rather than offset of the known anchor box. Anchor free reduces the number of box predictions to speeds up Non-Maximum Suppression (NMS) post processing. YOLOv8 is designed to be flexible, easy to use, fast and accurate compared to previous versions of YOLO framework, but still in the development stage. Regardless, the YOLO variants algorithm for fruit detection has a complicated network topology that is hard to understand, cannot estimate the area of fruit targets in an image, cannot properly address occlusions by leaves, branches or other clusters, and are anchor-based detectors excluding YOLOv8. Furthermore, the YOLOv8 network is yet to be experimented for fruit detection, including for fruit instance segmentation.

To approach fruit instance segmentation, several investigations have been conducted using Mask R-CNN *(He, Gkioxari, Dollár, & Girshick, 2017)* as two-stage detector. *Santos, et al., (2020),* addresses occlusions and recorded F_1-score up to 91%, and the DualSeg proposed by *Jinhai et al., (2023),* reported 83.7% for grape instance segmentation. *Chan et al., (2021),* demonstrated robustness against various illuminations and complex backgrounds, and yielded AP of 94.7% for mangoes instance segmentation. The amodal segmentation algorithm proposed by *Jordi et al., (2023)*, was designed to predict the complete shape of apple different growth stages under visible and occluded regions and it achieved an AP between 44% and 51% with a mean absolute error (MAE) of 4.5 mm. *Dandan & Dongjian, (2022)*, improved Mask RCNN by fusing an attention module into the backbone network to enhance feature extraction ability and apples were accurately segmented under various conditions, having a recall, precision, F_1-score, and segmentation mAP of 97.1%, 95.8%, 96.4% and 0.917, respectively, with average run-time of 4 fps. *Pengyu et al, (2021),* developed a suppression branch and added it

Mask R-CNN for apple segmentation. The experimental results showed a significantly enhanced F_1-score of 90.5% and detection time of 4 fps. The MASU R–CNN proposed by *Tian et al, (2020),* for instance segmentation of apple flowers reached precision of 96.43%, recall of 95.37%, F_1-score of 95.90%, and mAP of 59.4%, outperforming other state-of-the-art models. *Liu et al., (2019),* reported AP and inference time of 89.47% and 2.9 fps, respectively, on improved Mask-RCNN for cucumber instance segmentation. Nevertheless, the research experimented on Mask-RCNN for fruit instance segmentation tends to have a very large weight-size, which slower the detection speed. The detection speed of a single-stage is faster than a two-stage detector, according to *Koirala et al., (2019)* and *(Olarewaju M. Lawal, 2021)*. For this reason, *Kang & Chen, (2020),* developed single-stage DaSNet-v2 for fruit detection and instance segmentation, and semantic segmentation of branches under complex orchard environment. The results demonstrated a weight-size of 8.1 MB with speed of 18 fps, but still require further performance improvement. Recently, *Mubashiru, (2023),* designed YOLOv5-LiNet based on YOLOv5 for fruits instance segmentation, which achieved box AP of 89.3%, instance segmentation AP of 88.5%, and real-time speed of 385 fps with weight-size of 3.0 MB. However, there are a few experiments using YOLO framework, including anchor-free YOLOv8 for fruit instance segmentation. Therefore, this article developed YOLOseg-Jujube based on improved YOLOv8n architecture to real-time detect and segment fruit targets in the complex environment.

MATERIALS AND METHODS

Dataset description

The jujube fruit dataset used in this paper was obtained by *Defang et al., (2023)*, set for ripeness inspection method. According to *Defang et al., (2023)*, the images were collected from Gaolang Red Date Picking Garden, Linxian County, Luliang, Shanxi, China using Huawei mate30pro and mate40pro of resolution 1904×4096 and 2736×3648 pixels, respectively. With reference to white and crisp mature stage under complex environment such as leaf occlusion, overlap occlusion, dense target fruit, branch occlusion, illumination, earth background, sky background, and other fruit natural scenes, these images were taken in the morning, midday and afternoon with constantly changing shooting angle and distance. Table 1 describes the image dataset details under different conditions. A total of, 1959 images in JPG format and recorded video in mp4 were collected. Furthermore, these images were randomly divided into 80% train-set, 15% valid-set, and 5% test-set, and the ground truth bounding boxes of each target in an image were hand labeled into 80R (Crisp mature ripeness) and 70R (White mature ripeness). Nevertheless, the image dataset was improved for jujube fruit instance segmentation in this paper using Labelme annotation tool. Similarly, the supposed polygon shape of the fruit targets in an image was drawn without special attention to the condition of the image, and the annotation files were saved in COCO format. Then, the COCO format was converted into the Poly-YOLO txt format. The Poly-YOLO txt format takes target category followed by xy to xn yn for instance segmentation, where xy is the coordinate for n polygon point. A total of, 10912 and 1921 bounding polygons were created respectively from 1569 train-set and 292 valid-set, similar to the box's information of *Defang et al., (2023)*. The 98 test-set images and the provided video were not annotated, but rather treated as unseen data, used to measure the level of algorithm robustness towards generalization.

Table 1

Image dataset details under different conditions

Time taken	Occlusions	Dense targets	Close targets	illumination	Others
Morning	280	95	131	105	39
Midday	268	99	150	110	33
Afternoon	270	85	166	92	36

Source: (Defang et al., 2023)

YOLOseg-Jujube

The architecture of YOLOseg-Jujube makes use of some key components to perform both fruit detection and instance segmentation tasks according to Fig. 1. As a build on YOLOv8n, it consists of backbone, neck and head network. The backbone is basically a series of convolutional layers that extract relevant features from the input image. It comprised of Focus, CBS, Conv4cat, SPD, and SPPFr network.

Similar to YOLOv5, the Focus network performs a slicing operation to split high-resolution feature maps into multiple low-resolution feature maps of four times, to obtain every pixel in an image without information lost. In this way, the width (W), height (H) information is concatenated in the channel space, then convolved to a downsampled feature map according to Fig. 1.

As the 1st downsampling network in layer 0, it increases the generalization capability. The CBS is a convolution layer activated with SiLU *(Elfwing, Uchibe, & Doya, 2017)* after batch normalization (BN) layer. The placed CBS_3,2 in 1st layer is for downsampling to provide a more scalable approach, CBS_1,1 in 8th layer is for dimensionality reduction and retaining the salient features, and CBS_3,1 placed in 9th layer has the ability to learn features common to different situations for better generalization. The knowledge of integrated Conv4cat into 2nd, 4th and 6th layer of backbone was derived from *Defang et al., (2023)* and *Du et al., (2020)*, where the complementary features of low-layer concatenate high-layer to enable sharing of information and the ability to learn more diverse features. For having similar W and H, where C is the number of channels, the $X \in R^{H\times W\times C1}$ of feature maps in CBS_1,1, $Y \in R^{H\times W\times C2}$ of feature maps in CBS_3,1 and $Z \in R^{H\times W\times C3}$ of feature maps in CBS_1,1 concatenated to produced $O \in R^{H\times W\times (C1 + C2 + C3)}$ of features as indicated in Fig. 1 and stated in Eq. 1.

$$O = [X, Y, Z] \tag{1}$$

The space-to-depth (SPD) proposed by *Sunkara & Luo, (2022)*, shown in Fig. 2 was placed at the 3rd, 5th and 7th layer of the backbone to permutes the spatial blocks of the input into the depth dimension. This network was used to combine feature maps of different size without discarding any feature data. The idea of SPD was to solve the performance degradation with low-resolution images and small objects, and have shown to outperforms the state-of-the-art deep learning models using YOLOv5 detector. Since the image dataset is associated with dense fruit targets, SPD was employed serving both as a feature extractor and as downsampling operation. According to Fig. 2, the intermediate feature map X of size ($S \times S \times C_1$) in Fig. 2(b) is sliced into a sequence of sub-feature maps, each with a shape of ($S/2$, $S/2$, C_1). This operation effectively downsamples X by a factor of 2 in Fig. 2(c). These sub-feature maps concatenate along the channel dimension to obtain a feature map X' in Fig. 2(d) with a reduced spatial dimension by *scale* and an increased channel dimension by $scale^2$. After that, a non-strided convolution added to retain all the discriminative feature information X'' as in Fig. 2(e). The SPD feature transformation can be defined by Eq. 2.

$$X(S,\ S,\ C_1) \rightarrow X'\left(\frac{S}{scale}, \frac{S}{scale}, scale^2 C_1\right) \rightarrow X''\left(\frac{S}{scale}, \frac{S}{scale}, C_2\right) \tag{2}$$

The SPPF layer was originally used to speed up the computation of the network by pooling features of various scales into a fixed-size feature map. However, it experienced loss of feature information during learning, including a slower detection speed for having three maxpooling layers with a convolution layer being concatenated. For this reason, SPPFr was designed to have a single maxpooling layer concatenated with a convolution layer. As in the operation described by Equation (1), the feature maps from the CBS module are concatenated with those from the MaxPool layer, as shown in Figure 1. The SPPFr module, serving as the final layer of the backbone, was added at the 10th position to enhance feature representation, reduce missed detections, and improve detection speed.

YOLOseg-Jujube used similar neck network as YOLOv8n. The neck combines path aggregation network (PAN) and feature pyramid network (FPN) for multiscale feature fusion. The Upsample layers of 11th and 14th increase the resolution of the feature maps collected from the backbone and concatenated with 6th layer of Conv4cat and 4th layer of Conv4cat, respectively, followed by C2f module. The C2f module as shown in Fig. 1 combines the high-level features with contextual information to improve detection accuracy. It consists of two CBS_1,1, split and three Bottlenecks, which is placed at the 13th, 16th, 19th and 22nd layer of the neck. Meanwhile, CBS_3,2 in 17th and 20th layer does downsampling operation before being concatenated with 13th and 10th layers, respectively. Having obtained feature maps from backbone, the C2f 16th, 19th and 22nd layer of neck passes the information to detection module for small, medium and large scale.

Furthermore, the framework of YOLOseg-Jujube makes used of an anchor free paradigm whose head network is designed to be decoupled, meaning that it processes classification, and regression tasks independently. This enables each branch to focus on its respective task and to improve the overall accuracy of the algorithm.

The detection module is part of the head, and uses a set of convolution and linear layers to map high-dimensional features and predict bounding boxes and polygons, and class probabilities. During training, the loss function plays a critical role in updating the network's weights by measuring the difference between the predicted bounding boxes and the ground truth coordinates. For classification (Cls) loss, binary cross-entropy (BCE) was used, as shown in Figure 1.

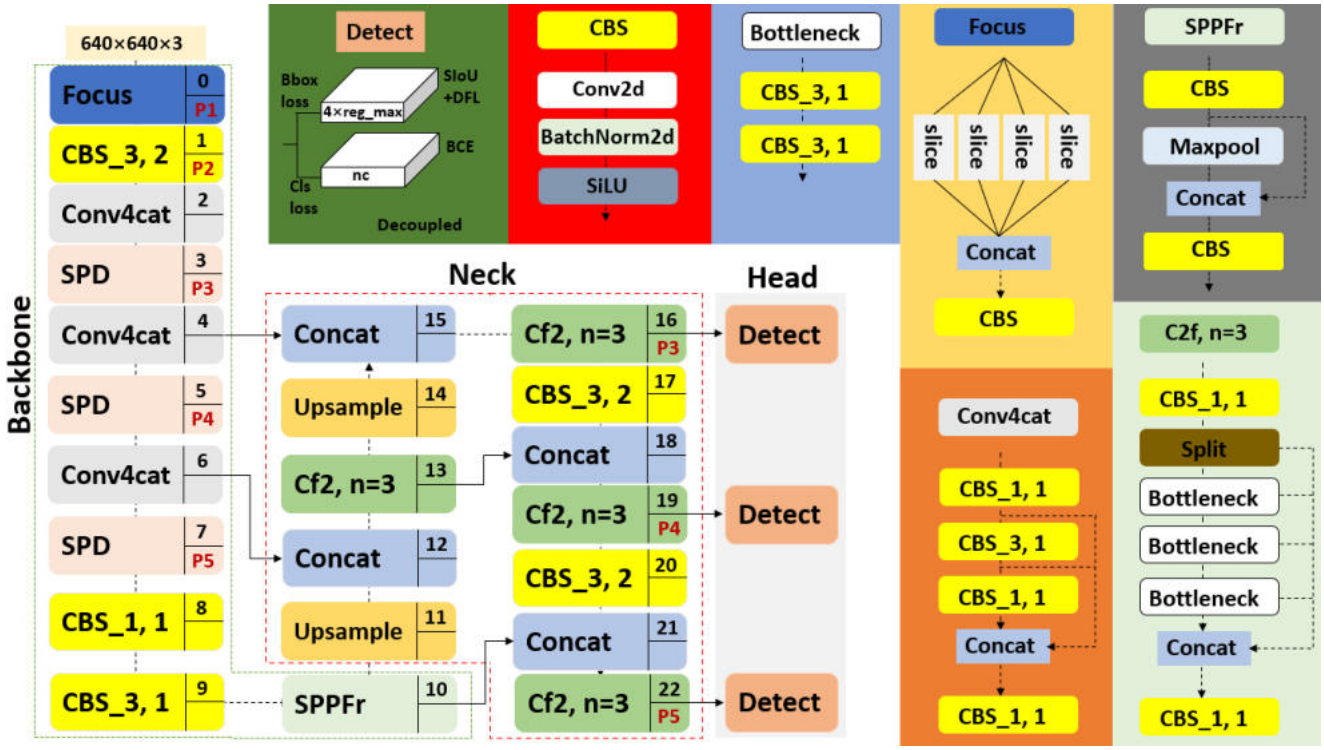


Fig. 1 - The network architecture of YOLOseg-Jujube

For regression loss, the proposed model adopts the SCYLLA-IoU (SIoU) loss function *(Gevorgyan, 2022)* combined with Distribution Focal Loss (DFL) *(Xiang et al., 2022)*, in contrast to the Complete IoU (CIoU) loss with DFL used in YOLOv8 *(Zheng et al., 2020)*. This substitution enhances bounding box regression by considering angle, distance, and shape alignment more effectively. SIoU loss improves the speed of training and the accuracy of inference depending on the cost of angular, distance, shape, and IoU. The loss function L_{box} embodies all the costs by Eq. 3, where the distance cost (Δ) takes into account the angle cost, shape cost (Ω) is unique for each dataset, and IoU is the difference between the predicted box (B) and real box (B^{gt}) with reference to union and intersection.

For DFL as shown in Eq. 4, it focuses on the distribution of the close to target location and enables probability density near the location. Here s_i is the sigmoid output, x_i and x_{i+1} is the interval, x is label.

$$L_{box} = 1 - \mathrm{IoU} + \frac{\Delta + \Omega}{2} \tag{3}$$

$$DFL_{(s_i, s_{i+1})} = -((x_{i+1} - x)\log(s_i) + (x - x_i)\log(s_{i+1})) \tag{4}$$

Finally, the overall architecture of YOLOseg-Jujube was designed to be low computation cost, fast, flexible, and efficient, while still achieving high fruit detection and instance segmentation accuracy.

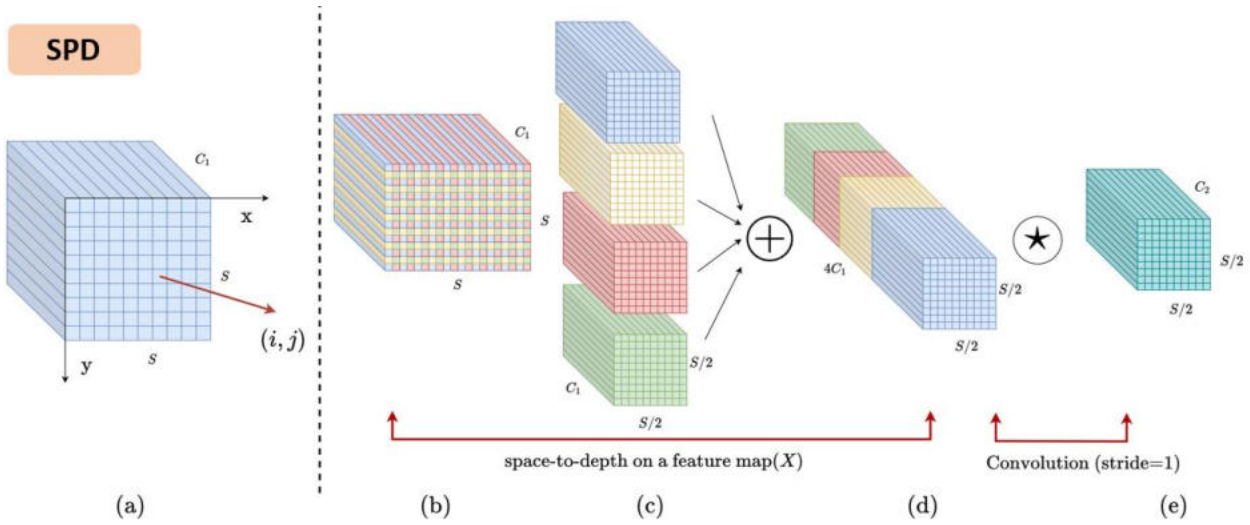


Fig. 2 - SPD-Conv for low resolution images and small objects (scale = 2, stride =1)
(Sunkara & Luo, 2022)

Experiment and evaluation

The training and testing of YOLOseg-Jujube, including compared YOLO-mainstream variants were implemented using YOLOv8.0.40 platform on hardware and environment information stated in Table 2. The algorithms received an input image of 640×640×3 pixels, 16 batch, 0.937 momentum, 0.0005 weight decay, 0.7 IoU, 0.015 hue, 0.7 saturation, 0.4 lightness, 1.0 mosaic, 0.5 scale, 0.1 translate, 7.5 Bbloss, 0.5 Clsloss, 1.5 DFloss, and 100 epochs for training from scratch. At the time, the weight for training the algorithms was randomly initialized from the scratch. The developed algorithms were exported from PyTorch (pt) to open neutral network exchange (ONNX), and to NCNN, developed by Tencent. The NCNN format was deployed using ncnn-android-yolov8 (Kang & Chen, 2020) on mobile phone. The NCNN was optimized to run faster than known frameworks on mobile phone CPUs.

Table 2

Hardware and environment description

Hardware	Configure	Environment	Version
System	Ubuntu20.04	Python	3.9.12
CPU	Core i7-12700F	Conda	23.1.0
GPU	RTX3060 (16G)	PyTorch	1.12.1
RAM	32G	CUDA	11.3.1
Hard-disk	1.0T	CUDNN	8.8.0

The algorithms were evaluated using the metrics stated in Eq. (5)-(11) respectively for precision (P), recall (R), average precision (AP), mean average precision (mAP), speed, number of parameters (params), and giga floating point operations per second (GFLOPs). TP is the true positive for correct detections, FN is the false negative for missed detections, FP is the false positive for incorrect detections, P(R) means that P is a function of R, AP is the area under curve (AUC) for single-class, mAP is mean AP values over multiclass, C is the total number of classes, j is the serial number, i is the input-size, k is the convolution kernel-size, o is the output-size and H×W is the size of outputted feature map. Speed is used to measure the real-time in frames per second (fps), params (10^6) is the number of trainable parameters, layer is the network topology, and GFLOPs estimate the number of floating-point arithmetic operations.

$$P = \frac{TP}{TP+FP} \tag{5}$$

$$R = \frac{TP}{TP+FN} \tag{6}$$

$$AP=\int_0^1 P_{(R)}dR \tag{7}$$

$$mAP = \frac{\sum_{j=1}^{C} AP_j}{C} \tag{8}$$

$$speed = frames/time \tag{9}$$

$$params = \left[i \times (k \times k) \times o\right] + o \tag{10}$$

$$GFLOPs = H \times W \times params \tag{11}$$

RESULTS AND DISCUSSION

Ablation studies on YOLOseg-Jujube

The ablation studies conducted on YOLOseg-Jujube are needed to find out what features of the algorithm are responsible for achieving a good performance. The process involves removing and adding some features of algorithm and seeing the effects on performance. Computation cost, detection accuracy, and speed were taken into consideration. Computation cost is simply based on the size of the algorithm in GFLOPs and params. While the layer 1–9 was held constant throughout the backbone network, Table 3 shows that changes in layer 0 and 10, including the neck network and loss function, caused a variation in computation cost. The added CBS_3,2/Focus and SPPF/SPPFr respectively in layer 0 and 10 of Method 1–12 show differences in params and GFLOPs. Moreover, the contribution to computation cost of methods with SPPFr is less than methods having SPPF. The shown number of layers in Table 3 as network topology is a support to this fact. Without no significant difference with the used loss function, the incorporated PAN-FPN constituted an increased in params and GFLOPs compared to the FPN. Using only params, the level of computation cost is measure as the equality of Method1, Method5 and Method6 is greater than the similarity of Method2–4, Method7 and Method10–12, and also higher than the equals of Method8 and Method9.

Table 3

Ablation studies on YOLOseg-Jujube based on computation cost

Algorithm	Layer 0	Layer 10	Neck	Loss	Layers	Params	GFLOPs
Method1	CBS_3,2	SPPF	PAN-FPN	CIoU	168	2.53	11.3
Method2	CBS_3,2	SPPFr	PAN-FPN	CIoU	167	2.49	11.2
Method3	CBS_3,2	SPPFr	PAN-FPN	SIoU	167	2.49	11.2
Method4	Focus	SPPFr	PAN-FPN	CIoU	169	2.49	11.3
Method5	Focus	SPPF	PAN-FPN	CIoU	170	2.53	11.4
Method6	Focus	SPPF	PAN-FPN	SIoU	170	2.53	11.4
Method7	Focus	SPPFr	PAN-FPN	SIoU	169	2.49	11.3
Method8	Focus	SPPFr	FPN	CIoU	153	2.16	11.0
Method9	Focus	SPPFr	FPN	SIoU	153	2.16	11.0
Method10	Focus	SPPFr	PAN-FPN	EIoU	169	2.49	11.3
Method11	Focus	SPPFr	PAN-FPN	DIoU	169	2.49	11.3
Method12	Focus	SPPFr	PAN-FPN	GIoU	169	2.49	11.3

The depicted validation losses in Fig. 3 are used to compliment computation cost and to predict the performance of Method1–12 by showing the consistence decreasing pattern. They measure the real position of fruit targets in an image during network training, where Fig. 3(a) is the bounding box, Fig. 3(a) is for instance segmentation via bounding polygon, Fig. 3(c) is for classification, and Fig. 3(d) is for DFL to enable general distribution of target position.

Having shown a closely related level of neural network depth among Method1–12, the validation of class loss is deeper than box loss, segment loss and DFL according. This is as a result of more correctness found in class loss compared to box loss, segment loss and DFL. Excluding Method10, which shows a less deep network in Fig. 3(a) because it has EIoU compared to others, it is difficult to examine the deepest and best performing network. But it can be addressed using Fig. 4 of mAP. This means that a decreasing loss of validation as algorithm learns is an increase in the mAP. Fig. 4(a) show that the aggregated mAP of 80R at 74.6% and 70R at 92.2% seen in Method7 is higher than other methods. Similarly, Figure 4(b) shows that Method 7 also achieves superior aggregated mAP values of 74.6% at 80R and 91.9% at 70R, further confirming its performance advantage over alternative approaches. Next to the mAP performance of Method7 is Method4, having scored 0.1% less under 80R with the same value under 70R of Fig. 4(a), and the same value under 80R with 0.1% less under 70R of Fig. 4(b). Despite having a similar backbone network, as indicated in Table 3, the improved mAP of Method7 was triggered with the added SIoU loss against the CIoU loss incorporated into Method4. The obtained results verify that the mAP level of Method7 is higher than the rest methods. For justification, the test-set images were tested on Method1–12 to investigate robustness towards generalization. And the sample of the tested image associated with sky background and occlusions is presented in Fig. 5. The methods were able to detect and segment a number of fruit targets perfectly, but were noted with difference in confidence score, including missed or false detection. For example, the confidence score of detected and segmented 70R target at the base of Fig. 5(g) recorded 62%, which is more than 59% of Fig. 5(a), 51% of Fig. 5(b), 34% of Fig. (c), 38% of Fig. 5(d), 29% of Fig. 5(e), 44% of Fig. 5(f), 47% of Fig. 5(h), 55% of Fig. 5(i), 33% of Fig. 5(j), 52% of Fig. 5(k), and 40% of Fig. 5(l). This demonstrated the superiority of Method7 over other methods.

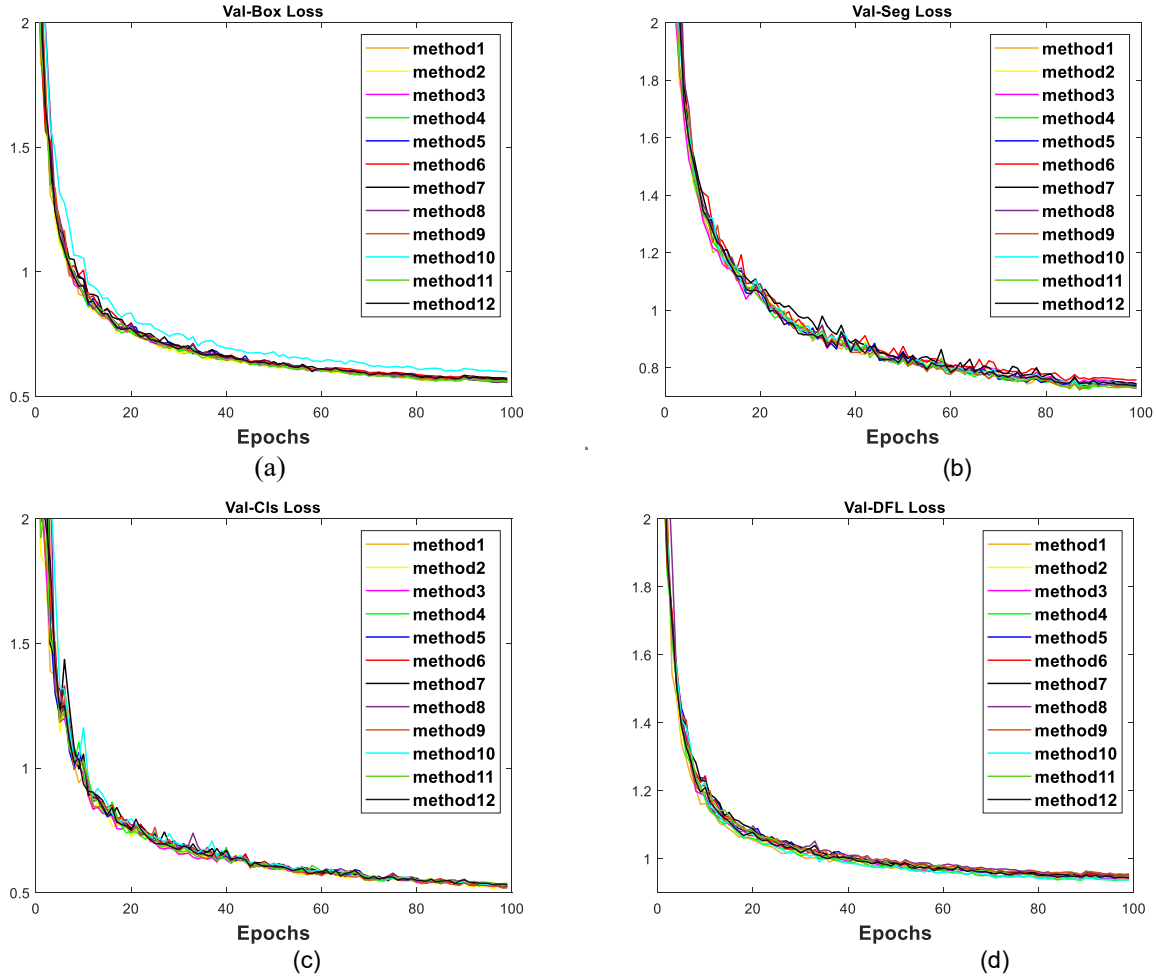


Fig. 3 - The validation of (a) box, (b) segmentation, (c) class, and (d) DFL loss during ablation on YOLOseg-Jujube

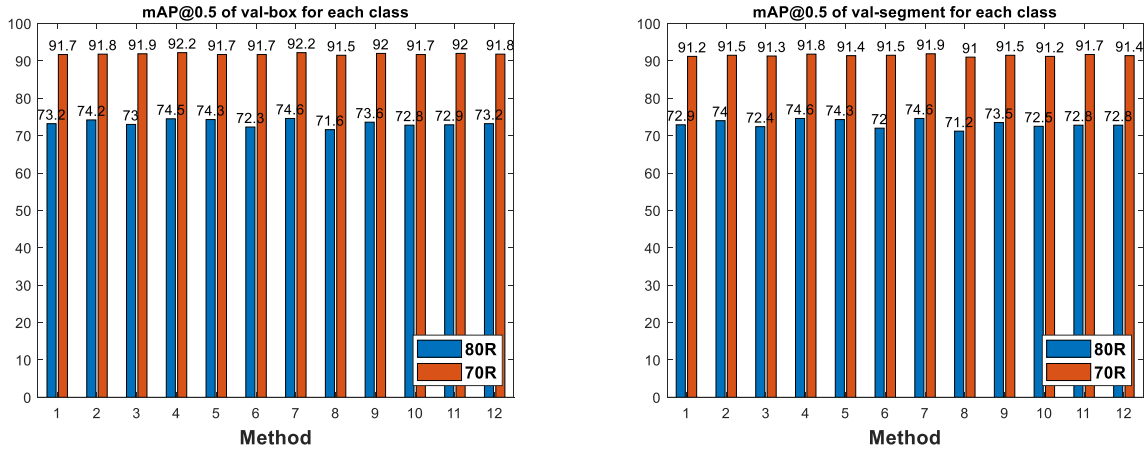


Fig. 4 - The mAP@50% of validation (a) box and (b) segmentation for each class during ablation on YOLOseg-Jujube



(a) (b) (c)



(d) (e) (f)



(g) (h) (i)

(j) (k) (l)

Fig. 5 - The detected and segmented fruit targets of class 80R and 70R obtained from an image with shy background and occlusions using (a)–(l) for Method1–12

Table 4 provides a comprehensive analysis of mAP for both box and segmentation, including speed, to show the outstanding performance of Method7 compared to Method1–6 and Method8–12. The mAP is more accurate because it measures the overall global relationship between P and R. Using Method7, the 83.5% of B_mAP is 1.1%, 0.5%, 1.0%, 0.2%, 0.5%, 1.5%, 1.9%, 0.7%, 1.2%, 1.0% and 1.1% more accurate respectively than Method1–6, Method8–12 under fruit targets detection, and 83.2% of S_mAP is 1.1%, 0.5%, 1.3%, 0.1%, 0.3%, 1.5%, 2.1%, 0.7%, 1.3%, 1.0% and 1.1% more accurate respectively than Method1–6, Method8–12 under fruit targets instance segmentation. Considering computation cost as a criterion for a faster detection speed, Method7 at 323 fps is faster than Method1 at 309 fps, Method2 at 315 fps, Method3 at 321 fps, Method4 at 320 fps, Method5 at 306 fps, Method6 at 317 fps, Method10 at 313 fps, Method11 at 319 fps, and Method12 at 318 fps, but not than Method8 at 342 fps and Method9 at 344 fps. The faster speed of Method8 and Method9 is attributed to applied FPN, unlike Method7 having PAN-FPN as shown in Table 4. Considering the overall performance of all methods, Method7 is the best and was chosen for our YOLOseg-Jujube after the ablation studies.

Table 4

Summary of Ablation study on YOLOseg-Jujube using valid-set and videos

Algorithm	B_P (%)	B_R (%)	B_ mAP (%)	S_P (%)	S_R (%)	S_ mAP (%)	Speed (fps)
Method1	78.8	76.4	82.4	78.3	76.8	82.1	309

Algorithm	B_P (%)	B_R (%)	B_ mAP (%)	S_P (%)	S_R (%)	S_ mAP (%)	Speed (fps)
Method2	77.1	79.6	83.0	77.2	79.3	82.7	315
Method3	82.4	74.7	82.5	82.2	74.6	81.9	321
Method4	83.8	74.3	83.3	83.9	74.3	83.1	320
Method5	80.8	75.7	83.0	80.8	75.4	82.9	306
Method6	81.3	76.3	82.0	81.2	76.1	81.7	317
Method7	80.1	77.7	83.5	80.4	77.2	83.2	323
Method8	79.8	74.5	81.6	79.7	74.1	81.1	342
Method9	76.4	80.3	82.8	81.6	75.4	82.5	344
Method10	77.1	77.9	82.3	77.6	77.3	81.9	313
Method11	78.8	76.6	82.5	78.8	76.7	82.2	319
Method12	78.4	78.4	82.5	78.0	78.2	82.1	318

Comparison with YOLO-mainstream variants

Having considered Method7 as YOLOseg-Jujube, its performance was compared to YOLO-mainstream variants as shown in Table 4. For computation cost, the obtained params from YOLOseg-Jujube are 62.8%, 9.8%, 73.9%, and 23.6% respectively less compared to YOLOv4-tiny, YOLOv5n, YOLOv7-tiny and YOLOv8n. In the case of GFLOPs, YOLOseg-Jujube is 82.7%, 83.8% and 5.8% lower than YOLOv4-tiny, YOLOv7-tiny and YOLOv8n, respectively, but not with YOLOv5n at -2.7%. With reference to B_mAP and S_mAP, the displayed results in Table 4 demonstrated the outstanding performance of YOLOseg-Jujube against YOLO-mainstream variants. For having 83.5% of B_mAP and 83.2% of S_mAP, YOLOseg-Jujube is 0.2% and 0.3%, 2.7% and 2.4%, 0.6% and 0.4%, and 2.1% and 1.9% more accurate than YOLOv4-tiny, YOLOv5n, YOLOv7-tiny and YOLOv8n, respectively. Furthermore, the algorithms were evaluated for their real-time detection speed using video as an important aspect of performance. The findings demonstrated that YOLOseg-Jujube is faster than YOLOv4-tiny YOLOv5n, YOLOv7-tiny and YOLOv8n as indicated in Table 4. Therefore, the aggregated performance in terms of reduced computation cost, accuracy and speed indicated that the algorithm of YOLOseg-Jujube was better than YOLOv4-tiny YOLOv5n, YOLOv7-tiny and YOLOv8n. YOLOseg-Jujube is robust against changeable environment and capable of understanding the ripeness stages of jujube fruit targets in an image.

Table 4

Performance comparison of algorithms using valid-set and videos

Algorithm	Params	GFLOPs	B_P %	B_R %	B_ mAP%	S_P %	S_R %	S_ mAP%	Speed (fps)
YOLOv4-tiny	6.70	65.5	76.5	79.3	83.2	76.4	78.8	82.9	297
YOLOv5n	2.76	11.0	79.3	75.5	80.8	79.2	75.7	80.8	273
YOLOv7-tiny	9.55	69.9	81.0	76.0	82.9	81.3	76.0	82.8	230
YOLOv8n	3.26	12.0	79.5	75.7	81.4	79.3	75.6	81.3	272
YOLOseg-Jujube	2.49	11.3	80.1	77.7	83.5	80.4	77.2	83.2	323

To establish the superiority of YOLOseg-Jujube to YOLO-mainstream variants, the algorithms were evaluated on test-set images with (1) fruit occlusions, (2) fruit clusters, and (3) dense targets, and were subjected to an estimation of the area of targets. Fig. 6 shows that the algorithms were able to segment and estimate the area of targets according to their classes very well, but there were some differences in the area value, including missed and false detections. Using the (1) fruit occlusion image, Fig. 6(a–c) of YOLOv4-tiny, YOLOv5n and YOLOv7-tiny were noted with two false detections unlike Fig. 6(d–e) of YOLOv8n and YOLOseg-Jujube with one false detection. Each segmented target is not completely drawn in the occlusion situation, which results in only an estimation of its area. Future investigation is required.

For (2) fruit clusters, all the algorithms segmented and estimated area perfectly, except for the difference in area value. Nevertheless, the obtained aggregated area values for YOLOseg-Jujube of Fig. 6(e) are higher than YOLOv4-tiny of Fig. 6(a), YOLOv5n of Fig. 6(b), YOLOv7-tiny of Fig. 6(c) and YOLOv8n of Fig. 6(d). This indicated that YOLOseg-Jujube instance segmentation is more robust than the YOLO-mainstream variants. In the case of

(3) dense targets, missed detections was observed in Fig. 6(a–c), but no missed detection was found in Fig. 6(d) of YOLOv8n and Fig. 6(e) of YOLOseg-Jujube. With this area calculation performance, YOLOseg-Jujube is the best candidate for the analysis of fruit-related phenotypic traits, such as number, size, shape and color.



(a)



(b)



(c)



(d)



(e)

Fig. 6 - The segmented targets with area obtained from images of (1) fruit occlusions, (2) fruit clusters, and (3) dense fruit evaluated on (a) YOLOv4-tiny, (b) YOLOv5n, (c) YOLOv7-tiny, (d) YOLOv8n and (e) YOLOseg-Jujube

Furthermore, the developed YOLOseg-Jujube algorithm was evaluated and compared with YOLO-mainstream variants on low-power computing device.

Table 5 provides details of the exported ONNX and NCNN model deployed on mobile phone. Table 5 shows that ONNX's size and exported time of YOLOseg-Jujube is smaller than YOLOv4-tiny YOLOv5n, YOLOv7-tiny and YOLOv8n. This is in support of the claims in Table 4 that the complexity of YOLOseg-Jujube is reduced compared to YOLO-mainstream variants.

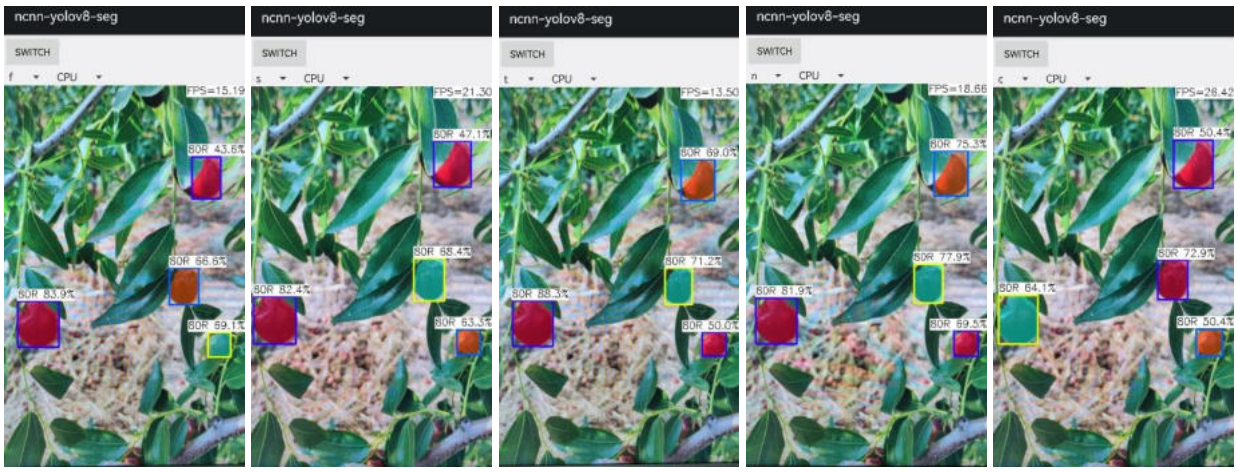
The obtained param and bin of the NCNN model also showed similar attributes, where the bin of YOLOseg-Jujube is 62.5%, 10.2%, 73.8% and 23.2% less than YOLOv4-tiny, YOLOv5n, YOLOv7-tiny and YOLOv8n, respectively. With reference to the displayed Fig. 7, the detection speed of algorithms was obtained. Subjecting the algorithms to real-time instance segmentation, a number of fruit targets were detected and segmented perfectly as shown in Fig. 6, but with a floating confidence score. Nevertheless, the real-time speed is very crucial to mobile phone.

Table 5 and Fig. 7(e) show that the real-time segmentation speed of YOLOseg-Jujube noted to be 26.24 fps is 73.9%, 24.0%, 95.7% and 41.6% faster than YOLOv4-tiny of Fig. 7(a), YOLOv5n of 7(b), YOLOv7-tiny of 7(c) and YOLOv8n of 7(d), respectively. This demonstrated that a decrease in bin results to an increase in speed. The obtained results also indicated that YOLOseg-Jujube is compatible and deployment friendly with low-power computing devices.

Table 5

Comparison of exported algorithms using simplified mode

ONNX	YOLOv4-tiny	YOLOv5n	YOLOv7-tiny	YOLOv8n	YOLOseg-Jujube
Add	3	7	–	6	–
BatchNormalization	3	–	–	–	–
Concat	13	19	20	19	22
Conv	59	87	85	75	66
Maxpool	3	3	6	3	2
Mul	47	78	76	66	57
Reshape	7	7	7	7	7
Resize	2	2	2	2	18
Sigmoid	47	78	76	66	57
Slice	–	–	–	8	4
Transpose	1	1	1	1	1
Size (MB)	25.6	10.5	36.5	12.5	9.5
Export (s)	10.7	8.9	8.3	3.9	3.4
NCNN					
Param (KB)	11.7	17.7	18.4	16.7	15.0
Bin (MB)	12.7	5.3	18.2	6.2	4.76
Speed (fps)	15.19	21.30	13.50	18.66	26.42



(a) (b) (c) (d) (e)

Fig. 7 - The output of fruit targets segmentation tested on a mobile phone using algorithm of (a) YOLOv4-tiny, (b) YOLOv5n, (c) YOLOv7-tiny, (d) YOLOv8n and (e) YOLOseg-Jujube

CONCLUSIONS AND FUTURE WORK

This paper explored the YOLOv8n based architecture to design YOLOseg-Jujube for fruit instance segmentation to consolidate fruit detection, including to solve the factors of complex environment faced by fruit detection. The ablation studies conducted on YOLOseg-Jujube resulted in the algorithm consisting of Focus, CBS, Conv4cat, SPD, and SPPFr as backbone network, and YOLOv8' head with SIoU loss as head network. The computation cost in terms of params show that YOLOseg-Jujube is 62.8%, 9.8%, 73.9%, and 23.6% less than YOLOv4-tiny, YOLOv5n, YOLOv7-tiny and YOLOv8n, respectively. Likewise, the 83.5% of B_mAP and 83.2% of S_mAP noted in YOLOseg-Jujube is 0.2% and 0.3%, 2.7% and 2.4%, 0.6% and 0.4%, and 2.1% and 1.9% more accurate than YOLOv4-tiny, YOLOv5n, YOLOv7-tiny and YOLOv8n, respectively. The real-time speed of YOLOseg-Jujube demonstrated to be faster than YOLOv4-tiny YOLOv5n, YOLOv7-tiny and YOLOv8n on computer with GPU-RTX3060 and mobile phone, including having to be the best candidate for the analysis of fruit-related phenotypic traits based on the conducted area calculation performance. The aggregated performance demonstrated that YOLOseg-Jujube is robust for generalization, low in computation cost, accurate, fast, flexible

for deployment on low-power computing devices, efficient and able to understand the ripeness stages of jujube fruit targets in an image and video. However, future investigations will require detection accuracy improvements, to solve each segmented target not completely drawn in the occlusion situation for proper area estimation, a simpler network topology, and the performance of other converted model format on mobile phones.

ACKNOWLEDGEMENTS

This research was funded by the Lvliang Key R&D Projects, grant number 2024NY03; The Basic Research Project of Shanxi Province, grant number 202103021223145 and College Student Innovation and Entrepreneurship Training Program, grant number 20-034.

REFERENCES

[1] Bin, Y., Pan, F., Xiaoyan, L., Zhijie, L., & Fuzeng, Y. (2021). A Real-Time Apple Targets Detection Method for Picking Robot Based on Improved YOLOv5. *Remote Sensing, 13*(9). https://doi.org/10.3390/rs13091619

[2] Bin, Z., Rongrong, W., Huiming, Z., Chenghai, Y., Yuyang, X., Meng, F., & Wei, F. (2022). Dragon fruit detection in natural orchard environment by integrating lightweight network and attention mechanism. *Frontiers in Plant Science, 13*. https://doi.org/10.3389/fpls.2022.1040923

[3] Bochkovskiy, A., Wang, C. Y., & Liao, H. (2020). YOLOv4: Optimal Speed and Accuracy of Object Detection. *arXiv preprint arXiv:2004.10934.* doi:https://doi.org/10.48550/arXiv.2004.10934:

[4] Borja, P. A. I., & Tofael, A. (2021). Real Time Pear Fruit Detection and Counting Using YOLOv4 Models and Deep SORT. *Sensors, 21*(14), 4803. https://doi.org/10.3390/s21144803

[5] Chan, Z., Pengfei, C., Jing, P., Xiaofan, Y., Changxin, C., Shuqin, T., & Yueju, X. (2021). A mango picking vision algorithm on instance segmentation and key point detection from RGB images in an open orchard. *Biosystems Engineering, 206*, 32-54. https://doi.org/10.1016/j.biosystemseng.2021.03.012

[6] Dandan, W., & Dongjian, H. (2022). Fusion of Mask RCNN and attention mechanism for instance segmentation of apples under complex background. *Computers and Electronics in Agriculture, 196*, 106864. https://doi.org/10.1016/j.compag.2022.106864

[7] Defang, X., Huamin, Z., Mubashiru, L. O., Xinyuan, L., Rui, R., & Shujuan, Z. (2023). An Automatic Jujube Fruit Detection and Ripeness Inspection Method in the Natural Environment. *Agronomy, 13*(2), 451. https://doi.org/10.3390/agronomy13020451

[8] Du, C., Wang, Y., Wang, C., Shi, C., & Xiao, B. (2020). Selective feature connection mechanism: Concatenating multi-layer CNN features with a feature selector. *Pattern Recognition Letters, 129*, 108-114. https://doi.org/10.1016/j.patrec.2019.11.015

[9] Elfwing, S., Uchibe, E., & Doya, K. (2017). Sigmoid-weighted linear units for neural network function approximation in reinforcement learning. *Neural Networks, 107*, 3-11. https://doi.org/10.1016/j.neunet.2017.12.012

[10] Fu, L., Feng, Y., Wu, J., Liu, Z., Gao, F., Majeed, Y., . . . Cui, Y. (2021). Fast and accurate detection of kiwifruit in orchard using improved YOLOv3-tiny model. *Precision Agriculture, 22*(3), 754-776. https://doi.org/10.1007/s11119-020-09754-y

[11] Gai, R., Li, M., & Chen, N. (2021). *Cherry detection algorithm based on improved YOLOv5s network*. Paper presented at the 2021 IEEE 23rd Int Conf on High Performance Computing & Communications; 7th Int Conf on Data Science & Systems; 19th Int Conf on Smart City; 7th Int Conf on Dependability in Sensor, Cloud & Big Data Systems & Application (HPCC/DSS/SmartCity/DependSys). https://ieeexplore.ieee.org/abstract/document/9780909

[12] Gevorgyan, Z. (2022). SIoU Loss: More Powerful Learning for Bounding Box Regression. *arXiv e-prints*, arXiv:2205.12740. https://ui.adsabs.harvard.edu/abs/2022arXiv220512740G

[13] He, K., Gkioxari, G., Dollár, P., & Girshick, R. (2017). Mask R-CNN. *arXiv e-prints*, arXiv:1703.06870. doi:10.48550/arXiv.1703.06870: https://ui.adsabs.harvard.edu/abs/2017arXiv170306870H

[14] Huang, M.-L., & Wu, Y.-s. (2023). GCS-YOLOV4-Tiny: A lightweight group convolution network for multi-stage fruit detection. *Mathematical biosciences and engineering : MBE, 20 1*, 241-268.

[15] Jinhai, W., Zongyin, Z., Lufeng, L., Huiling, W., Wei, W., Mingyou, C., & Shaoming, L. (2023). DualSeg: Fusing transformer and CNN structure for image segmentation in complex vineyard environment. *Computers and Electronics in Agriculture, 206*, 107682. https://doi.org/10.1016/j.compag.2023.107682

[16] Jocher, G., Chaurasia, A., & Qiu, J. (2023). ultralytics. https://github.com/ultralytics/ultralytics

[17] Jordi, G.-M., Mar, F.-F., Eduard, G., M., B. P., Jochen, H., Josep-Ramon, M., . . . Javier, R.-H. (2023). Looking behind occlusions: A study on amodal segmentation for robust on-tree apple fruit size estimation. *Computers and Electronics in Agriculture, 209*, 107854. https://doi.org/10.1016/j.compag.2023.107854

[18] Junyang, C., Hui, L., Yating, Z., Daike, Z., Hongkun, O., & Xiaoyan, C. (2022). A Multiscale Lightweight and Efficient Model Based on YOLOv7: Applied to Citrus Orchard. *Plants, 11*(23), 3260. https://doi.org/10.3390/plants11233260

[19] Kang, H., & Chen, C. (2020). Fruit detection, segmentation and 3D visualisation of environments in apple orchards. *Computers and Electronics in Agriculture, 171*, 105302. https://doi.org/10.1016/j.compag.2020.105302

[20] Koirala, A., Walsh, K. B., Wang, Z., & McCarthy, C. (2019). Deep learning for real-time fruit detection and orchard fruit load estimation: benchmarking of 'MangoYOLO'. *Precision Agriculture, 20*(6), 1107-1135. https://doi.org/10.1007/s11119-019-09642-0

[21] Lawal, O. M. (2021). Development of tomato detection model for robotic platform using deep learning. *Multimedia Tools and Applications, 80*(17), 26751-26772. https://doi.org/10.1007/s11042-021-10933-w

[22] Liu, G., Nouaze, J. C., Mbouembe, P. L. T., & Kim, J. H. (2020). YOLO-Tomato: A Robust Algorithm for Tomato Detection Based on YOLOv3. *Sensors, 20*(7), 2145. https://doi.org/10.3390/s20072145

[23] Liu, X., Zhao, D., Jia, W., Ji, W., Ruan, C., & Sun, Y. (2019). Cucumber Fruits Detection in Greenhouses Based on Instance Segmentation. *IEEE ACCESS, 7*, 139635-139642. https://ieeexplore.ieee.org/abstract/document/8843929

[24] Mubashiru, L. O. (2023). YOLOv5-LiNet: A lightweight network for fruits instance segmentation. *PloS one, 18*(3), e0282297. https://doi.org/10.1371/journal.pone.0282297

[25] Olarewaju M. Lawal. (2021). YOLOMuskmelon: Quest for Fruit Detection Speed and Accuracy Using Deep Learning. *IEEE ACCESS, 9*, 15221-15227. https://ieeexplore.ieee.org/abstract/document/9328755

[26] Peichao, C., Hao, F., Kunfeng, L., Jiachao, Z., & Shanda, L. (2023). MYOLO: A Lightweight Fresh Shiitake Mushroom Detection Model Based on YOLOv3. *Agriculture, 13*(2), 392. https://doi.org/10.3390/agriculture13020392

[27] Pengyu, C., Zhaojian, L., Kyle, L., Renfu, L., & Xiaoming, L. (2021). Deep Learning-based Apple Detection using a Suppression Mask R-CNN. *Pattern Recognition Letters*(147), 206-211. https://doi.org/10.1016/j.patrec.2021.04.022

[28] Redmon, J., & Farhadi, A. (2018). YOLOv3: An Incremental Improvement. *arXiv e-prints*, 1804.02767.

[29] Santos, T. T., Souza, L. L. d., Santos, A. A. d., & Avila, S. (2020). Grape detection, segmentation, and tracking using deep neural networks and three-dimensional association. *Computers and Electronics in Agriculture, 170*, 105247. https://doi.org/10.1016/j.compag.2020.105247

[30] Sunkara, R., & Luo, T. (2022). *No more strided convolutions or pooling: A new CNN building block for low-resolution images and small objects.* Paper presented at the Joint European conference on machine learning and knowledge discovery in databases.

[31] Tian, Y., Yang, G., Wang, Z., Li, E., & Liang, Z. (2020). Instance segmentation of apple flowers using the improved mask R–CNN model. *Biosystems Engineering, 193*, 264-278. https://doi.org/10.1016/j.biosystemseng.2020.03.008

[32] Wang, C.-Y., Bochkovskiy, A., & Liao, H.-Y. M. (2023). *YOLOv7: Trainable bag-of-freebies sets new state-of-the-art for real-time object detectors.* Paper presented at the Proceedings of the IEEE/CVF conference on computer vision and pattern recognition.

[33] Wang, Z., Walsh, K., & Koirala, A. (2019). Mango Fruit Load Estimation Using a Video Based MangoYOLO—Kalman Filter—Hungarian Algorithm Method. *Sensors, 19*(12), 2742. https://doi.org/10.3390/s19122742

[34] Wendong, G., Yakun, L., Jing, Z., & Gang, J. (2021). An improved Tiny YOLOv3 for real-time object detection. *Systems Science & Control Engineering, 9*(1), 314-321. https://doi.org/10.1080/21642583.2021.1901156

[35] Xiang, L., Chengqi, L., Wenhai, W., Gang, L., Lingfeng, Y., & Jian, Y. (2022). Generalized Focal Loss: Towards Efficient Representation Learning for Dense Object Detection. *IEEE transactions on pattern analysis and machine intelligence, 45*(3), 3139-3153. https://ieeexplore.ieee.org/abstract/document/9792391

[36] Yanchao, Z., Wenbo, Z., Jiya, Y., Leiying, H., Jianneng, C., & Yong, H. (2022). Complete and accurate holly fruits counting using YOLOX object detection. *Computers and Electronics in Agriculture, 198*, 107062. https://doi.org/10.1016/j.compag.2022.107062

[37] Yang-Yang, Zheng, Jian-Lei, Kong, Xue-Bo, Jin, . . . Zuo. (2019). CropDeep: The Crop Vision Dataset for Deep-Learning-Based Classification and Detection in Precision Agriculture. *Sensors, 19*(5), 1058. https://doi.org/10.3390/s19051058

[38] Yichen, Q., Yaohua, H., Zhouzhou, Z., Huanbo, Y., Kaili, Z., Juncai, H., & Jiapan, G. (2022). A Counting Method of Red Jujube Based on Improved YOLOv5s. *Agriculture, 12*(12), 2071. https://doi.org/10.3390/agriculture12122071

[39] Yunchao, T., Hao, Z., Hongjun, W., & Yunqi, Z. (2023). Fruit detection and positioning technology for a Camellia oleifera C. Abel orchard based on improved YOLOv4-tiny model and binocular stereo vision. *Expert Systems With Applications, 211*, 118573. https://doi.org/10.1016/j.eswa.2022.118573

[40] Zheng, Z., Wang, P., Liu, W., Li, J., Ye, R., & Ren, D. (2020). *Distance-IoU loss: Faster and better learning for bounding box regression.* Paper presented at the Proceedings of the AAAI Conference on Artificial Intelligence.

CLAM MEAT DETECTION ALGORITHM BASED ON IMPROVED YOLOv5s
/
基于改进 YOLOv5s 的蛤肉检测算法

Xinkai JIAO, Xiangcai ZHANG*), Zhongcai WEI, Xianliang WANG, Xiupei CHENG, Pingchuan MA
Shandong University of Technology, Institute of Modern Agricultural Equipment, ZiBo (255000), China
Tel: +86-15169235925; E-mail: zxcai0216@163.com

DOI: https://doi.org/10.35633/inmateh-76-52

Keywords: *machine vision; Ruditapes philippinarum; targeted detection; YOLO*

ABSTRACT

Intelligent and accurate shelling technology is essential for improving the quality of clam products. To enable the rapid and precise localization of clam meat in Ruditapes philippinarum (with half-shell) on an automated processing line, an improved clam meat detection algorithm - EET-YOLOv5, based on YOLOv5s - is proposed. This algorithm enables real-time detection and localization of clam meat on the production line. It integrates the Efficient Local Attention (ELA) mechanism to enhance target localization, adopts the EIoU loss function to reduce bounding box regression error, and replaces the original detection head with a TSCODE decoupled head to improve detection accuracy. The algorithm achieved a Precision of 93.03%, Recall of 97.03%, and mean Average Precision (mAP) of 93.55%, with a detection speed of 13.3 ms. Compared to YOLOv4, Faster R-CNN, SSD, and the standard YOLOv5 series, EET-YOLOv5 demonstrated superior performance. It was deployed on a test workbench for positioning experiments, achieving an average response time of 1.8 seconds and a positioning success rate of 92.7%, indicating its suitability for automated clam shell-meat separation production lines.

摘要

智能化、精确化的脱壳技术是提高蛤肉产品质量的关键。为了实现自动化加工生产线上对开半壳的菲律宾蛤仔中蛤肉的快速准确识别，提出了一种基于 YOLOv5s 改进而来的蛤肉检测算法（EET-YOLOv5），可以对生产线上的蛤肉进行实时定位识别。该算法融合 Efficient Local Attention（ELA）注意力机制，能够有效捕捉目标位置；采用 EIOU 损失函数，减少边界框回归损失；使用 TSCODE 解耦头替换原有检测头，提高检测准确率。该算法检测蛤肉的精确率、召回率和平均精度均值分别达到 93.03%，97.03%，93.55%，检测速度达到 13.3ms。将其与 YOLOv4、Faster-RCNN、SSD 和 YOLOv5 系列等算法比较具有明显优势。将其部署在实验台上进行定位试验，平均耗时 1.8 秒，成功率 92.7%，适用于自动化蛤仔壳肉分离生产线。

INTRODUCTION

As a bivalve shellfish with low farming cost and short cycle time, Philippine clams (*Ruditapes philippinarum*) are widely farmed worldwide for their high food and medicinal values (*Chang et al., 2007*). Global production exceeds 3 million tons annually (*Lin et al., 2022*), and this large volume has driven continuous advancements in its processing technology. Shell-flesh separation is an important part of Ruditapes philippinarum processing (*Zhao et al., 2023*). Manual shelling is time-consuming and laborious, so automatic shelling technology has emerged. The traditional automatic shell-meat separation method is mainly based on thermal shelling and mechanical shelling. Thermal shelling involves heating shellfish at high temperatures to inactivate or denature the adductor muscle fibers, thereby enabling the separation of the meat from the shell. In contrast, mechanical shelling uses mechanical methods to open the shell and extract the meat without the need for heat treatment, resulting in a fresher product. However, most current mechanical shelling methods suffer from limitations such as low accuracy and complex shell-clamping mechanisms, which hinder production efficiency. Additionally, thermal shelling significantly compromises the freshness of the shellfish, making it unsuitable for meeting market demands (*Zhang et al., 2013)*.

With the development of intelligent technology, the target detection network plays a key role in shellfish processing. Wang Haifeng proposed a new shellfish recognition algorithm, which uses Gabor filter combined with 2D PCA to extract shellfish image features. The average correct recognition rate of this method on the self-made data set reaches 96.7 % (*Wang et al., 2016*). *Feng Yiran et al., (2022)*, developed a shellfish recognition algorithm based on Faster R-CNN. DenseNet was used instead of the feature extraction module to fuse features at different levels, and the NMS algorithm was optimized to overcome the problems of shellfish overlap and omission, and the shellfish classification accuracy was improved by 4 %.

Zhang Yang et al., (2022), proposed the FCnet algorithm for accurate detection and recognition of multi-target shellfish. He added the AttResNet101 backbone network containing the multi-spectral channel attention mechanism to the DeFCN network to obtain rich information of the original features, and improved the feature extraction module to improve the accuracy of small target recognition. *Dong Zhaopeng et al., (2023),* used the CST-YOLOv5 algorithm to identify mussels, and the mAP index was improved by 1.583% compared with the original algorithm. *Yu Zhe et al., (2025),* developed a freshwater snail detection algorithm based on YOLOv8-OBB, which effectively improved the detection accuracy for small targets, and the mAP0.5 reached 80.6 %. *Liu Zhenlong et al., (2025),* used the YOLOv10-MECAS algorithm to identify sea cucumbers, effectively overcoming the problem of low underwater visibility. On their custom dataset, the algorithm achieved a mAP@0.5 of 90.4%.

Intelligent processing is the key technology to improve the production efficiency and product quality of shellfish. For the Ruditapes philippinarum, the clams that have been opened on the production line can be dynamically monitored in real time to accurately locate the clam meat and guide the clamping device to take it out, thereby improving the success rate of shell meat separation and ensuring the freshness of the clam meat. Therefore, a target detection network based on YOLOv5s is designed to detect clam meat on the production line and provide accurate positioning for the intelligent clamping device.

MATERIALS AND METHODS

Image acquisition

Shelled clams (Ruditapes philippinarum) were photographed, and the captured images were processed and used for training the network model. The images were taken in the Marine Products Processing Laboratory of Shandong University of Technology. The clams used in this study had naturally grown for 16 months after sowing. To replicate conditions on a processing line, the clams were placed naturally on a small conveyor belt with the shell openings facing upward. The clams were neither fixed in position nor stacked. To ensure diversity in the dataset, images were captured from various angles, distances, and under different lighting conditions. A smartphone was used as the imaging device. A total of 857 images were taken at a resolution of 4096 × 3072 pixels, from which 775 images were selected after screening. A sample of the collected clam meat images is shown in Figure 1.

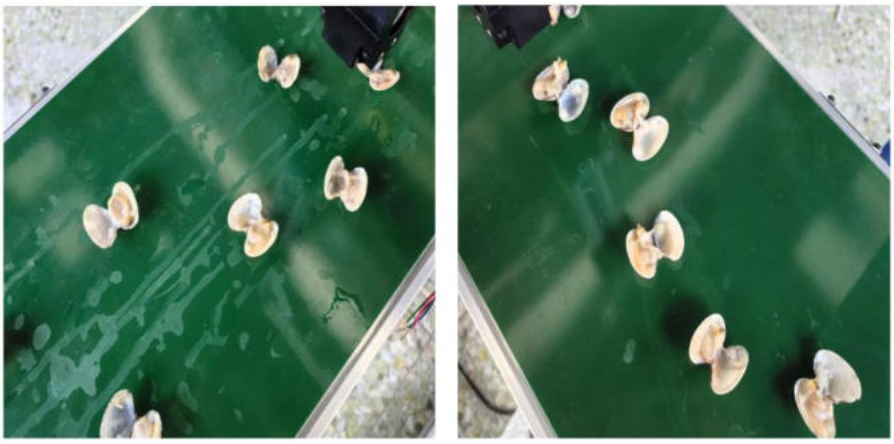


Fig. 1 - Part of the clam meat image collected

Data preprocessing and dataset construction

Before training the target detection network, the captured image data were preprocessed to construct a usable dataset. The LabelImg tool was used to annotate the location of clam meat targets by drawing bounding boxes. The corresponding location information was saved in TXT annotation files, and both the images and annotations were organized into a standard YOLO-format dataset. Since the manually captured images lacked sufficient scene complexity and quantity for effective model training, data augmentation was applied to expand and diversify the dataset. Augmentation techniques included random rotation, scaling, aspect ratio adjustment, contrast enhancement, and the addition of Gaussian noise. The final dataset consisted of 2,300 images, with 150 images designated as the test set. The remaining 2,150 images were randomly divided into a training set and a validation set at an 8:2 ratio, resulting in 1,720 training samples and 430 validation samples.

YOLOv5 algorithm

YOLOv5 is a single-stage object detection algorithm developed as an improvement over previous models in the YOLO series, particularly YOLOv4. In the input stage, YOLOv5 incorporates Mosaic data augmentation and an adaptive anchor box mechanism, which significantly enhance the detection performance, especially for small targets. The overall structure of YOLOv5 is illustrated in Figure 2.

In the backbone network, the CSP structure is employed to reduce the number of parameters. The SPPF module is integrated to improve the detection of objects at varying scales without compromising inference speed. In the neck, the FPN combined with PAN enables effective multi-scale feature fusion and target localization. With its high detection accuracy and low deployment cost, YOLOv5 is well-suited for rapid deployment on mobile and embedded devices. Therefore, it was selected as the base algorithm for target detection in this study.

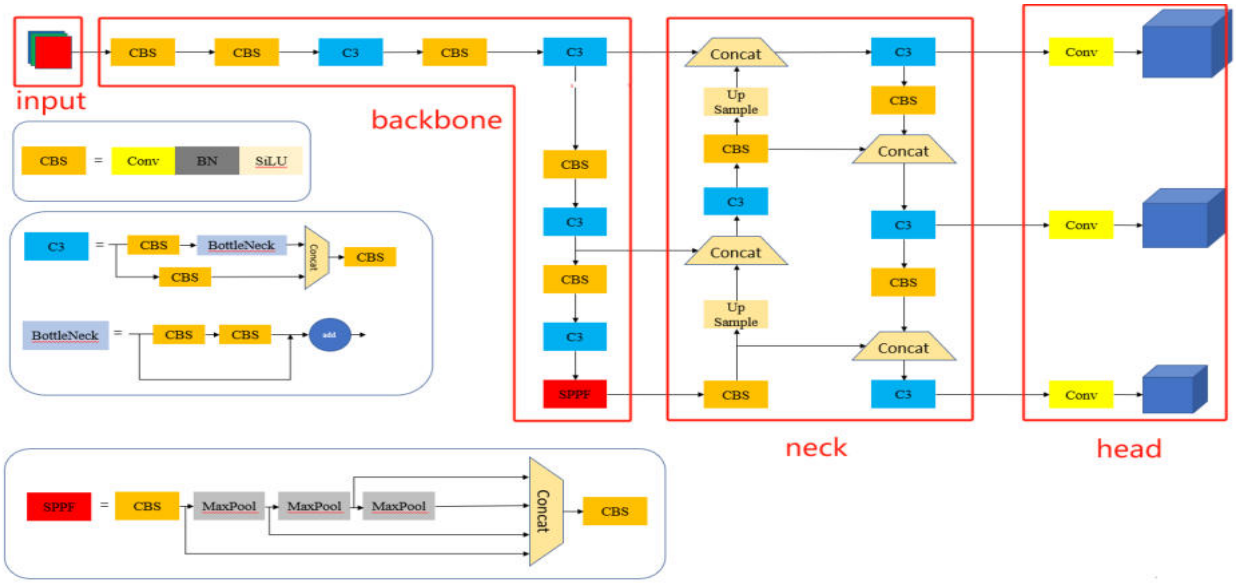


Fig. 2 - YOLOv5 network architecture diagram

Conv denotes the convolution operation; BN is normalization operation; SiLU is the Sigmoid Linear Unit activation function; Concat represents channel-wise concatenation and Add indicates element-wise addition

ELA attention mechanisms

Attention mechanisms enable networks to focus on meaningful parts of images. The attention mechanism can act on two dimensions of channel and space, namely channel attention and spatial attention. Common attention mechanisms include SEnet (*Hu et al., 2019*), ECA (*Wang et al., 2020*), CBAM (*Woo et al., 2018*), CA (*Hou et al., 2021*), ELA (*Xu et al., 2024*), etc.

In this study, the focus is on the localization of clam meat, which exhibits an irregular shape and a yellowish color after the shell is opened. Under varying lighting conditions, the clam meat often shares a similar color with the inner surface of the shell, making accurate localization challenging. To address this, it is crucial to minimize channel information loss during the extraction of spatial and channel features in order to obtain a clearer target contour. To achieve this, the Efficient Local Attention (ELA) module is introduced to enhance feature map processing and preserve critical information for more accurate contour detection.

ELA performs pooling operations along the width and height dimensions of the input tensor to extract global features in both directions. These features preserve both channel and spatial information, aiding the neural network in accurately locating target coordinates. Additionally, the pooling mechanism provides a global receptive field, enabling the establishment of long-range dependencies between elements. To further refine feature extraction while maintaining computational efficiency, one-dimensional convolution is applied. This approach ensures effective feature representation without reducing the number of channels.

GroupNorm is applied to normalize data batches (*Wu et al., 2018*), effectively mitigating the problem of vanishing gradients and enhancing the generalization capability of the network. Using the Sigmoid activation function, directional weight coefficients are computed and subsequently multiplied with the input feature map to refine the feature representation. Integrating the ELA module before the SPPF structure enables more accurate localization of regions of interest and improves the network's feature learning capacity. The architecture of this structure is illustrated in Figure 3.

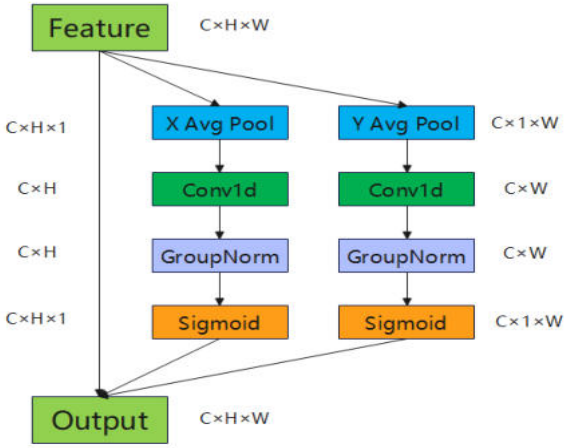


Fig. 3 - ELA attention mechanism architecture diagram.
X,Y Avg Pool is average pooling operation along the X and Y directions; Conv1d is one-dimensional convolution operation; GroupNorm is group normalization layer; Sigmoid is the sigmoid activation function

The ELA attention mechanism is calculated as follows:

$$Z_c^h(h) = \frac{1}{W}\sum_{0\le i<W} x_c(h,i) \quad (1)$$

$$Z_c^w(w) = \frac{1}{H}\sum_{0\le j<H} x_c(j,w) \quad (2)$$

$$y^h = \delta\left(G_n\left(F_h(z^h)\right)\right) \quad (3)$$

$$y^w = \delta\left(G_n\left(F_w(z^w)\right)\right) \quad (4)$$

$$Y = x_c \times y^h \times y^w \quad (5)$$

Here, $Z_c^h(h)$ is the pooled output of the c th channel at height h. W is the Width of input features. $x_c\,(i,j)$ is the elements at (i,j) in channel c. $Z_c^w(w)$ is the pooled output of the c-th channel at width w. H is the Width of input features. z^h is the characteristic map after pooling in the vertical direction. F_h is One-dimensional convolution in the vertical direction. G_n is grouping normalization. δ is sigmoid activation function. y^h is the vertical attention weights. z^w is the characteristic map after pooling in the vertical direction. F_w is One-dimensional convolution in the vertical direction. y^w is the vertical attention weights. Y is the output result.

Loss function optimization

The loss function is the core of the deep learning parameter optimization process. The model parameters are adjusted by minimizing the loss function to improve the prediction accuracy and generalization ability of the model. The loss function mainly considers the influence factors such as Euclidean distance, intersection over union and aspect ratio between the real box and the prediction box. The most widely used loss functions are GIOU (*Rezatofighi et al., 2019*), CIOU (*Zheng et al., 2020*), and SIOU (*Gevorgyan, 2022*), etc. The original network of YOLOv5 uses CIOU as the loss function. CIOU considers the overlap area, distance and aspect ratio of the predicted box and the ground truth box. However, the penalty term on the aspect ratio does not take into account the same aspect ratio of the two frames and the increase and decrease of the aspect gradient at the same time.

Therefore, this paper introduces EIOU to address this issue, which overcomes the limitations of conventional IoU-based losses by decomposing the aspect ratio penalty into two separate components - height and width - and calculating them independently. This approach enhances detection accuracy and accelerates network training. The EIoU loss is calculated as follows:

$$EIOU = IOU - \frac{\rho^2(b,b^{gt})}{(h^c)^2+(w^c)} - \frac{\rho^2(h,h^{gt})}{h^c} - \frac{\rho^2(w,w^{gt})}{w^c} \quad (6)$$

$$L_{EIOU} = 1 - EIOU \quad (7)$$

Here, IOU is the intersection over union of ground truth box and predicted box. h,h^{gt} is the height of gt-box (ground truth box) and p-box (predicted box). w,w^{gt} is the Width of gt-box and p-box. $\rho(b,b^{gt})$ is the Euclidean distance between the gt-box and p-box, and h^c, w^c is the height and width of the smallest external rectangle. L_{EIOU} is the Value of EIOU's losses.

Detection head improvement

Clam meat detection falls under the category of small target detection, with irregular and indistinct edges. Therefore, high localization accuracy is essential, and the TSCODE decoupled head is employed to enhance target detection performance. The YOLOv5 original network structure uses a coupled detection head to complete the classification and positioning tasks of the target at the same time. However, for some feature regions, there are rich semantic features inside and a lot of boundary texture on the boundary. The classification task needs to pay attention to the internal position, while the positioning task needs to pay attention to the boundary position. There is a conflict between the two requirements. If the same feature map is used, spatial misalignment may occur, affecting the positioning accuracy (*Song et al., 2020; Wu et al.,2020*). The TSCODE decoupled header enables the two to be performed separately. It uses the Semantic Context Encoding (SCE) module to generate feature encoding containing high semantic information, and Detail Preserving Encoding (DPE) to provide high-resolution feature maps containing edge information to perform the classification and localization tasks respectively. Its structure is shown in Fig. 4.

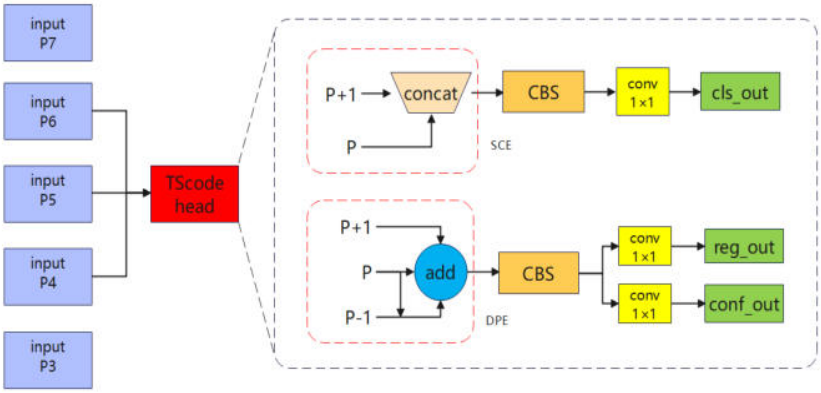


Fig. 4 - TSCODE decoupled head architecture diagram.

SCE is Semantic context encoding operation; DPE is Detail preserving encoding operation; cls_out is the classification results; reg_out is the Predicted Bounding Box location and size information; conf_out is the confidence for predicted bounding box

Set up the experimental platform

A test rig was constructed to verify the real-world deployment performance of the proposed algorithm. The test system consists of a small conveyor, a gantry-type test rig, an XY linear synchronous belt, a binocular camera, an Arduino control board, and a laser emitter. To accurately analyze the spatial relationship between the laser emitter and the clam meat, multiple coordinate systems were established: O_A at the position of the shell meat, O_B at the position of the laser emitter, O_C at the position of the binocular camera, and O_W at the base of the test bench. The configuration of the experimental setup and coordinate systems is illustrated in Fig. 5.

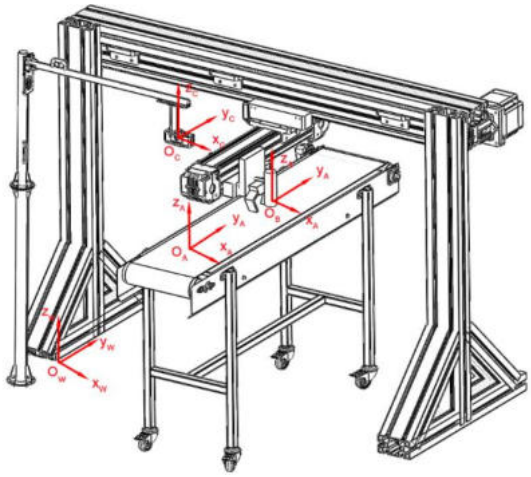


Fig. 5 - Test rig schematic diagram

RESULTS

Experimental environment

The core processor (CPU) used in this test was Intel I7-11700K, and the graphics card was NVIDIA RTX A4000 24G. The operating system was Win11, The deep learning framework was built using PyTorch 1.8.1, CUDA 11.1, and TensorFlow 2.4.1, with Python 3.8.19 as the programming language. At the beginning of training, the input image size was set to 640 * 640, the training was optimized by SGD, the maximum number of iterations was set to 1200 rounds, the batch_size was set to 8, and the maximum learning rate was set to 0.001. The cosine annealing learning rate adjustment algorithm was used to dynamically adjust the learning rate, so as to accelerate the convergence speed of the model and enhance the generalization ability of the model.

Evaluation indicators

To assess the model's real-world performance, several evaluation indicators are used, including Precision (P), Recall (R), mean Average Precision (mAP), number of model parameters, box loss (box_loss), and object loss (obj_loss). The calculation formulas are as follows:

$$P = \frac{TP}{TP + FP} \times 100\% \tag{8}$$

$$R = \frac{TP}{TP + FN} \times 100\% \tag{9}$$

$$AP = \int_0^1 P(R)dR \tag{10}$$

$$mAP = \frac{\sum AP}{N} \tag{11}$$

Here, TP (True Positives) represents the number of samples that were correctly rejected, FP (False Positives) represents the number of incorrectly rejected samples. FN represents the number of samples that were missed, AP represents the average precision of the model's assessment of a class of targets and mAP represents the mean accuracy of all categories of targets.

Box_loss represents the error between the ground truth box and the predicted box.

Obj_loss represents the probability of error in the model's judgement of the presence or absence of an object in the predicted box.

Comparison of ablation experimental performance

To evaluate the impact of individual improvements on the target detection performance, ablation experiments were conducted using YOLOv5s as the baseline model. Three components were tested: the ELA attention mechanism, the SIoU loss function, and the TSCODE decoupled head. Each component was added separately to the baseline, and then all were integrated to form the final improved YOLOv5s model. The results of the ablation experiments are summarized in Table 1, where "√" indicates that the corresponding component was applied, and "—" indicates that it was not.

Table 1

Results of the ablation experiment

ELA	EIOU	TSCODE	Precision	Recall	mAP_0.5*
			[%]	[%]	[%]
—	—	—	91.98	94,46	91.66
√	—	—	91.92	94.81	91.70
—	√	—	92.16	95.78	92.48
—	—	√	92.50	96.51	92.57
√	√	√	93.03	97.03	93.55

Note: * mAP_0.5 is the mean average precision of each category when the Intersection over Union threshold is 0.5

It can be observed from Table 1 that adding the ELA attention mechanism alone results in a change of -0.06% in Precision, and slight improvements of 0.35% in Recall and 0.04% in mAP. When the SIoU loss function is applied individually, the three indicators increase by 0.18%, 1.32%, and 0.82%, respectively.

The introduction of the TSCODE decoupled head alone leads to improvements of 0.52% in Precision, 2.05% in Recall, and 0.91% in mAP.

When the modalities for improvement are combined, the accuracy rate of the improved YOLOv5s model reaches 93.03 %, the recall rate is 97.03 %, and the mAP value is 93.55 %. Compared with YOLOV5s, it increased by 1.05 %, 2.57 % and 1.89 % respectively.

The results demonstrate that the use of the TSCODE detection head, which decouples classification and localization tasks, effectively prevents mutual interference between the two and significantly enhances detection accuracy. The SIoU loss function improves the convergence behavior of the detection frame. While the ELA attention mechanism enhances Recall, it causes a slight decrease in Precision. The most notable performance improvement is achieved when all three components are combined, yielding results that outperform the original YOLOv5s algorithm. Accordingly, the improved model is named EET-YOLOv5.

Performance comparison of YOLOv5 algorithms for different sizes

To evaluate whether the improved model maintains high detection accuracy while remaining lightweight, a performance comparison was conducted against more complex models from the YOLOv5 series. All models were tested under identical conditions. The comparison results are presented in Table 2.

Table 2

Comparative experimental results

Model	Precision	Recall	mAP_0.5	Model parameter quantity	Detection speed
	[%]	[%]	[%]	[M]	[ms]
EET-YOLOv5	93.03	97.03	93.55	11.62	13.3
YOLOv5m	95.92	96.72	93.32	21.23	14.4
YOLOv5l	92.03	95.73	89.83	46.51	20.8
YOLOv5x	96.01	95.81	95.01	86.77	39.5

Analysis of the results in the table shows that the average accuracy of EET-YOLOV5 is 0.23% higher than YOLOv5m and 1.46% lower than YOLOv5x. The number of model parameters is 54.7%, 25%, and 13.4% of the YOLOv5m, YOLOv5l, YOLOv5x, respectively. And the detection speed is 1.1 ms, 7.5 ms, and 26.2 ms faster than the three, respectively.

Based on the results, it can be seen that the EET-YOLOv5 algorithm exceeds the detection accuracy of YOLOV5m, approaches the detection accuracy of YOLOv5x, and has an advantage in detection speed, despite having fewer parameters. Its application in clam meat detection scenarios can ensure the detection accuracy while achieving model lightweight.

Performance comparison of different target detection models

In order to prove the superiority of EET-YOLOv5 algorithm, it is compared with other algorithms. Table 3 shows the performance parameters of the four networks.

Table 3

Comparative experimental results

Model	Precision	Recall	mAP_0.5	Model parameter quantity	Detection speed
	[%]	[%]	[%]	[M]	[ms]
EET-YOLOv5	93.03	97.03	93.55	11.62	13.3
YOLOv4	86.47	91.20	91.13	61.05	14.1
Faster-RCNN	88.50	90.24	89.06	63.09	52.9
SSD	81.31	86.78	81.43	10.71	8.4

Analysis of the data in the table shows that the average accuracy of EET-YOLOv5 is improved by 2.42%,4.49%,12.12% compared to YOLOv4, Faster-RCNN and SSD, respectively. The number of model parameters is 19.0%, 18.4% and 108.4% of the three, respectively. The detection speed is improved by 0.8 ms, 39.6 ms and decreased by 4.9 ms over SSD compared to the former two respectively.

The analysis based on the results is as follows:

1) Compared with YOLOv4, YOLOv5 applies the CSP structure more widely in Backbone and Neck modules, and can calculate the anchor frame size automatically, which improves the detection speed and reduces the model parameters while guaranteeing the accuracy, and the improved EET-YOLOv5 has a greater improvement in accuracy.

2) Faster-RCNN as a two-stage detection algorithm, has a significantly lower detection speed than EET-YOLOv5, which is a single-stage detection algorithm. Since the detection algorithm proposed in this study is intended for use on a dynamically operating production line, real-time performance is critical. The low detection speed of Faster R-CNN would negatively impact production efficiency, making it unsuitable for this application scenario.

3) The lightweight detection algorithm SSD demonstrates advantages over EET-YOLOv5 in terms of fewer parameters and faster detection speed. However, its detection accuracy is significantly lower than that of EET-YOLOv5.

To sum up, EET-YOLOv5 is more suitable for clam meat detection. The comparison of average precision across different models is illustrated in Figure 6.

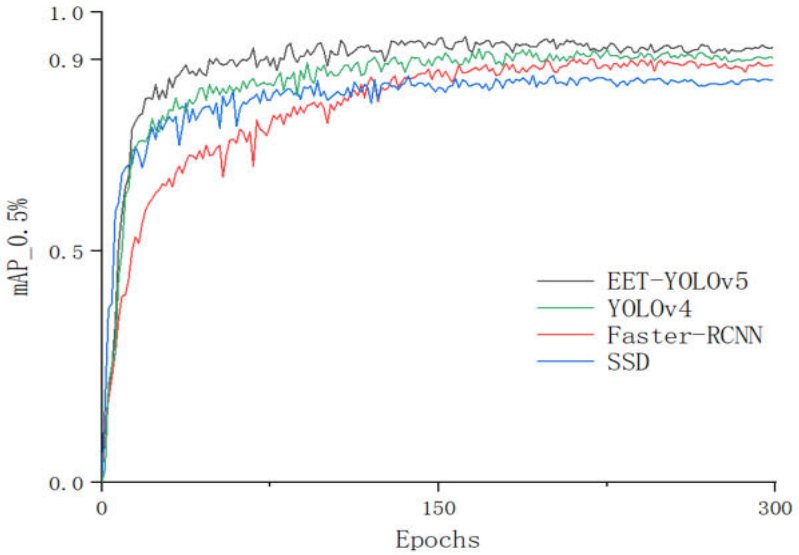


Fig. 6 - Mean average precision (mAP) curves of different target detection algorithms

Epochs is the number of training rounds

To provide a more intuitive comparison, the detection results of the four target detection algorithms on the same test set are visualized. The results are presented in Figure 7.

EET-YOLOv5





Fig. 7 - Results from various object detection networks

As shown in Figure 7, panels A and B represent detection results under normal illumination conditions. Under these conditions, YOLOv4 and SSD exhibit both missed and false detections, along with low confidence scores. While Faster R-CNN and EET-YOLOv5 successfully detect all targets, the confidence scores produced by Faster R-CNN are lower than those of EET-YOLOv5. Panel C shows detection performance under simulated strong indoor lighting. In this scenario, all detection networks except EET-YOLOv5 fail to detect one or more targets. EET-YOLOv5 successfully detects all clam meat instances with higher confidence than the other models. These comparative experiments demonstrate that EET-YOLOv5 achieves the best overall performance across varying lighting conditions. However, the experiments also revealed that in a few cases where clams were severely damaged during shelling, EET-YOLOv5 missed detections due to irregular shapes of the clam meat. This issue may be addressed by improving the shell-opening method and further optimizing the target detection network.

Workbench experiment

To validate the real-world deployment effectiveness of the proposed algorithm, a workbench experiment was conducted for clam meat positioning. A test bench was constructed, where a binocular vision system was used to capture the position parameters of the clam meat. Based on the detected coordinates, the system calculated the movement parameters for the XY synchronous belt, guiding a laser emitter to align precisely above the target. Successful laser irradiation of the clam meat indicated accurate positioning.

The experiment was conducted in the Marine Products Processing Laboratory at Shandong University of Technology. The setup is shown in Figure 8. A total of 120 positioning trials were carried out, achieving an average positioning time of 1.8 seconds and an average success rate of 92.7%, demonstrating the system's feasibility for practical application.

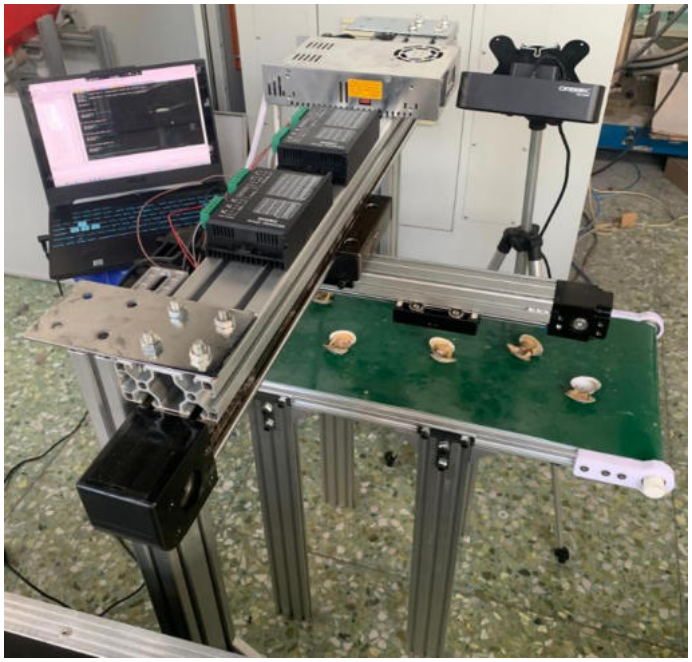


Fig. 8 - Workbench experiment

CONCLUSIONS

Intelligent shelling technology plays a key role in maintaining the freshness of clam meat while improving the efficiency of shell-meat separation, and it represents a promising development direction for the processing of *Ruditapes philippinarum*. In this study, an improved target detection network - EET-YOLOv5, based on YOLOv5 - was proposed for identifying clam meat on an automatic shelling production line.

Several enhancements were introduced to the original YOLOv5s architecture. The Efficient Local Attention (ELA) mechanism was added to the backbone network to suppress irrelevant information and enhance feature learning. The original CIoU loss function was replaced with the EIoU loss function to improve detection accuracy and network training speed. Additionally, the original detection head was replaced with the TSCODE decoupled head to improve both localization precision and classification accuracy. Ablation and comparative experiments were conducted to validate the effectiveness of these improvements. On a custom dataset, the proposed EET-YOLOv5 network achieved 93.03% precision, 97.03% recall, 93.55% mean average precision (mAP), and a detection speed of 13.3 ms, while maintaining high detection accuracy under varying lighting conditions. The main source of false detections was attributed to clam meat deformation caused by shelling, which can be addressed by improving the shell-opening process. The algorithm was deployed on a physical test bench for real-world positioning experiments, achieving an average positioning time of 1.8 seconds and a success rate of 92.7%. Although the model complexity of EET-YOLOv5 is slightly higher than that of the original YOLOv5s, the improvement in detection performance is substantial. Compared to other mainstream detection algorithms such as YOLOv4, Faster R-CNN, SSD, and models in the YOLOv5 series, EET-YOLOv5 shows clear advantages and is capable of meeting the demands of clam meat detection in production environments.

REFERENCES

[1] Chang Y.Q., (2008). *Shellfish enhancement* (水产养殖). China Agriculture Press., Chaoyang District, China.

[2] Dong Z. P., Yue X. X., Tian Z. X., Hou S.F., & Jiang L.S., (2023). Mussel detection algorithm based on YOLO (基于 YOLO 的贻贝检测算法). *Journal of Shanghai Ocean University. 32(5)*, 1015-1023. DOI：10.12024/ sou.20230604238

[3] Feng Y. R., Zhang X. D., & Tao X. H., (2022). Recognition and Detection of Shellfish Based on Improved Faster R-CNN（基于改进的 Faster R-CNN 贝类识别检测）. *Journal of Dalian Polytechnic University. 41(3)*, 208-213. DOI：10.19670/j.cnki.dlgydxxb.2022.0311

[4] Gevorgyan Z., (2022). SIoU loss: More powerful learning for bounding box regression. *arXiv:*2205.12740. DOI：10.48550/arXiv.2205.12740

[5] He K., Zhang X., Ren S., & Sun J., (2015). Spatial pyramid pooling in deep convolutional networks for visual recognition. *IEEE transactions on pattern analysis and machine intelligence. 37(9)*, 1904-1916. DOI: 10.1109/TPAMI.2015.2389824

[6] Hou Q., Zhou D., & Feng J., (2021). Coordinate attention for efficient mobile network design. *IEEE/CVF conference on computer vision and pattern recognition.* pp. 13713-13722. DOI: 10.48550/arXiv.2103.02907

[7] Hu J., Shen L., Albanie S., Sun G., & Wu E., (2019). Squeeze-and-Excitation Networks. *IEEE Transactions on Pattern Analysis and Machine Intelligence. 42(8)*, 2011-2023. DOI: 10.1109/TPAMI.2019.2913372

[8] Liu S., Qi L., Qin H., Shi J., & Jia J., Path aggregation network for instance segmentation. *IEEE conference on computer vision and pattern recognition*. pp. 8759-8768. DOI: 10.48550/arXiv.1803.01534

[9] Lin T. Y., Dollár P., Girshick R., He K., Hariharan B., & Belongie S., (2017). Feature pyramid networks for object detection. *IEEE conference on computer vision and pattern recognition.* pp. 2117-2125. DOI: 10.48550/arXiv.1612.03144

[10] Liu Z L., Wang J., & Mai R G., (2025). Detecting underwater sea cucumber in marine ranching using improved YOLOv10s. *Transactions of the Chinese Society of Agricultural Engineering. 41 (10):* 186-194. DOI: 10.11975/j.issn.1002-6819.202412109.

[11] Rezatofighi H., Tsoi N., Gwak J., Sadeghian A., Reid I., Savarese S., (2019). Generalized intersection over union: A metric and a loss for bounding box regression. IEEE/CVF conference on computer vision and pattern recognition. pp. 658-666.

[12] Song G., Liu Y., & Wang X., (2020). Revisiting the sibling head in object detector. *IEEE/CVF conference on computer vision and pattern recognition.* pp. 11563-11572. DOI:10.48550/arXiv.2003.07540

[13] Wang H. F., & Zhang K., (2016). Research on Shellfish Image Classification Algorithm based on Gabor Features. *The Journal of New Industrialization*. 6(2):59-62.

[14] Wang Q., Wu B., Zhu P., Li P., Zuo W., Hu Q., (2020). ECA-Net: Efficient channel attention for deep convolutional neural networks. IEEE/CVF conference on computer vision and pattern recognition. pp. 11534-11542.

[15] Wu Y., Chen Y., Yuan L., Liu Z., Wang L., Li H., & Fu Y., (2020). Rethinking classification and localization for object detection. *IEEE/CVF conference on computer vision and pattern recognition.* pp. 10186-10195. DOI:10.48550/arXiv.1904.06493

[16] Wu Y., & He K., (2018). Group normalization. *European conference on computer vision (ECCV).* pp. 3-19. DOI:10.48550/arXiv.1803.08494

[17] Woo S., Park J., Lee J. Y., & Kweon I. S., (2018). Cbam: Convolutional block attention module. *European conference on computer vision (ECCV)*. pp. 3-19. DOI:10.48550/arXiv.1807.06521

[18] Xing C., An Y., Chen J., Kong J. Y., & Liu G. Z., (2021). Marine Stewardship Council's strategy and practice of enhanced fisheries: Taking Ruditapes philippinarum fishery as a case study. *Fishery Information and Strategy. 36(4)*, 245-251.

[19] Xu W., & Wan Y., (2024). ELA: Efficient local attention for deep convolutional neural networks. *arXi,* 2403.01123. DOI: 10.48550/arXiv.2403.01123

[20] Yu Z., Wen L T., & Sun J., (2025). Dense small target detection algorithm for freshwater snails based on improved YOLOV8-OBB. *Acta hydrobiologica sinica.* 1-12 (2025-07-16). DOI: 10.7541/2025.2024.0497

[21] Zhang J., Yi J. G., Jiang H. Y., Wang J. Z., & Liu J. T., (2013). Shelling technique optimization of scallop by steam (蒸汽处理扇贝的剥壳技术优化). *Guangdong Agricultural Sciences. 40(14)*, 120-122.

[22] Zhang Y., Yue J., Jia S. X., Li Z. B., & Sheng G.R., (2022). Recognition of Shellfish Based on Visible Spectrum and Convolutional Neural Network (基于卷积神经网络的贝类识别方法研究). *Spectroscopy and Spectral Analysis. 42(10)*, 3298-3306.

[23] Zhao Y., Zhu X., Zhao J. B., & Fang G. A., (2024). Research Progress on Shell-Meat Separation Technology of Shelled Aquatic Products: A Review (带壳类水产品的壳肉分离技术研究进展). *Journal of Dalian Ocean University. 38(6)*, 1083. DOI:10. 16535/ j. cnki. dlhyxb. 2023-059

[24] Zheng Z., Wang P., Liu W., Li J., Ye R., & Ren D., (2020). Distance-IoU loss: Faster and better learning for bounding box regression. *AAAI conference on artificial intelligence. 34(07)*, 12993-13000. DOI:10.1609/aaai.v34i07.69

ANALYSIS OF THE CURRENT STATE OF RESEARCH WORLDWIDE ON SYSTEMS DESIGNED FOR IRRIGATION OF AGRICULTURAL CROPS
/
ANALIZA STADIULUI ACTUAL DE CERCETARE, PE PLAN MONDIAL, A SISTEMELOR DESTINATE IRIGĂRII CULTURILOR AGRICOLE

Dragos Mihail PREDA[1)], Adrian PANDELE*[1)], Bogdan Ovidiu DURAN[1)], Iuliana GAGEANU[2)], Gheorghe VOICU*[1)]
[1)]National University of Science and Technology POLITEHNICA Bucharest, Romania
[2)] INMA Bucharest - National Institute for Research and Development for Agricultural Machinery, Romania
Tel: +40 749998542, E-mail: dragospreda@yahoo.com; ghvoicu_2005@yahoo.com

DOI: https://doi.org/10.35633/inmateh-76-53

Keywords: *irrigation, energetic, independent, system, green energy*

ABSTRACT
This paper presents a comprehensive analysis of the global state of research and technological advancements in irrigation systems for agricultural crops, with a focus on the development of an energy-independent subsystem designed by the authors – SEMSI (Self-sustaining Energy Mobile Subsystem for Irrigation). SEMSI operates using renewable energy sources such as solar and wind power and is intended for use in areas lacking access to the electrical grid but with available water resources. To support the conceptualization and future optimization of this subsystem, the study outlines key principles of irrigation, reviews existing technologies and their performance, and analyses the functionality of both traditional and modern irrigation systems, including gravity, sprinkler, and drip methods. This documentation lays the groundwork for further development of the SEMSI system and serves as a reference base for theoretical modeling and experimental validation in future research stages.

REZUMAT
Lucrarea prezintă o analiză cuprinzătoare a stadiului actual al cercetării și al progreselor tehnologice la nivel global în domeniul sistemelor de irigații pentru culturile agricole, cu accent pe dezvoltarea unui subsistem energetic independent proiectat de autori – SEMSI (Subsistem Energetic Mobil Autonom pentru Irigații). SEMSI funcționează pe baza surselor de energie regenerabilă, precum energia solară și eoliană, și este destinat utilizării în zone fără acces la rețeaua electrică, dar cu resurse de apă disponibile. Pentru a sprijini conceptul și optimizarea viitoare a acestui subsistem, studiul prezintă principiile esențiale ale irigației, trece în revistă tehnologiile existente și performanțele acestora și analizează funcționarea atât a sistemelor tradiționale, cât și a celor moderne de irigație, inclusiv metodele gravitaționale, prin aspersiune și prin picurare. Această documentare oferă baza necesară pentru dezvoltările ulterioare ale sistemului SEMSI și servește ca punct de referință pentru modelarea teoretică și validarea experimentală în etapele viitoare ale cercetării.

INTRODUCTION
Globally, water management is becoming an increasingly sensitive issue. According to UN statistics, the world population is growing by 80 million people annually (*Alexandratos and Bruinsma, 2012*), implying an increase of 64 billion cubic meters of water needed for annual consumption. Currently, although the interest of the world's major powers is directed towards deposits, it is expected that in the long term the major global competition will be for water (*McVicker, 2024*).

Currently, about four billion people – almost half of the world's population – face a severe water shortage (*du Plessis, 2023*).

The demand for water for domestic and industrial use will increase rapidly and relatively slowly for agriculture. The developing world is expected to see a much greater increase in total water demand than the developed world, and approximately 93% of the additional demand will occur in developing countries (*Rosegrant and Cai, 2002*).

Water is the main limiting factor in agricultural production in regions where annual or seasonal rainfall is insufficient to meet crop water requirements (*Palma and Tomaz, 2024*). Globally, approximately 70% of all water withdrawn from water sources is used for irrigation (*Siebert et al., 2010*).

Irrigated agriculture plays a key role in feeding the world's population, accounting for 40% of global food production while occupying only 20% of global arable land (*Wang et al., 2022*).

Irrigation is the artificial application of water to crops to meet their requirements from the crown root initiation stage to maturity, in a controlled amount, according to the water requirements of the crop (*Askaraliev et al., 2024*).

Irrigation of agricultural crops refers to the process of controlled supply of water to cultivated plants, by various methods, to support their growth and development, especially in regions with insufficient rainfall, and aims to improve crop yield and quality (*Sabir et al., 2024*).

Proper water management in agriculture is essential for sustainable production, in the face of increasing water scarcity and climate change (*Ray and Majumder, 2024*). Climate change has a considerable impact on irrigated agriculture, which is vital for food and fibre production (*Gabr et al., 2024*).

Proper water management is achieved by drip irrigation systems, tubes and sprayers, as they can be used when natural water sources and rain are not sufficient to meet the water demand of plants and in areas where rainfall is irregular or drought periods are expected (*Shanu, 2024*).

Another type of sustainable water management is subsurface irrigation, which ensures the distribution of water within the soil layer, at a shallow depth, ensuring tailored results (*Rocha et al., 2024*). Subsurface irrigation eliminates surface evaporation, reduces the amount of salts, extends the life of the irrigation system by over 10 years, eliminates herbicide washout and its infiltration into the soil, reduces the need for personnel and reduces maintenance costs (*Codreanu and Malai, 2019*). Subsurface drip irrigation is recommended for cereal crops because it reduces evapotranspiration by about 25% compared to furrow irrigation and by about 15% compared to surface drip irrigation (*Umair et al., 2019*).

In these circumstances, sustainable irrigation - that is, irrigation for the production of healthy food through equitable use of water within planetary boundaries - is an important area of study, as it seeks to bring water systems and agricultural systems into balance, that is, harmonizing water use for food security, economic development and environmental sustainability (*Jain et al., 2021*).

Various precision irrigation methods such as sprinkler irrigation techniques, drip irrigation systems in combination with technological innovations and data-driven strategies such as satellite imagery, GIS, including the Internet of Things (IoT), remote sensing are being promoted to optimize water use and facilitate real-time environmental monitoring (*Xing and Wang, 2024*).

Advanced irrigation systems, together with soil conservation techniques and scheduling, hold promise for maximizing water efficiency and sustaining soil fertility while addressing the challenges of climate change, hunger, and environmental sustainability (*Enahoro-Ofagbe et al., 2024*).

The irrigation sector has changed significantly in the last 50 years due to climate change, drought problems, urbanization and population growth, and the trend is to search for and develop modern methods to optimize irrigation to achieve higher crop yields (*Lakhiar et al., 2024*).

The performance of irrigation systems is conditioned by the knowledge of geographical conditions, the physiology of the treated plants, the soil, in essence by an entire theoretical apparatus that provides the calculation bases for the start and maintenance of the irrigation system. A series of theoretical studies have laid the foundations of the necessary knowledge.

The water requirement of a crop, which must be satisfied through efficient water planning and management in order to obtain maximum yield, is obtained in the work *Saccon, (2018)*. *Popa, (2021)*, claims that the need to apply irrigation for a certain area is established according to the moisture deficit calculated as the difference between water consumption and water supply sources of the soil and plants. In Romania, *Corduneanu, (2018),* states that after calculating evapotranspiration using the Thornthwaite method and performing the water balance, it was concluded that in most areas there is a deficit, especially noted in the summer months.

The soil moisture should not fall below a certain minimum ceiling, i.e. the soil moisture should not be expected to reach the wilting coefficient. The minimum soil moisture ceiling (MHCPM) is located on medium soils, generally at half the active moisture range, on light soils at 1/3 of the Active Moisture Range (IUA), and on heavy soils at 2/3 of the I.U.A. The minimum ceiling (PM) was established depending on the texture, the field capacity CC and the wilting coefficient CO (*Grumeza et al., 1989; Canarache, 1990*). The time interval between waterings (T), according to *Botzan, (1972)*, represents the time between two waterings, and depends on the size of the applied watering norm, respectively on the average total daily moisture consumption through evapotranspiration. According to *Gaudin and Rapanoelina, (2003)*, the watering rate can be determined very easily, if a nomogram is built, the analysis of which will be done in theoretical research.

The paper presents a comprehensive analysis of current global research and technological trends in agricultural irrigation systems, with a focus on the design principles, functional characteristics, and integration of an innovative energy-independent mobile subsystem (SEMSI) powered by renewable sources.

MATERIAL AND METHODS

The working process of equipment intended for crop irrigation

In general, there are two irrigation methods: gravity (traditional method) and pressure-driven (modern method). *Brumă, (2004),* considers that the water regime of plants refers to the set of processes of water absorption, from the substrate and the atmosphere, to its circulation along the path of the plant body and to the elimination of the water current in the external environment through the processes of transpiration and guttation.

Domuţa et al., (2002), considers that supply irrigation is applied with the aim of ensuring the soil moisture necessary for uniform plant emergence and to create a water reserve that the plants will use in the following phases of development.

The amount of water in the plant organism varies with age, physiological state, geographical region, metabolic intensity, etc. in general, young tissues contain a greater amount of water than old ones (*Dry et al.,1999*).

Knowing the water consumption of crops, by developing maps of the actual water consumption of crops (*Roerink et al., 1997*) is of particular importance in irrigated agriculture, as it serves both to establish the water requirement in irrigation systems and to establish the timing of watering and irrigation norms.

Gravity irrigation is the supply of water at the end of an inclined channel built on a plot, to ensure the necessary amount of water through continuous gravitational flow in three phases: the advance phase, when the water flow is ensured on the dry edge, the storage phase, upon the arrival of the water wave until the interruption of the water supply and the recession phase, which is composed of two subphases, the first vertical recession upon the interruption of the water supply until the disappearance of the water and the horizontal recession upon the disappearance of the total water depth (*Chavez and Fuentes, 2019*).

Gravity irrigation is one of the oldest and simplest irrigation methods used in agriculture, which is based on harnessing the force of gravity to transport water from a source such as a river or reservoir, through canals, ditches or pipes, to fields located at a lower level. Most irrigation practices in southern Europe have been based on gravity-fed surface irrigation systems. For example, Figure 1 shows a gravity-fed surface irrigation system located in northern Italy. Currently, efforts are being made to encourage farmers to adopt more efficient gravity-fed irrigation practices, thus achieving both economic and environmental benefits (*Masseroni et al., 2017*).



Fig. 1 - Example of a gravity-fed surface irrigation system located in northern Italy

For flood irrigation, machines are used to dig canals, ditches and furrows, which create drainage channels on agricultural lands at risk of flooding or water stagnation, mini-irrigation canals, or irrigation furrows.

The furrows are made with special equipment, and figure 2 shows such agricultural equipment, which is composed of two guide wheels, five furrows and five compaction wheels for digging and compacting ditches for flood irrigation.

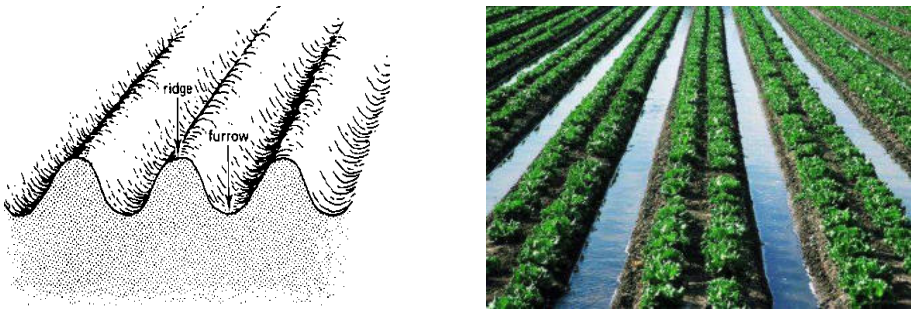
Flood irrigation requires a certain arrangement system (*Ivan et al., 2019*). The main technical elements of flood irrigation are the following: the thickness of the flood layer, the supply flow rate to achieve a certain thickness of the flood layer, the discharge flow rate (*Nicolaescu, 1981*). The design and evaluation of flood irrigation systems depend in part on the velocity at which water flows from the upper end of the furrow to the lower end, and knowledge of this velocity of advance for different flow rates allows the designer to choose the appropriate furrow length to achieve a certain uniformity of water distribution (*Davis, 1961*).



Fig. 2 - Aspects of an agricultural equipment for digging and tamping ditches for flood irrigation
(*https://www.centrulhidrauliccalarasi.ro/wp-content/uploads/2022/04/brazdar.jpg*)

In furrow irrigation (Fig. 3a), water reaches the plants by flowing along the natural slope, in the furrows that transport it due to the slope of the land between the crop rows, and it infiltrates into the soil as it moves along the slope (*Brouwer et al., 1988*).

Plants are usually grown on ridges between furrows. This method is intended for all row crops and for crops that cannot stand in water for long periods of time, such as corn, sugar beets, potatoes or vegetables. This method involves creating parallel furrows or grooves in the soil through which water is distributed to evenly moisten the soil around the roots of the plants.



a. b.

Fig. 3 - Furrow irrigation
a. top view and cross section of furrows and ridges; b. furrow-irrigated crop
(*https://www.fao.org/4/s8684e/s8684e04.htm*)

The management of gravity systems is not static, therefore farmers are supporting and experimenting with sophisticated systems, such as those based on computerization, automation and real-time optimization (*Singh, 2013*).

For example, a decision support system called SADREG has been developed to assist decision makers in the design and selection of furrow irrigation systems, which consists of a database, a simulation model, user-friendly interfaces and multi-criteria analysis models (*Gonçalves and Pereira, 2009*).

Pressure irrigation can be classified according to the way water is distributed to the plants and the type of equipment used.

Sprinkler irrigation. With this watering method, which is similar to natural rainfall, irrigation water is first sprayed into the air, from where the droplets fall as rain on plants and soil. Sprinkler irrigation is done with static, rotating or mobile sprinklers and is a modern irrigation system that uses water pressure to distribute water evenly and efficiently to agricultural crops or gardens. This method allows for more precise control of the amount of water applied, reducing waste and improving resource efficiency *(Nedelcu and Candea, 2009)*.

A significant example of sprinkler irrigation is represented by " **Irrigation system with ramp and watering cannon, IIRT"** (fig. 4), which is manufactured by Grup Romet SA Buzău for the irrigation of tall agricultural crops (corn, sunflower, hemp, etc.), medium (wheat, barley, rye, etc.) and low, sown in sparse rows (soybean, potato, alfalfa, clover, etc.) on medium and relatively large areas. The watering ramp mounted on the irrigation system ensures uniform water distribution, plant and soil protection, requires low pressures at the connection. In the case of using the watering cannon on the irrigation system, its working pressure is high to ensure optimal operation of the sprinkler.



Fig. 4 - Irrigation system with ramp and watering cannon, IIRT
(*https://www.romet.ro/resources/download/proiect_212_2008.htm*)

In aggregate with the 65 HP tractor on wheels, the installation is transported on the road arranged on the antenna line to one of the hydrants, where it will occupy two working positions. When it reaches the hydrant, the support legs and the jack are fixed in the working position and it is disconnected from the tractor.

The turret is pivoted, the drum is braked by manual operation and the hose is stretched with the help of the tractor. After the hose has been stretched, the operator releases the drum brake and tilts the ratchet on the gear ring; opens the ball valve on the main supply pipe and connects the installation to the hydrant; opens the hydrant and monitors the working pressure on the pressure gauge, adjusting it if necessary, using the connection.

The water intended for irrigation, under pressure, passes through the turbine and enters the drum shaft, then into the vertical pipe and further into the flexible polyethylene hose.

From here the water reaches the nozzles located on the ramp or in the watering cannon and is spread over the ground (watering circuit).

The turbine drives the reducer which in turn drives the drum with 4 speeds even with a low flow or pressure level, with minimal losses.

Rotating, the drum winds the hose and the trolley of the ramp or watering cannon moves towards the installation, the nozzles or cannon watering the ground on which it moves.

The rotational movement of the drum is transmitted via a chain to the device for setting the hose winding pitch. On the axis of the automatic stop device is the sensor for equalizing the speed of the trolley, which, depending on the number of layers of hose rolled on the drum, continuously adjusts the speed of the reducer through a system of levers.

When the trolley of the boom or watering gun has reached the drum, the electric motor is started by the programmable system of the work process, which drives the turbine bypass, stopping the water supply to the nozzles or watering gun. In this position, the installation is found by the operator, who raises the support legs and pivots the turret 180°.

The ramp or watering cannon will reach the other aisle, opposite the one where the previous watering was carried out and, using a mechanism with hydraulic cylinders operated by a manual hydraulic pump, the support legs are lowered. From this moment, the operations are resumed in the same order described and thus the second watering position is irrigated from the same hydrant (patent application RO126176A2, registration no. OSIM A00841/2009) (*http://pub.osim.ro/publication-server/pdf-document?PN=RO126176%20RO%20126176&iDocId=712&iepatch=.pdf*).

The drive mechanism of a pressure irrigation drum can be adjusted depending on the rotation speed of the drum and the movement of the sprinkler by:

- manual adjustment of the valve that changes the flow rate or pressure of the hydraulic motor;
- automatic adjustment, some installations being also equipped with a speed regulator to maintain a constant speed of movement of the sprinkler.

For example, the Bauer company uses the SmartRain application (fig. 5) to monitor the operation of the drum and hose sprinkler irrigation installations, which offers the possibility of controlling the drum and hose sprinkler irrigation installation from any location.

This obtains a remote overview with information about the real status, such as the remaining irrigation time, the remaining PE pipe, the time to change the irrigation tape and others, and the optimization of the installation can be done depending on the soil moisture and weather conditions through the irrigation management function.

It also receives error messages via SMS on the farmer's phone when the installation stops due to a malfunction or if it enters a dangerous area.



Fig. 5 - The SmartRain application developed by Bauer for monitoring the operation of sprinkler irrigation systems with a drum and hose
(*https://www.bauer-at.com/en/product/irrigation/smartrain/*)

Sprinkler irrigation is assessed using the following indices: irrigation uniformity, rain fineness and rain intensity (*Nagy and Luca, 1995*).

Irrigation uniformity is a particularly important index, because the way water is distributed on the land largely determines the quality of the irrigation, the efficiency of irrigation in the field, the uniformity and the increase in agricultural production.

Rain intensity, or pluviometry, represents the amount of water distributed by the ramp or irrigation cannon, per unit of time, per unit of surface area. It is expressed in mm/h, (*Luca and Nagy, 1999*).

The fineness of the rain from the ramp or the irrigation cannon of the irrigation system is determined by the size of the drops and is important in irrigation practice through the correlation that is made with the soil and the plant (*Nagy and Luca, 1995*).

In *Nedelcu, 2010*, it is stated that the duration of watering or the time of stationing, in a working position for applying the watering norm, depends on:

- the size of the watering norm;
- the pluviometry of the sprinkler;
- the chosen layout scheme.

The most common type of sprinkler system layout is shown in figure 5, consisting of a system of light aluminium or plastic pipes that are moved manually, and the rotating sprinklers are usually spaced 9-24 m along the side that is normally 5-12.5 cm in diameter, in order to be easily transported (*Brouwer et al., 1988*).



Fig. 5 - Sprinkler system with aluminium pipes

Watering ramps are mechanized systems used for pressure irrigation that are intended for drum and hose irrigation installations, in which water is transported through sections of metal pipes coupled together end to end and distributed to plants through nozzles or sprinklers. They consist of a movable arm (ramp) connected to a water source, which moves along a plot, evenly distributing water in the form of sprinkling or by other methods.

Figure 6 shows a TYPE-3 irrigation ramp, which consists of: a trolley for movement, a support structure for pre-assembled kits through which water is transported to the plants, kits that can be quickly mounted or dismantled on or off the support structure and that can be moved in the direction of increasing or decreasing the distance between them, depending on the distance between the rows of the irrigated crop, other pre-assembled kits for distributing water in the field depending on the chosen irrigation method, e.g. by continuous flow, by sprinkling, by dripping, the working height of the ramp can be adjusted using a manual winch system and some vertical slides with quick locking in position. To use the irrigation ramp (rain wing), the pressure at the entrance to the drum must be at least 2 bar. If the pressure is higher, the irrigation will be more intense, better in quality. The irrigation ramp is compatible with all irrigation drums on the market, with diameters of 90 mm, 110 mm, 125 mm, etc. The irrigation ramp (rain wing) can be equipped with nozzles, with different diameters: 4, 5, 6, 7, 8, 9, 10 mm (*Morimoto et al., 2021*).



Fig. 6 - Watering ramp TYPE-3
(https://www.apftrade.ro/spatii-verzi/rampa-de-udare-type-3.html)

Drip irrigation involves dripping water onto the soil in very small amounts (2-20 litres/hour) from a system of small-diameter plastic pipes fitted with holes called emitters or drippers. The water is applied close to the plants so that only a portion of the soil where the roots grow is wet (fig. 7), (*Marimoto and al., 2021*), unlike surface and sprinkler irrigation, which wet the entire soil profile. Drip irrigation water is applied more frequently (about 1...3 days) than other methods to ensure a high level of soil moisture favourable to agricultural crops.

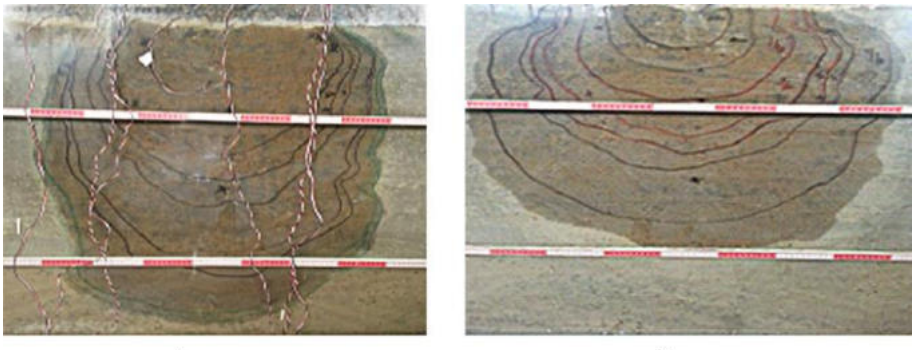


Fig. 7 - Comparison of soil moisture distribution in sandy soil with emitter flow rate of 2 L/h
A) Pulse drip irrigation; B) Continuous drip irrigation

Drip irrigation can be used on any agricultural crop. Normally, the crop should be planted along the contour of the water supply lines and pipes (laterals). However, drip irrigation is most suitable for row crops (vegetables), tree crops and vines. Figure 8 shows an automated drip irrigation and/or microsprinkler installation for greenhouses and solariums, which consists of a branch (1) for connection to a water storage tank (2), a self-priming electric pump (3), a water meter (4), a pressure gauge (5), some routing elements (6) for water transit through a control head (7) with a fertilizer tank and a filter (8) to a pipe (9) provided with some strips (10) with drippers incorporated in a bay (11) for drip irrigation/fertigation and/or to another pipe (12) provided with some microsprinklers (13) for foliar irrigation/fertigation, a humidity transducer (14), conductivity and temperature in connection with a Data Logger (15) provided with software for controlling solenoid valves (17) in the drip and/or micro-sprinkler irrigation/fertigation circuit, with another software for controlling a frequency converter (16) that controls the rotation speed of an electric pump (3) and with another software for controlling the application of drip and/or micro-sprinkler irrigation/fertigation based on preset programs, depending on the time factor, in the situation when the transducer (14) is inactive (defective) *(Marin et al., 2014)*, (*https://oaji.net/articles/2015/1672-1448748396.pdf*).

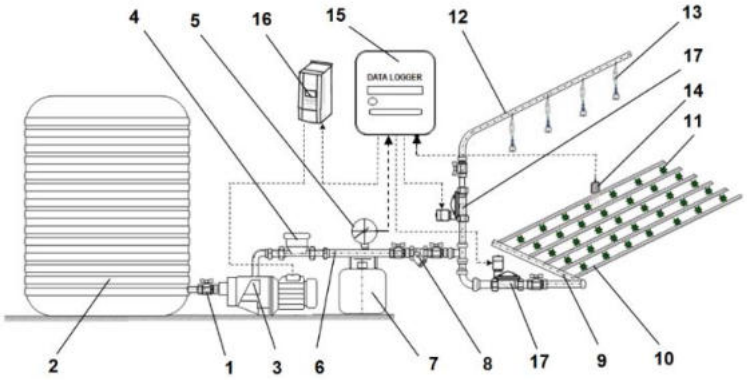


Fig. 8 - Automated drip and/or micro-sprinkler irrigation system

Subsurface drip irrigation (SDI) is the buried version of the traditional drip irrigation system, in which the drip line is buried below the soil surface, instead of being installed directly on the ground, supplying the plant with water directly at the root, and the precise monitoring of soil moisture levels in the plant root zone with the Internet of Things (IoT) ensures long-term productivity (*El-Sheshny et al., 2024*).

For example, an underground irrigation installation was implemented in an experimental plot with an area of 500 m2 (50 m long and 10 m wide) under a grant from the Romanian Ministry of Research and Innovation CCDI - UEFISCDI, Project "Innovative technologies for irrigation of agricultural crops in arid, semi-arid and subhumid-dry climates" (*Șovaiala et al., 2018*).

Figure 9 shows aspects of the irrigation lines being buried with special equipment (*Manea et al., 2021*), of a drip line that was placed in the soil at a depth of 20 cm and of the plot on which the underground irrigation system was installed for a sorghum crop located on the land of SCDCPN Dăbuleni. The distance between two adjacent drip lines was 1 m. The drip tubes that were used are with pressure-compensated and anti-siphon drippers, the distance between the drippers being 33 cm, and the outer diameter of the tube 16 mm. The underground irrigation system was supplied with water from an above-ground irrigation canal, using a Lorentz pump powered by electricity from a hybrid, solar and wind source.



a **b** **c**

Fig. 9 - Underground irrigation system implemented in a plot on the land of SCDCPN Dăbuleni

a) Equipment for burying underground irrigation lines; b) Underground irrigation line buried in the ground; c). Plot with underground irrigation system

Subsurface drip irrigation has significant economic effects by reducing water evaporation by about 25%, due to the fact that pH, P, K and Mg influence the structure of the microbial community, according to table 2 presented by Quach and extending the life cycle of the materials used in the entire system, (*Quach et al., 2022*). The advantages of subsurface drip irrigation are related to longevity - it can last up to 20-25 years without major repairs, minimal operational costs, reduced costs for crop maintenance and less use of water resources, which leads to the optimization of crop growth (*Cahn and Hutmacher, 2024*). The disadvantages are related to some external impacts that affect the irrigation system, the most important of which is the fact that, if in the case of an aboveground system, we can quickly notice any possible water loss due to a leaky joint, in the case of underground systems, this is more difficult to detect. Therefore, prior to actual burial of the components, it is necessary to conduct tests to confirm their proper functioning (*Wang et al., 2022*).

Other disadvantages of subsurface drip irrigation in commercial agriculture compared to alternative irrigation systems include higher capital cost per unit of land area (except for small plots of land), unfamiliar management and maintenance protocols that can exacerbate the potential for emitter clogging, visibility of system attributes (components and design) and performance characteristics, and susceptibility to damage (i.e., rodents and tillage) of subsurface drip lines. Despite these disadvantages, subsurface drip irrigation continues to be adopted in commercial agriculture in the US, and research efforts to evaluate and develop systems continue as well.

In the case of daily watering, the watering rate correlates with the daily water consumption, thus maintaining a constant soil water reserve, close to the field water capacity of the soil (*Grumeza and Kleps, 2005*, *Țenu, 2004*). Since the water pressure dissipated on the path to the dripper outlet is a determining factor for determining its flow rate, sophisticated passage models for high pressure dissipation have been developed (*Schwankl, 1992*).

- ***Specifications for mobile irrigation equipment***

Mobile irrigation equipment is a flexible and easy-to-move system, mainly used to irrigate large areas, but also for spot applications or on various terrains.

Table 1 presents some mobile irrigation equipment manufactured by IRRIMEC (*https://www.irrimec.com/?lang=en*).

Table 1

Mobile irrigation equipment manufactured by IRRIMEC -

	Model	Diameter [mm]	Hose length [m]
 Mini Rain AAg irrigation reel	50 TG	50	200
	63 TG	63	160 – 200 – 240
	70 TG	70	180 – 200 – 230
	75 TG	75	110 – 145
 Rain Sky A5 irrigation reel	50 F	150 50	150 – 180 – 200
	58 F	110 58	110
 Rain Sky AAA irrigation reel	40 F	110 40	110 – 130

 Eco Rain ST 2 irrigation reel	63 TG	63	250 – 280 – 300
	70 TG	70	220 – 240 – 270 – 300
	75 TG	75	200 – 220 – 230 – 245 – 250 – 300
	82 TG	82	180 – 200
 Eco Rain ST 3 irrigation reel	63 TG	63	280 – 350
	70 TG	70	265 – 280 – 300 – 310
	75 TG	75	245 – 300 – 320 – 350
	82 TG	82	220 – 270 – 300 –
	90 TG	90	200 – 230
 Opti Rain ST 4 irrigation reel	75 TG	75	350 – 400 – 430
	82 TG	82	350 – 380 – 400
	90 TG	90	300 – 320 – 340
	100 TG	100	240 – 270 – 300
	110 TG	110	200 – 230

Irrigation with drones is a cutting-edge technology that uses modern technology to improve irrigation efficiency and reduce water consumption, making it an ideal method for precision agriculture (*Khadse, 2021*).

This represents an important step towards sustainable and resource-efficient agriculture, and the choice of an irrigation drone should be based on the specific irrigation needs, land size, crop type, and available budget (*Rakhade et al., 2021*).

Types of drones:

- **DJI Agras**: DJI is a leader in drone technology, and its range **DJI Agras** offers specific drones for irrigation, with large water tanks and efficient spraying systems (*https://www.dji.com/global*).
- **Parrot Bluegrass**: Parrot is another brand well-known for its agricultural drones. The Parrot Bluegrass is equipped with multispectral cameras and can be used for crop monitoring as well as irrigation. (*https://www.parrot.com/en*).
- **XAG P150** (**table 2 row 3)**: An irrigation drone from China, which is used to spray water, pesticides and fertilizers on large agricultural fields (*https://hse-uav.com/products/xag-p150*).

DJI Agras T30 (table 2 row 1) is a great example of a spraying drone with a 30-liter tank and 16 nozzles that can be used for irrigation. Waterproof and equipped with a high-precision RTK system, this drone offers extensive coverage and optimized spraying, making it ideal for a variety of terrains, including farmland and orchards (*https://www.dji.com/global/t30*).

Table 2

Several types of agricultural drones used for crop irrigation

Crt. No.	Type of drones	Characteristics
1	 DJI Agras T30 (*https://www.dji.com/global/t30*)	- Operational efficiency (per hour) 16 hectares; - Spray tank volume 30 L (fixed tank); - High-precision radar; - AI intelligent engine for 3D operation planning; - High-precision flow meter; - Intelligent altitude control: Automatic altitude adjustment to maintain a constant height - Total weight (without battery): 26.4 kg

2	 ADT FALCON 50L (*https://appiadronetech.com/agricultural-and-farming-drones/adt-falcon-50l/*)	- Spraying efficiency up to 5280 m²/min - Liquid tank volume is 50 litres - Flight time 10-15 minutes - Flight range 0-1500 m - Flight height 0-20 m - Flight speed 0-10 m/s - Downward air flow 4-15 m/s - Wind resistance 10 m/s - Net weight 24.5 kg
3	 XAG P150 (*https://www.xa.com/en/p150/p150specs*)	- Maximum take-off weight: 96 Kg - Number of rotors: 4 - Liquid tank capacity: 50l - Maximum spraying flow rate: 22 l/min - Spraying width: 5...10 m - Solids tank capacity: 80 l - Spreading width: 3...7 m - Maximum distribution quantity: 150 kg/min

Pumping units can be motor pumps or electric pumps depending on the availability of the water resource, supplied directly from the source (irrigation canals, water courses) or reservoirs (metal basins, concrete or waterproofed basins), when the water resource is limited or taken from boreholes (*Alijanov et al., 2020*).

At irrigation pumping stations (unlike water supply pumping stations), the uniform operation of the pumping equipment is characterized by relatively constant flow and pressure over a certain period of time, and the pump must operate under optimal conditions with the highest efficiency (*Kan et al., 2020*).

The efficiency criterion of the pumping station is the degree of completeness of the coverage of the water consumption program by the water supply program, provided that minimum operating costs, health and safety requirements are met (*Platonov et al., 2019*).

In the works *Eckstein, 1990*, and *Al-Ibrahim, 1997,* a detailed theoretical analysis was developed to determine the characteristics of the motor and pump.

- ***Specifications regarding the commissioning and operation systems of irrigation installations***

The commissioning and operation of irrigation systems involves the use of pumps, which play an essential role in the operation of agricultural crop irrigation, with the main purpose of ensuring the circulation of water in the system, at the required pressure and flow rate (*Guler, 2001*).

There are many recognized brands that produce irrigation pumps, each with specifications adapted to various agricultural, horticultural or residential applications. Here is a list of the most popular brands of irrigation pumps and their characteristics:

Submersible pump Grundfos SP 9-11 is suitable for pumping clean water. Grundfos SP are stainless steel pumps, designed for pumping groundwater. It can be installed vertically or horizontally. This pump is approved for drinking water. The characteristics of the Grundfos SP 9-11 Rp2 4"3X380-415/50 2.2kW submersible pump are on: *https://www.pompe-grundfos.ro/pompe-apa-grundfos/sp9-11-rp2-43x380-41550-22kw-98699055*.

Submersible pump Grundfos SQE 2 – 100: is a 3" multistage submersible pump designed for domestic water supply, liquid transfer in tanks, irrigation and environmental applications. The pump has flooded impellers, each with its own tungsten carbide/ceramic bearing. The characteristics of the submersible pump - Grundfos SQE 2 – 100 are on: *https://www.pompe-grundfos.ro/pompe-apa-grundfos/pompe-grundfos-sq-sqe*.

Centrifugal pump Grundfos CR 5-3: the characteristics of the submersible pump - Grundfos CR 5-3 are presented on: *https://product-selection.grundfos.com/products/cr-cre-cri-crie-crn-crne-crt-crte/cr?tab=models*.

***Pedrollo CB2 - F 50/250A pressure groups*:** the pressure groups are composed of two pumps assembled in a ready-to-install unit. The groups are designed in such a way that at any request for pressure increase from the user, one or both pumps will automatically start in succession. The operation of the pumps is necessary to satisfy the water demand, significantly reducing energy consumption and the electronic circuits present in the electrical panel alternate the operation of the pumps. The characteristics of the pressure group Pedrollo CB2 - F 50/250A are: *https://pompesubmersibile.ro/grupuri-pompare-pedrollo/grup-pompare-pedrollo-CB2-F-50-200A*.

Submersible pump Wilo Sub-TWI 5 505: a multistage submersible pump for pumping clean water from tanks, cisterns, wells and shallow wells, up to an immersion depth of 17 m. Suitable for applications such as water supply, sprinkling, spraying, rainwater recovery. All components that come into contact with the pumped fluid are protected against corrosion. The pump characteristics Wilo Sub-TWI 5 505 (1~230 V, 50 Hz) are: *https://pompesubmersibile.ro/grupuri-pompare-pedrollo/grup-pompare-pedrollo-CB2-F-50-200A*.

Limiting noise and vibration of irrigation pumps is dictated by many circumstances, including direct technical requirements and operating conditions. Factors leading to damage to pumping units are: long-term static effects, stresses; static effects and repetitive stresses; noise and vibration effects; wear of the device design; corrosion and fatigue effects (*Bekchanov et al*., *2021*; *Chițoiu et al, 2020*) give an example of calculating the time-averaged sound pressure level for the noise source of a WTH 60 centrifugal pump equipped with an internal combustion engine.

With the increasing demand for energy worldwide, the generation of electricity based on solar energy produced by photovoltaic panels, which is based on the direct production of electricity through silicon cells, has become promising and suitable for pumping water for irrigation in agriculture (*Aliyu et al.*, *2018; Mateescu et al., 2023*).

The energy converted from the photovoltaic cell depends on the day-night cycle, the latitude of the place where it is captured, the seasons and the cloud cover. The photovoltaic array has an optimal operating state known as the maximum operating point (MPP), which is dependent on the level of irradiation, and when it shines and when the climatic conditions are favourable, the sun provides a power of 1 kW/m^2. Photovoltaic panels allow the direct conversion of 10 - 15% of this power into electricity (*Singh, 2013*). *Enescu et al., 2020,* conducted an analysis of the values recorded in the peak months (May-September) of a photovoltaic park for the supply of electricity to pumps at an irrigation system station and the values of the off-season months.

- **Factors influencing the process and qualitative indices of equipment intended for crop irrigation**

The irrigation process and the quality of irrigation equipment are influenced by a number of technical, economic and environmental factors. When choosing irrigation equipment for crops, it is essential to consider these factors to ensure the efficiency, durability and sustainability of the system.

The optimal design of a gravity irrigation network involves water availability, crop, soil characteristics, land topography and associated cost (*Holzapfel et al., 2009; Fouial et al., 2017; Duan et al., 2022*).

The main factors influencing the process and qualitative indices of crop irrigation equipment are:

- the type of crop because each crop has different requirements in terms of the amount of water needed, the type and characteristics of the soil, for example clay soils have a higher water retention capacity compared to sandy soils,
- climatic conditions and rainfall regime,
- the type and efficiency of the irrigation equipment, thus sprinkler irrigation is suitable for large fields, and drip irrigation offers precise water distribution,
- installation and maintenance costs, such as those by drip or automated sprinklers, may involve higher initial costs,
- access to the water source and its distribution and the durability and materials of the equipment, in order to have a long lifespan, they must be built from durable materials and resistant to UV, frost, extreme heat and humidity.

In *Pelea, (2021)*, the results of a study on the uniformity of irrigation application and water quality for irrigation within the local irrigation arrangement Emiliana West Rom Srl Plot Aranca are given. The main objective of the study was to analyse the uniformity of watering application for the linear and centre pivot type sprinkler irrigation installation.

Balaj, (2018), conducted studies and research on establishing the possibilities of using solar energy in land improvement arrangements, especially for local arrangements, on small areas especially in areas where there is adequate solar radiation and there is no electrical network to supply electric current to the pumps. For this purpose, Balaj used the Solar platform of the West University of Timișoara which includes a Solar Radiation Monitoring Station (SRMS) and three experimental stands dedicated to testing PV modules. The Solar Radiation Monitoring Station is equipped with first-class DeltaOHM pyranometers, in accordance with the ISO 9060 standard. The platform monitors global, diffuse, reflected and total solar irradiance. The measurement of all parameters (electrical, meteorological, radiometric) was made according to (*http://solar.physics.uvt.ro/srms/*).

Choudhury et al., (2011), considers that the passing wind drives the blades of a wind turbine, generating lift and exerting a turning force so that the blades rotate a shaft in a speed multiplier, which drives a generator to convert the rotational energy into electrical energy. In *Johari et al., (2018),* are described the results of some research on the performance of the HAWT wind turbine compared to the VAWT. The HAWT wind turbine has already been used since 5000 BC where people extracted energy from the wind to move boats along the Nile River.

Farrokhi & Parvaresh, (2022), consider that energy plays a vital role in ensuring security, development and economic stability within societies and especially given the fact that in the agricultural sector, the transition from surface irrigation to pressurized irrigation systems was adopted to increase the efficiency of water

consumption. This change led to an increase in energy consumption and the largest part, about 70% of energy consumption in the agricultural sector is pumps in pumping stations.

Qin et al., (2024), estimate that irrigation contributes 216 million metric tons of CO_2 emissions and consumes 1896 petajoules of energy annually, representing 15% of greenhouse gas emissions and energy used in agricultural operations, especially since only 40% of irrigated agriculture relies on groundwater sources, groundwater pumping represents 89% of total energy consumption in irrigation.

CONCLUSIONS

The research presented in this paper constitutes a foundational step in the development of SEMSI – an innovative, mobile, energy-independent subsystem designed for irrigation systems that operate without conventional energy sources. Through an extensive review of global irrigation practices, equipment types, and energy integration methods, the paper consolidates key knowledge required for the design and optimization of sustainable irrigation technologies.

This study contributes a structured synthesis of the operating principles, design specifications, and influencing factors of various irrigation systems, with a particular focus on mobile equipment and renewable energy integration. The collected data and theoretical background support the formulation of a mathematical model and provide essential inputs for the experimental research and validation phase of SEMSI.

Irrigation is an important technological measure, with the following effects:

- obtaining high yields, regardless of the amount of precipitation, because irrigation completes the water deficit, which is distributed in relation to the requirements of the plants;
- using fertilizers by plants with greater efficiency by increasing the degree of solubilization of substances;
- extending the vegetation period of plants and better staggered production.

A synthesis of studies conducted on the working process of equipment intended for crop irrigation and the factors that influence it was presented through a general analysis of the irrigation process, a study of the working process of equipment intended for irrigation, a study of some specifications regarding mobile irrigation equipment and systems for commissioning and actuating irrigation installations and finally, the factors that influence the process and qualitative indices of equipment intended for crop irrigation.

The findings highlight the importance of efficient water management in agriculture and the growing need for adaptable, energy-efficient irrigation solutions. Future work will build on this foundation to simulate, improve, and implement SEMSI in real-world scenarios, contributing to climate-resilient agricultural practices and sustainable rural development.

REFERENCES

[1] Abdurokhmonov, S., Umirov, N. (2020). Methods of regulating the work of units at irrigation pumping stations. *IOP Conference Series: Materials Science and Engineering*, *883*(1), 012117, IOP Publishing.

[2] Al-Ibrahim, A. M. (1997). *Optimum selection of direct-coupled photovoltaic pumping system in solar domestic hot water systems*. The University of Wisconsin-Madison.

[3] Alexandratos, N., Bruinsma, J. (2012). *World agriculture towards 2030/2050: the 2012 revision*.

[4] Alijanov, D., Abdurokhmonov, S., Umirov, N. (2020). Methods of regulating the work of units at irrigation pumping stations. *IOP Conference Series: Materials Science and Engineering*, *883*(1), 012117, IOP Publishing.

[5] Aliyu, M., Hassan, G., Said, S. A., Siddiqui, M. U., Alawami, A. T., Elamin, I. M. (2018). A review of solar-powered water pumping systems. *Renewable and Sustainable Energy Reviews*, *87*, 61-76.

[6] Askaraliev, B., Musabaeva, K., Koshmatov, B., Omurzakov, K., Dzhakshylykova, Z. (2024). Development of modern irrigation systems for improving efficiency, reducing water consumption and increasing yields. *Machinery & Energetics*, *15*(3), 47. https://doi.org/10.31548/machinery/3.2024.47

[7] Balaj, I. C. (2018). Possibilities for Using Solar Energy in Land Reclamation Arrangements (*Posibilități de utilizare a energiei solare în amenajările de îmbunătățiri funciare)* [Doctoral dissertation]. Timişoara: Politehnica Publishing.

[8] Bekchanov, F.A., Yusupov, F., Kholbutaev, M.O., Khayitov, B.K., & Ulashov, Q.C. (2021). Diagnostic model of great irrigation pump units. *IOP Conference Series: Earth and Environmental Science*, *868*(1), 012039, IOP Publishing.

[9] Biolan, I., Serbu, I., Sovăială, G., Mardare, F. (2010). Techniques and Technologies for Fertigation of Agricultural Crops (*Tehnici si tehnologii de fertirigare a culturilor Agricole)*. Publishing House AGIR, Bucharest.

[10] Botzan, M. (1972). Water Balance in Irrigated Soils (*Bilanţul apei în solurile irrigate)*. Romanian Academy Publishing House.
[11] Brouwer, C., Prins, K., Kay, M., Heibloem, M. (1988). *Irrigation water management: irrigation methods*. Training manual, 9(5), 5-7.
[12] Bruma, I. S. (2004). *Eco-friendly vegetable cultivation technologies (Tehnologii ecologice de cultivare a legumelor*) "TERRA NOSTRA" Publishing House Iasi, ISBN: 1584-0735.
[13] Cahn, M., & Hutmacher, R. (2024). Subsurface drip irrigation. *Microirrigation for Crop Production.* pp.257-301. Elsevier Science.
[14] Canarache, A. (1990). *Physics of agricultural soils* (*Fizica solurilor Agricole)*. Ceres Publishing House.
[15] Chavez, C., & Fuentes, C. (2019). Design and evaluation of surface irrigation systems applying an analytical formula in the irrigation district 085, La Begoña, Mexico. *Agricultural Water Management*, *221*, 279-285.
[16] Chiţoiu, M., Moiceanu, G., Paraschiv, G., Ştefan, M., Matache, A. (2020). Sound power determination for centrifugal pumps used for local agricultural irrigation in Romania. *E3S Web of Conferences* (Vol. 180, p. 03023). EDP Sciences.
[17] Choudhury, S., Mohanty, K.B., Babu, B.C. (2011). *Performance analysis of doubly-fed induction generator in wind energy conversion system* [Master of Technology in Electrical Engineering (Power Control & Drives) thesis]. National Institute of Technology Rourkela.
[18] Codreanu, I., Malai, S. (2019). The development of irrigation-based agriculture in the environmental conditions of the Nistru middle course districts on the territory of the Republic of Moldova. (Dezvoltarea agriculturii bazate pe irigare în condițiile de mediu ale raioanelor din cursul de mijloc al Nistrului de pe teritoriul Republicii Moldova)*. Acta et commentationes (Exact and Natural Sciences)*, *7*(1), 35-43.
[19] Corduneanu, O.R. (2018). *Research on optimizing the working process for fertilization and drip irrigation of vegetable crops (Cercetari privind optimizarea procesului de lucru pentru fertilizarea si irigarea prin picurare a culturilor legumicole)* (Doctoral dissertation), "Ion Ionescu de la Brad" University of Agricultural Sciences and Veterinary Medicine, Iaşi / Romania.
[20] Davis, J. R. (1961). *Estimating rate of advance for irrigation furrows,* Trans. ASCE Publishing House.
[21] Domuţa, C., Sabău, N. C., & Tusa, C. (2000). *Crop Irrigation*. *(Irigarea culturilor)* University of Oradea Publishing House.
[22] Dry, P. R., Stoll, M., Mc Carthy, M. G., & Loveys, B. R. (1999, June). Using plant physiology to improve the water use efficiency of horticultural crops. In *III International Symposium on Irrigation of Horticultural Crops. 537.* pp. 187-197.
[23] Duckworth, A. L., Quirk, A., Gallop, R., Hoyle, R. H., Kelly, D. R., & Matthews, M. D. (2019). Cognitive and noncognitive predictors of success. *Proceedings of the National Academy of Sciences, 116*(47), 23499–23504. USA. https://doi.org/10.1073/pnas.1910510116
[24] Duan, X., He, W., Wang, Y., Liu, Q., Tian, Y., & Shi, X. (2022). Optimization design method of a large-scale multilevel gravity drip irrigation pipe network system based on atom search optimization. *Journal of Irrigation and Drainage Engineering*, *148*(7), 04022023.
[25] Du Plessis, A. (2023). Water resources from a global perspective. In *South Africa's Water predicament: Freshwater's unceasing decline.* pp.1-25. Cham: Springer International Publishing.
[26] Eckstein, J. H. (1990). *Detailed modelling of photovoltaic system components* (Doctoral dissertation). University of Wisconsin, Madison.
[27] El-Sheshny, A. A., Elmesery, A. E. D. A., & Elsamra, E. A. (2024). Water management using internet of things with surface and sub-surface drip irrigation systems. *Al-Azhar Journal of Agricultural Engineering*, *7*(1).
[28] Enahoro-Ofagbe, F. E., Ewansiha, S. U., & Iwuozor, K. O. (2024). Integrating irrigation management and soil remediation practices for sustainable agricultural production: advances, challenges, and future directions. *Agroecology and Sustainable Food Systems*, 1-27.
[29] Enescu, F. M., Bizon, N., Onu, A., Răboacă, M. S., Thounthong, P., Mazare, A. G., & Șerban, G. (2020). Implementing blockchain technology in irrigation systems that integrate photovoltaic energy generation systems. *Sustainability*, *12*(4), 1540.
[30] Farrokhi, M., & Parvaresh Rizi, A. (2022). Energy Audit in Sprinkler Irrigation Systems: Methodology and Application. *Journal Of Iranian Water Engineering Research*, *2*(2), 79-91.
[31] Fouial, A., García, I. F., Bragalli, C., Brath, A., Lamaddalena, N., & Diaz, J. A. R. (2017). Optimal operation of pressurised irrigation distribution systems operating by gravity. *Agricultural Water Management*, *184*, 77-85.
[32] Gabr, M. E., Awad, A., & Farres, H. N. (2024). Irrigation Water Management in a Water-Scarce Environment in the Context of Climate Change. *Water, Air & Soil Pollution*, *235*(2), 127.

[33] Gaudin, R., & Rapanoelina, M. (2003). Irrigation based on a nomogram using soil suction measurements. *Agricultural Water Management*, *58*(1), 45-53.
[34] Gonçalves, J. M., & Pereira, L. S. (2009). Decision support system for surface irrigation design. *Journal of Irrigation and Drainage Engineering*, *135*(3), 343-356.
[35] Grady, J. S., Her, M., Moreno, G., Perez, C., & Yelinek, J. (2019). Emotions in storybooks: A comparison of storybooks that represent ethnic and racial groups in the United States. *Psychology of Popular Media Culture*, *8*(3), 207–217. https://doi.org/10.1037/ppm0000185
[36] Grant, P. (1989). *Device for Elementary Analyses*. Patent No. 123456. USA.
[37] Grumeza, N., & Klepș, C. (2005). *Irrigation arrangements in Romania (Amenajarile de irigatii din Romania)*. Ceres Publishing House, Bucharest, Romania
[38] Grumeza, N., Merculiev, O., & Klepș, C. (1989). *Forecast and programming of irrigation application in irrigation systems (Prognoza și programarea aplicării udărilor în sistemele de irigații)*. Ceres Publishing House, Bucharest, Romania.
[39] Guler, S. P. (2001). *Optimization of irrigation arrangements using unconventional energy (Optimizarea amenajărilor de irigaţii folosind energie neconvenţională)* (Doctoral dissertation). "Politehnica" University of Timișoara, Faculty of Hydrotechnical Engineering.
[40] Holzapfel, E. A., Pannunzio, A., Lorite, I., de Oliveira, A. S. S., & Farkas, I. (2009). Design and Management of Irrigation Systems. *Chilean Journal of Agricultural Research*, *69*(1), 17-25.
[41] International Organization for Standardization. (2018). *Occupational health and safety management systems—Requirements with guidance for use* (ISO Standard No. 45001:2018). https://www.iso.org/standard/63787.html
[42] Ivan, I., Bularda, M., & Ivan, E. (2019). The analyze of rice varieties behaviour and improvement under of global warming context, *An. I.N.C.D.A. Fundulea*, *vol. LXXXVII*, pp. 50-55.
[43] Jain, M., Fishman, R., Mondal, P., & Galford, G. L. (2021). Groundwater depletion will reduce cropping intensity in India. *Science Advances*, *7*(9), eabd2849.
[44] Johari, M. K., Jalil, M., & Shariff, M. F. M. (2018). Comparison of horizontal axis wind turbine (HAWT) and vertical axis wind turbine (VAWT). *International Journal of Engineering and Technology*, *7*(4.13), 74-80.
[45] Kan, E., Mukhammadiev, M., & Ikramov, N. (2020). Methods of regulating the work of units at irrigation pumping stations. In *IOP Conference Series: Materials Science and Engineering*. Vol. 869, No.4, p.042009). IOP Publishing.
[46] Khadse, K. (2021). To study applications of agricultural drones in irrigation and agriculture. *Bioscience Biotechnology Research Communications*, *14*(9), 81-86.
[47] Lakhiar, I.A.; Yan, H.; Zhang, C.; Wang, G.; He, B.; Hao, B.; Han, Y.; Wang, B.; Bao, R.; Syed, T.N.; Chauhdary J.N.; Rakibuzzaman Md. (2024). A review of precision irrigation water-saving technology under changing climate for enhancing water use efficiency, crop yield, and environmental footprints. *Agriculture*, *14*(7), 1141.
[48] Luca E., & Nagy, Z. (1999). *Crop irrigation (Irigarea culturilor)*. Genesis Publishing House, Cluj-Napoca, Romania.
[49] Manea, D., Draghici, I., Draghici, R., & Gidea, M. (2021, September). Research on subsurface drip irrigation of grain sorghum in sandy soils. *Engineering for Rural Development. Proceedings of the International Scientific Conference* (No. 20). Latvia University of Life Sciences and Technologies.
[50] Manea, D., Marin, E., Gheorghe, G., Persu, C., & Mitroi, R. (2021). Experimental research of equipment for burying in the ground the drip irrigation lines. *E3S Web of Conferences*. Vol. 286, p. 03011. EDP Sciences.
[51] Marin, E., Pirnă, I., Manea, D., Matache, M., & Popa, L. (2014). Innovative technology for irrigation and climate control in vegetable greenhouses. *INMATEH-Agricultural Engineering*, *44*(3), 43-50.
[52] Masseroni, D.; Ricart, S.; De Cartagena, F.R.; Monserrat, J.; Gonçalves, J.M.; De Lima, I.; Facchi, A.; Sali, G.; Gandolfi, C. (2017). Prospects for improving gravity-fed surface irrigation systems in Mediterranean European contexts. *Water*, *9*(1), 20.
[53] Mateescu M., Marin E., Manea D., Gheorghe G.V., Baltatu C., Dumitru D.N., Preda D.M., Duran B.O., Manoleli Preda O.D., Ceausu D.B. (2023). Research on the development of an innovative energy independent system for the irrigation of agricultural crops, *Proceedings of ISB-INMA THE 2023 International Symposium*, 5-6 October, Bucharest / Romania, ISSN 2344-4118, pp. 326-333.
[54] McVicker, E. (2024). Global perspectives on water management: an overview of action steps from the United Nations to local communities. *The Journal of Business*, *31*(1).

[55] Morimoto, G. E., Otto, A., & Burkholder, L. L. (2021). An innovative temporary escape ramp for deer and other wildlife. *California Fish and Game*, *107*(3), 213-228.
[56] Nagy, Z., Luca, E. (1995). *Crop Irrigation, Practical Works (Irigarea culturilor, Lucrări practice)*. Agronomic Publishing House. Cluj Napoca.
[57] Nedelcu, M. (2010). *Contributions to optimizing the operating regime of drum and hose sprinkler irrigation systems (Contributii privind optimizarea regimului de exploatare al instalatiilor de irigat prin aspersiune cu tambur si furtun)* [Doctoral dissertation]. Transilvania University of Brasov, Faculty of Mechanical Engineering.
[58] Nedelcu, M., & Candea, I. (2009). Study of water particles trajectories from the jet of wetting sprinklers. *Annals of the University of Craiova-Agriculture, Montanology, Cadastre Series*, *39*(2), 522-527.
[59] Nicolaescu, I. (1981). *Surface runoff irrigation (Irigaţii prin scurgere la suprafaţă)*. Ceres Publishing House, Bucharest, Romania.
[60] Palma, P., & Tomaz, A. (2024). Agricultural Practices to Improve Irrigation Sustainability. *Water*, *16*(6), 817.
[61] Pelea, G. N. (2021). *Current issues regarding the management of operation and maintenance of irrigation systems located in Western Romania (Probleme acutale privind managementul exploatării și întreținerii sistemelor de irigații aflate în vestul României)* [Doctoral dissertation]. Timişoara: Politehnica Publishing House.
[62] Platonov, V. V., Tsirkunenko, A. T., & Bukhanov, S. S. (2019, May). Control of energy-efficient electric drive of pumping stations. In *IOP Conference Series: Materials Science and Engineering*. Vol. 537, No.6, p. 062080. IOP Publishing.
[63] Popa, A. Ș. (2021). *Studies on updating the elements of the irrigation regime for corn and soybean crops in Mărtăcești locality, Brăila county, in the context of changing climatic conditions* (*Studii privind actualizarea elementelor regimului de irigare al culturilor de porumb și soia în localitatea Mărtăcești jud. Brăila, în contextul schimbărilor condițiilor climatice*). [Bachelor's thesis]. "Dunărea de Jos" University of Galați, Romania.
[64] Qin, J., Duan, W., Zou, S., Chen, Y., Huang, W., & Rosa, L. (2024). Global energy use and carbon emissions from irrigated agriculture. *Nature Communications*, *15*(1), 3084.
[65] Quach, M., Mele, P. M., Hayden, H. L., Marshall, A. J., Mann, L., Hu, H. W., & He, J. Z. (2022). Proximity to subsurface drip irrigation emitters altered soil microbial communities in two commercial processing tomato fields. *Applied Soil Ecology*, *171*, 104315.
[66] Rakhade, R.D., Patil, N.V., Pardeshi, M.R., Mhasde, C.S. (2021). Optimal choice of agricultural drone using MADM methods. *International Journal of Technology Innovation in Modern Engineering Science (IJTIMES)*, *7*(4), 2455-2585.
[67] Ray, S., Majumder, S. (2024). Water management in agriculture: Innovations for efficient irrigation. In P. Sil, P. Chhetri, S. Majumder, & D. T. Santosh (Eds.), *Modern Agronomy*. pp. 169-185.
[68] Rocha, M. O., de Miranda, A. G. S., da Silva, P. A., de Oliveira, J. T., & da Cunha, F. F. (2024). Growth Performance of Sabia Grass Irrigated by Drippers Installed in Subsurface. *AgriEngineering*, *6*(3), 3443.
[69] Roerink, G. J., Bastiaanssen, W. G., Chambouleyron, J., & Menenti, M. (1997). Relating crop water consumption to irrigation water supply by remote sensing. *Water Resources Management*, *11*(6), 445-465.
[70] Rosegrant, M. W., & Cai, X. (2002). Global water demand and supply projections: part 2. Results and prospects to 2025. *Water International*, *27*(2), 170-182.
[71] Sabir, R. M., Sarwar, A., Shoaib, M., Saleem, A., Alhousain, M. H., Wajid, S. A., Rasul, F., Shahid, M.A., Anjum, L., Safdar, M., Muhammad, N.E., Waqas, R.M., Zafar, U. Raza, A. (2024). Managing Water Resources for Sustainable Agricultural Production. *Transforming Agricultural Management for a Sustainable Future: Climate Change and Machine Learning Perspectives*. pp. 47-74. Cham: Springer Nature Switzerland.
[72] Saccon, P. (2018). Water for agriculture, irrigation management. *Applied Soil Ecology*, *123*, 793-796.
[73] Schwankl, L. (1992). *Maintenance of Microirrigation Systems*. University of California-Davis.
[74] Shanu, V. (2024). *High-Efficiency Irrigation Systems. Fundamentals And Innovations*, Chapter in Vegetanle Production: Fundamentals and Innovations, Stella International Publications, 1st Edition, ISBN:978-81-978397-3-3, India.
[75] Siebert, S., Burke, J., Faures, J. M., Frenken, K., Hoogeveen, J., Döll, P., & Portmann, F. T. (2010). Groundwater use for irrigation–a global inventory. *Hydrology and Earth System Sciences*, *14*(10), 1863-1880.
[76] Singh, G. K. (2013). Solar power generation by PV (photovoltaic) technology: A review. *Energy*, *53*, 1-13.

[77] Șovăială, G., Matache, G., Popescu, A. I., Popescu, A. M. C., Drăghici, I., Manea, D., & Septar, L. (2018). Considerations on irrigation and fertilization of agricultural crops on sandy soils in arid, semiarid and dry sub-humid climate. In *2018 International Conference on Hydraulics and Pneumatics–HERVEX,* Băile Govora, Romania. pp. 231-243.
[78] Țenu, I. (2004). *Irrigation Equipment (Echipamente pentru irigații)*. Cermi Publishing House, Iași / Romania.
[79] Umair, M., Hussain, T., Jiang, H., Ahmad, A., Yao, J., Qi, Y., Zhang, Y., Min, L., Shen, Y. (2019). Water-saving potential of subsurface drip irrigation for winter wheat. *Sustainability*, *11*(10), 2978.
[80] Wang, J., Du, Y., Niu, W., Han, J., Li, Y., & Yang, P. (2022). Drip irrigation mode affects tomato yield by regulating root–soil–microbe interactions. *Agricultural Water Management*, *260*, 107188.
[81] Xing, Y., & Wang, X. (2024). Precision Agriculture and Water Conservation Strategies for Sustainable Crop Production in Arid Regions. *Plants*, *13*(22), 3184.
[82] ***Innovative Independent Energy System for Irrigating Agricultural Crops in the Context of Current Climate Change *(Sistem Inovativ Independent Energetic Destinat Irigării Culturilor Agricole În Condițiile Schimbărilor Climatice Actuale)* financing contract no. 431/390107/07.02.2023, SMIS 156177. https://www.rolix.ro/proiecte_cercetare/pti_inma.htm
[83] *https://www.apftrade.ro/spatii-verzi/rampa-de-udare-type-3.html*
[84] *https://appiadronetech.com/agricultural-and-farming-drones/adt-falcon-50l/*
[85] *https://www.bauer-at.com/en/product/irrigation/smartrain/*
[86] *https://www.centrulhidrauliccalarasi.ro/wp-content/uploads/2022/04/brazdar.jpg*
[87] *https://www.dji.com/global*
[88] *https://www.dji.com/global/t30*
[89] *https://www.fao.org/4/s8684e/s8684e04.htm*
[90] *https://hse-uav.com/products/xag-p150*
[91] *https://www.irrimec.com/?lang=en*
[92] *https://oaji.net/articles/2015/1672-1448748396.pdf*
[93] *https://www.parrot.com/en*
[94] *https://www.pompe-grundfos.ro/pompe-apa-grundfos/pompe-grundfos-sq-sqe*
[95] *https://www.pompe-grundfos.ro/pompe-apa-grundfos/sp9-11-rp2-43x380-41550-22kw-98699055*
[96] *https://pompesubmersibile.ro/grupuri-pompare-pedrollo/grup-pompare-pedrollo-CB2-F-50-200A*
[97] *https://product-selection.grundfos.com/products/cr-cre-cri-crie-crn-crne-crt-crte/cr?tab=models*
[98] *http://pub.osim.ro/publication-server/pdf-document?PN=RO126176%20RO%20126176&iDocId=712&iepatch=.pdf*
[99] *https://ro.shop.wilo.com/ro/pompa-submersibila-sub-twi-5-505-1230-v-50-hz-4*
[100] *https://www.romet.ro/resources/download/proiect_212_2008.htm*
[101] *http://solar.physics.uvt.ro/srms/*
[102] *https://www.xa.com/en/p150/p150specs*

DISCRETE ELEMENT PARAMETER CALIBRATION AND OPTIMIZATION OF LAMINARIA JAPONICA BASED ON GP-PSO-XGBOOST MODEL

/

基于 GP-PSO-XGBOOST 模型的海带离散元参数校准与优化

Xian WANG[1,2,3], Hua ZHOU[*1,2,3], Duanyang GENG[1,2,3], Zehao ZHA[1,2,3], Zhengzhong LI[1,2,3]

[1]School of Agricultural Engineering and Food Science, Shandong University of Technology, Zibo/China.

[2] Institute of Modern Agricultural Equipment, Shandong University of Technology, Zibo/ China.

[3] Key Laboratory of Smart Agriculture Technology and Intelligent Agricultural Machinery Equipment for Field Crops in Shandong Province, Zibo / China.

Tel: +8615071529850; E-mail: zhouhua688@163.com

DOI: https://doi.org/10.35633/inmateh-76-54

Keywords: *Laminaria japonica, DEM, parameter calibration, simulation, XGBoost*

ABSTRACT

During the mechanized harvesting of Laminaria japonica, it is prone to breakage and damage, resulting in an increased loss rate. To accelerate the optimization of harvesting equipment for Laminaria japonica, this study established a simulation model based on the discrete element method. The Hertz-Mindlin with Bonding contact model was used, and parameters of Laminaria japonica were calibrated through shear tests. Using the maximum shear force (F_{max}) as the test indicator, the optimal parameters were obtained through Plackett-Burman test, the steepest climb test, Box-Behnken test, and the GP-PSO-XGBoost regression prediction model. The results indicated that when the coefficient of restitution of Laminaria japonica-steel was 0.45, the normal stiffness per unit area was 303 MN/m³, the shear stiffness per unit area was 378 MN/m³, and the bonding radius was 0.70 mm, the relative error of F_{max} was 0.75%. The average error of the F_{max} for samples at different thicknesses was 3.09%, and the relative error of the maximum puncture force in puncture test was 5.59%. Finally, a discrete element model of the whole Laminaria japonica was established. This study offers theoretical support for the development and optimization of harvesting equipment for Laminaria japonica.

摘要

海带在机械化采收过程中易出现破损和损伤，造成损失率增加。为了加速海带机械收获设备的研发，本研究基于离散元法建立了海带仿真模型。研究采用 Hertz-Mindlin with Bonding 接触模型，通过剪切试验对海带进行参数标定。以最大剪切力（F_{max}）为试验指标，通过 Plackett-Burman 检验、最陡爬坡检验、Box-Behnken 检验和 GP-PSO-XGBoost 回归预测模型得到最优参数。结果表明：当海带钢的恢复系数为 0.45，单位面积法向刚度为 303 MN/m³，单位面积剪切刚度为 378 MN/m³，粘接半径为 0.70 mm 时，F_{max} 的相对误差为 0.75%。不同厚度样品的 F_{max} 平均误差为 3.09%，穿刺试验中最大穿刺力的相对误差为 5.59%。最后，建立海带整体的离散元模型。本研究为海带收获设备的研发与优化提供理论支持。

INTRODUCTION

Laminaria japonica is rich in bioactive components such as fucoidan, mannitol, and iodine*(Li et al., 2023)*, making it a vital raw material in industries like pharmaceutical, healthcare, chemical, and agriculture *(He et al., 2020; Zhao et al., 2024)*. With the growing global demand for *Laminaria japonica*, its production has also been steadily rising *(Naylor et al., 2021)*. Against this backdrop, the development of mechanized harvesting equipment for *Laminaria japonica* is gradually becoming key to enhancing production efficiency and promoting the sustainable development of the *Laminaria japonica* industry *(Chang et al., 2018; Jiang et al., 2022; Tan et al., 2020)*. However, *Laminaria japonica* possesses unique morphological characteristics of being flat and flexible, which often leads to the issue of breakage and damage during the mechanical harvesting process. Addressing this challenge necessitates precise characterization of *Laminaria japonica*'s micromechanical fracture behavior.

Xian Wang, bachelor degree; Hua Zhou, Ph.D.; Duan-yang Geng, Prof. Ph.D.; Ze-hao Zha, bachelor degree; Zheng-zhong Li bachelor degree.*

The discrete element method (DEM) has proven effective in simulating the micromechanical behavior of particle-based materials *(Wachem et al., 2020; Zhao et al., 2023)* and has been widely applied in the mechanical modeling of various crops in agricultural engineering *(Gao et al., 2023; Tang et al., 2023)*. For example, the Hertz-Mindlin with bonding model has been used to construct breakable bonding models for tobacco leaves *(Tian et al., 2023)*, banana stems *(Guo et al., 2021)*, and wheat straw *(Li et al., 2024)*, with parameter calibration conducted through compression, shear, and three-point bending tests. These studies have provided key mechanical parameters for the design and development of harvesting and post-processing equipment. However, despite the extensive application of DEM in modeling terrestrial crops, research on aquatic macroalgae such as *Laminaria japonica* remains limited. Its markedly different mechanical behavior compared to terrestrial crops calls for further investigation into its fracture mechanisms.

This study aims to establish a damageable flexible model of *Laminaria japonica* based on the DEM. By integrating physical tests and simulation analysis, the fracture mechanism of *Laminaria japonica* is investigated. First, physical tests were conducted to determine the intrinsic parameters, contact parameters, and basic mechanical properties of *Laminaria japonica*, based on which a biomechanical model was developed. The Plackett-Burman design was employed to screen key parameters, followed by refinement of the parameter range using the steepest ascent method and Box-Behnken design. To improve calibration efficiency, a hybrid GP-PSO-XGBoost algorithm was introduced to construct a parameter prediction model. The accuracy of the model was validated through shear and puncture tests on *Laminaria japonica* of varying thicknesses. The results not only provide new insights into the study of the fracture mechanics of *Laminaria japonica*, but also offer theoretical support for the design and optimization of *Laminaria japonica* harvesting equipment.

MATERIALS AND METHODS

Sample preparation

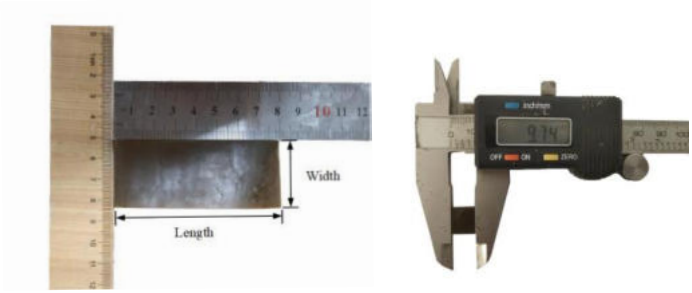
The *Laminaria japonica* samples selected for this study were sourced from the Ailun Bay marine ranch in Rongcheng, Shandong, China. The variety used is the No.205 at maturity, which is the primary species cultivated in Rongcheng. The *Laminaria japonica* is divided into upper, middle, and lower sections, as shown in Fig. 1.



Fig. 1 - The structure of fresh *Laminaria japonica*

During the harvesting process, it was observed that the middle section is the most susceptible to damage. Therefore, the middle section was selected as the research object for preparing *Laminaria japonica* samples for mechanical property analysis.

To acquire representative mechanical performance data, ten mature *Laminaria japonica* specimens were randomly selected, from which two types of rectangular test samples—sample 1 and sample 2—were prepared. Sample 1 measured approximately 80 × 33 mm (length × width), with a total of 40 samples produced; sample 2 measured approximately 10 × 10 mm, with 10 samples prepared in total, as shown in Fig 2. The thickness of each sample 1 was measured using a digital caliper, with a range from 0.8 to 5.2 mm.



(a) sample 1 *(b) sample 2*

Fig. 2 - Test sample of *Laminaria japonica*

Density measurement

Since there is no reference for the density of *Laminaria japonica*, it was measured using the pycnometer method. The pycnometer was cleaned, dried, and filled with distilled water, then weighed using a JCS-Z1 electronic balance (accuracy: 0.1 g). Subsequently, the *Laminaria japonica* was cut into uniform pieces and weighed. The *Laminaria japonica* was gently placed into the pycnometer, and any overflowed water was carefully wiped off with absorbent paper. The total mass of the pycnometer was measured again (Fig 3a). The density of the *Laminaria japonica* was calculated as follows:

$$\rho_g = \frac{m_g}{m_p + m_g - m_z} \rho_s \tag{1}$$

where: m_g is the mass of *Laminaria japonica* in air, kg; ρ_g is the density of *Laminaria japonica*, kg/m^3; ρ_s is the density of distilled water at room temperature, kg/m^3; m_P is the mass of the pycnometer filled with water, kg; and m_z is the total mass of the pycnometer containing the remaining water and *Laminaria japonica* after the overflowed water is wiped off, kg.

After multiple experiments, the density of *Laminaria japonica* was calculated to be 1263 kg/m^3.

Poisson's ratio and shear modulus

In this study, the multifunctional texture analyzer (ENS-DVU, range: 1000 N, accuracy: 0.01 N, Beijing Enovation Technology Development Co., Ltd.) (Fig 4a) was used to perform compression tests on sample 2 to determine the Poisson's ratio (v) and shear modulus (K) of *Laminaria japonica*, as shown in Fig 3b. The Poisson's ratio of *Laminaria japonica* was calculated using Eq (2).

$$v = \left|\frac{\varepsilon_1}{\varepsilon_2}\right| = \frac{L_1 - L_2}{H_1 - H_2} \tag{2}$$

where: ε_1 is the strain perpendicular to the load direction, ε_2 is the strain in the direction of the applied load, L_1 is the lateral dimension before compression, mm; L_2 is the lateral dimension after compression, mm; H_1 is the axial dimension before compression, mm; and H_2 is the axial dimension after compression, mm.

The shear modulus (K) can be calculated using Eq (3).

$$K = \frac{F \cdot L}{2(1+v) \cdot S \cdot \Delta L} \tag{3}$$

where: F is the maximum load during the elastic deformation phase of the test sample, N; L is the initial length of the test sample, mm; S is the cross-sectional area of the test sample, mm^2; and ΔL is the change in length before and after compression, mm.

After multiple tests, the Poisson's ratio of *Laminaria japonica* was determined to be 0.338, and its shear modulus was calculated as 5.43 MPa.

Coefficient of friction and coefficient of restitution

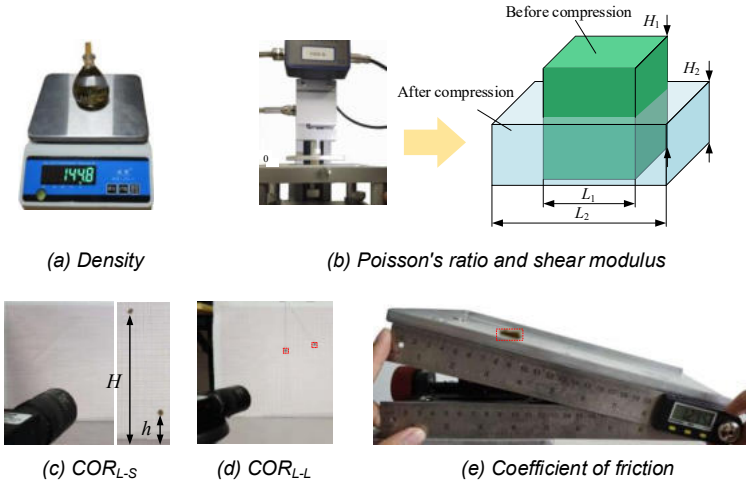
The coefficient of restitution of *Laminaria japonica*-steel ($COR_{L\text{-}S}$) was measured using a collision bounce test. A high-speed camera was used to record the collision between the *Laminaria japonica* and the steel plate (Fig.3c), and the coefficient of restitution (e) was calculated using Eq (4). The coefficient of restitution of *Laminaria japonica-Laminaria japonica* ($COR_{L\text{-}L}$) was measured using the fine wire suspension method (Fig.3d). The friction coefficient was measured using a friction tester (Fig 3e).

$$e = \left|\frac{v'}{v}\right| = \sqrt{\frac{2gh}{2gH}} = \sqrt{\frac{h}{H}} \tag{4}$$

where:

h is the height at which *Laminaria japonica* bounces up after falling, mm; H is the initial height of *Laminaria japonica*, mm.

After conducting multiple experiments, the average $COR_{L\text{-}L}$ and $COR_{L\text{-}S}$ were calculated to be 0.38 and 0.48, respectively. The average coefficient of static friction for *Laminaria japonica-Laminaria japonica* ($COS_{L\text{-}L}$) and the coefficient of static friction for *Laminaria japonica*-steel ($COS_{L\text{-}S}$) were calculated to be 0.84 and 0.72, respectively. The average coefficient of rolling friction for *Laminaria japonica-Laminaria japonica* ($COO_{L\text{-}L}$) and the coefficient of rolling friction for *Laminaria japonica*-steel ($COO_{L\text{-}S}$) were calculated to be 0.44 and 0.36, respectively.



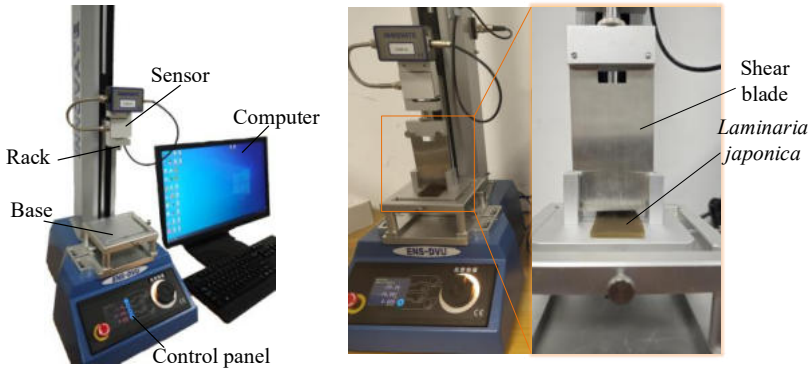
(a) Density (b) Poisson's ratio and shear modulus

(c) COR_{L-S} (d) COR_{L-L} (e) Coefficient of friction

Fig. 3 - Measurement of physical parameters of *Laminaria japonica*

Shear test

Shear test is a widely used method for determining the mechanical properties of materials and is frequently applied in the study of shear strength, rheological properties, and deformation behaviors of agricultural materials *(Li et al., 2017)*. In this study, shear test was performed using the multifunctional texture analyzer (Fig 4a). This equipment collects mechanical response data during the shear process of *Laminaria japonica* using a high-precision force-displacement sensor, making it suitable for experimental analysis of the shear mechanical properties of biological materials.



(a) Multifunctional texture analyser (b) Shearing process

Fig. 4 - Shear test of *Laminaria japonica*

A total of 30 fresh *Laminaria japonica* samples 1 were randomly selected for the shear tests. A shear blade with a thickness of 1.2 mm and a base gap of 1.5 mm, with a loading speed of 0.5 mm/s. A texture analyzer was employed to record the shear force–time curve in real time. The maximum shear force (F_{max}) of *Laminaria japonica* samples 1 with different thicknesses was measured and used as the key index for the calibration of discrete element model parameters, as shown in Fig 4b.

Particle radius and shear model construction

In the discrete element software EDEM, the behavior of the model is determined by several key parameters such as particle parameter, bonding parameters, and the computational time step. The actual thickness of *Laminaria japonica* ranges from 0.8 to 5.2 mm, and since its length is relatively large, the variation in thickness across the shear range can be considered negligible. Thus, a *Laminaria japonica* model with a thickness of its mean (3 mm) is established. To balance computational performance with simulation accuracy, uniform particles with a radius of 0.5 mm are selected as the basic particles, and a contact radius of 0.75 mm is chosen to ensure continuous bonds between particles. To ensure the accuracy of the subsequent calibration of discrete element parameters, the dimensions of the established discrete element model must match those of the physical test samples (Fig. 5). In the EDEM software, models for the shear blade and base with dimensions identical to those of the physical test are created. The discrete element model of *Laminaria japonica* sample is placed on the base, and the simulation test parameters are set to match those of the physical test (Fig 5). The detailed DEM simulation parameters are shown in Table 1.

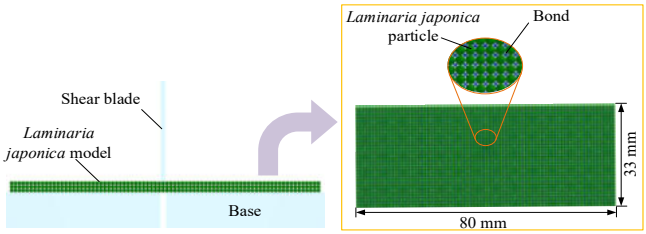


Fig. 5 - Discrete element model of *Laminaria japonica* sample

Table 1

Parameter table for *Laminaria japonica* simulated shear test

Types	Parameters	Values	Source
Intrinsic parameter	Density of *Laminaria japonica* (kg/m^3)	1263	Measurement
	Poisson's ratio of *Laminaria japonica*	0.338	Measurement
	Shear modulus of *Laminaria japonica* (MPa)	5.43	Measurement
	Density of steel (kg/m^3)	7865	*Zhang et al. (2023)*
	Poisson's ratio of steel	0.30	*Zhang et al. (2023)*
	Shear modulus of steel (GPa)	79	*Zhang et al. (2023)*
Contact parameter	$COR_{L\text{-}L}$	0.2~0.6	Calibration
	$COS_{L\text{-}L}$	0.4~1.2	Calibration
	$COO_{L\text{-}L}$	0.2~0.6	Calibration
	$COR_{L\text{-}S}$	0.3~0.7	Calibration
	$COS_{L\text{-}S}$	0.4~1.2	Calibration
	$COO_{L\text{-}S}$	0.2~0.6	Calibration
Bonding model parameters	Normal stiffness per unit area (MN/m^3)	100~900	Calibration
	Shear stiffness per unit area (MN/m^3)	100~900	Calibration
	Critical normal stress (MPa)	1~9	Calibration
	Critical shear stress (MPa)	1~9	Calibration
	Bonding radius (mm)	0.6~1	Calibration

Calibration of simulation parameters

Plackett-Burman test

In this study, Plackett-Burman test design was implemented using Design-Expert software. A total of 11 actual parameters and 8 virtual parameters were selected as experimental factors in this study. The actual parameters included: $COR_{L\text{-}L}$ (x_1), $COS_{L\text{-}L}$ (x_2), $COO_{L\text{-}L}$ (x_3), $COR_{L\text{-}S}$ (x_4), $COS_{L\text{-}S}$ (x_5), $COO_{L\text{-}S}$ (x_6), normal stiffness per unit area (x_7), shear stiffness per unit area (x_8), critical normal stress (x_9), critical shear stress (x_{10}), and bonding radius (x_{11}). Additionally, there were 8 virtual parameters (x_{12}~x_{19}). Each parameter was tested at two levels, high (+1) and low (-1). The performance indicator for the experiments was F_{max}. A total of 20 experiments were conducted. The detailed experimental design and simulation results are shown in Table 2 (columns for virtual parameters are omitted).

Table 2

Design and results of Plackett-Burman test

No.	Factors											F_{max}/N	No.	Factors										F_{max}/N
	x_1	x_2	x_3	x_4	x_5	x_6	x_7	x_8	x_9	x_{10}	x_{11}			x_1	x_2	x_3	x_4	x_5	x_6	x_7	x_8	x_9	x_{10}	x_{11}	
1	1	1	-1	-1	1	1	1	1	-1	1	-1	264.8	11	1	-1	1	-1	-1	-1	-1	1	1	-1	1	220.5
2	-1	1	1	-1	-1	1	1	1	1	-1	1	165.6	12	-1	1	-1	1	-1	-1	-1	-1	1	1	-1	42.6
3	1	-1	1	1	-1	-1	1	1	1	1	-1	304	13	1	-1	1	-1	1	-1	-1	-1	-1	1	1	133.8
4	1	1	-1	1	1	-1	-1	1	1	1	1	574.5	14	1	1	-1	1	-1	1	-1	-1	-1	-1	1	113.3
5	-1	1	1	-1	1	1	-1	-1	1	1	1	3.7	15	1	1	1	-1	1	-1	1	-1	-1	-1	-1	169.1
6	-1	-1	1	1	-1	1	1	-1	-1	1	1	321.5	16	1	1	1	1	-1	1	-1	1	-1	-1	-1	174.9
7	-1	-1	-1	1	1	-1	1	1	-1	-1	1	530	17	-1	1	1	1	1	-1	1	-1	1	-1	-1	170.3
8	-1	-1	-1	-1	1	1	-1	1	1	-1	-1	195.7	18	-1	-1	1	1	1	1	-1	1	-1	1	-1	259.4
9	1	-1	-1	-1	-1	1	1	-1	1	1	-1	116.5	19	1	-1	-1	1	1	1	1	-1	1	-1	1	264.8
10	-1	1	-1	-1	-1	-1	1	1	-1	1	1	388.7	20	-1	-1	-1	-1	-1	-1	-1	-1	-1	-1	-1	165.6

Steepest climb test

Based on the significant parameters selected from the Plackett-Burman test, a steepest climb test was conducted to further narrow the effective range of these parameters and quickly approach optimal values. Five groups of steepest climb test were designed, with the non-significant parameters set to their intermediate values.

Box-Behnken test

To establish a mathematical model between F_{max} and the discrete element simulation parameters in the simulation tests, and to find the optimal parameters for the *Laminaria japonica* model, Box-Behnken test designs were employed based on the results of the steepest climb test. This approach used a four-factor, three-level design to optimize significant parameters. The specific design and results of Box-Behnken test are shown in Table 3.

Table 3

Design and results of Box-Behnken test

No.	Factors				F_{max}/N	No.	Factors				F_{max}/N
	x_4	x_7	x_8	x_{11}			x_4	x_7	x_8	x_{11}	
1	0.4	0.6	0.4	0.8	122.8	16	0.5	1	0.5	0.8	226.5
2	0.6	0.6	0.4	0.8	143.6	17	0.4	0.8	0.3	0.8	100.6
3	0.4	1	0.4	0.8	178.3	18	0.6	0.8	0.3	0.8	102.2
4	0.6	1	0.4	0.8	206.5	19	0.4	0.8	0.5	0.8	186.2
5	0.5	0.8	0.3	0.7	73.5	20	0.6	0.8	0.5	0.8	221.7
6	0.5	0.8	0.5	0.7	167.8	21	0.5	0.6	0.4	0.7	106.4
7	0.5	0.8	0.3	0.9	135.4	22	0.5	1	0.4	0.7	155.5
8	0.5	0.8	0.5	0.9	236.5	23	0.5	0.6	0.4	0.9	159.2
9	0.4	0.8	0.4	0.7	128	24	0.5	1	0.4	0.9	226.1
10	0.6	0.8	0.4	0.7	142.5	25	0.5	0.8	0.4	0.8	170.1
11	0.4	0.8	0.4	0.9	177.9	26	0.5	0.8	0.4	0.8	168.2
12	0.6	0.8	0.4	0.9	211.4	27	0.5	0.8	0.4	0.8	158.2
13	0.5	0.6	0.3	0.8	66.4	28	0.5	0.8	0.4	0.8	168.8
14	0.5	1	0.3	0.8	131.6	29	0.5	0.8	0.4	0.8	167.9
15	0.5	0.6	0.5	0.8	173.3	-	-	-	-	-	-

Regression prediction of F_{max} based on the GP-PSO-XGBoost model

According to the analysis results of the Plackett-Burman and Box-Behnken tests, four factors (x_4, x_7, x_8, and x_{11}) were identified as having significant effects on F_{max}, with notable interactions observed among them. A GP-PSO-XGBoost regression prediction model was developed in the Python environment, integrating the eXtreme Gradient Boosting (XGBoost) algorithm with two heuristic optimization methods: Particle Swarm Optimization (PSO) and Gaussian Process-based Bayesian Optimization. This hybrid approach was designed to enhance both the model's capacity to capture complex data patterns and its nonlinear modeling capability. To further expand the feature space, second-order and interaction terms were generated using the Polynomial Features function.

In the GP-PSO-XGBoost model, x_4, x_7, x_8, and x_{11} were selected as input features, with F_{max} as the output target. Bayesian optimization was employed for global exploration in the parameter space, while PSO performed local search through iterative updates within the particle population, improving both the convergence speed and the robustness of the model. The hybrid optimization process is illustrated in Fig 6. Experimental data were divided into 60% for training, 20% for validation, and 20% for testing. The model performance was evaluated using the coefficient of determination R^2, R^2_{Adj}, and MAPE.

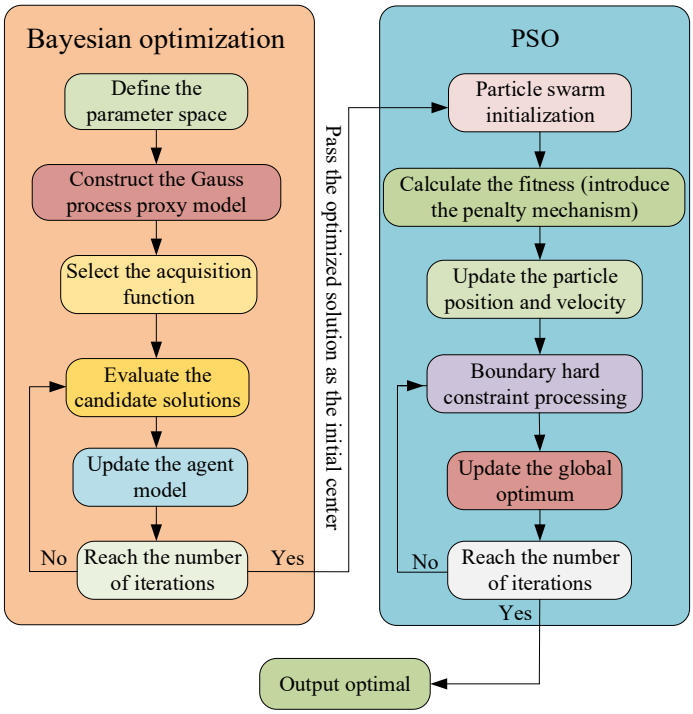


Fig. 6 - Hybrid optimization process

Validation of the Laminaria japonica model

To evaluate the accuracy of the calibrated model, experimental verification was conducted based on the prediction results of the GP-PSO-XGBoost model. Discrete element models of *Laminaria japonica* with different thicknesses were established, and their accuracy was assessed by comparing the simulation results with the predictions derived from the fitted equation. Puncture tests were further utilized for physical and simulation comparative analysis. The deformation and stress states of *Laminaria japonica* observed during the simulation were compared with those recorded in the physical tests. This comparison allowed for an assessment of the model's predictive accuracy, ensuring that the calibrated and optimized model delivers reliable and accurate results for practical applications.

Shear validation of Laminaria japonica models with different thicknesses

Based on the optimized parameters, discrete element models of *Laminaria japonica* with thicknesses of 1, 2, 3, 4, and 5 mm were constructed, and simulated shear tests were conducted for comparative validation against the equation fitting results.

Verification of puncture test results

To evaluate the adaptability of the discrete element model of *Laminaria japonica*, both physical and simulated puncture tests were conducted on *Laminaria japonica* sample 1 with a thickness of 3 mm and the corresponding discrete element model. In the physical test, the sample was placed on the base of the texture analyzer, ensuring that the sample was flat. The puncture probe of the texture analyzer moved downwards at a constant speed of 0.5 mm/s until it completely penetrated the sample *(Chen et al., 2024)*. The puncture force-displacement curves were recorded. The simulation tests were conducted under identical parameters.

RESULTS AND DISCUSSION

Shear test

Since the thickness of *Laminaria japonica* is not completely uniform, to obtain the corresponding F_{max} for the thickness (3 mm) of the *Laminaria japonica* discrete element model, a fitting relationship between thickness and F_{max} was established. First, data from 30 groups of *Laminaria japonica* shear tests were imported into Origin software to obtain the relationship between *Laminaria japonica* thickness and F_{max}. The fitted relationship curve is shown in Fig. 7, which approximates a linear relationship.

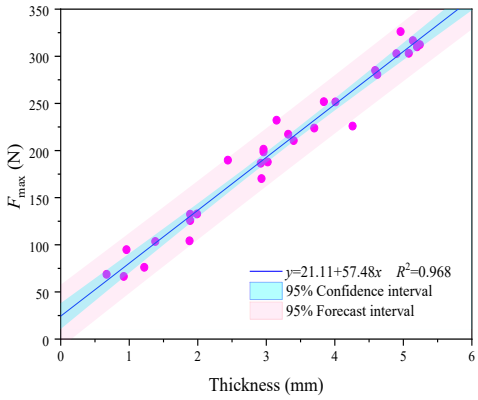


Fig. 7 - Relationship of F_{max}-thickness of *Laminaria japonica*

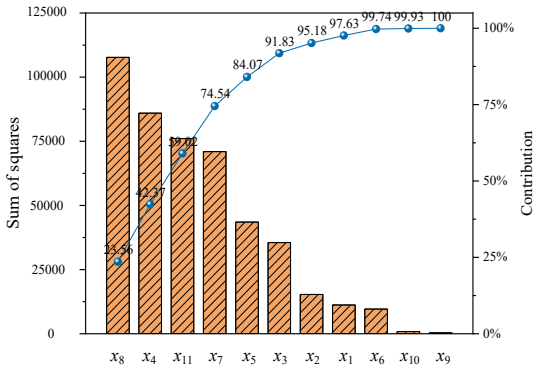


Fig. 8 - Pareto chart

Observations of the *Laminaria japonica* samples of 1 revealed that as the thickness of the *Laminaria japonica* increased, the internal structural organization increased, allowing it to withstand greater external forces. Additionally, the shear results indicated that F_{max} gradually increased with the thickness of the *Laminaria japonica*. Most of the data points for sample thickness and F_{max} fell within the 95% confidence interval, indicating that the fitted equation derived from the sample data was reliable. This equation can predict the F_{max} required for shear test of *Laminaria japonica* at various thicknesses. In the discrete element parameter calibration test, a *Laminaria japonica* model with a thickness of 3 mm was used. Substituting this thickness into the fitting equation yielded an F_{max} of 193.55 N.

Plackett-Burman test

After conducting an ANOVA on the experimental results, the significance effect of the 11 actual parameters on F_{max} was obtained. The Pareto chart visually illustrates the degree of influence of each factor, as shown in Fig 8. For cases with significant parameter variation, $COR_{L\text{-}S}$ (x_4), normal stiffness per unit area (x_7), bonding radius (x_{11}) and shear stiffness per unit area (x_8) collectively contributed to 75.54% of the total influence on F_{max}. These four parameters were found to have a significant effect on F_{max}, whereas the influence of the other parameters was relatively minor.

To further refine the range of significant parameters, steepest climb test and Box-Behnken test were employed in subsequent experiments. These experiments focused on the four significant parameters identified, while the remaining parameters, which showed no significant effect, were set to intermediate levels. The specific parameter settings were as follows: x_1=0.4, x_2=0.8, x_3=0.4, x_5=0.8, x_6=0.4, x_9=5 MPa, x_{10}=5 MPa.

Steepest climb test

The design and results of steepest climb test are shown in Table 4. According to the fitting equation, F_{max} was calculated to be 193.55 N for a *Laminaria japonica* thickness of 3 mm. This calculated value was compared with the simulation results to determine the percentage error.

The results of the steepest climb test showed that as x_4, x_7, x_8, and x_{11} increased, the F_{max} for *Laminaria japonica* also increased accordingly. The errors between the simulation and physical tests initially showed a decreasing trend, followed by an increasing trend. To further find the optimal parameter combination, the parameter settings from test 2 were used as the center point for subsequent tests, with tests 1 and 3 serving as references for low and high levels, respectively.

Table 4

Design and results of steepest climb test

No.	Factors				F_{max}/N	Error/%
	x_4	x_7	x_8	x_{11}		
1	0.3	100	100	0.6	48.3	-75.05
2	0.4	300	300	0.7	168.9	-12.74
3	0.5	500	500	0.8	305.7	57.94
4	0.6	700	700	0.9	435.0	124.75
5	0.7	900	900	1.0	460.4	137.87

Box-Behnken test

Based on the test results, ANOVA was conducted using the analysis fitting module in Design-Expert software, resulting in a quadratic regression equation with F_{max} as the response variable and x_4, x_7, x_8, and x_{11} as variables. This equation can predict the F_{max} based on these discrete element parameters. The fitted quadratic regression equation is as follows:

$$\begin{aligned} Y = {} & 166.64 + 11.17x_4 + 29.40x_7 + 50.19x_8 + 31.07x_{11} + 1.85x_4x_7 \\ & + 8.47x_4x_8 + 4.75x_4x_{11} - 3.00x_7x_8 + 4.45x_7x_{11} + 1.70x_8x_{11} - 0.60{x_4}^2 \\ & - 3.79{x_7}^2 - 13.10{x_8}^2 - 0.79{x_{11}}^2 \end{aligned} \quad (5)$$

To validate the accuracy of the quadratic regression model, residual analysis was performed. The normal probability plot of the residuals shows that the points are almost distributed along a straight line, indicating that the residuals are close to a normal distribution. Additionally, by comparing the actual and predicted values, it was found that most of the data points lie close to a straight line, further confirming the predictive accuracy of the model, as shown in Fig 9 and Fig 10. Therefore, the fitted quadratic regression model is accurate and reliable *(Awuah et al., 2022)*.

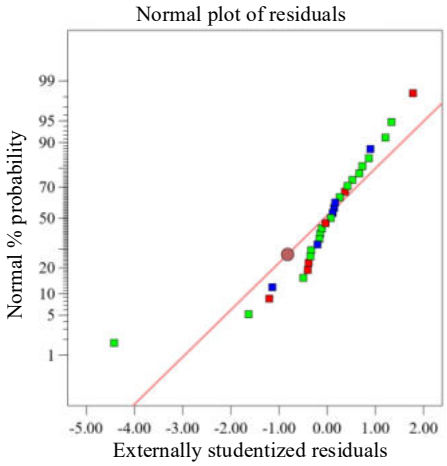


Fig. 9 - Residual normal distribution diagram

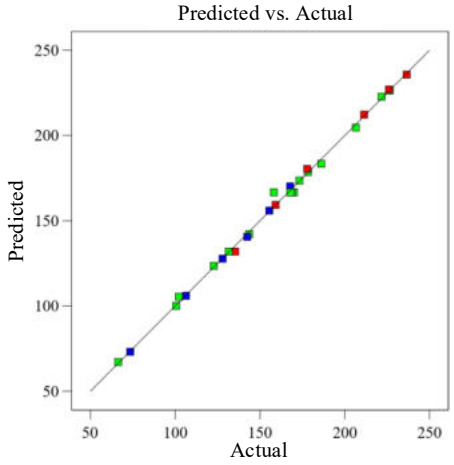


Fig. 10 - Correspondence between predicted value and actual value

From the ANOVA (Table 5), it was determined that the model was extremely significant statistical significance (P<0.0001), and the lack of fit was not significant. The model's R^2 value of 0.9973 and adjusted R^2_{Adj}value of 0.9947 indicated an excellent fit, effectively accounting for the variability in the data. ANOVA further indicated that x_4, x_7, x_8, x_{11}, x_4x_8, and ${x_8}^2$ had extremely significant effects on F_{max} (P<0.01), while x_4x_{11}, x_7x_{11}, and ${x_7}^2$ had significant effects (P<0.05).

Table 5

ANOVA of Box-Behnken test

Source	Sum of Squares	df	Mean Square	F-value	P-value
Model	55374.52	14	3955.32	373.71	< 0.0001
x_4	1498.57	1	1498.57	141.59	< 0.0001**
x_7	10372.32	1	10372.32	980.00	< 0.0001**
x_8	30230.44	1	30230.44	2856.24	< 0.0001**
x_{11}	11581.65	1	11581.65	1094.26	< 0.0001**
x_4x_7	13.69	1	13.69	1.29	0.2745
x_4x_8	287.30	1	287.30	27.14	0.0001**
x_4x_{11}	90.25	1	90.25	8.53	0.0112*
x_7x_8	36.00	1	36.00	3.40	0.0864
x_7x_{11}	79.21	1	79.21	7.48	0.0161*
x_8x_{11}	11.56	1	11.56	1.09	0.3137
${x_4}^2$	2.36	1	2.36	0.22	0.644
${x_7}^2$	93.21	1	93.21	8.81	0.0102*
${x_8}^2$	1113.71	1	1113.71	105.23	< 0.0001**
${x_{11}}^2$	4.06	1	4.06	0.38	0.5458
Residual	148.18	14	10.58		

Source	Sum of Squares	df	Mean Square	F-value	P-value
Lack of Fit	56.28	10	5.63	0.24	0.9676
Pure Error	91.89	4	22.97		
Cor Total	55522.70	28			
R^2=0.9973		R^2_{Adj}=0.9947			

*Note: * means significant difference (P<0.05), ** means extremely significant difference (P<0.01).*

Prediction results of the GP-PSO-XGBoost model

The predictive performance of the GP-PSO-XGBoost model is shown in Table 6. These results demonstrate that the model possesses excellent fitting performance and high generalization capability, with no signs of overfitting or underfitting. The XGBoost model, enhanced by the hybrid optimization framework, exhibits robust performance, delivering high accuracy, strong robustness, and remarkable generalization even under small-sample conditions. This provides a novel and effective framework for prediction and parameter optimization in future experimental studies.

Table 6

Comparison of model evaluation indicators

Evaluation type	Training set	Validation set	Test set
R^2	0.9991	0.9544	0.9727
R^2_{Adj}	0.9998	0.9895	0.9937
MAPE	0.57%	4.08%	3.16%

The result of parameter calibration

Prediction of optimal parameters for the *Laminaria japonica* shear model was made using the GP-PSO-XGBoost model. As a result, the optimal discrete element parameter combination for the *Laminaria japonica* model was determined as follows: CORL-S of 0.45, normal stiffness per unit area of 303 MN/m^3, shear stiffness per unit area of 378 MN/m^3, and bonding radius of 0.70 mm. Non-significant factors were assigned intermediate values. The final optimized discrete element parameters of the *Laminaria japonica* model are shown in Table 7.

Table 7

The final parameter calibration results of the discrete element model of *Laminaria japonica*

Factors	Parameters	Values
x_1	$COR_{L\text{-}L}$	0.40
x_2	$COS_{L\text{-}L}$	0.80
x_3	$COO_{L\text{-}L}$	0.40
x_4	$COR_{L\text{-}S}$	0.45
x_5	$COS_{L\text{-}S}$	0.80
x_6	$COO_{L\text{-}S}$	0.40
x_7	Normal stiffness per unit area (MN/m^3)	303
x_8	Shear stiffness per unit area (MN/m^3)	378
x_9	Critical normal stress (MPa)	500
x_{10}	Critical shear stress (MPa)	500
x_{11}	Bonding radius (mm)	0.70

Verification of parameter calibration results

The optimal combination of parameters was assigned to the discrete element model of *Laminaria japonica* with a thickness of 3 mm, and shear test was conducted under the same conditions. The measured F_{max} was 192.10 N, with a relative error of 0.75% compared to the fitted value (193.55 N), demonstrating close agreement between the simulation results and the fitted values. The simulation validation test was compared with the physical shear test of *Laminaria japonica* with a thickness of 3.02 mm (the closest experimental value to 3 mm). The shear force-displacement curves for both were extracted, as shown in Fig 11. The results showed high consistency in the shear force-displacement curves and deformation processes between the two tests. The *Laminaria japonica* samples of 1 in the shear tests exhibited three typical stages: (I) elastic stage, (II) local fracture stage, and (III) complete fracture stage.

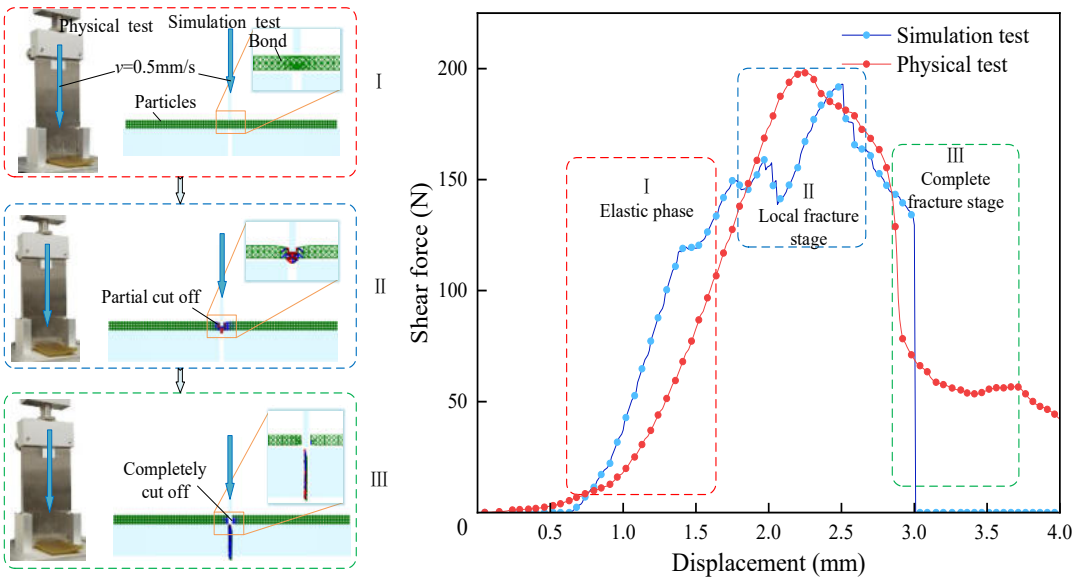


Fig. 11 - Shear test process and shear force-displacement curves

During both the simulated and physical shear test, as the shear blade moved downwards and compressed the surface of the *Laminaria japonica*, the shear force gradually increased, displaying a linear relationship with displacement within the elastic deformation range. The samples effectively resisted external forces, exhibiting prominent elastic properties (Stage I). As the shear blade continued its downward motion, the shear force increased further, and the sample began to fracture (with the bonds gradually stretching until rupture). At this stage, the internal structure of the *Laminaria japonica* began to deteriorate, with the shear force peaking and then starting to decline (Stage II). With continued displacement, the overall structure of the *Laminaria japonica* was completely compromised (the bonds were fully severed), leading to a rapid reduction in shear force as the sample lost its ability to resist external forces (Stage III). It is important to note that in the simulation test, the final shear force dropped to 0, whereas in the physical test, a residual force was observed. This discrepancy arises because the model in the simulation was cleanly cut by the shear blade, resulting in no further interaction with the blade after the cut (Fig. 12). Conversely, in the physical test, the *Laminaria japonica* was not cut neatly, it was divided into two segments that continued to interact with the shear blade, generating frictional forces and thus maintaining a residual shear force.

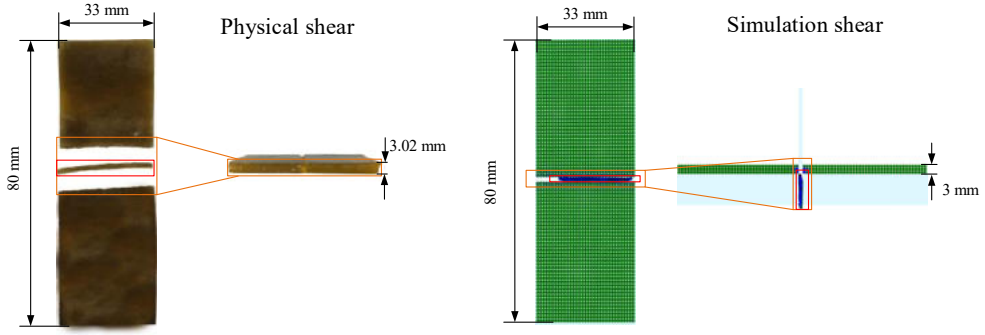


Fig. 12 - Samples after shear test

Shear validation of Laminaria japonica models with different thicknesses

The F_{max} errors of the *Laminaria japonica* models at different thicknesses are shown in Fig. 13. The average relative error across all models was 3.09%, with the maximum error occurring at a thickness of 5 mm, reaching 8.75%. This discrepancy is likely attributed to the increased complexity of the mechanical behavior in thicker samples, where pronounced non-uniformity or variations in bonding force distribution may arise. Nevertheless, the simulated predictive errors remain within an acceptable range. This indicates that the calibrated *Laminaria japonica* model exhibits excellent shear performance and adaptability. The model provides a reliable foundation for future research into the mechanical properties of *Laminaria japonica* and development of harvesting equipment for this species.

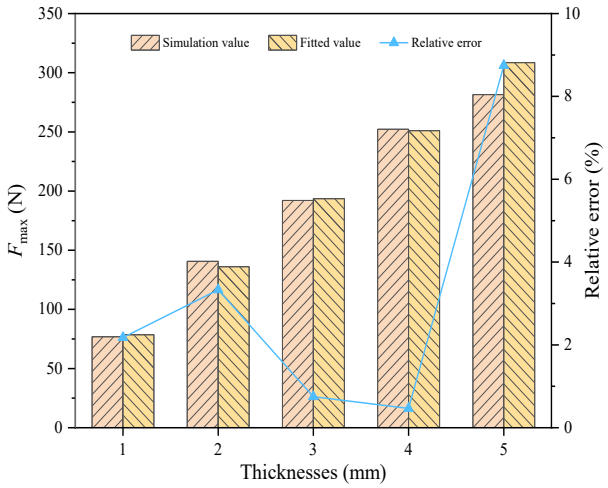


Fig. 13 - Relative error of F_{max} for different thickness models

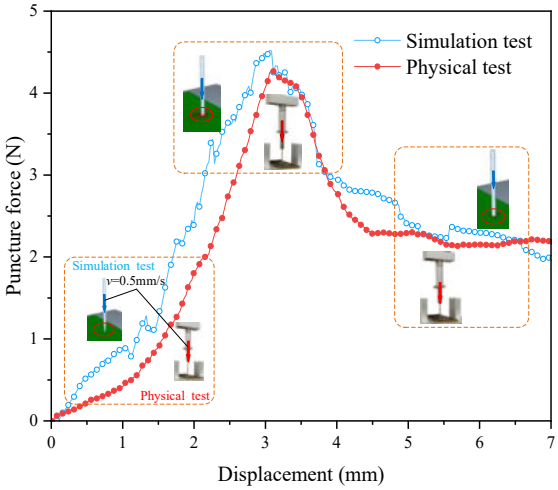


Fig. 14 - Puncture force-displacement curves

Verification of puncture test results

The puncture force-displacement curves for both simulation and physical tests are shown in Fig 14. A comparison of the two tests reveals that the overall trends of the puncture force-displacement curves are consistent. Both the simulation and physical tests indicate that as displacement increases, the force acting on the probe increases approximately linearly, reaching its maximum value when the probe fully penetrates the sample. The relative error at this point is 5.59%, suggesting a small error and strong agreement between the model and the *Laminaria japonica* samples. However, the simulation puncture force-displacement curve exhibits slight fluctuations compared to the physical test. This discrepancy is likely due to the larger particle radius used in the simulation model, which may introduce delays in the force response and slight oscillations during the transfer of collision forces between particles.

In summary, the established *Laminaria japonica* shear model effectively captures the mechanical properties of real *Laminaria japonica*, exhibiting strong predictive performance and accurately simulating the stress behavior of *Laminaria japonica* during mechanical harvesting. However, the mechanical properties of *Laminaria japonica* at the microscopic level are more complex. The model's assumptions about particle bonding may oversimplify these complexities. Future improvements in computational power are necessary to enhance calculation efficiency and enable further optimization of the model's microscopic parameters.

Establishment of the overall discrete element model for Laminaria japonica

Observations of a large number of *Laminaria japonica* samples revealed that its morphology is greatly influenced by the growth environment, especially in the edge regions. However, its thickness distribution generally follows a pattern of being thicker in the middle and thinner at the edges. To simplify the model, this study approximated *Laminaria japonica* as a flat structure while preserving its characteristic thickness distribution. Based on the Discrete Element Method (DEM), the model was filled with particles to generate a complete DEM model of *Laminaria japonica*, as shown in Fig. 15. This simplified design aims to provide a reference for mechanical harvesting and to lay the foundation for subsequent simulation tests and physical validation.

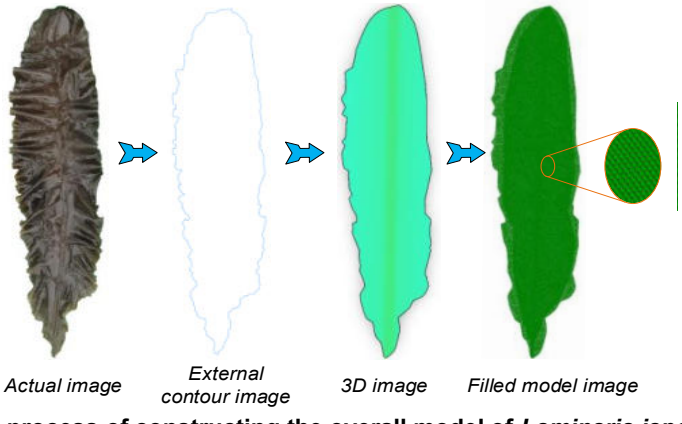


Fig. 15 - The process of constructing the overall model of *Laminaria japonica*

CONCLUSIONS

The physical, contact, and mechanical properties of Laminaria japonica were measured through physical experiments. Based on the Hertz-Mindlin with bonding model, a discrete element model of Laminaria japonica was developed by combining physical and simulation tests. Model parameter calibration was carried out, and the optimal parameter combination was obtained and validated. Using the F_{max} as the test indicator, the optimal parameters were obtained through Plackett-Burman test, the steepest climb test, Box-Behnken test, and the GP-PSO-XGBoost regression prediction model. The results indicated that when the coefficient of restitution of *Laminaria japonica*-steel was 0.45, the normal stiffness per unit area was 303 MN/m^3, the shear stiffness per unit area was 378 MN/m^3, and the bonding radius was 0.70 mm, the relative error of F_{max} was 0.75%. The average error of F_{max} across different thicknesses was 3.09%, and the relative error in maximum puncture force was 5.59%. These results demonstrate that the GP-PSO-XGBoost hybrid optimization and regression prediction model effectively captures complex inter-factor relationships, improves prediction accuracy and reliability, and provides strong support for parameter optimization in discrete element simulations. The discrete element model developed in this study lays a foundation for the design and optimization of Laminaria japonica harvesting equipment.

ACKNOWLEDGMENTS

This work was financially supported by the Key R&D Program Project in Shandong Province (Grant No. 2022CXGC020410).

REFERENCES

[1] Awuah, E., Zhou, J., Lian, Z. A., Aikins, K. A., Gbenontin, B. V., Mecha, P., & Makange, N. R. (2022). Parametric analysis and numerical optimisation of Jerusalem artichoke vibrating digging shovel using discrete element method. *Soil & Tillage Research*, 219, 105344. https://doi.org/10.1016/j.still.2022.105344

[2] Chang, Z., Zhang, Y., Zheng, Z., Wan, R., & Zhang, Z. (2018). Development status of the raft-cultivation harvesting devices for Laminaria japonica (筏式养殖海带收获装置的发展现状). *Fishery Modernization*, 45(1), 40-48. https://doi.org/10.3969/j.issn.1007-9580.2018.01.007 (in Chinese).

[3] Chen, H., Jin, L., Fang, C., Liu, L., Kačániová, M., Wang, J., Lu, J., & Ban, Z. (2024). Integration of puncture loading and finite element simulations to predict the mechanical responses for kiwifruit. *Postharvest Biology and Technology*, 217, 113102. https://doi.org/10.1016/j.postharvbio.2024.113102

[4] Gao, X., Xie, G., Li, J., Shi, G., Lai, Q., & Huang, Y. (2023). Design and validation of a centrifugal variable-diameter pneumatic high-speed precision seed-metering device for maize. *Biosystems Engineering*, 227, 161-181. https://doi.org/10.1016/j.biosystemseng.2023.02.004

[5] Guo, J., Karkee, M., Yang, Z., Fu, H., Li, J., Jiang, Y., Jiang, T., Liu, E., & Duan, J. (2021). Discrete element modeling and physical experiment research on the biomechanical properties of banana bunch stalk for postharvest machine development. *Computers and Electronics in Agriculture*, 188, 106308. https://doi.org/10.1016/j.compag.2021.106308

[6] He, B., Ming, Y., Pu, Y., Sun, Y., Jin, M., Yu, C., & Qi, H. (2020). The dual effects of riboflavin and Laminaria japonica polyphenol extracts on the gel properties of myofibrillar protein from Scomberomorus Niphonius under UVA irradiation. *Food Chemistry*, 332, 127373. https://doi.org/10.1016/j.foodchem.2020.127373

[7] Jiang, T., Hong, Y., Lu, L., Zhu, Y., Chen, Z., & Yang, M. (2022). Design and experiment of a new mode of mechanized harvesting of raft cultured Laminaria japonica. *Aquacultural Engineering*, 99, 102289. https://doi.org/10.1016/j.aquaeng.2022.102289

[8] Li, J., Bergman, K., Thomas, J., Gao, Y., & Gröndahl, F. (2023). Life Cycle Assessment of a large commercial Laminaria japonica farm in Shandong. *Science of The Total Environment*, 903, 166861. https://doi.org/10.1016/j.scitotenv.2023.166861

[9] Li, M., Xu, S., Yang, Y., Guo, L., & Tong, J. (2017). A 3D simulation model of corn stubble cutting using finite element method. *Soil & Tillage Research*, 166, 43-51. https://doi.org/10.1016/j.still.2016.10.003

[10] Li, S., Diao, P., Miao, H., Zhao, Y., Li, X., & Zhao, H. (2024). Modeling the fracture process of wheat straw using a discrete element approach. *Powder Technol*, 439, 119726. https://doi.org/10.1016/j.powtec.2024.119726

[11] Naylor, R. L., Hardy, R. W., Buschmann, A. H., Bush, S. R., Cao, L., Klinger, D. H., Little, D. C., Lubchenco, J., Shumway, S. E., & Troell, M. (2021). A 20-year retrospective review of global aquaculture. *Nature*, 591, 551-563. https://doi.org/10.1038/s41586-021-03308-6

[12] Tan, Y., Lou, S., & Chen, Z. (2020). Research on integrated specialized ship for Laminaria japonica harvesting, classifying and grading. *Aquacultural Engineering*, 91, 102121. https://doi.org/10.1016/j.aquaeng.2020.102121

[13] Tang, H., Xu, F., Xu, C., Zhao, J., & Wang, Y. (2023). The influence of a seed drop tube of the inside-filling air-blowing precision seed-metering device on seeding quality. *Computers and Electronics in Agriculture*, 204, 107555. https://doi.org/10.1016/j.compag.2022.107555

[14] Tian, Y., Zeng, Z., Gong, H., Zhou, Y., Qi, L., & Zhen, W. (2023). Simulation of tensile behavior of tobacco leaf using the discrete element method (DEM). *Computers and Electronics in Agriculture*, 205, 107570. https://doi.org/10.1016/j.compag.2022.107570

[15] Wachem, B., Thalberg, K., Nguyen, D., Juan, L., Remmelgas, J., & Niklasson-Bjorn, I. (2020). Analysis, modelling and simulation of the fragmentation of agglomerates. *Chemical Engineering Science*, 227, 115944. https://doi.org/10.1016/j.ces.2020.115944

[16] Zhang, Z., Mei, F., Xiao, P., Zhao, W., & Zhu, X. (2023). Discrete element modelling and simulation parameters calibration for the compacted straw cube. *Biosystems Engineering*, 230, 301-312. https://doi.org/10.1016/j.biosystemseng.2023.04.019

[17] Zhao, S., Pan, Z., Azarakhsh, N., Ramaswamy, H., Duan, H., & Wang, C. (2024). Effects of high-pressure processing on the physicochemical and adsorption properties, structural characteristics, and dietary fiber content of Laminaria japonica (Laminaria japonica), *Current Research in Food Science*, 8, 100671. https://doi.org/10.1016/j.crfs.2023.100671

[18] Zhao, J., Zhao, S., & Luding, S. (2023). The role of particle shape in computational modelling of granular matter. *Nature Reviews Physics*, 5(9), 505-525. https://doi.org/10.1038/s42254-023-00617-9

STUDY ON THE INFLUENCE OF VOLUTE WIDTH-DIAMETER RATIO ON THE PERFORMANCE OF MULTI-BLADE CLEANING FANS
/
蜗壳宽径比对多翼清选风机性能的影响研究

Yichen DONG[1,2,3], Zheng MA[1,2,3,*], Jie YU[1,2,3], Shuai WANG[1,2,3], Hongyan GAO[1,2,3], Yaoming LI[1,2,3]
[1)] School of Agricultural Engineering, Jiangsu University, Zhenjiang 212013, Jiangsu, China
[2)] Key Laboratory for Theory and Technology of Intelligent Agricultural Machinery and Equipment, Jiangsu University, Zhenjiang 212013, Jiangsu, China
[3)] Faculty of Agricultural Engineering, Jiangsu University, Zhenjiang 212013, Jiangsu, China
Tel: 18796087291; E-mail: mazheng123@ujs.edu.cn
DOI: https://doi.org/10.35633/inmateh-76-55

Keywords: *combine harvester, multi-blade centrifugal fan, volute width-diameter ratio, flow field characteristics, CFD*

ABSTRACT
Multi-blade centrifugal fans are regarded as an important direction for agricultural cleaning fans due to the advantages of compact structure, low noise and high efficiency. In view of the insufficient aerodynamic performance of traditional centrifugal fans in combine harvester cleaning devices caused by straight-blade structures, as well as the lack of design theory for multi-blade centrifugal fans, this study focused on a multi-blade centrifugal fan with wing-shaped blades. Using a combination of CFD numerical simulation and bench tests, the influence of the volute width-to-diameter ratio on fan performance and the internal flow field was investigated. The results showed that at a rated speed of 1000 r/min, the optimal volute width-to-diameter ratio was 1.3. Compared with the prototype fan, the optimized fan achieved a 7.13% increase in efficiency, a 6.53% increase in air volume, and a 16.63% improvement in air distribution uniformity. In addition, the internal flow of the optimized fan was improved, with reduced turbulence intensity in the tongue region of the volute. Furthermore, a volute width-to-diameter ratio–speed–air volume function model was established using MATLAB, providing a theoretical basis for the selection and design of high-performance multi-blade centrifugal fans.

摘要
多翼离心风机因结构紧凑、低噪高效等优势，被视为农业清选风机的重要方向。针对联合收获机清选装置中传统离心风机因平直叶片结构导致气动性能不足，以及多翼离心风机设计理论缺乏的问题，本研究以翼型叶片的多翼离心风机为研究对象，采用 CFD 数值模拟与台架试验相结合，探究了蜗壳宽径比对风机性能和内部流场的影响。结果表明：在额定转速 1000 r/min 下，最优风机蜗壳宽径比为 1.3；相较于原型风机，效率提升 7.13%，风量提升 6.53%，出风均匀性提升 16.63%；优化后的风机内部流动改善，蜗舌区域湍流强度减小。基于 MATLAB 建立蜗壳宽径比-转速-风量函数模型，本研究可为高性能多翼离心风机设计提供选型依据。

INTRODUCTION
With the increase of combine harvester feeding capacity and the popularization of multi-purpose mode, the agricultural production of combine harvester cleaning performance has put forward more stringent requirements. As the combine harvester's “digestive system”, the performance of the cleaning device directly determines the seed impurity rate and loss rate and other key indicators *(Liang et al., 2020; Almoslh et al., 2021)*. Currently, on the market, about 93% of combine harvester cleaning device use wind sieve type cleaning systems *(Ma et al., 2024; Wei et al., 2020)*. These systems utilize the synergistic effect of the centrifugal fan volute flow channel and impeller to generate an airflow field that meets the cleaning requirements. In close coordination with the sieve plate, they enable the precise and effective separation of grain from glumes, stalks, and other impurities *(Badretdinov et al., 2019; Zhang et al, 2025)*. The efficiency of the fan directly influences gas flow, pressure, and airflow stability. A highly efficient fan can deliver a more stable airflow, thereby enhancing cleaning performance. With the continuous growth of crop production and the increasing cutting width of combine harvesters, there is an urgent need to improve the efficiency of existing centrifugal fans to better meet the demands of modern, high-efficiency agricultural production.

Yichen Dong, Master's degree student; Zheng Ma, Professor; Jie Yu, Assistant Researcher; Shuai Wang, Assistant Researcher, Hongyan Gao, Assistant Researcher; Yaoming Li, Professor

In recent years, many scholars have utilized CFD numerical simulation methods to thoroughly study the influence of centrifugal fan structure on fan performance. *Varun et al, (2023),* designed a centrifugal fan model with 11 backward curved blades. The study found that when the number of blades increased to 14, the total pressure increased by 21.77% and the efficiency increased by 5.74%. In order to reduce the impact of uneven airflow distribution on the cleaning performance, *Chai et al, (2020),* optimized the blade parameters of the fan of the combine harvester using the response surface method, revealing the mechanism of the airflow distribution at the air outlet.

Wang et al, (2017), carried out numerical simulations of four agricultural fan models and discussed the effects of fan blade number and inclination angle on fan characteristics. *Liang and Wada, (2023),* studied the influence of the fan structure in the grain combine harvester on the airflow characteristics, explored the impact of the cleaning load on the flow rate of each air outlet of the fan, and optimized the fan structure.

Multi-blade centrifugal fan is regarded as an important development direction of future cleaning fan because of its advantages of large number of blades, low noise, large air volume and high pressure coefficient *(Yang et al., 2024; Ottersten et al., 2022; Acarer et al., 2020)*. At present, research on the structure of multi - blade centrifugal fans mainly focus on optimizing their impeller structure, while studies on the influence of volute structure on cleaning performance are relatively scarce. The geometric shape, dimensional parameters of the volute, and its matching relationship with the impeller directly affect the air flow distribution, pressure field, and velocity field, thereby determining the fan's efficiency and air flow uniformity (*Schäfer et al., 2020; Shim et al, 2020, Babubhai et al,2023)*. How to improve the fan's ability for efficient air flow separation and guidance through volute structure optimization is a technical problem urgently needing to be solved in the current fan design field.

This paper focuses on the optimization of the volute structure of multi-blade centrifugal fans, with the ratio of the volute width to the outer diameter of the impeller as the research variable. By setting four groups of values of the volute width and dimensionless processing of this parameter, the universality of the conclusions is enhanced, and the conversion according to the law of fan similarity can be applied to the prediction of the performance of fans with different specifications. CFD numerical simulation and bench test are combined to investigate the influence of the volute width-diameter ratio on the performance of the multi-blade centrifugal fan, focusing on the analysis of the parameter on the uniformity of the outlet airflow, air volume and the internal flow field of the mechanism, and design and build a performance test rig to verify the simulation results, with the aim of providing a basis for the subsequent multi-blade centrifugal fan design and optimization of the selection of the basis.

MATERIALS AND METHODS

Multi-blade centrifugal fan model construction

This paper takes the multi-blade centrifugal fan as the research object, and the structural model is shown in Fig. 1. The impeller consists of 16 wing fan-shaped blades, and the two sets of blades are back-to-back symmetrically mounted on the two sides of the center disk; the unequal basis element method is used to determine the size of the volute casing profile of the multi-blade centrifugal fan. The main structural dimensions of the fan are shown in Table 1.

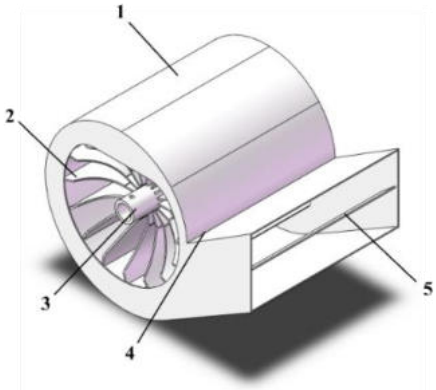


Fig. 1 - Schematic structure of multi-blade centrifugal fan

1 - Volute shell; 2 – Impeller; 3 - Impeller shaft; 4 - Volute tongue; 5 - Dividing plate

Table 1

Main structural parameters of the fan dimensions

Name	Sizes	Name	Sizes
Impeller inner diameter D_1	48 mm	Outer diameter of impeller D_2	262 mm
Number of blades Z	16	Inlet Diameter D_0	240 mm
Width of volute case B_k	314 mm	Height of air vents S	157 mm
Extended dimensions of the volute housing A_f	56 mm	Distance between impeller end face and housing f	5 mm
volute outlet length C	220 mm	Air outlet diffusion angle α	2°

Wind turbine similarity theory is an important theoretical basis used in the field of fluid mechanics to analyze and predict the performance of wind turbines. The theory provides a scientific basis for the design of wind turbines by establishing the geometrical, kinematic and dynamic similarity relationship between the model and the prototype *(Wang et al., 2012)*. This means that when the conclusions drawn in this study are applied to the actual design optimization of combine harvester fans, the parameters can be converted according to the similarity criterion to match the working condition requirements of different models. The relevant formulas of the similarity law for fans are shown in Table 2, where the formula labeled "'" indicates the known parameters.

Table 2

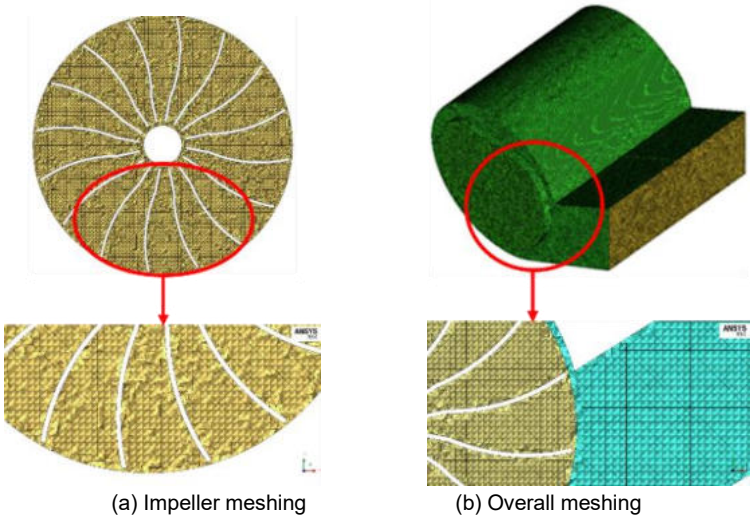
Calculation formulas based on wind turbine similarity theory

scientific law	calculation formula
Similarity law for flow rate	$\frac{Q}{Q'}=\frac{n}{n'}(\frac{D_2}{D_2'})^3$
Similarity law for full pressure	$\frac{P_{tF}}{P'_{tF}}=\frac{\rho}{\rho'}(\frac{n}{n'})^2(\frac{D_2}{D_2'})^2$
Similarity law for power	$\frac{N_i}{N'_i}=\frac{\rho}{\rho'}(\frac{n}{n'})^3(\frac{D_2}{D_2'})^5$
Similarity law for efficiency	$\eta_i=\eta'_i$

Where: Qv is the flow rate, m³/s; n is the rotational speed, r/min; D_2 is the outer diameter of the impeller, mm; P_{tF} is the total pressure, Pa; ρ is the density of the gas, kg/m³; P_{sh} is the shaft power, kW; η is the efficiency of the fan, %.

Grid Division

The flow channel model meshing is based on ICEM CFD in ANSYS 18.0. Structured meshes are used for the impeller channels and unstructured meshes are used for the volute shell channels. And the interface is set between the different flow channels to ensure the continuity of the flow at the interface. The Merge function is used to merge the two meshes, and the mesh schematic is shown in Fig. 2.



(a) Impeller meshing (b) Overall meshing

Fig. 2 - Effect of mesh division

Numerical Calculation Simulation Setup

Numerical simulations are performed based on Fluent in ANSYS 18.0, with steady state calculations first, and transient calculations after convergence of the calculations using the results of the constant calculations as initial values. The turbulence model is the RNG k-epsilon model, and the velocity-pressure coupling is done by SIMPLE algorithm with no-slip wall condition and enhanced wall function near the wall. The diffusion term, convection term and turbulent viscosity coefficients in the momentum equations are in second-order windward differential format. The inlet boundary is the pressure inlet with a value of 220 Pa, and the outlet boundary is the pressure outlet with a value of 0 Pa. The impeller speed is 1000 r/min, the maximum number of iteration steps is set to 20, the convergence residual is 10^{-3}, and the number of time steps is set to 250.

Numerical simulation validation

In order to verify the accuracy of the simulation results, a multi-blade centrifugal fan performance testing bench was built, as shown in Fig. 3. It mainly consists of multi-blade centrifugal fan, testing duct, sensor, motor, variable frequency controller, data acquisition system, and upper computer.

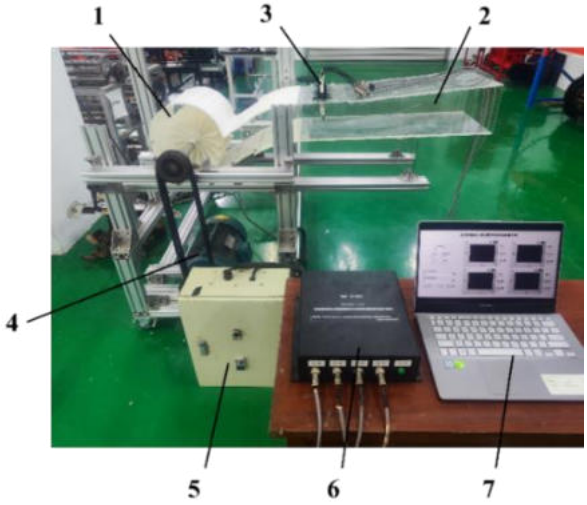


Fig. 3 - Multi-blade centrifugal fan performance testing bench

1 - Multi-blade centrifugal fan; 2 - Detection duct; 3 – Sensor; 4 – Motor; 5 - Frequency conversion controller; 6 - Data acquisition system; 7 - Upper computer

By numerical simulation of the fan under different working conditions, the simulation and test comparison curves of full pressure and efficiency are obtained as shown in Fig. 4. The results show that the numerical simulation results are in good agreement with the test data, with an error of no more than 10%, which verifies the reliability of the numerical simulation and can be used for subsequent simulation analysis.

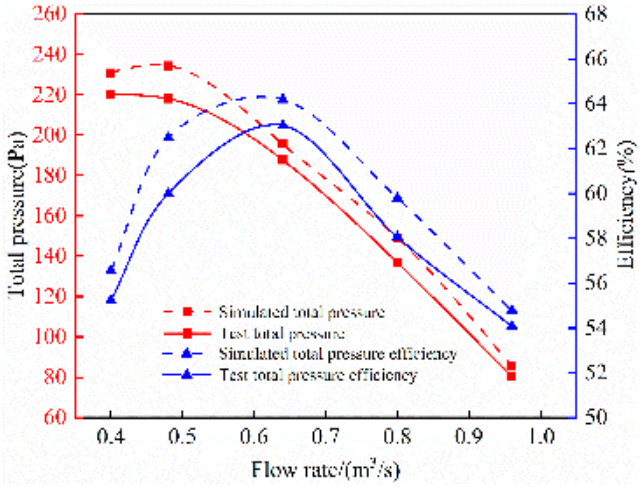


Fig. 4 - Comparison of numerical simulation and test results for prototype fan

Design of Matching Schemes for the Width-Diameter Ratio of Fan Volutes

Fig. 5 shows the axial structural schematic diagram of the volute and impeller of the multi-blade centrifugal fan. During the design of the scheme, the outer diameter and width of the impeller are kept unchanged, and only the width of the volute is changed to alter the axial matching between the volute and the impeller.

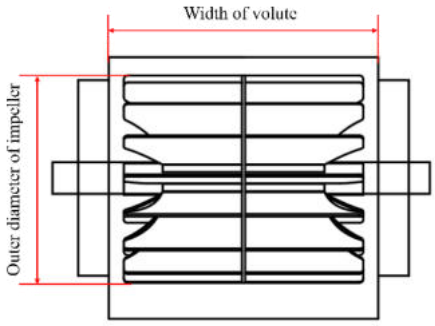


Fig. 5 - Schematic diagram of axial structure matching between volute and impeller

Since the size of the centrifugal fan will change with the change of the feeding amount of the combine harvester, in order to ensure the universality of the test results, the width of the volute is made dimensionless. The width-diameter ratio λ of the volute is defined as the ratio of the width of the volute to the outer diameter of the impeller, and the calculation formula is as follows:

$$\lambda = B_k / D_2 \quad (1)$$

where: B_k is the width of the volute, mm; D_2 is the outer diameter of the impeller, mm.

Four groups of test schemes are set up for grouped tests. The specific schemes are shown in Table 3.

Table 3

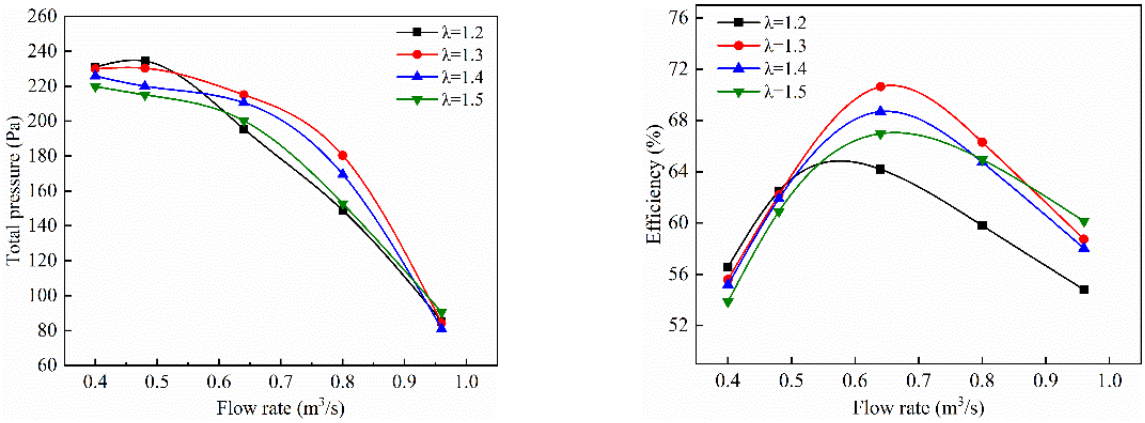
Experimental program for different volute width-to-diameter ratios

Experimental group	Outer diameter of impeller D_2 [mm]	Width of volute B_k [mm]	Volute width-diameter ratio λ /
1	262	314	1.2
2		340	1.3
3		366	1.4
4		393	1.5

RESULTS AND ANALYSIS

Performance Curves of Multi-blade Centrifugal Fans

The fan performance curve is used to characterize the relationship between the main performance parameters of the fan, such as air volume, air pressure, power and efficiency, etc., under a certain rotational speed and inlet conditions, reflecting the operating trend of the fan. In order to investigate the effect of different casing aspect ratios on the performance of centrifugal fans, this study uses CFD to numerically simulate the centrifugal fans with four casing designs at a rated speed of 1000 r/min, and obtains the total-pressure and efficiency performance curves of multi-blade centrifugal fans as shown in Fig. 6.



(a) Flow-Total Pressure Performance Curve (b) Flow-Efficiency Performance Curve

Fig. 6 - Schematic structure of multi-blade centrifugal fan

Fig. 6(a) illustrates that the total pressure of all four fan configurations generally decreases with increasing flow rate. The λ=1.3 fan exhibits superior total pressure across most flow ranges compared to other designs. The λ=1.2 configuration achieves peak total pressure at 0.48 m³/s through optimized kinetic-diffusion balance, yet its narrow flow path causes severe frictional losses at higher flows. Conversely, the λ=1.5 fan demonstrates higher pressure recovery in high-flow regimes (0.86~0.96 m³/s) due to reduced flow blockage from its enlarged cross-section.

The efficiency curves in Fig. 6(b) reveal parabolic trends with distinct peaks. The λ=1.3 configuration achieves maximum efficiency improvement (6.43% over the prototype), indicating optimal flow matching and minimal impact losses in the 1.3~1.4 width-diameter ratio range. The λ=1.2 fan shows left-shifted efficiency peaks, though efficiency plummets at higher flows due to axial spacing limitations. The λ=1.5 design excels in high-flow scenarios but suffers from vortex-induced losses at low flows due to incomplete diffusion.

Comprehensive analysis demonstrates that λ=1.3 provides balanced aerodynamic performance across operational ranges, making it ideal for general applications. The λ=1.2 configuration suits specialized low-flow/high-pressure scenarios, while λ=1.5 adapts to high-flow/low-loss requirements. Optimal width-diameter ratio selection requires balancing efficiency enhancement against potential aerodynamic losses, with 1.3~1.4 identified as the preferred range for multi-blade centrifugal fans in agricultural cleaning systems. These findings establish quantitative guidelines for fan geometry optimization under varying operational demands.

Comparative analysis of air velocity uniformity of outlet airflow

In grain cleaning operations, the airflow distribution characteristics of a multi-wing centrifugal fan directly affect the cleaning quality and operational efficiency. Studies have shown that when the airflow parameters (including flow rate, dynamic pressure and static pressure) at the air outlet of the fan show a uniform distribution along the impeller width direction, the grain cleanliness can be significantly improved and the sorting loss can be reduced *(Tang et al., 2007)*. The uniformity of the lateral distribution of wind speed at the air outlet is measured by the wind speed variance V, which is calculated as follows:

$$V = \frac{\sum_{i=1}^{n} (a_i - a)^2 \Big/ N-1}{a} \tag{2}$$

where: a_i is the wind speed value of the i-th measurement point, m/s; a is the average value of wind speed of the turbine, m/s; N is the number of measurement points of the turbine.

Under the rotational speed of 1000 r/min, three monitoring areas are divided at equal spacing in the vertical direction of the fan outlet, which are the upper L_1, middle L_2, and lower L_3, and 10 monitoring points are arranged at equal spacing on each monitoring line, and the distribution of the monitoring points is shown in the schematic diagram of Fig. 7.

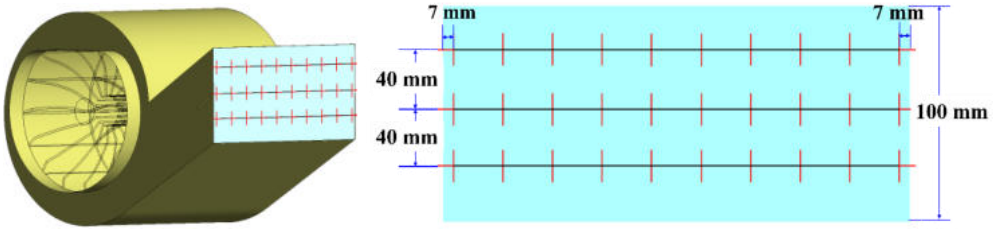


Fig. 7 - Schematic distribution of monitoring points of centrifugal fan outlet cross-section

According to the value of wind speed at the measurement point, the three-dimensional curve of wind speed at the air outlet is plotted, as shown in Fig. 8. It can be seen that the wind speed in the upper and middle layers is lower than that in the lower layer of the outlet, and the fluctuation is larger. The upper airflow curve shows a typical “W” distribution, with a high-speed jet protruding from the center axis region. The symmetric double-vortex structure is generated by the flow separation effect of the volute shell gap near the two sides of the volute shell wall, resulting in a sudden drop of the wind speed below 5 m/s. The wind speed of the upper layer is lower than that of the lower layer of the outlet, and the fluctuation is large. When λ increases from 1.2 to 1.5, the width share of the high-speed core area expands from 32% to 48%, but the peak wind speed decreases from 24.350 m/s to 22.175 m/s, which is a decrease of 8.93%, indicating that the increase of the width-to-diameter ratio weakens the centrifugal acceleration effect. The lower layer of the outlet is approximately “M” type distribution, the wind speed is higher overall, and the distribution is smoother.

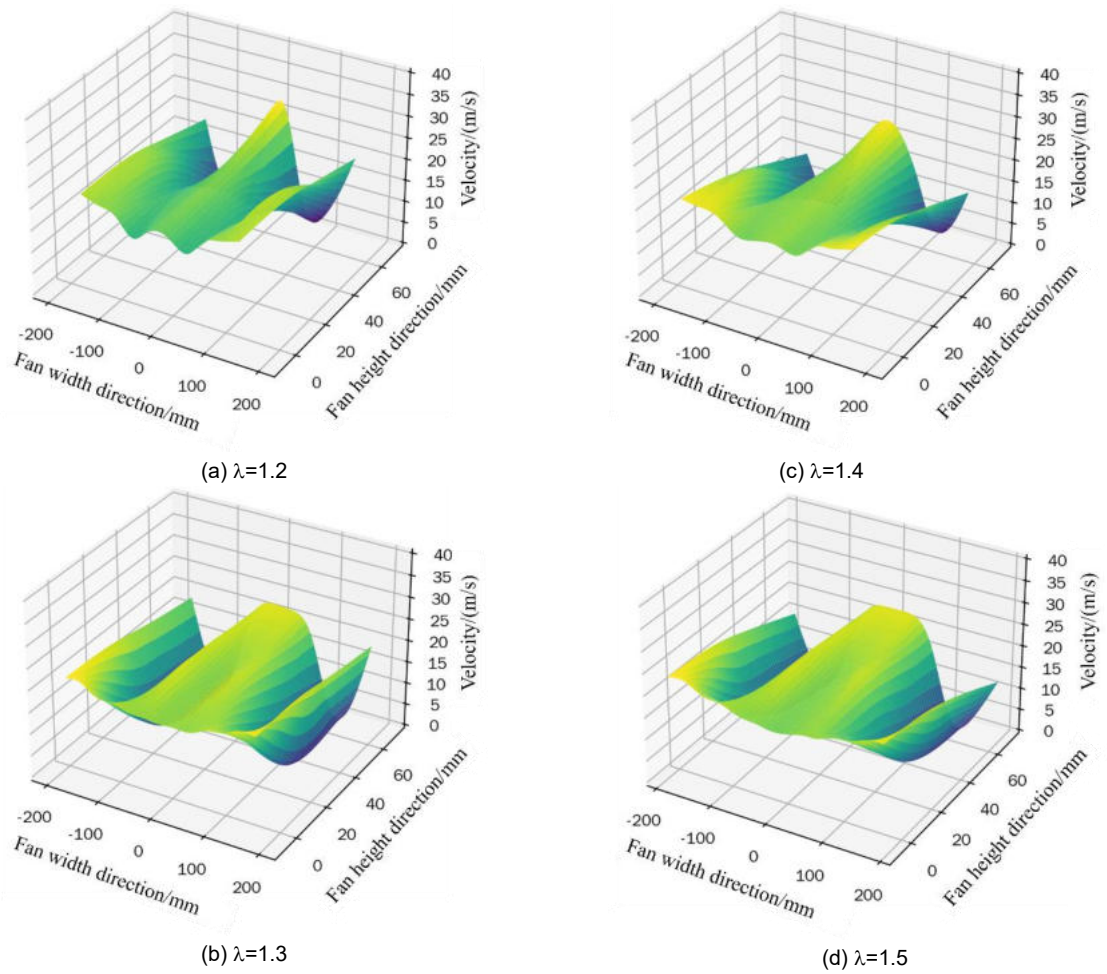


Fig. 8 - Three-dimensional curves of wind speed distribution at the outlet of fans with different fans

Calculating the wind speed variation values of the four fans is shown in Table 4, and the results show that the wind speed variation value of the fan with a λ of 1.3 is the smallest in the outlet section, which is 2.426, and is 16.63% lower than that of the prototype fan, which is 2.910, and the wind speed variation value of the fan with a λ of 1.5 is the largest, which is 3.496, namely 44.11% higher than that of the optimal structure, indicating that its wind speed distribution uniformity is the poorest. This suggests that the over-expanded volute flow channel exacerbates the flow separation and energy dissipation.

Table 4

Variability of air velocity at the outlet of four types of fans

Volute width-diameter ratio λ	Wind speed variability V
1.2	2.910
1.3	2.426
1.4	3.830
1.5	3.496

Comprehensive analysis of the above data shows that the change of the volute width-diameter ratio has a significant effect on the uniformity of the wind speed distribution at the fan outlet, and a suitable volute casing aspect ratio can effectively enhance the qualitative characteristics of the fan and improve the airflow uniformity inside the impeller. λ=1.3 is the optimal solution under the current design parameters, and the synergistic optimization of low turbulence dissipation and high uniformity is achieved by balancing the centrifugal effect and the flow channel geometry.

Modeling of volute width-diameter ratio-speed-air volume function based on MATLAB

According to the results of the numerical simulation, as the rotational speed of the fan changes, the relationship between the width-diameter ratio of the volute and the air volume will also change accordingly.

However, most of the existing studies focus on the influence of a single parameter on the performance of the fan, and there is a lack of quantitative characterization of the multi-dimensional correlation among λ, n, and Qv. This makes it difficult to precisely match the requirements of dynamic working conditions. Therefore, constructing an accurate function model to describe the interaction among the width-diameter ratio of the volute, the rotational speed, and the air volume can not only improve the working efficiency of the fan but also provide a theoretical basis for the design of the fan.

In order to achieve efficient model fitting and validation, the MATLAB R2022a platform is used, whose advantages are: MATLAB's library of nonlinear regression algorithms supports the parameter identification of complex physical models, its multivariate statistical toolbox function can synchronously assess the fitting excellence of polynomial regression and power law models, and with its powerful numerical calculation and visualization functions, it can intuitively reveal the interactive effects of each parameter. The multivariate fitting analysis of wind turbine parameters is efficiently completed. The fitted multivariate function model is:

$$Q_v = f(\lambda, n) = k \cdot \lambda^a \cdot n^b \tag{3}$$

where: k is a constant coefficient; a and b are power indices to be determined; and C is a constant term.

The discrete data were fitted using nonlinear least squares and the best k=0.0217, a=0.7948, b=0.4621 where Residual Sum of Squares=0.0053, Adj.R-Square=0.9444, the residual sum of squares is small, and the corrected coefficient of determination shows the success of the fit. The results of the fit are as follows:

$$Q_v = 0.0217 \cdot \lambda^{0.7948} \cdot n^{0.4621} \tag{4}$$

This functional relationship equation has the aspect ratio index a = 0.7948, which indicates that increasing the width-diameter ratio can enhance the airflow, but the gain decays with increasing λ. The three-dimensional surface plot of λ and n as independent variables and Q as dependent variable comprehensively shows the interrelationship between λ, n and Q as shown in Fig. 9.

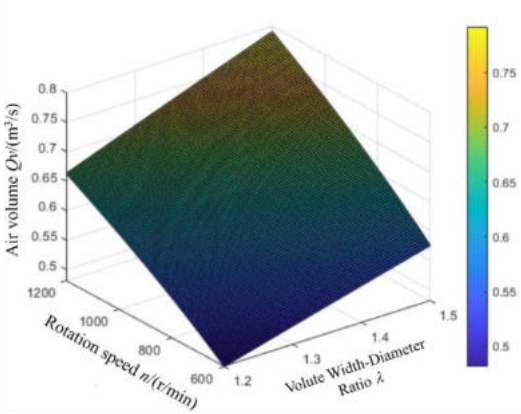
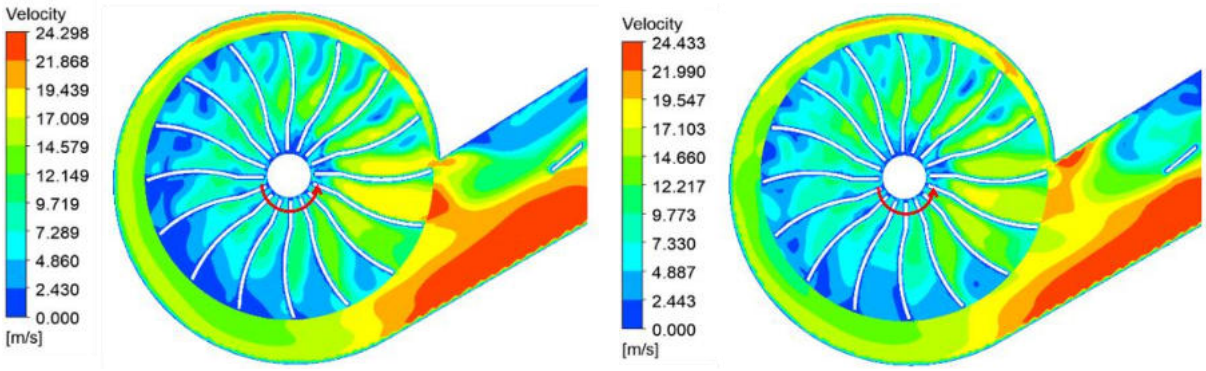


Fig. 9 - Three-dimensional surface diagram of the relationship between volute width-to-diameter ratio-speed-air volume

Simulation analysis of flow field of multi-blade centrifugal fan before and after optimization

Numerical simulation results show that the efficiency of the optimized fan with λ=1.3 reaches 70.61%, which is 6.43% higher than the 64.18% of the original fan. The air volume increases to 0.636 m³/s with a growth rate of 6.53%. This indicates that the optimization of the width-to-diameter ratio of the volute has achieved preliminary results, and the performance of the fan has been improved. The simulation results of multiblade centrifugal fan with λ=1.2 (original model) and λ=1.3 (optimized model) are selected for comparative analysis. Fig. 10 shows the comparison of the velocity clouds of the two centrifugal fans in the middle section.

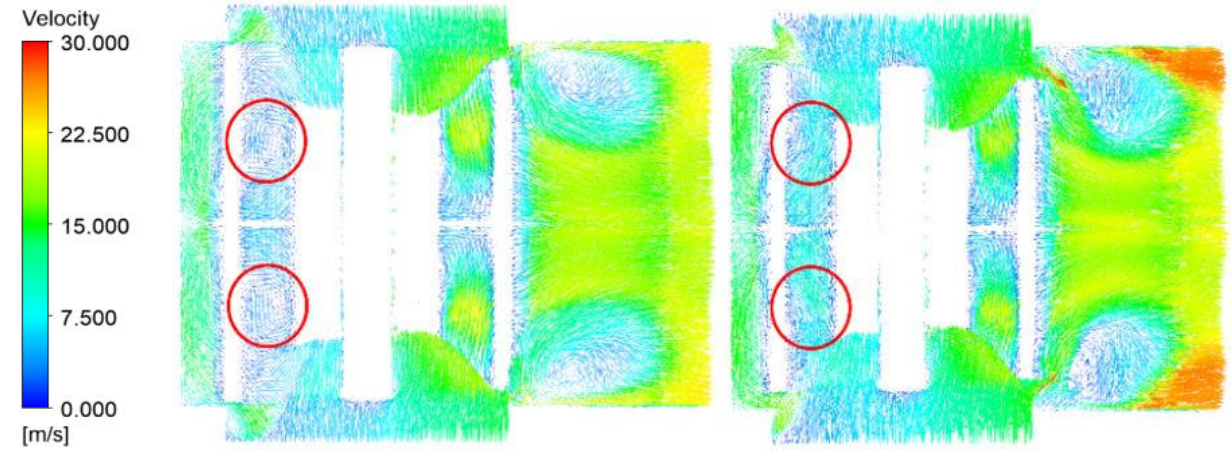
Through comparison, it can be found that the optimized velocity distribution has been significantly improved. The area of the low-velocity recirculation zone on the upper wall surface of the air outlet has been reduced, especially the low-velocity zone inside the impeller and the flow uniformity have been greatly improved. This improvement essentially stems from the fact that after optimizing the axial matching degree between the volute width and the impeller, the secondary flow of the airflow in the meridian plane has been effectively suppressed. Specifically, increasing the volute width reduces the radial velocity gradient and improves the matching between the airflow angle at the impeller outlet and the volute, thereby decreasing airflow impact losses. The phenomenon that the high-speed flow region with (v>21 m/s) concentrates towards the volute outlet confirms the reconstruction effect of the optimized width-diameter ratio of the volute on the jet-wake structure, effectively improving the conversion rate of the airflow kinetic energy.



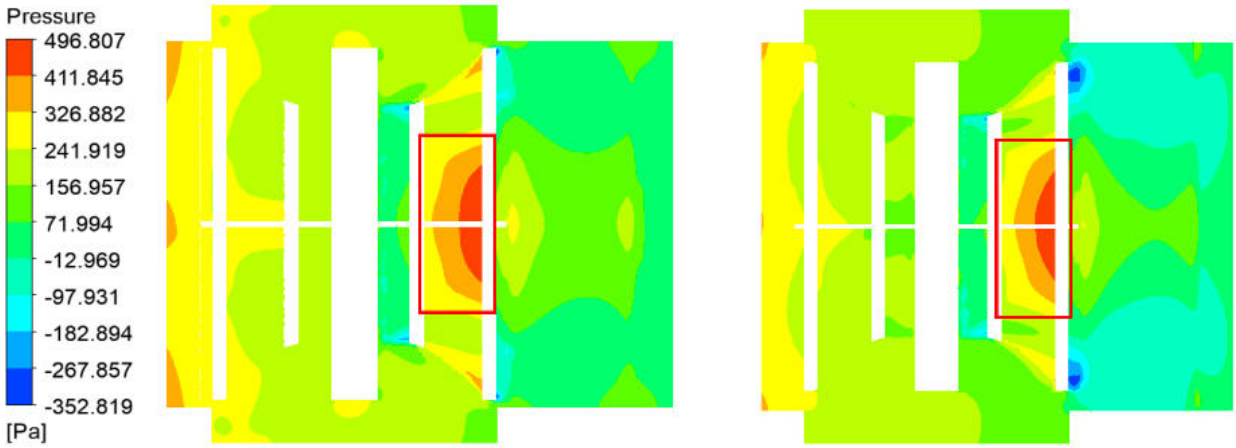
(a) Prototype fan (b) Optimizing fan

Fig. 10 - Velocity clouds on the middle section of the turbine before and after optimization of the volute width-to-diameter ratios

Fig. 11(a) and (b) present the velocity vector diagrams of the fan on the Y-Y plane. It can be clearly seen that the outlet velocity of the optimized fan has increased. The maximum velocity has increased from 24.18 m/s to 30.048 m/s, an increase of approximately 24%. In Fig. 11(a), the symmetrical vortex structure that existed in the middle of the suction surface of the original impeller has completely disappeared after optimization. The pressure nephograms in Fig. 11(c) and (d) show that the total pressure decreases to a certain extent along the direction of the volute outlet, indicating that kinetic energy dissipation occurs when the airflow flows in the volute. The reasons for this energy loss mainly come from two aspects: on one hand, there is frictional loss between the airflow and the volute wall and internal structures; on the other hand, the sudden change in the volute tongue structure leads to airflow separation and turbulent pulsation.



(a) Vector diagram of the speed of the prototype fan (b) Optimized fan speed vector plot

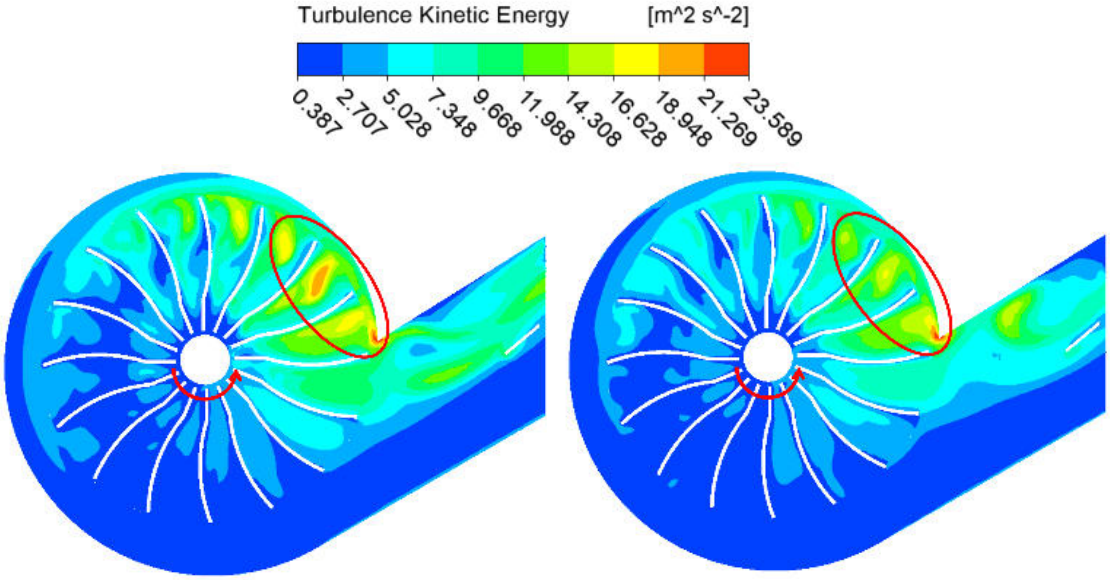


(c) Pressure distribution of the prototype fan (d) Optimization of fan pressure distribution

Fig. 11 - Y-Y plane velocity vector map and pressure cloud before and after optimization of volute width-to-diameter ratios

Turbulent Kinetic Energy (TKE) expresses the kinetic energy per unit mass of gas associated with the vortex in a turbulent flow. To some extent, it can reflect the stability of the airflow. Fig. 12 extracts the turbulent kinetic energy cloud for the middle section of the impeller of the multibladed centrifugal fan before and after optimization. The cloud diagram shows that the high energy consumption zone is mainly concentrated near the volute tongue, including the transition zone near the impeller front disk and downstream of the volute tongue, indicating that the fluid flow in this region is relatively complex.

The turbulence kinetic energy of the optimized volute casing decreases significantly compared with that of the prototype fan, and the turbulence of the airflow in the impeller channel and at the front end of the flow path improves significantly, indicating that the optimization of the volute casing width-to-diameter ratio makes the internal flow of the fan more smooth, and improves the stability and uniformity of the airflow, which is conducive to the generation of a more uniform airflow, and facilitates the effect of the cleaning action.

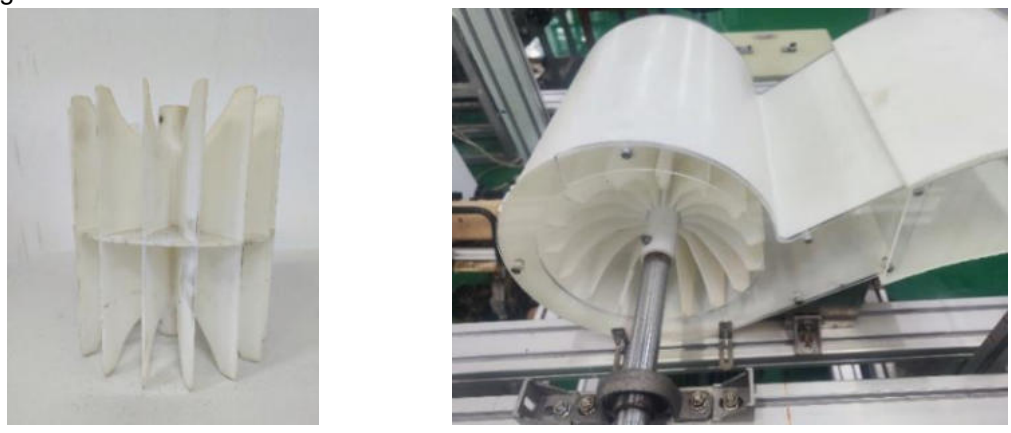


(a) Prototype fan (b) Optimizing fan

Fig. 12 - Turbulent kinetic energy distribution in the middle section of the fan before and after optimization

Experimental verification

To ensure the reliability of the optimized results, the optimized volute was machined and tested using 3D printing. All test conditions were the same as for the prototype. The physical diagram of the optimal fan is shown in Fig. 13.



(a) Fan impeller (b) Multi-blade centrifugal fan

Fig. 13 - 3D printed optimal fan physical drawing

Table 5 shows the comparison between the bench test data of the optimized solution for the multi-blade centrifugal fan volute structure and the data of the prototype fan.

As shown by the data in Table 5, the optimal fan achieved a 14.6% increase in air volume, an 11.8% increase in total pressure, and a 9.22% increase in efficiency compared with the prototype fan.

Although the shaft power increases by 3.8%, the increase in airflow, total pressure and efficiency confirms that the structural optimization not only improves the performance of the working conditions, but also expands the efficient working range of the fan, which indicates that the energy utilization is more reasonable. Moreover, the results of the bench test are similar to those of the numerical simulation, which verifies the reliability of the numerical simulation. The increase in air volume and full pressure of the optimal fan is due to the smoother flow of air in the fan after the optimization of the volute casing structure, which reduces the energy loss and enables the gas to be transported and pressurized more efficiently.

Table 5

Bench test comparison test data

Program	Air volume	Total pressure	Efficiency	Effective power	Shaft power
	[m^3/s]	[Pa]	[%]	[KW]	[KW]
Prototype fan	0.658	209.73	71.36	0.138	0.164
Optimizing fan	0.574	187.66	62.14	0.105	0.158

CONCLUSIONS

Aiming at the current situation of low efficiency of fans with flat blade structure in the agricultural field and less research and application of multi-blade centrifugal fans, this study analyzes the influence of the volute width-to-diameter ratio on the performance of agricultural cleaning centrifugal fans, aiming to provide a selection basis for the design and optimization of high-performance multi-blade centrifugal fans. At a rated speed of 1000 r/min, the multi-blade centrifugal fan with an aspect ratio of 1.3 has the best overall performance. Compared with the prototype fan, the efficiency is increased by 7.13%, the total pressure is increased by 10%, and the air volume is increased by 6.53%. At the same time, the fan has the smallest variance value of 2.426 for the outlet air velocity, which is 16.63% lower than that of 2.910 for the prototype fan, indicating that the optimization of the width of the volute casing improves the uniformity of the outlet airflow, which is conducive to the cleaning effect of the airflow. Based on the MATLAB platform, a multi-dimensional function model of the volute casing width-to-diameter ratio-speed-to-airflow is established, which fills the gap of the existing research focusing on a single parameter to quantitatively characterize the performance of the turbine. The validation results of the bench test show that the error between simulation and test is within 10%, which verifies the reliability of numerical simulation. According to the fan similarity theory, the universal law of the relationship between the width of the shell and the performance of the fan can be used for the optimization design of the shell of the combine harvester fan, which can be adapted to match different specifications of the models.

ACKNOWLEDGEMENT

This research was financially supported by National Natural Science Foundation of China (52375249), National Natural Science Foundation of China (32401690).

REFERENCES

[1] Acarer, S., Uyulan, Ç., & Karadeniz, Z. H. (2020). Optimization of radial inflow wind turbines for urban wind energy harvesting. *Energy*, *202*, 117772. https://doi.org/10.1016/j.energy.2020.117772

[2] Almoslh, A., Alobaid, F., Heinze, C., & Epple, B. (2021). Experimental Study of the Influence of Gas Flow Rate on Hydrodynamic Characteristics of Sieve Trays and Their Effect on CO2 Absorption. *Applied Sciences*, *11*(22), 10708. https://doi.org/10.3390/app112210708

[3] Babubhai, V. K. P., Chaudhari, A., Sharma, A., & Diwakar, V. (2023). Experimental and numerical study on the influence of flow passages in centrifugal fan using computational fluid dynamics. *Engineering Research Express*, *5*(2), 025030. https://doi.org/10.1088/2631-8695/accf00

[4] , I., Mudarisov, S., Lukmanov, R., Permyakov, V., Ibragimov, R., & Nasyrov, R. (2019). Mathematical modeling and research of the work of the grain combine harvester cleaning system. *Computers and Electronics in Agriculture*, *165*, 104966. https://doi.org/10.1016/j.compag.2019.104966

[5] Chai, X., Xu, L., Sun, Y., Liang, Z., Lu, E., & Li, Y. (2020). Development of a cleaning fan for a rice combine harvester using computational fluid dynamics and response surface methodology to optimise outlet airflow distribution. *Biosystems Engineering*, *192*, 232-244. https://doi.org/10.1016/j.biosystemseng.2019.12.016

[6] Liang, Z., & Wada, M. E. (2023). Development of cleaning systems for combine harvesters: A review. *Biosystems Engineering*, *236*, 79-102. https://doi.org/10.1016/j.biosystemseng.2023.10.018

[7] Liang, Z., Li, D., Li, J., & Tian, K. (2020). Effects of fan volute structure on airflow characteristics in rice combine harvesters. *Spanish Journal of Agricultural Research*, *18*(4), e0209-e0209. https://doi.org/10.5424/sjar/2020184-15426

[8] Ma, Z., Zhu, Y., Li, J., Song, Z., Yu, J., Li, Y., & Xu, L. (2024). Study on the performance of detection air duct and evaluation index of agricultural cleaning centrifugal fans. *Biosystems Engineering*, *239*, 81-97. https://doi.org/10.1016/j.biosystemseng.2024.01.015

[9] Ottersten, M., Yao, H. D., & Davidson, L. (2022). Inlet gap influence on low-frequency flow unsteadiness in a centrifugal fan. *Aerospace*, *9*(12), 846. https://doi.org/10.3390/aerospace9120846

[10] Schäfer, R., & Böhle, M. (2020). September. Validation of the lattice Boltzmann method for simulation of aerodynamics and aeroacoustics in a centrifugal fan. *In Acoustics*, *2*(4), 735-752. https://doi.org/10.3390/acoustics2040040

[11] Shim, H. S., & Kim, K. Y. (2020). Design optimization of the impeller and volute of a centrifugal pump to improve the hydraulic performance and flow stability. *Journal of Fluids Engineering*, *142*(10), 101211. https://doi.org/10.1115/1.4047539

[12] Sun Wen-sheng, Yi Shu-juan, Qi Hai-long, Li Yi-fei, Dai Zhi-bo, Zhang Yu-peng, Yuan Jia-sha, Wang Song. (2025). Design and Optimization of Air-Assisted Spiral Seed-Supply Device for High-Speed Dense Planting Maize Seeder. *INMATEH - Agricultural Engineering*, *75*(1), pp.13-25. https://doi.org/10.35633/inmateh-75-01

[13] Tang, C., Zhang, Ouyang, Z., Luo, H., Fang, Y., & Wu, B. (2007). Experimental research on the combined centrifuge-aerofoil grain cleaning fan *(离心—轴流组合式清粮风机的试验研究)*. *Transactions of the Chinese Society of Agricultural Engineering*, *23*(10), 117-120. https://doi.org/10.3321/j.issn:1002-6819.2007.10.020 *(In Chinese)*

[14] Varun Ch. S., Anantharaman, K., & Rajasekaran, G. (2023). Effect of blade number on the performance of centrifugal fan. *Materials Today: Proceedings*, *72*, 1143-1152. https://doi.org/10.1016/j.matpr.2022.09.185

[15] Wang, L., Gu, B., & Wang, T. (2012). Fast Calculation Model of Fan Performance Based on Similarity Theory *(基于相似理论的风机性能快速计算模型)*. *Fluid Machinery*, *40*(07), 24-28. https://doi.org/10.3969/j.issn.1005-0329.2012.07.006 *(In Chinese)*

[16] Wang, L., Jiao, Z., & Zhao, G. (2017). Simulation Analysis of Centrifugal Fan in Air Screen Type Cleaning Device *(风筛式清选装置离心风机气流场仿真分析)*. *Agricultural Equipment & Vehicle Engineering*, *55*(08), 10-14. https://doi.org/10.3969/j.issn.1673-3142.2017.08.003 *(In Chinese)*

[17] Wei, Y., Zhu, L., Zhang, W., & Wang, Z. (2020). Numerical and experimental investigations on the flow and noise characteristics in a centrifugal fan with step tongue volutes. *Proceedings of the Institution of Mechanical Engineers, Part C: Journal of Mechanical Engineering Science*, *234*(15), 2979-2993. https://doi.org/10.1177/0954406219890920

[18] Yang, L., Yaoming, L., Liya, L., & Maolin, S. (2024). Modeling and control methods of a multi-parameter system for threshing and cleaning in grain combine harvesters. *Computers and Electronics in Agriculture*, *225*, 109251. https://doi.org/10.1016/j.compag.2024.109251

APPLICATION OF DEM-BASED ANALYSIS IN THE OPTIMIZATION OF SHOVEL DESIGN FOR THE 1JS-200 ROCK PICKER

/

基于离散元法的 1JS-200 型捡石机起石铲的优化设计应用

Yasenjiang BAIKELI *[1,2], Jiaxi ZHANG [1,2], Jihuai GAO [3]; Haodong XU [1,2]

[1] College of Mechanical and Electrical Engineering, Xinjiang Agricultural University, Urumqi/ China;

[2] Key Laboratory of Xinjiang Intelligent Agricultural Equipment, Urumqi / China;

[3] Xinjiang Dafengge Agricultural Machinery Co., LTD, Bole / China;

Tel: 8613899827528; E-mail: yasin@zju.edu.cn

Corresponding author: Yasenjiang Baikeli

DOI: https://doi.org/10.35633/inmateh-76-56

Keywords: *Discrete element Method, Rock Picker, Shovel, Interaction, Optimization*

ABSTRACT

To enhance the operational efficiency and structural design accuracy of rock-picking machinery, this study proposes a Discrete Element Method (DEM)-based approach for the optimization of the lifting shovel in the 1JS-200 rock picker. A coupling simulation model of the shovel-soil-rock system was established to analyze the dynamic interaction mechanisms between the shovel and mixed granular media. Key parameters influencing excavation performance-including forward speed, digging depth, and shovel angle-were optimized using a Box-Behnken Design (BBD) response surface methodology. Regression models were constructed for torque and rock excavation efficiency (REE), and the optimal combination was determined to be a forward speed of 0.5 m/s, a digging depth of 170 mm, and a shovel angle of 40°, under which the predicted REE reached 88.1% with a torque of approximately 386 N·m. To validate the simulation results, field tests were conducted under optimal parameter conditions. The experimental results showed that REE values fluctuated within 2%, and torque errors remained within 4% of the predicted values, confirming the accuracy and applicability of the model. This research provides a practical, data-driven design method for rock-picking implements and offers theoretical and technical support for improving rock separation efficiency, reducing structural wear, and advancing the intelligent development of agricultural machinery.

摘要

为提升农田捡石机作业效率与结构设计的科学性，本文以 1JS-200 型捡石机的起石铲为对象，提出了一种基于离散元法（DEM）的结构优化方法。构建了起石铲–土壤–砾石系统的动力学模型，模拟分析了提升铲与混合颗粒介质之间的动态相互作用机制。在此基础上，采用 Box–Behnken 响应面设计方法，对作业速度、挖掘深度及铲角等关键参数进行优化，构建了扭矩与岩石清理效率（REE）的二次回归模型。结果表明，最优参数组合为作业速度 0.5 m/s、挖掘深度 170 mm、铲角 40°，在此条件下 REE 为 88.1%，扭矩约为 386 N·m。为验证模拟结果的可靠性，开展了田间验证试验。试验结果显示，实测 REE 波动范围控制在 2%，扭矩误差控制在 4%以内，验证了模型的准确性与适用性。研究成果为捡石作业设备的数据驱动式结构优化提供了实用路径，同时为提升捡石效率、降低设备磨损、推动农机装备智能化发展提供了理论依据与技术支撑。

INTRODUCTION

In modern agricultural mechanization, the widespread presence of rocks in farmland hinders operations like deep plowing, sowing, and harvesting, while accelerating wear and damage to machinery—ultimately limiting productivity and soil quality (*Mak & Chen, 2014*). Rock pickers are increasingly used in high-standard farmland construction, with the lifting shovel being the core component that directly affects rock-picking efficiency and machine stability. However, the 1JS-200 rock picker still suffers from low efficiency, high carryover, and severe wear, mainly due to its empirically driven design and lack of systematic analysis of the shovel's dynamic interaction with the soil–rock mixture under varying field conditions (*Coetzee, 2009; Fielke & Ucgul, 2013; Servin et al., 2020*). To address this, the Discrete Element Method (DEM) offers a robust approach to simulate shovel–material interactions and guide structural optimization (*Mak & Chen, 2014*).

**Yasenjiang Baikeli, Ph.D.Eng.; [1,2] Jiaxi Zhang, Prof.Ph.D.Eng.,[3] Jihuai Gao, Prof.Eng.; [1,2] Haodong Xu, M.S.Stud.Eng.*

Applying DEM to the 1JS-200 shovel structure is therefore essential for enhancing rock removal efficiency, improving machine intelligence, and advancing high-quality agricultural development.

In recent years, significant progress has been made in the simulation and design of soil-engaging tools through the application of the Discrete Element Method (DEM) and data-driven optimization techniques. For instance, *Franco et al. (2007*) and *Shmulevich et al. (2007)* made important contributions by using DEM to analyze the interaction between soil and bulldozer blades or wide cutting tools. Their work laid a theoretical foundation for modeling soil-tool contact mechanics and demonstrated the applicability of DEM in agricultural engineering. However, these studies primarily considered homogeneous soil conditions and simplified tool geometries, and they did not account for the coupled interactions between soil, rocks, and shovel surfaces. As a result, they fell short in capturing the complex dynamic behavior that occurs during rock-picking operations.

In terms of structural optimization, researchers such as *Zhang & Li*, *(2024)* successfully applied response surface methodologies to optimize tillage tool parameters, providing a more quantitative alternative to traditional trial-and-error approaches. Their studies demonstrated the effectiveness of Box–Behnken Design (BBD) and multi-factor analysis in improving tool performance. Nevertheless, most of these applications focused on relatively simple soil conditions and low-load scenarios. For high-resistance components such as lifting shovels in rock-picking equipment, the optimization process remains largely experience-based, lacking systematic multi-parameter analysis tailored to the mechanical demands of mixed soil–rock environments. Furthermore, there has been increasing interest in bridging the gap between virtual simulation and real-world testing. *Shmulevich et al. (2007)* and *Rizzardo et al. (2020)* explored virtual testing frameworks and discussed the limitations of simulation-to-reality (Sim2Real) transfer in agricultural machinery and robotics. These studies emphasized the importance of validation, but many existing works still treat simulation and field testing as separate processes. This often leads to discrepancies between predicted and actual performance, limiting the reliability and practical value of the models in field-scale applications such as rock separation under variable terrain and load conditions.

To overcome these limitations, this study proposes an integrated simulation and optimization framework for analyzing shovel-soil-rock interactions in rock-picking operations. A coupled modeling approach based on the Discrete Element Method (DEM) is developed to dynamically simulate the interaction between the lifting shovel and complex granular media, offering theoretical insight into the underlying mechanical processes. A structural optimization strategy using the Box–Behnken Design (BBD) is employed to systematically evaluate the influence of key parameters-such as operating speed, digging depth, and shovel angle-on performance. In addition, a performance verification method is established to validate the simulation results. This research not only enhances the theoretical methodology for agricultural equipment design optimization but also provides technical support for improving rock-picking efficiency, minimizing equipment wear, and advancing the intelligent development of rock-clearing machinery.

MATERIALS AND METHODS

Description of the 1JS-200 Rock Picker

The 1JS-200 is a chain-type rock picker designed for excavating, conveying, and collecting stones in agricultural fields. Its main structural parameters are listed in Table 1. As shown in Figure 1, the machine is composed of a towing frame *1*, rock-lifting shovel *2*, ground wheels *3*, stone collection box *4*, stone conveying mechanism *5* and chain drive system *6*.

During operation, the rock picker is towed forward by a tractor. The shovel cuts into the soil to dislodge stones, which are then lifted and conveyed via a chain-driven belt to the rear collection unit. The system is designed to separate larger stones from the soil while allowing finer particles to fall through during transport. The ground wheels provide mobility across varying field conditions.

The shovel is the key component responsible for stone excavation and directly affects the machine's overall efficiency. However, its current design faces challenges such as shallow digging capacity, instability on uneven terrain, and inefficient separation of stones from soil. These issues motivate the need for design optimization, where DEM-based analysis can be applied to simulate material interaction and improve performance.

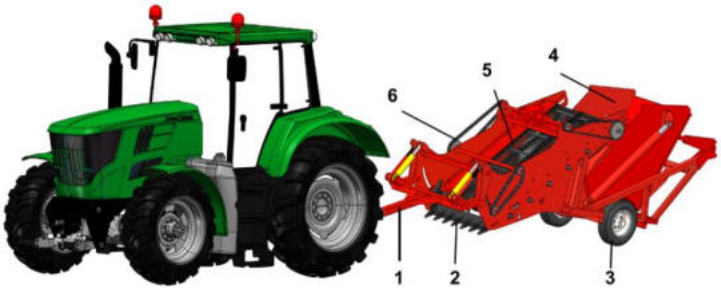


Fig. 1 - 1JS-200 Rock Picker Machine

Table 1

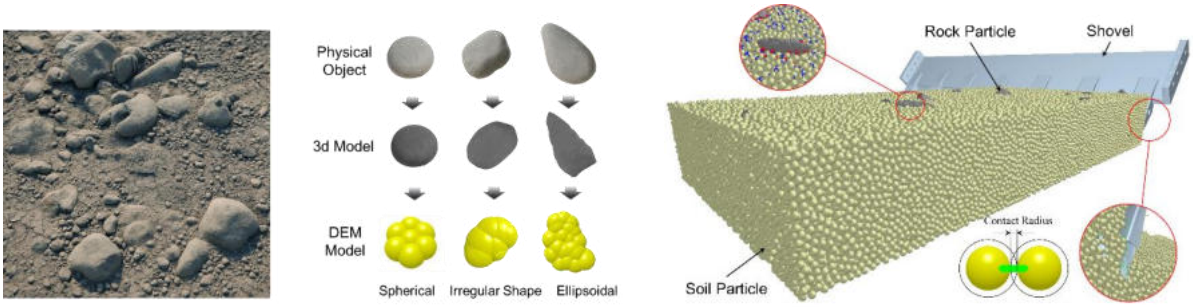
Discrete element model parameters of

Serial	Parameter	Value
1	Overall dimensions (L × W × H)	6250×1750×2150 mm
2	Structural weight	3500 kg
3	Required power	>40.5 KW (≥ 55 hp)
4	Working width	1300 mm
5	Suitable stone size range	600~700 mm
6	Operating speed	<5 km/h
7	Stone removal efficiency	>80 %

Shovel-Soil-Rock Interaction Modeling

Simulating shovel interactions with complex terrains composed of soil and embedded rocks presents challenges for conventional modeling methods, which often fail to capture the discrete, nonlinear behavior of granular media (*Servin, Berglund, & Nystedt, 2020*). The Discrete Element Method (DEM) offers a more suitable approach by modeling particle-scale interactions and contact dynamics, making it ideal for analyzing excavation processes in heterogeneous field conditions (*Coetzee, 2017*).

To simulate the mechanical behavior of multi-phase terrain during excavation, a discrete element modeling (DEM) framework was developed to represent the interaction between shovel tools, soil particles, and embedded rocks. As illustrated in Fig. 2, the modeling workflow begins with the physical characterization of soil and scattered surface rocks (Fig. 2a). These physical rock entities are digitally reconstructed, yielding a range of geometric types-spherical, irregular, and ellipsoidal shapes-to reflect natural variability (Fig. 2b). To balance geometric realism with computational efficiency, these three representative rock shapes were selected. This combination captures the essential morphological diversity observed in field conditions while ensuring manageable simulation complexity within the DEM framework. The final DEM framework integrates the reconstructed rock particles into a densely packed soil matrix and simulates the dynamic interaction as the shovel penetrates the terrain (Fig.2c). The model captures key behaviors such as contact force propagation, material displacement, and rock–soil separation. This enables quantitative evaluation of shovel performance under unstructured, heterogeneous field conditions and supports informed design optimization.



(a) Land of Soil - Rocks *(b) Modeling Process of Rocks* *(c) DEM Model of Shovel-Soil-Rock*

Fig. 2 - Discrete Element Model of Shovel-Soil-Rock Interaction

All parameters required for establishing the discrete element model in this section are set according to Table 2, where the contact parameters of the lifting shovel - soil - rocks (collision recovery coefficient, static friction coefficient, rolling friction coefficient) are obtained from the calibration tests and existing research literature, and other parameters are set with reference to previous studies.

Table 2

Discrete element model parameters

Type	Parameter	Value	Unit	Ref.
Rock	Density	2,500	kg/m³	*Zou et al., (2020); Camborde et al., (2000)*
	Young's Modulus	5.0E+10	Pa	*Zou et al., (2020); Camborde et al., (2000)*
	Poisson's Ratio	0.3	-	*Zou et al., (2020); Camborde et al., (2000)*
	Normal Stiffness	1.0E+7	N/m	*Zou et al., (2020); Camborde et al., (2000)*
	Tangential Stiffness	1.0E+6	N/m	*Zou et al., (2020); Camborde et al., (2000)*
	Friction Coefficient	0.4	-	*Zou et al., (2020); Camborde et al., (2000)*
Soil	Density	1,600	kg/m³	*Horn, (2004); Mak & Chen, (2014)*
	Young's Modulus	2.0E+7	Pa	*Horn, (2004); Mak & Chen, (2014)*
	Poisson's Ratio	0.35	-	*Horn, (2004); Mak & Chen, (2014)*
	Normal Stiffness	5.0E+6	N/m	*Horn, (2004); Mak & Chen, (2014)*
	Tangential Stiffness	5.0E+5	N/m	*Horn, (2004); Mak & Chen, (2014)*
	Friction Coefficient	0.35	-	*Horn, (2004); Mak & Chen, (2014)*
Shovel (Q235 Steel)	Density	7,850	kg/m³	*Feng et al., (2022); Zhang et al., (2023)*
	Young's Modulus	2.1E+11	Pa	*Feng et al., (2022); Zhang et al., (2023)*
	Poisson's Ratio	0.3	-	*Feng et al., (2022; Zhang et al., (2023)*
	Normal Stiffness	2.1E+11	N/m	*Feng et al., (2022); Zhang et al., (2023)*
	Tangential Stiffness	2.1E+10	N/m	*Feng et al., (2022); Zhang et al., (2023)*
	Friction Coefficient	0.3	-	*Feng et al., (2022); Zhang et al., (2023)*
Soil–Rock	Normal Stiffness	5.0E+6	N/m	*Zou et al., (2020)*
	Tangential Stiffness	5.0E+5	N/m	*Zou et al., (2020)*
	Friction Coefficient	0.35	-	*Zou et al., (2020)*
Shovel–Rock	Normal Stiffness	1.0E+8	N/m	*Fielke et al., (2013); Feng et al., (2022)*
	Tangential Stiffness	1.0E+7	N/m	*Fielke et al., (2013); Feng et al., (2022)*
	Friction Coefficient	0.30	-	*Fielke et al., (2013); Feng et al., (2022)*
Shovel–Soil	Normal Stiffness	5.0E+7	N/m	*Mak & Chen, (2014); Zhang et al., (2023)*
	Tangential Stiffness	5.0E+6	N/m	*Mak & Chen, (2014); Zhang et al., (2023)*
	Friction Coefficient	0.28	-	*Mak & Chen, (2014); Zhang et al., (2023)*

Shovel-Soil-Rock models for Discrete Element Simulation Test

In order to accurately simulate the process of pulling rocks by the lifting shovel of the 1JS-200 rock picker and analyze the rock picking efficiency and torque, a simulation model of the lifting shovel-soil-rock interaction is constructed based on the discrete element method, as shown in Figure 3.



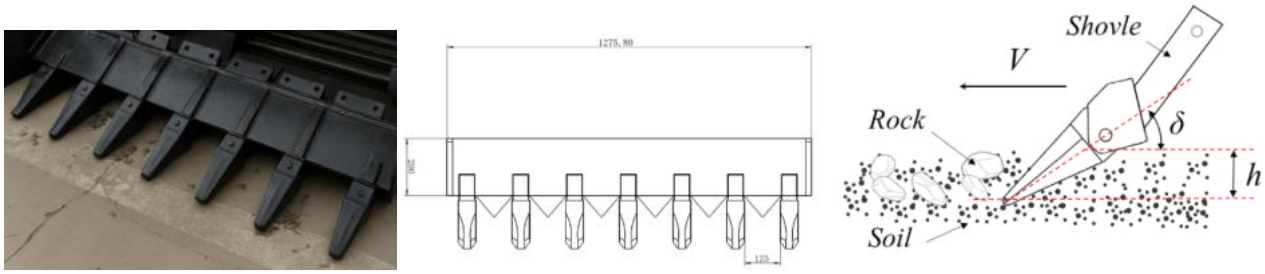
(a) Working View *(b) Shovel for DEM Simulation*

Fig. 3 - Discrete Element Simulation Model

Experimental Design and Performance Evaluation Methodology

Field experiments were conducted to test the operational effectiveness of the lifting shovel in the 1JS-200 rock picker under natural variability in the field. Fig 4(a) and Fig 4(b) show the structure and parameters of the Shovel, Fig 4(c) illustrates the interaction process between the lifting shovel**,** soil**,** and rock**.** As the lifting shovel moves forward, complex interactions occur between the shovel, soil particles, and rock particles.

The *V* in the figure represents the forward speed of the shovel, which directly impacts the disturbance caused to the soil and rock. *h* represents the digging depth, indicating the depth at which the shovel enters the soil, a critical factor affecting the soil-rock excavation efficiency. δ represents the angle between the shovel and the ground, which determines the direction of the forces acting on the soil and rock and the shovel's cutting behavior.



(a) Structure of Shovel *(b) Parameters of Shovel* *(c) Dynamic Parameters of Shovel*

Fig. 4 - Rock-Lifting Shovel

These conditions are of great significance to reduce experimental errors and ensure that the experimental results can be directly applied to improve the practical application performance of the rock picking device. In order to optimize the rock picking equipment, the effects of lifting shovel speed (X_1), digging depth (X_2), and angle (X_3) on the rock picking efficiency and operational torque were studied. Through Box-Behnken Design (BBD) experimental design, different speeds (X_1: 0.3 m/s to 0.7 m/s), digging depths (X_2: 160 mm to 200 mm), and angles (X_3: 30° to 50°) were set to simulate the interaction effects under different operating conditions. The experiment focused on recording the rock picking efficiency, operational torque, and evaluating the impact of X_1, X_2, and X_3 on performance. These results provide a reference basis for further optimizing the equipment. The selection of experimental factor levels is shown in Table 3.

Table 3

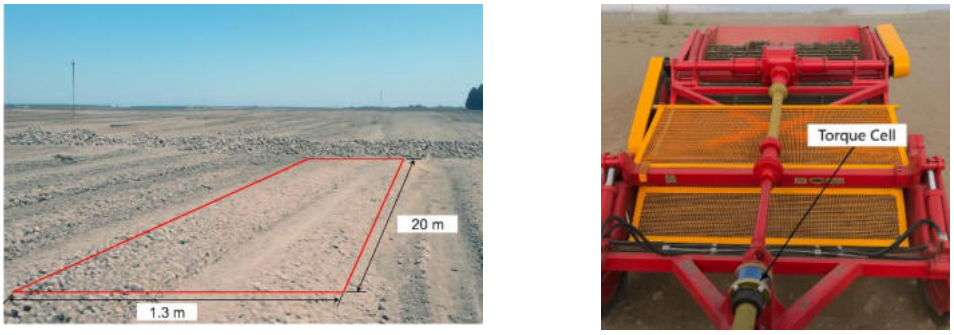
Experimental factor level design

Level	Factor		
	A (m/s)	B (mm)	C (°)
1	0.3	160	30
0	0.5	180	40
-1	0.7	200	50

Experimental Conditions and Performance Evaluation Metrics

To validate the effectiveness of the simulation-based optimization and evaluate the field performance of the 1JS-200 rock picker, a series of field experiments were conducted. The experimental site is located in Bole, Xinjiang, China (44.90° N, 81.69° E), within a typical farmland area commonly used for rock picking operations. The experimental equipment included the 1JS-200 rock picker, operated via a tractor, and the instrumentation focused on assessing rock excavation efficiency and operating torque under practical working conditions.

The field tests were designed in accordance with the Box-Behnken Design (BBD) optimization results. Key operating parameters-forward speed, digging depth, and shovel angle-were varied systematically within their respective ranges to evaluate their influence on performance metrics. Each test covered a fixed operation distance of 20 meters with a working width of 1.3 meters, as shown in Figure 5(a). These settings ensured comparable working volumes across trials, while still allowing the effects of the optimized parameters to be observed.



(a) Testing Field *(b) Torque Sensor*

Fig. 5 - Testing Field Method

After each trial, the total mass of collected rocks M_{rock} (*kg*) was measured using an electronic scale, and the operation time t (*s*) was recorded using a stopwatch. Operating torque and shaft speed were captured in real time using a Kistler Type 9051A rotary torque sensor installed on the machine's drive shaft, as shown in Figure 5(b). The average power *P* (*KW*) was calculated as:

$$P = \frac{T \cdot 2\pi \cdot RPM}{60 \times 1000} \quad (1)$$

Based on these measurements, the rock excavation efficiency (REE) was defined as the excavated rock mass per unit energy consumed:

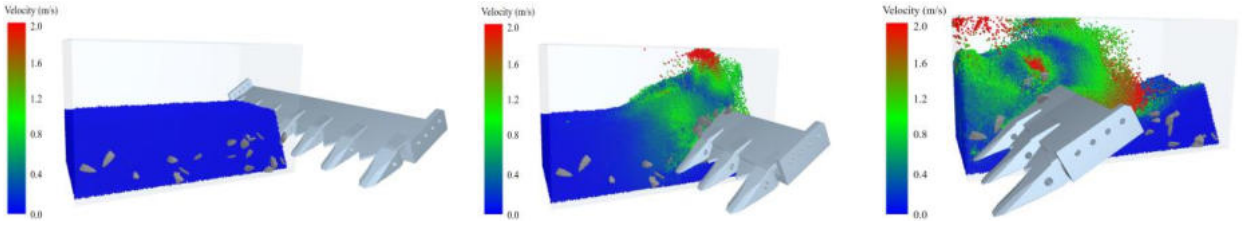
$$REE = \frac{M_{rock}}{t \cdot P} \quad (2)$$

Each parameter combination was tested three times to ensure repeatability. The field conditions were consistent with typical rock picking scenarios in the region, and the empirical results provided robust validation for the DEM-based optimization strategy.

RESULTS AND ANALYSIS

Simulation process of Rock-Lifting

Figure 6 shows the cross-sectional DEM simulation of the shovel–soil–rock interaction at 1 s, 5 s, and 9 s. At 1 s (Fig. 6a), the shovel initiates penetration with minimal soil disturbance. By 5 s (Fig. 6b), particle displacement and velocity increase significantly near the shovel edge. At 9 s (Fig. 6c), high-velocity regions (>1.6 m/s) appear, indicating active excavation and effective rock-soil separation. The results highlight the dynamic interaction process and the shovel's influence on material flow.



(a) 1 s *(b) 5 s* *(c) 9 s*

Fig. 6 - Cross-Sectional DEM Simulation of Shovel–Soil–Rock Interaction

Optimization Results Based on DEM and BBD Experiments

Discrete Element Method (DEM) simulations were conducted to analyze the influence of forward speed on the excavation performance of the 1JS-200 rock picker's shovel. Based on the Box-Behnken Design (BBD), three forward speeds were evaluated: 0.3 m/s, 0.5 m/s, and 0.7 m/s, while the other two parameters-digging depth and shovel angle-were held at their central values.

The simulation results, shown in Table 3, reveal a non-linear relationship between forward speed and rock excavation efficiency (REE). As the forward speed increases from 0.3 m/s to 0.5 m/s, the REE significantly improves, indicating enhanced soil-rock engagement and a more effective cutting-lifting interaction. At 0.5 m/s, the shovel achieves optimal contact with the soil-rock mixture, resulting in both high rock capture and relatively moderate energy consumption.

Table 4

Test factor level design

Serial Number	Forward speed (m/s)	REE (%)	Torque (N·m)
1	0.3	87.4	260.7
2	0.5	79.2	335.9
3	0.7	71.6	412.8

Three forward speeds were evaluated: 0.3 m/s, 0.5 m/s, and 0.7 m/s, as shown in Fig. 7. At 0.3 m/s (Fig. 7a), soil and rock movement is minimal, with most particles remaining in low-velocity zones (<0.4 m/s). At 0.5 m/s (Fig. 7b), material displacement increases, and a broader region of medium velocity (green) emerges. At the highest speed of 0.7 m/s (Fig. 7c), particle flow intensifies, with a clear expansion of high-velocity areas (>1.6 m/s) and increased rock-soil separation. These results suggest that higher operating speeds promote more efficient material disturbance, though potentially at the cost of increased energy input or wear.



(a) v= 0.3 m/s (b) v= 0.5 m/s (c) v= 0.7 m/s

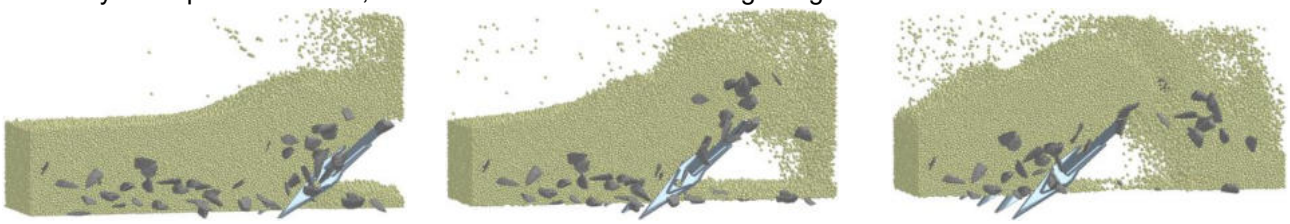
Fig. 7 – DEM Simulation of Soil and Rock Motion at Varying Shovel Speeds

Table 5

Test factor level design

Serial Number	Digging Depth (mm)	REE (%)	Torque (N·m)
1	160	82.6	310.3
2	180	79.2	335.9
3	200	75.4	362.1

As shown in Fig. 8, increasing the digging depth enhances shovel–rock contact, leading to greater rock displacement. At 160 mm, only shallow rocks are disturbed. At 180 mm, the shovel begins to lift embedded rocks, while at 200 mm, extensive rock separation occurs, indicating improved extraction. However, deeper excavation also increases soil disturbance and resistance. Thus, an optimal depth should balance rock-lifting efficiency and operational load, which can be determined through targeted DEM simulations.



(a) depth = 160 mm (b) depth = 180 mm (c) depth = 200 mm

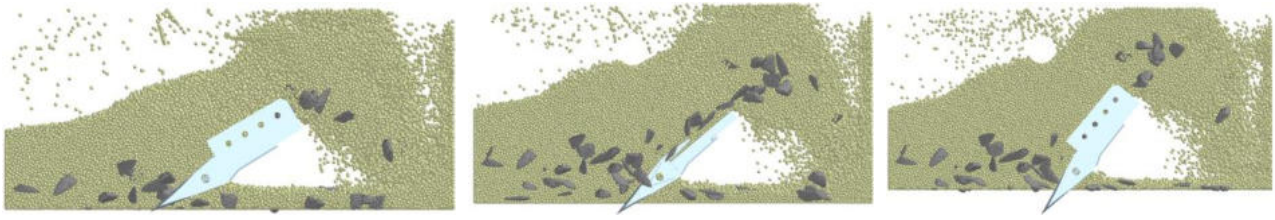
Fig. 8 - Rock Particle Motion at Different Working Depths

Table 6

Test factor level design

Serial Number	Angle (°)	REE (%)	Torque (N·m)
1	30°	83.8	315.4
2	40°	79.2	335.9
3	50°	73.9	358.6

Figure 9 illustrates rock particle motion at shovel angles of 30°, 40°, and 50°. At 30° (Fig. 9a), the shovel slides beneath the soil with limited rock engagement and minimal displacement. At 40° (Fig. 9b), the contact between the shovel and buried rocks increases significantly, causing noticeable lifting and separation. However, at 50° (Fig. 9c), the shovel penetrates steeply, pushing rocks laterally with less upward motion, which may reduce extraction efficiency. These results suggest that a moderate angle (around 40°) provides the best balance between penetration and rock-lifting effectiveness.



(a) degree = 30° (b) degree = 40° (c) degree = 50°

Fig. 9 - Rock Particle Motion at Different Working Degree

BBD response surface test results and analysis

To investigate the effects of three independent variables (A, B, and C) on response efficiency (REE) and torque, a Box–Behnken design (BBD) approach was employed. Table 7 presents the experimental design and results, including factor settings (A, B, and C), response efficiency (REE), and torque output.

The results indicate that Serial number 13 (center point with A=B=C=0) achieved the highest REE value (88.1%) and a relatively high torque output (386 N·m), suggesting a potential optimal combination near the center of the design space. In contrast, Serial number 7 (A=0, B=1, C=-1) recorded the lowest REE (64.5%) despite moderate torque (372 N·m), reflecting a condition less favorable for efficient energy utilization.

This variation in REE performance across runs can be attributed to the interaction effects among factors A, B, and C. For example, combinations where B and C had opposing signs (e.g., Serial 7 and 6) tended to show reduced REE, possibly due to conflicting effects on system dynamics. Conversely, center point conditions (Serial 13) may have benefited from a more balanced contribution of each factor, minimizing energy loss while maintaining torque. Additionally, Serial 12 (A=1, B=0, C=1) also produced high torque (421 N·m) with reasonably good REE (74.9%), indicating that positive settings of A and C may be favorable for torque output enhancement.

In conclusion, the BBD test results highlight that the optimal performance-in terms of both REE and torque-is likely located near the design center, and that specific combinations of factor levels significantly affect energy efficiency. These findings provide a basis for response surface modeling and further optimization of system parameters.

Table 7

Design of BBD response surface experiment

Serial number	A	B	C	REE (%)	Torque (N·m)
1	-1	-1	0	80.8	352
2	1	−1	0	74.8	368
3	−1	1	0	68.8	372
4	1	1	0	70.8	420
5	0	−1	−1	76.5	348
6	0	−1	1	69.5	360
7	0	1	−1	64.5	372
8	0	1	1	65.5	408
9	−1	0	−1	79.9	365
10	1	0	−1	76.7	391
11	−1	0	1	75.7	383
12	1	0	1	74.9	421
13	0	0	0	88.1	386

To evaluate the significance of the BBD response surface model and identify the key factors influencing REE, an ANOVA (analysis of variance) was performed. Table 8 presents the results, including the sum of squares, degrees of freedom, mean squares, F-values, and corresponding P-values for each factor and interaction term. The model was found to be highly significant ($P = 0.0005$), with a large F-value (28.53), indicating that the regression model explains a substantial portion of the variation in REE. Among the primary factors, A ($P = 0.0002$), B ($P = 0.0011$), and C ($P = 0.0021$) all showed statistically significant effects, with factor A exhibiting the strongest influence ($F = 57.85$).

In addition, the quadratic terms A^2 ($P = 0.0008$), B^2 ($P = 0.0015$), and C^2 ($P = 0.0043$) were also highly significant, suggesting strong curvature in the response surface and confirming the necessity of including second-order terms in the model. Conversely, the two-factor interaction terms (AB, AC, BC) were not statistically significant ($P > 0.05$), indicating that the combined effects of two factors did not significantly alter REE compared to their individual contributions. The lack-of-fit test was marginally non-significant ($P = 0.0514$), which supports the adequacy of the model, although minor unexplained variation may remain.

In conclusion, the ANOVA results confirm the validity of the BBD model and highlight that the individual and quadratic effects of factors A, B, and C are the main contributors to REE variation, while two-factor interactions are less influential. This justifies the use of a full quadratic model for accurate response prediction and optimization. This contributes a coupled shovel–soil–rock interaction with key design parameters, enabling data-driven optimization of shovel performance in rock-picking operations.

Table 8

BBD Response Surface Analysis Of Variance

Source	Sum of Squares	df	Mean Square	F-Value	P-Value
Model	30251.47	9	3361.27	28.53	0.0005
A	6812.73	1	6812.73	57.85	0.0002
B	4034.6	1	4034.6	34.24	0.0011
C	2961.22	1	2961.22	25.13	0.0021
AB	540.67	1	540.67	4.58	0.072
AC	302.88	1	302.88	2.56	0.1576
BC	612.44	1	612.44	5.2	0.0603
A^2	4908.32	1	4908.32	41.66	0.0008
B^2	3862.19	1	3862.19	32.8	0.0015
C^2	2216.42	1	2216.42	18.81	0.0043
Residual Error	822.7	3	274.23	-	-
Lack of Fit	791.24	2	395.62	18.36	0.0514
Pure Error	31.46	1	31.46	-	-
Total	31074.17	12	-	-	-

The regression equation for torque T based on the Box–Behnken design is expressed as follows:

$$T = 386 + 16A + 18B + 12C + 5A^2 + 8AB + 3AC - 13B^2 + 6BC - 1C^2 \quad (3)$$

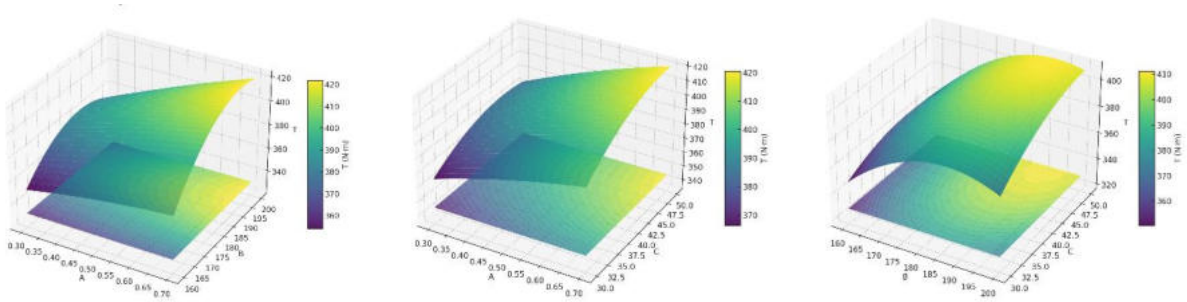
where: A represent forward speed (m/s), B - digging depth (mm), C - tool angle (°).

To visualize and interpret the interaction effects of variables A, B, and C on torque (T), 3D response surface plots were generated. Figure 10 illustrates the interactive influence of paired factors on torque while the third factor was held constant.

In Fig. 10(a), when C is fixed at 40°, torque increases steadily with the rise of both A and B, particularly showing a sharp increase at higher values of B. This suggests that B plays a dominant role in enhancing torque under these conditions. In Fig. 10(b), with B fixed at 180, torque again exhibits a strong positive correlation with A, and a nonlinear increasing trend with C, indicating that both A and C positively contribute to torque, though A's effect is more linear and consistent. Lastly, in Fig. 10(c), when A is fixed at 0.5, torque shows a clear curved response surface with respect to B and C, with a pronounced peak in the upper right region of the surface. This confirms a significant interaction between B and C in modulating torque output.

These surface plots are consistent with the ANOVA results, where primary factors A and B were significant, and the B² and C² terms showed strong quadratic effects. Although the interaction terms were not statistically significant in the ANOVA (P > 0.05), the curvature observed in the surfaces, especially in Fig. 10(c), suggests that visual inspection may still reveal synergistic tendencies not captured by isolated significance tests.

In summary, the response surface plots reinforce that A and B are the primary drivers of torque, with B-C interactions exhibiting practical relevance in shaping the torque response.



(a) T vs A and B(C = 40°) *(b) T vs A and C (B = 180)* *(c) T vs B and C (A = 0.5)*

Fig. 10 - Influence of the Interaction of Various Factors on the Torque Resistance

Field Performance Verification of the Rock Picker Machine

Fig.11 summarizes the field test results for REE, torque, and their respective errors across three test conditions. Among the three tests, Test 1 demonstrated the most efficient performance**,** combining high metabolic efficiency with stable torque output.

Specifically, Test 1 achieved the highest REE value (89.9%), accompanied by a modest positive REE error (+1.8%), and a torque output of 400.7 N·m with a 3.81% error. In contrast, Test 2 and Test 3 recorded lower REE values (86.2% and 86.7%, respectively), both with negative REE errors (−1.9% and −1.4%), and showed no clear advantage in torque.

Overall, the field test results not only reinforce the optimization trends observed in the simulation but also highlight the model's effectiveness in guiding real-world parameter selection for improved operational performance.

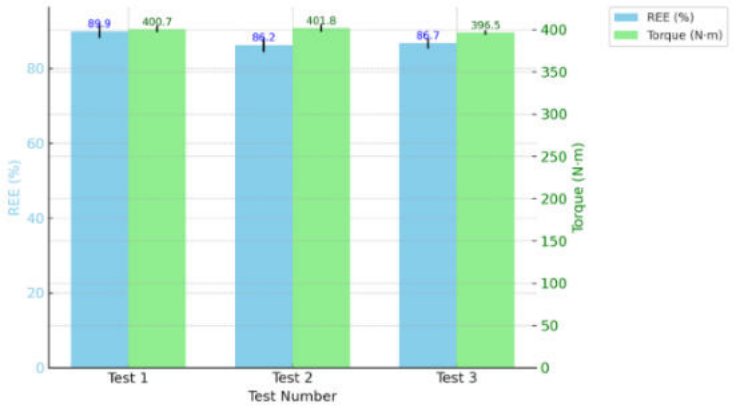


Fig. 11 - REE and Torque Performance Across Field Tests

Figure 12 illustrates the field-testing process and its outcomes. In Fig. 12(a), a tractor-mounted stone removal machine is shown operating in a rocky field, effectively clearing surface debris. Fig. 12(b) displays the result of this operation.



(a) Testing Operation *(b) The Effects Of Testing*

Fig. 12 - The Effects of Field Experiment Operation

Compared with previous studies that applied the Discrete Element Method (DEM) to shovel or soil-tool interaction analysis, this section contributes a more integrated and application-oriented framework. Prior work, such as *Asl and Singh (2009)* and *Zhang et al. (2023)*, focused on optimizing structural parameters-e.g., soil-opening angle, lifting angle, and camber angle-for improved straw burial and reduced resistance in tillage operations. Similarly, *Feng et al. (2022)* investigated DEM-based interactions between excavation tools and granular media on Earth-like terrains to enhance the performance of bucket-type soil removal systems.

Building upon these foundations, the present study expands the modeling scope by incorporating a wider set of physical and contact parameters, including static friction, rolling resistance, and restitution coefficients, which are critical in rock–soil environments. More importantly, these parameters are not only calibrated through simulation but also validated via field experiments-linking micro-scale material behavior with macro-scale equipment performance. This dual-layer validation improves the fidelity of the DEM model, making it more representative of real-world conditions involving complex rock–soil mixtures.

Unlike prior work that emphasized simulation precision in relatively homogeneous or less abrasive materials, this study targets a practical, PTO-driven rock picker operating in rugged agricultural environments. By integrating DEM-based interaction modeling with Box–Behnken Design (BBD) optimization and verifying key performance indicators such as torque and rock extraction efficiency (REE) in field tests, the research offers a systematic and validated approach for structural refinement. Specifically, it provides an effective method for optimizing the shovel design of the 1JS-200 rock picker, addressing both mechanical performance and energy efficiency under realistic working conditions.

CONCLUSIONS

(1) A coupling modeling framework was developed to simulate the interaction between soil, rock, and the lifting shovel using DEM. This model accurately captured the dynamic response of mixed granular media under working conditions and provided a theoretical basis for analyzing force transmission, material flow, and tool loading during rock-picking operations.

(2) A data-driven optimization method based on the Box–Behnken Design (BBD) was established, allowing the investigation of the effects of forward speed, digging depth, and shovel angle on key performance indicators. Response surface models were constructed for both torque and rock excavation efficiency (REE), revealing non-linear relationships and parameter interactions. The optimal parameter combination was determined as a forward speed of 0.5 m/s, a digging depth of 170 mm, and a shovel angle of 40°, under which the REE reached 88.1% with a predicted torque of approximately 386 N·m.

(3) A field validation framework was implemented to verify the simulation-based optimization results. The results of three field trials under the optimal parameter settings showed REE fluctuations within 2% and torque deviations within 4% of the predicted values, confirming the effectiveness and reliability of the model. These findings demonstrate that the optimized shovel design effectively reduces torque load while improving excavation efficiency.

ACKNOWLEDGEMENT

This study was supported by the Open Project of Key Laboratory of Intelligent Agricultural Equipment in Xinjiang (ND2N202302) and the Major Science and Technology Project of Xinjiang Autonomous Region (2022A02007-2-2)

REFERENCES

[1] Asl, J. H., & Singh, S. (2009). Optimization and evaluation of rotary tiller blades: Computer solution of mathematical relations. *Soil and Tillage Research*, 106(1), 1-7.

[2] Camborde, F., Mariotti, C., & Donzé, F. V. (2000). Numerical study of rock and concrete behaviour by discrete element modelling. *Computers and geotechnics*, 27(4), 225-247.

[3] Coetzee, C. J. (2009). The numerical modelling of excavator bucket filling using the discrete element method. *International Journal for Numerical and Analytical Methods in Geomechanics*, 33(11), 1337–1362. https://doi.org/10.1002/nag.771

[4] Coetzee, C. J. (2017). Review: Calibration of the discrete element method. *Powder Technology*, *310*, 104–142. https://doi.org/10.1016/j.powtec.2017.01.015

[5] Cundall, P. A. (1988). Formulation of a three-dimensional distinct element model—Part I. A scheme to detect and represent contacts in a system composed of many polyhedral blocks. In *International journal of rock mechanics and mining sciences & geomechanics abstracts.* Vol. 25, No.3, pp.107-116. Pergamon.

[6] Feng, Y., Wu, J., Guo, C., & Lin, B. (2022). Numerical simulation and experiment on excavating resistance of an electric cable shovel based on EDEM–RecurDyn co-simulation. *Machines*, 10(12), 1203. https://doi.org/10.3390/machines10121203

[7] Fielke, J. U., Ucgul, M., & Saunders, C. (2013). Discrete element modeling of soil-implement interaction considering soil plasticity, cohesion, and adhesion, *Transactions of the ASABE,* Paper No. 131618800. St. Joseph, Mich.: ASABE.

[8] Franco, Y., Rubinstein, D., & Shmulevich, I. (2007). Prediction of soil–bulldozer blade interaction using discrete element method. *Transactions of the ASABE*, 50(1), 345–353. https://doi.org/10.13031/2013.22354

[9] Horn R. Time dependence of soil mechanical properties and pore functions for arable soils[J]. *Soil Science Society of America Journal*, 2004, 68(4): 1131-1137.

[10] Liu, H., Yang, D., & Zhang, X. (2020). Application of discrete element modeling (DEM) for the mechanical analysis of construction materials. *Construction and Building Materials*, 246, 118473. https://doi.org/10.1016/j.conbuildmat.2020.118473

[11] Mak, T., & Chen, Y. (2014). Discrete element modeling of cultivator sweep-to-soil interaction. Journal of *Terramechanics*, 53, 1–10. https://doi.org/10.1016/j.jterra.2014.01.001

[12] Rizzardo, C., Katyara, S., Fernandes, M., & Chen, F. (2020). The importance and the limitations of Sim2Real for robotic manipulation in precision agriculture. *arXiv preprint arXiv:2008.03983*. https://arxiv.org/abs/2008.03983

[13] Shmulevich, I., Asaf, Z., & Rubinstein, D. (2007). Interaction between soil and a wide cutting blade using the discrete element method. *Soil and Tillage Research*, 97(1), 37–50. https://doi.org/10.1016/j.still.2007.08.004

[14] Servin, M., Berglund, T., & Nystedt, S. (2020). A multiscale model of terrain dynamics for real-time earthmoving simulation. *arXiv*. https://arxiv.org/abs/2011.00459

[15] Zou, J., Yang, W., & Han, J. (2020). Discrete element modeling of the effects of cutting parameters and rock properties on rock fragmentation. *IEEE Access*, 8, 136393-136408.

[16] Zhang J, Xia M, Chen W, Yuan D, Wu C, Zhu J. Simulation Analysis and Experiments for Blade-Soil-Straw Interaction under Deep Ploughing Based on the Discrete Element Method. *Agriculture*. 2023; 13(1):136. https://doi.org/10.3390/agriculture13010136

[17] Zhang, Y., & Li, L. (2024). Optimization of discrete element method model to obtain stable and reliable numerical results of mechanical response of granular materials. *Minerals, 14*(8), 758. https://doi.org/10.3390/min14080758

RESEARCH ON WEED RECOGNITION AND CROP ROW EXTRACTION TECHNOLOGY BASED ON DEEP LEARNING
/
基于深度学习的杂草识别与作物行提取技术研究

Tengxiang YANG; Chengqian JIN*); Youliang Ni; Man CHEN; Zhen LIU [1]
Nanjing Institute of Agricultural Mechanization, Ministry of Agriculture and Rural Affairs, Nanjing, Jiangsu / China
Tel: +8602584346113; E-mail: jinchengqian@126.com;
DOI: https://doi.org/10.35633/inmateh-76-57

Keywords: *semantic segmentation; image recognition; corn crop row recognition; precision agriculture;*

ABSTRACT

To address the limitation of existing agricultural unmanned plant protection equipment in perceiving crop growth status in real time during the maize seedling stage, this study proposes a crop row extraction method based on image processing. A crop semantic segmentation network was developed using the UNet framework, with VGG19 as the encoder and transposed convolution as the decoder. Model testing demonstrated that the segmentation network achieved accuracy rates of 0.9865 on the training set and 0.9864 on the validation set, with corresponding loss values of 0.0254 and 0.0270. In continuous processing scenarios, the average time for semantic segmentation per image was 120 milliseconds, while crop row extraction required 23 milliseconds.

摘要

为解决现有农用无人植保机具在玉米苗期作业时无法现场感知作物生长状况的问题，提出一种基于图像处理的玉米苗期作物行提取方法。基于 Unet 框架构建了作物语义分割网络，编码器为 VGG19，解码器为转置卷积，通过添加注意力机制来增强主要特征信息的权重。采用传统图像处理技术获取作物的轮廓、最小外接圆的圆心与半径等关键信息，引入数据缓存机制，增加用于作物行提取的作物数据量。运用苗带自动聚类算法，在作物行数量与位置不确定的情况下，自动对作物行的数量及其所包含的作物对象进行聚类。模型测试结果表明：作物语义分割模型在验证集与测试集上的准确率分别达到 0.9865 和 0.9864，损失率分别为 0.0254 和 0.0270。在实际连续处理过程中，单张图片的语义分割时间平均为 120 毫秒，作物行提取时间为 23 毫秒。

INTRODUCTION

Currently, unmanned field management machinery primarily relies on satellite navigation and inertial navigation systems for positioning during field operations. In practice, the machinery follows a predetermined absolute spatial trajectory without accounting for the relative spatial relationship between the machinery and the crops *(Wang et al., 2022; Xie et al., 2023)*. However, in actual agricultural production, field operations fundamentally involve direct interaction between the machinery and the crops. Therefore, it is essential to investigate crop row extraction technology to enhance the crop perception capabilities of unmanned agricultural machinery, thereby improving operational accuracy and efficiency while minimizing crop damage during autonomous operations.

Crop row extraction is a fundamental requirement for enabling unmanned plant protection operations in agricultural machinery. Existing studies generally adopt image processing methods for crop row extraction, typically comprising two main steps: crop recognition and crop row fitting. Traditional crop recognition approaches include the super-green method for crop segmentation *(Jiang et al., 2021)*, wavelet transform processing *(Habib et al., 2021)*, support vector machine classification *(Wu et al., 2023)*, and classification based on texture and color features *(Zhang et al., 2023)*. In recent years, with the rapid advancement of deep learning technologies, several classical neural network architectures have been applied to crop and weed classification tasks, such as Artificial Neural Networks (ANN) *(Monteiro et al., 2021)*, Convolutional Neural Networks (CNN) *(Jabir et al., 2021; Yang et al., 2023)*, Sum-Product Networks (SPN) *(Kumar Kempegowda et al., 2022; Wang S. et al., 2019)*, Transformers *(Feng et al., 2024; K. Jiang et al., 2022)*, and Probabilistic Neural Networks (PNN) *(Venkataraju et al., 2023)*.

[1] *Tengxiang Yang, Stud. Eng; Chengqian Jin, Prof. Ph.D. Eng.; Youliang Ni, Associate Prof. Ph.D. Eng.; Man Chen, Associate Prof. Ph.D. Eng.; Zhen Liu, Associate Prof. Ph.D. Eng.;*

Methods for fitting crop rows include the least squares method *(Diao et al., 2024)*, Hough transform *(Chen et al., 2019; Li et al., 2022)*, skeleton extraction *(Wu et al., 2024; Zhao et al., 2019)*, feature engineering *(Zhang et al., 2023)*, partition clustering *(Ma et al., 2021)*, Fast-SCNN *(Chen et al., 2021)*, and Mean-Shift *(Weibing, 2019)*.

However, existing methods face several limitations. When the angle between the camera and the ground is large or under backlit conditions, direct sunlight entering the image degrades image quality, making processing more difficult. In practical operations, weeds often cross or overlap with crops. Traditional methods relying on shallow features such as color, texture, and shape struggle to achieve accurate, robust, and generalizable segmentation. The crop information extracted from a single image is limited. The crop position data derived from it is susceptible to random errors, leading to significant fluctuations in measurement results.

To address these challenges, this study positioned the camera beneath the vehicle body with its central axis perpendicular to the ground to stabilize image acquisition and reduce interference from direct sunlight and reflections. For crop and weed segmentation, a deep learning-based semantic segmentation network was employed for initial crop recognition, followed by traditional image processing techniques to extract crop contour and positional information. During crop row extraction, contour information from the most recent five frames was collectively analyzed. An automatic seedling row clustering algorithm was then used to identify the seedling rows within the images, from which the crop row information was subsequently extracted.

MATERIALS AND METHODS

Data Acquisition and Processing

The dataset used in this study was collected by an onboard camera mounted at the bottom of a high-clearance boom sprayer, with a mounting height of 80 cm above ground level. The data acquisition was conducted on August 27, 2020, at the Baima Test Base of the Nanjing Research Institute for Agricultural Mechanization, Ministry of Agriculture and Rural Affairs. The vehicle-mounted camera employed was a RealWide USBFHD01M camera (maximum resolution: 1920×1080 pixels). A total of three video clips were recorded during the experiment. The first two video clips were used for model training, from which 1,436 images were obtained through frame extraction and cropping. The last video clip was reserved exclusively for testing purposes.

The crop objects in the images were annotated using the polygon tool in the image annotation software Labelme, where the crops were labeled as 1 and the rest as 0. The proposed method requires only crop image annotations, eliminating the need for weed classification labeling. The annotated data was divided into a training set and a validation set in an 8:2 ratio. The dataset was subjected to image data augmentation in the following ways with a 50% probability in sequence: random contrast adjustment, random brightness adjustment, random left-right flipping, and random noise addition. To facilitate training, the original image size obtained by the camera was adjusted to 512×512.

Semantic Segmentation Model Construction

The crop segmentation network was designed based on the classic semantic segmentation model UNet. The UNet model consisted of two main components: an encoder and a decoder. For the encoder, DenseNet121 served as the backbone network, extracting four top-level convolution maps with dimensions of 256×256, 128×128, 64×64, and 32×32 as feature maps. The decoder comprised two key elements: the Transition Layer and the UnSampling Layer. The Transition Layer followed a specific structure: CABM (Convolutional Block Attention Module) followed by 1×1 C2DT (Conv2Dtranspose), BN (Batch Normalization), and ReLU (Rectified Linear Unit). Meanwhile, the UnSampling Layer was structured as 2×2 C2DT + BN + ReLU. The overall network architecture is illustrated in Fig. 1.

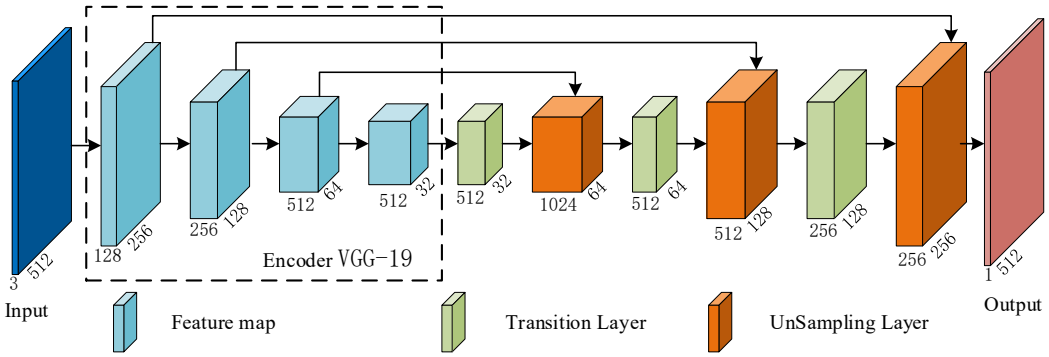


Fig. 1 - Network model of crop segmentation

The encoder employed VGG19 as its backbone network. VGG, an improved architecture derived from AlexNet, was developed by the Visual Geometry Group at the University of Oxford. This network came in two primary variants: VGG16, with 16 hidden layers (13 convolutional + 3 fully connected layers), and VGG19, featuring 19 hidden layers (16 convolutional + 3 fully connected layers). A key innovation of the VGG architecture was the use of smaller convolutional kernels, replacing a single 7×7 kernel with three consecutive 3×3 kernels and a 5×5 kernel with two 3×3 kernels. This design deepened the network while maintaining the same receptive field, enhancing feature extraction efficiency. In this study, four convolutional layers from VGG19—block5_conv1, block4_conv1, block3_conv1, and block2_conv1—were extracted as feature maps for crop segmentation. These layers had dimensions of 32×32×512, 64×64×512, 128×128×256, and 256×256×128, respectively.

The Transition Layer served as the preprocessing part of the decoder and comprised two components: the CABM attention module and the transposed convolution module. CABM represented the convolutional block attention mechanism, which functioned as a hybrid attention mechanism combining spatial attention and channel attention. The spatial attention mechanism consisted of three parts. CBAM demonstrated its advantage through dynamically focusing on key image regions by adaptively assigning weights to different positions, which significantly enhanced model performance. It automatically identified and enhanced task-relevant areas including target objects, edges, or textures while suppressing irrelevant backgrounds or noise, thereby improving the model's robustness to occlusion and complex environments. The first part involved channel pooling, where a tensor of size (h×w×c) was processed through maximum pooling and average pooling to yield a tensor of size (h×w×2). The second part performed a convolution operation on this tensor to produce an output tensor of size (h×w×1). The third part normalized this tensor through Batch Normalization and activated it with a Sigmoid function to obtain a spatial weight tensor, which was then multiplied by the input tensor to adjust the data weights in the spatial dimension. The channel attention mechanism was divided into four parts. The first part executed global maximum pooling and global average pooling on each channel, compressing each channel's data into one pixel to ultimately generate two tensors of size (1×1×c). The second part processed these tensors through two fully connected layers respectively to produce connection weights between channels, thereby enhancing channel connectivity. The third part stacked the two tensors from the previous step, activated them with a Sigmoid function, and multiplied them by the input tensor to modify each channel's weight levels. The transposed convolution employed a 3×3 kernel size with a stride of 1, maintaining the feature map's original size after processing.

The UnSampling Layer functioned as the upsampling component of the decoder and consisted of two parts: the transposed convolution module and feature fusion. The transposed convolution module employed a stride of 2, which doubled the image size after processing. Since transposition had already been performed in the preprocessing stage, the positional information within the feature map remained preserved during this operation. The resulting upsampled feature map subsequently underwent batch normalization and ReLU activation. Feature fusion represented a fundamental design characteristic of the UNet network architecture. This process concatenated the upsampled feature map produced by transposed convolution with the corresponding feature map of identical dimensions extracted from VGG19, thereby combining high-level abstract features from low-resolution data with low-level surface features from high-resolution data within the final feature map.

Loss Function Construction

The loss function L employed for model training in this study was computed through a weighted combination of Dice Loss and Binary Cross Entropy Loss. The calculation followed this formula:

$$L = w \times L_{\text{bce}} + L_{\text{dice}} \quad (1)$$

where:

The symbol w represents the weight, L_{bce} represents the Binary Cross Entropy loss, and L_{dice} represents the Dice Loss.

$$L_{bce}(\alpha,\beta) = -\frac{1}{N}\sum_{i=1}^{N}(\alpha \ln\left(\frac{1}{1+e^{-\beta}}\right) + (1-\beta)\ln\left(1-\frac{1}{1+e^{-\beta}}\right)) \quad (2)$$

where:

The symbol α is the actual label (0 or 1), and β is the probability predicted by the model.

$$L_{dice} = 1 - \frac{2|X\cap Y|+0.01}{|X|+|Y|+0.01} \quad (3)$$

where:

$|X \cap Y|$ represents the number of pixels in the intersection of the prediction result and the ground truth label. $|X|$ and $|Y|$ respectively denote the number of pixels in the prediction result and the ground truth label.

The model evaluation metrics are the average recognition *accuracy* and *mIOU*, and their calculation formulas are as follows:

$$Accuracy = \frac{1}{c}\sum_{j=1}^{c}\frac{n_{jj}}{n_j} \times 100\% \quad (4)$$

where: c denotes the number of categories, n_j represents the total number of samples in the j-th category, and n_{jj} indicates the number of correctly predicted samples for the j-th category.

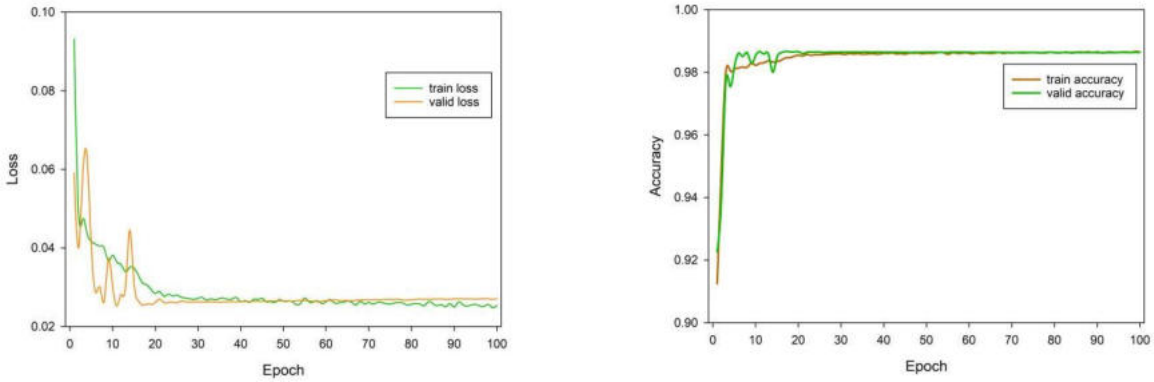
$$mIOU = \frac{1}{k+1}\sum_{i=0}^{k}\frac{p_{ii}}{\sum_{j=0}^{k}p_{ij}+\sum_{j=0}^{k}p_{ji}-p_{ii}} \quad (5)$$

where: p_{ii} represents the number of cases where the true value is i and it is predicted as i, which is the number of true positives; p_{ij} represents the number of cases where the true value is i but it is predicted as j, which is the number of false positives; p_{ji} represents the number of cases where the true value is j but it is predicted as i, which is the number of false negatives; k+1 represents the number of categories including the empty class. Since this study only distinguishes between crops and background, k =1.

Model Training

The model training platform was configured as follows: The CPU was an Intel Core i7 10700 with a main frequency of 4.8 GHz and 16 GB of memory, while the GPU was an Nvidia RTX 2060 with 11 GB of video memory. The operating environment consisted of Ubuntu 20.04 operating system, Python 3.9.0 programming language, and Tensorflow 2.5-GPU deep learning framework. The Adam optimization algorithm was employed for model training. The batch size was set to 8, with 150 training epochs and an initial learning rate of 0.01. A learning rate reduction mechanism was implemented where, if the loss remained unchanged for 5 consecutive epochs, the learning rate would decrease to 0.1 times its original value.

The training process completed 100 epochs, with the results presented in Fig. 2. Figure 2a demonstrated that the model started converging around the 25th epoch, ultimately achieving stabilized accuracies of 0.9865 for the training set and 0.9864 for the validation set. As shown in Fig. 2b, the loss rates similarly began converging around the 25th epoch, reaching values of 0.0254 (training) and 0.0270 (validation). After 70 epochs, the training loss became consistently lower than the validation loss, indicating the onset of model overfitting beyond this point.



a) - Training loss **b) - Training accuracy**

Fig. 2 - Process of model training

Weed Recognition

As illustrated in Fig. 3, after being processed by the crop-weed semantic segmentation network, a crop probability map was generated with a size of 512×512×1. The pixel values ranged from 0 to 1, representing the likelihood of each pixel belonging to a crop, where a value of 0 indicated background and a value of 1 indicated crop. To facilitate subsequent processing, the predicted map was binarized by considering pixels with probability values greater than 0.8 as crops, and those with values less than or equal to 0.8 as background.

The binarized predicted map exhibited spatial artifacts including isolated regions and fragmentation. To address these issues, a morphological opening operation was first applied using a 5×5 convolution kernel, which effectively removed isolated points, burrs, and bridging artifacts. Subsequently, a morphological closing operation with an identical 5×5 kernel size was performed to eliminate small holes, cracks, and surface pits in the processed image. This two-step morphological processing significantly improved the spatial coherence of the segmentation results while preserving the essential structural features of the crop distribution pattern.

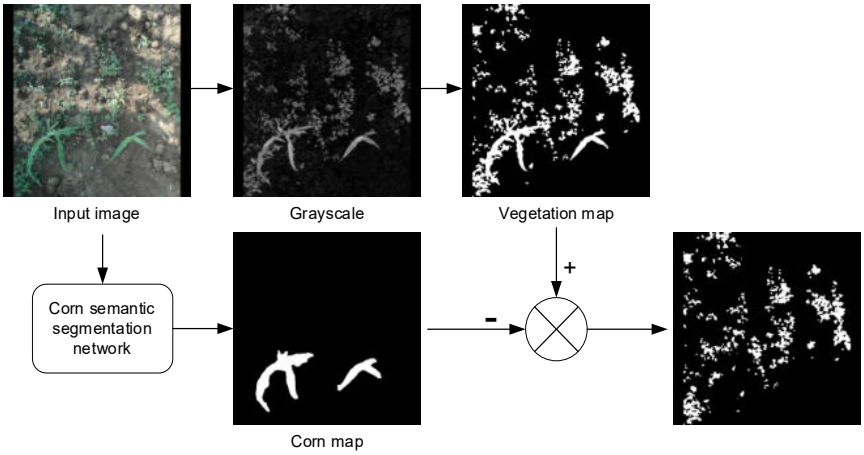


Fig. 3 - Process of weed extraction

Vegetation layer extraction was performed to obtain green vegetation information from images through specific processing methods. The image processing procedure consisted of the following steps. First, the red, green, and blue channels of the image were decomposed. The green channel was then enhanced using the super-green algorithm to produce a corresponding grayscale image, with pixel values constrained to the range of 0 to 255. Subsequently, the Otsu method (maximum inter-class variance method) was applied to perform binarization on the grayscale image, resulting in a binary image. Finally, a morphological opening operation was conducted using a 3×3 convolution kernel to generate the final vegetation layer. The super-green algorithm for green channel enhancement was calculated using the following formula:

$$G_{\mathrm{r}} = \min\left(255, \max\left(2G - B - R, 0\right)\right) \tag{5}$$

where: G_{r} represents the output grayscale image, while G, B, and R denote the green, blue, and red channels of the input image, respectively.

Crop row extraction

Contour detection was implemented using the findContours function from the OpenCV library. The detection mode was configured as RETR_EXTERNAL, ensuring only external contours were identified. For contour approximation, the CHAIN_APPROX_SIMPLE method was employed, which effectively compressed horizontal, vertical, and diagonal segments while preserving solely their endpoint coordinates.

The minimum enclosing circle corresponding to each contour was determined using the minEnclosingCircle function from the OpenCV library. This function automatically iterated through the 2D point set of each contour and calculated the precise center coordinates and radius of its minimum enclosing circle. The complete contour detection process, including this circle-fitting operation, was visually demonstrated in Fig. 4.

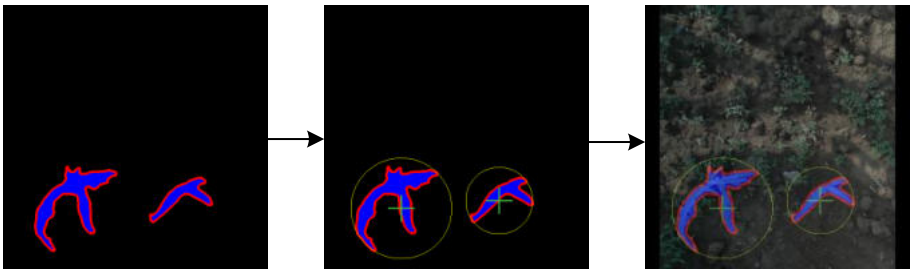


Fig. 4 - Process of crop positioning

The crop row positioning process was illustrated in Fig. 5. First, the semantic segmentation network extracted crop information from the input image, and the centers and radii of minimum enclosing circles for all crops were calculated and stored in memory. The system then verified whether the number of stored contour frames exceeded five; if so, the oldest frame was removed until the frame count satisfied the threshold requirement. Finally, all recorded crop contour data underwent clustering analysis. Upon identifying multiple seedling rows, the corresponding centerlines and boundary lines for each row were subsequently extracted.

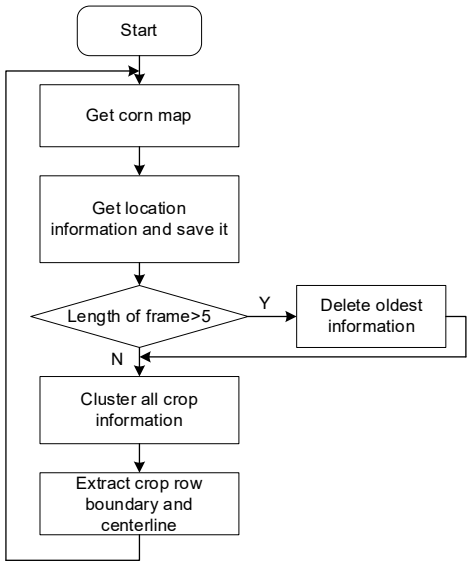


Fig. 5 - Process of crop row positioning

Due to the potential presence of multiple seedling rows within a single image, where both the quantity and spatial arrangement of these rows were unpredictable, the minimum-maximum distance algorithm was employed to perform clustering analysis on the contour coordinates. This clustering process enabled the determination of the exact number of seedling rows present in each image. As demonstrated in Fig. 6, the seedling row clustering algorithm operated according to the following procedure:

Algorithm 1: Crop row clustering

Data: set of point coordinates P, threshold of classification distance η, Minimum classification distance σ
Result: set of point classification Y

$center \leftarrow 0$;
$class \leftarrow 1$;
$Y \leftarrow \{1, 1, ..., 1\}$;
$maxDistance \leftarrow 0$;
calculate the points distance of P_1;
for $i \leftarrow 1$ **to** *Number of points* **do**
  $Di \leftarrow abs(P_{yi} - P_{y0})$;
  if $Di > max(D)$ **then**
    $maxDistance \leftarrow Di$;
    $center \leftarrow i$;
  end
end
while $max(D) > (maxDistance \times \eta)$ *and* $max(D) > \sigma$ **do**
  $class \leftarrow class + 1$;
  for $i \leftarrow 1$ **to** *Number of points* **do**
    $d \leftarrow abs(P_{yi} - P_{ycenter})$;
    if $Di > d$ **then**
      $Di \leftarrow d$;
      $Yi \leftarrow class$;
    end
  end
  $center \leftarrow$ *the index of max value in* D ;
end

Fig. 6 - Process of automatic seedling belt clustering

For a given input set of coordinate points $P=\{p_1, p_2, p_3, ..., p_n\}$, the algorithm selected p_1 as the initial clustering center. The distances from all points to p_1 were computed and stored in set D. The maximum value in D was identified as $maxDistance$, with its corresponding coordinate point designated as the next clustering center. Subsequently, the distance from each point to this new center was calculated and compared against the stored values in D. When a smaller distance was found, the point was assigned to the new cluster and its corresponding value in D was updated.

Following complete distance evaluation, the algorithm verified whether the maximum value in D satisfied the threshold condition: exceeding the minimum row spacing threshold *σ* while remaining below *η*×*maxDistance*, where *η* (a distance coefficient between 0 and 1) scaled the maximum classification threshold. If valid, the point associated with the current maximum distance became the subsequent clustering center, and the process iterated. Termination occurred when no values in *D* met the threshold criteria. The final output comprised classification set *Y* for point set *P*, representing the clustered results. The complete clustering procedure operated as follows:

Following point clustering, the classification set *Y* was obtained for the input set *P*, with values ranging from 1 to n (where n represented the maximum number of classifications, corresponding to the number of seedling rows). Through iterative traversal of set *Y*, the algorithm extracted the point set associated with each classification. Within each classified point set, the uppermost boundary (*LineA*) and lowermost boundary (*LineB*) of the contour were identified. The region bounded by these two lines constituted the seedling row area, while the midpoint between the upper and lower boundaries established the crop seedling row's centerline. This complete calculation process was illustrated in Fig. 7 and executed as follows:

Algorithm 1: Crop row extraction

Data: set of point coordinates P, set of point classification Y, set of circumcircle radius R
Result: Borderline $LineA, LineB$

calculate the number of crop rows;
for $i \leftarrow 1$ **to** *Number of categories* **do**
  for $j \leftarrow 1$ **to** *Number of points* **do**
    $LineA_i \leftarrow 0$;
    $LineB_i \leftarrow 512$;
    if $Y_j == i$ **then**
      $LineA_i \leftarrow max(LineA_i, P_{yj} + R_j)$;
      $LineB_i \leftarrow min(LineB_i, P_{yj} - R_j)$;
    end
  end
  $Line_i \leftarrow average(LineA_i, LineB_i)$;
end

Fig. 7 - Process of seedling belt boundary extraction

RESULTS

To validate the effectiveness and feasibility of the proposed algorithm, corresponding models and algorithms were constructed and verified using the third video clip collected during the experiment. The video recording specifications included a frame rate of 30 frames per second and an image resolution of 1920×1080 pixels. To accurately simulate the working environment, images were sequentially extracted from the video at 5-frame intervals. Each extracted image was then processed by cropping a central 1080×1080 area, which was subsequently resized to 512×512 pixels before being input into the algorithm for processing.

As shown in Fig. 8, the processing results of the first five extracted images during the experiment were presented. Horizontally, the images were arranged in chronological order, representing the first to the fifth image, with an interval of five frames between each. Vertically, the images were organized according to the processing steps: crop semantic segmentation, contour detection and localization, and navigation line extraction. Statistical analysis showed that the average processing time for crop semantic segmentation was 120 ms, while crop row extraction took an average of 23 ms.

From the crop semantic segmentation images, it was observed that corn was identified and segmented in all five images. The probability density was higher at the center of the leaves and lower at the edges, indicating better recognition performance in the core area and poorer performance at the leaf tips. Corn plants with two shoots per hole were recognized as a single plant, since the semantic segmentation network only classified objects by category without distinguishing individual instances. However, for optimal growth and increased yield per mu, single-plant-per-hole configurations were more desirable. Therefore, distinguishing individual seedlings was necessary to enable mechanized seedling removal operations.

In the contour segmentation images, the corn contours were accurately identified based on the segmented corn layer, and the center and radius of the minimum enclosing circles were calculated. Morphological operations and threshold filtering were applied to smooth the contours. When crops entered or exited the image frame, only partial contour information was captured, which limited the accuracy of the extracted contours. Thus, further refinement was required for contour optimization at the image boundaries to better reflect actual crop conditions.

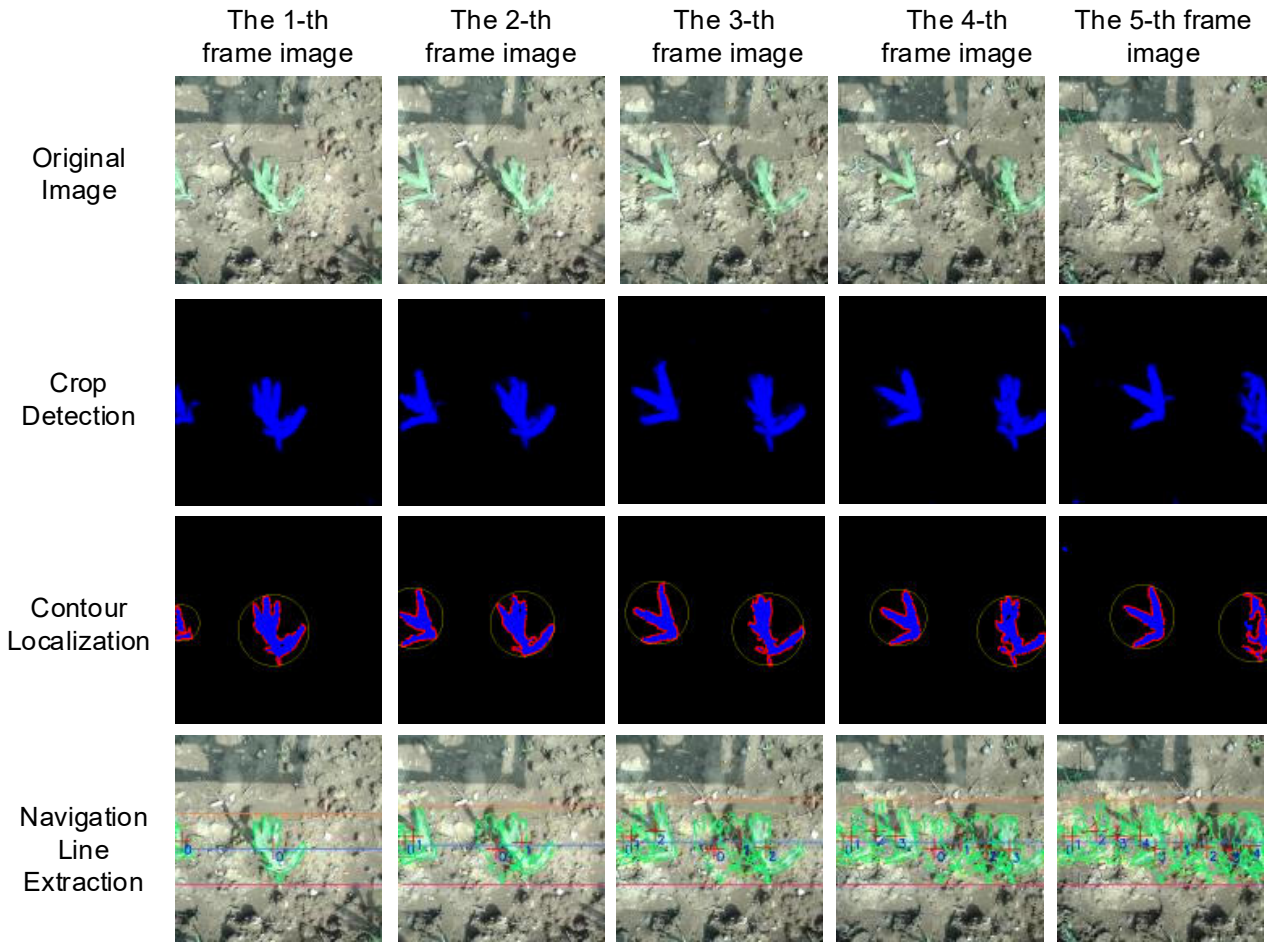


Fig. 8 - Algorithm testing results visualization

In the navigation line extraction images, the green dashed lines represented the crop contours, red crosses indicated the centers of the enclosing circles, yellow circles denoted the minimum enclosing circles, blue numbers marked the sequence of contour acquisition (i.e., the temporal order of contour generation), orange lines showed the upper boundaries of the seedling rows, dark red lines the lower boundaries, and blue lines the center lines. It was evident that seedling row information was extracted and the movement trajectories of the crops were tracked. Due to the asymmetrical shape of corn leaves, a deviation was observed between the enclosing circle center and the actual plant center. Additionally, differences in growth conditions led to vertical positional discrepancies even among adjacent plants. By comparing seedling row position data across the five images, the crop boundaries were successfully identified, reflecting the spatial distribution of the crops.

CONCLUSIONS

To address the challenges of crop recognition and segmentation in weedy field environments, this study proposed a crop recognition model based on a semantic segmentation network, enabling pixel-level differentiation between crops and weeds. From the segmented pure crop layer, the model extracted crop contour features and positional information to determine the location of the seedling rows in which the crops were situated.

A crop semantic segmentation network was constructed using semantic segmentation techniques. Model evaluation showed that the network achieved accuracy rates of 0.9865 on the training set and 0.9864 on the validation set, with corresponding loss values of 0.0254 and 0.0270. In real-time sequential processing, the average time required for semantic segmentation per image was 120 milliseconds, while crop row extraction took an average of 23 milliseconds.

By employing a multi-frame data caching strategy, the number of crop objects available for row extraction was increased in scenarios with sparse crop distribution, thereby enhancing the accuracy of crop row recognition.

ACKNOWLEDGEMENT

We greatly appreciate the careful and precise reviews by the anonymous reviewers and editors. This research was funded by the National Key Research and Development Plan project (2023YFD230050403) and the National Natural Science Foundation of China (32171911,32171911), and CAAS Center for Science in Smart Agriculture and Equipment (CAAS-SAE-202301).

REFERENCES

[1] Chen, Y., Geng, C., Wang, Y., Zhu, G., & Shen, R. (2021). Extraction method for centerlines of rice seedlings based on Fast-SCNN semantic segmentation. *INMATEH Agricultural Engineering*, Vol. 64, pp.335–344, Jiangsu/China.

[2] Chen Z., Li W., Zhang W., Li Y., Li M., & Li H. (2019). Research on Vegetable Crop Row Extraction Method Based on Automatic Hough Transform Accumulation Threshold (基于自动 Hough 变换累加阈值的蔬菜作物行提取方法研究). *Transactions of the Chinese Society of Agricultural Engineering*, Vol. 35, pp.314–322, Beijing/China.

[3] Diao, Z., Ma, S., Zhang, D., Zhang, J., Guo, P., He, Z., Zhao, S., & Zhang, B. (2024). Algorithm for Corn Crop Row Recognition during Different Growth Stages Based on ST-YOLOv8s Network. *Agronomy*, Vol.14, pp. 1466, Henan/China.

[4] Feng, X., Chen, D., & Yongke, L. (2024). Research on Cotton Seedling and Weed Detection Model Based on Improved Detection Transformer (基于改进 Detection Transformer 的棉花幼苗与杂草检测模型研究). *Computer & Digital Engineering*, Vol. 52, pp. 2176–2182, Xinjiang/China.

[5] Habib, S., Khan, I., Islam, M., Albattah, W., Mohammed Alyahya, S., Khan, S., & Kamrul Hassan, M. (2021). Wavelet Frequency Transformation for Specific Weeds Recognition. *2021 1st International Conference on Artificial Intelligence and Data Analytics* (CAIDA), Vol. 9, pp. 97–100, Saudi Arabia.

[6] Jabir, B., Rabhi, L., & Falih, N. (2021). RNN- and CNN-based weed detection for crop improvement: An overview. *Foods and Raw Materials*, Vol. 9, pp. 387–396, Morocco.

[7] Jiang, J., & Gao, M. (2021). Retraction Note: Agricultural super green image segmentation method based on Gaussian mixture model combined with Camshift. *Arabian Journal of Geosciences*, Vol. 14, pp. 2697, Zhejiang/China.

[8] Jiang, K., Afzaal, U., & Lee, J. (2022). Transformer-Based Weed Segmentation for Grass Management. *Sensors*, Vol. 23, pp. 65, Republic of Korea.

[9] Kumar Kempegowda, S., Rajeswari, R., Satyanarayana, L., & Matada Basavarajaiah, S. (2022). Hybrid features and ensembles of convolution neural networks for weed detection. *International Journal of Electrical and Computer Engineering (IJECE)*, Vol. 12, pp. 6756, India.

[10] Li, X., Lloyd, R., Ward, S., Cox, J., Coutts, S., & Fox, C. (2022). Robotic crop row tracking around weeds using cereal-specific features. *Computers and Electronics in Agriculture*, Vol. 197, pp. 106941, United Kingdom.

[11] Ma, Z., Tao, Z., Du, X., Yu, Y., & Wu, C. (2021). Automatic detection of crop root rows in paddy fields based on straight-line clustering algorithm and supervised learning method. *Biosystems Engineering*, Vol. 211, pp. 63–76, Zhejiang/China.

[12] Monteiro, A. L., de Freitas Souza, M., Lins, H. A., da Silva Teófilo, T. M., Júnior, A. P. B., Silva, D. V., & Mendonça, V. (2021). A new alternative to determine weed control in agricultural systems based on artificial neural networks (ANNs). *Field Crops Research*, Vol. 263, pp. 108075, Brazil.

[13] Venkataraju, A., Arumugam, D., Stepan, C., Kiran, R., & Peters, T. (2023). A review of machine learning techniques for identifying weeds in corn. *Smart Agricultural Technology*, Vol. 3, pp. 100102, United States.

[14] Wang S., Wang S., Zhang H., & Wen C. (2019). Weed Identification in Soybean Fields Based on Lightweight Sum-Product Network and UAV Remote Sensing Images (基于轻量和积网络及无人机遥感图像的大豆田杂草识别). *Transactions of the Chinese Society of Agricultural Engineering*, Vol. 35, pp. 81–89, Jiling/China.

[15] Wang, T., Chen, B., Zhang, Z., Li, H., & Zhang, M. (2022). Applications of machine vision in agricultural robot navigation: A review. *Computers and Electronics in Agriculture*, Vol. 198, pp. 107085, Beijing/China.

[16] Weibing, W. (2019). Target Detection and Analysis of Intelligent Agricultural Vehicle Movement Obstacle Based on Panoramic Vision. *INMATEH Agricultural Engineering*, Vol.59, pp. 277–284, Anhui/China.

[17] Wu, B. (2024). Virtual Reality-Integrated Solutions for Extracting Central Crop Row Skeleton Lines Using the Maximum Diamond Principle Algorithm. *Computer-Aided Design and Applications*, Vol. 17, pp. 37–48, Henan/China.

[18] Wu, Y., He, Y., & Wang, Y. (2023). Multi-Class Weed Recognition Using Hybrid CNN-SVM Classifier. *Sensors*, Vol. 23, pp. 7153, Tianjin/China.

[19] Xie, B., Jin, Y., Faheem, M., Gao, W., Liu, J., Jiang, H., Cai, L., & Li, Y. (2023). Research progress of autonomous navigation technology for multi-agricultural scenes. Computers and Electronics in *Agriculture*, Vol. 211, pp. 107963, Zhenjiang/China.

[20] Yang S., Zhang H., & Xing L. (2023). Improved MobileViT Network for Lightweight Field Weed Identification (改进 MobileViT 网络识别轻量化田间杂草). *Transactions of the Chinese Society of Agricultural Engineering*, Vol. 39, pp. 152–160, Heilongjiang/China.

[21] Zhang, L., Li, K., & Qi, Y. (2023). Recognition of crop leaf diseases based on multi-feature fusion and evolutionary algorithm optimisation. *International Journal of Bio-Inspired Computation*, Vol. 21, pp. 163–173. , Guangzhou/China.

[22] Zhang, S., Liu, Y., Xiong, K., Zhai, Z., & Du, Y. (2023). Field Crop Row Centerline Recognition Method Based on Feature Engineering (基于特征工程的大田作物行中心线识别方法). *Transactions of the Chinese Society for Agricultural Machinery*, Vol. 54, pp. 18–26, Beijing/China.

[23] Zhao, X., Ma, W., Gao, Y., & Zang, Y. (2019). Early Crop Row Detection in Drill-Seeded Crops Based on Inverse Perspective Transformation (基于逆透视变换的条播作物早期作物行识别). *Journal of Jiangsu University (Natural Science Edition)*, Vol. 40, pp. 668–375, Jiangsu/China.

DISCRETE ELEMENT SIMULATION CALIBRATION OF CONTACT PARAMETERS FOR MILLET SEEDS
/
谷子种子离散元仿真接触参数标定

Yang HE[1)], Xinxin JI[2)], Guoqiang DUN[2)], Xiaoyi LIU*[1)], Ankang MU[3)], Chunyu MA[1)]
[1)] Northeast Forestry University, College of Mechanical and Electrical Engineering, Harbin / China;
[2)] Harbin Cambridge University, Intelligent Agricultural Machinery Equipment Engineering Laboratory, Harbin / China;
[3)] Inner Mongolia Chifeng Academy of Agriculture and Animal Husbandry Sciences, Chifeng / China;
Tel: +86-18846771196; E-mail: liu_xy@nefu.edu.cn

DOI: https://doi.org/10.35633/inmateh-76-58

Keywords: *Millet seeds, Discrete Element Method, Repose angle, Parameter calibration, Seed shape*

ABSTRACT
In order to obtain accurate contact parameters for foxtail millet seeds in discrete element method (DEM) simulations, this study selected the Jinmiao K10 variety as the research object. Physical experiments and DEM simulations were integrated to calibrate the contact parameters. First, the restitution coefficient, static friction coefficient, and rolling friction coefficient between foxtail millet seeds and polylactic acid (PLA) material were measured using methods such as free-fall and inclined plane tests. Subsequently, based on the experimentally measured repose angle of 21.93°, a Plackett–Burman design was employed to screen the key parameters significantly influencing the repose angle. These included the inter-seed static friction coefficient, rolling friction coefficient, and restitution coefficient. The steepest ascent test was then conducted to determine the direction of parameter optimisation. A quadratic regression model was established using the Box–Behnken response surface methodology to determine the optimal combination of contact parameters: restitution coefficient of 0.512, static friction coefficient of 0.22, and rolling friction coefficient of 0.041. These parameters were imported into EDEM software for simulation validation. The simulated repose angle is 22.2°, with a relative error of 1.23%, demonstrating high accuracy and practical applicability of the calibrated parameters. This study provides reliable simulation parameter support for the design and optimization of critical components in foxtail millet seeding machinery.

摘要
为获取谷子种子在离散元仿真种精确的接触参数，本文以金苗K10谷子品种为研究对象，结合物理实验与离散元仿真方法开展接触参数标定研究。首先通过自由落体法、斜面法等方法测得谷子种子与PLA材料间的碰撞恢复系数、静摩擦系数及滚动摩擦系数范围；随后基于实际休止角角测量结果（21.93°），采用 Plackett-Burman 试验筛选出对休止角影响显著的关键参数，包括种间静摩擦系数、滚动摩擦系数和碰撞恢复系数；进一步通过最陡爬坡试验确定参数优化方向，并利用 Box-Behnken 响应面法建立二次回归模型，求解最优接触参数组合：种子间碰撞恢复系数为 0.512，静摩擦系数为 0.22，滚动摩擦系数为 0.041。将该组合导入 EDEM 软件进行仿真验证，所得休止角为 22.2°，相对误差为 1.23%，表明标定参数具有较高精度和实用性。研究成果可为谷子播种机械关键部件的设计与优化提供可靠的仿真参数支持。

INTRODUCTION
As a country with a large population, China feeds nearly 18% of the world's population with only about 9% of the world's arable land (*Liu et al., 2021*). Food is a strategic resource for China and is central to national security and the cornerstone of social stability. Millet is an important grain crop originating in China and is one of the earliest cereal crops to be domesticated and cultivated by humans (*Zhao and Diao, 2022*). Millet not only requires little water, but also has the advantages of being resistant to poor soil and rich in nutrients *(Xiao et al., 2022*). After being hulled, millet is known as Xiaomi, which has unique nutritional components and is easily digestible, making it particularly suitable for pregnant women, new mothers, and infants. According to data from the National Bureau of Statistics of China, the annual sowing area of millet in China is approximately 900,000 hectares, accounting for about 9% of China's total grain sowing area.

The advent of millet sowing machinery has promoted the transformation of China's millet industry from traditional small-scale farming methods relying on human and animal labour to modern industrial production methods (*Li et al., 2021*). In sowing machinery, the seed dispenser is a core component, and its performance directly affects sowing quality and efficiency (*Lai et al., 2020*). Traditional testing methods typically require the actual device to be manufactured for testing. This method is not only time-consuming and labour-intensive, but also difficult to observe the detailed interactions between millet seeds and seeders, as well as between millet seeds themselves, due to the complex contact relationships and mechanical interactions involved. With the widespread adoption and advancement of computer technology, the DEM has become an effective method for analysing and solving complex discrete system dynamics problems. Discrete element simulation can be used to obtain detailed parameters such as force, displacement, and velocity of seeds in mechanical devices, visualise the movement process of seeds, and provide intuitive references and theoretical basis for the structural design and optimisation of mechanical devices.

In discrete element simulation, the accuracy of contact parameters directly affects the reliability of the simulation (*Awuah et al., 2023; Aikins et al., 2021*). The shape of millet seeds is irregular, indicating low flatness, and the interaction between millet seeds is complex. This may lead to significant errors when directly measuring their contact parameters. Furthermore, some parameters are difficult to measure directly through testing. Many scholars have calibrated contact parameters by conducting simulated pile angle tests to measure and calibrate the contact parameters of materials (*Cui et al., 2025; Sun et al., 2022; Wang et al., 2023; Zheng et al., 2024*). *Ma et al. (2025)* calibrated the main contact parameters between Gansu winter wheat seeds and various materials. *Liang et al. (2025)* conducted experiments on the angle of repose of corn and PLA using the uplift and lateral collapse methods, and a mathematical regression model was established to optimise the combination of contact parameters for the corn-PLA pile angle. The relevant experiments showed that the discrete element method model has high accuracy. *Zhang et al. (2020)* performed parameter calibration of rice grains in the EDEM software, with the grains magnified to the same scale. The test structure showed that CPU time was reduced by 60% compared to the unmagnified model, and the test error was within 1%. The method of using the angle of repose to calibrate contact parameters is widely used in the study of large seeds such as beans, wheat, and corn, but there is a lack of relevant research on small seeds such as millet.

Therefore, this paper takes the Jinmiao K10 millet variety as the research object and combines physical experiments with EDEM discrete element simulation to conduct contact parameter calibration research. The range of contact parameters between seeds and PLA materials was determined through free-fall collision tests, inclined plane sliding and rolling friction tests. Based on this, key parameters were selected using Plackett-Burman test based on actual measured angle of repose, and parameter combinations were optimised using steepest climb test and Box-Behnken test. The accuracy of the parameters was verified through simulation, and the optimal contact parameters suitable for simulating the millet sowing process were ultimately obtained, providing a fundamental basis for the digital design and performance optimisation of millet sowing machinery in the future.

MATERIALS AND METHODS

Test materials and measurement of their physical parameters

Jinmiao K10 was selected as the millet variety for the experiment and was provided by the Inner Mongolia Chifeng Academy of Agriculture and Animal Husbandry Sciences. Considering that the moisture content of millet at the time of sowing is approximately 12% to 20%, and that moisture content has a significant impact on the physical parameters of millet (*Qiu et al., 2021*). In view of this, millet with a moisture content of 15% was selected as the measurement object in this study. The density of millet was measured using the drainage method, using anhydrous ethanol as the medium. The measurement was repeated five times, yielding a density of 1054 kg/m3. One hundred seeds were randomly selected and weighed using an electronic balance with an accuracy of 0.001 g. The measurement was repeated five times, resulting in a hundred-seed weight of 0.305 g.

To establish a simulation model of this variety of millet, the three mutually perpendicular dimensions of the millet were defined as characteristic dimensions based on its shape, namely the length (L), width (W), and thickness (T) of the millet, as shown in Figure 1. A random sample of 100 grains with a moisture content of 15% was selected from this variety. The L and W of the grains were measured using a digital vernier calliper (accuracy 0.01 mm), and the T was measured using a digital thickness gauge (accuracy 0.001 mm).

The K-S test was used to analyse the measurement results, which showed that the three-axis dimensions of this variety of millet seeds were normally distributed, as shown in Figure 2.

The average length of 100 millet seeds was 2.061 mm, the average width was 1.753 mm, and the average thickness was 1.342 mm.



(a) Characteristic dimensions of millet

(b) Measurement of millet thickness (T)

(c) Measurement of grain length (L) and width (W)

Fig. 1 - Characteristic dimensions of millet and measurement of characteristic dimensions

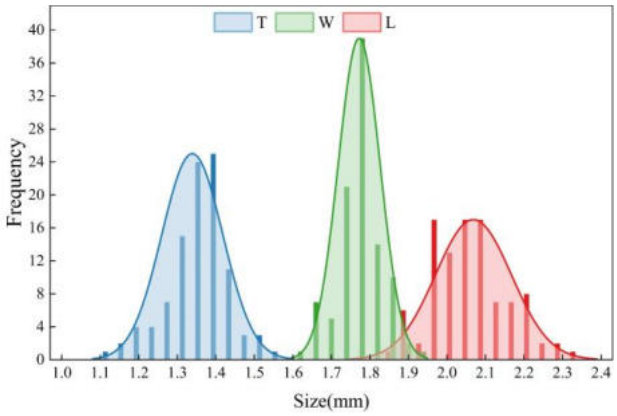


Fig. 2 - Normal distribution of the three-axis dimensions of millet: length, width, and thickness

Determination of seed-PLA contact parameters

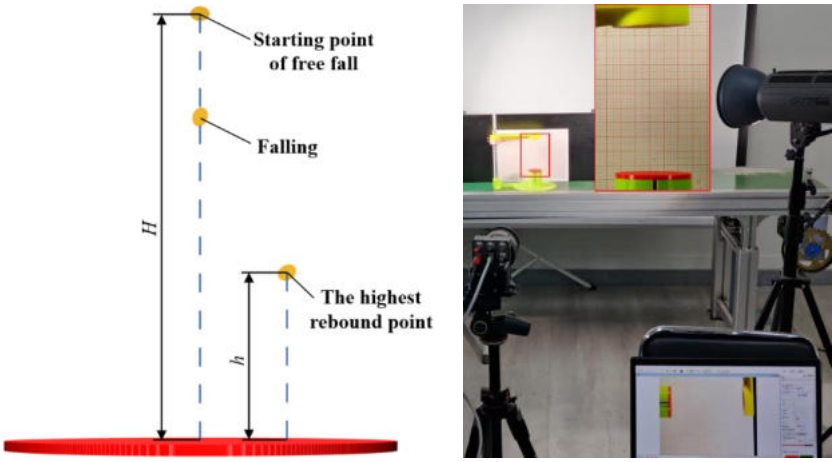
Determination of seed-PLA collision recovery coefficient

The collision recovery coefficient e_x is a parameter that measures the degree of rebound of two objects after a collision. It can be expressed as the ratio of the instantaneous separation velocities v_1 and v_2. That is, it is the ratio of the maximum rebound height h of the tested seed after colliding with the tested material to the initial falling height H.

The calculation formula is as follows:

$$e_x = \frac{v_1}{v_2} = \frac{\sqrt{2gh}}{\sqrt{2gH}} = \sqrt{\frac{h}{H}} \quad (1)$$

This experiment employed the free-fall collision method to determine the collision recovery coefficient between millet seeds and PLA plates (*Ding et al., 2023*). The measurement principle and experimental setup are shown in Figure 3. A seed was randomly selected using tweezers and released from a height of H = 100 mm directly above the PLA plate, allowing it to fall freely without initial velocity. The process, from the moment the tweezers were released until the seed collided with the PLA plate and rebounded to its highest point (h), was recorded using a high-speed camera with a resolution of 1280×720 and a frame rate of 1200 fps. After five repeated trials, the recorded data were substituted into Equation (1) to calculate the collision recovery coefficient, which ranged from 0.361 to 0.640, with an average value of 0.475.



(a) Test principle (b) Actual test

Fig. 3 - Seed and PLA collision recovery coefficient measurement test

Static friction coefficient between seeds and PLA

A homemade static friction angle measuring device was used to measure the static friction coefficient using the inclined plane method (*Wang et al., 2022*). The test apparatus is shown in Figure 4. The principle of the static friction test is that when the seed is at rest on the inclined plane, the force equilibrium formula is as follows:

$$\mu_s = \frac{f}{F} = \frac{mgsin\alpha}{mgcos\alpha} = tan\alpha \quad (2)$$

In the formula: μ_s is the static friction coefficient between the seed and PLA; f is the friction force between the seed and the PLA plate (N); F is the component of the seed's gravitational force perpendicular to the PLA plate (N); m is the mass of the seed (g); g is the gravitational force acting on the seed (N); α is the inclination angle of the PLA plate (°).

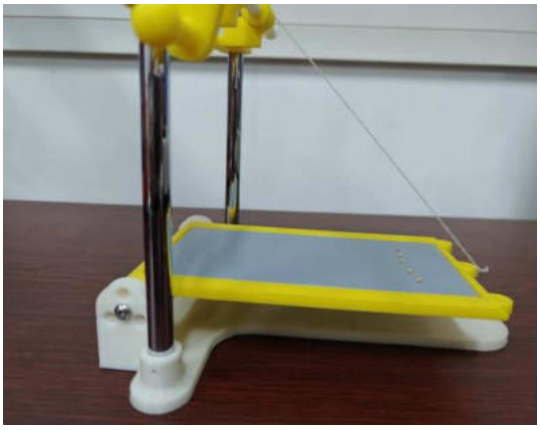


Fig. 4 - Homemade static friction angle measuring device

In each experiment, 10 seeds were randomly selected and placed on a PLA plane. The lifting device was then rotated at a constant speed to gradually tilt the plane. When more than three seeds began to slide, the rotation was immediately stopped, the plane was fixed, and the angle of the slope was measured. The experiment was repeated five times, and the static friction coefficient between the seeds and the PLA was found to be between 0.510 and 0.727, with an average value of 0.6224.

Determination of rolling friction coefficient between seeds and PLA

The rolling friction coefficient between seeds and PLA was determined using the inclined plane rolling method. The experimental diagram is shown in Figure 5. The experimental principle is to release seeds with an initial velocity of 0 from an inclined plane with an angle of inclination β. The seeds roll down the inclined plane with a length of S and roll a distance L on the horizontal plane. Assuming that the seeds roll purely during this process, they are only affected by rolling friction. According to the law of conservation of energy, it can be obtained:

$$\mu_r = \frac{mgSsin\beta}{mg(Ssin\beta + L)} = \frac{Ssin\beta}{Ssin\beta + L} \quad (3)$$

In the formula, μ_r is the rolling friction coefficient between the seed and PLA.

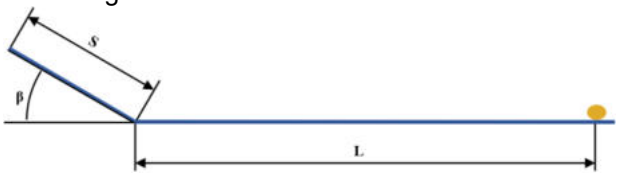


Fig. 5 - Schematic diagram of the inclined plane rolling test

Since millet seeds are not ideal spheres in shape, they tend to bounce and slide during rolling. To improve the accuracy of the test, after extensive preliminary testing and adjustments, the slope angle was set to 30° and the rolling distance on the slope to 30 mm. The above test was repeated 10 times, yielding a rolling friction coefficient range of 0.06 to 0.15 between the seeds and PLA, with an average value of 0.1.

Calibration of contact parameters between seeds

When calibrating inter-species contact parameters using the aforementioned experimental methods, seeds must be adhered together to form a seed plate. However, due to the inconsistent shapes and uneven surfaces of the seeds, using seed plates in experiments results in significant deviations in experimental outcomes. Particles accumulate on a horizontal surface under the influence of gravity, and the angle formed between the accumulated surface and the horizontal plane is referred to as the angle of repose. This angle reflects the friction characteristics and flowability of the particulate material. Therefore, this study is based on actual pile tests of millet seeds, using the measured pile angle as the response value, and the contact parameters between seeds and PLA material and inter-seed contact parameters as factors, to conduct Plackett-Burman tests, steepest ascent tests, and Box-Behnken tests. Through the tests, the optimal combination of contact parameters is obtained, and the combination parameters are verified through simulation.

Actual angle of repose test

The actual angle of repose test refers to GB/T 16913-2008, using the injection method to measure the angle of repose of millet seeds. The funnel's outlet has a cone angle of 70°, an inner diameter of 10 mm, and the distance between the outlet edge and the material tray surface is 50 mm. The diameter of the material tray is 50 mm. During the test, a shield is first used to cover the bottom of the outlet. 7.5g of seeds are then poured into the funnel. The shield is removed, allowing the seeds to flow out of the outlet. Once all the seeds have flowed out and the pile remains stable, a camera captures a frontal view image of the seed pile. This process is repeated five times. The captured images are processed using Python to generate a binary image, yielding the coordinate data of the boundary pixels of the seed pile. The pixel coordinate data is linearly fitted using the least squares method, and the tangent value of the slope of the fitted line represents the angle of repose. The angle of repose θ of the tested seeds is 21.93°, with the image processing process illustrated in Figure 6.

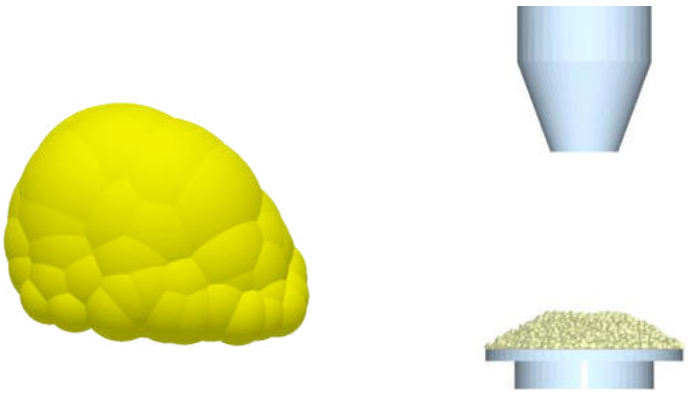


(a) Original image (b) Boundary Contour (c) Straight line fitting

Fig. 6 - Image processing of seed accumulation angle test

Discrete element simulation model and parameters

Based on the three-axis dimensions of the eight seed types and the morphological characteristics of millet measured in this study, a three-dimensional solid model of millet was created using SolidWorks software. The three-dimensional model was saved in STL format and imported into EDEM software. Using the software's built-in non-spherical particle automatic filling tool, the smoothness value was set to 4, the number of triaxial grids was set to 45, and the minimum spherical filling radius was set to 0.2 mm to complete the seed filling. Based on actual pile tests, models of the funnel, baffle, and material tray were created using SolidWorks software and imported into EDEM software in STEP format. The Seed Discrete Element Model and Angle of Repose Angle Test Simulation Model are shown in Figure 7.



(a)Seed Discrete Element Model (b)Angle of Repose Test Simulation Model

Fig. 7 - Seed Discrete Element Model and Angle of Repose Angle Test Simulation Model

In EDEM software, simulations of the angle of repose test for millet seeds were conducted. Based on relevant literature and previous experiments (*Dun et al., 2025; Ma et al., 2025; Zhang, 2023*), the simulation parameters for the angle of repose test were determined, as shown in Table 1.

Table 1

Discrete Element Method Angle of Repose Test Simulation Parameter Table

Simulation parameters	Value
Poisson's ratio of seeds	0.39
seed density (kg/m^3)	1054
Seed shear modulus (Pa)	5.252e+05
Poisson's ratio of PLA	0.3
PLA density (kg/m^3)	1290
PLA shear modulus (Pa)	1.04e+07
Seed-seed collision recovery coefficient	0.1~0.8
Seed - seed static friction coefficient	0.1~0.6
Seed - seed rolling friction coefficient	0~0.1
Seed-PLA collision recovery coefficient	0.361~0.64
Seed - PLA static friction coefficient	0.51~0.727
Seed-PLA rolling friction coefficient	0.06~0.29

Plackett—Burman Experiment

Since there are many parameters that affect the angle of repose, a Plackett-Burman test was used to screen out the parameters that have a greater impact on the angle of repose (*Kong et al., 2024*). The experiment used the measured angle of repose from actual experiments as the response value (*Yang et al., 2024*). Design-Expert software was used to design two-level factorial designs for different factors, as shown in Table 2. The experimental designs were randomly generated by the software, and simulations were conducted on each group according to the design sequence, with the angle of repose recorded. The experimental designs and results are shown in Table 3.

Table 2

Plackett-Burman Experiment parameter list

Simulation parameters	Low level (-1)	High level (+1)
Seed-seed collision recovery coefficient (A)	0.100	0.800
Seed - seed static friction coefficient （B）	0.100	0.600
Seed - seed rolling friction coefficient (C)	0.000	0.100
Seed-PLA collision recovery coefficient (D)	0.361	0.610
Seed - PLA static friction coefficient (E)	0.510	0.727
Seed-PLA rolling friction coefficient (F)	0.060	0.150

Table 3

Plackett-Burman Experiment design and results

Number	Simulation parameters						Simulation test angle of repose θ'/ (°)
	A	B	C	D	E	F	
1	+1	+1	-1	+1	+1	+1	24.710
2	-1	+1	+1	-1	+1	+1	35.770
3	+1	-1	+1	+1	-1	+1	15.995

Number	Simulation parameters						Simulation test angle of repose θ'/ (°)
	A	B	C	D	E	F	
4	-1	+1	-1	+1	+1	-1	26.865
5	-1	-1	+1	-1	+1	+1	16.340
6	-1	-1	-1	+1	-1	+1	13.410
7	+1	-1	-1	-1	+1	-1	11.700
8	+1	+1	-1	-1	-1	+1	24.225
9	+1	+1	+1	-1	-1	-1	31.350
10	-1	+1	+1	+1	-1	-1	34.820
11	+1	-1	+1	+1	+1	-1	7.650
12	-1	-1	-1	-1	-1	-1	11.9550
13	0	0	0	0	0	0	26.410

The results of the analysis of variance are shown in Table 4. As can be seen from the table, the three factors that have the greatest influence on the angle of repose are, in order of importance, the Seed - seed static friction coefficient B, the Seed - Seed rolling friction coefficient C, and the Seed-seed collision recovery coefficient A. Therefore, these three simulation parameters were selected for subsequent experiments. The remaining factors have a relatively minor influence on the angle of repose. Therefore, the average values from the previous experiments are used as the simulation values for the remaining factors (Seed-PLA collision recovery coefficient is 0.475, Seed - PLA static friction coefficient is 0.6224, and Seed-PLA rolling friction coefficient is 0.1).

Table 4

Significance analysis of Plackett-Burman Experiment parameters

Source	Standardized Effects	Sum of Squares	F-value	P-value
A	-3.92	46.12	4.70	0.0823
B	16.78	844.96	86.14	0.0002
C	4.84	70.35	7.17	0.0439
D	-1.31	5.18	0.53	0.5000
E	-1.45	6.34	0.65	0.4578
F	1.02	3.12	0.32	0.5974

Steepest Climb Experiment

The three simulation parameters identified in the previous experiment as having the greatest influence on the angle of repose were subjected to a Steepest Climb Experiment to further narrow the range of values for the experimental measurement parameters. This experiment began at the centre point of the Plackett-Burman Experiment and proceeded in the direction of decreasing angles, using the parameter with the most significant influence as the baseline, with a step size ratio of 0.2. The experiment was conducted using the relative error σ between the measured angle of repose θ and the simulated angle of repose θ' as the evaluation criterion. The experimental design and results are shown in Table 5. As can be seen from the table, the relative error caused by the angle of repose is the smallest at the 4th level. In the range from the 1st to the 6th level, the trend of the relative error caused by the angle of repose is from large to small and then back to large. Therefore, the 4th level is taken as the central point, with the 3rd and 5th levels as the low and high levels, respectively, for the subsequent Box-Behnken Experiment.

Table 5

Steepest Climb Experiment Plan and Results

Number	Seed-seed collision recovery coefficient (A)	Seed - Seed Static Friction Coefficient (B)	Seed - Seed rolling friction coefficient (C)	Simulation test angle of repose θ'/(°)	Relative error σ （%）
1	0.450	0.35	0.050	29.800	35.890
2	0.467	0.30	0.047	27.025	23.233
3	0.483	0.25	0.044	24.980	13.910
4	0.500	0.20	0.041	21.395	2.440
5	0.516	0.15	0.038	18.445	15.890
6	0.533	0.10	0.036	17.000	22.480

Box-Behnken Experiment

Using Design-Expert software, the three factors and three levels determined from the Steepest Climb Experiment were entered, and the software generated 17 randomized test plans. The test plans and corresponding results are presented in Table 6. Variance analysis was then performed on the experimental data to derive the quadratic regression equation for the angle of repose simulation test:

$$\theta' = 21.4039 + 2.108325A + 2.4703B + 0.775625C - 0.378AB - 1.17025AC + 0.1955BC + 1.030575A^2 + 0.825325B^2 + 0.600775C^2 \quad (1)$$

Table 6

Box-Behnken experiment design and results

Number	Seed-seed collision recovery coefficient (A)	Seed - seed static friction coefficient (B)	Seed - seed rolling friction coefficient (C)	Simulation test angle of repose θ'/(°)
1	0.516	0.15	0.041	18.4563
2	0.483	0.15	0.041	23.5629
3	0.516	0.25	0.041	23.7127
4	0.483	0.25	0.041	27.3073
5	0.516	0.20	0.038	19.0754
6	0.483	0.20	0.038	25.4986
7	0.516	0.20	0.044	22.9124
8	0.483	0.20	0.044	24.6546
9	0.500	0.15	0.038	19.5321
10	0.500	0.25	0.038	24.5219
11	0.500	0.15	0.044	20.7471
12	0.500	0.25	0.044	26.5189
13	0.500	0.20	0.041	21.5145
14	0.500	0.20	0.041	21.4555
15	0.500	0.20	0.041	21.3091
16	0.500	0.20	0.041	21.1330
17	0.500	0.20	0.041	21.6074

RESULTS

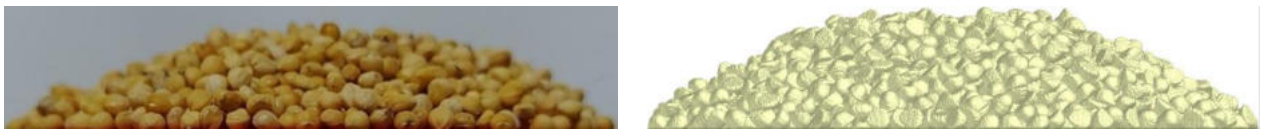
The analysis of variance for the quadratic regression model of the simulated angle of repose of millet seeds is shown in Table 7. As can be seen from the table, the model as a whole is highly significant ($p<0.0001$), and the main effects of factors A, B, and C, as well as the quadratic terms A2, B2, and C2, are all significant. The interaction effects of AB ($P=0.0329$) and AC ($P<0.0001$) are significant, The BC interaction effect is not significant ($P = 0.2123$), and the model shows no significant misfit ($P = 0.1022$), indicating that it can adequately explain the changes in the angle of repose. The determination coefficient $R^2 = 0.9946$, adjusted $R^2 = 0.9877$, and predictive $R^2 = 0.9330$ are all close to 1, indicating high model fit quality. The coefficient of variation CV = 1.26% indicates low data dispersion, and the signal-to-noise ratio is 41.9, indicating that the model has good reliability and accuracy.

Table 7

Variance analysis of the seed simulation angle of repose quadratic regression model

Source	Sum of Square	df	Mean Square	F-value	P-value
Model	105.23	9	11.69	144.07	<0.0001
A	35.56	1	35.56	438.16	<0.0001
B	48.82	1	48.82	601.52	<0.0001
C	4.81	1	4.81	59.3	0.0001
AB	0.5715	1	0.5715	7.04	0.0329
AC	5.48	1	5.48	67.5	<0.0001
BC	0.1529	1	0.1529	1.88	0.2123
A2	4.47	1	4.47	55.1	0.0001
B2	2.87	1	2.87	35.34	0.0006
C2	1.52	1	1.52	18.73	0.0034
Residual	0.5681	7	0.0812		
Lack of Fit	0.4294	3	0.1431	4.13	0.1022
Pure Error	0.1387	4	0.0347		
Cor Total	105.8	16			

Using the data analysis optimisation module of Design-Expert software, parameter optimisation was performed on the quadratic regression model, resulting in the optimal contact parameter combination: a Seed-seed collision recovery coefficient of 0.512, a Seed - seed static friction coefficient of 0.22, and a Seed - seed rolling friction coefficient of 0.041. These parameters were then input into EDEM software for simulation verification. The simulation results are compared with the actual test results as shown in Figure 8. The actual angle of repose was 21.93°, while the angle of repose in the simulation test was 22.2°, with an error of only 1.23% compared to the actual measured value, indicating that the parameters have high precision and reliability.



(a) Actual Test (b) Simulation Test

Fig. 8 - Comparison chart of millet seed accumulation angle tests

CONCLUSIONS

This study used the Jinmiao K10 variety as the reference sample, with a density of 1051 kg/m³ and a hundred-grain weight of 0.305 g when the moisture content was 15%. The three-axis dimensions of 100 seeds of this millet variety were also measured, with an average length of 2.061 mm, width of 1.753 mm, and thickness of 1.342 mm. All dimensions followed a normal distribution, providing a data basis for constructing a generalised millet grain model.

Physical tests were conducted to measure the Seed-PLA collision recovery coefficient, Seed - PLA static friction coefficient and Seed-PLA rolling friction coefficient range and average value between millet seeds and PLA. Based on the Plackett-Burman Experiment, three factors with a significant impact on the angle of repose were identified, in descending order of impact: Seed - seed static friction coefficient, the Seed - seed rolling friction coefficient, and the Seed-seed collision recovery coefficient. The average values of other factors were taken, namely, Seed-PLA collision recovery coefficient of 0.475, Seed - PLA static friction coefficient of 0.6224, and Seed-PLA rolling friction coefficient of 0.1.

Based on the results of the Steepest Climb Experiment and the Box-Behnken Experiment, a quadratic regression equation for the simulation test of the angle of repose was established. Optimisation was performed with the angle of repose measured in the actual test (21.93°) as the target, and the optimal contact parameters between millet seeds were determined to be a collision recovery coefficient is 0.512, static friction coefficient is 0.22, and rolling friction coefficient is 0.041. The parameters were entered into the EDEM software for simulation verification, and the angle of repose was obtained to be 22.2°, with an error of 1.23% from the actual measured value, further verifying the accuracy and practicality of the calibrated parameters, and also providing a certain reference and basis for the simulation optimisation of millet sowing machinery.

ACKNOWLEDGEMENT

This work was supported by the Key Scientific Research Application Research Project of Harbin Cambridge University (Grant No. JQZKY2022021) and the Heilongjiang Province Natural Science Foundation of China (Grant No. LH2023E025). The authors gratefully acknowledge the financial support provided by these institutions.

REFERENCES

[1] Aikins K.A., Ucgul M., Barr J.B., Jensen T.A., Antille D.L., Desbiolles J.M.A., (2021). Determination of discrete element model parameters for a cohesive soil and validation through narrow point opener performance analysis. *Soil and Tillage Research*, Vol. 213, Netherlands. DOI: https://doi.org/10.1016/j.still.2021.105123

[2] Awuah E., Aikins K.A., Antille D.L., Zhou J., Gbenontin BV., Mecha P., Liang Z., (2023). Discrete Element Method Simulation and Field Evaluation of a Vibrating Root-Tuber Shovel in Cohesive and Frictional Soils. *Agriculture*, Vol. 13, no. 8: 1525, Switzerland. DOI: https://doi.org/10.3390/agriculture13081525

[3] Cui Y., Ye S., Feng S., Zhang D., (2025). Calibration of Discrete Element Simulation Parameters for Buckwheat Seeds (荞麦种子离散元仿真参数标定). *INMATEH-Agricultural Engineering*, Vol. 75, no.1, pp. 110-120, Bucharest/Romania. DOI: https://doi.org/10.35633/inmateh-75-09

[4] Ding X., Wang B., He Z., Shi Y., Li K., Cui Y., Yang Q., (2023). Fast and precise DEM parameter calibration for Cucurbita ficifolia seeds. *Biosystems Engineering*, Vol. 236, pp. 258-276, England. DOI: https://doi.org/10.1016/j.biosystemseng.2023.11.004

[5] Dun G., Wei Y., Ji X., Gao S., Pei Y., He Y., Ma C., (2025). Design and Test of the Outside-Filling Chinese Chive Adjustable-Capacity Precision Seed-Metering Device. *Agronomy*, Vol. 15, issue 3, pp. 622. Switzerland. DOI: https://doi.org/10.3390/agronomy15030622

[6] Kong D., Ye Z., Tan X., Dai M., Zhao X., Kong D., (2024). Measurement of physical contact and discrete element simulation calibration of lettuce seeds (生菜种子物理接触参数测定与离散元仿真标定). *Acta Agriculturae Zhejiangensis,* Vol. 36, issue 4, pp. 932-942, Zhejiang/China. DOI: https://doi.org/10.3969/j.issn.1004-1524.20230649

[7] Lai Q., Jia G., Su W., Hong F., Zhao J., (2020). Design and Test of Ginseng Precision Special-hole Type Seed-metering Device with Convex Hull (凸包异形孔窝眼轮式人参精密排种器设计与试验). *Transactions of the Chinese Society for Agricultural Machinery*, Vol. 51, issue 7, pp. 60-71, Beijing/China. DOI: https://doi.org/10.6041/j.issn.1000-1298.2020.07.008

[8] Liu Z., Zhong H., Li Y., Wen Q., Liu X., Jian Y., (2021). Change in grain production in China and its impacts on spatial supply and demand distributions in recent two decades (近 20 年中国粮食生产变化特征及其对区域粮食供需格局的影响), *Journal of Natural Resources*, Vol. 36, issue 6, pp. 1413-1425, Beijing/China. DOI: https://doi.org/10.31497/zrzyxb.20210605

[9] Li S., Liu F., Liu M., Cheng R., Xia E., Diao X., (2021). Current Status and Future Prospective of Foxtail Millet Production and Seed Industry in China (中国谷子产业和种业发展现状与未来展望). *Scientia Agricultura Sinica*, Vol. 54, issue 3, pp. 459-470, Beijing/China. DOI: https://doi.org/10.3864/j.issn.0578-1752.2021.03.001

[10] Liang W., Meng W., Zhang B., Zhang H., Jin Y., Zhang J., (2025). Calibration method and experimental verification of corn discrete element parameters. *Measurement Science and Technology*, Vol. 36, issue 5, pp. 055003, England. DOI: https://doi.org/10.1088/1361-6501/adcad8

[11] Ma Q., Li T., Xu D., Wang Q., (2025). Determination of Physical Parameters of Pelleted Rice Seeds and Calibration of Discrete Element Simulation Parameters (丸粒化水稻种子物性参数测定与离散元仿真参数标定). *INMATEH Agricultural Engineering*, Vol. 75, no. 1, pp. 490-500, Bucharest/Romania. DOI: https://doi.org/10.35633/inmateh-75-42

[12] Ma Y., Wang Z., Shi L., Zhao W., Sun B., Dai F., Li H., (2025). Determination the intrinsic parameters and calibration of contact parameters for wheat seed particles (冬小麦种子颗粒离散元仿真参数标定). *Journal of China Agricultural University*, Vol.30, issue 3, pp.175-84, Beijing/China. DOI: https://doi.org/10.11841/j.issn.1007-4333.2025.03.16

[13] Qiu S., Li L., Cui Q., Zhang Y., Yang Z., Gou M., (2021). Study on tribological characteristics of buckwheat grain group (荞麦籽粒群摩擦力学特性研究). *Journal of Chinese Agricultural Mechanization*, Vol. 42, issue 9, pp. 90-95, Nanjing/China. DOI: https://doi.org/10.13733/j.jcam.issn.2095-5553.2021.09.13

[14] Sun K., Yu J., Liang L., Wang Y., Yan D., Zhou L., Yu Y., (2022). A DEM-based general modelling method and experimental verification for wheat seeds. Powder *Technology*, Vol. 401, Switzerland. DOI: https://doi.org/10.1016/j.powtec.2022.117353

[15] Wang S., Mengqing L., Liu X., Ji J., Chen P., (2022). Calibration and analysis of discrete element simulation parameters of Chinese cabbage seeds. *PLoS One*, Vol. 17, issue 6, pp. e0270415, United States. DOI: https://doi.org/10.1371/journal.pone.0270415

[16] Wang J., Chen L., Tang Y., Chen Z., Wu Q., Han D., (2023). Calibration and experiment of discrete element model parameters of Zanthoxylum bungeanum. *Frontiers in Mechanical Engineering*, Vol. 9, Switzerland. DOI: https://doi.org/10.3389/fmech.2023.1204659

[17] Xiao J., Liu Z., Xin Z., Li J., Chen G., Zhu X., Sun Z., (2022). Identification of drought tolerance in foxtail millet during its entire growth period based on principal component analysis and membership function (基于主成分分析和隶属函数的谷子全生育期耐旱性鉴定), *Agricultural Research in the Arid Areas*, Vol. 40, issue 6, pp. 34-44, Yangling/China. DOI: https://doi.org/10.7606/j.issn.1000-7601.2022.06.04

[18] Yang H., He J., Lu J., Wang T., Wang Y., Guo Y., (2024). Parameters Calibration for Discrete Element Model Simulation of White Kidney Bean Seeds (白芸豆种子离散元模型仿真参数标定). *INMATEH Agricultural Engineering*, Vol. 72, no. 1, pp. 77-86, Bucharest/Romania. DOI: https://doi.org/10.35633/inmateh-72-07

[19] Zhang S., Tekeste MZ., Li Y., Gaul A., Zhu D., Liao J., (2020). Scaled-up rice grain modelling for DEM calibration and the validation of hopper flow. *Biosystems Engineering*, Vol. 194, pp.196-212, England. DOI: https://doi.org/10.1016/j.biosystemseng.2020.03.018

[20] Zhao M., Diao X., (2022). Phylogeny of wild Setaria species and their utilization in foxtail millet breeding (谷子近缘野生种的亲缘关系及其利用研究), *Acta Agronomica Sinica*, Vol. 48, issue 2, pp. 267-279, Beijing/China. DOI: https://doi.org/10.3724/sp.J.1006.2022.14047

[21] Zhang D., (2023). *Study on Working Mechanism and experimental research of Cleaning Device for Millet (谷子风筛式清选装置筛分机理与试验研究)*, PhD Thesis, Heilongjiang Bayi Agricultural University, Harbin/China. DOI: https://doi.org/10.27122/d.cnki.ghlnu.2023.000002

[22] Zheng X., He X., Shang S., Wang W., Li C., Shi Y., Zhao Z., Lu Y., (2024). Journal of Agricultural Mechanization Research (油莎豆种子籽粒离散元仿真参数标定与试验). *Journal of Agricultural Mechanization Research*, Vol. 46, issue 2, pp. 172-8, Harbin/China. DOI: https://doi.org/10.13427/j.cnki.njyi.2024.02.028

STRAWBERRY FRUIT DETECTION METHOD BASED ON IMPROVED YOLOv8N
/
基于改进 YOLOv8N 的草莓果实检测方法

Zhenwei LI [1], Suyun LI [1], Wenting LAN [2], Shide LI [3], Yanguan CHEN [1], Pengcheng LV [4,*]

[1] Hezhou University, School of Artificial Intelligence, HeZhou, China
[2] Hezhou University, Academic Affairs Office, HeZhou, China
[3] Guangxi Medical University, School of Information and Management, NanNing, China
[4] Shandong University of Technology, College of Agricultural Engineering and Food Science, ZiBo, China
Tel: +86 13964379460; E-mail: wslpc1999@163.com
Corresponding author: Pengcheng LV

DOI: https://doi.org/10.35633/inmateh-76-59

Keywords: *Deep learning; attention mechanism; YOLOv8n; detection system*

ABSTRACT

As an economic crop of Rosaceae family, strawberry has the advantages of short reproductive cycle, wide ecological adaptability and significant economic benefits, and its planting industry has been rapidly developed in recent years. Aiming at the low efficiency and high labor cost of traditional manual picking detection methods in the intelligent transformation of strawberry industry, this study innovatively proposes a strawberry fruit intelligent detection system based on YOLOV8N. By introducing RFAConv dynamic sensory field convolution, SENet channel attention mechanism and InceptionNeXt lightweight structure, combined with Wise-IoU loss function and DIoU-NMS post-processing algorithm, the synergistic enhancement of detection accuracy and computational efficiency is realized. The ablation experiments show that the improved model has a precision rate of 95.92%, a recall rate of 95.45%, and a mAP50 of 98.29% on the strawberry dataset, which are 4.14%, 3.31%, and 1.55% higher than that of the baseline model, respectively, while the number of model parameters is compressed to 5.17 M (a reduction of 12.96%). This research can provide technical support for intelligent strawberry picking.

摘要

草莓作为蔷薇科经济作物，具有生育周期短、生态适应性广及经济效益显著等优势，其种植产业近年来得到了快速发展。本研究针对草莓产业智能化转型中传统人工采摘检测方法存在的效率低下、人工成本高等痛点，创新性提出一种基于 YOLOV8N 的草莓果实智能检测系统。通过引入 RFAConv 动态感受野卷积、SENet 通道注意力机制及 InceptionNeXt 轻量化结构，结合 Wise-IoU 损失函数与 DIoU-NMS 后处理算法，实现了检测精度与计算效率的协同提升。消融实验表明，改进后模型在草莓数据集上精确率达 95.92%、召回率为 95.45%、mAP50 达 98.29%，较基线模型分别提升 4.14%、3.31%和 1.55%，同时模型参数量压缩至 5.17M（减少 12.96%），该研究可为草莓智能化采摘提供技术支持。

INTRODUCTION

As a Rosaceae cash crop, strawberry has become the preferred crop for facility agriculture by virtue of its short reproductive cycle, wide ecological adaptability and significant economic benefits. Its fruit is generally small and dense. Dense canopy structure is easy to cause visual masking, coupled with the maturity gradient distribution phenomenon, resulting in the traditional artificial observation and picking both time-consuming and laborious, significantly increasing the difficulty of selective harvesting. Nowadays, the level of intelligence in China's strawberry industry is constantly improving, and the development of a high-precision fruit ripeness detection algorithm can not only accurately find out the distribution area of fruits with different ripeness levels, but also monitor and optimize the picking process.

With the iterative upgrading of computer vision technology, many innovative research results have emerged in the field of agricultural target detection, providing important technical support for intelligent crop management. In the direction of fruit multi-category recognition, *Wan et al., (2021)* constructed a multi-spectral visual analysis system based on the optimization of Faster R-CNN architecture, which effectively solved the feature confusion problem of apple, pear and peach fruits under the complex background of the orchard by reconfiguring the parameter distribution of the convolution kernel with the improvement of the downsampling strategy.

The experimental data show that the classification performance of the model for the above fruits reaches 92.51%, 88.94%, and 90.73%, respectively, and the overall mean average precision (mAP) is improved to 90.72%, which validates the generalization ability of deep networks in cross-species recognition tasks.

Notably, *Sharma et al., (2022),* developed a pineapple maturity analysis model based on the YOLOv5 framework for tropical crop characteristics, and constructed a three-stage discrimination system containing the green ripening stage, the color-turning stage, and the complete ripening stage by integrating spectral reflectance features and morphological parameters, and the classification accuracy of the final ripening stage discrimination exceeded 95%, which provided a new paradigm for the intelligent assessment of fruit quality.

In terms of feature enhancement technology path, *Lu et al., (2021),* researchers designed an attention-guided multi-scale feature fusion mechanism, which significantly improved the spatial localization accuracy of small-scale fruits by implementing cross-layer semantic enhancement to the shallow feature map of SSD network. The improved model mAP metrics improve by 29.2 percentage points from the baseline, especially the leakage rate in the fruit-dense region decreases by 18.6%, demonstrating excellent scene adaptability.

As for mobile deployment, the MobileNet lightweight architecture proposed by *Howard et al., (2019),* pioneered the use of depth-separable convolution instead of standard convolution operation, and compressed the model computation to about one-eighth of the traditional network by decoupling the feature learning process between the channel dimension and the spatial dimension, laying down a basic engineering framework for the development of embedded vision systems for orchard inspection UAVs.

The improved YOLOv5 model developed by *Peng et al., (2014)* introduces the Ghost module to reconfigure the feature extraction backbone network, combines the coordinate attention mechanism to strengthen the feature response in the key regions of the fruit, and also uses the SIoU loss function to optimize the bounding box regression process. After testing, the scheme achieves 94.8% mAP for strawberry target detection, the model volume is reduced to 67% of the original structure, and a real-time processing capability of 23.6 frames per second (FPS) is realized on the Jetson Nano embedded platform. These technological breakthroughs not only validate the application potential of the lightweight model in agricultural scenarios, but also provide key algorithmic components for the construction of a "cloud-edge-end" synergistic smart agriculture sensing system *(Elsayed et al., 2024; Hu et al., 2018; Hosna et al., 2022; Li et al., 2020).*

In this paper, a multi-source heterogeneous dataset for strawberry fruit detection under varying ripeness levels, lighting conditions, and complex backgrounds is first constructed, and a complete deep learning research framework is established. In the backbone network, RFAConv is used to replace the standard convolutional Conv to improve the performance of the network; the SENet attention mechanism is introduced to strengthen the learning ability of the backbone network on the color and shape features of strawberries, and at the same time, the design of the decoupling head is optimized to better adapt to the needs of classification and regression tasks. The InceptionNeXt neural network structure is introduced as the feature extraction network, and the convolution in Bottleneck in the Cf2 module of the neck network is replaced with the InceptionNeXt convolution, which effectively reduces the amount of computation. During the training process, the Wise-IoU loss function with dynamic nonmonotonic focusing mechanism is used to address the impact of low-quality samples on model performance in the target detection task. In the post-processing stage, DIoU-NMS is used to replace the traditional NMS algorithm to reduce the false deletion of overlapping target frames.

MATERIALS AND METHODS

Data Acquisition and Pre-processing

The data used in this study are mainly derived from online public data and strawberry garden collection data. This online public dataset was captured inside a greenhouse and contains 3,500 images. The advantage of strawberry orchard collection data is that these data reflect the actual farmland environment and crop growth conditions, with the advantage of authenticity and credibility.

The image acquisition device is the camera that comes with the Xiaomi 14 cell phone, and the effective pixel of the camera is 50 million. The shooting test data were images of strawberries with different growth cycles, such as front, side and shade, which were taken on February 4, 2024.

Figure 1 shows the strawberry image dataset.



Fig. 1 – Example graph of the strawberry dataset

In order to increase the speed of model training, the collected raw images are preprocessed with uniformity. At the same time, 500 typical samples were selected from a database of 3,500 annotated samples using a stratified random sampling method to implement a data augmentation strategy, and the dataset was expanded by pre-processing the images by rotating, panning, mirroring and adding noise. After augmentation, the total number of images increased to 5,500, with the enhanced portion contributing 2,000 images. The dataset contains 24619 labeled strawberry objects, including 19162 unripe strawberries, 4364 semi-ripe strawberries, and 5021 ripe strawberries. The statistical data are shown in Figure 2.

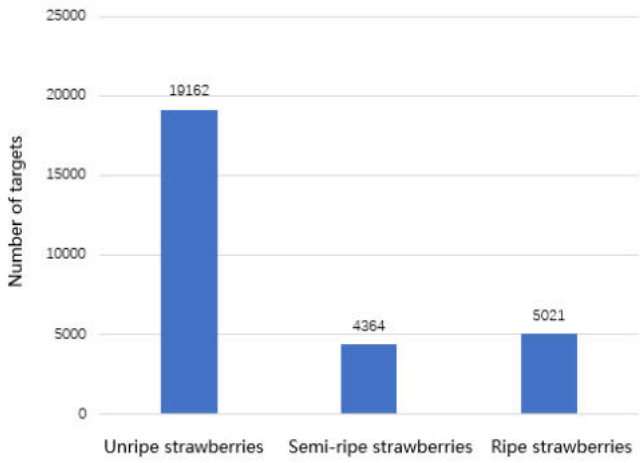


Fig. 2 – Strawberry fruit ripening statistics

The dataset was divided into training, validation and test sets according to the ratio of 8:1:1, i.e., 4400 images for the training set and 550 images each for the validation and test sets.

YOLOv8 Network Architecture

YOLOv8, an integrated and enhanced iteration of the YOLO series, incorporates a core feature of an anchor-free detection mechanism. This mechanism directly predicts the center position of the target without reliance on predefined anchor boxes, thereby simplifying the training process and accelerating the post-processing steps of non-maximum suppression (NMS). Depending on the depth and width of the network, different versions of YOLOv8n, YOLOv8s, YOLOv8m, YOLOv8l and YOLOv8x are used. Although the overall architecture of these models remains consistent, the number of modules and the configuration of the convolutional layers within each version differ significantly when implementing the network training process *(Vaswani et al., 2017; Wang et al., 2024; Zhu et al., 2024)*.

This difference mainly stems from considerations of model size, complexity, total number of parameters, computational burden, and training methods. By adjusting these factors, different versions of YOLOv8 are able to strike a unique balance between performance and computational resource consumption. The comparison data of different versions for detection on the public dataset COCO are shown in Table 1. In this study, YOLOv8n, which has a smaller weight file, faster inference speed, and is suitable for deployment to edge devices, is chosen as the base network.

Table 1

Comparison of data of different versions of YOLOv8

Mold	Depth	Width	Px	mAP	M	B
YOLOv8n	0.33	0.25	640	37.3	3.2	8.7
YOLOv8s	0.33	0.5	640	44.9	11.2	28.6
YOLOv8m	0.67	0.75	640	50.2	25.9	78.9
YOLOv8l	1.0	1.0	640	52.9	43.7	165.2
YOLOv8x	1.0	1.25	640	53.9	68.2	257.8

The structure of YOLOv8 consists of a backbone network, a neck network, and a predictive head network as shown in Figure 3.

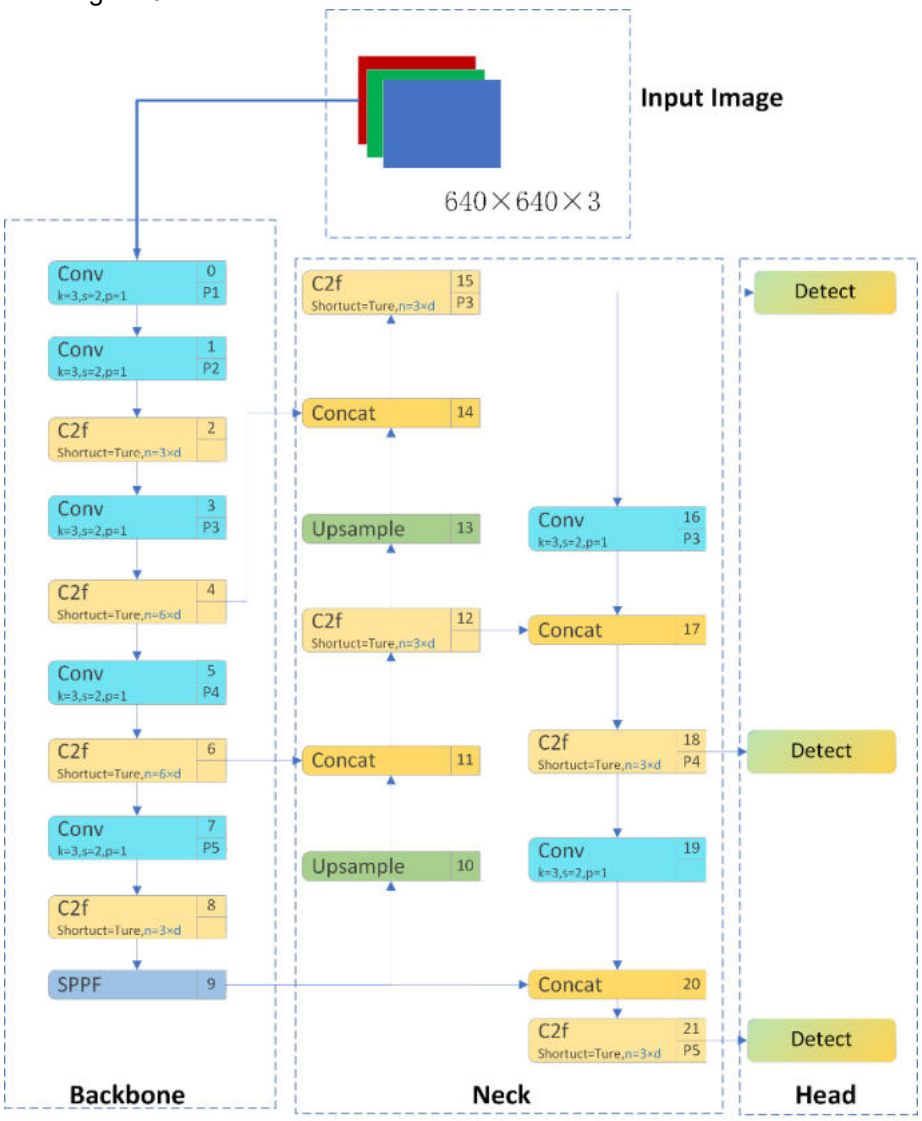


Fig. 3 – YOLOv8 network structure diagram

Study of Improved YOLOv8n Algorithm

For the strawberry fruit detection task, this study proposes a strawberry fruit detection method based on improved YOLOv8n to enhance the performance of the model in specific scenes. The use of receptive-field aware convolution RFAConv instead of standard convolution Conv in the backbone network improves the network performance, and the detection performance is significantly improved; the introduction of the SENet attention mechanism strengthens the learning ability of the backbone network for strawberry color and shape features, and the design of the decoupling head is also optimized to better adapt to the requirements of the classification and regression tasks. The InceptionNeXt neural network structure is introduced as the feature extraction network, and the convolution in Bottleneck in the Cf2 module of the neck network is replaced with the InceptionNeXt convolution, which effectively reduces the amount of computation. During the training process, the Wise-IoU loss function with dynamic nonmonotonic focusing mechanism is used to address the impact of low-quality samples on model performance in the target detection task. In the post-processing stage, DIoU-NMS is used to replace the traditional NMS algorithm to reduce the false deletion of overlapping target frames. The improved YOLOv8n network structure is shown in Fig. 4.

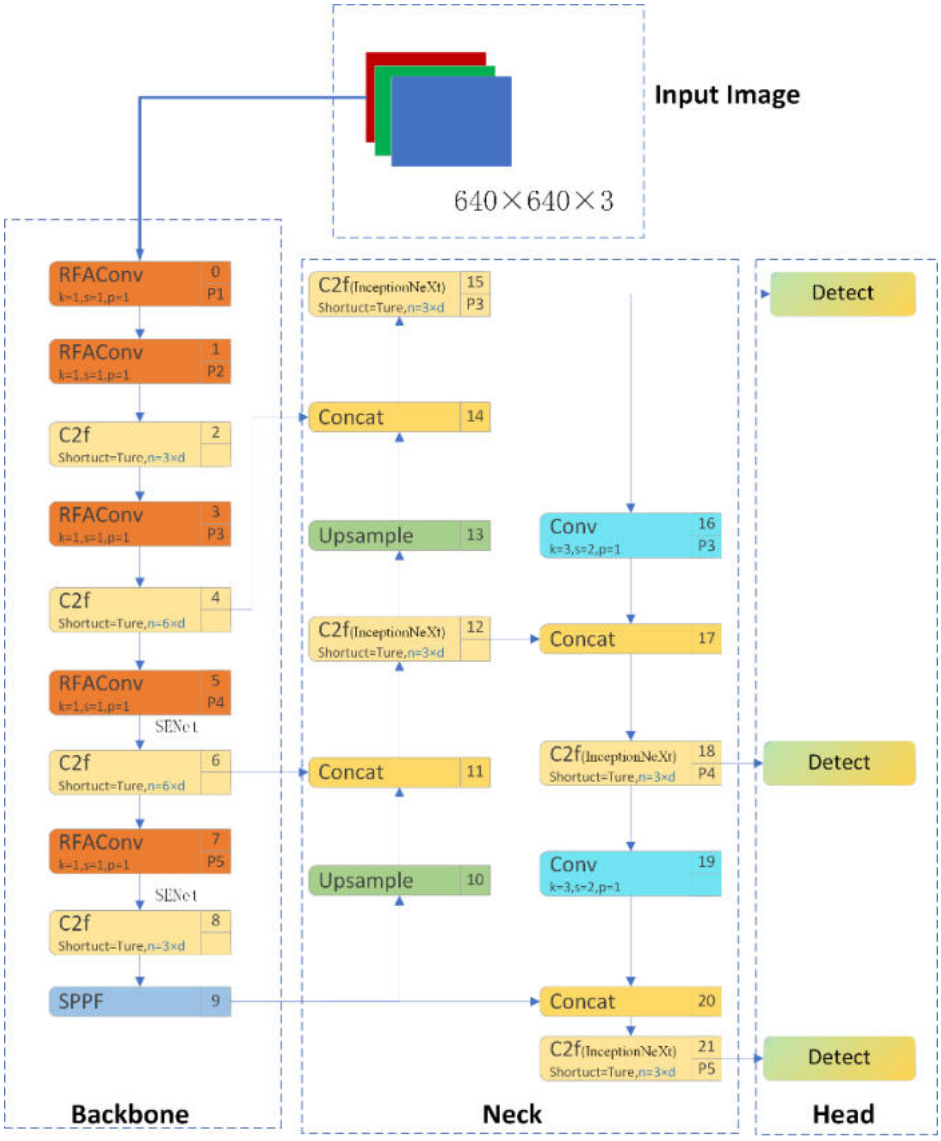


Fig. 4 – Improved YOLOv8n network architecture

Traditional convolution operation extracts local features through a fixed convolution kernel, and its receptive field is usually limited and fixed, which may lead to poor adaptability to multi-scale targets. RFAConv enables the convolution operation to adaptively adjust the size of the receptive field by introducing a dynamic receptive field mechanism and an attentional mechanism, so that it can better capture the target features at different scales. The principle of spatial feature transformation of the receptive field is shown in Fig. 5.

The original spatial feature has a size of C×H×W and is divided into non-overlapping sliding windows. When a 3×3 convolution kernel is applied, each 3×3 window in the receptive field corresponds to a local region of the input feature map. As a result, the converted spatial feature is expanded by a factor of three in both height and width, increasing its size to 3C×3H×3W. This enlargement effectively broadens the receptive field, enabling the capture of multi-scale information.

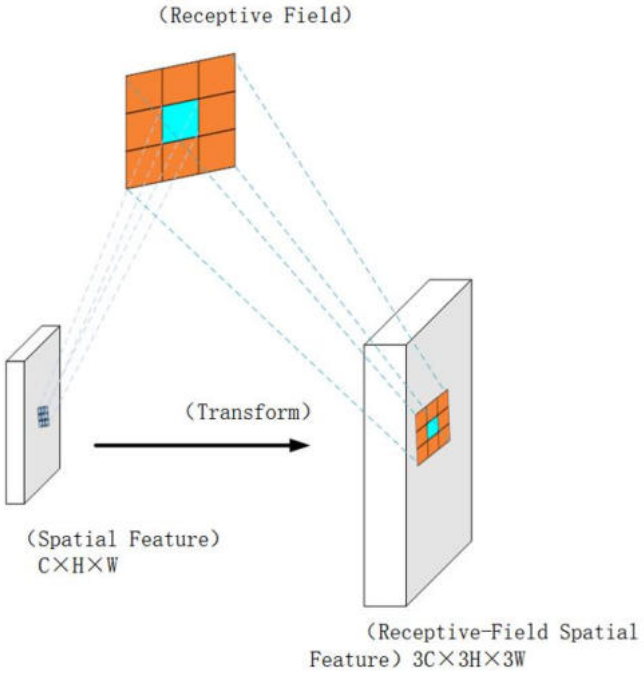


Fig. 5 – Principle of spatial feature transformation in the sensory field

Spatial attention mechanisms that focus on spatial features in the sensory field are combined with convolution to eliminate the problem of sharing convolution parameters. Current spatial attention mechanisms already consider long-range information, which can be obtained globally through global average pooling or global maximum pooling. In order to focus on feeling the wild spatial features, a k × k convolution operation with stride of k is used to extract feature information. Its specific structure is shown in Fig. 6.

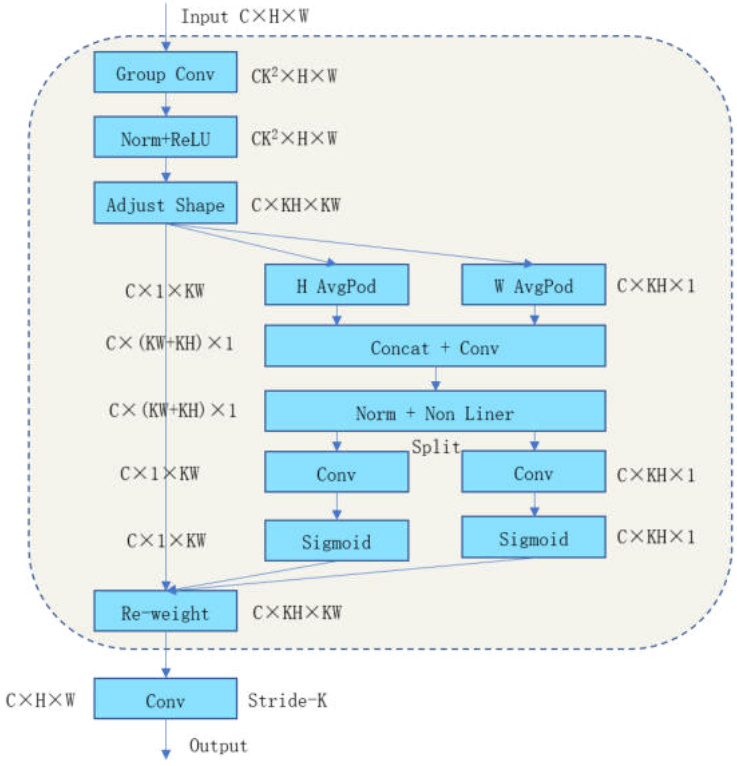


Fig. 6 – RFAConv structure

After the input feature map size of C×H×W enters the RFAConv module, the number of channels is extended to CK2 by a group convolution operation, generating a new feature map size of CK2×H×W. Subsequently, the feature map is further reshaped to C×KH×W after normalization with a nonlinear activation function, ReLU. To extract information along the spatial dimensions, average pooling is applied separately in the height and width directions, resulting in two intermediate feature maps with dimensions C × 1 × KW and C × KH × 1, respectively. These two feature maps are subsequently spliced together and fused by a convolutional layer to generate a new feature map with dimensions C × (KW + KH) × 1. After normalization and nonlinear transformation, this feature map is split into two parts corresponding to the information in the height and width directions, and each of them is passed through a convolution operation as well as a Sigmoid function to generate the final attention weight map. The generated attentional weight map is used to reweight the original input feature map through a final convolutional layer using a step size of K setting to generate the final output feature map.

SENet (Squeeze-and-Excitation Networks) is a convolutional neural network architecture that introduces an attentional mechanism in the channel dimension, aiming to improve the representation ability of the network by capturing the interdependencies between feature channels. It introduces an attention mechanism that significantly improves the image classification performance without significantly increasing the computational complexity. The core idea is to learn a weight for each feature channel to enhance useful features and weaken irrelevant features. Compared with traditional CNNs, SENet optimizes performance by introducing dynamic feature tuning through the SE module, which consists of two key operations: Squeeze and Excitation. In the compression phase, the SE module captures the global context information by compressing the spatial information of each channel into a single value through global average pooling. In the Excitation phase, a fully connected layer and a nonlinear activation function are utilized to learn the inter-channel dependencies and generate weights for each channel. These weights are used to recalibrate the responses of the feature channels, enhancing useful features and suppressing irrelevant features. This mechanism allows SENet to adaptively tune the feature representation and improve the performance of the model. The basic structure of SENet is shown in Fig. 7.

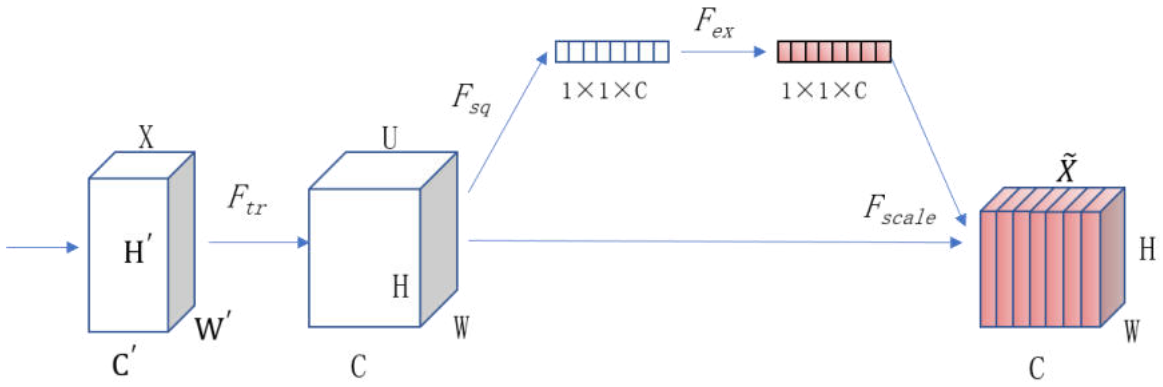


Fig. 7 – SENet module structure

For any transformation F_{tr} that maps an input X to a feature map U, where U ∈ RH×W×C, the corresponding SE block can be constructed for feature recalibration. First, the feature map U is aggregated in the spatial dimension (H × W) by the Squeeze operation to generate a channel descriptor. This descriptor is used to embed the global distribution of the channel-level feature responses, enabling the layers of the network to utilize the global sensory field information. The subsequent Excitation operation employs a self-selecting pass mechanism to generate per-channel modulation weights using the embedding as input. These weights are applied to the feature map U to generate SE block outputs that are passed directly to subsequent network layers.

Squeeze operation: the SE module generates a descriptor for each channel by aggregating the spatial dimensions (H×W) of the input feature map through a global average pooling operation. This operation compresses the global spatial information into channel vectors, capturing the global distribution of the channel feature responses and providing critical global information for subsequent recalibration. In the Squeeze operation, the input feature map is globally average pooled to compress the feature map with dimensions W × H × C into a 1 × 1 × C feature vector.

This process aggregates the spatial information of each 2D channel into a single value with a global receptive field. In this way, each channel is represented as a numerical value, removing the spatial distribution information and thus utilizing the inter-channel correlation more efficiently. Let ZC be the output vector of the Cth channel in the feature map after the Squeeze operation, and Fsq(UC) denotes the Squeeze operation performed on the input feature map UC of the Cth channel, where H and W denote the height and width of the feature map, respectively.

Excitation operation: after the Squeeze step, an Excitation mechanism is introduced, which is essentially a self-gating mechanism consisting of two fully connected layers and a nonlinear activation function. The first fully-connected layer processes the channel descriptors by dimensionality reduction and imposes the ReLU activation function; the second fully-connected layer maps them back to the original channel dimensions. This process effectively captures the nonlinear relationships between channels and generates a set of channel weights.

The SENet attention mechanism is able to fit the correlation between channels more efficiently and capture the dependencies and interactions between channels, thus optimizing the expression of feature weights. In addition, SENet is less parametric and computationally intensive, adding only a simple fully-connected layer and activation function after the convolutional layer, and thus does not incur significant additional overhead. Integrating it into YOLOv8n's backbone network enhances the model's ability to recognize strawberry features at the channel level and strengthens the extraction of key features while weakening the interference of irrelevant content and complex background. With the SENet attention mechanism, YOLOv8n can more fully utilize the inter-channel relationships to enhance feature differentiation and thus improve the accuracy of target detection.

The Backbone network structure contains a complex structure of ten layers, which is designed to extract features efficiently. Introducing the attention mechanism in each layer may significantly increase the computational burden and model complexity, which may be undesirable for resource-limited application scenarios, and the performance enhancement brought by the attention mechanism needs to be weighed against the computational cost in practical applications. In order to balance the accuracy and efficiency of the model, this paper designs three schemes to add the SENet attention module in the first and third layers, the third and fifth layers, and the fifth and seventh layers respectively, and selects the optimal introduction method as the basis for subsequent model improvement after comparison tests. The experimental results are shown in Table 2.

Table 2

Comparison of data of different versions of YOLOv8

Framework	Precision	Recall	mAP50
Unchanged	91.78%	92.14%	96.74%
Add in the first and third layers	91.25%	91.93%	96.82%
Add in the third and fifth layers	91.93%	92.32%	96.39%
Add in fifth and seventh layers	92.33%	92.87%	97.57%

The experimental data show that in the shallow layer structural adjustment, the improvement of the network module for the first and third layers makes the mAP50 rise slightly by 0.12%, but the Precision and Recall show a drop of 0.53% and 0.21%, respectively, which indicates that the shallow parameter adjustment, although it can improve the comprehensive detection performance to a limited extent, leads to negative fluctuation of the basic detection indexes. In the middle-layer network optimization experiments, enhancements to the five-layer structure increased Precision and Recall by 0.15% and 0.18%, respectively. However, mAP decreased by 0.35%, indicating that while this adjustment improved single-sample discriminative ability, it substantially weakened the model's overall detection performance on multi-scale targets. In contrast, the deep-network optimization scheme involving the fifth and seventh layers showed significant advantages. Precision and Recall improved by 0.55% and 0.73%, respectively, while mAP increased by 0.83%, verifying that optimizing deep feature extraction modules effectively enhances the model's multidimensional detection capability. Overall, the results demonstrate a clear depth-dependent characteristic of network structural optimization: the closer the adjustment is to the output layer, the more significant the enhancement in comprehensive performance. Based on these findings, architectural improvements were applied to the deep network module, with the SENet attention mechanism added to the fifth and seventh layers.

InceptionNeXt is an innovative convolutional neural network architecture that combines the multi-scale feature extraction idea of Inception with the large kernel deep convolution design feature of ConvNeXt. In recent years, although large kernel convolution can effectively expand the sensory field and improve the performance, its high memory access cost limits the efficiency of its application on high-performance devices. InceptionNeXt proposes a new deep convolutional structure that achieves a good balance of speed and performance by decomposing the large kernel into multiple small kernels and keeping some of the channels unchanged. This structure divides the channel into three parts, which are processed by 3×3, 1×k and k×1 convolutional kernels respectively, and the rest is passed directly through constant mapping, thus reducing the memory access cost while maintaining a large sense field. This design not only inherits the advantages of the classical Inception module, but also improves the efficiency by reducing the computational cost, solves the bottleneck of the traditional CNN in terms of speed and performance, and becomes the preferred model for efficient image categorization tasks in resource-constrained scenarios. Its structure is shown in Fig. 8.

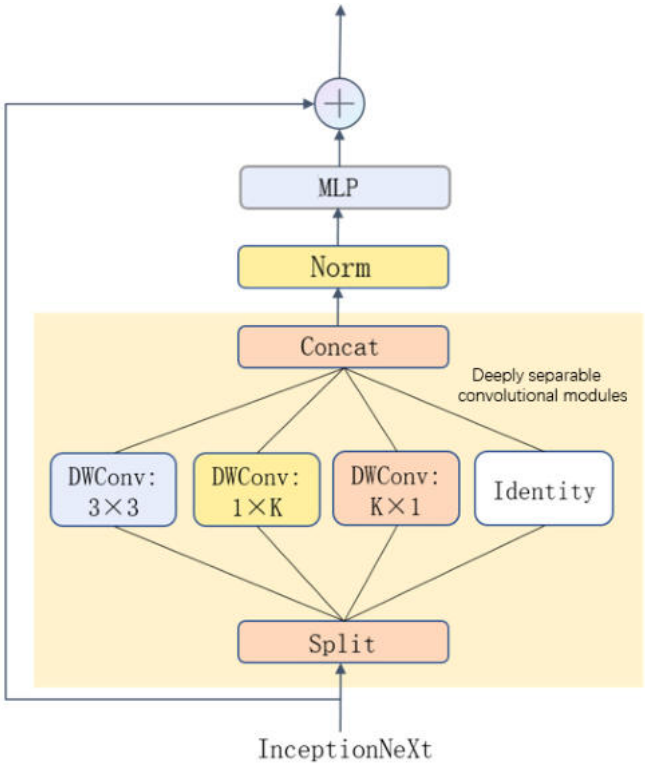


Fig. 8 – InceptionNeXt structure diagram

Distance Intersection over Union - Non Maximum Suppression (DIoU-NMS) is an improved non-maximum suppression algorithm for removing redundant bounding boxes in target detection tasks. In traditional NMS methods, IoU is the only suppression criterion, which may lead to false suppression in the case of occlusion. DIoU-NMS uses DIoU as a criterion for NMS and also considers the distance between the centroids of the two boxes as a judging criterion. Let the Euclidean distance between the centroids of the two bounding boxes be denoted as *d*, and the length of the diagonal of the smallest closure rectangle containing these two bounding boxes as *c*. Although the DIoU computation is more complex compared to the normal IoU, the performance gain it delivers far outweighs the impact of the additional computational cost, ensuring that the overall computational efficiency remains efficient. In terms of implementation details, DIoU-NMS typically consists of four steps: sorting, iterative selection, calculation of DIoU values, and filtering.

First, the prediction frames are sorted in descending order based on their confidence scores. Next, the best candidate frames that are currently unsuppressed are sequentially selected starting from the highest score and added to the final result set. For all the remaining candidate frames, their DIoU values are calculated separately with respect to the selected best frames. If the DIoU between a candidate and the selected best frames exceeds a predefined threshold, the candidate is suppressed; otherwise, it is retained for subsequent comparisons. This method is highly integrable and can be easily embedded with only minor code modifications.

RESULTS

The tests were conducted using a 64-bit Microsoft Windows 11 operating system. The central processor CPU was AMD Ryzen 7 6800H with Radeon Graphics at 3.2 GHz; the running memory (RAM) capacity was 16 GB, and the graphics processor (GPU) is NVIDIA GeForce RTX 3060 with 6 GB of video memory. The software platform was developed using the open-source deep learning framework PyTorch 2.2.1, with Python 3.9.12 as the programming language. The development environment utilized CUDA 11.7 (Compute Unified Device Architecture) and cuDNN 8.7.0 (CUDA Deep Neural Network library) for GPU acceleration. PyCharm and VScode served as the primary development tools.

Parameter settings

The YOLOv8n detection model training parameter settings are shown in Table 3. Because of the changes involved in the model, the model was uniformly constructed from scratch using the yaml file. High-resolution images, such as those with 50 million pixels, are captured to preserve details, while YOLOv8 selects 640×640 input images to improve inference speed and computing efficiency while ensuring detection accuracy.

Table 3

YOLOv8n test parameter settings

Parameter name	Parameter value
Image Input Size	640×640
Training batch	100
Batch size	8
Initial learning rate	0.001
Optimizer	Adam
Attenuation weight	0.0005
Number of processes	4
Learning rate warming	3

Loss Function Comparison

In the training process of deep learning models, the loss function plays a crucial role, which is not only used to quantify the gap between the model prediction results and the actual values, but also provides a direction guide for the optimization and adjustment of model parameters. For YOLOv8n, the design of its loss function plays a decisive role in improving its detection accuracy and computational efficiency. During model training, the loss function helps determine the model parameters that need to be adjusted and the magnitude of their adjustment by evaluating the deviation between the predicted output and the real label. In order to verify the performance of WIOU loss in strawberry target detection, EIoU, GIoU, DIoU, SIoU, and WIOU are used as the loss functions of YOLOv8n for comparative experiments on the strawberry dataset, respectively, and the test results are shown in Table 4.

Table 4

Comparison results of experiments with different loss functions

Mold	Loss function	Precision	Recall	mAP50
YOLOv8n	CIoU	91.78%	92.14%	96.74%
	GIoU	91.72%	92.04%	96.69%
	DIoU	91.93%	92.43%	96.89%
	SIoU	91.91%	92.36%	96.87%
	EIoU	90.94%	91.25%	95.63%
	WIoU	92.36%	93.19%	97.23%

The experimental comparison results show that WIOU using the dynamic non-monotonic focusing mechanism performs best over the other loss functions on this data, with an improvement of 0.58%, 1.05%, and 0.49% in precision, recall, and mean average precision, respectively, compared to the CIoU loss function used by default. WIOU enables YOLOv8n to ensure high-speed processing while also providing more accurate detection results, thus significantly improving overall performance.

Ablation experiment

In this paper, three main optimizations have been made in the structure of the YOLOv8n model. Firstly, the feeling field attention convolution RFAConv is used in the backbone network to replace the standard convolution Conv. Secondly, the SENet attention mechanism is introduced to strengthen the learning ability of the backbone network for strawberry color and shape features. Thirdly, the InceptionNeXt neural network structure is introduced as the feature extraction network, replacing the convolution in Bottleneck with InceptionNeXt convolution in the Cf2 module of the neck network. In order to verify the effectiveness of each improvement, ablation experiments are performed on the strawberry dataset, and the experimental environment as well as the parameters are consistent for each experiment. The experimental results are shown in Table 5.

Table 5

Results of ablation experiments

Model	RFAConv	SENet	Inception NeXt	Precision	Recall	mAP50	Size
YOLO v8n	×	×	×	91.78%	92.14%	96.74%	5.94M
	√	×	×	94.82%	94.15%	97.69%	7.84M
	×	√	×	93.73%	93.47%	97.57%	5.94M
	×	×	√	92.08%	92.27%	96.83%	4.22M
	√	√	×	95.79%	94.83%	97.91%	7.84M
	√	×	√	94.96%	94.33%	97.32%	5.17M
	×	√	√	95.24%	94.71%	97.78%	5.17M
	√	√	√	95.92%	95.45%	98.29%	5.17M

The triple co-optimization model proposed in this study demonstrates significant advantages in both performance and efficiency. By deeply integrating the feature enhancement module, dynamic attention module, and lightweight decoding module, the model achieves 95.92% precision, 95.45% recall, and 98.29% mAP50 value on the baseline dataset. Compared with the baseline model, the three core metrics are improved by 4.14%, 3.31% and 1.55% respectively, while the model size is compressed to 5.17M, which is 12.96% less than the original model. The experimental results show that this architectural innovation effectively solves the contradictory relationship between the number of parameters of the traditional model and the detection accuracy while maintaining the high-precision feature extraction capability, which provides support for the development of the subsequent detection system.

Visualization of detection results

As shown in Figure 9, the confusion matrix provides valuable information about the model's performance across different strawberry-related categories. The dataset contains three main categories: green, half_ripened, and fully_ripened, as well as a background category.

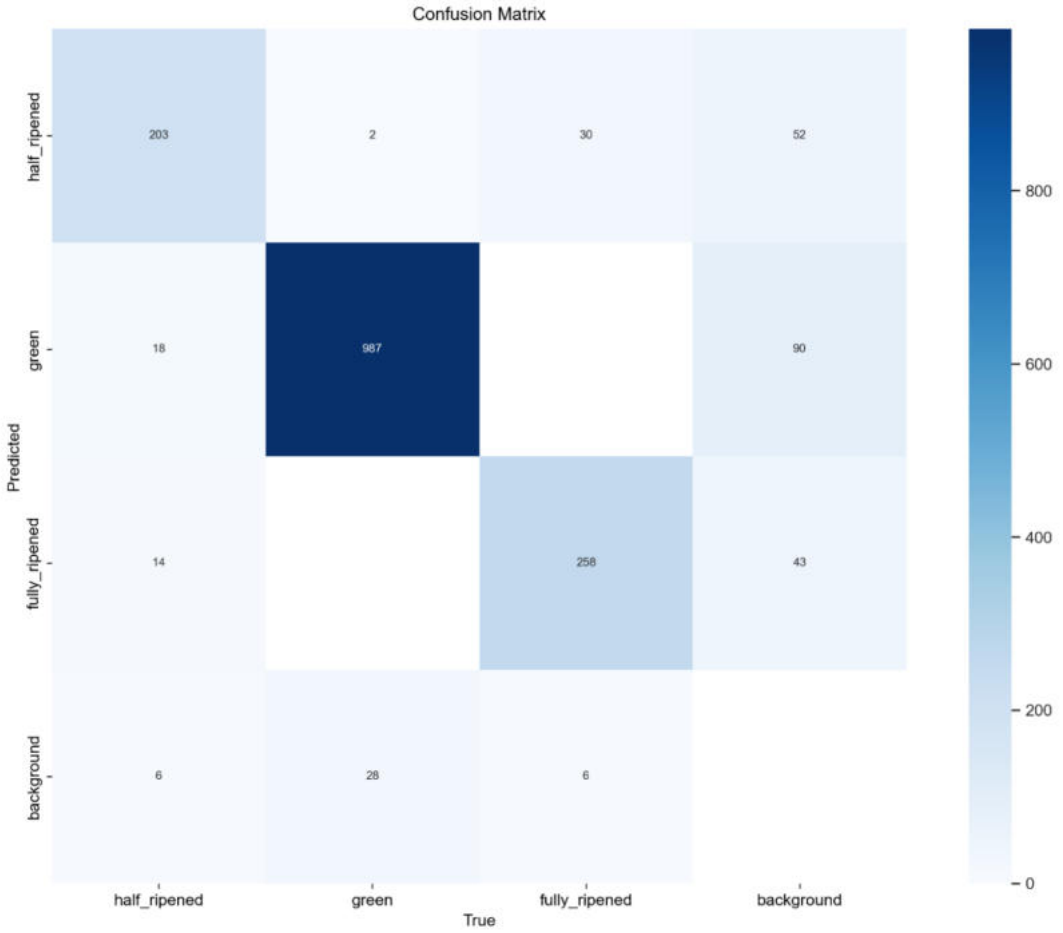


Fig. 9 –Confusion matrix after YOLO8N training

For the half-ripened category, the model demonstrated reasonable recognition capabilities, correctly classifying 203 samples. However, there were also some misclassifications, with six strawberries incorrectly labeled as background. This indicates that although the model can effectively recognize the characteristics of strawberries, there is still some confusion, possibly due to overlapping characteristics or visually similar elements between the strawberries and the background.

The green category achieved the highest recognition accuracy, with a total of 987 samples correctly identified. This high true positive rate indicates that the model effectively learned how to distinguish flowers. However, there are still a small number of misclassifications: 2 were misclassified as the half_ripened category, and 28 were classified as background. The proportion of strawberries misclassified as background is relatively high, indicating that in some cases, the model may have difficulty distinguishing between strawberries and non-strawberry elements, possibly influenced by environmental noise or scene complexity.

From the fully_ripened category, the model's recognition performance was moderate, correctly identifying 256 samples. There were a few misclassifications: 30 samples were misclassified as half_ripened, none were misclassified as green, and 6 were labeled as background. These errors indicate that while the model can identify strawberry ripeness to a certain extent, there is still room for improvement when dealing with ambiguous or unclear cases.

The strawberry dataset is validated using the optimized training model in this paper and the detection results are shown in Fig. 10. It can be seen that it performs well in detecting strawberries of different maturity levels.



Fig. 10 –Visualization of detection results

CONCLUSIONS

The study introduces RFAConv dynamic sensory field convolution, SENet channel attention mechanism and InceptionNeXt lightweight structure. It combines these with Wise-IoU loss function and DIoU-NMS post-processing algorithm. The result is a synergistic enhancement of detection accuracy and computational efficiency. The experimental findings demonstrate that the enhanced model exhibits a precision rate of 95.92%, a recall rate of 95.45%, and an mAP50 of 98.29% on the strawberry dataset. These metrics represent enhancements of 4.14%, 3.31%, and 1.55%, respectively, when compared to the baseline model. Additionally, the model's parameter count is reduced to 5.17M, marking a 12.96% decrease, which is of considerable importance in fostering the advancement of precision agriculture.

ACKNOWLEDGEMENT

This work was supported by the National Natural Science Foundation of China, grant no. 62366013

REFERENCES

[1] Elsayed M, Reda M, Mashaly A S. (2024) LERFNet: An enlarged effective receptive field backbone network for enhancing visual drone detection. *The Visual Computer,* 4: 1-14.

[2] Hu J, Shen L, Sun G. (2018). Squeeze-and-excitation networks. *IEEE conference on computer vision and pattern recognition*, 8: 7132-7141.

[3] Howard A, Sandler M, Chu G. (2019). Searching for mobilenetv3. *IEEE/CVF international conference on computer vision*, 4: 1314-1324.

[4] Hosna A, Merry E, Gyalmo J. (2022). Transfer learning: a friendly introduction. *Journal of Big Data*, 9(1): 102.

[5] Li W, Qi F, Tang M. (2020). Bidirectional LSTM with self-attention mechanism and multi-channel features for sentiment classification. *Neurocomputing*, 387: 63-77.

[6] Lu X, Ji J, Xing Z. (2021). Attention and feature fusion SSD for remote sensing object detection. *IEEE Transactions on Instrumentation and Measurement*, 70: 1-9.

[7] Peng H, Li B, Xiong W. (2014). RGBD salient object detection: A benchmark and algorithms. *Computer Vision–ECCV 2014: 13th European Conference*, 9: 92-109.

[8] Sharma A K, Nguyen H H C, Bui T X. (2022). An approach to ripening of pineapple fruit with model Yolo v5. *IEEE 7th international conference for convergence in technology (I2CT)*, 2: 1-5.
[9] Vaswani A, Shazeer N, Parmar N. (2017). Attention is All You Need. *Conference of Neural Information Processing Systems*,3:6000-6010.
[10] Wan L, Zhang J, Dong X. (2021). Unmanned aerial vehicle-based field phenotyping of crop biomass using growth traits retrieved from PROSAIL model. *Computers and Electronics in Agriculture*, 187: 106304.
[11] Wang J, Zhang Z, Dai B. (2024). Cow-YOLO: Automatic cow mounting detection based on non-local CSPDarknet53 and multiscale neck. *International Journal of Agricultural and Biological Engineering*, 17(3): 193-202.
[12] Zhu J, Hu T, Zheng L. (2024). YOLOv8-C2f-Faster-EMA: an improved underwater trash detection model based on YOLOv8. *Sensors*, 24(8): 2483.

EFFECT OF MECHANICAL SIDE DEEP FERTILIZATION TECHNOLOGY ON NUTRIENT ABSORPTION AND LOSS IN PADDY FIELDS
/
机械侧深施肥技术对水稻养分吸收及稻田养分损失的影响

Zhenhua XU [1,2], Haiying LIU [1,2], Yanmin YU [1,2], Changjun DAI [3], Jing WANG [3], Ping YAN [1,2*]
[1] Biotechnology Institute, Heilongjiang Academy of Agricultural Sciences, Harbin, 150028, China
[2] Northeast Branch of National Center of Technology Innovation for Saline-Alkali Tolerant Rice, Harbin, 150028, China
[3] Quality and Safety Institute of Agricultural Products, Heilongjiang Academy of Agricultural Sciences, Harbin, 150028, China
Corresponding author: Ping Yan; E-mail: yany1960928@sina.com

DOI: https://doi.org/10.35633/inmateh-76-60

Keywords: *Mechanical side deep fertilization, rice, nutrients, growth rate, dry material*

ABSTRACT
To investigate the effects of different fertilization treatments on rice growth, nutrient uptake, and nutrient loss in paddy fields, the study was conducted in Jiansanjiang Qixing Farm, Company 36, Jiamusi City, Heilongjiang Province as the experimental site. A total of six treatment groups (G1-G6) were set up with different fertilization methods and fertilizer application rates. The data demonstrated that the number of tillers increased by 61.4% in G2 and 80.4% in G3 compared to G1. The number of tillers in G6 was 489×104/hm2, which decreased by 13.6% compared to G3. During the tillering stage, the nitrogen content of G1, G2 and G3 stems was 2.08, 2.19 and 2.51%, respectively. The cumulative loss of potassium in paddy fields was 0.19 kg/hm2, 0.59 kg/hm2 and 0.41 kg/hm2 for G1, G2 and G3, respectively. The results indicated that the use of mechanical side deep fertilization could bring many advantages to rice compared to the traditional manual fertilization method, including an increase in the number of tillers and plant height, as well as an increase in the leaf area index and dry material accumulation. At the same level of fertilization, the mechanical side deep fertilization method resulted in less ammonia volatilization, which would contribute to reducing ammonia volatilization from the paddy field and allow more nitrogen to be stored by the paddy field. In addition, the cumulative loss of runoff from the paddy field was reduced by the mechanical side deep fertilization treatment compared to manual fertilization. The study provides a useful reference for optimizing rice cultivation techniques to improve yield and reduce nutrient losses.

摘要
为研究不同施肥处理对水稻生长、养分吸收和养分流失的影响，本研究以黑龙江省佳木斯市三十六连建三江七星农场为试验地。试验共设 6 个处理组（G1-G6），施肥方法和施肥量各不相同。数据表明，与 G1 相比，G2 的分蘖数增加了 61.4%，G3 增加了 80.4%。G6 的分蘖数为 489×104/hm²，比 G3 减少了 13.6%。在分蘖期，G1、G2 和 G3 茎的含氮量分别为 2.08%、2.19% 和 2.51%。G1、G2 和 G3 的稻田钾累积损失量分别为 0.19 kg/hm²、0.59 kg/hm² 和 0.41 kg/hm²。结果表明，与传统的人工施肥方法相比，使用机械侧深施肥能给水稻带来许多好处，包括增加分蘖数和株高、提高叶面积指数和干物质积累。在施肥量相同的情况下，机械侧深施肥法减少了氨的挥发，有助于减少稻田的氨挥发，使稻田储存更多的氮。此外，机械侧深层施肥处理还减少了水田径流的累积损失。

INTRODUCTION
With the continuous growth of global population and the acceleration of industrialization, the demand for food shows a continuous rise. In China, rice paddies are mainly distributed in regions such as Jiangnan and South China, where climatic conditions and water resources provide unique conditions for rice growth (*Mohidem et al., 2022*). However, the concentration of land resources in these areas has increased due to the growth of industrialization and urbanization. Therefore, it has become an important challenge in the field of agriculture to increase the unit yield of paddy fields (*Le Van and Jens, 2023; Xiao et al., 2022; Wu et al., 2023*). As one of the most important grains in China, the improvement of the yield of paddy fields is pivotal to ensure the food security of the country. To meet this need, scientists have devoted themselves to researching various methods to increase the yield and productivity of paddy fields so as to ensure a stable food supply for the country (*Jiaying et al., 2022*).

Urmi et al. (2022) used different treatment designs to investigate the impacts of integrated nutrient management on cropland's carbon sequestration, soil fertility, nutrient use efficiency, and rice yield. According to the findings, applying both organic and inorganic fertilizers at the same time increased soil fertility considerably and improved nutrient uptake and utilization efficiency. In a Basmati rice-wheat cropping system, Dhaliwal et al. evaluated the long-term impacts of applying fertilizer and manure together on wheat output, nutrient concentration, and absorption. The study's findings showed that applying farmyard manure in addition to 75% NPK considerably enhanced growth parameters and yield characteristics, as well as plant height, tiller count, chlorophyll content, and wheat yield (*Dhaliwal et al., 2023*). Using a greenhouse experiment, *Bhadwal et al. (2022)* assessed the impact of soil selenium treatment on metabolic alterations in rice under arsenic stress. According to the findings, selenium treatment greatly enhanced arsenic's harmful effects on grain yield, leaf dry weight, and rice plant height. *Litardo et al. (2022)* evaluated the effect of application of different mineral and organic amendments on rice growth and yield in saline soils of Yaguachi, Ecuador. The results indicated that the application of compost significantly increased rice yield and it promoted both nutritional and reproductive growth of rice. Therefore, it was considered as the best amendment in this type of soil. By comparing the varying nutrient consumption efficiencies of nitrogen, phosphorous, and potassium in rice and wheat under various integrated nutrient management regimes, Bihari et al. examined the impact of nutrient efficiency on crop yield. The findings showed that by enhancing soil fertility, raising sustainable crop yield, and enhancing nutrient uptake, the combined application of chemical and organic fertilizers can increase nutrient usage efficiency (*Bihari et al., 2022*).

However, traditional methods of fertilizer application in paddy fields often suffer from low nutrient utilization and serious fertilizer loss, which not only result in wastage of nutrients, but also cause pollution to the environment (*Lee et al., 2025*). Therefore, it is important to study new fertilization techniques to improve paddy yield and reduce environmental pollution. Paddy production has made extensive use of mechanical side deep fertilization (MSDF) techniques in recent years (*Assogba et al., 2025*). This technology enables fertilizer to be distributed more evenly in the paddy field by applying fertilizer at a depth of about 10 cm, thus improving the efficiency of nutrient utilization. *Wu et al.* compared the effects of manual versus mechanical side application of fertilizer under conventional tillage, minimum tillage and no-tillage conditions by machine transplanting rice. The results indicated that conservation tillage combined with mechanical side application of fertilizer can effectively improve fertilizer utilization, promote rice growth and increase yield (*Wu et al., 2022*). *Hou et al. (2023)* conducted a comparative experiment on different fertilizer depths using the side deep fertilization mode of machine transplanted rice. The results indicated that the optimum depth of side deep fertilization was 10 cm. This depth significantly increased rice yield and improved the efficiency of nitrogen and phosphorus utilization, while reducing nitrogen and phosphorus concentration and ammonia volatilization in surface water. Through field trials, *Zhong et al. (2024)* found that lateral depth fertilization of mechanically grown rice in double-season paddy fields in Hunan significantly reduced nitrogen losses. It also increased relative soil urease activity and reduced total N footprint. Using field tests and radioisotope tracer studies, *Wang et al. (2023)* investigated the effects of varying nitrogen fertilizer (NF) application rates on yield, nitrogen usage efficiency, and their physiological properties of mechanically potted rice transplants under deep-burrowing circumstances. According to the findings, rice output and NF use efficiency may be successfully increased by applying 135 kg N ha^{-1} of basal NF deep underground.

In summary, many studies have been done with many different designs and experiments for rice yield, nutrient utilization and mechanical fertilization, and results have been obtained. However, the impact of MSDF technology for rice growth and farmland nutrients is still controversial. In this context, the study will conduct experiments to analyze the specific impact effects of this technology, which will provide a scientific basis for paddy production, optimize paddy fertilization methods, increase paddy yield, and reduce environmental pollution. The innovativeness of the study is reflected in the fact that different ratios of the MSDF technology were used through field trials in Jiansanjiang Qixing Farm, Company 36, Jiamusi City, Heilongjiang Province. The nutrient uptake of rice and nutrient loss from paddy fields are also systematically measured and analyzed.

METHODS AND MATERIALS

Experimental sites and materials

A field trial was conducted between 2022 and 2023 at Jiansanjiang Qixing Farm (132°71′E, 47°28′N), Company 36, Jiamusi City, Heilongjiang Province, China. The annual average temperature in the area is 4.7 ℃, and the annual average precipitation is 567.3 millimeters, mainly concentrated in June, July, and August, accounting for 75% of the annual precipitation. The frost free period is about 120-140 days throughout the year.

The region has good agricultural conditions and is one of the important commodity grain bases in China (*Tang et al., 2022*). During the experiment, the rice varieties of Paddy Hualiang, Jilin Changbai Mountain Rice, and Heilongjiang Wuchang Rice were used. An aerial view of the experimental field is shown in Figure 1.



Fig. 1 – Bird's eye view of the test field

Compound fertilizer (slow-release fertilizer designed for rice) produced by Sinochem Fertilizer Co. Ltd. was selected as the base fertilizer. This fertilizer's composition of nitrogen, phosphorus, and potassium was 18:12:15., and the total nutrient content was not less than 45%. In addition, urea produced by Boda Field Fertilizer Co. Ltd. was used with a nitrogen content of not less than 46.4% (*Zhang et al., 2022*).

Experimental design

Six treatment groups were used in the setup of the experiment. Three replicated trials were implemented for each treatment group. The area of each trial was 150 square meters. These six treatment groups included: G1 i.e. no fertilization of crop as blank control group. G2 was fertilized manually. G3 was fertilized by MSDF with the same amount of fertilizer as G2 group. G4, G5 and G6 were all fertilized by MSDF, but the amount of fertilizer applied was reduced by 10%, 20% and 30% compared to G2 and G3, respectively. The experimental treatment scheme is shown in Table 1.

Table 1

Test treatment scheme

Group	Base fertilizer application method	Amount of base fertilizer applied	Urea Fertilization Methods	Amount of urea fertilizer applied
G1	/	0	/	0
G2	Artificial fertilization	700 kg/hm^2	Artificial fertilization	70 kg/hm^2
G3	Mechanical side deep fertilization	700 kg/hm^2	Artificial fertilization	70 kg/hm^2
G4	Mechanical side deep fertilization	630 kg/hm^2	Artificial fertilization	70 kg/hm^2
G5	Mechanical side deep fertilization	560 kg/hm^2	Artificial fertilization	70 kg/hm^2
G6	Mechanical side deep fertilization	490 kg/hm^2	Artificial fertilization	70 kg/hm^2

Measurements and calculations

Rice plant height and stem tiller formation were measured during the experiment. The rice plant height was measured by timed measurement method using a tape measure during the rice growth process. Using the counting approach, the stem tillers was determined (*Dumitru et al., 2024*). Leaf area index (LAI), an important parameter for measuring plant growth, was measured using the HM-G30 LAI meter (*Ren et al., 2023*). The effect of fertilization techniques on leaf growth of rice was analyzed by measuring the LAI at different growth stages of rice. The chlorophyll concentration was measured using the soil and plant analyzer development (SPAD) value, which is a measure of how well plants are able to absorb nutrients.

The study was conducted using a handheld SPAD meter for measurement. Rice leaves were randomly sampled at different periods of rice growth. The chlorophyll content was determined using the SPAD meter, which in turn analyzed the effect of fertilization techniques on nutrient uptake in rice (*Gu et al., 2024*).

Dry material accumulation was determined using the harvest method for rice dry material. Rice was harvested at different periods of time. After 0.5 hours of withering at 105 ℃, dry at 80 ℃ until the weight remains unchanged. The dry material was weighed after cooling. Rice growth rate was an important index for evaluating the growth status of rice, and the study was carried out using a rice growth rate meter. To assess the plant's nutrient uptake status, nutrient accumulation dynamics were crucial indications. The experiment employed the extraction method to ascertain the rice nutrients. At various periods of rice growth, rice was harvested and the straw was extracted to determine the content of total nitrogen, phosphate, potassium ions and other nutrients (*Wang et al., 2022*). Yield and its constituent factors were the important indexes for evaluating the efficiency of rice production. Rice was harvested at the maturity stage. Moisture content was determined using grain moisture meter. Paddy was dried using air drying method (*Găgeanu et al., 2024*). Then it was weighed to obtain the rice yield.

The formula for calculating nutrient accumulation is shown in equation (1).

$$A = \eta \cdot m \tag{1}$$

In equation (1), nutrient accumulation is A. Nutrient content is η. dry material mass is m. Rice biomass is calculated as shown in equation (2).

$$B = m_s \cdot \rho \tag{2}$$

In equation (2), the rice biomass is B. The dry weight of the stem is m_S. The rice planting density is ρ. The growth rate is calculated as shown in equation (3).

$$C = \frac{B_t - B_{t-1}}{T} \tag{3}$$

In equation (3), the growth rate is C. The t th biomass is B_t. The $(t\text{-}1)$-th biomass is B_{t-1}. The time interval is T. The study was conducted using an ammonia detector. The paddy fields were sampled at different periods of rice growth. Ammonia volatilization was determined using ammonia detector and thus the effect of fertilization techniques on the ecology of paddy field was analyzed (*Lin et al., 2022*). Nutrient runoff loss from paddy fields was an important indicator for evaluating nutrient loss from paddy fields, and was measured using the drainage collection method. During the growth of rice, the paddy field was drained. To examine the impact of fertilization methods on nutrient loss from paddy fields, drainage water was gathered and measured (*Jat et al., 2022*).

Equation (4) illustrates how the ammonia volatilization flux from the paddy field was determined.

$$E = \frac{M}{100 \cdot S \cdot d} \tag{4}$$

In equation (4), the ammonia volatilization flux is E. The measured ammonium nitrogen content is M. The cross-sectional area of the device is S. The continuous measurement time is d. The nutrient balance equation is shown in Eq. (5).

$$F = f_{in} - f_{out} \tag{5}$$

In equation (5), the nutrient in dynamic equilibrium is F. The output nutrient is f_m. The output nutrient is f_{out}. The output nutrient is calculated as shown in equation (6).

$$f_{out} = l_1 + l_2 + l_3 \tag{6}$$

In equation (6), nutrients removed by crops are l_1. Nutrients lost by ammonia volatilization are l_2. Nutrients lost by runoff are l_3.

Data processing methods

SPSS 26.0 software was used to process the experimental data. In the process of data processing, the data were first cleaned and organized, and outliers and missing data were eliminated. Then, descriptive statistics were applied to analyze the data, and statistical quantities such as mean, standard deviation, and correlation coefficient between groups were calculated (*Chinthamu and Karukuri, 2023*).

RESULTS

Rice growth and nutrient uptake

Figure 2 compares the quantity of rice tillers with plant height. Figure 2(a) displays the comparison of the number of tillers in rice at the peak tillering stage. In the control group, the number of tillers was 311×104/hm^2 in G1, 502×104/hm^2 in G2, and 566×104/hm^2 in G3. Compared with G1, the number of tillers increased by 61.4% in G2 and 80.4% in G3. Under MSDF, the number of tillers decreased in tandem with the amount of fertilizer applied. The number of tillers in G4 was 532×104/hm^2, which was 6.1% less compared to G3. The number of tillers in G5 was 501×104/hm^2, which was 11.5% less compared to G3. The number of tillers in G6 was 489 × 104/hm^2, which decreased by 13.6% compared to G3. Figure 2(b) shows the comparison of rice plant height in each period. At the tillering stage, the plant heights of G1, G2, G3, G4, G5, and G6 were 44.6 cm, 56.1 cm, 56.9 cm, 56.1 cm, 56.0 cm, and 55.3 cm, respectively. At the nodulation stage, the plant heights of G1, G2, G3, G4, G5, and G6 were 84.1 cm, 99.1 cm, 106.9 cm, 98.3 cm, 95.4 cm, and 92.1 cm. At the spike stage, the plant heights of G1, G2, G3, G4, G5, and G6 were 104.1 cm, 116.2 cm, 129.3 cm, 120.2 cm, 115.1 cm, and 113.2 cm, respectively. At the spike stage, the plant heights of G1, G2, G3, G4, G5, and G6 were 126.1 cm, 149.6 cm, 158.3 cm, 153.3 cm, 143.8 cm, and 140.3 cm. The findings indicated that, in comparison to the manual fertilization method and the blank control group, MSDF could greatly increase the number of stem tillers and plant height of rice.

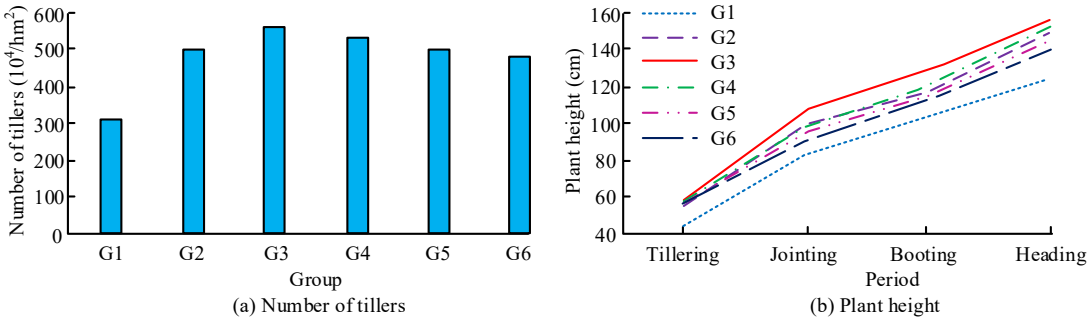


Fig. 2 - Rice contrast between tiller number and plant height

The variation of LAI in rice is shown in Figure 3. In the figure, 0-6 categorized rice growth into seven periods. 0 indicated the seedling stage, 1 indicated the tillering stage, 2 indicated the nodulation stage, 3 indicated the gestation stage, 4 indicated the tasseling stage, 5 indicated the milky ripening stage, and 6 indicated the maturity stage.

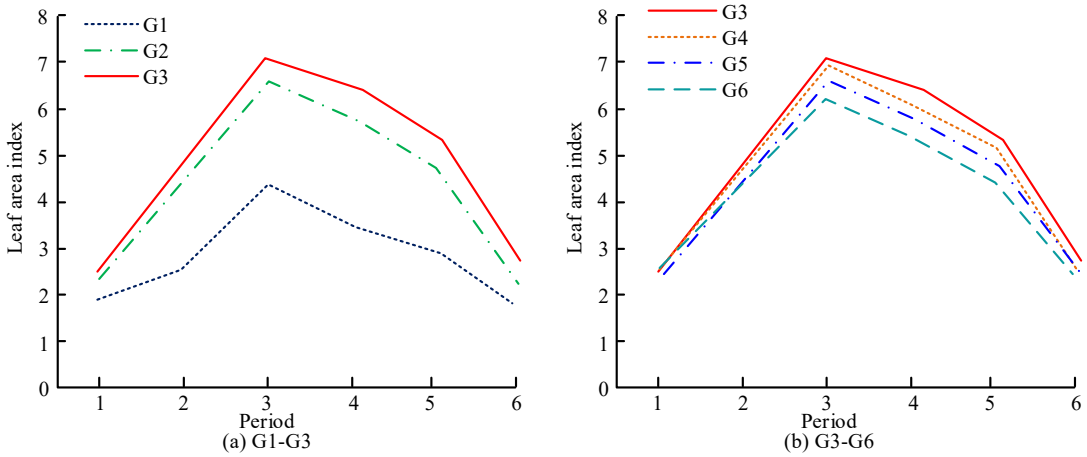


Fig. 3 - Leaf area index change in rice

Rice's LAI had an increasing and subsequently falling trend as it grew. The maximum value of rice LAI appeared at the pregnant spike stage. The rice leaf area indices of G1, G2, G3, G4, G5, and G6 were 4.51 cm, 6.62 cm, 7.19 cm, 6.88 cm, 6.19 cm, and 6.01 cm, respectively. Compared to G1, the rice leaf area indices of G2 at the pregnant spike stage increased by 2.11, and those of G3 increased by 2.68. At tillering and maturity stages, there was little difference in rice LAI between the groups. Compared with G1, the rice LAI increased by 1.81 for G2 at the nodulation stage and 2.23 for G3.

Compared with G1, the rice LAI increased by 2.39 for G2 at the tasseling stage and 3.12 for G3. The results indicated that the rice LAI varied with growth stages. During the gestation period, the rice LAI achieved its maximum value, and when the rice reached the growth stage, it steadily dropped. Additionally, rice LAI was impacted by the fertilization technique. Under MSDF, the rice LAI gradually decreased with the decrease of fertilizer application.

Figure 4 depicts the changes in SPAD in rice leaves. Figure 4(a) shows the comparison of G1, G2 and G3 groups. Figure 4(b) shows the comparison of G3, G4, G5 and G6 groups. With the growth of rice, SPAD showed an increase and then a decrease. The spike stage was when the value peaked, and the maturity stage was when the value decreased. At the gestation stage, the SPAD of rice leaves of G1, G2, G3, G4, G5, and G6 were 37.1, 40.9, 44.1, 43.3, 40.9, and 40.1, respectively. The outcomes indicated that MSDF could raise photosynthetic capability and chlorophyll content, which led to the development of high yield and high quality. However, reducing the fertilization amount would result in lower chlorophyll content, which might affect yield stabilization.

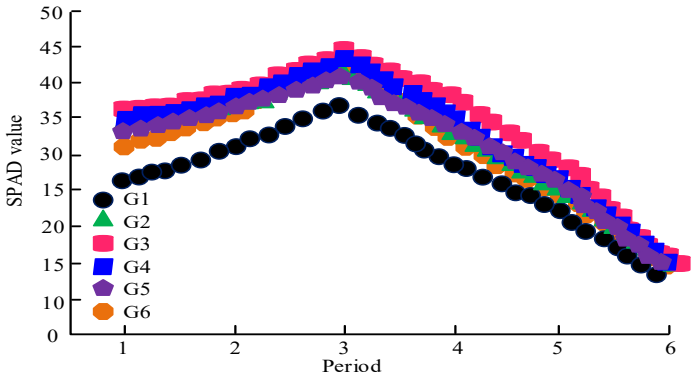


Fig. 4 - The SPAD changes in rice leaves

Figure 5 illustrates how the amount of dry particles that accumulated in rice fluctuated. As rice grew, the accumulation of dry material grew progressively and reached its maximum value at the maturity stage. The accumulation of dry material at the seedling stage was close to 0 in all groups. The accumulation of dry material at the tillering stage did not differ significantly in all groups. When entering the nodulation stage, the differences in the accumulation of dry material in rice became more obvious. At the nodulation stage, the accumulation of dry material in rice was 0.63 t/hm^2, 2.49 t/hm^2, 2.51 t/hm^2, 2.50 t/hm^2, 2.48 t/hm^2, 2.39 t/hm^2 in G1, G2, G3, G4, G5, and G6, respectively. At the maturity stage, the accumulation of dry material in rice in G1, G2, G3, G4, G5, and G6 were 5.58 t/hm^2, 9.93 t/hm^2, 11.72 t/hm^2, 10.97 t/hm^2, 10.29 t/hm^2, and 9.11 t/hm^2, respectively. The results showed that compared with the control group, all fertilizer treatments significantly increased the accumulation of aboveground dry material in rice. However, the decrease in the amount of MSDF resulted in lower dry material accumulation.

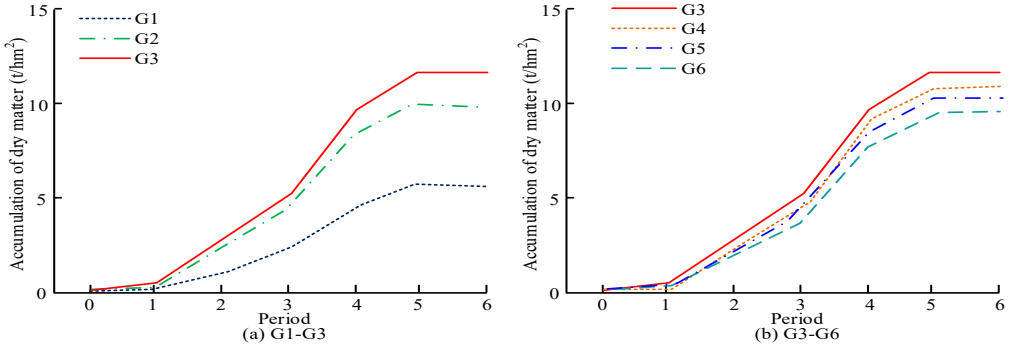


Fig. 5 - Accumulated change of dry material in rice

Rice growth rate comparisons are shown in Figure 6. Figure 6(a) shows the stem growth rate comparison. The maximum growth rate occurred from the tillering stage to the tasseling stage, and the growth rates of G1, G2, and G3 were 143.1 kg/hm^2/d, 249.6 kg/hm^2/d, and 271.3 kg/hm^2/d, respectively. Figure 6(b) shows the comparison of the growth rates of leaves. The maximum growth rate occurred from tillering stage to nodulation stage.

The growth rates of G1, G2, and G3 were 66.2kg/hm²/d, 159.7kg/hm²/d, and 183.2kg/hm²/d, respectively. Figure 6(c) shows the comparison of spike growth rates. The maximum growth rate occurred at the tasseling to milk maturity stage. The growth rates of G1, G2, and G3 were 99.3 kg/hm²/d, 154.9 kg/hm²/d, and 181.3 kg/hm²/d, respectively. The outcomes revealed that fertilizer application could promote the growth rates of rice stems, leaves, and spikes. Stem, leaf and spike growth rates increased significantly after MSDF treatment compared to manual fertilization treatment.

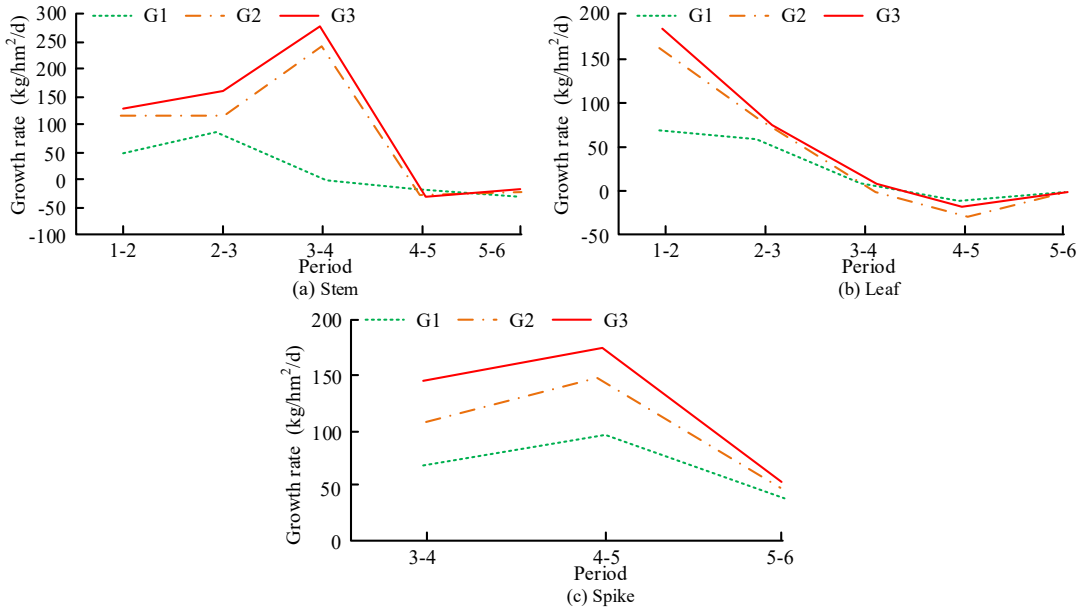


Fig. 6 - Comparison of rice growth rates

Figure 7 illustrates how the nutritious content of rice has changed.

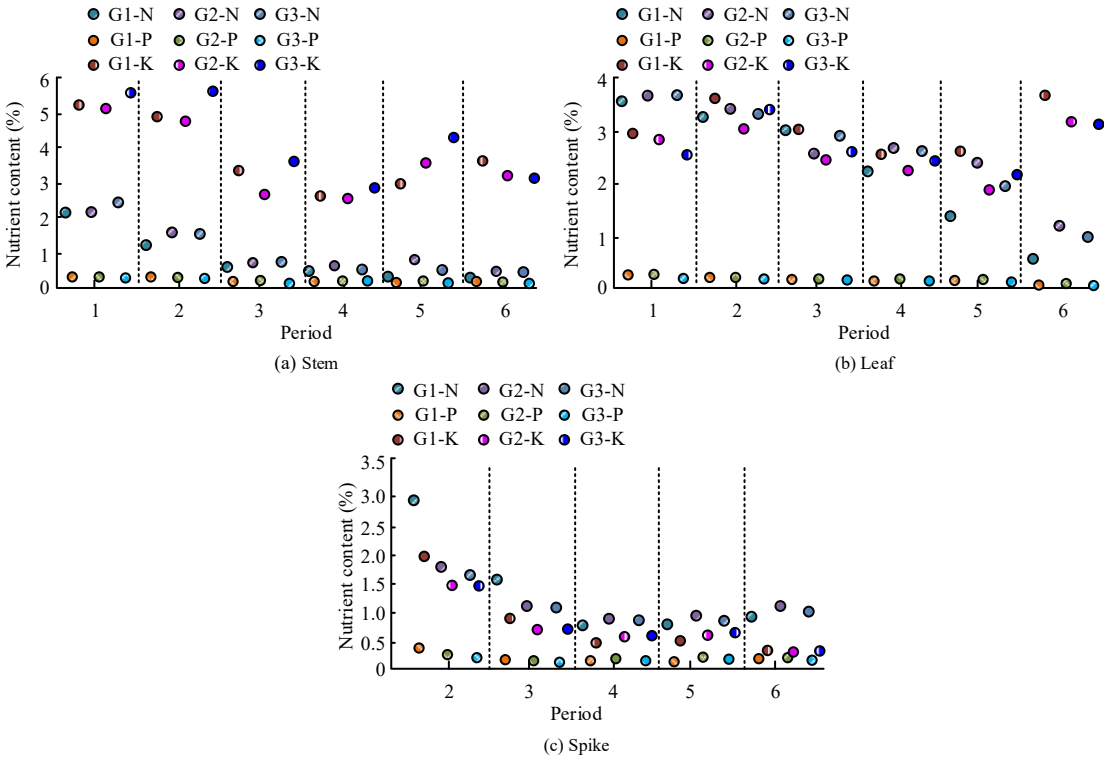


Fig. 7 - Changes in nutrient content in rice

Figure 7(a) displays the changes in nutrient content of stems in each period. Nitrogen, phosphorus and potassium contents in stems gradually decreased during rice growth. At the tillering stage, the nitrogen contents of G1, G2 and G3 were 2.08%, 2.19% and 2.51%, respectively.

At the tillering stage, the phosphorus contents of G1, G2, and G3 were 0.29%, 0.30%, and 0.28%, respectively, and their potassium contents were all around 5.5%. At the nodulation stage, the nitrogen contents of G1, G2 and G3 were 1.31%, 1.58% and 1.51%, respectively. The phosphorus content was all around 0.24%. Potassium content was 4.89, 4.91 and 5.53%, respectively. The G3 group outperformed the G2 group in promoting nitrogen uptake and utilization in the pre-emergent stems of rice at the same rate of fertilizer treatment. Figure 7(b) shows the variation of nutrient content of leaves in each period. Nitrogen content was greatest at the tillering stage, with 3.58%, 3.61% and 3.65% in G1, G2 and G3, respectively. Relative to manual fertilization treatments, MSDF resulted in an increase in rice leaf nitrogen content from at tillering to spike stage. However, its N content showed a decreasing trend in the remaining periods. Meanwhile, the phosphorus content of rice with MSDF decreased at all fertility stages, while the nitrogen content at the spike stage and potassium content at the tasseling and milking stages increased.

Figure 7(c) shows the variation of nutrient content in rice spike, which had reduced spike nitrogen content in G3 compared to G2. Meanwhile, phosphorus content decreased by 0.02% and 0.05% at the spike stage and maturity stage, respectively. However, potassium content increased by 0.02% and 0.05% at tasseling and milk maturity stages, respectively. The findings demonstrated that during the rice growth stage, fertilization treatments had a substantial impact on the nutritional levels of the stem, leaf, and spike. When compared to the manual fertilization treatment, the MSDF treatment greatly raised the N content of the stems and leaves of rice during the tillering and spike stage. However, its nitrogen, phosphorus and potassium contents were reduced at other growth stages.

Figure 8 depicts the buildup of nutrients in rice. Figure 8(a) displays the nutrient accumulation of stems, and nitrogen accumulation reached its maximum value at the tasseling stage. Compared to G2, the nitrogen accumulation in G3 increased by about 3.25 kg/hm2. Similarly, phosphorus accumulation reached its maximum value at the tasseling stage, and the phosphorus accumulation in G2 and G3 was almost the same. Compared to G1, phosphorus accumulation in G3 increased by 5.13 kg/hm^2. Potassium accumulation reached its maximum value at the milky stage. Compared with G1 and G2, potassium accumulation in G3 increased by 48.11 kg/hm^2 and 36.32 kg/hm^2, respectively.

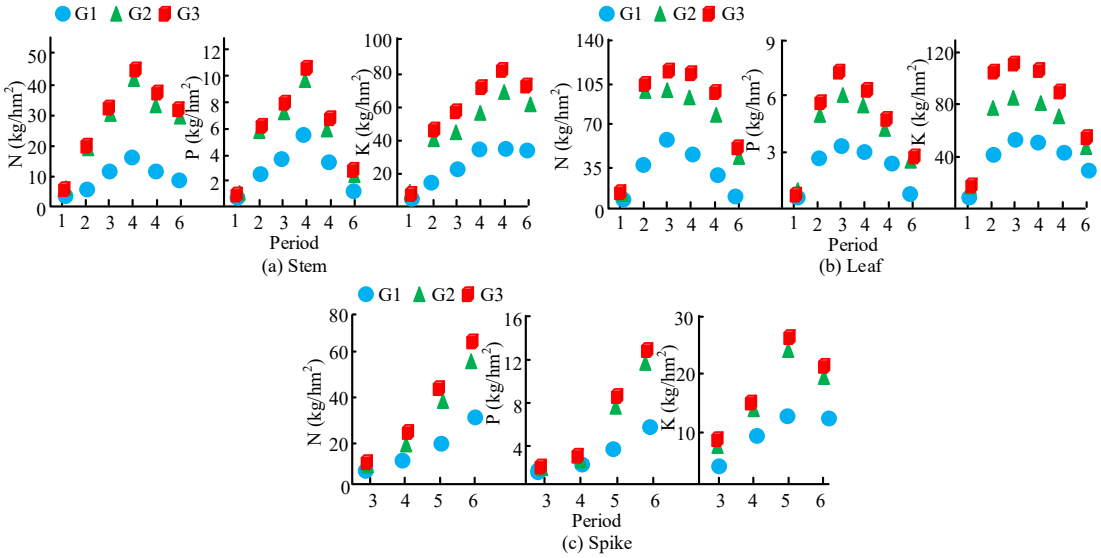


Fig. 8 - Nutrient accumulation in rice

Figure 8(b) shows the nutrient accumulation in leaves. Nitrogen accumulation reached its maximum at the nodulation stage, while phosphorus and potassium accumulation reached their maximum at the spike stage. At the nodulation stage, the nitrogen accumulation of G3 was 119.31 kg/hm^2, which was elevated by 9.37 kg/hm^2 and 59.52 kg/hm^2 compared with G1 and G2, respectively. At the spikelet stage, the phosphorus accumulation of G2 and G3 was basically the same, which was 7.41 kg/hm^2. At panicle initiation stage, potassium accumulation of G3 was 109.67 kg/hm^2, which was elevated by 56.56 kg/hm^2 and 20.83 kg/hm^2 compared to G1 and G2. Figure 8(c) shows the nutrient accumulation of spikes. Nitrogen and phosphorus accumulation both reached their maximum values at maturity, while potassium accumulation reached its maximum value at milk maturity. At the same fertilizer application rate, nitrogen, phosphorus and potassium accumulation of rice spikes increased in MSDF compared to manual fertilization, with an increase ranging from 10% to 19%.

Nutrient loss from paddy fields

Figure 9 displays the ammonia volatilization data from the paddy field. The ammonia volatilization flux from the paddy field is displayed in Figure 9(a). The ammonia volatilization flux of G1 was basically maintained around 0 due to the lack of fertilizer application. The ammonia volatilization flux of G2 reached the maximum value of 5.27 kg·N/hm²/d around day 5, and the ammonia volatilization flux of G3 reached the maximum value of 1.42 kg·N/hm²/d around day 8. Compared with G2, the ammonia volatilization flux of G3 decreased by 3.85 kg·N/hm²/d, which was 73.1%. Comparison of different fertilization treatments showed that MSDF was able to reduce ammonia volatilization loss, delay the peak appearance time, and reduce nitrogen loss. It showed its advantages in reducing ammonia volatilization loss in paddy system. Figure 9(b) shows the ammonia volatilization accumulation. The ammonia volatilization accumulation of G1, G2, and G3 were 2.01 kg·N/hm², 16.89 kg·N/hm², and 9.93 kg·N/hm², respectively. The results showed that the ammonia volatilization cumulative loss of G2 was the largest, followed by G3, and the smallest in G1 treatment. At the same N application rate, the artificial fertilizer spreading treatment had a substantially higher cumulative ammonia volatilization loss than the MSDF treatment. This suggested that the MSDF treatment had a higher effect on nitrogen retention, which could lower nitrogen loss and increase the rate at which NF is used, hence lessening the environmental impact.

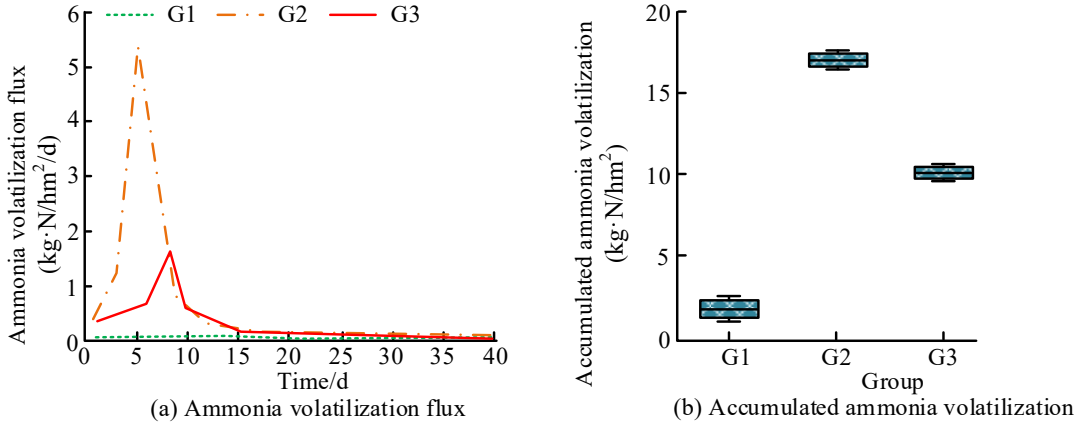


Fig. 9 - Results of ammonia volatilization flux in paddy fields

Figure 10 illustrates the change in the amount of nutrients in the stem flow water of a paddy field.

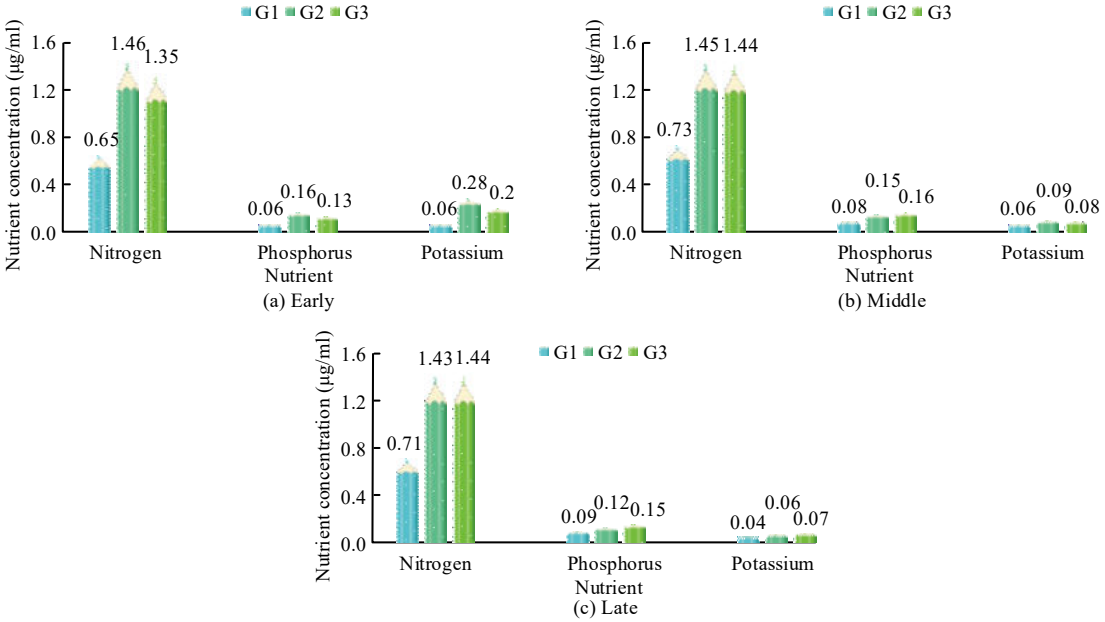


Fig. 10 - Changes in nutrient content of paddy field stem flowing water

Figure 10(a) displays the early drainage sampling. The nitrogen content of G1, G2, and G3 was 0.65, 1.46, and 1.35 μg/ml. The phosphorus content of G1, G2, and G3 was 0.06, 0.16, and 0.13 μg/ml. The potassium content of G1, G2, and G3 was 0.06, 0.28, and 0.20 μ g/ml. Figure 10(b) shows the mid-term drainage sampling.

The nitrogen content of G1, G2, and G3 was 0.73, 1.45, and 1.44 μg/ml, respectively. The phosphorus content of G1, G2, and G3 was 0.08, 0.15, and 0.16 μg/ml, respectively. The potassium content of G1, G2, and G3 was 0.06 μg/ml, 0.09 μg/ml, and 0.08 μ g/ml. Figure 10(c) shows the late drainage sampling. The nitrogen content of G1, G2, and G3 was 0.71, 1.43, and 1.44 μg/ml. The phosphorus content of G1, G2, and G3 was 0.09, 0.12, and 0.15 μg/ml, respectively. The potassium content of G1, G2, and G3 was 0.04, 0.06, and 0.07 μ g/ml.

Figure 11 illustrates the total amount of nutrient stem loss in paddy fields. Figure 11 (a) shows the cumulative loss of nitrogen, which was 1.79 kg/hm^2, 4.23 kg/hm^2, and 4.01 kg/hm^2 for G1, G2, and G3, respectively. Figure 11 (b) shows the cumulative loss of phosphorus, which was 0.18 kg/hm^2, 0.51 kg/hm^2, and 0.47 kg/hm^2 for G1, G2, and G3, respectively. Figure 11(c) shows the cumulative loss of potassium, which was 0.19 kg/hm^2, 0.59 kg/hm^2, and 0.41 kg/hm^2 for G1, G2, and G3, respectively. The findings demonstrated that nitrogen, phosphate, and potash losses in paddy fields were more likely to occur when fertilizer was applied, but the cumulative losses of these components in runoff water were effectively reduced by weight loss treatments. At the same fertilizer application rate, the cumulative loss in runoff from paddy field was reduced by MSDF treatment compared to manual fertilization.

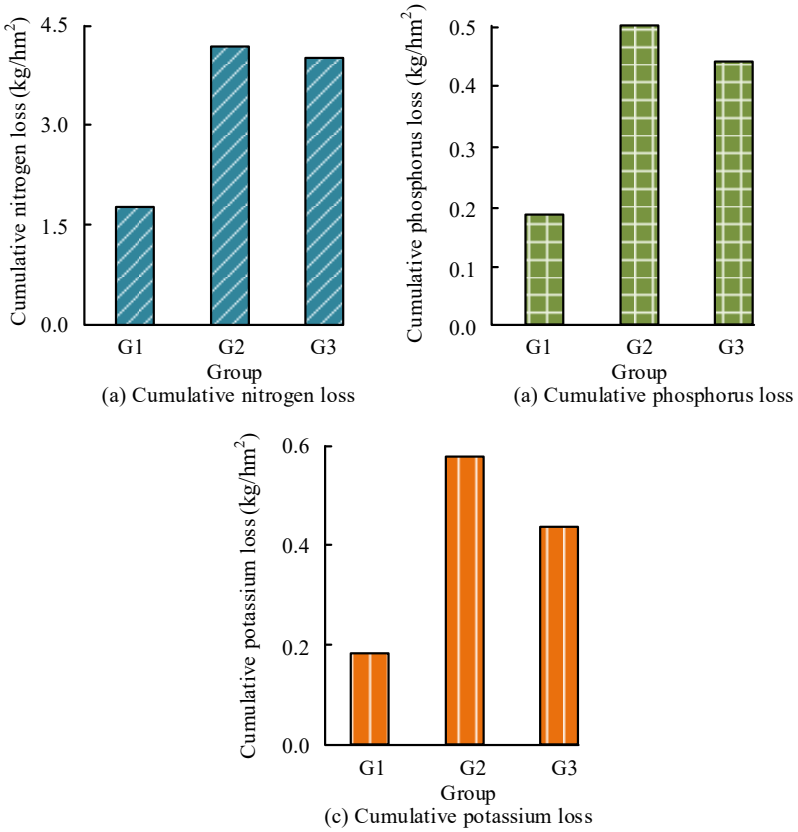


Fig. 11 - Accumulation of nutrient stem loss in paddy fields

CONCLUSIONS AND DISCUSSIONS

The study was conducted in a trial at Jiansanjiang Qixing Farm, Company 36, Jiamusi City, Heilongjiang Province. Nutrient changes in rice and fields were analyzed in combination with different fertilizer application methods and application rates. The outcomes indicated that the number of tillers was 311×104/hm^2 in G1, 502×104/hm^2 in G2, and 566×104/hm^2 in G3. Compared to G1, the rice LAI was improved by 2.39 in G2 and 3.12 for G3 at the tasseling stage. At the tasseling stage, the SPAD of rice leaves was 37.1, 40.9, 44.1, 43.3, 40.9, 40.1 for G1, G2, G3, G4, G5, and G6, respectively. At the maturity stage, G1, G2, G3, G4, and G5, G6 were 5.58 t/hm^2, 9.93 t/hm^2, 11.72 t/hm^2, 10.97 t/hm^2, 10.29 t/hm^2, and 9.11 t/hm^2, respectively. The cumulative loss of nitrogen in the paddy field of G1, G2, and G3 was 1.79 kg/hm^2, 4.23 kg/hm^2, and 4.01 kg/hm^2, respectively. Studies indicated that MSDF could significantly increase the number of stem tillers and plant height, increase the LAI, improve the chlorophyll content and photosynthetic capacity of rice, and create conditions for high yield and high quality. The MSDF treatment could effectively promote rice growth and improve nutrient absorption efficiency.

Compared with manual fertilization, MSDF significantly increased the nitrogen content of stems and leaves, and decreased the phosphorus and potassium content. It was found that the use of MSDF in paddy fields can effectively reduce ammonia volatilization and nutrient runoff losses. This can improve nitrogen utilization efficiency, which is important for environmental protection and sustainable agricultural development. Nevertheless, the study still had certain flaws and neglected to take into account how different rice cultivars affect nutrient uptake and loss. To improve fertilization methods, future research might examine how various rice cultivars and phases of growth affect nutrient uptake and loss.

ACKNOWLEDGEMENT

The research is supported by: The Innovation Project Grant Project of the Heilongjiang Academy of Agricultural Sciences, Breeding, Popularization and Industrial Application of New Medium-Late Maturing Rice Varieties with Excellent Eating Quality, (No. CX23ZD02); Project of the Heilongjiang Academy of Agricultural Sciences, The construction of cold-tolerant rice cDNA library and the mining of alkali stress-related genes, (No. CX23YQ15); Heilongjiang Province Key Research and Development Plan (Innovation Base), Northeast Branch of National Center of Technology Innovation for Saline-Alkali Tolerant Rice, (No. JD2023GJ04); National Technology System for Modern Agricultural Industry, Wuchang Integrated Test Station, (No. CARS-01-54).

REFERENCES

[1] Assogba, G. M., van de Ven, G. W., Rodenburg, J., Devkota, K. P., Dossou-Yovo, E. R., Giller, K. E. (2025). Tailoring fertilizer rates to catena positions improves nutrient use efficiency of rice in inland valleys of West Africa. *Field Crops Research*, Vol. 321, pp. 109679-109692.

[2] Bhadwal, S., Sharma, S. (2022). Selenium alleviates physiological traits, nutrient uptake and nitrogen metabolism in rice under arsenate stress. *Environmental Science and Pollution Research,* Vol. 29, pp. 70862-70881.

[3] Bihari, B., Singh, Y. K., Shambhavi, S., Mandal, J., Kumar, S., Kumar, R. (2022). Nutrient use efficiency indices of N, P, and K under rice-wheat cropping system in LTFE after 34th crop cycle. *Journal of Plant Nutrition,* Vol. 45, pp. 123-140.

[4] Chinthamu, N., Karukuri, M. (2023). Data Science and Applications. *Journal of Data Science and Intelligent Systems,* Vol. 1, pp. 83-91.

[5] Dhaliwal, S. S., Sharma, V., Shukla, A. K., Gupta, R. K., Verma, V., Kaur, M., Singh, P. (2023). Residual effect of organic and inorganic fertilizers on growth, yield and nutrient uptake in wheat under a basmati rice-wheat cropping system in North-Western India. *Agriculture,* Vol. 13, pp. 556-572.

[6] Dumitru, D. N., Marin, E., Gheorghe, G. V., Manea, D., Mateescu, M., Anghelache, D. N., Prisacariu, E., Harabagiu, A. (2024). Integration of EDEM by Altair simulations for efficient distribution of large and small seeds in agricultural systems of vineyards and fruit trees. *INMATEH-Agricultural Engineering*, Vol. 74, pp. 745-760.

[7] Găgeanu, I., Tăbăraşu, A. M., Persu, C., Gheorghe, G., Nițu, M., Cujbescu, D., Ionescu, A., Anghelache, D. (2024). Hydroponic vertical systems: enhancing climate resilience, water efficiency, and urban agriculture. *INMATEH-Agricultural Engineering*, Vol. 73, pp. 94-109.

[8] Gu, H., Wang, X., Zhang, M., Jing, W., Wu, H., Xiao, Z., Zhang, H. (2024). The response of roots and the rhizosphere environment to integrative cultivation practices in paddy rice (水稻根系和根圈环境对综合栽培措施的响应). *Journal of Integrative Agriculture,* Vol. 23, pp. 1879-1896, Jiangsu/China.

[9] Hou, K., Zhang, L., Liu, P., He, S., Rong, X., Peng, J., Han, Y. (2023). Side deep fertilization stabilizes double-cropping rice yield, increases N and P utilization, and reduces N and P losses (侧深施肥可稳定双季稻产量，提高氮磷利用率，减少氮磷损失). *Land,* Vol. 12, pp. 724-741, Hunan/China.

[10] Jat, D., Singh, K. P., Mathur, R. (2022). Optimization of tine spacing of seed drill for dual banding of fertilizer. *Journal of Scientific & Industrial Research,* Vol. 81, pp. 1073-1086.

[11] Jiaying, M. A., Tingting, C., Jie, L., Weimeng, F., Baohua, F., Guangyan, L., Guanfu, F. (2022). Functions of nitrogen, phosphorus and potassium in energy status and their influences on rice growth and development. *Rice Science,* Vol. 29, pp. 166-178.

[12] Le Van, C., Jens, R. J. (2023). Characteristics of local pump schemes reusing drainage water in a major rice-based irrigation and drainage area in the red river basin, Vietnam. *Water Conservation & Management (WCM),* Vol. 7, pp. 36-44.

[13] Lee, S. I., Ham, J. H., Baek, N., Kim, H. Y., Choi, W. J. (2025). Co-application of fly ash and zeolite increases N uptake but decreases P uptake and biomass of rice fertilized with fermented liquid manure. *Soil Science and Plant Nutritio*n, Vol. 71, pp. 269-281.

[14] Lin, L., Zheng, Z., Hua, T., Ashraf, U., Hamoud, Y. A., Xiangru, T., Shenggang, P. (2022). Nitrogen deep placement combined with straw mulch cultivation enhances physiological traits, grain yield and nitrogen use efficiency in mechanical pot-seedling transplanting rice (氮素深施与稻草覆盖栽培相结合可提高机械钵苗移栽水稻的生理性状、谷物产量和氮素利用效率). *Rice Science,* Vol. 29, pp. 89-100, Guangdong/China.

[15] Litardo, R. C. M., Bendezú, S. J. G., Zenteno, M. D. C., Pérez-Almeida, I. B., Parismoreno, L. L., García, E. D. L. (2022). Effect of mineral and organic amendments on rice growth and yield in saline soils. *Journal of the Saudi Society of Agricultural Sciences,* Vol. 21, pp. 29-37.

[16] Mohidem, N. A., Hashim, N., Shamsudin, R., Che Man, H. (2022). Rice for food security: Revisiting its production, diversity, rice milling process and nutrient content. *Agriculture,* Vol. 12, pp. 741-768

[17] Ren, Z. W., Kopittke, P. M., Zhao, F. J., Wang, P. (2023). Nutrient accumulation and transcriptome patterns during grain development in rice (水稻籽粒发育过程中的营养积累和转录组模式). *Journal of Experimental Botany,* Vol. 74, pp. 909-930, Jiangsu/China.

[18] Tang, M., Huang, Y., Zhang, W., Fu, T., Zeng, T., Huang, Y., Yang, X. (2022). Effects of microplastics on the mineral elements absorption and accumulation in hydroponic rice seedlings (Oryza sativa L.) (微塑料对水稻秧苗矿物质元素吸收和积累的影响). *Bulletin of Environmental Contamination and Toxicology,* Vol. 108, pp. 949-955, Chongqing/China.

[19] Urmi, T. A., Rahman, M. M., Islam, M. M., Islam, M. A., Jahan, N. A., Mia, M. A. B., Kalaji, H. M. (2022). Integrated nutrient management for rice yield, soil fertility, and carbon sequestration. *Plants,* Vol. 11, pp. 138-154.

[20] Wang, J., Wang, Z., Weng, W., Liu, Y., Fu, Z., Wang, J. (2022). Development status and trends in side deep fertilization of rice (水稻侧深施肥的发展现状与趋势). *Renewable Agriculture and Food Systems,* Vol. 37, pp. 550-575, Heilongjiang/China.

[21] Wang, Y., Li, Y., Xie, Y., Yang, X., He, Z., Tian, H., Pan, S. (2023). Effects of nitrogen fertilizer rate under deep placement on grain yield and nitrogen use efficiency in mechanical pot-seedling transplanting rice (氮肥深施率对机械钵育苗移栽水稻籽粒产量和氮素利用效率的影响). *Journal of Plant Growth Regulation,* Vol. 42, pp. 3100-3110, Guangdong/China.

[22] Wu, Q. X., Du, B., Jiang, S. C., Zhang, H. W., Zhu, J. Q. (2022). Side deep fertilizing of machine-transplanted rice to guarantee rice yield in conservation tillage (机插秧侧深施肥对保护性耕作水稻产量的保障作用). *Agriculture,* Vol. 12, pp. 528-539, Hubei/China.

PADDY RICE POROSITY PREDICTION BASED ON SNAKE ALGORITHM OPTIMIZED SUPPORT VECTOR REGRESSION

/

基于蛇算法优化支持向量回归的稻谷孔隙率预测

Zhi-Qi ZHANG[1,2], Lin WAN [*1,2], Gang CHE [*1,2], Hong-Chao WANG[1], Heng PAN[1], Shuo WANG[1]

[1]College of Engineering, Heilongjiang Bayi Agricultural University, Daqing / P.R.China

[2]Key Laboratory of Intelligent Agricultural Machinery Equipment in Heilongjiang Province, Daqing / P.R.China

Tel：+86-459-15245569595; E-mail: 895534729@qq.com

Corresponding author: Lin Wan

DOI: https://doi.org/10.35633/inmateh-76-61

Keywords: *paddy rice, image processing, snake algorithm, support vector regression*

ABSTRACT

During the paddy rice drying process, the uneven spatial distribution of pore spaces within drying chambers poses a significant challenge to accurate porosity characterization and results in inefficient energy utilization. To address this issue, this study proposes a porosity prediction model based on Support Vector Regression (SVR), aimed at effectively monitoring porosity variations during drying and enhancing energy efficiency. Using MATLAB based image processing, the porosity of paddy rice was quantitatively extracted. A Response Surface Methodology (RSM) was then employed to analyze the influence of geometric characteristics, moisture content, and grain bulk height on porosity during drying. To further improve the predictive performance, the SVR model was optimized using the Snake Optimizer (SO) algorithm. The resulting SO-SVR model was evaluated against porosity values derived from image analysis. Experimental results demonstrate that the SO-SVR model achieves high accuracy, with a Root Mean Square Error (RMSE) of 0.0095 and a coefficient of determination (R^2) of 0.9913. Compared to standard SVR and BP neural network models, the proposed model reduces RMSE by 0.0867 and 0.1663, and increases R^2 by 0.0449 and 0.1102, respectively. These findings indicate that the SO-SVR model provides a reliable and efficient approach for predicting paddy rice porosity during drying, offering valuable support for energy-saving and intelligent drying system design.

摘要

针对稻谷干燥过程中，干燥机内稻谷孔隙空间分布不均难以精准解析进而影响稻谷的干燥能耗的问题，建立一种基于支持向量回归（SVR）的稻谷孔隙率预测模型，高效检测稻谷干燥过程中孔隙率的变化，以达到节能效果。本文用 MATLAB 对稻谷图像处理得出稻谷孔隙率，用响应面（RSM）分析稻谷几何参数、含水率、粮堆厚度在稻谷干燥过程中对孔隙率的影响程度，利用蛇算法（SO）对支持向量回归（SVR）模型进行优化，建立稻谷孔隙率预测模型，并与基于图像处理后的稻谷孔隙率进行分析对比。结果表明： SO-SVR 模型的均方根误差（RMSE）为 0.0095、决定系数（R2）为 0.9913，相对于 SVR 和 BP 算法的 RMSE 降低了 0.0867 和 0.1663；R^2 提升了 0.0449 和 0.1102。实验数据表明该模型的预测误差较小，具有更高的准确性，可以有效预测稻谷在干燥过程的孔隙率。

INTRODUCTION

Grain security is a cornerstone of national economic stability and social development. Ensuring food security not only provides a solid foundation for stable economic development but also serves as a key factor in maintaining social stability and strengthening national security (*Fujimori et al., 2019*). According to data from the National Bureau of Statistics, China's total grain output reached 713 million tons in 2024, marking a 1.6% year-on-year increase, with rice accounting for 29.38% of the total grain production. To ensure rice quality, post-harvest high-moisture rice must undergo drying treatment. Porosity is one of the key parameters for understanding the drying process and energy consumption of rice (*Che et al., 2017*). During the drying process, porosity directly affects ventilation resistance, heat and moisture transfer coefficients, and the adjustment of drying process parameters (*Tong et al., 2023*), thereby influencing energy consumption, drying efficiency, and cost (*Oliveros et al., 2017*). Therefore, accurate detection of paddy rice porosity during drying is of great significance.

However, in practical production operations, there has been a lack of predictive research on paddy rice porosity, particularly in mixed-flow drying systems.

Currently, Moya conducted consolidation tests on paddy rice using a direct measurement method with an oedometer, and based on the experimental data, identified the relationship between porosity and vertical pressure (*Moya et al., 2013*). Martynenko through systematic experimental studies and theoretical analysis, established a relationship between moisture content and porosity, enabling the quantitative characterization of porous media structure parameters (*Martynenko et al., 2008*). Neethirajan employed computed tomography (CT) imaging technology to visualize the granular structures of wheat and pea seeds, calculating the spatial distribution of porosity and other features within the 3D images, including the degree of axial distortion and throat surface area (*Neethirajan et al., 2008*). Khalili proposed a mathematical model describing the relationship between porosity and bulk layer thickness based on experimental data (*Khalili et al., 2014*). Domestic scholars (*Chen et al., 2019)* have demonstrated, through both theoretical analysis and experimental validation, that porosity is influenced by the thickness of the material layer. Tang Fuyuan used an indirect gas displacement method to determine the porosity of paddy rice, analyzing density variations at different depths and establishing a mathematical model for porosity distribution in silo-stored rice (*Tang et al., 2017*). Cheno measured the permeability of two types of sandstone under varying confining pressures and determined their porosity using mercury intrusion porosimeters (MIP). By comparing the 3D geometrical structures of the pore spaces and flow-relevant pore characteristics, the study established a relationship between the differences in permeability and the porosity of the two sandstones (*Cheno et al., 2021*). Additionally, Ge Mengmeng combined the direct measurement method with liquid infiltration techniques to construct a quantitative model of porosity variation under different pressures. Their research further elucidated the relationship between bulk pressure and density, and analyzed the porosity and density distribution characteristics of rice stacks in flat warehouses (*Ge et al., 2021*). Despite significant progress made by researchers at home and abroad in the study of grain porosity, analytical methods currently in use often involve complex procedures and are time-intensive, thereby hindering their applicability and promotion in engineering practice.

In this study, a direct measurement method is employed to calculate paddy rice porosity based on surface images of rice stacks with varying height, using digital image processing techniques. The Design-Expert 13 software is utilized to analyze the influence of geometric parameters, moisture content, and stack height on porosity. Response Surface Methodology is further applied to evaluate and compare the variation in porosity under different influencing factors. A paddy rice porosity prediction model is then developed based on Support Vector Regression optimized by the Snake Algorithm. This model enables prediction of porosity during the rice drying process and provides key parameters for post-harvest drying and storage analysis of rice.

MATERIALS AND METHODS

Materials

The test material was the Songjing No. 16 rice variety, cultivated in Heilongjiang Province. After impurity removal, well-developed and uniformly shaped grains were selected for the experiment. The moisture content of the paddy rice was 2%, and the average grain length, based on measurements from 200 representative kernels, was 9.02 mm.

Mixed-Flow Paddy Drying Rice Experimental Apparatus

This study employed a self-developed bidirectional-ventilation mixed-flow paddy rice drying experimental platform. The overall structure of the mixed-flow dryer is illustrated in Fig. 1. Gravity-fed rice circulation is achieved through a free-flow feeding mechanism. Flow rate control valves are used to adjust the feeding speed, aligning it with the drying intensity to prevent uneven drying caused by excessively fast or slow grain flow. In the dryer, each drying unit comprises a layer of angular inlet ducts and a layer of angular outlet ducts, arranged in a vertically intersecting manner. The angular inlet ducts supply hot air from both sides, forming a mixed-flow drying pattern, while the outlet ducts vent the exhaust air unilaterally. This cross-layer configuration modifies the airflow path of paddy rice during drying, enabling effective balancing of wind pressure, air velocity, and temperature. Such a structural design improves the uniformity of the cyclic drying process.



Fig. 1 - Mixed-flow paddy rice drying experimental device

1. Mixed flow rice dryer; 2. Temperature and humidity sensor; 3. Air inlet pipeline; 4. Grain discharge motor; 5. Unloading device; 6. Control system cabinet; 7. Mixing pipeline; 8. Mixing device; 9. Hot air pipeline; 10. Electric heating control cabinet

The drying section process is shown in Fig. 2. In the drying operation, wet paddy rice is loaded into the dryer through the top inlet and gradually flows downward by gravity until the chamber is filled. The rice sequentially passes through the tempering-drying section, preheating-drying section, mixed-flow drying section, and discharge-drying section, initiating the cyclic drying process. Hot air ducts are connected on both sides of the drying sections. After setting the fan frequency and hot air temperature, heated air is supplied to the system via electric heaters and fans. A hot air mixing unit regulates the air temperature to ensure stable heat supply throughout the drying system.

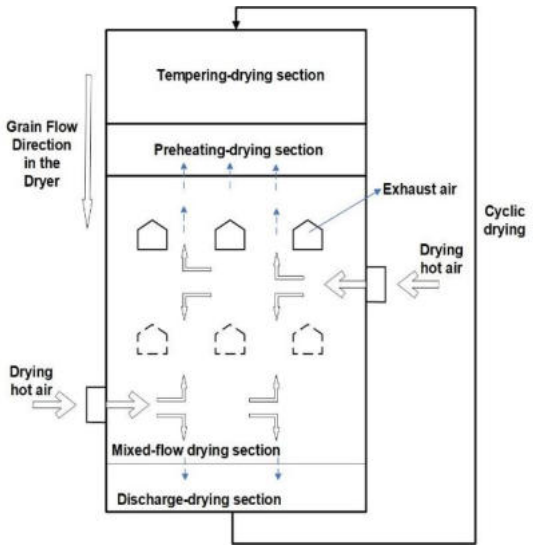


Fig. 2 - Mixed-Flow paddy rice drying process diagram

Additional Measurement Instruments

PM-8188New grain moisture tester; Canon EOS 5D Mark II; micrometer with a precision of 0.01 mm, and a measuring tape.

Data Collection Method

Paddy rice with an initial moisture content of 23.41% was dried to different target moisture levels. A moisture analyzer was used to measure the moisture content of each sample. Individual rice grains were randomly selected, and their lengths (L) were measured using a micrometer with a precision of 0.01 mm. For each group, the average length was calculated based on measurements of 100 intact grains. To simulate the pressure conditions within grain storage silos, incremental loads ranging from 0 to 200 kPa were applied to

the rice in the test container. The pressure applied to the grain bulk height was calculated using the hydrostatic pressure equation, as shown in Equation 1, this corresponded to adding 0-12 kg of rice incrementally.

A measuring tape was used to record the resulting grain pile height within the container. In total, 200 groups of data were collected, including measurements of moisture content, grain length, and grain bulk height, for use in subsequent analysis (*Prasad et al., 1973*).

$$P = \rho g h \tag{1}$$

where:

P is the pressure, [Pa];

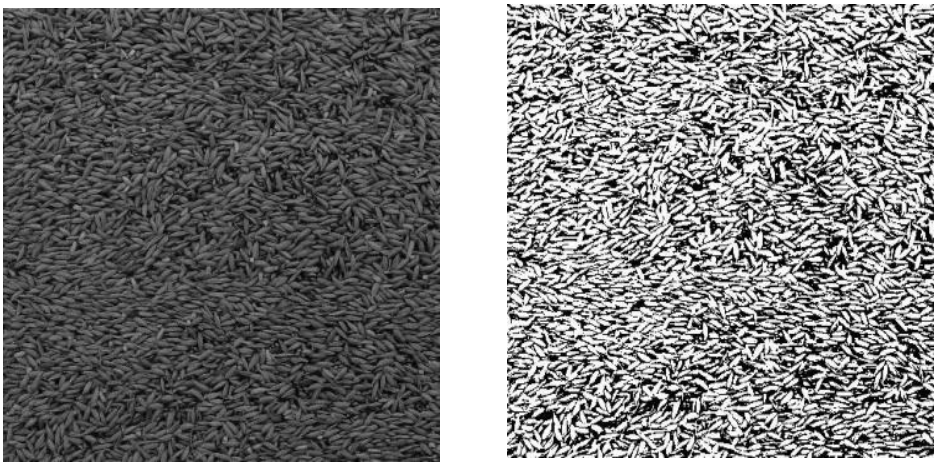
ρ is the density of paddy rice, [kg/m³];

g is the gravitational acceleration, [m/s²];

h is the grain bulk height, [m]

Porosity Measurement Method

To capture digital images of the grain bulk, a transparent glass test box was employed, featuring an embedded lid made of the same material. The internal dimensions of the box were 300 mm * 200 mm * 400 mm (length * width * height). The shortest dimension of the test container is 200 mm, which is over ten times greater than the average grain length of paddy rice (9.02 mm), thereby fully satisfying the spatial requirements for pressure testing (*Bian et al., 2021*). A Canon digital camera was used for image acquisition. Distortion correction was performed using the MathWorks calibration toolbox. For image segmentation, various thresholding algorithms were compared, and edge-based threshold segmentation was conducted using MATLAB to distinguish the target from the background, the grayscale image and the binarized image were obtained, as illustrated in Fig. 3. Morphological optimization was subsequently applied to the binarized image. Each grain was labeled based on the position of its pixel centroid, and the scaling factor of the imaging system was determined by correlating the pixel area to the actual physical area. Using this factor, the porosity of the paddy rice was calculated. To simulate pressure conditions within a rice silo, different weights of paddy rice were incrementally added to the box, and images were captured after each addition to determine the porosity under varying pressure levels.



a) The grayscale image *b) The binarized image*

Fig. 3 - The processed images of paddy rice

The porosity formula for paddy rice in their natural piled state is shown in Equation 2. The smaller the difference between the porosity value obtained through image processing and the one from the formula, the higher the accuracy, as illustrated in Fig. 4.

$$\varepsilon = \left(1 - \frac{\rho_b}{\rho_w}\right) \times 100\% \tag{2}$$

where:

ε - the porosity, [%];

ρ_b is the initial density of a paddy rice unit, [kg/m³];

ρ_w - the density of rice particles, [kg/m³]

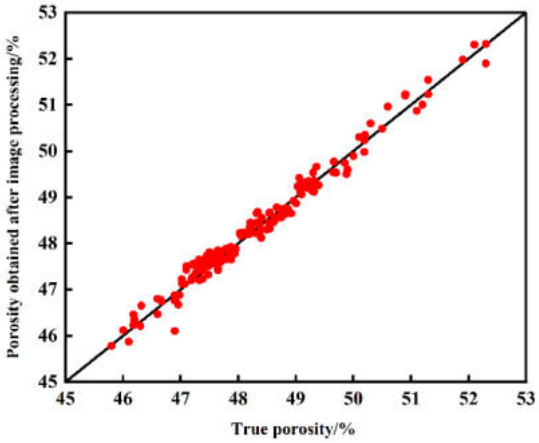


Fig. 4 - Fitting of porosity obtained after image processing to true values

Experimental Procedure

The rice drying experiment was conducted at the Intelligent Agricultural Machinery Equipment Laboratory of Heilongjiang Bayi Agricultural University. To simulate the actual conditions of rice after harvest, the paddy rice underwent moisture adjustment treatment, followed by sealed storage for a period of time and subsequent water spraying. After ensuring the rice absorbed enough moisture, the required rice samples for the experiment were obtained (*Chen et al., 2022*). First, the heat exchanger and fan were activated and allowed to stabilize before loading the rice. The drying process then began, with the dryer completing one cycle every 20 minutes based on real-time operating conditions. During both the early and late stages of the rice drying process, porosity measurements were taken at intervals of 20 minutes and 10 minutes, respectively, and compared with the predicted model. If the fit was satisfactory, the operating efficiency of the heat exchanger and fan was reduced to achieve energy savings. The experiment was then concluded.

Data Preprocessing

To mitigate the impact of differences between feature values on the prediction model, the $mapminmax$ function (*Liang et al., 2019*) was used to normalize the feature data, thereby ensuring the stability of the model's numerical values. The normalization formula is given by Equation 3.

$$y = \frac{(y_{max} - y_{min}) \times (x_{max} - x_{min})}{x_{max} - x_{min}} + y_{min} \quad (3)$$

where:

x_{max} is the maximum value in the original feature data;

x_{min} is the minimum value in the original feature data;

y_{max} is the maximum value after normalization, set to 1;

y_{min} is the minimum value after normalization, set to 0.

Orthogonal Experiment Design

The paddy rice moisture content, paddy rice grain length, and grain bulk height were selected as experimental factors, with paddy rice porosity set as the evaluation criterion. The experiment employed a three-factor, three-level quadratic regression orthogonal rotational combination design to analyze the effects of paddy rice moisture content, paddy rice grain length, and grain bulk height on paddy rice porosity and to construct a regression model. The factor level coding table is shown in Table 1.

Table 1

Encoding of orthogonal experimental factors

Serial Number	Encoding value	Paddy rice moisture content X_1 [%]	Paddy rice grain length X_2 [mm]	Grain bulk height X_3 [mm]
(+1)	+1	23.41	10.16	350
(0)	0	18.93	8.85	200
(−1)	−1	14.45	7.54	50

Development of the Prediction Model

SVR Model

The SVR model is trained using the training set $T= \{(x_1, y_1), \ldots, (x_n, y_n)\}$, they correspond to the input vector and output value of the sample, respectively. During the training process, SVR utilizes a nonlinear mapping $\phi(x)$ to map the training set from a low-dimensional space to a high-dimensional space (*Jin et al., 2024; Yang, 2023; Cui, 2023*). The expression of this process is shown in equation 4. A schematic diagram of the SVR prediction model is shown in Fig. 5.

$$f(x) = \omega\emptyset(x) + b \tag{4}$$

where: ω is the weight; b is the bias.

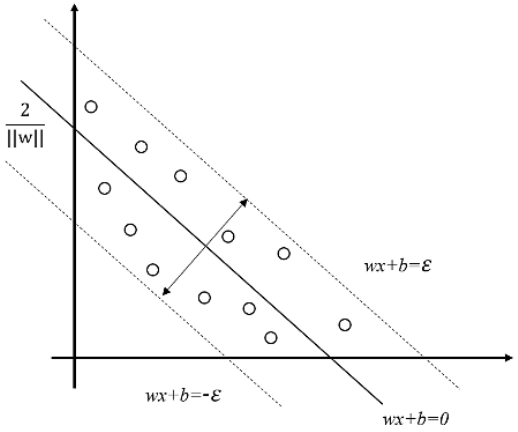


Fig. 5 - SVR prediction schematic diagram

The process of solving the SVR based on the principle of Structural Risk Minimization (SRM) can be represented as solving a constrained optimization problem, as shown in the following equation:

$$\min_{\omega,b} \frac{1}{2}||\omega||^2 + C\sum_{i=1}^{N}(\xi_i^{\Lambda} + \xi_i^{V}) \tag{5}$$

$$s.t. -(k + \xi_i^{V}) \le y_i - (\omega x_i + b) \le k + \xi_i^{\Lambda} \tag{6}$$

$$\xi_i^{\Lambda} \ge 0, \ i = 1,2,\cdots,N \tag{7}$$

$$\xi_i^{V} \ge 0, \ i = 1,2,\cdots,N \tag{8}$$

where:

C is the penalty parameter, which regulates the complexity of the sample regression model and the fitting accuracy;

ξ_i^{Λ} is the upper-bound slack variable;

ξ_i^{V} is the lower-bound slack variable;

k is the insensitive loss factor.

By introducing the Lagrange multiplier operator and the duality principle, the optimal Lagrange multiplier parameters $a^{\Lambda *}$ and a^{V*} are obtained through the Sequential Minimal Optimization (SMO) algorithm.

By incorporating the kernel function, the nonlinear mapping expression for the SVR is derived as:

$$f(x) = \omega\phi(x) + b = \sum_{i}^{N}(\alpha_i^{\Lambda *} - \alpha_i^{V*})K(x_i, x) \tag{9}$$

where: $K(x_i, x) = \phi(x_i)\phi(x)$ is the kernel function.

S0 Algorithm

Snake optimization, as a search strategy, effectively avoids getting trapped in local optima and exhibits a fast convergence rate when approaching the global optimum. The snake algorithm is a global optimization algorithm that simulates the combat and mating behaviors of snakes to achieve optimization. In the combat mode, male snakes compete to obtain the best female mate, while female snakes select the most suitable male for mating (*Su et al., 2022*). The specific process of the snake optimization algorithm is shown in Fig. 6.

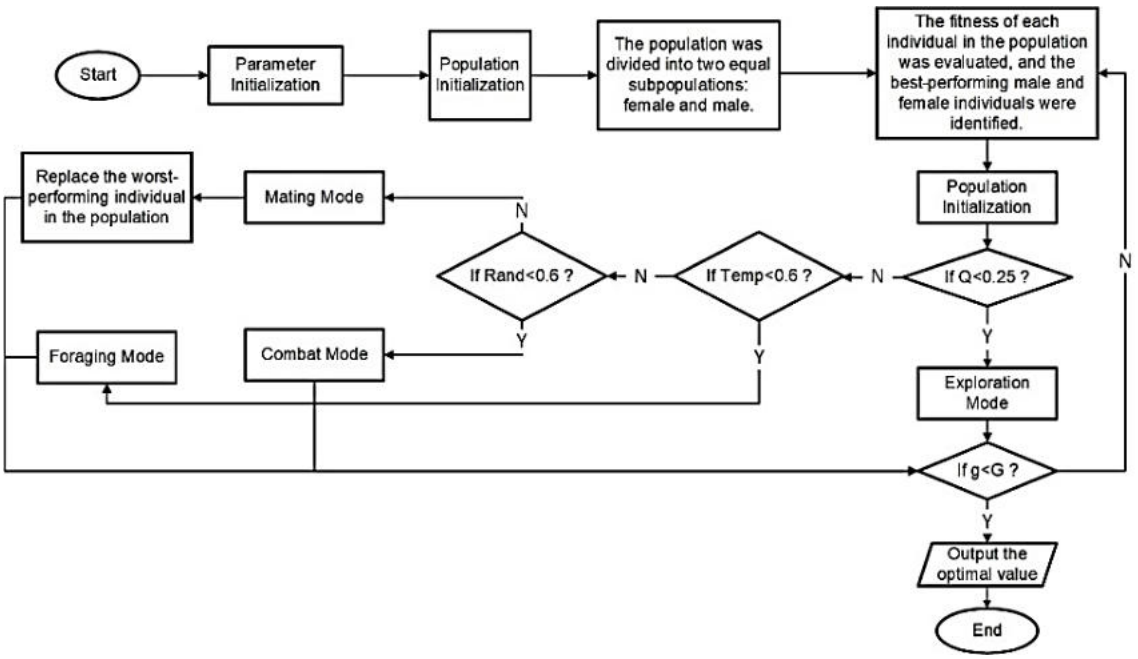


Fig. 6 - Snake algorithm optimization flowchart

Construction of the Paddy Rice Porosity Prediction Model:

The paddy rice moisture content, paddy rice grain length, and grain bulk height, which are three factors affecting porosity, are selected as input variables for the prediction model. The porosity of paddy rice serves as the output variable, and the SO-SVR model is constructed for predicting paddy rice porosity.

In the SVR model, the penalty parameter C and $gamma$ (the parameter of the radial basis function (*RBF*) kernel) are the key parameters influencing its prediction performance. The snake optimization algorithm generates N individuals randomly within the search space as the initial population for computation. The initial population is set to 100, with a maximum iteration count of 50 and a search range between [-1, 1]. The snake population X is divided into male snake group X_m and female snake group X_f. The fitness value of each snake individual is compared with its counterpart, and the individual with the lower fitness value is selected to form a new population.

During the optimization iterations, the parameter values of C and $gamma$ output in each iteration are input into the SVR model. The *Train* function is then called to calculate the fitness, and the output error is used as the fitness function, which is returned to the snake optimization for iterative optimization. This process continues until the fitness function converges.

In each iteration, the SO algorithm produces a new set of C and $gamma$ values. These new parameter combinations are used to train the SVR model, with the prediction error serving as an indicator to assess its performance. Based on the performance evaluation results, the combination of C and $gamma$ that provides the best performance for the SVR model is selected.

Model Accuracy Evaluation Metrics:

The coefficient of determination R^2 and the root mean square error (RMSE) are used to evaluate the accuracy of the neural network model (*Qiu et al., 2023*), as shown in Equations 9 and 10.

$$R^2 = \frac{(n\sum x_i \bullet y_i) - (\sum x_i \bullet \sum y_i)^2}{[n\sum x_i^2 - (\sum xi)^2 \bullet (n\sum y_i^2 - (\sum yi)^2)]} \quad (10)$$

$$RMSE = \sqrt{\frac{1}{n}\sum_{i=1}^{n}(y_i - x_i)^2} \quad (11)$$

where:

n is the number of prediction samples; y_i is the actual value; x_i is the predicted value.

RESULTS

Orthogonal experiment results and analysis

Table 2

Quadratic regression orthogonal rotation combination experiment and results

Number	Paddy rice moisture content X_1 [%]	Paddy rice grain length X_2 [mm]	Grain bulk height X_3 [mm]	Paddy rice porosity Y_1 [%]
1	-1	-1	0	48.37
2	1	-1	0	47.56
3	-1	1	0	48.55
4	1	1	0	47.88
5	-1	0	-1	49.32
6	1	0	-1	48.67
7	-1	0	1	46.91
8	1	0	1	46.18
9	0	-1	-1	49.17
10	0	1	-1	50.19
11	0	-1	1	47.19
12	0	1	1	47.35
13	0	0	0	48.12
14	0	0	0	47.96
15	0	0	0	47.93
16	0	0	0	47.94
17	0	0	0	47.92

The experimental results indicate that under the same conditions, the paddy rice moisture content, paddy rice grain length, and grain bulk height all have an impact on the paddy rice porosity. The analysis of the experimental results is shown in Table 3.

Table 3

Regression coefficient significance and ANOVA for paddy rice porosity model

Parameter	Paddy rice porosity [%]		
	Coefficient	F-value	P-value
Model	14.44	128.55	< 0.0001
X_1	1.02	81.92	< 0.0001
X_2	0.3528	28.27	0.0001
X_3	11.81	946.19	< 0.0001
$X_1 X_2$	0.0049	0.3926	0.5508
$X_1 X_3$	0.0016	0.1282	0.7309
$X_2 X_3$	0.1849	14.81	0.0063
X_1^2	0.3652	29.26	0.0010
X_2^2	0.7095	56.85	0.0001
X_3^2	0.0345	2.76	0.1404
Residual Sum of Squares		0.0874	
Pure Error Sum of Squares		0.0275	
Coefficient of Determination R^2		0.9940	
Adjusted R^2		0.9863	
Predicted R^2		0.9311	
C.V.%		0.2324	

The p-value of the model is less than 0.01, indicating that the regression model for paddy rice porosity is significant and statistically meaningful. The test result for the misfit terms is $p=0.1652$, which is not significant, demonstrating that the regression equation has a good fit and practical relevance. After removing the insignificant factors, the analysis of variance for porosity, shown in Table 3, presents the regression equation for porosity based on the factor coding:

$$Y_1 = 62.27 + 0.43X_1 - 3.97X_2 + 0.001X_3 - 0.001X_2X_3 - 0.01X_1^2 + 0.24X_2^2 \quad (12)$$

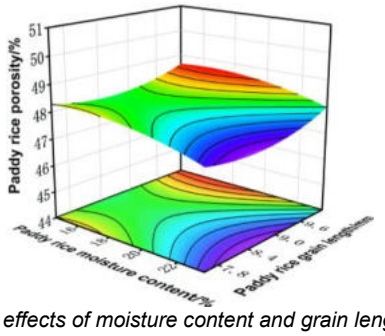
Response Surface Analysis

To further visualize and evaluate the influence of various factors on the response variable, Design-Expert 13 software was employed to generate response surface plots. These plots were used to investigate whether the interaction effects among paddy rice moisture content, paddy rice grain length, and grain bulk height lead to significant variations in the porosity of paddy rice.

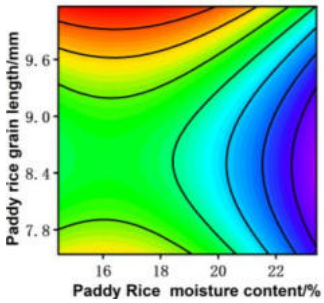
Fig. 7a illustrates the response surface depicting the interaction between paddy rice moisture content and grain length on paddy rice porosity, under the condition of a grain bulk height of 200 mm. As shown in the figure, porosity increases with grain length, suggesting that longer rice grains result in greater intergranular space within the bulk. In contrast, porosity decreases with increasing moisture content, indicating a negative correlation between moisture content and porosity.

Fig. 7b illustrates the response surface depicting the interaction between paddy rice moisture content and grain bulk height on paddy rice porosity, under the condition of a grain length of 8.85 mm. As shown in the figure, porosity decreases with increasing moisture content, indicating a negative correlation. Similarly, porosity also declines as grain bulk height increases, and the influence of grain bulk height on porosity is observed to be more pronounced than that of moisture content.

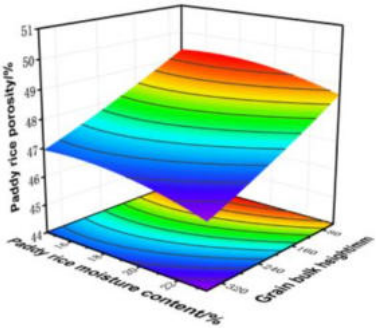
Fig. 7c illustrates the response surface depicting the interaction between paddy rice grain length and grain bulk height on paddy rice porosity, under the condition of a moisture content of 18.93%. As shown in the figure, porosity gradually decreases with increasing grain bulk height, when grain length is held constant. Moreover, the influence of grain bulk height on porosity is observed to be more significant than that of grain length.



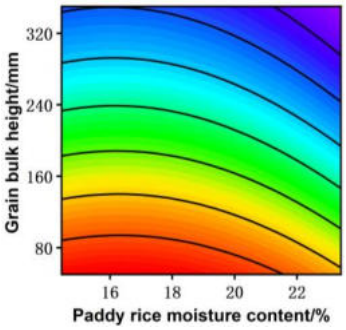
a) The effects of moisture content and grain length on the porosity of paddy rice



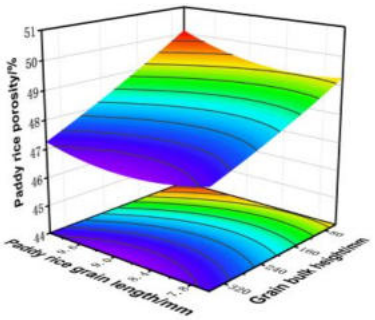
b) Contour plot showing the effects of moisture content and grain length on the porosity paddy rice



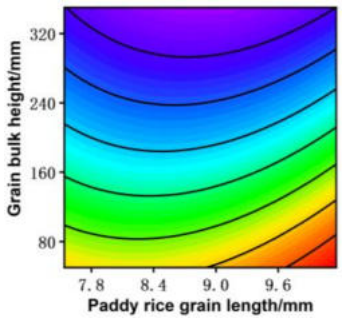
c) The effects of moisture content and grain bulk height on the porosity of paddy rice



d) Contour plot showing the effects of moisture content and grain bulk height on the porosity of paddy rice



e) The effects of grain length and grain bulk height on the porosity of paddy rice



f) Contour plot showing the effects of grain length and grain bulk height on the porosity of paddy rice

Fig. 7 - Effects of moisture content, grain length, and bulk height on paddy rice porosity

Prediction Model Results Analysis

A total of 200 data sets were selected as the sample size, with 80% used for training and 20% for testing. First, the training samples were divided into a training set and a testing set. The input and output samples were then normalized, and the parameters were initialized.

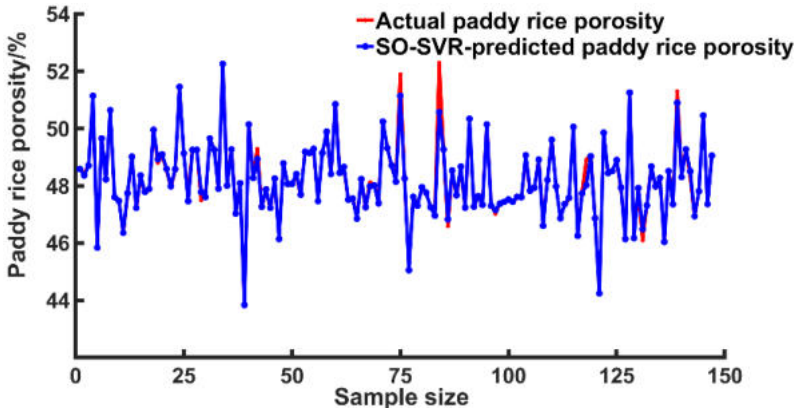
The comparison of rice porosity predicted by the three algorithms for both the training and testing sets is shown in Fig. 8. After training the model, the results were exported to the MATLAB workspace. The simulation results of the three prediction models are presented in Table 4. The R^2 of the SO-SVR algorithm is 0.9913, and the RMSE is 0.0095. Compared to the SVR and BP algorithms, the R^2 increased by 0.0449 and 0.1102, respectively, while the RMSE decreased by 0.0867 and 0.1663.

Table 4

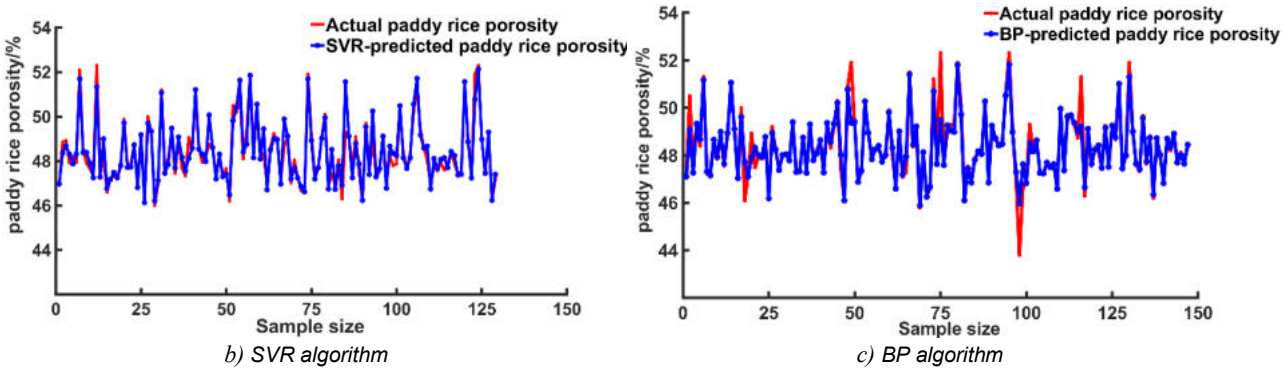
Simulation test results of three algorithms

Type	R^2	RMSE
SO-SVR	0.9913	0.0095
SVR	0.9464	0.0962
BP	0.8811	0.1758

Simulation experiments were conducted for the three prediction models, and the analysis shows that the SO-SVR algorithm demonstrates higher accuracy in predicting rice porosity compared to the SVR and BP algorithms.



a) SO-SVR algorithm



b) SVR algorithm *c) BP algorithm*

Fig. 8 - Comparison between actual paddy rice porosity and predicted values from three algorithms

Model Validation

The rice porosity data collected from the experiment were compared and analyzed against the rice porosity predictions made by the three algorithms. The maximum relative error and average relative error are shown in Table 5.

Table 5

Validation test results of three algorithms

Type	Maximum relative error [%]	Mean Relative Error [%]
SO-SVR	1.95	1.12
SVR	9.23	2.24
BP	14.62	4.36

The SO-SVR algorithm shows a reduction in the maximum relative error by 7.28% compared to SVR and by 12.67% compared to BP. The average relative error is also lower by 3.24% compared to SVR and by 1.12% compared to BP. The error between the rice porosity predicted by the SO-SVR model and the actual rice porosity is smaller, confirming the higher accuracy of the SO-SVR prediction model through experimental validation.

CONCLUSIONS

This study proposes a method for measuring the porosity of paddy rice based on image detection techniques. In the experiment, porosity was determined using an image-based approach, and the results were compared with those obtained from a theoretical method to verify the measurement accuracy. Furthermore, a paddy rice porosity prediction model based on SO-SVR was developed. The SO was used to identify the optimal combination of SVR hyperparameters C and $gamma$, which were then input into the SVR model to minimize prediction error. The optimal values of C and $gamma$ were found to be 4.00 and 3.99, respectively.

Simulation experiments for three rice porosity prediction models were conducted using MATLAB, with a total of 200 data sets selected as the sample size, 80% for training and 20% for testing. The coefficient of determination for SO-SVR was 0.9913, and the root mean square error was 0.0095. The iteration speed and prediction accuracy of the SO-SVR model were superior to those of the SVR and BP algorithms. The results of simulation experiments demonstrate that the SO-SVR-based model provides high accuracy in predicting paddy rice porosity.

Validation experiments were conducted for the three prediction models during the mixed flow drying process. The maximum relative error of the SO-SVR-based prediction model was 1.95%, and the average relative error was 1.12%, both of which were lower than those of the SVR and BP algorithms. The experimental results confirmed the accuracy of the SO-SVR-based rice porosity prediction model during the drying process, showing a good fit with the actual values and a small error. The predictive model proposed in this study enables estimation of paddy rice porosity and rapid assessment of drying degree throughout the drying process. It provides an effective means for monitoring drying performance, reducing energy waste, and optimizing drying operations, thereby improving overall energy efficiency.

ACKNOWLEDGEMENT

This project is supported by the Natural Science Foundation of Heilongjiang Province (LH2022E098).

REFERENCES

[1] Bian, H., Jiang, M. M., Liu, C. S., Yin, J. (2021). Study on the relationship between grain bulk pressure and porosity based on digital image technology (基于数字图像技术的粮堆压力与孔隙率关系研究). *Journal of Henan University of Technology (Natural Science Edition),* Vol.42(02), pp.107-111+120. Henan/China. DOI: 10.16433/j.1673-2383.2021.02.016.

[2] Che, G., Wu, C. S. (2017). Drying Technology and Intelligent Equipment for Typical Agricultural Products (典型农产品干燥技术与智能化装备). *Chemical Industry Press, Beijing, China.*

[3] Chen, Z. F., Che, G., Wan, L. (2022). Numerical simulation and experimental study of paddy rice four-way mixed-flow drying section (稻谷四向通风混流干燥段数值模拟与试验). *Transactions of the Chinese Society of Agricultural Engineering.* Vol.38(24), pp.237-247. Beijing/China.

[4] Chen, X., Cheng, X. D., Long, T. (2019). Study on porosity distribution of wheat bulk in a conical-hopper silo (带锥斗筒仓内小麦堆孔隙率分布研究). *Grain Science and Technology and Economy.* Vol.44(10), pp.48-52. Beijing/China.

[5] Cheon, D. S., Takahashi, M., Kim, T. (2021). Permeability differences based on three-dimensional geometrical information of void spaces. *Journal of Rock Mechanics and Geotechnical Engineering*, 13(2): 368–376.

[6] Cui, F. C., Mao, Z. C., Li, T. T., Li, J. R. (2023). Construction and application of a neural network-based shelf-life prediction model for fresh aquatic products (基于神经网络的生鲜水产品货架期预测模型的构建及应用). *Journal of Chinese Institute of Food Science and Technology.* Vol.23(11), pp.254–265. Beijing/China.

[7] Fujimori, S., Hasegawa, T., Krey, V., A multi-model assessment of food security implications of climate change mitigation[J]. *Nature Sustainability,* 2019, 2(5): 386 396.

[8] Ge, M. M., Chen, G. X., Liu, C. S., Zhang, H. W. (2021). Study on vertical pressure, porosity, and density of different grain types (不同粮种竖向压力孔隙度与密度研究). *Journal of Henan University of Technology (Natural Science Edition).* Vol.42(04), pp.89-95. Henan/China.

[9] Jin, H., Hu, Y. X., Ge, H. J., Hao, Z. P. (2024). Remaining useful life prediction of lithium-ion batteries based on improved GWO–SVR algorithm (基于改进 GWO–SVR 算法的锂电池剩余寿命预测). *Journal of Engineering Science.* Vol.46(03), pp.514–524. Beijing/China.

[10] Khalili, A., Morad, M. R., Matyka, M. (2014). Porosity variation below a fluid-porous interface. *Chemical Engineering Science,* 107: 311-316.

[11] Li, C. Y., Fang, Z. D., Mai, Z. W. (2014). Design and experiment of a porosity measurement device for bulk materials (散体物料孔隙度测定装置设计与试验). *Transactions of the Chinese Society for Agricultural Machinery.* Vol.45(10), pp.200–206. Beijing/China.

[12] Liang, Z. C., Guo, X. W., Song, Y. J., Ma, T. F., Wang, F. (2019). Optimization of polysaccharide extraction from Agaricus bisporus by response surface methodology and its in vitro antioxidant activity (响应面法优化双孢蘑菇多糖提取工艺及其体外抗氧化活性研究). *Journal of Agricultural Science and Technology.* Vol.21(08), pp.161–168. Beijing/China.

[13] Martynenko, A. (2008). The system of correlations between moisture, shrinkage, density, and porosity. *Drying Technology,* 26(12):1497-1500

[14] Moya, M., Aguado, P. J., Ayuga, F. (2013). Mechanical properties of some granular agricultural materials used in silo design. *International Agrophysics,* 27(2): 181-193.

[15] Neethirajan, S., Jayas, D. S., White, N. D. G., Zhang, H. (2008). Investigation of 3D geometry of bulk wheat and pea pores using X-ray computed tomography images. *Computers and Electronics in Agriculture,* 63(2):104–111.

[16] Oliveros, N. O., Hernández, J. A., Sierra-Espinosa, F. Z. (2017). Experimental study of dynamic porosity and its effects on simulation of the coffee beans roasting. *Journal of Food Engineering,* 199: 100-112.

[17] Prasad, S., Gupta, C.P., Behavior of paddy grains under quasi-static compressive loading[J]. *Transactions of the ASAE*, 16(2):328-330

[18] Qiu, J. D., Wang, T. X., Wan, F. X. (2023). Moisture content prediction of shiitake mushroom during vacuum far-infrared radiation drying based on improved BP neural network (基于改进 BP 神经网络的香菇真空远红外辐射干燥含水率预测). *Forestry Machinery & Woodworking Equipment.* Vol. 51(10), pp. 32-38. Beijing/China.

[19] Su, Z.Y. (2022). *Research on intelligent control system for circulating grain dryer (循环式粮食干燥机智能控制系统的研究).* Master's thesis, South China Agricultural University. Guangzhou/China.

[20] Tang, F. Y., Xu, Q., Cheng, X. D. (2017). Study on porosity distribution of paddy rice in silo (筒仓中稻谷的空隙度分布研究). *Journal of the Chinese Cereals and Oils Association.* Vol.32 (12), pp. 110–116. Beijing / China.

[21] Tong, J. J., Li, C. Y., Liu, M. H. (2023). Design and experiment of a porosity detection device for the flowing layer of paddy rice (稻谷流动层孔隙率检测装置设计与试验). *Journal of Chinese Agricultural Mechanization.* Vol. 44(11), pp. 26-31. Beijing/China. DOI: 10.13733/j.jcam.issn.2095-5553.2023.11.005.

[22] Yang, Y., Liu, J. Y., Chen, T. M. (2023). Short-term natural gas load forecasting based on the PSO-SVR model (基于 PSO-SVR 模型的短期天然气负荷预测). *Science Technology and Engineering.* Vol.23(35), pp.15210-15216. Beijing/China.

DEVELOPMENT AND EVALUATION OF AN ENHANCED SMALL-SCALE HYDROPONIC SYSTEM FOR INDOOR SEEDLING PRODUCTION
/
РАЗРАБОТВАНЕ И ОЦЕНКА НА ПОДОБРЕНА МАЛКА ХИДРОПОННА СИСТЕМА ЗА ПРОИЗВОДСТВО НА РАЗСАД НА ЗАКРИТО

Neiko V. NIKOLOV[1)], Atanas Z. ATANASOV*[1)] and Boris I. EVSTATIEV[2)]

[1)] Department of Agricultural Machinery, Agrarian and Industrial Faculty, University of Ruse "Angel Kanchev", 70017 Ruse, / BULGARIA

[2)] Department of Automatics and Electronics, Faculty of Electrical Engineering, Electronics and Automation, University of Ruse "Angel Kanchev", 7017 Ruse / BULGARIA

Tel: +359 885 497 406; E-mail: aatanasov@uni-ruse.bg

DOI: https://doi.org/10.35633/inmateh-76-62

Keywords: *hydroponic; IoT-based cultivation; indoor seedling production; low-cost smart farming*

ABSTRACT

This study presents the development and evaluation of an enhanced, modular, IoT-based hydroponic system for indoor seedling production. Designed to be low-cost and scalable, the system integrates automated lighting, irrigation, and environmental monitoring with cloud-based control. Its performance was validated using two tomato varieties, achieving 94–96% germination without added nutrient solution. A cost-benefit analysis indicated a payback period of under two years. While promising, the system has not yet been tested with other plant species, substrates, or nutrient solutions. Future research will focus on these variables to assess broader applicability and optimize performance.

РЕЗЮМЕ

Това проучване представя разработването и оценката на подобрена, модулна, базирана на интернет на нещата хидропонна система за производство на разсад на закрито. Проектирана да бъде нискобюджетна и мащабируема, системата интегрира автоматизирано осветление, напояване и мониторинг на околната среда с облачен контрол. Нейната производителност е валидирана с помощта на два сорта домати, постигайки 94–96% кълняемост без добавен хранителен разтвор. Анализът на разходите и ползите показва период на възвръщаемост под две години. Макар и обещаваща, системата все още не е тествана с други растителни видове, субстрати или хранителни разтвори. Бъдещите изследвания ще се фокусират върху тези променливи, за да се оцени по-широката приложимост и да се оптимизира производителността.

INTRODUCTION

One of the most pressing challenges for modern agriculture is ensuring food security for a rapidly growing global population. According to the *United Nations (2022)*, the world population is projected to exceed 10 billion by 2100, placing significant pressure on agricultural systems. This challenge is exacerbated by changing climatic conditions and limited arable land availability (*Rosenzweig and Tubiello, 1996; NOAA, n.d.; Peters et al., 1971; Wing et al., 2021; IPCC, 2021*).

Simultaneously, intensive agricultural practices are degrading soil quality and increasing the risk of contaminants entering food crops, with potential health consequences (*Alengebawy et al., 2021; Adil et al., 2023; Hossain et al., 2022*). Urbanization further compounds these issues, reducing the agricultural workforce and complicating food distribution networks (*United Nations, 2018*).

Given these combined pressures, new sustainable and space-efficient food production systems are required. Vegetable cultivation, particularly in urban settings, faces rising costs and declining feasibility due to climate variability and land limitations (*Hartwell et al., 2024; Rockström and Sukhdev, n.d.*). Urban agriculture solutions such as hydroponics and vertical farming have emerged as promising alternatives, offering optimized space utilization and resource efficiency (*Eigenbrod and Gruda, 2015*).

Hydroponic cultivation enables continuous, high-density vegetable production independent of soil and outdoor conditions. This method also facilitates automation and reduces reliance on manual labor (*van Delden et al., 2021; Cardoso et al., 2018; Alam et al., 2023; Ma et al., 2023; Chadwick et al., 2023*).

Recent advances integrate Internet of Things (IoT), computer vision, and mobile technologies to improve monitoring and control in hydroponic systems (*Nikolov et al., 2023; Hanafi et al., 2025; Duangpakdee*

and Thananta, 2024; Perara et al., 2024; Yessenamanova et al., 2023). Smart hydroponic systems designed for home or urban use have demonstrated the potential to enhance yield, water efficiency, and user accessibility (*Kushawaha et al., 2024; Stevens et al., 2024; Kim et al., 2024*). Examples include modular towers, intercropping setups, and crop-specific nutrient optimization (*Patel et al., 2004; Maucieri et al., 2017; Woznicki et al., 2021; Pieters et al., 2024; Elmulthum et al., 2023; Gutiérrez-Chávez et al., 2025; Luthuli et al., 2024; Ulas et al., 2024*).

Despite these innovations, many small-scale hydroponic systems remain either oversimplified or prohibitively expensive, lacking adaptability or full automation. Existing home solutions often fail to deliver adequate productivity or user control, while industrial systems are unsuitable for domestic use due to complexity and scale (*Khadijah et al., 2024; Hostalrich et al., 2022; Tatas et al., 2022; Lakshmiprabha and Govindaraju, 2019; Li et al., 2018*).

To address this gap, the present study aims to design and develop an enhanced version of a small, adaptive, high-tech hydroponic system suited for growing seedlings and vegetables in domestic environments. The system is modular, low-cost, and constructed from readily available components. It incorporates automated lighting, climate, irrigation control, cloud-based data logging, and video monitoring, offering users remote access and real-time adjustments.

It is anticipated that this system will provide an affordable and sustainable option for home-based food production, particularly in urban environments. The modular structure allows independent operation of units, enabling diverse crop cultivation. The present study seeks to validate the system's functionality, productivity, and economic viability through controlled experiments using tomato seedlings.

By bringing forward the research objective and clearly outlining the novel aspects of the developed system—including its affordability, modularity, and full IoT integration—this study contributes a practical solution to the challenges of small-scale urban agriculture.

MATERIALS AND METHODS

2.1. Architecture of the Hydroponic System

In this study, a hydroponic system was developed, whose architecture is summarized in Figure 1. The general management of all periphery is implemented by the control system, which operates according to predefined rules and assignments that were preliminary set by an operator. The control system receives feedback about its actions from several systems.

Microclimate monitoring system – collects data about the temperature and relative humidity of air inside the hydroponic system.

Water monitoring system – includes pH, electric conductivity (EC), and temperature sensors, used to monitor the key parameters of the water substrate.

Video monitoring system – provides a live stream so that the operator can change the system's operating parameters based not only on the abovementioned sensors but also on remote visual observations.

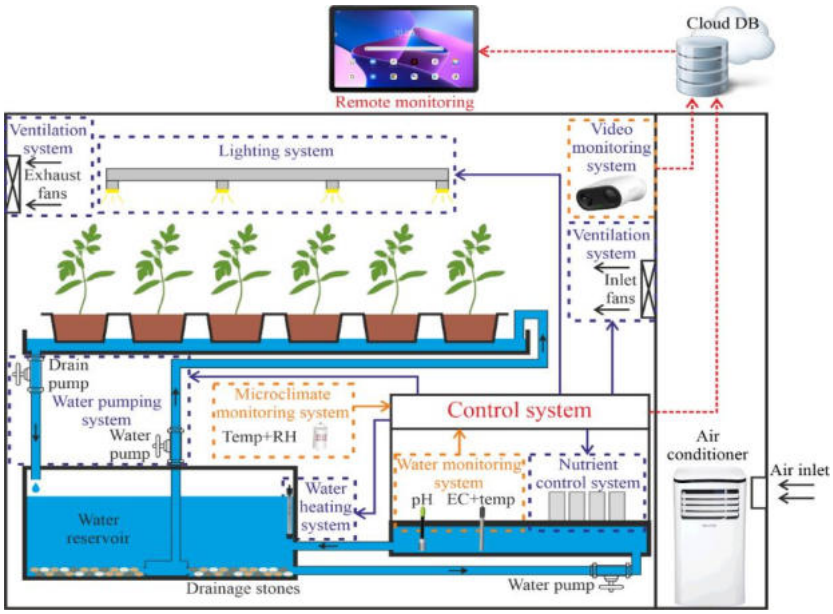


Fig. 1 - Architecture of the developed hydroponic system

The control system ensures the hydroponic system operates properly using several actuator subsystems:

a) Nutrient control systems – responsible for maintaining the fertilizer parameters following the operator-set requirements.
b) Water heating system – used to keep the water substrate temperature within acceptable boundaries.
c) Water pumping system – pumps the water through the different components of the hydroponic installation and includes at least three pumps: the first one is responsible for pushing the water through the nutrient system; the second one transfers the water from the reservoir to the plants; and the third one drains the water back to the reservoir. Furthermore, the water goes through drainage stones to ensure additional cleaning.
d) Lighting system – provides the plants with the necessary imitation of solar energy.
e) Ventilation system – used to replace the air inside the hydroponic installation and includes several parts:
   - an air conditioner is installed in a separate chamber of the system. It makes sure the air parameters in the chamber correspond to the necessary agro-technical requirements;
   - inlet fans for suctioning in the preliminary heated/cooled air from the air conditioner inside the chamber with the plants.;
   - exhaust fans – used to remove air from the plants' chamber.

All collected data, as well as the current states of all actuators, are stored in a remote cloud-based database and can be observed by an operator via a tablet device with the appropriate application installed. Naturally, the live stream from the video monitoring system is also accessible online.

To support a clearer understanding of the system architecture and the interconnections between sensors, actuators, and control elements, Table 1 summarizes the key components of the developed hydroponic system and their primary functions.

Table 1

Key components of the hydroponic system and their functions

System / Component	Function
Control Unit (NIDO ONE)	Central controller; manages irrigation, lighting, climate control, and data collection.
Microclimate Monitoring System	Measures air temperature and humidity; provides real-time data for environmental control.
Water Monitoring System	Monitors pH, EC, and temperature of the nutrient solution.
Video Monitoring System (WiFi Camera)	Enables visual inspection and remote system supervision.
Lighting System (Valoya LED L28)	Provides artificial light (16h/day); ensures proper photoperiod for seedling growth.
Irrigation System (GMAX Water Pump)	Delivers nutrient solution to trays; ensures even distribution across all levels.
Drainage System (Giant Drainage Pumps)	Removes excess water; recirculates it to the reservoir; ensures efficient water use.
Nutrient Control System	Maintains optimal concentration and composition of the nutrient solution.
Water Heating System (Water Master Heater)	Maintains optimal root zone temperature for nutrient uptake.
Aeration System (BOYU Pump & Air Stone)	Oxygenates nutrient solution to support root respiration and prevent pathogens.
Ventilation System (Blauberg Fans)	Provides fresh air; maintains uniform microclimate on all levels.
Air Conditioning Unit (AEG Comfort)	Controls air temperature; integrated into a separate chamber for optimal air handling.
Exhaust Fans (DF Extractor)	Removes warm/moist air; prevents condensation and maintains air quality.
Cloud Database & Tablet App	Stores sensor/actuator data; allows remote monitoring and control via app interface.
Cultivation Trays (Danish Trays)	Hold the plants; optimized size for productivity and ease of maintenance.

2.2. Hardware Implementation of the Hydroponic System

The improved version of our multifunctional small-scale hydroponic system was developed to address the constructive and technological shortcomings identified in the prototype small-scale hydroponic system for indoor sustainable farming of leafy vegetables, which was proposed in *Nikolov et al. (2023*). The general scheme of the improved hydroponic system is presented in Figure 2. Its key components are integrated into a structurally optimized external frame, which consists of three metal racks. Each rack includes supporting rails, measuring 1400 mm in length, on which trays for crop cultivation are arranged across three levels. A key improvement in the upgraded system is the increased tray size. The previous trays, measuring 600 mm in length and 400 mm in width (*Nikolov et al., 2023*), were replaced with new Danish trays (manufacturer: Danish Trays, China) with dimensions of 1100 mm in length and 630 mm in width. This modification enhanced the system's productivity by enabling the simultaneous distribution of nutrient solutions to plants at all levels, resulting in a simplified design and easier maintenance during operation.

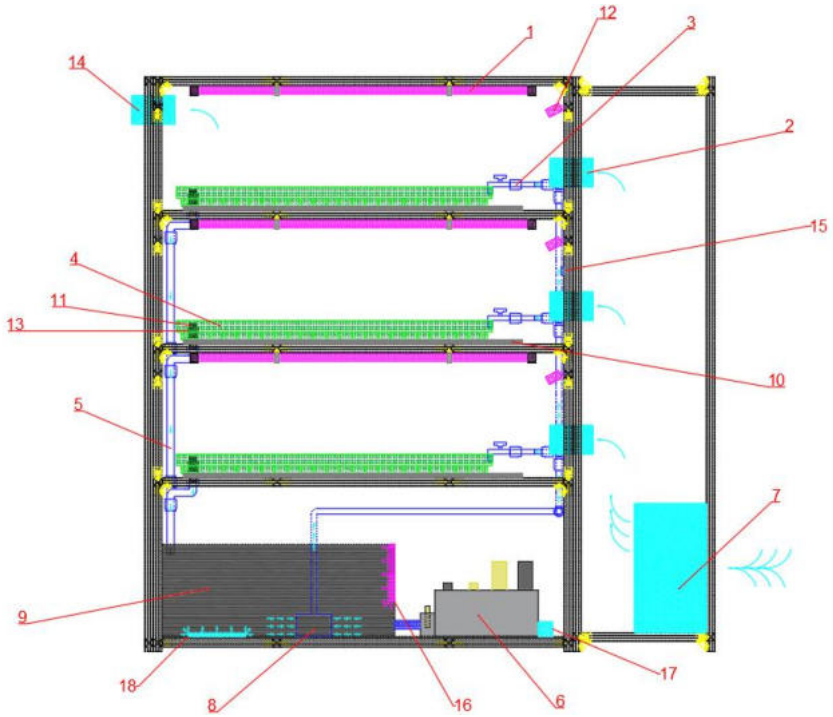


Fig. 2 - Scheme of the improved version of the multifunctional small-scale hydroponic system:
1) Full Spectrum led growing lights for vertical farming; 2) Inlet fans; 3) Irrigation system; 4) Growing trays; 5) Drainage system; 6) Computer NIDO ONE; 7) Mobile air conditioner; 8) Water pump; 9) Nutrient solution tank; 10) Plate for supporting and leveling the tray; 11) Drain head; 12) Surveillance camera; 13) Drainage pump; 14) Exhaust fan; 15) Temperature and humidity sensor; 16) Heater; 17) Air pump; 18) Air stone.

The nutrient solution is supplied to the trays by a GMAX Model Q400122 pressure water pump (manufacturer: GMAX Bulgaria) with a maximum flow rate of 9 m³/h, a maximum head of 8 m, and an installed power of 0.4 kW. A significant advantage of this pump is its ability to ensure uniform nutrient distribution across all levels of the system. Additionally, its operating parameters allow for future expansion of the prototype without requiring a more powerful pump. The lighting system is facilitated by LED lights from the Finnish company Valoya Ltd (Helsinki, Finland), specifically the Model L28, which has a power rating of 28 W and features the AP67, AP673L, G2, and NS12 spectra. These lights are positioned at 318 mm above each tray containing the cultivated plants. Artificial lighting was implemented for a specific photoperiod of 16 hours per day to simulate optimal day length conditions for seedling development.

An innovative feature of the constructed small-scale hydroponic system is the installation of three drainage pumps manufactured by Giant Electric Tech Inc. (Shenzhen, China) on each level of the system. These pumps have the following specifications: operating voltage of DC 6-12 V (maximum 1 A), IP68 grade, a maximum water column height of 3 m, a maximum static flow rate of 240 l/h, and dimensions of 54.4 mm in length, 52 mm in width, and 40.8 mm in height. Both the inlet and outlet have an outer diameter of 8.5 mm. These drainage pumps facilitate the remote and simultaneous drainage of all three levels.

Another novel element in the improved hydroponic system is the addition of three axial fans manufactured by Blauberg Ventilatoren GmbH (München, Germany) to supply fresh air to each level. Each fan has a capacity of 105 m³/h.

Additionally, the aeration system includes a BOYU Air Pump S-1000, which has a capacity of 252 l/h, operates at 3 W, and generates a pressure greater than 0.014 MPa. The outlet diameter is 1 x 4 mm, and it is equipped with a round ceramic air stone with a diameter of 200 mm manufactured by Guangdong BOYU Group Co., Ltd. (Chaozhou, Guangdong, China).

The primary purpose of the added BOYU Air Pump and Volume Air Round Ceramic Air Stone is to enrich the nutrient solution with oxygen, thereby supporting active root respiration in the plants and reducing the risk of mold and pathogen development. The exhaust air from the system is removed via exhaust ventilation, using a DF Extractor with a capacity of 350 m³/h, manufactured by Secret Jardin (Manage, Belgium). The airflow is heated by a mobile air conditioner model AEG Comfort 6000 BTU 9000, manufactured by AEG (Berlin, Germany). To optimize nutrient solution assimilation by the plant root system and maintain the solution at an optimal temperature, a Calentador Water Master heater (100W), manufactured by Guangzhou City Werierma Electrical Co., Ltd. (Guangzhou, Guangdong, China), was added inside the tank of the improved hydroponic system. For remote monitoring and control of plant vegetation at each level of the system, WiFi cameras, model IMOU Cell Go, with a microSD slot for storing video data up to 128GB, were installed. These cameras are manufactured by Hangzhou Huacheng Network Technology Co., Ltd. (Hangzhou, China). The air temperature and humidity monitoring is conducted using a combined sensor, manufactured by Nido S.r.l. (Carpineti, Italy).

The automation process relies on the NIDO ONE hydroponic controller system, manufactured by the Italian company Nido S.R.L. (Carpineti, Italy). The NIDO ONE controls the automatic regulation of nutrient solutions in hydroponic systems and manages climatic parameters in indoor cultivation environments. The NIDO control unit is also responsible for manipulating the lighting system via the NIDO Plug. Cloud and IoT technologies enable remote plant monitoring and facilitate the management of individual measurement parameters.

Nutrient solution monitoring is conducted using two types of sensors. The pH sensor measures acidity within a range of 4 to 10, with a resolution of 0.01 pH and an accuracy of 0.1 pH. The EC sensor measures electrical conductivity (EC) within a range of 0 to 5.0 mS/cm, with a resolution of 0.01 mS/cm and an accuracy of 0.1 mS/cm. Additionally, the EC sensor has an integrated temperature sensor used for EC/TDS temperature compensation.

The following main dimensions of the hydroponic system could be mentioned:

- Main chamber (where the seedlings are positioned): 2000 mm height, 1400 mm width, and 700 mm depth;
- Air conditioning chamber (where the air conditioner is kept): 2000 mm height, 435 mm width, and 700 mm depth;
- Distance between the lighting systems and the soil surface: 318 mm.

The assembly of the hydroponic system followed a logical sequence that ensured proper integration of all subsystems. The process included the construction of the supporting metal frame, installation of lighting, trays, irrigation and drainage systems, sensors, ventilation and air conditioning units, as well as the NIDO ONE control unit. The design emphasized modularity and ease of maintenance, enabling future upgrades and expansion.

2.3. Verification of the Functional Suitability of the System and Organization of the Experimental Investigations

To establish the functional suitability of the improved version of the designed system, experimental studies were conducted involving the cultivation of seedlings from two tomato varieties commonly used in Bulgaria: Florida F1 and Aleno Surtse. No nutrient solution was used during the seedling cultivation. Before the start of the experiment, the system was filled with 150 liters of clean spring water obtained from a local water source. Each tray contained 7 liters of water.

The sowing of seeds for all tomato varieties was carried out in nutrient cubes made from organic matter, with integrated fertilizer manufactured by HGA International B.V.- Eazy Plug (HJ Goirle, The Netherlands). The manufacturer did not disclose the specific ingredients of the nutrient component due to proprietary reasons. The nutrients present in the cubes are sufficient to support seedling growth for 15 days. For longer growing periods, it is necessary to replace the irrigation water with a nutrient solution, tailored to the specific needs of the cultivated crop.

The experiment took place from 01.08.2024 to 14.08.2024 and involved testing the system's performance with two tomato varieties - *Florida F1* and *Aleno Surtse*. Each variety was placed in a separate tray on a distinct level of the system.

Before initiating the experiment, the system was prepared by filling the water tank and checking all major components—irrigation, drainage, lighting, ventilation, sensors, and internet connectivity. Once verified, the trays were loaded with seeded nutrient cubes, and the automated control program was configured. The irrigation-drainage technological program for seedling cultivation was then launched. The irrigation-drainage technological protocol for seedling cultivation was established based on preliminary assessments of the substrate's physical properties, particularly its water retention capacity and drainage behavior (*Raviv et al., 2004*). The program parameters were defined to ensure optimal moisture conditions for seedling development under controlled environment cultivation. In this protocol, trays containing nutrient cubes are filled with water for 5 minutes to achieve field capacity without oversaturation. The timing was set based on the substrate's water absorption kinetics, ensuring sufficient hydration without waterlogging. After irrigation, trays are drained for 5 minutes to eliminate excess water, prevent hypoxic conditions, and enhance water-use efficiency (*Jones, 2013*). The collected surplus water is recirculated to promote resource conservation. Irrigation and drainage cycles are performed daily, with a total duration of 10 minutes. The protocol was uniformly applied to both tomato varieties to assess the functional suitability and adaptability of the constructed hydroponic system for varieties and species with differing vegetative requirements.

A total of 450 seed pots were used per variety. The reported germination percentages are based on this fixed number and correspond to the actual number of seedlings that emerged.

The selection of tomato seedlings (*Florida F1* and *Aleno Surtse*) as the test crop in this study was not intended for the production of fruiting plants, but rather to evaluate the functional suitability of the hydroponic system for seedling cultivation. Tomato seedlings were chosen due to their relatively high sensitivity to environmental conditions and nutritional requirements during early growth stages, making them a suitable model for assessing the system's performance, flexibility, and reliability. While leafy vegetables such as lettuce or spinach are more commonly used in hydroponic cultivation, tomatoes were intentionally selected to demonstrate the versatility of the system and its potential applicability to a broader range of crops in controlled environment agriculture.

Both tomato varieties used in the experiment were certified commercial seeds obtained from reputable suppliers. The germination degree was not independently measured before the experiment, as the manufacturer guarantees a germination rate exceeding 95% following international seed certification standards.

Throughout the 14-day test period, no functional faults or interruptions were observed. All components of the system—including pumps, aeration devices, lighting, and environmental sensors—operated autonomously and continuously under the control of the NIDO ONE unit. The modular structure of the system allowed for easy access to each component, and no maintenance interventions were required during the experimental phase. These results support the system's operational reliability for domestic or small-scale seedling production.

RESULTS

3.1. Experimental Measurements

After the initial checks and preparation of the system for operation, the cubes with the sown seeds were placed in the constructed improved small-scale hydroponic system Figure 3.



(a) (b)

Fig. 3 - Different views of the implemented small-scale hydroponic system for indoor vegetable growing

The measured germination rates (94–96%) reflect the effectiveness of the system in maintaining suitable microclimatic and water conditions during the seedling phase. Temperature and humidity variations, shown in Figures 4–6, align with the expected biological response of tomato seedlings under controlled cultivation and were obtained from the NIDOPRO software product (Nido S.r.l., Carpineti, Italy). The presented results are from the 1st to the 14th day after the tomato seeds were sown.

Figure 4 illustrates the variations in ambient temperature throughout the seedling cultivation period. From the first to the sixth day after sowing, the temperature fluctuated between 19°C and 44°C. It should be noted that even though an air conditioner was planned for the hydroponic system, it was still not installed during the experiment, which explains the high-temperature fluctuations. During the study, the minimal ambient temperatures (outside the container) varied between 18 and 23 °C, and the maximal ones between 28 and 34 °C. Considering that the hydroponic installation was placed inside a container heated by the sun, the maximal room temperatures were even higher, as seen from the experimental data.

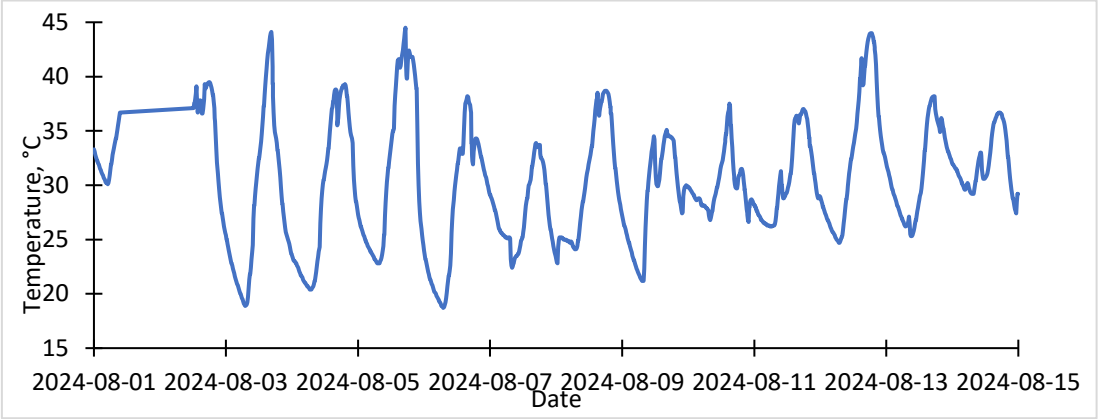


Fig. 4 - Time series of the ambient temperature

Maintaining elevated air temperatures during this initial phase is crucial, as it accelerates seed germination and enhances early seedling development. Optimal germination temperatures for tomatoes typically range between 20°C and 30°C, with higher temperatures promoting faster emergence but posing a risk of thermal stress if excessively high. However, considering that at the beginning of the period the plants were in the initial vegetation stage, the measured high temperature did not adversely affect their development. From the seventh day onward, the average temperature was around 30.4°C, though it varied significantly, following the environmental fluctuations. These observations show that having an air conditioning system that supports cooling is mandatory for the meteorological conditions in Bulgaria. It would allow for optimizing the temperature control and could help minimize extreme variations, reduce potential stress factors, and improve overall seedling uniformity and growth efficiency.

The time series of relative air humidity is shown in Figure 5. It exhibits variation throughout seedling cultivation. During the initial period, from sowing to the sixth day, high air temperatures led to intensive water evaporation, causing relative humidity to peak at 95.9% at nighttime when the temperatures were lower. This high humidity is typical during the early stages of vegetation when moisture levels are predominantly influenced by evaporation.

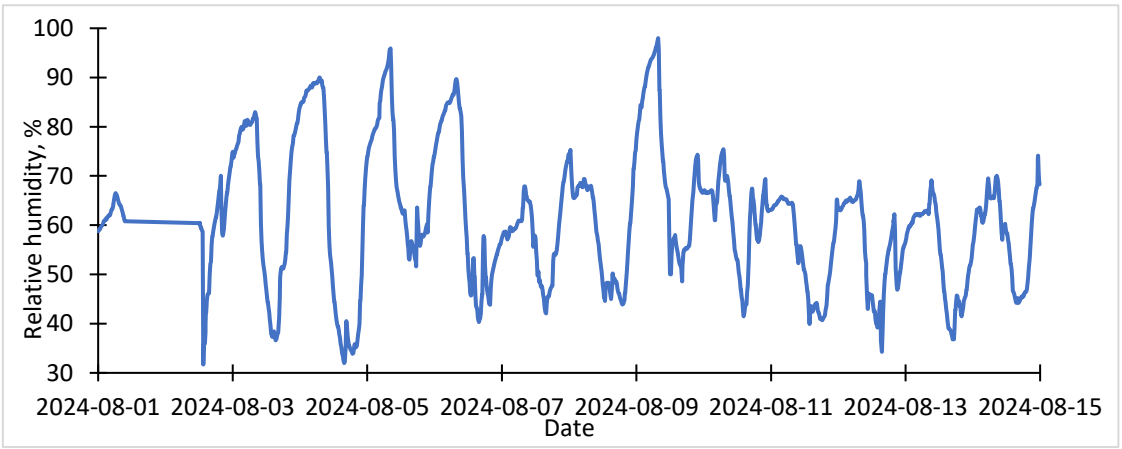


Fig. 5 - Time series of the air's relative humidity

From the seventh day onwards, the relative humidity in the system varied around an average value of 60.7 % with daily fluctuations following the air temperature variation. This moderate humidity level is more conducive to seedling growth, as excessive levels can encourage fungal diseases and hinder proper air circulation around the plants.

The regulation of air humidity within the system is implemented with ventilation holes incorporated into the enhanced prototype of the hydroponic system. These ventilation openings allow the expulsion of excess moisture from the air and improve overall air exchange, ensuring that humidity levels are kept within the optimal range for plant health. By controlling the airflow, the system helps maintain a balanced microclimate that supports the healthy development of seedlings.

During the entire cultivation period, the average water temperature in the system was 26.3 °C, with recorded values ranging from a minimum of 21.3 °C to a maximum of 32 °C (Figure 6).

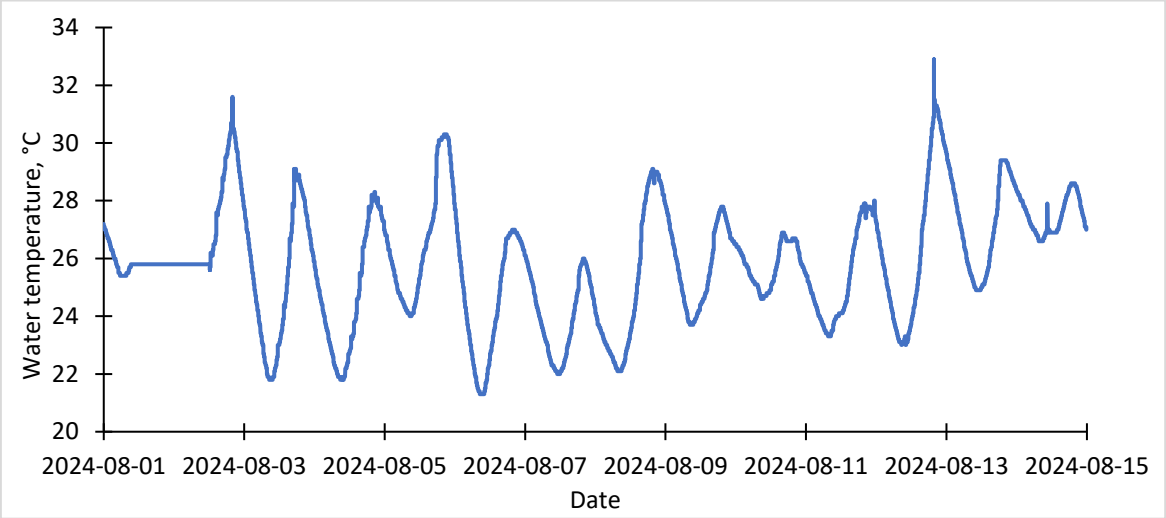


Fig. 6 - Time series of the temperature of the water

The variation in water temperature closely followed fluctuations in ambient air temperature, which served as the primary factor influencing thermal dynamics within the system. This passive heating and cooling mechanism effectively regulated the water temperature without the need for active intervention. The elevated water temperature had a positive effect on root system development, contributing to favorable growth conditions. As a result, no additional water heating was required during the experiment.

The measured environmental parameters demonstrated that the system maintained conditions generally favorable for tomato germination. For example, the average water temperature during the cultivation period was 26.3 °C, which aligns with optimal root-zone temperatures promoting rapid germination and root activity. Although ambient air temperatures exhibited higher fluctuations, germination was not adversely affected, and system productivity remained above 94%. These observations support the positive correlation between controlled water temperature and seedling emergence under hydroponic conditions.

This approach helped to avoid the temperature-related drawbacks observed in the previously designed system (*Nikolov et al., 2023*), where environmental influences affected the temperature of the working solution. According to *Yaling et al. (2015*), when growing tomatoes in soil, the temperature in the root zone should be maintained around 23°C to optimize root development and nutrient uptake. Additionally, *Miao et al. (2023*) have demonstrated the negative effects of low temperatures in the root zone on CO_2 assimilation and photosynthesis. Once again, the temperature variation shows that an air conditioner is mandatory for the meteorological conditions in Bulgaria if precise microclimate conditions are to be maintained within the hydroponic system.

To reduce the observed fluctuations in relative humidity and water temperature, future improvements will include precise microclimate control and better insulation of the nutrient tank. These upgrades aim to stabilize both parameters and maintain them within optimal ranges for plant growth.

In the implemented hydroponic system, the risk of pathogen development and reduced oxygen absorption by the roots, potentially caused by excessive temperatures in the root zone, is mitigated by the installed air stone. This ensures adequate oxygenation of the root zone, further promoting healthy root growth and minimizing the risks associated with high water temperatures.

A photo from the first day after sowing the seeds is shown in Figure 7. Mass germination of the tomato seeds was recorded on the 7th day of sowing, as shown in Figure 8. The recording was done on each shelf and tray for each tomato variety. After counting the successfully germinated seeds, it was found that the *Florida F1* hybrid had a 94% productivity of the hydroponic system. Promising results of 96% productivity were achieved for the *Aleno Surtse* variety.



Fig. 7 - Tomato seeds on day 1 from sowing

The productivity of the hydroponic system was evaluated based on the percentage of successfully germinated seeds relative to the total number of seeds sown—an established metric for assessing seedling cultivation efficiency under controlled environmental conditions (*Bugbee and White, 1984*). Although no external reference system (e.g., conventional soil-based cultivation or an alternative hydroponic setup) was included for direct comparison, the observed germination rates were assessed against standard benchmarks reported for optimal tomato seedling production in hydroponics, which typically exceed 90% under ideal conditions (*Resh, 2012*). The germination performance of the tomato hybrids *Florida F1* and *Aleno Surtse* was comparable to or surpassed these reference values, indicating effective system functionality.



Fig. 8 - Germination of tomato seeds on day 7 from sowing

An intermediate reading of the viability of the seedlings was carried out on the tenth day after sowing the seeds. It was established that all the growing plants developed well, as shown in Fig. 9.

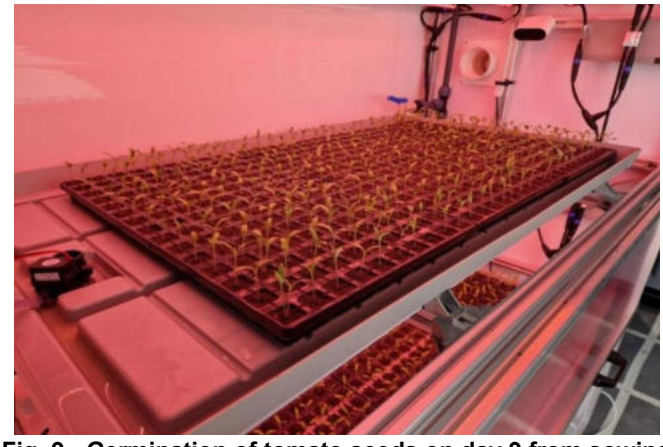


Fig. 9 - Germination of tomato seeds on day 9 from sowing

A fourth reading was carried out at the end of the growing period (Figure 10). It showed that all the sprouted tomato plants had retained their viability and were suitable for growing in a permanent place. The cultivation of tomatoes is not economically justified at a later stage in the hydroponic system due to its small volume and productivity.



Fig. 10 -The condition of tomato seedlings 15 days after sowing the seeds

3.2. Economic Evaluation of a Small-Scale Hydroponic System for Indoor Vegetable Growing

The economic evaluation is based on the observed seedling productivity, which serves as a proxy for functional system efficiency and potential income. The implementation costs of the prototype of the small-scale hydroponic system for indoor vegetable growing are summarized in Table 2. The total price of the facility is 9593 BGN or approximately 4900 EUR.

The operating costs in our study are based only on the production of tomato seedlings of the experimental varieties. The productivity of the hydroponic system is 1350 tomato seedlings in 15 days. From this productivity, 5% losses were observed due to the non-germination of the plants. The selling price of one plant is 1.00 BGN, and the system is expected to operate 120 days a year. The expected number of monthly plants is about 2700 minus 5% losses, with the price of integrated fertilizer being 0.18 BGN per plant, and the cost of purchasing tomato seeds for a single 15-day production cycle is 270 BGN. The price of electricity in Bulgaria is 0.23988 BGN/kWh daily rate and 0.14122 night rate. The daily electricity consumption is 5.219 kWh. The price of water is 0 BGN because it is from a self-owned source. Furthermore, no salary costs were foreseen for servicing the system because it was operated by the owner.

Table 2

Costs for constructing a small-scale hydroponic system for indoor vegetable growing

Product	Count, pcs	Price, BGN
Profile 30x30 with a length of 2000 mm	12	380.42
Profile 30x30 with a length of 1460 mm	8	188.00
Profile 30x30 with a length of 1400 mm	12	271.06
Profile 30x30 with a length of 700 mm	27	322.87
Profile 30x30 with a length of 435 mm	24	190.40
Profile 30x30 with a length of 405 mm	6	61.04
Corner connectors 30x30 with slot 8 nuts and bolts	206	526.78
IMOU Cell Go cameras	3	747.00
Nido One computer	1	2 223.98
Lighting Set Valoya L28 Clear AP673L	1	2 050.19
Drainage pump DC6-12V + Power supply	3	78.00
Irrigation pump GMAX Model Q400122	1	135.22
Ventilation Inlet - Axial fan 105 m^3/h, 100 mm	3	120

Product	Count, pcs	Price, BGN
Exhaust Ventilation – Secret Jardin DF Extractor T 150/250/350/ m^3/h	1	294
Scream parts 1		77.9
Scream parts 2		78.36
Danish tray 1100x630 mm	3	216
Total for planes and panels		530
WiFi Adapter 3840W	7	202.3
Tank: growTANK Food Tank 150 l.	1	129
Air pump + air stone: BOYU Air pump S-1000 252l/h +VolumeAir Round Ceramic Airstone 200mm - Aeration stone		63
Solution heater: CALENTADOR WATER MASTER 100W	1	22
Blum AVENTOS HL16 door mechanisms	3	686.28
Total All:		9593.8

A summary of all costs and benefits is presented in Table 3. The results of the economic analysis show that the small hydroponic system for growing tomato seedlings is cost-effective and can generate stable income for the owner. With a planned workload of 120 working days per year, the system is expected to produce approximately 10260 plants after adjusting for losses. The annual revenue from selling seedlings for 1 BGN per plant amounts to 10260 BGN (5245.85 EUR), while the total costs, including the costs of fertilizer, seeds, and electricity, are 4126.14 BGN (2109.66 EUR). This results in an annual net profit of 6133.86 BGN (3136.19 EUR).

The initial investment for the system is BGN 9593.80 (4905.23 EUR). At current revenues and expenses, the payback period is approximately 1.6 years (or about 19 months). This means that the system will start generating net profit in a relatively short period. Furthermore, assuming a depreciation period of 5 years, the annual depreciation costs will be around BGN 1918.76 (981.05 EUR), which further increases the predictability of financial results.

The profit will increase significantly once the investment is paid off, as depreciation costs will be eliminated. Furthermore, the profitability of the system can be improved by increasing the number of working days per year, including the production of seedlings of other vegetable crops, as well as the production of leafy vegetables, or by optimizing the production process, which would allow better resource management and reduction of losses.

Table 3

Results of economic evaluation of a small hydroponic system

Indicators	Value
Monthly number of plants	2565, pcs
Annual number of plants	10260, pcs
Monthly sales revenue	2565, BGN
Annual sales revenue	10260, BGN
Monthly fertilizer costs	461.7, BGN
Annual fertilizer costs	1846.8, BGN
Annual seed costs	2160, BGN
Monthly electricity cost	29.83, BGN
Annual expenses for electricity consumption	119.34, BGN
Total annual costs	4126.14, BGN
Annual profit	6133.86, BGN
Annual depreciation (assuming a 5-year term)	1918.76, BGN
Redemption period	≈19 months

The investment in this hydroponic system appears economically justified and has a high potential for return within less than two years. It provides an opportunity for a sustainable and profitable business model, especially for small producers who use self-owned water resources and can manage the system independently, without additional labor costs.

CONCLUSIONS

This study presented the design, development, and experimental validation of a modular, IoT-enabled hydroponic system intended for seedling cultivation in indoor environments. The system demonstrated high operational reliability and achieved a germination rate of 94–96% for two certified tomato varieties without the use of nutrient solution. These results confirm the system's ability to maintain favorable environmental and substrate conditions during early plant development.

While the study focused primarily on germination as a functional indicator, the observed environmental parameters—such as stable water temperature and controlled humidity—showed a positive correlation with seedling emergence. However, no detailed statistical analysis or phenological tracking was conducted, which limits the biological conclusions. These aspects will be addressed in upcoming studies with diverse crops and extended growth cycles.

The innovation of this system lies in its compact, modular structure, cloud-based control, and low-cost design, making it accessible for domestic users, urban gardeners, and small-scale producers. Its adaptability for different crops and potential for integration into home-based food production systems offer a practical solution for resilient agriculture in urban settings.

Further development will focus on refining environmental control, expanding biological monitoring, and evaluating long-term productivity and sustainability.

ACKNOWLEDGEMENT

This study was financed by the European Union—NextGenerationEU, through the National Recovery and Resilience Plan of the Republic of Bulgaria, project № BG-RRP-2.013-0001.

REFERENCES

[1] Adil N., Ashraf K., Munir M., Mohiuddin M., Abbasi A., Riaz U., Aslam A., Marey S.A., Hatamleh A.A., Zaman Q.u. (2023). Pesticides, Heavy Metals and Plasticizers: Contamination and Risk Assessment of Drinking-Water Quality. *Sustainability*, 15, 13263. https://doi.org/10.3390/su151713263

[2] Alam T., Haq Z.U., Ahmed M.A., Ikram M. (2023), Hydroponics as an advanced vegetable production technique: an overview, *Zoo Bot.,* 1(1), 29–42, https://doi.org/10.55627/zoobotanica.001.01.0630

[3] Alengebawy A., Abdelkhalek S.T., Qureshi S.R., Wang M.-Q. (2021). Heavy Metals and Pesticides Toxicity in Agricultural Soil and Plants: Ecological Risks and Human Health Implications. *Toxics*, 9(42). https://doi.org/10.3390/toxics9030042

[4] Bugbee B., White JW. (1984). Tomato growth as affected by root-zone temperature and the addition of gibberellic acid and kinetin to nutrient solutions. *J Am Soc Hortic Sci.,*109(1), 121-5. PMID: 11539775.

[5] Cardoso F.B., Martinez H.E.P., da Silva D.J.H., Milagres C.C., Barbosa J.G. (2018). Yield and quality of tomato grown in a hydroponic system, with different planting densities and number of bunches per plant. *Pesqui. Agropecuária Trop.,* 48, 340–349.

[6] Duangpakdee K., Thananta G. S. S. (2024). IoT enhanced deep water culture hydroponic system for optimizing Chinese celery yield and economic evaluation, *Smart Agricultural Technology*, 9, 100545, https://doi.org/10.1016/j.atech.2024.100545

[7] Eigenbrod C., Gruda N. (2015). Urban vegetable for food security in cities. A review. Agron. *Sustain. Dev*., 35, 483–498. https://doi.org/10.1007/s13593-014-0273-y

[8] Elmulthum N.A., Zeineldin F.I., Al-Khateeb S.A., Al-Barrak K.M., Mohammed T.A., Sattar M.N., Mohmand A.S. (2023). Water Use Efficiency and Economic Evaluation of the Hydroponic versus Conventional Cultivation Systems for Green Fodder Production in Saudi Arabia. *Sustainability*, 15(822). https://doi.org/10.3390/su15010822

[9] Gutiérrez-Chávez A., Robles-Hernández L., Guerrero B.I., González-Franco A.C., Medina-Pérez G., Acevedo-Barrera A.A., Hernández-Huerta J. (2025). Potential of Trichoderma asperellum as a Growth Promoter in Hydroponic Lettuce Cultivated in a Floating-Root System. *Plants*, 14(3). https://doi.org/10.3390/plants14030382

[10] Hanafi A., Hussien S., Elnahal D., Ahmed S. E., Salem M., Zainhum A., Elsayed A., Ibrahim M., Abdel Sattar Y. (2025). Revolutionizing Agriculture with IoT, Mobile Apps, and Computer Vision in Automated Hydroponic Greenhouses, *International Journal of Engineering and Applied Sciences-October 6 University*, 2(1), 1-16. https://doi.org/10.21608/ijeasou.2025.346170.1029

[11] Hartwell H., Bray J., Lavrushkina N., Lacey J., Rodrigues V.M., Fernandes A.C., Bernardo G.L., Martinelli S.S., Cavalli S.B., Proença R.P.d.C. (2024). Identifying key factors that encourage vegetable intake by young adults: using the health belief model", *British Food Journal*, 126(1), 453-470. https://doi.org/10.1108/BFJ-10-2022-0905

[12] Hossain M.E., Shahrukh S., Hossain S.A. (2022). Chemical Fertilizers and Pesticides: Impacts on Soil Degradation, Groundwater, and Human Health in Bangladesh. Springer, Cham, Water Science and Technology, 104. https://doi.org/10.1007/978-3-030-95542-7_4

[13] Hostalrich D., Pelegri-Sebastia J., Sogorb T., Pellicer V. (2022). Intelligent management of hydroponic systems based on IoT for agrifood processes. *Journal of Sensors*, 1, 9247965. https://doi.org/10.1155/2022/9247965

[14] Intergovernmental Panel on Climate Change. (2021). Climate Change 2021: The Physical Science Basis. Cambridge University Press. Available online: https://www.ipcc.ch/report/ar6/wg1/ (accessed on 26 February 2025).

[15] Chadwick J.J., Witteveen A., Zhang P., Lynch I. (2023). 10 - Hydroponics and alternative forms of agriculture: opportunities from nanotechnology, Nano-Enabled Sustainable and Precision Agriculture, Academic Press, 259-272, https://doi.org/10.1016/B978-0-323-91233-4.00018-1

[16] Jones H.G. (2013). Plants and Microclimate: A Quantitative Approach to Environmental Plant Physiology. 3rd ed. Cambridge University Press.

[17] Khadijah F. R., Thakur R., Roy S. (2024). Enhancing Hydroponic Farming Productivity Through IoT-Based Multi-Sensor Monitoring System. In *Proceedings of the 9th International Conference on Internet of Things, Big Data and Security (IoTBDS 2024)*, 351-357. http://doi.org/10.5220/0012741300003705

[18] Kim J., Park H., Seo C., Kim H., Choi G., Kim M., Kim B., Lee W. (2024). Sustainable and Inflatable Aeroponics Smart Farm System for Water Efficiency and High-Value Crop Production. *Appl. Sci*., 14(11). https://doi.org/10.3390/app14114931

[19] Kushawaha A., Shah D., Vora D., Zade N., Iyer K. (2024). Urban small-scale hydroponics: A compact, smart home-based hydroponics system, *MethodsX*, 13, 102998, https://doi.org/10.1016/j.mex.2024.102998

[20] Lakshmiprabha K. E., Govindaraju C. (2019). Hydroponic-based smart irrigation system using Internet of Things. *International Journal of Communication Systems*, 36(12), e4071. https://doi.org/doi:10.1002/dac.4071

[21] Li L., Li J., Wang H., Georgieva T., Ferentinos K. P., Arvanitis K. G., Sygrimis N. A. (2018). Sustainable energy management of solar greenhouses using open weather data on MACQU platform. *International Journal of Agricultural and Biological Engineering*, 11(1), 74-82. http://doi.org/10.25165/j.ijabe.20181101.2713

[22] Luthuli A., Magwaza L., Tesfay S., Magwaza S., Mditshwa A. (2024). Influence of Animal Manure Extracts on Physico-Chemical and Nutritional Quality of Tomatoes Grown in Soilless Cultivation. *Horticulturae*, 10, 1330. https://doi.org/10.3390/horticulturae10121330

[23] Ma L., Chai Ch., Wu W., Qi P., Liu X., Hao J. (2023). Hydrogels as the plant culture substrates: A review. *Carbohydrate Polymers*, 305, 120544, https://doi.org/10.1016/j.carbpol.2023.120544

[24] Mai C., Mojiri A., Palanisami S., Altaee A., Huang Y., Zhou J.L. (2023). Wastewater Hydroponics for Pollutant Removal and Food Production: Principles, Progress and Future Outlook. *Water*, 15, 2614. https://doi.org/10.3390/w15142614

[25] Maucieri C., Nicoletto C., Schmautz Z., Sambo P., Komives T., Borin M., Junge R. (2017). Vegetable Intercropping in a Small-Scale Aquaponic System. *Agronomy*, 7(63). https://doi.org/10.3390/agronomy7040063

[26] Miao Y., Ren J.-l., Zhang Y., Chen X., Qi M., Li T., Zhang G., Liu Y. (2023). Effect of low root-zone temperature on photosynthesis, root structure and mineral element absorption of tomato seedlings. Scientia *Horticulturae*, 315, 111956, https://doi.org/10.1016/j.scienta.2023.111956

[27] Nikolov N.V., Atanasov A.Z., Evstatiev B.I., Vladut V.N., Biris S.-S. (2023). Design of a Small-Scale Hydroponic System for Indoor Farming of Leafy Vegetables. *Agriculture*, 13, 1191. https://doi.org/10.3390/agriculture13061191

[28] NOAA (n.d.). Climate Change: Global Temperature. Available online: https://www.climate.gov/news-features/understanding-climate/climate-change-global-temperature (accessed on 21 February 2025).
[29] Patel K., Chauhan D., Mishra P., et al. (2024). Design and development of a modular hydroponic tower with topology optimization. *Int J Interact Des Manuf*., 19, 4243-4252. https://doi.org/10.1007/s12008-024-02052-1
[30] Perera M.N.T., et al. (2024). Intelligent Algorithm for Optimizing Hydroponic Solution in IoT-Integrated Agriculture Systems, *2024 Moratuwa Engineering Research Conference (MERCon)*, Moratuwa, Sri Lanka, 133-138. https://doi.org/10.1109/MERCon63886.2024.10689134
[31] Peters D.B., Pendleton J.W., Hageman R.H., Brown C.M. (1971). Effect of night air temperature on grain yield of corn, wheat, and soybeans. *Agron. J.,* 63, 809.
[32] Pieters A.J., Stürz S., Asch J., Asch F. A. (2024). Hydroponic System to Study the Effects of Root and Meristem Night Temperature on Growth, Photosynthesis Carbon Balance, and Antioxidant Enzymes in Rice. *Agriculture*, 14, 1574. https://doi.org/10.3390/agriculture14091574
[33] Raviv M., Wallach R., Blom T.J. (2004). The effect of physical properties of soilless media on plant performance - a review. *Acta Hortic*., 644, 251-259, https://doi.org/10.17660/ActaHortic.2004.644.34
[34] Redmond C., O'Mahoney R., Blanchard M., Coughlan N.E. (2025). Varied Growth Media Necessitate Different Light Regimes for Indoor Duckweed Cultivation. *Plants*, 14, 397.
[35] Resh H.M. (2012) Hydroponic Food Production, 8th ed.; CRC Press: Boca Raton, FL, USA.
[36] Rockström J., Sukhdev P. (n.d.) How food connects all the SDGs. Available online: https://www.stockholmresilience.org/research/research-news/2016-06-14-how-food-connects-all-the-sdgs.html (accessed on 28 February 2025).
[37] Rosenzweig C., Tubiello F.N. (1996). Effects of changes in minimum and maximum temperature on wheat yields in the central US A simulation study. *Agric. For. Meteorol*, 80, 215. https://doi.org/10.1016/0168-1923(95)02299-6
[38] Sela Saldinger S., Rodov V., Kenigsbuch D., Bar-Tal A. (2023). Hydroponic Agriculture and Microbial Safety of Vegetables: Promises, Challenges, and Solutions. *Horticulturae*, 9(51). https://doi.org/10.3390/horticulturae9010051
[39] Stevens JD., Murray D., Diepeveen D., Toohey D. (2024). A low-cost spectroscopic nutrient management system for Microscale Smart Hydroponic system. *PLoS ONE*, 19(5), e0302638. https://doi.org/10.1371/journal.pone.0302638
[40] Tatas K., Al-Zoubi A., Christofides N., Zannettis C., Chrysostomou M., Panteli S., Antoniou A. (2022). Reliable IoT-Based Monitoring and Control of Hydroponic Systems. *Technologies*, 10(26). https://doi.org/10.3390/technologies10010026
[41] Ulas F., Yücel Y.C., Ulas A. (2024). Physio-Morphological Traits Contributing to Genotypic Differences in Nitrogen Use Efficiency of Leafy Vegetable Species under Low N Stress. *Horticulturae*, 10(9). https://doi.org/10.3390/horticulturae10090984
[42] United Nations (2018). Goal 11: Make Cities Inclusive, Safe, Resilient and Sustainable. Available online: https://www.un.org/sustainabledevelopment/cities/ (accessed on 27 February 2025).
[43] United Nations (2022). World Population Prospects. The 2022 Revision of World Population Prospects. https://www.un.org/development/desa/pd/sites/www.un.org.development.desa.pd/files/wpp2022_summary_of_results.pdf (accessed on 17 February 2025).
[44] van Delden S.H., SharathKumar M., Butturini M., Graamans L.J.A., Heuvelink E., Kacira M., Kaiser E., Klamer R.S., Klerkx L., Kootstra G., et al. (2021). Current status and future challenges in implementing and upscaling vertical farming systems. *Nat. Food*, 2, 944–956. https://doi.org/10.1038/s43016-021-00402-w
[45] Wing I. S., Cian E. De., Malcolm N. (2021). Mistry. Global vulnerability of crop yields to climate change, *Journal of Environmental Economics and Management*, 109, 102462, https://doi.org/10.1016/j.jeem.2021.102462
[46] Woznicki T., Møllerhagen P.J., Heltoft P., Kusnierek K. (2021). Growing Potatoes (Solanum tuberosum L.) Hydroponically in Wood Fiber—A Preliminary Case-Study Report. *Agronomy*, 11, 1369. https://doi.org/10.3390/agronomy11071369
[47] Yaling L., Xiangzhen W., Liping L., Minli S. (2015). The effect of root-zone temperature on temperature difference between leaf and air in tomato plants. *Acta Hortic*., 1107, 251-256
[48] Yessenamanova M., Yessenamanova Z., Tlepbergenova A., Moldir M., Nurgul B. (2023). Optimization of acidity and electrical conductivity in hydroponic vegetable production: A STEM educational perspective. *International Journal of Design & Nature and Ecodynamics*, 18, 6, 1517-1524. https://doi.org/10.18280/ijdne.180627

DESIGN AND EVALUATION OF A NEW DEEP VERTICAL ROTARY TILLER FOR ENHANCED FIELD PERFORMANCE
/
新型深松立式旋耕机的设计与试验

Chao HE [1,2], Guiquan HAN[1], Tie YE[1], Mingyuan WEI[3], Chaofan SUN[1], Yiyuan CHENG[1]
[1] School of Intelligent Manufacturing and Electrical Engineering, Nanyang Normal University / China;
[2] Collaborative Innovation Center of Intelligent Explosion-proof Equipment, Henan Province / China;
[3] College of Engineering, China Agricultural University / China
Tel: 19937741208; E-mail: TB19050015B4@cumt.edu.cn
DOI: https://doi.org/10.35633/inmateh-76-63

Keyworks: *Vertical Rotary Tiller, Deep Tillage, Simulation, Field Trials*

ABSTRACT
Deep tillage is capable of penetrating the tough subsoil layers, while vertical rotary tillage improves soil aggregate structure and moisture retention. In this study, an innovative deep vertical rotary tiller was engineered. Utilizing ANSYS Workbench, stress simulation on the blade was conducted. The EDEM software was employed to explore how the machine's forward speed and the blade's rotational speed impact operational quality. Field trials of the developed prototype revealed that the tillage depth, tillage depth stability coefficient, and soil fragmentation rate all complied with the national standard GB/T 5668-2017 for rotary tiller testing. Comparative analysis with the current vertical rotary tiller confirmed that the tiller developed in this study exhibited superior performance, thereby facilitating the adoption and technological evolution of vertical rotary tillers.

摘要
深耕能打破坚硬的犁底层，而垂直旋耕能改善土壤团粒体结构和提高蓄水能力。本研究设计了一种新型深松立式旋耕机。利用 ANSYS Workbench 对旋耕刀进行了力学仿真。利用 EDEM 软件探究机具前进速度和旋耕刀转速对耕地质量的影响。所研制样机的田间试验表明：耕深、耕深稳定系数、土壤破碎率均符合旋耕机试验国家标准 GB/T 5668-2017。通过与现有立式旋耕机进行对比分析，证实了本研究中立式旋耕机性能的优越性，从而促进了立式旋耕机的技术发展。

INTRODUCTION

Due to the rolling by agricultural machinery and the long-term use of shallow tillage, hard subsoil compaction forms in most areas of the fields (*Hu et al., 2024*). Thick subsoil compaction is not conducive to energy transfer and downward extension of crop roots, meanwhile soil permeability and water storage capacity are significantly reduced, which further leads to increased chances of disease and reduced crop yields (*Bogunovic and Kisic, 2017; Yang et al., 2022; Huang et al., 2023*). To eliminate hard subsoil compaction, deep loosening and vertical rotary tillage techniques are required. These methods break subsoil compaction by increasing tillage depth and loosening the soil without turning it over (*Tarverdyan et al., 2017*), thereby improving soil granular structure while preserving the original soil layers and enhancing the soil's capacity for water storage, as well as its moisture and air permeability (*Chandrashekar et al., 2021; Gjoka et al., 2024*). *Bai et al., (2024),* further demonstrated that deep vertical rotary tillage is effective in mitigating soil salinity and significantly increasing seed cotton yield.

Tian have designed and tested a vertical strip rotary cultivator for conservation tillage and wide-narrow-row operation of straw (*Tian, 2023*).

Zhang (*2016*) developed a Y-shape vertical rotary cultivator and then proposed three design schemes for rotary blades. In order to reduce the resistance of the blade when cutting soil, *Liu et al. (2017)* put forward a vertical rotary blade with internal bending angle.

Chao He, Ph.D. Eng.; Guiquan Han, Ph.D. Eng.; Tie Ye, Ph.D. Agr.; Mingyuan Wei, M.S. Eng.; Chaofan Sun, Ph.D. Agr.; Yiyuan Cheng, Ph.D. Eng.

Zhai et al. (2022) designed various vertical rotary tillers with different structural forms, then they conducted a series of discrete element simulation experiments on the interaction between rotary tillers and soil. In results, the optimal structure and operating parameters of the rotary tiller were obtained to improve the tillage quality. A simulation model of a spiral cutter–soil system was established using Smoothed Particle Hydrodynamics (SPH) by *Yang et al. (2023*). Based on this model, the forces acting on the rotary cutter were thoroughly analyzed, providing an important basis for optimizing its design.

However, through literature search and market research, it can be found that scholars still have less research on vertical rotary tillers, and there are fewer types of vertical rotary tillers, with low popularity. On the other hand, the tillage depth of existing vertical rotary tillers is generally shallow (less than 200 mm). Therefore, in this work, a deep vertical rotary tiller has been developed, featuring a subsoiling depth of 350 mm, a rotary tillage depth of 250 mm, and a tillage width of approximately 2000 mm, which enhances the tillage efficiency and the soil quality, achieving the purpose of deep tillage and vertical rotary tillage.

This research introduces two innovative contributions: (1) Leveraging finite element and discrete element simulation techniques, an innovative vertical rotary blade was designed, achieving improvements in rotary tillage depth, stability coefficient, and soil fragmentation rate. (2) Deep tillage was combined with vertical rotary tillage to develop a novel deep vertical rotary tiller. Compared with existing vertical rotary tillers, this design enhances work performance in multiple aspects, thereby not only advancing the application of vertical rotary tillers but also providing crucial theoretical groundwork for future research in this field.

MATERIALS AND METHODS

Overall Design of the Deep Vertical Rotary Tiller

To achieve the objectives of deep plowing and vertical rotary tillage, the rotary tiller designed in this study primarily consists of a body frame, a reducer, a gearbox, 8 vertical rotary units, and 4 chisel-shaped subsoiling shovels. Its structural layout is schematically illustrated in Fig. 1.

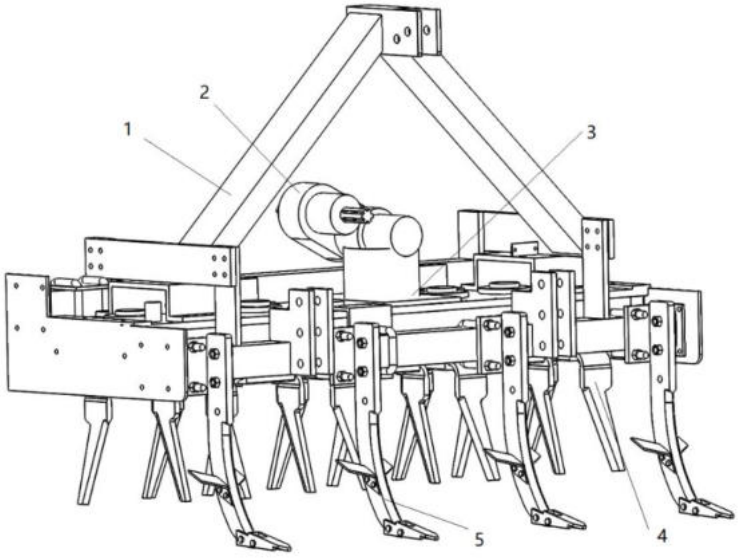


Fig. 1 - Structure diagram of vertical rotary tiller

1 - Body frame; 2 - Reducer; 3 - Gearboxes; 4 - Vertical rotary units; 5 - Chisel-shaped subsoiling shovels

The working principle of the machine is as follows: the power output from the tractor is transmitted to the reducer by the universal joint drive shaft, and then the reducer transmits the power downward to the gearbox through the bevel gear transmission. There are 8 cylindrical gears in the gear box, and each cylindrical gear drives a set of vertical rotary units to rotate. Each vertical rotary unit contains two vertical rotary blades, which are used to cut and break the soil, with tillage depth of 250 mm. Four chisel-shaped subsoiling shovels are installed in front of vertical rotary units, and the distance between two adjacent shovels is 580 mm and the subsoiling depth is 350 mm.

Design of the Chisel-shaped Subsoiling Shovel

The primary function of these shovels is to break the hard bottom layer of the soil and to reduce the cutting resistance of the vertical rotary blade. Each chisel-shaped subsoiling shovel consists of mounting holes, a shovel handle, a shovel handle blade and a shovel head, as illustrated in Fig. 2.

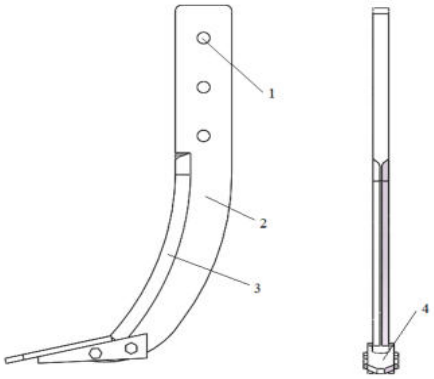


Fig. 2 - Schematic diagram of chisel-shaped subsoiling shovel

1 - Mounting holes; 2 - Shovel handle; 3 - Shovel handle blade; 4 - Shovel head

Design of Vertical Rotary Units

Vertical rotary units are divided into forward (clockwise rotation) vertical rotary units and reverse (counterclockwise rotation) vertical rotary units, each unit consists of blade box base, blade box, two same forward vertical rotary blades or two same reverse vertical rotary blades, as shown in Fig. 3, in which, the forward vertical rotary blade and reverse vertical rotary blade differ in opposite blade directions.

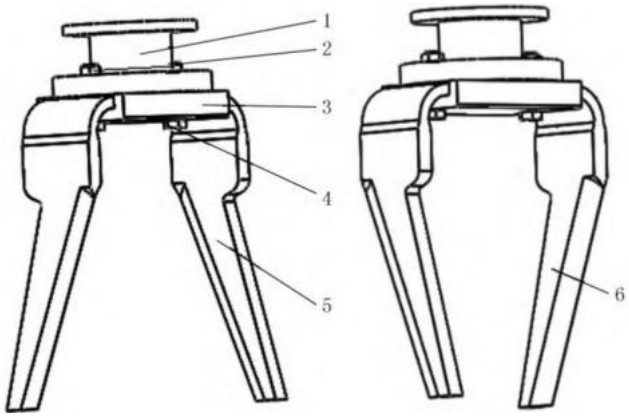


Fig. 3 - Forward vertical rotary units and reverse vertical rotary units

1 - Blade box base; 2 - Bolt; 3 - Blade box; 4 - Nut; 5 - Forward vertical rotary blade; 6 - Reverse vertical rotary blade

Structural Design of The Vertical Rotary Blade

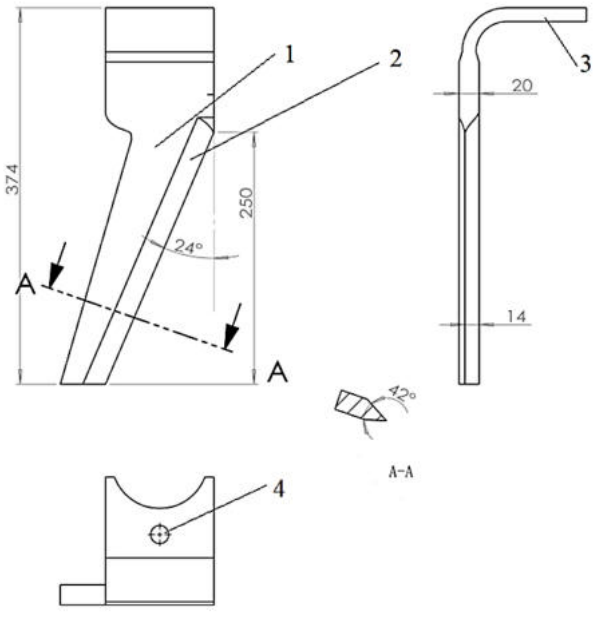


Fig. 4 - Structure of the forward vertical rotary blade

1 - Blade body; 2 - Cutting edge; 3 - Blade handle; 4 - Bolt hole

The vertical rotary blade is the execution part of the vertical rotary tiller, which is designed as shown in Fig. 4. In order to avoid deformation and breakage of the vertical rotary blade in work, it is necessary to ensure that the mechanical properties of the vertical rotary blade meet the work requirements. The material used in the designed blade is 65 Mn steel, and it is quenched and heat-treated to improve the hardness of the cutting edge and the comprehensive mechanical properties. To reduce cutting resistance and power consumption, the cutting edge of the vertical rotary blade is skewed at a certain angle to achieve a sliding cutting effect. Previous studies have reported that power consumption decreases when the sliding cut angle ranges between 22° and 55°. Accordingly, an angle α=24° was selected in the present work. The cutting edge of the designed blade is offset toward the outside of the blade body, being 6 mm from the outer side and 14 mm from the inner side. This configuration ensures that, during rotation in the soil, the blade body engages soil already fragmented by the cutting edge, thereby reducing soil resistance against the blade.

Finite Element Analysis of Vertical Rotary Blade Based on ANSYS Workbench

In SolidWorks software, the 3D model of the forward vertical rotary blade is saved in Parasolid format, and then imported into ANSYS Workbench software (*Jiang et al., 2013, Irsel, 2022*). The bending deformation of the vertical rotary blade mainly comes from the reaction force generated by the blade body penetrating the soil, which acts vertically on the blade body and causes the bending deformation of the blade (*Zhang et al., 2022; Zhang et al., 2024*). The force schematic of the blade body when penetrating the soil is presented in Fig.5, where *A* is the starting point of the vertical rotary blade, *B* is the bottom of the vertical rotary blade, *b* is the total length of the blade body, q is the vertical homogeneous load on the blade body, and w_B is the deformation value at the blade bottom.

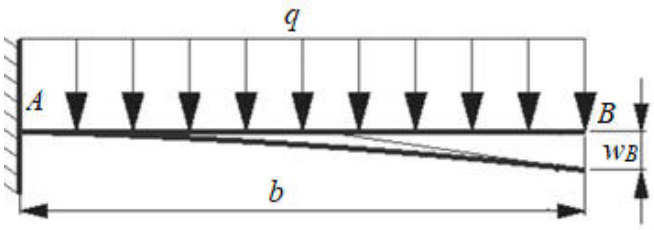


Fig. 5 - Force diagram of the blade body

The maximum force τ_{max} perpendicular to the blade body is:

$$\tau_{\max} = F_{\max} \sin \eta_{\max} = 561 \times \sin 42^{o} \approx 389N \quad (1)$$

where, F_{max} is maximum tangential resistance encountered by the vertical rotary blade, N; η_{max} is maximum cutting angle of the vertical rotary blade, °.

The area A_1 applied by τ_{max} on the blade body is 11246 mm², so the maximum pressure P_{max} is:

$$p_{\max} = \frac{\tau_{\max}}{A_1} \approx 3.46 \times 10^4 Pa \quad (2)$$

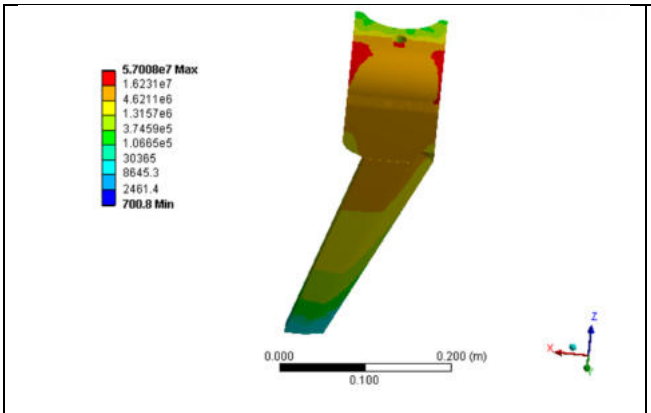


Fig. 6 - Stress distribution of the blade

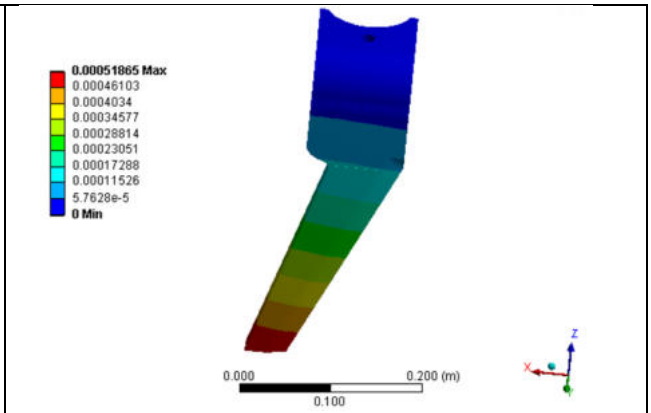


Fig. 7 - Deformation distribution of the blade

The vertical rotary blade model was sequentially defined with material properties, meshed, and constrained. A pressure load of 34600 Pa was then applied to the blade body. The resulting stress distribution is shown in Fig. 6, while the corresponding deformation distribution is presented in Fig. 7.

From Fig. 6 and Fig. 7, it can be concluded that the vertical rotary blade experiences a maximum stress of 57 MPa at the top arc and at the bolt hole. The maximum deformation of the blade occurs at the bottom of the blade tip, with a maximum deformation of 5.19×10^{-4}m. The material of the vertical rotary blade is 65Mn whose yield strength limit is $\sigma_s = 430$ MPa.

Taking the safety factor $n_s = 1.5$, the allowable stress $[\sigma]$ is:

$$[\sigma] = \frac{\sigma_s}{n_s} = 286 \text{ MPa} \quad (3)$$

The maximum stress suffered by the blade is 57 MPa < 286 MPa. The permissible deformation of 65Mn is 1.36×10^{-3}m, while the maximum deformation of the blade is 5.19×10^{-4}m$<1.36\times10^{-3}$m. Therefore, the vertical rotary blade can satisfy the strength demand during work.

Discrete Element Simulation Analysis

Aiming to investigate the influence of the rotational speed and forward speed for the vertical rotary blade on the soil fragmentation rate, EDEM software is utilized to simulate the operation process of the vertical rotary blade. A vertical rotary unit (including two blades) is selected as the model and imported into EDEM software.

The rotational speed of the blade and the forward speed of the machine are selected as the influencing factors for the simulation experiment. The forward speed is set to 0.45 m/s, 0.70 m/s, and 1.00 m/s, with corresponding blade rotational speeds of 309 r/min, 411 r/min, and 450 r/min, respectively. A series of orthogonal simulation experiments was subsequently conducted.

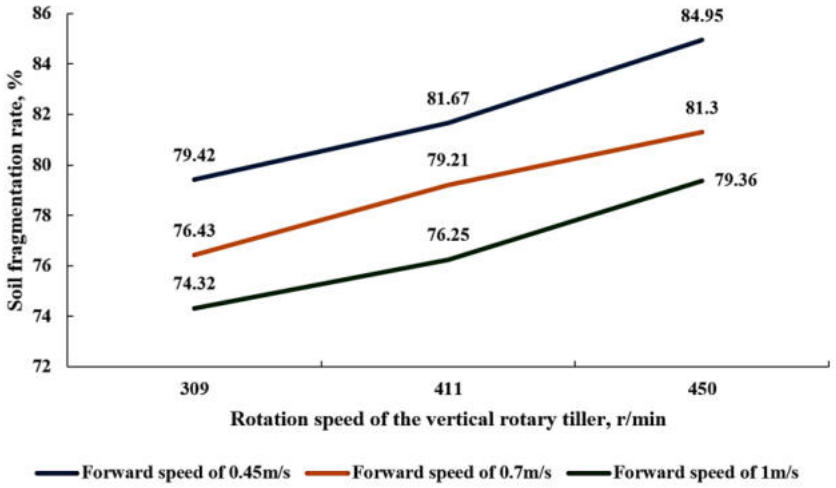


Fig. 8 - Simulation results of soil fragmentation rate

After each orthogonal experiment, the proportion of soil particles with the longest edge less than 40 mm is calculated in the post-processing module, which is the soil fragmentation rate (*Du et al 2020*). The simulation results under different working conditions are presented in Fig. 8. Through data analysis, it can be concluded that the forward speed is negatively correlated with the soil crushing rate, while the rotational speed of blades is positively correlated with the soil fragmentation rate. Therefore, a lower forward speed and a higher rotational speed should be selected for the vertical rotary blade during work.

Field Trials

Test conditions: The prototype vertical rotary tiller developed in this study was subjected to field testing in an experimental plot characterized by loamy soil with a moisture content of 16.7%. The prototype had dimensions of 1995 mm in width, a tillage depth of 250 mm, and a loosening depth of 350 mm, and was operated with a tractor providing 88.2 kW of power. During the testing phase, the tractor's forward speed was maintained at 0.45 m/s, while the blade rotational speed was set to 411 r/min. A visual overview of the field experiment is provided in Fig. 9.

Evaluation indexes: referring to NY/T 2456-2013 Technical Specifications for Quality Evaluation of Rotary Tillers (*NY/T 2456-2013 2013*), in combination with the actual working situation, the rotary tillage depth, stability coefficient of rotary tillage depth, soil fragmentation rate, and fuel consumption are adopted as the evaluation indexes for rotary tillers.



Fig. 9 - The field experiment of the prototype

Test scheme: in compliance with the testing requirements outlined in the national standard GB/T 5668-2017 Rotary Tillers (*GB/T 5668-2017 2017*), our prototype underwent a series of evaluations. The experimental setup consisted of five groups, each covering a distance of 20 meters. Within the scope of each trial, key evaluation indexes were measured and subjected to rigorous validation of the prototype's performance.

RESULTS

Test Results

The results of the field trials are presented in Table 1. The findings indicate that the tillage depth after the experiment is stable, ranging from 251 mm to 255 mm, with a mean depth of 253 mm. The stability coefficient of tillage depth is between 92.23 % and 93.94 %, averaging at 92.87 %. The soil fragmentation rate after the experiment is relatively pretty, ranging from 79.90 % to 82.38 %, with an average value of 81.28 %.

Table 1

Results of the field trials for prototype

	Tillage depth (mm)	Variation coefficient (%)	Stability coefficient (%)	Soil fragmentation rate (%)	Fuel consumption (g/kW·h)
1	251	7.51	92.49	80.06	18580
2	254	6.87	93.13	80.84	18364
3	254	6.98	93.02	83.36	18398
4	252	7.38	92.62	84.29	18411
5	254	6.91	93.09	77.85	18562
Average	253	7.13	92.87	81.28	18463

Comparative Test and Analysis

To substantiate the enhanced performance of the deep vertical rotary tiller crafted in this research, a comparative evaluation was undertaken against the prevalent ZBJQ-5 vertical rotary tiller available in the market. The ZBJQ-5 model, which is outfitted with 12 vertical rotary blades and 4 subsoiling shovels, has a tilling width of 1980 mm. The tests were conducted under uniform conditions, with a tractor power of 88.2 kW, a forward speed of 0.45 m/s, and a blade rotary speed of 411 r/min. The comparative test outcomes for the ZBJQ-5 vertical rotary tiller are detailed in Table 2.

Table 2

Comparative test results

	Average tillage depth (mm)	Stability coefficient (%)	Soil fragmentation rate (%)	Average fuel consumption (g/kW·h)
ZBJQ-5 tiller	205	89.92	72.53	19474
Tiller in this study	253	92.87	81.28	18463

Table 2 indicates that, in comparison to the ZBJQ-5 vertical rotary tiller, the average rotary tillage depth of the tiller designed in this study has increased by 47 mm. Additionally, the stability coefficient of tillage depth has improved by 2.95%, and the soil fragmentation rate has also risen by 12.06%. Moreover, under identical test conditions, the average fuel consumption was reduced by 3.55%. These results demonstrate the newly designed vertical rotary tiller exhibits superior working performance compared to the existing ZBJQ-5 tiller. These improvements are advantageous for root systems of crops, as they enhance the soil's capacity to retain water, moisture, and air permeability, which promotes a favorable environment for crop planting and growth.

Discussion

Further comparison with existing literature shows that, relative to the inner-curve-angle vertical rotary blade proposed by *Liu et al. (2017)*, the asymmetrical blade designed in this study (6 mm outward offset and 14 mm inward offset) demonstrates notable improvements based on finite element analysis. Specifically, the maximum stress was reduced by 17.52%, while tillage resistance decreased by 12.47%. Extensive testing further indicated a slight reduction in average fuel consumption, consistent with the findings of *Zhai et al. (2022)*, who reported that blade angle significantly affects energy efficiency. Compared with the Y-type vertical rotary tiller developed by *Zhang (2016)*, the bevel–cylindrical gear combination applied in this study achieved a 26.72% reduction in torque fluctuation. Additionally, relative to the spiral cutter that reached a soil fragmentation rate of 78% *(Yang et al., 2023)*, the optimized blade geometry in this study attained 81.28%, surpassing the optimal tillage standard of 75% proposed by *Bogunovic (2017)*. Under identical soil conditions (loamy soil, 16.7% moisture content), the working depth stability coefficient reached 92.87%, significantly exceeding the 85.2% reported by *Tian (2023)* for a strip-tilling cultivator. These results demonstrate that this research advances the technical development of vertical rotary tillers.

The deep vertical rotary tiller designed is ideally suited for plain areas. It may present challenges when applied to hilly areas. Therefore, in future research, flexible design methods can be introduced to design a deep vertical rotary tiller that meets the agronomic requirements of hilly areas.

CONCLUSIONS

(1) Ansys Workbench was employed to simulate the tiller's working state. The simulations revealed that the deformation and stress levels of the vertical rotary tiller fall within acceptable limits, signifying its capability to fulfill the operational demands.

(2) By simulating the operation process using EDEM software, it was found that the forward speed of the equipment and the rotational speed of the rotary blade have an impact on the soil fragmentation rate. Consequently, it is recommended to opt for a lower forward speed combined with a higher rotational speed to optimize the tilling process.

(3) The field test results highlight the vertical rotary tiller's impressive performance, characterized by an average tillage depth of 253 mm, a tillage depth stability coefficient of 92.87%, and a soil fragmentation rate of 81.28%, which meet the requirements of national standards GB/T 5668-2017.

(4) Compared to the existing ZBJQ-5 vertical rotary tiller on the market, the machine designed in this study demonstrates a 47 mm increase in rotary tilling depth, a 2.95% improvement in tilling depth stability coefficient, a 12.06% enhancement in soil fragmentation rate, and a 3.55% reduction in average fuel consumption. The vertical rotary tiller developed through this research unambiguously demonstrates its superior operational capabilities.

ACKNOWLEDGEMENT

This work was supported by Doctoral Special Project of Nanyang Normal University (Grant Number: 2024ZX030), Key Scientific and Technological Project of Henan Province (Grant Number: 242102230064), the Key Research Project of Higher Education Institutions of Henan Province (Grant Number: 25A460003), Natural Science Foundation of Henan Province in China (Grant Number: 242300420439), Key Scientific Research Project of Henan Province in China (Grant Number: 23A416005).

REFERENCES

[1] Bai, Z.T., Li, Z.J., Li, L., Li, P.F., Gong, P., Wang, T., Fan, J.L. & Liu, H.G. (2024). Deep vertical rotary tillage reduced soil salinity and improved seed cotton yield and water productivity under limited irrigation in saline-alkaline fields. *Industrial Crops and Products,* 218, 118943.

[2] Bogunovic & Kisic. (2017). Compaction of a clay loam soil in Pannonian region of Croatia under different tillage systems. *Journal of Agricultural Science and Technology,* 19 (2), 475-486.

[3] Chandrashekar, Reddy, H.K.V. & Singh, J. (2021). Evaluation of power tiller operated vertical rotary plough for tillage. *Indian Journal of Ecology,* (6), 48.

[4] GB/T 5668-2017. (2017). *Rotary tillers (GB/T5668-2008 旋耕机)*. Beijing: Standardization Administration of China.

[5] Du, X.W., Yang, X.L., Pang, J. & Ji, J.T. (2020). Design and test of automatic detection platform for soil fragmentation rate in rotary tillage. *International Journal of Agricultural and Biological Engineering,* 13 (5), 40-49.

[6] Gjoka, F., Shkurta, E. & Kasa, E. (2024). Soil compaction and maize yield in various plowing systems from a sustainability perspective *12th ed. Farm Machinery and Processes Management in Sustainable Agriculture (FMPMSA)*, Univ Life Sci, Lublin, POLAND, 159-164.

[7] Hu, R.W., Zheng, B.F., Liu, Y.J., Peng, S.G., Gong, J., Li, J.H., Qin, T., Liang, J.S., Xiong, K.L., Shao, L.J., Zheng, Z.Y., Yi, Z.X., Zhou, Q.M. & Li, J. (2024). Deep tillage enhances the spatial homogenization of bacterial communities by reducing deep soil compaction. *Soil & Tillage Research,* 239, 106062.

[8] Huang, S., Islam, M.U. & Jiang, F. (2023). The effect of deep-tillage depths on crop yield: A global meta-analysis. *Plant Soil and Environment,* 69 (3), 105-117.

[9] Irsel, G. (2022). Bevel gears strength calculation: Comparison ISO, AGMA, DIN, KISSsoft and ANSYS FEM methods. *Journal of the Chinese Society of Mechanical Engineers,* 43 (1), 315-323.

[10] Jiang, X.J., Zhu, Y.S., Hong, J., Zhang, Y.Y. & Kan, Q.H. (2013). Constitutive model for time-dependent ratchetting of ss304 stainless steel: Simulation and its finite element analysis. *Journal of Theoretical and Applied Mechanics,* 51 (1), 63-73.

[11] Liu, F., Mi, Y., Liao, N., Di, M., Liu, Y. & Liu, H. (2017). Research design of vertical rotary cultivator and experiment *(立式旋耕机研究设计与试验)*. *Journal of Agricultural Mechanization Research,* 39 (11), 81-84.

[12] NY/T 2456-2013. (2013). *Technical specifications for quality evaluation of rotary tillers (NY/T 2456-2013 旋耕机质量评价技术规范标准)*. Beijing: Ministry of Agriculture of the People's Republic of China.

[13] Tarverdyan, A.P., Sargsyan, S.F. & Altunyan, A.V. (2017). Investigation results of kinematic and dynamic indicators of tiller with vertical rotation axis in orchards soil cultivation. *Annals of agrarian science,* 15 (2), 163-168.

[14] Tian, Y. (2023). *Design and test of vertical strip rotary cultivator in straw return mode (秸秆归行模式下立式条带旋耕机设计及试验)*. Master Thesis. Jilin Agricultural University.

[15] Yang, J.J., Tan, W.J., Han, J.R., Li, F.M. & Zhang, F. (2022). Distribution pattern of rainwater in soil under vertical deep rotary tillage in dryland farmland. *Agricultural Water Management,* 273, 107891.

[16] Yang, W., Xiao, X., Pan, R.H., Guo, S.Y. & Yang, J. (2023). Numerical simulation of spiral cutter-soil interaction in deep vertical rotary tillage. *Agriculture-Basel,* 13 (9), 1850.

[17] Zhai, S., Shi, Y., Zhou, J., Liu, J., Huang, D., Zou, A. & Jiang, P. (2022). Simulation optimization and experimental study of the working performance of a vertical rotary tiller based on the discrete element method. *Actuators*, 342.

[18] Zhang, C. (2016). *Development of Y shape vertical rotary cultivator (Y 型立式旋耕机的研制)*. Master Thesis. Henan Agricultural University.

[19] Zhang, X.Y., Hu, X., Zhang, L.X. & Kheiry, A.N.O. (2024). Simulation and structural parameter optimization of rotary blade cutting soil based on SPH method. *International Journal of Agricultural and Biological Engineering,* 17 (3), 82-90.

[20] Zhang, X.Y., Zhang, L.X., Hu, X., Wang, H., Shi, X.B. & Ma, X. (2022). Simulation of soil cutting and power consumption optimization of a typical rotary tillage soil blade. *Applied Sciences-Basel,* 12 (16), 8177.

EXPERIMENTAL STUDY ON THE INFLUENCE OF STEAM PRESSURE DISTRIBUTION ON WOOD FIBER FEEDING

蒸汽压力分布对木纤维进给影响实验研究

Ao WANG [1], Guangwei CHEN [1], FaYi QU *[2], Yaoning YANG [1]
[1]Northeast Forestry University, College of Mechanical and Electrical Engineering, Harbin / China;
[2]Northeast Forestry University, Graduate School, Harbin / China.
DOI: https://doi.org/10.35633/inmateh-76-64

Keywords: *Heat mill; Grinding room; Saturated steam; Pressure distribution; Feed characteristics*

ABSTRACT

In this study, a non-invasive experimental method based on the shell temperature field was proposed to invert the internal steam pressure, aiming to investigate the distribution characteristics of saturated steam pressure within the mill chamber of the heat mill and its dynamic influence on the feed of wood fiber material feeding. The surface temperature field of the grinding chamber shell was measured by a high-precision infrared thermometer. Combined with the inverse heat conduction problem model and SteamTab software conversion, the cross-scale mapping relationship of "shell temperature-internal pressure" was constructed, and the pressure distribution cloud map was generated. The experimental materials consisted of mixed wood chips with a moisture content of 45±2%. After preheating and cooking at 160°C for 3 min, the chips were fed into the grinding chamber to analyze the coupling effect of the pressure field and the tooth shape parameters of the grinding disc. The results showed that the saturated steam pressure in the grinding chamber was significantly non-uniformly distributed along the radial direction, and the pressure gradient was mainly driven by the gradient change of the tooth shape parameters of the grinding disc. A solution to the problem of blocking backflow and excessive feed caused by non-uniform distribution of steam pressure was proposed in combination with the tooth profile parameters of the grinding plate.

摘要

本研究提出一种基于壳体温度场的非侵入式实验方法，通过反演磨室内部蒸汽压力，探究热磨机磨室内饱和蒸汽压力的分布特性及其对木质纤维原料进料的动态影响机制。采用高精度红外测温仪测量磨室壳体表面温度场，结合反热传导问题模型与 SteamTab 软件转换，构建"壳体温度-内部压力"的跨尺度映射关系，并生成压力分布云图。实验材料为含水率 45±2%的混合木片，经 160℃预热蒸煮 3 分钟后送入磨室，分析压力场与磨盘齿形参数的耦合效应。结果表明：磨室内饱和蒸汽压力沿径向呈显著非均匀分布，压力梯度主要受磨盘齿形参数的梯度变化驱动；结合磨盘齿廓参数特性，提出了解决蒸汽压力非均匀分布引发的堵塞回流与过量进料问题的技术方案。

INTRODUCTION

The hot mill is a key piece of equipment in the manufacturing of wood composite materials, particularly fiberboards *(Zhang et al., 2016*). Its operation relies on the synergistic effect of high-temperature saturated steam and mechanical refining to achieve the separation of wood fibers *(Wu et al., 2015*). During thermo-mechanical pulping, the spatial distribution of saturated steam pressure and temperature within the grinding chamber profoundly influences critical process parameters, including the degree of wood softening, fiber separation efficiency, and ultimately, the quality of the final products *(Xiong et al., 2014*).

Trairat Neimsuwan et al. (2008) focused on the effects of steam pressure on the performance of loblolly pine fibers during thermal refining. Their study revealed that higher steam pressure causes fiber surface damage, reducing moisture adsorption capacity and water activity but increasing crystallinity. In contrast, lower pressure maintains higher adsorption rates. *Fokko Schütt et al. (2011)* employed JMP software (SAS Institute) to design experiments, demonstrating that varying steam temperature and cooking duration during poplar wood steam pretreatment significantly alters fiber chemical composition. Based on this, they identified optimal cooking conditions.

Ao WANG, Postgraduates; GuangWei CHEN Assoc.Prof.; FaYi QU, Assistant Research Fellow; Yaoning YANG, Postgraduates.

Takasawa Ryosuke et al. (2011) investigated the impact of initial wood-chip moisture content and cooking time on the performance of medium-density fiberboard (MDF) manufactured from Acacia mangium. Their results indicated that high moisture content (90%) + short cooking (3–6 minutes) maximizes the comprehensive mechanical properties of Acacia mangium-based fiberboard.

While these studies emphasize steam's influence on fiber quality, production efficiency is equally critical in practice. This study thus targets the grinding chamber—the core component of thermal refiners—to examine how internal steam pressure distribution affects fiber feedstock feeding *(Liu et al., 2020*). However, the grinding chamber's harsh environment (high temperature/pressure, hermetic sealing, and complex geometry) impedes contact-based measurement of its internal steam pressure field. Consequently, the dynamic coupling mechanism between steam pressure distribution and fiber separation remains unclarified, severely limiting precise process control and optimization (*Wang et al., 2025*).

To address these limitations, a novel non-invasive experimental method is proposed to characterize saturated steam pressure distribution within the grinding chamber. The core innovation lies in deducing internal steam pressure from the shell's temperature field. Specifically: A high-precision infrared thermometer measures the shell surface temperature distribution. The Inverse Heat Conduction Problem (IHCP) method (*Min et al., 2022*) and SteamTab software (for saturated steam property conversion) analyze temperature data to establish a cross-scale mapping between the shell temperature field and internal steam pressure field. This approach enables the derivation and visualization of saturated steam pressure distribution.

Building on the inferred pressure distribution, this study further investigates the dynamic influence of this spatial pressure heterogeneity on the feeding behavior of fiber materials, particularly in relation to the geometric parameters of the grinding disc teeth. The main objectives are to:

- Quantitatively characterize the saturated steam pressure distribution within the operational grinding chamber.
- Systematically reveal the effect of this pressure field's spatial heterogeneity on fiber material feed dynamics.
- Propose targeted solutions to mitigate operational issues (e.g., backflow blockage, insufficient refining) arising from pressure non-uniformity.

The outcomes of this research have dual significance. Firstly, the developed non-invasive pressure inversion technique offers a new paradigm for analyzing multi-field coupling mechanisms within enclosed high-temperature, high-pressure industrial equipment like hot mills. Secondly, it enables online diagnosis of the internal pressure distribution through relatively simple shell temperature monitoring. This capability provides a direct scientific basis for optimizing production process parameters and refining grinding disc structural design *(Chen, 2012*), ultimately contributing to enhanced fiber separation uniformity and reduced unit energy consumption in the wood-based panel industry.

MATERIALS AND METHODS

Experiment equipment

The experiment was conducted in a hot mill at a wood-based panel plant in North China. The grinding disc had a diameter of 1.6 m, with a grinding disc gap ranging from 0.2 mm - 0.3 mm. A high-precision industrial infrared thermometer (Victory Instruments VC304F) was used to temperature measurements, with a measurement range of -40°C to 600°C, a temperature measurement frequency of 10 Hz, and employing 9-point laser positioning technology. The instrument was supplied by Suzhou Roebuck Measurement and Control Technology Co., Ltd., Suzhou, China.

Experiment materials

Poplar (60%) + pine (30%) + birch (10%) with a moisture content of 45±2% and a size of 15×15×5 mm) were preheated and cooked (160°C, 3 min).

Experimental methods and procedures

(1) Experiment purpose

To measure the temperature at the shell node of the grinding chamber and establish a cross-scale mapping model of the "shell temperature field–internal steam pressure field" by solving the inverse heat conduction problem, in order to investigate the distribution pattern of saturated steam pressure within the grinding chamber.

(2) Experimental operation flow

Preparation stage:

Observe the real-time monitoring and control panel of the hot mill to ensure the normal operation of the machine during the experiment; check whether the indoor temperature is within the allowable range of the temperature measuring instrument, and whether the reading of the temperature measuring instrument is normal.

Experimental stage:

Heat transfer from the interior to the exterior of the grinding chamber constitutes a multidimensional heat conduction process. During refining, frictional heat generation between the grinding disk and fibrous material occurs across the entire grinding disk surface, making this surface a distributed heat source.

Heat diffusion perpendicular to the normal direction is driven by local temperature gradients. However, in the planar direction, heat flow is supplemented and compensated by adjacent heat fluxes, resulting in minimal net lateral transfer. Therefore, when establishing a simplified thermal model for this system, primary attention can be directed to a one-dimensional heat conduction approximation perpendicular to the grinding disk surface (as illustrated in Fig. 1).

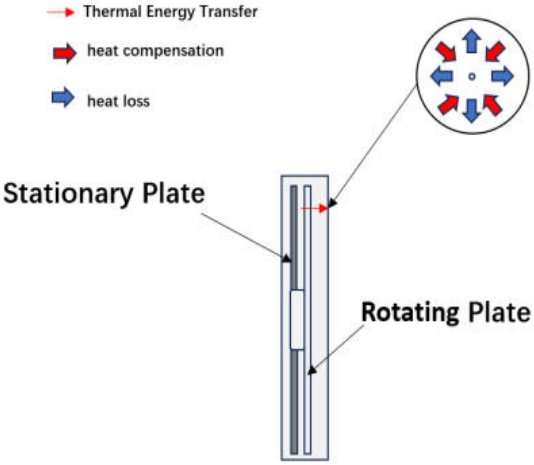


Fig. 1 - Grinding plate heat transfer analysis diagram

The pre-measurement points of the outer shell of the hot mill mode are divided. The outer circumference of the inlet is used as the initial measurement circumference, and the radius of the circumference is increased by 120 mm. Each measurement circumference is evenly distributed 12 points, a total of 84 measurement points, as shown in Fig. 2.

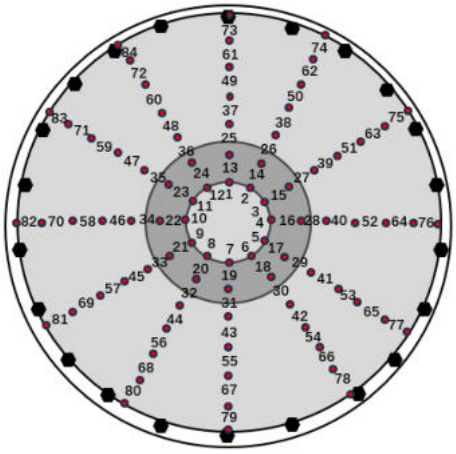


Fig. 2 - Experimental measurement point division

The temperatures at the above measurement points were measured using an industrial radiation thermometer positioned at 0.25 m from the measurement point (Fig. 3). Temperature data were recorded after the readings stabilized. Each measurement point was measured three times, and the average value was taken as the final recorded temperature.



Fig. 3 - Temperature measurement of outer shell of grinding chamber

The heat transfer from the interior of the grinding chamber to its shell is an extremely complex process. To simplify the problem and highlight the research focus *(Hua et al., 2015*), the following assumptions were made:

The shell of the hot mill grinding chamber has a uniform thickness.

The transient effect is neglected, and the heat conduction process is considered steady-state *(Chen et al., 2013)*.

Based on actual working conditions, the thermal conductivity of steam is treated as an average value.

The effects of friction and heat transfer between the fiber slurry and steam, as well as between the steam and the inner wall of the shell, are disregarded.

In the process of heat flux q transferring from the internal steam to the outer wall of the shell, two modes of heat transfer occur: (1) convection between the steam and the grinding disc of the hot mill, and (2) conduction from the grinding disc to the outer wall of the shell. These two heat transfer modes correspond to two kinds of thermal resistance, respectively, internal convective heat transfer thermal resistance - $Rconv=1/h_{in}A$ (h_{in} is the convective heat transfer coefficient between steam and inner wall, A is the heat transfer area), and wall thermal conductivity thermal resistance -d/kA (d is the thickness of wall and grinding disc, k is the thermal conductivity of grinding chamber wall).

Therefore, the total thermal resistance is as follows.

$$R_{\text{total}} = R_{\text{conv}} + R_{\text{cond}} = \frac{1}{h_{\text{in}} A} + \frac{d}{kA} \tag{1}$$

In steady state, the heat flux q satisfies.

$$q = \frac{T_{\text{steam}} - T_{\text{outer}}}{R_{\text{total}}} \tag{2}$$

where:

T_{steam} is the internal steam temperature corresponding to the measurement node;

T_{outer} is the experimental measurement node temperature.

Further combining the heat flux expressions $q=h_{in}$（T_{steam}- T_{inner}）and $T_{inner} = T_{outer}+qd/k$ (T_{inner} is the temperature of the inner wall of the disc), the internal steam temperature corresponding to the measurement node can be obtained by combining Formula (1) and Formula (2):

$$T_{\text{steam}} = T_{\text{outer}} \left(1 + \frac{h_{\text{in}} d}{k}\right) + \frac{qd}{k} \tag{3}$$

RESULTS

The temperature data of the measuring points are recorded as shown in Table 1.

Table 1

Temperatures of measuring points of outer shell of grinding chamber (°C)

Number of rounds/serial	1	2	3	4	5	6	7	8	9	10	11	12
1	133.6	132.5	133.7	134.6	135.9	131.2	131.8	133.6	133.9	135.9	135.6	135.0
2	135.5	137.6	137.4	135.9	140.0	138.9	137.6	139.6	136.7	137.5	140.0	136.6
3	150.6	152.5	157.5	157.7	156.5	155.4	152.3	155.6	156.4	152.5	155.3	157.5
4	160.6	166.4	167.4	163.2	166.9	166.4	167.2	162.3	164.9	165.3	167.3	168.3
5	177.4	177.3	172.5	174.7	179.0	176.5	179.2	173.4	178.8	175.0	176.9	174.9
6	170.0	170.0	169.5	170.0	168.8	167.5	170.0	168.9	169.4	168.3	170.0	169.4
7	165.6	163.9	165.0	163.3	164.5	165.0	163.3	164.3	164.2	165.0	163.4	164.7

According to Eq.(3) and industrial saturated steam pressure-temperature conversion software SteamTab, the experimental data of internal saturated steam temperature and pressure corresponding to the measurement points of the outer shell of the grinding chamber of the hot mill are obtained (as shown in Table 2).

Table 2

The measurement point of the outer shell of the grinding chamber corresponds to the internal saturated steam temperature / pressure table (°C/MPa)

Temperature / Pressure serial number	number of rounds	1	2	3	4	5	6	7
1		226.8/2.64	229.6/2.78	250.7/4.03	264.8/5.07	288.3/7.26	277.9/6.22	271.8/5.66
2		225.4/2.57	232.5/2.93	253.4/4.21	272.9/5.76	288.2/7.25	277.9/6.22	269.3/5.45
3		227/2.65	232.3/2.92	260.44.73	274.2/5.88	281.46.56	277.2/6.15	270.8/5.58
4		228.2/2.71	230.2/2.81	260.7/4.75	274.2/5.37	284.5/6.87	277.9/6.22	268.5/5.38
5		230/2.81	235.8/3.11	259/4.62	273.6/5.82	290.5/7.50	276.26.06	270.1/5.52
6		223.5/2.48	234.4/3.03	257.4/4.50	272.9/5.76	287/7.13	274.4/5.90	270.8/5.58
7		224.3/2.52	232,5/2.93	253.1/4.19	267.1/5.86	290.8/7.53	277.9/6.22	268.5/5.38
8		224.3/2.64	235.8/3.08	257.7/4.52	267.1/5.26	282.6/6.68	276.4/6.08	269.9/5.50
9		227.2/2.66	231.2/2.86	258.9/4.61	270.7/5.57	290.2/7.47	277/6.14	269.8/5.49
10		230.2/2.81	232.3/2.92	253.4/4.21	271.3/5.62	284.9/6.91	275.5/6.00	270.8/5.58
11		229.6/2.78	235.8/3.11	257.3/4.49	274.1/5.87	287.6/7.19	277.9/6.22	268.6/5.39
12		228.8/2.74	231.2/2.86	260.4/4.73	275.5/6.00	284.8/6.90	277/6.14	270.5/5.55

The temperature data at the entrance of the fiber slurry in the center of the grinding disc (as shown in Fig. 4) were obtained by measuring the junction point between the feeding spiral section and the entrance of the fiber slurry (215°C).

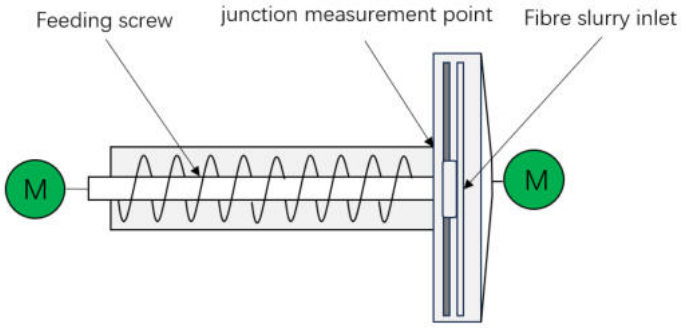


Fig. 4 - Schematic diagram of inlet end of fiber slurry

The afore-mentioned shell temperature and saturated steam pressure data of the mill chamber were imported into Origin software in the form of polar coordinates (ρ, θ, z). After matrix processing, the temperature distribution of the mill chamber shell and the internal saturated steam pressure distribution contour maps were generated, as shown in Fig. 5 and Fig. 6.

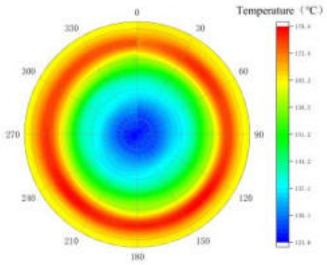


Fig. 5 - Temperature cloud diagram of grinding chamber shell

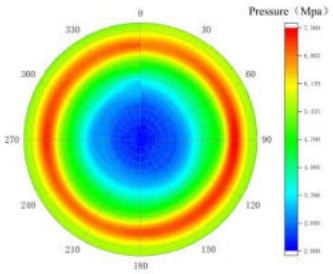


Fig. 6- The distribution of saturated steam pressure in the grinding chamber

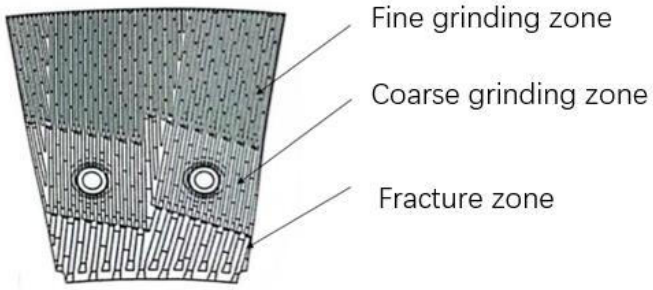


Fig. 7 - Grinding zone structure of grinding plate

Comparing the cloud image with the structure of the grinding area of the grinding disc (Fig. 7), the steam pressure shows a non-uniform distribution (first rising and then falling along the radial direction) in the crushing area, coarse grinding area and fine grinding area of the hot mill, which is due to the gradient change of the tooth shape parameters of the grinding disc (Table 3) and its synergistic regulation effect on the steam flow. The specific correlation mechanism is as follows:

Table 3

Grinding plate tooth profile parameters

Grinding plate partition	Tooth number	Tooth width [mm]	Tooth depth [mm]	Slot width [mm]	Tooth length [mm]	Tine angle [°]	Grinding gap [mm]
Fracture zone	48	8	10	21.2 ~36.3	95.1/259.2	56	0.30
Coarse grinding zone	312	4	9	5	18.9~148.0	39	0.25 ~0.27
Fine grinding zone	384	3	7	4	12.9~123.5	39	0.20

The tooth profile of the crushing zone is characterized by a wide tooth groove (the width of the groove is up to 21.2 ~ 36.3 mm, which is about 4 ~ 7 times that of the coarse grinding zone), the cross-sectional area of the steam channel (Ab = number of teeth × width of the groove × height of the tooth = 1.01 × 104 − 7.69 × 104mm^2) increases significantly, the flow resistance ($R \propto 1 / Ab^2$) decreases, and the large tooth inclination angle (φ = 56°) forms a divergent flow channel. The steam diffuses along the tooth surface, the pressure gradient is gentle (about 0.5 MPa/m), and the steam pressure has no obvious hindrance to the feed of the material. In this area, the centrifugal force plays a major role in the material. The overall material feed is stable and there is no risk of backflow.

When material reaches the primary grinding zone, the grinding gap narrows, subjecting coarse fibers to more intense and higher-frequency continuous dynamic loading. Concurrently, the presence of cross-bar teeth impedes rapid passage of steam and material within short timeframes. Consequently, rapid heat accumulation occurs within this confined space. At this time, the number of teeth increases to 312 (6.5 times of the crushing zone), the groove width decreases sharply to 5 mm, the cross-sectional area of the steam single channel decreases sharply (Ac = groove width × tooth height = 45mm^2), the cross-sectional area of the steam channel (Ab = tooth number × groove width × tooth height = 1.40 × 10^4), the flow resistance ($R \propto 1 / Ac^2$) is about 30 times higher than that of the crushing zone, and the pressure gradient reaches 3.6 MPa/m.

The saturated steam pressure reaches the peak at the junction of the coarse grinding zone and the fine grinding zone. The reason is that the material is changed from heat conduction to severe shear heating. According to the Clapeyron equation *(Liu et al., 2017*), the saturated vapor pressure has an exponential relationship with temperature ($P_{sat} \propto e - L/(RT)$, where L is the latent heat of vaporization).

Due to the centralized conversion of mechanical energy (from the kinetic energy of the disc rotor to thermal energy) and the location being at the junction where the cross-sectional area of the steam channel changes, material tends to accumulate in this region. This accumulation leads to a sharp local temperature increase, causing rapid vaporization of liquid water within the material. As a result, the steam generation rate in this area is significantly higher than in other regions. Under high pressure (8.5MPa), this can easily lead to material backflow along the radial direction of the grinding plate, ultimately causing blockages in material transmission.

When it reaches the fine grinding zone, the main component of the material is a small fiber bundle, and the way of heat generation is mainly concentrated in the high-speed crushing of the fiber bundle by the grinding teeth *(Hua et al., 2017*). The number of teeth in the fine grinding zone was further increased to 384 (23 % more than that in the coarse grinding zone), the gap between the grinding plates was reduced to 0.20 mm (80 % of that in the coarse grinding zone), and the cross-sectional area of the steam channel was reduced to 1.07 × 104 mm^2. However, due to the higher linear velocity in this region and the closer distance to the fiber outlet, the steam has enough centrifugal force to escape quickly from the outlet. When material reaches the primary grinding zone, the grinding gap narrows, subjecting coarse fibers to more intense and higher-frequency continuous dynamic loading. Concurrently, the presence of cross-bar teeth impedes rapid passage of steam and material within short timeframes. Consequently, rapid heat accumulation occurs within this confined space.

The sudden increase in tooth number density and the abrupt decrease in groove width in the rough grinding zone are the primary causes of the reverse pressure gradient. To prevent material blockage, the feed flow can be optimized by gradually increasing the tooth width and reducing the number of teeth in the rough grinding zone. To address the issue of overly fast feeding and insufficient fiber dissociation in the fine grinding zone, the number of grinding teeth in this area can be further increased to create multiple steam escape barriers, thereby slowing the steam escape rate. At the same time, the frequency of grinding tooth interaction with fiber is increased, promoting more thorough fiber dissociation.

CONCLUSIONS

The proposed non-invasive pressure inversion method overcomes the limitation of traditional invasive sensors, which cannot operate in harsh environments, and provides a new paradigm for multi-field coupling analysis of closed high-temperature and high-pressure equipment.

A cross-scale mapping model of “shell temperature field-internal steam pressure field” was established to analyze the distribution of saturated steam pressure in the grinding chamber and its influence on the feed of fiber materials. The results showed that the saturated steam pressure in the grinding chamber presented a non-uniform distribution along the radial direction of ”low pressure slow rise in the crushing zone (2.52-3.11 MPa)→ high pressure peak in the junction area between the coarse grinding zone and the fine grinding zone (6.00-7.53 MPa)→ rapid attenuation in the fine grinding zone (7.19-5.38 MPa)”. This phenomenon is due to the gradient change of the tooth shape parameters of the grinding disc. The fiber material is easy to cause the backflow blocking phenomenon in the coarse grinding area of the grinding plate, and the feed speed is too fast and the grinding is not sufficient in the fine grinding area. Solutions are proposed involving the use of progressive tooth width, reducing the number of teeth in the coarse grinding area, and increasing the number of teeth in the fine grinding area.

REFERENCES

[1] Chen G. (2012). *Model analysis and experimental study on the fiber separation mechanism of thermo-milling flakes (热磨法磨片纤维分离机理的模型分析与实验研究)* [D]. Northeast Forestry University.

[2] Chen K., Xu X., Ma K. (2013). Transient temperature field analysis of two-way gradient plate under heat flux / convective heat transfer boundary (热流密度/对流换热边界下双向梯度板的瞬态温度场分析) [J]. *Journal of Applied Mechanics*, Vol.30 (4), pp.563-568 + 648.

[3] Fokko S., Ju¨rgen P.,Bodo S.(2011). Optimization of steam pretreatment conditions for enzymatic hydrolysis of poplar wood *Eero [J]. *Holzforschung*, Vol. 65, pp. 453–459, 2011.

[4] Hua J., Chen G., Liu L. (2015). Numerical simulation of fiber flow in grinding flow field (纤维在研磨流场区域流动状况的数值模拟) [J]. *Journal of Northeast Forestry University*, Vol.43 (4), pp.113-118 + 130.

[5] Hua J., Lin X., Chen G. (2017). Establishment of fiber trajectory model in fine grinding zone and solution of grinding frequency (磨片精磨区纤维轨迹模型的建立及磨齿作用频数的求解) [J]. *Journal of Northeast Forestry University*, Vol.45 (04), pp.94-98.

[6] Liu F., Dong P., Wang G. (2020). New saturated vapor pressure and mass transfer coefficient test device (新型饱和蒸汽压及传质系数测试装置) [J]. *Laboratory research and exploration*, Vol, 39 (7), pp.71-73 + 83.

[7] Liu X., Lai H., Qu J. (2017) Discussion on the derivation of Clapeyron equation (关于 Clapeyron 方程推导的探讨) [J]. *Shandong Chemical Industry*, Vol.46 (16), pp.171 + 173.

[8] Min Ta, Han Y. (2022). Numerical solution of the inverse problem of initial conditions for two-dimensional heat conduction equations (二维热传导方程初始条件反问题的数值求解) [J]. *Mathematics*, Vol.42 (6), pp.513-522.

[9] Takasawa R., Shan N., Lin Z. (2019) The effect of initial moisture content and cooking time on the physical properties of MDF and cooking loss was studied (チップの初期含水率及び蒸煮時間が MDF 物性に及ぼす影響) [J]. *Journal of the Wood Society*, Vol. 65(1), pp.3-18.

[10] Trairat N., Siqun W., Xiaofei P.(2008). Effects of refining steam pressure on the properties of loblolly pine (Pinus taeda L.) fibers [J]. *Holzforschung*, Vol. 62, pp. 556-561.

[11] Wang C. (2025). Electrical Design of Grinding Disc Gap Control Based on Fiber Power Consumption (热磨机根据纤维功耗控制磨片间隙的电气设计) [J]. *China Wood-based Panels*, Vol.32 (2), pp.19-23.

[12] Wu J., Pan D., Huang L. (2015). Research, application and development of grinding plate of hot mill in China (我国热磨机磨片的研究应用及发展) [J]. *Casting technology*, Vol.36 (10), pp.2443-2447.

[13] Xiong J., Shen J., Song R. (2014). Factors affecting fiber quality during hot milling and solutions (热磨过程中影响纤维质量的因素及解决方法) [J]. *Forestry machinery and woodworking equipment*, Vol.42 (8), pp.38-39.

[14] Zhang S., Yan J., Hua J. (2016). Analysis of influencing factors of energy dissipation in fiber separation by hot milling (热磨法纤维分离能量耗散影响因素的分析) [J]. *Forestry industry*, Vol.43 (6), pp. 42-45.

CALIBRATION AND TESTING OF SIMULATION PARAMETERS FOR RAPESEED BLANKET SEEDLING SHEETS BASED ON DISCRETE ELEMENT METHOD
/
基于离散元法的油菜毯状苗的苗片仿真参数标定与测试

Qing TANG [1,2], Jing LUO[1], Minghui HUANG[2], Jun WU[1], Lan JIANG[*1], Zhewen SONG[2], Wei SHI[2], Yang WU[2]
[1] Nanjing Institute of Agricultural Mechanization, Ministry of Agriculture and Rural Affairs of China, Nanjing 210014 / China;
[2] Sinomach Changlin Company Limited, Changzhou 213002 / China;
Corresponding author: Lan JIANG
Tel: +86.17372778343; E-mail: jianglan@caas.cn

DOI: https://doi.org/10.35633/inmateh-76-65

Keywords: *discrete element simulation, maximum shear force, parameter calibration, EDEM, JKR Contact Model, rapeseed blanket seedlings*

ABSTRACT
It is difficult to accurately calculate the mutual force and seedling loss law between seedling needles and seedlings when conducting simulation analysis of cutting and transplanting rapeseed blanket seedlings with a transplanting machine due to a lack of reliable discrete element simulation parameters for rapeseed blanket seedlings. The physical and contact parameters of rapeseed blanket seedlings are calibrated in this study using the EDEM discrete element method. The Hertz Mindlin with JKR model in EDEM software was used to simulate the shear force of rapeseed blanket seedlings after conducting experiments to determine the density, shear modulus, Poisson's ratio, friction coefficient, and collision recovery coefficient between seedlings and steel materials. The surface energy parameters, recovery coefficient, static friction coefficient, and rolling friction coefficient between seedlings were used as experimental variables, with the maximum shear force of seedlings serving as the response value. Using Box Behnken's response surface optimization method, multiple regression fitting analysis was performed on the experimental results to obtain the regression model of seedling shear force, which was then optimized to obtain the parameter optimization solution for rapeseed blanket seedlings. Finally, the collision recovery coefficient was calculated to be 0.6. The ideal contact characteristics for seedlings are a static friction coefficient of 0.8, a rolling friction coefficient of 0.3, and a JRK surface energy of 12.3 J/m^2.

摘要
在进行油菜毯状苗移栽机切块取苗仿真分析时，由于缺乏可靠的油菜毯状苗的苗片离散元仿真参数，难以准确计算取苗秧针-苗片相互间受力和苗片损失规律。本研究基于 EDEM 离散元法对油菜毯状苗的苗片物理与接触参数进行标定。通过试验测定苗片密度、剪切模量、泊松比以及苗片-苗片、苗片-钢材料之间的摩擦系数和碰撞恢复系数，采用 EDEM 软件中的 Hertz-Mindlin with JKR 模型对油菜毯状苗的苗片进行剪切力仿真试验，以苗片间表面能参数、恢复系数、静摩擦系数、滚动摩擦系数为试验因素，以苗片最大剪切力为响应值，基于 Box-Behnken 的响应面优化方法，对试验结果进行多元回归拟合分析得到苗片剪切力的回归模型，并对回归模型进行寻优，得到油菜毯状苗苗片的参数优化解，最终确定碰撞恢复系数 0.6、静摩擦系数 0.8、滚动摩擦系数 0.3、JRK 表面能 12.3 J/m^2 是苗片的最优接触参数组合。

INTRODUCTION
The rapeseed blanket seedling transplanter accurately separates seedlings from seedlings while also improving the speed and efficiency of seedling extraction through mechanized operation *(Yu Gaohong et al., 2022)*. During the seedling-picking process, the seedling-picking mechanism splits the seedling pieces into seedling blocks, which can easily cause damage and impact planting quality. Traditional physical experiments fail to adequately determine the damage mechanism of seedling blocks during the seedling harvesting procedure. Virtual simulation is the only way to model the dynamic process of seedling particle mobility and interaction. Before employing the discrete element approach to simulate the interaction between soil-contacting components and seedlings, the simulation parameters between seedling particles must be calibrated.

In agricultural engineering, research on discrete element parameter calibration is mostly focused on soil and agricultural material particles *(Zeng et al., 2021; Chan et al., 2021)*. In the field of soil discrete element parameter calibration, for example, *Xiaoning He et al. (2024)* used Hertz Mindlin and Johnson Kendall Roberts (JKR) models to calibrate the contact parameters between saline soil particles as the test factor and soil accumulation angle as the test index and conducted saline soil contact parameter calibration experiments to determine the optimal combination of saline soil contact parameters. *Shaochuan LI et al. (2023)* studied no-till soil and determined the Edinburgh Elasto Plastic Adhesion (EEPA) model as the soil contact model by obtaining the relationship between loading force and deformation through uniaxial sealing compression tests. They used the Plackett Burman test and quadratic orthogonal rotation test to establish regression equations and analyze the interaction effects. The measured values of stacking angle and strain were obtained through the stacking angle test and uniaxial sealing compression test, and the optimal solution was obtained. The simulation values and measured values under the optimal parameters were compared and verified, and it was found that the error values were less than 1%. *Bin Chen et al. (2022)* calibrated the contact parameters between soil particles using the soil angle of repose test and between soil and machinery using the soil sliding test. The Hertz Mindlin JKR contact model was used for soil particles, and the Hertz Mindlin (no slip) contact model was used for soil particles and steel components. The errors between the simulation test and the physical test were 3.94% and 3.66%, respectively, through the stacking angle test and sliding angle test. These studies mainly focus on the discrete element parameters of pure soil, often using the JKR model and soil accumulation tests for parameter calibration. However, the actual soil is complex and often contains other biomass such as straw, roots, etc. Pure soil cannot fully reflect the actual soil state. *Zenghui GAO et al. (2022)* used the Hertz Mindlin with JKR contact model for parameter calibration of wheat straw soil mixture. The stacking angle test, Plackett Burman screening method, and steepest slope test were used to determine the optimal combination range of each parameter, and the Box Behnken test was used to find the optimal solution. *Shilin Zhang et al. (2022)* selected the Hertz Mindlin with JKR Cohesion contact model for maize root and soil mixtures and developed DEM models for maize single roots (SMR) and maize root soil mixtures (MRSM) with different diameters based on calibration parameters through angle of repose experiments. In the study of agricultural materials such as seeds and straw, *Guoqiang Dun et al. (2024)* selected the Hertz Mindlin no-contact model as the simulation contact model for Chinese cabbage seeds. Physical experiments were conducted to determine the basic physical and contact parameters of Chinese cabbage seeds. Based on the results of the physical experiments, the simulation parameter range was determined. The Plackett Burman experiment was used to screen the factors that significantly affect the stacking angle from each group of experimental parameters, and the optimal range of the two factors was further determined through the steepest climbing experiment. The regression equation between the significant parameters and the stacking angle is obtained through a second-order universal rotation combination test, and the optimal parameter combination is obtained by optimizing the measured stacking angle. *Min Fu et al. (2023)* used crushed corn stover as the research object and calibrated simulation parameters using a combination of physical measurements and virtual experiments. A Hertz Mindlin with JKR Cohesion contact model was used to establish a discrete element model for crushed corn stover, and virtual stacking experiments were conducted using EDEM software. The above research indicates that by comparing the simulated test angle of repose and the actual pile-up test angle of repose through pile-up experiments to determine the discrete element parameters, it can be found that such research objects are generally flowable bulk particles, but for materials that are not easy to flow, calibration cannot be completed through pile up experiments. Scholars at home and abroad have also researched this issue, *Guoyang Liu et al. (2021)* concatenated a nonlinear viscoplastic model with a Burgers model to form a nonlinear viscoelastic plastic model, and introduced creep test curves into the model for fitting. Through verification experiments, the nonlinear model was compared with the Burgers model, and the results showed that the fitting accuracy of the nonlinear model was better than that of the Burgers model. *Jiawei Xu et al. (2023)* combined Hertz Mindlin with bonding cohesive and Hertz Mindlin cohesive contact models (reflecting the cohesiveness and structure of soft clay, respectively) to reproduce the bonding process of clay, and established numerical models for lateral compression test, cross plate shear test, and triaxial test. The deformation and stress-strain development were in good agreement with the experimental results. *Syfur Rahman et al. (2020)* developed a discrete element model for cohesive soil mixtures using random irregular particle combinations with different microbonding strengths. The microscale model parameters are determined by macroscopic characteristics obtained from laboratory compression tests and calibrated based on actual stress-strain behavior. The indirect tensile test simulation is highly consistent with the actual stress-strain behavior of soil mixtures.

Hongbin Bai et al. (2023) applied the Hertz Mindlin with bonding model to model the matrix block, and used the maximum puncture force as the evaluation index. The two-level factorial test and steepest climbing test were used to screen for significant parameters and optimal intervals. Through the Box Behnken test and optimization solution, the optimal combination of bonding parameters for the matrix block particles was obtained. Simulation verification was carried out for the optimal parameter combination, and the relative error between the simulated value and the measured value of the maximum puncture force was 1.88%. These studies provide new parameter calibration experimental methods that can determine the optimal discrete element parameters through stress-strain comparison experiments.

Therefore, based on the characteristics of rapeseed blanket seedlings, physical experiments were used to determine the basic physical parameters of rapeseed blanket seedlings, including density, shear modulus, Poisson's ratio, as well as the friction coefficient and collision recovery coefficient between seedlings and steel materials, based on the shear force test of seedlings. Using EDEM software to construct a simulation model of seedlings, with maximum shear force as the evaluation index, using Design Expert software to determine the optimal values of seedling simulation parameters, and conducting calibration experiments on seedling contact parameters, providing basic parameters for the discrete element simulation of rapeseed blanket seedlings.

MATERIALS AND METHODS

Particle modeling of seedling sheets

The rapeseed variety is Ningza 1838. The seedling substrate is spread in plastic seedling trays with a length, width, and height of 300 mm, 600 mm, and 30 mm. The rapeseed seeds are sown according to the prescribed row spacing and plant spacing to cultivate carpet-like seedlings (Figure 1a). The seedling age is 30 days, the seedling height is 90 mm, and the seedling density is 3500 plants/m^2. The seedling substrate mainly includes substances such as coconut coir, peat, and vermiculite. After 30 days of growth, the root system and seedling substrate interweave to form a whole, forming seedling pieces with a thickness of 20 mm. The seedling piece sample used in the experiment is the part of the seedling above the cut seedling piece (Fig.1b).



(a) Rapeseed blanket seedling *(b) Seedling slice sample*

Fig. 1 - Rapeseed blanket seedling sheets

Density determination of seedling sheets

Select 10 samples of seedlings with dimensions of 30 mm × 30 mm × 20 mm, measure the mass of seedlings using a high-precision electronic scale, calculate the density of seedlings according to equation (1), and take the average value, that is, ρ=830 kg/m^3

$$.\rho = \frac{m}{V} \tag{1}$$

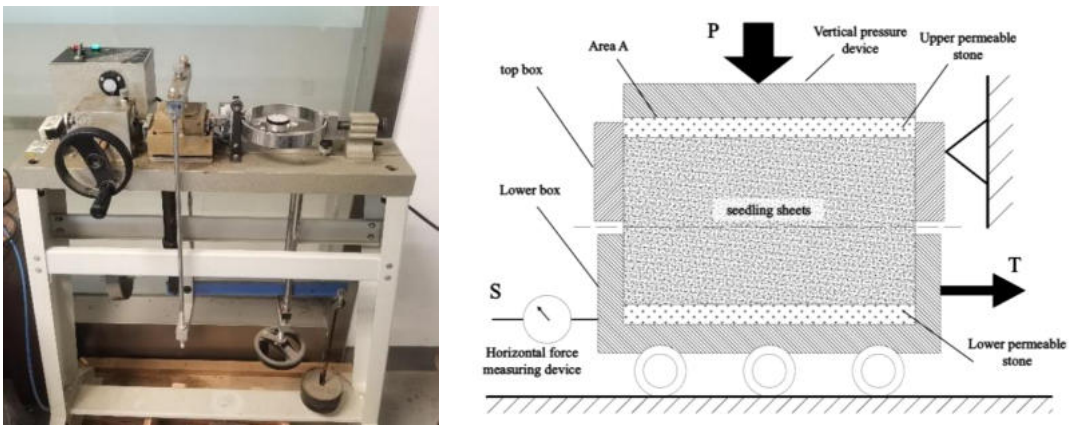
ρ is the density of seedlings, [kg/m^3]; m - mass of the seedling, [kg]; V - volume of the seedling sample, [m^3].

Shear modulus determination of seedling sheets

The TJ strain-controlled three-speed electric soil direct shear apparatus (Figure 2a) produced by Nanjing Soil Instrument Factory is used for seedling shear tests. The sampling ring knife provided with the direct shear apparatus is used to vertically press into the seedlings and take out a circular cake-shaped carpet-shaped seedling sample with a thickness of 20 mm and a cross-sectional area of 30 cm^2. It is placed between the upper and lower boxes (Figure 2b), loaded with a 1:12 lever, and two normal loads of 400kPa and 200kPa are used. A fast-cutting method with a cutting speed of 0.8 mm/min is adopted. The shear modulus of the seedlings calculated by formula (2) is G=0.22 MPa.

$$G = \frac{\tau}{\gamma} \tag{2}$$

where G is the shear modulus, [N/m^2]; τ is the shear stress, [N/m^2]; γ is the shear strain, dimensionless.



a) TJ Type Direct Shear Instrument *b) Shear Principle*

Fig. 2 - TJ type direct shearing instrument and shearing principle

Poisson's ratio of rapeseed blanket seedling sheets

Poisson's ratio refers to the ratio of lateral deformation to axial deformation of seedlings under unidirectional tension or compression and is an elastic index reflecting the lateral deformation of seedlings. During the experiment, the seedlings were made into standard cubic specimens with a side length of 20 mm, and the Poisson's ratio of the seedlings was calculated using formula (3) to obtain μ=0.3034.

$$\mu = \left|\frac{\delta_1}{\delta_2}\right| = \frac{W_1 - W_2}{L_1 - L_2} \quad (3)$$

where μ is Poisson's ratio, δ_1 is the lateral deformation amount, [mm]; δ_2 is the axial deformation amount, [mm]; W_1 and W_2 are the transverse dimensions before and after compression, [mm]; L_1 and L_2 are the axial dimensions of the seedlings before and after compression, [mm].

Friction coefficient

The static friction coefficient is the ratio of the maximum static friction force experienced by an object to the normal pressure. The inclined sliding method is used to measure the static friction coefficient between seedlings and steel plates, as well as between seedlings (Figure 3a). During the experiment, the stainless steel plate is adjusted to a horizontal state. When measuring the static friction coefficient between the seedling and the steel, the 20 mm cube seedling sample is directly placed on the stainless steel plate. When measuring the static friction coefficient between seedlings, lay the seedlings with a length x width of 580 mm x 280 mm flat on a stainless steel plate, and place a 20 mm cube seedling sample on the seedlings. Place the electronic angle meter on a stainless steel plate for easy observation of the angle degree. Slowly lift one end of the stainless steel plate to increase the tilt angle. When the seedling sample starts to slide down the slope, stop and record the angle α displayed on the electronic protractor. Apply formula (4) to calculate the static friction coefficient.

$$f_1 = \tan\alpha \quad (4)$$

where f_1 is the static friction coefficient; α is the critical angle of static friction, [°].

The rolling friction coefficient between seedlings and steel plates, as well as between seedlings, was measured using the inclined rolling method (Figure 3b). In two experiments, seedlings were made into 20 mm diameter spherical specimens and released at zero initial velocity on an inclined panel with an inclination angle of β=15 ° and a vertical height of H_2=80 mm.

The spherical specimens rolled downwards along the inclined panel for a distance S. Due to rolling friction, the spherical specimens finally rolled a distance L_2 on the horizontal panel and stopped. Assuming that the spherical specimens were ideal spheres, they were only affected by rolling friction during pure rolling, and the rolling friction coefficient was calculated according to equation (5).

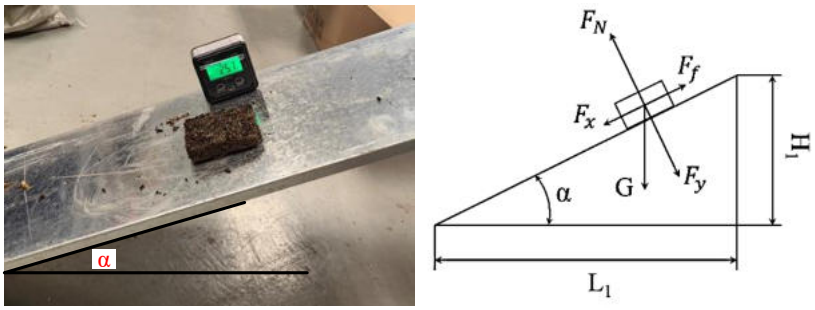
$$f_2 = \frac{S\sin\beta}{S\cos\beta + L_2} \quad (5)$$

where:

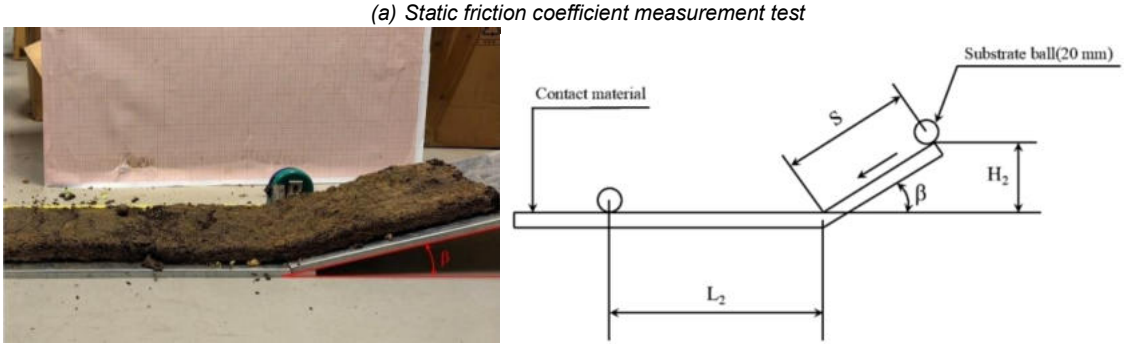
f_2 is the rolling friction coefficient;

β is the angle set for the stainless steel plate, [º];

L_2 is the horizontal rolling distance of the spherical sample, [mm].



(a) Static friction coefficient measurement test



(b) Rolling friction coefficient measurement test

Fig. 3 - Friction coefficient measurement test

The average static friction coefficient between the seedlings and the steel plate was calculated to be 0.441, and the rolling friction coefficient was 0.0621. The average static friction coefficient between seedlings is 1.0312, and the rolling friction coefficient is 0.4223.

Collision recovery coefficient

As shown in Figure 4, the collision recovery coefficients between seedlings and seedlings, as well as between seedlings and stainless steel plates, were measured using the free fall collision method. During the experiment, a 20 mm diameter spherical sample was released at a height of H=250 mm from the contact bottom surface. The entire release collision process was recorded by a high-speed camera. The spherical sample bounced back when it hit the contact material (seedling or stainless steel plate), and the highest rebound height h was recorded. The collision recovery coefficient ex is the ratio of the normal instantaneous separation velocity v_1 and instantaneous contact velocity v_0 at the collision contact point before and after the collision between the spherical sample and the contact material, that is, the ratio of the maximum collision rebound height h to the initial falling height H, calculated by formula (6).

$$e_x = \frac{v_1}{v_0} = \frac{\sqrt{2gh}}{\sqrt{2gH}} = \sqrt{\frac{h}{H}} \quad (6)$$

where e_x is the collision recovery coefficient; v_1 is the instantaneous normal velocity of the spherical specimen before collision, [mm/s]; v_0 is the instantaneous normal velocity of the spherical specimen after collision, [mm/s]; h is the initial release height of the spherical sample, [mm]; H is the initial release height of the spherical sample, [mm].

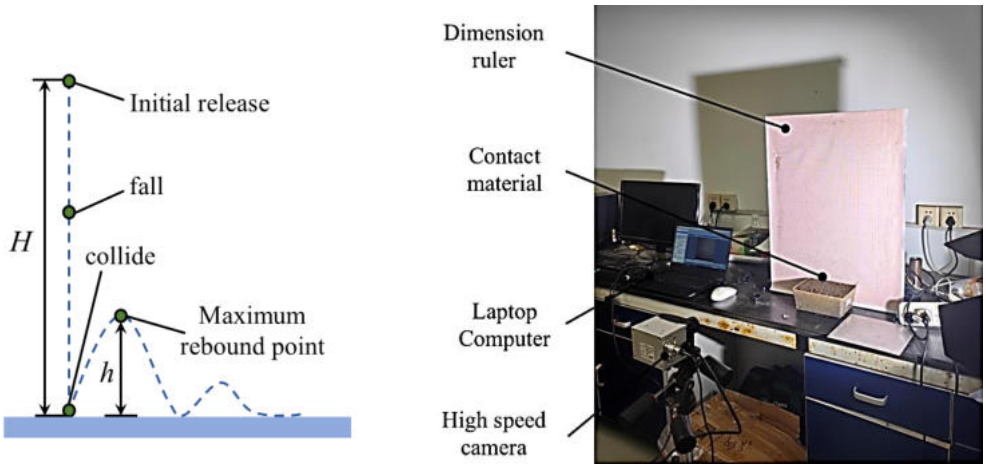


Fig. 4 - Collision Recovery Coefficient Measurement Test

Record the height before deployment and the height of the highest point after collision through high-speed photography, repeat each experiment 5 times, calculate the collision recovery coefficient using equation (6), and take the average of the results. The recovery coefficient for collision between seedlings and stainless steel plates is 0.728, and the recovery coefficient for collision between seedlings is 0.4129.

Determination of particle contact models for seedling sheets

The Hertz Mindlin with JKR model is a cohesive contact model that combines Hertz contact theory with JKR theory to consider the influence of interparticle bonding forces on particle motion. It is suitable for simulating materials with significant bonding and agglomeration between particles, such as crops and soil *(Sun Jingbin et al, 2022; Wu Tao et al, 2017; Tian Xinliang et al, 2021)*. For the large adhesion force between the seedlings of rapeseed blanket-like seedlings, this paper selects the Hertz Mindlin with the JKR model to simulate the seedlings and calibrate the contact model parameters accordingly. When simulating wet particles using the Hertz Mindlin with JKR contact model, the force required to separate two particles depends on the liquid surface tension γ_s and wetting angle, as shown in equation (7).

$$F_p = -2\pi\gamma_s\cos(\theta)\sqrt{R_i R_j} \quad (7)$$

where F_p is the force required to separate two particles, [N]; θ is the contact angle, [°]; R is the particle radius, [mm]. Equivalent this force to the maximum cohesive force of JKR $F_p = -\frac{3}{2}\pi\gamma R^*$, where γ is the surface energy and R^* is the equivalent radius. If EDEM particles are not scaled proportionally, parameter estimation of JKR surface energy can be performed.

Seedling sheets calibration test

The JKR contact parameters (coefficient of elastic recovery, coefficient of static friction, coefficient of kinetic friction, and JRK surface energy) between seedling particles were used as testing factors, and the maximum shear force was used as the testing indicator for seedling particle contact parameter testing. As shown in Figure 5, 5 seedling specimens with dimensions of 150 mm x 100 mm x 20 mm were taken and placed on a universal mechanical testing machine. The specimens were vertically cut with a cutting blade held in place, and the average maximum shear force was obtained as 35 N.



Fig. 5 - Seedling cutting test

The test level was set based on the values of the recovery coefficient, static friction coefficient, and rolling friction coefficient of the seedlings obtained from the measurement (Table 1). The surface energy of JKR was determined according to the reference literature *(Gao et al., 2022; L. Yang et al., 2024; Q. Yang et al., 2023)*, surface energy was set as reference values at levels of 5 J/m², 10 J/m², and 15 J/m².

Table 1

Factors and Levels of Shear Force Simulation Test

code	JKR surface energy A/ J/m²	Recovery coefficient B	Static friction coefficient C	Rolling friction coefficient D
-1	5	0.3	0.4	0.1
0	10	0.6	0.8	0.5
1	15	0.9	1.2	0.9

RESULTS

Simulation calibration test

The simulation model of seedling cutting is shown in Figure (6). The cutting blade used in the experiment is made of stainless steel material, and the material properties refer to the literature *(Zhu Yinghao et al., 2020)*. The density is 7.85 g/cm3, Poisson's ratio is 0.3, and the shear modulus is 79000MPa. By using EDEM software to construct the particle structure of seedlings, and following the Box Behnken four-factor three-level experimental design method, an experimental plan was developed using the factor levels listed in Table 1 using Design Expert 13.0 software. Vertical cutting simulation experiments of seedlings were conducted based on the experimental plan. To avoid calculation errors each time, each test group was repeated three times and the average value was taken as the test result. After determining the test results, determine the difference between the test results and the actual shear force of the seedlings. The test plan and its results are shown in Table 2.

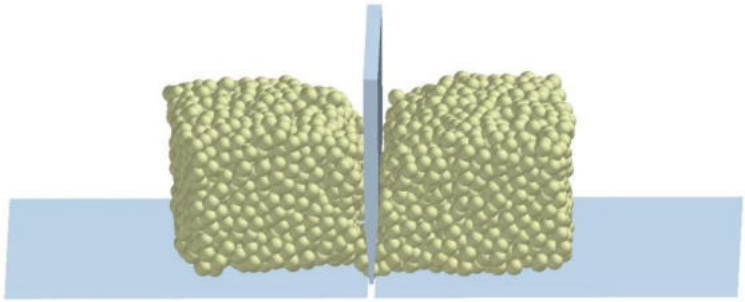


Fig. 6 - Simulation experiment of seedling cutting

Table 2

Design and Results of Shear Force Simulation Experiment on Rapeseed Blanket Seedlings Matrix

Test number	JKR surface energy A/ J/m^2	Recovery coefficient B	Static friction coefficient C	Rolling friction coefficient D	Shear force Y/N
1	10	0.3	0.8	0.1	10.17
2	10	0.3	1.2	0.5	12.97
3	10	0.6	1.2	0.1	9.89
4	5	0.9	0.8	0.5	34.46
5	10	0.9	0.8	0.1	9.62
6	10	0.6	0.4	0.1	30.55
7	5	0.6	0.4	0.5	34.93
8	10	0.6	0.8	0.5	71.73
9	15	0.9	0.8	0.5	35.2
10	10	0.3	0.8	0.9	10.19
11	10	0.3	0.4	0.5	15.12
12	10	0.6	1.2	0.9	17.93
13	10	0.9	0.8	0.9	13.03
14	10	0.9	1.2	0.5	10.39
15	5	0.6	1.2	0.5	27.37
16	5	0.3	0.8	0.5	25.56
17	10	0.6	0.8	0.5	69.13
18	15	0.6	0.4	0.5	46.6
19	15	0.6	0.8	0.9	42.3
20	5	0.6	0.8	0.1	33.92
21	15	0.6	1.2	0.5	40.4
22	15	0.6	0.8	0.1	39.4
23	10	0.6	0.8	0.5	71.72
24	10	0.6	0.4	0.9	21.57
25	15	0.3	0.8	0.5	36.7
26	10	0.6	0.8	0.5	69.69
27	5	0.6	0.8	0.9	24.55
28	10	0.9	0.4	0.5	27.03
29	10	0.6	0.8	0.5	68.43

Result analysis

According to the experimental factor levels in Table 2, shear force simulation experiments were conducted, and regression analysis of variance was performed on the experimental results. The results are shown in Table 3. Through multiple regression analysis of the experimental data, the shear force regression model for rapeseed blanket seedling substrate was obtained as follows:

$$Y = 70.14 + 4.98A + 1.58B - 4.74C - 0.3317D + 3.07AD - 3.62BC + 4.26CD - \\ -7.81A^2 - 30.43B^2 - 23.64C^2 - 27.59D^2 \quad (8)$$

Among them, coefficient of determination $R^2 = 0.9895$ and correction coefficient of determination $Adj - R^2 = 0.9827$.

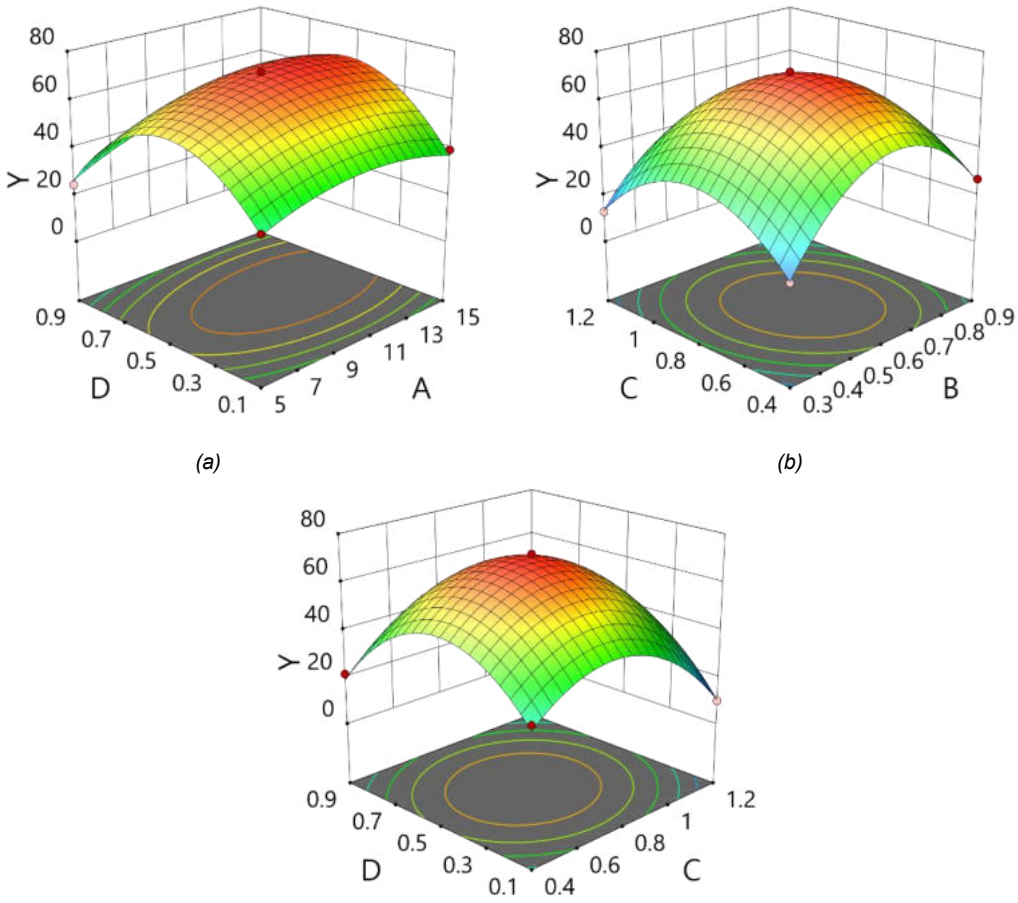
According to Table 3, the P-value of the model is less than 0.0001, indicating that the model is highly significant and can be used to predict the maximum shear force between matrices. Within the reference range of experimental factors, A, B, and C have a significant impact on the maximum shear force, with C being extremely significant. The rolling friction coefficient D has no significant impact on the maximum shear force, but D^2 is significant. The interaction between AD, BC, and CD is significant.

Table 3

Variance analysis of regression model for matrix shear force of rapeseed blanket seedlings

Source	Sum of Squares	df	Mean Square	F-value	p-value
Model	11517.43	14	822.67	125.78	< 0.0001
A	298.1	1	298.1	45.58	< 0.0001
B	30.15	1	30.15	4.61	0.0498
C	269.33	1	269.33	41.18	< 0.0001
D	1.32	1	1.32	0.2018	0.6601
AB	27.04	1	27.04	4.13	0.0614
AC	0.4624	1	0.4624	0.0707	0.7942
AD	37.64	1	37.64	5.75	0.0309
BC	52.49	1	52.49	8.03	0.0133
BD	2.87	1	2.87	0.4393	0.5182
CD	72.42	1	72.42	11.07	0.005
A^2	395.31	1	395.31	60.44	< 0.0001
B^2	6004.58	1	6004.58	918.06	< 0.0001
C^2	3623.95	1	3623.95	554.08	< 0.0001
D^2	4937.72	1	4937.72	754.94	< 0.0001
Residual	91.57	14	6.54		
Lack of Fit	82.4	10	8.24	3.59	0.1146
Pure Error	9.17	4	2.29		
Cor Total	11608.99	28			

To explore the interaction between the four testing factors and the response values, according to Table 3, the interaction between AD, BC, and CD has a significant impact on the maximum shear force and response surface and contour distribution of seedlings, as shown in Figure 7. The curvature of the response surface indicates that the order of the influence of interaction terms on the maximum shear force of seedlings is CD>BC>AD. As shown in Figure 7 (a), the maximum shear force of seedlings increases first and then decreases with the increase of dynamic friction coefficient and collision recovery coefficient. The maximum shear force of seedlings changes with the simultaneous increase of both, and the impact of the collision recovery coefficient on the maximum shear force of seedlings is minimal. From Figure 7 (b), it can be seen that the maximum shear force of seedlings increases first and then decreases with the increase of static friction coefficient and collision recovery coefficient, and the two interact with each other. The maximum shear force of seedlings changes with the simultaneous increase of both. Figure 7 (c) shows that the maximum shear force of seedlings increases first and then decreases with the increase of static friction coefficient and dynamic friction coefficient, and the two interact with each other. The maximum shear force of seedlings changes with the simultaneous increase of both.



(a) (b)

(c)

Fig. 7 - Maximum Shear Force Interaction of Seedlings

(a) AD Effect on maximum shear stress of matrix; (b) BC Effect on maximum shear stress of matrix; (c) CD Effect on maximum shear stress of matrix

Parameter optimization and validation

The maximum shear force physical experiment measured that the maximum shear force of the matrix sample under shear was 35 N. Through the optimization module of Design Expert software, the regression model was optimized with the maximum shear force of the matrix sample as the objective, and an optimized solution similar to the maximum shear force of the matrix sample was selected. The simulation results show that when the surface energy of JKR between matrices is 12.3 J/m^2, the recovery coefficient is 0.6, the static friction coefficient is 0.8, and the rolling friction coefficient is 0.3, the simulation result is 36.1 N, which is close to the average value of 35 N in physical experiments, with a relative error of 3.14% (Figure 8).

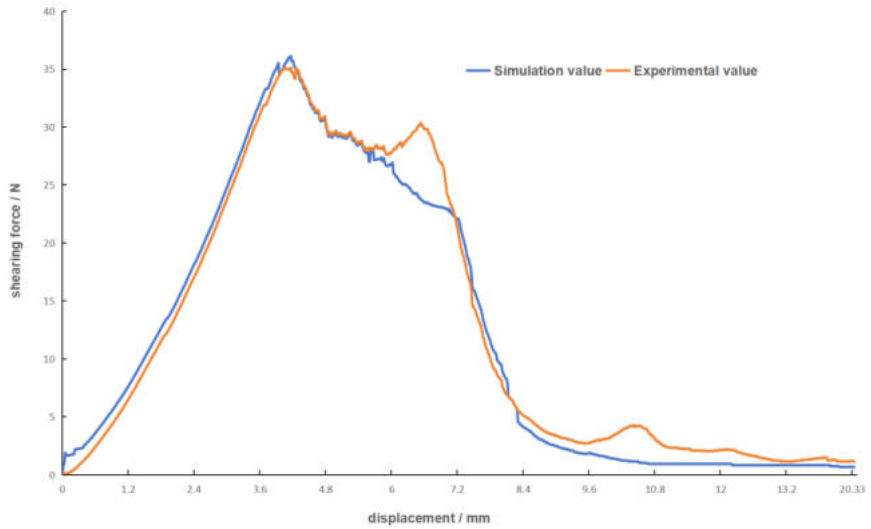


Fig. 8 - Comparison of Shear Force Test and Simulation Results of Seedlings

CONCLUSIONS

This study measured the physical parameters of rapeseed blanket seedlings and obtained a seedling density of 830 kg/m^3, a shear modulus of G=0.22 MPa, a Poisson's ratio of μ=0.3034, a static friction coefficient of 0.441 between seedlings and steel plates, a dynamic friction coefficient of 0.0621 between seedlings and steel plates, and a collision recovery coefficient of 0.728 between seedlings and steel plates. Based on the discrete element method, Hertz Mindlin with the JKR model was used to simulate the substrate suitable for planting rapeseed blanket seedlings. The simulation parameters of the contact model between substrate particles were calibrated through maximum shear force simulation experiments and compared with physical experiments to obtain the maximum shear force regression equation. The parameters of the contact model between seedlings were obtained using the response surface optimization method, which were: JKR surface energy of 12.3 J/m^2, recovery coefficient of 0.6, static friction coefficient of 0.8, and rolling friction coefficient of 0.3. When conducting relevant discrete element simulation experiments on the substrate suitable for planting rapeseed blanket seedlings, corresponding parameter values can be referred to.

This study has a certain role in the construction of a discrete element model for rapeseed blanket seedlings and the analysis of the interaction mechanism between seedlings and agricultural machinery seedling components, especially in the study of the mechanical properties of seedling particles and the changes in the physical properties of soil components in contact with seedlings during agricultural machinery operations such as transplanting and covering. However, this study mainly provides a method for constructing a discrete element particle contact model and parameter calibration of rapeseed blanket seedlings. The model parameters have complexity and variability under different seedling conditions and need to be reconstructed and calibrated based on factors such as substrate type, particle size composition, and moisture content.

ACKNOWLEDGEMENT

This research was supported by the China Postdoctoral Science Foundation (2023M740866); the National Key Research and Development Program of China (2023YFD2001001); the Jiangsu Province Modern Agricultural Machinery Equipment and Technology Demonstration and Promotion Project of China (NJ2024-01); the Jiangxi Province Agricultural Machinery Equipment, Manufacturing, Popularization and Application Integration Pilot Project (YCTY202403-02-02).

REFERENCES

[1] Bai H., Li X., Zeng F., Su Q., Cui J., Wang J., Zhang Y. (2023). Calibration and experiments of the simulation bonding parameters for plug seedling substrate block (穴盘苗基质块仿真粘结参数标定与试验), *INMATEH Agricultural Engineering*, Vol. 69, no.1, pp.617–625, Bucharest/Romania. DOI: https://doi.org/10.35633/inmateh-69-59

[2] Chen B., Liu Y., Yu Q., Chen X., Miao Y., He Y., Chen J., Zhang J. (2022). Calibration of soil discrete element contact parameter in rhizome medicinal materials planting area in hilly region (丘陵山地根茎类中药材种植区土壤离散元参数标定), *INMATEH Agricultural Engineering*, Vol. 68, no.3, pp.521–532, Bucharest/Romania. DOI: https://doi.org/10.35633/inmateh-68-51

[3] Chan L., Mou X., Pong Z. (2021). Application of Discrete Element Method in Agricultural Engineering (离散元法在农业工程中的应用). *Agricultural Engineering*, Vol. 11, no.8, pp.29-34, Beijing/China.

[4] Dun G., Zhang C., Ji X., Meng Q., Sheng Q., Wang L. (2024). Simulation parameter calibration and test of pak choi seeds based on discrete element method (基于离散元的小白菜种子仿真参数标定与试验), *INMATEH Agricultural Engineering*, Vol. 73, no.2, pp.391–405, Bucharest/Romania. DOI: https://doi.org/10.35633/inmateh-73-33

[5] Fu M., Chen X., Gao Z., Wang C., Xu B., Hao Y. (2023). Parameters calibration of discrete element model for crushed corn stalks (碎玉米秸秆离散元模型参数标定), *INMATEH Agricultural Engineering*, Vol. 69, no.1, pp.399–408, Bucharest/Romania. DOI: https://doi.org/10.35633/inmateh-69-37

[6] Gao Z., Shang S., Xu N., Wang D. (2022). Parameter calibration of discrete element simulation model of wheat straw-soil mixture in Huang Huai Hai production area (黄淮海产区小麦秸秆-土壤混合物的离散元仿真模型参数标定), *INMATEH Agricultural Engineering*, Vol. 66, no.1, pp.201–210, Bucharest/Romania. DOI: https://doi.org/10.35633/inmateh-66-20

[7] He X., Ma S., Liu Z., Wang D., Shang S., Li G., Li H. (2024). Calibration and testing of saline soil parameters based on EDEM discrete element methodology (基于 EDEM 离散元方法的盐碱土壤参数标定与测试), *INMATEH Agricultural Engineering*, Vol. 73, no.2, pp.822–833, Bucharest/Romania. DOI: https://doi.org/10.35633/inmateh-73-69

[8] Li S., Diao P., Zhao Y., Miao H., Li X., Zhao H. (2023). Calibration of discrete element parameter of soil in high-speed tillage (高速耕作条件下土壤离散元参数标定), *INMATEH Agricultural Engineering*, Vol. 71, no.3, pp.248–258, Bucharest/Romania. DOI: https://doi.org/10.35633/inmateh-71-21

[9] Liu G., Xia J., Zheng K., Cheng J., Jiang L., Guo L. (2021). Creep properties and prediction model of paddy soil under compression (水稻土受压蠕变特性及预测模型构建), *INMATEH Agricultural Engineering*, Vol. 65, no.3, pp.441–451, Bucharest/Romania. DOI: https://doi.org/10.356.33/inmateh-65-46

[10] Rahman S., Khattak M., Adhikari B., Adhikari S. (2020). Discrete element modeling of bonded soil mixtures under uniaxial compression and indirect tension test. *Transportation Geotechnics*, Vol 26, Netherlands. DOI: https://doi.org/10.1016/j.trgeo.2020.100438

[11] Sun J., Liu Q., Yang F., Liu Z., Wang Z. (2022). Calibration of Discrete Element Simulation Parameters of Sloping Soil on Loess Plateau and Its Interaction with Rotary Tillage Components (黄土高原坡地土壤与旋耕部件互作离散元仿真参数标定), *Transactions of the Chinese Society for Agricultural Machinery*, Vol 53, no.1, pp.63–73, Beijing/China. DOI: https://doi.org/10.6041/j.issn.1000-1298.2022.01.007

[12] Tian X., Cong X., Qi J., Guo H., Li M., Fan X. (2021). Parameter Calibration of Discrete Element Model for Corn Straw-Soil Mixture in Black Soil Areas (黑土区玉米秸秆－土壤混料离散元模型参数标定), *Transactions of the Chinese Society for Agricultural Machinery*, Vol 52, no.10, pp.100-108,242, Beijing/China. DOI: https://doi.org/10.6041/j.issn.1000-1298.2021.10.010

[13] Wu T., Huang W., Chen X., Ma X., Han Z., Pan T. (2017). Calibration of discrete element model parameters for cohesive soil considering the cohesion between particles (考虑颗粒间黏结力的黏性土壤离散元模型参数标定), *Journal of South China Agricultural University*, Vol 38, no.3, pp.93–98, Guangdong/China. DOI: https://doi.org/10.7671/j.issn.1001-411X.2017.03.015

[14] Xu J., Ye J., Sun J., Bian X. (2023). Discrete-element method modeling of structural clay. *Proceedings of the Institution of Civil Engineers-Geotechnical Engineering*, Vol 177, no.6, pp.717–732, London/England. DOI: https://doi.org/10.1680/jgeen.22.00224

[15] Yang L., Li J., Lai Q., Zhao L., Li J., Zeng R., Zhang Z. (2024). Discrete element contact model and parameter calibration for clayey soil particles in the Southwest hill and mountain region. *Journal of Terramechanics*, Vol 111, pp.73–87, Netherlands. DOI: https://doi.org/10.1016/j.jterra.2023.10.002

[16] Yang Q., Shi L., Shi A., He M., Zhao X., Zhang L., Addy M. (2023). Determination of key soil characteristic parameters using angle of repose and direct shear stress test. *International Journal of Agricultural and Biological Engineering*, Vol 16, no.3, pp.143–150, Beijing/China. DOI: https://doi.org/10.25165/j.ijabe.20231603.6293

[17] Yu G., Wang L., Sun L., Zhao X., Ye B. (2022). Advancement of Mechanized Transplanting Technology and Equipments for Field Crops. *Transactions of the Chinese Society for Agricultural Machinery*, Vol 53, no.9, pp.1–20, Beijing/China. DOI: https://doi.org/10.6041/j.issn.1000-1298.2022.09.001

[18] Zhang S., Yang F., Dong J., Chen X., Liu Y., Mi G., Wang T., Jia X., Huang Y., Wang X. (2022). Calibration of Discrete Element Parameters of Maize Root and Its Mixture with Soil. *Processes*, Vol 10, no.11, Switzerland. DOI: https://doi.org/10.3390/pr10112433

[19] Zeng Z., Ma X., Cao X., Li Z., Wang X. (2021). Critical Review of Applications of Discrete Element Method in Agricultural Engineering (离散元法在农业工程研究中的应用现状和展望). *Transactions of the Chinese Society for Agricultural Machinery*, Vol 52, no.4, pp.1-20, Beijing/China. DOI: https://doi.org/10.6041/j.issn.1000-1298.2021.04.001

[20] Zhu Y., Xia J., Zeng R., Zheng K., Du J., Liu Z. (2020). Prediction Model of Rotary Tillage Power Consumption in Paddy Stubble Field Based on Discrete Element Method (基于离散元的稻板田旋耕功耗预测模型研究), *Transactions of the Chinese Society for Agricultural Machinery*, Vol 51, no.10, pp.42–50, Beijing/China. DOI: https://doi.org/10.6041/j.issn.1000-1298.2020.10.006

RESEARCH ON CLASSIFICATION METHODS OF BARLEY PLANTS BASED ON TRANSFER LEARNING
/
基于迁移学习的大麦植株分类方法研究

Wenfeng GUO*[1], Yanwen LI[2], Xiaoying ZHANG[3], Linjuan WANG[1], Jiahao ZHANG[4], Guofang XING*[4]
[1] Department of Basic Science, Shanxi Agricultural University, Taigu, Shanxi / China;
[2] College of Information Science and Engineering, Shanxi Agricultural University, Taigu, Shanxi / China;
[3] College of Software, Shanxi Agricultural University, Taigu, Shanxi / China;
[4]College of Agriculture, Shanxi Agricultural University, Taigu, Shanxi / China;
Corresponding Authors: Guofang Xing; Tel: +86-15034661606; E-mail: gfxing@sxau.edu.cn
Wenfeng Guo; Tel: +86-18734409072; E-mail: wenfengguo@sxau.edu.cn
DOI: https://doi.org/10.35633/inmateh-76-66

***Keywords:** classification of barley plants; deep learning; transfer learning; Grad-CAM; EfficientNet-v2*

ABSTRACT
Classification of barley plants plays a crucial role in understanding barley varietal diversity and breeding. Traditional classification methods rely on expert experience and require significant manual effort. With the rise of deep learning based on machine vision technologies, particularly the emergence of transfer learning, the issue of model overfitting on small datasets has been mitigated, leading to enhanced generalization capabilities. This study employs a self-constructed barley plant image dataset to compare five state-of-the-art deep learning models, while analyzing the impacts of various factors - including image resolution and training-test split ratio - on classification accuracy. The results indicate that the DenseNet model achieves the best classification performance at an input resolution of 512×512 pixels, with an accuracy of 96.02%. Increasing the proportion of training data further improved performance, with the 80%:20% training-test split ratio yielding optimal results across all five models. Transfer learning models outperform training from scratch, with EfficientNet-v2 achieving the highest accuracy of 98.86%. Additionally, gradient-weighted class activation mapping (Grad-CAM) was utilized to generate heatmap visualizations of the decision-making processes in each transfer learning model. By applying deep learning for barley plant classification and selecting the optimal model, this research provides a reliable technical solution for barley variety identification and classification.

摘要
大麦植株分类对于理解大麦品种多样性和育种研究具有关键作用。传统分类方法依赖专家经验且需要大量人工操作。随着基于深度学习的机器视觉技术的兴起，尤其是迁移学习技术的出现，减轻了在小数据集上模型过拟合的现象，提高了模型的泛化能力。本研究采用自建的大麦植株图像数据集，对比了五种先进的深度学习模型，并分析了不同图像分辨率、不同训练集-测试集比例等因素对分类准确率的影响。研究结果表明：DenseNet 模型在 512×512 像素输入分辨率下表现最优，分类准确率达 96.02%；增加训练数据比例能提升模型性能，80%:20% 的训练-测试划分比例在五种模型中均取得最佳效果；使用迁移学习模型显著优于从头训练，其中 EfficientNet-v2 模型以 98.86%的准确率表现最佳。此外，研究还采用 Grad-CAM 技术对五种迁移学习模型的预测过程进行了热力图可视化分析。本研究通过深度学习技术实现大麦植株分类并优选最佳模型，为大麦品种鉴定与分类提供了可靠的技术方案。

INTRODUCTION
Barley is one of the world's most important cereal crops, and its cultivation plays a vital role in food security, feed supply, the brewing industry, economic development, and ecological benefits (*Ullrich, 2021*). The classification of barley plants holds significant importance for optimizing cultivation management, advancing breeding research, supporting precision agriculture, ensuring food security, and promoting industrial development (*Alahmad et al., 2022*).

The traditional methods for barley plant classification primarily rely on phenotypic data such as morphological traits, agronomic characteristics, and physiological properties. While these approaches can differentiate between varieties to some extent, they suffer from several limitations, including strong subjectivity, high labor intensity, significant environmental dependency, limited informative value, difficulties in distinguishing closely related varieties, dynamic variability, and lack of standardization (*Li et al., 2022*).

Deep learning models (e.g., Convolutional Neural Networks, CNNs) can automatically extract multi-level features from raw images, ranging from low-level edge and texture features to high-level semantic features (*Zhou et al., 2022*).

This end-to-end learning approach eliminates the laborious process of manual feature engineering required in traditional methods. Through deep network architectures and training on large-scale datasets, deep learning models can capture subtle differences in images, thereby achieving high-precision classification (*Nguyen et al., 2021*). These models autonomously learn features and patterns from data, reducing the need for human intervention and domain-specific expertise. Such automated learning capabilities make deep learning highly promising for a wide range of image classification tasks.

Deep learning has become a dominant approach for image-based classification tasks, with significant advancements in plant species identification and agricultural applications. Recent studies have explored various architectures to enhance classification accuracy and robustness. Comparative analyses of deep learning models have demonstrated the effectiveness of specific architectures for plant classification. For instance, DenseNet exhibited stable performance across multiple datasets, highlighting its robustness in feature reuse and gradient flow optimization (*Zhou et al., 2021*). Similarly, Xception outperformed InceptionV3 and VGG16 on the Plant Seeding Dataset, achieving 86.21% accuracy due to its depthwise separable convolutions (*Diaz et al., 2019*). In weed management, CNNs attained 97% accuracy in distinguishing crops (e.g., corn) from narrow- and broad-leaf weeds during early growth stages, critical for precision herbicide application (*Garibaldi-Márquez et al., 2022*). In addition, hybrid models can improve plant classification performance by combining the strengths of different architectures. Hybrid models, such as MIV-PlantNet, which integrates MobileNet, Inception, and VGG, achieved 99% accuracy on 10 Saudi Arabian plant species by leveraging complementary architectural strengths (*Amri et al., 2024*). Deep neural networks (DNNs) generally demand substantial amounts of training data to achieve optimal performance, as insufficient datasets often result in model overfitting and compromised generalization ability.

Transfer learning (TL) leverages pre-trained models from large-scale datasets (e.g., ImageNet) to transfer knowledge to target domains (e.g., plant classification), addressing challenges such as limited data, high training costs, and poor model generalization. In recent years, TL has achieved remarkable success in plant classification tasks, including species identification, disease detection, and leaf categorization. The most common implementation involves direct fine-tuning of pre-trained models for plant classification tasks. For instance, MobileNet pre-trained on ImageNet achieved 98.7% classification accuracy when fine-tuned on a custom medicinal plant dataset (*Duong-Trung et al., 2019*). Similarly, fine-tuned VGG16 models showed enhanced performance in agricultural disease detection, particularly for mildew classification in millet (*Coulibaly et al., 2019*). The exceptional 99.7% accuracy obtained by VGG-19 on the Swedish Leaf Dataset further validates TL's superiority in small-sample scenarios (*Siddharth et al., 2022*). Comparative studies have explored various architectures, including GoogLeNet and VGGNet with optimized TL parameters for the LifeCLEF 2015 challenge (*Ghazi et al., 2017*), while another investigation evaluated Inception V3, ResNet50 and VGG19 on 12 plant seedling categories (*Hassan et al., 2021*). Beyond direct fine-tuning, hybrid approaches combining deep learning with traditional methods have shown promising results. The integration of VGG19's deep features with handcrafted descriptors (e.g., texture and shape) achieved 93.73% accuracy using Random Forest classification (*Bansal et al., 2023*) Another study employed four pre-trained CNNs for feature extraction followed by Random Forest, significantly improving model interpretability (*Sachar et al., 2021*). These implementations demonstrate TL's dual advantage of reducing training time while enhancing classification accuracy by effectively transferring knowledge from large-scale datasets to specialized botanical applications.

As one of the world's most important crops, barley has received relatively limited research attention regarding plant classification. To address this gap, this study first systematically reviews the advantages and disadvantages of five deep learning approaches. Subsequently, comprehensive experiments are conducted on a self-constructed barley plant dataset, with evaluations focusing on: (1) input image resolution, (2) training-test split ratios, and (3) fine-tuning strategies based on transfer learning models. Finally, heatmap visualization is employed to analyze the critical regions identified by the five transfer learning models during prediction. These investigations aim to identify the optimal deep learning approach for barley plant classification and to provide technical support for the development of automated classification systems.

MATERIALS AND METHODS

Image dataset

The spike and awn morphology of different barley varieties exhibits significant differences, making them particularly suitable for computer-based classification tasks. The barley dataset used in this study was collected from the barley breeding experimental fields at Shanxi Agricultural University. Images of nine barley

varieties were captured during the heading and maturation stages, photographing individual plants (including partial stems, leaves, and spikes) against a white background using a smartphone in frontal parallel shooting mode.

To enhance dataset diversity, wheat plant images were included since wheat and barley share similar spike and awn structures. The final dataset comprised 896 RGB images across nine barley varieties and one wheat variety, with the number of images per variety ranging from 52 to 233.

In this study barley varieties were labeled as Barley_0 through Barley_8 and the wheat variety was designated as Wheat. Original image resolutions included 1276×1276 pixels, 2342×2342 pixels, and 3024×3024 pixels. Due to computational constraints, all images were uniformly resized to 1024×1024 pixels.

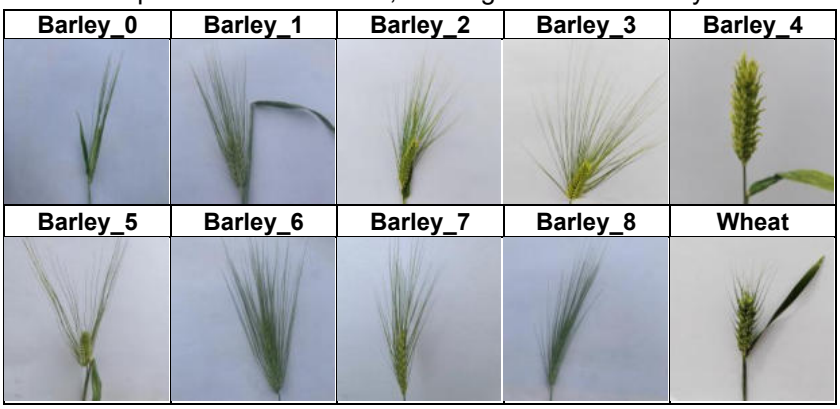


Fig. 1 - Characteristic specimens of all barley varieties and wheat

Figure 1 illustrates distinct phenotypic variations between different barley and wheat cultivars, primarily manifested in awn and spike characteristics. Awn morphology analysis demonstrates that the barley cultivar Barley_4 is classified as awn less, while the wheat cultivar Wheat exhibits short-awned characteristics, with all other barley cultivars displaying long-awned morphology. Regarding awn spatial distribution patterns, barley cultivars Barley_3 and Barley_5 show a scattered arrangement, whereas Barley_0, Barley_7, and Barley_8 present clustered awns. The intermediate awn distribution type is observed in barley cultivars Barley_1, Barley_2, and Barley_6. Spike architecture analysis indicates that barley cultivar Barley_5 possesses a distinctive two-rowed spike structure, contrasting with the six-rowed configuration of wheat. The remaining barley cultivars exhibit an intermediate four-rowed spike morphology.

Deep learning approaches for barley plant image classification

ResNet (Residual Network) was proposed by *He et al., (2016*), and achieved breakthrough performance in the ImageNet image classification competition. The core innovation of ResNet lies in its introduction of residual learning, which addresses the issues of gradient vanishing and network degradation in deep neural networks through residual connections (also known as skip connections). This architectural advancement enables the training of substantially deeper networks while enhancing their feature extraction capabilities. Due to hardware considerations, the ResNet-50 model with 50 layers was chosen as our baseline network.

DenseNet (Densely Connected Network) is a deep learning model proposed by *Huang et al., (2017*). The core innovation of DenseNet lies in its dense connection mechanism, where each layer's output is directly connected to all subsequent layers. This unique architecture significantly enhances feature propagation and reuse throughout the network while substantially reducing parameter redundancy and effectively alleviating vanishing gradient problems. DenseNet has demonstrated exceptional performance across various image classification tasks, showing particular advantages in scenarios with limited training data where its efficient feature utilization capability excels.

MobileNet-v2, developed by Google Research (*Sandler et al., 2018*), represents an optimized lightweight convolutional neural network specifically engineered for mobile and embedded devices. As an enhanced iteration of MobileNet-v1, this architecture incorporates two key innovations: inverted residual blocks and linear bottleneck layers, which collectively improve both computational efficiency and model performance.

ShuffleNet-v2, developed by Megvii Research (*Ma et al., 2018*), represents an optimized efficient convolutional neural network specifically designed for mobile and embedded devices. As an enhanced version of ShuffleNet, this architecture introduces two key improvements: an optimized network structure and a novel channel shuffle operation that reorganizes feature channels to enhance cross-group information exchange.

EfficientNet-v2, developed by Google Research (*Tan et al., 2021*), is an enhanced convolutional neural network that builds upon the EfficientNet series. This next-generation architecture achieves significant improvements through an integrated approach combining compound scaling and progressive learning strategies, which work synergistically to boost both training efficiency and model accuracy.

Evaluation metrics

This study evaluates the classification performance of the five deep learning methods using Top-1 accuracy, defined as the proportion of samples where the model's highest-probability prediction matches the true class label. To address class imbalance in the dataset, confusion matrix analysis was employed as a complementary evaluation metric. The confusion matrix provides a detailed breakdown of classification results, with rows representing actual classes, columns indicating predicted classes, diagonal entries showing correct classifications, and off-diagonal elements revealing specific misclassification patterns between classes. Additionally, this study uses the size of the model weight file as an indicator to determine the model size and employs inference speed to measure the computational efficiency of the model, excluding data loading time, with the unit in frames per second (FPS). Together, these metrics offer both quantitative performance measurement and qualitative insight into each model's classification behavior across all categories.

Training model

The experiments in this study were conducted on a Windows 10 system equipped with an Intel Core i7-12700F CPU (12 cores, 20 threads), 32GB RAM, and an ASUS TUF-GAMING RTX 3060 GPU with 12GB VRAM. For the experimental framework, OpenMMLab's MMPretrain (v1.0.0) was utilized, an open-source computer vision research platform that provides comprehensive transfer learning models and tools. As one of OpenMMLab's core libraries, MMPretrain specializes in image classification and feature extraction tasks while supporting various state-of-the-art deep learning models (*MMPretrain Contributors, 2023*).

To ensure the reliability of experimental results and achieve optimal classification performance, all five deep learning models were configured with the following unified parameter settings. The image input size was set to 1024×1024 pixels, and the batch size was set to 8. The Stochastic Gradient Descent (SGD) optimizer was selected, loss function was Cross-entropy Loss, and the training epochs were set to 100. The initial learning rate was 0.025, and the momentum parameter and the weight decay parameter were set to 0.9 and 0.0001, respectively.

The models process input images in RGB format with batch normalization applied during training. The training protocol consisted of 100 epochs with MultiStepLR learning rate scheduling, where the learning rate was reduced by a factor of 0.1 at epoch milestones 30, 60, and 90. This configuration maintains comparability across models while implementing established best practices for deep learning optimization.

RESULTS

The impact of image resolution on classification accuracy

Each image in the dataset contains only a single barley plant with a white background, and the plant occupies only a small portion of the image. Higher-resolution images can capture key structural features of barley, such as the spikes and awns. Three different input resolutions were examined: 128×128 pixels, 256×256 pixels, and 512×512 pixels, with an 80:20 train-test split ratios and models trained from scratch. The classification results are shown in Table 1.

Table 1

Classification performance of five models across different input resolutions with 80:20 training-test split

Resolution\Model	ResNet-50	DenseNet	MobileNet-v2	ShuffleNet-v2	EfficientNet-v2
128×128	82.39	94.32	92.05	81.25	94.32
256×256	85.23	95.45	93.19	84.1	92.61
512×512	93.75	96.02	92.61	90.91	95.45

The results showed that MobileNet-v2 achieved its best classification performance (93.19% accuracy) at 256×256 pixels resolution, while the other four models (ResNet-50, DenseNet, ShuffleNet-v2, and EfficientNet-v2) all performed best at the highest 512×512 pixels resolution, with classification accuracy generally improving as resolution increased. Specifically, ResNet-50 showed an 11.36% accuracy improvement, DenseNet improved by 1.7%, ShuffleNet-v2 by 9.66%, and EfficientNet-v2 by 1.13% when comparing the lowest and highest resolutions. At 512×512 pixels resolution, DenseNet delivered the strongest overall performance with 96.02% accuracy.

These findings demonstrate that higher resolutions generally enhance classification accuracy by preserving finer structural details, though the optimal resolution depends on model architecture. While most models benefited from increased resolution, MobileNet-v2's peak performance at 256×256 pixels suggests potential limitations in handling higher-resolution inputs. DenseNet's superior performance at the highest resolution indicates its effectiveness in leveraging detailed features for accurate classification.

For further error analysis, this study computed confusion matrices for all five classification models (as shown in Figure 2) at 512×512 pixels resolution. In the test set containing 176 images, ResNet-50 misclassified 11 images, DenseNet misclassified 7, MobileNet-v2 misclassified 13, ShuffleNet-v2 misclassified 16, and EfficientNet-v2 misclassified 8.

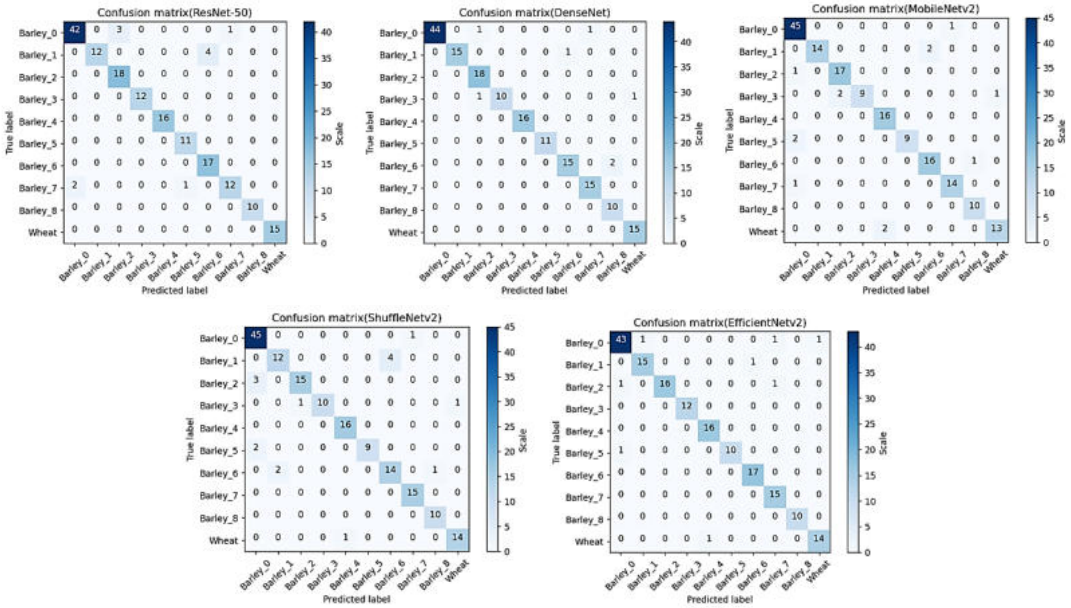


Fig. 2 - Confusion matrices of five models with 512×512 input resolution and 80:20 training-test split

A particularly notable error pattern was observed where both ResNet-50 and ShuffleNet-v2 models consistently misclassified 4 Barley_1 samples as Barley_6. This classification confusion likely stems from the morphological similarity between these two varieties, as both Barley_1 and Barley_6 possess characteristically long, spreading awns that create visual ambiguity in their distinguishing features.

The impact of different training-test split ratios on classification accuracy

The partitioning method of the training and test sets significantly influences the performance evaluation and generalization capability of the barley plant image classification model. Due to imbalanced sample sizes across different varieties in the dataset, this study employed stratified sampling to ensure that each category maintained a fixed proportion in both the training and test sets. Three different training-test split ratios were examined: 80%:20%, 70%:30%, and 60%:40%, using an input image resolution of 512×512 pixels and training the models from scratch. The classification results are presented in Table 2.

Table 2

Classification performance of five models with different training-test split ratios and 512×512 input resolution

Training-test split\Model	ResNet-50	DenseNet	MobileNet-v2	ShuffleNet-v2	EfficientNet-v2
70% : 30%	89.06	92.45	91.7	77.0	93.58
60% : 40%	87.08	90.45	91.57	78.93	90.73

Combined with Table 1, the analysis of the classification results revealed that when the training-test split ratio was 80%:20%, all five models achieved their optimal classification performance. Additionally, except for ShuffleNet-v2, the other models exhibited a trend where higher proportions of training data led to increased classification accuracy. Figure 3 presents the confusion matrices for all five classification models when the training-test split ratio was set to 70%:30%.

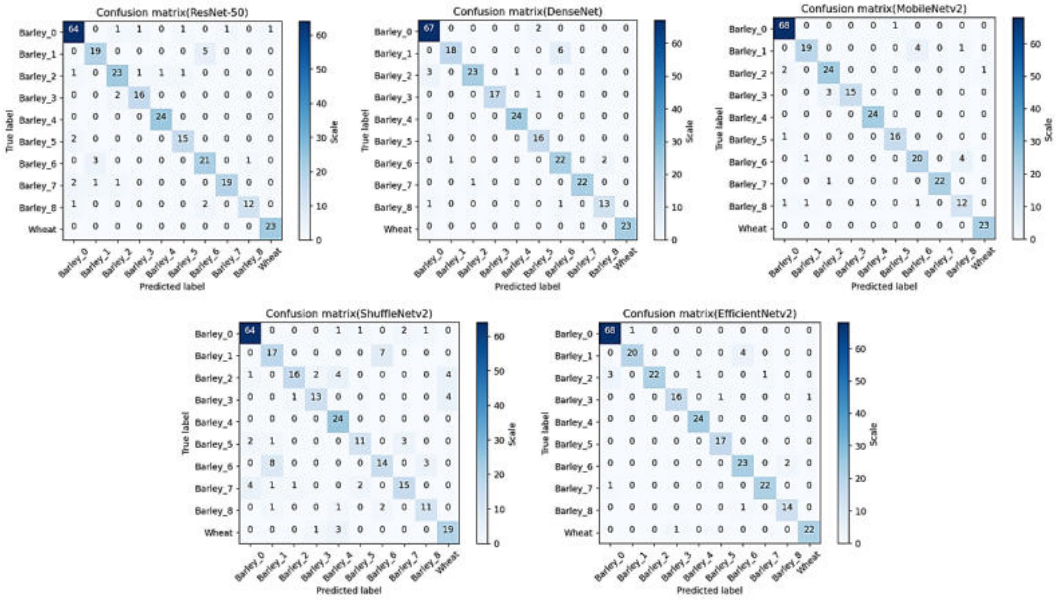


Fig. 3 - Confusion matrices of five models with 512×512 input resolution and 70:30 training-test split

When employing a 60% training and 40% testing data partition, the classification confusion matrices for all five models are illustrated in Figure 4.

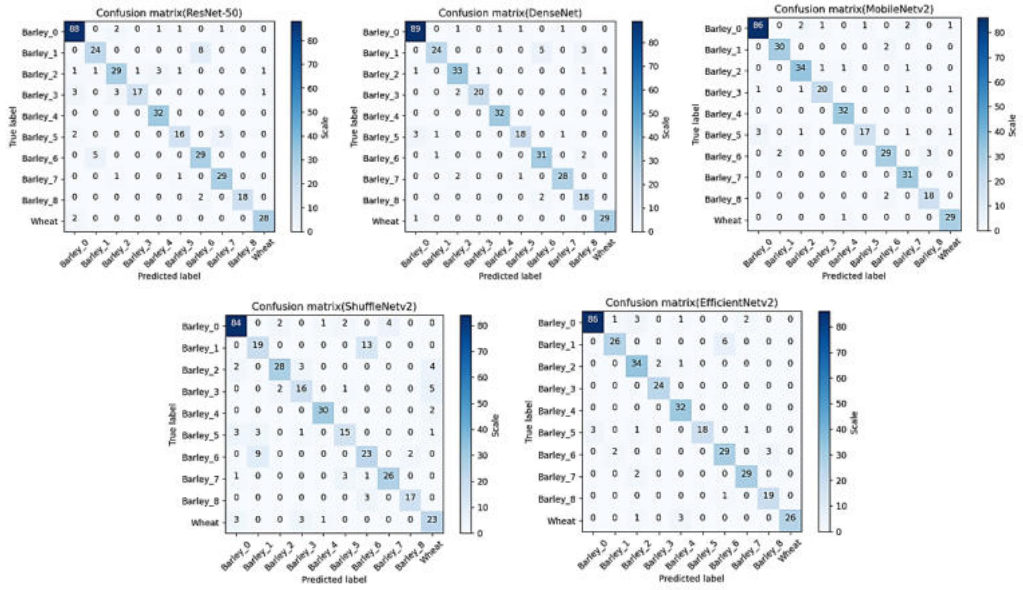


Fig. 4 - Confusion matrices of five models with 512×512 input resolution and 60:40 training-test split

The impact of transfer learning on classification accuracy

Transfer learning improves model performance by leveraging knowledge acquired from one task or domain and applying it to a related task, significantly reducing training time while enhancing accuracy (*Tan et al., 2018*). In this study, the models were initialized with weights pre-trained on the ImageNet-1k dataset and subsequently fine-tuned for barley plant image classification.

Using an 80%:20% training-test split ratio and an input resolution of 512×512 pixels, the classification results are presented in the Table 3, with corresponding confusion matrices shown in Figure 5. A comparison with Table 1 reveals that training based on ImageNet-1k transfer learning models yields better classification performance than training from scratch, with accuracy improvements of 1.70% (DenseNet), 7.39% (ShuffleNet-V2), and 3.41% (EfficientNet-V2). Among them, the transfer learning EfficientNet-V2 model achieved the highest classification accuracy at 98.86%. Its model size is moderate among the five models at 22.90 MB, while also delivering the fastest inference speed at 179 FPS. ShuffleNet-V2's classification accuracy is nearly comparable to EfficientNet-V2, yet it has the smallest model size among all five models and maintains a high inference speed (157 FPS).

Table 3

Classification performance of five pre-trained models with 80:20 training-test split and 512×512 input resolution

Evaluation metrics\Model	ResNet-50	DenseNet	MobileNet-v2	ShuffleNet-v2	EfficientNet-v2
Accuracy(%)	93.18	97.72	88.64	98.30	98.86
Size/MB	90.30	27.40	9.13	5.44	22.90
Speed/FPS	92	120	158	157	179

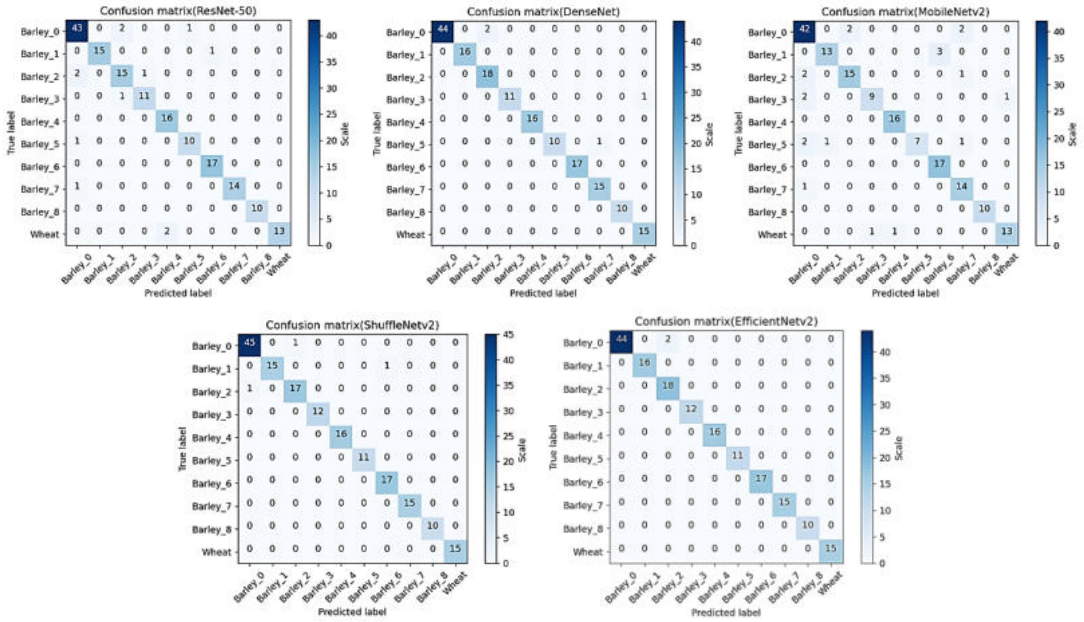
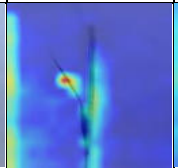
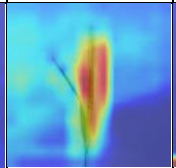
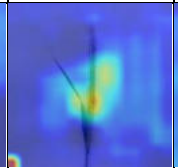
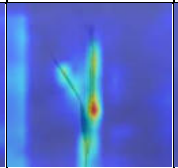
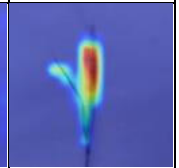
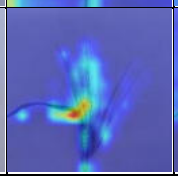
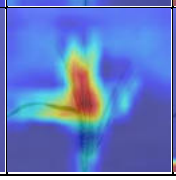
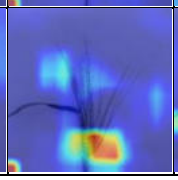
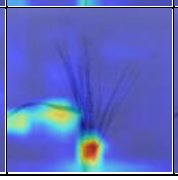
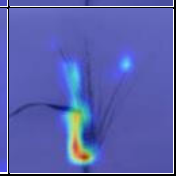


Fig. 5 - Confusion matrices of five pre-trained models with 512×512 input resolution and 80:20 training-test split

Comparative analysis of gradient-based heatmap visualization

Deep learning models demonstrate excellent performance in barley plant classification, yet their decision-making process remains opaque to end users. Gradient-based interpretation techniques, as attribution methods, utilize heatmaps to explain deep learning decisions. Grad-CAM (Gradient-weighted Class Activation Mapping) is a visualization technique that generates heatmaps to highlight image regions most influential to the model's predictions, thereby enhancing interpretability of the decision process (*Selvaraju et al., 2017*).

This study employs Grad-CAM to generate heatmaps for five transfer learning models, as shown in Figure 6. Overall, the heatmaps generated by the EfficientNet-v2 model exhibit higher response values in key structural features such as wheat spikes and awns, which aligns with the critical regions experts typically focus on during practical evaluations. This observation is consistent with the superior classification performance of EfficientNet-v2 demonstrated in earlier experiments. In contrast, some heatmaps from the DenseNet model (including varieties Barley_0, Barley_2, Barley_4, Barley_7, and Barley_8) predominantly highlight background regions. This phenomenon may stem from the gradient's inability to accurately reflect feature importance, leading to attention dispersion toward non-relevant background areas.

Class name	Original Image	ResNet-50	DenseNet	MobileNet-v2	ShuffleNet-v2	EfficientNet-v2
Barley_0						
Barley_1						

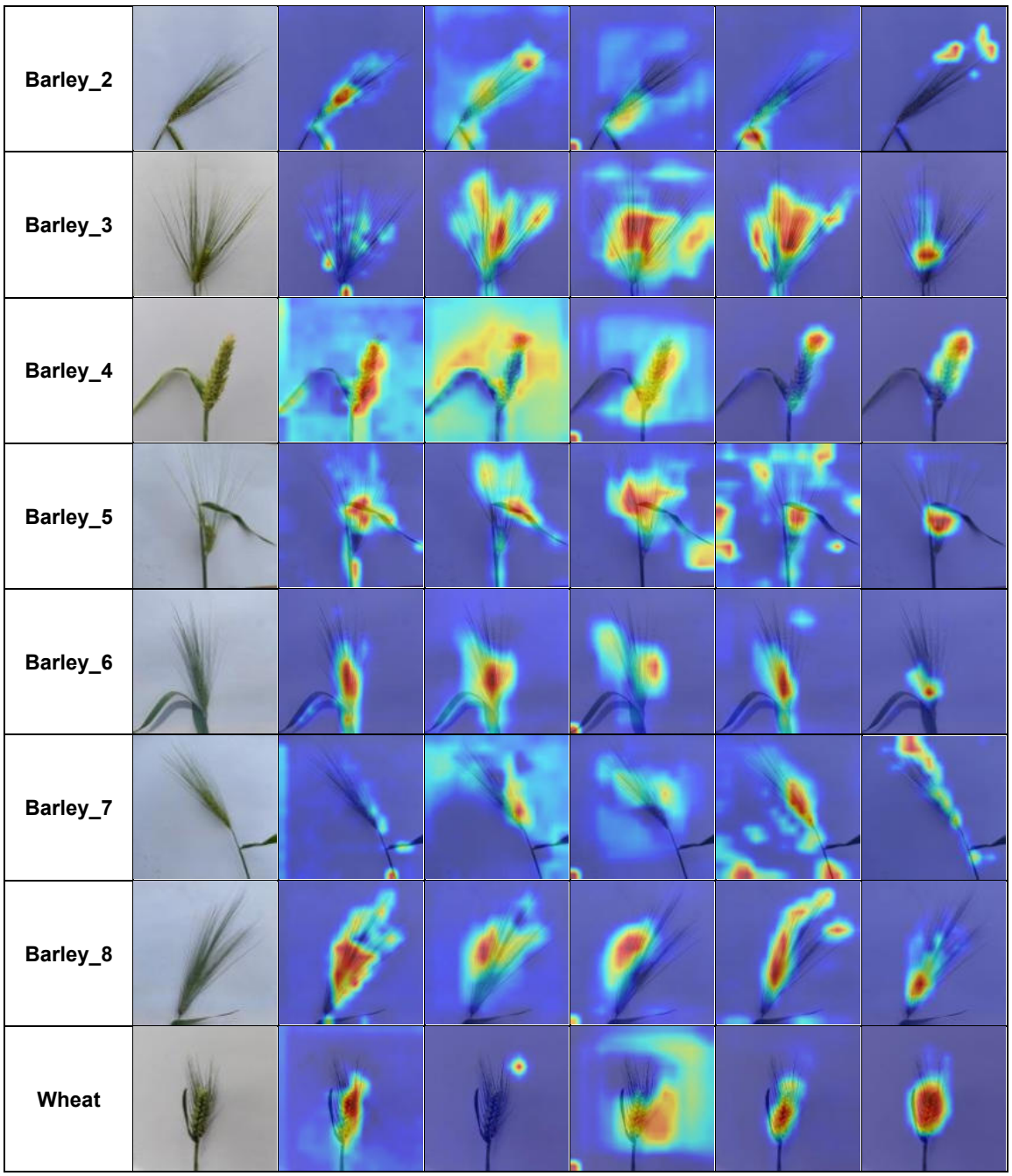


Fig. 6 - The output of the class activation maps for five transfer leaning models

CONCLUSIONS

This study reviewed recent research progress in plant classification using deep learning and evaluated the performance of five representative deep learning models. The core algorithmic concepts of these models were analyzed, along with their respective advantages and limitations. The models were then applied to a self-constructed barley plant dataset, and their classification performance was systematically assessed.

This study demonstrates that the EfficientNet-v2 model achieved the highest classification performance. Increasing the proportion of training data proved beneficial, as a larger sample size enabled the model to learn richer feature representations of barley plants. Transfer learning, through the use of knowledge acquired from large-scale datasets, not only accelerated model training but also enhanced classification accuracy. To further interpret the decision-making process, Gradient-weighted Class Activation Mapping (Grad-CAM) was employed to visualize regions of interest during prediction. The resulting heatmaps highlighted biologically significant areas, providing valuable references for plant classification analysis.

This work represents one of the few studies applying deep learning models to barley plant classification. Future research should focus on expanding the dataset with images from diverse growth stages and exploring advanced deep learning architectures to address remaining challenges in barley classification.

ACKNOWLEDGEMENT

This research was supported by the Fundamental Research Program of Shanxi Province (Grant NO. 202203021212450) and the Modern Agro-Industry Technology Research System of Shanxi Province, China (Grant NO. 2025CYJSTX03-19).

REFERENCES

[1] Alahmad, S., Chebotarov, D., Voss-Fels, K. P., Poland, J., & Hickey, L. T. (2022). High-throughput phenotyping for barley improvement. *Trends in Plant Science*. 27(5), 511-525.

[2] Amri, E., Gulzar, Y., Yeafi, A., Jendoubi, S., Dhawi, F., & Mir, M. S. (2024). Advancing automatic plant classification system in Saudi Arabia: introducing a novel dataset and ensemble deep learning approach. *Modeling Earth Systems and Environment*, *10*(2), 2693-2709.

[3] Bansal, M., Kumar, M., Sachdeva, M., & Mittal, A. (2023). Transfer learning for image classification using VGG19: Caltech-101 image data set. *Journal of ambient intelligence and humanized computing*, 1-12.

[4] Coulibaly, S., Kamsu-Foguem, B., Kamissoko, D., Traore, D. (2019). Deep neural networks with transfer learning in millet crop images. *Computers in industry*, 108, 115-120.

[5] Diaz, C. A. M., Castaneda, E. E. M., & Vassallo, C. A. M. (2019). Deep learning for plant classification in precision agriculture. In *2019 International Conference on Computer, Control, Informatics and its Applications (IC3INA)*. pp. 9-13. IEEE.

[6] Duong-Trung, N., Quach, L.D., Nguyen, M. H., & Nguyen, C.N. (2019). A combination of transfer learning and deep learning for medicinal plant classification. *In Proceedings of the 2019 4th International Conference on Intelligent Information Technology*. pp. 83-90.

[7] Garibaldi-Márquez, F., Flores, G., Mercado-Ravell, D. A., Ramírez-Pedraza, A., & Valentín-Coronado, L.M. (2022). Weed classification from natural corn field-multi-plant images based on shallow and deep learning. *Sensors*, *22*(8), 3021.

[8] Ghazi, M. M., Yanikoglu, B., & Aptoula, E. (2017). Plant identification using deep neural networks via optimization of transfer learning parameters. *Neurocomputing*, 235, 228-235.

[9] Hassan, E., Shams, M., Hikal, N. A., & Elmougy, S. (2021). Plant seedlings classification using transfer learning. *In 2021 International Conference on Electronic Engineering (ICEEM)*. pp. 1-7. IEEE.

[10] He, K., Zhang, X., Ren, S., Sun, J. (2016). Deep Residual Learning for Image Recognition. *CVPR 2016*.

[11] Huang, G., Liu, Z., Laurens, V. D. M., & Weinberger, K. Q. (2017). Densely Connected Convolutional Networks. *CVPR 2017*.

[12] Li, X., Wang, Y., Zhang, J., Liu, C., Chen, H., & Yang, D. (2022). Limitations of phenotypic characterization in barley breeding. *Plant Methods* 18:23.

[13] Ma, N., Zhang, X., Zheng, H. T., & Sun, J. (2018). ShuffleNet V2: Practical Guidelines for Efficient CNN Architecture Design. *ECCV 2018*.

[14] MMPretrain Contributors. (2023). MMPretrain: OpenMMLab's Pre-training Toolbox and Benchmark. *arXiv preprint*

[15] Nguyen, T.T., Smith, A.B., Johnson, C.D., Lee, E.F., Garcia, M.P., & Wilson, K.L. (2021). Domain-agnostic Feature Learning in Agriculture. *IEEE Transactions on AgriFood Electronics*. 7(3): 204-218.

[16] Sachar, S., & Kumar, A. (2021). Automatic plant identification using transfer learning. *In IOP conference series: materials science and engineering*. Vol. 1022, No. 1, p. 012086. IOP Publishing.

[17] Sandler, M., Howard, A., Zhu, M., Zhmoginov, A., & Chen, L.C. (2018). MobileNetV2: Inverted Residuals and Linear Bottlenecks. *CVPR 2018*.

[18] Selvaraju, R. R., Cogswell, M., Das, A., Vedantam, R., Parikh, D., & Batra, D. (2017). Grad-CAM: Visual Explanations from Deep Networks via Gradient-based Localization. *IEEE International Conference on Computer Vision (ICCV)*.

[19] Siddharth, T., Kirar, B. S., & Agrawal, D. K. (2022). Plant species classification using transfer learning by pretrained classifier VGG-19. *arxiv preprint arxiv*:2209.03076.

[20] Tan, C., Sun, F., Kong, T., Zhang, W., Yang, C., & Liu, C. (2018). A Survey on Deep Transfer Learning. *International Conference on Artificial Neural Networks (ICANN)*.
[21] Tan, M. & Le, Q.V. (2021). EfficientNetV2: Smaller Models and Faster Training. *ICML 2021*.
[22] Ullrich, S.E. (2021). Barley: Production, Improvement, and Uses. *Cereal Science and Technology*, 5(2), 112-130.
[23] Zhou, B., Khosla, A., Lapedriza, A., Oliva, A., & Torralba, A. (2022). Interpretable CNN for Plant Phenotyping. *IEEE Transactions on Pattern Analysis and Machine Intelligence.* 44(8): 4123-4136.
[24] Zhou, C. L., Ge, L. M., Guo, Y. B., Zhou, D. M., & Cun, Y. P. (2021). A comprehensive comparison on current deep learning approaches for plant image classification. In *Journal of Physics: Conference Series.* Vol. 1873, No. 1, p. 012002. IOP Publishing.

DESIGN AND TESTING OF A SINGLE-ROW FRESH CORN PICKING MECHANISM / 单行鲜食玉米摘穗机构的设计与试验

Bang JI [1,3,4], Yusong XIE [1], Long PAN [1], Zhukun WANG [1], Pu LI [*2], Xiushan WANG [*1,3]
[1] Hunan Agricultural University, College of Mechanical and Electrical Engineering, Changsha/China;
[2] Hunan Mechanical and Electrical Polytechnic, Changsha/China;
[3] State Key Laboratory of Agricultural Equipment Technology, Guangzhou /China
[4] Hunan Key Laboratory of Intelligent Agricultural Machinery and Equipment, Changsha/China.
Tel: +86 18711148341; Email: 494519721@qq.com
Corresponding author: 619741039@qq.com (Pu Li); 494519721@qq.com (Xiushan Wang)
DOI: https://doi.org/10.35633/inmateh-76-67

Keywords: *Corn-picking device, Fresh corn, Corn-ear-picking plate, High-speed camera*

ABSTRACT

To address the challenges of low mechanization in harvesting and the high damage rate of fresh corn, this paper proposes a cutter-stalk pulling roller type tassel picking mechanism designed to achieve low-damage tassel picking and fresh corn harvesting. Using high-speed camera technology and pressure testing, a kinematic analysis of the tassel picking process was conducted. A three-factor, three-level orthogonal experimental design was employed to systematically investigate the effects of forward speed, stalk-pulling roller rotational speed, and cutter clearance on operational quality. The results showed that the picker maintained the force at the bottom of the corn cob below 35 N, effectively reducing mechanical damage. Under the conditions of a forward speed of 0.40 m/s, stalk-pulling roller speed of 420 r/min, and cutter clearance of 34 mm, the cob damage rate was 0.05%, and the impurity rate was 0.62%. These findings provide a valuable basis for the optimization and further improvement of single-row fresh corn cob picking cutters.

摘要

针对鲜食玉米机械化采收程度不高且损伤率高的问题，本文设计了一款切刀－拉茎辊式摘穗机构，旨在实现对鲜食玉米低损伤摘穗收获。基于高速摄像技术和压力测试试验对摘穗过程进行运动学解析，采用三因素三水平正交试验设计，系统探究前进速度、拉茎辊转速和切刀间隙对作业质量的影响。试验结果表明：该摘穗机能够使玉米果穗底端受力控制在 35N 以下，能够有效减少机械损伤。当前进速度 0.4m/s、拉茎辊转速 420 r/min、切刀间隙 34mm，此时果穗损伤率为 0.05%，含杂率为 0.62%，研究结果可为单行鲜食玉米摘穗割台的优化改进提供依据与参考。

INTRODUCTION

Fresh corn was harvested during the milk-ripe stage for direct consumption. They can be divided into four categories: waxy corn, sweet corn, sweet waxy corn, and bamboo shoot corn *(Shi et al., 2022)*. However, fresh corn has high moisture content and brittle stalks during harvest. This leads to problems in mechanical harvesting, such as a high ear damage rate and a high impurity rate *(Zhou et al., 2024; Zhang et al., 2021)*.

In 2014, Zhang Zhilong et al. introduced a novel approach to corn ear picking with comb teeth and further explored the impact effect of the comb corn ear picking plate on corn ears, as well as the mechanical characteristics and movement of the ears when the mechanism acts on the ears *(Zhang et al., 2014; Zhang et al., 2020; Zhang et al., 2020)*. In 2015, Zhang Qiang et al. introduced a novel approach to bionic ear picking of corn and used ADAMS to simulate the ear-picking process of a new corn ear picking a plate and conducted experiments *(Zhang., 2015; Zhang et al., 2023)*. In 2020, Luo Huizhong verified through comparative tests that the flexible coupling structure could change the collision contact force parameters between the ear and the ear-picking part so as to reduce the damage caused by the collision between the corn ear and the ear-picking platform. In 2023, a fresh corn ear-picking plate with reverse bionic ear picking was proposed. This mechanism performs ear picking by applying deflection torque to the cob by pulling the stalk roller *(Luo et al., 2023; Luo et al., 2023)*. In 2023, Fu Qiankun et al. found that the fruit stalk changed from tensile fracture to bending fracture by applying force to the corn fruit stalk from different directions, which reduced the ear-picking force by more than 80% and significantly reduced the ear damage rate *(Fu et al., 2023)*.

In the same year, Qin Jiahao et al. verified the conclusion that a curved ear-picking plate can reduce mechanical damage to corn ears during ear-picking through simulation analysis and high-speed imaging *(Qin et al., 2020)*. In addition, Li et al, through the study of the corn ear-picking process, designed a shear-type Corn ear-picking plate that can reduce the loss and power consumption of corn ear-picking *(Li et al., 2023)*. Special corn ear harvesters mainly use a combination of a horizontal roller stalk-pulling roller and ear-picking plate and use conical small inclination angles to lengthen the stalk-pulling roller and an adaptive device for the ear-picking gap to achieve low-damage ear detachment *(Cui et al., 2019)*. These types of harvesters usually have the characteristics of a large size, high power, wide cutting width, large feed volume, and adjustable and equal machine chassis. For example, DRAGO in the United States has designed an ear-picking plate with a cushioning effect to effectively reduce collisions between corn ears and ear-picking mechanisms to reduce ear damage. The JOHN DEERE 700c series headers are equipped with hydraulic headers with adjustable working parameters to further reduce damage. The OXBO 3000 series headers feature conical cutter rollers, which reduce grain loss by reducing the impact acceleration of the ears and picking plates.

To solve the problems associated with small plots, a low degree of mechanized harvesting of fresh corn and a high damage rate during harvesting in hilly areas *(Su., 2021)*, a cutter-stalk-pulling roller ear-picking mechanism was designed. A high-speed camera was used to analyze the pressure on the corn plants during the ear-picking operation of the corn ear-picking plate. The feasibility of the cutting knife-stalk-pull roller-picking device was determined through a pressure test of the ear-picking plate. The parameters of the picking mechanism were optimized using three-factor and three-level orthogonal experiments.

MATERIALS AND METHODS

Morphological parameters of fresh corn

The test material was "Jin tian 13" corn, which has a high overall water content and significant brittleness in texture. Experimental protocols strictly followed GB/T 5262-2008 "General Provisions for Determination Methods of Experimental Conditions of Agricultural Machinery" *(Wang et al., 2024)*. The main measuring tools included rulers, tape measures, and vernier callipers.50 mature corn plants were randomly selected in the field using the five-point sampling method. The morphological characteristics of the fresh corn plants are shown in Table 1.

Table 1

Morphological characteristics of fresh corn plants

Parameter	Range [mm]	Mean [mm]
Height of the corn ear	530~890	737.72
Diameter of the bottom end of the corn ear	56.59~67	60.10
Diameter of the corn stalk	26.12~36.4	30.59
Length of the corn shank	32.19~63.33	48.19
Diameter of the corn shank	15.96~25.53	20.95

Structure and working principle of ear-picking machine

The stalk-pulling portion comprised a pair of stalk-pulling rollers arranged below the picking device and driven via the collection tank. The cob-picking device comprises a stalk-pulling part and a corn-picking part, and the overall structure is mounted at the front end of the cob-picking machinery. The stalk-pulling part consists of a pair of stalk-pulling rollers, which are arranged below the tassel-pulling device and driven by the tassel-pulling tank. The picking mechanism mainly consists of a picking plate and cutter, both of which are bolted to the frame on both sides of the stalk-pulling rollers.

The specific structure is shown in Fig. 1, and the main technical parameters of the fresh corn picker are listed in Table 2.

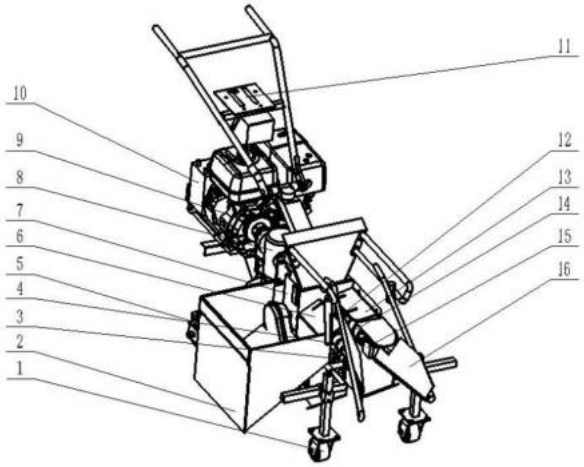


Fig. 1 – Schematic diagram of the single row fresh corn picking machine

1. Universal wheel; 2. Set spike tank; 3. Stalk cutting knife; 4. Lower stalk-pulling roller; 5. Track; 6. Left picking plate; 7. Collection tank 8. Speed tank; 9. Diesel engine; 10. Battery; 11. Operation desk; 12. Cutter; 13. Right picking plate; 14. Upper stalk-pulling roller; 15. Snapping rolls; 16. Grain separator

Table 2

Dimensional parameters of the whole machine

Parameter	Value
Overall dimensions	Length: 2150 mm, Width: 1350 mm
Minimum turning radius	0.8 m
Engine power	3.4 kW
Forward speed	0~2 km/h

The working process is illustrated in Fig. 2. During field operation, the front end of the tassel-picking machine advances along a row of fresh corn plants, guiding the stalks toward the machine's front end, where they are directed into the stalk-pulling roller gap by the snapping rolls. As the plants enter, the protruding structures on the surface of the stalk-pulling rollers drive the stalks backward into the upper picking plate gap, after which the lower portion of each stalk enters the roller gap. Here, the stalk is crushed in a way that avoids damaging the cob while reducing the tensile force required to break the stalk. The stalk rollers then continue pulling the stalk downward, while the cutter blocks the cob, enabling separation of the cob from the stalk. The detached cob subsequently falls through the lower side of the picking plate into the cob tank.

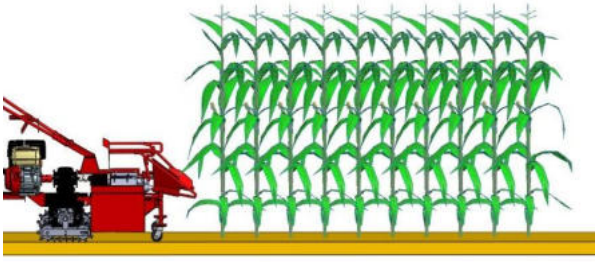


Fig. 2 – Working diagram of single row fresh corn picker

Design of functional components

The corn-ear-picking plate was the core component of the corn-ear-picking machine. Its primary function is to separate corn ears from plants directly. Therefore, its performance directly affects the overall operational performance of the corn ear-picking machine *(Zhu et al., 2023)*.

As shown in Fig. 3, a fresh corn ear-picking plate was designed to ensure ear integrity during mechanized harvesting. The mechanism consists of a cutter, an ear-picking plate, and upper and lower stalk-pulling rollers.

The ear-picking plate is positioned at a specific angle to work in coordination with the rollers, pulling the corn stalks downward. During the ear-picking process, the stalks tilt toward the side of the lower stalk-pulling roller, while the cutter severs the fruit stalk directly. This design prevents direct contact between the ear and the picking plate, thereby effectively achieving low-damage harvesting of fresh corn ears.

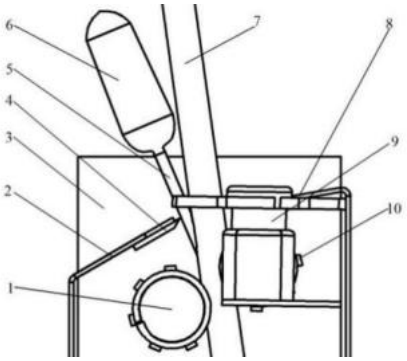


Fig. 3 – Working principle diagram of picking mechanism

1. Lower stalk pulling roller; 2. Left picking plate; 3. Collection Tank; 4. Cutter; 5. Shank; 6. Cob; 7. Corn stalk; 8. Right picking plate; 9. Pivoting wheel; 10. Upper stalk pulling roller

Test bench

In this study, a fresh corn ear-picking test bench was designed, and its structure is illustrated in Fig. 4. The test bench primarily comprises a mobile frame, a motor, an ear collection tank, a corn ear-picking plate, and a control system. The forward speed of the mobile frame was adjustable within the range of 0–5 m/s, with motor output regulated by an inverter. A separate three-phase motor, controlled by a frequency converter, provided a rotational speed of 0~450 rpm for the stalk-pulling roller. In addition, the gap of the corn ear-picking plate was adjustable to accommodate different test requirements.

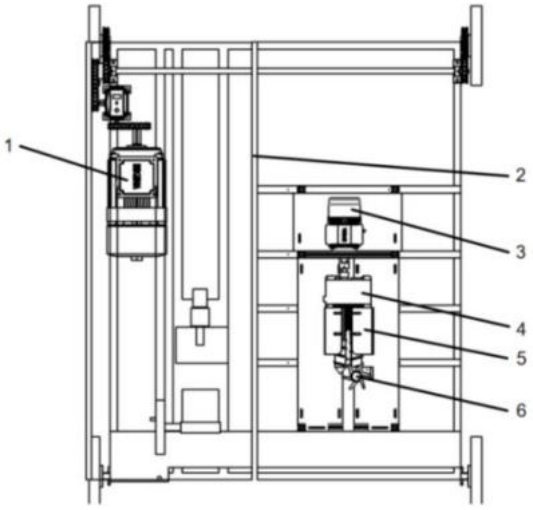


Fig. 4 – Schematic diagram of test stand structure

1. Motor 2. Frame 3. Auxiliary motor 4. Ear collection tank 5. Picking mechanism 6. Snapping rolls

High-speed camera

To explore whether the experimental device can achieve the expected effect, as illustrated in Fig 5, high-speed camera equipment was employed to record and analyze the working process of the corn ear-picking plate *(Li., 2023)*. The rotational speed of the stalk pulling roller (360, 390, 420, and 450 rpm) and cutting knife clearance (26, 28, 30, 32, and 34 mm) were used as variable factors for the single-factor tests. A control test without a cutter but with the same variable settings was also conducted. During the experiment, corn plants were manually fed individually, and each group of experiments was repeated twice.

Pressure test

To explore the impact of the corn ear-picking plate, as shown in Fig. 6, a thin-film pressure sensor was used to measure the force on the ear-picking plate during the ear-picking process with and without the installed cutter. A computer collected and recorded the pressure data in real-time. In the experiment, the rotational speed (390, 420, and 450 rpm), cutter installation gap, and ear-picking plate gap (28, 30, 32, and 34 mm) were used as factor variables. Each group of experiments involved feeding on a single corn plant, and the experiment was repeated twice. Finally, based on the recorded data, the pressure on the ear-picking plate was analyzed under different parameters.



Fig. 5 – Schematic layout of high-speed camera equipment



Fig. 6 – Schematic diagram of pressure test bench

1. Data display 2.FSR pressure sensor 3. Computer

Orthogonal experiment

The test was conducted in accordance with the national standard for corn harvesting machinery, GB/T 21962–2020 *(Li et al., 2024)*. During each trial on the test stand, five plants were fed into the mechanism. After operation, the harvested material was collected from the cob tank and the masses of corn stalks, leaves, other impurities, and damaged cob kernels, as well as the total mass of the harvested sample, were measured. The impurity content rate was calculated using formula (1), and the damage rate was calculated using formula (2).

$$H = \frac{m_2}{m_1} \times 100\% \quad (1)$$

$$Z = \frac{m_3}{m_1} \times 100\% \quad (2)$$

where:

H is the impurity content (%); Z is the damage rate (%); m_1 is the total mass of harvested material (g); m_2 is the total mass of impurities (g); m_3 is the damaged seed weight (g);

An orthogonal test method with three factors and three levels was used. The forward speed, cutter clearance, and stalk pulling roller speed were selected as the experimental factors, and the impurity content H and crushing rate Z were used as evaluation indices to conduct a three-factor, three-level, and two-index bench test. A, B, and C represent coded values for each factor in Table 3.

Table 3

Factor coding for orthogonal experiments

Level	Factor		
	A[m/s]	B[mm]	C[rpm]
1	0.2	30	390
2	0.3	32	420
3	0.4	34	450

Verification test

To verify the accuracy of the above-mentioned theory and experimental results, the optimal combination of structural parameters for the ear-picking mechanism was determined, and a verification test was conducted. The forward speed was set to 0.4m/s, the cutter clearance was 34 mm, and the rotational speed of the stalk-pulling roller was 420 rpm for the field test.

RESULTS

High-speed camera test

Tests were conducted under varying rotational speeds and cutter clearances. When the cutter clearance was set to 26 mm, the corn stalks were difficult to feed and frequently became clogged. As shown in Fig. 7, at a clearance of 28 mm, ears could be picked; however, they often became stuck between the ear-picking plates due to the narrow gap (Fig. 8). With a clearance of 34 mm, the contact position between the cutter and the fruit stalk shifted upward because of the increased gap, nearly reaching the base of the ear. Nevertheless, the larger end of the corn ear was not completely cut. In contrast, as illustrated in Fig. 9, most ear-picking devices without cutters directly contact the ear-picking plate, applying pressure. At a stalk-pulling roller speed of 360 rpm, direct ear-picking proved infeasible.

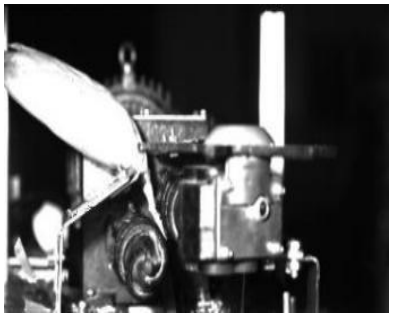


Fig. 7 – Fruit clogging diagram



Fig. 8 – Cutting position of the cutter



Fig. 9 – Force distribution on the cob in the absence of a cutter

The experiment indicated that, during the harvesting process, the fruit stalk was twisted off by the stalk-pulling roller, and the cutter under the ear-picking plate cut into the upper end of the fruit stalk, effectively preventing the fruit ear from being pulled down. The pressure points of the fruit ear were concentrated at the contact between the fruit stalk and the stalk pulling roller and the contact between the fruit stalk and the cutter, as shown in Fig.10.

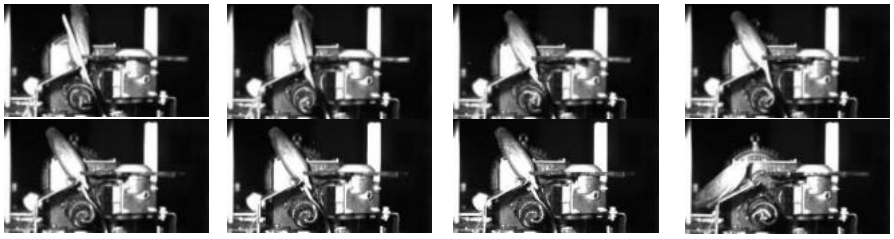


Fig. 10 – Corn picking flow chart

According to the high-speed camera analysis, when the installation gap of the cutting knife of the corn ear-picking plate was 30~34 mm, the ear-picking operation could be performed as expected. After the corn bracts were peeled off, no damage to the corn grains was observed. Moreover, the cutter could effectively prevent damage caused by direct contact between the large end of the corn ear and the ear-picking plate.

Pressure test

According to the final results, as shown in Fig.11, when no cutter was installed, the forces on the ear-picking plates were all greater than 30 N. The force change law was as follows: it increased with the increase in the stalk-pulling roller speed and first increased and then decreased with the increase in the ear-picking plate gap. However, the overall range of change was small, with the overall fluctuation range controlled within 5 N. At this time, the force on the ear-picking plate was generally higher than that when the cutter was installed. After installing the cutter, the force of the corn ear-picking plate was lower than 35 N, and the force first increased and then decreased slightly with an increase in the stalk-pulling roller speed. No ear damage was observed during this process.

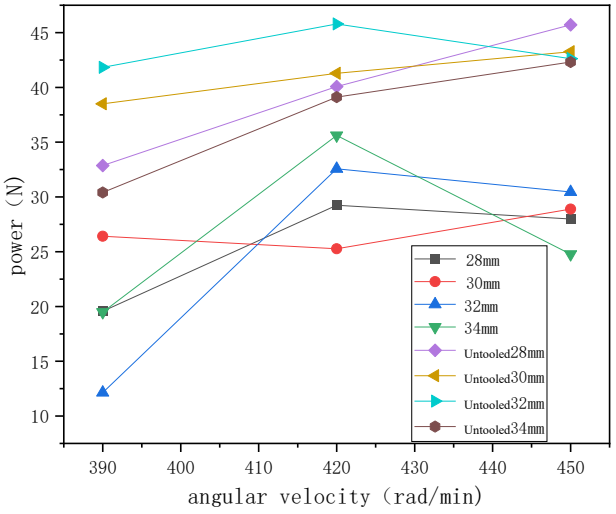


Fig. 11 - Force-speed line diagram

Thus, the reasonable value range for the cutter installation gap was 30~34 mm, and that for the stalk pulling roller speed was 390~450 rpm.

Analysis of Orthogonal Experiment Results

The designed orthogonal test is presented in Table 4. The impurity content and breakage rate of corn were used as evaluation indices and nine groups of tests were carried out. The impurity content ranged from 0.2% to 1.48%, and the breakage rate ranged from 0.02% to 0.2%. The test results were analyzed using SPSS. The primary and secondary factors affecting the impurity content were the cutter clearance, forward speed, and stalk-pulling roller speed, and the optimal combination was determined to be $A_1B_3C_3$. However, if this value is applied to actual work, the mechanical work efficiency will be too low. Therefore, after careful consideration, the best combination is $A_3B_3C_2$.

Table 4

Orthogonal experiments and results

Serial number		Test factors				H [%]	Z [%]
		A	B	C	D (Blank)		
1		1	1	1	1	1.2	0.13
2		1	2	2	2	0.67	0.05
3		1	3	3	3	0.2	0.02
4		2	1	2	3	1.34	0.14
5		2	2	3	1	0.88	0.1
6		2	3	1	2	0.65	0.06
7		3	1	3	2	1.48	0.2
8		3	2	1	3	1.21	0.14
9		3	3	2	1	0.6	0.05
Impurity content	Level 1	2.07	4.02	3.06	2.68		
	Level 2	2.87	2.76	2.61	2.8		
	Level 3	3.29	1.45	2.56	2.75		
	range	0.406	0.856	0.166	0.406		
	optimal combination			$A_1B_3C_3$			
	prioritize factors			B>A>C			

Serial number		Test factors				H [%]	Z [%]
		A	B	C	D (Blank)		
Kernel breakage rate	Level 1	0.2	0.47	0.33	0.28		
	Level 2	0.3	0.29	0.24	0.31		
	Level 3	0.39	0.13	0.32	0.3		
	range	0.0633	0.1133	0.0033	0.01		
	optimal combination	$A_1B_3C_3$					
	prioritize factors	B>A>C					

Note: H, Impurity content Z, Kernel breakage rate

From the analysis, it can be seen that the forward speed determines the feeding amount of the corn ear-picking plate. The larger the feeding amount, the greater the working pressure of the corn ear-picking plate, which is likely to cause multiple corn stalks to enter the gap of the stalk-pulling roller simultaneously, making it difficult to pick the corn ears smoothly and resulting in blockage. This blockage causes the corn ears to remain above the corn ear-picking plate for a long time, ultimately increasing the impurity and breakage rates.

The cutter clearance has a highly significant effect on both impurity and crushing rates. For the impurity rate, the larger the cutter installation clearance, the more favorable it is for the corn plant to be smoothly fed into the tassel picking mechanism for the corn stalk to pass through the stalk pulling roller gap, and ultimately to be crushed and returned to the field at the rear to reduce the impurity rate. For the crushing rate, within the range of the cutter installation gap, the larger the cutter installation gap, the smaller the possibility of clogging occurring when the cob-picking mechanism is working, and the more favorable it is for the corncobs to be smoothly stripped, thereby reducing the residence time of the cobs above the cob picking mechanism and lowering the probability of the cobs being damaged.

As can be seen from Table 5, the rotational speed of the stalk-pulling roller has a great influence on the impurity content. For a single-row fresh corn ear-picking plate, when the gap between the ear-picking plates and the forward speed is constant, the faster the rotation speed of the stalk-pulling roller, the lower the likelihood of blockage, and thus the lower the impurity content. However, the effect of the stalk-pulling roller speed on the ear breakage rate was insignificant. This is because the main causes of ear damage are excessive feed or a knife gap that is too small, which causes blockage, and contact between the large end of the ear and the cutter due to an unreasonable knife installation gap. The main function of the stalk-pulling roller is to provide force for picking the ears and pulling the corn stalks downward. As long as this basic requirement is met, its rotation speed has little impact on the change in the ear damage rate; therefore, it is not significant.

Table 5

Analysis of Variance results

Test indicators	Source of variation	Sum of Squares	Degrees of freedom	Mean square	F	P	Significance
Impurity content	A	0.256088	2	0.128044	105.7247	0.009369	**
	B	1.100955	2	0.550477	454.5229	0.002195	**
	C	0.050555	2	0.025277	20.87155	0.045721	*
	D(Blank)	0.002422	2	0.001211	1	0.5	
Kernel breakage rate	A	0.006022	2	0.003011	38.71428	0.025179	*
	B	0.019288	2	0.009644	124	0.008	**
	C	0.001622	2	0.000811	10.42857	0.0875	
	D(Blank)	0.000155	2	7.777E-05	1	0.5	

*Note: *indicates significant, **indicates highly significant.*

Verification test

The field results indicated that when the forward speed was 0.4 m/s, the cutter clearance was 34 mm, and the stalk-pulling roller speed was 420 rpm, the impurity content was 0.62%, and the ear damage rate was 0.05%, which were consistent with the expected values.

CONCLUSIONS

A corn tasseling test bench was developed, and a kinematic analysis of the tasseling process was conducted using high-speed camera technology and pressure testing to establish a reasonable range of operational parameters. The pressure test results indicated that the maximum contact force of the corn cob on the picking plate was 35 N, effectively reducing the impact force during cob picking.

An orthogonal test identified the optimal parameter combination as a forward speed of 0.40 m/s, a cutter clearance of 34 mm, and a stalk-pulling roller speed of 420 rpm. Under these conditions, the impurity content was 0.62% and the ear damage rate was 0.05%, both of which are below the thresholds specified by the national standard.

Overall, the single-row fresh corn ear-picking machine demonstrated the capability to complete harvesting in a single pass, achieving low-damage ear picking while enabling effective stalk return.

ACKNOWLEDGEMENT

This work is financially supported by the Hunan Provincial Natural Science Foundation Project (2024JJ6248), the open Fund of State Key Laboratory of Agricultural Equipment Technology (SKLAET-202406) and the Hunan Agriculture Research System (HARS-02)

REFERENCES

[1] Cui T., Fan C.L., Zhang D.X., Yang L., Li Y.B., Zhao H.H., (2019). Research Progress of Maize Mechanized Harvesting Technology (玉米机械化收获技术研究进展分析). *Transactions of the Chinese Society for Agricultural Machinery*, Vol. 50, pp .1-13, Beijing/China. DOI: 10.6041/j.issn.1000-1298.2019.12.001

[2] Fu Q., Fu J., Chen Z., (2023). Design and Experimental Study on a Corn Peking Device Based on the Fracture Mechanics of Corn Peduncle. *Journal of the ASABE*, Vol.66, pp.1067-1076， USA. DOI: 10.13031/JA.15105.

[3] Fu Q.K., Fu J., Wang F.D., Chen Z., Ren L.Q., (2019). Design and parameter optimization of corn head with wheel type rigid-flexible coupling snapping device to reduce loss (轮式刚柔耦合减损玉米摘穗割台的设计与参数优化). *Transactions of the Chinese Society of Agricultural Engineering*, Vol.35, pp.21-30, Jilin/China. DOI: 10.11975/j.issn.1002-6819.2019.07.003.

[4] Gao X., (2013). *experimental study of mechanical properties of corn stalks (玉米秸秆力学特性试验研究)*. MSc Thesis, Hua zhong Agricultural University, Hubei/China.

[5] Li F., (2023). Evaluation of the uncertainty of the drying method for determining the moisture content of corn stover (烘干法对测定玉米秸秆含水率不确定度的评定). *Xinjiang Agricultural Mechanization*, IS. (04), pp. 46-48, Xinjian/China. DOI: 10.13620/j.cnki.issn1007-7782.2023.04.013.

[6] Luo H.Z., Zuo P., Jiang X.X., Qiu Q.Y., Yuan S.L., Zhang L.H., (2023). Mechanical Simulation Experiment of Rigid Flexible Coupling Corn Plucking Based on ADAMS (基于 ADAMS 的刚柔耦合玉米摘穗力学仿真试验). Journal of Agricultural Mechanization Research, Vol.45, pp.147-153, Heilongjian/China. DOI: 10.13427/j.cnki.njyi.2023.01.029.

[7] Luo H., Nie J., Zhang L., (2023). Design and test of dislocation baffle roller bionic stripping device for fresh corn. *Agriculture*, Vol. 13, pp.991, Switzerland. DOI: 10.3390/agriculture13050991.

[8] Li T., Guan X., Zhou F., (2023). Mechanistic analysis and experimental study of a shear-type low-loss fresh corn ear-stripping mechanism. *Computers and Electronics in Agriculture*, Vol. 213, Netherlands. DOI: 10.1016/j.compag.2023.108191.

[9] LI Z.Y., (2023). *Research on key technologies and intelligent recognition for low-damaged-high-stripping peeling of corn ear harvester (玉米果穗收获机低损高净剥皮关键技术与智能识别研究)*. PhD dissertation, Jilin University, Jilin/China.

[10] Li Z.B., Ye T., Nie M.L., Lan H.T., Zhang X., Zhao W., (2024). Design and testing of 4yz-6 fresh corn harvester grain splitting front end component, *INMATEH Agricultural Engineering*, Vol.72, pp.820-829, Romania. DOI: https://doi.org/10.35633/inmateh-72-73.

[11] Qin J.H., Yin Y.P., Liu Z.G., Du Y.F., Wang G.Y., Zhu Z.X., Li Z., (2020). Optimisation of Maize Picking Mechanism by Simulation Analysis and High-Speed Video Experiments. *Biosystems Engineering*, Vol.189, pp. 84-89, Britain. DOI: 10.1016/j.biosystemseng.2019.11.010.

[12] Su L.J., (2021). Comparative Experiment of Fresh and Sweet Corn Varieties and Analysis of Meteorological Conditions in the Growing Period (鲜食甜玉米对比试验及生育期气象条件分析研究). *Chinese Agricultural Science Bulletin*, Vol. 37, pp. 7-12, Beijing /China. DOI: 10.11924/j.issn.1000-6850.casb2021-0276.

[13] Shi Z.S., Zhong X.M., (2016). Breeding Principle and Technical Skill of Fresh Corn Varieties (鲜食玉米新品种选育原理与技术技巧). *Journal of Maize Sciences*, Vol.24, pp.1-5, Jilin/China. DOI: 10.13597/j.cnki.maize.science.20160201.

[14] Wang H., Liu J., Chu W.C., Li X.L., Guo Z.X., Lan T.Q., Feng D.J., Yuan J.C., Kong F.L., (2024). Effect of Ear size on the Crushing Rate of Mechanical Corn Harvest (果穗大小对玉米机械粒收籽粒破碎率的影响). *Acta Agriculturae Boreali-Sinica*, Vol. 39, pp. 72-80, Hebei/China, DOI:10.7668/hbnxb.20194634

[15] Zhu G.Q., Li T.Y., Zhou F.J., Wang W.M., (2023). Design and experiment of bionic ear stripping device for fresh corn (鲜食玉米仿生摘穗装置设计与试验). *Journal of Jilin University*, Vol.53, pp.1231-1244, Heilongjian/China. DOI: 10.13229/j.cnki.jdxbgxb.20210767.

[16] Zhang L., (2015). *Theoretical Analysis and Simulation Research on Novel Bionic Com-ear Snapping Mechanism (新型仿生玉米摘穗机构理论分析与仿真研究).* MSc Thesis, Jilin University, Jilin/China.

[17] Zhang Z., Chi R., Du Y.F., Pan X., Dong N.X., Xie B., (2021). Experiments and modeling of mechanism analysis of maize stripping loss. *International Journal of Agricultural and Biological Engineering*, Vol.14, pp.11-19, Beijing / China. DOI: 10.25165/j.ijabe.20211401.5745.

[18] Zhang Z.L., Zhang D.X., Cui T., Yan L., Li K.H., (2014). Design and experiment of corn stripping monomer mechanism (玉米梳齿摘穗单体机构设计与试验). *Transactions of the Chinese Society of Agricultural Engineering*, Vol.30, pp.1-9, Beijing/ China. DOI: 10.3969/j.issn.1002-6819.2014.20.001.

[19] Zhang Z.L., Liu W., Hou J.L., Cui T., Geng A.J., Zhang J., (2020). Mechanical Analysis and High-speed Photograph Experiment of Corn in Stripping Process (玉米梳脱摘穗果穗受力分析与高速摄影试验). *Journal of Agricultural Mechanization Research*, Vol.42, pp. 123-129, Heilongjian / China. DOI: 10.13427/j.cnki.njyi.2020.06.021.

[20] Zhang Z.L., Cui T., Geng A.J., Zhang J., (2020). Design and simulation analysis of corn stripping head (玉米梳脱摘穗割台设计与仿真分析). Journal of Chinese Agricultural Mechanization, Vol.41, pp. 26-30, Beijing/China. DOI: 10.13733/j.jcam.issn.2095-5553.2020.05.005.

[21] Zhang L., Yu J.Q., Zhang Q., Fang W.W., (2023). Design and testing of a new bionic corn-ear-stripping test device. *Applied Sciences*, Vol.13, pp.838, Switzerland. DOI: https://doi.org/10.3390/app13020838.

DESIGN AND EXPERIMENT OF A NEW TYPE OF SORTING, EVISCERATION, AND CLEANING EQUIPMENT FOR SEA CUCUMBER

/

一种新型海参分拣除脏清洗设备的设计与试验

Lizheng JIANG*[1)], Zangping GUO[1)], Fangyuan SUN[1)]

[1)]Institute of Intelligent Manufacturing, Zhejiang Polytechnic University of Mechanical and Electrical Engineering, Hangzhou / China

Tel: +86-152-5887-8838; E-mail: jianglizheng@zime.edu.cn

DOI: https://doi.org/10.35633/inmateh-76-68

Keywords: *Sea Cucumber, Sorting, De-sanding and Organ Removing, Image Recognition, High-Pressure Water Jet Washing*

ABSTRACT

In sea cucumber production lines, manual sorting, de-sanding, and organ removing operations still predominated, severely limiting production efficiency and posing significant risks to product consistency and hygiene. This paper introduced a novel piece of equipment for sea cucumber sorting, de-sanding, organ removing, and washing. Employing an innovative process combining "automatic sand mouth removal + high-pressure water jet washing + hook-assisted organ removal," the equipment adapted well to sea cucumbers of various sizes and conditions, offering high versatility and facilitating an automated, efficient, and standardized processing workflow. Moreover, due to the high sensitivity to the sea cucumber's external shape and posture and the complexity of the background caused by residues during the de-sanding and organ removing process, which further complicated the recognition of the sea cucumber's sand mouth, this study proposed a sand mouth recognition algorithm for complex backgrounds. Utilizing tiered recognition technology, the algorithm precisely located the sea cucumber's sand mouth following the extraction of its position through artificial intelligence, significantly enhancing the success rate of recognition. Experimental results indicated that the prototype of this equipment increased the speed of de-sanding and organ removing by 107.8% compared to existing integrated sea cucumber washing and cutting equipment. The cleaning effectiveness was excellent, with a high sea cucumber cleaning acceptance rate of 91%, which was an increase of 6.125% over manual sorting, de-sanding, and organ re-moving methods, and the work efficiency increased more than ninefold, achieving the anticipated outcomes.

摘要

在海参生产线上，人工分拣除脏操作仍占据主导地位，这一现状严重制约了生产效率，也给产品的一致性和卫生带来了巨大风险。本文设计了一种新型海参分拣除脏清洗设备。通过“切割沙嘴 + 高压水冲洗 + 钩子辅助除脏”的创新工艺，对不同规格和状态的海参均具有良好的适应性，具备高度通用性，实现了海参的自动化、高效、标准化加工流程。同时，针对海参外形和姿态特征的高敏感度，以及除脏过程中产生的脏污导致背景复杂、海参沙嘴识别困难的问题，提出了一种复杂背景下的海参沙嘴识别算法。该算法利用分级识别技术，在提取海参位置后，通过人工智能精准定位海参沙嘴，显著提高了识别成功率。实验结果表明，该实物样机的除脏速度较现有海参清洗剖切一体化设备提升了 107.8%；清洗效果良好，海参清洗合格率高达 91%，较人工分拣除脏清洗合格率提高 6.125%，工作效率提高 9 倍以上，达到了预期效果。

INTRODUCTION

Sea cucumbers, recognized for their high protein and low fat content, are considered a marine delicacy with an increasingly growing market demand *(Xu et al., 2013)*. However, the processing of sea cucumbers is intricate, particularly in the stages of sorting, de-sanding, organ removal, and washing. These processes are predominantly manual, characterized by low efficiency and high labor intensity *(Liu et al., 2023)*. Impurities such as sand and internal organs within the sea cucumber, if not thoroughly removed, adversely affect the quality and palatability of the product *(Sun et al., 2019)*. Traditional manual methods of sorting, de-sanding, and organ removal not only are inefficient but also prone to damaging the sea cucumbers, leading to inconsistent product quality. Moreover, manual washing fails to ensure uniformity in the size of the cuts on the sea cucumbers, further impacting the standardization of subsequent processing steps (see Fig. 1).

In recent years, as the sea cucumber industry chain has evolved, numerous enterprises have begun to explore the research and application of mechanized and auto-mated processing equipment.



Fig. 1 - A manual labor scene of sea cucumber organ removal

Currently, in the processing of lightly dried sea cucumbers, the sequence involves temporary cultivation, manual de-sanding and organ re-moving (evisceration), flexible bubble automatic washing (*Xu et al., 2016*), multiple washes (including saltwater rinses), boiling (cooked in 85°C boiling water), followed by baking or sun-drying, steam drying, quality-based grading, and packaging (*Li et al., 2016*). Similarly, instant sea cucumbers undergo a process that includes temporary cultivation, evisceration, washing, blanching for shaping, curing, flash freezing, sealing, packaging, and refrigerated storage (*Tang et al., 2012*).

In recent years, as the industry chain has progressively upgraded, many sea cucumber processing enterprises have not only enhanced the construction of aquaculture bases but have also invested heavily in the establishment of automated sea cucumber processing lines (*Wang et al., 2020; Yu et al., 2016; Wu et al., 2023; He et al., 2019*). This has increased production capacity and continuously improved processing techniques, providing consumers with safe, healthy, and convenient sea cucumber products. However, existing devices still exhibit significant shortcomings in terms of cleaning quality, production efficiency, and automation level.

The cleaning equipment designed by Xu Wenqi et al., which employs compressed air bubbles emitted from the bottom of a tank, suffers from uncontrollable foam density and may induce stress responses in sea cucumbers, such as evisceration, thus compromising the quality of the cleaned sea cucumbers (*Xu et al., 2009*). The rotary brush cleaning device developed by Wang Hongyu et al., although capable of washing and slicing sea cucumbers, requires pre-treatment steps before pickling and cannot be applied directly to live sea cucumbers. Additionally, the rotary brush structure is highly likely to damage the ventral foot of the sea cucumbers (*Wang et al., 2018*).

Xu Jing et al. proposed a technique for shedding the skin of fresh or frozen East Sea sea cucumbers, covering steps such as fixation, mechanical abrasion, initial decontamination, enzymatic peeling, further de-contamination, and repeated enzymatic treatment. However, the enzymatic peeling strategy damages the superficial tissue characteristics of the sea cucumbers, affecting their appearance and taste (*Xu et al., 2013*).

Yang Sheng et al. (2024) developed an integrated sea cucumber washing and slicing machine that utilizes high-pressure water mist nozzles and ultrasonic generators to clean both the surface and internal sand of the sea cucumbers. Yet, this equipment requires multiple steps such as flipping, washing, and slicing during operation, leading to low work efficiency and failing to meet operational efficiency requirements. The injection-type equipment used in the Kansai region of Japan, although ensuring the quality of processed sea cucumbers, is cumbersome and unsuitable for assembly line production (*Xue et al., 2022*).

Notable advances include Ronel S. Pangan et al.'s processing technology package (preparation tables, boiling devices, etc.), which improves efficiency, quality, and cost-effectiveness (*Ronel et al., 2017*). Akhirman et al.'s new cleaning technology with soft brushes to reduce surface damage (*Akhirman et al., 2021*) and Xu Zhang et al.'s water jet cleaning technology, which removes impurities while preserving surface integrity - optimal results come from parameter optimization (pressure, target distance, etc.) (*Zhang et al., 2021*).

Consequently, the development of an efficient, automated sea cucumber processing equipment that performs sorting, de-sanding, organ removal, and washing is of significant importance for enhancing processing efficiency, reducing labor costs, and ensuring product quality in the sea cucumber industry.

This paper introduces a novel piece of equipment designed for these purposes, which utilizes an innovative process comprising "automatic sand mouth removal via cutting, high-pressure water jet washing, and hook-assisted organ removal." This equipment integrates machine vision technology with intelligent control systems to automate the sorting, de-sanding, organ removal, and washing of sea cucumbers.

Not only does this machine substantially increase production efficiency, but it also maintains the integrity of the sea cucumber's shape and the quality of its cleanliness, thereby providing a new solution for the automation of sea cucumber processing. This also provides feasible technological support for the advancement of agriculture 5.0 *(Taha et al., 2025; Adams et al., 2025)*.

MATERIALS AND METHODS

Structure and Principles of Sea Cucumber Sorting, De-sanding, Organ Removing, and Washing Equipment

In response to the rapid operational demands of the sea cucumber processing line, an innovative automated de-sanding, organ removing, and washing process has been developed. This process transitions from the traditional manual incision and hand removal of viscera to an automated system comprising automatic sand mouth removal, high-pressure water jet washing, and hook-assisted organ removal. The equipment designed for sorting, de-sanding, organ removing, and washing enables automated operations and combines machine vision for image recognition and processing *(Ma et al., 2009)*, intelligent control technologies, and mechanical execution mechanisms to ensure precise and rapid completion of large-scale sea cucumber cleaning tasks. The primary components of this equipment include a sorting feeding mechanism, a pressing conveyor mechanism, a de-sanding, organ removing, and washing mechanism, a washing transfer mechanism, and a frame platform, as illustrated in Fig. 2.

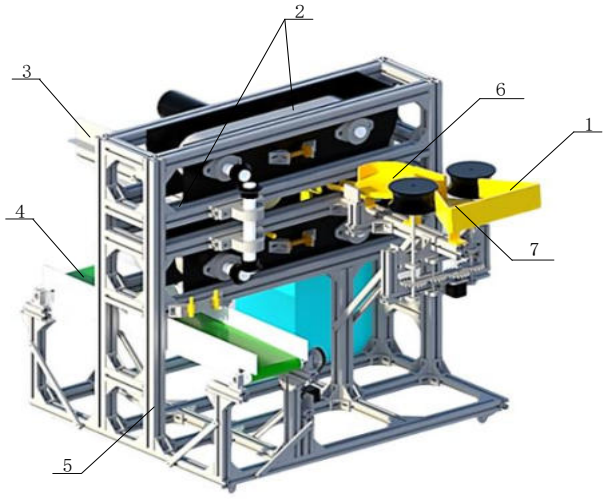


Fig. 2 - Schematic diagram of the sea cucumber sorting, de-sanding, organ removing, and washing equipment

1. Sorting feeding mechanism; 2. Pressing conveyor mechanism; 3. De-sanding, organ removing and washing mechanism; 4. Washing transfer mechanism; 5. Frame platform; 6. Turntable; 7. Chute.

A substantial quantity of sea cucumbers is deposited into the chute of the sorting feeding mechanism, where they are subsequently aligned on a turntable. Vision sensors identify and align the position of the sand mouth, after which they are transferred to the pressing conveyor mechanism. Here, the upper and lower claws of the pressing unit clamp the sea cucumber, positioning it for the cutting component of the de-sanding, organ removing, and washing mechanism to remove the sand mouth. The cleaning component then clears the viscera, and finally, the sea cucumber enters the washing transfer mechanism to complete the cleaning process. The functionality analysis of this equipment is depicted in Fig. 3.

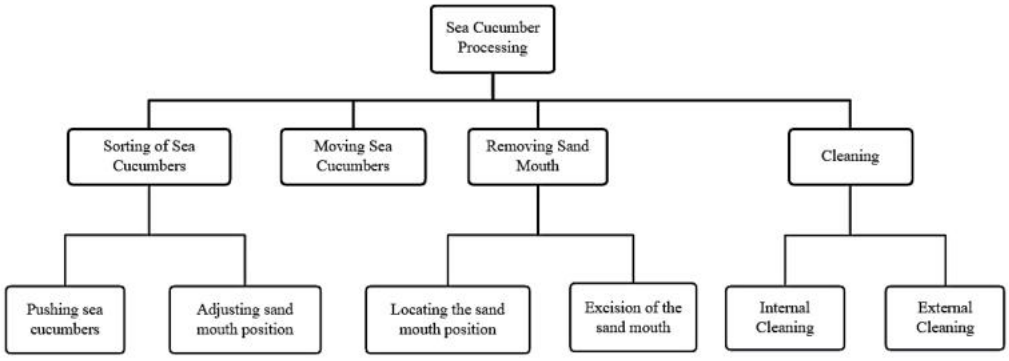


Fig. 3 - Functional analysis diagram of the sea cucumber sorting, de-sanding, organ removing, and washing equipment

Structural Design of Key Components

The key components of the sea cucumber sorting, de-sanding, organ removing, and washing equipment include the sorting feeding mechanism, pressing conveyor mechanism, and de-sanding, organ removing, and washing mechanism. The washing transfer mechanism and frame platform serve as auxiliary components and accessories, which facilitate the external rinsing and conveyance of processed sea cucumbers.

Sorting Feeding Mechanism

The sorting feeding mechanism primarily consists of six components: a vision module (1), a conveyor slide (2), a four-degree-of-freedom turntable (3), rollers (4), a chute (5), and gears (6). It is installed on the right side of the sorting, de-sanding, organ removing, and washing equipment for sea cucumbers. Positioned at the central part of the pressing conveyor mechanism, it aligns precisely with the positioning plate and the clamping claws (see Fig. 4).

The four-degree-of-freedom turntable collaborates with the vision recognition system not only to sort the sea cucumbers but also to adjust the orientation of the sand mouth, ensuring uniformity. During operation, the rotation of the rollers facilitates the rapid alignment of the sea cucumbers into a single row. The Hikvision SC6000 series camera captures the image information of the sea cucumbers and utilizes classification recognition technology to precisely locate the position of the sand mouth. Subsequently, the four-degree-of-freedom turntable rotates to align the sand mouths in a uniform direction, preparing for the subsequent de-sanding, organ removing, and washing processes. This camera is equipped with a 5-megapixel CMOS image sensor with a resolution of 1408×1204, positioned directly above the four-degree-of-freedom turntable, specifically for the recognition and positioning of the sand mouth. Its recognition performance is clear and reliable, efficiently identifying sea cucumbers and detecting the sand mouth from the captured images. Based on pre-set standards, the system grades the sea cucumbers and positions the sand mouth, subsequently sending commands to downstream devices.

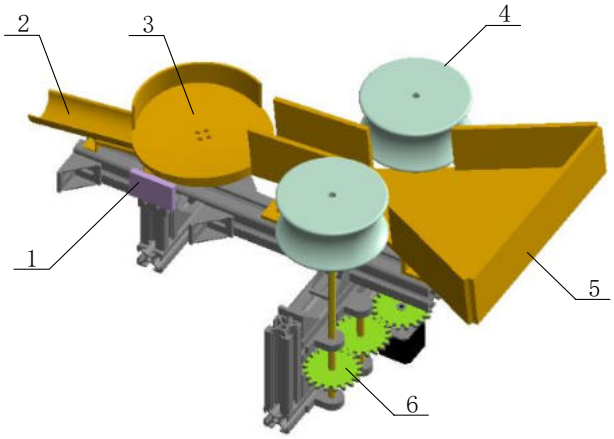


Fig. 4 - Structural schematic of the sorting feeding mechanism

1. Vision sensor; 2. Conveyor slide; 3. Four-degree-of-freedom turntable; 4. Rollers; 5. Chute; 6. Gears.

Pressing Conveyor Mechanism

The pressing conveyor mechanism primarily consists of components such as a sprocket (1), a fixed plate (2), a large pulley (3), a drive motor (4), a small pulley (5), a timing belt (6), bevel gears (7), a conveyor chain (8), an arcuate claw compression plate (9), an upper claw (10), and a lower claw (11). The structure of this mechanism is depicted in Fig. 5(a).

This system utilizes a collaborative transmission between the timing belt and the bevel gears to facilitate synchronous movement of the conveyor chain. The configuration of the four bevel gears ensures that the conveyor chain moves in opposing directions. The pressing assembly, as shown in Fig. 5(b) and 5(c), is chiefly responsible for compressing and clamping the sea cucumbers, thereby ensuring their stability during transportation and minimizing displacement. This assembly comprises an arcuate claw compression plate, an upper claw equipped with an internal spring secured by a pin to prevent dislocation, and a lower claw. The pressing assembly is mounted on the exterior of the conveyor chain with the claws affixed to the chain, while the arcuate claw compression plate is positioned at the front, closely conforming to the curved surfaces of the fixed plates located on either side.

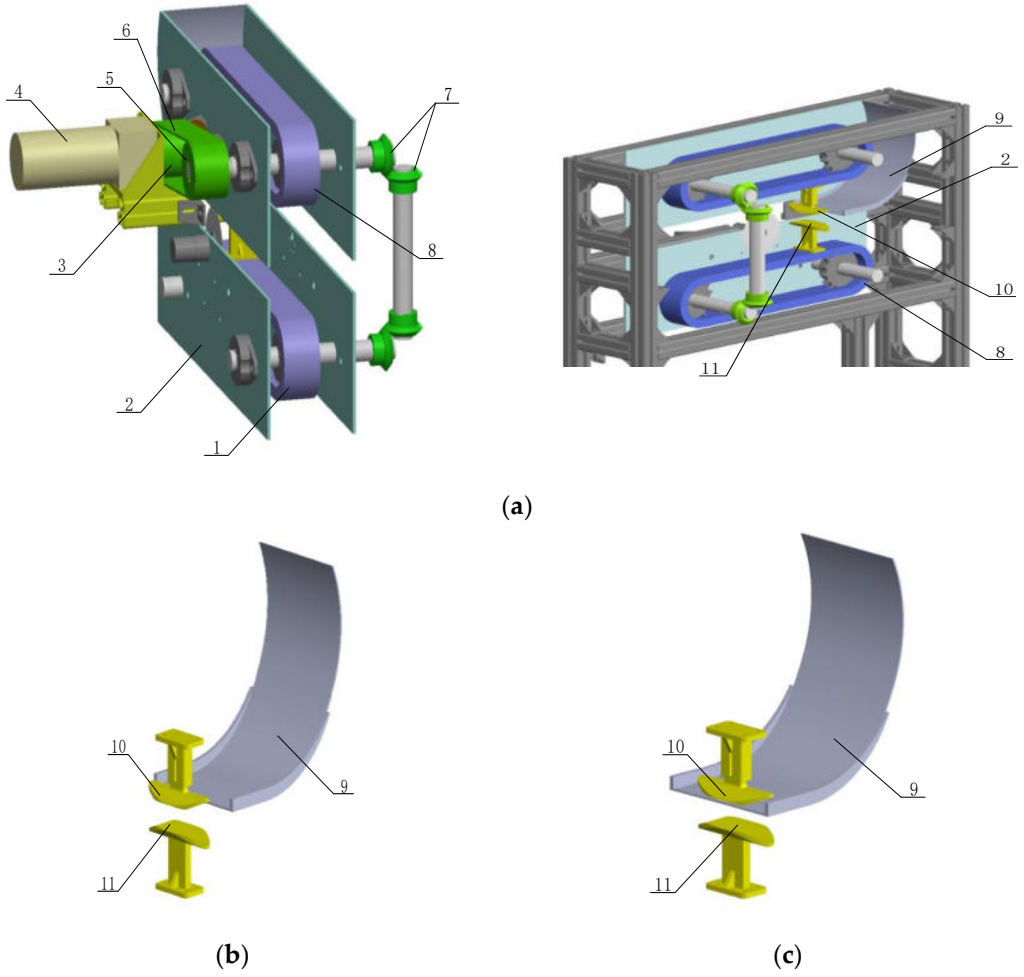


Fig. 5 - Structure and pressing state of the pressing conveyor mechanism.
(a) Schematic of the Pressing Conveyor Mechanism; (b) Compressed State of the Pressing Assembly; (c) Extended State of the Pressing Assembly.
1. Sprocket; 2. Fixed plate; 3. Large pulley; 4. Drive motor; 5. Small pulley; 6. Timing belt; 7. Bevel gear; 8. Conveyor chain; 9. Arcuate claw compression plate; 10. Upper claw; 11. Lower claw.

Design and Verification of Clamping Force

The selected material for the springs is SUS304 stainless steel, characterized by a wire diameter (d) of 0.8 mm, a mean diameter (D) of 9 mm, and a total of 10 coils. The initial length (L_0) of the spring is 110 mm, with compressed lengths of 29 mm (L_1) and 9 mm (L_2), resulting in compression displacements of s_1 = 81 mm and s_2 = 101 mm, respectively.

The formula for spring deformation is denoted as:

$$s = \frac{8FnD^3}{Gd^4} \quad (1)$$

From which, the force (F) can be derived:

$$F = \frac{SGd^4}{8nD^3} \quad (2)$$

The shear modulus (G) of SUS304 material is 7000 kgf/mm2 ≈ 68600 MPa. Using this value, the range of clamping force can be calculated by:

$$F_1 = \frac{s_1 Gd^4}{8nD^3} = \frac{81 \times 68600 \times 0.8^4}{8 \times 10 \times 9^3} = 39.004N \quad (3)$$

$$F_2 = \frac{s_2 Gd^4}{8nD^3} = \frac{101 \times 68600 \times 0.8^4}{8 \times 10 \times 9^3} = 48.706N \quad (4)$$

Given that each gripper incorporates two springs, the range of clamping force for the gripper assembly is given by:

$$F_{min} = 2F1 = 78.008N \quad (5)$$

$$F_{max} = 2F2 = 97.412N \quad (6)$$

The friction force formula "$f=F\mu$" is utilized, assuming a friction coefficient (μ) of 0.05 between the sea cucumber and the grippers, and a contact area of 6000 mm^2. Consequently, the friction force range between the sea cucumber and the grippers is calculated as:

$$f_{min} = F_{min}\mu=78.008\times0.05=3.9N \quad (7)$$

$$f_{max} = F_{max}\mu=97.412\times0.05=4.87N \quad (8)$$

The claws can provide a maximum friction force of 4.87 N and a minimum of 3.9 N, which satisfies the design requirements.

Selection and Verification of Conveyor Belt Motor

The conveyor belt is designed to handle a maximum load of 50 kg and operates at a speed of 60 m/min, with a roller diameter of 30 mm. The overall efficiency (η) is set at 75%, with a friction coefficient of 0.2 and a safety factor (k) of 1.8. The timing belt pulleys are specified with teeth counts Z_1 = 10 and Z_2 = 30.

The friction force required is calculated by:

$$f=F\mu=mg\mu=50\times10\times0.2=100\ \mathrm{N} \quad (9)$$

The power required for the conveyor belt is given by:

$$P=\frac{fVk}{\mu}=\frac{100\times1\times1.8}{0.75}=0.24\ \mathrm{kW} \quad (10)$$

The rotation speed of the larger shaft is:

$$n=\frac{v}{2\pi r}=\frac{1}{2\times3.14\times0.015}=10.6\ \mathrm{r/s}=636\ \mathrm{r/min} \quad (11)$$

The torque required for the motor is:

$$T=9550P/n=9550\times\frac{0.24}{636}=3.6\ \mathrm{N\cdot m} \quad (12)$$

Based on the relationship defined in:

$$i=\frac{Z2}{Z1}=\frac{30}{10}=3 \quad (13)$$

The actual power required for the motor is determined by:

$$T_0=\frac{T}{i}=\frac{3.6}{3}=1.2\ \mathrm{W} \quad (14)$$

The actual rotation speed of the motor is calculated as:

$$n_0=ni=636\times3=1908\ \mathrm{r/min} \quad (15)$$

De-sanding, Organ Removing, and Washing Mechanism

The de-sanding, organ removing, and washing mechanism comprises a positioning and cutting assembly and an internal cleaning assembly. As depicted in Fig. 6, the positioning and cutting assembly's layout incorporates a conveyor slide (1) precisely aligned with adjustable components and secured on a frame platform. A motor (3) is mounted on the adjustable component, connecting to a circular blade (2) positioned to the right of the adjustable component at a precise distance equivalent to the width of a "sand mouth." Under the cooperative action of the pressing conveyor mechanism, the head and tail of the sea cucumber are compressed, allowing the cutting assembly to precisely execute cutting and expanding operations on the sand mouth. Moreover, the adjustable component facilitates the flexible positioning of the motor, effectively minimizing the removal volume of the sea cucumber, thereby preserving the integrity of its edible portions to the greatest extent.

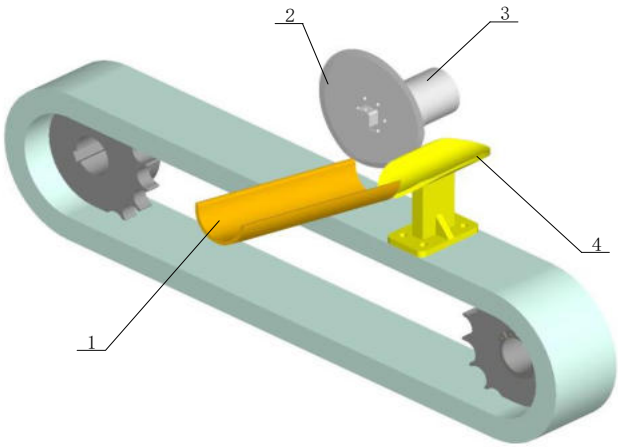


Fig. 6 - Structural schematic of the installation position of the cutting assembly

1. Conveyor slide; 2. Circular blade; 3. Motor; 4. Lower claw.

The internal cleaning assembly, as illustrated in Fig. 7, consists of a slide rail (1), slide rail support (2), water spray pipe (3), three-way block (4), and push rod (5). This assembly facilitates the "automatic sand mouth removal + high-pressure water jet washing + hook-assisted organ removal" cleaning operations for the sea cucumber. The push rod, in conjunction with the nozzle structure, enters the sea cucumber through the cut made post-sand mouth removal to perform internal cleaning, thereby maximally preserving the structural integrity of the sea cucumber. During the cleaning process, the upper and lower claws clamp the sea cucumber and move it toward the front of the cleaning assembly. A high-pressure diaphragm pump draws water, which is then directed through the three-way block to the water spray pipe. Water is ejected from lateral orifices in the water spray pipe. A hook mounted at the front of the water spray pipe aids in the removal of internal organs. Through its reciprocating linear motion, the hook enables repeated high-pressure rinses within the sea cucumber, effectively eliminating internal contents and achieving a thorough cleaning.

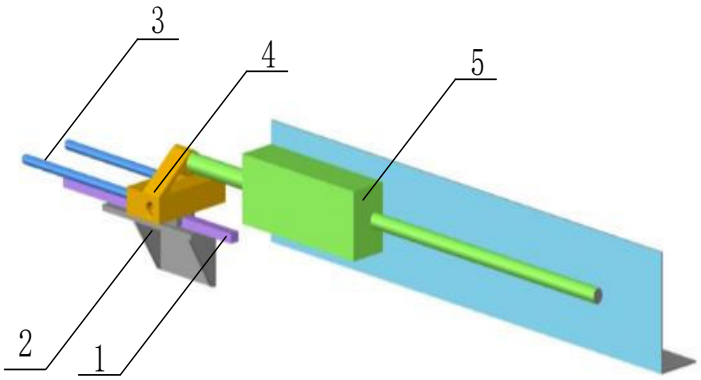
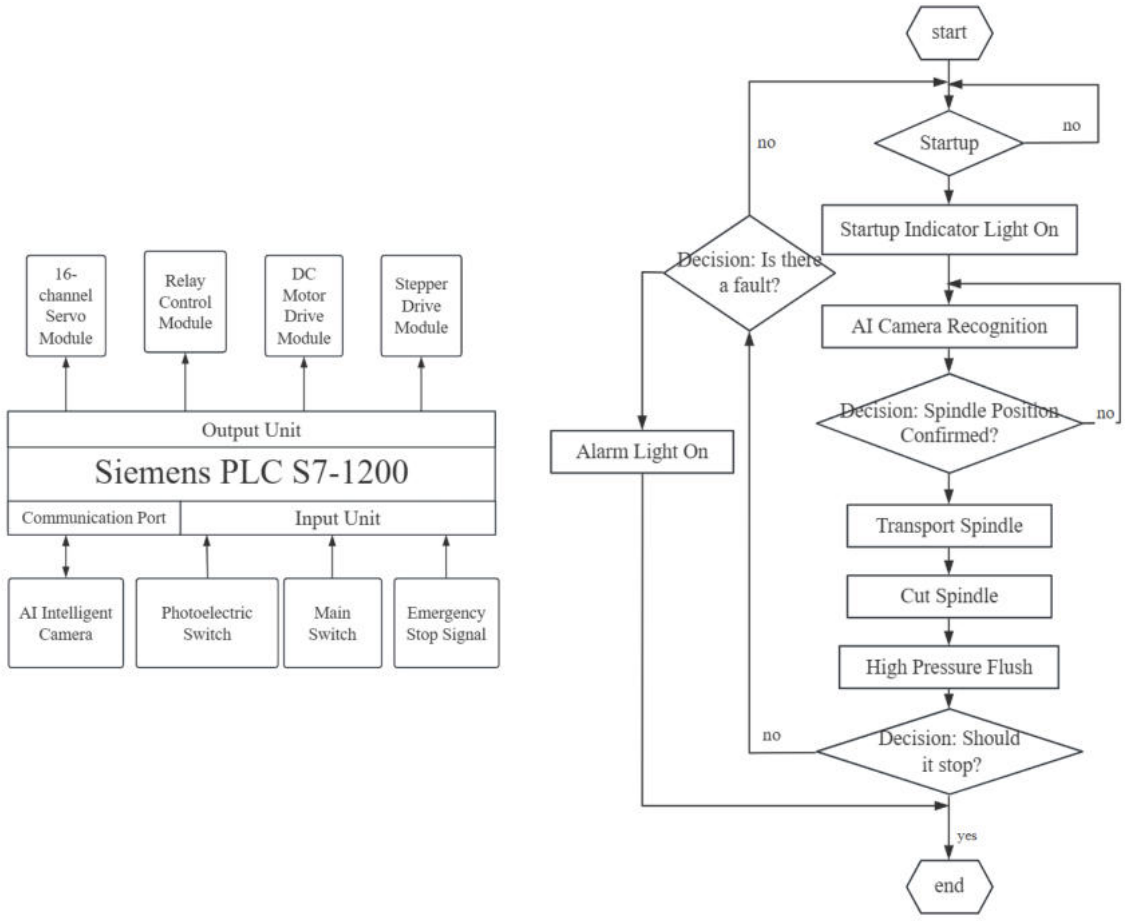


Fig. 7 - Structural schematic of the installation position of the cleaning assembly

1. Slide rail; 2. Slide rail support; 3. Water spray pipe; 4. Three-way block; 5. Push rod.

Design of Control Systems

The comprehensive design of the electrical control system is illustrated in Fig. 8(a). This system is centered around the Siemens S7-1200 PLC as the core controller, which coordinates the operation of various electrical components such as DC motors, stepper motors, servos, high-pressure diaphragm pumps, and solenoid valves. The system operates in a semi-automatic control mode, requiring manual intervention only to activate/deactivate start/stop buttons and emergency stop functions, while other functionalities (including vision recognition and photoelectric switch controls) are executed automatically through pre-set logic, as shown in the control flow diagram in Fig. 8(b).



(a) (b)

Fig. 8 - Schematic of the electrical control system design and control flow diagram.
(a) Schematic of the electrical control system design; (b) Control flow diagram

The vision recognition control module is primarily utilized for sorting operations, identifying the position and orientation of the sea cucumber's sand mouth, thereby enabling precise sorting without the need for human intervention. Conversely, the photoelectric switch control module is employed in cleaning operations, where photo-electric sensors detect the presence of sea cucumbers at designated cleaning stations, subsequently triggering the cleaning process. The PLC, serving as the system's central control unit, is responsible for programming and executing the overall work logic.

During the sorting process of sea cucumbers, the PLC first controls the stepper motor to transport the sea cucumbers to the servo-operated area; subsequently, the AI smart camera module recognizes the sea cucumbers and their sand mouth positions. This data is transmitted in real-time to the PLC via the Profinet communication protocol. Based on the received data, the PLC controls a 16-channel servo module to carry out precise sorting and ordering operations, ensuring the sea cucumbers proceed in a pre-determined sequence to the next stage. For the position-specific cutting of sea cu-cumbers, the PLC controls AC motor drives through relay modules and L298N DC motor driver modules, managing the upper and lower conveyor chains. Concurrently, the PLC activates the blade's DC motor to rotate at a set speed. Through the collaborative operation of these components, the system efficiently completes the precise cutting of the sea cucumber's sand mouth.

In the subsequent internal cleaning process, when a sea cucumber is conveyed to a specified cleaning position, the photoelectric switch is activated and sends a signal to the PLC. Upon receiving this signal, the PLC immediately controls the relay module to cease the operation of the AC motors while initiating the diaphragm pump for spray cleaning. Furthermore, the PLC also controls the crank slider mechanism of the motor intermittently, ensuring a thorough internal cleaning of the sea cucumbers.

RESULTS

Experimental Design

To validate the efficacy of each module of the sea cucumber sorting, de-sanding, organ removing, and washing equipment, as well as the operational stability, reliability, and processing outcomes, this study was based on the structural and operational principles of the sea cucumber processing equipment. The construction involved machining and assembling critical modules including the sorting feeding mechanism, pressing conveyor mechanism, and the de-sanding, organ removing, and washing mechanism, along with the washing transfer mechanism. These modules were integrated with an electrical control system and subsequently calibrated, as illustrated in Fig. 9.

The experimental study was divided into four parts.

(1) Sea Cucumber Identification and Sand Mouth Detection Algorithm Efficacy Experiment: This phase aimed to validate the applicability and reliability of the intelligent recognition algorithm and to verify its superiority in operation within the equipment through the accuracy of identification.

(2) Processing Effectiveness Experiment for Various Factors: This part focused on validating the overall system's applicability and reliability, as well as each module's effectiveness. Independent factor experiments were conducted to determine the optimal operational parameters for the equipment.

(3) Comparative Experiment with Other Equipment: Building on the optimal process parameters established in the first part, this experiment compared those parameters with those of existing equipment to affirm the superiority of the proposed design.

(4) Comparison Experiment with Manual Processing: This experiment involved actual production measurements to further validate the stability of the system and the quality of the processing results.



Fig. 9 - Exterior view of the prototype of the sea cucumber sorting, de-sanding, organ removing, and washing equipment

Experimental Evaluation of Sea Cucumber Identification and Sand Mouth Detection Algorithms

As depicted in Fig. 10(a), the sea cucumber identification algorithm proposed in this study demonstrates significant efficacy when applied on a turntable. When sea cucumbers are situated against a clean background, this facilitates the more precise extraction of deep features during the feature extraction process, thereby rendering the features of the sea cucumbers more complete and significantly enhancing the confidence of identification, with confidence levels exceeding 90%. Conversely, for sea cucumbers against a dirty background, the complexity of the image background complicates the distinction between the sea cucumbers and the background. Although the algorithm still successfully detects the sea cucumbers, the confidence levels are typically below 80%, but still surpass 60%, as shown in Fig. 10(b). This performance is sufficient to meet the basic requirements for sea cucumber identification. Furthermore, as shown in Fig. 10(c), through a tiered recognition approach, high-confidence sea cucumbers can be precisely identified for their sand mouth location using artificial intelligence technology, and this identification also exhibits high confidence.

Simultaneously, for sea cucumbers on dirty turntables, the post-tiered processing results for sand mouth location detection are favorable, with confidence levels also reaching above 65%, as illustrated in Fig. 10(d). Therefore, the sea cucumber sand mouth detection algorithm developed in this study demonstrates good applicability and reliability for use in sea cucumber sorting, dirt removal, and cleaning equipment.

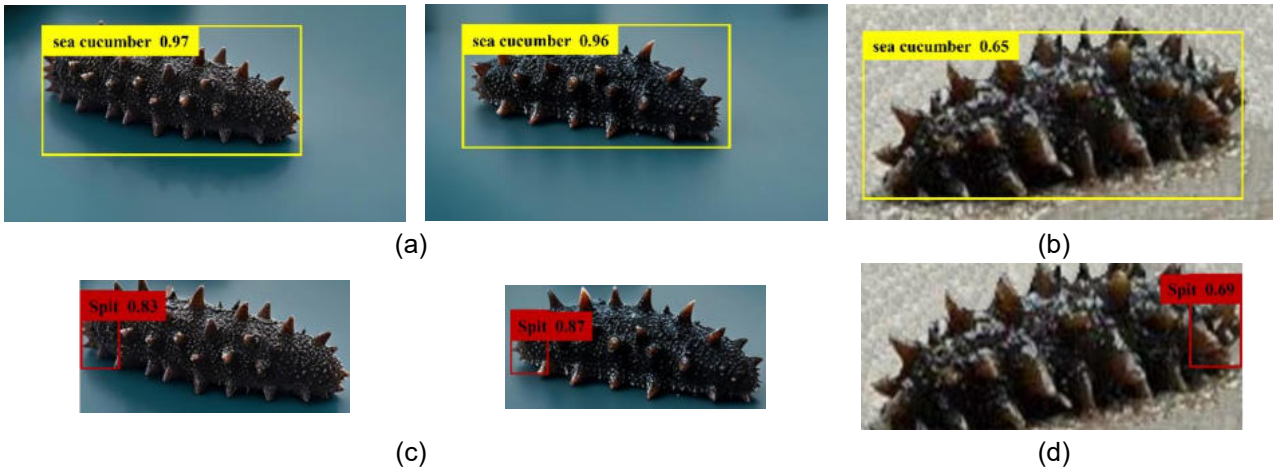


Fig. 10 - Effects of sea cucumber identification and sand mouth detection.

(a) Identification of sea cucumbers against a clean background; (b) Identification of sea cucumbers against a dirty background; (c) Detection of sand mouth against a clean background; (d) Detection of sand mouth against a dirty background.

Experimental Analysis of Factorial Processing Effects

The operational speeds of the sorting feeding mechanism, pressing conveyor mechanism, and washing transfer mechanism are critical determinants affecting the efficiency of sea cucumber cleaning processes, with notable interactions existing among these factors. This study employed a single-factor experimental approach to independently investigate the impact of each mechanism on the cleaning speed of sea cucumbers. Initially, the research focused on the sorting feeding mechanism. The study isolated the feeding rate during the sorting process as the sole variable. Each trial involved the use of 200 sea cucumbers of varying sizes. Evaluation metrics such as the stack count, parallel alignment, miscellaneous issues (including incidents of sea cucumbers falling off or jams preventing operation), sorting completion rate, and time consumption were considered. The outcomes of these experiments are illustrated in Fig. 11. Subsequently, attention was directed towards the pressing conveyor mechanism. Building on the optimal feeding rate established earlier, the pressing force was varied to assess its influence on the efficacy of pressing sea cucumbers. The metrics for evaluation included the rate of damage and the completion rate of pressing, with results depicted in Fig. 12. Finally, the study examined the washing transfer mechanism. Different transfer speeds during the washing phase were analyzed for their effect on the cleaning outcomes of sea cucumbers. Metrics such as the cleaning qualification rate and time consumption were used as evaluative criteria, and the findings are presented in Fig. 13.

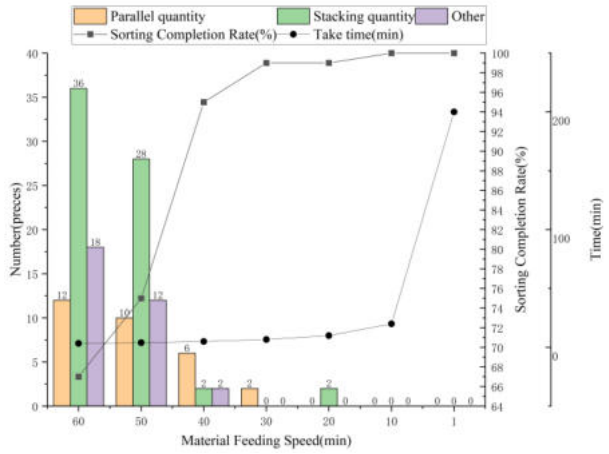


Fig. 11 - Experiment on feeding speed

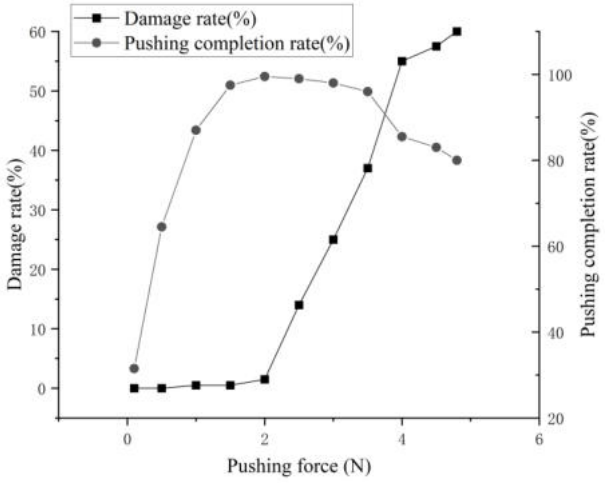


Fig. 12 - Experiment on pushing speed

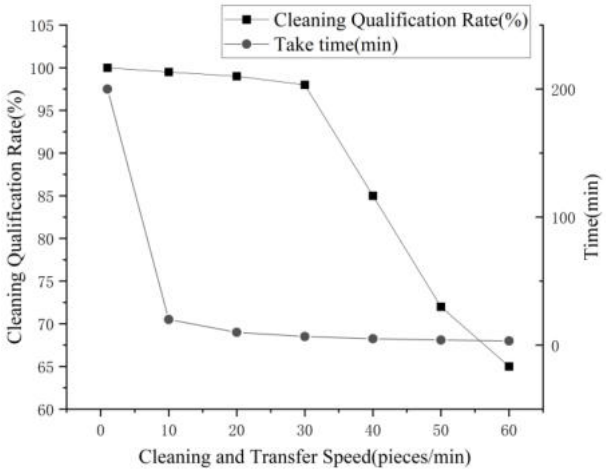


Fig. 13 - Experiment on transfer speed

The experimental results depicted in Fig. 11 indicate that under conditions of high feeding rates (60, 50, and 40 units/min), the sorting feeding mechanism is prone to issues of sea cucumber stacking, alongside prominent problems of sea cucumbers falling and jamming. Despite achieving a high sorting efficiency, the overall sorting performance is suboptimal. When the feeding rate is reduced to 10 units/min or less, the completion rate of sorting can reach 100%, but the efficiency significantly decreases. At feeding rates of 30 units/min and 20 units/min, the completion rates are both 99%, with reduced time consumption, thereby identifying 30 units/min as the optimal speed for the feeding mechanism. The experimental results presented in Fig. 12 show that under the influence of substantial pressing forces (≥2.5N) during the pressing process, sea cucumbers are highly susceptible to damage due to irreversible deformation caused by excessive pressure. Additionally, slight disturbances or inaccuracies in the pressing location can easily result in the sea cucumbers slipping out. When the pressing force is reduced to 2.0N or below, the damage rate decreases to 1.5% or lower. However, when the pressing force is less than 1.5N, there is a sharp decline in the completion rate of pressing, primarily due to the sea cucumbers detaching during the pressing and conveying process. Thus, the optimal pressing force for the pressing mechanism is determined to be 2.0N or less. Fig. 13 illustrates that during high-speed cleaning and transfer processes, the sea cucumbers are not thoroughly cleaned if the cleaning time is insufficient, leaving mud, sand, and stains on their surfaces. By reducing the speed of cleaning and transfer to 30 units/min or less, the rate of adequate cleaning reaches 98% or higher. Therefore, the optimal speed for the washing transfer mechanism is set at 30 units/min, with a cleaning duration of 2 seconds per sea cucumber. Fig.14 displays the functional verification results of the prototype. These results demonstrate that key components such as the sorting feeding mechanism, pressing conveyor mechanism, and the de-sanding, organ removing, and washing mechanism, as well as the washing transfer mechanism, exhibit satisfactory performance, effectively supporting the automated workflow. Based on the comprehensive experimental results, the optimal process parameters for the equipment are set with both feeding and cleaning transfer speeds at 30 units/min and the pressing force at 2.0N.



(a) (b) (c) (d)

Fig. 14 - A schematic representation of the functional verification of the prototype model.
(a) Sorting feeding mechanism, (b) Pressing conveyor mechanism,
(c) De-sanding, organ removing, and washing mechanism, (d)washing transfer mechanism

Comparative Experiment with Other Devices

In the comparative experiments with other devices, the newly developed sea cucumber sorting, de-sanding, organ removing, and washing equipment was evaluated against the integrated sea cucumber washing and cutting equipment. Each trial utilized 200 live sea cucumbers of varying sizes. Both machines operated under optimal conditions, with the following process parameters for the integrated equipment: a conveyor belt speed of 0.03 m/s and a vertical gap of 30 mm between the upper and lower rollers of the cutting device. The cleaning efficacy of both devices was compared, as detailed in Table 1. The criteria for damage were defined as physical harm to the sea cucumber's body, and the criteria for inadequate cleaning were defined as incomplete removal of sand from the sea cucumber's mouth.

Table 1

Comparative experiment of sea cucumber cleaning equipment.

Equipment	Total Number	Damaged	Inadequately Cleaned	Time (min)
New sea cucumber sorting, de-sanding, organ removing, and washing equipment	200	4	1	32
Integrated sea cucumber washing and cutting equipment	200	6	0	66.5

The results indicated that the sea cucumber cleaning equipment designed in this study achieved a 1% reduction in damage rate compared to the integrated washing and cutting equipment. However, there was an increase of one in the count of inadequately cleaned sea cucumbers. Moreover, the time taken to complete the same cleaning tasks was reduced by more than 50%. The sorting feeding mechanism and pressing mechanism organized irregularly positioned sea cucumbers neatly, significantly enhancing the cleaning efficiency. The experiments demonstrated that the new sea cucumber sorting, de-sanding, organ removing, and washing equipment significantly improved the automation efficiency of sea cucumber processing, with a reduced damage rate and almost no increase in the number of inadequately cleaned sea cucumbers.

Comparative Experiment with Manual Labor

In the comparative experiments with manual labor, the new sea cucumber sorting, de-sanding, organ removing, and washing equipment was tested against the manual processing of 200 live sea cucumbers of varying sizes by four workers on a production line. The equipment operated under optimal conditions, and the results are summarized in Table 2. The standards for cleaning rate, damage rate, and acceptance rate were de-fined as the number of sea cucumbers cleaned/total sea cucumbers processed, the number of sea cucumbers damaged/total sea cucumbers processed, and the number of sea cucumbers properly cleaned without damage/total sea cucumbers processed, respectively.

Table 2

Comparison of new sea cucumber sorting, de-sanding, organ removing, and washing equipment with manual cleaning

Experiment ID	Cleaning Rate (%)	Damage Rate (%)	Acceptance Rate (%)	Efficiency (units/h)
New Equipment	96	2	91	375
Worker 1	95	9	86.5	33
Worker 2	93	13	80.0	28
Worker 3	96	12	84.5	32
Worker 4	98	10	88.5	30

The experimental results demonstrate that the sea cucumber cleaning equipment designed in this study shows a slight reduction in cleaning rate by 0.5% compared to manual cleaning. However, it significantly reduces the damage rate by 9% and increases the acceptance rate by 6.125%, with an overall efficiency improvement of more than ninefold. The new sea cucumber sorting, de-sanding, organ removing, and washing equipment substantially enhances the efficiency of automated sea cucumber processing. Concurrently, compared to manual methods, it improves the integrity of the sea cu-cumber's form and cleanliness after washing and mitigates the issues commonly associated with manual processing, such as inconsistency in the sea cucumber's form and cleaning quality, as well as safety incidents.

CONCLUSIONS

The application of the sea cucumber sorting, de-sanding, organ removing, and washing equipment represents a significant advancement over the traditional manual sorting and cleaning processes, playing a crucial role in transforming the production paradigm of traditional sea cucumber processing towards standardization and large-scale production. This equipment reduces labor demands, alleviates worker stress, and eliminates reliance on manual experience for quality control, offering a cost-effective solution with a favorable cost-performance ratio. It can serve as a model for the development of similar equipment within the sea cucumber processing line.

(1) The equipment innovates a "automatic sand mouth removal + high-pressure water jet washing + hook-assisted organ removal" method for sea cucumber cleaning, which is considered advanced and effectively speeds up the process of gut cleaning while preserving the integrity of the sea cucumber.

(2) Utilizing machine vision and image recognition technology, a four-degree-of-freedom turntable adjusts the position of the sand mouth, facilitating precise, subsequent cutting operations.

(3) The clever and stable mechanical design features a movable conveyor chain and upper and lower clamps, enabling synchronous transportation of sea cucumbers.

Future research will focus on enhancing the application of image recognition technology to improve the speed and accuracy of cutting and aligning the sand mouth, thereby further increasing the efficiency of sorting and cleaning processes.

REFERENCES

[1] Adams, Z.; Modi, A.T.; Kuria, S.K. (2025). Multidimensional Perspective of Sustainable Agroecosystems and the Impact on Crop Production: A Review. *Agriculture*, 15, 581.

[2] Akhirman, Lia Suprihartini, Dian Putri Ramadhani (2021). The Role of Partnership Guidance on Increasing the Economy of Workers the Sea Cucumber Business in Benan Village Katang Bidare District Lingga Regency. EAI, 9.24.

[3] He, X.D.; Li, H.S.; He, L.Y.; Kong, F.Z.; Wang, B. (2019). Present Situation of Marine Farming and Processing Equipment in Shandong Province and Its Urgent Need for Development. *Agricultural Equipment & Vehicle Engineering*, 57(2), 4.

[4] Li, J.; Wang, J.Y.; Guan, C.T.; Yang L.X.; Teng, Y.; Wang, C.L. (2016). Brief on structure effect and processing technology of sea cucumber. *Farm Products Processing*, (5), 4.

[5] Liu, W.L.; Zhou, Y.B.; Zeng, R.J.; San, Y.J.; Huang, S.Y.; Li, J. (2023). Difficulties and Countermeasures in the Intensive Processing of Sea Cucumber Viscera. *Science and Technology of Food Industry*, 44(20), 458-466.

[6] Ma X.Y.; Li, M.; Xiong, W.C.; Liu, Y.S.; Liu, X.Z.; Yu, Y.C.; Yang, J.D. (2009). Design of sea cucumber grading and counting equipment based on technology of image recognition. *Journal of Dalian fisheries university*, 24(6), 549-552.

[7] Ronel S. Pangan, Kevin F. Yaptenco, Sharmaine N. Pardua and Jonnel Andrew C. Duque (2017). Development of an Alternative Technology Package for Processing Sea Cucumber [J]. *Philippine Journal of Agricultural and Biosystems Engineering*, 13(2):16-29.

[8] Sun, Y. (2019). *Design of Deep Cleaning Technology and Equipment for Sea Cucumbers Based on Water Jet*. Dalian Polytechnic University, Dalian.

[9] Taha, M.F.; Mao, H.; Zhang, Z.; Elmasry, G.; Awad, M.A.; Abdalla, A.; Mousa, S.; Elwakeel, A.E.; Elsherbiny, O. (2025). Emerging Technologies for Precision Crop Management Towards Agriculture 5.0: A Comprehensive Overview. *Agriculture*, 15, 582.

[10] Tang, J.L.; Wu, C.Y.; Liu, S.J.; Su, Y.C.; Wang, Y. (2012). Researches on instant sea cucumber processing technology. *Journal of Fujian Fisheries*, 34(1), 31-35.

[11] Wang, H.Y. (2018). *Design of a Roller Brush Cleaning Method and Equipment for Sea Cucumbers*. Dalian Polytechnic University, Dalian.

[12] Wang, Q.; Wang, G.D.; Sun, Q.; Wang, X.T. (2020). *A sea cucumber processing equipment*. CN 111480679 A. 2020-08-04.

[13] Wu, H.Y.; Bao H.X; Yao, L.Q.; Lv, G.; Gao, D.S.; Su, N.J.; Chang, S.K.; Meng, X.K. (2023). *An automated mechanism and method for removing sea cucumber intestines*. CN 114568655 A.2023-06-03.

[14] Xu, J.; Su, L.J.; Xu, Y.L.; Cheng, Q.Q.; Zhang J.; Li, Q.H.; Li, Y.; Hu, X. (2013). A rapid peeling method for East China Sea sea cucumbers CN 103027321 A.

[15] Xu, W.Q.; Shen, J. (2016). Research on mechanized processing technology of sea cucumbers and its application progress. *Food and Machinery*, 32(2), 215-218.
[16] Xu, W.Q.; Shen, J.; Xue C.H.; Cai, S.J.; Lin W. (2009). Experimental Study on the Cleaning Process of Fresh Sea Cucumbers. *Fishery Modernization*, 3(6), 42-45.
[17] Xu, Y.D.; Li, K.W. (2013). Analysis of the current situation of China's sea cucumber industry. Fishery Information and Strategy, 28(2), 117-122.
[18] Xu Zhang, Changyuan Zhang, Fei Gao, Weiwei Xia, Peng Zhang and Zixiang Xu(2021). Optimization design of sea cucumber cleaning parameters by water jet. American Journal of Biochemistry and Biotechnology, 17(1): 67-75.
[19] Xue, C. H.; Jiang, X. M. (2022). The pretreatment technology of raw sea cucumber and new processing technology of salted sea cucumber. *Fish & Shellfish Immunology*, 125(1), 145-169.
[20] Yang, S.; Sun, Y.J.; Ju, W.M.; Yan, C.Z.; Li, G.Z.; Wang, K.G.; Wang, S.S. (2024). Design of an integrated equipment for cleaning and cutting sea cucumbers. *Fishery Modernization*, 51(1), 98-105.
[21] Yu, H.W. (2016). *An integrated device for sea cucumber processing*. CN 205093521U .2016-03-23.

DESIGN AND SIMULATION OF SCREW CONVEYOR FOR SESAME COMBINE HARVESTER CUTTING TABLE

/

芝麻联合收获机割台螺旋输送装置的设计与仿真

Longze GUO[1)], Shuqi SHANG*[1)], Xiaoning HE[1)], Mingtao JIA[1)], Zengcun CHANG[2)], Haipeng YAN[2)], Lin GU[1)], Fuwen YAO[1)], Zhentao SONG[1)]

[1)] College of Mechanical and Electrical Engineering, Qingdao Agricultural University, Shandong / China

[2)] Dongying Yellow River Delta Intelligent Agricultural Machinery and Equipment Industry Research Institute/ China

Tel: +86-15106988621; E-mail: 995966736@qq.com

Corresponding author: Shuqi Shang

DOI: https://doi.org/10.35633/inmateh-76-69

Keywords: *Cutting table, Screw conveyor; Sesame capsule, EDEM simulation*

ABSTRACT

Aiming at the problems of high crushing rate and severe loss of sesame capsules caused by mechanical collision in the conveying link of the header of the traditional sesame combine harvester, a low-damage screw conveying device has been optimized and designed. This study analyzed the operation mechanism of the low-damage screw conveyor based on the characteristics of the sesame capsule and determined the key parameters affecting the crushing rate of the sesame capsule, including diameter, pitch and rotational speed. Taking the crushing rate as the evaluation index and with the aid of EDEM discrete element simulation technology, the interaction model of sesame capsule - sesame stem - low-damage screw conveying device was constructed, and the single-factor and Box-Behnken response surface experimental designs were systematically carried out. Through simulation analysis and optimization, the optimal parameter combination of the low-damage screw conveyor device was determined: diameter 302 mm, pitch 422 mm, and rotational speed 200 r/min. Under these conditions, the crushing rate of sesame capsules can be reduced to less than 3%. This study provides a theoretical basis and technical reference for the structural optimization of the screw conveyor device of the sesame combine harvester and the reduction of the header loss rate.

摘要

针对传统芝麻联合收获机割台输送环节因机械碰撞导致的芝麻蒴果破碎率高、损失严重等问题，优化设计了一种低损伤螺旋输送装置。本研究基于芝麻蒴果特性分析了低损伤螺旋输送装置的作业机理，确定了影响芝麻蒴果破碎率的关键参数，包括直径、螺距和转速。以破碎率作为评价指标，借助 EDEM 离散元仿真技术，构建了芝麻蒴果-芝麻茎秆-低损伤螺旋输送装置的互作模型，系统开展了单因素和 Box-Behnken 响应面试验设计。通过仿真分析与优化，确定了低损伤螺旋输送装置的最优参数组合：直径 302mm、螺距 422mm、转速 200r/min，此条件下，芝麻蒴果破碎率可降至 3%以下。本研究为芝麻联合收获机螺旋输送装置的结构优化与割台损失率的降低提供了理论依据和技术参考。

INTRODUCTION

Sesame as a high economic value of oil crops, its mechanized harvesting has been a difficult point in agricultural production *(Wang et al., 2024; Dou, 2025; Tian et al., 2025)*. During the harvesting process of traditional combine harvester, the cutting table conveyor is prone to cause violent collision and extrusion of sesame pods, resulting in high seed breakage rate, high loss rate and other problems, which seriously affects the quality and yield of sesame *(Lian et al., 2023)*. The existing harvester has serious seed breakage, which is difficult to meet the demand of fine agriculture *(Ni et al., 2023; Xiaoyuan et al., 2025; Pezo M. et al., 2025)*. Therefore, designing a cutting table conveyor with low crushing rate is of great significance to realize efficient and low-loss harvesting of sesame. At present, domestic and foreign research for sesame harvesting machinery mainly focuses on the optimization of cutting table structure and the improvement of threshing system, while the analysis of the mechanical characteristics of the seeds in the conveying process is insufficient, resulting in the lack of theoretical support for low damage conveying technology *(Liu et al., 2021)*. Derald Ray Langham bred the non-cracking (ND) sesame variety S55. The capsule does not crack and has a high seed retention rate, reducing the loss of sesame seeds (*Derald Ray Langham*., *2011*).

Developed countries represented by the United States have achieved the reduction of sesame seed loss and the increase of sesame yield by screening non-cracked (ND) sesame varieties and replacing the header of the harvester.

Although the Quantum series of combine harvesters from Wintersteiger in Austria are not specifically designed for sesame, they can be compatible with small-grain crops such as sesame by changing the header and adjusting parameters (such as low-speed flexible threshing and air flow cleaning system)

To address this problem, this study combines the biological characteristics and mechanical properties of the sesame plant to design a low-crushing rate cutting table conveying device, three-dimensional modeling of the screw conveying device through SolidWorks, to determine the diameter, rotational speed, pitch, and other parameters and dimensions, and the use of the EDEM discrete element model, to obtain the optimal parameters of the low-crushing rate, for the low-damage conveying of the sesame combine harvester to provide the technological Reference.

This study aims to solve the key bottleneck in the mechanized harvesting of sesame, to provide new ideas for the research and development of low-damage harvesting equipment for crops with high oil content, and to promote the development of mechanization of special economic crops with practical application value.

MATERIALS AND METHODS

Overall structure of the cutting table

The overall structure of the operating platform is shown in Fig. 1.

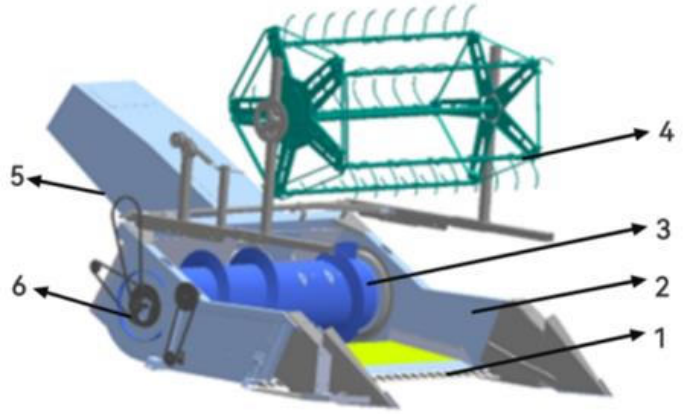


Fig. 1 - Overall structure of cutting table

1 – cutter; 2 - baffle; 3 - screw conveyor; 4 - paddle wheel; 5 - conveyor chute; 6 - drive system

Principle of operation

When working, the machine travels forward, the pivoting wheel rotates, and its popping teeth are inserted into the sesame plant clumps, pivoting backward and downward and supporting the plant to guide it steadily to the cutter. The guided plant stalks enter between the moving and fixed blades of the cutter and are cleanly cut off. The pivoting wheel continues to rotate, pivoting the freshly severed plant away from the cutting area and backward, so that it lays relatively neatly on the cutting platform. The screw conveyor rotates, and the screw blades at both ends of the screw conveyor will spread the sesame plants on the left and right sides of the cutting platform to the center area to be quickly pushed and concentrated, and concentrated backward to the conveyor chute for backward movement for subsequent processing.

Static analysis of sesame capsule

As shown in Fig. 2 in the horizontal screw conveying device, the sesame capsule conveying process is realized under the combined action of the propulsion and friction of the screw blades, as well as the friction of the bottom plate wall. The action of these forces on the sesame capsule is actually very complex. In this study, in order to simplify the analysis, a single-mass model is used to describe the forces on the sesame capsule, and the surface of the screw blade is assumed to be an inclined plane *(Zhao, 2024; Song et al., 2016; Song et al., 2016)*. When the seeds are stationary in the screw conveyor, they are in static equilibrium under the force of gravity G and the support force N provided by the tube wall. When the spiral blades begin to rotate, the seeds begin to move under the positive thrust F_n of the blades and the frictional force f.

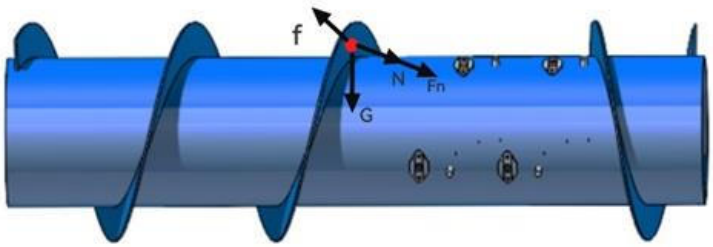


Fig. 2 - Conveying state of sesame capsule in screw conveyor device

Dynamic analysis of sesame capsule

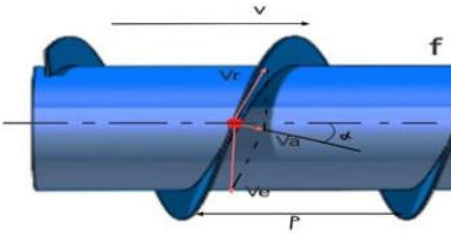


Fig. 3 - Kinematic modeling of sesame capsule in screw conveyor device

As shown in Fig.3, the relative, implicit and absolute speeds of the sesame capsule are related not only to the rotational speed of the spiral shaft, but also to the pitch of the spiral blades. In the same pitch, the more against the outer edge of the spiral blade, the faster the conveying speed.

$$\begin{aligned} v_e &= \frac{2\pi nR}{60} = \frac{\pi nR}{30} \\ v_a &= v_e \sin\alpha = \frac{\pi nR}{30}\sin\alpha \\ v_r &= v_e \cos\alpha = \frac{\pi nR}{30}\cos\alpha \\ \alpha &= arc\tan\frac{P}{\pi D} \end{aligned} \tag{1}$$

where:

v_a is the absolute velocity of the sesame capsule, [m/s]; v_e is the entanglement speed of the sesame capsule, [m/s]; v_r is the relative velocity of the sesame-capsule fruit, [m/s]; α is the helix angle, [°]; R is the radius of the screw conveyor device, [mm].

Determination of diameter

The formula for the diameter is:

$$D = \sqrt{\frac{4Q}{\pi v \varphi \rho}} \tag{2}$$

where:

D is the diameter of the roller of the screw conveyor device, [mm];Q is the value of screw conveying capacity, [kg/s]; v is the axial movement speed of the sesame capsule, [m/s]; φ is the fill factor; ρ is the density of the material pile, [kg/m³]

In this paper, the screw conveying capacity Q=2.58~5.65kg/s; v≤0.5m/s; ρ=450~550kg/m³ is selected to get the range of diameter values from 270 to 400 mm.

Determination of pitch

The pitch formula is:

$$P = k\,D \tag{3}$$

where: k is the coefficient of proportionality between pitch and helical blade diameter.

Agricultural fiber material k takes the value range of 0.5~2.0 *(Zhao et al., 2025; Zhao et al., 2018)*, in this paper k takes 1.1 to get the range of pitch values 297~440 mm.

Determination of rotational speed

The formula for calculating the spiral speed is:

$$n = \frac{Q \times 1000}{60 A v \rho \eta} \quad (4)$$

where: n is the value of the rotational speed, [r/min];

A is the cross-sectional area of the screw conveyor, $A = \frac{\pi (D^2 - d^2)}{4}$, [m²]; η is conveying efficiency.

After calculation and design criteria to obtain the speed range of about 150~250 r/min.

Research based on EDEM conveying process simulation analysis

In this study, the crushing behavior of sesame capsules was analyzed using the Discrete Element Method (DEM). The crushing process was simulated by applying external force to the sesame capsules *(Qing et al., 2024; Jia X et al., 2025; Zhou et al., 2024)*. During the crushing, the capsules come into contact with the force-applying object. The Hertz-Mindlin with Bonding V2 contact model was employed to simulate this process, forming bonding interactions between particles *(Wang et al., 2021; Hou et al., 2018; Cheng et al., 2024)*. The crushing degree was evaluated by calculating the ratio of broken bonds to the total number of bonding interactions.

Based on the study of the seed crushing rate in the screw conveyor device, a solid model of the device was created using SolidWorks 3D software and imported into EDEM in *stl* format. The resulting simulation model is shown in Fig. 4. In order to facilitate the processing, the overall material of the screw conveyor device was set to be 65Mn steel. Based on the morphology and characteristics of the sesame seed capsule a realistic capsule model was constructed. Using the Bonding V2 contact model, a meta-particle was employed to represent the sesame seed capsule, as shown in Fig. 5.

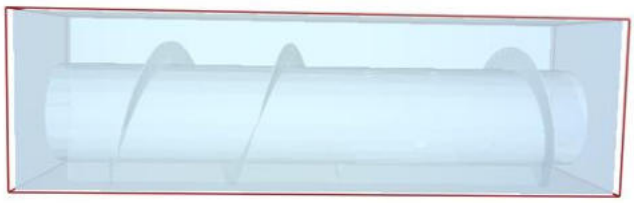
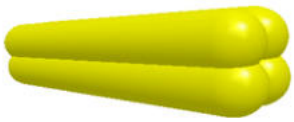


Fig. 4 - Simulation model of screw conveyor



（a）Discrete metamodeling of sesame stalks and capsules



（b）Discrete metamodeling of the sesame capsule

Fig. 5 - Simulation of the simulation model

The simulated material is a sesame seed capsule, and its mechanical properties were obtained from experimental tests and references *(Wang et al., 2018; Zhao et al., 2022; Zhang et al., 2020)* and the specific properties are shown in Table 1.

Table 1

Basic parameters of the discrete element simulation model

Parameters	Numerical value
Sesame density [kg·m^{-3}]	350
Sesame Poisson's ratio	0.25
Sesame shear modulus [Pa]	8×10^6
Steel density [kg·m^{-3}]	7850

Parameters	Numerical value
Steel Poisson's ratio	0.3
Steel shear modulus [Pa]	2×10^{11}
Sesame-Sesame coefficient of restitution	0.2
Sesame-Sesame static friction coefficient	0.6
Sesame-Sesame dynamic friction coefficient	0.05
Sesame-Steel coefficient of restitution	0.5
Sesame-Steel static friction coefficient	0.6
Sesame-Steel kinetic friction coefficient	0.01

Single-factor simulation test

Through theoretical analysis, the key parameters of the spiral conveying device - screw roller diameter *D*, pitch *P*, and rotational speed *n* were selected as test factors to analyze their influence on the crushing rate of sesame capsules and determine appropriate value ranges. Based on the results, the diameter range was set between 270 - 400 mm, the pitch between 297 - 440 mm, and the speed between 150 - 250 r/min. To meet the performance requirements for minimizing the crushing rate, the intermediate levels for the single-factor tests were defined as 335 mm for diameter, 368 mm for pitch, and 225 r/min for speed. During the single-factor tests, the other two parameters were maintained at their respective intermediate levels. The specific factor levels used in the single-factor experiments are shown in Table 2.

Table 2

Factor levels of one-way simulation test

Level	Diameter [mm]	Pitch [mm]	Speed [r/min]
1	270	297	185
2	302	332	200
3	335	368	225
4	368	404	235
5	400	440	250

Box-Behnken Design Simulation tests

In order to further determine the optimal combination of the parameters of the screw conveyor device with the best effect on the crushing rate of sesame capsules in this design, on the basis of the one-factor test, three key factors affecting the crushing rate (diameter *D*, pitch *P*, rotational speed *n*) were selected as the test factors, and a three-factor, three-level Box - Behnken design was used to study the relationship between the key factors and the test indicators. The relationship between the key factors and the test indexes was investigated using a three-factor, three-level Box-Behnken design. According to the previous theoretical analysis and the results of one-factor simulation test, the diameter of the spiral drum is 302~335 mm, the pitch is 404~440 mm, and the rotational speed is 200~235 r/min. The coding of the test factors is shown in Table 3, and the test program and results are shown in Table 4.

Table 3

Coding of test factors

Encodings	Considerations		
	D / [mm]	P / [mm]	n / [r/min]
-1	302	404	200
0	335	422	217.5
1	368	440	235

Table 4

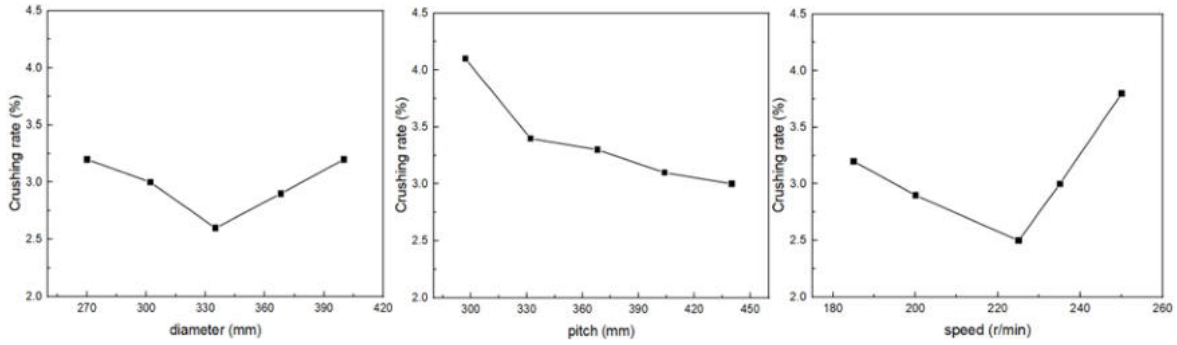
Pilot program and result

Serial Number	Considerations			Crushing rate / [%]
	D / [mm]	P / [mm]	n / [r/min]	
1	302	404	217.5	3.1
2	302	440	217.5	2.5
3	368	404	217.5	3.2
4	368	440	200	3.1
5	335	404	200	3.3
6	335	440	235	3.2
7	335	404	235	3.0
8	335	440	200	2.5
9	302	422	200	2.9
10	368	422	235	3.7
11	302	422	235	2.8
12	368	422	217.5	3.0
13	335	422	217.5	3.0
14	335	422	217.5	2.9
15	335	422	217.5	3.1
16	335	422	217.5	3.0
17	335	422	217.5	3.1

RESULTS

Analysis of single-factor test results

The results of the single-factor test are shown in Fig.6.



(a) Diameter **(b) Pitch** **(c) Speed**

Fig. 6 - Results of single-factor simulation test

(1) The influence of screw roller diameter on the crushing rate of sesame capsules was analyzed for diameters of 270, 302, 335, 368, and 400 mm. When the diameter is less than 280 mm, the rotation of the spiral blade causes the sesame capsules to move outward due to centrifugal force. However, because of the smaller diameter, the outer edge of the blade is close to the pipe wall, which forces the capsules to collide frequently with the pipe wall, leading to a higher crushing rate. Conversely, when the diameter exceeds 380 mm, the increased size of the screw roller results in a larger contact area with the sesame capsules, again causing a higher crushing rate due to more frequent and intense collisions.

(2) The effect of screw conveyor pitch on the crushing rate of sesame capsules was analyzed using pitch values of 297, 332, 368, 404, and 440 mm. When the pitch is less than 400 mm, the spiral blade exerts a stronger rubbing effect on the sesame capsules, which significantly increases mechanical stress. Additionally, the smaller pitch results in a higher filling rate, causing the capsules to become wedged in the narrow gaps between the blade and the pipe wall. This leads to compression and extrusion of the capsules, ultimately resulting in a higher crushing rate.

(3) The influence of screw conveyor speed on the crushing rate of sesame capsules was investigated using rotational speeds of 185, 200, 225, 235, and 250 r/min. At speeds below 200 r/min, the conveying time is extended, leading to material accumulation at the inlet and potential blockages. This prolonged compression causes the sesame capsules to experience sustained pressure, resulting in fatigue fractures and a high crushing rate. Conversely, when the speed exceeds 235 r/min, the centrifugal force acting on the capsules increases significantly, causing them to be flung against the inner wall of the pipe at high velocity. The resulting impact energy surpasses the structural limit of the capsules, leading to a marked increase in the crushing rate.

Analysis of Box-Behnken Design tests results

The experiment was analyzed using Design-Expert software. The variance analysis of the simulation test of the screw conveyor device is shown in Table 5. Analysis of variance shows that the diameter, pitch and rotational speed of the spiral device have extremely significant effects, and the regression equation between the breakage rate A and the diameter *D*, pitch *P* and rotational speed *n* is obtained:

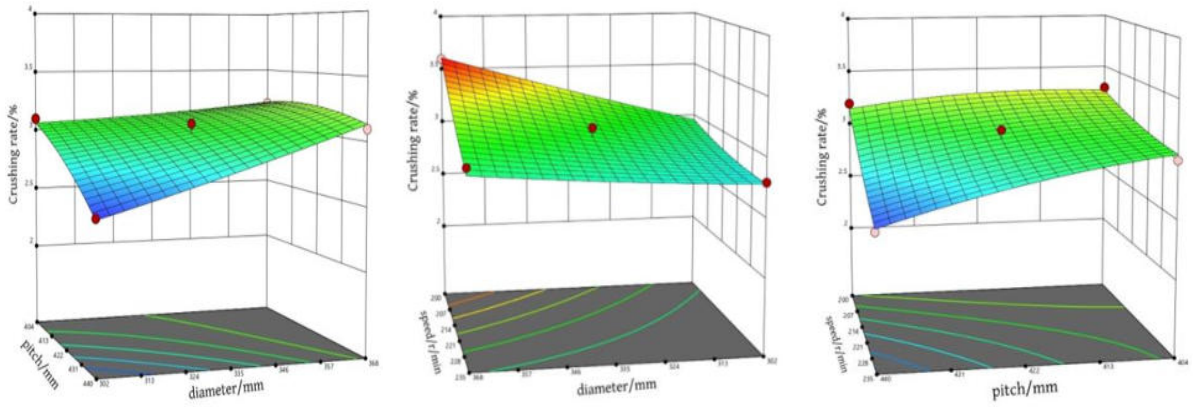
$$A=3.02-0.1625D+0.2P-0.2125n+0.125DP-0.1Dn-0.125Pn-0.06D^2+0.015P^2+0.04n^2 \quad (5)$$

To further analyze the interaction effects of key parameters on the crushing rate of sesame capsules in the screw conveyor device, the test data were processed using Design-Expert software. This enabled the generation of response surface plots illustrating the interactive influences of screw roller diameter, pitch, and rotational speed on the crushing rate (denoted as A), as shown in Fig. 7. From Fig. 7a, it can be observed that with a fixed diameter, the crushing rate decreases as the pitch increases. Conversely, when the pitch is held constant, the crushing rate tends to increase with larger diameters, although the increase is relatively modest. Fig. 7b shows that when the diameter is fixed, the crushing rate decreases with increasing rotational speed, while at a constant speed, the crushing rate increases with the diameter. Finally, Fig. 7c indicates that when the pitch is held constant, the crushing rate initially increases and then decreases with increasing speed; meanwhile, at a constant speed, the crushing rate consistently decreases as the pitch increases.

Table 5

Analysis of variance of crushing rate simulation experiment

Source	Sum of Squares	df	Mean Square	F-value	P-value
Model	1.08	9	0.1199	18.45	0.0004
D	0.2113	1	0.2113	32.50	0.0007
P	0.3200	1	0.3200	49.23	0.0002
n	0.3613	1	0.3613	55.28	0.0001
DP	0.0625	1	0.0625	9.62	0.0173
Dn	0.0400	1	0.0400	6.15	0.0422
Pn	0.0625	`	0.0625	9.62	0.0173
D2	0.0152	1	0.0152	2.33	0.1706
P2	0.0009	1	0.0009	0.1457	0.7140
n2	0.0067	1	0.0067	1.04	0.3425
Residual	0.0455	7	0.0065	-	-
Lack of Fit	0.0175	3	0.0058	0.8333	0.5413
Pure Error	0.0280	4	0.0070	-	-
Cor Total	1.12	16	-	-	-



（a） （b） （c）

Fig. 7 - Response surface for the effect of interaction of factors on crushing rate

The test results show that the changes of diameter, pitch and rotational speed will all affect the breakage rate of sesame capsule. In order to obtain the optimal structural parameters of the screw conveyor device, the structural parameters were optimized by using the optimization module of Design-expert data analysis software. When *D*=302 mm, *P*=422 mm, *n*=200 mm, the crushing rate is 2.9%

CONCLUSIONS

(1) SolidWorks was used to construct a 3D model of the cutting table screw conveyor, followed by design calculations for its diameter, pitch, and rotational speed to determine the key structural parameters and their respective ranges. The determined ranges were: diameter 270~400 mm, pitch 297~440 mm, and rotational speed 185~250r/min.

(2) Using EDEM discrete element modeling, sesame capsules were selected as the simulation object. Single-factor tests were conducted with screw conveyor diameter, pitch, and rotational speed as test factors, and the crushing rate as the evaluation index. Analysis of the influence of each factor on the crushing rate determined that optimal parameter ranges were: diameter 302-368 mm, pitch 404-440 mm, and rotational speed 200-235 r/min.

(3) A Box-Behnken Design simulation test was conducted to explore the interactions between factors. The influence of each factor on crushing rate, in descending order of significance, was: rotational speed, diameter, and pitch. The optimal parameter combination - diameter of 302 mm, pitch of 422 mm, and rotational speed of 200 r/min - resulted in a predicted crushing rate of 2.9%.

ACKNOWLEDGEMENT

The research was funded by the National Key Research and Development Program of China (No. 2022YFD2300100).

REFERENCES

[1] Cheng W., Yu F., Lei Z., (2024). Study on macroscopic and micromechanical behavior of rock particle fragmentation based on discrete element method (基于离散元法的岩石颗粒破碎宏微观力学行为研究). *Journal of Engineering Geology*, Vol. 32, no. 6, pp. 2130-2142, Beijing/China

[2] Derald Ray Langham. (2011). Non-dehiscent sesame variety Sesaco27[P]. USA: 07964768.

[3] Dou X., (2025). Co-innovation of mechanized sesame production technology in Fuyang, Anhui (安徽阜阳芝麻全程机械化生产技术的协同创新). *China Seed Industry*, no. 6, pp. 57-59+64, Beijing/China.

[4] Hou S., Wang Z., Wang W., (2018). Study on the shear expansion characteristics of particles at friction interface based on Hertz-Mindlin contact model (基于 Hertz-Mindlin 接触模型的摩擦界面颗粒剪切膨胀特性研究). *Journal of Hefei University of Technology (Natural Science Edition)*, Vol. 41, no. 12, pp. 1601-1605, Anhui/China.

[5] Jia X., Zheng X., Chen L., Liu C., Song J., (2025), Discrete element flexible modeling and experimental verification of rice blanket seedling root blanket. *Computers and Electronics in Agriculture*, Vol. 233, pp. 110155-110155, UK.

[6] Liu J., Wang D., He X., Shang S., Xu N., (2021). Design and test of threshing device of sesame combine harvester (芝麻联合收获机脱粒装置的设计与试验). *Agricultural Mechanization Research,* Vol. 43, no. 12, pp. 110-114+122, Heilongjiang/China.

[7] Lian G., Zong W., Feng W., Ma L., Cheng Y., (2023). Design and test of integrated cutting platform for combined harvesting of sunflower (食葵联合收获割脱一体式割台设计与试验). *Journal of Agricultural Machinery*, Vol. 54, no. 08, pp. 122-131+154, Beijing/China.

[8] Ni Y., (2023). Research on crushing mechanism and low-loss harvesting technology of soybean machine harvesting (大豆机收破碎机理与低损收获技术研究). *Chinese Academy of Agricultural Sciences*, Beijing/China.

[9] Pezo M., Pezo L., Lončar B., Kojić P., Ilić M., Jovanović A., (2025). Granular flow in screw conveyors: a review of experiments and discrete element method (DEM) studies. *Powder Technology*, no. 459, pp. 121040-121040, Switzerland.

[10] Qingqiu C., Shengwei Z., Tao L., Gaixia Z., Hongfang Y., (2024). Discrete element modelling and mechanical properties and cutting experiments of Caragana korshinskii Kom. stems. *Frontiers in Plant Science*, Vol. 15, pp. 1457243-1457243, Switzerland.

[11] Song H., (2016). Optimized design and simulation of quantitative screw conveyor (定量螺旋输送机的优化设计及模拟). *Qingdao University of Science and Technology*, Shandong/China.

[12] Song H., LI Y., Ma Y., Liu W., (2016). Optimization study of quantitative screw conveyor based on discrete element method (基于离散元法的定量螺旋输送机的优化研究). *Hoisting and Conveying Machinery*, no. 2, pp. 30-34, Beijing/China.

[13] Tian H., Xie F., Yan X., Wang F., Zhang W., (2025). Key technologies and applications of whole process mechanized production of sesame (芝麻全程机械化生产关键技术与应用). *Heilongjiang Agricultural Sciences*, no. 5, pp. 114-119, Heilongjiang/China.

[14] Wang X., Xue Y., Liu J., Yang J., Zhou S., Guan Z., Li J., (2021). Discrete element multi-particle adhesion modeling technique based on drop weight test (基于落重试验的离散元多颗粒黏结建模技术). *Chinese Journal of Nonferrous Metals*, Vol. 31, no. 8, pp. 2258-2268, Hunan/China.

[15] Wang Z., Zhang C., Li M., Yang X., Li H., Liu X., Guo P., Ma Z., (2024). Mechanical characterization of sesame at harvesting stage (针对分段收获适收期芝麻力学特性). *Journal of Anhui Institute of Science and Technology*, Vol. 38, no. 6, pp. 71-76, Anhui/China.

[16] Wang Z., Zhou F., Yang Y., Zhou T., Liu H., (2024). Progress of key agronomic traits suitable for mechanized planting and harvesting of sesame in China (我国芝麻适宜机械化种植与收获的关键农艺性状研究进展). *China Seed Industry*, no. 1, pp. 22-31, Beijing/China.

[17] Xiaoyuan Z., Baoan W., Yanfeng Z., (2025). Characterization of screw conveyor based on discrete element method. *Journal of Electrotechnology, Electrical Engineering and Management*, Vol. 8, no. 1, Germany.

[18] Zhao F., (2018). Experimental and optimal design of screw conveying device for agricultural fiber materials (农业纤维物料螺旋输送装置试验与优化设计). *Inner Mongolia Agricultural University*, Neimenggu/China.

[19] Zhao G., Liu X., Wu H., Chen A., Zhang Q., Song Q., Xing W., Zhang H., (2025). Design and test of key components of conveyor device for corn stover baler (玉米秸秆打捆机输送装置关键部件的设计与试验). *Agricultural Mechanization Research*, Vol. 47, no. 5, pp. 82-87, Heilongjiang/China.

[20] Zhao H., (2024). Design and test of spiral seed conveying device for soybean combine harvester (大豆联合收获机螺旋式籽粒输送装置设计与试验). *Shenyang Agricultural University*, Liaoning/China.

[21] Zhao J., Wei T., Cheng Q., Liu F., (2022). Experimental study on shear mechanical properties of sesame seeds (芝麻籽粒的剪切力学特性试验研究). *Journal of Jiamusi University (Natural Science Edition)*, Vol. 40, no. 4, pp. 112-115+119, Liaoning/China.

[22] Zhang N., Wang D., Shang S., Liu J., Su X., (2020). Experimental study on mechanical properties of sesame stalk and capsule (芝麻茎秆及蒴果力学特性试验研究). *Agricultural Mechanization Research*, Vol. 42, no. 9, pp. 181-185, Heilongjiang/China.

[23] Zhou S., Wan Z., Wang Y., Li G., Ma Y., Xie L., (2024). Study on Feeding Performance of Screw Feeder Based on Discrete Element Simulation (基于离散元仿真模拟的螺杆加料机加料性能研究). *China Plastics*, Vol. 38, no. 9, pp. 60-65, Beijing/China.

OPTIMIZATION OF THE STRUCTURE OF THE MILK POWDER CONVEYING DEVICE FOR CALF FEEDING EQUIPMENT BASED ON DISCRETE ELEMENT SIMULATION
/
基于离散元仿真的犊牛饲喂装备代乳粉料输送装置结构的优化

Yang BAI[1)2)], Yanguo CHEN[3)], Fuxiang XIE*[1)], Yanjun LI[1)], Song JIAN[1)], Wang KAI[1)]
[1)] School of Machinery and Automation, Weifang University, Weifang/China;
[2)] Shandong Key Laboratory of Intelligent Manufacturing Technology for Advanced Power Equipment
[3)] ShanDong Administration for Market Regulation
Tel: 13260170996; E-mail: baiyang19891014@163.com
Correspondent author: Fuxiang XIE
DOI: https://doi.org/10.35633/inmateh-76-70

Keywords: *precision calf feeding, milk replacer, scraper conveyor, virtual simulation, EDEM*

ABSTRACT
In the intelligent transformation of global animal husbandry, precise calf feeding faces challenges like arching and flow fluctuations during milk replacer delivery, leading to inaccurate feeding, diarrhea and higher costs. This study aims to enhance the precision and stability of milk replacer delivery via structural innovation. Through shear tests, the internal friction angle of milk replacer was measured at 23.76° and the external friction angle at 23.97°. Combined with discrete element simulation and orthogonal experiments, the scraper conveyor device was optimized. A particle model of milk replacer was established using the discrete element method to analyze the effects of blade curvature, number of blades and guide plate tangent angle on conveying performance. Optimal parameters were determined through orthogonal experiments. Results showed that the guide plate tangent angle most significantly affected conveying rate, with peak efficiency at 45°. The number of blades was the main factor for operational stability, with 8 blades reducing delivery fluctuations. The optimal combination was found to be curved blades, 8 blades and a 45° guide plate tangent angle. Validation tests showed a stable conveying rate of 7.50 - 8.48 g/s, a standard deviation below 0.43 g, and operational stability of 71.80% - 75.96%, effectively solving arching and flow fluctuation issues. This study offers theoretical support for developing precise powder delivery equipment and core technological support for domestic smart feeding equipment. It directly helps reduce calf morbidity and improve ranch economic efficiency.

摘要
面对全球智能化转型中犊牛精准饲喂的技术瓶颈，针对代乳粉输送过程因结拱、流量波动导致的饲喂精度不足、犊牛腹泻率上升及养殖成本增加等突出问题，本研究旨在通过结构创新提升犊牛饲喂过程中代乳粉料输送精确性和稳定性。通过直剪试验测定代乳粉内摩擦角为23.76°、外摩擦角为23.97°的实测数据，结合离散元仿真与正交试验，系统优化刮板式输送装置。采用离散元法建立代乳粉颗粒模型，系统分析叶片曲率变化、叶片数量及导流板切向角对输送性能的影响规律，并通过正交试验确定最优参数组合。结果表明：导流板切向角对输送速率影响最为显著，切向角为 45°时效率最高；叶片数量是运行稳定性的主控因素，8 片叶片工况下有利于降低粉料输送的波动率。最终确定圆弧叶片、8叶片、45°导流板切向角为最优组合，试验验证显示输送平均速率稳定于 7.50-8.48g/s，标准偏差小于 0.43g，运行稳定性达 71.80%-75.96%，有效解决了结拱与流量波动问题。本研究为高黏性粉料精准输送装备开发提供了理论依据。为智能饲喂装备国产化提供核心技术支持，对降低犊牛发病率、提升牧场经济效益具有直接应用价值。

INTRODUCTION
As the global livestock industry accelerates its transformation towards intensification and digitalization, precision feeding technology for dairy cows has emerged as a key component in enhancing both farm production efficiency and animal welfare standards *(Meng et al., 2013)*. The vital role of scientific precision feeding for calves in promoting rumen development and reducing feeding costs has become a critical component of modern ranch management *(Zeng et al., 2017)*. Traditional bucket-based management models relying on manual operations present challenges such as significant temperature fluctuations during feeding, inconsistent feed quantities, and hygiene management difficulties, which may lead to health risks including calf diarrhea and impaired growth. Livestock and poultry breeding feeding robot technology faces both challenges and opportunities in improving feeding efficiency and enhancing animal health levels *(Dmytriv Vasyl et al., 2020, Dmytriv Ihor et al., 2021, Bin et al., 2021)*.

Companies such as Germany-based FörsterTechnik and Sweden's DeLaval have developed intelligent feeding systems for calves, utilizing RFID and distributed control systems to achieve individualized feeding protocols (*Zhao et al., 2015, Janzekovic M. et al., 2011, Sutherland M. et al., 2018). Yang et al., (2016), Cai et al., (2014), Zhang et al., (2016),* have conducted comprehensive research and analysis on automated feeding systems for sheep, meat pigeons, hogs, and other livestock species, significantly contributing to the technological advancement of intelligent feeding devices. The intelligent calf feeding apparatus designed by *Qi et al., (2014),* enables customized control parameter settings based on individual calf biometrics, achieving precise water volume metering, temperature-regulated formula preparation, and automated incorporation of measured milk replacer doses, with liquid feed homogenization accomplished through an integrated agitation mechanism. *Jin et al., (2014),* designed a liquid feeding control system for calves, utilizing a MCU as the central control system. It employs DS1820 sensors to monitor and regulate temperature through feedback mechanisms, achieving precise control of milk temperature. *Shi et al., (2016),* have successfully developed a precision calf feeding control system based on a host-slave architecture, achieving fully automated temperature-stabilized and quantity-regulated feeding of regular milk. *He et al., (2022),* developed a dynamic temperature control system based on a fuzzy PID control algorithm to achieve precise regulation of reconstituted milk replacer solution temperature during calf feeding processes, significantly improving the control accuracy of heat exchanger temperature. The team has currently designed a B/S architecture-based calf feeding information management system for operational data management, while constructing predictive models for milk allowance and replacer concentration parameters. These advancements collectively enhance intelligent and precision management levels in calf rearing operations at dairy farms *(He et al., 2022)*.

As the core nutritional carrier for calves, milk replacer requires precise conveyance and metered feeding that directly influence calf growth performance and health status. However, technical bottlenecks persist in achieving uniformity and controllability of replacer delivery systems, leading to recurrent bridging phenomena and discharge fluctuations. These operational instabilities compromise feeding accuracy and indirectly hinder precision management protocols in calf rearing operations. Current research on conveying equipment predominantly focuses on conventional configurations such as screw-type and vibratory-type systems. While screw conveyors feature simple structural configurations, they exhibit proneness to bridging tendencies when handling poor-flowability powder materials. Additionally, insufficient precision in motor speed regulation results in discharge quantity deviations *(Meng et al., 2015, Wang et al., 2011)*. While vibratory conveyors can mitigate bridging issues in powder conveyance, they are prone to excessive material spillage that causes environmental contamination and feed wastage *(Su et al., 2013)*. In comparison, scraper-type conveyors demonstrate potential through their uniform material propulsion and low residual accumulation characteristics. However, prevalent designs suffer from material adhesion issues and premature scraper blade wear. Research by *Li et al., (2014),* has demonstrated that the nonlinear relationship between scraper rotational speed and conveying rate is prone to induce flow fluctuations. *Qiao et al., (2014),* have identified that the optimization of scraper spacing constitutes a critical factor in enhancing operational efficiency.

Current research lacks systematic investigation into the coupling mechanisms between key parameters of scraper-type conveyors and powder motion characteristics, particularly for materials like milk replacer with distinctive frictional properties. The optimization of conveying efficiency and stability for such materials remains inadequately supported by theoretical foundations. This study addresses these gaps by employing the Discrete Element Method (DEM) to investigate discharge uniformity in milk replacer feeding systems. A systematic analysis has been conducted on the effects of flow-guiding baffles and conveyor structural configurations on conveying rates and operational stability within storage units. Optimal operational parameters for calf feeding machine conveying systems have been determined through parametric analysis. The resolution of dynamic bridging phenomena during milk replacer conveyance establishes a generalizable methodological framework for precision conveying system design of complex powdered materials. These findings provide practical significance for enhancing intelligent livestock equipment and advancing industrial transformation.

MATERIALS AND METHODS

Milk replacer material characteristics

The experimental material was calf-specific milk replacer with a moisture content of 5.84 wt.% (Brand: Nongdali; Composition: concentrated whey protein, whey powder, fat, vitamins, minerals, amino acids, enzymatic preparations).

The design of milk replacer conveying systems necessitates comprehensive understanding of the tribological properties of the stored material. Stress analysis was performed on the hopper assembly and agitator blades based on these frictional characteristics, as experimentally validated in Fig. 1, thereby enabling rational structural design of the powder conveying system.

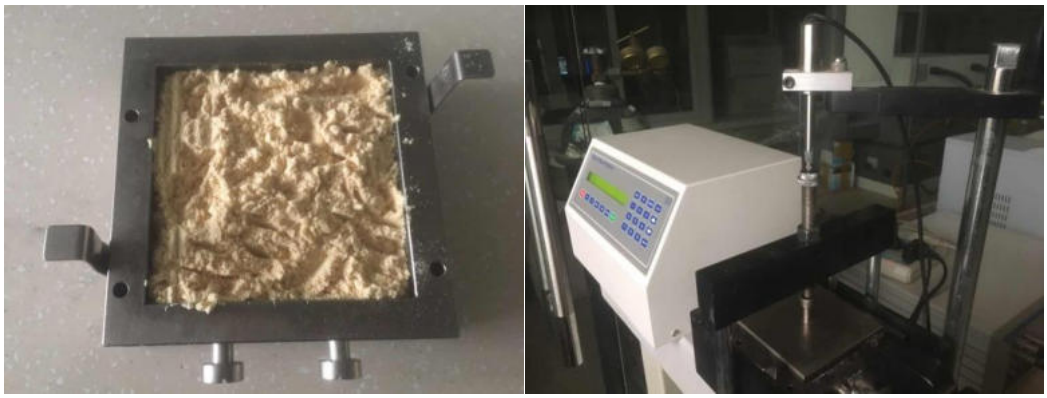


Fig. 1 – Milk replacer and direct shear test apparatus diagram

Experimental measurements of the internal friction characteristics of milk replacer powder and its external friction characteristics against stainless steel plates were conducted. Through linear regression analysis, the internal friction angle of the material was determined as 23.76°, with the wall friction angle measuring 23.97°.

Model development and parameter configuration of scraper-type conveyor systems

The design of the conveying system primarily considers three aspects: effective conveying volume, the resultant radial forces exerted by blades and flow-guiding baffles on materials, and the influence of the number of blades on conveying speed fluctuations. The scraper-type conveyor is shown in Fig.2.

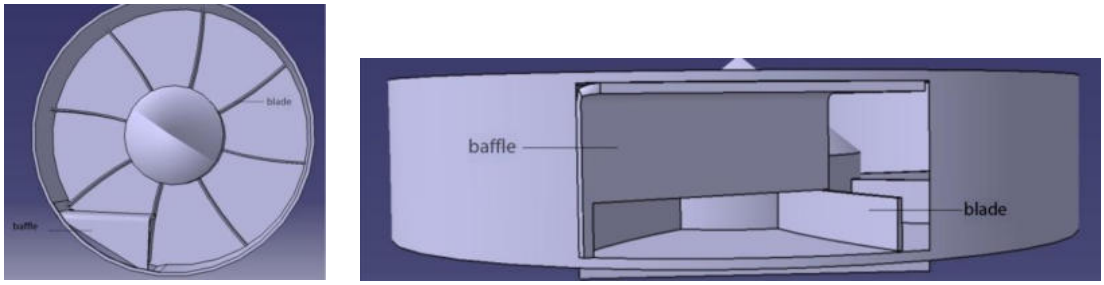


Fig. 2 – Milk replacer and direct shear test apparatus diagram

For effective conveying volume, since the height of the discharge port is fixed, it is mainly determined by the projected area variation along the axial direction of the hopper formed by the blades and baffles. The baffle angle and blade shape both affect this effective area.

Regarding the resultant radial forces from blades and baffles, when the angle between the baffle and the radial direction of the hopper decreases, the radial component force exerted by the baffle on the material also decreases. Although this increases the effective conveying volume, insufficient radial force leads to reduced conveying efficiency. Excessively large baffle angles diminish the effective working volume by affecting material guidance. Similarly, blade effects on conveying must also consider their radial force components.

Analysis of the impact of blade number on conveying speed fluctuations. During material conveyance by the hopper's conveying system, the discharge rate exhibits non-uniform fluctuations influenced by blade geometry, flow-guiding baffle angles, and the number of blades. As the blades are uniformly distributed circumferentially, these fluctuations demonstrate periodic characteristics. Increasing the number of blades reduces the fluctuation period. Under ideal conditions with identical blade configurations and baffle angles, fluctuation profiles remain consistent over equivalent operational durations. Extended blade engagement periods result in prolonged fluctuation cycles, where amplitude variations exceed or equal those observed in systems with higher number of blades (shorter cycles).

Given the potential influence of blade curvature radius on discharge rate and uniformity, the factor levels were designed based on the curvature radius parameters of the blades. The polar coordinate equation of the logarithmic spiral is

$$\rho(\theta) = ae^{\theta cot\alpha} \quad (1)$$

where : ρ is the radial distance;

θ – the polar angle;

α – the helix angle;

a – the scale factor.

The logarithmic spiral is a curve where the radius of curvature is proportional to the polar radius. When α is 90°, the curve degenerates into a circular arc. The inlet setting angle for blades relative to the inner circumference is uniformly configured at 90°.

The mathematical formulation of logarithmic spirals and their engineering implementation in blade profile design are detailed as follows:

$$\begin{cases} x = 40cos(t)exp(tan\alpha \cdot t) \\ y = 40sin(t)exp(tan\alpha \cdot t) \end{cases} \quad (2)$$

where α is the helix angle;

x –the abscissa of blade curve;

y – the ordinate of blade curve;

t – the intermediate variable.

Particle characteristic parameter configuration and particle factory establishment

The milk replacer model complies with GB/T 20715-2006 standards for calf milk replacer. The parameters for Replacing particles and Stainless steel are shown in Table 1. The established particle is shown in Fig. 3. A region was established above the scraper-type conveyor model to accommodate the particle factory, as indicated by the green area in Fig 4. The particle factory generated 10,000 particles within 2 seconds.

Table 1

The parameters for Replacing particles and Stainless steel

Parameter	Values
Poisson's ratio of milk replacer particles	0.45
Bulk density of milk replacer particles /(kg·m^{-3})	500
Density of stainless steel /(kg·m^{-3})	7930
Shear modulus of stainless steel / (GPa)	77
Coefficient of restitution between milk replacer particles	0.01
Coefficient of restitution between milk replacer particles and stainless-steel	0.01
Sliding friction coefficient between milk replacer particles	0.44
Sliding friction coefficient between milk replacer particles and stainless-steel	0.4446

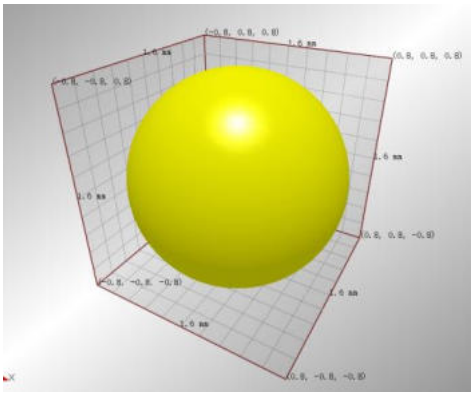


Fig. 3 – The established particle

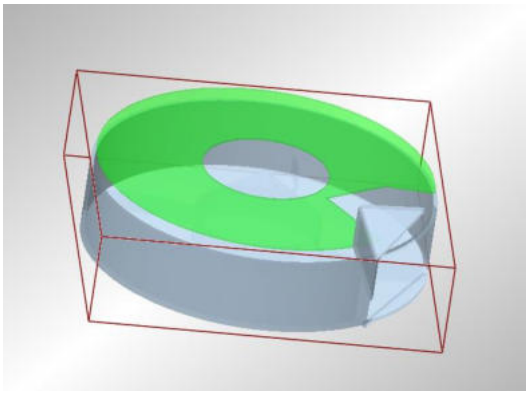


Fig. 4 – The particle factory

Discrete Element simulation of powder conveying

Based on the preceding analysis, a factor-level table has been established with variations in blade curvature radius, number of blades, and tangential angle between flow-guiding baffles and the conveyor as experimental factors, as detailed in Table 2. Simulation trials were conducted, with the computational process illustrated in Fig. 5.

Table 2

Factor-level table

Factors	A	B	C
	The blade curvature radius (α) (°)	Number of blades (unit)	Tangential angle between flow-guiding baffles and conveyor (°)
-1	30，gradually decrease	4	15
0	0	6	30
1	30，gradually increase	8	45

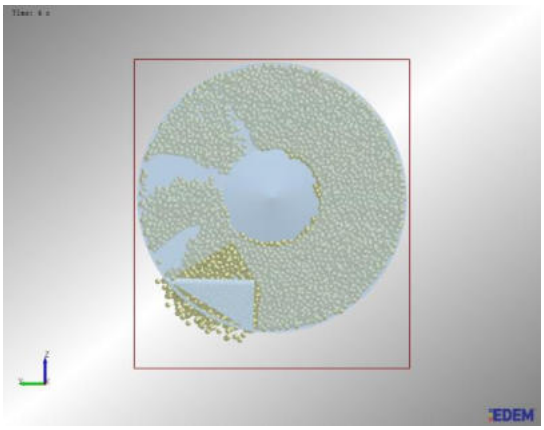
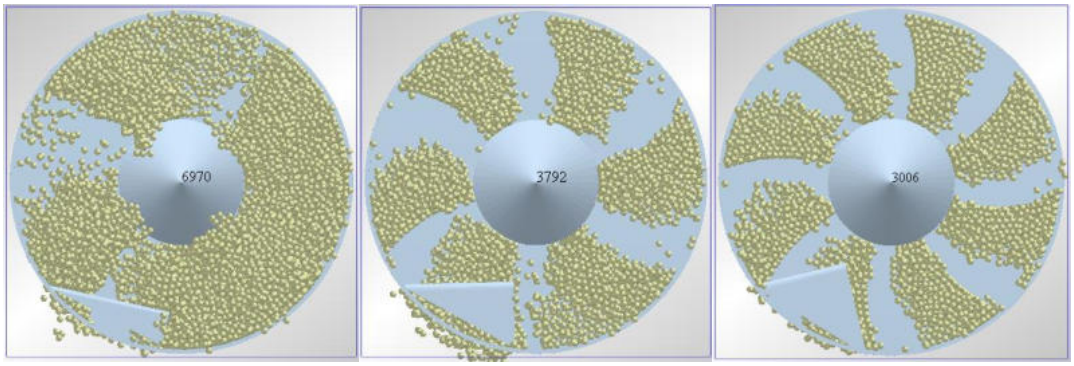


Fig. 5 – Powder conveying simulation process

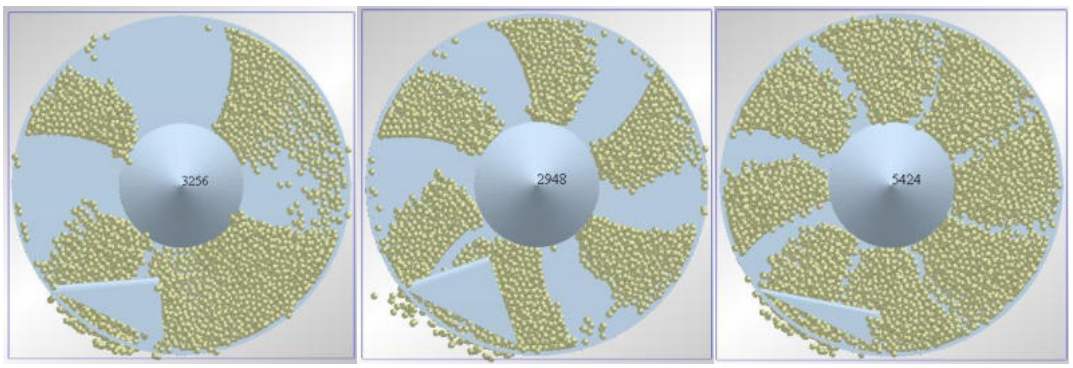
RESULTS

Discrete Element simulation results of powder conveying

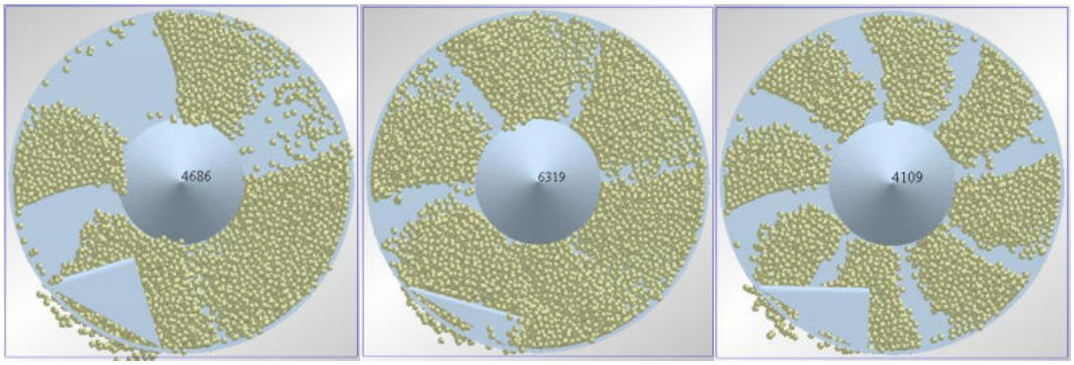
The intermediate phase was defined from 3.5 s to 9.5 s, during which the scraper blades completed exactly one full 360° phase rotation, i.e., all blades executed one operational cycle. Fig. 6 illustrates the residual material within the conveyor at 9.5 s.



A(-1)-B(0)-C(-1) A(-1)-B(0)-C(0) A(-1)-B(1)-C(1)



A(0)-B(-1)-C(0) A(0)-B(0)-C(1) A(0)-B(1)-C(-1)



A(1)-B(-1)-C(1) A(1)-B(0)-C(-1) A(1)-B(1)-C(0)

Fig. 6 – Residual material within the conveyor at 9.5 s

Simulation results indicate that when the tangential angle between flow-guiding baffles and the conveyor is 15°, residual material volume within the conveyor remains significantly higher. This demonstrates that the 15° configuration results in an excessively small effective conveying volume, impeding material transport. Conversely, negligible differences in performance are observed at 30° and 45° angles.

To determine the primary and secondary influences of each factor on powder conveying rate and operational stability, identify optimal levels, and ascertain the optimal parameter combination, a range analysis was performed on the simulation trials. The results are presented in Table 3.

Table 3

Orthogonal simulation results and range analysis

Indicator	Trial sequence number	A	B	C	Mid-term rate/(g/s)	Mid-term stability/(%)
	1	-1	-1	-1	21.36	36.96
	2	-1	0	0	46.6	73.77
	3	-1	1	1	47.09	65.26
	4	0	-1	0	28.34	37.24
	5	0	0	1	52.27	75.14
	6	0	1	-1	33.84	71.69
	7	1	-1	1	40.85	52.29
	8	1	0	-1	27.45	31.16
	9	1	1	0	43.51	69.01
Mid-term rate	K1	38.35	30.18	27.55		
	K2	38.15	42.11	39.48		
	K3	37.27	41.48	46.74		
	R	1.08	11.92	19.19		
Mid-term stability	K1	58.66	42.16	46.60		
	K2	61.36	60.02	60.01		
	K3	50.82	68.65	64.23		
	R	10.54	26.49	17.63		

Based on the mid-term experimental results, the optimal parameter combination includes a blade curvature radius of 30° with a gradual decrease, six blades, and a tangential angle of 45° between the flow-guiding baffles and the conveyor. Among the factors analyzed, the tangential angle had the greatest influence on conveying performance, followed by the number of blades, while blade curvature radius showed the least significant effect.

Based on mid-term stability results, the optimal parameter combination features a blade curvature radius of 0°, 8 blades, and a 45° tangential angle between flow-guiding baffles and conveyor, with the number of blades exhibiting the most pronounced effect on stability, followed by the baffle tangential angle, while blade curvature radius demonstrates the lowest significance.

The results of the orthogonal experiment ANOVA are presented in Table 4. Using mid-term conveying rate as the evaluation index and treating the empty column as the error term at a 0.05 significance level, the analysis shows that the flow-guiding baffle angle has a statistically significant effect on the conveying rate. The number of blades exhibits a noticeable influence, with confidence levels exceeding 80%, while the blade curvature radius has a minimal impact, as its confidence level remains below 80%.

Table 4

Analysis of variance

Indicator	Source of variation	SS	df	MS	F	sig.
Mid-term rate	Variation in blade curvature radius	1.981	2	0.991	0.032	0.969
	Number of blades	270.173	2	135.087	4.346	0.187
	Tangential angle between flow-guiding baffles and conveyor	563.144	2	281.572	9.059	0.099
	Residual	62.166	2	31.083		
Mid-term stability	Variation in blade curvature radius	179.793	2	89.897	0.244	0.804
	Number of blades	1095.177	2	547.589	1.485	0.402
	Tangential angle between flow-guiding baffles and conveyor	508.185	2	254.093	0.689	0.592
	Residual	737.325	2	368.663		

Based on the optimization analysis of the blades and flow-guiding baffles, the conveying system of the calf feeding machine adopts circular-arc blades (with a curvature radius variation of 0°), incorporates 8 blades, and sets the tangential angle between the flow-guiding baffles and the conveyor at 45°.

Structural measurement test of milk replacer conveying device

The test first switched the system to manual mode, selected the "hopper feeding function" on the interface, and utilized load cells installed beneath the agitation mechanism for data acquisition. Collected data were stored in .txt format files. Three discharge trials were repeated. Fig. 7 shows the conveying section of the hopper assembly equipped with circular-arc blades (8 blades) and 45° flow-guiding baffles. Fig. 8 illustrates the agitation mechanism with load cells mounted underneath.

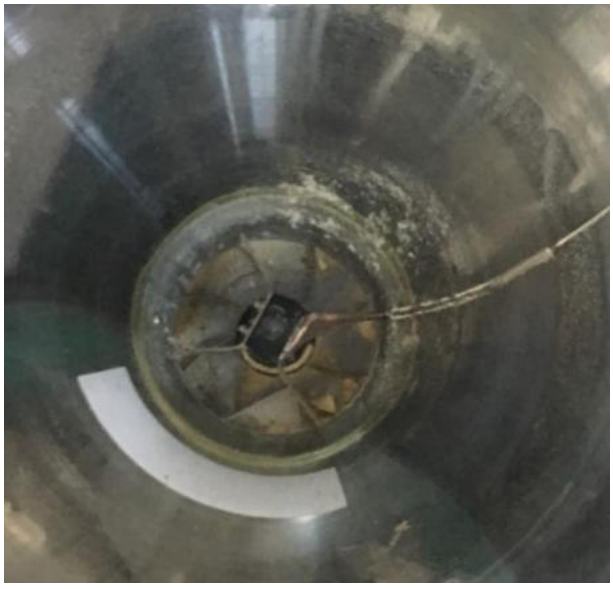


Fig. 7 – Circular-arc-8-blade conveying device with 45° flow-guiding baffles



Fig. 8 – Milk replacer agitation mechanism with load cell

After subtracting the initial weight of the agitation mechanism at 0 s from all data, the processed data were analyzed. The discharge quantity versus time curve is plotted in Fig. 9.

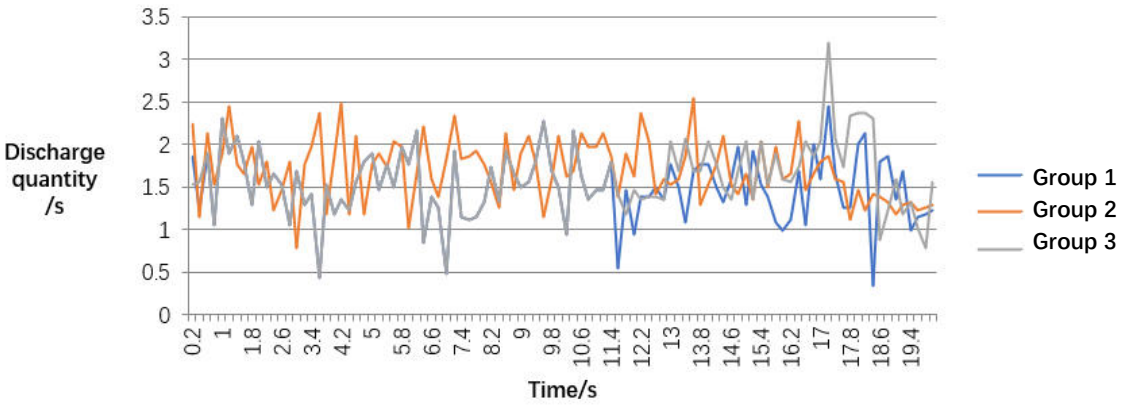


Fig. 9 – Discharge quantity versus time curves for three replicate trials of the feeding mechanism

Based on three replicate trials, the mean value, standard deviation, and operational stability of the discharge quantity are presented in Table 5.

Table 5

Discharge quantity standard deviation analysis table

Trial sequence number	Mean discharge quantity (g/s)	Standard deviation	Operational stability
1	7.50	0.40	73.31%
2	8.48	0.36	75.96%
3	8.01	0.43	71.80%

Table 4 indicates a low standard deviation in discharge quantity, demonstrating high operational stability. The mean discharge rate remains within 7.50 ~ 8.48 g/s, confirming that the feeding mechanism maintains consistent material conveyance during testing. This discharge rate complies with design specifications and ensures feeding continuity.

CONCLUSIONS

(1) Through friction characteristic testing of milk replacer material in the storage device, the internal friction angle was measured as 23.76° and the external friction angle as 23.97°. Based on the frictional characteristics, a scraper-type milk replacer conveying device for calf feeding equipment was designed.

(2) The movement of powder material inside the conveyor was simulated, and tests were performed to analyze the results. The findings show that, regarding the factors influencing the average conveying rate over time, the most important factor is the angle between the flow-guiding baffles and the conveyor, followed by the number of blades, and then the curvature radius of the blades. When it comes to the factors affecting the stability of powder conveying during the same period, the number of blades is the most significant, followed by the angle of the flow-guiding baffles, and lastly the variation in blade curvature radius. At a 0.05 significance level, the tangential angle between flow-guiding baffles and conveyor significantly affects the mid-term rate. The optimal parameters for the calf feeding machine conveying device are: circular-arc blades, 8 blades, and a 45° tangential angle between flow-guiding baffles and conveyor.

(3) Field trials of the conveying device verified discharge stability for the milk replacer system. The mean feeding rate remained within 7.50–8.48 g/s, confirming stable material conveyance by the feeding structure during testing. This discharge rate complied with design requirements and ensured operational continuity.

REFERENCES

[1] Bin Li, Mingjun Ma, Chaoju Yang. (2021). Study on Precise Feeding Control of Dairy Cows Based on Wireless Communication Technology and Dairy Cow Information Management Technology. *INMATEH-Agricultural Engineering*, Vol. 65, no. 3: pp.173-182, doi: https://doi.org/10.35633/inmateh-65-18

[2] Cai Jichen, (2014). *Design of Automatic Feeding Equipment for Large-scale Meat Pigeon Farming (肉鸽规模化养殖自动饲喂设备的设计)*. Master's Thesis, Shandong Agricultural University;

[3] Dmytriv Ihor. (2021). The Functional Controllability of Milk Ejection of the Adaptive Milking System. *INMATEH-Agricultural Engineering*, Vol. 65, No.3, pp.399-409, doi: https://doi.org/10.35633/inmateh-65-42

[4] Dmytriv Vasyl, Dmytriv Ihor, Horodetskyy Ivan, Yatsunskyi Petro (2020). Adaptive Cyber-Physical System of the Milk Production Process. *INMATEH-Agricultural Engineering*, Vol. 61, No.2, pp. 199-208, doi: https://doi.org/10.35633/inmateh-61-22;

[5] He Gang, Cai Xiaohua, Bai Yang. (2022). Design and Experiment of Calf Milk Replacer Temperature Control System Based on Fuzzy PID (基于模糊 PID 的犊牛代乳粉奶液温度控制系统设计与试验). *Journal of Agricultural Machinery*, Vol.53, no.3, pp.266–276, doi: 10.6041/j.issn.1000-1298.2022.03.028

[6] He Gang, Zhai Guixia, Zhu Tianyu. (2022). Design of Calf Feeding Information System and Research on Milk Volume Prediction (犊牛饲喂信息系统设计与给奶量预测研究). *Journal of Agricultural Machinery*, Vol. 53, no. S2: pp. 241–248, doi: 10.6041/j.issn.1000-1298.2022.S2.028

[7] Janzekovic M., Mursec B., Janzekovic I., (2011). Automatic and conventional system for feeding calves. *Manufacturing and Processing*, Vol. 49, no.2: pp.566~572;

[8] Jin Mixiao, Li Yamin, Zeng Zhihua. (2014). Design of Calf Feeding Control System (一种犊牛饲喂控制系统的设计). *Journal of Zhejiang Agricultural Sciences*, Vol. 26, no.01: pp. 206–209;

[9] Li Yongjun, Yi Weiming, Bai Xueyuan, Li Zhihe, He Fang. (2014). Analysis on Feeding Characteristics of Scraper-type Biomass Powder Feeder (刮板式生物质粉喂料机的喂料特性分析). *Acta Energiae Solaris Sinica*, Vol. 35, no.02: pp. 355 – 359,doi: 10.3969/j.issn.0254-0096.2014.02.028

[10] Meng Hewei, Kan Za, Li Yaping. (2008). Design and 3D Modeling of Screw Conveyor in Cattle Feeding Device (奶牛饲喂装置中螺旋输送器的设计及三维造型). *Agricultural Mechanization Research*, no.10: pp. 61–63, doi: 10.3969/j.issn.1003-188X.2008.10.018

[11] Meng Xiurong, Li Wenbo, Wang Yijiang, Wang Mengyue. (2013). The change of calf feeding and management mode (犊牛饲养管理模式的变革). *China Dairy Cattle*, no.10: pp. 59–61, doi: 10.3969/j.issn.1004-4264.2013.02.016

[12] Qi Jiangtao, Li Chengsong, Li Yaping, Kan Za, Lin Hai, He Miao. (2014). Design of Intelligent Feeding Device for Calves (犊牛智能化饲喂装置的设计). *Agricultural Mechanization Research*, Vol. 36, no.10: pp. 127-130. doi: 10.13427/j.cnki.njyi.2014.10.031

[13] Qiao Yu, Liang Qi. (2014). Research on Driving Load of Scraper Conveyor Based on Granular Mechanics (基于散体力学的刮板输送机驱动负载研究). *Coal Mine Machinery*, Vol. 35, no.05: pp.65 – 67, doi: 10.13436/j.mkjx.201405030

[14] Shi Chengcheng (2016). *Design of Automatic Control System for Precise Calf Feeding Equipment (*犊牛精确饲喂装备自动控制系统的设计*)*. Master's Thesis, Shihezi University*;*

[15] Su Jiang, Yang Zhigang, Tian Fengjun. (2013). Inertial Piezoelectric Vibration Feeder (惯性式压电振动送料器). *Journal of Agricultural Machinery*, Vol. 44, no.08: pp.281–286, doi: 10.6041/j.issn.1000-1298.2013.08.048

[16] Sutherland, M. A., Lowe, G. L., Huddart, F.J., Waas, J.R., & Stewart, M. (2018). *Measurement of dairy calf behavior prior to onset of clinical disease and in response to disbudding using automated calf feeders and accelerometers. Journal of Dairy Science,* Vol. 101, no.09: pp. 8208-8216, doi:10.3168/jds.2017-14207

[17] Wang Jiwei, Yu Wenjuan, Jiang Yuanzhi. (2010). Analysis on Types and Conveying Principles of Screw Conveyors (螺旋输送器的类型及输送机理分析). *Grain and Oil Processing (Electronic Edition)*, no.7, pp.158–160, doi: CNKI:SUN:NJSP.0.2010-07-055

[18] Yang Jianning. (2016). *Design research on key devices of automatic feeding vehicle for sheep farming in facilities (*设施养羊自动饲喂车关键装置的设计研究*).* Master's Thesis, Inner Mongolia Agricultural University;

[19] Zeng Jinghua, Meng Xiancheng. (2017). Matters needing attention in calf feeding and management in dairy farms (奶牛场犊牛饲养管理应注意的问题). *China Animal Husbandry and Veterinary Medicine Digest*, Vol. 33, no.12, pp.83, doi: 10.19305/j.cnki.11-3009/s.2023.05.001

[20] Zhang Hui. (2016). *Research and Implementation of Key Technologies in Organic Pig Intelligent Feeding System (*有机生猪智能化综合饲养系统中关键技术的研究及实现*). Master's Thesis, Anhui University;*

[21] Zhao Xinyu, Feng Dengzhen, Wu Qiang. (2015). Matters needing attention in calf feeding and management in dairy farms (奶牛场犊牛饲养管理应注意的问题). *Agricultural Science Research*, Vol. 36, no.01: pp.78–81, doi: 10.13907/j.cnki.nykxyj.2015.01.017

DEM-BASED MODELING AND CONTACT PARAMETER CALIBRATION OF HAZELNUTS
/
基于 DEM 榛子建模与接触参数标定

Chun WANG[1)], Hailin KUI[1)], Xiaoli WU[1)], Yongchao SHAO[2)], Minggang FU[*1)]
[1)]College of Biological and Agricultural Engineering, Jilin University, Changchun 130000, China;
[2)]College of Mechanical Electrical Engineering, Northwest A&F University, Yangling 712100, China
Tel: +86-15584156891; E-mail: kuihl@jlu.edu.cn
DOI: https://doi.org/10.35633/inmateh-76-71

Keywords: *hazelnuts, discrete element, simulation parameter, calibration, repose angle*

ABSTRACT
To address the lack of contact parameters in designing hazelnut harvesting machinery, this study measured the physical properties of hazelnuts through experiments and obtained a 3D model via scanning. A DEM model was established accordingly. Contact parameters between hazelnuts and steel were calibrated through physical and simulated tests, yielding a restitution coefficient of 0.31, static friction of 0.39, and rolling friction of 0.04. Using the relative error of repose angle as the response variable and hazelnut–hazelnut contact parameters as factors, a quadratic regression model was developed by steepest ascent and Central Composite tests. The optimal contact parameters of hazelnuts were 0.11 (restitution), 0.21 (static friction), and 0.04 (rolling friction), with a 1.84% error.

摘要
为解决设计，优化榛子收获机械中缺乏接触参数的问题，本文通过试验测试得到了它的基本物理参数。通过 3D 技术得到了榛子的三维模型并建立了 DEM 模型。通过物理及模拟接触参数试验，测量及校准了榛子与钢的接触参数：恢复率 0.31，静摩擦率 0.39，滚动摩擦率 0.04。以物理与模拟堆积角的相对误差为响应值，以榛子间的接触参数为影响因子，通过最陡爬坡试验及中心组合试验建立二次回归模型，通过求解方程得到榛子间的最佳接触参数组合为：恢复系数 0.11，静摩擦系数 0.21，滚动摩擦系数 0.04，相对误差为 1.84%。

INTRODUCTION
Hazelnuts *(Corylus spp., family Betulaceae)* are among the world's four major nuts and serve as a vital oilseed crop. Their kernels are rich in essential amino acids, minerals, and unsaturated fatty acids that help lower blood lipids and support cardiovascular health *(Kruk et al., 2024; Bonisoil et al., 2015; Delprete et al., 2014)*. With recognized nutritional and medicinal value, hazelnuts are in growing demand globally. Rising health awareness and improved economic conditions have further boosted hazelnuts consumption. China is a leading producer, with output reaching 0.6 million tons in 2023 and showing steady annual growth *(Zhao et al., 2023; Guo et al., 2024)*.

The growing hazelnut market has driven the development of related machinery, with mechanization seen as a key solution to labor shortages intensified by China's aging population. However, equipment in this field remains in its early stages, lacking standardization and widespread adoption. To address terrain challenges, *Ren et al. (Ren et al., 2022; Ren et al., 2024)* developed a pneumatic harvester achieving a 96.332% picking rate with only 1.679% foreign material content. Further improvements enhanced operational stability. For shelling, *He et al., (2024),* proposed a conical sheller capable of processing hazelnuts of varying sizes, effectively improving shelling efficiency and reducing kernel breakage. The design and optimization of hazelnut-related machinery increasingly rely on computer-aided technologies such as DEM, CAE, and CAD, which streamline development and shorten design cycles. The Discrete Element Method (DEM), widely used in civil engineering, mining, and agricultural machinery, enables accurate simulation of granular material behavior. For example, *Zhang et al., (2024)*, developed a DEM model for alfalfa seeds, calibrating contact parameters via repose angle comparisons. Similarly, *Zhang et al., (2024),* established a safflower seed model using the Hertz–Mindlin (no slip) contact model and orthogonal testing. *Shi et al., (2024),* proposed a DEM model for cotton seeds, achieving accurate simulation of coated seed behavior for planting applications.

Mohammad et al., (2024), proposed a comprehensive five-step framework of a DEM grain model calibration and validation of flow and grain impacts on equipment was investigated. The flow model of corn during hopper unloading of the harvester was established and verified.

Currently, no studies have reported the development of a discrete element model (DEM) for hazelnuts or the calibration of their contact parameters, despite their importance for machinery design and optimization. In this study, the basic physical properties of hazelnuts were obtained through experimental measurement and theoretical calculation *(Sun et al., 2022)*. Contact parameters between hazelnuts and steel - including restitution, static friction, and rolling friction coefficients - were measured and calibrated using physical and simulated repose tests *(Wang et al., 2022; Xu et al, 2021, Xu et al., 2022)*. Using the relative error of repose angles as the response variable, and inter-hazelnut contact parameters as factors, the optimal parameter combination was identified through steepest ascent and the central composite tests *(Xu et al., 2018)*. Further validation confirmed the accuracy and reliability of the DEM model and calibrated parameters.

MATERIALS AND METHODS

Size Parameters

This study focuses on *Corylus avellana* (European hazelnut) as the target material. The hazelnut exhibits an approximately elliptical shape, with a nearly circular center that tapers toward both ends. Based on morphological features, the husk end is defined as the bottom and the pointed end as the top. During maturation, natural linear textures form along the husk surface. As shown in Figure 1, a three-dimensional rectangular coordinate system was established: the distance between the two vertices is defined as length (*L*), the axis along the husk's linear texture as width (*W*), and the axis perpendicular to it as thickness (*T*). A total of 200 hazelnuts were randomly selected for dimensional analysis. Using a digital caliper with 0.01 mm precision, the average values measured were 22.48 ± 0.96 mm (*L*), 18.23 ± 0.78 mm (*W*), and 17.46 ± 0.81 mm (*T*).

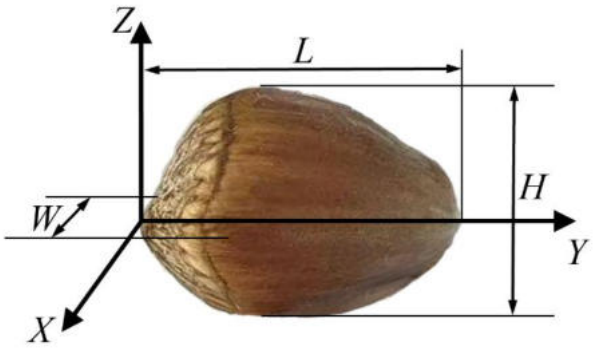


Fig. 1 – Schematic diagram of size characteristics of hazelnut

The density of hazelnuts

The mass of the hazelnuts was measured using an electronic balance with a precision of 0.01 g. Volume was determined via the liquid displacement method using a graduated cylinder (0.1 mL precision) filled with 99% ethanol. To minimize splashing and measurement error, the cylinder was tilted, and each hazelnut was gently introduced at the opening, allowing it to slide in slowly and become fully submerged. The hazelnut volume was calculated as the absolute difference between the initial and final liquid volumes. Ten hazelnuts were randomly selected, and the test was repeated five times per sample, with the average taken as the final result. Based on the standard formula for density *(Liu et al., 2025)*, the average density of hazelnuts was calculated to be 851 ± 15.37 kg/m³.

The Young's modulus and Poisson's ratio of hazelnuts

The Young's modulus is a measure of a material's ability to resist deformation under tension or compression and is one of the key mechanical properties of the hazelnut. The Young's modulus of the hazelnut was measured using a texture analyzer, as shown in Figure 2. The hazelnut was placed horizontally on the platform of the texture analyzer, and the hydraulic probe was manually adjusted to a suitable position above the hazelnut. The loading speed was set to 10 mm/s and pressure was applied until the breaking force in the dislocation-force curve in the computer reached its peak and decreased sharply, at which point the test was stopped.

The post-processing module of computer software was used to obtain the force-displacement curve during the seed compression test, as shown in Fig. 3(b). The indentation method is used to calculate the contact area, the surface of the hazelnut is coated with pigment, compressed to leave a near circular pattern on the hydraulic probe, and the contact area is calculated by the formula $A = \pi r^2$. The test was repeated seven times, and the average value was calculated. The Young's modulus of the hazelnut was then determined by Equation (1), yielding E = 1.254×10^9 Pa.

$$E = (\frac{\sigma}{A}) / v \tag{1}$$

where:

E is the Young's modulus of hazelnuts, Pa; σ represents the maximum compressive stress, Pa;

A represents the contact area of the compression head with the hazelnut, m^2; v is the line strain.

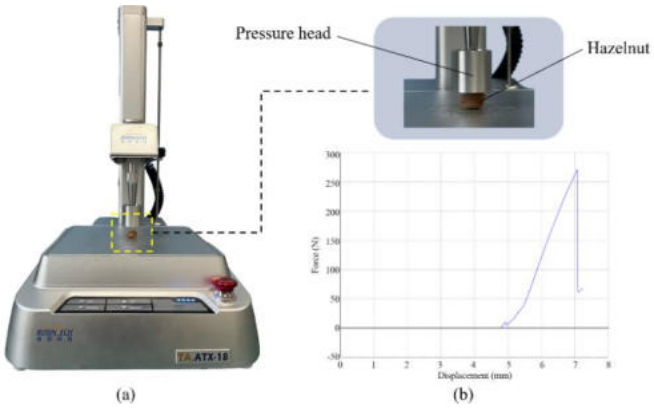


Fig. 2 – Hazelnuts mechanical properties test

(a) Hazelnuts compression test; (b) Load-displacement curve

Poisson's ratio is defined as the ratio of lateral strain to axial strain under uniaxial compression, and it is a key mechanical property of hazelnuts. In this study, a texture analyzer was used to perform compression deformation tests. Five hazelnuts were randomly selected, and their initial width and thickness were measured using a digital caliper. Each sample was placed on the test platform, and a hydraulic probe was manually positioned until it contacted the surface. The loading rate was set to 0.5 mm/s for a duration of 4 seconds. After compression, the width deformation was recorded. The test was repeated five times, and the average was used to calculate Poisson's ratio based on thickness and width changes. The resulting Poisson's ratio of hazelnuts was determined to be 0.38.

$$\lambda = \frac{\Delta T / T}{\Delta W / W} \tag{2}$$

where:

λ is Poisson's ratio of hazelnut; ΔT is the absolute deformation in the direction of the thickness of hazelnuts, mm; T is the original thickness of hazelnuts, mm; ΔW is the absolute deformation in the direction of the width of hazelnuts, mm; W is the original length in the direction of the width of hazelnuts, mm.

Discrete element method model

In this study, a three-dimensional model of a hazelnut was obtained using 3D scanning technology. A sample with dimensions close to the average was selected (Figure 3a), and its surface geometry was captured and smoothed using Materialise Magics 28.0 (Figure 3b). The processed model was exported in STL format and imported into EDEM 2022 (Figure 3c), where a discrete element model was generated using the automatic filling method (Figure 3d). This approach preserves the geometric fidelity and physical characteristics of the hazelnut, improving the accuracy and realism of simulation results for harvesting and processing applications. Contact interactions between hazelnuts and between hazelnuts and equipment surfaces were simulated using the Hertz–Mindlin (no slip) contact model. This model incorporates both elastic and frictional properties of materials, enabling accurate representation of collision and contact behaviors in the discrete element framework *(Li et al., 2024, Fan et al., 2021)*.

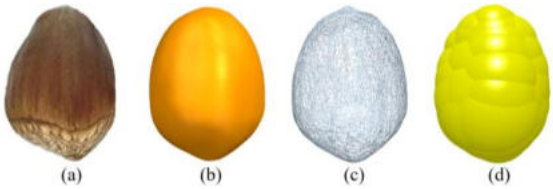


Fig. 3 – Hazelnut model

(a) Actual hazelnut; (b) Hazelnut scanning model, (c) Hazelnut profile model; (d) Hazelnut discrete element model

Determination and calibration of restitution coefficient

The collision restitution coefficient is defined as the ratio of separation velocity to approach velocity in the normal direction of contact and is influenced by the material properties of the colliding bodies. As illustrated in Fig. 4a, the restitution coefficient between hazelnuts and a steel plate was determined via a free-fall test. A hazelnut was released from a height of 500 mm above a horizontal steel surface, with vertical grid paper used for reference. The rebound motion was recorded using a high-speed camera, and the rebound height (h) was measured accordingly. This test was repeated ten times, yielding an average rebound height of 9.42 mm. The restitution coefficient was calculated using Equations 3–5, resulting in a value of 0.14 for the hazelnut–steel interaction.

$$e = \frac{v_4 - v_3}{v_2 - v_1} \tag{3}$$

$$v_4 = \sqrt{2gh} \tag{4}$$

$$v_2 = \sqrt{2gH} \tag{5}$$

where, e is the collision restitution coefficient between hazelnuts and steel; v_1 is the velocity of the steel before the collision, v_2 is the velocity of hazelnuts before the collision, mm·s^{-1}; v_3 is the velocity of the steel after the collision, mm·s^{-1}; v_4 is the velocity of hazelnuts after the collision, mm·s^{-1}; H is the height from which the object is dropped before free fall, mm; h is the rebound height, mm; g is the gravity acceleration, m·s^{-2}.

Due to deviations between physically measured and simulation-required restitution coefficients [30], calibration is necessary before applying values in DEM. As shown in Figure 4b, a simulation was conducted in EDEM 2022 under the same conditions as the physical free-fall test. The restitution coefficient ranged from 0.01 to 0.41 in steps of 0.05, while the static and rolling friction coefficients were fixed at measured values. Nine simulations were performed with a 5 s duration and a 0.001 s time step. A quadratic fit of the results is shown in Figure 5a. Substituting the physical rebound height (9.42 mm) into Equation (6) yielded a calibrated restitution coefficient of 0.31. This value was then verified through five repeated simulations, producing an average rebound height of 9.13 mm and a relative error of 3.08%. These results confirm that the calibrated coefficient closely reflects actual behavior and is suitable for further DEM simulations.

$$y_1 = 1.403 - 42.794x_1 + 217.095x_1^2 \tag{6}$$

where, x_1 is the restitution coefficient; y_1 is the rebound height, mm.

Determination and calibration of static friction coefficient

The static friction coefficient is defined as the ratio of the maximum static friction force to the normal force between two contact surfaces. It is influenced by material properties and surface roughness. In this study, the inclined plane method was used to measure the static friction coefficient between hazelnuts and a steel plate (Fig.4c). To prevent rolling, two hazelnuts were bonded together using adhesive. The inclined plane angle was gradually increased at a constant rate using a hand-cranked mechanism until the hazelnut assembly began to slide. The critical angle at the onset of sliding was recorded. This test was repeated 10 times, and the average value was calculated. The resulting average maximum static friction angle between the hazelnuts and the steel surface was 22.70°.

$$f = G\sin\theta \tag{7}$$

$$F_N = G\cos\theta \tag{8}$$

$$\mu = \frac{F_N}{f} \tag{9}$$

where: f is the frictional force acting on hazelnuts, N; G is the gravitational force on hazelnuts, N; F_N is the support force acting on hazelnuts, N; μ is the static friction coefficient; θ is the angle between the inclined plane and the horizontal surface, °.

The static friction coefficient was calculated using Equations (7)-(9), yielding a measured value of 0.42 for the hazelnut–steel interface. Calibration followed a similar procedure to that of the restitution coefficient. As shown in Figure 4d, a simulation of the inclined plane test was constructed in EDEM 2022 using the same initial and boundary conditions as the physical test. The restitution and rolling friction coefficients were fixed at previously determined values, while the static friction coefficient varied from 0.1 to 0.5 in 0.05 increments, requiring nine simulations. Each simulation lasted 15 s, with the plane rotating at 2°/s and a time step of 0.01s. The simulation results and quadratic fitting curve are shown in Figure 5b. Substituting the physical result (y_2 = 22.70°) into Equation (10), the calibrated static friction coefficient was determined to be 0.39. Repeated simulations yielded an average friction angle of 23.16°, with a relative error of 2.03%, confirming the calibration's accuracy.

$$y_2 = 0.944 + 59.548x_2 - 7.836x_2^{\,2} \tag{10}$$

where, x_2 is the static friction coefficient; y_2 is the maximum static friction angle,°.

Determination and calibration of rolling friction coefficient

Rolling friction refers to the resistance encountered when an object rolls over a surface without slipping, primarily caused by surface deformation at the contact interface. In this study, the bevel rolling method was used to determine the rolling friction coefficient between hazelnuts and a steel plate. As illustrated in Figure 4e, the inclined plane formed a 20° angle with the horizontal. Each hazelnut was placed at a distance of S = 150 mm from the incline's base and released from rest (initial velocity = 0 m/s). The hazelnut rolled freely until it came to a stop, and the horizontal rolling distance L was recorded. The test was repeated 10 times, and the average rolling distance was calculated to be 322.81 mm.

$$\mu' = \frac{GL\sin\beta}{G(L\cos\beta + S)} \tag{11}$$

where, G is the gravitational force on the hazelnut, N; β is the angle of inclination of the inclined plane, °; S is the distance traveled by the hazelnut while rolling on a flat surface, mm; L is the distance traveled by the hazelnut while rolling on an inclined plane, mm; μ' is the rolling friction coefficient of the hazelnut and steel plate.

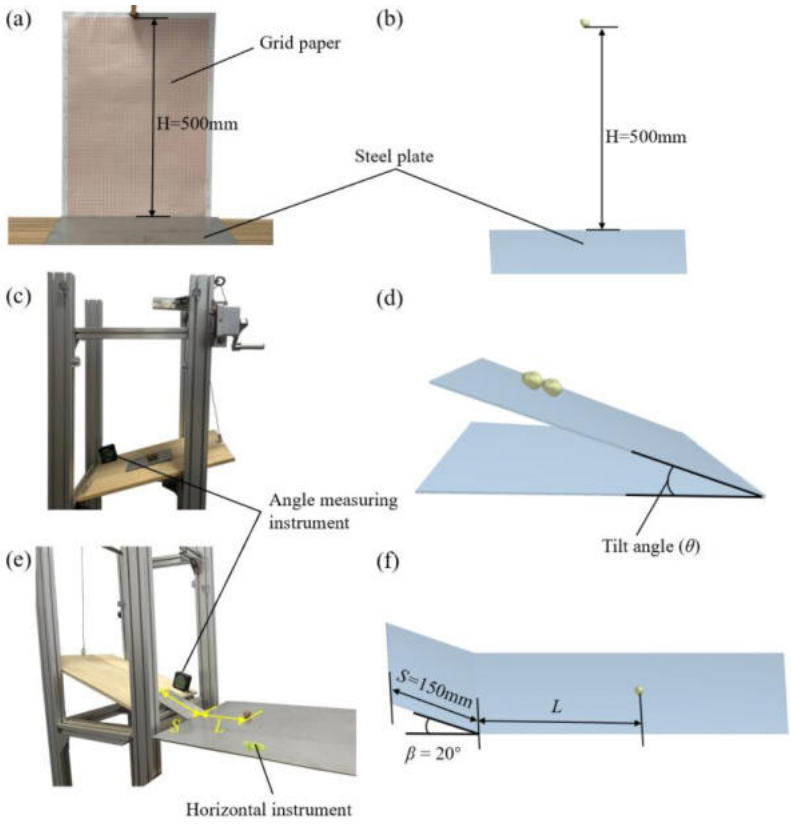


Fig. 4 - Physical test and simulated test for measuring contact parameters of hazelnuts and steel

(a) Physical collision test; (b) Simulated collision test; (c) Physical static friction coefficient test; (d) Simulated static friction coefficient test; (e) Physical rolling friction coefficient test; (f) Simulated rolling friction coefficient test.

The rolling friction coefficient is calculated using Equation (11). The rolling friction coefficient between hazelnuts and the steel plate is calculated to be 0.11.

A simulation test replicating the physical rolling friction experiment was constructed in EDEM 2022, as shown in Figure 4f. The restitution and static friction coefficients were fixed at their calibrated values. The rolling friction coefficient was varied from 0.01 to 0.17 in 0.02 increments, resulting in nine simulations. The simulation results and the corresponding quadratic fitting curve are presented in Figure 5c. By substituting the physical rolling distance (y_3 = 322.81 mm) into Equation (12), the calibrated rolling friction coefficient was determined to be 0.04. This value was then applied in a second round of simulations (n = 10), producing an average rolling distance of 313.46 mm. The relative error between the physical and simulated results was 2.90%, confirming that the calibrated rolling friction coefficient closely reflects actual behavior and is reliable for subsequent discrete element simulations.

$$y_3 = 345.71 - 680.14x_3 + 2059.71x_3^2 \quad (12)$$

where, x_3 is the rolling friction coefficient; y_3 is the rolling distance, mm.

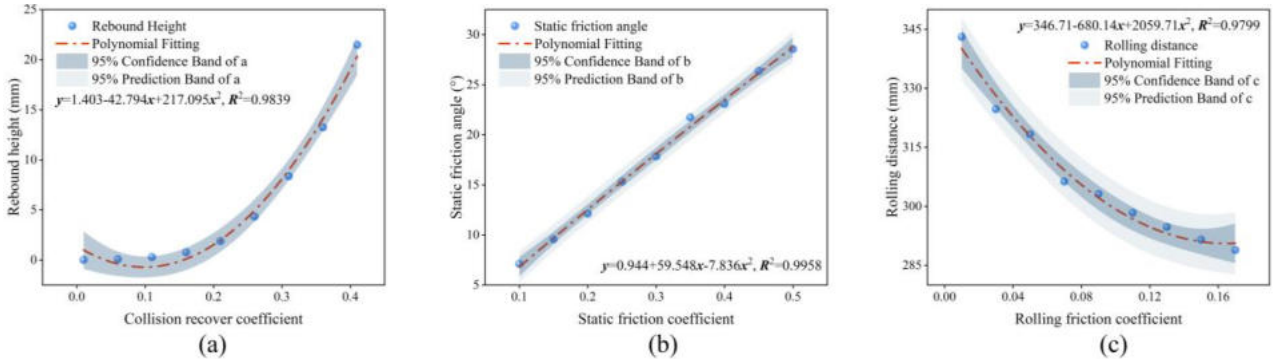


Fig. 5 - Simulation results of hazelnut and steel contact parameters and polynomial fitting

(a) Simulation results of restitution coefficient test and quadratic fitting; (b) Simulation results of static friction coefficient test and quadratic fitting; (c) Simulation results of rolling friction coefficient test and quadratic fitting.

Calibration of contact parameters between hazelnuts

Direct measurement of contact parameters between hazelnuts using conventional methods is challenging. Therefore, this study employs a combined approach of physical and simulated repose angle tests for calibration. The relative error between physical and simulated repose angles serves as the response variable, while the restitution coefficient, static friction coefficient, and rolling friction coefficient between hazelnuts are treated as experimental factors. Using steepest ascent and orthogonal test methods, a regression model is established, and the optimal combination of inter-hazelnut contact parameters is determined for accurate discrete element simulation *(Ucgul et al., 2018, Gu et al. 2020)*.

Physical repose test

The physical repose angle tests were conducted using the cylindrical lifting method. The test apparatus comprised a steel cylinder (100 mm diameter, 400 mm height) and a steel plate (400 × 400 mm, 2 mm thick). Before testing, the cylinder was placed at the center of the plate and filled with hazelnuts. It was then lifted vertically at a constant speed of 30 mm/s, allowing the hazelnuts to form a natural pile, as shown in Figure 6a. Image processing was performed in MATLAB, including binarization, hole filling (Figure 6b), edge extraction, and linear fitting using the least squares method to determine the slope on both sides of the pile (Figures 6c and 6d). Due to asymmetry, the average of the absolute values of both side slopes was taken as the repose angle for each test. The procedure was repeated 10 times, yielding an average repose angle of 23.38 ± 0.72°.

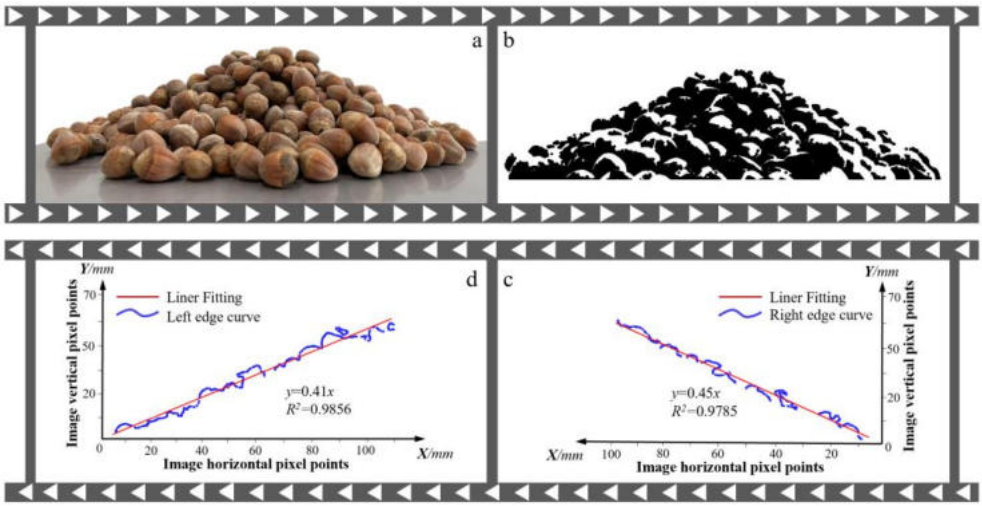


Fig. 6 - Physical repose tests and experimental processing.

(a) Physical angle of repose test; (b) Using MATLAB to process the figures; (c) Right side repose curve; (d) Left side repose curve.

Simulation repose test

A simulated repose angle test replicating the physical test was established in EDEM 2022, as shown in Figure 7a. Contact parameters between hazelnuts and the steel tube/plate were set according to values listed in Table 2. The lifting direction of the steel tube was aligned with the positive z-axis, at a velocity of 0.03 m/s. The total simulation time was set to 8 s, with a data-saving interval of 0.1 s, as only the final repose state was of interest. The simulation process and resulting particle pile formation are illustrated in Figures 7b–7d. For analysis, the post-processing view was set to the XZ plane, and particle color was rendered black. The final pile shape was processed using MATLAB, where edge detection and least squares fitting were performed to extract the slope values, as shown in Figure 7e.

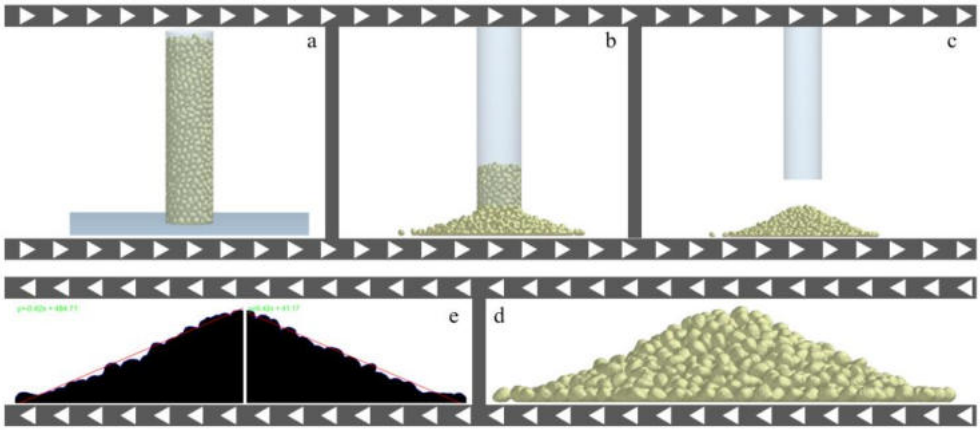


Fig. 7 - Simulated Repose Tests and Experimental Processing.

(a) Before simulated tests; (b) During simulated tests; (c) After simulated tests; (d) Hazelnuts stacking; (e) Repose angle measurement

The steepest climb test

The steepest ascent method was employed to quickly approach the optimal range of these significant factors. The experimental design is shown in Table 1.

Table 1

Design of the steepest climb test

NO.	Test factors		
	X_1	X_2	X_3
1	0.1	0.1	0.01
2	0.2	0.2	0.02
3	0.3	0.3	0.03
4	0.4	0.4	0.04
5	0.5	0.5	0.05

Central composite design with quadratic orthogonal rotations

Based on the optimal factor ranges determined from the steepest ascent test, three levels of restitution coefficient, static friction coefficient, and rolling friction coefficient were selected for a central composite design with quadratic orthogonal rotation. A response surface model was then established using the experimental results, and a regression equation was derived. This equation was used to predict the optimal combination of contact parameters between hazelnuts that best approximates the actual repose angle, enabling improved accuracy in the discrete element simulation.

RESULTS

Results of the steepest climb test

The results of the steepest ascent test are presented in Figure 8. As the restitution coefficient, static friction coefficient, and rolling friction coefficient increased, the relative error between simulated and physical repose angles initially decreased and then increased. Test Group No. 2 produced the lowest relative error of 2.61% and was therefore selected as the zero level for the subsequent response surface design. The optimal range of factor levels was determined to lie between those of Group No. 1 and Group No. 3, providing the basis for refined parameter optimization.

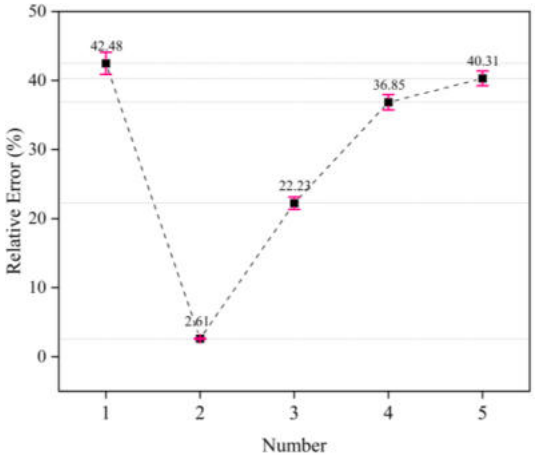


Fig. 8 – Results of the steepest climb test

Results of the quadratic orthogonal rotating combination test

The results and analysis of variance for the three-factor, five-level orthogonal rotating combination test are presented in Table 2 and Table 3.

Table 2

Test result of the central composite test

No.	X_1	X_2	X_3	Relative Error (Y)
1	-1	-1	-1	48.10
2	1	-1	-1	51.65
3	-1	1	-1	3.63
4	1	1	-1	3.55
5	-1	-1	1	24.16
6	1	-1	1	20.78
7	-1	1	1	1.54
8	1	1	1	19.37
9	-1.682	0	0	2.52
10	1.682	0	0	0.51
11	0	-1.682	0	64.73
12	0	1.682	0	0.51
13	0	0	-1.682	26.38
14	0	0	1.682	19.37
15	0	0	0	0.51
16	0	0	0	11.03
17	0	0	0	0.51
18	0	0	0	2.61
19	0	0	0	0.56
20	0	0	0	0.51

The data in Table 4 were analyzed using Design-Expert 13.0. A regression model was established to describe the relative error of repose angle as a function of the restitution coefficient (X_1), static friction coefficient (X_2), and rolling friction coefficient (X_3) between hazelnuts. The fitted regression equation is shown in Equation (13).

$$Y = 2.57 + 1.06X_1 - 16.45X_2 - 3.87X_3 + 2.20X_1X_2 + 1.37X_1X_3 + 8.57X_2X_3 - 0.05X_1^2 + 10.94X_2^2 + 7.50X_3^2 \quad (13)$$

The ANOVA results for the regression model (Equation 13) are summarized in Table 5. A P-value < 0.0001 indicates the model is highly significant, while the lack of fit (P = 0.1813) is not significant, confirming the model's adequacy. The coefficient of determination (R^2) is 0.9586, indicating strong predictive reliability. Among the factors, the static friction coefficient (X_2) has a highly significant effect, followed by the rolling friction coefficient (X_3), while the restitution coefficient (X_1) shows no significant impact. Only the interaction between X_2X_3 is statistically significant. The response surface of X_2X_3 (Figure 10) shows that as both static and rolling friction coefficients increase, the relative error first decreases and then rises. The steeper, denser contours of X_2 indicate its greater influence, consistent with the ANOVA findings. The factors affecting repose angle error, in order of significance, are X_2, X_3, and X_1 *(Zhuang et al, 2023)*.

Table 3

ANOVA for quadratic equation model

Parameters	Sum of Squares	Df	Mean square	F value	P value
Modal	6922.69	9	769.19	25.74	<0.0001**
X_1	15.48	1	15.48	0.5181	0.4882
X_2	3693.92	1	3693.92	123.63	<0.0001**
X_3	204.67	1	204.67	6.85	0.0257*
X_1X_2	38.63	1	38.63	1.29	0.2820
X_1X_3	15.07	1	15.07	0.5044	0.4938
X_2X_3	587.22	1	587.22	19.65	0.0013**
X_1^2	0.0413	1	0.0413	0.0014	0.9711
X_2^2	1725.98	1	1725.98	57.76	<0.0001*
X_3^2	810.28	1	810.28	27.12	0.0004**
Residual	298.79	10	29.88		
Lack of Fit	210.47	5	42.09	2.38	0.1813
Pure Error	88.33	5	17.67		
Cor Total	7221.49	19			

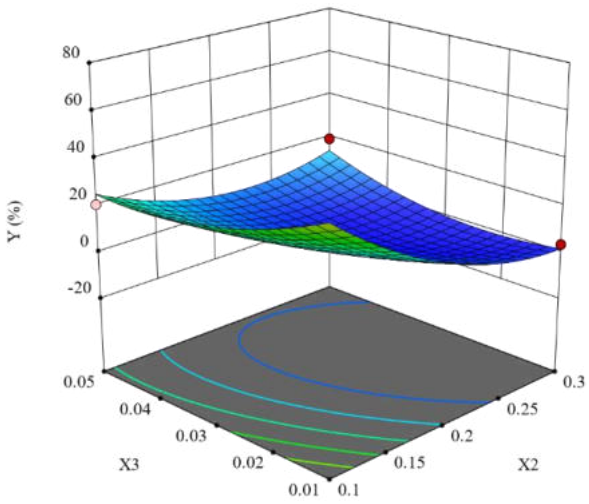


Fig. 10 - Effect of static friction coefficient and rolling friction coefficient on the relative error

Parameter optimization

Based on the experimental data and regression equation, the optimization module in Design-Expert 13.0 was used to minimize the relative error (Y). The software identified the optimal combination of significant factors that resulted in the lowest predicted error, providing the best-fit contact parameters for accurate repose angle simulation.

The objective function and constraints are as following equation (14):

$$\begin{cases} \min Y(X_1, X_2, X_3) \\ \begin{cases} 0.1 \le X_1 \le 0.3 \\ 0.1 \le X_2 \le 0.3 \\ 0.01 \le X_3 \le 0.05 \end{cases} \end{cases} \quad (14)$$

The optimized contact parameters between hazelnuts were: restitution coefficient 0.11, static friction coefficient 0.21, and rolling friction coefficient 0.04. These values were applied in EDEM, and 10 simulated repose angle trials were conducted. The average simulated repose angle was 23.82°, with a relative error of only 1.84 ± 0.009%. This confirms that the optimized parameter set is highly accurate and suitable for use in subsequent discrete element simulations.

CONCLUSIONS

1. The fundamental physical properties of hazelnuts—including size, density, Young's modulus, and Poisson's ratio—were measured through physical testing. Contact parameters between hazelnuts and steel were obtained and calibrated using a combination of experiments and simulations. A 3D model was built via scanning, and a DEM model was generated using the automatic filling method. The calibrated parameters were: restitution coefficient 0.31, static friction 0.39, and rolling friction 0.04.

2. Contact parameters between hazelnuts were calibrated using combined physical and simulated repose tests. Image analysis in MATLAB enabled accurate measurement of the repose angle. A steepest ascent test identified optimal parameter ranges, followed by response surface optimization. The final calibrated values were 0.11 (restitution), 0.21 (static friction), and 0.04 (rolling friction), yielding a relative error of 1.84 ± 0.009% in validation tests—demonstrating high model accuracy.

3. The calibrated contact parameters provide a reliable foundation for DEM-based design and optimization of hazelnut harvesting, handling, and cleaning machinery, helping reduce development costs and improve efficiency.

ACKNOWLEDGEMENT

This work was supported financially by the Natural Science Foundation of Jilin Province (No. 0250102113JC)

REFERENCES

[1] Bonisoil, E.; Delprete, C.; Sesana, R.; Tamburro, A.; Tornincasa, S. (2015). Testing and Simulation of the three point bending anisotropic behaviour of hazelnut shells. *Biosyst. Eng.,* Vol.129, pp: 134–141;

[2] Chen, X. Y., Wang, X. Z., Bai, J., Fang, W. Q., Hong, T. Y., Zang, N., Wang, G. L. (2024). Virtual parameter calibration of pod pepper seeds based on discrete element simulation. *Heliyon*, Vol.10, Issue 11, e31686

[3] Delprete, C.; Sesana, R. (2014). Mechanical characterization of kernel and shell of hazelnuts: Proposal of an experimental procedure. *J. Food Eng.*, Vol.124, pp: 28–34;

[4] Fan, R., Cui, Q. L., Zhang, Y. Q., Lu, Q. (2021). Analysis and calibration of parameters of buckwheat grain based on the repose experiment. *INMATEH-Agricultural Engineering*, Vol.64, Issue 2, pp: 467-476

[5] Gu, Z. Y., Cao, M. C. (2024). Analysis of unstable block by discrete element method during blasting excavation of fractured rock mass in underground mine. *Heliyon,* Vol.9, Issue 11, e22558

[6] Guo, Y., Chen, Q. S., Xia, Y. D., Westover, T., Eksioglu, S., Roni, M. (2020). Discrete element modeling of switchgrass particles under compression and rotational shear. *Biomass and Bioenergy*, Vol.141, 105649

[7] He, T., Liu, K., Zhang, R., Ren, G. Y., Liu, Z. H., (2024). Development of high efficiency hazelnut shell breaking machine. *Food & Machinery*, Vol. 40, Issue 5, pp: 88-95;

[8] Kruk, M., Ponder, A., Horoszewicz, J., Poplawski, D., Krol, K., Leszczynska, J., Jaworska, D., Trzaskowska, M. (2024). By-product hazelnut seed skin characteristics and properties in terms of use in food processing and human nutrition. *Scientific Reports*, Vol.14, Issue 1, 18835;

[9] Liu, J., Lu, T., Zheng, S., Tian, Y., Han, M., Tai, M., He, X., Li, H., Wang, D., Zhao, Z. (2025). Parameter Calibration Method for Discrete Element Simulation of Soil-Wheat Crop Residues in Saline-Alkali Coastal Land. *Agriculture*, Vol.15, Issue 2, 129;

[10] Li, Y. F., Zhou, W. Q., Ma, C. C., Feng, Z. H., Wang, J. W., Yi, S. J., Wang, S. (2024). Design and optimization of the seed conveying system for belt-type highspeed corn seed guiding device. *International Journal of Agricultural and Biological Engineering*, Vol.17, Issue 02, pp: 123-131;
[11] Mohammad, M., Mehari Z.T. (2024). Systematic Calibration and Validation Approach for Discrete element Method (DEM) Modeling of Corn under Varying Moisture Contents (MC). *J. ASABE*, Vol.67, Issue 2, pp: 259-274;
[12] Ren, D. Z., Yu, H. L., Zhang, R., Li, J. Q., Zhao, Y. B., Liu, F. B., Zhang, J. H., Wang, W. (2024). Topology Optimization Design and Modal Analysis of Hazelnut Picking and Sorting Machine. *Journal of Agricultural Mechanization Research*, Vol.46, Issue 05, pp: 19-25;
[13] Ren, D. Z., Yu, H. L., Zhang, R., Li, J. Q., Zhao, Y. B., Liu, F. B., Zhang, J. H., Wang, W. (2022). Research and experiments of hazelnut harvesting machine based on CFD-DEM analysis. *Agriculture*, Vol.12, Issue 12, 2115;
[14] Sun, K., Yu, J. Q., Liang, L. S., Wang, Y., Yan, D. X., Zhou, L., Yu, Y. J. (2022). A DEM-based general modelling method and experimental verification for wheat seeds. *Powder Technology*, Vol. 401, 117353;
[15] Ucgul, M., Saunders, C., Fielke, J. M. (2018). Comparison of the discrete element and finite element methods to model the interaction of soil and tool cutting edge. *Biosystems Engineering*, Vol.169, pp: 199-208;
[16] Wang, S., Yu, Z. H., Aorigele, Zhang, W. J. (2022). Study on the modeling method of sunflower seed particles based on the discrete element method. *Computers and Electronics in Agriculture*, Vol.198, 107012;
[17] Xu, B., Zhang, Y. Q., Cui, Q. L., Ye, S. B., Zhao, F. (2021). Construction of a discrete element model of buckwheat seeds and calibration of parameters. *INMATEH-Agricultural Engineering*, Vol.64, Issue 02, pp: 175-184;
[18] Xu, B., Zheng, D. C., Cui, Q. L. (2022). Experimental research on three-level vibrating screening of buckwheat based on discrete element method. *INMATEH-Agricultural Engineering*, Vol.68, Issue 03, pp: 191-200;
[19] Xu, T. Y., Yu, J. Q., Yu, Y. J., Wang, Y. (2018). A modelling and verification approach for soybean seed particles using the discrete element method. *Advanced Powder Technology*, Vol.29, Issue 12, pp: 3274-3290;
[20] Zhao, J. R., Wang, X. H., Lin, H., Lin, Z. (2023). A comprehensive review of nutrition, phytochemical profile, extraction, bioactivities and applications. *Food Chemistry*, Vol.413, 135576;
[21] Zhang, X. J., Wang, H. T., Wang, F. Y., Lian, Z. G. (2024). Parameter calibration of discrete element model for alfalfa seeds based on EDEM simulation experiments. *International Journal of Agricultural and Biological Engineering*, Vol.17, Issue 3, pp: 33-38;
[22] Zhang, Z. G., Zeng, C., Xing, Z. Y., Xu, P., Guo, Q. F., Shi, R. M., Wang, Y. Z. (2024). Discrete element modeling and parameter calibration of safflower biomechanical properties. *International Journal of Agricultural and Biological Engineering*, Vol.17, Issue 2, pp: 37-46;
[23] Zhuang, H. Y., Wang, X. L., Zhang, X. C., Cheng, X. P., Wei, Z. C. (2023). Discrete element-based design of key parameters for wheel rut tillage devices. *Engenharia Agricola*, Vol.43, Issue 3, e20230039;
[24] Zhao, J. W., Yu, J. Q., Sun, K., Wang, Y., Liang, L. S., Sun, Y. C., Zhou, L., Yu, Y. J. (2024). A discrete element method model and experimental verification for wheat root systems. *Biosystems Engineering*, Vol.244, pp: 146-165.

A STUDY ON THE INFLUENCING FACTORS OF CORN KERNEL COLLISION RESTITUTION COEFFICIENT BASED ON THE OBLIQUE IMPACT COLLISION THEORY

/

基于斜撞击碰撞理论的玉米籽粒碰撞恢复系数影响因素研究

Zhongqi HE[1)], Mingxu WANG*[1,2)], Ziyan ZHAO[1)], Yingxin XIE[1)], Mengfei LIU[1)]

[1)]College of Mechanical and Electrical Engineering, Henan University of Technology, Zhengzhou, Henan/China

[2)]Henan Key Laboratory of Grain & Oil Storage Building and Safety, Henan University of Technology, Henan/China

Tel: +86-18937087621; E-mail: wmx20032002@163.com

Corresponding author: Mingxu Wang

DOI: https://doi.org/10.35633/inmateh-76-72

Keywords: *oblique impact collision theory, corn kernels, rotation, restitution coefficient*

ABSTRACT

Corn kernels collide with the pipe wall during pneumatic conveying, which affects their quality. Based on the theory of oblique impact collision dynamics, this paper investigates the breakage of corn kernels at impact angles ranging from 10°~40° and impact velocities ranging from 6 ~ 28m/s. The results show that secondary collisions have a significant effect on the normal restitution coefficient. As the impact angle increases, all three restitution coefficients tend to increase. At impact angles of 40° and above, the normal and overall restitution coefficients are related to the initial velocity, while the tangential restitution coefficient is not. At impact angles of 30° and above, the normal restitution coefficient is smaller at the top and larger in the middle, and the tangential and overall restitution coefficients are independent of the collision location. The three restitution coefficients when the rotation direction is in the same plane are all smaller than those when rotation occurs perpendicular to the translational plane, with the normal restitution coefficient being most affected by the direction. When the impact angle is between 30°~40°, the tangential restitution coefficient of corn kernels increases with increasing rotational speed. When the impact angle is between 20°~40°, the normal restitution coefficient decreases with increasing rotational speed. When the impact angle is between 10°~40°, the overall restitution coefficient is independent of the rotational speed.

摘要

玉米籽粒在气力输送中会与管壁碰撞进而影响自身质量，本文基于斜撞击碰撞动力学理论，研究了 10°~40°撞击角度下玉米籽粒的破碎情况。结果表明：二次碰撞对法向恢复系数影响较大；随着碰撞角度增加，三种恢复系数均呈增大趋势；40°及以上时，法向及整体恢复系数与初速度相关，切向恢复系数与其无关；30°及以上时，法向恢复系数顶部小、腹部大，切向及整体恢复系数与碰撞部位无关；旋转方向在同一平面内的三个恢复系数均小于在垂直于平动面内发生旋转时的恢复系数，其中法向恢复系数受方向影响最大；30°~40°时，玉米籽粒切向恢复系数随转速增大而增大，20°~40°时，法向恢复系数随转速增大而减小，10°~40°时，整体恢复系数与转速无关。

INTRODUCTION

Particle collisions are widespread in the field of agricultural engineering and hold universal significance. The restitution coefficient, a crucial physical parameter, reflects the ability of particles to recover from deformation and the extent of energy loss.

Currently, dilute-phase pneumatic conveying is widely used for agricultural products, but it has problems such as impact damage to corn kernels (*Zhao et al., 2017*), and high breakage rates (*Wang et al., 2018*). Since grains generally have irregular shapes, the forces they experience during pneumatic conveying are uneven and change randomly, making collisions and breakage behaviors complex (*Yang et al., 2025*). Among various grains, corn is particularly susceptible to damage from collision-induced breakage (*Wang et al., 2024*). Therefore, this study focuses specifically on corn kernels.

During the pneumatic conveying phase, collisions between corn kernels and the pipe wall are inevitable. Extensive research has been conducted on the mechanical characteristics of the collision process. Li designed a drop impact test and found that the ability of corn kernels to withstand impact forces varies significantly depending on the impact location (*Li et al., 2009*). Zhao used discrete element simulation software to create an ellipsoidal rice kernel model to study the mechanical characteristics of the collision process (*Zhao et al., 2013*).

Ozturk experimentally analyzed the restitution coefficients of chickpea and pea seeds (*Ozturk et al., 2010*). Wang experimentally investigated the restitution coefficients of different shaped corn kernels at speeds of 2-4 m/s and impact angles of 30-90° (*Wang et al., 2015*). Chen used the free-fall method and inclined plane method, combined with discrete element simulation and benchmark analysis, to measure the restitution coefficients of spherical soybeans (*Chen et al., 2024*). Wang determined the restitution coefficients of wheat kernels under different influencing factors in a two-dimensional plane based on the principle of kinematic equations (*Wang et al., 2012*). Liu used a high-speed camera to measure and analyze the effects of different influencing factors on the restitution coefficients of sunflower seeds (*Liu et al., 2020*). Current studies on the restitution coefficients of materials mainly focus on experimental and simulation research without considering rotation and low-angle collisions. By approximating the research objects as spherical or ellipsoidal shapes and studying central collisions, the normal restitution coefficient is obtained by examining the ratio of the normal approach velocity to the separation velocity of the kernels before and after the collision (*Feng et al., 2017*). However, for pneumatic conveying, the normal restitution coefficient alone cannot fully describe the state before and after the collision when the impact angle is small (*Wang et al., 2015*). Especially for non-spherical particles like corn kernels, the rebound during low-angle collisions is highly random and accompanied by rotation. Therefore, using only the normal restitution coefficient to represent the state before and after the collision is inaccurate. The tangential restitution coefficient and the effect of rotation should be considered comprehensively.

Previous finite element studies on grains have often made extensive simplifications. However, the geometric characteristics of grains are important parameters, and excessive simplification can affect the accuracy of the solution. Therefore, this paper selects corn kernels with a constant moisture content as the research object. Based on a pneumatic high-speed collision testing platform for agricultural products, and combining the theory of oblique impact collision dynamics, this study comprehensively considers the effects of different collision locations, angles, velocities, and post-collision rotational speeds and directions on the restitution coefficient during low-angle collisions. The study solves for the effects of these factors on the tangential, normal, and overall restitution coefficients from a momentum–energy perspective, providing a reference for the research on the restitution coefficient of corn kernel collisions.

MATERIALS AND METHODS

Experimental materials and Methods

The corn kernel variety examined in this study is “Zhengdan 958”.To reduce the influence of shape differences on the collision test results, trapezoidal corn kernels with a thousand-kernel weight of 316.4 g, a bottom width of 8.5±0.5 mm, a top width of 6.3±0.4 mm, a height of 12±0.8 mm, and a thickness of 3.6±0.3 mm were selected as the objects for low-angle collision tests. The names of the kernel parts are shown in Figure 1. Four hundred plump kernels were selected, and the moisture content was measured to be 12.2%.

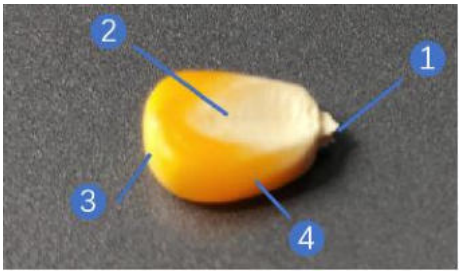


Fig. 1 - “Zhengdan 958”corn seed

1 - Top of the grain; 2 - Middle of the grain; 3 - Bottom of the grain; 4 - Side of the grain

Before the experiment, two flat plates with graduated coordinates were placed at a 90° angle on a horizontal table to simulate a three-dimensional coordinate system. After the collision, the corn kernels would move outside the collision plane. To obtain the velocity trajectory of the particles in the spatial coordinates, an interchangeable impact indentation capture paper was placed at the end of the collision path. By observing the indentations on the coordinate paper caused by the collisions of the corn kernels, the motion trajectory of the kernels outside the collision plane in space after the collision could be observed, as shown in Figure 2.

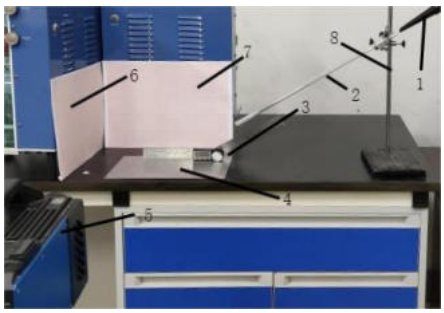


Fig. 2 - Pneumatic high-speed collision platform for agricultural products
1 - Air blower; 2 - Transparent tube; 3 - Digital protractor; 4 - Stainless steel plate; 5 - High speed camera; 6 - Dent catching paper; 7 - Graph paper; 8 - Fixing bracket

Figure 3 shows the entire process of a single corn kernel colliding with and rebounding from a wall under a high-speed camera. S1-S4 and S5-S8 are the four trajectories closest to the wall before and after the collision, respectively. Angles a and b represent the impact and rebound angles. To minimize deviation, the distances between three coordinates before and after the collision were selected and averaged to obtain the actual distance of the particle's motion. Dividing the spatial distance of the particle's motion by the time interval of the high-speed camera's capture yields the true velocity of the corn kernel. The impact angle a and the rebound angle b can be determined by recording the angle between the trajectory of the corn kernel and the wall.

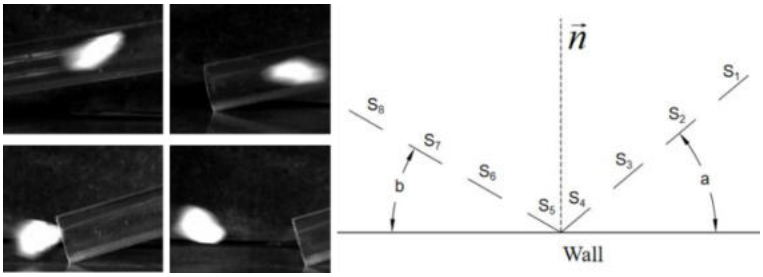


Fig. 3 - Diagram of the collision process of corn kernels

Experimental Principle and Design

Because corn kernels are non-spherical particles, different collision locations can make the post-collision trajectories of the particles very complex, with random rebounds accompanied by rotation (*Ma et al., 2020*). To measure the energy process of corn kernels during collisions, a three-dimensional spatial coordinate system is used to determine the restitution coefficient of corn kernel collisions. This approach takes into account the deformation of the corn kernel and the changes in kinetic energy due to rotation during the collision process.

This paper focuses on the changes in the motion state of corn seeds before and after collisions with the pipe wall during pneumatic conveying. The analysis is conducted based on the changes in tangential velocity, normal velocity, overall velocity, and angular velocity before and after the impact. A restitution coefficient model is employed to normalize the experimental results. Under low-angle inclined impacts, the effects of collisions on the tangential velocity of corn kernels are revealed. Therefore, this experiment needs to consider the tangential restitution coefficient, normal restitution coefficient, and overall restitution coefficient simultaneously. The characteristics of post-collision rebound in the oblique impact collision model established by Maw were used for formula derivation, and the velocity vectors during the collision process were analyzed (*Maw et al., 1976*).

Tangential restitution coefficient:

$$e_t = \frac{V_{nr}}{V_{ni}} = \frac{V_r sinb}{V_i sina} \quad (1)$$

Normal restitution coefficient:

$$e_n = \frac{V_{tr}}{V_{ti}} = \frac{V_r cosb}{V_i cosa} \quad (2)$$

In this context, V_i represents the impact velocity vector of the corn kernel, which is determined by the experimental setup and lies within the XOZ plane. V_r denotes the rebound velocity vector of the corn kernel. Given that corn kernels are non-spherical particles, even when colliding with a flat steel plate, irregular rebounds can still occur. V_{ti} and V_{ni} are the tangential and normal components of the impact velocity vector V_i, respectively, while V_{tr} and V_{ni} are the tangential and normal components of the rebound velocity vector V_r, respectively.

The elbow section is the region with the highest collision intensity in a dilute-phase pneumatic conveying pipeline, where particle-particle and particle-wall collisions are the main forms of breakage. Based on preliminary experiments, this paper investigates the breakage and motion states of collisions at angles ranging from 10 to 40°.

Two collision directions of corn kernels, top-first and bottom-first, were designed, and 80 trials were conducted for each angle. A second trial was used to ensure that the collision angle of each corn kernel deviated from the set angle by ±1°, ultimately obtaining valid experimental data for each of the four angles, consisting of 80 sets each. The speed and angle of the corn kernels before collision, the collision location of each kernel, and the rotational speed, rotational direction, displacement speed, and rebound angle of the corn kernels after collision were all documented. The experimental results were processed using fractal statistical principles, and the conditions for different collisions were summarized. The results were then subjected to fractal processing, and the Pearson correlation coefficient was calculated to draw conclusions (*Han et al., 2019*).

This paper employs air jet ejection to meet the requirement of high initial collision velocity. However, this method causes the post-collision velocity of corn kernels to be more influenced by the airflow than their actual rebound velocity. To address this issue, corn kernels were placed stationary near the collision site. The post-collision velocity of the initially stationary kernels was computed. By subtracting the velocity of the stationary kernels from that of the incident kernels, the corrected rebound velocity was obtained.

RESULTS

To address the issue that the force direction during collisions of non-spherical particles is not perpendicular, the overall and tangential restitution coefficients are introduced to assess the impact of the collision location on the restitution coefficient under different angles and initial velocities.

The impact of secondary collisions

It was observed that the probability of secondary collisions of corn kernels with the steel plate at four angles accounted for a high proportion of the total experiments and should be included in the restitution coefficient of small-angle collisions between corn kernels and the steel plate.

The essence of secondary collisions is that the rebound height of the corn kernel after the first collision is insufficient (the distance from the centroid to the next collision point does not exceed the rotational radius of the kernel). Secondary collisions manifest in two ways: The first is when the separation velocity of the corn kernel after the collision is small and the rotational velocity is large, causing the kernel to collide with the steel plate again due to rotation, during which the rotational velocity decreases and the separation velocity increases. The second scenario occurs when the corn kernel already has a relatively high initial velocity after the first collision. The secondary collision only changes the posture after rebounding (the path after rebounding, rotational state, etc.), and the impact on velocity is minimal.

Statistics show that the restitution coefficients during secondary collisions are smaller than those during primary collisions, but the differences are small: The deviation rates of the tangential, normal, and velocity restitution coefficients (calculated as the difference between the single-collision value and the combined value, divided by the combined value) are 0.21%, 0.98%, and 0.29%, respectively. Secondary collisions mainly involve the transformation of high rotational velocity into translational velocity, with the force direction primarily being normal, leading to the greatest impact on the normal restitution coefficient. Given that secondary collisions between corn kernels and the pipe wall are inevitable, the restitution coefficients of secondary collisions should be included in the overall consideration to derive a comprehensive collision restitution coefficient.

The impact of collision angle

This paper employs fractal statistical methods to summarize the patterns. The single-factor analysis indicates that under the condition of collision angles ≤40°, the tangential, normal, and velocity restitution coefficients all decrease as the collision angle increases.

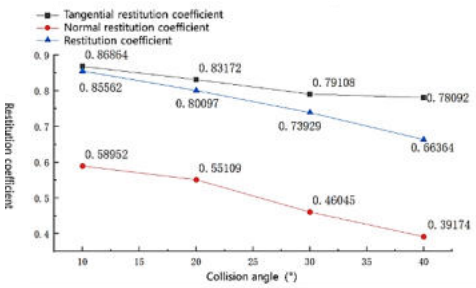


Fig. 4 - The Effect of Collision Angle on the Restitution Coefficient

By analyzing the intersection extended from three frames before and after the collision of corn kernels, it was found that there was no slip during the collision. When the collision angle is within the range of 10 - 40°, all three restitution coefficients decrease as the angle increases, with the tangential having the smallest rate of decrease and the normal having the largest rate of decrease. The reason is that as the collision angle increases, the elastic deformation of the corn kernel increases, leading to a decrease in the normal restitution coefficient. The reason for the decrease in the tangential restitution coefficient is that during the collision, there is a tangential frictional force that increases with the normal contact force, indicating that the angle has a smaller effect on the tangential restitution coefficient. The overall restitution coefficient decreases due to the decrease in both the normal and tangential restitution coefficients.

The impact of initial velocity

The tangential component of the velocity in this paper is much greater than the normal component within the 10° to 30° range. The Pearson correlation between the tangential restitution coefficient and the tangential component of the initial velocity was calculated for each of the four angles, as shown in Figure 5 and Table 1.

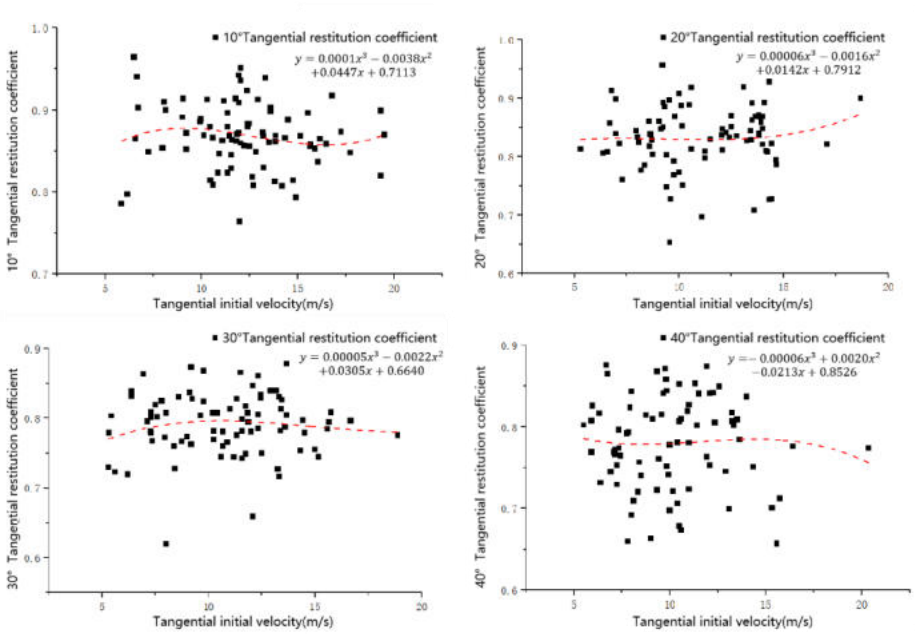


Fig. 5 - Distribution of tangential restitution coefficients at different angles

Table 1

Tangential restitution coefficient and the tangential component of the initial velocity

Collision angle	Significance level of correlation P	Degree of correlation
10	0.37224	Not correlated
20	0.64339	Not correlated
30	0.67643	Not correlated
40	0.96503	Not correlated

Based on the kinetic analysis, it can be concluded that in the case of low-angle oblique collisions, due to the small friction coefficient between the corn kernels and the steel plate and the relatively small normal impact force at low angles, according to equation (3), the effect of tangential friction can be neglected. This leads to the tangential restitution coefficient being independent of the tangential component of the initial velocity.

$$f = \mu\left(\frac{mV_r - mV_i}{\Delta t}\right) \quad (3)$$

By comparing the experimental results of the four groups of angles and analyzing the relationship between the normal restitution coefficient and the normal component of the initial velocity, it was found that at 10° and 20°, there is no definite relationship between the normal restitution coefficient of corn kernels and the normal component of the initial velocity.

At 30° and 40°, the normal restitution coefficient decreases with the increase of the normal initial velocity. The Pearson correlation between the normal restitution coefficient and the normal component of the initial velocity was calculated for the four angles, and the results are shown in Figure 6 and Table 2.

Table 2

The normal restitution coefficients and the normal components of the initial velocity for the four angles

Collision angle	Significance level of correlation P	Degree of correlation	Correlation coefficient R^2
10	0.99131	Not correlated	
20	0.11398	Not significant	
30	0.14945	Not significant	
40	0.00683	Significant	-0.30201 Weak correlation

In oblique collisions, corn kernels undergo eccentric collisions and rotation, resulting in a reduction of the normal contact force. At small angles, the normal component of the velocity is small, the normal contact force is small, and the primary effect is the generation of a torque that causes the kernel to rotate. At large angles, part of the energy loss is manifested as the contact force of normal elastic deformation, and at this time, the normal contact coefficient is significantly correlated with the normal component of the initial velocity. However, at angles of 30° and below, the normal restitution coefficient is not significantly correlated with the normal component of the initial velocity.

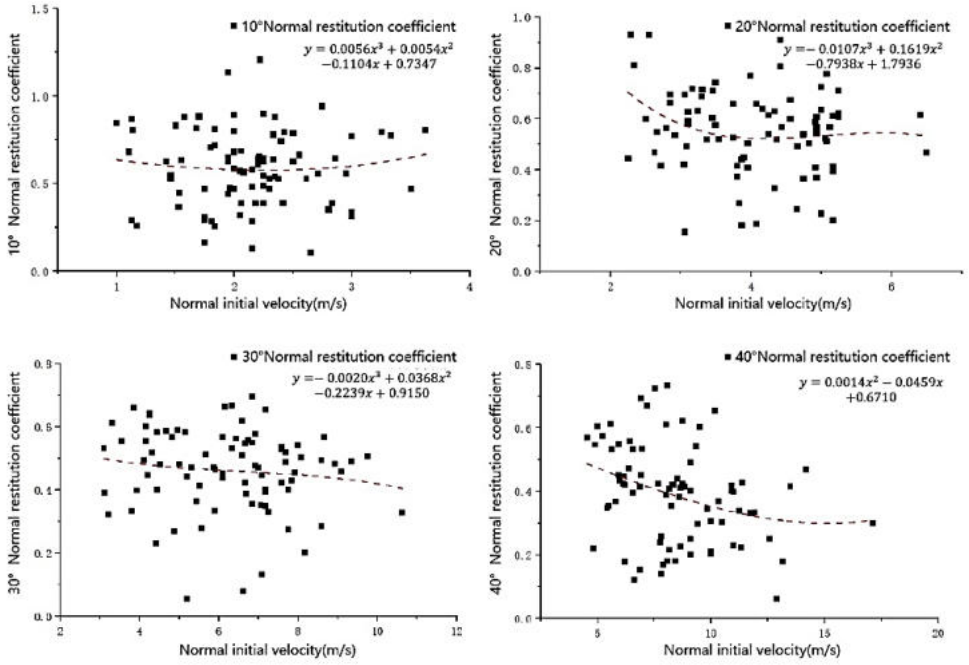


Fig. 6 - Distribution of normal restitution coefficients at different angles

The Pearson correlation between the overall restitution coefficient and the initial velocity was calculated for each of the four angles, as shown in Table 3. Based on the principles of kinematics, a significant correlation between the overall restitution coefficient and the initial velocity only appears when the collision angle is greater than or equal to 40°.

Table 3

The correlation between the overall restitution coefficient and the initial velocity for the four angles

Collision angle	Significance level of correlation P	Degree of correlation	Correlation coefficient r
10	0.41191	Not correlated	
20	0.8482	Not correlated	
30	0.79048	Not correlated	
40	0.07907	Significant	-0.20877 Weak correlation

The impact of collision location

The collision sites of corn kernels with the steel plate were divided into the head, ventral side, base, and side. The collision site at the moment of impact was recorded, and the restitution coefficients and deviations from the overall restitution coefficient at different sites and angles were statistically analyzed, as shown in Figure 7. Collisions at 10° and 20° were ignored in the analysis due to the small normal contact force and significant shape influence. The results showed that the normal restitution coefficient had the highest deviation rate and was most affected by the collision site. When the head collided, the normal restitution coefficient was lower than the overall value due to the soft and easily deformable pedicel. When the ventral side collided, the normal restitution coefficient was higher than the overall value because of the dense and hard endosperm tissue. When the side and base collided, the normal restitution coefficient was slightly higher than the overall value. The tangential restitution coefficient was greatly affected by friction and rotation, but since the friction coefficients were the same at all sites, the influence was relatively small when the angle was the same. The tangential restitution coefficient of the head was slightly lower than the overall tangential restitution coefficient, while that of the base was slightly higher. The overall restitution coefficient was less affected by the collision site.

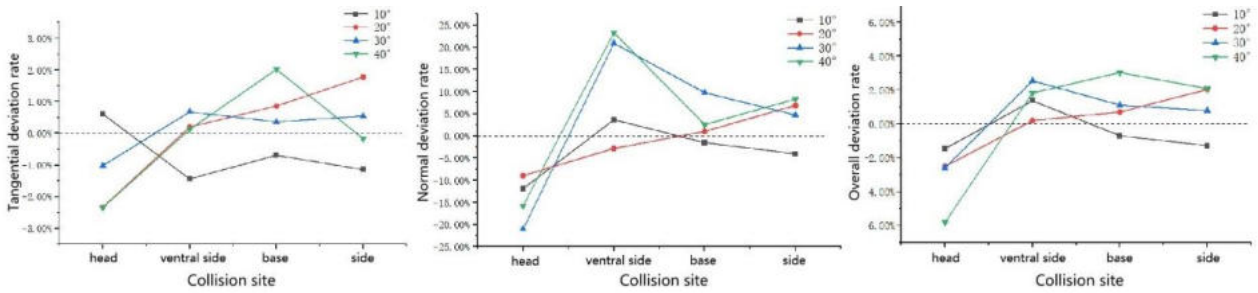


Fig. 7 - Overall restitution coefficient at different collision sites and angles

The impact of rotation after collision

In the experiment, 99.1% of the corn kernels rotated after collision. Therefore, the rotation direction and speed of the corn kernels after collision were recorded. The experimental results show that the rotation state of the corn kernels after collision is mainly related to the instantaneous posture, position, angle of the collision, and the angle between the axis through the center of mass of the kernel and the collision surface.

The kinetic energy of a rigid body in planar motion is equal to the sum of the translational kinetic energy of the center of mass and the rotational kinetic energy about the center of mass.

$$T = 1/2mv_c^2 + 1/2J_C\omega^2 \quad (4)$$

The shape of the corn kernel is approximately a trapezoidal prism, which has geometrical symmetry. Taking the x, y, and z axes through the center of mass (point o), the trapezoidal prism can rotate about the x, y, and z axes. The top edge of the trapezoidal prism is set at 6.5 mm, the bottom edge at 9.5 mm, the height at 12 mm, and the thickness at 3 mm. Using the mass projection method, the moment of inertia about the z-axis is calculated as $J_z = 9.04\times10^{-13} kg\cdot m^2$, about the y-axis as $J_y = 1.76\times10^{-12} kg\cdot m^2$, and about the x-axis as $J_x = 1.51\times10^{-12} kg\cdot m^2$. The average kinetic energy due to rotation is 2.85×10^{-5} J, and the average kinetic energy due to translation is 1.6×10^{-2} J. The ratio of rotation to translation is 561. It can be concluded that for high-speed oblique collisions of corn kernels, the kinetic energy generated by rotation can be neglected, and the kinetic energy due to translation is the dominant kinetic energy.

The impact of rotation direction

Observations revealed that after collision, corn kernels would rotate in two different directions due to the varying collision sites, as shown in Figure 8. One type of rotation occurs within the xoz plane, around an axis parallel to the y-axis, termed parallel-plane rotation (A). The other type takes place within the zoy plane, around an axis parallel to the x-axis, known as perpendicular-plane rotation (B).

Statistics indicated that, apart from the 30° angle where the proportion of co-directional rotation accounted for 53% of the total, the proportion of co-directional rotation at other angles was 33±2%. When rotating in the same direction, all three restitution coefficients were lower than when rotating in the opposite direction.

However, the ratios of the differences between the restitution coefficients in different directions and the combined restitution coefficients varied. Figure 9 shows the ratio of the difference between the restitution coefficients in the perpendicular plane and those in the parallel plane to the combined restitution coefficient. It can be seen that the tangential restitution coefficient is least affected by the rotation direction, while the normal restitution coefficient is most affected. The fluctuation in the combined normal restitution coefficient caused by counter-directional and co-directional rotations reaches 8.95%. Since all three restitution coefficients follow the order of $40° > 10° > 30° > 20°$, it is concluded that the effect of rotation direction on the restitution coefficients is independent of the angle. The reason why the restitution coefficients are lower during perpendicular-plane rotation than during parallel-plane rotation remains to be investigated. The conclusion is that during low-angle oblique collisions, the tangential, normal, and overall restitution coefficients for parallel-plane rotation are all lower than those for perpendicular-plane rotation, with the normal restitution coefficient being most affected by the rotation direction.

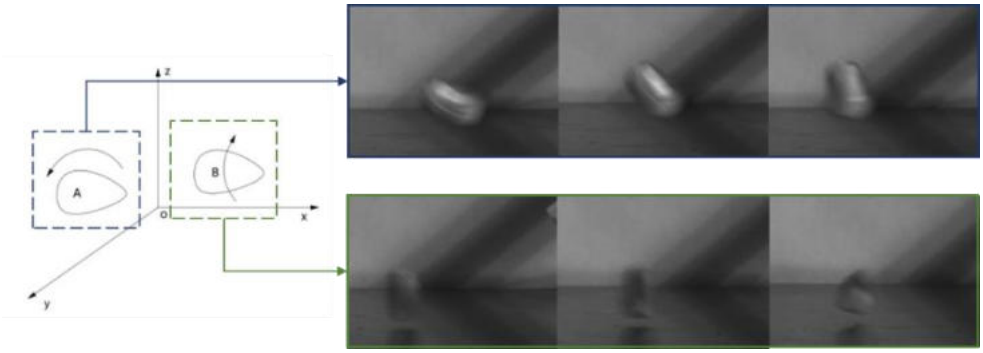


Fig. 8 - Actual images of different rotation directions

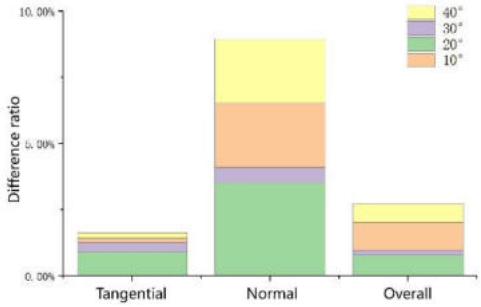


Fig. 9 - The ratio of the difference between the two directions of rotation to the combined value

The impact of rotational speed

As shown in Figure 10, when the collision angle increases, the rotational speed of the corn kernel after collision accelerates, leading to energy transfer. Although the kinetic energy generated by rotation is much smaller than that by translation, the influence of rotation on energy transfer grows as the rotational speed increases.

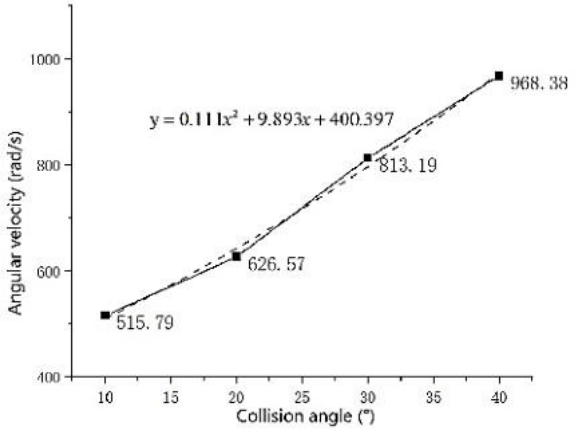


Fig. 10 - Relationship between rotational speed and collision angle

The correlation between the restitution coefficients at each of the four angles and the rotational speed was statistically calculated, as shown in Table 4.

Table 4

The restitution coefficients at each of the four angles and rotational speed

Restitution coefficient	Collision angle	Significance level of correlation P	Degree of correlation	Correlation coefficient r
Tangential	10	0.36051	Not correlated	
	20	0.16958	Not correlated	
	30	0.10069	Relatively significant	0.18143 Extremely weak correlation
	40	0.00236	Significant	0.33537 Weak correlation
Normal	10	0.55983	Not correlated	
	20	0.0194	Significant	-0.28293 Weak correlation
	30	0.0003	Significant	-0.4181 Moderate correlation
	40	0.0001	Significant	-0.4381 Moderate correlation
Overall	10	0.3415	Not correlated	
	20	0.1607	Not correlated	
	30	0.7538	Not correlated	
	40	0.9287	Not correlated	

That is, within the range of 30°~40°, the greater the rotational speed, the greater the normal restitution coefficient, while within the range of 20°~40°, the greater the rotational speed, the smaller the normal restitution coefficient, as shown in Figure 11, which illustrates the relationship between the normal restitution coefficient at 30° and the angular velocity. Since the tangential restitution coefficient increases with increasing rotational speed, while the normal restitution coefficient decreases with increasing rotational speed, there is no correlation between the overall velocity restitution coefficient and the rotational speed.

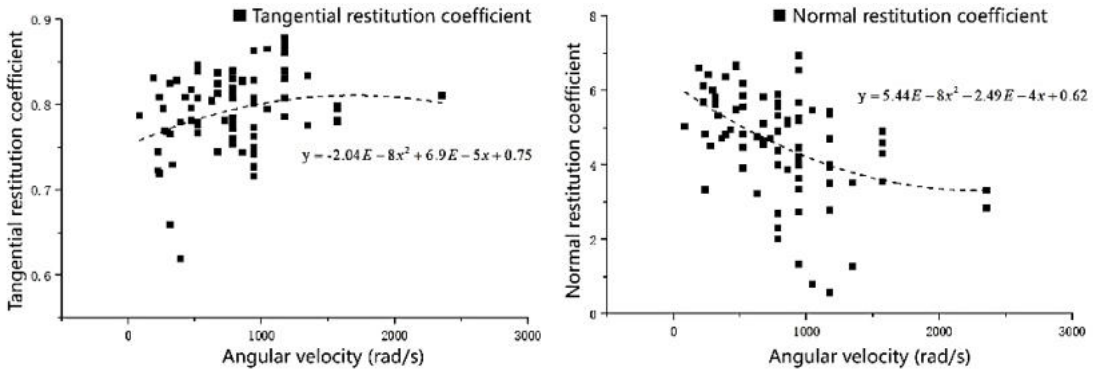


Fig. 11 - Relationship between coefficient of restitution and angular velocity at 30° collision angle

Simulation analysis

The impact analysis was conducted in ANSYS Workbench 2021 R1 using the explicit dynamics solver LS-DYNA. Following the LS-DYNA Material Selection Manual, the maize kernel was modeled as an elastic-plastic material with a density of 1120 kg/m3, an elastic modulus of 246.72 MPa, a Poisson's ratio of 0.32, and a yield strength of 37 MPa. The initial velocity of the particles was set at 21 m/s, and the collision angles were approximately 10° and 40°. An oblique impact test was conducted by filling the acceleration tube with corn kernels to obtain the results.

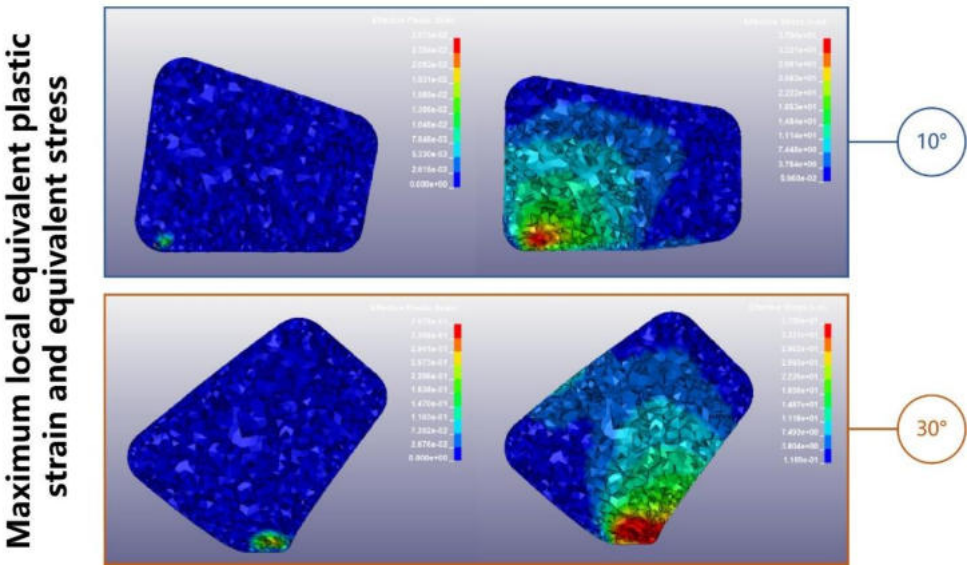


Fig. 12 - Simulation at collision angles of 10° and 30°

As can be seen from Figure 12, the distribution of the maximum equivalent plastic strain is consistent with that of the corresponding equivalent stress distribution, both being concentrated on the inner side of the collision point. The combined analysis indicates that this is due to the superposition of the reaction force from the steel plate on the corn kernel and the inertia of the corn kernel itself, resulting in a concentrated compressive stress at this location. It was found that both the maximum local equivalent plastic strain and the equivalent stress increase with the increase of the collision angle, which verifies the conclusion that the restitution coefficient decreases with the increase of the collision angle.

CONCLUSIONS

1）All three restitution coefficients decrease with increasing collision angle, with the normal coefficient being more affected by the angle than the tangential coefficient.

2）Secondary collisions mainly affect the normal restitution coefficient and should be included in the comprehensive consideration of the collision restitution coefficient.

3）The tangential restitution coefficient is independent of the tangential component of the initial velocity. The normal and overall restitution coefficients only decrease with increasing velocity when the angle is greater than or equal to 40°.

4）The collision location significantly impacts the normal restitution coefficient. When the angle is greater than or equal to 30°, the normal restitution coefficient is lower than the average value for top collisions and higher for abdominal collisions. The tangential and overall coefficients are less affected by the collision location.

5）The tangential, normal, and overall restitution coefficients are all lower for parallel-plane rotation than for perpendicular-plane rotation, with the normal restitution coefficient being most affected by the rotation direction. When the collision angle is between 30° and 40°, the tangential restitution coefficient tends to increase with increasing rotational speed. When the angle is between 20° and 40°, the normal restitution coefficient decreases with increasing rotational speed. Within the range of 10° to 40°, the overall restitution coefficient is independent of the rotational speed.

ACKNOWLEDGEMENT

This research was supported by the “Opening subject of Henan key laboratory of grain and oil storage construction and safety” (No.2021KF-B02), the “Henan Provincial Science and Technology Research Project” (No. 232103810084) and the “Science and Technology Key Research Program of Henan Provincial Department of Education” (No.24A460004).

REFERENCES

[1] Chen G.W., Li F.X., Qu F.Y., & Zhang C.J., (2024). Parameter calibration and experiment of discrete element simulation of spherical-like soybean based on DEM. *INMATEH Agricultural Engineering*, Vol.74, no.3, pp. 303-315, Bucharest/Romania. https://doi.org/10.35633/inmateh-74-26

[2] Feng B., Sun W., Shi L.R., Sun B.G., & Zhang T., (2017). Determination of restitution coefficient of potato tubers collision in harvest and analysis of its influence factors (收获期马铃薯块茎碰撞恢复系数测定与影响因素分析). *Transactions of the Chinese Society of Agricultural Engineering (Transactions of the CSAE)*, Vol. 33, no.13, pp. 50-57, Beijing/China.

[3] Han S., Han J.Z., Zhao X., Wang X.X., & Fan L.H., (2019). Pearson correlation coefficient and application of distance weight improvement (距离权重改进的 Pearson 相关系数及应用). *Oil Geophysical Prospecting*, Vol. 54, no.6, pp. 1363-1370, Hebei/China.

[4] Li X.P., Ma F.L., & Gao L.X., (2009). Drop impact test of corn seeds (玉米种子的跌落式冲击试验). *Transactions of the Chinese Society of Agricultural Engineering (Transactions of the CSAE)*, Vol. 25, no.1, pp. 113-116, Beijing/China.

[5] Liu Y., Zong W.Y., Ma L.N., Huang X.M., & Li M., (2020). Determination of three-dimensional collision restitution coefficient of oil sunflower seeds by high-speed photography technology (采用高速摄影技术测定油葵籽粒三维碰撞恢复系数). *Transactions of the Chinese Society of Agricultural Engineering (Transactions of the CSAE)*, Vol. 36, no.4, pp. 44-53, Beijing/China.

[6] Ma S.L., Zhao Z.H., Yan C., & Chen W., (2020). Simulation research on the rebound characteristics of sand and dust on typical metal walls (砂尘在典型金属壁面上的反弹特性仿真研究). *Journal of Nanjing University of Aeronautics and Astronautics*, Vol. 52, no.1, pp. 142-149, Jiangsu/China.

[7] Maw N., Barber J.R., & Fawcett J.N., (1976). The oblique impact of elastic spheres. *Wear*, Vol. 38, no.1, pp. 101-114, Netherlands.

[8] Niu J.J., Wang S.F., & Li P.F., (2018). Experimental study on the rebound distribution characteristics of non-spherical particles (非球形粒子反弹分布特性试验探究). *Journal of Propulsion Technology*, Vol. 39, no.3, pp. 638-644, Beijing/China.

[9] Ozturk I., Kara M., Uygan F., & Kalkan, F., (2010). Restitution coefficient of chick pea and lentil seeds. *International Agrophysics*, Vol. 24, no.2, pp. 209-211, Warsaw/Poland.

[10] Wang B., Wang J., & Du D.D., (2018). Finite element analysis of the dynamic process of corn kernel collision damage based on Hyper-Mesh and LS-DYNA (基于 HyperMesh 和 LS-DYNA 的玉米籽粒碰撞损伤动态过程的有限元分析). *Journal of Zhejiang University (Agriculture and Life Sciences)*, Vol. 44, no.4, pp. 465-475, Zhejiang/China.

[11] Wang C.J., Li Y.M., Ma L.Z., & Ma Z., (2012). Experimental study on measurement of restitution coefficient of wheat seeds in collision models (小麦籽粒碰撞模型中恢复系数的测定). *Transactions of the Chinese Society of Agricultural Engineering*, Vol. 28, no.11, pp. 274-278, Beijing/China.

[12] Wang L.J., Zhou W.X., Ding Z.J., Li X.X., & Zhang C.G., (2015). Experimental determination of parameter effects on the coefficient of restitution of differently shaped maize in three-dimensions. *Powder Technology*, Vol. 284, pp. 187–194, Switzerland.

[13] Wang M.X., Ouyang J.F., Zhao Z.Y., & Wu R.Z., (2024). Research on the anti-crushing mechanism of corn grain pneumatic conveying process under the influence of multi-parameter coupling. *INMATEH Agricultural Engineering*, Vol.72, no.1, pp. 87-95, Bucharest/Romania. https://doi.org/10.35633/inmateh-72-08

[14] Yang L., Wang L., Zhang Y.Y., Li Y.P., & Xu X.M., (2025). Research on the Flow Field Characteristics of Pneumatic Conveying of Bulk Grain in a Cyclone Pipeline (散粮管道旋流气力输送流场特性研究). *Chinese Journal of Agricultural Mechanization*, Vol. 46, no.1, pp. 99-104, Jiangsu/China.

[15] Zhao Z., Li Y.M., Chen Y., Liang Z.W., & Liu L.X., (2013). Research on the mechanical properties of rice grain collision (水稻籽粒碰撞力学特性研究). *Transactions of the Chinese Society for Agricultural Machinery*, Vol. 44, no.6, pp. 88-92, Beijing/China.

[16] Zhou J.W., Liu Y., Du C.L., & Liu S.Y., (2017). Effect of the particle shape and swirling intensity on the breakage of lump coal particle in pneumatic conveying. *Powder Technology*, Vol. 317, pp. 438-448, Switzerland.

A LIGHTWEIGHT WEED IDENTIFICATION METHOD FOR CHINESE CABBAGE FIELDS BASED ON THE IMPROVED YOLOv11

基于改进 YOLOv11 的轻量化白菜地杂草识别方法

Shunshun JI[1)], Jiajun SUN[1)], Chao ZHANG[1,*)]
[1)] College of Information Science and Engineering, Shandong Agricultural University, TaiAn, Shandong/China
Tel: +86-15621550101; E-mail: zhangch@sdau.edu.cn
DOI: https://doi.org/10.35633/inmateh-76-73

Keywords: *YOLO-LMSW, Object detection, Weed recognition, Lightweight*

ABSTRACT

Accurate and real-time weed identification was a key technology for ensuring the efficient operation of field weeding robots. It played a vital role in reducing pesticide usage, minimizing environmental pollution, and protecting the agricultural ecosystem. In response to these demands, this paper proposed a lightweight and high-precision weed recognition method, YOLO-LMSW, tailored for Chinese cabbage field scenarios. Firstly, a lightweight multi-scale convolutional module (LMSConv) was designed, upon which the LMSC3k2 structure was constructed to reduce computational complexity and enhance multi-scale feature extraction capabilities. In terms of network architecture, a lightweight backbone network, LMSNet, was built to significantly reduce model parameters while maintaining detection accuracy. Additionally, a detection head, LMSHead, was designed to further optimize the model structure. To improve localization accuracy and convergence speed, the Wise-IoU (WIoU) loss function was introduced. Experimental results demonstrated that, compared to YOLOv11n, YOLO-LMSW achieved improvements of 1.2%, 1.0%, and 0.6% in precision, recall, and mAP50 respectively, while reducing the Params and FLOPs by 34.6% and 36.5%, respectively. Furthermore, the model was deployed on a Jetson Orin Nano (4GB) embedded device, where it achieved an average inference time of 117 ms per image. These results demonstrated its application potential in the actual deployment of field weeding robots.

摘要

精准且实时的杂草识别是保障田间除草机器人高效运行的关键技术，对于减少农药施用、降低环境污染以及保护农业生态环境具有重要意义。针对上述需求，本文提出了一种适用于白菜地场景的轻量化高精度杂草识别方法 YOLO-LMSW。本方法首先设计了一种轻量化多尺度卷积模块（LMSConv），并在此基础上构建了 LMSC3k2，用以降低计算复杂度并增强多尺度特征提取能力。在网络架构方面，构建了轻量化主干网络 LMSNet，以在保持检测精度的同时显著减少模型参数量。此外，设计了检测头 LMSHead，进一步优化模型结构。为提升定位精度与收敛速度，引入了 Wise-IoU（WIoU）作为损失函数。试验结果表明，相较于 YOLOv11n，YOLO-LMSW 在精确率、召回率与 mAP50 上分别提升了 1.2%、1.0%和 0.6%，参数量与每秒浮点运算数分别减少了 34.6%和 36.5%。此外，该模型被部署于 Jetson Orin Nano（4GB）嵌入式设备上，单张图像的平均推理时间为 117 毫秒。这些结果展示了其在田间除草机器人实际部署中的应用潜力。

INTRODUCTION

Chinese cabbage was an essential component of the daily diet and held a significant position in the agricultural industry *(Hasan et al., 2023)*. However, the presence of weeds during its growth period severely affected both yield and quality *(Khan et al., 2021; Xiang et al., 2024)*. Weeds demonstrated high resilience and adaptability to agricultural environments. Their root systems were often more developed than those of crops, allowing them to compete more effectively for nutrients *(Darbyshire et al., 2024)*. Moreover, weeds reproduced rapidly, and without timely intervention, could cause substantial yield losses. Manual weeding was labor-intensive and inefficient, while chemical herbicides introduced harmful residues, making them unsuitable for the production of organic vegetables. Furthermore, chemical usage contributed to environmental pollution. As a result, achieving green, efficient, and intelligent weeding became a critical need *(Praveenraj et al., 2024; Zhang et al., 2025)*. Computer vision-based automatic weed recognition provided accurate spatial information about weed distribution, enabling more precise and automated weeding operations.

At that time, researchers both domestically and internationally conducted extensive studies on weed recognition, encompassing traditional and deep learning-based approaches *(Chen et al., 2022)*. Traditional methods typically relied on color, shape, and texture features, which were extracted using conventional image processing techniques. These features were then fed into classical classifiers such as support vector machines (SVMs), achieving a certain degree of success *(Hua et al., 2022; Sabzi et al., 2020)*. However, such methods often suffered from poor robustness under complex field conditions. With the advancement of artificial intelligence, deep learning techniques were increasingly applied in the field of weed recognition *(Zhang et al., 2024)*. *Shang et al., (2022),* improved the Faster R-CNN algorithm by incorporating an enhanced double-threshold non-maximum suppression algorithm and employing transfer learning. The improved model achieved a precision of 96.58%, a recall of 94.82%, and an F1 score of 95.06%. *Cai et al., (2023),* proposed a semi-supervised semantic segmentation network for weed recognition in pineapple fields and evaluated the model's effectiveness by placing the attention mechanism at different network layers.

The methods proposed by the aforementioned scholars demonstrated promising recognition performance; however, many of their models were overly complex, making them unsuitable for real-time operation on weeding robots. As a result, single-stage object detectors such as the YOLO series gained popularity due to their high inference speed and accuracy *(Yan et al., 2025)*. *Ji et al., (2024),* conducted lightweighting research on the YOLOv5 algorithm. In their study, the lightweight network PP-LCNet was employed to redesign the feature extraction backbone, thereby reducing the model's parameter count. They introduced the Ghost convolution module to lightweight the feature fusion network and incorporated a standardized attention module at the end of the fusion stage. As a result, the memory usage of the weed recognition model was reduced to 6.23 MB. *Shao et al., (2023),* proposed GTCBS-YOLOv5s, a lightweight model for weed recognition in rice fields. This model achieved both reduced complexity and improved accuracy, attaining an average precision of 91.1% and a recognition speed of 85.7 FPS. *Hu et al., (2024),* designed an efficient deep learning model for lettuce field weed detection and severity classification. They reduced the size of the YOLOv7 network using a scaling factor ($\tau = 0.5$), and further enhanced the model by integrating ECA and CA attention mechanisms. They also introduced ELAN-B3 and DownC modules to construct the Multimodule-YOLOv7-L framework, which was applied in a real-time mechanical–laser collaborative weeding robot.

Despite these advancements, three major challenges remained unresolved: (1) the high computational complexity of deep networks, (2) low detection accuracy for small or occluded weed targets, and (3) limited feasibility of real-time deployment on low-power embedded devices. To address these issues, this study proposed a lightweight weed detection algorithm for Chinese cabbage fields, named YOLO-LMSW, based on YOLOv11n. The proposed method introduced a novel lightweight backbone network (LMSNet) and a simplified detection head (LMSHead), which together significantly reduced computational cost while preserving high detection accuracy. In addition, the Wise-IoU (WIoU) loss function was employed to enhance localization performance and accelerate convergence. The effectiveness of each module was validated through ablation and comparison experiments. Furthermore, the model was deployed on a Jetson Orin Nano embedded device, where it achieved an average inference time of 117 ms per image, confirming its potential for real-time, field-level application in intelligent weeding systems.

MATERIALS AND METHODS

Data Collection and Preprocessing

The dataset used in this study was collected from Shandong Xiangniao Ecological Farm, located in Qihe County, Dezhou City, Shandong Province (116°46′E, 36°39′N), as shown in Figure 1(a). The images were captured using a Redmi K60 smartphone during the months of September and October. A total of 850 images were collected, covering Chinese cabbage and several representative weed species, mainly including Portulaca oleracea, Eleusine indica, Cirsium setosum, Chenopodium album, and Amaranthus retroflexus. The images were captured under diverse lighting conditions, including strong sunlight and shadows. The images were annotated using the open-source tool Labelme, with labels divided into two categories: crop and weed. Representative sample images were presented in Figure 1(b). The dataset was subsequently divided into training, validation, and test sets in a 7:2:1 ratio. Considering the limited number of original samples, which could have led to model overfitting, four methods were used to enhance the dataset: image flipping, rotation, noise addition, and brightness adjustment. After augmentation, the total number of images increased to 3400.

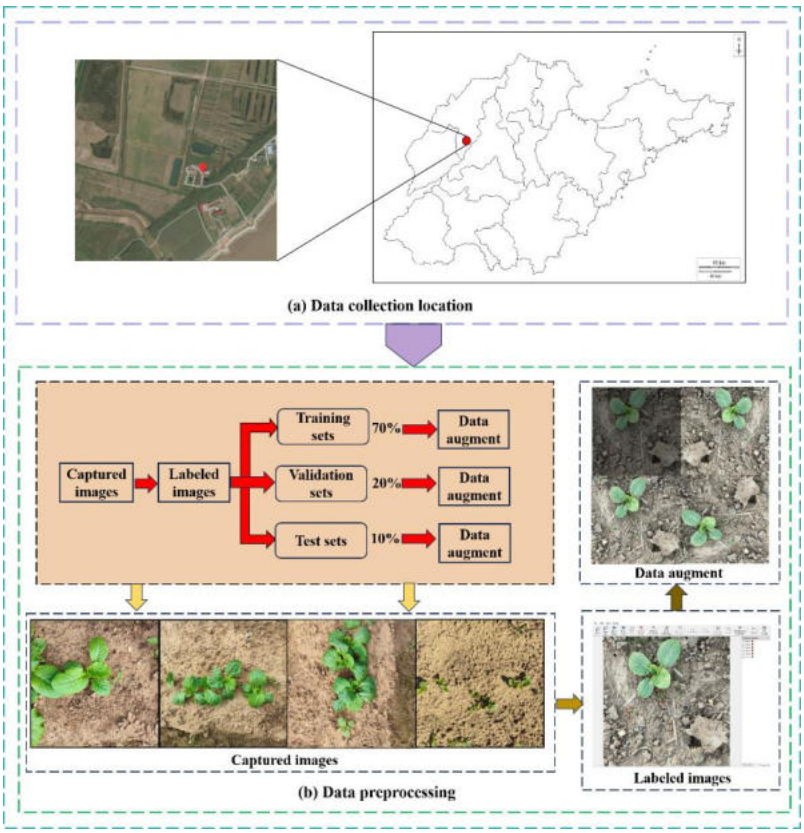


Fig. 1 - Data acquisition and preprocessing flow chart

YOLO-LMSW

YOLOv11 was one of the classic algorithms in the YOLO (You Only Look Once) series *(Redmon et al., 2016)*. As a single-stage object detection algorithm, it balanced accuracy and real-time performance. The overall architecture of YOLOv11 comprised three main components: the backbone, neck, and detection head. The backbone was responsible for extracting fundamental features from the input image, the neck facilitated multi-scale feature fusion, and the head performed the final tasks of object localization and classification. However, the conventional YOLOv11 model entailed a relatively large computational burden, making it difficult to meet the real-time inference requirements of embedded devices.

To address this, and with the aim of improving both detection accuracy and inference speed, this study proposed a lightweight optimization of YOLOv11n. Firstly, a lightweight convolutional module with multi-scale feature extraction capability, LMSConv, was designed, upon which the LMSC3k2 structure was built to form the lightweight backbone network, LMSNet. Subsequently, a lightweight detection head, LMSHead, was proposed to further reduce the model size while maintaining accuracy. Finally, the loss function was replaced with WIoU to enhance the model's regression performance and accelerate convergence during training. The final YOLO-LMSW network architecture, illustrated in Figure 2, achieved significantly improved real-time performance and deployment efficiency, while preserving high detection accuracy.

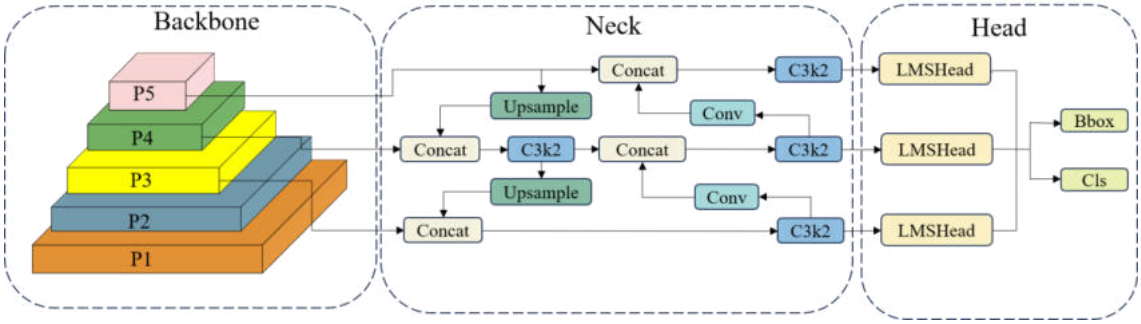


Fig. 2 - YOLO-LMSW Network Architecture

LMSNet

To address the high computational cost of the conventional YOLOv11 backbone and its performance bottlenecks on edge devices—particularly in the context of Chinese cabbage and weed targets that exhibited similar color and significant scale variation—this study proposed a structurally optimized, lightweight multi-scale backbone network, termed LMSNet. The architecture of LMSNet was illustrated in Figure 3.

Firstly, a convolutional module named LMSConv was designed, which combined lightweight characteristics with effective multi-scale feature extraction capabilities. This module replaced part of the Standard Convolution (SC) operations to reduce model complexity. Building upon LMSConv, the LMSC3k2 module was constructed to further enhance the representation of multi-scale features. In the LMSNet backbone, the P1 and P2 layers retained SC operations to ensure sufficient extraction of high-resolution features. In contrast, the P3, P4, and P5 layers incorporated LMSConv and LMSC3k2 modules to achieve more efficient multi-scale feature extraction while alleviating the computational burden. Additionally, the original SPPF and C2PSA modules from YOLOv11 were preserved to strengthen feature extraction and fusion capabilities, ensuring that the lightweight design did not compromise the robustness and accuracy of the model in weed recognition tasks.

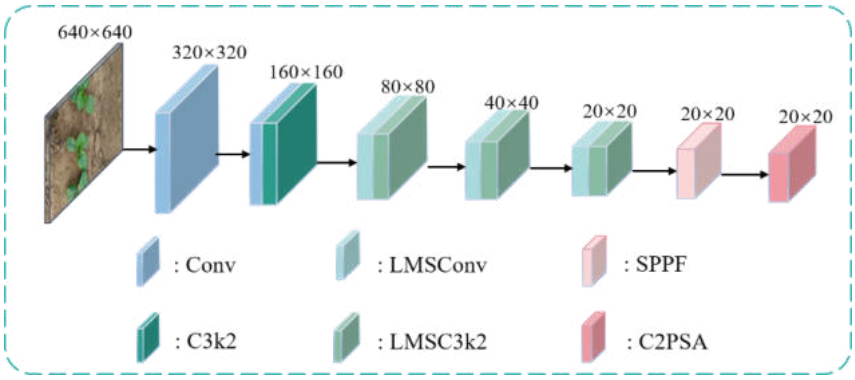


Fig. 3 - LMSNet structure

While SC performed well in feature extraction, their high computational complexity made them less suitable for lightweight models on edge devices. Moreover, due to the significant scale variation between Chinese cabbage and weeds in field environments, single-scale convolution operations struggled to effectively capture features of multi-scale targets.

To address these issues, this study drew inspiration from the ShuffleNet *(Ma et al., 2018)* and Xception *(Chollet, 2017)* architectures and proposed a lightweight multi-scale convolutional module, termed LMSConv. This module significantly reduced the number of parameters and computational load while maintaining model accuracy. Specifically, the input feature map was first split along the channel dimension into two parts. One part was processed with a 3×3 Depthwise Convolution (DWConv) to capture fine-grained details and enhance the perception of small-scale targets; the other part was processed with a 5×5 DWConv to obtain a larger receptive field, thereby improving contextual modelling of large-scale objects. As a typical lightweight convolution operator, DWConv substantially reduced the computational cost and number of parameters compared to SC, making it well-suited for mobile and embedded scenarios. The structure was illustrated in Figure 4(a). Following the application of different-scale DWConv, the resulting feature maps were concatenated along the channel dimension to restore the original number of channels. A 1×1 SC was then applied for channel fusion, enabling cross-channel multi-scale feature interaction and further enhancing feature representation. The complete structure of LMSConv was depicted in Figure 4(b).

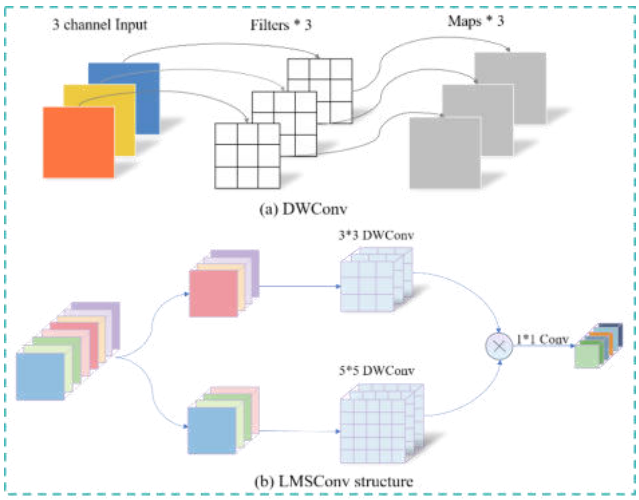


Fig. 4 - The structures of DWConv and LMSConv

Compared to SC, LMSConv significantly reduced computational complexity while enhancing feature representation through the introduction of multi-scale convolutional branches. To quantitatively assess the difference in computational cost between LMSConv and SC, the ratio of their FLOPs was calculated in this study.

$$r_{LMSConv} = \frac{C_{in} \times C_{out} \times H \times W \times 3 \times 3}{\frac{C_{in}}{2} \times 3 \times 3 + \frac{C_{in}}{2} \times 5 \times 5 + C_{in} \times C_{out}} = \frac{9C_{out}}{17 + C_{out}} \quad (1)$$

As shown in formula (1), the gap in FLOPs between LMSConv and SC widened progressively with an increase in the number of output channels, further validating the proposed module's advantage in achieving lightweight computation.

Building upon LMSConv, the Bottleneck structure within the original C3k2 module was modified by replacing its two SC with LMSConv, resulting in a new module termed Bottleneck_LMS. This module retained the original structure's feature extraction capability while significantly reducing the computational load. Subsequently, a Multidimensional Collaborative Attention *(Yu et al., 2023)* (MCA) module was introduced at the output of the C3k2 module to enhance the global modelling capacity of feature representations. MCA integrated information across the channel, height, and width dimensions, thereby improving the network's ability to perceive fine-grained targets and enhancing recognition accuracy. The structure of the MCA module was shown in Figure 5(a).

By placing the MCA attention module after the 1×1 SC within the C3k2 module, the fused channel features were further refined and enhanced, effectively improving the model's ability to perceive global contextual information. The final constructed LMSC3k2 module, illustrated in Figure 5(b), maintained strong feature extraction capabilities while significantly reducing the number of parameters, thereby achieving an improved balance between lightweight design and representational power.

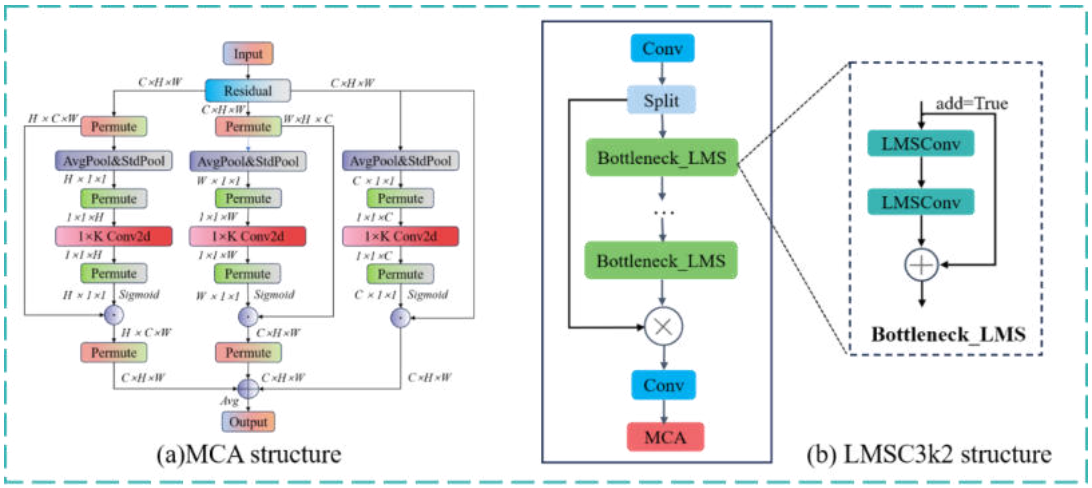


Fig. 5 - The structure of MCA and LMSC3k2

LMSHead

The traditional YOLOv11 detection head consisted of two branches: one branch comprising two 3×3 SC layers and the other employing two 3×3 Depthwise Separable Convolution (DSConv) layers, each of which was processed and then output via a 1×1 Conv2d module. However, this structure resulted in high computational complexity and a large parameter count.

To address this issue, this research redesigned the detection head and proposed LMSHead. LMSConv was introduced into LMSHead, and the original parallel structure was changed to a sequential structure, thus significantly reducing the number of parameters and computational complexity. Specifically, a 3×3 LMSConv was used to replace the original two 3×3 SC layers and two 3×3 DSConv layers. The feature maps transmitted by the neck network first passed through the LMSConv, followed by a 1×1 Conv2d layer, which separately output the regression and classification results. This design simplified the original four convolution operations into one, reducing the number of parameters in the detection head by approximately 72% without sacrificing accuracy. The LMSHead structure was illustrated in Figure 6.

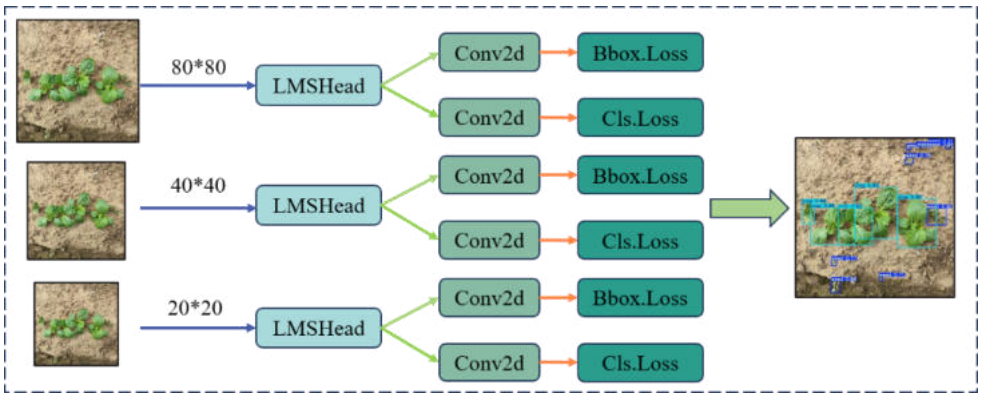


Fig. 6 - LMSHead structure

WIoU

YOLOv11 employed Complete Intersection over Union (CIoU) as its bounding box regression loss function *(Zheng et al., 2022)*. CIoU enhanced the evaluation of predicted boxes by incorporating penalties for the distance between center points, aspect ratio discrepancies, and the IoU itself, thereby providing a more comprehensive assessment of bounding box quality. However, in real-world field environments, Chinese cabbage and weeds often differed significantly in scale, and a substantial proportion of weed instances appeared as small objects. These small targets were prone to being confused with the background, making them difficult to annotate and detect accurately, and thus more likely to be treated as low-quality samples. The use of CIoU exacerbated the penalization of such samples, which in turn impaired the model's recognition capability. To address this issue, this study introduced the WIoU loss *(Tong et al., 2023)*. WIoU incorporated a dynamic, non-monotonic focusing mechanism along with gradient gain to mitigate the negative effects of penalizing low-quality samples, thereby enhancing the model's overall detection performance.

The calculation method of WIoU was presented in formula (2):

$$L_{WIoU} = rR_{WIoU}L_{IoU} \tag{2}$$

$$R_{WIoU} = exp\left(\frac{(a-a_{gt})^2 + (b-b_{gt})^2}{(W_{min}^2 + H_{min}^2)}\right) \tag{3}$$

where: L_{IoU} denoted the IoU-based bounding box loss, R_{WIoU} represented distance attention, a and b represented the horizontal and vertical coordinates of the predicted box center point, respectively, and a_{at} and b_{at} represented the horizontal and vertical coordinates of the real box center point, respectively. W_{min} and H_{min} indicated the width and height of the minimum bounding rectangle between the predicted box and the real box, respectively.

The quality of anchor boxes was characterized by the outlier degree β, defined as:

$$\beta = \frac{L_{IoU}^*}{L_{IoU}}, r = \frac{\beta}{\delta\alpha^{\beta-\delta}} \tag{4}$$

where: * denoted the separation operation. r was the gradient gain, and α and δ were hyperparameters.

Training Platform and Parameters

The model was executed on an experimental platform with a 64-bit Windows 10 operating system and was equipped with CUDA version 12.1. The development environment was PyCharm, running Python version 3.8 and PyTorch version 2.4.1, with an NVIDIA Tesla T4 GPU. The training configuration included 200 epochs, a batch size of 32, an image size of 640 × 640, an initial learning rate of 0.01, and a momentum factor of 0.937. Stochastic Gradient Descent (SGD) was employed as the optimizer.

Performance evaluation indicators

This study used Precision (P), Recall (R), and mean average precision (mAP) as evaluation metrics for model recognition accuracy. The IoU threshold for mAP was set to 0.5. The mAP50, commonly referred to as mAP50, was adopted as a standard metric to facilitate comparison with other models and to provide a more comprehensive assessment of model performance. Floating Point Operations per Second (FLOPs) and the number of Parameters (Params) were used to evaluate model lightweighting. The formulas for P, R, and mAP were defined as follows:

$$P = \frac{TP}{TP + FP} \tag{5}$$

$$R = \frac{TP}{TP + FN} \tag{6}$$

$$mAP = \frac{1}{k}\sum_{i=1}^{k} AP_i \tag{7}$$

where: TP stood for true case, FP for false positive case, FN for false negative case. k denoted the total number of detected object categories.

RESULTS

Ablation experiments

To assess the specific contribution of each proposed module to the model's performance, a series of ablation experiments were conducted, and the results were presented in Table 1. A tick mark "√" indicated that the corresponding module was incorporated in a given experimental configuration. YOLOv11n was used as the baseline model in the first group of experiments. In the second and third groups, the LMSNet backbone and the LMSHead detection head were introduced individually. The results showed that both modules significantly reduced the Params and FLOPs, while improving detection accuracy. In the fourth experiment, the WIoU loss function was introduced independently. Although this module had a minimal impact on computational cost, it contributed to a certain improvement in detection accuracy, verifying its effectiveness in enhancing localization performance. The fifth, sixth and seventh groups of experiments combined two of the three modules respectively, and the final comprehensive performance was all better than that of the benchmark model. In the eighth experiment, all three modules—LMSNet, LMSHead, and WIoU—were integrated. This configuration achieved improvements of 1.2%, 1.0%, and 0.6% in P, R, and mAP50, respectively, while reducing the Params and FLOPs by 34.6% and 36.5%. These results fully validated the effectiveness and practicality of the proposed method in enhancing detection accuracy and accelerating inference speed.

Table 1

Ablation experiments

LMSNet	LMSHead	WIoU	P(%)	R(%)	mAP50(%)	Params(M)	FLOPs(G)
			93.8	91.3	96.4	2.6	6.3
√			94.1	91.4	96.8	2.0	5.4
	√		93.3	92.3	96.6	2.3	4.9
		√	94.7	90.7	96.7	2.6	6.3
√	√		94.0	91.1	96.5	1.7	4.0
√		√	93.1	93.0	96.8	2.0	5.4
	√	√	93.4	91.9	96.7	2.3	4.9
√	√	√	95.0	92.3	97.0	1.7	4.0

As shown in Figure 7, the loss of YOLO-LMSW on both the training and validation sets consistently remained lower than that of YOLOv11n, indicating improved localization accuracy and a faster convergence rate. These results demonstrated the effectiveness of the proposed model in enhancing regression performance.

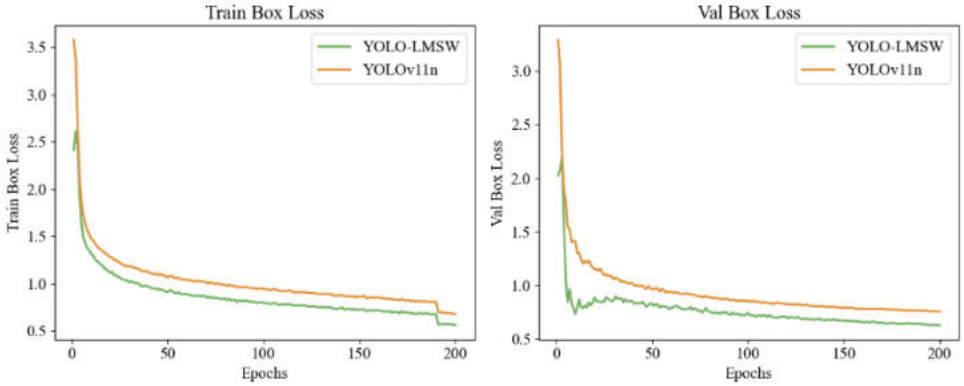


Fig. 7 - Convergence curve of loss function

Comparison experiments

To comprehensively evaluate the detection performance of the proposed YOLO-LMSW algorithm, a series of comparative experiments were conducted against several state-of-the-art one-stage object detection models. The results were summarized in Table 2. The findings indicated that YOLO-LMSW outperformed all competing methods across key evaluation metrics. Compared with YOLOv5, YOLO-LMSW achieved improvements of 0.9%, 2.2%, and 1.0% in P, R, and mAP50, respectively. When compared to YOLOv8, the respective gains were 0.7%, 1.2%, and 0.9%. Relative to YOLOv7-tiny, the performance advantages were even more pronounced, with increases of 4.2% in P, 4.9% in R, and 2.9% in mAP50. Furthermore, YOLO-LMSW demonstrated superior performance over both YOLOv11 and YOLOv12, achieving gains of 1.2%, 1.0%, and 0.6%, and 0.7%, 0.9%, and 0.2%, respectively, across the same three metrics. Compared to RT-DETR, YOLO-LMSW consistently exhibited outstanding results in all evaluated aspects, confirming its competitive advantage.

Table 2

Comparison experiments

Model	P(%)	R(%)	mAP50(%)	Params(M)	FLOPs(G)
YOLOv5n	94.1	90.1	96.0	1.8	4.1
YOLOv7-tiny	90.8	87.4	94.1	6.0	13.0
YOLOv8n	94.3	91.1	96.1	3.0	8.1
YOLOv11n	93.8	91.3	96.4	2.6	6.3
YOLOv12n	94.3	91.4	96.8	2.6	6.3
RT-DETR	87.4	81.6	89.9	27.9	89.2
YOLO-LMSW	95.0	92.3	97.0	1.7	4.0

As illustrated in Figure 8, a qualitative analysis was conducted using several high-performing detection models. In the visualizations, red bounding boxes denoted false positives, while black boxes represented false negatives. The results showed that YOLO-LMSW exhibited markedly superior localization accuracy and recognition performance, particularly in detecting small objects. It also significantly reduced both false positives and false negatives. For large object detection tasks, the model's performance was comparable to that of other benchmark algorithms. These findings clearly indicated that YOLO-LMSW not only maintained strong accuracy for large-scale targets but also significantly enhanced the detection of small-scale objects, thereby validating the robustness and adaptability of the proposed method in multi-scale field scenarios.

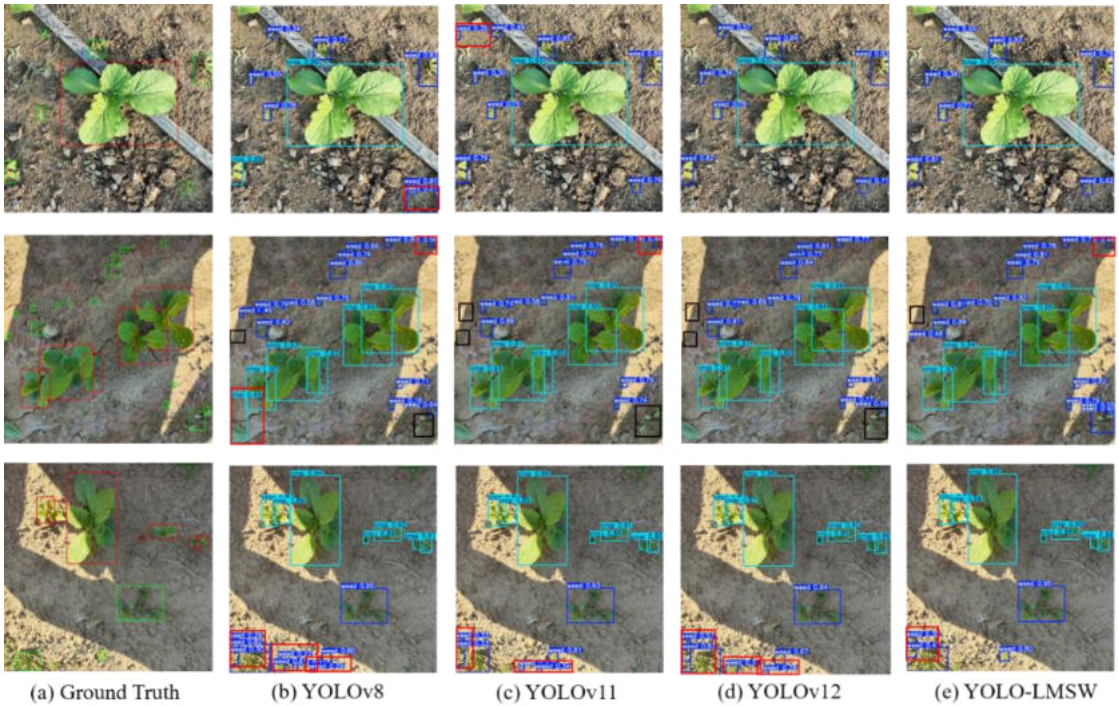


Fig. 8 - Detection effect diagram of different models

Deployment of edge devices

To further evaluate the practical deployment potential of the proposed model, it was deployed on a Jetson Orin Nano (4GB) embedded device. During the deployment test, an independent test set unrelated to the training data was used for inference validation, with the input image size set to 640×640. The inference time for each image and the number of detected instances for each category were recorded throughout the test. The experimental results showed that the model achieved an average inference time of 117 ms per image on the test set. The number of detected targets for each category closely matched the actual quantities, demonstrating the model's capability for real-time detection and its strong robustness in terms of accuracy. The inference performance is illustrated in Figure 9.

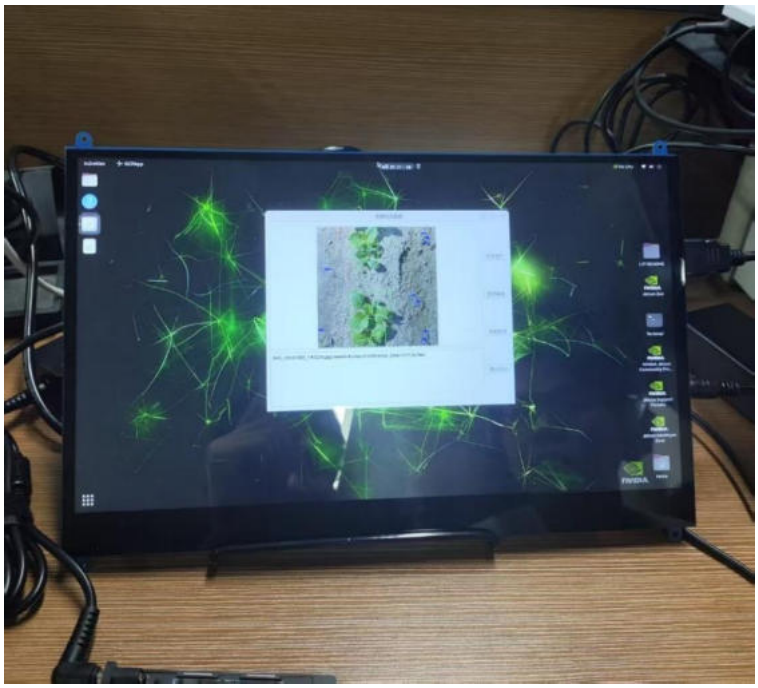


Fig. 9 - Edge device inference effect diagram

CONCLUSIONS

In this study, an improved YOLO-LMSW algorithm based on YOLOv11 was proposed to achieve a balance between speed and accuracy. Firstly, LMSConv was introduced, and the LMSC3k2 module was designed to enhance feature extraction capability and reduce computational load. Subsequently, LMSNet was constructed as the lightweight backbone network of YOLOv11. At the same time, LMSHead was developed as the detection head to make the model structure more efficient. To improve target localization accuracy without increasing computational cost, the WIoU loss function was adopted. The effectiveness of each module was verified through comprehensive ablation and comparison experiments. The experimental results showed that YOLO-LMSW outperformed the baseline models in terms of P, R, and mAP50, while maintaining significantly fewer Params and lower FLOPs. The model achieved an average inference time of 117 ms per image when deployed on a Jetson Orin Nano (4GB) embedded device, confirming its capability for real-time detection. Furthermore, the detection results closely matched the ground truth annotations, demonstrating the robustness and reliability of the model in practical scenarios. These results highlighted the strong potential of YOLO-LMSW for real-time weed detection applications, especially in resource-constrained environments. In future work, the model is planned to be integrated into a weeding robot to further evaluate its performance under real-world agricultural conditions.

ACKNOWLEDGEMENT

This research was supported by the development of a laser weed removal technology system for farmland (381941).

REFERENCES

[1] Cai, Y. L., Zeng, F. G., Xiao, J. Y., Ai, W. J., Kang, G. B., Lin, Y. D., Cai, Z. X., Shi, H. W., Zhong, S. X.,Yue, X. J., (2023). Attention-aided semantic segmentation network for weed identification in pineapple field. *Computers and Electronics in Agriculture, 210*, 107881. doi:https://doi.org/10.1016/j.compag.2023.107881

[2] Chen, J. Q., Wang, H. B., Zhang, H. D., Luo, T., Wei, D. P., Long, T.,Wang, Z. K., (2022). Weed detection in sesame fields using a YOLO model with an enhanced attention mechanism and feature fusion. *Computers and Electronics in Agriculture, 202*, 107412. doi:https://doi.org/10.1016/j.compag.2022.107412

[3] Chollet, F., (2017). Xception: Deep Learning with Depthwise Separable Convolutions. *Paper presented at the 2017 IEEE Conference on Computer Vision and Pattern Recognition (CVPR)*. doi:10.1109/CVPR.2017.195

[4] Darbyshire, M., Coutts, S., Bosilj, P., Sklar, E.,Parsons, S., (2024). Review of weed recognition: A global agriculture perspective. *Computers and Electronics in Agriculture, 227*, 109499. doi:https://doi.org/10.1016/j.compag.2024.109499

[5] Hasan, A. S. M. M., Diepeveen, D., Laga, H., Jones, M. G. K.,Sohel, F., (2023). Image patch-based deep learning approach for crop and weed recognition. *Ecological Informatics, 78*, 102361. doi:https://doi.org/10.1016/j.ecoinf.2023.102361

[6] Hu, R., Su, W. H., Li, J. L.,Peng, Y. K., (2024). Real-time lettuce-weed localization and weed severity classification based on lightweight YOLO convolutional neural networks for intelligent intra-row weed control. *Computers and Electronics in Agriculture, 226*, 109404. doi:https://doi.org/10.1016/j.compag.2024.109404

[7] Hua, C. J., Zhang, A. R., Jiang, Y., Yu, J. F.,Chen, Y., (2022). Lawn weed recognition based on improved fuzzy C-means clustering algorithm(基于改进模糊C均值聚类算法的草坪杂草识别). *Journal of South China Agricultural University, 43*(3), 107-115. doi:10.7671/j.issn.1001-411X.202109005

[8] Ji, W. L., Liu, Z.,Xing, H. H., (2024). Lightweight Method for Identifying Farmland Weeds Based on YOLO v5(基于YOLO v5的农田杂草识别轻量化方法研究). *Transactions of the Chinese Society for Agricultural Machinery, 55*(1), 212-222，293. doi:10.6041/j.issn.1000-1298.2024.01.020

[9] Khan, S., Tufail, M., Khan, M. T., Khan, Z. A., Anwar, S., (2021). Deep learning-based identification system of weeds and crops in strawberry and pea fields for a precision agriculture sprayer. *Precision Agriculture, 22*(6), 1711-1727. doi:https://doi.org/10.1007/s11119-021-09808-9

[10] Ma, N., Zhang, X., Zheng, H. T.,Sun, J., (2018). ShuffleNet V2: Practical Guidelines for Efficient CNN Architecture Design. *Paper presented at the Computer Vision – ECCV 2018*, Cham. doi:https://doi.org/10.1007/978-3-030-01264-9_8

[11] Praveenraj, R., Ramya, R., Thanu, S.,Aswinkumar, R., (2024). Computer Vision based Smart Bot for Weed Detection and Removal in Vegetable Crop Fields. *Paper presented at the 2024 International Conference on Inventive Computation Technologies (ICICT)*. doi:10.1109/ICICT60155.2024.10544594

[12] Redmon, J., Divvala, S., Girshick, R.,Farhadi, A., (2016). You Only Look Once: Unified, Real-Time Object Detection. *Paper presented at the 2016 IEEE Conference on Computer Vision and Pattern Recognition (CVPR)*. doi:10.1109/CVPR.2016.91

[13] Sabzi, S., Abbaspour-Gilandeh, Y.,Arribas, J. I., (2020). An automatic visible-range video weed detection, segmentation and classification prototype in potato field. *Heliyon, 6*(5), e03685. doi:https://doi.org/10.1016/j.heliyon.2020.e03685

[14] Shang, W. Q.,Qi, H. B., (2022). Identification algorithm of field weeds based on improved Faster R-CNN and transfer learning (基于改进Faster R-CNN与迁移学习的农田杂草识别算法). *Journal of Chinese Agricultural Mechanization, 43*(10), 176-182. doi:10.13733/j.jcam.issn.2095-5553.2022.10.025

[15] Shao, Y. Y., Guan, X. L., Xuan, G. T., Gao, F. R., Feng, W. J., Gao, G. L., Wang, Q. Y., Huang, X. C.,Li, J. C., (2023). GTCBS-YOLOv5s: A lightweight model for weed species identification in paddy fields. *Computers and Electronics in Agriculture, 215*, 108461. doi:https://doi.org/10.1016/j.compag.2023.108461

[16] Tong, Z. J., Chen, Y. H., Xu, Z. W.,Yu, R., (2023). Wise-IoU: Bounding Box Regression Loss with Dynamic Focusing Mechanism. doi:abs/2301.10051

[17] Xiang, M., Gao, X., Wang, G., Qi, J., Qu, M., Ma, Z., Chen, X., Zhou, Z.,Song, K., (2024). An application oriented all-round intelligent weeding machine with enhanced YOLOv5. *Biosystems Engineering, 248*, 269-282. doi:https://doi.org/10.1016/j.biosystemseng.2024.11.009

[18] Yan, J. L., Zhai, Z. K., Feng, Z. X.,Yang, J., (2025). A lightweight millet downy mildew spore detection method based on improved YOLOv8s. *INMATEH-Agricultural Engineering, 75*(1).

[19] Yu, Y., Zhang, Y., Cheng, Z. Y., Song, Z.,Tang, C. K., (2023). MCA: Multidimensional collaborative attention in deep convolutional neural networks for image recognition. *Engineering Applications of Artificial Intelligence, 126*, 107079. doi:https://doi.org/10.1016/j.engappai.2023.107079

[20] Zhang, J. W., Peng, Q. J., Kang, J. M., Di, Z. F., Wang, S. W., Chen, Y. K.,Chen, Y. L., (2025). Design and experiment of a corn inter-plant weeding machine based on visual recognition. *INMATEH-Agricultural Engineering, 75*(1).

[21] Zhang, X., Wang, Q., Wang, C., Wang, X., Xu, Z.,Lu, C., (2024). Guidelines for mechanical weeding: Developing weed control lines through point extraction at maize root zones. *Biosystems Engineering, 248*, 321-336. doi:https://doi.org/10.1016/j.biosystemseng.2024.11.003

[22] Zheng, Z. H., Wang, P., Ren, D. W., Liu, W., Ye, R. G., Hu, Q. H.,Zuo, W. M., (2022). Enhancing Geometric Factors in Model Learning and Inference for Object Detection and Instance Segmentation. *IEEE Transactions on Cybernetics, 52*(8), 8574-8586. doi:10.1109/TCYB.2021.3095305

EXPERIMENTAL AND DEM-BASED ANALYSIS OF LATERAL STRESS AND SOIL PARTICLE DISPLACEMENT UNDER THE ACTION OF A SUBSOILER
/
基于试验和离散元仿真模拟方法对深松铲下土壤侧向应力与侧向位移的研究

Jun GE, Xu ZHU, Chengmao CAO, Liangfei FANG, Yan SUN, Kuan QIN *), Weidong GAO, Junjie LU [1]
School of Engineering, Anhui Agricultural University, Hefei, Anhui/China
Phone: 86-18855102551; E-mail: qinkuan@ahau.edu.cn
Corresponding author: Qin Kuan
DOI: https://doi.org/10.35633/inmateh-76-74

Keywords: *subsoiler, discrete element simulation, soil lateral stress, soil lateral displacement*

ABSTRACT
The lateral stress on the soil in the lateral position during the operation of a subsoiler directly affects the soil displacement and quality of operation. In this study, soil pressure sensors are used to measure the soil lateral stress at the lateral position of the subsoiler in the soil trough, and a discrete element simulation is used to explore the relationship between the change pattern of the soil lateral stress and soil displacement. The test results show that the soil at the lateral position of the subsoiler is subjected to lateral stress, which leads to the generation of lateral displacements. The lateral stress lasts no longer than 3.5 s, the lateral displacement lasts no longer than 3 s, and both exhibit a fluctuating pattern of peaks and troughs over time. The positive peaks are significantly larger than the troughs, indicating that the positive peaks are the main factor generating soil disturbance. The lateral stress and lateral displacement changes are consistent on the timeline, with the lateral displacement moving in the positive (negative) direction when the lateral stress direction is positive (negative). Both values tend to decrease linearly with increasing transmission distance.

摘要
松土机作业过程中土壤侧向应力直接影响土壤位移及作业质量。本研究通过土槽试验，利用土压力传感器测量松土机侧向位置土壤所受侧向应力，并结合离散元仿真探究土壤侧向应力变化规律与土壤位移的关联性。试验结果表明：松土机侧向位置土壤受侧向应力作用产生侧向位移，侧向应力作用时长不超过 3.5 s，侧向位移持续时长不超过 3 s，二者均呈现"波峰-波谷"交替的波动规律，且正向波峰幅值显著高于波谷，表明正向应力峰是引发土壤扰动的主要因素；侧向应力与侧向位移在时序上具有一致性，侧向应力方向为正（负）时，侧向位移沿正（负）方向运动；二者均随传递距离增大呈线性衰减趋势。研究结果为优化松土机结构参数与作业模式提供了理论依据。

INTRODUCTION
Deep-loosening tillage is an effective method for improving soil physical properties and increasing crop yield (*Arvidsson et al., 2010*). The subsoiler disturbs the soil laterally, increasing its ability to hold water and moisture (*Wang et al., 2020*). Lateral disturbances are caused by stresses placed on the soil by the subsoiler when it contacts the soil and are transmitted laterally (*Ibrahmi et al., 2014*). This process is accompanied by soil displacement and deformation, which disrupt the original structure of the soil on both sides of the subsoiler (*Li et al., 2016*).

Scholars around the world have conducted relevant studies (*Li et al., 2023*) to determine how lateral stresses are generated during subsoiler operations and how they affect soil displacement and disturbance (*Ma et al., 2019*). Research has shown that the subsoiler creates lateral stresses on the soil on both sides through shear and compression. *Huang et al. (2016)* further found that the shearing and squeezing of the soil by the subsoiler shovel originated from the shovel tip flanks and that the shearing of the soil by the shovel tip flanks produced soil failure that resulted in soil slippage. Moreover, the stress exerted on the soil increased with proximity to the shovel tip flanks.

[1] *Ge Jun, Lecturer PhD. Eng.; Zhu Xu, M.S. Stud. Eng.; Cao Chengmao, Prof. PhD. Eng.; Fang Liangfei, Lecturer PhD. Eng.; Sun Yan, Assoc. Prof. M.S. Eng.; Qin Kuan*, Assoc. Prof. PhD. Eng.; Gao Weidong, M.S. Stud. Eng.; Lu Junjie, M.S. Stud. Eng.*

Liu et al. (2017) found that lateral stresses caused soil loosening and fragmentation and that soils at different depths were subjected to stresses of different magnitudes. The above findings show that scholars have clearly studied how lateral stresses are generated in the process of deep loosening and that the magnitudes of lateral stresses vary in different locations of the soil. However, it is not clear exactly how lateral stresses change at different soil lateral locations and what the exact magnitudes are. This is important for analyzing how lateral stresses drive the entire lateral soil movement. If the variation rule of the lateral stress at different lateral soil locations can be explored, the lateral soil displacement law can be further analyzed. Scholars have studied soil displacement patterns in deep pine operations. *Ding et al. (2017a)* found that during deep subsoiler operation, the soil above the flanks of the shovel tip was first lifted to the sides along the forward direction of the deep subsoiler after a force was applied. Then, the soil was moved to the sides. The soil below the flanks of the shovel tip was extruded laterally by the subsoiler to form a rectangular groove approximately equal in width to that of the shovel. *Ding et al. (2017b)* and *Hang et al. (2017)* also found that the lateral displacements were significantly greater for shallow soils than for soils in other locations and that deeper soils had the least lateral displacements. *Zhang (2018)* used the discrete element method with a soil trough test to study the effect of a deep subsoiler on soil displacement and found that the disturbance of the soil by the deep subsoiler extends from the tip of the shovel to the surface of the soil on both sides, at which time the soil on both sides forms a soil barrier and moves to both sides under the actions of lateral stresses. However, there is a lack of analysis of the causes of lateral displacement from a force perspective, and it is not clear how lateral stresses specifically affect lateral displacement.

In summary, this study aims to determine both the change rule of the soil lateral stress at the lateral position during the operation of a subsoiler. In this study, using a soil trough and soil pressure sensor in combination with a discrete element simulation test, a fixed-point layered analysis of the lateral position of the soil lateral stress and lateral displacement change rule of the subsoiler is conducted, and the lateral stress change rule of the lateral displacement and perturbation of the impact are analyzed. This provides a theoretical basis for improving the quality of deep pine operations (*Li et al., 2021; Zhang et al., 2021*)

MATERIALS AND METHODS

Test subsoiler

The test subsoiler is a double-wing subsoiler, which consists of two parts: the tip and handle. The tip is the main working part of the subsoiler, the structure and dimensions of which is shown in Fig. 1.

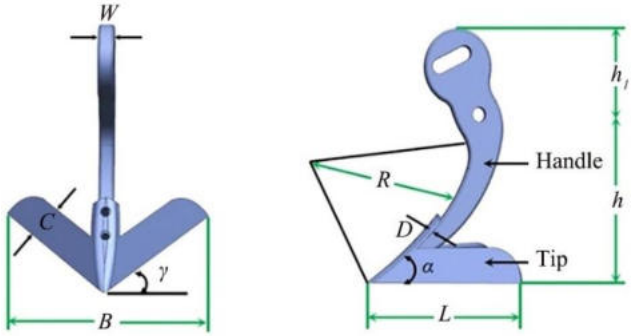


Fig. 1 – Schematic drawing of the subsoiler

In Fig.1, R represents the radius of curvature of the shovel shank in mm. W is the thickness of the shovel shank in mm. $h+h1$ is the height of the tillage tool shank in mm. B is the width of the shovel tip in mm. C is the width of the shovel tip flange in mm. L is the length of the shovel tip flange in mm. D is the thickness of the tillage tool tip in mm. α is the angle of the tangent edge in degrees. γ is the angle of the tillage tool tip flange tension in degrees.

Table 1

Parameters of the subsoiler.

Parameter	*R* (mm)	*W* (mm)	*h* (mm)	h_1 (mm)	*B* (mm)	*C* (mm)	*D* (mm)	*L* (mm)	*α* (°)	*γ* (°)
Value	100	15	160	50	220	30	3	190	30	45

Table 1 shows the tillage tool tip and tillage tool handle structure parameters according to the standard JB/T 9788-1999, “Subsoiler and share shaft”. The subsoiler was made of 65Mn, as specified in GB/T700, and

the blade was quenched to achieve a hardness of 48–56 HRC. The shovel handle was bolted to the shovel tip, and the upper part of the shovel handle contained bolt holes for connecting and fixing it to the test bench.

Soil bin experimental device

Fig. 2 shows the schematic of the test bench and sensor system, which mainly consisted of a soil trough, gear motor, test bogie, bogie guide rail, gears, rack, control cabinet, and subsoiler. The basic parameters of the soil trough were as follows: length = 4,000 mm; width = 1,000 mm; and height = 800 mm. The gear motor provides power for deep-loosening operations. The gear motor was integrated with a 130ST-M15025 servo motor with a power of 3.8 kW and a three-stage gear ratio planetary reducer. The gears were mounted on the output shaft of the reducer for transmission. The gear rack was installed in the side frame of the soil trough, the bogie rail was installed in the side frame on both sides of the trough, the gear motor was fixed to the test bogie, and the test bogie was driven by the gear rack to move in a straight line along the rail.

The bogie moved in the range of 0–1.6 m/s. The subsoiler was fixed to the suspension under the test bogie using bolts and moved forward or backward with the bogie at a uniform speed. No. 8 in Fig. 2 is the self-made sensor-fixing device. The sensor-fixing device has an inverted L-shape structure (300 height × 2 thick, mm). The upper end is bolted to the body frame, and the lower end can fix the sensor. The test sensor adopted was a high-precision cylindrical point-type soil pressure sensor (DMTY model, Nanjing Dan Mor Electronic Technology Co.). This pressure sensor has a diameter of 16 mm, thickness of 4.8 mm, range of 0.05 to 10 MPa, and sensitivity of 2 mV/V. The polished side of the sensor was the stress sensing surface, and the unpolished side was the support surface. The electrical signal collected by the sensor was converted into a pressure value using Equation 1:

$$P_i = K(F_i - F_0) \tag{1}$$

where P_i is the real-time pressure value to which the sensor is subjected (kPa), F_i is the output electrical signal strain value corresponding to P_i in μV, F_0 is the electrical signal strain value output at the sensor's zero point in μV, and K is the sensor calibration factor of 0.152 kPa/μV. The measured pressure values were converted into pressure values using Equation 2:

$$F = P_i \times \pi r^2 \tag{2}$$

where F is the stress collected by the sensor in N and r is the radius of the sensor (8 mm).

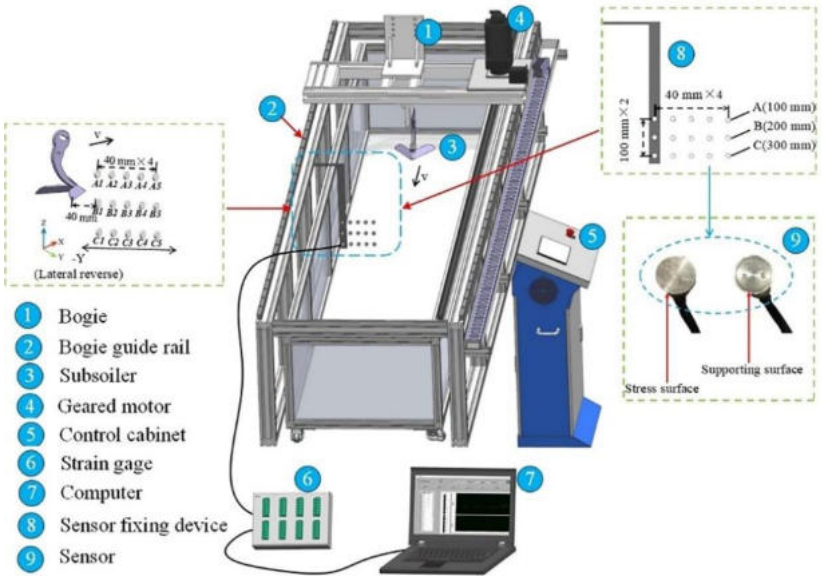


Fig. 2 – Schematic illustration of the soil bin device and sensor system

Soil preparation

The test soil in the soil trough was sandy loam, and the soil physical parameters were determined before the test using a GHHB-009-485-1 soil moisture meter (moisture accuracy ± 0.3% RH), ring knife, and TYD-2 soil firmness meter (accuracy ± 1%) to determine the soil moisture content, bulk weight, and soil firmness in the shallow (soil depth range of 0–150 mm), middle (150–270 mm), and deep (270–320 mm) soil layers, respectively. Table 2 lists the obtained soil water content, bulk weight, soil firmness, and soil physical parameters.

Table 2

Basic physical soil parameters.

Soil depth (mm)	Soil density (kg/m³)	Moisture content (%)	Soil hardness (kg/cm²)
0–150	1310	11.21	14.4
150–270	1420	12.32	16.8
270–320	1610	14.31	20.3

Experimental methods design

The soil at the lateral position of the subsoiler was divided into shallow (0–150 mm), middle (150–270 mm), and deep (270–320 mm) layers. According to its distance from the subsoiler, each layer was further divided into five areas, for a total of 15 areas within the three layers. The test was conducted by burying the sensor in the area above and determining the lateral stress on the soil at the lateral position in a point-by-point manner. The sensor was set up in the soil trough, as shown in Fig. 2, and the sensor was buried at depths in the shallow, middle, and deep layers, corresponding to the depths of layers A, B, and C, respectively. The distances of the sensor from the edge of the wing shovel of the subsoiler used were 40, 80, 120, 160, and 200 mm (in order of 40 mm increases), corresponding to the five lateral positions: 1, 2, 3, 4, and 5. Based on the preliminary pre-test, there is almost no lateral stress response after exceeding a lateral distance of 200 mm. Therefore, the maximum lateral distance determination point was set to 200 mm. The soil pressure sensors were calibrated using a potentiometer-based calibration method prior to testing (*Lamande et al., 2015*). The sensor was buried behind the measurement point and calibrated to zero. As shown in Fig. 3, the operating depth of the subsoiler was 200 mm, and the operating speed was 0.2 m/s during the test. The middle section of the 1,000 mm soil trough was used as the stabilization measurement area. The subsoiler was moved from the beginning of the soil trough to the end of the soil trough for each test stroke. After each test, the subsoiler was reset, the soil in the soil trough was reprepared, and the soil parameters were controlled within 100% ± 5% relative error. Each stroke was repeated five times, and the average value of the test results was taken. The test was completed when all five lateral positions of the soil layers A, B, and C were measured.

The response start time was set to be the point when the first stress change value was captured for each test stroke, and the response cutoff time was when the final stress value stabilized. When all tests were completed, the collected voltage signals were converted to stress values using Equations 1 and 2, and the law of lateral stresses was applied to each lateral position in layers A, B, and C of the soil and obtained as a function of time. During the test, an I-SPEED high-speed camera was used to record the deep pine process and obtain soil disturbance images at specific time points. Fig. 3 shows the high-speed photograph arrangement.

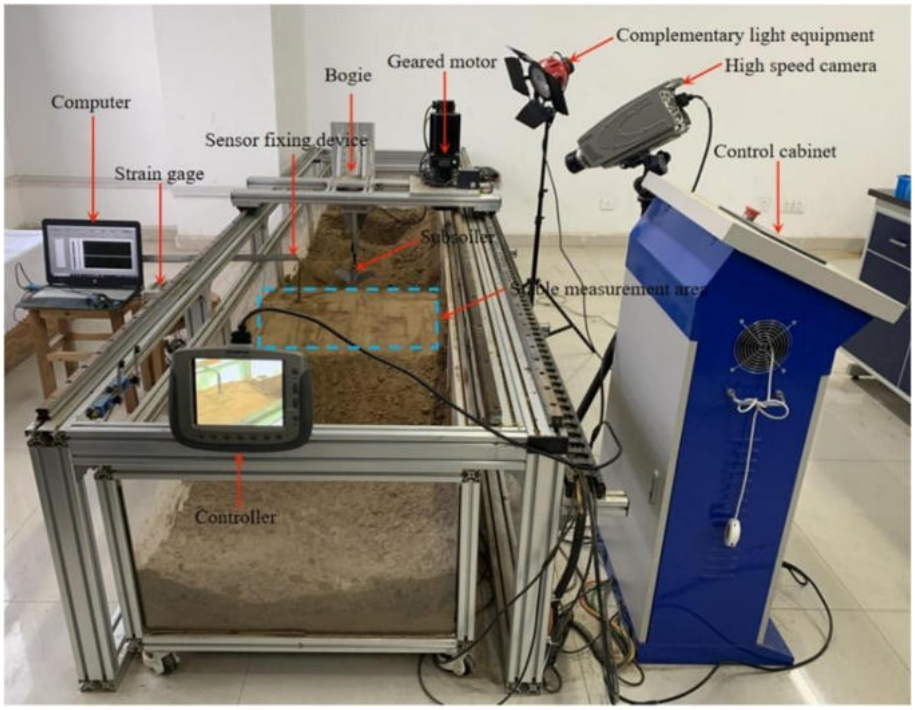


Fig. 3 – Soil trough test procedure

Discrete element simulation

A three-dimensional model of the subsoiler and a soil model identical to the actual soil trough test were created. As shown in Fig. 4, a soil model with a length × width × height of 1,000 mm × 800 mm × 320 mm was created using the EDEM. Shallow soil (0–150 mm) is shown in blue, medium soil (150–270 mm) in green, and deep soil (270–320 mm) in red.

To ensure that the discrete element simulation model was consistent with the actual soil, the Hertz-Mindlin model with the JKR model was selected as the particle contact model. The Hertz-Mindlin (no-slip) contact model between the soil particles and the tip of the subsoiler was selected, and basic spherical soil particles with a radius of 4 mm were chosen for this study.

The established soil model and model parameters were mainly divided into material and contact parameters, which included the density, Poisson's ratio, and shear modulus of the soil and subsoiler (65Mn), which mainly included the friction factor and coefficient of restitution between the materials. The soil density was obtained through actual measurements, and the other parameters were determined from the literature. Table 3 lists the simulation parameters.

Table 3

Basic discrete element model parameters

Parameter	Shallow soil	Middle soil	Deep soil
Soil Poisson's ratio	0.40	0.42	0.43
Soil shear modulus (Pa)	1×10^6	1.4×10^6	1.6×10^6
Soil density (kg/m^3)	1,370	1,492	1,705
Restitution coefficient between soils	0.2	0.2	0.15
Static friction coefficient between soils	0.4	0.4	0.3
Dynamic friction coefficient between soils	0.3	0.3	0.2
Restitution coefficient of soil and 65Mn	0.2	0.2	0.17
Static friction coefficient of soil and 65Mn	0.5	0.5	0.4
Dynamic friction coefficient of soil and 65Mn	0.3	0.2	0.09
Soil surface energy	4.4	5.1	6.2
65Mn Poisson's ratio	0.35		
65Mn shear modulus (Pa)	7.27×10^{10}		
65Mn density (kg/m^3)	7,830		
Total number of soil particles	610,000		
Gravity acceleration (m·s^{-2})	9.81		

The clipping module of the EDEM was utilized to select soil-particle clusters (particle clusters consisting of five soil particles) in the soil model, as shown in Fig. 4, where the soil-particle cluster locations were the same as those of the soil trough test sensor measurement points.

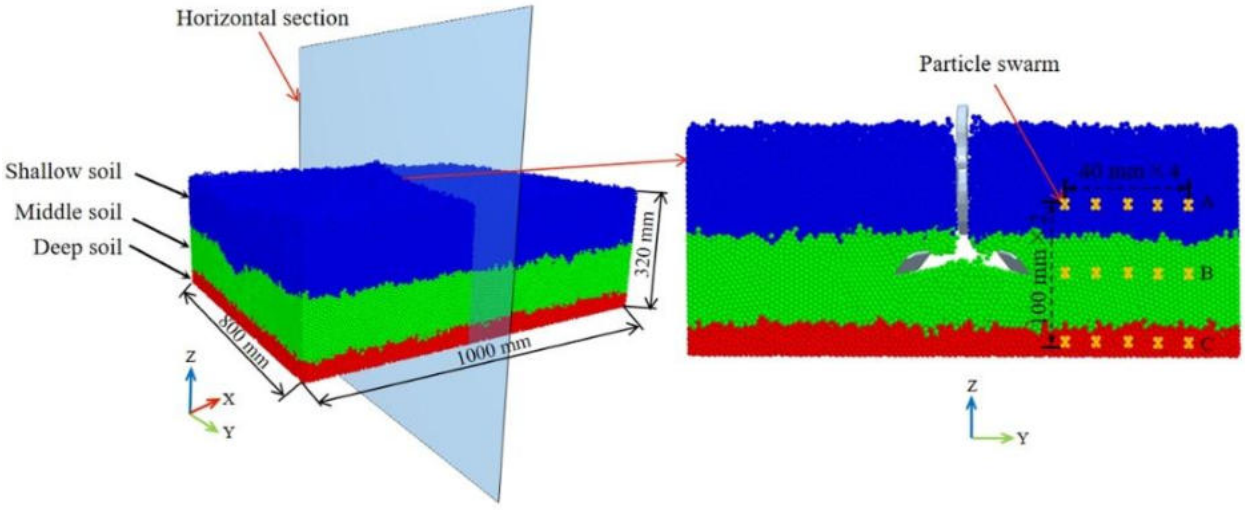


Fig. 4 – Simulation modelling with soil particle swarms

The entire discrete element simulation test procedure was consistent with that of the soil-trough test. After the test, the lateral displacement data of the soil particle population were counted (the data were

averaged) to obtain the change rule of the lateral displacement of the soil at the five lateral positions of the soil in layers A, B, and C. The soil model was also dissected along the lateral direction through the clipping module to observe the disturbance state of the soil at different lateral locations during the deep pine operation.

RESULTS

Basic laws of lateral soil stresses and lateral soil displacements

Fig. 5a shows that lateral stresses are generated during the operation of the subsoiler. The lateral stresses are transmitted to various locations in the lateral soil, and the lateral stresses show a fluctuating pattern with time changes (*Qin et al., 2022*). The entire duration of the fluctuation did not exceed 3.5 s. This result is in agreement with the findings of *El Kahi et al. (2020)* and *Lutz et al. (2017)*, who both found that the lateral stress transfer process in soil can have fluctuating characteristics. Lateral stress fluctuation exists in two cases. The first case is an initial rise and a subsequent fall; that is, the fluctuation only exists at a peak. The second case is an initial rise, a subsequent fall, and a subsequent rise; that is, the curve exists in a peak and a trough. In this case, the value of the wave peak is much larger than that of the trough, which indicates that the wave peak is the main reason for the lateral displacement of the soil affected by the lateral stress.
Fig. 5b shows that the lateral soil displacement caused by the subsoiler exhibited a fluctuating pattern over time and that the entire fluctuation duration did not exceed 3 s. The lateral displacement exhibited the same two fluctuations as those of the lateral stress. This indicates that the two change patterns were consistent in the process of lateral displacement caused by lateral stress.

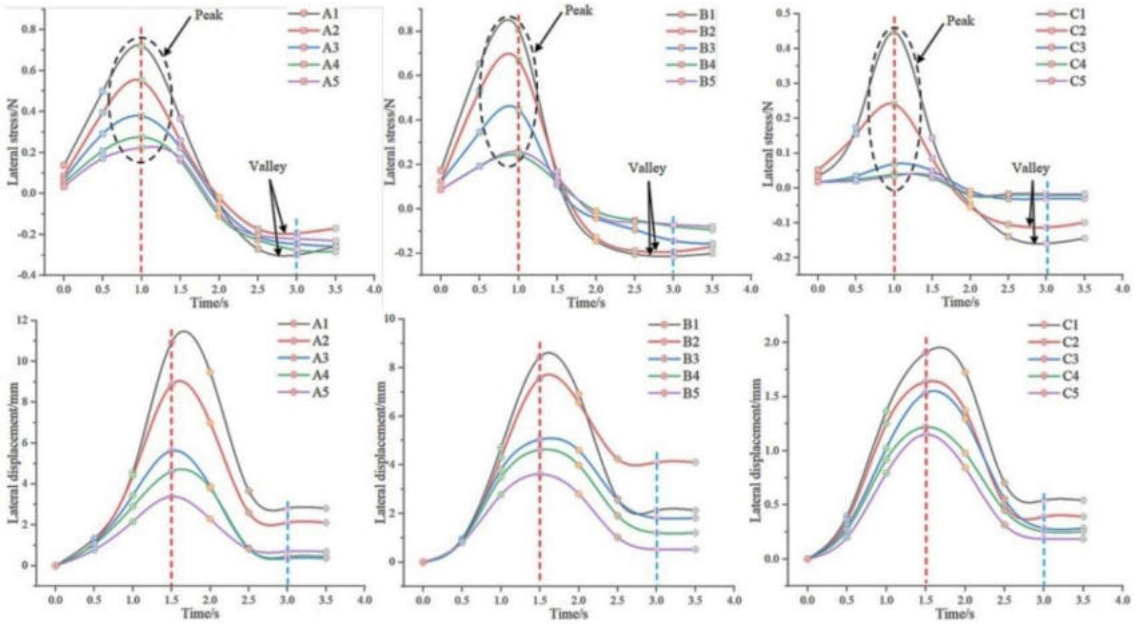


Fig. 5 – Change laws of lateral stress and displacement over time during subsoiler operation
(a) Change law of lateral stress on the soil over time during subsoiler operation
(b) Change law of lateral soil displacement over time during subsoiler operation

Analysis of soil lateral stress and lateral displacement extremes

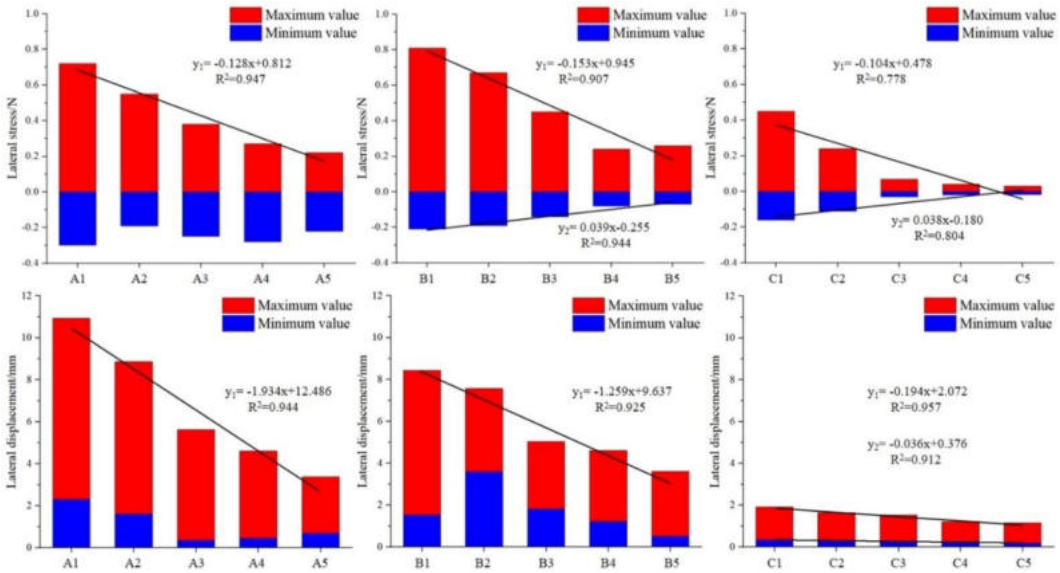
Fig. 6 illustrates the analysis of the maximum and minimum values of lateral stress and lateral displacement. The maximum values represent the highest points during the variation of lateral stress and displacement and typically occur at the peaks of the waveform. Conversely, the minimum values are the lowest points, occurring at the troughs or endpoints of the waveform. The sign (positive or negative) of each extreme value indicates the direction of the force or displacement, while the magnitude reflects its intensity. As shown in Fig. 6, the maximum (positive) values of lateral stress and displacement are significantly greater in magnitude than the minimum (negative) values. This suggests that positive-direction lateral stress and displacement are dominant over those in the negative direction.

The extreme values of lateral soil stress showed a linear decreasing trend with increasing transmission distance, particularly in soil layers B and C. Similarly, the large (positive) values of lateral soil displacement also decreased linearly with transmission distance, while the small (negative) values of displacement exhibited a linear decrease primarily in the C horizon.

These results indicate that, in the positive direction, both lateral force and displacement effects diminish linearly as the transmission distance increases (*Jude et al., 2012*). However, in the negative direction, no consistent pattern of change was observed.

The maximum and minimum values of lateral force and lateral displacement were analyzed for each layer. In soil layer A, the maximum and minimum values of the lateral force of A1 were the largest, being observed at 0.72 N and -0.30 N, respectively. In layer B, the maximum and minimum values of the lateral force of B1 were the largest, at 0.81 N and -0.21 N, respectively. In layer C, the maximum and minimum values of the lateral force of C1 were the largest, at 0.45 N and -0.16 N, respectively. In layer A, the maximum and minimum values of A1 were 10.93 mm and 2.31 mm, respectively. In layer A, the maximum and minimum values of A1 were 10.93 mm and 2.31 mm, respectively. In soil layer A, A1 had the largest maximum and minimum values of lateral displacement, at 10.93 mm and 2.31 mm, respectively. In soil layer B, B1 had the largest maximum value of lateral displacement and B2 had the largest minimum value, which were 8.44 mm and 3.60 mm, respectively. In soil layer C, C1 had the largest maximum and minimum values of lateral displacement, at 1.91 mm and 0.34 mm, respectively.

From the above results, it can be seen that the maximum extreme value of lateral soil stress occurred in layer B, followed by layer A, and was lowest in layer C. The minimum value of the lateral stress in soil layer A was the highest, followed by those in layers B and C. The maximum extreme values of lateral displacement were observed in layer A, followed by layer B, with the lowest in layer C. In contrast, the highest minimum (negative) values of lateral displacement occurred in layer B, followed by layer A, and were lowest in layer C. Regarding lateral stress, the maximum positive values were recorded in layer B, followed by layer A, and were lowest in layer C. These findings suggest that layer B experienced the highest lateral stress, while layer A exhibited the greatest lateral displacement.



(a)

(b)

Fig. 6 – Analysis of lateral force and soil displacement extremes

(a) Lateral stress extremes, and (b) Lateral displacement extremes

Timeline correspondence of lateral stresses driving changes in soil lateral displacement

Fig. 7 shows that the lateral stress increases from 0–1 s and decreases from 1.0–1.5 s, and that the direction of the lateral stress is positive from 0–1.5 s. The lateral stress decreases from 0–1.7 s, and the direction of the lateral stress changes from positive to negative. The lateral stress decreases from 1.7–3.0 s, and the direction of lateral stress is negative. The range of 3.0–3.5 s is a special time period in which the phenomenon of lateral stress rebound appeared in the A1, A2, B1, B2, C1, and C2 positions. The direction is still negative, and the lateral stress remains unchanged in the C3, C4, and C5 positions. In the other positions, the lateral stress continues to decrease.

The lateral displacement increased from 0–1.5 s and moved in the positive direction. At approximately 1.7 s, the direction of movement started to change from positive to negative, and from 1.7–3.0 s, the lateral stress started to decrease and move in the negative direction. By 3.0 s, the lateral displacement stopped moving. These results show that lateral displacement and lateral stress remain consistent on the time line.

From 0–1.7 s, the direction of lateral stress is positive, and the lateral displacement moves in the positive direction. From 1.7–3.0 s, the direction of lateral stress is negative, and the lateral displacement moves in the negative direction. The range of 3.0–3.5 s is a special time period in which there is still a change of negative lateral stress at all lateral locations, but the stress is no longer able to push the soil to move laterally.

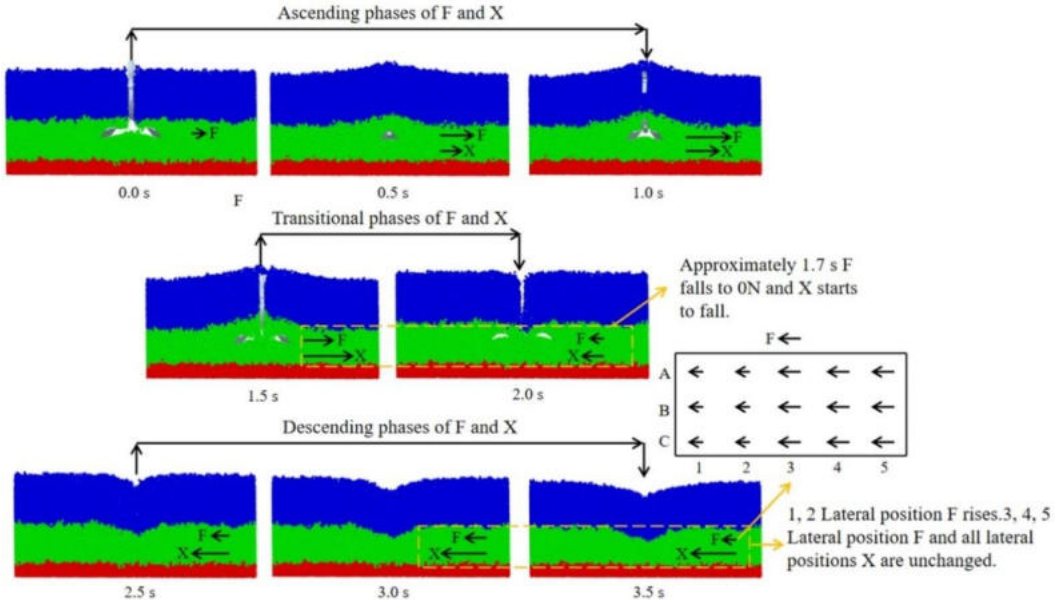
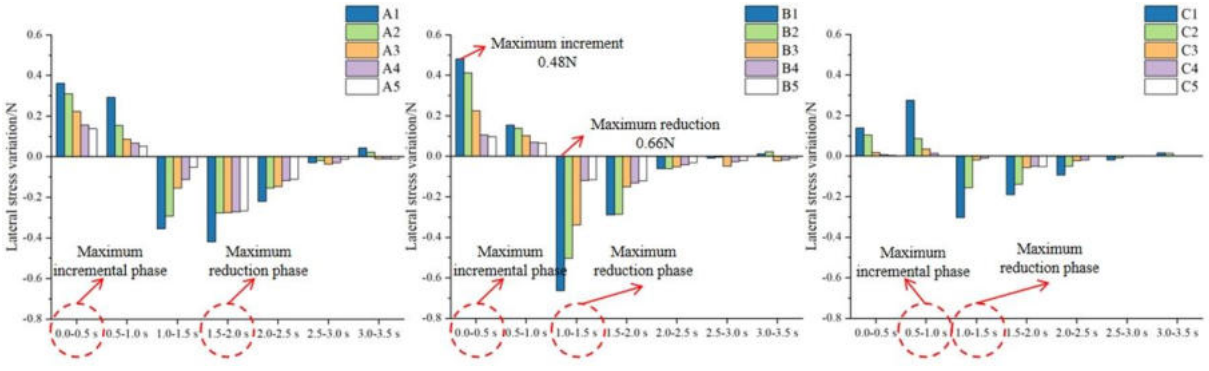


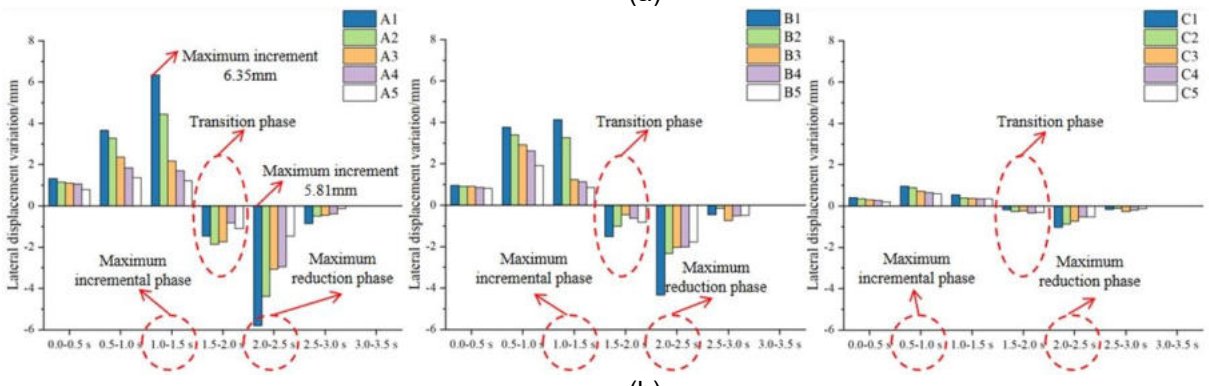
Fig. 7 – Direction of lateral stress and lateral displacement with timeline

Lateral stress and lateral displacement with the time incremental (decremental) change rule of law

Fig. 8a shows that both the increment and decrement of the lateral stress in soil layer B were the largest, and this was followed by those in layers A and C. The maximum increase and decrease in lateral stress in layer B were the largest. The maximum value of the lateral stress increment occurs at position B1 from 0–0.5 s, with a maximum increment of 0.48 N. The minimum value of the decrement occurs at position B1 from 1–1.5 s, with a maximum decrement of 0.66 N. The maximum value of the decrement occurred at position B1 from 1–1.5 s, with a maximum decrement of 0.66 N.



(a)



(b)

Fig. 8 – Increase (decrease) in lateral stress and soil displacement at different time intervals

(a) Increase (decrease) in lateral stress at different time intervals

(b) Increase (decrease) in lateral displacement at different time intervals

Both the increment and decrement in the lateral displacement of the soil in layer A were the largest, followed by those in layers B and C. The maximum increment and decrement of the lateral displacement occurred at location A1 from 1.0–1.5 s. The maximum value of the lateral displacement increment occurred at position A1 from 1.0–1.5 s with a maximum increment of 6.35 mm. The minimum value of the decrement occurred at position A1 from 2.0–2.5 s, with a maximum decrement of 5.81 mm.

The above results indicate that the change in the lateral stress on the soil in layer B was the largest; however, this change does not cause the largest change in lateral displacement in layer B, instead causing the largest change in lateral displacement in layer A. In addition, the magnitude of the change in lateral stress does not directly correspond to the magnitude of the change in lateral displacement on the same timeline; e.g., the maximum increment in lateral stress is within the range of 0–0.5 s for layers A and B, but the maximum increment in lateral displacement is caused only in the range of 1.0–1.5 s. The maximum decrements in layers A and B are within the ranges of 1.5–2.0 s and 1–1.5 s, respectively, but the maximum decrement in lateral displacement is caused only within the range of 2.0–2.5 s, which indicates that the change in lateral displacement has a certain hysteresis relative to the lateral stress.

CONCLUSIONS

In this study, the variation patterns of soil lateral stress and displacement at the lateral position of a subsoiler were analyzed using soil trough experiments and discrete element simulations conducted at fixed points.

(1) The peak (positive) values of lateral stress and lateral displacement were significantly higher than their corresponding trough (negative) values. Both positive lateral stress and displacement showed a linear decreasing trend with increasing transmission distance. Among the soil layers, the highest positive lateral stress was observed in the B layer, while the highest positive lateral displacement occurred in the A layer.

(2) The directions of lateral stress and displacement were consistent over time. From 0 to 1.7 s, the lateral stress was positive, and the corresponding displacement occurred in the positive direction. Between 1.7 and 3.0 s, the lateral stress became negative, causing the displacement to shift in the negative direction. From 3.0 to 3.5 s, although the lateral stress remained negative at the lateral position, it was no longer sufficient to induce further lateral soil movement.

(3) The soil in the B layer experienced the greatest change in lateral stress; however, this did not result in the greatest lateral displacement within the same layer. Instead, the A layer exhibited the largest change in lateral displacement. Additionally, the variation in lateral displacement corresponded to the changes in lateral stress, but with a noticeable hysteresis, indicating that the displacement response lagged behind the stress changes.

ACKNOWLEDGEMENT

The authors were supported by Anhui Provincial Natural Science Foundation (2308085ME160).

REFERENCES

[1] Arvidsson, J., Hillerström, O. (2010). Specific draught, soil fragmentation and straw incorporation for different tine and share types. *Soil & Tillage Research,* Vol. 110, pp. 154–160, Sweden.

[2] Ding, Q., Ge, S., Ren, J., Li, Y. He R. (2017a). Characteristics of Subsoiler Traction and Soil Disturbance in Paddy Soil (水稻土深松阻力与土壤扰动效果研究). *Transactions of the Chinese Society for Agricultural Machinery.* Vol. 48, pp 47-56, Nanjing/China.

[3] Ding, Q., Ren, J., BELAL, E., Zhao, J., Ge, S., Li, Y. (2017b). Discrete element analysis of deep loosening process in wet clay rice soils (湿粘水稻土深松过程离散元分析). *Transactions of the Chinese Society of Agricultural Machinery*, Vol. 48, pp. 39-47, Nanjing/China.

[4] El Kahi, E., Deck, O., Khouri, M., Mehdizadeh, R., Rahme, P. (2020). A new simplified meta-model to evaluate the transmission of ground movements to structures integrating the elastoplastic soil behavior – Science Direct. *Structures.* Vol. 23, pp. 324-334, France.

[5] Hang, C., Huang, Y., Zhu, R. (2017). Analysis of the movement behaviour of soil between subsoilers based on the discrete element method. *Journal of Terramechanics,* Vol. 74, pp. 35–43, Yangling/China.

[6] Huang, Y., Hang, C., Yuan, M., Wang, B., Zhu, R. (2016). Discrete Element Simulation and Experiment on Disturbance Behavior of Subsoiling (深松土壤扰动行为的离散元仿真与试验). *Transactions of the Chinese Society for Agricultural Machinery*. Vol. 47, pp. 80-88, Yangling/China.

[7] Ibrahmi, A., Bentaher, H., Maalej, A. (2014). Soil-blade orientation effect on tillage forces determined by 3D finite element models. *Spanish Journal of Agricultural Research*, Vol. 12, pp. 941–951, Tunisia.

[8] Jude, L., Radhey, L. K. (2012). Effect of travel speed and vertical load on the subsoil force and displacement under a smooth steel roller. *Journal of Terramechanics*, Vol. 49, pp. 263–270, USA.

[9] Lamandé, M., Keller, T., Berisso, F., Stettler, M., Schjønning, P. (2015). Accuracy of soil stress measurements as affected by transducer dimensions and shape. *Soil & Tillage Research*, Vol. 145, pp.72–77, Denmark.

[10] Li, B., Chen, Y., Chen, J. (2016). Modeling of soil-claw interaction using the discrete element method (DEM). *Soil and Tillage Research*, Vol. 158, pp. 177–185, Yangling/China.

[11] Li, H., Zhang, Z.G., Xue, J.A., Li, Y.L. (2021). Effect of different tillage practices on soil environment and maize yield and efficiency (不同耕作方式对土壤环境及玉米产量与效益的影响). *Journal of Maize Sciences*. Vol. 28, pp. 70-77, Shanxi/China.

[12] Li, J., Sun, K.P., Zhang, Y.H., Zhang, T.H. (2023). Simulation of Tillage Behavior of Double Winged Subsoiler Based on Discrete Element Method (基于离散元法的双翼深松铲耕作行为的仿真分析). *Journal of Inner Mongolia Agricultural University (Natural Science Edition)*. Vol. 44, pp. 67-75, Yunnan/China.

[13] Liu, X.H., Qiu, L.C. (2017). Finite element simulation analysis of soil cutting by vibratory subsoiler-based on ANSYS/LS-DYNA (振动深松铲土壤切削有限元模拟分析). *Journal of Agricultural Mechanization Research*. 1, pp. 19-24, Shengyang/China.

[14] Lutz, Auersch. (2017). Mitigation of railway induced vibration at the track, in the transmission path through the soil and at the building. *Procedia Engineering*, Vol. 199, pp. 2312–2317, Germany.

[15] Ma, Y., Wang, A., Zhao, J., Hao, J., Li, J., Ma, L., Zhao, W., Wu, Y. (2019). Simulation analysis and experiment of drag reduction effect of convex blade subsoiler based on discrete element method (基于离散元法的凸圆刃式深松铲减阻效果仿真分析与试验). Transactions of the Chinese Society of Agricultural Engineering. Vol. 35, pp. 16-23, Hebei/China.

[16] Qin, K., Zhao, Y., Zhang, Y., Cao, C., Shen, Z. (2022). Lateral stress and its transmission law caused by operation of a double-wing subsoiler in sandy loam soil. *Frontiers in Environmental Science*, Vol.10, No. 986361, Anhui/China.

[17] Wang, Y., Zhang, D., Yang L., & Zhong, X., (2020). Modeling the interaction of soil and a vibrating subsoiler using the discrete element method. *Computers and Electronics in Agriculture,* Vol. 174, No. 105518, Nanjing/ China

[18] Zhang, S.L. (2018). Simulations and experiments of soil disturbance as affected by the dislocation arrangement of subsoilers (深松铲错位布置对土壤扰动影响的仿真与试验研究). *North West Agriculture and Forestry University,* Dissertation, Yangling/China.

[19] Zhang, Z., Gan, S., Zuo, G., Tong, J. (2021). Bionic Design and Performance Experiment of Sandfish Head Inspired Subsoiler Tine (以砂鱼蜥头部为原型的仿生深松铲尖设计与离散元仿真). *Transactions of the Chinese Society of Agricultural Machinery*. Vol. 52, pp. 33-42, Yunnan/China.

ESTABLISHMENT AND PARAMETER CALIBRATION OF QUINOA SEED-SOIL CONTACT MODEL BASED ON DISCRETE ELEMENT METHOD
/
基于离散元法的藜麦种子-土壤接触模型建立及参数标定

Wenxue DONG, Xuan ZHAO, Fei LIU*), Hongbin BAI, Dezheng XUAN, Anbin ZHANG, Yuxing REN
College of Mechanical and Electrical Engineering, Inner Mongolia Agricultural University, Hohhot 010010, China;
Tel: 13238446338; E-mail: dong18403045597@163.com; afei2208@imau.edu.cn
DOI: https://doi.org/10.35633/inmateh-76-75

Keywords: *Parameter calibration; Quinoa seed-soil; Contact model; Dynamic angle of repose*

ABSTRACT
This study provides valuable insights into the interaction between seeds and soil, specifically focusing on quinoa seeds. Accurate discrete element contact models and parameters have been lacking in this area, which has somewhat hindered the optimization and improvement of seeders. By analyzing the collision process between quinoa seeds and soil through contact experiments, the study finds that the adhesive force of the soil on quinoa seeds is much greater than the gravitational force on the seeds and increases with higher soil moisture content. The load-displacement curve obtained from the experiments closely resembles the loading-displacement curve of the JKR (Johnson-Kendall-Roberts) model, leading to the selection of the JKR contact model for simulating the quinoa seed-soil mixture. Using Plackett-Burman experiments, the study identifies the key factors that significantly affect the dynamic angle of repose: soil surface energy, quinoa seed-soil surface energy, and the static friction coefficient between quinoa seeds and soil. Based on the principles of Box-Behnken experimental design, regression analysis and parameter optimization are conducted on these significant factors, resulting in optimal parameter combinations under varying soil moisture content. The verification experiment shows an error of within 1.9%, demonstrating the accuracy of the calibrated parameters. This research provides a solid theoretical foundation for discrete element simulation of seed-soil contact, offering a reference for improving the design and efficiency of seeders.

摘要
种子-土壤相互作用的研究中缺乏准确的离散元接触模型和参数，在一定程度上限制了播种机具的优化改进。本文以藜麦种子与土壤为研究对象，通过接触试验分析藜麦种子与土壤接触碰撞过程，发现土壤对藜麦种子的粘附力远大于种子重力并随土壤含水率的增加而增加。试验所得加载位移曲线与 JKR 模型加载位移曲线规律相似，因此选用 JKR 接触模型作为藜麦种子-土壤混料接触模型。通过 Plackett-Burman 试验筛选出了对动态休止角影响显著的因素。通过 Box-Behnken 试验得到了不同土壤含水率下的较优参数组合。验证试验误差在 1.9% 以内，证明了标定参数的准确性。这为种子与土壤接触的离散元仿真提供了理论参考。

INTRODUCTION
The balanced distribution of nutrients and water in the soil is crucial for crop growth (*Cay et al., 2018*), while uniform seed spacing in the field directly influences crop yield (*Pareek et al., 2023; Sun et al., 2022*). However, the actual grain spacing achieved by precision seeders in field operations often deviates from uniformity due to accumulated errors (*Abdolahzare et al., 2018; Xie et al., 2023; Liu et al., 2022*). One significant factor affecting seed spacing uniformity is the seed bounce displacement caused by the impact of seeds with the soil in the seed furrow during their release from the seed metering device (*Li et al., 2022; Yan et al., 2020*). Thus, a comprehensive and systematic investigation into the mechanisms of seed-soil contact collision and the key factors influencing seed bounce displacement is essential. Such research holds substantial theoretical and practical importance for enhancing seed spacing uniformity. Physical experiments studying seed-soil collision processes are heavily influenced by seasonal climate conditions, making it challenging to obtain accurate measurements of parameters like collision contact force, collision speed, and bounce displacement. These parameters are critical for the design and optimization of seed metering devices. The discrete element method (DEM), a numerical simulation technique, offers an effective solution for examining seed-soil contact and collision processes (*Lei et al., 2021; Liao et al., 2023*).

Before conducting DEM simulation tests, it is necessary to establish a discrete element contact model and calibrate corresponding contact parameters (e.g., collision restitution coefficient, static friction coefficient, dynamic friction coefficient, surface energy) (*Zhao et al., 2022*).

Research to date has successfully calibrated DEM simulation parameters for various seeds, including corn (*Liu et al., 2021; Wang et al., 2016; Shi et al., 2023*), rice (*Zhang et al., 2020*), wheat (*Horabik et al., 2020; Sun et al., 2022*), and notoginseng (*Yu et al., 2020*). Findings suggest that the Hertz-Mindlin (no-slip) contact mechanics model is particularly suitable for calibrating parameters of dry seed particles, although contact parameters vary significantly between different seed types. During the sowing period, soil moisture content typically ranges from 15% to 20%, which introduces a degree of adhesion (*Wang et al., 2021*). To address this, many researchers use models like the Johnson-Kendall-Roberts (JKR) model (*Yang et al., 2024*), the Edinburgh Elasto-Plastic Adhesive (EEPA) model (*Chen et al., 2023*), or the Hertz-Mindlin with Bonding model (*Song et al., 2022; Zhou et al., 2023*) for soil parameter correction. However, modeling seeds or soil independently does not accurately reflect the seed-soil contact and collision dynamics, emphasizing the need for a suitable seed-soil mixture contact model.

Mixture contact models are crucial for accurately describing interactions between different particles and understanding the interaction mechanisms (*Zhang et al., 2023; Fang et al., 2022; Jiang et al., 2023*). These models are generally categorized into non-viscous and viscous contact models. Non-viscous models, such as the Hertz-Mindlin (no-slip) model, are typically used for dry particles (*Liao et al., 2022*). For mixtures involving viscous particles, models like JKR and EEPA are more appropriate (*Ma et al., 2022; Tian et al., 2021*). Although there has been progress in developing mixture contact models, theoretical research, particularly regarding model selection, remains insufficient (*Walunj et al., 2023*). For instance, *Zhou et al.* (*2023*) used the EEPA model to calibrate parameters for soil cohesion in a corn seed-soil contact test, highlighting the rationale behind choosing this model. Given the substantial differences in size and shape between quinoa and corn seeds, it remains unclear whether the EEPA model is suitable for smaller seeds like quinoa. Hence, further investigation into the contact models and parameter calibration for small-sized seeds and soil is necessary for accurately studying seed-soil collision during seed placement.

Addressing these issues, this study focuses on quinoa seeds and the specific soil used for quinoa cultivation, examining the contact process between quinoa seeds and soil. It aims to identify the most suitable contact model for quinoa seed-soil mixtures and calibrate relevant contact parameters. This research provides a theoretical foundation for developing contact models for small-sized seeds and offers valuable insights for studying mixture contact collisions.

MATERIALS AND METHODS

Quinoa Seed-soil Contact Test

During sowing, soil typically contains a certain level of moisture. Capillary water between soil particles forms discontinuous liquid bridges, creating adhesion between the particles. However, whether this adhesion force needs to be considered when establishing a collision contact model for small-sized seeds like quinoa and soil requires further investigation.

In this experiment, a texture analyzer was used to study the adhesion of quinoa seeds to soil when the seeds were in vertical contact with the soil, as shown in Figure 1. Six quinoa seeds of similar size (2.15 mm in length, 2.10 mm in width, and 1.28 mm in thickness) were attached to a probe, and soil was placed in a tray. The experiment was conducted with soil moisture content as the test variable. Considering that the ideal soil moisture content for quinoa sowing ranges from 15% to 20%, tests were performed at moisture levels of 15%, 17.5%, and 20%. Each experimental condition was repeated three times for accuracy.

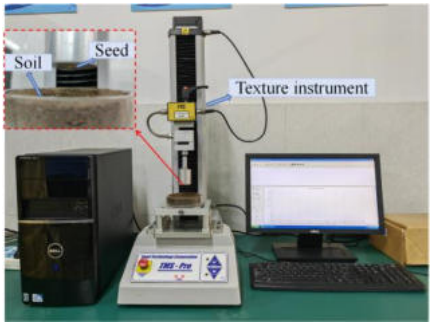


Fig. 1 - Quinoa seed-soil contact test device

During the test, the probe descends vertically at a speed of 30 mm/min. When it comes into contact with the soil, it continues to compress the soil until it reaches 30% deformation. Afterward, it starts the unloading phase, retracting at the same speed of 30 mm/min.

If the adhesion force of the soil on the quinoa seeds is greater than the gravitational force acting on the seeds, it shows that soil adhesion significantly affects the contact and collision dynamics between quinoa seeds and soil. In such cases, the adhesion force should be taken into account when creating a quinoa seed-soil contact model.

Physical Experiment of Quinoa Seed-soil Dynamic Angle of Repose

The dynamic angle of repose refers to the maximum angle between the slope of an accumulated pile of particles and the horizontal plane before the particles begin to collapse. This occurs when the inter-particle forces can no longer balance with gravity during the rotation of the particles within the drum. Figure 2 illustrates a custom-built device for measuring the dynamic angle of repose. This device consists of a drum (200 mm in diameter, 100 mm in length, made of organic glass), a coupling, a motor, and a controller.

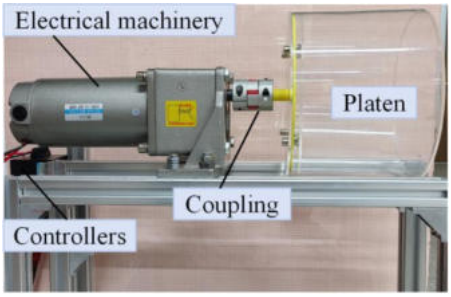


Fig. 2 - Measuring device for dynamic angle of repose

In the experiment, a quinoa seed-soil mixture was prepared with a seed-to-soil ratio of 1:4. The motor speed was set to 20 r/min. Once the speed stabilized, the dynamic angle of repose of the quinoa seed-soil mixture was recorded in real-time. Three experimental groups were established, with soil moisture content set at 15%, 17.5%, and 20% for each group, respectively. Each test was repeated three times, and the average value was taken for analysis.

Simulation Test of Quinoa Seed-soil Dynamic Angle of Repose

(1) JKR Contact Theory

The Hertz-Mindlin with JKR contact model is a cohesive model, whose surface energy can simulate the cohesive force between particles. The model is suitable for simulating wet viscous particles and agglomerated materials. The viscoelastic characteristics between particles can be expressed by the normal elastic force in the model. The normal elastic force is based on the normal overlap and surface energy:

$$F_{JKR} = -4\sqrt{\pi U_S E^*}\, a^{\frac{3}{2}} + \frac{4E^*\alpha^3}{3R^*} \quad (1)$$

$$\gamma = \frac{\alpha^2}{R^*} - \sqrt{\frac{4\pi U_S \alpha}{E^*}} \quad (2)$$

$$\frac{1}{E^*} = \frac{1-\nu_1^2}{E_1} + \frac{1-\nu_2^2}{E_2} \quad (3)$$

$$\frac{1}{R^*} = \frac{1}{R_1} + \frac{1}{R_2} \quad (4)$$

In the formula, F_{JKR} is JKR normal elastic force, N; U_S is the surface energy, (N/m), E^* is the equivalent elastic modulus, Pa; γ is the normal overlap between two contact particles, m; α is the radius of contact circle between two contact particles, mm; R^* is the equivalent contact radius, mm; R_1, R_2 is the contact radius of two particles, mm; ν_1, ν_2 is the Poisson 's ratio of two particles; E_1, E_2 is the elastic modulus of two contact particles, Pa.

When U_S is 0, the normal force of JKR can be simplified to Hertz-Mindlin normal force F_{Hertz}.

$$F_{JKR} = F_{Hertz} = \frac{4E^* \sqrt{R^*} \gamma^{\frac{3}{2}}}{3} \quad (5)$$

If the two particles are not in direct contact, the JKR model can provide attractive cohesion. At this time, the maximum gap between the two particles is:

$$\gamma_c = \frac{\alpha_c^2}{R^*} - \sqrt{\frac{4\pi U_S \alpha_c}{E^*}} \quad (6)$$

$$\alpha_c = \left[\frac{9\pi U_S R^*}{2E^*} - \left(\frac{3}{4} - \frac{1}{\sqrt{2}} \right) \right]^{\frac{1}{3}} \quad (7)$$

In the formula, γ_c is the maximum normal gap between particles with non-zero cohesion, mm; α_c is the maximum tangential gap when there is non-zero cohesion between particles, mm.

When the particles are in non-actual contact and the gap is less than or equal to γ_c, the cohesion of the JKR model reaches the maximum.

$$F_{pullout} = -\frac{3}{2} \pi U_S R^* \quad (8)$$

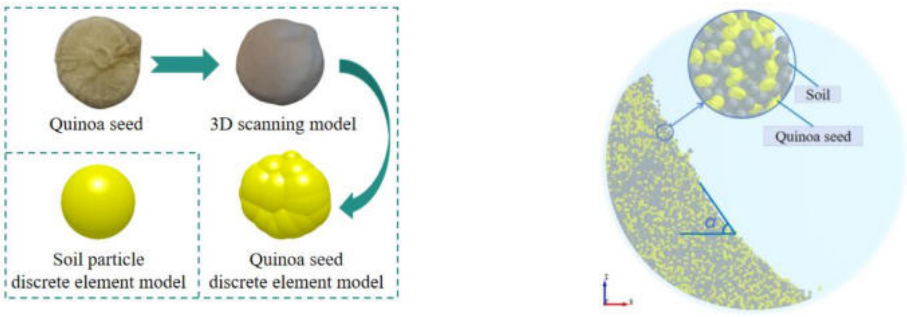
At this time, the adhesion between particles is in a critical state, and if the tension is increased, the two particles are separated. Therefore, the maximum tensile force F_l that separates the two particles is:

$$F_l = -\frac{3}{2} \pi U_S R^* \quad (9)$$

In order to accurately express the adhesion phenomenon, the Hertz-Mindlin with JKR contact model was selected to construct the quinoa seed-soil interaction model, and the discrete element parameters of the quinoa seed-soil mixture were calibrated.

(2) Shear Modulus Measurement

In this paper, the seeds of Mengli No.1 were selected for experiment. Because the seed size is small and the difference between the seeds is small, it is assumed that the seed size is the same in the simulation. The quinoa seeds were scanned and sampled by a three-dimensional scanner to obtain a quinoa seed model, which was imported into the EDEM simulation software for filling. This process yielded a quinoa seed model closely matching the real seed. The soil of quinoa planting area in Inner Mongolia was selected, and the soil was screened by 2 mm fine sieve to obtain soil particles with uniform particle size. A soil model was established using spherical particles in EDEM, as shown in Figure 3(a). In the dynamic angle of repose simulation test, the size of the rotating drum is consistent with the actual size, as shown in Figure 3(b). According to the literature, the parameters of this simulation are determined, as shown in Table 1. During the test, the particles are generated by the particle factory. After the particles reach a stable state, the drum rotates at a speed of 20 r/min.



(a) **(b)**

Fig. 3 - Dynamic angle of repose simulation model

Table 1

Simulation parameter

Parameters	Numerical values
Poisson 's ratio of soil	0.46
Shear modulus of soil / Pa	4.3×10^{10}
Soil density / (g/cm^{-3})	2.65
Poisson 's ratio of quinoa	0.2
Shear modulus of quinoa / Pa	3.9×10^{8}
Quinoa density / (g/cm^{-3})	0.87
Poisson 's ratio of organic glass	0.37
Shear modulus of organic glass / Pa	2.3×10^{9}
Organic glass density / (g/cm^{-3})	1.15
Restitution coefficient of soil-organic glass collision	0.4
Quinoa seed-organic glass collision recovery coefficient	0.45
Quinoa seed-organic glass static friction coefficient	0.55
Dynamic friction coefficient of quinoa seed-organic glass	0.12

Based on the previous repeated experiments and the parameter selection range of reference (*Dong et al., 2023*), the variation range of quinoa seed-soil contact physical parameters was determined as shown in table 2.

Table 2

Discrete element simulation parameters

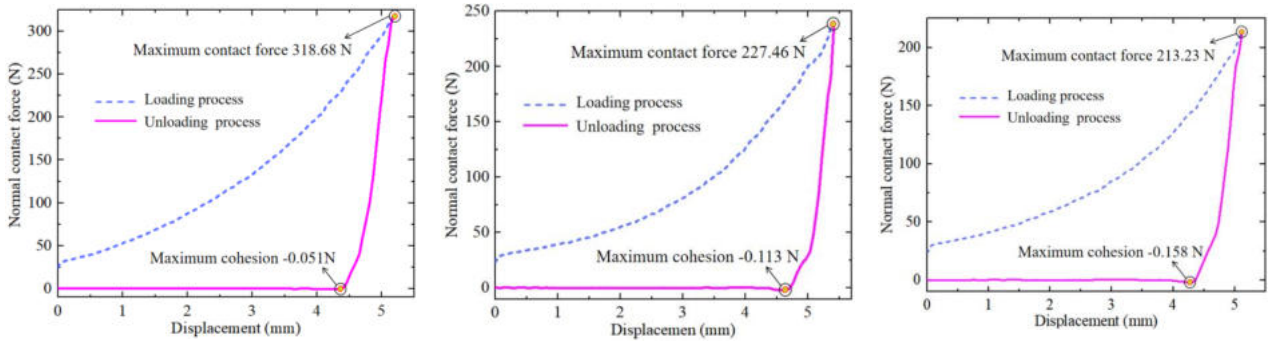
Factor	Level	
	-1	1
Quinoa seed-soil collision recovery coefficient *A*	0.2	0.6
Quinoa seed-soil static friction coefficient *B*	0.3	0.7
Quinoa seed-soil dynamic friction coefficient *C*	0.05	0.25
Soil-soil collision recovery coefficient *D*	0.2	0.6
Soil-soil static friction coefficient *E*	0.2	1
Soil-soil dynamic friction coefficient *F*	0.05	0.25
Soil-organic glass static friction coefficient *G*	0.3	0.9
Soil-organic glass dynamic friction coefficient *H*	0.05	0.25
Soil surface energy *I* / (J·m^2)	0.2	0.8
Quinoa seed-soil surface energy *J* / (J·m^2)	0.3	0.7

Plackett-Burman screening test was designed by Design-Expert software. The dynamic angle of repose of quinoa seed-soil mixture was used as the test index to screen out the parameters that had a significant impact on the index. On the basis of analyzing the results of Plackett-Burman screening test, the steepest ascent test was carried out on the selected factors with greater contribution. According to the principle of Box-Behnken test, the simulation parameters were calibrated and optimized. Finally, the dynamic angle of repose is measured by the image recognition method.

RESULTS

Analysis of Contact Between Quinoa Seeds and Soil

Figure 4 illustrates the load-displacement curve of quinoa seeds in contact with soil at three different moisture contents. In this figure, the x-axis represents the displacement of the seed caused by the probe, while the y-axis indicates the contact force between the quinoa seed and the soil. A negative contact force value signifies the bonding force between the quinoa seeds and soil during the upward movement of the seeds with the probe. The quinoa seeds were weighed using an electronic balance with an accuracy of 0.01 grams, with each seed's mass measured at 0.03 grams. The combined weight of six seeds was calculated to be 0.002 N. From Figure 4, it can be observed that when the soil moisture content is 15%, the maximum bonding force between the quinoa seeds and the soil is 0.051 N. At a soil moisture content of 17.5%, the maximum bonding force increases to 0.113 N. When the soil moisture content reaches 20%, the maximum bonding force further rises to 0.158 N. It is evident that the cohesive force between the quinoa seeds and the soil is significantly greater than the gravitational force acting on the seeds themselves. Therefore, when developing a contact model for quinoa seeds and soil, the adhesion between the seeds and soil must be taken into account.



(**a**) (**b**) (**c**)

Fig. 4 - Load displacement curves under different water content

(a) The soil moisture content is 15%; (b) The soil moisture content is 17.5%; (c) The soil moisture content is 20%.

During the loading phase, the load-displacement curve resembles the non-viscous contact behavior described by the Hertz model. In contrast, during the unloading phase, the load-displacement curve follows a pattern similar to the Boussinesq linear relationship, particularly as the seed is about to detach from the soil surface, indicating a critical bonding point between the seed and the soil. Based on this observation, it is inferred that the JKR model could effectively describe the quinoa seed-soil contact interaction. Consequently, the Hertz-Mindlin model, incorporating the JKR contact mechanics, was selected to construct the quinoa seed-soil interaction model.

Physical Test Results of Quinoa Seed-soil Dynamic Angle of Repose

The physical test of the dynamic angle of repose of quinoa seed-soil mixture is shown in Figure 5. The test results are shown in Table 3. When the soil moisture content is in the range of 15% to 20%, the dynamic angle of repose increases as the soil moisture content rises.

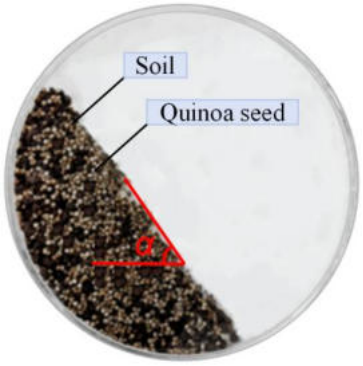


Fig. 5 - Physical test of dynamic angle of repose

Table 3

Physical test results of dynamic angle of repose

Moisture content / %	Dynamic angle of repose / (°)	Mean value
15	54.2 53.8 54.9	54.3
17.5	55.0 55.7 54.6	55.1
20	56.1 57.2 56.4	56.7

Simulated Test Results of Quinoa Seed-soil Dynamic Angle of Repose

(1) Plackett-Burman Test Results

The design and results of Plackett-Burman screening test are shown in Table 3. The Design-Expert software was used to process the data in Table 4, and the significant order of the influence of each parameter on the dynamic angle of repose was shown in Table 5.

Table 4

Results of response surface test

Test	Factor										Dynamic angle of repose / (°)
	A	*B*	*C*	*D*	*E*	*F*	*G*	*H*	*I*	*J*	
1	1	-1	1	1	-1	-1	-1	1	-1	1	55.5
2	-1	-1	-1	-1	-1	-1	-1	-1	-1	-1	48.3
3	1	-1	1	-1	1	1	1	-1	-1	-1	57.2
4	1	1	-1	1	1	1	-1	-1	-1	1	58.9
5	-1	-1	-1	1	-1	1	1	-1	1	1	64.7
6	-1	-1	1	-1	1	1	-1	1	1	1	69.9
7	1	-1	-1	1	1	-1	1	1	1	-1	58.1
8	-1	1	1	1	1	-1	-1	-1	1	-1	59.7
9	-1	1	1	1	-1	1	1	1	-1	-1	42.7
10	-1	1	-1	-1	1	-1	1	1	-1	1	46.8
11	1	1	1	-1	-1	-1	1	-1	1	1	61.5
12	1	1	-1	-1	-1	1	-1	1	1	-1	57.2

Table 5

Significance analysis of Plackett-Burman screening test results

Source of Variance	Sum of Squares	Freedom	Mean Square	*F*-Value	*P*-Value	Significance
Model	643.35	64.33	10	267.13	0.0476	*
A	22.14	22.14	1	91.93	0.0662	
B	60.30	60.30	1	250.38	0.0402	*
C	13.02	13.02	1	54.07	0.0861	
D	0.1408	0.1408	1	0.5848	0.5844	
E	35.71	35.71	1	148.27	0.0522	
F	35.71	35.71	1	148.27	0.0522	
G	28.52	28.52	1	118.43	0.0583	
H	33.67	33.67	1	139.80	0.0537	
I	317.24	317.24	1	1317.26	0.0175	*
J	96.90	96.90	1	402.36	0.0317	*
Residuals	0.2408	0.2408	1	267.13	0.0476	*
Cor Total	643.59		11			

According to the relevant data in Table 5, the Pareto diagram is drawn, as shown in Figure 6. It can be seen from Table 4 and Figure 7 that the significance of the influence of each contact parameter on the dynamic angle of repose is ranked from large to small: soil surface energy, quinoa seed-soil surface energy, quinoa seed-soil static friction coefficient, soil-soil static friction coefficient, soil-soil dynamic friction coefficient, soil-organic glass dynamic friction coefficient, soil-organic glass static friction coefficient, quinoa seed-soil collision recovery coefficient, quinoa seed-soil dynamic friction coefficient, soil-soil collision recovery coefficient. Among them, the three factors of soil surface energy, quinoa seed-soil surface energy and quinoa seed-soil static friction coefficient had significant effects, and the total contribution rate was 73.75%. The other seven factors were not significant. Therefore, three factors of soil surface energy, quinoa seed-soil surface energy and quinoa seed-soil static friction coefficient were selected for the steepest climbing test.

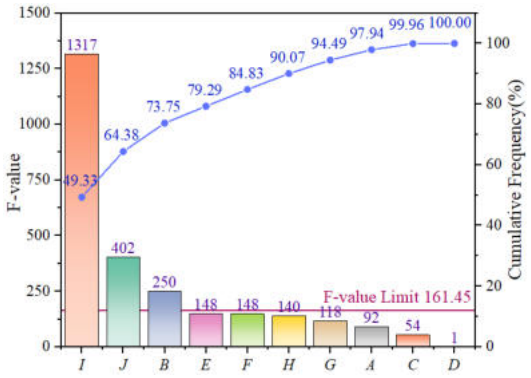


Fig. 6 - Pareto chart of PB design

(2) **Steepest climbing test Results**

Based on the analysis of the results of Plackett-Burman test, the steepest ascent test was carried out on the three significant factors. The relative error between the actual dynamic repose angle and the simulated dynamic repose angle is calculated to determine the optimal range of the simulation parameters. In the simulation process, the parameters that have no significant effect are removed from the intermediate level: Soil-soil static friction coefficient 0.6, soil-soil dynamic friction coefficient 0.15, soil-organic glass dynamic friction coefficient 0.15, soil-organic glass static friction coefficient 0.6, quinoa seed-soil collision recovery coefficient 0.4, quinoa seed-soil dynamic friction coefficient 0.15, soil-soil collision recovery coefficient 0.4.

The design and results of the steepest climbing test are shown in Table 6. The results show that the dynamic repose angle error is the smallest in the second group of tests, and the optimal interval can be determined near the second group of parameter values. Therefore, the Box-Behnken test was carried out with the second group of parameter values as the intermediate level, and the third group of parameter values of the first group as the low level and the high level respectively.

Table 6

Steepest climbing test design and results

Test	Soil surface energy / (J·m^2)	Quinoa seed-soil surface energy / (J·m^2)	Quinoa seed-soil static friction coefficient	Dynamic angle of repose / (°)	Relative error / %
1	0.3	0.2	0.3	52.6	-4.5
2	0.4	0.35	0.4	56.4	2.4
3	0.5	0.5	0.5	60.1	8.1
4	0.6	0.65	0.6	64.3	16.7
5	0.7	0.8	0.7	69.4	26.0

(3) **Box-Behnken Test Results**

In order to find the optimal parameter combination of soil surface energy, quinoa seed-soil surface energy and quinoa seed-soil static friction coefficient in the simulation test. Based on the steepest climbing test, the dynamic angle of repose was used as the test index, and the three-factor three-level response surface test was carried out according to the Box-Behnken test principle. The experimental design and results are shown in Table 7.

Table 7

Box-Behnken experimental design and results

Test	Factor			Dynamic angle of repose *Y* / (°)
	I	*J*	*B*	
1	-1	0	1	53.1
2	0	0	0	54.6
3	-1	-1	0	52.4
4	-1	1	0	56.1
5	0	0	0	55.7
6	-1	0	-1	53.6
7	1	0	-1	54.2
8	0	-1	1	53.7

Test	Factor			Dynamic angle of repose *Y* / (°)
	I	*J*	*B*	
9	0	-1	-1	54.1
10	1	1	0	60.3
11	1	0	1	58.9
12	1	-1	0	54.7
13	0	1	1	58.6
14	0	0	0	55.3
15	0	1	-1	56.2
16	0	0	0	55.6
17	0	0	0	54.9

The regression analysis of the test results was carried out by Design-Expert software, as shown in Table 8, and the regression equation of the qualified rate *Y* was obtained:

$$Y = 55.22 + 1.61I + 2.04J + 0.775B + 0.475IJ + 1.3IB + 0.7JB - 0.0225I^2 + 0.6775J^2 - 0.2475B^2 \quad (10)$$

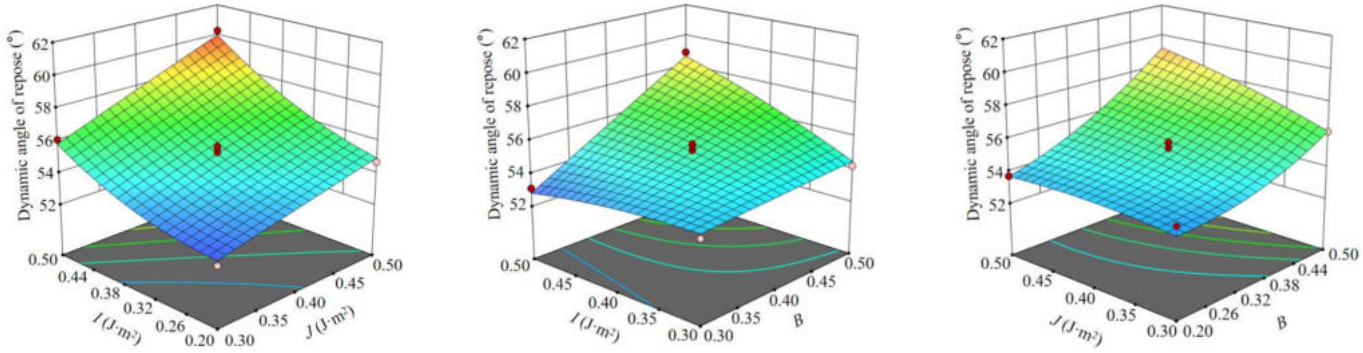
Table 8

Analysis of variance

Source of Variance	Sum of Squares	Mean Square	Freedom	*F*-Value	*P*-Value	Significance
Model	70.56	9	7.84	25.70	0.0001	**
I	20.80	1	20.80	68.18	< 0.0001	**
J	33.21	1	33.21	108.86	< 0.0001	**
B	4.81	1	4.81	15.75	0.0054	**
IJ	0.9025	1	0.9025	2.96	0.1291	
IB	6.76	1	6.76	22.16	0.0022	**
JB	1.96	1	1.96	6.42	0.0390	*
I^2	0.0021	1	0.0021	0.0070	0.9357	
J^2	1.93	1	1.93	6.34	0.0400	*
B^2	0.2579	1	0.2579	0.8454	0.3884	
Residuals	2.14	7	0.3051			
Lack of fit	1.27	3	0.4225	1.95	0.2639	
Pure error	0.8680	4	0.2170			
Cor total	72.70	16				

It can be seen from the results of variance analysis that the three factors of soil surface energy, quinoa seed-soil surface energy and quinoa seed-soil static friction coefficient have extremely significant effects on the dynamic angle of repose, and some factors have pairwise interactions. The regression model fitting degree of the evaluation index was extremely significant, and the lack of fit item $P > 0.05$, indicating that there were no other factors affecting the evaluation index. Through the regression coefficient test, the primary and secondary order of the factors affecting the dynamic angle of repose is quinoa seed-soil surface energy *J*, soil surface energy *I* and quinoa seed-soil static friction coefficient *B*.

According to the regression equation, the surface diagram of the influence of the factors with significant interaction on the evaluation index is drawn, as shown in Figure 7. From Figure 7(a), it can be seen that compared with quinoa seed-soil surface energy *J*, the soil surface energy *I* curve is steeper, indicating that it has a more significant impact on the dynamic angle of repose. It can be seen from Figure 7(b) that the soil surface energy *I* is similar to the trend of the quinoa seed-soil static friction coefficient *B* curve, indicating that the two factors have a more significant effect on the dynamic angle of repose. It can be seen from Figure 7(c) that compared with the quinoa seed-soil surface energy *J*, the quinoa seed-soil static friction coefficient *B* curve is steeper, indicating that it has a more significant effect on the dynamic angle of repose.



(a) (b) (c)

Fig. 7 - The effect of interaction on dynamic angle of repose

(4) Parameter Optimization and Simulation Verification Results

In order to obtain the best combination of parameters, the optimization module of Design-Expert software was used to optimize the analysis within the range of factor levels with 54.3°, 55.1° and 56.7° as the target values. The optimal parameter combination was determined. When the soil moisture content was 15%, the soil surface energy was 0.351 J·m^2, the quinoa seed-soil surface energy was 0.347 J·m^2, and the quinoa seed-soil static friction coefficient was 0.489. When the soil moisture content was 17.5%, the soil surface energy was 0.343 J·m^2, the quinoa seed-soil surface energy was 0.409 J·m^2, and the quinoa seed-soil static friction coefficient was 0.400. When the soil moisture content was 20%, the soil surface energy was 0.473 J·m^2, the quinoa seed-soil surface energy was 0.354 J·m^2, and the quinoa seed-soil static friction coefficient was 0.415.

The optimized parameters were used for verification test. The verification test results are shown in Figure 8, and the errors with the physical test are -1.8%, 0.9%, and 1.9%, respectively. The error is small, which proves the accuracy of the calibration parameters.

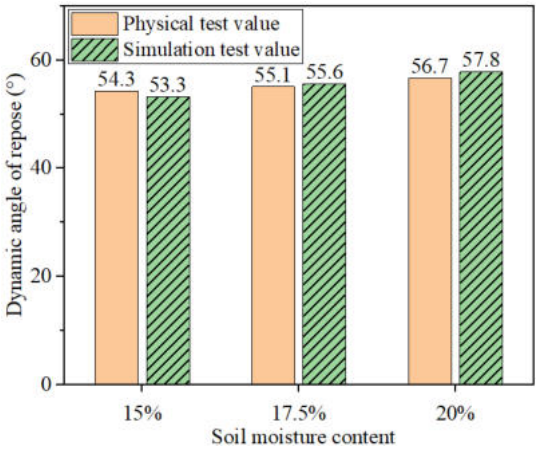
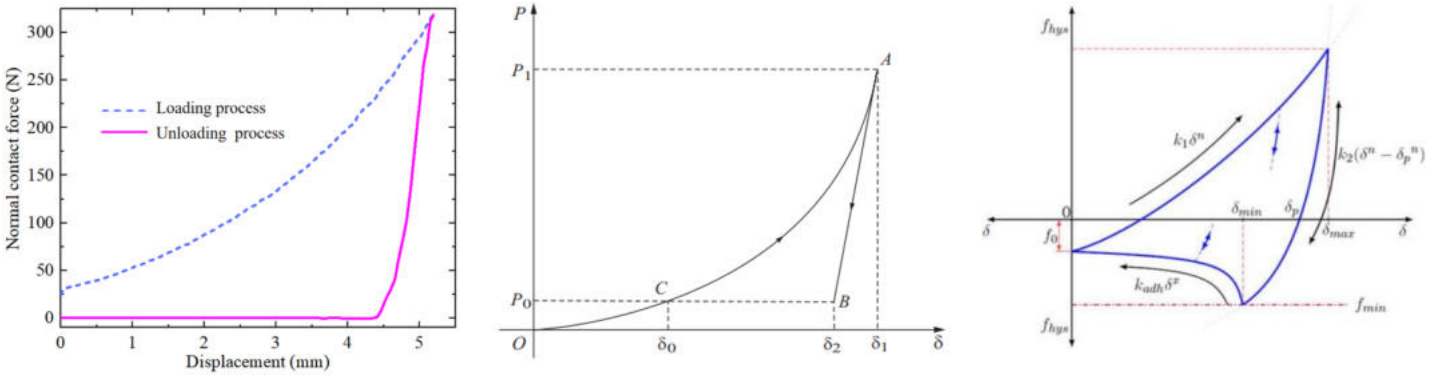


Fig. 8 - Comparison diagram of verification test and physical test

DISCUSSION

In recent years, as the discrete element (DEM) simulation is not limited by seasonal climate, more and more scholars use simulation to simulate the seeding process (*Tang et al., 2022; Luo et al., 2023*). The biggest difficulty of using DEM simulation is to select the correct model and the corresponding contact parameters (*Chen et al., 2023*). In this study, the contact process between quinoa seeds and soil under different soil water contents was analyzed by contact test. In the loading process, the load-displacement curve is similar to the non-viscous contact relationship of Hertz model. During the unloading process, the load-displacement curve is similar to the Boussinesq linear relationship when the seed is about to leave the soil surface to the critical bonding between the seed and the soil. This is consistent with the theoretical analysis results of Borodich, F.M.et al. (*Borodich et al., 2014*) JKR model. Compared with the load-displacement curve of the EEPA model, the load-displacement curve of the contact test is closer to the load-displacement curve of the JKR model, as shown in Figure 9. Therefore, the JKR model was selected as the quinoa seed-soil contact model. According to the agronomic requirements of quinoa planting, the soil moisture content should be between 15% and 20%. Therefore, it is of practical significance to select the soil moisture content range of 15% -20%.

In this range, the adhesion of soil to quinoa seeds increased with the increase of soil moisture content, which was consistent with the results of Zhou et al. (*Zhou et al., 2023*). In the process of sowing, it can be considered to appropriately increase the soil moisture content and increase the adhesion of the soil to the seed to reduce the bounce of the seed and the soil, thereby improving the uniformity of sowing.



(a) (b) (c)

Fig. 9 - Load displacement curve comparison diagram

(Zhou et al., 2023; Borodich et al., 2014)

(a) Load-displacement curve of contact test; (b) Load-displacement curve of JKR model; (c) Load-displacement curve of EEPA model.

At present, the calibration of discrete element simulation parameters mostly uses static angle of repose as a macro index (*Fang et al., 2022; Shi et al., 2022*). In the seeding operation, when the seed collides with the soil, most of the soil particles are in a moving state under the action of the opener, and the static angle of repose is not enough to fully characterize the rheological properties of the soil. Therefore, this paper chooses the dynamic angle of repose as the macro index. In the physical experiment of dynamic angle of repose, the dynamic angle of repose increases with the increase of soil moisture content. Seeds and soil particles are difficult to separate due to adhesion. The greater the adhesion is, the more difficult it is to separate, and the greater the dynamic angle of repose is. *Zhou et al.* (*2023*) concluded that the angle of repose does not increase with the increase of soil moisture content. There are two main reasons for the differences in the conclusions. First, the macro indicators are different. In this paper, the dynamic angle of repose is used as the macro indicator, and *Zhou Long et al.* used the static angle of repose as the macro indicator, as shown in Figure 10. Secondly, the range of sudden moisture content is different. The range of soil moisture content in this paper is 15% -20%, and the range of soil moisture content such as Zhou long is 15% -25%. In the static angle of repose test, when the soil moisture content exceeds 20%, the larger adhesion force of the soil to the seeds prevents the free scattering of particles, and the angle of repose formed by direct collapse in the final stage is smaller. In the dynamic angle of repose test, the seeds and soil particles rotate uniformly in the drum, avoiding the occurrence of sudden collapse.

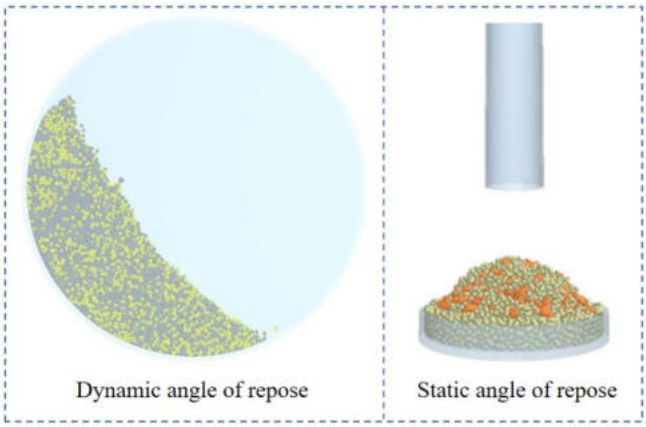


Fig. 10 - Comparison of dynamic static angle of repose (Zhou et al., 2023)

By comparing the calibration results of different scholars' JKR model parameters, it is found that the particle surface energy has a significant effect on the test index (*Qiu et al., 2022; Zeng et al., 2023*). In this study, the Plackett-Burman test was used to screen out the factors that had a significant effect on the dynamic

angle of repose, which were soil surface energy, quinoa seed-soil surface energy, and quinoa seed-soil static friction coefficient. Based on the analysis and optimization of Box-Behnken test, the optimal parameter combination under different water content was determined. Compared with the physical test results, the error was within 1.9%. This proves the feasibility and accuracy of the JKR model as a quinoa seed-soil mixture contact model.

CONCLUSIONS

This study investigated the contact process between seeds and soil. The adhesion force of the soil to the seeds is significantly greater than the seeds' own force, and it increases with the soil's moisture content. The load-displacement curves obtained from the experiments are similar to those of the JKR (Johnson-Kendall-Roberts) adhesion model. Consequently, the JKR model is deemed suitable for use as a discrete element model for seeds with small diameters, such as quinoa, interacting with soil mixtures.

Through a physical experiment measuring the dynamic angle of repose, it was observed that the dynamic angle of repose increases as the soil moisture content increases.

The Plackett-Burman test was designed by Design-Expert software using the method of combining physical test and simulation test. The factors that significantly affected the dynamic angle of repose were soil surface energy, quinoa seed-soil surface energy and quinoa seed-soil static friction coefficient. Through the Box-Behnken test, a second-order regression model between the dynamic angle of repose and the three factors was established and the variance and regression model interaction effects were analyzed. The influence parameters are optimized to obtain the best parameter combination. When the soil moisture content was 15%, the soil surface energy was 0.351 J·m^2, the quinoa seed-soil surface energy was 0.347 J·m^2, and the quinoa seed-soil static friction coefficient was 0.489. When the soil moisture content was 17.5%, the soil surface energy was 0.343 J·m^2, the quinoa seed-soil surface energy was 0.409 J·m^2, and the quinoa seed-soil static friction coefficient was 0.400. When the soil moisture content was 20%, the soil surface energy was 0.473 J·m^2, the quinoa seed-soil surface energy was 0.354 J·m^2, and the quinoa seed-soil static friction coefficient was 0.415.

ACKNOWLEDGEMENT

This work was funded by The National Natural Science Foundation of China (32060418), The National Key Research and Development Program of China (2023YFD1600701), Inner Mongolia Autonomous Region Science and Technology Planning Project (2023YFDZ0024), Inner Mongolia Autonomous Region Science and Technology Planning Project (2025YFHH0133), Inner Mongolia Autonomous Region 'first-class discipline scientific research special project' (YLXKZX-NND-046) and Key R & D project of Ordos City (YF20232341).

REFERENCES

[1] Abdolahzare, Z., & Mehdizadeh, S. A. (2018). Real time laboratory and field monitoring of the effect of the operational parameters on seed falling speed and trajectory of pneumatic planter. *Computers and Electronics in Agriculture*, 145, 187-198. https://doi.org/10.1016/j.compag.2018.01.001.

[2] Borodich, F. M., Galanov, B. A., Keer, L. M., & Suarez-Alvarez, M. M. (2014). The JKR-type adhesive contact problems for transversely isotropic elastic solids. *Mechanics of Materials*, 75, 34-44. http://dx.doi.org/10.1016/j.mechmat.2014.03.011.

[3] Cay, A., Kocabiyik, H., & May, S. (2018). Development of an electro-mechanic control system for seed-metering unit of single seed corn planters Part I: Design and laboratory simulation. *Computers and Electronics in Agriculture*, 144, 71-79. https://doi.org/10.1016/j.compag.2017.11.035.

[4] Chen, X., Gu, F., Hu, Z., Wu, F., Luo, W., & Guo, K. (2023). The calibration of soil simulation parameters for wheat grown after rice in the Yangtze River Basin of China. *Sustainability*, 15(15079). https://doi.org/10.3390/su152015079.

[5] Dong, W. X., Li, N., Liu, F., Zhao, X., Wang, L. H., Xuan, D. Z., Zhong, W. D., Hu, H. T., Kong, X., Meng, X. Y., & Li, M. Y., Duan, Z. J. (2023). Study on vibration adsorption characteristics of small particle size seeds based on DEM. *INMATEH-Agricultural Engineering*, 71(3). https://doi.org/10.35633/inmateh-71-35.

[6] Fang, M., Yu, Z. H., Zhang, W. J., Gao, J., & Liu, W. H. (2022). Friction coefficient calibration of corn stalk particle mixtures using Plackett-Burman design and response surface methodology. *Powder Technology*, 396, 731-742. https://doi.org/10.1016/j.powtec.2021.10.040.

[7] Fang, W., Wang, X., Han, D., & Chen, X. (2022). Review of material parameter calibration method. *Agriculture*, 12(706). https://doi.org/10.3390/agriculture12050706.

[8] Horabik, J., Wiacek, J., Parafiniuk, P., Banda, M., Kobylka, R., & Stasiak, M., & Molenda, M. (2020). Calibration of discrete-element-method model parameters of bulk wheat for storage. *Biosystems Engineering*, 200, 298-314. https://doi.org/10.1016/j.biosystemseng.2020.10.010.

[9] Jiang, D., Chen, X., Yan, L., Gou, H., Yang, J., & Li, Y. (2023). Parameter calibration of discrete element model for cotton rootstalk-soil mixture at harvest stage in Xinjiang cotton field. *Agriculture*, 13(1344). https://doi.org/10.3390/agriculture13071344.

[10] Lei, X. L., Hu, H. J., Wu, W. C., Liu, H. N., Liu, L. Y., Yang, W. H., Zhou, Z. L., & Ren, W. J. (2021). Seed motion characteristics and seeding performance of a centralised seed metering system for rapeseed investigated by DEM simulation and bench testing. *Biosystems Engineering*, 203, 22-33. https://doi.org/10.1016/j.biosystemseng.2020.12.017.

[11] Li, S. P., Pan, J. F., Zhong, J. Q., Huang, Z. X., & Gan, F. F. (2022). Design and experiment of furrow opener for transversal sugarcane planter based on effective seeding space. *Transactions of the Chinese Society for Agricultural Machinery*, 53(7), 162-170. https://doi.org/10.6041/j.issn.1000-1298.2022.07.016.

[12] Liao, Y. Y., You, Y., Wang, D. C., Zhang, X. N., Zhang, H. F., & Ma, W. P. (2022). Parameter calibration and experiment of discrete element model for mixed seeds of oat and arrow pea. *Transactions of the Chinese Society for Agricultural Machinery*, 53(8), 14-22. https://doi.org/10.6041/j.issn.1000-1298.2022.08.002.

[13] Liao, Y., You, Y., Hui, Y., Zhang, X., & Wang, D. (2023). Mixed seeds of oat and vetch based on DEM-Fluent coupling motion simulation in a Venturi tube. *Processes*, 11(1095). https://doi.org/10.3390/pr11041095.

[14] Liu, R., Liu, L., Li, Y., Liu, Z., Zhao, J., Liu, Y., & Zhang, X. (2022). Numerical simulation of seed-movement characteristics in new maize delivery device. *Agriculture*, 12(1944). https://doi.org/10.3390/agriculture12111944.

[15] Liu, R., Li, Y. J., Liu, Z. J., Liu, L. J., & Lv, H. T. (2021). Analysis and calibration of discrete element parameters of coated maize seed. *Transactions of the Chinese Society for Agricultural Machinery*, 52(S1), 1-8+18. https://doi.org/10.6041/j.issn.1000-1298.2021.S0.006.

[16] Luo, W., Chen, X., Guo, K., Qin, M., Wu, F., Gu, F., & Hu, Z. (2023). Optimization and accuracy analysis of a soil–planter model during the sowing period of wheat after a rice stubble based discrete element method. *Agriculture*, 13(2036). https://doi.org/10.3390/agriculture13102036.

[17] Ma, X. J., Liu, M., Hou, Z., Li, J., Gao, X., Bai, Y., & Guo, M. (2022). Calibration and experimental studies on the mixing parameters of red clover seeds and coated powders. *Processes*, 10(2280). https://doi.org/10.3390/pr10112280.

[18] Pareek, C. M., Tewari, V. K., & Brajesh, N. (2023). A mechatronic seed metering control system for improving sowing uniformity of planters. *Journal of Engineering Research*. Available online 3 November 2023. https://doi.org/10.1016/j.jer.2023.10.041.

[19] Qiu, Y., Guo, Z., Jin, X., Zhang, P., Si, S., & Guo, F. (2022). Calibration and verification test of cinnamon soil simulation parameters based on discrete element method. *Agriculture*, 12(1082). https://doi.org/10.3390/agriculture12081082.

[20] Shi, G., Li, J., Ding, L., Zhang, Z., Ding, H., Li, N., & Kan, Z. (2022). Calibration and tests for the discrete element simulation parameters of fallen jujube fruit. *Agriculture*, 12(38). https://doi.org/10.3390/agriculture12010038.

[21] Shi, L., Zhao, W., Rao, G., Guo, J., & Wang, Z. (2023). Modeling of typically shaped corn seeds and calibration of the coefficient of rolling friction. *Agronomy*, 13(1573). https://doi.org/10.3390/agronomy13061573.

[22] Song, Z. H., Li, H., Yan, Y. F., Tian, F. Y., Li, Y. D., & Li, F. D. (2022). Calibration method of contact characteristic parameters of soil in mulberry field based on unequal-diameter particles DEM theory. *Transactions of the Chinese Society for Agricultural Machinery*, 53(6), 21-33. https://doi.org/10.6041/j.issn.1000-1298.2022.06.002.

[23] Sun, K., Yu, J. Q., Liang, L. S., Wang, Y., Yan, D. X., Zhou, L., & Yu, Y. J. (2022). A DEM-based general modelling method and experimental verification for wheat seeds. *Powder Technology*, 401, 117353. https://doi.org/10.1016/j.powtec.2022.117353.

[24] Sun, J., Zhang, Y., Zhang, Y., Li, P., & Teng, G. (2022). Precision seeding compensation and positioning based on multisensors. *Sensors*, 22(7228). https://doi.org/10.3390/s22197228.

[25] Tang, H., Xu, F. D., Xu, C. S., Zhao, J. L., & Wang, Y. J. (2023). The influence of a seed drop tube of the inside-filling air-blowing precision seed-metering device on seeding quality. *Computers and Electronics in Agriculture*, 204(107555). https://doi.org/10.1016/j.compag.2022.107555.

[26] Tian, X. L., Cong, X., Qi, J. T., Guo, H., Li, M., & Fan, X. H. (2021). Parameter calibration of discrete element model for corn straw-soil mixture in black soil areas. *Transactions of the Chinese Society for Agricultural Machinery*, 52(10), 100-108+242. https://doi.org/10.6041/j.issn.1000-1298.2021.10.010.

[27] Wang, X. L., Zhong, X. K., Geng, Y. L., Wei, Z. C., Hu, H., Geng, D. Y., & Zhang, X. C. (2021). Construction and parameter calibration of the nonlinear elastoplastic discrete element model for no-tillage soil compaction. *Transactions of the Chinese Society of Agricultural Engineering*, 37(23), 100-107. https://doi.org/10.11975/j.issn.1002-6819.2021.23.012.

[28] Wang, Y. X., Liang, Z. J., Zhang, D. X., Cui, T., Shi, S., Li, K. H., & Yang, L. (2016). Calibration method of contact characteristic parameters for corn seeds based on EDEM. *Transactions of the Chinese Society of Agricultural Engineering*, 32(22), 36-42. https://doi.org/10.11975/j.issn.1002-6819.2016.22.005.

[29] Walunj, A., Chen, Y., Tian, Y., & Zeng, Z. (2023). Modeling soil–plant–machine dynamics using discrete element method: A review. *Agronomy*, 13(1260). https://doi.org/10.3390/agronomy13051260.

[30] Xie, C., Zhang, D., Yang, L., Cui, T., He, X., Du, Z., & Xiao, T. (2023). Research and analysis on the influence of different speed measurement methods on the monitoring accuracy of seed spacing. *Agriculture*, 13(128). https://doi.org/10.3390/agriculture13010128.

[31] Yan, B. X., Wu, G. W., Fu, W. Q., Gao, N. N., Meng, Z. J., & Zhu, P. (2020). Influencing factors of corn implantation distribution for high-height planting based on EDEM. *Transactions of the Chinese Society for Agricultural Machinery*, 51(S2), 47-54. https://doi.org/10.6041/j.issn.1000-1298.2020.S2.006.

[32] Yang, L., Li, J. W., Lai, Q. H., Zhao, L. L., Li, J. J., Zeng, R. H., & Zhang, Z. H. (2024). Discrete element contact model and parameter calibration for clayey soil particles in the Southwest hill and mountain region. *Journal of Terramechanics*, 111, 73-87. https://doi.org/10.1016/j.jterra.2023.10.002.

[33] Yu, Q. X., Liu, Y., Chen, X. B., Sun, K., & Lai, Q. H. (2020). Simulation parameter calibration and experiment of Panax notoginseng seeds based on discrete element. *Transactions of the Chinese Society for Agricultural Machinery*, 51(2), 123-132. https://doi.org/10.6041/j.issn.1000-1298.2020.02.014.

[34] Zeng, Y., Chen, C., Quan, W., Xie, S., Shi, F., Ma, Z., & Wu, M. (2023). Calibration parameter of soil discrete element based on area difference method. *Agriculture*, 13(648). https://doi.org/10.3390/agriculture13030648.

[35] Zhang, R. F., Jiao, W., Zhou, J. L., Qi, B., Liu, H., & Xia, Q. Q. (2020). Parameter calibration and experiment of rice seeds discrete element model with different filling particle radius. *Transactions of the Chinese Society for Agricultural Machinery*, 51(S1), 227-235. https://doi.org/10.6041/j.issn.1000-1298.2020.S1.026.

[36] Zhang, S., Yang, F., Dong, J., Chen, X., Liu, Y., Mi, G., Wang, T., Jia, X., Huang, Y., & Wang, X. (2022). Calibration of discrete element parameters of maize root and its mixture with soil. *Processes*, 10(2433). https://doi.org/10.3390/pr10112433.

[37] Zhao, L., Zhou, H. P., Xu, L. Y., Song, S. Y., Zhang, C., & Yu, Q. X. (2022). Parameter calibration of coconut bran substrate simulation model based on discrete element and response surface methodology. *Powder Technology*, 395, 183-194. https://doi.org/10.1016/j.powtec.2021.09.065.

[38] Zhou, L., Dong, Q., Yu, J., Wang, Y., Chen, Y., Li, M., Wang, W., Yu, Y., & Yuan, J. (2023). Validation and calibration of maize seed-soil inter-parameters based on the discrete element method. *Agronomy*, 13(2115). https://doi.org/10.3390/agronomy13082115.

[39] Zhou, H., Chen, H. L., Geng, D. Y., Chen, M. Z., & Zhang, M. P. (2023). Discrete element modeling and parameter calibration of typical soil in maize field tillage layer. *Transactions of the Chinese Society for Agricultural Machinery*, 54(11), 49-60+113. https://doi.org/10.6041/j.issn.1000-1298.2023.11.005.

PROFILING DESIGN AND OPTIMIZATION OF END-EFFECTOR FOR PINEAPPLE EYE REMOVAL
/
菠萝去眼末端执行机构仿形设计与优化

Xingzao MA, Manfeng GONG*), Hua LI, Shuai WANG
School of Mechanical and Electrical, Lingnan Normal University, Zhanjiang 524048, China
Tel: 13414898351; E-mail: gongmanfeng@163.com
DOI: https://doi.org/10.35633/inmateh-76-76

Keywords: *pineapple, end-effector, profiling design, structural optimization design, finite element analysis, pineapple eye removal device*

ABSTRACT
To address the issues of high labor intensity, low efficiency, and excessive flesh loss in pineapple eye removal, a design scheme of pineapple eye removal end-effector based on mechanical arm was proposed according to the analysis results of pineapple eye morphological characteristics. Based on the experimental determination of the elastic modulus of the pineapple fruit eye area, the design of the end-effector mechanism for pineapple eye removal, kinematic and dynamic simulation analysis, and finite element optimization design of the eye removal gripper were carried out. Finally, a pineapple eye removal device was built for experimental verification. The simulation results indicated that the optimal length of the driving link of the pineapple eye removal end-effector mechanism was 23 mm. The eye removal trajectory of the gripper tip was highly consistent with the morphological contours of pineapple eyes. The maximum contact forces between gears and at the gripper-pineapple interface reached 33.13 N and 78.64 N, respectively. Under this condition, the maximum stress and maximum deformation of the gripper tip were 532.15 MPa and 0.17 mm, respectively, and there was a significant stress concentration phenomenon. After structural optimization, the maximum stress and deformation were reduced to 133.13 MPa and 0.12 mm, with reduction rates of approximately 75% and 29.4%, respectively. These improvements effectively enhanced the structural stress distribution and deformation behavior, meeting the material strength requirements. The experimental results showed that pineapple eye removal operations were efficiently completed by the end-effector mechanism, with an eye removal success rate of 98%. The research results provide theoretical and technical reference for the development of pineapple automatic processing equipment.

摘要
针对菠萝去眼劳动强度大、效率低、果肉损耗率偏高等问题，依据菠萝果眼形态特征分析结果，提出了一种基于机械臂的菠萝去眼末端执行机构设计方案。在试验测定菠萝果眼区域的弹性模量的基础上，开展菠萝去眼末端执行机构设计、运动学与动力学仿真分析及去眼手爪有限元优化设计，最后搭建菠萝去眼装置进行试验验证。仿真结果表明，菠萝去眼末端执行机构的原动件杆最优杆长为 23 mm，手爪尖点的去眼轨迹与菠萝果眼形态高度吻合，齿轮间最大接触力达 33.13 N，手爪与菠萝最大接触力为78.64 N，在此工况下，手爪尖点的最大应力与最大变形量分别为532.15 MPa 和0.17 mm，存在显著的应力集中现象。经结构优化后，最大应力和最大变形分别为 133.13 MPa 和 0.12 mm，降幅分别约为 75%和 29.4%，有效改善了结构应力分布与变形情况，满足材料强度要求。试验结果显示，该末端执行机构可高效完成菠萝去眼作业，去眼成功率达 98%。研究成果可为菠萝自动化加工装备研发提供理论支撑与技术参考。

INTRODUCTION
Pineapples are rich in nutrients, including fructose and vitamins, and have a unique flavor that is widely appreciated (*Deng et al., 2018*). However, fresh pineapples have a short shelf life, and their market prices vary significantly. To provide growers with stable income, most harvested pineapples were processed (*Fang, 2023; Gong, 2020*), with eye removal being the most time-consuming and labor-intensive aspect of post-harvest handling (*Liu et al., 2022*).

To date, numerous researchers have reported advancements in machinery for pineapple eye removal. *Kumar P. (2021)* developed a new device for easing the process specifically for removing eyes and evaluated the device by compared with the present tool. *Liu (*2020*) designed* a novel pineapple eye removal device based on a V-shaped blade, which performs eye removal by pulling the handle to enhance operational smoothness. *Zhang et al (2018)* from Dezhou University developed a "Detachable Pineapple Peeling and Eye Removal Machine" and *Wen et al (2021)* from Tianjin University of Technology designed a "Pineapple Peeling

and Eye Removal Machine". Both schemes achieved semi-mechanized peeling and eye removal through innovative structural designs. Such devices have a simple structure, low working efficiency, and high labor intensity, making them unsuitable for widespread adoption.

With the development and maturation of computer image processing, artificial intelligence, and electronic technology, some researchers have integrated computer vision technology with the requirements of pineapple eye removal. *Trieu N. M. et al (2022)* designed an automatic pineapple eye removal machine that fixed the pineapple in place, used a camera to identify the eye positions, and removed them with a rotating cutter. Additionally, *Zhang et al (2021)* from the Institute of Automation, Chinese Academy of Sciences, invented the "Automatic Pineapple Eye Removal Device," which automates mechanical peeling and eye removal. This device employed a camera to recognize the spiral trajectory of the pineapple eyes, generating control instructions to guide the pineapple knife along the spiral path to remove the eyes. *Liu et al (2024)* designed a machine for automatic pineapple eye removal based on machine vision, which used an industrial camera to identify pineapple eyes. The modified eye removal forceps were mounted on a tool-closing cylinder, and the eye removal function was realized through the operation of the closing cylinder. *Gong et al. (2025)* used a depth camera to locate the pineapple eyes and installed the eye-removal gripper on the XZ-axis sliding platform to realize the pineapple eye removal operation. *Qian et al (2024)* used 3D reconstruction technology to acquire surface data of the pineapple and applied a trajectory-searching algorithm to obtain the trajectory path. The tool was then guided along the planned trajectory to perform spiral eye removal on the pineapple. However, existing research on pineapple eye removal predominantly concentrates on operational implementation and process control, whereas systematic studies focusing on the optimization design of the end-effector mechanism itself are rarely addressed.

With the excellent flexibility, environmental adaptability and high-precision operation characteristics，the mechanical arm demonstrates significant advantages in reducing labor costs and enhancing production efficiency, while exhibiting application potential for multi-machine collaborative operation *(Wu et al., 2024; Li et al., 2024; Duan et al., 2021; Zhang et al., 2024)*. However, the research on the application of pineapple eye removal is still blank. Therefore, a mechanical-arm-based end-effector mechanism design for pineapple eye removal was proposed in this study. Specifically, 3D modeling was accomplished using SolidWorks; kinematic and dynamic simulation analyses were conducted via ADAMS software; structural optimization of the removal gripper was implemented through ANSYS finite element analysis; and a pineapple eye removal test device was ultimately constructed for experimental validation. The research results can provide theoretical support and technical guidance for the design and manufacture of pineapple eye removal equipment and addressing key technical challenges in this field.

MATERIALS AND METHODS

Physical properties of pineapple

China has a diverse range of pineapple varieties, with the Bali variety occupying the largest planting area, accounting for approximately 76% of total pineapple cultivation. This variety currently serves as the primary source for pineapple processing (*Jin, 2021*). The pineapples used in this experiment were purchased from farmers near Zhanjiang City, Guangdong Province, in early January. Forty pineapples with varying degrees of maturity and sizes were selected for morphological measurements, as detailed in Table 1. To ensure the eye-removal gripper conformed to the shape of the pineapple eyes and achieved optimal removal efficiency, measurements were taken of the physical characteristics of the pineapple eye area, including cross-sectional shape, depth range, angle range, and elastic modulus.

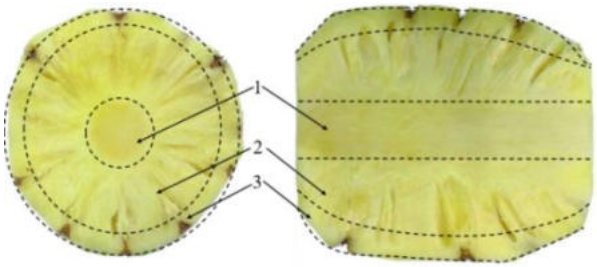
Table 1

Statistical table of characteristic parameters of pineapple (Bali)

Unpeeled mass [g]	Peeled mass [g]	Fruit longitudinal diameter [mm]	Fruit equatorial diameter [mm]	Number of fruit eyes
1252.5±187	897.5±162	124.7±12.7	105.94±5.5	97±7

Shape characteristics of pineapple eye

The structure of the pineapple fruit, as shown in Figure 1, was radially divided into three concentric layers from the interior to the exterior: the core, pulp, and eye. The core had a compact structure, while the pulp layer was relatively loose. The eye layer formed the outermost surface of the pulp, encompassing the entire fruit.

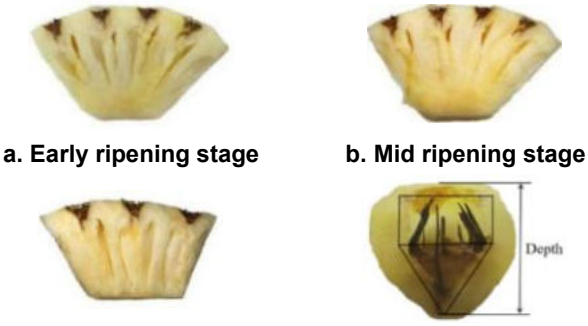


a. Radial cross-section **b. Axial cross-section**

Fig. 1 - Pineapple fruit structure

1-core area; 2-pulp area; 3-eye area.

Pineapples were classified into three ripeness stages: early ripening stage, mid ripening stage, and late ripening stage. Cross-sectional images of pineapple eyes at each maturity stage were presented in Figure 2. The shape of pineapple eyes remained generally consistent across different ripeness stages. Examination of individual pineapple eye profiles revealed a structure characterized by a frustum shape at the top and a cone-shaped pit at the base, with a distinct dark brown color. A total of 300 pineapple eyes representing the different ripeness stages were selected, and their depth and cone angles were measured. The depth and cone angle ranges of the pineapple eyes were shown in Figures 3 and 4, respectively.

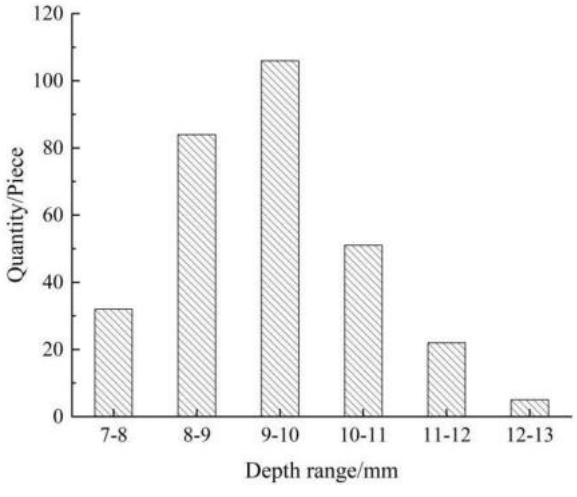


a. Early ripening stage **b. Mid ripening stage**

c. Late ripening stage **d. Single fruit eye**

Fig. 2 -Cross-section of a pineapple eye

As shown in Figures 3 and 4, the depth of the pineapple eyes was primarily distributed between 9~10 mm, with a maximum depth of 13 mm. The angle distribution mainly fell between 28°~32°, reaching a maximum angle of 40°. In the structural design, to meet the design requirements and ensure the complete removal of all pineapple eyes, the depth of the eye-removal gripper on the end-effector had to be at least 13 mm, with an angle of no less than 40°.



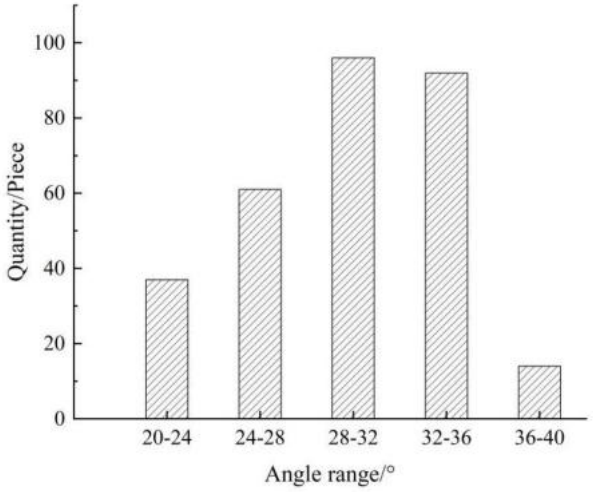
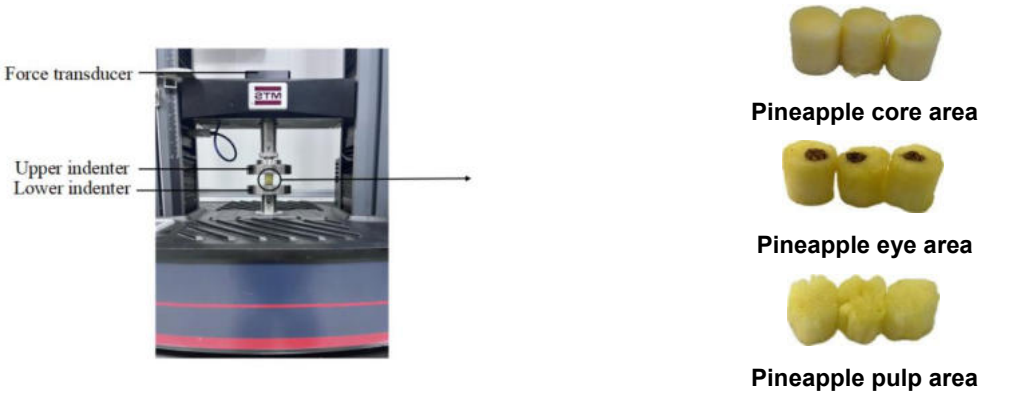


Fig. 3 -Depth distribution diagram of pineapple eyes **4 -Angle distribution diagram of pineapple eyes**

Compression test

The compression test was conducted using an electronic universal testing machine (MTS Exceed E43) with a maximum load capacity of 10 kN and an effective compression space of 1000 mm. A rigid plate indenter was employed, and the loading rate was maintained at 1 mm/min. Compression tests were performed on samples taken from the eye area, pulp area, and core area of each pineapple, as shown in Figure 5. Collected data were analyzed to calculate the elastic modulus for different regions of the pineapple at each maturity stage. The test results were presented in Figure 6.



a. Compression test apparatus **b. Compression test sample**

Fig. 5 - Compression test

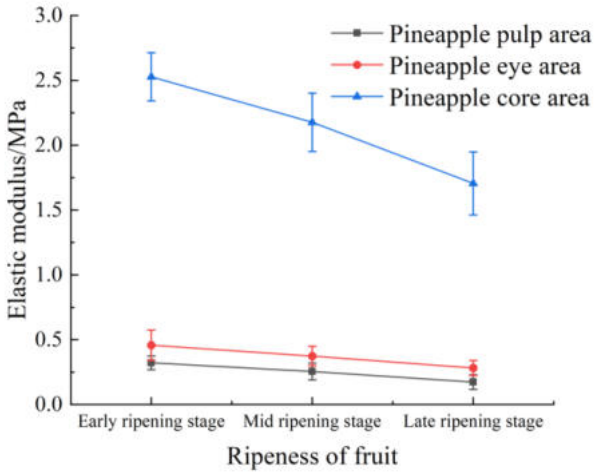


Fig. 6 -Elastic modulus of different regions of pineapple

Figure 6 showed that under identical ripeness conditions, the elastic modulus of the core region was significantly higher than that of the other two regions, while the eye and flesh regions exhibited little difference in elastic modulus. Elastic modulus across regions differed substantially among pineapples of varying ripeness. Early ripening pineapples demonstrated higher elastic modulus in all regions compared to other ripeness levels, with the highest value of 2.53 MPa observed in the early ripening core region. Conversely, the lowest modulus of 0.17 MPa occurred in the flesh of late ripening pineapples. These experimental results aligned with conclusions from compression tests on pineapples reported by *Xue Zhong et al. (2024)* from the Chinese Academy of Tropical Agricultural Sciences. Since mid-ripening pineapples dominated industrial processing, this study adopted the elastic modulus of the eye region (0.37 MPa) in mid ripening pineapples as the ADAMS simulation parameter.

The overall structure scheme

Based on the morphological characteristics of the pineapple eye, which featured a frustum-shaped top and a conical depression at the base, with a maximum depth of 13 mm and a base cone angle of 40°, the eye-removal gripper of the end-effector was designed with a profiling approach to match this shape and enhance

removal efficiency. Drawing inspiration from the pineapple eye's geometry, a pyramidal configuration was adopted, resulting in a semi-conical shape for the gripper. The dimensions were adjusted to fit the pineapple eye, with a depth of 15 mm and an angle of 21° to meet the design specifications. The opening and closing motion of the gripper was regulated by a gear mechanism, to which it was attached via a revolute joint. To ensure consistent motion, a limiting component was incorporated between the gripper and the gear mechanism to restrict its movement trajectory. The end-effector is shown in Figure 7.

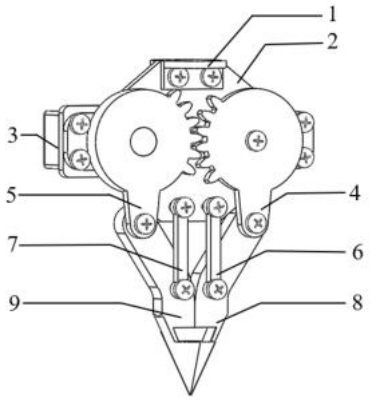


Fig. 7 - Schematic diagram of the end-effector

1- Clasp; 2-Bottom board; 3-Camel; 4-First gear mechanism; 5-Second gear mechanism; 6-First limit switch; 7-Second limit switch; 8-First eye removal gripper; 9-Second eye removal gripper

Structural parameter design

Since the designed end-effector was symmetrical about the central plane, the structure on one side of the centerline was selected for analysis (*Ye et al., 2011*). The structural diagram of the mechanism was shown in Figure 8, based on the configuration depicted in Figure 7.

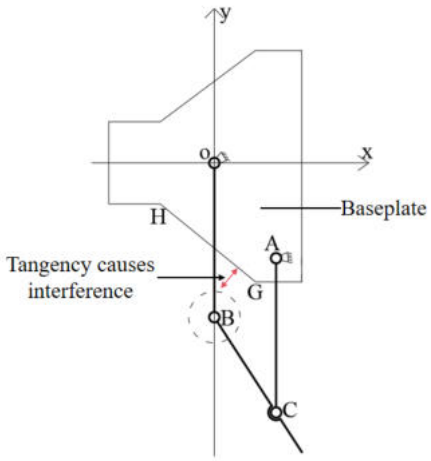


Fig. 8 - Structural diagram of the eye removal end-effector

Points O and A were fixed joints, consisting of the gear mechanism, limit element, and base plate, respectively. Points B and C were rotating joints, comprising the gear mechanism, limit element, and eye-removal gripper. HG represented the lower bevel of the base plate. As illustrated in Figure 9, when the length of the OB rod decreased below a certain value, interference occurred between the BC rod and the lower bevel HG of the base plate, thus requiring a minimum length for the BC rod. The rod width was modeled as a circle centered at point B with a radius of 5 mm. When this circle was tangent to the bevel HG, the BC rod was at its minimum achievable length. A rectangular coordinate system was established with point O as the origin. Given the coordinates of point H as (x_1,y_1) and point G as (x_2,y_2), the slope k of line l_{GH} was determined by:

$$k = \frac{y_2 - y_1}{x_2 - x_1} \tag{1}$$

Considering that the linear equation of l_{GH} was:

$$y - y_1 = k(x - x_1) \tag{2}$$

Point B was located on the y-axis, with coordinates $(0,y)$. According to the formula for the distance from a point to a line

$$d = \frac{|Ax_0 + By_0 + C|}{\sqrt{A^2 + B^2}} \quad (3)$$

Substituting the coordinates of point H (-10.5, 8.0) and point G (8.0, -22.5) yielded

$$y \approx -22.58 \text{ mm} \quad (4)$$

Therefore, the length of the OB rod was required to be at least 22.58 mm. It was rounded, and 23 mm was selected as its rod length.

The movement of the pineapple eye-removal gripper was controlled by a gear mechanism, where the rotation angle of the gear influenced the opening and closing distance of the gripper. Consequently, the relationship between the rotation angle of the gear and the opening and closing distance of the gripper was analyzed. The motion diagram for this mechanism was shown in Figure 9.

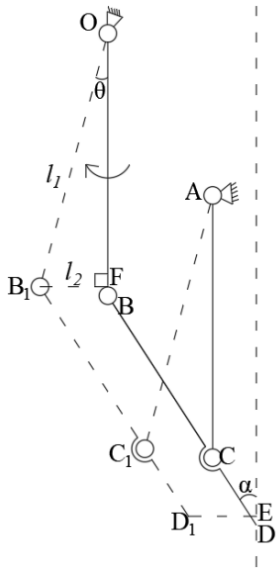


Fig. 9 - Motion diagram of the eye removal end-effector

In the figure, point D represented the initial position of the eye-removal gripper. Points B_1, C_1, and D_1 denoted the positions of points B, C, and D, respectively, after the OB rod had rotated by an θ angle. Point F was the perpendicular projection of B_1 onto the OB rod, while point E was the perpendicular projection of D_1 onto the central axis. The length of the OB rod was denoted as l_1, and the length of B_1F was denoted as l_2. Establishing the relationship between the rotation angle and the opening-closing distance was equivalent to identifying the relationship between the length D_1E and the parameter θ. The OB rod was parallel and equal in length to the AC rod. When the OB rod rotated by an angle θ, the AC rod rotated by the same angle θ under the motion of the OB rod, which results in the following relationship:

$$l_{D_1E} = l_{B_1F} = l_2 \quad (5)$$

In the right triangle OB_1F:

$$l_2 = l_1 \times \sin\theta \quad (6)$$

Thus, it was calculated:

$$\theta = arc\,sin\frac{l_2}{l_1} \quad (7)$$

Simulation optimization of rod length

Since the pineapple eye removal end-effector mechanism could not operate independently and required integration with a mechanical arm, a simplified test device was constructed. Based on the motion requirements and parameter settings of each structure, 3D modeling was completed in SolidWorks. After simplification, the model was imported into ADAMS (*Xia et al., 2021*).

Within ADAMS, material properties, constraints, external forces, and other factors were applied to various model components, and dynamic parameters were defined. The main body of the prototype model utilized aluminum alloy material. Physical property parameters for the pineapple were based on data obtained from compression tests, with material parameters listed in Table 2. The virtual prototype was shown in Figure 10. To optimize the OB link length, a series of simulations were performed in ADAMS software according to actual pineapple eye removal paths. By controlling two variables—eye removal time and rotational angular velocity—simulations for different link lengths were conducted to analyze the influence of driving link length on contact forces during eye removal and gear torque. This methodology determined the optimal OB link length. As previously analyzed, the minimum achievable OB link length was 22.58 mm. Considering practical constraints, this value was rounded to 23 mm. Starting from this minimum length as the initial value, the link length was incremented by 5 mm in successive simulations until reaching 43 mm. Simulation results for different link lengths were presented in Figure 11.

Table 2

Material property parameters

Parameter type	Aluminum alloy	Pineapple fruit eye
Material density [kg·m^{-3}]	7.85×10^{3}	1.09×10^{3}
Elastic modulus [MPa]	$2.\times10^{5}$	0.37
Poisson ratio	0.3	0.46

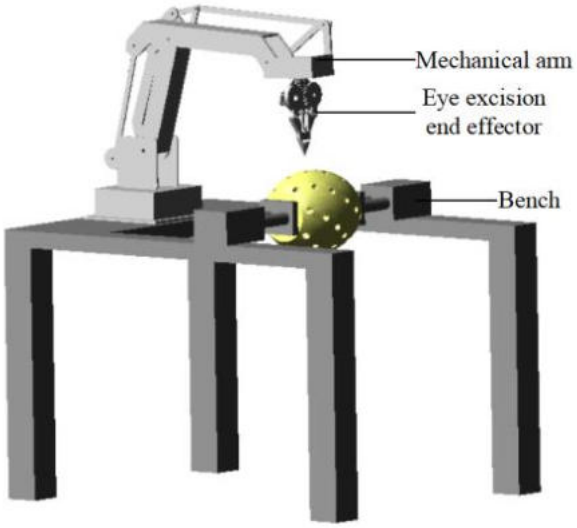
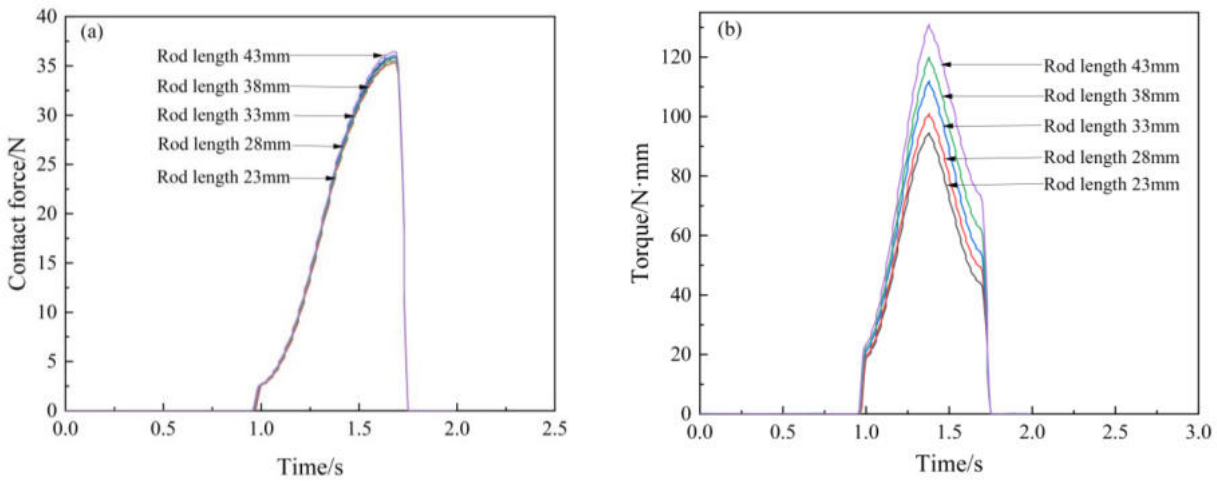
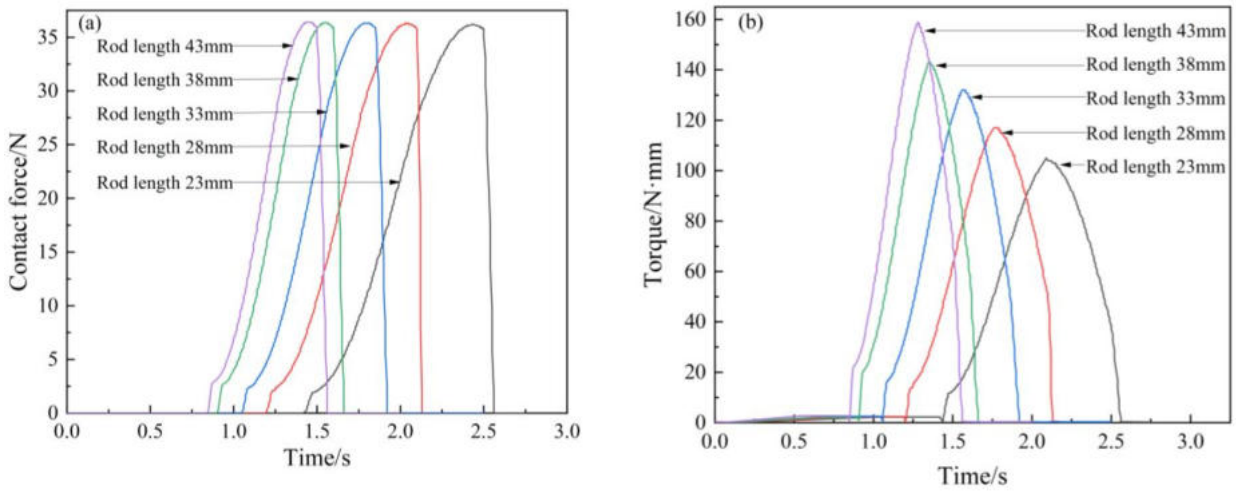


Fig. 10 - Virtual prototype built based on ADAMS



a. Eye removal time was the same



b. Rotational angular velocity was the same

Fig. 11 - Simulation results of different rod lengths

Figure 11 showed that when eye removal time or rotational angular velocity remained constant, contact forces were insensitive to changes in link length, while torque increased with longer link lengths. Simulation results revealed that shorter link lengths required lower torque, indicating that the minimum achievable OB link length constituted the optimal design length.

Kinematic and Dynamic Simulation Analysis

Within the ADAMS Simulation module, appropriate driving functions were applied to the prototype. The simulation time was set to 7 seconds with 2000 steps, modeling eye removal operations at three different locations. During the eye removal process, the gripper opened to a suitable angle via gear mechanism rotation. Driven by the mechanical arm, it positioned itself within the eye region. Upon reaching the top of the conical eye pit, the gripper closed to separate the pineapple eye. Following gripper closure, the mechanical arm rapidly ascended to complete the operation. The eye removal trajectory was shown in Figure 12.

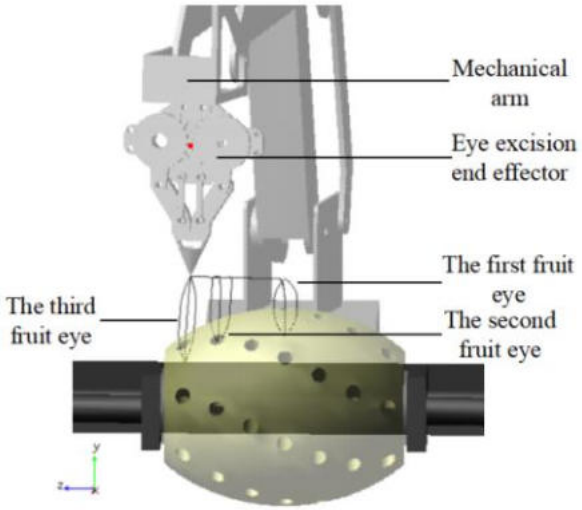


Fig. 12 - Eye removal trajectory

Figure 12 showed that the eye removal trajectory of the gripper tip highly aligned with the morphological profile of the pineapple eye, demonstrating the rationality of the designed end-effector solution.

To obtain mechanical parameters at critical positions during pineapple eye removal, the kinematics and dynamics simulation analysis of the contact force between the gears and the contact force between the eye removal gripper and the pineapple were carried out. The simulation results were shown in Figures 13 and 14.

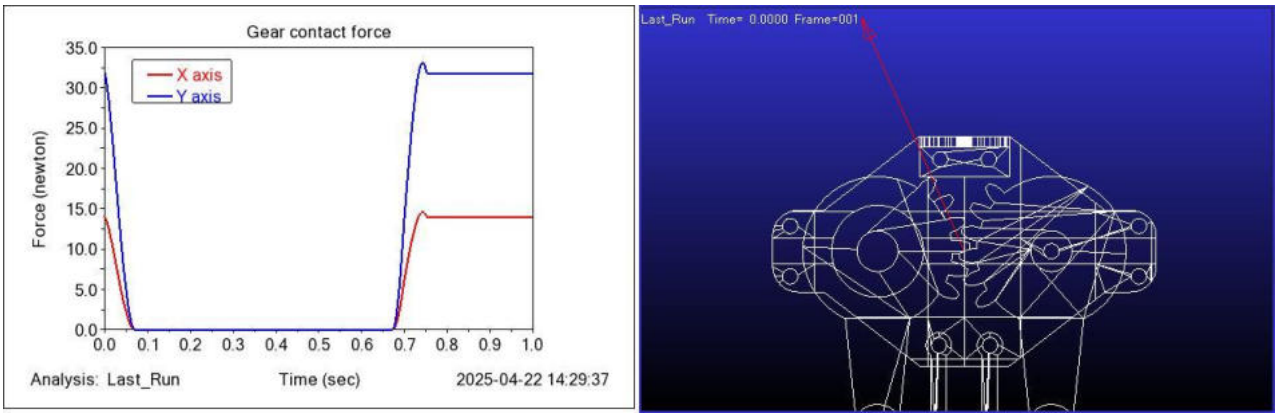


Fig. 13 -The contact force between the left and right gears

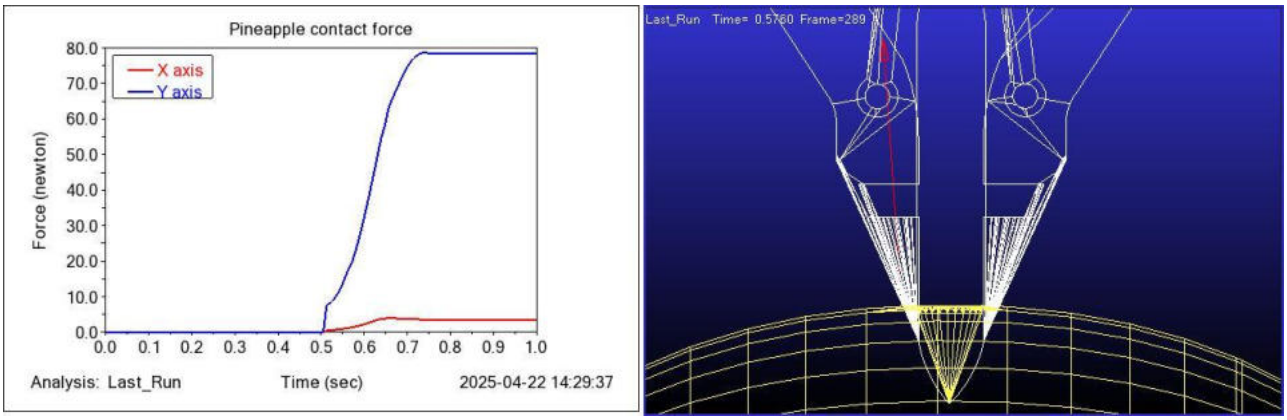


Fig. 14 -The contact force between the gripper and the pineapple flesh.

Figures 13 and 14 showed that at the instant the gripper contacted the pineapple, a contact reaction force was generated between the left and right gears, resulting in rapid contact force variation. This force changed by 33.25 N within 0.1 s. The maximum contact force between the gripper and the pineapple reached 78.64 N, with uniform overall variation, meeting the required shear force for pineapple eye removal.

To obtain the displacement curve along the eye removal direction (y-axis) and the rising phase velocity curve of the eye-removal gripper, the center of mass of the base plate and the contact point between the gripper and pineapple were analyzed. The results were shown in Figures 15 and 16.

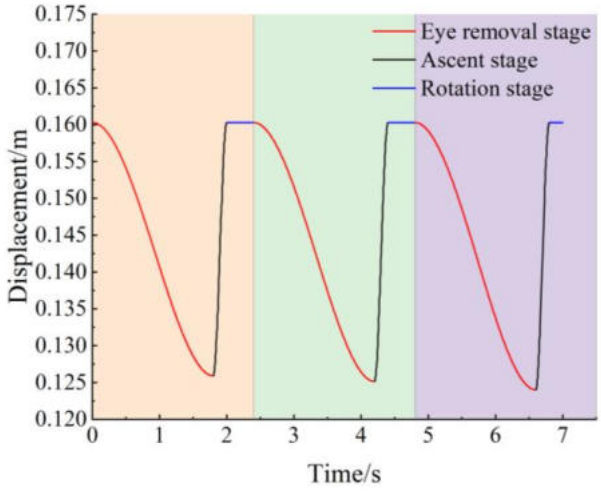


Fig. 15 -The y-axis displacement curve of the end-effector of eye removal

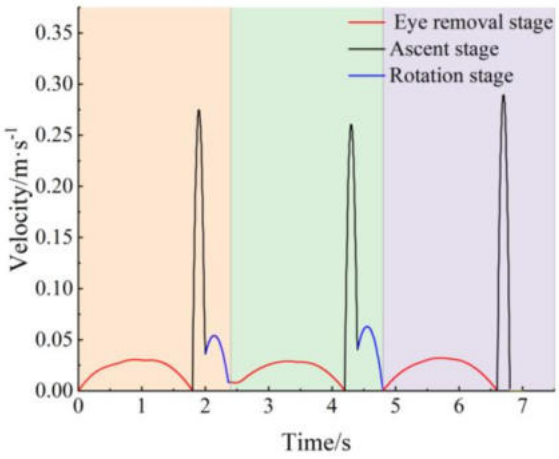


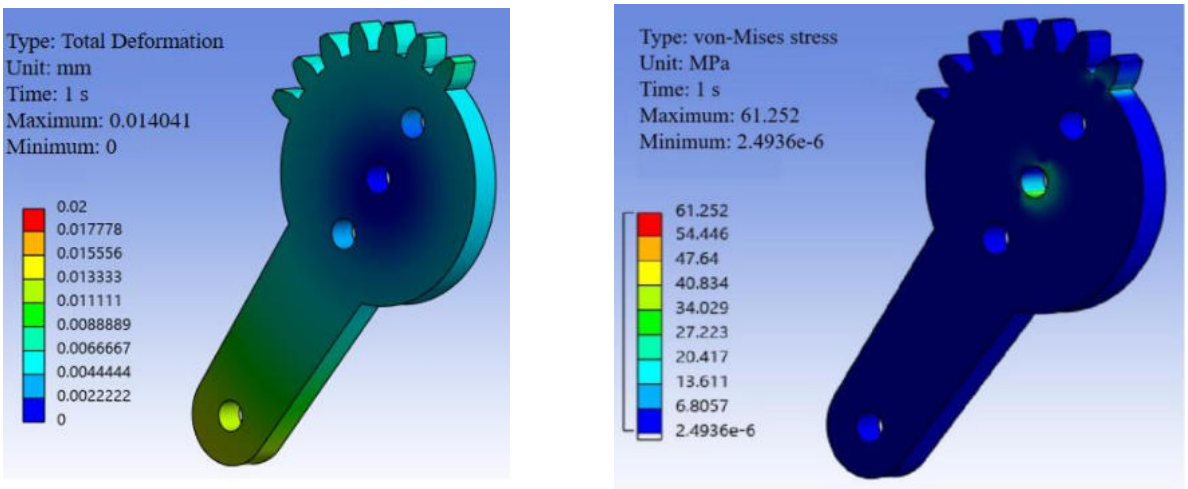
Fig. 16 - Amplification velocity curve of the pineapple-eye-removing end-effector

Figure 15 showed that during 0.0~2.4 s, the first pineapple eye (located at the center-top position) was removed, requiring the smallest downward displacement of the end-effector. From 2.4~4.8 s, the second eye (positioned laterally at a lower height) was removed, necessitating deeper end-effector displacement. During 4.8~7.0 s, the third eye (at the outermost and lowest position) was removed, demanding the maximum downward displacement. Figure 16 revealed similar velocity curves during three intervals: 0.00~1.75 s, 2.40~4.15 s, and 4.80~6.55 s, corresponding to gripper opening/closing motions for eye removal. Between 2.00~2.40 s and 4.40~4.80 s, variations occurred in the rising phase velocity of the gripper while the mechanical arm drove its rotation.

Simulation analysis of the eye removal process validated that the end-effector mechanism possessed effective displacement and velocity control capabilities during the removal of eyes at different positions. The simulation results demonstrated stable operational performance of the end-effector mechanism. The opening/closing and rotating motions of the eye-removal gripper exhibited high precision and repeatability in simulations, providing theoretical support for practical application of the device.

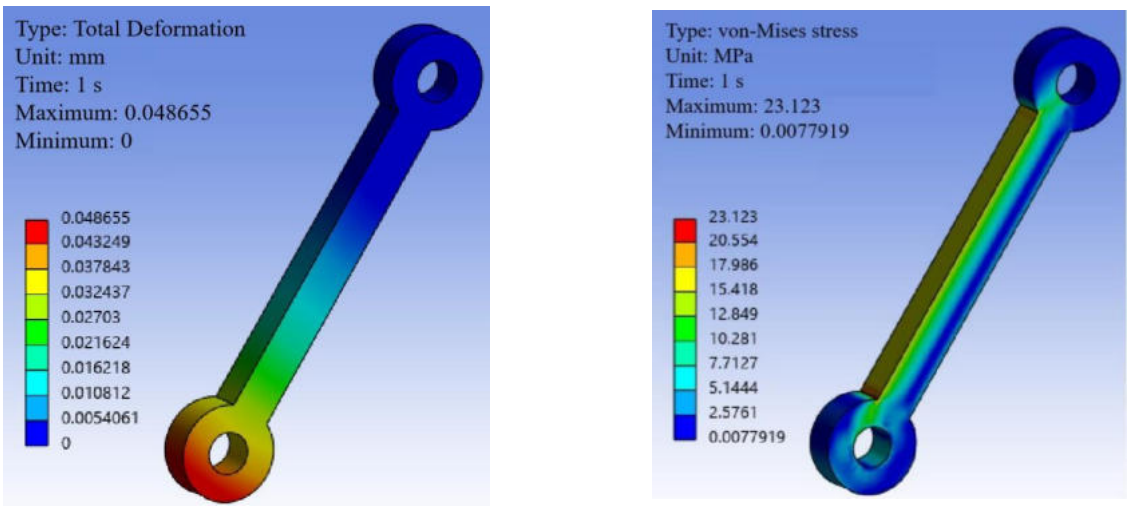
Finite element simulation analysis and structural optimization

To prevent stress concentration in components, ANSYS software was employed for finite element simulation analysis of the device. Aluminum alloy material properties were selected from the engineering database. Parts were discretized with a mesh size of 0.5 mm. Fixed constraints were applied to gears and the limit rocker arm, while constraint loads simulating actual working conditions were imposed. After applying all loads, the solution was computed. Total deformation contour plots and equivalent stress contour plots for the gear mechanism, limit components, and eye-removal gripper were obtained, as were shown in Figures 17-19.



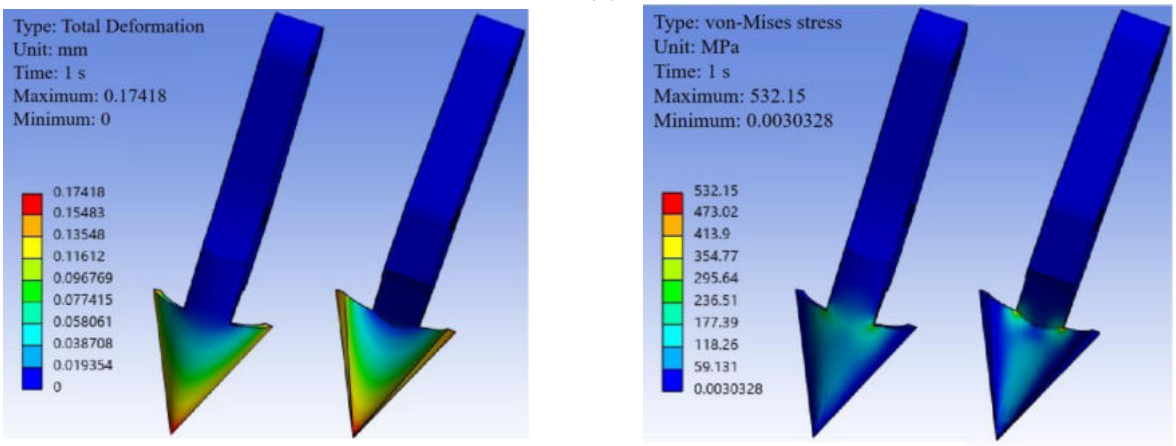
(a) (b)

Fig. 17 - Gear Mechanism Simulation Results
(a) Total deformation diagram; (b) Equivalent stress diagram



(a) **(b)**

Fig. 18 - Limiting component simulation results
(a) **Total deformation diagram**; **(b) Equivalent stress diagram**
(b)



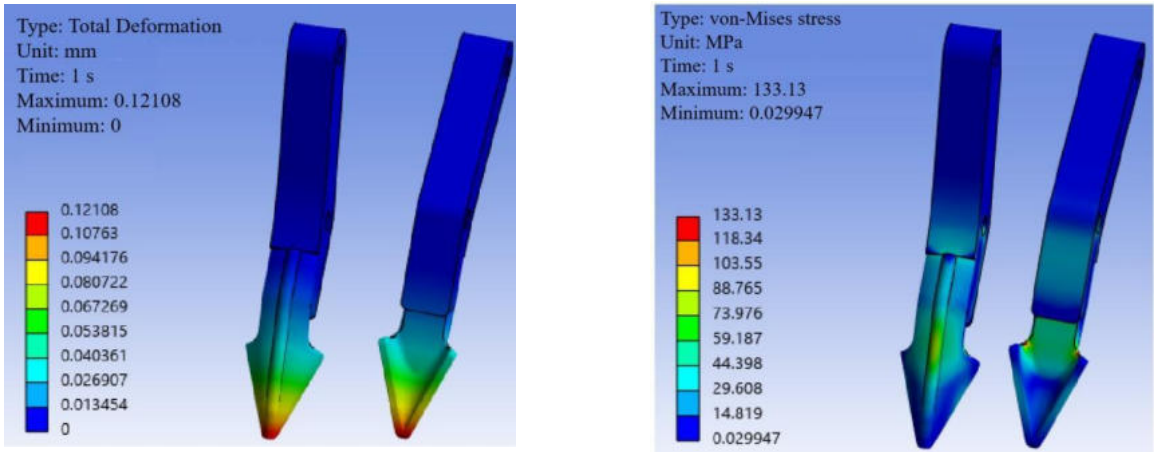
(a) **(b)**

Fig. 19 - Eye-removal gripper simulation results
(a) Total deformation diagram; (b) Equivalent stress diagram

Figures 17-19 showed that the maximum achievable stress at the gear tooth roots was 61.25 MPa, and the maximum achievable stress in the limit components was 23.12 MPa. For the eye-removal gripper, the maximum stress occurred at the blade tip, which was the contact force point with pineapple flesh, aligning with design expectations. However, the maximum deformation measured 0.17 mm and the maximum stress reached 532.15 MPa, exceeding the yield strength of aluminum alloy.

To address this issue, structural optimization was performed on the gripper. Focusing on contact force distribution, the original point-convergence blade tip design was modified to a linear-convergence configuration. By expanding the contact area with the flesh, the originally concentrated point load was distributed across a linear zone, effectively dispersing stress, improving overall load uniformity, and reducing local stress peaks. Analysis of the gripper body structure revealed insufficient wall thickness and inadequate bending stiffness. Additionally, stiffeners were confined to the transition area between the gripper and shank, leaving the main blade structure unsupported, further compromising overall rigidity. Consequently, structural improvements included thickening the main gripper body and adding cylindrical stiffeners along the curved outer edge toward the blade tip to enhance global stiffness and bending resistance. Fillet processing was applied to critical transition regions (gripper-shank junctions, stiffener-body connections) to prevent new stress concentrations at sharp corners.

The overall contour curvature and surface smoothness were optimized to improve mechanical performance and machining stability. Under identical constraints, the modified gripper was analyzed, with total deformation and equivalent stress contour plots shown in Figure 20.



(a) **(b)**

Fig. 20 - The improved eye-removal gripper simulation results.
(a) Total deformation diagram; (b) Equivalent stress diagram

Figure 20 showed that for the optimized eye-removal gripper, deformation at the blade tip decreased from 0.17 mm to 0.12 mm, and maximum stress reduced from 532.15 MPa to 133.13 MPa, representing reductions of approximately 75% and 29.4% respectively. The maximum stress was less than the yield strength of aluminum alloy (276 MPa), satisfying structural strength and stiffness design requirements.

RESULTS AND DISCUSSION

To verify the feasibility of the end-effector mechanism, a JETSON NANO mechanical arm was selected as the execution carrier. The self-designed eye-removal end-effector mechanism was mounted at its end to construct a pineapple eye removal mechanical test device. Experimental validation was conducted as shown in Figure 21. The mechanical arm was equipped with an HTS-35H steering engine to ensure the eye-removal gripper could penetrate the eye accurately. Based on the gear torque requirement (≥105 N·mm) determined from optimal link length simulations, a TBSN-K20 steering engine was selected to provide drive power for the eye-removal gripper.

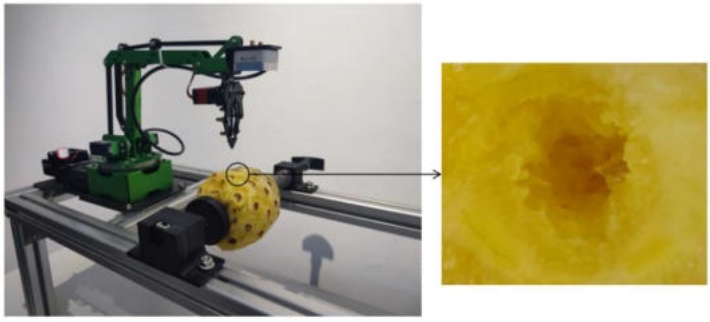


Fig. 21 - Pineapple eye removal test device and resulting eye removal effect

The experiment utilized five medium-sized pineapples at mid ripening as test materials, completing 50 eye removals total. After configuring the test device's operating program, the eye-removal gripper was manually aligned with target eyes. The automatic removal program was then executed: the mechanical arm descended autonomously with the gripper opening during descent. Upon reaching the top of the pineapple eye pit, the gripper began closing. After full closure, the mechanical arm ascended, thereby removing the eye. Experimental results were presented in Table 3.

Table 3

Eye removal test

Fruit maturation	Number of fruit eyes	The average time of eye removal[s]	Rate of success [%]
Mid ripening stage	50	2.5	98

Table 3 showed that during 50 eye removal operations by the mechanical arm with the end-effector, a success rate of 98% was achieved with an average removal time of 2.5 s per eye, validating the rationality of the structural design and operational reliability of the device. The experimental results demonstrated fundamental agreement with simulated trajectories and velocity responses, demonstrating the practical guidance value of kinematic and dynamic simulation parameters obtained from ADAMS.

ADAMS simulation results indicated an optimal driving link length of 23 mm for the end-effector mechanism. The eye removal trajectory of the gripper tip was highly consistent with the morphological contours of pineapple eyes. The maximum contact force between left/right gears reached 33.13 N, and the maximum contact force at the gripper-pineapple interface measured 78.64 N, both satisfying fundamental mechanical requirements for eye removal. However, ANSYS finite element analysis further clarified stress distribution and deformation characteristics in critical structures: the original gripper design exhibited stress concentration at the blade tip, with maximum stress reaching 532.15 MPa, exceeding the yield strength of aluminum alloy. After implementing structural optimization via blade tip modification (point-to-linear convergence), stiffener addition, and fillet processing, the maximum stress was reduced to 133.13 MPa and the deformation to 0.12 mm, thereby satisfying structural strength and stiffness requirements. Meanwhile, despite successful eye removal, the cut fruit flesh surface displayed irregularity with bruising and rough cutting surfaces. This might stem from suboptimal blade sharpness, edge angle, or material stiffness, causing excessive compression of the flesh. Additionally, the current semi-automatic test device requiring manual eye alignment exhibited low automation levels, limiting its applicability in industrial production lines.

Therefore, subsequent research would focus on two aspects: optimizing gripper material and blade edge angle to reduce flesh compression and improve cut surface smoothness, and integrating a vision module to achieve automatic eye recognition and positioning, thereby enhancing system intelligence and automation levels to provide more comprehensive technical support for practical applications.

CONCLUSIONS

Geometric characterization confirmed pineapple eyes exhibit a composite concave structure with frustum-shaped tops and conical bases. Compression tests revealed significant elastic modulus variations across pineapple regions at different ripeness levels: the core of early ripening pineapples showed the highest modulus (2.53 MPa), while late ripening flesh exhibited the lowest (0.17 MPa). The elastic modulus of eye regions in industrially preferred mid ripening pineapples (0.37 MPa) was adopted for simulations. Morphology-informed design yielded a mechanical-arm-based end-effector, with theoretical analysis establishing the gear system's minimum link length and the correlation between gear rotation and gripper opening distance. ADAMS simulations determined 23 mm as the optimal driving link length, demonstrated high consistency between the gripper tip's eye-removal trajectory and pineapple eyes' morphological contours, and confirmed maximum contact forces of 33.13 N (inter-gear) and 78.64 N (gripper-pineapple), satisfying shear removal force requirements. After structural optimization via blade tip modification (point-to-linear convergence), stiffener addition, and fillet processing, the eye-removal gripper achieved a maximum stress of 133.13 MPa and a deformation of 0.12 mm, satisfying structural strength and stiffness requirements. Experimental validation proved the design can effectively realize the pineapple eye removal operation and basically meet the design requirements. However, there is a problem of insufficient smoothness in the pit section of the eye. The follow-up research will focus on the optimization of the material and edge angle parameters of the eye-removal gripper to further improve the surface quality of the eye-removal.

ACKNOWLEDGEMENT

Thanks to the Innovation team of intelligence and key technology research for agricultural machinery and equipment in Western of Guangdong province (Grant No. 2020KCXTD039), the Key Field Project of Guangdong Provincial Universities (2024ZDZX4025), the Competitive Allocation Project of the Special Fund for Science and Technology Development of Zhanjiang City (2022A01058).

REFERENCES

[1] Deng C., Liu Y., Liang W., Ye L. (2018). Development status and countermeasures of Pineapple Industry in China (我国菠萝产业发展现状及对策). *Journal of Shanxi Agricultural Sciences*, vol. 46, no.6, pp. 1031-1034.

[2] Duan J., Wang Z., Ye L., Yang Z. (2021). Research progress and development trend of motion planning for fruit picking robotic arms (水果采摘机械臂运动规划研究进展与发展趋势). *Journal of Intelligent Agricultural Mechanization*, vol. 2, no.2, pp. 7-17.

[3] Fang W. (2023). Present situation and development suggestions of pineapple industry in Guangdong Province (广东省菠萝产业现状及发展建议). *Chinese Fruit,* no. 6, pp. 123-126.

[4] Gong M., Wang S., Ma X., Li H., Tu C., Guo Z. (2025). Design and Experiment of Pineapple Eye Removal Device Based on Machine Vision. Machines. vol. 13, no. 6, pp. 479-492.

[5] Gong Y. (2020). *Research on Strategies for Optimization and Upgrading of Pineapple Industry in Zhanjiang* (湛江市菠萝产业优化升级对策研究). MSc Thesis, Guangdong Ocean University, school of economics.

[6] Jin Y. (2021). Investigation and Analysis Report of Pineapple Market and Industry in China (我国菠萝市场与产业调查分析报告). *Market for Farm Products*, no. 8, pp. 46-47.

[7] Liu X. (2020). A Novel Pineapple Eye Removal Device (一种新型菠萝去眼器). CN211130616U, 21 Jul, 2020.

[8] Liu A., Xiang Y., Li Y., Hu Z., Dai X., Lei X., Tang Z. (2022). 3D Positioning Method for Pineapple Eyes Based on Multiangle Image Stereo-Matching. *Agriculture*, vol. 12, no. 12, pp. 2039.

[9] Liu A., Xie F., Xiang Y., Li Y., Lei X. (2024). Automatic pineapple eye removal Method and experiment based on machine vision (基于机器视觉的菠萝自动去眼方法与试验). *Journal of Agricultural Engineering*, vol. 40, no. 1, pp. 89-89.

[10] Li D., Hong K., Liu N., Wang G. (2024). Research on multi-action cooperative grasping strategy of manipulator in complex scene (复杂场景下机械臂多动作协同抓取策略方法研究). *Information and Co*ntrol, no. 4, pp. 619-631+643.

[11] Trieu N. M., Thinh N T. Pineapple Eyes Removal System in Peeling Processing Based on Image Processing[M]//Mobile Computing and Sustainable Informatics: Proceedings of ICMCSI 2022. Singapore: Springer Nature Singapore, 2022: 843-853.

[12] Kumar P. (2021). Design of Pineapple Eye-Removing Device, Advances in Manufacturing Technology and Management: *Proceedings of 6th International Conference on Advanced Production and Industrial Engineering (ICAPIE)—2021*. Singapore: Springer Nature Singapore, 2022: 142-148.

[13] Qian S., Zhao M., Chen H., Liang X., Wei Y. (2024). Method and experiment of spiral pineapple thorn removal based on 3D reconstruction (基于三维重建的菠萝螺旋去刺方法与实验). *Experimental Technology and Management*, vol. 41, no. 8, pp. 73-83.

[14] Wen B., Li C-Y. (2021). *A pineapple peel off eye integrated machine* (一种菠萝去皮去眼一体机). CN212307524U, 8 Jan, 2021.

[15] Wu Q., Wang Z., Yang Y., Lu Y., Liu G., Shi X., Bao P. (2024). Review of the development and application of mechanical arm structure (机械臂结构的发展与应用综述). *Aviation Science,* vol. 35, no.5, pp. 60-73.

[16] Xue Z., Zhang X., Chen R. (2024). Experimental study on morphology and mechanical properties of pineapple fruit (菠萝果形态及力学特性试验研究). *Journal of Agricultural Mechanization Research*, vol.46, no. 5, pp. 170-174.

[17] Xia W., Zhang Y. (2021). Research on co-simulation of six-degree-of-freedom manipulator based on SolidWorks and ADMAS (基于 SolidWorks 和 ADMAS 的六自由度机械臂联合仿真研究). *Mechanical Engineering and Automation*, no. 5, pp. 79-81.

[18] Ye M., Zhou X., Cai P., Zou H. (2011). Design of universal clamping mechanism for fruit picking robot (水果采摘机器人通用夹持机构设计). *Transactions of the Chinese Society of Agricultural Machinery*, vol.42, no.S1, pp. 177-180.

[19] Zhang D., Wang Z. (2018). Removable pineapple peel off eye integrated machine (可拆卸菠萝削皮去眼一体机). *Hebei Agricultural Machinery*, no.1, pp. 59.

[20] Zhang H., Wang Y., Hu J. (2021). Automatic pineapple eye removal device and method (菠萝自动去眼装置及菠萝自动去眼方法). CN113412954A, 21 Sep, 2021.

[21] Zhang M. (2024). Research on dual-arm collaborative control system (基于双机械臂协同控制系统的研究). *Electronic Production*, vol. 32, no. 20, pp. 29-31.

PREPARATION OF BIOMASS SEEDLING TRAYS USING LIGNIN BONDING PROPERTIES AND DESIGN OF HEATING COMPRESSION FORMING MOLD
/
基于木质素粘结特性的生物质育苗盘制备及热压成型模具设计

Jin-yang LI[1)], Wei ZHANG[*2)], Chun-tao YU[2)], Li-qiang QI[2)] , Bo ZHANG[1)]
[1)]College of Information and Electrical Engineering, Heilongjiang Bayi Agricultural University, Daqing/P.R.China
[2)]College of Engineering, Heilongjiang Bayi Agricultural University, Daqing/P.R.China
Tel: +86-459-15246110999; E-mail: zhang66wei@126.com

DOI: https://doi.org/10.35633/inmateh-76-77

Keywords: *Biomass; Seedling trays; Heating compression forming; Mold; Lignin; Degradable material*

ABSTRACT
In the current agricultural production, widely used plastic seedling trays suffer from poor air permeability, poor water permeability, and slow degradation. Therefore, this study proposes the preparation of degradable seedling trays utilizing the bonding effect of lignin, and the design of a heating compression forming mold according to the size and forming requirements of the trays. Flexural strength of seedling trays and seedling experiments were conducted to verify the effectiveness of the preparation process and mold design. The experiment results showed that the heating function requirements of the mold can be achieved when the heating power of the electromagnetic induction heater was set to 3000 W, and the heating time of the frame was 60 s. The heating compression mold designed can ensure that the seedling trays were heated uniformly and have excellent mechanical properties during the forming process. Biomass seedling trays prepared using lignin bonding and specific raw material ratios performed well in terms of compressive strength, water resistance and degradability. During the seedling cycle, no rupture occurred in the seedling trays, and the growth of maize seedlings was good enough to meet the actual seedling needs. The results of the study provide new ideas and methods for the preparation of lignin bonding degradable biomass seedling trays, and the application of heating compression forming mold provides technical support for the efficient and large-scale production of seedling trays.

摘要
针对当前农业生产中广泛使用的塑料育苗盘存在透气性差、透水性不佳以及难以降解等问题，本研究提出了利用木质素粘结作用制备可降解育苗盘，根据育苗盘的尺寸和成型需求，设计加热压缩成型模具。为验证制备工艺和模具设计有效性，进行了育苗盘抗弯强度及育苗试验。试验结果表明，在电磁感应加热器的加热功率设置为3000 W，料框加热时间为60 s 时，可达到模具加热功能要求。本研究设计的加热压缩成型模具能够确保育苗盘在成型过程中受热均匀并具有优异力学性能。利用木质素粘结及特定原料配比制备的生物质育苗盘在抗压强度、耐水性和生物降解性等方面均表现出色。在育苗周期内，育苗盘未发生破裂现象，玉米苗长势良好，能够满足实际育苗需求。研究结果为木质素粘结型可降解生物质育苗盘的制备提供了新的思路和方法，加热压缩成型模具的应用为育苗盘高效、规模化生产提供了技术支持。

INTRODUCTION
Maize is an important food crop and feed crop with large production potential and high economic benefits, and has an important strategic position in guaranteeing food security. Transplanting can prolong the growing period and improve the quality of maize, and the use of transplanting methods can solve the problems of short frost-free period, large temperature difference and low maturity of maize in the process of planting maize, so as to achieve stable and high yields of maize planting. The role of seedling trays in crop seedling and crop growth period has become particularly important.

Nowadays, the most used seedling trays are made of plastic, but the air permeability and water permeability of plastic are not satisfactory, and also has the disadvantage of difficult to degrade and cause pollution to the environment. In recent years, experts around the world have devoted more attention to the research and development of seedling containers using biodegradable materials.

[1]*Jin-yang LI, Ph.D.; Wei ZHANG, Prof. Ph.D.; Chun-tao YU, Ph.D.; Li-qiang QI, Ph.D.; Bo ZHANG, Ph.D.*

Biodegradable materials are characterized by non-toxicity, biocompatibility, and biodegradability, and are able to break down over time in the natural environment, doing so more rapidly than traditional materials *(Chen et al., 2023)*. Seedling trays prepared from this material have good water permeability and air permeability. The degradation of seedling trays can increase the content of soil organic matter and soil fertility in the late stage *(Choudhary et al., 2023)*. At the same time, waste resources can be effectively utilized by finding degradable materials to replace the original production materials *(Guerrini et al., 2017)*.

Biomass materials are an important branch of biodegradable materials, mainly derived from agricultural crops and their processing residues and wastes, and can be used to prepare seedling trays *(Li et al., 2022)*. Recent studies have further advanced the processing of agricultural waste. *Cheng et al. (2025)* developed a twin-screw straw pulping machine, which provides efficient technical solutions for converting straw into moldable substrates, laying a foundation for the large-scale production of biomass seedling trays.

The development of compression forming for biomass materials has enabled the effective conversion of what might otherwise be bulky and misshapen agricultural waste into seedling containers with standard dimensions and excellent physical properties. When the material is compressed and molded, the void space between each particle will change due to pressure *(Komine et al., 2023)*. After filling the mold with the material in the experiment, the elastic deformation of the particles will result in the destruction of the physical structure due to the positional changes produced by the original particles to achieve full filling *(Clemmer et al., 2023)*.

Li et al. (2014) used oligosaccharides production waste as the main raw material to prepare degradable seedling trays with good mechanical strength and water absorption by hot pressing process. *Wan et al. (2020)* prepared lycopene biomass seedling trays using rice straw and cow dung. *Juanga-Labayen et al. (2021)* used textile wastes mixed with paper scraps to make biodegradable seedling trays, which met the commercial standards in terms of compressive strength, degradability and seed germination.

Biomass solids forming processes can be classified into wet compression, carbonization, and heating compression forming *(Jian et al., 2013; Wang et al., 2017)*. The characteristics of the three forming processes can be found in the literature *(Xie et al., 2020; Guo et al., 2023)*. The heating compression forming is currently the most widely used process for biomass compression forming. Existing biomass heating compression forming process is mainly for biomass fuel pellet forming, and its main forming relies on the internal fiber structure of the mechanical mosaic, so it has a low moisture content, and the adhesive effect of lignin will avoid the expansion of the particles after the forming of the phenomenon of flaccidity. Meanwhile, efforts to optimize forming parameters have been made. *Yaheliuk et al. (2025)* optimized the technological parameters for producing fuel rolls from crop stem biomass, which offers insights into improving the forming efficiency and stability of biomass materials in thermal compression processes, including seedling trays.

The strength of particles after compression includes adhesion, inter-particle attraction, collision force, surface tension, solid bridging force and capillary force *(Rumpf et al., 2023)*. Compared with biomass forming fuel pellets, the structure of the seedling trays is complex, low moisture content of the material heating compression forming method cannot meet the needs of its structural filling, the need for the material in the compression process with a certain degree of mobility, and to make the biomass material within the lignin to a greater extent to play its role in the adhesion. Relevant research on composite materials has shown that the mechanical properties of agricultural waste-based composites can be adjusted by regulating additive concentrations *(Farcaș-Flamaropol et al., 2024)*, which guides the design of biomass seedling tray formulations to meet strength requirements.

Therefore, the purpose of this paper is to design a new biomass seedling trays forming mold for maize seedling transplantation. It is necessary to meet the requirements of forming dimensions and forming conditions for the preparation of biomass seedling trays without the addition of adhesives. After the completion of the equipment, the testing of the equipment includes the use of the equipment to make seedling trays, the bending resistance test and seedling test of the seedling trays to ensure that the seedling trays made through the mold can be used in practice.

MATERIALS AND METHODS

Selection and treatment of materials for seedling trays preparation

The cow dung and rice straw are suitable for use as seedling trays because they have the advantages of a wide range of material sources, a simple preparation process, and do not pollute the soil. Therefore, in this paper, cow dung and rice straw were selected as the raw materials for the preparation of biomass seedling trays. Cow dung and rice straw are mainly composed of lignin, cellulose, and hemicellulose, which together form the structural skeleton that supports plant cells and structures.

Lignin is a complex structure that is insoluble in water in an acidic environment and cannot be hydrolyzed. It is a polymer aggregate with glass transition properties *(Luo et al., 2019)*. When the heating temperature increases to the critical point, the unique glass transition characteristics of lignin will produce good adhesion, which can be used as a binder to achieve bonding effect in biomass compression molding *(Wang et al., 2016)*.

The cow dung was obtained from Beingmei Industrialized Dairy Cattle Breeding Base, Anda City, Heilongjiang Province, China (46°27′3" N, 125°22′50" E). The rice straw was obtained from Wutong River Farm, Tangyuan County, Jiamusi City, Heilongjiang Province, China (47°12′56" N, 130°49′15" E). The concentrations of lignin, cellulose and hemicellulose in cow dung and rice straw used in the experiment are shown in Table 1.

Table 1

Concentrations of lignin, cellulose and hemicellulose in cow dung and rice straw

Ingredient	Cow dung	Rice straw
Lignin (%)	26.43 ± 0.46	14.72 ± 0.26
Cellulose (%)	17.67 ± 0.72	39.35 ± 0.31
Hemicellulose (%)	21.10 ± 1.41	36.08 ± 0.42

The natural drying method was used to treat the rice straw, and the drying treatment was finished when the moisture content of the straw detected by the moisture content detector (SFY, Guanya Electronic Science and Technology Co., Ltd., Shenzhen, China) reached less than 15%. The dried rice straw was placed in hammer mill (Filtra, FML2000, Spain) and filtered using a 5 mm round-hole sieve accompanying the machine, resulting in a final crushed stalk length of 5 mm±1 mm. Cow dung samples were taken and placed in a light-proof and ventilated environment for shade drying to reduce the moisture content, until the cow dung was in the form of lumps and the moisture content was 23%±1%. The dried cow dung and crushed rice straw were put into a mixer (Bingcheng, BH-12.5, Harbin, China), with a mixing speed of 20 r/min and a mixing time of 10 min, until the cow dung was in a loose state, at which time the looseness was 0.42 t/m^3. The mass ratio of the cow dung to the rice straw was 90% and the moisture content of the experimental prepared biomass material detected using the drying method was 21%±0.6%.

Dimensions of biomass seedling trays

Based on market research and maize seedling agronomic requirements, seedling tray dimensions were determined as follows: considering the tray bottom thickness and water - storage need during seeding, the height was set at 35 mm (with a 3.5 mm - thick tray, the effective depth is 31.5 mm to keep seedlings intact after transplantation). Referring to common market plastic tray sizes, the longitudinal dimension was 42 mm. Thus, each cell size is 35 × 42 × 31.5 mm.

Current automated rice transplanting equipment is well-developed. In designing maize seedling trays, the maximum lateral space (285 mm) of the most widely used rice transplanter's tray holder was adopted. Combined with the pre-determined single pot volume range and need for 6 pots per row, the final single tray length is 276.5 mm, giving an overall size of 276.5 × 42 × 35 mm. Specific parameters are shown in Fig.1.

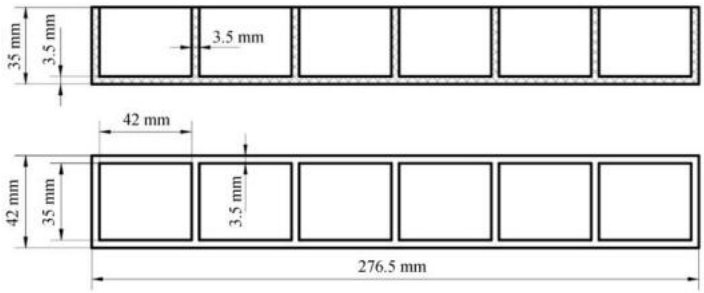


Fig. 1 - The parameter design of seedling tray

The mold design for biomass seedling trays

Biomass materials with cow dung and rice straw as the main raw materials are viscoelastic materials, and it is a large deformation process to compress them from a loose state into seedling trays with a certain shape and degree of compactness. Biomass material has the nature of a fluid, but its fluidity is poorer than bulk, worse than fluid, so it is not a fluid, also different from bulk. In view of its characteristics, it is a more feasible way to design the forming molds for biomass seedling trays by using a closed forming structure.

According to the function in the forming process, the basic composition of the mold was mainly divided into forming parts and structural parts. The forming parts included convex mold, concave mold, frame, withdrawal plate and base. They were in indirect contact with the synthetic material of the seedling tray and completed the main functions during the forming process. The structural parts included long tie rods, upper limit levers, lower limit levers, sprung assemblies and limit pins. They were not in direct contact with the material and played a role in mounting and positioning. The schematic diagram of the basic structure of the mold and the final design of the mold's physical effect are shown in Fig. 2.



（a）The basic structure of the mold （b）The final design of the mold's physical effect

Fig. 2 - The schematic diagram of the basic structure of the mold

The heating function design for mold

The existing forming molds for maize seedling trays have a compression forming process that is usually carried out at room temperature. However, during the process of biomass material being compressed, although the extrusion and friction between particles will lead to some increase in the temperature of the material, this temperature increase is far from the required temperature (170 ℃) for the accelerated softening of lignin *(Jiang et al., 2015)*. As a result, the lignin within the compressed biomass material cannot be liquefied and precipitated under the existing forming pressure. In order to enable the biomass material to reach the glass transition temperature of lignin after compression, further design and incorporation of heating function is required on top of the compression function of the existing mold. This enables the mold to warm up the internal material when compressing the biomass material, ensuring that the material reaches the required softening temperature and thus optimizing the forming effect.

The electromagnetic induction heating is a heating method that acts directly on the metal material. This method acts directly on the metal material without the need for a heat transfer medium, making it possible to achieve higher heating efficiency and energy utilization *(Li et al., 2024)*. Therefore, the electromagnetic induction heating was chosen as the heating method for mold warming in order to achieve a more efficient heating effect and energy utilization.

The operating frequency of electromagnetic induction heating has a close relationship with the position of the eddy current heating depth of the electromagnetic coil. Different operating frequencies lead to different heating depths, as shown in equation (1) for the calculation process of heating depth.

$$\delta = \frac{30}{\sqrt{f}} \tag{1}$$

where: f is the frequency, [kHz]; δ is the heating depth, [mm].

The heating simulation of the frame

In order to simulate the heating power of the electromagnetic induction heater and the temperature troughs and distribution of the inner wall of the frame after heating, and to provide a reference for the adjustment of the power range of the electromagnetic induction heater at a later stage, the heating simulation of the frame was carried out. The SolidWorks Simulation function module was used to simulate the heating process of the frame.

The model was drawn to the frame's actual dimensions (373 × 182 × 80 mm), with total transient time set to 60 s and time increment of 6 s. Ordinary carbon steel, consistent with the part's actual material properties, was defined for the frame.

For the temperature setting, the ambient temperature was set to 300 K (26.85 ℃). For the heat setting, the four sides of the inside of the frame were selected as contact surfaces to ensure that the heat could be transferred accurately. Based on the characteristics of air heat transfer, the heat dissipation on the inner surface was set to 0.2 W to ensure uniform heat distribution.

It should be noted that this value of 0.2 W was determined through multiple repeated experiments, where different heat dissipation values were continuously tested and the corresponding heat distribution effects were observed, ultimately being confirmed that 0.2W could achieve the desired uniform heat distribution.

In addition, in order to simulate the convection effect during the actual heating process, the convection option in the thermal load was selected and the convection coefficient was set to 25 W/(m^2·K) for the four faces on the outside of the mold. Similarly, this convection coefficient of 25 W/(m^2·K) was obtained through a series of repeated experiments. Numerous tests were conducted with various convection coefficient values, the simulation results were compared with the actual heating conditions, and after repeated verification and adjustment, it was determined that 25 W/(m^2·K) was the most suitable value to simulate the actual convection effect. The corresponding total ambient temperature for external heating was set according to the power of the induction heating unit. When the power was 2000 W, the ambient temperature was set to 430 K; when the power was 3000 W, the ambient temperature was adjusted to 600 K; and when the power reached 5000 W, the ambient temperature was set to 960 K.

Preparation of biomass seedling trays

For the preparation of compression formed maize biomass seedling trays at room temperature, 300 g of treated biomass material (90% mass ratio of cow dung to rice straw and 23% moisture content) was placed in the forming mold. The mold was compressed using electronic universal testing machine and pressure of 25 MPa was selected to ensure that the material was fully compressed and shaped in the mold.

In preparing compression formed maize biomass seedling trays under heated conditions, the induction coil of electromagnetic induction heater was tightly wound around the outer surface of the mold frame. By precisely adjusting the current output of the electromagnetic induction heater, the inner surface of the mold was heated to 240 ℃ and this temperature was kept constant. Other than that, the rest of the operation steps remained the same as the preparation process under room temperature conditions. After compression and holding for 20 s, waiting for the temperature of the mold to naturally drop to below 50 ℃ before carrying out the demolding operation. This procedure ensured the stable quality of the formed seedling trays, with regular dimensions, intact structures, and no obvious defects.

Flexural strength test of seedling trays

This study aimed to investigate the source of strength of biomass seedling trays and the role of lignin in the forming process through a comparative analysis of the changes in flexural strength between room-temperature compression forming and heating compression forming of the trays. The seedling trays were placed on the test platform of electronic universal testing machine (WDW-200EIII, Jinan Golden Age Testing and Measuring Machine Co., Ltd., Jinan, China), which complied with GB/T 16491-2008 standard. Fig. 3 shows the flexural strength test of seedling trays using electronic universal testing machine. The test was based on GB/T 1449-2005, using unconstrained support to destroy the seedling trays by three-point bending at a constant loading rate of 10 mm/min. The termination position at the closed loop control was set to 6 mm with a hold time of 10 s. The span and the position of the upper press head were adjusted to 0.5 mm, and the span used in this test was 210 mm.



Fig. 3 - The flexural strength test of seedling trays using electronic universal testing machine

Seedling experiments using seedling trays

The purpose of the seedling experiments was to verify the applicability and effectiveness of the seedling trays in practical use, and to determine whether they could withstand the pressure exerted by plant growth. In addition, the performance data of the seedling trays provided a basis for subsequent improvement and optimization.

The maize variety selected for this experiment was Demeria 3, a maize hybrid selected by KWS, Germany. Two to three days before sowing, the maize seeds were soaked in warm water at 28 to 30 ℃ for 12 hours, fished out and filtered dry of excess water. The treated maize seeds were evenly spread in culture trays with a layer of non-woven fabric fully saturated with water at the bottom of the trays. The seeds and trays were placed in a thermostat at 30℃ for 24 hours for germination. After germination was completed, 20 mm thick subsoil was placed in the holes of the seedling trays. One maize seed was inserted into each hole and filled with topsoil until it was level with the upper edge of the seedling trays. Water was poured into the trays until the soil was completely saturated. The ambient temperature of the trays was controlled at 25℃ ± 3℃ throughout the seedling process. Ventilation was carried out regularly on a daily basis and watering was carried out once in the morning from 8 to 9 am to ensure proper growth of the maize seeds.

RESULTS

Analysis of the heating location

According to the structural characteristics of the maize seedling trays, theoretically, heating from the inner wall and outer wall of the seedling tray hole can most effectively achieve the common heat inside and outside, so that the seedling tray as a whole reaches the glass transition temperature, and ensure the most uniform temperature distribution. The parts in contact with the maize seedling tray mainly include the top plate core, withdrawal plate, frame and base. Among them, the top plate core was in contact with the inner wall, the frame was in contact with the outer wall, and the base was in contact with the bottom of the seedling tray. Therefore, the heating efficiency of the maize seedling tray can be significantly improved by heating the top plate core and the frame specifically.

After the seedling tray has been compressed, direct internal heating is difficult to achieve because the top plate core is located inside the mold. If heating is attempted from the outer edges of the top plate core, there will be a large energy loss in the process of heat transfer to the top plate core, so this heating method is not ideal. Comparatively speaking, the inner wall of the formed frame and the outer wall of the seedling tray are in close proximity to each other, and the inner wall of the frame has the largest area of contact with the compressed biomass material, except for the top plate core. By heating the frame, the heat can be effectively and uniformly transferred to the maize seedling tray. Therefore, the electromagnetic induction coil was wound on the outer surface of the frame, and the electromagnetic induction principle was used to heat up the frame, so as to achieve the purpose of heating the internal biomass material.

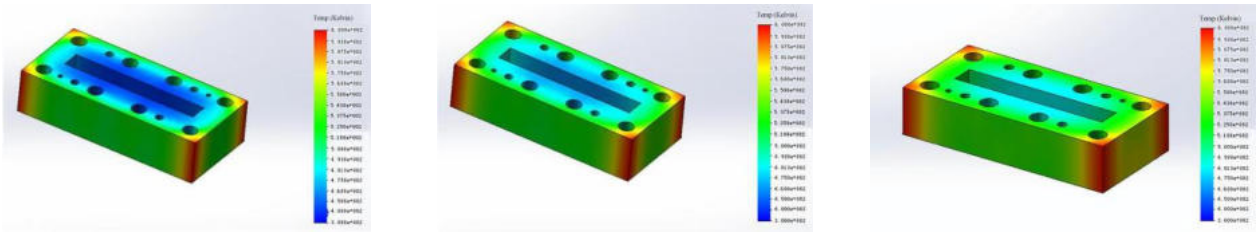
In order to penetrate the 5 mm thick glass insulation cotton outside the mold and form an effective vortex heating layer in the outer frame of the mold, an operating frequency of 20 kHz was selected according to the frequency adjustment range of the electromagnetic induction heater. The heating depth at this frequency can reach 6.7 mm, which fully meets the heating demand.

Results of the heating simulation of the frame

In the preliminary simulation, at a heating temperature of 430 K, it took up to 103 s to reach the target temperature of 170℃ to 270℃ at each point of the inner wall of the frame, which was obviously not satisfactory. In the simulation conditions of 960 K, although the heating speed of the frame significantly increased, only 24 s the highest temperature exceeded 270℃, but at the same time, the lowest point of the temperature failed to reach 170℃, the temperature difference between the inner wall of the frame was significant, and could not meet the requirements of the uniform heating of the material. In view of this, this paper adopted the heating temperature of 600 K to simulate the frame. After 30 steps of iterative solution, the heating process of the frame in 60 s was obtained. The heat distribution of the frame at 20 s, 40 s, and 60 s of heating was plotted, as shown in Fig. 4, to visualize the distribution at different heating stages.

From the Fig.4, it can be seen that within the first 20 s heating, the temperature had not yet penetrated deep into the frame, but was mainly concentrated in the outer corners. Due to the dense electromagnetic induction lines in these areas, the temperature rapidly rose to the peak heating temperature of 600 K. As the heating time progressed, by 40 s, the color inside the frame gradually shifted from dark blue to light blue, indicating that the temperature had steadily increased to approximately 460 K.

When heating reached 60 s, the temperature change in the frame gradually stabilized, and the heat distribution on the inner wall became more uniform. This fully demonstrated the stability of the heating process and the evenness of heat distribution.



（a）Heat distribution at 20 s （b）Heat distribution at 40 s （c）Heat distribution at 60 s

Fig. 4 - Heat distribution after heating of the frame

In order to accurately detect the temperature of the frame, based on the characteristics of the temperature change of the inner wall of the frame during the heating simulation, the center of the two sides of the inner wall of the frame and the center of the diagonal were selected as the key detection points for continuous monitoring of the temperature changes. The location distribution of the detection points and the detection results of temperature points are shown in Fig. 5.



（a）The location distribution of the detection points （b）The detection results of temperature points

Fig. 5 - The location distribution of the detection points and the detection results of temperature points

Point 1 was the high temperature point of the inner wall of the frame, and point 2 was the midpoint of the heating of the outer end surface of the seedling tray. Point 3 was the midpoint of the side heating of the seedling tray and was the lowest point of the heat distribution of the whole frame. The simulation time of the three points was 60 s. The temperature changes of point 1, point 2 and point 3 show a linear trend with the heating time. When the heating time was in the range of 0-20 s, the temperature rise of all three points was slow. After the heating time exceeded 20 s, the temperature began to rise rapidly. When the heating time was 60 s, the temperature of point 1 was between 480 K (about 207 ℃) and 540 K (about 267 ℃), which was between 200 ℃ and 270 ℃ in the heating requirement of the inner wall.

Therefore, the heating power of the electromagnetic induction heater was set to 3000 W, and the heating time for the frame at room temperature was set to 60 s, which could meet the heating function requirements of the mold. The infrared camera was used to monitor temperature changes and distribution of the frame. The imaging results of mold heating are shown in Fig. 6.

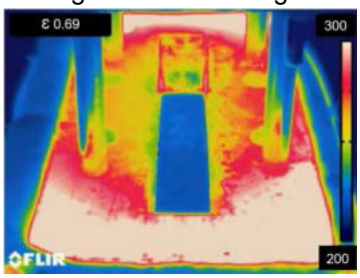
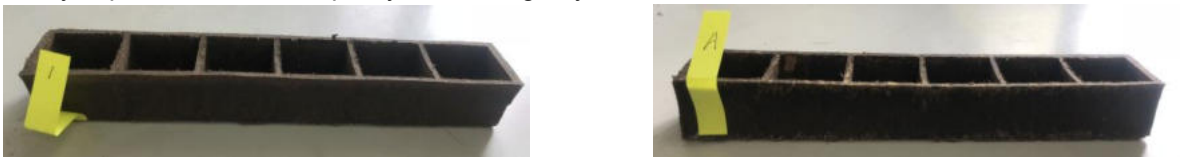


Fig. 6 - The imaging results of mold heating

As can be seen in Fig. 6, heating between 40 s-60 s, the high point temperature of the inner surface of the frame varied from 209 ℃ to 266 ℃, and the low point temperature varied from 174 ℃ to 217 ℃, which was within the range of the glass transition and pyrolysis temperature of lignin. The imaging results of mold heating were basically consistent with the simulation results, and the heating performance of the mold met the heating and compression forming requirements of biomass materials.

Results of biomass seedling trays preparation

The seedling trays prepared by two different processes, room temperature compression and heating compression are shown in Fig.7. In terms of color characteristics, the heated compressed seedling trays had a slightly darker color compared with the room temperature compressed product. Further micro-analysis revealed that the room-temperature compression trays showed tiny gaps along the sides, generated by friction between the material and the side wall during extrusion - an unavoidable physical phenomenon in the room-temperature compression forming process. The surface of the heated compressed seedling trays exhibited a much smoother quality, making it almost impossible to observe visible imperfections. Therefore, the heated compression process has significant advantages in the preparation of seedling trays and can effectively improve the surface quality of seedling trays.

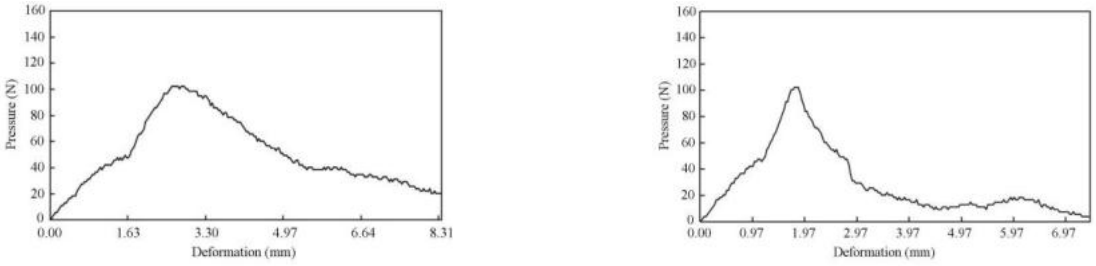


（a）The room temperature compression （b）The heating compression

Fig. 7 - The seedling trays prepared by two different processes

Results of flexural strength test for seedling trays

The results of flexural strength test for seedling trays of room temperature compression forming and heating compression forming are shown in Fig. 8, the test was repeated 10 times for each treatment.



（a）The room temperature compression （b）The heating compression

Fig. 8 - The results of flexural strength test

When the pressure of the heated compression formed seedling trays reached 100 N, the pressure value dropped rapidly. The room temperature compression formed seedling trays showed a smoother decrease in pressure value when subjected to the same pressure. Although the heated compression formed seedling trays exhibited a greater magnitude of elastic deformation, the difference between the two was not significant in terms of strength.

Results of seedling experiments

After sowing maize in seedling trays, the seeds broke the ground and emerged in 3-4 days and grew to 3 leaves and 1 core in about 18-22 days to meet transplanting requirements. Status of seedling trays at different times after sowing are shown in Fig. 9. None of the seedling trays broke during this seedling cycle, and the maize seedlings grew well.



（a）Status after first watering （b）Status after 5 days （c）State of final growth before transplanting

Fig. 9 - Status of seedling trays at different times after sowing

CONCLUSIONS

In this study, a heating compression forming mold was designed to meet the requirements of forming dimensions and conditions for the preparation of biomass seedling trays for maize transplantation without the addition of adhesives. The preparation of seedling trays, flexural strength test and seedling nursery test were carried out using the designed heating compression forming mold. The surface of the seedling trays was smoother due to the full flow and bonding of lignin during heating compression forming to fill up the gaps caused by friction. The seedling trays obtained by heating compression forming have greater elastic deformation, which improves the elasticity and plasticity of the seedling trays. During the seedling cycle, no rupture occurred in the seedling tray, and the maize seedlings grew well. The designed mold is practical and feasible, and can provide an efficient and environmentally friendly solution for maize seedling transplantation. Lignin, as an important binder, effectively improves the forming effect of seedling trays, which is expected to replace the traditional plastic seedling trays and provide ideas for the resourceful use of agricultural waste.

ACKNOWLEDGEMENT

This work was supported by China Agriculture Research System of MOF and MARA (CARS-04-PS30); Guiding Science and Technology Plan Project in Daqing City (zd-2024-24).

REFERENCES

[1] Chen, Z., Aziz, T., Sun, H., Ullah, A., Ali, A., Cheng, L., Ullah, R., & Khan, F. U. (2023). Advances and applications of cellulose bio-composites in biodegradable materials. *Journal of Polymers and the Environment*, 31(6), 2273-2284.

[2] Choudhary, V., & Machavaram, R. (2023). A comprehensive review of sustainable soil organic growing media for mat-type paddy seedling nurseries under Indian agronomical condition. *Journal of Soil Science and Plant Nutrition*, 23(2), 1515-1534.

[3] Cheng, H., Zhao, N., Ren, D., Wang, W., Gong, Y., & Huang W. (2025). Design and experimental study on twin-screw straw pulping machine. *INMATEH - Agricultural Engineering*, 75(1), 178-189.

[4] Clemmer, J. T., Long, K. N., & Brown, J. A. (2023). Exploring pressure-dependent inelastic deformation and failure in bonded granular composites: An energetic materials perspective. *Mechanics of Materials*, 184, 104693.

[5] Farcaş-Flamaropol, D. C., Surdu, E., Iatan, R. I., Cârdei, P., Enăchescu, G., Prodea, I., & Durbacă, I. (2024). Mechanical and thermal properties of composite materials obtained with sludge matrix and agricultural waste inserts. *INMATEH - Agricultural Engineering*, 73(2), 427-434.

[6] Guerrini, S., Borreani, G., & Voojis, H. (2017). Biodegradable materials in agriculture: case histories and perspectives. In *Soil degradable bioplastics for a sustainable modern agriculture* (pp. 35-65). Berlin, Heidelberg: Springer Berlin Heidelberg.

[7] Guo, M., Li, J., & Tang, K. (2023). Research Progress on Biomass Solid Briquettes (生物质固体成型燃料研究进展). *China Forest Products Industry*, 60(10), 40-44.

[8] Juanga-Labayen, J. P., & Yuan, Q. (2021). Making biodegradable seedling pots from textile and paper waste—Part B: Development and evaluation of seedling pots. *International Journal of Environmental Research and Public Health*, 18(14), 7609.

[9] Jian, X., & Liu, S. (2013). Research status and development prospect of densified biofuel (生物质固体成型燃料研究现状及发展前景). *Biomass Chemical Engineering*, 47(2), 54-58.

[10] Jiang, S., Huang, L., Peng, H., Tang, F., & Yao, K. (2015). Thermo gravimetric analysis and kinetics of biomass briquette fuels (生物质成型燃料的热重分析及动力学研究). *Advances in New and Renewable Energy*, 3(2), 81-87.

[11] Komine, R., Yasuda, S., Kajihara, M., & Yonezu, A. (2023). Material parameters in constitutive equation for plastic deformation at a high strain rate estimated by high-velocity microparticle collisions. *Journal of Materials Engineering and Performance*, 32(12), 5627-5637.

[12] Li, D., Wang, X., Jing, Q., Si, S., Li, J., & Li, S. (2014). Preparation of xylooligosaccharides producing solid waste based biodegradable seedling pots (低聚木糖生产废渣基可降解育苗钵研究). *Transactions of the Chinese society for agricultural machinery*, 45(S1), 207-212.

[13] Li, H., Wang, C., Zou, H., Sun, H., Wang, H., Yu, Z., Shi, J., & Liu, X. (2022). Structural Design and Performance Test of Biomass-Based Nursery Trays. *Sustainability*, 14(15), 9101.

[14] Luo, F., Lin, L., Li Z., Li, W., Chen, X., Sha, S., & Luo, T. (2019). Electrochemical reactions and reactors for biomass valorisation. *CIESC Journal*, 70(3), 801.

[15] Li, X., Wang, H., & Zuo, S. (2024). A novel flexible catheter with integrated magnetic variable stiffness and actuation. *Smart Materials and Structures*, 33(2), 025028.
[16] Rumpf, H. C. H. (1970). On the theory of tensile strength of agglomerates during force transmission at contact points (Zur theorie der zugfestigkeit von agglomeraten bei kraftuebertragung an kontaktpunkten). *Chemie Ingenieur Technik*, 42(8), 538-540.
[17] Wan, P., Ma, Y., Zhang, B., Shang, J., & Zhang, Y. (2020). Experimental research on process parameters for animal manure and straw prepared briquet (动物粪便与秸秆成型坯块制备工艺参数试验研究). *Renewable Energy Resources*, 38(4), 427-433.
[18] Wang, J., Tang, H., & Wang, J. (2017). Comprehensive utilization status and development analysis of crop straw resource in Northeast China (东北地区作物秸秆资源综合利用现状与发展分析). *Transactions of the Chinese Society for Agricultural Machinery*, 48(5), 1-21.
[19] Wang, G., Jiang, Y., Li, W., & Yin, X. (2016). Process optimization of corn stover compression molding experiments based on response surface method (基于响应面法的玉米秸秆成型工艺优化). *Transactions of the Chinese Society of Agricultural Engineering*, 32(13), 223-227.
[20] Xie, T., Wang, Y., Cong, H., Zhao, L., Qiu, L., Yao, Z., Kang, K., Zhu, M., Zhang, T., Huo, L., & Yuan, Y. (2020). Experiment on combustion characteristic and densified biomass pellets from maize stalk char mixing typical agricultural wastes (玉米秸秆炭和典型农业废弃物混合成型与燃烧特性试验). *Transactions of the Chinese Society of Agricultural Engineering*, 36(15), 227-234.
[21] Yaheliuk, S., Didukh, V., Fomich, M., Yaheliuk, O., Kuzmina, T., & Boiko, G. (2025). Optimization of technological parameters for fuel roll production using agricultural crop stem biomass. *INMATEH -Agricultural Engineering*, 75(1), 243-252.

DESIGN AND TESTING OF A WINGED SUBSOILER SHOVEL FOR STRIP MINIMUM-TILLAGE DEEP LOOSENING FERTILISER MACHINE
/
条带少耕深松施肥机带翼式深松铲设计与试验

Shi-cheng XU [1]; Gui-xiang TAO *[1]; Shu-juan YI [1]; Song WANG [1]; Yu-hang SAN [1]
College of Engineering, Heilongjiang Bayi Agricultural University, Daqing/P. R. China
Tel: +86-459-13836961877; E-mile: 15628820228@163.COM;
Corresponding author: Gui-xiang TAO
DOI: https://doi.org/10.35633/inmateh-76-78

Keywords: *strip minimum tillage; subsoiling fertilizer applicators; winged subsoiler shovels; discrete element method*

ABSTRACT
To address issues such as soil compaction, plough layer damage, and hardpan formation caused by long-term use of rotary tillage and conventional ploughing, a winged subsoiler shovel was designed based on the soil characteristics of the black soil region in Northeast China. A mechanical contact model between the subsoiler shovel and soil was established to identify the design factors affecting the operational quality of the shovel. Using discrete element simulation technology, a shovel-soil interaction model was constructed. Through a quadratic regression rotational orthogonal design test, the effects of shovel structural parameters on soil disturbance area were determined. Taking the maximization of soil disturbance area as the objective, the shovel parameters were optimized. The optimal parameter combination was obtained as follows: shovel tip entry angle of 21°, wing inclination angle of 28°, and wing width of 104 mm, resulting in a maximum soil disturbance area of 1699.80 cm². A bench verification test was subsequently conducted, showing an actual soil disturbance area of 1666.08 cm². The test results were consistent with the simulation optimization results, confirming that the optimal parameter combination meets operational requirements and satisfies agronomic needs for deep loosening.

摘要
针对于长期使用旋耕、翻耕等耕整地方式造成土壤板结、犁地层破坏、犁底层板结等问题，基于中国东北黑土区土壤特性设计了一种带翼式深松铲。建立了深松铲与土壤间的力学接触模型，确定了影响深松铲作业质量的深松铲设计因素。应用离散元仿真技术，建立了深松铲-土壤仿真模型，通过二次回归旋转正交组合试验，确定了深松铲结构参数对土壤扰动面积的影响规律，以土壤扰动面积最大化为目标，对深松铲参数进行优化求解，深松铲的最优参数组合为：铲尖入地角为 21°、铲翼倾角为 28°、铲翼宽度为 104mm 时，土壤扰动面积最大，土壤扰动面积为 1699.80cm²。得出最优参数后进行台架验证试验，台架试验结果表明：实际土壤扰动面积为 1666.08cm²，试验结果与仿真优化结果基本一致，最优参数组合符合作业要求，满足深松农艺要求。

INTRODUCTION
Since the 1980s, the mode of ploughing operation has been transitioning from the full-tillage operation with a large amount of soil movement to the no-tillage operation mode such as less-tillage and no-tillage (*Zhang et al., 2024*). Among them, less tillage provides a certain degree of soil disturbance, which can improve soil aeration, effectively prevent soil sloughing, and improve the degree of plough subsoil sloughing and damage (*Wang et al., 2021*). Strip minimum tillage is mainly to return the straw to the rows, so that the surface of the ground to form a strip to be sown (*Gao et al., 2023*). During strip minimum tillage, the subsoiler shovel further optimizes the soil tillage structure. Subsoiling loosens the soil along predetermined strips, increasing the depth and range of soil loosening, which can better break up the plough pan, promote deep root growth of crops, and thereby increase crop yields.

[1] *Shi-cheng Xu, M.S.; Gui-xiang Tao, Prof. Ph.D.; Shu-juan Yi, Prof. Ph.D.; Song Wang, Ph.D.; Yu-hang San, Ms.*

At present, limited research has been conducted on the winged subsoiler shovel used in strip minimum-tillage deep loosening fertilizer machines *(Zhao et al., 2018)*. Most related studies focus on the structural design and optimization of subsoiler shovels used in ploughing components, with particular emphasis on the structural design of the shovel itself. *Zheng et al., (2016*), designed a subsoiler shovel with a folded breaking edge for effective drag reduction and consumption reduction through discrete element simulation and field tests. *Manuwa, (2009),* investigated the effects of different subsoiler shovel tip designs and entry angles on soil disturbance. *Li et al., (2018),* conducted a comparative analysis of two types of subsoiler shovels, with and without wings. The results showed that winged subsoiler shovels exhibited better performance in terms of ploughing resistance and soil disturbance compared with non-winged shovels. Specifically, the tillage resistance and disturbed area of winged subsoiler shovels were more than twice those of non-winged shovels. However, existing research has not yet integrated the strip minimum tillage mode to develop specialized subsoiler shovels, and conventional designs demonstrate poor adaptability, thereby reducing the quality of machine operation.

Based on the soil characteristics of the black soil region in Northeast China, this study designs a subsoiler shovel adapted to the strip minimum tillage mode. Discrete element method (DEM) simulation was used to optimize the structural parameters of the subsoiler shovel, aiming to develop a winged design that maximizes soil disturbance. The optimal parameters were verified through bench testing, confirming the effectiveness of the proposed winged subsoiler shovel.

MATERIALS AND METHODS

Structure and working principle

The strip minimum-tillage deep loosening fertilizing machine consists of a straw-clearing and cutting mechanism and a subsoiling mechanism. The winged subsoiler shovel is composed of a shovel tip, shovel handle, and shovel wings, and is mounted onto the subsoiling mechanism after the straw-clearing and cutting unit. The subsoiling mechanism is connected to the rear of the straw-clearing and cutting mechanism via a connecting frame. The subsoiler shovel is fixed to the mounting handle, which is in turn secured to the connecting frame of the subsoiling mechanism using bolts. The working depth of the subsoiler shovel can be adjusted by selecting different mounting holes on the handle, allowing adaptation to various agronomic requirements. The structural design of the strip minimum-tillage fertilizing machine and the winged subsoiler shovel is illustrated in Fig. 1.

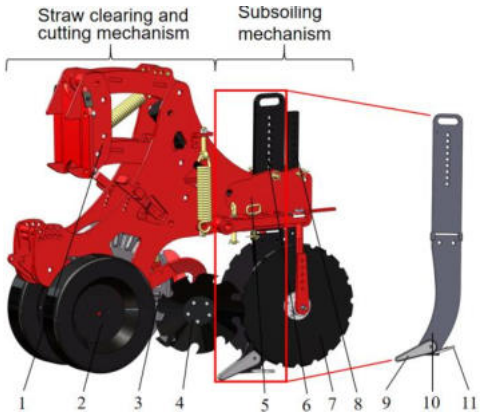


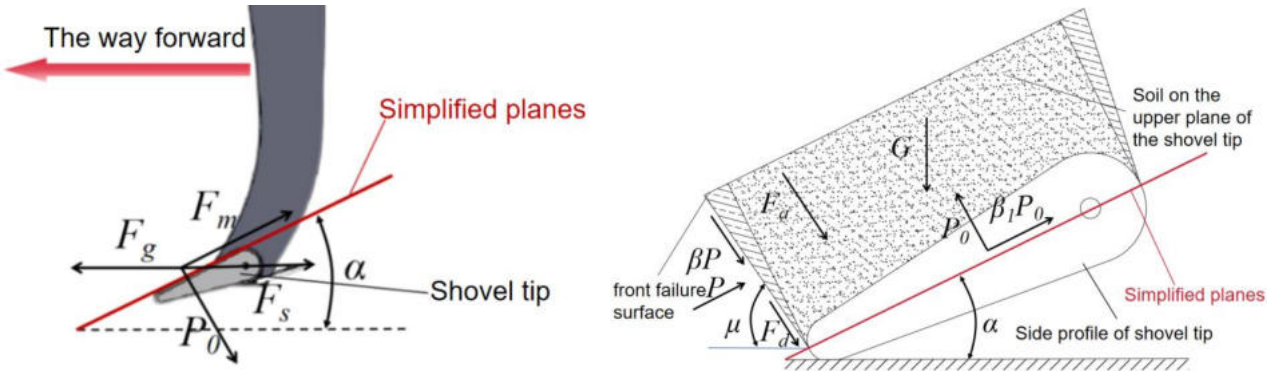
Fig. 1 – Structure of the strip minimum-tillage deep loosening fertilizing machine and winged subsoiler shovel

1. Four-link connecting bracket; 2. Depth-limiting wheel; 3. Stubble-cutting disc knife; 4. Notched straw-clearing disc; 5. Subsoiling mechanism connecting frame; 6. Subsoiler shovel; 7. Disc harrow; 8. Fertilizer tube; 9. Shovel tip; 10. Shovel handle; 11. Shovel wings

When the subsoiler shovel carries out deep loosening operation, under the action of traction force, the subsoiler shovel cuts into the soil at a certain angle and moves forward, continuously squeezes the soil in front of it, and produces a continuous shear force on the soil, and under the action of the shear force, the soil gradually breaks up and loosens, and pushes the soil to the two sides to form a loose ridge, thus arriving at the effect of soil loosening. At the same time, the side and bottom of the subsoiler shovel will also produce extrusion and friction on the soil, which can further break the soil. The cutting and crushing action of the subsoiler shovel on the soil can make the soil particles rearrange, increase the soil porosity and improve the soil structure.

Mechanical analysis of the subsoiling process

To investigate the forces acting on the subsoiler shovel during the subsoiling process, a mechanical analysis of the shovel tip is conducted, and a mechanical contact model between the shovel tip and the soil is established, as shown in Fig. 2(a). The shovel tip of the subsoiler is simplified as an inclined plane subjected to force. When this inclined plane is pushed forward horizontally in the soil, shear failure occurs on the soil surface in front of the shovel tip as well as in the soil above it (*Zhang, 2013*).



(a) Analysis of forces in subsoiler shovel tip operation (b) Analysis of soil forces in the upper plane of the shovel tip

Fig. 2 – Force analysis diagram of shovel tip

According to Fig. 2(a), the equilibrium equation of force on shovel tip can be obtained:

$$\begin{aligned} F_q &= P_0 \sin\alpha + F_m \cos\alpha + F_s \\ F_m &= P_0\beta \end{aligned} \quad (1)$$

where: F_q is the traction force, N; P_0 is the normal load of the soil on the shovel tip, N; α is the angle of shovel tip into the ground, (°); F_m is the friction of the soil on the upper plane of the shovel tip, N; F_s is the cutting resistance of the soil on the shovel tip, N; and β_1 is the friction factor between the soil and the shovel tip.

The soil cutting resistance is negligible due to the fact that there are fewer hard stones and other hard debris in normal ploughed soils during subsoiling, and the cutting resistance of the soil is small (*Ma, 2022*). Therefore, from Equation (1), it can be seen that the traction force is related to the normal load of the soil on the shovel tip, the friction factor between the soil and the shovel tip, and the shovel tip entry angle. The traction force and the horizontal ploughing resistance of shovel tip are equilibrium forces, so the horizontal ploughing resistance is related to the normal load of soil on the shovel tip, the friction factor between soil and shovel tip, and the angle of shovel tip into the ground.

In order to deeply investigate the influence mechanism of the structural parameters of the shovel tip on the effect of subsoiler shovelling operation, it is necessary to carry out a mechanical analysis of the soil on the plane of the shovel tip, as shown in Fig. 2 (b).

According to Fig. 2 (b) and Eq. (1), the equilibrium equation for the force on the plane soil on the shovel tip can be obtained:

$$F_q = P(\sin\mu + \beta\cos\mu) + (F_d + F_a)\cos\mu \quad (2)$$

$$F_q\left(\frac{\cos\alpha - \beta_1\sin\alpha}{\sin\alpha + \cos\alpha} + \frac{\cos\mu - \beta\sin\mu}{\sin\mu + \beta\cos\mu}\right) = G + (F_d + F_a)\sin\mu + (F_d - F_a)\sin\mu\frac{\cos\mu - \beta\sin\mu}{\sin\mu + \beta\cos\mu} \quad (3)$$

where: P is the normal load of the soil front failure surface on the shovel tip, N; μ is the inclination angle of the soil front failure surface on the shovel tip, (°); β is the internal friction factor of the soil; F_d is the cohesion force of the soil, N; F_a is the acceleration force of the soil, N; G is the gravity force of the soil on the shovel tip, N.

Where the soil gravity in the plane on the shovel tip in equation (3) can be calculated from the volume of soil supported by the shovel tip (*Zhou, 2006*), the soil gravity is calculated as:

$$G = \rho g C_k H\left(\frac{\sin(\alpha+\mu)}{\sin\mu}\right)\left\{C_l + H\frac{[\cos(\alpha+\mu) + \tan\alpha\sin(\alpha+\mu)]}{2\sin\mu}\right\} \quad (4)$$

where: ρ is the soil density, kg/m^3; H is the depth of subsoiler shovelling, mm; C_k is the width of shovel tip, mm; C_l is the length of shovel tip, mm.

Based on the formula for soil cohesion, a theoretical expression for soil cohesion can be derived:

$$F_d = d\frac{HL}{\sin\mu} \quad (5)$$

where:

d is the soil cohesion per unit of shear failure surface, Pa;

L is the arc length of the front plane of the shovel tip, mm.

Based on the theoretical derivation of the soil acceleration force by Newton's second law, the cutting failure process of the Subsoiling shovel on the soil during ploughing can be regarded as a quasi-static continuous motion process, so the acceleration force on the soil can be characterized as a steady state acceleration force, and its magnitude can be calculated by the mass of the accelerated soil per unit of time, and the calculation formula:

$$F_a = \rho C_k HVV_1 \quad (6)$$

where: V is the speed of subsoiler shovel, m/s; V_1 is the instantaneous speed of subsoiler shovel tip, m/s.

The equilibrium equation was derived by substituting Equations (4), (5), and (6) into Equation (3):

$$F_q = P(\sin\mu + \beta\cos\mu) + \left(d\frac{HL}{\sin\mu} + \rho C_K HVV_1\right)\cos\mu \quad (7)$$

$$F_q\left(\frac{\cos\alpha - \beta_1\sin\alpha}{\sin\alpha + \cos\alpha} + \frac{\cos\mu - \beta\sin\mu}{\sin\mu + \beta\mu}\right) = \rho g C_k H\left(\frac{\sin(\alpha+\mu)}{\sin\mu}\right)\left\{C_l + H\frac{[\cos(\alpha+\mu) + \tan\alpha\sin(\alpha+\mu)]}{2\sin\mu}\right\}$$

$$+\left[d\frac{HL}{\sin\mu} + \rho C_K HVV_1\right]\sin\mu + \left[d\frac{HL}{\sin\mu} - \rho C_K HVV_1\right]\sin\mu\frac{\cos\mu - \beta\sin\mu}{\sin\mu + \beta\cos\mu} \quad (8)$$

Based on the shear failure theory in soil mechanics, the angle of inclination of the front failure surface of the soil on the upper plane of the shovel tip can be studied and derived, resulting in a theoretical expression for the angle of inclination of the front failure surface of the soil.

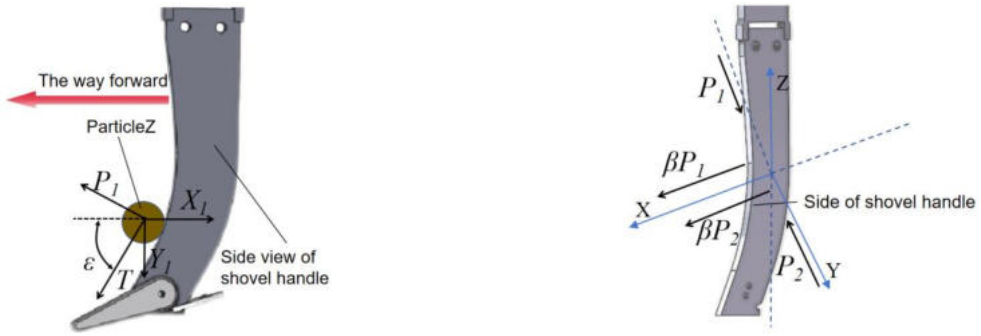
The expression is:

$$\mu = \frac{\pi}{2} - \arctan\frac{\varpi}{2} \quad (9)$$

where: ϖ is the angle of internal friction of the soil, (°).

Based on the analysis of the mechanical contact model, the soil disturbance range of the shovel tip and the tillage resistance can be determined by soil mechanical parameters (e.g., cohesion, internal friction angle, density), tillage condition parameters (e.g., tillage depth, tillage speed), and geometric parameters of the shovel tip (e.g., entry angle, width, and length). Since soil mechanical properties are generally uncontrollable during the design process, the influence of the shovel tip on soil disturbance primarily depends on its geometric parameters, particularly key variables such as the entry angle, width, and length. According to *Zhou (2006)*, among these parameters, the soil entry angle exerts the most significant influence on the performance of the subsoiler shovel. Selecting an appropriate entry angle can effectively reduce ploughing resistance and enhance soil disturbance. In contrast, the width and length of the shovel tip have relatively smaller effects, mainly influencing the uniformity of soil fragmentation and the stability of ploughing.

The shovel handle exerts a cutting effect on the soil primarily through frictional resistance and contact resistance. For the force analysis, soil particles along the curve of the shovel handle were treated as mass points. The mechanical contact model between the soil and the shovel handle is illustrated in Fig. 3(a).



(a) Analysis of forces on soil mass points of shovel handle (b) Shovel handle side force analysis

Fig. 3 – Force analysis of shovel handle

Assuming the soil is homogeneous, the interaction force between soil particles follows Coulomb's law. According to Coulomb's friction law, the frictional force and normal pressure between soil particles are proportional. Thus, the relationship between the normal pressure and tangential force at the soil particle mass point can be expressed as:

$$T = F_d + P_1 \tan \varpi \quad (10)$$

where: T is the tangential force of the shovel handle on the soil particle mass point, N; P_1 is the positive pressure of the curved shovel handle on the soil particle mass point, N.

According to Fig. 3 (a) as well as Eq. (10), the equilibrium equations of force on the soil mass are obtained:

$$X_1 = \left(P_1 + F_d + P_1 \tan \varpi\right)\cos \varepsilon \quad (11)$$

$$Y_1 = (P_1 - F_d - P_1 \tan \varpi)\sin \varepsilon \quad (12)$$

where: X_1 is the horizontal force of the resistance given by the soil particles around the soil particle mass point, N; P_1 is the positive pressure of the curved shovel handle on the soil particle mass point, N; Y_1 is the vertical force of the resistance given by the soil particles around the soil particle mass point, N; ε is the angle of tangency between the soil particle mass point and the shovel handle, (°).

According to Equations (11) and (12), the force acting on soil particle mass point Z consists of the tangential component, determined by the push tangent angle (ε) between the soil particle and the shovel handle, and the resistance exerted by the surrounding soil particles in the vertical direction. As the soil particle mass point moves along the shovel handle, the push tangent angle reaches its maximum when the particle is at the vertical position, at which point Y_1 is maximized and X_1 minimized. Owing to the principle of action and reaction, the force exerted on the soil particle by the shovel handle generates an equal and opposite reaction force from the soil particle onto the shovel handle.

To further examine the influence of shovel handle side width on tillage resistance, the forces acting on both sides of the shovel handle were analysed. The side-force diagram of the shovel handle is presented in Fig. 3(b). Based on Fig. 3(b), the equilibrium equation for the forces on the shovel handle side can be derived as follows:

$$F_c = \beta P_1 + \beta P_2 \quad (13)$$

where:

F_c is the shovel handle side friction resistance, N; P_1, P_2 is the soil on the shovel handle side normal load, N.

The shovel handle is a symmetrical structure with equal areas on both sides, so the pressure on both sides is equal.

$$P_1 = P_2 = S_1 U$$
$$F_c = 2\beta\, S_1 U \quad (14)$$

where:

S_1 is the side area of shovel handle, mm^2; U is the coefficient of friction between soil and side of shovel handle.

The frictional resistance on both sides of the subsoiler shovel handle, as described by Equation (14), is influenced by the side surface area. Therefore, the side area should not be excessively large, as it would increase tillage resistance. However, according to the analysis based on Equations (11) and (12), the shovel handle is prone to stress concentration. Additionally, it is subjected to alternating bending loads and torsional loads caused by soil resistance eccentricity. If the side area is too small, the structural load-bearing capacity of the shovel handle is reduced, increasing the risk of mechanical failure. Thus, an appropriate balance must be maintained to optimize both resistance and structural integrity.

In the force analysis of the shovel wings, they are simplified as an inclined plane, with force conditions analogous to those of the shovel tip. Therefore, the parameters influencing the performance of the shovel wings can be referenced from those of the shovel tip.

Subsoiler shovel design

The chisel-type shovel tip penetrates the soil more effectively, with reduced extrusion of the surrounding soil. This allows it to quickly break through the plough pan while ensuring uniform lateral movement of the soil, thereby achieving more consistent loosening and enhancing the subsoiling effect. Given the high soil density and compact plough pan in the black soil region of Northeast China, a chisel-type shovel tip was selected. According to the JB/T9788–2020 standard "*Subsoiler Shovel and Subsoiler Shovel Handle"*, the shovel tip length and width were set at 165 mm and 40 mm, respectively. The structure of the shovel tip is illustrated in Fig. 4(a).



(a) Shovel tip structure drawing (b) Shovel handle structure drawing

Fig. 4 – Structure of shovel tip and shovel handle

According to the mechanical contact model between the soil and the shovel tip, the entry angle of the shovel tip determines both the contact area with the soil and the cutting force. When the entry angle is moderate, the subsoiler shovel can effectively penetrate the soil while maintaining low resistance, thereby achieving efficient deep loosening operations. Since the shovel wings are subjected to the same forces as the shovel tip, their entry angle likewise has a significant influence on the soil disturbance area. Moreover, because the wings are wider than the tip, shovel wing width also strongly affects the disturbance area. Therefore, selecting an appropriate shovel tip entry angle, shovel wing inclination, and wing width is critical to optimizing subsoiler shovel performance. The optimal parameters will be determined through subsequent simulation experiments.

According to the mechanical contact model between the soil and the shovel handle, an arc-shaped shovel handle reduces the push-cut angle between the soil particle mass point and the shovel handle compared to a vertical shovel handle. This reduction in the push-cut angle effectively lowers ploughing resistance and mitigates stress concentration, helping to prevent shovel handle failure. Additionally, in contrast to traditional straight designs, the arc-shaped shovel handle better conforms to the natural flow of soil, reducing resistance during soil entry and facilitating smoother soil movement during subsoiling operations. The shovel handle width is most effective when the ratio of the shovel handle width to the shovel tip length is between 0.68 and 1.04. Therefore, based on a shovel tip length of 160 mm and the optimal ratio range, the shovel handle width is calculated to be 110 mm. As noted in the literature (*Chen et al., 2021*), shovel handle thickness also affects tillage resistance. Excessive thickness increases traction resistance, while insufficient thickness reduces the soil-crushing effect and increases the risk of structural failure. Referring to the JB/T 9788–2020 "*Subsoiler Shovel and Subsoiler Shovel Handle"* standard, the shovel handle thickness is set to 18 mm. The height of the shovel handle depends on the subsoiling depth, and for the target working depth, it is calculated to be 380 mm.

Discrete element simulation experiment for subsoiling operation

Operational modelling

Soil parameter determination was conducted using samples from the black soil region of Northeast China to obtain accurate soil characteristic values. Based on these measured parameters, a soil particle model was established. Pre-tests showed that enlarging the particle diameter by a factor of 1 to 10 had no significant impact on the simulation results, allowing the model to be simplified accordingly. To more accurately simulate real soil behaviour, the Hertz-Mindlin with JKR contact model was selected, as it effectively captures soil cohesion and bonding phenomena (*Zang et al., 2022*). A soil trench was created in EDEM 2022, and a particle factory was used to populate the trench with a bed of soil particles.

To ensure efficient and accurate simulation, the full machine model was simplified by retaining only the subsoiler shovel for analysis. This reduction in model complexity significantly decreased computational load, enabling more efficient simulations (*Wang et al., 2017*). The subsoiler shovel model, created in SolidWorks 2023, was exported in *.slt* format and imported into EDEM 2022 software. The material of the subsoiler shovel was defined as 65-gauge steel, with a density of 7850 kg/m^3, a Poisson's ratio of 0.3, and a shear modulus of 7.8×10^{10} Pa.

The established soil particle model and subsoiler shovel model were imported into EDEM 2022 software. Contact parameters between soil particles, as well as between soil particles and the subsoiler shovel, were defined based on relevant literature (*Wang et al., 2017*) and parameters obtained from physical testing. This setup resulted in the subsoiling operation model shown in Fig. 5. The specific simulation parameters are listed in Table 1.

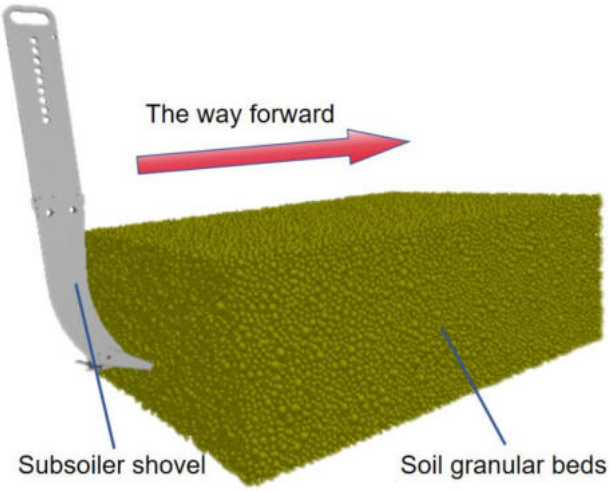


Fig. 5 – Modelling of subsoiling operations

Table 1

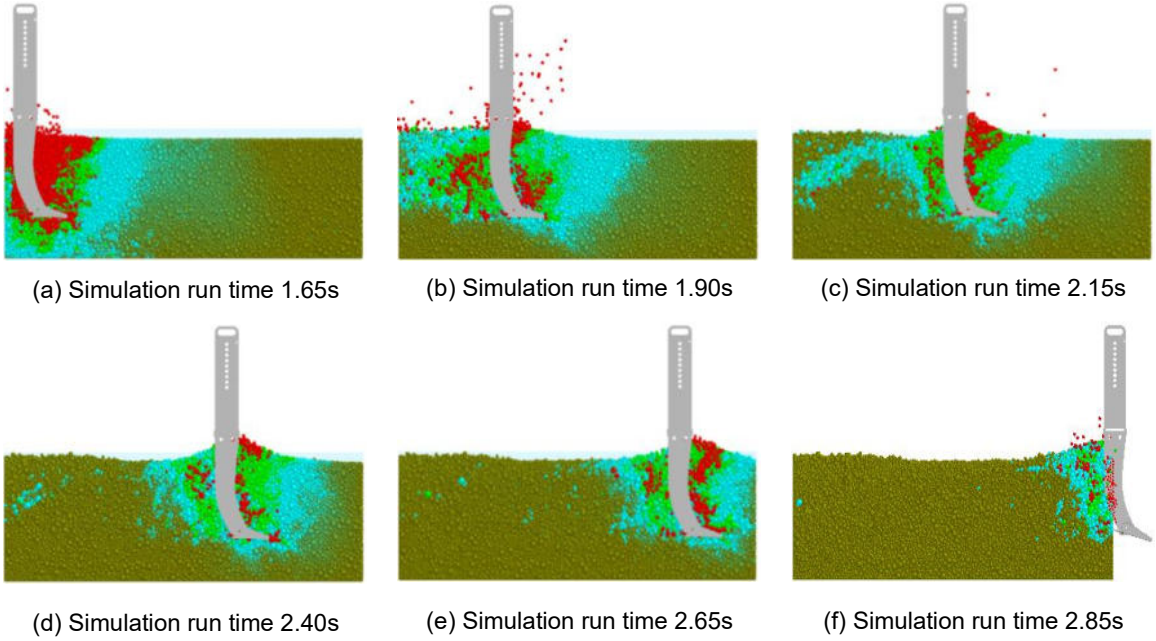
Simulation test parameters

Parameter class	Numerical value	Parameter class	Numerical value
Poisson's ratio of soil particles	0.30	Particle-65 steel dynamic friction	0.15
Soil particle density (kg/m^3)	1600	Poisson's ratio of 65 steel	0.35
Soil particle shear modulus (Pa)	1×107	Density of 65 steel (kg/m^3)	7850
Particle-particle coefficient of recovery	0.3	Sear modulus of 65 steel (Pa)	7.8×1010
Particle-particle static friction coefficient	0.7	Soil particle bed thickness (mm)	450
Particle-particle kinetic friction	0.2	Subsoiler shovel horizontal speed (m/s)	1.5
Particle-65 steel restitution coefficient	0.35	Subsoiling depth (mm)	320
Particle-65 steel static friction	0.6	Grid size (mm)	24

Simulation process analysis

After configuring the parameters of the subsoiling operation model, the subsoiling simulation was conducted. Upon completion, soil disturbance was evaluated by dissecting the soil trench using the post-processing module in EDEM 2022. Transverse cross-sections of the soil disturbance at multiple time points during the subsoiling process are shown in Fig. 6.

In the simulation, particle velocity is represented by colour: red particles indicate the highest velocities, followed by green, and then blue, which represent progressively lower speeds. The variation in particle velocity arises from differences in acceleration caused by contact with the subsoiler shovel. Particles in direct contact with the shovel experience greater acceleration, while the acceleration - and thus the particle velocity - gradually decreases with increasing distance from the shovel.



(a) Simulation run time 1.65s (b) Simulation run time 1.90s (c) Simulation run time 2.15s

(d) Simulation run time 2.40s (e) Simulation run time 2.65s (f) Simulation run time 2.85s

Fig. 6 – Transverse section of subsoiling operation

As shown in Fig. 6, when the subsoiler shovel enters the soil particle bed, it undergoes a brief period of instability. This initial disturbance occurs during the early stage of soil contact but dissipates as the shovel continues to move forward. Upon reaching the right side of the soil trench, localized soil particle extrusion is observed. The simulation results indicate that a stable operational phase occurs between 1.90 s and 2.60 s of simulation time.

To accurately evaluate the performance of the subsoiler shovel, it is also necessary to analyse its resistance during operation. Using the post-processing function of EDEM 2022, ploughing resistance data were extracted at different time points. The resulting resistance trend is illustrated in Fig. 7.

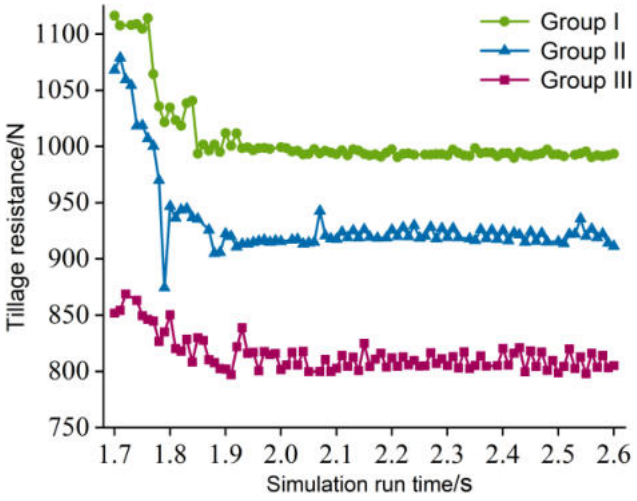


Fig. 7 – Comparison of ploughing resistance in three groups

As shown in Fig. 7, the ploughing resistance is more stable during the simulation time interval from 1.90 s to 2.50 s.

Simulation test design

The mechanical contact model between the subsoiler shovel and soil established earlier identified the primary factors influencing the soil disturbance area. These key factors include the shovel tip entry angle, the inclination angle of the shovel wings, and the width of the shovel wings. To assess their effects on the soil disturbance area Y_1, a multifactor interaction test was conducted. Based on mechanical analysis and pre-tests, the following parameter ranges were selected: shovel tip entry angle X_1 (5°~25°), shovel wing inclination angle X_2 (10°~30°), and shovel wing width X_3 (100mm~120mm). The objective of this test is to determine the optimal structural parameters of the subsoiler shovel under a fixed operational speed; therefore, operating speed was not considered a variable. Based on field conditions and operational experience, the working speed was set to 5 km/h.

A coding table for the test factors was established and is presented in Table 2.

Table 2

Test factor code

Coding	Factor		
	Shovel tip entry angle X_1 (º)	Inclination of shovel wings X_2 (º)	Width of shovel wings X_3 (mm)
1.682	25	30	120
1	21	26	116
0	15	20	110
-1	9	14	104
-1.682	5	10	100

RESULTS AND DISCUSSIONS

Discrete element simulation test results

A multifactor optimization simulation experiment was designed using a quadratic orthogonal rotational combination design. The simulation tests were conducted accordingly, and the evaluation index - soil disturbance area - was measured and recorded at the end of each simulation. The specific test design and corresponding results are presented in Table 3.

Table 3

Pilot programme and results

Number	Factor			Area of soil disturbance Y_1/cm^2
	X_1	X_2	X_3	
1	-1	-1	-1	1645.42
2	1	-1	-1	1305.03
3	-1	1	-1	1516.34
4	1	1	-1	1523.24
5	-1	-1	1	1458.9
6	1	-1	1	1379.36
7	-1	1	1	1405.14
8	1	1	1	1689.5
9	-1.682	0	0	1552.17
10	1.682	0	0	1496.53
11	0	-1.682	0	1400.11
12	0	1.682	0	1551.65
13	0	0	-1.682	1543.28
14	0	0	1.682	1510.96
15	0	0	0	1564.28
16	0	0	0	1574.31
17	0	0	0	1572.44
18	0	0	0	1562.96
19	0	0	0	1550.17
20	0	0	0	1570.56
21	0	0	0	1556.49

Number	Factor			Area of soil disturbance Y_1/cm^2
	X_1	X_2	X_3	
22	0	0	0	1553.63
23	0	0	0	1567.35

Analysis of test results

Regression analysis and analysis of variance (ANOVA) were conducted on the experimental data from Table 3 using Design-Expert 13.0 software. A significance test was applied to identify the most influential factors. Regression equations describing the relationships between the multiple factors and both soil disturbance area and tillage resistance were established. The detailed results of the statistical analysis are presented in Table 4.

Table 4

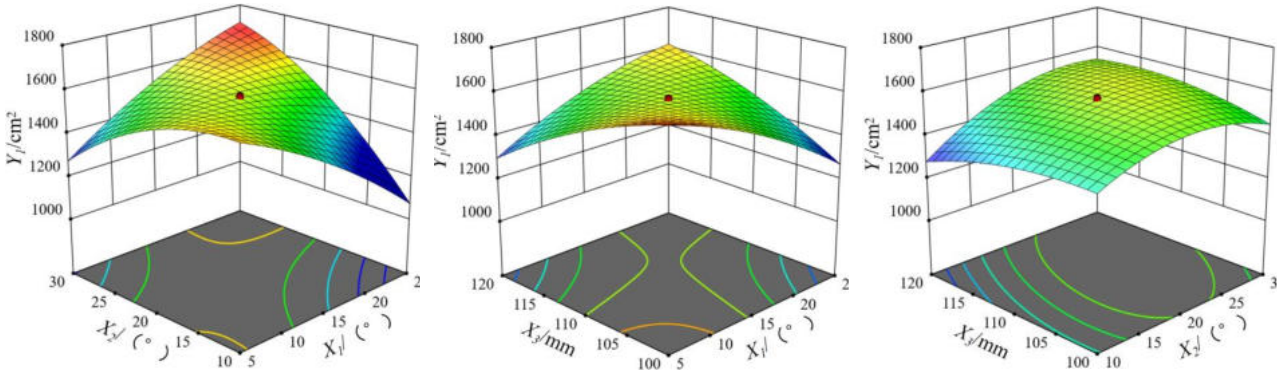
Analysis of variance for regression modelling of soil disturbance area

Norm	Source of variance	Sum of squares	Degree of freedom	F	P	Significance
Area of soil disturbance Y_1	Model	160896.97	9	57.43	<	**
	X_1	3616.71	1	33.20	<	**
	X_2	26392.81	1	242.31	<	**
	X_3	910.09	1	8.36	0.0123	*
	X_1X_2	63223.90	1	580.46	<	**
	X_1X_3	36222.21	1	332.56	<	**
	X_2X_3	3496.57	1	32.10	<	**
	X_1^2	4630.84	1	42.52	<	**
	X_2^2	18594.01	1	170.71	<	**
	X_3^2	4114.77	1	37.78	<	**
	Residual	1415.96	13			
	Lack of fit	829.42	5	2.26	0.1458	
	Error	586.54	8			
	Sum total	162312.93	22			

As can be seen from Table 4, the regression model P-values are less than 0.01, indicating that the models are all highly significant. In the regression model of soil disturbance area, X_1, X_2, X_1X_2, X_1X_3, X_2X_3, X_1^2, X_2^2, X_3^2 have a highly significant effect on the soil disturbance area, and X_3 has a significant effect on the soil disturbance area. Based on these results, a regression equation relating the factors to soil disturbance area was established.

$$\begin{aligned} Y_1 = {} & 1563.91 - 16.27X_1 + 43.96X_2 - 8.16X_3 \\ & + 88.90X_1X_2 + 67.29X_1X_3 + 20.91X_2X_3 \\ & - 17.07X_1^2 - 34.21X_2^2 - 16.09X_3^2 \end{aligned} \quad (15)$$

To facilitate visual analysis of the relationships between the influencing factors and the evaluation index, response surface plots were generated using Design-Expert 13.0 software. The resulting response surfaces are shown in Fig. 8.



(a) (b) (c)

Fig. 8 – Response surface plots between factors and area of soil disturbance

As can be seen from Fig. 8(a), with the gradual increase of shovel tip entry angle and shovel wing inclination angle, the soil disturbance area shows a trend of small decrease and then large increase. When the shovel tip entry angle changes, the soil disturbance area change interval is larger, so the effect of the shovel tip entry angle on the soil disturbance area is more significant compared to the shovel wings inclination angle. As can be seen from Fig. 8(b), with the gradual increase of shovel tip entry angle and shovel wing width, the soil disturbance area shows a trend of large decrease and then small increase. When the shovel tip entry angle varies, the variation interval of soil disturbance area is larger, so the effect of shovel tip entry angle on soil disturbance area is more significant compared with shovel wings width. From Fig. 8(c), it can be seen that as the shovel wings inclination angle and shovel wings width gradually increase, the soil disturbance area appears to increase firstly and then tends to flatten the change trend. When the shovel wings inclination angle and shovel wings width change, the change interval of soil disturbance area is basically the same, so the influence of shovel wings inclination angle and shovel wings width on soil disturbance area is basically the same.

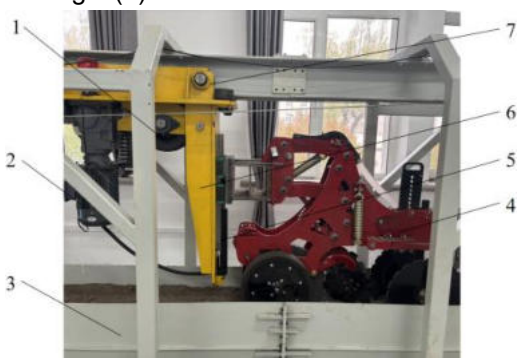
To determine the optimal combination of influencing factors, an optimization design was carried out. A parametric mathematical model was established based on the boundary conditions of the test factors. Following the objective of maximizing the soil disturbance area, a nonlinear programming model was constructed:

$$\begin{cases} \max Y_1 = (X_1, X_2, X_3) \\ s.t. \begin{cases} 5 < X_1 < 25 \\ 10 < X_2 < 30 \\ 100 < X_3 < 120 \end{cases} \end{cases} \quad (16)$$

The multi-objective optimization module in Design-Expert 13.0 was used to optimize the parameter combinations. Through this process, the optimal structural parameters for the subsoiler shovel were obtained. Based on the optimisation results, a reasonable combination of parameters was selected. When the shovel tip entry angle X_1 is 20.68°, the shovel wing inclination angle X_2 is 27.54°, and the shovel wing width X_3 is 103.72 mm, the soil disturbance area $Y_1$is optimal reaching 1699.80 cm^2. After the optimisation results, in order to facilitate the post-processing, the shovel tip entry angle X_1 is taken as 21°, the shovel wing inclination angle X_2 as 28°, and the shovel wing width X_3 as 104 mm. The optimised parameters are simulated and the soil disturbance area Y_1 is 1690.34cm^2, which is basically consistent with the optimised results.

Benchtop validation experiments

To validate the optimal parameter combination of the subsoiler shovel obtained from the discrete element simulation, a benchtop testing apparatus was developed. The test bench includes components such as a connecting arm, drive motor, single-axis lifting mechanism, guide rail, soil tank, control system, and travelling wheels. The soil tank was pre-filled with representative black soil from Northeast China to replicate actual field conditions. The structural layout of the strip minimum tillage subsoiling and fertilizing test bench is shown in Fig. 9(a).



(a) Structural diagram of the pedestal

1.Travelling wheel; 2 Drive motor; 3.Soil tank; 4.Strip minimum tillage subsoiling fertilizer applicator; 5.Single-axis lifting mechanism; 6.Connecting arm; 7.Guide rail



(b) Actual working conditions of subsoiler shovel in the tillage layer

1. Soil; 2. Shovel handle; 3. Shovel wings; 4. Shovel tip

Fig. 9 – Structural layout of the benchtop platform and working conditions of the subsoiler shovel

Based on the optimal working parameters for the subsoiler shovel obtained from the simulation tests, a winged subsoiler shovel was fabricated. Since the optimized parameters included decimal values, they were rounded for ease of manufacturing: the entry angle was set to 21°, the shovel wing inclination to 28°, and the shovel wing width to 104 mm. The manufactured subsoiler shovel was then mounted on the strip minimum tillage deep loosening fertilization machine. The fertilization machine was connected to the mounting arm, and the insertion depth of the subsoiler shovel into the soil was adjusted accordingly. To observe the in-soil behaviour of the subsoiler shovel, the surrounding soil was cleared after placement. The working condition of the shovel in the tillage layer is shown in Fig. 9(b).

To measure the actual soil disturbance area, it was necessary to extract the disturbed furrow profile after testing. A point within the stable velocity phase was selected as the furrow extraction location. The soil in front of this point was excavated to create a vertical cross-section perpendicular to the trench bottom. The disturbed soil was then carefully cleaned to expose the complete furrow profile. A flexible marker tape was positioned along the trench wall to delineate the profile, and imaging equipment was placed horizontally in front of the exposed cross-section to capture a clear image of the disturbance pattern. The captured image was imported into MATLAB 2020b to extract coordinate data representing the soil disturbance contour, as shown in Fig. 10(a) and (b). These coordinates were then imported into ORIGIN 2021 software to reconstruct the furrow profile and calculate the corresponding soil disturbance area. The final disturbance pattern is illustrated in Fig. 10(c).



(a) Original image (b) Extraction of furrow images (c) ORIGIN maps soil disturbance furrow patterns

Fig. 10 – Flowchart for obtaining area of soil disturbance

Three bench tests were conducted on 3 April 2025, with the soil surface levelled after each trial to ensure consistent initial conditions. Following each test, the soil disturbance area was calculated using ORIGIN2021 software. The disturbance areas recorded for the three trials were 1653.67cm^2, 1665.23cm^2, and 1649.35cm^2, respectively, yielding an average value of 1666.08cm^2. It should be noted that while the discrete element simulation assumed uniform soil particle density and compaction, the actual test conditions introduced variability. In practice, the soil density was not completely uniform across the test plots, and the presence of soil clods introduced inconsistencies in compaction. These factors contributed to the discrepancy between the simulated and measured results. The difference between the average actual disturbance area and the simulated result was -34.26cm^2, which falls within an acceptable error range.

CONCLUSIONS

(1) Based on the prevalent soil compaction issues in the black soil region of Northeast China and the requirements of the strip minimum-tillage cropping pattern, a novel winged subsoiler shovel was designed. This design enhances soil disturbance and effectively addresses existing soil structure problems while maintaining compatibility with strip-tillage operations.

(2) A mechanical contact model between the subsoiler shovel and soil was established to analyse the operational forces acting on the shovel. Key design parameters influencing subsoiling quality were identified through this model.

(3) A discrete element method (DEM) simulation was conducted to model subsoiling operations. An orthogonal experimental design was implemented using the shovel tip angle, wing inclination angle, and wing width as test factors, with the soil disturbance area as the primary evaluation index. Based on the simulation results and response surface optimization, the optimal structural parameters of the subsoiler shovel were determined. A bench-scale validation test confirmed the effectiveness of the optimized design, with the average actual soil disturbance area measured at 1666.08 cm², closely aligning with the simulation results and meeting the operational requirements for minimum tillage subsoiling.

ACKNOWLEDGEMENT

This paper was supported by the National Key Research and Development Programme of China (2023YFD1501005-06) and the Heilongjiang Provincial Key Research and Development Programme (2022ZX05B05-01).

REFERENCES

[1] Chen J., Liang X., Qi G., Zhang Y., Wang S., & Xing S. (2021). Optimization of mechanical structure of soil subsoiling and operation test (土壤深松机械结构优化及作业试验) [J]. *Tianjin Agriculture and Forestry Science and Technology*, Issue 4, pp. 8-10.

[2] Gao Z., Lu C., Wei X., Li H., He J., & Wei Q. (2023). Design and Experiment of Co-stirring Combined Corn Strip-Straw Cleaning Device (协拨组合式玉米条带秸秆清理装置设计与试验) [J]. *Transactions of the Chinese Society for Agricultural Machinery*, Vol. 54, Issue 10, pp. 68-79.

[3] Li B., Chen Y., & Chen J. (2018). Comparison of Two Subsoiler Designs Using the Discrete Element Method (DEM). *Transactions of the ASABE*, Vol. 61, Issue 5, pp. 1529-1537.

[4] Manuwa, S I. (2009). Performance evaluation of tillage tines operating under different depths in a sandy clay loam soil. *Soil & Tillage Research*, Vol. 103, Issue 2, pp. 399-405.

[5] Ma C. (2022). Design and experiment of deep fertilization strip tillage device for corn in Northeast China (东北玉米区深施肥带状耕作装置设计与试验). *Chinese Academy of Agricultural Mechanization Sciences*.

[6] Wang Q., Cao X., Wang C., Li H., He J., Lu C. (2021). Research Progress of No/Minimum Tillage Corn Seeding Technology and Machine in Northeast Black Land of China (东北黑土地玉米免少耕播种技术与机具研究进展) [J]. *Transactions of the Chinese Society for Agricultural Machinery*, Vol. 52, Issue 10, pp.1-15.

[7] Wang J., Tang H., Wang J., Huang H., Lin N., Zhao Y. (2017). Numerical Analysis and Performance Optimization Experiment on Hanging Unilateral Ridger for Paddy Field (悬挂式水田单侧修筑埂机数值模拟分析与性能优化) [J]. *Transactions of the Chinese Society for Agricultural Machinery*, Vol. 48, Issue 8, pp. 72-80.

[8] Zhang Z., Yin Z., Yu P., Qi Z., Wei Y., Li A. (2024). Effects of Soil and Water Conservation Measures on Soil Physical and Chemical Properties in Slope Farmland in Black Soil Region (黑土区坡耕地水土保持耕作措施对土壤理化性状的影响) [J]. *Transactions of the Chinese Society for Agricultural Machinery*, Vol. 55, Issue 1, pp.282-293.

[9] Zhao S., Wang J., Chen J., Yang Y., & Tan H. (2018). Design and Experiment of Fitting Curve Subsoiler of Conservation Tillage (保护性耕作拟合曲线型深松铲设计与试验) [J]. *Transactions of the Chinese Society for Agricultural Machinery*, Vol. 49, Issue 2, pp. 82-92.

[10] Zheng K., He J., Li H., Diao P., Wang Q., & Zhao H. (2016). Research on Polyline Soil-breaking Blade Subsoiler Based on Subsoiling Soil Model Using Discrete Element Method (基于离散元深松土壤模型的折线破土刃深松铲研究) [J]. *Transactions of the Chinese Society for Agricultural Machinery*, Vol. 47, Issue 9, pp. 62-72.

[11] Zhang L. (2013). Study on Resistance Reduction Technology of Subsoilers (深松铲减阻技术). *Jilin University.*

[12] Zhou Y. (2006). Force Mathematical model and computer simulation of subsoiling (深松铲受力数学模型与计算机模拟). *Henan Agricultural University.*

[13] Zhang X., You Y., Wang D., Wang Z., Liao Y., Lv J. (2022). Design and Experiment of Soil-breaking and Root-cutting Cutter Based on Discrete Element Method (基于离散元法的板结草地破土切根刀优化设计与试验) [J]. *Transactions of the Chinese Society for Agricultural Machinery*, Vol. 53, Issue 11, pp.176-187.

RESEARCH ON THE INFLUENCE OF GRINDING TIME ON THE PARTICLE SIZE DISTRIBUTION WHEN OBTAINING ROSEHIPS POWDER
/
CERCETĂRI PRIVIND INFLUENȚA TIMPULUI DE MĂCINARE ASUPRA DISTRIBUȚIEI DIMENSIUNII PARTICULELOR LA OBȚINEREA PULBERII DE MĂCEȘE

Alina-Daiana IONESCU, Gheorghe VOICU*), Gabriel-Alexandru CONSTANTIN*), George IPATE, Elena Mădălina ȘTEFAN, Mihaela BEGEA, Gabriel MUȘUROI, Mihaela-Florentina DUȚU, Iulian-Claudiu DUȚU, Magdalena-Laura TOMA, Sorin-Dan IORDACHE
National University of Science and Technology POLITEHNICA Bucharest –
Faculty of Biotechnical Systems Engineering / Romania;
*Tel: 0724 715 585, 0727651064; *E-mail: ghvoicu_2005@yahoo.com, gabriel.constantin@upb.ro*
DOI: https://doi.org/10.35633/inmateh-76-79

Keywords: *rosehips powder, grinding time, sieves, particle size distribution, average particle diameter*

ABSTRACT
This study evaluates the influence of grinding time on the particle size distribution of rosehip powder. A universal mill based on the cutting principle was used, equipped with four sieves with different mesh sizes (0.2 mm, 0.5 mm, 1 mm, and 4 mm). The grinding durations were set at 30 seconds, 60 seconds, 90 seconds, 120 seconds, and 150 seconds. Each grinding stage was followed by particle separation using a set of sieves to determine the particle size distribution. The results indicated that both the grinding duration and the mesh size of the sieves significantly impacted the particle size distribution. The 0.5 mm sieve associated with a grinding time of 90 seconds provides an optimal balance between achieving a reduced average particle diameter, high specific surface area, and energy efficiency. These findings have important implications for the production and quality control of rosehips powder in various applications, including food, nutraceutical, and pharmaceutical products. Understanding the granulometric behavior of rosehip powder can help improve the solubility, stability, and bioavailability of the product. This research establishes the groundwork for further studies focused on optimizing grinding processes and developing rosehip powder products with customized particle size distributions to meet the specific demands of various industries.

REZUMAT
Acesta lucrare evaluează influența timpului de măcinare asupra distribuției dimensiunii particulelor pulberii de măcește. A fost utilizată o moară universală bazată pe principiul de tăiere, echipată cu patru site cu dimensiuni diferite ale ochiurilor (0.2 mm,0.5 mm, 1 mm și 4 mm), iar timpii de funcționare au fost de (30 secunde, 60 secunde, 90 secunde, 120 secunde și respectiv 150 secunde). Fiecare etapă de măcinare a fost urmată de separarea particulelor printr-un set de site pentru a determina distribuția dimensiunii acestora. Rezultatele au indicat faptul că atât durata de măcinare, cât și dimensiunea ochiului sitei au avut un impact semnificativ asupra distribuției dimensiunii particulelor. Sita de 0,5 mm asociată cu un timp de măcinare de 90 de secunde oferă un echilibru optim între obținerea unui diametru mediu redus al particulelor, suprafață specifică mare și eficiență energetică. Aspectele prezentate constituie implicații importante pentru producția și controlul calității pulberii de măcește în diverse aplicații, inclusiv în alimentație, obținerea de produse nutraceutice și farmaceutice. Înțelegerea comportamentului granulometric al pulberii de măceș poate ajuta la îmbunătățirea solubilității, stabilității și indisponibilității produsului. Această cercetare pune bazele pentru studii ulterioare privind optimizarea proceselor de măcinare și dezvoltarea produselor sub formă de pulbere de măcește cu distribuții adaptate a dimensiunii particulelor pentru a îndeplini cerințele specifice ale industriei.

INTRODUCTION
Rosehip, or *Rosa canina L.*, is a plant that is widely used in cosmetics, medicines, and nutrition. Growing wild in regions including Asia, North America, Europe, and the Middle East, it is a member of the *Rosaceae* family and belongs to the *Rosa genus*. The health-promoting qualities of rosehip are attributed to its considerable levels of bioactive substances, which include vitamins, minerals, antioxidants, and phenolic compounds (*Igual et al., 2022; Patel, 2017; Belkhelladi & Bougrine, 2024; Ghendov-Mosanu, 2020).* Rosehip is a fruit that is high in nutrients and it is considered to be of significant scientific importance.

Phenolic acids (gallic acid, ellagic acid, caffeic acid, p-coumaric acid), carotenoids (lycopene, β-carotene, zeaxanthin), anthocyanins, tocopherols (α- and β-tocopherols), tannins, and flavonoids (flavan-3-ols) are the primary bioactive components of rosehip (*Igual et al., 2021; Negrean et al., 2024; Lustrup & Winther, 2022; Peña et al., 2023; Koczka et al., 2018; Nađpal et al., 2016*).

Rosehips can be used for much more than just jams and infusions; drying the fruits and then grinding them into a powder is one of the best ways to utilize them. The obtaining of product in powder form would increase its uses as reconstituted juice or infusion, or added to breakfast, ice cream, dairy products, baked goods, smoothies, shakes, salads, snacks, and more. It could even be used to directly enhance any food with bioactive ingredients *(Igual et al., 2021)*. Rosehip powder can be consumed as capsules, which come in a variety of brands (*Götz et al., 2011*).

A patent has revealed an innovative technology for processing rosehip powder, enabling the production of particles with extremely small dimensions, which are critical for efficient integration into food and beverage products. This advanced micronization method optimizes the dispersibility and solubility of the powder, thereby ensuring superior performance in food formulations where homogeneity and fine texture are essential. Additionally, this finely milled powder enhances the stability of the final products, preventing sedimentation and offering a refined sensory experience for the consumer. The resulting powder contains no particles larger than 600 micrometers, with approximately 50% of the particles measuring between 100 and 150 micrometers. US Patent 6,024,960 to Kharazmi et al. describes how rose hips are transformed into a fine, dry powder with small particles (less than 1 mm, ideally between 0.1 and 0.5 mm). This technology is used to produce the powders HYBEN-VITAL and i-FLEX, which are used in food products and nutritional supplements. Additionally, patent US 2007/0184164 examines the use of rose hip powder with particles of 841 microns or smaller in food premixes, enriched with essential nutrients such as alpha-linolenic acid, dietary fiber, and antioxidants, demonstrating the versatility of this powder in various food formulations. The Japanese patent Kokai 2004275015 (K. Emoto, 2004) reveals the use of rose hip powder with an average particle size of less than 2 mm as a gelling agent in the production of fruit jams. The Chinese patent 101040833 (Tianjin Yumelijing Group Co., Ltd) describes a cosmetic product that incorporates rose hip pulp among other ingredients, with particle sizes varying from 5 mesh (4000 microns) to 200 mesh (90 microns). The patents discussed underscore the critical role particle size plays in the formulation of products across various industries, including food, pharmaceuticals, and cosmetics. The precise control of particle size, whether in rose hip powders used as gelling agents in fruit jams, as nutritional supplements, or as components in cosmetic products, directly influences the texture, stability, and bioavailability of the final product. This highlights the importance of selecting and processing ingredients to specific particle sizes to optimize their functional properties and efficacy in diverse applications (*Götz. et al., 2011*).

Specifications involving finer particles and stricter control over the mean particle size, or the width and cut-off of the particle size distribution, have been increasingly rigorous in recent years, especially in the food and pharmaceutical industries *(Tangirala et al., 2014; Silva et al., 2013; Shekunov et al., 2007)*. Particle-size distribution (PSD) is a mathematical function or a list of numbers that indicates the relative amount (usually expressed in mass) of particles present based on size in a powder, granular material, or particles distributed in fluid. Grain size distribution is an alternative name for PSD (*Ujam & Enebe, 2013; Bayat et al., 2015; Islam et al., 2022*). Particle size distribution is a crucial factor since it affects several product attributes, including density, flowability, compressibility, segregation, and rehydration. Nevertheless, it can be difficult to find the appropriate PSD. Accidentally modifications to the PSD, such as attrition of particles, or deliberate modifications, such as grinding, can occur downstream *(Carpin et al., 2017; Servais et al., 2002; Guo et al., 2024)*. Another product attribute that can be affected by the PSD of the powder is caking, which is the unintentional agglomeration of powder particles visible as lumps of different sizes and hardness (*Carpin et al., 2017*).

Several methods are employed to determine PSD, each suited to different types of materials and particle sizes. Common techniques include laser diffraction, dynamic light scattering (DLS), image analysis, and sieve analysis. Each method offers unique advantages and insights. For instance, laser diffraction is highly effective for a wide range of particle sizes and provides rapid results, while DLS is often used for sub-micron particles in colloidal suspensions (*Li et al., 2005; Lyu et al., 2020; Fuaâ & Tajdari, 2011; Nijhu et al, 2024; Ma S. et al., 2024).* Sieve analysis, one of the oldest and most straightforward methods, remains widely used (*Dodds, 2024*). However, for a more precise analysis of fine particles or for samples that may cause sieve clogging, more advanced alternative methods may be necessary.

This technique involves passing the powder through a series of sieves with progressively smaller mesh sizes, allowing for the separation and quantification of particles based on size. When analyzing particle size distribution (PSD) using sieve analysis, the method offers simplicity, cost-effectiveness, and the ability to handle large sample volumes. However, sieve analysis has limitations, especially with finer particles, where problems such as agglomeration and reduced separation efficiency can lead to inaccuracies (*Kroetsch & Wang, 2008; Fahrenholz et al., 2010; Patwa et al., 2010; Liu et al., 2023)*. Additional advantages and limitations of sieve analysis are illustrated in Figure 1, which provides a detailed visual representation of the method's overall effectiveness. (*Igathinathane et al., 2009; Sonaye S. Y., & Baxi, 2012*).

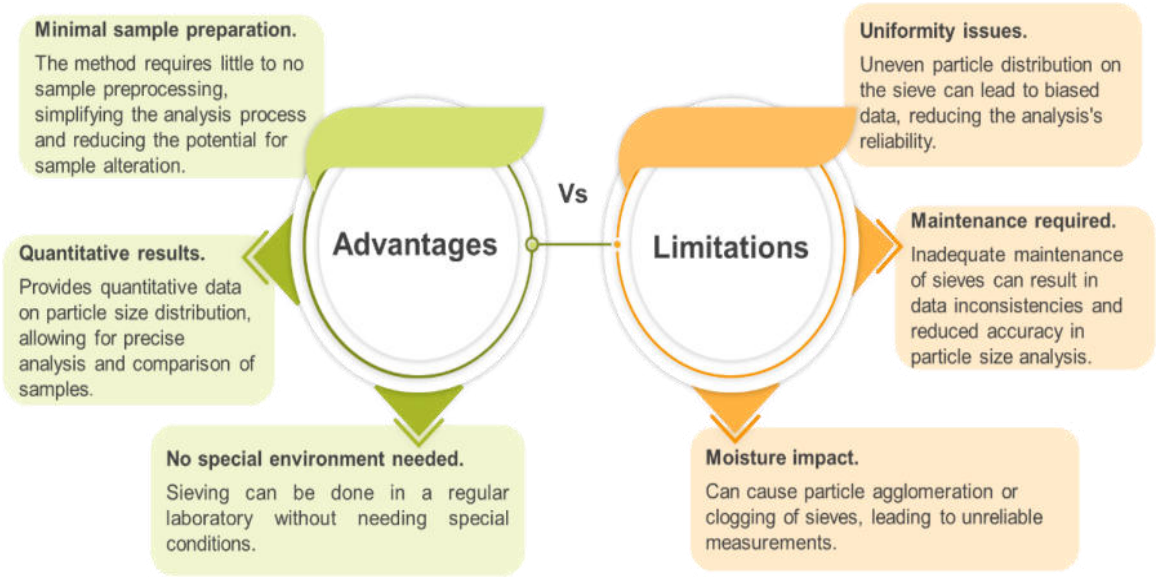


Fig. 1 - Overview of advantages and limitations in particle size distribution analysis using the sieving method (*Igathinathane et al., 2009; Sonaye & Baxi, 2012*)

Grinding time significantly influences the particle size distribution of rosehip powder. As the grinding time increases, larger particles are broken down into smaller ones, leading to a finer distribution. Initially, the reduction in particle size is rapid, but over time, the rate of size reduction slows as the particles become smaller and harder to break down further. Extended grinding can also lead to the agglomeration of fine particles due to increased surface energy, which may affect the uniformity of the particle size distribution. Therefore, optimizing grinding time is crucial for achieving the desired particle size distribution (*Liu et al., 2016; Kumar et al., 2021; Liu et al., 2022; Shuhua et al., 2021; Hanumanthappa et al., 2020).*

The objectives of this study are to analyze the effect of varying grinding times on the particle size distribution of rosehips powder and to determine the optimal grinding time needed to achieve the desired fineness and uniformity. Additionally, the study aims to investigate the relationship between prolonged grinding and the potential for particle agglomeration. By addressing these objectives, the study aims to provide valuable insights into the grinding process for rosehips powder, helping to optimize the production parameters for achieving a high-quality product.

MATERIALS AND METHODS

Rosehip fruits of the *Rosa canina* variety were carefully hand-picked from a wooded area in Vâlcea County at the beginning of September. The fruits were fully ripe, exhibiting a vibrant light red color, and were meticulously selected to be free of mold, blemishes, and other impurities. After harvesting, the rosehips were thoroughly washed and then dried in a laboratory-controlled environment at 40°C until they reached a moisture content of 5%. This drying process was crucial to prevent microbial growth and ensure long-term storage stability. The dried rosehips were then stored in moisture-proof polyethylene bags and kept in a refrigerator at 5°C to preserve their moisture content and overall quality for subsequent studies. For the experimental tests, a total of 600 grams of dried rosehips were prepared, ensuring an ample supply for repeated trials and consistent results. From this batch, a sample size of 30 grams was selected for each individual experiment. The whole fruits, including peel, pulp, and seeds, were subjected to the grinding process to obtain a powder that retains the full nutritional value of the rosehip.

This approach was taken to ensure that the powder captured the complete range of natural compounds present in each component of the fruit, maximizing its potential health benefits and functional properties. Additionally, the inclusion of seeds and peel in the grinding process contributes to a richer profile of bioactive compounds, such as antioxidants, vitamins, and fatty acids, which are essential for the comprehensive evaluation of the powder's quality and efficacy in various applications. The five key experimental steps and corresponding equipment were illustrated in Figure 2.



Fig. 2 - Experimental protocol for particle size characterization as a function of grinding time and milling sieve mesh dimensions

Grinding process was carried out using a Fritsch Pulverisette 19 mill, specifically designed for processing hard materials. This mill operates on the cutting principle, where the material is finely ground through the interaction between the rotor's cutting edges and the stationary knives within the grinding chamber. The mill can present a maximum feed size of 70 x 80 mm, boasts a flow rate of up to 60 liters per hour, and operates at a rotor speed of 2800 rpm. The design of the grinding chamber is optimized for efficiency, featuring smooth inner walls that prevent the formation of dead spaces, which also simplifies and accelerates the cleaning process. The mill is engineered for easy maintenance; the rotor and sieve cassette can be quickly detached for thorough cleaning. The rotor itself is constructed from hardened stainless steel and is equipped with four straight cutting edges aligned parallel to the stationary knives. These knives feature two cutting edges and can be reversed when necessary, effectively doubling the operational lifespan of the rotor.

Material was introduced into the grinding chamber, where it was allowed to flow freely and was shredded as it passed between the cutting edges of the rotor and the stationary blades. The final particle size was controlled using four different sieve cassettes, each with cells of varying dimensions: 4 mm, 1 mm, 0.5 mm, and 0.2 mm. Grinding durations for each sieve size were set at 30, 60, 90, 120, and 150 seconds, respectively. Time was accurately measured using a precise stopwatch. Once the material reached the desired fineness, the particles passed through the sieve openings and were collected in a designated vessel.

The sieves had trapezoidal perforations for the 0.2 mm, 0.5 mm, and 1 mm sizes, which provided an additional shredding effect due to the increased shear forces compared to the square perforations used of the 4 mm sieve. This design improved grinding efficiency by facilitating additional size reduction of the material before it passed through the sieve and into the collection vessel.

The particle size distribution analysis was conducted using the Analysette 3 Spartan Vertical Vibrating Laboratory Sieve Shaker (Fritsch, Idar-Oberstein, Germany), a high-precision instrument designed for accurate particle separation and classification based on size. This equipment operates on the principle of vertical vibration, which ensures that the material is evenly distributed across the sieve surfaces. This even distribution allows particles to pass efficiently through a series of sieves arranged in a stack, where each sieve has a progressively smaller mesh size from top to bottom. Process begins by placing the sample in the top sieve, which has the largest mesh size. The shaker then subjects the stack of sieves to mechanical agitation, causing the particles to move through the sieves. As the particles travel downward, they are separated according to their size: larger particles are retained on the upper sieves, while smaller particles pass through to the lower ones. By collecting and weighing the material retained on each sieve, a detailed particle size distribution profile is generated. This profile is crucial for assessing the granulometry of the rosehip powder, as it provides insight into the proportion of particles within specific size ranges. The equipment's adjustable vibration settings further enhance the accuracy of the sieving process, ensuring consistent and reliable results across different samples.

The average particle size (d_m) is typically calculated using a mathematical formula based on the distribution of particle sizes in a sample. One common method is the weighted arithmetic mean size, which can be expressed as follow (*Ionescu et al., 2024*):

$$d_m = \frac{\sum a_i\,(\%) \times d_i}{100}\ (mm) \tag{1}$$

Specific surface area (S_{sm}) of a set of particles is a critical parameter that describes the total surface area of particles per unit mass or volume. This measurement is particularly useful in powder technology, as it significantly influences the reactivity, dissolution rate, and overall stability of materials in powder form, which is especially important in the food and pharmaceutical industries (*Ionescu et al., 2024*).

$$S_{sm} = \frac{6}{100 \times \rho} \sum_{di}^{n+1} \frac{a_i}{d_i} \left(\frac{m^2}{kg}\right) \tag{2}$$

where:

d_m-average particle diameter (mm); a_i- percentage of material with a size between dimensions l_i and l_{i+1} of the adjacent sieves (mm); d_i-average particle size of fraction (mm), ρ- density of the particle material (kg/m³); S_{sm}- specific surface area (m²/kg);

To obtain the trend lines of the average particle diameter as a function of grinding time, as well as the specific surface area as a function of grinding time, for all four sieves used during the grinding process of dried rose hips, a statistical package Microsoft Excel Version 2406 64-bit was used. This methodical approach facilitated a comprehensive analysis of the grinding kinetics, revealing distinct trends for each sieve type, which were essential for understanding how grinding parameters affect particle morphology. Consequently, this facilitated a deeper insight into the interplay between particle size distribution and grinding duration, guiding the optimization of grinding conditions.

RESULTS

Within this section are presented and analyzed the experimental results obtained from grinding the material using sieves of different sizes (0.2 mm, 0.5 mm, 1 mm, and 4 mm) and for various grinding durations. The purpose of this analysis is to highlight how grinding time influences the *average particle diameter* and to identify specific behaviors for each sieve size, including possible particle agglomeration phenomena at extended grinding times. Average diameter variation graph (Figure 3) as a function of grinding time is used to illustrate the trends observed for each sieve. Each trend lines is described in detail using regression equations to quantify the correlation between the analyzed variables. The coefficient of determination (R^2) values are also discussed to evaluate the degree of model fit to the experimental data and to provide a clear picture of the accuracy and relevance of the obtained results.

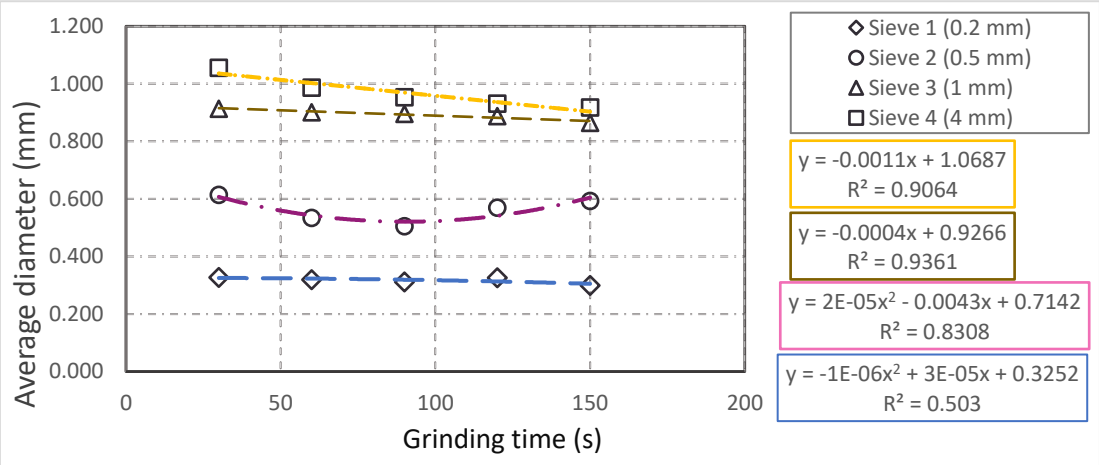


Fig. 3 - Variation of average particle diameter with grinding time for different sieve sizes

For the finest fraction passing through Sieve 1 (0.2 mm), the polynomial regression of second degree exhibits a low coefficient of determination (R^2 = 0.503), indicating substantial variability and limited predictive accuracy. This curve suggests a dynamic equilibrium between particle fragmentation and agglomeration phenomena. As grinding continues, particle size reduction approaches a physical limit dictated by material properties and grinding efficiency, while concurrent agglomeration or reaggregation processes lead to slight increases in effective particle diameter.

The particle size evolution for the fraction passing through Sieve 2 (0.5 mm) is described by the same second-degree polynomial regression with a coefficient of determination R=0.831. The positive quadratic and negative linear coefficients define a concave upward curve, indicating an initial decrease in mean particle diameter during grinding, followed by a slight increase at extended grinding times.

Analyzing the polynomial regression equations for Sieves 1 and 2 (with aperture sizes of 0.2 mm and 0.5 mm, respectively), it can be observed that the coefficient of the quadratic term (x^2) is very small. This suggests that a linear relationship between the parameters, mean particle diameter and grinding time, can still be considered. To support this assumption, linear regression equations were also determined: for Sieve 1, $y=-0.0002x+0.3322$ with $R^2=0.4764$, and for Sieve 2, $y=-2x10^{-5}x+0.5652$, with $R^2=0.0005$. However, the coefficient of determination (R^2) remains relatively low when applying a linear regression model, indicating a limited explanatory power despite the apparent linear trend.

Furthermore, the linear trend line for Sieve 3 (1 mm), with a coefficient of determination $R^2=0.9361$, demonstrates a strong and well-defined correlation between grinding time and the reduction in average particle size. This indicates that as grinding time increases, particle size consistently and predictably decreases. High coefficient of determination suggests that the linear model accounts for nearly 94% of the variation in particle size. The constant reduction in size implies an efficient grinding process that does not result in significant particle agglomeration, indicating that the particles do not become small enough to cause agglomeration issues.

The linear trend line for sieve 4 (4 mm), with a coefficient of determination of $R^2=0.9064$, indicates a clear and strong correlation between grinding time and the reduction in average particle size. This suggests that as the grinding time increases, there is a continuous fragmentation of larger particles into smaller ones. The high value of R^2 reflects a robust relationship, meaning that the model effectively explains the variation in particle size. Although the particles are consistently broken down into smaller sizes, they do not reach dimensions small enough to cause significant agglomeration. Thus, the grinding process is effective in reducing particle size without leading to problems associated with particle clustering.

The varying behavior of particles based on sieve size highlights the complexity of the grinding process. For fine particles (0.2 mm and 0.5 mm), extending the grinding time does not necessarily result in a continuous reduction in size due to the phenomenon of agglomeration. Optimizing the process to achieve a specific particle size distribution requires careful consideration of the dynamic balance between grinding and agglomeration, especially for finer particles. Controlling parameters such as moisture, temperature, or grinding energy is crucial for managing this balance. Prolonged grinding can heat the material, affecting its properties and potentially influencing its grinding behavior. Even though the same amount (30 g) was used for each experiment, the exact composition of the rosehip samples may vary from batch to batch, adding another layer of complexity to the process.

The graph in Figure 4 presents a detailed analysis of how sieve mesh size and sieving time affect the average particle diameter. Each set of columns in the graph represents the average diameter of particles (in millimeters) that have passed through sieves of different sizes (0.2 mm, 0.5 mm, 1 mm, and 4 mm) at different time intervals (30, 60, 90, 120, and 150 seconds). The mean particle diameter of ground rosehip increases linearly with the increase in sieve aperture size.

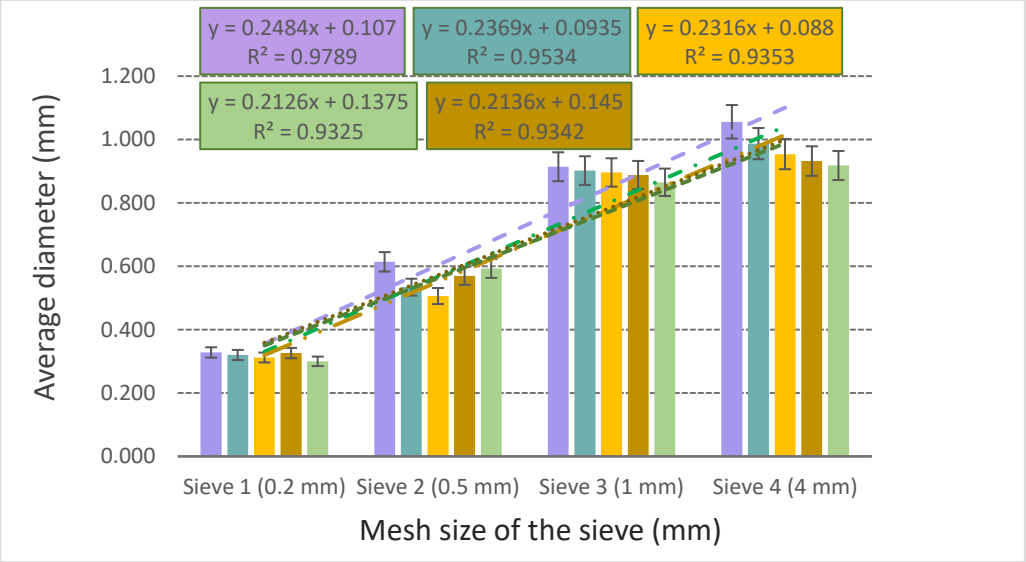


Fig. 4 - The relationship between sieve mesh size and particle diameter evolution based on grinding time

Analysis of sieve 1, which has a nominal size of 0.2 mm, shows that the average particle diameter is approximately 0.3 mm. This indicates a notable deviation from the nominal sieve size, suggesting that the resulting particles are larger than the specified dimension. The minor variations in particle size related to grinding time emphasize that, although the grinding process affects particle size, it does not consistently achieve the precise nominal sieve size.

Also, for sieve 2, with a nominal size of 0.5 mm, the average particle diameter increases notably, ranging from approximately 0.5 to 0.6 mm. Additionally, there is a greater variability in particle size relative to the grinding time, with a general trend showing that particles tend to be smaller with longer grinding durations. This suggests that extended grinding periods can reduce the size of the particles, but there remains a notable deviation from the nominal sieve size.

Additionally, for sieve 3, with a nominal size of 1 mm, the average particle diameter increases substantially, reaching values between 0.85 and 1.05 mm. The variation in particle size related to the grinding time is more pronounced, showing a clear trend of decreasing average diameter as the grinding duration increases. This indicates that while the sieve is designed to retain particles up to 1 mm, the actual particle sizes can vary, with longer grinding times resulting in smaller average particle diameters.

In the same way, for sieve 4, with a nominal size of 4 mm, the average particle diameter reaches its highest values, ranging between 0.9 and 1.1 mm. The most significant variation in particle size is observed based on grinding time, with a notable decrease in the average diameter as the grinding duration is extended. This suggests that, despite the sieve's large nominal size, the actual particle sizes are smaller, and longer grinding times lead to a more pronounced reduction in average particle diameter.

A valuable observation from the analysis of the graph is that for sieves with larger dimensions, the efficiency of the grinding process is often reduced, as the ground particles tend to be larger compared to the nominal sieve size. This is manifested by a greater difference between the sieve size and the average particle diameter, indicating that the particles are not fully fragmented to meet the specifications. Thus, as the sieve size increases, it becomes more challenging to achieve an average particle diameter close to the nominal sieve size, which can impact the quality and consistency of the final product. The duration of grinding plays a crucial role in determining particle size, as extended grinding allows particles to undergo additional cycles of fragmentation. For sieves with larger dimensions, where particles may initially have a diameter close to the nominal sieve size, extending the grinding time helps achieve a finer particle size. This adjustment in grinding time allows for better control over particle dimensions, thereby optimizing the grinding process.

According to theory, the specific surface area is inversely proportional to the particle diameter, a relationship that is also demonstrated by our results. The average specific surface area reflects the total surface area available per unit mass of the particles, and generally, a higher specific surface area is desirable because it enhances the product's functionality. Typically, an increase in grinding time leads to a reduction in particle size, which in turn increases the specific surface area, thereby improving the physicochemical properties of the rosehip powder. Figure 5 illustrates the graph showing the variation in the average specific surface area of particles as a function of grinding time for particles passed through sieves of different sizes: 0.2 mm, 0.5 mm, 1 mm, and 4 mm.

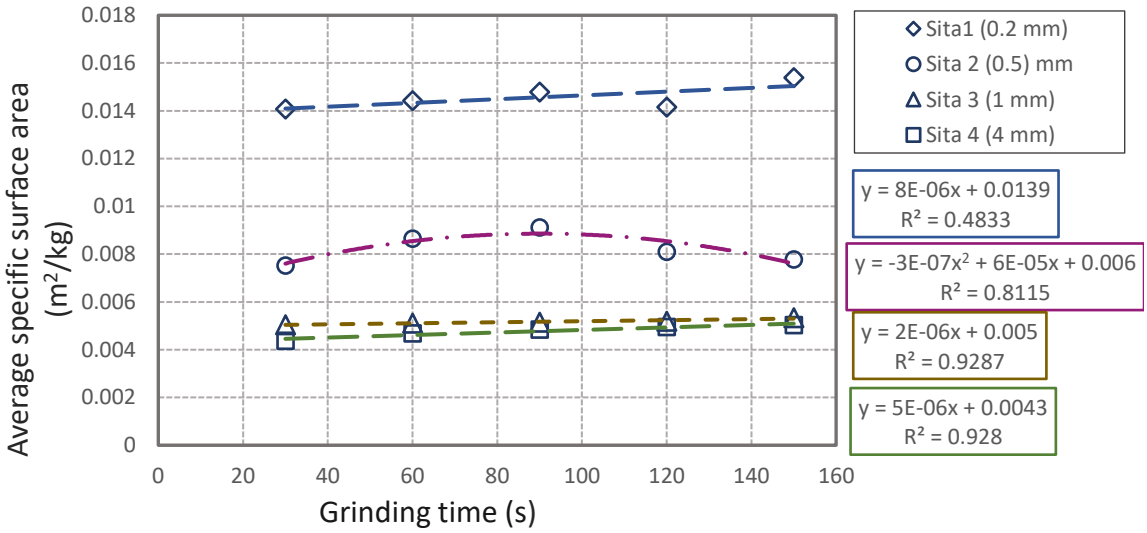


Fig. 5 - Variation of average specific area with grinding time for different sieve sizes

For the 0.2 mm sieve, a clear upward trend in the average specific surface area is observed as the grinding time increases. The positive slope of the equation (8E-06) indicates a consistent rate of increase in specific surface area, meaning that particle size gradually decreases as grinding time is extended. However, the moderate R^2 value suggests that while the overall trend is upward, there is some variability in the measured data, likely due to the complex phenomena of fine particle agglomeration.

The evolution of the curve corresponding to the 0.5 mm sieve exhibits a parabolic behavior, characterized by an initial increase in specific surface area followed by a subsequent decrease, indicating an optimal grinding efficiency around the peak value. This phenomenon can be attributed to particle size reduction reaching a critical threshold, beyond which agglomeration or structural changes may occur, leading to a decrease in exposed surface area. Therefore, the grinding time must be carefully optimized to prevent the adverse effects of over-grinding. The distinct behavior of this sieve highlights a heightened sensitivity to the duration of the grinding process.

Furthermore, regarding the 1 mm sieve the trend line has a slightly positive slope and a high coefficient of determination ($R \approx 0.93$). This suggests a strong correlation between the grinding time and the average specific surface area, with the specific surface area increasing slightly as the grinding time increases. The data are very well explained by this trend line, indicating a clear linear relationship.

Similarly, for the 4 mm sieve, the trend line has a positive slope and a very high coefficient of determination ($R \approx 0.93$). This indicates a strong correlation, with the average specific surface area increasing significantly as the grinding time increases. Much like with the 1 mm sieve, the data are very well explained by this trend line, demonstrating a consistent and predictable increase in specific surface area.

Overall, this graph illustrates how sieve size influences the dynamics between grinding and agglomeration during the milling process. For fine particles (sieve of 0.2 mm and 0.5 mm), the agglomeration phenomenon plays a more significant role, slowing down the decrease in particle size and, consequently, leading to a more pronounced increase in the mean specific surface area. On the other hand, for larger particles (sieve of 1 mm and 4 mm), the grinding process predominates, resulting in a linear and steady increase in the mean specific surface area as grinding time increases. This in-depth analysis of the relationship between grinding time, sieve size, and mean specific surface area provides a valuable overview of the complex dynamics occurring within the milling process. It can be used to optimize process parameters and achieve the desired particle size distribution based on specific application requirements.

In Figure 6, the graph illustrates the relationship between sieve mesh size and the evolution of average specific surface area as a function of grinding time. The following general trends can be observed: the average specific surface area decreases as the sieve size increases, from sieve 1 (0.2 mm) to sieve 4 (4 mm), and for each sieve, there are variations in the specific surface area depending on the grinding time. Additionally, the average specific surface area of the ground material decreases linearly with the increase in sieve aperture size.

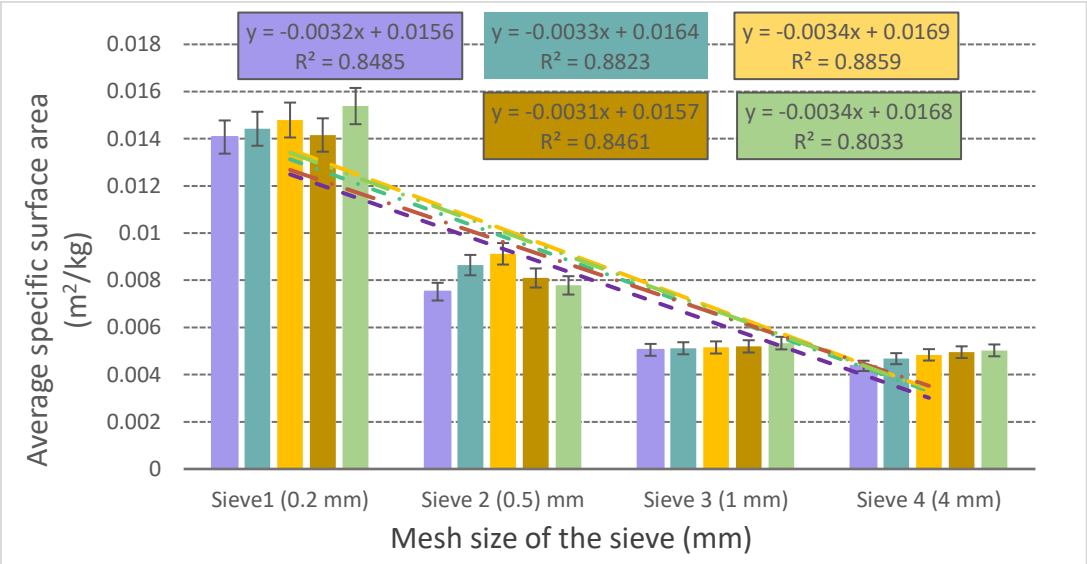


Fig. 6 - The relationship between sieve mesh size and average specific area evolution based on grinding time

Sieve 1 presents the highest average specific surface area, ranging from approximately 0.014 to 0.0154 m²/kg. There is a general trend of increasing specific surface area with longer grinding times, with a slight decrease observed at 120 seconds. The maximum value of the specific surface area is reached at 150 seconds of grinding.

Also, sieve 2 shows a significantly lower average specific surface area compared to Sieve 1, ranging from approximately 0.0075 to 0.0091m²/kg. There is an increase in the specific surface area up to 90 seconds, followed by a decrease for longer grinding times.

Increasing the grinding time has a positive but limited effect on the specific surface area for this Sieve 3 size. Even after 150 seconds of grinding, the specific surface area remains significantly lower than that obtained with finer sieves (Sieve 1 and Sieve 2), but slightly higher than for Sieve 4. Extending the grinding time from 30 to 150 seconds can be beneficial, but the gains are less significant compared to switching to a finer sieve. These larger particles may be preferred in certain applications for their physical properties.

Although Sieve 4 produces particles with the smallest specific surface area, the relative increase with grinding time is more pronounced compared to the finer sieves. This suggests that for larger particles, grinding time has a proportionally greater impact on the specific surface area. However, increasing the grinding time involves higher energy consumption. It is important to evaluate whether the benefit of increased specific surface area justifies the additional energy cost. Longer grinding times may also lead to increased equipment wear, which should be considered in process planning. A potential avenue for further research would be to investigate whether the observed trend of increasing specific surface area continues beyond 150 seconds or if it reaches a plateau. The behavior of Sieve 4 demonstrates that, even for larger particles, there are significant opportunities to optimize the specific surface area by adjusting the grinding time.

CONCLUSIONS

This study highlights the critical role of both grinding time and sieve size in determining the average particle diameter, specific surface area, and overall particle size distribution of rosehip powder. The 0.2 mm sieve, combined with a grinding time of 150 seconds, was found to be the most effective in producing the smallest average particle diameter and the highest specific surface area, making it ideal for applications requiring maximum reactivity or solubility. However, this approach also results in higher energy demands and potential equipment wear, underscoring the need for a balanced approach. The 0.5 mm sieve at 90 seconds of grinding offers a more energy-efficient alternative, achieving a moderately small average particle diameter and a high specific surface area while minimizing the negative impacts of prolonged grinding.

This makes it a suitable choice for applications where a balance between fine particle size, energy efficiency, and operational practicality is required. Conversely, larger sieves (1 mm and 4 mm) demonstrated that while extended grinding can decrease the average particle diameter and increase the specific surface area, these gains are incremental and come with significantly higher energy consumption and wear on the equipment. This study suggests that for most applications, a mid-range sieve size like 0.5 mm, paired with a moderate grinding duration, provides an optimal balance between reducing particle diameter, enhancing specific surface area, and maintaining energy efficiency and equipment durability. Further research is recommended to explore the potential benefits of extending grinding time beyond 150 seconds, particularly for coarser sieves, to determine if further reductions in average particle diameter and increases in specific surface area are possible or if a plateau is reached.

ACKNOWLEDGEMENT

This work has been funded from the project CNFIS-FDI-2025-F-0108 “Ensuring the sustainability of an application base for biotechnical systems in orchards, vineyards, gardens and solariums (SISBIOSUS)”, from the Ministry of Education and Research through the Executive Agency for Financing Higher Education, Research, Development and Innovation.

REFERENCES

[1] Bayat H., Rastgo M., Zadeh M. M., & Vereecken H. (2015). Particle size distribution models, their characteristics and fitting capability. *Journal of hydrology*, 529, 872-889.

[2] Belkhelladi M., & Bougrine A. (2024). Rosehip extract and wound healing: A review. *Journal of Cosmetic Dermatology*, 23(1), 62-67.

[3] Carpin M., Bertelsen H., Dalberg A., Bech J. K., Risbo J., Schuck P., & Jeantet, R. (2017). How does particle size influence caking in lactose powder. *Journal of Food Engineering,* 209, 61-67.

[4] Dodds J. (2024). Techniques to analyse particle size of food powders. *In Handbook of food powders* (pp. 249-268). Woodhead Publishing.

[5] Fahrenholz A. C., McKinney L. J., Wurth C. E., & Behnke, K. C. (2010). The importance of defining the method in particle size analysis by sieving. Swine Day Report 2012. Kansas State University Agricultural Experiment Station & Cooperative Extension Service. Progress Report 1038, p.316.

[6] Fuaâ M., & Tajdari T. (2011). Particle size measurement techniques: A review of methods and applications. *Jurnal Teknologi*, 137â-149.

[7] Ghendov-Mosanu A., Cristea E., Patras A., Sturza R., & Niculaua M. (2020). Rose hips, a valuable source of antioxidants to improve gingerbread characteristics. *Molecules*, 25(23), 5659.

[8] Götz N., Kranzer U., & Wolfram S. (2011). U.S. Patent Application No. 12/988,143.

[9] Guo, W., Guo, K., Kou, Z., Wang, Z., Xing, Y., & Gui, X. (2024). The effects of processing parameters on the shape of particle size distribution and grinding rate in a stirred mill. Particulate Science and Technology, 1-10.

[10] Hanumanthappa H., Vardhan H., Mandela G. R., Kaza M., Sah, R., & Shanmugam B. K. (2020). Estimation of grinding time for desired particle size distribution and for hematite liberation based on ore retention time in the mill. Mining, *Metallurgy & Exploration*, 37(2), 481-492.

[11] Igual M., García-Herrera P., Cámara, R. M., Martínez-Monzó J., García-Segovia P., & Cámara M. (2022). Bioactive compounds in rosehip (Rosa canina) powder with encapsulating agents. *Molecules*, 27(15), 4737

[12] Igual M., Chiş MS., Păucean A., Vodnar DC., Muste S., Man S., Martínez-Monzó J., García-Segovia P. Valorization of Rose Hip (Rosa canina) Puree Co-Product in Enriched Corn Extrudates. *Foods*. (2021); 10(11):2787. https://doi.org/10.3390/foods10112787

[13] Igathinathane C., Pordesimo L. O., Columbus E. P., Batchelor W. D., & Sokhansanj S. (2009). Sieveless particle size distribution analysis of particulate materials through computer vision. *Computers and Electronics in Agriculture*, 66(2), 147-158.

[14] Ionescu A-D., Ferdeș M., Voicu G., Ipate G., Constantin G-A., Ștefan E-M, Begea M. (2024). Effect of Grinding and Successive Sieving on the Distribution of Active Biological Compounds in the Obtained Fractions of Blackthorn Berries. *Applied Sciences*; 14(16):7133. https://doi.org/10.3390/app14167133

[15] Islam S. F., Hawkins S. M., Meyer J. L., & Sharman A. R. (2022). Evaluation of different particle size distribution and morphology characterization techniques. *Additive Manufacturing Letters*, 3, 100077.

[16] Koczka N., Stefanovits-Bányai É., & Ombódi A. (2018). Total polyphenol content and antioxidant capacity of rosehips of some Rosa species. *Medicines*, 5(3), 84.
[17] Kroetsch D., & Wang C. (2008). Particle size distribution. Soil sampling and methods of analysis, 2, 713-725.
[18] Kumar S., Park H. S., & Nedelcu, D. (2021). Development of real-time grinding process monitoring and analysis system. *International Journal of Precision Engineering and Manufacturing*, 22, 1345-1355.
[19] Li M., Wilkinson D., & Patchigolla K. (2005). Comparison of particle size distributions measured using different techniques. *Particulate Science and Technology*, 23(3), 265-284.
[20] Liu D., O'Sullivan C., & Carraro J. A. H. (2023). The influence of particle size distribution on the stress distribution in granular materials. *Géotechnique*, 73(3), 250-264.
[21] Liu P., Zou W., Peng J., & Xiao F. (2022). Investigating the Effect of Grinding Time on High-Speed Grinding of Rails by a Passive Grinding Test Machine. *Micromachines*, 13(12), 2118.
[22] Liu S., Li Q., Xie G., Li L., & Xiao H. (2016). Effect of grinding time on the particle characteristics of glass powder. *Powder Technology*, 295, 133-141
[23] Lustrup D. C., & Winther K. (2022). Rose Hip as a Nutraceutical. *In Medicinal Plants*. IntechOpen. Vol. 18, 395–420. https://doi.org/10.5772/intechopen.105392
[24] Lyu F., Thomas M., Hendriks W. H., & Van der Poel A. F. B. (2020). Size reduction in feed technology and methods for determining, expressing and predicting particle size: A review. *Animal Feed Science and Technology*, 261, 114347.
[25] Ma S., Song Y., Liu J., Kang X., & Yue Z. Q. (2024). Extended wet sieving method for determination of complete particle size distribution of general soils. *Journal of Rock Mechanics and Geotechnical Engineering*, 16(1), 242-257.
[26] Nađpal J. D., Lesjak M. M., Šibul F. S., Anačkov G. T., Četojević-Simin D. D., Mimica-Dukić N. M., & Beara I. N. (2016). Comparative study of biological activities and phytochemical composition of two rose hips and their preserves: Rosa canina L. and Rosa arvensis Huds. *Food chemistry*, 192, 907-914.
[27] Negrean O. R., Farcas A. C., Nemes S. A., Cic D. E., & Socaci S. A. (2024). Recent advances and insights into the bioactive properties and applications of Rosa canina L. and its by-products. Heliyon.
[28] Sultana, R., Khatun A., & Hossen M. F. (2024). A comprehensive review of particle size analysis techniques. *International Journal of Pharmaceutical Research and Development*, 6(1), 01-05.
[29] Patel S. (2017). Rose hip as an underutilized functional food: Evidence-based review. *Trends in Food Science & Technology*, 63, 29-38.
[30] Patwa A., Malcolm B., Wilson J., & Ambrose K. R. (2014). Particle size analysis of two distinct classes of wheat flour by sieving. *Transactions of the ASABE*, 57(1), 151-159.
[31] Peña F., Valencia S., Tereucán G., Nahuelcura J., Jiménez-Aspee F., Cornejo P., & Ruiz A. (2023). Bioactive compounds and antioxidant activity in the fruit of rosehip (*Rosa canina L*. and *Rosa rubiginosa L*.). *Molecules*, 28(8), 3544.
[32] Servais C., Jones R., & Roberts I. (2002). The influence of particle size distribution on the processing of food. *Journal of food engineering*, 51(3), 201-208.
[33] Shekunov B. Y., Chattopadhyay P., Tong H. H., & Chow A. H. (2007). Particle size analysis in pharmaceutics: principles, methods and applications. *Pharmaceutical research*, 24, 203-227.
[34] Shuhua L. I. U., Hao W.A. N. G., & Hongling W.A.N. G. (2021). Effect of grinding time on the particle size distribution characteristics of tuff powder. *Materials Science*, 27(2), 205-209.
[35] Silva A. F., Burggraeve A., Denon Q., Van der Meeren P., Sandler N., Van Den Kerkhof T., ... & De Beer T. (2013). Particle sizing measurements in pharmaceutical applications: Comparison of in-process methods versus off-line methods. *European journal of pharmaceutics and biopharmaceutics*, 85(3), 1006-1018.
[36] Sonaye S. Y., & Baxi R. N. (2012). Particle size measurement and analysis of flour. lung, 2(3).
[37] Tangirala A. S., Charithkumar K. & Goswami T. K. (2014). Modeling of size reduction, particle size analysis and flow characterisation of spice powders ground in hammer and pin mills. *Int. J. Res. Eng. Technol*, 3, 296-309.
[38] Ujam A. J., & Enebe K. O. (2013). Experimental analysis of particle size distribution using electromagnetic sieve. *American J. Eng. Research*, 2(10), 77-85.

DESIGN AND RESEARCH ON THE TRIGGERING MECHANISM OF ROPE FEEDING IN REED BALING DEVICE
/
芦苇打捆装置触发送绳机构的设计和研究

Yang BAI[1)], Xiang ZHENG[2)], Kun LU[3)], Yanjun LI[1)], Jian SONG[1)], Fuxiang XIE*[1)]
[1)]School of Machinery and Automation, Weifang University, Weifang/China;
[2)]BEIQI FOTON MOTOR CO., LTD
[3)]The Affiliated Qingdao Third People's Hospital of Qingdao University
Tel: 13260170996; E-mail: baiyang19891014@163.com
Correspondent author: Fuxiang XIE

DOI: https://doi.org/10.35633/inmateh-76-80

Keywords: *Rope-Feeding Trigger, Reed, Baling, Orthogonal, Kinematic simulation*

ABSTRACT
To enhance the efficiency and quality of whole-stalk reed harvesting and baling while addressing the issues of low efficiency, reed damage, and high fragmentation rate in manual baling, existing mechanical research primarily focuses on harvesting improvements and straw baling equipment optimization. However, it has not yet resolved the coordination problem of achieving both low damage and high efficiency during whole-stalk reed baling. This paper concentrates on a key aspect of reed baling devices by designing and optimizing a trigger rope-feeding mechanism. This mechanism comprises a triggering mechanism and a rope-feeding mechanism. The triggering mechanism employs a combination of a rocker-slider mechanism and springs to achieve reliable triggering and resetting of the baling action. The rope-feeding mechanism utilizes a crank-rocker mechanism to drive the rope-feeding needle, completing tasks such as rope delivery, knotting initiation, and reed compression to enhance bale compactness. A 3D model of the mechanism was established using SolidWorks, and kinematic simulation and parameter optimization were performed using ADAMS. The key parameter combinations for the trigger mechanism rocker length of 100 mm, connecting rod length of 30 mm, offset distance of 90 mm, and the rope feeding mechanism crank length of 160 mm, rocker length of 175 mm, and connecting rod length of 630 mm were determined. Based on the optimization results, orthogonal experiments were conducted with rope type, operating speed, and pre-tightening force as factors. The results indicate that the optimal parameter combination is nylon rope, operating speed of 90 r/min, and pre-tightening force of 123 N. Experimental analysis revealed that operating speed has the most significant impact on productivity, pre-tightening force is the dominant factor influencing the damage rate, and rope type primarily affects the bale forming rate. Bench tests verified that this trigger rope-feeding mechanism effectively enables low-damage, high-efficiency reed baling, significantly improving bale density and operational efficiency, providing new technical insights for the development of reed baling devices.

摘要
为提升芦苇整杆收获打捆的效率与质量，解决人工打捆效率低、易损伤芦苇且破碎率高的问题，现有机械研究主要集中于收割环节及秸秆打捆设备改进，尚未解决整秆芦苇成捆时的低损伤与高效协同问题，本文聚焦芦苇打捆装置的关键环节，设计并优化了一种触发送绳机构。该机构由触发机构和送绳机构组成，触发机构采用摇杆滑块机构与弹簧的组合，实现打捆动作的可靠触发与复位；送绳机构基于曲柄摇杆机构驱动送绳针，完成捆绳递送、打结触发以及对芦苇的挤压，增强草捆紧实度。利用 SolidWorks 建立机构三维模型，通过 ADAMS 进行运动学仿真与参数优化，确定了触发机构摇杆长度 100 mm，连杆长度 30 mm，偏置距离 90 mm，以及送绳机构曲柄长度 160 mm，摇杆长度 175 mm，连杆长度 630 mm 的关键参数组合。基于优化结果，以捆绳类型、工作转速和预紧力为试验因素，进行正交试验。结果表明，最优参数组合为尼龙绳、工作转速 90 r/min、预紧力 123N。试验分析显示工作转速对生产率影响最显著，预紧力是损伤率的主控因素，捆绳类型则主要影响成捆率。台架试验验证了该触发送绳机构能够有效实现芦苇的低损伤高效打捆，显著提高草捆密度和作业效率，为芦苇打捆装置的研发提供了新的技术思路。

INTRODUCTION

Reed, as a high-quality biological resource, has extensive applications in ecology, landscaping, animal husbandry, and other fields *(Zhao et al., 2021)*. Large-scale reed cultivation presents challenges not only in harvesting but also in post-harvest baling. Harvesting whole, intact reed stalks maximizes the strength, fiber integrity, and appearance of the raw material for uses such as weaving and papermaking, while also facilitating efficient storage, transportation, and processing, thereby optimizing resource utilization and economic benefits *(Wang et al., 2023)*. Current reed baling devices are far from meeting baling demands, with manual baling being predominant. Manual baling is not only inefficient but also prone to causing injuries.

Progress has been made in reed harvesting technology through innovative designs. *Du et al. (2024)* developed a reed clamping and conveying device, conducted modal analysis on its frame structure to identify natural frequencies and comprehensively assess external excitation impacts, ultimately validating the design effectiveness through comparative analysis. *Li et al. (2020)* addressed the practical problem of entanglement between reeds and weeds during harvesting by designing a reed harvesting device that links spatial and planar linkage mechanisms. This device achieves synchronous horizontal and vertical cutting within one rotation of the crank shaft, completing coordinated cutting through trajectory analysis of reciprocating vertical and horizontal blades. Their concept of separating transverse reed cutting from longitudinal weed cutting offers insights for aquatic weed cleaning machinery design. *Li et al. (2021)* further studied the conveying tines and motion mechanism post-cutting in reed harvesters, planning a crank-link mechanism with quick-return characteristics to achieve an arcuate trajectory for the tines and validating frame stability through simulation. Considering the characteristics of reeds in southern China, designed a crawler self-propelled reed harvester with a dedicated clamping and conveying device. They analyzed key components, enabling the transport of cut reeds from the front header to the rear, and determined the optimal working parameter combination for the conveying device *(Yin et al., 2023)*. Based on reed compression characteristic experiments, *Chen et al. (2020)* determined the theoretical optimal compression density and corresponding pressure, conducted parametric design of a compression baling device, verified mechanism strength, and identified potential resonance frequencies.

Research on the bundling, compression, and twine feeding stage of reeds, both domestically and internationally, remains relatively scarce, necessitating reference to the structural optimization of bundling mechanisms in other equipment (*Zhong Chengyi et al., 2023, Flick et al., 2019, Nalobina et al., 2024*). Regarding the load issue of the knotter's key component, the knotter jaw, twine tension data and application points were obtained through straw baling tests combined with comprehensive measurement methods. A load conversion model was constructed, revealing that the upper jaw bears the maximum load reaching... Based on this, finite element analysis was conducted, identifying high stress concentrations at the roller shaft mounting point and the corner of the upper jaw (*Chen et al., 2015*). *Zhang et al. (2022)* addressed vibration issues caused by large inertial forces in the reciprocating compression mechanism of large square balers using model optimization, achieving a bale density of 230 kg/m³. *Wang et al. (2021)* utilized MATLAB for kinematic simulation analysis of the feeding mechanism in a 4YF-1300 large square baler, improving the filling capacity of the pre-compression and compression chambers to enhance efficiency. Based on the working principle of the square baler's compression mechanism, combined with motion simulation analysis of the constructed model using ADAMS, the bale density and operational efficiency of the baler were enhanced conducted static and modal simulation analysis on the feeding mechanism and validated the results through field tests *(Zhang et al., 2024; Wang et al. 2025)*. The results indicated stable operation of the feeding mechanism, with no resonance phenomena, faults, and the formation of straw bales with regular shape and high density after operation.

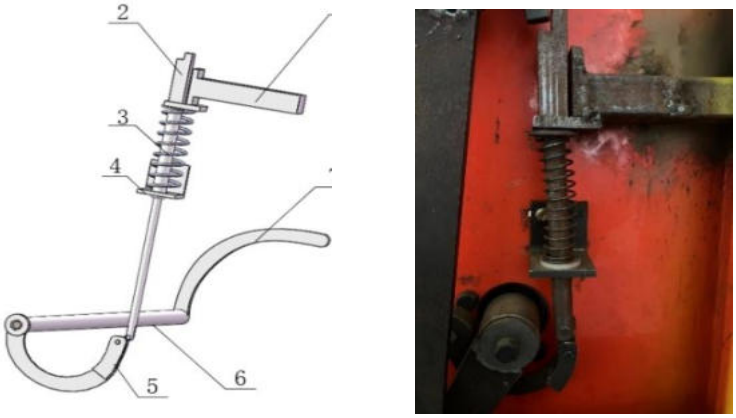
Unlike fragmented forage baling, whole-stalk reed baling requires consideration of baling success rate and fragmentation. More importantly, effectively achieving low-damage, whole-stalk reed harvesting in practice still poses significant technical challenges. This paper addresses the reed baling problem by developing a trigger rope-feeding mechanism for a reed baling device. The trajectory was validated through simulation, and the mechanism was optimized based on reed physical properties. Parameters were optimized, and the baling process was verified through orthogonal experiments considering three factors: rope type, operating speed, and pre-tightening force. This approach aims to improve reed baling efficiency, reduce labor intensity, minimize reed damage during baling, enhance baling efficiency and quality, and validate the mechanism through bench tests, providing new ideas for reed baling device design.

MATERIALS AND METHODS

Design of the Trigger Rope-Feeding Mechanism for Reed Baling Device

The trigger rope-feeding mechanism is a critical component of the reed baling device, and its rationality directly affects baling success. It mainly consists of a triggering mechanism and a rope-feeding mechanism. The triggering mechanism includes a transmission part and springs, while the rope-feeding mechanism comprises a transmission part and a rope-feeding needle. Its primary function is to ensure intermittent motion of the rope-feeding mechanism. This study focuses on kinematic simulation and parameter optimization of the transmission mechanism within the triggering mechanism.

For the triggering mechanism, considering the structural characteristics of the four-bar linkage, the design requirements of the reed baling device, and the design intent requiring the trigger crank to rotate no more than 40°, a combination of a rocker-slider mechanism and springs was adopted. The 3D model and physical diagram of the triggering mechanism are shown in Fig. 1.



(a) SolidWorks 3D model (b) Physical prototype

Fig. 1 – Trigger mechanism assembly

1. Blocking bracket;2. Blocking rod; 3. Spring; 4. Spring stop block; 5. Connecting plate; 6. Shaft; 7. Trigger crank

The rope-feeding mechanism primarily consists of a crank-rocker mechanism, a rope-feeding needle connecting shaft, and the rope-feeding needle itself. Its 3D assembly is shown in Fig. 2. This mechanism is mainly used to deliver one end of the binding rope into the knotter to complete knotting and simultaneously compress the reed stalks during knotting to enhance bale compactness. The rope-feeding needle is fixed to a rotating shaft. When baling is triggered, the shaft, driven by the crank-rocker mechanism, causes the rope-feeding needle to rotate 90°, delivering the rope into the D-type knotter while simultaneously driving the gear disc *(Cen et al., 2020)*. After knotting is completed, the rope-feeding needle returns to its original position. An additional function of the rope-feeding needle is that its tip blocks reeds fed by the tine, preventing them from being pulled back.

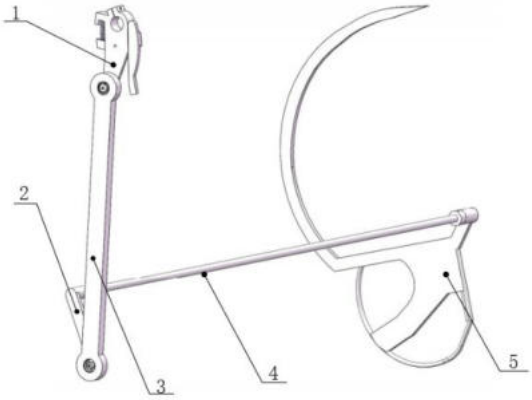
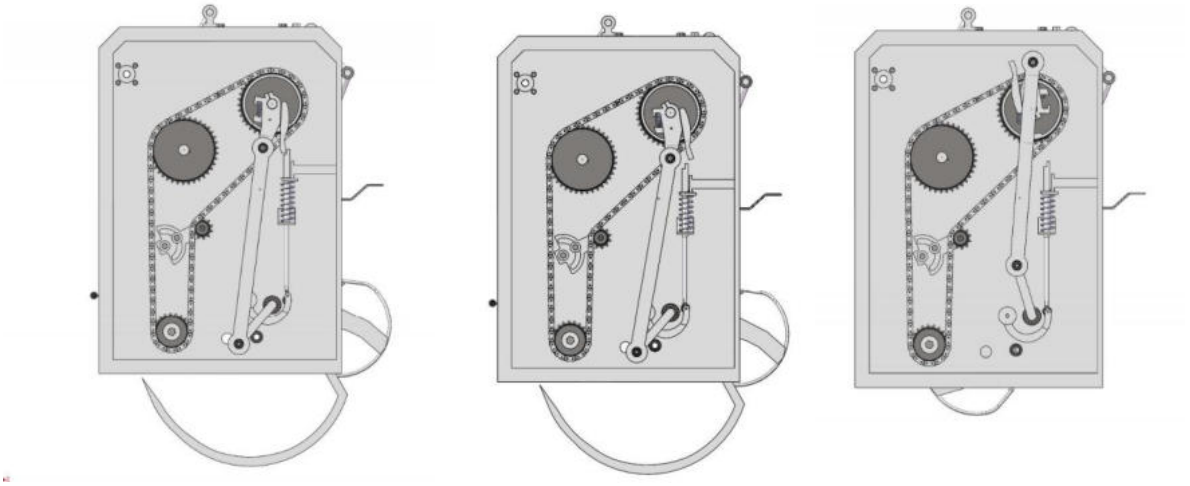


Fig. 2 – Rope-feeding mechanism assembly

1. Crank; 2. Rocker; 3. Connecting rod; 4. Shaft; 5. Rope-feeding needle

The crank of the rope-feeding mechanism is a key component controlling its operation; its shape and size critically affect the successful operation of baling. When the reed reaches the baling weight, the spring on the blocking rod is compressed to its working length, causing the blocking rod in the trigger mechanism to lose its blocking effect on the crank, thus triggering baling. The dimensions of the crank, rocker, and connecting rod were designed based on crank-rocker mechanism calculation formulas, resulting in a crank length of 160 mm, connecting rod length of 630 mm, and rocker length of 175 mm. The rope-feeding needle was designed according to the knotter position. Its main functions are to deliver the rope into the knotter and compress the reeds during baling to make the bale tighter and denser. Therefore, it requires a reasonable curvature and a hollow center for threading the rope *(He et al., 2017)*. Based on the designed 3D model, the working process of the trigger rope-feeding mechanism is shown in Fig. 3.



(a) Trigger mechanism blocking crank (b) Trigger mechanism triggering (c) Rope feeding needle feeding rope

Fig. 3 – Triggering the working process of the rope feeding mechanism

Simulation Analysis of Trigger Rope-Feeding Mechanism

The primary function of the triggering mechanism is to pull down the stop block when the trigger crank rotates, initiating the baling action, and then return to the initial position. A combination of an offset rocker-slider mechanism and springs was selected for this purpose. When the force on the trigger crank is transmitted to the rocker, it pulls down the blocking block via the connecting rod, triggering the baling mechanism. Subsequently, the elastic deformation of the spring returns the blocking block to its original position. Since the mechanism includes a spring, it must be mounted vertically with one end fixed during operation to prevent spring offset affecting the experiment. A Cartesian coordinate system for the rocker-slider mechanism was established, as shown in Fig. 4. The geometric relationships of the parameters are according to relation (1).

$$\left(x_B - x_C\right)^2 + \left(y_B - y_C\right)^2 = b^2 \tag{1}$$

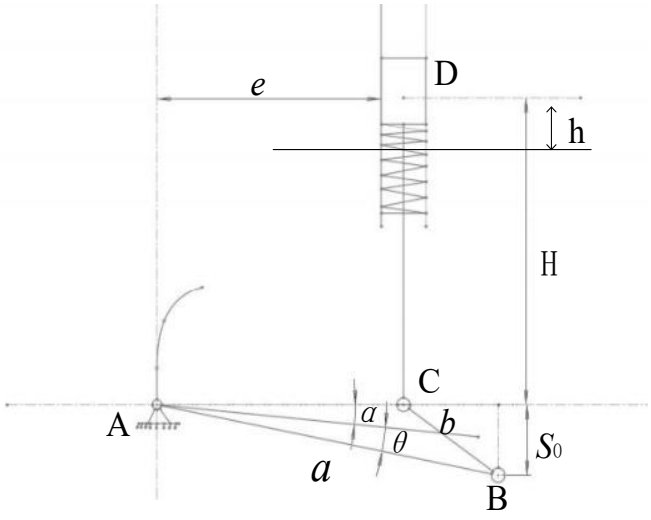


Fig. 4 – Motion diagram of trigger mechanism

In the figure, a is the length between AB, b is the length between BC, α is the initial rotation angle of the rocker, θ is the angle of rotation of the rocker. The coordinate of point B is: $(x_B = a\cos\theta; y_B = a\sin\theta)$, point C is (e, S_0), and point D is (e, H) as shown in Table 1.

Substituting the coordinate values into Eq. (1) yields the relationship between the parameters to be determined and the given parameters. To determine the five unknown parameters a, b, e, α and S_0, the solving process is simplified by setting $\alpha = 0$, $S_0 = 0$, reducing the unknowns to three. The simplified equation is according to relation (2).

$$2aH\cos\theta - 2ae\sin\theta - \left(a^2 + e^2 - b^2\right) = H^2 \quad (2)$$

Table 1

Design point constraint condition

Design point	X/mm	Y/mm	Z
A	0	0	0
B	$a\cos\theta$	$a\sin\theta$	0
C	*e*	S_0	0
D	*e*	*H*	0

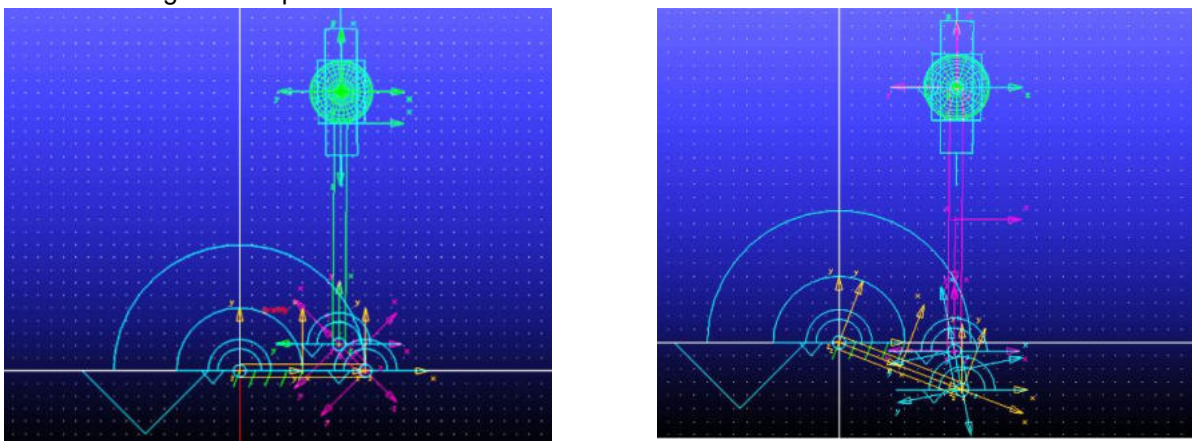
The design variable H = 200 mm. Initial values and variation ranges of each design variable are listed in Table 2. The optimized link lengths must fall within the specified ranges.

Table 2

Initial value of design variable and its constraint conditions

Design point	X/mm	Constraint conditions
a/mm	100	-20.0; 20.0
b/mm	50	-20.0; 20.0
e/mm	100	-20.0; 20.0
θ /°	20.0	0; 40.0

The tension on the blocking block during operation originates from the torque transmitted from the trigger crank to the rocker. The design lengths of *a*, *b*, and *e* affect the force exerted by the transmission mechanism on the spring. Therefore, ADAMS software was used to simulate the mechanism, with the link lengths of the transmission mechanism as optimization targets, to investigate the influence of design variables on trigger mechanism performance. Using Fig. 4 and Tables 1 & 2, a virtual prototype of the trigger mechanism was built. After adding constraints and setting the rocker as the driving part, simulation was performed. Fig.5(a) shows the initial working position of the transmission mechanism; (b) shows the rocker at the working position, where the blocking block is pulled down 15 mm.



(a) Initial position of joystick (b) Working position of joystick

Fig. 5 – Working position of transmission mechanism

Based on force calculations for the feeding mechanism tines, the torque on the trigger crank during triggering was approximately 14.6 N·m. Pre-calculation indicated that the resistance force on the blocking block was about 150 N, originating from the spring force. An external load opposing the motion direction was applied to the blocking block.

The simulation observes variations in mechanism performance under different parameters by altering the values of design variables. By comparing the sensitivity of design variables, it identifies the primary variables influencing mechanism performance. The design variables are listed in Table 2. In ADAMS, the measurement variable is set as MOTION_1_MEN_1.

With the simulation step size set to Steps=200, establish the measured torque value *T* as the optimization objective in the "Simulation/Design Evaluation" command to optimize the lengths of *a, b*, and *e*. During simulation, variables were changed individually to study the variation of driving torque *T* with the lengths of *a, b*, and *e*. Fifty sets of experiments were conducted within the variable ranges. Nine representative sets showing the change of driving torque *T* with variable a were selected, as shown in Table 3. The average sensitivity of driving torque *T* to the three variables is shown in Table 4.

Table 3

Change of the value of driving force distance *T* with *a*

Test No.	*T* (N·m)	*a* (mm)	Sensitivity
1	16.152	80	-21107
2	15.702	85	-2.1511
3	15.453	90	-2.2278
4	14.996	95	-2.2974
5	14.610	100	-2.3623
6	14.122	105	-2.4328
7	13.548	110	-2.4538
8	13.014	115	-2.4576
9	12.675	120	-2.4593

Table 4

Sensitivity of design variables

Design Variable	Sensitivity to Driving Torque
a	-2.28956
b	120.532
e	-104.77

Based on the data from Tables 3 and 4, among the three design variables, *a* has the lowest sensitivity to driving torque *T*, indicating it has a smaller influence on the driving torque. Variables *b* and *e* have a significant influence, making them the main factors affecting the change in driving torque.

Through ADAMS simulation analysis, with the torque on the trigger crank being 14.6 N·m, simulation of the trigger mechanism showed that when *a* = 100 mm, *b* = 30 mm, and *e* = 90 mm (integer values), and the force on the slider is 150 N, the output torque on the driving rocker is closest to 14.6 N·m. The design of the rotating crank connected to the shaft needs to be reasonable; it can be connected to the blocking rod via a connecting plate. Through design calculations and motion analysis, the rocker length was set to 100 mm. To prevent interference with the rocker of the rope-feeding mechanism, the rotating crank was approximated as a semicircle with a diameter of 100 mm.

Spring Dynamic Analysis and Selection

Calculated based on the minimum torque of the tines, the force the trigger mechanism can withstand at this moment reaches its maximum. The friction coefficient μ for straw-like materials is 0.4–0.47 *(Wang et al., 2017)*. According to the friction formula $F_f = \mu N$, where *N* is the weight of the reeds, the friction force $F_f = 15N$ generated by a full bin of reeds, which is small and negligible. The minimum force exerted by the tine on the reeds is *F*=915 N. The trigger crank is 8 cm above the base plate, so the force exerted by the tine on the reeds acting on the trigger crank is F_3=2*F*/5=366 N. Assuming uniform force distribution on the trigger crank, the force from the reeds acts at the centroid of the crank. The torque at this point, calculated using the torque formula, is M_3=14.64 N·m. Since the simplified crank 3 rotates simultaneously with the trigger crank, the torque magnitude is the same. The trigger crank is connected to the trigger mechanism via a shaft. The simplified force model of the trigger mechanism is shown in Fig. 6. With the rocker length *L* = 100 mm, *F* = 146.4 N is obtained. Therefore, calculated based on minimizing reed damage, the maximum force *F* required to pull the spring to the trigger position is 146.4 N.

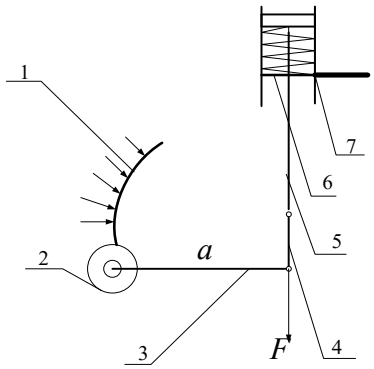


Fig. 6 – Trigger simplified model

1. Trigger crank 2. Shaft connection 3. Simplified crank 4. Connecting block 5. Blocking rod 6. Spring 7. Stop block bracket

The triggering mechanism requires a matching compression spring. The spring is crucial for determining whether triggering occurs. A spring with too low stiffness may cause premature triggering, reducing bale density, while excessive stiffness may lead to reed accumulation in the bin, potentially causing reed damage or failure to trigger. Therefore, spring selection must meet the following requirements: the distance between the blocking bracket and spring stop block is 100 mm, requiring a spring compression stroke $h > 15$ mm. To ensure that the spring meets operational and installation requirements, its free length H_0 should be $100 \leq H_0 \leq 140$ mm. The blocking rod diameter is 15 mm, requiring the spring inner diameter $D\text{-}d > 15$ mm. The spring stop block size is 50 mm × 50 mm, requiring the spring outer diameter $D+d < 50$ mm. The force $F = 146.4$ N. To minimize reed damage, the spring's maximum working load should be $110 \text{ N} \leq F \leq 146.4$ N. For comparative tests, a maximum working load $F < 170$ N was selected, i.e., the spring working load range is $110 \text{ N} \leq F \leq 170$ N. At this point, the spring compression equals the initial length H of 85 mm.

The spring's working load is the tension it experiences when pulled down to the trigger position. Different spring working loads result in different bale densities, affecting the net hourly productivity of the entire device. Subsequent experiments used different pre-tightening forces caused by the spring as a factor to verify the bale forming rate, bale density, and net hourly productivity of the baling device.

Single-Factor Experiment and Analysis of Pre-tightening Force

Reeds collected in November from the Zhuo River in Weifang City were used for this experiment. Collected reeds were trimmed according to the feeding port size of the test device, retaining the middle section of the reed stalks (1.2 m–2.6 m). The measured average moisture content was 20.7%, consistent with material test results. After multiple measurements using an electronic scale, the average weight of a single trimmed reed was approximately 13 g. Fig. 7 shows the prepared test materials.



Fig. 7 – Experimental materials



Fig. 8 – Binder test stand

The pre-tightening force is controlled by the spring in the triggering mechanism. The spring is the key component determining when baling is triggered. A higher spring stiffness (greater force) makes triggering harder, resulting in a higher weight per bale. Five springs with relatively evenly spaced maximum working loads were selected for the single-factor experiment. The experiment fixed the operating speed at 90 r/min and used nylon rope. Damage rate, bale forming rate, and single bale weight were evaluation indicators. Reeds were fed manually and uniformly during the test. The experiment was conducted synchronously with the single-factor speed test. After testing each spring, it was replaced before proceeding. The results for damage rate, bale forming rate, and single bale weight are shown in Table 5.

Table 5

Pre-tightening test results

Pre-tightening Force (N)	123	136.5	145.5	156	165
Damage Rate (%)	3.29	3.59	3.88	4.98	5.22
Single Bale Weight (kg)	4.14	4.31	4.44	4.51	4.55
Bale Forming Rate (%)	100	98	96	92	90

The test data shows that, under different spring conditions, a higher pre-tightening force results in higher bale density. This is because the reeds are compressed during baling and expand due to stress relaxation afterward. A higher pre-tightening force delays triggering, allowing more reeds to accumulate in the bin. Since the volume of the formed bale is similar, reeds expand more after baling with higher pre-tightening forces, leading to higher density. Net hourly productivity also increases with higher pre-tightening force. The pre-tightening force has a limited effect on bale density and forming rate. However, experiments showed that increased pre-tightening force caused more reed damage, with a higher number of surface creases in the formed bales compared to lower pre-tightening forces. Therefore, to ensure reed quality while meeting net hourly productivity and bale density requirements, springs resulting in higher productivity and density were selected. However, when the pre-tightening force increased from 145.5 N to 156 N, the damage rate increased sharply. Considering factors like damage rate, the pre-tightening force range was set at 123 N, 136.5 N, and 145.5 N.

Orthogonal Experiment for Reed Baling

Preliminary experiments indicated that the bale forming rate, bale density, damage rate, and other test results are related to rope type, motor operating speed, and spring pre-tightening force. Therefore, these three factors were used to establish an orthogonal experiment factor-level table, detailed in Table 6.

Table 6

Test factors and levels

Factor		Level		
		1	2	3
A	Rope Type (Diameter 1.5mm)	Hemp rope	Nylon rope	Cotton rope
B	Operating Speed (r/min)	80	90	100
C	Pre-tightening Force (N)	123	136.5	145.5

RESULTS

The results of the orthogonal experiment are shown in Table 7.

Table 7

Testing results and analysis

No.	Factor Level			Indicator Values		
	Rope Type A	Operating Speed B	Pre-tightening Force C	Net Hourly Productivity (t/h)	Damage Rate (%)	Bale Forming Rate (%)
1	1	1	1	0.548	3.38	99
2	1	2	2	0.561	3.68	96
3	1	3	3	0.573	3.97	93
4	2	1	1	0.547	3.28	100
5	2	2	2	0.56	3.59	98
6	2	3	3	0.574	3.86	96
7	3	1	2	0.55	3.62	97
8	3	2	3	0.563	3.9	95
9	3	3	1	0.571	3.34	100
10	1	1	3	0.549	3.98	93
11	1	2	1	0.559	3.39	100

No.	Factor Level			Indicator Values		
	Rope Type A	Operating Speed B	Pre-tightening Force C	Net Hourly Productivity (t/h)	Damage Rate (%)	Bale Forming Rate (%)
12	1	3	2	0.574	3.66	97
13	2	1	2	0.549	3.55	98
14	2	2	3	0.564	3.88	96
15	2	3	1	0.573	3.29	100
16	3	1	3	0.548	3.92	95
17	3	2	1	0.562	3.36	100
18	3	3	2	0.575	3.63	98

Variance analysis was performed on the experimental data, and the results are presented in Table 8. Analysis of Table 8 reveals that since the P-values for rope type, operating speed, and pre-tightening force are all less than 0.05, these factors exhibit statistically significant effects on the target metrics. Further comparison of the F-values in the ANOVA indicates the following primary-secondary order of influencing factors: For net hourly productivity: B (Operating Speed) > C (Pre-tightening Force) > A (Rope Type). For damage rate: C (Pre-tightening Force) > A (Rope Type) > B (Operating Speed). For bale forming rate: A (Rope Type) > C (Pre-tightening Force) > B (Operating Speed).

Table 8

ANOVA Results

Source	Dependent Variable	Type III Sum of Squares	df	Mean Square	F	Sig.
Intercept	productivity	5.667	1	5.667	3319852.071	0.000
	Damage rate	236.749	1	236.749	1370650.947	0.000
	Bundling rate	170333.389	1	170333.389	475014.239	0.000
A	productivity	2.111×10^{-6}	2	1.056×10^{-6}	.618	0.047
	Damage rate	0.031	2	0.016	89.833	0.000
		8.778	2	4.389	12.239	0.002
B	productivity	0.002	2	0.001	542.287	0.000
	Damage rate	0.000	2	0.000	1.254	0.033
	Bundling rate	0.778	2	0.389	1.085	0.032
C	productivity	1.144×10^{-5}	2	5.722×10^{-6}	3.352	0.043
	Damage rate	1.004	2	0.502	2905.254	0.000
	Bundling rate	80.111	2	40.056	11.704	0.000
Error	productivity	1.878×10^{-5}	11	1.707×10^{-6}		
	Damage rate	0.002	11	0.000		
	Bundling rate	3.944	11	0.359		
Total	productivity	5.669	18			
	Damage rate	237.786	18			
	Bundling rate	170427.000	18			
Corrected Total	productivity	0.002	17			
	Damage rate	1.037	17			
	Bundling rate	93.611	17			

For Rope Type (A), level 2 (Nylon rope) yields the lowest damage rate (3.575%) and highest bale forming rate (98.0%). Thus the Nylon rope is optimal. For Operating Speed (B), damage rate (3.622–3.633%) and bale forming rate (97.0–97.5%) show minimal variation across levels. Level 3 (100 r/min) achieves the highest net hourly productivity (0.573 t/h). Thus 100 r/min is optimal. For Pre-tightening Force (C), level 1 (123 N) delivers the lowest damage rate (3.340%) and highest bale forming rate (99.833%). Thus 123 N is optimal. The optimal parameter combination is Nylon rope, 100 r/min operating speed, and 123 N pre-tightening force.

CONCLUSIONS

(1) This study developed a triggering rope-feeding mechanism for a reed bundling device. Its core innovation lies in employing a rocker-slider mechanism combined with springs to achieve automatic triggering, while utilizing a crank-rocker mechanism to drive the hollow rope-feeding needle. The mechanism initiates the bundling process by sensing accumulated reed weight. During operation, the rope-feeding needle simultaneously performs three critical functions: routing the rope into the knotter, compressing reeds to enhance bundle tightness, and blocking subsequent reed retraction. This provides a foundational mechanical solution for efficient and low-damage whole-stalk reed bundling.

(2) Based on ADAMS, parameterized simulation optimization of the triggering mechanism is carried out, and the key influencing factors of the rod length parameters *b* and *e* are determined through sensitivity analysis of the driving torque to obtain the optimal rod length combination. Based on the analysis of spring dynamics, the critical value of spring working load of 146.4 N and selection parameters were established, providing a design basis for reducing the driving torque of the mechanism and mitigating reed damage.

(3) The influence of rope type, working speed, and pre tension on bundling performance was verified through orthogonal experiments: working speed has the most significant impact on pure working hour productivity, pre tension dominates damage rate, and rope type determines bundling rate. The optimal combination is nylon rope, working speed of 100 r/min, and pre tension force of 123 N, achieving low damage and efficient bundling of reed whole poles.

REFERENCES

[1] Cen Haitang, Song Yu, Wei Ruitao, Li Ling, Qin Jianbin (2020). Reliability Design of Knotter Cam Gear for D-type Knotter. *IOP Conference Series: Materials Science and Engineering*, Vol. 784 no.1, pp. 012020, doi:10.1088/1757-899X/784/1/012020;

[2] Chen Kesheng (2020). *Design and Research of Reed Compression Characteristics and Compression Packing Device (芦苇压缩特性及其压缩打包装置设计与研究).* Master's Thesis, Shihezi University, doi:10.27332/d.cnki.gshzu.2020.000290;

[3] Chen Longjian, Li Cheng, Zhang Anqi, Li Haitao, Zhang Shaoying (2015). Load Test Analysis of Knotter Jaw During Straw Baling Process (秸秆捆扎过程中打结钳嘴载荷试验分析). *Transactions of the Chinese Society for Agricultural Machinery*, Vol. 46 no.9, pp. 128-134, doi: 10.6041/j.issn.1000-1298.2015.09.019;

[4] Zhong Chengyi, Yin Wenqing, Liu Dejiang, Yao Keheng, Chen Wei, Xing Zitao, Jin Fan (2023). Design and experiment of self-propelled highland barley harvesting and baling machine. *INMATEH-Agricultural Engineering,* Vol. 70 no.2, pp. 423-430, doi: https://doi.org/10.35633/inmateh-70-41;

[5] Du Tuo, Li Yaoming, Yin Qiang, Ji Binbin (2024). Static and Modal Analysis of Reed Clamping Conveying Device Frame (芦苇夹持输送装置台架的静力学及模态分析). *Journal of Agricultural Mechanization Research*, Vol. 46 no.8, pp. 70-74, doi: 10.13427/j.cnki.njyi.2024.08.023;

[6] Flick D., Nigon M. C., Shinners K.J. Friede J. C. (2019). Control system for a continuous compaction large square baler. *Computers and Electronics in Agriculture,* Vol. 2 no.7, pp.519-528, doi: https:// 10.1016/j.compag.2019.104969;

[7] He Ming (2017). *Design Research of Baling Device for Rapeseed Binding Harvester (油菜割捆机打捆装置的设计研究).* Master's Thesis, Hunan Agricultural University*;*

[8] Li Yancong, Wang Yonghong, Guo Junwang, Li Shuhuan, Wei Yong (2021). Simulation Design of Reed Harvester Rake Mechanism (芦苇收割机拨齿机构仿真设计). *Journal of Agricultural Engineering*, Vol.11 no.6, pp. 94-98, doi: 10.3969/j.issn.2095-1795.2021.06.021;

[9] Li Yancong, Wei Yong, Zhang Hao, Song Xin, Liu Yule (2020). Design and Kinematic Analysis of Key Components for Reed Harvester (芦苇收割机关键部件设计及运动分析). *Journal of Chinese Agricultural Mechanization*, Vol. 41 no.12, pp. 20-23, doi:10.13733/j.jcam.issn.2095-5553.2020.12.005;

[10] Nalobina O., Holotiuk M., Bundza O., Shymko A., Puts V., Martyniuk V. (2024). Machine for technological spring harvesting of technical hemp, *INMATEH-Agricultural Engineering,* Vol. 74 no.3, pp. 25-32, doi: https://doi.org/10.35633/inmateh-74-02;

[11] Wang Defu, Jiang Zhiguo, Li Baiqiu, Wang Guofu, Jiang Yiyuan (2017). Experiment on Sliding Friction Characteristics Between Rice Straw and Baler Steel-Roll (稻秆与圆捆机钢辊间滑动摩擦特性试验). *Transactions of the Chinese Society of Agricultural Engineering (Transactions of the CSAE)*, Vol. 33 no.21, pp. 44-51, doi: 10.11975/j.issn.1002-6819.2017.21.005;

[12] Wang Haichao, Sun Xiaotian, Liu Yu, Pei Zhiyong, Guo Gensheng (2021). Motion Simulation Analysis and Optimization of Feeding Mechanism for 4YF-1300 Large Square Baler Based on MATLAB (基于 MATLAB 的 4YF-1300 型大方捆打捆机喂入机构运动仿真分析与优化). *Journal of Chinese Agricultural Mechanization*, Vol. 42 no.2, pp. 31-36, doi:10.13733/j.jcam.issn.2095-5553.2021.02.005;

[13] Wang Qi, Li Chenqi, Zhang Xuesong, Wang Chunming, Pan Yufeng (2023). Application and Development Trend of Reed Fiber Materials (芦苇纤维材料的应用及发展趋势). *Forestry Science and Technology*, Vol. 48 no.5, pp. 60-62, doi: 10.19750/j.cnki.1001-9499.2023.05.014;

[14] Wang Xiang, Gao Lei, Bao Zhiliang, Guo Xiyan, Meng Yu (2025). Design and Experiment of Feeding Mechanism for Square Baler Based on SolidWorks (基于 SolidWorks 的方捆机喂入机构设计与试验). *Journal of Chinese Agricultural Mechanization*, Vol.46 no.2, pp.35-40+47, doi: 10.13733/j.jcam.issn.2095-5553.2025.02.006;

[15] Yin Qiang, Li Yaoming, Ji Binbin, Chen Lipeng (2023). Design and Experiment of Clamping Conveying Device for Self-Propelled Reed Harvester (自走式芦苇收获机夹持输送装置的设计与试验). *Journal of Agricultural Mechanization Research*, Vol. 45 no.4, pp. 113-118, doi:10.13427/j.cnki.njyi.2023.04.046;

[16] Zhang Fu, Lou Limin, Qian Dan, Wang Shiqiang, Feng Chunling, Zhao Yirong (2024). Optimum design and test of compression mechanism of big square baler (大方捆打捆机压缩机构优化设计及试验). *Journal of Jilin University (Engineering and Technology Edition)*, Vol. 54 no.4, pp. 1166-1174, doi: 10.13229/j.cnki.jdxbgxb.20221139;

[17] Zhang Xiaojun (2024). Motion Simulation and Experiment of Compression Mechanism for Six-Twine Large Square Baler (六道捆绳大方捆打捆机压缩机构运动仿真与试验). *Journal of Agricultural Equipment and Vehicle Engineering*, Vol. 62 no.12, pp. 29-32;

[18] Zhao Xue (2021). *Modification of reed and its design application in furniture decoration (芦苇茎秆改性及其在家具装饰设计中的应用研究).* Doctoral Dissertation, Beijing Forestry University, doi: 10.26949/d.cnki.gblyu.2021.000990.

WHEAT HARVESTING QUALITY ONLINE DETECTION SYSTEM AND EXPERIMENTAL VERIFICATION
/
小麦收获质量在线检测系统与试验验证

Yue QIN [1], Man CHEN [1,2*], Tengxiang YANG [1], Guangyue ZHANG [1], Chengqian JIN [1*], Gongwu MO [3]
[1] Nanjing Institute of Agricultural Mechanization, Ministry of Agriculture and Rural Affairs, Nanjing, Jiangsu / China;
[2] National Digital Agriculture Equipment (South China Intelligence Agricultural Machine) Innovation Sub-center, Nanjing, Jiangsu / China;
[3] Jiangsu Agricultural Machinery Testing and Appraisal Station, Jiangsu / China;
Tel: +8602584346113; E-mail: chenman@caas.cn; jinchengqian@caas.cn
DOI: https://doi.org/10.35633/inmateh-76-81

Keywords: *Wheat; Harvesting quality; Online; Detection system; Experimental verification*

ABSTRACT
Harvest quality is one of the key indicators for evaluating the performance of mechanized wheat harvesting. To enable real-time monitoring of harvest quality during the wheat combine harvesting process, this study integrates an online detection system specifically designed for wheat harvest quality. The system is capable of real-time monitoring of threshing and cleaning losses, breakage rate, and impurity rate. To assess the effectiveness of the online detection system, field experiments were conducted. The experimental results showed that the average threshing and cleaning loss rates of the harvester measured manually were 0.69% and 0.75%, respectively, while those detected by the online system were 0.52% and 0.50%, respectively. The average grain breakage rates obtained through manual measurement were 0.67% and 0.58%, whereas the system detected breakage rates of 0.49% and 0.52%, respectively. For impurity rate, manual measurements yielded average values of 0.81% and 0.69%, while the system recorded 0.73% and 0.67%, respectively. The results demonstrate that the developed online wheat harvest quality detection system can effectively perform real-time assessments of harvest quality during combine harvesting operations.

摘要
收获质量是衡量小麦机械化收获性能的关键指标之一。为了实现对小麦机收过程中收获质量的实时监控，本文集成了小麦收获质量在线检测系统，该系统能够对脱粒清选损失、破碎率、含杂率进行实时检测。为了评估小麦收获质量在线检测系统的效能，进行了田间试验。试验结果显示：人工检测收获机清选脱粒损失率的平均值分别为0.69%和0.75%，而小麦收获质量在线检测系统检测到的收获机清选脱粒损失率的平均值分别为0.52%和0.50%；人工检测收获机破碎率的平均值分别为0.67%和0.58%，系统检测到的收获机破碎率的平均值分别为0.49%和0.52%；人工检测收获机含杂率的平均值分别为0.81%和0.69%，系统检测到的含杂率的平均值分别为0.73%和0.67%。本研究开发的小麦收获质量在线检测系统能够有效地完成收割机小麦收获作业质量的检测任务。

INTRODUCTION
China is one of the largest wheat-producing countries in the world, with wheat cultivation widely distributed across the country *(Zhao et al., 2024)*. The major wheat-growing regions include the Huang-Huai-Hai Plain, the middle and lower reaches of the Yangtze River, and the inland areas of Northwest China *(Zhao et al., 2025)*. Among these, the Huang-Huai-Hai region serves as the core wheat production zone, accounting for over 60% of the national planting area and total output. Wheat production in China is dominated by winter wheat, supplemented by spring wheat, with typical cropping systems including double cropping per year or rice-wheat rotation *(Wang et al., 2024)*. In recent years, with the continuous advancement of agricultural modernization, the level of mechanization in wheat production has increased significantly *(Li et al., 2025; Li et al., 2024; Vlădut et al., 2023)*.

Yue Qin, Stud. Eng.; Man Chen, Prof. Ph.D. Eng.; Tengxiang Yang, Research Associate. Ph.D. Eng; Guangyue Zhang Research Associate. Ph.D. Eng; Chengqian Jin, Prof. Ph.D. Eng; Gongwu Mo, Prof. Ph.D. Eng.

The comprehensive mechanization rate of tillage, sowing, and harvesting has surpassed 95% *(Zhang et al., 2024; Chen et al., 2023)*. In particular, during the harvest stage, the widespread adoption of combine harvesters enables centralized and efficient harvesting, substantially enhancing both harvest efficiency and timeliness.

Online detection of wheat harvest quality is a key component in achieving intelligent and precise management in modern agriculture *(Xie et al., 2024; Liao et al., 2025)*. It plays a vital role in ensuring grain quality and enhancing economic benefits *(Geng et al., 2024)*. During the harvesting process, factors affecting wheat quality include impurity rate, breakage rate, and loss rate. Traditional manual sampling methods can no longer meet the demands for rapid, continuous, and high-precision monitoring. By leveraging online detection technologies, real-time acquisition of quality data throughout the harvesting process becomes possible *(Gu et al., 2025)*. This enables timely identification of issues and dynamic adjustment of operational parameters. Intelligent regulation of critical processes—such as threshing, screening, and air separation—can thus be achieved, effectively reducing harvest losses and grain breakage, while improving the whole kernel rate and net content *(Ding et al., 2025; Liu et al., 2023)*.

With the continuous advancement of agricultural equipment intelligence, online detection of wheat harvest quality is expected to become one of the key functional modules of combine harvesters *(Audu et al., 2021)*. It will play a significant role in safeguarding national food security and promoting the development of smart agriculture in China *(Wang et al., 2024)*. Zhang Qi et al. proposed a method for detecting wheat breakage rate and impurity rate based on the DeepLab EDA semantic segmentation model and developed a corresponding detection system. The average errors in detecting wheat breakage rate and impurity rate were 13.32% and 9.77%, respectively *(Zhang et al., 2024)*. Chen Man et al. introduced an online detection method for wheat impurity rate during mechanical harvesting, based on an improved U-Net model integrated with attention mechanisms. In both bench and field tests, the average impurity rates detected online were 1.69% and 1.48%, which were 0.26 and 0.13 percentage points higher than the manually measured values, respectively *(Chen et al., 2023)*. Tang Zhong et al. utilized an array-type polypropylene fluoride (PVDF) piezoelectric film sensor to measure the grain quantity beneath the toothed longitudinal axial-flow drum of a longitudinal flow combine harvester during field operation. By applying a separation matrix equation, the entertainment loss mass was calculated, with a measurement error ranging from –4.82% to –5.87% *(Tang et al., 2012)*. Li Yibo et al. combined time-frequency images of granular vibration piezoelectric signals with machine learning techniques to classify grains and impurities and evaluate corn cleaning loss. The piezoelectric detection unit based on the optimal Naïve Bayes (NB) model was able to control the absolute error of grain loss rate within 0.43% *(Li et al., 2024)*. Wu Zhiping et al. developed a lightweight detection system for measuring impurity content and breakage rate in rice, and optimized the corresponding computational models. The relative errors for impurity content and breakage rate detection were 7.99% and 8.46%, respectively *(Wu et al., 2024)*. Liu Lei et al. designed a machine vision–based monitoring device for impurity rate and proposed a dedicated CPU-Net semantic segmentation model tailored for corn impurity detection. The average relative measurement error was 4.64% *(Liu et al., 2022)*. Although significant progress has been made in single-point technologies for measuring threshing and cleaning loss rate, breakage rate, and impurity rate, a comprehensive evaluation system for wheat harvest quality remains underdeveloped. Moreover, given the wide variety of wheat cultivars and harvesting machinery types in China, how to construct a robust online wheat harvest quality detection system has become a key focus of this study.

Therefore, to enable real-time monitoring of harvest quality during the wheat combine harvesting process, this study integrates an online wheat harvest quality detection system and conducts field experiments to verify its feasibility.

MATERIALS AND METHODS

System Composition

The online wheat harvest quality detection system consists of an entrainment loss sensor, a cleaning loss sensor, a breakage rate sensor, an impurity rate sensor, a threshing and cleaning loss data acquisition controller, a breakage and impurity data acquisition controller, a human–machine interaction (HMI) system, and a 12V power supply unit. The system block diagram is shown in Figure 1. Specifically, the entrainment loss sensor and the cleaning loss sensor detect the impact of lost grains on the sensitive plates during combine harvester operation and output corresponding electrical signals. The threshing and cleaning loss acquisition controller receives the electrical signals from both sensors and performs real-time online detection of grain loss per unit area over time.

Based on its built-in algorithm, it calculates and outputs the real-time threshing and cleaning loss rate, which is transmitted to the HMI system via the CAN bus. The breakage rate sensor and impurity rate sensor are responsible for real-time acquisition of grain image data during harvesting, outputting dynamic grain images. The breakage and impurity data acquisition controller receives these image signals and conducts online segmentation and identification of whole grains, broken grains, and impurities in the images. It then calculates and outputs the real-time breakage rate and impurity rate based on its internal algorithm, and sends the data to the HMI system via the CAN bus. The HMI system allows for the configuration of both harvester parameters and crop parameters. Once set, these parameters are transmitted via the CAN bus to the threshing and cleaning loss acquisition controller and the breakage and impurity acquisition controller. The 12 V power supply unit provides a stable 12 V output voltage to ensure the reliable operation of the entire wheat harvest quality detection system.

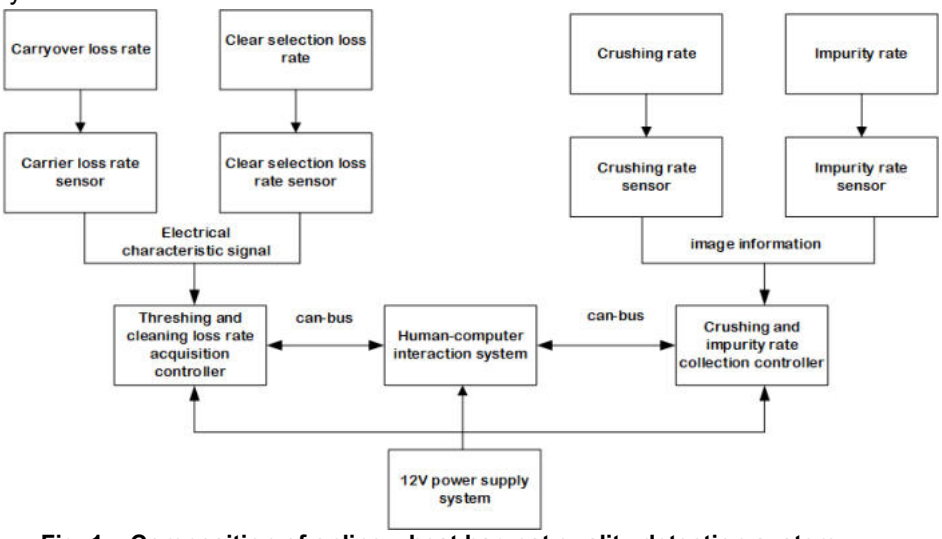


Fig. 1 – Composition of online wheat harvest quality detection system

Field Validation Experiment Design

During the optimal harvest period for wheat, experimental plots were selected that were firm underfoot and free of standing water. Prior to the experiment, the plots were trimmed and leveled, and three regular-shaped test areas were prepared. Before the trial, the wheat cultivar planted in the test area was confirmed. Representative samples were collected to determine plant height, thousand kernel weight, moisture content, and the number of naturally shed grains per unit area. Environmental data such as ambient temperature and humidity were also recorded. In addition, the basic parameters of the combine harvester to be tested were confirmed and documented. The online wheat harvest quality detection system was installed on the combine harvester under test. The system was then calibrated and debugged to ensure proper functioning. The operator conducted two harvesting operations in the designated plots using two standard operating gears of the combine harvester according to the product specifications. During the harvesting process, the quality detection system performed real-time monitoring and recorded the operational quality data, generating detection results automatically. Manual sampling and measurements were performed concurrently. The results obtained by the online wheat harvest quality detection system were compared with those from manual inspection to evaluate the system's detection accuracy and effectiveness.

Field Survey

On June 7, 2024, a wheat harvest experiment was carried out in Dantu District, Danyang City, Jiangsu Province (119°17′11.969″E, 32°12′50.263″N). Three test plots with dimensions of 40 m in length and 25 m in width were prepared. Two plots were randomly chosen for the experiments and labeled as Test Group 1 and Test Group 2. The field survey data are presented in Table 1.

Table 1

Field investigation record

Item	*Parameter*	*Item*	*Parameter*
Variety	Yangmai 33	Plant height / cm	84.6
Spike length / cm	9.8	1000-seed weight / g	43.2
Moisture content / %	18.1	Yield / kg/m^2	0.74

The test site photos are shown in Figure 2. The combine harvester used in this experiment was the WoDe 4LZ-6.0ME(Q)(G4) RuiLong Cross-Region Enhanced Edition, manufactured by Jiangsu WoDe Agricultural Machinery Co., Ltd. This model is equipped with a 125-horsepower, National IV (China IV) high-pressure common rail engine, a 45cc large-displacement hydraulic transmission (HST), and an 85-strengthened dedicated gearbox. The engine's rated power is 92 kW, with a rated speed of 2400 rpm. The minimum ground clearance reaches 43.5 cm. It features a "riding" style chassis wheel system with 53-section, 500 mm wide high-tooth tracks. The cutter header has a working width of 2.10 m and a feed rate of 6 kg/s. It is equipped with lengthened and thickened reel teeth with spring fingers, a reinforced anti-grass entanglement divider, and a floating feed inlet design. The operational hourly productivity ranges from 0.27 to 1.0 hectares per hour. The threshing drum is extended to 2.01 m, and the fish-scale sieve has six adjustable openings. Both airflow volume and direction can be regulated. The harvester supports a 360° extended rotary grain unloading system.



a) Testing site: *b) Manual sampling inspection*

Fig. 2 – Wheat harvest experiment

Data Acquisition and Processing Methods

The threshing and cleaning loss rate, breakage rate, and impurity rate of the combine harvester during the experiment were obtained through manual sampling inspection. During the harvesting operation, three random harvesting passes were selected. For each pass, a 20-meter section of the material discharged from the rear of the combine was collected. The lost grains were separated from the straw, and the quantity of lost grains was measured. By converting this to a per unit yield basis, the threshing and cleaning loss rate of the combine harvester for the test process was calculated.

From the grain tank of the combine harvester, three random grain samples were taken, each weighing no less than 1 kg. The non-grain materials and broken grains were manually separated and counted, allowing for the determination of the breakage rate and impurity rate of the combine harvester during the test.

Simultaneously, the wheat harvest quality online detection system performed real-time monitoring throughout the experiment, saving detection data at each time point. After the test, the relevant data were exported from the system for performance analysis.

The detection performance of the system was analyzed statistically by calculating the maximum, minimum, mean, standard deviation, and coefficient of variation of the measured indicators: threshing and cleaning loss rate, breakage rate, and impurity rate.

Table 2

Statistical table of manual detection data on threshing and cleaning loss rate

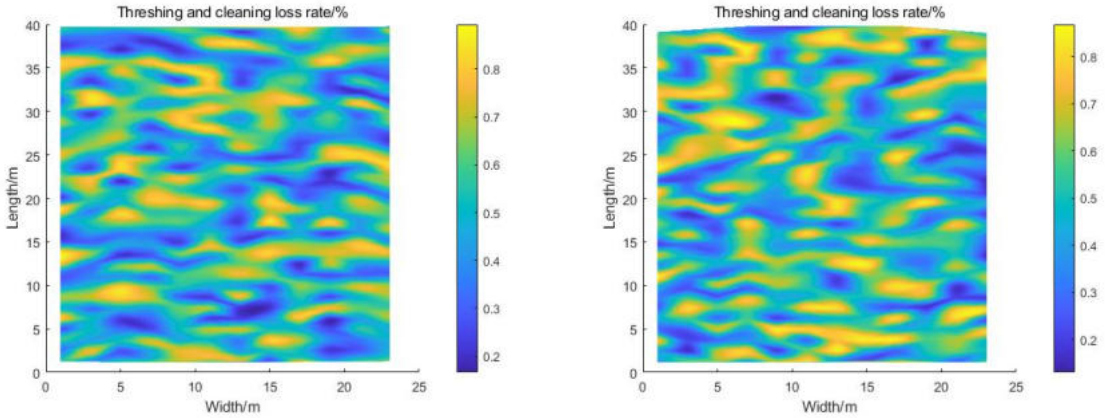
Test group	**Threshing and cleaning loss rate / %**			
1	Measured data	0.76	0.81	0.49
	Maximum value	0.81	Minimum value	0.49
	Average value	0.69	Standard deviation	0.14
	Coefficient of variation		20.29	
2	Measured data	0.63	0.76	0.86
	Maximum value	0.86	Minimum value	0.63
	Average value	0.75	Standard deviation	0.09
	Coefficient of variation		12.00	

The results were processed by Microsoft Office Excel (version 2021, Microsoft Corp., USA) and Matlab (version 2021a, MathWorks Corp., USA). Single factor analysis of variance (ANOVA) was carried out with IBM SPSS Statistics (version 24, IBM Corp., USA).

RESULTS

Results and Analysis of Threshing and Cleaning Loss Rate Detection

The statistical results of the threshing and cleaning loss rate obtained by manual sampling inspection are presented in Table 2. During the test, in Plot 1, the manually measured threshing and cleaning loss rate had a maximum value of 0.81%, a minimum value of 0.49%, an average value of 0.69%, a standard deviation of 0.14%, and a coefficient of variation of 20.29%. In Plot 2, the manually measured threshing and cleaning loss rate had a maximum value of 0.86%, a minimum value of 0.63%, an average value of 0.75%, a standard deviation of 0.09%, and a coefficient of variation of 12.00%.



a) Experimental Zone 1: *b) Experimental Zone 2*

Fig. 3 – Distribution map of threshing and cleaning losses in harvest experimental area

The experimental data from the online detection system for wheat harvest quality indicate that the overall threshing and cleaning loss rates in the first and second experimental fields are at a relatively low level (with a maximum value not exceeding 0.85%). Specifically, the average loss rate in the first field is 0.52% (standard deviation: 0.18%, coefficient of variation: 34.62%), and that in the second field is 0.50% (standard deviation: 0.20%, coefficient of variation: 40.00%). The loss rates in both fields exhibit significant fluctuations (with coefficients of variation exceeding 34%); however, the overall means are close and remain within a low range, which reflects the consistency and reliability of the system's online detection results for threshing and cleaning losses.

Table 3

Statistical table of system detection data on threshing and cleaning loss rate

Test group	Threshing and cleaning loss rate / %			
1	Maximum value	0.85	Minimum value	0.19
	Average value	0.52	Standard deviation	0.18
	Coefficient of variation		34.62	
2	Maximum value	0.84	Minimum value	0.16
	Average value	0.50	Standard deviation	0.20
	Coefficient of variation		40.00	

In this trial, the average threshing and cleaning loss rate of the Worde 4LZ-6.0ME(Q)(G4) Ruilong Cross-Region Enhanced Combine Harvester measured by manual random sampling was 0.72%, while the average instantaneous threshing and cleaning loss rate detected by the system was 0.51%. The absolute error between manual detection and system detection based on the average values was 0.21%.

Results and Analysis of Crushing Rate Detection

Statistical analysis of the damage rate obtained through manual sampling inspection reveals that the overall grain damage rate in Experimental Area 1 and Experimental Area 2 is at a moderately low level (with the maximum value not exceeding 0.82%). The mean damage rate in Experimental Area 1 is 0.67% (standard deviation: 0.14%, coefficient of variation: 20.90%), while that in Experimental Area 2 is 0.58% (standard deviation: 0.17%, coefficient of variation: 29.31%). A comparison of the data between the two experimental areas indicates that the mean damage rate in Experimental Area 1 is approximately 0.09 percentage points higher than that in Experimental Area 2, and the coefficient of variation is lower, suggesting that the fluctuation of the damage rate in Experimental Area 1 is relatively minor and the stability is superior. Although the mean damage rate in Experimental Area 2 is lower, individual differences are more pronounced (with a higher standard deviation and coefficient of variation), which may be associated with disparities in local operating conditions or uneven sampling distribution in the field.

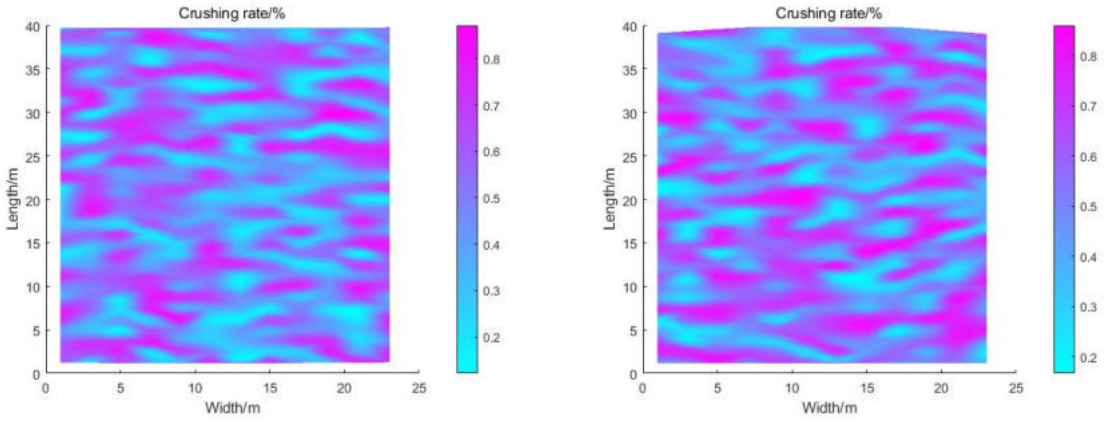
Overall, the results of manual sampling reflect the central tendency and dispersion characteristics of grain damage rates in different experimental areas, offering crucial references for evaluating the quality of harvesting operations.

Table 4

Statistical table of manual detection data on crushing rate

Test group	Crushing rate / %			
1	Measured data	0.69	0.49	0.82
	Maximum value	0.82	Minimum value	0.49
	Average value	0.67	Standard deviation	0.14
	Coefficient of variation		20.90	
2	Measured data	0.81	0.39	0.54
	Maximum value	0.81	Minimum value	0.39
	Average value	0.58	Standard deviation	0.17
	Coefficient of variation		29.31	

The statistical data of broken rate detected by the system are shown in Figure 4 and Table 5. During the trial, in Plot 1, the maximum broken rate detected by the system was 0.83%, the minimum was 0.14%, the average was 0.49%, the standard deviation was 0.19%, and the coefficient of variation was 38.78%. In Plot 2, the maximum broken rate was 0.84%, the minimum was 0.19%, the average was 0.52%, the standard deviation was 0.18%, and the coefficient of variation was 34.62%.



a) Experimental Zone 1 *b) Experimental Zone 2*

Fig. 4 – Distribution map of crushing in harvest experimental area

In this trial, the average broken rate of the Jiangsu Wode 4LZ-6.0ME(Q)(G4) RuiLong Cross-Regional Enhanced Version combine harvester detected by manual random sampling was 0.63%, while the system detected an average instantaneous broken rate of 0.51%. Based on the average values, the absolute error between manual detection and system detection was 0.12%.

Table 5

Statistical table of system detection data on crushing rate

Test group	Crushing rate / %			
1	Maximum value	0.83	Minimum value	0.14
	Average value	0.49	Standard deviation	0.19
	Coefficient of variation		38.78	
2	Maximum value	0.84	Minimum value	0.19
	Average value	0.52	Standard deviation	0.18
	Coefficient of variation		34.62	

Results and Analysis of Impurity Rate Detection

The statistical results of impurity rate detected by manual sampling are shown in Table 6. During the trial, in Plot 1, the maximum impurity rate detected by manual sampling was 0.97%, the minimum was 0.68%, the average was 0.81%, the standard deviation was 0.12%, and the coefficient of variation was 14.81%. In Plot 2, the maximum impurity rate was 1.03%, the minimum was 0.46%, the average was 0.69%, the standard deviation was 0.24%, and the coefficient of variation was 34.78%.

Table 6

Statistical table of manual detection data on impurity rate

Test group	Impurity rate / %			
1	Measured data	0.78	0.68	0.97
	Maximum value	0.97	Minimum value	0.68
	Average value	0.81	Standard deviation	0.12
	Coefficient of variation		14.81	
2	Measured data	0.59	1.03	0.46
	Maximum value	1.03	Minimum value	0.46
	Average value	0.69	Standard deviation	0.24
	Coefficient of variation		34.78	

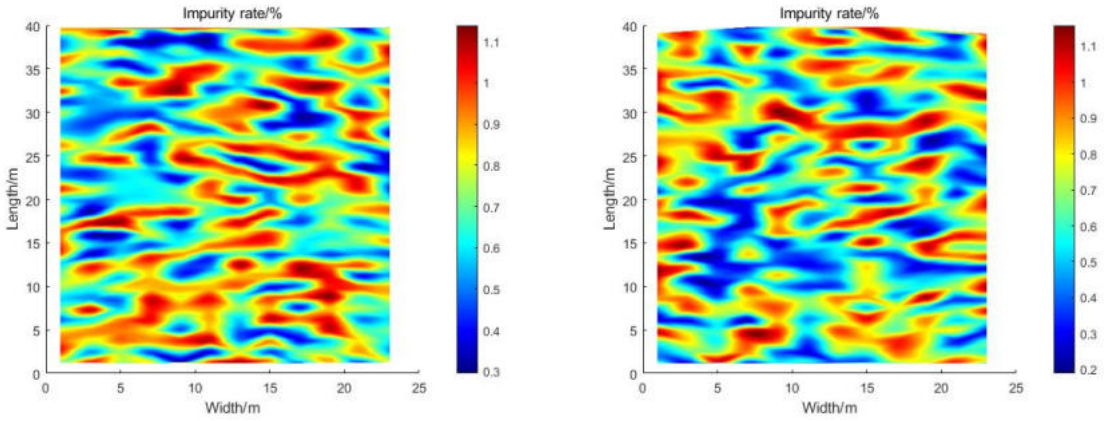
The statistical results of impurity rate detected by the online detection system are shown in Figure 5 and Table 7. During the trial, in Plot 1, the system detected a maximum impurity rate of 1.11%, a minimum of 0.32%, an average of 0.73%, a standard deviation of 0.22%, and a coefficient of variation of 30.14%. In Plot 2, the system detected a maximum impurity rate of 1.13%, a minimum of 0.23%, an average of 0.67%, a standard deviation of 0.26%, and a coefficient of variation of 38.81%.

Table 7

Statistical table of system detection data on impurity rate

Test group	Impurity rate / %			
1	Maximum value	1.11	Minimum value	0.32
	Average value	0.73	Standard deviation	0.22
	Coefficient of variation		30.14	
2	Maximum value	1.13	Minimum value	0.23
	Average value	0.67	Standard deviation	0.26
	Coefficient of variation		38.81	

In this trial, the average impurity rate of the Jiangsu Word 4LZ-6.0ME(Q)(G4) RuiLong cross-region enhanced version combine harvester measured by manual random sampling was 0.75%, while the average instantaneous impurity rate detected by the system was 0.70%. The absolute error between manual detection and system detection based on the average values was 0.05%.



a) Experimental Zone 1: *b) Experimental Zone 2*

Fig. 5 – Distribution map of impurity in harvest experimental area

Results and Analysis of Overall Machine Operation Quality Detection

In this evaluation trial, the results of manual sampling detection showed that the maximum threshing and cleaning loss rate of the Jiangsu Word 4LZ-6.0ME(Q)(G4) RuiLong cross-region enhanced version combine harvester was 0.86%, the maximum breakage rate was 0.82%, and the maximum impurity rate was 1.03%. The digital quality evaluation system for combine harvester operation detected a maximum threshing and cleaning loss rate of 0.85%, a maximum breakage rate of 0.84%, and a maximum impurity rate of 1.13% for the same combine harvester model. Both detection methods confirmed that the three indicators—threshing and cleaning loss rate, breakage rate, and impurity rate-of the 4LZ-6.0ME(Q)(G4) RuiLong combine harvester meet the relevant technical requirements, demonstrating that the performance of this combine harvester complies with the specified standards.

CONCLUSIONS

To verify the detection performance of the wheat harvesting quality online detection system, a validation test scheme was developed specifically for wheat harvesting. Field trials were conducted in Jiangsu Province. The test results showed that:

(1) The average threshing and cleaning loss rates measured by manual sampling were 0.69% and 0.75%, while the online detection system measured average loss rates of 0.52% and 0.50%;

(2) The average breakage rates measured manually were 0.67% and 0.58%, compared to 0.49% and 0.52% detected by the online system;

(3) The average impurity rates from manual detection were 0.81% and 0.69%, whereas the online detection system measured 0.73% and 0.67%.

Compared with manual sampling results, the maximum absolute errors of the online detection system were 0.25% for threshing and cleaning loss rate, 0.16% for breakage rate, and 0.08% for impurity rate. The wheat harvesting quality online detection system developed in this study can effectively perform real-time quality monitoring of combine harvester operations during wheat harvesting.

ACKNOWLEDGEMENT

We greatly appreciate the careful and precise reviews by the anonymous reviewers and editors. This research was financially supported by the National Key Research and Development Program of China, grant number 2021YFD2000503; the National Natural Science Foundation of China, grant number 32272004; the Basic Research Center, Innovation Program of Chinese Academy of Agricultural Sciences (CAAS-BRC-SAE-2025-02).

REFERENCES

[1] Audu, J., Aremu, A.K. (2021). Development, evaluation, and optimization of an automated device for quality detection and separation of cowpea seeds. *Artificial Intelligence in Agriculture*, Vol.5, pp.240-251. DOI: 10.1016/j.aiia.2021.10.003

[2] Chen M., Cheng G., Xu J., Zhang G., Jin C. (2023). Online detection system for crushed rate and impurity rate of mechanized soybean based on DEEPLABV3+, *INMATEH - Agricultural Engineering* Vol.70, pp. 497-506, DOI: https://doi.org/10.35633/inmateh-70-48

[3] Chen, M. Jin, C.Q., Mo, G.W., Liu, S.K. & Xu, J.S. (2023). Online detection method of impurity rate in wheat mechanized harvesting based on improved U-Net model (基于改进 U-Net 模型的小麦收获含杂率在线检测方法). *Transactions of the Chinese Society of Agricultural Machinery*, Vol.54, pp.73-82. DOI: 10.6041/j.issn.1000-1298.2023.02.007

[4] Ding, Z.Z., Mei, W., Hu, B., Chen, Z.W., & Dong, C.W. (2025). Impurity detection of premium green tea based on improved lightweight deep learning model. *Food Research International*, Vol.200, pp.115516. DOI: 10.1016/j.foodres.2024.115516

[5] Geng, D.Y., Kang, Y.Y., Wang, W.L., Zhang, Y.M., Zhu, J.K. & Wang, X.L. (2024). Design and test of high sped seeding system for wheat wide seedling belt (小麦宽苗带高速排种系统设计与试验). *Journal of Chinese Agricultural Mechanization*, Vol. 45, pp.17-24. DOI: 10.13733/j.jcam.issn,2095-5553.2024.10.003

[6] Gu, M., Shen, H.Y., Ling, J., Yu, Z.Y., Luo, W.W., Wu, F., Gu, F.W. & Hu, Z.C. (2025). Online detection of broken and impurity rates in half-feed peanut combine harvesters based on improved YOLOv8-Seg. *Computers and Electronics in Agriculture*, Vol.237, pp.110494. DOI: 10.1016/j.compag.2025.110494

[7] Li, C.P., Wang, M.S., Chen, X., Ji, H., Huang, W.K. & Wang, W.Z. (2025). Design of a wheat yield detection system based on PVDF and co-planar curved surface capacitors (基于 PVDF 和同面弧面电容的小麦产量检测系统设计). *Journal of Chinese Agricultural Mechanization*, Vol.46, pp.230-237. DOI: 10.13733/j.jcam.issn,2095-5553.2025.03.034

[8] Li, B.G., Wang, H., Song, Y., Ren, Z.W., Liu, Y.H. & Xu, L.C. (2024). Stereo visual perception system based on unmanned wheat harvester (基于无人驾驶小麦收割机立体视觉感知系统). *Journal of Chinese Agricultural Mechanization*, Vol.45, pp.244-249. DOI: 10.13733/j.jcam.issn,2095-5553.2024.09.037

[9] Li, Y.B., Hou, Y.X., Cui, T., Tan, D.S., Xu, Y., Zhang, D.X., Qiao, M.M., & Xiong, L.J. (2024). Classifying grain and impurity to assess maize cleaning loss using time-frequency images of vibro-piezoelectric signals coupling machine learning. *Computers and Electronics in Agriculture*, Vol.227, pp.109583. DOI: 10.1016/j.compag.2024.109583

[10] Liao, Y.T., Shi, B.B., Wang, C.Q., Liao, Q.X., Wu, A.Y. & Ou, Y.H. (2025). Development status and trend of mechanization of rapeseed and wheat sowing in hilly and mountainous region of southern China (南方丘陵山地油菜和小麦播种机械化发展现状与趋势). *Transactions of the Chinese Society of Agricultural Engineering (Transactions of the CSAE)*, Vol.41, pp.12-26, DOI: 10.11975/j.issn.1002-6819.202406121

[11] Liu, Q.H., Liu, W.K., Liu, Y.S., Zhe, T.T., Ding, B.C. & Liang, Z.W. (2023). Rice grains and grain impurity segmentation method based on a deep learning algorithm-NAM-EfficientNetv2. *Computers and Electronics in Agriculture*, Vol.209, pp.107824. DOI: 10.1016/j.compag.2023.107824

[12] Liu, L., Du, Y.F., Chen, D., Li, Y.B., Li, X.Y., Zhao, X.M., Li, G.R. & Mao, E.R. (2022). Impurity monitoring study for corn kernel harvesting based on machine vision and CPU-Net. *Computers and Electronics in Agriculture*, Vol.202, pp.107436. DOI: 10.1016/j.compag.2022.107436

[13] Tang, Z. Li, Y.M., Zhao, Z., Xu, L.Z. & Li, H.C. (2012). Test and analysis of wheat entrainment loss for tangential-longitudinal-axial combine harvester (切纵流联合收获机小麦夹带损失检测试验与分析). *Transactions of the Chinese Society of Agricultural Engineering (Transactions of the CSAE)*, Vol.28, pp.11-16. DOI: 10.3969/j.issn.1002-6819.2012.01.003

[14] Vlădut N.-V., Ungureanu N., Biris S.St., Voicea I., Nenciu F., Găgeanu I., Cujbescu D., Popa L.-D., Boruz S., Matei G., Ekielski A., Teliban G.C. (2023). Research on the identification of some optimal threshing and separation regimes in the axial flow apparatus, *Agriculture*, Vol.13, pp.838, DOI: 10.3390/agriculture13040838

[15] Wang, F.M., Ni, X.D., Zhang, Q., Tao, W., Chen, D. & Mao, X. (2024). Online classification and identification method of winter wheat maturity under mechanical harvesting scenario based on MobileNetV2-CBAMl (基于 MobileNetV2-CBAM 的机收场景下冬小麦成熟期在线分类识别方法). *Transactions of the Chinese Society of Agricultural Machinery*, Vol.55, pp.71-80. DOI: 10.6041/j.issn.1000-1298.2024.S1.008

[16] Wang, Y.L., Ou, X.Q., He, H.J. & Kamruzzaman, M. (2024). Advancements, limitations and challenges in hyperspectral imaging for comprehensive assessment of wheat quality: An up-to-date review. *Food Chemistry: X*, Vol.21, pp.101235. DOI: 10.1016/j.fochx.2024.101235

[17] Wu, Z.P., Chen, J., Ma, Z., Li, Y.M., & Zhu, Y.L. (2024). Development of a lightweight online detection system for impurity content and broken rate in rice for combine harvesters. *Computers and Electronics in Agriculture*, Vol.218, pp.108689. DOI: 10.1016/j.compag.2024.108689

[18] Xie, J.H., Zhang, H.L., Feng, H., Huang, W.L., Jin, J.Y. & Ma, W.B. (2024). Design and experiment of friction adjustable precision seed feeder device for wheat experimental sowing (摩擦调节式小区小麦精密排种器设计与试验). *Transactions of the Chinese Society of Agricultural Machinery*, Vol.56, pp.164-173. DOI: 10.6041/j.issn.1000-1298.2025.01.017

[19] Zhang, P., Wang, Y., Zhang, J., LIU, H.Y., Ding, Y.Q. & Liu, Y.Y. (2024). Investigation and analysis of the present status of unmanned wheat sowing operation in Jiangsu farms (江苏农场小麦播种无人化作业现状调研及分析). *Journal of Chinese Agricultural Mechanization*, Vol.45, pp.272-277. DOI: 10.13733/j.jcam.issn,2095-5553.2024.11.042

[20] Zhang, Q., Wang, L., Ni, X.D., Wang, F.M., Chen D. & Wang, S.M. (2024). Research on wheat broken rate and impurity rate detection method based on DeepLab-EDA model and system construction. *Computers and Electronics in Agriculture*, Vol.226, pp.109375. DOI: 10.1016/j.compag.2024.109375

[21] Zhao, P.F., Ju, X.T., Yang, P.K., Zheng, Z.Q., Huang, Y.X., Gao, Z.Y. & Shi, J.T. (2024). Design and experiment of fertilizer pipe front-mounted wheat wide seedling belt rotary tillage fertilization planter (肥管前置式小麦宽苗带旋耕施肥播种机设计与试验). *Transactions of the Chinese Society of Agricultural Engineering (Transactions of the CSAE)*, Vol.40, pp.12-21, DOI: 10.11975/j.issn.1002-6819.202405006

[22] Zhao, J.W., Yu, J.Q., Sun, K., Sun, Y.C., Wang, Y., Liang, L.S. & Yu, Y.J. (2025). Modeling and verifying wheat roots using AgriDEM (基于 AgriDEM 软件的小麦根系建模与试验验证). *Transactions of the Chinese Society of Agricultural Engineering (Transactions of the CSAE)*, Vol.41, pp.63-72, DOI: 10.11975/j.issn.1002-6819.202406180.

OPTIMIZATION DESIGN AND PERFORMANCE ANALYSIS OF A NOVEL BIONIC ROTARY CUTTER FOR A WEEDING MACHINE
/
新型除草机仿生旋转刀具的优化设计与性能分析

Wenjuan SHUN[2)], Jun GE*[1)], Kuan QIN[1)], Chengmao CAO[1)], Yan SUN[1)], Liangfei FANG[1)], Xu ZHU[1)], Junjie LU[1)], Weidong GAO[1)] [1]
[1)] School of Engineering, Anhui Agricultural University, Hefei, Anhui / China
[2)] College of Food and Nutrition, Anhui Agricultural University, Hefei, Anhui / China
Corresponding authors: Jun Ge; Tel: +8615077912067; E-mail: gejunahau@ahau.edu.cn
DOI: https://doi.org/10.35633/inmateh-76-82

Keywords: *weeding cutter, bionic, cicada nymph, DEM, three-direction resistance*

ABSTRACT
In a weeding machine, the weeder component determines overall working performance, while the weeding blade influences soil-cutting quality, weeding efficiency, resistance, and power consumption. In this paper, a bionic design for a weeding cutter inspired by the soil-cutting process of the cicada nymph has been proposed and the intent is to promote the performance of the bionic design. The weeding cutter introduced in this paper has been equipped with lightweight and simplified rotary robotic-machinery commonly utilized in hilly and mountainous areas. To assess the performance of the bio-mimetic weeding cutter during rotary, the forces in 3 directions (X, Y & Z) and the resistance torque have been investigated. An experimental platform with a 4 m long soil bin has been utilized for tests indoors. Meanwhile, the discrete element method (DEM) simulations with different conditions like the operated angle, the rotation speed, the forward velocity, and different cutting edges, have been carried out. Either the experimental result or the simulative result indicated that the bio-mimetic weeding blade ameliorated the performance of soil-cutting, energy consumption and weeding efficiency. Specifically, the bio-mimetic weeding blade exhibits a notable reduction of 14.19% in average torque and 14.95% in horizontal resistance compared to the traditional weeding blade. Finally, it could be found that the bionic rotary cutter proposed in this research could be a better choice for the weeder machine used in hilly and mountainous areas.

摘要
对于旋耕除草机械来说，除草刀是决定其工作性能的关键因素。具体而言，除草刀片决定了土壤切割的质量、除草效率、阻力和功耗。本文提出了一种受蝉若虫土壤切割过程启发的除草刀仿生设计，旨在提高除草刀的性能表现。本文介绍的除草机配备在丘陵山区常用的轻量化旋耕除草机械上。本研究为了评估仿生除草刀在旋转过程中的表现，研究了 3 个方向（X、Y 和 Z）的力和阻力扭矩。试验主要在 4 米长土槽平台中进行，之后，在参数标定的基础上进行了不同条件下的离散元法（DEM）模拟，主要变量包含操作角度、转速、前进速度和不同的切削刃。无论是土槽试验结果还是仿真模拟结果都表明，仿生除草刀片改善了土壤切割性能、能耗和除草效率。具体而言，与传统除草刀片相比，仿生除草刀片的平均扭矩显著降低了 14.19%，水平阻力显著降低了 14.95%。整体而言，本研究提出的仿生旋转切割器可能是丘陵山区除草机的更好选择。

INTRODUCTION
Peucedanum praeruptorum Dunn, known as Qianhu in Chinese, is the herb with high medicinal value in traditional Chinese medicine (*Chen et al., 2021*). In decades, the quality of Qian Hu has declined due to the excessive use of herbicides through chemical weeding (*Mayerová et al., 2018*). Generally speaking, there are three ways to remove the herbs in the field: manual weeding, chemical herbicide, and mechanical weeding. As a traditional method, weeding by hand has apparent limitations such as labor-intensive and time-consuming. Furthermore, the chemical way has the problem of herbicide residue which is strictly prohibited in the medical herb.

Wenjuan Shu, Stud. Eng.; Jun Ge, Lecturer PhD. Eng.; Xu Zhu, M.S. Stud. Eng.; Chengmao Cao, Prof. PhD. Eng.; Yan Sun, Assoc. Prof. M.S. Eng.; Liangfei Fang, Assoc. Prof. PhD. Eng.; Kuan Qin, Assoc. Prof. PhD. Eng.; Junjie Lu, M.S. Stud. Eng.; Weidong Gao, M.S. Stud. Eng.*

Different from the above two ways, mechanical weeding, serving as a chemical-free and environmentally friendly weed control method, has gained widespread recognition for effectively managing weed growth in various crops (*Richard et al., 2023; Fishkis & Koch, 2023; Liu, et al., 2023*).

Ning Qianhu, named after the Ningguo City (N 30°16′ - 30°47′, E 118°36′ - 119°24′), a hilly mountainous area in Anhui Province, China, is always cultivated in hilly mountainous regions. Due to the challenging terrain of steep mountains, large and medium-sized machinery is unsuitable for agricultural operations in this region. As a result, lightweight and simplified machinery is commonly employed *(Cao et al., 2023*). Micro-tillers are equipped with a maximum engine power of 6.5 kW which can effectively remove weeds in crop rows by the drove weeding wheels. The weeding wheel, a key component of micro-tillage machines, consists of multiple metal weeding blades transversely welded to the wheel hub. When a certain torque is applied, the weeding wheel tills the topsoil and removes weeds. However, traditional weeding wheels face challenges such as high resistance and power consumption during weeding operations. These issues lead to low weeding efficiency and high costs, which hinder the widespread adoption of agricultural mechanization *(Wang, et al., 2021)*. In recent years, researchers and scholars have focused on designing new weeders to enhance mechanization in hilly mountainous areas. Their efforts aim to optimize weeder performance, improve weeding efficiency, and reduce the cost of mechanical weeding. For instance, *Wang et al. (2011)* developed a novel 3ZS-150 tillage weeder for weed control in paddy fields. That innovative machine enables simultaneous weeding between rows and seedlings. The study conducted a systematic analysis of the machine's structure and working principles, introducing a novel design of the weeding spring tooth for effective removal of intra-row weeds and inter-row cultivation. Furthermore, *Wang et al. (2017)* developed a simplified 3SCJ-2 paddy inter-row weeder, focusing on a more comprehensive analysis of the structural design and power distribution of a small-scale weeding machine. The study established a mechanical model of the weeding wheel, determining essential working and structural parameters. These efforts resulted in a lightweight and straightforward weeding machine design that ensures low power consumption and high efficiency. The optimization of the geometric structure of the rotary cutter, along with the relevant operating and structural parameters, has been a prominent focus of research within the context of previous studies on rotary cultivator design. For instance, *Matin, Fielke, and Desbiolles (2014)* have explored the impact of the geometric shape and operating speed of the rotary cultivator on torque, energy consumption, and the soil cutting and throwing process. The research has investigated the interaction between the cutting edges of the blades and the soil to determine the optimal design for the rotary cultivator. Efforts to optimize the geometric structure of the weeding wheel and its associated parameters are crucial for enhancing the overall performance and efficiency of the weeding process *(Matin et al., 2014, 2015, 2020).*

In summary, to address the challenge of high resistance in weeding blades used in micro-tillage weeders operating in hilly mountainous areas, this paper presents a novel bionic rotary weeding cutter inspired by the serrated characteristics of the forelimbs of nymphal cicadas, which holds promise for improving the performance of weeding wheels in micro-tillage weeders. Furthermore, a mechanical model of soil-weeding cutter interaction was established to further study the resistance change of the rotary cutter in the process of cutting soil.

MATERIALS AND METHODS

This paper proposed a bionic design approach for developing weeders suitable for hilly mountainous areas. Figure 1 illustrates the robotic micro-tillage weeder machine specifically designed for the Ning Qianhu. The machine contains a separated roll-cutting weeding wheel for inter-row weeding. During the weeding process, the weeding blades shear and break the topsoil, effectively removing the weeds embedded in the soil. Therefore, the soil and weeds are propelled backwards with the weeding blades rotating *(Tian et al., 2022)*.

Extracting and fitting the serrated structure

Samples of *Cicadas nymphs* were collected from Anhui, China, to study the excavating process, as shown in Figure 1. The tibia continuously opened, retracted, and drove the serrated structure, effectively cutting through the sediment *(Smith & Hasiotis, 2008)*. These serrations exhibited a cutting angle that extended beyond the friction angle, providing a slip-cutting effect. That characteristic was crucial for achieving efficient cutting and reducing cutting resistance during the emergence of *Cicadas nymphs* and it shares many similarities with rotary tillage tools in terms of soil cutting *(Chang et al., 2016)*. Enlarged photographs of the serrated structures of *Cicada Nymphs* were captured using an electron microscope. To enhance the quality of the images and reduce noise, a combination of Gaussian filtering and the Laplace operator was applied as a preprocessing step. Subsequently, image binarization was performed, followed by the utilization of the Canny

edge detection operator, which enabled accurate positioning and robust resistance to interference. Finally, the Find function was employed to extract the contour pixel coordinates. The results of the contour extraction are illustrated in Fig. 2. A total of 3969-pixel coordinate points were extracted in this figure. The contour curves of the cicada's saw-tooth structure exhibited four distinct curves, namely A, B, C, and D. Among those curves, in terms of manufacture and curvature, curve D was more feasible and suitable for the bionic saw-tooth profile in this study. Subsequently, the accorded dimensions for manufacturing the bio-mimetic blade teeth are shown in Figure 3 and manufactured products are shown in Fig. 4.

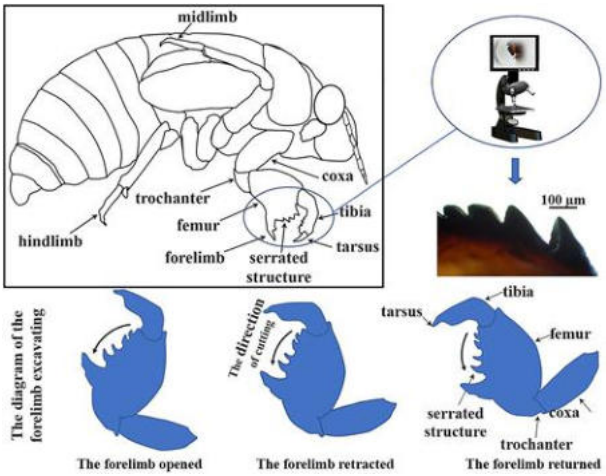


Fig. 1 – Serrated structure of the cicada nymph

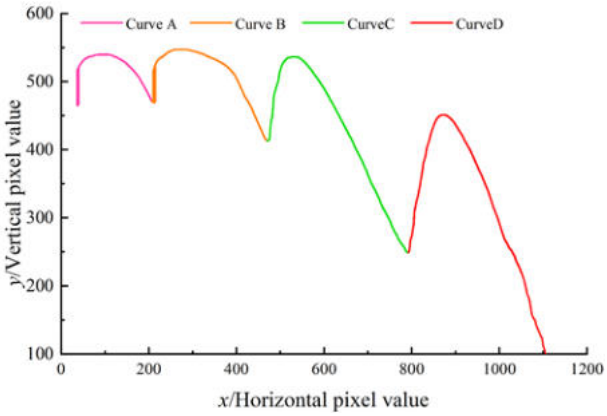
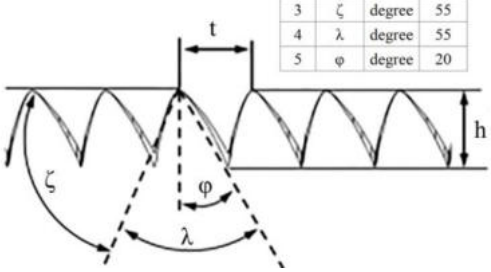


Fig. 2 – Pixel chart for the saw-tooth profile on forelimbs of the cicada nymph

No.	Items	Unit	Value
1	t	mm	6.3
2	h	mm	4.6
3	ζ	degree	55
4	λ	degree	55
5	φ	degree	20



Note: t, distance between teeth; h, teeth height; ζ, teeth tilted angle with horizontal line; λ, angle of the teeth profile; φ, angle between the right side of teeth profile and vertical line

Fig. 3 – Teeth dimensions of the bio-mimetic weeding blade

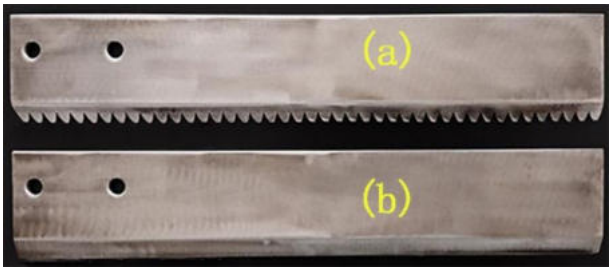


Fig. 4 – Physical picture of bio-mimetic (a) and traditional weeding blade (b)

Weeding blade parameter and resistance analysis

The mounted angle of the blade *α*, defined as the angle between the tangent to the radius of rotation and the blade, is a significant parameter for soil entry and exit, as illustrated in Fig. 5. When the blade enters the soil, the entry angle *β* should be noted; it varies with the mounted angle α, as shown in Fig. 5(a) and 5(c). Fig. 5(a) is a normal situation whereas Fig. 5(c) has a perpendicular *β*. In Fig. 5(a), the contacted F_N has been decomposed into F_{Nx} in the tangent direction and F_{Ny} in the normal direction. F_{Nx} is mainly affected by the angle *β*, while F_{Ny} is relevant to the weight and the slip ratio of the weeder machine. The relationship between F_N, F_{Nx} and F_{Nxy} could be expressed as follows:

$$\begin{cases} F_{Nx} = F_N \cos\beta \\ F_{Ny} = F_N \sin\beta \end{cases} \quad (1)$$

The maximum weeding depth is h, the blade width is L, and the trajectory radii of the blade top and end are R_1 and R_2. In this study, the blade width L, depth h, and R_1 were 40 mm, 40 mm and 123 mm, respectively. Meanwhile, the entry angle *β* was set at 90° for a minimum penetration resistance. The following Eqs. (2), (3) were then obtained:

$$\frac{1}{2} R_1 + L + h \ = R_1 + L \times \sin\alpha \quad (2)$$

$$\alpha = \sin^{-1}\frac{L + h - \frac{1}{2}R_1}{L} \tag{3}$$

A microscopic view of the forces acting on a soil particle is shown in Figure 5(b). The abscissa *x'* is parallel to the blade surface, while the longitudinal axis *y'* passes through the center of the particle and is perpendicular to *x'*. The force F on the soil particle is the resultant of the frictional force and the support force; F_a and F_n are the components of F in the directions of *x'* and *y'*, respectively. F_a can be calculated using Eq. (4).

$$F_a = \cos\alpha \;\; F \tag{4}$$

Generally speaking, F_a is affected by the angle *α* of the weeding blades *(Zhang et al., 2022)*. Based on Eq. (4), a smaller α makes a greater F_a. On the other hand, it means greater soil adhesion and power consumption as the blade moves. Therefore, an appropriate angle α should be assigned in the first place.

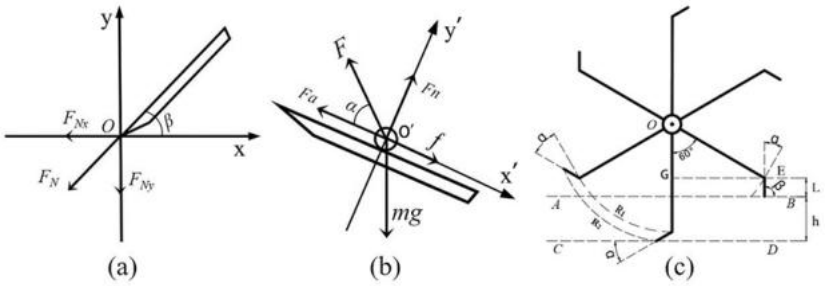


Fig. 5 – Mechanics analysis for soil-blade interaction system

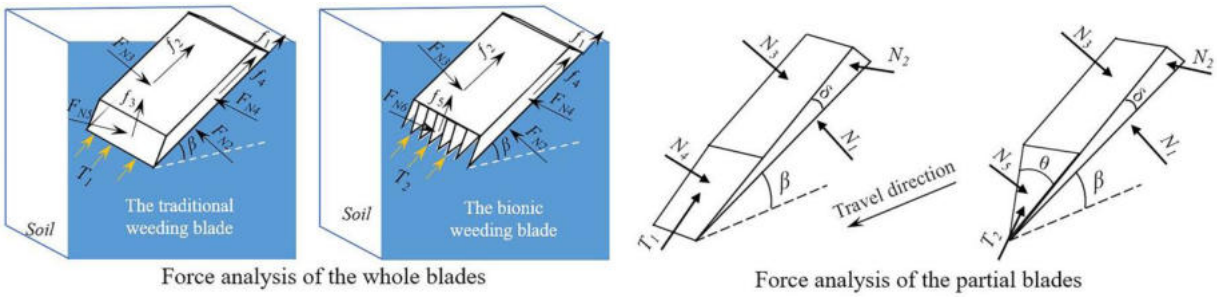


Fig. 6 – Respective mechanic analysis for traditional and bionic weeding blade

Figure 6 diagrammatically compares the forces generated by traditional and bionic weeding blades as they are contacting with soil, respectively. To compare the resistance of the two blades, both the bionic blade and traditional blades were divided into several units. The bionic blade edge can be approximated as a triangular shape that serves as the unique profile of the bionic saw-tooth. Figure 6 intuitively reflects the difference in force between these two blades. In the figure, N_1, N_2, N_3, N_4 and N_5 were pressures acting on different faces of the blades' element. T_1, T_2 were the pure cutting resistances, and *θ* represented the sharpness angle of the blade head. According to the cutting model of Kostritsyn *(Zeng, 1995)*, the forces in Figure 6 could be expressed as follows:

$$P_1 = \cos\delta\left(\frac{M_1\cos\beta}{\tan(\delta+\beta)} + M_1\cos\beta\,\mu\right) + \cos\delta\left(\frac{N_3}{\tan\beta} + N_3\mu + 2N_2\mu\right) + \frac{mse}{cos(\delta + tan^{-1}\mu)}S_1\mu + kb_1 \tag{5}$$

$$P_2 = \cos\delta\left(\frac{M_1\cos\beta}{\tan(\delta+\beta)} + M_1\cos\beta\,\mu\right) + \cos\delta\left(\frac{N_3}{\tan\beta} + N_3\mu + 2N_2\mu\right) + \frac{mse}{cos(\delta + tan^{-1}\mu)}S_2\mu + kb_2 \tag{6}$$

where:

P_1 was the resistance of the traditional blade along the direction of the blade edge.

P_2 was the resistance of the bionic blade along the direction of the blade edge.

According to Eq. 5 and Eq. 6, the resistance of the bionic blade should be less than that of the traditional blade due to $b_1 > b_2$ and $S_1 > S_2$.

Calibration of DEM parameters

Soil parameters determined the accuracy of DEM simulation *(Wu et al., 2021)*. In the field, the five-point sampling method was employed to assess the density and water content of the soil within the 0-250 mm depth range. As a result, the tested soil has a density of 1.51 g·cm^{-3} and water content of 18.15%. The vibratory sieving method revealed the distribution of soil particle sizes: the sand particles were more than 20% and the powder particles were less than 40%. According to the Chinese Soil Texture Classification, the sandy loam could be an appropriate result for the test soil. Moreover, the repose angle of soil, shown in Figure 7(a), (b) and (c), yielded an average value of 33.7°.

Table 1

Parameters utilized in DEM simulation

Type of parameter	Values	Type of parameter	Values
Soil particle diameter (mm)	4	Soil-soil static friction coefficient	0.6
Soil density (g·cm^{-3})	1.51	Soil-soil rolling friction coefficient	0.3
Soil shear modulus	1e+06	Soil-soil restitution coefficient	0.5
Soil Poisson's ratio	0.35	JKR with surface energy (J·m^{-2})	1
Weeding blades density (g·cm^{-3})	7.89	Soil- blades friction coefficient	0.5
Weeding blades shear modulus (Pa)	2.1e+11	Soil- blades rolling friction coefficient	0.05
Weeding blades Poisson's ratio	0.3	Soil- blades restitution coefficient	0.5

Based on the field tests, the calibration process/tests should be replicated in the DEM simulations to try the parameters of soil particles. Because of the cohesive force between soil particles, the Hertz-Mindlin model with the JKR soil contact model was chosen to simulate the binding and agglomeration forces between the soil particles *(Zhang et al., 2022, 2023)*. As Figure 7(d) shows, there was a cylinder and a circular plate to implement the repose angle test in the DEM simulation. In terms of the calibration result, the calibrated parameters of the soil particles used in DEM tests, such as the soil collision coefficient, soil rolling friction coefficient, soil static friction coefficient, and JKR surface energy, are shown in Table 1.

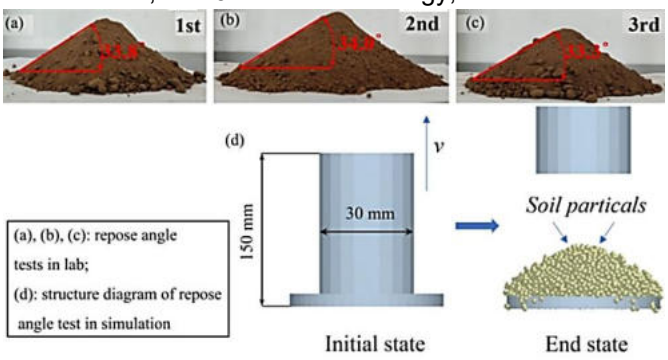


Fig. 7 – Repose angle test in lab and simulation for parameters calibration

Condition of Soil bin test

Due to the relatively stable performance of repeated experiments, the soil bin test is widely used for soil-related studies. In this study, a soil bin experiment was also conducted for comparison with the DEM simulation. In the soil bin test, both the traditional and bionic weeding wheels were represented by a single blade.

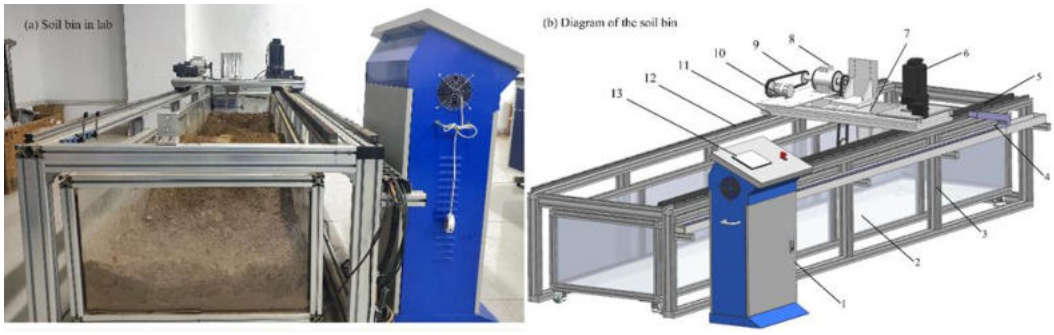


Fig. 8 – Experimental site picture and structural diagram of the soil bin

1. Electrical control box; 2. Soil tank; 3. Body frame; 4. Wire trays; 5. Forward guides (left side); 6. Electric motor for forward motion; 7. Three-direction force sensor; 8. Torque transducer; 9. Chain; 10. Electric motor for blade drive; 11. Moving platform; 12. Forward guides (right side); 13. Human–machine interface

As Fig. 8 shows, the experimental device contains thirteen main parts and the details have been noted below the figure, respectively. The soil bin has a length of 4 m, a width of 1 m and a depth of 0.8 m. Experimental soil, whose properties were stated in the last section, was collected from the Ning Qianhu plantation area. The moving platform (11 in Fig. 8(b)) could be moved with speeds ranging from 0 to 1.5 m·s-1 along the guiding chute. The three-direction forces sensor (7 in Fig.8(b)) was positioned beneath the movement mechanism. The rotation of weeding blade could be controlled by a speed controller and adjacent to the soil bin, a control cabinet was installed, enabling the setting of forward speed and displacement of the test device, as well as a real-time data display. The settings and parameters are shown in Table 2.

Table 2

The values of the test parameters

Type of parameter	values	Type of parameter	values
Forward speed /(m·s^{-1})	0.3	Blade width /(mm)	40
Rotational speed /(rpm)	150	Blade thickness /(mm)	3
Test length /(mm)	1000	Weeding depth /(mm)	40
Mass of the weeding blade /(g)	220	Weeding width /(mm)	217

RESULTS AND DISCUSSION

Simulation tests7

As mentioned above, the torque and three-direction forces were significant factors in indicating resistance when the weeding blade contacted the soil. Therefore, the DEM simulation of traditional and bionic blades focused on the comparison of the torque and three-direction forces by these two blades, too.

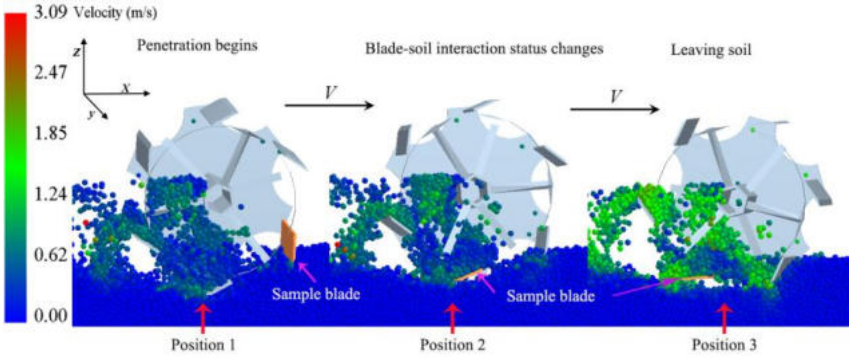


Fig. 9 – Blade-soil interaction and the movement of soil particles at different positions during weeder rotation in the DEM simulation

The blade interacted with the soil in different states during wheel rotation. As illustrated in Fig. 9, position 1 corresponds to the sample blade just penetrating the soil surface; position 2 represents the blade at the trough point of the trajectory curve; and position 3 shows the blade beginning to throw the soil away. Based on Fig. 9, soil particle disturbance increased from a mild degree at position 1 to the highest level at position 3. Hereinafter, the traditional weeding blade and the biomimetic blade are compared in terms of torque and three-directional forces based on the experimental results.

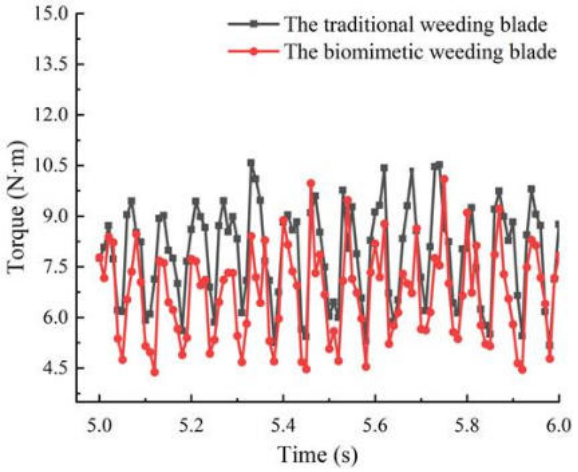


Fig. 10 – Difference between traditional and biomimetic weeding blades in torque on one blade during the blade touch with soil

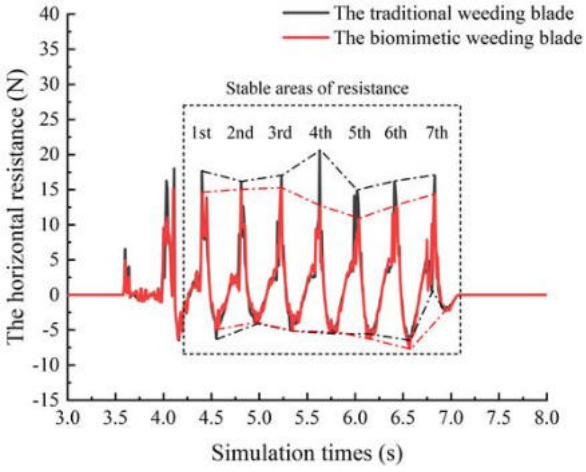


Fig. 11 – Horizontal resistance of the sample blade during the whole process in simulation

Figure 10 shows the variation in torque for the two types of weed wheels. As the figure shows, both the biomimetic weeding wheel and the traditional weeding wheel exhibited regular fluctuations. However, the biomimetic weeding wheel required less torque than the traditional weeding wheel for rotating the wheel. The results indicated that the average torque required for the traditional weed wheel was 7.89 N·m. In comparison, the biomimetic weeding blade exhibited a lower average torque of 6.71 N·m, representing a reduction of 14.95%. To facilitate a clear observation of the force variations during the simulation, the direction of the three-direction resistance on the weeding wheel is defined as follows: horizontal along the X-axis (aligned with the forward direction), vertical along the Z-axis, and lateral along the Y-axis.

As Figure 11 shows, the horizontal resistance of the weeding blade aligns with the forward direction, resulting in a positive horizontal resistance. Based on the previous analysis, the horizontal resistance of the weeding blade primarily arises from the shear resistance and friction of the soil. The variation in horizontal resistance can be observed for the two different weeding blades in the soil. At the moment of 5.05 s, the weeding blade contacts with the soil. As the depth of the weeding blade increases, the amount of soil adjacent to the weeding blade also increases, and it caused the angle between the weeding blade and the horizontal surface to be decreased to an acute angle. Consequently, the soil pressure, shear resistance, and frictional force against the weeding blade gradually increased, resulting in a progressive rise in horizontal resistance. This horizontal resistance represents the resistance encountered by the weeding blade during soil penetration and primarily depends on the depth of penetration. The graph indicates that the peak positive horizontal resistance occurred at 5.09 s, corresponding to the moment when the weeding blade reaches its maximum depth. Comparing the peak resistance values of the different weeding blades in simulation, it can be found that the peak resistance for the traditional weeding blade during soil penetration ranges from 12.27 N to 20.50 N, while for the biomimetic weeding blade, the peak resistance ranges from 9.31 N to 13.89 N.

The variation of horizontal force during a full rotation of a blade with the wheel is shown in Fig. 12.

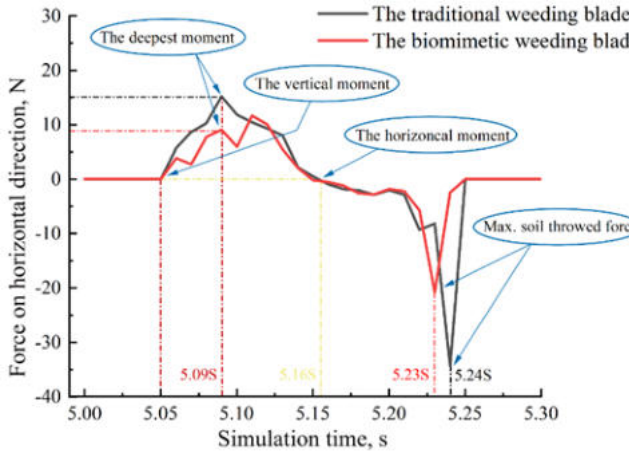


Fig. 12 – Horizontal resistance of blades over time

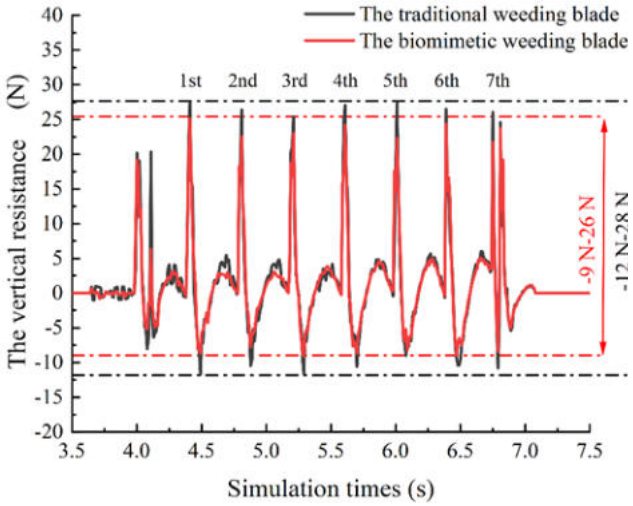


Fig. 13 – Vertical resistance of blades

During the simulation, the weeding blade was moved at a speed of 0.3 m·s-1 and rotated at 150 rpm, resulting in ten cycles of entering and leaving the ground. As illustrated in Figure 12, starting from the 3.46 s mark, the weeding blade entered the soil every 0.4 s, resulting in ten successive periodic variations. However, only seven of these variations in resistance were continuous. By calculating the average horizontal resistance value, it was found that the traditional blades had an average value of 8.17 N, while the bionic blades had an average value of 7.01 N. As a result, the bionic blades showed a reduction in horizontal resistance of approximately 14.19%. After reaching the peak resistance value, the angle between the blade and the horizontal surface gradually decreases. Consequently, the soil pressure in the horizontal component also gradually decreases, leading to a decrease in the horizontal resistance until it reaches 0 N. Meanwhile, the force in the vertical direction also reached its peak value. The variation in vertical resistance over the simulation time is shown in Fig. 13.

As depicted in Fig. 13, at this stage, the vertical resistance observed is the result of the weeding blades throwing off the soil, as the angle between the weeding blade and the horizontal surface becomes negative. Both types of resistance are influenced by similar forces, primarily the shear resistance of the soil, gravity, and

friction. Consequently, they exhibit similar fluctuations, increasing and decreasing in a synchronized manner. In addition, positive values indicate the reaction force of the soil on the blade, while negative values represent the resistance caused by the gravity and adhesion of the soil. The average vertical resistance surpasses the average horizontal resistance, highlighting that the primary resistance faced by the weeding wheel during the weeding process is vertical. The maximum vertical force recorded for the traditional weeding blade was 31.06 N, while the bionic weeding blade was 35.58 N. Additionally, the average vertical resistance in the forward direction was 11.90 N for the traditional blade and 12.75 N for the bionic blade, while the vertical resistance in the backward direction was 8.7 N.

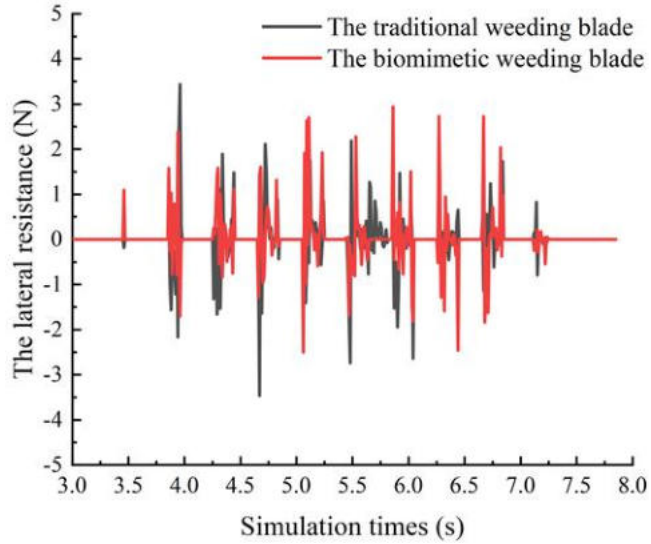


Fig. 14 – Lateral resistance of the blades

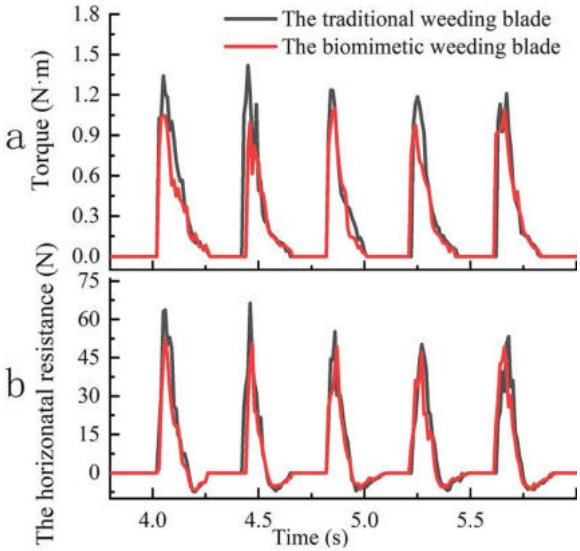


Fig.15 – Soil bin test result curve

Fig. 14 displays the lateral force diagram of the weeding blade. It is evident that lateral resistance also exhibits ten-fold variations. However, the maximum lateral resistance for the traditional weeding blade was 3.46 N, whereas, for the biomimetic weeding blade, it was 3.39 N. The average lateral resistance for the traditional weeding blade was 0.582 N, and for the bionic weeding blade, it was 0.585 N. The lateral resistance of the weeding blade primarily arises from the small amount of soil present and the friction and lateral pressure exerted by the soil during blade movement. Consequently, the lateral resistance values are small and remain consistent.

Overall, the weeding blade experiences two main types of resistance during operation: vertical resistance and horizontal resistance. The magnitude of both depends on the depth of blade penetration and the angle formed with the horizontal surface, with deeper penetration and smaller angles resulting in increased resistance. When comparing the two blade types, the average horizontal resistance of the biomimetic weeding blade was 14.19% lower than that of the traditional blade. The difference in vertical resistance was relatively small, at 11.90 N and 12.75 N, respectively.

Soil bin experiment

During weed control, the performance of different weed blades can be evaluated by comparing their torque. The torque of a weed blade indicates the amount of power required and is directly proportional to the resistance encountered during penetration.

Fig. 15(a) shows the soil bin test torque results comparing the traditional weeding blade and the biomimetic weeding blade. The eight obvious fluctuations in Figure 15(a) represent the eight times that the weeding blade cut the soil. Each torque fluctuation has a sudden rise stage, after reaching the peak, there is a fluctuating decline to 0 N. On the whole, individual weeding blade torque consumption was low on average, and the bionic weeding blade was always lower than the traditional weeding blade. The simulation of the weed blade revealed a significant difference between the two types of blades, primarily in terms of horizontal resistance, while the vertical and lateral resistances were similar to each other. Fig. 15(b) presents the variation in horizontal resistance between the two blades. In Fig. 15(b), the change in horizontal resistance follows the same trend as the change in torque in Fig. 15(a).

As shown in Table 3, the average torque value for the traditional weeding blade was 0.2097 N·m, while the average torque value for the biomimetic weeding blade was 0.1782 N·m, representing a 15.02% reduction in average torque. The total torque applied to the weeding wheel is the sum of the torques exerted by each blade on the weeding wheel. Therefore, the biomimetic weeding blade performs better in terms of average torque.

Summing up, it is known that the average horizontal resistance of the bionic weeding blade was reduced by 14.99% compared to the traditional weeding blade and 15.02% in average torque. Thus, the bionic weeding blade outperforms the traditional weeding blade in terms of both torque and resistance reduction. Additionally, in terms of horizontal resistance reduction and torque reduction, the results of the soil bin test and simulation experiment were consistent and the error was within the controllable range.

Table 3

The test result of torque and horizontal resistance in the soil bin

No. of test	Average horizontal resistance of traditional weeding blade /N	Average horizontal resistance of biomimetic weeding blade / N	Average torque of traditional weeding blade /N·m	Average torque of biomimetic weeding blade / N·m
The 1st	15.85 N	13.54 N	0.2033 N·m	0.1747 N·m
The 2nd	15.17 N	12.96 N	0.2056 N·m	0.1760 N·m
The 3rd	17.68 N	14.90 N	0.2202 N·m	0.1840 N·m
Average values	16.24 N	13.80 N	0.2097 N·m	0.1782 N·m

CONCLUSIONS

The forelimbs of the cicada nymphs were observed and photographed using a microscope to capture its sawtooth structure. The image processing technique was employed to extract the contour curve of the sawtooth structure, which was then fitted by using Origin2021. The fitted function underwent analysis of its second-order derivatives and curvature. The resulting contour curve, referred to as D, was chosen as the basis for the bionic sawtooth. Subsequently, a 3D model of the bionic weeding blade was designed.

The basic parameters of the soil in Ningguo City's Qianhu plantation were determined. To simulate the sandy loam soil found in Ningguo City, situated in the hilly mountainous region of southern Anhui, a simulation model was established. The DEM simulation employed the Hertz-Mindlin contact model with JKR as the soil contact model.

Weeding blade simulation tests were conducted to compare the performance of the bionic weeding blade and the traditional weeding blade. The simulations revealed that the bionic weeding blade required 14.95% less torque than the traditional weeding blade. The difference between the two types of blades depended on the depth of penetration into the soil and the angle between the blades and the horizontal plane. Deeper penetration and smaller angles resulted in increased horizontal and vertical resistance. The bionic weeding blade demonstrated an average reduction of 14.19% in horizontal resistance compared to the traditional weeding blade under specific conditions.

Comparative soil trough tests were performed using the weed blade to further evaluate its performance. The results of these tests confirmed the trend observed in the simulation tests. The average torque applied to the bionic weeding blade was lower than that of the traditional weeding blade, showing a reduction of 15.02%. The horizontal resistance showed a reduction of 14.99%.

ACKNOWLEDGEMENT

The authors were supported by Anhui Provincial Natural Science Foundation (2308085ME160).

REFERENCES

[1] Chang, Z., Liu, W., Tong, J., Guo, L., Xie, H., Yang, X., Mu, H., Chen, D. (2016). Design and experiments of biomimetic stubble cutter. *Journal of Bionic Engineering*, Vol.13, Iss.2, pp. 335-343, Jilin/China.

[2] Chen, F., Tu, L., Liu, D., Ma, J., Luo, Y. (2021). Chemical constituents from the roots of *Peucedanum praeruptorum* Dunn and their chemotaxonomic significance. *Biochemical Systematics and Ecology,* Vol. 99, No. 104355, Nanchang/China.

[3] Cao, C., Xiang, W., Luo, K., Wu Z., Zhang, X., Qin, K. (2023). Design and experiment of *Radix Peucedani* weeding machine separating weeds and soil with combination of throwing and pushing (抛推组合式草土分离前胡除草机设计与试验). *Transactions of the Chinese Society for Agricultural Machinery*, Vol. 54, Iss. 03, pp. 106-114, Hefei/China.

[4] Fishkis, O., Koch, H. (2023). Effect of mechanical weeding on soil erosion and earthworm abundance in sugar beet (Beta vulgaris L.). *Soil and Tillage Research*. Vol. 225, No.105548, Germany.
[5] Liu, C., Yang, K., Chen, Y., Gong, H., Feng, X., Tang, Z., Fu, D., Qi, L. (2023). Benefits of mechanical weeding for weed control, rice growth characteristics and yield in paddy fields. *Field Crops Research*, Vol. 293, No. 108852, Guangzhou/China.
[6] Matin, M.A., Fielke, J.M., Desbiolles, J. (2014). Furrow parameters in rotary strip-tillage: Effect of blade geometry and rotary speed. *Biosystems Engineering*, Vol. 118, pp. 7-15, Australia.
[7] Matin, M.A., Fielke, J.M., Desbiolles, J. (2015). Torque and energy characteristics for strip-tillage cultivation when cutting furrows using three designs of rotary blade. *Biosystems Engineering*, Vol. 129, pp. 329-340, Australia.
[8] Mayerová, M., Madaras, M., Soukup, J. (2018). Effect of chemical weed control on crop yields in different crop rotations in a long-term field trial. *Crop Protection*, Vol. 114, pp. 215-222, Czech.
[9] Matin, M.A., Hossain, M.I., Gathala, M.K., Timsina, J., Krupnik, T.J. (2020). Optimal design and setting of rotary strip-tiller blades to intensify dry season cropping in Asian wet clay soil conditions. *Soil and Tillage Research*, Vol. 207, No. 104854, Bangladesh.
[10] Richard, D., Leimbrock-Rosch, L., Keßler, S., Stoll, E., Zimmer, S. (2023). Soybean Yield Response to Different Mechanical Weed Control Methods in Organic Agriculture in Luxembourg. *SSRN Electronic Journal*, Vol. 147, No. 126842, Germany.
[11] Smith, J.J., Hasiotis, S.T. (2008). Traces and burrowing behaviors of the cicada nymph Cicadetta calliope: Neoichnology and paleoecological significance of extant soil-dwelling insects. *Society for Sedimentary Geology*, Vol. 23, pp. 503-513, USA.
[12] Wang, J., Niu, C., Zhang, C., Wei, C., Chen, Z. (2011). Design and experiment of 3ZS-150 paddy weeding-cultivating machine (3ZS-150 型水稻中耕除草机设计与试验). *Transactions of the Chinese Society for Agricultural Machinery*, Vol. 42, Iss. 02, pp. 75-79, Harbin/China.
[13] Wang, J., Wang, J., Yan, D., Tang, H., Zhou, W. (2017). Design and experiment of 3SCJ-2 type row weeding machine for paddy field (3SCJ-2 型水田行间除草机设计与试验). *Transactions of the Chinese Society for Agricultural Machinery*, Vol.48,Iss. 06, pp. 71-78, Harbin/China.
[14] Wu, Z., Wang, X., Liu, D., Xie, F., Ashwehmbom, L.G., Zhang, Z., Tang, Q. (2021). Calibration of discrete element parameters and experimental verification for modelling subsurface soils. *Biosystems Engineering*, Vol. 212, pp. 215-227, Hunan/China.
[15] Wang, J., Ma, X., Tang, H., Tang, H., Wang, Q., Wu, Y., Zhang, Z. (2021). Design and experiment of curved-tooth oblique type inter-row weeding device for paddy field (曲面轮齿斜置式稻田行间除草装置设计与试验). *Transactions of the Chinese Society for Agricultural Machinery*, Vol. 52, Iss. 04, pp.91-100, Harbin/China.
[16] Zeng, D. (1995). Soil Machine Dynamics. China: *Bejing Science and Technology Publishing Co.,Ltd*, pp. 414-438, Beijing/China.
[17] Zhang, Y., Tian, L., Cao, C., Zhu, C., Qin, K., Ge, J. (2022). Optimization and validation of blade parameters for inter-row weeding wheel in paddy fields. *Frontiers in Plant Science*, Vol. 13, No. 1003471, Hefei/China.
[18] Zhang, Z., Xue, H., Wang, Y., Xie, K., Deng, Y. (2022). Design and experiment Panax notoginseng bionic excavating shovel based on EDEM (基于离散元法的三七仿生挖掘铲设计与试验). *Transactions of the Chinese Society for Agricultural Machinery*, Vol. 53, Iss. 5, pp. 100-111, Kunming/China.
[19] Zhang, S., Zhao, H., Wang, X., Dong, J., Zhao, P., Yang, F., Chen, X., Liu, F., Huang, Y. (2023). Discrete element modeling and shear properties of the maize stubble-soil complex. *Comput. Electron. Agric.*, Vol. 204, No.107519, Yangling/China.

RESEARCH ON OPTIMIZATION OF VIBRATION EAR PICKING PARAMETERS BASED ON CORN PLANT VIBRATION RESPONSE CHARACTERISTICS AND FINITE ELEMENT ANALYSIS

/

基于玉米植株振动响应特性与有限元分析的激振摘穗参数优化研究

Pengxuan GUAN[1,2,3], Yipeng CUI[1,2,3], Jianning YIN[1,2,3], Zehao ZHA[1,2,3], Qiming YU[1,2,3], Duanyang GENG[1,2,3*)]

[1)] College of Agricultural Engineering and Food Science, Shandong University of Technology, Zibo 255000, China;

[2)] Institute of Modern Agricultural Equipment, Shandong University of Technology, Zibo255091, China

[3)] Shandong Provincial Key Laboratory of Smart Agricultural Technology and Intelligent Agricultural Machinery and Equipment for Field Crops, Shandong University of Technology, Zibo255091, China;

Tel: +86-13668641238; E-mail: dygxt@sdut.edu.cn

DOI: https://doi.org/10.35633/inmateh-76-83

Keywords: *Finite element analysis; Vibration ear-picking; Vibration characteristics; Maize plant*

ABSTRACT

To reduce maize ear damage caused by ear-picking rollers during maize harvesting and to improve ear-picking efficiency, this study investigates the vibration response characteristics of maize plants and conducts comprehensive experimental research. Current research on vibration ear-picking predominantly conducts on the structural design and parameter optimization of ear-picking mechanisms, with comparatively limited attention given to the dynamic response patterns of maize plants under vibrational excitation. Therefore, it is essential to conduct an in-depth investigation into the mechanical behavior and vibration response characteristics of maize plants during the maize ear detachment process. In this study, the mechanical behavior of ear-bearing maize plants during the vibration ear-picking process was first analyzed, and a theoretical model was established. The optimal acceleration range for low-damage and high-efficiency ear-plant separation was identified, and the key parameters affecting ear-picking performance—namely amplitude, frequency, and clamping position—were determined. Based on the slope algorithm and response surface methodology, combined with finite element analysis, this study quantitatively evaluates the influence of various vibration parameters on the acceleration score S_z at the ear-bearing region. A predictive model was established using a Box-Behnken experimental design, identifying the optimal parameter combination as an amplitude of 8 mm, a frequency of 18 Hz, and a clamping position of 106 mm. This model enables the quantitative analysis of excitation forces acting on the ear during the ear-picking process and provides a theoretical foundation for optimizing the structure of the excitation waveform, thereby offering valuable guidance for the subsequent optimization and design of vibration ear-picking systems.

摘要

为了减少玉米收获过程摘穗辊对果穗的啃伤，提升摘穗效果，本研究以玉米植株的振动响应特性为切入点，开展了相关试验研究。当前关于激振摘穗的研究多聚焦于摘穗机构结构与参数优化，而对玉米植株在激振条件下的动力学响应规律关注较少，故需深入探讨玉米植株在果穗分离过程中的力学行为变化规则与振动响应特性。本研究首先分析了激振摘穗过程中带穗植株的力学行为变化规则，建立了理论模型，明确了果穗-植株分离低损高效分离的加速度范围，确定了影响摘穗效果的关键参数：振幅、频率和夹持位置。基于斜率算法与响应面法，结合有限元分析，量化分析了不同激振参数对结穗处加速度得分 S_z 的影响。根据 Box-Behnken 设计试验建立预测模型，确定最优参数组合为振幅 8mm、频率 18hz、夹持位置 106mm。该模型能定量分析摘穗过程中果穗的激振力，用于优化激振波结构，为后续激振摘穗的优化设计提供理论指导。

INTRODUCTION

Maize harvesting is a critical stage in the production process, and the quality of harvesting directly affects both the yield and the quality of maize *(Jun et al., 2024; Shulun et al. 2024)*. Maize ear damage not only affects the appearance quality of maize but also leads to yield reduction due to physical injury and increases the risk of mold growth during storage, thus becoming a major bottleneck that limits improvements in harvest quality *(Qihuan et al., 2025; Shulun et al., 2024)*. Therefore, reducing ear damage has become a critical measure for enhancing maize harvest quality.

To address the issue of maize ear damage caused by ear-picking rollers during the harvesting process, expert scholars have conducted extensive research *(Qiankun et al., 2020; Shanglong et al., 2023)*. For example, Tong Jin employed a bionic ear-picking roller combined with differential loading, which altered the loading direction and contact area during the ear-stalk separation process, thereby reducing maize ear damage during harvesting *(Feng, 2007)*. Hongyu Yan developed a vertical roller maize ear-picking technology, which allows the detached maize ears to leave the ear-picking rollers and thereby prevents secondary damage to the maize ears, effectively improving the overall harvest quality of maize *(Hongyu et al., 2009)*. Building upon the foundation of vertical roller ear-picking technology, our research team has developed a vibration ear-picking technique, in which high-frequency vibrations are applied to the maize stalk during the clamping and conveying process to achieve ear-stalk separation *(Xiaoqi et al., 2020)*. This approach avoids direct contact between the maize ear and the picking mechanism, effectively reducing maize ear damage, and has been successfully promoted and applied in companies such as Shandong DIMA and Jindafeng. However, it has been observed in practical production that excessive inertial force applied to the maize ear can result in premature breakage of maize plants and, in severe cases, lead to header blockages *(Wenxue et al., 2024; Ranbing et al., 2021)*. Conversely, insufficient inertial force may cause difficulties in separating the maize ear from the plant, thereby hindering the effectiveness of vibration ear-picking *(Zhang et al., 2022)*.Therefore, to improve ear-picking performance, it is necessary to accurately understand the variation of inertial forces acting on the maize ear during the vibration process and their relationship with operational parameters. Given that these inertial forces are directly dependent on the vibration response characteristics of maize plants under vibrational excitation, conducting research on the dynamic behavior of maize plants in such conditions is of great significance for revealing the mechanism of vibration ear-picking and guiding parameter optimization to enhance harvest efficiency and quality.

The separation of the maize ear from the plant during the vibration ear-picking process can be described as occurring when the inertial force generated by the acceleration of the maize ear exceeds the bonding force between the maize ear and the peduncle, thereby enabling effective detachment of the maize ear from the plant. Current research on vibration ear-picking primarily focuses on the structural design and parameter optimization of the ear-picking mechanism, while the dynamic response patterns of maize plants under vibrational excitation have received comparatively little attention *(Xiaoqi et al., 2020)*. This is mainly due to the complexity of effective excitation force transmission and the dynamic response characteristics of the plant, making it difficult to accurately capture the response patterns of maize plants using conventional experimental methods alone. To address this issue, the finite element analysis method provides an effective means of simulating the response patterns of maize plants to various excitation parameters. In recent years, this method, owing to its outstanding capability in simulating the dynamic behavior of complex structures, has been widely applied to the study of vibration responses and mechanical harvesting processes in agricultural and forestry crops *(Pereira et al., 2025; Delin et al., 2022)*. Longsheng Fu utilized finite element analysis software to investigate the vibration-based harvesting mechanism of sea buckthorn *(Longsheng et al., 2016)*. Guofeng Zhang optimized the vibration parameters for the mechanical harvesting of camellia fruit by integrating finite element analysis with dynamic modeling *(Kaizhan et al., 2019)*. Linyun Xu employed the finite element method to study the effects of ginkgo canopy structure on vibration response characteristics *(Xuan et al., 2021)*. However, finite element analysis studies focusing on the dynamic response patterns of maize plants under vibrational excitation remain limited.

In summary, although vibration ear-picking technology has already been applied in production, issues such as plant breakage and header blockages persist. Therefore, it is essential to further analyze the vibration response characteristics of maize plants and optimize the key parameters of the vibration ear-picking process. In this study, a theoretical analysis of the vibration ear-picking process was initially conducted to identify the key parameters influencing ear harvest quality and efficiency. Subsequently, finite element simulation software was utilized to numerically investigate the vibration response characteristics of maize plants, thereby determining the optimal ranges of critical operational parameters. Finally, an orthogonal experiment was performed to establish the optimal parameter combination, which was further validated through bench testing, confirming the accuracy and practical applicability of the research findings.

MATERIALS AND METHODS

Working Principle of Vibration Ear-Picking

The Overall Structure

As shown in Fig. 1(a), the vibration ear-picking header primarily consists of a crop divider, crop press

bar, ear-picking mechanism, conveyor belt, gathering chain and cutter bar. Its core component is the ear-picking roller assembly, which features symmetrically shaped, non-equilateral polygonal rollers (non-equilateral octagonal rollers), as shown in Fig. 1(b). During operation, ear-bearing maize plants are conveyed rearward under the clamping action of the rotating ear-picking roller assembly. In this process, the irregular polygonal edges of the rollers impart periodic excitation forces to the ear-bearing maize plants, inducing high-frequency lateral oscillations, as illustrated in Fig. 1(c).During the reciprocating oscillation, when the inertial force exerted on the maize ear exceeds the bonding force between the maize ear and the peduncle, the maize ear is separated from the stalk, thereby achieving effective detachment of the maize ear from the plant, as shown in Fig. 1(d).

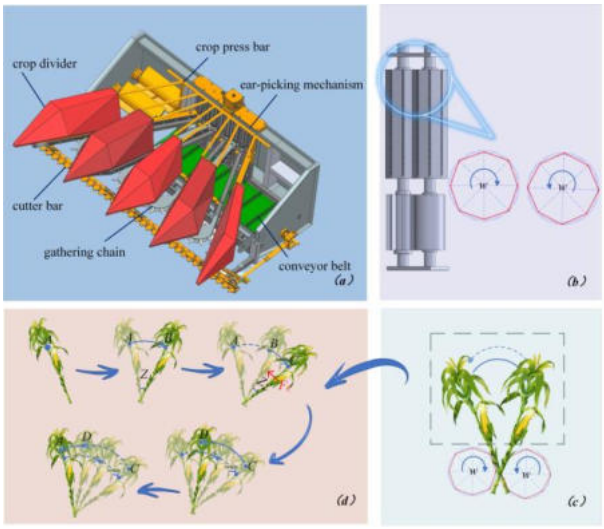


Fig. 1 - Schematic diagrams of harvesting principle

(a) the vibration ear-picking header; (b) the ear-picking mechanism; (c) the geometry and working principle of the ear-picking roller; and (d) the movement of the maize plant (the solid line represents the displacement during forward travel, while the dashed line denotes the displacement at the corresponding step).

Theoretical Model

Fig. 1(d) presents a complete cycle of the reciprocating motion of the maize plant during the vibration ear-picking process. Under the action of the ear-picking rollers, the ear-bearing plant undergoes simple harmonic vibration, which can be described by the following kinematic equation:

$$\theta = Z\sin(\omega t + \phi) \tag{1}$$

Under the influence of the excitation waveform, the ear-bearing maize plant accelerates from point A to point B. When the direction of vibration reverses, the velocity of the maize ear rapidly drops to zero due to inertia, and the plant moves from point B to point C. The process from point C to point D and back to point A is the exact reverse of the previous motion. Since the motion is symmetrical within a single cycle, only the dynamics within a half-cycle are analyzed.

Since the angle of motion differs during the acceleration and deceleration phases, when the maize ear is initially at rest, the equation of motion for the maize ear during the phase from A to B is as follows:

$$\theta_{AB} = Z_1\sin(\omega_1 t) \tag{2}$$

where, θ_{AB} is the angular displacement of the maize ear from point A to point B, Z_1 is the maximum angular amplitude during this phase, and w_1 is the angular velocity during the acceleration from A to B. The equation of motion for the maize ear during the phase from point B to point C is as follows:

$$\theta_{BC} = Z2\sin\left[\omega_2\left(t - \frac{\pi}{2\omega_1}\right)\right] \tag{3}$$

where, θ_{BC} is the angular displacement of the maize ear from point B to point C, Z_2 is the maximum angular amplitude during this phase, and w_2 is the angular frequency during the rapid attenuation phase from B to C.

According to the Eq. (1), the angular acceleration of the maize ear is given by:

$$\varepsilon = \frac{d\theta}{dt} = \omega Z\cos(\omega t + \phi) \tag{4}$$

Therefore, the maximum angular acceleration of the maize ear is:

$$\varepsilon_{\max} = \omega Z \tag{5}$$

According to the theorem of simple harmonic motion, acceleration attains its maximum value at the endpoints. Specifically, at point C, the maximum acceleration is acting on the maize ear. The maximum acceleration of the maize ear is:

$$a_{\max} = r\varepsilon_{\max} = r\omega_2 Z2 \quad (6)$$

Let β be defined as the ratio of the angular amplitude Z_2 during the deceleration phase to the total angular amplitude Z from point A to point C, as expressed by:

$$\beta = \frac{Z2}{Z} \quad (7)$$

When the motion period T = 2π/ω=1/f, according to Eq. (6), the maximum acceleration of the maize ear, a_{max}, can be expressed as:

$$a_{\max} = 2\pi \mathrm{r}\, fZ\beta \quad (8)$$

where, r is the distance from the clamping position to the maize ear, f is the vibration frequency of the ear-bearing plant, Z is the angular amplitude of the maize ear from point A to point C, and β is the ratio of the angular amplitude Z_2 during the deceleration phase to the total angular amplitude Z from point A to point C.

According to Newton's second law and Eq. (8), the maximum force acting on the maize ear during the motion is given by:

$$F_C = ma_{\max} = 2\pi \,\mathrm{r}\, m\, f\, Z\, \beta \quad (9)$$

where m is the mass of the maize ear, β is the ratio of the angular amplitude Z_2 during the deceleration phase to the total angular amplitude Z from point A to point C, Z is the angular amplitude of the maize ear from point A to point C, f is the vibration frequency of the ear-bearing plant, and r is the distance from the clamping position to the maize ear.

Based on the above theoretical analysis, it can be concluded that the primary factors influencing the excitation force are the vibration frequency f, the vibration amplitude Z, and the clamping position r.

Development of a Simplified Maize Plant Model

Material Properties of the Maize Plant

To investigate the vibration response characteristics of maize plants, the physical parameters of the plants were measured. In this study, the widely cultivated maize variety "Xianyu 335" from Shandong Province was selected as the experimental subject.

The measurement methods were as follows: the instruments used included a tape measure, ruler, vernier caliper, high-precision electronic balance, push-pull force gauge, and texture analyzer. The measured parameters encompassed the fundamental structural characteristics of the maize plant and the maize ear, including plant height, stem diameter, plant breaking force, ear-bearing height, maize ear mass, and peduncle bonding force.

Table 1

Physical Parameters of the Maize Plant

	Plant height (mm)	Stem Diameter (mm)	Breaking Force (N)	Ear-Bearing Height (mm)	Maize Ear Mass (g)	Peduncle Bonding Force (N)
Min	2495	19.2	89	975	205	48
Max	2663	21.4	136	1035	263	60
Mean	2500.42	20.24	103.5	1026.56	243.39	53.5

Measurement of Material Properties

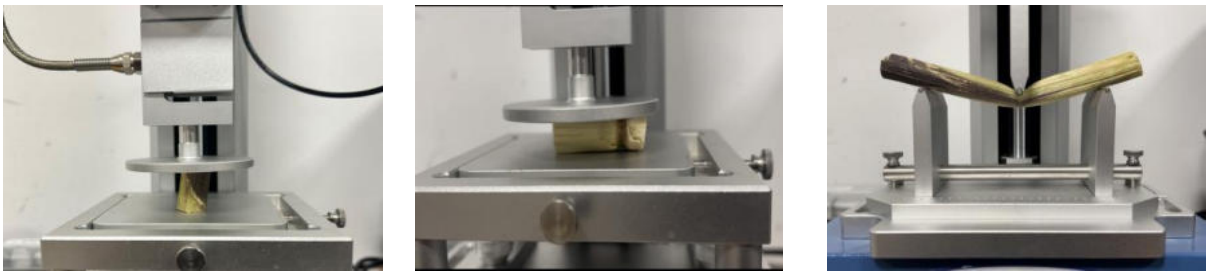
The density of maize plants was determined using the water displacement method *(Zijie et al., 2022)*. Specifically, the plant volume was measured by displacement, and the mass was measured using an electronic balance with a precision of 0.01 g. The density was then calculated as the ratio of mass to volume. To improve measurement accuracy, the collected plant samples were divided into ten groups, with the volume and corresponding mass of each group measured separately. The average value of the calculated densities was taken, resulting in an average density of 1003 kg/m³.

To determine additional engineering parameters of the maize plant, the de-eared plant was simplified as a cylindrical structure. The center of the cylinder's base was defined as the origin of the coordinate system, with the base lying on the X-Y plane and the plant's axial direction aligned with the Z-axis, thereby constructing a geometric model of the plant in the X-Y-Z coordinate system. In this model, it was assumed that the material was uniformly distributed and exhibited consistent mechanical properties throughout.

Thus, the simplified maize plant could be regarded as an orthotropic material, characterized by nine engineering parameters: the radial elastic modulus E_x and E_y, axial elastic modulus E_z, radial shear modulus G_{yz} and G_{xz}, axial shear modulus G_{xy}, Poisson's ratio β_{xy}, β_{yz} and β_{xz}), and the relationship for the engineering parameters of orthotropic materials is expressed using Eq. (10)

$$\begin{cases} E_x = E_y \\ G_{yz} = G_{xz} \\ \beta_{yz} = \beta_{xz} \\ G_{xy} = \dfrac{E_x}{2(1+\beta_{xy})} \end{cases} \tag{10}$$

To obtain the engineering parameters of the maize plant, compression and three-point bending tests were conducted using a texture analyzer (Fig. 2), with the compression and bending head speeds controlled at 3 mm/s and 5 mm/s, respectively.



（a） （b） （c）

Fig. 2 - Measurement of engineering parameters using a texture analyzer

According to the reference *(Jian et al., 2021)*, the elastic modulus of the sample can be calculated as follows:

The compressive stress of the tested material is calculated as:

$$\sigma = \frac{F}{A_0} \tag{11}$$

The strain equation of the tested material is given by:

$$\varepsilon = \frac{\Delta l}{l_0} \tag{12}$$

Thus, the elastic modulus of the tested material is:

$$E = \frac{\sigma}{\varepsilon} = \frac{F}{\Delta l} \cdot \frac{l_0}{A_0} = \frac{k \cdot l_0}{A_0} \tag{13}$$

where F is the applied load (N), A_o is the cross-sectional area of the plant (mm^2), σ is the stress (MPa), ε is the strain, Δl is the deformation length(mm), l_o is the initial length of the sample(mm), and k is the slope of the load-displacement curve (N/mm).

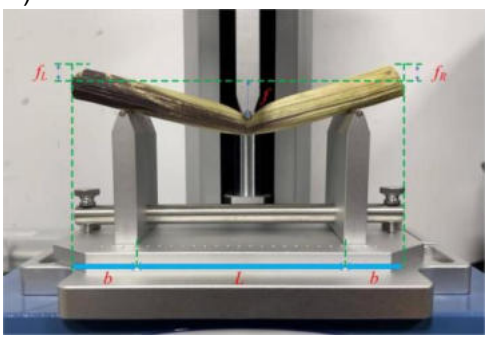


Fig. 3 - Schematic diagram of the three-point bending shear test and parameter annotations.

The three-point bending test was used to calculate the radial shear modulus (Fig. 3) *(Jian et al., 2021)*. The radial shear modulus of the sample can be determined using Eq. s (15) to (16).

$$f_1 = \frac{f_L + f_R}{2} \quad (14)$$

$$H = \frac{\Delta p \cdot L^4}{f - \frac{f_1 \cdot L^3}{b}} \quad (15)$$

$$G_{yz} = \frac{4H}{\pi D^2} \quad (16)$$

Where $\triangle p$ is the load increment during the elastic deformation stage (N); f_i is the extension deviation increment (mm); L is the span between the supports (mm); b is the extension length (mm); f is the midspan deflection increment (mm); H is the shear stiffness (N/mm); D is the diameter of the tested sample (mm) and f_L and f_R are the extension deflection increments on the left and right sides, respectively (mm).

According to the relevant literature, the Poisson's ratio β_{xy} of the isotropic plane is defined as 0.3 (*Zhouzhou et al., 2024*). The relationship between the Poisson's ratio β_{xy} of the isotropic plane and the Poisson's ratio β_{yz} of the orthotropic plane is expressed by Eq. (17).

$$\beta_{yz} < \frac{1}{2} \cdot \beta_{xy} \cdot \frac{E_x}{E_z} \quad (17)$$

Although most existing studies treat maize stalks as having identical material properties, this approach may not be sufficiently accurate for the present study and could compromise the reliability of the simulation results. Therefore, axial compression, radial compression, and three-point bending shear tests were conducted on maize plants (Fig.2). Based on the aforementioned measurement methods, the nine engineering parameters required for simulation were calculated, as summarized in Table 2.

Table2

Material Property Parameters of the Maize Plant

E_x/MPa	E_y/MPa	E_z/MPa	G_{xy}/MPa	G_{xz}/MPa	G_{yz}/MPa	β_{xy}	β_{xz}	β_{yz}	ρ(kg/m^3)
373.58	373.58	5773.6	145.5	2886.8	2886.8	0.3	0.019	0.019	1003

Vibration Response Simulation

To determine the acceleration response of the maize ear under specific operating conditions, this study employed 3D modeling software and finite element analysis software (SolidWorks/Ansys) to conduct numerical simulations of the vibration response characteristics of maize plants. Specifically, a geometric model of the maize plant was first created using SolidWorks, and the relevant structural parameters were subsequently imported into Ansys for dynamic simulation analysis, thereby obtaining the vibration response characteristics of the maize stalk.

In this study, finite element analysis software (*Ansys Workbench, 2021-R1*) was used to perform dynamic simulations in order to replicate the kinematic behavior of actual maize plants under identical conditions. During the simulation process, the maize plant model was first established in SolidWorks (2020) based on the average geometric dimensions provided in Table1. Subsequently, the model was imported into the finite element analysis software for mesh generation, with the element size set to 10 mm, and the material properties obtained from Table 2 were assigned to the model accordingly. Since the excitation force is transmitted to the maize ear through the plant, this study focuses solely on analyzing the vibration acceleration at the measurement points near the ear-bearing position. Considering the inherent variability in maize ear-bearing height, to enhance the accuracy of the simulation results, seven measurement points were evenly distributed along the plant's axial direction at 10 mm intervals around the ear-bearing region. The response acceleration at each measurement point was extracted using acceleration probes in the post-processing module, as shown in Fig. 4.

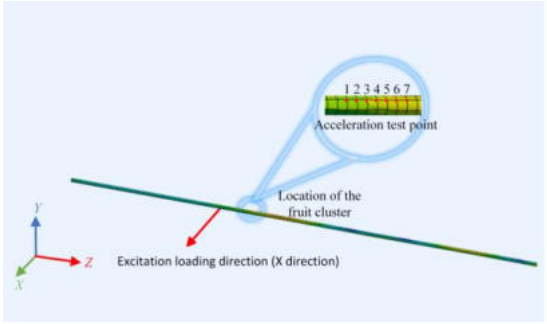


Fig. 4 - Simulation model of the maize plant and distribution of measurement points

The simulation conditions illustrated in Figure 4 are as follows: to study the effect of different clamping positions on the acceleration response at the ear-bearing region, the excitation amplitude and frequency were kept constant while only the position of the applied vibration load was varied, thereby analyzing the relationship between clamping position and acceleration response. When investigating the effects of different amplitudes and frequencies on the acceleration response at the ear-bearing region, the clamping position was fixed. The excitation amplitude and frequency were adjusted by modifying the displacement and frequency settings in the harmonic response analysis module. A periodic sinusoidal excitation force was applied along the X-axis to the clamping region of the plant model. The acceleration responses at the ear-bearing region under various amplitudes and frequencies were then obtained, allowing the identification of the variation patterns between excitation frequency, amplitude, and acceleration response.

To evaluate the inertial forces acting on the maize ear under different excitation parameters and their effects on the separation performance, the harmonic response analysis module was employed to simulate the acceleration response characteristics of the maize plant under various combinations of excitation parameters. Based on the degree of influence of each parameter on maize ear–stalk separation, amplitude, frequency, and clamping position were selected as the experimental factors to investigate their effects on the acceleration score index Sz. For amplitude, if it is too small, the resulting acceleration may be insufficient to achieve maize ear–stalk separation; conversely, an excessively large amplitude may cause premature breakage of the maize plant. Based on relevant studies *(Duanayng et al., 2019)*, the amplitude range was selected between 5 mm and 15 mm. For frequency, excessively low values may result in an insignificant excitation effect, while excessively high values could induce maize plant fatigue failure. Based on relevant studies *(Duanyang et al., 2017)*, the frequency range was set between 16 Hz and 20 Hz. The clamping position was optimized within the range of 50 mm to 170 mm based on the team's previous research *(Qian et al., 2018)*. The levels of the experimental factors are shown in Table 2.

Table 2

Factors and levels of experiment

Level	Factor		
	Amplitude (mm)	Frequency (Hz)	Clamping position (mm)
1	5	16	50
2	7.5	17	80
3	10	18	110
4	12.5	19	140
5	15	20	170

This section established an accurate finite element model of the maize plant based on its actual geometric structure and material properties. Harmonic response analysis was conducted to simulate the acceleration characteristics of the ear-bearing region under varying amplitude, frequency, and clamping position. The results provide essential data support for the subsequent development of an evaluation index system centered on ear acceleration.

Evaluation Index

Considering that insufficient acceleration of the maize ear under excitation may hinder effective ear-stalk separation, while excessive acceleration may lead to premature plant breakage-resulting not only in the failure of ear-stalk separation but also in potential header blockages—it is essential to optimize the vibration parameters for the ear-picking process. Given that the elastic modulus calculation in Eq. (13) involves the load-displacement slope k, a slope-based scoring algorithm was introduced to evaluate and rank the acceleration at each measurement point *(Peng et al., 2022)*. In this study, the vibration acceleration at the measurement points near the ear-bearing region was quantified using the scoring method, and the average acceleration score S, across all points was adopted as the evaluation index. Specifically, the difference between the acceleration at each measurement point and the critical acceleration a_{min} (the minimum acceleration required for ear-stalk separation) was used as the basis for determining the score at each measurement point.

Assuming the acceleration required for ear-stalk separation is ai, the acceleration range for ear-stalk separation can be expressed by Eq. (18):

$$\frac{f_a}{m} \le a_i \le \frac{f_b}{m} \tag{18}$$

where:

m is the average mass of the maize ear; f_a is the maximum peduncle bonding force (N);

f_b is the minimum plant breaking force (N);

a_i is the acceleration required for ear-stalk separation (m/s^2).

By substituting the data from Table1 into Eq. (16), the calculated acceleration range that satisfies ear-stalk separation without causing plant breakage is obtained as follows: the minimum acceleration a_{min}=246.52m/s^2 and the maximum acceleration a_{max}=365.67m/s^2.

The specific scoring criteria are illustrated in Fig. 5. For each measurement point near the ear-bearing region, the maximum score was set at 100 points. When the acceleration at a measurement point equals a_{min}, it is considered optimal—achieving ear-stalk separation without causing premature plant breakage—and thus the score for that point is defined as 100 points. If the acceleration is less than a_{min}, the score is assigned as O points. If the acceleration exceeds a_{min}, the score is proportionally reduced based on the degree of exceedance. The average score S_z, across all measurement points is used as the evaluation index to assess the overall vibration effect. The score for each measurement points within the ear-bearing region and the average score S_z, can be calculated using Eq. s (19)-(20), respectively, as follows:

$$S_i = 100 - \frac{(a_i - a_{\min})}{a_{\max} - a_{\min}} \times 100 \quad (19)$$

The vibration acceleration score at each measurement point within the ear-bearing region is calculated according to Eq. (19), and the average score across all measurement points can be expressed as:

$$S_z = \frac{1}{n}\sum_{i=1}^{n} S_i \quad (20)$$

where:

S_i — score of an individual measurement point;

S_z — average score of all measurement points;

a_{max} — maximum allowable separation acceleration (m/s²);

a_i — acceleration at the measurement point to be scored (m/s²);

a_{min} — minimum required separation acceleration (m/s²).

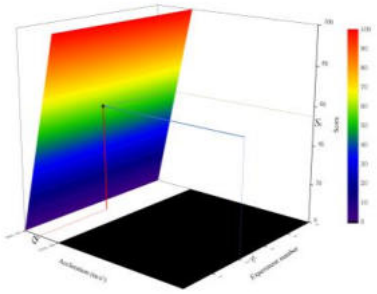


Fig. 5 - Schematic diagram of the slope-based scoring algorithm

Bench verification test

The effectiveness of the optimized parameter combination was verified using an image acquisition platform specifically constructed for the maize vibration ear-picking process. This platform consists of four main components: a test bench, a high-speed camera (X150, Revealer Company), a computer, and a fill light (EF-200, Shanghai Jinbei Company), as shown in Fig. 6. The test bench primarily includes a motor (Model: YE2-100L-2, speed range: 0–2870 r/min), a frequency converter, an ear-picking mechanism, a gathering chain, a crop press plate, and a reciprocating cutter bar. The motor provides the power source for the ear-picking rollers while simultaneously driving the gathering chain.

During the experiment, several maize plants of the "Xianyu 335" variety with similar ear-bearing heights were selected as test materials. To accurately capture the acceleration during ear–stalk separation, the high-speed camera was set to a frame rate of 1000 frames per second, an exposure time of 999 μs, and a resolution of 2560 × 1920 pixels. After starting the test bench, observations continued until the maize ear detached from the plant. The separation acceleration was analyzed using high-speed imaging analysis software (Revealer Company), and the acceleration score was evaluated based on the slope-based scoring algorithm. The experiment was repeated five times.

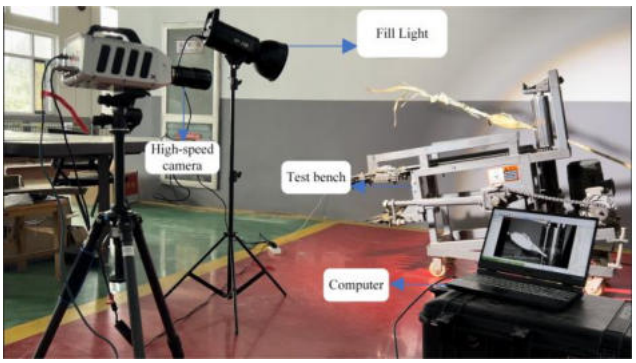


Fig. 6 - Verification Test Setup

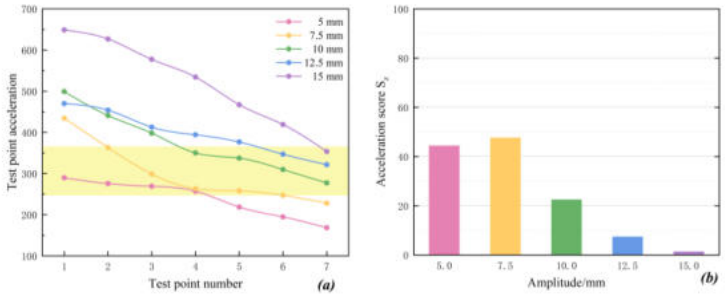
RESULTS

Single-Factor Experimental Analysis

To determine the appropriate level ranges for the orthogonal experiment, single-factor tests were conducted based on the experimental method described in Section 2.4, using the average acceleration score S_z as the performance evaluation criterion to investigate the influence patterns of each factor on the ear-picking performance.

Influence of Amplitude on the Acceleration

The effect of amplitude on acceleration was obtained through experiments, as shown in Fig. 7. As illustrated in Fig. 7(b), the influence of amplitude on the average acceleration score S_z exhibits a trend of first increasing and then decreasing. When the amplitude is less than 7.5 mm, the score S_z increases with the increase in amplitude; however, when the amplitude exceeds 7.5 mm, the score S_z decreases significantly. The underlying reason, as shown in Fig. 7(a), is that at lower amplitudes, the acceleration at some measurement points does not reach the acceleration scoring range, resulting in a lower S_z. As the amplitude increases to 7.5 mm, more measurement points achieve acceleration values within the scoring range, leading to an improvement in S_z and reaching its peak. When the amplitude is further increased, the acceleration at some measurement points exceeds the upper limit of the scoring range, causing a decline in S_z. Considering these results, an amplitude range of 5–10 mm is deemed appropriate for the orthogonal experiment.



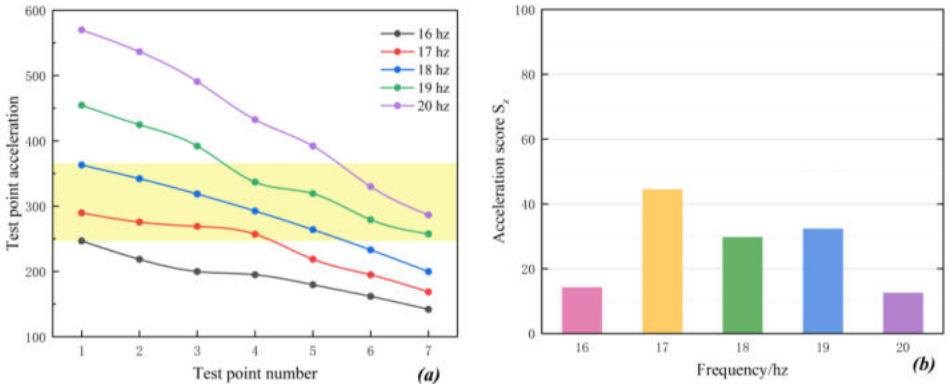
Note: The yellow-shaded area represents the acceleration scoring range.

Fig. 7 - Experimental results for amplitude

(a) acceleration at each measurement point; (b) average acceleration score.

Influence of Frequency on the Acceleration

The effect of frequency on acceleration was obtained through experiments, as shown in Fig. 8. As illustrated in Fig. 8(b), the influence of frequency on the average acceleration score S_z exhibits a trend of first increasing and then decreasing. When the frequency is below 17 Hz, the score S_z increases with rising frequency; however, when the frequency exceeds 17 Hz, the score S_z decreases as the frequency continues to increase. The underlying reason, as shown in Fig. 8(a), is that at lower frequencies, the excitation-induced acceleration is relatively low, causing some measurement points to fall below the acceleration scoring range and resulting in a lower S_z. As the frequency increases, more measurement points enter the acceleration scoring range, thereby leading to an increase in S_z. However, when the frequency further increases, the acceleration at some points significantly deviates from the scoring range, ultimately causing a decline in S_z. Considering these results, a frequency range of 17–19 Hz is considered appropriate for the orthogonal experiment.



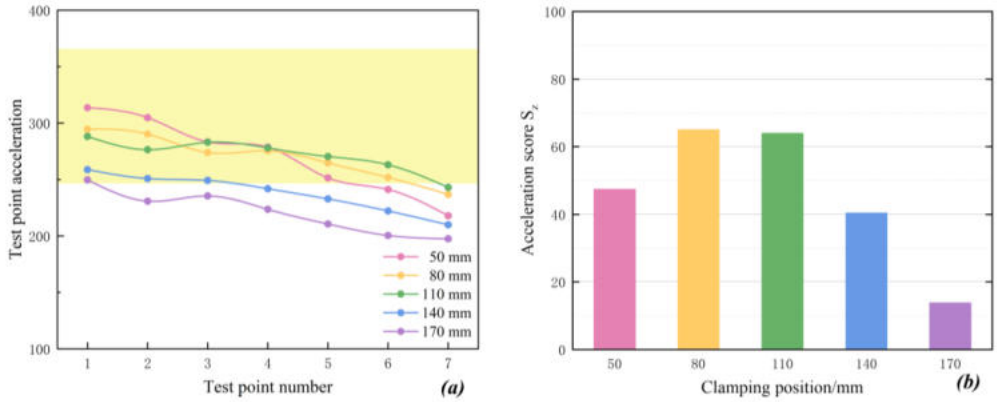
Note: The yellow-shaded area represents the acceleration scoring range.

Fig. 8 - Experimental results for frequency

(a) acceleration at each measurement point; (b) average acceleration score.

Influence of clamping position on the Acceleration

The effect of clamping position on acceleration was obtained through experiments, as shown in Fig. 9. As illustrated in Fig. 9(b), the influence of clamping position on the average acceleration score S_z exhibits a trend of first increasing and then decreasing. When the clamping position is less than 80 mm, the score S_z increases with increasing clamping distance; however, when the clamping position exceeds 80 mm, the score S_z decreases with further increases in clamping distance. The underlying reason, as shown in Fig. 9(a), is that when the clamping position is too close to the maize ear, the transmitted acceleration in the ear-bearing region becomes excessively large, causing some measurement points to deviate significantly from the optimal acceleration a_{min}, thereby reducing the score S_z. Conversely, when the clamping position is too far, the propagation distance of the excitation wave increases, leading to a gradual reduction in acceleration at some points, eventually falling below the scoring range and resulting in a lower S_z. Considering these results, a clamping position range of 50–140 mm is considered appropriate for the orthogonal experiment.



Note: The yellow-shaded area represents the acceleration scoring range.

Fig. 9 - Experimental results for clamping position

(a) acceleration at each measurement point; (b) average acceleration score.

Considering that vibration ear-picking relies on the combined effects of the three parameters to achieve maize ear–stalk separation, further optimization of the operating parameters is necessary to obtain the optimal parameter combination for the vibration ear-picking process.

Optimal Parameter Combination

To obtain the optimal operating parameters for vibration ear-picking, a three-factor, three-level orthogonal experiment was conducted on the three parameters that significantly affect the average acceleration score S_z. In this experiment, the average acceleration score S_z was used as the performance evaluation index, with amplitude X_1, frequency X_2, and clamping position X_3 selected as the experimental factors. The test factors and their corresponding levels are listed in Table 3.

Table 3

Factor Coding

Level	Amplitude X_1 (mm)	Frequency X_2 (Hz)	Clamping position X_3 (mm)
-1	5	17	50
0	7.5	18	95
1	10	19	140

The Box-Behnken experimental design method was used to determine 17 sets of simulation test results for vibration ear-picking. The simulation data were then subjected to second-order multiple regression analysis using Design Expert software to study the effects of amplitude, frequency, and clamping position on the test index S_Z Ultimately, the optimal combination of vibration ear-picking parameters was determined.

Table 4

Orthogonal Test Results

Test No.	Amplitude X_1 (mm)	Frequency X_2 (Hz)	Clamping Position X_3 (mm)	Average Acceleration Score S_Z
1	0	0	0	90.8
2	-1	-1	0	10.2
3	-1	1	0	69.32
4	1	1	0	76.55
5	-1	0	1	54.38
6	0	0	0	89.9
7	0	-1	-1	12.5
8	0	1	-1	83.4
9	1	0	1	81.26
10	0	0	0	91.4
11	0	1	1	74.23
12	0	0	0	86.39
13	0	0	0	89.5
14	1	0	-1	43.65
15	-1	0	-1	45.36
16	0	-1	1	67.35
17	1	-1	0	33.68

Table 5

Analysis of Variance (ANOVA)

Source	Sum of squares	Degree of freedom	Mean square	*F*-value	*P*-value	significant level
Model	11486.84	9	1276.32	96.80	< 0.0001	**
X_1	390.32	1	390.32	29.60	0.0010	*
X_2	4039.66	1	4039.66	306.37	< 0.0001	**
X_3	1065.14	1	1065.14	80.78	< 0.0001	**
X_1X_2	66.02	1	66.02	5.01	0.0603	
X_1X_3	204.35	1	204.35	15.50	0.0056	*
X_2X_3	1024.64	1	1024.64	77.71	< 0.0001	**
X_1^2	2166.58	1	2166.58	164.32	< 0.0001	**
X_2^2	1597.20	1	1597.20	121.13	< 0.0001	**
X_3^2	486.71	1	486.71	36.91	0.0005	*
Residual	92.30	7	13.19			
Lack of Fit	77.21	3	25.74	6.83	0.0473	
Pure Error	15.08	4	3.77			
Cor Total	11579.14	16				

*Note: P<0.01 (Highly significant), 0.01≤P<0.05 (Significant). ** indicates highly significant, * indicates significant.*

As shown in Table 5, for the S_z model, P<0.0001 indicates that the quadratic multiple regression model is highly significant. The lack-of-fit term is not significant, suggesting that the experimental error is small and the regression equation fits the data well. In the average acceleration score model, P<0.01 for X_2, X_3, X_2X_3, X_1^2, and X_2^2 indicates that these factors have a highly significant effect on the regression model within a 99% confidence interval. From the analysis of the regression coefficients, the sequence of factor significance on the acceleration score model is: frequency, clamping position, and amplitude. For X_1, X_1X_3, and X_3^2, P<0.05 shows that their influence on the regression model is significant within a 95% confidence interval. Other terms have P values greater than 0.05, indicating that their effect on the regression model is not significant. After eliminating the non-significant terms and performing variance fitting, the final multiple quadratic regression equation for the acceleration score S_z is:

$$S_z = 89.60 + 6.98x_1 + 22.47x_2 + 11.54x_3 + 7.15x_1x_3 - 16.00x_2x_3 - 22.68x_1^2 - 19.48x_2^2 - 10.75x_3^2 \quad (21)$$

Response Surface Analysis

Figure 10a illustrates the response surface of frequency and amplitude. As both frequency and amplitude increase, the acceleration score S_z initially rises and then declines. Interaction analysis reveals that under low frequency and small amplitude, the overall acceleration of the plant is insufficient, causing most test points to fall outside the scoring range, resulting in a low S_z. As frequency and amplitude increase, the acceleration values at various test points gradually enter the effective scoring range, leading to a sharp increase in S_z. However, when the excitation intensity becomes excessive, some test points exceed the scoring range, causing a reduction in S_z.

Figure 10b presents the response surface of amplitude and clamping position. As clamping position and amplitude increase, S_z shows a rising trend followed by a decline. Interaction analysis indicates that increasing the clamping position extends the transmission distance, which reduces the acceleration transmitted to the maize ear. Conversely, increasing amplitude enhances the overall plant acceleration. Therefore, under the combined effect of both factors, a moderate clamping position and amplitude bring the acceleration near the critical threshold, resulting in an increased S_z.

Figure 10c depicts the response surface of frequency and clamping position. With increasing clamping position and frequency, S_z rapidly increases and then stabilizes. Interaction analysis shows that at low frequency or short clamping distance, the acceleration often falls outside the scoring range, resulting in low S_z. As frequency increases or clamping distance moderately extends, more test points fall within the effective range, leading to a significant improvement in S_z. However, if frequency or clamping distance becomes too large, some test points again deviate from the scoring range, and S_z growth slows.

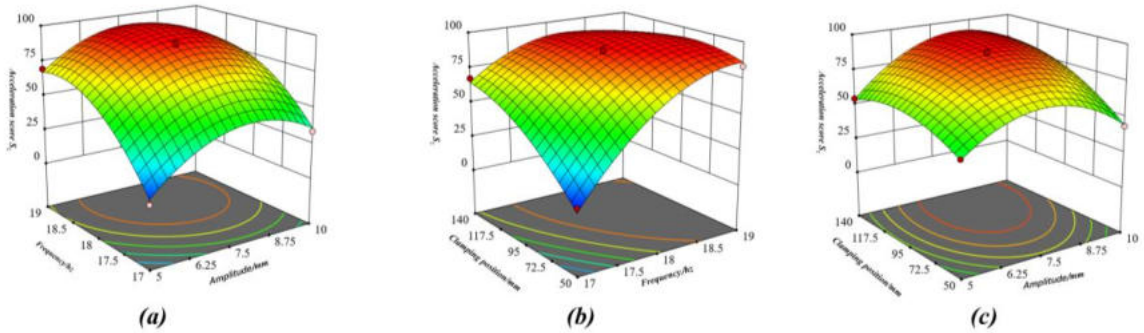


Fig. 10 - Response Surface Analysis of Acceleration Score

Parameter Optimization and verification test

Taking amplitude, frequency, and clamping position as optimization variables, the optimal parameter combination was determined using the average acceleration score S_z as the evaluation index. The optimal combination for effective ear-picking was found to be an amplitude of 7.88 mm, a frequency of 18.46 Hz, and a clamping position of 105.94 mm, corresponding to an acceleration score S_z of 96.71. To verify the reliability of the simulation results, the parameters were rounded to an amplitude of 8 mm, a frequency of 18 Hz, and a clamping position of 106 mm.

Bench tests were conducted five times using a self-developed image acquisition platform for vibration ear-picking of maize. The results showed a maximum score of 97.31, a minimum score of 90.68, and an average score of 93.61. The error between test and simulation results was 2.36%, confirming the predictive accuracy of the model and the practical applicability of the optimized parameters.

Table 6

Verification Results of Bench Tests

Indicator	Minimum value	Maximum	Average value	SD	Error (%)
average acceleration score S_z	90.68	97.31	93.61	2.72	3.21

CONCLUSIONS

Based on the finite element analysis method, simulation tests were conducted to analyze the acceleration amplitude response of maize plants under different excitation parameters. The ear-picking process and its main influencing factors were examined, and the reliability and accuracy of the simulation results were validated through bench tests. The main conclusions are as follows:

(1) By analyzing the changes in the mechanical behavior of maize plants during the ear-picking process, it was determined that the main factors influencing ear-picking performance are amplitude, frequency, and clamping position. This provides a theoretical foundation for subsequent analyses of the vibration response characteristics of maize plants.

(2) The vibration response characteristics of maize plants were explored, providing a basis for the calculation and prediction of the excitation forces acting on the maize ear under different working parameters.

(3) Single-factor tests for amplitude, frequency, and clamping position were conducted using simulation software to determine the influence of these three variables on the acceleration score. Furthermore, using these parameters as test factors, a three-factor, three-level orthogonal experiment and response surface analysis were carried out with acceleration score as the evaluation criterion. A slope-based scoring algorithm was employed to assist in decision-making. The optimal parameter combination was determined to be amplitude of 7.88 mm, frequency of 18.46 Hz, and clamping position of 105.94 mm, which yielded the best ear-picking performance. After rounding the optimal parameters and conducting verification tests, the average acceleration score S_z was found to be 93.61, indicating that the verification test results closely matched the optimized regression prediction values. This confirmed the reliability of the simulation results and provided new insights for vibration ear-picking.

ACKNOWLEDGEMENT

This work was supported financially by the National Natural Science Foundation of China under Grant No. 32372008.

REFERENCES

[1] Chen, K., Du, X., Zhang, G., & Zhou, R. (2019). Analysis on dynamics characteristics of vibratory harvesting for oil-tea Camellia fruit. Paper presented at the *2019 ASABE Annual International Meeting*, Boston, Massachusetts, July 7–10.

[2] Dong, W., Wu, Y., Liu, F., Hu, H., Yan, J., Bai, H., & Zhao, X. (2024). Design and experiment of a harvesting header for wide–narrow-row corn. *Applied Sciences*, 14(3), Article 1309. https://doi.org/10.3390/app14031309

[3] Fu, J., Zhang, M., Cheng, C., Zhao, H., & Ren, L. (2024). Thickness monitoring of threshing mixture on the oscillating plate of corn grain harvester. *Computers and Electronics agriculture*, 227, 109485. https://doi.org/10.1016/j.compag.2024.109485

[4] Fu, L., Peng, J., Nan, Q., He, D., Yang, Y., & Cui, Y. (2016). Simulation of vibration harvesting mechanism for sea buckthorn. *Engineering in Agriculture, Environment and Food*, 9(1), 10-108. https://doi.org/10.1016/j.eaef.2015.08.003

[5] Fu, Q., Fu, J., Chen, Z., & Ren, L. (2020). Analysis and experiment on the mechanism of rigid-flexible coupling loss reduction of corn ear-picking header (玉米摘穗割台刚柔耦合减损机理分析与试验). *Transactions of the Chinese Society of Agricultural Machinery*, 51(4), 60–68.

[6] Geng, D., Li, Y., Meng, F., Meng, P., Ni, G., & Zhang, M. (2017). Design and experiment of multi-sided vertical roller ear picking device for corn harvester (玉米收获机多棱立辊式摘穗装置设计与试验). *Transactions of the Chinese Society of Agricultural Machinery*, 48(3), 84–91.

[7] Geng, D., Wang, Q., Lu, X., Yu, X., Liu, Y., & Jin, C. (2019). Design and experiment of corn multi-ribbed ear picking roller based on excitation theory (基于激振理论的玉米多棱摘穗辊设计与试验). *Transactions of the Chinese Society of Agricultural Machinery*, 50(5), 124–132.

[8] Ji, X., Geng, D., Yao, Y., Du, J., Zhu, J., & Xu, H. (2020). Design and experiment of vibration ear-picking device for corn harvester (玉米收获机激振摘穗装置设计与试验). *Transactions of the Chinese Society of Agricultural Machinery*, 51(S2), 126–133.

[9] Liu, F. (2007). Research on key components of vertical ear-removing roller corn harvester for harvesting both ears and stems [Master's thesis, Jilin University].

[10] Pereira, M. R., Santos, F.L., Scinocca, F., Tinoco, H. A., & Villibor, G.P. (2025). Evaluation of the transmissibility of vibration and dynamic behaviour of coffee plants under field conditions. *Biosystems Engineering*, 250, 225–235. https://doi.org/10.1016/j.biosystemseng.2025.01.002

[11] Wang, Q., He, K., Jin, C., Lu, X., Geng, D., & Zhang, G. (2018). Analysis on the mechanism of corn vibration ear picking and optimization of parameter experiments (玉米激振摘穗机理分析与参数试验优化). *Transactions of the Chinese Society of Agricultural Machinery*, 49(S1), 249–257.

[12] Wang, Q., He, Q., Yue, D., Li, D., Yin, J., Guan, P., & Wang, Z. (2025). Dynamic real-time detection for corn kernel breakage rate based on deep learning and sliding window technology. *Computers and Electronics in Agriculture*, 232, 109926. https://doi.org/10.1016/j.compag.2025.109926

[13] Wu, D., Zhao, E., Fang, D., Jiang, S., Wu, C., Wang, W., & Wang, R. (2022). Determination of vibration picking parameters of Camellia oleifera fruit based on acceleration and strain response of branches. *Agriculture*, 12(8), Article 1222. https://doi.org/10.3390/agriculture12081222

[14] Xing, S., Cui, T., Zhang, D., Yang, L., He, X., Li, C., & Du, Z. (2024). Design and optimization for a longitudinal-flow corn ear threshing device of low loss and low energy consumption. *Computers and Electronics in Agriculture*, 226, 109328. https://doi.org/10.1016/j.compag.2024.109328

[15] Xing, S., Cui, T., Zhang, D., Yang, L., He, X., Wang, Z., & Jing, M. (2024). Design and experiment of the simulated electronic corn ear based on UWB/IMU technology. *Computers and Electronics in Agriculture*, 217, 108567. https://doi.org/10.1016/j.compag.2023.108567

[16] Xuan, Y., Xu, L., Liu, G., & Zhou, J. (2021). The potential influence of tree crown structure on the ginkgo harvest. *Forests*, 12(3), Article 366. https://doi.org/10.3390/f12030366

[17] Xin, S., Zhao, W., Shi, L., Dai, F., Feng, B., Yan, Z., & Lü, D. (2023). Design and experiment of the clamping and conveying device of the vertical roller corn harvesting header (立辊式玉米收获割台夹持输送装置设计与试验). *Transactions of the Chinese Society of Agricultural Engineering*, 39(9), 34–43.

[18] Yan, H., Wu, W., Han, F., & Liu, F. (2009). Effect of the roller type of corn harvester's ear picking roller on its working performance (立辊型玉米收获机摘穗辊辊型对工作性能的影响). *Transactions of the Chinese Society of Agricultural Machinery*, 40(5), 76–80.

[19] Yang, R., Chen, D., Zha, X., Pan, Z., & Shang, S. (2021). Optimization design and experiment of ear-picking and threshing devices of corn plot kernel harvester. *Agriculture*, 11(9), Article 904. https://doi.org/10.3390/agriculture11090904

[20] Zhao, J., Ma, T., Inagaki, T., Chen, Q., Gao, Z., Sun, L., & Chen, J. (2021). Finite element method simulations and experiments of detachments of Lycium barbarum L. *Forests*, 12(6), Article 699. https://doi.org/10.3390/f12060699

[21] Zhao, J., Tsuchikawa, S., Ma, T., Hu, G., Chen, Y., Wang, Z., & Chen, J. (2021). Modal analysis and experiment of a *Lycium barbarum L*. shrub for efficient vibration harvesting of fruit. *Agriculture*, 11(6), Article 519. https://doi.org/10.3390/agriculture11060519

[22] Zheng, Z., Hu, Y., Dong, J., Zhao, P., Liu, Y., Jiang, X., & Huang, Y. (2024). Characterising vibration patterns of winter jujube trees to optimise automated fruit harvesting. *Biosystems Engineering*, 248, 255–268. https://doi.org/10.1016/j.biosystemseng.2024.11.004

[23] Zhuo, P., Li, Y., Wang, B., Jiao, H., Wang, P., Li, C., & Wang, L. (2022). Analysis and experimental study on vibration response characteristics of mechanical harvesting of jujube. *Computers and Electronics in Agriculture*, 203, 107446. https://doi.org/10.1016/j.compag.2022.107446

CALIBRATION AND OPTIMIZATION OF DISCRETE ELEMENT PARAMETERS FOR TIGER NUTS

/

油莎豆种子离散元素参数的标定与优化

Yangyang SHI, Xuejun ZHANG, Jinshan YAN*), Xu MA, Huazhi LI, Changjie HAN
College of Mechanical and Electrical Engineering, Xinjiang Agricultural University, Urumqi 830052, China
Tel: +8615894618255; E-mail: jshan.yan@xjau.edu.cn
Corresponding author: Jinshan Yan
DOI: https://doi.org/10.35633/inmateh-76-84

Keywords: *tiger nuts; contact parameter; Plackett-Burman test; discrete element; simulation*
[1]

ABSTRACT

To improve the accuracy of discrete element simulation parameters for tiger nuts, this study suggests the measurement of the triaxial dimensions of tiger nuts using MATLAB. This method exhibited a maximum error of no more than 0.16% compared to the traditional measurement techniques. Experimental measurements were used to obtain the basic physical parameters of the seeds. Physical tests on the angle of stacking of tiger nuts were conducted. A discrete element model for tiger nuts was constructed. The Plackett-Burman test and the steepest climb test were used to identify critical parameters affecting the angle of accretion and to delineate the optimal range of parameters impacting larger parameters proportionately. The optimum values for the coefficient of static and rolling friction between tiger nuts were established at 0.32 and 0.24, respectively, using response surface methodology. The average tangent of the simulated stacking angle obtained was 0.731 from three tests that carried out using the optimized parameters, representing a mere 0.41% deviation from the physical test average of 0.734. The experimental outcomes confirm that these parameters can provide reliable data for discrete element simulation experiments involving tiger nuts.

摘要

为提高油莎豆种子离散元模拟参数的准确性，本研究提出使用 MATLAB 测量油莎豆种子的三轴尺寸。事实证明，与传统测量技术相比，该方法的最大误差不超过 0.16%。试验测量用于获得种子的基本物理参数。对油莎豆种子的堆积角进行了物理测试。构建了油莎豆种子的离散元模型。利用 Plackett-Burman 试验和最陡爬坡试验确定了影响堆积角的关键参数，并划定了影响较大参数比例的最佳参数范围。利用响应面方法确定了油莎豆种子间静摩擦系数和滚动摩擦系数的最佳值，分别为 0.32 和 0.24。在使用优化参数进行的三次试验中，模拟堆积角的平均正切值为 0.731，与物理试验的平均值 0.734 相比，偏差仅为 0.41%。试验结果证实，这些参数可为有关油莎豆种子的离散元模拟试验提供可靠数据。

INTRODUCTION

Tiger nut, a crop notable for its substantial oil content, is endowed with considerable nutritional value and exhibits a robust adaptability to arid and sandy areas (*Guo et al., 2021*). In recent years, there has been a growing demand for edible oil in China, and the tiger nut, with its uniquely high oil yield, has strategically aligned with national needs. Additionally, its large cultivable area and high harvest rate offer a promising foundation for extensive research (*Li et al., 2022*).

The mechanized sowing of tiger nuts using precision planters introduces intricate interactions among the seeds themselves, and between the seeds and the planter. The constrained dimensions within the seed dispenser render the analysis of these dynamics challenging, necessitating an operational investigation encompassing seed filling, clearing, transporting, and dissemination processes (*Peng et al., 2022; Zhang et al., 2023*). During the seeding process, particles exhibit distinct motion traits individually, along with characteristics of continuous fluid motion, demonstrating pronounced bulk particle dynamics (*Tsa et al., 2021*). The discrete element method is the leading technique for studying the motion of bulk particles, enabling effective simulation of their dynamics and force interactions.

[1] *Yangyang Shi, M.S. Stud.; Xuejun Zhang, Prof. Ph.D.; Jinshan Yan, Prof. Ph.D.; Xu Ma, Prof. Ph.D.; Huazhi Li, M.S. Stud.*

It is widely used in the design of specialized seeders. Due to the irregular surface texture of the tiger nut, both in shape and material properties, it is unsuitable for conventional seeding techniques. To devise a seeder tailored for tiger nuts, an initial investigation into the material properties of these nuts is essential to refine the structural parameters of the specialized seeder, thereby enhancing sowing precision (*Zhang et al., 2021; Xu et al., 2020*).

In seed characterization studies, employing the discrete element EDEM simulation necessitates calibration of several critical parameters, such as inter-particle friction, friction between particles and surfaces, and restitution coefficients (*Chen et al., 2012; Chen et al., 2017; Zhou et al., 2018; Hou et al., 2020*). Some researchers have developed a mung bean model using the bonding model approach, calibrating contact parameters in EDEM simulations to minimizing discrepancies between simulation results and physical testing, thereby refining parameter accuracy (*Zhang et al., 2022*). Some researchers have employed reverse engineering techniques to create discrete element models for cotton seeds, calibrating the contact parameters and aligning the discrepancies in the angle of repose between physical and simulation tests, thereby optimizing the parameters and improve the simulation accuracy (*Wang et al., 2022*). Some researchers have used a rotating drum apparatus to ascertain the contact parameters and angles of repose for cotton seeds, employed these contact parameters as indicators for the mathematical model, and solved the multifactorial optimization through response surface methodology, which proved the reliability and consistency of the discrete element simulation method combined with physical test method (*Hu et al., 2022; Zeng et al., 2021*).

To augment the precision of meta-parameters for tiger nuts, this study proposes integrating theoretical analysis with experimental measurements to derive the seeds' geometrical characteristics, contact parameters and physical properties. Physical and simulation tests were conducted on tiger nuts . Using the Plackett-Burman design, parameters significantly impacting the stacking angle - considered a key evaluation index - were identified. Hill-climbing tests were employed to fine-tune the experimental parameters and obtain the best combination of important parameters, similar to the real-world conditions, for experimental validation. This research provides theoretical references for the study of precision sowing of tiger nuts and the structural parameters of the seeder.

MATERIAL AND METHODS

Rapid calculation of triaxial dimensions of tiger nuts based on image detection

Currently, vernier gauges are predominantly utilized to measure the three-axis dimensions of seeds (*Peng et al., 2022*), a method characterized by low-precision, high labor cost and time-consuming nature. In this study, a MATLAB-based image processing technique is used to ascertain the three-axis dimensions (length L, width W, and thickness T) of tiger nutss, providing sufficient data for EDEM simulation, as illustrated in Fig. 1. Predominantly, tiger nuts exhibit an oval geometry with elongated or abbreviated semiaxes, but also instances of round or irregularly shaped beans occur in random samples. Seeds were sourced from Jiyoudou 21 (JYD-21), a cultivar native to the southern periphery of the Xinjiang Uygur Autonomous Region, China. Considering the practicality and in order to enhance germination efficacy, seeds randomly selected for testing underwent a hydration process, immersing them in water for 4 days before sowing (*Zheng et al., 2024*).

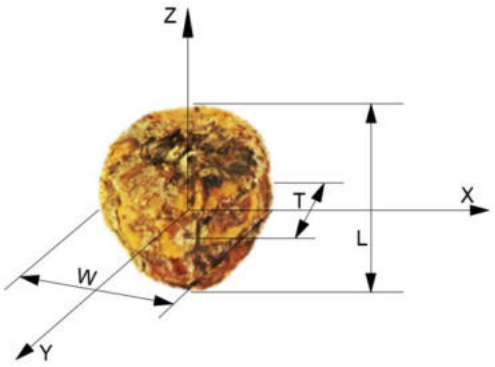


Fig.1 - Schematic diagram of tiger nut characteristic size

Note: L, W, and T are the length, width and thickness of tiger nuts particles)

Seeds were positioned on a shooting plane, photographed by a high-definition industrial camera, and uploaded to a computer (Lenovo R7000p_3050ti) for further analysis with MATLAB. Some of the functions used are not included in the MATLAB library but are still applicable. First of all, the use of function imread was deployed to import the image, as depicted in Fig. 2 (a). Subsequently, the rgb2gray function was applied for grey scale processing, as shown in Fig. 2 (b). The function im2bw was then applied to binarize image processing, as seen in Fig. 2 (c). Owing to significant noise inherent in the image due to capture conditions, a two-dimensional median filtering function medfilt was utilized to denoise the image, as demonstrated in Fig. 2 (d). Considering only the peripheries of the tiger nuts, the use of fill function imfill on the image of the structural elements of the expansion of the processing, as illustrated in Fig. 2 (e). Finally, the use of the regionprops function of the image was calibrated, with the boundaries marked by the red box, as shown in Fig. 2 (f). The centroid, width and length of the depicted tiger nuts were analyzed using the MajorAxisLength and MinorAxisLength functions. The image was scaled in pixel units, with the pixel scale calibrated to a 1 mm unit ratio using the getpois function, which in turn gave the length (mm) and width (mm) dimensions of the tiger nuts. To ascertain the thickness, seeds were positioned on a flat surface in the direction of the thickness and measured in the same way as above.

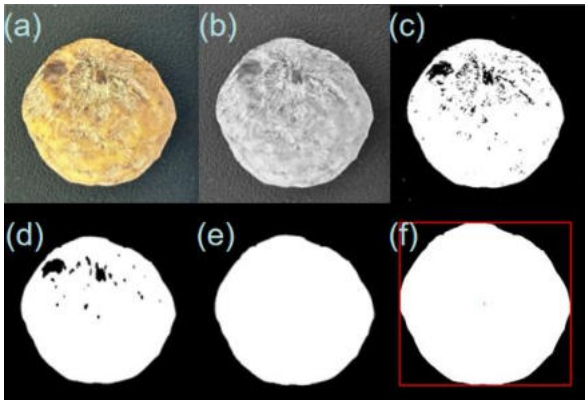


Fig. 2 - Seed image calibration process

In the extant body of research concerning the triaxial dimensional analysis of seeds, vernier gauges are predominantly employed, with no alternative measurement methodologies reported. In order to ascertain the reliability of the data, 60 tiger nuts were randomly selected from a sample of 100 for analysis. The resultant measurements were averaged and contrasted with those typically recorded using vernier gauges, as detailed in existing literature. In this study, compared with the vernier gauge (German SYNTEK digital vernier gauge, accuracy of 0.01 mm), as depicted in Table 1, the measurement errors of the three-axis dimensions (length L (mm), width W (mm), and thickness T (mm) are 0.16 mm, 0.06 mm, and 0.13 mm, respectively, averaging 0.12 mm. In tiger nuts, given the minimal variation in measurement positioning, the occurrence of small discrepancies is expected, however, the rapidity and appropriateness of this method align with the measurement requirements of this paper.

Table 1

Comparison of three-axis dimensional measurements of tiger nuts

Parametric	Length L (mm)	Breadth W (mm)	Thickness T (mm)
Image Inspection/Vernier Calipers	13.07/13.00	12.38/12.33	8.48/8.45
	14.77/14.73	13.67/13.61	7.24/7.16
	14.39/14.11	12.66/12.66	9.28/9.22
	14.46/14.00	13.22/13.02	7.12/7.10
	12.88/12.88	12.17/12.15	8.12/8.02
	13.04/13.02	12.63/12.52	10.11/10.04
Average error in length, width and thickness	0.16	0.06	0.13

Basic physical parameters of tiger nuts

For this study, two hundred seeds were randomly selected and analyzed. Each seed was photographed, and its three-axis dimensions - length (L), width (W), and thickness (T) - were measured. As shown in Table 2, the average values were 12.43 mm, 11.68 mm, and 9.14 mm, respectively, with standard deviations of 1.52 mm, 1.33 mm, and 1.01 mm.

The distribution of these dimensions, illustrated in Fig. 3, follows a bell-shaped curve, i.e., most values are concentrated near the mean, with a gradual decrease and convergence as the values move away from the mean - indicating a normal distribution.

Equation 1 demonstrates that when the size of the three axes is larger, the sphericity is higher, the volume is larger, and the mobility is greater; consequently, the collision force generated by the collision will also increase. Therefore, the selection of materials for seeders needs to be considered to avoid causing significant collision damage to the seeds.

Table 2

Tiger nuts triaxial dimensions

Parametric	Length L (mm)	Breadth W (mm)	Thickness T (mm)
maximum value	15.21	14.11	12.32
minimum value	9.97	8.91	7.01
average value	12.43	11.68	9.14
standard deviation	1.51	1.33	1.01

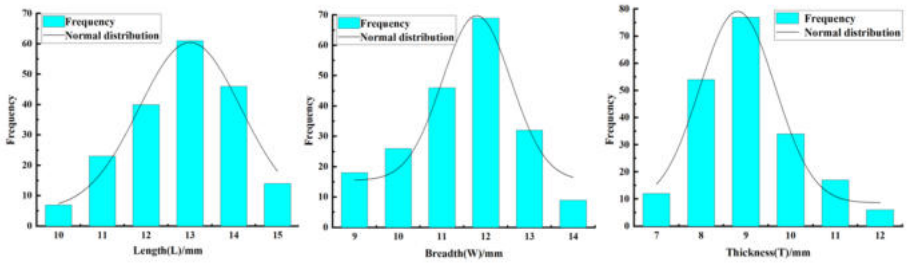


Fig. 3 - Normal distribution of triaxial dimensions of tiger nuts

The volume V, equivalent grain size d, and sphericity S_p of tiger nuts were calculated, with sphericity approaching 100% indicating fuller seeds that more closely approximate a spherical shape (*Chen et al., 2023; Ma et al., 2015*). Repeated 20 times, the mean values of tiger nuts volume V, equivalent particle size d and sphericity S were 1.54 cm^3, 11.15 mm and 85%, respectively, with corresponding standard deviations of 0.12 cm^3, 0.71 mm and 0.97% as listed in Table 3.

The weighing method was used to randomly measure 10 tiger nuts using an MTB1000D-B high precision electronic balance (minimum reading accuracy of 0.01 g). Using a 350 ml beaker, 10 seeds were placed in sequence after the addition of 200 ml of water, ensuring that no air bubbles were present when recording the results of the rise in water level. This process was repeated 10 times, and the average density of tiger nuts was determined to be 1062.22 kg/m^3 (*Chen et al., 2023*). This value is similar to those reported in the relevant literature and is used in this paper to set the structural parameters for subsequent simulations.

A high-precision electronic balance scale (accuracy 0.01 g) was employed to determine the thousand-seed weight, which averaged 789.32 g after 10 repetitions, as shown in Table 3.

$$\begin{cases} V = LWT \\ d = \sqrt[3]{LWT} \\ S_P = \dfrac{d}{L} \times 100\% \end{cases} \quad (1)$$

where: V - volume of tiger nuts, cm^3; L - length of tiger nuts, mm; W - width of tiger nuts, mm; T - thickness of tiger nuts, mm; d - equivalent particle size of tiger nuts, mm; S_p - sphericity of tiger nuts, %.

Table 3

Basic physical parameters of tiger nuts

Parametric	Maximum value	Minimum value	Average value	Standard deviation
Volumetric/(cm^3)	2.64	0.62	1.54	0.12
Equivalent particle size/(mm)	13.83	8.54	11.15	0.71
Sphericity/(%)	91	81	85	0.97
Particle density/(kg m^3)	1063.03	1060.46	1062.22	0.78
Kernel mass/(g)	791.20	787.99	789.32	0.52

Elastic Modulus

The elastic modulus, critical for simulation studies, was assessed using the RGM - 4002 universal testing machine (*Sun et al., 2017*), as shown in Fig. 4. Twenty seeds underwent compression testing along the seed thickness axis (*Chen et al., 2023*). The compression test was conducted on the seed along its thickness direction. The speeds were maintained at 2 mm/s before loading, reduced to 0.02 mm/s during loading, and then restored to 2 mm/s after loading. The elastic modulus is calculated as:

$$E = \frac{\sigma}{\upsilon} = \frac{Fl_o}{\Delta l S_o} \tag{2}$$

where: E - elastic modulus of tiger nuts, MPa; σ - compressive stress of tiger nuts, Pa; υ - compressive strain of tiger nuts, Pa; F - exert external force of tiger nuts, N; l_o - initial compression direction length of tiger nuts, mm; Δl - length distortion distance of tiger nuts, mm; S_o - initial cross-sectional area of tiger nuts, mm^2.

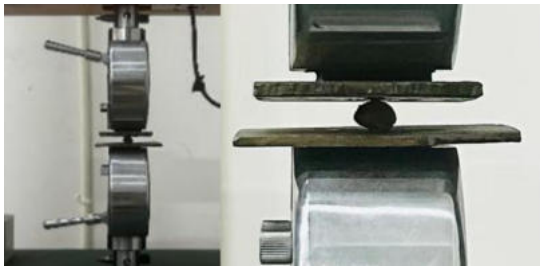


Fig. 4 - Seed compression test of tiger nuts

The experiment was replicated 10 times and the elastic modulus of the tiger nuts was 8.22×106Pa.

Table 4

Elastic modulus of tiger nuts

Parametric	Maximum value	Minimum value	Average value	Standard deviation
Elastic modulus/Pa	9.68×106	6.37×106	8.22×106	0.97

Poisson's ratio and shear modulus

For this experiment, 10 tiger nuts were randomly selected and subjected to a mechanical test using the RGM - 4002 universal testing machine. The seeds were loaded gradually at a speed of 0.2 mm/s in the length direction. Loading was halted when the display indicated that seeds had reached their rupture breakpoints. Simultaneously, a camera mounted parallel to the seed loading platform captured the deformation. The deformations were analyzed using MATLAB, in a manner consistent with the three-axis dimensional measurements, to record the deformation in both the length and the thickness directions (*Khodabakhshian, 2012*). Poisson's ratio was calculated as follows:

$$\delta = \left| \frac{\Upsilon_1}{\Upsilon_2} \right| = \frac{\Delta l / l}{\Delta t / t} \tag{3}$$

where: δ - Poisson's ratio; γ_1 - lengthwise strain of tiger nuts, mm; γ_2 - thickness direction strain of tiger nuts, mm; Δl - longitudinal deformation value of tiger nuts, mm; l - original dimensions in length direction of tiger nuts, mm; Δt - deformation values in the thickness direction of tiger nuts, mm; T - original dimensions in thickness direction of tiger nuts, mm.

Subsequent analysis revealed the shear modulus of the tiger nuts can be obtained. The shear modulus was derived as:

$$G = \frac{E}{2(1+\delta)} \tag{4}$$

where:

G - shear modulus of tiger nuts, Pa; E - elastic modulus of tiger nuts, Pa;

δ - Poisson's ratio of tiger nuts.

As shown in Table 5, the experiment was repeated 10 times and the mean values of Poisson's ratio and shear modulus of tiger nuts were taken as 0.39 and 3.03×106Pa, respectively.

Table 5

Poisson's ratio and elastic modulus of tiger nuts

Parametric	Maximum value	Minimum value	Average value	Standard deviation
Poisson's ratio	0.51	0.28	0.39	0.94
Elastic modulus/P_a	3.58×106	1.97×106	3.03×106	1.10

Friction factor and coefficient of restitution

The determination of the static coefficient of friction between the tiger nuts and various materials - namely the steel plate, acrylic plate, PE polyethylene, and hard plastic plate - was conducted using the oblique measurement method. The experimental setup is depicted in Fig. 5. The seed was placed on the selected material plate, and the handle was rotated to slowly raise the plate. When the seed was about to roll but did not, the rotation of the handle was stopped. The angle between the material plate and the plane α was recorded. The static coefficient of friction was calculated as follows:

$$k = \tan\alpha \tag{5}$$

where: k - static friction factor of tiger nuts; α - angle between the material plate and the plane, °.

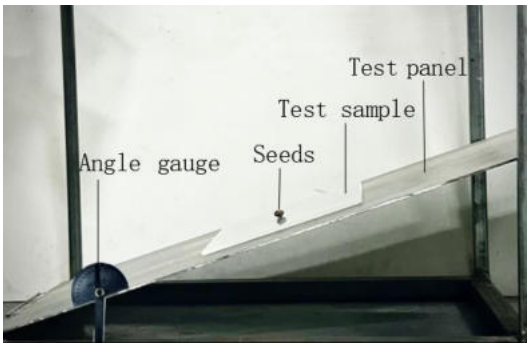


Fig. 5 - Static friction test of tiger nuts

Static friction between the tiger nuts is essential for the accuracy of EDEM simulations. As illustrated in Fig 6, A4 paper was employed as the sample plate, to which double-sided adhesive tape was applied. Randomly selected tiger nuts of comparable size were randomly distributed on the sample plate, which was subsequently positioned on the test bench. The handle was rotated until the seeds demonstrated a tendency to roll downwards without actual rolling. At this juncture, the rotation of the handle was stopped. The angle between the seed plate and the plane was recorded α, which could be substituted into the aforementioned equation (*Wu et al., 2020; Shi et al 2019*). The static friction between the seeds can be obtained by substituting into the above equation. The tests involving tiger nuts and various materials were repeated 20 times. The results are shown in Table 6. The resultant mean static friction values for tiger nuts in contact with steel, acrylic, plastic and seed plates were 0.40, 0.41, 0.57 and 0.49 respectively.

Table 6

Static friction factor of tiger nuts

Parametric	Maximum value	Minimum value	Average value	Standard deviation
tiger nuts - steel plate	0.43	0.37	0.40	0.45
tiger nuts - acrylic sheet	0.49	0.23	0.41	0.51
tiger nuts - plastic sheet	0.63	0.51	0.57	0.49
tiger nuts - seed board	0.58	0.36	0.49	0.53

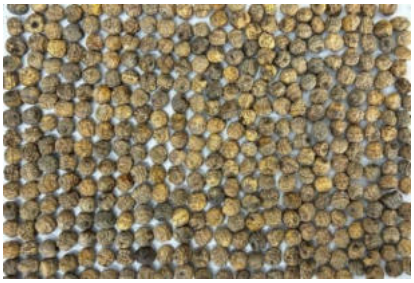


Fig. 6 - Tiger nuts board

Determination of rolling friction factor of tiger nuts

The rolling friction factor of tiger nuts correlates with their size, volume and sphericity. In this study, 10 tiger nuts with a high degree of sphericity were assessed using the oblique measurement method. Steel, acrylic, plastic and seed boards were selected for the test. On the test bench, different test plates were positioned, and the seed was placed on the material plate. The handle was then turned to gradually increase the angle between the experimental plate and the horizontal plane. The adjustment was halted when the seeds appeared to roll, and the angle of the inclined plane at this time was recorded as β. This angle was then substituted into equation 5 to calculate the rolling friction factor.

The above tests were replicated 20 times for each group, as shown in Table 7, with the mean rolling friction factors being 0.24, 0.21, 0.17, and 0.27 for steel, acrylic, plastic and seed plates, respectively.

Table 7

Rolling friction factor of tiger nuts

Parametric	Maximum value	Minimum value	Average value	Standard deviation
Tiger nuts - steel plate	0.31	0.17	0.24	0.63
Tiger nuts - acrylic sheet	0.25	0.16	0.21	0.56
Tiger nuts - plastic sheet	0.24	0.11	0.17	0.55
Tiger nuts - seed board	0.33	0.19	0.27	0.59

Coefficient of restitution for tiger nuts

The coefficient of restitution was defined as the ratio of the relative normal separation velocity post-collision to that prior to collision (i.e., the ratio of the maximum height of rebound of the tiger nuts after collision with an object to the initial height of fall). The coefficient of restitution significantly influences the realism of EDEM simulation metrics (*Yu et al., 2020*). In this study, the seeds were allowed to freely fall and collide with a plate, with their trajectories subsequently recorded. Before the test, coordinate-scale paper was placed at 90° to the material plate, forming a two-dimensional spatial coordinate system. Seeds were released from a height of 250 mm above the plate. An iPhone 14 was employed to capture the rebound at a slow-motion frame rate of 120fps, as depicted in Fig. 7, thereby facilitating accurate rebound height measurements. The coefficient of restitution equation is:

$$e = \left|\frac{v'}{v}\right| = \left|\frac{v_2' - v_1'}{v_1 - v_2}\right| = \left|\frac{-\sqrt{2gh'}}{\sqrt{2gh}}\right| = \sqrt{\frac{h'}{h}} \tag{6}$$

where: e - coefficient of restitution of tiger nuts; $v`$ - instantaneous velocity of tiger nuts in the normal direction before collision, mm/s; $v$ - instantaneous velocity of tiger nuts before collision, mm/s; $v_1`$ - velocity of tiger nuts before collision, mm/s; $v_2`$ - velocity of material before collision, mm/s; $v_1$ - velocity of tiger nuts after collision, mm/s; $v_2$ - velocity of material after collision, mm/s; $g$ - gravitational acceleration; $h$ - initial drop height of tiger nuts, mm; $h`$ - maximum rebound height of tiger nuts after collision, mm.

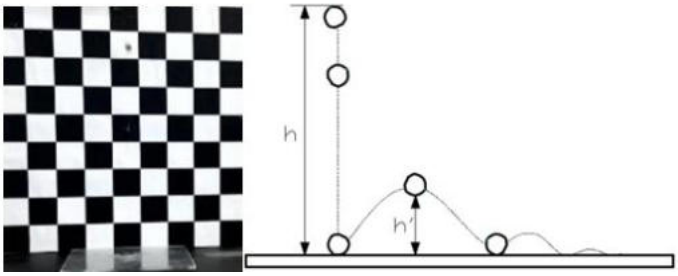


Fig. 7 - Seed coefficient of restitution tests of tiger nuts

Observations indicate that when the rebound effect is not the desired effect, it notably affects the coefficient of restitution test. Given the irregular geometry of the tiger nuts, it is difficult for them to rebound vertically upwards after hitting a flat plate. Consequently, extensive testing is required to investigate this phenomenon.

The results of 20 tests in which the rebound path was parallel to the fall path are selected for analysis. The average value from these tests was used in the above formula for calculation. As shown in Table 8, the mean coefficients of restitution for collisions between tiger nuts and various materials — steel plate, acrylic plate, plastic plate, and seed plate — were 0.63, 0.58, 0.55, and 0.53, respectively, with corresponding standard deviations of 0.61, 0.56, 0.63, and 0.58.

Table 8

Coefficient of restitution of tiger nuts

Parametric	Maximum value	Minimum value	Average value	Standard deviation
Tiger nuts - steel plate	0.81	0.47	0.63	0.61
Tiger nuts -acrylic sheet	0.78	0.37	0.58	0.56
Tiger nuts - plastic sheet	0.76	0.34	0.55	0.63
Tiger nuts - seed board	0.77	0.28	0.53	0.58

Physical stacking angle tests

The stacking angle embodies the comprehensive performance of seeds, including inter-crop mobility and crop-material mobility, as well as inter-crop friction and crop-material friction properties (*Xia et al., 2019; Hamzah et al., 2018; Ma et al., 2020*), which are pivotal for achieving accurate results in EDEM simulations. The parameters for a single seed model, particularly for diverse shapes like those of tiger nuts, are not universally applicable. In the present study, physical experiments were integrated with EDEM simulations to calibrate the parameters of the seed stacking angle of tiger nuts for the above characteristics.

The determination of the stacking angle was performed using the draw plate method (*Yu et al., 2021*). The testing apparatus comprised a stainless steel cylindrical drum, 130 mm in outer diameter, 125 mm in inner diameter, and 150 mm in height, without a lid. This drum was positioned on a flat test bed and filled to the brim with tiger nuts. As the cylinder was gradually raised, the seed freely formed a conical shape, and the angle of the resultant seed slope was recorded as the stacking angle when no further seed flow was observed, as shown in Fig. 8 (a).

In this study, the stacking angle was documented utilizing a MATLAB image processing technique (*Müller et al., 2021*). As illustrated in Fig. 8 (a), the image was captured using the imread function, Fig. 8 (b) shows the image grayscale, and as shown in Fig. 8 (c), the grayscale image was binarized using the im2bw function by selecting the appropriate threshold. As shown in Fig. 8 (d), the image, characterized by large internal gaps and incoherent structures at the edges, was refined using the imfill function to improve the definition of structural elements. The binarized contours were extracted with the bwperim function, as indicated in Fig. 8 (e). Half of the edge information was imported into Origin and analyzed using the image digitization tool to determine the tangent, as shown in Fig. 9.

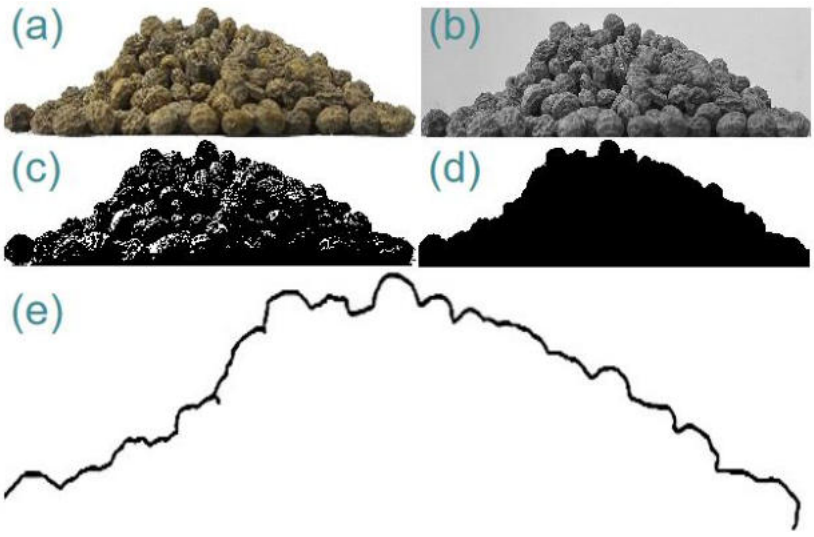


Fig. 8 - Stacked corner contour extraction process

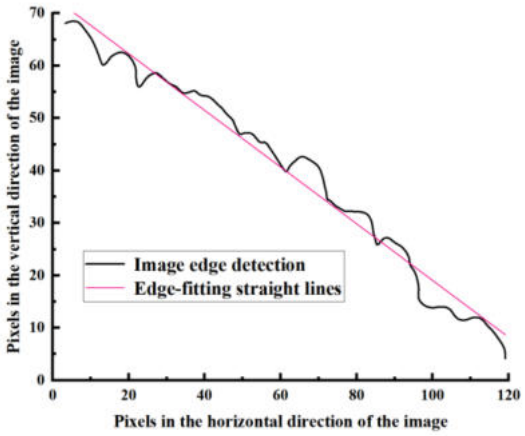


Fig. 9 - Tangent value fit

The experiment was replicated across 10 groups, and the results of the physical slope tangent τ measurements of seed stacking angle are presented in Table 9, with an average value of 0.734 recorded.

Table 9

Measurements of the angle of accumulation of tiger nuts

Test number	1	2	3	4	5	6	7	8	9	10
Stacking angle tangent	0.71	0.74	0.73	0.71	0.69	0.74	0.77	0.75	0.74	0.76

Stacking angle simulation test

From the data of 200 measurements, most of the tiger nuts were predominantly of an oblate-spheroid shape, with variations within 3 mm in thickness. A seed model was constructed using SolidWorks, as illustrated in Fig. 10 (b). Considering the variability in seed sizes, 50 percent of the seeds were model at dimensions of 13.5 mm in height, 12 mm in width, and 8.15 mm in thickness, while 25 percent of the seeds were scaled down by a factor of 0.9 and 0.8 respectively. The model was converted to STL format and imported into EDEM, filled with particles no smaller than 1 mm with the smoothing value set to 1, culminating in 245 different particles, as shown in Fig. 10 (c).

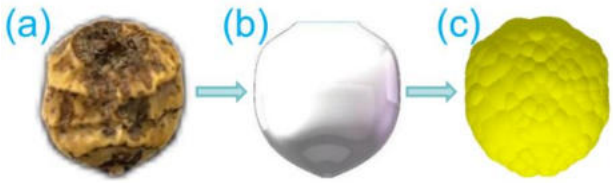


Fig. 10 - Seed model building process

To ensure consistency between the simulation process and the physical experiment, the material dimensions used in the simulation are identical to those used in the physical experiment in SOLIDWORKS, the material properties selected in EDEM are the same as the actual situation, and the input parameters are consistent with the measured data. The different materials are shown in Table 10. In this study, 500 particles were selected for generation and subsequently deposited for a duration of 1.5 s. The cylindrical container was elevated vertically at a velocity of 0.03 m/s, facilitating the autonomous flow of seeds, thereby forming a stacking angle. The total simulation was conducted over a period of 6 s. The simulation outcomes were documented upon completion. The results of the test are shown in Fig. 11. The resultant images were processed in MATLAB and analyzed using the image digitization tool to derive the tangent values in Fig. 12.

Table 10

Contact material simulation parameters

Parametric	Average parameters of steel plates	Average parameters of plastic plates
Poisson's ratio	0.30	0.34
Density/kg m^{-3}	7800	1160
shear modulus/MPa	79100	9420

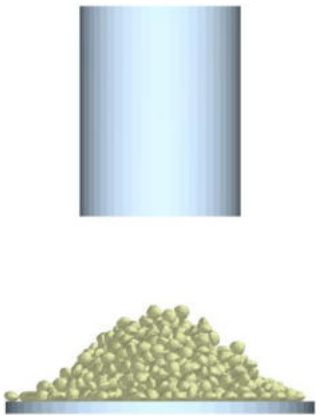


Fig. 11 - Simulation results before parameter optimization

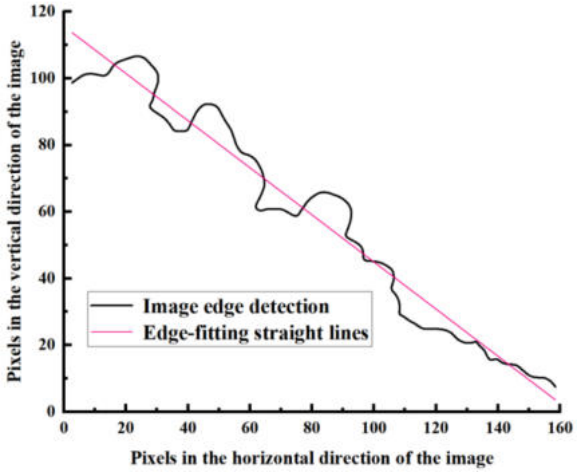


Fig. 12 - Simulation of the fitted image

Parameter optimization for discrete element simulation

Plackett-Burman design was employed for the screening test, utilizing Design-Expert 13 software. This design encompassed a multi-parametric experiment with two levels, nine principal factors, and two dummy factors to assess interactions between tiger nuts and various materials. The main effects of the factors were estimated using the minimum number of trials required to identify those with significant influence on the indicators being examined (*Yuan et al., 2022; Liu et al., 2016*).

Determination of significant impact parameters

X_1~X_8 represent the primary characteristics of tiger nuts, while X_9~X_{11} denote horizontally replicated tests. The maximum and minimum settings of the 12 test parameters were coded as +1 and -1, based on literature review and empirical data (e.g., Table 11) for each of the 12 sets of tests. Using the stacking angle as the principal factor under investigation, the images obtained from each group of tests were analyzed using MATLAB and the image digitization tool to record the values, as shown in Table 12.

Table 11

Plackett-Burman Test Parameter Range Tables

Symbols	Test parameters	Low level (-1)	Hight level (+1)
X_1	Poisson's ratio of tiger nuts	0.25	0.45
X_2	tiger nuts shear modulus/MPa	25.9	35.9
X_3	Tiger nuts - tiger nuts rolling friction coefficient	0.21	0.31
X_4	Tiger nuts - tiger nuts coefficient of static friction	0.28	0.68
X_5	Tiger nuts - tiger nuts coefficient of restitution	0.28	0.78
X_6	Tiger nuts - acrylics plate coefficient of restitution	0.37	0.78
X_7	Tiger nuts - acrylics plate static friction coefficient	0.23	0.49
X_8	Tiger nuts - acrylics plate rolling friction coefficient	0.17	0.23
$X_{9, 10, 11}$	Tiger nuts -nylon Horizontal repetition test	—	—

Table 12

Plackett-Burman test program and results

No.	X_1	X_2	X_3	X_4	X_5	X_6/X_9	X_7/X_{10}	X_8/X_{11}	Stacking angle tangent
1	1	1	-1	1	1	1/-1	-1/1	-1/-1	0.72
2	-1	1	1	-1	1	1/-1	1/-1	-1/1	0.87
3	1	-1	1	1	-1	1/-1	1/-1	1/-1	1.21
4	-1	1	-1	1	1	-1/1	1/-1	1/-1	0.71
5	-1	-1	1	-1	1	1/1	-1/1	1/-1	0.96
6	-1	-1	-1	1	-1	1/1	1/1	-1/1	0.76
7	1	-1	-1	-1	1	-1/-1	1/1	1/1	0.69
8	1	1	-1	-1	-1	1/1	-1/-1	1/1	0.73
9	1	1	1	-1	-1	-1/1	1/1	-1/-1	0.79
10	-1	1	1	1	-1	-1/-1	-1/1	1/1	1.09
11	1	-1	1	1	1	-1/1	-1/-1	-1/1	1.10
12	-1	-1	-1	-1	-1	-1/-1	-1/-1	-1/-1	0.71

Analysis of the results indicates that when the P-value is greater than 0.05, it signifies an absence of significant influence on the stacking angle, whereas a P-value less than 0.05 denotes a substantial influence on the stacking angle. As illustrated in Table 13, the P-values for X_1, X_2, X_5~ X_8 exceeded 0.05, with corresponding effects on the stacking angle of 0.36%, 5.66%, 1.33%, 0.75%, 1.90% and 4.16%, respectively. The influence of X_3 and X_4 accounted for 64.89 percent and 16.08 percent, respectively. Compared with other individual factors, X_3 and X_4 emerged as the predominant influences, collectively accounting for 80.97 percent of the influence factors, thereby confirming them as the main influence factors. By comparing the values, the primary and secondary order of parameter is: X_3, X_4, X_2, X_8, X_7, X_5, X_6, X_1.

Table 13

Significance analysis of Plackett-Burman test parameters

Parameters	Standardization effect	Sum of squares	Contribution rate/%	F value	P value
model		0.35		8.91	0.04
X_1	0.21	0.01	0.36	0.27	0.64
X_2	-0.08	0.02	5.66	4.24	0.13
X_3	0.28	0.24	64.89	48.61	0.01
X_4	0.14	0.06	16.08	12.05	0.04
X_5	-0.04	0.01	1.33	1.00	0.39
X_6	0.03	0.01	0.75	0.56	0.51
X_7	-0.05	0.01	1.90	1.42	0.32
X_8	0.07	0.02	4.16	3.11	0.18

*Note: * indicates a significant impact (0.01<P<0.05) ; ** indicates that the effect is extremely significant (P≤0.01).*

Steepest climb test based on the Plackett-Burman test

It was determined from the significance influence parameter test that X_3 and X_4 exerted the most substantial impact on the stacking angle; hence, they were selected as the test factors in the steepest climb test. The remaining parameters were modeled based on the values derived from the physical experiment results. X_3, X_4 showed that the standardized effect was positive, so it was incrementally increased at a fixed step size during the steepest climb test. The relative error 3 was calculated by bringing the steepest climb test stack angle tangent θ and the physical test stack angle tangent τ into Eq. 7.

The results of the steepest climb test are shown in Table 14, in which the rolling friction coefficients and static friction coefficients between the seeds were taken as 0.21~0.31 and 0.28~0.68, respectively, and the relative error of test 2 of the test results was the smallest, so test 2 was chosen as the center of the subsequent center-conformity response surface test. The optimal intervals are the values in the vicinity where the error is minimized: test 1 and test 3, the low and high values, respectively.

$$\ell = \frac{|\tau - \theta|}{\tau} \times 100\% \quad (7)$$

Table 14

Steepest Climb Test Program and Results

No.	X_3	X_4	Climbing test stacking angle tangent	Relative error/%
1	0.21	0.28	0.72	2.09
2	0.24	0.38	0.76	1.48
3	0.26	0.48	0.78	5.41
4	0.29	0.58	0.80	8.37
5	0.31	0.68	0.82	10.27

RESULTS AND DISCUSSION

Analysis of simulation results

Based on the range of interval values of rolling and static friction factors selected for tiger nuts in the steepest climb test using Design-Expert 13, the central composite test was conducted in Design-Expert 13. Stacking angle tests were performed for 11 sets of parameters. In order to increase the precision and reliability of the test and to reduce the effect of random errors on the test results, three of the groups of parameters were horizontally repeated tests. This was done to assess the impact of the rolling friction factor X_3 and static friction factor X_4 on the response surface optimization test for the formation of stacking angle of tiger nuts. The coding of the test factors and the results are displayed in Table 15. The maximum error in this test result was 4.84%, which is a substantial reduction of 5.43% relative to the maximum error of 10.27% for the steepest climb test. The minimum error of 0.12% is 1.35% less than the minimum error of 1.47% for the steepest climb test. The results show a substantial increase in the accuracy and reliability of the results obtained in this interval.

Table 15

Centre composite test results

No.	X_3	X_4	Stacking angle tangent	Errors/%
1	-1	-1	0.75	2.54
2	1	-1	0.73	0.55
3	-1	1	0.75	3.19
4	1	1	0.76	4.84
5	-1.41	0	0.75	2.80
6	1.41	0	0.75	2.54
7	0	-1.41	0.74	0.12
8	0	1.41	0.76	4.59
9	0	0	0.74	1.49
10	0	0	0.74	1.36
11	0	0	0.74	1.49

Multiple regression fitting by Design-Expert 13-centre composite test yielded the second-order regression equations for the coefficients of rolling and static friction between the simulation test stacking angle and the tiger nuts as:

$$\theta = 0.918 + 0.0844\,X_3 + 0.0284\,X_4 - 0.0785\,X_3X_4 - 0.0575\,X_3^2 - 0.084X_4^2 \quad (8)$$

As can be seen from Table 16, the P-value for the tiger nuts model is less than 0.0001. The misfit direction P is 0.8422, and the coefficient of determination R^2 is 0.9992, which is close to 1, indicating an extremely significant regression equation. A comparison between the adjusted coefficient of determination Adjusted R^2 and Predicted R^2 is 0.013, which is less than 0.2. The coefficient of variation (CV) is relatively small at 5.8%, which indicates a higher reliability of the model, as evidenced by these experimental results. It is concluded that the regression model not only accurately captures the real situation but also effectively predicts the stacking angle of tiger nuts.

Table 16

Analysis of variance results of the central composite response surface regression model

Parameters	Sum of squares	Degrees of freedom	Mean square	F value	P value
model	0.0011	5	0.0002	1204.94	＜0.0001
X_3	0.000003	1	0.000002	15.47	0.0110
X_4	0.0007	1	0.00007	3710.36	＜0.0001

Parameters	Sum of squares	Degrees of freedom	Mean square	F value	P value
X_3X_4	0.0002	1	0.0002	1040.67	＜0.0001
X_3^2	0.0001	1	0.0001	652.97	＜0.0001
X_4^2	0.0002	1	0.0002	962.79	＜0.0001
residual	0.0000009	5	0.0000002	/	/
lost proposal	0.0000003	3	0.0000001	0.2750	0.8422
pure error	0.0011	2	0.0000003	/	/

*Note: * indicates a significant impact (0.01<P<0.05) ; ** indicates that the effect is extremely significant (P≤0.01).*

The stacking angle response surface is depicted in Fig. 13, where variations in the effect on the stacking angle are associated with changes in dynamic and static friction. The coefficient of rolling friction has a small interval of variation, whereas an increase in the coefficient of static friction correlates with an increase in the stacking angle. The most pronounced impact on the stacking angle occurs when the rolling friction coefficient is 0.21 and the static friction coefficient is 0.48. When the rolling friction coefficient is between 0.23~0.26, the model shows a slowly increasing trend. When the static friction of the seeds increases, the effect on their stacking angle is greater regardless of whether the rolling friction is smaller or greater. This indicates that the coefficient of static friction has a greater effect on the change in the value of the tiger nuts stacking angle compared to the coefficient of dynamic friction. Combined with the previous analyses in this paper, the significance of the influence of static friction and rolling friction on the stacking angle between the tiger nuts were better verified.

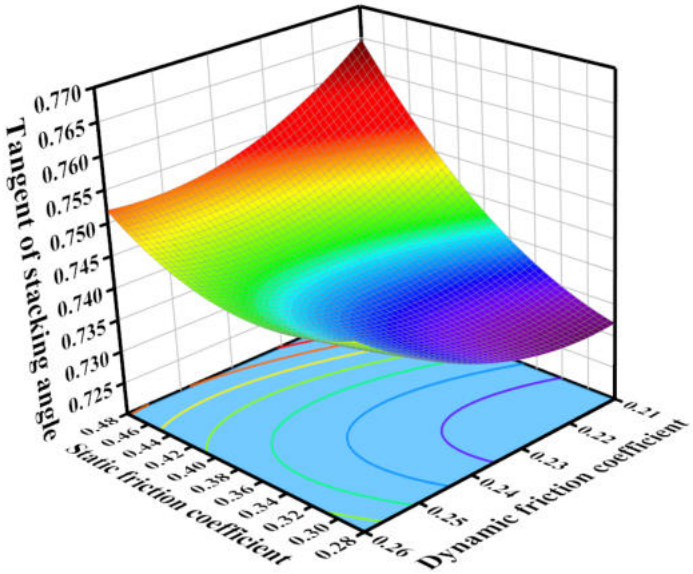


Fig. 13 - Stacking angle response surface plot

Experimental verification

In order to make the simulated stacking angle close to the physical experiment, this analysis is based on the central composite test and the second-order regression equation. From the objective of minimizing the error of the test results, the optimal solution analysis is carried out for the rolling friction and static friction between the seeds, which have the most influence in the test. The objective function and constraints are set as follows:

$$\begin{cases} \min \omega(X_3, X_4) \\ s.t. \begin{cases} 0.21 \le X_3 \le 0.26 \\ 0.28 \le X_4 \le 0.48 \end{cases} \end{cases} \quad (9)$$

The optimal parameters for static and rolling friction between tiger nuts were identified as 0.32 and 0.24, respectively. The stacking angle of the simulation test is closest to the stacking angle of the physical test, indicating that this combination is the best parameter combination to be used in the simulation test.

To confirm the reliability of the parameter results, the optimal parameters were applied to simulation tests in EDEM, and the tests were replicated three times, yielding the simulation stacking angle tangent values of 0.720, 0.732, and 0.741, respectively. The error between the simulation test stacking angle mean value of 0.731 and the result from the physical test, recorded at 0.734 is 0.41%. A high degree of congruence is observed between the physical test 14(a) and the simulation of stacking angle 14(b) employing the selected optimal parameters, with no significant difference evident. This suggests that the parameters of this simulation test are set with precision. This result further validates the reliability and realism of the simulation test.

Compared with existing studies, this paper improves the accuracy of the model through a combination of physical and simulation tests. The obtained parameters can be directly used in the testing of tiger nutsing tools and provide a reliable discrete element parameter model.

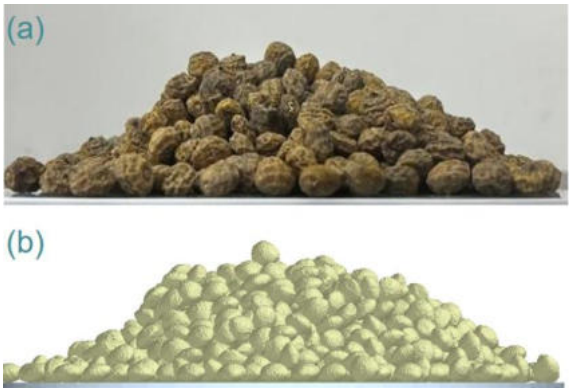


Fig. 14 - Simulation of stacking angle after parameter optimization of tiger nuts

CONCLUSIONS

In this study, MATLAB was used to make accurate and fast measurements of the three dimensions of tiger nuts to obtain reliable discrete meta-model dimensions. The average density and thousand grain weight of tiger nuts were measured to be 1062.22 kg/m^3 and 789.32 g, respectively. The average volume, equivalent particle diameter and sphericity were 1.54 cm^3, 11.15 mm and 85%, respectively. The modulus of elasticity, Poisson's ratio and shear modulus of tiger nuts were measured in physical tests: 8.22×106 Pa, 0.39, 3.03×106 Pa.

Dimensional measurements and physical tests of tiger nuts were used as a basis for selecting parameters for simulation tests. Through the Plackett-Berman screening experiment and the steepest-climbing test, the parameter intervals that had a large influence on the stacking angle were identified: inter-seed rolling friction (0.21 to 0.31), and inter-seed static friction (0.28 to 0.68). The optimal simulation parameters were obtained from the central composite response surface test: inter-seed rolling friction of 0.24 and inter-seed static friction of 0.32, the relative error in the stacking angle was minimized.

In this paper, the relevant parameters obtained from the discrete element calibration test using tiger nuts can be used as the parameters for tiger nuts simulation, and can be used as a reference for the optimized design of tiger nuts sowing machine structure. By simulating the process of stacking angle formation of tiger nuts, it is possible to predict the pass rate and breakage rate of sown seeds under different factors. This optimizes the structure of the tiger nuts planter, reduces the number of physical pre-tests, avoids the problem of not being able to conduct seeding tests due to external environmental factors, reduces production costs, and improves research efficiency.

ACKNOWLEDGEMENT

The authors were funded for this project by the Ministry of Agriculture and Rural Affairs Specialty Oilseed (Oil Sesame) Crop Full Mechanization Base, and the Key R&D Tasks in the Autonomous Region (2023B02032).

REFERENCES

[1] Chen X., Zhong L. (2012). Design and testing of air-absorbent seed dischargers with seed guides (气吸式排种器带式导种装置的设计与试验). *Journal of Agricultural Engineering*, Vol. 28(22), pp. 8-15, China.

[2] Chen Y., Gao X., Jin X., Ma X., Hu B., Zhang X. (2023). Calibration and test of discrete element simulation parameters for tiger nut seeds (油莎豆排种离散元仿真参数标定与试验). *Journal of Agricultural Machinery*, Vol. 54(12), pp. 58-69, China.

[3] Chen Y., Wang K., Luo X., Li J., Hu B., Zhang H. (2017). Theoretical analysis of adsorption seed pick-up in air-blown suspended seed supply drum planters (气吹悬浮供种滚筒式播种机吸附取种理论分析). *Agricultural mechanization research*, Vol. 39(04), pp. 21-26, China. DOI: 10.13427/j.cnki.njyi.2017.04.004.

[4] Guo T., Wan C., Huang F., Wei C., Hu Z. (2021). Progress of research on the main nutrients and physiological functions of tiger nut seeds (油莎豆主要营养成分及生理功能研究进展). *Chinese Journal of Oil Crops*, Vol. 43(06), pp. 1007-9084, China DOI: 10.19802/j.issn.1007-9084.2020145.

[5] Hamzah M., Beakawi A, H., Omar S. (2018). A review on the angle of repose of granular materials. *Powder Technology*, Vol. 330(03), pp. 397-417.

[6] Hou Z., Dai N., Chen Z., Xu Y., Zhang X. (2020). Determination of physical property parameters of iceplant seeds and calibration of parameters for discrete element simulation (冰草种子物性参数测定与离散元仿真参数标定). *Journal of Agricultural Engineering*, Vol. 36(04), pp. 44-53, China.

[7] Hu M., Xia J., Zhou Y., Luo C., Zhou M., Liu Z. (2022). Measurement and Calibration of the Discrete Element Parameters of Coated Delinted Cotton Seeds (涂层脱绒棉籽离散元素参数的测量与校准). *Agriculture*, Vol. 12, 286, China. https://doi.org/10.3390/agriculture12020286

[8] Khodabakhshian R. (2012). Poisson's ratio of pumpkin seeds and their kernels as a function of variety, size, moisture content and loading rate. Agricultural Engineering International: *The CIGR e-journal*, Vol. 14(3), pp. 3-14.

[9] Li Z., Wang J., Liu H., Wang P., Wu X., Ma C., Zhang D. (2022). Status of tiger nut seeds Industry Development and Suggestions (油莎豆产业发展现状及建议). *Modern agricultural science and technology*, Vol. 22(08), pp. 225-231, China.

[10] Liu F., Zhang J., Li B., Chen J. (2016). Discrete elemental parameter analysis and calibration of wheat based on stacking tests (基于堆积试验的小麦离散元素参数分析及标定). *Journal of Agricultural Engineering*, Vol. 32(12), pp. 247-253, China.

[11] Ma Y. (2015). *Agricultural material science (农业材料科学).* Beijing: Chemical Industry Press, 2015, China.

[12] Ma Y., Song C., Xuan C., Wang H., Yang S., Wu P. (2020). Calibration of discrete element model parameters for alfalfa straw compression simulation (苜蓿秸秆压缩仿真离散元模型参数标定). *Journal of Agricultural Engineering*, Vol. 36(11), pp. 22-30, China.

[13] Muller D., Fimbinger E., Brand C. (2021). Algorithm for the determination of the angle of repose in bulk material analysis. *Powder Technology*, Vol. 383(01), pp. 598-605. https://doi.org/10.1016/j.powtec.2021.01.010

[14] Peng F., Wang J., Zhang L., Wei C., Liu W. (2022). Improvement and parameter optimisation of air suction cup seed discharger for tiger nut seeds (油莎豆气吸盘式排种器改进和参数优化). *Agricultural Engineering*, Vol. 12(12), pp. 98-103, China. DOI: 10.19998/j.cnki.2095-1795.2022.12.017.

[15] Shi L., Ma Z., Zhao W., Yang X., Sun B., Zhang J. (2019). Calibration of discrete meta-simulation parameters and experimental validation of seed rowing in caraway seeds (胡麻籽粒离散元仿真参数标定与排种试验验证). *Journal of Agricultural Engineering*, Vol. 35(20), pp. 25-33, China.

[16] Sun J., Yang Z., Guo Y., Cui Q., Wu X., Zhang Y. (2017). Mechanical properties of compression and damage crack formation mechanism in cereal grains (谷子籽粒压缩力学性质及损伤裂纹形成机理). *Journal of Agricultural Engineering*, Vol. 33(18), pp. 306-314, China.

[17] Tsa B., Rf B., Er B. (2021). Classification of granular materials via flowability-based clustering with application to bulk feeding. *Powder Technology*, Vol. 378(02), pp. 288-302. https://doi.org/10.1016/j.powtec.2020.09.022

[18] Wang L., He X., Hu C., Guo W., Wang X., Xing J., Hou S. (2022). Determination of physical property parameters of dressed cotton seeds and calibration of parameters for discrete element simulation (包衣棉种物性参数测定与离散元仿真参数标定). *Journal of China Agricultural University*, Vol. 27(06), pp. 71-82, China.

[19] Wu M., Cong J., Yan Q., Zhu T., Peng X., Wang Y. (2020). Calibration and experimentation of parameters for discrete meta-simulation of peanut seed particles (花生种子颗粒离散元仿真参数标定与试验). *Journal of Agricultural Engineering*, Vol. 36(23), pp. 30-38, China.

[20] Xia R., Li B., Wang X., Li T., Yang Z. (2019). Measurement and calibration of the discrete element parameters of wet bulk coal (湿煤颗粒离散元素参数的测量与校准). *ScienceDirect. Measurement*, Vol. 142(2019), pp. 84-95, China. https://doi.org/10.1016/j.measurement.2019.04.069

[21] Xu Z., Zhou Y., Hu M., Ke H., Zhang M., Lv W. (2020). Simulation test on seed discharge of internal seed filling type cotton seed discharger based on EDEM (基于 EDEM 的内充种式棉花排种器排种仿真试验). *Journal of Gansu Agricultural University*, Vol. 55(04), pp. 175-183, China. DOI: 10.13432/j.cnki.jgsau.2020.04.025.

[22] Yu C., Duan H., Cai X., Xu T., Yao F., Chen Z., Yan Q. (2021). Determination of micro potato materials based on discrete element simulation parameters (基于离散元仿真参数的微型薯物料测定). *Journal of Central China Agricultural University*, Vol. 40(01), pp. 210-217, China. DOI: 10.13300/j.cnki.hnlkxb.2021.01.026.

[23] Yu Q., Liu Y., Chen X. (2020). Calibration and testing of simulation parameters of Panax pseudoginseng seeds based on discrete elements (基于离散元的三七种子仿真参数标定与试验). *Journal of Agricultural Machinery*, Vol. 51(02), pp. 123-132, China.

[24] Yuan J., Zhang H., Yang S., Song Q., Zhang J. (2022). Discrete meta-parameter calibration of grass carp feeds based on stacking tests (基于堆叠试验的草鱼饲料离散元参数校准). *Manufacturing automation*, Vol 44(12), pp. 61-67, China.

[25] Zeng Z., Ma X., Cao X., Li Z., Wang X. (2021). Current status and perspectives of the application of the discrete element method in agricultural engineering research (离散元法在农业工程研究中的应用现状和展望). *Journal of Agricultural Machinery*, Vol. 52(04), pp. 1-20, China.

[26] Zhang S., Zhang R., Chen T., Fu J., Yuan H. (2022). Mung bean seed discrete meta-simulation parameter calibration and seed scheduling test (绿豆种子离散元仿真参数标定与排种试验). *Journal of Agricultural Machinery*, Vol. 53(03), pp. 71-79, China.

[27] Zhang X., Chen Y., Shi Z., Jin W., Zhang H., Fu H., Wang D. (2021). Design and experiment of double-storage turntable cotton vertical disc hole seeding and metering device (双仓转盘式棉花竖直圆盘穴播排种器设计与试验). *Transactions of the Chinese Society of Agricultural Engineering*, Vol. 37(19), pp. 27-36, China.

[28] Zhang X., Cheng J., Shi Z., Wang M., Fu H., Wu H. (2023). Simulation and experiment of seed taking performance of swing clamp type maize precision seed-metering device (摆动夹取式玉米精量排种器取种性能仿真与试验). *Transactions of the Chinese Society of Agricultural Machinery*, Vol. 54(04), pp. 38-50, China.

[29] Zheng X., He X., Shang S., Wang D., Li C., Shi Y., Zhao Z., Lu Y. (2024). Calibration and test of discrete element simulation parameters for tiger nut seeds grain (油莎豆种子籽粒离散元仿真参数标定与试 验). *Agricultural Mechanisation Research*, Vol. 46(2), pp. 172-178, China. DOI:10.13427/j.cnki.njyi.2024.02.028.

[30] Zhou H., Hu Z., Chen J., Lv X., Xie N. (2018). Calibration of DEM models for irregular particles based on experimental Check for design method and bulk experiments (基于实验数据校准不规则颗粒的数字高程模型（DEM）验证设计方法和体积试验). *Powder Technology*, Vol. 33(02), pp. 210-223, China. https://doi.org/10.1016/j.powtec.2018.03.064.

DESIGN AND EXPERIMENTAL OF A SEED METERING DEVICE FOR SMALL SIZED VEGETABLE SEEDS
/
小粒径蔬菜种子排种器的设计与试验

Qichao LI*, Guoqin XU, Jinlong FENG
College of Mechanical and Electrical, Lingnan Normal University, Cunjin Street, Zhanjiang 524048, China
E-mail: qc_lee@126.com (correspondent author)
DOI: https://doi.org/10.35633/inmateh-76-85

Keywords: *Vegetable seeds, cabbage, separation type of picking and dropping, seed metering device*

ABSTRACT
To address the seeding difficulty and low precision of small sized vegetable seeds, a new precision seed metering device with separated seed picking and dropping functions was developed. The structure and working principle of the device were analyzed. The mass, three-axis dimensions, and angle of repose of three cabbage seed varieties were measured to analyze the statistical patterns of their orientation distribution. The structural parameters of key components including the seed picking wheel, seed dropping wheel, and separator plate were designed using numerical calculation methods. Bench performance tests were conducted for parameter optimization. The experiment adopted a quadratic orthogonal rotation composite design, with the working speed and tilt angle of the measuring device as experimental factors, and the qualified seed spacing index and coefficient of variation as evaluation indicators. The results indicated that when the working speed was 0.40-0.63 r/s and the tilt angle was 5.32-9.67°, the seeding qualified index can exceed 90% and the variation coefficient was smaller than 12%, meeting the requirements of good seeding standards. This study used a separated harvesting vegetable seed metering device to sow small vegetable seeds, providing a new concept and theoretical reference for precision vegetable seed metering devices.

中文摘要
针对小粒径蔬菜种子播种难度大，精度低等问题，研制一种新型取投分离式小粒径蔬菜种子精密排种器，分析排种器的结构和工作原理。分别测试三种甘蓝种子质量、三轴尺寸和自然休止角，并分析了姿态分布规律，利用数值计算方法，设计了取种轮盘、投种轮盘、分隔板等关键部件结构参数。通过台架性能试验进行参数优选，以排种器工作转速和倾斜角度为因素，播种粒距合格指数和变异系数为指标，采用多因素二次正交旋转组合设计试验。结果表明：排种器工作转速 0.40~0.63 r/min，倾斜角度 5.32~9.67°时，播种合格指数>90%，变异系数<12%，达到播种优等标准要求。该研究利用取投分离式排种器播种小粒径蔬菜种子，为蔬菜精密排种器的创制提供了新思路和理论参考。

INTRODUCTION
Vegetable production requires mechanization, and planting technology is a main link in mechanized vegetable production. Current vegetable planting methods are categorized into seedling transplanting and mechanical direct seeding *(Zamuco et al., 2023; Hensh et al., 2024; Sharma et al., 2024; Li et al., 2022; Sun et al., 2024)*. Seedling transplanting can effectively preserve seeds and control pests, diseases and weeds. However, the transplanting process is labor-intensive and the planting cost is high *(Paudel et al., 2024; Saqib et al., 2025; Liu et al., 2025)*. Mechanical direct seeding can simplify the transplanting process and reduce planting cost. Due to the small particle size and low mass of most vegetable seeds, the development of mechanical direct seeding technology is constrained *(Li and Feng, 2024; Sharaby et al., 2019; Sharma and Khar, 2024; Basit et al., 2021)*. The key component for vegetable seeding is the seed metering device. Its structure and working principle determine the seeding quality, directly affecting vegetable yield and quality *(Yang et al., 2024; Valentin et al., 2024)*.

Sharaby et al. (2022) predicted the outflow process of sesame seeds from the oscillating seed meter. The optimal values for the main parameters of the oscillating seed metering device for sowing sesame seeds are a seed hole clearance of 9 mm, an oscillation angle of 20°, and an opening time of 0.022 s, and a sesame seed rate of 2.7 kg/ha. This provides a reference for the design and optimization of oscillating seeders for small seeds.

Qichao LI, Associate professor, Ph.D.; Guoqin XU, Undergraduate student; Jinlong FENG, Associate professor, Ph.D.

Hensh and Raheman (2022) designed an electromagnetic driven seeder driven by a push-pull solenoid valve. The seeds are transported through a rectangular hole wheel disc and thrown out at the outlet to improve seeding accuracy. *Valentin et al. (2023)* developed a carrot seeder that uses a cylindrical component as seed metering device. The seeder precisely places seeds into hills at a uniform interval along a straight row over the plant bed. *Patel et al. (2024)* developed a radish pneumatic planter. The parameters for variables nozzle hole were designed, and the operating parameters including forward speed, vacuum pressure, and nozzle hole diameter were optimized to achieve the desired performance of the planter. *Kus and Yildirim (2021)* designed a slotted wheel seeder device. Through optimizing the design of the slotted wheel, the damage to the seeder was reduced. *Mintesinot and Khurana (2025)* designed a fluted roller-type metering devices with trapezoidal and asymmetric grooves, as well as an indented cell-type roller metering mechanism for berseem and lucerne crops. *Liao et al. (2024)* designed a roller-type precision seed metering device featuring device specifically for rapeseed, which combined positive-negative pressure and lateral seed filling. This design can reduce the pressure applied to the bottom seed mass in the filling zone, effectively preventing seed mass entrainment and accumulation.

These studies on vegetable seed metering devices mainly focused on the mechanism of a single seed disc with simultaneous seed picking and dropping operations. The devices that use two separate components for seed picking and seed dropping are limited. This separation method can directly implement two-stage seed filling and dropping processes in the device, thereby improving seeding precision. This study designed a precision seed metering device with separated picking and dropping functions for vegetable seeds. The structure and working principle of the device were analyzed, and structural parameters of its key components were optimized. This work can provide a theoretical foundation and a new concept for advancing vegetable seeding technology, and also provide an essential sowing machinery to support the mechanized production and large-scale cultivation of vegetables.

MATERIALS AND METHODS

Selection and Physical Properties of Tested Vegetable Seeds

The geometric properties of seeds determine their flow ability and seed filling performance within seeding devices, and are key references for designing key structural parameters of seed metering devices. Due to variations in the morphological characteristics of different seeds, the axial dimension method was used to measure the triaxial dimensions of three cabbage seed varieties to ensure seeding precision and broaden the applicable seeding range. The seed length (l), width (w), and thickness (h) were defined to represent their overall shape and size. In the experiment, three cabbage varieties: Zhonggan 21, Jingfeng 1, and Dongguan, suitable for cultivation in the Heilongjiang region were selected. One hundred seeds were randomly sampled from each variety for triaxial dimension measurement. The overall mean values and standard deviations were calculated, as shown in Table 1.

Table 1

Three-dimensional dimension of cabbage seeds

Varieties	Thousand kernel weight (g)	Length *L* (mm)	Standard deviation s(%)	Width *w* (mm)	Standard deviation (%)	Thickness *h* (mm)	Standard deviation (%)	Angle of repose *β*(°)
Zhonggan 21	3.59	1.72	0.13	1.68	0.15	1.22	0.08	25
Jingfeng 1	3.76	1.78	0.28	1.72	0.11	1.18	0.13	28
Dongguan	4.11	1.76	0.22	1.69	0.18	1.29	0.24	30

Table 2

Probability of postures of cabbage seeds in seed container

Varieties	Supine Orientation /%	Lateral Recumbent Orientation /%	Vertical Orientation /%
Zhonggan 21	41.06	29.82	29.12
Jingfeng 1	42.57	29.21	28.22
Dongguan	40.06	30.58	29.36

As shown in Table 2, the orientation distribution of the three types of tested seeds in the seed picking spoons showed that the supine orientation was the most common, accounting for over 40%. The lateral and vertical orientations were equivalent, each accounting for about 29%.

Structure Design of the Seed Metering Device

The structure of the separated picking and dropping vegetable seed metering device is shown in Fig. 1. It mainly consists of housing, seed picking wheel, separator plate, seed dropping wheel, metering shaft, seed cleaning brush, and end cover. The seed picking wheel, separator plate, and seed dropping wheel are sequentially mounted on the metering shaft with an axial clearance of 0.5 mm. The separation plate is rigidly fixed to the device housing. There are 12 evenly distributed seed picking spoons installed on the seed picking wheel, which correspond one-to-one with the 12 seed receiving units on the seed dropping wheel. The functional area for picking and dropping operations is physically isolated, achieving a series of functions such as seed collection and discharge. The seed cleaning brush is installed inside the end cover, and there is a threaded adjustment mechanism on the brush holder.

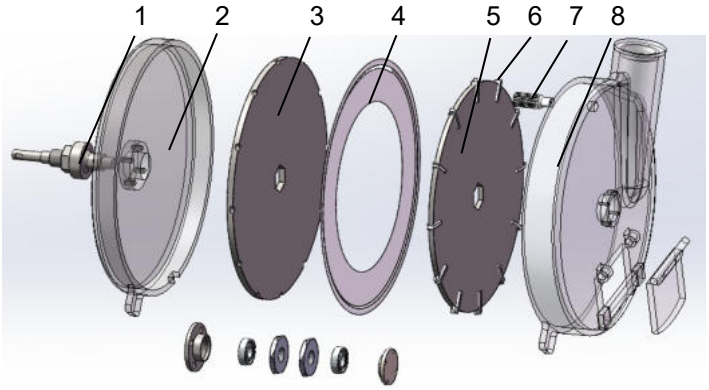


Fig. 1 - External structure of seed metering device
1 - Metering shaft; 2 - End cover; 3 - Seed dropping wheel; 4 - Separator plate; 5 - Seed picking wheel; 6 - Seed spoon; 7 - Seed cleaning brush; 8 - Housing

The operational cycle of the seed metering device includes six sequential stages: seed filling, unstable seed shedding, seed transfer, seed cleaning, seed transport, and seed sowing, as shown in Fig. 2.

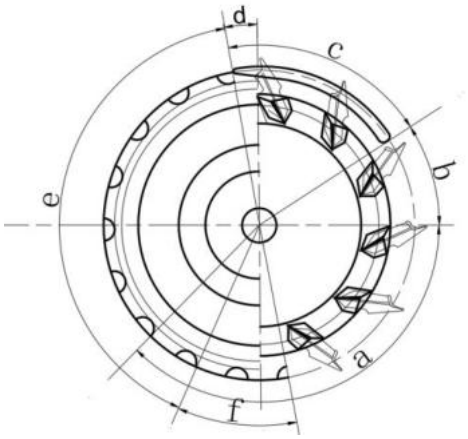


Fig. 2 - Schematic diagram of functional zones in seed metering device
a - Seed filling zone; b - Unstable seed shedding zone; c - Seed transfer zone; d - Seed cleaning zone; e - Seed guiding zone; f - Seed sowing zone

Vegetable seeds flow into the filling zone through the seed inlet channel. Under the drive of external power, the seed metering shaft rotates and activates the seed picking wheel and seed dropping wheel at the same time. Each seed picking spoon and separation plate form a seed-holding cavity. In the filling zone, a spoon scoops out multiple seeds from the seed mass, completely occupying their cavities before leaving the seed mass, and entering the sow zone after seed filling. In the shedding zone, unstably retained seeds detach from the spoons under dynamic forces and fall back into the seed mass of the filling zone. Spoons carrying stabilized seed quantities rotate to the transfer port of the separator plate. The seeds are fed into the corresponding seed receiving cells of the dropping wheel. Since each cell only accommodate one seed, the excess seeds are left in the spoon, completing the seed transfer process. At the end of the transfer zone, the seed cleaning brush removes residual seeds from the spoon. If the receiving cell is empty, the brushed seed supplements it. If the receiving cell is occupied, the brushed seeds will be returned to the seed mass in the filling zone.

The dropping wheel advances to the seed guiding zone. The seeds inside the receiving cells are fixed by the separator plate and housing guard, and can stably move to the discharge port at the bottom of the shell to complete seed guiding. At the discharge port, seeds are sprayed at a horizontal velocity opposite to the direction of machine movement. This balances the horizontal velocity during descent, achieving near-zero relative ground speed for precise placement onto the prepared seedbed to complete sowing.

Structural design of the seed picking wheel

The seed picking wheel is used as the seed collection and transfer component of the seed metering device. It mainly consists of seed picking spoons, spoon sockets, and the wheel disc, as shown in Fig. 3. The spoon sockets are fixed onto the wheel disc, and the seed picking spoons are plugged into the sockets. To improve the seed filling and transfer performance of the metering device and ensure broad adaptability to different vegetable seeds, the structural parameters of the seed picking spoons should be designed based on the physical properties of vegetable seeds.

This study uses the geometric parameters and orientation distribution probabilities of cabbage seeds to design the structural dimensions of the seed picking spoons. A multi-curvature combined-arc seed picking spoon has been developed, including three concave arc surfaces: the oblique-cut seed picking arc surface, the seed-holding transition arc surface, and the balanced seed-retention arc surface, as shown in Fig. 4. Oblique-cut seed picking arc surface: formed by the oblique intersection of an inclined cylinder and the cylindrical body at the spoon tip. Its inclination angle is determined based on the depth of the seed-holding cavity of the spoon. During seed mass filling and transport, this surface facilitates tangential seed separation and longitudinal seed guidance. Seed-holding transition arc surface: a spatial surface formed by sweeping a parabolic curve. It can effectively balance the seed weight, enhance stability during seed holding and transporting, and strengthen the seed cleaning effect of gravity. Balanced seed-retention arc surface: it supports seeds during transport, maintaining them in a state of dynamic equilibrium, as well as minimize seed damage during filling, transport and transfer. Consequently, the main structural parameters designed for the seed picking spoon include its length L, depth H, and wrap angle γ.

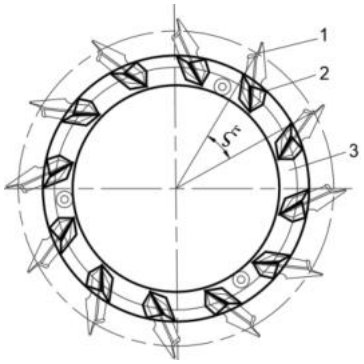


Fig. 3 - Structure diagram of the Seed Picking Wheel
1 - seed picking spoons; 2 - spoon sockets; 3 - wheel disc

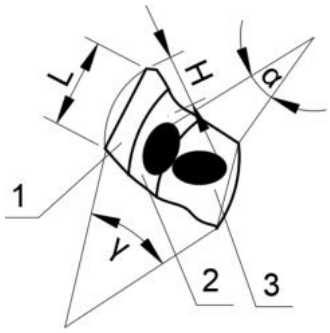


Fig. 4 - Structure diagram of seed picking spoons
1 - Oblique-cut seed picking arc surface; 2 - Seed-holding transition arc surface; 3 - Balanced seed-retention arc surface

The seed-holding space is a cavity formed by the three arc surfaces of the seed picking spoon and the planar surface of the seed separator plate. The volume of this cavity depends on the structural parameters of the seed picking spoon. Specifically, the length (*L*) and depth (*H*) are related to the triaxial dimensions of the cabbage seeds and their orientation when captured in the cavity, whereas the wrap angle is related to the angle of repose (*β*) of the seed mass. To ensure optimal seed filling and transfer performance of the seed picking spoon, the seed transfer angle (*α*) is designed.

The geometric parameter design follows the following principles:

$$\begin{cases} l < L < (1 + cos\alpha)l \\ w < H < (1 + sin\alpha)w \\ \beta > \gamma > atctan\left[1 + \left(\frac{H}{L}\right)^2\right]^{-1} \end{cases} \quad (1)$$

The outermost seeds at the critical edge are the most unstable. Therefore, a kinetic analysis is conducted on a single outermost seed, as shown in Fig. 5. Based on D'Alembert's principle, the equilibrium force system equations are established as follows:

$$\begin{cases} mgsin(\varphi+\omega t)+F_s=F_{N_1}+F_e \\ mgcos(\varphi+\omega t)-F_{N_2}=ma_\tau \\ F_e=mR\omega^2 \\ F_s=\mu F_{N_2} \end{cases} \quad (2)$$

where, m is the seed mass, g; a_τ is the tangential acceleration of cabbage seeds, m/s^2; ω is the angular speed of spoon movement, rad/s; (φ+ωt) is the rotation angle of seed collecting spoon (0, π/2), °; μ is the coefficient of friction between seeds; F_{N1} is the bearing force of seeds, N; F_{N2} is the push force of the spoon, N; F_s is the flying friction of the grains at the peripheral, N, and F_e is the centrifugal force of seeds, N.

Solving the second derivative of the radial decomposition force in Equation (2), then:

$$\frac{d^2F_{N_1}}{d\omega^2}=-Gt^2[sin(\varphi+\omega t)+\mu cos(\varphi+\omega t)]-2mR \quad (3)$$

Within the rotation angle interval (0, π/2) of the seed spoon, the second derivative value in Eq. (4) is consistently negative. This indicates that the radial force controlling seed retention in the spoon follows a downward-convex curve. Consequently, as the operational speed of the seed spoon increases, the radial force acting on the seed initially increases and subsequently decreases. Therefore, ensuring force balance at the inflection point is critical.

The seed picking wheel is designed with a rotational diameter of 200 mm and equipped with 12 seed picking spoons. To ensure effective single-seed feeding into the seed receiving cells of the seed dropping wheel, the seed picking spoons are designed to pick 1-2 seeds. Based on the principles of controlling seed orientation within the seed-holding cavity and the established spoon dimension design criteria, the structural parameters are determined: length L=3 mm, depth H=2 mm, wrap angle γ=(20~30)°, seed transfer angle α=(45~50)°.

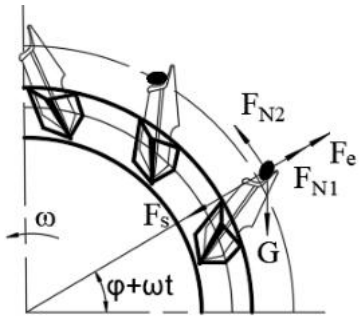


Fig. 5 - Diagram of the force applied to the moving seed

Structural design of the seed dropping wheel

The seed dropping wheel is used as the seed transport and discharge component of the seed metering device. Its function is to transport seeds fed from the receiving cells of the seed picking spoon to the discharge port area for release. The structural performance of the seed dropping wheel directly impacts seeding quality. An optimal seed transport and discharge trajectory facilitates zero-speed seeding. The seed receiving cells adopt a short isochronous curve contour, which can promote smooth seed feeding and discharging, ensure uniform seed spacing, and improve the accuracy of seed soft landing. This study investigates the motion trajectory of seeds during the delivery-to-landing process and designs a seed dropping wheel structure based on the brachistochrone principle. When a seed is discharged from the seed receiving cell at the discharge point, in a plane parallel to the central axis of the wheel (side view, O-XZ plane), the seed has a lateral horizontal velocity component with the initial speed v_x. The seed possesses a horizontal velocity component opposite to the forward direction of the wheel, with the initial speed v_y at the discharge port. In the vertical direction: due to the deviation between the seed position within the discharge cell and the centerline of the wheel, different centrifugal force components act on the seed during spraying. Therefore, the parabolic trajectory of the sprayed seeds requires spatial kinematic analysis. To analyze the motion of vegetable seeds during landing, a three-dimensional Cartesian coordinate system was established. The coordinate origin O is located at the initial seed release point, vertically aligned with the center of the seed-metering wheel. The cartesian coordinate system XOZ is established on the plane parallel to the central axis of the seed-metering wheel, and a Cartesian coordinate system YOZ is defined on the plane perpendicular to the central axis of the seed-metering wheel, as shown in Fig. 6.

The specific velocity equations are as follows:

$$\begin{cases} v=\varpi R \\ v_y = v\cos\sigma \\ v_z = v\sin\sigma \end{cases} \quad (4)$$

where, v is the linear speed of seeding wheel rotation, m/s; v_x is the component in the side horizontal direction of the sowing speed, m/s; v_y is the component in the front horizontal direction of the sowing speed, m/s; v_z is the component in vertical direction of the sowing speed, m/s; ω is the angular speed of seeding wheel rotation, rad/s; σ is the horizontal contained angle of seed throwing speed, °, and R is radius of the seed wheel, mm.

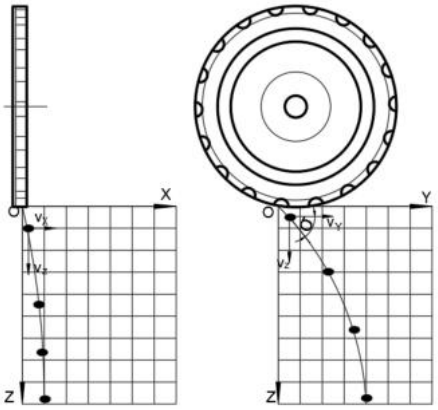


Fig. 6 - Kinematic analysis in dropping seed phase

Ignoring the influences of other factors in the sowing process, according to the momentum theorem, it could be obtained:

$$Ft_0 = mR\omega^2 t_0 = mv_x \quad (5)$$

Combining Eqs. (4) and (5), the trajectory equation of seed sowing could be obtained as follows:

$$\begin{cases} X=\varpi^2 \mathrm{R}t_0 t \\ Y=\varpi Rt\cos\sigma \\ Z=\varpi Rt\sin\sigma+\frac{1}{2}gt^2 \end{cases} \quad (6)$$

where, X is the horizontal displacement in the forward direction, mm; Y is the horizontal displacement in the lateral direction, mm; Z is the displacement in vertical direction, mm; t is the delivering time of the thrown seeds, s; t_0 is the time for the seeds to drop from the seeding wheel, s.

The kinematic analysis of the seed trajectory reveals that the release speed of the seeding device is opposite to the forward movement of the machine in the horizontal direction, thereby reducing horizontal velocity, lowering the release height, decreasing the vertical velocity at seed-soil contact in the vertical direction, and minimizing seed movement. According to the seeding quality standards and the principle of zero-speed seeding requirement, the horizontal displacement components are $X \approx 0$, $Y \approx 0$. The rotational linear velocity of the seed-metering wheel should be equal the travel speed of the seeder to ensure the shortest seed separation time. Using seed geometric parameters and orientation distribution probabilities as design inputs, and applying the principle of short-term curve truncation, the seed-cell structure of the metering wheel was designed. Through rotational scanning optimization of the truncated curve, the seed receiving cell is optimized to have a nearly spherical crown profile. The structural parameters include the cell opening diameter D, cell depth H, and parameters of the swept truncated curve. The design follows the principles: $D > H > l$.

The short-time truncation curve of the seed receiving cell surface is analyzed considering a mass point M rolling from the starting point O to the endpoint K, where K is not directly lower than O. When a circle with a radius *r* rolls along different paths, the trajectory traced by point M on its circumference is a short-time line that minimizes the travel time between O and K. The curve I in Fig. 7 shows this short-term line, let θ be the rotation angle of the circumference. The parametric equations of the brachistochrone trajectory are as follows *(Akhshik et al., 2015)*:

$$\begin{cases} x = r(\theta - \sin\theta) \\ z = r(1-\cos\theta) \end{cases} \qquad \theta \in [0, \pi/2] \quad (7)$$

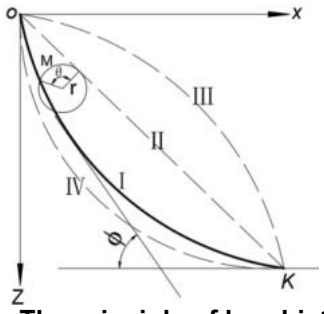


Fig. 7 - The principle of brachistochrone

Based on the kinematic model of seeds feeding into the cell during filling, when a seed rolls down at a height h, (where the maximum value equals the cell depth H), its lateral displacement is $\frac{1-\cos\theta}{\sin\theta}h$.

The work done by friction F_s along the brachistochrone path to the cell base is as follows:

$$\int_0^{\frac{1-\cos\theta}{\sin\theta}h} mg\cos\phi\tan\varphi dx = mgh\cos\phi\tan\varphi\frac{1-\cos\theta}{\sin\theta} \quad (8)$$

where, ϕ is the tangent inclination angle of the truncated curve at the sliding point, (°), and φ is the friction angle between seed and spoon, (°).

According to the law of conservation of energy, that is:

$$\frac{1}{2}m(v_z^2 - v_x^2) + mgh = mgh\,cos\,\phi\,tan\,\varphi\,\frac{1-cos\,\theta}{sin\,\theta} \quad (9)$$

where v_z is the initial descent speed of seeds, (m/s), and v_x is the seed termination horizontal speed, (m/s).

Combining and simplifying Eqs. (7) - (9), it can be obtained:

$$\frac{dz}{dx} = \frac{2gh\,\cos\phi\tan\varphi}{v_z^2 - v_x^2 + 2gh} \quad (10)$$

From this, the tangent inclination angle ϕ is as follows:

$$\phi = \arcsin\left[\sqrt{1 + \left(\frac{v_z^2 - v_x^2 + 2gh}{4gh\tan\varphi}\right)^2} - \frac{v_z^2 - v_x^2 + 2gh}{4gh\tan\varphi}\right] \quad (11)$$

The friction angle between the seed and the seed receiving cell is φ=20º-28º. Under ideal conditions with an initial seed velocity of v_z=0m/s and a final velocity at the cell base of v_x=0 m/s, a tangent inclination angle of ϕ =23º is obtained by substituting into Eq. (11).

Therefore, the design specifications of the seed dropping wheel are an outer contour diameter of 198 mm, an opening diameter D=2.0 mm of the seed receiving cell, a cell depth H=1.8 mm, and a tangent inclination angle of the cell surface ϕ =23º. The 12 seed receiving cells are evenly distributed.

Structural design of the separator plate

The separation plate located between the seed picking wheel and seed dropping wheel is an annular disc-shaped component made of 1.5 mm thick stamped steel sheet. The annular groove of the separator plate interfaces with the seed picking spoons to form the seed-picking cavity. During seeding, this plate remains stationary and does not rotate with the seed picking wheel or the seed dropping wheel. The plate has a sector shaped seed transfer port with an opening angle of θ, a tapered convergence angle δ at the port terminus, an opening width of b, as shown in Fig. 8. Adjacent seed picking spoons separated by an angle ξ fully feed seeds into the seed receiving cells of the dropping wheel in this port region.

This design prevents seed backflow and missed seeding events, according the following principles:

$$\begin{cases} 2\xi < \theta < 3\xi \\ \frac{3}{4}\xi \le \delta \le \xi \\ l < b < H \end{cases} \quad (12)$$

The separation plate is designed for safe installation in the shell, with a diameter of 204 mm. Its sector-shaped port has an opening angle of 70°, with a tapered convergence angle of 20° at the terminus and an opening width of 2 mm.

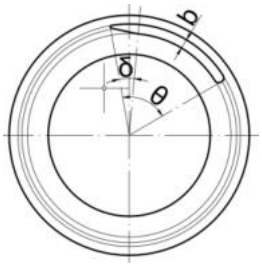


Fig. 8 - Structure diagram of the separator plate

Experimental Method

Experimental materials include the widely cultivated cabbage variety "Zhonggan 21"in Heilongjiang Province. The trials were conducted at the Seeding Performance Laboratory of Northeast Agricultural University. The experimental equipment includes a vegetable seeder with a separated type of picking and dropping and a JPS-12 computer vision seed metering performance test bench, as shown in Fig. 9.

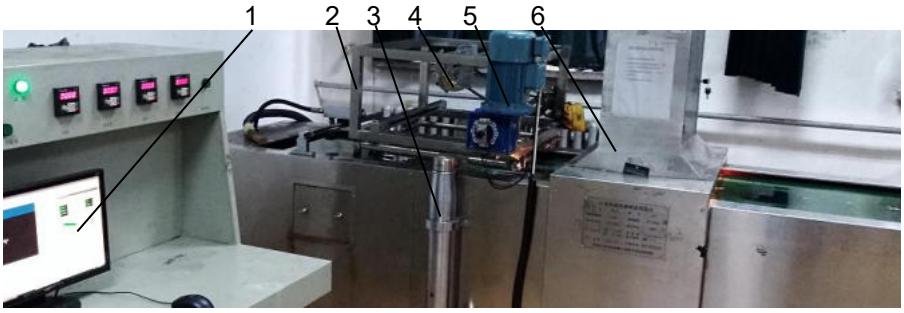


Fig. 9 - JPS-12 computer vision seed metering performance test bench

1 - Data analysis system; 2 - Mounting bracket; 3 - Frame lever; 4 - Seed metering device; 5 – Motor; 6 - Image acquisition system;

According to the structural principles and operational process of the seed metering device, the main factors influencing seeding quality and adaptable seeding range are the speed and tilt angle. Consequently, an optimization study focusing on these two factors was conducted. Referring to GB/T6973-2005 "Test methods for single seed drills " and JB/T1029-2001 "Specifications for single seed drills ", the seeding qualified index and coefficient of variation were selected as the test indicators to evaluate the performance of the seeder. A two-factor, five-level quadratic regression orthogonal rotational composite design was employed to determine the optimal operating parameters. The working speed v of the seeder is set in the range of 0.3 - 0.9 r/s, and the tilt angle ε was set in the range of -20~20° (Negative: tilted toward seed-picking wheel; Positive: tilted toward seed-dropping wheel).

RESULTS AND ANALYSIS

The working speed and tilt angle of the seed metering device were adjusted using the testing bench of the seed metering device. The seed distribution pattern observed during the tests is illustrated in Fig. 10. The experimental design scheme and measurement results are shown in Table 3. Design Expert 8.0.6 software was used for analysis, as shown in Table 4.

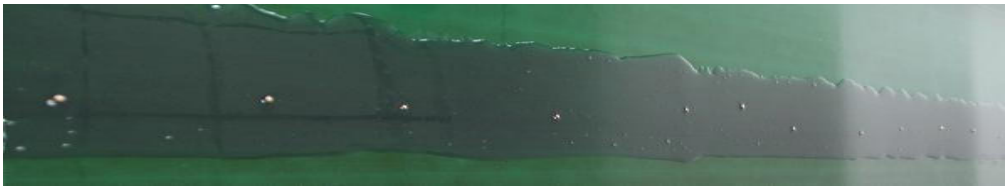


Fig. 10 - Distribution of seeds

Table 3

Experimental design and results

Number	Experimental factors			Performance indexes	
	working speed v / (r/s)	tilt angle ε / (°)		qualified index S / (%)	variable coefficient C / (%)
1	-1	-1		84.21	14.97
2	+1	-1		70.59	19.67
3	-1	+1		82.08	13.95
4	+1	+1		85.48	12.56

5	-1.414	0		89.35	10.32
6	+1.414	0		72.23	17.65
7	0	-1.414		76.81	16.69
8	0	+1.414		85.16	13.78
9	0	0		86.86	13.21
10	0	0		90.62	9.36
11	0	0		90.52	9.93
12	0	0		89.19	10.34
13	0	0		88.45	13.51
14	0	0		91.35	10.41
15	0	0		90.06	11.76
16	0	0		92.31	10.37

Table 4

Measured test data for variance analysis

Indexes	Sources	Sum of squares	df	Mean square	*F*	*P*
Qualified index	Model	633.28	5	126.66	27.87	< 0.0001
	v	148.19	1	148.19	32.61	0.0002
	ε	75.45	1	75.459	16.60	0.0022
	$v\,\varepsilon$	72.42	1	72.429	15.93	0.0026
	v^2	172.19	1	172.199	37.89	0.0001
	ε^2	165.03	1	165.03	36.31	0.0001
	Residual	45.44	10	4.54		
	Lack of Fit	24.76	3	8.25	2.79	0.1188
	Pure Error	20.68	7	2.95		
	Cor Total	678.73	15			
Variable coefficient	Model	111.86	5	22.37	8.66	0.0021
	v	23.38	1	23.38	9.05	0.0132
	ε	18.74	1	18.74	7.26	0.0226
	$v\,\varepsilon$	9.27	1	9.27	3.59	0.0874
	v^2	20.64	1	20.64	7.99	0.0180
	ε^2	39.83	1	39.83	15.42	0.0028
	Residual	25.83	10	2.58		
	Lack of Fit	9.16	3	3.05	1.28	0.3529
	Pure Error	16.68	7	2.38		
	Cor Total	137.70	15			

Note: ** means extremely significant (P < 0.01); * means significant (0.01 < P < 0.05), same as below.

As shown in Table 4, the working speed and tilt angle have an extremely significant impact on the sowing qualified index and coefficient of variation performance indicators. The regression equations for fitting the seeding qualified index and coefficient of variation are as follows:

$$S = 64.98+103.43v\text{-}0.63\varepsilon+1.42v\varepsilon-103.10v^2-0.02\varepsilon^2 \quad (13)$$

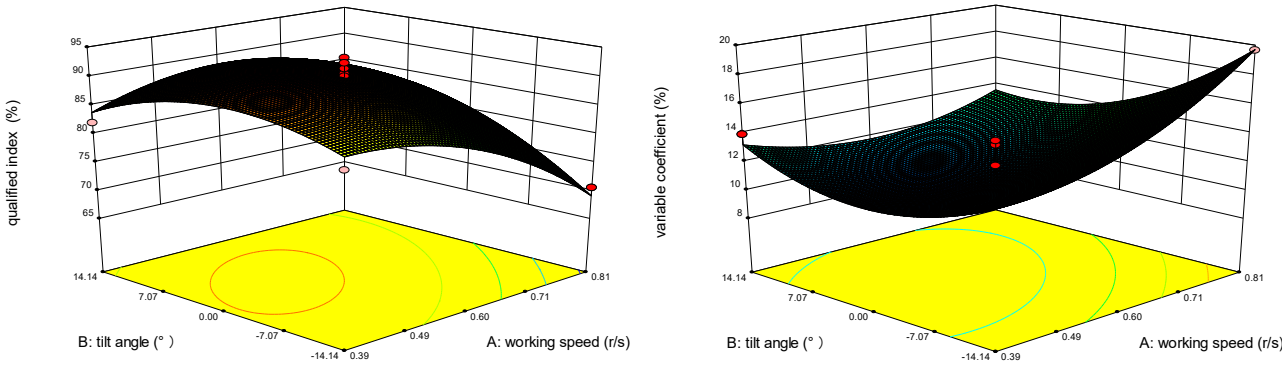
$$C = 19.13\text{-}34.77v+0.20\varepsilon-0.51v\varepsilon+35.69v^2+0.01\varepsilon^2 \quad (14)$$

To intuitively analyze the relationship between sowing indicators and experimental factors, Design Expert software is used to establish corresponding surfaces between the indicators and the two factors, as shown in Fig. 11.

Based on the regression Eq. (13) and the corresponding response surface plot in Fig. 11(a), the following relationships are observed: as the speed increases, the qualified index of seed spacing initially increases then decreases. When the working speed is low, the change in the qualified index is gentle, and when it is high, the change increases significantly. The main reason is that the relatively fast rotational speed leads to a decrease in seed filling rate, making it easy to miss seeds. As the tilt angle changes from negative to positive, the qualified index first increases and then decreases. When the tilt angle is negative, the seed picking spoons tilts outward, and the effective volume of the seed picking cavity decreases, resulting in a decrease in filling rate. Seeds are not easily fed into the falling wheel cells and are not easily missed during sowing. When the tilt angle is positive, the seed picking spoons tilts inward, and the effective volume of the seed picking cavity relatively increases, resulting in an increase in filling rate. The seeds are easy to be fed into the dropping wheel cells for re-seeding. When the working speed is about 0.50 r/s and the tilt angle is about 4°, the qualified index is the highest.

Based on the regression Eq. (14) and the corresponding response surface plot in Fig. 11(b), the following relationships are observed: as the speed increases, the variable coefficient of seed spacing decreases first and then increases.

When the working speed is low, the variation in the coefficient of variation is relatively small and stable; however, as the speed increases, the variation grows significantly. This is mainly due to an increased likelihood of missed seeding events at higher speeds. As the tilt angle changes from negative to positive, the qualified index first decreases and then increases. When the tilt angle is negative, the variable coefficient of uniformity changes rapidly, and when it is positive, the change is gentle. When the working speed is about 0.5 r/s and the tilt angle is about 3°, the variable coefficient is the smallest.



(a) Effects of working speed and tilt angle on the qualified index *(b) Effects of working speed and tilt angle on the variable coefficient*

Fig. 11 - Effects of working parameters on indexes

Based on of the experimental data, the optimal working parameters are determined, and each factor is subjected to optimization design. A parameterized mathematical model was established based on the agronomic requirements of vegetable sowing operations, taking into account the boundary conditions of various factors. Using a multi-objective optimization method, the regression equations for the qualified index of seed spacing and the coefficient of variation were analyzed to formulate the following nonlinear programming parametric model:

$$\begin{cases} \max S = f_1(r,\varepsilon) \\ \min C = f_2(r,\varepsilon) \\ s.t. \quad 0.30 \le v \le 0.90\ r \cdot s^{-1} \\ \qquad -20 \le \varepsilon \le 20° \\ \qquad 90\% \le S \le 100\% \\ \qquad 0 \le C \le 12\% \end{cases} \tag{15}$$

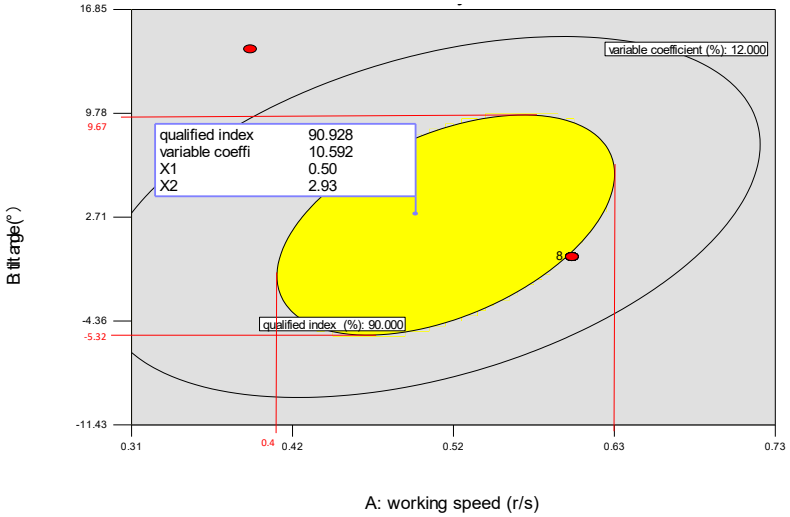


Fig. 12 - Diagram of parameters analysis

Based on optimization principles, Design-Expert software is used for parameter optimization The results demonstrate that the seed metering device can achieve optimal performance at an operational speed of 0.50 r/s and a tilt angle of 2.93°, with a qualified index of 90.93% and a variation coefficient of 10.59%. According to the optimization analysis, the optimal parameter combination interval is shown in Fig. 12. It is found that when the working speed is 0.40-0.63 r/s and the tilt angle is -5.32-9.67°, the qualified index of sowing distance is greater than 90%, and the variation coefficient is less than 12%.

CONCLUSIONS

Vegetable planter is an important component of mechanized vegetable cultivation, which directly affects the sowing quality and yield of vegetables. This study addresses the scarcity of mechanical seed metering devices suitable for small sized vegetable seeds. Through theoretical analysis, mechanical design, and prototype performance testing, the mechanism of a vegetable seed metering device was designed and analyzed. The main conclusions are as follows:

(1) Based on the physical properties of small-sized vegetable seeds (cabbage), a new precision seed metering device with separated seed picking and dropping functions was designed. Structural parameters of key components including the seed picking wheel, seed dropping wheel, and separator plate were analyzed and optimized;

(2) Bench tests identified the optimal operational parameter combination of working speed and tilt angle. Mathematical models correlating seeding performance metrics with experimental parameters were established. At an optimal operating condition of 0.5 r/s and a tilt angle of 2.93°, the device can achieve a qualified index of 90.93% and a variation coefficient of 10.59%. Optimization on the regression models confirmed that in the operational speed range of 0.40-0.63r/s and tilt angle range of -5.32-9.67°, the qualified index of seed spacing can exceed 90% and the Variation coefficient remained smaller than 12%, meeting seeding standards;

(3) The seed picking and dropping functions were performed by two separate components. The picking unit initially filled the seed-receiving cells of the dropping unit, which then transported the seeds to the discharge port for release. This two-stage precision metering process enabled continuous seed filling and discharge, significantly improving seeding accuracy. This innovative approach provided a new conceptual framework for the development of advanced vegetable seed metering technology.

ACKNOWLEDGEMENTS

Thanks to the Engineering Technology Research Center for High-Efficiency Precision Machining and Intelligent Management and Control of Hard-to-Machine Material Components in Western of Guangdong province (GrantNo.2024GCZX008), Horizontal project of intelligent seeder (Grant No.23060351600030), University Special talent projects (Grant No. ZL22023).

REFERENCES

[1] Akhshik, S., Behzad, M., & Rajabi, M. (2015). CFD-DEM approach to investigate the effect of drill pipe rotation on cuttings transport behavior. *Journal of Petroleum Science and Engineering*, *127*, 229-244. https://doi.org/10.1016/j.petrol.2015.01.017

[2] Basit, A., Zahid, A., Shah, S.T., Ullah, I., Ullah, S., Nawaz, M.K., Khalid, M.A., Ullah, I., Ali, F., & Ali, S. (2021). Effect of sowing methods and picking intervals on fresh yield and seed production of okra (Abelmoschus esculentus L.). *Pakistan Journal of Weed Science Research*, *27*(3), 407-418. http://dx.doi.org/10.28941/pjwsr.v27i3.885

[3] Hensh, S., & Raheman, H. (2022). Laboratory Evaluation of a Solenoid-Operated Hill Dropping Seed Metering Mechanism for Pre-germinated Paddy Seeds. *Journal of Biosystems Engineering, 47*(1), 1-12. https://doi.org/10.1007/s42853-021-00124-8

[4] Hensh, S., Raheman, H., Upadhyay, G., & Bera, S. (2024). Comparative analysis of a remotely-controlled wetland paddy seeder and conventional drum seeder. *Sādhanā*, *49*(4), 260. https://doi.org/10.1007/s12046-024-02604-x

[5] Kus, E., & Yildirim, Y. (2021). Laboratory Scale of Seed Damage of Coarse-Grain Depending on Groove Diameter and Depth in Roller Devices. *Applied Engineering in Agriculture*, 37(3), 411-416. https://doi.org/10.13031/aea.14484

[6] Li, Q.C., & Feng, J.L. (2024). Design and Experimental Analysis of Rotary Spoon Soybean Precision Seeder. *INMATEH - Agricultural Engineering*, *74*(3), 13-24. https://doi.org/10.35633/inmateh-74-01

[7] Li, Q.C., Feng, J.L., & Jiang, W. (2022). Design and Experiment on Precision Seed Metering Device for Narrow-Row and Dense Planting of Soybean. *INMATEH - Agricultural Engineering*, *67*(2), 353-363. https://doi.org/10.35633/inmateh-67-36

[8] Liao, Y.T., Liu, J.C., Liao, Q.X., Zheng, J., Li, T., & Jiang, S. (2024). Design and Test of Positive and Negative Pressure Combination Roller Type Precision Seed-metering Device for Rapeseed (正负气压组合滚轮式油菜精密排种器设计与试验). *Transactions of the Chinese Society for Agricultural Machinery*, *55*(5), 63-76. *(In Chinese)*. http://dx.doi.org/10.6041/j.issn.1000-1298.2024.05.006

[9] Liu, H., Du, Z., Guo, X., Li, H., Ma, X.Y., & Liao, Y.T. (2025). Progress on technology and equipment of precision and direct seeding for vegetable seeds (蔬菜种子精量直播技术与装备研究进展). *Journal of Huazhong Agricultural University*, *44*(1), 225-238. *(In Chinese).* https://doi.org/10.13300/j.cnki.hnlkxb.2025.01.025

[10] Mintesinot, S.M., & Khurana, R. (2025). Development and Evaluation of Metering Mechanism for Sowing of Berseem (*Trifolium alexandrinum L.*) and Lucerne (*Medicagosativa*) Crops. *Green Energy and Technology*. 148, 95-110. https://doi.org/10.1007/978-3-031-77339-6_6

[11] Patel, S.K., Bhimani, J.B., Yaduvanshi, B.K., Gupta, P. (2024). Radish (Raphanus raphanistrum subsp. sativus) Seed Planter Parameters Optimization using Response Surface Methodology. *Journal of Scientific & Industrial Research (JSIR)*, *83*(5), 483-489. https://doi.org/10.56042/jsir.v83i5.2823

[12] Paudel, B., Basak, J.K., Jeon, S.W., Lee, G.H., Deb, N.C., Karki, S., & Kim, H.T. (2024). Working speed optimization of the fully automated vegetable seedling transplanter. *Journal of Agricultural Engineering*. *55*(2), 1569. https://doi.org/10.4081/jae.2024.1569

[13] Saqib, M., Haram, A., Akbar, A., & Anjum, M. A. (2025). Methods of Open Field Cultivation of Vegetables. *Sustainable and Innovative Vegetable Production in times of Climate Change*, *6*, 89-100. https://doi.org/10.1007/978-981-96-6283-8_6

[14] Sharaby, N.，Doroshenko, A., & Butovchenko, A. (2022). Modelling and verification of sesame seed particles using the discrete element method. *Journal of Agricultural Engineering*. 53(2), 1286. https://doi.org/10.4081/jae.2022.1286Copy to clipboard

[15] Sharaby, N., Doroshenko, A., Butovchenko, A., & Legkonogih, A. (2019). A comparative analysis of precision seed planters. *E3S Web of Conferences*, *135*, 01080. https://doi.org/10.1051/e3sconf/201913501080

[16] Sharma, A., & Khar, S. (2024). Design and development of a vegetable plug seedling transplanting mechanism for a semi-automatic transplanter. *Scientia Horticulturae*, *326*, 112773. https://doi.org/10.1016/j.scienta.2023.112773

[17] Sharma, A., Prakash, A., Bhambota, S., & Kumar, S. (2024). Investigations of precision agriculture technologies with application to developing countries. *Environment, Development and Sustainability*, *27*, 15135-15171. https://doi.org/10.1007/s10668-024-04572-y

[18] Sun, S., Hu, B., Ma, J.H., Wu, X.M., Luo, X., Xu, X.Y., & Xu, L.C. (2024). Mechanism of high-voltage electrostatic adsorption seeding for vegetable seedlings and optimization of system parameters. *Transactions of the Chinese Society of Agricultural Engineering (Transactions of the CSAE)*, *40*(9), 26-38. https://doi.org/10.11975/j.issn.1002-6819.202311136

[19] Valentin, M.T., Białowiec, A., Karayel, D., Jasinskas, A., Ciolkosz, D., & Lavarias, J.A. (2023). Investigation of the performance of a cylindrical hopper and metering device of a carrot seeder. *Scientific Reports*. *13*(1), 813. https://doi.org/10.1038/s41598-022-25798-8

[20] Valentin, M.T., Pagnas, K.M., Suclad, R.L.M., Jasinskas, A., Domeika, R., & Šarauskis, E. (2024). Development of a cell-type cylindrical carrot seeder. *Heliyon*, *10*(23), e39605. https://doi.org/10.1016/j.heliyon.2024.e39605

[21] Yang, W.C., Tian, Z.Y., Pan, W.J., Zhao, J., Zhang, H.D., & Li, G.R. (2024). Design and experiment of seed cleaning device of vegetable plug seedling seeder (蔬菜穴盘育苗播种机清种装置的设计与试验). *Journal of South China Agricultural University*, *45*(1), 116-126. *(In Chinese).* http://dx.doi.org/10.7671/j.issn.1001-411X.202208041

[22] Zamuco, C.T., Amongo, R.M.C., Suministrado, D.C., & Peralta, E.K. (2023). Development of an automated precision planter for solanaceous vegetable seeds. *IOP Conference Series: Earth and Environmental Science*, *1241*(1), 012063. https://doi.org/10.1088/1755-1315/1241/1/012063

DETERMINATION AND ANALYSIS OF BIOMECHANICAL PROPERTIES OF POD PEPPERS UNDER DIFFERENT MOISTURE CONTENTS FOR MECHANIZED HARVESTING

/

不同含水量下机械化收获朝天椒的生物力学特性的测定与分析

Zhiqiang SONG *[1, 2], Yibao CHEN[3], Xiang DU [1], Zhong TANG [1], Shuyun LIN [4], Yunxiang YE *[2]

[1] School of Agricultural Engineering, Jiangsu University, Zhenjiang, Jiangsu / China;

[2] Key Laboratory of Agricultural Equipment for Hilly and Mountainous Areas in Southeastern China (Co-construction by Ministry and Province), Ministry of Agriculture and Rural Affairs, Hangzhou, Zhejiang / China;

[3] School of Navigation, Xiamen Ocean Vocational College, Xiamen, Fujian / China;

[4] Guizhou Institute of Mountain Agricultural Machinery, Guiyang, Guizhou / China

Tel: +8618303107879; E-mail: 666szq888@163.com; Corresponding author: Yunxiang YE

DOI: https://doi.org/10.35633/inmateh-76-86

Keywords: *pod pepper, moisture content, mechanized harvesting, experimental determination, tensile resistance*

ABSTRACT

Pod pepper is widely cultivated worldwide and serves diverse agricultural and industrial value. To reduce the loss and damage rate of mechanized harvesting of pod peppers, this study conducted multiple measurement experiments on the planting modes and biomechanical characteristics of pod peppers under different moisture contents. The experimental results are as follows: the average size of pod pepper fruit is 63.2 mm in length and 10.5 mm in diameter, the average density is 0.82×10³ kg·m⁻³, and the elastic modulus is 9.6 MPa. The maximum tensile force required for detaching pod pepper stalks from stems is 13.85 N, and the average value is 11.62 N; whereas the maximum tensile force required for separating pepper fruit from stalk ranges from 16.0N to 35.0 N, indicating that the fruit-stalk connection is stronger than the stalk-stem connection. In addition, the moisture content has a significant effect on the biomechanical properties of pod peppers. Within a certain range, the compressive resistance of pod peppers increases first and then decreases with the decrease of moisture content.

摘要

朝天椒在世界范围内广泛种植，具有多种农业和工业价值。为了降低机械化收获辣椒的损失和损坏率，本研究对朝天椒的种植模式和不同含水量下的生物力学特性进行了多次测量实验。实验结果如下：朝天椒果实的平均尺寸为长 63.2 毫米，直径 10.5 毫米，平均密度为 0.82×10³ 千克/立方米，弹性模量为 9.6 兆帕。从茎杆上分离果柄所需的最大拉力为 13.85 N，平均值为 11.62N；而分离朝天椒果实与果柄所需的最大拉力范围为 16.0 N 至 35.0 N，可见果实与果柄之间的连接力大于果柄与茎杆之间的连接力。此外，水分含量对朝天椒的生物力学性能有显著影响，在一定范围内，朝天椒的抗压强度随着含水量的降低先增加后减小。

INTRODUCTION

Pod pepper is not only a kind of vegetable with a spicy taste and multiple nutrients, but also a raw material for extracting industrial pigments *(Do Nascimento et al., 2014; Zhang et al., 2021)*. Therefore, pod pepper is widely cultivated in the globally with the global area reached 2.83 million hectares (ha) in 2020 *(FAOSTAT, 2025)*. Especially, China is a major producer and consumer of chili peppers, and China's demand for chili peppers is also growing with the development of industrial level and a large population. Pepper harvesters are replacing manual harvesting of chili peppers due to their high efficiency *(Zou et al., 2022; Han et al., 2024)*.

To improve the mechanized harvesting performance of pod pepper, reducing loss and damage rates, the biomechanical properties of pod pepper should be determined before a harvester is developed. This helps to explore the optimal structural and motion parameters of a pepper harvester. The geometric characteristics of pod pepper are of great significance for the harvesting performance of pepper harvesters. Currently, there are two mainstream structural forms of pod pepper harvesters, one structure is to use a toothed roller device to comb pod peppers, and the other structure is to use a double spiral rod to pull pod peppers *(Tai et al., 2025)*. During the mechanized harvesting of pod peppers, the forces exerted by mechanical components on the pepper fruits should exceed the connecting force between the fruit and stalk to detach from the main stems. If the force is exerted heavily, the pepper fruits may be damaged *(Kang et al., 2016; Song et al., 2024)*.

In recent years, many scholars have conducted research on the biological and mechanical properties of chili peppers. For example, *Du et al. (2023)* obtained some contact parameters of pod pepper through direct discrete element models (DEM). *Chen et al. (2024)* determined the static friction coefficient and coefficient of restitution between the seeds and steel plates through incline and free-fall tests. *Wang et al. (2024)* studied the damage mechanism of collision between pod pepper and comb teeth based on Hertz theory. *Han D. et al. (2024)* developed an inclined double-spiral pod pepper harvester to improve the harvest rate and reduce loss rate. To meet the power requirements of operations in hilly and mountainous areas, *Wu D. et al. (2023)* analyzed the load sensitivity of the hydraulic system of the pod pepper picking machine, and *Wang et al. (2023)* analyzed the vibration characteristics of a pepper harvester under different operating conditions.

To summarize the existing research, they focused on the biological and mechanical properties of pigmented chili peppers and string chili peppers in the mature stage. While, there is a lack of research on the biological and mechanical properties of pod peppers under different moisture contents. To address this gap, this study will conduct experimental measurements and analysis of the biological and mechanical properties of pod peppers under different moisture contents, including pepper density, compressive resistance of chili fruits, and the connection force between fruits and stems. It will provide basic data for the structural development of pod pepper harvesting equipment (e.g., picking devices, cleaning and separation devices) and the optimization of harvesting quality.

MATERIALS AND METHODS

Selection of pod pepper samples

The pod pepper samples were selected for experiments from a field in Shouxian Town, Xuzhou City, Jiangsu Province, as shown in Fig. 1. The row spacing was 70 cm, the plant spacing was 25 cm, the planting density was approximate 71700 plants per hectare, and the height of pod pepper plants measured using a tape measure was within 550 mm to 810 mm, the average plant height was 653 mm. The average plant width was 228 mm.



a) ***b)***

Fig. 1 – Pod pepper samples

a) Pod pepper plants; b) Measurement of pod pepper plant height

Geometric measurements of pod pepper

A total of 300 pod pepper samples were randomly collected from the experimental field. The length (*L*) and diameter (*D*) of the pod pepper fruits were measured using a vernier caliper with an accuracy of 0.02 mm, as shown in Fig. 2.



a) ***b)***

Fig. 2 – Determination of pod pepper's geometric characteristics

a) Pod pepper samples; b) Determination of the length (L) and diameter (D) of pod pepper fruits.

Determination of pod peppers' density

To determine the density of the pod peppers, the total masses and volume of several pod peppers should be measured first. Then, the density can be obtained based on the density calculation formula (1).

$$\rho_b = \frac{m}{V_t} \quad (1)$$

Eight pod peppers were randomly selected, and the total masses of them were measured by an electronic balance and denoted as m.

To measure the total volume of these pod peppers, drainage method was used in this study due to the irregular shape and size of the pod peppers. First, an appropriate amount of water was added to a graduated cylinder (with the volume sufficient to submerge the pod peppers), and the initial water volume in the cylinder was recorded as v_1. Then, these pod peppers were put into the cylinder, as shown in Fig. 3.

Since the density of pod pepper is lower than that of water, pod pepper would float on the water surface. To prevent pod peppers from floating, slight pressing force was applied to the eight pod peppers in the cylinder. After this operation, these pod peppers did not float in the cylinder, which was prevented by the compressive forces between the peppers and between the peppers and the cylinder wall. The water volume in the cylinder after submersion was recorded as v_2.

The total volume of the eight pod peppers was thus calculated as $V_t = v_2 - v_1$. To minimize experimental measurement errors, five identical tests were conducted. Then the density of the pod pepper samples was derived using Equation (1).



a) ***b)***

Fig. 3 – Determination of pod pepper's density

a) Measuring the total masses of pod peppers; b) Pod peppers put into the cylinder.

Determination of the moisture content of pod pepper fruits

The moisture content of pod pepper fruits has a significant impact on their mechanical properties, and moisture content can be used to characterize the maturity of pod peppers. Therefore, moisture content is an important material characteristic. To determine the moisture content of pod peppers and prepare for different moisture contents of pod pepper samples, the relevant determination method was conducted in accordance with the method of determining grain moisture content specified in GB/T 5262-2008 *(China Machinery Industry Federation, 2008)*.

A total of 100 pod pepper samples were randomly selected and evenly divided into five groups (20 samples per group). Before drying, the weight of each group of pod peppers fruits was weighed. Then, these pod pepper samples were placed into evaporating dishes, and the total mass of pod peppers in each dish was measured separately using a balance. The five groups of pod pepper samples were then simultaneously placed into a DHG-9053A electric constant temperature blast drying oven (Fig. 4 (a)) for constant-temperature drying. The temperature was set at 105°C.

After drying for 30 minutes, pod peppers samples of Group 1 were taken out and placed into a sealed desiccator to cool to room temperature, and their masses were weighed. After drying for 60 minutes, pod pepper samples of Group 2 were taken out again. After it cooled to room temperature, and the mass was weighed. The same processing method as described above was referred to record as Group 3, Group 4, and Group 5, respectively. Especially, the mass of group 5 was measured every 30 minutes until the mass difference between two consecutive measurements was no more than 0.05 g. The pod pepper that has not undergone drying treatment was recorded as sample Group 0.

In this way, six groups of pod pepper samples with different moisture content gradients were obtained for subsequent mechanical measurement experiments, as shown in Fig. 4 (b). The average moisture content of the pod peppers was calculated for five sets of experiments using Equation (2):

$$m_d = \frac{w_{si} - w_{gi}}{w_{si}} \times 100\% \quad (2)$$

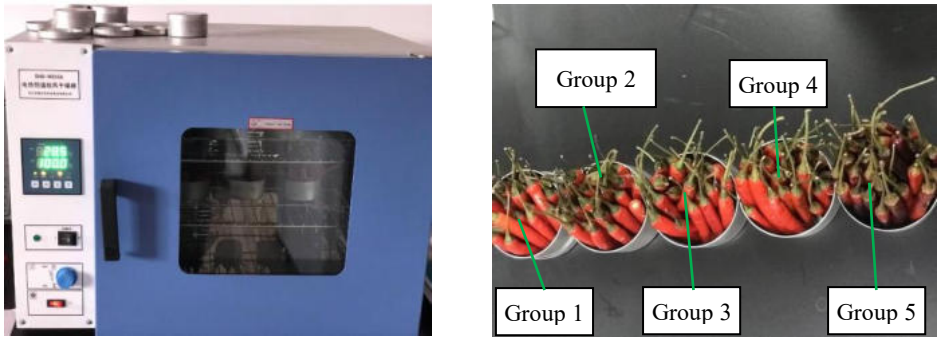
where:

m_d - moisture content of pod pepper, %;

w_{si} - the mass of the i-th group of pod peppers before drying, in grams;

w_{gi} - the mass of dried chili peppers in group i, measured in grams;

i - group i experiment, i = 1, 2, 3, 4, 5.



a) *b)*

Fig. 4 – Drying five groups of pod pepper samples with varying degrees of moisture content

a) A DHG-9053A electric constant temperature blast drying oven; b) Five groups of pod pepper samples with different moisture content.

Measurement of static friction contact coefficient

An angle tilt platform was used to measure the static friction coefficient of a pod pepper, the structure of which consists of a working surface, a frame, and an angle adjustment mechanism, as shown in Fig. 5. The tilt angle formed by the slope and the horizontal plane can be adjusted by the angle adjustment mechanism.

The measurement principle is that the gravity G of an object stationary on the working surface can be decomposed into two forces: a force F parallel to the slope downwards and a force T perpendicular to the slope downward, as shown in Fig. 6. If the tilt angle α of the working surface is less than the sliding critical angle, F is less than the static friction force between the pod pepper and the working surface, and the pod pepper is still in a relatively static state. As the tilt angle α increases, F becomes larger, if α exceeds the sliding critical angle of the pod pepper, it will begin to slide down along the tilt direction.

During the measuring process, a pod pepper was placed on the working surface of the angle tilt platform, then the tilt angle was adjusted, until the pod pepper was about to slide down but hasn't slid yet, the tilt angle formed by the slope and the horizontal plane was considered as the friction angle, and its tangent value was the measured friction coefficient of the pod pepper.

The relationship between the static friction coefficient μ_s and the tilt angle α is shown in Equation (3) *(Zhang et al., 2023)*.

$$\mu_s = \frac{f}{F} = \frac{mg\sin\alpha}{mg\cos\alpha} = \tan\alpha \quad (3)$$



Fig. 5 – Angle tilt platform (SXGX65) and digital display instrument

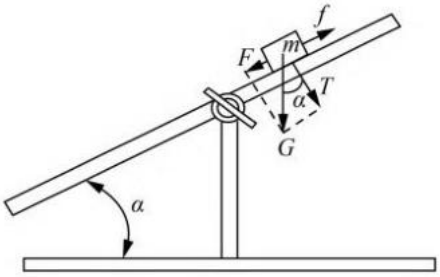


Fig. 6 – Schematic diagram of measuring the friction coefficient of an object

Measurement of rolling friction contact coefficient

To measure the rolling friction coefficient of the pod pepper, a pod pepper at a specific height on the angle tilt platform was released from rest to roll downward and subsequently transitions onto a horizontal steel plate. Then, the pod pepper rolled a certain distance on the horizontal surface before it stopped to rest. The test required that the pod pepper underwent pure rolling motion, with the static friction effect neglected during the rolling process, such that the resistance was treated as rolling friction resistance. The rolling distance along the incline was measured as S, and the rolling distance on the horizontal steel plate was measured as B. Based on the law of conservation of energy, the rolling friction coefficient was calculated using Equation (4):

$$\mu_r = \frac{mgS\sin\alpha}{mg\left(S\cos\alpha + B\right)} = \frac{S\sin\alpha}{S\cos\alpha + B} \tag{4}$$

Determination of restitution coefficient

The method of the free-fall collision rebound test was used determine the restitution coefficient of the pod pepper. During the free-fall collision rebound test, a pod pepper was initially released from a relative height H_1, allowing it to fell freely under gravity until it collided with a collision plate (steel or rubber) *(Kong et al., 2019; Huang et al., 2014)*. After the collision, the pod pepper rebounded, and the maximum relative rebound height H_2 was recorded. And the collision process was captured using a high-speed image acquisition system (i-SPEED TR, Olympus Corporation, Tokyo, Japan) at a frame rate of 100 fps. The restitution coefficient e of the pod pepper with a collision plate was calculated using Equation (5). To ensure reliability, the test is repeated five times using five different pod peppers per trial.

$$e = \frac{v_2}{v_1} = \frac{\sqrt{2gH_2}}{\sqrt{2gH_1}} = \frac{\sqrt{H_2}}{\sqrt{H_1}} \tag{5}$$

where, e denotes the restitution coefficient of the pod pepper collision with contact material; v_1 represents the instantaneous velocity of the pod pepper prior to the collision; v_2 represents the instantaneous velocity of the pod pepper after the collision.

Application methods of texture analyzer

A Texture Analyzer (TA. XT plus, UK) was used to measure the tensile, compressive, and shear stresses of pod peppers. Prior to conducting experiments, height correction and force correction should be performed. Height correction aims to calibrate the probe's zero reference point relative to the platform base, facilitating precise calculation of the sample's height when the probe makes contact. Force correction ensures the accuracy and traceability of test data by validating the precision of the sensor's measurements.

To configure the test, the "Return to Start" mode was selected. Within this mode, the "Go-to-Distance" method was employed, with "Force" designated as the primary measurement parameter. This configuration ensured that upon activation, the probe would move to the preset distance (Distance) and automatically return to its initial position after measurement. Additionally, the x-axis was configured to record distance (or time), whereas the y-axis was set to record force, aligning with experimental requirements to capture stress-strain relationships during mechanical testing of pod pepper samples. During these tests, the Texture Analyzer applied progressively increasing force, and the force sensed by the sensor was transmitted to a computer workstation and generated real-time force-displacement curves. These curves allow for the extraction of key parameters, including maximum tensile strength, elastic modulus, and elongation at fracture.

The schematic diagram of the TA.XT plus Texture Analyzer is presented in Fig. 7.

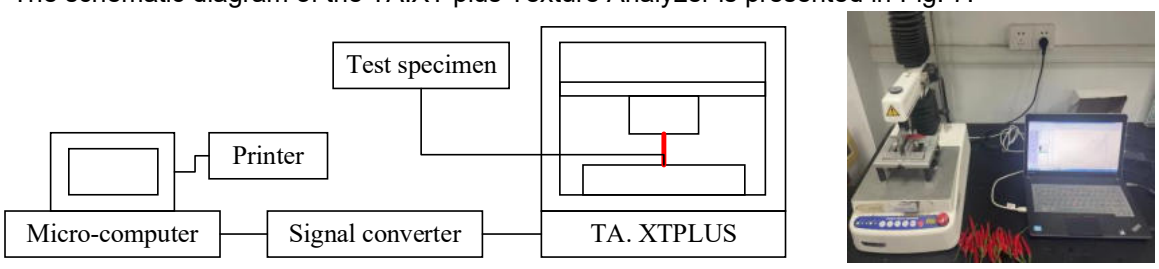


Fig. 7 – Structure schematic diagram of the Texture Analyzer.

a) Structure schematic diagram; b) TA. XT plus Texture Analyzer.

Determination of test speed

Testing speed (i.e., strain rate, defined as strain per unit time) significantly influences the mechanical response of materials and is critical for evaluating their mechanical behavior under different loading rates. Therefore, the selection of testing speed for tensile/compressive tests using a TA. XT plus texture analyzer must be based on material properties and experimental objectives. For instance, slow loading scenarios (e.g., material creep testing) typically require a testing speed of 0.1–1.0 mm/s, whereas high-speed scenarios (e.g., simulating impact or rapid deformation, such as material tear resistance) generally use relatively high speeds of 5.0–20.0 mm/s.

The purpose of this study is to analyze the impact and shear forces applied to pod peppers by a toothed drum. Therefore, high-speed testing was chosen for conducting tensile/compression tests. Nine pod pepper samples were randomly selected to undergo tensile testing at three testing speeds: 5 mm/s, 10 mm/s, and 15 mm/s. Each speed condition was conducted in triplicate, and the resultant curves with tensile-displacement are presented in Fig. 8.

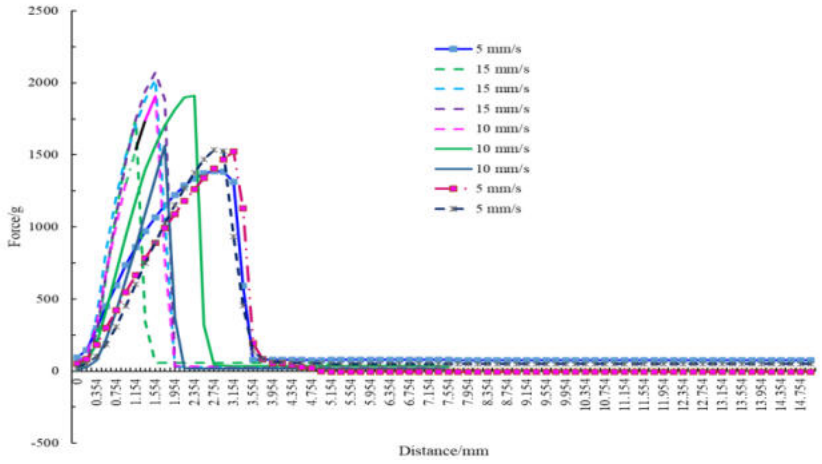
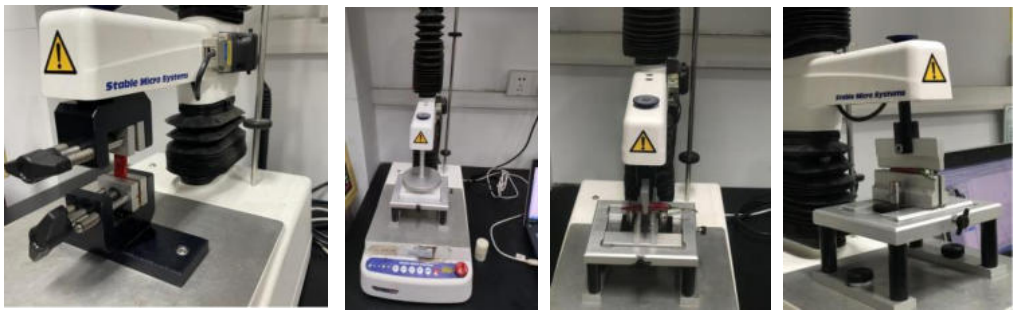


Fig. 8 – Tensile force-displacement curves at different speeds

As illustrated in Fig. 8, when the stretching speed was increased to 15 mm/s, the force-displacement curve become steeper, indicating a higher fracture strength. Under this high-speed condition, the pod chili pepper samples lack sufficient time for plastic deformation and energy absorption. Conversely, at a stretching speed of 5 mm/s, the force-displacement curve exhibited a relatively flatter profile with lower fracture strength, which better reflected the intrinsic mechanical response characteristics of pod chili peppers.

Determination of the mechanical properties of pod peppers

Tensile testing, compression testing, and shear testing are the three most commonly used testing methods in the study of material mechanical properties. Before the experiment, it is necessary to replace the texture analyzer probe corresponding to the specific testing method and configure the testing mode and speed parameters. Tensile tests were used to apply tensile loads to the stems and peels of pod pepper samples to characterize their tensile properties. Before testing, the A/TG clamping probe was used to clamp both ends of the pod pepper samples, as shown in Fig. 9 (a). The tensile distance was set to 15 mm, and the tensile speed was adjusted to 5 mm/s. To minimize experimental variability, five replicate tests were conducted.



a) ***b)*** ***c)*** ***d)***

Fig. 9 – Mechanical property test of pod chili pepper

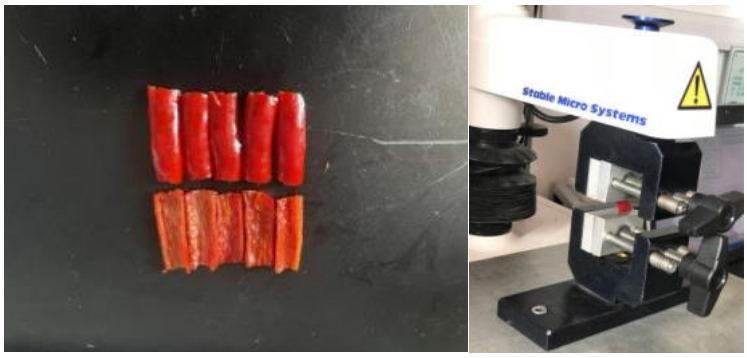
a) Tensile test; b) Compression test; c) Shear test; d) Longitudinal shear test

During compression tests, a pod pepper sample was positioned centrally on the testing platform of the texture analyzer, and the P/100 disc compression probe was used to compress pod pepper samples at a speed of 2 mm/s to acquire compressive force-displacement data curves. After testing, the pod pepper sample was replaced, and five replicate experiments were conducted to ensure reproducibility.

During shear testing, a pod pepper sample was placed on the support platform in a way that it spanned both ends of the platform, with care taken to position the pepper sample as symmetrically as possible relative to the shear probe's centerline to prevent relative sliding. To minimize experimental errors, five shear tests were conducted using the same method.

Tensile test of pod pepper peel

To carry out tensile test of pod pepper peel, pod pepper samples were selected from Group 0, and the seeds and placenta inside the fruit cavity were removed. Then the pod pepper peel was cut into rectangular strip samples with a length of 50 mm and a width of 10 mm, as shown in Fig. 10. Each strip sample was numbered, and its thickness was measured and recorded. To reduce experimental errors, four replicate experiments were conducted. In addition, pod pepper samples were selected from Group 1, Group 3, Group 5 to conduct tensile tests of pod pepper peel with different moisture contents.



a) ***b)***

Fig. 10 – Tensile test of pod pepper peel

a) Strip-like thin slices; b) Tensile test

Poisson's ratio and Elastic modulus

In addition, the Poisson's ratio and Elastic modulus of pod peppers were derived based on these test results, providing a scientific reference for optimizing the structural and motion parameters of harvesting devices. Poisson's ratio describes the absolute value ratio of the transverse normal strain to the axial normal strain of a material under uniaxial tension or compression, denoted by the Greek letter *v*. For most isotropic materials, the Poisson's ratio ranges between 0 and 0.5. The definition formula of Poisson's ratio is:

$$\nu = -\frac{\varepsilon_l}{\varepsilon} = -\frac{\Delta D/D_0}{\Delta L/L_0} = -\frac{(D-D_0)/D_0}{(L_1-L_0)/L_0} \quad (6)$$

where, ν is the Poisson's ratio of pod pepper; denotes the transverse normal strain; represents the axial normal strain; D_0 is the radial diameter of the pod pepper before loading; D is the radial diameter of the pod pepper after breakage; L_0 is the axial length of the pod pepper before loading; and L_1 is the axial length of the pod pepper after breakage.

Young's modulus (E) specifically describes the elastic stiffness of a material under uniaxial tension or compression, characterizing the relationship between normal stress and normal strain. The calculation formula for Young's modulus is,

$$E = \frac{\sigma}{\varepsilon} \quad (7)$$

RESULTS

Determining the biological properties of pod peppers

The external shape feature of pod peppers is that their diameters are the largest near the fruit base, gradually decreases from the base to the tip, and sharply decreases from the area near the tip to the tip. The fruit length was classified at intervals of 5.0 mm, and the diameter was classified at intervals of 1.0 mm. The measurement results of geometric dimensions of pod pepper are shown in Table 1.

Table 1

Classification of shape and determination of length and diameter of pod pepper fruits

Length (mm)	Diameter (mm)	Frequency	Proportion (%)
(35, 40]	(6.0, 7.0]	5	1.67
(40, 45]	(7.0, 8.0]	35	11.67
(45, 50]	(8.0, 9.0]	36	12.00
(50, 55]	(9.0, 10.0]	38	12.66
(55, 65]	(10.0, 11.0]	130	43.33
(65, 70]	(11.0, 12.0]	56	18.67

The density of pod pepper calculated by the drainage method is presented in Table 2. Due to the irregular shape and presence of cavities in pod peppers, the density is not an absolute density, but a bulk density.

Table 2

The density data of pod pepper measured

No. Item	1	2	3	4	5	Average density g/cm^3
Weight /g	22.576	25.230	20.869	22.423	26.597	
Volume /ml	27.0	31.0	25.0	28.0	32.0	0.823
Density g/cm^3	0.836	0.814	0.835	0.801	0.831	

The data of moisture content of pod pepper fruits obtained from five groups of measuring experiment and the average values are shown in Table 3.

Table 3

Moisture content of pod pepper

Item \ Test No.	1	2	3	4	5	Average moisture content /%
Quality before drying（w_s）/g	64.42	59.99	57.81	60.28	58.82	/
Quality after drying（w_g）/g	24.80	22.10	16.01	23.98	18.25	/
Moisture content /%	61.50	63.17	72.31	60.21	68.97	65.23

Determination of contact coefficients of pod pepper

Table 4 presents the experimental results of the static friction coefficient, rolling friction coefficient, and coefficient of restitution between pod pepper and steel plate in the above experiment.

Table 4

The contact coefficient between pod pepper and steel plate

Material	Static friction coefficient	Rolling friction coefficient	Coefficient of restitution
Pod pepper-steel plate	0.42	0.24	0.42

Determination of mechanical properties of pod peppers

Fig.11 shows the force displacement curve of the fruit-stalk fracture for pod pepper samples from Group 0. In order to further determine the tensile strength of pod peppers with different moisture contents, three pod pepper samples were randomly selected from Group 1 to Group 5 (with decreasing moisture content from Group 1 to Group 5), and subjected to fruit-stalk tensile tests on these pod pepper samples. The obtained tensile displacement curves are shown in Fig. 12.

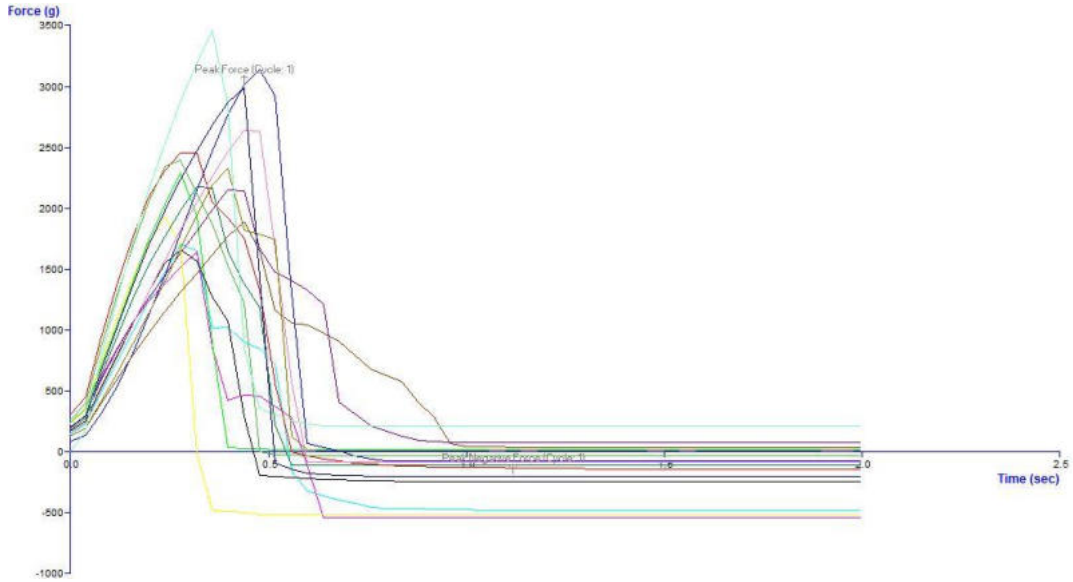


Fig. 11 – Tensile force-displacement curves

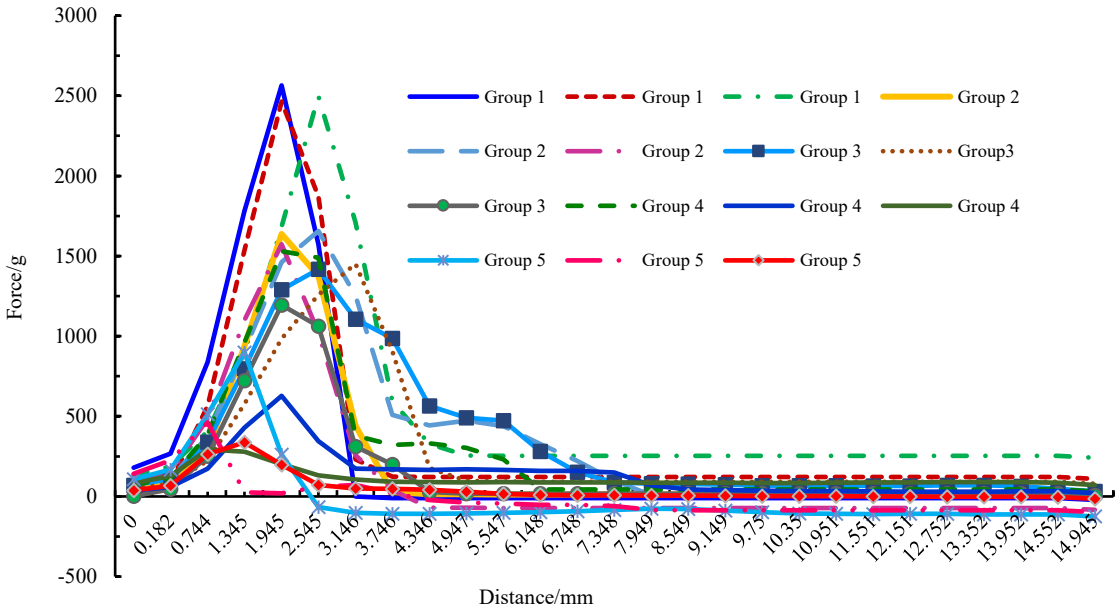


Fig. 12 – Tensile displacement curves at different moisture contents

The results of the tensile test of strip-shaped pod pepper peels

Table 5 presents the relevant tensile test data of strip-shaped pod pepper peel with different thicknesses. Fig. 13 shows the tensile force-displacement curve with varying moisture contents. It can be seen from Fig. 13 that the lower the moisture content, the lower the maximum tensile force required during stretching.

Table 5

Tensile test data of strip-shaped pod pepper peel with different thicknesses

Item \ Number	1	2	3	4	Average	Tensile stress/ MPa	E/ MPa
Thickness /mm	1.22	1.58	1.58	1.40	1.45	0.76	9.60
Tensile force /N	8.6	12.3	12.0	11.2	11.0		
ΔL /mm	3.5	4.3	4.2	4.0	4.0	/	
Strain ε	0.07	0.09	0.08	0.08	0.08	/	

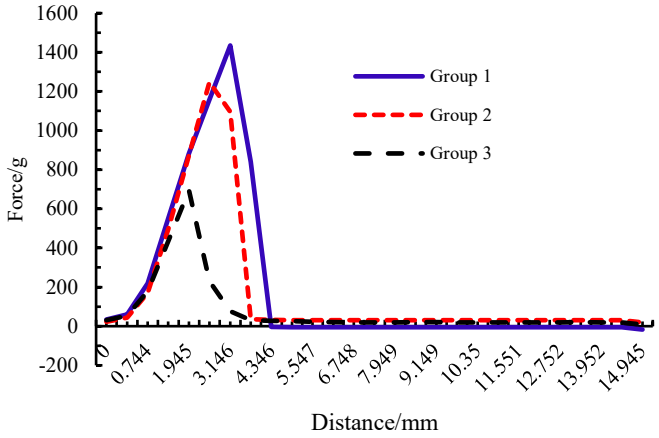


Fig. 13 – Tensile force-displacement curve with varying moisture contents

The results of the pod pepper compression tests

Fig. 14 presents the compressive force-displacement curve of pod pepper samples from Group 0. As shown in Fig. 14, the maximum compressive force that pod peppers can withstand ranges from 13 kg to 40 kg, indicating a yield-point behavior. Prior to reaching the yield point, the compressive force increases approximately linearly with deformation. Once the maximum compressive force is reached, the force decreases sharply with further deformation *(Seok et al., 2018)*.

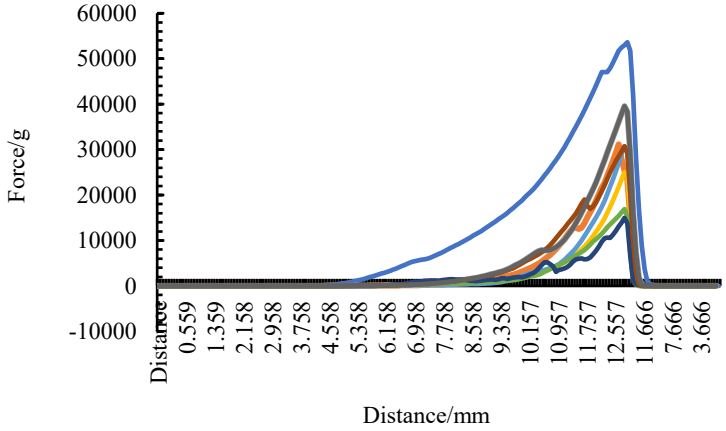
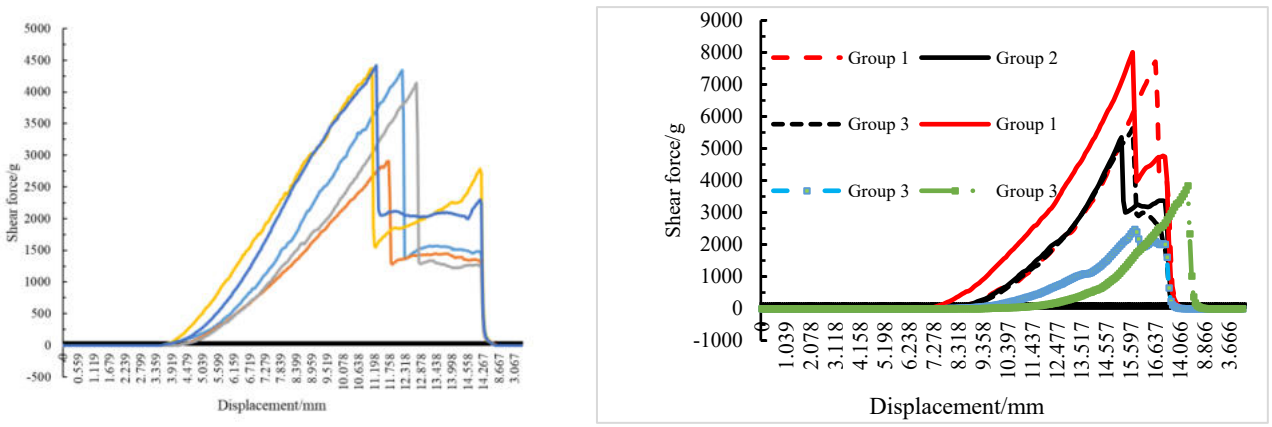


Fig. 14 – The compressive force-displacement curve of pod pepper samples from Group 0

The results of the pod pepper shear tests

Fig. 15(a) presents the shear force-displacement data curves of six test sets, and Fig. 15(b) presents the shear force-displacement curves of pod pepper samples under different moisture contents.



a) ***b)***

Fig. 15 – Shear force-displacement curve

As shown in Fig. 15(a), the maximum shear force ranges from 30.0 N to 45.0 N, corresponding to the plastic deformation of pod pepper, specifically, the yield point. Before reaching the yield point, the shear force increases gradually with deformation, showing a direct proportionality between the two, which is characteristic of elastic deformation. From Fig. 15(b), it can be observed that within a specific moisture content range (50%–70%), pod pepper samples with lower moisture content exhibit greater shear force at rupture. This is primarily because pod pepper becomes more brittle at higher moisture contents but demonstrates increased toughness as moisture content decreases.

DISCUSSION

The contact coefficients between pod pepper and steel plate are determined in this study as following: a static friction coefficient of 0.42, a rolling friction coefficient of 0.24, and a coefficient of restitution of 0.42. For comparison, *Du et al. (2023)* reported the following values from their experiments: the restitution coefficient was 0.42 ± 0.082, the static friction coefficient was 0.39, and the rolling friction coefficient was 0.19. Similarly, *Zhang et al. (2023)* reported the following values from their experiments: a restitution coefficient of 0.43, a static friction coefficient of 0.56, and a rolling friction coefficient of 0.31. Comparing these results reveals that the average static and rolling friction coefficients are not entirely consistent across different studies. The primary source of this discrepancy is likely attributed to variations in the surface roughness of the steel plates used in the respective experimental setups.

The maximum tensile force required for separating pepper fruit from stalk ranges from 16 N to 35 N in Fig. 11. In addition, pod pepper samples with lower moisture content (e.g., Group 5) require a smaller maximum tensile force to separate, whereas pod pepper samples with higher moisture content (e.g., Group 1) exhibit a larger maximum tensile force at the breaking point, as shown in Fig. 12. This study result aligns with the result reported by other scholars, and their results showed that the average tensile force for separation fruit from stalk decreases as the moisture content decreases with maturity level *(Liu et al., 2022; Wu et al., 2021; Xu et al., 2018)*. The higher the maturity level, the lower the required tensile force for separation, making it easier to separate. Conversely, the higher the required tensile force, the more difficult it is to separate *(Zhang et al., 2025)*. These test results confirm that the moisture content of pod pepper fruits has a notable influence on their tensile/compressive stress characteristics.

The maximum tensile force required to detach pod pepper stalks from stems was 13.85 N, with an average value of 11.62 N obtained in this study. Compared with the results reported by *Zhang et al. (2023)*, the average connection force between fruit and stalk was 11.54 N, while that between stalk and stem was 10.11 N, indicating that the fruit-stalk connection is stronger than the stalk-stem connection.

Elastic modulus is defined as the ratio of stress to strain under elastic loading, and it reflects the material's stiffness. A higher E value indicates greater resistance to stretching or compression (e.g., diamond exhibits an E of approximately 1000 GPa). Using relevant mechanical formulas, the Young's modulus of the pod pepper peel is calculated as 9.6 MPa.

This study focuses on exploring the planting mode and biomechanical characteristics of pod peppers in northern Jiangsu province. The results of this study are not entirely consistent with those of other scholars, and of course, the differences are not significant. It can be inferred that different regional terrains and climates in China have led to tailored planting patterns, which in turn affect the biomechanical properties of pod pepper plants.

CONCLUSIONS

This study investigated the biological and mechanical properties of pod pepper through experimental measurements combined with a review of relevant literature. The research aimed to enhance harvesting performance and reduce damage rates by integrating principles of agricultural machinery and agronomy. The findings provide foundational data to support the design and development of specialized harvesting machinery and equipment for pod pepper.

The main conclusions drawn are as follows: (1) Plant height, pepper length, pepper diameter are the main factors affecting the structural parameters of harvesting mechanisms. (2) The moisture content of pod peppers has a significant impact on their biological and mechanical properties. When the moisture content is around 50%, the pod peppers have the highest resistance to damage, making it the best period for mechanized harvesting. (3) The connection force between pepper fruit and stalk, between stalk and stem are the main factors affecting the motion parameters of a harvesting mechanism.

ACKNOWLEDGEMENT

This work was supported by the 14th Five Year Plan National Key R&D Program Project (2024YFD2300301), and "Key Laboratory of Agricultural Equipment for Hilly and Mountainous Areas in South-eastern China (Co-construction by Ministry and Province), Ministry of Agriculture and Rural Affairs Project, grant number (KFKT2024005)", and the "Jiangsu Province Education Science Planning Project (B/2023/01/60)", and "Guizhou Pepper Industry Technology System (GZLJCYJSTX-05)", and "Qiankehe Platform ZSYS (2025) 013 Guizhou Province Key Laboratory of Mountain Intelligent Agricultural Machinery".

REFERENCES

[1] Chen, X., Bai, J., Wang, X., Fang, W., Hong, T., Zang, N., Fang, L., Wang, G. (2024). Calibration and Testing of Discrete Elemental Simulation Parameters for Pod Pepper Seeds. *Agriculture-Basel,* 14, 831.

[2] China Machinery Industry Federation. (2008). *Agricultural machinery testing conditions-general rules for measuring methods (农业机械 试验条件测定方法的一般规定),* GB/T 5262—2008. Beijing/China.

[3] Do Nascimento, N. F. F., do Rêgo, E.R., Nascimento, M. F. , Bruckner, C. H. , Finger, F. L. , & do Rêgo, M.M. (2014). Combining ability for yield and fruit quality in the pepper capsicum annuum. *Genetics & Molecular Research, 13*(2), 3237-3249.

[4] Du, C., Han, D., Song, Z., Chen, Y., Chen, X., Wang, X. (2023). Calibration of contact parameters for complex shaped fruits based on discrete element method: the case of pod pepper (*Capsicum annuum*). *Biosystems Engineering, 226*, 43-54.

[5] FAOSTAT. (2025). *Food and Agriculture Organization of the United Nations: 2025*. Available online: https://www.fao.org/faostat/zh/#data/qcl (accessed on 7 May 2025).

[6] Han, D., Zhang, H., Li, G., Wang, G., Wang, X., Chen, Y., Chen, X., Wen, X., Yang, Q., Zhao, R. (2024) Development of a Bionic Picking Device for High Harvest and Low Loss Rate Pod Pepper Harvesting and Related Working Parameter Optimization Details. *Agriculture-Basel*, 14, 859. Switzerland.

[7] Huang, X., Zha, X., Pan, H, Zong, W., Chen, H. (2014). Measurement and analysis of rapeseeds' restitution coefficient in point-to-plate collision. *Transactions of the Chinese Society of Agricultural Engineering*, 30, 22–29.

[8] Kang, K., Park, H., Park, S., Kang, Y., Kim, D. (2016). Study on Optimal Working Conditions for Picking Head of Self-Propelled Pepper Harvester by Factorial Test. *Journal of Biosystems Engineering,41*(1), 12-20.

[9] Kong F., Shi L., Zhang Y., Chen C., Sun Y., Xie Q. (2019). Determination and Analysis of Recovery Coefficient in Seed Cotton Collision Model. *Journal of Agricultural Science and Technology*. 21, 92–99.

[10] Liu, Y., Zhang, X., Zhu, X., Ma, S. (2022). Vibration Separation Mechanism and Experimental Study of Pigment of Chile (色素辣椒机械振动分离机理及试验研究). *Journal of Agricultural Mechanization Research.* 44, 7-13, Harbin/China.

[11] Seok, N.J., Byun, J.-H.; Hyung, K.T., Kim, M.H., Dae-Cheol, K. (2018). Measurement of mechanical and physical properties of pepper for particle behavior analysis. *Journal of Biosystems Engineering.* 43, 173–184.

[12] Song, Z., Du, C., Chen, Y., Han, D., Wang, X. (2024) Development and test of a spring-finger roller-type hot pepper picking header. *Journal of Agricultural Engineering, 55*(2), 1562.

[13] Tai, S., Tang, Z., Li, B., Wang, S., Guo, X. (2025). Intelligent Recognition and Automated Production of Chili Peppers: A Review Addressing Varietal Diversity and Technological Requirements. *Agriculture-Basel*, 15, 1200, Switzerland.

[14] Wang, G., He, B., Han, D., Zhang, H., Wang, X., Chen, Y., Chen, X., Zhao, R., Li, G. (2024). Investigation of Collision Damage Mechanisms and Reduction Methods for Pod Pepper. *Agriculture-Basel,* 14, 117.

[15] Wang, X., Cao, Y., Fang, W., Sheng, H. (2023). Vibration Test and Analysis of Crawler Pepper Harvester under Multiple Working Conditions. *Sustainability,* 15, 8112.

[16] Wu, D., Ma, Z., Zhang, J., Xu, W., He, H., Li, Z. (2023). Simulation analysis of working circuit performance of mountain pepper harvester based on improved load-sensitive system. *Applied Sciences-Basel*, 13(18), 15.

[17] Wu, L. (2021). *Design and analysis of small hand supported pepper harvester (小型手扶式辣椒收获机设计与分析).* [Master's thesis], Chengdu University.

[18] Xu, D. (2018). *Design and research of small pepper picking machine (线辣椒收获机的设计与研究).* [Master's thesis], Gansu Agricultural University.
[19] Zhang, D., Sun, X., Battino, M., Wei, X., Shi, J., Zhao, L., Liu, S., Xiao, J., Shi, B., Zou, X. (2021). A comparative overview on chili pepper (*Capsicum genus*) and Sichuan pepper (*Zanthoxylum genus*): from pungent spices to pharma-foods. *Trends in Food Science & Technology*, 117 (16):148–162.
[20] Zhang, D., Tang, Y., Zhang, J., Lin, S., Zhang, T., Xu, W. (2023). Determination and simulation analysis of material properties of Chaotian pepper mixture (朝天椒混合物物料特性的测定与仿真分析). *Journal of Chinese Agricultural Mechanization*. 44(05):35-41+57. Nanjing/China.
[21] Zhang, S., Sun, Y., Zhang, Y., Dai, M., Miao, H., Zhang, Y., Gao J. (2025). Experimental study on the biomechanical characteristics of millet pepper (小米椒生物力学特性试验研究). *Journal of Agricultural Mechanization Research*. 47, 151–159, Harbin/China.
[22] Zou D., Alym·M., Han C., Li Q., Li Y., Zhang J., (2022). Design and Experiment of Picking Table of Pepper Harvester（辣椒收获机采摘台的设计与试验）. *Journal of Agricultural Mechanization Research*. 44 (08): 105–109. Harbin/China

DESIGN AND EXPERIMENTAL RESEARCH ON THE END EFFECTOR OF FRUIT ORCHARD COMB-TYPE FLOWER THINNING

/

果园梳齿式疏花末端执行器设计与试验研究

Caiqi HU*[1,2], Yechao HAN[1,2], Yichen LI[1,2], Junhao LI[1,2], Pengyu LIU[1,2], Siyuan ZHENG[1,2]
[1)] College of Mechanical and Electrical Engineering, Qingdao Agricultural University, Shandong / China
[2)] Shandong Provincial Key Laboratory of Smart Agricultural Equipment for Protected Horticulture
Tel: 8613616397874; E-mail : hucaiqi@163.com
Corresponding author: Caiqi HU
DOI: https://doi.org/10.35633/inmateh-76-87

Keywords: *mechanical flower thinning; simulation analysis; orchard test; smart horticulture*

ABSTRACT

Flower thinning is an important agricultural process in orchards. To address issues such as insufficient thinning accuracy and the need for secondary operations in traditional orchard thinning mechanisms, and to meet the agricultural demands for precise flower thinning, this study designs a comb-type flower thinning end effector based on the physical characteristics of the flowers and the agronomic requirements for thinning. This study adopts a flower thinning method combining thinning leaf spring piece and comb teeth. By optimizing the design of the spring piece dimensions, the study first systematically analyzes the force characteristics of the spring piece during the working process, as well as the force conditions of the flowers under different operating conditions, to identify the key factors affecting flower abscission. Next, ADAMS software is used for rigid-flexible coupling dynamic simulation analysis to determine the optimal working speed of the key flower thinning device as 230–250 r/min. Finally, field tests were conducted to verify the working reliability of the flower thinning machine. The test results show that the machine meets the expected design goals, providing technical support for efficient and precise flower thinning operations in orchards.

摘要

疏花是果园工作中重要的农艺过程，为解决传统果园疏花机构存在的疏花精度不足、需二次作业等问题，满足果园精确疏花的农艺需求，本研究基于花朵物理特性与疏花农艺要求，设计了梳齿式疏花末端执行机构。本研究采用疏花弹片与梳齿相结合的疏花形式，通过对弹片尺寸进行优化设计，首先系统分析弹片在工作过程中的受力特性，以及花朵在不同作业工况下的受力情况，明确影响花朵脱落的关键影响因素。其次，运用 ADAMS 软件进行刚柔耦合动力学仿真分析，确定疏花关键装置的最佳工作转速为 230~250r/min。最终通过田间试验对疏花机的工作可靠性进行验证，试验结果表明该疏花机达到预期设计目标，为果园高效精准疏花作业提供了技术支撑。

INTRODUCTION

Flower thinning is an important step in the growth process of apple trees; it can not only improve fruit quality *(Dennis et al., 2011)* but also effectively prevent the problem of yield reduction caused by excessive fruit load that burdens the tree *(Liu et al.,2018)*. Currently, traditional manual flower thinning methods mainly rely on manual operations, including pinching and flower sequence rubbing methods *(Cheng et al., 2018; Wang and Liu, 2020; Cheng et al., 2020)*. Manual flower thinning has high labor intensity and low efficiency *(Pan et al., 2021)*. Chemical flower thinning has issues with pesticide residues and is easily influenced by environmental factors, fruit varieties, and other variables *(Robinson and Lakso, 2011; Cheryl and Karen, 2011)*. Manual flower thinning still plays an important role in modern orchard management, but it can no longer meet the demands of modern agriculture for fruit quality and production efficiency *(Sui et al., 2024)*. To address this issue, mechanized flower and fruit management has become one of the urgent problems that farmers need to solve. Among them, the development and application of flower thinning machines has become a hot topic in modern orchard management *(Lan et al., 2020; Chen et al., 2018; Kang et al., 2019)*.

Currently, flower thinning devices are mainly classified into three types: manual, semi-automatic, and intelligent *(Lei et al., 2023)*. The development of orchard flower thinning machinery in China is still immature, and existing research has mainly focused on the development of airborne flower thinning mechanisms.

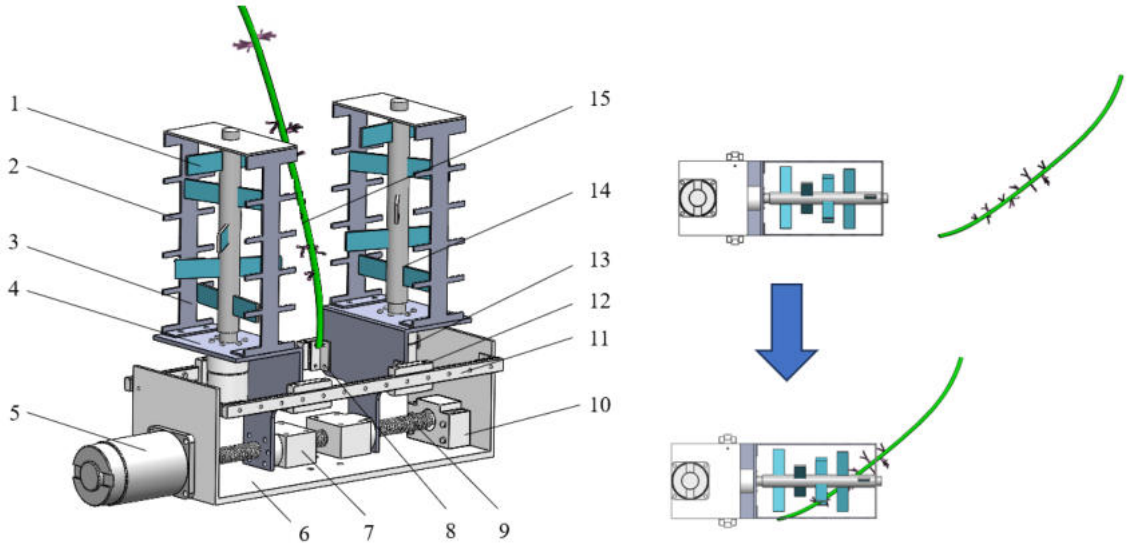
Li Jun et al. from South China Agricultural University *(Li et al., 2016)* designed a suspended electric flexible flower thinning machine. Wang Qiang et al. from Hebei Agricultural University *(Wang et al., 2018)* developed a mechanical flower thinning device for northern dwarf rootstock high-density orchards. Liu Huanwei et al. from Qingdao Agricultural University *(Liu et al., 2025)* developed a crawler-type double-arm apple flower thinning machine based on profile theory. Research on flower thinning machinery started earlier abroad. Recently, *Alberto et al., (2018),* developed a large flower thinning machine. Lyons et al., *(2015),* designed a selective automatic flower thinning device and a novel AI controller for a mechanical flower thinning device has been proposed *(Matache et al., 2024),* which integrates the ZED 3D camera and a custom-trained YOLO9 algorithm. It can detect and count flowers in real-time and automatically adjust the thinning rotor speed based on density to achieve the desired thinning ratio.

Currently, mainstream flower thinning equipment faces prominent issues such as poor selectivity, large body size, and high mechanical damage rates. To improve the accuracy of mechanical flower thinning, this study designed a comb-tooth type flower thinning end effector. Through research and analysis of the mechanical characteristics of flowers in the field, a flower thinning structure combining a spring piece and comb teeth was designed. It can complete the flower thinning operation within a specified range by being mounted on a robotic arm. Meanwhile, a prototype of the flower thinning end effector was fabricated, and field tests were conducted to verify its operational performance.

MATERIALS AND METHODS

Design of the End Effector

The end effector mainly consists of a motor, support base, flower-thinning shaft support, flower-thinning shaft, guide rail, bi-directional lead screw, flower-thinning spring piece, and comb-teeth column. The bi-directional lead screw is fixed to the base, the flower-thinning shaft support is fixed to the bi-directional lead screw, and the comb-teeth column is fixed to the flower-thinning shaft support. The flower-thinning shaft is connected to the drive motor via a coupling. Its 3D model is shown in Figure 1.



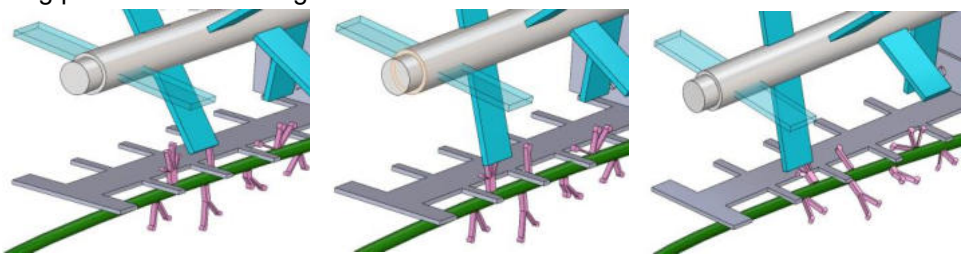
(a) End effector (b) End effector work process

Fig. 1 - 3D diagram of the end effector and its working principle

1) Flower thinning spring piece; 2 - Comb teeth; 3 - Comb teeth column; 4 - Flower thinning shaft base; 5 - Lead screw motor; 6 – Base; 7 - Lead screw nut; 8 - Angle iron; 9 - Bi-directional lead screw; 10 - Lead screw base; 11 - Guide rail; 12 - Guide rail support; 13 - Flower thinning shaft motor; 14 - Flower thinning shaft; 15 – Branch

The working principle is as follows: during the flower thinning operation, the flower clusters are identified by the visual recognition system. Under the control of the system, the robotic arm moves the end effector to the appropriate position, as shown in Figure 1. The motor drives the bi-directional lead screw to move the flower thinning shaft to the appropriate position, exerting a fixed effect on the branches. The flower thinning shaft motor is then activated, causing the flower thinning spring piece to rotate. Some flowers fall off due to the shear force when they come into contact with the spring pieces.

The remaining flowers, under the limiting effect of the comb teeth, are positioned at the front end in the direction of rotation. The flower pedicels are within the gap between the flower thinning spring piece and the comb teeth. As the flower thinning spring piece moves forward during rotation, the flower pedicels trapped between the comb teeth are better subjected to the shear force exerted by the spring piece. The flowers fall off due to the shear force. During this process, multiple spring pieces on the two flower thinning shafts perform flower thinning work simultaneously. After all flowers in the working area have been thinned, the system moves to the next thinning point, continuing until the entire flower thinning operation is complete. The process of flower removal by the spring piece is shown in Figure 2.



(a) (b) (c)

Fig. 2 - Schematic diagram of flower thinning

(a) Flower entering the comb teeth; (b) Spring piece contacts the flower; (c) The flower pedicel gradually breaks

Force Analysis of Key Components in the Flower Thinning Process

During the flower thinning operation, the flower thinning shaft drives the flower thinning spring piece to rotate, causing it to interact with the flowers, flower pedicels, and branches of the fruit tree. To facilitate the analysis of this process, the flower model is simplified into a force model used in engineering. According to engineering analysis theory, it can be considered that external shear forces cause the flower pedicel to break, allowing the flowers to fall off the branches. When the flower thinning spring piece makes contact with the flower pedicel, the instantaneous force applied to the flower pedicel can be approximated as a uniform force. Since the contact area of this force is much smaller than the surface area of the flower pedicel, it can be regarded as a concentrated force acting at a specific point on the flower pedicel. In the force model of the flower, the connection node between the flower pedicel and the branch is regarded as a fixed end. When the force is applied to the contact point on the flower pedicel, it will deform in the direction of the applied force. When the deformation exceeds a certain threshold, the structure of the flower pedicel will experience displacement, eventually leading to the breakage of the flower pedicel. During the entire flower thinning process, the flower thinning spring piece must not only bear its own weight but also overcome work resistance, centrifugal force, and the frictional resistance generated during the cutting of the flower pedicel by the spring piece. Considering that work resistance, centrifugal force, and other factors significantly affect the performance of the components during operation, a simplified model of the flower thinning device is used for force analysis. In this simplified model, point b is the center of mass of the spring piece, point d is the farthest end of the spring piece from the shaft, point c is the contact point between the spring piece and the flower pedicel, and point a is the fastening point between the flower thinning spring piece and the flower thinning shaft. Using the impulse-moment theorem and D'Alembert's principle, an in-depth analysis of the forces acting on the flower thinning component when it contacts the flower pedicel is conducted, and the following conclusions can be drawn.

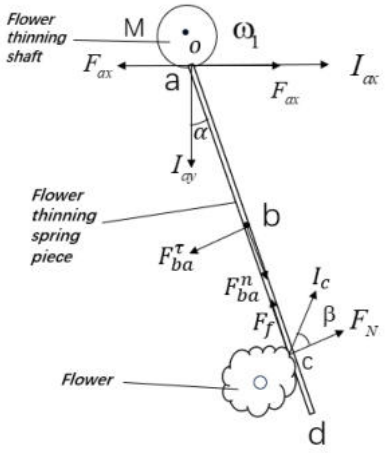


Fig. 3 - Schematic diagram of the force of the flower thinning component

$$\begin{cases} I_{ay}\sin\alpha - I_{\alpha x}\cos\alpha - I_{c}\cos\beta = m_2(\omega_2^{'} - \omega_2)L_x \\ J(\omega_2^{'} - \omega) = I_{\alpha y}\sin\alpha L_{\alpha b} - I_{\alpha x}\cos\alpha L_{\alpha c} - I_{c}L_{oc}\cos\beta \\ M - F_{\alpha x}L_{o\alpha} = 0 \\ F'_{\alpha x} + F^{\tau}_{b\alpha}\cos\alpha - F^{n}_{b\alpha}\sin\alpha + F_f\sin\alpha - F_N\cos(\alpha+\beta) = 0 \\ J_b a^{'}{}_2 + F^{\tau}_{b\alpha}L_{\alpha b} + F^{\tau}_{b\alpha}L_{\alpha b}\sin\alpha - F_N(L_{\alpha b} + L_{bc})\cos\beta + \frac{1}{2}F_y\delta = 0 \\ \omega_1 L_{o\alpha}\cos\alpha - \omega^{'}{}_2 L_{\alpha c} - V_m\cos\alpha = 0 \end{cases} \quad (1)$$

M is the torque of the flower thinning shaft, $N{\cdot}m$. ω_1 is the angular velocity of the flower thinning shaft, rad/s. m_2 is the mass of the spring piece, kg. β is the angle between the spring piece and the vertical direction of the plane, °. r is the angle between the direction of the collision impulse and the collision surface, °. ω_2 is the angular velocity of the spring piece before colliding with the flower pedicel, rad/s. ω_2' is the angular velocity of the spring piece after colliding with the flower pedicel, rad/s. I_{ax} is the horizontal component of the impulse exerted by the spring piece on point A, $N{\cdot}S$. I_{ay} is the vertical component of the impulse exerted by the spring piece on point A, $N{\cdot}S$. I_c is the impulse exerted by the spring piece on point C, $N{\cdot}S$. F_{ax} is the horizontal constraint force acting on point A, $N{\cdot}S$. F_N is the working resistance force of the spring piece, N. F_{ba}^{n} is the tangential adhesive force of the spring piece, N. F_{ba}^{τ} is the normal adhesive force of the spring piece, N. F_f is the frictional force generated between the spring piece and the flower pedicel leaf, N. L_{ad} is the length of the spring piece, m. L_{ab} is the distance from the hinge point of the spring piece to its center of mass, m. L_{oa} is the distance from the hinge point of the spring piece to the center of the thinning axis, m. L_{bc} is the distance from the contact point of the spring piece with the flower pedicel to its center of mass, m. a_2' is the acceleration of the spring piece after collision with the flower pedicel, m/s^2. J_c is the moment of inertia of the spring piece, $kg \cdot m^2$.

Due to the rotational operation of the spring piece on the flower thinning shaft during the process, in order to improve work efficiency, the impulse at the fastening point between the flower thinning spring piece and the flower thinning shaft is considered to be zero. Substituting this into the equation yields the following result.

$$L_{bc} = \frac{J_c}{m_2 L_{ab}} \quad (2)$$

$$F_N = \frac{(J_b + m_2L_{ab}^2)(m_2\omega_2 L_{ab}\sin\alpha - \frac{M}{L_{o\alpha}}) + m_2L_{ab}^2\sin\alpha\cos\alpha m_2\omega_1^2 L_{oa}}{m_2L_{\alpha b}\cos\alpha(L_{\alpha c} - \frac{1}{2}f\delta) + [J_b + m_2(L_{ad} + L_{bd})^2](\cos\alpha - f\cos\alpha)} \quad (3)$$

$$\omega^{'}{}_2 = \frac{\omega_1 L_{o\alpha}\cos\beta - V_m\cos\beta}{L_{\alpha b}} \quad (4)$$

Through force analysis of the flower thinning component, it can be determined that the impact position of the spring piece on the flower pedicel is related to the rotational inertia J_c, the mass of the spring piece m_2, and the position of the center of mass. The impact force of the spring piece on the flower pedicel is influenced by parameters such as the angular velocity of the flower thinning shaft ω_1, the mass of the spring piece m_2, the length of the spring piece L_{ad} and the torque M.

Different Work Processes of the Flower Thinning Operation and Flower Force Analysis

When the flower thinning shaft drives the spring piece to operate, the flower thinning spring piece strikes the flower, causing it to fall off. The force-induced flower detachment can be divided into two situations.

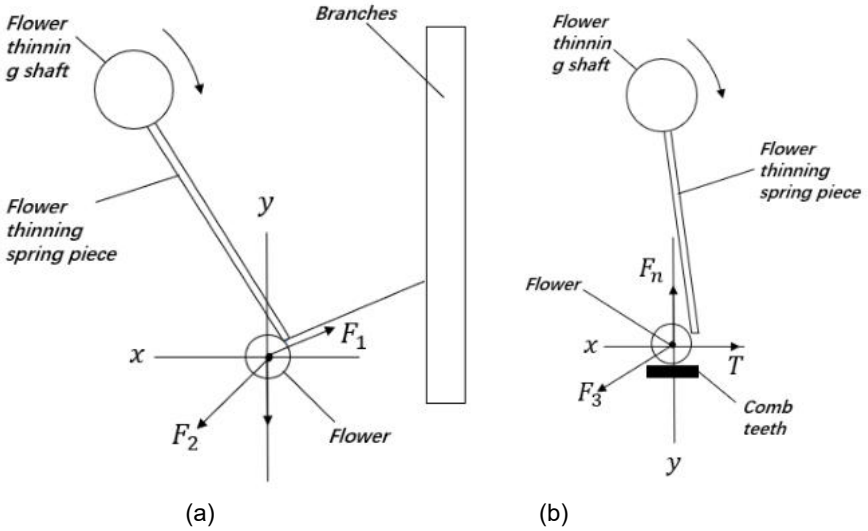


Fig. 4 - Force analysis of the flower under different working conditions

(a) Working condition 1. Simplified diagram of flower stress; (b) Working condition 2. Simplified diagram of flower stress

When a few flowers are only affected by the flower thinning spring piece and are knocked off, the flower pedicel comes into contact with the spring piece and is straightened. At this moment, the flower and the spring piece are relatively stationary, and the force is balanced. The flower is subjected to shear and frictional forces from the spring piece. The force diagram for this scenario is shown in figure 4.

When the flower thinning shaft rotates at a constant angular velocity ω, the speed at which the flower thinning spring piece strikes the flower is:

$$v_1 = \omega R \tag{5}$$

In the equation, R represents the distance from the flower to the flower thinning shaft, m.

At this moment, the acceleration at the force application point on the flower is:

$$a_1 = \frac{v_1^2}{R} = w^2 R \tag{6}$$

The impact force of the spring piece on the flower is:

$$F_2 = M_1 a_1 = M_1 w^2 R \tag{7}$$

In the equation, M_1 represents the mass of the spring piece, N.

When there is no relative displacement between the flower and the branch, the flower is in force equilibrium, and the force acting on the flower in the horizontal direction is:

$$F_2 \sin\theta_1 = F_1 \sin\theta_2 \tag{8}$$

In the equation, θ_1 is the angle between F_2 and the y-axis, θ_2 is the angle between F_1 and the y-axis, and F_1 is the force exerted by the flower pedicel on the flower, N.

When the flower thinning shaft drives the spring piece to rotate and the rotation speed exceeds a certain value, the connection point between the flower and the flower pedicel experiences a fracture under the action of shear force, causing the flower to fall off.

In actual flower thinning operations, due to the good elasticity of the flower pedicel, the force exerted by the spring piece often cannot completely detach the flower. Therefore, under the action of the comb teeth, a limiting effect is applied to the flower and pedicel, allowing the flower to better receive the force from the spring piece. The flower is subjected to the combined effect of the spring piece and the comb teeth. The force diagram is shown in figure 4.

When the flower thinning shaft rotates at a constant angular velocity ω, the speed at which the flower thinning spring piece strikes the flower is:

$$v_2 = \omega R_1 \tag{9}$$

In the equation, R_1 represents the distance from the flower to the flower thinning shaft, m

At this moment, the acceleration at the force application point on the flower is:

$$a_2 = \frac{v_2^2}{R_1} = w^2 R_1 \tag{10}$$

The impact force of the spring piece on the flower is:

$$F_3 = M_1 a_2 = M_1 w^2 R_1 \tag{11}$$

In the equation, θ_3 is the angle between F_3 and the y-axis.

The frictional force T exerted by the comb teeth on the flower is the resultant force in the horizontal direction.

$$T = \mu F_3 \sin\theta_3 = \mu M_1 w^2 R_1 \sin\theta_3 \tag{12}$$

In the equation, μ represents the coefficient of friction between the comb teeth and the flower, N.

When there is no displacement between the flower and the branch, the flower is in force equilibrium, and the force acting on the flower in the vertical direction is:

$$F_3 \cos\theta_3 + G = F_n \tag{13}$$

When the horizontal shear force applied to the flower exceeds a certain value, the flower falls off.

Through the force analysis of the flower thinning working components and the flower under different operating conditions, it can be concluded that when the material is fixed, the impact force exerted by the spring piece on the flower pedicel is related to parameters such as the angular velocity ω_1 of the flower thinning shaft, the mass M of the spring piece, the length L_{ad} of the spring piece, and the torque M. The greater the normal force F_N, the better the thinning performance of the spring piece on the flower, which is more favorable for the flower thinning operation.

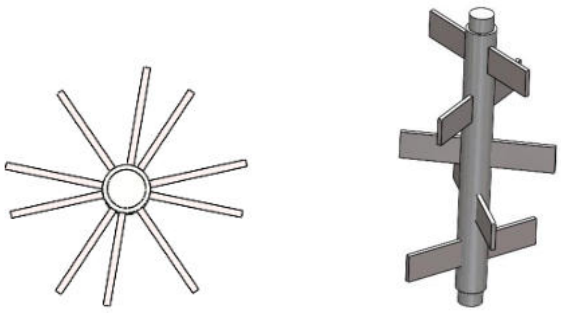
Design of Relevant Parameters for the End Effector

When designing the overall dimensions, it is necessary to consider the actual situation of the flowers and fruit trees. Research was conducted in the orchard, and flower samples were taken. Measurements showed that the flower diameter ranges from 26 to 35 mm, and the flower pedicel length ranges from 28 to 56 mm. Based on this data, to ensure that the spring piece can effectively remove the flowers while leaving a certain parameter margin, the size of the flower thinning spring piece is designed to be 65 mm in length and 32 mm in width. The choice of material for the spring piece is also crucial.

For this study, the material used for the flower thinning spring piece is polypropylene, which ensures effective flower thinning while minimizing damage to the branches.

The flower thinning shaft plays a role in driving the spring piece in flower thinning operations. It is one of the key components and major force-bearing parts of the operation, and its structural design has a significant impact on the operational outcome. Its mass should be as small as possible, so a hollow tube is selected as the material for the flower thinning shaft. To improve flower thinning efficiency, the length is set at 260 mm, which is twice the distance between flower clusters. Five flower thinning spring pieces are evenly installed on the shaft, with a certain gap between each pair of spring pieces, ensuring that the flower removal rate reaches about fifty percent, as required by agricultural standards. When determining the arrangement of the spring pieces on the flower thinning shaft, a rotary tiller-like arrangement was used, so the spring pieces are arranged in a spiral pattern on the shaft, as shown in Figure 5.

During one full rotation of the flower thinning shaft, only one spring piece is at the same phase angle at a time. This ensures that the torque is more balanced, reduces torque fluctuations, increases operational stability, and ensures even load distribution. The flower thinning spring pieces have a certain width and a reasonable arrangement to minimize the occurrence of missed hits.



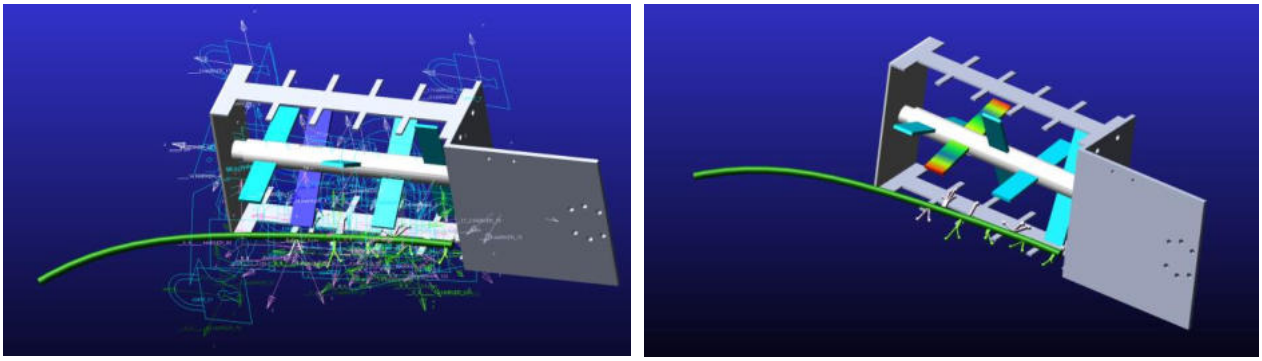
(a) (b)

Fig. 5 - Arrangement of spring plates on the thinning shaft

(a) Top view of the flower thinning mechanism; (b) Axonometric view of the arrangement

Simulation Analysis of Key Flower Thinning Components

It has been measured that the shear force range for the apple flower pedicel fracture is 3.69–4.79 N, with an average shear force of 4.18 N. To simulate the working process of the flower thinning end effector and analyze the impact force exerted by the spring piece on the flower at different rotational speeds, an ADAMS rigid-flexible coupling simulation analysis is performed on the end effector. During flower thinning operations, the flower thinning device must have a certain level of stiffness and flexibility to ensure effective flower thinning while minimizing damage to the branches. In this simulation, polypropylene is selected as the material for the spring piece, while the other components are made of aluminum. Then, constraints are applied to the model based on the motion relationships between the various parts of the flower thinning machine. Figure 6 shows the diagram of the applied constraints.



(a) (b)

Fig. 6 - ADAMS simulation

(a) Schematic diagram of constraint application; (b) Spring piece flexible settings

To simplify the flexible dynamics simulation model, based on the periodic repetitive impact characteristics of the flower thinning spring piece, one spring piece system on one side of the flower thinning shaft is selected as the research object. The model is constrained and driven based on the actual motion state of the flower thinning mechanism. The applied constraints are shown in Table 1.

Table 1

Constraint conditions

Serial number	Kinematic pair	Constrained components
1	Rotary pair	Flower thinning shaft + flower thinning shaft base
2	Fixed pair	Comb-tooth column + flower thinning shaft base
3	Fixed pair	Flower thinning spring piece + flower thinning shaft

RESULTS

Simulation results and data

The rotational speed of the flower thinning shaft was set to 150-250 r/min. Based on the relatively low geometric complexity of the mechanism, the ADAMS/Flex module was used to generate a flexible body: in the ViewFlex module, the spring piece that needed to be made flexible was selected, with the material defined as polypropylene. The flexible body type was set to geometric appearance, with entity mesh parameters having a reference size of 5 mm, a minimum element size of 1 mm, and a size gradient coefficient of 1.5. The remaining options were kept at their default values. After performing mesh division, flexible body creation was completed through automatic contact point recognition, and the final output was the flexible model of the polypropylene material flower thinning spring piece, showing its nonlinear deformation characteristics. The spring piece's flexibility was shown in Figure 6.

The flower thinning spring piece, after undergoing flexible treatment, made contact and collided with the branches and flowers. Due to the inertia and elasticity of the flower thinning spring piece, swinging occurred after it underwent flexible deformation. Subsequently, the flower thinning spring piece continued to rotate under the drive of the flower thinning shaft.

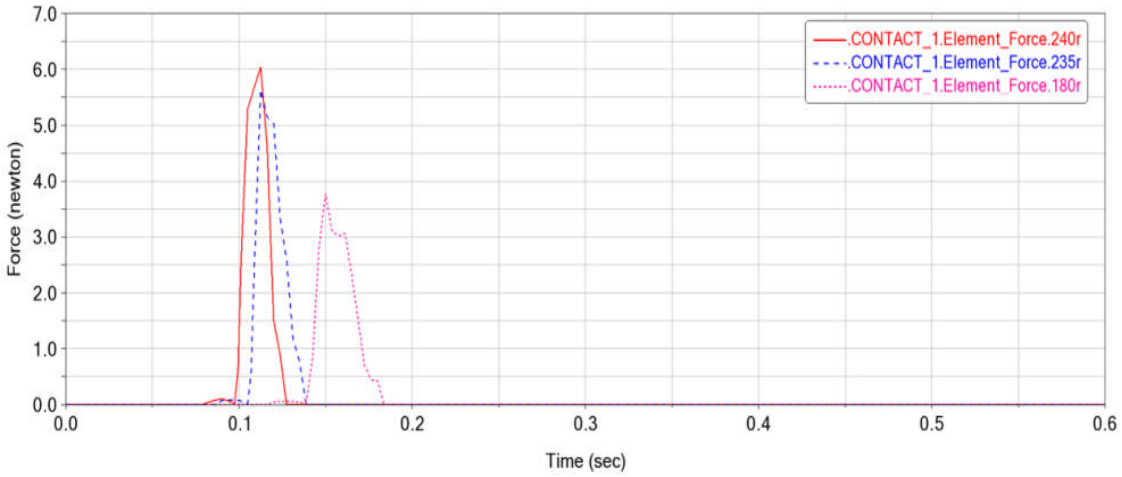


Fig. 7 - Contact force curves of spring piece at different speeds

Table 2

Impact force simulation results

Rotational speed / $r \cdot min^{-1}$	150	180	230	235	240	250
Applied force / N	2.76	3.82	4.91	5.59	5.98	6.76

The rotational speed range of the flower thinning shaft was set between 150 r/min and 250 r/min. The contact force of the flower thinning spring piece was calculated through simulation. The simulation results were shown in Table 2. From Table 2, it could be seen that the contact force increased as the rotational speed increased. From Figure 7, it was clear that when the rotational speed was at 180 r/min, during the stage when the flower thinning spring piece had not yet come into contact with the flower, the force remained at 0. At 0.14 s, the flower thinning spring piece began to contact the flower, and the contact force gradually increased, reaching a peak value of 3.82 N. However, the force still did not meet the flower thinning standards.

When the rotational speed of the flower thinning shaft reached 240 r/min, the flower thinning spring piece made contact with the flower at 0.09 s, and the contact force gradually increased to 5.98 N. The simulation results showed that at lower rotational speeds, the force curve fluctuated significantly within a short period and even produced several force peaks. However, at higher rotational speeds, the force curve was more stable with only one peak. Analysis indicated that at slower rotational speeds, the simulation process was slower, and after the flexible flower thinning spring piece contacted the target, certain deformation occurred, leading to multiple force peaks detected at the contact point. When the deformation exceeded the maximum value, the flower thinning spring piece completed the impact on the target and continued to rotate.

The maximum force value in the curve represented the accurate force under that rotational speed. Based on the previous analysis, the range of shear force required to break the apple flower's pedicel was between 3.69 N and 4.79 N. During the flower thinning operation, the force exerted by the flower thinning spring piece had to be greater than 4.79 N. When the rotational speed of the flower thinning shaft was between 230 and 250 r/min, it met the force requirements for the flower thinning operation.

Prototype Manufacturing and Field Testing

To evaluate the performance of the end effector, based on the analysis and parameter optimization results of the various components of the whole machine mentioned earlier, the flower thinning end effector was modeled using 3D design software. The rationality of each component was checked, and the prototype was manufactured for testing.

In this study, the manufactured prototype was installed at the end of the robotic arm. During operation, a binocular camera captured the overall information of the fruit trees, and the central control machine analyzed and processed the information. After processing, it provided the solution and working coordinates. The robotic arm, upon receiving the coordinates of the working position via internal communication, moved to the designated point. The motor of the end effector started rotating to remove the flowers that needed thinning. Afterward, it moved to the next position point that required flower thinning, repeating the operation. After completing the flower thinning for one fruit tree, the entire machine moved to the next fruit tree and repeated the process. The movement between trees was mapped in advance by radar, allowing for fixed-point cruising of each tree in the orchard. After completing the entire orchard or a row of trees, the machine moved to the set orchard origin point and waited.



Fig. 8 - Field experiment on flower thinning

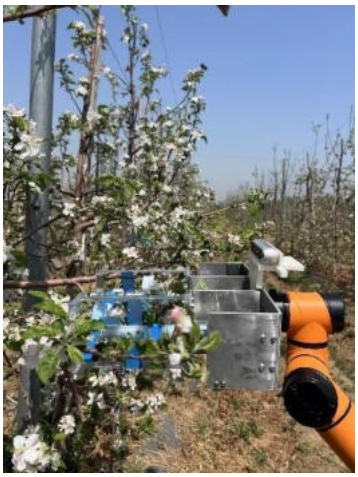


Fig. 9 - End Effector in field operation

To verify the flower thinning effect of the end effector and assess the rationality of the end effector's structure, the flower thinning rate was calculated, and field tests were conducted on the end effector. After completing the operation, the flower thinning rate for each branch was calculated, which was the ratio of the remaining flowers on each branch before and after flower thinning.

The calculation formula is

$$k = 1 - \frac{Z_1}{Z} \times 100\% \tag{14}$$

where Z_1 is the number of remaining flowers after the operation is completed, and Z is the original number of flowers on the branch.

Table 3

Test results of flower thinning and branch damage rate

Branch number	Number of flowers/piece	Number of flowers thinned/piece	Thinning rate/%	Branch surface area/mm²	Damage area/mm²	Damage rate/%
1	22	13	59.1	783.91	27.43	3.5
2	16	7	43.8	652.37	9.89	1.5
3	23	10	43.4	897.04	11.66	1.3

Branch number	Number of flowers/piece	Number of flowers thinned/piece	Thinning rate/%	Branch surface area/mm²	Damage area/mm²	Damage rate/%
4	9	5	55.6	615.28	17.23	2.8
5	19	9	47.4	848.75	30.56	3.6
6	13	7	53.8	721.59	11.53	1.6
7	19	10	52.6	669.43	15.39	2.3

To ensure accuracy in the experiment, multiple branches from different plants were selected. During flower thinning, it was also important to ensure that the branches were not damaged by the end effector's operation. Based on previous experience and expert advice, the epidermal damage area of the branches was kept to less than 4% of the total area of the branch. The rotational speed of the flower thinning shaft was set to 240 r/min, and the following results were obtained through the experiment.

According to agronomic requirements and past experience, a flower thinning rate of around 50% was considered the optimal thinning rate. As shown in Table 3, this basically met the agronomic requirements for flower thinning.

CONCLUSIONS

This study presents the design of an orchard flower thinning machine equipped with a comb-tooth end effector, developed according to the physical properties of flowers and the requirements of the thinning process. The thinning method combines spring pieces with comb teeth. By optimizing the size of the spring pieces, selecting suitable materials, and analyzing their force characteristics during operation, as well as the mechanical response of flowers under different working conditions, the key factors influencing flower detachment were identified. Through ADAMS rigid-flexible coupled dynamic simulation, the optimal rotational speed range of the end effector's key components was determined to be 230-250 r/min. Field experiments confirmed that the design met agronomic requirements for flower thinning. Overall, the results demonstrate that the proposed design provides effective technical support for improving the efficiency and precision of flower-thinning operations in orchards.

ACKNOWLEDGEMENT

This research was funded by the National Natural Science Foundation of China (No:31971801), the Natural Science Foundation of Shandong Province of China (No: ZR2020ME252, ZR2020ME250) and Qingdao Science and Technology Benefit-the-People Demonstration Project(25-1-5-xdny-33-nsh).

REFERENCES

[1] Alberto A., Daniela G., Mattia C., Sandro S., Gianluca B., Giuseppina C. (2018). Evaluation of a new machine for flower and fruit thinning in stone fruits. *Sustainability*, Vol. 10, pp. 4088-4088, Italy.

[2] Chen G., Li J., Chen H., An Y. (2018). Research Progress of Artificial Intelligence Technology in the Agricultural Field in the Era of Big Data (大数据时代人工智能技术在农业领域的研究进展), *Journal of Jilin Agricultural University*, Vol. 40, pp. 502-510, Jilin/China.

[3] Cheng D., Chen J., Gu H., (2018). Efficient and Labor-Saving Grape Clusters Thinning Technology (葡萄省工高效整穗疏果技术), *Fruit Grower's Friend*, Vol. 04, pp. 13-14, Henan/China.

[4] Cheng D., He S., Li M., (2020). The Effect of Different Flower Cluster Shaping Methods on the Fruit Quality of Zhengyan Seedless' Grapes (不同花穗整形方式对'郑艳无核'葡萄果实品质的影响), *China Fruit Trees*, Vol. 04, pp. 18-22, Henan/China.

[5] Cheryl H., Karen B., (2011). Efficacy of blossom thinning treatments to reduce fruit set and increase fruit size of Ambrosia and Aurora Golden Gala apples. *Canadian Journal of Plant Science*, Vol. 91, No. 6, Canada.

[6] Dennis H., Ines H., Karen L., Jim M., Michael B. (2011). Mechanical flower thinning improves fruit quality of apples and promotes consistent bearing. *Scientia Horticulturae*, Vol. 134, pp. 241-244, United States.

[7] Kang M., Wang X., Hua J., Wang H., Wang F. (2019) Parallel Agriculture: Intelligent Technologies Leading to Smart Agriculture (平行农业:迈向智慧农业的智能技术), *Journal of Intelligent Science and Technology*, Vol. 1, pp. 107-117, Shandong/China.

[8] Lan Y., Wang T., Chen S., D. (2020). Agricultural Artificial Intelligence Technology: The Wings of Modern Agricultural Science and Technology (农业人工智能技术: 现代农业科技的翅膀), *Journal of South China Agricultural University*, Vol. 41, pp. 1-13, Guangdong/China.

[9] Lei X., Yuan Q., Xyu T., Qi Y., Zeng J., Huang K., Sun Y., Herbst A., Lyu X. (2023). Technologies and Equipment of Mechanized Blossom Thinning in Orchards: A Review. *Agronomy*, Vol. 13, Jiangsu/China.

[10] Li J., Xu Y., Xu J., Yang Z., Lu H. (2016). Design and Experiment of Control System for Suspended Electric Flexible Flower Thinning Machine (悬挂式电动柔性疏花机控制系统设计与试验), *Transactions of the Chinese Society of Agricultural Engineering*, Vol. 32, pp. 61-66, Guangdong/China.

[11] Liu H., Chi J., Liang Q., Liu T., Wang H., Li S., Hu C. (2025). Design and Simulation Analysis of a Crawler-type Double-arm Apple Flower Thinning Machine (履带式双节臂苹果疏花机的设计与仿真分析), *Journal of Agricultural Mechanization Research*, Vol. 47, pp. 35-41, Shandong/China.

[12] Liu L., Nie L., Zhao H., Cao Y., Sun A., (2018). Research on the Technical Issues of Apple Flower Thinning and Fruit Thinning (苹果疏花疏果技术问题研究), *Shaanxi Agricultural Science*. Vol. 64, pp. 88-91, Shaanxi/China.

[13] Lyons D. J., Heinemann P. H.; Schupp J. R., Baugher T. A., Liu J. (2015). Development of a selective automated blossom thinning system for peaches. *Transactions of the ASABE*, Vol. 58, pp. 41-42, United States.

[14] Matache M. G., Cristea R., Zaica A., Ciupercă R., Iosif A., Voicu Gh. (2024). Real-time mechanical flower thinning equipment, controlled by artificial intelligence, *INMATEH Agricultural Engineering*, Vol. 74, No. 3, pp. 875-884.

[15] Pan Y., Zhou Y., He L., Wang Q., Song Z., Song L., (2021). Research Progress on Flower Thinning and Fruit Thinning in Orchard Management (果园管理工作中疏花疏果的研究进展), *Journal of Agricultural Mechanization Chemistry*, Vol. 42, pp.198-204, Xinjiang/China.

[16] Robinson T.L., Lakso A.N., (2011). Predicting chemical thinner response with a carbohydrate model. *Acta Horticulturae*, Vol. 903, pp.743-750.

[17] Sui S., Li M., Li Z., Zhao Y., Wang C., Du W., Li X., Liu P. (2024). A comb-type end-effector for inflorescence thinning of table grapes. *Computers and Electronics in Agriculture*, Vol. 217, Shandong/China.

[18] Wang L., Liu R., (2020). The Effect of Different Cluster Thinning Methods on the Quality of Facility-Grown Red Baraldo Grapes (不同整穗方式对设施葡萄红巴拉多品质的影响), *Agriculture and Technology*, Vol. 40, pp. 41-43, Gansu/China.

[19] Wang Q. (2018) *Design and Research of Flower Thinning Device for Dwarf Dense Fruit Trees* (矮密果树疏花装置设计及研究), Hebei Agricultural University, Master's Thesis, Hebei/China.

EXPERIMENTAL STUDY ON VARIABLE TEMPERATURE DRYING PROCESS OF PADDY BASED ON GLASS TRANSITION

/

基于玻璃化转变的稻谷变温干燥工艺及试验研究

Hongchao WANG [1]; Jing WANG [1]; Ziyu WANG *[2]; Lin WAN [1]; Gang CHE *[1]; Shuo WANG [1]; Zhengfa CHEN [1]

[1] College of Engineering, Heilongjiang Bayi Agricultural University, Daqing 163319, China

[2] College of Information and Electrical Engineering, Heilongjiang Bayi Agricultural University, Daqing 163319, China

Tel: 18645949778; E-mail: 295684617@qq.com

DOI: https://doi.org/10.35633/inmateh-76-88

Keywords: *paddy, variable-temperature drying, glass transition, experiment*

ABSTRACT

To improve the quality of paddy, reduce post-production losses, and ensure processing efficiency, this paper proposes a variable-temperature drying process based on the glass transition phenomenon, using the relationship between paddy moisture content and glass transition temperature. An optical three-dimensional scanning method was employed to obtain the paddy grain particle model. Subsequently, a heat and mass transfer model for paddy was constructed to analyze the temperature distribution and moisture migration behavior during drying. Experiments were conducted using a constant temperature of 40 ℃ and heating amplitudes of 5 ℃, 10 ℃, and 15 ℃ to investigate the drying characteristics and quality evolution of paddy. The simulation results showed that the average errors for moisture content and temperature were 1.58% and 2.66%, respectively. Compared with constant temperature drying at 40 ℃, the variable-temperature drying with heating amplitudes of 5 ℃, 10℃, and 15℃ reduced the drying time by 19, 58, and 63 minutes, respectively. Among the tested conditions, the 5 °C heating amplitude yielded the best results, with a crack increase rate of only 2.5% and a head rice yield of 68.3%. These findings offer valuable insights for understanding the mechanism of variable-temperature drying and for optimizing the drying process of paddy.

摘要

为提高稻谷品质、减少产后损失、保障加工质量等方面，本文通过稻谷含水率与玻璃化转变温度之间的关系，提出基于玻璃化转变的变温干燥工艺。采用光学三维扫描方法获取稻谷颗粒模型，再次基础上构建稻谷传热传质模型解析稻谷温度、水分的迁移规律。以 40℃恒温及 5℃、10℃、15℃的加热幅度为变量，开展试验探究稻谷干燥特性及其品质变化趋势。研究结果显示，模型模拟含水率的平均误差为 1.58%，温度的平均误差为 2.66%。与 40℃恒温干燥相比，5℃、10℃和 15℃升温幅度分别使干燥时间缩短了 19 分钟、58 分钟和 63 分钟。其中，5℃升温幅度的干燥工艺裂纹增率仅为 2.5%，整精米率达到 68.3%。研究结果为变温干燥机理及工艺优化提供参考。

INTRODUCTION

As one of the major staple foods in China, paddy production has remained above 200 million tons according to the 2024 national paddy production data released by the National Bureau of Statistics (*Islam et al., 2024*). However, annual post-harvest losses due to untimely or insufficient drying are estimated to be as high as 3–5% (*Tola et al., 2024*). Therefore, to prevent spoilage caused by mold, germination, and other deterioration processes, it is essential to dry and treat paddy promptly and adequately after harvest to ensure both yield and grain quality (*Zhang et al., 2024*).

Currently, hot-air drying is the most widely used method in commercial drying systems (*Okeyo et al., 2024*). It utilizes the temperature difference between hot air and the paddy to accelerate internal moisture evaporation. Using higher hot-air temperatures can effectively enhance drying efficiency (*Liu et al., 2024*).

However, if the temperature is not properly controlled, it may lead to a high incidence of grain cracking, which can severely impact the nutritional value and marketability of rice.

---

[1] *Hongchao Wang, Ph.D.*; *Jing Wang, master degree*; *Ziyu Wang, master degree*; *Lin Wan, Prof. Ph.D.*; *Gang Che, Prof. Ph.D.; Shuo Wang, Ph.D.*; *Zhengfa Chen, Ph.D.*

Paddy, as a polymeric material, undergoes a glass transition during the drying process due to temperature fluctuations (*Owusu et al., 2024*). When the temperature of the paddy is below its glass transition temperature, it enters a glassy state, characterized by low elasticity and high resistance to moisture diffusion. Conversely, at temperatures above the glass transition point, the grain enters a rubbery state, which exhibits higher elasticity and enhanced moisture diffusivity (*Wang et al., 2022*). Often, both glassy and rubbery states may coexist within the same grain, leading to internal structural changes and mechanical stress that may ultimately result in cracking. As temperature and moisture content vary throughout the drying process, the physical state of paddy dynamically shifts between the glassy and rubbery phases. According to the principles of glass transition, careful regulation of drying temperature to maintain a relatively stable physical state can significantly reduce the occurrence of cracking phenomena. While higher temperatures can maintain the rice in a rubbery state and promote rapid drying, they also increase the risk of cracking. In contrast, maintaining a glassy state through low-temperature drying helps minimize cracking but results in longer drying times and reduced efficiency (*Smith et al., 2024*). To balance drying efficiency and grain quality, variable-temperature hot-air drying has been widely adopted (*Rashid et al., 2023*). By adjusting the drying temperature over time, this approach helps minimize cracking while preserving post-drying grain quality (*Zhang et al., 2024*). However, the practical application of variable-temperature drying still faces several challenges, such as the accurate determination of temperature transition points and the prediction of quality changes during the process, which require further investigation and optimization.

Therefore, this study aims to establish a relationship between the glass transition temperature of paddy and moisture content and to analyze the coupled heat and mass transfer behavior during drying. By comparing constant-temperature drying with variable-temperature drying, the effects on drying characteristics, *head rice yield*, and crack increase rate are systematically explored.

MATERIALS AND METHODS

Experimental materials and equipment

In this experiment, paddy grains of the Suidao 3 variety from Heilongjiang Province were used. After harvesting in September 2024, the initial moisture content of the grains was approximately 22%. Following threshing, de-awning, and impurity removal, the paddy grains were sealed, packaged, and stored in a freezer at 2 ~ 4 °C for subsequent experiments. The hot-air drying experiment device was used in this study, as shown in Figure 1.

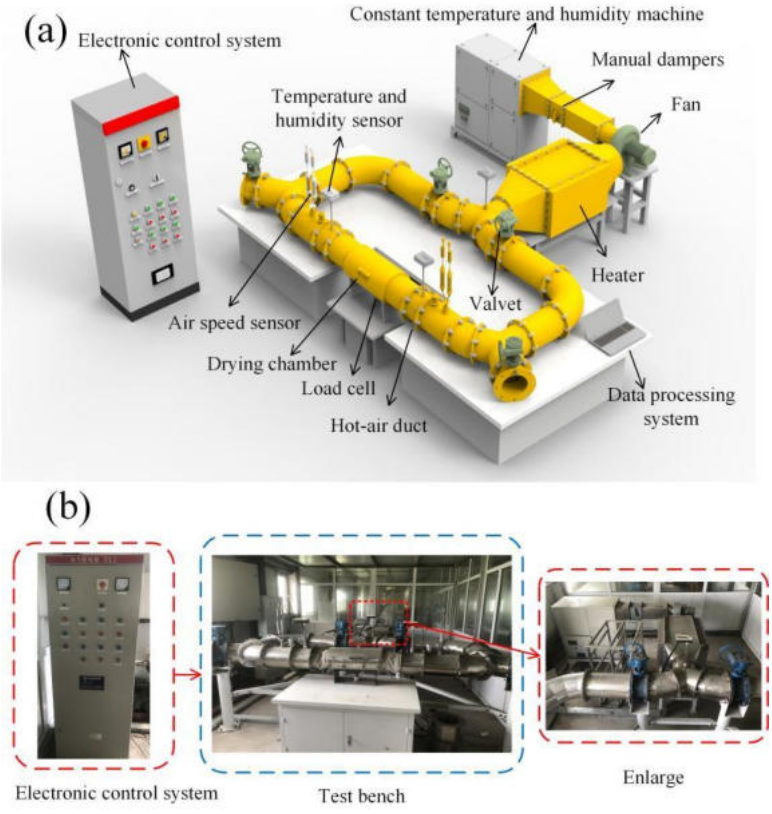


Fig. 1 - The hot-air drying experiment device

The device is capable of accurately controlling the temperature and air velocity, combined with a control system for recording and detecting data changes. The system is equipped with temperature and humidity sensors to dynamically detect the air temperature and humidity status at each pipe location, while the control unit makes rapid adjustments based on the set parameters. For each experiment, 200 grams of paddy were put into the drying area for processing. The hot air velocity was set at a constant 0.1 m/s, which remained constant throughout the drying process. A load cell was set at the bottom of the drying bin to continuously record the changes in sample mass.

Hot-air drying numerical simulation

Geometric modeling of paddy grain

In this study, the Suidao 3 variety was used as the test sample, and three-dimensional scanning technology was employed to obtain its geometric feature parameters. The test utilized an OKIO-5M 3D scanning device, which is based on the principle of structured light projection. The system captures the surface characteristics of the object using an image sensor and applies a phase resolution algorithm to accurately reconstruct the three-dimensional coordinate information of the sample surface. In the data processing stage, the raw point cloud data were processed with outlier removal and noise filtering, and then the morphological parameters of the sample were calculated, including the maximum projected area, equivalent volume and center of mass position. Subsequently, the final three-dimensional model is obtained for subsequent simulation operations by coloring, merging and correcting the model, as shown in Fig. 2.

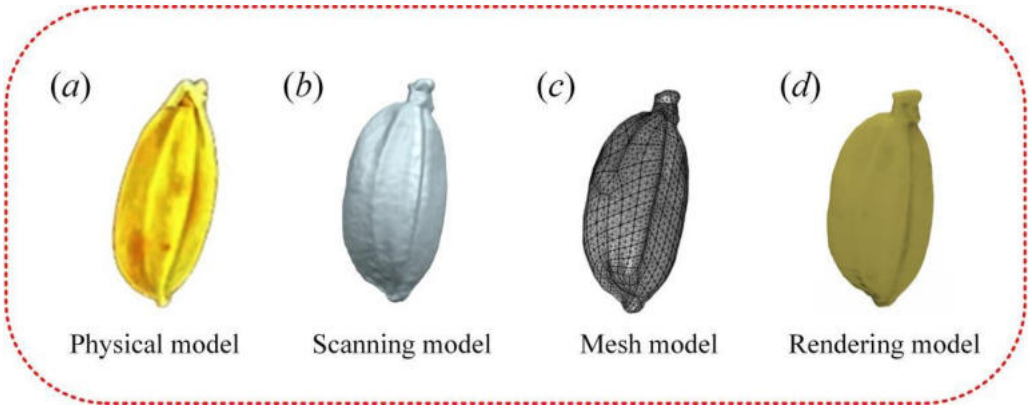


Fig. 2 - The three-dimensional geometric modeling of paddy grain

Model Assumptions

Modeling assumptions are required before numerical simulation modeling in this study (*Zhao et al., 2019*). (1) The paddy is regarded as an isotropic continuous medium material, and the initial state satisfies the conditions of uniform distribution of temperature and moisture in the paddy. (2) The drying process paddy diffuses in both liquid water and gaseous water. (3) Medium parameters in the drying process to maintain a steady state, ignoring the impact of fluctuations in environmental parameters (*Wang et al., 2024*).

Heat Transfer Equation

Based on the theory of energy conservation in a three-dimensional spatial coordinate system (x, y, z), the heat transfer phenomenon describing the hot-air drying process of paddy can be expressed by the following equations.

$$\rho C_p \frac{\partial T}{\partial t} = \lambda\left(\frac{\partial^2 T}{\partial x^2} + \frac{\partial^2 T}{\partial y^2} + \frac{\partial^2 T}{\partial z^2}\right) + h_g \rho \frac{\partial M}{\partial t} \quad (1)$$

The corresponding initial and boundary conditions are shown in equation (2).

$$\begin{cases} t = 0, \quad T = T_0 \\ -\lambda \dfrac{\partial T}{\partial t} = h_t\left(T - T_a\right) \end{cases} \quad (2)$$

where ρ is the density of paddy, (kg/m^3); C_p is the specific heat capacity of paddy, (J/kg·K); T is the temperature of paddy, ($^\circ$C); t is the time, (s); h_g is the latent heat of vaporization of paddy, (J/kg); M is the wet base moisture content of paddy, (kg/kg); T_0 is the initial temperature of paddy, (K); λ is the thermal conductivity of paddy, (W/m·K); T_a is the temperature of hot air, ($^\circ$C); h_t is the convective heat transfer coefficient, (W/m^2·K).

The h_t in the hot-air drying process can generally be calculated by the Nussel number (Nu), as shown in equation (3).

$$\begin{cases} Nu = \dfrac{h_t d}{\lambda_a} = 2 + 0.552\,\mathrm{Re}^{0.53}\,\mathrm{Pr}^{\left(\frac{1}{3}\right)} \\ \mathrm{Re} = \dfrac{v_a \rho_a d}{\mu_a} \\ Pr = \dfrac{\mu_a C_a}{\lambda_a} \end{cases} \quad (3)$$

where d is the equivalent diameter of paddy, (m); λ_a is the thermal conductivity of hot air, (W/m·K); Re is the Reynolds number; Pr is the Prandtl number; v_a is the velocity of hot air, (m/s); ρ_a is the density of hot air, (kg/m^3); μ_a is the dynamic viscosity of hot air, (Pa·s); C_a is the specific heat capacity of hot air, (J/kg·K).

Mass Transfer Equation

The heat transfer mechanism of hot-air drying of paddy covers convection and diffusion, and based on the mass conservation equation, the mathematical model of its internal moisture transport in a three-dimensional coordinate system can be described as follows:

$$\frac{\partial M}{\partial t} = D_{eff}\left(\frac{\partial^2 M}{\partial x^2} + \frac{\partial^2 M}{\partial y^2} + \frac{\partial^2 M}{\partial z^2}\right) \quad (4)$$

The initial and boundary conditions are set as follows:

$$\begin{cases} t = 0, \quad M = M_0 \\ -\lambda \dfrac{\partial M}{\partial t} = h_m\left(M - M_e\right) \end{cases} \quad (5)$$

where D_{eff} is the effective diffusion coefficient of moisture in paddy, (m^2/s); h_m is the convective mass transfer coefficient, (m/s); M_e is the equilibrium moisture content of paddy, (kg/kg); M_0 is the initial moisture content of paddy, (kg/kg).

The convective mass transfer coefficient (h_m) of paddy grain can generally be obtained by Sherwood number (Sh) calculation.

$$\begin{cases} Sh = \dfrac{h_m d}{D_a} = 2 + 0.552\mathrm{Re}^{0.53}\,Sc^{\left(\frac{1}{3}\right)} \\ Sc = \dfrac{\mu_a}{\rho_a D_a} \end{cases} \quad (6)$$

where D_a is the moisture diffusion coefficient in air, (m²/s); Sc is the Schmidt number.

Model solving

COMSOL Multiphysics software was used to select the fluid heat transfer and dilute matter transfer modules for the numerical simulation of the variable-temperature drying process of paddy. The grid independence was verified before solving, and the number and size of the grid were determined. The time step of the calculation was set to 10 seconds, and the simulation was done on a Dell 7810 workstation (Windows 10 system) equipped with 64 GB of RAM.

Experimental methods

Determination of glass transition temperature of paddy

Paddy samples weighing 500 g were randomly selected and dried under controlled conditions, with a constant temperature of 45 °C and a fixed air velocity of 0.5 m/s. The samples were taken at 10 min intervals and the moisture content was measured by a moisture meter, and then pulverized and placed in the refrigerator (2~4℃) for use. Paddy powders with different wet basis moisture content levels (10.1%, 12.5%, 14.3%, 16.2%, 18.3%, 20.4%, and 22.2%) were selected as test samples, and the glass transition temperature was determined by using a differential scanning calorimeter (*Chayjan et al., 2018*). Each sample with the same moisture content was tested three times, and the final glass transition temperature was obtained by averaging the results.

Variable-temperature hot-air drying experiment of Paddy

To investigate the influence of variable-temperature drying conditions on paddy drying quality, this study maintained a constant hot-air velocity and initial moisture content, while adjusting only the drying temperature during the variable-temperature experiments. The initial hot-air temperature was set at 40 °C, with temperature increments of 5 °C, 10 °C, and 15 °C applied in separate trials. Samples were taken at 10-minute intervals, and their moisture content was measured using a moisture meter until the safe storage standard of 14.0–14.5% was reached. When the moisture content of the paddy exceeded the value corresponding to the glass transition temperature by more than 4%, the drying temperature was increased to the next level according to the predefined increment. This protocol ensured that the paddy remained in the rubbery state throughout the entire drying process.

Indicator determination and calculation

Determination of initial moisture content of paddy refers to the use of grain, oilseed test Moisture Determination Method (GB/T 5497-1985), the paddy sample is placed in the drying box, and the weight of the paddy is measured several times at intervals of 1 h until the weight change is not more than 2 mg. The calculation of the wet-base moisture content of paddy at any moment of the drying process (M_t) is as shown in Equation (7) (*Nosrati et al., 2021*).

$$M_t = \frac{W_t - W_d}{W_t} \tag{7}$$

where W_t is the mass of the sample at time t, (g); t is the drying time, (s); W_d is the dry matter mass of the paddy sample, (g) (The paddy was dried at 105 °C until the change in weight was less than 0.02 g.).

The drying rate of paddy at different stages of the drying process was calculated by Equation (8).

$$DR = \frac{M_{t1} - M_{t2}}{t_2 - t_1} \tag{8}$$

where DR is the drying rate, (%/min); M_{t1} is the wet basis moisture content of paddy at time t_1, (%); M_{t2} is the wet basis moisture content of paddy at time t_2, (%).

After drying, the paddy was placed in a self-sealing bag and stored at room temperature for 48 h. It was then hulled, and the resulting brown rice was placed on a glass plate, where cracks were observed under a waist lamp. The cracking increase rate (F_{in}) was calculated according to equation (9).

$$F_{in} = \frac{n_f}{n} \tag{9}$$

where n is the number of paddy grains selected; n_f the number of paddy cracks.

The head rice yield was calculated according to equation (10).

$$HRY = \frac{m}{m_0} \times 100\% \tag{10}$$

where HRY is the head rice yield, (%); m_0 is the mass of paddy sample, (g); m is the mass of whole refined paddy, (g).

RESULTS AND DISCUSSIONS

Determination of the glass transition temperature of paddy

The glass transition curve of the Suidao 3 variety is shown in Fig. 3. This curve serves as a boundary that divides the paddy into two distinct physical states. In the region above the fitted curve, the paddy is in the rubbery state; conversely, in the region below the curve, the paddy is in the glassy state. By modeling this relationship, it becomes possible to predict and control the physical state of the paddy. Fluctuations in moisture content and temperature can cause transitions between these two states or maintain the current state, thereby influencing the physical and chemical properties of the paddy. This behavior aligns with the known plasticizing effect in polymeric materials, where a decrease in moisture content leads to an increase in the glass transition temperature. In this study, the variable-temperature drying process based on glass transition theory was defined to maintain the paddy in the rubbery state throughout the entire drying cycle (*Nasrnia et al., 2021*). As the moisture content of the paddy decreased from 22.2% to 10.1%, the glass transition temperature increased from 30.16 °C to 58.86 °C. A significant negative correlation was observed between the moisture content and the glass transition temperature.

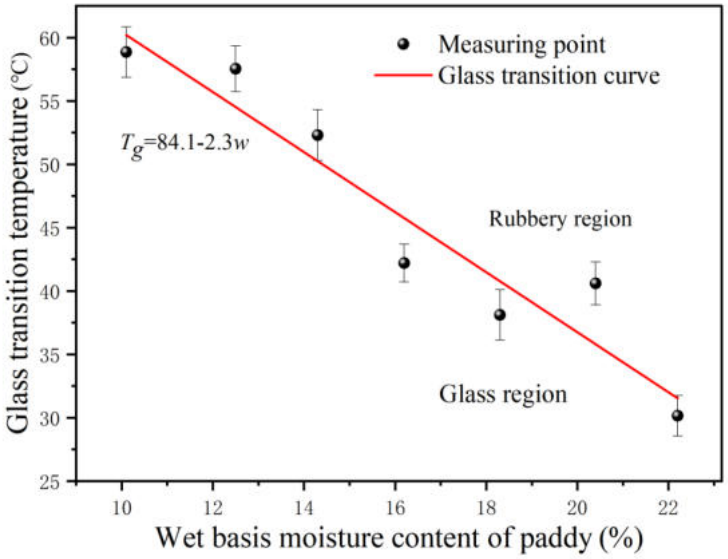
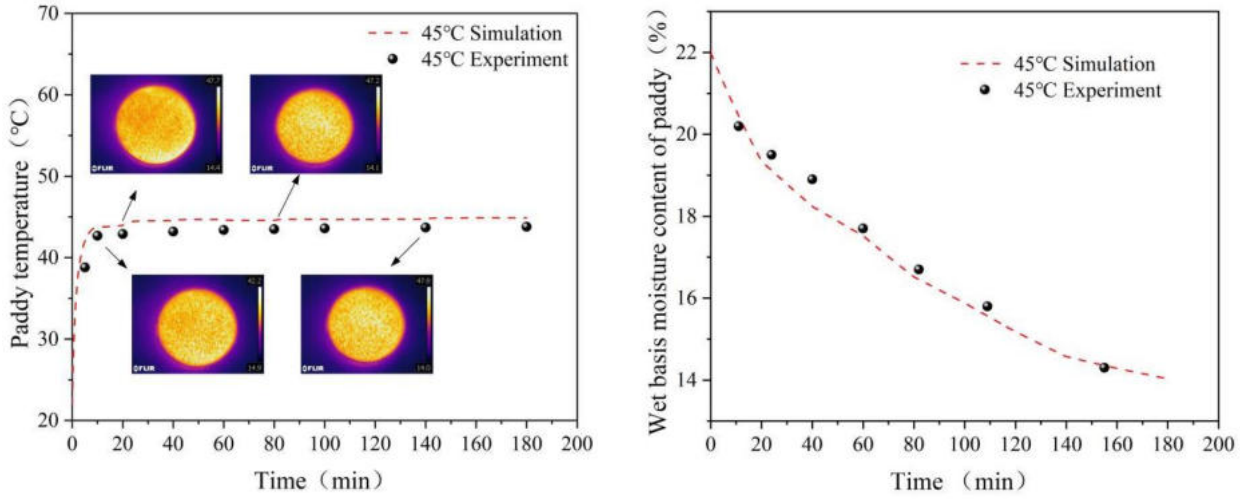


Fig. 3 - Fitted curve of moisture content and glass transition temperature for the Suidao 3 variety

Validation of the simulation model of paddy

Drying curves for the average moisture content and average temperature of paddy grains were obtained through numerical simulation. To ensure the accuracy of the comparison, the simulation and experimental drying conditions were kept consistent. The drying temperature was set to 45 °C, with an air velocity of 0.5 m/s. The comparison between the simulation and experimental results of the paddy drying process is shown in Fig. 4. As observed from the curves, paddy grains exhibited rapid moisture diffusion in the initial stage, followed by a slower diffusion rate as drying progressed. Meanwhile, the temperature of the paddy also rose rapidly, gradually reaching 45 °C. The simulated drying curves, derived from a three-dimensional scanning-based multi-physical field coupled model, showed a trend consistent with the experimental results. This indicates that the model effectively captures the changes in moisture and temperature during the drying process. The average error in simulated moisture content was 1.58%, with a mean square error of 0.11. For temperature, the average error was 2.66%, with an MSE of 1.35. According to previous studies, the acceptable error range for numerical simulations of paddy drying lies within 0–15% (*Zhao et al., 2019*). Therefore, the error range of the proposed model falls within acceptable limits, validating the accuracy and reliability of the established simulation model.



(a) Temperature variation of paddy (b) Moisture content variation of paddy

Fig. 4 - The comparison between the simulation and experimental results of the paddy drying process

Analysis of temperature and moisture changes in the paddy drying process

Under the initial conditions of an air velocity of 0.5 m/s and a moisture content of 22%, the drying process of paddy was simulated at a constant temperature of 40 °C, as well as with heating amplitude of 5 °C, 10 °C, and 15 °C. The internal temperature distributions of paddy grains under different drying conditions are shown in Fig. 5. At the initial stage of drying, the temperature of the paddy grains gradually increased upon exposure to hot air, eventually approaching the hot-air drying temperature asymptotically (*Li et al., 2024*). As shown in Fig. 5 (a)–(d), all four drying conditions maintained a grain surface temperature of approximately 40 °C at the 10-minute mark. The temperature of the outer layers increased more rapidly than that of the inner layers and progressively propagated inward. By the 30-minute mark, temperature differences among the four drying strategies began to emerge. In all cases, however, the outer layer temperature remained higher than that of the inner core. At 90 minutes, the internal temperature of the paddy grains approached the target drying temperature more closely across all test conditions. According to the law of conservation of energy, a portion of the input energy is consumed for moisture evaporation, resulting in the internal paddy temperature being slightly lower than the hot-air temperature throughout the process.

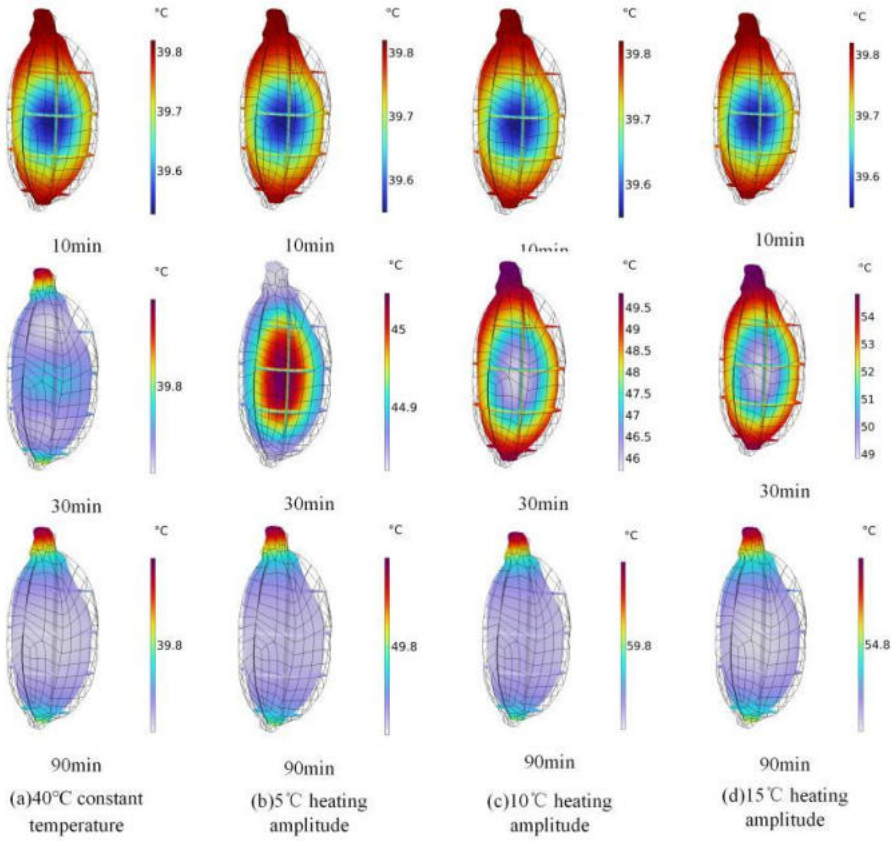


Fig. 5 - Internal temperature distribution of paddy under different hot-air drying conditions

Fig. 6 illustrates the internal moisture distribution of paddy under different hot-air drying conditions. Before the drying treatment, the internal temperature and moisture of the paddy grains were uniformly distributed. Moisture diffuses from the interior to the surface, which is the opposite direction of heat transfer (*Liu et al., 2022*). As shown in Figures 6(a)–(d), during the first 10 minutes of the drying process, the moisture distribution of all samples under the four drying conditions was generally consistent. During this initial stage, as the paddy grains came into contact with the hot air, internal moisture began to diffuse gradually toward the outer layers. By 30 minutes, the moisture distribution began to diverge across the different drying conditions. The rate and extent of internal moisture diffusion varied depending on the applied temperature gradient, resulting in noticeable differences in overall moisture content among the four treatments. At 90 minutes, during the later stage of drying, the internal moisture content of the grains decreased at a slower rate. The trends observed in the visualized moisture distribution were largely consistent with the experimental results, validating the accuracy of the simulation.

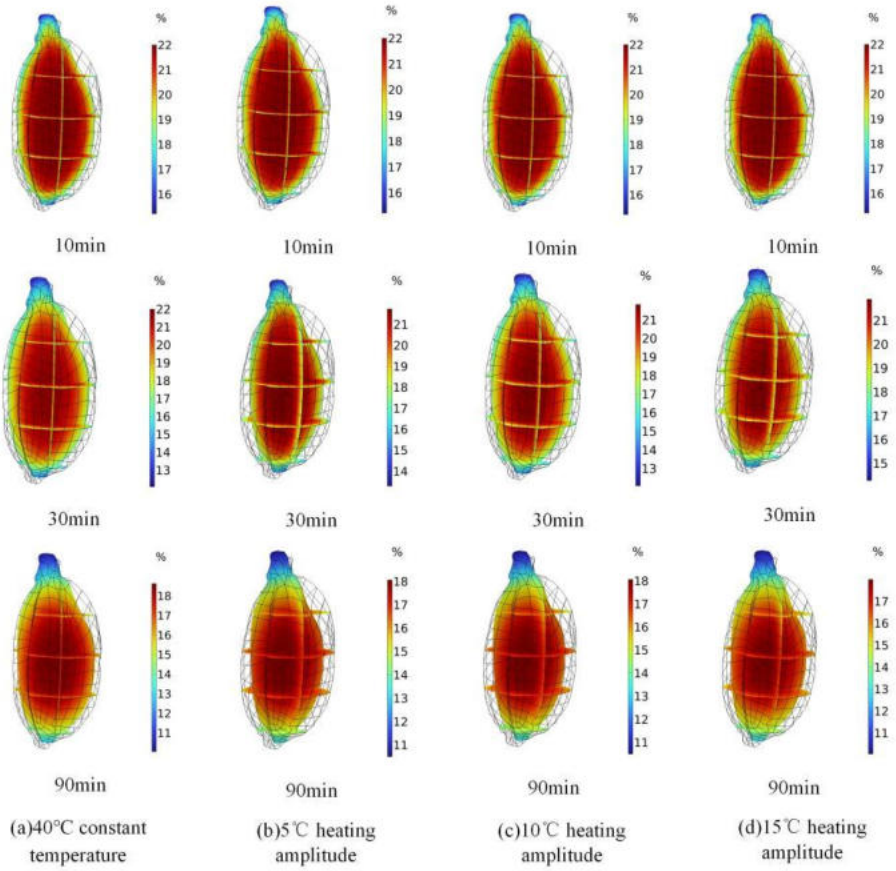


Fig. 6 - Internal moisture distribution of paddy grains under different hot-air drying conditions

Analysis of paddy drying characteristics

Fig. 7 illustrates the drying curves of paddy under different hot-air drying conditions.

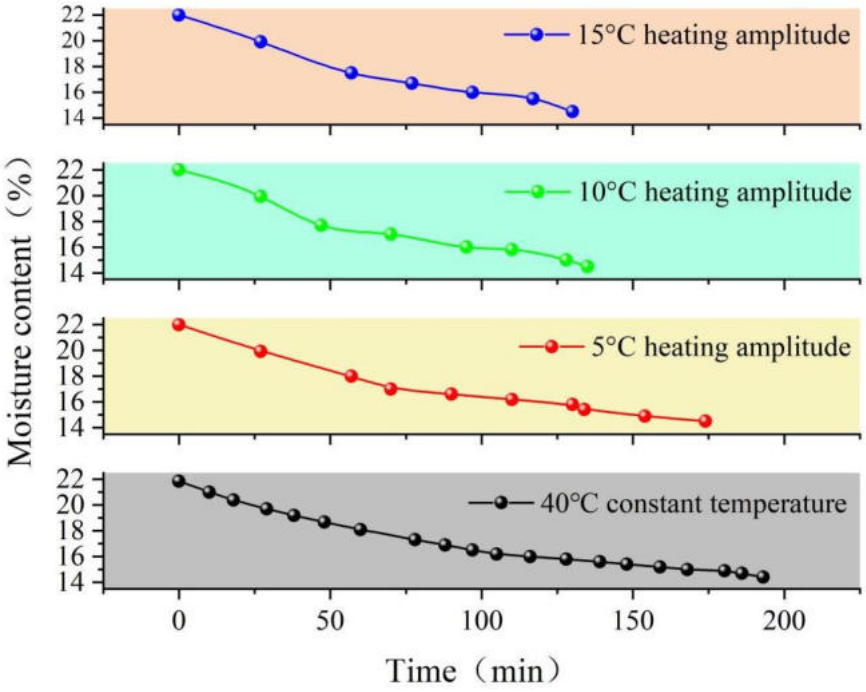


Fig. 7 - Drying curves of paddy under different hot-air drying conditions.

As shown in the figure, the moisture content exhibits a gradual decreasing trend. The turning point in the temperature change corresponds to the fitted curve of the glass transition temperature of the paddy. To ensure that the paddy remains in the rubbery state throughout the drying process, the initial drying temperature of 40 °C was followed by increases of 5 °C, 10 °C, and 15 °C in separate tests.

The longest drying time (174 min) was required when the air velocity was 0.5 m/s, the initial wet-base moisture content of paddy was 22%, and the heating amplitude was 5°C, while the shortest drying time (130 min) was required when the heating amplitude was 15°C. These results demonstrate that greater temperature increments lead to shorter drying durations. During the hot-air drying process, heat is transferred to the paddy primarily through convection and conduction. A temperature difference exists between the drying medium and the paddy, leading to heat absorption at the surface and its subsequent conduction into the interior. This promotes internal moisture evaporation. The larger the initial temperature increase, the greater the moisture gradient between the interior and exterior of the grain, resulting in a faster overall drying rate (*Guo et al., 2024*). This phenomenon can be attributed to the fact that, in the early stage of drying, the evaporation primarily involves non-bound water and moisture within the paddy husk. During this period, moisture diffusion and evaporation from the surface layer occur more rapidly, thereby accelerating the initial drying rate.

Fig.8 illustrates the drying rate curves of paddy under different hot-air drying conditions. As shown, the drying rate of paddy continuously changes throughout the drying process (*Sun et al., 2023*). In the initial stage, the drying rate increases rapidly due to the quick dissipation of surface moisture. In the middle and later stages, the drying rate exhibits minimal fluctuation. The fastest increase in drying rate was observed under the condition where the initial drying temperature was 40 °C with the heating amplitude of 15 °C. Conversely, when the heating amplitude was 5 °C, the drying rate increased at the slowest pace. During the constant-rate drying phase, differences in drying rate across conditions were relatively small. This is primarily due to the multi-layered structure of the paddy, which affects the evaporation and diffusion of moisture. At the beginning of the drying process, moisture in the paddy husk and non-bound water are removed first. Water diffuses from the interior of the grain to the surface and evaporates rapidly. As the moisture content decreases, internal water diffusion resistance increases, resulting in a decline in the drying rate during the later stages.

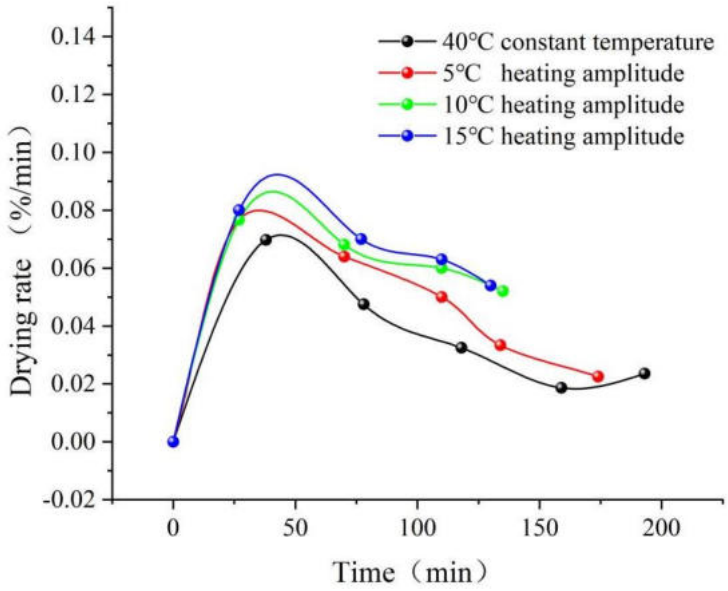


Fig. 8 - Drying rate curves of paddy under different hot-air drying conditions

Cracking increase rate

The effect of different hot-air drying conditions on the cracking increase rate of paddy is illustrated in Fig. 9. As shown in the figure, the cracking increase rate of paddy grain under varying drying conditions ranged from 2.5% to 6%. The cracking increase rate increased with the heating amplitude, reaching a maximum value of 6% under the drying condition with a 15 °C heating amplitude. It is noteworthy that when the cracking increase rate exceeds 3%, the paddy is more prone to breakage during the milling process, resulting in economic losses due to reduced yield of intact paddy. Compared to constant temperature drying at 40 °C, the drying condition with a 5 °C heating amplitude reduced the cracking increase rate by 0.3%. This indicates that variable temperature drying can effectively mitigate paddy cracking. The reduced cracking under the 5 °C heating amplitude is attributed to the absence of a glass transition in the paddy grain during drying, thereby minimizing internal stress and crack formation. However, when the heating amplitude increased to 10 °C and 15 °C, the cracking increase rate rose correspondingly. This trend is likely due to the development of more pronounced moisture gradients within the paddy grain at higher drying temperatures.

Even in the absence of a glass transition, these elevated gradients induce greater moisture stress, which in turn promotes cracking (*Mahmood et al., 2022*). Therefore, it can be concluded that excessive drying temperatures or large temperature increments are detrimental to paddy grain integrity. A carefully controlled heating range during hot air drying is crucial for minimizing grain cracking and ensuring post-processing quality.

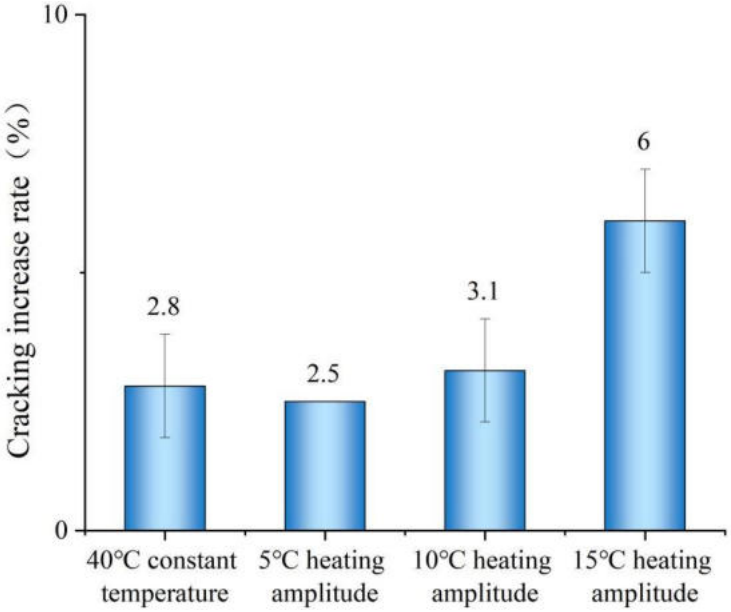


Fig. 9 - Effect of different hot-air drying conditions on the cracking increase rate of paddy

Head Rice Yield

Fig. 10 illustrates the effect of different hot-air drying conditions on the head rice yield of paddy. As shown in the figure, the HRY under various drying conditions ranged from 65.0% to 68.3%. Under the same initial drying temperature, a larger heating amplitude resulted in a lower HRY, with the maximum difference reaching 3.3%. This indicates a clear negative correlation between the temperature increase and head rice yield (*Mondal & Sarker, 2024*). The primary reason is that greater heating amplitudes lead to larger internal moisture gradients within the rice kernels, which promote grain fissuring during drying. These internal cracks increase the likelihood of grain breakage during milling, thereby reducing the final HRY. Compared to constant temperature drying at 40 °C, the HRY increased by 0.8% under a 5 °C heating amplitude. This result suggests that moderate variable-temperature drying can enhance the structural integrity of the grain and improve milling outcomes. HRY is not only a key indicator of the economic value of milled rice but also closely related to its sensory quality and nutritional attributes. Therefore, selecting optimal drying parameters, particularly in terms of heating amplitude, plays a vital role in maintaining and enhancing the processing quality of paddy.

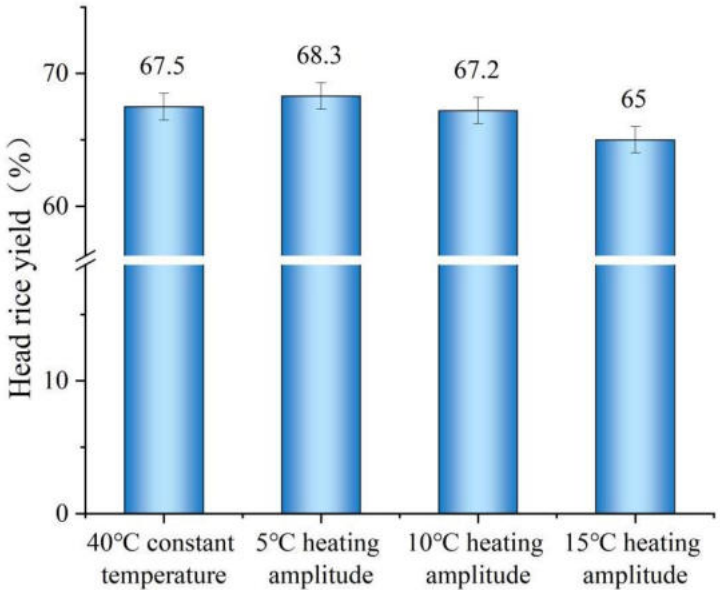


Fig. 10 - Effect of different hot-air drying conditions on the head rice yield of paddy

CONCLUSIONS

(1) Optical three-dimensional scanning was employed to obtain the three-dimensional geometric model of paddy. This method offers higher compatibility with the actual tri-axial dimensions of paddy and allows for a more realistic simulation of the drying process. By solving the heat and mass transfer models, the simulation of variable-temperature drying was successfully achieved. The simulation results showed high accuracy, with an average error of 1.58% and a mean square error of 0.11 for moisture content prediction, and an average error of 2.66% and MSE of 1.35 for temperature prediction.

(2) Glass transition curves were constructed based on the glass transition temperatures of paddy at different moisture contents. As the wet basis moisture content decreased from 22.0% to 10.1%, the glass transition temperature increased from 31.5 °C to 60.0 °C. Based on these curves, variable-temperature drying processes with heating amplitudes of 5 °C, 10 °C, and 15 °C were proposed. Compared with constant temperature drying, the variable-temperature drying processes reduced drying time by 19 min, 58 min, and 63 min, respectively. Among them, the process with a 5 °C heating amplitude showed the best performance, yielding a cracking increase rate of only 2.5% and a head paddy yield of 68.3%.

ACKNOWLEDGEMENT

This research was funded by the Daqing Municipal Directed Science and Technology Program, grant number zd-2025-032; the China Postdoctoral Science Foundation, grant number 2024MD763975; the School Orientation Training Research Initiation Fund Program, grant number XYB202307; the Heilongjiang Provincial Postdoctoral General Funding Project, grant number LBH-Z24250.

REFERENCES

[1] Chayjan R., Ghasemi A., & Sadeghi M. (2018). Stress fissuring and process duration during rough rice convective drying affected by continuous and stepwise changes in air temperature. *Drying Technology*, 37(2), 198-207. https://doi.org/10.1080/07373937.2018.1445637

[2] Guo, W., Cheng, S., Cui, Z., He, D., Zhang, X., Shi, T., & Du, J. (2024). Dynamic drying characteristics of alfalfa under solar energy-heat pump combined drying conditions. *INMATEH Agricultural Engineering*, 73(2), 569-580. https://doi.org/10.35633/inmateh-73-48

[3] Islam M. H., Momin A., Saha C. K., Alam M. M., & Islam S. (2024). Techno-economic analysis of BAU-STR dryer for rice drying: An approach to accelerate adoption. *Sustainability*, 16(22), 9846. https://doi.org/10.3390/su16229846

[4] Li X., Yang K., Wang Y., & Du X. (2024). Study on heat and moisture transfer of nonspherical rice during hot-air drying in thin-layer grain pile. *Journal of Food Process Engineering*, 47(4), e14597. https://doi.org/10.1111/jfpe.14597

[5] Liu H., He Y., Tang T., & Zhai M. (2022). Cracking prediction of germinated brown rice based on intragranular drying kinetics. *Powder Technology*, 406, 117587. https://doi.org/10.1016/j.powtec.2022.117587

[6] Liu Z., Che G., Wan L., Wang H., Chen Z., & Wang H. (2024). Design and experimental verification of self-priming hot air temperature changing device for grain dryer. *INMATEH Agricultural Engineering*, 73(2), 310-323. https://doi.org/10.35633/inmateh-73-26

[7] Mahmood N., Liu Y., Munir Z., Zhang Y., & Niazi B. (2022). Effects of hot air assisted radio frequency drying on heating uniformity, drying characteristics and quality of paddy. *Lwt-Food Science and Technology*, 158, 113131. https://doi.org/10.1016/j.lwt.2022.113131

[8] Mondal M., & Sarker M. (2024). Comprehensive energy analysis and environmental sustainability of industrial grain drying. Renewable and Sustainable *Energy Reviews*, 199, 114442. https://doi.org/10.1016/j.rser.2024.114442

[9] Nasrnia E., Sadeghi M., Raeisi Isa-Abadi A., & Mireei S. (2024). A novel simulation model to analyze rice intermittent drying considering glass transition concept. *Journal of Food Engineering*, 364, 111819. https://doi.org/10.1016/j.jfoodeng.2023.111819

[10] Nosrati M., Zare D., Nassiri S. M., Chen G., & Jafari A. (2021). Experimental and numerical study of intermittent drying of rough rice in a combined FIR-dryer. *Drying Technology*, 40(10), 1967-1979. https://doi.org/10.1080/07373937.2021.1898418

[11] Okeyo A. A., Luthra K., Vazquez A. R., & Atungulu G. G. (2024). Quality characteristic of instant rice produced using microwave-assisted hot air drying. *Cereal Chemistry*, 101(3), 641-653. https://doi.org/10.1002/cche.10770

[12] Owusu E. A., Luthra K., & Atungulu G. (2024). Material state diagrams for informed decision-making during drying of contemporary rice cultivars. *Drying Technology*, 42(5), 917-925. https://doi.org/10.1080/07373937.2024.2322110

[13] Smith D., Wason S., Atungulu G., & Bruce R. (2024). Radiofrequency (RF) drying of paddy rice and its effects on fissure formation and milling quality. *Applied Engineering in Agriculture*, 40(6), 697-714. https://doi.org/10.13031/aea.15966

[14] Rashid M. T., Liu K. L., Wei D. Z., Jatoi M. A., Li Q. Y., & Sarpong F. (2023). Drying kinetics and quality dynamics of ultrasound-assisted dried selenium-enriched germinated black rice. *Ultrasonics Sonochemistry*, 98, 106468. https://doi.org/10.1016/j.ultsonch.2023.106468

[15] Sun X., Guo Z., Wang G., Cai C., & Wang Z. (2023). Hot air drying, impact of infrared drying, and combined hot air-infrared drying on alfalfa drying quality and performance. *INMATEH Agricultural Engineering*, 71(3), 441-450. https://doi.org/10.35633/inmateh-71-38

[16] Wang C., Pei Y., Mu Z., Fan L., Kong J., Tian G., & Qiu H. (2024). Simulation analysis of 3-D airflow and temperature uniformity of paddy in a laboratory drying oven. *Foods*, 13(21), 3466. https://doi.org/10.3390/foods13213466

[17] Wang H., Che G., Wan L., & Tang H. (2022). Effects of drying approaches combined with variable temperature and tempering on the physicochemical quality of rice. *Drying Technology*, 41(7), 1199-1213. https://doi.org/10.1080/07373937.2022.2133140

[18] Zhang L., Jiang L., Adnouni M., Li S., & Zhang X. (2024). Numerical study on the variable-temperature drying and rehydration of shiitake. *Foods*, 13(21), 3356. https://doi.org/10.3390/foods13213356

[19] Zhang P., Li B., Hu Z., Zhang Q., Zhu Y., & Hao W. (2024). Effects of ultrasonic and microwave treatment on color, quality and drying characteristics of rice. *Journal of Cereal Science*, 116, 103856. https://doi.org/10.1016/j.jcs.2024.103856

[20] Zhao L., Yang J., Wang S., & Wu Z. (2019). Investigation of glass transition behavior in a rice kernel drying process by mathematical modeling. *Drying Technology*, 38(8), 1092-1105. https://doi.org/10.1080/07373937.2019.1612427

DESIGN AND EXPERIMENT OF TRACTION PERFORMANCE TEST EQUIPMENT FOR AGRICULTURAL TIRES
/
农用轮胎牵引性能试验设备的设计与试验

Jianguo YAN, Genglong GUO, Jiayao LI, Yaotai LI, Lijuan WANG*)
College of Mechanical and Electrical Engineering, Inner Mongolia Agricultural University, Hohhot 010018, China
Tel: +86 - 15848371910; E-mail: wanglijuan_qq@163.com
Corresponding author: Lijuan Wang
DOI: https://doi.org/10.35633/inmateh-76-89

Keywords: *agricultural tires; traction performance; tire-soil coupling; simulation analysis; field experiment*

ABSTRACT
To address the challenges of testing traction performance parameters of agricultural tires under varying soil types, tire specifications, and operational conditions, a dedicated test platform was developed to improve efficiency and reduce workload. The system includes a hydraulic drive with adjustable torque and speed, and a data acquisition module. Key components were selected based on design requirements and the frame was modeled and analyzed using ANSYS for both stress strain behavior and sixth-order modal characteristics, confirming structural integrity and absence of resonance. Field experiments were conducted using a 12.4-24 agricultural tire in accordance with the Chinese national standard GB/T 14828-2003, under three test surfaces: asphalt, withered grass field, and tilled soil. Results indicate that the developed equipment performs reliably through these conditions, demonstrating good stability and accurate data acquisition. The system's main specifications include external dimensions of 3155 mm x 1750 mm x 1385 mm, a total mass of 835.5 kg (1308.5 kg fully loaded), a variable speed range of 0-12 km/h, and a maximum driving torque exceeding 1000 N·m. These findings support the effectiveness and practical applicability of the device in agricultural tire traction performance testing.

摘要
针对农用轮胎在不同土壤类型、轮胎规格及运行条件下牵引性能参数测试存在的难题，本研究开发了一套专用试验平台系统以提高测试效率并降低工作强度。该系统配备扭矩与转速可调的液压驱动装置及数据采集模块，关键部件依据设计要求选型，并采用 ANSYS 对机架进行应力应变分析和六阶模态特性仿真，验证了结构完整性且无共振风险。按照中国国家标准 GB/T 14828-2003，选用 12.4-24 型农用轮胎在沥青路面、枯草地及翻耕地三种测试地面开展田间试验。结果表明：所研制设备在不同工况下运行可靠，稳定性良好且数据采集精确。该系统主要技术参数包括：外形尺寸 3155㎜×1750㎜×1385㎜，整机质量 835.5kg（满载 1308.5kg），测试速度范围 0-12km/h，最大驱动扭矩超 1000N·m。研究证实该装置在农用轮胎牵引性能测试中具有良好实效性与工程适用性。

INTRODUCTION
Agricultural production necessitates traction power, and the traction performance of agricultural tires, which are the primary components of wheeled agricultural machinery for achieving traction, is directly linked to the operational efficiency of such machinery *(Angelucci et al., 2025; Tekeste et al., 2023; Jjagwe et al., 2023)*. Significant energy losses occur during power transmission: studies report only 50-70% of tractor power reaches traction implements (dropping to 50% in soft soils), while 20-55% dissipates at the tire-soil interface due to rolling resistance/slippage *(Zeng et al., 2024; Farhadi et al., 2020; Kim et al 2018)*. These losses are compounded by tractor-implement compatibility issues and soil variability, causing unpredictable energy depletion *(Czarneck et al., 2019; Osinenko et al., 2015)*. Consequently, resolving tire-soil interactions is critical to mitigate slippage, fuel waste, and soil compaction *(Jasoliya et al., 2024; Małecka et al., 2024; Xi et al., 2024; Li et al., 2024)*. However, traction performance involves complex multi-factor coupling (soil type/tire parameters/operating conditions), demanding efficient testing methodologies for diverse scenario combinations *(Janulevičius et al., 2022; Zeng et al., 2025; Alkhalifa et al., 2024; Zeng et al.,2020)*.

Existing testing solutions face key limitations. Although soil-bin equipment dominates indoor research *(Taghavifar et al., 2014)* and was used in 63 studies conducted globally between 1968 and 2015 *(Ani et al., 2018)*, it inadequately replicates field conditions due to simplified soils and constrained operational parameters *(Jie et al., 2023; Kumar et al., 2019)*.

Field-capable devices often lack versatility, focusing on specific terrains like stubble fields *(Ekinci et al., 2015; Ekinci et al., 2017)*, plowed soils *(Abdolmaleki et al., 2015)*, or forest grounds *(Cudzik et al., 2018)*. In China, research is further hindered by reliance on tractor-towed systems or simulations, limiting field-validation capabilities *(Lun et al., 2016; Zhao et al., 2022; Huang et al., 2021; Wu et al., 2014)*. To address these gaps, this study develops novel traction testing equipment with four integrated innovations:

1. Self-contained operation via onboard power and steering control, enabling autonomous mobility;
2. Real-time parameter control of driving torque, speed, and wheel load through hydraulic-counterweight integration;
3. Modular single-wheel design with interchangeable tires for structural parametric studies;
4. This system uniquely supports both indoor soil-bin and field environments, overcoming prior device limitations.

The objective of this study is to design, fabricate, and experimentally validate this multifunctional equipment, establishing a standardized platform for quantifying tire-soil interactions under real-world conditions.

MATERIALS AND METHODS

Machine Structure and Operational Fundamentals

The traction performance tester consists of three main components: the frame, the power drive system, and the data acquisition system. These components are assembled as illustrated in fig. 1 (side view) and Fig. 2 (top view). The frame supports the entire test assembly rig and enables control of the travel direction via the turning mechanism. The test equipment adopts a single-wheel structure with interchangeable test tires, facilitating the study of the influence of tire structural parameters on traction performance. The power drive system includes: the diesel engine that drives the hydraulic pump, a hydraulic system, a deceleration sprocket group, and test tires. etc. This system collaboratively delivers required speed and torque outputs for tire traction testing. Driving torque is adjusted through the relief valve to control test tire torque output. Travel speed is regulated via the flow control valve to adjust the driving speed and control the slip rate of the test tires. The data acquisition system collects and processes all traction performance data from the test tires.

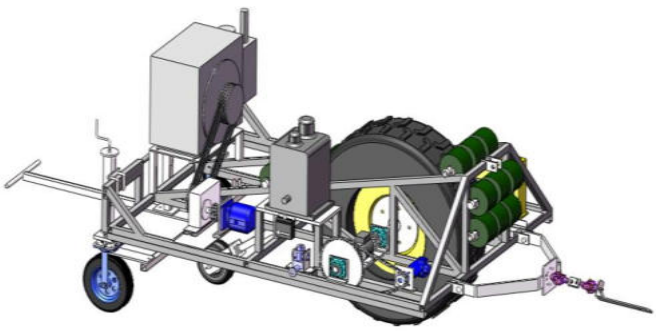


Fig. 1 - Assembly side view of agricultural tire traction performance tester

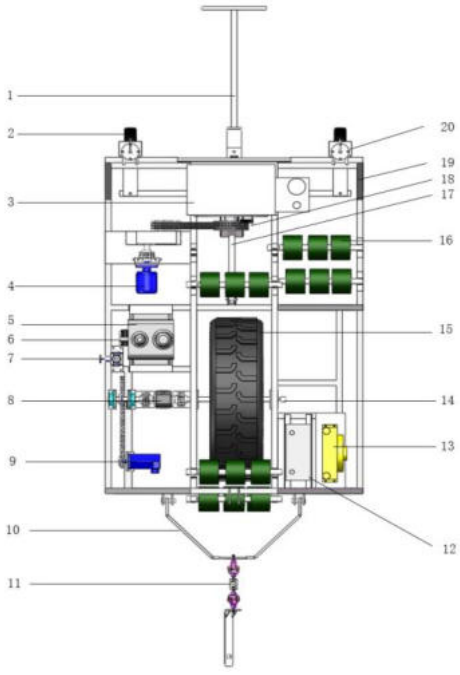


Fig. 2 - Assembly top view of agricultural tire traction performance tester

1.turning mechanism; 2.turning wheel; 3.diesel engine; 4.hydraulic pump; 5.hydraulic oil tank; 6.flow regulating valve; 7.relief valve; 8.torque sensor; 9.hydraulic motor; 10.pulling frame; 11.pulling sensor; 12.power supply; 13.hydraulic oil radiator; 14.driving wheel speed sensor; 15.test tire; 16.counterweight block; 17.driven wheel mechanism; 18.driven wheel speed sensor; 19.frame; 20.load sensor

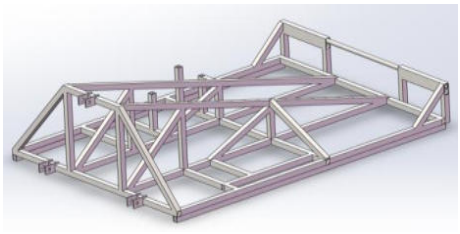
Design of Key Components

- **Design of Frame**

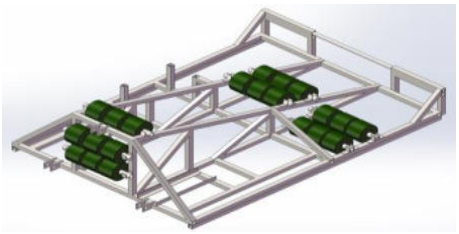
The test equipment frame requires high strength and sufficient space to mount power components, test tires, and counterweights (Fig. 3(a)). The frame is constructed from 40 mm × 40 mm × 4 mm Q235 square steel welded into a grid structure. Intersecting supports ensure uniform load distribution, while triangular reinforcements at high-stress areas dissipate impacts and vibrations, guaranteeing long-term stability. Counterweight modules (three 68 kg blocks each) are fixed to the frame via angle steel (Fig. 3(b)).

The steering mechanism includes a screw lifting device, sleeve, steering wheel, and steering rod. The planar linkage mechanism (pivoted at the sleeve) is secured to both sides of the frame with U-bolts. Adjusting the steering wheel angle controls travel direction (Fig. 3(c)-(d)).

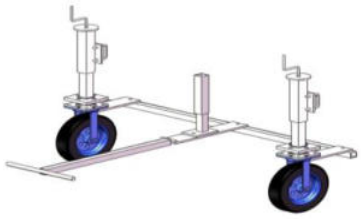
The traction mechanism comprises a traction frame, universal joints, tension sensors, and traction rods. The rods connect the tractor to the frame's suspension points via pins, enabling rolling resistance measurement under varying speeds, loads, and tire pressures (Fig. 3(e)-(f)).



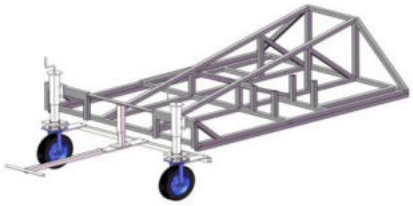
(a) Structure of frame



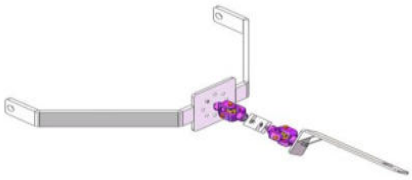
(b) Counterweights on the frame



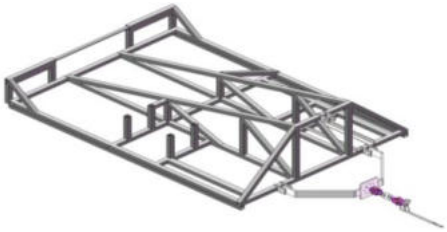
(c) Structure of turning mechanism



(d) Assembly scheme of turning mechanism on the frame



(e) Structure of pulling mechanism



(f) Assembly scheme of pulling mechanism on the frame

Fig. 3 - Overall structure diagram of frame

- **Design of Power Drive System**

The system is primarily composed of a diesel engine, hydraulic system, reduction sprocket group, and test tires. By appropriately selecting component parameters, the system ensures that its output speed and torque meet the requirements for tire traction performance testing. The driving torque of the tire is calculated using Equation (1).

$$T_t = F_N \cdot \varphi \cdot r \cdot k \quad (1)$$

Where:

T_t is the tire driving torque (N·m), F_N is the vertical tire load (N), φ is the attachment coefficient, F_f is the rolling resistance (N), r is the tire radius, (m), k is the sliding bearing friction coefficient.

Selected 12.4-24 agricultural tires as the basis for the design of the power system; the main parameters of the tires are shown in Table 1. According to equation (1), the maximum driving torque of the test tire is calculated to be 868 N·m.

Table1

Parameters of the 12.4-24 agricultural tire

Tire Specification	Number of tire ply	Section width (mm)	Diameter (mm)	Load capacity (kg)	Maximum tire pressure (kPa)
12.4-24	8	315	1160	1415	230

The BM5-315 cycloidal hydraulic motor is selected due to its high torque density and smooth low-speed operation—critical for precise traction control in off-road testing. Its parameters are listed in Table 2. While the motor's maximum torque (900 N·m) meets requirements, its minimum speed falls short of the required 8 r/min. Therefore, a reduction sprocket assembly is integrated.

Table 2

Parameters of the BM5-315 cycloidal hydraulic motor

Type specification	Displacement (ml/r)	Maximum torque (N·m)	Speed range (r/min)	Maximum pressure (MPa)	Weight (kg)
BM5-315	296	900	15-600	20	10

The test tire 12.4-24 outer diameter is 1160 mm. To simulate the general working speed of agricultural machinery 1~15 km/h, the corresponding tire rotational speed is calculated in Equation (2):

$$n = \frac{60v}{D\pi} \tag{2}$$

where:

n is the tire rotational speed (r/min), v is the tire linear velocity (m/s), D is the diameter of the test tire (m).

To meet the tire speed requirement (4–60 r/min), a reduction device with a ratio of 3.75:1 is calculated using Equation (3).

$$i = \frac{n_1}{n_2} = \frac{Z_2}{Z_1} \tag{3}$$

Where:

i is the reduction ratio, n_1 is the input speed (r/min), take 15 r/min, n_2 is the output speed (r/min), take 4 r/min, Z_1 is the number of teeth of the main wheel, Z_2 is the number of teeth of the driven wheel,

A sprocket combination of 17 and 65 teeth is ultimately selected, providing a reduction ratio of approximately 3.8:1, which satisfies both the minimum speed and slip rate adjustment requirements.

Table 3

Parameters of JHP-2080 high pressure gear pump

Type specification	Maximum pressure (MPa)	Displacement (ml/r)	Maximum speed (r/min)	Weight (kg)
JHP-2080	25	83	2000	30

The JHP-2080 high-pressure gear pump is chosen for its volumetric efficiency and pressure stability under variable loads. Parameters are listed in Table 3. Pump displacement is calculated using Equation (4), with power demand determined via Equation (5).

$$V_2 = \frac{V_1 \cdot n_1}{n_2} \tag{4}$$

$$P = V \cdot n \cdot p \times 10^{-6} \times 1.2 \tag{5}$$

Where:

V_2 is the hydraulic pump displacement (ml/r), V_1 is the hydraulic motor displacement (ml/r), n_1 is the hydraulic motor speed (r/min), n_2 is the hydraulic pump speed (r/min), P is the hydraulic pump power (kW), V is the hydraulic pump displacement (ml/r), N is the hydraulic pump speed (r/min), p is the hydraulic pump pressure (MPa).

Based on the hydraulic pump's power demand, the ZS195 diesel engine is selected, providing robust power delivery in field environments. Specifications are detailed in Table 4.

Table 4

Parameters of ZS195 diesel engine

Type specification	Maximum power (kW)	Maximum speed (r/min)	Sizes (mm)	Weight (kg)
ZS195	10.8	2200	830×380×670	145

The hydraulic system consists of a hydraulic oil tank, hydraulic pump, relief valve, flow control valve, bidirectional hydraulic motor, and temperature-controlled electronic radiator. The principle of the hydraulic system is shown in Fig. 4. The diesel engine drives the hydraulic pump, which delivers hydraulic oil through a filter to the hydraulic motor, producing output speed and torque that meet performance requirements. The system regulates driving torque via the relief valve, adjusts speed through the flow control valve, and maintains normal hydraulic oil temperature using the temperature-controlled radiator, ensuring continuous operation and system stability.

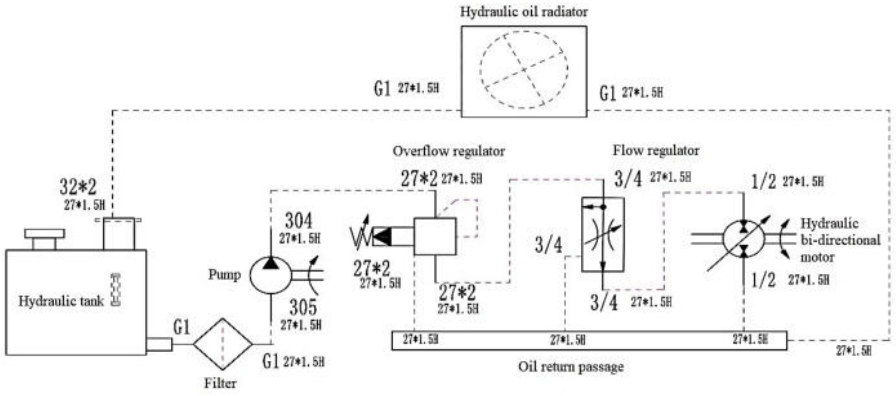


Fig. 4 - Hydraulic schematic diagram

● Design of Data Acquisition System

The system architecture consists of sensors, a data acquisition processor, a communication module, and a central PC interface. Sensors include a test tire RPM sensor and following wheel RPM sensor (both connected directly to the data acquisition processor's input ports), along with a torque sensor, left/right turning wheel load sensors, and a pulling sensor – these are connected to the processor's input ports via transmitters. The data acquisition processor collects and processes signals from all sensors before transmitting the output data through an RS232 serial communication interface to the central PC. The PC then receives and displays all measurement data in real time. Power is supplied to all sensors and the data acquisition processor by a dedicated power management module.

According to the RPM speed requirements of the tester power drive system, the DW3806 RPM sensor is selected (Fig. 5(a)), with parameters detailed in Table 5. The tire RPM sensor measures the rotational speed of the driven tire, while the follower wheel RPM sensor determines the actual linear travel speed of the platform. This configuration enables slip calculation by comparing theoretical travel speed (derived from driven tire rotation) with actual linear movement. The tire RPM sensor is installed at the end of the tire drive shaft (Fig. 5(b)), and the follower wheel RPM sensor is mounted at the end of the follower wheel shaft (Fig. 5(c)). Both sensors are coupled to their respective shafts via winding couplings, with mounting positions secured by positioning plates.

Table 5

Parameters of the DW3806 RPM sensor

Para-meters	Dimensions (OD mm x H mm)	Shaft diameter (mm)	Radial load (N)	Axial load (N)	Starting torque (N·m)	Maximum speed (r/min)	Moment of inertia (g/cm^2)	Allowable angular acceleration (rad/s)	Weight (kg)
Value	37 x 52	6	≤30	≤20	≤2×10^{-3}	6000	20	2 x 10^4	0.1



(a) RPM sensor *(b) Test tire RPM sensor* *(c) Following wheel RPM sensor*

Fig. 5 - RPM sensor and assembly scheme

The torque sensor is used to test the driving torque of the test tire, installed on the tire drive shaft. According to the output torque designed for the power drive system of the tester, the JN-DN4 torque sensor is selected for its ability to provide accurate real-time measurement to test the driving torque of the test tire, and the relevant parameters of the torque sensor are shown in Table 6. In order to achieve the purpose of real-time measurement during operation, the sensor is fixed between the sprocket power output shaft and the drive tire shaft, and both sides are connected through roller chain coupling, as shown in Fig. 6.

Table 6

Parameters of JN-DN4 torque sensor

Parameters	Overall dimensions (L mm × W mm × H mm)	Shaft diameter (mm)	Range (N·m)	Combined accuracy (%)	Rated speed (r/min)	Maximum speed (r/min)	Safe overload (%)	Operating environment (℃)
Value	230 x 127 x 168.5	38	0~5000	± 0.3	4000	6000	120	-10~+60



(a) Torque sensor



(b) Torque sensor assembly scheme

Fig. 6 - Torque sensor and assembly scheme

The left and right turning wheel load sensors are used to test the loads of the left and right turning wheels, which are used to calculate the actual loads of the tire under test, and are mounted between each ground wheel and the bottom of the test frame. The full load weight of the test set is about 1308.5 kg, and the overall weight is borne by the driving tire and the two turning wheels, with the test tire as the main load-bearing wheel. The ZNLBU-I load cell is selected due to its robust design and suitability for the anticipated load range to measure the load of the turning wheels, as shown in Fig. 7(a), and the relevant parameters of the load cell are shown in Table 7. In order to facilitate the disassembly and installation of the cell and the load test, the upper mounting plate can slide up and down through the positioning guide pillar, and the turning wheel rotor shaft is provided with a structure for mounting the load cell, as shown in Fig. 7(b). This mounting structure allows for straightforward calibration and maintenance.

Table 7

Parameters of ZNLBU-I load sensor

Parameters	Overall dimensions (O.D. mm × H. mm)	Range (kg)	Sensitivity (mv/V)	Combined accuracy (%)	Operating temperature range (°C)	Thread size (mm)	Allowable overload (%)	Sealing grade
Value	72 x 27	600	1.2	0.05	-20~+70	M12×1.75	120	IP66



(a) Load sensor



(b) Load sensor assembly scheme

Fig. 7 - Load sensor and assembly scheme

A pulling sensor is used to test the rolling resistance of the tire under test. According to the rolling resistance estimation under the maximum load of the test tire, it is determined that the ZNLBS-I pulling sensor

is selected, as its measurement range and accuracy are appropriate for the expected rolling resistance forces, as shown in Fig. 8 (a). The parameters of the sensor are shown in Table 8, and the sensor is mounted on the pulling bar during the towing test and coupled with the pulling mechanism of the tractor, as shown in Fig. 8 (b).

Table 8

Parameters of ZNLBS-I pulling sensor

Parameters	Dimensions (L mm x W mm x H mm)	Range (N)	Sensitivity (mv/V)	Operating temperature range (°C)	Thread Size (mm)	Allowable overload (%)	Sealing Grade
Value	51 x 19 x 76	5000	2	-20~+70	M12×1.75	150	IP67



(a) Pulling sensor *(b) Pulling sensor assembly scheme*

Fig. 8 - Pulling sensor and assembly scheme

The circuit diagram of the data acquisition system is shown in Fig. 9. A 24 V lithium battery pack powers the system for sustained outdoor operation, simultaneously supplying the data acquisition processor and all sensors. Voltage regulators mitigate battery voltage fluctuations, while a fuse protects against short circuits or overloads. The rotational speed sensors' encoders generate pulse signals (sampled at 1 kHz with ±0.1% accuracy) from the test tire and follower wheel axles, transmitted to the PLC's X0–X3 high-speed input ports. Analog-output sensors (left/right wheel load, torque, and pulling sensors) convert physical quantities to voltage signals (0–10 V range, 16-bit resolution), routed to the PLC's AD0–AD3 ports for synchronized analog-to-digital conversion at 500 Hz. All channels are sampled simultaneously via PLC scan-cycle synchronization to ensure temporal alignment for slip/force calculations. Processed data is sent via RS232 to a Human Machine Interface (HMI) for real-time numerical display, enabling intuitive monitoring. A USB interface facilitates data download for post-processing.

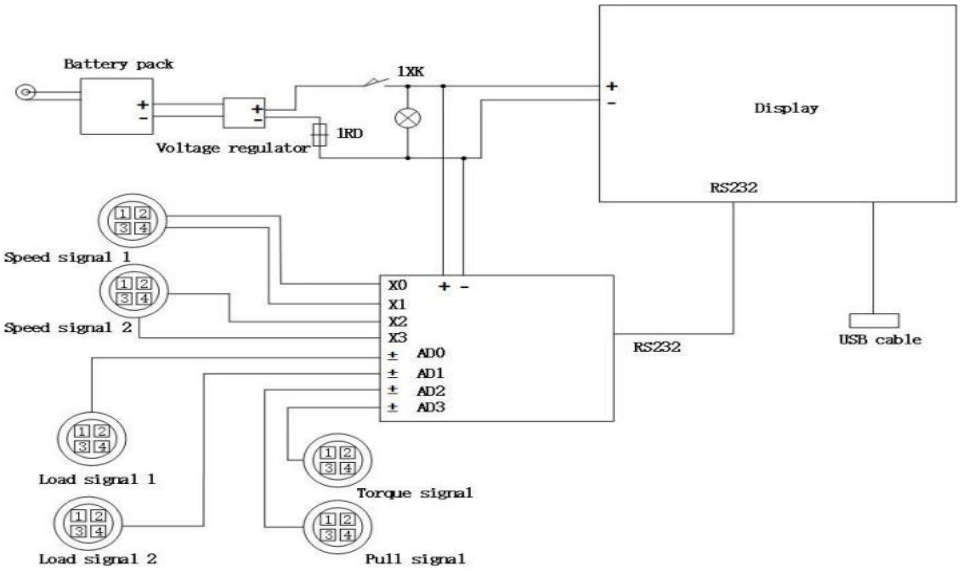
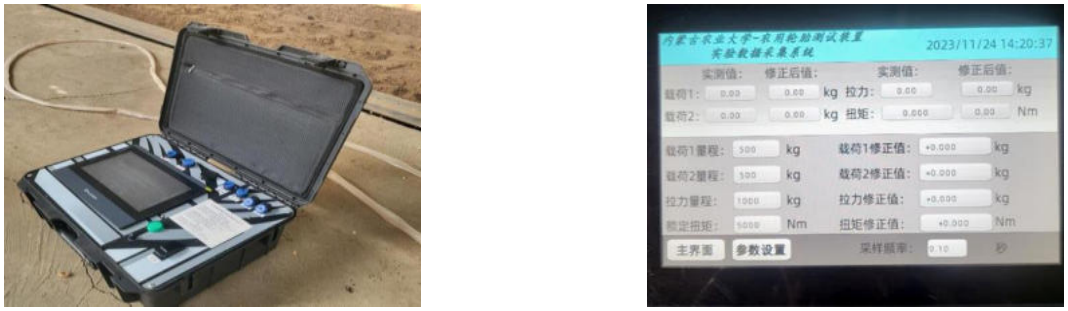


Fig. 9 - Circuit diagram of data acquisition system

The designed and fabricated data acquisition instrument is shown in Fig. 10(a), and the working interface of the data acquisition instrument is shown in Fig. 10(b). The data acquisition instrument is used to display and save the output of each sensor test data.



(a) Data acquisition instrument *(b) Working interface of data acquisition instrument*

Fig. 10 - Data acquisition instrument and working interface

The designed systems were integrated, and the developed agricultural tire traction performance test equipment is shown in Fig.11.



Fig. 11 - Agricultural tire traction performance test equipment

Experiment Scheme

- **Simulation Experiment**

ANSYS was used for carrying out static analysis of the frame to check whether the strength of the frame meets the requirements. In addition, the frame is installed with a diesel engine driving the hydraulic pump. In order to check whether the coercive vibration generated in the operation of the engine will cause resonance problems in the frame, modal analysis of the frame is needed.

By elucidating the dynamic characteristics and vibrational modes of the equipment, modal analysis facilitates the identification of critical frequencies and potential resonance points that could adversely affect the precision and reliability of traction measurements. SolidWorks software is used to establish a three-dimensional structural model of the frame, and the frame model is imported into ANSYS Workbench to construct a finite element model. The material of the frame is Q235A carbon structural steel, and the relevant mechanical parameters are listed in Table 9. The two bearing surfaces of the test tires and the mounting plates of the two steering wheels are defined as "fixed supports" in the fixed support setting. The overall load on the frame is distributed between the fuel tank $(24\ \mathrm{kg})$, the diesel engine $(145\ \mathrm{kg})$, hydraulic pump $(30\ \mathrm{kg})$, hydraulic motor $(10\ \mathrm{kg})$, electric battery $(18\ \mathrm{kg})$, hydraulic oil radiator and fan $(15\ \mathrm{kg})$, and 7 sets of counterweights $(7 \times 68\ \mathrm{kg})$ are applied, so the frame force is the gravity of each of these components. The setup applies loads to each of the above components at the corresponding mounting part of the frame and performs the computational solution.

Table 9

Material properties of Q235A

Material	Density (kg/m^3)	Young's modulus (Pa)	Yield strength (Pa)	Tangent modulus (Pa)	Poisson's ratio
Q235A	7860	2.12 x 10^{11}	2.35 x 10^8	6.1 x 10^9	0.288

● **Field Experiment**

A field experiment covering three aspects was conducted to verify whether the working performance of the developed tester could meet the expected goals. Firstly, test the ability of the test equipment to work stably, including the stability of the travel speed and the ability to adapt to the work of different terrain conditions. Secondly, according to the Chinese national standard "GB_T14828-2003 Agricultural Tire Traction Performance Test Method," the relationship between tire tractive efficiency and slip rate with traction coefficient under different terrain conditions was investigated. Finally, a field experiment was carried out to investigate the effects of tire load and pressure on traction force and rolling resistance under different terrain conditions.

The experiment was conducted at the experimental base of Inner Mongolia Agricultural University. The asphalt road, withered grass field, and tillage were selected as the terrain conditions, as shown in Fig. 12. The experiment was conducted in October 2024. The soil parameters of withered grass fields and tillage are shown in Table 10.



(a) Asphalt road



(b) Withered grass field



(c) Tillage

Fig. 12 - Three experimental terrain conditions

Table 10

Soil parameters of withered grass field and tillage

Withered grass field		Tillage	
parameter	**value**	**parameter**	**value**
Moisture content (%) (0-20 cm)	3-5	Moisture content (%) (0-20 cm)	16-18
Penetration resistance ($N \cdot cm^{-2}$) (0-20cm)	312.4	Penetration resistance ($N \cdot cm^{-2}$) (0-20cm)	135.2
Shearing strength ($kN \cdot m^{-2}$)	36.91	Shearing strength ($kN \cdot m^{-2}$)	7.89

Experiment of the stable working capacity of the tester:

In order to verify the stability of the travel speed of the tester and its adaptability to work under three kinds of terrain conditions, the tester was maneuvered to travel more than 50 meters under the conditions of loaded 340 kg counterweight block (full load 13085 N) and unloaded counterweight (8355 N). A total of 16 sets of speed data were tested on each kind of terrain, including 8 sets under the conditions of full load and 8 sets under the conditions of unloaded counterweight. In the test, the turning mechanism controls the tester to keep traveling in a straight line as far as possible. The travel speed of the test tire was changed by the flow-regulating valve in the hydraulic system. The data collection was started after the travel speed of the tester was stabilized in each test. The travel speed of the tester was measured by the following wheel speed sensor. At the same time, the GPS-based VBOX data acquisition system (produced by RaceLogic, UK, with a speed measurement accuracy of 0.1km/h) was used for measuring the travel speed of the tester. The travel speed stability and terrain adaptation ability of the tester were evaluated by comparing the difference in speed between the two measurements.

(2) Experiment on the traction performance of agricultural tire based on Chinese national standard GB_T14828-2003:

According to the "GB_T14828-2003 test method for traction performance of agricultural tires" (*GB/T 14828-2003*), the experiment on the relationship between the slip rate of agricultural tires, tractive efficiency, and traction coefficient was carried out, which could check whether the driving torque of the tester and the adjusting range can meet the test requirements.

The calculations of tire slip rate S, tractive efficiency TE, and traction coefficient TC are shown in Equations (6)-(10):

Tire travel reduction (S). $S = (1 - \frac{v_a}{v_t}) \times 100\%$ (6)

Traction coefficient $TC = \frac{F_t}{G}$ (7)

Drawbar power. $P_D = F_t \cdot v_a$ (8)

Axle power (kW). $P_a = \frac{T \cdot n}{9550}$ (9)

Tractive efficiency. $TE = \frac{P_D}{P_a} \times 100\%$ (10)

where:

v_a is the tire actual velocity (m/s), v_t is the tire theoretical velocity (m/s), F_t is the traction force of tire (N), G is the vertical load of tire (N), T is the tire axle torque (N.m), n is the tire rotation speed (rpm).

The relief valve of the hydraulic system was used to adjust the driving torque of the test tire. As the driving torque of the test tire increases gradually from small to large, the traction coefficient increases with the driving torque of the tire. As the traction coefficient increases, the slip component of the tire roll increases gradually, and the tire tractive efficiency will also change.

Therefore, by carrying out the agricultural tire traction performance experiment, it was examined whether the tester could complete the tire traction test under the three different terrain conditions according to the Chinese national standard GB_T14828-2003.

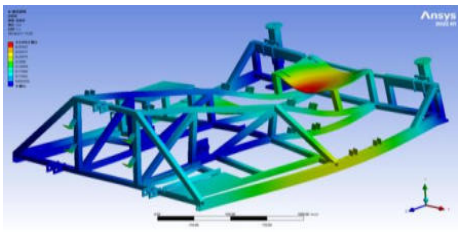
(3) Experiment on the effect of tire load and pressure on tire traction performance:

The effect of tire load and pressure on rolling resistance and traction was investigated under three terrain conditions. The tire load was adjusted by using counterweights, and the vertical loads of the tire were 8355 N, 10395 N, 11755 N, and 13085 N, respectively, while the tire pressure was set to 120 kPa. The tire pressure could be adjusted by inflation and deflation, and the tire pressure was set to 80 kPa, 120 kPa, 160 kPa, and 200 kPa, respectively. At the same time, the tire load was set to 8355 N. The travel speed of the tester was kept stable during the test, and the test was repeated three times under each test condition, and the average value of the data from the three repeated tests was taken as the final test value. The average travel speeds of the tester measured during the tests on asphalt roads, field withered grass, and tillage were 3.56 km/h, 3.25 km/h, and 2.51 km/h, respectively.

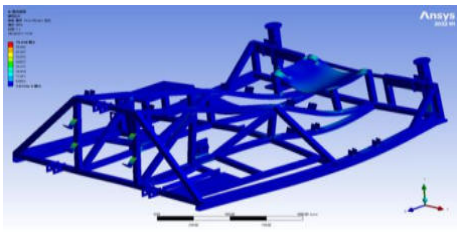
RESULTS AND ANALYSIS

Analysis of Simulation Results

Through static analysis, the frame exhibits a maximum total deformation of 0.53963 mm at the diesel engine mounting plate (Fig. 13a) and a maximum equivalent stress of 79.248 MPa at the engine mounting holes and counterweight block groove (Fig. 13b). This deformation magnitude is functionally acceptable since, under dynamic field conditions (e.g., tractor-induced vibrations exceeding ±3 mm per ISO 5008), the 0.53963 mm static deflection is negligible relative to system-level displacements. The material of the frame is Q235A. The Q235A steel frame's maximum stress (79.248 MPa) remains below the material's 235 MPa yield strength (GB/T 700-2006), confirming a safety factor >2.96. Thus, the frame's structural adequacy is validated for all operational scenarios.



(a) Deformation cloud image of the frame



(b) Equivalent stress cloud image of the frame

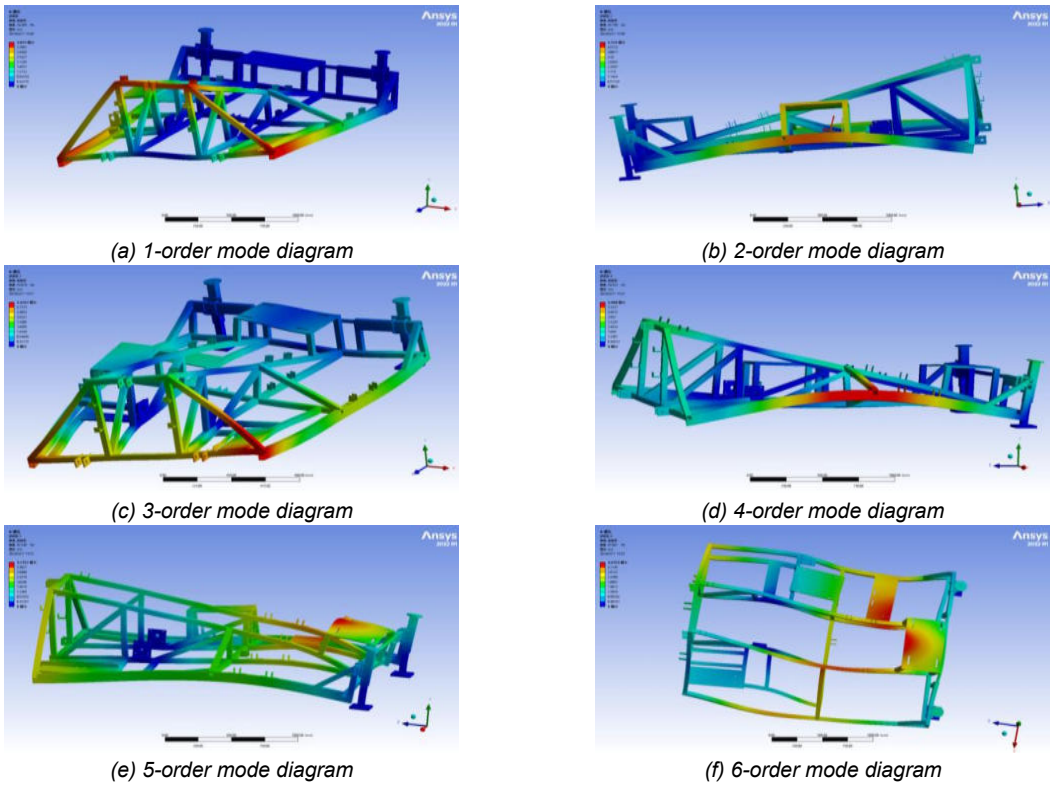
Fig. 13 - Deformation cloud and equivalent stress cloud image of the frame

Modal analysis confirmed the structural integrity of the frame under dynamic loads. Table 11 lists the first six orders of intrinsic frequencies obtained through solving the frame modes. Fig. 14 presents the results of the first six-order modal analysis. The natural frequencies differ across orders, resulting in correspondingly distinct deformations of the frame at each frequency. Higher deformation amplitudes occurred at the mounting points (diesel engine, oil tank, hydraulic pump, counterweight), exhibiting reciprocating and torsional deformation modes.

Table 11

Intrinsic frequencies of the first 6 orders of modes of the frame

Order	1	2	3	4	5	6
Intrinsic frequency value (Hz)	26.389	42.769	52.076	56.613	62.348	67.081



(a) 1-order mode diagram (b) 2-order mode diagram

(c) 3-order mode diagram (d) 4-order mode diagram

(e) 5-order mode diagram (f) 6-order mode diagram

Fig. 14 - First 6 order modal diagram of the frame

The main vibration excitation to the frame is from the vibration generated by the operation of the diesel engine. The selected diesel engine is a single-cylinder 4-stroke engine, and the engine excitation frequency is calculated as Equation (11):

$$f = \frac{2nz}{60k} \quad (11)$$

where:

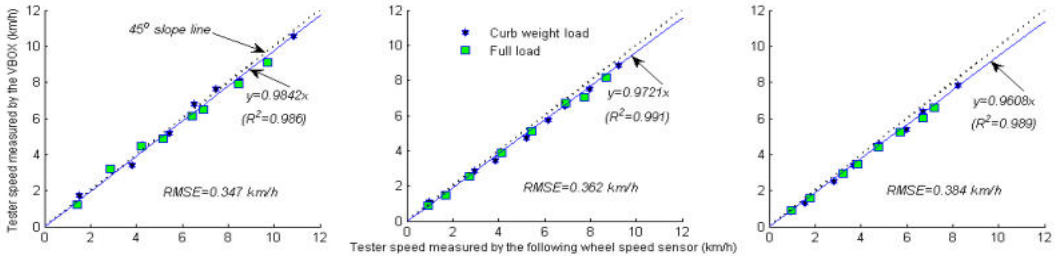
f is the engine excitation frequency (Hz), n is the engine speed (r/min), z is the number of engine cylinders, k is the number of engine strokes.

The engine idle speed is 800 r/min, so the excitation frequency of the engine is calculated to be 6.67 Hz. The maximum speed of the engine is 2200 r/min, and the vibration frequency is 18.33 Hz. It can be seen from Table 10 that the lowest intrinsic frequency of the frame is 26.389 Hz, which is higher than the maximum excitation frequency of the engine. So, there is no resonance occurring in the frame. While the magnitude of deformation increases with the modal order, all values remain within safe limits.

Analysis of Field Experiment Results

- **Experiment of the stable working capacity of the tester**

The test results of the tester in three terrain conditions with different travel speeds are shown in Fig. 15.



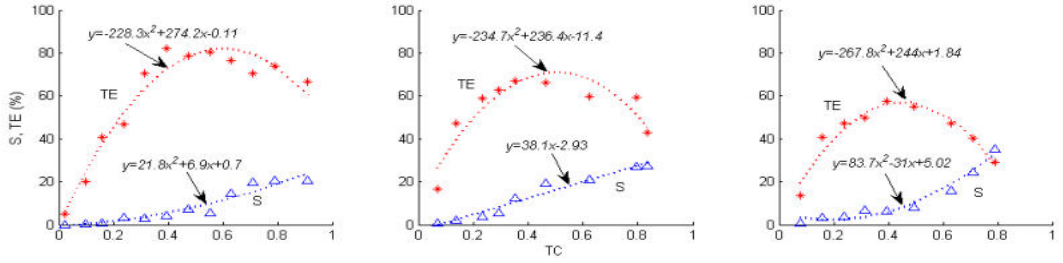
(a) Asphalt road *(b) Withered grass field* *(c) Tillage*

Fig. 15 - Test results for different travel speeds

As shown in Figure 15, the travel speeds measured by the tester's RPM sensor and the VBOX reference system show good agreement under both curb weight and full load conditions. RMSE values were 0.347 km/h (asphalt), 0.362 km/h (withered grass), and 0.384 km/h (tillage). A consistent minor overestimation by the RPM sensor (<0.4 km/h RMSE), attributed to wheel bounce on rough terrain, is operationally negligible. This discrepancy does not impact core functions (stability assessment, maneuverability) and falls within acceptable tolerances for agricultural machinery testing.

- **Experiment on the traction performance of agricultural tire based on national standard GB_T14828-2003**

The experimental results of tire tractive efficiency and slip rate versus traction coefficient are shown in Fig. 16.



(a) Asphalt road *(b) Withered grass field* *(c) Tillage*

Fig. 16 - Relationship between tractive efficiency TE, slip rate S and traction coefficient TC

As can be seen from Fig. 16, under the three terrain conditions, tire tractive efficiency and slip rate vary with traction coefficient, but the trends are basically the same. That is, the slip rate increases with the increase of the traction coefficient, and the tractive efficiency increases and then decreases with the increase of the traction coefficient, which conforms to the trend of the relationship between the tractive efficiency and slip rate with the traction coefficient in GB_T14828-2003. It shows that the driving torque output characteristics and adjustment range of the tester can meet the road and field test environment and can be used to carry out agricultural tire traction performance tests, which lays a foundation for the study of tire-soil coupling mechanisms.

- **Experiment on the effect of tire load and pressure on tire traction performance**

Based on the analysis of the test data, the effects of load and tire pressure on the tire traction force are shown in Fig. 17, and the effects of load and tire pressure on the rolling resistance of the tire are shown in Fig. 18.

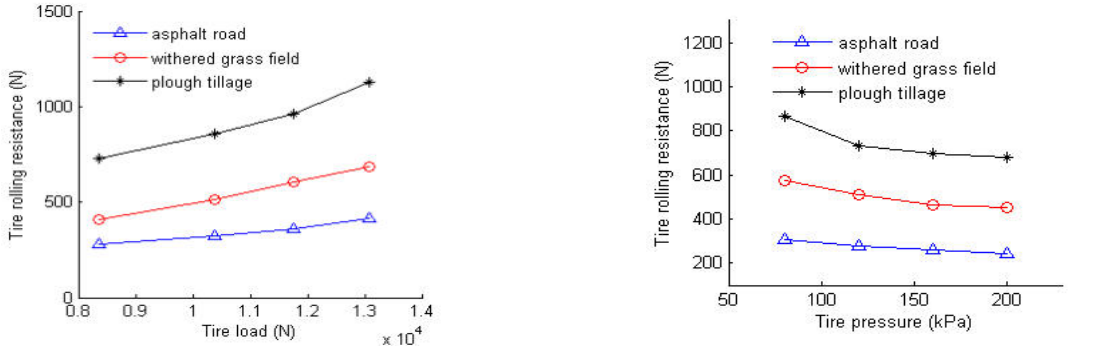


(a) Effect of load on tire traction *(b) Effect of tire pressure on tire traction*

Fig. 17 - Effect of Load and Tire Pressure on Tire Traction

From Fig. 17(a), it can be seen that the traction force of a tire at the same load is the largest on an asphalt road and the smallest on tillage. The traction force of agricultural tires traveling on asphalt roads, withered grass fields and tillage is increasing as the tire load increases from 8355 N to 13085 N. This is consistent with the conclusion obtained through experimental data fitting in reference (*Zhu et al., 2020*), that is, the traction force of the tire increases with the increase of vertical load on the axle. In addition, compared with tillage, the traction force of tires traveling on asphalt roads and withered grass fields increases more significantly with the increase in load.

From Fig. 17(b), it can be seen that with the increase of tire pressure from 80 kPa to 200 kPa, the traction force of agricultural tires traveling on asphalt roads, withered grass fields and tillage decreases gradually, among which the traction force traveling on tillage decreases more obviously with the increase of tire pressure. Zhu et al. investigated the effect of the tire vertical load with the tire pressure on tractor traction performance. The results show that the tire traction force is linearly related to the vertical load on the axle, the maximum traction force of the tire is somewhat linearly related to the vertical load on the axle, and the tire deformation displacement increases with the increase of the tire driving force. With the increase of vertical load and the decrease of tire pressure, the adhesion performance of the tire is improved.



(a) Effect of load on tire rolling resistance *(b) Effect of tire pressure on tire rolling resistance*

Fig. 18 - Effect of load and tire pressure on tire rolling resistance

From Fig. 18(a), it can be seen that the rolling resistance of tires on tillage is the largest and the rolling resistance on asphalt roads is the smallest for the same load. The rolling resistance of agricultural tires running on asphalt roads, withered grass fields and tillage is increasing as the tire load is increased from 8355 N to 13085 N. The rolling resistance of agricultural tires running on asphalt roads and asphalt roads is increasing with increasing load. The increase in rolling resistance with increasing load is more pronounced for tires running on tillage compared to asphalt roads and withered grass fields.

As can be seen from Fig. 18(b), the rolling resistance of agricultural tires running on asphalt roads, withered grass fields and tillage decreases gradually as the tire pressure increases from 80 kPa to 200 kPa. The rolling resistance of running on the tillage decreases more obviously with the increase of the tire pressure. By means of an experimental method, *Čiplienė et al., (2019*), investigated the effect of front and rear tire pressure combinations on tractor traction performance. The results showed that a traction advantage of about 2% could be produced by setting the front and rear tire pressure combinations appropriately.

CONCLUSIONS

In this study, an agricultural tire traction performance tester was designed. The structure parameters and the key components of the frame, the power drive system, and the data acquisition system were determined. The tester can be used to carry out experimental tests in indoor soil tanks and fields for testing traction performance parameters such as rolling resistance, traction force, slip rate, traction efficiency and traction power consumption of agricultural tires. The tester adopts a single tire structure and can replace different specifications of the test tire. Also, the tester comes with a power source to achieve self-propelled function. The turning mechanism is designed to achieve control of the traveling direction. Most importantly, a wide range of test conditions can be generated depending on tire parameters, soil type, and driving conditions.

Taking 12.4-24 agricultural tire as the test object, according to Chinese national standard "GB_T14828-2003 test method for traction performance of agricultural tires," the experiment was conducted under asphalt roads, withered grass fields and tillage conditions. The travel speeds of the tester measured by the RPM sensor of the tester and the travel speeds measured by the VBOX are in good agreement, both under the conditions of curb weight load and full load. The RMSE values for travel speeds on asphalt roads, withered grass fields and tillage are 0.347 km/h, 0.362 km/h and 0.384 km/h, respectively. The results verified that the tester has the ability to work stably, including the stability of travel speed and the ability to adapt to different terrain conditions. The driving torque output characteristics and adjustment range of the tester can meet the road and field test environment, which indicates that the design of the tester is scientific and practical. That lays the foundation for the subsequent in-depth research on the mechanism of agricultural tire-soil coupling. It is important to note that when conducting experimental operations using this equipment, direction control is essential. When the speed exceeds 5 km/h, a sufficiently long test section must be allocated. Particularly when conducting experiments in indoor soil bins, the test speed should be appropriately regulated based on the length of the soil bin to ensure the safety of both the equipment and the operating personnel.

In future research, this equipment will be utilized to conduct traction performance tests for agricultural tires, aiming to investigate the coupling mechanism between agricultural tires and various types of farmland soil. Based on soil conditions, the study will propose the optimal matching relationship between tire structural parameters and operating conditions to achieve efficient and low-energy-consumption traction behavior. This research will provide a basis for the rational selection of agricultural tires and the effective regulation of their traction performance.

ACKNOWLEDGEMENT

This research was funded by the National Natural Science Foundation of China (52362056), Inner Mongolia Natural Science Foundation (2023LHMS05006), Inner Mongolia Natural Science Foundation (2025MS05131), the Program for improving the Scientific Research Ability of Youth Teachers of Inner Mongolia Agricultural University (BR230126), and Inner Mongolia Autonomous Region “First-Class Discipline Research Special Project” (Creation of Intelligent Equipment for the Whole Industrial Chain of Grass Industry and Special Economic Mixed Grain, No. YLXKZX-NND-046).

REFERENCES

[1] Angelucci, L., Pinet, F., Vertua, A., & Mattetti, M. (2025). Towards more efficient tractors: Assessing and refining traction test procedures for agricultural tractors. *Journal of Terramechanics*, Vol.117, pp.101018, Italy. https://doi.org/10.1016/j.jterra.2024.101018

[2] Tekeste, M. Z., Way, T. R., Birkenholz, W., & Brodbeck, S. (2023). Effect of increased deflection tire technology on soil compaction. *Journal of the ASABE*, Vol.66, issue 1, pp.75-84, American. https://doi.org/10.13031/2013.21335

[3] Jjagwe, P., Tekeste, M. Z., Alkhalifa, N., & Way, T. R. (2023). Modeling tire-soil compression resistance on artificial soil using the scaling law of pressure-soil sinkage relationship. *Journal of Terramechanics*, Vol.108, pp.7-19, USA. https://doi.org/10.1016/j.jterra.2023.02.002

[4] Zeng, H., Tang, X., Chen, S., & Qi, H. (2024). Numerical investigations of traction behaviors of a pneumatic tire on wet granular terrains: DE/FE simulations. *Journal of Terramechanics*, Vol.113, pp.10-22, China. https://doi.org/10.1016/j.jterra.2024.100972

[5] Farhadi, P., Golmohammadi, A., Malvajerdi, A. S., & Shahgholi, G. (2020). Tire and soil effects on power loss: Measurement and comparison with finite element model results. *Journal of Terramechanics*, Vol.92, pp.13-22, Iran. https://doi.org/10.1016/j.jterra.2020.09.004

[6] Kim, Y. S., Lee, S. D., Kim, Y. J., Kim, Y. J., & Choi, C. H. (2018). Effect of tractor travelling speed on a tire slip. *Korean Journal of Agricultural Science*, Vol.45, issue 1, pp.120-127, Korea. https://doi.org/10.7744/kjoas.20180002

[7] Czarnecki, J., Brennensthul, M., Białczyk, W., Ptak, W., & Gil, Ł. (2019). Analysis of traction properties and power of wheels used on various agricultural soils. *Agricultural Engineering*, Vol.23, issue 1, pp.13-23, Poland. doi:10.1515/agriceng-2019-0002. https://doi.org/10.1515/agriceng-2019-0002

[8] Osinenko, P. V., Geissler, M., & Herlitzius, T. (2015). A method of optimal traction control for farm tractors with feedback of drive torque. *Biosystems engineering*, Vol.129, pp.20-33, Germany. https://doi.org/10.1016/j.biosystemseng.2014.09.009

[9] Jasoliya, D., Untaroiu, A., & Untaroiu, C. (2024). A review of soil modeling for numerical simulations of soil-tire/agricultural tools interaction. *Journal of Terramechanics*, Vol.111, pp.41-64, USA. https://doi.org/10.1016/j.jterra.2023.09.003

[10] Małecka, A., Brennensthul, M., Ptak, W., Czarnecki, J., & Lejman, K. (2024). Evaluation of the Changes in Dimensions of the Footprint of Agricultural Tires under Various Exploitation Conditions. *Applied Sciences*, Vol.14, issue 12, pp.5228, Poland. https://doi.org/10.3390/app14125228

[11] Xi, Z., Feng, T., Liu, Z., Xu, H., Zheng, J., & Xu, L. (2024). Estimation of Soil Characteristic Parameters for Electric Mountain Tractor Based on Gauss–Newton Iteration Method. *World Electric Vehicle Journal*, Vol.15, issue 5, pp.217, China. https://doi.org/10.3390/wevj15050217

[12] Li, S., Wu, J., Wan, Y., Su, B., & Wang, Y. (2024). Numerical Study of Tangential Traction Mechanism between Pattern Blocks of Agricultural Radial Tires and Soft Soil. *Materials*, Vol.17, issue 16, pp.1-18, China. https://doi.org/10.3390/ma17163906

[13] Janulevičius, A., & Damanauskas, V. (2022). Prediction of tractor drive tire slippage under different inflation pressures. *Journal of Terramechanics*, Vol.101, pp.23-31, Lithuania. https://doi.org/10.1016/j.jterra.2022.03.001

[14] Zeng, H., Lin, Z., Huang, G., Yang, X., Li, Y., Su, J., & Xu, W. (2025). Parameter identification of DEM-FEM coupling model to simulate traction behavior of tire-soil interaction. *Journal of Terramechanics*, Vol.117, pp.101012, China. https://doi.org/10.1016/j.jterra.2024.101012

[15] Alkhalifa, N., Tekeste, M. Z., Jjagwe, P., & Way, T. R. (2024). Effects of vertical load and inflation pressure on tire-soil interaction on artificial soil. *Journal of Terramechanics*, Vol.112, pp.19-34, USA. https://doi.org/10.1016/j.jterra.2023.11.002

[16] Zeng, H., Xu, W., Zang, M., & Yang, P. (2020). Experimental and numerical investigations of tractive performance of off-road tires on gravel terrain. *International Journal of Computational Methods*, Vol.17, issue 08, pp.1950055, China. https://doi.org/10.1142/S0219876219500555

[17] Taghavifar, H., & Mardani, A. (2014). Analyses of energy dissipation of run-off-road wheeled vehicles utilizing controlled soil bin facility environment. *Energy*, Vol.66, pp.973-980, Iran. https://doi.org/10.1016/j.energy.2014.01.076

[18] Ani, O.A., Uzoejinwa, B.B., Ezeama, A O., Onwualu, A.P., Ugwu, S.N., & Ohagwu, C.J. (2018). Overview of soil-machine interaction studies in soil bins. *Soil and Tillage Research*, Vol.175, issue 1, pp.13-27, Nigeria. https://doi.org/10.1016/j.still.2017.08.002

[19] Wang, J., Shang, L., Xu L., & Tang Q. (2023). Evaluation of traction characteristics of tractor tires on loose soils: simulation and experimental research. *INMATEH-Agricultural Engineering*, Vol.71, issue 3, pp.379-390, https://doi.org/10.35633/inmateh-71-33

[20] Kumar, S., Noori, M. T., & Pandey, K. P. (2019). Performance characteristics of mode of ballast on energy efficiency indices of agricultural tyre in different terrain condition in controlled soil bin environment. *Energy*, Vol.182, issue 1, pp.48-56, India. https://doi.org/10.1016/j.energy.2019.06.043

[21] Ekinci, Ş., Çarman, K., & Kahramanlı, H. (2015). Investigation and modeling of the tractive performance of radial tires using off-road vehicles. *Energy*, Vol.93, issue 2, pp.1953-1963, Turkey. https://doi.org/10.1016/j.energy.2015.10.070

[22] Ekinci, Ş., & Çarman, K. (2017). Effects of some properties of drive tires used in horticultural tractors on tractive performance. *Journal of Agricultural Sciences*, Vol.23, pp.84-94, Turkey.

[23] Abdolmaleki, H., Jafari, A., Tabatabaeifar, A., Hajiahmad, A., & Goli, H. (2015). Development and evaluation of an in-situ tire testing facility with variable side slip angles. *Journal of Terramechanics*, Vol.59, pp.49-58, Iran. https://doi.org/10.1016/j.jterra.2015.03.002

[24] Cudzik, A., Brennensthul, M., Białczyk, W., & Czarnecki, J. (2018). Tractive performance of tyres in forest conditions–impact assessment of ground and tyres parameters. *Croatian Journal of Forest Engineering*, Vol.39, issue 1, pp.85-96, Poland.

[25] Lun, J., & Yang, L. (2016). *Experimental and Finite Element Analysis of Tire-Soil Contact Based on Tire.* Sinkage Doctoral dissertation, Northwest A&F University, Yangling, China.

[26] Zhao, Y. (2022). *Design and Experiment of Tire-soil Interaction Research Platform*. Master's Thesis, Northwest A&F University. Yangling, China. https://doi.org/10.27409/d.cnki.gxbnu.2022.000569

[27] Huang, K. (2021). *Numerical simulation of the interaction of tractor tyre with soft ground*. Master's Thesis. Jilin. University. Changchun, China. https://doi.org/10.27162/d.cnki.gjlin.2021.005385

[28] Wu, X., Xie, B., Song, Z., Shang, G., Mao, E., Li, W. (2014). Design and optimization of a single wheel tester for agricultural machinery drive tires. *Journal of China Agricultural University*. Vol.19, issue 5, pp.146-152, China. https://doi.org/10.11841/j.issn.1007-4333.2014.05.20

[29] GB/T 14828-2003. *Test method for measuring traction performance of agricultural tyres*. Beijing. Standards. Press of China. https://www.antpedia.com/standard/567682-1.html

[30] Zhu, Z., Chen, L., Xia, C., & Cai, Y. (2020). Test research on the adhesive and tractive performance of a wheeled tractor. *International journal of heavy vehicle systems*, Vol.27, issue 1/2, pp.65, China. https://doi.org/10.1504/IJHVS.2020.104425

[31] Čiplienė, A., Gurevičius, P., Janulevičius, A., & Damanauskas, V. (2019). Experimental validation of tyre inflation pressure model to reduce fuel consumption during soil tillage. *Biosystems engineering*, Vol.186, pp.45-59, Lithuania. https://doi.org/10.1016/j.biosystemseng.2019.06.023

A BLOCKCHAIN-BASED PRIVACY-PRESERVING SOLUTION FOR AGRICULTURAL PRODUCT TRACEABILITY BASED ON GROUP SIGNATURES
/
基于群签名的区块链农产品溯源隐私保护方案

Jiarui ZHANG, Jianyu CHEN, Xuanyu CAO, Shuo LIU, Hao JI, Yongshuai YANG, Lijun CHENG*)
College of Software, Shanxi Agricultural University, Taigu, Shanxi / China;
Corresponding authors: Lijun CHENG; Tel: +86-13835441585; E-mail: cljzyb@sxau.edu.cn
DOI: https://doi.org/10.35633/inmateh-76-90

Keywords: *Blockchain; Group signatures; Agricultural-product traceability; Privacy preservation*

ABSTRACT

Traceability is a crucial component in ensuring the secure sharing of information throughout the entire supply chain of agricultural products. However, existing blockchain-based traceability solutions lack identity anonymity, face challenges in regulatory traceability, and lack dynamic member management capabilities. This paper proposes a blockchain privacy protection scheme integrating group signatures, pseudonymity mechanisms, and revocable accumulators to address these issues. The core design of this scheme encompasses three key aspects: first, this study introduces a dynamic group signature algorithm to balance the anonymity of data signatures with the traceability of responsibility, ensuring both privacy protection and accountability for data sources. Second, this study designs a pseudonym-based identity-hiding and authentication-obfuscation mechanism to enhance privacy protection further, improve resistance to on-chain analysis, and prevent the leakage of user identities. Finally, an efficient dynamic member management protocol is constructed to support rapid node joining and flexible revocation, thereby addressing frequent member changes in agricultural supply chains. Security analysis indicates that the scheme meets stringent security requirements regarding anonymity, non-repudiation, and traceability. Experimental results show that the proposed scheme outperforms existing solutions regarding signature verification overhead, communication costs, and operational efficiency, demonstrating good practicality and scalability, and providing practical support for privacy protection and digital regulation in agricultural supply chains.

摘要

溯源是保障农产品全流程信息安全共享的重要部分。然而，现有基于区块链的溯源方案不具备身份匿名性、监管可追溯性困难以及缺少动态成员管理方面。为了解决这些问题，本文提出了一种融合群签名、伪名机制与可撤销累加器的区块链隐私保护方案。该方案的核心设计包括以下三个方面：首先，引入了动态群签名算法，以实现数据签名的匿名性与责任可追溯性的平衡，确保数据源的隐私保护与责任追溯；其次，设计了基于伪名的身份隐藏与认证混淆机制，进一步加强了隐私保护，提升了抗链上分析的能力，防止用户身份泄露；最后，构建了高效的动态成员管理协议，支持节点的快速加入与灵活撤销，从而应对农业供应链中频繁的成员变动。安全性分析表明，该方案在匿名性、不可伪造性和可追溯性等方面满足严格的安全要求。实验结果显示，本文方案在签名验证开销、通信成本以及运行效率上优于现有方案，具备较好的实用性与可扩展性，为农业供应链中的隐私保护与数字监管提供了有效的支持。

INTRODUCTION

With the ongoing digitalisation of agriculture and the deepening of supply-chain management, enabling trustworthy, end-to-end data sharing and traceability for agricultural products has become a prominent research focus in food-safety governance (*Demestichas et al., 2020; Bermeo-Almeida et al., 2018*). Owing to its decentralisation, immutability and verifiable auditability, blockchain technology provides a technical foundation for multi-stakeholder collaboration “from farm to table.” It has already shown promise in organic certification, geographical-indication protection and cold-chain logistics supervision (*Stranieri et al., 2021; Sharma et al., 2023; Zhang et al., 2020*). Nevertheless, when agricultural participants change frequently, blockchain-based traceability schemes reveal several limitations, including static identity management, weak compatibility between tamper resistance and privacy, and insufficient data trustworthiness (*Xu et al., 2022*). Consequently, devising a privacy-preserving solution that simultaneously offers member anonymity, regulatory traceability, and dynamic identity management has become a pressing challenge.

Current privacy-enhanced blockchain traceability schemes concentrate on three core capabilities—identity authentication, identity anonymity and member management—but still display conspicuous shortcomings in agricultural scenarios. First, group authentication often lacks efficiency, hindering the rapid onboarding of large numbers of nodes. Second, sensitive information may leak during authentication, resulting in inadequate privacy protection. Third, efficient dynamic member management is absent, so permission updates lag in the face of frequent node churn. Therefore, a comprehensive solution that integrates group authentication, advanced privacy preservation and dynamic member management is needed to improve both the applicability and reliability of blockchain traceability in agricultural supply chains. To clarify the practical roots of this demand, representative recent studies are reviewed and assessed below.

In identity authentication, Li et al combined RFID with smart contracts to map physical-tag IDs to on-chain accounts, enabling rapid, correct confirmation across production, storage and sales stages (*Li et al., 2024*). Soy et al merged decentralised identifiers (DIDs) with zero-knowledge proofs to create a one-registration, multi-verification cycle (*Soy et al., 2025*). Gong et al designed a certificate-less lightweight protocol that bridges terminals, gateways and a Hyperledger Fabric blockchain via ABAC and a three-way handshake (*Gong et al., 2024*). Although these schemes shorten initial access latency and increase throughput, they generally rely on static certificates or hardware identifiers. When nodes change frequently, keys must still be reissued or rotated; systems usually broadcast revocation and update operations on-chain or store them in auxiliary tables, compromising real-time performance and cost efficiency. Accordingly, authentication bottlenecks remain unresolved under highly concurrent, group-oriented conditions.

For identity-anonymity protection, Zhang et al proposed a fine-grained and flexible terminal-data access-control scheme based on ciphertext-policy attribute-based encryption (CP-ABE) and a hybrid data-encryption method that supports multi-dimensional sharing by “crop type–batch–role” (*Zhang et al., 2022*). Zhang et al built a multi-chain blockchain architecture supported by zero-knowledge proofs for inter-chain data collaboration and privacy preservation in food supply chains (*Zhang et al., 2023*). Wang et al adopted ring signatures to conceal signer identity and origin, strengthening the anonymity of on-chain information release. While these approaches reinforce the principle of minimal disclosure, they exhibit common weaknesses (*Wang et al., 2024*). As access policies, participants, or the number of chains grow, encryption and proof costs escalate sharply, impeding deployment on resource-constrained agricultural terminals; moreover, strong anonymity often sacrifices accountability, because few schemes offer an optional identity-decryption window for compliance audits, making it challenging to balance privacy with regulatory needs.

Regarding member management, Wang et al presented a blockchain-based proxy re-encryption access-control method (BBPR-AC) that protects agro-biological risk information by defining attributes for each supply-chain stage, establishing policies and executing them via smart contracts to achieve decentralised, automated authorization (*Wang et al., 2024*). Peng et al developed a dynamic supervision model driven by smart contracts to revoke real-time members, enhancing transparency and quality assurance in the rice supply chain (*Peng et al., 2022*). Sun et al designed a provenance-aware dynamic access-control scheme with a fast lookup table for member control (*Sun et al., 2023*). Although these studies improve permission-configuration flexibility, they still face common challenges: on-chain revocation operations can cause congestion and high gas costs; centralised permission logic may become a performance bottleneck; and “expired identities” must be synchronised off-chain. Low-cost yet real-time dynamic-management capability remains insufficient for agricultural scenarios with high node-turnover rates. In summary, existing research has not yet achieved coordinated optimisation across the triple dimensions of large-scale group authentication, strong privacy protection and efficient dynamic management, leaving room for a comprehensive framework that reconciles anonymity, accountability and scalability.

To address the deficiencies in identity anonymity, traceability and member revocation, this paper makes the following contributions from the perspectives of group signatures, pseudonym protection and dynamic identity management:

1. Group signature for agricultural traceability. A group-signature scheme tailored to agricultural product traceability that combines blockchain verifiability with signature anonymity is proposed. While protecting the identities of ordinary users, designated authorities can decrypt identity information and revoke signatures, thereby achieving an effective balance between privacy preservation and accountability. The scheme enhances the traceability of responsibilities under strict privacy requirements.

2. Pseudonym-based identity-mapping and dynamic-obfuscation mechanism. A pseudonym-identity mapping mechanism that dynamically obfuscates authentication information during data interactions is introduced. This mechanism prevents on-chain behavioural pattern tracking, boosts resistance to analytical

attacks and enforces business-data separation, guaranteeing anonymity in traceability information while deterring the abuse of malicious behavioural tracking.

3. Lightweight member-management protocol. Given the frequent node changes in agricultural supply chains, a lightweight member-management protocol that supports rapid node admission, flexible revocation and synchronised key-state updates is designed. Through group key-agreement and authentication-reconstruction algorithms, the protocol ensures security and consistency while providing scalability and robustness. It effectively meets the demands of dynamic network environments, improving the adaptability and flexibility of blockchain traceability systems in agriculture.

The notation used throughout this paper is defined in Table 1.

Table 1

Symbol Definition

Symbol	Meaning
G_1, G_2, G_T	Pairing source and target groups ($e: G_1 \times G_2 \rightarrow G_T$)
q	G_1, G_2, G_T of order of a large integer prime
P_1 , P_2	Generators of groups G_1, G_2 ($\varphi(P_2) = P_1$)
P_{pub}	System master public key ($P_{pub} = s \cdot P_1$)
$H(\cdot)$	Collision-resistant hash function
L	Table of real identities
P	Pseudonymised table of identities
id_i	User's real identities
PID	Pseudonymised identities ($PID = H(id_i) \cdot P_1$)
ACC_0	Initial accumulator ($ACC_0 = r \cdot P_2$)

MATERIALS AND METHODS

System model

Figure 1 illustrates the structure of each functional role in this scheme and its specific responsibilities within the agricultural product traceability system.

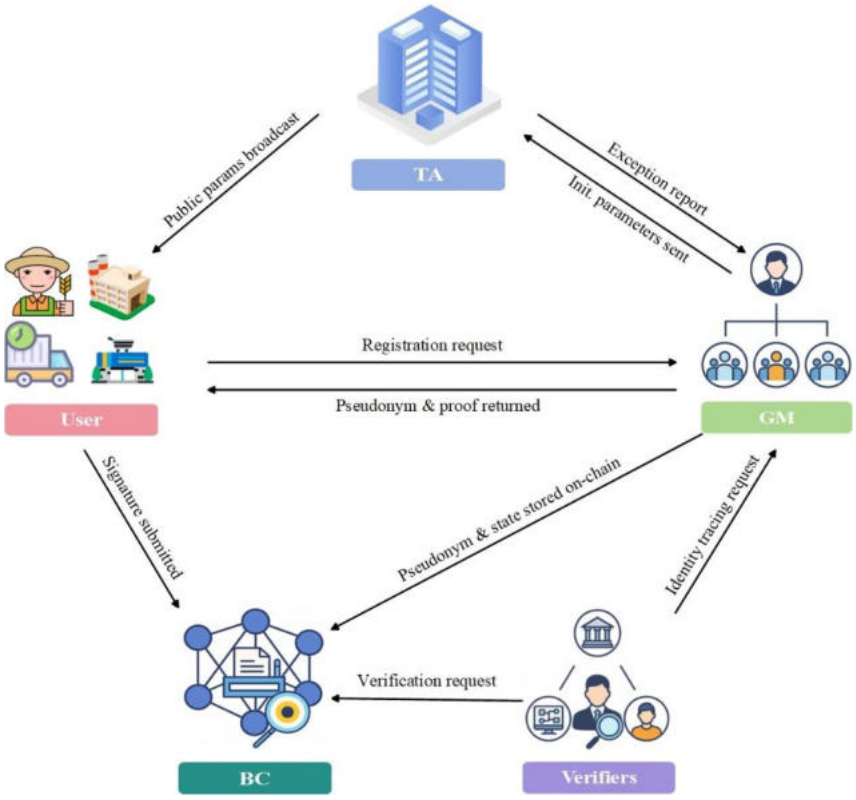


Fig. 1 - System Model

The diagram defines five primary roles:

Trusted Authority (TA): Responsible for generating and publishing cryptographic parameters during the initialisation phase of the scheme, coordinating user identity registration processes, distributing authentication

credentials, and managing dynamic updates to group keys when network members change. The TA is assumed to be a fully trusted entity operating offline, participating in system operations only when necessary.

Group Manager (GM): Responsible for user joining and revocation, signature validity verification, and identity de-anonymisation when necessary. Typically authorised and generated by the TA, the GM assumes daily identity management and audit responsibilities during regular system operation.

Users (U): Entities or organisations involved in various stages of the supply chain, including agricultural product cultivation, processing, transportation, and sales. Users obtain anonymous authentication credentials during registration and use them for traceability data signing operations. The scheme supports dynamic user joining and secure exit mechanisms to ensure long-term scalability.

Verifiers (V): Verification entities, including regulatory authorities, traceability platforms, and end consumers. Their primary tasks are to verify the validity and integrity of on-chain data signatures and determine the validity of the signer's identity. Among these, regulatory authorities serve as privileged verifiers, able to decrypt member identities and trace abnormal behaviour once they meet the required conditions.

Blockchain (BC): As a distributed storage infrastructure, it is responsible for recording and storing signature information and hash summaries of traceability data. The blockchain network only stores cryptographic proofs required for verification and does not contain plaintext identity information, effectively combining data auditability with identity anonymity.

Scheme Overview

Combining the requirements for secure sharing and privacy protection of agricultural product data in traceability scenarios, the traceability authentication scheme based on group signatures proposed in this paper consists of the following six probabilistic polynomial-time algorithms:

$Setup(1^{\lambda}) \rightarrow (params, msk)$: System initialisation algorithm. Under security parameter λ, it generates bilinear group parameters, hash functions, and accumulator initial values, outputs system public parameters params and master key msk, and publishes $params$ to the blockchain.

$Join(U_i, T_1, \sigma_{id_i}) \rightarrow (PID_i, W_i, ACC_j)$: User U_i sends a registration request. After the group administrator verifies the identity signature σ_{id_i} it assigns a pseudonym PID_i and membership proof W_i to the user and updates the accumulator state ACC_j.

$Sign(sk_i, M) \rightarrow \sigma$: The user U_i uses their private key sk_i to generate an anonymous group signature $= \{M, T_1, T_2, T_3, A, c, S_1, S_2\}$ for message M, ensuring the integrity and anonymity of the traceable data.

$Verify(\sigma, params, \mathcal{P}) \rightarrow \{0,1\}$: The verifier checks the integrity and validity of the signature structure based on the public parameters and pseudonym list P to confirm whether the signature comes from a valid, non-revoked member.

$Open(\sigma, s) \rightarrow id_i$: The group administrator uses the private parameter s from the master key to recover the corresponding pseudonym from the signature σ and searches the identity list to restore the real identity id_i, thereby achieving traceability of behaviour.

$Revoke(id_k, L) \rightarrow (ACC, W_i)$: When member id_k is revoked, the system calculates the update factor based on their identity information, updates the accumulator state ACC and the proof values W_i of the remaining members, ensuring the security of subsequent signatures.

Scheme Construction

(1) System Initialisation

During the initial deployment phase of the system, the TA is responsible for generating global public parameters and the system's initial state. This corresponds to the standard setup algorithm $Setup(1^{\lambda}) \rightarrow (params, msk)$. To reduce trust dependencies, this scheme centralises the initialisation responsibilities in the TA, which performs a one-time execution. After publishing the parameters, the TA transitions to an offline state, and subsequent operations are handled by the GM. The initialisation steps are as follows:

First, the TA sets a finite field $\mathbb{F}_q$. It constructs groups G_1 and G_2 and defines a bilinear mapping $e: G_1 \times G_2 \rightarrow G_T$. It randomly selects P_1 and P_2 such that there exists a homomorphic mapping φ that maps group G_2 to group G_1, satisfying $\varphi(P_2) = P_1$. Next, the TA randomly selects two non-zero integers $s, r \in \mathbb{Z}_q^*$, where s does the GM hold the system master private key. Based on this, $P_{pub} = s \cdot P_1$ is calculated, and the accumulator state is initialised as $ACC_0 = r \cdot P_2$, providing verifiable support for subsequent user registration and revocation operations. To enhance identity privacy protection, a collision-resistant hash function $H(\cdot)$ is introduced for identity pseudonymisation processing.

The system maintains two types of identity mapping tables to efficiently manage user identity states:

① Real Identity list L: The record format is a quintuple $< id_i, PID, join/delete, W_i, ACC_j >$, where id_i is the user's real identity identifier, and the pseudonym PID is calculated using the formula $PID = H(id_i) \cdot P_1$ to protect the user's real identity information;

② Pseudonym identity list P: The record format is $< PID, join/delete, W_i, ACC_j >$, used to publish the user's registration and revocation status publicly. This list is stored on-chain via blockchain, providing external verifiers with an auditable, tamper-proof mechanism for querying revocation status.

TA ultimately discloses the following parameter set to the system:

$$params = \{q, G_1, G_2, G_T, e, P_1, P_2, P_{pub}, ACC_0, H(\,)\}$$

(2) User Registration Phase

The user registration phase corresponds to the Join algorithm $Join(U_i, T_1, \sigma_{id_i}) \rightarrow (PID_i, W_i, ACC_j)$. Users first submit a registration request during the user registration phase by generating a private value and an authentication signature. The GM verifies the user's identity and generates a pseudonymous identity identifier based on the accumulator mechanism. Next, the GM writes the relevant information into the real Identity list L and synchronises it with the blockchain to ensure the system's transparency and auditability. The user ultimately receives the private key triplet via a secure channel, which is used for subsequent agricultural product traceability data signing and privacy protection. As shown in Figure 2, the detailed steps of the user registration phase are presented.

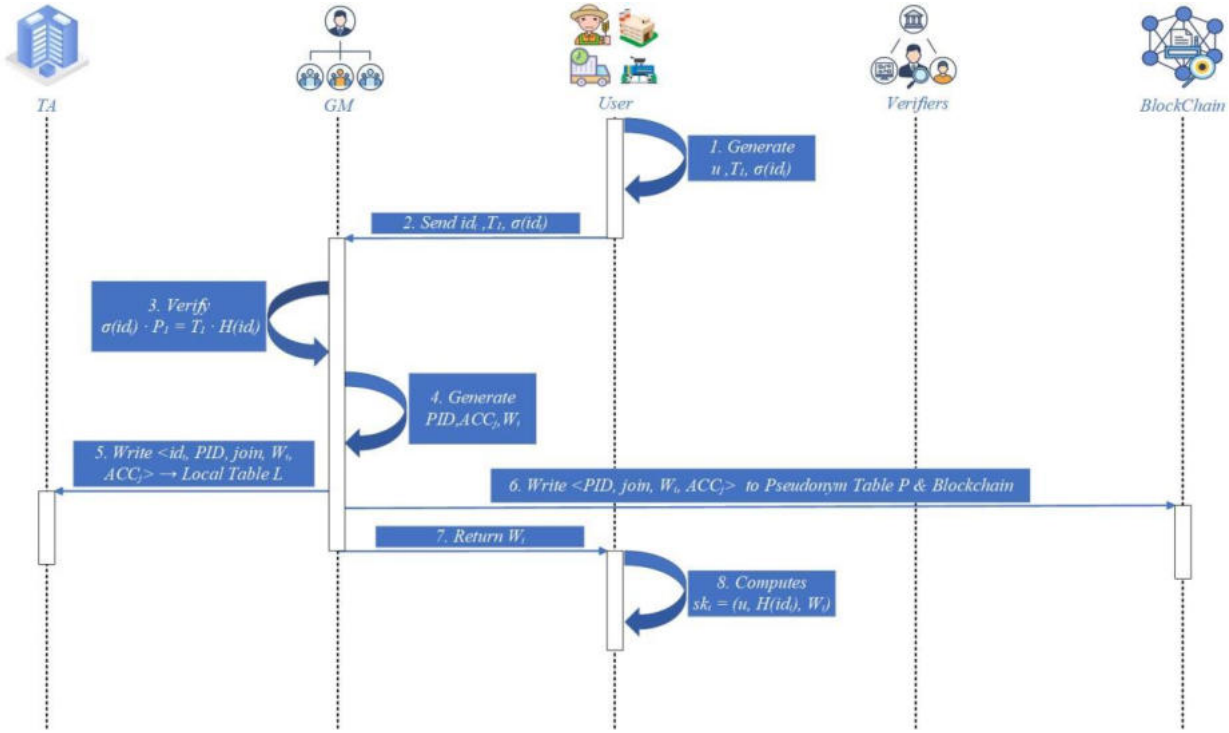


Fig. 2 - User Registration Phase

If U_i wishes to become a chain-based authentication entity and obtain legitimate signing permissions, it must submit a registration request to GM. The specific registration phase is as follows:

Step 1: U_i first randomly selects a private value $u \in \mathbb{Z}_q^*$, calculates the authentication parameter $T_1 = u \cdot P_1$, and generates an authentication signature $\sigma_{id_i} = u \cdot H(id_i)$ based on its identity identifier.

Step 2: Subsequently, U_i submits the authentication triplet $\{\sigma_{id_i}, id_i, T_1\}$ to GM, which verifies its validity through $\sigma_{id_i} \cdot P_1 = T_1 \cdot H(id_i)$. If the verification is successful, it indicates that U_i is valid in the local regulatory whitelist and proceeds to the next stage.

Step 3: GM generates a pseudonymous identity identifier $PID = H(id_i) \cdot P_1$ for $U_i$based on this, and updates the system state according to the accumulator mechanism to generate a new accumulator value $ACC_j = (H(id_i) + s) \cdot ACC_{j-1}$. At the same time, $W_i = ACC_{j-1}$ is recorded as the membership proof value for U_i. Subsequent signature verification relies on this value to ensure that its identity has not been revoked.

Step 4: The GM writes the five-tuple $< id_i, PID, join, W_i, ACC_j >$ into the local real identity list L, while recording the pseudonymous identity information $< PID, join/delete, W_i, ACC_j >$ in the pseudonym identity list P and synchronously writing it to the blockchain. This enables the registration status of participants in the traceability system to be queried in real time by upstream and downstream enterprises, consumers, and regulatory authorities, thereby enhancing the system's transparency and auditability.

Step 5: The GM returns W_i to U_i via a secure channel. U_i combines its private key parameters to locally generate the final private key triplet $sk_i = (u, H(id_i), W_i)$. This key will be used in subsequent data signing to achieve responsibility signing and privacy protection for agricultural product traceability data.

(3) Signature Generation Phase

The signature generation phase corresponds to the Sign algorithm $Sign(sk_i, M) \rightarrow \sigma$. After completing registration and obtaining legal member status, U_i can perform group signature operations on any message M to achieve identity authentication and accountability tracing under anonymity. As shown in Figure 3, the specific steps for generating group signatures and the information exchange process between participating parties are illustrated.

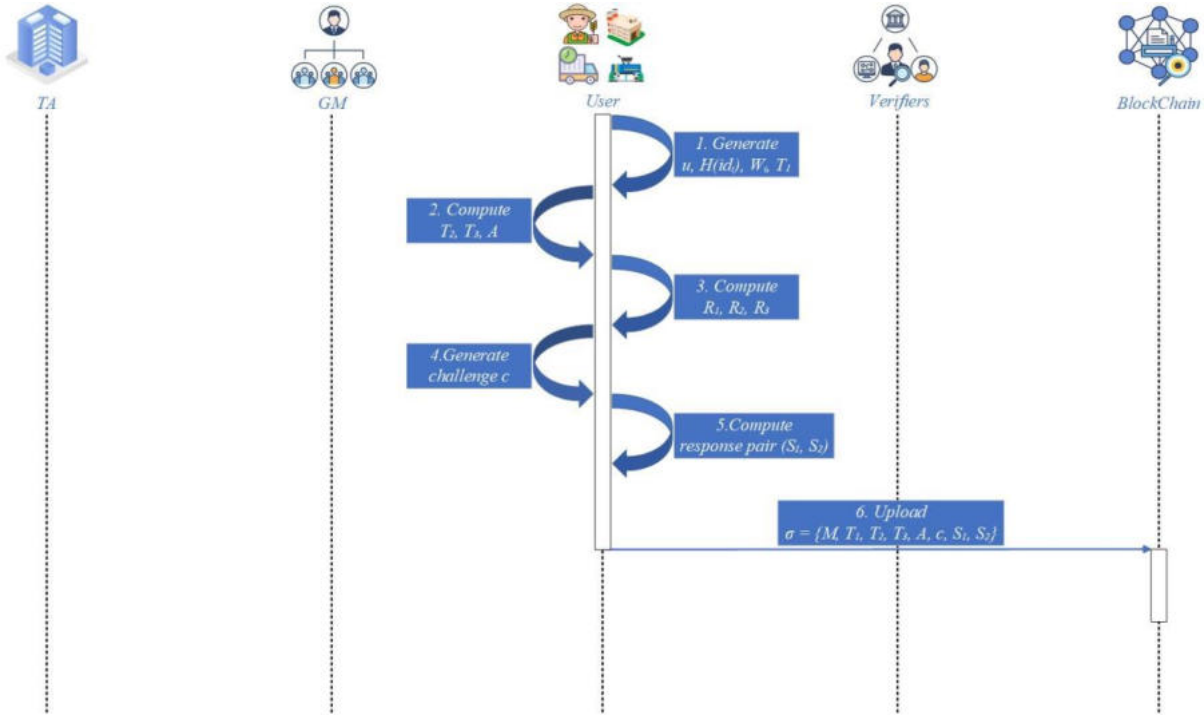


Fig. 3 - Group Signature Generation Phase

The group signature generation phase proceeds as follows:

Step 1: User U_i first uses the membership proof value W_i generated in the registration stage, the identity hash value $H(id_i)$, and the private parameter $u \in \mathbb{Z}_q^*$ to construct the following signature auxiliary quantities. Where $T_1 = u \cdot P_1$ is an intermediate variable generated and retained by U_i during the registration phase, followed by the calculation of $T_2 = H(id_i) \cdot P_1 + u \cdot P_{pub}$, $T_3 = u \cdot P_{pub}, A = u \cdot W_i$.

Step 2: Randomly select v from group $\mathbb{Z}_q^*$ to calculate the intermediate values $R_1 = v \cdot P_1$, $R_2 = e(P_{pub}, A) \cdot e(T_1, W_i)^{H(id_i)}$, $R_3 = v \cdot P_1 + v \cdot P_{pub}$.

Step 3: Based on the above intermediate values, U_i uses the hash function $H()$ to calculate the challenge value $c = H(M, T_1, T_2, T_3, A, R_1, R_2, R_3)$. Subsequently, U_i calculates the signature response pair $S_1 = v + c \cdot u$, $S_2 = v + c \cdot H(id_i)$.

Step 4: User U_i constructs the final group signature result as $\sigma = \{M, T_1, T_2, T_3, A, c, S_1, S_2\}$and uploads it to the blockchain. Since the signature does not contain the user's real identity information, it ensures that the data records of the participants in the supply chain are traceable but not disclosed.

At the same time, the on-chain records also serve as irrefutable evidence for subsequent audits, meeting the comprehensive requirements of the agricultural product traceability system for data security, anonymity, and verifiability. The verifier V can complete the verification process by simply accessing the blockchain, without needing to contact the signers or GM, thereby significantly enhancing the system's scalability.

(4) Signature Verification Phase

The signature verification phase corresponds to the Verify algorithm $Verify(M, \sigma, params) \rightarrow \{0,1\}$.The verifier V only needs to access the blockchain to complete the verification operation, without contacting the signer or GM, thereby enhancing the system's scalability. As shown in Figure 4, the specific steps of the signature verification process and the information exchange process between the parties involved are illustrated. Through this sequence diagram, readers can clearly understand the execution order of each step and the detailed process of signature verification.

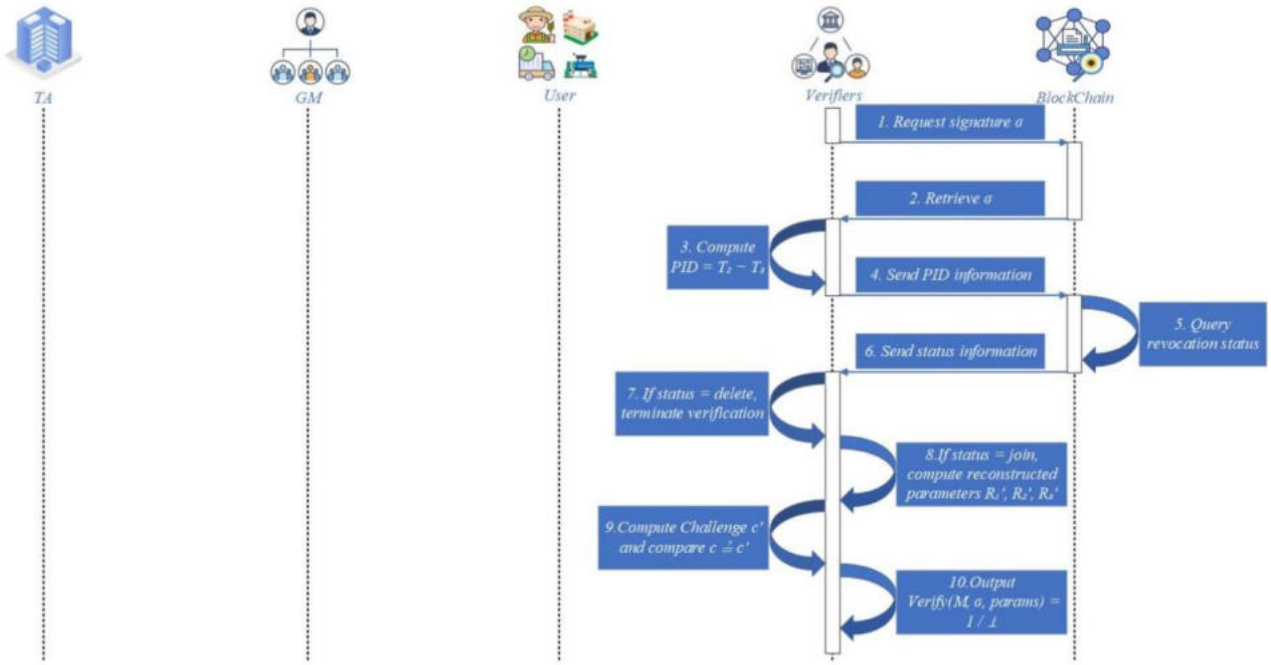


Fig. 4 - Signature Verification Phase

When the verifier obtains the signature $\sigma = \{\mathrm{M}, \mathrm{T}_1, \mathrm{T}_2, \mathrm{T}_3, \mathrm{A}, \mathrm{c}, \mathrm{S}_1, \mathrm{S}_2\}$ from the blockchain, the following steps must be performed in sequence to confirm its validity and the validity of the member's identity:

Step 1: The verifier V performs a pseudonym extraction and revocation status query. Based on the intermediate variables in the signature, the verifier calculates the user's pseudonym $PID = T_2 - T_3$. Then, the verifier searches the pseudonym identity list P maintained by the system for a matching record in the format $< \mathrm{PID}, \mathrm{join/delete}, \mathrm{W_i}, \mathrm{ACC_j} >$. If the current record status is deleted, it indicates that the member has been revoked, and the verification process terminates; otherwise, the following step is executed.

Step 2: Verifier V reconstructs the intermediate variables that should be generated during the signing process based on the public parameters and the signature response value, and calculates $R_1' = S_1 \cdot P_1 - c \cdot T_1$, $R_2' = e(T_1, ACC_j)$, $R_3' = S_2 \cdot P_1 + S_1 \cdot P_{pub} - c \cdot T_2$. Where ACC_j is the current accumulator state obtained from the pseudonymous identity list.

Step 3: Perform a hash consistency check. Verifier V inputs the message and intermediate parameters into the hash function to calculate the challenge value $c' = H(M, T_1, T_2, T_3, A, R_1', R_2', R_3')$. Next, compare the challenge value c' with the original challenge value c carried in the signature. If $c = c'$, it indicates that the signature was indeed generated by a legitimate member in accordance with the protocol specifications, the content has not been tampered with, and the associated pseudonym has not been revoked; otherwise, it is considered an invalid signature.

Step 4: If the consistency verification is valid, i.e., $c = c'$ the verification passes, and the output result is $Verify(M, \sigma, params) = 1$, indicating that the signature is valid and effective. If it is not valid, i.e., $c \neq c'$, the verification fails, and the output result is $Verify(M, \sigma, params) = 0$, indicating that the signature is invalid or the signer's identity has been revoked.

(5) Signature De-anonymisation Phase

The Signature de-anonymization phase corresponds to the Open algorithm $Open(\sigma, s) \rightarrow id_i$. Figure 5 illustrates the specific steps of the de-anonymisation process and the information exchange flow between parties.

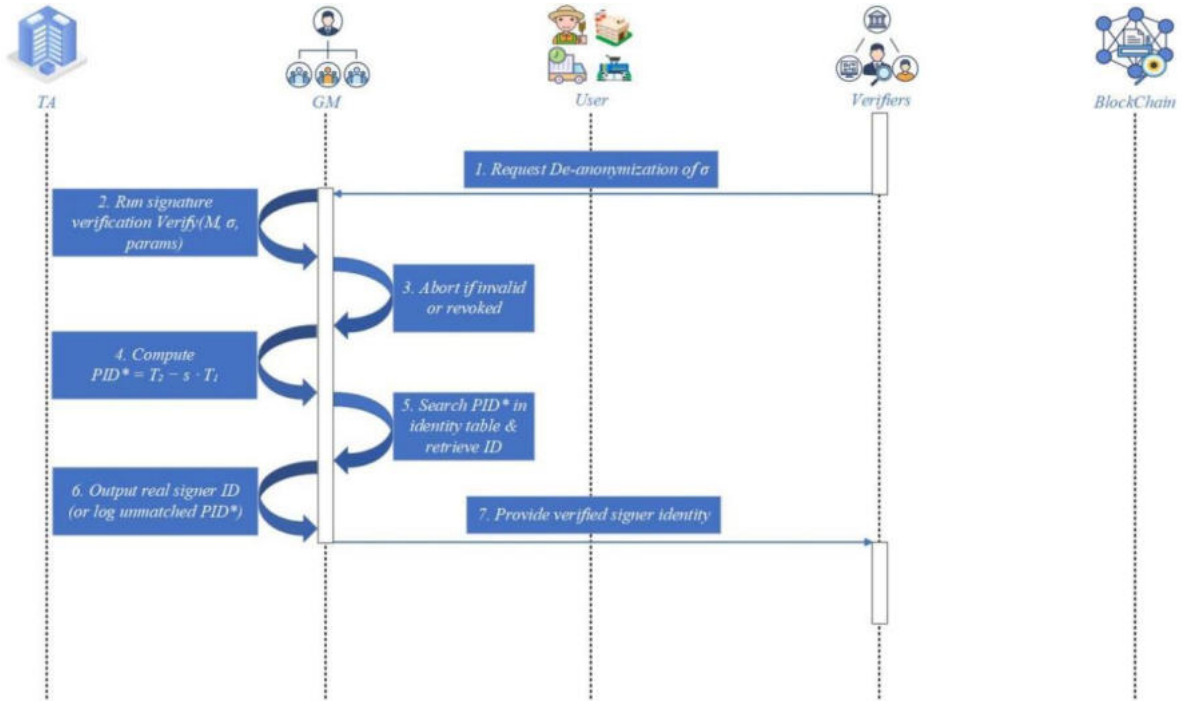


Fig. 5 - De-anonymization Operation Process

When the regulatory authority needs to perform de-anonymization on a chain signature $\sigma = \{M, T_1, T_2, T_3, A, c, S_1, S_2\}$ to trace the identity of the actual signer, the following steps must be executed:

Step 1: Before performing de-anonymization, the GM first calls the verification algorithm $Verify(M, \sigma, params)$ to validate the signature's validity. If the result is $\perp$, indicating the signature is invalid or the member has been revoked, the de-anonymization process is terminated, and the signer's identity is not disclosed; otherwise, the process continues to the next step.

Step 2: After verifying the signature's validity, the GM calculates the signer's pseudonym identifier based on the system master private key s generated during system initialisation, combined with the intermediate variables T_1 and T_2 contained in the signature $PID_* = T_2 - s \cdot T_1 = H(id_*) \cdot P_1$. Here, PID_* is the pseudonym bound to the signer's identity, used to locate their identity record in the member list.

Step 3: The GM then traverses the real identity list L maintained by the system to find the record item $< id_*, PID_*, join, W_i, ACC_k >$ corresponding to PID_*. If a match is found, the real identity i id_* of the signer can be restored, completing the traceable authentication of the signature behavior, thereby enabling the regulatory authority to implement accountability mechanisms for the behaviour of group members. If no match is found, it may indicate that the signature did not originate from a current valid member, posing risks such as signature forgery, member revocation, or protocol inconsistency. The system refuses to recognize the signature in such cases and logs the relevant data for subsequent audit and traceability analysis.

(6) Membership Revocation Phase

The membership revocation phase corresponds to the Revoke algorithm $Revoke(id_k, L) \rightarrow (ACC, W_i)$.To ensure the security and verifiability of the group signature system under dynamic changes in member identities, when the regulatory authority identifies violations, identity anomalies, or termination of cooperation involving a supply chain participant (such as a farmer, transporter, or seller) and decides to revoke their signature permissions, the system must execute the following steps to dynamically update the status, thereby ensuring the reliability and consistency of identity management across all nodes in the agricultural product traceability chain. As shown in Figure 6, the specific steps of the cancellation operation and the information exchange process among all parties are elaborated in detail.

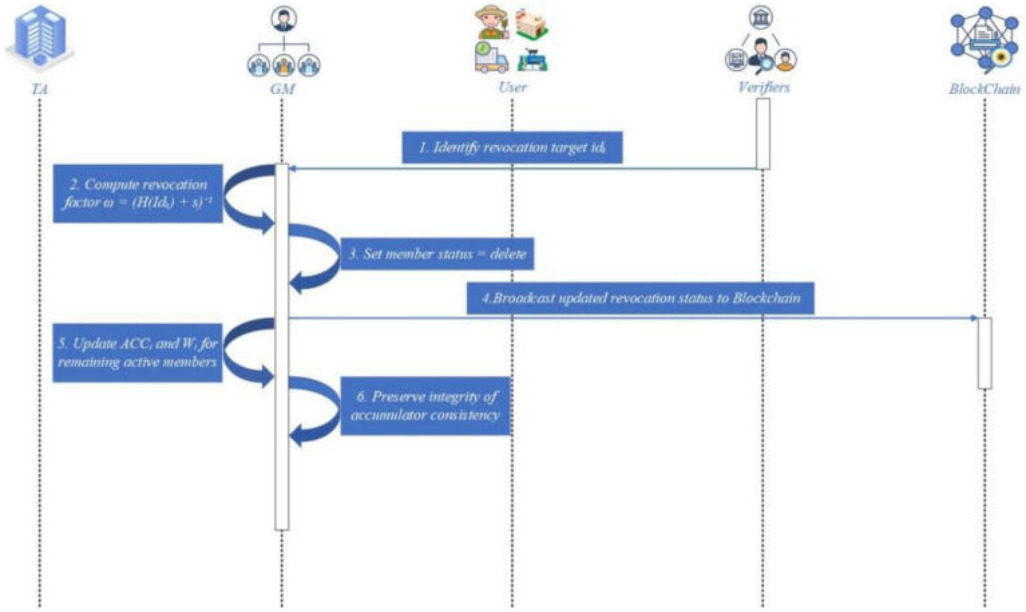


Fig. 6 - Revocation Operation Process

For the member entity l_k to be revoked, it should be a valid member in the current identity table L.

Step 1: The GM calculates the update factor $\omega = (H(id_k) + s)^{-1}$ required for revocation based on the identity identifier id_k of the member to be revoked and the system master private key s. This factor is used to adjust the current accumulator state and completely remove the member's valid contribution from the system state.

Step 2: The GM sets the status of member l_k to "$delete$". The updated pseudonym status quadruple $< PID_k, delete, W_i, ACC_j >$ is written to the pseudonym identity list P and synchronously broadcast to the blockchain network. This process ensures that all validators (such as government regulatory nodes and downstream enterprises) can obtain real-time updates on member status changes, preventing revoked members from continuing to perform signing operations, thereby enhancing the system's regulatory capabilities and transparency.

Step 3: To avoid the continued impact of revoked members on the system's signature logic, the GM must recalculate the accumulator state and proof value $ACC_i = ACC_i \cdot \omega, W_i = W_i \cdot \omega$ for all subsequent members in the member list with index $i \in [k+1, n]$ and current status as "$join$". This process ensures the mathematical consistency of the revocation operation, ensuring that the accumulator states and proof values of all valid members are synchronized with the current system state, thereby preventing revoked entities from bypassing the verification mechanism through historical signatures or leaked information.

RESULTS

Security Analysis

(1) Correctness Proof

The following equation can be used to derive the correctness of this group signature scheme:

$$\begin{aligned} e(P_{pub}, A) \cdot e(T_1, A)^{H(id_i)} &= e(s \cdot P_1, u \cdot W_i) \cdot e(u \cdot P_1, W_i)^{H(id_i)} \\ &= e(T_1, W_i)^s \cdot e(T_1, W_i)^{H(id_i)} \\ &= e(T_1, W_i)^{s+H(id_i)} \\ &= e(T_1, ACC_j) \end{aligned} \quad (1)$$

The above derivation shows that if the signature is generated by a legitimate member based on the protocol, the submitted signature data satisfies the final pairing equation, which completes the validation of the signature's legitimacy.

(2) Anonymity

Theorem 1: Assuming the hash function $H(\,)$ is modeled as a random oracle and the underlying bilinear map satisfies the Decisional Bilinear Diffie–Hellman (DBDH) assumption (*Boneh et al., 2001*), the proposed group-signature scheme achieves the anonymity security goal.

Proof of Theorem 1: Assuming a polynomial-time adversary $\mathcal{A}$, capable of attacking anonymity with a non-negligible probabilistic advantage, an algorithm $\mathcal{B}$ is constructed that solves the DBDH problem with $\mathcal{A}$ as a subroutine, thus inducing a contradiction.

To portray the ability of the adversary, the following challenge game $\mathcal{G}_{anon}^{\mathcal{A}}$ is defined:

① System initialisation: the adversary $\mathcal{A}$ obtains the system parameter params and can optionally initiate queries such as registration and signature.

② Challenge phase: the adversary $\mathcal{A}$ specifies two legitimate members U_0, U_1 and a message M^*, and the system randomly selects $b \in \{0,1\}$, and the signature U_b is generated σ^*.

③ Guessing phase: the adversary $\mathcal{A}$ outputs a guess b', and the challenge succeeds if $b' = b$.

The advantage of adversary $\mathcal{A}$ is defined as:

$$\mathrm{Adv}_{\Pi}^{anon}(\mathcal{A}) = \left| Pr[\, b' = b] - \frac{1}{2} \right| \tag{2}$$

If for any PPT (Probabilistic Polynomial Time) adversary $\mathcal{A}$, there is $\mathrm{Adv}_{\Pi}^{anon}(\mathcal{A}) \leq \mu(\lambda)$, where $\mu(\lambda)$ is a negligible function, then the scheme satisfies anonymity.

Based on the above game, construct Algorithm B to perform the following simulation:

① Input instances: Algorithm B receives DBDH instances (g, g^a, g^b, g^c, Z), and the goal is to determine whether $Z = e(g,g)^{abc}$ or $Z \in R \in G_T$.

② Parameter simulation: Algorithm B constructs the group signature system with the public parameters $P_1 = g, P_2 = g^a, P_{pub} = g^b$, and the initial accumulator is $ACC_0 = g^{ar}$, where $r \in \mathbb{Z}_q^*$ is randomly generated. Subsequently, the system parameter $params$ is returned to the adversary $\mathcal{A}$.

③ Query simulation: Algorithm $\mathcal{B}$ simulates the registration and signature operations, and models the hash function $H(\cdot)$ as a random predicator, which returns consistent random values for each hash query and maintains query consistency.

④ Challenge phase: adversary $\mathcal{A}$ submits (U_0, U_1, M^*). Algorithm $\mathcal{B}$ randomly selects $b \in \{0,1\}$, constructs a signature using member U_b, and embeds the DBDH instance parameters. Let $T_3 = g^c = u \cdot P_{pub}$, $T_2 = PID_b + T_3$, $A = u \cdot W_b$, where $r \in \mathbb{Z}_q^*$ is randomly generated and the pairing term $R_2 = Z = e(g,g)^{abc}$, and finally construct the signature $\sigma^* = \{M^*, T_1, T_2, T_3, A, c, S_1, S_2\}$ and return it to the adversary $\mathcal{A}$.

⑤ Judgment of the output: If adversary $\mathcal{A}$outputs guess b', algorithm B decides accordingly: if $b' = b$ then output 1, considering $Z = e(g,g)^{abc}$. If $b' \neq b$, then output 0, considering $Z \in R \in G_T$ as a random element.

⑥ Successfulness analysis: if $Z = e(g,g)^{abc}$, the signature structure is legitimate and $\mathcal{A}$ cannot distinguish the membership; if $Z \in R \in G_T$, the pairing term R_2 is a random value, the signature does not satisfy the verification condition, and the adversary cannot obtain valid information. Therefore, if $\mathcal{A}$ has a non-negligible advantage ϵ to distinguish b, then $\mathcal{B}$ can distinguish DBDH instances from random values with the same advantage, which yields:

$$\mathrm{Adv}_{DBDH}^{\mathcal{B}} = |Pr[\mathcal{B}(Z = e(g,g)^{abc}) = 1] - Pr[\mathcal{B}(Z \in R \in G_T) = 1]| = \epsilon \tag{3}$$

This contradicts the DBDH assumption, so the original assumption is not valid. In summary, this group signature scheme satisfies the anonymity security requirement under the defined anonymity challenge model. The proof is complete.

(3) Unforgeability

Theorem 2: If the Discrete Logarithm Problem (DLP) is challenging in a cyclic group G_1 and the adversary has no access to the private keys of the legitimate members, then the signature scheme of this group satisfies existential unforgeability under the Choice Message Attack (EUF-CMA) model (*Bellare et al., 2003*).

Proof of Theorem 2: Assuming that a polynomial-time adversary $\mathcal{A}$ that can successfully forge an unqueried legitimate signature with non-negligible probability, an algorithm $\mathcal{B}$ is constructed that solves the DLP problem with $\mathcal{A}$ as a subroutine, thus inducing a contradiction.

To portray the ability of the adversary, the following challenge game $\mathcal{G}_{\mathrm{ufg}}^{\mathcal{A}}$ is defined:

① System initialisation: the system generates the parameter $params$ and registers multiple members. The adversary $\mathcal{A}$ obtains all public parameters and pseudonym information, but cannot obtain the private key of a challenge member.

② Query phase: adversary $\mathcal{A}$ can initiate registration, signature and hash function $H(\cdot)$ queries.

③ Output phase: Adversary $\mathcal{A}$ outputs a forged signature $\sigma^* = \{M^*, T_1^*, T_2^*, T_3^*, A^*, c^*, S_1^*, S_2^*\}$, where M^* has not been queried and the signature corresponds to a challenge member but is not generated by it. The forgery success probability of adversary $\mathcal{A}$ is:

$$\mathrm{Adv}_{\Pi}^{\mathrm{ufg}}(\mathcal{A}) = \Pr[\mathcal{A}\mathrm{wins}\mathcal{G}_{\mathrm{ufg}}^{\mathcal{A}}] \quad (4)$$

If for any PPT adversary $\mathcal{A}$, there is $\mathrm{Adv}_{\Pi}^{\mathrm{ufg}}(\mathcal{A}) \leq \mu(\lambda)$, where $\mu(\lambda)$ is a negligible function, then this scheme satisfies EUF-CMA unforgeability.

Based on the above game, construct Algorithm $\mathcal{B}$ to perform the following simulation:

① Input instance: algorithm $\mathcal{B}$ receives a DLP instance $(P_1, P_{pub} = s \cdot P_1)$, and the goal is to compute $s \in \mathbb{Z}_q^*$.

② Parameter simulation: Algorithm $\mathcal{B}$ designates P_1 as a generator in the DLP instance, randomly chooses $r \in \mathbb{Z}_q^*$, and sets the initial accumulator to be $ACC_0 = r \cdot P_2$. The rest of the parameters, such as P_2, G_2, G_T, e, are randomly set by Algorithm $\mathcal{B}$. The hash function $H(\,)$ is modeled as a random oracle, with all queries recorded to ensure consistency. Eventually, Algorithm B returns the system parameter $params$ to the adversary $\mathcal{A}$.

③ Simulated querying: Algorithm $\mathcal{B}$ completely simulates all the registration and signature requests of $\mathcal{A}$; autonomously assigns the pseudo-name PID_i and computes the accumulator state; constructs a legitimate signature using the simulated membership key $(u_i, H(id_i), W_i)$, and specifically marks a challenge member U^*, for which it does not return the private key and does not accept signature request.

④ Forged signature and private key extraction: when the adversary $\mathcal{A}$ outputs a legitimate signature σ^* for the message M^*, if it satisfies the verification conditions and is attributed to the challenge member U^*, then from the signature parameter relationship, it can be seen that $T_1^* = u^* \cdot P_1, T_3^* = u^* \cdot P_{pub} = u^* \cdot s \cdot P_1$. Since T_1^* and T_3^* are in the same subgroup of the generator P_1, there exists a unique scalar s satisfying $T_3^* = s \cdot T_1^*$. Therefore, $\mathcal{B}$ can solve the DLP by the following formula:

$$T_3^* = s \cdot T_1^* \Rightarrow s = \frac{T_3^*}{T_1^*} \quad (5)$$

⑤ Successfulness analysis: if the probability of success of the forgery of the adversary $\mathcal{A}$ is ϵ, the algorithm $\mathcal{B}$ solves the DLP with the same advantage, which is in contradiction with the DLP assumption.

Therefore, assuming the DLP assumption is valid and the adversary cannot access the private keys of legitimate members, this group signature scheme satisfies existential unforgeability under the EUF-CMA model. The proof is complete.

(4) Traceability

Given any group signature $\sigma = \{M, T_1, T_2, T_3, A, c, S_1, S_2\}$, and only the GM owns the master private key s in the system, the pseudonym identity of the signer can be recovered by calculating the $PID_* = T_2 - s \cdot T_1$, and combining with the local identity mapping table to uniquely locate the real identity id_i, to achieve the effective traceability of the signer. Each valid signature corresponds to a unique identity identifier to ensure the accuracy of the traceability result. In the process of signature generation, the random factor u introduced each time makes that even if the same member generates signatures for many times, the parameters of its signature components T_1, T_2, etc. remain random in distribution, ensuring the uniqueness and unpredictability of each signature. Only if the signature is verified and confirmed to be valid, the GM performs the de-anonymisation operation, thus restoring the real identity and completing the traceability. This mechanism ensures that all signatures can be effectively traced back to the corresponding authentic signer in the produce traceability system.

(5) Forward-backward unlinkability

Suppose member U_i is revoked and the attacker holds the updated parameter ACC_j'. Since ACC_j' is inconsistent with $\mathrm{ACC_j}$ used for historical signatures and PID_i is no longer publicly available, the verifier is unable to obtain W_i, and thus is unable to associate the signature with U_i, thus verifying forward privacy.

Assuming that the new member U_k tries to identify the signer of the old signature σ_i, since the new member's key does not contain $H(id_i)$ or W_i and u in $T_3 = u \cdot P_{pub}$ was generated by the old member, the new member is unable to construct signatures that can validate this signature structure, and thus cannot distinguish historical identities.

Thus, forward privacy arises from the binding of the historical accumulator snapshot $\mathrm{ACC_j}$ in the signature structure, while backward privacy relies on the unidirectional evolution of the accumulator with the

irreversibility of the hash function. As long as the hash function is collision-resistant and the accumulator is irreversible, the present swarm signature system satisfies forward and backward privacy.

Performance Analysis

(1) Experimental Environment

This experiment was conducted on a high-performance platform with a hardware configuration of an Intel Core™ i7-9750H (2.60 GHz) central processor, an NVIDIA GeForce GTX 1650 graphics processor, and 16 GB of operating memory. The software environment comprised the Windows 11 operating system, IntelliJ IDEA 2023.2.1 development tool, and Java programming language. In addition, the JPBC library (version 2.0.0) was used in the experiments and the cryptographic operations were performed based on type A pairing profiles (a.properties) with a 512-bit base field. The key generation process used the SHA-256 hash algorithm, and the encryption algorithm used the AES encryption standard. All experiments were conducted under uniform hardware and software conditions to ensure the reproducibility of the experimental results.

The content of Table 2 demonstrates the execution time statistics of the cryptographic operations used in this experiment:

Table 2

Cryptographic Operational Definitions and Average Runtime

Symbol Definition	Type of operation	Execution time (average)
T_{bp}	Bilinear pairing operation execution time	22ms
T_{Ex}	Power operation execution time	16ms
T_{Mu}	Multiplication operation execution time	0.06ms
T_h	Hash operation execution time	0.056ms

(2) Functionality Comparison

There exist multiple blockchain-based privacy-preserving schemes for agricultural-product traceability; representative examples include a zero-knowledge-proof–based model, ProChain (*Li et al., 2024*), a proxy re-encryption (PRE) approach (*Wang et al., 2024*), and an attribute-based encryption (ABE) scheme (*Yang et al., 2024*). In addition, Cai et al and Zeng et al propose efficient group-signature–based authentication frameworks in non-agricultural settings (*Cai et al., 2023; Zeng et al., 2024*). Although developed for different domains, their cryptographic designs are largely transferable and thus informative for our setting.

Table 3

Functionality comparison table

Programme	Privacy-preserving mechanisms	Signature anonymity	Signature traceability Member	Revocation mechanism
Yang et al.,2024	ABE	×	×	×
Wang et al., 2024	PRE	×	√	×
Li et al., 2024	Zero-knowledge proofs	√	√	×
Cai et al., 2023	Group signatures	√	√	×
Zeng et al., 2024	Group signatures	√	√	√
Ours	Group signatures + pseudonyms + revocable accumulators	√	√	√

Table 3 contrasts these studies along key functional dimensions—underlying mechanism, support for signature anonymity and traceability, and the presence of a membership-revocation mechanism. Guided by the characteristics of agricultural supply chains, a scheme is designed that integrates group signatures, pseudonyms, and revocable accumulator, which is better suited to the privacy and identity-management requirements of agricultural-product traceability.

(3) Computational Overhead

To systematically assess the computational efficiency of our scheme, benchmarks are conducted against two representative group-signature–based authentication schemes—*Cai et al. (2023)* and *Zeng et al. (2024)*. Table 4 compares the algorithmic complexity of different schemes in the Signature Generation, Signature Verification, and Membership Revocation phases.

Table 4

Comparison of algorithmic complexity of different schemes

Programme	Signature	Verification
Cai et al., 2023	$11T_{Mu} + T_{bp} + T_{Ex} + 2T_h$	$2T_{Mu} + 4T_{bp} + T_{Ex} + 2T_h$
Zeng et al., 2024	$12T_{Mu} + 2T_{bp} + 2T_{Ex} + T_h$	$9T_{Mu} + 3T_{bp} + 3T_{Ex} + T_h$
Ours	$10T_{Mu} + 2T_{bp} + T_{Ex} + T_h$	$5T_{Mu} + T_{bp} + T_h$

As shown in Table 4, our scheme has lower computational complexity in the Signature Generation phase than *Cai et al. (2023)* and is slightly higher than *Zeng et al. (2024)*. In the Signature Verification phase, our scheme enjoys a clear advantage: it requires only one bilinear pairing and one hash evaluation, thereby reducing the computational load and improving response time. Both our scheme and *Zeng et al. (2024)* support dynamic membership revocation with comparable revocation complexity, whereas *Cai et al. (2023)* does not provide a revocation mechanism, which limits its practicality and flexibility in dynamic settings. Fig. 7 compares the measured average time overheads for Signature Generation, Signature Verification, and Membership Revocation.

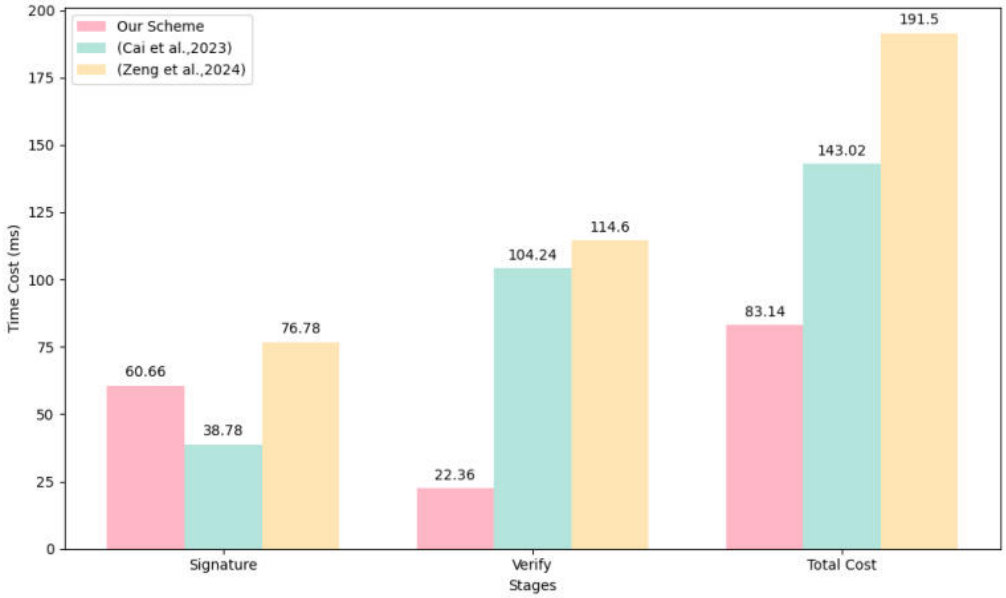


Fig. 7 - Comparison of average time overhead of different group signature schemes in signature and verification phases

As shown in Fig. 7, our scheme achieves an average Signature Generation time of 60.66 ms, lower than Zeng et al. (2024) (76.78 ms) and higher than *Cai et al. (2023)* (38.78 ms). In the Signature Verification phase, our scheme performs best at 22.36 ms, substantially outperforming *Cai et al. (2023)* (104.24 ms) and Zeng et al. (2024) (114.60 ms). For Membership Revocation, our scheme and *Zeng et al. (2024)* exhibit comparable time costs, indicating efficient support for dynamic membership management, whereas Cai et al. (2023) does not implement revocation. Aggregating the three phases, the total measured overhead of our scheme is 83.14 ms, markedly below *Cai et al. (2023)* (143.02 ms) and *Zeng et al. (2024)* (191.50 ms), while maintaining equivalent security guarantees.

(4) Communication Overhead

In blockchain-based agricultural traceability, communication overhead is dominated by signature transmission. Signature sizes are quantified for our scheme and are compared with *Cai et al. (2023)* and *Zeng et al. (2024)*. Results are shown in Table 5.

Table 5

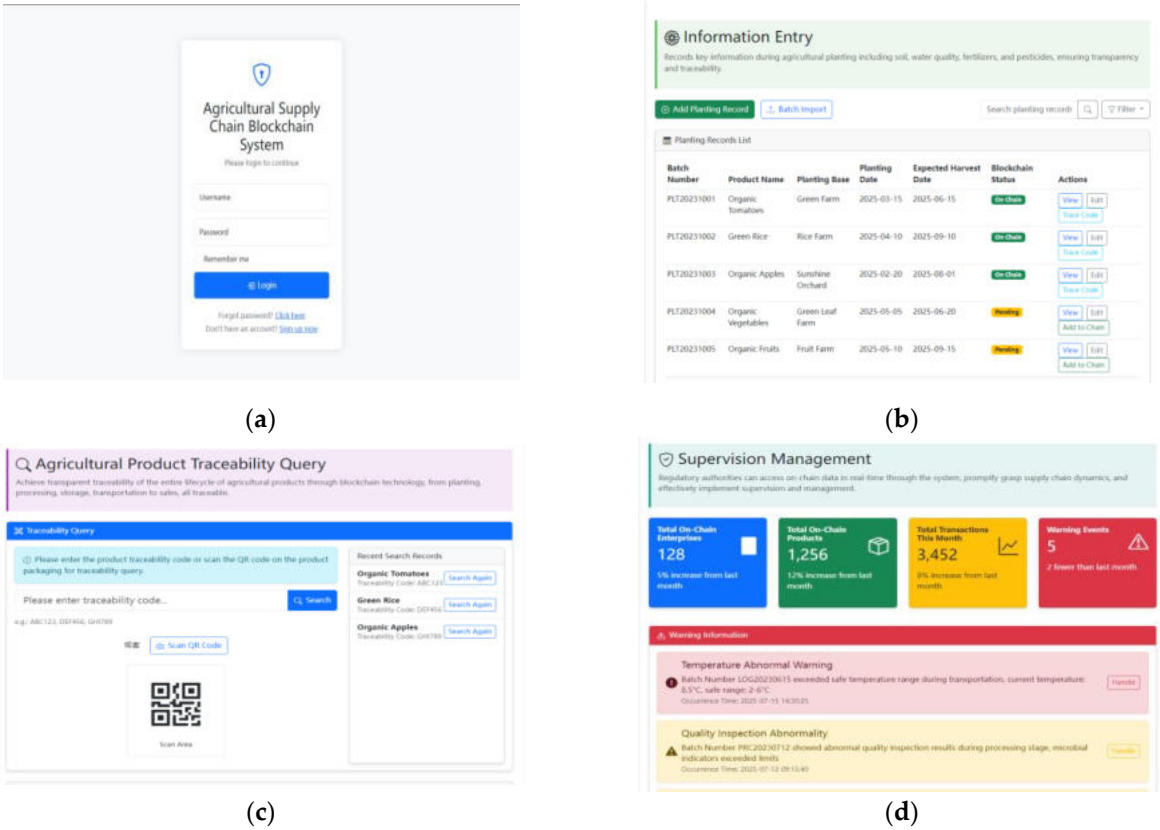
Signature communication overhead comparison table

Programme	Signature size	Byte size
Cai et al., 2023	4|G|+|H|	532B
Zeng et al., 2024	5|G|+|H|+2|Zr|	700B
Ours	4|G|+|H|+2|Zr|	572B

From Table 5, it can be seen that the signature size of this paper's scheme is 572 bytes, 128 bytes less than that of the *Zeng et al. (2024)*, and is more advantageous in transmission efficiency. However, there is a slight increase compared with the *Cai et al. (2023);* overall, it is still in the acceptable range. The difference mainly stems from the additional parameters necessary to introduce a revocable mechanism in the signature structure in this paper. It is worth noting that the scheme in this paper achieves an effective trade-off between security and efficiency by integrating anonymity, traceability and revocation mechanisms in the signature structure, and keeping the communication burden moderate while expanding the functionality. Comprehensively, this paper effectively controls the communication overhead to ensure the integrity of the signature function and demonstrates better practicality and system performance.

(5) Subsubsection

The prototype system, which embodies the proposed group-signature-based blockchain privacy-protection scheme, was developed with the open-source Hyperledger Fabric 2.1 framework. It covers the four pivotal stages of the agricultural supply chain—cultivation, processing, storage and transport, and retail—each corresponding to a distinct stakeholder group. The system significantly accelerates consumer queries for traceability information, strengthening trust in agricultural products. Regulatory bodies gain real-time access to on-chain data, enabling them to monitor supply-chain dynamics and enforce oversight effectively. Agricultural enterprises, meanwhile, can exploit the scheme's authorisation and privacy mechanisms to achieve secure, efficient data exchange and sharing, thus promoting the digitalisation and intelligent upgrading of the sector. The implementation and user interface of the system are illustrated in Fig. 8.



(a) (b)

(c) (d)

Fig. 8 - Selected system function interfaces

(a) login page (b) enterprise information entry (c) consumer traceability query and verification (d) regulatory authority maintenance

Figure 8(a) shows the system's login interface: enterprise users and regulatory authorities sign in with account credentials, whereas consumers can proceed directly to the traceability query module. Figure 8(b) depicts the enterprise data-entry interface, where stakeholders at each supply-chain stage upload traceability data to guarantee the authenticity and traceability of product information. Figure 8(c) presents the consumer query interface, enabling users to retrieve product traceability details by scanning a QR code or entering a traceability code. Figure 8(d) illustrates the supervisory-authority management interface, through which regulators monitor and manage traceability data across the entire process, ensuring secure and stable system operation.

CONCLUSIONS

This study addresses the critical issues of privacy leakage, inflexible identity management, and inadequate auditability in agricultural-product traceability systems by introducing a blockchain-based privacy-protection scheme grounded in group signatures. The proposed design integrates a revocable accumulator, pseudonym mapping, and dynamic membership management to maintain signature anonymity while ensuring regulatory traceability and identity consistency amid frequent node changes. Six polynomial-time algorithms and a corresponding security-property model collectively support user registration, signing, verification, de-anonymisation, and revocation, forming a comprehensive privacy-enhanced authentication framework for traceability. Formal analysis confirms that the scheme guarantees anonymity, signature unforgeability, traceability, and forward and backwards privacy. Experimental results demonstrate superior computational efficiency, lower communication overhead, and better blockchain performance than several existing benchmarks—most notably in verification latency and revocation responsiveness. The scheme offers a viable technical route and theoretical foundation for secure, accountable data sharing in multi-stakeholder agricultural supply chains.

Although the prototype performs well in small- to medium-scale networks, the communication complexity and latency of the classical PBFT consensus protocol become bottlenecks as network size grows or conditions fluctuate. Future work will focus on tailored optimisations of PBFT, specifically: (i) compressing communication costs through threshold signatures and batch verification; (ii) employing hierarchical or partitioned consensus to enable parallel execution and reduce overall complexity; and (iii) designing adaptive view-change mechanisms that leverage latency monitoring and reputation evaluation to swiftly exclude faulty nodes, thereby enhancing scalability and robustness in large, heterogeneous networks.

ACKNOWLEDGEMENT

We would like to express our sincere gratitude to all authors for their support and contributions to this manuscript. This research is supported by the Shanxi Province Basic Research Program for Young Scientists (NO. 202303021222039).

REFERENCES

[1] Bellare, Namprempre, Pointcheval, & Semanko. (2003). The one-more-RSA-inversion problems and the security of Chaum's blind signature scheme. *Journal of Cryptology*,*16*(3), 185-215.

[2] Bermeo-Almeida, O., Cardenas-Rodriguez, M., Samaniego-Cobo, T., Ferruzola-Gómez, E., Cabezas-Cabezas, R., & Bazán-Vera, W. (2018). Blockchain in agriculture: A systematic literature review. In *International conference on technologies and innovation.* pp. 44-56. Springer, Cham.

[3] Boneh, D., & Franklin, M. (2001, August). Identity-based encryption from the Weil pairing. In *Annual international cryptology conference.* pp. 213-229. Berlin, Heidelberg: Springer Berlin Heidelberg.

[4] Cai, J., Tao, X., & Wang, C. (2023). Cooperative authentication scheme for heterogeneous networks based on identity group signature and blockchain. *IEEE Transactions on Vehicular Technology*, *73*(1), 1394-1399.

[5] Demestichas, K., Peppes, N., Alexakis, T., & Adamopoulou, E. (2020). Blockchain in agriculture traceability systems: A review. *Applied Sciences* ,*10*(12), 4113.

[6] Gong, Q., Zhang, J., Wei, Z., Wang, X., Zhang, X., Yan, X., Liu, Y & Dong, L. (2024). Sdacs: Blockchain-based secure and dynamic access control scheme for internet of things. *Sensors*, *24*(7), 2267.

[7] Li, J., Wang, Z., Guan, S., & Cao, Y. (2024). ProChain: A privacy-preserving blockchain-based supply chain traceability system model. *Computers & Industrial Engineering*, *187*, 109831.

[8] Li, L., Tian, P., Dai, J., & Miao, F. (2024). Design of agricultural product traceability system based on blockchain and RFID. *Scientific Reports*, *14*(1), 23599.

[9] Peng, X., Zhang, X., Wang, X., Li, H., Xu, J., & Zhao, Z. (2022). Construction of rice supply chain supervision model driven by blockchain smart contract. *Scientific Reports*, *12*(1), 20984.

[10] Sharma, M. G. (2023). Supply chain, geographical indicator and blockchain: provenance model for commodity. *International Journal of Productivity and Performance Management*, *72*(1), 92-108.

[11] Soy, A., & Balkrishna, S. M. (2025). Blockchain Integration in Agriculture for Transparent Farm-to-Fork Supply Chains: Leveraging IoT and Decentralized Identity for Enhanced Traceability and Security. In *SHS Web of Conferences* (Vol. 216, p. 01073). EDP Sciences.

[12] Stranieri, S., Riccardi, F., Meuwissen, M. P., & Soregaroli, C. (2021). Exploring the impact of blockchain on the performance of agri-food supply chains. *Food control*, *119*, 107495.

[13] Sun, L., Zhou, D., Liu, D., Tang, J., & Li, Y. (2023). BPDAC: A Blockchain Based and Provenance Enabled Dynamic Access Control Scheme. *IEEE Access*,*11*, 142552-142568.
[14] Wang, L., Peng, C., & Tan, W. (2023). Secure ring signature scheme for privacy-preserving blockchain. *Entropy*, *25*(9), 1334.
[15] Wang, S., Luo, N., Xing, B., Sun, Z., Zhang, H., & Sun, C. (2024). Blockchain-based proxy re-encryption access control method for biological risk privacy protection of agricultural products. *Scientific Reports*, *14*(1), 20048.
[16] Xu, Y., Li, X., Zeng, X., Cao, J., & Jiang, W. (2022). Application of blockchain technology in food safety control: current trends and future prospects. *Critical reviews in food science and nutrition*, *62*(10), 2800-2819.
[17] Yang, S., Li, S., Chen, W., & Zhao, Y. (2024). A redactable blockchain-based data management scheme for agricultural product traceability. *Sensors*, *24*(5), 1667.
[18] Zeng, M., Cui, J., Zhang, Q., Zhong, H., & He, D. (2024). Efficient revocable cross-domain anonymous authentication scheme for IIoT. *IEEE Transactions on Information Forensics and Security*.
[19] Zhang, B., Xu, J., Wang, X., Zhao, Z., Chen, S., & Zhang, X. (2023). Research on the construction of grain food multi-chain blockchain based on zero-knowledge proof. *Foods*, *12*(8), 1600.
[20] Zhang, G., Chen, X., Zhang, L., Feng, B., Guo, X., Ling, J., & Zhang, Y. (2022). STAIBT: Blockchain and CP-ABE empowered secure and trusted agricultural IoT blockchain terminal. *IJIMAI*, *7*(5), 66-75.
[21] Zhang, S., Ye, J., & Li, G. (2020). Research and implementation of blockchain technology scheme for cold chain logistics. *Computer Engineering and Applications*, *56*(3), 19-27.

LIGHTWEIGHT RESEARCH OF FORESTRY UNMANNED VEHICLE SWING ARMS BASED ON MULTI-CONDITION TOPOLOGY OPTIMIZATION OF CONTINUUM STRUCTURES
/
基于连续体结构多工况拓扑优化的林业无人车辆摆臂轻量化研究

Yihan QIN, Yilu ZHAO, Qiang CHEN, Ji WU, Zhongjia CHEN, Qingchun WANG, Xiangyue YUAN*)
The School of Technology, Beijing Forestry University, Beijing / China
Tel: +086-13366903021; E-mail: yuanxiangyue@bjfu.edu.cn
Corresponding author: Xiangyue Yuan
DOI: https://doi.org/10.35633/inmateh-76-91

Keywords: *Dynamics Simulation; Structure Optimization; Finite Element Analysis; Modal Test*

ABSTRACT
To meet the demanding terrain of China's forest regions—characterized by obstacles, gullies, and uneven ground—a wheel-leg hybrid chassis is proposed for a three-axle unmanned electric forestry vehicle. Parametric modelling in SolidWorks and dynamic simulations in MSC Adams quantified the critical load cases on the swing arms during obstacle negotiation. The Analytic Hierarchy Process (AHP) assigned optimal weights for multi-scenario topology optimization. A finite-element model of the arms was built in HyperMesh/OptiStruct; post-optimisation analyses confirmed structural integrity. Masses of the front and rear arms reduced to 31.3 kg each, and the middle arm to 39.44 kg, realizing weight reductions of 29.1 % and 21.7 %, respectively, with no loss in performance.

摘要
为应对中国大陆林区存在众多障碍物和沟壑等林业作业条件所带来的挑战，本文提出了一种适用于林业三轴无人电动车辆的轮腿式混合行走机构。利用 SolidWorks 和 MSC Adams 软件进行了参数化建模和动力学仿真，以分析车辆摆臂在越障过程中所经历的多种典型载荷工况，运用层次分析法（AHP）确定了多工况拓扑优化的最优权重系数分配。使用 Hypermesh-Optistruct 软件建立了摆臂的有限元模型，并对优化后的摆臂进行了有限元分析。优化后的前、后摆臂重量均为 31.3 千克，中摆臂重量为 39.44 千克，重量分别降低了 29.1%和 21.7%，取得了良好的轻量化效果。

INTRODUCTION

Currently, forest engineering vehicles in China face the challenge of off-road capabilities when operating in forested areas. The operating environment in forest regions is more complex and difficult than ordinary environments. Since forestry production vehicles often need to operate on non-structured terrains in the forest, ordinary wheeled or tracked vehicles struggle to meet the obstacle-crossing performance requirements in complex site conditions, such as numerous ravines and vertical obstacles (*Sun et al., 2019*). This paper, based on a 6×6 wheel-hub motor driven, tri-axle electric unmanned vehicle, studies a walking mechanism that integrates strong obstacle-crossing capabilities, combining the advantages of wheeled vehicles for high-speed travel and legged structures for superior terrain adaptability. This mechanism is designed to meet the random changes in forest terrain and road conditions.

Chen et al. proposed a structural optimization scheme for tree transplanters designed for hilly and mountainous environments to enhance their stability and maneuverability during climbing, obstacle crossing, and trench crossing. Simulation and real-vehicle testing, conducted using the RecurDyn V9R4 dynamic analysis software, demonstrated that the design meets driving performance requirements (*Chen et al., 2024*). Mergl et al. studied the performance of a hydraulic harvester crane operating on slopes with varying inclines and investigated the impact of slewing bearing angles on slewing torque using MSC Adams simulations (*Mergl & Kašpárek, 2022*).

Wang et al. proposed a passive morphing wheel-legged robot design for obstacle crossing. Kinematic simulations of the robot's morphing and obstacle-crossing processes were conducted using MSC Adams, and the design's feasibility was validated through physical prototype experiments (*Wang Y. et al., 2024*). *Zhou, Liu at al.* have utilized Adams software for kinematic and dynamic analyses of mechanisms, studying both their dynamic and static characteristics (*Huaitang et al., 2024; Liu, 2020*). Chen et al. developed an independent strut-type air suspension system for high-clearance self-propelled sprayers, employing HyperMesh for finite element analysis of critical components like vertical shafts and steering arms. Their design achieved effective vibration damping through air spring optimization and additional air chamber damping, demonstrating a 20-inch vibration reduction stroke while maintaining structural integrity under extreme conditions such as side slip and emergency braking (*Chenwei et al., 2023*). *Wentao et al.* proposed a novel high-clearance chassis design for weeding robots featuring cross-floating suspension mechanisms. Through dynamic simulations and field tests, they achieved 800 mm ground clearance with 22° longitudinal and 32° transverse slope stability, while maintaining structural integrity under 134.88 MPa stress during emergency braking conditions through optimized beam connections *(Wentao et al., 2025*).

The swing arm of a tri-axle unmanned vehicle, as a critical component of the drive system, primarily absorbs impact forces from the ground when driving on complex terrain and overcoming vertical obstacles. Therefore, the structural strength and stiffness of the swing arm are key technical indicators in the design process. Lightweight design, while ensuring the structural strength of the swing arm, can reduce the resistance from the ground, enhance obstacle-crossing performance on challenging terrain, and improve the battery life of an electric vehicle. This ultimately increases their practical application value in forestry operations. With the rapid advancement of optimization algorithms, continuum structure topology optimization has gradually become one of the main approaches to achieving lightweight structural design (*Qiang et al., 2024*).

Wang et al. proposed an improved Solid Isotropic Material with Penalization (SIMP) method and introduced a sensitivity filtering method based on Gaussian weighting functions. The new topology optimization method has advantages such as faster convergence speed and suppression of grayscale elements (*Jing-liang et al., 2022*). Meng et al. applied fuzzy and probabilistic theory to handle cognitive and stochastic uncertainties and studied the flexibility reliability optimization of continuum structures (*Meng et al., 2020*). *Li et al.* proposed a topology optimization method for continuum structures under stress constraints with non-periodic loads, based on the Bidirectional Evolutionary Structural Optimization (BESO) method, which is suitable for dynamic stress under non-periodic loads with iterative periodic updates (*Li et al., 2023*). *Xia et al.* established a non-probabilistic reliability topology optimization model considering local strength characteristics of structures, based on stress influence functions (*Xia & Qiu, 2022*). *Xiaokai et al.* proposed a multi-material topology optimization method for shell/fill structures for automotive control arms, establishing a material interpolation model to achieve better lightweighting results (*Xiaokai et al., 2021*). *Zhang, Wang et al.* developed an integrated lightweight method for steel-aluminum hybrid materials based on sensitivity analysis, reducing the cabin mass by 12.8% and the frame mass by 5.6% (*Wang C. et al., 2024; Zhang et al., 2020*). *Xiong et al.* employed a multi-objective particle swarm optimization algorithm to reduce the weight of the body-in-white by 4.12 kg while ensuring other mechanical properties *(Xiong et al., 2018*). In recent years, many researchers have introduced deep learning models into the topology optimization process, using initial iterative structural density distributions and gradient values as starting information to quickly obtain reliable topological configurations, thereby improving the efficiency of topology optimization (*Padhi et al., 2024; Qiu et al., 2021*).

In summary, this paper focuses on the lightweight design and vertical obstacle-crossing performance of a tri-axle unmanned vehicle. It conducts a vehicle dynamic simulation, with the swing arm as the research object, to analyze the force conditions under various operating conditions. Subsequently, a multi-condition topology optimization design is performed, and a finite element model of the swing arm is established to analyze and verify the performance of the optimized structure (*Kešner et al., 2021; Niu et al., 2022*). A test bench for the swing arm is built to conduct static analysis and modal analysis on the swing arm specimens. The calculated results are compared with experimental data to validate the effectiveness of the topology optimization model and the accuracy of the finite element analysis (*Zhao et al., 2025*).

MATERIALS AND METHODS

Structure Composition and Dynamic Simulation

The structure of the unmanned vehicle consists of three pairs of symmetrically arranged deformable swing arms and a frame-type vehicle body. The drive electric cylinders, hinged to the vehicle body, control the swing arm angles to switch between the wheeled mode and the legged mode, thus achieving the objectives of off-road and vertical obstacle-crossing. For the specific condition of vertical obstacle-crossing, the vehicle needs to smoothly cross a high platform with a maximum height of 1 meter. A simplified dynamic model of the entire vehicle will be established and simulated in the MSC Adams for analysis.

Establishment of the Vehicle Dynamic Simulation Model

The simplified dynamic model after importing is shown in Fig 1, with the main components including the vehicle frame, drive electric cylinders and piston rods, tri-axle swing arms, and wheels. According to the preliminary design requirements, the total mass of the vehicle frame, swing arms, arm drive devices, and related components should be kept within 745 kg, with the mass of a single swing arm not exceeding 42 kg. Considering that modules such as batteries, perception systems, and auxiliary power systems also need to be installed on the vehicle frame, the frame in the model is defined as 1650 kg, and the total weight of the unmanned vehicle is controlled at around 2650 kg, with a single swing arm weighing 42 kg. This ensures the accuracy of the simulation results. The vehicle dimensions and weight parameters are shown in Table 1.

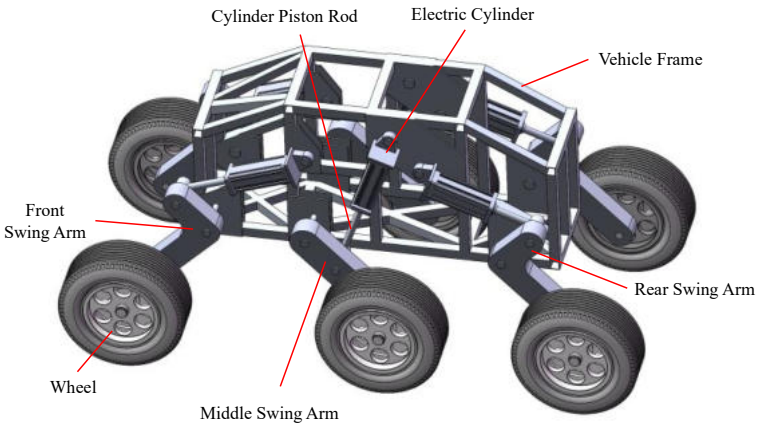


Fig. 1 - The simplified dynamic model of the vehicle

Table 1

The parameters of the vehicle model

Parameter	Value
Vehicle Dimensions(mm)	4130 × 1970 × 1960
Vehicle Weight(kg)	2650
Vehicle Frame Weight(kg)	1650
Single Swing Arm Weight(kg)	42
Single Drive Cylinder Weight(kg)	30
Single Wheel Weight(kg)	100

Through the simulation, the main connections in the unmanned vehicle's dynamic model are as follows:

1. A rotational joint between the lower end of the swing arm and the wheel;
2. A rotational joint between the middle of the swing arm and the vehicle frame;
3. A rotational joint between the upper end of the swing arm and the electric cylinder's piston rod;
4. A translational joint between the electric cylinder's piston rod and the cylinder body;
5. A rotational joint between the end of the electric cylinder and the vehicle frame.

The contact between the wheels, the ground, and obstacles is added using an im-pact function method, with Coulomb friction between the wheels and the ground. The parameters are shown in Table 2.

Table 2

The parameters of the contact

Parameter	Value
Stiffness(N/mm)	1.0×10^4
Collision index	2.2
Damping(N·s/mm)	10
Penetration depth /mm	0.1
Static friction coefficient	0.8
Dynamic friction coefficient	0.1

Dynamic Simulation Process and Results

During the obstacle-crossing process, due to the relatively heavy weight of the unmanned vehicle, in order to prevent excessive force on the swing arm drive electric cylinders, the wheel drive speed is set to 0.2 m/s, and the obstacle-crossing rotational speed is set to 0.04 m/s. The off-road performance of the entire vehicle is then verified. The simulation results are shown in Fig. 2, with the obstacle-crossing process completed within 200 seconds.

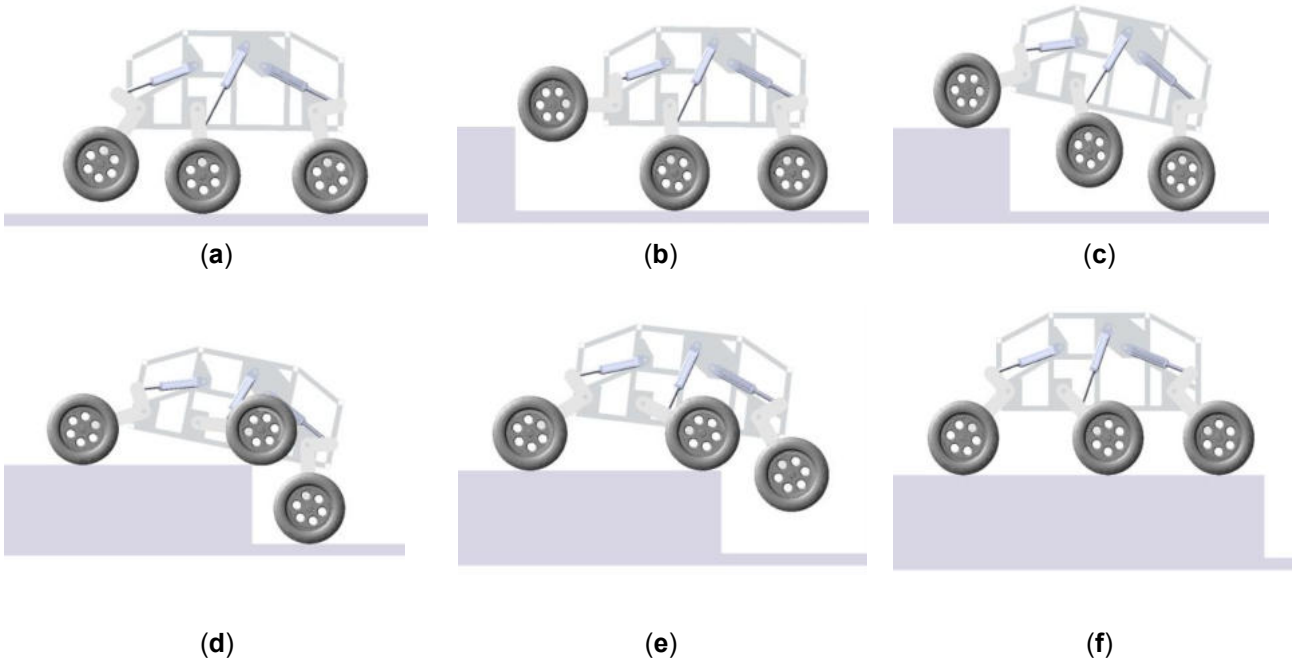


Fig. 2 - The obstacle-crossing process schematic diagram

*(**a**) The middle/rear arm raises to lift the vehicle's posture; (**b**) The front arm is raised to a horizontal angle, approaching the obstacle; (**c**) The front wheel crosses the obstacle while the front arm begins to retract; (**d**) The middle wheel crosses the obstacle while the middle arm begins to retract; (**e**) The middle/rear arm returns to the normal driving angle; (**f**) The vehicle completes the obstacle-crossing.*

In Fig. 3, the gray curve represents the change in the center of mass position of the unmanned vehicle along the vertical direction. This curve indicates that the vehicle maintains overall stability during the wheel-leg transition, wheeled movement, and obstacle-crossing process. The red curve represents the center of mass velocity curve of the vehicle, and the blue curve represents the center of mass acceleration curve. From 0 to 10 seconds, all three-axles swing arms are raised to improve the vehicle's posture, causing the center of mass to rise and resulting in a sudden change in velocity and acceleration. From 10 to 50 seconds, the vehicle approaches the obstacle platform, and its center of mass velocity and acceleration gradually stabilizes. After 50 seconds, the vehicle begins to cross the obstacle and climb the slope, with its center of mass acceleration approaching zero, indicating that its motion is relatively stable.

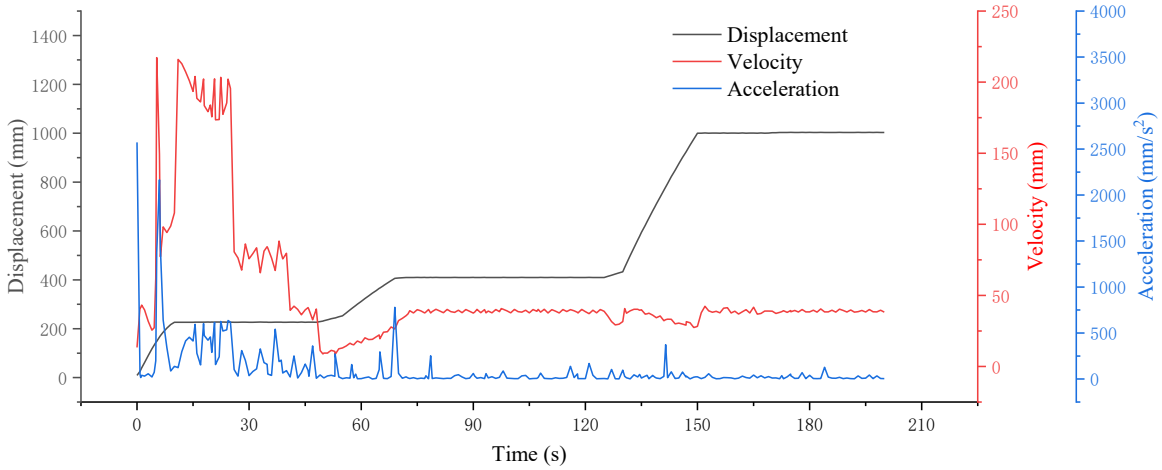


Fig. 3 - The center of mass displacement, velocity, and acceleration curves of the unmanned vehicle during the obstacle-crossing process

The lifting of the swing arm is achieved by controlling the driving cylinder. During the entire obstacle-crossing process, the drive cylinder needs to provide sufficient thrust and pull to enable the wheel-leg transformation of the unmanned vehicle and withstand the impact forces encountered during the obstacle-crossing. Therefore, the force conditions at the connection between each swing arm and the cylinder rod were also studied in Adams software, as shown in Fig. 4, which provides more reference for the subsequent structural topology optimization loading conditions.

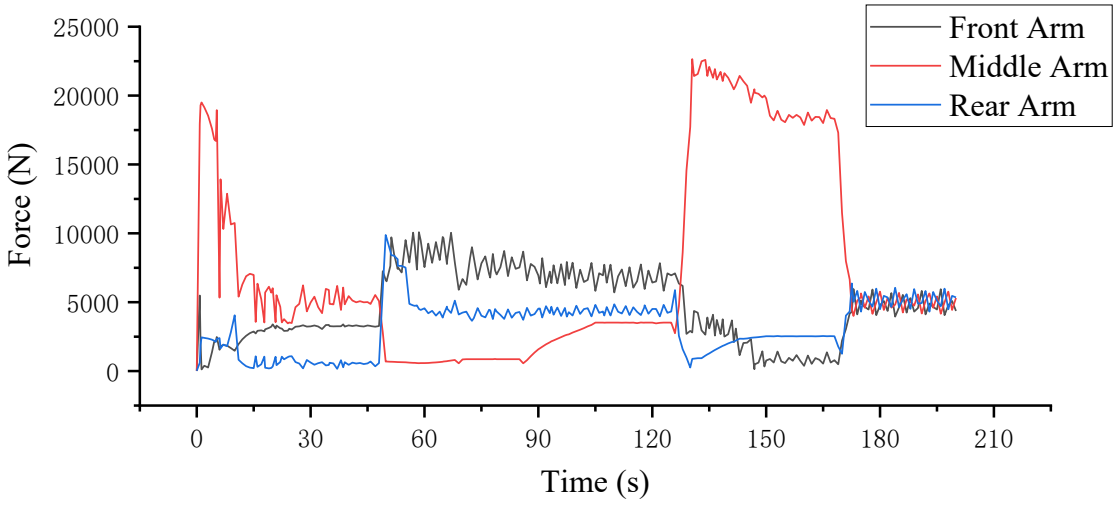


Fig. 4 - Force diagram at the connection between each axle Swing Arm and the Drive Cylinder Rod

From Fig. 4, it can be seen that the force conditions of the front/rear swing arms during the wheel-leg transformation and obstacle-climbing stages are quite similar, and the load they bear is smaller compared to the middle swing arm. Considering the interchangeability of the structure, the front/rear swing arms can be merged in the subsequent design. The middle swing arm, however, bears the primary load during the vehicle posture transformation and obstacle-crossing process. Therefore, its structural strength at the connection points with the frame and the cylinder push rod should be carefully ensured in the optimization design to guarantee the operational safety of the forestry unmanned vehicle.

Introduction to Topology Optimization

The concept of structural topology optimization originated from Michell's study on truss structure design. In the entire design optimization process, it belongs to the conceptual design phase, which determines the design direction. Topology optimization can, based on the given boundary conditions and loading scenarios, find the optimal material distribution or load path within the design space, thus achieving the lightest design while satisfying various performance criteria.

This paper uses the density method for material modeling based on OptiStruct topology optimization *(Tan et al., 2022*). In this method, each element in the finite element model design space is assigned to a relative density ρ_i as an optimization design variable, with a value range of $0 \leq \rho_i \leq 1$. When $\rho_i = 0$, it indicates that material is removed; when $\rho_i = 1$, it indicates that material is retained. This converts the structural topology optimization problem into an optimal material distribution problem, which is solved using mathematical programming methods.

Common material interpolation models in the density method include Solid Isotropic Material with Penalization (SIMP) and Rational Approximation of Material Properties (RAMP) *(Bai et al., 2024; Wang et al., 2021*). The OptiStruct solver uses the SIMP method, which introduces a penalty factor to penalize intermediate density values, causing the density values to converge toward 0 or 1. This results in a clear 0-1 optimization, approximating solid or void material distributions.

Analysis of Typical Swing Arm Loading Conditions

Due to the similar shapes and symmetric structures of the front and rear suspension arms, they can be analyzed together for their loading conditions. By analyzing the unmanned vehicle's movement and obstacle-crossing process, five typical loading conditions for the front/rear swing arms can be identified:

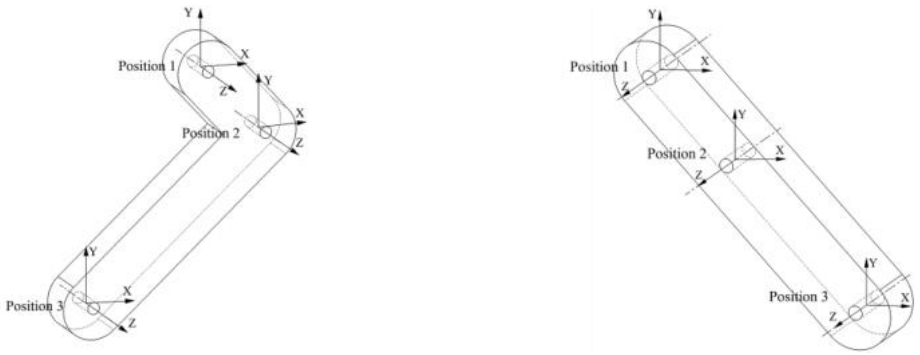
1. Static state loading condition;
2. Obstacle overcoming loading condition;
3. Under electric cylinder action condition;
4. Differential steering condition;
5. Emergency braking condition.

Similarly, five typical loading conditions can be identified for the middle swing arm:

1. Static state loading condition;
2. Arm raised loading condition;
3. Under electric cylinder action condition;
4. Arm returning after crossing obstacle loading condition;
5. Differential steering condition.

The load conditions of differential steering and emergency braking are calculated using the inertia release method (*Huang et al., 2025*), while the load conditions for others are derived from the dynamic simulation results in MSC Adams.

All the load conditions are shown in Table 3, where F_x, F_y, F_z represent the forces in the X, Y, and Z directions. The coordinate system for each axis swing arm is shown in Fig. 5.



(a) (b)

Fig. 5 - Swing arm coordinate system
(a) Front/rear arm; (b) Middle arm

Table 3

Load conditions for each scenario

Condition	Front/Rear Arm			Middle Arm		
	Position 1	Position 2	Position 3	Position 1	Position 2	Position 3
1	Constrained	$F_y = -4166N$	$F_y = 4166N$	$F_y = -4166N$	Constrained	$F_y = 4166N$
2	$F_x = -9660N$ $F_y = -1700N$ $F_z = 1400N$	Constrained	$F_x = 2167N$ $F_y = 3383N$	$F_x = 1400N$ $F_y = -4200N$ $F_z = 4000N$	Constrained	$F_y = 8000N$
3	$F_x = 9339N$ $F_y = -2550N$ $F_z = 1500N$	Constrained	$F_x = 2200N$ $F_y = 3383N$	Constrained	$F_x = 11000N$ $F_y = 22000N$ $F_z = -4800N$	Constrained
4	Constrained	$F_y = -8333N$ $F_z = -6666N$	$F_y = 8333N$ $F_z = 6666N$	$F_x = 10242N$ $F_y = -12261N$ $F_z = -3900N$	Constrained	$F_y = 9400N$
5	Constrained	$F_x = -12500N$ $F_y = 12500N$	$F_x = 12500N$ $F_y = 12500N$	$F_y = -8177N$ $F_z = -6533N$	Constrained	$F_y = 8177N$ $F_z = 6533N$

Swing Arm Topology Optimization Mathematical Model

In multi-condition continuum structure topology optimization, the weighted compromise programming method is used. Based on the weight coefficients for each condition, the objective function values for each individual condition are linearly weighted, transforming the multi-condition topology optimization problem into a single-condition topology optimization problem (*Guo-fei et al., 2018*). Based on the variable density method, where the relative density of the elements is taken as the design variable, the objective is to minimize the structural compliance (flexibility) under different loading conditions.

The mathematical model for the swing arm's compliance minimization topology optimization under multiple conditions is formulated as follows:

$$\begin{cases} X = (X_1, X_2, \dots, X_n)^T, \min\limits_X C(X) = \sum\limits_{k=1}^{n} \omega_k C_k(X) \\ Subject\ to: \begin{cases} \sum\limits_{i=1}^{n} x_i v_i - f_v V_0 \le 0 \\ 0 < \rho_{min} \le \rho_i \le 1 \\ k = 1,2,\dots,n \end{cases} \end{cases} \quad (1)$$

where X is the relative density of the elements in the design domain, which is the design variable; $C(X)$ is the weighted compliance of the swing arm structure, which is the objective function; $C_k(X)$ is the objective function for the k-th loading condition; ω_k is the weight coefficient for the k -th condition; n is the total number of discrete elements; k is the number of loading conditions; ρ_i is the relative density of the i-th element; v_i is the volume of the i-th element; f_v is the volume fraction corresponding to the volume constraint of the optimization objective; and V_0 is the initial volume.

The Analytic Hierarchy Process (*Kayet et al., 2020*) is used to perform pairwise comparisons of the k conditions and construct a decision matrix to determine the weight coefficient ω_k for each condition. From the mathematical model of compliance minimization, it is clear that the optimal compliance values for the initial topology optimization model under each individual condition determine the corresponding weight coefficients for multi-condition topology optimization. The initial topology optimization model for the swing arm is optimized separately under each condition to obtain the optimal compliance values α_k for each condition, and a decision matrix is then constructed.

$$M = \begin{pmatrix} \frac{\alpha_1}{\alpha_1} & \frac{\alpha_1}{\alpha_2} & \cdots & \frac{\alpha_1}{\alpha_k} \\ \frac{\alpha_2}{\alpha_1} & \frac{\alpha_2}{\alpha_2} & \cdots & \frac{\alpha_2}{\alpha_k} \\ \vdots & \vdots & \ddots & \vdots \\ \frac{\alpha_k}{\alpha_1} & \frac{\alpha_k}{\alpha_2} & \cdots & \frac{\alpha_k}{\alpha_k} \end{pmatrix} \quad (2)$$

The maximum eigenvalue λ_{max} of the decision matrix M is solved, and the corresponding eigenvector $a = [\omega_1, \omega_2, \ldots, \omega_k]$ is obtained. Normalizing the eigenvector gives the weight coefficients ω_k for each condition in the objective function.

Swing Arm Structure Topology Optimization

The profile models of the front, middle, and rear swing arms are created using SolidWorks. Based on the force conditions at key nodes from the dynamic simulation described, the OptiStruct solver on the HyperMesh platform is used to perform topology optimization on the swing arms for each axle.

Considering the interchangeability of the front and rear swing arm structures, the front and rear arm models are combined to improve computational efficiency. Based on the mounting positions of the swing arms, vehicle frame, wheels, and drive cylinder rods, the initial topology optimization models for the front/rear arm and the middle arm are established. The mounting positions of the swing arms on the frame, wheels, and drive cylinder rods are designated as non-design regions. This means that the material in non-design regions is kept fixed during the optimization process, while other regions are designated as design regions.

Fig. 6 shows the initial topology optimization model for the swing arm. Due to its symmetrical shape and relatively regular structure, a 4mm hexahedral element mesh is used for discretization. The parameters for the topology optimization model are listed in Table 4.

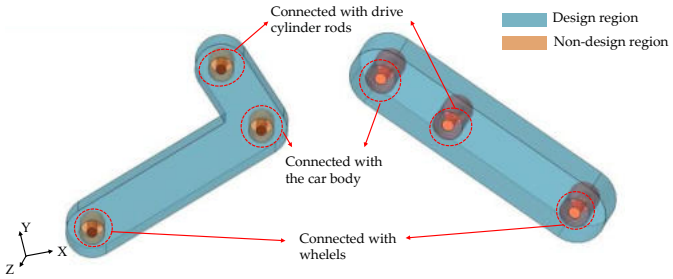


Fig. 6 - Initial topology optimization models for front/rear arm and middle arm

Table 4

Topology optimization model material parameters

Parameter	Value
Material	7A58AL
Density (kg/m^3)	2.78 × 10^3
Young's Modulus (MPa)	6.89 × 10^4
Poisson's Ratio	0.33
Shear modulus (MPa)	2.6 × 10^4
Yield Strength (MPa)	345

The initial topology optimization models for the front/rear arm and the middle arm are optimized individually under five different conditions. The optimal compliance values for the front/rear arm under each condition are denoted as $\alpha_1 = 118979Nmm, \alpha_2 = 361640Nmm, \alpha_3 = 421899Nmm, \alpha_4 = 1200140Nmm$ and $\alpha_5 = 368721Nmm$.

The optimal compliance values for the middle arm under each condition are denoted as $\beta_1 = 374471Nmm, \beta_2 = 1391650N \cdot mm, \beta_3 = 1043790N \cdot mm, \beta_4 = 1001620N \cdot mm$ and $\beta_5 = 2780710N \cdot mm$.

The α values are then used to construct the decision matrix for the topology optimization objective function for the front/rear swing arm.

$$M_1 = \begin{pmatrix} 1.00 & 0.33 & 0.28 & 0.10 & 0.32 \\ 3.04 & 1.00 & 0.86 & 0.30 & 0.98 \\ 3.55 & 1.17 & 1.00 & 0.35 & 1.14 \\ 10.09 & 3032 & 2.84 & 1.00 & 3.26 \\ 3.10 & 1.02 & 0.87 & 0.31 & 1.00 \end{pmatrix} \quad (3)$$

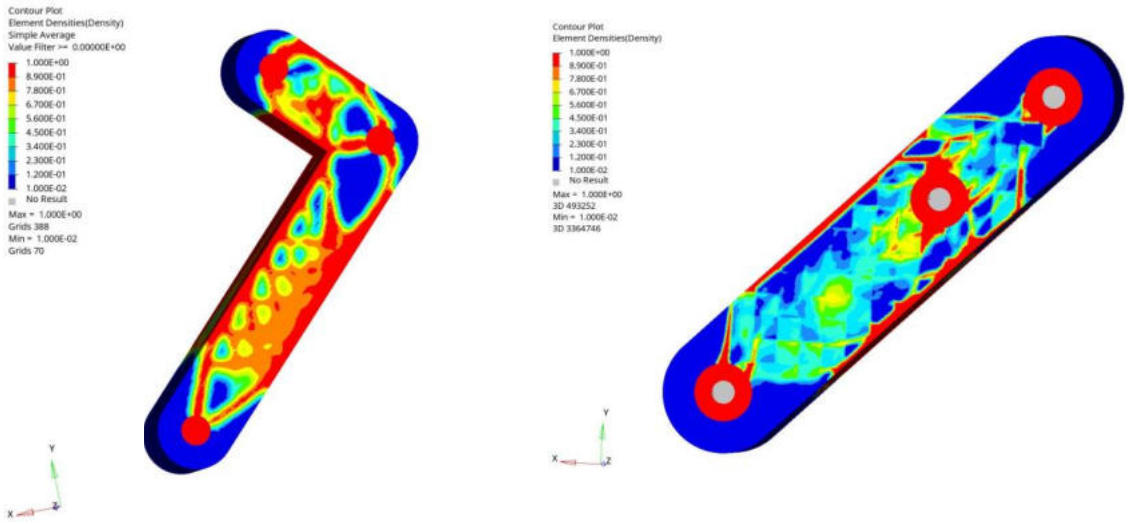
The maximum eigenvalue $\lambda_1 = 5$ of matrix M_1 is solved, and corresponding eigenvector $a_1 = [0.086\ 0.26\ 0.31\ 0.87\ 0.27]$ is obtained. By normalizing the eigenvector, the weight coefficients of the front/rear arm for the five conditions are determined as 0.048, 0.15, 0.17, 0.49, 0.15.

Then the β values are then used to construct the decision matrix for the topology optimization objective function for the middle swing arm.

$$M_1 = \begin{pmatrix} 1.00 & 0.27 & 0.36 & 0.37 & 0.14 \\ 3.72 & 1.00 & 1.33 & 1.39 & 0.50 \\ 2.79 & 0.75 & 1.00 & 1.04 & 0.38 \\ 3.68 & 0.72 & 0.96 & 1.00 & 3.26 \\ 7.43 & 2.00 & 2.67 & 2.78 & 1.00 \end{pmatrix} \quad (4)$$

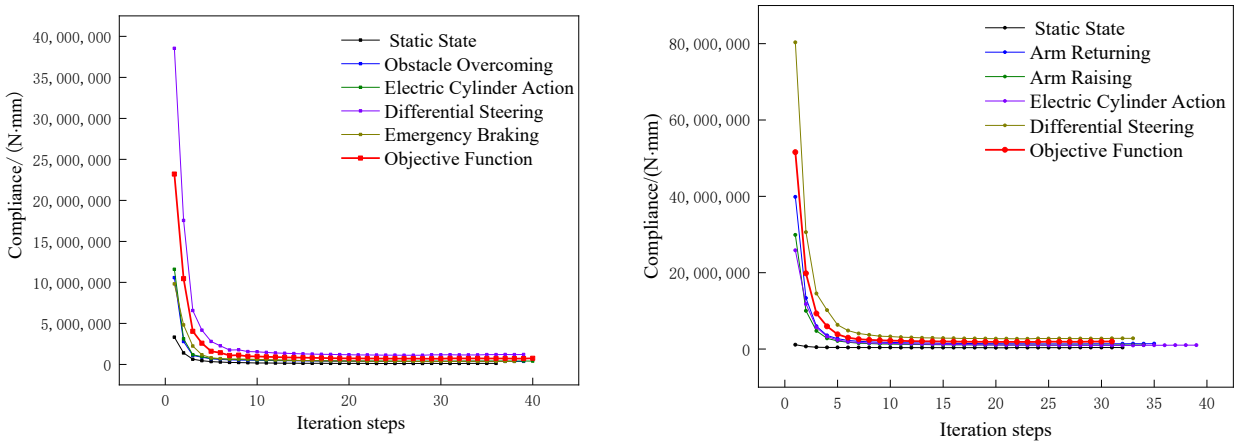
The maximum eigenvalue $\lambda_2 = 5$ of matrix M_2 is solved, and corresponding eigenvector $a_2 = [0.11\ 0.40\ 0.30\ 0.29\ 0.81]$ is obtained. By normalizing the eigenvector, the weight coefficients of the front/rear arm for the five conditions are determined as 0.06, 0.21, 0.16, 0.15, 0.42.

The mass fraction and weighted strain energy are defined as constraint conditions. The optimized mass of the front/rear swing arm is set to not exceed 30% of the initial model, and the optimized mass of the middle swing arm is set to not exceed 40% of the initial model. Additionally, the maximum stress is limited to 276 MPa, which is 80% of the yield strength of 7A58 aluminum. A symmetry constraint is also applied to the plane. The calculation is performed using the Optistruct solver, and after 40 iterations, the solution converges, yielding the topology optimization results as shown in Fig. 7. The iteration process of the objective function and compliance values under various conditions is shown in Fig. 8.



(**a**) (**b**)

Fig. 7 - Topology optimization results for swing arms
(a) Result for the front/rear arm; (b) Result for the middle arm.



(**a**) (**b**)

Fig. 8 - Objective function and compliance iteration process of each loading condition

(a) Compliance iteration process of the front/rear arm. (b) Compliance iteration process of the middle arm.

Based on the results of the swing arm multi-condition topology optimization, the swing arm structure is geometrically reconstructed. The reconstruction process is divided into the following three steps:

1. Retain the main structural features as much as possible to obtain the external shape of the structure;
2. Weight reduction is primarily applied to the outer sides of the front/rear arms, while retaining a solid structure in the middle. For the middle arm, additional cover plates are added to both outer sides to prevent foreign objects from getting trapped inside the arm during vehicle operation;
3. The middle swing arm should ensure sufficient strength at the middle and both ends where it connects to other structures.

The final geometric models of the swing arms for each axis are shown in Fig. 9.

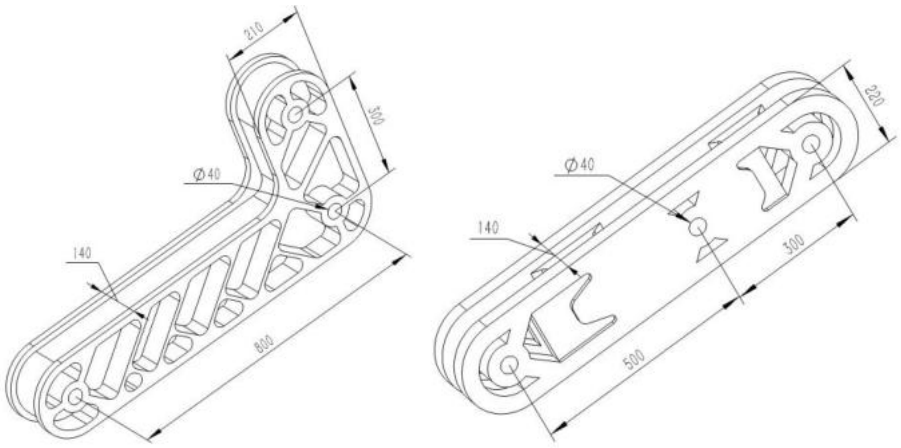


Fig. 9 - Reconstructed geometric models of the swing arms

Performance Verification of the Optimized Swing Arm Model

To verify whether the performance of the swing arms after topology optimization meets the requirements, a performance check is conducted on the optimized swing arm model. In HyperMesh software, a tetrahedral mesh with a size of 4 mm is used for discretization. Constraints are applied to the connection holes using RBE2 elements, and the load application positions are defined with RBE3 elements. The constraint conditions corresponding to the five scenarios are the same as those in Table 3 and the finite element model is illustrated in the Fig 10.

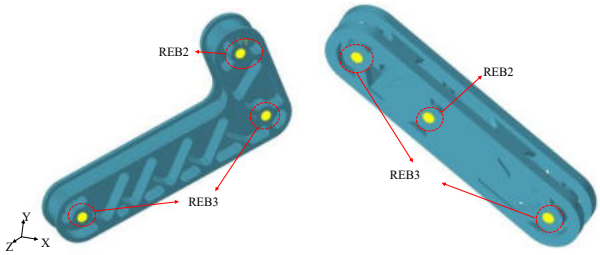


Fig. 10 - Finite element models of the swing arms

The calculations are performed using the OptiStruct solver, and stress contour maps for the swing arms under each condition are shown in Fig.11 and Fig.12. Table 4 summarizes the specific stress distribution.

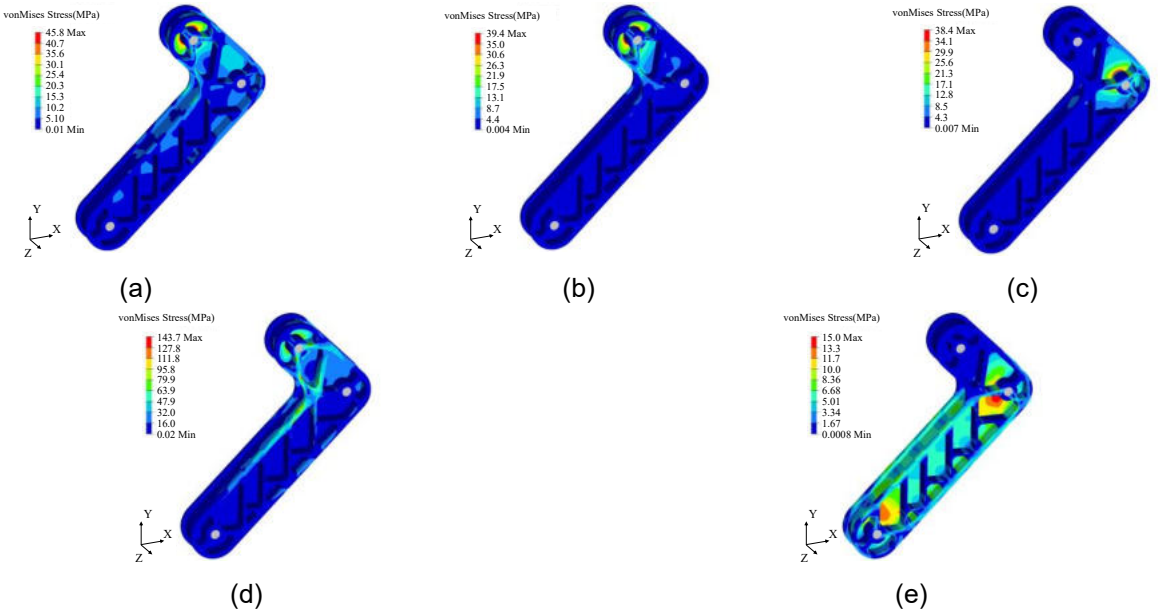


Fig. 11 - Stress contour map of the front/rear arm under five loading conditions

*(**a**) Static state loading condition; (**b**) Obstacle overcoming condition; (**c**) Electric cylinder action condition; (**d**) Differential steering condition; (**e**) Emergency braking condition.*

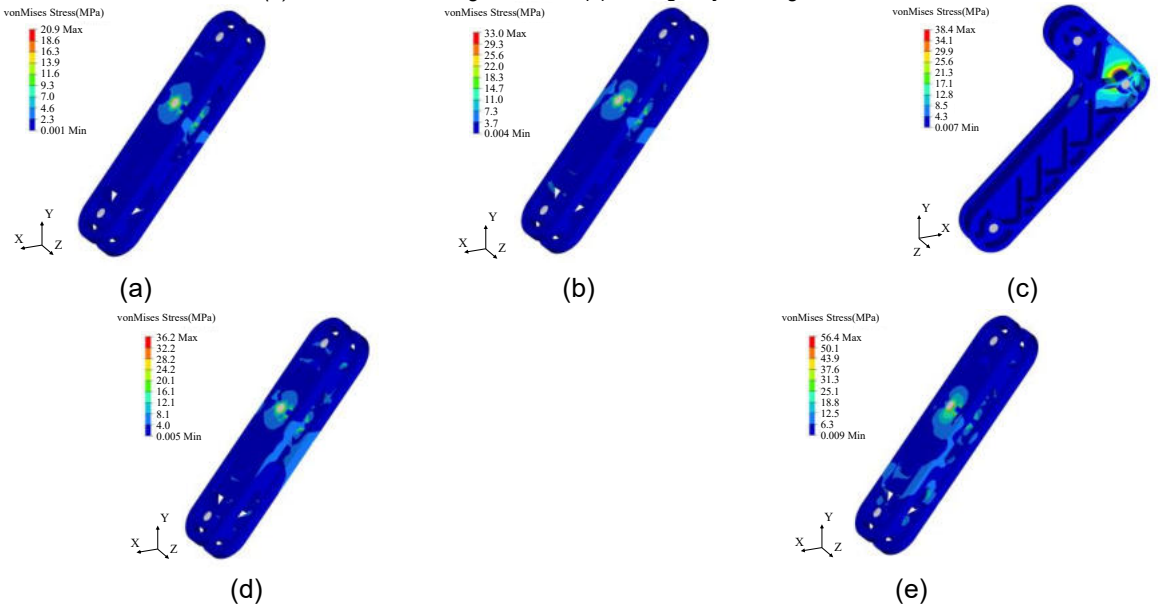


Fig. 12 - Stress contour map of the middle arm under five loading conditions

*(**a**) Static state loading condition; (**b**) Arm raised loading condition; (**c**) Electric cylinder action condition; (**d**) Arm returning condition; (**e**) Differential steering condition.*

Table 5

Maximum stress of the swing arms for each axle under five conditions

Condition	Maximum stress of the front/rear arm (MPa)	Maximum stress of the middle arm (MPa)
1	45.8	20.9
2	39.4	33.0
3	38.4	25.9
4	143.7	36.2
5	15.0	56.4

It is clearly shown in Table 5 that the maximum stresses for the two types of swing arms under five typical working conditions are 143.7 MPa and 56.41 MPa. These maximum stresses are mainly located at the connection points between the swing arms of each axle and the cylinder push rod under steering conditions, which account for 41.65% and 16.35% of the maximum allowable stress, respectively. Considering the possibility of extreme working conditions, the minimum safety factor of the swing arms is set around 2.4. Through finite element mesh calculations, the optimized weights are 31.3 kg for the front/rear swing arms and 39.44 kg for the middle swing arm. In comparison to the initial model weights of 44.12 kg and 49.47 kg for the swing arms, the weight reduction rates are 29.1% and 20.28%.

RESULTS

Experimental Verification and Results Analysis of the Aluminum Swing Arms Specimen

Due to the high manufacturing costs of the unmanned vehicle swing arms and frame, along with limitations in testing conditions, performing an aluminum alloy swing arm test that simulates real-world operational conditions is very challenging. Therefore, the tests in this paper, within the allowed conditions, include free vibration modal testing and static mechanical testing under bending conditions for each axle of the swing arm. While these tests cannot fully represent the actual working conditions of the swing arm, they provide valuable experimental data on the mechanical behavior and response of aluminum alloy swing arms. This data can be compared and evaluated against finite element analysis results to verify the accuracy of the finite element analysis and provide insights and directions for future research.

Modal Testing

Modal testing is a method used to determine the inherent characteristics of a vibrating system. The goal is to obtain the system's modal parameters, including natural frequency, damping ratio, vibration modes, and modal mass, all of which describe the intrinsic properties of the system in the frequency domain. Through vibration modal analysis, the natural vibration modes of the structure can be revealed, helping to identify potential vibration issues, fatigue life, and structural safety (*Qingge et al., 2025*). Additionally, vibration modal analysis serves as a basis for structural health monitoring, fault detection, and prediction (*Zou et al., 2023*).

In the vibration modal test of the swing arm, the DH5922N dynamic signal testing system is used for precise measurement and analysis. This system can accurately record and analyze the vibration response of the swing arm under hammer impact excitation. By applying impact excitation at different positions and recording the corresponding vibration signals, the vibration modes of the swing arm at different frequencies can be obtained. These vibration modes include the natural frequencies and vibration shapes of free vibrations, revealing the structural characteristics and vibration behavior of the swing arm.

Before the test begins, as shown in Fig 13 above, elastic cords are tied to both ends of the swing arm and suspended from a load-bearing frame, allowing the swing arm to be in a free-floating state to ensure its free modal condition.

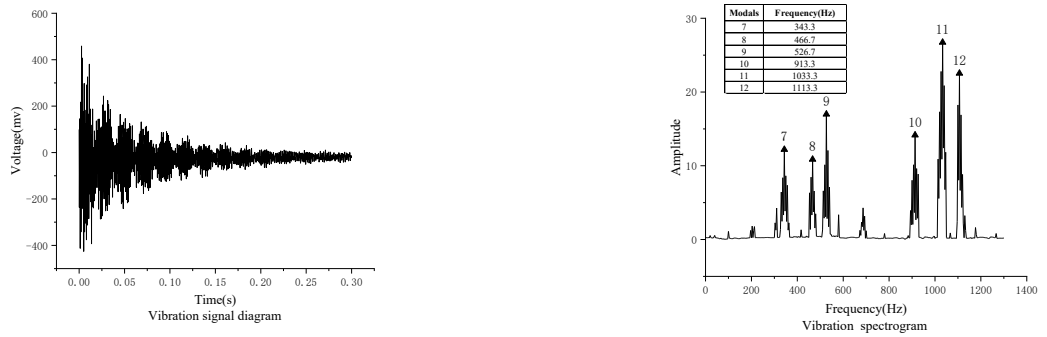


(**a**) (**b**) (**c**)

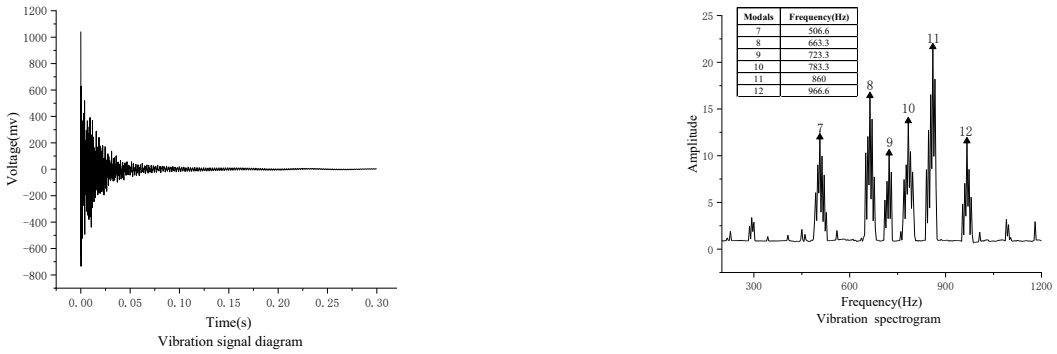
Fig. 13 - Modal test photographs

(a) Test for front/rear arm; (b) Test for middle arm; (c) DH5922N Dynamic Signal Testing and Analysis System.

It is important to ensure that the distance between the swing points of the swing arm and the elastic cords is sufficiently large to reduce the impact of the increased stiffness caused by tightening the elastic cords, thus improving the accuracy of the test results. The DH5922N system establishes a connection with the swing arm through a piezoelectric velocity sensor. A force hammer is used to strike the swing arm to induce vibration and excite its natural frequency. Through the system's data acquisition function, the time-domain signal of the swing arm's vibration is recorded in real time. A Fast Fourier Transform (FFT) is then performed to convert the time-domain signal into a frequency-domain signal (*Chen & Li, 2019*), from which the peak values of the frequency-domain signal are extracted, representing the natural frequencies of the swing arm, as shown in Fig.14.



(**a**)



(**b**)

Fig. 14 - Modal test results of each axle swing arm

(a) Front/rear arm; (b) Middle arm.

After the test, a finite element model of the swing arm specimen was established, and a 12-order vibration modal analysis was conducted. Since the first six modes are rigid body vibration modes, only the 7th to 12th modes are shown. The vibration mod-al frequencies obtained from the test were compared with the finite element simulation results under the same test conditions, and the specific results are shown in Table 6.

The results indicate that the relative error between the two for each mode is less than 10%, demonstrating that the modal analysis process of the finite element model closely fits the actual test data.

Table 6

Maximum stress of the swing arms for each axle under five conditions

Modals	Front/Rear Arm			Middle Arm		
	Calculated Frequency (Hz)	Experimental Frequency (Hz)	Relative Error	Calculated Frequency (Hz)	Experimental Frequency (Hz)	Relative Error
7	344.7	343.3	0.41%	508.4	506.6	0.35%
8	459.3	466.7	-1.61%	730.6	663.3	9.21%
9	513.1	526.7	-2.65%	732.0	723.3	1.19%
10	973.1	913.3	6.15%	864.1	783.3	9.35%
11	1040.6	1033.3	0.70%	887.6	860	3.11%
12	1055.1	1113.3	-5.52%	895.9	966.6	-7.89%

The modal analysis results show that the 7th vibration mode frequencies of the swing arms for each axle are 344.7 Hz and 508.4 Hz, respectively. Under normal conditions, the road surface excitation frequency is typically up to 28 Hz, while the hub motor excitation frequency ranges from 50-60 Hz (*Zhang et al., 2019*). Since the natural frequencies of the swing arms are much higher than the upper limit of their excitation frequencies, it can be confirmed that resonance will not occur between the two.

Static Testing

Due to testing constraints, it was not possible to simulate the actual motion conditions of the swing arms. Therefore, a simple bending condition was designed, where the upper end of the swing arm is fixed, and a load is applied at the lower end. This condition has simple boundary constraints, making the experiment easier to control and measure, which improves the repeatability and accuracy of the test, thereby better verifying the rationality of the finite element analysis. The strain of the specimen under static load conditions is precisely measured using the resistance method.

After establishing the finite element model for the swing arm, strain gauges were applied at the locations where stress verification was required, based on the stress contour maps. On the test bench, the swing arm specimen's top and middle were fixed by locking the angle of the electric cylinder and the cylinder rod length, while the load was applied at the bottom of the specimen using standard weight blocks, simulating the constraints and loads from the static analysis. The specific locations for strain gauge application, fixation, and loading are shown in Fig. 15 and Fig. 16.

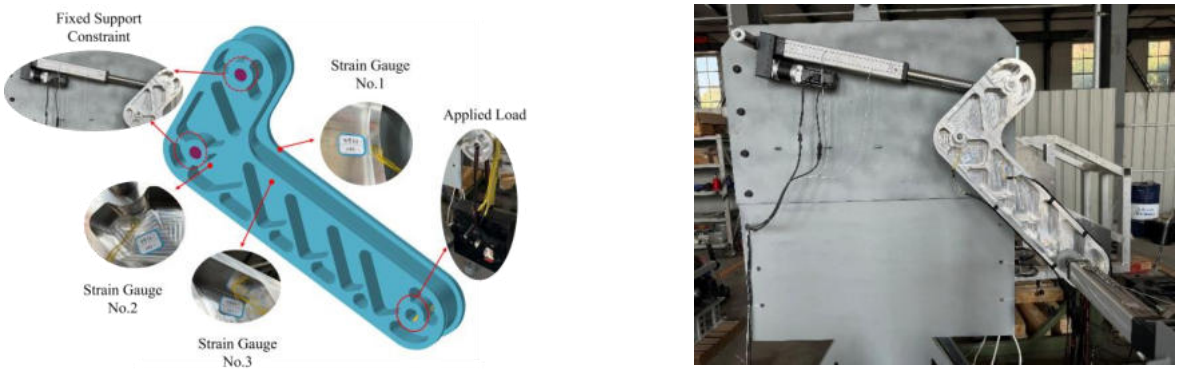
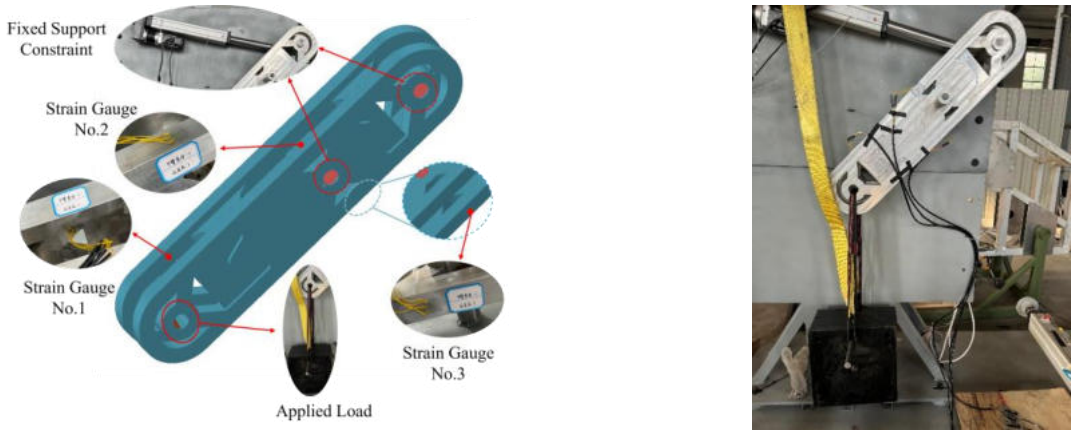


Fig. 15. Static test of front/rear arm specimen

(a) Strain gauges placement locations for swing arm specimen stress test; (b) Static test photograph.



(a) **(b)**

Fig. 16 - Static test of middle arm specimen

*(**a**) Strain gauges placement locations for swing arm specimen stress test; (**b**) Static test photograph.*

Strain gauges at each measurement location were connected to the DH5922N system via a strain indicator, measuring the strain in three directions: $\varepsilon_{0°}$, $\varepsilon_{45°}$ and $\varepsilon_{90°}$. To minimize errors, the specimen underwent three test trials. After the tests, the measured strain values were exported and substituted into the following formula to calculate the von Mises stress for each strain gauge location (*Chen et al., 2025*).

$$\sigma = \frac{E(\varepsilon_{0°} - \varepsilon_{90°})}{2(1-\mu)} + \frac{\sqrt{(\varepsilon_{0°} - \varepsilon_{45°})^2 + 2(\varepsilon_{45°} - \varepsilon_{90°})^2}}{\sqrt{2}(1+\mu)} \quad (5)$$

The von Mises stress results from the finite element model at corresponding locations in HyperView were compared with the experimental data, as shown in Table 7.

Table 7

Comparison of static test results for each axle swing arm specimen

Arm Specimen	Strain Gauge Number	Applied load (N)	Calculated Stress (MPa)	Experimental Stress (MPa)	Relative Error
Front/Rear	1-1	1500	5.64	5.38	-4.61%
Front/Rear	1-2	1500	3.42	3.23	-5.56%
Front/Rear	1-3	1500	4.25	4.03	-5.18%
Front/Rear	2-1	2500	9.39	9.55	1.70%
Front/Rear	2-2	2500	5.7	6.11	7.19%
Front/Rear	2-3	2500	7.08	7.35	3.81%
Middle	1-1	1500	1.06	1.02	-3.77%
Middle	1-2	1500	0.91	0.95	4.40%
Middle	1-3	1500	0.84	0.81	-3.57%
Middle	2-1	2500	1.67	1.61	-3.59%
Middle	2-2	2500	1.52	1.59	4.61%
Middle	2-3	2500	1.41	1.51	7.09%

The test results show that the maximum relative error between the stress calculated by finite element analysis and the test stress is 7.19%, indicating that the accuracy of the static analysis process in the finite element model is relatively high.

CONCLUSIONS

This paper presents the design of a tri-axle unmanned vehicle with a swing arm and wheel-leg hybrid configuration, optimized for excellent obstacle-crossing performance under forestry production site conditions. After conducting dynamic simulations to obtain the different loading conditions for the swing arms, optimization was per-formed. Using the Analytic Hierarchy Process (AHP), the five typical loading conditions of the swing arms were weighted and analyzed. The swing arms were then subjected to multi-condition topology optimization and lightweight design using the Hypermesh-Optistruct software. The optimized mass of the front/rear swing arms and the middle swing arm are 31.3 kg and 39.44 kg, respectively, with weight reduction rates of 29.1% and 20.27%, meeting the lightweight requirements.

Static and vibration modal tests were conducted on the processed swing arm specimens, verifying the effectiveness and accuracy of the finite element analysis. The relevant conclusions of this study provide valuable references for the topology optimization and lightweight design of the continuous body structure of forestry unmanned vehicles.

ACKNOWLEDGEMENT

The authors were funded for this project by the National Natural Science Foundation of China (NSFC) (No.51475255).

REFERENCES

[1] Bai, H., Xing, P.-f., & Wu, M.-w. (2024). Research on Topology Optimization and Lightweight Design of Continuum Structures under Multiple Serving Conditions (连续体结构多工况拓扑优化与轻量化设计研究). *Tractor & Farm Transporter*, *51*(2), 76-83.

[2] Chen, G., & Li, X. (2019). Modal analysis on the linear module with ball screw (滚珠丝杠直线模组的模态分析). *Journal of Machine Design*, *36*(03), 56-61. https://doi.org/10.13841/j.cnki.jxsj.2019.03.010

[3] Chen, Q., Zhao, Y., Wang, D., Chen, Z., Wang, Q., & Yuan, X. (2025). Multi-Level Matching Optimization Design of Thin-Walled Beam Cross-Section for Tri-Axle Unmanned Forestry Vehicle Frame. *Forests*, *16*(1), 69. https://doi.org/10.3390/f16010069

[4] Chen, Y., Zhu, J., Yao, L., Yang, Z., Hu, Z., Xu, L., & Yao, L. (2024). Analysis and Optimization of Driving Performance for Tree Transplanting Machine in Hilly Mountainous Areas. *Forests*, *15*(12). https://doi.org/10.3390/f15122128

[5] Chenwei, H., Jiayu, C., Yu, C., & Liquan, L. (2023). Design and Analysis of Independent Strut Type Air Suspension Applied to High Clearance Self-Propelled Sprayer (应用于高地隙自走式喷雾机的独立式立轴空气悬架设计与分析). *INMATEH-Agricultural Engineering*, *71*(3). https://doi.org/10.35633/inmateh-71-04

[6] Guo-fei, Y., Hai-bing, W., Fei, H., & Zhong-wu, W. (2018). Topology Optimization Design with the Globalization of Stress Constrains and Analytic Hierarchy Process (结合应力全局化与层次分析的拓扑优化设计). *Machinery Design & Manufacture*(06), 200-202+206. https://doi.org/10.19356/j.cnki.1001-3997.2018.06.053

[7] Huaitang, Z., Zilong, D., Tiemin, G., & Yan, H. (2024). Dynamics Simulation Analysis on Configuration Change of Metamorphic Lifting Mechanism Based on ADAMS(基于 ADAMS 变胞升降机构构态变换动力学仿真分析). *Journal of Liaoning University of Petroleum & Chemical Technology*, *44*(4), 60. https://doi.org/10.12422/j.issn.1672-6952.2024.04.008

[8] Huang, Y., Peng, W., Li, H., Lin, L., Shao, Y., & Shen, H. (2025). Finite Element Analysis of Structural Strength of Complex Aluminum Alloy Knuckle Under Multiple Working Conditions and Load Channels (多载荷通道复杂铝合金转向节的多工况结构强度有限元分析). *Mechanical Science and Technology for Aerospace Engineering*, *44*(5), 857-867. https://doi.org/10.13433/j.cnki.1003-8728.20230230

[9] Jing-liang, W., Tian-cheng, Z., Long-biao, Z., & Fei-yun, X. (2022). Research on variable density topology optimization method for continuum structure (连续体结构的变密度拓扑优化方法研究). *Chinese Journal of Engineering Design*, *29*(3), 279-285. https://doi.org/https://doi.org/10.3785/j.issn.1006-754X.2022.00.039

[10] Kayet, N., Chakrabarty, A., Pathak, K., Sahoo, S., Dutta, T., & Hatai, B. K. (2020). Comparative analysis of multi-criteria probabilistic FR and AHP models for forest fire risk (FFR) mapping in Melghat Tiger Reserve (MTR) forest. *Journal of forestry research*, *31*(2), 565-579. https://doi.org/10.1007/s11676-018-0826-z

[11] Kešner, A., Chotěborský, R., Linda, M., Hromasová, M., Katinas, E., & Sutanto, H. (2021). Stress distribution on a soil tillage machine frame segment with a chisel shank simulated using discrete element and finite element methods and validate by experiment. *Biosystems Engineering*, *209*, 125-138. https://doi.org/10.1016/j.biosystemseng.2021.06.012

[12] Li, Y., Chang, T., Kong, W., Wu, F., & Kong, X. (2023). Topological Optimization of Bi-Directional Progressive Structures with Dynamic Stress Constraints under Aperiodic Load. *Applied Sciences*, *14*(1), 322. https://doi.org/10.3390/app14010322

[13] Liu, L. (2020). Design and servo characteristics of two-dimensional turntable(二维转台设计和伺服特性研究) [masters, Chengdu University of Technology]. https://doi.org/10.26986/d.cnki.gcdlc.2020.000529

[14] Meng, Z., Pang, Y., Pu, Y., & Wang, X. (2020). New hybrid reliability-based topology optimization method combining fuzzy and probabilistic models for handling epistemic and aleatory uncertainties. *Computer Methods in Applied Mechanics and Engineering*, *363*, 112886. https://doi.org/10.1016/j.cma.2020.112886

[15] Mergl, V., & Kašpárek, J. (2022). Verifying the Lifting and Slewing Dynamics of a Harvester Crane with Possible Levelling When Operating on Sloping Grounds. *Forests*, *13*(2). https://doi.org/10.3390/f13020357

[16] Niu, Z., Xu, Z., Deng, J., Zhang, J., Pan, S., & Mu, H. (2022). Optimal vibration parameters for olive harvesting from finite element analysis and vibration tests. *Biosystems Engineering*, *215*, 228-238. https://doi.org/10.1016/j.biosystemseng.2022.01.002

[17] Padhi, A. P., Chakraborty, S., Chakrabarti, A., & Chowdhury, R. (2024). Deep learning accelerated efficient framework for topology optimization. *Engineering Applications of Artificial Intelligence*, *133*, 108559. https://doi.org/10.1016/j.engappai.2024.108559

[18] Qiang, G., Jian, W., Yan, Z., Xuyang, Z., LÜ Hao, & Guodong, Y. (2024). Topology Optimization Approaches and Its Application and Prospect in Transportation Engineering (拓扑优化方法及其在运载工程中的应用与展望). *Journal of Mechanical Engineering*, *60*(4), 369-390. https://doi.org/10.3901/jme.2024.04.369

[19] Qingge, L., Haitao, L., Fengxia, H., Yuxin, L., & Yanbin, L. (2025). Model test and dynamic similarity study of large space truss structure (空间大型桁架结构模型试验与动力相似研究). *Manufacturing Technology & Machine Tool,* (01), 33-40. https://doi.org/10.19287/j.mtmt.1005-2402.2025.01.005

[20] Qiu, C., Du, S., & Yang, J. (2021). A deep learning approach for efficient topology optimization based on the element removal strategy. *Materials & Design*, *212*, 110179. https://doi.org/10.1016/j.matdes.2021.110179

[21] Sun, S., Zhang, S., Li, Y., Wu, J., & Chu, J. (2019). Studies of several large-scale forestry operating vehicles at home and abroad and prospect of vehicle type design(国内外林区几种大型作业车辆研究进展及车型设计展望). *Journal of Beijing Forestry University*, *41*(6), 154-166. https://doi.org/10.13332/j.1000-1522.20190048

[22] Tan, L., Cheng, B., Jia, D., & Gao, D.-w. (2022). Topology Optimization Design of an Aeroengine Bracket under Multiple Load Cases (多工况下的发动机支架拓扑优化设计). *Aeroengine*(2), 90-95. https://doi.org/10.13477/j.cnki.aeroengine.2022.02.013

[23] Wang, C., Li, M., Cheng, A., He, Z., & Yu, W. (2024). Lightweight Design of Material-Structure for Steel-Aluminum Hybrid Cab (钢-铝混合驾驶室材料-结构轻量化设计). *Automotive Engineering*, *46*(4), 735-744. https://doi.org/10.19562/j.chinasae.qcgc.2024.04.019

[24] Wang, X., Liu, H., Kang, Z., Long, K., & Meng, Z. (2021). Topology optimization for minimum stress design with embedded movable holes. *Computers & structures*, *244*, 106455. https://doi.org/10.1016/j.compstruc.2020.106455

[25] Wang, Y., Tan, X., Ban, X., Li, D., & Yue, S. (2024). Research on a wheel-legged obstacle-crossing robot (一种轮腿式越障机器人的研究) [J]. *Journal of Mechanical Transmission*, *48*(01), 128-134. https://doi.org/10.16578/j.issn.1004.2539.2024.01.019

[26] Wentao, X., Lei, H., Yanhua, M., Tao, L., & Wen, L. (2025). Design and Experimental Study of a High Ground Clearance Weeding Robot Chassis (高地隙跨垄除草机器人底盘设计与试验). *INMATEH-Agricultural Engineering*, *75*(1). https://doi.org/https://doi.org/10.35633/inmateh-75-93

[27] Xia, H., & Qiu, Z. (2022). An efficient sequential strategy for non-probabilistic reliability-based topology optimization (NRBTO) of continuum structures with stress constraints. *Applied Mathematical Modelling*, *110*, 723-747. https://doi.org/10.1016/j.apm.2022.06.021

[28] Xiaokai, C., Chao, L., Yingchun, B., & Zifa, Y. (2021). Multi-material Topology Optimization of Automotive Control Arm(汽车多材料控制臂拓扑优化方法). *Automotive Engineering 43*(07), 1088-1095. https://doi.org/10.19562/j.chinasae.qcgc.2021.07.016

[29] Xiong, F., Wang, D., Ma, Z., Chen, S., Lv, T., & Lu, F. (2018). Structure-material integrated multi-objective lightweight design of the front end structure of automobile body. *Structural and Multidisciplinary Optimization*, *57*(2), 829-847. https://doi.org/10.1007/s00158-017-1778-1

[30] Zhang, J., Chen, K., & Dai, Y. (2019). Design and Modal Analysis of Electric Vehicle Frame for Modern Agricultural Manor (面向现代农业庄园的电动车车架设计及模态分析). *Journal of Chinese Agricultural Mechanization*, *40*(2), 109-112. https://doi.org/10.13733/j.jcam.issn.2095-5553.2019.02.17

[31] Zhang, K., LI, S., & Sun, M. (2020). Lightweight optimization design of commercial vehicle frames combined by steel and aluminum materials under multiple working conditions (钢铝材料结合的商用车车架多工况轻量化优化设计). *China Mechanical Engineering*, *31*(18), 2206.

[32] Zhao, X., Zhao, J., Zhao, J., Ma, Z., Li, J., Dai, B., An, M., Wang, J., & Hao, J. (2025). Optimisation design and experimental analysis of rotary blade reinforcing ribs using DEM-FEM techniques. *Biosystems Engineering*, *249*, 1-17. https://doi.org/10.1016/j.biosystemseng.2024.11.015

[33] Zou, X., Gou, L., Fu, L., Jiang, H., & Liu, L. (2023). Finite Element Analysis and Lightweight Design of the Lower Control Arm for All-Terrain Vehicle Suspension (全域车悬架下控制臂有限元分析及轻量化设计). *Journal of Highway and Transportation Research and Development*, *40*(12), 227-235. https://doi.org/10.3969/j.issn.1002-0268.2023.12.026

DESIGN AND EXPERIMENT OF A BUILT-IN SCREEN-TYPE CYCLONE SEPARATION CLEANING SYSTEM FOR A SMALL-SCALE WHEAT COMBINE HARVESTER

/

小型小麦联合收获机内置筛网式旋风分离清选系统设计与试验

Yangang LI [1)], Xiaoyu CHAI [1)], Jinpeng HU [1)], Zhiqiang SONG [1)], Yuzhe WANG [1)], Lizhang XU [1,*)]

[1)] College of Agricultural Engineering, Jiangsu University, Zhenjiang 212013, China

**Corresponding author's Email: justxlz@ujs.edu.cn*

DOI: https://doi.org/10.35633/inmateh-76-92

Keywords: *Small Combine Harvester; Wheat; Cleaning System; Screen; CFD-DEM*

ABSTRACT

To address the issues of high grain impurity rate and low cleaning efficiency in the cyclone separation cleaning system of small wheat combines harvesters in hilly and mountainous areas, this study proposes an internally screened cyclone separation cleaning system. Using the CFD-DEM coupled simulation method, the effect of the screen structure on the motion trajectory and separation behavior of the threshed material was systematically analyzed. A response surface methodology was applied to analyze the impact of interaction factors on cleaning performance. The optimal working parameters were determined to be: fan speed of 4020 r/min, scraper shaft speed of 340 r/min, clearance between the screen and the chamber wall of 37 mm, and mesh size of 29 mm. Under these parameters, the simulation results showed a grain impurity rate of 2.99% and a cleaning loss rate of 1.10%, while the field experiment results were 3.08% and 1.14%, respectively. The field experiment results indicate that the designed cleaning system improved the cleaning performance and operational efficiency of the small combine harvester, providing both theoretical support and engineering guidance for the optimized design of cleaning system in small combine harvesters for hilly regions.

摘要

针对丘陵山区小型联合收获机旋风分离清选系统小麦清选时籽粒含杂率高、清选效率低等问题，本文提出一种内置筛网式旋风分离清选系统。采用 CFD-DEM 耦合仿真方法，系统分析筛网结构对脱出物运动轨迹及分离规律的影响。并采用响应面试验方法，分析了各交互因素对清选性能的影响，得出优化工作参数组合为：风机转速 4020 r/min、刮板转轴转速 340 r/min、筛网到筒壁间隙 37 mm、网格间距 29 mm。在此参数组合下，仿真结果显示籽粒含杂率为 2.99%，清选损失率为 1.10%；田间试验为籽粒含杂率 3.08%，清选损失率 1.14%。田间试验结果表明，所设计清选系统提高了小型联合收获机的清选性能与作业效率，为丘陵山区小型联合收获机清选系统的优化设计提供了理论依据与工程指导。

INTRODUCTION

Hilly and mountainous areas are important regions for the production of grains and specialty agricultural products in China, with the arable land in these areas accounting for 34.62% of the total arable land in the country. However, due to the terrain constraints, the promotion and application of large combine harvesters in these areas face significant challenges *(Mandler et al., 2025)*. Small combine harvesters (with a feeding rate of less than 1.5 kg/s) have become one of the main pieces of equipment in hilly and mountainous areas, thanks to their compact structure and flexible operation. Among these, the cleaning system, as a key component of the harvester, directly affects the overall performance of the machine *(Ding et al., 2022)*. Small combine harvesters generally use cyclone separation cleaning systems *(Wan et al., 2018)*, which rely solely on airflow to separate grains from impurities. When the proportion of impurities in the discharged material, such as wheat, is high, these systems often face issues such as high impurity rates and low cleaning efficiency, limiting the overall machine performance and requiring targeted optimization.

Yangang Li, Student; Xiaoyu Chai, Lecturer; Jinpeng Hu, Student; Zhiqiang Song, Lecturer; Yuzhe Wang, Student; Lizhang Xu, Professor.

For air-sieve cleaning system *Mirzazadeh et al, (2022)* used response surface methodology to optimize the mathematical model of feed rate, fan speed, and sieve opening. *Lovchikov and Ognev (2022)* analyzed the impact of screen type and airflow velocity on cleaning efficiency, providing theoretical support for the optimization of cleaning systems. *Badretdinov et al. (2022)* used mathematical modeling to analyze the impact of uneven airflow distribution on cleaning performance and proposed an improvement plan. For the cyclone separation cleaning device of small combine harvesters, *Liu et al. (2015)* designed an airflow-based cleaning device for wheat harvesting, but field tests could only meet the feeding rate requirement below 0.5 kg/s. *Bizuneh and Abate (2024)* studied the performance of cyclone separators for peas and lentils, analyzing their efficiency in impurity separation and cleaning. *Shi et al. (2022)* proposed a compound cleaning system and optimized the internal flow field for flax harvesting in hilly terrain. *Shu et al. (2024)* improved cyclone cleaning systems with airflow feeding for rapeseed harvesting. These studies indicate that air-sieve cleaning systems are well-developed and have good cleaning performance, but the large size and complex structure of such systems make them difficult to apply in small combine harvesters with limited space. Small combine harvesters generally use blower or pneumatic conveying combined with cyclone separation, which can only meet the feeding rate requirements below 0.5 kg/s when processing high-impurity crops. Although compound cleaning systems have improved efficiency, their complex structure still limits their widespread application in small machines.

In summary, this study proposes an internally screened cyclone separation cleaning system. The system ensures stable and orderly material feeding through the scraper conveyor and optimizes the separation path of impurities by combining the synergistic effect of the screen and airflow. Using CFD-DEM coupled simulations, the impact of the screen structure on the motion trajectory and separation behavior of the threshed material was analyzed. The optimal parameter combination for the cleaning system was determined through response surface methodology, and its performance was verified through field experiments. This study provides theoretical support and engineering guidance for the optimized design of cleaning systems for small combine harvesters in hilly and mountainous areas.

MATERIALS AND METHODS

Overall Structure and Working Principle

The overall structure of combine harvester

This study focuses on the 4LZ-1.0LC combine harvester, which is equipped with a KD1100FB4-2 National IV diesel engine. The harvester primarily consists of a double-layer cutting and feeding system, a conveying system, a threshing system, a cleaning system, a power drive system, a crawler walking system, and a hydraulic control system. The main structure is shown in Fig. 1, and the key technical specifications are listed in Table 1.

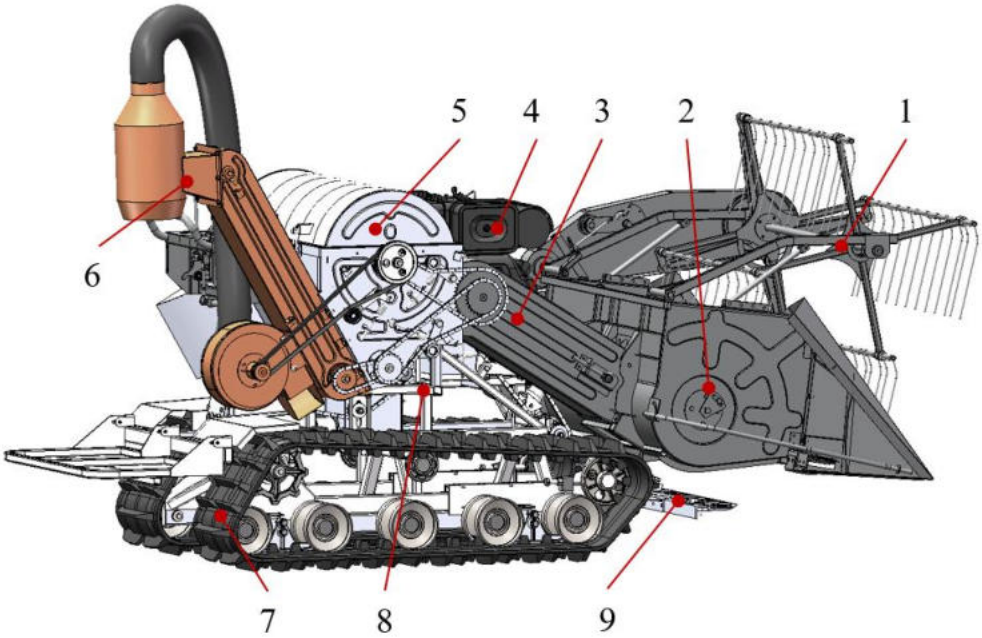


Fig. 1 - Schematic diagram of the structure of small wheat combine harvester
1 - Reel; 2 – Header; 3 - Spiral conveyor; 4 – Engine; 5 - Threshing system; 6 - Cleaning system; 7 - Crawler track; 8 - Chassis frame; 9 - Lower cutter

Table 1

Main parameters of combine harvester

Item	Parameter
Structure Type	Full-feed, crawler-type
Engine Power/kW	9.8
Dimensions (L×W×H)/mm	3100×1500×1700
Total Weight/kg	645
Cutting Platform Clearance/mm	1200
Rated Feeding Amount/(kg/s)	1.0
Operating Speed/(m/s)	0.4~1.2
Production Efficiency/(hm^2/h)	≥0.06

Structure and working principle of the cleaning system

To address the poor cleaning performance of conventional airflow-based cleaning systems when processing discharged material with a high proportion of impurities, this study proposes an internally screened cyclone separation cleaning system. As shown in Fig. 2, the system mainly consists of a scraper conveyor, a separation chamber, a screen, and a centrifugal impurity-extraction fan. During operation, the threshed wheat mixture is uniformly fed into the separation chamber at a constant speed under the action of the scraper conveyor. Light impurities are directly carried out of the chamber by the high-speed airflow. Stalks and other heavier impurities are constrained by the screen and lifted upward by the continuous airflow before being discharged. In contrast, the grains pass through the screen and fall along the chamber wall to the grain outlet, thereby achieving effective separation of grains and impurities.

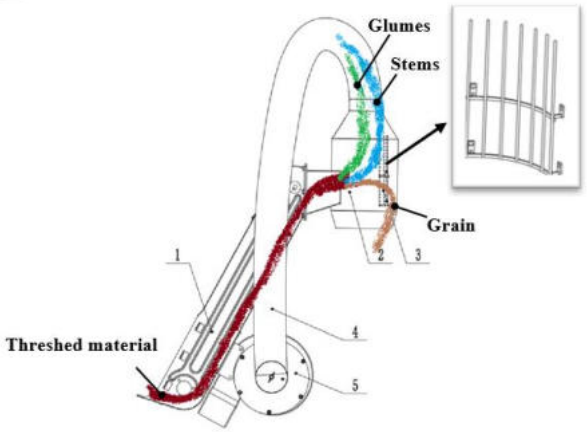


Fig. 2 - Cleaning system structure and working principle diagram

1 - Scraper conveying; 2 - Separation cylinder; 3 – Screen; 4 - Suction pipe; 5 - Suction centrifugal fan

Dynamic and kinematic analysis of threshed material

As shown in Fig. 3, the airflow in the separation chamber flows upward, with higher airflow velocities in the upper and lower conical sections and lower velocities near the chamber walls.

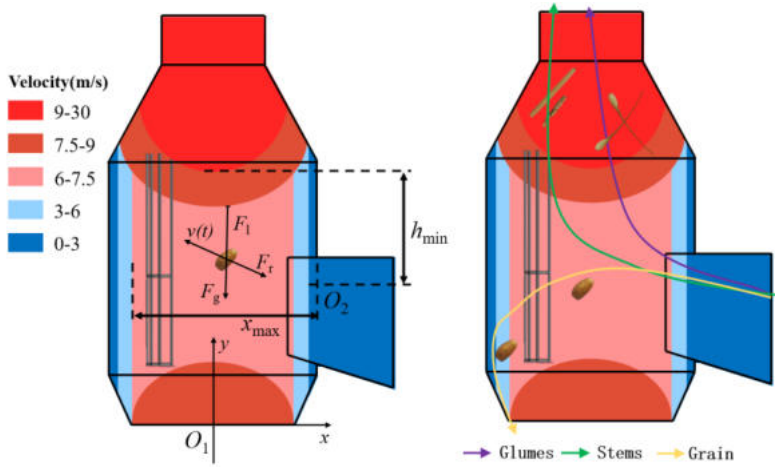


Fig. 3 - Schematic diagram of the force and motion analysis of the threshed material

When the threshed material is conveyed into the separation chamber at a certain speed by the scraper, the forces acting on it can be expressed as follows:

$$\begin{cases} F_r = -kv(t) \\ F_l = kv_{air}(x(t), y(t)) \\ F_g = -mg \end{cases} \quad (1)$$

In the equation, F_r represents the aerodynamic drag force, N; F_l represents the lift force generated by the airflow, N; F_g represents the gravitational force, N; k represents the aerodynamic drag coefficient; m is the mass of the threshed material, kg; g is the gravitational acceleration, 9.81 m/s².

The motion velocity of the threshed material can be expressed as:

$$\begin{cases} m\dfrac{dv_x}{dt} = -k\left(v_x(t) - u(x(t), y(t))\right) \\ m\dfrac{dv_y}{dt} = -k\left(v_y(t) - v(x(t), y(t))\right) - mg \end{cases} \quad (2)$$

The displacement expression can be obtained by integrating the velocity:

$$\begin{cases} x(t) = x_0 + \int_0^t v_x(\tau)d\tau \\ y(t) = y_0 + \int_0^t v_y(\tau)d\tau \end{cases} \quad (3)$$

To achieve effective separation of impurities from the threshed material, the impurities must reach the high-speed airflow region in the upper conical section before entering the low-speed airflow region on the left side. Therefore, their motion trajectory must satisfy the following conditions:

$$\begin{cases} |x(t_f) - x_0| < x_{max} \\ y(t_f) - y_0 \geq h_{min} \end{cases} \quad (4)$$

In the equation, x_{max} represents the maximum horizontal displacement of the impurities, m; h_{min} represents the minimum vertical displacement of the impurities, m.

By combining the above velocity and motion equations, the integral expression for the motion of the threshed material is obtained as follows:

$$\begin{cases} \left| \int_0^{t_f} \left[v_{x0} + \int_0^{\tau} \left(-\dfrac{k}{m}(v_x(s) - u(x(s), y(s))) \right) ds \right] d\tau \right| < x_{max} \\ \int_0^{t_f} \left[v_{y0} + \int_0^{\tau} \left(-\dfrac{k}{m}(v_y(s) - v(x(s), y(s))) - g \right) ds \right] d\tau \geq h_{min} \end{cases} \quad (5)$$

After adding a properly sized screen to the separation chamber, the screen blocks the horizontal movement of impurities. At this point, the forces and displacement of the impurities are expressed as follows:

$$\begin{cases} \dot{F_l} = k_l(t)\dot{v}_{air}(x(t), y(t)) \\ \dot{F_g} = -mg\dot{j} \end{cases} \qquad \begin{cases} x(t) = 0 \\ y(t) = y_{t_0} + \int_{t_0}^{t} v_y(\tau)d\tau \end{cases} \quad (6)$$

In the equation, t_0 represents the time taken for the impurities to reach the screen, *s*.

The above analysis indicates that the motion trajectory of the threshed material in the airflow field is jointly influenced by its physical properties, the airflow distribution, and its initial velocity and position. By installing a screen in the separation chamber, the horizontal displacement of impurities is restricted while being expelled upward under the action of high-speed airflow, thereby improving separation efficiency.

Design of Key Components

Separation chamber

As shown in Fig. 4, the performance of the separation chamber is primarily determined by the airflow rate and the diameter of the separation chamber. The required airflow rate for cleaning, Q, is given by the equation 7 *(Geng et al., 2011; Zhao et al., 2024)*:

$$Q = \frac{\gamma q}{\mu \rho} \quad (7)$$

In the equation, γ represents the proportion of impurities in the total feeding rate of the harvester; q represents the feeding rate, kg/s; ρ represents the air density, kg/m³; μ represents the concentration ratio of the airflow carrying impurities.

The diameter of the middle section of the separation chamber and the diameter of the grain outlet are determined by the following equations:

$$D = \sqrt{\frac{4Q}{\pi V}} \tag{8}$$

In the equation, V represents the airflow velocity inside the separation chamber, m/s.

Based on calculations and the overall machine layout, the diameter of the middle section of the separation chamber was determined to be D = 225 mm, the diameter of the grain outlet was 190 mm, and the total height of the separation chamber was 440 mm.

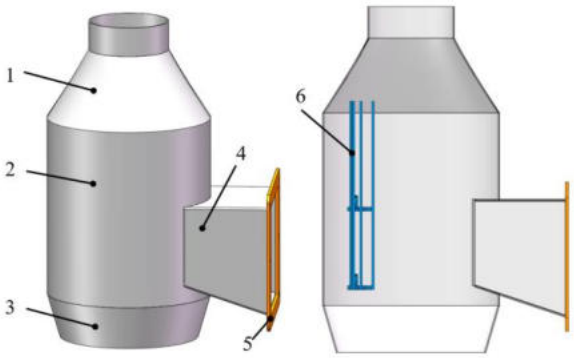


Fig. 4 - Schematic diagram of the separation cylinder structure

1 - Upper conical section; 2 - Middle section; 3 - Lower conical section; 4 - Feeding section; 5 - Connecting flange; 6 - Screen

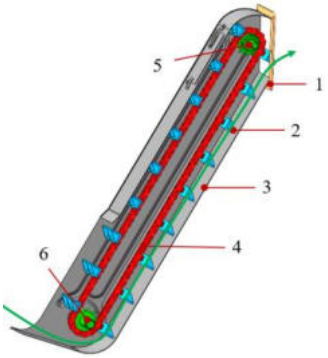


Fig. 5 - Structure diagram of scraper conveyor

1 - Discharge flange; 2 – Scraper; 3 – Housing; 4 – Chain; 5 - Driven shaft and sprocket; 6 - Driving shaft and sprocket

Scraper conveyor

Based on the overall spatial layout of the harvester and practical application requirements, a bottom-scraping type scraper conveyor was selected. Its structure is shown in Fig. 5.

To prevent blockage in the scraper conveyor and ensure smooth material conveying, the discharge outlet length *l* is determined by the following equation *(Geng et al., 2011)*:

$$l = v_g \sqrt{\frac{2H_t \cos\varphi}{g\cos(\beta+\varphi)}} \tag{9}$$

In the equation, v_g represents the conveying speed of the scraper, 1.5 m/s; H_t represents the lifting height of the threshed material, m. β represents the inclination angle of the conveyor relative to the horizontal plane; φ represents the friction angle between the material and the scraper.

The conveying capacity of the scraper conveyor is determined by the following equation:

$$Q_w = L_g B_g v_g m_g \psi k_1 \tag{10}$$

In the equation, L_g, B_g represents the length and width of the scraper, m; m_g represents the bulk density of the material, kg/m³; ψ represents the filling coefficient; k_1 represents the inclination coefficient.

After calculation and considering the actual structure of the combine harvester, the scraper length is 125 mm, width is 25 mm, the discharge outlet length *l* is 150 mm, and the inclination angle is 30°.

Coupled Simulation of CFD-DEM

CFD and DEM model establishment

To ensure that the simulation reflects real-world conditions while reducing computational load, the simulation model retained the fan and scraper conveyor components but shortened the conveying stroke of the scraper. After constructing the flow channel model of the cleaning system in SolidWorks, the model was exported in .x_t format and imported into the Workbench Mesh module. An unstructured tetrahedral mesh, suitable for complex geometries, was used for meshing the flow channel. Local mesh refinement was applied to the geometrically complex regions, such as the screen and fan blades.

A total of 762, 707 mesh elements were generated. The mesh quality was evaluated to be satisfactory, meeting the simulation requirements. The mesh is shown in Fig. 6.

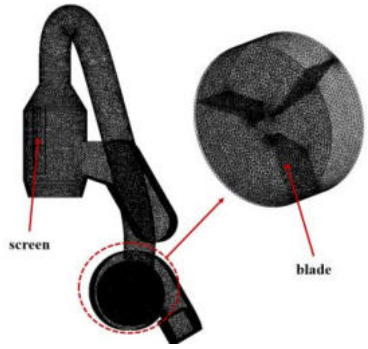


Fig. 6 - Meshing

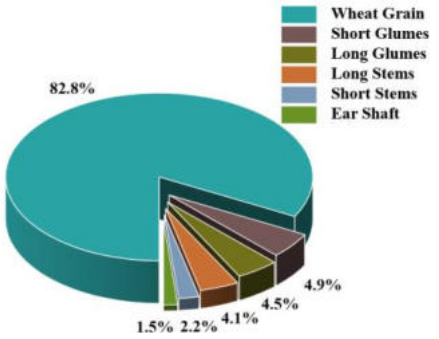


Fig. 7 - Mass ratio of threshed material

Based on field experiment measurements, the mass proportions of different components in the threshed wheat material from the small combine harvester were obtained, as shown in Fig. 7. Given the significant proportion of glumes, this study incorporated a glume model into the existing discrete element modeling of wheat grains and stems by previous scholars to enhance the reliability of the simulation. *(Schramm and Tekeste, 2022; Wiącek et al., 2023)*. The average geometric dimensions of the components were measured using a vernier caliper, and DEM models for each component were constructed in EDEM, as shown in Fig. 8. The material property parameters for the particle models, including material density, Poisson's ratio, and shear modulus, were set based on the research team's existing data *(Li, 2017)*. A particle factory was established on the scraper, with the following particle generation rates: grains at 436.71 g/s, long stems at 21.62 g/s, short stems at 11.60 g/s, rachis at 7.91 g/s, long glumes at 23.73 g/s, and short glumes at 25.84 g/s.

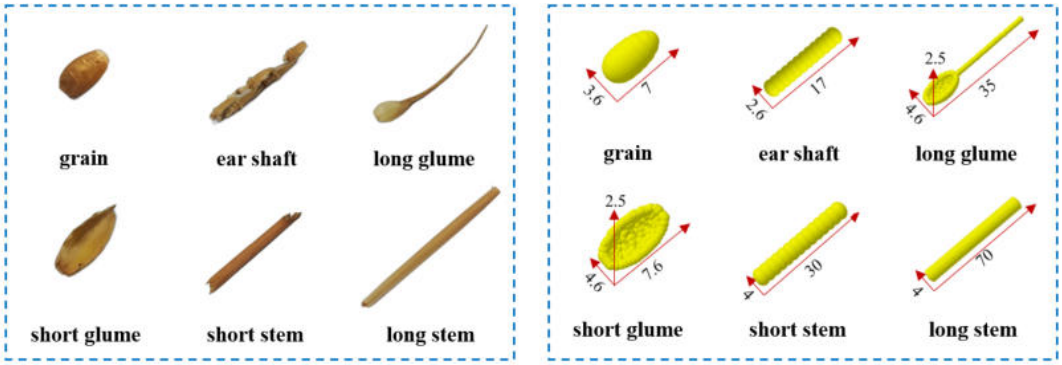


Fig. 8 - DEM model of threshed material

Parameter setting of CFD-DEM

In Fluent, the standard turbulence model was employed, and the mesh region corresponding to the centrifugal impurity-extraction fan impeller was defined as a Multiple Reference Frame rotational zone *(Zhou et al., 2025; Mircea et al., 2020)*, with a set rotational speed of 4000 r/min. The inlet boundary of the airflow in the cleaning system was set as a pressure inlet, while the outlet was set as a pressure outlet. In EDEM, the motion parameters of the scraper were defined according to a scraper shaft speed of 350 r/min. The contact interactions between particles and between particles and geometry were modeled using the Hertz-Mindlin (no slip) contact model and the Standard Rolling Friction model. The Eulerian model was used for the numerical simulation of gas-solid two-phase flow. After multiple tests, the EDEM time step was set to 5×10^{-7} s and the Fluent time step was set to 5×10^{-5} s. A total of 30,000-time steps were calculated, with a total simulation time of 1.5 s.

Simulation Test of Response Surface Method

Based on Section 2.1.3 and the simulation analysis results, fan speed, scraper shaft speed, the clearance between the screen and the separation chamber wall, and the screen mesh size were selected as experimental factors, with grain impurity rate Y_1 and cleaning loss rate Y_2 as the evaluation indices. The coding of each experimental factor is shown in Table 2.

A four-factor, three-level response surface experiment was designed using the Box-Behnken method *(Ayorinde and Owolarafe, 2023; Kushwah et al., 2023)*.

Table 2

Test factor level and coding table

Code	Factor			
	Fan Speed X_1/(r/min)	Scraper Shaft Speed X_2/(r/min)	Screen Gap X_3/(mm)	Grid Spacing X_4/(mm)
-1	3600	300	30	15
0	4000	400	45	25
1	4400	500	60	35

RESULTS AND ANALYSIS

Simulation Results and Analysis

Airflow field analysis

After the simulation was completed, the vertical central plane and several horizontal cross-sections at different heights of the separation chamber were extracted in CFD-Post to obtain airflow velocity contour maps, as shown in Fig. 9.

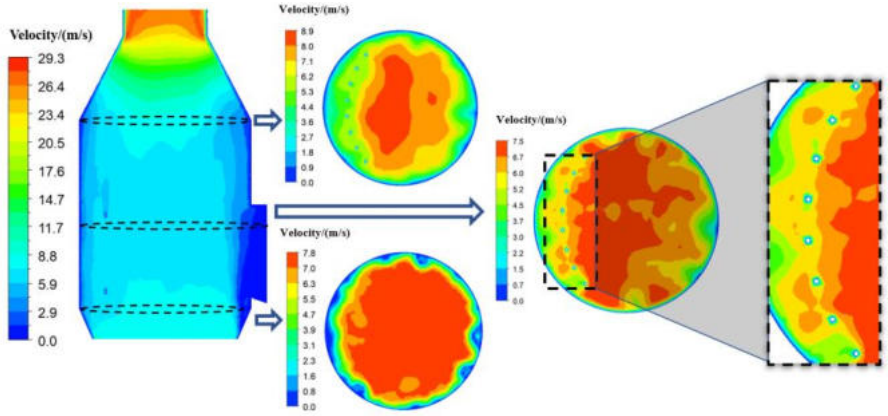
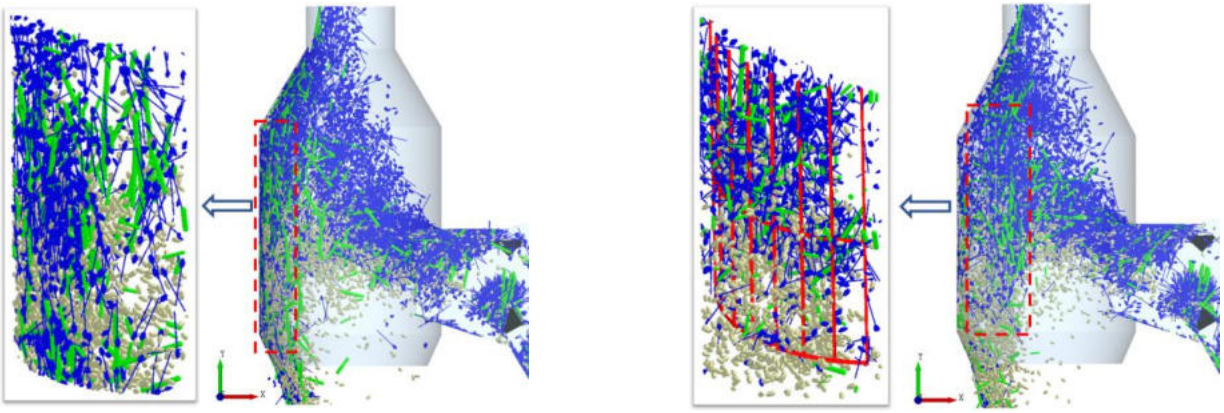


Fig. 9 - Velocity cloud diagram of different sections of the separation cylinder

Overall, the airflow field exhibited distinct high- and low-velocity regions: the airflow velocity was relatively high in the upper and lower conical sections, relatively uniform in the middle section, and significantly lower near the chamber walls. The spatial distribution characteristics of the airflow field were generally consistent with the initial design expectations, verifying the rationality of the separation chamber structure. The airflow velocity on the right side of the screen was significantly higher than on the left. The high-velocity region on the right side facilitates efficient separation of grains and impurities, while the low-velocity region on the left promotes rapid sedimentation of the grains.

Screen function analysis

To clarify the specific functional mechanism of the screen during the cleaning process, a comparative analysis was conducted between the material motion near the left wall of the separation chamber under the no-screen condition and the motion on both sides of the screen when the screen was installed. The particle motion in the selected regions is shown in Fig. 10.



(a) Without Screen *(b) With Screen*

Fig. 10 - Analysis of particle movement in cleaning process

Fig. 10(a) shows the particle motion under the no-screen condition. After the threshed material is conveyed into the separation chamber by the scraper, a large amount of glumes, along with some rachis and stalks, is directly extracted by the airflow, while a considerable amount of material accumulates along the chamber wall. In the selected chamber wall region, both impurities and grains are discharged together through the grain outlet, resulting in poor cleaning performance. Fig. 10(b) illustrates the particle motion with the screen installed. In the extracted screen region, only a small amount of impurities passes through the screen. Most impurities are blocked by the screen and remain within the central high-speed airflow region, which reduces mixing with grains and allows more impurities to be extracted by the airflow.

To further quantify the impact of the screen structure on cleaning performance, two particle mass statistics regions were defined in the EDEM post-processing: one below the grain outlet and the other above the impurity outlet. These were used to calculate the grain impurity rate and cleaning loss rate. The simulation results showed that, without the screen, the impurity rate was 5.23% and the cleaning loss rate was 1.09%; after installing the screen, the impurity rate decreased to 3.10%, while the loss rate remained stable at 1.07%. In summary, the screen structure effectively optimized the movement path of large-particle impurities such as stalks, improving the separation efficiency between grains and impurities, and reducing the impurity rate by more than 40%.

Analysis of the centroid velocity of threshed material particles

To further analyze the motion behavior of the threshed material during the cleaning process, and in consideration of the working characteristics of the separation chamber, this study focuses on the variation pattern of centroid velocity in the Y direction (vertical direction). Since analyzing individual particles involves a high degree of subjectivity and cannot fully represent the motion characteristics of an entire particle type, the Y-direction velocity vectors of all threshed material particles within the separation chamber were extracted over time. The summed velocity vectors were used to generate time-series curves of the centroid velocity in the Y direction for each particle group.

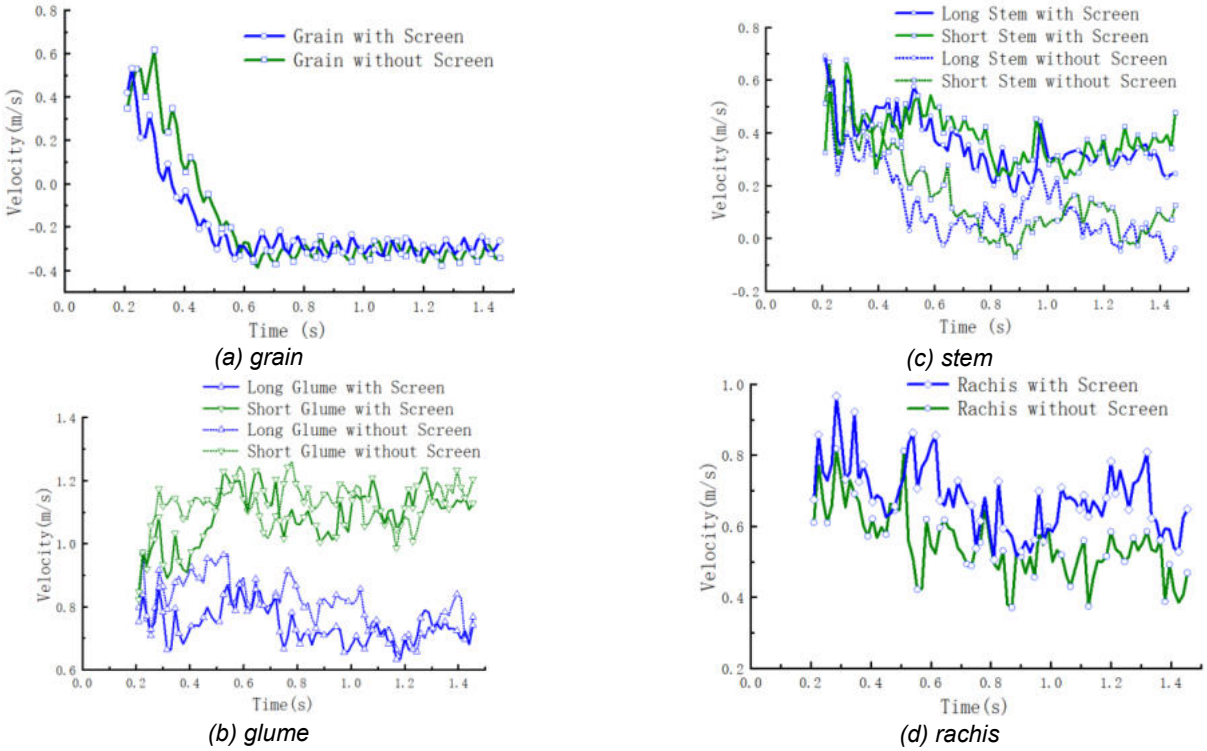


Fig. 11 - Relationship between the velocity of particle swarm centroid motion and time in the Y direction

As shown in Fig. 11(a), it takes 0.2 s for the wheat grains to move from the particle factory to the separation chamber, and after 0.6 s, the velocity gradually stabilizes. Once the cleaning process stabilizes, the grain velocity under both conditions becomes nearly identical, indicating that the screen structure has a minimal effect on grain movement, and the grains can easily pass through the screen. As shown in Fig. 11(b), under both conditions, the velocity of short glumes gradually increases after entering the separation chamber and stabilizes, indicating that after entering the chamber, short glumes are quickly expelled upward through the impurity outlet under the action of airflow. The velocity of long glumes decreases after cleaning stabilizes.

Combining this with the analysis of the cleaning simulation process, under the no-screen condition, a large amount of impurities accumulate in the left region of the separation chamber, leading to the difficulty in expelling some glumes, which results in a reduced overall glume velocity. As shown in Fig. 11(c) and Fig. 11(d), in the screen-equipped cleaning system, the centroid velocity of the rachis and stem particles in the Y direction is higher than that under the no-screen condition. The average velocities of stems and rachis during the stable phase were calculated: under the no-screen condition, the velocities of the rachis, long stems, and short stems were 0.51 m/s, 0.06 m/s, and 0.07 m/s, respectively; under the screen-equipped condition, the corresponding velocities were 0.65 m/s, 0.2 m/s, and 0.24 m/s, representing increases of 27.45%, 233.33%, and 242.86%, respectively.

In summary, the screen structure significantly increased the upward velocity of the rachis and stems, effectively improving the separation efficiency between grains and impurities and enhancing the overall cleaning performance of the cleaning device.

Analysis of Response Surface Experiment Results

Regression model building and testing

The results of the response surface experiment are shown in Table 3. Based on the response surface experimental data, variance analysis was performed on the regression models for the impurity rate Y_1 and cleaning loss rate Y_2. The analysis results are shown in Table 4. The quadratic polynomial regression models for Y_1 and Y_2 are:

$$Y_1 = 2.97 - 1.85X_1 + 0.22X_2 + 0.73X_3 - 0.17X_4 - 0.11X_1X_2 - 0.3X_1X_3 + 0.09X_1X_4 + 0.2X_1^2 + 0.76X_2^2 + 0.87X_3^2 + 0.92X_4^2 \quad (11)$$

$$Y_2 = 1.45 + 0.85X_1 + 0.40X_2 + 0.23X_3 - 0.25X_4 + 0.24X_1X_2 + 0.13X_1X_3 - 0.1X_1X_4 + 0.21X_1^2 + 0.06X_2^2 + 0.1X_3^2 \quad (12)$$

Table 3

Results of response surface experiment

Experiment	X_1	X_2	X_3	X_4	Y_1/%	Y_2/%	Experiment	X_1	X_2	X_3	X_4	Y_1/%	Y_2/%
1	-1	0	-1	0	4.96	0.75	15	0	1	0	1	4.68	1.55
2	0	0	-1	1	3.88	1.08	16	0	0	0	0	3.03	1.42
3	-1	1	0	0	6.04	1.01	17	0	-1	1	0	5.05	1.38
4	0	1	0	-1	5.11	2.12	18	1	0	0	-1	2.21	2.82
5	1	0	0	1	2.11	1.96	19	1	0	-1	0	1.84	2.25
6	0	-1	0	1	4.25	0.93	20	-1	0	1	0	6.86	1.03
7	0	-1	0	-1	4.61	1.25	21	0	0	-1	-1	4.12	1.5
8	0	0	0	0	2.91	1.48	22	-1	0	0	1	5.71	0.68
9	0	-1	-1	0	3.59	1.03	23	0	0	0	0	2.96	1.45
10	0	1	1	0	5.61	2.33	24	-1	-1	0	0	5.45	0.65
11	0	0	1	1	5.32	1.42	25	1	0	1	0	2.56	3.04
12	1	1	0	0	2.21	3.25	26	0	1	-1	0	3.99	1.74
13	-1	0	0	-1	6.17	0.94	27	1	-1	0	0	2.04	1.94
14	0	0	1	-1	5.75	1.94							

Table 4

Analysis of variance for regression equations

Source	Impurity Rate of Grain					Cleaning Loss Rate				
	Sum of Squares	DF	Mean Square	F	P	Sum of Squares	DF	Mean Square	F	P
Model	56.58	14	4.04	601.41	<0.0001**	12.75	14	0.91	229.87	<0.0001**
X_1	41.14	1	41.14	6122.5	<0.0001**	8.67	1	8.67	2188.40	<0.0001**
X_2	0.59	1	0.59	87.08	<0.0001**	1.94	1	1.94	488.67	<0.0001**
X_3	6.41	1	6.41	953.76	<0.0001**	0.65	1	0.65	163.73	<0.0001**
X_4	0.34	1	0.34	50.60	<0.0001**	0.73	1	0.73	183.05	<0.0001**
X_1X_2	0.044	1	0.04	6.56	0.0249*	0.23	1	0.23	56.95	<0.0001**
X_1X_3	0.35	1	0.35	51.80	<0.0001**	0.065	1	0.065	16.41	0.0016**
X_1X_4	0.032	1	0.032	4.82	0.0485*	0.090	1	0.090	22.72	0.0005**
X_2X_3	0.0064	1	0.0064	0.95	0.3484	0.014	1	0.014	3.63	0.0808
X_2X_4	0.0012	1	0.0012	0.18	0.6770	0.016	1	0.016	3.94	0.0704
X_3X_4	0.0090	1	0.0090	1.34	0.2691	0.0025	1	0.0025	0.63	0.4424
X_1^2	0.21	1	0.21	31.22	0.0001**	0.23	1	0.23	57.73	<0.0001**
X_2^2	3.06	1	3.06	454.89	<0.0001**	0.02	1	0.02	5.61	0.0354*
X_3^2	4.03	1	4.03	600.13	<0.0001**	0.057	1	0.057	14.37	0.0026**

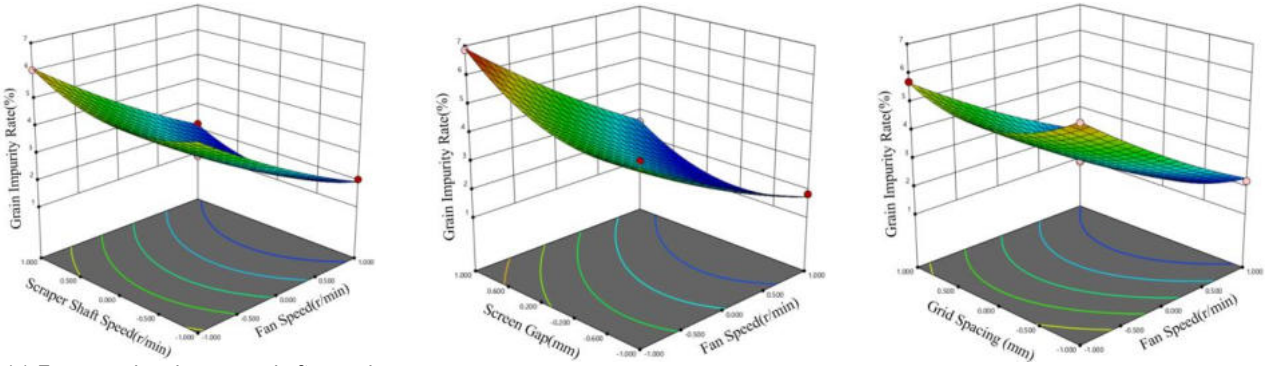
Source	Impurity Rate of Grain					Cleaning Loss Rate				
	Sum of Squares	DF	Mean Square	F	P	Sum of Squares	DF	Mean Square	F	P
X_4^2	4.50	1	4.50	669.30	<0.0001**	0.0187	1	0.0187	4.71	0.0507
Residual	0.081	12	0.0067			0.048	12	0.0040		
Lack of fit	0.073	10	0.0073	2.02	0.3763	0.046	10	0.0046	5.08	0.1755
Pure Error	0.0073	2	0.0036			0.0018	2	0.0009		
Cor Total	56.66	26				12.80	26			

Note: ** indicates extremely significant difference (P ≤ 0.01); * indicates significant difference (P ≤ 0.05).

As shown in Table 4, the p-value of the regression models for grain impurity rate and cleaning loss rate is less than 0.0001, indicating that the model is highly significant overall. The p-value for the lack-of-fit term is greater than 0.05, suggesting that the fitted quadratic regression equation matches well with the actual data. For the grain impurity rate, the effects of X_1, X_2, X_3, X_4, X_1X_3, X_1^2, X_2^2, X_3^2 and X_4^2 were extremely significant. For the cleaning loss rate, the effects of X_1, X_2, X_3, X_4, X_1X_2, X_1X_3, X_1X_4, X_1^2 and X_3^2 were extremely significant. According to the magnitude of the regression coefficients, the order of importance of the factors affecting the grain impurity rate was: fan speed, clearance between the screen and the separation chamber wall, scraper shaft speed, and screen mesh size. For the cleaning loss rate, the order of influence was: fan speed, scraper shaft speed, screen mesh size, and clearance between the screen and the chamber wall.

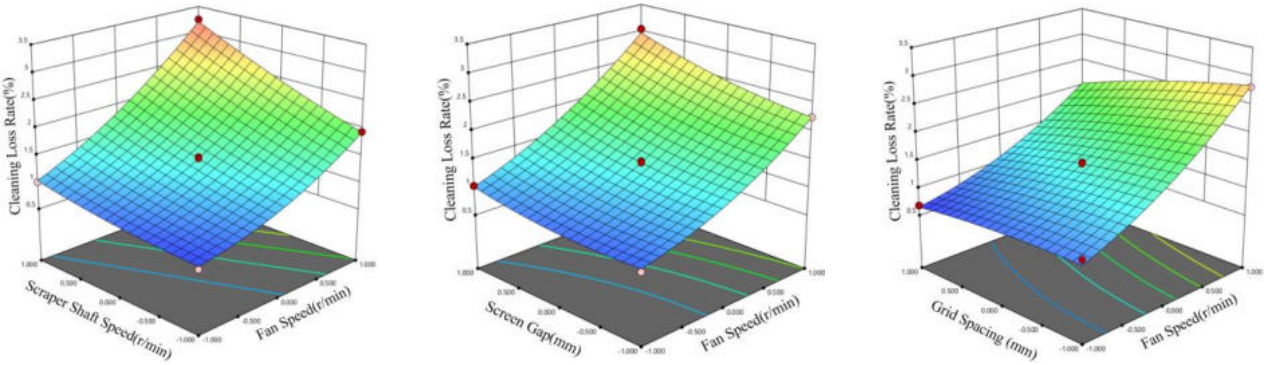
Influence of interaction factors on cleaning performance

To visually analyze the impact of interaction factors on the grain impurity rate and cleaning efficiency, response surface plots of the regression model were generated, as shown in Fig. 12 and Fig. 13.



(a) Fan speed and scraper shaft speed *(b) Fan speed and screen gap* *(c) Fan speed and grid spacing*

Fig. 12 - The influence of interactive factors on the impurity content rate of grains



(a) Fan speed and scraper shaft speed *(b) Fan speed and screen gap* *(c) Fan speed and grid spacing*

Fig. 13 - The influence of interactive factors on the cleaning loss rate

The optimal working parameters are determined

To further improve cleaning performance, the minimum values of grain impurity rate and cleaning loss rate were used as optimization indices. Considering that small combine harvesters focus more on reducing the loss rate, weights of 0.4 and 0.6 were assigned to the grain impurity rate and cleaning loss rate, respectively. Under the constraint conditions of the experimental factor levels, target optimization was performed to determine the optimal working parameters. The regression model was optimized to solve for the target parameters. Considering practical factors, the optimal working parameter combination was determined as follows: fan speed of 4020 r/min, scraper shaft speed of 340 r/min, clearance between the

screen and the chamber wall of 37 mm, and mesh size of 29 mm. Three repeated simulation tests were conducted under this parameter combination, yielding an average grain impurity rate of 2.99% and an average cleaning loss rate of 1.10%.

Field Experiment Verification

To verify the cleaning performance of the cleaning device under the optimal working parameters in hilly and mountainous areas, a field experiment was conducted from May 8 to 11, 2024, in Shehong City, Sichuan Province, according to the relevant provisions of GB/T 8097-2008 Test Methods for Combine Harvesters and JB/T 13544-2018 Micro Full-Feed Combine Harvesters. The wheat variety used in the experiment was “Chuannong 30,” with an average plant height of 823 mm, a thousand-kernel weight of 45.1 g, and a grain moisture content of 18.12%. The experimental field was divided into three straight 15-meter sections. The combine harvester operated at full cutting width and a constant speed. Grains were collected below the grain outlet using woven bags, and impurities were collected using nylon mesh bags. After each test, the collected materials were separated, and the weight of each component was measured using a high-precision electronic scale. The grain impurity rate and cleaning loss rate were then calculated. The test procedure is shown in Fig. 14. The experiment results are shown in Table 5.



Fig. 14 - Field experiment and cleaning performance

Table 5

Field experiment results

Experiment Number	Collected Material Mass (g)	Collected Grain Mass (g)	Loss Mass (g)	Impurity Rate (%)	Loss Rate (%)
1	8538.53	8290.68	94.71	2.90	1.13
2	9433.63	9142.91	97.58	3.08	1.06
3	9237.78	8936.88	110.55	3.26	1.22

The average grain impurity rate was 3.08%, and the cleaning loss rate was 1.14%. Compared to the simulation results, the relative error for the impurity rate was 2.92%, and the relative error for the loss rate was 3.51%. These errors mainly arise from the complexity of field environmental factors and differences in operator performance. Overall, the relative errors were small, indicating that the simulation model has high accuracy and reliability. This validates the effectiveness and feasibility of the designed built-in screen cyclone separation cleaning system in improving cleaning performance and operational efficiency.

CONCLUSIONS

To address the issues of high grain impurity rates and low cleaning efficiency in small combine harvesters during wheat harvesting, an internally screened cyclone separation cleaning system is proposed. This system combines the synergistic effects of the screen and airflow, effectively improving the separation efficiency between grains and impurities, as well as the overall cleaning performance. Through CFD-DEM coupled simulation technology, the impact of the screen structure on the motion trajectory and separation behavior of the threshed material was systematically analyzed. Using response surface methodology, regression models were established for the factors and evaluation indices, and the optimal working parameter combination was determined: fan speed of 4020 r/min, scraper shaft speed of 340 r/min, clearance between the screen and the chamber wall of 37 mm, and mesh size of 29 mm. Under this parameter combination, the simulation results showed a grain impurity rate of 2.99% and a cleaning loss rate of 1.10%. Field test results showed a grain impurity rate of 3.08% and a cleaning loss rate of 1.14%, verifying the accuracy of the simulation model. The designed cleaning device meets the wheat cleaning performance standards for small combine harvesters in hilly and mountainous areas.

ACKNOWLEDGEMENT

Key R&D Program of Shandong Province, China(2022SFGC0201); The National Natural Science Foundation of China (52405271), and The Natural Science Foundation of Jiangsu Province (BK20230544).

REFERENCES

[1] Ayorinde, T. A., Owolarafe, O. K. (2023). Effect of operational parameters on the performance of a kenaf harvester. *Spanish Journal of Agricultural Research, Vol. 21*(4), pp. e0209-e0209. https://orcid.org/0000-0002-6748-8704

[2] Badretdinov, I. D., Mudarisov, S. G. & Khaliullin, D. T. (2022). Examination of the Airflow Uneven Distribution over the Combine Harvester Cleaning System. *Mathematical Modelling of Engineering Problems*, *Vol. 9*(2), pp. 371-378. https://doi.org/10.18280/mmep.090210

[3] Bizuneh, Y. E. Abate, L. A. (2024). Experimental investigation on the separation and cleaning efficiency of pea & lentil split chaffs using cyclone cleaner. *Case Studies in Thermal Engineering*, *Vol. 61*, pp. 104875. https://doi.org/10.1016/j.csite.2024.104875

[4] Ding, B., Liang, Z., Qi, Y., Ye, Z. & Zhou, J. (2022). Improving cleaning performance of rice combine harvesters by DEM–CFD coupling technology. *Agriculture*, *Vol. 12*(9), pp. 1457. https://doi.org/10.3390/agriculture12091457

[5] Geng, D., Zhang, D., Wang, X. & Yang, Z. (2011). *New Edition of Agricultural Machinery Science* (新编农业机械学). Beijing: National Defense Industry Press. *(In Chinese)*. ISBN: 9787118075281.

[6] Kushwah, A., Sharma, P. K., Mani, I., Kushwaha, H. L., Sahoo, R. N., Sarkar, S. K., Sharma, B. B., Carpenter, G., Singh, N., Yadav. R., Nag, R. H. (2023). Parameter optimization for selective harvesting in cauliflower (Brassica oleracea) using response surface methodology. *The Indian Journal of Agricultural Sciences*, *Vol. 93*(8), pp. 912-918. https://doi.org/10.56093/IJAS.V93I8.136898

[7] Li Y. (2017). Numerical simulation and experiment of gas-solid two-phase flow in multi-duct cleaning device (多风道清洗装置中气固两相流的数值模拟与试验). *Zhenjiang: Jiangsu University*. *(In Chinese).*

[8] Liu, Z., Zheng, Y., Wang, Z., Chen, D., Wang, J. (2015). Study on airflow cleaning device of micro rice-wheat combine harvester (微型稻麦联合收获机气流式清选装置研究). *Transactions of the Chinese Society for Agricultural Machinery*, *Vol. 46*(7), pp. 102-108. *(In Chinese).* https://doi.org/10.6041/j.issn.1000-1298.2015.07.016

[9] Lovchikov, A.P., Ognev, I.I. (2022). Theoretical background for combination of sieves of combine harvester cleaning system. *AIP Conference Proceedings*. *AIP Publishing, Vol. 2503*(1). https://doi.org/10.1063/5.0099726

[10] Mandler, A., Becce, L., Carabin, G., Gronauer, A., Mazzetto, F. (2025). Mechanisation of Mountain Farming. Observations on Grain Production in the Alps. In: Sartori, L., Tarolli, P., Guerrini, L., Zuecco, G., Pezzuolo, A. (eds) Biosystems Engineering Promoting Resilience to Climate Change - AIIA 2024 - Mid-Term Conference. MID-TERM AIIA 2024. *Lecture Notes in Civil Engineering, Vol 586,* pp. 807-815. Springer, Cham. https://doi.org/10.1007/978-3-031-84212-2_100

[11] Mircea, C., Nenciu, F., Vlăduț, V., Voicu, G., Gageanu, I., Cujbescu, D. (2020). Increasing the performance of cylindrical separators for cereal cleaning, by using an inner helical coil, *INMATEH - Agricultural Engineering, Vol. 62*(3), pp. 249-258, https://doi.org/10.35633/inmateh-62-26.

[12] Mirzazadeh, A., Abdollahpour, S. Hakimzadeh, M. (2022). Optimized Mathematical Model of a Grain Cleaning System Functioning in a Combine Harvester using Response Surface Methodology. *Acta Technol. Agric*, *Vol. 25*, pp. 20-26. https://doi.org/10.2478/ata-2022-0004

[13] Schramm, M., Tekeste, M. Z. (2022). Wheat straw direct shear simulation using discrete element method of fibrous bonded model. *Biosystems engineering, Vol. 213*, pp. 1-12. https://doi.org/10.1016/j.biosystemseng.2021.10.010

[14] Shi, R., Dai, F., Zhao, W., Liu, X., Wang, T., Zhao, Y. (2022). Simulation Optimization and Experiment on Compound Cleaning System of Hilly Area Flax Combine Harvester (丘陵山地胡麻联合收获机复式清选系统仿真优化与试验). *Transactions of the Chinese Society for Agricultural Machinery*, *Vol. 53*(8), pp. 93-102+113. *(In Chinese)*. http://dx.doi.org/710.6041/j.issn.1000-1298.2022.08.010

[15] Shu, C., Yang, J., Liao, Q., Wan, X., Yuan, J. (2024). Design and experiment of guide-type dual-cyclone separation cleaning device for rapeseed combine harvester (油菜联合收获导流式双筒旋风分离清选装置设计及试验). *Journal of Jilin University (Engineering and Technology Edition)*, *Vol. 54*(6),

pp. 1807-1820. *(In Chinese)*. https://doi.org/10.13229/j.cnki.jdxbgxb.20220860

[16] Wan, X., Liao, Q., Xu, Y., Yuan, J., Li, H. (2018). Design and evaluation of cyclone separation cleaning devices using a conical sieve for rape combine harvesters. *Applied Engineering in Agriculture*, *Vol. 34*(4), pp. 677-686. https://doi.org/10.13031/aea.12502

[17] Wiącek, J., Parafiniuk, P., Molenda, M., Horabik, J., Gallego, E. (2023). DEM study of microstructural effects in friction of wheat on corrugated steel surface. *Tribology International, Vol. 183*: 108435. https://doi.org/10.1016/j.triboint.2023.108435

[18] Zhao, H., Li, X., Zhao, Y., Li, S., Diao, P. (2024). Simulation analysis and experiment of cleaning mechanism for track-type combine harvester based on CFD-DEM. *INMATEH - Agricultural Engineering, Vol. 74*(3), pp. 603-614, https://doi.org/10.35633/inmateh-74-54

[19] Zhou, B., Ma, S., Li, W., Wu, Z., Qian, J., Huo, P., Yang, S. (2025). CFD-DEM coupling simulation and parameter optimisation of sugarcane harvester extractor. *Biosystems Engineering, Vol. 250*, pp. 80-93. https://doi.org/10.1016/j.biosystemseng.2024.12.003

DESIGN AND EXPERIMENT OF DEEP TOPDRESSING APPLICATOR FOR WINTER WHEAT
/
冬小麦深施追肥机的设计与试验

Huimin FENG[1)], Jianhui NIE[2)], Baohui XU[1)], Yuming GUO[*3)]
[1)] Mechanical and Electrical Engineering Department, Yuncheng University, Yuncheng 044000, China;
[2)]Intelligent Equipment Research Center, Beijing Academy of Agriculture and Forestry Sciences, Beijing 100097, China;
[3)] College of Agricultural Engineering, Shanxi Agricultural University, Taigu 030801, China
Tel: +86-0354-6286869; E-mail: guoyuming99@sina.com
Corresponding author: Yu-ming Guo
DOI: https://doi.org/10.35633/inmateh-76-93

Keywords: *row spacing; structural parameters; row alignment; topdressing; winter wheat*

ABSTRACT
To achieve mechanized deep topdressing for winter wheat, the planting pattern of narrow and wide row spacing of (10+20) cm was proposed and the topdressing applicator was designed to implement deep topdressing in the 20 wide row. The numerical simulation was conducted to evaluate the soil disturbance of furrow opener, the precision fertilization control system was attached to improve the fertilization accuracy, the precision row alignment system was attached to furnish support for the operation between the rows, the field experiments were conducted to evaluate the performance of topdressing applicator and the effect of deep topdressing fertilization on grain yield and yield trait parameters after harvest. The simulation results showed that the double-disc furrow opener with parameters of disc diameter 350 mm, disc angle 10° and offset angle 25° caused the soil disturbance within the ± (5-15) cm range along with a heave less than 2 cm at a furrowing depth of 10 cm, the row alignment deviation values of guideline alignment and cross-track deviation under flat ground were mostly distributed within ±3 cm at a tractor speed of 3 km/h. The field experimental results indicated that at a working speed of 3 km/h, the topdressing applicator can accomplish 10 cm deep topdressing in the 20 cm wide row along with the row alignment deviation largely distributed with in ±5 cm, the GNs, TKW and grain yield were higher than broadcasting group, which verifies the feasibility of the planting pattern of (10+20) cm and the practicality of the deep topdressing applicator.

摘要
为实现冬小麦机械化追肥作业，本文提出了一种（10+20）cm 宽窄行种植在 20cm 宽行内追肥的作业模式，以此为依据设计了深施追肥机。通过离散元仿真分析了开沟器对于土壤的扰动作用，通过加装精量排肥系统提高施肥均匀性，通过加装对行作业系统提高深施肥作业对行精度，通过田间实验对作业方案和样机性能进行了验证。仿真结果表明，当双圆盘开沟器结构参数为：直径 350mm，圆盘夹角 10°，圆盘偏角 25°，在开沟深度为 10cm 时，土壤扰动范围为± (5-15) cm 且有低于 2cm 的土壤垄起；当作业速度为 3km/h，平地条件下追肥机具的对行作业偏差和接行作业偏差值基本分布在±3cm 内。田间追肥试验表明：作业速度为 3km/h，在宽窄行种植模式下追肥机可以实现在 20cm 宽行内进行 10cm 深施追肥作业且对行作业偏差基本分布在±5cm 内。深施追肥组小麦穗粒数、千粒重及小麦产量均高于表层撒施组，表明宽窄行模式下冬小麦机械化深施追肥方案可行。

INTRODUCTION
Topdressing winter wheat with fertilizer N is an important process to compositing for any deficiencies and giving wheat an extra boost to enhance winter wheat production and profitability *(Wang Y., 2020; Yang W., 2024*). The Nitrogen (*N*) fertilizer was reported as a crucial process of nutrient dynamics for plant growth (*Shen X., 2024*). Rational amount and suitable placement of N fertilizer were proposed to increase N utilization and improve the grain yield.

Broadcasting fertilization is the most common way for wheat topdressing, which is usually implemented by centrifugal disc spreader (*Assad Y., 2020*) or drones.

Huimin Feng, Lec. Ph.D., Eng.; Jianhui Nie, Engineer, Master, Eng.; Baohui Xu, Prof. Ph.D. Eng.; Yuming Guo, Prof. Ph.D. Eng.

However, the structural parameters of the spreading equipment and the operational parameters of these two fertilization methods exert substantial influence on fertilization uniformity, under specific operational conditions, the coefficient of variation (CV) values of fertilizer distribution can reach 10%-15% (*Ren W., 2021*). Additionally, for broadcasting, neither application can effectively reduce the total nitrogen application rate.

Fertilizer subsurface was studied to be an effective approach to realize high grain yield with moderate fertilizer amount, which also along with a superior fertilizer utilization rate *(Anurag P., 2020; Zhu W., 2023*). *Nkebiwe P. et al. (2016)* suggested that deep subsurface fertilizer placement may be an additional tool for the mitigation of negative consequences of increasingly frequent extreme weather events like high temperatures to improve the fertilizer utilization. *Liu T. et al., (2015*) studied deep Nitrogen placement can effectively decrease NH_3 volatilization and increase N utilization in no-tillage paddy fields.

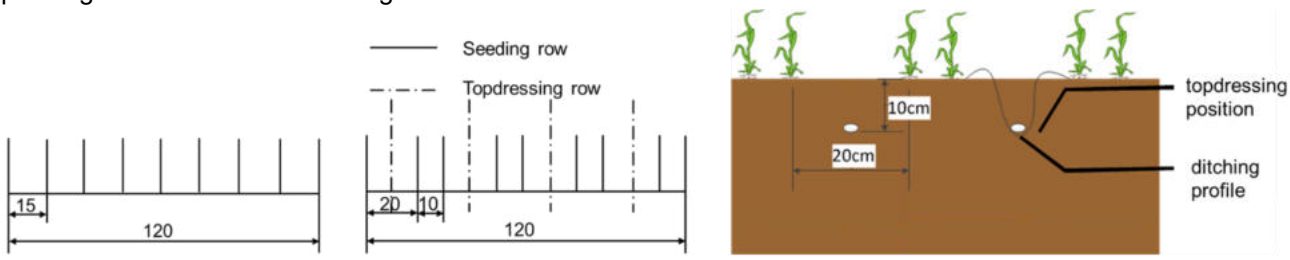
For winter wheat, the 15 cm uniform row spacing planting pattern makes topdressing impractical to mechanize deep fertilization during the green-up stage or jointing stage. To realize deep fertilization, adaptable inter-row spacing (*Guo M., 2015; Mabio C.,2016*) and ditch tools should be taken into consideration. MHDSR-NF combined with a furrower opener enables puddling, seeding, and fertilizer application operations simultaneously were designed to examine the effects of mechanical deep placement of fertilizer on N use efficiency (*Pan S. et al., 2017*). *Kargbo M. et al.* (*2016*) reported that deep fertilizer with precision hill-drilling machine in super rice has a higher efficiency and labor saving. A syringe through two tubules was used to place soil solution at 5 cm and 12 cm depths (*Wu M. et al., 2017*).

In summary, research on mechanized deep topdressing for winter wheat, few studies have analyzed planting row spacing and topdressing depth simultaneously as influencing factors to provide an effective and rational design of topdressing machine. Therefore, the objective of this study is to propose a planting pattern to apply deep topdressing for winter wheat. Based on an automatic navigation system and precision fertilization system, the applicator was designed to perform inter-row deep topdressing for winter wheat, which can apply nitrogen fertilizer to a specific depth between the seedling rows. Additionally, through experimental analysis, the operation performance of the deep topdressing applicator, as well as the impact of deep topdressing on grain yield and yield trait parameters were evaluated.

MATERIALS AND METHODS

Planting pattern and topdressing fertilization strategy

The traditional wheat planting method is drill seeding with an equal row spacing of 15 cm, based on the previous research (*Feng H. et al, 2017*), the narrow and wide row spacing of (10+20) cm was proposed to apply deep topdressing in the middle of 20 cm wide row, which can ensure that the wheat seeding density and the fertilizer amount are consistent with those in the traditional planting method. The schematic diagrams of planting method are shown in Fig. 1.



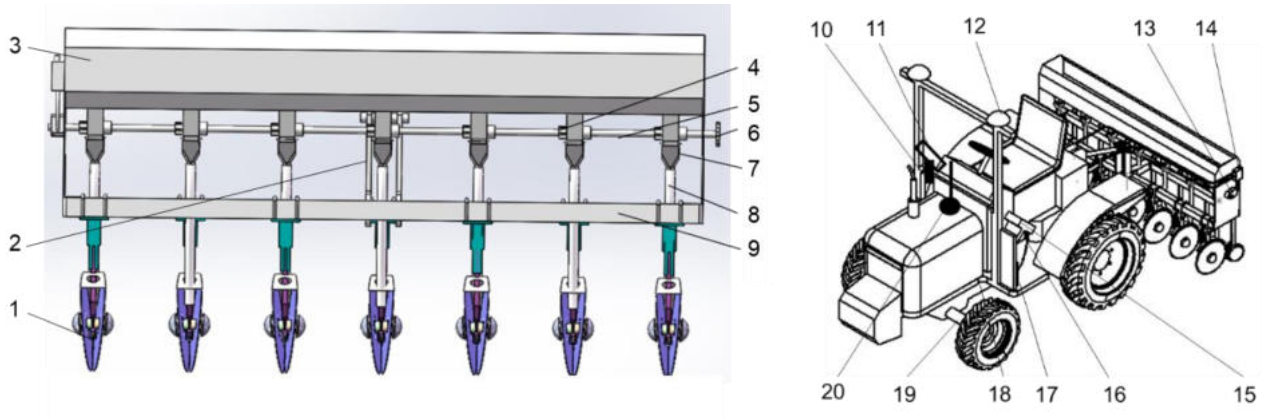
(a) uniform row spacing of 15 cm (b) row spacing of (10+20) cm (c) deep topdressing solution

Fig. 1 - The schemes of planting pattern and deep topdressing operation

Overall structure and working principle

The structure of the deep topdressing applicator is shown in Fig.2a, all the components are installed and fixed on the machine frame. The topdressing fertilization applicator is used in conjunction with a 14 - row wheat seeder, therefore, 7 sets of fertilizer metering devices of 30 cm interval were installed in a staggered front - to - back direction to realize deep topdressing application. The precision row alignment system was equipped to improve inter-row operation accuracy, which can effectively reduce cutting damage of the furrow opener to wheat roots as well as tire compaction damage to wheat seedlings, the precision fertilization control system was added to enhance uniform fertilizer distribution, the overall structure scheme is shown in Fig. 2b.

The row alignment system is composed of navigation terminal, RTK-GNSS controller, angular sensor, steering valve and other components; the fertilization control system is mainly composed of fertilization terminal, fertilization controller, hydraulic valve and motor.



(a) Schematic diagram of topdressing applicator (b) The overall structure of applicator

Fig. 2 - Overall design of topdressing applicator

(a) 1. Double - disc furrow opener; 2. Three-point hitch; 3. Fertilizer tank; 4. Fertilizer apparatus; 5. Fertilizer metering shaft; 6. Screw mechanism; 7. Fertilizer discharge box; 8. Fertilizer tube; 9. Machine frame

(b) 10. Fertilization controller; 11. Fertilization terminal; 12. RTK - GNSS antenna; 13. Hydraulic motor; 14. Electro - hydraulic valve; 15. Navigation terminal; 16. RTK - GNSS receiver; 17. Navigation controller; 18. Steering valve; 19. Angular sensor; 20. Radio antenna

The applicator is attached to tractor through a three-point hitch, the fertilization power is provided by the tractor's hydraulic system, the row alignment system and fertilization control system are separately installed on the tractor body, the hydraulic motor is connected to the fertilizer distribution shaft through a hexagonal shaft, the electro-hydraulic valve is installed on the side of the motor to shorten the hydraulic circuit and improve the operation efficiency.

Parameter design of furrow opener

The structural parameters of double-disc furrow opener were designed to evaluate the soil disturbance during deep topdressing operation, as shown in Fig.3. The main parameters studied are as follows: disc diameter D, disc angle θ and offset angle *β* (*Ye R., 2023*). The above structural parameters determine the position of the pinch point *m*.

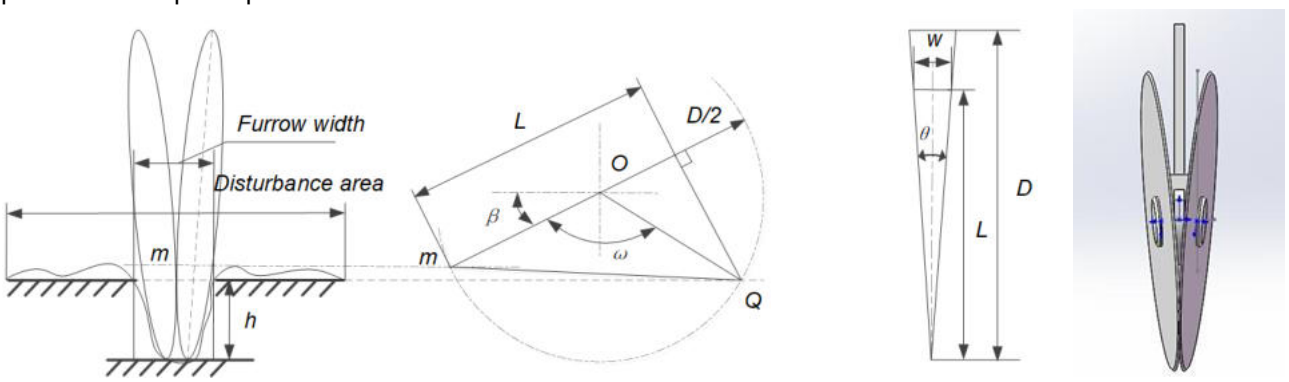


Fig. 3 - Structural parameters of double-disc furrow opener

Based on the structure scheme, the theoretical furrow width can be calculated as following:

$$\begin{cases} \omega = (90° - \beta) + \arccos(\dfrac{D/2 - h}{D/2}) \\ L = \dfrac{D}{2} + \dfrac{D}{2}\cos(180° - \omega) \quad 90° < \omega \le 180° \\ w = 2L\sin(\dfrac{\theta}{2}) \end{cases} \tag{1}$$

where: h is the depth of furrowing operation, mm; Q is the intersection point of the disc edge with the ground; *ω* is the angle between Q and the convergence point *m* at a certain depth, (°); L is the length of the projection of line *Qm* onto the diameter where the convergence point lies, mm; w is the furrow width, mm.

According to the requirements of the agricultural machinery design manual, four different parameter combinations in Table 1 were set up to conduct comparative analysis of disturbance effects of various furrow openers on soil, the SolidWorks and EDEM software were used to perform modeling and simulation process (*Wang Y., 2019*). The DEM parameters were classified as material, interaction and bond properties, the detailed descriptions of these properties are presented in Table 2. The soil disturbance area and the soil backfilling profile were selected as evaluation indicators to determine the final structural parameters of the double-disc furrow opener.

Table 1

The 4 sets parameters of double disc furrow opener

Type		Parameter		
		D / mm	B / °	θ / °
Double disc furrow opener	D_{disc1}	350	25	10
	D_{disc2}	350	15	10
	D_{disc3}	350	15	15
	D_{disc4}	300	15	10

Table 2

The properties parameters of DEM simulation

Parameter	Value
Soil density (kg·m^{-3})	2600
Steel density (kg·m^{-3})	7865
Soil shear modulus (MPa)	26
Steel shear modulus (MPa)	7.9×10^{4}
Soil Poisson's ratio	0.25
Steel Poisson's ratio	0.3
Particle-particle friction coefficient	0.6
Particle-steel friction coefficient	0.6
Soil restitution coefficient	0.6
Steel restitution coefficient	0.6
Particle-particle rolling friction coefficient	0.28
Particle-steel rolling friction coefficient	0.05

The precision fertilization control system

The precision fertilization control system has two major design requirements: one is to realize real-time control of the hydraulic motor rotational speed based on the tractor's driving speed, precisely regulate the rotational speed of the fertilizer distribution shaft to achieve the required control accuracy for the fertilizer application rate. The other one is to determine the optimal working length and rotational speed of the fertilizer apparatus based on the target fertilizer amount and the tractor's driving speed, thereby defining the fertilizer discharge per revolution of the apparatus to improve the uniformity of fertilizer application. Based on these requirements, the precision fertilization control system was designed.

The precision fertilization control system is shown in Fig. 4. The fertilization terminal obtains location information from the RTK-GNSS receiver and calculates the current driving speed of vehicle, and then determines the target rotational speed of hydraulic motor based on the fertilizer control model. The controller adjusts the opening degree of the valve according to the current signal output to regulate the flow through valve, which drives hydraulic motor to rotate, thus achieving precisely control over the rotational speed of hydraulic motor and fertilizer distribution shaft. Simultaneously, an encoder monitors the actual rotational speed signal of the hydraulic motor to form a closed-loop control circuit, the controller uses a PID algorithm to adjust system current in real time, fine-tuning the hydraulic motor speed to achieve accurate control of the fertilizer application rate. The apparatus parameters control method (*Feng H., 2020*) was used to improve fertilization uniformity.



Fig. 4 - Precision fertilizer distribution control system

1. RTK - GNSS antenna; 2. RTK - GNSS receiver; 3. Fertilization terminal; 4. Fertilization controller; 5. Electro - hydraulic valve; 6. Hydraulic motor; 7. Fertilizer apparatus

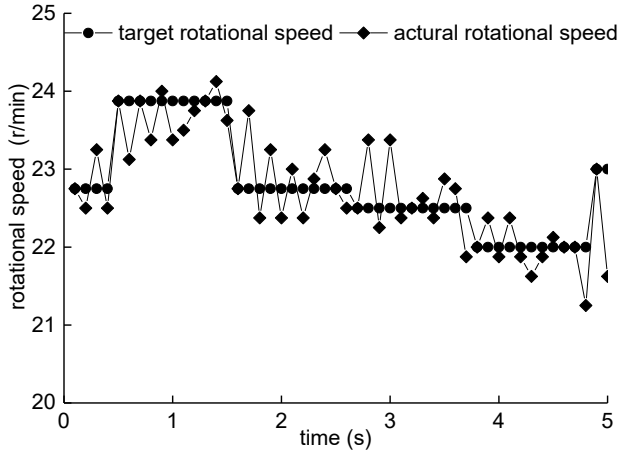


Fig. 5 - Control accuracy of rotational speed of hydraulic motor

The standard PID algorithm was used to calculate and control the rotational speed of the hydraulic motor in real - time. The control accuracy of the motor's rotational speed was analyzed in Fig. 5. Under dynamic conditions, the upper - computer sends a rotational speed command every 1 second at a tractor's forward speed of 5 km/h. The serial port sends back a command every 100 ms and records the rotational speed of motor. The results indicate that under dynamic conditions, the PID control system can complete the rotational speed adjustment within 0.2 seconds, the average control error of the motor's rotational speed is 1.52%, and the maximum control error is 10.2%. The results show that the system can meet the requirements of precisely fertilizer distribution.

Under the premise that fertilizer application rates remain consistent, the model of fertilizer amount was established by formula (2), and the target rotational speed of hydraulic motor is calculated using formula (3):

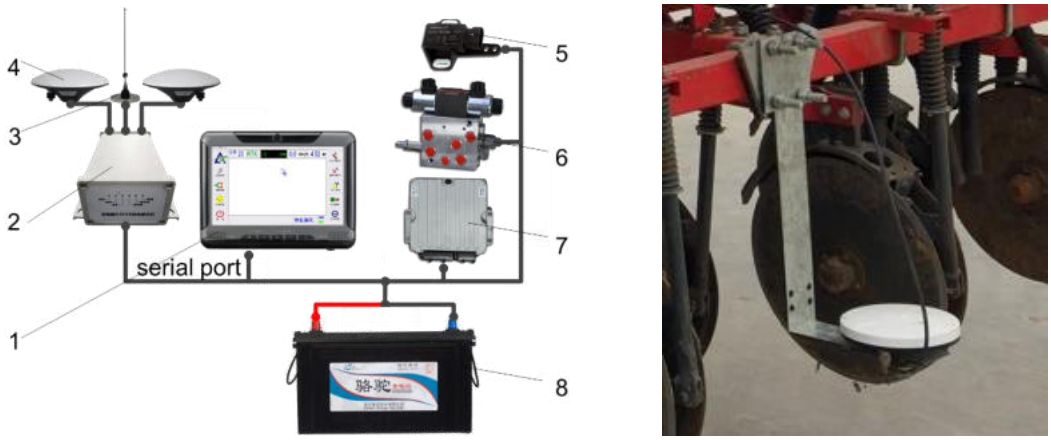
$$\begin{cases} \mathrm{d}S(t) = \dfrac{1000}{60} \times 10^{-4} V_G(t) W \mathrm{d}t \\ \mathrm{d}Q_0(t) = Q_0 \mathrm{d}S(t) \\ \mathrm{d}Q_0(t) = N_\mathrm{T} q R_0(t) \mathrm{d}t \end{cases} \tag{2}$$

$$R_0(t) = \frac{1000 V_G(t) W Q_0}{60 N_\mathrm{T} q} \times 10^{-4} \tag{3}$$

where: $S(t)$ is the operation area at time *t*, hm^2; $V_G(t)$ is the tractor's driving speed at time *t*, km/h; W is the operating width, m; Q_0 is topdressing amount per unit area, kg/hm^2; $Q_0(t)$ – topdressing amount at time *t*; $R_0(t)$ is the target rotational speed of hydraulic motor, r/min; q is the fertilizer discharge per revolution, kg/r; N_T is the amount of fertilizer tube.

The precision row alignment system

The precision row alignment system consists of a navigation control system, a steering control system, and an executive mechanism, as shown in Fig. 6(a). The target steering angle of the tractor's steering wheels is calculated in real - time by operation parameters and the tractor's driving speed measured and calculated by the GNSS, after receiving the steering command, the steering controller compares the target steering angle with the actual steering angle of the front wheels, and runs the PID control program to control the electro - hydraulic valve to drive steering. Due to the influence of tractor vibration and field flatness, the row-alignment accuracy of the topdressing applicator requires further testing, a GNSS antenna is installed at the middle position of the topdressing frame by using a right - angle fixing bracket to collect the machine's trajectory data, as shown in Fig. 6(b).

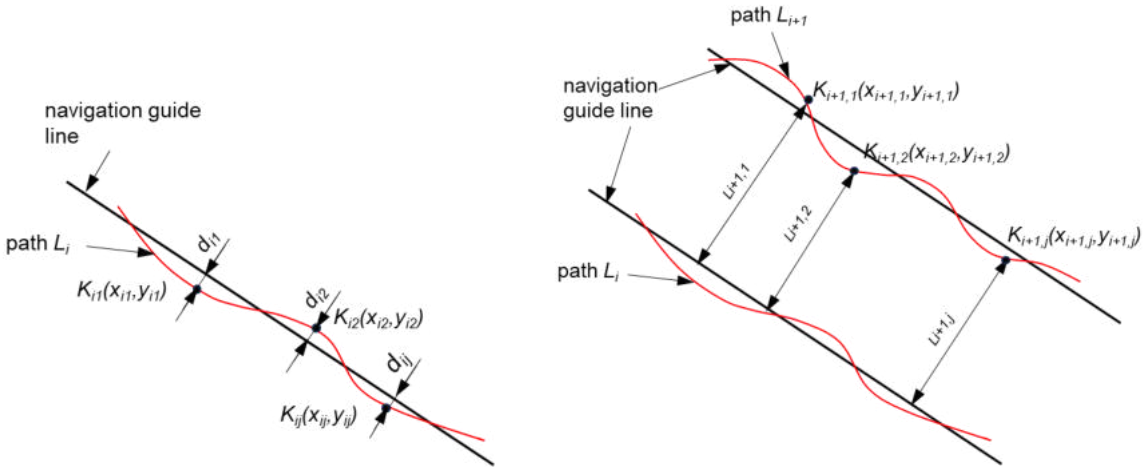


(a) Row alignment control system (b) Antenna installed on the applicator

Fig. 6 - Scheme of precision row alignment system

1. Navigation terminal; 2. RTK - GNSS receiver; 3. Radio antenna; 4. RTK - GNSS antenna; 5 Angular sensor; 6. Steering valve; 7. Navigation controller; 8. Power supply

The guidance alignment deviation and cross-track deviation were used to evaluate the row-alignment accuracy of the topdressing applicator, as shown in Fig.7.



(a) Guidance alignment deviation (b) Cross-track deviation

Fig. 7 - Schematic diagram of row alignment deviation

The equation of the navigation guide line can be obtained by converting the latitude and longitude of reference points on the guide line. The guidance alignment deviation d_{ij} is calculated by the lateral deviation from the sampling points on the machine trajectory to the navigation guide line, according to:

$$d_{ij} = \frac{A_i x_{ij} + B_i y_{ij} + C_i}{\sqrt{A_i^2 + B_i^2}} \quad (4)$$

The cross-track deviation $D_{i+1,j}$ is calculated by subtracting the operating width from the lateral deviation from the sampling points on the machine trajectory within the adjacent working width to the navigation guide line, according to:

$$D_{i+1,j} = \frac{A_i x_{i+1,j} + B_i y_{i+1,j} + C_i}{\sqrt{A_i^2 + B_i^2}} - W \quad (5)$$

The navigation accuracy of the tractor is an important factor affecting the row alignment accuracy of the topdressing applicator. When the driving speed is 5 km/h, three sets data of row alignment operation were processed and analyzed.

Field experimental design and treatments

The experiments were conducted to evaluated the operation performance at National Experiment Station for Precision Agriculture located in Changping, Beijing, China. The topdressing experiments were conducted in accordance with GB/T 20346.2—2006 *Fertilizing Machinery—Test Methods—Part 2: Inter-row Topdressing Machines* and JB/T 7864—2013 *Cultivator-Topdressing applicator*.

The wheat is planted in a wide-narrow row mode of (10+20) cm, with deep topdressing applied within the 20 cm wide rows at a depth of 10 cm, the uniform row planting of (15+15) cm with broadcasting topdressing was set as control group. Urea is used as the fertilizer, with a topdressing rate of 225 kg N ha^{-1} for all treatments (*Muhammad S., 2021*). The topdressing operation is conducted at a speed of 3 km/h, and each experiment group includes 3 replicate plots.

The trajectory data of topdressing applicator is recorded to analyze the row-alignment accuracy, the soil disturbance after topdressing is measured and analyzed to verify the effect of the double-disc opener on seedling area.

After harvest, the yield trait parameters were measured to evaluate the effect of deep topdressing on wheat yield, the spike number per unit area (SN), grain number per spike (GNs) and thousand grain weight (TGW) were measured by the average values of 10 random plants from each plot, and the grain weight per m² were obtained by weighing, wheats were manually harvested at mature stage from 3 representative unit areas (1 m^2). The Origin (OriginLab, USA) and SAS statistical Software (SAS Institute, USA) were used to process data analysis.

RESULTS AND DISCUSSIONS

The effects of structural parameters on soil disturbance

The DEM simulation results of $Ddisc3$ were shown in Fig. 8, the moment with the largest soil disturbance area in each group was selected to determine the maximum soil disturbance range, the curve of the maximum disturbed soil range was determined by identifying the boundary where the particle velocity was zero. The soil backfill profile was determined by selecting the moment when the velocity of all particles was zero in each group. the comparative analyses of the maximum soil disturbance area and soil backfill profile were shown in Fig.8. The disturbance process for each cross-sectional soil layer lasted less than 2 seconds. The curve shape outside the ±15 cm range on the x-axis in the figure represents the initial shape of the soil bin, which has no impact on the soil disturbance analysis. The effect of soil heave caused by furrowing on seedlings was analyzed through the final soil backfill profile.

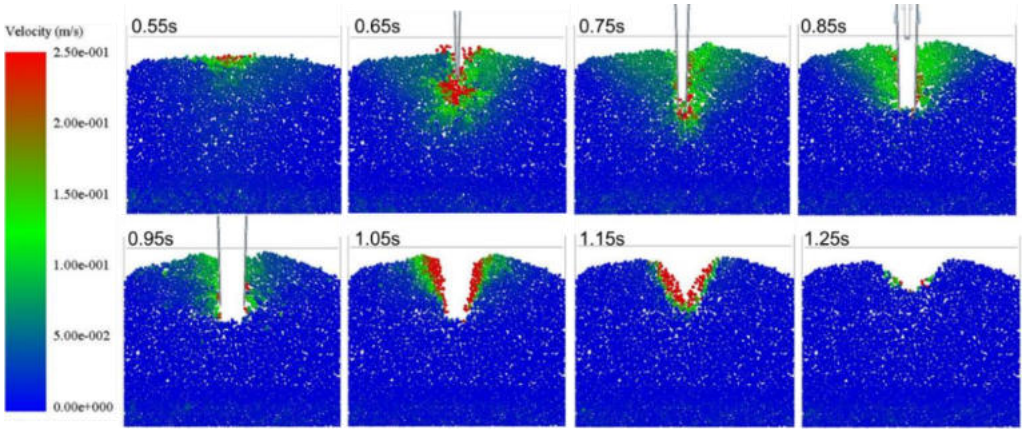
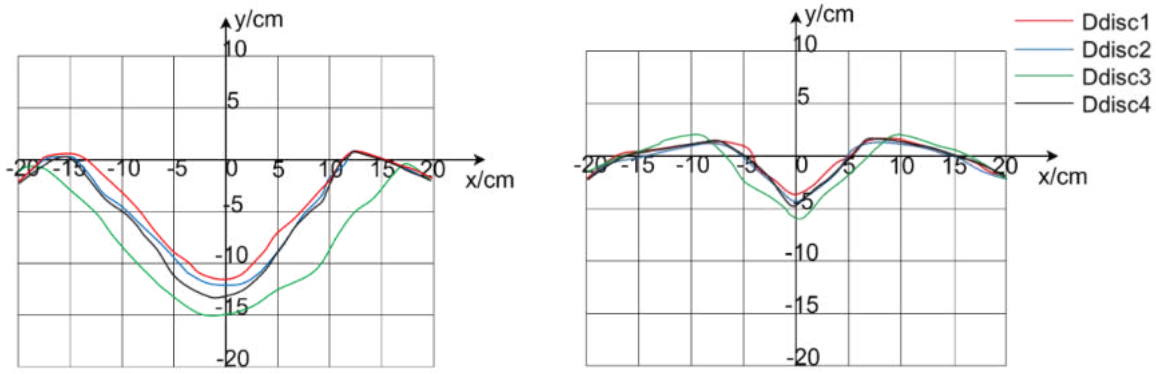


Fig. 8 - Soil disturbance process of double-disc opener

The simulation results of the soil disturbance area and soil backfill profile of four furrow openers are shown in Fig. 9. The soil disturbance area by opener *Ddisc3* is significantly larger than 3 other types openers, thus, the comparation analyses were conducted for the other 3 groups. As can be seen in Fig. 9(a), when the furrowing depth is 10 cm, the soil disturbance ranges of the three groups are from - 15 cm to 15 cm, the disturbance ranges are not completely symmetrical which is due to the random errors during the soil particle generation process. Although the particles nearby the boundary were disturbed, the velocity of the particles is only about 0.05 m/s, and the duration of the disturbance process is less than 2 s, therefore, the soil cover impact of the furrow process on the wheat seedlings can be ignored.

As can be seen in Fig. 9(b), after the furrowing operation is completed, there is a soil heave within the ± (5-15) cm range on both sides of the ground, the height of the heave is less than 2 cm, and the highest point is within ±10 cm, which has minimal impact on the coverage of seedlings on both sides. Comparing the simulation results, Ddisc1 exhibits the smallest soil disturbance area and soil backfill profile.



(a) Soil disturbance area (b) Soil backfill profile

Fig. 9 - Soil disturbance area and soil backfill profile of four furrow openers

Combined with the formula 1, at a certain depth, for a given disc diameter D and included angle θ, as the offset angle β increases, the vertical position of pinch point decreases, thus leads to an increase in the theoretical furrow width; for a given disc diameter D and offset angle β, as the included angle θ decreases, the theoretical furrow width decreases.

Based on the above analysis, the parameters of the double-disc furrow opener are selected as follows: disc diameter D is 350 mm, disc angle θ is 10° and offset angle β is 25°, at a furrowing depth of 10 cm, the theoretical furrow width is calculated as 55.12 mm, which can avoid the furrow opener from cutting the wheat roots when the planting row spacing is greater than 20 cm.

The row alignment deviation analysis of topdressing applicator

The guidance alignment deviation distribution diagrams of tractor path and three sets of applicator paths were shown in Fig.10. As can be seen, the overall guideline alignment deviation of tractor path exhibits a normal distribution within ±1.5 cm, the overall guideline alignment deviations of row following (RF) paths exhibit a normal distribution and over 90% of deviations fall within ±3 cm, which can fully meet the accuracy requirements at an operating row width of 20 cm.

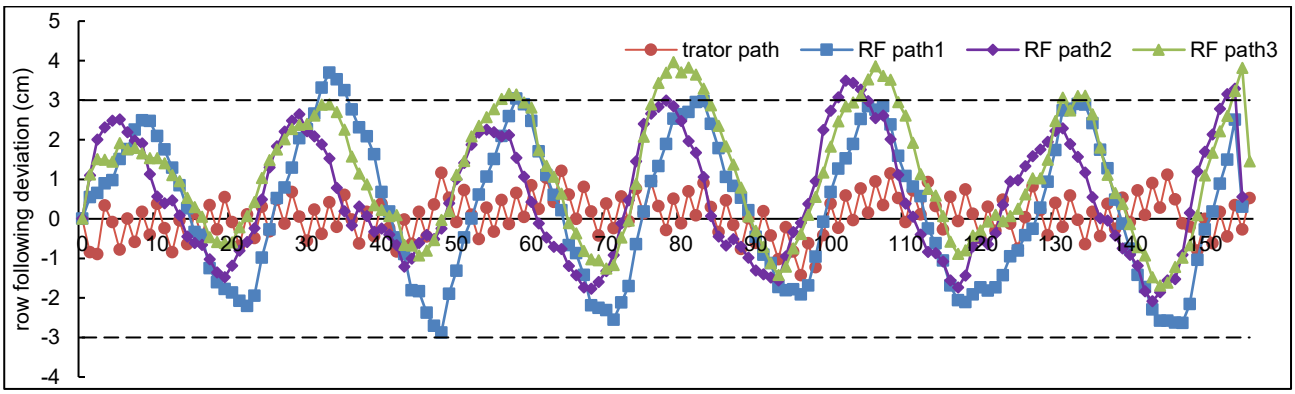
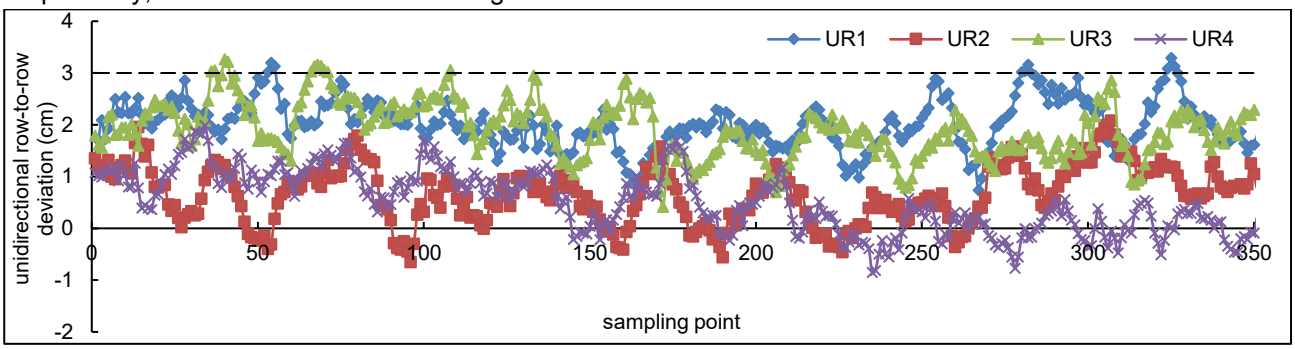
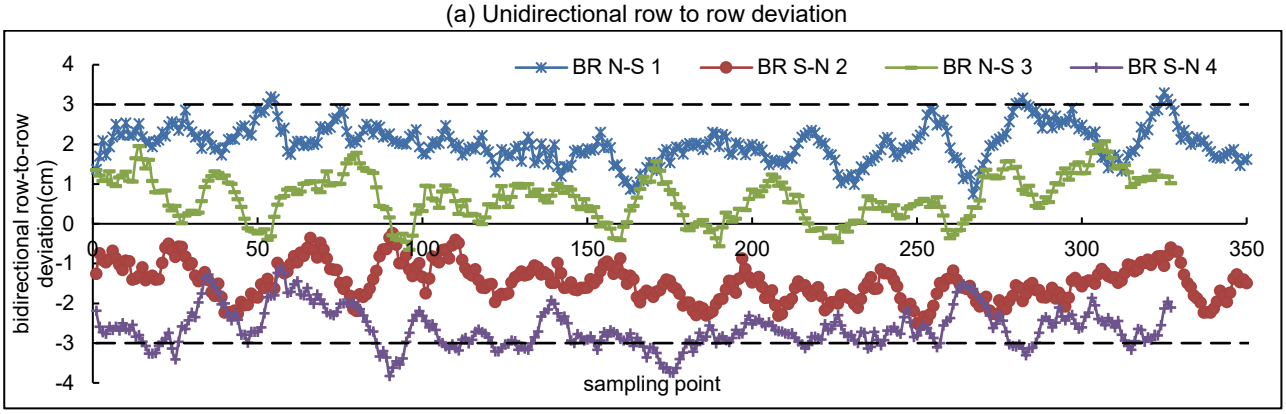


Fig. 10 - Guidance alignment deviation distribution of row following path

The cross-track alignment deviation includes unidirectional row-to-row deviation and bidirectional row-to-row deviation. At a driving speed of 3 km/h, the trajectory data of the topdressing applicator from 4 paths of unidirectional row-to-row operations and 4 paths of bidirectional row-to-row operations were analyzed respectively, the results were shown in Fig. 11.



(a) Unidirectional row to row deviation



(b) Bidirectional row to row deviation

Fig. 11 – Cross-track alignment deviation

As shown in Fig.11, the unidirectional row-to-row deviations exhibits certain fluctuations without an obvious normal distribution, and the tend to shift to one side of the guide line. In contrast, the bidirectional row-to-row deviations of the back-and-forth paths along the north-south direction are distributed on both sides of the navigation guide line. The distribution range of both cross-track deviations were essentially within ±3 cm. By comparison, the distribution of cross-track deviation shows a distinct bias, which can be attributed to machinery offset errors caused by row alignment calibration. Therefore, the cross-track deviation can be reduced by repeating the calibration process.

The results under field experiments

The field experiments and yield traits parameters measurement were carried out, as shown in Fig.12. Subsequently, the relevant experimental results were analyzed.



Fig. 12 – Field experiments

Soil disturbance under field condition

The furrow profile and soil disturbance range during topdressing furrowing at a depth of 10 cm were shown in Fig.13. The disturbance to the soil layers is a smooth inclined plane on both sides during furrowing, and it exhibits good soil backfilling due to the loose soil during topdressing period, which can effectively reduce damage to wheat roots and nitrogen volatilization.

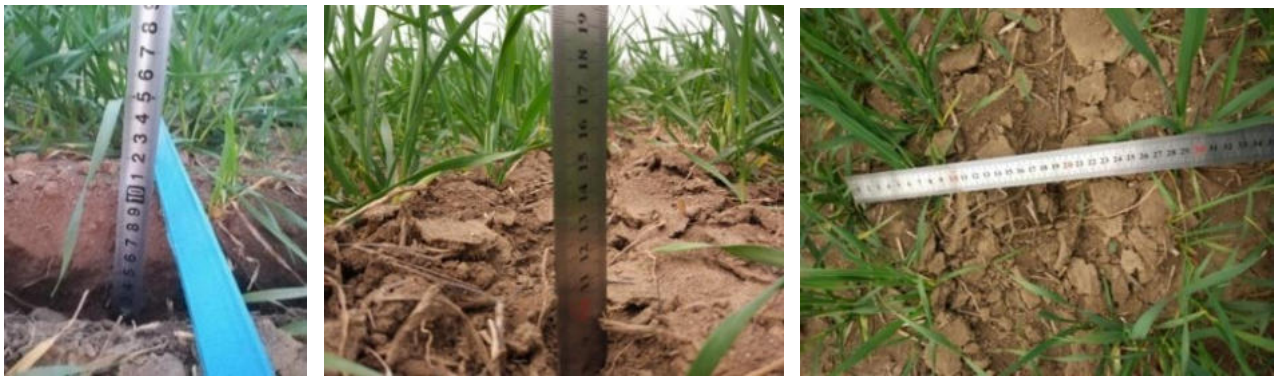


Fig.13 – Soil disturbance during topdressing furrowing at depth of 10 cm

Within the same furrow row, 10 points were randomly selected to measure the soil disturbance range, the farthest fracture point of the surface soil observed was selected as the boundary, and the results show that the surface soil disturbance range is between 27 and 31 cm. Due to the soil compaction, the movement of soil particles and disturbance range during actual furrowing operations differ from the simulation results, although the surface disturbance range increases, it did not form excessive soil heaving, resulting in a slight impact on seedling coverage.

Row alignment deviation of applicator under field condition

The trajectories data of 5 working paths were obtained to analyze the row alignment deviation of the topdressing applicator. Taking the first path navigation guide line as reference, the row alignment deviation of the first path and the cross-track deviation of the other four paths are analyzed. The deviations are calculated according to the formula (4) and (5), the results are shown in Fig. 14.

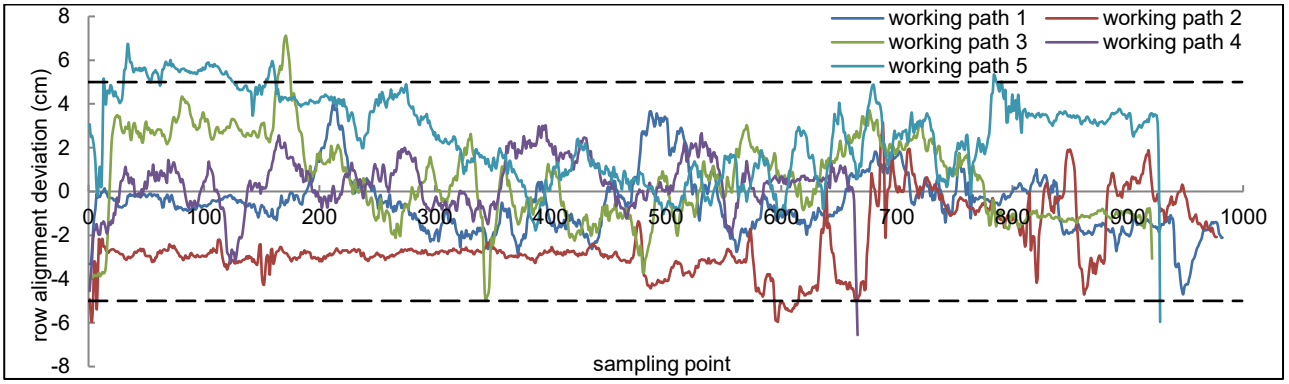


Fig. 14 - Row alignment deviation of 5 working paths

As can be seen in Fig. 14, the deviation ranges of the row alignment operation for the first working width to the fifth working width are -4.7~4.03 cm, -5.95~3.1 cm, -4.99~7.11 cm, -6.56~3.01 cm and -5.96~6.75 cm, respectively. The positive and negative deviations of the first working path are relatively evenly distributed, the largest cross track deviations of the working pass 2 and 4 are on the negative side of the coordinate axis, the largest cross track deviations of the working pass 3 and 5 are on the positive side of the coordinate axis, which is caused by the difference of steering direction. Except for a few data points with excessively large deviations, the row alignment deviations of the topdressing machine were basically distributed within the range of ±5 cm, this result can meet the requirements of mechanized deep topdressing operations.

During topdressing, the flatness of the field has a significant impact on the operational stability of the topdressing applicator. When carrying out the operation, the working speed of the tractor can be adjusted according to the soil flatness to decrease the row alignment deviation caused by vibration.

Effect of deep topdressing on grain yield and yield trait parameters of winter wheat

The grain yield (GY) and yield trait parameters after harvest in the two groups are comparatively analyzed, including spike number per unit area (SN), grain number per spike (GNs) and thousand grain weight (TGW). The results are presented in table 3.

Table 3

The grain yield and yield trait parameters of two groups

	SN/units	GNs/units	TGW/g	GY/kg·ha-2
Experimental group	317	35.23	45.11	4075.75
Control group	321	34.3	42.75	3544.5

The GNs, TWG and GY values of the experimental group are higher than the control group, the theoretical grain yield of experimental group is about 500 kg higher than the control group, which has a similar conclusion with the *He Y. (2020)* study that deep topdressing treatment could significantly improve the grain yield of winter wheat. The results show that deep topdressing application is beneficial to the wheat heading and grain filling, which can increase the wheat yield to a certain extent.

CONCLUSIONS

This study provided a feasible solution to the problem of mechanized deep topdressing application of winter wheat, and the main conclusions are as follows.

(1) The planting pattern of (10+20) cm row spacing were proposed, the topdressing applicator attached precision fertilization control system and precision row alignment system was designed to implement deep topdressing fertilization in the 20 cm wide row.

(2) The DEM simulations were performed to evaluate the soil disturbance of double disc furrow opener at a furrowing depth of 10cm. The results showed that with a disc diameter D of 350 mm, a disc angle θ of 10° and an offset angle β of 25°, the opener caused minimal soil disturbance within a range of approximately ± (5-15) cm, with a soil backfill heave of less than 2 cm.

(3) The row alignment accuracy of topdressing applicator was analyzed by guideline alignment deviation and cross-track alignment deviation. At an operation speed of 3 km/h, the deviation values were basically distributed within ±3 cm under flat ground conditions.

(4) Under field conditions, the topdressing applicator was validated as effective, achieving 10 cm deep topdressing within the 20 cm row spacing. The resulting soil disturbance had a negligible effect on seedling coverage, and the row alignment deviations were generally distributed within ±5 cm at an operating speed of 3 km/h. Yield analysis indicated that mechanized deep topdressing positively influenced both the yield trait parameters and the overall grain yield.

ACKNOWLEDGEMENT

This research was funded by the National Key Research and Development Program of China (2016YFD0200600), Scientific and Technological Innovation Projects of Higher Education Institutions (2021L482), Doctoral Research Start Project of Yuncheng University (YQ-2021006) and Special Scientific Research Project for Outstanding Doctors Coming to Shanxi Province of Yuncheng University (QZX - 2021014).

REFERENCES

[1] Anurag, P., RC, S., & Ashok, T. (2020). Development and testing of tractor operated variable depth fertilizer applicator on application of granular urea in wheat crop planted on beds. *International Journal of Chemical Studies*, Vol. 8, issue 5, pp. 989-996. https://doi.org/10.22271/chemi.2020.v8.i5n.10426

[2] Assad Y., Majed S., & Salim A. (2020). Modulating a centrifuge spreader disc and evaluating performance under some different operating factors. *International Journal of Agricultural and Statistical Sciences*. Vol. 16, pp. 1799-1805. https://connectjournals.com/03899.2020.16.1799

[3] Feng H., Gao N., Li Y., & Meng Z. (2017). Effects of topdressing depth and row spacing on the SPAD and plant height of winter wheat. *2017 ASABE Annual International Meeting*. pp. 201700924. https://doi.org/10.13031/aim.201700924

[4] Feng, H., Gao, N., Li, Y., Fu, W., & Guo, Y. (2020). Control method for parameters coordinate match of fluted roller fertilizer apparatus. *INMATEH-Agricultural Engineering*. Vol. 60, issue 1, pp. 211-220. https://doi.org/10.35633/inmateh-60-24

[5] Guo M., Z. G., Guo W., Chang X., Wang D., Yang Y., Wang M., Fan Z., Qi Z., Wang Y., & Liu X. (2015). Effects of nitrogen rate and row spacing on winter wheat grain quality (施氮量与行距对冬小麦品质性状的调控效应). *Chinese Journal of Eco-Agriculture*, Vol.23, issue 6, pp. 668-675. https://doi.org/10.13930/j.cnki.cjea.150014

[6] He, Y., Zhao X., Dou, H., Gao Y., Wang, X., Li, C., &Li J. (2020). Effect of different top-dressing methods and nitrogen level on growth and yield of winter wheat. *Bangladesh Botanical Society*, Vol. 49, issue 3, pp. 769-776.

[7] Kargbo, M., Pan S., Mo Z., Wang Z., Luo X., & Tian H. (2016). Physiological Basis of Improved Performance of Super Rice (Oryza sativa) to Deep Placed Fertilizer with Precision Hill-drilling Machine. *International Journal of Agriculture and Biology*, Vol. 18, issue 4, pp. 797-804. https://doi.org/10.17957/IJAB/15.0173

[8] Liu, T., Fan, D., Zhang, X., Chen J., Li, C., & Cao, C. (2015). Deep placement of nitrogen fertilizers reduces ammonia volatilization and increases nitrogen utilization efficiency in no-tillage paddy fields in central China. *Field Crops Research*, Vol. 184, pp. 80-90. https://doi.org/10.1016/j.fcr.2015.09.011

[9] Mabio, C., Adriano, N. (2016). Effects of row spacing and nitrogen topdressing fertilization on the yield of upland rice in a no-tillage system. *Acta Scientiarum Agronomy*, Vol. 38, issue 4, pp. 493-502. https://doi.org/10.4025/actasciagron.v38i4.30855

[10] Muhammad, S., Feng M., Samy S., Akhtar H., Nadir A., Hidayat U., et al (2021). Agronomical traits associated with yield and yield components of winter wheat as affected by nitrogen managements, *Saudi Journal of Biological Sciences*, Vol. 28, Issue 9, pp. 4852-4858. https://doi.org/10.1016/j.sjbs.2021.07.027

[11] Nkebiwe, P., Weinmann, M., Bar-Tal A., & Mulle, T. (2016). Fertilizer placement to improve crop nutrient acquisition and yield: A review and meta-analysis. *Field Crops Research*, Vol. 196, pp. 389-401. https://doi.org/10.1016/j.fcr.2016.07.018

[12] Pan, S., Wen X., Wang Z., Ashaf U., Tian H., & Duan M. (2017). Benefits of mechanized deep placement of nitrogen fertilizer in direct-seeded rice in South China. *Field Crops Research*, Vol. 203, pp. 139-149. https://doi.org/10.1016/j.fcr.2016.12.011

[13] Ren, W., Wu, Z., Li, M., Lei, X., Zhu, S., & Chen, Y. (2021). Design and Experiment of UAV Fertilization Spreader System for Rice (水稻无人机撒肥系统设计与试验). *Transactions of the Chinese Society for Agricultural Machinery*, Vol. 52, issue 3, pp. 88-98. http://doi.org/10.6041/j.issn.1000-1298.2021.03.009

[14] Shen X., Liu J., Liu L., Zeleke K., Yi R., Zhang X., Gao, Y., & Liang Y. (2024). Effects of irrigation and nitrogen topdressing on water and nitrogen use efficiency for winter wheat with micro-sprinkling hose irrigation in North China. *Agricultural Water Management*, Vol. 302, pp.109005, https://doi.org/10.1016/j.agwat.2024.109005.

[15] Wang, Y., Xue, W., Ma, Y., Tong, J., Liu, X., & Sun, J. (2019). DEM and soil bin study on a biomimetic disc furrow opener. *Computers and Electronics in Agriculture.* Vol. 156, pp. 209-216. https://doi.org/10.1016/j.compag.2018.11.023

[16] Wang, Y., Ye, Y., Huang, Y., Zhao, Y., Ning, R., Wen, F. & Yue, S. (2020). Development of Nitrogen Fertilizer Topdressing Model for Winter Wheat Based on Critical Nitrogen Dilution Curve. *International Journal of Plant Production*, Vol. 14, pp. 165–175. https://doi.org/10.1007/s42106-019-00076-2

[17] Wu, M., Li, G., Li, W., Liu J., Liu, M. & Jiang C. (2017). Nitrogen Fertilizer Deep Placement for Increased Grain Yield and Nitrogen Recovery Efficiency in Rice Grown in Subtropical China. *Frontiers in Plant Science.* Vol. 8, pp. 01227. https://doi.org/10.3389/fpls.2017.01227

[18] Yang W., Yang M., Guo S., Song S., Chen y., Wang S., &Zhao H. (2024). Effects of reducing nitrogen fertilizer combined with biochar on the yield and quality of wheat and carbon sequestration and emission reduction in Northern Xinjiang of China (减氮配施生物炭对北疆小麦产量品质及固碳减排的影响). *Transactions of the Chinese Society of Agricultural Engineering (Transactions of the CSAE)*, Vol 40, issue 4, pp. 108-115. http://doi.org/10.11975/j.issn.1002-6819.202307171

[19] Ye, R., Ma, X., Zhao, J., Liao, J., Liu, X., Xi, L., & Su, G. (2023). Optimization and Design of Disc-Type Furrow Opener of No-Till Seeder for Green Manure Crops in South Xinjiang Orchards. *Agriculture*, Vol. 13, issue. 8, pp. 1474. https://doi.org/10.3390/agriculture13081474

[20] Zhu, W., Zeng, K., Tian, Y., Zhang, C., Li, X., Ge, R., & Yin, B. (2023). Effects of Different Deep Fertilization Methods on Ammonia Volatilization and Nitrogen Use Efficiency in Rice Fields in Taihu Lake Region, *Soils*, Vol. 55, Issue 4, pp. 729-738. https://doi.org/10.13758/j.cnki.tr.2023.04.005

STUDY ON THE CHARACTERISTICS OF SAND AND WIND FLOW OF A NEW TYPE OF SAND BARRIER BASED ON NUMERICAL SIMULATION AND EXPERIMENT

/

基于数值模拟和实验的新型沙障的风沙流特征研究

Sibin ZHANG, Weiqiang ZHENG*), Liping ZHANG
[1)]College of Mechanical Engineering, Xinjiang University, Urumqi 830046 / China
Tel: +86-18384082033; E-mail: xjzwq@xju.edu.cn
DOI: https://doi.org/10.35633/inmateh-76-94

Keywords: *Numerical simulation, agricultural security, new sand barrier, windproof efficiency, field experiment, wind-blown sand*

ABSTRACT

The natural conditions in northwestern China are extremely harsh, with severe desertification. Frequent sandstorms cause significant damage to transportation infrastructure along desert margins, agricultural cash crops, and the local ecological environment. This study proposes a novel high vertical curved sand barrier system. Field experiments were conducted to validate numerical simulation results, and the properties of wind-driven sand movement and protective efficiency of these barriers were analyzed. Furthermore, double-row sand barriers with varying spacing were investigated to determine the optimal arrangement. The research demonstrates that the flow deflection angle of the high vertical curved sand barrier relative to the vertical direction significantly impacts its protective efficiency, showing a fluctuating pattern with changing angles. When the inlet airflow speed reaches 10 m/s with a barrier inclination angle of 75°, the leeward deceleration zone achieves an area of 25.450 m² with a coverage range of 19.31H (where H represents barrier height), resulting in optimal overall protective efficiency. For double-row sand barriers, the protective efficiency is influenced by inter-barrier spacing. As the spacing between two rows increases, the protective efficiency initially improves before declining. The system reaches peak overall protective efficiency when the inter-barrier spacing is set at 20H.

摘要

中国西北地区的自然条件恶劣，荒漠化较为严重。沙尘暴天气频发，对沙漠边缘交通设施、农业经济作物和当地生态环境造成破坏。本文提出一种新型高立式曲线沙障，通过野外实验验证了数值模拟结果，并分析了高立式曲线沙障的风沙流特征和防护效率。对不同间距下的双排沙障进行研究，得出最优铺设间距。研究表明，高立式曲线沙障相对于垂直方向的角度显著影响新型沙障的防护效率，其防护效率随着角度的改变呈现波动格局。当入口风速为 10m/s，沙障倾斜角度为 75°时，沙障后方的减速区面积达到 25.450 m²，覆盖范围为 19.31H，沙障整体防护效率最佳。双排沙障的防护效率受到沙障间距的影响，随着两排沙障间距的增强，防护效率先增加后减小。当两排沙障间距达到 20H 时，沙障整体防护效率最优。

INTRODUCTION

Desertification is a critical global ecological issue that significantly impacts human survival and development. According to UNCCD assessments, China is classified among the top-tier countries most severely impacted by desertification on a global scale, with its northwestern region being particularly vulnerable due to harsh natural conditions and scarce land resources, making it a typical example of an ecologically fragile zone (*Yifei C. et al., 2024*). Xinjiang is the largest province in China's northwest region and the area most severely affected by desertification, with the greatest expanse of desertified land in the country. It has long been influenced by the westerlies, the Siberian High, and a continental arid climate (*Bingqi Z. et al., 2014*). The sandstorms carry massive amounts of sand particles that can bury vast areas of farmland. Through sand burial, wind erosion, and windblown sand attacks, they cause ecological degradation and significant losses to people's lives and property (*Chuijie W. et al., 2008*).

Desertification control interventions are primarily functionally partitioned into mechanical sand control and biological sand control. Sand control projects can protect local desert vegetation and farmlands, and prevent further expansion of desertification. Among desertification control measures, engineering measures address the symptoms, while biological measures tackle the root causes.

The systematic integration of both engineering and biological measures offers a fundamental solution for effective wind and sand control (*Muning Z. et al., 2006; Jianjun Y., 2007*).

Mechanical sand control measures demonstrate faster effectiveness compared to biological approaches. By altering underlying surface properties and increasing ground roughness, mechanical sand barriers effectively reduce sand flow volume and erosion intensity, thereby achieving rapid stabilization of mobile sands (*Jing S. et al., 2023*).

Straw checkerboard barriers constitute the canonical aeolian sand control infrastructure, demonstrating maximum implementation density along desertification fronts worldwide. It plays an irreplaceable role in wind prevention and sand fixation, precipitation interception, reduction of water evaporation, and nutrient provision for sandy soil (*Jiayuan D. and Xiangyun Q., 2019*).

The direct effect of straw checkerboard sand barriers is to increase surface roughness. Sand particles tend to accumulate around the barriers, promoting the formation of concave surfaces (*Na Z. et al., 2014; Xiaohong D., 2015*). *Li L. and Tianli B., (2015*), conducted experimental and numerical studies on the design of checkerboard sand barriers for desertification control projects. Field observation results demonstrated that the installation of checkerboard barriers induces substantial airflow deceleration behind sand dunes. The size and shape of straw checkerboard sand barriers significantly influence sand flow patterns and near-surface wind speed distribution (*Ze M. et al., 2024; Jianjun Qet et al., 2007; Kecun Zet et al., 2012; Chunlai Zet et al., 2016*).

The installation of straw checkerboard sand barriers gradually alters the surface aeolian sand structure, effectively inhibiting sand drift and playing a vital role in local ecological restoration (*Yanfu Let et al., 2017; Yuqiu G. et al., 2004*).

For critical windproof and sand-blocking areas such as railways, highways, and farmland, high vertical sand barriers demonstrate excellent wind and sand control effectiveness. *Cheng X et al., (2021),* conducted field studies on the windproof and sand-blocking characteristics of high vertical nylon net sand barriers. Under low wind speed conditions (below 12 m/s), the effective protection distance was measured at 3H (where H represents the barrier height) for single-row barriers, while double-row barriers exhibited a leeward protection zone extending to 12H. The windproof fence barrier induces measurable velocity attenuation across the 100-220 meters behind the barrier, but it has no significant impact on the overall airflow distribution (*Jianhua X. et al., 2022; Tao W. et al., 2018*). *Li Kaichong et al., (2017),* examined the influence of aperture configuration on the sand-blocking efficiency of sand barriers. When the wall aperture angle was set at 135°, both the accumulated sand volume and the barrier's sand-blocking efficiency reached their optimal levels. *Chen Boyu et al., (2019),* investigated perforated sand fences with different aperture sizes and found that the variation in aperture diameter is a key parameter affecting the flow acceleration domain, the length of the leeward vortex region, and the distribution of surrounding sediments. *Zhang Kai et al., (2021),* conducted indoor wind tunnel experiments to analyze the flow field characteristics, porosity, and sand-blocking effectiveness of single-row vertical sand barriers made of HDPE panels. The results indicated that the sand-blocking efficiency of a single-row HDPE barrier was lower than that of multi-row sand barriers. *Wang Fang et al., (2023),* conducted numerical simulations using Fluent software to analyze the spacing and height of double-row sand barriers. The results revealed a positive correlation between barrier height and protective performance. Optimal windproof efficiency was achieved when the barrier height ranged between 1.5~2 m with a spacing of 2H (where H represents the barrier height).

In summary, scholars worldwide have conducted extensive research on the windproof and sand-blocking performance and mechanisms of sand barriers, accumulating substantial technical and engineering application experience. Low vertical barriers such as straw checkerboards can be deployed over large areas to effectively increase surface roughness and prevent desertification erosion. However, such barriers require long-term ecological restoration and cannot immediately establish effective wind and sand control for farmlands, railways, and highways at desert margins. In areas with severe wind-sand hazards, tall vertical barriers can effectively block sand-laden winds below the barrier height while creating a deceleration zone behind the barrier, thereby providing timely protection for desert highways, railways, and ecological farmlands against wind-sand damage.

Therefore, this study focuses on a novel tall vertical curved sand barrier as the research subject. Through numerical simulation methods complemented by field experiments to validate the simulation results, the protective efficiency of the curved sand barrier under various parameters was systematically investigated. The findings aim to provide theoretical design foundations for windproof and sand-control projects in regions severely affected by wind-sand hazards.

MATERIAL AND METHODS

Description of the study area

As shown in Figure 1, the study area is located in Nanhuzi Sand Hill next to the S235 highway in Yizhou District, Hami City, Xinjiang Uygur Autonomous Region, geographically situated at longitude 93°12'9.137" East and latitude 42°29'27.028" North. The study area is rich in sand sources, with frequent sandstorms, and the wind direction of sand initiation is mostly SE and SW winds. The area has a variety of sand dunes and is characterized by a typical temperate continental arid climate. The climate is dry, with annual precipitation below 30 mm and evaporation exceeding 3,000 mm; the mean temperature is 5.0°C; the soil is typical wind-sand soil, and the vegetation is basically absent. The experimental area was artificially leveled in the early stage, and the terrain is relatively flat and open with little human traffic, making it an ideal location for observing sand prevention measures.

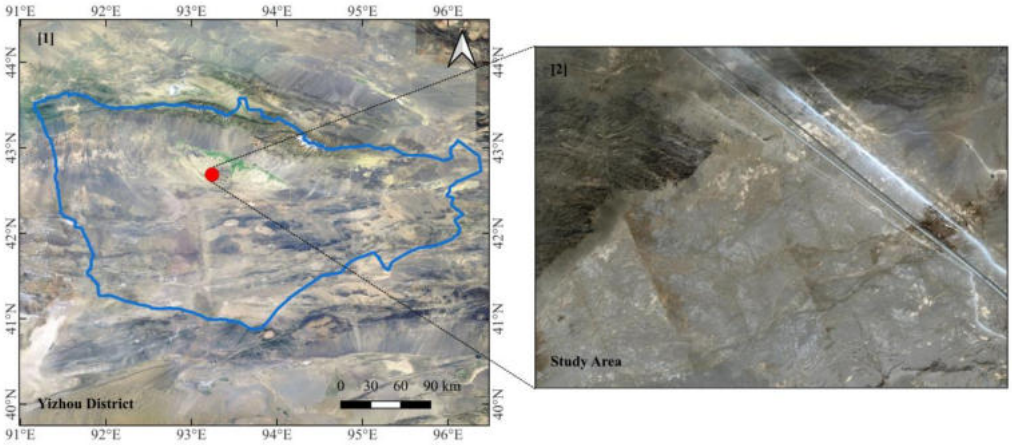


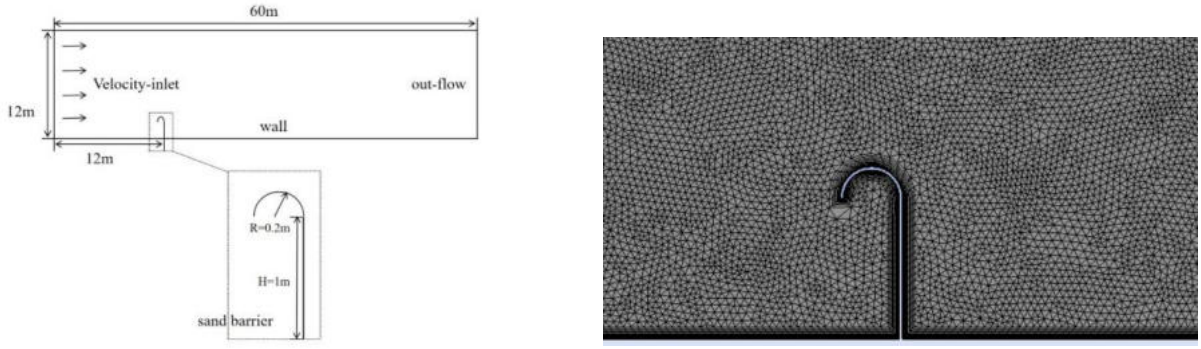
Fig. 1 - Map of the study area in the sandy hills of Nanhuzi, Hami, China

Numerical simulation

Geometric modelling and meshing

In natural environments, there exists a three-dimensional coupled wind-sand field. Theoretically, larger simulation domains allow for more complete airflow development, thereby reducing errors caused by vortices and airflow deflection around sand barriers. However, considering practical working conditions, sand particle motion is primarily governed by three forces: fluid drag force, lift force, and particle gravity. Under the action of airflow, these forces usually act within the same plane, so it is permissible to solve the problem as a two-dimensional problem (*Yan W et al., 2024*).

The computational domain of this study has a length of 60 m and a height of 12 m, as shown in Figure 2a. The height of the tall curved sand barrier is 1 m, the radius is 0.2 m, and the thickness is 0.02 m. The entrance is 12 m away from the sand barrier, and the speed exit is 48 m away from the sand barrier. The size of the flow field is consistent with the field experiment. The railway is located 48 m behind the sand barrier, and the height is set at 12 m, which is conducive to observing the airflow distribution above the sand barrier. An unstructured grid method was employed to divide the domain into triangular meshes. As shown in Figure 2b, a triangular element type was employed with approximately 600,000 elements. The grid skewness is less than 0.85, meeting the criteria for numerical simulation.



a) **b)**

Fig. 2 - Numerical simulation model diagram

a) Calculate regional distribution map; b) Grid partitioning diagram

Theoretical governing equation

The standard k-ε turbulence model was used to simulate the wind field, providing more accurate results for flows with significant streamline curvature and offering higher computational precision (*Bailiang Land and Douglas J.S., 2015*). The Eulerian model (two-fluid model) was selected for the multiphase flow simulation, which treats both the continuous and discrete phases as continua. It establishes continuity and momentum equations for each phase and solves them through coupled calculations of pressure and interphase exchange coefficients. The SIMPLE algorithm was then employed to solve for pressure and velocity (*Guowei X. et al., 2021; Lzael A.L. et al., 2020*).

The following equation represents the windproof efficiency:

$$\mathbf{f_{xz}} = \frac{\mathbf{v_{xz}} - \acute{\mathbf{v}}_{\mathbf{xz}}}{\acute{\mathbf{v}}_{\mathbf{xz}}} \times \mathbf{100}\% \quad (\mathbf{1})$$

where: $\mathbf{f_{xz}}$ is wind protection efficiency; x is the distance from the sand barriers; z is the height above ground level (expressed as a multiple of the height of the sand barriers); $\acute{\mathbf{v}}_{\mathbf{xz}}$ is the wind speed relative to the wall surface under sand barrier protection; $\mathbf{v_{xz}}$ is the wind speed relative to the wall surface without sand barrier protection (*Yana L. et al, 2025; Jing S. et al, 2024*).

The following equation shows the retention rate of sand particles:

$$\boldsymbol{n} = \frac{\mathbf{W} - \mathbf{Q}}{\mathbf{W}} \times \mathbf{100}\% \quad (\mathbf{2})$$

where: **n** is the sand barrier retention rate; **W** is the amount of sand transported in the wilderness for the same wind speed and altitude (g·cm^{-2}·min^{-1}); **Q** is the sand transport flux of sand particles behind the sand barrier (g·cm^{-2}·min^{-1}).

Calculated parameter

Boundary conditions for numerical simulation: the left side is a velocity inlet (constant), the right side is an outlet (free outflow), the bottom is a wall, and the top is a symmetry plane (*Yang D. et al., 2021; Ascanio D.A. et al., 2013*). as detailed in Table 1.

Table 1

Numerical simulation of calculated parameters

Variable	Parameters	Variable	Parameters
Air density/(kg·m^3)	1.225	Sand diameter/m	1×10^{-4}
Air viscosity/Pa·s	1.7894×10^{-5}	Sand viscosity/(kg/m·s)	0.047
Turbulence intensity	0.05	Sand Volume fraction/%	0.02
Temperature/K	256.95	Sand density/(kg·m^3)	2650
Mach number	<0.3	Convergence criteria	<10^{-5}

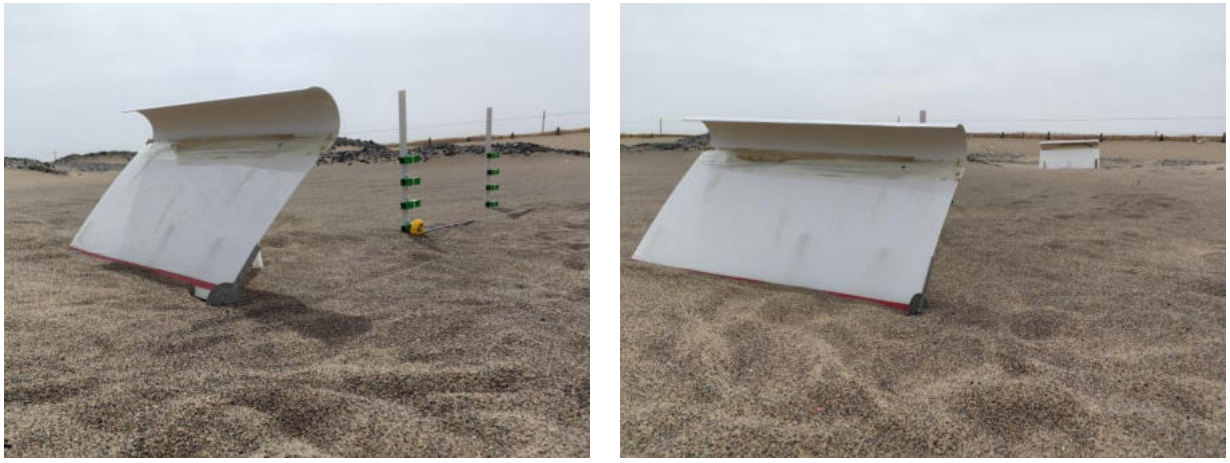
Field experiment design

As shown in Figure 3, the sand barriers used in this experiment were fabricated with PLA material at a 2:1 scale reduction to verify the windproof and sand-blocking performance of barriers with a 75° inclination angle. The actual height of the sand barrier is 0.6 m, and its width is 0.5 m. Field experimental equipment included a sand trap, an electronic balance (0.01 g precision), calipers (1 mm precision), and an anemometer (0.1 m/s precision).

To obtain accurate wind speed data, the research team collected nearly one year of local environmental data through online databases and conducted on-site wind measurements from May 6 to May 9, 2025. Wind speed measurements were taken using a smart anemometer at heights of 10 cm, 30 cm, and 50 cm. The measurement protocol involved 10 readings per hour over 5-hour periods each day for three consecutive days, with the final wind speed averages calculated from this dataset.

The measurement results showed average wind speeds of 7 m/s (range: 3-10 m/s) at 10 cm height, 10m/s (range: 5-14 m/s) at 30 cm height, and 15 m/s (range: 6-20 m/s) at 50 cm height. The data analysis revealed that wind speed variations were not significant below 30 cm height, where low wind speeds occurred more frequently, while noticeable wind speed fluctuations were observed at the 50 cm height.

The sand trap employed was a stepped collector with four height layers. Measurements revealed the following average aeolian sand transport fluxes in open terrain: 3.91 g·cm^{-2}·min^{-1} at 0-10 cm height, 2.82 g cm^{-2}·min^{-1} at 10-20 cm height, 1.41 g cm^{-2}·min^{-1} at 20-30 cm height, and 0.53 g cm^{-2}·min^{-1} at 30-40 cm height. Figure 3 shows the on-site installation layout of the sand barriers.



a) b)

Fig. 3 - Sand barrier layout diagram

a) Single-row sand barrier; b) Double-row sand barriers

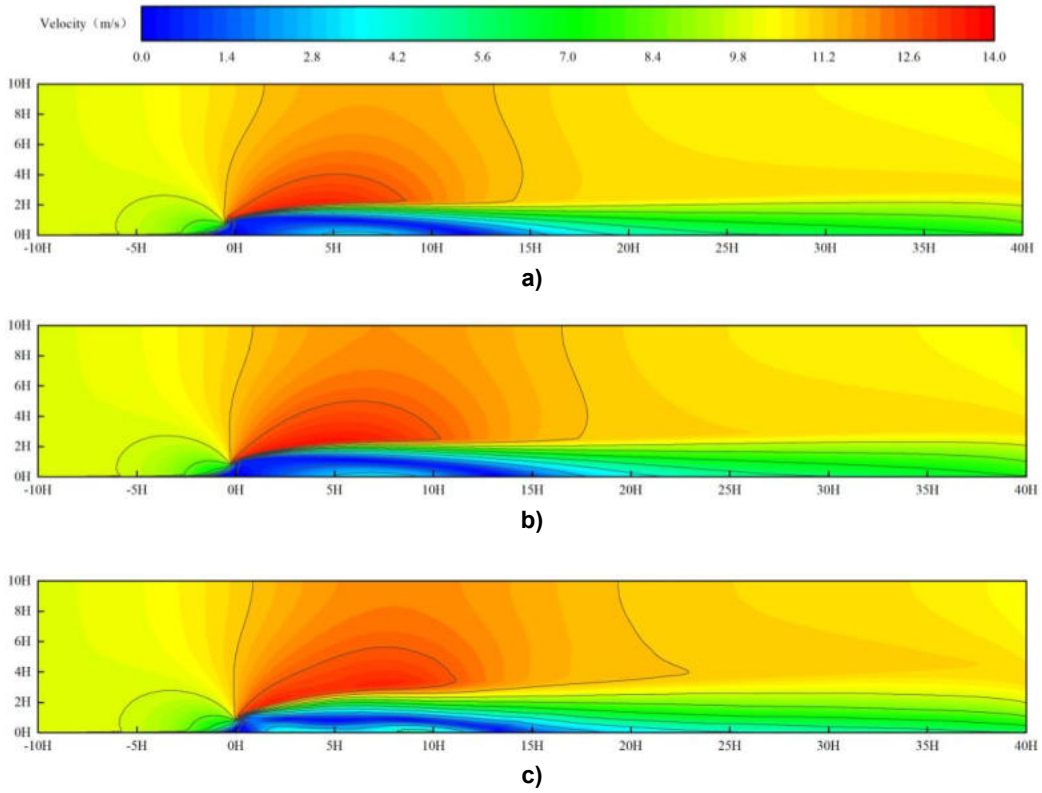
RESULTS

- **Numerical simulation results and analysis**

The influence of sand barrier inclination angle on windproof effectiveness

Figure 4 shows the wind velocity contour plots of sand barriers with five different inclination angles under an incident flow velocity of 10 m/s. Specifically: Figure 4a displays the wind velocity contour for a 90° inclination angle, Figure 4b for 75°, Figure 4c for 60°, Figure 4d for 45°, and Figure 4e for 30°.

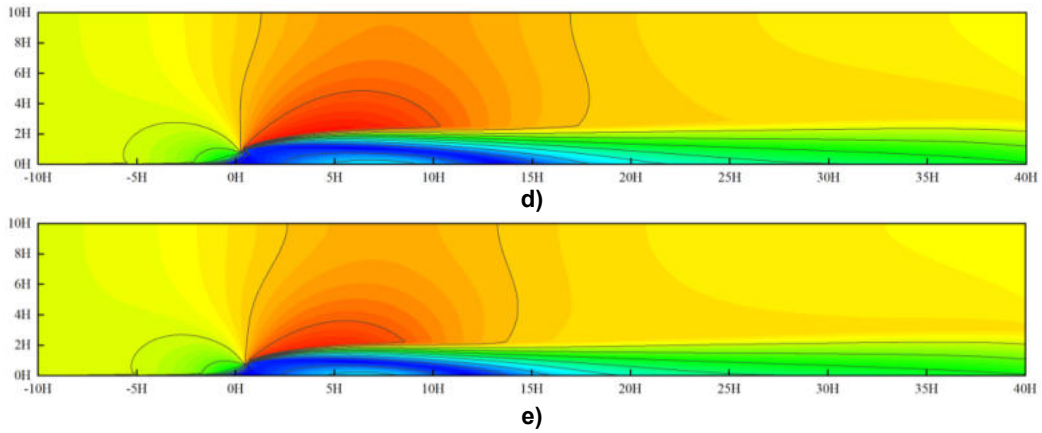
As illustrated in Figure 4, the novel sand barrier exhibits a wind velocity distribution pattern similar to vertical sand barriers. When airflow encounters the barrier, it obstructs the approaching wind, creating three distinct zones: small deceleration zones are formed on the windward side of the sand barrier, acceleration zones are formed at the top of the sand barrier, and turbulence zones are formed on the leeward side of the sand barrier. The innovative design of this sand barrier prevents direct perpendicular wind force. Notably, variations in the barrier's inclination angle dynamically modify the spatial dimensions of both the crest acceleration zone and the leeward deceleration zone.



a)

b)

c)



d)

e)

Fig. 4 - Airflow velocity contour of single-row sand barrier

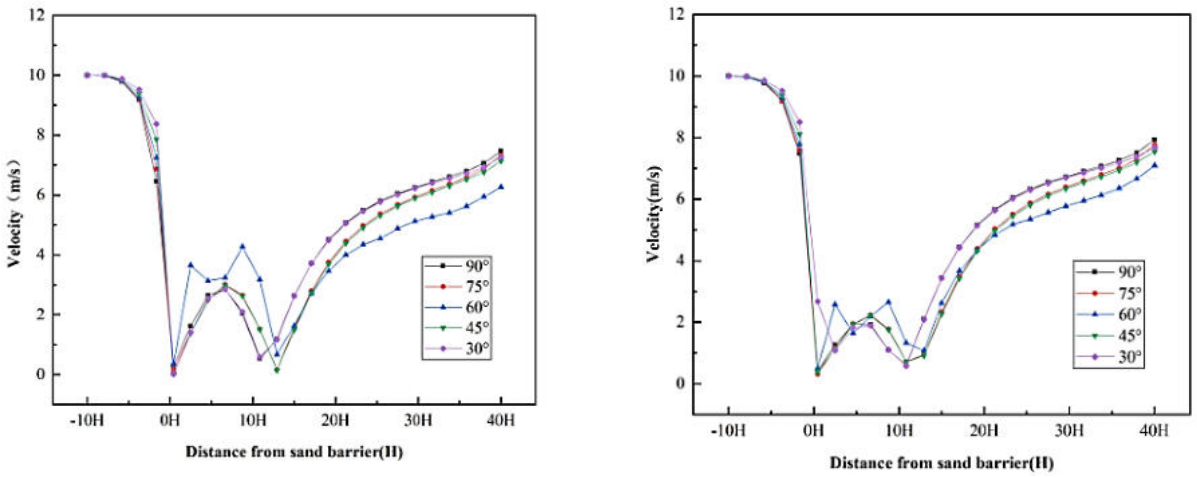
a) α=90°; b) α=75°; c) α=60°; d) α=45°; e) α=30°

A comparative analysis of sand barriers with different inclination angles in Figure 4 was conducted using 2.5 m/s as the minimum threshold wind speed for sand particle entrainment. The areas with wind speeds below 2.5 m/s for barriers inclined at 90° to 30° measured 21.515m^2, 25.450m^2, 17.332m^2, 24.299m^2, and 19.039m^2 respectively. The protective area of the turbulent zone behind the barriers exhibited an initial increase followed by a decreasing trend. The horizontal coverage ranges of the 2.5 m/s wind speed contour behind the sand barriers were 17.51H, 19.31H, 19.64H, 19.03H, and 17.49H, respectively. The size of the deceleration zone generally showed an initial increase followed by a decreasing trend. Overall, the 75° inclined sand barrier demonstrated better protective effectiveness under 10 m/s wind conditions.

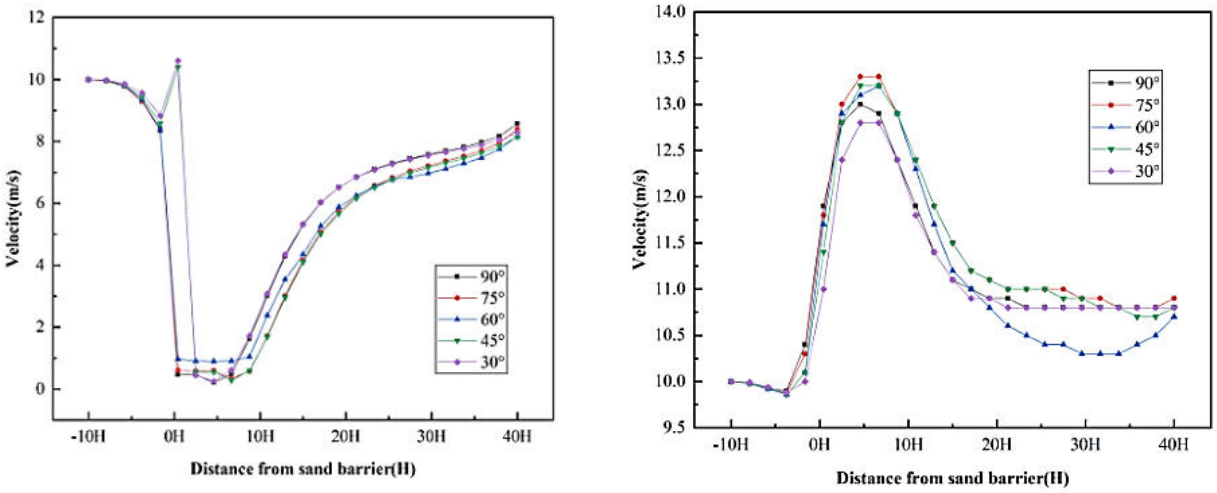
Flow field patterns around sand barriers

Figure 5 shows the horizontal wind speed distribution characteristics around the new sand barrier at different inclination angles. Figures 5a to 5d show the horizontal wind speed diagrams at heights of 0.2H, 0.5H, 1H, and 3H above ground level.

At heights of 0.2H and 0.5H above ground level, the horizontal velocity variation demonstrates an initial decrease followed by an increase, exhibiting an approximately "W"-shaped distribution along the distance. Due to the effect of sand barriers blocking airflow, the airflow velocity decreases sharply in front of the barrier. In the leeward region, the combined effects of low pressure and turbulence cause the velocity to first increase and then decrease. As the distance between the airflow and the sand barrier increases, the wind speed behind the sand barrier gradually recovers. Below the barrier height (1H), the wind speeds behind sand barriers with inclination angles from 90° to 30° are reduced to 6.09 m/s, 5.70 m/s, 5.79 m/s, 6.06 m/s, and 6.52 m/s, respectively. These results indicate that at a 75° inclination angle, the airflow velocity is lowest under 10 m/s wind conditions, demonstrating optimal protective effectiveness.



a) b)



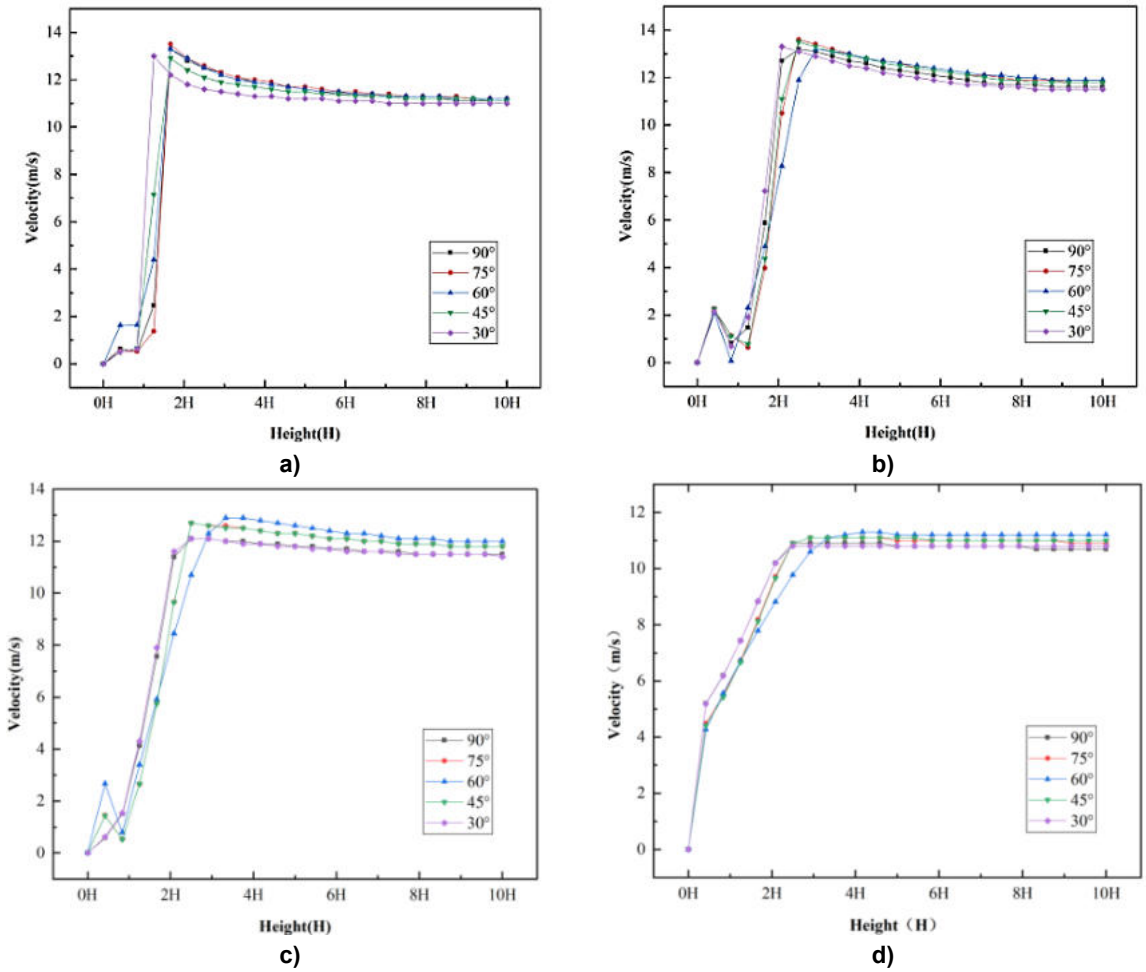
c) d)

Fig. 5 - Planar wind speed profiles for differently inclined sand barriers

a) D =0.2H; b) D =0.5H; c) D =1H; d) D=3H

Figure 5d demonstrates that the velocity variation at 3H height above ground follows the same pattern as observed at the other three elevations, exhibiting an inverted "V"-shaped distribution characteristic. This indicates that the windproof is less effective at a height of 3H and that the protective height of the windproof is lower than its own height.

Figure 6 presents the vertical wind speed characteristics around the novel sand barriers at different inclination angles.



a) b)

c) d)

Fig. 6 - Vertical velocity distribution patterns for variably inclined sand barriers

a) D=1H; b) D =5H; c) D =10H; d) D =20H

Figures 6a to 6d display the vertical wind speeds at distances of 1H, 5H, 10H, and 20H from the barriers. The sand barrier exhibits similar wind speed variation patterns at 1H, 5H, 10H, and 20H distances, though the variation trends are significantly influenced by elevation height. Below the height of 1H, wind speed first increases and then decreases as the height above ground increases; between the heights of 1H and 2H, the wind speed gradually increases, the wind protection effect decreases, and it enters into the acceleration zone. When the height above the ground exceeds 2H, the wind-blocking effect of the sand barriers on the incoming wind decreases, and the airflow behind the barriers comes into contact with the external airflow, so that the wind speed gradually tends to stabilize.

Windproof efficiency variation patterns of sand barriers

Figure 7 selects wind speeds at four heights: 0.2H, 0.5H, 1H, and 3H above the ground. Based on the windproof efficiency formula (1), the windproof efficiency of sand barriers at different tilt angles is calculated, with the overall distribution trend showing an "M" shape. At three heights: 0.2H, 0.5H, and 1H, the windproof efficiency first increases and then decreases, indicating that the main protective range of the sand barriers is in the area below the height of the barriers. At a height of 3H, the sand barrier has no effect on blocking airflow, so the windproof efficiency becomes negative. The movement of sand particles in the desert mostly occurs near the surface.

This study focuses on the analysis below the height of the sand barrier (1H). The average windproof efficiencies of sand barriers with tilt angles ranging from 90° to 45° are 39.1%, 43.0%, 42.1%, and 39.4%. Windproof efficiency fluctuates with changes in the angle of the sand barrier, increasing at first and then decreasing, reaching its optimum at 75°.

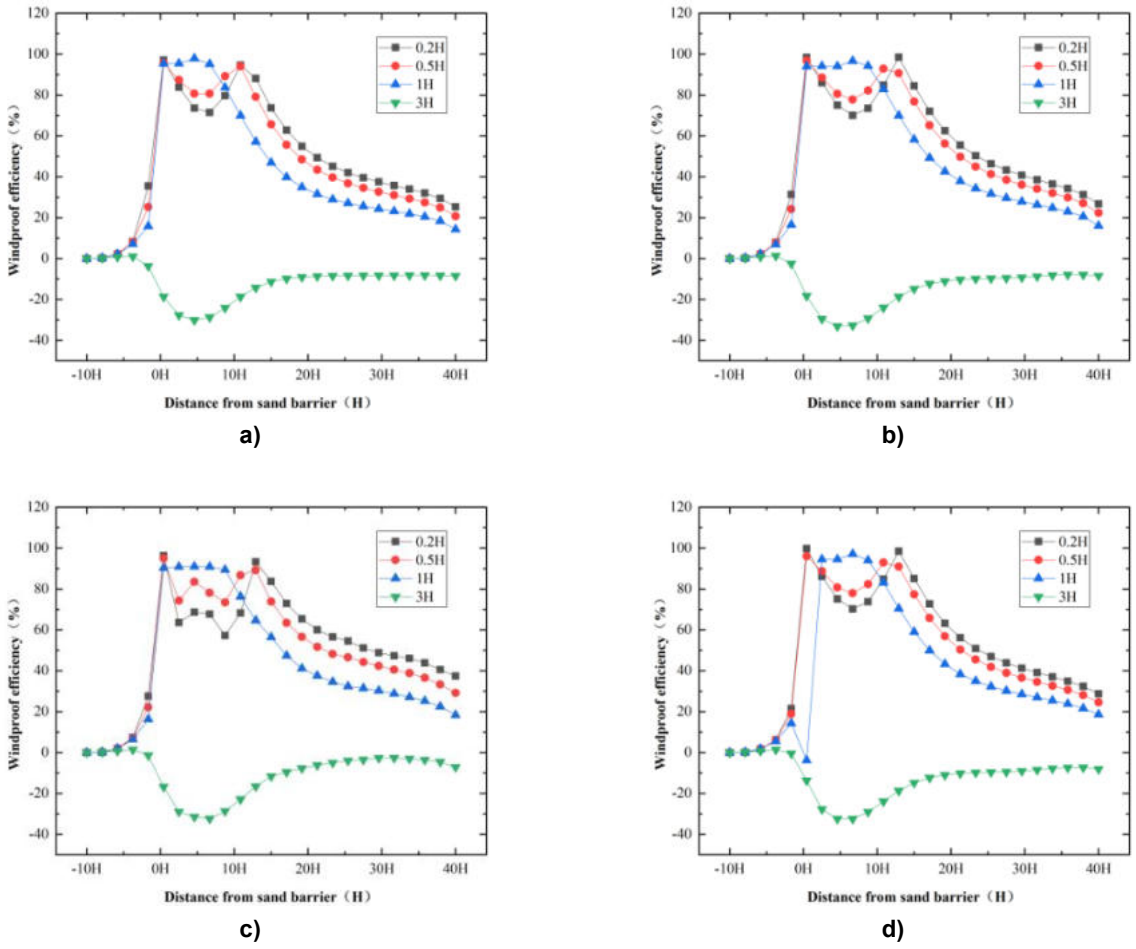


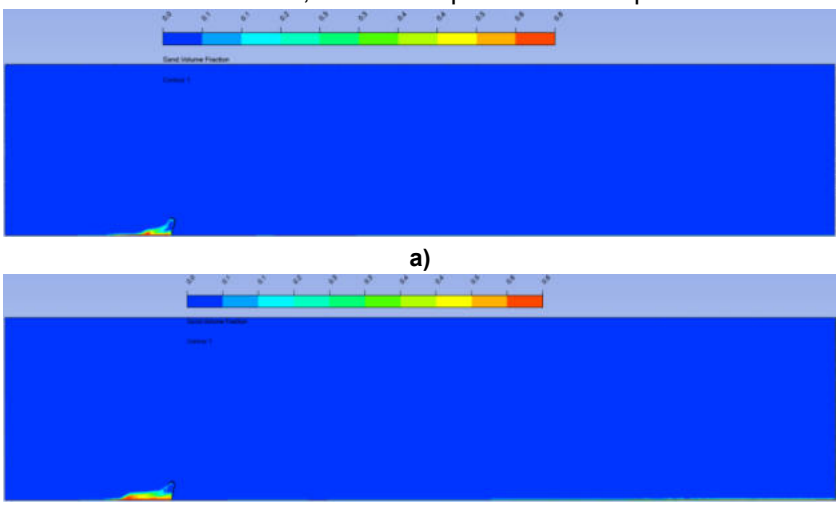
Fig. 7 - Windproof efficiency diagram of sand barriers at different tilt angles

a) α=90°; b) α=75°; c) α=60°; d) α=45°

The sediment distribution of sand barriers

Due to the significant mass difference between sand particles and air, when wind-sand flow reaches the vicinity of a sand barrier, a pressure difference is created, generating localized resistance.

This can substantially reduce the transit speed of the airflow and weaken the energy of the wind-sand flow, causing some sand particles to deposit around the sand barrier. The study on the windproof efficiency and protective distance of sand barriers shows that a tilt angle of 75° yields better results. At this angle, the volumetric distribution of sand particles in the flow field is illustrated in Figure 8. As the volume fraction of sand particles and the accumulation time increase, more sand particles are deposited around the sand barrier.



a)

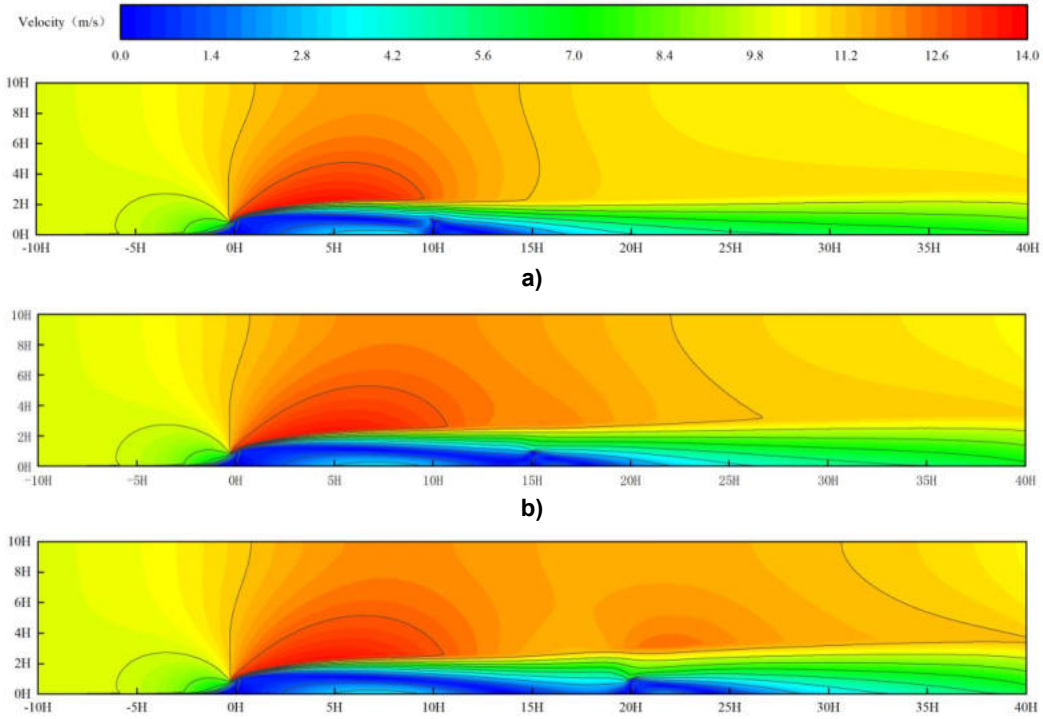
b)

Fig. 8 - Contour plot of sand accumulation at the sand barrier

a) t=4s; b) t=8s

Flow distribution characteristics of double-row sand barriers

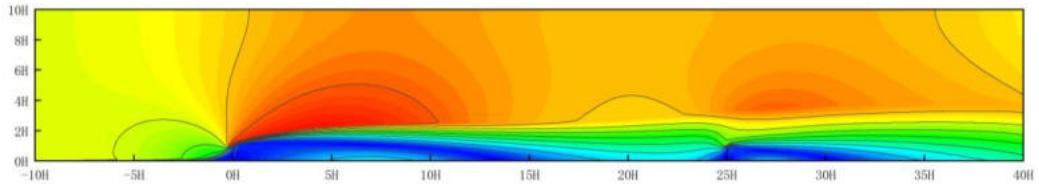
Figure 9 displays the wind speed contour plots of double-row sand barriers with spacings of 10H, 15H, 20H, and 25H at a wind speed of 10 m/s. D represents the distance between double rows of sand barriers. When the airflow reaches the first row of sand barriers, a deceleration zone forms in front of the barriers due to their blocking effect, while an acceleration zone develops above the barriers. The two rows of barriers create a vortex zone, leading to sand deposition. When the airflow reaches the second row of barriers, the wind speed is already reduced, resulting in a smaller acceleration zone. The distance between the two rows of barriers influences the overall windproof and sand-blocking effectiveness.



a)

b)

c)



d)

Fig. 9 - Wind speed contour maps of double-row sand barriers with different spacings

a) D=10H; b) D=15H; c) D=20H; d) D=25H

The double-row sand barriers exhibit a bimodal airflow fluctuation pattern. For barriers with spacings of 10H to 25H, the areas with wind speeds below 2.5 m/s measure 22.971m^2, 31.916 m^2, 37.326m^2, and 36.693m^2, respectively. The protective area of the turbulent zone behind the barriers shows an initial increase followed by a fluctuating decrease. Overall, the double-row sand barriers with a 20H spacing demonstrate better protective effectiveness at a wind speed of 10 m/s.

Variation characteristics of windproof efficiency in double-row sand barriers

Figure 10 illustrates the windproof efficiency of double-row sand barriers with spacings of 10H, 15H, 20H, and 25H. As shown in Figures 13a~b, the overall trend of windproof efficiency for double-row sand barriers with spacings of 10H and 15H is consistent, exhibiting an initial increase followed by a decrease. From Figures 13c~d, it can be observed that the windproof efficiency for double-row sand barriers with spacings of 20H and 25H features a longer transition zone. Among sand barriers with different spacing, those with a spacing of 20H have the best overall windproof efficiency and the optimal effective protection distance.

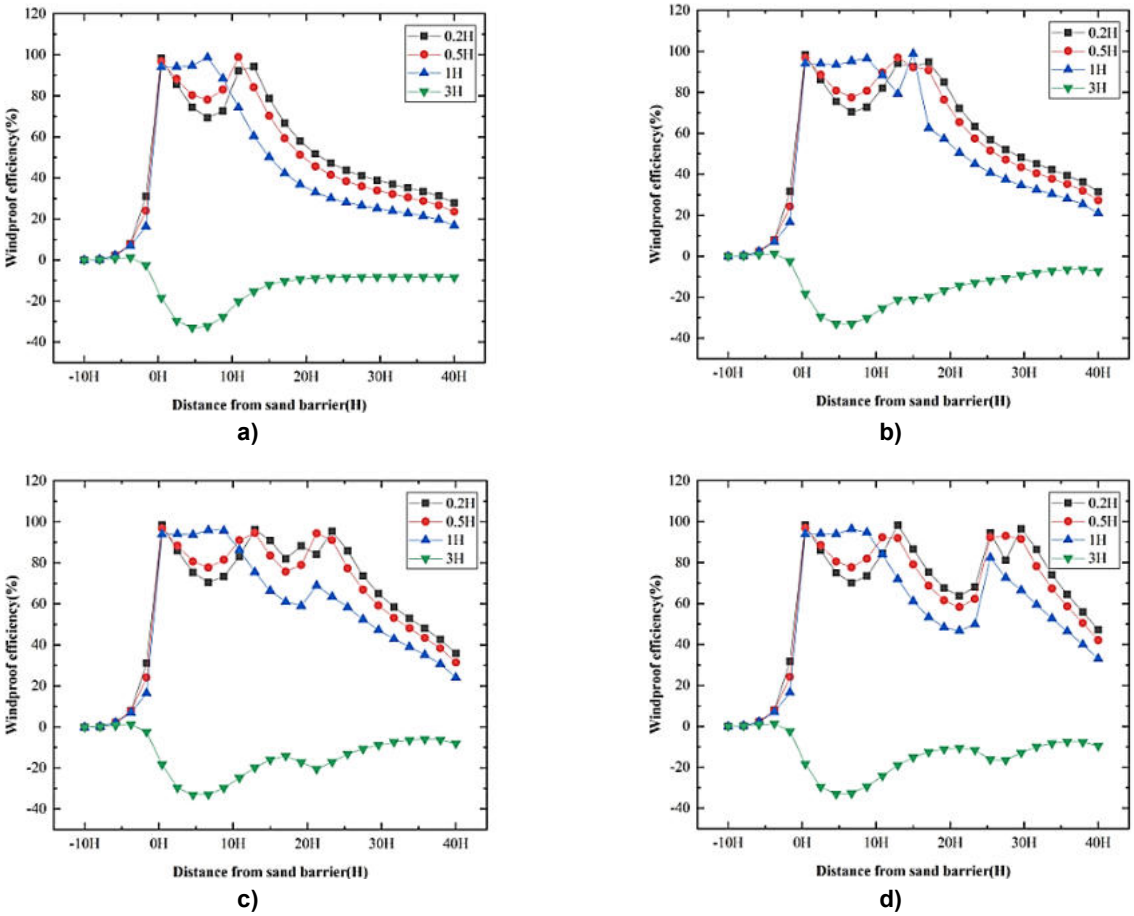


Fig. 10 - Windproof efficiency diagram of double-row sand barriers

a) D=10H; b) D=15H; c) D=20H; d) D=25H

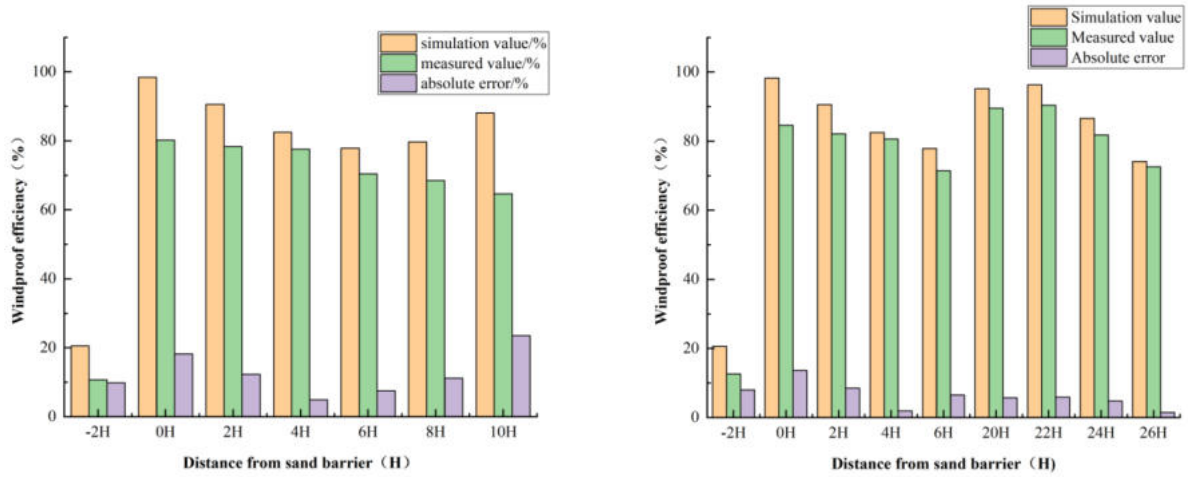
➢ **Results and analysis of field experiments**

Comparative analysis of wind speed in field experiments

In field environments, wind speed variations are significant and unstable, with differences observed even at the same altitude level. Therefore, instead of directly comparing wind speed values, the windbreak efficiency is calculated using the measured wind velocity data from the open area in front of the sand barrier and the measured wind speed data behind the sand barrier. This approach allows for a more intuitive comparative analysis.

Using the 30 cm (0.5H) height layer as the comparison level, Figure 11a shows that there are certain discrepancies between the field experiment and simulation results. The maximum absolute error is 23.5%, primarily because the measurement points were located at a considerable distance from the sand barrier, and the rear measurement points were significantly affected by lateral winds, leading to a larger error. The minimum error is 4.9%, with all other errors being less than 20%. Overall, the field experiment data align well with the numerical simulation data.

As shown in Figure 11b, the maximum error is 13.6%, the minimum is 1.9%, and all other errors are less than 10%. Overall, the error distribution indicates that double-row sand barriers exhibit smaller discrepancies compared to single-row barriers and align more closely with the numerical simulation results. This further validates the reliability of numerical simulation and can accurately display the patterns of airflow.



a) b)

Fig. 11 - Comparison of errors between field experiments and numerical simulations

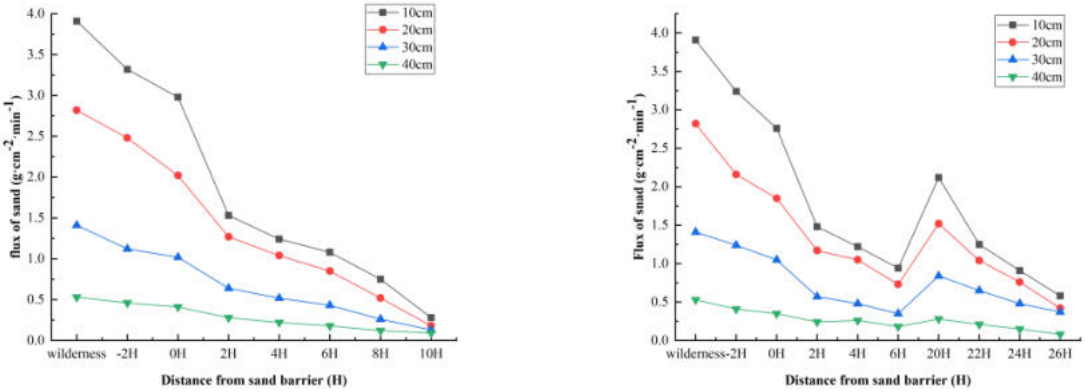
a) Single-row sand barrier; b) Double-row sand barriers

Analysis of sand deposition in field experiments

Figure 12 shows the measurement and analysis of sand deposition in the experimental area. The main area for sand grain migration is within the 0-10 cm height span, where the sand transport flux is greatest. As the height increases, the sand transport flux decreases significantly. The average sand transport flux at a height of 0-10 cm was 3.91 g cm^{-2}·min^{-1}. For every 10 cm increase in height, the sand transport flux gradually decreases to 2.82 g cm^{-2}·min^{-1}, 1.41 g cm^{-2}·min^{-1}, and 0.53 g cm^{-2}·min^{-1}, respectively.

As shown in Figure 12a, the 0-10 cm height range is the primary zone for sand saltation, with the maximum sand particle interception rate reaching 92.83%. As the height increases, the maximum interception rate at 20 cm is 93.61%, at 30 cm it is 90.78%, and at 40 cm it is 83.01%. This further confirms that the sand transport flux weakens with increasing height, and wind-sand activity is predominantly concentrated near the ground surface.

Figure 12b shows sand particle deposition in a double row of sand barriers. Their sand-blocking characteristics are similar to those of the single-row barriers. After sand particles collide with the barriers, most of them deposit in front of the barriers, while some particles pass over them. The sand transport flux decreases with increasing distance from the barriers. Due to the blocking effect of the first row of barriers, the sand transport flux in front of the second row is significantly reduced compared to the first row. As the row number of sand barriers increases, the wind speed in the area between the double-row barriers becomes lower, making it less likely for sand particles to saltate. Overall, the double-row sand barriers exhibit better sand-blocking effectiveness.



a) **b)**

Fig. 12 - Sand deposition diagrams from field experiments

a) Single-row sand barrier; b) Double-row sand barriers

CONCLUSIONS

To address the shortcomings of traditional vertical sand barriers, this study proposes a new type of curved vertical sand barrier. Using Fluent numerical simulations, the characteristics of wind-sand flow around the curved vertical sand barrier and its protective efficiency were analyzed. Finally, the results of the numerical simulation were verified through field trials, leading to the following conclusions:

1. The angle of the horizontal vertical curved sand barrier relative to the vertical direction significantly affects the protective efficiency of the new barrier. The protective efficiency of the barrier exhibits a fluctuating pattern as the angle changes. At an inlet wind speed of 10 m/s, when the barrier's tilt angle is 75°, the area of the deceleration zone behind the barrier is 25.450 m², with a coverage range of 19.31H, indicating overall better protective effectiveness. The protective efficiency begins to decline when the angle exceeds 75°.

2. The height of the vertical curved sand barrier affects the effective protection range of the sand barrier. The barrier cannot effectively intercept sand particles exceeding its height. In the vertical direction, sand particles are primarily distributed in the area below the barrier height, while in the horizontal direction, they mainly deposit in front of the barrier.

3. The overall protective efficiency of double rows of sand barriers is affected by the distance between the double rows of sand barriers. The overall protective area of double rows of sand barriers shows a fluctuating trend of first increasing and then decreasing as the distance between the sand barriers increases. When the spacing between two lines is 20H, the area with wind velocity below 2.5 m/s within the double-row barriers reaches its maximum at 37.326 m². When the spacing exceeds 20H, the overall protective area of the sand barriers begins to decrease, and the protective efficiency decreases.

Railways, highways, farmlands, and ecological restoration areas are abundant in Northwest China. Severe sandstorms can bury railways and highways under sand, reduce crop yields, and damage the local ecological environment. This study provides a solid foundation for the development of transportation infrastructure and sand prevention projects in desertification areas. Finally, the dimensions of the sand barriers can be further optimized to ensure their protective effect on agricultural areas under extreme weather conditions. Research can also be conducted on the accumulation of sand particles in front of the sand barriers to avoid affecting their effectiveness.

ACKNOWLEDGMENTS

The authors were funded for this project by the National Natural Sciences Foundation of China (NSFC), Grant/Award Number: 52265039.

REFERENCES

[1] Ascanio D.A., Eric J.R., Thorsten P., Jose S.A., Hans J.S. (2013), Numerical modeling of the wind flow over a transverse dune, *Scientific Reports*, Vol.3, pp.2858, Hangzhou/China. Fortaleza/Brazil.

[2] Bingqi Z., Jingjie Y., Xiaoguang Q., Patrick R., Yichi Z., Heigang X. (2014), Formation and evolution of sand deserts in Xinjiang, Northwest China: II. The palaeo-environmental reconstruction. *Journal of Geographical Sciences*, Vol.24(3), pp.539-559, Beijing/China.

[3] Boyu C., Jianjun C., Lingui X., Rui W., (2019), Effectiveness of hole plate-type sand barriers in reducing aeolian sediment flux: Evaluation of effect of hole size, *Aeolian Research*, Vol.38, pp.1-12, Xinjiang/China.
[4] Bailiang L., Douglas J.S., (2015), Aerodynamics and morphodynamics of sand fences: A review. *Aeolian Research*, Vol.17, pp.33-48, Suzhou/China.
[5] Chuijie W., Ming W., Liang W., (2008), Large-eddy simulation of formation of three-dimensional aeolian sand ripples in a turbulent field. *Science in China Series G: Physics, Mechanics & Astronomy*, Vol.51(8), pp.945-960, China.
[6] Chunlai Z., Qing L., Na Z., Jiaqiong Z., Liqiang K., Yaping S., Wenru J., (2016), Field observations of wind profiles and sand fluxes above the windward slope of a sand dune before and after the establishment of semi-buried straw checkerboard barriers, *Aeolian Research*, Vol.20, pp.59-70, Beijing/China.
[7] Cheng X., Hejun Z., Haibing W., Min Y., Guangpu J., (2021), Wind-proof and sand-blocking characteristics of high vertical nylon mesh sand barrier and its rational allocation (高立式尼龙网沙障防风阻沙特征及其合理配置), *Arid Zone Research*, Vol.38(3), pp.882-891, Hohhot/China.
[8] Fang W., Shixiao L., Yujia J., Weijia D., (2023), Research on the Effect of Sand Barriers on Highways in Desert Areas on Sand Control, *Sustainability*, Vol.15, pp.13906, Yinchuan/China.
[9] Guowei X., Ning H., Jie Z., Hongchao D., (2021), Investigations into the design of sand control fence for Gobi buildings, *Aeolian Research*, Vol.49, pp.100662, Lanzhou/China.
[10] Jianjun Y., (2007), Discussion on Several Problems in the Projects of Slope Ecological Protection Engineering (边坡生态防护工程中的若干问题探讨), *Research of Soil and Water Conservation*, Vol.14(5), pp.333-335, Hubei/China.
[11] Jing S., Jun W., Hailong W., Junzhe H., Shaoyun Z., (2023), Wind tunnel test study on windbreak and sand fixing effect of porous sand fixing brick grid mechanical sand barrier (多孔固沙砖机械沙障防风固沙效果的风洞试验研究), *Journal of Vibration and Shock*, Vol.42(19), pp.266-274, Zhangjiakou/China.
[12] Jiayuan D., Xiangyun Q., (2019). Application of Grass Square Sand Barrierin Windbreak and Sand Fixation (草方格沙障在防风固沙中的应用), *Construction Technology*, Vol.11(21), pp.205-207, Guangzhou/China.
[13] Jianjun Q., Ruiping Z., Kecun Z., Haiyan F., (2007), Field observations on the protective effect of semi-buried checkerboard sand barriers, *Geomorphology*, Vol.88(1-2), pp.193-200, Lanzhou/China.
[14] Jianhua X., Dongting Y., Xiaosong X., Zhengyi Y., Jianjun Q., Benli L., (2022), Numerical simulation of the airflow at the world's largest concentrated solar power plant in a desert region, *Solar Energy*, Vol.232, pp.421-432, Lanzhou/China.
[15] Jing S., Shen W., Yongzhi L., Junjie M., Junzhe H., Jun W., Pu C., Hongbo L., Boyang Z., Yong L., (2024), Experimental study on a combined sand barrier: Integration of porous mesh plate and novel porous sand-fixing bricks, *Journal of Wind Engineering & Industrial Aerodynamics*, Vol.251, pp.105809, Zhangjiakou/China.
[16] Kecun Z., Jianjun Q., Zhishan A., (2012), Characteristics of wind-blown sand and near-surface wind regime in the Tengger Desert, China, *Aeolian Research*, Vol.6, pp.83-88, Lanzhou/China.
[17] Kaichong L., Long S., Fuqiang J., Chunxiao X., Lingwei K., (2017), Research on the Relationship between Perforated Sand - blocking Wall and Sand - blocking Effect (挡沙墙开孔方式与阻沙效果的关系研究), *Journal of Railway Engineering Society*, Vol.11, pp.005-009, Lanzhou/China.
[18] Kai Z., Peiwen Z., Jianchang Z., Xingxin Z., (2021), Protective effect of multi-row HDPE board sand fences: A wind tunnel study, *International Soil and Water Conservation Research*, Vol.9(1), pp.103-115, Lanzhou/China.
[19] Li L., Tianli B., (2015), Effects of checkerboard sand barrier belt on sand transport and dune advance, *Aeolian Research*, Vol.42, pp.100546, Lanzhou/China.
[20] Lzael A.L., Eric J.R.P., Yaping S., (2020), CFD simulation of the wind field over a terrain with sand fences: Critical spacing for the wind shear velocity, *Aeolian Research*, Vol.43, pp.100574, Fortaleza/Brazil.
[21] Muning Z., Dingqiang L., Yuji Z., (2006), Study on Soil and Water Conservation Effect of Bioengineering Techniques for Slope Protection in Highway (高速公路生态护坡技术的水土保持效应研究), *Journal of Soil and Water Conservation*, Vol.21(1), pp.164-167, Guangzhou/China.

[22] Na Z., Chunlai Z., Jinlu T., Liqiang K., (2014), Flow field controlling the concave surface of the semi-buried checkerboards and its characterization by grain sizes of sediments (半隐蔽式草方格沙障凹曲面形成的流场解析及沉积表征), *Geographical Research*, Vol.33(11), pp.2145-2156, Beijing/China.

[23] Tao W., Jianjun Q., Yuquan L., Benli L., Jianhua X., (2018), Shelter effect efficacy of sand fences: A comparison of systems in a wind tunnel, *Aeolian Research*, Vol.30, pp.32-40, Lanzhou/China.

[24] Xiaohong D., Yong G., Yi Y., et al., (2015), Windproof efficiency with new biodegradable PLA sand barrier and traditional straw sand barrier (新型生物可降解 PLA 沙障与传统草方格沙障防风效益), *Journal of Beijing Forestry University*, Vol.37(3), pp.118-125, Hohhot/China.

[25] Yifei C., Feng W., Xubin P., Fangmin Z., Guoyu R., Qi L., (2024), 150-year shift of potential geographical distribution of desertification in China: Past, present and future (中国荒漠化潜在发生区域 150 年变迁:过去、现在和未来), *Chinese Science Bulletin*, Vol.69(31), pp.4637-4650, Beijing/China.

[26] Yanfu L., Zhiwei L., Zhaoyin W., Wenlong W., Yanhong J., Shimin T., (2017), Impacts of artificially planted vegetation on the ecological restoration of movable sand dunes in the Mugetan Desert, northeastern Qinghai-Tibet Plateau, *International Journal of Sediment Research*, Vol.32, pp.277-287, Nanjing/China.

[27] Yuqiu G., In-Bok L., Hideyuki S., Yong G., Guodong D., (2004), Principles of sand dune fixation with straw checkerboard technology and its effects on the environment, *Journal of Arid Environments*, Vol.53(3), pp.449-464, Beijing/China.

[28] Yang D., Shuangxi Z., Yongqi W., Tonglin Y., Jingliang D., (2021), Influence of Wind Speed, Wind Direction and Turbulence Model for Bridge Hanger: A Case Study, *Symmetry*, Vol.13, pp.1633, Hangzhou/China.

[29] Yana L., Yinxiang L., Xiaoqiang H., Quanwang Y., Daimin Y., Haijun T., (2025), Analysis of the effectiveness of four types of banded sand barriers in the Ulan Buh Desert (乌兰布和沙漠 4 种带状沙障建设成效分析), *Journal of Inner Mongolia Forestry Science & Technology*, Vol.51(1), pp.1-6, Hohhot/China.

[30] Yan W., Afang J., Jianzhou J., (2024), Numerical Simulation and Parameter Optimization of a New Slant Insertion-Opening Combination Sand Fence, *Sustainability*, Vol.16, pp.8651, Urumqi/China.

[31] Ze M., Zhongju M., Jianguo L., Alatengtaogesu., Dongying Z., (2024), Wind-prevention and Sand Fixation Effects of Checkerboard Sand Barrier Along Typical Yellow River Bank in Ulan Buh Desert (乌兰布和沙漠典型沿黄段格状沙障防风固沙效应), *Bulletin of Soil and Water Conservation*, Vol.44(2), pp.001-010, Hohhot/China.

EFFECTS OF DIFFERENT MICROBIAL FERMENTATION PROCESSES OF RICE STRAW ON ITS QUALITY AS LIVESTOCK FEED
/
水稻秸秆发酵特性及饲料化利用

Liyan WU[1)], Tianyi ZHANG[1)], Zheng JIN[1)], Fangming CUI[1)], Zhicheng ZHANG[*2)]
[1)] College of Engineering, Shenyang Agricultural University, Shenyang 110866 / China;
[2)] Department of Logistics Support, Jilin Agricultural University, Changchun 130118 / China
Tel: +86043184533410; E-mail: zhangzhicheng8644@jlau.edu.cn
Corresponding author: Zhicheng Zhang
DOI: https://doi.org/10.35633/inmateh-76-95

Keywords: *rice straw feed, microbial fermentation, intake rate*

ABSTRACT
Rice straw's poor palatability and low nutrition limit its utilization as livestock feed, resulting in low intake rates. To address this, three fermentation treatments (compound bacteria, compound bacteria + enzymes, lactic acid bacteria) were tested over 25, 45, and 65 days, analyzing crude fiber, soluble sugar, and protein to evaluate quality. Results showed compound bacteria + enzymes performed best at 65 days: crude fiber reduced to 34.83%, crude protein increased to 9.45%, and soluble sugar reached 1.89%. Feeding trials with Simmental cattle revealed a 93% intake rate for fermented straw—65% higher than unfermented. This study establishes a microbial degradation technology for rice straw, identifies optimal starters, and forms a feed production process, laying a foundation for enhanced rice straw utilization as livestock feed.

摘要
水稻秸秆适口性差、营养价值低，使其作为畜禽饲料的利用率受限，导致采食率偏低。针对这一问题，本研究采用三种发酵处理方式（复合菌、复合菌 + 酶、乳酸菌），分别发酵 25 天、45 天和 65 天，并通过分析粗纤维、可溶性糖和蛋白质含量来评估饲料品质。结果显示，复合菌 + 酶处理在 65 天时效果最佳：粗纤维含量降至 34.83%，粗蛋白含量提升至 9.45%，可溶性糖含量达 1.89%。对西门塔尔牛的饲喂试验表明，发酵秸秆的采食率为 93%，较未发酵秸秆提高 65%。本研究建立了水稻秸秆的微生物降解技术，筛选出了适宜的发酵剂，形成了秸秆饲料生产工艺，为提升水稻秸秆作为畜禽饲料的利用率奠定了基础。

INTRODUCTION
China is a major rice - producing country, with an annual output of 210 million tons of rice straw (*Lu et al., 2022*). The main components of rice straw, namely cellulose, hemicellulose, and lignin, are difficult to decompose within a short period. The carbon - nitrogen (C/N) ratio usually ranges from 60:1 to 100:1, leading to poor palatability, low nutritional value, and low intake rates for cattle and sheep (*Xu et al., 2020*). Microorganisms can secrete cellulase, hemicellulase, and other enzymes. These enzymes break down complex carbohydrates in straw such as crude fiber and lignin, which are difficult for animals to digest directly - into small - molecule substances like glucose and xylose, thereby improving the digestibility of straw (*Du et al., 2025*). In addition, some microorganisms (e.g., lactic acid bacteria and yeast) utilize carbon and nitrogen sources in straw for metabolism during fermentation, synthesizing nutrients such as proteins, amino acids, and vitamins (e.g., B vitamins). This process increases the content of crude protein, soluble sugars, and other components in straw. For instance, yeast can convert sugars in straw into proteins, significantly enhancing the protein level of straw feed. However, for crop straw with a high C/N ratio, such as rice straw, factors like microbial species, fermentation time, and moisture content during the fermentation process exert a significant impact on fermentation efficiency (*Zheng et al., 2019*). There remains a lack of clear conclusions regarding the optimization of fermentation for rice straw with a high C/N ratio, such as the compatibility between specific microbial agent combinations and fermentation cycles, which in turn affects livestock intake rates.

Liyan Wu, Prof. Ph.D.; Tianyi Zhang, M.S. Stud.; Zheng Jin, M.S. Stud. Eng.; Fangming Cui, Ph.D. Eng.; Zhicheng Zhang, M.S. Assistant research fellow, Eng.

Microbial fermentation technology, when applied with probiotics, can effectively improve the biological and physicochemical properties of rice straw. This process degrades lignin and crude fiber in the straw, thereby increasing the content of nutrients such as protein. Additionally, the softened rice straw can enhance palatability and boost the intake rates of livestock *(Liu et al., 2024*). The strategies of "returning straw to the field through cattle digestion" and "transforming straw into beef and milk via cattle" can contribute to carbon reduction and sequestration, achieving a carbon sequestration rate of 20 - 30% (*Huo et al., 2021, 2022*). Evidently, microbial fermentation of straw is currently the most favorable approach for the comprehensive utilization of rice straw. Exploring the utilization of rice straw as animal feed can not only expand the feed resources for animal husbandry and reduce feed costs but also alleviate the environmental pollution caused by the outdoor stacking and burning of rice straw. This practice is of great significance for increasing farmers' income, and promoting sustainable agricultural development (*Cong et al., 2019; Kyawt et al., 2024*).

Therefore, the present study aimed to explore microbial fermentation technology for the production of rice straw feed and to investigate the effects of different starter cultures and the optimal fermentation duration. By comparing the effects of three treatments—"compound bacteria", "compound bacteria + enzyme", and "lactic acid bacteria"—over fermentation periods of 25 days, 45 days, and 65 days, and integrating nutritional indicators (such as crude fiber and protein) with cattle feeding rate data, this study reveals the efficient degradation effect of rice straw by the synergy of bacteria and enzyme. Key indicators, including the pH value, crude fiber content, crude protein content, soluble sugar levels in the straw after fermentation were evaluated. The results of this study are expected to lay a solid foundation for the further development and utilization of rice straw feed.

MATERIALS AND METHODS

Materials

The rice straw utilized in this study was sourced from the rice field of Shenyang Agricultural University, China. The rice was harvested using a mechanical harvester, resulting in partial mechanical rubbing of the straw during the threshing process. This mechanical treatment affected the straw's physical structure to some extent. The moisture content of the straw was measured to be approximately 35%–45%, which was within a typical range for freshly harvested rice straw and could influence subsequent fermentation processes. Three distinct starter culture treatments were employed:

A compound bacterial mixture consisting of lactic acid bacteria at a concentration of 5×10^5 colony - forming units (cfu) per gram and yeast at 1×10^5 cfu per gram;

A compound enzymatic mixture comprising lactic acid bacteria (5×10^5 cfu /g) and cellulase (3×10^5 cfu /g);

Lactic acid bacteria alone, with a concentration of 5×10^5 cfu per gram.

Methods

To systematically investigate the effects of different starter cultures on rice straw feed quality, a four-factor, three-level experiment was designed. Fermentation durations (A1, A2, A3) corresponded to 25, 45, and 65 days, respectively. Starter culture treatments included: B1 (compound bacteria of lactic acid bacteria + yeast), B2 (compound bacteria + cellulase), B3 (lactic acid bacteria alone), and CK (no starter, control). Detailed experimental configurations are shown in Table 1.

Table 1

Experimental scheme for rice straw fermentation

Factor A	Factor B			
	B1	B2	B3	CK
A1	A1B1	A1B2	A1B3	A1CK
A2	A2B1	A2B2	A2B3	A2CK
A3	A3B1	A3B2	A3B3	A3CK

Preparation of starter cultures

To prepare starter cultures, brown sugar was dissolved in boiling water, cooled to 40°C, then mixed with starter cultures to homogeneity. The mixture (starter:sugar:water = 1:5:50, mass ratio) was sealed and activated for 3 days before spraying.

1) Starter cultures spraying

Three starter culture types were uniformly sprayed onto each straw piles at a rate of ~0.2 g per 100 g straw, adjusting the straw moisture content to 50% - 65%. Then the straw was sealed with plastic strip and incubated in a temperature - controlled climate chamber, with the temperature regime simulating northern China's autumn conditions: 5 °C (0:00–8:00), 10 °C (8:00–12:00), 15 °C (12:00–17:00), and 5 °C (17:00–24:00).

2) Content analysis

Rice straw samples from different fermentation treatments were dried at 105 °C, then grounded into powder using a high-speed pulverizer, followed by fine grinding with a planetary ball mill and sieving. Samples for crude protein and soluble sugar analysis were sieved to 80 - 100 mesh, while those for crude fiber analysis were 20 - 30 mesh.

The content of crude fiber

The analysis was carried out in strict compliance with the national standard GB/T 5009.10-2003.

The content of crude protein

The analysis was carried out using the elemental analysis method (*Xiao et al., 2018*).

The content of soluble sugar

The analysis was conducted in accordance with the national standard NY/T 1278-2007 (*Wang et al., 2007*).

3) Experimental indices

pH value

To avoid parameter changes from prolonged air exposure, fermented straw samples were collected immediately after opening the packs. After thorough mixing, 10 g of straw was weighed into a wide-mouth bottle, mixed with 100 mL distilled water, and sealed. The bottle was incubated at 10 °C for 12 h, then filtered. The pH of the filtrate was measured using a calibrated pH meter. The pH value is a pivotal metric for evaluating fermentation efficiency. According to established standards (Wang et al., 2011), a pH of ≤3.8 signifies excellent fermentation quality, 3.9–4.1 indicates good quality, 4.2–4.7 denotes moderate quality, and ≥4.8 represents poor quality.

Sensory evaluation

On-site sensory evaluation represents the most straightforward, practical, and efficient approach for gauging the quality of straw feed. Fermented straw sensory evaluation followed the Deutsche Landwirtschafts-Gesellschaft scoring method, assessing odor, texture, and color (*Ai et al., 2020*). An evaluation panel comprising ten trained professionals (five males and five females, aged between 25 and 45 years) was assembled to conduct the sensory assessments. Based on total scores, feeds were classified into four quality grades (excellent, good, medium, poor). Detailed scoring criteria are in Table 2.

Table 2

Sensory evaluation criteria of Deutsche Landwirtschafts-Gesellschaft

Indicators	Criteria	Score
Odor	No acid odor, with aromatic fruit or obvious bread aroma	14
	A weak acid odor, a strong sour odor or a weak aromatic smell	10
	A quite strong acid taste or a pungent sticky or musty odor	4
	A strong ammonia odor or almost no acidity	2
Texture	Good stem and leaf structure	4
	Poor maintenance of stem and leaf structure	2
	The preservation of stem and leaf structures is extremely poor, or there is slight mold contamination	1
	Stem and leaf decay or severe pollution	0

Indicators	Criteria				Score
Color and luster	Similar to the raw material, turning light brown after drying Slightly discolored, appearing light yellow or brownish Severe discoloration, dark green or brown in yellow, with a strong musty odor				2 1 0
Total score	16-20	10-15	5-9	0-4	
Level	Excellent (Level 1)	Good (Level 2)	Medium (Level 3)	Bad (Level 4)	

RESULTS

Following a designated fermentation period, subtle white flocculent colonies of lactic acid bacteria emerged within the plastic packaging bags, presenting a distinct visual contrast. In stark contrast, the control group (CK) remained unaltered, showing no discernible changes to the naked eye.

The pH value

Figure 1 depicts the dynamic changes in pH values over time for straw samples treated with various starter cultures. Significantly, all three treatment groups with different starter cultures showed notably lower pH values than the control group (CK). The control group maintained pH levels consistently above 5.0 throughout the experiment. Among them, the compound enzyme treatment (B2) stood out with the lowest pH range (3.90–3.93), underscoring its exceptional acidification capability.

These findings strongly suggest that starter cultures promote the fermentation of rice straw by generating substantial amounts of organic acids, thereby effectively reducing pH values. Moreover, organic acids function not only as flavor enhancers to improve feed palatability but also play crucial roles in regulating digestive processes and enhancing animal health (*Wu et al., 2022*).

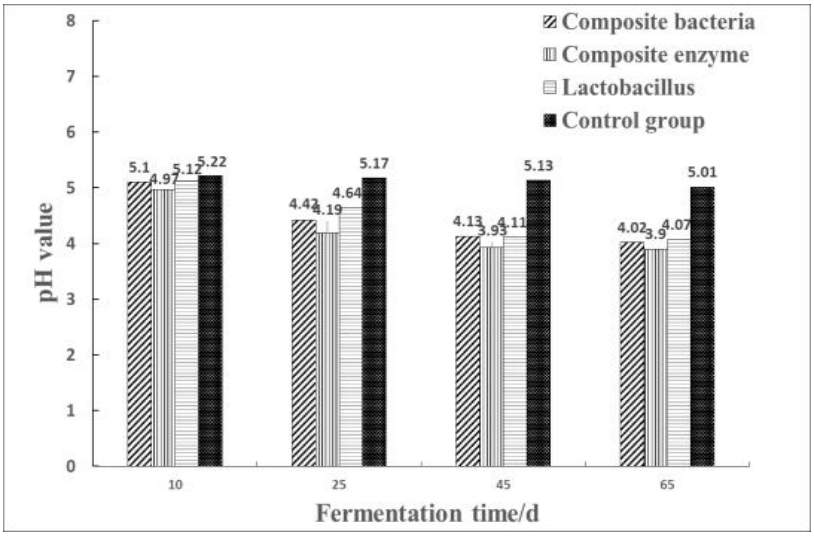


Fig. 1 – Variation of pH values of different groups

Sensory evaluation

As clearly illustrated in Table 3, the three treatment groups outperformed the control group (CK) significantly, registering notably higher sensory scores. Samples rated at Level 1 (Excellent) were characterized by the complete absence of acidic odors, instead exuding a distinct, pleasant aroma reminiscent of fresh bread or natural fragrances, while maintaining an intact texture and structure. Level 2 (Good) samples, though lacking any sour smell, retained a discernible aroma, and the straw underwent a color transformation to light brown. Level 3 (Moderate) samples were marked by a pungent sour odor, a faint aromatic presence, compromised structural stability, and a light yellowish hue. In contrast, Level 4 (Poor) samples emitted strong musty and sour odors, displayed a decomposed texture, and exhibited severe discoloration.

The evaluation outcomes revealed that across all starter cultures tested, a fermentation duration of 45–65 days consistently yielded the highest sensory scores. These comprehensive findings collectively underscore that the application of starter cultures not only elevates the sensory appeal of straw feed but also expedites the degradation of fibers, optimizing its overall quality.

Table 3

Sensory scores under the criteria of the Deutsche Landwirtschafts-Gesellschaft

Treatment group	Starter culture	Scores of indicators			Total score	Quality level
		Odor	Texture	Color and luster		
25d	CK	2	2	0	4	Poor
	B1	10	2	1	13	Good
	B2	14	4	2	20	Excellent
	B3	10	2	1	13	Good
45d	CK	2	2	0	4	Poor
	B1	14	4	0	18	Excellent
	B2	14	4	2	20	Excellent
	B3	14	4	2	20	Excellent
65d	CK	2	1	0	3	Poor
	B1	12	4	0	16	Excellent
	B2	12	4	2	18	Excellent
	B3	12	4	2	18	Excellent

Nutritional indicators

As shown in Table 4, a detailed summary of the nutritional parameters of rice straw from different treatment groups is provided. Statistical analysis was shown in Table 5.

Table 4

Nutritional indicators of rice straw feed (%)

Treatment group		Nutritional indicators		
		Crude fiber	Crude protein	Soluble sugar
25d	B1	39.41±3.05Ac	8.10±0.00Bc	1.55±0.00Aa
45d	B1	37.97±2.22ABc	9.10±0.06Aa	1.57±0.43Ab
65d	B1	36.75±1.30Bc	9.38±0.02Aa	1.56±0.17Ab
25d	B2	37.67±3.40Ad	8.34±0.03Ba	1.52±0.12Ba
45d	B2	36.96±2.13Ad	8.94±0.01Bab	1.78±0.01Aa
65d	B2	34.83±0.58Bd	9.45±0.35Aa	1.89±0.01Aa
25d	B3	41.71±0.86Ab	8.25±0.45Bb	1.22±0.00Bb
45d	B3	40.41±1.92Bb	8.59±0.26Ab	1.49±0.00Ab
65d	B3	38.41±2.22Cb	8.79±0.00Ab	1.44±0.10Ab
25d	CK	43.25±1.82Aa	5.87±0.02Ac	1.10±0.00Ac
45d	CK	43.73±2.36Aa	5.39±0.03Ac	1.14±0.02Ac
65d	CK	42.39±3.18Aa	5.36±0.15Ac	1.25±0.16Ac

Note: Capital letters are employed to denote significant variations in the impact of fermentation time on nutritional indicators when the same starter culture treatments are applied. Conversely, lowercase letters signify significant disparities in the effects of different starter culture types on nutritional indicators under identical fermentation time conditions.

Table 5

Analysis of variance for nutritional indicators

Source of variation	Dependent variable	Sum of squares	degree of freedom	Mean square	F-value	P-value
Treatment group	Crude fiber	36.723	4	18.362	3.630	0.042
	Crude protein	2.227	4	1.114	31.714	0.000
	Soluble sugar	0.234	4	0.117	5.311	0.012
Starter cultures	Crude fiber	223.031	6	74.344	14.697	0.000
	Crude protein	71.182	6	23.727	675.673	0.000
	Soluble sugar	1.591	6	0.530	24.071	0.000
Treatment group * Starter cultures	Crude fiber	6.367	12	1.061	0.210	0.970
	Crude protein	3.280	12	0.547	15.568	0.000
	Soluble sugar	0.143	12	0.024	1.083	0.400
Error	Crude fiber	121.406	48	5.059		
	Crude protein	0.843	48	0.035		
	Soluble sugar	0.529	48	0.022		
Total	Crude fiber	56435.722	72			
	Crude protein	2360.461	72			
	Soluble sugar	79.147	72			

The changes in the content of crude fiber

During the entire fermentation process, the crude fiber content in treatment groups B1 (compound bacteria), B2 (compound enzyme), and B3 (lactic acid bacteria) was significantly lower than that in the control group (CK) ($P<0.05$). Notably, treatment B2 consistently showed the lowest crude fiber content across all fermentation stages. After 65 days of fermentation, its crude fiber content reached a minimum of 34.83%, representing a 13.56% reduction compared to the CK group. Statistical analysis revealed that, with the extension of fermentation time, the crude fiber content exhibited a significant decreasing trend ($P < 0.05$), while the fermentation duration exerted no significant effect on the CK group. Collectively, these findings strongly suggest that the application of starter cultures effectively promotes straw degradation, consequently leading to a notable reduction in the crude fiber content of the final feed product.

Crude protein

The choice of starter cultures exerted a pronounced influence on the crude protein content of the straw feed. Across all treatments involving starter cultures, the levels of crude protein increased steadily as fermentation progressed, culminating in a peak at the 65 day mark. Notably, the B1 treatment group achieved a crude protein content of 9.38%, the B2 group reached 9.45%, and the B3 group recorded 8.79%. In stark contrast, the control group (CK) experienced a marginal decrease, with its crude protein content dropping to 8.38% by the 65th day of fermentation. These findings unequivocally indicate that the application of starter cultures facilitates the accumulation of crude protein in rice straw, thereby substantially enhancing the nutritional profile of the feed. The main reasons for the increase in crude protein include:

Soluble sugar

During the fermentation process, a significant upward trend in soluble sugar content was observed across all treatment groups, whereas the control group (CK) remained unchanged. Statistical analysis confirmed that starter cultures exerted a significant influence on soluble sugar levels ($P < 0.05$) compared to the CK. In treatment group B1, the soluble sugar content increased initially and plateaued between 45 and 65 days of fermentation. In contrast, treatment group B2 exhibited a continuous increase, with significantly higher soluble sugar values than groups B1 and B3 at both 45 and 65 days. These results suggest that starter cultures enhance straw fermentation by increasing the soluble sugar content in the feed. Comparative analysis indicated that the B2 treatment achieved the optimal fermentation results during the 45 - 65-day period.

As mentioned in the text, compared with the control group (CK), the addition of the starter culture significantly affects the level of soluble sugars ($P < 0.05$). The microorganisms in different types of starter cultures (such as treatment groups B1 and B2) have different species and metabolic characteristics, which can promote the decomposition of polysaccharides in the substrate or the synthesis of soluble sugars. Certain microorganisms in the starter culture (such as yeasts and lactic acid bacteria) can secrete relevant enzymes (such as amylase and cellulase). These enzymes can hydrolyze polysaccharides (such as starch, cellulose, hemicellulose, etc.) in raw materials like straw into soluble sugars (such as glucose and xylose), thereby increasing the content of soluble sugars in the fermentation system (*Jabbour et al., 2013; Guo. et al., 2022*).

Feeding Experiment of Cattle

The production process of rice straw feed was conducted as follows: the preparation of the starter culture adhered to the same protocol described in Part 2. Following the spraying of the starter culture, the moisture content of the rice straw was adjusted to approximately 50%–65%. The feed production apparatus included a baling machine and a sealing machine. A spraying device was installed at the inlet of the baling machine, enabling a sequential operation workflow that included starter culture spraying, baling, and plastic sealing. The resultant straw bales were standardized with dimensions of 80 cm in diameter and 80 cm in length, achieving a consistent density of 480 kg/m^3. Each bale was packaged with three layers of plastic to ensure integrity during storage and handling. For experimental purposes, rice straw fermented for 65 days with the combined treatment of compound bacteria and enzymes was designated as the experimental feed. In contrast, untreated rice straw was employed as the control group (CK). All samples were derived from the Shennong 9903 rice cultivar, ensuring uniformity in the raw material source for accurate experimental comparison.

The study subjects consisted of 20 Simmental cattle originating from Longpao Village, Qingyuan County, Liaoning Province, China. These cattle were approximately 4 months old, demonstrated normal growth patterns, had moderate fat deposition, were in good health condition, and their body weights ranged from 140 to 185 kg.

The feeding protocol was divided into two distinct phases: a preparation phase lasting for 3 days and an experimental phase spanning 3 weeks. The twenty cattle were randomly assigned into two groups, with 10 cattle in each group. The control group was fed unfermented rice straw, while the experimental group was provided with fermented rice straw.

During the experimental period, the daily diet of the cattle consisted of both coarse feed and concentrated feed. Specifically, the coarse feed was corn silage, with each group being supplied 75 kg of it daily. The concentrated feed was commercial fattening-cattle feed, with 8 kg provided to each group per day. These two types of feed were mixed and administered to the cattle twice a day, at 6:00 a.m. and 6:00 p.m. For the control group (CK), the coarse feed was substituted with unfermented rice straw, whereas the experimental group received fermented rice straw. Throughout the entire trial, the concentrated feed remained unchanged for both groups.

The daily amounts of coarse and concentrated feed remained consistent across all groups, and the feeding schedules were strictly adhered to. Throughout the experiment, the cattle were ensured unrestricted access to drinking water and feed. During the preparation phase, the coarse feed was gradually replaced with either unfermented rice straw (in the control group, CK) or fermented rice straw (in the experimental group). One-third of the coarse feed was replaced daily until a complete substitution was achieved. By the first day of the experimental phase, the coarse feed was fully replaced with rice-straw feed. Daily, the coarse and concentrated feeds were homogeneously blended according to the prescribed proportions. The remaining coarse feed from the previous day was weighed to calculate the intake rates (refer to Equation 1).

$$Intake\ rate = \frac{Total\ amount - Remaining\ amount}{Totalamount} \times 100\% \quad (1)$$

Table 6

Results of feeding experiment

Groups	Week 1		Week 2		Week 3		Average intake / kg	Average intake rate / %
	Feeding amount / kg	Residual amount / kg	Feeding amount / kg	Residual amount / kg	Feeding amount / kg	Residual amount / kg		
Control group	75.0	57.6	75.0	52.3	75.0	51.1	21.33	28
Experimental group	75.0	1.30	75.0	1.83	75.0	2.12	69.75	93

Table 6 illustrates that fermented rice straw proved to be more advantageous for Simmental cattle. In contrast, unfermented rice straw displayed suboptimal palatability, leading to lower acceptance by the cattle. Notably, the intake rate of fermented rice straw reached an impressive 93%, marking a substantial 65% increase when compared to the mere 28% intake rate of unfermented rice straw.

Discussion

This study assessed three starter cultures (compound bacteria, compound bacteria + enzymes, lactic acid bacteria) on rice straw fermentation over 25, 45, 65 days, focusing on nutrition and intake rates. Findings show microbial fermentation enhances feed quality, with 65-day compound bacteria + enzyme (B2) most effective.

Treated groups (especially B2) had significantly reduced crude fiber, with B2 reaching 34.83% at 65 days (13.56% lower than CK), due to cellulase hydrolyzing cellulose β-1,4-glycosidic bonds and disrupting hemicellulose-lignin interactions (*Su et al., 2012; Tem et al., 2019*). B2's continuous crude fiber decline indicates sustained enzymatic activity, unlike CK's stability.

B2's crude protein peaked at 9.45% at 65 days, via microbial-enzyme synergy: lactic acid bacteria/yeast use straw nitrogen for microbial proteins (*Zhu et al., 2021*), while cellulase aids carbon access and nitrogen conversion (*Hall et al., 2001*), outperforming B1 (9.38%) and B3 (8.79%).

B2's soluble sugar (1.89% at 65 days) rose continuously, unlike B1's plateau, due to microbial cellulase/amylase hydrolyzing polysaccharides into glucose/xylose (*Jabbour et al., 2013; Guo et al., 2022*), boosting nutrition and palatability.

pH and sensory attributes: Treated groups had a lower pH than CK (pH > 5.0); Specifically, the B2 group had a pH of 3.90–3.93 (excellent quality) (*Wang et al., 2011*).

This quality advantage is attributed to the spoilage-inhibiting effect of lactic acid (*Sun, 2023; Zhang et al., 2021*). B2 scored highest in sensory evaluation (bread-like aroma, intact texture, raw material-like color), contributing to 93% intake rate (*Liu et al., 2024*).

Feeding trial implications. Fermented straw's 93% intake rate (vs. 28% unfermented) stems from reduced crude fiber, increased soluble sugars, and improved texture, addressing low straw utilization in ruminants (*Xu et al., 2020*). Standardized production (50%–65% moisture, 480 kg/m³ density, 65-day B2) supports scalability, aligning with carbon sequestration via "straw-to-feed" (*Huo et al., 2021, 2022*).

Findings support microbial fermentation's role (*Du et al., 2025; Feng et al., 2021*), but B2's superiority highlights microbe-enzyme synergy, contrasting with microbial-only studies (*Zheng et al., 2019*) and emphasizing exogenous enzymes in high C/N substrates.

Limitations: unanalyzed microbial dynamics, intake rate-focused feeding trial, single rice cultivar (Shennong 9903). Future work: metagenomic analysis of microbe-enzyme interactions, long-term large-cohort trials, parameter optimization for scaling. In summary, 65-day B2 optimizes rice straw feed quality (reduced crude fiber, increased nutrients, enhanced palatability) with 93% intake rate, supporting sustainable straw use in livestock.

CONCLUSIONS

This study systematically explored the impacts of starter cultures, specifically compound bacteria and enzymes, along with fermentation duration, on the nutritional characteristics of rice straw. The key findings are comprehensively summarized as follows:

(1) The microbial degradation experiment provided compelling evidence of significant enhancements in the sensory indicators of rice straw. Compared with the control group (CK), the treated samples exhibited marked improvements. Notably, the pH values of the groups treated with starter cultures decreased substantially relative to the CK, with the compound bacteria - enzyme treatment group achieving the lowest pH value of 3.90. Moreover, pronounced differences were detected in the contents of crude fiber and soluble sugar after the application of starter cultures. At the 65 - day fermentation mark, the compound bacteria - enzyme treatment yielded the most outstanding results: it achieved the highest levels of crude protein (9.45%) and soluble sugar (1.89%), while simultaneously presenting the lowest crude fiber content (34.83%). The addition of the three types of starter cultures effectively enhanced the aromatic profile, softened the texture, and significantly elevated the overall quality of the straw feed. Among these, the compound bacteria - enzyme treatment emerged as the most effective approach, attaining optimal outcomes.

(2) The feeding experiment conducted on Simmental steers yielded remarkable results. Fermented straw feed demonstrated an impressively high intake rate of 93%, in stark contrast to the mere 28% intake rate of unfermented rice straw. Collectively, these findings clearly demonstrate that rice straw feed treated with starter cultures undergoes notable improvements in sensory quality, palatability, and nutritional parameters. More importantly, it significantly boosts the intake rate in ruminant livestock, highlighting the practical significance and potential of this treatment method in animal husbandry applications.

ACKNOWLEDGEMENT

This work was financially supported by the National Key Research and Development Plan (2023YFD2301605), the Natural Science Foundation of Liaoning Province (2020MS203), and the Basic Research Project of the Education Department of Liaoning Province (LJKZ0694).

REFERENCES

[1] Ai, Q., Jiang, H., Guo, R., Jiang, T., Su, H., (2020). Effects of adding defective apple fermentation in rice straw on quality and microbial numbers of mixed silage (添加残次苹果发酵物对稻草青贮品质及其微生物数量的影响). *Transactions of the Chinese Society of Agricultural Engineering*, Vol. 36, 316-323, Beijing/China. DOI: 10.11975/j.issn.1002-6819.2020.20.035

[2] Cong, H., Yao, Z., Zhao, L., Meng, H., Wang, J., Huo, L., Yuan, Y., Jia, J., Xie, T., Wu, Y., (2019). Analysis of long-term mechanism for development of straw industry in northeast China under guidance of "Green-concept" (中国农作物秸秆资源分布及其产业体系与利用路径). *Transactions of the Chinese Society of Agricultural Engineering*, Vol. 36, pp. 132-140, Beijing/China. DOI: CNKI:SUN:NYGU.0.2019-22-015:

[3] Du, S., Xu, L., Jiang. C., Xiao, Y., (2025). Novel strategy to understand the bacteria-enzyme synergy action regulates the ensiling performance of wheat straw silage by multi-omics analysis, *International*

Journal of Biological Macromolecules, Vol. 289, pp. 138864, Netherlands, DOI: org/10.1016/j.ijbiomac.2024.138864

[4] Feng, P., Wu, H., Meng, F., Zheng, H., Yang, Z., Wang, J., Shen, Z., (2021). Effects of different compatible biological agents on quality and feeding value of rice straw silage (不同配伍生物制剂对水稻秸秆青贮品质及饲喂价值的影响). *China Feed*, Vol. 17, pp. 122-128., Beijing/China. DOI: 10.15906/j.cnki.cn11-2975/s.20211725

[5] Guo, Z., Wang, L., Yu, C., (2022). Increasing the glucose metabolism enhances the bioelectricity generation in microbial fuel cells. *Acta Biochimica et Biophysica Sinica*, Vol 54. pp. 1566-1567. DOI: 10.3724/abbs.2022129

[6] Hall M.B., Herejk C., Differences in Yields of Microbial Crude Protein from In Vitro Fermentation of Carbohydrates, (2001). *Journal of Dairy Science*, Vol 84, pp. 2486-2493. DOI: 10.3168/jds.S0022-0302(01)74699-1

[7] Huo, L., Yao, Z., Zhao, L., Luo, J., Zhang, P., (2022). Contribution and Potential of Comprehensive Utilization of Straw in GHG Emission Reduction and Carbon Sequestration (秸秆综合利用减排固碳贡献与潜力研究). *Transactions of the Chinese Society for Agricultural Machinery*, Vol. 53, pp. 349-359, Beijing/China.

[8] Huo, L., Zhao, L., Yao, Z., Luo, J., Zhang, P., Xie, T., Jia, J., Deng Y., Wei, X., (2021). Potentiality of agricultural biomass energy for greenhouse gas emission reduction (农业生物质能温室气体减排潜力). *Transactions of the Chinese Society of Agricultural Engineering*, Vol. 37, pp. 179-187, Beijing/China.

[9] Jinpeng, Z., Jie, Z., Junfeng, L., Zhihao, D., Lei, C., Yunfeng, B., Yushan, J., Tao, S., n.d. (2019). Effect of different additives on fermentation quality and structural carbohydrates compositions of rice straw silage (不同添加剂对水稻秸秆青贮发酵品质和结构性碳水化合物组分的影响). *Journal of Nanjing Agricultural University*, Vol. 42(1), pp. 152-159, Nanjng/China. DOI: 10.7685/jnau.201803011

[10] Jabbour, D., Borrusch, M. S., Goutami B., Jonathan D. W. (2013). Enhancement of fermentable sugar yields by α-xylosidase supplementation of commercial cellulases. *Biotechnology for Biofuels*, Vol. 6:58. DOI:10.1186/1754-6834-6-58

[11] Kyawt, Y., Aung, M., Xu, Y., Sun, Z., Zhou, Y., Zhu, W., Padmakumar, V., Tan, Z., Cheng, Y., (2024). Dynamic changes of rumen microbiota and serum metabolome revealed increases in meat quality and growth performances of sheep fed bio-fermented rice straw. *Journal of Animal Science and Biotechnology*, Vol. 15, Beijing/China. DOI: 10.1186/s40104-023-00983-5

[12] Liu, E.Y., Wang, Shuiping, Wang, Shibo, Khan, N.A., Zhou, X., Tang, S., Zhou, C., Tan, Z., Liu, Y., (2024). Bacterial inoculants and enzymes based silage cocktails boost the ensiling quality of biomasses from reed, corn and rice straw. *Chem. Biol. Technol. Agric*, Vol. 11, England. DOI: 10.1186/s40538-024-00549-1

[13] Lu, H., Chen, Y., Zhang, P., Huan, H., Xie, H., Hu, H., (2022). Impacts of farmland size and benefit expectations on the utilization of straw resources: Evidence from crop straw incorporation in China. *Soil Use and Management*, Vol. 38, pp. 929–939, England. DOI: 10.1111/sum.12739

[14] Su Y., Zhao G., Wei Z., Yan C., Liu S. (2012). Mutation of Cellulose Synthase Gene Improves the Nutritive Value of Rice Straw, *Asian - Australasian Journal of Animal Science*, Vol. 25, pp. 800-805. DOI: 10.5713/ajas.2011.11409

[15] Sun, Y., Sun, Q.L., Tang, Y., Li, Q., Tian, C., Sun, H., (2023). Integrated microbiology and metabolomic analysis reveal the improvement of rice straw silage quality by inoculation of Lactobacillus brevis, *Biotechnology for Biofuels and Bioproducts,* Vol. 16, England. DOI: 10.1186/s13068-023-02431-y

[16] Tem T. D., Thava V., (2019). Modification of rice bran dietary fiber concentrates using enzyme and extrusion cooking. *Food Hydrocolloids*, Vol 89, pp. 773-782. DOI: 10.1016/j.foodhyd.2018.11.024

[17] Wang, D., Buckmaster, D.R., Jiang, Y., Hua, J., n.d., (2011). Experimental study on baling rice straw silage. *International Journal of Agricultural and Biological Engineering*, Vol.4, Beijing/China. DOI: 10.3965/ijabe.v4i1.262

[18] Wang, X., Liu, S., Liu, Z., Yang, M., Chen, N., (2007). *Determination of Soluble Sugars in Vegetables and Their Products by Copper-Reduction Iodometric Method (NY/T 1278-2007)(蔬菜及其制品中可溶性糖的测定铜还原碘量法)*, Ministry of Agriculture of the People's Republic of China, Beijing. 2007: 1 - 4

[19] Wu, Y., Ding, H., Shao, T., Zhao, J., Dong, D., Dai, T., Yin, X., Zong, C., Li, J., (2022). Effects of enzyme preparation on fermentation quality and in vitro digestion characteristics of rice straw silage (酶制剂对水

稻秸秆青贮发酵品质及体外消化特性的影响). *Acta Prataculturae Sinica*, Vol. 31, pp. 167-177, Gansu/China. DOI: 10.11686/cyxb2021312

[20] Xiao, Z., Fan, X., Ma, D., Li, L., Wang, S., Jia, Z., Liu, X., Wang, Z., Liu, J., (2018). GB/T6432-2018, Determination of crude protein in feeds—Kjeldahl method (饲料中粗蛋白的测定-凯氏定氮法), National Feed Quality Supervision and Testing Center (Beijing)

[21] Xu, C., Yuan, Q., Zhao, S., He, T., Song, N., (2020). Effects of pretreatments on physical and chemical characteristics of wheat straw used as a maintenance-free compressed green roof substrate material. *Journal of Cleaner Production*, Vol. 277, United States. DOI: 10.1016/j.jclepro.2020.123381

[22] Zhang, H., Cheng, X., Elsabagh, M., Lin, B., Wang, H., (2021). Effects of formic acid and corn flour supplementation of banana pseudostem silages on nutritional quality of silage, growth, digestion, rumen fermentation and cellulolytic bacterial community of Nubian black goats. *Journal of Integrative Agriculture*, Vol. 20, pp. 2214-2226, Beijing/China. DOI: 10.1016/s2095-3119(20)63470-0

[23] Zheng, G., Zhou, C., Yin, T., Lu, Z., & Ai, S., (2019). Optimization of fermentation factors to enhance rice straw degradation ability using a microbial consortium lzf-12. *International Journal of Agricultural and Biological Engineering*. Beijing/China, DOI: 10.25165/ijabe.v12i3.4638

[24] Zhu X., Wang L., Zhang Z., Ding L., Hang S. (2021). Combination of fiber-degrading enzymatic hydrolysis and lactobacilli fermentation enhances utilization of fiber and protein in rapeseed meal as revealed in simulated pig digestion and fermentation in vitro. *Animal Feed Science and Technology*, Vol. 278, pp. 115001-. DOI: 10.1016/j.anifeedsci.2021.115001

ELECTRIC RED BEAN PRECISION SEEDING CONTROL SYSTEM BASED ON IHBA-LADRC

/

基于 IHBA-LADRC 的电驱动红豆精量播种控制系统

Yi-fei LI [1,2], Guang-yu WANG [1]; Lin ZHAO [3], Shu-juan YI *[1]
[1] College of Engineering, Heilongjiang Bayi Agricultural University, Daqing, Heilongjiang/ China
[2] College of Engineering, Northeast Agricultural University, Harbin Heilongjiang/ China
[3] College of Basic Education, Beijing Polytechnic University, Beijing/ China
Tel: +86-459-13836961877; E-mile: yishujuan@byau.edu.cn;
Corresponding author: Shu-juan Yi
DOI: https://doi.org/10.35633/inmateh-76-96

Keywords: *red bean, electric precision seeding, control system, IHBA, LADRC*

ABSTRACT

This study proposes an improved honey badger algorithm (IHBA) and a linear active disturbance rejection controller (LADRC) for the electric red bean precision seeder control system to solve high sowing missing rates and uneven sowing in high-density red bean precision sowing. The research details the design process of the intelligent control system, the improvement of the honey badger algorithm, and the intelligent adjustment method for key parameters of the LADRC controller. Simulation experiments show that the IHBA-LADRC based control system has no overshoot, short adjustment time, minimal steady-state error, no oscillation, and strong anti-interference ability. The system achieves an adjustment time of 0.79 seconds, almost zero static error, and an interference recovery time of 0.22 seconds. Bench tests indicate that compared to traditional PID electronic control sowing, the IHBA-LADRC system improves the pass index by 1.32 percentage points, reduces the multiple index by 0.49 percentage points, and lowers the missed sowing index by 0.76 percentage points. The overall variation coefficient decreases by 6.30 percentage points, and the variation coefficient of qualified plant spacing drops by 5.43 percentage points. This system reduces the discrepancy between the actual and theoretical plant spacing of red beans.

摘要

本研究针对高密度红豆精播中的高漏播率和播种不均匀问题，提出了一种改进的蜜獾算法（IHBA）和线性自抗扰控制器（LADRC）用于电动红豆精播机控制系统。该研究详细阐述了智能控制系统的设计、蜜獾算法的改进以及 LADRC 关键参数的智能调整方法。模拟实验表明，基于 IHBA-LADRC 的控制系统具有无超调、调整时间短、稳态误差小、无振荡和抗干扰能力强的特点。该系统实现了 0.79 秒的调整时间，几乎无静态误差和 0.22 秒的干扰恢复时间。台架测试结果表明，与传统的 PID 电子控制播种相比，IHBA-LADRC 系统使格指数整体提高了 1.32 个百分点，重播指数降低了 0.49 个百分点，漏播指数降低了 0.76 个百分点。总体变异系数降低了 6.30 个百分点，合格株距的变异系数降低了 5.43 个百分点。该系统减小了实际株距与理论株距之间的差异。

INTRODUCTION

As an important legume crop, red bean holds a significant place in China's agricultural production. With the advancement of agricultural modernization, red bean seeding technology is continually improving and evolving (*Ma et al, 2022*). To improve the planting efficiency and yield of red beans, electric precision sowing technology ensures that red beans are sown into the soil according to the set spacing, thereby optimizing the allocation of seed resources and increasing crop yield (*Xu et al, 2024*). However, the planting distance of red beans is usually small, and the qualified operational range is narrow, requiring higher control accuracy of the control system. An effective control strategy for the seed discharge motor can improve the performance of the control system (*Li et al ,2024; Ma et al, 2023; Chen et al, 2022*), and many scholars have conducted extensive research in this area (*Wang et al, 2024; Mangus et al, 2017; Ranta et al, 2012*).

Jafari et al. (2010) studied a cereal seeder with variable speed control of a DC motor. The system uses an incremental PID controller to perform closed-loop control. Test results show that the motor can fully adapt to changes in travel speed and reach the set speed in about 6 seconds.

Kamgar et al. (2013) designed an electromechanical transmission system for a conventional row seeder. Their research focused on real-time regulation of the seeding disk's rotation speed through PID control based on speed measurements from a vehicle speed monitoring module. Tests demonstrated that this system can improve the seeding qualification index and reduce missed sowing and variation coefficient. *Cay et al. (2018)* investigated a motor drive system for a single-grain precision seeder. The system comprises an encoder, a brushless DC motor, and its drive module, using pulse width modulation and PID technology for motor control, with a feedback mechanism.

Wang et al. (2022) developed a fuzzy PID control strategy for electric seeding based on GAPSO optimization. GAPSO was used to optimize the two quantization factors, three scaling factors of the fuzzy controller, and the initial values of the three characteristic functions of the PID, leading to improved control system performance. *Ding et al. (2021)* designed a single driver for a corn variable seeder, utilizing the incremental PID algorithm as the control algorithm for the BLDC motor, achieving PID closed-loop control of the seeding motor.

Currently, various electric seeding control methods, both domestically and internationally, mainly use PID control. However, the PID controller has low accuracy and poor anti-interference ability. LADRC can perform real-time feedback compensation for internal and external disturbances in the system. It has the advantage of not relying on an accurate mathematical model of the seeding motor and does not require explicit external interference information for the control system of the electric red bean precision seeder. However, the controller parameter setting is complex, necessitating the introduction of intelligent optimization algorithms. An electric red bean precision seeding control system based on IHBA-LADRC was studied.

MATERIALS AND METHODS

System design

The control system of the electric red bean precision seeder based on IHBA-LADRC mainly consists of the switching power supply, main controller, DC brushless motor, DC motor driver, human-computer interaction interface, air-suction red bean seed metering device, and photoelectric monitoring seed guide tube. The overall structure of the system is shown in Fig. 1.

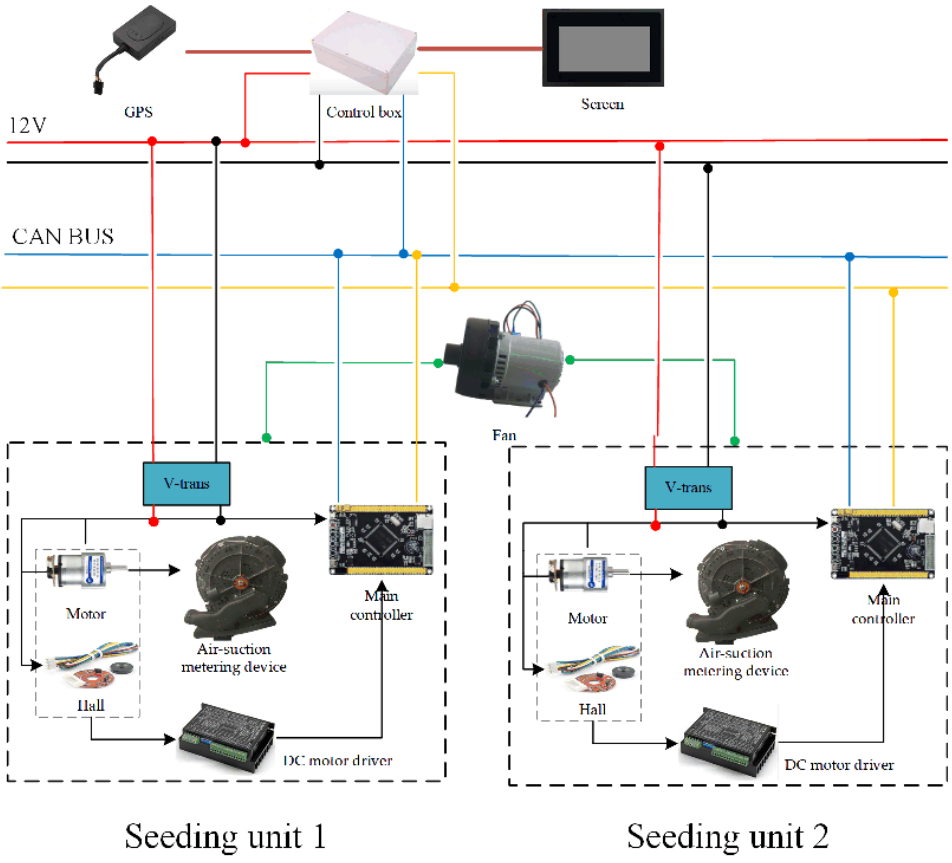


Fig. 1 - Overall system composition diagram

The air-suction red bean seed metering device uses the vSet air-suction seed metering device from Precision Planting Company. The seeding motor is a JGB37-520-CE DC brushless motor produced by ASLONG Company, with a working voltage of 12 V, a no-load speed of 110 r/min, and a rated torque of 0.85Nm. This is greater than the maximum load torque of 0.8 Nm measured by the torque meter when the seed metering device is suctioning, fully meeting the needs of subsequent research. The encoder equipped with the seeding motor is an SCX-Type 520 Hall encoder, a two-channel incremental magnetic encoder suitable for various harsh working conditions, with output in two-way square waves. The main parameters of the seeding motor are shown in Table 1.

Table 1

Motor key parameters of JGB37-520-CE

Motor parameters	Values
Damping coefficient/(N·m·s/rad)	0.0036
Armature resistance/(Ω)	4.3
Armature inductance/(mH)	7.1
Moment of inertia/(kg·cm^2)	220
Rotational acceleration/(rad/s^2)	55

The system's main controller is the STM32F103ZET6 microcontroller, which has 13 communication ports, 144 external pins, integrates 14 timers, and 23 external interrupt controllers, fully meeting current research and future development needs. The human-computer interaction interface uses the DMT10600T070_01W industrial serial screen developed by Beijing Diwen Company, which offers high reliability, good stability, and strong anti-interference ability. The simulated locomotive operating speed and plant distance control seeding motor speed are input through the serial screen. The seeding motor driver uses the MC-FBLD-6600 DC motor driver. The theoretical speed is used as the step input of the closed-loop control, and the speed collected by the encoder serves as the feedback for the closed-loop system, ultimately achieving closed-loop control of the motor speed. The control system circuit of the electric red bean precision seeder is shown in Fig. 2.

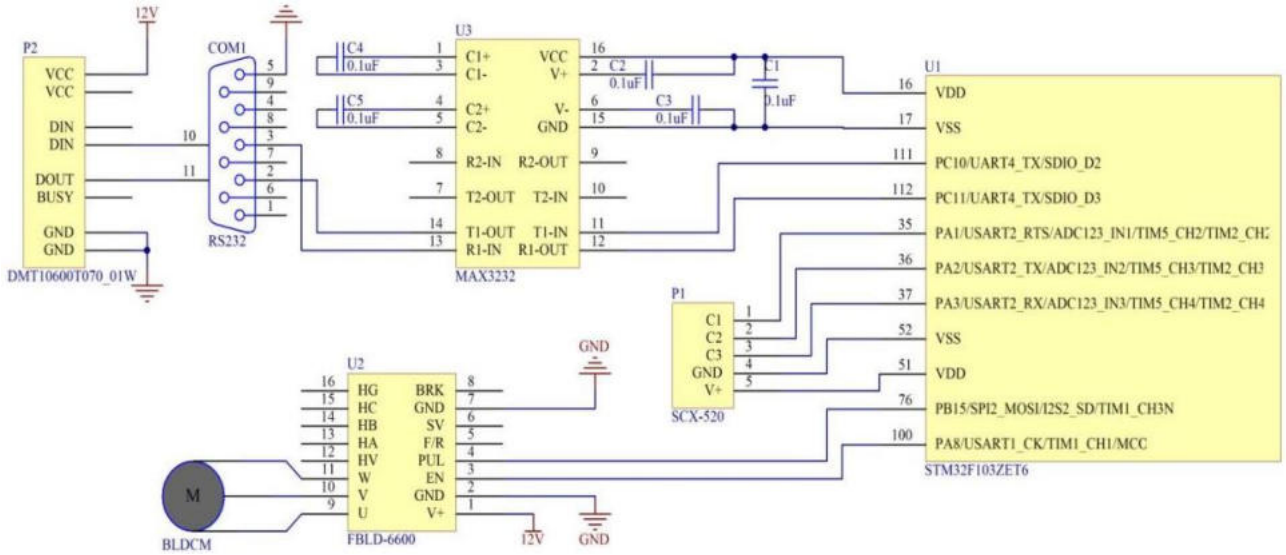


Fig. 2 - Control system circuit of motorized red bean precision planter

Modeling of the seed-rowing motor

To determine the relationship between the motor speed and the operating speed, it is necessary to derive the mathematical relationship between the seeding motor and the machine's traveling speed. The study focuses on an air-suction red bean seed metering device. Assuming there are *m* seed suction holes on the seed plate, the time difference between the dropping of two adjacent red bean seeds is:

$$\Delta t = \frac{60}{nm} \tag{1}$$

where: n is the rotation speed of the seed metering device, r/min.

The formula for calculating the spacing of red bean plants is:

$$Z = 277.78v\Delta t = \frac{1.67\times10^4 v}{nm} \tag{2}$$

where: v is the travel speed of the machine, km/h.

The number of holes in the red bean seed plate of the vSet precision seed metering device selected for the study is 27. Substituting m=27 into the formula (2), the mathematical relationship between the seeding motor and the machine's travel speed can be obtained as:

$$n = \frac{618.52v}{Z} \tag{3}$$

To conduct simulation experiments on the seeding motor control system based on IHBA-LADRC, a physical model of the seeding motor is first established. Compared to the transfer function, the state changes and electrical characteristics of the motor physical model are more similar to the actual seeding motor's changing characteristics and can better simulate the functions and properties of the brushless DC motor (*Zhang et al, 2022; Yousri et al, 2020*). The voltage balance equation of the brushless DC motor is:

$$\begin{bmatrix} U_a \\ U_b \\ U_c \end{bmatrix} = \begin{bmatrix} R & 0 & 0 \\ 0 & R & 0 \\ 0 & 0 & R \end{bmatrix} \begin{bmatrix} i_a \\ i_b \\ i_c \end{bmatrix} + \begin{bmatrix} L-M & 0 & 0 \\ 0 & L-M & 0 \\ 0 & 0 & L-M \end{bmatrix} \begin{bmatrix} \frac{\mathrm{d}i_a}{\mathrm{d}t} \\ \frac{\mathrm{d}i_b}{\mathrm{d}t} \\ \frac{\mathrm{d}i_c}{\mathrm{d}t} \end{bmatrix} + \begin{bmatrix} e_a \\ e_b \\ e_c \end{bmatrix} \tag{4}$$

where:

U_a, U_b, U_c is the phase voltage between windings, *V*; R is the winding phase resistance, Ω; i_a, i_b, i_c is the three-phase phase current, A; L is the stator phase winding self-inductance, H; M is the stator phase winding mutual inductance, H; e_a, e_b, e_c is the three opposite electromotive forces, V.

The expression for the electromagnetic torque of a platoon motor is given by.

$$T_e = \frac{e_a i_a + e_b i_b + e_c i_c}{\omega} \tag{5}$$

where: T_e is the electromagnetic torque, N·m; w is the rotational acceleration, rad/s^2

The rotational acceleration expression is given by:

$$\omega = \frac{2\pi}{60} n' \tag{6}$$

where: n' is the motor rotation speed, r/min

During motor operation, only two of the motor's three-phase windings are active at any moment. Due to the symmetry of the windings, the two active windings have equal amplitude but opposite direction of the reverse electromotive force and phase current. Therefore, it can be derived that:

$$e_a i_a + e_b i_b + e_c i_c = 2E_s I_s \tag{7}$$

$$E_S = \frac{PN}{60}\Phi_m n \tag{8}$$

where:

E_s is the stator voltage, V; I_s is the stator current, A; P is the number of pole pairs of permanent magnets; N is the total number of conductors; Φ_m is the main magnetic flux.

According to Eqs. (6), (7) and (8) the expression for the electromagnetic torque of the platoon motor can be rewritten as.

$$T_e = \frac{2E_s I_s}{\omega} = \frac{PN}{\pi}\Phi_m I_s = C'\Phi_m I_s \tag{9}$$

where: C' is the electromagnetic torque constant

From formula (9), it can be seen that P and N of the seeding motor are constants determined by the motor's inherent properties. The electromagnetic torque T_e of the motor is directly proportional to the main magnetic flux Φ_m and the stator current I_s. Therefore, the motor torque can be adjusted by changing the three-phase stator winding current. The equations of equilibrium of motion of the motor rotor are:

$$T_L = T_e - B\omega + J\frac{\mathrm{d}\omega}{\mathrm{d}t} \tag{10}$$

where:

T_L is the load torque, N·m; B is the damping coefficient, N·m·s/rad; J is the moment of inertia, kg·m^2

When the seeding motor reaches a steady state, the armature windings of any two phases are active, from which the armature circuit voltage loop equation can be derived.

$$U_d = R_s i_a + (L-M)\frac{\mathrm{d}i_a}{\mathrm{d}t} + k_e\omega - \left((L-M)\frac{\mathrm{d}i_b}{\mathrm{d}t} + R_s i_b\right) \tag{11}$$

where: U_d is the bus voltage, V; R_s is the equivalent resistance of each stator winding, Ω

When phases a and b are active, the equivalent resistance and inductance can be established as $R_a=2R_s$ and $L_a=2(L-M)$, because the currents are in opposite directions, $i_p=i_a=-i_b$, so formula (11) can be simplified.

$$U_d = R_a i_p + L_a\frac{\mathrm{d}i_p}{\mathrm{d}t} + k_e\omega \tag{12}$$

The phase voltage of the seeding motor is the input parameter of the control system, and the rotational speed of the seeding motor is the output parameter.

The mathematical model of the seed-rowing motor can be derived as follows.

$$\omega(s) = \frac{K_T U_d(s) - (r_a + L_a s)T_L(s)}{L_a J s^2 + (r_a J + L_a B)s + (r_a B + k_e K_T)} \tag{13}$$

where: K_T is the torque constant of seeding motor.

The equivalent circuit of the brushless DC motor is shown in Fig. 3.

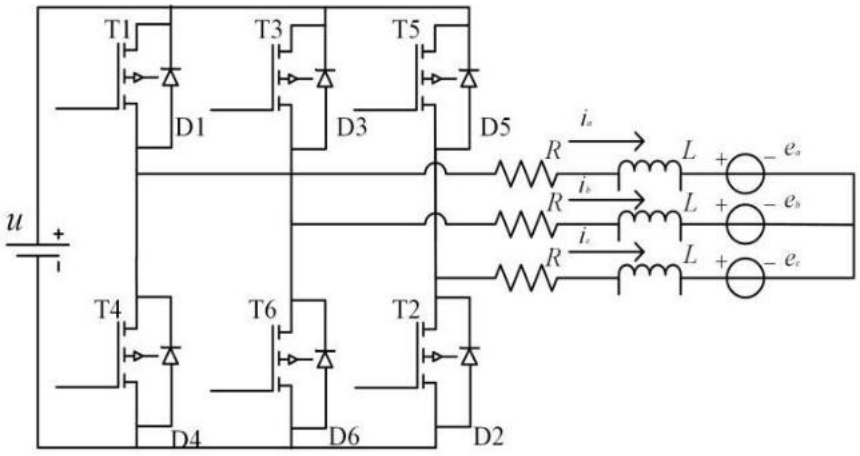


Fig. 3 - Equivalent circuit of the brushless DC motor

Selection of parameters to be optimized by the controller

An active disturbance rejection controller (ADRC) primarily consists of three components: a tracking differentiator (TD), an extended state observer (ESO), and nonlinear state error feedback (NLSEF). Unlike the PID controller, ADRC incorporates the interference signal into the system as a state variable, and then considers interference compensation to minimize the impact of disturbance on the system.

However, ADRC has many components, and there are typically 11 parameters that need adjustment for each component. Manual trial and error is too cumbersome (*Chen, 2008*). Even with optimization algorithms for offline optimization, the complex mathematical model and the number of parameters can lead to excessive computation and long iteration times. Therefore, the literature (*Gao, 2003*) proposes a LADRC, which consists of a TD, a LESO, and a LSEF. LESO is the core control link of LADRC, capable of performing real-time feedback compensation for internal and external disturbances. It does not rely on an accurate mathematical model of the seeding motor, nor does it require clear external interference information for the control system of the electric red bean precision seeder. This greatly reduces the number of parameters that need tuning. Since the DC motor is a second-order system, the expression of the second-order uncertain linear system is:

$$y = f(x_1, x_2, \omega(t)) + bu \tag{14}$$

where: y is the system output; x_1,x_2 is the system parameters; $w(t)$ is the external disturbance; b is the control gain; u is the system input.

The third-order LESO mathematical model can be derived from the second-order linear system state equation:

$$\begin{cases} \dot{z}_1 = z_2 - \beta_1(z_1 - y) \\ \dot{z}_2 = z_3 - \beta_2(z_1 - y) + b_0 u \\ \dot{z}_3 = -\beta_3(z_1 - y) \end{cases} \tag{15}$$

where: β_1, β_2, β_3 is the gain coefficient of LESO,

A PD (proportional-derivative) controller is introduced on the basis of NLSEF to linearize the nonlinear system. Compared with the traditional PD controller, the obtained LSEF reduces the overshoot probability caused by signal mutation. The difference between LSEF and disturbance compensation is:

$$\begin{cases} e_1 = v_0 - z_1 \\ e_2 = -z_2 \\ u_0 = k_p(v_0 - z_1) - k_d z_2 \\ u = (u_0 - z_3)/b \end{cases} \tag{16}$$

where: v_0 is the given value of the controlled object; e_1 is the error input signal; e_2 is the error differential signal; k_p is the proportional coefficient of e_1; k_d is the differential coefficient of e_2.

From equations (8) and (9), it is evident that the performance of the LADRC control system is directly related to the rationalization of the control gain b_0, the gain coefficients β_1, β_2, β_3 of LESO, and the error proportional coefficient k_p and differential coefficient k_d of LSEF. Since there is currently no widely adopted parameter tuning method for LADRC besides the trial and error method, the improved honey badger algorithm is introduced to optimize these six parameters to improve the performance of the control system.

Improving the honey badger algorithm

HBA is a metaheuristic optimization algorithm that simulates the foraging behavior of honey badgers in nature (*Fatma et al, 2021*). Honey badgers are not adept at locating hives, while honey guide birds are not good at opening hives (*Sercan et al, 2023*). HBA is divided into two stages: the excavation stage and the honey collection stage.

The position update formula for the excavation stage is expressed as:

$$x_{new} = x_{prey} + F\beta I x_{prey} + F r_1 w d_i \left|\cos(2\pi r_2)\left[1 - \cos(2\pi r_3)\right]\right| \tag{17}$$

where: x_{prey} is the global optimal position of the prey; $\beta \in [1, \infty)$ represents the honey badger's ability to obtain food, usually set to 6; d_i is the distance between the prey and the i-th honey badger; r_1, r_2, r_3 are three different random numbers in the range of (0,1); I is the odor intensity of the prey, determined by equation (18); w is the update density factor, determined by Eq.(21); F is the sign of changing the search direction, determined by Eq.(22).

$$I = r_4 \frac{S}{4\pi d_i^2} \tag{18}$$

$$S = (x_i - x_{i+1})^2 \tag{19}$$

$$d_i = x_{prey} - x_i \tag{20}$$

$$w = C\exp\left(-\frac{t}{t_{\max}}\right) \tag{21}$$

$$F = \begin{cases} 1, r_5 \le 0.5 \\ -1, \text{else} \end{cases} \tag{22}$$

where: r_4 is a random number within (0,1); S is the source intensity or prey concentration intensity; t_{max} is the maximum number of iterations; C is a constant greater than 1, usually set to 2; and r_5 is a random number within (0,1).

The position update equation for the nectar harvesting phase can be expressed as follows:

$$x_{\text{new}} = x_{\text{prey}} + Fr_6 wd_i \tag{23}$$

where: x_{new} is the new position of the honey badger; x_{prey} is the position of the prey; and r_6 is a random number within (0,1).

The original honey badger algorithm has issues such as slow convergence and a tendency to get trapped in local optima. To address these problems, this paper proposes an IHBA based on a multi-strategy approach. The chaotic mapping algorithm is added in the initialization phase to enable the population to search for the initial operators globally (*Priyadarshi et al, 2023*). Moreover, the human golden ratio segmentation algorithm is added in the variation phase to make the algorithm avoid falling into the local optima (*Anandhakumar et al, 2024*). The density update factor of this algorithm is expressed as:

$$w = 2\left[1 - \sin\left(\left(\frac{t}{t_{\max}}\right)^2 \frac{\pi}{2}\right)\right] \tag{24}$$

The location update equation for the excavation phase is given by

$$x_{\text{new}} = x_{\text{prey}} + F\beta I x_{\text{prey}} + Fr_1 ad_i \left|\cos(2\pi r_2)\left[1 - \cos(2\pi r_3)\right]\right| x_{\text{gnew}} \tag{25}$$

$$x_{\text{gnew}} = x_i \left|\sin(r_7)\right| - r_8 \sin(r_8)\left|c_1 x_b - c_2 x_i\right| \tag{26}$$

$$c_1 = a(1-h) + bh \tag{27}$$

$$c_2 = ah + b(1-h) \tag{28}$$

where: x_{gnew} is the position of the individual after iteration; x_b is the optimal position of the individual; a and b are the initial values of the golden section coefficients, with a=π and b=-π; h is the golden section ratio, approximately 0.6183.

The characteristic parameter process of IHBA optimization of LADRC in Simulink is shown in Fig. 4.

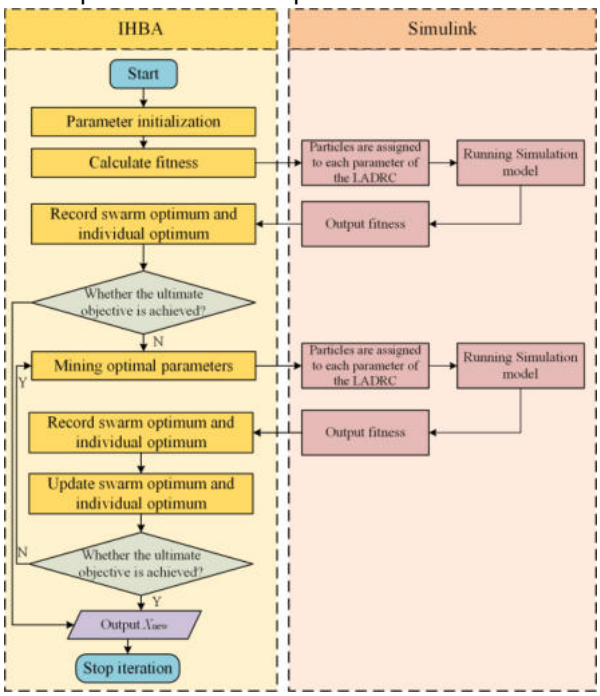


Fig. 4 - IHBA optimization feature parameter process of LADRC in Simulink

IHBA-LADRC controller design

The system objective function used in this study is the ITAE comprehensive evaluation index. This index integrates the product of the running time and the absolute value of the system's steady-state error as the fitness function. A lower ITAE value indicates better control system performance. A control system designed according to this criterion exhibits smaller transient response oscillations and offers good selectivity for parameters. The ITAE calculation formula serves as the fitness function formula:

$$J_{\mathrm{ITAE}} = \int_0^{+\infty} t\left|e(t)\right| \mathrm{d}t \tag{29}$$

where: t is the system running time, s; $e(t)$ is the system steady-state error.

The ITAE index comprehensively evaluates the static and dynamic performance of the control system, including rapidity, accuracy, and stability. This feature helps achieve ideal optimization effects on the steady-state error and adjustment time of the seeding motor.

The input signal should be the expected speed of the seeding motor, calculated by equation (3), and the system control object is the brushless DC motor that drives the red bean precision seeding device. IHBA optimizes the control gain b_0 of LADRC, the gain coefficients β_1, β_2, β_3 of LESO, and the error proportional coefficient k_p and differential coefficient k_d of LSEF. The feedback value of the control system should be the rotor speed of the motor. By comparing the expected speed of the metering device with the actual rotor speed, the speed error e_1 can be obtained. Differentiating this error provides the error change rate e_2. IHBA calculates and evaluates the control system using the ITAE index based on the system error e_1. This process yields the optimal response curve for seeding motor control within the set number of iterations. The IHBA-optimized air-suction electric-driven red bean precision seeder control system LADRC parameter flowchart is shown in Fig.5.

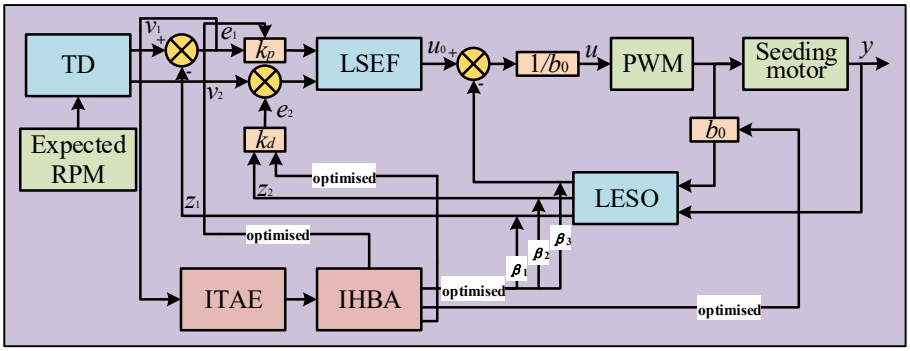


Fig. 5 - IHBA optimized air-suction electric-driven red bean precision seeder system LADRC parameter flowchart

RESULTS

Simulation experiments

The simulation experiment for the electric red bean precision seeder control system, based on the IHBA-LADRC algorithm, uses MATLAB 2022b/Simulink as the test environment. The LADRC-based seeding motor control system is constructed as shown in Fig. 6. Both HBA and IHBA are used to optimize six key LADRC parameters. The experiment compares three seeding motor control strategies: IHBA-LADRC control, empirically tuned PID control, empirically tuned LADRC control, and HBA-LADRC control. This comparison aims to demonstrate the superiority of the IHBA-LADRC-based intelligent control system for the electric red bean precision seeder. In the Simulink simulation, the system running time t is used as the independent variable, the seeding motor speed as the system input, and the unit step response as the output.

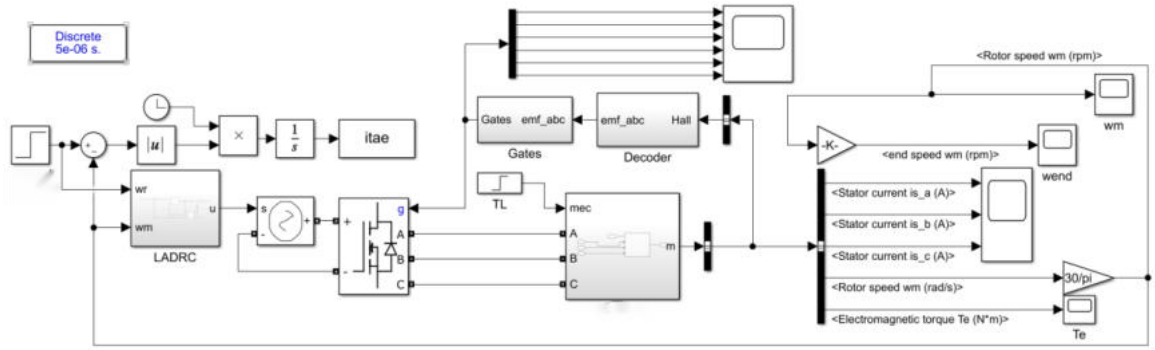


Fig. 6 - Seeding motor control system based on LADRC

Since the simulation experiment involves six optimization parameters, to avoid prolonged simulation times, the optimization scope is narrowed to save time. Before starting the simulation experiment, the six parameters were optimized based on previous empirical adjustments of LADRC parameters. The optimization ranges were set as follows: b_0∈[0.0001,1000], β_1∈[0.0001,1000], β_2∈[0.0001,1000], β_3∈[0.0001,1000], k_p∈[0.0001,1000], k_d∈[0.0001,1000]. The population size for HBA and IHBA is set to 40, and the maximum number of iterations is 100 generations. During sowing operations, various external interferences such as machine tool oscillation and internal interference caused by inconsistent friction factors in different areas inside the seed metering device are common. To evaluate the anti-interference capabilities of the four control strategies, a step disturbance with an intensity of 5 default unit strengths and a disturbance time of 0.2 s was added to the system at 5 s.

The simulation experiments were conducted on an AMD EPYC TM 7642-48C-96T CPU @ 3.0GHz system with 256GB of RAM, running a 64-bit Windows 10 operating system. The simulation software used was MATLAB 2022b/Simulink. Fig. 7 presents the step response curve comparison of the four control strategies, Fig. 7 shows the fitness-iteration number change curve for the two intelligent algorithms, and Table 2 summarizes the control performance indicators for the four control strategies.

Table 2

Comparison of control performance indicators of four control strategies

Control strategies	Overshooting volume δ/%	Adjustment time t_s/s	Steady-state error/ e_{ss}	Interference recovery time t_k/s	Disturbed vibration peak value z/(r·min^{-1})	Adaptation
PID	5.12	0.94	0.012	1.01	45.65	
LADRC	0.37	1.58	0.002	0.45	40.92	
HBA-LADRC	0.02	1.24	0.008	0.20	40.66	3.2036
IHBA-LADRC	0	0.79	0.001	0.22	40.72	1.7611

From Fig. 7 and Table 2, it is evident that the performance indicators of the electric red bean precision seeder control system based on IHBA-LADRC demonstrate significant advantages over the other three control strategies in terms of overshoot, adjustment time, and steady-state error. Specifically, the IHBA-LADRC system exhibits no overshoot, an adjustment time of 0.79 s, almost no static error, a recovery time after interference of 0.22 s, and no oscillation or static error after reaching a steady state again. Although HBA-LADRC and LADRC significantly improve overshoot and steady-state error compared to traditional PID, their anti-interference abilities are not as robust as the IHBA-LADRC. However, there are still certain limitations in optimizing the adjustment time, which remains much greater than that achieved by the IHBA-LADRC algorithm. The anti-interference capabilities of the three LADRCs are significantly better than those of PID. Although the t_k and z values of HBA-LADRC are better than those of IHBA-LADRC, the disturbed vibration peak of IHBA-LADRC is lower. Moreover, there is almost no static difference after it returns to steady state, resulting in better overall stability.

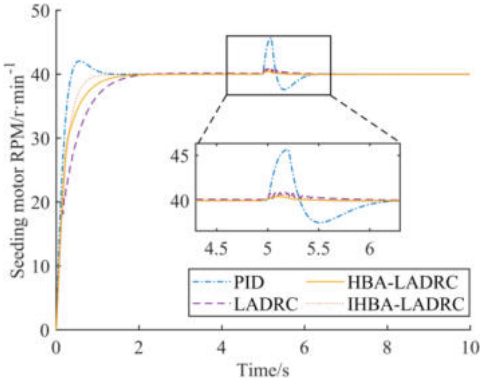


Fig. 7 - Comparison of step response curves of four control strategies

As seen in Fig. 8 and Table 2, the LADRC parameters optimized using IHBA reached the optimal value at the 72nd iteration, with a fitness of 1.7611. In contrast, the LADRC parameters optimized using HBA reached the optimal value at the 85th iteration, with a fitness of 3.2036. IHBA-LADRC demonstrates more iterations and a smaller fitness value, indicating a better control system compared to HBA-LADRC. This validates the improvements made to the HBA in this study.

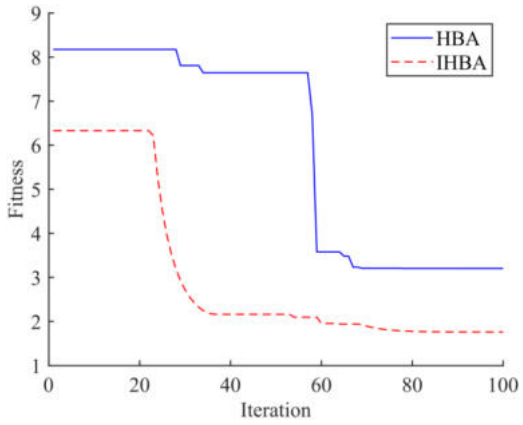
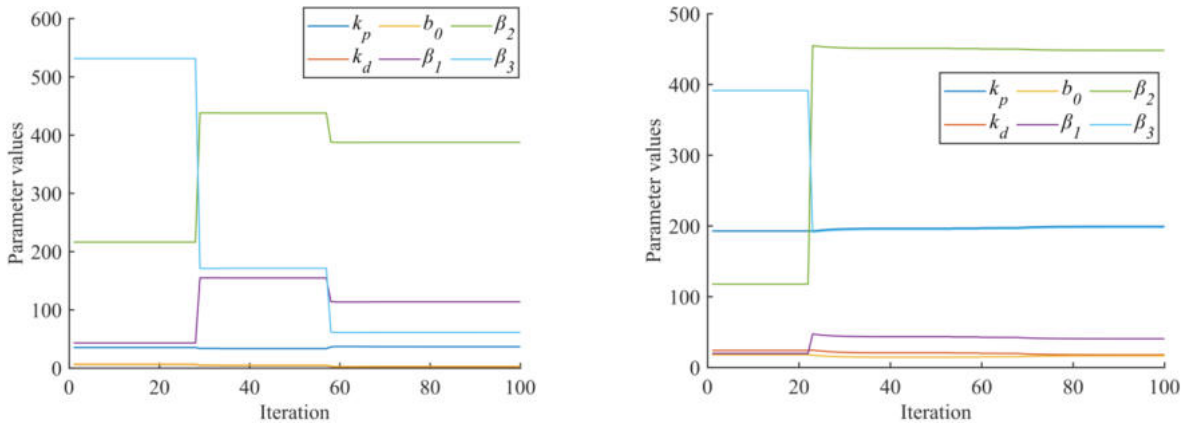


Fig. 8 - Fitness-iterations curve of two intelligent algorithms

Fig. 9 shows the change curves of six key parameters of the LADRC controller optimized by the two intelligent algorithms. As shown in Fig. 9(a), the six parameters of HBA-optimized LADRC are as follows: b_0 reaches the optimal value in the 72nd generation, with an optimal value of 36.7034; k_p reaches the optimal value in the 72nd generation, with an optimal value of 2.3106; k_d reaches the optimal value in the 72nd generation, with an optimal value of 2.8586; β_1 reaches the optimal value in the 72nd generation, with an optimal value of 113.5999; β_2 reaches the optimal value in the 72nd generation, with an optimal value of 387.4995; β_3 reaches the optimal value in the 72nd generation, with the optimal value being 61.2449. As shown in Fig. 9(b),the six parameters of IHBA-optimized LADRC are as follows: b_0 reaches the optimal value in the 85th generation, with an optimal value of 199.3519; k_p reaches the optimal value in the 85th generation, with an optimal value of 17.8458; k_d reaches the optimal value in the 85th generation, with an optimal value of 16.4955; β_1 reaches the optimal value in the 85th generation, with an optimal value of 40.5441; β_2 reaches the optimal value in the 85th generation, with an optimal value of 448.2168; β_3 reaches the optimal value in the 85th generation, with the optimal value being 197.8834.



(a) HBA optimized LADRC parameter change curve (b) IHBA optimized LADRC parameter change curve

Fig. 9 - Iterative diagram of two intelligent algorithms optimizing the six key parameters of the LADRC

Seed displacer speed accuracy test

To evaluate the speed accuracy of the control system for the electric air-suction red bean precision seeder, a seed metering speed accuracy test was conducted. The test took place on March 26, 2024, in the High-speed Precision Seeding Laboratory of Heilongjiang Bayi Agricultural University. Using the DT-2234A photoelectric speedometer (accuracy: ±0.1 r/min) developed by the Lutron Company, the actual rotation speed of the seed metering device was collected. This was done when the theoretical plant spacing was 100 mm and the operating speed was set at 3, 5, 7, 9 km/h. The speed of the seeding motor was recorded 30 seconds after stabilizing, and the average speed *N* of the seeding device was calculated. Each set of speeds was repeated 8 times (N1~N8), and the coefficient of variation of the actual speed of the seeding device was determined. Table 3 presents the results of the seed metering speed accuracy verification test.

Table 3

Verification experiment table of speed accuracy of seed metering device

Working speed/(km·h^{-1})	Theoretical speed/(r·min^{-1})	Actual speed/(r·min^{-1})								Average speed/(r·min^{-1})	Coefficient of variation/%
		N_1	N_2	N_3	N_4	N_5	N_6	N_7	N_8		
3	18.6	19.0	18.1	19.5	18.2	19.4	18.3	18.0	19.2	18.7	3.34
5	31.0	30.1	31.8	31.5	30.4	32.2	30.2	31.7	30.3	31.0	2.76
7	43.3	42.6	44.5	42.6	42.7	43.8	42.7	43.2	42.4	43.1	1.61
9	55.7	54.4	57.7	53.9	54.0	53.5	56.8	53.4	58.1	55.2	3.56

As shown in Table 3, the electric red bean precision seeder control system based on IHBA-LADRC shows superior seed metering speed accuracy and uniformity, with seed metering speed variation coefficients of less than 4%. At operating speed of 9 km/h, the coefficient of variation of the actual rotation speed of the seed metering device reaches a maximum of 3.56%. At operating speed of 7 km/h, this coefficient reaches a minimum of 1.61%. When operating at 9 km/h, N_5 shows the maximum speed deviation, with a deviation rate of 4.31%. At 7 km/h, N_5 shows the minimum speed deviation, with a deviation rate of 0.23%.

Seed discharge performance static test

To further verify the superiority of the IHBA-LADRC intelligent control strategy obtained from the simulation experiments, a bench comparison test was conducted. This test compared the performance of the intelligent electric seeding system, the traditional PID electric seeding system, and the sprocket seeding system. The test took place in the High-speed Precision Seeding Laboratory of Heilongjiang Bayi Agricultural University from April 5 to April 7, 2024. The test materials included the red bean hybrid "Jihong No. 7,". This hybrid has a moisture content of (13.1±0.87)%, a thousand-grain weight of (202.2±0.85)g, a density of (1.24±0.06) g·cm^{-3}, and a seed clarity of 97.96%. The seeds are ellipsoid in shape, with a sphericity of 80.1%, and dimensions of (8.09±0.78) mm in length, (5.81±0.40) mm in width, and (5.78±0.40) mm in height. The test was conducted on April 30, 2024, in the Seeding Equipment Laboratory of the Heilongjiang Bayi Agricultural University. The laboratory is equipped with a JPS-12 computer vision seed metering device performance testing device. The seeding performance test setup is shown in Fig. 10.



Fig. 10 - Seeding performance experiment device

Red beans are planted at densities where the distance between plants is determined to be 100~150 mm according to the indicators. After preliminary testing and calibration, it was found that seeds can be planted evenly when the operating speed is below 10 km/h and the wind pressure in the seed suction room is between -1~-1.5 kPa. To minimize variables and reduce the number of test groups in the comparison test, the fan's negative pressure was fixed at -1.5 kPa, and the seeding height was set at 50 mm. Three different groups of sowing at plant spacings of 100 and 150 mm were selected at four different operating speeds of 3, 5, 7, and 9 km/h. These were used to compare the performance of chain-driven and electric-driven red bean precision sowing operations, following GB/T 6973-2005 "Test Method for Single-Seed (Precision) Seeder"(*Yi et al, 2025; Sun et al, 2024; Wang et al, 2024*). The qualified index, multiple index, missing index, and coefficient of variation were used as evaluation indices. Additionally, the coefficient of variation for qualified spacing was introduced to determine the stability of the electric seeding control system designed in this study.

The coefficient of variation for qualified spacing measures the variation in spacing among qualified seeds, excluding reseeding and missed seeding caused by seed arranging device defects and external interference. This metric helps to determine the uniformity of sowing qualified red bean seeds, thereby validating the superiority of the designed control system. Ideal spacing uniformity is crucial for subsequent field management activities such as fertilization and spraying. In each bench test, 30 consecutive spacing samples were selected from the seed bed after the stable operation of the electronic control system. Each test group was repeated three times, resulting in 90 spacing samples for analysis and calculation of operational indexes. The results of the bench test are shown in Table 4.

Table 4

Bench experiment results

Working distance / mm	Operational indicators	Seeding operation speed (chain drive)/(km·h^{-1})				Seeding operation speed (PID electric drive)/(km·h^{1})				Seeding operation speed (intelligent electric drive)/(km·h^{-1})			
		3	5	7	9	3	5	7	9	3	5	7	9
100	Qualified index	92.22	93.33	93.33	90.56	94.45	93.89	95.56	94.45	94.45	96.11	97.22	94.45
	Multiple index	1.11	2.22	2.22	3.33	2.22	2.22	1.11	2.22	2.22	1.11	0.56	2.22
	Missing index	6.67	4.45	4.45	6.11	3.33	3.89	3.33	3.33	3.33	2.78	2.78	3.33
	CV	26.56	27.89	26.96	29.39	23.89	24.00	22.94	26.18	20.21	16.95	13.63	20.05
	CV of spacing	19.91	19.08	18.24	20.73	15.45	15.13	15.95	19.26	9.62	12.13	7.83	12.07
150	Qualified index	94.45	95.56	95.56	93.34	96.11	95.56	95.56	95.00	96.67	97.78	97.78	96.67
	Multiple index	2.22	1.11	1.11	2.22	1.11	2.22	2.22	1.11	1.11	1.11	1.11	1.11
	Missing index	3.33	3.33	3.33	4.44	2.78	2.22	2.22	3.89	2.22	1.11	1.11	2.22
	CV	23.04	21.56	22.73	26.04	20.88	21.59	20.11	22.49	16.84	13.90	12.46	17.67
	CV of spacing	15.87	16.18	17.07	19.39	14.98	13.86	12.53	15.30	9.56	8.46	7.91	11.52

As seen in Table 4, the IHBA-LADRC-based electric red bean precision seeder control system significantly improves various sowing operation indicators compared to the traditional sprocket seeding system and the traditional PID electric seeding system. At four different operating speeds, when the theoretical plant spacing of red beans is 100 mm, the average passing index of the intelligent electric-driven sowing system is 3.20 percentage points higher than that of the sprocket sowing system. The average multiple index is reduced by 0.69 percentage points, and the average missing index is reduced by 2.36 percentage points. Additionally, the average coefficient of variation decreased by 9.99 percentage points, and the average coefficient of variation for qualified plant spacing decreased by 9.08 percentage points. Compared to the traditional PID electric seeding system, the intelligent electric seeding system's average qualified index increased by 0.97 percentage points, the average reseeding index decreased by 0.41 percentage points, and the average missed sowing index decreased by 0.41 percentage points. The average variation coefficient decreased by 6.54 percentage points, and the average variation coefficient for qualified plant spacing decreased by 6.04 percentage points.

When the theoretical plant spacing of red beans is 150 mm, the average qualified index of the intelligent electric seeding system is 2.50 percentage points higher than that of the sprocket seeding system. The average reseeding index is reduced by 0.56 percentage points, the average missed sowing index is reduced by 1.94 percentage points, and the average variation coefficient is reduced by 8.12 percentage points. The average variation coefficient for qualified plant spacing decreased by 7.77 percentage points. Compared to the traditional PID electric-driven sowing system, the average qualified index of the intelligent electric-driven sowing system increased by 1.67 percentage points, the average multiple index decreased by 0.56 percentage points, the average missed sowing index decreased by 1.11 percentage points, the average variation coefficient decreased by 6.05 percentage points, and the average qualified plant spacing variation coefficient decreased by 4.81 percentage points.

The data above demonstrates that compared to the chain-driven seeding system, the intelligent electric seeding system shows an overall improvement of 2.85 percentage points in the qualified index, a reduction of 0.63 percentage points in the multiple index, and a reduction of 2.15 percentage points in the missed seeding index across different plant spacings and operating speeds.

Additionally, the overall coefficient of variation decreased by 9.06 percentage points, and the coefficient of variation for qualified plant spacing decreased by 8.43 percentage points. Compared to the traditional PID electric seeding system, the intelligent electric seeding system exhibits an overall improvement of 1.32 percentage points in the qualified index, a reduction of 0.49 percentage points in the multiple index, and a reduction of 0.76 percentage points in the missed seeding index across different plant spacings and operating speeds. The overall coefficient of variation decreased by 6.30 percentage points, and the coefficient of variation for qualified plant spacing decreased by 5.43 percentage points.

Compared to the sprocket-driven seeding system and the PID electric-driven seeding system, the intelligent electric seeding system significantly reduces the missed seeding rate and coefficient of variation in the red bean seeding process. It also improves the uniformity of the spacing of qualified red bean plants, as evidenced by the significantly reduced variation coefficient of qualified plant spacing. This improvement ensures that the actual planting of red beans is less variable than the theoretical plant spacing, resulting in evenly aligned seeds between ridges and consistent plant numbers. This uniformity facilitates follow-up field management for farmers.

CONCLUSIONS

(1) To address the high sowing missing rate and uneven sowing due to small theoretical plant spacing, narrow qualified range, and internal and external interference during precision sowing of red beans in high-density planting, an electric red bean precision seeder control system based on IHBA-LADRC was studied. The design process of the intelligent control system, the improvement of the honey badger algorithm, and the intelligent tuning method of key parameters in the LADRC controller are explained. This system addresses the issues of long adjustment time, large overshoot, significant steady-state error, and poor anti-interference ability in general electric seeding systems.

(2) The simulation experiment results demonstrate that the control system of the electric red bean precision seeder based on IHBA-LADRC exhibits no overshoot, short adjustment time, minimal steady-state error, no oscillation, and strong anti-interference ability. Among the four algorithms tested, the dynamic response characteristics are optimal. The IHBA algorithm enables the optimal intelligent control strategy in the electric seeder control system. The system reaches steady state with an adjustment time of 0.79 s, shows nearly zero steady-state error, recovers from disturbances within 0.22 s, and maintains stability without oscillations after returning to steady state.

(3) Bench test results show that under four different operating speeds and three different theoretical plant spacings, the electric red bean precision seeder control system based on IHBA-LADRC outperforms the sprocket seeding system in various seeding performance indicators. The overall qualified index increased by 2.85 percentage points, the reseeding index decreased by 0.63 percentage points, the missed seeding index decreased by 2.15 percentage points, the coefficient of variation decreased by 9.06 percentage points, and the variation coefficient of qualified plant spacing decreased by 8.43 percentage points. Compared to traditional PID electronically controlled sowing, the IHBA-LADRC system also showed improvements: the overall qualified index increased by 1.32 percentage points, the reseeding index decreased by 0.49 percentage points, the missed sowing index decreased by 0.76 percentage points, the overall coefficient of variation decreased by 6.30 percentage points, and the variation coefficient of qualified plant spacing decreased by 5.43 percentage points. The IHBA-LADRC-based control system for the electric red bean precision seeder ensures that the actual plant spacing closely matches the theoretical set value. This high level of operational accuracy provides a foundation for implementing precise intercropping between different rows in future applications, thereby further improving land utilization efficiency.

ACKNOWLEDGEMENT

This study was supported by the Key Research and Development Plan Project of Heilongjiang Province (2022ZX05B02), the Heilongjiang Provincial Natural Science Foundation Joint Guidance Project (LH2024E103), and the Heilongjiang Bayi Agricultural University Graduate Innovative Research Project (YJSCX2024-Z02、YJSCX2024-Y12、YJSCX2024-Y13).

REFERENCES

[1] Anandhakumar, C., Murugan, N. S. S., & Kumaresan, K. (2024). Extreme learning machine model with honey badger algorithm based state-of-charge estimation of lithium-ion battery. *Expert Systems with Applications*, 238, 121609. https://doi.org/10.1016/j.eswa.2023.121609

[2] Cay, A., Kocabiyik, H., & May, S. (2018). Development of an electro-mechanic control system for seed-metering unit of single seed corn planters part i: Design and laboratory simulation. *Computers and Electronics in Agriculture*, 144, 71–79. https://doi.org/10.1016/j.compag.2017.11.035

[3] Cay, A., Kocabiyik, H., & May, S. (2018). Development of an electro-mechanic control system for seed-metering unit of single seed corn planters part ii: Field performance. *Computers and Electronics in Agriculture*, 145, 11–17. https://doi.org/10.1016/j.compag.2017.12.021

[4] Chen, J., Zhang, H., Pan, F., Du, M., & Ji, C. (2022). Control system of a motor-driven precision no-tillage maize planter based on the CANopen protocol. *Agriculture*, 12(7), 932. https://doi.org/10.3390/agriculture12070932

[5] Chen, X. (2008). *Automatic disturbance rejection controller parameter tuning method and its application in thermal process* [PhD thesis]. Tsinghua University.

[6] Ding, Y., Li, Y., Zhang, D., Cui, T., Li, Y., Zhong, X., Xie, C., & Ding, Z. (2021). Novel low-cost control system for large high-speed corn precision planters. *International Journal of Agricultural and Biological Engineering*, 14(2), 151-158. https://doi.org/10.25165/j.ijabe.20211402.6053

[7] Gao, Z. (2003). Scaling and bandwidth-parameterization based controller tuning. In *Proceedings of the American Control Conference* (Vol. 6, pp. 4989–4996). Denver, CO, USA.

[8] Hashim, F. A., Houssein, E. H., Hussain, K., Mabrouk, M. S., & Atabany, W. (2021). Honey badger algorithm: New metaheuristic algorithm for solving optimization problems. *Mathematics and Computers in Simulation*, 192, 84-110. https://doi.org/10.1016/j.matcom.2021.08.013

[9] Jafari, M., Hemmat, A., & Sadeghi, M. (2010). Development and performance assessment of a dc electric variable-rate controller for use on grain drills. *Computers and Electronics in Agriculture*, 73(1), 56–65. https://doi.org/10.1016/j.compag.2010.04.004

[10] Kamgar, S., Eslami, M. J., & Maharlouie, M. M. (2013). Design, development and evaluation of a mechatronic transmission system to improve the performance of a conventional row crop planter. Dallas, Texas, July 29-august.2012. https://doi.org/10.13031/2013.41987

[11] Li, Y., Zhou, W., Ma, C., Feng, Z., Wang, J., Yi, S., & Song, W. (2024). Design and optimization of the seed conveying system for belt-type high-speed corn seed guiding device. *International Journal of Agricultural & Biological Engineering*, 17(2), 123-131. https://doi.org/10.25165/j.ijabe.20241702.8427

[12] Ma, C., Yi, S., Tao, G., Li, Y., Wang, S., Wang, G., & Gao, F. (2023). Research on receiving seeds performance of belt-type high-speed corn seed guiding device based on discrete element method. *Agriculture*, 13(5), 1085. https://doi.org/10.3390/agriculture13051085

[13] Ma, J., Khan, N., Gong, J., Hao, X., Cheng, X., Chen, X., Chang, J., & Zhang, H. (2022). From an introduced pulse variety to the principal local agricultural industry: A case study of red kidney beans in Kelan, China. *Agronomy*, 12(7), 1717. https://doi.org/10.3390/agronomy12071717

[14] Mangus, D. L., Sharda, A., Flippo, D., Strasser, R., & Griffin, T. (2017). Development of high-speed camera hardware and software package to evaluate real-time electric seed meter accuracy of a variable rate planter. *Computers and Electronics in Agriculture*, 142, 314–325. https://doi.org/10.1016/j.compag.2017.09.014

[15] Ozumcan, S., Ozturk, A., Vuran, M., & Andic, C. (2023). A novel honey badger algorithm based load frequency controller design of a two-area system with renewable energy sources. *Energy Reports*, 9(12), 272-279. https://doi.org/10.1016/j.egyr.2023.10.002

[16] Priyadarshi, A., Yadav, K., & Rathore, V. (2023). Synchrophasor assisted load frequency control of interconnected system with multiple fuel inputs using honey badger algorithm. *Int. J. Model. Identif. Control*, 43, 54–63. https://doi.org/10.1504/IJMIC.2023.132109

[17] Ranta, O., Drocas, I., Stanila, S., Molnar, A., Muntean, M., Marian, O. (2012). The main advantages of E-drive system used for precision seeding. *Bulletin of the University of Agricultural Sciences and Veterinary Medicine Cluj-Napoca. Agriculture*, 69(1). https://doi.org/10.15835/buasvmcn-agr:8685

[18] Sun, W., Yi, S., Qi, H., Li, Y., Dai, Z., Zhang, Y., & Wang, S. (2024). Design and experiment of progressive seed-cleaning mechanism for air-pressure maize precision seed-metering device. *INMATEH - Agricultural Engineering*, 73, 473-486. https://doi.org/10.35633/inmateh-73-40

[19] Wang, S., Zhao, B., Yi, S., Zhou, Z., & Zhao X. (2022). GAPSO-optimized fuzzy PID controller for electric-driven seeding. *Sensors*, 22(17), 6678. https://doi.org/10.3390/s22176678

[20] Wang, S., Yi, S., Zhao, B., Li, Y., Li, S., Tao, G., Mao, X., & Sun, W. (2024). Sowing depth monitoring system for high-speed precision planters based on multi-sensor data fusion. *Sensors*, 24(19), 6331. https://doi.org/10.3390/s24196331

[21] Wang, S., Yi, S., Zhao, B., Li, Y., Wang, G., Li, S., & Sun, W. (2024). Photoelectric sensor-based belt-type high-speed seed guiding device performance monitoring method and system. *Computers and Electronics in Agriculture*, 227, 109489. https://doi.org/10.1016/j.compag.2024.109489

[22] Xu, T., Fu, H., Yu, J., Li, C., Wang, J., & Zhang, R. (2024). Determination of ellipsoidal seed–soil interaction parameters for DEM simulation. *Agriculture*, 14(3), 376. https://doi.org/10.3390/agriculture14030376

[23] Yi, S., Wang, G., Li, Y., Wang, S., Li, S., & Wei, R. (2025). Design and Experiment of Seed Orientation Correction Element for High-speed Belt-type Soybean Seeding Device. *Transactions of the Chinese Society for Agricultural Machinery*, 56(5), 268–278+424. https://doi.org/10.6041/j.issn.1000-1298.2025.05.025

[24] Yousri, D., Allam, D., Eteiba, M. B. (2019). Chaotic heterogeneous comprehensive learning particle swarm optimizer variants for permanent magnet synchronous motor. *Applied Soft Computing*, 74, 479–503. https://doi.org/10.1016/j.asoc.2018.10.032

[25] Zhang, Y., Sun, W., Yu, H., Geng, X., Fan, M., & Qin, M. (2022). An improved model-free predictive current control method for PMSM drives based on extended control set and fast current difference updating. *IEEE Energy Conversion Congress and Exposition (ECCE)*, Detroit, MI, USA, 2022, 1-8, *https://doi.org/10.1109/ECCE50734.2022.9947757*

YOLO-LSD: A LIGHTWEIGHT MODEL FOR HIGH-ACCURACY MULTI-BREED SHEEP FACE DETECTION

/

YOLO-LSD：一种轻量级的高精度多品种羊脸检测模型

Xiwen ZHANG[1,2]; Zelin NIU[1]; Yanxin GUO[1,3], Yu CAI[3], Ruiyan SUN[1,3*]
[1] Jiangsu Maritime Institute, College of Marine Electrical and Intelligent Engineering, Nanjing, China
[2] Inner Mongolia Agricultural University, College of Mechanical and Electrical Engineering, Inner Mongolia, China
[3] Industrial Center, Nanjing Institute of Technology, Nanjing, China
*Tel: 0471-4309215; *)Corresponding author E-mail: nit_sry@126.com*
DOI: https://doi.org/10.35633/inmateh-76-97

Keywords: *Sheep face detection; Deep learning; High-accuracy model; YOLOv11; Multi-breed*

ABSTRACT

Sheep face detection is critical for intelligent livestock management and breeding, yet existing models often struggle in complex farm scenarios due to inadequate multi-scale feature utilization and high computational demands. To address these challenges, this study proposes a lightweight multi-breed sheep face detection framework named YOLO-LSD (Lightweight Sheep Face Detection), achieving an optimal balance between detection accuracy and computational efficiency through multi-dimensional optimizations. At the feature enhancement level, the lightweight channel attention mechanism Efficient Channel Attention (ECA) is embedded into the backbone network to dynamically strengthen the channel responses of key facial features through local cross-channel interactions. Concurrently, Ghost convolution is introduced to replace traditional convolutional layers, leveraging feature redundancy mining technology to substantially reduce computational complexity while maintaining the ability to represent diverse facial features across sheep and goat breeds. To address the limited sample diversity in multi-breed datasets, a transfer learning strategy is employed, involving directional fine-tuning of breed-specific facial features based on large-scale pre-trained models to enhance the model's generalization ability across diverse sheep and goat varieties. Experimental results demonstrate that YOLO-LSD achieves a mAP@0.5 of 99.29% on a self-constructed multi-breed sheep face dataset, marking a 0.59% improvement over the baseline YOLOv11. Notably, the parameter count of YOLO-LSD is only 2.4×10^6, while achieving an inference speed of 60 FPS and 6.3 Flops. This study presents a high-precision, lightweight solution for intelligent livestock monitoring systems, offering practical insights for the deployment of multi-breed sheep face detection models in real-world farm applications.

摘要

绵羊面部检测是智能畜牧管理和养殖的关键，但由于多尺度特征利用不足和计算需求高，现有模型在复杂的农场场景中往往难以实现。为了解决这些挑战，本研究提出了一种轻量级的多品种羊人脸检测框架，名为YOLO-LSD (lightweight sheep face detection)，通过多维优化实现了检测精度和计算效率之间的最佳平衡。在特征增强层面，将轻量级通道注意机制ECA嵌入骨干网络，通过局部跨通道交互，动态增强关键面部特征的通道响应。同时，引入Ghost卷积来取代传统的卷积层，利用特征冗余挖掘技术大幅降低计算复杂性，同时保持表示绵羊和山羊品种不同面部特征的能力。为了解决多品种数据集样本多样性有限的问题，采用迁移学习策略，在大规模预训练模型的基础上对特定品种的面部特征进行定向微调，以提高模型在不同绵羊和山羊品种间的泛化能力。实验结果表明，YOLO-LSD在自构建的多品种绵羊面部数据集上的mAP@0.5 达到了 99.29%，比基线YOLOv11提高了0.59%。值得注意的是，YOLO-LSD的参数量仅为 2.4×10^6，同时实现了 60 FPS和6.3 Flops的推理速度。本研究提出了一种高精度、轻量级的智能牲畜监测系统解决方案，为在实际农场应用中部署多品种绵羊面部检测模型提供了实用的见解。

INTRODUCTION

With the increasing advancement of intelligent livestock farming, including intensive breeding, breed improvement, and precision animal health management, the demand for accurate identification and monitoring of sheep, as key livestock resources, has emerged as a critical research focus in agricultural technology (*Sharma et al., 2020*).

Against the backdrop of rapid developments in smart farming systems, high-precision sheep face detection techniques serve not only as a foundational enabler for individual animal tracking and breed classification but also as core technology for optimizing feeding strategies and ensuring animal welfare (*Xue et al., 2024*). The accurate detection of sheep face targets is directly linked to the efficiency of farm management, and its significance becomes particularly pronounced in real-time scenarios such as automated feeding and health monitoring (*Zhang et al., 2024*). However, traditional manual sheep identification methods suffer from notable drawbacks, such as low efficiency, poor real-time performance, susceptibility to false negatives and positives in complex farm environments, and high labor costs (*Hao et al., 2024*).

Traditional manual sheep detection methods have manifested numerous deficiencies in practical applications. The visual screening approach is highly inefficient, rendering it unable to handle the massive volume of monitoring data generated in large-scale farms and falling short of real-time management requirements (*Salama et al., 2019*). In time-sensitive scenarios such as disease outbreak response, the inherent delays in manual identification can lead to untimely intervention, thereby increasing the risk of epidemic spread (*Hitelman et al., 2022*). Moreover, this method is heavily reliant on human resources, with labor costs increasing non-linearly as the farming scale expands. These limitations have become increasingly prominent in the face of the urgent demand for automated and high-precision management in smart agriculture, prompting both academia and industry to explore intelligent detection technologies based on deep learning to overcome the long-standing bottlenecks in efficiency, accuracy, and scalability associated with traditional methods (*Peruzzi et al., 2025*).

In the early stages of sheep face detection, two-stage object detection algorithms, such as Faster R-CNN, were commonly employed (*Zhang et al., 2022*). These algorithms generate candidate bounding boxes through region proposal networks and conduct fine-grained classification for each box, enabling high detection accuracy in complex farm scenarios (*Deng et al., 2022*). Nevertheless, the two-stage cascaded architecture leads to high computational complexity and slow inference speed (*Deng et al., 2021*). Additionally, the manually designed anchor boxes struggle to adapt to the multi-scale facial features across different sheep breeds, often resulting in missed detection of small targets and positioning deviations for large targets. As a result, these algorithms fail to meet the requirements of real-time farm monitoring.

As a typical representative of single-stage object detection algorithms, the YOLO series transforms object detection into a problem of directly predicting the coordinates of grid cells and class probabilities through an end-to-end regression architecture (*He et al., 2016*). This approach avoids the redundant calculation of candidate bounding box generation in two-stage algorithms, significantly improving inference efficiency while maintaining detection accuracy. On this basis, the YOLOv11 algorithm further optimizes the backbone network structure. By adopting the CSPDarknet lightweight feature extraction module and the efficient Feature Pyramid Network (FPN), it maintains the multi-scale feature representation ability while reducing the number of parameters. It is particularly suitable for complex farm scenarios where small distant sheep faces and large close-up faces coexist. Its improved anchor box adaptation mechanism learns the aspect ratio priors of the sheep face dataset through K-means clustering, enhancing the matching degree between the anchor boxes and the actual facial shapes of different breeds (*Zhang et al., 2023*). This effectively alleviates the adaptation deviation problem of traditional manually designed anchor boxes for varied facial characteristics, such as the rounder faces of some sheep breeds versus the more angular features of others. These characteristics endow YOLOv11 with strong engineering practicality in farm monitoring, making it an ideal baseline model for real-time sheep face detection.

In summary, to overcome the challenges of complex scale variation, cluttered farm backgrounds, and limited sample diversity in multi-breed sheep face detection, this work presents YOLO-LSD, a lightweight enhancement of YOLOv11. Specifically, we embed the ECA module into the backbone to adaptively amplify key facial features and suppress interference from farm backgrounds. Then, we replace standard convolutional layers with Ghost convolution blocks, mining feature redundancy to slash both model parameters and FLOPs without sacrificing multi-scale representation. Finally, the strategy of transfer learning pre-training is adopted. Through pre-training on large-scale animal facial datasets, the learning ability of the model for sheep facial features is further enhanced. Through these multi-dimensional optimizations, YOLO-LSD strikes an optimal balance between detection accuracy and computational efficiency, offering a practical, high-precision solution for real-world farm surveillance.

MATERIALS AND METHODS

Dataset

The dataset constructed in this study integrates two categories: sheep and goats, forming a composite multi-breed sheep face dataset. The sheep samples specifically belong to the Small-tailed Han breed, with a total of 50 individuals selected for data collection. These facial images were acquired in May 2024 at a farm operated by Beiqi Technology Co., Ltd. In Hohhot, Inner Mongolia, China. Image capture was performed using a Canon EOS 600D digital single-lens reflex (DSLR) camera (manufactured by Canon Inc., Tokyo, Japan), with all images stored in JPG format at a resolution of 2736×1824 pixels. For each sheep in the experiment, 50 original facial images were collected.

The goat dataset was sourced from an open-access repository, which contains manually captured images of 10 dairy goats from a farm in China for facial recognition purposes, amounting to 1311 goat face images in total (*Billah et al., 2023*). Data collection took place outdoors over a three-month period, encompassing variations in weather and seasonal conditions. Each goat was photographed individually in three distinct pens and across three-time segments: morning, midday, and afternoon. Each goat collected approximately 80 to 150 raw face images. Both the sheep and goat datasets were collected in real-world outdoor farm environments, encompassing diverse collection conditions such as varying lighting (e.g., morning sunlight, overcast afternoons), seasonal changes, and typical farm backgrounds (e.g., fences, feeding areas). These conditions effectively simulate the complex environments encountered in real-time sheep face detection tasks, ensuring that the proposed method in this study possesses strong practicality and effectiveness in actual application scenarios. Examples of original facial samples from both sheep and goats are presented in Fig.1.



Fig. 1 – Sample images of the sheep and goat faces

To improve the model's adaptability to complex farm environments, data augmentation was applied to the collected sheep face images. Specific operations included: modulating image brightness within a range of -45% to 45%, adjusting contrast by ±45%, rotating images by 45 degrees left and right, and performing vertical flipping. Through these augmentation strategies, augmented images were generated for each sheep in the experiment, effectively expanding the training data volume. Ultimately, each sheep retained 150 facial images (including original and augmented samples), forming the complete multi-breed sheep face image dataset. In addition, to ensure accurate target localization during model training, all images (both original and augmented) were annotated using the Make Sense online tool. For each image, a bounding box was manually drawn to precisely enclose the sheep face region, with the category label uniformly set as "Sheep Face" to standardize the annotation format. The sample annotation diagrams are shown in Fig.2.



Fig. 2 – Sample annotation diagrams

The final multi-breed sheep face dataset was randomly partitioned into training, validation, and test sets at a ratio of 8:1:1. Detailed configuration parameters of the dataset are presented in Table 1.

Table 1

The multi-breed sheep face dataset

Dataset	Images	Proportion
Training	7200	80%
Verification	900	10%
Testing	900	10%
Total	9000	100%

YOLOv11

The state-of-the-art single-stage object detection algorithm YOLOv11 is composed of three main components: backbone network, neck network, and detection head, which are optimized for detection scenarios to achieve efficient sheep face detection (*Li et al., 2025*). The backbone network employs an optimized CSPDarknet architecture, where the basic module CBS consists of a convolution, batch normalization, and activation function (*Jo et al., 2024*). A novel feature preprocessing module is deployed at the front end to process high-resolution images more efficiently, minimizing information loss compared to traditional downsampling. During the feature extraction stage, an improved spatial pyramid pooling (SPP) structure is utilized to finely capture multi-scale spatial features, enhancing adaptability to sheep face targets of different sizes (*Kumar et al., 2023*). The CSPLayer, through optimizing the residual structure, effectively integrates gradient changes of feature maps into the output results, not only reducing the total number of network parameters and computational complexity but also delivering high-quality features to the neck network, thus serving as a core component for efficient feature extraction (*Chen et al., 2025*).

The neck network of YOLOv11 adopts an adaptive feature fusion architecture to dynamically optimize multi-scale feature weights. Through an innovative cross-layer connection mechanism, high-resolution detail features from shallow layers are deeply fused with semantic-rich features from deep layers to construct a more representative feature pyramid. This design enhances the model's detection capability for both distant small targets and nearshore large targets, effectively addressing the challenge of extreme scale distribution of sheep face targets in complex scenarios, and lays a foundation for the accurate prediction of the detection head.

The detection head employs a decoupled design, separating the target classification and localization regression tasks into independent branches. The classification branch outputs multi-class probabilities for sheep face detection, while the localization regression branch optimizes the prediction accuracy of bounding box coordinates and confidence scores by integrating improved loss functions. Multi-scale feature maps are fused to cover sheep face targets of different scales, and anchor boxes adapted to the aspect ratio distribution of sheep faces are generated through K-means++ clustering, replacing manually preset anchors to improve matching efficiency. In the prediction stage, confidence screening and non-maximum suppression (NMS) are used to reduce false positives in complex backgrounds, and dynamic sample matching strategies are employed to balance positive and negative samples, achieving precise detection and localization of multiple sheep face types while maintaining end-to-end efficient inference.

ECA attention

To enhance the model's discriminative ability for sheep face targets in complex backgrounds, this study embeds a lightweight channel attention mechanism, ECA, into the backbone network of YOLOv11. This mechanism adaptively strengthens channel responses related to sheep features, through a local cross-channel interaction strategy, all with almost no additional computational cost (*Peng et al., 2020*).

For the feature map $X \in \mathbb{R}^{H \times W \times C}$ (where $H \times W$ is the spatial dimension and C is the number of input channels) output by the backbone network, spatial dimension information is first aggregated via global average pooling to generate a channel-level descriptor $Z \in \mathbb{R}^{C}$, calculated as:

$$Z_C = \frac{1}{H \times W} \sum_{i=1}^{H} \sum_{j=1}^{W} X_c(i,j) \quad (1)$$

This compresses spatial features into global response values in the channel dimension, providing a basis for channel attention calculation.

Unlike traditional channel attention mechanisms, SE-Net, which rely on fully connected layers and incur high computational costs, ECA achieves lightweight local cross-channel interactions via a 1D convolution with kernel size k. Here, k is adaptively determined by the number of channels C using:

$$k = |\log_2(C) + 1|_{odd} \quad (2)$$

where, $|\cdot|_{odd}$ denotes adjusting the result to the nearest odd integer (e.g., $k = 5$, when $C = 32$) to ensure convolution symmetry and avoid global redundant calculations. After extracting local channel correlations via this 1D convolution, channel attention weights $w_c \in [0,1]$ are generated through a sigmoid function to quantify the importance of each channel for sheep face detection. Among them, weights close to 1 enhance responses in critical feature channels, while weights approaching 0 suppress noise in background interference channels.

Finally, channel attention weights are multiplied element-wise with the original feature map to obtain the enhanced feature map $\hat{X}_c = w_c \cdot X_c$. This design introduces only linear complexity parameters $O(kC)$. While maintaining efficient model inference, it dynamically adjusts the channel interaction range for scale differences of sheep face targets in scenarios: smaller k values focus on high-frequency detail features, whereas larger k values integrate low-frequency semantic features, significantly improving feature discriminability in complex backgrounds and providing more distinguishable inputs for subsequent multi-scale feature fusion and target detection (*Xue et al., 2025*). The structure diagram of the ECA module is shown in Fig. 3.

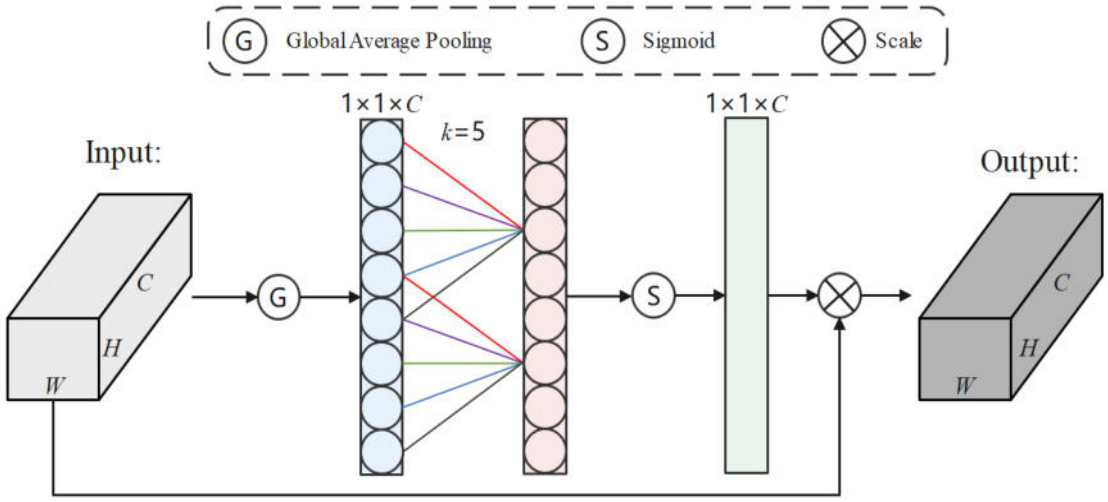


Fig. 3 - The structure diagram of the ECA module

Ghost convolution

To address the issue of low computational efficiency of traditional convolutions in sheep face detection, this study introduces Ghost Convolution into the backbone network of YOLOv11 to achieve lightweight feature extraction by exploiting feature map redundancy. Ghost Convolution decomposes traditional convolution into two stages: intrinsic feature extraction and Ghost feature generation, significantly reducing parameter overhead while preserving critical target semantics (*Dai et al., 2024*).

For an input feature map $X \in \mathbb{R}^{H \times W \times C_{in}}$ (where $H \times W$ is the spatial dimension and C_{in} is the number of input channels), Ghost Convolution first generates a channel-reduced intrinsic feature $F_{int} \in \mathbb{R}^{H \times W \times m} (m \ll C_{in})$, calculated as:

$$F_{int} = Conv(X,\ k,\ m,\ s = 1,\ p = 1) \quad (3)$$

where, k is the convolution kernel size (set to 3×3 in this study) for capturing basic spatial semantic information, such as sheep face contours and textures. Subsequently, lightweight linear transformations are applied to the intrinsic features to generate s-1 groups of Ghost features F_{gh} (s is the expansion factor, set to 2 in this study to balance efficiency and feature diversity).

The output feature map is obtained by concatenating intrinsic and Ghost features:

$$F_{out} = Concat(F_{int}, F_{gh}) \in R^{H \times W \times ms} \quad (4)$$

Compared to traditional convolutions with C_{out} output channels (parameter count: $C_{in} \cdot k^2 \cdot C_{out}$), Ghost Convolution has a parameter count of:

$$Params_{GhostConv} = C_{in} \cdot k^2 \cdot m + m \cdot k^2 \cdot (s - 1) \quad (5)$$

When $s = 2$ and $m = C_{out}/2$, this achieves a significant reduction in computational complexity without loss of feature dimensions.

In this study, replacing traditional convolutions in the backbone with Ghost Convolution is particularly suitable for down sampling high-resolution images. By reusing the spatial correlation of intrinsic features, the generated diverse Ghost features effectively enhance the edge detail representation of distant small sheep faces and the structural semantic expression of nearshore large sheep faces. This lightweight design enables efficient inference on edge devices while retaining the feature discriminability required for sheep face detection in complex scenarios, making it a key technical module for balancing detection accuracy and computational efficiency. The structure diagram of the Ghost module is shown in Fig.4.

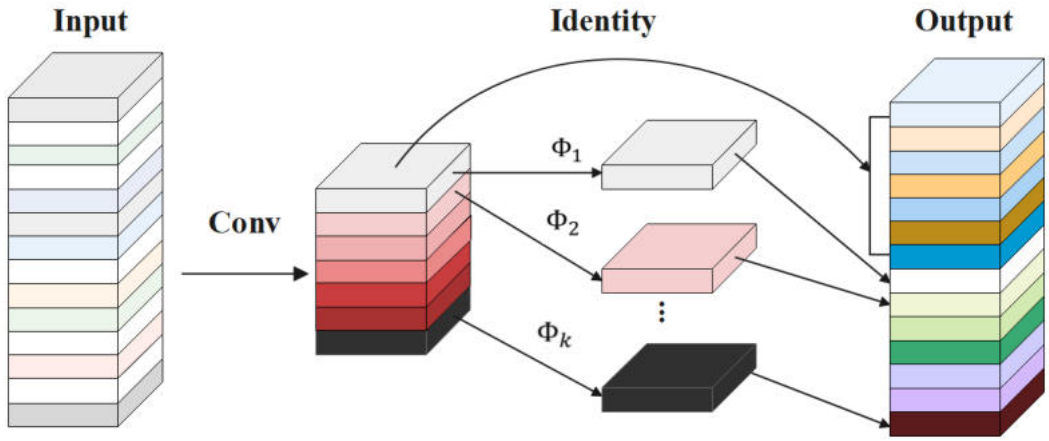


Fig. 4 - The structure diagram of the Ghost module

Transfer learning

To address the challenges of scarce high-quality labeled data and insufficient model generalization in few-shot scenarios for sheep face detection, this study employs a transfer learning strategy to efficiently transfer pre-trained knowledge to the sheep face detection task. Specifically, the constructed multi-breed sheep face dataset was first split into two subsets, A and B, ensuring a balanced distribution of breeds, lighting conditions, and shooting angles in both subsets. Cross-pre-training was then performed: subset A was used as the pre-training dataset, and the model was trained from scratch to obtain pre-trained weights, which were subsequently used as initial weights for training subset B. Conversely, subset B was employed for pre-training to generate weights, which served as the starting point for training subset A. During each pre-training phase, the optimizer's learning rate was adjusted and shallow network layers were frozen to enable the model to gradually learn breed-specific facial features (e.g., muzzle contours, ear shapes) and adapt to variations in farm environments. This cross-pre-training strategy enabled the limited labeled data to be fully leveraged, accelerated convergence in subsequent training, and enhanced generalization ability across different sheep face samples. Finally, the average of the two sets of training results was taken as the final detection performance, effectively mitigating the impact of data imbalance and improving both detection accuracy and robustness.

YOLO-LSD

The YOLO-LSD model builds on YOLOv11 with two targeted modifications, the ECA attention mechanism and Ghost convolutions. Specifically, an ECA module was added immediately before the SPPF block in the backbone and before every C3k2 block in the neck, so channel-wise sheep face features such as hull contours and superstructure lines are adaptively amplified and distinctions between container sheep faces and other classes are enhanced. Meanwhile, the final convolution in the backbone and all convolutions in the neck were replaced with Ghost convolution blocks. Each Ghost layer decomposes a standard convolution into intrinsic feature extraction and lightweight transformation, reusing spatial correlations to preserve multi-scale detail for distant small sheep faces while reducing parameters and computational complexity for fast and resource-efficient inference. The overall structure diagram of YOLO-LSD is shown in Fig. 5.

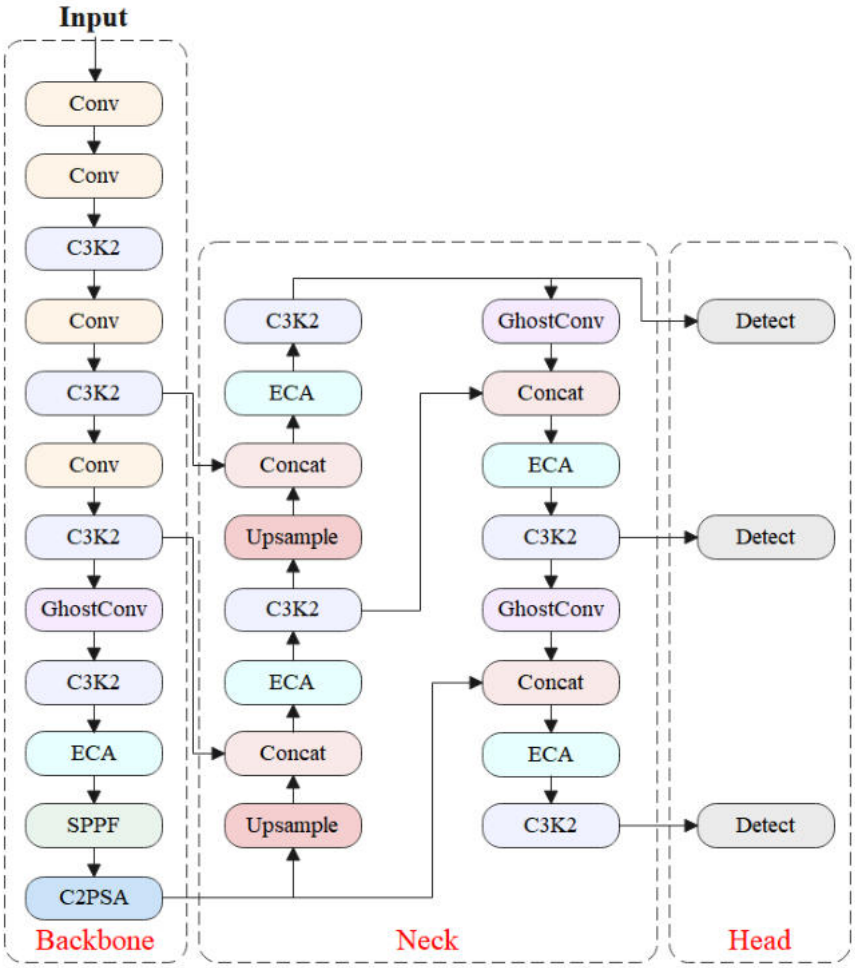


Fig. 5 - The overall structure of YOLO-LSD

Training platform and hyperparameters

The experiment was conducted on a Windows 11 operating system with a hardware platform configured with an i7-9700 processor (3.0 GHz clock speed), 16 GB of RAM, and an NVIDIA GeForce RTX 2080 Ti discrete graphics card, which provided efficient computational support for model training and inference. The algorithm was implemented using the PyTorch 1.12.0 deep learning framework in a Python 3.8 development environment, with GPU computing performance optimized via CUDA 11.6 and cuDNN acceleration technologies to ensure training efficiency for complex models. During training, a batch size of 16, 200 epochs, and a stochastic gradient descent (SGD) optimizer with a momentum parameter of 0.937 were set, balancing model convergence speed and parameter optimization stability while providing a standardized hyperparameter configuration foundation for the multi-module collaborative training of the improved YOLOv11 model.

Evaluation Metrics

For the sheep face detection task in complex environments, this study employs Precision, Recall, F1-score, mean Average Precision (mAP@0.5), FPS, GFLOPs, and Parameters as core evaluation metrics to construct a comprehensive evaluation system from three aspects: detection accuracy, efficiency, and model complexity.

Parameters reflect the total number of trainable parameters in the model, used to quantify the complexity of the network structure. Precision is defined as the ratio of the number of correctly detected sheep face samples to the total number of samples detected as sheep face. True negative, true positive, and false negative are the sample numbers of TN, TP, and FN. The calculation formula is:

$$\text{Precision}=\text{TP}/(\text{TP}+\text{FP}) \quad (6)$$

Recall is defined as the ratio of the number of correctly detected sheep face samples to the total number of actual sheep face samples, with the formula:

$$\text{Recall} = \text{TP}/(\text{TP} + \text{FN}) \quad (7)$$

The F1-score provides a balanced evaluation metric that accounts for both precision and recall through their harmonic mean, with the calculation formula:

$$\text{F1-score} = (2 \times \text{Precision} \times \text{Recall})/(\text{Precision} + \text{Recall}) \quad (8)$$

FPS refers to the number of images processed by the model per second, used to measure the algorithm's real-time response capability to dynamic complex scenarios. GFLOPs is used to quantify the model complexity, reflecting the number of floating-point operations required for a single forward pass.

mAP@0.5 calculates the mean average precision for sheep face at an intersection-over-union (IOU) threshold of 0.5, with the formula:

$$\text{AP} = \int_0^1 \text{P(R)d R} \quad (9)$$

where, the average precision (AP) for a single category is obtained by integrating the precision-recall curve:

$$\text{mAP} = \sum_{i=1}^{N}(\text{AP}_i/\text{N}) \quad (10)$$

where, N is the total number of identification types.

RESULTS AND DISCUSSIONS

Comparison experiments of YOLO series algorithms

To further evaluate the detection performance of models for subsequent improvement strategy integration, comparative experiments with YOLO series algorithms were carried out. Representative YOLO models were selected including YOLOv4-tiny, YOLOv5s, YOLOv7-tiny, YOLOv8n, YOLOv10n, and YOLOv11n for comparison. All models were tested under consistent settings, and the results are presented in Table 2.

As Table 2 shows, YOLOv11n demonstrates excellent performance across multiple metrics. In terms of Precision, it achieves 98.56%, outperforming YOLOv4-tiny (89.03%) by 9.53 percentage points, YOLOv5s (90.95%) by 7.61 percentage points, YOLOv7-tiny (92.85%) by 5.71 percentage points, YOLOv8n (95.99%) by 2.57 percentage points, and YOLOv10n (98.28%) by 0.28 percentage points. For Recall, YOLOv11n reaches 96.12%, showing improvements of 5.46 percentage points over YOLOv4-tiny (90.66%), 5.37 percentage points over YOLOv5s (90.75%), 4.15 percentage points over YOLOv7-tiny (91.97%), 0.57 percentage points over YOLOv8n (95.55%), and 0.34 percentage points over YOLOv10n (95.78%).

In terms of the F1-score, which comprehensively reflects the balance between Precision and Recall, YOLOv11n attains 97.32%. It surpasses YOLOv4-tiny (89.82%) by 7.5 percentage points, YOLOv5s (90.84%) by 6.48 percentage points, YOLOv7-tiny (92.40%) by 4.92 percentage points, YOLOv8n (95.78%) by 1.54 percentage points, and YOLOv10n (97.02%) by 0.3 percentage points. For the critical mAP@0.5 metric, YOLOv11n scores 98.70%, outshining YOLOv4-tiny (89.88%) by 8.82 percentage points, YOLOv5s (90.32%) by 8.38 percentage points, YOLOv7-tiny (94.55%) by 4.15 percentage points, YOLOv8n (97.76%) by 0.94 percentage points, and YOLOv10n (98.52%) by 0.18 percentage points. Additionally, regarding model volume (Params), YOLOv11n has only 2.6×10^6 parameters. It is more lightweight compared to YOLOv4-tiny (6.0×10^6), YOLOv5s (7.2×10^6), YOLOv7-tiny (6.3×10^6), YOLOv8n (3.0×10^6), and YOLOv10n (2.7×10^6). These results indicate that YOLOv11n exhibits significant advantages in model performance, detection comprehensiveness, and model volume. Therefore, this study takes YOLOv11n as the benchmark model, and subsequent improvement strategies will be added based on it to further enhance detection capabilities while maintaining its lightweight characteristics.

Table 2

The training results of the YOLO series algorithms

Model	Precision (%)	Recall (%)	F1-score (%)	mAP@0.5 (%)	Params (10^6)
YOLOv4-tiny	89.03	90.66	89.82	89.88	6.0
YOLOv5s	90.95	90.75	90.84	90.32	7.2
YOLOv7-tiny	92.85	91.97	92.40	94.55	6.3
YOLOv8n	95.99	95.55	95.78	97.76	3.0
YOLOv10n	98.28	95.78	97.02	98.52	2.7
YOLOv11n	98.56	96.12	97.32	98.70	2.6

Ablation Experiment

To assess the impact of individual and combined improvements on model performance, ablation experiments were carried out, with results presented in Table 3.

Table 3

The ablation results of YOLO-LSD

Method	ECA	Ghost convolution	F1-score (%)	mAP@0.5 (%)	Params (10^6)	FPS	GFLOPs
1	×	×	97.32	98.70	2.6	56	6.4
2	√	×	97.90	98.88	2.6	50	6.6
3	×	√	97.12	98.31	2.4	62	6.2
4	√	√	97.98	98.96	2.4	60	6.3

The effects of integrating the ECA attention mechanism and Ghost module into the baseline YOLOv11n (Method 1) were analyzed, to evaluate their contributions to key metrics: F1-score, mAP@0.5, model complexity (Params), inference speed (FPS), and computational cost (GFLOPs).

As shown in Table 3, Method 2 introduces only the ECA attention mechanism. Compared to the baseline (Method 1), it improves the F1-score from 97.32% to 97.90% and mAP@0.5 from 98.70% to 98.88%. However, this comes with a trade-off: FPS decreases from 56 to 50 and GFLOPs increase from 6.4 to 6.6, while model parameters (Params) remain unchanged at 2.6×10^6. This indicates ECA enhances feature attention for better accuracy but adds marginal computational overhead.

Method 3 incorporates only the Ghost module. Relative to the baseline, it reduces model parameters to 2.4×10^6 and increases FPS to 62. However, detection performance slightly degrades: F1-score drops to 97.12% and mAP@0.5 to 98.31%. The Ghost module effectively streamlines model complexity for efficiency but sacrifices minor accuracy, highlighting a classic accuracy-efficiency trade-off.

Method 4 combines both ECA and Ghost modules. It achieves a balanced improvement: F1-score reaches 97.98%, mAP@0.5 rises to 98.96%. Meanwhile, model parameters were reduced to 2.4×10^6, and GFLOPs to 6.3. FPS is 60, which is faster than Method 1 and balances the speed loss from ECA alone. This synergy shows ECA compensates for Ghost's accuracy loss, while Ghost offsets ECA's computational overhead, resulting in a more robust model.

In summary, the ECA module boosts accuracy but adds computational cost, while the Ghost module enhances efficiency but slightly reduces accuracy. Their combination (Method 4) achieves the best balance: improved F1-score (+0.66%), mAP@0.5 (+0.26%), lighter parameters (2.4×10^6), and reasonable speed (60 FPS). Thus, integrating both ECA and Ghost modules optimizes the trade-off between performance and efficiency, validating their synergistic value for enhancing YOLOv11n in subsequent refinements.

Comparative experiment of transfer learning

To evaluate the influence of transfer learning on model performance, comparative experiments were conducted, and the results are presented in Table 4. As shown in Table 4, the baseline model (YOLOv11n) achieves an F1-score of 97.98% and an mAP@0.5 of 98.96%, with 2.4×10^6 parameters, 60 FPS, and 6.3 GFLOPs. When transfer learning is introduced, the F1-score improves from 97.98% to 98.12%, and the mAP@0.5 rises from 98.96% to 99.29%.

Importantly, transfer learning does not bring any negative impacts on model complexity and efficiency. The number of parameters remains unchanged at 2.4×10^6, and both FPS and GFLOPs stay the same as the baseline. This indicates that transfer learning can effectively leverage pre-trained knowledge to enhance the model's feature representation and generalization ability, thereby improving detection accuracy without increasing computational overhead or model size.

Table 4

The training results of transfer learning

Model	F1-score (%)	mAP@0.5 (%)	Params (10^6)	FPS	GFLOPs
YOLO-LSD	97.98	98.96	2.4	60	6.3
+ Transfer learning	98.12	99.29	2.4	60	6.3

The training curves of YOLO-LSD are shown in Fig.6. From the training curves, it can be seen that as the number of iterations progresses, train/box_loss, train/cls_loss, and train/dfi_loss all show a significant and stable downward trend. The corresponding losses on the validation set (val/box_loss, val/cls_loss, val/dfi_loss) also decrease synchronously, indicating that the model's learning of sheep face features is continuously deepening and the gradient update is stable. Meanwhile, metrics/precision and metrics/recall rise rapidly and then tend to be stable. Metrics/mAP50 is close to 1.0, and metrics/mAP50-95 also increase steadily, reflecting the gradual maturity of the model's classification and positioning capabilities and good generalization.

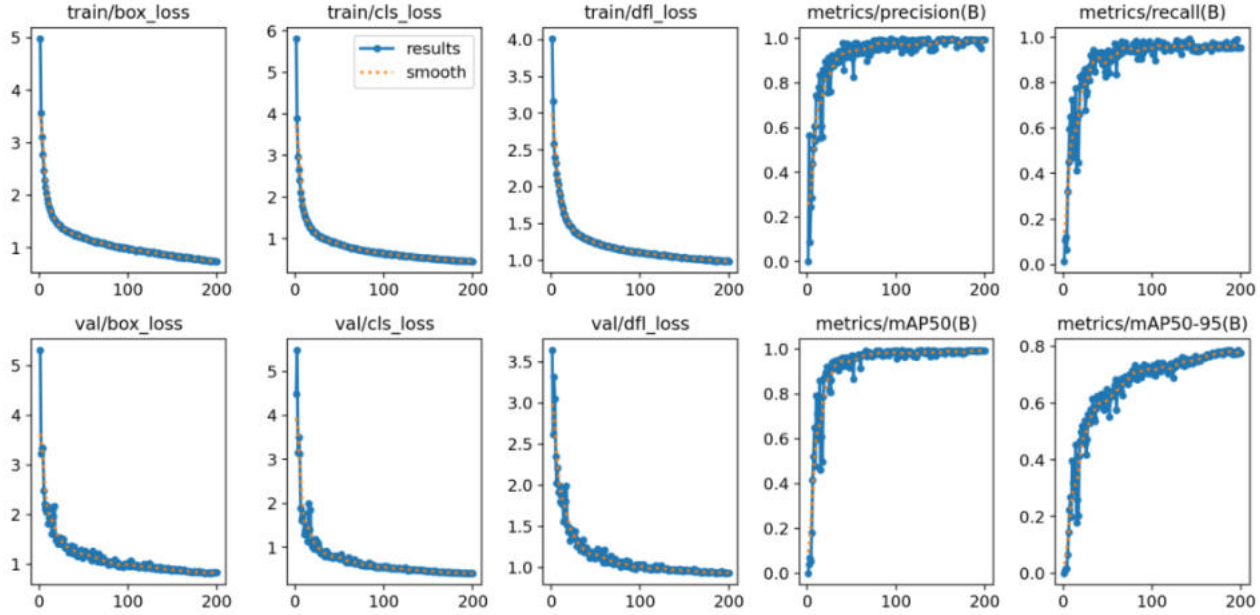


Fig. 6 - The training curves of YOLO-LSD

The detection effect of YOLO-LSD on individual sheep is shown in Fig. 7, and the effect on groups of sheep is shown in Fig. 8. By observing the specific detection results, it can be found that in different time periods and farm environments, the model can accurately identify the 'Sheep Face' category. For individual sheep detection, whether in close-up or long-distance shots, the bounding boxes show a high degree of fitting, and the confidence of category prediction is mostly above 0.80. When testing flocks of sheep, the confidence of each sheep face is above 0.75, and all sheep faces are effectively detected. The test results demonstrate that the proposed YOLO-LSD model has strong adaptability to complex farm environments.

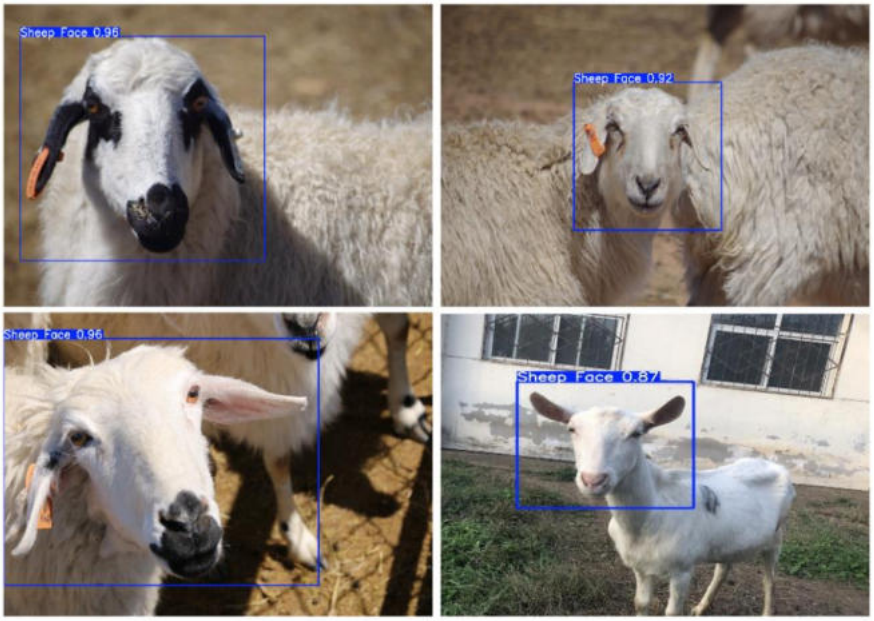


Fig. 7 - Sample images of individual sheep face detection results

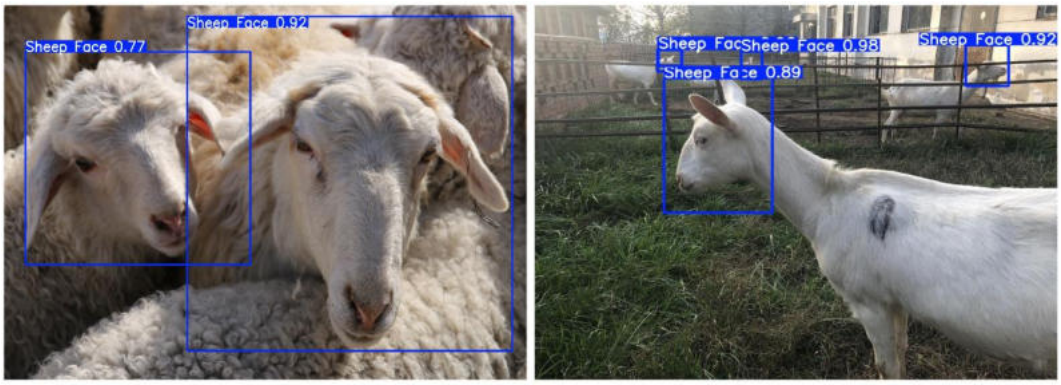


Fig. 8 - Sample images of detection results for groups of sheep

Comprehensively considering the convergence of the training curves and the recognition effect of the detection diagrams, the YOLO-LSD model proposed in this study has effectively completed the training task, constructed a stable and generalizable feature learning system, and can efficiently perform sheep face detection tasks. It provides reliable technical support for scenarios such as intelligent livestock management and farm monitoring, and fully verifies the practicality and effectiveness of the model design in sheep face detection tasks.

To demonstrate the practical deployment of the YOLO-LSD model, a real-time sheep face detection system was developed using LabVIEW 2018, as shown in Fig. 9. This system was tested in an actual farm breeding environment, specifically capturing the scenario where sheep pass through a detection channel, which naturally simulates the complex backgrounds (e.g., fences, vegetation) and variable lighting conditions encountered in real-time monitoring. The target detection interface within the system visualizes results on high-resolution RGB images, where two sheep faces are accurately identified, with confidence scores of 0.82 and 0.71, and bounding boxes fitting tightly to the facial regions even in a semi-overlapping situation. The parameter setting module allows for the configuration of the image path, processing type, and automatic timestamping, while the identification result module records detection quantities, staff information, and identification dates, and provides functions for data clearing, screenshot capturing, and result saving. Overall, this system not only validates the YOLO-LSD model's strong adaptability to complex farm environments for multi-target detection but also supports practical livestock management tasks like rapid flock counting and individual health monitoring, bridging the gap between algorithm development and on-site application.

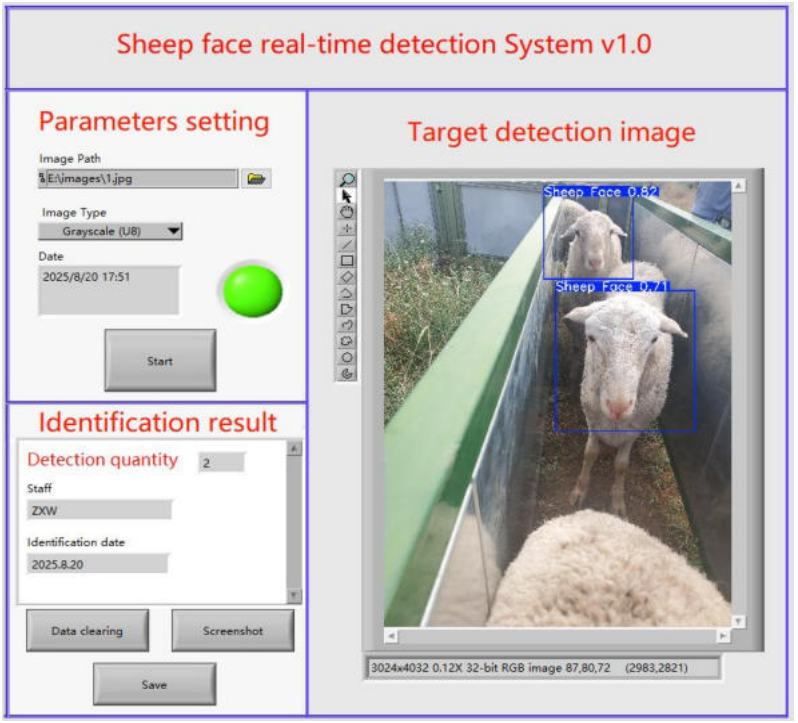


Fig. 9 - Operation diagram of the real-time sheep face detection system

CONCLUSIONS

This study proposes YOLO-LSD, a lightweight sheep face detection model developed based on YOLOv11. Through multi-dimensional optimizations-including feature enhancement, lightweight inference optimization, and few-shot generalization enhancement—the model effectively addresses the issues of insufficient multi-scale feature utilization and low computational efficiency in complex farm scenarios. Experimental results on the self-constructed multi-breed sheep face dataset show that YOLO-LSD achieves 99.29% mAP@0.5, with optimized model parameters and computational overhead, and a competitive inference speed on edge devices (e.g., farm-mounted embedded systems). Beyond technical performance, the model's practical deployment demonstrates tangible value for livestock management: by enabling automated, real-time monitoring of individual and group sheep, YOLO-LSD alleviates labor-intensive manual inspection, enhances the timeliness and precision of health and behavior assessment, and supports data-driven decision-making in farm operations. By synergizing these optimization strategies, YOLO-LSD breaks through the performance bottlenecks of traditional models in farm scenarios, providing a solution that balances performance and computational efficiency for intelligent livestock management systems—ultimately advancing operational efficiency, animal welfare, and data-informed practices in modern agriculture. Future research will focus on further lightweight optimization for low-power devices and multi-modal detection, integrating infrared data to enhance detection robustness in low-light or nighttime conditions, promoting the application of sheep face detection models in broader agricultural engineering scenarios.

ACKNOWLEDGEMENTS

We acknowledge that this work was supported by the Doctoral Research Start-up Fund Project of Jiangsu Maritime College (2024BSKY18).

REFERENCES

[1] Billah M., Wang X., Jiang Y., (2022), Real-time goat face recognition using convolutional neural network. *Computers and Electronics in Agriculture*, Vol 194, pp. 106730.

[2] Chen J., Yu R., Yang M., Che W., Ning Y., Zhan Y. (2025). SN-YOLO: A Rotation Detection Method for Tomato Harvest in Greenhouses. *Electronics*, Vol 14, pp. 3243.

[3] Dai D., Wu H., Wang Y., Ji P. (2024). LHSDNet: A Lightweight and High-Accuracy SAR Ship Object Detection Algorithm. *Remote Sens*., Vol 16, pp. 4527.

[4] Deng X., Yan X., Hou Y., Wu H., Feng C., Chen L., Bi M., Shao Y. (2021). Detection of behaviour and posture of sheep based on YOLOv3. *INMATEH-Agricultural Engineering*, Vol 64, Issue 2, pp. 457-466. DOI: https://doi.org/10.35633/inmateh-64-45

[5] Deng X., Zhang S., Shao Y., Yan X., (2022). A real-time sheep counting detection system based on machine learning. *INMATEH-Agricultural Engineering*, Vol 67, Issue 2, pp. 85-94. DOI: https://doi.org/10.35633/inmateh-67-08

[6] Hao M., Sun Q., Xuan C., Zhang X., Zhao M., Song S. (2024). Lightweight Small-Tailed Han Sheep Facial Recognition Based on Improved SSD Algorithm. *Agriculture*, Vol 14, pp. 468.

[7] He K., Zhang X., Ren S., Sun J., (2016). Deep residual learning for image recognition. In *IEEE Conference on Computer Vision and Pattern Recognition (CVPR)*, pp. 770-778.

[8] Hitelman A., Edan Y., Godo A., Berenstein R., Lepar J., Halachmi I. (2022). Biometric identification of sheep via a machine-vision system. *Computers and Electronics in Agriculture*, Vol 194, pp. 106713. https://doi.org/10.1016/j.compag.2022.106713

[9] Jo S., Woo J., Kang C.H., & Kim S.Y. (2024) Damage detection and segmentation in disaster environments using combined YOLO and Deeplab [J]. *Remote sensing*, 16(22), 4267.

[10] Kumar D., & Muhammad N. (2023) Object Detection in Adverse Weather for Autonomous Driving through Data Merging and YOLOv8 [J]. *Sensors*, 23(20), 8471.

[11] Li S., Wang R., Wang S., Yue P., Guo G. (2025). YOLO-FFRD: Dynamic Small-Scale Pedestrian Detection Algorithm Based on Feature Fusion and Rediffusion Structure. *Sensors*, Vol 25, pp. 5106, China.

[12] Peng, Z. H., Li, Q., & Liang, S. (2020) Multi-Scale Dense Selective Kernel Spatial Attention Network for Single Image De-raining [C]. 2020 *IEEE 5th International Conference on Cloud Computing and Big Data Analytics (ICCCBDA)*, *IEEE*, 341-347.

[13] Peruzzi, G., Galli, A., Giorgi G., & Pozzebon, A. (2025) Sleep posture detection via embedded machine learning on reduced set of pressure sensors [J]. *Sensors*, 25(2), 458.

[14] Salama A., Hassanien A.E., Fahmy A.A., (2019). Sheep identification using a hybrid deep learning and bayesian optimization approach. *IEEE Access*, Vol 7, pp. 31681-31687.
[15] Sharma A., Jain A., Gupta P., (2020). Machine learning applications for precision agriculture: A comprehensive review. IEEE Access, Vol 9, pp. 4843-4873.
[16] Xue H., Liu L., Wu Q., He J., Fan Y. (2025). Defect Detection Algorithm for Photovoltaic Cells Based on SEC-YOLOv8. Processes, Vol 13, pp. 2425.
[17] Xue J., Hou Z., Xuan C., Ma Y., Sun Q., Zhang X., Zhong L., (2024), A Sheep Identification Method Based on Three-Dimensional Sheep Face Reconstruction and Feature Point Matching. Animals, Vol 14, Issue 13, pp. 1923.
[18] Zhang X., Hou Z., Xuan C., (2022). Design and experiment of recognition system for coated red clover seeds based on machine vision. *INMATEH-Agricultural Engineering*, Vol 66, Issue 1, pp. 62-72. DOI: https://doi.org/10.35633/inmateh-66-06
[19] Zhang X., Xuan C., Ma Y., Su H., (2023). A high-precision facial recognition method for small-tailed Han sheep based on an optimised Vision Transformer, *Animal*, Vol 17, pp. 100886.
[20] Zhang X., Xuan C., Ma Y., Tang Z., Gao X., (2024), An efficient method for multi-view sheep face recognition. *Engineering Applications of Artificial Intelligence*, Vol 134, pp.108697.

DESIGN AND EXPERIMENT OF AN INTEGRATED PRUNING, THRESHING AND BRANCH CHOPPING MACHINE FOR GREEN PRICKLY ASH
/
青花椒整枝脱粒碎枝一体机设计与试验

Hao WANG[1]; Yanjun ZHOU*[1]; Chuanyao LIN[1]; Jian WU[1]; Jia DENG[1]; Xiaobo ZHOU[1]
[1] Sichuan Academy of Agricultural Machinery Science / China;
Tel: +86-15281031885; E-mail: 1550698497@qq.com
DOI: https://doi.org/10.35633/inmateh-76-98

Keywords: *Green prickly ash; Structural Design; Finite Element Analysis; Response Surface Experiment*

ABSTRACT
Aiming at the difficulty and low efficiency of threshing green prickly ash, a small-sized integrated pruning, threshing and branch chopping machine driven by a DC motor was designed and studied. The dynamic and static analyses of the tubular straight-cut threshing device and the clamping traction roller-cutting device were carried out respectively. The results show that the maximum shear stress on the green prickly ash branch during the cutting and separation process is 0.156 MPa. The maximum stress on the cutting blade of the clamping traction roller-cutting device is 333.99 MPa, and the maximum strain is 0.0017, which fully meets the usage requirements. The response surface analysis experiment was conducted with the moisture content of green prickly ash branches and the motor speed as the influencing factors and the undamaged threshing rate as the index. After optimization and solution, it was found that when the moisture content of green prickly ash branches was 43% and the motor speed was 1488 r/min, the undamaged threshing rate reached 95.9%, and the integrated pruning, threshing and branch chopping machine for green prickly ash reached the optimal working state.

摘要
针对青花椒脱粒困难，效率较低，设计研究了一款采用直流电机驱动的小型整枝脱粒碎枝一体机。分别对管状直切脱粒装置和夹持式牵引滚切装置进行显示动力学和静力学分析，其结果表明，在切割分离过程中花椒穗枝受到的最大剪切应力为 0.156MPa。夹持式牵引滚切装置的切割刀片所受的最大应力为 333.99MPa，最大应变为0.0017，完全满足使用要求。以花椒穗枝含水率和电机转速为影响因素，以花椒未损伤摘净率为指标进行响应面分析试验，优化求解后得到在花椒穗枝含水率为 43%，电机转速为 1488r/min 时，花椒未损伤摘净率达到 95.9%，青花椒整枝脱粒碎枝一体机达到最优工作状态。

INTRODUCTION
Green prickly ash, as a distinctive crop, is rich in nutritional and medicinal value. Due to its strong adaptability, high demand, good economic benefits and easy cultivation, the planting area and output of prickly ash in Sichuan Province have been expanding at an annual rate of about 30%. When harvesting green prickly ash, the branches bearing fruits are cut together with the fruits, which not only improves the harvesting efficiency but also promotes the growth of the prickly ash trees in the following year. The harvested branches are then subjected to threshing to complete the harvesting process *(Zhibo X. et al., 2022)*.

At present, the threshing of green prickly ash is mainly done manually, by beating the dried green prickly ash with bamboo sticks or wooden rods. This method is labor-intensive and inefficient and cannot meet the rapid development of the prickly ash industry. Therefore, it is necessary to design and develop more lightweight, easy-to-operate, reliable, high-threshing efficiency and low-damage rate prickly ash threshing equipment. *Yang L. et al.* designed a rotary shearing type green prickly ash harvesting device, which uses a reciprocating cutter to achieve the shearing function. They built a simulation model of the prickly ash branch shearing using ANSYS/LS-DYNA, determined the optimal tooth shape parameters, and verified through a three-factor quadratic regression orthogonal combination experimental that under the optimal working parameters, the average harvesting efficiency of green prickly ash per person per branch was 10.95kg/h, the average cleaning rate was 95.57%, and the average damage rate was 12.87% *(Yang L. et al., 2024)*.

Hao Wang, Assistant Engineer; Yanjun Zhou, Senior Engineer; Chuanyao Lin, Engineer;
Jian Wu, Engineer; Jia Deng, Senior Agronomist; Xiaobo Zhou, Senior Agronomist;

Jiang Q. et al. designed an automatic recognition prickly ash harvester, mainly including the visual recognition part, the mechanical arm movement part, the fruit storage part, and the vehicle drive part. Through dynamic simulation, the parts can be coordinated to achieve visual recognition and positioning harvesting of prickly ash fruits. Based on the existing structure, the picking device, transmission device and other components were designed and analyzed based on the principle of comb brushing. Using ADAMS software, the response surface simulation analysis experimental was conducted with the rotational speed of the comb brushing roller, the distance between the comb brushing roller and the feeding port, and the distance between the two comb brushing rollers as the influencing factors, and the undamaged cleaning rate of prickly ash fruits as the detection target. Under the optimal parameters, the undamaged cleaning rate of prickly ash fruits was 96.6% *(Jiang Q. et al., 2023)*.

This paper focuses on the design and development of a small-sized integrated machine for pruning, threshing and crushing branches for the green prickly ash harvesting process, with the aim of providing certain references and inspirations for the design of mechanical equipment in the green prickly ash harvesting process.

MATERIAL AND METHODS

Main Structural Components

The overall design of the machine is based on the "cutting at the base" of the green prickly ash. After converting the pepper tree into pepper branches, the branches are processed for fruit picking and branch crushing using a rotary tubular cutting technology *(Shao W., et al., 2023; Yexin L., et al., 2022)*. The pepper fruits are obtained, and the crushed branches are used as fertilizer and returned to the field. The overall structure is shown in Fig. 1, mainly consisting of a frame, a clamping traction roller cutting device, a reversing reducer, a transmission chain, a tubular straight-cutting and threshing device, a transmission belt, a motor, etc.

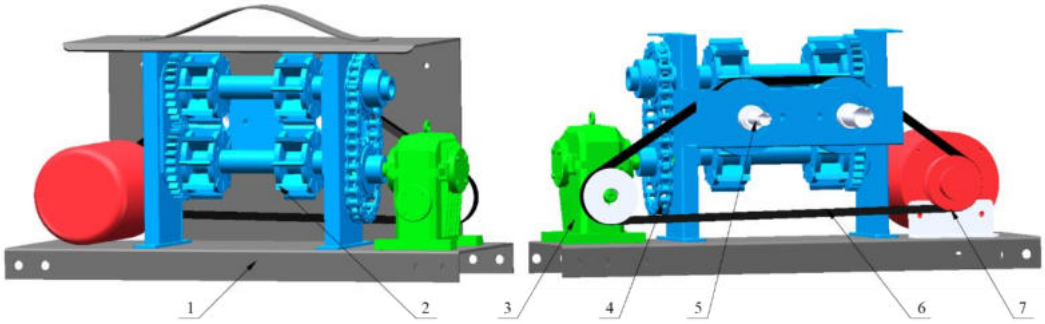


Fig. 1 - Structure Diagram of the Integrated Machine for Branch Pruning, Threshing and Branch Crushing of Green Prickly Ash

1-Frame; 2-Clamping Traction and Rolling Cutting Device; 3-Reversing Reducer; 4-Transmission Chain; 5-Tubular Straight Cutting and Threshing Device; 6-Transmission Belt; 7-Motor

Working Principle

An Integrated Pruning, Threshing and Branch Chopping Machine for Green Prickly Ash uses a DC motor as the power source, equipped with a battery, which is convenient for use in the field without AC power. It adopts belt drive, worm gear drive and gear drive mechanisms to drive the tubular straight-cutting destemming device and the clamping traction roller cutting device respectively. During operation, the pruned branches of green prickly ash are fixed by the clamping wheels and move in a fixed direction driven by the chain. When passing through the tubular cutting knife, the prickly ash fruits are cut off from the branches by the low-speed rotation and feeding process of the tubular knife, completing the picking of prickly ash. The branches are crushed after passing through the clamping knife *(Du P., et al., 2024; Li R., 2022)*. This picking device can achieve destemming and crushing of branches of different thicknesses by changing the diameter of the tubular knife. At the same time, it can feed multiple branches simultaneously to increase the picking efficiency.

Design of Key Components

Tubular Straight Cutting and Threshing Device

The threshing device uses a serrated tubular cutting knife. The circular ring with teeth and cutting edge type tool is fixed in the bearing sleeve on the bearing seat through a threaded connection and rotates at high speed driven by a DC high-speed motor via belt drive, separating the clusters and branches. During operation, the force analysis of the device is shown in Fig. 2.

In the figure, β is the cutting edge angle of the tool, θ is the friction angle of the tool, F_N is the pressure of the prickly ash clusters and branches on the wedge surface of the cutting edge during cutting, F_s is the pressure of the clusters and branches on the bottom surface of the cutting edge during cutting, F_1 is the resistance force on the cutting edge, F_2 is the cutting force required for cutting the prickly ash clusters and branches, f_1 is the friction force on the bottom surface of the cutting edge, and f_2 is the friction force on the wedge surface of the cutting edge. The required cutting force F_2 during operation is given by equation (1).

$$F_2 = F_1 + F_S \tan\theta + F_N(\tan\theta\cos\beta + \sin\beta) \quad (1)$$

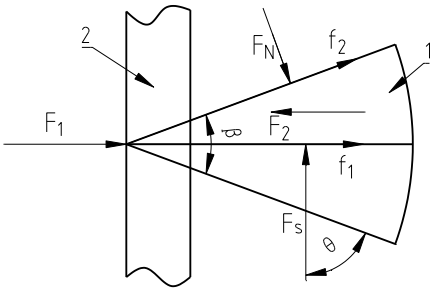


Fig. 2 - Force Analysis Diagram of Tubular Direct Cutting Threshing Device
1 - Cutting Tool; 2 - Pepper Spike Branch

Clamping Traction and Rolling Cutting Device

The structural diagram of the clamping traction rolling cutting device is shown in Fig. 3. It uses two rollers rotating in opposite directions. The surface of the rollers is processed with anti-slip teeth. The pepper branches are clamped between the rollers. The rollers rotate to pull the branches along, avoiding the branches from slipping due to rotation. The cutting device installs a fixed knife on the frame and a cutting knife on the rotating roller. During the rotation of the roller, the cutting knife and the fixed knife interact with each other to crush and cut the branches after the green prickly ash fruits are removed.

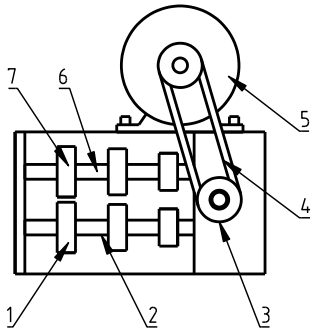


Fig. 3 - Structural schematic diagram of the clamping-type traction and cutting device
1-Lower clamping wheel; 2-Lower clamping wheel drive shaft; 3-Pulley; 4-Belt;
5-Drive motor;6-Upper clamping wheel drive shaft; 7-Upper clamping wheel

Main Technical Parameters

This design takes the rate of intact and undamaged pepper pods harvested and the rate of crushing of pepper branches as the main performance indicators of the entire machine. Based on the geometric and physical parameters as well as the growth and physiological characteristics of green prickly ash, the main technical parameters of the integrated machine for pruning, threshing and crushing of green prickly ash are shown in Table 1.

Table 1

Main Technical Parameters of the Integrated Machine for Pruning, Threshing and Crushing of Green Prickly Ash

Parameter Name	Parameter Value
Overall dimensions (L×W×H)/(mm)	480×250×650
Overall machine weight/(kg)	24
Motor power/(kW)	550
Gear ratio of reversing reducer	1:20
Rated rotational speed of cutting blade/(r/min)	2000
Rated rotational speed of clamping wheel/(r/min)	100
Feed speed of pepper branches/(mm/s)	400
Applicable diameter of pepper branches/(mm)	10~25
Applicable length of pepper branches/(mm)	150~2000

RESULTS

PERFORMANCE SIMULATION ANALYSIS OF TUBULAR STRAIGHT CUTTING THRESHING DEVICE

Simulation Model

A tubular straight cutting threshing device operation model was established using SolidWorks 2020, and it was simplified. The length direction of the pepper branches was regarded as a standard cylinder, and the bending and taper changes of the branches were ignored. The influence of the sharp spines and the surface of the branches was also ignored, as well as the influence of the pepper fruits and branches and leaves. A branch and spike separation model was established *(Li Y., 2023; Shan H., et al., 2022)*. According to the geometric and physical parameters of pepper, the diameter of the pepper branch was set to 12 mm, the diameter of the pepper spike branch was set to 4 mm, and the diameter of the circular cutting knife holes was set to 22 mm.

The model was established using SolidWorks 2020. The model was imported into the Workbench 19.2 LS-DYNA module. The material properties of the pepper branches are shown in Table 2. The material of the circular cutting knife was selected as structural steel. The model was divided into grids, with tetrahedral elements as the basic type. The size was set at 2 mm. After the division, there were 6066 nodes and 22,250 elements. The simulation conditions are shown in Table 3.

Table 2

Properties of Cinnamon Branch Materials

Parameter Name / Measure unit	**Value**
Density / (kg/m^3)	850
Young's Modulus X direction / (MPa)	115
Young's Modulus Y direction / (MPa)	17.25
Young's Modulus Z direction / (MPa)	8.63
Poisson's Ratio XY / (r/min)	0.38
Poisson's Ratio YZ / (r/min)	0.038
Poisson's Ratio XZ / (mm/s)	0.038
Shear Modulus XY / (MPa)	41.67
Shear Modulus YZ / (MPa)	4.16
Shear Modulus XZ / (MPa)	8.31
Maximum Equivalent Plastic Strain EPS	0.1

Table 3

Simulation Initial Conditions Table

Parameter Name	**Value**
Type	Frictional
Friction Coefficient	0.4
Dynamic Coefficient	0.3
Erosion algorithm	Single Surface
Velocity / (mm/s)	400
Rigid Body Rotation / (r/min)	2000
End Time / (s)	0.5

Simulation Results and Analysis

The shear stress exerted on the pepper sprout branches during the cutting and separation process is shown in Fig. 4. When the circular cutter initially starts to cut the pepper sprout branches, the shear stress on the sprout branches is 0. As the circular cutter cuts into the pepper sprout branches, the high-speed rotation of the circular cutter generates a significant shear force on the sprout branches, causing the shear stress to rapidly increase and reach a peak of 0.156 MPa at 0.05 s. At this point, the sprout branches undergo deformation. After the axial coarse fibers of the pepper sprout stem are cut off, the shear stress drops sharply and finally approaches a horizontal line. The contact moment of the circular cutter during the cutting and separation process is shown in Fig. 5.

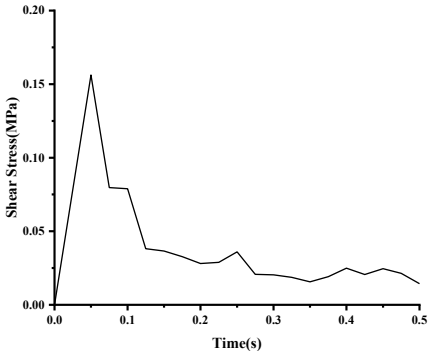


Fig. 4 - Shear Stress Change Curve

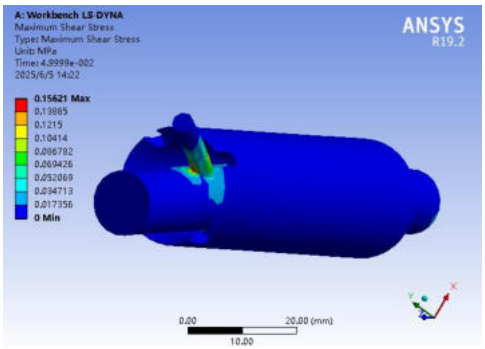


Fig. 5 - Cutting Contact Instantaneous Diagram

PERFORMANCE SIMULATION ANALYSIS OF THE CLAMPING TRACTION ROLLING CUTTING DEVICE

The clamping traction rolling cutting device, as one of the core components of the entire machine, experiences varying degrees of bending deformation on the blades on the clamping conveyor wheels during actual operation. Therefore, it is the most prone part to failure in the entire machine. To verify whether it meets the design requirements, a static analysis was conducted using the ANSYS Workbench simulation software.

Model Establishment

The clamping traction rolling cutting device operation model was established using SolidWorks 2020, and the material was selected as 45 steel. The model was imported into the software and meshed. The basic type of the mesh was tetrahedral elements, with a size of 1 mm. After meshing, there were 287638 nodes and 59612 elements. There were a total of 8 blades on the clamping traction rolling cutting device, but only one blade was in operation during the cutting process. Therefore, only one blade was subjected to load for static analysis. Based on the displayed dynamic model simulation results, boundary conditions were set to ensure the stability and reliability of the device. A driving torque of 100 N·mm was applied to the clamping conveyor wheel, and a vertical force of 2000 N was applied to the blade of the clamping conveyor wheel.

Simulation Results

A finite element analysis was conducted on the clamping traction rolling cutting device. The total displacement analysis cloud map is shown in Fig. 6. From the figure, it can be seen that the displacement variation at any point in the middle of the cutting blade is very small, and the maximum displacement occurs at the middle, but it is only 0.0033 mm. The stress analysis cloud map is shown in Fig. 7, and the maximum stress on the part is 333.99 MPa, which is at the thinnest part of the cutting blade. The strain analysis cloud map is shown in Fig. 8, and the maximum strain is 0.0017, which is also concentrated at the thinnest part of the cutting blade. Based on the yield strength of 45 steel ≥ 355 MPa and the tensile strength of 600 MPa, it can be known that the designed part can fully meet the usage requirements.

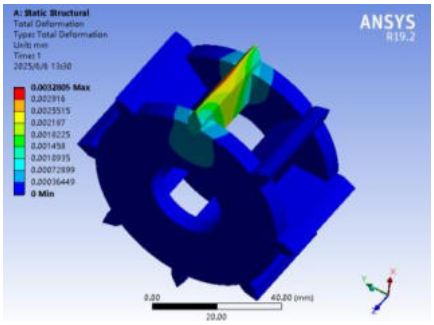


Fig. 6 - Total Displacement Analysis Cloud Image

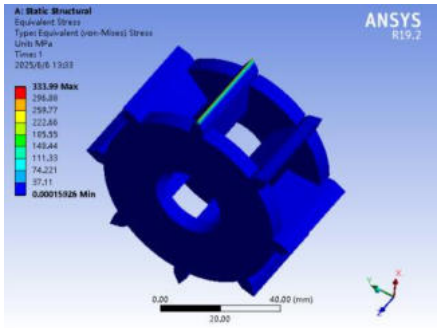


Fig. 7 - Stress Analysis Nephogram

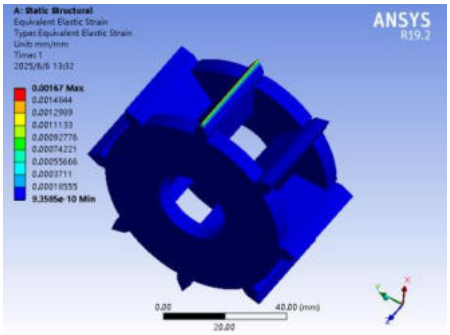


Fig. 8 - Strain Analysis Cloud Image

EXPERIMENTAL VERIFICATION

Experimental Indicators and Measurement Methods

In this experiment, the moisture content of the pepper branches and the motor speed were taken as the influencing factors, and the undamaged and clean yield of the pepper was used as the evaluation indicator *(Zhang Y., 2024; Shao W., et al., 2020)*. The calculation formula for the evaluation indicators is shown in equation (2).

$$Y = \frac{n_1 - n_2}{n} \times 100\% \quad (2)$$

where:

Y - Unharmed yield rate, [%];

n_1 - Separated quantity, [pieces];

n_2 - Damaged quantity, [pieces];

n - Total quantity, [pieces];

The response surface simulation analysis experiment was designed using the Design-Expert12 software. All the experimental factors were represented by the three levels of coding -1(low), 0(medium), and +1(high). The factor coding table is shown in Table 4.

Table 4

Coding Table of Experimental Factors

Code	Factor	
	Water content of pepper fruit branches X_1/(%)	**Motor speed X_2/(*r/min*)**
-1.414	25.8579	1075.74
-1	30	1200
0	40	1500
1	50	1800
1.414	54.1421	1924.26

Experimental Results and Analysis

Experimental Results

The Experimental plan and results are shown in Table 5.

Table 5

Experimental Plan and Results

Experimental Number	Water content of pepper fruit branches X_1/(%)	Motor speed X_2/(*r/min*)	Unharmed yield rate Y/(%)
1	25.8579	1500	95.9
2	30	1800	94.9
3	30	1200	94.6
4	40	1500	96.2
5	40	1500	96.6
6	40	1075.74	94.5
7	40	1500	95.7
8	40	1500	96.7
9	40	1500	96.5
10	40	1924.26	93.8
11	50	1200	94.1
12	50	1800	93.9
13	54.1421	1500	94.3

According to the data in Table 3, using the Design-Exper12 software, a variance regression analysis was conducted on the undamaged and stripped yield rate of pepper, and the regression equation model reflecting the relationship of its change with the experimental factors was obtained, as shown in equation (3).

$$Y = 96.34 - 0.4703X_1 - 0.1112X_2 - 0.1250X_1X_2 - 0.6825X_1^2 - 1.16X_2^2 \quad (3)$$

Analysis of Variance

Based on the experimental data, an analysis of variance was conducted and the results after removing the insignificant items are shown in Table 6.

Table 6

Analysis of Variance Table for the Uninjured and Cleaned Rate of Pepper

Source	Sum of Squares	df	Mean Square	F-value	P-value
Model	13.25	5	2.65	18.58	0.0006
X_1	1.77	1	1.77	12.41	0.0097
X_2	0.0990	1	0.0990	0.6942	0.4322
X_1X_2	0.0625	1	0.0625	0.4383	0.5291
X_1^2	3.24	1	3.24	22.72	0.0020
X_2^2	9.32	1	9.32	65.36	< 0.0001
Residual	0.9982	7	0.1426		
Lack of Fit	0.3462	3	0.1154	0.7080	0.5956
Pure Error	0.6520	4	0.1630		
R^2	0.9299				
Cor Total	14.25	12			

From the variance analysis of the undamaged and cleaned rate of the pepper in Table 4, it can be seen that the order of the magnitude of the influence of the interaction effects among the various factors on the impurity rate is X_2^2, X_1^2, X_1, X_2, X_1X_2. X_2^2, X_1^2, X_1, X_2 (the influence is extremely significant, P<0.01), and X_1X_2 has a relatively significant influence(0.05≤P<0.1). The residual sum of squares P=0.5956 is not significant (P>0.1), which proves that there are no other main factors that affect the experimental indicators.

Response Surface Analysis

The moisture content of the pepper branches X_1, the motor speed X_2, and their interaction have significant effects on the undamaged and cleaned rate of the pepper. The response surface of the interaction between the moisture content of the pepper branches and the motor speed obtained using the Design-Exper12 software is shown in Fig. 9.

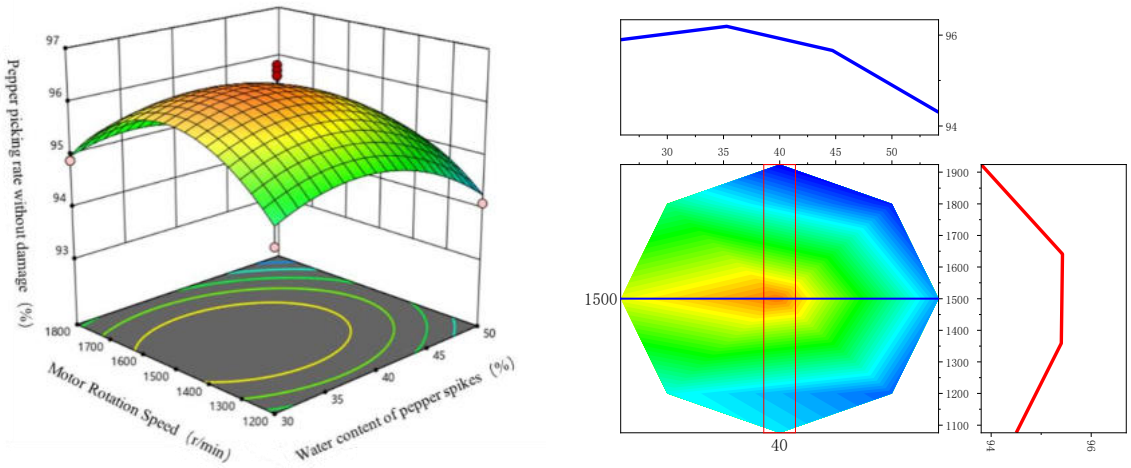


Fig. 9 - Influence of Factor Interaction on Impurity Content

The interaction effect of the moisture content of the pepper branches and the motor speed has a significant impact on the unharmed threshing rate of the pepper *(Li C., et al., 2024; Guo J., et al., 2023)*. When both factors are at their lowest levels, the unharmed threshing rate of the pepper reaches its minimum within the depicted range; when the moisture content of the pepper branches is at its lowest level, the unharmed threshing rate of the pepper is within a higher range; when the moisture content of the pepper branches is at its highest level, the unharmed threshing rate of the pepper is within a lower range. Under the same moisture content of the pepper branches, as the motor speed increases, the unharmed threshing rate of the pepper shows a trend of first increasing and then decreasing; under the same motor speed factor, as the moisture content of the pepper branches increases, the unharmed threshing rate of the pepper still shows a trend of first increasing and then decreasing.

Parameter Optimization and Verification Experiments

To achieve the optimal operating state of the integrated pruning, threshing, and branch-chopping machine for green prickly ash and to maintain a high undamaged threshing rate, the optimization module in Design-Expert 12 software was used to optimize and solve the regression model *(Huang Y., et al., 2024; Sun H., 2022)*.

To verify the above experimental conclusions, multiple verification experiments were conducted under the optimal working conditions, and the results are shown in Table 7. The experimental error is small and within the acceptable range, indicating that the regression equation is in good agreement with the actual situation and the model is reliable.

Table 6

Prediction and Verification Results Table

Parameters	Water content of pepper fruit branches X_1 / (%)	Motor speed X_2 / (r/min)	Unharmed yield rate Y / (%)
Predicted value	43	1488	96.1413
Verification value			95.9

CONCLUSIONS

Due to the difficulty and low efficiency in threshing of green prickly ash, a small-sized integrated machine for pruning, threshing and crushing of pepper branches was designed. It is driven by a DC motor. The pipe-shaped straight-cut threshing device and the clamping traction and rolling cutting device cooperate with each other to cut off the pepper fruit clusters, completing the pepper picking process while crushing the branches.

Finite element analyses were conducted on the pipe-shaped straight-cut threshing device and the clamping traction and rolling cutting device. The results showed that the maximum shear stress on the pepper clusters during the cutting and separation process was 0.156 MPa. The maximum displacement changes on the cutting blades of the clamping traction and rolling cutting device was only 0.0033 mm, and the maximum stress was 333.99 MPa, with a maximum strain of 0.0017, all concentrated at the thinnest part of the blade. Based on the material structure properties, the entire machine can fully meet the usage requirements.

Taking the moisture content of pepper clusters and the motor speed as influencing factors and using the undamaged and fully picked pepper rate as the index, a response surface simulation analysis experiment was designed. The regression equation model of the relationship with the changes of the experimental factors was obtained and optimized. When the moisture content of the pepper clusters was 43% and the motor speed was 1488 r/min, the undamaged and fully picked rate of the pepper reached 95.9%, which was the optimal working state of the designed integrated machine for pruning, threshing and crushing of green prickly ash branches.

REFERENCES

[1] Du P., Chen S., Li X., (2024). Green Prickly Ash Fruits Counting Based on Improved Deep Sort and Optimized Yolov5s. *Frontiers in Plant Science*, Vol. 15, pp. 151417682-1417682, DOI: 10.3389/FPLS.2024.1417682

[2] Guo J., Xiao X., Miao J. (2023). Design and Experiment of a Visual Detection System for Zanthoxylum-Harvesting Robot Based on Improved YOLOv5 Model. *Agriculture*, Vol. 13, Issue 4, pp, DOI: 10.3390/AGRICULTURE13040821

[3] Huang Y., Zhong Y., Zhong D., (2024). Pepper-YOLO: a lightweight model for green pepper detection and picking point localization in complex environments. *Frontiers in Plant Science*, Vol. 15, pp. 3151508258-1508258, DOI: 10.3389/FPLS.2024.1508258

[4] Jiang Q., Wan Z., Wang W. (2023). Design of Zanthoxylum Bungeanum Picker (花椒采摘机设计). *Agricultural Machinery Using & Maintenance*, Vol. 12, pp. 1-3+9, DOI: 10.14031/j.cnki.njwx.2023.12.001

[5] Li C., Shang S., Wang D., (2024). Peppercorn Harvester Design and Experiment (花椒采收机设计与试验). *Journal of Agricultural Mechanization Research*, Vol. 46, pp. 145-152, DOI: 10.13427/j.cnki.njyi.2024.10.013

[6] Li R., (2022). *Structure design and experiment of green Sichuan pepper picker based on branch trimming off (基于下桩的青花椒采摘机结构设计与试验).* (Degree Dissertation). Southwest University, Chongqing/China, DOI: 10.27684/d.cnki.gxndx.2022.001562

[7] Li Y. (2023). *Research on the cutting mechanism of green prickly ash branches and cutting device based on mechanical numerical model (基于力学数值模型的青花椒枝条切割机理和切枝装置研究). (*Degree Dissertation). Southwest University, Chongqing/China, DOI: 10.27684/d.cnki.gxndx.2023.003277

[8] Shan H., Bin L., Yuanzhe A. (2022). Comprehensive study on nutritional, flavour and metabolite characteristics of green prickly ash (*Zanthoxylum schinifolium*) at different picking stages. *International Journal of Food Science & Technology*, Vol. 57, pp. 7961-7973, DOI: 10.1111/IJFS.16154

[9] Shao W., Wu Y., (2020). Design and Experiment of Device for Ring-cut Cluster Branch Separation Unit of Green Prickly ash Picking Machine (青花椒采收机环切式穗枝分离装置设计与试验). *Agricultural Engineering*, Vol. 10, pp. 78-83;

[10] Shao W., Wu Y., Zhang L., (2023). Design and Experiment of Automatic Feeding Device for Harvester of *Zanthoxylum schinifolium* (青花椒采收机自动喂入装置设计与试验). *Agricultural Technology & Equipment*, Vol. 10, pp. 57-59

[11] Sun H., (2022). *Optimal design and research of a comb-tooth-air-suction pepper harvester* (梳齿-气吸式花椒采收机优化设计与研究). (Degree Dissertation). Gansu Agricultural University, Gansu/China, DOI: 10.27025/d.cnki.ggsnu.2022.000109

[12] Yang L., Zhang Y., He Z. (2024). Design and experiment of the rotating shear picking device for green Sichuan peppers (旋转剪切式青花椒采摘装置设计与试验). *Transactions of the Chinese Society of Agricultural Engineering*, Vol. 40, pp. 72-83, DOI: 10.11975/j.issn.1002-6819.202310135

[13] Yexin L., Binjie L., Yiyao J. (2022). Study on the Dynamic Cutting Mechanism of Green Prickly Ash (*Zanthoxylum armatum*) Branches under Optimal Tool Parameters. *Agriculture*, Vol. 12, pp. 1165-1165, DOI: 10.3390/Agriculture 12081165

[14] Zhang Y. (2024). *Design and experiment of a rotating shear picking device for green Sichuan pepper based on down-pile* (基于下桩的旋转剪切式青花椒采摘装置设计与试验). (Degree Dissertation). Southwest University, Chongqing/China, DOI: 10.27684/d.cnki.gxndx.2024.002746

[15] Zhibo X., Xiaopeng H., Yuan H. (2022). A Real-Time Zanthoxylum Target Detection Method for an Intelligent Picking Robot under a Complex Background, Based on an Improved YOLOv5s Architecture. *Sensors*, Vol. 22, pp. 682-682, DOI: 10.3390/S22020682

DESIGN AND EXPERIMENTAL STUDY OF A SHAFTLESS DOUBLE-SCREW FERTILIZER SPREADER FOR RICE
/
无轴双螺旋式水稻排肥器的设计与试验研究

Ziyu WANG[1]; Deyu HONG[1]; Hongchao WANG*[2]; Chengyang LIU[2]; Zanfeng MA[2]; Xingkang LIU[2]; Wentao LI[2]

[1] College of Information and Electrical Engineering, Heilongjiang Bayi Agricultural University, Daqing 163319, China
[2] College of Engineering, Heilongjiang Bayi Agricultural University, Daqing 163319, China
Tel: 16645548678; E-mail: 452713509@qq.com
DOI: https://doi.org/10.35633/inmateh-76-99

Keywords: *rice, spiral, fertilizer spreader, design, experiment*

ABSTRACT
To address the problems of poor fertilizer distribution uniformity and low application accuracy during the operation of rice fertilizer spreaders, this paper presents the design of a shaftless double–screw fertilizer spreader for rice. Dynamic methods were combined to analyze the filling stage and discharge stage of the fertilizer spreader and to investigate the impact of its structural parameters on the uniformity of fertilizer discharge. The fertilizer distribution process was simulated using EDEM software, and single–factor experiments were conducted to analyze the effects of spiral blade outer diameter, pitch, and rotational speed on fertilizer distribution uniformity. Furthermore, a two–factor orthogonal rotational combination experiment was carried out under different structural parameter conditions to analyze the interactions between influencing factors and determine the optimal parameter combination. The optimal parameters were found to be an outer diameter of 23.3 mm, a pitch of 23.6 mm, and a rotational speed of 149.2 r/min, yielding a uniformity coefficient of variation of 6.1%. Bench test results showed that the relative error between the simulation and experimental uniformity coefficient was 0.7%, indicating strong agreement. The results meet the agronomic requirements for fertilization and ensure stable fertilizer supply. These findings provide a reference for the design optimization of spiral fertilizer spreaders.

摘要
针对水稻排肥器作业时存在施肥均匀性差和施肥精度等问题，本文设计了一种无轴双螺旋式水稻排肥器。结合动力学方法对排肥器的充肥阶段与排肥阶段进行分析，探究其结构参数对排肥均匀性的影响。利用EDEM软件对排肥过程进行仿真，通过单因素试验分析螺旋叶片外径、螺距和螺旋转速对排肥均匀性的影响。此外，在不同结构参数条件下进行二次正交旋转组合试验，分析各影响因素之间交互作用并确定最佳参数组合。最优参数组合为当螺旋叶片外径为23.3mm，螺距为23.6mm，转速为149.2r/min，均匀性变异系数为6.1%。台架试验结果表明：均匀性变异系数仿真试验相对误差为 0.7%，仿真与台架试验吻合度较好，满足施肥农艺及供肥稳定性要求。研究结果可为螺旋式排肥器设计优化提供参考。

INTRODUCTION
Rice, as the main staple crop in China, requires efficient agricultural management practices to ensure the stability of its production and supply. Fertilization is a key agronomic practice for increasing rice yields and improving soil fertility *(Qi et al., 2024)*. However, improper fertilization can result in yield reduction, resource waste, and environmental pollution. Precision fertilization technology enables the quantitative and accurate application of fertilizers by adjusting the operational parameters of fertilization devices, thereby significantly improving grain yield and quality while promoting sustainable agricultural development *(Wang et al., 2022)*.

Currently, the most widely used fertilizer spreaders on the market are mainly of the external slot–wheel type and screw type, but they generally suffer from uneven fertilizer distribution, making it difficult to achieve precise and quantitative fertilization results *(Yan et al., 2024)*. In response to these issues, researchers in China and abroad have conducted extensive studies.

Wang Jinfeng et al. (2018) analyzed improvements to the external slot wheel fertilizer spreader of a fertilizer applicator using kinematic and dynamic methods, concluding that higher rotation speeds of the fertilizer wheel are more conducive to improving distribution uniformity.

Song Cancan et al. (2021) designed slot wheel fertilizer distributors with different groove shapes and varying numbers of groove rows, and, through simulation and experimentation, determined reasonable structural parameters. Their results indicated that an external 4-row slot wheel achieved better performance when distributing compound fertilizer. *Dun Guoqiang et al. (2025)* designed a spiral fertilizer spreader with notched blades and analyzed the main factors affecting fertilizer uniformity using discrete element simulation and bench tests. They further optimized the parameters of the regression model through multi-objective optimization and verified the fertilization effects with different fertilizer particles. Similarly, *Song Xuefeng et al. (2023)* constructed a bonding model for fertilizer blocks using the discrete element method to examine the effects of screw rotation speed, cross-sectional shape, and screw pitch angle on the performance of a spiral groove fertilizer spreader. *Fang Longyu et al. (2024)* developed an eccentric spiral tooth fertilizer application device based on rice fertilization agronomic requirements and fertilizer particle movement patterns and conducted experiments incorporating structural parameter combinations. The results showed that the diameter of the fertilizer wheel, the number of spiral teeth, and the tooth height directly influenced device performance. *Wang Yu et al. (2023)* investigated the effects of spiral angle and installation angle on the application performance of a spiral spline drum fertilizer applicator, finding that when the spiral angle was 45° and the installation angle was 40°, the device exhibited excellent fertilization performance. Most existing studies have focused on the design optimization of sprocket structures and single–screw fertilizer spreaders, with no reported innovative designs for shaftless double-screw fertilizer spreaders. In traditional single–screw fertilizer spreaders, changes in the position of the screw blade tip at the fertilizer discharge port result in varying sizes of fertilizer storage spaces between the blade and the housing. This change has led to a periodic fluctuation in the emission of fertilizer granules, reducing the effectiveness of fertilization.

To improve the operational stability of rice fertilizer spreaders, this study proposes a shaftless double-screw fertilizer dispenser for rice, designed to meet the agronomic requirements of rice cultivation. Using EDEM, a three–factor, five–level orthogonal combination experiment was conducted to analyze the effects of spiral blade outer diameter, pitch, and rotational speed on fertilizer discharge performance. Based on the experimental results, the structural parameters of the dispenser were optimized, and bench tests were performed to further verify its operational performance.

MATERIALS AND METHODS

Main structure and working principle of the shaftless double–screw fertilizer spreader

The shaftless double–screw fertilizer spreader consists primarily of end covers, drive gears, spiral blades, and a housing (Fig. 1). Two sets of shaftless double-screw blades are arranged in parallel inside the spreader, forming a continuous material-conveying plane. The housing adopts an inverted “8”–shaped cavity design, ensuring that the screw blades remain in close contact with the housing. This configuration effectively reduces fertilizer residue and promotes stable material flow.

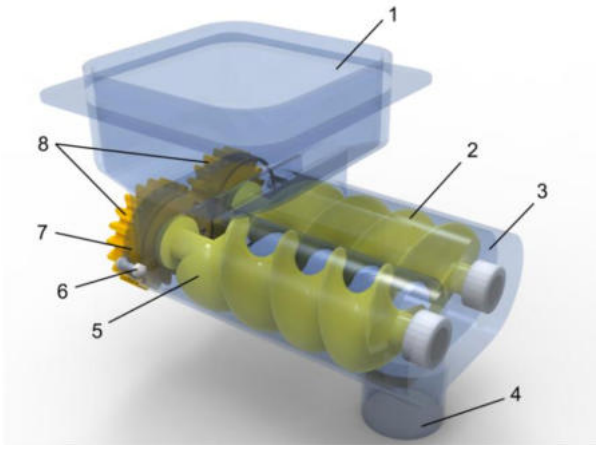


Fig. 1 - The experimental bench for synchronized corn seeding and precision hole fertilization

1. feed inlet; 2. left–hand spiral blade; 3. housing; 4. discharge outlet; 5. right–hand spiral blade; 6. bolt; 7. end cover; 8. drive gear.

The fertilizer spreader is mounted at the bottom of the hopper. During operation, fertilizer enters the housing through the feed port. Power from the tractor is transmitted via the drive shaft to the gearbox, which drives the two sets of spirals to rotate at the same speed but in opposite directions. Under the combined action of the dual spiral blades, layered advancement and dynamic mixing of fertilizer particles are achieved.

The continuous rotation of the blades generates axial thrust, pushing the fertilizer toward the discharge port. The phase-complementary motion of the dual spirals eliminates the periodic fluctuations typically observed in single-screw fertilizer spreaders, thereby ensuring uniform material conveyance. Finally, the fertilizer is evenly delivered to the discharge port through the coordinated action of the dual spirals and discharged via the outlet piping.

Modeling of fertilizer loading and discharge dynamics

Mechanical analysis of the fertilizer loading stage

The fertilizer loading stage is the critical process in which fertilizer particles are transferred from the hopper into the housing and undergo initial filling. At the beginning of this stage, the particles in the hopper are in a piled state. When the spiral mechanism is activated, the particles are propelled forward by the combined effects of gravity, the thrust generated by the dual spiral blades, and interparticle forces during blade rotation. The force analysis of fertilizer particles is illustrated in Figure 2.

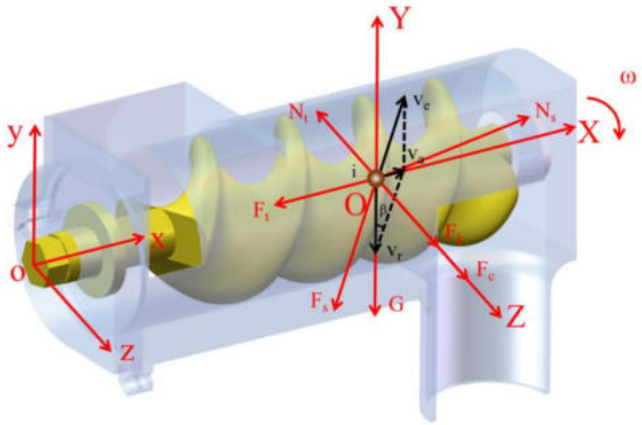


Fig. 2 - The force analysis of fertilizer particles

As shown in Figure 2, a fixed reference frame O-XYZ is established with the spiral shaft axis aligned with the X–axis and the opposite direction of gravity aligned with the Y–axis. A moving reference frame o–xyz, rotating periodically with the spiral blades, is also defined. Ignoring the interaction between adjacent particles, the motion trajectory of a representative particle i during the filling stage can be observed.

The dynamic equilibrium equation for the particles can be expressed as:

$$G + N_s + F_s + F_c + N_t + F_t + F_k = mg + N_s + \mu N_s + m\omega^2 R + m\omega^2 R + \mu N_t + 2m\omega v_i = 0 \quad (1)$$

where G is the gravitational force acting on fertilizer particle i during the fertilization process (N); N_s is the normal support force of the spiral surface (N); F_s is the sliding friction force on the spiral surface (N); F_c is the centrifugal inertial force (N); N_t is the support force from the wall of the fertilizer discharge pipe (N); F_t is the friction force of the fertilizer discharge pipe (N); F_k is the Coriolis inertial force (N); m is the mass of a single fertilizer particle (kg); ω is the angular velocity of the shaftless double spiral blade (rad/s); R is the distance from the center of mass of particle i to the Y-axis (m); μ is the friction coefficient between particle i and the surface of the shaftless double spiral blade; v_i is the relative velocity between particle i and the outer edge of the screw blade (m/s); v_a is the absolute velocity of particle i (m/s); v_e is the relative velocity of particle i (m/s); v_r is the entrainment velocity of particle i (m/s); and β is the helix angle of the screw blade (°).

The X components of the sliding friction force (F_s), normal support force (N_s), and fertilizer discharge pipe friction force F_t are shown in Equation (2).

$$F_s \sin\beta + F_t = N_s \cos\beta \quad (2)$$

The Y components of the gravitational force G, normal support force N_s, and sliding friction force F_s are shown in Equation (3).

$$G + F_s \cos\beta = N_s \sin\beta \quad (3)$$

The Z-components of the drag inertia force F, fertilizer discharge pipe support force N_t, and Coriolis force F_k are shown in Equation (4).

$$F_k + F_C = N_t \tag{4}$$

Combining equations (1) to (4), equation (5) is obtained.

$$\begin{cases} \mu N_s \sin\beta + \mu m\omega^2 R = N_s \cos\beta \\ mg + \mu N_s \cos\beta = N_s \sin\beta \\ 2m\omega v_i + m\omega^2 R = N_t \end{cases} \tag{5}$$

In practical operation, the relative velocity v_e of the particles is small, and thus the Coriolis force F_k can be neglected. Setting $F_k \approx 0$ simplifies the expression to Equation (6).

$$R = \frac{mg(\cos\beta - \mu\sin\beta)}{\mu m\omega^2(\sin\beta - \mu\cos\beta)} \tag{6}$$

In summary, according to Equation (6), the motion of fertilizer particles during the fertilization process is influenced by the angular velocity of the shaftless spiral blade, the distance from the particle's center of mass to the Y-axis, and the helix angle of the spiral surface.

Kinematic model of the fertilizer discharge stage

During the fertilizer discharge stage, when fertilizer particles detach from the spiral blades and fall into the fertilizer discharge pipe, their velocity is equal to the tangential velocity of the spiral blades (v_R). Under the combined effects of their own gravity, centrifugal and inertial forces, and air resistance (F_f), the particles fall into the fertilizer discharge pipe, performing a projectile motion with a parabolic trajectory as shown in Figure 3.

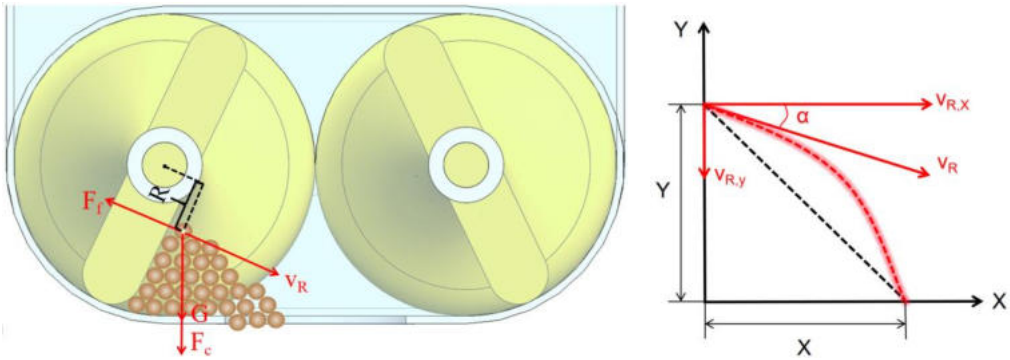


Fig. 3 - The force analysis of fertilizer particles

The tangential velocity of the spiral blades is the product of the distance from the center of mass of the fertilizer particles to the spiral axis and the angular velocity of the spiral blades.

$$v_R = \omega R \tag{7}$$

The components in the X-axis and Y-axis directions are shown in Equation (8).

$$v_{R,X} = v_R \cos\alpha \tag{8}$$

$$v_{R,Y} = v_R \sin\alpha \tag{9}$$

where α is the angle between the tangential velocity of the spiral blades and the horizontal direction, °.

According to Newton's second law, the differential equation of motion for the inclined projectile motion of fertilizer is established, as shown in Equation (10).

$$\begin{cases} m\dfrac{d^2x}{dt} = 0 \\ m\dfrac{d^2y}{dt} = mg \end{cases} \tag{10}$$

where m is the mass of the fertilizer particle, kg; x is the displacement of the fertilizer particle in the X-axis direction, m; y is the displacement of the fertilizer particle in the Y-axis direction, m.

At this point, the equation of motion for the fertilizer is shown in Equation (11).

$$\begin{cases} x = v_R \cos\alpha \cdot t \\ y = v_R \sin\alpha \cdot t + \frac{1}{2} g t^2 \end{cases} \quad (11)$$

The trajectory equation is given by Equation (12).

$$y = x\tan\alpha + \frac{g}{2\omega^2 R^2 \cos^2\alpha} x^2 \quad (12)$$

From Equation (12), although increasing the rotational speed can enhance the tangential velocity, it also intensifies the centrifugal effect, causing particles to aggregate toward the outer edge and potentially disrupting the uniformity of filling. During actual fertilizer discharge, it is necessary to optimize the spiral outer diameter and rotational speed to make most particles approach a certain average value, thereby balancing centrifugal force and conveying efficiency.

Structural Design

From the analysis of the working process of the spiral fertilizer spreader, it can be concluded that the parameters most significantly affecting its fertilization performance are the outer diameter (D), the pitch (S), and the rotational speed (n). The main geometric parameters of the fertilizer supply spiral are shown in Figure 4.

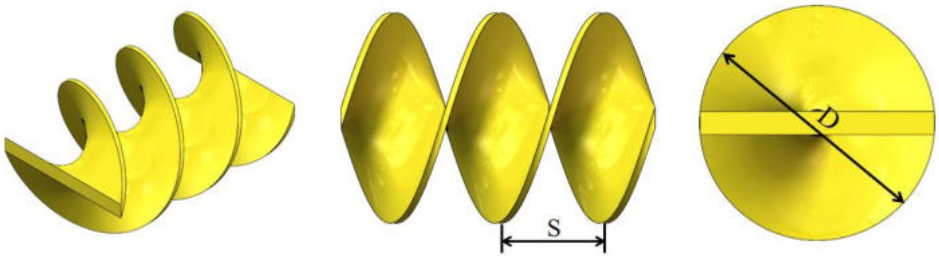


Fig. 4 - The main geometric parameters of the fertilizer supply spiral

The outer diameter of the spiral blades, as the core parameter of the spiral fertilizer spreader, directly influences fertilizer output, operational stability, and power consumption. Its design should be determined comprehensively by considering material characteristics, agronomic requirements, and structural constraints. Based on empirical formulas and literature data, the quantitative relationship between the target fertilizer output (Q) and the outer diameter of the spiral blades can be expressed as shown in Equations (13)–(15).

$$Q = 47 K_1 A \varphi \lambda \varepsilon D^{\frac{5}{2}} \quad (13)$$

$$K = \left(\frac{1}{47 K_1 A} \right)^{\frac{5}{2}} \quad (14)$$

$$D \geq K \left[\frac{Q}{\phi \lambda \varepsilon} \right]^{\frac{2}{5}} \quad (15)$$

where K is the characteristic coefficient of the fertilizer particles; K_1 is the ratio coefficient of pitch to diameter; A is the comprehensive characteristic coefficient of the material; φ is the filling coefficient; λ is the unit volume mass of the material (t/m³); ψ is the filling coefficient; ε is the spiral inclination angle coefficient.

Considering the agronomic requirements for fertilization in the Heilongjiang region, the influence of the screw structure volume on the fertilizer discharge rate, and stability concerns at high discharge speeds *(Wang et al., 2018)*, the standard integer series of screw conveyor diameters was calculated. As a result, the design range for the screw blade outer diameter D was adjusted to 18–44 mm

The pitch size not only determines the helix angle but also affects the slip surface morphology and velocity distribution of fertilizer movement under a given filling coefficient, thereby directly influencing the continuity and stability of material conveyance *(Xu et al., 2024)*. The selection of an appropriate pitch requires comprehensive consideration of the frictional characteristics between the screw surface and the material, as well as the compatibility of the velocity components. The pitch is typically determined using the empirical formula in Equation (16).

$$D \geq K\left[\frac{Q}{\phi\lambda\varepsilon}\right]^{\frac{2}{5}} \quad (16)$$

where K_1 is a coefficient, typically ranging from 0.8 to 1.0. In this design, since the shaftless spiral blades are arranged parallel to the horizontal plane, and based on existing experience and comprehensive analysis, K_1 is set to 0.9. Consequently, the pitch range is determined to be 16.2–39.6 mm.

With a fixed screw shaft structure, adjustment of the fertilizer discharge volume is often achieved by changing the rotational speed. Increasing the rotational speed increases the discharge volume; however, it must be kept within a reasonable range. Excessively high speeds can cause fertilizer particles to be thrown outward by centrifugal force, resulting in discharge blockage, reduced filling time, a lower filling coefficient, and deterioration of discharge stability. Therefore, it is necessary to ensure that the inertial centrifugal force acting on the fertilizer particles does not exceed their gravitational force, thereby preventing particles from scattering outward and failing be conveyed properly.

$$n_{\max} = \frac{30K\sqrt{2g}}{\pi\sqrt{D}} \quad (17)$$

$$A = \frac{30K\sqrt{2g}}{\pi} \quad (18)$$

$$n_{\max} = \frac{A}{\sqrt{D}} \quad (19)$$

where K_0 is the comprehensive material property coefficient; $n_{\max}$ is the maximum rotational speed of the screw conveyor; A is the comprehensive material property coefficient. For granular fertilizers, A is taken as 28, resulting in a calculated range for the actual rotational speed of the screw blades of 134–209 r/min.

Simulation model and parameter settings

To investigate the fertilizer distribution performance of a shaftless double-screw fertilizer spreader, simulation experiments were conducted using the Rocky–DEM discrete element software *(Sugirbay et al., 2020)*. To improve computational efficiency, secondary structural components that do not meet fertilizer particles were removed from the shaftless double-screw fertilizer spreader model, retaining only the core functional components. A simplified three–dimensional model was constructed in SolidWorks, comprising five main components: the fertilizer hopper, double-screw blades, housing, end caps, and fertilizer collection trough. The model was then exported in STL format and imported into Rocky-DEM. The simulation model of the shaftless double-screw fertilizer spreader is shown in Figure 5.

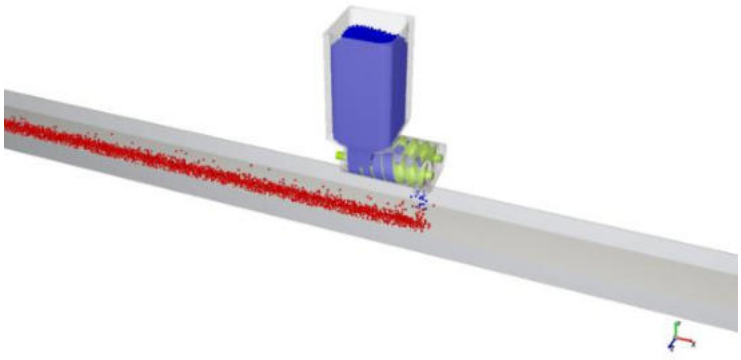


Fig. 5 - Simulation model of the shaftless double-screw fertilizer spreader

The core working principle of the shaftless double-screw fertilizer spreader is based on the dynamic contact and interaction between fertilizer particles and the rotating spiral blade surfaces, the particles and the housing cavity walls, and between the particles themselves. In this study, the Hertz–Mindlin (no slip) contact model and the Linear Spring Coulomb Limit model were selected to describe the normal and tangential contact forces, thereby accurately representing particle collisions and simulating the actual operating environment of the spreader. Referring to relevant literature and experimental methods, actual fertilizer particles were sampled

and measured (n = 100). The particle size distribution was found to follow a normal distribution, with an average diameter of 3.28 mm and a standard deviation of 0.41 mm. For the purposes of simulation, the fertilizer particle model was simplified to a perfect sphere, and the particle density was set to 1670 kg/m³ based on measured values. According to the experimental measurement results, the parameters are set as shown in Table 1.

Table 1

Parameters required for discrete element simulation

Item	Property	Value
Fertilizer particles	Poisson's ratio	0.25
	Shear modulus (Pa)	1.0×10^{7}
	Density (kg/m^3)	1670
PLA plastic	Poisson's ratio	0.3
	Shear modulus (Pa)	4.0×10^{8}
	Density (kg/m^3)	1255
Particle to particle	Recovery factor	0.52
	Static friction coefficient	0.48
	Rolling friction coefficient	0.28
Particle to discharging wheel and shell	Recovery factor	0.51
	Static friction coefficient	0.23
	Rolling friction coefficient	0.18

Experimental design

A total of 5 kg of fertilizer granules were generated in the fertilizer box using the volume filling method and filled uniformly within 1 s to simulate the fertilizer filling process *(Tian et al., 2024)*. Once all particles were generated, the shaftless double–screw blades were started at a preset speed, while the fertilizer dispenser moved at a speed of 0.20 m/s along a straight line to simulate the operating conditions of a rice transplanting machine. The discharged fertilizer particles fell into a fertilizer collection trough with a width of 100 mm and a length of 2000 mm. The specific calculations were performed according to the following formulas.

$$\overline{\mathrm{X}} = \frac{\sum_{i=1}^{m_0} \mathrm{X}_i}{m_0} \tag{20}$$

$$\overline{\mathrm{Y}} = \frac{\sum_{i=1}^{m_0} \mathrm{Y}_i}{m_0} \tag{21}$$

$$\sigma = \sqrt{\frac{\sum_{i=1}^{m_0} (X_i - X)^2}{m_0 - 1}} \tag{22}$$

$$V = \frac{\sigma}{X} \times 100\% \tag{23}$$

Where:

m is the number of measurements; Y_{i} is the total fertilizer discharge volume for each test, g; $\overline{Y}$ is the average stability of the total fertilizer discharge volume for each test, g; X_{i} is the mass of fertilizer particles in the i–th grid, g; $\overline{X}$ is the average mass of fertilizer particles in all grid units; σ is the standard deviation between grid cells, g; V is the coefficient of variation of fertilizer uniformity between individual grid cells, %.

Based on the grid method principle, 10 equally spaced grid units were set up in the stable operating section of the conveyor belt, with each grid unit measuring 100 mm × 100 mm. The specific configuration of the simulated mass statistical grid is shown in Figure 6 *(Sugirbay et al., 2020)*. After calculating the fertilizer mass within each grid, the mean stability and coefficient of variation of uniformity were determined *(Chen et al., 2021)*.

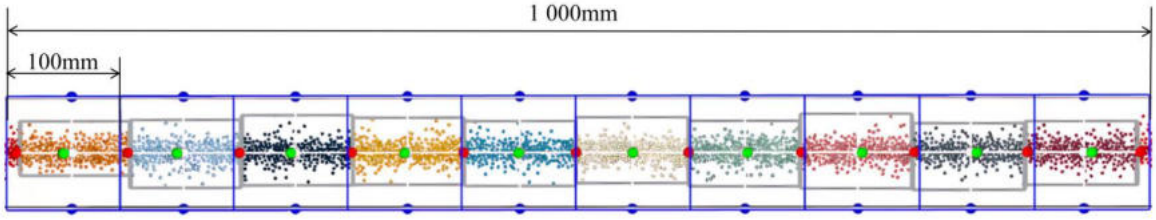


Fig. 6 - The specific configuration of the simulated mass statistical grid

Three sets of single-factor experiments were designed. Under fixed conditions of spiral blade outer diameter (42 mm) and pitch (30 mm), the performance was tested at six rotational speed levels: 140, 155, 170, 185, 200, and 215 r/min. Second, under fixed pitch (30 mm) and rotational speed (180 r/min) conditions, performance was tested at six levels of diameter: 18, 24, 30, 36, 42, and 48 mm. Under fixed rotational speed (180 r/min) and diameter (42 mm) conditions, the performance was tested at six levels of lead: 16, 22, 28, 34, 40, and 46 mm.

The mean stability of fertilizer application rate and the coefficient of variation of fertilizer application uniformity were used as experimental evaluation indicators, and a quadratic regression orthogonal rotated combination experiment was conducted *(Chen et al., 2021)*. The factor level coding table is shown in Table 2.

Table 2

The factor level coding

Coded value	Factor		
	The outer diameter (mm)	The pitch (mm)	The rotational speed (r/min)
1.682	44	39.6	209
1	38.7	34.9	193.8
0	31	27.9	171.5
–1	23.3	20.7	149.2
–1.682	18	16.2	134

RESULTS AND DISCUSSIONS

Effect of spiral blade outer diameter on fertilizer distribution performance

As shown in Figure 7, the experimental results indicate that as the outer diameter of the spiral blades increases, the coefficient of variation of uniformity gradually decreases, with the overall range of variation in the uniformity coefficient spanning from 2.56% to 14.85%. Additionally, as the spiral blade outer diameter increases, the mean stability value progressively increases, showing a strong linear correlation. The goodness of fit, $R^2 = 0.98$, indicates a high level of accuracy. Therefore, precise fertilization can be achieved by adjusting the outer diameter of the spiral blades.

Effect of pitch on fertilizer distribution performance

As shown in Figure 8, the experimental results indicate that as the pitch of the spiral blades increases, the coefficient of variation of uniformity exhibits fluctuating changes. Specifically, the coefficient of variation initially decreases gradually, then increases, reaching a peak near a pitch of 32 mm, and subsequently shows a decreasing trend. The coefficient of variation reaches a maximum of 12.32% and a minimum of 3.46%. Additionally, as the pitch of the spiral blades increases, the mean stability value generally increases, although it decreases between 34 mm and 40 mm.

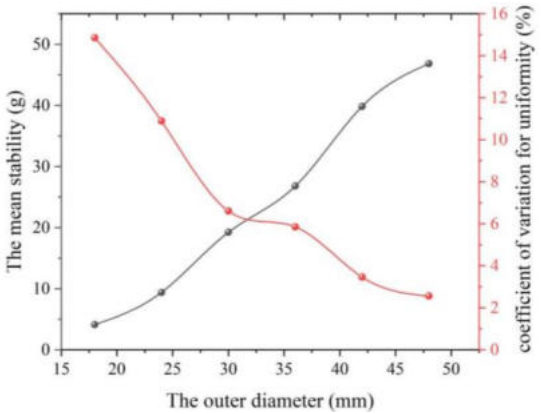


Fig. 7 - Effect of spiral blade outer diameter on fertilizer distribution performance

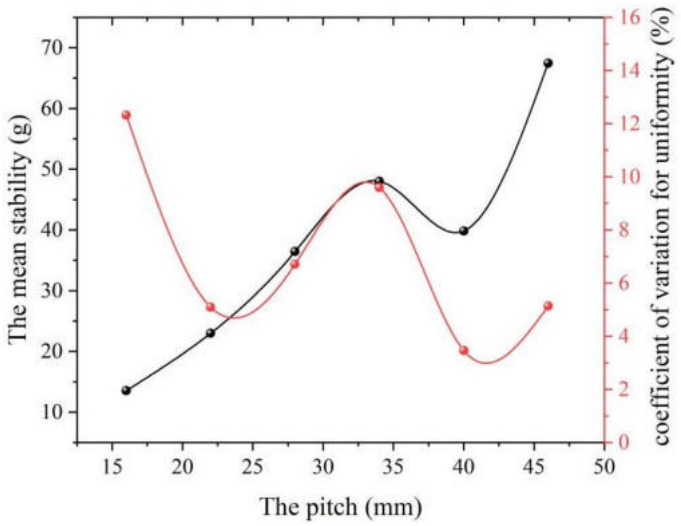


Fig. 8 - Effect of pitch on fertilizer distribution performance

Effect of rotational speed on fertilizer distribution performance

As shown in Figure 9, the experimental results indicate that as the rotational speed of the spiral blades increases, the coefficient of variation of uniformity first decreases, with the overall range of variation being 5.44% to 14.33% between 185 and 220 r/min. Additionally, as the screw blade speed increases, the mean stability value gradually increases, exhibiting a good linear relationship with a high degree of fit ($R^2 = 0.97$). This suggests that precise fertilizer application can be achieved by adjusting the screw speed.

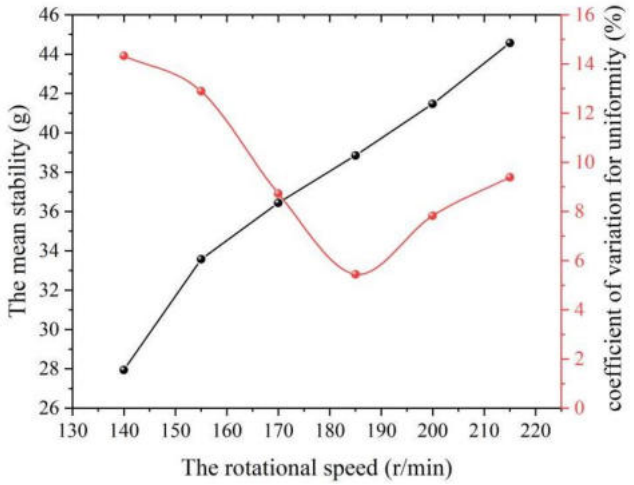


Fig. 9 - Effect of rotational speed on fertilizer distribution performance

Multi-factor Parameter Optimization Analysis

The coefficient of variation for uniformity is a key indicator for evaluating fertilizer performance. Therefore, this study focuses on analyzing the effects of interaction between various factors on the coefficient of variation for uniformity. After performing multiple regression analysis using Design–Expert 8.0.6 software, regression equations for each factor's influence on the coefficient of variation for uniformity were derived (*Adilet et al., 2023*). The results of the analysis of variance (ANOVA) and significance are shown in Table 3. All regression equations were highly significant ($P < 0.01$). Additionally, the P–value for misfit was not significant, indicating that the equations fit well. In the ANOVA results for the coefficient of variation of uniformity, the P-value for misfit was 0.59, indicating that no other factors had an influence. Under the conditions that all models are significant and the misfit term is not significant, the insignificant factors are removed, and the factor coded value regression equation is established, as shown in Equation (24).

$$y_1 = -3.78 - 0.26x_3 - 0.03x_1x_2 - 0.03x_1^2 + 0.03x_2^2 \quad (24)$$

where:

y_1 is the coefficient of variation of uniformity, %; x_1 is the outer diameter of the spiral blade, mm; x_2 is the pitch of the spiral blade, mm; x_3 is the rotational speed of the spiral blade, r/min.

Table 3

The results of the analysis of variance for the regression equations

Source of variance	Coefficient of variation for uniformity (%)			
	Square sum	Degrees of freedom	*F*	*P*
Model	169.27	9	5.72	0.0026**
x_1	0.0168	1	0.0051	0.9441
x_2	7.31	1	2.22	0.1598
x_3	40.19	1	12.22	0.0039*
x_1x_2	15.70	1	4.78	0.0478*
x_1x_3	0.0010	1	0.0003	0.9863
x_2x_3	2.53	1	0.7702	0.3961
x_1^2	61.62	1	18.74	0.0008*
x_2^2	21.49	1	6.54	0.0239*
x_3^2	1.14	1	0.3459	0.5665
Residual	42.74	13		
Lost proposal	14.07	5	0.7853	0.59
Errors	28.67	8		
Sum of all	212.01	22		

Note: * indicates significant (P < 0.05) and ** indicates highly significant (P < 0.01).

Figure 10 shows the effect of rotational speed and pitch on the coefficient of variation for fertilizer uniformity under the condition of a spiral blade outer diameter of 31 mm. As indicated in the figure, when the rotational speed remains constant, the coefficient of variation first decreases and then increases as the pitch gradually increases. This suggests that there is an optimal pitch range within which fertilizer uniformity is maximized. A pitch that is too small may cause material blockage or unstable output, while a pitch that is too large can lead to a discontinuous fertilization rhythm, thereby reducing uniformity. On the other hand, when the pitch is fixed, the coefficient of variation increases monotonically with increasing rotational speed, implying that higher rotational speeds weaken the stability and uniformity of fertilization. This could be due to high-speed rotation causing the fertilizer to be ejected too quickly, which hinders uniform distribution and may lead to material jumping or intermittent flow issues *(Wang et al., 2022)*.

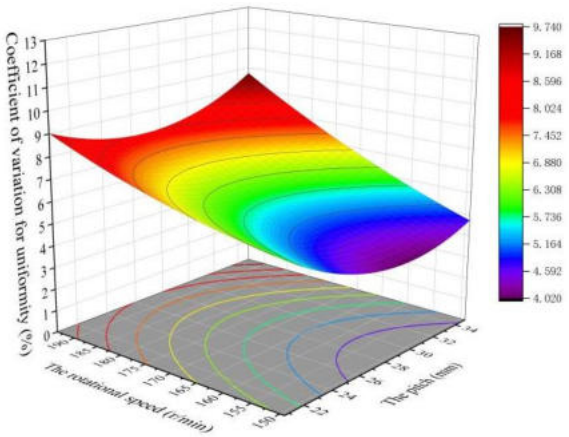


Fig. 10 - Effect of rotational speed and pitch on the coefficient of variation for uniformity

Figure 11 illustrates the effects of pitch and outer diameter on the coefficient of variation of uniformity under a spiral blade rotational speed of 171.5 r/min. The figure clearly shows the distinct influence patterns of the two parameters on fertilizer application uniformity. When the pitch remains constant, the coefficient of variation increases and then decreases as the spiral blade outer diameter increases. In contrast, when the outer diameter remains constant, the coefficient of variation continuously increases as the pitch increases. This indicates that while a larger pitch may increase the fertilizer application rate per unit time, it is more likely to cause intermittent or concentrated material output during transmission, disrupting the stability of fertilizer application and thus reducing uniformity.

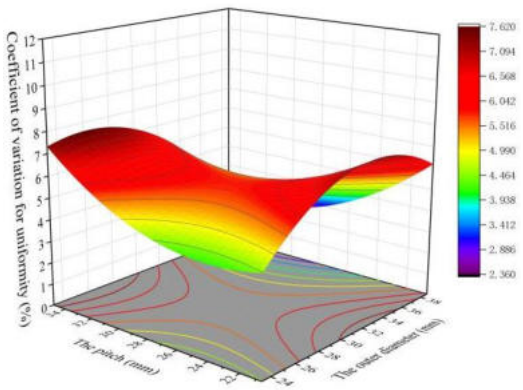


Fig. 11 - Influence of pitch and outer diameter on the coefficient of variation for uniformity

Figure 12 shows the relationship between rotational speed and outer diameter on the coefficient of variation of uniformity, with the pitch fixed at 27.8 mm. As can be seen from the figure, when the rotational speed remains constant, the coefficient of variation of uniformity first increases and then decreases as the outer diameter of the spiral blades increases. Additionally, under fixed outer diameter conditions, as the rotational speed increases, the coefficient of variation shows a continuous upward trend, indicating that higher rotational speeds are more likely to cause unstable material dispersion and disordered distribution, which negatively impacts fertilizer uniformity.

To determine the optimal parameter combination, boundary conditions must be set and a mathematical model established using software *(Dun et al., 2021)*. The mathematical model obtained through analysis is given in Equation (25).

$$\begin{cases} \min\ y_1 \\ s.t. \begin{cases} 18\text{mm} \le x_1 \le 44\text{mm} \\ 16.2\text{mm} \le x_2 \le 39.6\text{mm} \\ 134\,\text{r/min} \le x_3 \le 209\,\text{r/min} \end{cases} \end{cases} \tag{25}$$

Optimization using the Design–Expert optimization module yields the following optimal combination: spiral blade outer diameter of 23.3 mm, pitch of 23.6 mm, and rotational speed of 149.2 r/min, resulting in a uniformity coefficient of variation of 5.64%. Simulation verification of the optimized parameters yielded a uniformity coefficient of variation of 6.1%, which is in good agreement with the optimization results. To verify the fertilizer supply performance of the fertilizer dispenser, bench tests were conducted on the shaftless double-screw fertilizer spreader, as shown in Figure 13. The bench test was conducted using the optimal parameter combination, with the average value taken from three repeated experiments. The measured coefficient of variation for uniformity was 6.7%, differing by 0.6% from the simulation results. The deviation may be attributed to measurement errors in manual measurements and the impact of vibrations during the test process on fertilizer supply performance. Nevertheless, the fertilizer supply performance met the agronomic requirements.

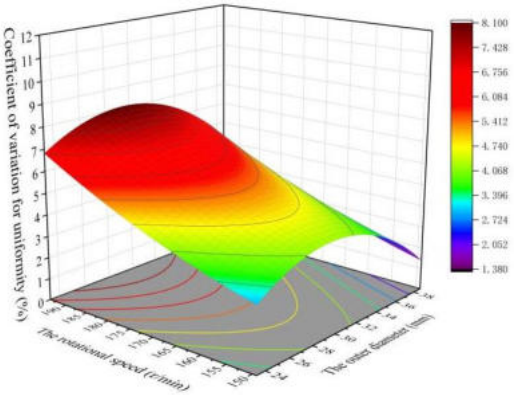


Fig. 12 - Influence of rotational speed and outer diameter on the coefficient of variation for uniformity

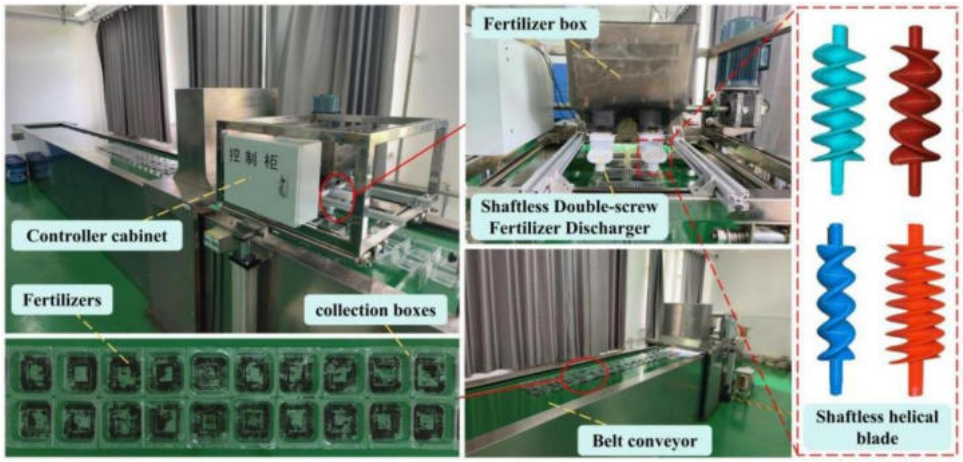


Fig. 13 - Bench test of the shaftless double-screw fertilizer spreader

CONCLUSIONS

This paper designs a shaftless double–helix rice fertilizer spreader and conducts a theoretical analysis of its fertilizer supply performance to identify the primary factors influencing its performance. Single-factor simulation test results indicate that the outer diameter, pitch, and rotational speed of the spiral blades all affect fertilizer distribution. By reasonably adjusting the outer diameter, pitch, and rotational speed of the spiral blades, a precise fertilizer supply can be achieved.

A quadratic regression orthogonal rotation combination experiment was conducted. Using Design–Expert software, variance and response surface analysis were performed on the results of the orthogonal rotation combination experiment. The results indicate that the regression equations are highly significant ($P < 0.01$). Optimization of the fertilization performance indicators was performed. When the outer diameter of the spiral blades was 23.3 mm, the pitch was 23.6 mm, and the rotational speed was 149.2 r/min, simulation results indicated a uniformity coefficient of variation of 6.1%. Bench verification tests showed a uniformity coefficient of variation of 6.7%, demonstrating that fertilization performance met agronomic requirements.

ACKNOWLEDGEMENT

This research was funded by the China Postdoctoral Science Foundation, grant number 2024MD763975; the School Orientation Training Research Initiation Fund Program, grant number XYB202307; the Heilongjiang Provincial Postdoctoral General Funding Project, grant number LBH-Z24250; the National Key Research and Development Program, grant number 2016YFD0200600.

REFERENCES

[1] Adilet S., Zhao K., Liu G., Sayakhat N., Chen J., Hu G., Marat M. (2023). Investigation of the pin-roller metering device and tube effect for wheat seeds and granular fertilizers based on DEM. *International Journal of Agricultural and Biological Engineering, 16*(2), 103–114. https://doi.rog/10.25165/j.ijabe.20231602.7721

[2] Chen H., Zheng J., Lu S., Zeng S., Wei S. (2021). Design and experiment of vertical pneumatic fertilization system with spiral Geneva mechanism. *International Journal of Agricultural and Biological Engineering, 14*(3), 135–144. doi:10.25165/j.ijabe.20211404.6575

[3] Dun G., Gao Z., Liu Y., Ji W., Mao N., Wu X., Liu W. (2021). Optimization design of fertilizer apparatus owned arc gears based on discrete element method. *International Journal of Agricultural and Biological Engineering, 14*(2), 97–105. https://doi.rog/10.25165/j.ijabe.20211402.5719

[4] Dun G., Sheng Q., Ji X., Li H., Ma C., Li X., Sun H., Wang L., Ma C., Wang H. (2025). Parameter optimization of the notched blade spiral fertilizer discharger for pineapple orchards based on DEM. *Frontiers in Mechanical Engineering, 11*, 1535013. https://doi.rog/10.3389/fmech.2025.1535013

[5] Fang L., Yang W., Luo X., Guo H., Song S., Liu Q., Li G. (2024). Development and optimization of an offset spiral tooth fertilizer discharge device. *Agriculture, 14*(2), 329. https://doi.rog/10.3390/agriculture14020329

[6] Qi Z., Liu C., Wang Y., Zhang Z., Sun X. (2024). Design and experimentation of targeted deep fertilization device for corn cultivation. *Agriculture, 14*(9), 1645. https://doi.rog/10.3390/agriculture14091645

[7] Song C., Zhou Z., Wang G., Wang X., Zang Ying. (2021). Optimization of the groove wheel structural parameters of UAV-based fertilizer apparatus. *Transactions of the Chinese Society of Agricultural Engineering*, *37*(22), 1–10. https://doi.rog/10.11975/j.issn.1002-6819.2021.22.001

[8] Song X., Dai F., Zhang X., Gao W., Li X., Zhang F., Zhao, W. (2023). Simulation and experiment of fertilizer discharge characteristics of spiral grooved wheel with different working parameters. *Sustainability, 15*(14), 118309. https://doi.rog/10.3390/su151411309

[9] Sugirbay A., Zhao J., Nukeshev S., Chen J. (2020). Determination of pin-roller parameters and evaluation of the uniformity of granular fertilizer application metering devices in precision farming. *Computers and Electronics in Agriculture, 179*, 105835. https://doi.rog/10.1016/j.compag.2020.105835

[10] Tian L., Li H., Zhang X., Liu, C. (2024). Discrete Element Method simulation of rice grain stacking characteristics. *INMATEH Agricultural Engineering*, *74*(3), 554-561. https://doi.rog/10.35633/inmateh-74-49

[11] Wang J., Gao G., Weng W., Wang J., Yan D., Chen B. (2018). Design and Experiment of Key Components of Side Deep Fertilization Device for Paddy Field. *Transactions of the Chinese Society for Agricultural Machinery*, *49*(6), 92–104. https://doi.rog/10.6041/j.issn.1000-1298.2018.06.011

[12] Wang J., Wang Z., Weng W., Liu Y., Fu Z., Wang, J. (2022). Development status and trends in side-deep fertilization of rice. *Renewable Agriculture and Food Systems, 37*(5), 550–575. https://doi.rog/10.1017/s1742170522000151

[13] Wang Y., Tan Y., Wei S., Liao M., Zang, Y., Zeng, S. (2023). Design and experimental study of the fertilizer applicator with vertical spiral fluted rollers. *International Journal of Agricultural and Biological Engineering, 16*(5), 80–87. https://doi.rog/10.25165/j.ijabe.20231605.7555

[14] Yan S., Zhong W., Wu G., Bai X., Di J., Zhao X. (2024). Optimisation and testing of structural parameters of internal tangent circle external grooved wheele fertiliser discharger. *INMATEH Agricultural Engineering*, *74*(3), 895–907. https://doi.rog/10.35633/inmateh-74-79

[15] Xu W., Yuan Q., Zeng J., Lü X. (2024) Design and experiment of four-head inclined spiral precision fertilizer dischargers in orchard. *Transactions of the Chinese Society for Agricultural Machinery*, *55*(s2), 30–40. https://doi.rog/10.6041/j.issn.1000-1298.2024.S2.004

STUDY AND EXPERIMENT ON A CORN FLEXIBLE THRESHING TECHNOLOGY WITH SINGLE-POINT HINGED STRUCTURE BASED ON DEM-MBD COUPLING

/

基于 DEM-MBD 耦合的单点铰接玉米柔性脱粒技术研究与试验

Qiming YU[1)], Jianning YIN[1)], Yipeng CUI[1)], Zehao ZHA[1)], Pengxuan GUAN[1)], Yang WANG[1)], Xinxin WANG[1)], Duanyang GENG[1*)]

[1)] School of Agricultural Engineering and Food Science, Shandong University of Technology, Zibo 255000, China

** Corresponding authors. Tel.: +86 13668641238; E-mail address: dygxt@sdut.edu.cn (D.Y. Geng)*

DOI: https://doi.org/10.35633/inmateh-76-100

Keywords: *DEM-MBD coupled simulation; corn; flexible threshing; kernel breakage rate; threshing device*

ABSTRACT

To address the issues of high kernel breakage rate and poor adaptability in threshing devices for direct corn kernel harvesting, this study proposes a flexible threshing device based on a single-point hinged structure. In this design, the threshing elements are flexibly mounted via single–point hinges, allowing them to rotate upon impacting corn kernels. This rotational motion provides an impact-buffering effect during the threshing process, thereby reducing the risk of kernel breakage. By comparing the dynamic characteristics of the single-point hinged flexible structure with those of a rigid structure, the superiority of the proposed device is confirmed. A contact force model is established to analyze key parameters influencing threshing performance, identifying the mass of the threshing element, rotational speed, and structural configuration as the primary factors. A coupled simulation model was developed using RecurDyn and EDEM software to investigate the effects of threshing element mass, rotational speed, and structural configuration on the kernel breakage rate and unthreshed grain rate of the device, and to determine the optimal parameter range. Based on a three-factor, three-level orthogonal experimental design, the optimal working parameters of the device were identified as follows: threshing element mass of 200 g, rotational speed of 600 r/min, and a composite structural configuration. Under these conditions, the kernel breakage rate was 3.95% and the unthreshed grain rate was 0.88%, meeting the practical requirements for harvesting performance. This study provides theoretical support and a technical pathway for the design of high-efficiency, low-damage threshing devices for direct corn kernel harvesting.

摘 要

为解决玉米籽粒直收中脱粒装置对籽粒破碎率高、柔性适应性差等问题，本文提出了一种基于单点铰接结构的玉米柔性脱粒装置。该装置通过将脱粒元件以单点铰接的形式柔性安装，让脱粒元件在冲击玉米籽粒的同时可以回转，旋转脱粒过程具有缓冲冲击能力，以降低籽粒破碎风险。通过将单点铰接柔性结构与刚性结构脱粒时的动力学特性进行对比，确定该装置的优越性。建立接触力模型并分析影响脱粒效果的关键参数，确定了脱粒元件质量、转速和结构形式作为主要影响因素。基于 RecurDyn 和 EDEM 软件构建了耦合仿真模型，探究了该装置中脱粒元件的质量、转速以及结构形式对籽粒破碎率和未脱净率的影响规律，并确定了较优参数区间。通过三因素三水平正交试验，确定了该装置的最佳工作参数为：脱粒元件质量为 200g、转速为 600 r/min、结构形式为组合型，此时籽粒破碎率为 3.95%，未脱净率为 0.88%，作业性能满足了实际收获需求。本研究为高效、低损伤的玉米籽粒直收脱粒装置设计提供了理论支持和技术路径。

INTRODUCTION

Direct corn kernel harvesting has emerged as a major developmental trend in China's corn production due to its advantages such as high operational efficiency, reduced mechanical losses, and decreased dependence on post-harvest drying and manual labor *(Jun et al., 2018, Mircea et al., 2020, Nenciu et al., 2021)*. This method has been widely promoted across key corn-producing regions, including Northeast China and the Huang–Huai–Hai Plain *(Meizhou et al., 2020, Qing et al., 2024)*. However, due to the relatively high moisture content of corn at harvest, the performance requirements for the threshing device in kernel–direct harvesting systems have become more stringent-particularly in achieving a high threshing rate while effectively controlling the kernel breakage rate. To reduce kernel breakage, many researchers in China have proposed flexible threshing technologies.

For example, a bionic flexible threshing technology was developed, inspired by the biomechanics of the human thumb, which significantly reduces kernel damage while maintaining a high threshing rate *(Jiale et al., 2023)*. Similarly, a flexible resin hammer-claw threshing system was developed, achieving low-damage threshing for corn *(Zhanbin et al., 2020)*. A novel composite threshing device incorporating flexible teeth and dual-torsion-spring short rasp bars was designed, enabling segmented flexible threshing that further reduces kernel breakage *(Meizhou et al., 2020)*. Clearly, flexible threshing has proven effective in reducing kernel damage. However, challenges such as component fatigue and wear have limited its large-scale application *(Lin et al., 2024; Vlăduț et al., 2022; Vlăduț et al., 2023)*. To address this, the present study proposes a flexible threshing technology in which the threshing element is hinged to the threshing rod. A mechanical model of the contact force between the flexible threshing element and corn kernels is established to identify key parameters. Using a DEM–MBD coupled simulation, the effects of different threshing element masses, rotational speeds, and structural configurations on the contact performance with corn ears are investigated. Furthermore, bench-scale experiments are conducted to determine the optimal parameters. This study provides theoretical support for the development of high-efficiency, low-damage corn kernel direct harvesting technologies.

MATERIALS AND METHODS

Overall structure and working principle

As shown in Figure 1, the single-point hinged flexible corn threshing device mainly consists of threshing elements, a drive shaft, upper cover, perforated screen, torque sensor, feed inlet, V–belt transmission system, gearbox, frame, and motor. During the threshing process, corn ears are fed through the feed inlet. The motor drives the drive shaft via the V–belt, which in turn rotates the threshing elements. Under the repeated action of the rotating threshing elements, the kernels are separated from the cob. The detached corn kernels pass through the perforated screen, achieving separation from the cob, while the cob is discharged from the machine by the continuous action of the helically arranged threshing elements. During this process, when the high-speed rotating threshing element strikes a corn kernel, it undergoes reverse rotation around the hinge axis due to resistance from the corn ear, as illustrated in Figure 2. This reverse rotation acts as a buffer against the impact load on the kernel, thereby reducing kernel damage. The structural parameters of the threshing test bench are shown in Table 1.

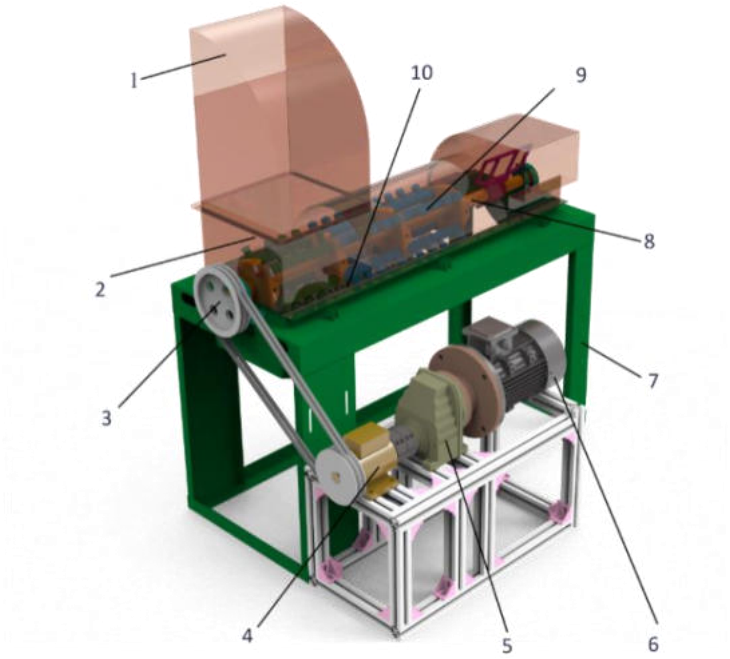


Fig. 1 - Schematic structure of the single-point hinged flexible corn threshing test bench
1 - Feeding inlet; 2 - Upper cover plate; 3 - V-belt drive system; 4 - Torque sensor; 5 - Reducer; 6 - Motor; 7 - Rack; 8 - Drive shaft; 9 - Threshing element; 10 - Hole punching sieve

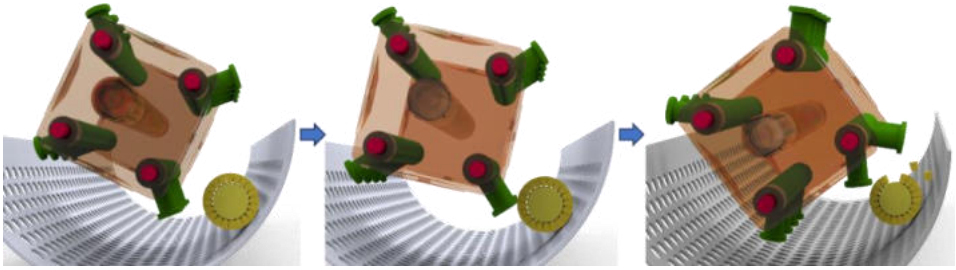


Fig. 2 - Schematic diagram of the threshing process of the single-point hinged flexible device

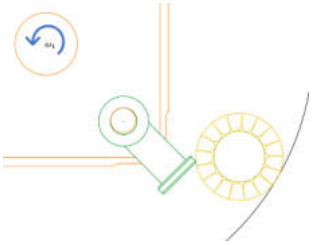
Table 1

Structural Parameters of the Threshing Test Bench

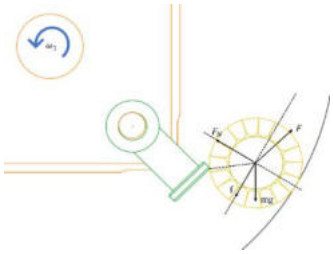
Parameter	Value
Dimensions (L × W × H) (mm)	1200 × 510 × 1400
Rotational speed of threshing drum (r/min)	0–1000
Threshing clearance (mm)	40
Feeding rate (kg/s)	2

Threshing Load Analysis of Corn Ears in a Single-Point Hinged Structure

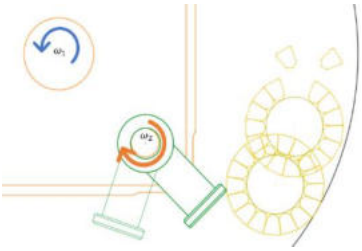
To determine the threshing load exerted on the corn ear during the flexible threshing process, a comparative analysis was conducted between the load–bearing conditions rigid (where the threshing element is rigidly fixed to the connecting shaft) and flexible threshing configurations *(Kiniulis et al., 2018)*. As shown in Figure 3(a), the threshing element is in a critical pre-collision state, about to impact the corn ear. At this moment, the motion states of both the rigid and single-point hinged flexible threshing elements are essentially the same. Figure 3(b) illustrates the scenario in which the rigid threshing element comes into contact with the corn ear. In this case, F represents the contact force on the corn ear, directed tangentially to the circular motion of the threshing element; F_N is the supporting force from the concave screen; mg denotes the gravitational force of the corn ear; and f is the frictional force from the concave screen acting on the ear. During rigid threshing, the threshing element is fixed and non-flexible, directly exerting an impact force on the corn ear. This impact is transmitted rapidly and in a concentrated manner over a relatively long duration, often resulting in strong localized pressure on the corn ear and causing kernel breakage *(Duane et al., 1972)*. In contrast, Figure 3(c) shows the flexible threshing process. When the threshing element strikes the corn ear, it undergoes reverse buffering due to its ability to rotate about the hinge axis. This prevents continuous compression of the corn ear, significantly reducing the threshing load applied by the element and minimizing kernel damage.



(a) critical moment before collision



(b) Mechanical Analysis of the Contact Process in Rigid Threshing



(c) Mechanical Analysis of the Contact Process in Single-Point Hinged Flexible Threshing

Fig. 3 - Comparison of Contact Mechanics: Single-Point Hinged Flexible vs. Rigid Threshing

Contact Force Analysis

In the threshing process, the separation of kernels from the cob depends on the impact load applied by the threshing component to the corn kernels. It is evident that the greater the applied force, the more favorable the separation of kernels from the cob becomes. However, an excessive force may lead to an increased kernel breakage rate *(Yajun et al., 2021)*. Conversely, if the applied force is too small, it may result in a higher unthreshed rate. Therefore, it is necessary to analyze the impact load exerted by the threshing component on the corn ear. Based on the threshing process of the device (Figure 3), the following assumptions are made *(Zhenjie et al., 2021)*:

（1）Initial velocity of corn ear v_c=0.

（2）There is no friction between the threshing element and the corn kernel.

（3）At the critical moment before the collision, the threshing element and the maize are considered as a system, ignoring the influence of other components.

Momentum change of the threshing element before and after the collision Δp_h:

$$\Delta p_h = m_h(v_h' - v_h) \tag{1}$$

In the formula, m_h—Thresher element mass;

v_h—Pre-collision velocity of the threshing element;

v_h'—Post-collision velocity of the threshing element.

Momentum change of the corn before and after the collision Δp_c:

$$\Delta p_c = m_c(v_c' - v_c) \tag{2}$$

In the formula, m_c—Mass of the corn;

v_c—Corn pre-collision velocity;

v_c'—Velocity of the corn after collision.

During the collision process, the total momentum of the system is conserved, and thus we can derive:

$$m_h v_h + m_c v_c = m_h v_h' + m_c v_c' \tag{3}$$

Simplifying:

$$m_h(v_h - v_h') = m_c(v_c' - v_c) \tag{4}$$

The contact force F can be expressed according to the impulse-momentum theorem as:

$$F \cdot t = \Delta p_h$$

In the equation, *t* represents the collision time. It can be concluded that:

$$F = \frac{\Delta p_h}{t} = \frac{m_h(v_h' - v_h)}{t} \tag{5}$$

Assuming the collision is an inelastic collision, the collision coefficient $e(0 \le e \le 1)$ is defined as:

$$e = \frac{v_c' - v_h'}{v_h - v_c} \tag{6}$$

The coefficient of restitution e is defined as:

e=1 represents a perfectly elastic collision, meaning there is no energy loss and kinetic energy is conserved.

e=0 represents a perfectly inelastic collision, where the objects stick together after the collision, resulting in the maximum kinetic energy loss.

0< e <1 represents a partially elastic collision, where some of the kinetic energy is converted into other forms of energy, such as heat or deformation energy.

By combining Equation (4) with Equation (6):

$$v_h' = \frac{(1+e)m_c v_c + (m_h - em_c)v_h}{m_h + m_c} - v_h \tag{7}$$

Substituting Equation (7) into Equation (5), we obtain:

$$F = \frac{m_h}{t}\left[\frac{(1+em_c v_c + (m_h - em_c)v_h}{m_h + m_c} - v_h\right] \tag{8}$$

After simplification:

$$F = \frac{m_h}{t(m_h + m_c)}[(1+e)m_c(v_c - v_h) - em_c v_h] \tag{9}$$

Assuming the initial velocity of the corn ear:

$$F = \frac{m_h m_c (1+e)}{t(m_h+m_c)} v_h \quad (10)$$

The initial velocity of the threshing element v_h can be expressed as:

$$v_h = \frac{2\pi r_h n}{60} \quad (11)$$

where: n –rotational speed of the element;

r_h – the rotational radius of the threshing element.

Substituting Equation (11) into Equation (10), we obtain:

$$F = \frac{m_h m_c (1+e) 2\pi r_h n}{60t(m_h+m_c)} \quad (12)$$

It is evident that, without altering the structural configuration of the threshing element, adjusting the mass m_h and angular velocity ω_h of the threshing element allows for regulation of the impact load, thereby achieving the objective of reducing kernel damage.

Determination of Experimental Factors

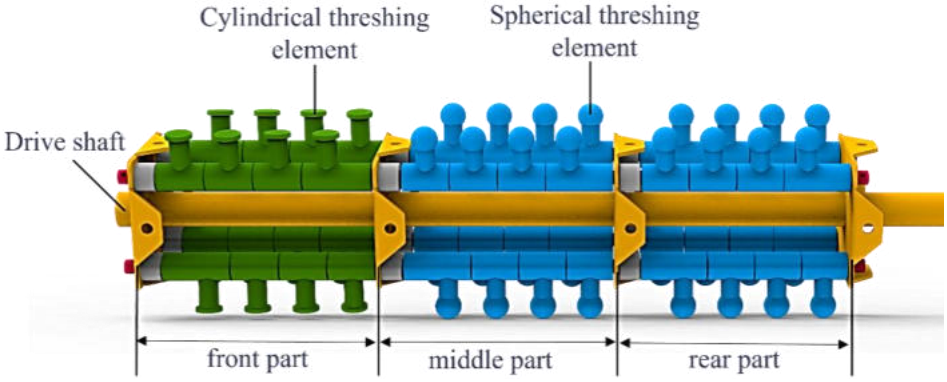


Fig. 4 - Arrangement of Combination-Type Threshing Elements

In this study, the threshing components were fabricated from medium–carbon steel (No. 45 steel), which provides high wear resistance and sufficient structural strength under prolonged operation. To reduce the aggressiveness of the threshing component surface and mitigate kernel damage, the working surfaces were polished to a smooth finish and all edges were chamfered with a rounded radius of 2 mm. These treatments reduce localized stress concentrations upon contact with kernels, thereby lowering the risk of visible cracks or peeling while maintaining the necessary threshing performance. The threshing components are available in two forms: flat–head and ball–head. The flat-head threshing component has a stronger ability to grab and transport the corn ears, which leads to a larger contact force on the corn kernels. On the other hand, the ball-head threshing component has a weaker ability to grab and transport the corn ears, but it is gentler during the threshing process *(Yuan et al., 2021)*. Considering that the impact load is larger when the kernels are not yet detached, and once a kernel is partially separated, the impact load on adjacent kernels decreases significantly, it is necessary to enhance the grabbing and transporting ability in the feeding section. Therefore, the front feeding section uses flat–head threshing components, while the middle and rear sections use ball-head threshing components (as shown in Fig. 4). In comparison to using a single type of threshing component, the combination of different forms in the threshing component theoretically ensures both high threshing efficiency and reduced damage to the corn ears in the middle and rear sections of the threshing zone. To verify the superiority of the combination–type threshing component, both simulation and bench tests were conducted, comparing single-type components with the combined-type components. Based on the analysis in Section “Contact Force Analysis”, the mass and speed of the threshing components are selected as experimental factors. According to the literature, experiments were conducted at rotational speeds of 400 r/min, 500 r/min, 600 r/min, 700 r/min, and 800 r/min *(Xin Ping, 2021)*. At low speeds, the mass must be large enough to ensure that the unthreshed rate meets the requirements. At high speeds, the mass should not be too large to avoid excessive kernel breakage. Preliminary experiments determined that at 400 r/min, a threshing component mass of 260 g meets the unthreshed rate requirement, while at 800 r/min, a mass of 140g meets the breakage rate requirement. Therefore, five mass levels (260 g, 230 g, 200 g, 170 g, and 140 g) were selected for the experiment. First, simulation tests were performed to determine the optimal range, and then, based on bench orthogonal experiments, the optimal parameters were identified.

DEM-MBD COUPLED MODEL AND SIMULATION TEST

Establishment of the DEM Model

To accurately establish a Discrete Element Method (DEM) model of corn, 50 corn ears of the widely cultivated variety "Zhengdan 958" in Shandong Province were selected, and their morphological and structural dimensions were measured, as shown in table 2. Based on the diameter and length of the cob, a coordinate sketch of the corn kernels was created in SolidWorks, and the kernel coordinates were exported using a macro command and then imported into EDEM software to construct a complete corn ear model *(Mousaviraad and Tekeste, 2024; Xiaoyu et al., 2022)*, as shown in Figure 6.

To determine the influence of the flexible threshing device on the contact force acting on the corn ear, the ear model was simplified by replacing the corn kernels with spherical particles. The characteristic parameters of the corn ear and the threshing device materials are shown in Table 3 and Table 4 *(Dandan et al., 2021; Horabik et al., 2017; Zhe et al., 2018)*.

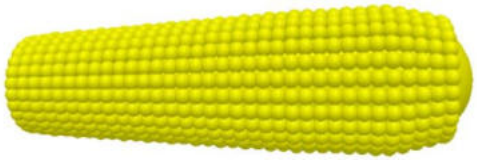


Fig. 5 - Corn Cob Model

Table 2

Dimensions of Corn Ear and Cob Shaft

Item	Corn ear		Maize Cob		Axial Length (mm)
	Large End Diameter (mm)	Small End Diameter (mm)	Large End Diameter (mm)	Small end diameter(mm)	
Maximum	56.47	47.31	36.18	28.78	203
Minimum	45.34	39.68	27.45	21.56	145
Mean	52.35	45.69	31.46	25.47	176
Standard Deviation	2.14	1.87	1.63	1.43	9.44

Table 3

Parameters of materials

Attributes	Ear of Corn	Steel
Poisson ratio	0.4	0.3
shear modulus (MPa)	127	7.9×10^4
Density（kg/m^3）	1197	7850

Table 4

Parameters of mutual materials

Contact Form	Corn–Corn	Corn–Steel
Coefficient of restitution	0.086	0.332
Coefficient of static friction	0.484	0.512
Coefficient of rolling friction	0.103	0.097

DEM-MBD Coupled Model Construction

To expedite the simulation process and minimize the settings for constraint and contact parameters, unnecessary components in the simulation model of the threshing test rig were eliminated. A simplified model of the threshing device, incorporating three different combinations of threshing elements, was developed using SolidWorks and imported into RecurDyn software in STEP format, as shown in Figure 6. Based on the operational process of the single-point hinged maize threshing test rig, constraint and motion conditions between the components were defined in RecurDyn. Using Ground as the reference, fixed constraints were applied to the housing and the perforated screen of the threshing device. Fixed constraints were also established between the connection shaft of the threshing elements and the drive shaft. Rotational constraints were assigned to both the main shaft and the threshing elements, referencing their respective rotational axes.

Additionally, a motion function was applied to the drive shaft's rotational joint using the Motion module to ensure that the drive shaft rotated at a constant speed, as specified. After finalizing the parameter settings in RecurDyn, the simulation model was exported as a wall file format via the External SPI module.

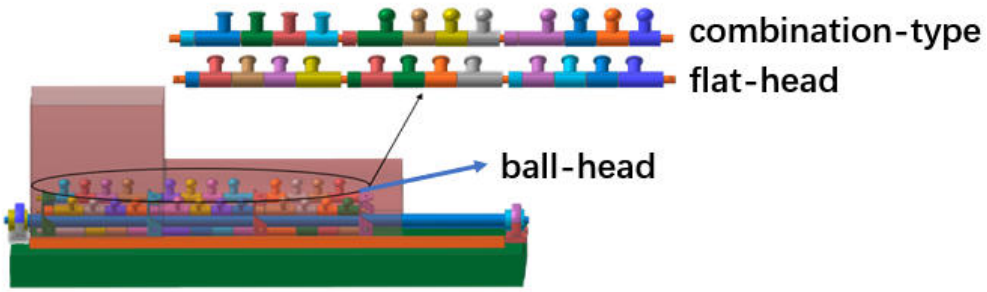


Fig. 6 - MBD Simulation Models of Three Structural Forms

Simulation Experiment

To reflect the differences in the threshing process for different types of threshing elements and to determine the optimal parameter range for rotational speed and threshing element mass for the bench test, coupled simulation experiments were conducted. Based on the analysis in section “Determination of Experimental Factors”**,** the experimental factors chosen were the type of threshing element structure, rotational speed, and the mass of the threshing element. The threshing element structures include cylindrical, spherical, and combined types. Rotational speeds of 400 r/min, 500 r/min, 600 r/min, 700 r/min, and 800 r/min were selected, and the masses of the threshing elements were set at 260 g, 230g, 200 g, 170 g, and 140 g.

During the simulation process, part attributes were set in RecurDyn software, and the user input option was used to set different threshing element masses. The speed of the rotating axis was controlled by adjusting the “motion” module to achieve different rotational speeds. A particle factory was added at the feed inlet, with the feeding rate set to 2 kg/s. The gravitational direction was set to the -Z direction. The total simulation time was set to 6 seconds with a time step of 19.17%, and data was saved every 0.1 seconds. The simulation process is shown in Figure 7.

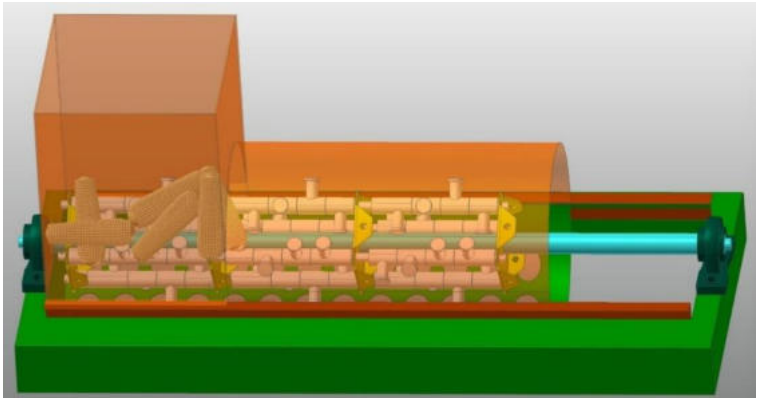


Fig. 7 - Coupled Simulation Model

Bench Test

The single–point hinged corn flexible threshing test stand was used for the bench test, conducted at the experimental field in Hejiayan Tuan Village, Juxian, Rizhao City, Shandong Province (Figure 8a). The threshing device uses a scraper-type conveyor for feeding, with a torque sensor connected at the small pulley to monitor the torque change at the input end of the threshing process in real-time. The cylindrical and spherical threshing components used in the bench test are shown in Figure 8b. The initial mass of the threshing components is 230g, which is reduced to the required mass by drilling holes in the components for the test. The motor speed is controlled by a frequency converter, and a grain collection box is placed at the bottom. The corn variety used in the test is Zheng dan 958, with a moisture content of 28.36%.

According to (GB/T21962-2020) Technical Regulations for Corn Harvesting Machinery and (GB/T5982-2017) Threshing Machine Testing Methods, the test factors include threshing component mass, drum speed, and threshing component structure. Corn ears are fed at a rate of 2 kg/s, and the test evaluation indices are kernel breakage rate and the unthreshed rate. Each test group is repeated three times, and the average value is taken.

The formula for calculating the indices is as follows:

$$Z_s = \frac{W_s}{W_i} \times 100\%$$

Let Z_s denote the kernel damage rate (%), where W_s represents the mass of damaged kernels (g), defined as the total mass of kernels exhibiting visible cracks or peeled surfaces, and W_i is the total mass of kernels in the sample (g).

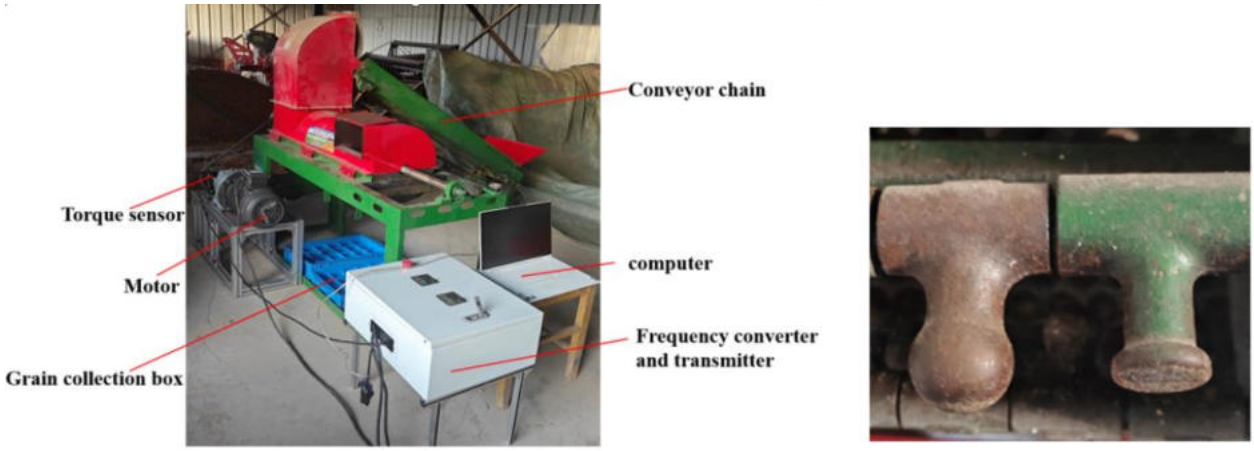
The threshing performance index is defined as follows:

$$S_w = \frac{W_j}{W_z} \times 100\%$$

where: S_w – threshing completeness rate (%);

W_j – total mass of kernels remaining on the cob (g);

W_z – total mass of all kernels, including both threshed and unthreshed ones (g).

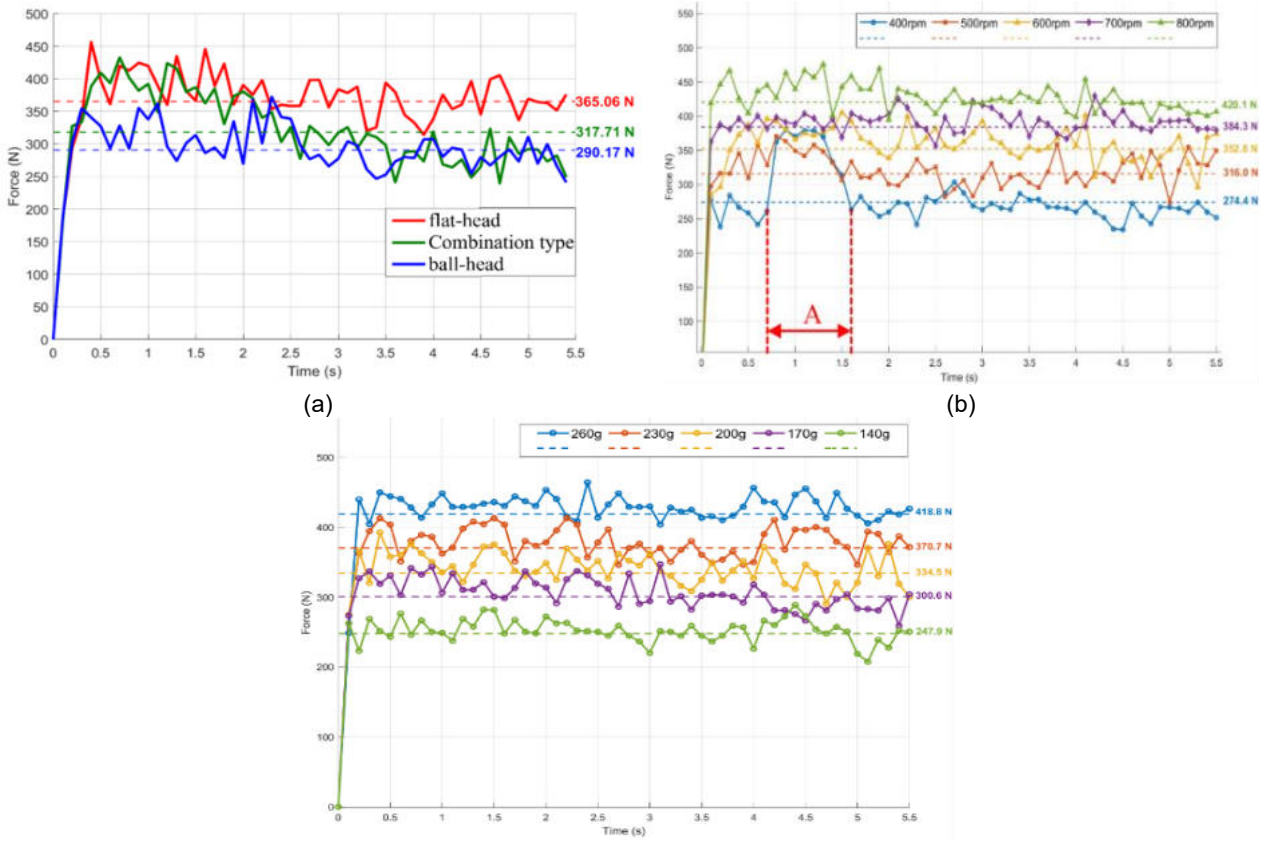


(a) (b)

Fig. 8 - Test Stand for Threshing Device

RESULTS AND DISCUSSION

Analysis of Single-Factor Simulation Results



(a) (b)

(c)

Fig. 9 - Simulation Test Results

Figure 9a shows the variation curves of the contact force between different threshing elements and corn ears over time. In terms of overall trends, the flat–head threshing element consistently generates a relatively high contact force throughout the threshing process, with an average value of 365.06 N. In contrast, the ball–head threshing element maintains a lower contact force, averaging 290.17 N. This indicates that under the same conditions, the flat-head element exerts a greater force on the kernels, making kernel damage more likely.

In the combination configuration, flat–head elements are arranged at the front section, while ball–head elements are installed in the middle and rear sections. As a result, before 2.5 s, when the corn ear is in the front section, the contact force is higher; after 2.5 s, as it moves to the middle and rear sections, the contact force decreases. The overall average contact force in this configuration is 317.71 N. The simulation results align with expectations: the combination setup exhibits strong contact in the flat–head section and gentler contact in the ball–head section. Compared to a fully flat–head configuration, it reduces the overall contact intensity; compared to a fully ball–head configuration, it improves threshing efficiency. Thus, this configuration demonstrates the best performance among all structures in the single–factor experiment, providing a theoretical basis for structural optimization of the threshing device.

Figure 9b illustrates the effect of threshing element rotational speed (from 400 r/min to 800 r/min) on contact force with corn ears. As shown, the contact force spikes sharply at the beginning, because initially, it is difficult to detach the kernels from the cob, leading to a surge in contact force. Subsequently, the force fluctuates within a range – this is because once some kernels around a corn ear are detached, the threshing load required to remove the remaining kernels decreases. Therefore, as the threshing element acts on different parts of the ear, the contact force exhibits fluctuations and a general downward trend. It can also be seen from Figure 9b that the contact force increases with higher rotational speeds of the threshing element. Specifically, when the drum speed is 800 r/min, the average maximum contact force reaches 420.1 N, while at 400 r/min, it is only 274.4 N. This is because a higher drum speed results in a higher velocity of the threshing elements, thus increasing the impact load on the corn ears; conversely, lower speeds reduce the impact load. In addition, under the condition of 400 r/min, an abnormally high contact force is observed in Region A. This suggests that when the speed is too low, the flexible threshing element is unable to immediately separate the kernels from the cob. Only when the element deforms to its limit, or even transitions to a rigid state, can separation occur, resulting in a sustained high contact force over time. This also indicates that excessively low drum speeds are not suitable for flexible threshing. According to the literature, if the contact force on corn kernels during threshing exceeds 400 N, the risk of kernel breakage increases significantly *(Dandan et al., 2021)*. Considering both breakage rate and threshing efficiency, rotational speeds of 500 r/min, 600 r/min, and 700 r/min are identified as optimal.

Figure 9c presents the simulation results for threshing elements of different masses. As the mass of the threshing element increases, the impact force generated during contact with the corn kernels increases significantly. A comprehensive analysis shows that although increasing the element mass helps enhance the threshing intensity, an excessively high mass substantially increases the contact force, which may lead to a higher kernel breakage rate. Conversely, a mass that is too low results in insufficient threshing capacity, thus increasing grain loss. Compared to other masses, threshing elements weighing 230 g, 200 g, and 170 g demonstrate a better balance between achieving higher threshing efficiency and maintaining a lower breakage probability.

Based on the results of the single–factor simulation experiments, the selected range of rotational speed parameters is set to 500 r/min, 600 r/min, and 700 r/min, while the selected range of mass parameters is 230 g, 200 g, and 170 g. According to the simulation data on the effect of the threshing element structural form on threshing performance, the combination configuration outperforms the other two single-element configurations. This provides a theoretical basis for further validation through bench-scale experiments.

Orthogonal Experiment and Verification

To determine the optimal combination of operating parameters, a three-factor, three-level Box-Behnken response surface design was developed based on the results of single-factor experiments. Within the optimized parameter ranges identified through simulation testing, rotational speeds of 500 r/min, 600 r/min, and 700 r/min, and threshing component masses of 170 g, 200 g, and 230 g were selected for the trials. The coded levels of the experimental factors are shown in Table 5.

Table 5

Coding table of test factors

Level	Factor		
	Rotational Speed X_1(r/min)	Quality X_2 (g)	Component Structure X_3
-1	500	170	ball-head
0	600	200	Combination type
1	700	230	flat-head

The experimental design and results are shown in Table 6, where X1, X2 and X3, represent the coded values of the experimental rotational speed, threshing element mass, and threshing component combination respectively, Y1 and Y2 respectively represent the kernel breakage rate and the unthreshed rate.

Table 6

Design and results of simulation test

Test number	Rotational Speed X_1(r/min)	Quality X_2(g)	Component Structure X_3	Y1/%	Y2/%
1	-1	1	0	5.65	1.89
2	0	0	0	3.88	0.88
3	0	-1	-1	4.58	2.14
4	-1	-1	0	4.72	1.95
5	0	0	0	4.05	1.04
6	-1	0	1	4.31	1.81
7	-1	0	-1	4.42	2.18
8	1	0	-1	4.53	1.68
9	1	0	1	5.22	0.41
10	0	0	0	3.95	0.96
11	1	-1	0	5.83	2.01
12	0	1	1	5.39	0.82
13	0	0	0	4.05	0.75
14	0	1	-1	5.42	1.14
15	0	0	0	3.95	0.84
16	0	-1	1	4.90	1.41
17	1	1	0	5.94	0.33

Analysis of Experimental Results

To analyze the significance of rotational speed, threshing element mass, and threshing component combination on each evaluation index, analysis of variance (ANOVA) and significance testing were performed on the kernel breakage rate and threshing loss rate using Design-Expert software. The results are presented in Table 7.

Table 7

Analysis of airflow velocity in front of screen

Analysis of variance

Source	df	Grain breakage rate Y1		Unthreshed grain rate Y2	
		F Value	P-value	F Value	P-value
Model	9	113.1	< 0.0001	39.73	< 0.0001
X1	1	78.39	< 0.0001**	87.31	< 0.0001**
X2	1	81.37	< 0.0001**	83.76	< 0.0001**
X3	1	10.61	0.0139*	54.66	0.0002**
X1 X2	1	18.08	0.0038	39.65	0.0004
X1X3	1	22.32	0.0021	12.24	0.01
X2 X3	1	7.38	0.0299	2.54	0.1551
X12	1	179.01	< 0.0001	40.05	0.0004
X22	1	566.52	< 0.0001	16.45	0.0048
X32	1	4.97	0.061	13.37	0.0081
Residual	7				
Lack of fit	3	1.78	0.2908	1.79	0.289
Pure error	4				
Total error	16				

Note: *significant (P<0.05), **very significant (P<0.01)

Based on the data in Tables 7, the rotational speed, threshing component mass, and threshing component combination form exhibit varying degrees of influence on the grain breakage rate and threshing loss rate. All three parameters are significant factors affecting both the breakage rate and the threshing loss rate of corn kernels. Among them, the primary to secondary factors influencing the breakage rate (Y1), in descending order of importance, are: threshing component mass > rotational speed > component combination form. For the threshing loss rate (Y2), the order of influence is: rotational speed > threshing component mass > component combination form.

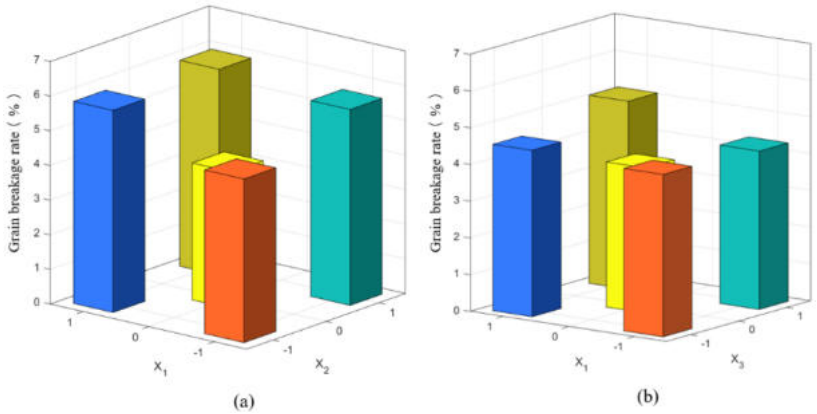


Fig. 10 - Response Surface Diagram of Interaction Factors for Kernel Breakage Rate

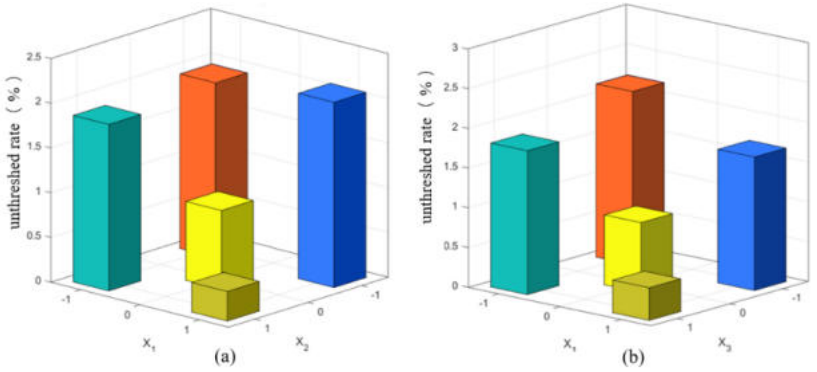


Fig. 11 - Response Surface Diagram of Interaction Factors for Unthreshed Rate

As shown in Figure 10a, the kernel breakage rate initially decreases and then increases with the rise in both the rotational speed and mass of the threshing element. The highest breakage rate occurs when both speed and mass are at high levels, while the lowest breakage rate is observed when these parameters are at moderate levels. Notably, a higher breakage rate is also observed under low–speed and low–mass conditions. This trend can be attributed to the fact that increasing the rotational speed raises the linear velocity of the threshing element, thereby increasing the impact kinetic energy. Simultaneously, an increase in mass amplifies the inertial force, resulting in greater instantaneous impact loads on the kernels. When both speed and mass are elevated, the combined impact intensity significantly increases, making the kernels more susceptible to breakage. Conversely, at low speed and mass, the flexible threshing effect is reduced, leading to higher stress on the kernels and thus greater breakage.

Figure 10b shows that under constant mass conditions, the influence of the threshing element's structural configuration on kernel breakage rate becomes more pronounced with increasing rotational speed. As the structure transitions from spherical to composite and cylindrical forms, the breakage rate increases accordingly. The cylindrical threshing element exhibits consistently higher breakage rates across all rotational speeds. In general, the higher the speed, the greater the structural configuration's impact on kernel breakage rate.

As shown in Figure 11a, the unthreshed rate decreases with increasing threshing element rotational speed and mass, indicating a negative correlation between these two factors and the unthreshed rate. The underlying reason is that a higher rotational speed increases the number of contacts between the threshing element and the corn ear, facilitating the detachment of kernels. Likewise, an increase in the element' s mass enhances the impact force, thereby improving threshing completeness.

In Figure 11b, under the same mass condition (200 g), notable differences in threshing performance are observed among different structural configurations of the threshing elements. The cylindrical structure results in the lowest unthreshed rate, suggesting that its smaller contact surface generates a more concentrated impact force, significantly improving threshing efficiency. Conversely, the spherical structure yields the highest unthreshed rate, likely due to its larger contact area, which weakens the impact and leaves some kernels unthreshed. At lower rotational speeds, the structural configuration of the threshing element has a greater effect on the unthreshed rate.

The optimal combination of parameters for this threshing device is: rotational speed of 600 r/min, threshing element mass of 200 g, and a combination-type configuration.

CONCLUSIONS

This study investigates a novel flexible corn threshing technology and develops an experimental bench in which threshing elements are hinged to the threshing rods. A series of single–factor simulations and multifactor orthogonal experiments were conducted, leading to the following conclusions:

By analyzing the impact loads during the operation of both rigid and flexible structures, the superiority of the single–point hinged flexible configuration over the rigid one was demonstrated. A contact force model between the flexible threshing element and the corn ear was established, and key operational parameters were identified.

Using the DEM–MBD coupled simulation method, the effects of threshing element mass, rotational speed, and structural configuration on contact force and adhesive bond failure between kernels and cobs were systematically analyzed. The results provided the basis for determining the test parameter range for bench-scale experiments.

Response Surface Methodology (RSM) optimization experiments revealed that the primary factors affecting the kernel breakage rate are: threshing element mass > rotational speed > structural configuration; while for the unthreshed rate, the order of influence is: rotational speed > mass > configuration. Considering both kernel breakage and unthreshed rate, the optimal working parameters were identified as a threshing element mass of 200 g, rotational speed of 600 r/min, and a combination-type configuration. Under these conditions, the kernel breakage rate was 3.95%, and the unthreshed rate was 0.88%.

The threshing principle and structural approach proposed in this study effectively mitigate the high breakage rate caused by traditional rigid-impact methods. This research provides a feasible solution for efficient and low-damage direct harvesting of corn kernels and offers valuable insights for the development and engineering application of flexible threshing devices.

ACKNOWLEDGEMENT

This research was funded by the National Key R&D Program of China, grant 569 number 2021YFD2000502, and the Modern Agricultural Industrial System of 570 Shandong Province, grant number SDAIT-02-12.

REFERENCES

[1] Dandan H., Yang Z., Junshan N., Qiqiang L., Lin C., Qi C., Lihua Z. (2024). DEM model acquisition of the corn ear with bonded particle model and its simulated parameters calibration. *Granular Matter*, 26(2), 54.

[2] Duane L., Harry H., Ted H. (1972). Corn kernel damage due to high velocity impact. *Transactions of the ASAE*, 12(1), 330–331.

[3] Horabik J., Beczek M., Mazur R., Parafiniuk P., Ryżak M., Molenda M. (2017). Determination of the restitution coefficient of seeds and coefficients of visco-elastic Hertz contact models for DEM simulations. *Biosystems Engineering*, 161, 106–119.

[4] Jiale Z., Hainan Z., Han T., Xiaogeng W., Yajun Y. (2023). Bionic threshing component optimized based on MBD-DEM coupling simulation significantly improves corn kernel harvesting rate. *Computers and Electronics in Agriculture*, 212, 10672.

[5] Jun F., Zhi C., Lujia H., Luquan R. (2018). Review of grain threshing theory and technology. *International Journal of Agricultural and Biological Engineering*, 11(3), 12–20.

[6] Kiniulis V., Steponavičius D., Kemzūraitė A., Andriušis A., Juknevičius D. (2018). Dynamic indicators of a corn ear threshing process influenced by the threshing-separation unit load. *Mechanics*, 24(4), 412–421.

[7] Lin N., Zehao Z., Haoran Y., Jie M., Qinghao H., Yanan W., Duanyang G. (2024). Design and Experiment of Flexible Threshing Device with Variable Stiffness for Corn. *Agriculture*, 14(6), 836.
[8] Meizhou C., Guangfei X., Chuansu W., Peisong D., Yinping Z., Guodong N. (2020). Design and experiment of roller-type combined longitudinal axial flow flexible threshing and separating device for corn. *Transactions of the Chinese Society for Agricultural Machinery*, 51(10), 123–131.
[9] Mircea C., Nenciu F., Vlăduț V., Voicu Gh., Găgeanu I., Cujbescu D. (2020). Increasing the performance of cylindrical separators for cereal cleaning, by using an inner helical coil. *INMATEH – Agricultural Engineering*, 62(3), 249–258.
[10] Mousaviraad M., Tekeste M. (2024). Systematic calibration and validation approach for Discrete Element Method (DEM) modeling of corn under varying moisture contents (MC). *Journal of the ASABE*, 67(2), 259–274.
[11] Nenciu F., Mircea C., Vlăduţ V., Belc N., Berca L. (2021). Evaluation of wheat seed separation performances for new design of rotating cylindrical sieve, equipped with customizable homogenization coil, *20th International Scientific Conference Engineering for Rural Development*, vol. 20, pp. 1478-148, Jelgava, Latvia.
[12] Tang Q., Jiang L., Yu W., Wu J., Wang G. (2024). Design and experiment of high moisture corn threshing device with low damage. *INMATEH - Agricultural Engineering*, 74(3), 172–183.
[13] Vlădut N.-V., Biris S.St., Cârdei P., Găgeanu I., Cujbescu D., Ungureanu N., Popa L.-D., Perişoară L., Matei G., Teliban G.-C. (2022). Contributions to the mathematical modeling of the threshing and separation process in an axial flow combine. *Agriculture,* 12(10), 1520.
[14] Vlădut N.-V., Ungureanu N., Biris S.St., Voicea I., Nenciu F., Găgeanu I., Cujbescu D., Popa L.-D., Boruz S., Matei G., Ekielski A., Teliban G.C. (2023). Research on the identification of some optimal threshing şi separation regimes in the axial flow apparatus. *Agriculture,* 13(4), 838.
[15] Xiaoyu L., Yuefeng D., Lei L., Enrong M., Fan Y., Jun F., Liang Z. (2022). Research on the constitutive model of low-damage corn threshing based on DEM. *Computers and Electronics in Agriculture*, 194, 10672.
[16] Xiaoyu L., Yuefeng D., Jinglin G., Enrong M. (2020). Design, simulation, and test of a new threshing cylinder for high moisture content corn. *Applied Sciences*, 10(14).
[17] Xin Ping L. (2013). Study on relationship of feeding form and threshing-cleaning rate of corn ears. *Advanced Materials Research*, 753, 1462–1466.
[18] Yajun Y., Liangshan L., Jiale Z., Xiangeng W., Jun F. (2021). Optimal design and simulation analysis of spike tooth threshing component based on DEM. *Processes*, 9(7), 1163.
[19] Yuan S., Hao L., Yang X., Tao C., Zhe Q., Dongxing Z. (2018). Optimization and experiment of spike-tooth elements of axial flow corn threshing device (轴流式玉米脱粒装置钉齿元件优化与试验). *Transactions of the Chinese Society for Agricultural Machinery*, 49(S1), 258–265.
[20] Zhanbin, W., Zhenwei, W., Yinping, Z., Wenxi, Y., Yanjie, C., Chengqiang, L. (2020). Design and test of longitudinal axial flexible hammer-claw corn thresher (纵轴流柔性锤爪式玉米脱粒装置设计与试验). *Transactions of the Chinese Society for Agricultural Machinery*, 51(S2), 109–117.
[21] Zhe Q., Dongxing Z., Li Y., Tianliang Z., Zhendong W.,Tao C. (2018). Experiment on feed rate and cylinder speed of longitudinal axial flow threshing and separating device for maize (纵轴流玉米脱粒分离装置喂入量与滚筒转速试验). T*ransactions of the Chinese Society for Agricultural Machinery*, 49(2), 58–65.
[22] Zhenjie Q., Chengqian J., Dingguo, Z. (2017). Multiple frictional impact dynamics of threshing process between flexible tooth and grain kernel. *Computers and Electronics in Agricultur*e, 141, 276–285.

OPTIMIZATION OF VERTICAL ROTARY TILLAGE BLADE PARAMETERS FOR SALINE-ALKALI LAND IMPROVEMENT

/

面向盐碱地改良的立式旋耕刀结构参数优化

Xuan LUO, He SUN, Haoran BAI*)
College of Mechanical and Electrical Engineering, Qingdao Agricultural University Qingdao /China
Tel: +86 13854285625; E-mail: baihaoran111@126.com
Corresponding author: Haoran BAI
DOI: https://doi.org/10.35633/inmateh-76-101

Keywords: *saline–alkali land, vertical rotary tiller blades, tool speed ratio, discrete element method, soil fragmentation, tillage simulation*

ABSTRACT

To address the limitations of conventional tillage machinery in compacted, high–viscosity saline–alkali lands, this study designed a vertical rotary tiller tool structure suitable for deep fragmentation operations in saline-alkali lands, aiming to improve soil fragmentation efficiency and reduce operational resistance. Employing orthogonal experiments and response surface methodology (RSM), this study established a quadratic regression model correlating soil fragmentation rate and blade force, utilizing the tool camber angle, blade inclination angle, and internal bending angle as key variables. On this basis, a kinematic model of the cutting tool was constructed, and the correlation between the speed ratio and operating conditions was elucidated. Based on the EDEM simulation platform, the dynamic characteristics of cutting force, torque, particle flow velocity, and particle force during one complete rotation of the cutting tool in saline–alkali land were simulated and analyzed. Results indicated that the tool camber angle and internal bending angle exerted the most significant influence on operational effectiveness, with a notable interaction effect observed between them. An optimal parameter combination was ultimately derived through optimization: camber angle of 8.06°, blade–inclination angle of 7.48°, internal bending angle of 7.46°, resulting in a force of 2295.27 N and a soil fragmentation rate of 91.59%. The results established a theoretical foundation for optimizing vertical tiller blade design, while practical guidance for saline-alkali land tillage was developed through studies on soil fragmentation and energy use.

摘要

针对盐碱地土壤板结严重、黏重性高等特点导致传统耕整机械适应性差的问题，本文设计了一种适用于盐碱地深层破碎作业的立式旋耕机刀具结构，旨在提高碎土率和降低作业阻力。研究选取刀具外倾角、刀刃倾角和内折弯角作为主要影响因素，结合正交试验与响应面分析方法，建立了碎土率和刀具受力的二次回归模型。在此基础上，构建刀具运动学模型，明确了速度比与作业工况之间的匹配关系。基于 EDEM 仿真平台，模拟分析刀具在盐碱地中旋转一周内的受力、扭矩、颗粒流速与颗粒力的动态变化特性。结果表明，刀具外倾角和内折弯角对作业性能影响显著，且二者间存在交互作用。优化结果显示，当外倾角为 8.06°、刀刃倾角 7.48°、内折弯角为 7.46° 时，刀具受力为 2295.27 N，碎土率为 91.59%。研究为立式旋耕刀具的结构优化提供了理论依据，并通过碎土率和能耗特性的研究，为改善盐碱地机械化整地作业质量提供了实践指导。

INTRODUCTION

China possesses diverse land resource types, yet high–quality cultivated land is relatively scarce. Saline–alkali land accounts for over 10% of the total cultivated land area in the country. According to statistics from the National Plan for Saline-Alkali Land Resource Utilization (2021–2030), more than 100 million mu (approximately 6.67 million hectares) of saline-alkali land nationwide is available for development, characterized by wide distribution and significant potential *(Chang et al., 2025)*. However, saline–alkali lands are universally characterized by high soil hardness, severe compaction, and elevated viscosity, which result in increased operational resistance and poor soil fragmentation when conventional tillage machinery was employed, severely constraining reclamation efficiency. The amelioration of saline–alkali lands has been recognized as a critical measure for enhancing agricultural productivity and ensuring food security.

In recent years, multiple techniques, including biological, chemical, physical, and integrated agronomic approaches have been explored through research and practical applications *(Vlăduţoiu et al., 2017; Popescu et al., 2022)*.

Among these, the development of high–efficiency tillage equipment adapted to saline–alkali land conditions was identified as a vital pathway for improving operational efficiency and reclamation outcomes. Concurrently, relevant studies provided methodological and theoretical references from the perspectives of machinery selection, structural optimization, and soil–tool interaction mechanisms *(Ungureanu et al., 2015; Vlăduţ et al., 2017)*.

In the mechanized reclamation of saline-alkali lands, rotary tillage equipment was widely adopted due to its demonstrated capabilities in soil fragmentation and cultivation layer improvement. As a new type of tillage machinery, the vertical rotary tiller breaks up the soil structure from multiple angles after the blades cut vertically into the soil, making it more suitable for deep soil compaction improvement than traditional horizontal rotary tillers. Meanwhile, its detailed working effect, uniform tillage layer, low energy consumption, and strong adaptability have made it one of the important technical directions for the mechanized improvement of saline-alkali land *(Fang et al., 2016; Zhang et al., 2013)*. However, most existing vertical rotary tillers are designed for general use, and their blade structures have not been systematically optimized for the complex soil conditions of saline-alkali land, which limits further improvements in their operational performance.

In response to this issue, some scholars have conducted research on tool structure optimization. *Yang et al. (2025)* analyzed the impact of the outward tilt angle on the force distribution and operational quality of the Sangyuan power harrow, while *Wang et al. (2019)* optimized the operational parameters of the vertical-driven shallow rotary harrow based on tool kinematics and dynamics. These studies provide references for the optimization of vertical rotary tillage tools; however, there remains a gap in specialized adaptive design tailored for saline-alkali soils. Therefore, this paper aims to improve saline–alkali land by designing a vertical rotary tillage tool adapted to saline-alkali land working environments, establishing a cutting kinematic model, analyzing the impact of structural parameters on operational performance, and selecting the optimal parameter combinations that reduce power consumption and improve operational quality through discrete element simulation and field trials, thereby providing a theoretical basis and technical support for the efficient mechanized improvement of saline-alkali land *(Ucgul et al., 2020; Makange et al., 2021)*.

MATERIALS AND METHODS

Vertical rotary tiller structure design and working principle

The cutter assembly functions as the working component of the vertical rotary tiller, making direct contact with the soil. The blades are mounted vertically and rotate about individual axes. The implement performance depends on cutting tool characteristics, and the cutter assembly was 3D–modeled in SolidWorks 2022, with its full structure shown in Figure 1.

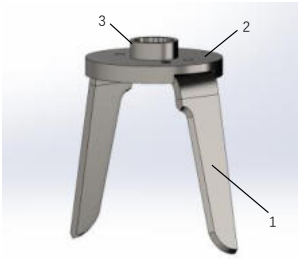


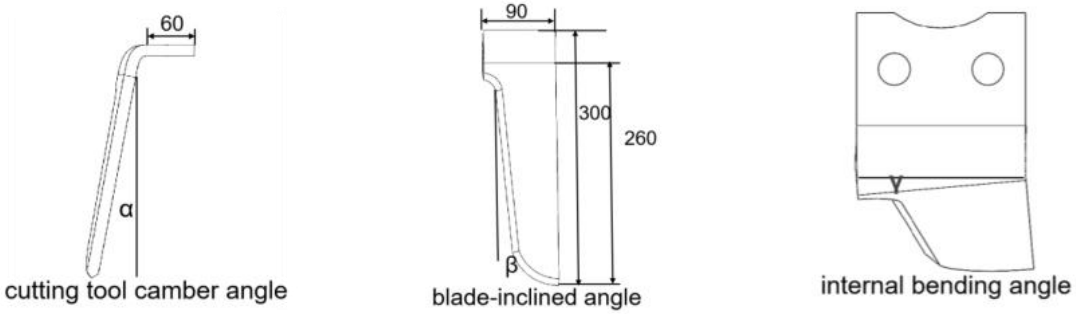
Fig. 1 –Diagram of the cutter assembly structure

1 - Tool; 2 - Base; 3 - Tool axis

The rake knife on the rotor has a swivel diameter of 240 mm (material: 65Mn steel), and the thickness of the non-cutting area at the front end is designed to be 7 mm to ensure the structural strength of the cutting edge. To avoid cutter assembly interference and missed plowing, the width of the cutter assembly is 90 mm, the length is 60 mm, and the thickness is 15 mm, in accordance with the size of the cutter disc and the installation distance between the rotors. Considering the characteristics of saline-alkali land with serious soil compaction and a deeper plowing layer, the plowing depth needs to reach 200–250 mm, so the total height of the tool is set to 300 mm, of which the length of the cutting edge is 260 mm (Fig. 2).

The structural parameters of the cutting tool are designed as follows: α is the camber angle of the cutting tool, which affects its working coverage area. By adjusting the camber angle, the overlap rate between rotors can be optimized, effectively preventing leakage and improving the uniformity of soil fragmentation, thereby enhancing operational efficiency and controlling energy consumption.

β is the blade–inclined angle, which affects the soil penetration performance of the cutting tool. A larger inclination angle helps reduce soil penetration resistance but may decrease the soil contact area, thereby affecting the effectiveness of soil fragmentation. Therefore, its value must be balanced according to actual soil conditions. γ is the internal bending angle, which plays a key role in the dynamic performance of the cutting tool. Without an internal bending angle, the back of the cutter in contact with the soil is prone to the phenomenon of "anti-soil," which increases operating resistance and machine vibration.



(a) Main view *(b) Side view* *(c) Top view*

Fig. 2 – Schematic diagram of the cutting tool structure

Kinematic analysis of soil cutting

The trajectory of the blade at any point is depicted in Figure 3. The cutter movement of the vertical rotary tiller consists of two parts: one is the linear movement that advances with the whole machine, and the other was the circular rotary movement around its own axis, and the two are superimposed to form a spiral ground–cutting path.

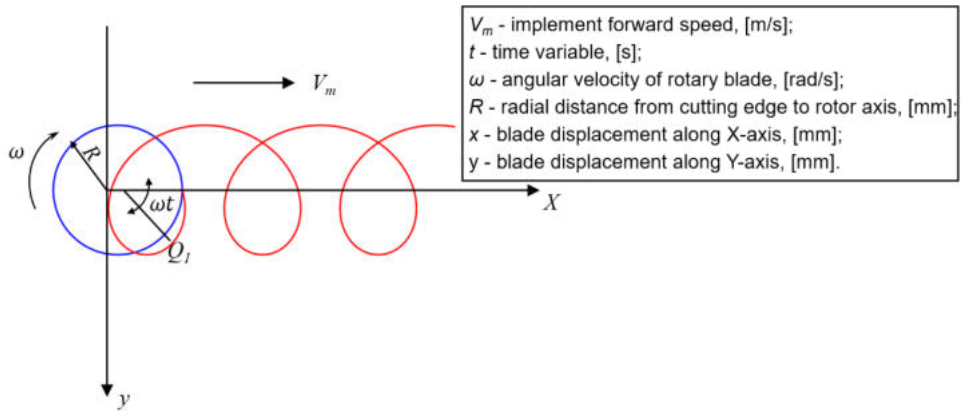


Fig. 3 – Diagram of the cutting tool motion trajectory

The kinematic trajectory of the blade tip after time t was described by the following Equations (1-2):

$$x = R\cos\omega t + V_m \text{ t} \quad (1)$$

$$y = -R\sin\omega t \quad (2)$$

The tool speed ratio λ is defined as the ratio of the implement forward velocity V_m to the product of the blade rotational angular velocity ω and the cutting radius R. Set the tool speed ratio Equation (3):

$$\lambda = \frac{\omega R}{V_m} \quad (3)$$

The angular velocity Equation (4) is:

$$\theta = \omega t \quad (4)$$

Substituting λ and θ yields:

$$x = R\left(\frac{\lambda}{\theta} + cos\theta\right) \quad (5)$$

$$y = -Rsin\theta \quad (6)$$

where:

V_m is the implement forward speed, [m/s];

t – time variable, [s];

ω – angular velocity of rotary blade, [rad/s];

R – radial distance from cutting edge to rotor axis, [mm];

x – blade displacement along X-axis, [mm];

y – blade displacement along Y-axis, [mm];

θ – angle, [°];

λ – tool speed ratio.

From this, the motion trajectory was a pendulum motion. Equations (1–2) were analyzed using Python. The simulation parameters comprised: (1) cutting edge radius R = 110 mm (rotor axis to blade tip, (2) operational conditions with V_m = 1 m/s forward speed the rotary cutter and three rotational velocities (0.5,1, and 1.5 rev/s), and (3) temporal domain limited to t = 1 s. The three motion trajectories are shown in Figure 4.

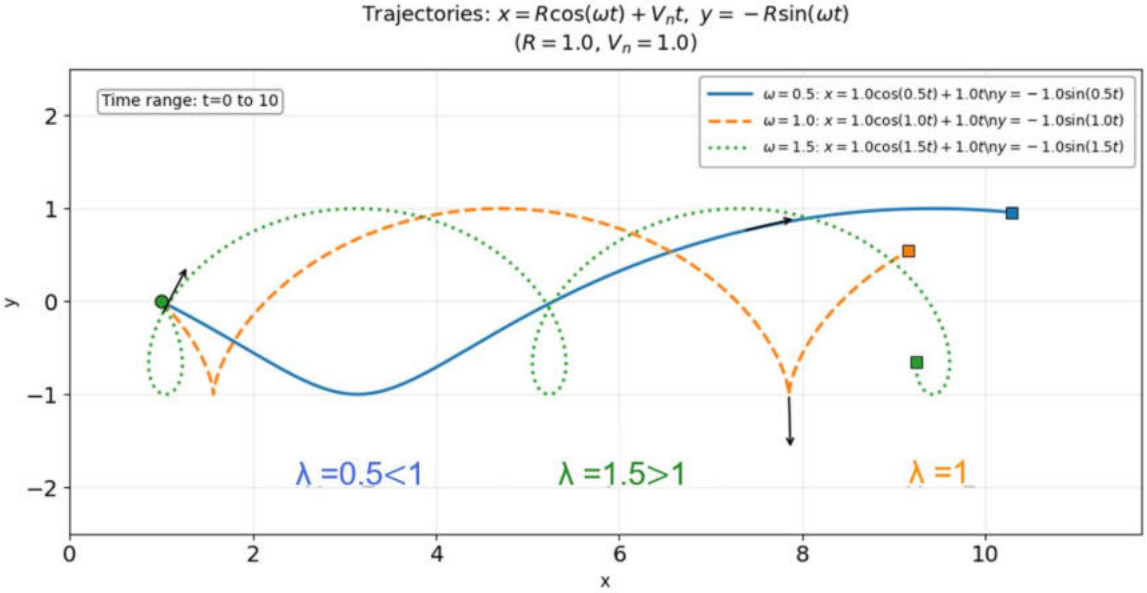


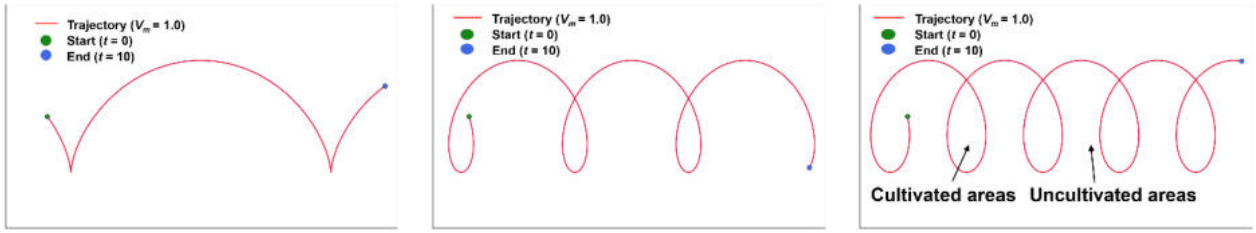
Fig. 4 – Three types of motion trajectory diagrams

When λ < 1, the trajectory is a short pendulum and the blade plays a role in pushing the soil.

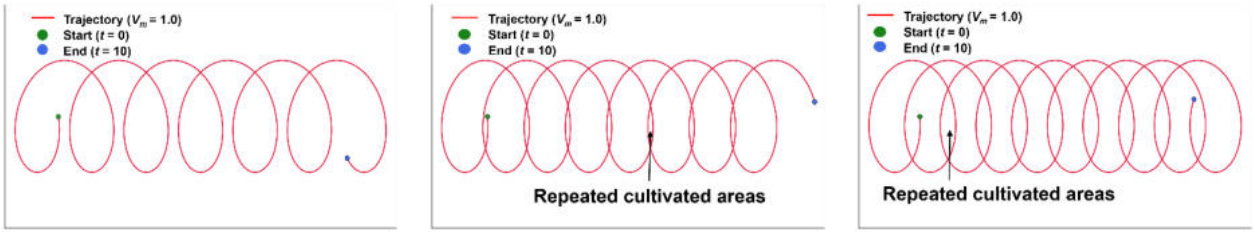
When λ = 1, the trajectory is a standard pendulum and the blade plays a role in piercing the soil.

When λ > 1, the trajectory is a long pendulum line, the blade plays a role in crushing the soil.

Therefore, λ >1, the vertical tiller normal operation of the sufficient conditions, the rotational speed of the tool should be greater than the forward speed of the tiller.



(a) λ=1 *(b) λ=2* *(c) λ=3*



(d) λ=4 *(e) λ=5* *(f) λ=6*

Fig. 5 – Motion trajectory under different speed ratios

Figure 5 shows that as λ increased, the overlapping area of the harrow blade movement trajectory line increases, which means that as λ increases, the plowed area increases and the unplowed area decreases. When λ > 4, the area of repeated plowing appeared. To avoid unnecessary power consumption, the structure, power consumption and productivity of the vertical rotary tiller should be considered, and the value range of λ should be $1 < \lambda < 4$.

Simulation based on EDEM

Soil modeling

With notable variations in particle size, shape, and physical characteristics, soil was a highly heterogeneous discrete particle medium. To facilitate simulation modeling and improve computational efficiency, this paper simplifies soil particles using smooth solid spheres to approximate the unit particles. Spherical particles not only simplify contact calculations but also effectively enhance simulation stability.

In discrete element simulations, the choice of particle size directly affects the computational load and simulation accuracy. The number of contact calculations decreases with larger particle sizes while the simulation speed increases, but this results in a less accurate description of the actual soil details. Considering the balance between simulation accuracy and efficiency, the radius of soil particles in the EDEM software was set to 5 mm in EDEM 2022 software, allowing the simulation model to better reflect the mechanical response of real soil.

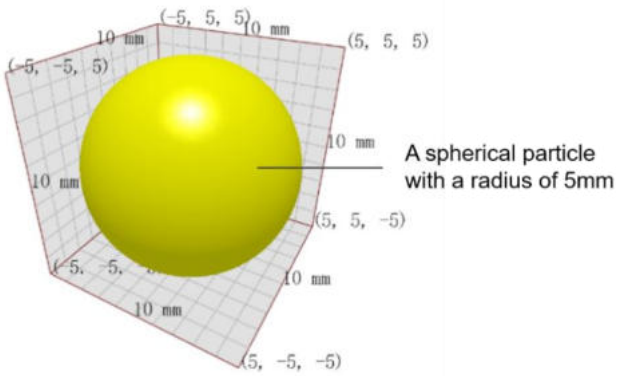


Fig. 6 – Particle model

To accurately describe the interactions between soil particles and between particles and tools, the Hertz–Mindlin with JKR model and the Hertz–Mindlin with Bonding model were chosen as particle contact models. The Hertz–Mindlin with JKR model was mainly used to describe the nonlinear elastic contact behavior with adhesion, suitable for the bonding phenomenon between fine particles caused by surface energy, especially under saline–alkali land conditions. Its contact force included three components: elastic force, damping force, and adhesive force. To further simulate the fragmentation process of soil structures under external forces, the Hertz–Mindlin with Bonding model was introduced. Based on the basic elastic contact, the "bonding bond" was added in this model, which broke after meeting certain fracture criteria to simulate the rupture of soil aggregates. This model could accurately reflect the process of soil evolving from a clustered state to a discrete state when disturbed by a tool, thereby accurately predicting the soil fragmentation effect *(Ucgul et al., 2018; Sun et al., 2018)*.

Simulation parameter setting

Soil test samples were taken from the saline-alkali agricultural trial demonstration base in the Yellow Delta Agricultural Highland Zone, Dongying City, Shandong Province, with a pH value of 8.2. By reviewing the relevant literature *(Wang et al., 2024)*, the specific parameters of the discrete meta-simulation were determined as shown in Table 1.

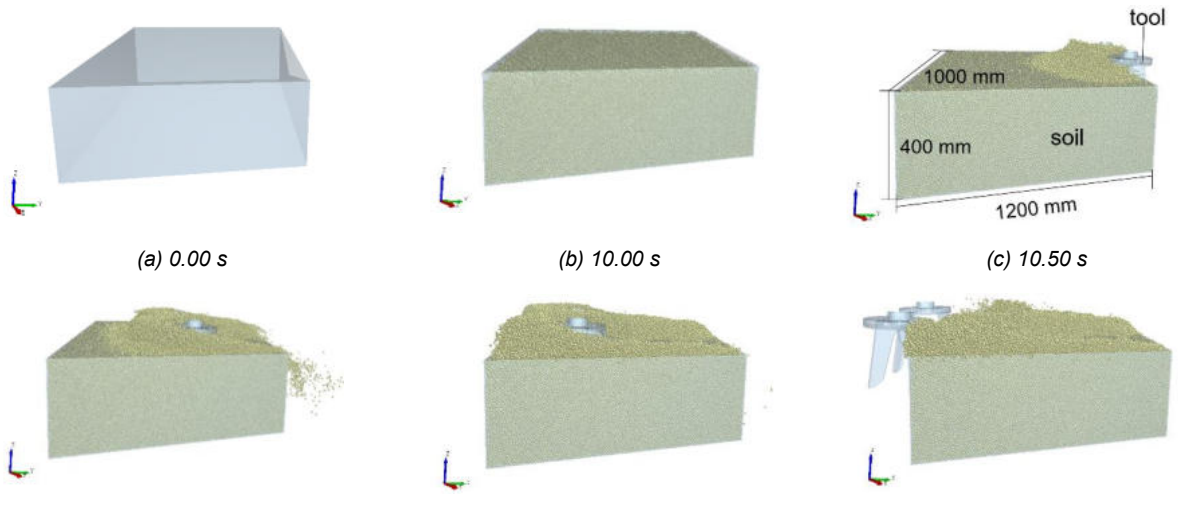
Table 1

Setting of simulation parameters of soil model

Project	Property	Unit	Parameter Value
Soil particles	Poisson's ratio		0.32
	Shear module	Pa	1.2×10^{8}
	Density	kg/m^3	2270
Blade	Poisson's ratio		0.3
	Shear module	Pa	7.9×10^{10}
	Density	kg/m^3	7865
Soil particles-rake knife	Coefficient of restitution		0.3
	Static friction factor		0.5
	Kinetic friction factor		0.1
Soil particles-soil particles	Coefficient of restitution		0.358
	Static friction factor		0.546
	Kinetic friction factor		0.15
Soil JKR surface energy		J/m^2	3.207

Construction of soil tank model and simulation process

A three–dimensional model of vertical rotary tiller blades was developed using SolidWorks 2022 software and exported in the STL file format. The model was subsequently imported into EDEM 2022 software, where a complete simulation system was established to conduct operational simulations of the vertical rotary tillage tools. Considering that during actual vertical tiller operation, adjacent blades had to employ identical rotational speeds but opposite rotational directions to maintain operational stability, two tillage blades were configured as a functional group in the simulation model for modeling and analytical purposes. According to the simulation of actual saline soil cultivation conditions, considering the actual working size and the influence of the simulation boundary, the length of the soil tank was set to 1200 mm, the width of the soil tank at 1000 mm, and the height of the soil tank to 400 mm. The simulation process of the vertical rotary tiller was shown in Figure 7. Based on previous kinematic analysis of soil cutting, the simulation parameters were set to a 1.2 m/s forward speed, 4 r/s rotational speed and 250 mm working depth for plow pan disruption in saline–alkali lands. The total duration of the simulation was set to 12 s, during which the soil particles were arranged according to the random filling mode in 0–10 s, and the natural accumulation was accomplished by gravity settling to ensure the reasonable distribution of the particles and the contact stability to meet the requirements of the initial simulation conditions. The vertical rotary tillage blade was used for normal rotary tillage operation in 10–12 s.



(a) 0.00 s *(b) 10.00 s* *(c) 10.50 s*

(d) 11.00 s *(e)11.50 s* *(f) 12.00 s*

Fig. 7 – Simulation process of a vertical rotary tiller

RESULTS AND DISCUSSIONS

Analysis of force and torque variations in rotary tillage tools

To thoroughly investigate the force characteristics and soil response during vertical rotary tillage operations in saline-alkali soils, dynamic simulation analysis was conducted on the total tool force, torque, particle flow velocity, and particle force over a complete rotation cycle. By comparing the mechanical responses between two consecutive cycles (10.60–11.10 s), the periodic patterns and synergistic effects during tool-soil interaction were examined, revealing the influence of high cohesion and aggregation properties of saline-alkali lands on particle motion transmission and energy dissipation, which provides theoretical guidance for tool structural optimization and operational parameter matching. As depicted in Figures 8 and 9, distinct periodic fluctuations in tool force were observed during the 10.6–11.1 s interval, with each complete rotation corresponding to one full cycle of force variation. Specifically, the first rotational cycle (10.60–10.85 s) was characterized by multiple peaks and troughs in both force and torque curves, indicating significant load variations when cutting through soils of different compaction levels. The second cycle (10.85–11.10 s) exhibited essentially identical fluctuation patterns to the first, confirming stable tool-soil interaction characteristics. Based on these findings, subsequent orthogonal experiments could be performed using single-cycle simulations to conserve computational resources.

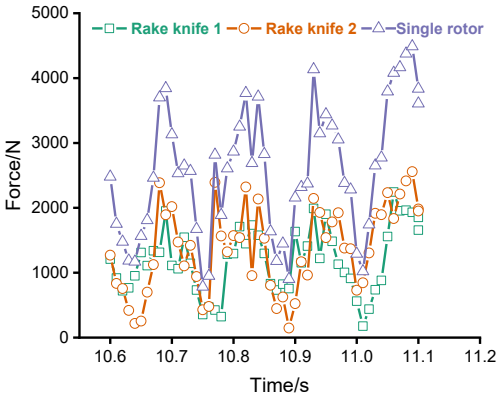


Fig. 8 – Curve of force versus time

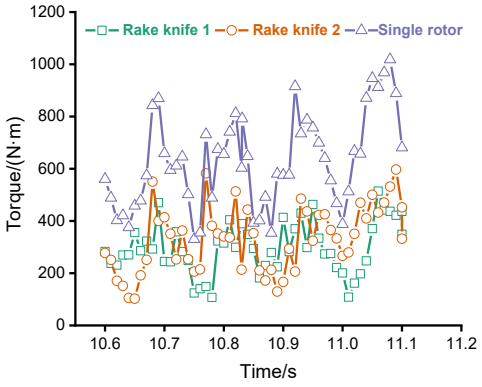


Fig. 9 – Curve of torque versus time

Trends in particle flow rate and particle force

During tool rotation, the dynamic response of soil perturbation was reflected through concurrent variations in particle flow velocity and particle force. Analysis of two complete rotational cycles (10.60–11.10 s) demonstrated high temporal synchronization between these parameters (Fig. 10 and Fig. 11).

The overall trend indicated that after soil engagement and incision by the tool, particle force underwent rapid intensification, resulting in elevated particle flow velocity; upon progressive tool retraction from the active zone, particle force and flow velocity exhibited a synchronous decrease, manifesting characteristic cyclic variation. In the first cycle (10.60–10.85 s), the particle flow velocity and force reached a trough around 10.64 s, followed by a synchronized rapid increase to a local peak with a flow velocity of 0.1845 m/s and particle force of 0.0847 N around 10.70 s, indicating that at this time, the depth of tool penetration and the soil reaction force were synchronously enhanced. In the second cycle (10.85–11.10 s), the two continued to maintain synergistic fluctuations, indicating that the perturbation rhythm had a certain regularity.

As the saline-alkali soil had the characteristics of high cohesion and strong agglomeration, which made the cohesion between particles larger in the disturbance process, the particle flow rate enhancement lagged the force enhancement, and the damping effect in the particle movement process was more obvious. The rigid characteristics of the soil structure led to the fluctuation of particle force before and after the peak value being larger than the fluctuation of flow rate, reflecting the influence of saline soil structure on the particle motion transfer process.

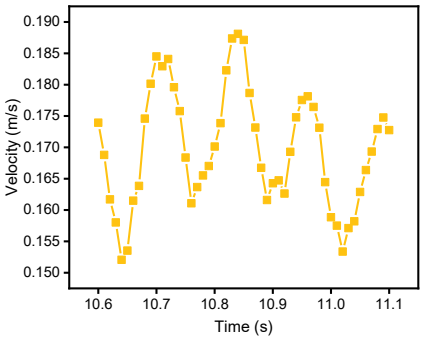


Fig. 10 – Curve of velocity versus time

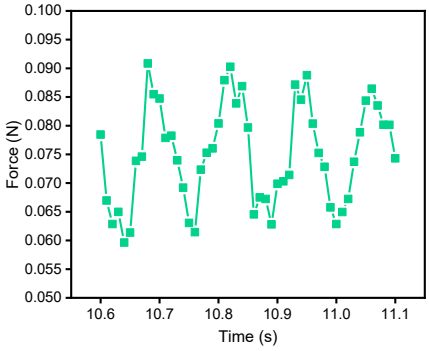


Fig.11 – Curve of force versus time

Results of the multi-factor experiments

An investigation into the effects of tool camber, blade–inclined, and internal bending angles on soil crushing rate and force distribution was conducted employing the orthogonal test methodology; response surface methodology was subsequently applied to establish quantitative relationships between these structural parameters and tillage performance through mathematical modeling; finally, a three–factor, three–level orthogonal experiment was conducted to identify the key influencing factors through significance analysis and optimize the tool parameter combination. From the previous trend of force and torque changes, it was observed that the fluctuation of the tool's force and torque in each motion cycle was smooth, so the following orthogonal test only needed to perform the simulation process of one motion cycle *(Chen et al., 2025)*. The factor levels of the test tool were displayed in Table 2, and the test results were shown in Table 3.

Table 2

Simulation test factors and levels

Encodings	Tool camber angle A	Blade-inclined angle B	Internal bending angle C
a	0	0	0
b	5	5	5
c	10	10	10

Table 3

Structural parameter results and analysis of vertical rotary tiller

Standards	Tool camber angle	Blade-inclined angle	Internal bending angle	Force	Soil fracture rate
1	b	b	b	2294.33	91.92
2	c	b	c	2231.12	91.12
3	c	a	b	2300.14	89.25
4	a	c	b	2478.65	90.76
5	c	b	a	2390.56	89.32
6	b	b	b	2310.52	91.71
7	b	a	a	2543.75	88.52
8	b	b	b	2305.20	91.45
9	b	c	c	2270.65	90.42
10	b	b	b	2280.64	91.72
11	a	b	c	2300.68	92.65
12	b	a	c	2269.50	93.50
13	a	b	a	2612.25	91.25

Standards	Tool camber angle	Blade-inclined angle	Internal bending angle	Force	Soil fracture rate
14	b	c	a	2425.65	90.45
15	b	b	b	2285.68	91.14
16	a	a	b	2601.25	92.56
17	c	c	b	2386.10	87.50

Regression modeling and response surface analysis of forces were performed using Design–expert 13.0 software. Quadratic regression analysis was done on the tillage resistance of vertical rotary tiller to obtain the response surface regression model.

$$F=2295.27-85.61A-112.53C+52.15AB+38.03AC+76.27A^2+70.00B^2 \quad (7)$$

As can be seen from Table 3, the regression model between the vertical rotary tiller forces and the test factors was highly significant (P < 0.01), indicating that the model was able to explain the force variations well. The out-of-fit term was not significant (P=0.0799 > 0.01), suggesting that the model fits well and can be used for prediction. The results showed that the combined effect of tool camber, blade-inclined, and internal bending angle were the main factors affecting the force on vertical rotary tiller, followed by blade-inclined, and there was a significant interaction between the factors.

Table 4

ANOVA of the force regression model

Source	Sum of squares	Freedom	Mean of squares	F-value	P-value	Significance
Model	2.325×10^5	9	25829.33	60.82	＜0.0001	Significant
A	58630.86	1	58630.86	138.05	＜0.0001	
B	2947.20	1	2947.20	6.94	0.0337	
C	1.013×10^5	1	10.013×10^5	238.53	＜0.0001	
AB	10878.49	1	10878.49	25.61	0.0015	
AC	5785.88	1	5785.88	13.62	0.0077	
BC	3555.14	1	3555.14	8.37	0.0232	
A^2	24491.82	1	24491.82	57.67	0.0001	
B^2	20633.35	1	20633.35	48.58	0.0002	
C^2	617.53	1	617.53	1.45	0.2671	
Residual	2973.01	7	424.72			
Lack of fit	2334.95	3	778.32	4.88	0.0799	Insignificant
Pure Error	638.06	4	159.51			
Cor Total	2.354×10^5	16				

Note: P<0.01 (indicates highly significant);

Regression modeling and response surface analysis of soil fracture rate using Design–expert 13.0 software. A quadratic regression analysis was done on the soil fragmentation rate of vertical rotary tiller to obtain a response surface regression model.

$$W=91.59-1.25A+1.02C-1.25BC-0.9640B^2 \quad (8)$$

Table 5

Analysis of variance for regression modeling of soil fracture rate

Source	Sum of squares	Freedom	Mean of squares	F-value	P-value	Significance
Model	35.59	9	3.95	10.46	0.0027	Significant
A	12.53	1	12.53	33.13	0.0007	

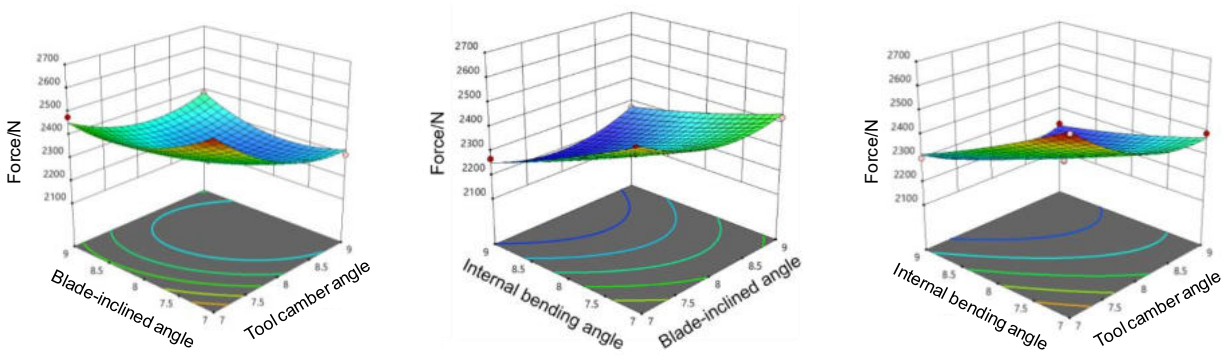
Source	Sum of squares	Freedom	Mean of squares	F-value	P-value	Significance
B	2.74	1	2.74	7.24	0.0310	
C	8.30	1	8.30	21.96	0.0022	
AB	0.0012	1	0.0012	0.0032	0.9562	
AC	0.0400	1	0.0400	0.1058	0.7545	
BC	6.28	1	6.28	16.60	0.0047	
A^2	1.52	1	1.52	4.03	0.0847	
B^2	3.91	1	3.91	10.35	0.0147	
C^2	0.0409	1	0.0409	0.1080	0.7520	
Residual	2.65	7	0.3781			
Lack of fit	2.28	3	0.7615	8.41	0.0335	Insignificant
Pure Error	0.3623	4	0.0906			
Cor Total	38.24	16				

Note: P<0.01 (indicates highly significant);

As shown in Table 5, the model of the relationship between the soil fracture rate of the vertical rotary tiller and the test factors was highly significant (P < 0.01), indicating the model could explain the soil fracture rate well. Meanwhile, the lack-of-fit term was not significant (P=0.0335 > 0.01), suggesting the model was well fitted. This proved the modified model was superior and could be used for prediction. The results showed that under the combined effect of tool camber, blade–inclined angle, and internal bending angle, tool camber and internal bending angle had the most significant effect on the soil fracture rate, followed by blade-inclined.

Influence of interaction factors on operational effectiveness

The force response surface was shown in Figure 12. Both the contact area at the tool-material interface and resultant force direction were determined by blade-inclined angle, while force distribution pattern and transmission pathway were governed by tool camber angle. The surface shape reflected their interaction: the peak area indicated significant force trend change under specific combinations, caused by superposition of contact area and force distribution. Internal bending angles affected tool rigidity and cutting path, with contour distribution revealing its greater sensitivity to force effects compared to tool camber angle. It directly altered cutting edge effective length and stress concentration degree. Cutting edge geometry and material removal mechanisms were jointly influenced by internal bending angle and tool camber. The surface trend demonstrated that blade-inclined increased with internal bending angle, cooperatively changing cutting edge entry angle and material deformation zone distribution.

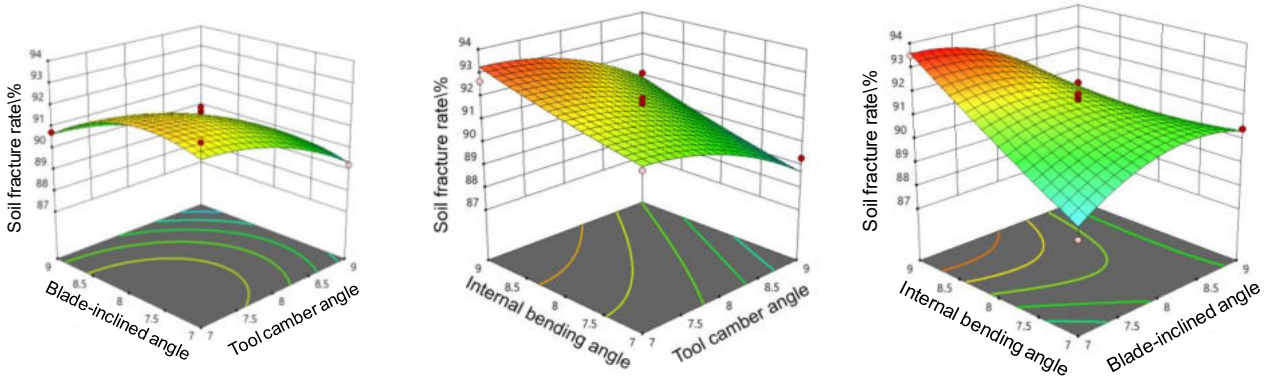


(a) AB *(b) BC* *(c) AC*

Fig. 12 –The surface on which the interaction responds to the force

A - Tool camber angle; B -Blade-inclined angle; C - Internal bending angle; AB - The impact of A and B on force; AC - The impact of A and C on force; BC - The impact of B and C on force

The soil fracturing rate response surface was shown in Figure 13. The contact angle between cutting edge and soil was determined by blade-inclined angle, influencing soil crushing efficiency. The tool camber angle altered lateral cutting–edge distribution, modifying soil crushing coverage. The surface showed higher soil fragmentation in the middle region, indicating parameter interaction. The shear crushing effect on soil was directly influenced by blade-inclined angle, while lateral soil extrusion and crushing range were affected by tool camber angle. The aggregation and crushing paths of the tool on soil were affected by internal bending angle, with crushing rate first increasing then decreasing as internal bending angles increased. With tool camber angle variation, small internal bending angles exhibited crushing rate constrained by camber angle, whereas near peak areas demonstrated enhanced parameter interaction jointly determining crushing rate improvement. Soil breakage rate sensitivity to tool camber response increased with internal bending angle.



(a) AB *(b) AC* *(c) BC*

Fig. 13 – Response surfaces for the effect of interaction terms on the soil fracture rate

A - Tool camber angle; B - Blade-inclined angle; C - Internal bending angle; AB - The impact of A and B on force; AC - The impact of A and C on force; BC - The impact of B and C on force

In order to obtain the optimal combination of operating parameters of vertical rotary tiller, two regression models were optimized and solved by using the Numerical module of Design–Expert 13.0 software. In saline-alkali land, the force of vertical rotary tiller was 2295.27 and the soil breakage rate was 91.59% with the tool camber angle of 8.06°, the tool camber angle of 7.48°, and the internal bending angle of 7.46°.

Field trial

To validate the field performance of the simulation–optimized structural parameters of the vertical rotary tiller blades in saline–alkali soil conditions, field tests were conducted to validate the optimized vertical rotary tiller performance in saline-alkali lands at the Yellow River Delta Agricultural High-tech Zone, Dongying City, Shandong Province.



Fig. 14 – Field trial process

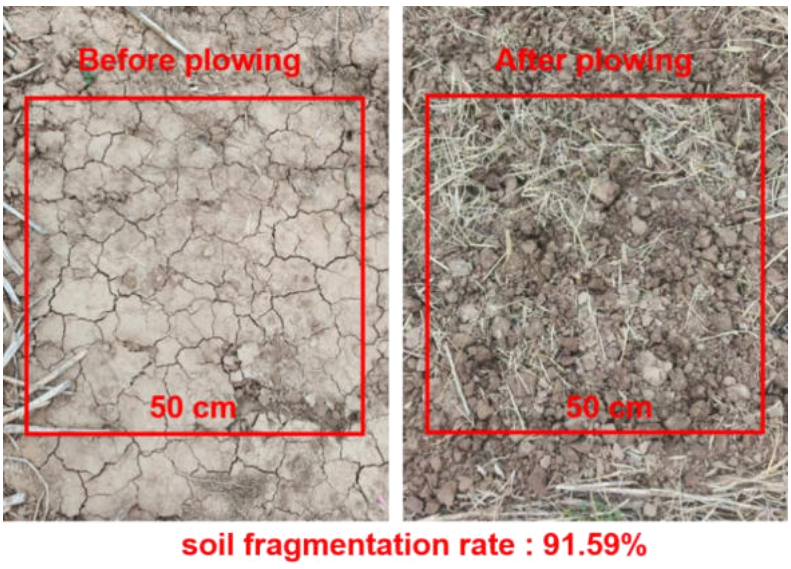


Fig. 15 – Field trial effect

A Deutz–Fahr 1804 tractor was used with 1.2 m/s forward speed and 240 rpm blade rotation. The experimental site was characterized by moderate saline-alkali soil with severe surface compaction, unimplemented spring tillage, and flat terrain (50 m length × 10 m width). The cultivated layer exhibited significant soil hardness *(Gao et al., 2023; Zhang et al., 2024; Qin et al., 2016)*. The measurement equipment included: an electronic balance (maximum capacity: 2500 g, accuracy: 0.1 g), a steel tape measure (range: 5 m, accuracy: 0.1 cm), and a steel ruler (range: 50 cm, accuracy: 0.5 mm). The tests were performed in mid-March 2025 under clear weather conditions, following identical experimental protocols as previously described.

The tests were conducted to validate the simulation optimization combinations (external inclination angle of 8.06°, blade–inclined angle of 7.48°, and internal bending angle of 7.46°), respectively, and the evaluation index was the soil fragmentation rate. In the test area, a 50 × 50 cm area was taken every 5 m in a trip (3 areas in total) and a 50 × 50 cm self-made frame was placed. At the same time, the soil quality of the cultivated layer and the soil block quality greater than 4 cm in the frame were weighed, and the soil fragmentation rate of the 3 areas was calculated respectively, and the average value was obtained *(Xiao et al., 2024; Ucgul et al., 2017*).

The soil fragmentation rate can be obtained from Equation (9):

$$F = \frac{M_t - M_d}{M_t} \times 100\% \quad (9)$$

where:

F is the soil fragmentation rate, [%];

M_t – the mass of all the soils, [g];

M_d - the mass of the soil block with the longest length larger than 4 cm, [g].

Table 6

Validation test results

Test conditions	Soil fracture rate (%)
1	88.55
2	89.14
3	90.21
Average value	89.30
Predicted value	91.59
Mean relative error/%	2.29

The results suggested that the soil fracture rate of the optimized structural combination reached 91.59%, and the results of the field validation test were shown in Table 7, which showed that the soil fracture rate after the test was 89.30%, and the mean relative error of the average value was 2.29% compared with the results of the simulation test, which might be due to the fact that the vibration of the machine in the actual operation process led to a lower soil fracture efficiency than that of the simulation test. However, the deviation was in line with the simulation and actual error range, so it could be considered that the simulation test results were basically consistent with the field test results. The knives had no obvious wear and tear or grass tangling phenomenon under continuous operation conditions, and the operation stability was excellent.

Comprehensive analysis indicated that the simulation-optimized tool structure not only performed well in the discrete element simulation, but also had the characteristics of high soil crushing efficiency, low energy consumption, and high adaptability in the actual saline-alkali land operation, which verified the engineering feasibility and practicability of the simulation and the response surface optimization model, providing theoretical and practical support for the subsequent product promotion and mechanized operation.

CONCLUSIONS

This paper focused on the application requirements of vertical rotary tiller in saline–alkali land improvement operation and carried out the research on optimization of blade structure parameters and simulation analysis of operation performance. By establishing the kinematic model of the tool, the relationship between the tool speed ratio and the operating quality was clarified, which provided a theoretical basis for the reasonable determination of the operating parameters.

Based on EDEM discrete element simulation software, Hertz-Mindlin with JKR and Bonding contact model was adopted to establish a soil simulation system for saline land cultivation. The simulation results demonstrated that the vertical rotary tiller blades exhibited significant periodic fluctuations in both force and torque during operation, with highly consistent variation trends across different cycles, indicating stable tool-soil interaction. Particle flow velocity was found to be synchronized and coordinated with force variations.

Combined with orthogonal experimental design and response surface analysis, the effects of tool camber, blade-inclined, and internal bending angle on the operating force and soil fragmentation rate were investigated. The operating effect was demonstrated by the regression model and significance analysis to be primarily determined by the tool camber angle and internal bending angle, while the resultant force and soil crushing rate variation were significantly influenced by their interaction.

Through parameter optimization, the optimal combination of three key parameters was determined: an 8.06° camber angle, 7.48° blade-inclined angle and 7.46° internal bending angle. Subsequent field validation tests demonstrated that the optimized tool achieved a cutting force of 2295.27 N and a soil fragmentation rate of 91.59%, both exceeding relevant national standards.

ACKNOWLEDGEMENT

This work was supported by National Key Research and Development Program of China (Project no. 2023YFD2001400), National Key R&D Program of China (Project no.2022YFE0125800).

REFERENCES

[1] Chang Y., Ge Y., Cao Z. (2025). Analysis of distribution characteristics and improvement practices of saline-alkali land in China (我国盐碱地分布特征及改良实践分析). *Journal of Agricultural Catastrophology*, 15(1), 244–246.

[2] Chen X., Chen L., Cai Z., Wang Q. (2025). Design and parameter optimization of a seed storage device of a wheat plot seeder (小麦小区播种机存种装置的设计与参数优化). *INMATEH - Agricultural Engineering*, 76(2), 121–130.

[3] Fang H., Ji C., Zhang Q., Guo J. (2016). Force analysis of rotary blade based on distinct element method (基于离散元法的旋耕刀受力分析). *Transactions of the Chinese Society of Agricultural Engineering*, 32(21), 54–59.

[4] Gao Z., Lu C., Wei X., Liu H., He J., Wang Q. (2023). Design and experiment of co-stirring combined corn strip straw cleaning device (协拨组合式玉米条带秸秆清理装置设计与试验). *Transactions of the Chinese Society for Agricultural Machinery*, 54(10), 68–79.

[5] Makange N., Ji C., Nyalala I. (2021). Prediction of precise subsoiling based on analytical method, discrete element simulation and experimental data from soil bin. *Scientific Reports*, 11(1), 11082.

[6] Popescu E., Nenciu F., Vlădut V. (2022). A new strategic approach used for the regeneration of soil fertility, in order to improve the productivity in ecological systems, *Scientific Papers. Series E. Land Reclamation, Earth Observation & Surveying, Environmental Engineering,* XI, 277–284.

[7] Qin K., Ding W., Fang Z., Du T., Zhao S., Wang Z. (2016). Design and experiment of ploughing and rotary tillage combined machine (犁翻旋耕复式作业耕整机的设计与试验). *Transactions of the Chinese Society of Agricultural Engineering*, 32(16), 7–16.

[8] Sun J., Wang Y., Ma Y., Tong J., Zhang Z. (2018). DEM simulation of bionic subsoilers (tillage depth > 40 cm) with drag reduction and lower soil disturbance characteristics. *Advances in Engineering Software*, 119(5), 30–37.

[9] Ucgul M., Saunders C. (2020). Simulation of tillage forces and furrow profile during soil-mouldboard plough interaction using discrete element modelling. *Biosystems Engineering*, 190, 58–70.

[10] Ucgul M., Saunders C., Fielke J.M. (2017). Discrete element modelling of top soil burial using a full-scale mouldboard plough under field conditions. *Biosystems Engineering*, 160, 140–153.

[11] Ucgul M., Saunders C., Li P., Lee S., Desbiolles J. (2018). Analyzing the mixing performance of a rotary spader using digital image processing and discrete element modelling (DEM). *Computers & Electronics in Agriculture*, 151, 1–10.

[12] Ungureanu N., Croitoru Şt., Biriş S., Voicu Gh., Vlăduţ V., Selvi K.Ç., Boruz S., Marin E., Matache M., Manea D., Constantin G., Ionescu M. (2015). Agricultural soil compaction under the action of agricultural machinery. *Proceedings of the 43rd International Symposium on Agricultural Engineering "Actual Tasks on Agricultural Engineering"*, 31–42, Opatija, Croaţia.

[13] Vlăduţ V., Gheorghe G., Marin E., Biriş S.Șt., Paraschiv G., Cujbescu D., Ungureanu N., Găgeanu I., Moise V., Boruz S. (2017). Kinetostatic analysis of the mechanism of deep loosening system of arable soil. *Proceedings of the 45th International Symposium on Agricultural Engineering "Actual Tasks on Agricultural Engineering"*, 217–228, Opatija, Croaţia.

[14] Vlăduţoiu L., Cârdei P., Vlăduţ V., Fechete L. (2017). Modern trends in designing and selecting the machine / equipment for soil deep tillage. 16th International Scientific Conference "Engineering for Rural Development", 1415–1420, Jelgava, Latvia.

[15] Wang D., Lu T., Zhao Z., Shang S., Zheng S., Liu J. (2024). Calibration of discrete element simulation parameters for cultivated soil layer in coastal saline alkali soil (滨海盐碱地耕作层土壤离散元仿真参数标定方法). *Transactions of the Chinese Society for Agricultural Machinery*, 55(11), 240–249.

[16] Wang Y., Rong G., Li H., Wang Q., He J., Lu C., (2019). Design and parameter optimization of vertical driving-type surface rotary tillage machine (立式驱动浅旋耙设计与参数优化). *Transactions of the Chinese Society of Agricultural Engineering*, 35(9), 38–47.

[17] Xiao W., Niu P., Wang P., Xie Y., Xia F. (2024). Simulation analysis and optimization of soil cutting of rotary blade by ANSYS/LS-DYNA (基于 ANSYS/LS-Dyna 旋耕刀切土仿真分析及优化). *INMATEH - Agricultural Engineering*, 72(1), 22–32.

[18] Yang Q., Lyu Z., Yan Y., Yang S., Li F., Song Z., Chen Y. (2025). Optimal design and experiment of vertical rotary harrow for mulberry plantation (桑园立式旋转动力耙优化设计与试验). *Transactions of the Chinese Society for Agricultural Machinery*, 56(1), 210–220.

[19] Zhang M., Wu C., Chen C. (2013). Drive system design and blade motion analysis of vertical rotary cultivator (立式旋耕机传动系统设计及旋刀运动分析). *Journal of Chinese Agricultural Mechanization*, 34(1), 66–69.

[20] Zhang S., Huang Y., Zhao H., Fu Z., Liu Z., Shi J. (2024). Design and experiment of cutting and throwing combined anti-blocking device for wide-seedbed seeding of wheat (切抛组合式小麦宽幅沟播破茬清秸防堵装置设计与试验). *Transactions of the Chinese Society for Agricultural Machinery*, 55(5), 40–52.

OPTIMIZATION OF ORGANIC FERTILIZER DISTRIBUTION USING EDEM SIMULATION ANALYSIS
/
OPTIMIZAREA DISTRIBUȚIEI ÎNGRĂȘĂMINTELOR ORGANICE UTILIZÂND ANALIZA PRIN SIMULARE EDEM

Vasilica ȘTEFAN[1)], Lucreția POPA[1)], Alin HARABAGIU [*1)], Radu CIUPERCĂ[1)], Ana ZAICA[1)], Alexandra VIȘAN[1)]
[1)] National Institute of Research – Development for Machines and Installations Designed for Agriculture and Food Industry – INMA Bucharest / Romania
Corresponding author: Alin Harabagiu; E-mail: alinhara04@gmail.com
DOI: https://doi.org/10.35633/inmateh-76-102

Keywords: *fertilizer, spreader, EDEM, simulation, optimization*

ABSTRACT
This study investigates the distribution performance of solid organic fertilizers using vertical helical rotor equipment, focusing on the optimization of spreading uniformity. EDEM simulations were employed to analyse the particle flow and distribution patterns under varying rotor speeds (360, 440, and 540 rpm) and inclination angles (75°, 80°, and 85°). The results indicate that the most uniform distribution is achieved at 540 rpm with a 75° rotor inclination. The study was extended to a configuration with four rotors, simulating field-like conditions. Although a good lateral and longitudinal spread was observed, material concentration along the machine's central axis suggests a second pass is needed for complete field coverage. These findings contribute to the design optimization of fertilizer spreading equipment to improve efficiency and application precision.

REZUMAT
Această lucrare investighează performanța de distribuire a îngrășămintelor organice solide utilizând echipamente cu rotoare verticale elicoidale, cu accent pe optimizarea uniformității de împrăștiere. Simulările realizate în EDEM au permis analiza fluxului de particule și a modelului de distribuție în funcție de viteza rotorului (360, 440 și 540 rpm) și unghiul de înclinare (75°, 80° și 85°). Rezultatele au indicat că distribuția cea mai uniformă se obține la 540 rpm și un unghi de 75°. Studiul a fost extins la o configurație cu patru rotoare, simulând condiții reale de lucru. Deși s-a observat o bună extindere a împrăștierii pe direcțiile transversală și longitudinală, concentrarea materialului pe axa centrală a echipamentului sugerează necesitatea unei a doua treceri pentru acoperire completă. Concluziile contribuie la optimizarea proiectării echipamentelor de împrăștiere a îngrășămintelor pentru creșterea eficienței și a preciziei aplicării.

INTRODUCTION
In recent years, there has been a growing recognition of the critical role that solid organic fertilizers play in sustainable agriculture. These fertilizers not only enhance soil fertility and structure but also promote biodiversity and improve water retention, ultimately leading to increased crop yields. Effective distribution of organic fertilizers across soil surfaces is vital for ensuring uniform application, which maximizes their benefits while minimizing environmental impacts *(Dang et al., 2022; Ramadan, 2023; Katchali et al., 2025; Sánchez-Monedero et al., 2019).*

Traditionally, the design of equipment for distributing solid organic fertilizers relied on empirical methods and hands-on experience. However, as agricultural technology advances, the need for precision and efficiency has led to the integration of computational tools in the design process. Software platforms such as EDEM, which utilize discrete element modelling (DEM), allow engineers to simulate and analyse the behaviour of granular materials under various conditions. This parametric modelling provides insights into the dynamics of fertilizer distribution, enabling the optimization of equipment design through precise calculations (*Ou et al, 2025; Xu et al, 2023; Zinkevičienė et. al*, *2021).*

By comparing classical design approaches with modern computational methods, one can observe a significant improvement in both the precision and efficiency of fertilizer application. The parametric modelling offered by EDEM facilitates the identification of optimal parameters for equipment operation, such as flow rates, distribution patterns, and contact forces, which are critical for achieving consistent application rates across varying soil types and terrain *(Debska et al, 2022).*

The integration of advanced modelling software into the design of organic fertilizer distribution systems represents a significant advancement over traditional methods. This synergy of technology and agriculture not only enhances the effectiveness of fertilizer application but also supports sustainable agricultural practices by improving soil health and productivity.

Traditionally, organic manure was distributed manually, which was labour-intensive and time-consuming. To improve efficiency, various types of fertilizer spreaders have been developed across the world, that reduce labour requirements while ensuring uniform application rates. The primary performance criterion for these spreaders is the uniformity of distribution across diverse conditions, which is influenced by the design and functionality of the metering devices used *(Thirion et al., 1997, Liu et al., 2022).*

EDEM software, powered by the Discrete Element Method (DEM), has been effectively utilized in agricultural applications to enhance the distribution of fertilizers and seeds, sowing precision, parameter calibration (*Wenzheng et al., 2018; Du et al.,* 2019; *Yang et al, 2018, Walunj et al, 2023).* Some notable examples are presented below.

According to *Yang et. al,2008,* spreading uniformity is a key factor in evaluating the performance of a fertilizer spreader. The varying size parameters of different fertilizers available on the market - such as average particle mass, particle diameter, and surface roughness - directly influence the uniformity of distribution. Given these differences, achieving optimal design for a variable-rate fertilizer machine equipped with crop sensing, data analysis, and a fertilizer controller is crucial. Using the laboratory's existing disc variable fertilizer applicator as a prototype, their study employs EDEM simulations to model the fertilization process of various commercially available fertilizers and analyses their distribution patterns. This study simulates the spread of potassium chloride, potassium sulphate, and urea using EDEM in a centrifugal disc variable-rate fertilizer applicator. The lateral homogeneity variation coefficients are 43.34%, 26.26%, and 39.21%, respectively. Results indicate that the spreading uniformity does not meet the standard, highlighting the need for further research to enhance machine performance.

Hai Ding et.al (2017) designed a new fertilizer guide device to improve the uniformity of base fertilizer application (Figs. 1, 2). Using EDEM simulations, they analysed factors such as the installation angle of the fertilizer guide groove and the opening angle of shunt components. The simulation results provided valuable insights for optimizing the design parameters, leading to improved fertilizer distribution uniformity.

The fertilizer particles were modelled as spheres. The material density of the fertilizer particles was determined using the following equation.

$$\rho_f = \frac{m_f}{V_f} = \frac{m_f}{\frac{4}{3}\pi\left(\frac{D_f}{2}\right)^3} = \frac{6m_f}{\pi {D_f}^3} \quad (1)$$

where:

ρ_f is the particle density, g/cm^3 ; m_f - particle mass, g; V_f - particle volume, mm^3;

D_f - average particle diameter, mm;

Average particle density ρ_f=1.861 g/cm^3; bulk density of fertilizer particle was 0.982 g/cm^3

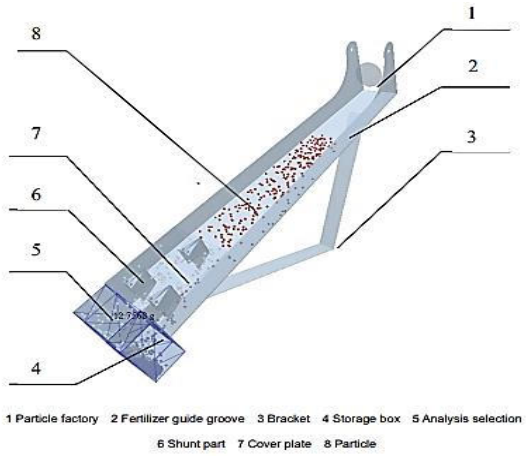


Fig. 1 - EDEM simulation model of fertilizer application

Item	Property	Value
particles	Poisson ratio	0.25
	Shear modulus/ Pa	1.0×107
	density/(kg·m^{-3})	1861
Grooved wheel, housing	Poisson ratio	0.394
	Shear modulus	3.189×10^8
	density/(kg·m^{-3})	1335
particle-particle	Coefficient of restitution	0.6
	Coefficient of static friction	0.4
	Coefficient of kinetic friction	0.01
Particle-grooved wheel, housing	Coefficient of restitution	0.5
	Coefficient of static friction	0.5
	Coefficient of kinetic friction	0.01

Fig. 2 - Pre-treatment parameter setting

Shan et al, (2024), designed a soil compaction mechanism suitable for rice seedbeds and simulated its performance using EDEM - RecurDyn software (Figs. 3, 4). The study verified that integrating an eccentric vibration mechanism with spring support into seedbed levelling machines enhances soil compaction effectiveness. This design ensures compliance with agronomic standards while improving operational performance in modern rice seedling greenhouse systems. Field trials confirmed the model's accuracy, with a relative error of less than 5% between simulated and measured results, thereby demonstrating the effectiveness of the optimized compaction mechanism.

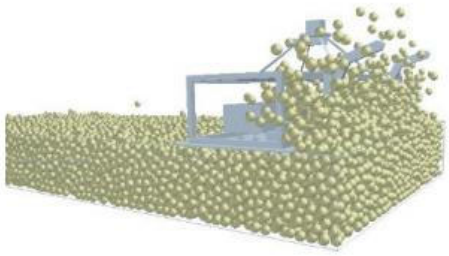


Fig. 3 - Effect of machine forward speed on seedbed

Main Parameters of the Soil Particle Model

Parameter name	Value
Soil particles density [kg/m^3]	2740
Soil particle shear modulus [Pa]	1.55e+08
Soil particle Poisson's ratio	0.29
Coefficient of restitution between soil particles	0.4
Static friction coefficient between soil particles	0.4
Dynamic friction coefficient between soil particles	0.11
Surface energy between soil particles [J/m^2]	0.159
Static friction coefficient between soil and leveling machine	0.5
Soil-Separate Rubbing coefficient between the leveling machines	0.48
Dynamic friction coefficient between soil and leveling machine	0.21

Fig. 4 - Main Parameters of the Soil Particle Model
Shan et al, (2024)

Wang et al., (2022), conducted a study on the seed-filling process in a sugarcane seed-metering device using EDEM simulation. A geometric model of the device, a particle model, and a contact model were established to analyse billet movement and interactions. In their EDEM model, a single-bud billet, originally cylindrical in shape, was approximated using three overlapping spheres to represent its geometry and mass distribution. This particle clustering method effectively maintained the mechanical behaviour of the billet while allowing the simulation to remain computationally feasible. Experimental validation showed a 6.67% relative error in the angle of repose, confirming the accuracy of material parameters. The seed-filling experiment yielded linear correlation coefficients of 0.762 for qualification filling rate S_q and 0.869 for the missed filling rate S_e, verifying the simulation's reliability. Analysis of particle velocity and force revealed two circulation circles in the seed box, with larger circles facilitating billet entry into the rake bar. The findings provide a theoretical basis for optimizing sugarcane billet planter design (Figs. 5-7).

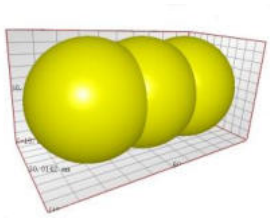


Fig. 5 - Model diagram of single-bud billet

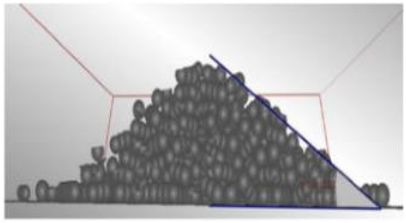


Fig. 6 - Generation of a pile of single-bud billet models for simulation

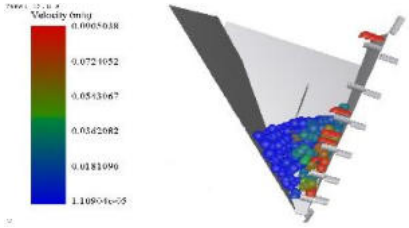


Fig. 7 - Motion simulation results

Dumitru et al. (2024) used EDEM software in order to design and simulate the processes to develop an efficient seed distributor. Using SolidWorks modelling software, the spreader was designed to ensure uniform seed distribution by considering factors such as seed size, distribution speed, and soil type (Fig. 8-9). SolidWorks enabled precise structural analysis and performance evaluation of the distributor components. To validate its efficiency, EDEM software, based on the discrete element method (DEM), was employed to simulate seed movement and interaction with the soil. The simulation provided detailed insights into seed trajectory, fall speed, and distribution patterns. Based on these results, iterative modifications were made in SolidWorks and re-tested in EDEM, allowing for continuous optimization. This iterative approach ensured the distributor met the efficiency and reliability requirements for real-world agricultural applications.

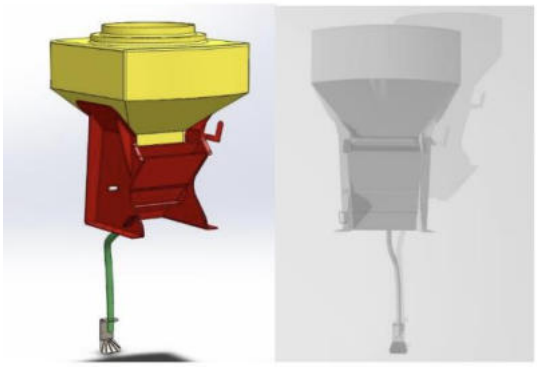


Fig. 8 - Seed distributor with SolidWorks Software

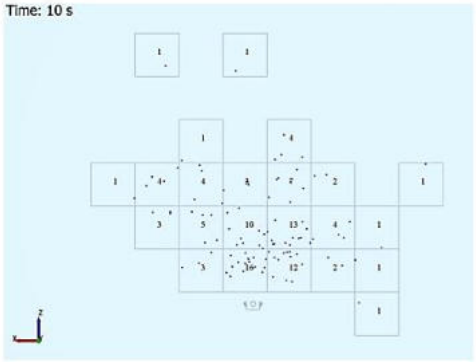


Fig. 9 - 3D Scatter plot for the seeds

MATERIALS AND METHODS

Equipment for distributing solid organic fertilizers with vertical rotors (helical) is among the most widespread and commonly used in agriculture due to their efficiency and versatility. These machines are essential for the effective management of fertilizers, particularly manure and compost, as they allow for uniform and rapid distribution over large areas of land.

The vertical rotor distribution units work by utilizing rotors equipped with helical spirals or blades, which are mounted on a frame and powered by the tractor's power take-off (PTO). These rotors are usually arranged in pairs (two or four), and each rotor rotates in opposite directions - typically one rotor in a counterclockwise direction and the other in a clockwise direction (Fig. 10). This setup helps to fragment and distribute the material over a wide area. At the base of the rotors, there are discs with blades that pick up any material not processed by the helical spirals or that falls from the conveyor.

One of the main characteristics that make these machines so popular is their large working width and ability to distribute material over considerable distances. For example, rotors tilted away from the vertical plane can significantly increase the distribution range, thereby providing wider coverage and reducing the working time. Furthermore, this technology minimizes the risk of clogging or overloading the transmission system, a common issue with other types of fertilizer distributors *(Popa L., 2009; Ștefan et al., 2019).*



a) two vertical rotors HR 250 Model
(https://www.pikrite.com/spreaders/vertical-beaters/#)



b) 4 vertical rotors MG 5 Experimental model
(Popa L, 2009; Ștefan, 2023)

Fig. 10 - Types of machines that use vertical rotors for distributing fertilizers

The rotors work by fragmenting the material and throwing it onto the soil in an even layer, which is crucial for ensuring proper fertilization. Additionally, modern systems allow for the adjustment of the throwing angle, the distribution width, and the distance between the rotors, offering precise control over the distribution process.

Another significant advantage is that the machine's own volume does not significantly affect the usable space on the platform, thus allowing for greater loading capacity. The tilted rotor arrangement also contributes to more efficient fertilizer distribution.

EDEM allows for the simulation of the material flow within the fertilizer spreader. By modelling the behaviour of solid organic fertilizers (which are often irregularly shaped and have different sizes, densities, and moisture contents), it is possible to optimize the distribution pattern. This ensures a uniform spread across the field, which is crucial for effective fertilization, preventing over- or under-application in different areas of the land.

EDEM was employed to conduct a series of simulations aimed at optimizing the uniformity of material distribution on the ground. By utilizing advanced simulation software, the behaviour of particles under varying conditions can be modelled, enabling fine-tuning of the distribution process. Simulations were first conducted using a single distribution rotor, after which the results were scaled up by incorporating four identical rotors across the full width of the machine's hopper. This approach allowed performance assessment of a single rotor before extending the findings to a multi-rotor system, thereby providing a more accurate representation of material distribution across the entire equipment width. In this way, optimal efficiency and uniformity of the distribution process can be ensured under full operational conditions.

For the study of fertilizer distribution on the soil surface by a helical rotor (Fig. 11) arranged in the vertical plane, the following initial data were considered:

- Rotor speed n = 360, 440 and 540 rpm;
- Outer diameter of the helical spiral D_{out}= 0.345 m;
- Inner diameter of the helical spiral d_{in} =0.115 m;
- Pitch of the helical spiral p = 0.3 m;
- Rotor length l = 0.9 m;
- Distance between rotor and soil: h = 1.2 m
- Rotor inclination relative to the vertical axis α = 85°, 80°, and 75°;
- Coefficient of friction with the metal surface μ = 0.5;
- Fertilizer type: compost;
- Simulation time, t=25 s.

The simulations will be conducted in a stationary position and will focus on the quantitative distribution on the soil, under different working conditions, to determine the optimal distribution variant, with distribution uniformity as the main indicator.

Distribution uniformity illustrates how the material is spread across the working width of the machine and along the direction of travel.

Transversal uniformity represents the percentage at which the amount of material reaching the soil remains constant along the direction perpendicular to the machine's travel direction. If the material amounts deposited on the soil per square meter vary significantly from the central area, it is necessary to overlap the boundary zones during adjacent passes of the machine in order to maintain this uniformity.

$$U = \left[1 - \frac{\sqrt{\frac{\sum_{i=1}^{j}(\sigma_i - \sigma_m)^2}{j-1}}}{\sigma_m}\right] \cdot 100 \quad (2)$$

where: U is the distribution uniformity degree across the effective working width, [%];

σ_m– is the average amount of manure falling into a collector along the effective working width, [kg];

σ_i – is the actual amount falling into each collector along the effective working width, [kg];

n – is the number of collectors in each row, placed across the effective working width.

Effective working width is the width where the spreader actually applies fertilizer uniformly to the soil. This is often smaller than the total working width because uniform distribution depends on factors like machine adjustment, operational condition, and field conditions. In many cases, to achieve uniform application, overlapping of adjacent passes is required, which reduces the effective working width compared to the total working width.

In our previous study, a mathematical model was developed to describe the motion of organic fertilizers (manure) during the distribution process, using equations derived from force equilibrium and based on classical mechanics principles *(Ștefan et al., 2018; Ștefan et al., 2019)* The particle trajectory was divided into two distinct phases: movement along the helical rotor surface and subsequent parabolic flight through the air. The model incorporated the relationships between the machine's design parameters and the material properties, providing explicit equations for calculating the time required for the material to reach the soil.

Building upon this theoretical foundation, the current paper advances the analysis by employing discrete element method (DEM) simulations using EDEM software. This approach enables a more detailed and realistic representation of the distribution process, taking into account particle interactions and the variability in particle size, shape, and moisture content.

Fig. 11 shows the model of the organic fertilizer spreader rotor designed in SolidWorks, similar with its version in STL format, ready to be imported into the EDEM by Altair simulation software. For the simulation, a type of material (compost) was selected to be imported into the software. The rotor dimensions were proposed based on research into existing market solutions for distribution equipment.

Table 1 contains the values of the physical parameters necessary for DEM (Discrete Element Method) simulations in the EDEM software taken from literature for similar material type *(Han et. al, 2023; Yu et al., 2020)*. These parameters define the behaviour of the materials involved - especially steel and particles - within the simulations, including the interactions between particles and between particles and steel surfaces. The material selected for simulations is compost, with the properties mentioned above. The particles are spherical in shape, with a diameter ranging between 5 and 10 mm. The EDEM software was configured to randomly distribute particles within this range, meaning that the initial positions of the particles were assigned without a predefined pattern, adhering only to the imposed boundaries (Fig. 12).

In the present simulation, organic fertilizer particles were approximated as spheres, primarily due to computational limitations and the current capabilities of EDEM software. This method is commonly used in preliminary design studies *(Yang et al., 2018; Wang et al., 2022),* with the aim of identifying trends rather than achieving precise replication of physical experiments. This simplification is a widely accepted approach in discrete element modelling (DEM), particularly for simulations requiring large particle counts and efficient computation.

To simulate the cohesive behaviour of moist organic fertilizer (compost), the default contact model in EDEM was replaced with the Hertz-Mindlin with JKR contact model. This advanced model accounts for particle adhesion through surface energy, allowing particles to stick together and form clusters, which more accurately represents the real flow behaviour of compost.

Mathematically, the normal force F_n includes both elastic deformation and adhesive pull-off forces:

$$F_n = \frac{4}{3}E^*\sqrt{R^*}\delta^{3/2} - 3\pi\gamma R^* \quad (3)$$

where:

E^* is the equivalent Young's modulus;

R^* is the effective radius;

δ is the overlap;

γ is the surface energy.

The tangential force F_t is limited by friction:

$$F_t \leq \mu F_n \quad (4)$$

In the simulation, this model allowed the particles to behave more like wet compost, leading to more realistic spreading patterns, better cluster formation, and improved correlation with observed field behaviour. By adjusting parameters such as surface energy, Poisson's ratio, and shear modulus, the simulation was calibrated to match the expected compost flow characteristics.

The horizontal axis *(X)* represents the particle diameter, ranging from 0 to 10 cm, indicating that the simulated particles were generated with sizes distributed within this interval.

The vertical axis *(Y)* represents the number of particles corresponding to each diameter range.

The graph shows a decreasing distribution, suggesting that smaller particles are more numerous, while larger particles are less frequent. This type of distribution is commonly observed in granular material handling processes, where finer particles tend to be present in greater numbers compared to coarser ones.

Such a distribution can significantly influence material behaviour in the simulation, affecting phenomena such as granular flow, compaction, or particle segregation.

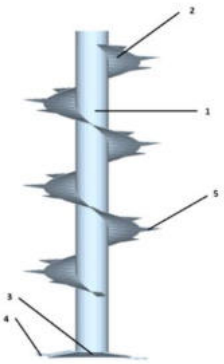


Fig. 11 - Rotor vertical helicoidal (SolidWorks)
1. shaft, 2. helical spiral, 3. disc, 4. spreader blade, 5. cutting knife

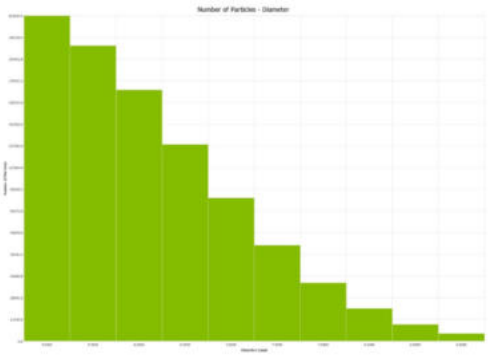


Fig. 12 – Particle size distribution

Table 1

Parameters required for EDEM simulation

EDEM Parameters	Materials	Value	Materials	Value
Density (kg·m^{-3})	Steel	7850 *(Han et al., 2023; You et al, 2020)*	Compost	550 *(You et al, 2020)*
Poisson's ratio	Steel	0.3 *(Han et al., 2023; You et al, 2020)*	Compost	0.5 *(Yu et al, 2020)*
Shear modulus (Pa)	Steel	7.9x10^{10} *(Han et al., 2023; You et al, 2020)*	Compost	1x10^{6} *(Yu et al, 2020)*
Coefficient of restitution	Compost-Steel	0.1 *(Yu et al, 2020)*	Compost - Compost	0.1 *(Yu et al, 2020)*
Coefficient of static friction	Compost - Steel	0.59 *(Yu et al, 2020)*	Compost - Compost	0.2 *(Yu et al, 2020)*
Coefficient of rolling friction	Compost - Steel	0.04 *(Yu et al, 2020)*	Compost - Compost	0.5 *(Yu et al, 2020)*
Surface energy (J m^{-2})			Compost - Compost	3.5 *(Yu et al, 2020)*

In the creator tree presented in Fig.13, a *15 x 15 m* polygon is used to model the soil which serves as the primary environment where the fertilizer will be dispersed. This polygon outlines the boundaries of the soil area, providing a clear visual representation of the terrain in which the simulation occurs.

For modelling the compost factory, a box is created (Fig.14). The box dimension is *L x l x h* = 2.3 x 0.5 x 1.15 m. The box is then filled with material (particles) for a more realistic and accurate representation (Fig.15).

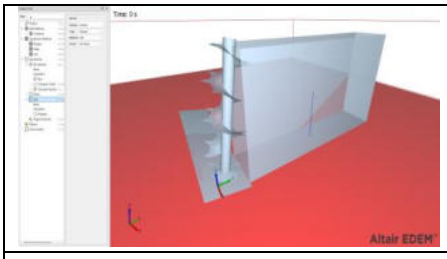


Fig. 13 - Soil area representation

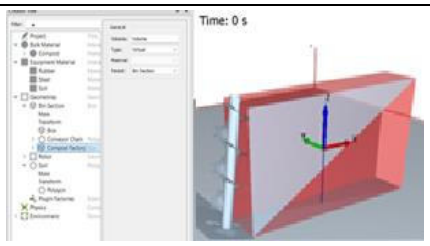


Fig. 14 - Compost factory (box)

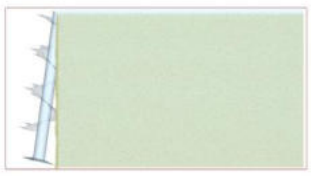
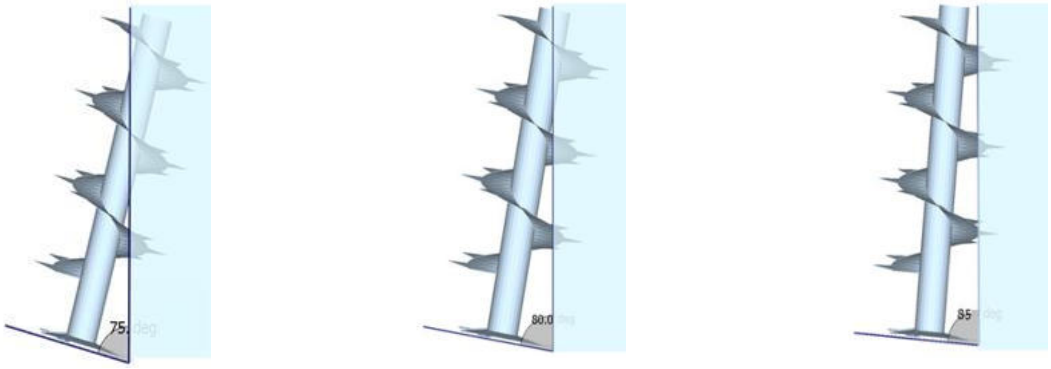


Fig. 15 – Box filled with compost particles

Additionally, another polygon is created to represent the conveyor chain inside the trailer. To enhance realism, a sinusoidal translation is applied to this polygon, simulating the movement of the conveyor system. These polygons are essential for defining the spatial elements of the simulation and ensuring a more accurate representation of material distribution. Once these components are in place, the simulation is initiated, allowing for a detailed visualization of the material flow and its dispersion over the soil. For the simulations, the chain speed is considered 0.006 m/s.

The rotor is positioned at different angles between vertical axis and rotor base (Fig. 16), which plays a critical role in directing the material as it makes contact with the rotor blade. This angle helps ensure that the manure is efficiently distributed across the soil surface by optimizing their trajectory after collision, promoting a more uniform spread. The 75º, 80º and 85º inclinations are specifically chosen to balance the forces acting on the particles during impact, minimizing bounce or clumping and enhancing overall spreading efficiency.



a) 75° inclination angle *b) 80° inclination angle* *c) 85° inclination angle*

Fig. 16 – Rotor inclination relative to the vertical axis

RESULTS

In this section, the results of a 3D scatter plot representing the spatial distribution of material within the defined area are presented. A detailed quantitative analysis has been conducted, focusing on several key aspects: density analysis, variance in material distribution, hotspot identification, and standard deviation.

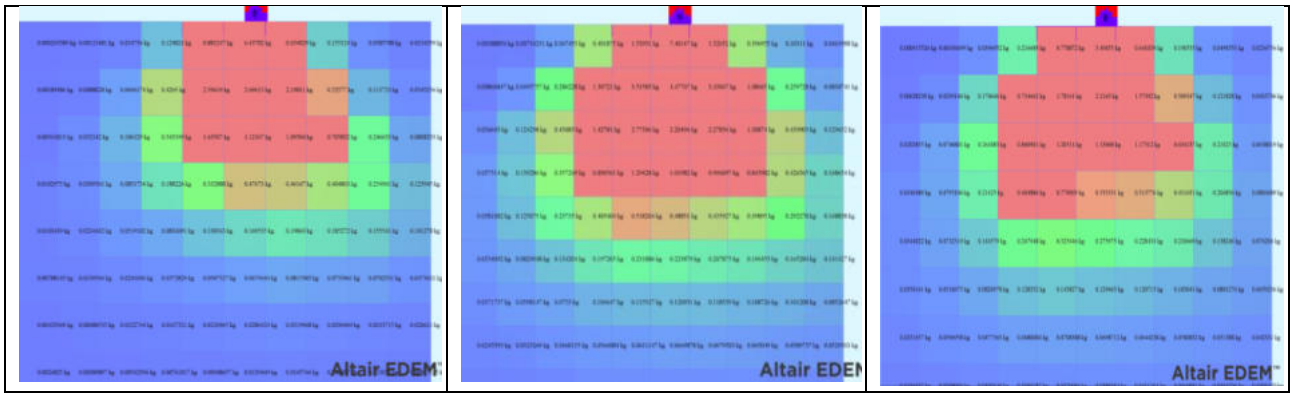
The scatter plot is divided in sections of *1 x 1 m* for an easier interpretation.

A quantitative analysis was performed using a 3D scatter plot of material distribution, generated with EDEM software. The 3D material deposition data was converted into a simplified 2D grid format, as shown, where each cell represents the amount of manure deposited in the corresponding area. This visualization helps assess the uniformity of the spreading process and identify potential areas of over- or under-application.

Figure 17 c) presents a grid-based visualization of material distribution, where each square represents a specific area and the amount of material deposited within it. The colour gradient transitions from red (high accumulation) to blue (low accumulation), illustrating the spreading efficiency. The central region remains the most concentrated, while the periphery shows a sparser distribution, meanwhile material accumulation on the soil happens further from the release point.

In Fig. 17 (a) and (b), the highest material concentration appears in the central region of the distribution area, the colour gradient shifts from red (high accumulation) to blue (low accumulation), which signifies the greatest deposited mass per grid cell. The distribution pattern suggests a localized accumulation near the release point, gradually decreasing outward.

Compared to Figs. 17 (a) and (b), which show significant material buildup near the release point, fig. 17 (c) represents a more favourable distribution. Large accumulations near the rotor are reduced, and the material is spread more evenly over a greater distance. This improved dispersion enhances uniformity and minimizes excessive deposition in the immediate vicinity of the rotor.



a) inclination 80° for 360 rpm *b) inclination 80° for 440 rpm* *c) inclination 80° for 540 rpm*

Fig. 17 - Material distribution patterns

The images provided depict the manure distribution results using a spreading system with rotors set at an 80-degree angle while operating at three different rotational speeds: 360 rpm, 440 rpm, and 540 rpm. Each image represents the distribution pattern through a color-coded grid, where higher concentrations of manure appear in red, while lower deposition areas transition into green and blue shades. By analysing these patterns, it can be determined how effectively each rotational speed disperses the manure across the field.

At 360 RPM, the first image shows a highly concentrated manure distribution in the central region, with a significant buildup of material in the middle of the spread area. The outer sections receive considerably less manure, indicating a less uniform spreading pattern. The deposition appears asymmetrical, with much of the material failing to disperse widely, suggesting that at this lower speed, the spreading system struggles to distribute manure effectively across a larger surface area. This results in an uneven application, which could lead to over-fertilization in some areas while leaving others under-treated.

Increasing the speed to 440 rpm, as shown in the second image, results in a more balanced distribution compared to the 360 rpm setting. The accumulation in the centre is still present but appears less pronounced, with the spread extending further outward. The manure is dispersed more evenly, covering a broader area with a smoother transition in concentration. While there is still some central buildup, the overall pattern suggests improved field coverage, reducing the risk of excessive material being deposited in one location while ensuring more consistent application across the spread zone.

The final image, representing the highest speed of 540 rpm, demonstrates the most effective manure distribution. The central accumulation is significantly reduced, and the material is spread much more uniformly across the field. The colour gradient transitions more gradually, indicating that manure is distributed more consistently rather than being concentrated in a single area. The spread reaches its widest extent in this scenario, covering a larger portion of the field and achieving a more optimal application. This suggests that operating at a higher rotational speed allows for better manure dispersion, minimizing uneven patches and promoting a more efficient fertilization process.

Although the simulation was carried out under stationary conditions, the results can be used to estimate the distribution in dynamic operation, assuming that the material is discharged uniformly over time and that the machine's movement merely shifts this distribution spatially. Thus, by temporally overlapping the values along the direction of travel, a realistic estimation of the field spreading pattern is obtained.

In each case (for each rotor speed), the behaviour of the particles was simulated in a setup where the machine remained stationary while the rotors were active. The space around the machine was divided into transverse sectors, and the mass of particles collected in each sector was recorded.

The collected data were summed column-wise (along the longitudinal axis) to simulate the equivalent behaviour of the machine moving at a constant speed of 1 m/s. This approach allows the transformation of the stationary distribution into a distributed band model, similar to what would be observed in actual field conditions.

The resulting distribution for each simulation was represented in Fig. 18, where:

- the *X*-axis corresponds to the lateral distance from the machine's central axis,
- the *Y*-axis indicates the relative amount of material distributed across each transverse band.

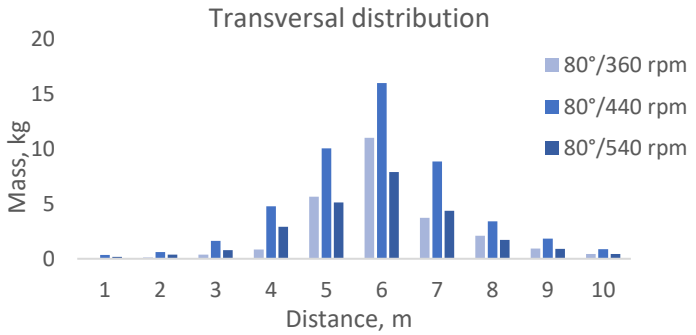


Fig. 18 - Transversal distribution at different rotational speeds

From these results, it is evident that 540 rpm offers the best overall distribution, as it reduces central buildup while increasing uniformity across the entire spread area. In contrast, 360 rpm leads to a highly concentrated and inefficient distribution, while 440 rpm shows some improvement but still does not achieve the same level of coverage as the highest speed. Therefore, for optimal manure spreading with rotors set at an angle of 80°, using 540 rpm is the most effective choice, ensuring a more even and efficient application across the field.

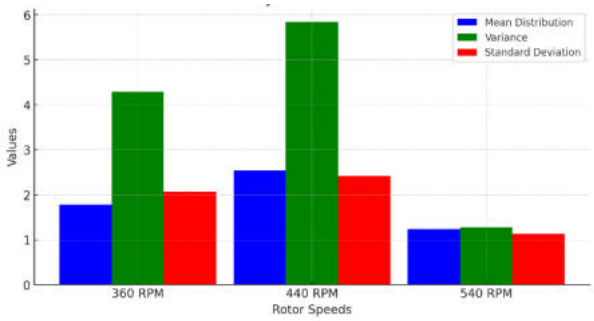
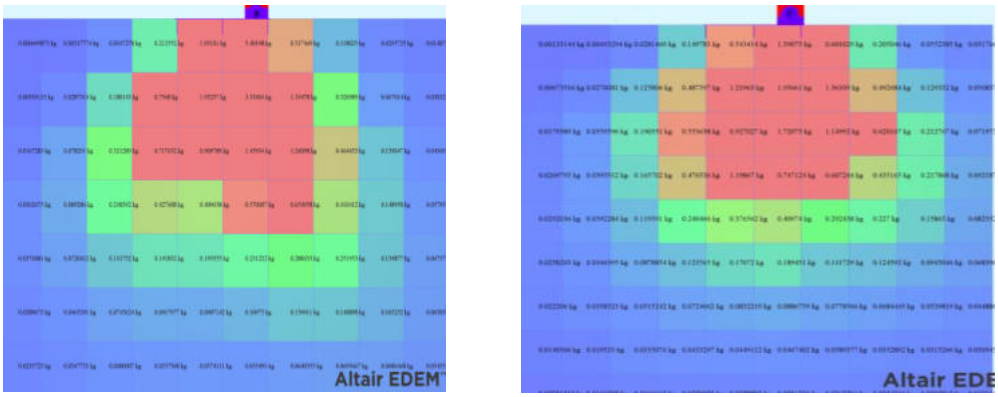


Fig. 19 – Statistical analysis of compost distribution

A statistical analysis of manure distribution at different rotor speeds (360 rpm, 440 rpm, and 540 rpm) is given in Fig. 19. The blue bars indicate the mean distribution, showing the average spread of manure at each speed. The green bars represent variance, which measures how much the distribution varies from the mean. The red bars depict the standard deviation, illustrating the extent of deviation from the average spread. The data suggests that at 440 rpm, there is the highest variance and standard deviation, indicating an uneven spread. In contrast, 540 rpm achieves a more uniform spread, making it the best choice for consistency.

Given that 540 rpm provided the most consistent material distribution with the lowest variance and standard deviation, two additional simulations were conducted where the rotor angle was modified to assess its impact on spreading performance. Adjusting the rotor angle was intended to further optimize both the coverage and uniformity of manure distribution. The simulations enabled analysis of whether slight variations in rotor inclination could improve efficiency or introduce new variations in the spreading pattern. The results from these additional tests, shown in Fig. 20 a) and b), help determine the optimal combination of speed and angle for the most effective manure distribution.



a) 75-degree, 540 RPM *b) 85-degree ,540 RPM*

Fig. 20 - Compost distribution at 540 RPM

The conclusion drawn from the additional simulations highlighted the significant impact of the rotor angle on manure distribution. By comparing the different angle settings, it was observed that minor adjustments in rotor inclination had notable effects on coverage and uniformity. However, the 75° angle setting demonstrated the best balance between coverage and uniformity, providing a more even distribution and broader coverage compared to the other angles tested. In conclusion, choosing a 75° angle in combination with a speed of 540 RPM represents the optimal solution for ensuring an efficient and uniform manure distribution, maximizing equipment performance in terms of both coverage and variability.

Following the stationary simulations, the results were extrapolated to estimate the distribution in dynamic operation at a speed of 1 m/s. It was found that at 75° inclination, the distribution was the most uniform, with no significant peaks in the central area, ensuring a more consistent spread of material during dynamic operation. This adjustment helped reduce the central concentration of particles, which is commonly observed at lower inclination angles.

The obtained results of the distributions at different rotor inclination angles are shown in Fig. 21, confirming that the 75° provided the most optimal spreading pattern.

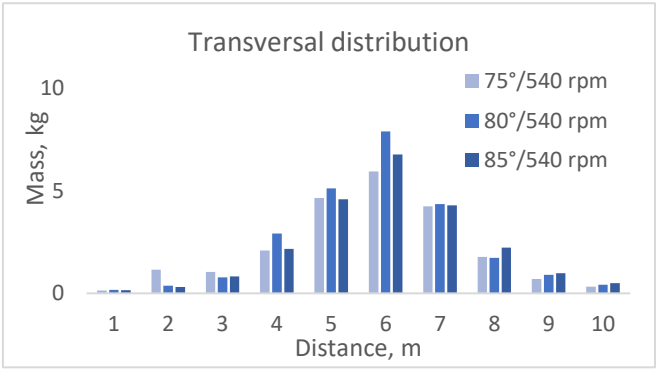


Fig. 21 - Transversal distribution at different inclination angles

The simulations were performed over a period of 25 seconds under stationary conditions. However, in reality, the material flow rate is much lower when the machine is in motion. The simulations primarily provide insight into the profile of the distribution curve but do not necessarily represent the actual quantities of material being spread.

The quantities of fertilizer distributed on the soil can be adjusted based on the machine's working speed. Specifically, as the machine moves slower, a greater quantity of fertilizer is deposited per unit area, since the material has more time to spread across the field. Conversely, when the machine moves at a higher speed, the amount of solid fertilizer reaching the soil decreases, as the material is spread over a larger area in a shorter time.

This relationship between the machine speed and the quantity of material distributed is essential for real-world applications. By controlling the working speed of the machine, it is possible to achieve the desired amount of fertilizer applied to the field, optimizing the application rate for different soil types and conditions.

After determining the optimal parameters for a single rotor, the performance of a fertilizer distributor equipped with four vertical rotors, spaced 0.5 m apart, was simulated. The width of the hopper in this design is 2 meters, which corresponds to the average width of an agricultural trailer. The direction of rotation of the four rotors, each inclined at 75° relative to the horizontal axis, directed towards the interior of the machine, is shown in Fig. 22 (two rotors rotate to the left and two to the right).

The optimal distribution identified previously should have a uniform profile, with a smooth transition between areas of high and low particle concentration.

For the machine with four rotors, a high concentration of particles is observed along the central axis of the equipment, indicating an overlap of the material flow streams.

A noticeable expansion of the particle distribution occurs both transversely and longitudinally, which is beneficial as it results in wider coverage of the area (Figs. 23, 24). The area covered by the machine is increased. Transversely, the coverage extends from 7 meters to 15 meters, and longitudinally, it ranges from 10 meters to 15 meters. This expansion of the covered area further enhances the uniformity of fertilizer distribution across the field. Even the maximum spreading width increases very much, the actual effective working width is about 5 m. The transversal spreading uniformity reported to the effective width, is about 88%.

To further uniformize the lateral zones, a second pass is necessary to achieve an overlap of the material deposited on the ground, ensuring a more even spread of fertilizer.

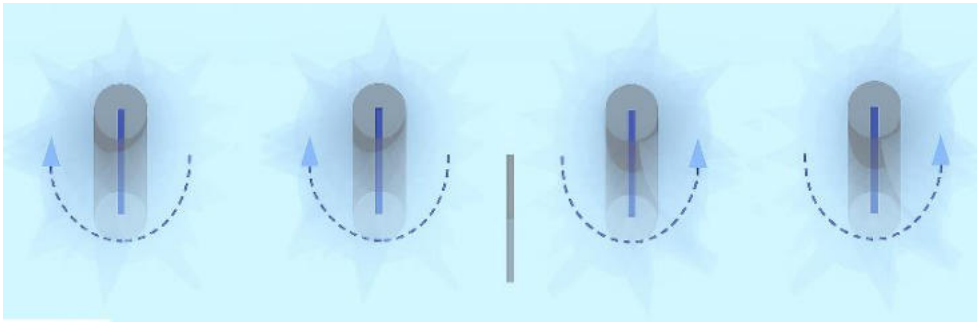


Fig. 22 – Direction of rotor rotational speed

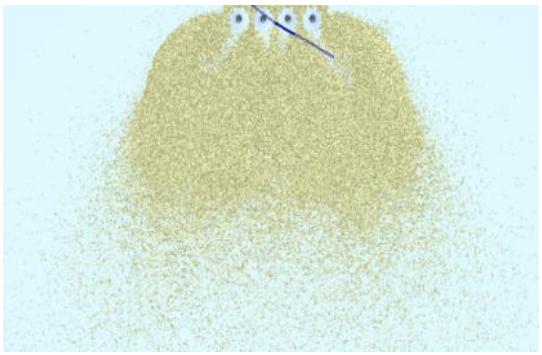


Fig. 23 - Particle distribution – top view

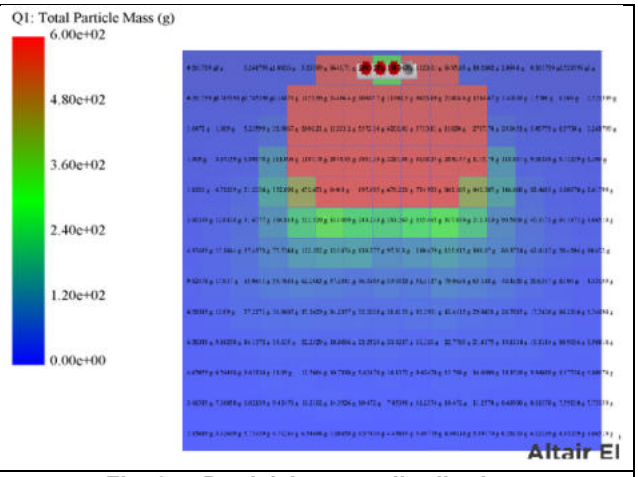


Fig. 24 - Particle's mass distribution

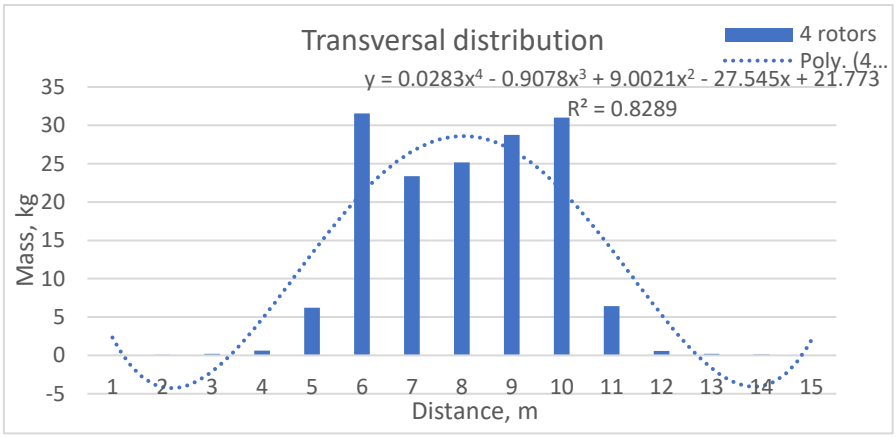


Fig. 25 – Simulated transversal distribution

It is important to emphasize that a four-rotor system not only ensures a wider working width and a more uniform coverage (Fig. 25) but also offers a significant advantage in fragmenting the organic fertilizer (manure). With four rotors, the material is broken down more effectively, allowing for better dispersion and finer fragmentation, which is crucial for proper incorporation into the soil. Therefore, using four rotors is recommended not just for achieving an even distribution but also for improving the quality of material processing, which enhances fertilizer efficiency.

To further uniformize the lateral zones, a second pass is necessary to achieve an overlap of the material deposited on the ground, ensuring a more even spread of fertilizer.

CONCLUSIONS

The integration of EDEM software into the design process of fertilizer spreaders demonstrated a significant improvement in application precision and efficiency, with parametric modelling facilitating the identification of optimal operating parameters. Detailed analysis of fertilizer distribution at different rotor rotation speeds showed that while 360 rpm resulted in a highly concentrated and inefficient distribution, and 440 rpm showed some improvement but with suboptimal uniformity, 540 rpm offered the most efficient and uniform distribution, significantly reducing central accumulation and ensuring a more consistent spread over a larger area.

At 540 rpm, additional simulations revealed that a 75° angle provided the best balance between coverage and uniformity, minimizing excessive concentrations in the central area.

Although simulations were performed under stationary conditions, the results can be extrapolated to estimate distribution in dynamic operation (at a speed of 1 m/s), indicating that a 75° inclination ensures the most uniform distribution during movement. It was also confirmed that the machine's working speed directly influences the quantity of fertilizer deposited per unit area: a lower speed allows for the deposition of a larger quantity, while a higher speed reduces the quantity per unit area. Simulating a distribution system with four vertical rotors (inclined at 75°, spaced 0.5 meters apart) indicated a significant increase in working width and more uniform coverage (extension from 7 to 15 meters transversely and 10 to 15 meters longitudinally).

Furthermore, a four-rotor system contributes to more efficient fragmentation of organic fertilizer, ensuring finer dispersion and optimal incorporation into the soil, thereby maximizing fertilization efficiency. To further uniformize the lateral zones and ensure a more consistent spread of fertilizer on the ground, a second pass of the machine is necessary to achieve an overlap of the deposited material.

In conclusion, the use of EDEM simulations allowed for the optimization of key parameters for the design and operation of organic fertilizer distribution equipment. It was established that a rotation speed of 540 rpm and a rotor inclination angle of 75°, combined with a four-rotor system, represent the optimal configuration for efficient, uniform distribution and superior material fragmentation, essential for improving soil health and agricultural productivity.

REFERENCES

[1] Dang, Y., Ma, H., Wang, J., Zhou, Z., Xu, Z. (2022). An improved multi-objective optimization decision method using NSGA-III for a bivariate precision fertilizer applicator. *Agriculture*, *12*(9), 1492. https://doi.org/10.3390/agriculture12091492

[2] Debska B., Kotwica K., Banach-Szott M., Spychaj-Fabisiak E., Tobiašová E. (2022). Soil fertility improvement and carbon sequestration through exogenous organic matter and biostimulant application. *Agriculture*, *12*(9), 1478. https://doi.org/10.3390/agriculture12091478

[3] Du Y., Cui T., Zhang D., Wei Y., Yang R., Wu H.(2019). Establishment and Parameter Calibration of Broad Bean Seeds Simulation Particles in EDEM. In *2019 ASABE Annual International Meeting; American Society of Agricultural and Biological Engineers*: St. Joseph, MI, USA; Volume 1.

[4] Dumitru D.N., Marin E., Gheorghe G.V., Manea D., Mateescu M., Anghelache D.N., Prisacariu E., Harabagiu A. (2024). Integration of EDEM by Altair simulations for efficient distribution of large and small seeds in agricultural systems of vineyards and fruit trees, *INMATEH - Agricultural Engineering*, 74(3), DOI: https://doi.org/10.35633/inmateh-74-66

[5] Hai D., Xiaofei A, Guangwei W., Liwei L., Qingzhen Z. (2017). Optimization and Simulation of Fertilizer Guide Device Parameters Based on EDEM Software. *11th International Conference on Computer and Computing Technologies in Agriculture (CCTA)*, pp.377-388

[6] Han, S., Li, Y., Zhou, X., Kan, Z., Meng, H., & Qi, J. (2023). DEM Simulation and Experimental Validation of the Performance of an Orchard Deep Applicator for Manure. *Applied Sciences*, *13*(6), 3709. https://doi.org/10.3390/app13063709

[7] Katchali M., Richard E., Tonnang H.E.Z., Tanga C.M., Beesigamukama D. And Senagi, K. (2025). Mathematical and computational modeling for organic and insect frass fertilizer production: a systematic review. *Plos One*, 20(1)

[8] Landry H., Thirion F., Laguë C., Roberge M. (2006). Numerical modeling of the flow of organic fertilizers in land application equipment, *Computers and Electronics in Agriculture,* 51(1-2), 35-53. https://doi.org/10.1016/j.compag.2005.11.001

[9] Liu M., Wu Y., Huang S., Yang Y., Li Y., Wang L., Xi Y., Zhang J., Chen Q. (2022). Effects of organic fertilization rates on surface water nitrogen and phosphorus concentrations in paddy fields. *Agriculture*, *12*(9), 1466. https://doi.org/10.3390/agriculture12091466

[10] Ou M., Wang G., Lu Y., Zhang Z., Pan H., Jia W., Dong X. (2025). Structure optimization and performance compaction device of seedbed leveling machine *INMATEH - Agricultural Engineering*, 74(3), 42-56

[11] Popa L. (2009). Development of the ecological fertilisation technologies by implementing a new manure spreader. *Environmental Engineering and Management Journal.* Vol. 8, Issue 1, pp.146-146

[12] Ștefan V., Cârdei P., Vlăduț N.V., Popa L., Ciupercă R., Ungureanu N. (2018). Mathematical model for particle motion applied on a manure spreading apparatus used in environmentally friendly technology. *Environmental Engineering and Management Journal*, Gheorghe Asachi Technical University, Iași, 17, 217-227

[13] Ștefan V., Cârdei P., Popa L., David L., Ciupercă R. (2019). Influence of the manure spreading machines' working parameters on the qualitative performances of the fertilization process, *INMATEH Agricultural Engineering,* 58 (2), 115-120, DOI: https://doi.org/10.35633/inmateh-58-12

[14] Ștefan V., *Distribution of organic fertilizers on soil. (2023).* Printech Publishing House, Bucharest

[15] Thirion F., Chabot F., Andler D. (1997). Physical characterization of animal manure, *98-FAO:8th,* pp. 457-468

[16] Xu B., Cui Q., Zheng D. (2023). Improvement design and simulation analysis on centrifugal disc organic fertilizer spreader. *INMATEH Agricultural Engineering*, Vol. 70, 328–336. https://doi.org/10.35633/inmateh-70-32

[17] Yang L., Chen L., Zhang J., Liu H, Sun Z., Sun H., Zheng L. (2018). Fertilizer sowing simulation of a variable-rate fertilizer applicator based on EDEM, *IFAC-PapersOnLine*, 51(17), 418-423, DOI: https://doi.org/10.1016/j.ifacol.2018.08.185.

[18] Yu W., Liu R., Yang W. (2020). Parameter Calibration of Pig Manure with Discrete Element Method Based on JKR Contact Model.*AgriEngineering*, 2, 367–377. doi:10.3390/agriengineering2030025

[19] Walunj A., Chen Y., Tian Y., Zeng Z. (2023). Modeling soil–plant–machine dynamics using discrete element method: A Review. *Agronomy*, *13*(5), 1260. https://doi.org/10.3390/agronomy13051260

[20] Wang M, Liu Q, Ou Y, Zou X. (2022). Numerical Simulation and Verification of Seed-Filling Performance of Single-Bud Billet Sugarcane Seed-Metering Device Based on EDEM. *Agriculture.* 12(7): 983. https://doi.org/10.3390/agriculture12070983

[21] Wenzheng L., Jin H., Hongwen L., Xueqiang L.I., Kan Z.H., Zhongcai W.E. (2018). Calibration of simulation parameters for potato minituber based on EDEM. *Trans. Chin. Soc. Agric.* 49, 125–135.

[22] Zinkevičienė R., Jotautienė E., Juostas A., Comparetti A., Vaiciukevičius, E. (2021). Simulation of granular organic fertilizer application by centrifugal spreader. *Agronomy*, 11(2), 247. https://doi.org/10.3390/agronomy11020247

[23] *** https://www.pikrite.com/spreaders/vertical-beaters/#

PARAMETER OPTIMIZATION AND EXPERIMENT OF A SINGLE LONGITUDINAL AXIAL FLOW FULL-CIRCUMFERENCE SEPARATION THRESHING DEVICE FOR RAPESEED HARVESTER

/

油菜收割机单纵轴流全周分离脱粒装置参数优化与试验

Min ZHANG, Chenke XU, Chengpeng LI, Gang WANG, Yao YANG, Tao JIANG
Nanjing Institute of Agricultural Mechanization, Ministry of Agriculture and Rural Affairs of China, Nanjing 210014, China
Tel: +86.15366092917; E-mail: zhm0912@126.com
DOI: https://doi.org/10.35633/inmateh-76-103

Keywords: *rapeseed, combine harvester, threshing device, EDEM, parameter optimization*

ABSTRACT

A discrete element model (DEM) of rapeseed threshing and separation was established based on EDEM software. The simulation results were compared with bench test data, showing an absolute error of 0.33% and a relative error of 55% for threshing loss. The relative errors for the proportion of threshed material on the sieve surface and the left–right distribution ratio of threshed material on the sieve surface were 1.21% and 2.38%, respectively, verifying the accuracy of the simulation model. Secondly, a three-factor, three-level Box–Behnken experimental design was conducted, with threshing drum speed, guide plate angle, and threshing gap as test factors, and threshing loss, proportion of threshed material on the sieve surface, and left–right distribution ratio of the threshed material as evaluation indicators. The influence of each factor on the evaluation indicators was analyzed, and regression models between the test factors and evaluation indicators were established. Through a multi-objective optimization solution, combined with consideration of the actual operating conditions and processing requirements of the rapeseed combine harvester, the optimal parameter combination was determined as: drum speed of 550 r/min, guide plate angle of 75°, and threshing gap of 8 mm. Finally, a prototype was developed based on the optimized structure and operating parameters, and its rapeseed harvesting performance was tested by a third-party inspection agency. Field tests showed a total harvest loss rate of 5.6%, impurity rate of 2.3%, breakage rate of 0.4%, and an operational productivity of 0.57 hm²/h. The performance exceeded the requirements of industry standards. This study provides a valuable reference for the performance optimization of threshing devices.

摘要

基于 EDEM 软件构建了油菜脱粒分离离散元模型，仿真结果和台架对比试验表明，脱粒损失绝对误差为 0.33%，相对误差为 55%，筛面脱出物占比和筛面脱出物左右比值的相对误差分别为 1.21%和 2.38%，验证了仿真模型的准确新。以脱粒滚筒转速、导草板角度和脱粒间隙为试验因素，以脱粒损失、筛面脱出物占比和筛面脱出物左右分布比值为评价指标，开展了三因素三水平 Box-Behnken 试验，分析了各因素对评价指标的影响关系，建立了试验因素与评价指标之间的回归数学模型，通过多目标优化求解，结合油菜联合收割机实际工况和加工要求，确定优化后的参参数组合为：滚筒转速 550 r/min，导草板角度 75°，脱粒间隙 8 mm。在最优结构和工作参数下，试制了样机并委托第三方检测机构对油菜收获作业性能进行了检测，田间实测收获总损失率 5.6%、含杂率 2.3%、破碎率 0.4%，作业小时生产率 0.57hm²/h，作业性能优于行业标准要求。该研究可为脱粒装置性能优化提供参考。

INTRODUCTION

The threshing device is the core working component of a rapeseed combine harvester. Based on its configuration, it can be categorized into transverse axial–flow and longitudinal axial-flow types. When the device is arranged transversely, the threshing and separation capacity is limited by the horizontal length of the threshing drum. In contrast, a longitudinal configuration allows for unrestricted drum length, offering advantages such as higher efficiency and better economic performance (*Yang et al., 2018; Tang et al., 2013*). However, longitudinal axial-flow threshing devices also face challenges such as excessive stalk breakage due to delayed separation of threshed material, a high proportion of threshed material that increases the cleaning load, and low utilization of the sieve surface.

To enhance the processing capacity and cleaning efficiency of threshing devices, internationally renowned combine harvester manufacturers such as John Deere, CLAAS, and Geringhoff have developed advanced threshing systems, including tangential–axial flow combination types and dual axial-flow threshing and separation drums. These multi-drum configurations increase the threshing path and separation area, improving material throughput and screen penetration (*Dong et al., 2023; Teng et al., 2020; Mirzazadeh et al. 2012; Yuan et al., 2024*). Additionally, features such as segmented sieve boxes, material guide plates, and intelligent control technologies that adjust the vibration state of the cleaning sieve help achieve more uniform material distribution on the sieve surface, thereby improving post-threshing cleaning performance. However, these systems also present challenges, including structural complexity and large overall geometry, making them suitable only for large scale harvesters (*Xu et al., 2011; Qian et al., 2017; Yang et al., 2010*). Miu et al. developed a variable diameter threshing device that adjusts the threshing gap by changing the drum diameter during operation. This allows for the regulation of threshing intensity at different stages, thereby reducing grain damage and breakage of threshed material (*Miu et al., 2007; Wang et al., 2020; Trollope et al., 1982; Tang et al., 2012*). *Xu et al.* (*2020*) designed a combined tangential–axial flow double-drum threshing device for rapeseed, where easily threshed parts undergo preliminary threshing, and the more difficult parts enter a longitudinal axial-flow threshing drum (*Xu et al., 2014; Wu et al., 2024; Fang et al., 2024)*. This design reduces threshing damage, decreases the frequency of threshed material impact, and improves both threshing and cleaning efficiency. The above studies indicate that increasing the separation area of the threshing device, accelerating the separation of threshed material *(Fu et al., 2024; Yang et al., 2024; Dai et al., 2022; Jiang et al., 2023)*, reducing the frequency of threshed material impact, and minimizing material fragmentation and the proportion of threshed material can not only enhance the performance of the threshing device but also contribute to improving the cleaning efficiency in the subsequent cleaning process.

Our team previously designed a single longitudinal axial–flow full–circle separation threshing device for rapeseed harvesting by increasing the separation area of the threshing device and employing a concave screen that rotates counter to the threshing drum to enhance rubbing and reduce material impact intensity. Preliminary tests were conducted using evaluation indicators such as the left–right distribution of threshed material on the sieve surface and the left–right distribution ratio of threshed material. Key parameters such as drum speed, guide plate angle, and threshing gap were analyzed to identify the main factors affecting threshing and separation performance and to determine the optimal parameter combination, and experimental verification was carried out.

MATERIALS AND METHODS

STRUCTURE AND WORKING PRINCIPLE OF THE THRESHING DEVICE

The structure of the single longitudinal axial-flow full-circle separation threshing device for rapeseed combine harvesters is shown in Figure 1. It mainly consists of a spiral conveyor, a rasp bar–spike tooth threshing drum, a full-circle separation concave screen, a guide plate, and a transmission system. The threshing drum rotates driven by the main engine of the combine harvester, while the concave screen is driven by the sprocket reducer to rotate in the opposite direction relative to the threshing drum. The working principle of this threshing device is as follows: material is fed into the threshing device by the spiral conveyor. Through the rotation of the threshing drum and the reverse rotation of the concave screen, the rapeseed material is subjected to impact and rubbing actions from the threshing components. This causes stalks to break and the grains to separate from the pod shells. Short stalks, residues, and grains pass through the concave screen and fall downward, while long stalks and large impurities are discharged from the rear end of the threshing device.

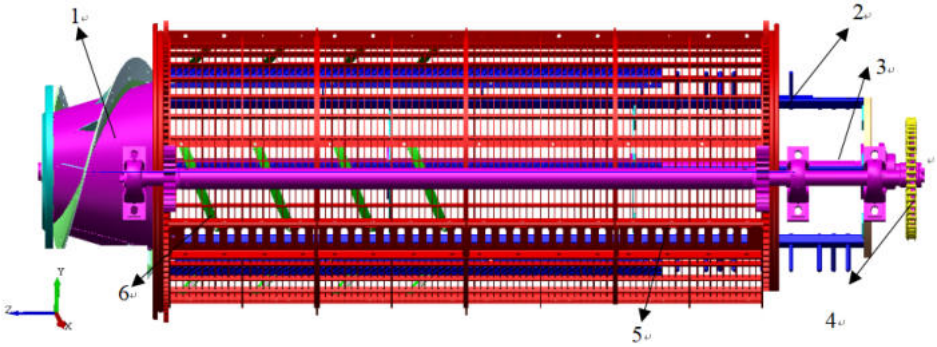


Fig. 1 - Single Longitudinal Axial-Flow Full-Circle Separation Threshing Device

1. Spiral Conveyor; 2. Rasp Bar–Spike Tooth Threshing Drum; 3. Sprocket Transmission System; 4. Full-Circle Concave Screen; 5. Guide Plate

Threshing gap, guide plate angle, and the rotational speeds of the threshing drum and concave screen are the core structural parameters of this threshing device. The threshing drum is designed with a diameter of 628 mm and a length of 1770 mm. The concave screen has a diameter of 705 mm and a length of 1542 mm. The spike teeth are 115 mm in height, with a total of 30 teeth. The rasp bars are 1240 mm long, with six bars in total. The threshing drum has six rod teeth, with the rasp bars and spike teeth evenly distributed across these six rods.

SIMULATION ANALYSIS OF THE THRESHING AND SEPARATION PROCESS

The discrete element method (DEM) was used to conduct simulation analysis in order to analyze the threshing and separation performance of the single longitudinal axial-flow full-circle separation threshing device, aiming to determine the optimal combination of structural parameters for the threshing device.

DISCRETE ELEMENT MODEL OF THE THRESHING DEVICE

Using the EDEM discrete element method, the material flow distribution during the rapeseed threshing process was analyzed. The single longitudinal axial–flow full–circle separation threshing device was modeled and simplified in the 3D modeling software SolidWorks, and components such as bearings and sprockets that did do not affect the simulation results were removed. Receiving boxes were placed below and behind the threshing system to collect and quantify the mass and composition of the material falling into each collection area. The components were grouped into five parts: the housing cover, threshing drum, counter-rotating concave screen, receiving box, and particle factory. The Hertz–Mindlin contact model was selected for the simulation. Both the threshing drum and concave screen were set to rotational motion and remained in continuous motion throughout the entire simulation, as shown in Figure 2.

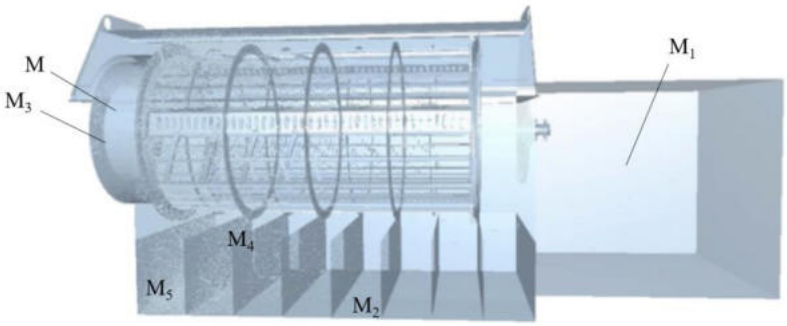


Fig. 2 - Simplified Model of the Threshing Device

DETERMINATION OF SIMULATION PARAMETERS

The collision and movement of rapeseed threshed material within the threshing device are complex. This study employs a soft-particle contact model, which simplifies the normal forces between particles into springs and dampers, and the tangential forces into springs, dampers, and sliders. In the soft–sphere contact model, the elastic and damping coefficients are determined based on Hertz contact theory. The threshed material in the threshing device consists of three components: grains, pods, and stalks. Taking the rapeseed variety Qinyou No. 10 as the research object and based on field preliminary experiments, the rapeseed grain model is simplified as a sphere with a diameter of 2 mm. The short stalks are simplified as cylinders with a diameter of 10 mm, which were randomly generated between 50.4-84 mm in length. The pods are randomly generated between 35-50 mm in length. A schematic diagram of the simplified rapeseed material model is shown in Figure 3.

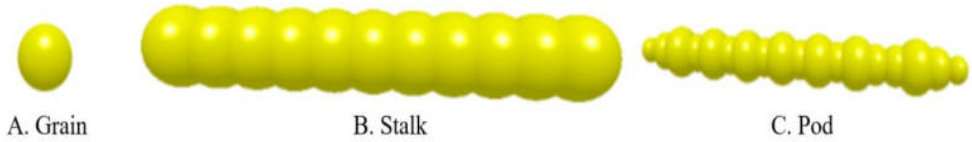


Fig. 3 - Schematic Diagram of the Simplified Threshed Material Model

This study primarily focuses on the distribution patterns of threshed material during rapeseed combined harvesting. The threshing device is made of 45# steel, and the simulation uses the previously determined basic Hertz–Mindlin particle model parameters. The material properties and contact simulation parameters between materials are listed in Tables 1 and 2.

A cylindrical virtual particle factory is set up around the spiral feeding inlet to generate material particles. The particle factory type is set to dynamic, and the material generation mode is configured as Total Mass.

Table 1

Simulation Parameters of the Material

Material Name	Poisson's Ratio	Density (kg/m^3)	Shear Modulus (MPa)
Grain	0.30	1069	7
Pod	0.33	894	1.8
Stalk	0.38	586	66.69
Threshing Device	0.30	7850	70000

Table 2

Contact Parameters Between Materials

Name	Restitution Coefficient	Static Friction Coefficient	Rolling Friction Coefficient
Grain–Grain	0.41	0.52	0.01
Grain–Pod	0.30	0.45	0.01
Grain–Stalk	0.33	0.35	0.01
Grain–Threshing Device	0.50	0.30	0.01
Pod–Pod	0.3	0.35	0.01
Pod–Stalk	0.35	0.33	0.01
Pod–Threshing Device	0.35	0.45	0.01
Stalk–Stalk	0.42	0.31	0.01
Stalk–Threshing Device	0.35	0.40	0.01

PERFORMANCE EVALUATION INDICATORS OF THE THRESHING DEVICE

(1) Threshing Loss Rate

In the EDEM post-processing, a material box with a Grid Bin Group of 1×1×1 is set up at the rear end of the threshing device to collect and count the grains discharged from the rear end of the threshing device. The threshing loss rate is calculated using the following formula:

$$Y_1 = \frac{M_1}{M} \times 100\% \quad (1)$$

Where: Y_1 – threshing loss rate, %; M_1 – mass of rapeseed collected in the material box at the rear end of the threshing device, g; M – total mass of rapeseed fed into the threshing device, g.

(2) Proportion of Threshed Material on the Sieve Surface

In the EDEM post-processing, a calculation region with a Grid Bin Group of 1×1×1 is established below the concave sieve to measure the mass of threshed material separated from the concave sieve-that is, the mass of threshed material falling onto the cleaning sieve surface. The proportion of residues on the sieve surface is calculated using the following formula:

$$Y_2 = \frac{M_2}{M_3} \times 100\% \quad (2)$$

where: Y_2 – proportion of threshed material on the sieve surface; M_2 – mass of threshed material in the material box below the concave sieve, g; M_3 – total mass of material fed into the threshing device, g.

(3) Left–right Distribution Ratio of Threshed Material on the Sieve Surface

In the EDEM post-processing, two collection regions with Grid Bin Groups of 2×1×1 are established on the left and right sides below the concave sieve to measure the weight of threshed material separated by the concave sieve on the left and right sides of the cleaning sieve surface.

The left–right distribution ratio of threshed material on the sieve surface is calculated using the following formula:

$$Y_3 = \frac{M_4}{M_5} \times 100\% \quad (3)$$

where:

Y_3 – left–right distribution ratio of threshed material on the sieve surface; M_4 – mass of threshed material in the right region of the sieve surface, g; M_5 – mass of threshed material in the left region of the sieve surface, g.

SIMULATION MODEL VALIDATION

A 3D model of the full-perimeter concave separation threshing device was established with a straw guide plate angle of 76° and a threshing gap of 7 mm. In the discrete element simulation model, the threshing drum speed was set to 650 rpm, and the reverse rotation speed of the concave sieve was set to 40 rpm, rotating in the opposite direction to the threshing drum. A tracked-type rapeseed combine harvester was used for preliminary testing, with overall dimensions (L × W × H) of 5120 × 2520 × 2720 mm and an engine power of 73 kW. According to preliminary field tests, the mass proportions of grains, pods, and short stalks in the threshed material were set as 25%, 30%, and 45%, respectively. The grain seed generation rate was set at 0.375 kg/s, the pod generation rate was set at 0.45 kg/s, and the short stalk stem generation rate was set at 0.675 kg/s, resulting in a total feed rate of 1.5 kg/s. The mass of lost rapeseed during threshing and the mass of the threshed material on the sieve surface obtained through simulation were 3.08144 g and 2215.94 g, respectively. Using the evaluation methods for the threshing device, the calculated loss rate of threshing entrainment was 0.27%, the proportion of threshed material residues on the sieve surface was 49.24%, and the left–right distribution ratio of threshed material residues on the sieve surface was 0.82.

To verify the accuracy of the simulation model, a field test device was designed and fabricated based on the structural dimensions of the designed full-perimeter rapeseed separation threshing device, as shown in Figure 4.

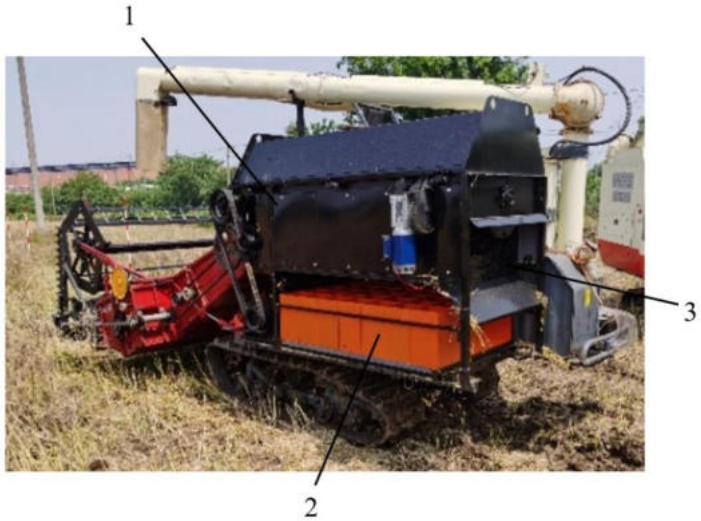


Fig. 4 - Test Platform of the Rapeseed Single Axial-Flow Full-Perimeter Separation Threshing Device
1. Threshing Drum Exit; 2. Sample Collection Box; 3. Separation and Cleaning Outlet

On May 24, 2024, a field experiment was conducted in Shiyezhou Town, Dantu District, Zhenjiang City, Jiangsu Province, to investigate threshing loss, the proportion of threshed material on the sieve surface, and the left–right distribution ratio of threshed material on the sieve surface. The test device operated with a cylinder rotation speed of 650 r/min, concave screen rotation speed of 40 r/min, a straw guide plate angle of 76°, and a threshing gap of 7 mm. The rapeseed variety used was Qin You 10, with grain moisture content at 24.2% and stalk moisture content at 65.7% during the test. The feeding rate was manually controlled at 1.5 kg/s. The field test results measured that the threshing loss rate was 0.60%, a proportion of threshed material on the sieve surface was 48.65%, and the left–right ratio of threshed material on the sieve surface was 0.84.

The absolute error of the threshing loss rate was 0.33%, and the relative error was 55%. The absolute errors of the proportion of threshed material on the sieve surface and the left–right distribution ratio of threshed material on the sieve surface were small, with relative errors of 1.21% and 2.38%, respectively. Compared with the field test results, the simulation analysis showed small absolute errors. Although the relative error for threshing loss was relatively larger, none of the errors exceeded an order of magnitude. Therefore, the established discrete element model of the rapeseed single axial-flow full-perimeter separation threshing device can be used for subsequent optimization of structural parameters.

EXPERIMENTAL DESIGN FOR PARAMETER OPTIMIZATION

Based on the established and validated discrete element model (DEM) of the single axial-flow full-perimeter separation threshing device for a rapeseed harvester, three key structural and operational parameters，namely threshing drum speed, straw guide plate angle, and threshing gap, were selected as

experimental factors. Multiple single-factor simulation analyses were conducted using three evaluation indicators: threshing loss rate, proportion of threshed material on the sieve surface, and the left–right distribution ratio of threshed material on the sieve surface.

Through a comprehensive assessment of the effects of each factor on the performance of the threshing device, the preliminary optimal ranges were determined as follows: threshing drum speed between 450 r/min and 650 r/min, straw guide plate angle between 74° and 78°, and threshing gap between 5 mm and 9 mm.

To further optimize the structural parameters of the single axial–flow full–perimeter separation threshing device for rapeseed, a three-factor, three-level Box-Behnken experimental design was employed to investigate the effects of threshing drum speed, straw guide plate angle, and threshing gap on the threshing loss rate, proportion of threshed material on the sieve surface, and the left–right distribution ratio of threshed material on the sieve surface. A comprehensive evaluation method was used to select the optimal parameter combination. The levels of the experimental factors are shown in Table 3.

Table 3

Levels of Factors in the Three-Factor, Three-Level Box-Behnken Experiment

Leve	Test Factors		
	Drum Speed *A* (r/min)	Straw Guide Plate Angle *B* (°)	Threshing Gap *C* (mm)
-1	450	74	5
0	550	76	7
1	650	78	9

RESULTS AND ANALYSIS

RESULTS AND ANALYSIS OF THE BOX-BEHNKEN EXPERIMENT

To analyze the significance of the effects of experimental factors on the evaluation indicators, the proportions of grains, siliques, and stalks generated in the particle factory during each simulation were randomly generated following a normal distribution to ensure the randomness and independence of the simulation test conditions.

The simulation duration was set to 3 seconds, and the material parameters for the simulation tests were configured according to the calibrated model parameters. The results of the three-factor, three-level Box-Behnken experiment are shown in Table 4.

Table 4

Results of the Three-Factor, Three-Level Box-Behnken Experiment

Test No.	Test Factors and Levels			Test Indicators		
	A (r/min)	*B* (°)	*C* (mm)	Y_1 (%)	Y_2 (%)	Y_3
1	450	76	5	0.32	47.54	0.80
2	450	74	7	0.37	45.79	0.90
3	450	78	7	0.33	48.42	0.84
4	450	76	9	0.36	44.78	0.86
5	550	74	5	0.32	47.39	0.92
6	550	78	5	0.27	49.86	0.77
7	550	76	7	0.29	47.17	0.88
8	550	76	7	0.29	46.97	0.88
9	550	76	7	0.29	47.07	0.87
10	550	76	7	0.29	47.07	0.87
11	550	76	7	0.30	47.07	0.88
12	550	74	9	0.34	45.83	0.93
13	550	78	9	0.31	47.12	0.83
14	650	76	5	0.25	49.54	0.80
15	650	74	7	0.28	48.82	0.92
16	650	78	7	0.25	50.55	0.75
17	650	76	9	0.27	48.14	0.82

The experimental results were analyzed using the Box-Behnken module in Design Expert 13. The analysis of variance (ANOVA) results for threshing loss rate, proportion of threshed material on the sieve surface, and the left–right distribution ratio of threshed material on the sieve surface discharge are shown in Tables 5, 6, and 7, respectively.

Table 5

Analysis of Variance for Threshing Loss Rate

Source	df	SS	MS	*F-value*	*P-value*
Model	9	0.0193	0.0021	143.27	< 0.0001
A	1	0.0136	0.0136	907.50	< 0.0001
B	1	0.0028	0.0028	187.50	< 0.0001
C	1	0.0018	0.0018	120.00	< 0.0001
AB	1	0.00001	0.00001	1.67	0.2377
AC	1	0.0001	0.0001	6.67	0.0364
BC	1	0.0001	0.0001	6.67	0.0364
A^2	1	0.0000	0.0000	2.12	0.1885
B^2	1	0.0007	0.0007	45.63	0.0003
C^2	1	0.0001	0.0001	7.74	0.0272
Residual	7	0.0001	0.0000		
Lack of Fit	3	0.0000	0.000008333	0.4167	0.751
Pure Error	4	0.0001	0.00001		
Total	16	0.0194			
R^2	0.9946				

Note: $p < 0.01$ indicates a highly significant effect; $0.01 < p < 0.05$ indicates a significant effect; $p > 0.05$ indicates no significant effect. Same below.

Table 6

Analysis of Variance for Proportion of Threshed Material from the Sieve Surface

Source	df	SS	MS	*F-value*	*P-value*
Model	9	36.02	4.00	386.66	< 0.0001
A	1	13.83	13.83	1336.60	< 0.0001
B	1	8.24	8.24	796.31	< 0.0001
C	1	8.95	8.95	864.39	< 0.0001
AB	1	0.2025	0.2025	19.57	0.0031
AC	1	0.4624	0.4624	44.68	0.0003
BC	1	0.3481	0.3481	33.63	0.0007
A^2	1	1.71	1.71	165.33	< 0.0001
B^2	1	1.99	1.99	192.28	< 0.0001
C^2	1	0.1813	0.1813	17.52	0.0041
Residual	7	0.0725	0.0104		
Lack of Fit	3	0.0525	0.0175	3.50	0.129
Pure Error	4	0.0200	0.0050		
Total	16	36.09			
R^2	0.998				

Table 7

Analysis of Variance for Left–right Distribution Ratio of Threshed Material on the Sieve Surface

Source	df	SS	MS	*F-value*	*P-value*
Model	9	0.0445	0.0049	117.37	< 0.0001
A	1	0.0015	0.0015	35.89	0.0005
B	1	0.0288	0.0288	683.39	< 0.0001
C	1	0.0028	0.0028	66.74	< 0.0001
AB	1	0.0030	0.0030	71.78	< 0.0001
AC	1	0.0004	0.0004	9.49	0.0178
BC	1	0.0006	0.0006	14.83	0.0063
A^2	1	0.0046	0.0046	108.80	< 0.0001
B^2	1	0.0004	0.0004	9.02	0.0199
C^2	1	0.0022	0.0022	52.85	0.0002
Residual	7	0.0003	0.00004		

Lack of Fit	3	0.0002	0.0001	1.94	0.2643
Pure Error	4	0.0001	0.00003		
Total	16	0.0448			
R^2	0.9934				

According to the ANOVA results in Tables 5, 6, and 7, the p-values for the models of threshing loss rate, proportion of threshed material on the sieve surface, and the left–right distribution ratio of threshed material on the sieve surface are all less than 0.0001, which is far below the conventional significance level of 0.05. This indicates that the assumed linear relationships in the models are reasonable. The coefficient of determination (R^2) for the threshing loss rate model is 0.9946, for the proportion of threshed material on the sieve surface is 0.998, and for the left–right distribution ratio of threshed material on the sieve surface is 0.9934, indicating that the regression models have a good fit. Regression equations describing the relationships between threshing loss rate, proportion of threshed material on the sieve surface, and left–right distribution ratio of threshed material on the sieve surface and the drum speed, straw guide plate angle, and threshing gap were obtained using Design Expert 13 software.

The regression equation for the threshing loss rate is shown in Equation (4).

$$R_1 = 21.57968 - 0.00149A - 0.50950B - 0.09213C - 0.00003AC + 0.00125BC + 0.00319B^2 + 0.00131C^2 \quad (4)$$

The regression equation for the proportion of threshed material on the sieve surface is shown in Equation (5).

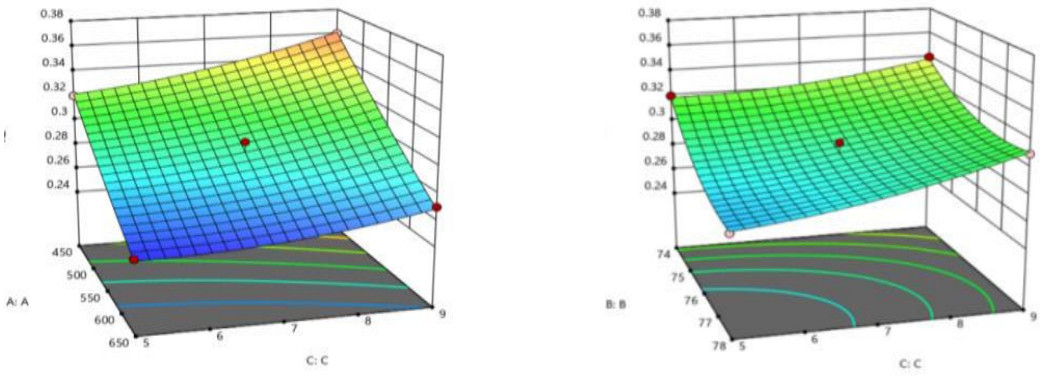
$$R_2 = 934.74625 + 0.01663A - 24.4825B + 4.8675C - 0.00113AB + 0.0017AC - 0.07375BC + 0.00006A^2 + 0.17188B^2 - 0.05188C^2 \quad (5)$$

The regression equation for the left–right distribution ratio of threshed material on the sieve surface is shown in Equation (6).

$$R_3 = 11.3265 + 0.01429A - 0.33725B - 0.12013C - 0.00014AB - 0.00005AC + 0.00313BC - 0.00238B^2 - 0.00575C^2 \quad (6)$$

(1) ANALYSIS OF FACTORS AFFECTING THRESHING LOSS

The effects of drum speed, straw guide plate angle, and threshing gap on the threshing loss rate are shown in Figure 5. When the straw guide plate angle is at the central horizontal position (76°) and the drum speed is fixed, the threshing loss increases as the threshing gap becomes larger. When the threshing gap is fixed, the threshing loss decreases as the drum speed increases. When the drum speed is at the central horizontal position (550 r/min) and the threshing gap is fixed, the threshing loss increases as the straw guide plate angle becomes larger. When the straw guide plate angle is fixed, the threshing loss also increases with the increase of the threshing gap. After optimizing the parameters, the combination that minimizes threshing loss was obtained: drum speed of 648.675 r/min, straw guide plate angle of 77.860°, and threshing gap of 6.452 mm. At this point, the threshing loss rate is 0.246%.



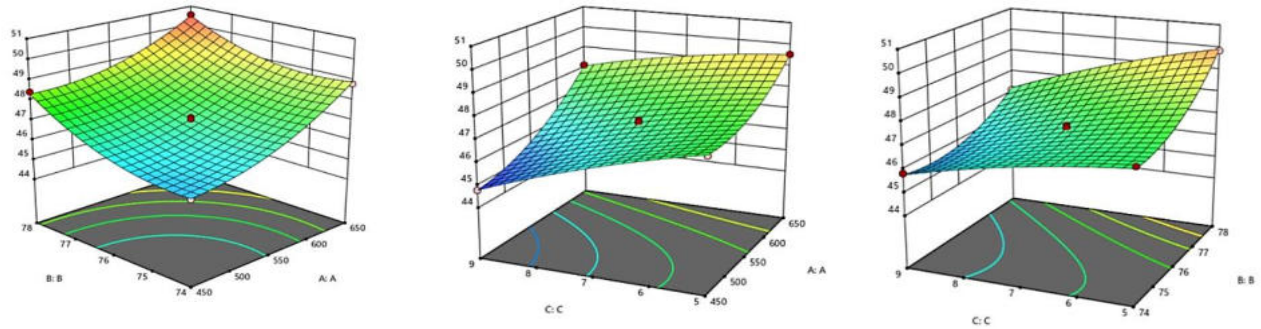
(a) Interaction Effect between Drum Speed and Threshing Gap

(b) Interaction Effect between Straw Guide Plate Angle and Threshing Gap

Fig. 5 - Effects of Drum Speed, Straw Guide Plate Angle, and Threshing Gap on Threshing Loss Rate

(2) ANALYSIS OF FACTORS AFFECTING THE PROPORTION OF THRESHED MATERIAL ON THE SIEVE SURFACE

The effects of drum speed, straw guide plate angle, and threshing gap on the proportion of material passing through the sieve surface are shown in Figure 6. When the threshing gap is at the central level (7 mm) and the drum speed is fixed, the proportion of material passing through the sieve decreases as the straw guide plate angle increases. When the straw guide plate angle is fixed, the proportion of material passing through the sieve increases with the increase in the drum speed. When the straw guide plate angle is at the central level (76°) and the drum speed is fixed, the proportion of material passing through the sieve decreases as the threshing gap becomes larger. When the threshing gap is fixed, the proportion of material passing through the sieve increases as the drum speed increases. When the drum speed is at the central level (550 r/min) and the threshing gap is fixed, the proportion of material passing through the sieve increases as the straw guide plate angle becomes larger. When the straw guide plate angle is fixed, the proportion of material passing through the sieve decreases as the threshing gap increases. After optimizing the parameters, the combination that minimizes the proportion of material passing through the sieve was obtained: drum speed of 461.41 r/min, straw guide plate angle of 74.090°, and threshing gap of 8.794 mm. At this point, the proportion of material passing through the sieve is 44.74%.

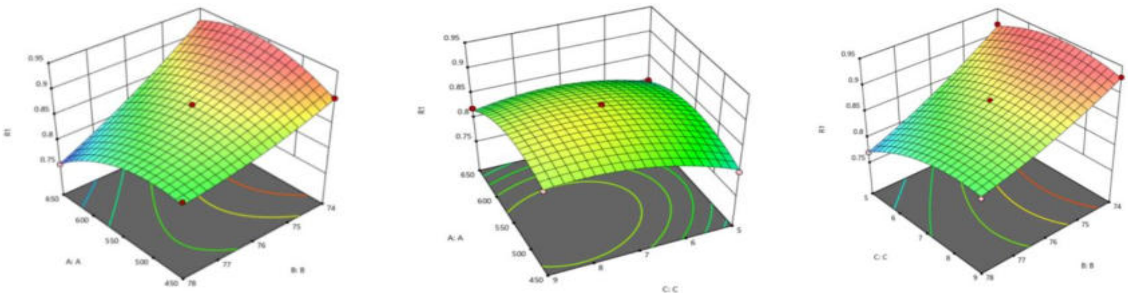


(a) Interaction Effect between Drum Speed and Straw Guide Plate Angle *(b) Interaction Effect between Drum Speed and Threshing Gap* *(c) Interaction Effect between Straw Guide Plate Angle and Threshing Gap*

Fig. 6 - Effects of Drum Speed, Straw Guide Plate Angle, and Threshing Gap on the Proportion of Material Passing Through the Sieve Surface

(3) ANALYSIS OF FACTORS AFFECTING THE LEFT–RIGHT DISTRIBUTION RATIO OF THRESHED MATERIAL ON THE SIEVE SURFACE

The effects of drum speed, straw guide plate angle, and threshing gap on the left–right distribution ratio of threshed material on the sieve surface are shown in Figure 7. When the threshing gap is at the central level (7 mm) and the drum speed is fixed, the left–right distribution ratio of threshed material on the sieve surface increases as the straw guide plate angle becomes larger, indicating a more uniform distribution of material across the sieve surface. When the straw guide plate angle is fixed, the uniformity of the left–right material distribution first improves and then deteriorates as the drum speed increases. When the straw guide plate angle is at the central level (76°) and the drum speed is fixed, the left–right distribution ratio of threshed material on the sieve surface initially increases and then decreases as the threshing gap becomes larger, indicating that the uniformity of material distribution across the sieve surface first improves and then declines. When the threshing gap is fixed, the uniformity of left–right material distribution first increases and then decreases as the drum speed increases. When the drum speed is at the central level (550 r/min) and the threshing gap is fixed, the left–right distribution ratio of threshed material on the sieve surface increases as the straw guide plate angle becomes larger. When the straw guide plate angle is fixed, the uniformity of the left–right material distribution first increases and then decreases as the threshing gap increases. After optimizing the parameters, the combination that maximizes the left–right distribution ratio of threshed material on the sieve surface was found to be: drum speed of 558.197 r/min, straw guide plate angle of 74.296°, and threshing gap of 7.195 mm. At this point, the left–right distribution ratio of threshed material on the sieve surface is 0.935.



(a) Interaction Effect between Drum Speed and Straw Guide Plate Angle

(b) Interaction Effect between Drum Speed and Threshing Gap

(c) Interaction Effect between Straw Guide Plate Angle and Threshing Gap

Fig. 7 - Effects of Drum Speed, Straw Guide Plate Angle, and Threshing Gap on the Left–right Distribution Ratio of Material Passing Through the Sieve Surface

PARAMETER OPTIMIZATION

The interactions among drum speed, straw guide plate angle, and threshing gap in the single longitudinal axial flow full-periphery separation threshing device of the rapeseed harvester have different effects on threshing loss, the proportion of threshed material on the sieve surface, and the left–right distribution ratio of threshed material on the sieve surface. Under the conditions of minimal threshing loss, the proportion of threshed material on the sieve surface is minimized, and a larger left–right distribution ratio of threshed material on the sieve surface can improve the handling capacity and cleaning efficiency of the sieve surface material. Therefore, it is necessary to further optimize the relevant structure and operating parameters of the threshing device to achieve a comprehensive improvement. To identify the optimal solutions for the relevant factors, regression models relating threshing loss rate, proportion of threshed material on the sieve surface, and the left–right distribution ratio of threshed material on the sieve surface, and drum speed, straw guide plate angle, and threshing gap were established as objective functions. The solved parameter ranges were used as constraints, and the optimal solutions of the objective functions were obtained using Design Expert software. The optimization objectives and constraints are shown in Equation (7).

$$\begin{cases} \min\ Y_1 Y_2(A,B,C), \max\ Y_3(A,B,C) \\ s.t. \begin{cases} 450r/\min \le A \le 650r/\min \\ 74^\circ \le B \le 78^\circ \\ 5mm \le C \le 9mm \end{cases} \end{cases} \tag{7}$$

The optimal operating parameters were determined as follows: drum speed of 576.479 r/min, straw guide plate angle of 74.797°, and threshing gap of 7.687 mm. Under these conditions, the threshing loss rate was 0.301%, the proportion of threshed material on the sieve surface was 46.841%, and the left–right distribution ratio of threshed material on the sieve surface was 0.914. Considering the actual working conditions and processing requirements of the combine harvester, the optimized parameter set was adjusted to: drum speed of 550 r/min, straw guide plate angle of 75°, and threshing gap of 8 mm.

FIELD TEST EVALUATION

Based on the chassis, cutter bar, and cleaning system of the Xingguang 4LZY-4.0Z rapeseed combine harvester, the single longitudinal axial flow full-periphery separation threshing device designed in this study was installed. The main structure and technical parameters of the Xingguang 4LZY-4.0Z rapeseed combine harvester are shown in Table 8.

Table 8

Main Structure and Technical Parameters of the 4LZY-4.0Z Rapeseed Combine Harvester

Parameter	Value
Overall Dimensions (L × W × H) / （mm×mm×mm）	5190×2640×2980
Structural Type	Full-Feeding Crawler Self-Propelled Type
Engine Power (kW)	73.5
Rated Engine Speed (r·min^{-1})	2400
Working Cutting Width (m)	2.1
Feeding Rate (kg·s^{-1})	0–4
Operating Speed (km·h^{-1})	0–5.69

On May 29, 2025, in Shiyezhou Town, Dantu District, Zhenjiang City, Jiangsu Province, a third-party testing agency, Zhejiang Electromechanical Product Quality Institute Co., Ltd., was commissioned to conduct performance tests. The tests were carried out in accordance with the Chinese national standards GB/T 8097-2008 “Harvesting Machinery – Combine Harvester Test Methods” and DG/T 057-2019 “Rapeseed Harvester,” as well as agricultural machinery appraisal procedures. The field performance test setup is shown in Figure 8, and the testing conditions are listed in Table 9. According to the third-party performance test, the total loss rate was 5.6%, impurity rate 2.3%, and breakage rate 0.4%, with an operational hourly productivity of 0.57 hm²/h. These performance indicators exceed the requirements specified in NY/T 2199-2012 “Quality Standards for Rapeseed Combine Harvester Operations”.



Fig. 8 - Field Performance Test of the Rapeseed Single Longitudinal Axial Flow Full-Periphery Separation Harvester

Table 9

Field Test Conditions

Test Items	Unit	Test Result
Weather	/	Overcast
Temperature	℃	19.9–23.3
Humidity	RH/%	59.4–62.7
Test Field (Length × Width)	m	70×30
Slope and Ground Conditions	/	Flat Terrain
Crop Variety	/	Yueyou 1510
Maturity Stage	/	Fully Mature Stage
Natural Height	mm	1712
Lowest Pod Height	mm	650
Root Diameter	mm	10
Canopy Diameter	mm	600
Grain Moisture Content	%	15.1
Operating Speed	km/h	2.93
Working Width	mm	2100

DISCUSSION

The threshing device is the core working component of the rapeseed harvester. Optimizing the performance of the threshing device solely by evaluating threshing loss is insufficient. In the extreme case where all the material entering the threshing system is completely crushed and separated by concave screens to fall onto the cleaning sieves, the threshing loss would be zero. However, on the one hand, a large amount of threshed material then falls onto the cleaning sieves, which leads to excessive material load on the sieve surface. This results in untimely cleaning and increased cleaning losses, thereby adversely affecting the overall harvesting loss. On the other hand, if the threshed material are unevenly distributed on the cleaning sieve surface, local accumulation of threshed material in certain areas will make grain separation more difficult. Similarly, areas with fewer threshed material cannot fully utilize the separation capacity of the cleaning sieve. Therefore, optimizing the performance of the threshing device should not focus solely on the loss during the threshing stage. It is also necessary to comprehensively consider the proportion of threshed material and the distribution of threshed material on the sieve surface, which optimizes the performance of the threshing device through a multi-criteria approach.

The movement and forces acting on the material inside the threshing device during threshing are complex. Field experiments for optimization require high labor intensity and long testing periods. Additionally, the material properties of the crop vary significantly with the harvesting period, resulting in considerable errors when combining experimental data. This study attempts to use EDEM software to build a discrete element model (DEM) of rapeseed threshing and separation, establishing an evaluation and optimization model for the performance of the threshing device. The model was validated through comparison with field experiments.

The relative error in threshing loss was relatively large, while the relative errors in the proportion of threshed material on the sieve surface and the left–right distribution ratio of threshed material on the sieve surface were relatively small. This is mainly because grain separation and material carryover are affected by particle contact parameters and material distribution states, whereas the distribution of threshed material is less influenced by the intrinsic properties of the material. These findings also indicate that relying solely on simulation analysis to accurately evaluate threshing loss is challenging. This study conducted a simulation analysis of threshing loss by combining preliminary experiments with the composition of the threshing residues. The absolute error in the threshing loss rate was small, while the relative error was larger, though it did not exceed an order of magnitude. Therefore, it is still feasible to carry out parameter optimization based on the trend of changes in the threshing loss rate.

CONCLUSIONS

To optimize the performance of the single axial-flow full-perimeter separation threshing device of the rapeseed harvester, a comprehensive evaluation method was proposed using three indicators: threshing loss, proportion of threshed material on the sieve surface, and the left–right distribution ratio of threshed material on the sieve surface. A discrete element model (DEM) of rapeseed threshing and separation was established based on EDEM software. Comparison between simulation results and bench tests showed that the absolute error of threshing loss was 0.33%, with a relative error of 55%. The relative errors for the proportion of threshed material on the sieve surface and the left–right distribution ratio of threshed material were 1.21% and 2.38%, respectively. All errors between simulation and bench tests were within one order of magnitude, validating the feasibility of using the discrete element method to analyze and optimize the threshing device.

Using threshing drum speed, straw guide plate angle, and threshing gap as experimental factors, and threshing loss, proportion of threshed material on the sieve surface, and the left–right distribution ratio of threshed material on the sieve surface as evaluation indicators, a three-factor, three-level Box-Behnken experiment was conducted. Regression models were established between experimental factors and evaluation indicators. Through multi-objective optimization and considering the actual working conditions and processing requirements of the rapeseed combine harvester, the optimized parameter combination was determined as: drum speed of 550 r/min, straw guide plate angle of 75°, and threshing gap of 8 mm.

Under the optimal structure and operating parameters, a prototype was fabricated and entrusted to a third-party testing agency to evaluate the rapeseed harvesting operation. Field measurements showed a total harvesting loss rate of 5.6%, impurity rate of 2.3%, and grain breakage rate of 0.4%, with an operational productivity of 0.57 ha/h. The performance exceeded industry standard requirements, validating the feasibility and accuracy of the optimization method and results through field testing.

ACKNOWLEDGEMENT

This research was supported by National Key R&D Program of China (2023YFD2001000) and Funds for Modern Agricultural Industry Technology System Construction of China (CARS-12)

REFERENCES

[1] Dai F., Song X.F., Shi R.J., Guo W.J., Zhao Y.M., Wang F., Zhao W.Y. (2022). Movement law of the threshing material in threshing and cleaning machine for plot-bred wheat. *International Journal of Agricultural and Biological Engineering*,15(3), 100–106.

[2] Dong J. Q., Zhang D. X., Yang L., Cui T., Zhang K. L., He X. T., Wang Z. D., Jing M. S. (2023). Discrete element method optimization of threshing components to reduce maize kernel damage at high moisture content. *Biosystems Engineering*, 233, 221–240.

[3] Fang X.W., Zhang J.S., Zhao X.L., Zhang L., Zhou D.Y., Yu C.S., Hu W., Zhang Q. (2024). Optimising maize threshing by integrating DEM simulation and interpretive enhanced predictive modelling. *Biosystems Engineering*, 244, 93–106.

[4] Fu J., Zhang J.L., Liu F.S. (2024). Enhanced sieving mechanism of novel cleaning screen and investigation of particle movement characteristics on the screen. *Powder Technology*, 431, 119043.

[5] Jiang T., Li H.T., Guan Z.H., Mu S.L., Wu C.Y., Zhang M. (2023). Design and experiments of material uniform dispersion and diversion device on cleaning screen surface for oilseed harvesting. *Transactions of the Chinese Society for Agricultural Machinery*, 54(1), 164–176.

[6] Mirzazadeh Ali, Abdollahpour Shamsollah, Mahmoudi Asghar, Bukat A.R. (2012). Intelligent modeling of material separation in combine harvester's thresher by ANN. *International Journal of Agriculture and Crop Sciences*, 4(23), 1767–1777.

[7] Miu PI，Kutzbach HD. (2007). Mathematical model of material kinematics in an axial threshing unit[J]. *Computers and Electronics in Agriculture*, 58(2), 93–99.

[8] Qian Z.J., Jin C.Q., Zhang D.G. (2017). Multiple frictional impact dynamics of threshing process between flexible tooth and grain kernel. *Computers and Electronics in Agriculture*, 141, 276–285.

[9] Tang Z., Li Y. M., Wang C. H. (2013). Experiments on variable-mass threshing of rice in the tangential-longitudinal-flow combine harvester. *Journal of Agricultural Science and Technology*, 15(4), 1319–1334.

[10] Tang Z., Li Y.M., Xu L.Z., Pang J., Li H.C., (2012). Experimental study on wheat rate of tangential-axial combine harvester. *Transaction of the Chinese Society of Agricultural Engineering*, 28(5), 26–31.

[11] Teng Y.J., Jin C.Q., Chen Y.P., Liu P., Yin X., Wang T.E., Yu K. (2020). Design and optimization of segmented threshing device of combine harvester for rice and wheat. *Transactions of the Chinese Society of Agricultural Engineering*, 36(12), 1–12.

[12] Trollope J.R. (1982). A mathematical model of the threshing process in a conventional combine thresher. *Journal of Agricultural Engineering Research*, 27(2), 119–130.

[13] Wang Q.R., Mao H.P., Li Q.L. (2020). Modelling and simulation of the grain threshing drum for rice combine harvester using MBD-DEM coupling simulation. *Computers and Electronics in Agriculture*, 178, 106859.

[14] Wu Z., Chen J., Ma Z. (2024). Development of a lightweight online detection system for impurity content and broken rate in rice for combine harvesters. *Computers and Electronics in Agriculture*, 218:18689.

[15] Xu L.Z., Li Y.M. (2011). Modeling and experiment to threshing unit of stripper combine. *African Journal of Biotechnology*, 10(20), 4106–4113.

[16] Xu L.Z., Li Y.M., Chai X.Y. (2020). Numerical simulation of gas-solid two-phase flow to predict the cleaning performance of rice combine harvesters. *Biosystems Engineering*, 190, 11–24.

[17] Xu L.Z., Li Y.M., Wang C.H., Xue Z. (2014). A combinational threshing and separating unit of combine harvester with a transverse tangential cylinder and an axial rotor. *Transactions of the Chinese Society for Agricultural Machinery*, 45(02), 105–108,135.

[18] Yang F.F., Yan C.L. (2018). Movement analysis of cereal in axial flow threshing roller space. *Transactions of the Chinese Society for Agricultural Machinery*, 39(11), 48–50.

[19] Yang F.F., Yan C.L., Yang B.N., Yi S.J., Jiang N. (2010). Simulation and testing of cereal motion in threshing unit of combine harvester with axial feeding. *Transactions of the Chinese Society for Agricultural Machinery*, 41 (12), 67–81, 88.

[20] Yang L., Zhang X.L., Li Y.M., Lv L.Y., Shi M.L. (2024). Modeling and control methods of a multi-parameter system for threshing and cleaning in grain combine harvesters. *Computers and Electronics in Agriculture*, 225, 109251.

[21] Yuan L.H., He X., Zhu C.H, Wang W.Z., Wang M.L, Wu S.J. (2024). Design and test of tangential and longitudinal-axial threshing and separating unit for wheat. *Microelectronics Journal*, 21, 101774.

STRUCTURAL DESIGN AND PERFORMANCE STUDY OF SALT-ALKALI SOIL ROTARY BLADE BASED ON DISCRETE ELEMENTS
/
基于离散元的盐碱地旋耕刀结构设计与性能研究

Shuai ZHENG[1)], Ahmed F. El-SHAFIE[2)], Jie LIU[1)], Abouelnardar SALME[3)], Jing ZHANG[4)] Haoran BAI*[1)]
[1)] College of Mechanical and Electrical Engineering, Qingdao Agricultural University, Qingdao / China;
[2)] National Center of Technology Innovation for Comprehensive Utilization of Saline-Alkali Land, Dongying / China;
[3)] Yellow River Delta Intelligent Agricultural Machinery Equipment Industry Academy, Dongying / China
[4)] Academician Workstation of Agricultural High-tech Industrial Area of the Yellow River Delta,
[5)] Dongying Vocational College School of Ecology and Biology, Dongying / China
Corresponding author: Haoran Bai
Tel: +86-19558970989; E-mail: 20232111061@stu.qau.edu.cn
DOI: https://doi.org/10.35633/inmateh-76-104

Keywords: *rotary blade, saline-alkaline soil, operating power consumption, structural design*

ABSTRACT
Aiming at the issues of high energy consumption and poor tillage quality caused by soil compaction and heavy clay in the saline-alkali soils of the Yellow River Delta, this study systematically analyzes the dynamic interaction between rotary tiller blades and soil, investigates the influence of structural parameters on tillage performance, designs a blade edge curve based on the shearing effect, and identifies the primary factors affecting energy consumption and their respective ranges. Using EDEM software in combination with a quadratic orthogonal rotational combination test, with bending angle, working width, and tangential surface height as the experimental factors and operational power consumption as the evaluation index, the optimal structural parameters were determined through Design-Expert 13 optimization: bending angle of 136.49°, working width of 34.20 mm, and tangential surface height of 42.3 mm, corresponding to a theoretical power consumption of 36.64 kW. Field experiments demonstrated that the designed rotary tiller blade consumed 38.49 kW under the same operating conditions, representing a 16.07% reduction compared with traditional blades, thereby validating the effectiveness of the design. The findings provide a theoretical basis for the utilization of saline-alkali land as well as for resistance reduction and efficiency improvement in rotary tillers.

摘 要
针对黄河三角洲盐碱地土壤板结黏重导致旋耕功耗高、质量差等问题，本文系统分析了旋耕刀-土壤动力学特性，探究旋耕刀结构参数对耕作性能的影响规律，设计了一种基于滑切效果的刃口曲线，明确了影响功耗的主要因素及取值范围。利用EDEM软件和二次正交旋转组合试验，以弯折角、工作幅宽、正切面高度为因素，作业功耗为试验指标，结合Design-Expert 13优化得出最佳结构参数为弯折角136.49°、作业幅宽34.20mm、正切面高度42.3mm，对应理论功耗36.64kW。田间试验表明，所设计旋耕刀在相同工况下功耗为38.49kW，较传统刀具降低16.07%，验证了设计的有效性。研究成果为盐碱地开发利用及旋耕机减阻增效提供了理论依据。

INTRODUCTION
Rotary tillage is the primary cultivation method in the Yellow River Delta region, enabling plowing, efficient soil fragmentation, and land preparation in a single operation. After rotary tillage, the soil surface becomes flat and loose, creating seedbed conditions suitable for sowing, improving soil aeration and water retention capacity, and effectively breaking up and burying crop residues (*Zhao et al., 2025; Liu et al., 2022*). However, compared with other soils, those in this region exhibit high salinity and alkalinity, low organic matter content, and a tendency for underground salts to migrate to the surface, which causes soil hardening and compaction (*Zhu et al., 2024*). As a result, soil fragmentation is poor, and the cutting resistance is high. In practice, rotary tillers often need to rework the soil to achieve the seedbed requirements for sowing, which greatly increases power consumption.

In order to improve the operational efficiency of rotary tillers and reduce blade working resistance, optimizing the geometric structure of rotary tiller blades to reduce power consumption has been an important research direction for scholars in recent years. Recently, the interaction process between rotary tiller blades and soil using the SPH method was simulated, the structural parameters that generate resistance in rotary tiller blades was determined, and their design was optimized.

Time comparison tests showed that the power consumption of the optimized rotary tiller blades was reduced by 9.52%, providing a reference for reducing resistance and saving energy in rotary tiller blades (*Zhang et al., 2024*).

In 2019, a wedge-shaped drag-reducing rotary tiller blade was designed to address the issues of high resistance and energy consumption during rotary tilling operations. Field comparison tests showed that the wedge-shaped rotary tiller blade reduced average torque by 11.35% and average power consumption by 9.29% compared to the national standard rotary tiller blade, effectively reducing tillage energy consumption (*Hao et al., 2019*). By studying the three-directional working resistance experienced by rotary tiller blades and its variation patterns, the experimental factors influencing the three-directional resistance of rotary tiller blades were determined to be the bending angle, blade width, tilling depth, phase angle, and forward speed (*Xiong et al., 2018*).

In 2021, in response to the issues of high resistance and high energy consumption during oilseed rape cultivation, a counter-rotating rotary tiller blade and soil model were established. Through a combination of discrete element simulation and field comparison experiments, the optimal structural parameters of the blade were determined (*He et al., 2022*). In recent years, relevant scholars have studied the impact of the geometric and operational motion parameters of L-shaped rotary tiller blades on the dynamic performance of rotary tillers. They found that changing the sweeper angle can significantly reduce the power consumption of the operation while improving the mixing and burial effect (*Nalawade et al., 2024*).

This paper designs a new type of rotary tiller blade suitable for saline-alkali heavy clay soil. Through kinematic and structural parameter analysis of the rotary tiller blade, a rotary tiller blade-soil dynamic model is constructed. Using EDEM simulation experiments, the study investigated the influence of different structural parameter combinations on operational power consumption. Through orthogonal experiments, the optimal structural parameter combination for the blades was determined. Field comparison experiments were conducted to validate the accuracy of the simulation, aiming to provide references for reducing resistance and improving efficiency in saline-alkali soil cultivation.

MATERIALS AND METHODS

DYNAMIC ANALYSIS AND STRUCTURAL DESIGN OF ROTARY TILLAGE BLADES

Analysis of Rotary Tiller Blade Working Parameters

During rotary tilling operations, the rotary tiller blades rotate around the blade axis center at an angular velocity *ω* while moving forward with the rotary tiller at a linear velocity v_m. Therefore, the absolute motion of the rotary tiller blades is the combination of these two types of motion (*Zhang et al., 2019*). A rectangular coordinate system was established, as shown in Fig. 1, where *O* is the center of rotation of the blade shaft, the positive direction of the *x*-axis is the same as the forward direction of the rotary tiller, and the positive direction of the *y*-axis is perpendicular to the soil surface and downward. The tip of the blade is the point on the blade that can reach the maximum tilling depth. Assuming that the starting position of the blade tip is on the positive *x*-axis, the equation of motion of the blade tip can be expressed as:

$$\begin{cases} x = R\cos\omega t + v_m t \\ y = R\sin\omega t \end{cases} \quad (1)$$

where:

R is the radius of rotation of the blade tip, [mm]; ω - the angular velocity of rotation of the blade shaft, [rad]; v_m - the forward speed of the rotary tiller, [m/s]; t - the operating time, [s].

The end point motion trajectory of the rotary tiller blade is a cycloid. Taking point *A* as either end point of the blade's motion trajectory, the horizontal component velocity v_x and vertical component velocity v_y of point *A* motion are respectively:

$$\begin{cases} v_x = v_m - R\omega\sin\omega t \\ v_y = R\omega\cos\omega t \end{cases} \quad (2)$$

Therefore, the absolute movement speed of the blade tip is:

$$v = \sqrt{v_x^2 + v_y^2} = \sqrt{v_m^2 + R^2\omega^2 - 2v_m R\omega\sin\omega t} \quad (3)$$

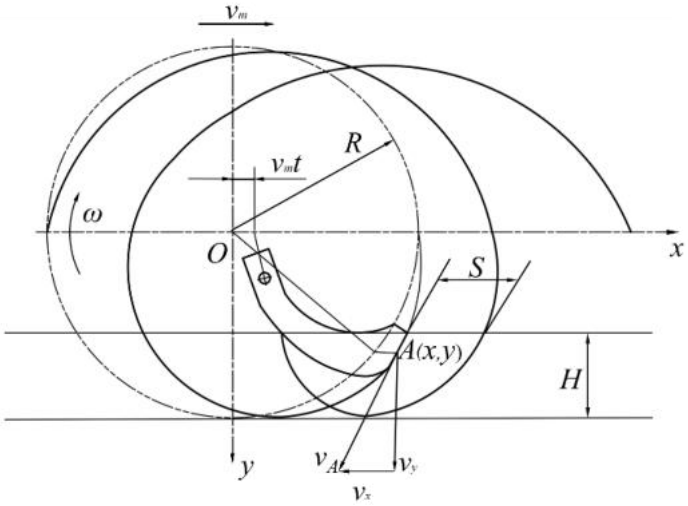


Fig. 1 - Rotary tiller blade working trajectory diagram

Curve Design of Rotary Tiller Blade Edge

When cutting soil, the rotary tiller blade cuts the soil longitudinally with its side cutting edge. Typically, the cutting edge near the center begins to cut the soil, then gradually penetrates the soil from near to far, and finally cuts the soil horizontally with its tangential cutting edge. When designing the cutting edge of a rotary tiller blade, it is important to ensure that the blade curve does not become entangled with grass. The blade should operate according to the principle of sliding achieving the cutting operations, capable of cutting straw or soil clumps with moderate sliding cutting force. If immediate cutting is not possible, the blade should be able to slide along the cutting edge and disengage, preventing grass entanglement and blockages, thereby achieving smooth cutting and minimizing power consumption (*Guan et al., 2021; Zhang et al., 2022*). Therefore, the sliding angle is used as an important basis for the design of the rotary tiller blade edge curve, and the Archimedean spiral is used for the design of the rotary tiller blade edge curve.

Curve Design of Side Cutting Edge of Rotary Tiller Blade

The angle between the velocity vector at a point on the cutting edge of a rotary tiller and the tangent plane of the cutting edge curve at that point, as shown in Fig. 2, is called the slip angle τ at point A on the side cutting edge curve. When the blade rotates only around the blade axis, τ is the static slip angle.

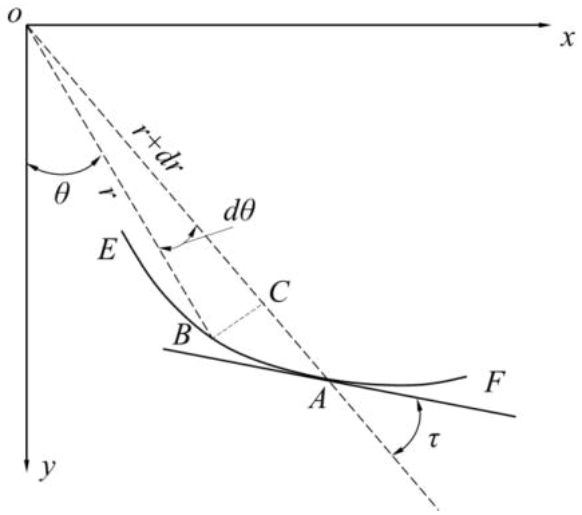


Fig. 2 - Diagram of the sliding cutting action of a rotary tiller blade

Due to the different operating speeds of rotary tillers, the speed direction and magnitude at a point on the side cutting edge curve vary, so the sliding angle value at that point also varies. Therefore, it is necessary to consider the effect of the dynamic sliding angle on the blade. The value of the dynamic sliding angle τ' is (*Liang et al., 2016*):

$$\tau' = \tau - arctan\left(\frac{cos\theta}{\lambda\frac{r}{R} - sin\theta}\right) \quad (4)$$

where: θ is the polar angle, [rad]; λ is the rotary tiller speed ratio.

The Archimedes spiral line has the characteristic of gradually increasing sliding cutting action, cutting soil from near to far. The feed rate of the blade in the radial direction is uniform, thereby achieving reasonable load distribution and stable operation (*Zhang et al., 2023*). Therefore, the Archimedes spiral line is used as the side cutting edge curve design of the rotary tiller blade. The Archimedean spiral equation for the design is:

$$r = r_0 + \Delta r\theta \quad (5)$$

where: r_0 is the initial polar radius, [mm]; Δr - the increase in the polar radius *r,* when the helix increases by 1rad, [mm].

The initial radius r_0 of the side cutting edge is one of the basic parameters for designing a rotary tiller blade. Based on the current status of rotary tillage in saline-alkali soil and the agronomic requirements for sowing subsequent crops, the tillage depth H is set to 120 mm to ensure stable tillage. The maximum radius of rotation R of the blade is set to 195 mm. According to the Agricultural Machinery Design Manual, when the soil is highly viscous and has a low moisture content, the cutting pitch S can be set to 60-90 mm. To ensure effective soil fragmentation, the cutting pitch should not be too large. It can be appropriately reduced to improve soil fragmentation.

The cutting pitch S is set to 80 mm.

$$r_0 = \sqrt{R^2 + S^2 - 2S\sqrt{2RH - H^2}} \quad (6)$$

Substituting the design values of R, H, and S into equation (6) yields an initial polar radius r_0 of 125 mm for the side cutting edge curve. To ensure that the side cutting edge curve transitions smoothly with the tangential cutting edge, thereby achieving a smooth soil penetration effect, the r_1 value is generally 10-20 mm smaller than the rotational radius R of the rotary tiller blade. In this case, it is set to 185 mm. The extreme angle θ_1 at the end of the cutting edge curve is:

$$\theta_1 = \frac{r_1 - r_0}{r_1} tan\tau_1 \quad (7)$$

where:

τ_1 is the static shear angle at the end of the side cutting edge curve, [°].

The size of the sliding angle is directly related to the resistance of the operation. If it is too large, it will increase the power consumption of the operation; if it is too small, it will not be possible to push soil clumps and straw out of the cutting edge. Considering the saline-alkali soil operating environment, the static sliding angle τ_1 at the endpoint of the cutting edge curve is designed to be 60°. Then, the terminal extreme angle θ_1 is 0.56 rad. From equation (5), it can be seen that the independent parameters include the polar radius r_0 of the starting point of the cutting edge curve and the polar radius increment Δr. Given the initial polar radius r_0 and the terminal polar radius θ_1 of the cutting edge curve of the rotary tiller, the above parameters can be substituted into equation (8).

$$\Delta r = \frac{r_1 - r_0}{\theta_1} \quad (8)$$

The increase in the helix angle Δr is 1.87, at which point the side cutting edge of the rotary tiller blade is:

$$r = 125 + 1.87\theta \quad (9)$$

Analysis of Rotary Tiller Blade Structural Parameters

Based on the analysis of the rotary tiller blade curve described above, a new rotary tiller blade was designed using the constructed curve. Its structural parameters are shown in Fig. 3.

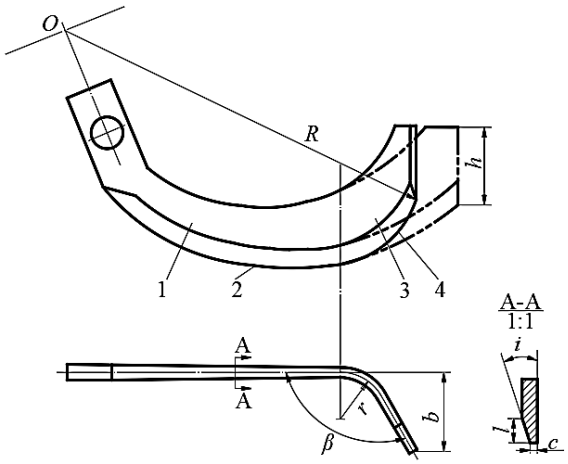


Fig. 3 - Diagram of the sliding cutting action of a rotary tiller blade

1 - side cutting surface; 2 - side cutting edge; 3 - tangential cutting surface; 4 - tangential cutting edge; R - blade rotation radius; h - tangential cutting surface height; β - bending angle; r - bending radius; b - working width; l - cutting edge width; c - cutting edge thickness.

Rotary tiller blade structural parameter design:

1. Blade rotation radius R. The design of the rotation radius R is based on factors such as working depth and soil properties. A larger rotation radius increases the working range of the blade, improving working efficiency, but also increases working resistance and power consumption; a smaller rotation radius helps reduce energy consumption and is suitable for harder soils, but may affect soil fragmentation effectiveness. Based on the designed working depth H = 120 mm in this paper, the blade rotation radius R = 195 mm is selected in this design (*Qin et al., 2021*).

2. Tangential height h. When the tangential height of the rotary tiller blade is too small, the quality of soil tossing and soil fragmentation deteriorates, and it cannot meet the requirements of agricultural cultivation. When the tangential height of the rotary tiller blade is too large, the tilling resistance of the rotary tiller blade increases, and the bent section is prone to breakage. Referring to relevant research content and combining the saline-alkali soil working environment, the tangential height is selected to be 35-65 mm (*He et al., 2021*).

3. Bending angle *β*. The angle formed between the tangential surface and the lateral surface of the rotary tiller blade after bending. If the bending angle of the rotary tiller blade is too large, the tip of the tangential blade will first come into contact with the soil and straw, increasing tillage resistance and reducing the service life of the tillage blade. If the bending angle is too small, the bent portion of the tillage blade will first contact the soil, resulting in better sliding cutting performance, but it will increase the contact area between the tangential surface and the soil, thereby increasing cutting resistance. According to the requirements for reducing resistance and combining operational requirements, a bending angle of 115° to 145° should be selected (*Xiao et al., 2024*).

4. Working width b. When the working width of the blade is too large, it will increase the resistance of single-blade operation. When the working width is too small, it will affect the quality of cultivation. Therefore, under the premise of meeting agronomic requirements, the working width *b* of the blade should be selected as 35-55 mm (*Yang et al., 2024*).

Based on the above analysis, the key parameters affecting the cutting resistance of rotary tiller blades in their structural design are the bending angle *β*, tangential height *h*, working width *b*, and rotational radius R, which have a significant impact on the operational performance of rotary tiller blades. Among them, the turning radius R has been determined. Changes in the bending angle *β*, tangential height *h*, and working width *b* have a direct impact on the power consumption and quality of rotary tillage operations. Therefore, these three parameters were selected as experimental factors. Combined with the requirements for preparing seedbeds in saline-alkali soil, a second-order orthogonal rotated center combination experiment was conducted on the three experimental factors to determine the optimal combination parameters and further analyze the power consumption during rotary tillage operations.

ESTABLISHMENT OF DISCRETE ELEMENT MODELS

Soil Model Settings

This experiment was conducted at the Agricultural Experiment and Demonstration Base for Saline-Alkali Land in the Yellow River Delta Agricultural High-Tech Industrial Demonstration Zone in Shandong Province. Using EDEM software, a soil discrete element model was established. The soil particle contact model selected was Hertz-Mindlin with Bonding, which can simulate the bonding action of soil particles, forming bonding action between particles until the limit of bonding rupture is reached (*Makange et al., 2020; Asl et al., 2020*).

The soil particle radius was set to 5 mm. The particle bonding radius is calculated based on soil density and moisture content. The rotary tiller blades are made of 65 Mn steel. To simulate actual working conditions, the forward speed is set to 1.38 m/s, the rotation speed to 330 r/min, and a tillage depth of 12 cm. A soil trench with dimensions of (length × width × height) 2000 mm × 1100 mm × 400 mm was established in the model, and a particle factory was set up above the soil trench to generate 401,800 soil particles using the gravity deposition method. The particles were bonded together via linking bonds, and the simplified rotary tiller blade model was imported. Simulation parameters were selected based on preliminary studies of the mechanical properties and contact parameters of saline-alkali soil, and the intrinsic parameters and contact parameters of each material required for the simulation model were determined through experiments (*Mak et al., 2012; Wang et al., 2024; Xu et al., 2025*). The simulation contact model parameters and simulation contact parameters are shown in Tables 1 and 2.

Table 1

Simulation model parameters

Materials	soil	65Mn
Density [kg·m^{-3}]	1.58×10^{3}	7.85×10^{3}
Poisson's ratio	0.32	0.30
Shear modulus [Pa]	7.25×10^{6}	7.90×10^{9}

Table 2

Simulated contact parameters

Materials	soil
Soil-soil recovery factor	0.35
Soil-soil static friction factor	0.5
Soil-soil rolling-friction facto	0.15
Soil-steel recovery factor	0.3
Soil-steel static friction factor	1.15
Soil-steel rolling friction factor	0.15
Normal rigidity [N·m^{-3}]	5×10^{8}
Tangential rigidity [N·m^{-3}]	5×10^{8}
Critical normal stress [Pa]	3×10^{6}
Critical tangential stress [Pa]	3×10^{6}

Experimental Design

Based on the above research, this experiment selected X1 bend angle, X2 tangent plane height, and X3 working width as experimental factors. According to the analysis of the experimental factors mentioned above, the bending angle was set at 115-145°, the tangent surface height at 35-65 mm, and the working width at 34-56 mm. An orthogonal rotation center combination experiment was conducted, and the experimental factor codes are shown in Table 3.

Table 3

Experimental factors and level coding

code	factors		
	X1	X2	X3
-1.353	110	30	30
-1	115	35	34
0	130	50	45
1	145	65	56
1.353	150	70	60

During the process of rotary tillage blades cutting soil, according to the principles of theoretical mechanics, changes in the torque of the blade shaft can reflect power consumption. Power consumption during rotary tillage operations can be calculated using equation (10).

$$P = \frac{n}{9550} \times M \tag{10}$$

where:

P is the power consumption, [kW]; n is the blade shaft speed, [r/min]; M is the blade shaft torque, [N·m].

Therefore, during rotary tilling operations, simply recording the torque and rotational speed of the blade shaft allows for the calculation of power consumption by the rotary tilling blades during operation.

RESULTS

Simulation Process Analysis

The total simulation duration is set to 3 seconds, with 0-1 seconds designated as the particle generation time and 1.1 seconds as the start time for the rotary tiller blade movement. A fixed time step size of 10% is set, and the grid size is set to 2.5 times the average particle radius, which corresponds to Rayleigh's value of $8.56e+10^{-6}$. Data is saved every 0.01 seconds. The simulation model is shown in Fig. 4.

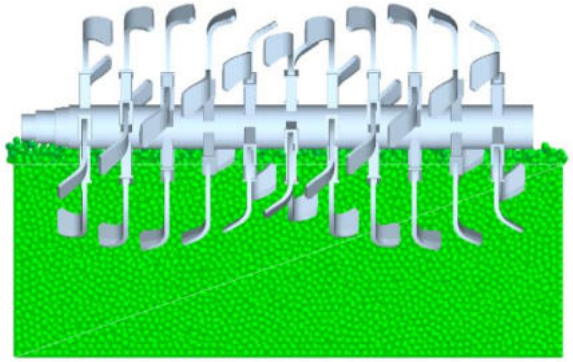


Fig. 4 - Rotary tiller blade - Discrete element simulation model for saline-alkali soil

During the simulation process, the torque applied to the rotary tiller blade shaft is recorded to calculate the power consumption of the rotary tiller during operation. The power consumption curve during the rotary tilling process is shown in Fig. 5.

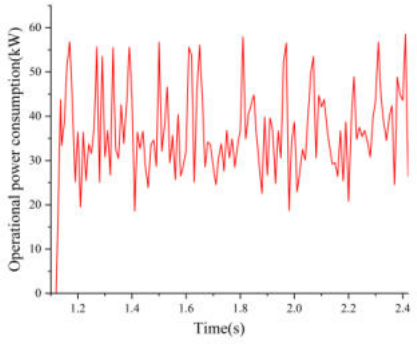


Fig. 5 - Power consumption curve diagram for rotary tiller operation

In the rotary blade simulation process, EDEM simulation post-processing can be used to analyze the dynamic contact process between the blade and the soil at different times, as shown in Fig. 6. As the blade shaft continues to move forward, the side cutting edge of the rotary tiller blade first contacts and cuts into the uncultivated soil in front of it. Under the combined action of cutting force and thrust, the soil particles accelerate. The tangential surface area of the blade forms a localized high-speed soil ejection zone. Soil particles are subjected to intense disturbance under the movement of the blade, moving backward and forward in a projectile-like manner, and the soil particles appear red in color. Overall, the velocity vectors of soil particles exhibit distinct layered characteristics. Particles at the leading edge of the blade move violently, primarily consisting of soil fragmentation and ejection movements. Particles below the blade move slowly, primarily involving compression and shear movements. Therefore, under the reciprocating action of the rotary tiller blade, soil particles are both disrupted and ejected, completing the entire cutting process. At the same time, the movement of soil particles also reflects the soil cutting mechanism of rotary tillers in actual operation and indicates that blade structural parameters have a significant impact on soil disturbance and energy consumption.

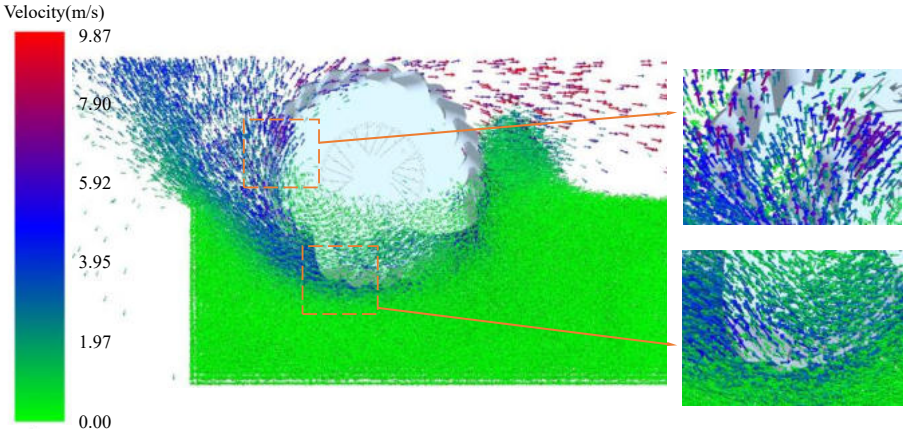


Fig. 6 – Rotary tiller cutting operation vector diagram

Through 17 simulation tests on EDEM, with bending angle, tangent height, and working width as test factors, and operating power consumption Y as the evaluation index, the measurement results are shown in Table 4.

Table 4

Experimental Results

Number	Factor			Operating power consumption Y [kW]
	X1 [°]	X2 [mm]	X3 [mm]	
1	-1	-1	-1	43.6
2	1	1	-1	36.8
3	-1	1	-1	53.5
4	1	-1	-1	39.8
5	-1	-1	1	44.8
6	1	1	1	42.7
7	-1	1	1	58.6
8	1	0	1	47.6
9	-1.353	0	0	52.4
10	1.353	-1.353	0	39.4
11	0	1.353	0	38.6
12	0	0	0	47.2
13	0	0	-1.353	38.8
14	0	0	1.353	45.3
15	0	0	0	40.8
16	0	0	0	40.6
17	0	-1	0	41.5

Analysis of Test Results

The test results were analyzed using Design-Expert 13 software to perform significance tests and variance analysis on the experimental data in Table 4, yielding the significance test results for the Y power consumption regression model in Table 5. As shown in Table 5, the analysis of operational power consumption $Y1$ indicates that at the P < 0.05 significance level, $X1$, $X2$, $X3$, $X1X2$, $X1^2$ and $X2^2$ are highly significant model terms; $X1X3$, $X2X3$, and $X3^2$ for significant model terms. The overall model P-value and coefficient of determination R^2 are <0.0001 and 0.9932, respectively, while the P-value for the non-significant terms is 0.2610. This indicates that the model is highly significant and has a very high fitting accuracy, with the non-significant terms not being statistically significant, and the regression being valid. The regression equation for operational power consumption Y is obtained.

$$Y = 40.78 - 4.39X1 + 3.71X2 + 2.47X3 - 1.98X1X2 + 0.9250X1X3 + 0.7250X2X3 + 2.93X1^2 + 1.29X2^2 + 0.8226X3^2 \quad (11)$$

Table 5

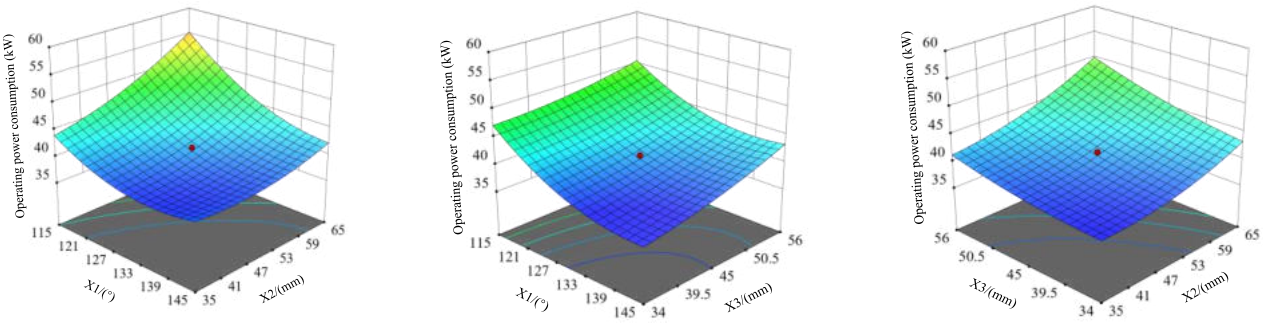
Analysis of variance of power consumption Y

Source	Sum of Squares	Freedom	Mean Square	F	P-Value
Model	571.38	9	63.49	113.36	<0.0001**
X1	224.70	1	224.70	401.21	<0.0001**
X2	160.30	1	160.30	286.22	<0.0001**
X3	71.10	1	71.10	126.95	<0.0001**
X1X2	31.20	1	31.20	55.72	0.0001**
X1X3	6.85	1	6.85	12.22	0.0100*
X2X3	4.21	1	4.21	7.51	0.0289*
$X1^2$	57.38	1	57.38	102.45	<0.0001**
$X2^2$	11.10	1	11.10	19.82	0.0030**
$X3^2$	4.54	1	4.54	8.10	0.0248*
Residual	3.92	7	0.5601		
Lack of Fit	3.47	5	0.6948	3.11	0.2610
Pure Error	0.4467	5	0.2233		
Cor Total	575.30	16			

Note: * indicates a significant effect (P<0.05), ** indicates a highly significant effect (P<0.01).

Response Surface Analysis

The response surface plots of the operating power consumption for any two factors, namely the bending angle, tangential height, and working width, as interaction factors are shown in Fig. 7.



(a) The interaction of X1 and X2 factors *(b) The interaction of X1 and X3 factors* *(c) The interaction of X2 and X3 factors*

Fig. 7 - Response surface analysis of power consumption during rotary tillage

As shown in Fig. 7a, when the working width is at the zero level, the operational power consumption increases as the bending angle decreases and the tangential height increases. As shown in Fig. 7b, when the tangential surface height is at the zero level, the operational power consumption decreases as the working width decreases and the bending angle increases. Additionally, the operational power consumption changes more rapidly with the direction of the bending angle than with the direction of the working width.

Therefore, during rotary tillage operations, the bending angle has a greater influence on operational power consumption than the working width. As shown in Fig. 7c, when the bending angle is at the zero level, the operational power consumption increases with the increase in working width and tangential surface height.

As shown in Table 5, the F values in the table indicate the influence of each influencing factor on the test indicators. The larger the F value, the greater the influence on the test indicators. The degree of influence of each test factor on the operational power consumption Y, from greatest to least, is as follows: $X1$ bend angle, $X2$ tangential face height, and $X3$ working width.

Optimal Design of Experimental Combinations

To determine the optimal combination of rotary tiller blade parameters while ensuring rotary tilling quality, an optimization design was conducted for each experimental factor. By combining the boundary conditions of each factor, the goal of reducing blade cutting resistance and improving rotary tilling quality was achieved. The objective function and constraint function were determined as follows:

$$\begin{cases} Y_{min} \\ s.t. \begin{cases} 110° \le X1 \le 150° \\ 30mm \le X2 \le 70mm \\ 30mm \le X3 \le 60mm \end{cases} \end{cases} \quad (12)$$

Using Design-Expert 13 software for analysis and solution, the optimal parameter combination affecting the power consumption of the operation was obtained as follows: bending angle 136.49°, working width 34.20 mm, and tangent height 42.23 mm. At this point, the power consumption of the operation was 36.64 kW. To verify the accuracy of the optimization results, performance verification tests were conducted on the optimized rotary tiller blades. Three measurements were taken and averaged, resulting in an average operating power consumption of 37.48 kW. The test results show that the maximum error between the theoretical value and the test value is 2.24%. The simulation test results are basically consistent with the theoretical results, indicating that the regression equation is accurate.

Results validation

The experimental field is located at the Saline-Alkali Land Agricultural Experiment and Demonstration Base in the Yellow River Delta Agricultural High-Tech Industrial Demonstration Zone, Dongying City, Shandong Province (118°65E, 38°32′N). It has a warm temperate semi-humid monsoon climate with distinct seasons, an annual average temperature of 12.3°C, an annual average precipitation of 587.4 mm, an annual average sunshine duration of 2,234 hours, and a frost-free period of 198 days. The soil at this experimental base is coastal saline-alkali soil, with soil salinity levels ranging from 1‰ to 10‰, encompassing three categories of saline-alkali land: mild, moderate, and severe. This experiment was conducted on mild saline-alkali land.

Field Trial Conditions

During field trials, the test field was divided into five plots, each 50 m long and 1.5 times the width of the machinery. The first 10 m of each plot was designated as the acceleration zone for the machinery, and the middle 20 m was designated as the stable forward movement zone for the machinery. The testing equipment primarily includes a Deutz-Fahr 1804 tractor, a rotary tiller prototype, a ring blade, a measuring tape (3m), steel ruler (300 mm), electronic scale, sealed bags, tape measure (50 m), 0.5 m × 0.5 m square frame, TOP CLOUD-AGRI TECHNOLOGY CO (TJSD-750-II) soil compaction meter, and TOP CLOUD-AGRI TECHNOLOGY CO (TZS-1K-G) soil moisture rapid tester.

The working environment conditions during field trials are shown in Table 6. During field trials, the testing methods for machinery are based on NY/T499-2013 “Rotary Tiller Operational Quality” and GB/T5668-2017 “Rotary Tiller,” with operational power consumption as the testing criterion. Power consumption was measured using an HCNJ-101 dynamic torque sensor (torque range: 0.05-2000 N·m; speed range: 2000 r/min) and a three-point tension sensor (SBT620TF-10T). The field test process is shown in Fig. 8.

Table 6

Test environmental characteristics

Measurement item	Argument
Soil moisture content [%]	18.58
Volume weight of soil [g·cm^{-3}]	1.45
Soil compactness [kg/cm^2]	26.72
Soil pH value	7.86



(a) Rotary tiller operation diagram *(b) Torque sensor installation diagram*

Fig. 8 – Field trial effect diagram

Analysis of Field Trial Results

During field trials, the designed rotary tiller blades were compared with traditional rotary tiller blades (GB/T 5669-2017 Rotary Tiller Blade IIT195, bending angle 120°, tangential surface height 50 mm, working width 50 mm) for experimental comparison. Due to the complex field conditions of saline-alkali soil, there was a certain degree of error between the experimental results and the simulation values. Therefore, the power consumption data from five tests within the specified time period were recorded, and their average value was taken as the experimental measurement result. Under identical initial simulation parameters (i.e., bending angle of 136.49°, working width of 34.20 mm, and tangential height of 42.23 mm), the measured average power consumption of the rotary tiller was 38.49 kW, which resulted in a measurement error of 4.81 % compared to the simulated average power consumption of 36.64 kW. Further validation of simulation accuracy is provided by the field test results shown in Table 7. The actual test values are higher than the simulation test values, consistent with the results obtained by other scholars in soil shear tests (*Kang et al., 2016*).

Table 7

Field trial comparison results

Serial number	Design of rotary blades		Traditional rotary blade	
	torque value M [Nm]	Operating power consumption Y [kW]	torque value M [Nm]	Operating power consumption Y [kW]
1	1103.45	38.13	1254.16	43.34
2	1094.06	37.81	1308.64	45.22
3	984.35	34.01	1322.73	45.71
4	1147.62	39.66	1426.18	49.28
5	1238.73	42.86	1324.37	45.76
Average	1113.64	38.49	1327.22	45.86

As shown in the experimental results of Table 8, the maximum power consumption value of the designed rotary tiller blade during field operations was 42.86 kW, the minimum was 34.01 kW, and the average was 38.49 kW. The error between the simulated values and the theoretical values was less than 10%, indicating that the simulated power consumption has high accuracy.

Under the same operational conditions, the power consumption of the traditional rotary tiller blade ranged from a maximum of 49.28 kW to a minimum of 45.22 kW, with an average value of 45.86 kW. Compared to the results of the traditional rotary tiller blade, the power consumption of the designed rotary tiller blade during operation was reduced by 16.07%. The results indicate that by optimizing the structural parameters of the rotary tiller blade, the resistance during operation can be effectively reduced.

CONCLUSIONS

1) In response to the high energy consumption and poor quality of rotary tillage operations caused by the compacted and heavy soil in the saline-alkali lands of the Yellow River Delta, this paper systematically analyzes the dynamic characteristics of rotary tillage blades and soil, investigates the influence of rotary tillage blade structural parameters on the tillage performance of saline-alkali soils, and designs a blade edge curve based on the sliding cutting effect. It clarifies that the bending angle, tangent plane height, and working width are the primary factors influencing operational energy consumption.

2) Through orthogonal center combination experiments and discrete element simulation analysis, the optimal parameter combination was obtained: bending angle 136.49°, working width 34.20 mm, tangent height 42.23 mm, corresponding to an operating power consumption of 37.80 kW. Performance verification tests showed that the maximum error between the theoretical value and the test value was 2.24%, and the regression model was accurate.

3) Field comparison tests showed that under conditions of soil hardness of 26.72 kg/cm², moisture content of 18.58%, and pH value of 7.86, the average power consumption of the designed rotary blade was 38.49 kW. Compared with traditional rotary blade, power consumption is reduced by 16.07%, meeting the requirements for tilling heavy, sticky soil on saline-alkali land. This provides theoretical reference for the development of saline-alkali land and the optimization of rotary tillers.

ACKNOWLEDGEMENT

This research is supported by the National Key Research and Development Program of China (Project no. 2023YFD2001400); Shandong Province Key Research and Development Program (Science and Technology Demonstration Project): Creation and Industrial Application of Fertilizer and Intelligent Equipment for Improving the Fertility of Saline-Alkali Soil (2024SFGC0405); National Key R&D Program of China (Project no.2022YFE0125800); Development of Key Components for High-Efficiency Tillage Equipment for Saline-Alkali Soil (Y20240055); Research and Development of High-Quality Tillage and Composite Operations Technology and Equipment for Saline-Alkali Land (WSR2023093).

REFERENCES

[1] Asl, J. H., & Singh, S. (2009). Optimization and evaluation of rotary tiller blades: Computer solution of mathematical relations. *Soil and Tillage Research*, *106*(1), 1-7. https://doi.org/10.1016/j.still.2009.09.011

[2] Guan C. (2021). *Basic Research on the Layered Tillage Technology by biaxial rotary tillage component for vegetable bed former (双轴分层旋耕碎土起垄技术基础研究)*. [Doctoral dissertation, Jiangsu University]. https://link.cnki.net/doi/10.27170/d.cnki.gjsuu.2021.000032. Jiangsu/China

[3] Guan, C., Fu, J., Cui, Z., Wang, S., Gao, Q., & Yang, Y. (2021). Evaluation of the tribological and anti-adhesive properties of different materials coated rotary tillage blades. *Soil and Tillage Research*, *209*, 104933.

[4] Hao J., Yu H., Zhao J., Li J., Ma Z., & Cai J. (2019). Design and test of wedge drag reduction rotary blade (楔形减阻旋耕刀设计与试验). *Transactions of the Chinese Society of Agricultural Engineering (Transactions of the CSAE)*, 35(8): 55-64. Hebei/China.

[5] He X., Zhang X., Zhao Z., Shang S., Wang D., & Yang S. (2022). Design and optimization tests of reverse spin-throwing cyperus edulis starting device (反向旋抛式油莎豆起挖装置设计与试验). *Transactions of the Chinese Society for Agricultural Machinery*, 53(05), 34-43. Wulumuqi/China

[6] He X., Zhang X., Zhao Z., Shang S., Wang D., & Yuan X., (2021). Design and test of resistance-reducing excavation device of Cyperus edulis based on discrete element method (基于离散元法的油莎豆降阻挖掘装置设计与试验). *Transactions of the Chinese Society for Agricultural Machinery*, 52(12), 124-133. doi:10.6041/j.issn.1000-1298.2021.12.013. Wulumuqi/China

[7] Kang J., Li S., Yang X, & Liu L. (2016). Structure parameters optimization of sine exponential curve type ditching blade (正弦指数曲线型开沟刀片结构参数优化). *Transactions of the Chinese Society for Agricultural Machinery*, 47(11), 91-99+17. doi:10.6041/j.issn.1000-1298.2016.11.012. Beijing/China

[8] Liang F., Wang D. C., You Y., Wang G., Zhang X., He C. B., & Li S. (2016). Design and optimization of the edge curve of root-cutting blade in grassland (草地破土切根刀具的刃口曲线设计与优化). *Journal of China Agricultural University*, 21(06),100-107. Beijing/China

[9] Liu G., Xia J., Zheng K., Cheng J., & Wei Y. (2022). Design and experiments of the barrier type rotary anti-adhesion blade roller with vibration crosspiece (振动横挡阻隔式旋耕防粘结刀辊设计与试验). *Transactions of the Chinese Society of Agricultural Engineering*. Vol. 38(23), pp. 29-40. Wuhan/China

[10] Makange, N. R., Ji, C., & Torotwa, I. (2020). Prediction of cutting forces and soil behavior with discrete element simulation. *Computers and Electronics in Agriculture*, *179*, 105848. https://doi.org/10.1016/j.compag.2020.105848

[11] Mak, J., Chen, Y., & Sadek, M. A. (2012). Determining parameters of a discrete element model for soil–tool interaction. *Soil and Tillage Research*, *118*, 117-122. https://doi.org/10.1016/j.still.2011.10.019.

[12] Nalawade, R. D., Singh, K. P., Roul, A. K., Agrawal, K. N., Sonawane, S., Mahore, A., & Elbeltagi, A. (2024). Study on the effect of geometrical and operational parameters on performance dynamics of modified rotary blades using DEM. *Scientific Reports*, 14(1), 19239. https://doi.org/10.1038/s41598-024-69803-8

[13] Qin K., Liang X., Cao C. M., Ding W., Wu Z., & Fang L. (2021). Design and experiment of combined cutting and throwing ditching blade for tea garden (茶园切抛组合式开沟刀设计与试验). *Transactions of the Chinese Society for Agricultural Machinery*, 52(05), 74-82. Anhui/China

[14] Wang D., Lu T., Zhao Z., Shang S., Zheng S., & Liu J. (2024). Calibration of discrete element simulation parameters for cultivated soil layer in coastal saline alkali soil (滨海盐碱地耕作层土壤离散元仿真参数标定方法). *Transactions of the Chinese Society for Agricultural Machinery*, 55(11),240-249. https://link.cnki.net/urlid/11.1964.S.20240903.1531.002. Qingdao/China

[15] Xiong P., Yang Z., Sun Z., Zhang Q., Huang Y., & Zhang Z. (2018). Simulation analysis and experiment for three-axis working resistances of rotary blade based on discrete element method (基于离散元法的旋耕刀三向工作阻力仿真分析与试验). *Transactions of the Chinese Society of Agricultural Engineering (Transactions of the CSAE)*, 34(18): 113-121. doi: 10.11975/j.issn.1002-6819.2018.18.014. Guangzhou/China

[16] Xiao W., Niu, Wang P., Xie Y., Xia F. (2024). Simulation ANSYS and optimization of soil cutting of rataty blade by ANSYS/LS-DYNA (基于 ANSYS/LS-Dyna 旋耕刀切土仿真分析及优化). *INMATEH-Agricultural Engineering*, 72(1):22-32. DOI: https://doi.org/10.35633/inmateh-72-02

[17] Xu, N., Xin, Z., Yuan, J., Gao, Z., Tian, Y., Xia, C., Liu, X., & Wang, D. (2025). Calibration of Discrete Element Simulation Parameters and Model Construction for the Interaction Between Coastal Saline Alkali Soil and Soil-Engaging Components. *Agriculture*, 15(1), 7. https://doi.org/10.3390/agriculture15010007

[18] Yang D., Cai W., Wu R., Zhang X., He Y., He L., & Xiong A. (2024). Optimization design of rotary cultivator blade structure parameters for tea garden micro-tillers based on discrete element method (基于离散元法茶园微耕机旋耕刀结构参数优化设计). *Southern Agricultural Machinery*, 55(01),7-10+15. doi:10.3969/j.issn.1672-3872.2024.01.002. Nanchang/China

[19] Zhao, Z., Hou, J., Guo, P., Xia, C., Yan, H., & Wang, D. (2025). Analysis of Soil–Straw Movement Behavior in Saline–Alkali Soil Under Dual-Axis Rotary Tillage Based on EDEM. *Agriculture*, *15*(3), 337.

[20] Zhu, W., Gu, S., Jiang, R., Zhang, X., & Hatano, R. (2024). Saline–alkali soil reclamation contributes to soil health improvement in China. *Agriculture*, *14*(8), 1210.

[21] Zhang X., Hu X., Zhang L. & Kheiry A. (2024). Simulation and structural parameter optimization of rotary blade cutting soil based on SPH method. *International Journal of Agricultural and Biological Engineering*, 17(3):82-90. doi: 10.25165/j.ijabe.20241703.8470.

[22] Zhang C., Xia J., Zhang J., Zhou H., Zhu Y., & Wang J. (2019). Design and experiment of knife roller for six-head spiral straw returning cultivator (六头螺旋秸秆还田耕整机刀辊设计与试验). *Transactions of the Chinese Society for Agricultural Machinery*, 50(3):25-34. https://doi:10.6041/j.issn.1000-1298.2019.03.003. Wuhan/China

[23] Zhang, X., Zhang, L., Hu, X., Wang, H., Shi, X., & Ma, X. (2022). Simulation of soil cutting and power consumption optimization of a typical rotary tillage soil blade. *Applied Sciences*, *12*(16), 8177.

[24] Zhang Q.S., Qi T., Ao Q., Shu C. X., Liao Y., & Liao Q. (2023). Design and experiment of rapeseed direct seeding machine with furrow opener and shallow plowing (油菜机械直播机开沟浅旋装置设计与试验). *Transactions of the Chinese Society for Agricultural Machinery*, 54(10), 58-67+104. doi:10.6041/j.issn.1000-1298.2023.10.005. Wuhan/China

RESEARCH ON GRADING METHOD OF PEPPER PLUG SEEDLINGS BASED ON MACHINE VISION
/
基于机器视觉的辣椒穴盘苗分级方法研究

Fengwei YUAN[1)], Shuaiyin CHEN[1)], Zhang XIAO[*1)], Erjie SUN[1)], Guoning MA[1)], Gengzhen REN[1)], Zhenlong LI[1)] Zhenhong ZOU[2)], Xiangjiang WANG[1)]

[1)] College of Mechanical Engineering, University of South China, Hengyang/China.

[2)] Hengyang Vegetable Seeds Co. Hengyang/ China.

Tel: +8615200596268; E-mail: 2013000885@usc.edu.cn

DOI: https://doi.org/10.35633/inmateh-76-105

Keywords: *Machine vision, Plug seedlings, Image segmentation, Grading methods*

ABSTRACT

This study proposes a grading method using combined target detection and segmentation models to enhance grading accuracy for pepper plug seedlings. We constructed separate datasets for target detection and image segmentation of pepper plug seedlings, then trained various detection models including EfficientDet, Faster R-CNN, SSD, and YOLO-series architectures. After comprehensive evaluation, YOLOv5 achieved optimal performance with 99.5% mAP, a compact 3.8 MB model size, and rapid 5.33ms inference time per image. To avoid the impact of the culture medium and adjacent pepper seedlings on the image, we developed an improved U-Net model incorporating an Efficient Channel Attention (ECA) mechanism, enhancing segmentation accuracy by 1.29% to 93.01% while reducing processing time by 69.7% (33.32 ms). Subsequent feature extraction analysed lateral area, height, stem thickness, hypocotyl length, and divergence degree from segmented images. Using these extracted features, grading models were trained employing support vector machines, k-nearest neighbours, and random forests. The random forest model achieved a grading accuracy of 99.33%, validating that this method meets the accuracy requirements for pepper seedling grading.

摘要

为了提高辣椒穴盘苗分级检测精度，本研究提出了一种基于目标检测和分割模型相结合的辣椒穴盘苗分级方法。首先，构建辣椒穴盘苗目标检测和图像分割两个数据集；其次，训练了 Efficientdet，Faster-Rcnn，SSD 以及 YOLO 系列目标检测模型，经过综合对比 YOLOv5 检测效果最好，平均精度均值（mean average precision，mAP）达到 99.5%，模型大小 3.8 MB，单张图像检测时间 5.53ms；然后，为了避免培养基质以及相邻辣椒苗对图像的影响，使用 U-Net 算法作为本文的图像处理算法的基础模型，并引入通道注意力机制 ECA（Efficient Channel Attention Network）进行改进，与 U-Net 相比改进后模型分割准确率提高 1.29%，达到 93.01%，检测时间缩短 69.7%，为 33.32ms；最后基于图像分割算法处理后的图像，提取了辣椒穴盘苗面积，高度，茎粗，下胚轴长度和发散程度等参数，并利用提取的特征参数完成了支持向量机，K 最邻近算法，和随机森林算法的分级模型训练，其中随机森林模型分级准确率为 99.33%，验证了该方法能够满足辣椒穴盘苗分级精度要求。

INTRODUCTION

During the cultivation process of plug seedlings, factors such as seed quality, temperature, sunlight, and soil conditions can cause large differences in seedling morphology, which in turn affect subsequent transplanting and sales. Currently, the grading of plug seedlings primarily relies on manual labor, which is characterized by inconsistent grading standards and relatively high costs. Therefore, achieving automated grading for plug seedlings is a crucial task.

Subo Tian et al., (2017), expressed the cumulative maximum of 0 grey value pixels within a certain range of rows as the diameter of the seedling to achieve grading of melon seedlings. *Li Mingyong et al., (2021),* extracted two characteristics of leaf area and greenness per unit leaf area for grading of pepper plug seedling. *Jiang Huanyu et al., (2009),* determined whether the transplanting criteria were met by extracting the leaf area and perimeter of plug seedlings, with an identification accuracy of 98%. *Tong Junhua et al.,* (*2018*), used the centroid method and watershed algorithm to extract leaf area and the number of seedling leaves in a string red tray image for quality evaluation. *Fu Wei et al.,* (*2022*), employed threshold segmentation, erosion, dilation, and area division to extract the leaf area of lettuce seedlings in terms of pixel values, which was subsequently used to assess seedling quality.

Although the aforementioned literature obtained different methods for grading plug seedlings by obtaining phenotypic parameters, the algorithms such as threshold segmentation used are not suitable for changing environmental conditions and have low robustness.

In recent years, deep learning algorithms continue to develop, and convolutional neural networks are beginning to be widely used in grading detection, recognition and segmentation of plug seedlings. *Zhang Xiuhua et al., (2022)*, used spatial pyramid pooling and introduced the SAM spatial attention mechanism to improve the YOLOv3-Tiny model, with an average accuracy of 98.22% for tomato seedling robustness detection. *Xu Shengyong et al., (2023),* collected height and leaf area data of watermelon seedlings in the tray for the first three days, and used the LSTM neural network to predict the height and leaf area on the sixth day for grading, achieving an accuracy rate of 84%. *Li Yatao et al., (2024),* utilized a multi-layer perceptron neural network for image segmentation and calculated the area of plug seedlings by connected component centroid coordinates for grading, achieving an accuracy rate of 96.9%. The aforementioned studies indicate that there are various methods for grading plug seedlings; however, most of these methods focus primarily on seedlings with fewer than five leaves, which do not meet the requirements for sale.

To address this issue, this paper proposes a phenotypic parameter acquisition method for pepper plug seedlings, which combines target detection and segmentation models. The target detection model processes the entire row of pepper seedlings into individual states, thereby reducing the complexity and computational load of subsequent image processing. The segmentation algorithm is then used to segment the images processed by the detection model, avoiding the influence of the background and adjacent pepper seedlings. Feature extraction methods are utilized to obtain five parameters of the pepper plug seedlings, including lateral area, height, stem thickness, hypocotyl length, and divergence degree. By comparing the experimental results of various grading models, the random forest model, which has the highest accuracy, is selected to achieve accurate grading of pepper plug seedlings.

MATERIALS AND METHODS

Data set construction

A size of 5×10 was selected for the plug seedlings in this study. The images were captured using an industrial camera MI-230U150C, with a resolution of 1920px by 1200px. To comprehensively acquire the phenotypic parameters of the pepper seedlings, the camera is positioned at an inclined angle above the seedlings to avoid interference from the back row of seedlings. The target detection dataset comprised a total of 200 images of pepper seedling trays, while the image segmentation dataset, derived from the individual seedling trays processed by the target detection algorithm, contained 1000 images. Both datasets were proportioned into training and validation sets with a 7:3 ratio. The processing flow is shown in Fig. 1.

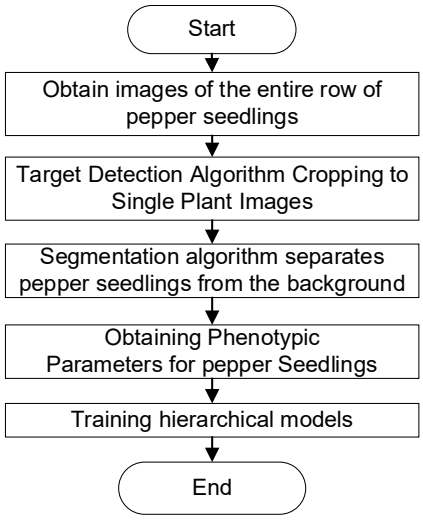


Fig. 1 - Flow chart of hierarchical processing

Algorithm for detection of pepper plug seedlings

In large scale nursery enterprises, most of them use plug seedlings, and the research object of this paper is to meet the transplanting conditions of pepper plug seedlings. The seedlings in the current growth cycle exhibit dense foliage, resulting in significant mutual shading between plants. Processing an entire row of seedlings into individual plants can effectively reduce the complexity of subsequent image processing.

After comprehensive comparison, this study adopts the YOLOv5 model for the detection of pepper plug seedlings. The backbone network of YOLOv5 employs a hopping fusion technique based on the Darknet architecture, which effectively enhances the information transfer efficiency of the network, allowing the model to learn rich feature information in a shorter period of time, thereby improving overall detection performance.

Segmentation Algorithm for Pepper plug Seedlings

The single target image is segmented based on the bounding box coordinates of the pepper seedling detected by YOLOv5. Since robust seedlings occupy a significant amount of space, the leaves of other seedlings may appear in the individual image of the pepper seedlings. Traditional segmentation algorithms that rely on features such as color, shape, and contour are incapable of distinguishing the leaves of other seedlings. In contrast, the improved U-Net segmentation algorithm, which is trained on convolutional neural networks, automatically learns the feature representation within the images, leading to superior segmentation outcomes. It effectively manages more intricate and delicate boundaries.

Network Architecture of Pepper Plug Seedling Segmentation Algorithm

The left side of the U-Net network structure comprises the contracting path, which doubles the feature channels and halves the image dimensions after each down sampling through convolutional layers and max pooling layers, primarily serving to extract shallow features of the target. The right side consists of the expansive path, which performs the inverse operation of down sampling through transposed convolution, meaning that the feature channels are halved while the image dimensions are doubled. The results of the transposed convolution are then concatenated with the corresponding parts of the feature map on the left side. This structure serves two main purposes: first, to extract the deep features of the image and perform feature fusion; second, to resize all extracted features back to the original image dimensions. Additionally, due to the inherent limitation of skip connections in the U-Net model for capturing long-range dependencies, an Efficient Channel Attention module (ECA)(*Wang et al.*, *2020*) is integrated between each pooling layer and subsequent convolutional layer on the contracting path (left side) of the U-Net architecture. This integration aims to strengthen inter-channel dependencies and enhance the model's capability to extract fine-grained surface features of seedlings. The enhanced U-Net network architecture is illustrated in Fig. 2.

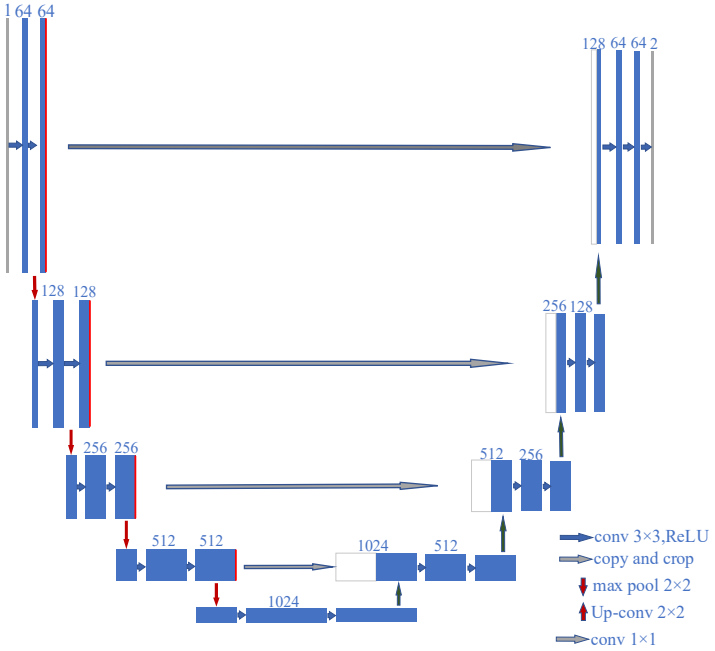


Fig. 2 - Enhanced U-Net network structure diagram

ECA Attention Mechanism

This study integrates ECA mechanism into the down-sampling part of the U-Net, effectively capturing channel interactions while avoiding dimensionality reduction. The inspiration for this attention mechanism is derived from the SE attention mechanism (*Hu et al.*, *2018*). The ECA, modified based on this foundation, does not increase the model's complexity and enhances the overall network performance. The ECA module initially computes the size of the one-dimensional convolutional kernel adaptively as indicated in Equation (1).

$$\left[k = \left| \frac{\log_2(C)}{\gamma} + \frac{b}{r} \right|_{odd} \right] \quad (1)$$

In the equation, C denotes the channel count of the input features, while γ and b are the hyperparameters. The process of taking the absolute value and then rounding down to the nearest odd integer guarantees that the kernel size remains odd. The ECA module utilizes a one-dimensional convolution on the input features, as illustrated in Equation (2).

$$[out = Conv1D_k(in)] \quad (2)$$

The illustration of the attention mechanism is illustrated in Fig. 3.

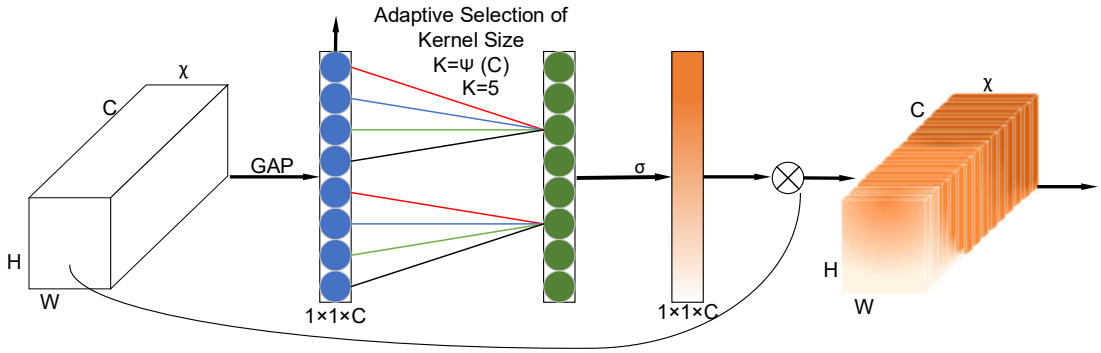


Fig. 3 - Schematic diagram of the ECA attention mechanism

Pepper plug Seedlings Feature Parameter Extraction

The characteristic parameters of plug seedlings serve as the basis for quality grading. Before transplanting the seedlings, it is essential to assess their quality based on these parameters to ensure that seedlings transplanted into the same tray are of uniform quality. In accordance with the agricultural industry standard of China, NY/T 3952-2021 (*Ministry of Agriculture and Rural Affairs of the People's Republic of China*, *2021*), this study selects five characteristic parameters for grading plug seedlings: lateral area, plant height, stem thickness, hypocotyl length, and divergence degree.

Parameter extraction of lateral area

This study employs the findContours function from the OpenCV vision library to detect the contours of pepper seedlings. This function retrieves all contours in the cv2.RETR_TREE mode, which prevents the inability to recognize internal contours due to overlapping leaves, thereby increasing the lateral area of the seedlings. The contourArea function is then used to count the pixel points and calculate the lateral area. The calculation formula is as follows:

$$A_i = contourArea(contours_i) \quad (3)$$

$$A = \sum_{i=1}^{n} A_i \quad (4)$$

Within the formula, Ai refers to the area of the ith contour, A signifies the aggregate area, and n indicates the total count of contours.

Extraction of height parameters

The method for extracting the height parameter typically involves locating the smallest enclosing rectangle around the plug seedlings and using the height of this rectangle as the plant height. Since the images of the plug seedling captured from a frontal view can have part of the stem obscured by the tray, this study tilted the camera at a certain angle during image acquisition, as shown in Fig. 4.

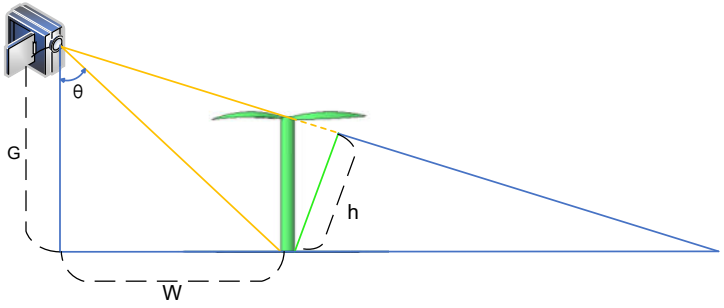


Fig. 4 - Schematic diagram of the plug seedling height error

(θ is the camera shooting angle; G is the camera height; W is the distance between the camera and the plug seedling; h is the plug seedling shooting height).

As can be discerned from Figure 4, the height of the plug seedlings depicted in the image, which is due to the angle of photography, represents the projection of their actual height. Prior to the training of the grading model, it is essential to perform a height correction on the tray seedlings to mitigate errors. The formula for height correction is presented as Equation (5).

$$H = \frac{h}{\cos(\sin^{-1}(\frac{\sqrt{G+W^2-h^2}}{\sqrt{G+W^2}})-\theta)} \quad (5)$$

The height parameter of the plug seedling is based on the contour calculation method during the extraction of the area parameter. Based on the known contour of the pepper seedling, the minimum rectangular bounding box of the seedling is calculated by using the boundingRect function in the OpenCV vision library, and the height of this rectangle is approximated as the height of the pepper seedling.

Extraction of width parameters

The stem thickness of plug seedlings can serve as an indicator of the "robustness" of the seedlings to a certain degree. In this study, the Canny edge detection algorithm is employed to initially identify the root location of the pepper seedlings. Following this, the contours within the area between the root and 20 pixels above it are detected. Then, using the root and the 20 pixels above as reference points, and the detected contours as criteria, the minimum bounding rectangle of the stem section is fitted to represent the stem thickness of the pepper seedlings, offering enhanced stability.

Extraction of Hypocotyl Parameters

Image scanning begins at the bottom of the seedling image, where the lowest pixel row generally has a value of 0 (black). At the root position, the pixel value changes from 0 to 1 (white) and then back to 0, which is recorded as two transitions (0 → 1 → 0). The row at which the first transition occurs is taken as the root position. Scanning continues upward, and the distance to the first true leaf is defined by the number of transitions encountered, normally equal to two. The line showing a different number of transitions is recorded as the first leaf position, and the vertical pixel distance between the root row and the leaf row represents the hypocotyl length. To avoid errors caused by occluded or deformed stems, a threshold is introduced: if the hypocotyl length is calculated to be less than 10 pixels, scanning proceeds further upward until a valid leaf position is identified. This procedure ensures accurate and reliable determination of hypocotyl length. The calculation method is shown in Equation 6. For each pixel point P_{ij}, in row i, it is checked whether it differs from the previous pixel point $P_{i(j-1)}$.

$$C_i = \sum_{j=1}^{W} P_{ij} \neq P_{i(j-1)} \quad (6)$$

During scanning, the current line number is recorded when C_i equals 2, after which the upward scan continues. If C_i is not equal to 2 and the distance between two consecutive lines exceeds 10 pixels, the vertical difference between these lines is considered the measured hypocotyl length.

Extraction of the dispersion degree parameters

n this paper, the image of a single seedling is obtained using a target detection algorithm and a segmentation algorithm, and the resulting image contains the overall characteristics of the seedling. In fact, the dispersion degree of the seedling leaves can also indicate the 'strength' of the seedling in a certain aspect. Considering that representing the dispersion degree of plug seedlings solely through the minimum bounding rectangle is susceptible to the accuracy of contour detection results, and individual plug seedling images are obtained via object detection algorithms, this paper proposes to utilize the total pixel area of the entire individual plug seedling image as the parameter to characterize the dispersion degree of single-pepper plug seedlings.

Grading of plug seedlings

Data standardisation

This study utilizes the measured lateral area, plant height, stem thickness, hypocotyl length, and dispersal degree of plug seedlings as grading criteria. The extracted pixel values for the lateral area of the seedlings typically range from 5 to 6 digits, while the pixel values for plant height generally consist of 3 digits, and stem thickness is represented by only 2 digits.

The substantial differences among these five parameters can easily lead to situations where larger parameters overshadow the characteristics of smaller ones during the training of the grading model. To mitigate this issue, it is necessary to standardize these five feature parameters.

In this paper, the StandardScaler method was used to normalise the data with the processing equation:

$$X^* = \frac{x-\mu}{\sigma} \quad (7)$$

In the equation, x denotes the original feature value, μ represents the mean of the feature, and σ signifies the standard deviation of the feature.

Classification methodology

As the research subjects of this paper are pepper seedlings that have already satisfied the requirements for transplanting, there are essentially no empty slots. Therefore, this paper divides the plug seedlings into two categories: Grade 1 and Grade 2. In machine learning, a variety of classification algorithms have shown good performance on binary classification issues. This paper discusses Support Vector Machines (SVM), Random Forest (RF) classification algorithms, and K-Nearest Neighbor (KNN) classification algorithms, with the aim of training a grading model that is most suitable for this project.

Scikit-learn (Sklearn) is a third-party machine learning library for Python that is both simple and efficient, including a range of machine learning algorithms such as Support Vector Machines, K-Nearest Neighbor classification algorithms, and Random Forest. This paper employs Sklearn directly for the training of the grading model.

RESULTS

Evaluation indicators

This research aims to identify a suitable target detection model by assessing model performance based on precision (P), recall (R), mean average precision (mAP), mean intersection over union (MIOU), model size in megabytes (MB), and detection time in milliseconds (ms). The metrics calculation formulas are presented below:

$$p = \frac{TP}{TP+FP} \times 100\% \quad (7)$$

$$R = \frac{TP}{TP+FN} \times 100\% \quad (8)$$

$$AP = \frac{1}{n}\int_0^1 P(R)dR \quad (9)$$

$$mAP = \sum_{i=1}^{N} \frac{AP_i}{N} \quad (10)$$

$$MIOU = \frac{1}{k+1}\sum_{i=0}^{k} \frac{TP}{TP+FP+FN} \quad (11)$$

In the equation, TP denotes the true positive samples, FP denotes the false positive samples, FN denotes the false negative samples, and N refers to the number of detection categories.

Comparison of detection algorithm results

With the continuous development of computer hardware, machine vision-based object detection methods have entered a prosperous period. The current mainstream object detection algorithms include EfficientDet (*Tan et al.*, *2020*), Faster R-CNN (*Ren et al.*, *2015*), SSD (*Liu et al.*, *2016*), and the YOLO (*Bochkovskiy et al.*, *2020; Ge et al.*, *2021; glenn-Jocherglenn-Jocher*, *2022; Redmon & Farhadi*, *2018; Ultralytics*, *2023; Wang et al.*, *2023*) series of algorithms. We conducted experimental comparisons of these popular object detection models, and the results are presented in Table 1.

Table 1

Performance of mainstream target detection models on pepper seedling dataset

Model	Precision	Recall	mAP	Parameter	Inference Time
	[%]	[%]	[%]	[MB]	[ms]
Efficientdet	77.54	84	82.29	15.8	14.83
Faster-Rcnn	96.86	99.35	99.92	113.4	39.24
SSD	92.68	98.06	98.81	95.1	5.88

Model	Precision [%]	Recall [%]	mAP [%]	Parameter [MB]	Inference Time [ms]
YOLOv3	94.86	89.35	95.76	246.5	9.77
YOLOv4	99.67	98.39	99.69	256.3	12.85
YOLOv5	99.10	99.10	99.50	3.8	5.33
YOLOv7	100	99.70	99.60	74.8	19.60
YOLOv8	99.03	99.03	99.33	44.8	6.11
YOLOX	99.68	99.03	99.03	36.1	6.52

Experimental results demonstrate that YOLOv5 exhibits outstanding comprehensive performance in pepper seedling detection: achieving a precision rate of 99.10% and a mean average precision (mAP) of 99.50% while maintaining high accuracy, with a model size of only 3.8 MB (representing a reduction exceeding 95% compared to YOLOv4/YOLOv7) and an inference speed of 5.33 ms per frame (equivalent to 187.6 FPS). Compared to SSD, it achieves a 6.42% precision improvement alongside a 25-fold reduction in model size (3.8 MB vs. 95.17 MB). When benchmarked against Faster-RCNN, YOLOv5 operates 7.36 times faster (5.33 ms vs. 39.24 ms) with merely a 0.42% decline in mAP. This model provides an efficient, resource-optimized, and lightweight detection solution for agricultural robotics applications requiring high robustness and low-power deployment.



Fig. 5 - YOLOv5 test result chart

Comparison of different segmentation algorithms

To systematically evaluate the practical application performance of the enhanced U-Net model, this study adopts the Mean Intersection over Union (MIoU) and pixel-wise accuracy as core metrics for assessing segmentation precision, while additionally incorporating model size and single-frame detection time to characterize hardware deployment characteristics of segmentation performance. The improved U-Net was compared with other segmentation models, including U-Net(*Ronneberger et al.*, *2015*), U-Net++(*Zhou et al.*, *2018*), U-Net+++(*Huang et al.*, *2020*), SegNet (*Badrinarayanan et al.*, *2017*), DeepLabv3+(*Chen et al.*, *2018*), and AGNet (*Zhang et al.*, *2019*). The performance of these segmentation models on the seedling tray dataset is detailed in Table 2.

Table 2

Performance of different segmentation models on pepper seedling dataset

Model	MIoU [%]	Precision [%]	Parameter [MB]	Inference Time [ms]
U-Net	86.30	91.72	53.65	110.01
UNet++	81.51	91.15	12.16	64.98
UNet+++	77.34	87.73	16.15	55.43
SegNet	85.28	92.95	117.9	26.36
DeepLabv3+	85.01	91.40	238	22.84
AGNet	83.60	91.73	37.34	45.41
improved U-Net	86.94 (↑0.6%)	93.01 (↑1.29%)	81.69	33.32

The experimental results presented in Table 2 indicate that the accuracy of the U-Net model with the ECA module improved by 1.9% compared to the original model. Most importantly, the detection time decreased substantially from 110 ms to 33.32 ms, thus better satisfying practical application requirements. The images processed by the segmentation algorithm are shown in Fig.6. It is clear that the improved U-Net model demonstrates superior control over the contour details of pepper seedling segmentation compared to other models. By enhancing its focus on surface feature information, the improved U-Net effectively captures the intricate details of the pepper seedling contours, resulting in better segmentation performance. This model can effectively distinguish adjacent plug seedlings and handles both the target seedling contours and interference features with notable efficacy, achieving segmentation results that closely approximate those of manual segmentation.



Fig. 6 - Comparison of segmentation results of different algorithms

Parameter extraction results

This study extracts feature parameters of plug seedlings from images that were pre-processed using target detection and segmentation algorithms. Parameters such as the lateral area, plant height, stem thickness, and hypocotyl length of the seedlings are extracted based on pixel points. Because the resolution of individual pepper seedling images segmented by the detection algorithm was inconsistent, all images used for feature extraction in this study were standardized to a uniform resolution of 640 × 640 pixels to avoid error accumulation. If the resolution of an image intended for feature extraction is below the target resolution, linear interpolation is used for upscaling. Conversely, if the resolution exceeds the target, area interpolation is applied for downscaling. All diagrams for parameter extraction are depicted in Fig.7.

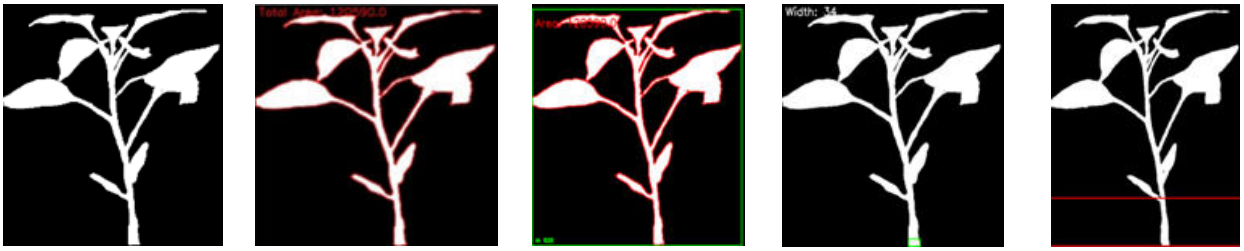


Fig. 7 - Parameter extraction

Classification results

150 images of pepper plug seedlings were selected, which were firstly classified into first-grade and second grade seedlings according to the technical regulations of pepper greenhouse cultivation (*Hunan Provincial Administration for Market Regulation*, *2022*) as well as the opinions of relevant growers.

Parameter data such as height, stem thickness, lateral area, hypocotyl length and degree of dispersion of pepper seedlings were obtained using feature extraction methods, and they were divided into training set and validation set according to the ratio of 8:2. The accuracy and recall of Support Vector Machine, K Nearest Neighbour Classification Model and Random Forest Classification Model for grading the 150 pepper dataset are presented in Table 3.

Table 3

Performance of three classification models on the pepper dataset

	Precision	Recall
SVM	96.67%	90.42%
KNN	98%	93.74%
Random Forest	99.33%	99.62%

The results in Table 3 demonstrate that the Random Forest classification algorithm achieves higher accuracy and recall across all datasets, surpassing the performance of the other two classification algorithms. Moreover, the overall speed of the algorithm is efficient, making it suitable for the grading algorithm proposed in this paper.

CONCLUSIONS

The paper begins with the application of the YOLOv5 algorithm to detect and automatically crop entire rows of pepper seedlings into individual plant states. Subsequently, a channel attention mechanism is integrated into the down sampling section of the U-Net architecture to enhance the extraction of surface features of the seedlings, thereby facilitating their segmentation. Finally, feature extraction methods are employed to derive five parameters—side area, plant height, stem thickness, hypocotyl length, and dispersal degree—of the plug seedlings. These parameters are then used to train a Random Forest classification model for the grading of plug seedlings. The main conclusions are as follows:

1) The training results of the U-Net model enhanced with ECA attention on the pepper seedling dataset cropped by YOLOv5 indicate that the accuracy of the improved U-Net segmentation algorithm reached 93.01%, an increase of 1.29 percentage points. The image processing time was 33.32 ms, only 30% of that of the original model, demonstrating a significant speed advantage.

2) By employing feature extraction techniques to derive parameters such as area, height, stem diameter, hypocotyl length, and divergence degree of pepper plug seedlings, a grading model was trained using the random forest classification algorithm. This resulted in an impressive grading accuracy of 99.33%, facilitating the swift and precise classification of pepper plug seedlings in real-world agricultural applications.

ACKNOWLEDGEMENT

This paper was supported by the Hunan Provincial Natural Science Foundation(2023JJ50125) and Hengyang Science and Technology Innovation Programme Projects (202330066437).

REFERENCES

[1] Badrinarayanan, V., Kendall, A., Cipolla, R. (2017). Segnet: A deep convolutional encoder-decoder architecture for image segmentation. *IEEE transactions on pattern analysis and machine intelligence,* 39(12), 2481-2495.

[2] Bochkovskiy, A., Wang, C.-Y., Liao, H.-Y. M. (2020). Yolov4: Optimal speed and accuracy of object detection. *arXiv preprint arXiv:2004.10934*.

[3] Chen, L.-C., Zhu, Y., Papandreou, G., Schroff, F., Adam, H. (2018). Encoder-decoder with atrous separable convolution for semantic image segmentation. *Proceedings of the European conference on computer vision (ECCV)*.

[4] Fu, W., Gao, J., Zhao, C., Jiang, K., Zheng, W., Tian, Y. (2022). Detection method and experimental research of leafy vegetable seedlings transplanting based on a machine vision. *Agronomy,* 12(11), 2899.

[5] Ge, Z., Liu, S., Wang, F., Li, Z., Sun, J. (2021). Yolox: Exceeding yolo series in 2021. *arXiv preprint arXiv:2107.08430*.

[6] glenn-Jocherglenn-Jocher. (2022). YOLOv5 by Ultralytics (Version v7.0). *https://github.com/ultralytics/yolov5*

[7] Hu, J., Shen, L., Sun, G. (2018). Squeeze-and-excitation networks. *Proceedings of the IEEE conference on computer vision and pattern recognition*.

[8] Huang, H., Lin, L., Tong, R., Hu, H., Zhang, Q., Iwamoto, Y., Han, X., Chen, Y.-W., Wu, J. (2020). Unet 3+: A full-scale connected unet for medical image segmentation. *ICASSP 2020-2020 IEEE international conference on acoustics, speech and signal processing (ICASSP)*.

[9] Hunan Provincial Administration for Market Regulation. (2022). *Technical regulations for medium cultivation of chili pepper production (DB43/T 2396-2022)*. Hunan Provincial Administration for Market Regulation.

[10] Jiang, H., Shi, J., Ren, Y., Ying, Y. (2009). Application of machine vision on automatic seedling transplanting. *Transactions of the Chinese Society of Agricultural Engineering,* 25(5), 127-131.

[11] Li, M., Jin, X., Ji, J., Li, P., Du, X. (2021). Design and experiment of intelligent sorting and transplanting system for healthy vegetable seedlings. *International Journal of Agricultural and Biological Engineering,* 14(4), 208-216.

[12] Li, Y., Wei, H., Tong, J., Qiu, Z., Wu, C. (2024). Evaluation of health identification method for plug seedling transplantation robots in greenhouse environment. *Biosystems engineering,* 240, 33-45.

[13] Liu, W., Anguelov, D., Erhan, D., Szegedy, C., Reed, S., Fu, C.-Y., Berg, A. C. (2016). Ssd: Single shot multibox detector. *Computer Vision–ECCV 2016: 14th European Conference,* Amsterdam, The Netherlands, October 11–14, 2016, Proceedings, Part I 14.

[14] Ministry of Agriculture and Rural Affairs of the People's Republic of China. (2021). *General technical requirements for whole industrial chain management of pepper in solar greenhouses (NY/T 3952-2021)*. Ministry of Agriculture and Rural Affairs of the People's Republic of China. https://hbba.sacinfo.org.cn/attachment/onlineRead/b9c4af4f9f64a23f98509674b4f50b6648583ad9f97e06e8cbea99538098fcb8

[15] Redmon, J., Farhadi, A. (2018). Yolov3: An incremental improvement. *arXiv preprint arXiv:1804.02767*.

[16] Ren, S., He, K., Girshick, R., & Sun, J. (2015). Faster r-cnn: Towards real-time object detection with region proposal networks. *Advances in neural information processing systems,* 28.

[17] Ronneberger, O., Fischer, P., Brox, T. (2015). U-net: Convolutional networks for biomedical image segmentation. *Medical image computing and computer-assisted intervention–MICCAI 2015: 18th international conference,*. Munich, Germany, October 5-9, 2015, proceedings, part III 18.

[18] Tan, M., Pang, R., Le, Q. V. (2020). Efficientdet: Scalable and efficient object detection. *Proceedings of the IEEE/CVF conference on computer vision and pattern recognition*.

[19] Tian, S., Wang, Z., Yang, J., Huang, Z., Wang, R., Wang, L., Dong, J. (2017). Development of an automatic visual grading system for grafting seedlings. *Advances in Mechanical Engineering,* 9(1), 1687814016686265.

[20] Tong, J., Shi, H., Wu, C., Jiang, H., Yang, T. (2018). Skewness correction and quality evaluation of plug seedling images based on Canny operator and Hough transform. *Computers and electronics in agriculture,* 155, 461-472.

[21] Ultralytics. (2023). YOLOv8 by Ultralytics. *https://github.com/ultralytics/ultralytics/tree/main/ultralytics/models/v8.*

[22] Wang, C.-Y., Bochkovskiy, A., Liao, H.-Y. M. (2023). YOLOv7: Trainable bag-of-freebies sets new state-of-the-art for real-time object detectors. *Proceedings of the IEEE/CVF conference on computer vision and pattern recognition*.

[23] Wang, Q., Wu, B., Zhu, P., Li, P., Zuo, W., Hu, Q. (2020). ECA-Net: Efficient channel attention for deep convolutional neural networks. *Proceedings of the IEEE/CVF conference on computer vision and pattern recognition*.

[24] Xu, S., Zhang, Y., Dong, W., Bie, Z., Peng, C., Huang, Y. (2023). Early identification and localization algorithm for weak seedlings based on phenotype detection and machine learning. *Agriculture,* 13(1), 212.

[25] Zhang, S., Fu, H., Yan, Y., Zhang, Y., Wu, Q., Yang, M., Tan, M., & Xu, Y. (2019). Attention guided network for retinal image segmentation. *Medical Image Computing and Computer Assisted Intervention–MICCAI 2019: 22nd International Conference, Shenzhen*. China, October 13–17, 2019, Proceedings, Part I 22.

[26] Zhang, X., Jing, M., Yuan, Y., Yin, Y., Li, K., Wang, C. (2022). Tomato seedling classification detection using improved YOLOv3-Tiny. *Trans. Chin. Soc. Agric. Eng,* 38(1).

[27] Zhou, Z., Rahman Siddiquee, M. M., Tajbakhsh, N., Liang, J. (2018). Unet++: A nested u-net architecture for medical image segmentation. *Deep Learning in Medical Image Analysis and Multimodal Learning for Clinical Decision Support: 4th International Workshop, DLMIA 2018, and 8th International Workshop, ML-CDS 2018, Held in Conjunction with MICCAI 2018*. Granada, Spain,September 20, 2018, Proceedings 4.

EXPERIMENTAL AND THEORETICAL STUDY ON STRAIGHTNESS IMPROVEMENT IN AGRICULTURAL MACHINERY MOVEMENT

/

EKSPERIMENTĀLS UN TEORĒTISKS PĒTĪJUMS PAR LINEARITĀTES UZLABOŠANU LAUKSAIMNIECĪBAS MAŠĪNU KUSTĪBĀ

Volodymyr BULGAKOV[1)], Adolfs RUCINS*[2)], Lucretia POPA[3)], Roman ANTOSHCHENKOV[4)], Mykyta KUSKOV[4)], Mariia RUZHYLO[1)], Mykhailo CHERNOVOL[5)], Ivan HOLOVACH[1)], Oleksandra TROKHANIAK[1)]

[1)]National University of Life and Environmental Sciences of Ukraine / Ukraine;
[2)]Latvia University of Life Sciences and Technologies / Latvia;
[3)]National Institute of Research–Development for Machines and Installations Designed for Agriculture and Food Industry–INMA, Bucharest / Romania
[4)]State Biotechnological University / Ukraine; [5)] Central Ukrainian National Technical University / Ukraine
*Corresponding author's E-mail: adolfs.rucins@lbtu.lv

DOI: https://doi.org/10.35633/inmateh-76-106

Keywords: *mathematical model, dynamics, trajectory of the movement, design parameters, seeding machine-tractor system (SMTS)*

ABSTRACT

This research was conducted for enhancing the linearity (or straightness) of the movement of a seeding machine-tractor system (SMTS), encompassing both theoretical and experimental studies. The experimental studies were conducted using a SMTS as part of a classic all-wheel drive tractor and a pneumatic trailed seeder. Theoretical research of the SMTS was carried out for three versions of the initial parameters of the mathematical model. In the first version the speed of movement was v = 2.5 m·s^{-1}, the distance from the point of the seeder trailer to the centre of mass of the seeder was l_5 = 2 m, and the pressure in the pneumatic tires of the tractor wheels was P_w = 0.10 MPa. In the second one, the speed of the unit is increased to v = 2.8 m·s^{-1}, the distance from the point of the seeder trailer to the centre of mass of the seeder is increased to l_5 = 3 m, and the pressure in the tractor's tires is P_w = 0.10 MPa. In the third versions, the pressure in the tractor tires is increased to 0.12 MPa. The difference between values $O_{(1)(T)}$, $O_{(2)(T)}$ of the trajectory of the movement of the centres of mass of the tractor and the seeder, determined during the theoretical research, and determined during the experimental research is 11%, and the discrepancy between the values of the rotation angles of the centres of mass is 9%; therefore, the mathematical model of the dynamics of the SMTS may be considered adequate.

Kopsavilkums

Šajā darbā tika pārbaudīta metode sēšanas mašīnas–traktora vienības (SMTV) kustības linearitātes uzlabošanai, izstrādājot kustības dinamisko vienādojumu, piemērojot otrā veida Lagranža vienādojumus un veicot teorētiskus un eksperimentālus pētījumus. Eksperimentālie pētījumi tika veikti, izmantojot SMTV, kā traktora un piekabināmas pneimatiskās sējmašīnas kombināciju, bet teorētiskie pētījumi tika veikti trīs matemātiskā modeļa sākotnējo parametru variantiem. Pirmajā variantā kustības ātrums bija v = 2.5 m·s^{-1}, attālums no sējmašīnas piekabes punkta līdz sējmašīnas masas centram bija l_5 = 2 m, un spiediens traktora riteņu pneimatiskajās riepās bija Pw = 0.10 MPa. Otrajā variantā vienības ātrums palielināts līdz v = 2.8 m·s^{-1}, attālums no sējmašīnas piekabes punkta līdz sējmašīnas masas centram palielināts līdz l_5 = 3 m, un spiediens traktora riepās ir P_w = 0.10 MPa. Trešajā variantā spiediens traktora riepās palielināts līdz 0.12 MPa. Teorētiskajos pētījumos noteiktās traktora un sējmašīnas masu centru kustības trajektorijas vērtības $O_{(1)(T)}$, $O_{(2)(T)}$ un eksperimentālos pētījumos noteiktās vērtības atšķiras par 11 %, bet masu centru rotācijas leņķu vērtības atšķiras par 9 %; tādēļ SMTS dinamikas matemātiskais modelis var tikt uzskatīts par atbilstošu.

INTRODUCTION

In modern agriculture, the efficiency of agronomic processes largely depends on the use of modern equipment, seeding machine-tractor units in particular. Therefore, the relevance of the conducted research is determined by the need to improve the accuracy and stability of the movement of the SMTS, which directly affects the efficiency of technological operations in the conditions of precision farming and changing climate.

The plane-parallel movement of the SMTS is crucial to ensure seeding accuracy and quality, as well as to optimize the resource costs. The research presented in this work aimed to develop a mathematical model describing the movement of a classic all-wheel drive tractor in combination with a seeder. This model will allow a deeper understanding of the mechanics of interaction between the elements of the unit, as well as the influence of various parameters on the stability of movement and productivity. The relevance of this study is determined by the need to improve the efficiency of agricultural operations, which is especially important in the context of growing competition and changing climatic conditions.

Analysis of the latest research and publications shows that in agricultural production, especially in precision farming, there is a growing need to improve the efficiency and productivity of the seeding operations. An important aspect is to ensure stability and precision of movement of the SMTSs that perform these operations (*Adamchuk et.al., 2023*). In particular, the research of the plane-parallel movement of the SMTS, consisting of all-wheel drive tractors of classical design and seeders, is an urgent task since it allows optimizing the sowing process, reducing the resource costs and increasing the yields *(Parihar et.al., 2024*).

Instability of movement may lead to uneven seed distribution, increased skips and double sowings, which negatively affects the quality of sowing and the yield (*Sun et.al., 2022*).

Contemporary research in the field of the SMTS dynamics is focused on the development of mathematical models that consider various factors influencing the motion of the unit (*Ivanovs et.al., 2020; Startcev et.al., 2021*). Mathematical modelling allows analysis of the stability of movement, determining the optimal design parameters and operating modes of the SMTS, and develop automatic control systems that ensure high accuracy and stability of movement (*Adamchuk et.al., 2023*).

This paper presents the results of research of the plane-parallel movement of a SMTS, consisting of a classic-configuration all-wheel drive tractor and a seeder. The purpose of this research is to develop a mathematical model, describing the movement dynamics of the unit in a horizontal plane, taking into account the design parameters of the tractor and the seeder, as well as external forces, acting upon the SMTS. The developed mathematical model allows evaluation of the impact of various factors upon the movement stability of the unit and determination of the optimal parameters that ensure high precision and stability of the sowing operations (*Babaei et.al., 2024*).

All-wheel drive tractors remain essential in modern agriculture due to their adaptability to diverse soil conditions. Their integration into smart mobile systems (SMTS) requires careful analysis of movement stability to ensure precise and efficient field operations (*Li et.al., 2024*). In this regard, the development of a mathematical model that takes into account the design features of such tractors and their interaction with the seeder is a pressing task (*Prasanna Kumar et.al., 2009*).

In some previous investigations there was considered the improvement of the dynamic properties of the machine-tractor *system*, achieved through theoretical studies of their dynamics, assessment of the linearity (straightness) of the movement, stability and controllability (*Wang et.al., 2024a; Antoshchenkov et.al., 2023; Antoshchenkov et.al., 2022; Bulgakov et.al., 2017, 2022*).

In the above investigations an analysis of the movement of the SMTS was made, the dynamic models of which were presented in the form of spatial and plane-parallel models with two or more elements (masses).

Other studies have confirmed the topicality of this task; for example, a model of a mouldboard-less seeder with a semi-active shock absorber, based on magnetorheological fluid, has been developed, which allows the movement of the unit to be adapted to the uneven soil surfaces and vibrations, which increases the accuracy of sowing and the stability of movement (*Sharipov, 2019*).

An energy analysis of a wide-cut seeder was also performed, showing that up to 90.8% of the tractor power is spent on overcoming the traction resistance, which emphasizes the importance to optimize the design of the unit in order to increase its efficiency (*Tulegenov et.al., 2020*).

In another investigation, the effect of vibration upon the accuracy of a pneumatic seeder at different speeds of travel is examined. A CFD–DEM model was used, confirming that the vibrations significantly affect the accuracy of the seed sowing and the stability of the movement of the seeding unit (*Wang et.al., 2024b*). *Findura and Ruman (2024*) have studied the manoeuvrability of a three-module seeding unit, based on a reversible tractor. The theoretical and experimental investigations have shown that increasing the length of the

drawbar of the side seeders and the width of the tractor track allows for a reduction in the turning radius of the seeding unit and an increase in the stability of its movement on the headland.

The improvement of the dynamic properties of the SMTS needs theoretical studies of the plane-parallel movement of a two-mass unit with four degrees of freedom.

Seeders are an integral part of the SMTS, playing an important role in ensuring uniform seed distribution. Their design features and parameters also affect the dynamics of the movement of the unit. Therefore, when developing a mathematical model, it is necessary to take these factors into account to obtain accurate results (*Wang et.al., 2024a*).

The purpose of the research is to increase the linearity (straightness) of the movement of the SMTS as part of an all-wheel drive tractor and a seeder by theoretically substantiation pf the design parameters and operating modes.

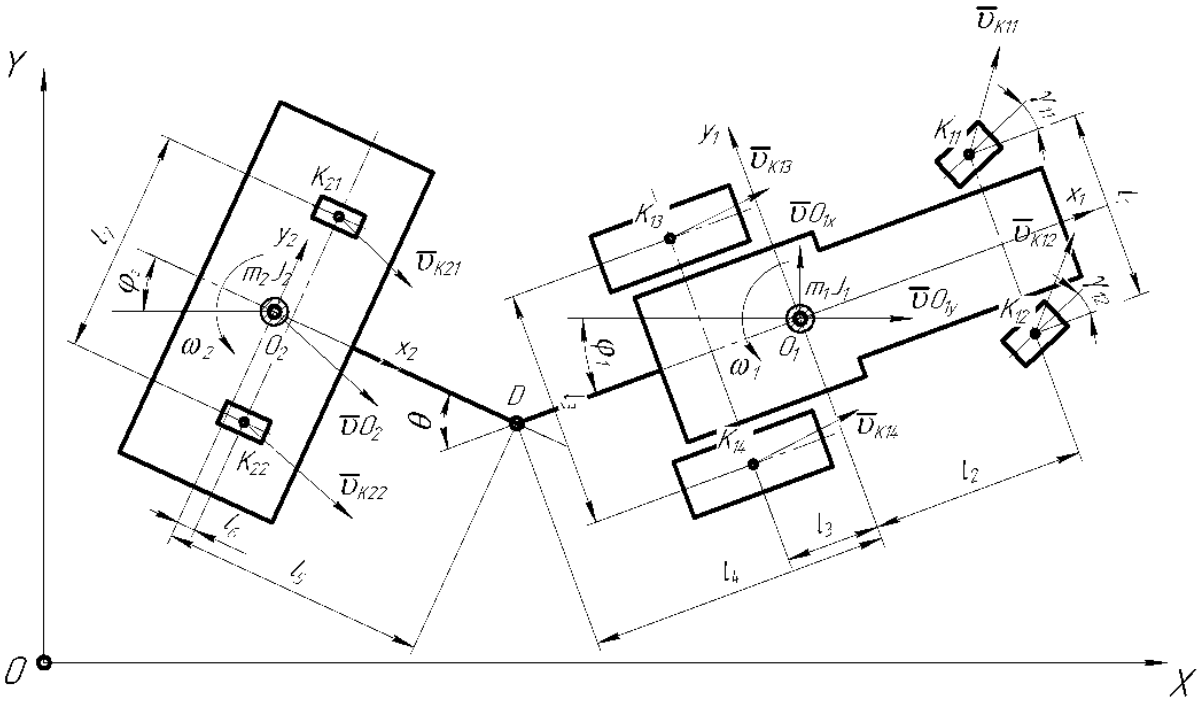
MATERIALS AND METHODS

Theoretical investigations have been conducted using a SMTS as part of an all-wheel drive tractor and a *pneumatic* trailed seeder. Classic-design tractor, all-wheel drive 79 kW, trailed pneumatic seeder, which is designed for the simultaneous sowing of two crops.

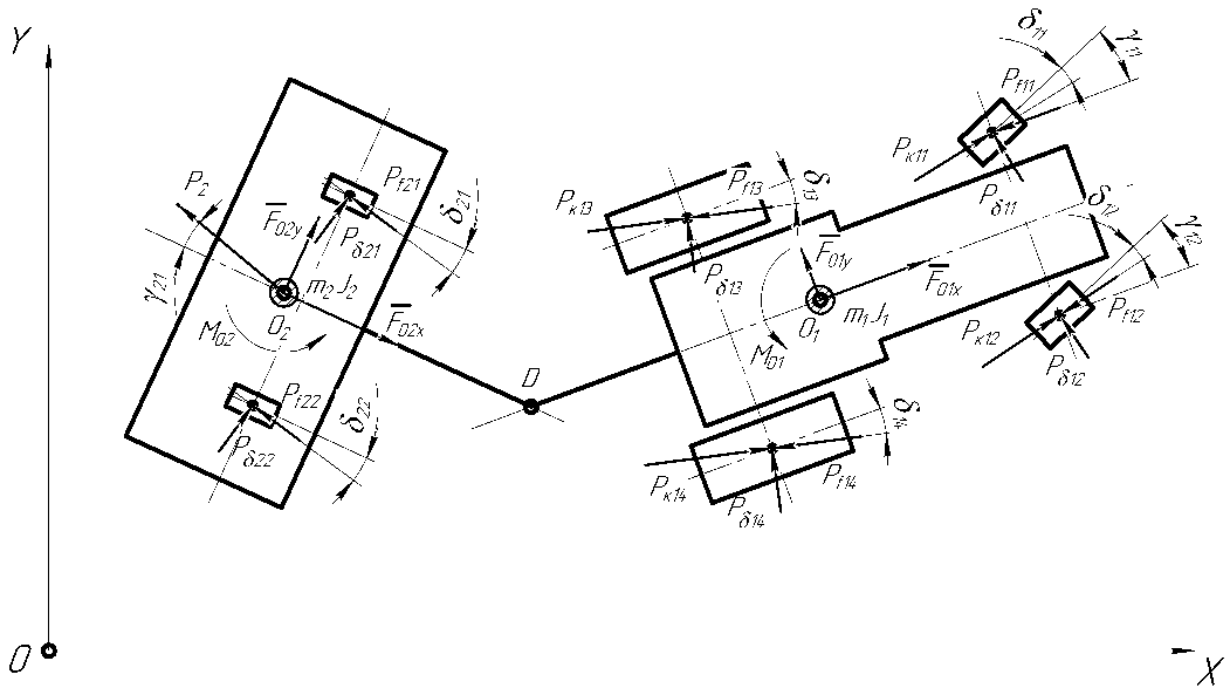
Formation of the equations of the movement of the unit requires making assumptions that will simplify the solution of the problem, as well as discarding factors that complicate mathematical modelling and do not affect the calculation. The following assumptions were introduced: plane-parallel movement of the unit was considered; in the process of compiling the mathematical model, the deferent (plane-parallel movement of the unit in the *XOZ* plane) and the roll (plane-parallel movement of the unit in the *YOZ* plane) were not taken into account; the processes that occur in the hydraulic steering drive were not taken into account; the processes that occur in the transmission were not taken into account; the dynamic characteristics of the engine during acceleration and braking of the unit were not taken into account; the frames of the sections are absolutely rigid bodies, and the entire unit is symmetrical relative to the longitudinal plane; the rolling resistance forces are considered constant; the lateral forces onto the tires are limited by the adhesion of the wheels to the road. The rolling resistance of the tractor and the seeder wheels is calculated depending on the vertical load on the corresponding wheel (*Damme et.al., 2021*).

The accepted assumptions allow representation of the SMTS as a flat dynamic system in the horizontal plane *XOY*, since in this plane there are projections of forces that form loads upon the elements of the unit, the coupling device, the resistance force of the seeder, the resistance force to rolling of the machine, lateral forces and driving forces.

The equivalent scheme (Fig. 1) is a dynamic model of the plane-parallel movement of a two-element (two-mass) SMTS, consisting of two parts: a tractor and a seeder.



a)



b)

Fig. 1 – A kinematic (a) and a dynamic (b) model of plane-parallel movement of a two-element (two-mass) SMTS

When compiling a mathematical model, the case of movement along a curvilinear trajectory is used, which corresponds to the actual trajectory of movement of the seeding units across the field (*Antoshchenkov et.al., 2024*). During movement, the leading wheels are the front and the rear wheels of the tractor. The loads that the unit experiences in this case are not critical and are typical for the technological process of sowing. A distinctive feature of the developed mathematical model is that it allows analysis of the trajectories of the movement of the unit elements, deviations and frequencies depending on the control action and design parameters.

The following designations are used in the diagram of the kinematic and the dynamic model of plane-parallel movement of a two-element (two-mass) SMTS (Fig. 1): *XOY* – the global (fixed) coordinate system; O_1 – the centre of mass of the tractor; O_2 – the centre of mass of the seeder; $x_1O_1y_1$ – the connected (moving) coordinate system of the tractor, passing through the centre of mass, point O_1; $x_2O_2y_2$ – the connected (moving) coordinate system of the seeder, passing through the centre of mass, point O_2; point *D* – the coupling device (the connection point of the tractor and the seeder); φ_1 – the turning angle of the tractor frame around the vertical axis; φ_2 – the turning angle of the seeder frame around the vertical axis; ω_1 – the angular velocity of turning of the tractor frame around the vertical axis z; ω_2 – the angular velocity of turning of the seeder frame around the vertical axis z; γ_{11} – the turning angle of the steered front left wheel of the tractor; γ_{12} – the turning angle of the steered front right wheel of the tractor; δ_{11}, δ_{12}, δ_{13}, δ_{14} – l lateral slip angle of the front left, front right, rear left and rear right wheels of the tractor; the lateral slip angle of the front left, front right, rear left and rear right wheels of the tractor; δ_{21}, δ_{22} – the lateral slip angle of the left and the right wheels of the seeder; θ – the bend angle (the angle between the longitudinal axes of the tractor and the seeder); l_1 – the track of the front wheels of the tractor; l_2 – the distance from the front wheels to the centre of mass of the tractor; l_3 – the distance from the centre of mass to the axis of the rear wheels of the tractor; l_4 – the distance from the centre of mass of the tractor to the attachment point of the seeder; l_5 – the distance from the attachment point of the seeder to the centre of mass; l_6 – the distance from the centre of mass of the seeder to the axis of the wheel; l_7 – the track of the seeder wheel; m_1 – mass of the tractor; J_1 – the moment of inertia of the tractor; m_2 – mass of the seeder; J_2 – the moment of inertia of the seeder; $P_{\kappa 11}$, $P_{\kappa 12}$, $P_{\kappa 13}$, $P_{\kappa 14}$ – the tangential traction force of the front left, front right, rear left and rear right wheels of the tractor; P_{f11}, P_{f12}, P_{f13}, P_{f14} – the rolling resistance force of the front left, front right, rear left and rear right wheels of the tractor; $P_{\delta 11}$, $P_{\delta 12}$, $P_{\delta 13}$, $P_{\delta 14}$ – the lateral slip force of the front left, front right, rear left and rear right wheels of the tractor; P_2 – the vector of the traction resistance forces of the seeder; γ_{21} – rotation angle of the vector of the seeder's traction resistance forces; P_{f21}, P_{f22} – the rolling resistance force of the left and right wheels of the seeder; $P_{\delta 21}$, $P_{\delta 22}$ – the lateral slip force of the left and the

right wheels of the seeder; F_{O1x}, F_{O1y}, F_{O2x}, F_{O2y} – the projections of the main vector of forces from the side of the support surface for the tractor and seeder; M_{O1}, M_{O2} – the main point of disturbing effects from the side of the supporting surface for the tractor and seeder.

The position of the dynamic system "tractor-seeder" will be determined by four generalized coordinates: O_{1x} – the projection of the speed of the center of mass of the tractor onto axle *x*; O_{1y} – the projection of the speed of the center of mass of the tractor onto axle *y*; φ_1 – the turning angle of the tractor frame around the vertical axis *z*; φ_2 – the turning angle of the seeder frame around the vertical axis *z*.

As a mathematical apparatus for the compilation of differential equations of movement of a two-element (two-mass) seeding unit, consisting of a tractor and a seeder, the Lagrange dynamics equations of the second kind were adopted (*Antoshchenkov et.al., 2024*):

$$\frac{d}{dt}\left(\frac{\partial T}{\partial \dot{q}_k}\right) - \frac{\partial T}{\partial q_k} = Q_k, k = 1,2,3,4 \quad (1)$$

where: T – the kinetic energy of the system; Q – the generalized forces of the system; q_k – the generalized coordinates of the system.

The Lagrange equations of the second order, describing the dynamics of the seeding unit, are formed relative to the following generalized coordinates: O_{1x} and O_{1y} – the centre of mass of the tractor (point O_1); the turning angles of the tractor frame φ_1 and the seeder φ_2 around axle *z*. The equations of the dynamics of the unit in the general case have the following form:

$$\begin{cases} \frac{d}{dt}\left(\frac{\partial T}{\partial \dot{x}_{O_1}}\right) - \frac{\partial T}{\partial x_{O_1}} = Q_{O1x} \\ \frac{d}{dt}\left(\frac{\partial T}{\partial \dot{y}_{O_1}}\right) - \frac{\partial T}{\partial y_{O_1}} = Q_{Oy1} \\ \frac{d}{dt}\left(\frac{\partial T}{\partial \dot{\varphi}_1}\right) - \frac{\partial T}{\partial \varphi_1} = Q_{\varphi_1} \\ \frac{d}{dt}\left(\frac{\partial T}{\partial \dot{\varphi}_2}\right) - \frac{\partial T}{\partial \varphi_2} = Q_{\varphi_2} \end{cases} \quad (2)$$

where:

Q_{O1x}, Q_{O1y}, $Q_{\varphi 1}$, $Q_{\varphi 2}$ – generalized forces of the corresponding generalized coordinates.

The kinetic energy of the SMTS consists of the kinetic energy of the tractor and the seeder and is determined from the expression:

$$T = \frac{m_1 v_{O_1}^2}{2} + \frac{J_{O_1}\omega_1^2}{2} + \frac{m_2 v_{O_2}^2}{2} + \frac{J_{O_2}\omega_2^2}{2}, \quad (3)$$

where: v_{O1}, v_{O2} – the velocities of the centres of mass of the tractor and the seeder; ω_1, ω_2 – the angular velocities of the tractor and the seeder relative to the corresponding vertical axes *z*; J_{O1}, J_{O2} – the moments of inertia of the tractor and the seeder relative to the corresponding vertical axes *z*.

To use the numerical method for solving a system of differential equations (a modified Runge-Kutta method of 4-5 order), it is necessary to reduce system (2) to the Cauchy form.

To reduce equations (1) – (3) to the Cauchy form and numerically solve the system of linear algebraic equations (SLAE) using Cramer's method, the MatLab 2021a mathematical software package (*Shior et.al., 2024*) was used and the following variables were introduced:

$$\begin{cases} a_{11} = m_1 + m_2; a_{12} = 0; a_{13} = m_2 l_4 \sin\varphi_1; a_{14} = m_2 l_5 \sin\varphi_2; \\ a_{21} = 0; a_{22} = m_1 + m_2; a_{23} = -m_2 l_4 \cos\varphi_1; a_{24} = -m_2 l_5 \cos\varphi_2; \\ a_{31} = m_2 l_4 \sin\varphi_1; a_{32} = -m_2 l_4 \cos\varphi_1; a_{33} = J_1 + m_2 l_4^2; a_{34} = m_2 l_4 l_5; \\ a_{41} = m_2 l_5 \sin\varphi_2; a_{42} = -m_2 l_5 \cos\varphi_2; a_{43} = m_2 l_5 l_4 \cos(\varphi_1 - \varphi_2); a_{44} = J_2 + m_2 l_5^2. \end{cases} \quad (4)$$

Considering equations (1)– (3), after performing the necessary groupings and transformations, the Lagrange equations are obtained, with the form:

$$\begin{cases} a_{11}\ddot{x}_{O_1} + a_{12} y_{O_1} + a_{13}\ddot{\varphi}_1 + a_{14}\ddot{\varphi}_2 = Q_{x_{O_1}}; \\ a_{21}\ddot{x}_{O_1} + a_{22} y_{O_1} + a_{23}\ddot{\varphi}_1 + a_{24}\ddot{\varphi}_2 = Q_{y_{O_1}}; \\ a_{31}\ddot{x}_{O_1} + a_{32} y_{O_1} + a_{33}\ddot{\varphi}_1 + a_{34}\ddot{\varphi}_2 = Q_{\varphi_1}; \\ a_{41}\ddot{x}_{O_1} + a_{42} y_{O_1} + a_{43}\ddot{\varphi}_1 + a_{44}\ddot{\varphi}_2 = Q_{\varphi_2}. \end{cases} \quad (5)$$

The coefficients of the second derivative systems (5) and generalized forces are functions of the mass, geometric, operational parameters of the tractor and the unit, generalized coordinates and speeds. The equation of the motion of the SMTS is a system of four inhomogeneous second-order differential equations.

Generalized forces contain such characteristics of the unit as tangential traction forces of the tractor wheels; rolling resistance forces of the tractor wheels; lateral input forces of the tractor wheels; vector traction resistance force of the seeder; rolling resistance forces of the seeder wheels; lateral input forces of the seeder wheels; projections of the main vector of forces from the support surface for the tractor and seeder; the main moment of the disturbing effects from the supporting surface for the tractor and the seeder. The type and conditions of the soil affect the rolling resistance forces of the tractor wheels; the lateral input forces of the tractor wheels; traction force of the seeder; the forces of the seeder's traction resistance; the rolling resistance forces of the seeder wheels; lateral wheel slip of forces of the seeder.

The developed mathematical model allows studying the dynamics (movement) of the SMTS elements in a longitudinally parallel plane and determining the impact of the geometric parameters of the unit upon its dynamics, the oscillations of the elements around a straight trajectory and the stability of movement.

The experimental research of the SMTS is aimed to confirm the adequacy of the developed mathematical model of the dynamics of the seeding unit. During the experimental investigations of the SMTS a measuring system for the dynamics and energy of mobile machines was used (*Antoshchenkov et.al., 2023*). The measuring system for the dynamics and energy of mobile machines (MSDEMM) is a technical means of measurement for testing, diagnostics and operational control. The measuring system (MS) is designed to determine the kinematic, dynamic, power and energy characteristics of mobile machines and their elements during road, field and bench tests (*Antoshchenkov et.al., 2022*).

When conducting experimental investigations of the SMTS, the following sensors are used as part of the measuring system:

– an inertial measurement device (IMD), consisting of a microcontroller, accelerometer, gyroscope and magnetometer, being designed to determine accelerations, angular velocities, the strength of the Earth's magnetic field, the orientation angles, vibration, and the actual trajectory of movement in three planes (*Bulgakov et.al., 2022*);

– the wheel dynamics sensor (WDS), consisting of a microcontroller, accelerometer, gyroscope and magnetometer and being designed to determine accelerations, the angular velocities, the orientation angles, vibration, and the wheel rotation speed;

– the GPS receiver, determining the actual speed of the unit, its geographic location, and the angle of the direction of movement.

During the experimental investigations, the impact of the design parameters of the unit upon the dynamics and vibrations of the elements was determined, as well as to confirm the adequacy of the developed mathematical model of the unit dynamics. The location of the sensors on the SMTS during the experimental research is shown in Fig. 2. The placement of sensors on the SMTS during experimental investigations is shown in Fig. 2.

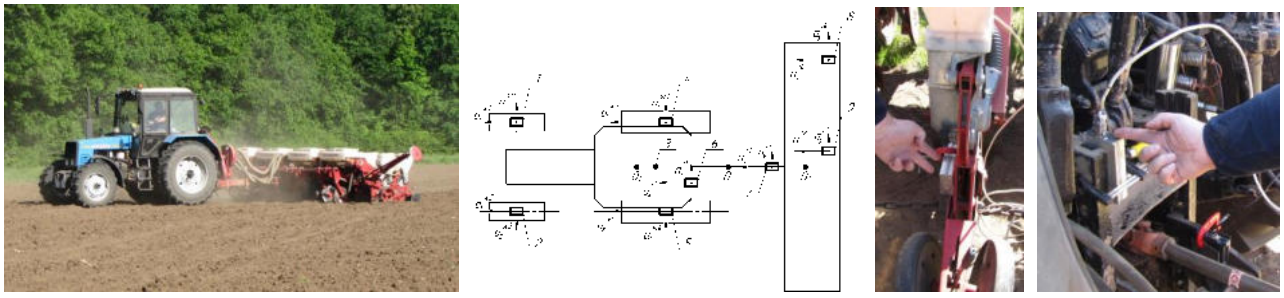


Fig. 2 – The placement of sensors on the SMTS during experimental investigations

1 – the wheel dynamics sensor 1 (the front right wheel of the tractor); 2 – the wheel dynamics sensor 2 (the front left wheel of the tractor); 3 – the GPS receiver antenna; 4 – the wheel dynamics sensor 3 (the rear right wheel of the tractor); 5 – the wheel dynamics sensor 4 (the rear left wheel of the tractor); 6 – the inertial measuring device 1; 7 – the inertial measuring device 3; 8 – the inertial measuring device 4; 9 – the inertial measuring device 2

The wheel dynamics sensor 1 was located on the front right wheel of the tractor. The wheel dynamics sensor 2 was located on the front left wheel of the tractor. The GPS receiver antenna was located on the roof of the tractor (in the longitudinal-horizontal plane in the centre of mass of the tractor). The wheel dynamics sensor 3 was located on the rear right wheel of the tractor. The wheel dynamics sensor 4 – on the rear left wheel of the tractor. The inertial measuring device 1 – on the tractor frame; the inertial IMD-3 – on the rear of the seeder; the IMD - on the extreme (eighth) section of the seeder; the IMD-2– on the fourth section of the seeder.

A methodology for conducting experimental studies, using modelling and simulation of dynamic experimental measurement method (MSDEMM) is described in detail in the works by *Antoshchenkov et.al., (2022); Antoshchenkov et.al., (2023.*)

The methodology of experimental research includes three stages. In the first stage, the measuring equipment is located on the elements of the unit. The second stage allows to exclude the influence of extraneous factors. The elimination of random factors is achieved by repeating each experiment three times. To eliminate the influence of the technical condition, it is necessary to carry out routine maintenance at the beginning of the shift. To eliminate the influence of the field relief, experiments are carried out in one and the opposite direction (this is considered a separate experiment). When conducting experiments, two fields with the most characteristic soil structure are selected, which differ sharply in their physical and mechanical properties. The same type of experiments are carried out in two fields during one shift. At the third stage, after the completion of operations to prepare the unit for research, information is collected. The soil properties (physical and mechanical properties and moisture) and environmental parameters are determined. The computing module is turned on to collect information. The required number of experiments is conducted, and after each experiment the obtained data is stored on the hard drive for further processing. After completion of the research, the measuring system is switched off and dismantled from the unit.

Experimental studies are conducted in the fields of the experimental farm (50.041266, 36.485128) with an area of 54 hectares. The sowing of combined crops of corn, soybeans and sorghum was performed, using highly productive varieties: corn “Solominskaya 298 SR”, soybeans – “Khutoryanochka”, which had high laboratory seed germination: 98% and 94%. The sorghum variety, sown together with soybeans, is called “Samurai”, the seeds of which also had a high laboratory germination rate – 98%.

The soil condition indicators meet the conditions for sowing grain crops. The soil hardness in spherical layers 0-5 cm – 1.1 MPa; 5-10 cm – 1.4 MPa; 10-15 cm – 1.7 MPa. The soil moisture in the 0-5 cm layers was 21.4%; 5-10 cm – 23.9%, 10-15 cm – 22.9%. Sowing was carried out after pre-sowing soil cultivation, using a 240 HP tractor and a John Deere 10 m cultivator, the cultivation depth 7-11 cm.

By experimental research the trajectories of the centres of mass of the unit elements and the turning angles were determined.

RESULTS

The theoretical investigations of the SMTS were conducted for three versions of the initial parameters of the mathematical model. In the first version, the speed of movement was v = 2.5 m·s^{-1}; the distance from the point of the seeder trailer to the centre of mass of the seeder was l_5 = 2 m; the pressure in the tires of the tractor wheels was P_w = 0.10 MPa. In the second version, the speed of the unit is increased to v = 2.8 m·s^{-1}; the distance from the seeder trailer point to the seeder’s center of mass is increased to l_5 = 3 m; the pressure in the tractor wheels – P_w = 0.10 MPa. In the third variant, the pressure in the tractor tires is increased to P_w = 0.12 MPa.

The trajectories of the centres of mass of the tractor O_1 and the seeder O_2 (Fig. 3), the dependences of the turning angles of the centres of mass of the tractor γ_1 and the seeder γ_2 around the vertical axis on the distance traveled (Fig. 4), and the spectral densities of the trajectories of the centres of mass of the tractor $S(O_1)$ and the seeder $S(O_2)$ (Fig. 5) were determined and compared.

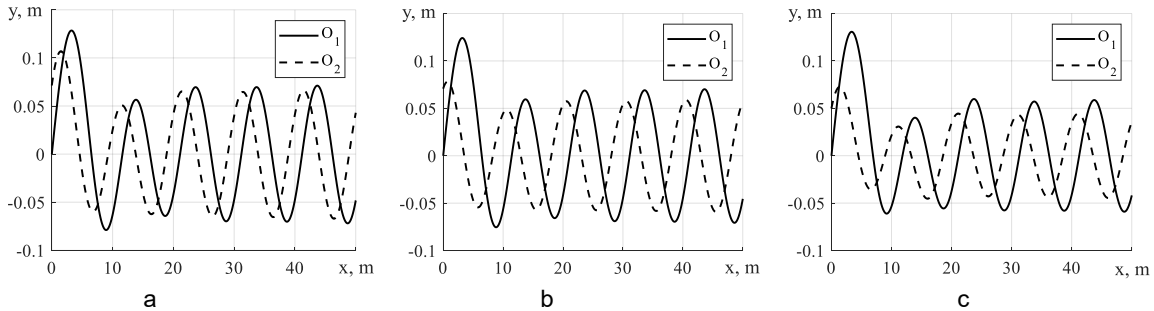


Fig. 3 – Trajectories of the centres of mass of the tractor
O_1 and the seeder O_2 (a – v = 2.5 m·s^{-1}, l_5 = 2 m, P_w = 0.10 MPa; b – v = 2.8 m·s^{-1}, l_5 = 3 m, P_w = 0.10 MPa; c – v = 2.8 m·s^{-1}, l_5 = 3 m, P_w = 0.12 MPa)

The maximum deviation of the centre of mass of the tractor from a straight-line trajectory is 0.125 m (Fig. 3, a), and for other design parameters of the SMTS – 0.12 m. The range of oscillations of the centre of mass of the tractor is 0.12 m (at v = 2.5 m·s^{-1}, l_5 = 2 m, P_w = 0.10 MPa). An increase in the travel speed to 2.8 m·s^{-1} and an increase in the pressure in the tractor tires to 0.12 MPa lead to a decrease in the amplitude of the tractor frame oscillations to 0.11 m (Fig. 3, c).

The range of oscillations of the centre of mass of the seeder decreases from 0.11 m (at v = 2.5 m·s^{-1}, l_5 = 2 m, P_w = 0.10 MPa, Fig. 3, a) to 0.08 m (at v = 2.8 m·s^{-1}, l_5 = 3 m, P_w = 0.12 MPa, Fig. 3, c).

Increasing the travel speed to 2.8 m·s^{-1}, increasing the distance from the seeder trailer point to the center of mass of the seeder l_5 to 3 m, and increasing the tire pressure of the tractor wheels to 0.12 MPa have a positive effect on the linearity (straightness) of the movement of the elements of this seeding unit.

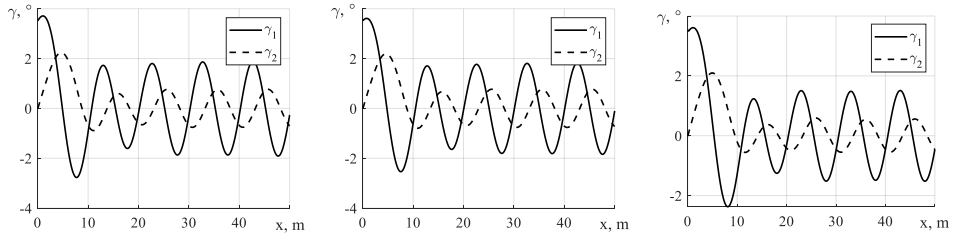


Fig. 4 – Dependences of the turning angles of the centres of mass of the tractor γ_1 and the seeder γ_2 around the vertical axis on the distance travelled

a – v = 2.5 m·s^{-1}, l_5 = 2 m, P_w = 0.10 MPa P; b – v = 2.8 m·s^{-1}, l_5 = 3 m, Pw = 0.10 MPa; c – v = 2.8 m·s^{-1}, l_5 = 3 m, Pw = 0.12 MPa

The maximum range of values of the turning angle of the tractor frame around the vertical axis is 5.8 degrees (at v = 2.5 m·s^{-1}, l_5 = 2 m, P_w = 0.10 MPa, Fig. 4, a). The range of oscillations of the seeder frame angle for this case is 2.2 deg. An increase in the speed of the SMTS and an increase in the length of the seeder linkage leads to a decrease in the angle of the tractor and seeder to 2.8 degrees and 1.8 degrees, respectively (at v = 2.8 m·s^{-1}, l_5 = 3 m, P_w = 0.12 MPa, Fig. 4, c).

A complex indicator for the assessment of the dynamics of the elements of this seeding unit is the spectral densities of the trajectories of the centres of mass of the tractor and the seeder (*Antoshchenkov, et.al., 2022; Bulgakov, et.al., 2022*). The spectral densities of the trajectories of the centres of mass of the tractor $S(O_1)$ and the seeder $S(O_2)$ were calculated for three variants of the design parameters of the SMTS (Fig. 5).

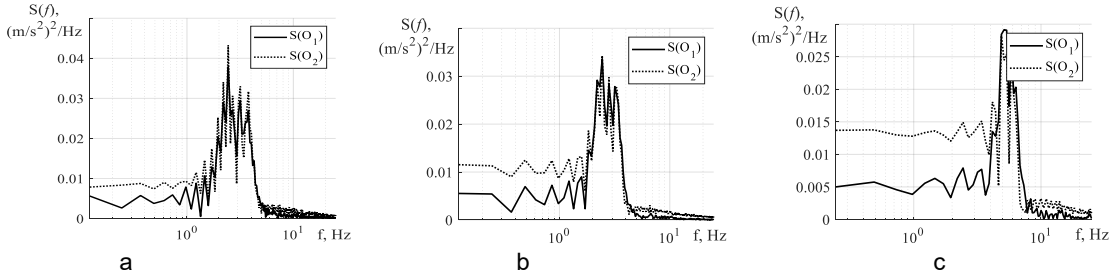


Fig. 5 – Spectral densities of trajectories of the centres of mass of the tractor $S(O_1)$ and the seeder $S(O_2)$

a – v = 2.5 m·s^{-1}, l_5 = 2 m, P_w = 0.10 MPa; b – v = 2.8 m·s^{-1}, l_5 = 3 m, P_w = 0.10 MPa; c – v = 2.8 m·s^{-1}, l_5 = 3 m, P_w = 0.12 MPa

The spectral density of the trajectory of the centre of mass of the tractor has the highest amplitude: 0.045 (m·s^{-2})^2·Hz^{-1} at a frequency of 3.1 Hz; the spectral density of the trajectory of the seeder's centre of mass is 0.032 (m·s^{-2})^2·Hz^{-1} at frequencies of 2.5–4 Hz (Fig. 5, a). Increasing the speed of the SMTS to 2.8 m·s^{-1} leads to a decrease in the amplitude of the spectral density of the trajectory of the centre of mass of the tractor and the seeder to 0.032 (m·s^{-2})^2·Hz^{-1}·at frequencies of 2.5–5 Hz (at v = 2.8 m·s^{-1}, l_5 = 3 m, P_w = 0.10 MPa, Fig. 5, b). The decrease in amplitudes to 0.028 (m·s^{-2})^2·Hz^{-1} at frequencies of 5–7 Hz occurs at v = 2.8 m·s^{-1}, l_5 = 3 m, P_w = 0.12 MPa (Fig. 5, c).

To test the adequacy of the mathematical model of the dynamics of the SMTS, experimental investigations were conducted in which the trajectories of the movement of the centres of mass of the tractor and the seeder were determined and compared with the theoretical ones for two movement speeds of 2.5 and 2.8 m·s^{-1} (Fig. 6). The trajectories of the movement of the centres of mass of the investigated SMTS are a complex parameter for assessing the adequacy of the mathematical model of movement (*Bulgakov et.al., 2022*).

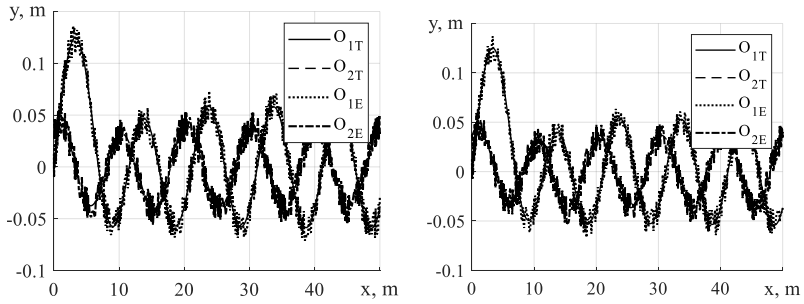


Fig. 6 – The trajectories of the centres of mass of the tractor and the seeder were determined during the theoretical investigations O_{1T}, O_{2T} and were verified during the experimental studies O_{1E}, O_{2E}
a – v = 2.8 m·s^{-1}; b – v = 2.8 m·s^{-1}

Additionally, a comparison between the turning angles of the centres of mass of the tractor and the seeder around the vertical axes was made, being determined during the theoretical research γ_{1T}, γ_{2T} and during the experimental studies (Fig. 7), using the methodology that has shown efficiency in the previous works (*Antoshchenkov et.al., 2022; Bulgakov et.al., 2022; Antoshchenkov et.al., 2024*).

The discrepancies between the values of the trajectory of the movement of the centres of mass of the tractor and the seeder, determined during the theoretical research O_{1T}, O_{2T} and determined during the experimental studies is 11%, and the discrepancy between the values of the turning angles of the centres of mass is 9%; therefore, the mathematical model of the dynamics of the SMTS can be considered adequate.

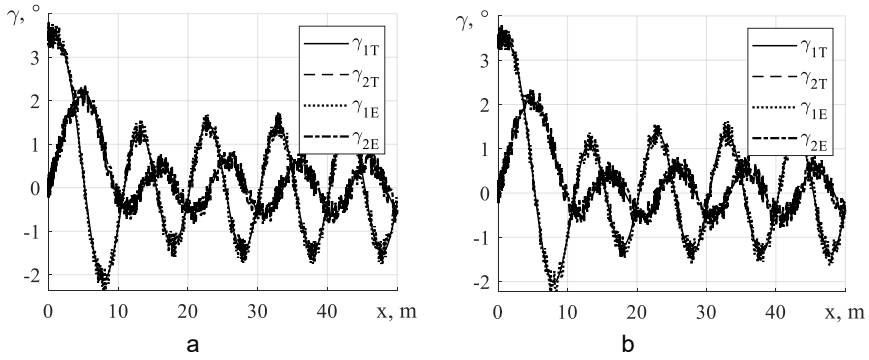


Fig. 7 – The turning angles of the centres of mass of the tractor and the seeder around the vertical axes, determined during theoretical research γ_{1T}, γ_{2T} and verified during experimental studies γ_{1E}, γ_{2E}
a – v = 2.5 m·s^{-1}; b – v = 2.8 m·s^{-1}

The results of the research of the movement of the SMTS for three different sets of parameters showed that an increase in the speed of the movement and the pressure in the pneumatic tires of the running wheels has a positive impact upon the linearity (straightness) of the movement of this seeding unit. The maximum deviation of the centre of mass of the tractor from the preset trajectory of movement decreased from 0.125 m to 0.11 m, and the amplitude of oscillations of the centre of mass of the seeder decreased from 0.11 m to 0.08 m. This indicates an increase in the stability and accuracy of sowing.

For a comprehensive assessment of stability, spectral analysis of the trajectories of the centres of mass was used. The spectral density of the movement centre of mass of the tractor decreased from 0.045 $(m \cdot s^{-2})^2 \cdot Hz^{-1}$ at a frequency of 3.1 Hz to 0.028 $(m \cdot s^{-2})^2 \cdot Hz^{-1}$ at a frequency of 5–7 Hz. Similar changes were recorded for the seeder. This means that the system exhibits reduced dynamic instability under optimal driving conditions.

Comparison of the theoretical and the experimental data made it possible to evaluate the adequacy of the developed model. The average deviation in trajectories was 11%, and in the turning angles – 9%, which is within the acceptable limits of engineering modelling.

In other studies, it was pointed out to similar trends, for example, a research conducted in Germany, showed that the introduction of magnetorheological shock absorbers reduces vibrations and improves the controllability of the SMTS when sowing on uneven soil surfaces (*Sharipov, 2019*).

During a research in China CFD–DEM modelling was applied to analyse vibrations for seed dosing accuracy in pneumatic seed drills. It was found that increasing the travel speed with proper design settings reduces the negative impact of vibrations upon sowing (*Wang et.al., 2024b*).

The authors of another study analysed the energy distribution in a wide-cut SMTS and determined that up to 90.8% of the power of the tractor is spent on overcoming resistance, emphasizing the importance of optimizing the design of the unit (*Tulegenov et.al., 2020*).

The authors of theoretical and experimental investigations of three-module sowing machine-tractor system studied the impact of the length of the drawbar of the side seeder and the track width upon the stability of the unit when it is turned. The results confirmed that changing the geometry of the SMTS increases its stability (*Findura et.al., 2024*).

The results of modelling, presented in the work of *Marcinkiewicz et.al., (2019*), demonstrate high accuracy of the analysis of the seeder elements using the discrete element method (DEM), which made it possible to evaluate in detail the interaction of components during the sowing process. These approaches are well compatible with the results of our study, where the use of Lagrange equations of the second kind provided a reliable description of the plane-parallel movement of an aggregating wheeled tractor and a trailed seeder. Both approaches confirm that digital modelling – whether DEM or classical mechanics – allows optimizing the design parameters of the seeding unit, reducing dynamic vibrations and increasing the accuracy of the seeding process in real field conditions.

Thus, the obtained results confirm the efficiency of the proposed mathematical model and show its applicability for optimizing the movement of a sowing machine-tractor system. The conducted comparison with the studies by foreign authors confirms that, considering the geometric parameters, pressure in the pneumatic tires of the running wheels, the speed of movement and spectral characteristics, is an important condition for increasing the accuracy and reliability of the technological process of sowing various agricultural crops.

CONCLUSIONS

It was determined that the maximum value of deviation of the tractor's centre of mass from a straight-line trajectory is 0.125 m (v = 2.5 m·s^{-1}, l_5 = 2 m, P_w = 0.10 MPa; v = 2.8 m·s^{-1}, l_5 = 3 m, P_w = 0.10 MPa) and 0.12 m (v = 2.5 m·s^{-1}, l_5 = 2 m, P_w = 0.10 MPa). The length of the range of oscillations of the tractor's centre of mass is 0.12 m (at v = 2.5 m·s^{-1}, l_5 = 2 m, P_w = 0.10 MPa).

Increasing the travel speed to 2.8 m·s^{-1} and increasing the pressure in the tractor tires to 0.12 MPa lead to a decrease in the amplitude of the oscillations of the tractor's centre of mass to 0.11 m.

The range of oscillations of the centre of mass of the seeder decreases from 0.11 m (at v = 2.5 m·s^{-1}, l_5 = 2 m, P_w = 0.10 MPa, to 0.08 m (at v = 2.8 m·s^{-1}, l_5 = 3 m, P_w = 0.12 MPa). The maximum turning angle of the tractor frame around the vertical axis is 5.8 degrees (at v = 2.5 m·s^{-1}, l_5 = 2 m, P_w = 0.10 MPa). The turning angle of the seeder frame for this case is 2.2 deg.

Increasing the speed of the SMTS and increasing the length of the seeder hitch leads to a decrease in the angle φ_1 of the tractor and seeder to 2.8 degrees and 1.8 degrees, respectively (at v = 2.8 m·s^{-1}, l_5 = 3 m, P_w = 0.12 MPa).

Increasing the speed of movement to 2.8 m·s^{-1}, increasing the distance from the seeder trailer point to the centre of mass of the seeder l_5 to 3 m, and increasing the pressure in the tractor wheels to 0.12 MPa have a positive effect on the linearity (straightness) of the movement of the SMTS elements.

It has been established that the discrepancy between the values of the trajectory of the movement of the centres of mass of the tractor and the seeder, determined during the theoretical research O_{1T}, O_{2T} and determined during the experimental studies is 11%, and the discrepancy between the values of the rotation angles of the centres of mass is 9%; therefore, the mathematical model of the dynamics of the SMTS can be considered adequate.

REFERENCES

[1] Adamchuk V., Bulgakov V., Nadykto V., Trohaniak O., & Chorna T. (2023). Theoretical study of the stability of asymmetric movement sowing machine-tractor aggregate. *Bulletin of Agricultural Science*, 101(5), 57–64. https://doi.org/10.31073/agrovisnyk202305-08

[2] Antoshchenkov R., Halych I., Nikiforov A., Cherevatenko H., Chyzhykov I., Sushko S., Ponomarenko N., Diundi S., Tsebriuk I. (2022). Determining the influence of geometric parameters of the traction-transportation vehicle's frame on its tractive capacity and energy indicators. *Eastern-European Journal of Enterprise Technologies*, 2, (7-116), 60-61. DOI: 10.15587/1729-4061.2022.254688

[3] Antoshchenko R.V., Cherevatenko G.I., Zadorozhny V.P., Svitlychny O.V., Kuskov M.A. (2023). Research on the dynamics of an all-wheel drive traction and transport machine. *Ukrainian Journal of Applied Economics and Technology*, 7(3). 125–135.

[4] Antoshchenkov R., Halych I., Antoshchenkov V., Nykyforov A., Kis-Korkishchenko L., Cherevatenko H., Smitskov D. (2024). Measuring system of dynamics and energy of mobile machines: monograph. – Katowice: *Wydawnictwo Uniwersytetu Śląskiego*. 150 p.

[5] Babaei Robat A., Arezoo K., Alipour K., & Tarvirdizadeh B. (2024). Dynamics modelling and path following controller of tractor-trailer-wheeled robots considering wheels slip. *ISA Transactions*, 148, 45–63. https://doi.org/10.1016/j.isatra.2024.03.004

[6] Bulgakov V., Adamchuk V., Ivanovs S., Ihnatiev Y. (2017). Theoretical investigation of aggregation of top removal machine frontally mounted on wheeled tractor. *Engineering for Rural Development*, 16, 273–280. https://www.iitf.lbtu.lv/conference/proceedings2017/Papers/N054.pdf

[7] Bulgakov V., Antoshchenkov R., Adamchuk V., Halych I., Ihnatiev Y., Beloev I., Ivanovs S. (2022). Investigation ofwhats the tractor performance when ballasting its rear half-frame. *INMATEH – Agricultural Engineering*, 68(3), 533–542. http://dx.doi.org/10.35633/inmateh-68-52

[8] Dammeten L., Schjonning P., J. Munkholm L., Green O., K. Nielsen S., & Lamandé M. (2021). Traction and repeated wheeling – effects on contact area characteristics and stresses in the upper subsoil. *Soil and Tillage Research*. 211, Article 105020. https://doi.org/10.1016/j.still.2021.105020

[9] Ivanovs S., Bulgakov V., Nadykto V., Ihnatiev Ye., Smolinskyi S., Kiernicki Z. (2020). Experimental study of the movement control-lability of a machine-and-tractor aggregate of the modular type. *INMATEH – Agricultural Engineering,* 61(2), 9–16. https://doi.org/10.35633/inmateh-61-01

[10] Findura P., Kollárová K., Nadykto V., Kyurchev V., Zhokin I. (2024). Turning Research of a Sowing Unit Based on Reversible Tractor. *Acta Technologica Agriculturae*. 27. 194-202. http://dx.doi.org/10.2478/ata-2024-0026

[11] Li X., Xu L., Liu M., Yan X., & Zhang M. (2024). Research on torque cooperative control of distributed drive system for fuel cell electric tractor. *Computers and Electronics in Agriculture*, 219, 108811. https://doi.org/10.1016/j.compag.2024.108811

[12] Marcinkiewicz J., Selech J., Staszak Ż., Gierz Ł., Ulbrich D., & Romek D. (2019). DEM simulation research of selected sowing unit elements used in a mechanical seeding drill. *MATEC Web of Conferences*, 254, 02021. https://doi.org/10.1051/matecconf/201925402021

[13] Parihar N.S., Sharma S., & Khar S. (2024). Factors Affecting the Performance of a Potato Digger – A Review. *Potato Research*, 67(4), 1563–1580. https://doi.org/10.1007/s11540-024-09704-5.

[14] Prasanna Kumar G.V., Srivastava B., & Nagesh D.S. (2009). Modelling and optimization of parameters of flow rate of paddy rice grains through the horizontal rotating cylindrical drum of drum seeder. *Computers and Electronics in Agriculture*, 65(1), 26–35. https://doi.org/10.1016/j.compag.2008.07.006

[15] Sharipov M.G. (2019). *Modelling and Optimization of No-Till Seeder Dynamics*. [Dissertation Submitted in fulfilment of the regulations to acquire the degree "Doktor der Agrarwissenschaften"], https://scispace.com/pdf/modelling-and-optimisation-of-no-till-seeder-dynamics-for-gfa7s97zi9.pdf

[16] Shior M.M., Agbata B.C., Gbor G.D., Ezugorie I.U., & Topman N.N. (2024). Solution of First Order Ordinary Differential Equations Using Fourth Order Runge-Kutta Method with MATLAB. *International Journal of Mathematics and Statistics Studies*, 12(1), 54–63. https://doi.org/10.37745/ijmss.13/vol12n15463

[17] Startcev A., Romanov S., & Vagina O. (2021). Research into the Course Stability of a Four-Wheel Drive Wheeled Machine–Tractor Unit. In *Lecture Notes in Mechanical Engineering*, Springer International Publishing. 607–614. https://doi.org/10.1007/978-3-030-54814-8_70

[18] Sun J., Zhang Y., Zhang Y., Li P., & Teng G. (2022). Precision Seeding Compensation and Positioning Based on Multisensors. *Sensors*, 22(19), 7228. https://doi.org/10.3390/s22197228

[19] Wang L., Zhu J., Liu F., He Z., Lai Q., Zhu Z., Song Z., & Li Z. (2024a). Algorithm and scale experiment of gyro-based tractor rollover control towards hilly farmland application. *Computers and Electronics in Agriculture*, 220, 108925. https://doi.org/10.1016/j.compag.2024.108925

[20] Wang Y., Zhang W., Luo, X., Zang Y., Ma L., Zhang W., Liu, J., & Zeng S. (2024b). Effect of Vibration Conditions on the Seed Suction Performance of an Air-Suction Precision Seeder for Small Seeds. *Agriculture*, 14(4), 559. https://doi.org/10.3390/agriculture14040559

STUDY ON THE MOVEMENT CHARACTERISTICS OF RAPESEED THRESHING MATERIALS BASED ON DEM SIMULATION AND HIGH-SPEED IMAGING
/
基于 DEM 和高速摄影技术的油菜籽脱粒物料迁移特性研究

Guangchao ZHAN*[1)], Wei LIU[2)], Peng ZHANG[1)]
[1)] School of Electromechanical and Intelligent Manufacturing, Huanggang Normal University, Huanggang 438000, Hubei, China
[2)] Jiangshan Heavy Industries Research Institute Co., Ltd., Norinco Group, Xiangyang Hubei 441005, China
Tel: +86-180-8650-1301; E-mail: guangchaozhan@hgnu.edu.cn
DOI: https://doi.org/10.35633/inmateh-76-107

Keywords: *rapeseed; threshing drum; DEM simulation; high-speed imaging; movement characteristics*

ABSTRACT
To investigate the movement characteristics and distribution patterns of materials inside the threshing drum during the rapeseed threshing process, a simplified DEM model was established using three typical particle types: seeds, pods, and stalks. A simulation system of the drum's internal environment was constructed, and combined with high-speed photography experiments to analyse the material distribution and dynamic movement trajectories. The results showed that materials primarily migrated in a helical pattern along the outer edge of the drum. Seeds and pods were mainly concentrated in collection box 2, accounting for 33.6% and 27.6% of the total, respectively. The material quantity gradually decreased from collection boxes 2 to 6, while 56.5% of the partially unbroken stalks were discharged from the straw outlet and collected in box 7. To verify the accuracy of the simulation, a test platform was built and high-speed photography experiments were conducted, showing that the actual material trajectories closely matched the simulation. Both simulation and experimental results indicated the highest material concentration in collection box 2, at 24.6% and 19.2%, respectively, and the lowest in box 6, at 5.1% and 6.8%. These findings provide theoretical support and technical guidance for optimizing drum structure, achieving precise threshing control, and advancing intelligent agricultural machinery design.

摘要
为研究油菜籽脱粒过程中脱粒滚筒内部物料的迁移特征和分布规律，建立了籽粒、果荚和茎秆三种典型颗粒简化的 DEM 模型。建立了脱粒滚筒内部环境模拟系统，并结合高速摄影实验对物料分布和动态迁移轨迹进行了分析。结果表明，物料主要沿滚筒外缘呈螺旋状迁移。种子和豆荚主要集中在 2 号收集箱，分别占总量的 33.6% 和 27.6%。从 2 号收集箱到 6 号收集箱，物料量逐渐减少，56.5% 的部分未破碎茎秆从秸秆出口排出，被收集到 7 号收集箱。为了验证模拟的准确性，我们搭建了一个测试平台，并进行了高速摄影实验，结果表明实际的物料轨迹与模拟非常吻合。模拟和实验结果都表明，2 号收集箱的物料浓度最高，分别为 24.6% 和 19.2%，6 号收集箱的物料浓度最低，分别为 5.1% 和 6.8%。这些发现为优化滚筒结构、实现精确脱粒控制和推进智能农机设计提供了理论支持和技术指导。

INTRODUCTION
As a critical stage in the mechanized harvesting of rapeseed, the performance of threshing directly affects key indicators such as seed loss rate, damage rate, and threshing efficiency *(Qing, 2021; Kuai, 2015; Pari, 2012)*. At present, mainstream rapeseed threshing devices both domestically and internationally predominantly adopt axial-flow or transverse-flow drum structures *(Yuan, 2024; Vlădut, 2023)*. Among them, axial-flow drums are widely applied in China's major rapeseed-producing areas due to their advantages in layered threshing and high efficiency *(Wan, 2018; Tang, 2024)*.

To enhance threshing performance, recent research efforts in China have focused on structural optimization of rapeseed threshing drums. Innovations include composite threshing devices, conical drum structures, variable-diameter drums *(Wang, 2023; Li, 2020; Chen, 2025)*, and differential-speed threshing mechanisms. These designs aim to develop a threshing unit with strong adaptability, low loss, and high versatility *(Wang, 2017; Xu, 2019; Wan, 2023)*.

[1] *Guangchao Zhan, Lecture, Ph.D; Wei Liu, Engineer, Ph.D; Peng Zhang, Lecture, Ph.D.*

However, most of the existing studies emphasize rotor or threshing component optimization and parameter regulation, while the impact of internal material movement characteristics on threshing performance remains largely underexplored. Given the significant variability in ripeness, moisture content, and plant morphology across different rapeseed fields *(Bruce, 2001; Ma, 2015; Liao, 2019)*, the mixture of seeds, pods, and stalks during the threshing process frequently leads to issues such as material clogging, accumulation, and repeated striking and over-crushing of stalks *(Mircea, 2020)*. These problems severely hinder threshing and separation efficiency during the combine harvesting process.

To overcome the limitations of traditional experimental methods in observing internal particle movement, DEM has been widely adopted in agricultural machinery simulation. *Wu et al. (2022)* developed a DEM-based rapeseed threshing model for parameter optimization. *Guan et al (2022)* proposed a flexible stalk model to improve simulation accuracy. *Fu et al (2021)* analysed the distribution characteristics of mixed materials in axial-flow drums, and other researchers investigated the mechanism of threshing loss, offering reference for simulation parameter settings *(Tang, 2024; Lee, 2009; Vlădut, 2022)*. Nonetheless, current research still lacks dynamic tracking of spatial movement, path variation, and residence behaviour of materials inside the drum. Furthermore, simulation result validation methods remain limited, which compromises the credibility and generalizability of the models.

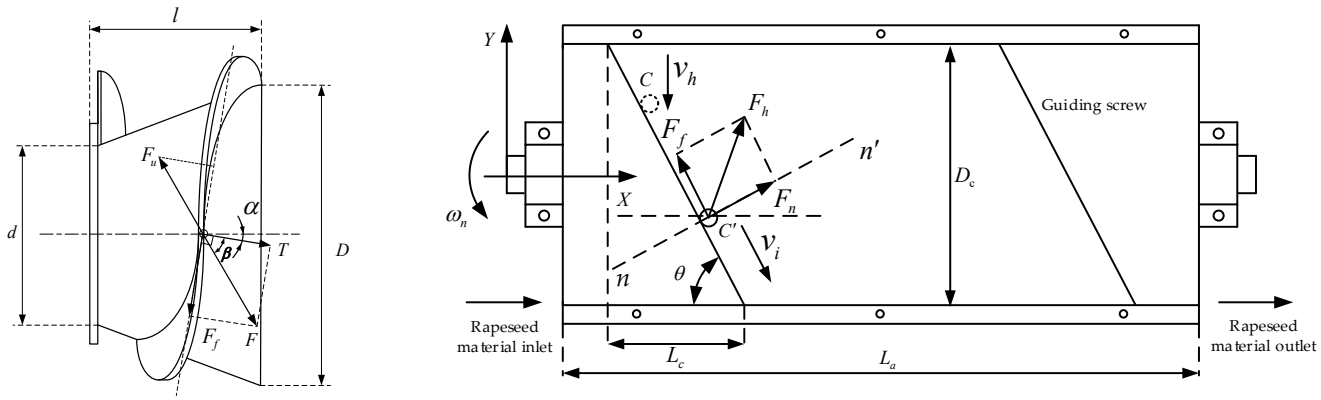
High-speed photography, a non-contact and instantaneous visualization technique, has recently been applied to monitor agricultural operations and track particle motion. *Zhan et al (2022)* studied the dynamic response of rapeseed plants under vibration using high-speed imaging. Other researchers used high-speed cameras to evaluate the impact of different threshing elements on seed damage *(Ma, 2020; Lian, 2022)*. Some researchers combined image analysis to investigate the motion trajectories and threshing states of stalks and seeds, demonstrating the potential of high-speed photography in particle motion studies *(Zong, 2013; Zuo, 2014; Li, 2021)*. However, due to limitations such as restricted viewing angles, image occlusion, and high particle density, high-speed imaging alone is insufficient to fully reveal internal motion mechanisms.

In summary, although the research on rapeseed threshing devices has made notable progress, the internal movement mechanism of materials, particle movement paths, and residence distribution inside the drum remain under-investigated. Additionally, there is a lack of a high-confidence modelling and validation framework. Therefore, this study proposes a combined approach using DEM simulation and high-speed visual analysis. A simulation model of rapeseed threshing materials is developed to analyse their dynamic movement within the drum. Experimental validation is conducted through bench tests coupled with high-speed photography, aiming to reveal the material movement characteristics during the threshing process. This study provides theoretical support for structural optimization of the threshing drum and the design of intelligent agricultural machinery.

MATERIALS AND METHODS

Theoretical analysis

During the rapeseed threshing process, the axial movement of materials mainly relies on the spiral feeding head and the guiding spiral. The determination of the key parameter, screw angle, directly affects the efficiency of axial material movement. A force analysis showing how the spiral feeding head and guiding spiral act on the materials is presented in Figure 1.



(a) Screw feed head of threshing drum *(b) Upper cover of rapeseed threshing drum*

Fig. 1 - Force analysis of guiding components in the rapeseed threshing drum

In Figure 1(*a*), T represents the normal thrust exerted by the helical blade on the rapeseed material, and its direction is perpendicular to the blade surface. When conveying the material, the helical blade generates a friction force F_f with the material, which lies in the blade surface and is perpendicular to the normal thrust T. The resultant force F is the combination of T and F_f. F_u is the resistance force acting on the material. The angle between the normal thrust T and the horizontal axis of the helical feed head is denoted as α, and the friction angle β between the rapeseed material and the helical blade is the angle between F and T. The angle α, corresponding to the helix angle, plays a critical role in feed performance. If the angle is too small, material feeding becomes slow and prone to clogging. Conversely, an excessively large angle can lead to unstable and pulsating feed flow, which is particularly unfavourable for lightweight crops such as rapeseed. Based on empirical data, the helix angle is typically within the range of 15° to 30°. In this design, the angle is set to 25°.

To facilitate observation of the actual threshing process of rapeseed, the upper cover is made transparent using organic glass. When the threshing device operates, the drum rotates at a high speed ω_n, and after the rapeseed material enters the threshing drum, it is subjected to high-speed striking and agitation by the threshing beaters mounted on the drum. Under this disturbance, the material moves in a circular path in the radial direction of the drum. Meanwhile, the guiding spiral conveys the material axially.

As shown in figure 1 (*b*), the rapeseed material, with mass m_c, contacts point C on the guiding spiral with an initial velocity v_h, then slides to point C', reaching a velocity v_i at that point. To enable the rapeseed material to slide and be conveyed along the axial direction of the drum, the angle between the guide spiral and the Y-axis must be less than the sliding friction angle of the rapeseed material, namely:

$$\begin{cases} 90° - \theta \le \varphi \\ \varphi \approx arctan\, \mu_c \end{cases} \quad (1)$$

In the equation, the symbol φ represents the sliding friction angle between the rapeseed material and the guiding spiral; while θ denotes the angle between the guiding spiral and the axial direction of the drum; and μ_c is the friction coefficient of the rapeseed material.

By simplifying Equation (1), the following is obtained:

$$\theta \ge 90° - arctan\, \mu_c \quad (2)$$

In the Yangtze River region of China, rapeseed is typically harvested with a relatively high moisture content. Under such conditions, the coefficient of friction of the material is taken as 0.58, thus, $\theta \ge 60°$. Furthermore, if angle θ is too large, the guiding efficiency of the spiral decreases, requiring additional guide spirals to achieve the desired conveying effect, therefore :

$$\begin{cases} tan\, \theta = \dfrac{D_c}{L_c} \\ L_c \ge \dfrac{L_a}{K_c} \end{cases} \quad (3)$$

where: D_c represents the width of the upper cover of the threshing drum, L_c denotes the lead of a single guiding spiral, L_a is the total length of the upper cover of the threshing drum, and K_c refers to the number of guiding spirals. Simplifying equation (3), the following is obtained:

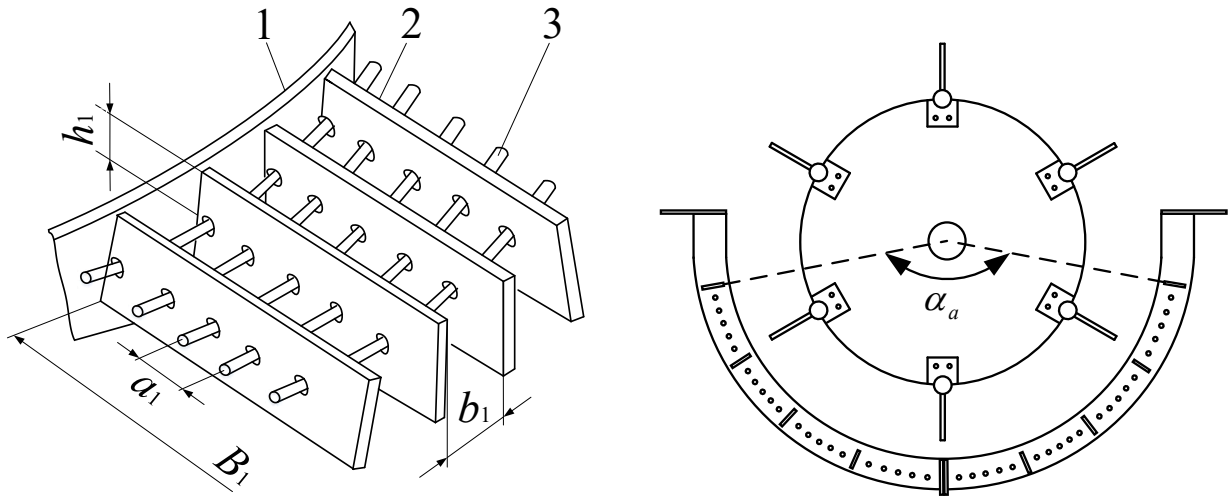
$$\theta \le arctan \frac{K_c \cdot D_c}{L_a} \quad (4)$$

The width of the threshing drum upper cover D_c is directly determined by the threshing drum and is taken as 680 mm. The number of guiding spirals K_c is set to 8, and the length of the threshing drum upper cover L_a is 2.03 m. Therefore, $\theta \le 69.3°$. Considering all factors comprehensively, the helix angle θ of the guiding spiral is selected as 65°.

As shown in figure 2 (a), the grid-type concave screen generally consists of several components, including the side curved plates, transverse plates, and grate bars. Here, b_1 represents the spacing between adjacent transverse plates when they are evenly distributed, typically ranging from 30 to 40 mm; in this study, it is set to 40 mm. h_1 denotes the height by which the edge of a cross slat protrudes above the grate bars, which serves to assist in the threshing process. However, an excessive height may cause severe damage to the rapeseed stems. Therefore, h_1 is usually within the range of 5-15 mm, and is set to 10 mm in this design. a_1 indicates the spacing between grate bars. A smaller spacing may reduce the separation efficiency of the concave screen, while a larger spacing may lead to an increased loss of unthreshed pods and stalks falling through. Typically, the spacing ranges from 8 to 15 mm.

Considering that the material density at the front end of the threshing drum is higher than that at the rear end during operation, a two-section concave screen is adopted in this study: the front section has a spacing of 12 mm, and the rear section is set to 15 mm.

The wrap angle of the concave screen is illustrated in figure 2 (b). Since the wrap angle of the concave screen in rapeseed threshing devices is generally less than 180°, a wrap angle α_a of 150° is selected in accordance with the dimensions of the existing structure.



(a) Schematic diagram of the grid-type concave screen (b) Cross-sectional view of the concave screen

Fig. 2 - Schematic diagram of threshing elements

1. Side curved plate; 2. Transverse plate; 3. Grate bar

Material Modelling and Parameter Settings

Given the complex composition of materials involved in the actual threshing process, the simulation simplified the materials into three representative particle types: seeds, pods, and stalks. The seed model was simplified to a spherical particle with a diameter of 2 mm, based on the actual size of rapeseed grains. The stalks were modelled as cylindrical particles with a defined diameter, while the pods were simplified based on their actual morphological features. The simplified model is shown in the figure 3.



Seeds Pods Stalks

Fig. 3 - Simplified material model

The physical properties of each particle type were determined based on existing literature and experimental measurements. Detailed parameters are listed in Table 1 *(Shi, 2018)*.

Table 1

Parameter value of material simulation

Item	Poisson's Ratio	Density (kg·m^{-3})	Shear Modulus (MPa)
Seed	0.28	1060	11
Pods	0.30	1000	11
Stalks	0.30	809	47
Drum	0.30	7800	7000

Since all parts of the threshing drum were made of the same material, it was only necessary to define the contact parameters among the four types of materials: stalks, pods, seeds, and drum. The interaction parameters used in the contact simulation between these materials are listed in Table 2 *(Liao,2020)*. The main parameters include the coefficient of restitution between components, the static friction coefficient, and the rolling friction coefficient.

Table 2

Contact simulation parameters between materials

Item	Restitution Coefficient	Static Friction Coefficient	Rolling Friction Coefficient
Seed-Seed	0.41	0.54	0.01
Seed-Pod	0.30	0.47	0.01
Seed-Stalk	0.37	0.37	0.01
Seed-Drum	0.53	0.30	0.01
Pod-Pod	0.31	0.37	0.01
Pod-Stalk	0.35	0.32	0.01
Pod-Drum	0.34	0.43	0.01
Stalk-Stalk	0.41	0.29	0.01
Stalk-Drum	0.39	0.40	0.01

Based on the actual structural dimensions of the threshing drum, a simplified simulation model was constructed, including the drum, concave sieve, and guiding structures. Key parameters such as the drum diameter, length, and the arrangement of threshing beaters were set according to specifications commonly found in rapeseed threshing devices, with support for adjustable rotational speed to simulate different working conditions. In this study, the required materials were generated using a virtual factory approach, in which particles were introduced at a controlled rate over time. To better observe and compare the material distribution during the threshing process, the generation rate of particles was determined based on the actual feeding rate of rapeseed in field harvesting. Since the typical feeding rate of rapeseed is ≥2 kg/s and the harvesting speed is ≥0.9 m/s, the feeding rate was set to 20 rapeseed plants per second in the simulation. Statistical analysis of rapeseed plants shows that each plant contains approximately 254-478 pods, with each silique containing 12-33 seeds. A single plant has 8-12 branches, with branch lengths ranging from 46 to 87 mm. Considering these material characteristics and field operating parameters of rapeseed combine harvesters, the simulation was configured with a silique generation rate of 4,000 pods per second, a seed generation rate of 80,000 seeds per second, and a stalk generation rate of 100 stalks per second (with each stalk having a length of 200 mm).

Table 3

Statistical parameters of rape plant characters

Item	Numerical range	Average
Number of seeds (single pod)	12~33	21
Number of pods (single plant)	254~478	383
Number of branches (single plant)	8~12	10
Length of branch (mm)	46~87	64

High-Speed Photography Experiment



Fig. 4 - Main parameters of threshing test bench

1. Receiving plate; 2. Discharge port; 3. Concave screen; 4. Upper cover; 5. Threshing nail beater; 6. Guide screw; 7. Toothed rod; 8. Spiral feeding head; 9. Feeding port; 10. Drive motor; 11. Slide rail; 12. Electric push rod

The actual drum structure was consistent with the simulation model. The upper cover of the threshing drum was made transparent using organic glass to facilitate observation of the internal material movement by a high-speed camera. A receiving tray was placed below the drum to collect materials, and after threshing, manual screening was conducted to determine the distribution of seeds and other materials. The experimental setup is shown in figure 4.

By conducting high-speed photography observations of stalk breakage along the axial direction during the rapeseed threshing process, the motion trajectories and distribution of materials within the threshing unit can be intuitively understood. This method also enables the visualization of the interactions between rapeseed materials and key threshing components such as the rasp bars and guiding helices. Six collection boxes, each 200 mm in width, are arranged side by side beneath the drum sieve, with an additional box positioned at the end of the straw outlet. Figure 5 shows the experimental setup for axial observation during the rapeseed threshing process.



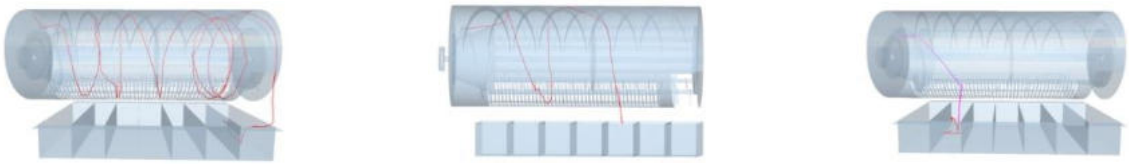
Fig. 5 - Test site of rape threshing process observed from axial direction

RESULTS

Simulation Results Analysis

To facilitate the observation of material movement trajectories, the simulation model was simplified by hiding the internal structure of the threshing drum rotor. After continuous feeding for 5 seconds, the materials inside the drum reached a relatively stable state. At this stage, randomly selected materials were observed to track their motion trajectories.

To better track individual particle movements, a single rapeseed stalk, pod, and seed were marked, and their motion trajectories were recorded. As shown in figure 6, the stalk, due to its larger size, could not easily pass through the concave sieve and exhibited a more complex trajectory before being discharged from the straw outlet at the end of the drum. In contrast, the smaller pods and seeds fell through the sieve more readily, showing simpler trajectories with distribution mainly concentrated in the front section of the sieve.

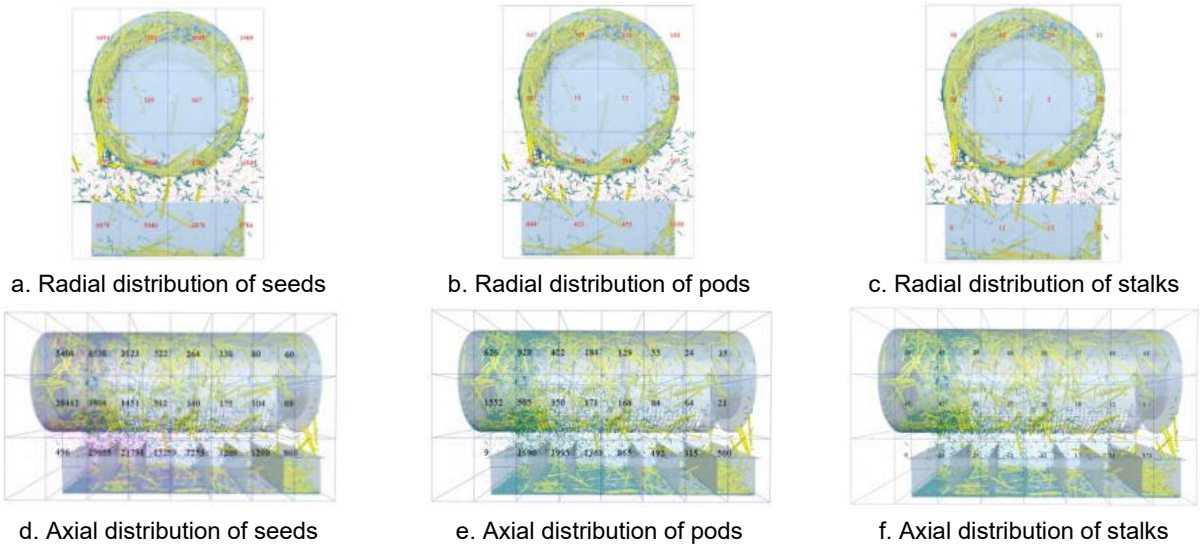


a. Trajectory of stalk b. Trajectory of pod c. Trajectory of seed

Fig. 6 - Motion trajectories of rapeseed materials inside the threshing drum

Keeping the material feeding rate constant, the simulation time was set to 5 seconds with a data saving interval of 0.01 seconds. After the simulation concluded, the process was paused at the 5-second mark. The DEM computational domain was divided into 8 × 1 × 3 regions along the axial, horizontal radial, and vertical directions of the threshing drum. The material distribution in each region was statistically analysed.

To investigate the distribution of stalks discharged from the drum, only the stalk distribution in the receiving box beneath the concave screen was considered. To reduce random errors, each simulation scenario was repeated three times, and the average values were taken. Figure 7 shows the material distribution diagram. In the figure, magenta particles represent rapeseed grains, green particles represent pods, and yellow particles represent stalks.



a. Radial distribution of seeds b. Radial distribution of pods c. Radial distribution of stalks

d. Axial distribution of seeds e. Axial distribution of pods f. Axial distribution of stalks

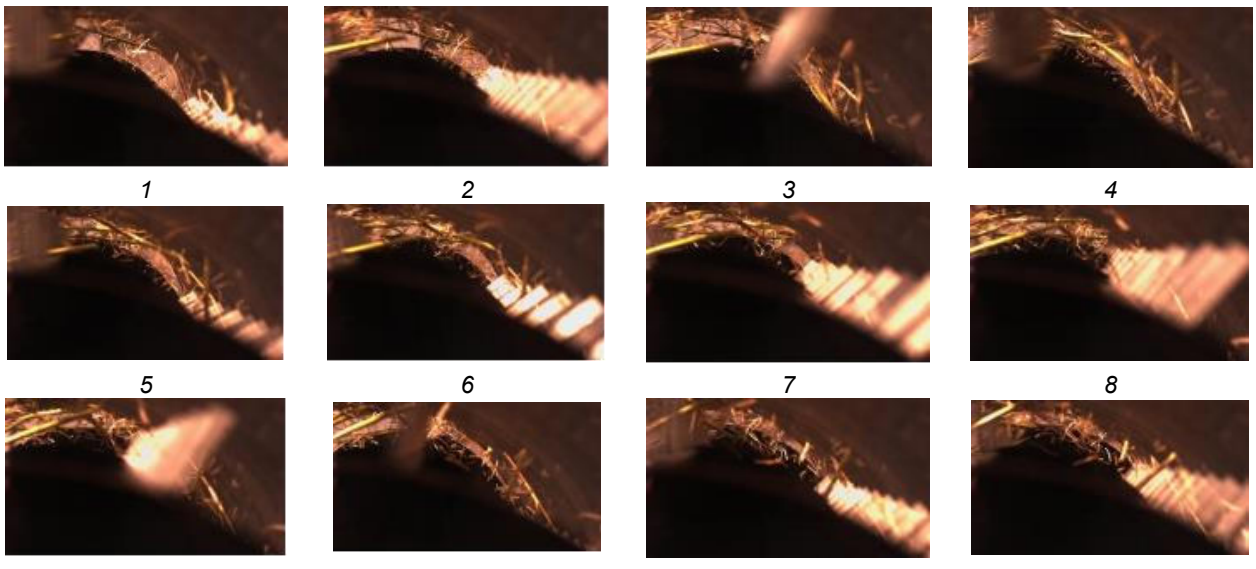
Fig. 7 - Distribution of rapeseed materials in the threshing drum

Figure 7 presents the simulated material distribution within the threshing drum. The simulation results indicate that the radial distribution of materials is primarily concentrated near the outer periphery of the drum, with fewer materials located near the drum centre. Axially, the distribution of seeds and pods shows a clear decreasing trend from the front to the rear part of the drum.

Due to their larger size and frequent contact with the concave screen and threshing components inside the drum, the stalks exhibit the longest residence time and are mainly discharged from the straw outlet at the rear part of the drum. The pods rank second in residence time, with materials primarily distributed in the front half of the drum. The rapeseed grains, being the smallest, are the easiest to be discharged and have the shortest residence time inside the drum. These differences are directly related to threshing efficiency and separation performance.

High-Speed Photography Experimental Results

High-speed photography was used to observe and analyse the rapeseed threshing process. Figure 8 shows the axial movement and distribution of materials within the threshing drum. The high-speed photography experiments revealed that during the threshing process, materials were mainly distributed along the outer region of the drum. Under the combined action of threshing beaters and rods, the rapeseed materials migrated along the periphery of the threshing drum. The results of this experiment are in general agreement with the simulation.



1 2 3 4

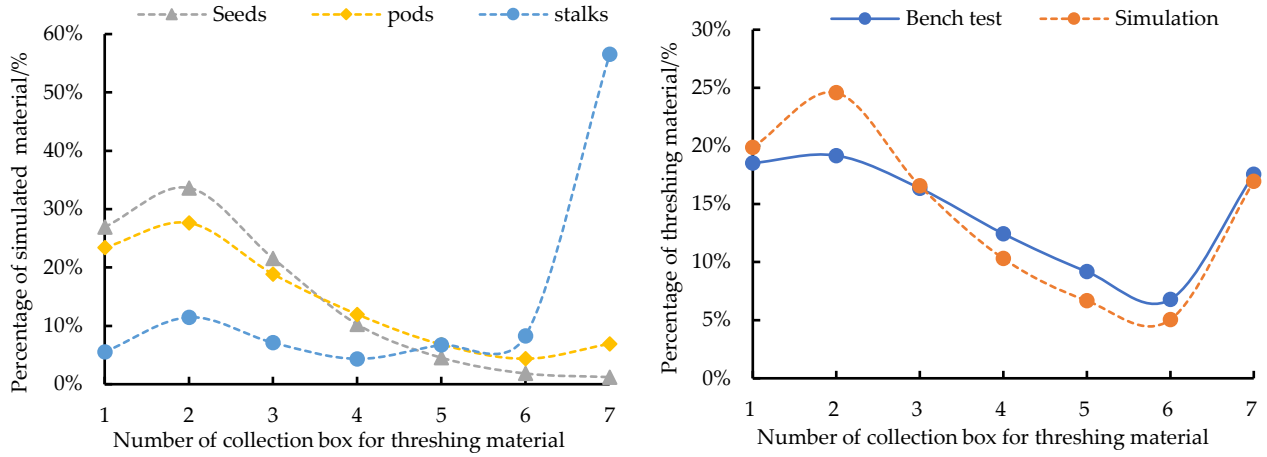
5 6 7 8

9 10 11 12

Fig. 8 - High-speed photography of material movement as rapeseed separates from the threshing drum

The distribution of materials in the collection bins after separation is shown in figure 9. Figure 9(*a*) shows the distribution of seeds, pods and stalks during the simulation process. To better replicate the real feeding process from the conveyor to the threshing drum, a horizontal initial velocity was assigned to the materials in the simulation. This velocity caused a portion of the materials to travel further before settling, resulting in a smaller quantity in collection box 1 and a greater accumulation in collection box 2. Seeds and pods were concentrated in collection box 2 with 33.6 % and 27.6%, respectively. From collection box 2 to box 6, the material amount shows a decreasing trend, and 56.5% of the partially unbroken stalks are discharged from the straw outlet of the threshing drum and fall into collection box 7, which contains the largest mass of material.

To estimate the mass of seeds, pods, and stalks in the simulation, the physical materials were scaled according to the dimensions used in the simulation model. Given that the thousand-grain weight of rapeseed is approximately 3.5 g, the mass of a single seed is about 0.0035 g. A single pod weighs approximately 0.5 g, and a mature 200 mm-long rapeseed stalk weighs about 5 g. Based on the material counts in each collection box, the corresponding mass distribution of different materials in the simulation was calculated. This simulated mass distribution was then compared with the results obtained from the actual threshing experiments.



(*a*) Simulation of material distribution (*b*) Comparison of simulated and experimental

Fig. 9 - Threshing material distribution of collection boxes

Test results are shown in figure 9(b). The increase in material quantity from collection box 1 to box 2 is mainly because the materials are relatively intact upon entering the threshing drum; at this stage, pods and stalks have not yet fully separated, so the materials are less likely to fall into the bins. From Collection box 2 to 6, both the simulation and the bench-scale threshing experiment exhibit a gradual decrease in material quantity. The material distribution from both simulation and experiment was highest in collection box 2, accounting for 24.6% and 19.2%, respectively, while the lowest mass was observed in collection box 6, with 5.1% and 6.8%, respectively.

CONCLUSIONS

Based on DEM simulation and high-speed imaging visualization experiments, this study systematically investigated the movement characteristics and motion patterns of materials inside the rapeseed threshing drum. The results show that materials are mainly distributed around the beater bars near the drum periphery, with movement trajectories following a spiral motion along the drum's outer edge. The spiral direction is generally consistent with the guiding helix on the drum cover.

Significant differences in motion states were observed among different particle types within the drum. Stalks, due to their large size and frequent contact with the internal drum structures, exhibit the longest residence time; pods rank second; and seeds, being small and light, have the shortest residence time. The high-speed photography experiments validated the simulation model's accuracy and reliability regarding particle trajectories, velocity variation trends, and residence time distribution, ensuring the credibility of the simulation results. The distribution of rapeseed seeds and pods beneath the concave sieve exhibited a pattern of initial increase followed by a decrease, while the distribution of rapeseed stalks was relatively uniform.

However, there was a noticeable rise in stalk material near the discharge outlet, with 57% of the stalks exiting through this opening. A comparison between the bench test and simulation results revealed a consistent distribution trend, thereby confirming the reliability of the findings.

This study proposes a “simulation + visualization validation” methodological framework, providing new insights into the movement mechanisms of materials inside rapeseed threshing drums. The findings lay a technical foundation for developing efficient and low-loss intelligent threshing equipment. Future work could integrate intelligent sensing and control technologies to achieve real-time monitoring and adaptive regulation of the threshing process, promoting the intelligent and efficient development of rapeseed harvesting machinery.

ACKNOWLEDGEMENT

The authors gratefully acknowledge the support of the affiliated institution and the technical assistance provided during the research. Appreciation is also extended to the research group members for their valuable discussions. This project was funded by the Young Faculty Career Elevation Project (204202315604), and the University Distinguished Doctoral Research Program (2042023014).

REFERENCES

[1] Bruce, D., Hobson, R., Morgan, C., & Child, R. (2001). Threshability of shatter-resistant seed pods in oilseed rape. *Journal of Agricultural Engineering Research*, 80(4). 343–350. https://doi.org/10.1006/jaer.2001.0748

[2] Chen, L., Zhang, L., Li, L., & Zhang, L. (2025). Design and experiment of a low-damage threshing drum for corn with stepless taper adjustment. *Agriculture*, 15(1), 4. https://doi.org/10.3390/agriculture15010004

[3] Fu, J., Xie, G., Ji, C., Wang, W., Zhou, Y., Zhang, G., Zha, X., Abdeen, M. (2021). Study on the distribution pattern of threshed mixture by drum-shape bar-tooth longitudinal axial flow threshing and separating device. *Agriculture*, 11. https://doi.org/10.3390/agriculture11080756

[4] Guan, Z., Mu, S., Li, H., Jiang, T., Zhang, M., & Wu, C. (2022). Flexible DEM model development and parameter calibration for rape stem. *Applied Sciences*, 12(17). https://doi.org/10.3390/app12178394

[5] Kuai, J., Sun, Y., Zuo, Q., Huang, H., Liao, Q., Wu, C., Lu, J., Wu, J., & Zhou, G. (2015). The yield of mechanically harvested rapeseed (*Brassica napus L.*) can be increased by optimum plant density and row spacing. *Scientific Reports*, 5, 18835. https://doi.org/10.1038/srep18835

[6] Lee, C., Choi, Y., Jun, H., Lee, S., Moon, S., & Kim, S. (2009). Development of a rapeseed reaping equipment attachable to a conventional combine (III) – Analysis of principal factor for loss reduction of rapeseed mechanical harvesting. *Journal of Biosystems Engineering*, 34(2), 114–119. https://doi.org/10.5307/JBE.2009.34.2.114

[7] Li, X., Du, Y., Guo, J., & Mao, E. (2020). Design, simulation, and test of a new threshing cylinder for high moisture content corn. *Applied Sciences*, 10(14), 4925. https://doi.org/10.3390/app10144925

[8] Li, X., Wang, W., Zhao, G., Sun, C., Hu, P., & Ji, J. (2021). Design and experiment of longitudinal axial flow double flexible rolling and kneading threshing device for millet. *Transactions of the Chinese Society of Agricultural Machinery*, 52(7), 113–123. https://doi.org/10.6041/j.issn.1000-1298.2021.07.011

[9] Lian, G. D., Wei, X. X., Ma, L. N., Zhou, G. H., & Zong, W. Y. (2022). Design and experiments of the axial-flow spiral-drum threshing device for the edible sunflower. *Transactions of the Chinese Society of Agricultural Engineering*, 38, 42–51. DOI: 10.11975/j.issn.1002-6819.2022.17.005

[10] Liao, Q., Xu, Y., Yuan, J., Wan, X., & Jiang, Y. (2019). Design and experiment on combined cutting and throwing longitudinal axial flow threshing and separating device of rape combine harvester. *Transactions of the Chinese Society of Agricultural Machinery*, 50(7): 140-150. https://doi.org/10.6041/j.issn.1000-1298.2019.07.001

[11] Liao, Y., Liao, Q., Zhou, Y., Wang, Z., Jiang, Y., & Liang, F. (2020). Parameters calibration of discrete element model of fodder rape crop harvest in bolting stage. *Transactions of the Chinese Society of Agricultural Machinery*, 51(06):73-82. https://doi.org/10.6041/j.issn.1000-1298.2020.06.008

[12] Ma, Z., Han, M., Li, Y., Yu, S., & Chandio, A. (2020). Comparing kernel damage of different threshing components using high-speed cameras. *International Journal of Agricultural and Biological Engineering*, 06. 013. https://doi.org/10.25165/j.ijabe.20201306.5395

[13] Ma, Z., Li, Y., & Xu, L. (2015). Experimental study of reciprocating friction between rape stalk and bionic non-smooth surface units. *Applied Bionics and Biomechanics*, 627960. https://doi.org/10.1155/2015/627960

[14] Mircea, C., Nenciu, F., Vlăduț, V., Voicu, G., Gageanu, I., & Cujbescu, D. (2020). Increasing the performance of cylindrical separators for cereal cleaning by using an inner helical coil. *INMATEH – Agricultural Engineering*, 62(3), 249-258. https://doi.org/10.35633/inmateh-62-26.

[15] Pari, L., Assirelli, A., Suardi, A., Civitarese, V., Giudice, A., Costa, C., & Santangelo, E. (2012). The harvest of oilseed rape (Brassica napus L.): The effective yield losses at on-farm scale in the Italian area. *Biomass Bioenergy*, 46: 453-458. https://doi.org/10.1016/j.biombioe.2012.07.014

[16] Qing, Y., Li, Y., Xu, L., & Ma, Z. (2021). Screen Oilseed Rape (Brassica napus) Suitable for Low-Loss Mechanized Harvesting. *Agriculture,* 11(6), 504; https://doi.org/10.3390/agriculture11060504

[17] Shi, X., Wu, C., Li, H.; Qi, X., Yuan, J., Mei, Z., & Hu, T. (2018). Measurement and analysis of physical mechanical properties and aerodynamic characteristics of harvesting extractions from two rape varieties. *Jiangxi Agricultural Sciences*, 30(6). https://doi.org/10.19386/j.cnki.jxnyxb.2018.06.22

[18] Tang, Q., Jiang, L., Yu, W., Wu, J., & Wang, G. (2024). Design and experiment of high moisture corn threshing device with low damage. *INMATEH – Agricultural Engineering*, 74(3), 172-183. https://doi.org/10.35633/inmateh-74-15

[19] Vlădut, N., Biris, S., Cârdei, P., Găgeanu, I., Cujbescu, D., Ungureanu, N., Popa, L., Perişoară, L., Matei, G., & Teliban, G. (2022). Contributions to the mathematical modeling of the threshing and separation process in an axial flow combine. *Agriculture*, 12(10), 1520. https://doi.org/10.3390/agriculture12101520

[20] Vlădut, N., Ungureanu, N., Biris, S., Voicea, I., Nenciu, F., Găgeanu, I., Cujbescu, D., Popa, L., Boruz, S., Matei, G., Ekielski, A., & Teliban, G. (2023). Research on the identification of some optimal threshing and separation regimes in the axial flow apparatus. *Agriculture*, 13(4), 838. https://doi.org/10.3390/agriculture13040838

[21] Wan, X., Shu, C., Xu, Y., Y, J., Li, H., & Liao, Q. (2018). Design and experiment on cylinder sieve with different rotational speed in cleaning system for rape combine harvesters. *Transactions of the Chinese Society of Agricultural Engineering*, 34(14), 27–35. https://doi.org/10.11975/j.issn.1002-6819.2018.14.004

[22] Wan, X., Yuan, J., Yang, J., Liao, Y., & Liao, Q. (2023). Effects of working parameters on the performance of cyclone separator for rapeseed combine harvester based on CFD. *International Journal of Agricultural and Biological Engineering*, 16(1), 128–135. https://doi.org/10.25165/j.ijabe.20231601.7253

[23] Wang, F., Liu, Y., Li, Y., & Ji, K. (2023). Research and experiment on variable-diameter threshing drum with movable radial plates for combine harvester. *Agriculture*, 13(8), 1487. https://doi.org/10.3390/agriculture13081487

[24] Wang, G., Guan, Z., Mu, S., Tang, Q., & Wu, C. (2017). Optimization of operating parameter and structure for seed thresher device for rape combine harvester. *Transactions of the Chinese Society of Agricultural Engineering*, 33(24):52-57. https://doi.org/10.11975/j.issn.1002-6819.2017.24.008

[25] Wu, J., Tang, Q., Mu, S., Jiang, L., & Hu, Z. (2022). Test and optimization of oilseed rape (*Brassica napus L.*) threshing device based on DEM. *Agriculture*, 12(10), 1580. https://doi.org/10.3390/agriculture12101580

[26] Xu, L., Wei, C., Liang, Z., & Li, Y. (2019). Development of rapeseed cleaning loss monitoring system and experiments in a combine harvester. *Biosystems Engineering*, 178, 118–130. https://doi.org/10.1016/j.biosystemseng.2018.11.001

[27] Yuan, J, Liao, Q., Wan, X., Yang, J., & Shu, C. (2024). Parameter matching and experiment of the combined cyclone separation and cylinder sieve cleaning system for rape combine harvester. *International Journal of Agricultural & Biological Engineering*, 17(1), 128–136. https://doi.org/10.25165/j.ijabe.20241701.7739

[28] Zhan, G., Ma, L., Zong, W., Liu, W., Deng, D., & Lian, G. (2022). Study on the vibration characteristics of rape plants based on high-speed photography and image recognition. *Agriculture*, 12(5),727. https://doi.org/10.3390/agriculture12050727

[29] Zong, W., Liao, Q., Huang, P., Li, H., & Chen, L. (2013). Design of combined rape threshing device and analysis of rape cane movement trail. *Transactions of the Chinese Society of Agricultural Machinery*, 44:41-46. https://doi.org/10.6041/j.issn.1000-1298.2013. S2.009

[30] Zuo, Q., Huang, H., Cao, S., Yang, S., Liao, Q., Leng, S., Wu, J., & Zhou, G. (2014). Effects of harvesting date on yield loss percentage of mechanical harvesting and seed quality in rapeseed. *Acta Agronomica Sinica*, 40(04): 650-656. https://doi.org/10.3724/SP.J.1006.2014.00650

DEVELOPMENT OF TRACTOR FRONT MOUNTED CONVEYOR BASED PULSES CROP HARVESTER

/

ट्रैक्टर फ्रंट माउंटेड कन्वेयर आधारित दलहन फसल हार्वेस्टर का विकास

Tanmoy DAS[1)], Sanjay KUMAR PATEL[1)], Bibek ISHORE[1)], Jaya SINHA[1)] and Sanjay KUMAR[1)]

[1)] Department of Farm Machinery and Power Engineering, College of Agricultural Engineering and Technology, Dr. Rajendra Prasad Central Agricultural University, Pusa, Samastipur, Bihar, India

Corresponding Author: Sanjay Kumar Patel, Email: sppiari@gmail.com

DOI: https://doi.org/10.35633/inmateh-76-108

Keywords: Pulse crop, mechanical harvesting, pulse harvester

ABSTRACT

The aim of the study was to develop an efficient and cost-effective tractor-front-mounted conveyor-based pulse crop harvester to meet the increasing demand for mechanized harvesting methods, particularly for crops like chickpeas, lentils, and black gram. The research is based on the principles of agricultural mechanization, focusing on optimizing key crop parameters such as cutting force requirements, plant spacing, row spacing, and stem diameter. These factors are crucial in selecting appropriate motors and cutting blades to enhance harvesting efficiency of pulse crops. The study involves torque calculations to determine the power requirements for cutting and conveying units, with results showing 1.24 Nm and 7.06 Nm, respectively. A gear motor was employed to ensure the proper conveyance of cut crops at a linear speed of 0.54 m/s. Field tests were conducted in a black gram field to evaluate the harvester's effectiveness under varying conditions. Field tests demonstrated the harvester's ability to handle premature crops, with cutting efficiency ranging from 71.04% to 75.06% at different forward speeds. The harvester achieved a maximum field capacity of 0.225 ha/h at a speed of 1.50 km/h, with a corresponding field efficiency of 75.02%. The working capacity varied from 0.831 ha/day to 1.80 ha/day, proving its suitability for pulse harvesting. Power consumption analysis indicated a total power requirement of 0.569 kW, enabling the harvester to operate for approximately 4 hours on a fully charged 12V, 200 Ah batteries. The developed harvester provides a viable solution for pulse crop harvesting, addressing the need for mechanization in pulse cultivation. Its efficiency and economic feasibility make it an attractive option for widespread adoption, contributing to improved productivity in Indian agriculture.

सारांश:

अध्ययन का उद्देश्य एक कुशल और किफायती ट्रैक्टर-फ्रंट-माउंटेड कन्वेयर-आधारित दलहनी फसल हार्वेस्टर का विकास करना है, ताकि चना, मसूर और उड़द जैसी फसलों के यंत्रीकृत कटाई तरीकों की बढ़ती मांग को पूरा किया जा सके। यह अनुसंधान कृषि यंत्रीकरण के सिद्धांतों पर आधारित है, जिसमें कटाई बल की आवश्यकता, पौधों की दूरी, कतारों की दूरी और तने के व्यास जैसे प्रमुख फसल मापदंडों के अनुकूलन पर ध्यान केंद्रित किया गया है। ये कारक उपयुक्त मोटर और काटने वाले ब्लेड के चयन में महत्वपूर्ण भूमिका निभाते हैं, जिससे दलहनी फसलों की कटाई की दक्षता बढ़ाई जा सके। अध्ययन में कटाई और कन्वेइंग यूनिट्स की शक्ति आवश्यकताओं को निर्धारित करने के लिए टॉर्क गणनाएं शामिल हैं, जिनके परिणाम क्रमशः 1.24 एन-मी और 7.06 एन-मी पाए गए। कटे हुए फसलों को 0.54 मीटर/सेकंड की रेखीय गति से ठीक प्रकार से स्थानांतरित करने के लिए एक गियर मोटर का उपयोग किया गया है। फील्ड परीक्षण उड़द की फसल में किए गए ताकि विभिन्न परिस्थितियों में हार्वेस्टर की प्रभावशीलता का मूल्यांकन किया जा सके। परीक्षणों में यह पाया गया कि हार्वेस्टर अधपकी फसलों को भी संभालने में सक्षम है, जिसमें कटाई दक्षता विभिन्न आगे की गति पर 71.04% से 75.06% तक पाई गई। हार्वेस्टर 1.50 किमी/घंटा की गति पर 0.225 हेक्टेयर/घंटा की अधिकतम क्षेत्र क्षमता प्राप्त करता है, जिसके साथ 75.02% क्षेत्र दक्षता पाई गई। इसकी कार्य क्षमता 0.831 हेक्टेयर/दिन से 1.80 हेक्टेयर/दिन तक भिन्न पाई गई, जो इसे दलहनी फसलों की कटाई के लिए उपयुक्त बनाती है। विद्युत खपत विश्लेषण से कुल 0.569 किलोवाट की शक्ति आवश्यकता पाई गई, जिससे हार्वेस्टर एक पूर्ण चार्ज की गई 12 वोल्ट, 200 एएच बैटरी पर लगभग 4 घंटे तक संचालित हो सकता है। यह विकसित हार्वेस्टर दलहनी फसल कटाई के लिए एक व्यावहारिक समाधान प्रदान करता है, जो दलहन उत्पादन में यंत्रीकरण की आवश्यकता को पूरा करता है। इसकी दक्षता और आर्थिक व्यवहार्यता इसे व्यापक रूप से अपनाने के लिए एक आकर्षक विकल्प बनाती है, जिससे भारतीय कृषि में उत्पादकता में सुधार हो सकता है।

1. INTRODUCTION

Agriculture is a cornerstone of India's economy, serving as a primary livelihood source for a substantial portion of the population. Within the agricultural sector, cereals, pulses, and oilseeds constitute the core of crop production. Consequently, enhancing pulse production has become a strategic priority due to its dual importance in nutritional security and economic viability. Pulses are recognized for their high nutritional value, being rich in dietary fiber and having a low glycemic index, which helps mitigate health issues such as hypertension and cholesterol *(Curran et al., 2012)*. These crops can fix atmospheric nitrogen and enhance soil fertility, and they are well-suited for inter-cropping and crop rotation, making them an economically and environmentally sustainable choice. Prominent pulse crops in India, including Bengal gram, black gram, chickpea, lentil, and others, are cultivated across diverse agro-climatic regions, depending on the seasonality of each crop. In states like Rajasthan, Madhya Pradesh, Maharashtra, and Uttar Pradesh, pulses are grown mostly. In fiscal years 2019–20, 2020–21, and 2021–22, total pulse production was 23.25, 25.46, and 27.30 million tons, respectively. The targeted pulse production in India during the financial year 2022–23 was 29.550 million tons. Approximately 20% of India's agricultural land, with India being the world's largest pulse producer (*FAO-2017 Report*). A crucial stage of pulse production faces considerable challenges, particularly in the area of harvesting. Mostly, the sowing to harvesting of pulses is carried out using traditional methods. Manual harvesting remains the predominant method due to the unique morphological characteristics of pulses, such as their shrubby growth and low plant height, which complicate mechanical harvesting efforts. In a study, it was found that the farm mechanization status of pulses like chickpeas is about 30-40% in terms of harvesting and threshing *(Patel et al., 2020)*. Manual harvesting of chickpeas and lentils requires 98.76 man·h/ha and 163.58 man·h/ha, respectively *(Dutt, 2021)*.

Pulse crops are grown in most of the states in India, and the production is also ratcheting year by year. In the states of Bihar, Jharkhand, and West Bengal, pulses like lentil, chickpea, and black gram have comparatively higher yields than other pulses. It is known that the harvesting machines developed in other countries, like America, Canada, and Australia, are expensive and/or unavailable in India, which is not feasible for small to marginal-scale farmers. For this reason, most harvesting of pulses is done using the manual method. A two-row battery-operated manually push type two-row harvester was utilized and required only 56.81 man·h/ha for lentils and 68.46 man·h/ha for chickpeas (*Dutt*, *2021*). However, the two-row battery harvester requires comparable man-hours with manual labor, takes time, and covers only two rows in a single pass. Hence, a tractor-operated, front-mounted harvester-cum-windrower is needed to improve the efficiency of pulse harvesting by reducing human labor through mechanization and by increasing field coverage within a single pass. It will also be cost-effective, considering the adaptability of the small and marginal scale farmers on a custom hire basis. While machine harvesting necessitates more experienced workers to operate the machine and more space for operation, manual harvesting is time-consuming and ineffective. In order to boost yields, contemporary farms now combine computers with satellite imagery and GPS guiding systems. Compared to manual harvesting, this way of operation saves 50–60% labour costs and 60–70% harvesting costs *(Yogaraj et al., 2022)*.

Mechanization of crop harvesting has received increasing attention worldwide due to rising labor costs, declining availability of farm workers, and the demand for higher field efficiency. Considerable progress has been made in developing specialized harvesting machinery for different cropping systems. For example, integrated harvesting in intercropping systems has been an active area of research. The practice of separate harvesting is useful in regions where maize and soybeans have different harvesting seasons. Separate harvesting techniques, however, pose serious difficulties in areas where maize and soybeans are harvested concurrently. Harvesters used for one crop may unintentionally harm another, causing losses. Additionally, customers must purchase separate corn and soybean machines, which results in significant labour and equipment expenses. Separate processes also result in repeated land compaction, increased labour intensity, and decreased labour efficiency. These disadvantages show that separate harvesting is not very adaptable to soybean-corn strip composite planting methods. Creating a low-loss, high-efficiency integrated harvester especially for the soybean-corn strip composite planting system is crucial to overcoming these obstacles. To further this technology, a customised header for soybean-corn integrated harvesters was developed. In addition to increasing labour efficiency and offering strong equipment support for the mechanised harvesting of soybean-corn strip planting systems, this innovation was essential for improving the mechanisation of soybean-corn integrated harvesting *(XU, et al., 2025)*.

Similar challenges are also observed in other crops, such as root and tuber harvesting, where soil and climatic conditions complicate efficient separation of produce from the soil. Around the world, 30 to 35 million

hectares of land are currently used for the planting and cultivation of root crops *(Leff, et al., 2004)*. In practically every nation, growing and collecting root crops constitutes a significant part of agricultural productivity. The creation of extremely effective and resource-saving technical tools that guarantee root crop digging with the least amount of energy consumption is also given a lot of attention *(Ibrahim, et al., 2011; Ulyanov, et al., 2022)*. Harvesting root crops presents a number of challenges due to the diverse climates, soil types, and water supplies found in every location of the world *(Xaliqulov et al., 2023)*. For example, under Uzbekistan's soil and climatic conditions—marked by high summer temperatures, low relative humidity, and soil compaction following irrigation—the tuberous layer tends to disintegrate into large, hardened clods during root-crop harvesting. These clods are more resistant than the root crops themselves, making separation at the lifting stage difficult. This challenge constitutes the primary obstacle to the widespread implementation of root and tuber harvesters *(Norchayev, et al., 2021)*. Depending on the season, it is preferable to employ the appropriate methods for harvesting the root fruit crop *(Norchayev, et al., 2022)*. Harvesting tuberous roots imply the following steps: removing the tops a few weeks before harvesting, extracting the roots from the soil and separating them from it, and then loading the harvested material onto a vehicle to transport it to the location for sorting and storage *(Ulyanov et al., 2022)*. Harvesting is completed by either loading the crop into storage facilities (in-line technology) or putting it in temporary storage clamps before sending it to a sorting station for storage, depending on the technique used to cultivate tuberous roots *(Uspensky, et al., 2014)*.

The Government of India has implemented various initiatives to promote agricultural mechanization, but the adoption of mechanical harvesting for pulses is still limited, primarily due to the unavailability of suitable machinery and the high labor costs associated with manual harvesting. Addressing these challenges by developing cost-effective and efficient harvesting technologies is essential to support small and marginal farmers and ensure the long-term viability and profitability of pulse cultivation in India. In other developed nations, there are some modified machineries available for pulse harvesting. The third kind of combine harvesters with unique drum configurations for pulse harvesting is commercially accessible in Europe and the US, but not in India *(Dogra, 2018; Singh, 2018)*.

Research on pulse harvesting is still ongoing, but it is not commercially available to date. Sidahmed and Jaber *(Sidahmed, 2004; Jaber, 2004)* designed a cutter bar to harvest lentils. Field performance tests revealed that lentil crops with an average height of 0.59 m were suitable for harvesting using the harvester. Dange and Thakare *(Dange, 2010; Thakare, 2010)* developed a tractor front-mounted stem cutter for harvesting pigeon peas. The power transmission arrangement consisted of the tractor power take-off (PTO) connected to a gearbox, which was coupled with a motor and a hydraulic cylinder. The conveyor arrangement was also utilized to carry out crop cutting.

Golpira, (2013), modified passive fingers with V-shaped slots to develop a tractor-operated mechanical harvester. The width of the machine was 1.0 meters, reel index was 1.6, reel velocity was 50 rotations per minute, and slot width was 0.04 meters. *Mehetre et al., (2014),* examined the performance of a self-propelled riding-type vertical conveyor reaper (VCR) for harvesting soybean crops. The study revealed that the reaper had an effective field capacity of 0.17 ha/h and a field efficiency of 60% when operated at a speed of 1.70 km/h. *Wahane, (2017),* conducted a performance evaluation for the chickpea and wheat crops using a reaper. In chickpea fields, the reaper recorded a field capacity of 0.249 ha/h with 89.00% efficiency, while in wheat it achieved 0.360 ha/h with 91.76% efficiency. *Kiran et al., (2017),* developed a battery-powered reaper, having an effective width of 0.6 m. Performance evaluation revealed that the reaper achieved an effective field capacity of 0.13 ha/h and an average cutting efficiency of 98.24%. *Kumar, (2020),* developed a battery-powered vertical conveyor-based mini paddy harvester, which required 0.160 kW for cutting and conveying, having a width of the cutter bar of 0.53 m. *Dutt, (2021),* developed a manually push-type battery-powered lentil and chickpea harvester for two rows. The harvester's cutting unit operated through the clockwise and counterclockwise rotation of the cutting blade. It was tested on chickpea and lentil crops, with a cutting width of 0.45 m. The field capacity was 0.0221 ha/h at 89.04% efficiency for chickpea, and 0.0176 ha/h at 86.50% efficiency for lentil. Based on these results, the present research was undertaken to develop a tractor front-mounted conveyor-based pulse harvester.

2. MATERIALS AND METHODS

2.1. Description of the Harvester

The tractor front-mounted conveyor harvester was specifically developed for pulse crop harvesting, targeting species such as chickpea, lentil, black gram, and Bengal gram etc. The harvester mainly consisted of the cutting unit, conveying unit, power transmission unit, and machine holding cum adjusting unit, which

were assembled on the main frame. The components of the harvester are presented in Fig.1. The Top view and side view of the harvester are shown in Fig.2.

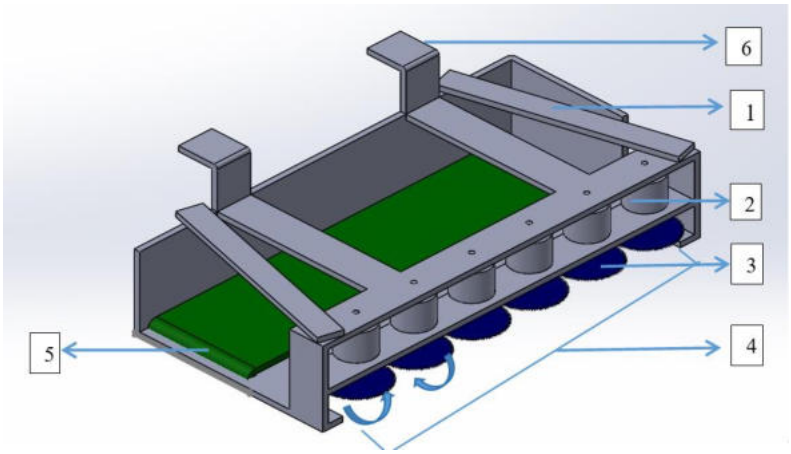
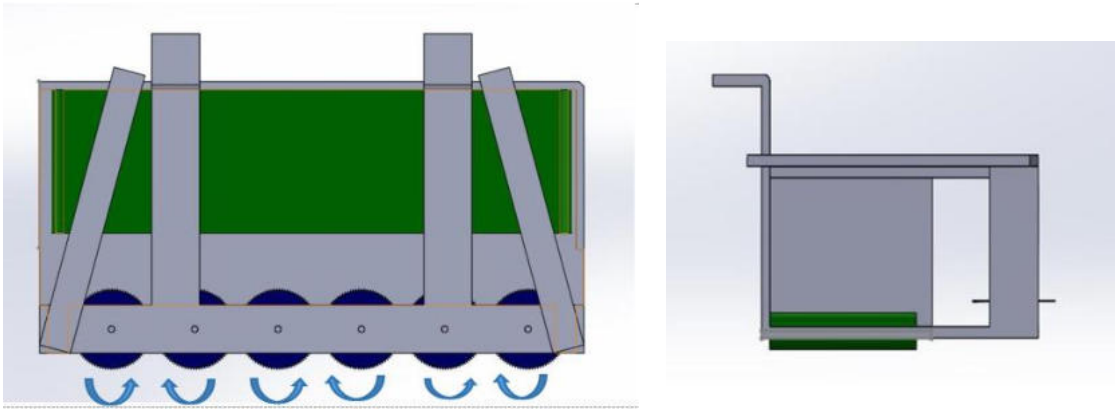


Fig. 1 - Conceptual design of the developed harvester by CAD software

1. Main Frame; 2. Motor for cutting; 3. Cutting blade; 4. Cutting unit; 5. Conveying unit; 6. Machine holding attachment



Top view of the harvester Side view of the harvester

Fig. 2 -Top view and side view of the harvester

2.1.1 Main Frame

The main frame of the harvester, with a length of 2.00 m, supports all the components of the harvesting unit, namely the motors and saw blades, the conveying unit, and the power transmission unit. The frame was also shielded with an MS sheet. Its dimensions were designed to accommodate six motor-driven blades, enabling the coverage of six crop rows.

2.1.2 Cutting unit of the harvester

The cutting unit of the harvester was attached to the front of the mainframe, consisting of six assemblies, each one formed by a 12 V DC motor and a cutting saw blade. The saw blades were connected to the motors using a spindle, rotating clockwise and in anti-clockwise direction alternatively. Six motors were used for the cutting unit of the harvester, having the cutting blades rotate alternatively to create centrifugal force, which leads the crop to be cut onto the conveyor. Each of the motors generated 1.24 Nm of torque at 917 rpm, which was able to cut the crops, such as chickpea, lentil, and black gram. The saw blade was designed with a diameter of 0.254 m, with 100 teeth, considering the maximum stem diameter of 25 mm.

2.1.3 Conveying unit of the harvester

The conveying unit was mounted directly behind the cutting unit of the harvester, directing the crop into a windrow on the right side of the tractor. It consisted of a pulley-driven conveyor belt. The material of the conveyor belt was rubber-blended, to produce a better grip on the conveyor roller or pulley. The conveying unit was powered by one gear motor using a chain sprocket. The ratio of the driver and driven pulley was 2:1 to achieve the required linear speed of 0.54 m/s with the reduced 175 rpm of the motor. The gear motor had a torque generation capacity of 8.18 Nm (as per specifications). Under laboratory conditions, the torque required to operate the conveyor with a 22 kg load was 7.76 Nm. Therefore, the selected motor was deemed compatible for operating the conveyor.

2.1.4 Machine holding attachment cum height adjuster

The harvester's holding attachment was mounted on the main frame after the conveying unit. This attachment secured the main frame to the tractor and allowed adjustment of the cutting height in field conditions as required. It was constructed with a screw lever mechanism, enabling height adjustment from 0.05–0.07 m at the lowest setting to 0.35–0.40 m above ground level, thereby ensuring smooth operation and stability of the harvester.

2.1.5 Power source to the cutting and conveying unit

The cutting and conveying units of the harvester were powered by a 2.4 kW rated battery. The battery was selected to ensure continuous operation of both units for at least 4–5 hours on a single charge. In case of battery discharge, power could alternatively be drawn from the tractor.

2.2. Field evaluation of the harvester

The performance evaluation of the harvester was carried out on a premature black gram crop in an experimental field measuring 65 m × 35 m at the Tirhut College of Agriculture, Dholi Parisar, Bihar. The harvester was tested at four tractor's speed: 0.75, 1.00, 1.25, and 1.50 km/h and a fixed 917 rpm cutting speed. For performance evaluation of the harvester, the following parameters were considered: effective width of the harvester, operation speed, cutting efficiency, theoretical field capacity, effective field capacity and field efficiency. The effective working width of the harvester was determined after harvesting a predetermined 25 m² area of the experimental field, with the width measured at three different points within the selected area. Cutting efficiency was calculated based on the ratio of the number of plants before harvesting to the number of uncut plants over a 10 m² section of the field. Field efficiency was expressed as the percentage of the machine's theoretical field capacity achieved under actual operating conditions, considering factors such as turning, machine adjustments, and reduced operational width. Crop parameters, such as plant height, spacing between rows, height of the lowest branch, minimum height of the pod from the ground, number of branches, and diameters of the plants, were measured. The plant height was taken from the base of the plant to the apical bud. The spacing between rows for black gram was measured between two adjacent rows at ten different locations using a measuring tape. Also, the height of the black gram plants was measured using the measuring tape. Plants height were measured from ten random places within the standing crop at the maturity time. Diameters of the black gram plant stems were taken also from ten random locations from the selected field crop. Measurement of stem diameter was done using Vernier calipers. This paper presents the average data for all measured performance parameters, derived from field evaluation of the harvester.

3. RESULTS AND DISCUSSIONS

A tractor was used to support the harvester, whose main power source was a 2.4 kW battery. The harvester measured 2.00 m in length, 0.609 m in height, and 0.452 m in width. The conveyor had a length of 4.267 m, a width of 0.254 m, and a thickness of 0.8 mm. The conveyor roller measured 0.254 m in length and 0.06 m in diameter. The attachment of the harvester to the tractor bumper was fabricated from a 0.304 m square pipe welded to a 0.304 m threaded shaft. After assembly, the total weight of the harvester was 83 kg. The developed harvester is presented in Fig. 8, and the specifications of the harvester are shown in Table 1.



Fig. 8 - General view of the developed harvester

Table 1

Specifications of the tractor-mounted harvester

Sl. No.	Machine components	Specification
1.	**Main frame** Frame length Frame width Frame height	 2.00 m 0.609 m 0.452 cm
2.	**Machine holding attachment** Square pipe Threaded shaft length Attached MS flat	 0.304 m 0.304 m 0.12 m
3.	**Power source** a) Battery	 200Ah, 2.4 kW
4.	**Power transmitting unit** **I. Cutting unit** DC motor No. of motors Shaft diameter Length Blade diameter Blade-to-blade distance **II. Conveying unit** **a) Conveying belt (Rubber blended)** Length Width Thickness **b) Pulley or roller (MS pipe)** Roller length Number of rollers Roller diameter Spacing of rollers **c) Gear motor**	 0.12 kW, 917 rpm 6 nos. 0.025 m 0.060 m 0.254 m 0.510 m 4.267 m 0.254 m 0.008 m 0.304 m 4 nos. 0.060 m 0.500 m 0.25 kW, 350 rated rpm

3.1. Field performance of the harvester

3.1.1 *Crop parameters of the black gram crop harvester*

The field data of black gram was taken before harvesting the crop and is presented in Table 2. It was observed that the spacing between crop rows had a maximum of 280 mm and a minimum of 240 mm. The maximum and minimum height of the plant were found to be 200 mm and 350 mm, respectively. The maximum and minimum diameter of the stem was found to be 1.2 and 1.4 mm, respectively. Therefore, the biometric data of the crop was suitable for harvesting using the developed harvester. Sidahmed and Jaber also reported that the lentil crop height of 59 mm from the ground was suitable for harvesting the crop *(Sidahmed, 2004; Jaber, 2004)*. In the same line, *Mehetre et al., (2014),* also reported that soybean was harvested at a plant height of 550 to 600 mm. Lower plant height and excessive dryness of the stem increase vibration and shattering losses, thereby reducing the effective cutting efficiency. Conversely, if the crop is too green due to delayed maturity, it creates an extra load on the knife section, which results in incomplete cutting and lodging of uncut stems *(Kumar, 2021; Maji, 2021)*.

Table 2

Crop parameters of black gram in the experimental field

Sl. No.	Crop parameters	Minimum (mm)	Maximum (mm)	Average (mm)
1.	Spacing between rows	240	280	260
2.	Height of the plant	200	350	275
3.	Height of the lowest branch	63	78	70.5
4.	Minimum height of the pod from the ground	60	83	71.5
5.	Number of branches	7	12	9.5
6.	Diameter of the stem	1.23	1.42	1.32

3.1.2 Power requirement for the cutting and conveying unit

During harvesting, the power drawn from the battery was measured. The cutting unit required 0.479 kW at a current of 39.96 A for six motors, while the conveying unit required 0.089 kW at a current of 7.46 A. Thus, the harvester consumed a total of 0.569 kW at a constant supply of 12 V (Table 3).

Other authors also reported that the power requirement for pulse harvesting units ranges from 1.7–3.0 kW, with 1.2–2.0 kW used for cutting due to tough stems and 0.5–1.0 kW for conveying *(Singh, 2018; Verma, 2018; Patel et al., 2020; Chauhan, 2019; Sharma, 2019; Mandal et al., 2021)*. Serrated blades reduce energy demand and improve efficiency.

Table 3

Power consumption of both units (cutting and conveying)

Sl. No.	Function	Measured current, A	Voltage, V	Power, kW
1.	Cutting (for six motors)	39.96	12	0.479
2.	Conveying (one-gear motor)	7.46	12	0.089
Total power required				0.569

3.1.3 Torque developed by the cutting and conveying unit at field conditions

The torque developed by each motor from the cutting unit was 1.24 N·m. The conveying unit gear motor developed 7.06 N·m of torque needed to run the conveyor with 20 kg of premature black gram crop load. Torque requirement was influenced by stem hardness and cutting blade load. Pulses need 25–40 N·m torque for effective cutting at 600–900 strokes/min *(Chauhan et al., 2018)*. Insufficient torque causes choking. Moderate speed and sharp blades maintain efficiency *(Kumar, 2019; Singh, 2019; Mandal, 2020; Verma, 2020; Patel et al., 2021)*.

3.1.4 Effect of forward speed on different performance parameters

The speed of operation of the harvester was measured in four replications: 0.75, 1.00, 1.25, and 1.50 km/h. The operation speed, namely the tractor forward speed, governed the harvester's performance. The cutting efficiency, theoretical field capacity, and effective field capacity of the harvester were calculated under optimized conditions, and the results are presented as follows:

3.1.5 Cutting efficiency of the harvester

The cutting efficiency of the harvester was influenced by the forward speed of operation. The maximum efficiency was 75.06% at the lowest trial speed of 0.75 km/h, while the minimum efficiency was 71.04% at the highest trial speed of 1.50 km/h. This result occurred because the cutting blade operated at a fixed speed of 917 rpm, irrespective of the forward speed. The results are presented in Table 4, and Fig. 9 clearly illustrates the variation in cutting efficiency under field conditions. High cutting efficiency is generally difficult to achieve in pulse crops due to their non-uniform plant height, hard stem structure, and lodging tendency at maturity (*Sundaram and Singh, 2017*). Studies reported that the cutting efficiency of mechanical reapers or harvesters in pulses usually ranges between 85% and 95% depending on crop variety, moisture condition, cutter bar design, and forward speed of the machine (*Patel et al., 2019*).

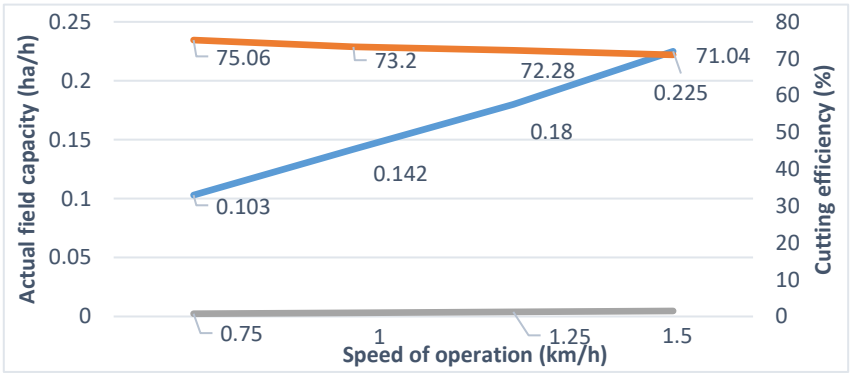


Fig. 9 - Effect of operational speed on actual field capacity and cutting efficiency

Table 4

Cutting efficiency at different speeds of operation

Sl. No.	Particulars	Values			
1.	Speed of operation (km/h)	0.75	1.00	1.25	1.50
2.	Cutting efficiency (%)	75.06	73.20	72.28	71.04

The cutting efficiency declined as the forward speed increased, likely due to the fixed speed of the cutting blade, which did not vary with the operational speed. However, Tanti *(Tanti, 2019)* observed the opposite trend, where the cutter bar speed increased along with the operational speed. These results highlight the need to optimize the fixed cutting blade speed in relation to the forward speed of operation to improve harvesting efficiency.



Fig. 10 - Pictorial representation of the harvested crop rows following harvester operation

3.1.6 Effective Field capacity and Field efficiency of the developed harvester

The field efficiency and effective field capacity of the developed harvester were assessed at four speed replications: 0.75, 1.00, 1.25, and 1.50 km/h. The results showed that the harvester's theoretical field capacity (TFC) ranged from a minimum of 0.150 ha/h to a maximum of 0.300 ha/h. The actual field capacity varied from a minimum of 0.103 ha/h, corresponding to a field efficiency of 69.30%, to a maximum of 0.225 ha/h, with a field efficiency of 75.02%. Overall, the field efficiency of the operation was between 69.30% and 75.02%. On an 8-hour workday basis, the harvester's maximum capacity was 1.80 ha, while the minimum capacity was 0.831 ha (shown in Table 5).

Table 5

Performance evaluation parameters

Particulars	Values			
Forward Speed(km/h)	0.75	1.00	1.25	1.50
Effective width (m)	2.00	2.00	2.00	2.00
Theoretical field capacity (ha/h)	0.150	0.200	0.250	0.300
Field efficiency (%)	69.30	71.20	72.38	75.02
Actual field capacity (ha/h)	0.103	0.142	0.180	0.225
The capacity of the harvester on a day 8h basis (ha)	0.831	1.136	1.440	1.800

Moreover, changes in operating speed, whether an increase or a decrease, also led to corresponding changes in both effective field capacity and field efficiency. These parameters were further influenced by factors such as crop type, plant spacing, and plant population during cutting. Maharana *(Maharana et al., 2018)* reported similar findings. The effective field capacity of reapers used for pulses generally varies from 0.3 to 0.6 ha/h, depending on machine width, forward speed, and turning losses (*Kumar and Singh, 2018*). Field efficiency typically ranges between 65% and 80%, largely affected by field size, crop density, operator skill, and time lost in maneuvering and clogging (*Patel et al., 2020*). Higher forward speeds increase theoretical capacity but often reduce field efficiency because of missed plants and frequent blockages. Irregular field boundaries and lodging of crop cause additional turning time and idle run, thereby reducing effective field capacity. Studies have shown that self-propelled reapers achieve higher field efficiency compared to tractor-mounted types due to better maneuverability and reduced turning radius (*Sharma and Verma, 2019*). Selection of appropriate machine width and optimum speed (around 2.5–3.5 km/h) was recommended to improve field capacity without compromising the harvest quality (*Chand et al., 2017*).

4. CONCLUSIONS

The study revealed that the mechanical harvesting of pulses not only reduced labor hours but also harvesting time. The developed harvester was found to be cost-effective for small and marginal-scale farmers. A tractor front-mounted pulse harvester was found suitable for harvesting the black gram. Although the harvester was developed to harvest pulses, such as Chickpea, lentil, and black gram, the performance was evaluated only in premature black gram. All the harvester's parameters, field capacity, field efficiency, and speed of operation, were determined under optimized conditions. Hence, the tractor front-mounted pulse harvester was found suitable for small and marginal farmers as an alternative to manual harvesting.

Declaration

All authors have read, understood, and complied as applicable with the statement on "Ethical responsibilities of Authors" as found in the instructions for authors.

REFERENCES

[1] Chand, P., Meena, R., & Sharma, V., (2017). Evaluation of field efficiency of reaper for pulse crop harvesting. *Agricultural Mechanization in Asia, Africa and Latin America*, 48(1), pp. 62–66. India.

[2] Chauhan, R., & Sharma, V., (2019). Power consumption in conveyor units of pulse crop harvesters. *Journal of Agricultural Engineering and Technology*, 6(2), pp. 55–60, India.

[3] Chauhan, H., Yadav, M., & Sharma, K., (2018). Torque characteristics of cutter bar mechanisms for pulse crops. *Journal of Agricultural Machinery*, 10(2), pp. 44–48, India.

[4] Curran, J., (2012). The nutritional value and health benefits of pulses about obesity, diabetes, heart disease, and cancer. *British Journal of Nutrition*, *108*, S1-S2, Canada.

[5] Dange, A. R., & Thakare, S. K., (2010). Development and Performance Evaluation of Tractor Front-Mounted Pigeon-Pea Stem Cutter. *Iranian (Iranica) Journal of Energy & Environment*, 2010, Vol. 1, pp. 200-204, India.

[6] Dogra, B., & Singh, N. K., (2018). Efficient Machinery for Harvesting and Threshing of Pulse Crops. *Farm Mechanization for Production,* pp. 46-56, India.

[7] Dutt, S., (2021). *Development of Lentil (Lens culinaries) and Chickpea (Cicer arientinum) Harvester. Unpublished M.T. Tech. Thesis*, RPCAU, India.

[8] Golpira, H., (2013). Conceptual design of a chickpea harvesting header. *Spanish Journal of Agricultural Research,* Vol. 11, pp. 635-641, Iran.

[9] Ibrahim, M.M., & Attia, M.F. (2011). Development and evaluation of potato digger suitable for smallholdings

[10] Kiran, I. K. M., Awal, Md. A., & Ali, Md. R., (2017). Development and performance evaluation of a battery-operated small-scale reaper. *Agricultural Engineering International: CIGR Journal,* Vol. 19, pp. 217-223, Bangladesh.

[11] Kumar, B., (2020). *Development of Battery-Operated Mini Paddy Harvester*. *Unpublished M. Tech. Thesis*, RPCAU, India.

[12] Kumar, A., & Maji, S., (2021). Losses in mechanical harvesting of black gram using tractor-operated reaper. *Journal of Agricultural Machinery*, 12(1), 34–39, India.

[13] Kumar, A., & Singh, J., (2018). Field performance of self-propelled reaper in harvesting of lentil crop. *Journal of Agricultural Engineering*, 55(3), pp. 15–20, India.

[14] Kumar, V., & Singh, J., (2019). Power and torque requirement for harvesting chickpea using mechanical reaper. *Indian Journal of Agricultural Engineering*, 26(1), pp. 73–76, India.

[15] Leff, B., Ramankutty, N., & Foley, J.A., (2004). Glob. Biogeochem. *Cycles*, Vol. 18(1).

[16] Maharana, S., Goel, A. K., Behera, D., & Mahapatra, M., (2018). Development and Evaluation of a Self-Propelled Pulse Reaper. *Int.J.Curr.Microbiol.App.Sci.*, Vol. 7, pp. 1983-1991, India.

[17] Mandal, A., & Verma, R., (2020). Vibration and torque analysis of cutter bar systems in pulse crop harvesters. *Agricultural Engineering Today*, 44(3), 60–65, India.

[18] Mandal, A., Patel, S.K., & Yadav, R., (2021). Energy requirement analysis of small-scale mechanical harvesters for pulses*. International Journal of Farm Machinery Science*, 12(3), 39–44, India.

[19] Mehetre, S. A., Ghatge, J. S., & Bandgar, P. S., (2014). Performance Evaluation of Self-Propelled Riding Type Vertical Conveyor Reaper. *Journal of Agricultural Engineering. ISAE*, Vol. 1, pp. 38-41, India.

[20] Norchayev, D.R., Xaliqulov, M.A., Shermuxamedov, X.P., & Lbragimova, G.N., (2021). *IOP Conf. Ser. Earth Environ. Sci.,* Vol. 868(1).

[21] Norchayev, D.R., Xaliqulov, M.A., Turkmenov, X.I., Shermuxamedov, X.P., Ibragimova, G.N., (2022). IOP Conf. Ser. Earth Environ. Sci. Vol. 1076(1)

[22] Patel, L., Sharma, R., & Yadav, P., (2020). Analysis of field capacity during mechanical harvesting of black gram. *International Journal of Farm Machinery*, Vol. 14(2), pp. 42–47, India.

[23] Patel, L., Singh, M., & Jha, P., (2020). Comparative study of cutter bar designs on power and fuel requirement in pulse harvesting. *Agricultural Mechanization Research*, Vol. 8(1), pp. 22–27, India.

[24] Patel, S. K., Tiwari, R., & Sen, A., (2021). Performance evaluation of a tractor-operated reaper for pulse harvesting. *International Journal of Farm Tools and Machinery*, 15(1), pp. 29–34, India.

[25] Patel, S. K., Yadav, R., & Singh, B., (2019). Field evaluation of self-propelled reaper for pulse crops. *International Journal of Agricultural Engineering*, Vol. 11(1), pp. 89–94, India.
[26] Patel, S. K., Yaduvanshi, B. K., & Sundaram, P. K., (2020). Advances in Farm Mechanization in India. In New India Publishing Agency (Eds.), *Advances in Crop Production and Climate Change*, pp. 329-366, India.
[27] Sharma, R., & Verma, S., (2019). Comparative study of tractor-operated and self-propelled reapers in pulse crops. *Journal of Farm Equipment*, Vol. 12(4), pp. 30–35, India.
[28] Sidahmed, M. M., & Jaber, N. S., (2004). The design and testing of a cutter and feeder mechanism for the mechanical harvesting of lentils. *Biosystems Engineering*, 2004, Vol. *88*, pp. 295-304, Beirut.
[29] Singh, R., & Verma, J., (2018). Estimation of cutting power for chickpea harvesting. *Indian Journal of Agricultural Machinery*, Vol. 45(4), pp. 18–22, India.
[30] Sundaram, J., & Singh, J., (2017). Harvesting issues in pulse crops – A review. *Agricultural Reviews*, Vol. 38(4), pp. 280–286, India.
[31] Tanti, D. P., Jhala, K. B., & Jadav, C. V., (2019). Performance Evaluation of Battery Powered Reaper. *Int. J. Curr. Microbiology App. Sci.,* Vol. 8, pp. 1998-2005, India.
[32] Ulyanov, M.V., Skripkin, D.V., Kharlashin, A. V., Ulyanova, A. V., Ayugin, N.P., & Khalimov, R.Sh., (2022). Improving the design of a root crop harvester in order to increase the sustainability of agriculture. *Earth and Environmental Science*, 965, pp. 01-07, Russia.
[33] Uspensky, I. A., Yukhin, I. A, & Zhukov, K. A., (2014). Ways to reduce the traumativeness of fruit and vegetable products during on-farm transportation. *Polythematic Network Electronic Scientific Journal*, Vol. 96 (02), pp. 01-07, Russia.
[34] Wahane, T., (2017). *Modification and Performance Evaluation on Self-propelled Vertical Conveyor Reaper for Harvesting Chickpea and Wheat*. Unpublished M. Tech. Thesis, PDKV, India.
[35] Xaliqulov, M., Kannazarova, Z., Norchayev, D., Juliev, M., Turkmenov, X., Shermuxamedov, X., Ibragimova, G., Abduraxmonova, S., (2023). Root harvester machine: a review of papers from the Scopus database published in English for the period of 1982-2022. *E3S Web of Conferences,* 402, pp. 01-13, Uzbekistan.
[36] Xu, J., Jin, C., Chen, Q., NI, Y., Chen, M., Zhang, G., & Yang, T., (2025). Research and development of an integrated header for soybean corn combined harvesters adapted to strip intercropping. *INMATEH-Agricultural Engineering*, Vol. 76(2), pp. 58-68, China. DOI: https://doi.org/10.35633/inmateh-76-05
[37] Yogaraj, D., Subesh, T., Devaraj, A., Chowdary, K.S.P., Khakha, U., Alone, S.P., & Sharma, A. (2022). *Design and analysis of compact paddy harvester machine*. *Materials Today: Proceedings*, 62, pp.1430-1434, India.

FACTORS INFLUENCING THE COMPOSTING PROCESS OF VEGETAL WASTE: A REVIEW
/
FACTORI CARE INFLUENȚEAZĂ COMPOSTAREA DEȘEURILOR VEGETALE: O ANALIZĂ DE SINTEZĂ

Elena-Melania CISMARU[1)], Ana-Maria TĂBĂRAȘU[1*)], Nicolae-Valentin VLĂDUȚ[1)], Gabriel-Valentin GHEORGHE[1)], Ana ZAICA[1)], Dragoș-Nicolae DUMITRU[1)], Alin-Nicolae HARABAGIU[1)], Elena-Mădălina ȘTEFAN[2*)], Mirela Nicoleta DINCĂ[2)]

[1)]National Institute of Research-Development for Machines and Installations Designed to Agriculture and Food Industry, Romania;

[2)] National University of Science and Technology POLITEHNICA Bucharest, Romania

Tel: +40 730 417 449; E-mail: anamariatabarasu22@yahoo.com

Tel: +40 726 043 458; E-mail: stefanelenamadalina@gmail.com

DOI: https://doi.org/10.35633/inmateh-76-109

Keywords: *composting process, organic waste management, aerobic biodegradation, compost quality, sustainable waste management*

ABSTRACT

Although composting is a well-established method for the biological stabilization of organic matter, in recent years advanced technologies and optimized operational strategies have been introduced, that are aimed at enhancing both compost quality and processing efficiency. These innovations, ranging from improved aeration and moisture control systems to the use of bio-activators and process monitoring tools, have significantly reduced decomposition time, while ensuring a more homogeneous, nutrient-rich final product. The aim of the paper is to systematically centralize relevant information from the literature with the purpose of identifying the key parameters that most significantly influence the composting process and evaluate the advantages and disadvantages of the most widely used composting technologies. Experimental results reported in the literature indicate that emerging processing technologies offer faster composting and improved compost quality, by enabling more efficient optimization of operating parameters. By producing higher-quality compost, these technologies enhance soil fertility, structure, and microbial activity, leading to improved nutrient cycling and water retention. In the long term, it can play a crucial role in promoting sustainable soil management, restoring degraded soils, and enhancing carbon sequestration, thereby contributing to climate change mitigation.

REZUMAT

Deși compostarea este o metodă bine stabilită pentru stabilizarea biologică a materiei organice, în ultimii ani au fost introduse tehnologii avansate și strategii operaționale optimizate, menite să îmbunătățească atât calitatea compostului, cât și eficiența procesului. Aceste inovații – de la sisteme îmbunătățite de aerare și control al umidității, până la utilizarea bioactivatorilor și a instrumentelor de monitorizare a procesului – au redus semnificativ timpul de descompunere, asigurând totodată un produs final mai omogen și mai bogat în nutrienți. Scopul lucrării a fost de a centraliza în mod sistematic informațiile relevante din literatura de specialitate, în vederea identificării parametrilor-cheie care influențează cel mai puternic procesul de compostare și a evaluării avantajelor și dezavantajelor celor mai utilizate tehnologii de compostare. Rezultatele experimentale raportate în literatura de specialitate indică faptul că tehnologiile emergente de procesare oferă o compostare mai rapidă și o calitate superioară a compostului, printr-o optimizare mai eficientă a parametrilor de operare. Prin obținerea unui compost de calitate ridicată, aceste tehnologii sporesc fertilitatea, structura și activitatea microbiană a solului, îmbunătățind ciclul nutrienților și retenția apei. Pe termen lung, compostarea poate juca un rol esențial în promovarea gestionării durabile a solului, restaurarea terenurilor degradate și creșterea sechestrării carbonului, contribuind astfel la atenuarea schimbărilor climatice.

[1)]Elena-Melania Cismaru, PhD.Stud.; [1)]Ana-Maria Tăbărașu, SR III; [1)]Nicolae-Valentin Vlăduț, SR I; [1)]Gabriel-Valentin Gheorghe, SR III.; [1)]Ana Zaica, SR III; [1)]Dragoș-Nicolae Dumitru, SR; [1)]Alin-Nicolae Harabagiu, Research Assistant; [2*]Elena-Mădălina Ștefan, Lecturer PhD. Eng.; [2)]Mirela Nicoleta Dincă, Lecturer PhD. Eng.*

INTRODUCTION

Since the Green Revolution of the 1960s, the intensive use of chemical fertilizers has played a pivotal role in meeting the growing global food demand by significantly boosting agricultural productivity. While this approach has undeniably increased crop yields, it has also led to serious environmental challenges, including nutrient imbalances, soil degradation, loss of microbial biodiversity, and water pollution. In response to these issues, composting of plant residues has emerged as a promising and sustainable organic waste management strategy. This method recycles valuable nutrients back into the soil, improves soil structure and long-term fertility, and supports microbial diversity, all while maintaining a considerably lower ecological footprint compared to synthetic inputs *(Rehman et al., 2023; Sathiyapriya et al., 2024; Caba et al., 2019)*. Moreover, targeted supplementation with nutrients or microorganisms can enhance both the efficiency of the composting process and the quality of the final product by stabilizing microbial communities and optimizing nutrient dynamics *(Sánchez et al., 2017)*.

Composting is a controlled aerobic process in which organic materials, such as plant residues, food waste, or manure, are biologically decomposed into a stable, nutrient-rich product that can improve soil health and fertility. The process comprises four main stages: the initial mesophilic phase, the thermophilic phase, a second mesophilic phase, and a maturation phase. Successful composting depends on multiple factors, including the carbon-to-nitrogen (C/N) ratio, moisture content, temperature, substrate particle size, pH, oxygen availability, and the composition of the microbial community.

Microorganisms such as bacteria, fungi, and actinomycetes serve as the main decomposers, converting complex organic molecules like lignin, cellulose, and hemicellulose into carbon dioxide, heat, water, humus, and a relatively stable final product compost *(Nemet et al., 2021)*.

Composting is a sustainable alternative or complement to chemical fertilizers, offering significant environmental benefits by mitigating issues such as soil acidification, nitrate leaching, and greenhouse gas emissions. The efficiency of the composting process depends on multiple key factors, including pH, carbon-to-nitrogen (C/N) ratio, moisture content, oxygen availability, raw material type, particle size, and the composting technology employed *(Manea and Popescu, 2022; Poornima et al., 2024; Nenciu et al., 2022)*.

Optimal composting conditions typically include a C/N ratio of around 30:1, moisture content between 50–60%, and adequate aeration to maintain microbial activity and accelerate decomposition *(Manea and Popescu, 2022; Parihar and Sharma, 2021)*. Among these, aeration and temperature are critical: thermophilic conditions between 50 and 60 °C not only speed up compost stabilization but also ensure pathogen destruction.

Several studies also contrast composting with conventional agricultural practices, noting that modern intensive farming relies heavily on synthetic inputs such as chemical fertilizers, pesticides, and herbicides. While these substances can boost short-term yields, their excessive use contributes to soil degradation, reduced microbial biodiversity, groundwater depletion, and increased environmental pollution *(Zainudin et al., 2022; Nemet et al., 2021; Lu Zhang et al., 2018)*.

Globally, composting currently processes around 40% of organic waste streams, reducing dependence on synthetic fertilizers, improving soil health and water retention, and lowering greenhouse gas emissions. Methods such as passive or transitional stacks and closed reactors improve biodegradation by controlling aeration, temperature, and moisture *(Argun et al., 2017)*. In regions such as Morocco, composting is increasingly applied to manage agricultural residues like crop waste and livestock manure. By transforming these materials into nutrient-rich compost, farmers not only enhance soil fertility but also reduce their dependency on costly synthetic inputs. Moreover, composting mitigates greenhouse gas emissions that would otherwise result from traditional practices like open-air burning or anaerobic decay, thus contributing to broader climate change mitigation goals *(Oueld Lhaj et al., 2024).*

Traditional aerobic composting methods, such as the Indore process, produce high-quality compost through regular turning of large piles, while modern approaches, like municipal solid waste (MSW) composting, are more suited to urban waste streams *(Niladri et al., 2019)*. The integration of microbial inoculants and anaerobic digestion technologies can further improve process efficiency. *(Manea et al., 2024)*. For example, composting vegetable waste from food markets can yield high-quality compost within 60 days, supporting sustainable agricultural practices *(Puntsag et al., 2022)*.

Aerobic composting methods are effective in reducing greenhouse gas emissions, whereas anaerobic processes can produce biogas but may emit methane if not carefully managed *(Esparza et al., 2020)*.

Effective composting requires the implementation of key management practices that sustain microbial activity, maximize process efficiency, and ensure high-quality final compost.

According to *Ansar et al. (2025)*, essential management practices include maintaining optimal thermophilic temperatures, controlling moisture content, ensuring regular aeration, applying microbial inoculants, and continuous monitoring of compost quality. Furthermore, the adoption of advanced composting technologies alongside supportive policy and regulatory frameworks can improve operational efficiency and enhance economic viability.

By diverting organic waste from landfills, reducing greenhouse gas emissions, and recycling nutrients back into the soil, composting directly supports the principles of a circular economy and plays a vital role in regenerative agriculture *(Obuobi et al., 2022; Sánchez et al., 2022; Hidalgo et al., 2021)* (illustrated in Fig.1).

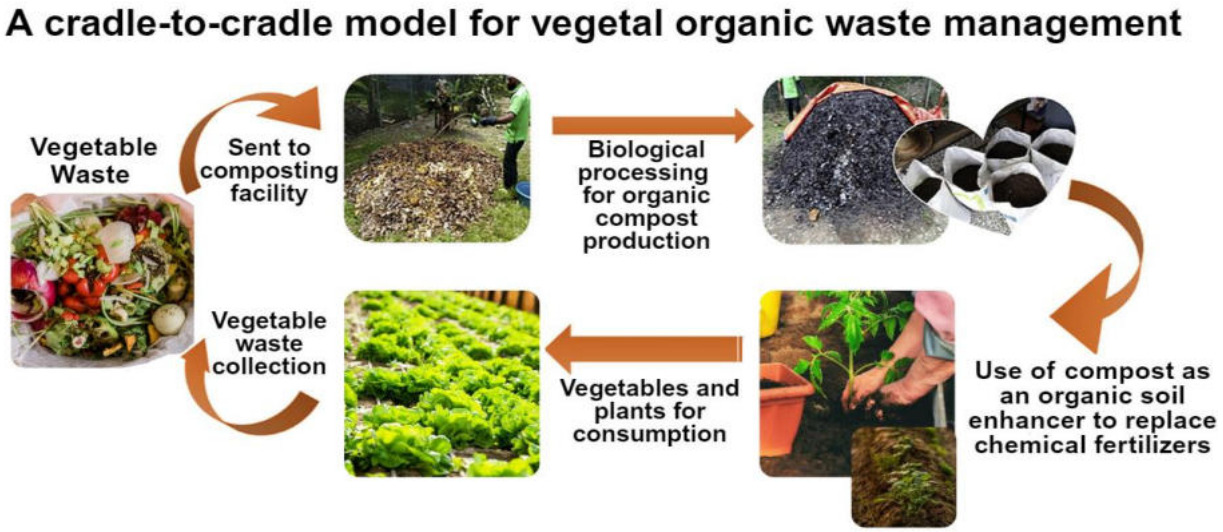


Fig. 1 - A cradle-to-cradle model for vegetal organic waste management
(adapted from Zi Xiang Keng et al., 2020)

The aim of the paper was to systematically centralize relevant information from the literature in order to identify the key parameters that most significantly influence the composting process and to evaluate the advantages and disadvantages of the most widely used composting technologies. To this end, relevant literature from major academic databases (Web of Science and Scopus) has been evaluated. Research papers with solid experimental models have been selected.

RESULTS

The efficiency of microbial activity during composting is governed by several key factors, including temperature, moisture content, the carbon-to-nitrogen (C/N) ratio, oxygen availability, and the characteristics of the plant material being composted *(Azim et al., 2018; Luo et al., 2024)*. The interdependence of these factors in the composting process is illustrated in Figure 2(a), adapted from *Kluczek-Turpeinen et al. (2007)*. Maintaining adequate oxygen levels (above 10%) through natural or forced aeration is essential to prevent anaerobic conditions, reduce harmful gas emissions such as methane and ammonia, and consequently improve compost quality while contributing to climate change mitigation *(Zelong Liu et al., 2025; Li M. et al., 2023)*. Various composting technologies, including aerated static piles, windrows, and in-vessel systems, play a significant role in determining the degradation rate and the final quality of the compost, as shown in Figure 2(b) *(Tiquia-Arashiro and Tam, 2002; Rajin et al., 2025)*. Recent technological advancements, such as automated aeration and real-time monitoring, have enhanced energy efficiency and microbial performance. Furthermore, pre-treatment methods, including particle size reduction and homogenization, facilitate microbial access to the substrate and accelerate the decomposition process *(Ponsá et al., 2009)*.

Composting proves particularly effective for managing plant-based organic waste, such as peels, crop residues, and pruning materials, which are rich in cellulose and hemicellulose. These materials, however, also present challenges due to high moisture content and variable C/N ratios *(Gezu et al., 2024; Plazzotta et al., 2017; Liu et al., 2025)*. Nevertheless, mature compost provides numerous agronomic and environmental benefits: it restores degraded soils, enhances fertility, promotes carbon sequestration, suppresses plant diseases, and improves soil water retention *(Pergola et al., 2018; Miyamoto et al., 2022; Pane et al., 2016)*.

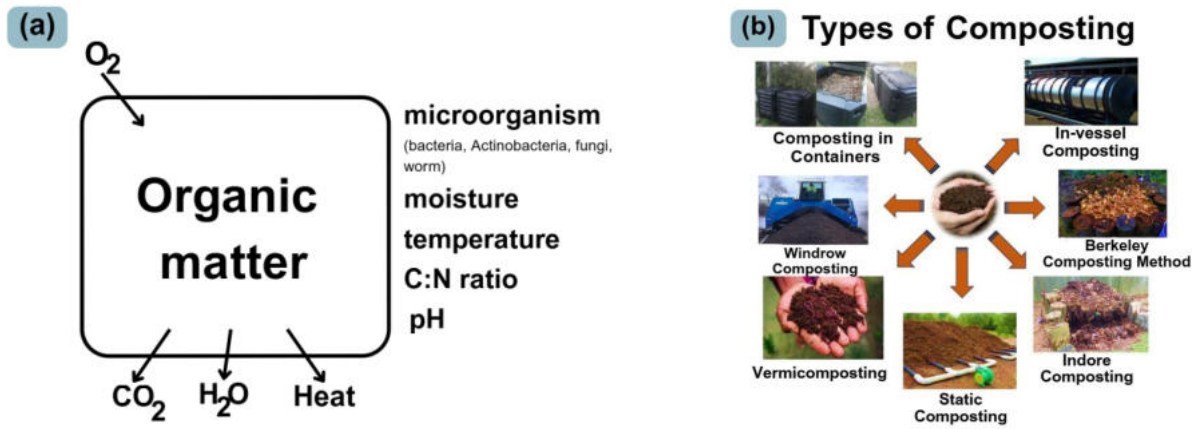


Fig. 2 - Overview of the composting process and associated technologies:
(a) The composting process and key factors affecting it *(adapted from Kluczek-Turpeinen et al., 2007)*
(b) Types of composting technologies *(adapted from Chakravorty et al., 2024)*

Moreover, it reduces dependence on chemical fertilizers and pesticides, thereby lowering production costs and minimizing environmental impact *(Ștefan et al., 2021)*. Nevertheless, current composting technologies remain insufficiently standardized for vegetal waste streams, making process optimization essential for improving compost quality and maximizing ecological benefits.

Sustainable organic waste management through composting, combined with complementary treatments, facilitates circular nutrient flows and contributes to the development of sustainable agriculture *(Mancuso et al., 2024)*. This review highlights the key factors influencing the composting of plant-based waste, offering a synthesis of recent technological innovations, microbial dynamics, and operational challenges. Special attention is given to optimizing conditions such as moisture, aeration, and the C/N ratio, specifically tailored to plant-based substrates.

By integrating these elements, the review supports the advancement of efficient and sustainable composting practices for both agricultural and urban applications *(Manea and Popescu, 2022; Aguilar-Paredes et al., 2023)*. This biologically driven thermogenic process is powered by the intense respiration of thermophilic bacteria and fungi, which naturally heat the organic mass. Consequently, it facilitates rapid decomposition of organic matter, destruction of pathogens and parasites (including helminth eggs and larvae), and the formation of stable humic substances, an indicator of compost maturity *(Avramović and Janković, 2018; Finore et al., 2023; Voicea et al., 2024)*.

KEY PARAMETERS INFLUENCING COMPOSTING EFFICIENCY

The reviewed literature highlights that temperature, along with other key factors such as the carbon-to-nitrogen ratio, moisture content, aeration frequency, and microbial activity, plays a significant role in determining both the quality and duration of the composting process *(El-mrini et al., 2022; Adugna, 2018)*. Effective composting practices typically involve regular turning of the pile, temperature monitoring, and careful management of thermal phases, ensuring that the final product is mature, stable, and biologically safe *(El-mrini et al., 2022; Adugna, 2018; El Boudihi et al., 2024)*. Depending on these variables and the nature of the raw materials, composting durations range from 1 to 12 months. Recent advancements have further improved composting efficiency. These include the use of microbial inoculants, vermicomposting, and various pre-treatment methods, all contributing to enhanced nutrient transformation, faster decomposition rates, and improved oxygen diffusion within the compost matrix *(Parihar and Sharma, 2021; Vladut et al., 2024)*. Additionally, biochar amendments have been shown to enhance compost quality by improving aeration and stabilizing nutrients, offering a promising strategy for organic waste management *(Poornima et al., 2024)*.

However, challenges persist, particularly concerning the management of contaminants such as heavy metals and microplastics, which can compromise the safety and agronomic value of the final compost product *(Mengistu et al., 2018)*.

Carbon-to-nitrogen ratio

During composting, carbon (C) and nitrogen (N) are key nutrients for microorganisms. Carbon provides energy, while nitrogen is essential for building cellular structures. If nitrogen is deficient, microbial growth and carbon decomposition slow down. If nitrogen is excessive, it can cause ammonia emissions and harmful salt accumulation. Microorganisms consume carbon 30 to 35 times faster than nitrogen, so maintaining an optimal C/N ratio is critical. A low C/N ratio leads to nitrogen loss as ammonia gas, while a high C/N ratio limits microbial activity and slows composting. To adjust the initial C/N ratio, materials like rice husks, wood chips, peanut shells, and urea are often added. Overall, the initial C/N ratio strongly influences organic matter mineralization and nitrification during composting *(Tianming Chen et al., 2020)*.

The carbon-to-nitrogen ratio (C/N) is widely acknowledged as a key parameter in composting, influencing both process efficiency and the quality of the final product. Most studies agree that the optimal C/N ratio lies between 25:1 and 30:1, though some standards accept a broader range of 20:1 to 30:1 *(Zhang et al., 2024; El-mrini et al., 2022)*. Maintaining a ratio within this range promotes microbial activity, accelerates organic matter degradation, and supports nutrient cycling, all contributing to the production of stable, mature compost *(Zhang et al., 2024; Sole-Mauri et al., 2007)*. A lower C/N ratio, particularly values around 15–16:1, has been shown to raise composting temperatures and prolong the thermophilic phase, thus enhancing pathogen elimination and organic breakdown *(Cai et al., 2024; Vladut et al., 2023a)*. However, excessively low ratios may increase ammonia (NH_3) emissions and reduce nitrogen retention *(El-mrini et al., 2022)*.

Conversely, higher C/N ratios can delay the onset of composting and extend the overall process. Still, they support the breakdown of lignocellulosic materials like hemicellulose and contribute to sulphur retention, improving plant nutrient availability *(Cai et al., 2024)*. Additionally, a C/N ratio of approximately 25 has been linked to reduced mobility of heavy metals such as copper and zinc, despite a potential increase in their total concentration during composting. Biochemically, the C/N ratio influences enzymatic activity, such as urease function, by affecting metal ion availability. It also plays a role in organic matter and nitrogen losses, although it does not significantly impact pH or temperature trends throughout the composting process *(El-mrini et al., 2022)*. In practice, managing the C/N ratio alone is not sufficient. Other operational factors, such as moisture content, aeration, and pH, must also be carefully controlled to maintain process stability *(Cerda et al., 2018)*.

While the ideal C/N ratio is typically cited as 25–30, studies have also reported successful composting outcomes outside this range. For example, ratios as high as 45 or as low as 15 can still produce mature compost if supplementary strategies such as enhanced aeration, microbial additives, or extended processing time are applied *(Bo Shen et al., 2024)*. However, these adjustments may lead to increased nutrient loss, higher costs, and inconsistency in compost quality. The diversity of input materials and methodologies further complicates the comparative evaluation of the C/N ratio's effects Ultimately, integrated C/N ratio management, combined with optimized operational parameters, not only supports compost maturity and pathogen reduction, but also minimizes harmful emissions like hydrogen sulphide (H_2S) *(Mengistu et al., 2018)*, contributing to sustainable agriculture and the principles of the circular economy *(Sole-Mauri et al., 2007; El-mrini et al., 2022)*.

Table 1

Impact of C/N ratio on composting efficiency

Impact	Description	Reference
Microbial Efficiency	Microorganisms require carbon for energy and nitrogen for growth. A balanced ratio ensures rapid and complete decomposition.	*Sun et al., 2025*
Compost Maturity	Compost with a proper C/N ratio matures faster and has lower phytotoxicity. Ratios of 25:1 showed better germination index and root development.	*Alkoaik et al., 2015*
Pathogen Reduction	C/N ratios influence temperature and microbial dynamics, which affect pathogen elimination. Ratios around 22:1 were most effective in reducing *Salmonella* and helminth eggs.	*Macias-Corral et al., 2019*
Material Selection	Different organic materials have varying C/N ratios. For example, sawdust has a high C/N (~400:1), while manure is low (~15:1). Mixing them balances the overall ratio.	*Qasim et al., 2018*

Temperature and moisture content

The composting process generates a significant amount of heat, particularly during the early stages, due to the rapid breakdown of organic matter. This heat production raises the compost temperature, promoting the activity of thermophilic microorganisms that accelerate decomposition and effectively eliminate pathogens.

Maintaining an optimal temperature range, typically between 40 and 65 °C, is essential for efficient composting and high-quality end products *(Shiyang Fan et al., 2021; Amuah et al., 2022; Assandri et al., 2021)*.

Temperatures above 55 °C are particularly important for pathogen destruction, with recommended thresholds of 65 °C sustained for several hours or 70 °C for 30 minutes to ensure proper sanitization.

Moisture content is another critical factor influencing microbial activity and overall process efficiency. Adequate moisture levels, generally between 40 and 60%, facilitate microbial metabolism by supporting nutrient solubilization, gas exchange, and preventing conditions detrimental to aerobic decomposition. Insufficient moisture causes drying and microbial inactivity, while excess moisture results in waterlogging, creating anaerobic zones that slow down the process and generate unpleasant odours *(Shiyang Fan et al., 2021; Ebrahimi et al., 2024; Ghinea and Leahu, 2020; Vladut et al., 2023)*. Therefore, maintaining optimal moisture is crucial for balancing these conditions and optimizing both the decomposition rate and the quality of the final compost. Temperature significantly impacts composting progress, affecting the four main phases and microbial populations. Most methods begin with Phase I – Mesophilic Phase (Initiation phase), where temperatures rise from ambient levels to around 40 °C, driven by mesophilic microorganisms metabolizing simple compounds such as sugars and amino acids *(Amuah et al., 2022)*. This is followed by Phase II – Thermophilic Phase, characterized by temperatures ranging from 40 to 70 °C, during which thermophilic bacteria and fungi degrade more complex organic compounds, ensuring pathogen inactivation *(Assandri et al., 2021)*. Subsequently, temperatures decline during Phase III – Mesophilic Cooling Phase, as microbial activity slows and mesophilic organisms recolonize the compost. This phase continues until the temperature stabilizes at ambient levels for at least three consecutive days *(opanatura.com)*. Finally, Phase IV – Maturation Phase involves the stabilization of humic substances and overall compost quality over a period of 30 to 60 days or longer, depending on the composting materials and conditions *(Amuah et al., 2022)*.

Figure 3 illustrates the dynamics of temperature and microbial communities throughout the composting process, highlighting the transitions between the active, cooling, and maturation phases. The figure *(Kluczek-Turpeinen et al., 2007)* demonstrates how temperature fluctuations drive microbial succession and the transformation of organic compounds, from initial decomposition to the final stabilization of humified material.

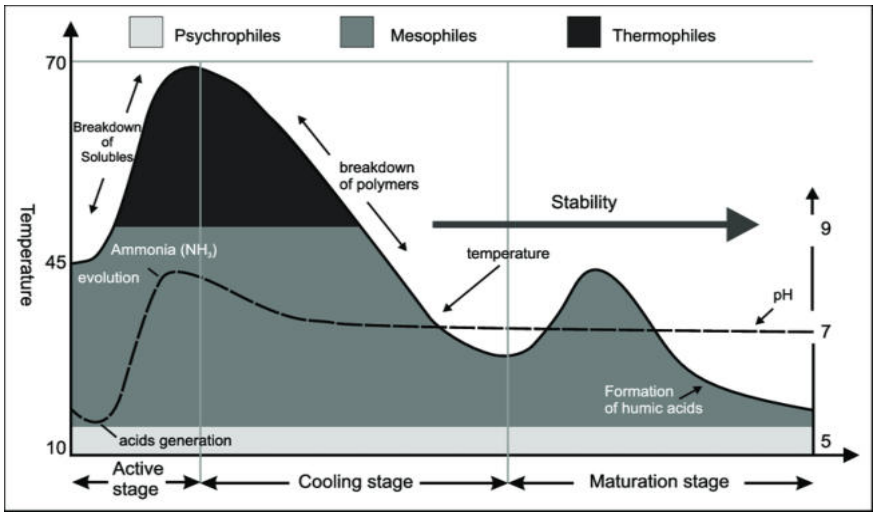


Fig. 3 - Dynamics of Temperature and Microbial Community during Composting

(Kluczek-Turpeinen et al., 2007)

In large-scale operations, piling is considered one of the most effective techniques for maintaining optimal temperature and moisture levels, ensuring faster degradation and the production of high-quality compost *(Rawoteea et al., 2017)*.

Aeration and particle size

Aeration and particle size are two interdependent parameters that critically influence the efficiency of composting processes for vegetal waste. An adequate oxygen supply is essential for microbial respiration and the degradation of organic matter. This is typically achieved through physical mixing, natural convection, or forced aeration, each with specific implications for process efficiency, depending on the system type.

In enclosed composting systems, forced aeration becomes necessary due to the absence of natural airflow. In contrast, units with perforated sidewalls allow passive air diffusion, reducing energy costs while maintaining aerobic conditions, which is highly relevant for optimizing system performance *(Vilela et al., 2022)*.

The aeration rate must be carefully controlled: insufficient oxygen leads to anaerobic zones, reducing efficiency, while excessive airflow can cool the compost mass and inhibit microbial activity.

Effective aeration rates reported for agricultural waste range between 0.3 and 1.16 L·min^{-1}·kg organic matter^{-1}, and for municipal solid waste between 0.06 and 0.5 L·min^{-1}·kg waste^{-1} *(Rasapoor et al., 2009)*. Specifically, a flow of 2.6 L·kg^{-1} dry solid·min^{-1} combined with intermittent agitation has been shown to markedly improve microbial efficiency and accelerate decomposition *(Sarkar et al., 2016)*. In addition to controlling aeration, the use of strategic additives can optimize the composting environment. Materials such as sawdust and microbial inoculants help maintain porosity and create favourable conditions for microbial growth, thereby promoting faster organic matter breakdown *(Borkute and Hedaoo, 2022; Azim et al., 2018)*. Furthermore, amendments like biochar and zeolite improve aeration, reduce greenhouse gas emissions, and enhance nutrient cycling. These benefits contribute to more sustainable and agriculturally valuable compost, which is especially important for reducing the environmental footprint of composting *(Ayilara et al., 2020; Nenciu et al., 2021)*.

Particle size also plays a crucial role in composting efficiency. Smaller particles offer a greater surface-area-to-volume ratio, enhancing microbial colonization and enzymatic activity, which accelerates degradation rates *(Somera et al., 2023)*. Shredding fibrous materials such as leaves, grass, and small branches improves the structural uniformity of the compost mass, supports moisture retention, and promotes even aeration. Finer particles release more nitrogen and phosphorus and degrade at nearly twice the rate of coarser materials. Recommended particle sizes range from 1.3 to 7.6 cm, although many studies classify them broadly as "small" (under 1 cm) or "large" (over 5 cm), which is relevant for practical composting strategies. Despite general agreement on the benefits of smaller particles, research gaps remain, particularly concerning the impact of particle size on rapid composting of garden waste using microbial inoculants and vessel composting systems. Further investigation is needed to determine how different particle sizes influence the physicochemical and biological parameters of compost, which remains a significant topic for advancing composting technologies *(Mishra and Yadav, 2022)*. Moreover, particle size affects not only composting efficiency but also the properties of the final compost and its interaction with soil. Smaller particles tend to increase microbial biomass and phosphorus availability due to higher degradability, while larger fractions have shown stronger potential for disease suppression.

Soil characteristics such as pH, electrical conductivity, organic matter content, nutrient levels, and heavy metal concentrations are also influenced by compost granulation. However, limited research exists on how particle size affects the physical properties of soil and whether these effects vary depending on raw materials and application rates, making this an important area for future study *(Głąb et al., 2025)*.

When aeration is properly managed, particle size is optimized, and additives are strategically used, the composting process results in faster decomposition, improved microbial efficiency, and higher-quality compost with considerable environmental and agronomic benefits. These factors are highly relevant for sustainable waste management and soil health *(Barthod et al., 2018)*. Given this complexity, advanced treatment technologies such as nitrification-denitrification, biofiltration, activated carbon adsorption, and advanced oxidation processes are essential to reduce toxicity and enable safe disposal or reuse of leachate *(Brown et al., 2013)*.

Nutritional composition and compost maturity

Compost quality is essential for sustainable agriculture, influencing soil fertility, plant nutrition, microbial dynamics, and disease suppression. Key nutrient-related parameters of high-quality compost include increased nitrogen and potassium levels, a balanced pH (6.5 to 9.4), and reduced electrical conductivity (EC), all of which contribute to improved plant and soil *health (Borkute and Hedaoo, 2022; Ghinea and Leahu, 2020; Popa et al., 2023)*. Compost-amended soils (CAS) not only provide essential nutrients but also enhance microbial communities that outcompete pathogens such as Rhizoctonia and Fusarium, through nutrient competition and antimicrobial production, contributing to overall soil health *(Mehta et al., 2014)*. For instance, the application of CAS in spinach cultivation led to increased phenolics and flavonoids and reduced nitrate content, improving both plant quality and safety *(Hernández-Lara et al., 2023)*.

Similarly, food waste compost (FOWC) and vermicompost improved radish growth by enhancing the uptake of nitrogen, phosphorus, and potassium while maintaining a favourable soil pH *(Almaramah et al., 2024)*.

Composting techniques and raw material sources significantly influence nutrient outcomes. Successive composting of vegetable waste, for example, sustained thermophilic temperatures (55-68°C) and increased

nitrogen content from 9.4% to 32.4%, highlighting its potential as a potent organic amendment *(Kim E.Y. et al., 2018)*. Plant-based composts, especially from agricultural residues, enhance soil structure and nutrient content. Methods such as windrow composting have proven effective, increasing nitrogen by 37–71% in soybean-based composts and potassium by 7-37% in maize-based composts *(Adediran et al., 2003)*.

The maturity of compost is a defining quality criterion, as immature compost may compete with plants for oxygen and nitrogen and release phytotoxic compounds (e.g., ammonia, organic acids) that inhibit seed germination and plant growth. Thus, only mature and stable compost should be used in agriculture and landscaping *(Chang Y-T et al., 2023)*. Various indicators have been developed to assess compost maturity, grouped into physical, chemical, biological, and spectroscopic methods. Physical indicators like temperature, colour, odour, and moisture offer qualitative but sometimes subjective insights *(Zaghloul et al., 2019)*. Chemical indicators such as pH, EC, carbon-to-nitrogen (C/N) ratio, and the humic acid to fulvic acid ratio (HA/FA) provide quantifiable information, though they must be interpreted in relation to raw material types and composting conditions. For example, high EC values might not necessarily reflect immaturity depending on feedstock composition *(Chang Y-T et al., 2023; Abaker et al., 2025; Kong Y. et al., 2024)*.

Biological indicators such as germination index (GI), nitrification potential, microbial respiration, and enzyme activities like dehydrogenase offer insights into microbial activity and compost stability *(Mahapatra et al., 2022)*. More recently, spectroscopic techniques like 3D fluorescence excitation-emission matrix (EEM) analysis have enabled detailed, non-destructive characterization of organic matter evolution during composting. Additionally, dissolved organic matter (DOM) profiling reveals valuable information on the humification process, a key aspect of compost maturity *(Kong Y. et al., 2024; Chang Y-T et al., 2023)*. However, no single indicator is universally applicable due to the variability of feedstocks and composting conditions, underscoring the need for integrated evaluation methods *(Antil et al., 2014)*.

Recent studies have applied these indicators with promising results. In a 60-day composting trial using pig and chicken manure alongside agricultural by-products, *Chang et al. (2023)* monitored parameters such as temperature, pH, EC, C/N ratio, E4/E6 absorbance, humic substances, HIX, and GI. They found that by day 30, the C/N ratio, humic substances, and GI stabilized, with most indicators plateauing by day 45, indicating full compost maturity. The study further validated fluorescence spectroscopy as a valuable complement to traditional assessments.

Similarly, *Lončarić et al. (2024)* evaluated compost derived from vegetal waste, combining chemical indicators like C/N ratio and ammonium/nitrate ratio with germination tests. While diluted extracts (1:10 v/v) stimulated growth in dicotyledonous species (*Lepidium sativum*, *Cucumis sativus*), higher concentrations (1:2.5 v/v) caused phytotoxicity in monocots (*Hordeum vulgare*, ×*Triticosecale*), highlighting the species-specific nature of phytotoxic responses and the need for multi-species bioassays when evaluating compost maturity.

Table 2

Degree of compost maturity and their properties

Characteristic	Immature	Mature	Fully Mature
Toxicity	High	Moderate	Absent
Composting Progress	Incomplete	Substantial	Complete
Nitrogen Impact	Strong	Minimal	None
Odour	Strong and Unpleasant	Slight and Earthy	Neutral or None

Maturity and stability are distinct yet interrelated aspects of compost quality. Maturity reflects the completeness of organic matter transformation, while stability refers to the resistance to further microbial degradation and the potential release of phytotoxins *(Martín-Ramos and Martín-Gil, 2020)*. Mature compost is characterized by minimal odour, low phytotoxicity, and negligible nitrogen immobilization, whereas immature compost can exhibit strong odours, unstable temperatures, and high microbial respiration. Table 3 summarizes the stages of compost maturity, highlighting toxicity, composting progress, nitrogen impact, and odour. Table 4 presents the commonly used indicators for assessing compost maturity and stability, including organic matter content, temperature profile, germination test results, nitrifying activity, microbial respiration, dehydrogenase enzyme activity, the Bc/Bn ratio (cellulolytic to nitrifying bacteria), and the C/N ratio, which typically stabilizes around 10–15 in mature compost.

Table 3

Key indicators for assessing compost maturity and stability

Indicator	Description
Organic Matter	Reflects the degree of organic matter decomposition; mature compost has low and stable OM content.
Temperature Profile	Tracks temperature changes over time; maturation is marked by a decline in temperature.
Germination Test	Measures indirect seed toxicity; mature compost does not inhibit germination.
Nitrifying Activity	Assesses the conversion of ammonium to nitrates, indicating beneficial biological activity.
Microbial Respiration	Microbial respiration rates (e.g., CO_2) reflect biological stability.
Dehydrogenase Activity	Enzyme activity indicating the intensity of microbial decomposition processes.
Bc/Bn Ratio	Ratio of cellulolytic bacteria (Bc) to nitrifying bacteria (Bn); balanced values indicate maturity.
C/N Ratio	Carbon-to-nitrogen ratio; mature compost typically has values around 10–15, showing nutrient balance.

Microbial processes in composting

Composting is mediated by diverse microbial communities that decompose organic matter into stable compounds and precursors of humic substances *(Sánchez et al., 2017)*. These microbial agents, including bacteria, fungi, and actinomycetes, operate in succession throughout the composting stages *(Nemet et al., 2021)*, each performing distinct enzymatic and metabolic roles in transforming waste into nutrient-rich compost. Macro-organisms, such as worms, also support microbial activity.

During the initial mesophilic and thermophilic phases, bacteria dominate the microbial community, actively degrading easily biodegradable compounds such as sugars and proteins. Their rapid metabolism generates substantial heat, which sanitizes the compost and creates favourable conditions for thermotolerant microorganisms *(Aguilar Paredes et al., 2023)*. Thermophilic bacteria, particularly from the genera *Bacillus* and *Thermus*, play a key role by secreting thermostable enzymes including proteases, ureases, cellulases, and lignin modifying enzymes that are essential for breaking down complex biomolecules such as fats, lignin, and cellulose *(Finore et al., 2023)*.

As the compost cools, fungi become increasingly active, contributing to the decomposition of recalcitrant compounds that bacteria cannot efficiently degrade. Their enzymatic activity, especially during the maturation phase, is crucial for nutrient mineralization and humus formation *(Aguilar-Paredes et al., 2023)*. *Actinomycetes*, filamentous bacteria with fungal-like characteristics, also emerge at this stage. They further degrade resistant organics, release antimicrobial compounds that suppress pathogens, and are responsible for the earthy smell associated with mature compost *(Aguilar-Paredes et al., 2023; Nemet et al., 2021)*. Collectively, these microbial dynamics are fundamental to transforming organic waste into nutrient-rich and stable compost.

Optimal moisture and pH levels support enzymatic functions, and a balanced C/N ratio supplies essential nutrients for microbial proliferation. Maintaining these parameters within ideal ranges is crucial for producing stable, mature compost *(Nemet et al., 2021; Luo et al., 2023)*. Maintaining optimal environmental conditions significantly enhances microbial metabolism, thereby improving the efficiency and effectiveness of the composting process. Microorganisms not only drive the rapid decomposition of organic matter but also improve the biological stability and nutrient content of the final product, making compost a high-quality amendment for agricultural and horticultural *applications (Zainudin et al., 2022; Tianming Chen et al., 2020)*.

Recent advances demonstrate how microbial management strategies can accelerate the composting process. *Somera et al. (2023)* showed that the addition of vegetable waste as a bio-activator enriched beneficial microbes such as *Streptococcus* and *Lactobacillus*, which produce lactic acid. This acidification process suppresses pathogenic organisms and enhances nutrient availability.

When combined with precise process control measures such as a seeding rate of 14.5%, air suction of 2.6 L/kg dry solids per minute, and alternating agitation cycles, these conditions allow compost to mature in just four days, achieving a carbon conversion rate of 14.54%.

Another strategy to improve composting performance involves the use of microbial inoculants *(Huang et al., 2022)*, either as pure strains or mixed cultures. These inoculants, typically composed of bacteria, fungi, or actinobacteria, can significantly accelerate the degradation of lignocellulosic materials, improve compost quality, and reduce the required maturation time *(Babett Greff et al., 2022; Zainudin et al., 2022)*.

However, their effectiveness depends on selecting strains compatible with specific substrates and environmental conditions, and practical application must also consider production and implementation costs.

The incorporation of vegetable waste as a bio-activator further promotes microbial proliferation, especially of lactic acid producing bacteria that both suppress pathogens and enhance compost stabilization.

Microbial activity is also essential in composting-based bioremediation, facilitating the breakdown of organic pollutants into non-toxic compounds such as carbon dioxide and water. Under thermophilic conditions, achieved through proper temperature management, microbial metabolism is enhanced, while the compost matrix immobilizes pollutants, reducing their bioavailability and environmental impact *(Girish et al., 2020)*. Compost particle size influences microbial dynamics and phosphorus availability. *Verma and Marschner (2013)* demonstrated that finer fractions (<3 mm or <2 mm) increased microbial biomass carbon (MBC) and phosphorus (MBP) more effectively than coarser particles (>5 mm), likely due to improved microbial colonization. Soil properties, such as organic matter content, pH, and texture, also affect phosphorus pools. Organic-rich soils had higher Fe/Al-bound and organic phosphorus, while alkaline soils favoured Ca-bound phosphorus. These findings highlight the complex interactions between compost characteristics, soil properties, and microbial activity. The microbial community's enzymatic potential is central to compost transformation. *Finore et al. (2023)* highlighted thermophilic bacteria, particularly *Bacillus* and *Thermus*, as major producers of thermostable enzymes such as proteases, ureases, cellulases, hemicelluloses, and esterases. These enzymes catalyse the breakdown of complex polymers into simpler compounds. Advances in metagenomics have provided deeper insight into these microbial communities and their functional capabilities, enabling the optimization of composting conditions for higher efficiency. For instance, the Life Tirsav Plus project demonstrated effective composting of olive oil waste using both dynamic and static methods, resulting in high-quality compost within controlled environments.

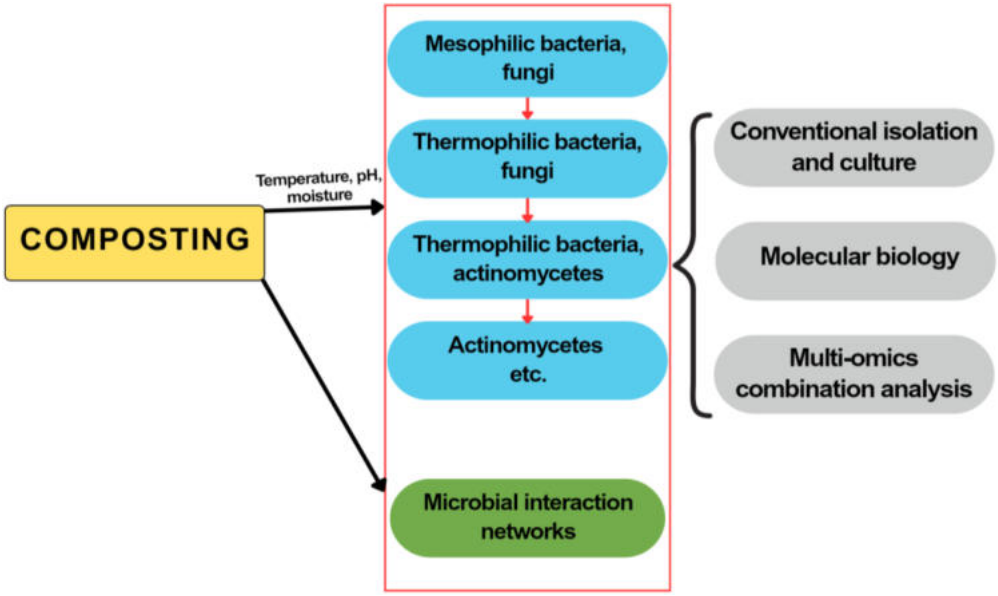


Fig. 4 - Outlines of microbial communities in composting process and related biological technologies
(adapted from Luo et al., 2023)

Composting is thus a multi-stage, microbially mediated process that involves successive actions by bacteria, actinomycetes, and fungi. Initially, mesophilic bacteria metabolize sugars, elevating the temperature. *Thermophilic bacteria* and actinomycetes subsequently degrade cellulose, followed by fungal decomposition of lignin. Composting methods vary in terms of oxygen availability and biological agents used, ranging from anaerobic systems (several months), aerobic methods (including heap, pit, and Berkeley techniques), to vermicomposting with earthworms. For effective composting, conditions such as oxygen availability, moisture, and temperatures up to 75 °C are crucial, ensuring both microbial efficiency and pathogen suppression *(Zafar, 2022)*.

COMPOSTING TECHNOLOGIES AND OPTIMIZATION APPROACHES

Traditional composting still has some disadvantages, such as nitrogen loss, leachate generation, odour problems, greenhouse gas emissions (CH_4 and N_2O), heavy metal (HM) mobility, antibiotic residues, and the diffusion of antibiotic resistance genes.

During the composting process, between 9.6% and 46% of the initial total nitrogen (N) is lost due to NH_3 volatilization, which not only decreases the quality of the compost but also worsens air pollution *(Wang, Q. et al., 2018)*.

To overcome these drawbacks, recent advances in composting technologies have greatly enhanced the production of high-quality organic fertilizers, supporting sustainable agriculture and improving soil health.

For example, vegetable waste composting, particularly when combined with amendments such as sawdust, meets agricultural safety standards while improving soil properties *(Somera et al., 2023; Leahu, 2020)*.

Food waste composting has been shown to reduce harmful emissions and increase the nutrient content of vegetables *(Guo et al., 2018)*. Furthermore, the application of bioinoculants, as demonstrated by the National Institute of Plant Health Management, has shortened composting times and promoted better plant growth *(Girish et al., 2020)*.

Additional organic amendments, including insect frass and shiitake mushroom compost, have been reported to improve tree growth and water retention, although their effectiveness in pathogen suppression may vary *(Somera et al., 2023)*. For instance, technologies such as windrow composting (WC) and windrow-vermicomposting (WVC) can achieve thermophilic temperatures (> 45 °C) within just 2-3 days. The WVC method has been found more effective in meeting WHO safety standards and in reducing volatile solids, organic carbon, and the C/N ratio *(Mengistu et al., 2018)*. During composting, carbon and ammonium (NH_4^+) concentrations typically decline, while pH decreases in the early stages and later rises as the compost reaches maturity. Microbial metabolism converts organic substrates into humic substances, releasing by-products such as CO_2, H_2O, NH_3, SO_4^{2-}, and heat, the latter serving as a key indicator of microbial activity *(Manea and Popescu, 2022)*. Composting methods strongly influence temperature and moisture control. Windrow-vermicomposting (WVC) quickly reaches and sustains thermophilic conditions, improving pathogen destruction rates and accelerating the process. By contrast, slower techniques like pit composting (PC) require longer maturation periods due to limited aeration and reduced turning *(Mengistu et al., 2018)*. Both laboratory-scale and co-composting studies emphasize that controlled aeration, appropriate moisture, and balanced substrate composition are critical for maximizing microbial activity and carbon conversion efficiency *(Somera et al., 2023; Amiruddin et al., 2023)*. The main differences among composting technologies are summarized in Table 4.

Table 4

Composting methods overview: temperature, moisture, and process timing

Method	Thermophilic Onset	Duration	Maturity Time	Notes	References
Windrow composting	2-3 days	15-19 days	~60 days	High microbial activity, efficient pathogen removal	*Mengistu et al., 2018*
Static Composting	Delayed	Short	~80 days	Poor aeration, slower degradation	*Mengistu et al., 2018*
In-Vessel Bioreactor	Controlled	Variable	~50 days	Allows precise control of temperature and moisture	*Chang et al., 2023; Rawoteea et al., 2017*
Vermicomposting	No thermophilic phase	Continuous	~45–60 days	Uses earthworms; ideal for organic kitchen waste; low odour	*Vuković et al., 2021; Nemli et al., 2008*
Berkeley Composting Method	1-2 days	18 days	~30 days	Rapid composting with frequent turning; high temperature maintained	*De Almeida Leal et al., 2022*
Indore Composting	3-5 days	20–25 days	~90 days	Traditional method; layered approach; moderate temperature rise	*Pathak et al., 2025; Kanaujiya et al., 2020*
Composting in Containers	2-4 days	10–20 days	~60 days	Suitable for small-scale urban composting; temperature varies	*Schrader et al., 2015; Mengistu et al., 2018*

Windrow composting

Windrow composting is an aerobic technique for treating organic waste, in which the material is arranged in long, narrow piles (windrows). These rows are periodically turned in order to maintain oxygen levels,

stimulate microbial activity, and promote efficient decomposition. The method is widely adopted for large-scale composting of agricultural residues, municipal solid waste, and industrial organic by-products.

Typically, a windrow represents a stack of raw materials organized in elongated rows. For effective composting, the piles should be kept relatively small, generally not exceeding 6 feet in height, and sufficiently porous to allow proper air exchange *(Mengistu et al., 2018; Degefe et al., 2025)*.

Turning is usually performed mechanically, with the help of windrow turners, manure spreaders, or bucket loaders. This operation improves aeration, ensures uniform decomposition, and exposes all material to microbial colonization. During the process, heat, water vapour, and gases are released from the pile. Despite its advantages, windrow composting also has drawbacks: it requires high labour input, and both temperature and moisture content are difficult to control effectively *(Lynch and Cherry, 1996; Hashim et al., 2024)*.

To overcome these limitations, in-vessel composting systems have been developed. These systems improve process efficiency by providing controlled aeration, better regulation of temperature, and faster stabilization of the final product. Two common types of in-vessel systems include *(Manyapu et al., 2017)*:

- Passively Aerated Windrow System (PAWS);
- Forced Aerated Static Piles (FASP).

Passively Aerated Windrow System (PAWS) represents a modified method of windrow composting designed to enhance aeration without the need for frequent mechanical turning. In this system, perforated pipes are strategically placed at the base of the windrow, enabling natural convective airflow to pass through the compost pile and maintain aerobic conditions essential for microbial activity. Prior to layering the organic substrates over the pipes, the materials are thoroughly mixed to ensure homogeneity and promote uniform decomposition. To sustain thermophilic conditions and minimize heat loss, the outer surface of the windrow is covered with a layer of finished compost, which also serves to reduce odour emissions and prevent excessive moisture evaporation. Research has shown that the effectiveness of PAWS depends heavily on factors such as feedstock composition, compaction, porosity, and permeability, which influence airflow and temperature regulation within the pile *(Veeken et al., 2003)*. Studies also confirm that passive aeration can achieve composting temperatures above 57°C, comparable to forced aeration systems, while saving energy and reducing operational complexity. Additionally, PAWS has been successfully applied in emergency composting scenarios, such as animal mortality management, due to its ability to inactivate pathogens and limit environmental contamination *(Manyapu et al., 2017)*.

Table 5

Advantages of the PAWS system

Benefit	Explanation
Efficient aeration	No energy consumption for mechanical turning
Reduced costs	Less labour and fewer equipment required
Odour control	Mature compost acts as a bioactive cover
Moisture conservation	Reduced evaporation, maintaining ideal conditions for composting
Biological safety	High temperatures destroy pathogens and weed seeds

Forced Aerated Static Piles (FASP) is a composting method derived from the Passively Aerated Windrow System, but improved through the use of forced aeration. In this system, perforated pipes are connected to blowers that actively regulate airflow, ensuring adequate oxygen supply and maintaining thermophilic conditions. Airflow is typically controlled based on temperature feedback, with blowers activated around 65°C to optimize microbial activity, accelerate decomposition, and ensure pathogen inactivation. By eliminating the need for manual turning, FASP increases process efficiency, reduces labour requirements, and produces a uniform and stable compost product *(Manyapu et al., 2017; Oñiguez et al., 2018)*.

This setup enables forced aeration, which aerates the compost pile by a fan or blower to maintain adequate oxygen levels. The forced air passes through the pile via the network of pipes, enhancing microbial activity and accelerating decomposition without the need for manual turning *(Riaz et al., 2021)*.

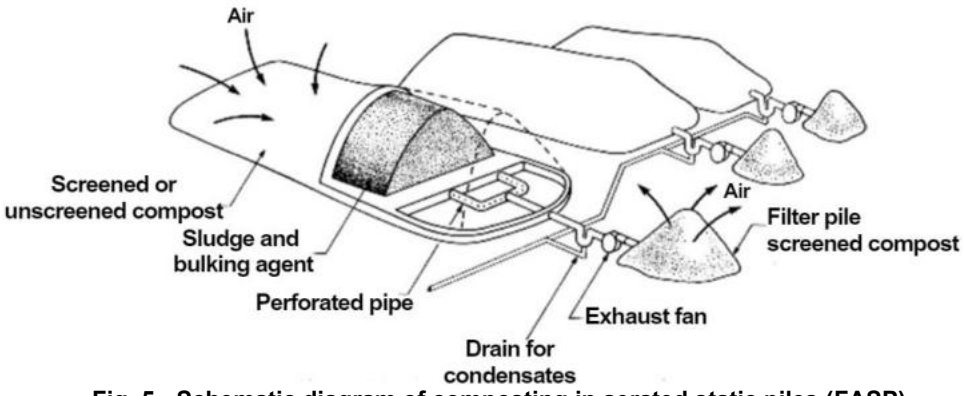


Fig. 5 - Schematic diagram of composting in aerated static piles (FASP)
(Riaz et al., 2021)

Table 6

Comparative evaluation of in-vessel composting system
(adapted from, Manyapu et al., 2017)

Sl. No.	Parameters	PAWS	FASP
1	Moisture control	Partial	Full
2	Temperature control	Partial	Full
3	Aeration control	Yes	Yes
4	Exhaust air control	No	Yes
5	Climate suitability	Best in warm and dry climates	Suitable for both warm and cold climates
6	Risk of recontamination	Possible if poorly managed	Minimal
7	Occupational risks	Low	Low
8	Odour emissions	Low	Low
9	Space requirement	Medium	Medium
10	Skill level required	Moderate	Moderate
11	System design complexity	Simple	Moderate
12	Processing time	Long (8-12 weeks)	Fast (2-4 weeks)
13	Operational cost	Low	Moderate

Vermicomposting

Vermicomposting is an eco-friendly biotechnological method that transforms organic waste into nutrient-rich fertilizer, significantly improving soil fertility through the production of vermicompost with a low carbon-to-nitrogen (C/N) ratio. This process addresses common challenges in organic waste management, such as phytotoxicity and nitrogen leaching, thereby producing a safer and more effective fertilizer for agricultural applications. By reducing environmental impacts and supporting sustainable farming practices, vermicomposting aligns with the European Union's circular economy objectives *(Gabur et al., 2024)*.

Economically, vermicomposting offers multiple benefits: it produces valuable organic fertilizers that enhance nutrient availability, accelerates organic matter decomposition, and serves as a sustainable alternative to conventional chemical fertilizers *(Borkute and Hedaoo, 2022; Savage, 1996; Gabur et al., 2024)*.

Unlike traditional composting, vermicomposting utilizes earthworms, commonly species such as *Eisenia fetida*, that biologically digest organic waste within an optimal temperature range of 10 °C to 32 °C. This biological activity significantly improves decomposition efficiency. However, important knowledge gaps remain regarding ammonia volatilization and greenhouse gas emissions during vermicomposting, particularly in the context of plant residues and manure in mountainous regions. While organic waste management and manure reuse have been extensively studied, research on gas emissions specific to vermicomposting is still limited, thus requiring further investigation. Gaining a deeper understanding of these emissions is essential for developing alternative waste management strategies and ensuring the long-term sustainability of organic waste recycling *(Raza et al., 2022)*.

Economically, vermicomposting offers multiple benefits: it produces valuable organic fertilizers that enhance nutrient availability, accelerates organic matter decomposition, and serves as a viable sustainable alternative to conventional chemical fertilizers *(Borkute and Hedaoo, 2022; Savage, 1996; Gabur et al., 2024)*.

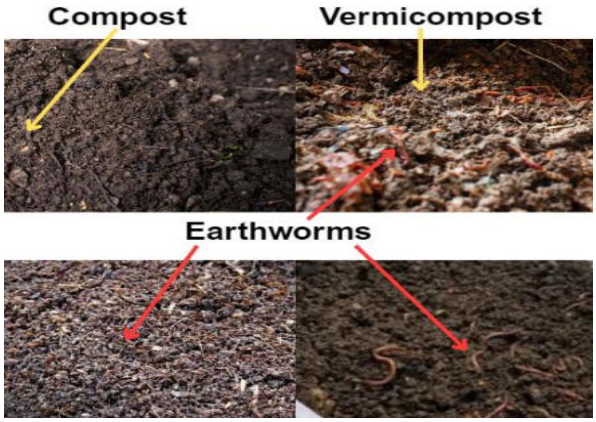


Fig. 6 - Appearance of compost and vermicompost
(adapted from Raza et al., 2022)

Vermicompost results from synergistic interactions between earthworms and microorganisms, leading to a non-thermophilic stabilization of organic materials. It is recognized as an environmentally friendly method for recycling organic waste and acts as a potent soil amendment that promotes plant growth. Additionally, vermiculture involves the mass production of earthworms in waste environments, which supports large-scale vermicomposting operations *(Raza et al., 2022)*. The vermicomposting process typically takes place in containers with perforated bottoms to allow drainage of nutrient rich leachate, commonly referred to as "compost tea." The procedure involves layering cow manure, introducing earthworms, covering with shredded food waste, and maintaining moisture through regular watering. Earthworms efficiently convert a variety of organic substrates including sludge, manure, and household waste into nutrient rich compost that is beneficial for agricultural and horticultural applications *(Waqas et al., 2023)*.

Table 7

Benefits of vermicomposting

Benefit	Description	Scientific Source
Soil Fertility Enhancement	Improves nutrient availability (N, P, K, Ca, Mg), humic substances, and enzymes	*Cruz et al., 2024*
Improved Soil Structure	Enhances porosity, water retention, and aggregate stability	*Patra and Parihar, 2023*
Plant Growth Promotion	Boosts germination, root development, and crop yield	*Blouin et al., 2019*
Microbial Activity Increase	Enriches soil with beneficial microbes (e.g. nitrogen fixers, phosphate solubilizers)	*Vuković et al., 2021*
Eco-Friendly Waste Management	Converts organic waste into valuable fertilizer, reducing landfill burden	*Thakur et al., 2021*
Disease Suppression	Vermicompost suppresses soil-borne pathogens and pests	*Mohite et al., 2024*
Rapid Processing Time	Faster than traditional composting; produces stable compost in < 2 months	*Cruz et al., 2024*
Heavy Metal Immobilization	Reduces bioavailability of toxic metals in soil	*Vuković et al., 2021*

Comparative evaluation of the main composting technologies

Composting methods differ considerably in terms of efficiency, processing time, and environmental impact. Traditional windrow composting can require 120–150 days to complete, whereas modern technologies, such as in-vessel composting, can complete the composting process in as little as 10 days *(Stentiford and Sánchez-Monedero, 2016)*. The incorporation of organic amendments, including vermicompost and vegetable peels, can further reduce composting time to 45–75 days *(Borkute and Hedaoo, 2022)*.

An important aspect of composting management is the treatment of leachate, the nutrient-rich but pollutant-laden liquid formed by water percolating through waste.

Leachate contains high organic loads (measured by biochemical oxygen demand, BOD_5, and chemical oxygen demand, COD), toxic ammoniacal nitrogen, heavy metals (e.g., Zn, Pb, Hg), phenols, and other recalcitrant compounds that threaten soil and groundwater quality *(Siciliano et al., 2019; Sanadi et al., 2019)*.

Static pile systems, although often challenged by difficulties in maintaining thermophilic conditions, can yield compost of comparable quality to industrial systems when properly managed. Additionally, they offer advantages such as lower greenhouse gas emissions and the absence of plastic contamination *(Sánchez, 2022)*.

Efficient separation of organic waste also plays a critical role in improving compost quality by increasing nutrient content and minimizing contaminants *(Savage, 1996)*. Microbial inoculants and organic additives accelerate the decomposition process and improve overall compost quality. For instance, the 'heaping' composting method, which can achieve temperatures up to 65.9°C, ensures effective pathogen sanitization *(Manea et al., 2024; Sarkar et al., 2016)*. Supplementing compost with microbial agents and organic amendments has also been shown to enhance degradation rates and product quality *(Sun et al., 2021)*.

Table 8

Compost management practices and their main objectives

Management Practice	Main Objective
Thermophilic temperature	Eliminates pathogens and weed seeds
Moisture control	Prevents microbial inhibition and undesirable emissions
Regular aeration	Maintains aerobic conditions and prevents foul odours
Microbial inoculants	Enhances organic matter degradation
Compost quality monitoring	Ensures product safety and improves soil quality
Advanced composting technologies	Increases efficiency, control, and energy optimization
Policy and regulatory support	Facilitates scalability and economic viability

CONCLUSIONS

Composting of plant waste is a complex process that relies on microbial activity and several essential parameters. The most critical factors include the carbon-to-nitrogen ratio, temperature, humidity, aeration, pH, and the characteristics of the materials used. When these factors are properly controlled, the composting process develops efficiently, producing a stable compost that is free of harmful bacteria and rich in nutrients, making it ideal for soil fertilization.

The composting process can be further optimized through modern technologies that enable rapid and efficient transformation of waste into high-quality compost. These include automatic aeration systems that supply oxygen necessary for microbial activity without manual turning, as well as grinding and sorting equipment that prepare the waste for uniform decomposition. Pretreatment techniques, such as controlled fermentation or soaking of dry materials, facilitate faster microbial degradation. Vermicomposting, which employs decomposer worms to convert organic residues into natural fertilizer, represents another highly efficient and environmentally friendly approach. Collectively, these technologies make composting faster, cleaner, and less labour-intensive. While these technological advancements offer significant advantages, they also affect compost quality and processing time, and may increase overall operational costs. Future perspectives should focus on balancing efficiency and quality while minimizing expenses.

In conclusion, producing efficient compost from plant waste requires an integrated approach that combines scientific knowledge with practical process management. Composting thus serves not only as an effective method for valorising plant waste but also as a key strategy for promoting sustainable agriculture and advancing circular economy objectives by closing resource loops and reducing environmental impact.

ACKNOWLEDGEMENT

This work was funded by ADER Program - Ministry of Agriculture and Rural Development (MADR) - Contract ADER 24.1.3/17.07.2023 and by Ministry of Research, Innovation and Digitalization, within the NUCLEU Program, through Project 9N/ 01.01.2023.

REFERENCES

[1] Abaker, M., Redon, R., Théraulaz, F., Raynaud, M., Prudent, P., Vassalo, L., Martino, C., Domeizel, M., and Mounier, S. (2025). Composting process monitoring and maturity prediction by spectroscopic measurement and PLS modelling. *International Journal of Environmental Research*, 19, article 108. https://doi.org/10.1007/s41742-025-00753-3.

[2] Abbas, R. I., and Flayeh, H. M. (2024). Aerobic composting of organic waste, alternative and an efficient solid waste management solution. *Asian Journal of Water, Environment and Pollution*, 21(4), 101–111. https://doi.org/10.3233/AJW240051.

[3] Adediran, J. A., Taiwo, L. B., Sobulo, R. A. (2003). Effect of organic wastes and method of composting on compost maturity, nutrient composition of compost and yields of two vegetable crops. *Journal of Sustainable Agriculture*, 22(4), 95–109. https://doi.org/10.1300/J064v22n04_08.

[4] Adugna, G. (2018). A review on impact of compost on soil properties, water use and crop productivity. *Agricultural Science Research Journal*, 4(3), 93–104. https://doi.org/10.14662/ARJASR2016.010.

[5] Aguilar-Paredes, A., Valdés, G., Araneda, N., Valdebenito, E., Hansen, F., Nuti, M. (2023). Microbial community in the composting process and its positive impact on the soil biota in sustainable agriculture. *Agronomy*, 13(2), 542. https://doi.org/10.3390/agronomy13020542.

[6] Alkoaik, F., Khalil, A., Al-Mahasneh, M., Fulleros, R., and El-Waziry, A. (2015). Changes in colour and germination index as indicators for compost maturity. https://doi.org/10.13140/RG.2.1.5120.7840.

[7] Almaramah, S. B., Abu-Elsaoud, A. M., Alteneiji, W. A., Albedwawi, S. T., El-Tarabily, K. A., Al Raish, S. M. (2024). The impact of food waste compost, vermicompost, and chemical fertilizers on the growth measurement of red radish (*Raphanus sativus*): A sustainability perspective in the United Arab Emirates. *Foods*, 13(11), 1608. https://doi.org/10.3390/foods13111608.

[8] Amiruddin, N., Rozamri, N., Baharudin, F., Mohamad, I. (2023). A study on household food waste management and composting practice. *IOP Conference Series: Earth and Environmental Science*, 1205, 012018. https://doi.org/10.1088/1755-1315/1205/1/012018.

[9] Amuah, E. E. Y., Fei-Baffoe, B., Sackey, L. N. A., Douti, N. B., and Kazapoe, R. W. (2022). A review of the principles of composting: understanding the processes, methods, merits, and demerits. Organic Agriculture, 12, 547–562. https://doi.org/10.1007/s13165-022-00408-z.

[10] Ansar, A., Du, J., Javed, Q., Adnan, M., Javaid, I. (2025). Biodegradable waste in compost production: A review of its economic potential. *Nitrogen*, 6(2), 24. https://doi.org/10.3390/nitrogen6020024.

[11] Antil, R. S., Raj, D., Abdalla, N., Inubushi, K. (2014). Physical, chemical and biological parameters for compost maturity assessment: A review. https://doi.org/10.1007/978-3-319-08004-8_5.

[12] Argun, Y. A., Karacali, A., Calisir, U., Kilinc, N. (2017). Composting as a waste management method. *Journal of International Environmental Application and Science*, 12(3), 244–255. https://doi.org/10.1007/s11756-017-0091-4.

[13] Assandri, D., Zara, G., Cavallo, E., Marilena, B. Composting technology of brewer's grains. *Encyclopedia*. https://encyclopedia.pub/entry/6177.

[14] Avramović, D., Janković, S. (2018). Composting as a method of biodegradable waste management. *Facta Universitatis, Series: Working and Living Environmental Protection*, 15(3), 137–148. https://casopisi.junis.ni.ac.rs/index.php/FUWorkLivEnvProt/article/viewFile/3866/2676.

[15] Ayilara, M. S., Olanrewaju, O. S., Babalola, O. O., Odeyemi, O. (2020). Waste management through composting: Challenges and potentials. *Sustainability*, 12(11), 4456. https://doi.org/10.3390/su12114456.

[16] Azim, K., Soudi, B., Boukhari, S., Perissol, C., Roussos, S., and Thami Alami, I. (2018). Composting parameters and compost quality: A literature review. *Organic Agriculture*, 8, 141–158. https://doi.org/10.1007/s13165-017-0180-z.

[17] Barthod, J., Rumpel, C., and Dignac, M.-F. (2018). Composting with additives to improve organic amendments: A review. *Agronomy for Sustainable Development*, 38(17). https://doi.org/10.1007/s13593-018-0491-9.

[18] Blouin, M., Barrere, J., Meyer, N., Lartigue, S., Barot, S., and Mathieu, J. (2019). Vermicompost significantly affects plant growth. A meta-analysis. *Agronomy for Sustainable Development*, 39, Article 34. https://doi.org/10.1007/s13593-019-0579-x.

[19] Borkute, P. A., and Hedaoo, M. N. (2022). Study on composting of vegetable waste. *Journal of Emerging Technologies and Innovative Research (JETIR)*, 9(11), b31–b36. https://www.jetir.org/papers/JETIR2211120.pdf.

[20] Brown, K., Ghoshdastidar, A. J., Hanmore, J., Frazee, J., Tong, A. Z. (2013). Membrane bioreactor technology: a novel approach to the treatment of compost leachate. *Waste Management*, 33(11), 2188-2194. https://doi.org/10.1016/j.wasman.2013.04.006.

[21] Caba, I. L., Bordean, D., Matei, G., Matei, M., and Pavel, I. (2019). Improving the composting of waste materials from agricultural farms, a step towards sustainable agriculture. *8th International Conference on Thermal Equipment, Renewable Energy and Rural Development (TE-RE-RD 2019), E3S Web of Conferences, 112*, 03025. https://doi.org/10.1051/e3sconf/201911203025.

[22] Cai, S., Ma, Y., Bao, Z., Yang, Z., Niu, X., Meng, Q., Qin, D., Wang, Y., Wan, J., Guo, X. (2024). The Impacts of the C/N Ratio on Hydrogen Sulfide Emission and Microbial Community Characteristics during Chicken Manure Composting with Wheat Straw. *Agriculture*, 14(6), 948. https://doi.org/10.3390/agriculture14060948.

[23] Cerda, A., Artola, A., Font, X., Barrena, R., Gea, T., Sánchez, A. (2018). Composting of food wastes: Status and challenges. *Bioresource Technology*, 248 (Pt A), 57-67. https://doi.org/10.1016/j.biortech.2017.06.133.

[24] Chakravorty, S., Panda, S., Jain, M. S. (2024). Chapter 8 - A review of rapid composting techniques and optimization of parameters for the management of organic waste. In R. Singh, S. Mohapatra, and M.-C.

Jong (Eds.), Waste and the Environment: Underlying Burdens and Management Strategies, Solid Waste Management for Resource-Efficient Systems (pp. 163–177). *Elsevier*. ISBN 9780443237751.

[25] Chang, Y.-T., Lee, C.-H., Hsieh, C.-Y., Chen, T.-C., Jien, S.-H. (2023). Using Fluorescence Spectroscopy to Assess Compost Maturity Degree during Composting. *Agronomy*, 13(7), 1870, https://doi.org/10.3390/agronomy13071870.

[26] Chen, T., Zhang, S., Yuan, Z. (2020). Adoption of solid organic waste composting products: A critical review. *Journal of Cleaner Production*, 272, 122712. https://doi.org/10.1016/j.jclepro.2020.122712.

[27] Cruz García-Santiago, J., Pérez Hernández, H., Sánchez Vega, M., and Alonso Méndez López, A. (2024). Benefits of vermicompost in agriculture and factors affecting its nutrient content. *Journal of Soil Science and Plant Nutrition*, 24, 4898–4917. https://doi.org/10.1007/s42729-024-01880-0.

[28] De Almeida Leal, M. A., Leal, M. A., França De Oliveira, D., and García, A. C. (2022). Chemical and spectroscopy characterization of a compost from food waste applying the hot composting Berkeley method. *International Journal of Recycling of Organic Waste in Agriculture*, *11*(2). https://doi.org/10.30486/ijrowa.2021.1897439.1052.

[29] Degefe, G., Ayele, C., Shimekit, F. (2025). Windrow composting: A viable option for the management and conversion of various agro-industrial organic wastes in Ethiopia. *Journal of Applied and Natural Science, 17*(2), 671–676. https://doi.org/10.31018/jans.v17i2.6310.

[30] Ebrahimi, M., Gholipour, S., Mostafaii, G., Yousefian, F. (2024). Biochar-amended food waste compost: A review of properties. *Results in Engineering*, 24, 103118. https://doi.org/10.1016/j.rineng.2024.103118.

[31] El Boudihi, H., Kifani-Sahban, F., Wahby, I., Fihri, M. (2024). Study of temperature dynamics and influencing factors during composting process. *International Journal of Chemical Reactor Engineering*, 22(10), 1183-1198. https://doi.org/10.1515/ijcre-2024-0133.

[32] El-mrini, S., Aboutayeb, R., Zouhri, A. (2022). Effect of initial C/N ratio and turning frequency on quality of final compost of turkey manure and olive pomace. *Journal of Engineering and Applied Sciences*, 69, 37. https://doi.org/10.1186/s44147-022-00092-6.

[33] Esparza, I., Jiménez-Moreno, N., Bimbela, F., Ancín-Azpilicueta, C., and Gandía, L. M. (2020). Fruit and vegetable waste management: Conventional and emerging approaches. *Journal of Environmental Management*, 265, 110510. https://doi.org/10.1016/j.jenvman.2020.110510.

[34] Fan, S., Li, A., ter Heijne, A., Buisman, C.J.N., Chen, W.-S. (2021). Heat potential, generation, recovery and utilization from composting: A review. *Resources, Conservation and Recycling*, 175, 105850. https://doi.org/10.1016/j.resconrec.2021.105850.

[35] Finore, I., Feola, A., Russo, L., Cattaneo, A., Di Donato, P., Nicolaus, B., Poli, A., and Romano, I. (2023). Thermophilic bacteria and their thermozymes in composting processes: A review. *Chemical and Biological Technologies in Agriculture*, 10, Article 7. https://doi.org/10.1186/s40538-023-00381-z.

[36] Gabur, G.-D., Teodosiu, C., Fighir, D., Cotea, V. V., Gabur, I. (2024). From Waste to Value in Circular Economy: Valorizing Grape Pomace Waste through Vermicomposting. *Agriculture*, 14(9), 1529. https://doi.org/10.3390/agriculture14091529.

[37] Gezu, S., Kim, D.-G., Yimer, F., Tadesse, M. (2024). Exploring compost production potential and its economic benefits and greenhouse gas mitigation in Addis Ababa, Ethiopia. *Science of The Total Environment*, 955, 176617. https://doi.org/10.1016/j.scitotenv.2024.176617.

[38] Ghinea, C., and Leahu, A. (2020). Monitoring of fruit and vegetable waste composting process: Relationship between microorganisms and physico-chemical parameters. *Processes*, 8(3), 302. https://doi.org/10.3390/pr8030302.

[39] Girish, A., Palaniyandi, S., and Sujeetha, A. R. P. (2020). A new method of compost preparation from vegetable waste and dried leaf litters. *International Journal of Current Microbiology and Applied Sciences*, 9, 281–290. https://doi.org/10.20546/ijcmas.2020.908.033.

[40] Głąb, T., Gondek, K., and Mierzwa-Hersztek, M. (2025). Enhancing soil physical quality with compost amendments: Effects of particle size and additives. *Agronomy*, 15(2), 458. https://doi.org/10.3390/agronomy15020458.

[41] Greff, B., Szigeti, J., Nagy, Á., Lakatos, E., Varga, L. (2022). Influence of microbial inoculants on co-composting of lignocellulosic crop residues with farm animal manure: A review. *Journal of Environmental Management*, 302 Part B, 114088. https://doi.org/10.1016/j.jenvman.2021.114088.

[42] Gökay Nemli, S., Yıldız, S., and Gezer, D. E. (2008). The potential for using the needle litter of Scotch pine (*Pinus sylvestris* L.) as a raw material for particleboard manufacturing. *Bioresource Technology*, 99(14), 6054–6058. https://doi.org/10.1016/j.biortech.2007.12.044.

[43] Guo, W., Zhou, Y., Zhu, N., Hu, H., Shen, W., Huang, X., Zhang, T., Wu, P., and Li, Z. (2018). On site composting of food waste: A pilot scale case study in China. Resources, Conservation *and Recycling*. 132:130-138. https://doi.org/10.1016/j.resconrec.2018.01.033.

[44] Hashim, S., Bashir, R., Khan, A. A., Mirani, A. A., Shoaib, M., Razzaq, A., Ehsan, F., and Munir, F. (2024). Performance evaluation of compost of windrow turner machine using agriculture waste materials. *Sustainability*, 16(17), 7779. https://doi.org/10.3390/su16177779.

[45] Hernández-Lara, A., Ros, M., Giménez, A., Moreno, D. A., Díaz-Galiano, F. J., Martínez-Bueno, M. J., Lozano-Pastor, P., and Pascual, J. A. (2023). Organic amendment for disinfecting soil alters the metabolites in Spinacia oleracea. *Agriculture*.13(12):2227. https://doi.org/10.3390/agriculture13122227.

[46] Hidalg, D., Corona, F., and Martín-Marroquín, J. M. (2021). Nutrient recycling: From waste to crop. *Biomass Conversion and Biorefinery*, 11, 207–217. https://doi.org/10.1007/s13399-019-00590-3.

[47] Huang, D., Gao, L., Cheng, M., Yan, M., Zhang, G., Chen, S., Du, L., Wang, G., Li, R., Tao, J., Zhou, W., and Yin, L. (2022). Carbon and N conservation during composting: A review. *Sci Total Environ*. 840:156355. doi: 10.1016/j.scitotenv.2022.156355. Epub 2022 May 30. PMID: 35654189.

[48] Karimi, S., Raza, T., and Mechri, M. (2024). Composting and Vermitechnology in Organic Waste Management. In: Kumar V, Bhat SA, Kumar S, Verma P, editors. *Environmental Engineering and Waste Management*. Cham: Springer; p. 1–20. https://doi.org/10.1007/978-3-031-58441-1_16.

[49] Keng, Z.X., Chong, S., Ng, C.G., Ridzuan, N.I., Hanson, S., Pan, G.-T., Lau, P.L., Supramaniam, C.V., Singh, A., Chin, C.F., Lam, H.L. (2020). Community-scale composting for food waste: A life-cycle assessment-supported case study. *Journal of Cleaner Production*, 261, 121220. https://doi.org/10.1016/j.jclepro.2020.121220.

[50] Kim, E. Y., Hong, Y. K., Lee, C. H., Oh, T. K., and Kim, S. C. (2018). Effect of organic compost manufactured with vegetable waste on nutrient supply and phytotoxicity. *Applied Biological Chemistry*, 61, 509–521. https://doi.org/10.1007/s13765-018-0386-0.

[51] Kluczek-Turpeinen, B., Maijala, P., Hofrichter, M., and Hatakka, A. (2007). Degradation and enzymatic activities of three Paecilomyces inflatus strains grown on diverse lignocellulosic substrates. *International Biodeterioration and Biodegradation*. 59:283–291. https://doi.org/10.1016/j.ibiod.2006.09.007.

[52] Kong Y, Zhang J, Zhang X, Gao X, Yin J, Wang G, Li J, Li G, Cui Z, Yuan J. (2024). Applicability and limitation of compost maturity evaluation indicators: A review. *Chemical Engineering Journal*. 489:151386. https://doi.org/10.1016/j.cej.2024.151386.

[53] Li, M., Li, S., Chen, S., Meng, Q., Wang, Y., Yang, W., Shi, L., Ding, F., Zhu, J., Ma, R., and Guo, X. (2023). Measures for Controlling Gaseous Emissions during Composting: A Review. *International Journal of Environmental Research and Public Health*, 20(4): 3587. https://doi.org/10.3390/ijerph20043587.

[54] Liao, L., Jia, J., Tang, L., Yang, Z., Shen, D., and Long, Y. (2024). Effect of Ventilation Modes on Microplastic Flow During Perishable Waste Composting. *Waste and Biomass Valorization*, 15, 6891–6902. https://doi.org/10.1007/s12649-024-02632-y.

[55] Liu, Z., Zhang, X., Wang, F., Bai, Z., Wang, X., Ma, L. (2025). Stratified aeration supplied an effective way for ammonia and greenhouse gas mitigation in composting. *Environmental Technology and Innovation*, 37, 104055. https://doi.org/10.1016/j.eti.2025.104055.

[56] Lončarić, Z., Galić, V., Nemet, F., Perić, K., Galić, L., Ragályi, P., Uzinger, N., and Rékasi, M. (2024). The Evaluation of Compost Maturity and Ammonium Toxicity Using Different Plant Species in a Germination Test. *Agronomy*. 14(11):2636. https://doi.org/10.3390/agronomy14112636.

[57] Luo, Y., Shen, J., Wang, X., Xiao, H., Yaser, A., and Fu, J. (2024). Recent advances in research on microbial community in the composting process. *Biomass Conv Bioref*. 14:23319–23333. https://doi.org/10.1007/s13399-023-04616-9.

[58] Lynch, N.J., Cherry, R.S. (1996). Design of Passively Aerated Compost Piles: Vertical Air Velocities between the Pipes. In: de Bertoldi, M., Sequi, P., Lemmes, B., Papi, T. (eds) *The Science of Composting. Springer, Dordrecht*. https://doi.org/10.1007/978-94-009-1569-5_93.

[59] Macias-Corral, M. A.; Cueto-Wong, J. A.; Morán-Martínez, J.; Reynoso-Cuevas, L. (2019). Effect of different initial C/N ratio of cow manure and straw on microbial quality of compost. *International Journal*

of Recycling of Organic Waste in Agriculture, 8 (Suppl 1), 357–365. https://doi.org/10.1007/s40093-019-00308-5.

[60] Mahapatra, S., Ali, M. H., Samal, K. (2022). Assessment of compost maturity-stability indices and recent development of composting bin. *Energy Nexus*, 6, 100062. https://doi.org/10.1016/j.nexus.2022.100062.

[61] Mancuso, G., Habchi, S., Maraldi, M., Valenti, F., El Bari, H. (2024). Comprehensive review of technologies for separate digestate treatment and agricultural valorisation within circular and green economy. *Bioresource Technology*, 409, Article 131252. https://doi.org/10.1016/j.biortech.2024.131252.

[62] Manea, E. E., and Popescu, L. M. (2022). Composting as a sustainable method for organic waste management: A review. *Environmental Advances*, 9, Article 100033. https://doi.org/10.1016/j.envadv.2022.100033.

[63] Manea, E. E., Bumbac, C., Dinu, L. R., Bumbac, M., Nicolescu, C. M. (2024). Composting as a sustainable solution for organic solid waste management: Current practices and potential improvements. *Sustainability*, 16(15), 6329. https://doi.org/10.3390/su16156329.

[64] Manyapu, V., Sh, S., Kumar, S., and Rajendra, K. (2017). In-vessel composting: a rapid technology for conversion of biowaste into compost. *Open Access International Journal of Science and Engineering.* 2. 58-63.

[65] Martín-Ramos, P., Martín-Gil, J. (2020). Facile monitoring of the stability and maturity of compost through fast analytical instrumental techniques. In M. Meghvansi and A. Varma (Eds.), *Biology of Composts* (Soil Biology), Vol. 58. Springer, Cham. https://doi.org/10.1007/978-3-030-39173-7_8.

[66] Mehta, C. M., Palni, U., Franke-Whittle, I. H., Sharma, A. K. (2014). Compost: Its role, mechanism and impact on reducing soil-borne plant diseases. *Waste Management*, 34(3), 607–622. https://doi.org/10.1016/j.wasman.2013.11.012.

[67] Mengistu, T., Gebrekidan, H., Kibret, K., Woldetsadik, K., Shimelis, B., and Yadav, H. (2018). Comparative effectiveness of different composting methods on the stabilization, maturation and sanitization of municipal organic solid wastes and dried faecal sludge mixtures. *Environmental Systems Research*, 6, Article 5. https://doi.org/10.1186/s40068-017-0079-4.

[68] Mishra, S.K., Yadav, K.D. (2022). Assessment of the effect of particle size and selected physico-chemical and biological parameters on the efficiency and quality of composting of garden waste. *Journal of Environmental Chemical Engineering*, *10*(3), 107925. https://doi.org/10.1016/j.jece.2022.107925.

[69] Miyamoto, H., Suda, W., Kodama, H., Takahashi, H., Nakanishi, Y., Moriya, S., Adachi, K., Kiriyama, N., Wada, M., Sudo, D., Ito, S., Shibata, M., Wada, S., Murano, T., Taguchi, H., Shindo, C., Tsuboi, A., Tsuji, N., Matsuura, M., and Ohno, H. (2022). A novel sustainable role of compost as a universal protective substitute for fish, chicken, pig, and cattle, and its estimation by structural equation modeling. 10.48550/arXiv.2201.10895.

[70] Mohite, D. D., Chavan, S. S., Jadhav, V. S., Kanase, T., Kadam, M. A., and Singh, A. S. (2024). Vermicomposting: A holistic approach for sustainable crop production, nutrient-rich bio fertilizer, and environmental restoration. *Discover Sustainability*, 5, article 60. https://doi.org/10.1007/s43621-024-00245-y.

[71] Nemet, F., Perić, K., Lončarić, Z. (2021). Microbiological activities in the composting process – A review. *COLUMELLA – Journal of Agricultural and Environmental Sciences*, 8(2), 41–53. https://doi.org/10.18380/SZIE.COLUM.2021.8.2.41.

[72] Nenciu, F., Stanciulescu, I., Vlad, H., Gabur, A., Turcu, O. L., Apostol, T., Vladut, V. N., Cocarta, D., and Stan, C. (2022). Decentralized Processing Performance of Fruit and Vegetable Waste Discarded from Retail, Using an Automated Thermophilic Composting Technology, *Sustainability*, Volume: 14 (5), Article Number: 2835, https://doi.org/10.3390/su14052835.

[73] Nenciu, F., Vladut, V. (2021). Studies on the perspectives of replacing the classic energy plants with Jerusalem artichoke and sweet sorghum, analyzing the impact on the conservation of ecosystems. In IOP *Conference Series: Earth and Environmental Science*, Vol. 635, Article 012002*). IOP Publishing*. https://doi.org/10.1088/1755-1315/635/1/012002.

[74] Niladri, P., Giri, U., Roy, G. (2019). Composting. *IntechOpen*. doi: 10.5772/intechopen.88753.

[75] Obuobi, B., Zhang, Y., Adu-Gyamfi, G., Nketiah, E., Grant, M., Adjei, M., Cudjoe, D. (2022). Fruits and vegetable waste management behavior among retailers in Kumasi, Ghana. *Journal of Retailing and Consumer Services*, 67, 102971. https://doi.org/10.1016/j.jretconser.2022.102971.

[76] Oueld Lhaj, M., Moussadek, R., Zouahri, A., Sanad, H., Saafadi, L., Mdarhri Alaoui, M., Mouhir, L. (2024). Sustainable agriculture through agricultural waste management: A comprehensive review of composting's impact on soil health in Moroccan agricultural ecosystems. *Agriculture*, 14(12), 2356. https://doi.org/10.3390/agriculture14122356.

[77] Oñiguez, G., Gomez Rizo, R., Ramírez-Meda, W., and Bernal-Casillas, J. (2018). Composting of Food and Yard Wastes under the Static Aerated Pile Method. *Advances in Chemical Engineering and Science*. 08. 271-279. https://doi.org/10.4236/aces.2018.84019.

[78] Pane, C., Palese, A., Spaccini, R., Piccolo, A., Celano, G., and Zaccardelli, M. (2016). Enhancing sustainability of a processing tomato cultivation system by using bioactive compost teas. *Scientia Horticulturae*, 202, 117–124. https://doi.org/10.1016/j.scienta.2016.02.034.

[79] Parihar, P., and Sharma, S. (2021). Composting: A better alternative of chemical fertilizer. *IOP Conference Series: Earth and Environmental Science*, 795, 012038. https://doi.org/10.1088/1755-1315/795/1/012038.

[80] Pathak, S., Pipariya, S. (2025). Impact of Indore's waste management practices on environmental sustainability. *International Journal of Arts, Humanities and Social Science*, 7(1), 447–450. https://doi.org/10.33545/26648652.2025.v7.i1f.207.

[81] Patra, K., Parihar, R. (2023). Enhancing soil fertility and crop nutrition through vermicomposting. *International Journal of Agriculture and Nutrition*, 5(2), 114–117. https://doi.org/10.33545/26646064.2023.v5.i2b.168.

[82] Pergola, M., Persiani, A., Palese, A. M., Di Meo, V., Pastore, V., D'Adamo, C., Celano, G. (2018). Composting: The way for a sustainable agriculture. *Applied Soil Ecology*, 123, 744–750. https://doi.org/10.1016/j.apsoil.2017.10.016.

[83] Plazzotta, S., Manzocco, L., Nicoli, M. (2017). Fruit and vegetable waste management and the challenge of fresh-cut salad. *Trends in Food Science and Technology*, *63*. https://doi.org/10.1016/j.tifs.2017.02.013.

[84] Ponsá, S., Pagans, E., Sánchez, A. (2009). Composting of dewatered wastewater sludge with various ratios of pruning waste used as a bulking agent and monitored by respirometer. *Biosystems Engineering*, *102*, 433-443. https://doi.org/10.1016/j.biosystemseng.2009.01.002.

[85] Popa, L.-D., Isticioaia, S.-F., Vladut, N.-V., Matei, G., Leonte, A., Gageanu, I., Nenciu, F., Pintilie, P.-L., Pintilie, A.-S., and Milea, O. (2023). The multiple applications of industrial hemp (cannabis sativa l.) in the context of sustainable development. *INMATEH - Agricultural Engineering*, 75(1). DOI: https://doi.org/10.35633/inmateh-75-88.

[86] Poornima, S., Dadi, M., Subash, S., Manikandan, S., Karthik, V., Deena, S.R., Balachandar, R., Kumaran, S.K.N., and Subbaiya, R. (2024). Review on advances in toxic pollutants remediation by solid waste composting and vermicomposting. *Scientific African*, *23*, e02100. https://doi.org/10.1016/j.sciaf.2024.e02100.

[87] Puntsag, O., Olzii, M., Altansuvd, J. (2022). The evaluation of fertilizer made from vegetable waste from the food markets in Ulaanbaatar, Mongolia. *International Journal of Advanced Research*, *10*(1), 715–720. https://www.journalijar.com.

[88] Pragati, K., and Devendra, D. (2020). Study of Composting for Municipal Organic Waste A Review, *International journal of engineering research and technology* (IJERT). 9(11).

[89] Qasim, W., Lee, M. H., Moon, B. E., Okyere, F. G., Khan, F., Nafees, M., and Kim, H. T. (2018). Composting of chicken manure with a mixture of sawdust and wood shavings under forced aeration in a closed reactor system. *International Journal of Recycling of Organic Waste in Agriculture*, *7*, 261–267. https://doi.org/10.1007/s40093-018-0212-z.

[90] Rajin, M., Saalah, S., Atinin, E. S., and Shafizan, S. N. M. (2025). Mesophilic Composting of Vegetable Waste Using a Passive Aerated Static Bioreactor: Simultaneous Production of Compost and Leachate. În: Yaser, A.Z.; Abu Samah, M.A.; Ariffin, F.; Haghi, A.K. (eds), *Controlling Environmental Pollution*, pp. 341–353. Springer, Singapore. https://doi.org/10.1007/978-981-97-8931-3_19.

[91] Rasapoor, M.; Nasrabadi, T.; Kamali, M.; Hoveidi, H. (2009). The effects of aeration rate on generated compost quality, using aerated static pile method. Waste Management, 29(2), 570–573. https://doi.org/10.1016/j.wasman.2008.04.012.

[92] Rawoteea, S.A., Mudhoo, A., Kumar, S. (2017). Co-composting of vegetable wastes and carton: Effect of carton composition and parameter variations. *Bioresource Technology*, *227*, 171–178. https://doi.org/10.1016/j.biortech.2016.12.019.

[93] Raza, S.T., Wu, J., Rene, E.R., Ali, Z., Chen, Z. (2022). Reuse of agricultural wastes, manure, and biochar as an organic amendment: A review on its implications for vermicomposting technology. *Journal of Cleaner Production*, 360, 132200. https://doi.org/10.1016/j.jclepro.2022.132200.

[94] Rehman, S., De Castro, F., Aprile, A., Benedetti, M., Fanizzi, F.P. (2023). Vermicompost: Enhancing Plant Growth and Combating Abiotic and Biotic Stress. *Agronomy*, *13*(4), 1134. https://doi.org/10.3390/agronomy13041134.

[95] Riaz, U., Iqbal, S., Rafi, F., Batool, M., Manzoor, N., Ashraf, W., Murtaza, G. (2021). Values of Composting. In *Environmental Engineering and Waste Management*. Springer. https://doi.org/10.1007/978-3-030-61010-4_9.

[96] Sanadi, N.F.A., Fan, Y.V., Lee, C.T., Ibrahim, N., Li, C., Gao, Y., Ong, P.Y., and Klemes, J.J. (2019). Nutrient in Leachate of Biowaste Compost and its Availability for Plants. *Chemical Engineering Transactions*, *76*, 1369–1374. https://doi.org/10.3303/CET1976229.

[97] Sánchez, A. (2022). Decentralized Composting of Food Waste: A Perspective on Scientific Knowledge. *Frontiers in Chemical Engineering*, *4*, 850308. https://doi.org/10.3389/fceng.2022.850308.

[98] Sánchez, Ó.J., Ospina, D.A., and Montoya, S. (2017). Compost supplementation with nutrients and microorganisms in composting process. *Waste Management*, *69*, 136–153. https://doi.org/10.1016/j.wasman.2017.08.012.

[99] Sarkar, S., Pal, S., Chanda, S. (2016). Optimization of a vegetable waste composting process with a significant thermophilic phase. *Procedia Environmental Sciences*, *35*, 435–440. https://doi.org/10.1016/j.proenv.2016.07.026.

[100] Sathiyapriya, S., Prabhaharan, J., Samuel, S., Anandham, R., Ilamaran, M. (2024). Nutrient recycling through composting: Harnessing agricultural wastes for sustainable crop production. *Plant Science Today*, *11*. https://doi.org/10.14719/pst.5627.

[101] Savage, G.M. (1996). The Importance of Waste Characteristics and Processing in the Production of Quality Compost. In de Bertoldi, M., Sequi, P., Lemmes, B., and Papi, T. (Eds.), *The Science of Composting*. Springer, Dordrecht. https://doi.org/10.1007/978-94-009-1569-5_76.

[102] Schrader, J., McCabe, K., Grewell, D., and Graves, W. (2015). Bioplastics and biocomposites for sustainable horticultural containers: Performance and biodegradation in home compost. *Acta horticulturae, In press*. https://doi.org/10.17660/ActaHortic.2017.1170.142.

[103] Shen, B., Zheng, L., Zheng, X., Yang, Y., Xiao, D., Wang, Y., Sheng, Z., Ai, B. (2024). Insights from meta-analysis on carbon to nitrogen ratios in aerobic composting of agricultural residues. *Bioresource Technology*, 413, 131416. https://doi.org/10.1016/j.biortech.2024.131416.

[104] Siciliano, A., Limonti, C., Curcio, G.M., Calabrò, V. (2019). Biogas Generation through Anaerobic Digestion of Compost Leachate in Semi-Continuous Completely Stirred Tank Reactors. *Processes*, 7(9), 635. https://doi.org/10.3390/pr7090635.

[105] Sole-Mauri, F., Illa, J., Magrí, A., Prenafeta-Boldú, F.X., Flotats, X. (2007). An integrated biochemical and physical model for the composting process. *Bioresource Technology*, 98(17), 3278–3293. https://doi.org/10.1016/j.biortech.2006.07.012.

[106] Somera, T., Mazzola, M., Cook, C. (2023). Directing the Apple Rhizobiome toward Resiliency Post-Fumigation. *Agriculture*, 13(11), 2104. https://doi.org/10.3390/agriculture13112104.

[107] Stentiford, E., Sánchez-Monedero, M.A. (2016). Past, present, and future of composting research. *Acta Hortic.*, (1146). https://doi.org/10.17660/ActaHortic.2016.1146.1.

[108] Sun, L., Guan, W., Tai, X., Qi, W., Zhang, Y., Ma, Y., Sun, X., Lu, Y., and Lin, D. (2025). Research Progress on Microbial Nitrogen Conservation Technology and Mechanism of Microorganisms in Aerobic Composting. *Microbial Ecology*, 88, article 19. https://doi.org/10.1007/s00248-025-02513-4.

[109] Sun, L., Long, M., Li, J., Wu, R., Ma, L., Tang, D., Lu, Y., and Wang, Z. (2021). Different Effects of Thermophilic Microbiological Inoculation With and Without Biochar on Physicochemical Characteristics and Bacterial Communities in Pig Manure Composting. *Frontiers in Microbiology*, 12:746718. https://doi.org/10.3389/fmicb.2021.746718.

[110] Ștefan, V., Zaica, A., Iosif, A. (2021). Research on the uniformity degree of solid organic fertilizers distribution. *INMATEH Agricultural Engineering*. 495-504. https://doi.org/10.35633/inmateh-65-51.

[111] Thakur, A., Kumar, A., Chava, V., Kumar, B., Kiran, S., Kumar, V., Athokpam, V. (2021). A Review on Vermicomposting: By-products and Its Importance. *Plant Cell Biotechnology and Molecular Biology*, 22, 156–164.

[112] Tiquia-Arashiro, S., Tam, N. (2002). Characterization and composting of poultry litter in forced aeration piles. *Process Biochemistry*, 37, 869–880. https://doi.org/10.1016/S0032-9592(01)00274-6.
[113] Verma, S., Marschner, P. (2013). Compost effects on microbial biomass and soil P pools as affected by particle size and soil properties. *Journal of Soil Science and Plant Nutrition*, 13, 313–328. https://doi.org/10.4067/S0718-95162013005000026.
[114] Veeken, A. H. M., Timmermans, J., Szanto, G. L., and Hamelers, H. V. M. (2003). Design of passively aerated compost systems on the basis of compaction–porosity–permeability data. In ORBIT 2003, Biological Processing of Organics (pp. 75–85).
[115] Vilela, R.N.S., Orrico, A.C.A., Orrico Junior, M.A.P., Borquis, R.R.A., Tomazi, M., Oliveira, J.D., Ávila, M.R., dos Santos, F.T., Leite, B.K.V. (2022). Effects of aeration and season on the composting of slaughterhouse waste. *Environmental Technology and Innovation*, *27*, 102505. https://doi.org/10.1016/j.eti.2022.102505.
[116] Vladut, N.-V., Ungureanu, N., Biriş, S.-Ş., Voicea, I., Nenciu, F., Găgeanu, I., Cujbescu, D., Popa, L.-D., Boruz, S., Matei, G., Ekielski, A., and Teliban, G.-C. (2023b). Research on the identification of some optimal threshing and separation regimes in the axial flow apparatus. *Agriculture*, 13(4). https://doi.org/10.3390/agriculture13040838
[117] Vladut, N.-V., Atanasov, A., Ungureanu, N., Ivascu, L.-V., Cioca, L.-I., Popa, L.-D., Matei, G., Boruz, S., Cerempei, V., Titei, V., Nenciu, F., Milea, O.-E., Dumitru, S., and Caba, I. (2024). Trends in the development of conservation/ecological agriculture in the context of current climate change – A review. INMATEH – *Agricultural Engineering*, 74(3). https://doi.org/10.35633/inmateh-74-86.
[118] Vladut, N.-V., Biriş, S.-Şt., Paraschiv, G., Ungureanu, N., Bungescu, S.-T., Voicea, I., Cujbescu, D., Găgeanu, I., Laza, E., Popa, L.-D., Matei, G., Lateş, D., and Atanasov, A. (2023). Considerations regarding the effects of shock and vibration on operators of self-propelled agricultural equipment. *INMATEH – Agricultural Engineering* 71 (3), pp. 823-836. https://doi.org/10.35633/inmateh-71-74.
[119] Voicea, I., Nenciu, F., Vladut, N.-V., Matache, M.-G., Persu, C., Cujbescu, D. (2024). Exploring a Self-Sufficiency Approach within a Sustainable Integrated Pisciculture Farming System. *Sustainability*, 16(18), 8055. https://doi.org/10.3390/su16188055.
[120] Vuković, A., Velki, M., Ečimović, S., Vuković, R., Štolfa Čamagajevac, I., Lončarić, Z. (2021). Vermicomposting-Facts, Benefits and Knowledge Gaps. *Agronomy*, 11(10), 1952. https://doi.org/10.3390/agronomy11101952.
[121] Wang, Q., Awasthi, M. K., Ren, X., Zhao, J., Wang, M., Chen, H., and Zhang, Z. (2018). Recent Advances in Composting of Organic and Hazardous Waste: A Road Map to Safer Environment. În: Varjani, S., Parameswaran, B., Kumar, S., Khare, S. (eds), *Biosynthetic Technology and Environmental Challenges (Energy, Environment, and Sustainability)*, pp. 307–329. Springer, Singapore. https://doi.org/10.1007/978-981-10-7434-9_17.
[122] Waqas, M., Hashim, S., Humphries, U.W., Ahmad, S., Noor, R., Shoaib, M., Naseem, A., Hlaing, P.T., Lin, H.A. (2023). Composting Processes for Agricultural Waste Management: A Comprehensive Review. *Processes*, 11(3), 731. https://doi.org/10.3390/pr11030731.
[123] Zafar, S. (2022). Introduction to composting. *EcoMENA*. https://www.ecomena.org/composting/.
[124] Zaghloul, A., Saber, M., Abd-El-Hady, M. (2019). Physical indicators for pollution detection in terrestrial and aquatic ecosystems. *Bull Natl Res Cent*, 43, 120. https://doi.org/10.1186/s42269-019-0162-2.
[125] Zainudin, M.H.M., Zulkarnain, A., Azmi, A.S., Muniandy, S., Sakai, K., Shirai, Y., Hassan, M.A. (2022). Enhancement of Agro-Industrial Waste Composting Process via the Microbial Inoculation: A Brief Review. *Agronomy*, 12(1), 198. https://doi.org/10.3390/agronomy12010198.
[126] Zhang, L., Yan, C., Guo, Q., Zhang, J., and Ruiz-Menjivar, J. (2018). The impact of agricultural chemical inputs on environment: global evidence from informetrics analysis and visualization. *Int J Low-Carbon Technol*. 338–352. https://doi.org/10.1093/ijlct/cty039.
[127] Zhang, Z., Zu, G., Liu, Q., Liu, Y., Xi, B., Dang, Q., Su, J. (2024). Confirming the key factors influencing the biosynthesis and regulation of organic nitrogen in composting. *SSRN*. https://ssrn.com/abstract=5035589 or http://dx.doi.org/10.2139/ssrn.5035589.
[128] Zhang, Z., Zu, G., Liu, Q., Liu, Y., Xi, B., Dang, Q., and Su, J. (2025). Confirming the key factors influencing the biosynthesis and regulation of organic nitrogen in composting. *J Environ Manage*. https://doi.org/10.1016/j.jenvman.2025.124436.
[129] ***Opanatura. (n.d.). Compost and composting. Retrieved from https://opanatura.com/compost-and-composting/.

RESEARCH AND EXPERIMENT OF RAPID DISENGAGEMENT SYSTEM FOR KELP SEEDLING ROPES BASED ON A LOCKING DEVICE

/

基于锁扣结构的海带苗绳快速脱扣技术研究与试验

Zehao ZHA[1)], Jianning YIN[1)], Qiming YU[1)], Pengxuan GUAN[1)], Yipeng CUI[1)], Xian WANG[1)], Xinxin WANG[1)], Tongfei SHENG[2)], Duanyang GENG[1*)]

[1)] School of Agricultural Engineering and Food Science, Shandong University of Technology, Zibo 255000, China

[2)] Weihai Renhe Electromechanical Co., Ltd., Weihai Shandong 264200, China

[*)] *Corresponding authors. Tel.: +86 13668641238; E-mail address: dygxt@sdut.edu.cn (D.Y. Geng).*

DOI: https://doi.org/10.35633/inmateh-76-110

Keywords: *kelp harvesting, locking device, disengagement device, seedling rope disengagement, Programmable Logic Controller (PLC) control*

ABSTRACT

In China's algae farming, ropes are widely used for seedling cultivation and suspension, requiring fast and reliable uncoupling during harvest. However, current kelp harvesting faces issues like complex rope connections, low unlocking efficiency, and poor reusability. To address this, a PLC-controlled rapid disengagement system was developed. The proposed system employs a button with self-locking functionality, coupled with a magnetically controlled disengagement device, to achieve automated unfastening of seedling ropes without damaging the suspension rope. The paper presents the components and operating principle of the locking device. To address the force characteristics of the seedling rope during the disengagement process, a dual-fingered pusher configuration was designed. The use of an involute trajectory enabled stable extraction of the rope from the locking groove. A Delta PLC was employed as the central controller, and an execution system comprising of an electric push rod, proximity sensors, magnetic adsorption module, and rope-pulling motor was developed to achieve automated control of lock correction, magnetic positioning, unlocking, and rope disengagement. Experimental results indicated that the system achieved the highest disengagement success rate of 96.67% when the guiding slot clearance was 14 mm, the haulage rope speed was 40 mm/s, and the pusher length was 45 mm, demonstrating stable and reliable device performance.

摘 要

在我国海藻养殖过程中，绳索广泛应用于苗体的吊挂和培育，收获阶段对苗绳与绠绳的快速可靠脱扣提出了更高要求。然而，当前海带收获普遍存在连接方式复杂、解扣效率低、结构不可重复使用等问题。为此，本文开发了一种基于 PLC 控制的海带苗绳快速脱扣系统。该系统采用具有自锁功能的按钮结构，结合磁控脱扣装置，实现苗绳在不损伤吊绳的前提下自动解扣。文中介绍了锁扣结构的组成与工作原理。针对苗绳在脱扣过程中的受力特性，设计了双拨指结构，并利用渐开线轨迹实现苗绳从挂接槽中的稳定拨出。控制系统以台达 PLC 为核心，配套电动推杆、接近传感器、磁吸模块及拨绳电机，实现了锁扣矫正、磁吸定位、解锁与苗绳脱出的全流程自动控制。试验结果表明，当导向槽间隙为 14 mm、绠绳行进速度为 40 mm/s、拨指长度为 45 mm 时，系统脱扣成功率最高可达 96.67%，装置运行稳定可靠。

INTRODUCTION

Kelp is a type of large brown seaweed that primarily grows in cold marine environments and represents one of the most important economic algal resources *(Branch et al. 2023; Forbes et al. 2022; Grebe et al. 2019)*. In recent years, with the rapid development of the kelp industry, the scale of aquaculture has expanded annually, positioning China as the global leader in kelp production *(Hewei et al., 2020; Zimin et al., 2021)*. According to statistics, China's total kelp output reached 1.6 million tonnes in 2022, accounting for 89.4% of the global production, which presents significant technical challenges for kelp cultivation and harvesting *(Zimin et al. 2023)*. Currently, kelp harvesting largely depends on manual labor or semi-mechanized equipment *(Mac Monagail et al., 2017; Tullberg et al., 2022)*. Particularly, the connection and disconnection between seedling ropes and haulage or suspension ropes are commonly performed through manual knotting and unfastening. This process is not only labor-intensive, time-consuming, and inefficient, but also poses safety risks *(Mac Monagail et al., 2017; Yongming et al., 2020)*, making it inadequate for meeting the development needs of the modern kelp industry *(Bak et al., 2018)*. Therefore, the development of a rapid disengagement system for seedling ropes from haulage and suspension ropes is crucial to addressing these challenges.

Extensive research has been conducted by both domestic and international scholars to address the technical challenges associated with mechanizing kelp harvesting. For instance, in Norway was developed an articulated crane system for the efficient harvesting of wild kelp *(Peteiro et al., 2016; Vea and Ask, 2010)*, which is suitable only for naturally grown kelp without seedling ropes and thus is ineffective for China's flat-raft kelp cultivation model *(Zongyu et al., 2018)*. In China, various kelp harvesting machines have also been developed, such as rope-hook integrated harvesters, yet the separation of seedling ropes from haulage ropes still relies entirely on manual operation. Jiang Tao's team developed an automatic towing-type kelp harvesting vessel and a kelp harvest and transfer device *(Tao et al., 2020; Tao et al., 2022; Yongming et al., 2018)*, but it is poorly compatible with standard flat-raft cultivation systems. Liu Hewei and colleagues designed a bionic kelp harvester based on the motion analysis of manual harvesting *(Hewei and Bin, 2020)*. These devices enable large-scale kelp harvesting, but still face issues in practice, such as difficulties in separating seedling or suspension ropes from haulage ropes and unstable operational performance. Clearly, with the rapid advancement of automation and intelligent technologies, developing an integrated automated and mechanized rapid unlocking system is crucial for the efficient separation of seedling and haulage ropes.

In light of these challenges, this study aims to develop a rapid disengagement system for seedling ropes to improve the efficiency, automation, and reliability of kelp harvesting. The proposed solution focuses on enabling automated separation between seedling and haulage ropes under complex working conditions, ensuring operational stability while reducing labor intensity and time consumption. By addressing the bottleneck of manual disengagement, the research provides a practical foundation for the mechanization and intelligent transformation of kelp harvesting processes.

MATERIALS AND METHODS

Overall structure and working principle

As shown in Figure 1, the test platform for the rapid disengagement of kelp seedling ropes mainly consists of a motor, flared guiding slot, electric push rod, magnet, proximity sensor, and control unit.

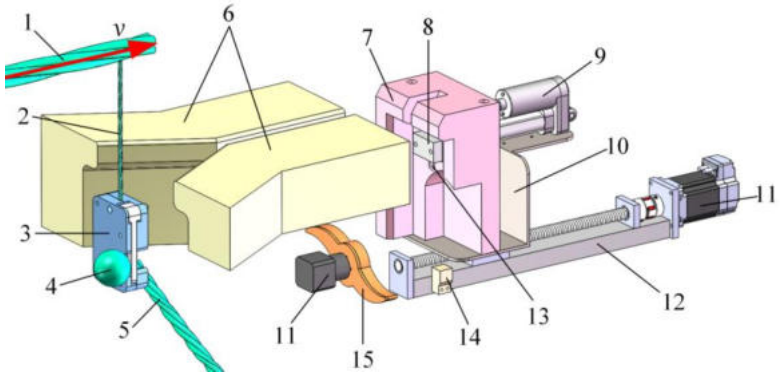


Fig. 1 - Schematic diagram of the complete machine structure

1 - Haulage rope; 2 - Suspension rope; 3 - Locking device; 4 - Seedling rope knot; 5 - Seedling rope; 6 - Flared guiding slot; 7 - Blocking plate; 8 - Magnet; 9 - Electric push rod; 10 - Supporting plate; 11 - Stepper motor; 12 - Lead screw; 13 - Proximity sensor; 14 - Metal sensing switch; 15 - Pusher

During the simulation operation, the winch system drives the haulage rope forward, the lead screw moves the blocking plate to the initial position, and the locking device connected to the haulage rope enters the flared guiding slot. It is then guided into a slot of equal width to the quick-locking device under the constraint of the flared slot. Since both ends of the seedling rope are connected to the suspension rope via locking devices, its posture can only be maintained with the contact point oriented forward. This ensures that the locking device enters the disengagement region on the blocking plate with the same posture. When the locking device enters the effective magnetic range, it is attracted to the blocking plate aligned with the electric push rod. The electric push rod then drives the locking device toward the blocking plate, and upon contact, the blocking plate applies pressure to the button on the locking device, triggering the release of the internal locking device and completing the unlocking operation. Once the locking device engages the proximity sensor, the motor drives the pusher to rotate, dislodging the knotted seedling rope from the unlocked locking device. After disengagement, the lead screw retracts the blocking plate, releasing the locking device from the magnetic holding area and restoring its freedom of movement. Then, the haulage rope moves diagonally upward, carrying the disengaged locking device away from the device, thus preparing space for the next disengagement operation.

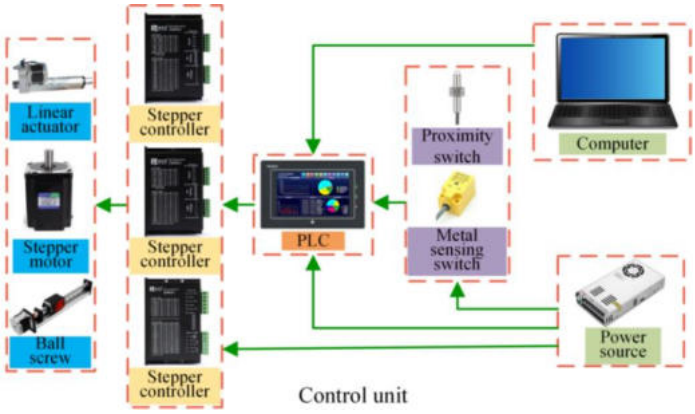
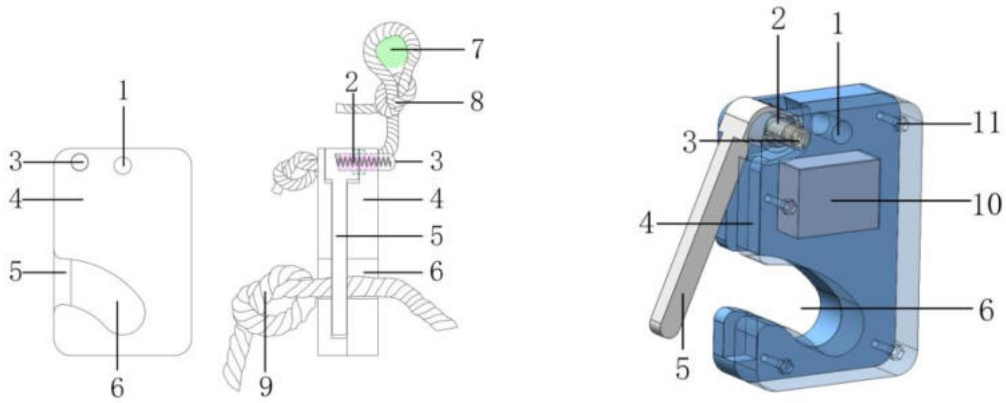


Fig. 2 - Control unit of the disengagement device

Study of key components and mechanisms

Determination of the locking device

To achieve rapid disengagement of the seedling rope from the haulage rope, a quick-release structure, as illustrated in Figure 3, was developed. It mainly consists of a housing, button, torsion spring, latch, and iron block. The locking device functions through a button-triggered quick-release mechanism. When external pressure is applied to the button, its internal protrusion disengages from the limit groove in the housing. This disengagement removes the mechanical constraint on the latch, allowing it to rotate under the restoring force of the torsion spring. As the latch opens, the seedling rope locking channel is released, enabling the pusher to separate the rope from the haulage system. It can significantly improve the efficiency of separating the seedling rope from the haulage rope.



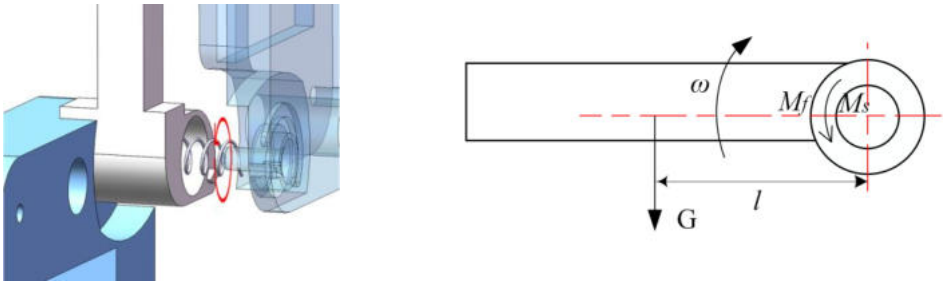
(a) Schematic diagram of the planar structure (b) Schematic diagram of the 3D structure

Fig. 3 - Structural diagram of the locking device for kelp seedling ropes

1 - Suspension rope connection hole; 2 - Torsion spring; 3 - Button; 4 - Housing; 5 - Latch; 6 - Seedling rope locking groove; 7 - Haulage rope; 8 - Suspension rope; 9 - Seedling rope; 10 - Iron block; 11 - Housing mounting hole

Analysis of torsion spring torque and button loading

From the above structure, the torsion spring is the key to the instantaneous opening of the latch, as shown in Figure 4 and Figure 5. During operation, when the locking structure moves to the position of the magnet-equipped blocking plate, it is firmly attracted to the plate by magnetic force. The plate then depresses the button on the locking structure, driving the internal protrusion out of the button limiting slot in the housing. The latch thereby loses the constraint of the protrusion and, under the torque of the torsion spring, instantly rotates by an angle, thus opening the seedling-rope engagement channel.



(a) Pre-rotational installation of torsion spring (b) Simplified force diagram of the latch

Fig. 4 - Diagram of torsion spring installation and latch force analysis

Evidently, the torsional moment of the torsion spring is critical to reliably opening the seedling-rope engagement channel. To ensure the spring has sufficient capacity to actuate the latch, a torque analysis of the latch is conducted:

$$\begin{cases} M_g = Gl \\ M_s = k\theta \\ M_s = M_g + M_f \end{cases} \quad (1)$$

where: M_g is the gravitational torque caused by its own weight, Nm; G is the weight of the latch, N; l is the distance from the latch centroid to the rotation center, m; M_s is the torsion spring moment, Nm; k is the torsional stiffness of the torsion spring, N·m/(°); θ is the torsional angle of the spring, (°); M_f is the frictional moment at the latch ends, Nm.

During rotation, only the two end faces of the latch seat contact the housing, so friction and a corresponding frictional torque act at these faces. To ensure that the latch opens stably and holds its position—and to avoid re-closure even in the event of a sudden torsion-spring failure—the minimum frictional torque between the latch and the housing should equal the gravitational torque of the latch; thus, we have:

$$M_f = M_g \quad (2)$$

To compute the minimum torsion-spring torque, substituting Equation (2) into Equation (1) yields the spring torque as:

$$M_s = M_g + M_f = 2M_g \quad (3)$$

Considering system reliability and the influence of the operating environment, we set:

$$M_s = n(M_g + M_f) = 2nM_g \quad (4)$$

where: n is the safety factor for system operation, and in this study, considering both the load magnitude and the working environment, n is set to 2.5. Thus, we have:

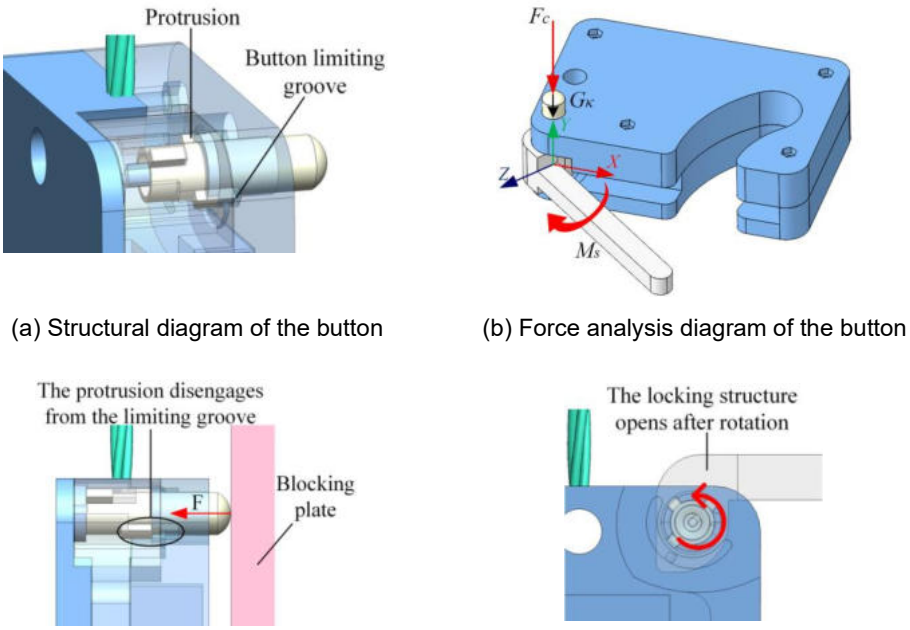
$$M_s = k\theta = 5M_g \quad (5)$$

According to the torque calculation formula of the torsion spring, it results:

$$k = \frac{5Gl}{\theta} \quad (6)$$

For simplicity, it is assumed that once the latch-locking button is released, the latch can rotate by 90°. Clearly, the longer the latch, the greater its weight and the larger the required torsion-spring stiffness coefficient k; conversely, a shorter latch requires a smaller stiffness k.

The detailed structure of the button is shown in Figure 5(a). The button is the key component for unlocking the locking structure. Its core function is to apply pressure to the button, causing the protrusion on it to disengage from the button limiting slot inside the locking structure housing, allowing the torsion spring to release its rotational force, transferring the force to the button. The button then drives the latch to rotate, opening the locking structure. As shown in Figure 5(b), the button is mainly influenced by the pressure from the blocking plate, its own weight, and the torsion spring moment.



(a) Structural diagram of the button

(b) Force analysis diagram of the button

(c) The blocking plate applying pressure to the button

(d) Rotation to open after disengaging from the limiting groove

Fig. 5 - Schematic diagram of the button structure and unlocking process

As shown in Figure 5(c), when the button contacts the blocking plate, it is subjected to a compressive load determined by the contact force between the button and the plate. Thus:

$$F_c = k_\delta \cdot \Delta x \tag{7}$$

where: F_c is the compressive force applied by the blocking plate to the button, N; k_δ is the contact stiffness coefficient, N/m; Δx is the displacement of the button under the applied load, m.

The contact stiffness is:

$$k_\delta = \frac{G_\delta d^4}{8D^3\eta} \tag{8}$$

where:

G_δ is the shear modulus of the material, MPa; d is the spring wire diameter, m; D is the mean coil diameter, m; and η is the number of active turns.

Since the button's position within the button limiting slot is influenced by external forces, the vertical force on the button can be estimated as:

$$F_0 = \frac{G_\delta d^4}{8D^3\eta} \cdot \Delta x + G_\kappa \tag{9}$$

where:

F_0 is the force exerted by the button in the vertical direction, N; G_κ is the self-gravity of the button, N.

Study on the Rapid Disengagement Device

Study on the Flared Guiding Slot

During the kelp harvesting process, the seedling rope is kept under tension with the locking device due to the weight of the kelp, which causes the locking device to assume a tilted angle. To ensure a smooth transition of the locking device from its inclined initial posture to the vertical constrained disengagement position, the flared guiding slot must have continuous posture adjustment capability. Therefore, the inner surface of the flared guiding slot is designed as a helical surface with spatially varying geometry, incorporating a bivariate design that controls both angular orientation and radial offset, to enhance the stability of lock insertion and the precision of disengagement.

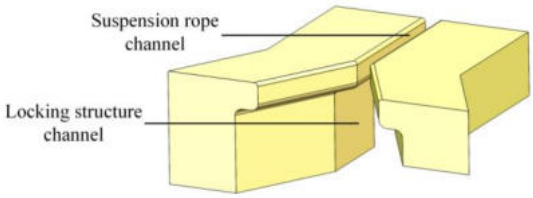
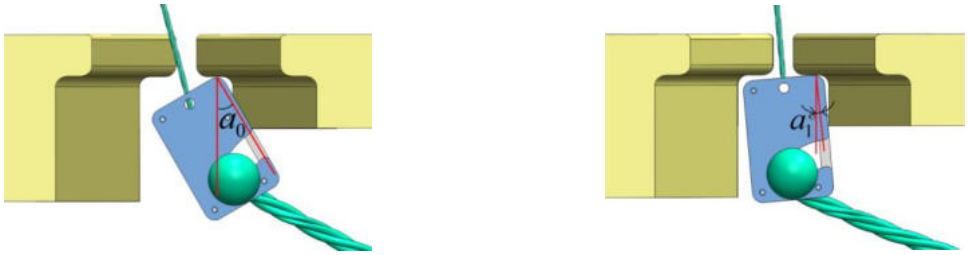


Fig. 6 - Structure of the flared guiding slot



(a) Initial angle of the locking device

(b) Angle of the locking device after being guided through the constricted slot

Fig. 7 - Comparison of the locking device before and after posture adjustment in the guiding slot

Having L as the length of the guiding slot, and defining a parametric surface over u that belongs to $[0, L]$, then a helical surface with simultaneous variation in radial distance and angular orientation is obtained.

$$\begin{cases} x(u,v) = u \\ y(u,v) = r(u)\cos(\theta(u)) + v \cdot \cos(\theta(u)) \\ z(u,v) = r(u)\sin(\theta(u)) + v \cdot \sin(\theta(u)) \end{cases} \tag{10}$$

where: u is the advancement coordinate of the locking device along the guiding slot, v belongs to $[-w/2, w/2]$ is the variable along the width direction of the guiding slot wall surface, $r(u)$ is the radial offset function between the guiding slot wall and the central axis, $\theta(u)$ is the angular orientation function of the posture, w is the maximum lateral dimension of the locking device.

To achieve a smooth transition of the angle from a_0 to a_1 (see fig.7), a fifth-order Bezier function is introduced.

$$\theta(u) = \sum_{i=0}^{5} B_{i,5}(t) \cdot \theta_i, t = \frac{u}{L} \tag{11}$$

where: θ_i are the six control angle points of the fifth-order Bezier curve, The variable t ranges from [0, 1] and controls the distribution of points along the curve between the given control points, $B_{i,5}(t)$ is the Bernstein basis function, defined as:

$$B_{i,5}(t) = \binom{5}{i}(1-t)^{5-i} t^i \tag{12}$$

Similarly, to achieve a gradually narrowing design of the guiding slot width, the radial offset function $r(u)$ is expressed using a second-order Bezier curve.

$$r(u) = (1-t)^2 r_0 + 2(1-t)t r_m + t^2 r_1, t = \frac{u}{L} \tag{13}$$

where: r_0 is the radius at the entrance of the guiding slot, r_m is the radius at the middle section of the guiding slot, r_1 is the radius at the end of the guiding slot.

Study on the Pusher Configuration and Motor Selection

The pusher configuration is one of the key components of the entire disengagement device, and its function is to ensure that the seedling rope can be smoothly disengaged from the locking device, thereby enabling the automated unlocking process *(Min et al., 2023; Yiren et al., 2021)*. To ensure the operational stability of the pusher configuration, a dual-pusher design was adopted.

To ensure that the motion trajectory of the pusher matches the trajectory of the locking groove on the locking device, the design of the pusher configuration must incorporate the involute curve equation. The involute equation can be expressed as:

$$\begin{cases} x = r(\theta - \sin\theta) \\ y = r(1 - \cos\theta) \end{cases} \quad (14)$$

where: r is the radius of the pusher, θ is the rotation angle of the pusher.

By optimizing the involute curve, the trajectory of the pusher can be made consistent with that of the locking groove on the locking device, effectively avoiding rope jamming caused by trajectory mismatch.

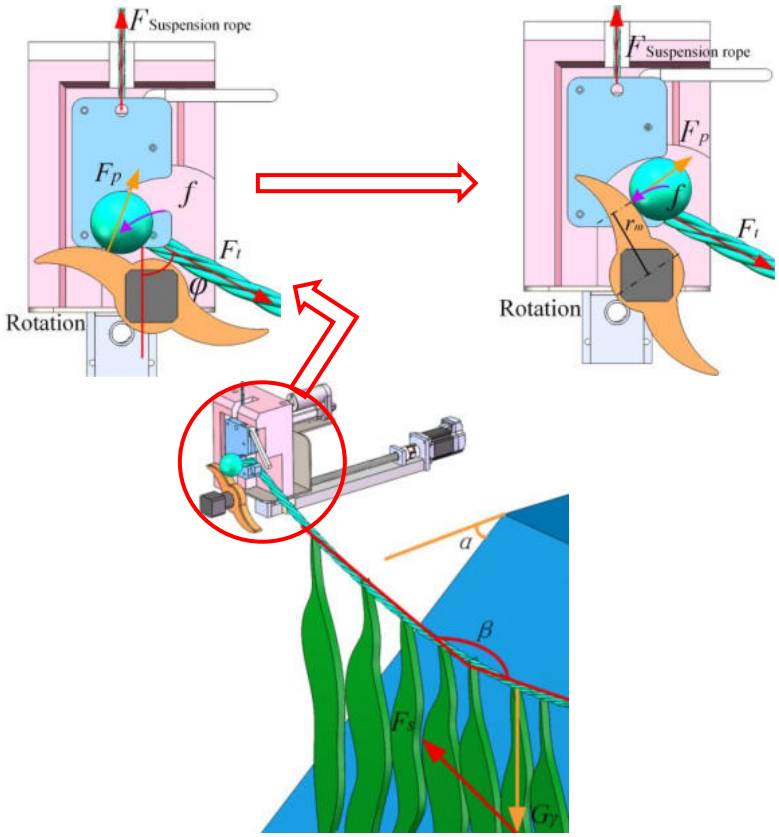


Fig. 8 - Schematic diagram of the pusher configuration and force analysis

After the locking device is unlocked, the pusher, driven by the motor, performs the rope disengagement operation. For successful disengagement, the pushing force applied by the pusher must be greater than the sum of the tensile force in the rope and the frictional force between the rope and the locking groove:

$$F_p > F_t + f \quad (15)$$

where: F_p is the pushing force applied by the pusher, N; F_t is the tensile force in the rope, N; f is the frictional force between the rope and the locking groove, N.

During the unlocking process, the pusher must overcome the combined weight of the seedling rope and kelp, as well as the frictional force between the seedling rope and the locking groove, to ensure successful disengagement of the seedling rope. During harvesting, the kelp is first lifted onto the hauling platform before rope disengagement is performed, thus, the platform provides partial support to the kelp, and the rope disengagement is carried out simultaneously by rapid disengagement devices on both sides, so the load should be considered as equally distributed. When the kelp contacts the hauling platform, it is saturated with water and tends to adhere to the surface, and the effect of friction is neglected in this analysis. The conveyor belt exerts a supporting force on the kelp, which is related to the installation inclination angle α of the conveyor belt, thus:

$$F_s = G_\gamma \cdot \cos\alpha \quad (16)$$

where:

F_s is the supporting force, N; G_γ is the weight of the kelp and rope, N;

α is the inclination angle of the hauling platform, (°).

Since the rope is a flexible body, the point of force application is assumed to be at its midpoint. When the included angle between the seedling rope ends is β, the normal force acting on a single side locking device is:

$$F_n = 2F_s \cdot \cos\frac{\beta}{2} \quad (17)$$

where: F_n is the normal force acting on a single side locking device, N; β is the included angle of the seedling rope, (°).

Since the pusher must overcome the friction between the seedling rope and the arc-shaped groove of the locking device to disengage the rope, and there is an inclination angle between the seedling rope and the locking device, then the frictional force that the pusher needs to overcome is:

$$f = \mu \cdot F_n \cdot \cos\varphi \quad (18)$$

where: μ is the coefficient of friction between the seedling rope and the locking device, taken as 0.3, φ is the angle between the seedling rope and the locking device, (°).

Since the pusher mechanism is designed based on the involute curve of the locking device, the distance from the pusher's rotation axis to the point of force application is considered the moment arm, and the required torque can be calculated accordingly:

$$M = F_p \cdot r_m \quad (19)$$

where:

M is the required rotational torque, Nm;

r_m is the moment arm length from the pusher's rotation axis to the point of force application, m.

Control System Design

Hardware Design of the Control System

The control system is centered on the Delta DVP-ES2 series PLC (Programmable Logic Controller), and its hardware configuration is shown in Figure 9, mainly consisting of a Delta PLC controller, a 24V switching power supply, a Pufeide driver, a ball screw, a stepper motor, a stepper electric push rod, a metal sensing switch, and a proximity sensor.

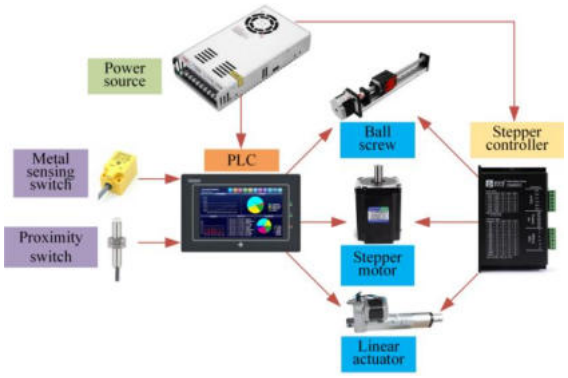


Fig. 9 - Hardware configuration diagram of the control system

The power supply required by each component in the control system is provided by a switching power supply, and a proximity sensor is used to determine whether the locking device is correctly positioned, with its feedback signal sent to the PLC controller for logical evaluation *(Xin et al., 2018)*. A metal sensing switch is used to detect whether the quick-release blocking device has reached the designated position, and the sensing signal triggers subsequent actions of the disengagement device. The ball screw assembly, driven by the motor, enables the forward and backward reciprocating movement of the quick-release blocking plate, thereby controlling the engagement and release of the quick-release structure. The stepper electric push rod is used to apply a pushing force, creating the necessary compressive force between the quick-release locking device and the blocking plate, thereby enabling automatic unlocking. All actuators are current-regulated and pulse-controlled by the Pufeide stepper motor driver, achieving precise control of displacement and speed. The PLC controller is programmed with predefined logic, which makes real-time decisions based on sensor input signals, and controls the timing of motor and push rod operations. The control panel provides parameter setting and operation status monitoring via a human-machine interface (HMI), facilitating on-site commissioning and operation.

Program Design of the Control System

Based on the operation process of rapid disengagement of kelp seedling ropes, a complete automatic control program was developed for the control system. The overall control flow of the system is illustrated in Figure 10. The program is coordinated by a PLC controller to manage the operation of all modules, in conjunction with hardware components including the electric push rod, motor, proximity sensor, metal sensing switch, and magnetic attraction module, to achieve precise unlocking of the locking device and the disengagement of the seedling rope. After initialization, the system automatically resets all components and awaits operation commands via the user interface to begin the process.

The locking device moves with the haulage rope into the flared guiding slot, where the magnetic module is activated to strongly attract the locking device and stabilize its posture. Subsequently, the electric push rod drives the locking device toward the blocking plate, until the proximity sensor detects contact between the locking device and the blocking plate, indicating that the unlocking has been completed. The PLC then drives the pusher configuration to rotate. After the rope is disengaged, the control system reverses the movement of the lead screw, moving the disengagement zone backward. Throughout the entire control process, the PLC continuously monitors the status of all sensors, and the execution completion signals, enabling precise and coordinated control, improving the efficiency and success rate of the disengagement operation.

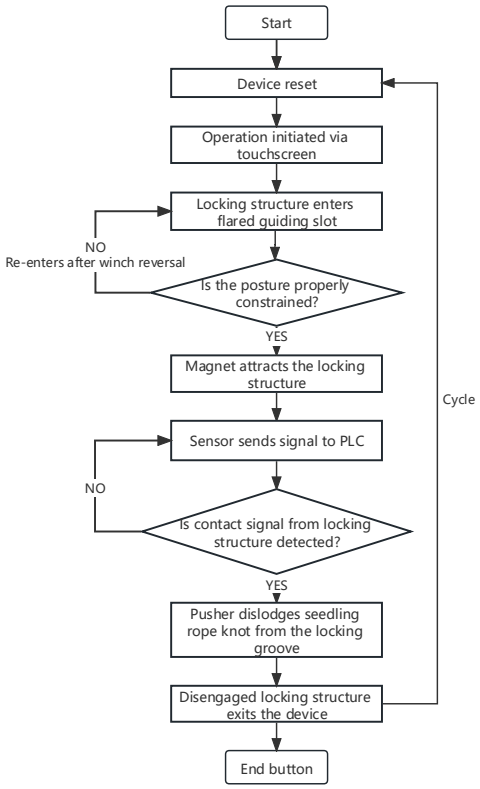


Fig. 10 - Control system flowchart.

EXPERIMENT AND ANALYSIS

Experimental Method



(a) (b)

Fig. 11 - Bench test diagram

To verify the reliability of the PLC-controlled rapid disengagement device for kelp seedling ropes under various operating conditions, key components were fabricated using 3D printing, and a bench-scale testing system was constructed. The disengagement success rate was used as the evaluation index, and an orthogonal experiment was conducted using three variables—guiding slot clearance, haulage rope speed, and pusher length to optimize structural parameters and enhance operational stability. Guiding slot clearance directly affects posture constraints and frictional behavior of the locking device; therefore, its lower limit was set slightly greater than the suspension rope diameter, and the upper limit was defined by effective posture restriction. Based on structural considerations, clearance levels were set from 8 to 24 mm.

Haulage rope speed determines the effectiveness of positioning and rope disengagement. According to the coordination between vessel speed and disengagement speed during harvesting, the range was set to 20-100 mm/s. Pusher length, which affects disengagement effectiveness, was set between 40 and 50 mm.

Orthogonal Experiment and Verification

Given that the performance of the rapid disengagement device is the result of multiple interacting factors and based on the results of the previously conducted single-factor experiments, an orthogonal optimization experiment was conducted with guiding slot clearance, haulage rope speed, and pusher length as experimental factors, and the factor level coding table is presented in Table 1.

Table 1

Coding table of test factors

Level	Factor		
	Guide slot gap a / mm	Speed of rope movement b / mm·s^{-1}	Length of dial finger c / mm
-1	10	20	40
0	14	40	45
1	18	60	50

The disengagement success rate was used as the evaluation index for assessing the performance of the disengagement device, and the experimental design and results are shown in Table 2.

For each test condition, 30 repeated trials were conducted, recording whether the seedling rope could be smoothly disengaged from the locking groove after unlocking, and the number of successful cases was counted to calculate the success rate of disengagement.

$$P = \frac{n}{n_0} \cdot 100\% \tag{20}$$

Where: P is the disengagement success rate, n is the number of successful disengagements, n_0 is the total number of trials.

Table 2

Design and results of simulation test

Test number	Guide slot gap a / mm	Speed of rope movement b / mm·s^{-1}	Length of dial finger c / mm	Success rate of disengagement R1 / %
1	14	60	40	70
2	10	40	50	66.67
3	14	40	45	96.67
4	14	60	50	50
5	18	40	40	66.67
6	14	40	45	93.33
7	10	40	40	73.33
8	18	20	45	83.33
9	14	20	40	86.67
10	18	40	50	53.33
11	10	60	45	70
12	14	40	45	96.67
13	14	40	45	86.67
14	14	40	45	96.67
15	18	60	45	50
16	10	20	45	80
17	14	20	50	83.33

Analysis of Experimental Results

Based on the experimental results in Table 2, an analysis of variance (ANOVA) was conducted on the disengagement success rate, and the results are shown in Table 3. The regression equation for the disengagement success rate is expressed as follows:

$$R_1 = 94 - 4.58a - 11.67b - 5.42c - 5.83ab - 1.67ac - 4.16bc - 15.33a^2 - 7.83b^2 - 13.67c^2 \quad (21)$$

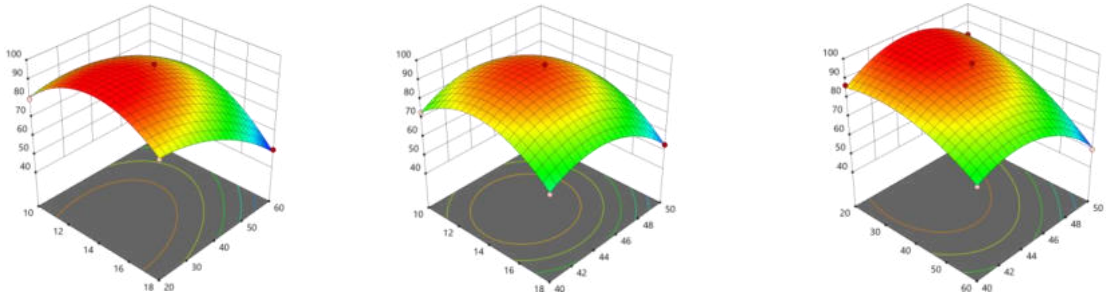
Table 3

Analysis of variance for the regression model

Index	Source	Sum of squares	Degree of freedom	Mean square	F-value	P-value
Success rate of disengagement	Model	3960.92	9	440.10	36.72	< 0.0001**
	a	168.09	1	168.09	14.02	0.0072**
	b	1088.81	1	1088.81	90.84	< 0.0001**
	c	234.79	1	234.79	19.59	0.0031**
	ab	136.07	1	136.07	11.35	0.0119*
	ac	11.16	1	11.16	0.9307	0.3668
	bc	69.39	1	69.39	5.79	0.0470*
	a^2	990.12	1	990.12	82.60	< 0.0001**
	b^2	258.46	1	258.46	21.56	0.0024**
	c^2	786.50	1	786.50	65.61	< 0.0001**
	Residual	83.91	7	11.99		
	Lack of Fit	8.34	3	2.78	0.1472	0.9263
	Pure Error	75.56	4	18.89		
	Cor Total	4044.82	16			

Note :**indicates P≤0.01 (highly significant), *indicates P≤0.05 (significant).

As shown in Table 3, the P-value for the disengagement success rate model is less than 0.01, indicating that the regression model is highly significant. The coefficient of determination (R^2) is 0.9793, indicating that model R_1 explains most of the variability in the response value. The lack of fit P-value is 0.9263, which is greater than 0.05, suggesting that the experimental error is small and the model is reasonable, and that model R_1 can be used to predict the trend of disengagement success rate. The influence of operating parameters on disengagement success rate can be assessed based on the F-values, the influence of operating parameters on disengagement success rate can be assessed based on the F-values, and the order of significance of the factors is as follows: haulage rope speed > pusher length > guiding slot clearance.



(a) (b) (c)

Fig. 12 - Response surface analysis of significant interaction terms on disengagement success rate

Parameter Optimization

To determine the optimal operating parameter combination for the rapid disengagement device, the Optimization module built into the Design-Expert software was used, to optimize the regression model. Considering both operating efficiency and effectiveness, the disengagement success rate was set as the objective to be maximized, with constraints applied to the objective function as shown in Equation (22).

$$\begin{cases} \max R_1(a,b,c) \\ \text{s.t.} \begin{cases} 10\text{mm} \le a \le 14\text{mm} \\ 20\text{mm/s} \le b \le 60\text{mm/s} \\ 40\text{mm} \le c \le 50\text{mm} \end{cases} \end{cases} \quad (22)$$

Based on the defined constraints, the objective function was optimized, resulting in the optimal parameter combination for the rapid disengagement device: guiding slot clearance of 14 mm, haulage rope speed of 40 mm/s, and pusher length of 45 mm, with a predicted disengagement success rate of 96.67% under the optimal parameters.

To verify the predictive accuracy of the response models and the overall performance of the prototype under the optimal parameter combination, a validation test was conducted, to confirm the accuracy of the regression model and the reliability of the optimization results derived from the orthogonal experiment. The operating parameters were: guiding slot clearance of 14 mm, haulage rope speed of 40 mm/s, and pusher length of 45 mm, with five repeated trials conducted under these conditions and the results averaged, the test results are shown in Table 7.

Table 7

Effect of haulage rope speed on disengagement success rate

Items	Experimental values		Predicted values
Success rate of disengagement	1	96.67	96.67
	2	93.33	
	3	90	
	4	96.67	
	5	96.67	

CONCLUSIONS

Based on the posture variation and force characteristics of the locking device during the disengagement of kelp seedling ropes, a rapid disengagement device was developed, consisting of a flared guiding slot for constraint, a magnet for positioning, an electric push rod for unlocking, and a pusher for rope disengagement. Three key structural parameters were identified: guiding slot clearance, haulage rope speed, and pusher length. The structural design was used to ensure both stable operation of the locking device and smooth release of the seedling rope, offering good operability and adaptability.

A response surface model was established, an orthogonal experiment was conducted, and a second-order polynomial regression model was developed using Design-Expert software. The analysis revealed that the influence of the three factors on disengagement success rate followed the order: haulage rope speed > pusher length > guiding slot clearance, resulting in the optimal parameter combination: guiding slot clearance of 14 mm, haulage rope speed of 40 mm/s, and pusher length of 45 mm. Under these parameters, the quick-release device operated stably with a high unlocking success rate, and the predicted disengagement success rate was 96.67%.

The research results provide a theoretical basis and data support for the structural optimization and parameter selection of the rapid disengagement mechanism, laying a foundation for the subsequent realization of automatic separation, intelligent control, and efficient harvesting of kelp seedling ropes.

ACKNOWLEDGEMENT

This research was funded by the Key R&D Program Project in Shandong Province, grant number 2022CXGC020410.

REFERENCES

[1] Bak, U.G., Mols-Mortensen, A., Gregersen, O. (2018). Production method and cost of commercial-scale offshore cultivation of kelp in the Faroe Islands using multiple partial harvesting. *Algal Research*, Vol.33, pp.36-47. https://doi.org/10.1016/j.algal.2018.05.001

[2] Branch, R., Rose, D., Grear, M., Briggs, C., Rollano, F.T. (2023). Powering the Blue Economy: Marine Energy at Kelp Farm Sites. *Marine Technology Society Journal*, Vol.57, no.4, pp.6-14.

[3] Forbes, H., Shelamoff, V., Visch, W., Layton, C. (2022). Farms and forests: evaluating the biodiversity benefits of kelp aquaculture. *Journal of Applied Phycology*, Vol.34, no.6, pp.3059-3067. https://doi.org/10.1007/s10811-022-02822-y

[4] Grebe, G.S., Byron, C.J., Gelais, A.S., Kotowicz, D. M., Olson, T.K. (2019). An ecosystem approach to kelp aquaculture in the Americas and Europe. *Aquaculture Reports*, Vol.15.

[5] Hewei, L., Bin, H. (2020). Research on bionic kelp harvesting device (仿生型海带采收装置的研究). *Journal of Fisheries Research*, Vol.42, no.5, pp.445-452.

[6] Mac Monagail, M., Cornish, L., Morrison, L., Araújo, R., Critchley, A.T. (2017). Sustainable harvesting of wild seaweed resources. *European Journal of Phycology*, Vol.52, no.4, pp.371-390. https://doi.org/10.1080/09670262.2017.1365273

[7] Min, Z., Gang, L., Yao, Y., Mei, J., Tao, J. (2023). Design and Parameter Optimization of Variable Speed Reel for Oilseed Rape Combine Harvester. *Agriculture*, Vol.13, no.8. https://doi.org/10.3390/agriculture13081521

[8] Peteiro, C., Sánchez, N., Martínez, B. (2016). Mariculture of the Asian kelp Undaria pinnatifida and the native kelp Saccharina latissima along the Atlantic coast of Southern Europe: An overview. *Algal Research*, Vol.15, pp.9-23.

[9] Tao, J., Yang, H., Longfei, L., Ye, Z., Zhixin, C., Meng, Y. (2022). Design and experiment of a new mode of mechanized harvesting of raft cultured kelp. *Aquacultural Engineering*, Vol.99. https://doi.org/10.1016/j.aquaeng.2022.102289

[10] Tao, J., Zhixin, C., Ye, Z., Yang, H., Haishen, Z., Yongming, T., Wei, Y. (2020). Design of kelp harvest and transfer device (海带收获转运装置设计). *Fishery modernization*, Vol.47, no.1, pp.16-23.

[11] Tullberg, R.M., Nguyen, H.P., Wang, C.M. (2022). Review of the Status and Developments in Seaweed Farming Infrastructure. *Journal of Marine Science and Engineering*, Vol.10, no.10. https://doi.org/10.3390/jmse10101447

[12] Vea, J., Ask, E. (2010). Creating a sustainable commercial harvest of *Laminaria hyperborea*, in Norway. *Journal of Applied Phycology*, Vol.23, no.3, pp.489-494. https://doi.org/10.1007/s10811-010-9610-y

[13] Xin, J., Kaixuan, Z., Jiangtao, J., Xinwu, D., Hao, M., Zhaomei, Q. (2018). Design and implementation of Intelligent transplanting system based on photoelectric sensor and PLC. *Future Generation Computer Systems*, Vol.88, pp.127-139. https://doi.org/10.1016/j.future.2018.05.034

[14] Yiren, Q., Yaoming, L., Yi, Y., Lizhang, X., Zheng, M. (2021). Development and experiments on reel with improved tine trajectory for harvesting oilseed rape. *Biosystems Engineering*, Vol.206, pp.19-31. https://doi.org/10.1016/j.biosystemseng.2021.02.016

[15] Yongming, T., Shangyou, L., Zhixin, C. (2020). Research on integrated specialized ship for kelp harvesting, classifying and grading. *Aquacultural Engineering*, Vol.91. https://doi.org/10.1016/j.aquaeng.2020.102121

[16] Yongming, T., Zhixin, C., Shupo, C., Shangyou, L., Tao, J. (2018). Design of automatic drafting and hanging kelp harvesting vessel (自动拖拽转挂式海带采收船的设计). *Fishery modernization*, Vol.45, vol.5, 69-74.

[17] Zimin, H., Tifeng, S., Jie, Z., Quansheng, Z., Critchley, A. T., Choi, H. G., Yotsukura, N., Fuli, L., & Delin, D. (2021). Kelp aquaculture in China: a retrospective and future prospects. Reviews in Aquaculture, Vol.13, no.3, pp.1324-1351. https://doi.org/10.1111/raq.12524

[18] Zimin, H., Tifeng, S., Quansheng, Z., Fuli, L., Jueterbock, A., Gaoge, W., Zhongmin, S., Xiangyu, W., Weizhou, C., Critchley, A.T., Naihao, Y. (2023). Kelp breeding in China: Challenges and opportunities for solutions. *Reviews in Aquaculture*, Vol.16, no.2, pp.855-871. https://doi.org/10.1111/raq.12871

[19] Zongyu, C., Yang, Z., Zhongqiang, Z., Rong, W., Zhixin, Z. (2018). Development status of the raft－cultivation harvesting devices for kelp (筏式养殖海带收获装置的发展现状). *Fishery modernization*, Vol.45, no.1, pp.40-48.

PARAMETER OPTIMIZATION AND EXPERIMENT OF AN INSIDE-FILLING PNEUMATIC HIGH-SPEED PRECISION SEED-METERING DEVICE FOR COTTON
/
内充气力式棉花高速精量排种器参数优化与试验

Meng-jie HU*[1,2]; Jia-qi ZHANG[1]; Yao CHEN[1]; Chu-zhen XU[1]; Bao-jia LI[1]
[1]School of Animal Science and Nutritional Engineering, Wuhan Polytechnic University, Wuhan/P.R.China
[2]Key Laboratory of Agricultural Equipment in Mid-Lower Yangtze River, Ministry of Agriculture and Rural Affairs, Wuhan/P.R.China
Tel: +86-027-15527930805; E-mail: humj@whpu.edu.cn
DOI https://doi.org/10.35633/inmateh-76-111

Keywords: *cotton, inside-filling pneumatic high-speed precision seed-metering device, parameter optimization, CFD, DEM-CFD*

ABSTRACT
To address the poor seeding effect of inside-filling pneumatic high-speed precision seed-metering device for cotton, Computational Fluid Dynamics (CFD) and Discrete Element Method–Computational Fluid Dynamics (DEM-CFD) approaches were employed for simulation and optimization. The CFD technique was applied to analyze the influence of key structural parameters of the negative-pressure air chamber on the adsorption performance of the suction holes, while the DEM-CFD approach was used to investigate the motion of cotton seeds inside the seed-metering device during the seed-throwing stage. Based on these analyses, the optimal combination of structural and performance parameters of the seed-metering device was obtained. The simulation-optimized parameters were then validated through bench tests, which showed that at a suction hole diameter of 3.1 mm, a forward speed of 2.33 m/s (8.4 km/h), and a negative pressure of 3,178 Pa, the evaluation indexes were optimal: 96.25% qualification index, 1.83% multiple sowing index, and 1.92% missed sowing index. Further high-speed adaptability test showed that when the forward speed was 1.67~3.33 m/s (6~12 km/h), the qualification index remained greater than 91%, and both the multiple and missed sowing index were less than 5%, meeting the agronomic requirements of high-speed precision seeding for cotton.

摘要
针对内充气力式棉花高速精量排种器排种效果不佳的问题，采用 CFD 和 DEM-CFD 仿真分析方法对其进行了模拟与优化。利用 CFD 仿真分析了负压气室关键结构参数对吸孔吸附性能的影响，采用 DEM-CFD 气固耦合方法探究了投种环节排种器内部棉花种子运动规律，并获得了排种器关键结构与性能参数最佳组合。仿真优化后的参数经台架排种性能试验表明，当吸孔直径为 3.1 mm、前进速度为 2.33 m/s (8.4 km/h)、负压为 3178 Pa 时，其试验指标最优且为合格指数 96.25%，重播指数 1.83%，漏播指数 1.92%。进一步经高速适应性试验表明，当前进速度为 1.67~3.33 m/s (6~12 km/h) 时，合格指数均大于 91%，重播与漏播指数均小于 5%，满足棉花高速精播农艺要求。

INTRODUCTION
Cotton is an important economic crop in China, with a long history of cultivation *(Bie et al., 2018)*. With the acceleration of agricultural modernization, cotton growers are increasingly demanding high-speed and efficient agricultural machinery *(Dong et al., 2025)*. Sowing represents the first step of planting, the seed-metering device being a seeder key component, its seeding quality directly affecting the operational performance of the machine *(Li et al., 2025; Cortez et al., 2020)*. Cotton seed-metering devices are mainly classified into mechanical and pneumatic types. Mechanical seed-metering devices have simple structures but require high seed shape uniformity, having a tendency to damage seeds and suffer from low seeding accuracy under high-speed operation *(Yang et al., 2024; Li et al., 2025; Li et al., 2024)*. In contrast, pneumatic seed-metering devices, although structurally more complex, exhibit better adaptability to seed shape variations, higher seeding precision, and less seed damage, making them more suitable for high-speed seeding operations *(Zang et al., 2024; Li et al., 2021; Gao et al., 2023; Li et al., 2020; Yatskul & Lemiere, 2018; Pareek et al., 2023)*. At present, existing cotton precision seed-metering devices still suffer from poor seed-filling performance under high-speed conditions, with a typical missed sowing index greater than 10%, a qualification index lower than 75%, and the forward speed generally limited to less than 1.11 m/s (4 km/h) *(Zhang et al., 2021; Zhang et al., 2022; Xu, 2018)*.

Since the seed inside-filling type can make use of gravity, centrifugal force, and inter-seed interaction forces to improve the seed-filling performance, our research group previously designed an inside-filling pneumatic cotton high-speed precision seed-metering device. However, experimental results revealed that although the seed-filling performance was improved, the device still exhibited problems such as unstable seed adsorption and poor seed throwing quality under high-speed operation, leading to poor seeding performance. Therefore, the structural parameters of the seed-metering device still require further investigation and optimization.

In recent years, the Computational Fluid Dynamics (CFD) and Discrete Element Method–Computational Fluid Dynamics (DEM-CFD) techniques have been widely applied in the development of seed-metering devices *(Wang et al., 2025; Sun et al., 2025; Wan et al., 2022; Zhou et al., 2024; Guzman et al., 2020; Bustos-Gaytán et al., 2025)*. Guzman validated the feasibility of using DEM-CFD technique to simulate pneumatic seeder planting green field peas through the combination of simulation and experimentation, and investigated the effects of scaled-down seed tank and fluted roller, single run of a horizontal distributor tube, horizontal-vertical tube transition, and vertical seed manifold on the seed movement *(Guzman, 2024)*. Zha et al. designed a branched air-chamber type pneumatic seed-metering device to meet the varying seed rate requirements for different rice varieties, employing CFD technique to optimize the key structural parameters of the branched air chamber casing *(Zha et al., 2024)*. Cao et al. aimed to improve the operational performance of the mixing component in a horizontal air-assisted centralized wheat metering device. Using CFD and DEM-CFD methods, they investigated the influence of key structural parameters of the mixing component on internal airflow distribution and wheat conveying performance, and determined the optimal parameter combination *(Gao et al., 2024)*. Hussain et al. aimed to optimize the working performance of an air-suction maize seed metering device. CFD was used to investigate the effects of vacuum pressure, suction hole diameter, and seed disk speed on device performance, and the optimal parameter combination was obtained. This was subsequently validated through DEM-CFD coupling simulations and bench tests. At a vacuum pressure of 3.5 kPa, an operating speed of 1.94 m/s (7 km/h), and a suction hole diameter of 4 mm, the qualified index reached 95.98%, while the missed index was 1.5% *(Hussain et al., 2025)*. Zhao et al. combined the DEM-CFD gas-solid coupling method and high-speed camera to investigate the effects of key structural and performance parameters of a novel high-speed precision maize seed-metering device on the seeding performance, determining the optimal combination of operating parameters, and verifying the reliability of the seed-metering device under high-speed operation through bench and field tests *(Zhao et al., 2024)*. In summary, simulation techniques are currently widely applied in the development of seed-metering devices for grain crops such as peas, rice, wheat, and maize, while their application in the research and development of high-speed cotton seed-metering devices is not very developed. Moreover, existing studies have not clarified how the air chamber geometry affect the pressure uniformity at suction hole endface for inside-filling pneumatic seed-metering devices, nor have the DEM-CFD coupling simulation been utilized to define the seed throwing pressure and seed throwing port position angle required for stable seed throwing. Therefore, this study uniquely addresses these gaps by combining CFD and DEM-CFD simulations with experimental research to improve the seeding performance of inside-filling pneumatic cotton high-speed precision seed-metering device.

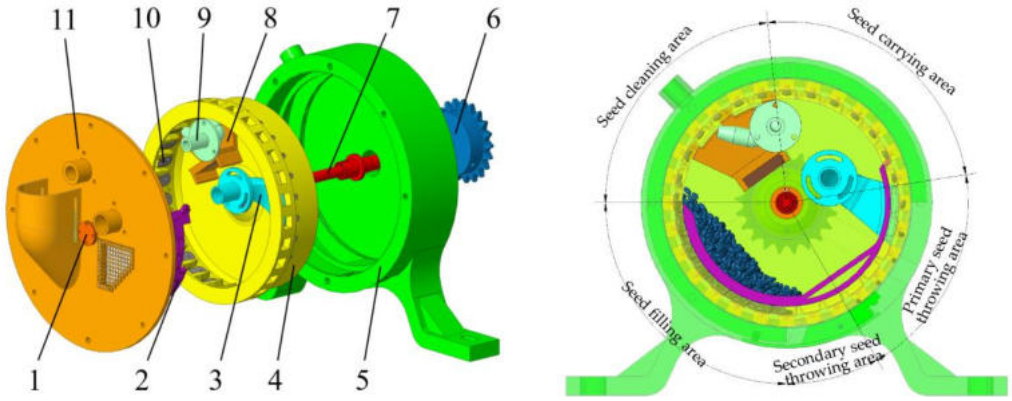
To improve the operational performance of an inside-filling pneumatic high-speed precision cotton seed-metering device, CFD simulations were conducted to analyze the influence of key structural parameters of the negative-pressure air chamber on the pressure at the suction hole end face, and the optimal parameter combination was determined. The DEM-CFD gas–solid coupling technique was then applied to investigate the motion behavior of cotton seeds inside the device during the seed-throwing stage, analyzing the effects of seed-throwing pressure on the initial and stable contact angles between the seeds and the inner wall of the back shell, and determining the optimal seed-throwing pressure and port position. Bench tests of the optimized device were carried out to identify the best combination of performance parameters affecting seeding quality, followed by high-speed adaptability verification. This study provides a reference for the optimization and further improvement of precision seed-metering devices.

MATERIALS AND METHODS

Overall structure and working principle

The inside-filling pneumatic high-speed precision cotton seed-metering device mainly consists of the front shell, seeding plate, suction-hole replacement plate, seed protection board, scraper, seed-cleaning air nozzle, seed-throwing air nozzle, seeding shaft, and back shell, as shown in Fig. 1(a).

As shown in Fig. 1, an arc-shaped groove is arranged on the inner wall of the back shell, which is assembled with the outer wall of the seeding plate to form an air chamber. The back shell is provided with an air outlet hole, which is connected to the air chamber and externally connected to a fan, so that the air chamber can be filled with negative pressure airflow. After cotton seeds enter the inner cavity of the seed-metering device through the seed inlet on the front shell, a seed cluster is formed. The cotton seeds in the lower layer of the seed cluster are adsorbed onto the suction holes under the action of airflow and rotate clockwise with the seeding plate. When the suction hole rotates into the seed cleaning area, excess seeds surrounding the suction hole are removed by the combined action of the scraper and seed cleaning air nozzle, falling back into the seed cluster. The single cotton seed stably adsorbed onto the suction hole is carried by the seeding plate through the seed carrying area and reaches the primary seed throwing area, where it is blown into the collection hole under the action of airflow from the seed throwing air nozzle. As the collection hole continues to move into the secondary seed throwing area, the seed is thrown out through the seed throwing port of back shell, thereby completing the entire seeding process.



(a) (b)

Fig. 1 - Structural schematic diagram of inside-filling pneumatic cotton high-speed precision seed-metering device

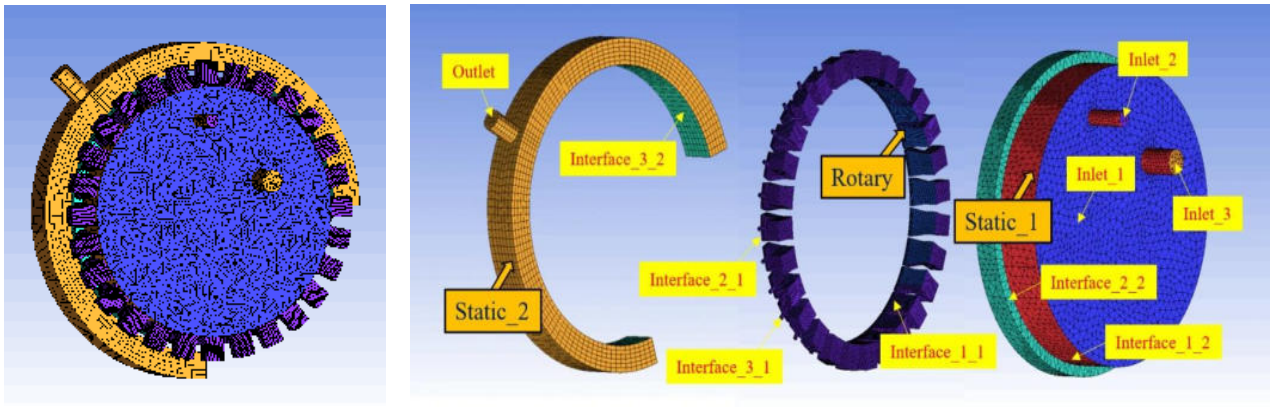
(a) Exploded view diagram of the seed-metering device, (b) Schematic diagram of the working principle of the seed-metering device 1. Bearing end cover; 2. Seed protection board; 3. Seed throwing air nozzle; 4. Seeding plate; 5. Back shell; 6. Sprocket; 7. Seeding shaft; 8. Scraper; 9. Seed cleaning air nozzle; 10. Suction hole replacement plate; 11. Front shell

Simulation analysis method

CFD simulation method for the negative pressure air chamber

Construction and validation of the airflow field model

Using ANSYS Fluent 18.0 software to simulate the airflow field of the negative pressure air chamber, the airflow field model needs to be constructed firstly according to the actual structure and working principle of the seed-metering device, as shown in Fig. 2(a).



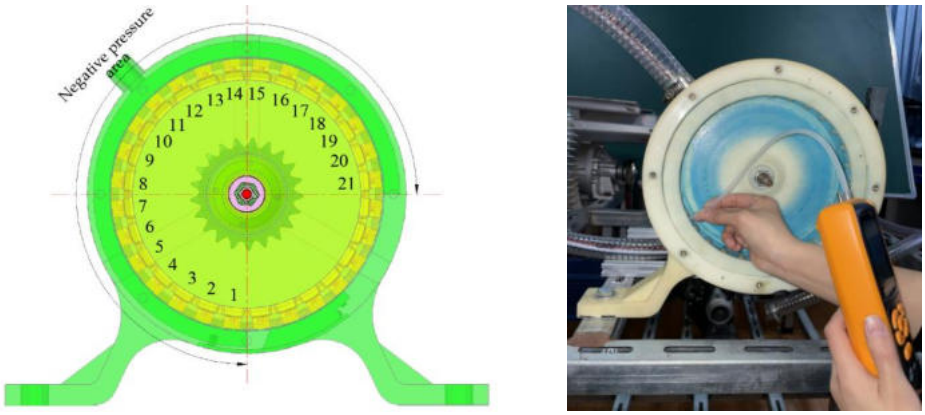
(a) (b)

Fig. 2 - Airflow field mesh model of the seed-metering device

(a) Overall schematic diagram of the mesh model, (b) Exploded schematic diagram of the mesh model

To improve the simulation efficiency, components such as the seeding shaft, seed protection plate, and scraper were omitted to simplify the computational domain. Based on the working principle of the seed-metering device, the airflow field model was divided into one dynamic zone (Rotary) and two static zones (Static_1 and Static_2), as shown in Fig. 2(b). According to the sliding mesh technique, pairs of interfaces were set up between the dynamic and static zones to realize the airflow communication and data exchange across the different regions. Due to the relatively regular geometry of the airflow field in the Rotary and Static_2 zones, structured meshes were applied in these regions. However, the airflow field in the Static_1 zone contains embedded seed cleaning and throwing air nozzles, making it unsuitable for structured meshes, therefore, instead were used unstructured meshes. After meshing the airflow field, the total number of cells was 342356, with the maximum skewness of 0.68. To verify the mesh-independence, two refined meshes with 459749 and 576813 cells were generated for simulation. The pressure differences at the suction hole endface among the three meshes were all less than 5%, indicating that the mesh density had little influence on the pressure at the suction hole endface and that mesh was independent.

In order to test the accuracy of the airflow field model of the seed-metering device, the pressure at the suction hole endface was selected as the evaluation index to carry out the airflow field simulation and physical comparison verification test. Before the test, the central plane of the partition plate between any two adjacent type holes was aligned with the vertical central axis of the seed-metering device, so that the 21 suction holes on the seeding plate were symmetrically and evenly distributed within the negative pressure zone, and sequentially numbered in a clockwise direction, as shown in Fig. 3(a). In the physical test, the pressure at the suction hole endface was measured using a digital differential pressure gauge (Shenzhen Wintact Electronics Co., Ltd., GM520 type, accuracy ±0.3% FSO (factory calibration within 12 months)), and the measurement method was illustrated in Fig. 3(b). The negative pressure at the air outlet was adjusted to –3000 Pa, and after the airflow stabilized, the pressure at suction holes 1–21 was measured and recorded in sequence. The simulation tests were conducted with reference to the physical test, and the boundary conditions were set as follows: the Outlet was set as a pressure outlet with a value of −3000 Pa, the Inlet_1, Inlet_2, and Inlet_3 were set as pressure inlets with the value of 0 Pa, and the rotation speed of dynamic zone was set to 0 r/min. The endface of the suction hole at the measurement points was set as wall. The standard k-ε turbulence model was employed and the pressure-based type solver was selected. The residual convergence criterion was set to 10^{-4}, and the time step was set to 0.003571429, with a total of 500 time steps. After both the physical and simulation tests were completed, the suction holes endface pressure values were compared to verify the accuracy of the airflow field model of the seed-metering device.



(a) **(b)**

Fig. 3 - Measurement of the pressure at the suction hole endface with the negative pressure setpoint of −3000 Pa

(a) Schematic diagram of suction hole numbering (1~21) in the negative pressure area,
(b) Schematic diagram of physical measurement method
Note: 1. Simulation settings: standard k–ε turbulence model, pressure-based solver, Outlet −3000 Pa, Inlet(s) 0 Pa, dynamic zone rotation speed 0 r/min, residual convergence 10^{-4}, time step 0.003571429 s, 500 steps.
2. Test repeats for 3 times.

Simulation method

The negative pressure air chamber is directly connected to the suction holes, providing the required negative pressure to ensure that cotton seeds remain stably adsorbed on the suction hole endface during the normal operation of the seed metering device. The pressure at the suction hole endface can reflect the adsorption performance of suction hole, and investigating the effects of the structural parameters of the

negative pressure air chamber on the pressure at the suction hole endface can provide a basis for optimizing the parameters of the seed-metering device. The key structural parameters of the negative pressure air chamber mainly include the angle and position of the air outlet hole, and the width and thickness of the negative pressure air chamber.

(1) Effect of Air Outlet Hole Angle and Position on Suction Hole Endface Pressure

The air outlet hole serves as the airflow exit of the seed-metering device, with its angle and position parameters directly affecting airflow direction. These include the position angle, vertical inclination angle, and longitudinal (front–rear) inclination angle, which were therefore selected as test factors to investigate their effect on the pressure at the suction hole endface. Because the suction hole endface pressure is the key factor for stable adsorption of cotton seeds, increasing the endface pressure in the seed-filling area improved the filling performance of the seed-metering device, while reducing pressure variation between suction holes in the seed-cleaning and seed-carrying areas helped prevent missed seeding caused by abrupt pressure changes. Therefore, the average endface pressure in the seed-filling area and the standard deviation of endface pressure in the seed-cleaning and seed-carrying areas were selected as evaluation indexes, and a three-factor, three-level orthogonal test was conducted. The levels of each factor are shown in Table 1, and the angle arrangement was illustrated in Fig. 4. In the numerical simulation, the relevant parameters were set as follows: the Outlet was set as a pressure outlet with a value of −3000 Pa, the Inlet_1, Inlet_2, and Inlet_3 were set as pressure inlets with the value of 0 Pa, and the rotation speed of dynamic zone was set to 30 r/min. The standard k-ε turbulence model was employed and the pressure-based type solver was selected. The residual convergence criterion was set to 10^{-4}, the time step was set to 0.003571429, and the number of time steps was 570.

Table 1

The levels of test factors for orthogonal test

Levels	Test factors		
	Position angle θ_a / (°)	Up and down inclination angle θ_b / (°)	Front and rear inclination angle θ_c / (°)
1	45	-45	-45
2	135	0	0
3	225	45	45

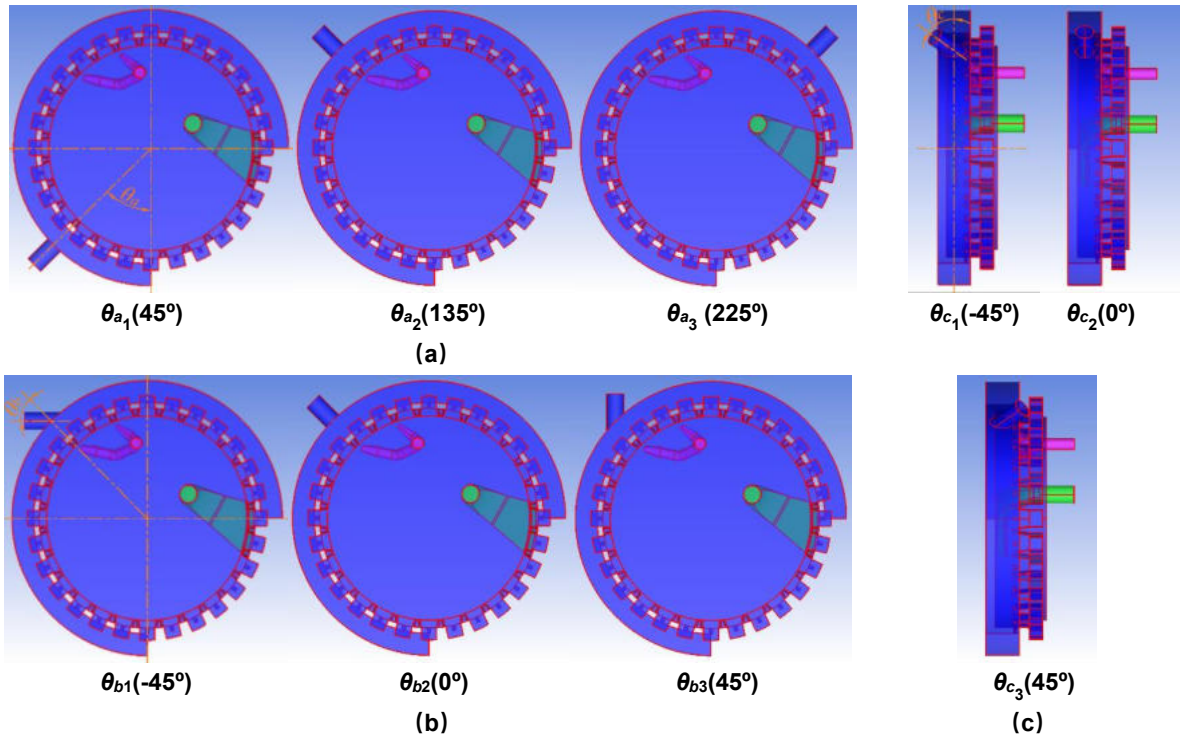


Fig. 4 - Schematic diagram of the angle arrangement of each factor

(a) Position angle, (b) Up and down inclination angle, (c) Front and rear inclination angle

Note: 1. Simulation settings: standard k–ε turbulence model, pressure-based solver, Outlet −3000 Pa, Inlet(s) 0 Pa, dynamic zone rotation speed 30 r/min, residual convergence 10^{-4}, time step 0.003571429 s, 570 steps.

2. Test repeats for 3 times.

(2) Effect of Negative Pressure Air Chamber Width and Thickness on Suction Hole Endface Pressure

The thickness and width of the negative pressure air chamber determine the volume of the air chamber, as shown in Fig. 5, and its influence on the pressure at the suction hole endface can be explored to provide a reference for the optimization of the structural parameters of the seed-metering device. In the simulation test, the air chamber thickness and width were taken as test factors, and the pressure average at the suction hole endface in the seed filling area and pressure standard deviation at the suction hole endface in the seed cleaning and carrying areas were taken as evaluation indexes to carry out a two-factor test.

Based on the actual size of the seed-metering device, the air chamber width b_0 was set at three levels: 22 mm, 26 mm, and 30 mm, while the thickness c_0 was set at 12 mm, 16 mm, and 20 mm. In the flow field model, the position angle, up and down inclination angle, and front and rear inclination angle of the air outlet hole were all set to the optimal levels determined in the previous experiments. All relevant parameters in the Fluent software were kept consistent with the above orthogonal test.

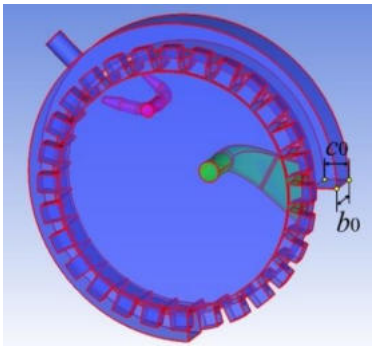


Fig. 5 - Schematic diagram of the width and thickness of the negative pressure air chamber

Note: 1. Simulation settings: standard k–ε turbulence model, pressure-based solver, Outlet −3000 Pa, Inlet(s) 0 Pa, dynamic zone rotation speed 30 r/min, residual convergence 10^{-4}, time step 0.003571429 s, 570 steps. 2. Test repeats for 3 times.

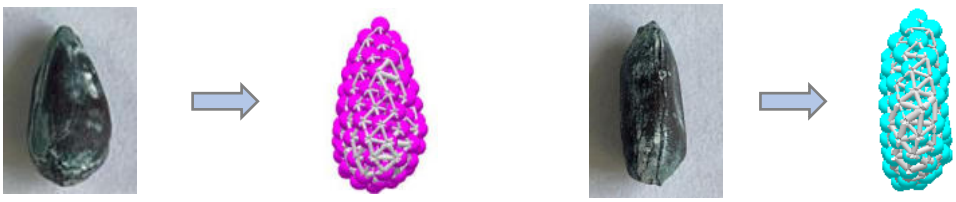
DEM-CFD simulation method for the seed throwing link

In the primary seed throwing area, the cotton seeds adsorbed on the suction hole endface are blown from the filling hole into the collection holes under the airflow action from the seed throwing air nozzle outlet, and then rotated with the seeding plate to the secondary seed throwing area, and finally thrown out through the seed throwing port. The seed throwing air nozzle pressure determines whether cotton seeds can be smoothly blown into the collection hole. To reduce the required air pressure, the seed throwing air nozzle pressure should be selected as low as possible while ensuring the normal operation of the seed-metering device. After cotton seeds fall from the filling hole into the collection hole, collisions between them may cause a certain degree of bouncing. To avoid the impact of bouncing on the seeding performance of seed-metering device, the starting position angle (the angle between the plane formed by the starting edge of the seed throwing port and the center axis of the seeding plate, and the vertical center plane of the seeding plate) of the seed throwing port should be determined to ensure that the seeds have no significant bouncing against the inner wall of the back shell before seed throwing. Since the seeding plate is made of opaque toughness photosensitive resin, and the cotton seeds are coated, the external seed coating agent is easy to adhere to its contact and interfere with the line of sight, so it is not feasible to directly observe the movement of the seeds in the seed throwing area. Therefore, the DEM-CFD gas-solid coupling simulation test method was adopted.

Construction and validation of the cotton seed particle model

EDEM 2018 and ANSYS Fluent 18.0 software were used to perform DEM-CFD gas–solid coupling simulations of the seed-metering device. Bonded particle model (BPM) was adopted to construct cotton seed particles, meaning a single cotton seed consists of several independent fraction particles bonded together. The contact model between fraction particles was set as Hertz-Mindlin with bonding model, and a particle radius of 0.45 mm was chosen. In this study, the E`kangmian-10 cotton seeds (moisture content 11.06% wb, mass of 1000 cotton seeds 94.50 g, length 9.27±0.67 mm, width 5.14±0.37 mm, and thickness 4.50±0.33 mm) were selected as the test material, which can be divided into two categories of ellipsoidal and flat cotton seeds, with the quantity ratio of 22:3, the simulation model being shown in Fig. 6. The ellipsoidal and flat cotton seeds were composed of 146 and 127 fraction particles, respectively. The key components of the seed-metering device were all generated by 3D printing technology with resin materials. Among them, the front shell and seed protection board were made of fully transparent photosensitive resin, while the remaining parts were made of tough photosensitive resin.

Based on previous research and preliminary experiments, the intrinsic material parameters, contact parameters, and main computational parameters used in the coupling simulation are listed in Table 2 *(Hu et al., 2022)*.



(a) **(b)**

Fig. 6 - The physical and simulation particle models of cotton seeds

(a) Ellipsoidal cotton seed, (b) Flat cotton seed

Table 2

DEM-CFD coupling simulation parameters

Program	Parameter	Value
cotton seed	Poisson's ratio	0.14
	Shear modulus/(Pa)	4.01
	Density/(kg/m^3)	917
Tough photosensitive resin	Poisson's ratio	0.42
	Shear modulus/(Pa)	1.04×10^9
	Density/(kg/m^3)	1140
Fully transparent photosensitive resin	Poisson's ratio	0.41
	Shear modulus/(Pa)	9.49×10^8
	Density/(kg/m^3)	1268
cotton seed - cotton seed	Restitution coefficient	0.06
	Static friction coefficient	0.10
	Dynamic friction coefficient	0
cotton seed - Tough photosensitive resin	Restitution coefficient	0.13
	Static friction coefficient	0.33
	Dynamic friction coefficient	0
cotton seed - Fully transparent photosensitive resin	Restitution coefficient	0.12
	Static friction coefficient	0.29
	Dynamic friction coefficient	0
EDEM	Solid time step/(s)	3×10^{-7}
	Gravity acceleration/(m/s^2))	9.81
CFD	Fluid	Air
	Density/(kg/m^3)	1.23
	Fluid time step/(s)	3×10^{-5}

Simulation method

Since the number of particles significantly affects the coupling simulation speed, one ellipsoidal and flat cotton seed was used in the DEM-CFD simulation for calculation, respectively. The seed-throwing pressure was selected as the test factor and set at four levels (500, 1000, 1500, and 2000 Pa) based on pre-tests. The initial contact angle—defined as the angle between the vertical center plane of the seeding plate and the vertical line connecting the center of the bonded particle closest to the vertical center plane with the centerline of the seeding plate at the moment the cotton seed first contacts the inner wall of the back shell—and the stable contact angle—measured when the seed shows no significant rebound after contact—were chosen as evaluation indices. These parameters were then used to conduct the coupling simulation test. Since a higher seeding plate rotational speed reduces the time during which the cotton seed is exposed to the airflow from the seed throwing air nozzle in the primary seed throwing area, making it more difficult for the seed to be smoothly blown into the collection hole, the rotational speed of the seeding plate was set to 35.71 r/min (corresponding to the designed maximum forward speed of 3.33 m/s (12 km/h)) to ensure the normal operation of the seed-metering device.

The remaining parameters were set as follows: the Inlet_1 and Inlet_2 were set as pressure inlets with the value of 0 Pa, the Outlet was set as pressure outlet with the value of -3000 Pa. The number of time steps was 100,000 and the simulation time was 3 s. The structural parameters of the negative pressure air chamber were set to the optimal combinations determined from the previous airflow field simulation tests.

The DEM-CFD coupling frequency was set to 3×10^{-5} s, the turbulence–particle coupling was set to two-way data transfer, and the Freestream model was adopted as the drag model. Each cotton seed type was simulated 10 times, the mean was used as the evaluation index, and the minimum value was used as the diagnostic indicator.

Seeding performance test method of the seed-metering device

To investigate the working effect of the simulation-optimized seed-metering device under high-speed operation, the seeding performance tests were conducted.

Test equipment

The test equipment consisted of a self-built performance test platform for the seed-metering device. The main components of the device were fabricated by 3D printing and installed on the platform, as shown in Fig. 7. The seed-metering device was driven by a DC motor through a speed reducer. The detection system employed a self-developed seed-metering device performance testing device for medium and large seeds, which mainly consisted of an LED photoelectric sensing system and a pulse recognition monitoring system, enabling real time monitoring and display of the seeding operation status *(Liu et al., 2021)*.

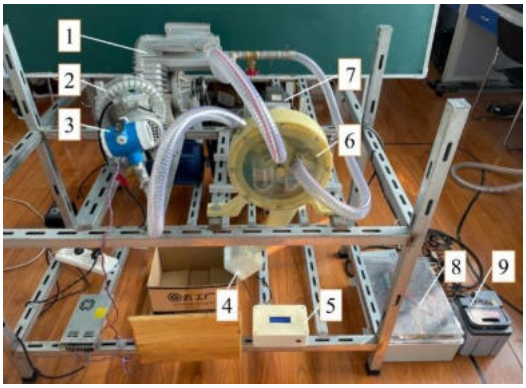


Fig. 7 - Seed-metering device performance test platform

1. Fan Ⅰ; 2. Fan Ⅱ; 3. Pressure gauge; 4. LED photoelectric sensing system; 5. Pulse recognition monitoring system; 6. Seed-metering device; 7. DC motor; 8. Control system; 9. Lithium battery

Test method and evaluation indexes

Referring to GB/T 6973-2005 “Testing Methods of Single Seed Drills (Precision Drills)”, the seed-metering device performance testing device for medium and large seeds continuously detected and recorded the seeding time intervals under stable operation conditions. Every 251 seeds constituted one test group, and each group was repeated 3 times. The qualification index A_1, multiple sowing index D_1 and missed sowing index M_1 were taken as the evaluation indexes, and their calculation formulas were as follows:

$$\begin{cases} A_1 = \dfrac{n_1}{N}\times 100\% \\ D_1 = \dfrac{n_2}{N}\times 100\% \\ M_1 = \dfrac{n_3}{N}\times 100\% \end{cases} \quad (1)$$

where: n_1 is the number of seedings with the seeding time interval between 0.5 and 1.5 times the theoretical value; n_2 is the number of seedings with the seeding time interval less than 0.5 times the theoretical value; n_3 is the number of seedings with the seeding time interval greater than 1.5 times the theoretical value; N is the total number of seedings.

The experimental environmental conditions were a temperature of 25±2℃ and a relative humidity of 50±5%. All experimental runs were randomized.

Test design

Based on previous studies and pre-test, the main factors affecting the seeding performance of the seed-metering device are suction hole diameter, forward speed, and negative pressure. Among them, the conversion formula between forward speed and seeding plate rotational speed was as follows:

$$V_m = \frac{nKI_z}{60} \quad (2)$$

where: V_m is the forward speed, m/s; n is the rotational speed of seeding plate, r/min; K is the number of suction holes, value 28; I_z is the theoretical seed spacing, value 0.2 m.

Therefore, the above three factors were selected as test factors, and the qualification index A_1, multiple sowing index D_1, and missed sowing index M_1 were used as evaluation indexes to conduct the seeding performance tests of the seed-metering device.

(1) A Box-Behnken central combination test was carried out to investigate the effects of each test factor on the evaluation indexes and to determine the optimal parameter combination. According to the pre-test, it was found that the seeding performance was good when the suction hole diameter, forward speed and negative pressure were set to 2.7~3.5 mm, 1.67~3.33 m/s (6.0~12.0 km/h), and 2000~4000 Pa, respectively. Therefore, the levels of each test factor were selected as shown in Table 3. A total of 17 test groups were conducted, with each group repeated 3 times, and the average value was taken as the final evaluation index.

Table 3

The levels of test factors for Box-Behnken test

Levels	Test factors		
	Suction hole diameter X_1 / (mm)	Forward speed X_2 / (m/s)	Negative pressure X_3 / (Pa)
-1	2.7	1.67	2000
0	3.1	2.5	3000
1	3.5	3.33	4000

(2) Based on the optimal parameter combination obtained from the above tests, four levels of 1.67, 2.22, 2.78 and 3.33 m/s (6, 8, 10 and 12 km/h) were selected to carry out the high-speed adaptability test of the seed-metering device with forward speed as the test factor. Each group of tests was repeated 3 times, and the average of the results was taken as the final evaluation index.

RESULTS AND DISCUSSION

Validation of the airflow field model

The pressure registered values at the suction hole endface in both physical and simulation tests are shown in Fig. 8.

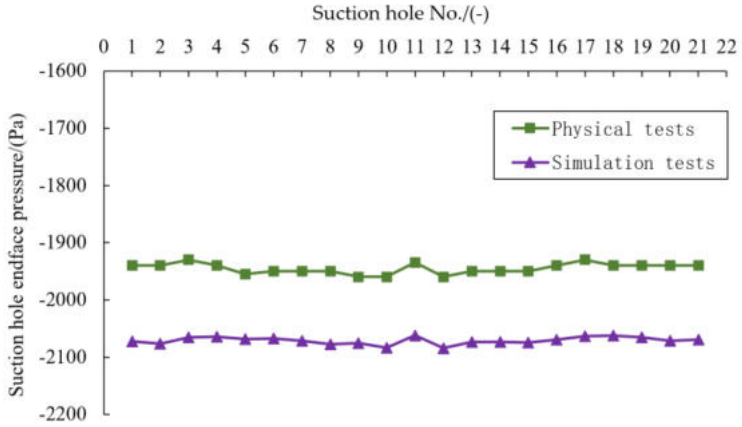


Fig. 8 – Pressure values at the suction hole endface in both physical and simulation tests

Note: 1. Simulation settings: Outlet −3000 Pa, Inlet(s) 0 Pa, dynamic zone rotation speed 0 r/min, residual convergence 10^{-4}, time step 0.003571429 s, 500 steps.
2. Test repeats for 3 times.

As can be seen from Fig. 8, the absolute values of the pressure at the suction hole endface in the physical tests were lower than the simulation values, which was mainly due to the airflow loss caused by the gap between the seeding plate and back shell. Since the seeding plate and the back shell were in axial linear contact, considering the difficulty of ensuring coaxiality due to the limited precision of 3D printing, a clearance of 0.6 mm was reserved between the back shell and the seeding plate to allow the seeding plate smooth rotation. Therefore, the absolute pressure values measured in the physical tests were all lower than those obtained from the simulation tests, but the relative errors between them were all less than 7.04%, indicating that the airflow field model was suitable for the subsequent simulation analysis of the seed-metering device.

Simulation analysis results

CFD simulation results *for the negative pressure air chamber*

Effect of Air Outlet Hole Angle and Position on the Suction Hole Endface Pressure

The design and results of the orthogonal test on the air outlet hole angle and position of the negative pressure air chamber are shown in Table 4, and the results of extreme difference analysis are shown in Table 5. As shown in the table, the factors influencing the pressure average at the suction hole endface in the seed filling area ranked in the following order: front and rear inclination angle θ_c, up and down inclination angle θ_b and position angle θ_a, and for this evaluation index, the optimal combination was $\theta_{c_2}\theta_{b_2}\theta_{a_1}$. The factors influencing the pressure standard deviation at the suction hole endface in the seed cleaning and carrying areas ranked in the following order: position angle θ_a, front and rear inclination angle θ_c and up and down inclination angle θ_b, and for this evaluation index, the optimal combination was $\theta_{a_2}\theta_{c_2}\theta_{b_2}$. Therefore, it can be concluded that the up and down inclination angle should be set to level θ_{b_2}, and the front and rear inclination angle should be set to level θ_{c_2}. However, the optimal value for the position angle remains uncertain and requires further determination through analysis of variance.

Table 4

Orthogonal test design and results

Test serial number	Test factors			Evaluation indexes	
	θ_a	θ_b	θ_c	Pressure average at the suction hole endface in the seed filling area Y_1/(Pa)	Pressure standard deviation at the suction hole endface in the seed cleaning and carrying areas Y_2/(Pa)
1	1	1	1	1207.69	81.11
2	1	2	2	1354.77	70.72
3	1	3	3	1077.77	90.99
4	2	2	3	1145.55	30.06
5	2	3	1	1206.23	31.07
6	2	1	2	1164.85	29.31
7	3	3	2	1190.64	101.31
8	3	1	3	1055.01	113.00
9	3	2	1	1275.71	91.20

Note: 1. Simulation settings: Outlet −3000 Pa, Inlet(s) 0 Pa, dynamic zone rotation speed 30 r/min, time step 0.003571429 s, 570 steps. 2. Test repeats for 3 times.

Table 5

Extreme difference analysis of orthogonal test results

Evaluation indexes	Test factors	Factor levels averages			Maximum difference/(Pa)	Optimal parameter combination
		Level 1/(Pa)	Level 2/(Pa)	Level 3/(Pa)		
Pressure average at the suction hole endface in the seed filling area Y_1/(Pa)	θ_a	1213.41	1172.21	1173.79	41.20	$\theta_{c_2}\theta_{b_2}\theta_{a_1}$
	θ_b	1142.52	1258.68	1158.21	116.16	
	θ_c	1229.88	1236.75	1092.78	143.97	
Pressure standard deviation at the suction hole endface in the seed cleaning and carrying areas Y_2/(Pa)	θ_a	80.94	30.15	101.84	71.69	$\theta_{a_2}\theta_{c_2}\theta_{b_2}$
	θ_b	74.47	63.99	74.46	10.48	
	θ_c	67.79	67.11	78.02	10.91	

Note: 1. Simulation settings: Outlet −3000 Pa, Inlet(s) 0 Pa, dynamic zone rotation speed 30 r/min, time step 0.003571429 s, 570 steps. 2. Test repeats for 3 times.

The results of variance analysis are shown in Table 6. As can be seen from the table, for the pressure average at the suction hole endface in the seed filling area, the front and rear inclination angle had a significant effect on it, and the remaining two factors have no significant effect. For the pressure standard deviation at the suction hole endface in the seed cleaning and carrying areas, all the test factors had a highly significant effect, which was consistent with the results of the extreme difference analysis. Among the three test factors, the position angle had no significant effect on the pressure average at the suction hole endface in the seed filling area, with a contribution rate of 4.78%. However, it had a highly significant effect on the pressure standard deviation at the suction hole endface in the seed cleaning and carrying areas, with a contribution rate as high as 94.83%. Therefore, the selection of the position angle should be primarily based on the pressure standard deviation. Combined with the results of the extreme difference analysis, the optimal level for the air outlet position angle was determined to be θ_{a_2}. Since the factor combination $\theta_{a_2}\theta_{b_2}\theta_{c_2}$ was not included in the orthogonal test design, a simulation verification test was conducted for the airflow field model under this combination using the same method. After the simulation, statistical analysis showed that the pressure average at the suction hole endface in the seed filling area was 1257.64 Pa, which was lower than that of groups 2 and 9 in the orthogonal test, with a maximum pressure difference of 97.13 Pa. The pressure standard deviation at the suction hole endface in the seed cleaning and carrying areas was 8.92 Pa, which was lower than all standard deviations in the orthogonal test. This indicated that when the air outlet was located in the central plane of the negative pressure air chamber, the pressure at the suction hole endface in the seed filling area was not the highest, but the pressure variation in the seed cleaning and seed carrying areas was minimized, resulting in the most stable cotton seed adsorption. Since increasing pressure at the suction hole endface in the seed filling area can be achieved by adjusting the air outlet negative pressure, while reducing the pressure standard deviation at the suction hole endface in the seed cleaning and carrying areas was difficult to accomplish through changing external parameters, the optimal combination of air outlet angle and position was determined to be $\theta_{a_2}\theta_{b_2}\theta_{c_2}$, namely, the position angle of 135°, up and down inclination angle of 0°, front and rear inclination angle of 0°.

Table 6

Variance analysis of orthogonal test results

Source of variation	Pressure average at the suction hole endface in the seed filling area				Pressure standard deviation at the suction hole endface in the seed cleaning and carrying areas			
	Sum of squares	Degree of freedom	*F*-value	Contribution /(%)	Sum of squares	Degree of freedom	*F*-value	Contribution /(%)
θ_a	3269.93	2	1.91	4.78	8156.42	2	4301.73**	94.83
θ_b	23832.41	2	13.93	34.85	219.28	2	115.65**	2.55
θ_c	39572.98	2	23.13*	57.87	223.89	2	118.08**	2.60
Error	1710.77	2		2.50	1.90	2		0.02
Cor total	68386.09	8			8601.49	8		

*Note: 1. Simulation settings: Outlet −3000 Pa, Inlet(s) 0 Pa, dynamic zone rotation speed 30 r/min, time step 0.003571429 s, 570 steps; 2. Test repeats for 3 times; 3. * represents the factor with a significant influence on the index, ** represents factor with a highly significant influence on the index.*

Effect of Negative Pressure Air Chamber Width and Thickness on the Suction Hole Endface Pressure

The results of the two-factor test on the negative pressure air chamber width and thickness are shown in Table 7. As observed, with the increase of thickness, the pressure average at the suction hole endface in the seed filling area gradually increased, while the pressure standard deviation at the suction hole endface in the seed cleaning and carrying areas gradually decreased. This was primarily because an increase in thickness enlarged the airflow circulation area within the air chamber. According to fundamental fluid dynamics theory, a smaller airflow circulation area results in greater resistance losses. Therefore, increasing the thickness of the negative pressure air chamber was conducive to reducing airflow losses and promoting the uniform distribution of suction hole endface pressure. As the width increased, the trend of the average pressure at the suction hole endface in the seed-filling area was not obvious, with only small differences observed, while the pressure standard deviation at the suction hole endface in the seed-cleaning and seed-carrying areas gradually decreased. The main reason is that the suction holes are located along the width of the air chamber, and their diameter is much smaller than the chamber width. Thus, airflow in this direction remained smooth. Consequently, width changes had little effect on the average pressure at the suction hole endface in the seed-filling area, whereas the increased circulation area promoted a more uniform pressure distribution. The results of variance analysis are shown in Table 8.

As can be seen from the table, thickness had a greater influence than width on both the pressure average at the suction hole endface in the seed filling area and the standard deviation in the seed cleaning and carrying areas, which was consistent with the above analysis. In order to obtain a higher pressure average at the suction hole endface in the seed filling area and a lower pressure standard deviation at the suction hole endface in the seed cleaning and carrying areas, the width and thickness of the negative pressure air chamber were selected as 30 mm and 20 mm, respectively.

Table 7

Two-factor test results

Thickness c_0/(mm) / Width b_0/(mm)	Pressure average at the suction hole endface in the seed filling area Y_1/(Pa)			Pressure standard deviation at the suction hole endface in the seed cleaning and carrying areas Y_2/(Pa)		
	12	16	20	12	16	20
22	1229.35	1248.70	1254.92	52.02	22.48	21.16
26	1233.53	1249.32	1257.01	25.22	11.13	10.93
30	1238.97	1246.61	1257.64	23.78	10.65	8.92

Note: 1. Simulation settings: Outlet −3000 Pa, Inlet(s) 0 Pa, dynamic zone rotation speed 30 r/min, time step 0.003571429 s, 570 steps; 2. Test repeats for 3 times.

Table 8

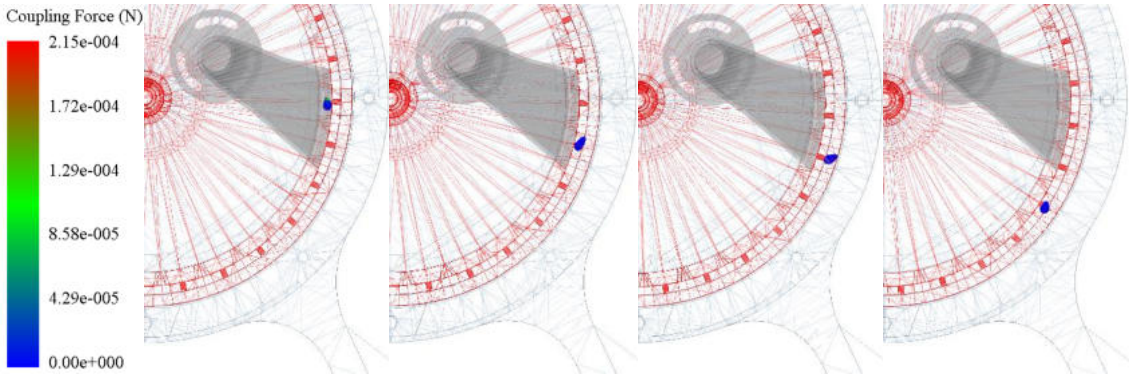
Variance analysis of two-factor test results

Source of variation	Pressure average at the suction hole endface in the seed filling area				Pressure standard deviation at the suction hole endface in the seed cleaning and carrying areas			
	Sum of squares	Degree of freedom	*F*-value	Contribution /(%)	Sum of squares	Degree of freedom	*F*-value	Contribution /(%)
b_0	18.20	2	1.00	2.18	565.82	2	9.76*	39.26
c_0	782.01	2	42.94**	93.47	759.27	2	13.10*	52.69
Error	36.43	4		4.35	115.96	4		8.05
Cor Total	836.64	8			1441.05	8		

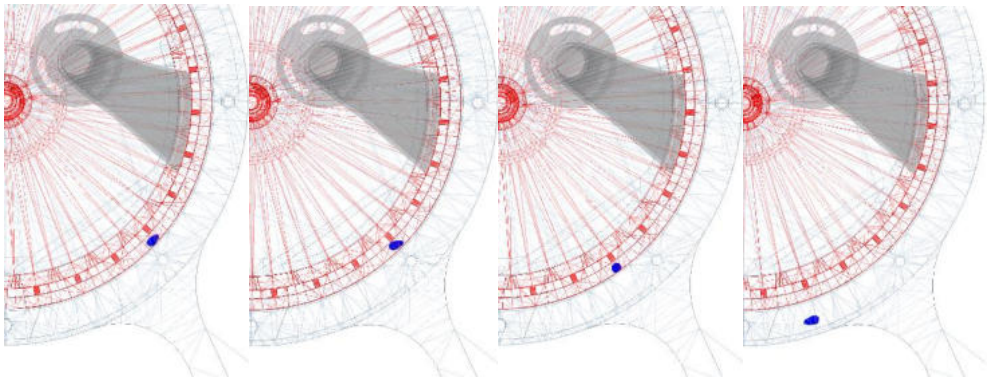
Note: 1. Simulation settings: Outlet −3000 Pa, Inlet(s) 0 Pa, dynamic zone rotation speed 30 r/min, time step 0.003571429 s, 570 steps; 2. Test repeats for 3 times.

DEM-CFD coupling simulation results for the seed throwing link

The single cotton seed throwing process is shown in Fig. 9. As illustrated in the figure, when the positive pressure of the seed throwing air nozzle was 1500 Pa, the cotton seed at the suction hole endface was blown into the collection hole under the drag force of the seed throwing air nozzle. At 1.581 s, the seed makes its first contact and collision with the inner wall of the back shell, and was subsequently bounced upward, followed by a second and third collision with the inner wall at 1.695 s and 1.752 s, respectively. After that, the seed no longer exhibited obvious bouncing behavior but instead moved along the inner wall until it was discharged at the seed-throwing port. This simulation phenomenon indicated that, after entering the collection hole, the cotton seed underwent multiple contacts and collisions with the inner wall of the back shell. Therefore, the starting position angle of the seed-throwing port should be set slightly backward to avoid degraded seeding performance caused by seed bouncing.



(a) (b) (c) (d)



(e) (f) (g) (h)

Fig. 9 - Seed throwing process for single cotton seed

(a) 1.506 s, (b) 1.566 s, (c) 1.581 s, (d) 1.656 s, (e) 1.695 s, (f) 1.707 s, (g) 1.752 s, (h) 1.830 s

Note: 1. Simulation settings: Freestream model, Outlet −3000 Pa, Inlet_1 0 Pa, Inlet_2 0 Pa, Inlet_3 1500 Pa, dynamic zone rotation speed 35.71 r/min, solid time step 3×10^{-7} s, fluid time step 3×10^{-5} s, 100000 steps; 2. Test repeats for 10 times.

The DEM–CFD coupling simulation results for the seed-throwing process are presented in Table 9. As shown, when the seed-throwing pressure was 500 Pa, the outlet velocity of the seed-throwing air nozzle was 19.54 m/s, which was insufficient to blow the cotton seed into the collection hole. When the pressure was ≥1000 Pa, seeds were blown smoothly into the collection hole, and with increasing pressure, the nozzle outlet airflow rate also increased, accelerating seed entry. Consequently, the initial contact angle increased gradually, while the stable contact angles were consistently ≥37.23°, although no clear variation pattern was observed. Simulation and post-processing analyses further revealed no obvious regularity in the bouncing behavior of seeds within the collection hole. Based on this analysis, the seed-throwing pressure should be no less than 1000 Pa to ensure smooth seed delivery. However, considering the gap between the seeding plate and the back shell during actual operation, residual adsorption forces may still act on the seeds at the suction-hole end face after leaving the negative-pressure air chamber. Therefore, the seed-throwing pressure should be appropriately increased, and in this study, a value of 1500 Pa was selected. In addition, to minimize the bouncing of seeds in the collection hole and avoid adverse effects on seeding performance, the starting position angle of the seed-throwing port should be smaller than the minimum stable contact angle of the seeds (37.23°). Accordingly, an angle of 30° was adopted.

Table 9

Simulation test results of seed throwing link

Seed throwing pressure/(Pa)	Outlet velocity of seed throwing air nozzle/(m/s)	Initial contact angle / (°)	Initial contact angle minimum / (°)	Stable contact angle /(°)	Stable contact angle minimum / (°)
500	19.54				
1000	27.85	69.23±1.82	67.1	41.03±1.95	38.03
1500	34.29	75.37±1.43	72.18	39.87±1.46	37.23
2000	39.65	77.84±1.56	75.17	40.26±1.52	37.77

Note: 1. Simulation settings: Freestream model, Outlet −3000 Pa, Inlet_1 0 Pa, Inlet_2 0 Pa, Inlet_3 1500 Pa, dynamic zone rotation speed 35.71 r/min, solid time step 3×10^{-7} s, fluid time step 3×10^{-5} s, 100000 steps; 2. Test repeats for 10 times.

Seeding performance test results of the seed-metering device

Box-Behnken Test

The protocol and results of the Box-Behnken test are shown in Table 10.

Table 10

Box-Behnken test protocol and results

Test serial number	Test factors			Evaluation indexes		
	X_1	X_2	X_3	Qualification index A_1/(%)	Multiple sowing index D_1/(%)	Missed sowing index M_1/(%)
1	-1	-1	0	90.25	3.32	6.43
2	-1	0	-1	81.38	1.06	17.56
3	-1	0	1	91.36	2.78	5.86
4	-1	1	0	88.64	3.69	7.67
5	0	-1	-1	86.78	2.69	10.53
6	0	-1	1	89.46	6.15	4.39

Test serial number	Test factors			Evaluation indexes		
	X_1	X_2	X_3	Qualification index A_1/(%)	Multiple sowing index D_1/(%)	Missed sowing index M_1/(%)
7	0	0	0	97.19	1.19	1.62
8	0	0	0	96.54	1.85	1.61
9	0	0	0	95.93	1.59	2.48
10	0	0	0	94.26	2.53	3.21
11	0	0	0	96.88	1.70	1.42
12	0	1	-1	77.00	4.43	18.57
13	0	1	1	86.98	6.29	6.73
14	1	-1	0	91.13	5.65	3.22
15	1	0	-1	86.92	2.74	10.34
16	1	0	1	88.93	8.52	2.55
17	1	1	0	88.17	6.18	5.65

Note: 1. Air outlet hole position angle 135°, up and down inclination angle 0° and front and rear inclination angle 0°; air chamber thickness 20 mm and width 30 mm; seed throwing pressure 1500 Pa, seed throwing port starting position angle 30°; 2. Test repeats for 3 times.

In order to further analyze the significance of the effect of each test factor and its interaction on the evaluation indexes, Design-Expert 10.0.4 was used to carry out a multiple regression analysis on the test results and establish a quadratic regression model between the test factors and evaluation indexes. The significance analysis results are shown in Table 11. As can be seen from the table, the regression models were all highly significant (P≤0.01) and the lack of fit were all insignificant (P>0.05), so the regression equations were well fitted to the test data. For the qualification index, the linear terms X_2, X_3 and quadratic term X_2^2, X_3^2 had a highly significant effect on it (P≤0.01), interaction term X_1X_3, X_2X_3 and quadratic term X_1^2 had a significant effect on it (0.01<P≤0.05), and the remaining terms had no significant effect on it (P>0.05). For the multiple sowing index, the linear terms X_1, X_3 and quadratic term X_2^2, X_3^2 had a highly significant effect on it (P≤0.01), interaction term X_1X_3 and quadratic term X_1^2 had a significant effect on it (0.01<P≤0.05), and the remaining terms had no significant effect on it (P>0.05). For the missed sowing index, all the linear terms and quadratic term X_2^2, X_3^2 had a highly significant effect on it (P≤0.01) and the remaining terms had no significant effect on it (P>0.05). Moreover, the order of test factors affecting the qualification index was: negative pressure>forward speed>suction hole diameter. And the order of test factors affecting the multiple sowing index and missed sowing index was: negative pressure>suction hole diameter>forward speed. The quadratic regression equations between the test factors and evaluation indexes are as follows:

$$A_1 = 96.16 + 0.44X_1 - 2.10X_2 + 3.08X_3 - 0.34X_1X_2 - 1.99X_1X_3 + 1.83X_2X_3 - 2.26X_1^2 - 4.35X_2^2 - 6.75X_3^2 \quad (3)$$

$$D_1 = 1.77 + 1.53X_1 + 0.35X_2 + 1.6X_3 + 0.04X_1X_2 + 1.01X_1X_3 - 0.4X_2X_3 + 0.91X_1^2 + 2.03X_2^2 + 1.09X_3^2 \quad (4)$$

$$M_1 = 2.07 - 1.97X_1 + 1.76X_2 - 4.68X_3 + 0.3X_1X_2 + 0.98X_1X_3 - 1.42X_2X_3 + 1.35X_1^2 + 2.33X_2^2 + 5.66X_3^2 \quad (5)$$

where:

X_1, X_2 and X_3 represent the coded levels (−1, 0, +1), and the coding of actual factor levels is shown in Table 3.

Table 11

Variance analysis of Box-Behnken test results

Source of variation	Qualification index			Multiple sowing index			Missed sowing index		
	Sum of squares	F-value	P-value	Sum of squares	F-value	P-value	Sum of squares	F-value	P-value
Model	463.19	26.21	0.0001**	73.34	22.66	0.0002**	421.13	27.93	0.0001**
X_1	1.55	0.79	0.4040	18.73	52.09	0.0002**	31.05	18.53	0.0035**
X_2	35.41	18.03	0.0038**	0.97	2.69	0.1452	24.68	14.73	0.0064**
X_3	75.95	38.68	0.0004**	20.54	57.14	0.0001**	175.50	104.74	<0.0001**
X_1X_2	0.46	0.23	0.6447	0.01	0.018	0.8976	0.35	0.21	0.6597
X_1X_3	15.88	8.09	0.0249*	4.12	11.46	0.0117*	3.82	2.28	0.1747
X_2X_3	13.32	6.78	0.0352*	0.64	1.78	0.2239	8.12	4.85	0.0636
X_1^2	21.51	10.95	0.0130*	3.50	9.73	0.0169*	7.66	4.57	0.0699
X_2^2	79.77	40.62	0.0004**	17.29	48.09	0.0002**	22.78	13.60	0.0078**
X_3^2	191.98	97.77	<0.0001**	5.02	13.95	0.0073**	134.93	80.53	<0.0001**
Residual	13.75			2.52			11.73		

Source of variation	Qualification index			Multiple sowing index			Missed sowing index		
	Sum of squares	*F*-value	*P*-value	Sum of squares	*F*-value	*P*-value	Sum of squares	*F*-value	*P*-value
Lack of Fit	8.36	2.07	0.2470	1.56	2.17	0.2341	9.42	5.45	0.0674
Pure Error	5.39			0.96			2.31		
Cor Total	476.93			75.86			432.86		

*Note: 1. Air outlet hole position angle 135°, up and down inclination angle 0° and front and rear inclination angle 0°; air chamber thickness 20 mm and width 30 mm; seed throwing pressure 1500 Pa, seed throwing port starting position angle 30°; 2. Test repeats for 3 times; 3. P ≤ 0.01 (Highly significant, **); 0.01 < P ≤ 0.05 (Significant, *).*

So as to obtain the best combination of test factors, taking the maximum qualification index and the minimum multiple and missed sowing index as the final optimization objective, combined with the boundary conditions of each test factor, the established quadratic regression models were solved by multi-factor optimization.

The objective functions and constraints are as follows:

$$\begin{cases} \max A_1(x_1, x_2, x_3) \\ \min D_1(x_1, x_2, x_3) \\ \min M_1(x_1, x_2, x_3) \\ s.t. \begin{cases} 2.7\ mm \le x_1 \le 3.5\ mm \\ 1.67\ m/s \le x_2 \le 3.33\ m/s \\ 2000\ Pa \le x_3 \le 4000\ Pa \end{cases} \end{cases} \quad (6)$$

Using the optimization module of Design-Expert 10.0.4, the best combination of parameters was determined to be: suction hole diameter of 3.1 mm, forward speed of 2.33 m/s (8.4 km/h), and negative pressure of 3178 Pa. Under these conditions, the seeding performance was optimal, with a qualification index of 96.67%, multiple sowing index of 2.04%, and missed sowing index of 1.29%. To verify the reliability of the optimized parameters, the seeding performance test of seed-metering device was conducted for three repetitions. The average values of the evaluation indexes were as follows: qualification index of 96.25%, multiple sowing index of 1.83%, and missed sowing index of 1.92%, which were generally consistent with the predicted values from the software.

High-speed Adaptability Test

The high-speed adaptability test results of the inside-filling pneumatic cotton high-speed precision seed-metering device are shown in Table 12. As shown in the table, with increasing forward speed, the qualification index first increased and then decreased, the multiple sowing index first decreased and then increased, while the missed sowing index gradually increased, which was consistent with the previous analysis. When the forward speed ranged from 1.67 to 3.33 m/s (6–12 km/h), the qualification index exceeded 91%, and both the multiple sowing index and the missed sowing index remained below 5%. These values were superior to the agronomic requirements specified in JB/T 10293-2013 'Specifications for Single Seed Drills (Precision Drills),' which require a qualification index ≥75%, a multiple sowing index ≤20%, and a missed sowing index ≤10%. This indicates that the optimized seed-metering device meets the high-speed sowing requirements for cotton.

Table 12

High-speed adaptability test results

Forward speed/(m/s)	Qualification index/(%)	Multiple sowing index/(%)	Missed sowing index/(%)
1.67	94.34	3.98	1.68
2.22	95.66	2.61	1.73
2.33	96.25	1.83	1.92
2.78	94.81	2.75	2.44
3.33	91.43	4.55	4.02

Note: 1. Air outlet hole position angle 135°, up and down inclination angle 0° and front and rear inclination angle 0°; air chamber thickness 20 mm and width 30 mm; seed throwing pressure 1500 Pa, seed throwing port starting position angle 30°; 2. Test repeats for 3 times.

CONCLUSIONS

(1) The CFD simulation results of the negative-pressure air chamber showed that, in the orthogonal test of air outlet hole angle and position, the order of influence on the average pressure at the suction hole end face in the seed-filling area was: front–rear inclination angle > vertical inclination angle > position angle. For the pressure standard deviation in the seed-cleaning and seed-carrying areas, the order was: position angle > front–rear inclination angle > vertical inclination angle. The optimal parameter combination was a position angle of 135°, a vertical inclination angle of 0°, and a front–rear inclination angle of 0°. In the two-factor test of chamber thickness and width, thickness had a greater effect than width on both the average pressure in the seed-filling area and the standard deviation in the seed-cleaning and seed-carrying areas, with the optimal combination being a thickness of 20 mm and a width of 30 mm.

(2) The DEM–CFD simulation results of the seed-throwing process showed that, after falling into the collection hole, cotton seeds underwent multiple collisions with the inner wall of the back shell before moving along it. At a seed-throwing pressure of 1500 Pa, the seeds could be smoothly blown into the collection hole. Setting the starting position angle of the seed-throwing port to 30° reduced the adverse effects of seed bouncing within the collection hole on the seed-throwing performance.

(3) The results of the Box–Behnken test indicated that the factors influencing the qualification index ranked in the following order: negative pressure > forward speed > suction hole diameter. For the multiple sowing index and missed sowing index, the order was: negative pressure > suction hole diameter > forward speed. The optimal parameter combination was a suction hole diameter of 3.1 mm, a forward speed of 2.33 m/s (8.4 km/h), and a negative pressure of 3178 Pa. Bench tests verified the corresponding evaluation indexes, yielding a qualification index of 96.25%, a multiple sowing index of 1.83%, and a missed sowing index of 1.92%.

(4) The results of the high-speed adaptability test showed that, as forward speed increased, the qualification index first increased and then decreased, the multiple sowing index first decreased and then increased, and the missed sowing index gradually increased. When the forward speed was 1.67–3.33 m/s (6–12 km/h), the qualification index remained above 91%, while both the multiple and missed sowing indices were below 5%, thereby meeting the agronomic requirements for high-speed precision cotton seeding.

ACKNOWLEDGEMENT

This study was supported by the Research Funding of Wuhan Polytechnic University (2024RZ081; XQ2025006) and Double First Class School Funding - Discipline Building (01003009).

REFERENCES

[1] Bie, S. & Zhang, J.H. (2018). Cotton green light and simple efficient cultivation technology. 1rd ed., *Hubei Science and Technology Press*, Wuhan, China, pp. 1-2.

[2] Bustos-Gaytán, A., Saldaña-Robles, N., Joya-Cárdenas, D.R., Gutiérrez-Vaca, C., Alfaro-Ayala, J.A., Barco-Burgos, J., & Saldaña-Robles, A. (2025). Advancements in pneumatic seed-metering devices: A review of numerical and experimental approaches. *Results in Engineering*, *26*, 105626. https://doi.org/10.1016/j.rineng.2025.105626

[3] Cao, X.Y., Wang, L., Liao, Q.X., & Liao, Y.T. (2024). Simulation of the mixing component of a horizontal air-assisted centralised wheat metering device. *Biosystems Engineering*, *243*, 13-26. https://doi.org/10.1016/j.biosystemseng.2024.05.002

[4] Cortez, J.W., Anghinoni, M., & Arcoverde, S.N. (2020). Seed metering mechanisms and tractor-seeder forward speed on corn agronomic components. *Engenharia Agrícola*, *40(1)*, 61-68. https://doi.org/10.1590/1809-4430-Eng.Agric.v40n1p61-68/2020

[5] Dong, J., Wu, J., Zhu, Y., & Gao, X. (2025). Investigation on Seed-Filling Effect of Quantitative Precision Filling High-Speed Seed-Metering Device for Maize. *Agriculture*, *15*(14), 1517. https://doi.org/10.3390/agriculture15141517

[6] Gao, X.J., Yu, L.Y., Wu, X.P., Huang, Y.X., & Yan, X.L. (2023). Design and Experiment of Intelligent Seed Supply System of Air-assisted High Speed Precision Maize Seed Metering Device. *Transactions of the Chinese Society for Agricultural Machinery*, *54*(s1), 66-75. https://doi.org/10.6041/j.issn.1000-1298.2023.S1.008

[7] Guzman, L. (2024). *Simulation of Agricultural Air Seeding Systems Using the Discrete Element Method and Computational Fluid Dynamics* [Doctoral dissertation, University of Manitoba]. University of Manitoba's Institutional Repository. http://hdl.handle.net/1993/38061

[8] Guzman, L., Chen, Y., & Landry, H. (2020). Coupled CFD-DEM Simulation of Seed Flow in an Air Seeder Distributor Tube. *Processes*, *8(12)*, 1597. https://doi.org/10.3390/pr8121597

[9] Hu, M.J., Xia, J.F., Zhou, Y., Luo, C.M., Zhou, M.K., & Liu, Z.Y. (2022). Measurement and Calibration of the Discrete Element Parameters of Coated Delinted Cotton Seeds. *Agriculture*, *12*(2), 286. https://doi.org/10.3390/agriculture12020286

[10] Hussain, S., Chen, Y., Yu, X., Farid, M.U., Ghafoor, A., Alshamali, S.J., Munir, T., & Hu, J. (2025). Design Optimization and Aerodynamic Investigations of Air Suction Seed Metering Systems through CFD-DEM Approach. *Smart Agricultural Technology*, *12*, 101082. https://doi.org/10.1016/j.atech.2025.101082

[11] Li, C., Zhang, D.X., Yang, L., Cui, T., He, X.T., Zhang, K.L., Li, Z.M., Li, H.S., Xing, S.L., Dong, J.Q., Jiang, Y.Y., Zhang, X.S., Wu W., & Zhang, C.K. (2025). Design of a streamlined structure to minimize seed damage in high-speed centrifugal seed metering devices. *Powder Technology*, *464*, 121251. https://doi.org/10.1016/j.powtec.2025.121251

[12] Li, M.S., Wang, P., Yan, Y.L., Xie, S.Y., Liu, Z.J., Liu, F.Y., & Chen, X.Z. (2025). Design and experiment of chain-spoon type maize precision seed metering device. *Transactions of the Chinese Society of Agricultural Engineering*, 447-459.

[13] Li, Y.H., Yang, L., Zhang, D.X., Cui, T., Zhang, K.L., Xie, C.J., & Yang, R.M. (2020). Analysis and test of linear seeding process of maize high speed precision metering device with air suction. *Transactions of the Chinese Society of Agricultural Engineering*, *36*(9), 26-35. https://doi.org/10.11975/j.issn.1002-6819.2020.09.003

[14] Li, Y.H., Zhao, S., Yang, L., Song, Q., Li, B.G., & Yang, F.Z. (2024). Design and Test of High-speed Precision Seeder of Independent Fractionated Soybean Double-row Brush. *Transactions of the Chinese Society for Agricultural Machinery*, *55*(06), 101-110. https://doi.org/10.6041/j.issn.1000-1298.2024.06.010

[15] Li, Z.D., He, S., Zhong, J.Y., Han, J.F., Chen, Y.X., & Song, Y. (2021). Parameter optimization and experiment of the disturbance pneumatic plate hole metering device for rapeseed. *Transactions of the Chinese Society of Agricultural Engineering*, *37*(17), 1-11. https://doi.org/10.11975/j.issn.1002-6819.2021.17.001

[16] Liu, Z.Y., Xia, J.F., Hu, M.J., Du, J., Luo, C.M., & Zheng, K. (2021). Design and analysis of a performance monitoring system for a seed metering device based on pulse width recognition. *Plos one*, *16*(12), e0261593. https://doi.org/10.1371/journal.pone.0261593

[17] Pareek, C.M., Tewari, V.K., & Machavaram R. (2023). Multi-objective optimization of seeding performance of a pneumatic precision seed metering device using integrated ANN-MOPSO approach. *Engineering Applications of Artificial Intelligence*, *117*, 105559. https://doi.org/10.1016/j.engappai.2022.105559

[18] Sun, W.S., Yi, S.J., Qi, H.L., Li, Y.F., Dai, Z.B., Zhang, Y.P., Yuan, J.S. & Wang, S. (2025). Design and optimization of air-assisted spiral seed-supply device for high-speed dense planting maize seeder. *INMATEH - Agricultural Engineering*, *75*(1), 13-25. https://doi.org/10.35633/inmateh-75-01

[19] Wan, L., Wang, H.C., Che, G., Sun, W.S., & Chen, Z.F. (2022). Design and performance test of spoiler blades of the direct seed-metering device for rice. *INMATEH - Agricultural Engineering*, *68*(3), 60-70. https://doi.org/10.35633/inmateh-68-06

[20] Wang, W.W., Song, L.Z., An, X., Quan, L.Z., Xie, D.B., Chen, Y.X., Li, Z.D., Wu, Z.C., & Chen, L.Q. (2025). Optimizing seed filling performance of the double-filling air suction maize and soybean seed metering device based on DEM-CFD coupling method. *Computers and Electronics in Agriculture*, *237*, 110586. https://doi.org/10.1016/j.compag.2025.110586

[21] Xu, G.J. (2018). *Design and experiment of pneumatic cylinder array precision seed-metering device for cotton*. [Master dissertation, Shihezi University]. Shihezi University Campus Repository.

[22] Yang, L., Li, Z.M., Zhang, D.X., Li, C., Cui, T., & He, X.T. (2024). Design and test of the T-shaped hole of centrifugal high-speed maize precision seed metering device. *Transactions of the Chinese Society of Agricultural Engineering*, *40*(07), 50-60. https://doi.org/10.11975/j.issn.1002-6819.202312208

[23] Yatskul, A., & Lemiere, J.P. (2018). Establishing the conveying parameters required for the air-seeders. *Biosystems Engineering*, *166*, 1-12. https://doi.org/10.1016/j.biosystemseng.2017.11.001

[24] Zang, Y, Huang, Z.S., Qin, W., He, S.Y., Qian, C., Jiang, Y.C., Tao, W.Y., Zhang, M.L., & Wang, Z.M. (2024). Design of hybrid rice air-suction single-seed metering device. *Transactions of the Chinese*

Society of Agricultural Engineering, *40*(6), 181-191. https://doi.org/10.11975/j.issn.1002-6819.202310212

[25] Zha, X.T., Chen, L., Chen, D.Q., He, Y.P., & Yang, R.B. (2024). Design and Testing of a Branched Air-Chamber Type Pneumatic Seed Metering Device for Rice. *Agriculture*, *14*(11), 1934. https://doi.org/10.3390/agriculture14111934

[26] Zhang, C.Y., Kang, J.M., Peng, Q.J., Zhang, N.N., Wang, X.Y., & Jian, S.C. (2021). Design and Test of Secondary Seed Feeding Mechanism of Air-suction Roller Dibbler for Cotton. *Transactions of the Chinese Society for Agricultural Machinery*, *52*(6), 106-116. https://doi.org/10.6041/j.issn.1000-1298.2021.06.011

[27] Zhang, X.J., Zhang, H.T., Shi, Z.L., Jin, W., Chen, Y., & Yu, Y.L. (2022). Design and experiments of seed pickup status monitoring system for cotton precision dibblers. *Transactions of the Chinese Society of Agricultural Engineering*, *38*(5), 9-19. https://doi.org/10.11975/j.issn.1002-6819.2022.05.002

[28] Zhao, P.F., Gao, X.J., Su, Y., Xu, Y., & Huang, Y.X. (2024). Investigation of Seeding Performance of a Novel High-speed Precision Seed Metering Device Based on Numerical Simulation and High-speed Camera. *Computers and Electronics in Agriculture*, *217*, 108563. https://doi.org/10.1016/j.compag.2023.108563

[29] Zhou, H.J., Zhang, C.L., Liu, T., Wang, Y.Z., Fang, J., & Hu, A.T. (2024). Design and experiment of annular air-blowing assisted seed guiding device for corn no-till seeder. *INMATEH - Agricultural Engineering*, *73*(2),50-62. https://doi.org/10.35633/inmateh-73-04

NOVEL SOLUTIONS FOR MITIGATING DROUGHT IMPACT AND RESTORING SOIL FUNCTIONALITY IN AGRICULTURE
/
SOLUȚII NOI PENTRU ATENUAREA IMPACTULUI SECETEI ȘI RESTABILIREA FUNCȚIONALITĂȚII SOLULUI ÎN AGRICULTURĂ

Nicoleta-Alexandra VANGHELE[1), 2)], Nicolae-Valentin VLĂDUȚ[1)], Augustina PRUTEANU*[1)], Andreea MATACHEI[1)], Laurentiu-Constantin VLĂDUȚOIU[1)], Nicoleta-Olimpia VRÂNCEANU[3)]

[1)]The National Institute of Research-Development for Machines and Installations Designed for Agriculture and Food Industry-INMA Bucharest, Ion Ionescu de la Brad -6, Sector 1, Bucharest, 013813 Romania

[2)]Politehnica University of Bucharest, Splaiul Independentei no. 313, sector 6, Bucharest, 060042, Romania

[3)]National Institute for Research and Development for Pedology, Agrochemistry and Environmental Protection – ICPA, Mărăști, no. 61, Sector 1, Bucharest

E-mail: pruteanu_augustina@yahoo.com

DOI: https://doi.org/10.35633/inmateh-76-112

Keywords: *climate change, novel agroecological approaches, sustainable agriculture, water conservation techniques, restore soil functionality*

ABSTRACT

Drought and soil degradation represent critical challenges to sustainable agriculture and global food security, because they limit crop productivity and disrupt ecosystem services. The paper explores novel solutions designed to mitigate the impacts of drought and restore soil functionality in agricultural systems. The proposed approaches integrate innovative soil amendments, such as biochar and compost-based bioproducts, with advanced water conservation techniques and biological interventions aimed at improving soil structure, fertility, and moisture retention. Furthermore, the study examines the role of microbial inoculants and organic matter management in enhancing soil resilience to climatic stressors. This paper focuses on the analysis of case studies that illustrate notable advances in mitigating the effects of drought and improving the quality of agricultural soils through the use of unconventional and innovative technologies. The results highlight the effectiveness of integrating biological, physical, and chemical strategies, carefully adapted to specific site conditions. The adoption of these novel approaches has the potential to enhance the resilience of agricultural systems to climate variability, while simultaneously supporting productivity and long-term sustainability. This research supports the development of climate-smart agricultural approaches that harmonize productive farming with long-term environmental sustainability. This paper synthesizes and critically evaluates the most effective and current strategies identified in recent literature, offering a comprehensive overview aimed at advancing efforts to combat climate change.

REZUMAT

Seceta și degradarea solului reprezintă provocări critice pentru agricultura durabilă și securitatea alimentară globală, deoarece limitează productivitatea culturilor și perturbă serviciile ecosistemice. Lucrarea explorează soluții noi concepute pentru a atenua impactul secetei și a restabili funcționalitatea solului în sistemele agricole. Abordările propuse integrează amendamente inovatoare ale solului, cum ar fi biocharul și produsele bio pe bază de compost, cu tehnici avansate de conservare a apei și intervenții biologice menite să îmbunătățească structura, fertilitatea și retenția umidității solului. În plus, studiul examinează rolul inoculanților microbieni și al gestionării materiei organice în îmbunătățirea rezistenței solului la factorii de stres climatic. Această lucrare se concentrează pe analiza studiilor de caz care ilustrează progrese notabile în atenuarea efectelor secetei și îmbunătățirea calității solurilor agricole prin utilizarea tehnologiilor neconvenționale și inovatoare. Rezultatele evidențiază eficacitatea integrării strategiilor biologice, fizice și chimice, atent adaptate la condițiile specifice ale amplasamentului. Adoptarea acestor abordări noi are potențialul de a spori rezistența sistemelor agricole la variabilitatea climatică, sprijinind în același timp productivitatea și sustenabilitatea pe termen lung. Această cercetare sprijină dezvoltarea unor abordări agricole inteligente din punct de vedere climatic care armonizează agricultura productivă cu sustenabilitatea mediului pe termen lung.

[1)]Nicoleta-Alexandra Vanghele, PhDStud.; Nicolae-Valentin Vlăduț, PhD.; Augustina Pruteanu, PhD.; Andreea Matache Eng.; Laurentiu-Constantin Vlăduțoiu, PhD.; Nicoleta-Olimpia Vrânceanu, PhD.*

INTRODUCTION

The increasing severity and frequency of drought events, coupled with ongoing land degradation, have emerged as major threats to agricultural sustainability and global food security. Drought impacts are manifesting not only as temporary reductions in crop yield but also as long-term degradation of soil quality (*Teliban et al., 2022; Vlăduţ et al., 2017; Vlăduţ et al., 2018*), structure, and ecosystem function (*Nadeem et al., 2018; Bularda et al., 2020; Cârdei et al., 2021a; Cârdei et al., 2021b; Biriş. et al., 2021; Marin et al., 2024; Vlăduţ et al., 2013; Vlăduţ et al., 2023a; Nenciu, et al., 2022a-d).* Understanding this problem requires a critical examination of the underlying drivers and consequences, situated within the broader context of environmental, social, and technological systems (*Khan et al., 2024; Nenciu et al., 2020; Oprescu et al., 2023; Voicea, et al., 2024*).

The degradation of soils under drought conditions is fundamentally driven by the combined effects of natural climate variability and human activities. Extended periods of low precipitation, intensified by climate changes, result in declining soil moisture, reduced infiltration, and loss of organic matter, which collectively impair the soil's capacity to support plant growth (*Ashraf et al., 2019; Mircea et al., 2020; Ciobotaru et al., 2013*). Furthermore, inappropriate land management practices, such as overgrazing, excessive tillage, monocropping, and the removal of vegetative cover, exacerbate the vulnerability of soils to erosion, compaction, and salinization. These processes diminish the productive capacity of soils and undermine their role as carbon sequestration sources and regulators of hydrological cycles (*Oncescu et al., 2025; Tienda et al., 2024; Tarniţă et al., 2025*). The complexity of this domain is highlighted by the intricate interplay between biophysical and socio-economic factors, which collectively shape both the underlying challenges and the pathways to potential solutions. From a biophysical perspective, soils exhibit considerable heterogeneity in terms of texture, structure, organic matter content, and microbial dynamics-attributes that critically influence their capacity to withstand and recover from drought stress. Furthermore, the variability among agro-ecological zones leads to diverse soil-water-plant interactions, necessitating tailored, site-specific management strategies to enhance resilience. Concurrently, socio-economic constraints-such as insecure land tenure, insufficient access to credit and financial services, weak extension and advisory systems, and gaps in supportive policy frameworks—significantly limit the ability of farmers, particularly smallholders and resource-poor producers, to implement sustainable land management practices (*Cujbescu et al., 2023; Vlăduț et al., 2024; Nenciu et al., 2014*). These interdependencies underscore the need for integrated approaches that simultaneously address environmental, technical, and socio-economic dimensions to effectively mitigate soil degradation and enhance agricultural sustainability.

An in-depth exploration of the domain also reveals that knowledge and technology transfer remain critical bottlenecks. Although innovative technologies and equipment for drought mitigation and soil restoration have been developed and tested in experimental settings, their widespread adoption has been slow. Farmers often face barriers such as high initial costs, lack of technical know-how, and uncertainties about the long-term benefits of these innovations. Bridging this gap requires not only technological improvements, but also institutional support mechanisms, capacity building, and participatory approaches that engage farmers as active stakeholders (*Stan et al., 2024; Vlăduţ et al., 2022; Vlăduț et al., 2023b; Voicea et al., 2022*).

From a systems perspective, soil degradation and drought impact multiple dimensions of sustainability-environmental, economic, and social-requiring holistic and interdisciplinary solutions. Restoring degraded soils entails more than physical or chemical amendments; it involves rebuilding soil biological activity (*Tudora et al., 2024a; Tudora eta al., 2025*), enhancing water retention, improving nutrient cycling, and increasing biodiversity (*Nenciu et al., 2023; Voicea et al., 2021*). Similarly, mitigating drought impacts goes beyond providing irrigation infrastructure, encompassing water-use efficiency, crop diversification, and landscape-level interventions that enhance resilience.

Furthermore, the domain's complexity is heightened by the uncertainty inherent in climate projections and the non-linear, often irreversible, nature of soil degradation processes. Tipping points can be crossed, beyond which soil recovery becomes extremely difficult or impossible. This underscores the urgency of implementing preventive and adaptive measures before critical thresholds are reached.

Considering these challenges, it becomes apparent that a critical analysis of the problem must move beyond symptom treatment to address root causes and structural constraints. It calls for an integrative approach that combines scientific research, technological innovation, policy reform, and stakeholder participation. The development and deployment of innovative equipment and systems for soil restoration and drought mitigation must be embedded within broader strategies that promote sustainable land use, strengthen institutional capacities, and build adaptive capacity at the community level.

This research therefore lays the groundwork for identifying and evaluating such innovative solutions by providing a nuanced understanding of the problem and the intricacies of the domain. By critically examining both the drivers of soil degradation and the barriers to implementing effective solutions, better interventions can be designed, that are not only technically sound but also socially acceptable, economically viable, and environmentally sustainable.

Addressing the dual challenge of drought and soil degradation requires recognizing that soils are living systems embedded within complex socio-ecological networks. Their restoration is not merely a technical task but a transformative process that demands systemic thinking, long-term commitment, and collective action. The subsequent sections of this article build on this critical analysis to propose and discuss specific technologies, equipment, and integrated systems that align with these principles and offer tangible pathways toward sustainable land management and agricultural resilience.

The most recent solutions proposed for mitigating the effects of drought and restoring soil functionality in agriculture are, in most cases, either developed within an overly theoretical framework, lacking direct correlation with on-field realities, or based on highly specific experimental models that are difficult to replicate or adapt to other agricultural systems. This lack of general applicability limits technology transfer and the large-scale adoption of such solutions. Moreover, the scientific literature is considerably fragmented, being dominated by studies addressing related topics - such as fertilization, land rehabilitation, or water management - but which fail to provide integrated and novel solutions dedicated exclusively to improving soil quality.

Furthermore, truly interdisciplinary approaches are often absent or insufficiently supported by relevant experimental data adapted to current agro-ecological conditions. As a result, there is an urgent need for the development of scalable technologies, tested under real-world conditions, that can respond to the multiple challenges imposed by climate change. High-impact solutions should encompass not only the biological and physicochemical aspects of soil but also innovative technological components that allow real-time monitoring and adaptation. Another major obstacle is the lack of standardized methodologies that would enable comparative assessment of the effectiveness of various technologies.

Therefore, our objective is to critically analyze the scientific literature and identify the most relevant and impactful research in this field. Despite the growing body of research on climate change mitigation and soil management, there remains a notable lack of consolidated evaluations that systematically compare the effectiveness of different strategies within this domain.

- **Context and research approach**

The review employed a systematic selection process, identifying relevant research papers through comprehensive searches of major academic databases (Web of Science, Scopus, ScienceDirect) using predefined keywords related to climate change and soil management. Inclusion criteria prioritized recent peer-reviewed studies emphasizing the practical applicability of mitigation strategies, while studies lacking field experimental research were excluded.

Numerous strategies have been proposed and investigated in recent years to mitigate the negative effects of climate change on agriculture, however all these measures remain insufficiently structured and synthesized. Consequently, their practical application by farmers is often limited, fragmented, or ineffective. The lack of a coherent and accessible framework impedes the adoption of innovative practices that could effectively enhance resilience and sustainability in agricultural systems. Addressing this gap is crucial, given the accelerating rates of soil degradation, declining fertility, and the expansion of desertified areas, which together threaten global food security and rural livelihoods (*Rugege et al., 2017; Alvar-Beltrán et al. 2021; Vlăduțoiu et al., 2025*).

The main objective of the current research paper is to present, in a unified, scientifically grounded, and practically oriented manner, a set of innovative technologies, equipment, and integrated systems that have demonstrated potential in mitigating drought impacts and restoring degraded agricultural soils. By consolidating knowledge from recent research and field applications, the paper aims to provide a comprehensive synthesis that facilitates decision-making at farm level and informs policy development.

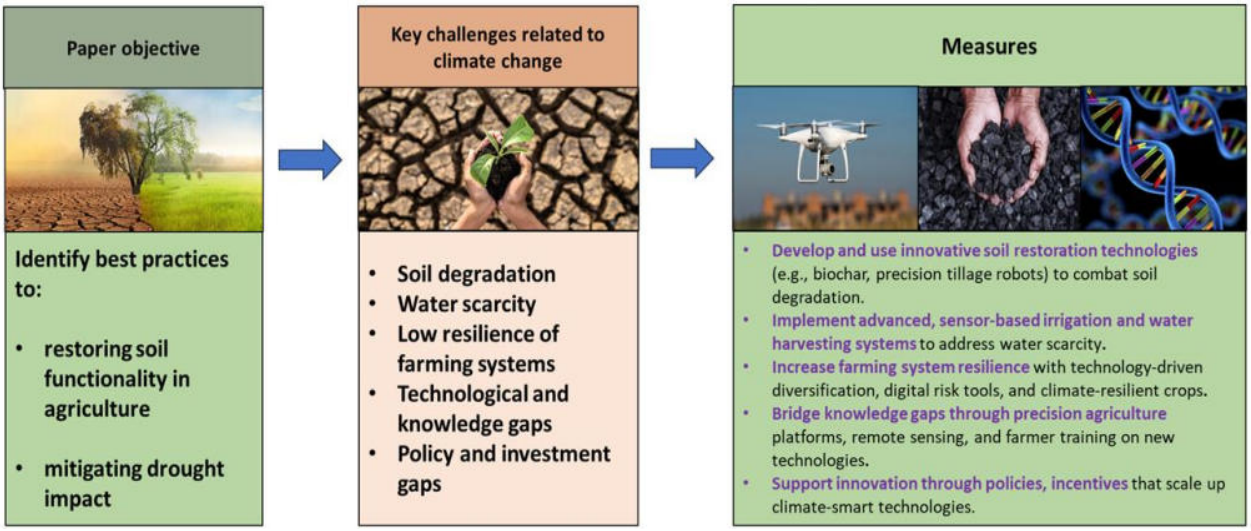


Fig. 1 - Experimental approach for mitigating drought impact and restoring soil functionality in agriculture

Furthermore, the article highlights the critical importance of soil as a highly valuable resource underpinning agricultural productivity and ecosystem services. Climate-induced stressors, such as prolonged droughts, increased evapotranspiration, and extreme weather events, exacerbate existing pressures from unsustainable land use, overgrazing, and excessive tillage. Without targeted interventions, these processes can lead to irreversible losses in soil structure, organic matter, and biodiversity (*Teiba et al., 2024; Popa et al., 2023*).

The paper also seeks to explore the synergies between technological innovation and traditional soil conservation practices, demonstrating how modern precision agriculture tools, remote sensing, and automated irrigation systems can complement time-tested measures like mulching, crop rotation, and cover cropping. Emphasis is placed on cost-effectiveness, scalability, and adaptability to diverse agro-climatic zones, ensuring that the proposed solutions are accessible not only to large-scale commercial farms but also to smallholder and subsistence farmers.

In addition, the discussion includes an assessment of implementation barriers, such as financial constraints, lack of technical knowledge, and institutional weaknesses, proposing pathways to overcome these challenges through capacity building, policy incentives, and multi-stakeholder collaboration. Ultimately, this article aspires to contribute to the broader discourse on sustainable land management by offering actionable insights and evidence-based recommendations for reversing soil degradation trends and enhancing agricultural resilience in the face of climate change.

✓ ***The Impact of Climate Change on Agricultural Productivity***

Global agricultural productivity is changing as a result of climate change, both directly and indirectly. Reduced crop yields, decreased soil fertility, and increasing unpredictability in farming techniques are all being caused by rising temperatures, changing growing seasons, altered precipitation patterns, and an increase in the frequency of extreme weather events. Temperature changes, droughts, and floods are examples of extreme weather phenomena that are progressively upsetting worldwide agricultural systems. Crop yields, food security, and the livelihoods of farmers worldwide are all directly threatened by these events. The frequency and intensity of these events are predicted to increase in tandem with climate change, presenting serious obstacles to agriculture and the ability to continue producing food in a sustainable manner.

Extreme events like drought and aridity are a result of global climate change, which has been increasingly prevalent in recent years. It has been demonstrated over time that severe drought episodes in a given location not only result in high rates of death and economic losses but also negatively impact the biological system, human life, economic activity, and water supplies (*Fye et al., 2010 Schwalmet al., 2017; Popescu et al., 2012*).

Agriculture is characterized by a complex web of structures and interactions among diverse components, producing concerns over its future viability, especially in a climate that offers considerable hazards to food security. As a result, it's critical to assess how climate change is negatively affecting agricultural productivity and develop fresh approaches to these problems (*Rahman et al., 2018*).

Numerous global-scale assessments have been conducted regarding the impact of climate change on agriculture; however, these assessments frequently fail to capture the uncertainties inherent in climate projections and fail to account for important factors like changes in pest and disease dynamics and extreme weather events. Furthermore, different criteria lead to dramatically varied estimations of future risks about the best ways to quantify the impacts of climate change on drought from an agricultural perspective (*Gornall et al., 2010*).

✓ ***The Impact of Extreme Weather Events on Global Agriculture***

The study of the impact of future climate change on agriculture has become one of the hottest issues in the current field of climate change research. This is because there is no guarantee about the future impact of climate change on crops and the importance of agricultural production (*Xiao et al., 2020; Zilli et al., 2020*). Extreme events, such as drought, floods, and heat waves, can affect agricultural production by decreasing crop yields, livelihoods, and community food security.

Rapid climate change is having a significant impact on agricultural production, which is essential for human survival and development *(Annie et al., 2023*). It also disrupts the ecological balance and has an impact on the prevention and management of agricultural diseases and pests (*Yang et al., 2023; Tudora et al., 2022; Tudora et al., 2024b*). In addition, soil degradation and lack of land resources have been caused by climate change, which has had a negative effect on the progress of agricultural production in the long term (*Eekhout et al., 2022*).

In addition to the areas directly affected by the event, other areas around the world may be affected by indirect consequences, such as rising food prices and declining exports of agricultural products.

Understanding the impact of extreme weather events on crop yields in both the current and previous climates is essential to ensure and optimize yields in a changing climate (*Vogel et al., 2019*). Strong international cooperation and inventive solutions are needed to meet this challenge. The joint efforts of nations can promote the development of sustainable technologies and significantly reduce greenhouse gas emissions by combating the effects of climate change.

✓ ***Mitigation approaches***

Several studies have identified viable methods to minimize the effects of climate change on agricultural productivity using new approaches and agricultural practices. Among the most frequently explored approaches are conservation agriculture, precision farming, crop diversification, and integrated nutrient - water management. Researchers usually emphasize the importance of adapting crop varieties to changing climatic conditions, improving soil health through organic amendments, and implementing climate-smart irrigation techniques.

Additionally, there is growing interest in agroecological practices and regenerative agriculture, which not only reduce greenhouse gas emissions, but also increase carbon sequestration in soils and vegetation. The integration of digital technologies, such as remote sensing and AI-based monitoring, further supports the optimization of resource use and risk mitigation in the face of weather variability. Numerous studies also underline the role of policy frameworks and farmer education in scaling up these adaptive practices. Ultimately, a multidisciplinary approach combining agronomy, environmental science, and socio-economic analysis is essential for developing resilient agricultural systems in the era of climate change.

Emission avoidance strategies that generate a positive carbon sequestration and improve input usage efficiency include conservation agriculture, controlled traffic, precision farming, and soil-specific management. Climate change adaptation options in agriculture include producing massive quantities of biomass even in the context of rising temperatures, less effective precipitation, an increase in the frequency and severity of extreme events, and increased pest and pathogen pressure (*Yang et al, 2023*). The net balance between carbon gains and losses determines the dynamic equilibrium of the soil carbon pool. The application of organic amendments (such as compost, manure, and biochar), the deposition of carbonaceous substances (both organic and inorganic) by wind and water, and biomass inputs (such as plant and animal waste) all contribute to carbon gains. Thus, the addition of carbon in the soil stabilizes it against microbial attack through the formation of structural aggregates, the transformation of simple organic compounds into complex humic substances, the transfer of carbon into the subsoil (illuviation), and the transformation of that carbon into decomposition-resistant substances (recalcitration). Grazing, harvesting, and burning all physically remove biomass from the soil, which results in carbon losses. Additionally, decomposition, mineralization, leaching of dissolved carbon molecules, and rapid erosion (from wind, water, tillage, and gravity) all reduce soil carbon. By making carbon gains larger than carbon losses, the aim is to produce a positive carbon budget (*Lal et al., 2010*).

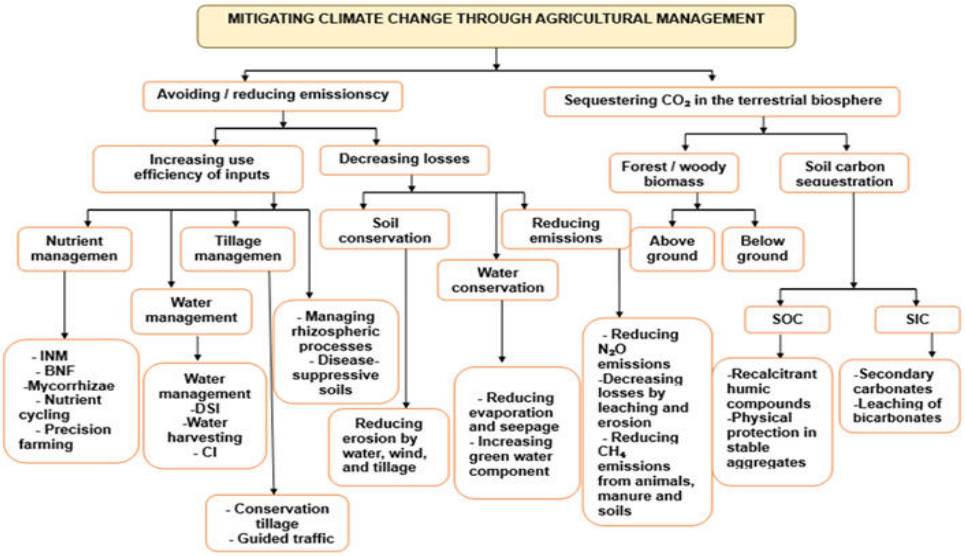


Fig. 2 - Sustainable agricultural techniques to mitigate climate change

**Where: INM = Integrated Nutrient Management; BNF = Biological Nitrogen Fixation; DSI = Deficit Soil Irrigation; CI = Conjunctive Irrigation (the combined use of surface water and groundwater resources for irrigation); SOC = Soil Organic Carbon; SIC = Soil Inorganic Carbon (carbon stored in soils as carbonates and bicarbonates)*

Agriculture and global warming are interconnected, forming a two-way relationship in which agricultural practices both influence and are influenced by climate change. Modern farming technologies contribute significantly to greenhouse gas emissions and environmental degradation, yet they also hold immense potential to mitigate climate change through the adoption of sustainable techniques, as illustrated in Figure 2.

By implementing practices such as efficient nutrient and water management, conservation tillage, and improved soil carbon sequestration, agriculture can play a pivotal role in reducing its ecological footprint. Enhancing soil health, preserving water resources, and increasing biomass also contribute to atmospheric carbon removal and climate resilience. Furthermore, these strategies not only curb emissions, but also improve long-term productivity, food security, and ecosystem stability. The diagram highlights how targeted interventions-both above and below ground create synergies between agricultural productivity and environmental stewardship. Ultimately, transforming agriculture into a climate-smart sector is essential for meeting global sustainability goals and ensuring the resilience of food systems in the face of climate change.

Figure 3 illustrates key strategies for enhancing agricultural adaptation to climate change, in order to maintain productivity at advanced levels, but in a sustainable way.

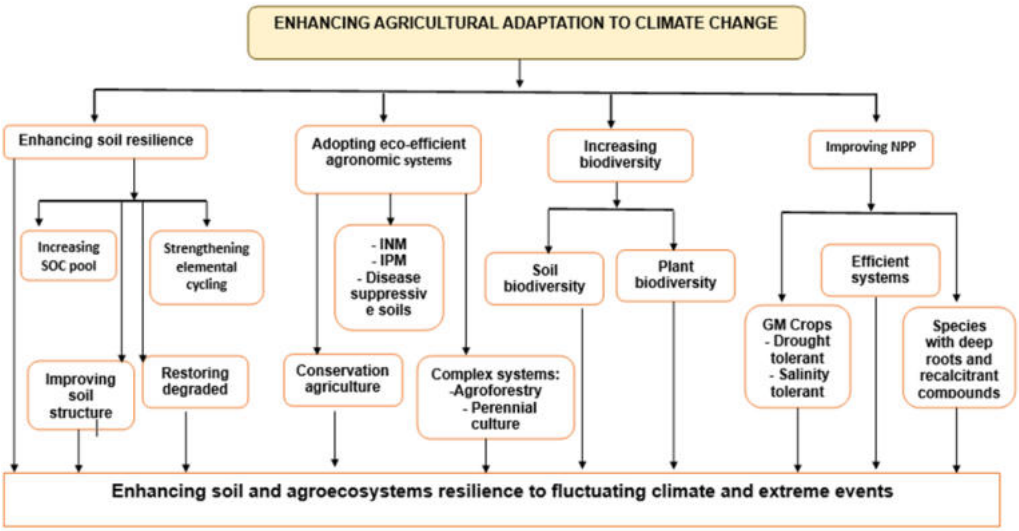


Fig. 3 - Sustainable agricultural techniques to mitigate climate change

**Where: SOC = Soil Organic Carbon; INM = Integrated Nutrient Management (a balanced approach to plant nutrition that combines organic, inorganic, and biological sources of nutrients to improve efficiency and sustainability); IPM = Integrated Pest Management (a strategy for controlling pests and diseases using a combination of biological, cultural, physical, and chemical tools in a way that minimizes risks to health and the environment); NPP = Net Primary Productivity (the rate at which plants accumulate biomass (carbon) through photosynthesis minus the carbon they respire, representing the growth and productivity of vegetation); GM Crops = Genetically Modified Crops (Crops that have been genetically engineered for drought or salinity tolerance, pest resistance, or improved yield)*

As showed above, a major pathway is enhancing soil resilience, achieved by increasing the soil organic carbon (SOC) pool, improving soil structure, and restoring degraded soils. Strengthening elemental cycling and improving soil health are critical to maintaining soil productivity under stress conditions. Therefore, adopting eco-efficient agronomic systems is another cornerstone, which includes integrated nutrient management (INM), integrated pest management (IPM), and fostering disease-suppressive soils.

These practices are supported by conservation agriculture, which minimizes soil disturbance and preserves resources. Increasing biodiversity is highlighted through both soil and plant biodiversity, which improve ecosystem functions and stability.

Complex systems such as agroforestry and perennial cropping systems contribute significantly to biodiversity and resilience. However, the measures must not affect productivity. Improving net primary productivity (NPP) is also essential, and can be performed without affecting productivity by deploying genetically modified (GM) crops that are drought and salinity tolerant. In addition, efficient production systems that optimize resource use and reduce losses further enhance climate resilience.

These approaches build synergistic benefits for soils, plants, and ecosystems. They aim not only to mitigate the negative impacts of climate change, but also to sustain agricultural productivity in the long term. The integration of these practices strengthens agroecosystem sustainability and food security.

- **The chemical challenge in agriculture: understanding the impact of agrochemicals on soil health and sustainability**

About 95% of global food production is supported by soil, a non-renewable resource that provides ecosystem services such as biomass production, pollutant removal, and mass and energy transfer between continents. Soil natural resources are threatened by unsustainable management practices and climate change, especially in the Mediterranean region, where growing populations, rapid land-use changes, associated socio-economic activities and climate change are putting significant pressure on shallow soils. Even though there is evidence that soil is highly susceptible to degradation and desertification, it is unclear how severe soil degradation is (*Ferreira et al., 2022*).

To meet the food needs of a rapidly growing global population, the use of various agrochemicals is essential for contemporary agriculture. These products contribute significantly to increasing the economical and efficient production of crops. Agrochemicals are used in agriculture to bridge the gap between food production and consumption to meet the growing demand for food. However, the improper use of agrochemicals causes environmental degradation and raises a number of problems for soil health and agricultural ecosystems. Microorganisms help with nutrient cycling and improve soil health and crop productivity. Soil degradation caused by the excessive use of agrochemicals threatens global livelihoods, soil health and food security. In addition to numerous other biotic and abiotic factors, including soil characteristics and crop varieties, agrochemicals have a significant impact on how microbial populations and communities of microorganisms in soil evolve (*Mandal et al. 2020*).

Soil degradation causes landslides, floods, desertification, water contamination, and a decline in food production globally. Meanwhile, there are a number of direct consequences that affect the agricultural sector every day.

In agriculture, the continuous use of agrochemicals can also have other harmful effects such as: soil salinization and acidification, loss of organic matter, soil compaction, loss of biodiversity, etc.

Preventing land degradation will help keep farmland productive enough to feed an expanding population. Land conservation supports ecosystems and biodiversity. In addition, healthy soils sequester carbon dioxide and help mitigate climate change.

A global adoption of soil conservation practices will protect natural resources and ensure the long-term viability of agriculture (*Nunes et al., 2020; * ESDAC*).

It is also essential to adopt alternative treatment solutions, such as plant extracts, which are rich in bioactive compounds, to reduce dependence on synthetic chemicals in agriculture (*Tăbărașu et al., 2024 a, b; Isticioaia et al., 2024; Stan et al., 2024*).

- **Climate change challenges in agriculture**

Climate change affects crops in many ways, but some important factors stand out due to their significant influence and are widely acknowledged as crucial in the specialized literature. The aforementioned factors, which have an immediate impact on plant development, soil health, and water availability, include rising temperatures, changing precipitation patterns, and an increase in the frequency of extreme weather events.

A comprehensive grasp of these crucial elements is important for evaluating the vulnerability of agricultural systems and designing appropriate adaptive solutions. In this section, the most significant climate-related elements that promote losses in crop yield and agricultural sustainability will be analyzed, as discovered in recent studies.

Table 1

Climate change impact on agriculture: key factors and responses

Phenomenon	Impact	Counteraction	References
Heat stress on crops	- Higher average temperatures lead to heat stress in crops, reducing photosynthesis and slowing growth rates. - Reduce plant resistance to diseases.	- Development of heat stress tolerant crop plants through environmental and genetic interactions; - Use of detection sensors to expand genetic databases in abiotic stress breeding programs; -The use of viruses, bacteria and fungi to enhance the resistance of crops to heat stress; -Use of transgenic crops	Nadeem, 2018; Teiba, 2024; Kan, 2023; Ashraf, 2019; Khan, 2024; Mukhtar, 2023; Duarte, 2024; Fanai, 2024
Accelerated growth cycles	Warmer temperatures can cause crops to mature faster, reducing the time available for grains, fruits, or vegetables to fully develop, thus decreasing overall productivity and nutritional quality. - The occurrence of eutrophication	- Use of physical, chemical and biological control techniques such as ultrasound, micro-current or ultraviolet, coagulation/flocculation; - Physical shading is a method by which the process of photosynthesis is prevented or slowed down, thus preventing growth. - Adsorption and ion exchange method	Wang, 2024; Moore, 2021 Yang, 2020; Simkin, 2020; Foste, 2021; Hwang, 2020; Akinnawo, 2023; Ajala, 2023
Drought	- Prolonged periods of drought deplete soil moisture and water availability, severely affecting both rainfed and irrigated crops.	- Increasing the soil's capacity to retain water, through practices that lead to the increase of organic matter in the soil (biochar, mulching); - Crop change and rotation; - Management and conservation of resources -The use of cover crops; - Use of biofertilizers, stimulators, -Irrigation - Cloud seeding; - Increase in relative water content, soil protein, antioxidant enzyme activity, sugars through the use of microorganisms	Hunter, 2021; Sarma, 2024; Ali, 2017; Zhang, 2020; He, 2024; Tăbărașu, 2024a; Dastogeer, 2018; Vílchez, 2018; Chaín, 2020; Paul, 2024; Sharan, 2024; Nenciu, 2021b
Flood	- Increased rainfall and flooding can damage crops, wash away nutrient-rich soil, and disrupt planting seasons. - High-intensity storms can cause significant physical damage to crops, uproot plants, and damage critical agricultural infrastructure.	- Rational land management, - Use of drainage ditches, storm drains, embankments, dams; - Planting green belts, leguminous plants or other plants adapted to excessive water stress such as rice, willow, reed, etc. - For nutrient losses, perennials with long root roots can be used, which also stabilize the soil	Jager, 2020; Schilling, 2019; McCarthy, 2021; Jager, 2018; Tiend, 2024; Careers, 2023; Nenciu, 2022d
Pests and diseases	- Warmer temperatures and humidity create ideal conditions for many agricultural pests and diseases to thrive. - Climate change is allowing pests and diseases to spread to new areas.	- Modified Integrated Pest Management (IPM) practices. - Modified cultivation practices and adapted management strategies: planting more varieties, planting at different times of the year, increasing biodiversity at the edges of the field to reduce the number of natural enemies - The use of allelochemicals and pheromones, bioinsecticides.	Barzman, 2015; Lamichhane, 2015; Shrestha, 2019; Heuskin, 2011; Nihal, 2020; Stan, 2022; Alfizar, 2024; Nitta, 2024; Priya, 2024;
Soil health and fertility	- Increased temperatures and erratic rainfall can exacerbate soil erosion, degrade soil structure, and reduce organic matter content. - Heavy rainfall can lead to nutrient leaching, where essential minerals like nitrogen and phosphorus are washed out from the soil.	-Seed bombing on difficult or inaccessible terrain, such as steep slopes or remote areas, which are difficult for traditional planting methods. This method is useful in carbon sequestration, rapid ecosystem recovery, reduced erosion and improving soil health accelerates the reforestation process. - Conservation agriculture technology by reducing the degree of soil disturbance and diversification of plant species, preservation of crop residues from the previous year on fields before and after planting new crops. - Improving soil health and fertility by using biofertilizers, compost, biochar, mulch. - Precision soil fertilization using various smart methods.	Sarma, 2024; Rosmawati, 2023; Talukdar, 2023; Dutta, 2023; Cordovil, 2020; Nenciu, 2014 a, b; Kong, 2024; Mohawesh, 2021; Hernandez-Charpak, 2024; Calcan, 2022

Changing growing seasons	- With unpredictable seasonal changes, farmers may have difficulty timing their planting and harvesting. -Temperature changes can disrupt the timing between crop flowering and pollinator activity such as bees, reducing pollination success and crop yield.	- Crop improvement through the integration of biotechnologies. - Use of simulated historical crop calendars. - Adjustment of sowing dates. - Using Computer Crop Simulation (CSM) methods, productivity ca be assessed by using physiological processes in relation to factors affecting production. - Conservation of pollinators through strategies such as: integrated pest and pollinator management (IPPM); crop rotation; including a wide range of plants for different flowering times, sustainable pest control strategies.	Shamim, 2024; Minoși, 2022; Annie, 2023, Lundin, 2021; Guzmán, 2019; Sidhu, 2016; Long, 2016; Agbehadji, 2023; Ortiz-Bobea, 2021; Yoon, 2020
Impact on animal productivity	-Changes in crop productivity have a direct impact on the availability and price of animal feed. -Rising temperatures negatively affect animal health, reproduction and productivity.	- Using new climate-resistant crops - Improving growth practices by improving nutrition, assisted reproduction strategies, etc. - Reducing greenhouse gases by implementing different technologies and practices for carbon sequestration, improving diets to reduce enteric fermentation and using fertilizers more efficiently	Soumya, 2022; Jawhar, 2024; Llonch, 2017; Rojas-Downing, 2017; Sossidou., 2014

- **Synthesis and contextualization of validated solutions to combat the effects of climate change**

The solutions identified in the literature are largely convergent, however they are often adapted and contextualized to address the particularities of specific agro-ecological settings and thematic domains. This reflects the recognition that while the fundamental mechanisms of soil restoration and climate change mitigation are widely understood, their effective implementation requires tailoring to local biophysical conditions, socio-economic realities, and institutional capacities. In the following section, the most prevalent and empirically validated solutions reported in the scientific literature are systematically assessed and synthesized, which have demonstrated substantial potential to deliver long-term benefits in mitigating the adverse impacts of climate change on agriculture and soils. An overview of these solutions is presented in Table 2.

Table 2

Key mitigation measures reported in the literature for addressing the impact of climate change in agriculture

No.	Recommended measures	Action	References
1.	**Management of agricultural practices, no-till systems**	These measures include improving soil organic content, improving farmland management methods, improving indigenous genetic diversity, optimizing livestock farming techniques, integrating cropping and livestock systems, using diversified cropping methods, improving grazing land management, increasing agricultural productivity, mitigating soil erosion, and implementing agroecological techniques; use of planting and weed control technologies without tillage.	Yin, 2024; Dmuchowski, 2024; Liebhard, 2022; Vlăduț, 2024;
2.	**Land/soil and water management**	Adaptation to climate fluctuations is facilitated by the implementation of sustainable land management approaches, such as conservation agriculture, agroforestry, sustainable intensification and optimized cropping systems. The use of sustainable agriculture through integrated methods of managing pests and soil fertility, as well as better and more efficient use of water and nutrients.	Khatav, 2024; Hatfield, 2001; Tume, 2024; Ungureanu, 2020
3.	**Crop diversification and optimization of the harvesting system**	A reasonable and cost-effective approach to increase the resilience of the agricultural system to climate change is crop rotation, and the use of a variety of production methods is essential to ensure ecosystem regulation. For example, soil erosion control, greenhouse gas emission reduction, nutrient cycling, carbon sequestration and control of hydrological processes.	Magesa. 2023; Dawood, 2024; Nenciu, 2022c, d; Chamberlain, 2020; Huggins, 2007
4.	**Sequestration of organic carbon from the soil**	Annual cropping systems can capture unused carbon. In addition to reducing greenhouse gas (GHG) emissions, negative emissions (NET) technologies, also known as active removal techniques of CO_2 from the atmosphere, are needed to achieve net decreases in CO_2 and prevent the most dangerous consequences of climate change. Agricultural soils have the capacity to store all the CO_2 in the atmosphere, even though the level of carbon in the soil has obviously decreased in the last century.	Eckardt, 2023; Northrup, 2021; McClelland, 2021; Ogle, 2019; Nazir, 2024

No.	Recommended measures	Action	References
5.	**Development of resistant varieties**	Climate-resilient crops and varieties offer farmers a way to cope with climate change. Under new environmental conditions, these crops have a better yield, avoiding decreased productivity and crop failure	Kopeć, 2024; Matei, 2020; Nenciu, 2022 a, b
6.	**Remote sensing and satellite imagery**	The impact of climate change on agriculture can be predicted using remote sensing. For example, satellites equipped with sensors can be used to monitor vegetation and determine different indices.	El Jazouli, 2019; Kazemi Garajeh, 2023; Beeson, 2016
7.	**Use of cover crops, crop residues, mulch, compost and biochar**	In conservation agriculture, the use of cover crops is one of the basic tasks. Plant species known as cover crops are introduced into crop rotations to provide benefits to the agro-ecosystem. Cover crops can be grouped according to the role they play on the farm. They can be annuals and function as live mulch, grown either alternately or at the same time as the crop. They have a role in improving porosity and aeration and drainage of the soil, reduce nitrogen losses and help sequester carbon. The use of mulch, crop residues and biochar have proven to be beneficial for both the soil and the crop.	Zhou, 2018; Hively, 2020; Mesgaran, 2017; Sun, 2019; Dissanayaka, 2024; Yousefi, 2024; Yuan. 2022; Gholizadeh, 2021; Sachdev, 2023; Safari, 2022; Agegnehu,2016; Mak-Mensah, 2021

This synthesis provides a foundation for informed decision-making and strategic planning, linking scientific knowledge to actionable pathways for resilience and sustainability. In the next sub-chapters, a selection and evaluation of the most significant case studies with empirically validated outcomes have been undertaken to analyze recent advancements in mitigating the adverse effects of drought and enhancing the quality and functionality of agricultural soils. These case studies were chosen based on their demonstrated efficacy and relevance across diverse agroecological contexts. Specially integrated solutions that combine cutting-edge technological innovations with sustainable land management practices were selected. This approach addresses immediate drought-related challenges and promotes long-term soil resilience and productivity.

- **Solutions, equipment and technological systems for mitigating the impact of drought and restoring agricultural soils**

As climate change accelerates and intensifies the frequency and severity of droughts, the urgency for innovative and integrated solutions to preserve and restore soil health has never been greater. Traditional farming practices, while productive in the short term, have often contributed to soil degradation, diminishing its ability to retain water, store nutrients, and support resilient crop growth. This degradation undermines the natural buffering capacity of soils against climatic extremes and threatens long-term agricultural productivity. Addressing these challenges requires a shift toward sustainable soil and water management practices supported by modern equipment and advanced technological systems.

This section explores a range of scientifically validated strategies and technologies that have proven effective in mitigating the adverse impacts of drought while enhancing soil quality and functionality. These include conservation agriculture techniques such as no-till and strip-till systems, precision irrigation equipment designed to optimize water use efficiency, and soil amendments like biochar and organic composts to improve soil structure and water-holding capacity. Additionally, the adoption of sensor-based monitoring systems, geographic information systems (GIS), and decision-support tools enables real-time assessment of soil moisture, fertility, and crop health, facilitating targeted interventions and efficient resource allocation. By integrating such solutions and technologies into agricultural practices, farmers can improve the resilience of agroecosystems, reduce vulnerability to drought, and promote the restoration and long-term sustainability of agricultural soils. This holistic approach not only safeguards productivity in the face of climate stress but also contributes to broader environmental and food security goals.

✓ ***Biochar production technologies and its role in mitigating the impact of drought***

Many studies (*Yuan et al., 2019; Patwardhan et al., 2022; Guo 2021; Malyan et al., 2021; González-Pernas et al., 2022 etc.*) have suggested biochar, (a carbon-rich substance obtained from the pyrolysis of different organic materials), as a possible technical option to deal with the numerous problems caused by drought in agricultural activities. Its characteristics have a significant impact, particularly in arid and semi-arid locations, and improve soil fertility and water retention in specific settings. In order to produce biochar, biomass must be thermally decomposed in a low-oxygen environment, turning organic molecules into a stable form of carbon. This method can lower greenhouse gas emissions, aid in the absorption of carbon, and turn agricultural waste into a useful soil amendment.

Biochar can be added to soil to greatly improve its chemical and physical characteristics, such as increased microbial activity, nutrient retention, and porosity.

This section examines different approaches for producing biochar, the technology tools needed, and the systems that make it easier to use in agricultural settings. The ways in which biochar helps restore degraded soils and lessens the effects of drought is evaluated, emphasizing its significance in supporting sustainable farming methods (*Vlăduțoiu et al., 2025*).



Fig. 4 - Equipment for biochar production to enhance soil moisture retention

Technologies used in biochar production

Biochar is a solid carbon-rich product obtained by heating biomass raw materials in a controlled process, with or without a limited oxidizing agent. In general, carbon makes up about 70% of the weight of biochar. In addition to the mineral components in the ash, the remaining fragments include hydrogen, sulfur, oxygen, nitrogen. The operating conditions, the characteristics of the raw material and the technologies used in the production process are just some of the many factors that influence the performance and properties of biochar (*Anton-Herrero et al., 2018; Li et al., 2018; Wang et al. 2020; Diatta et al. 2020).*

Biochar can be obtained from a variety of organic sources, mainly wheat straw, corn straw, wood chips, melon seed shell, peanut shell, rice husk, biomass energy crops, agricultural waste, manure, sewage sludge, organic kitchen waste, and so on (*Patwardhan et al., 2022; Tanet al., 2017*).

In general, biochar is produced through different thermochemical conversion processes, under different process parameters. The main processes of obtaining biochar are: slow pyrolysis, rapid pyrolysis, torrefaction and gasification (*Leng et al, 2019*).

Slow pyrolysis is described as a process in which the decomposition of biomass occurs at a relatively moderate temperature, in an oxygen-limited or oxygen-free environment, with typical heating rates between 1 and 30 °C min -1 (*Lua et al, 2004*). The name slow refers to a low rate of heating. Through the slow pyrolysis process, pyrolysis vapors are released from biomass and exhibit both condensable and non-condensable components. These components are collected in the form of by-products. The condensable components can be recovered in the form of bio-oil, which is also called "wood vinegar", the name coming from the acetic acid content (*Setter et al., 2020*).

Rapid pyrolysis is carried out at very high heating rates of up to 1000 °C/min. In this rapid pyrolysis process, the biomass undergoes rapid decomposition resulting in the generation of pyrolysis vapor and biochar (10-15%). In other words, in the rapid pyrolysis process, the main product obtained is bio-oil, and biochar is a by-product (*Choi et al., 2017*).

Gasification is the process by which biomass undergoes incomplete combustion. This process occurs at temperatures between 700-1000 °C in the presence of gasifying agents. These agents can be air, pure oxygen, or steam and oxygen to obtain a gaseous product (*Benedetti et al., 2018*).

Torrefaction is a heat pretreatment process that improves biomass properties. The main chemical roasting process develops in the absence of oxygen to obtain a solid product that is used as a solid fuel or as a soil amendment. Torrefied biomass that has a lower O/C ratio compared to the original biomass (*Barskov et al., 2019*). Typically, the spinning process is achieved by directly or indirectly heating the biomass to temperatures between 200 and 300 °C at a low heating rate of up to 50 °C/min over a period of time between 20–120 min (*Wang, et al., 2017*).

Biological charcoal has different physical and chemical properties, depending on the thermochemical parameters of operation and the intrinsic nature of the biomass. In order to achieve a higher yield and a better quality of the desired product, several plants, furnaces and reactors were built for the production of biomass. Although these reactors have a common principle, the oxygen use, heating rate, and final temperature are different. This can affect the quality and distribution of final products.

Regardless of the biochar equipment used, the main stages of the production process are the same: shredding the biomass, carbonizing it at different temperatures to obtain the biochar, cooling the biochar (*Zaman et al., 2017; Antal et al., 2003*).

Biochar mechanisms for drought mitigation and soil restoration

Agricultural productivity has long been affected by inefficient land management practices, climate change and unsustainable use of fresh water. To reduce the impact of climate change on agricultural crops and stop or reverse desertification and the systematic loss of food quantity and quality, farmers can manage healthy soils without using harmful chemicals. Regenerative management methods, such as minimal tillage technologies, cover crops and mulching, microorganism inoculation, nutrient cycling, organic fertilizer balance, or foliar application, help manage healthy soils (*Popescu et al., 2022*).

Recognized as a promising product for carbon storage, biochar improves soil's ability to retain nutrients and water, creates energy-dense energy carriers, and improves the environment by reducing greenhouse gas emissions (*Safarian et al. 2022*).

The redefinition of contaminated soil was carried out using a variety of remediation techniques, including chemical leaching, adsorption and immobilization, electrochemical remediation, phytoremediation, bioremediation, and others. Of these, the biochar adsorption technique is considered a promising technology for remediation of in situ immobilization. This is because it is easy to use, very effective, and environmentally friendly (*Gholizadeh et al., 2021; Sachdeva et al., 2023; Lin et al., 2021*).

First, biochar occurs in the soil in the form of loose discrete particles that are not bound to the soil. Subsequently, it interacts with the different parts of the soil to form denser and more stable complexes that are involved in the soil preparation process. Biochar can be mixed with different soil components in different ways. Soil micro-agglomerates are then formed from these organic-mineral complexes by electrostatic attraction, salt bridge, and van der Waals forces (*Nkoh et al., 2021*). Finally, biological secretions serve as binders to grow micro-agglomerates in the soil, and as a result, stable macro-agglomerates are formed in the soil. Despite the complexity of the process of biochar involvement in soil agglomerates, adhesion patterns between biochar and soil components can be observed during the formation of agglomerates by the use of scanning electron microscopy (SEM) (*Bai et al., 2020*).

Biochar also has the ability to physically adsorb and chemically interact with soil elements, resulting in an organic-mineral complex (*Sun et al., 2021*). To form a porous organic-mineral complex, functional groups C and N on the surface of the biochar interact with multivalent iron oxide particles (*Archanjo et al., 2017*). Finally, electrostatic attraction, salt bridge, and van de Waals forces cause these organic-mineral complexes to merge.

In other words, biochar, through its interactions with soil components, has the ability to influence the formation of soil aggregates. The interaction between biochar and soil components is based on seven possible mechanisms. These mechanisms can be listed as follows: the first is ligand exchange and electrostatic attraction between biochar-negatively charged functional groups and positively charged mineral surfaces; the second is ligand exchange and electrostatic attraction between negatively charged soil minerals and positively charged mineral surfaces; and the third is the hydrophobic and electro-phobic interaction between soil organic matter (SOM)/microorganism the fourth is the relationship between biochar, soil minerals and SOM/soil microorganisms and dissolved organic carbon (DOC); fifth, electrostatic interactions and ligand exchange between SOMs/soil microorganisms and positively charged minerals; sixth, electrostatic interactions that take place between negatively charged soil minerals, multivalent ions and negatively charged biochar; and seventh, electrostatic interactions between positively charged mineral surfaces, multivalent ions, and negatively charged biochar functional groups (*Nkoh et al., 2021; Yuan et al., 2022; Deng et al., 2022; Bai et al., 2020*).

Various studies have shown that biochar is used to combat the effects of climate change, to remediate soils that have been contaminated with potentially toxic elements (PTE); it is used to immobilize PTEs, improve soil quality, and increase crop yields. The effect of PTE adsorption of biochar is influenced by two main factors: the choice of raw material and the pyrolysis temperature of biological charcoal. Also, the application dose and incorporation time determine the remedial effect of biological charcoal in the soil (*Bousdra et al., 2023; Ji et al., 2022; Golia et al., 2022; Calcan et al., 2022; Hussein and Alaa Hasan 2024; Osman et al., 2024*).

Even though the number of studies referring to biochar is increasing, research on its long-term effects on the environment has been far fewer than in other areas of research, such as its use as a soil improver. To better understand how aging due to abiotic and microbial processes in soil will affect the C-sequestration capacity of biochar, further research is needed. This is because the results of specific field studies differ from those of corresponding field studies due to differences in soil properties under actual environmental conditions *(Singh et al. 2022*).

In general, most studies on the soil-biochar relationship are carried out either in a laboratory or in a greenhouse setting, and less in the field. For this reason, it is imperative to carry out additional field experiments. When it comes to assessing the effects of biochar on soil properties, most studies have been conducted in less than two years (*Zeba et al., 2022*).

- ✓ ***New tillage technologies and equipment designed to mitigate the impact of drought and restore agricultural soils***

Most of the main causes of soil degradation are natural, such as climate change (soil degradation caused by wind, sun, drought or heavy rains that favor fertile soil washing) and human activities (overgrazing, deforestation, excessive use of chemical fertilizers, pesticides, herbicides, bare soils, overconsumption of groundwater, etc.) (*Popescu et al. 2022a; Popescu et al., 2022b*).

Nowadays, the main theme of agricultural discussions is to increase productivity so that it matches or exceeds traditional tillage systems in terms of energy efficiency, water conservation, soil conservation, and crop quality. As tillage directly influences the stability and susceptibility of the soil to erosion, tillage is essential for the production of agricultural crops. Despite the fact that traditional soil tillage methods are more widespread, both in Europe and in Romania, a number of studies and practical applications have shown that systems with minimal tillage are effective. In contrast to traditional soil cultivation methods, soil conservation work is a method that has a significant carbon absorption effect and uses agricultural machinery that is more friendly to both the soil and the environment (*Bogdan et al., 2024; Li et al., 2024*).

Currently, to meet the water needs for irrigation, diesel and electric pumps are used; however, these traditional systems are inefficient and expensive. In these circumstances, it is imperative to develop new methods of crop irrigation that are both economical and less harmful to the environment. Such a model is the prototype made by INMA Bucharest in collaboration with ROLIX IMPEX SERIES SRL. The innovative prototype of the system includes a photovoltaic panel frame, a 2000kg two-axle automotive platform, several 85Ah gel solar batteries, a 5kW off-grid solar inverter, a Lorentz PS2-1800 CS-F4-6 solar pump, a PS2-1800 CS-F4-6 pump controller, an intelligent irrigation management and scheduling system, and a helix vertical wind turbine, 1000W, 600 rpm. The system can be quickly transferred to rural areas where there is no other source of electricity, and the pumping of water for irrigation is carried out by a photovoltaic surface pump, reducing the annual costs of a diesel motor pump (*Mateescu et al., 2023*).

Conservation soil tillage equipment and methods

The main methods for mitigating soil degradation due to climate change and agricultural practices are: conservative tillage; biological fertilization; directly sowing or in narrow strips; biological control of weeds, diseases and pests.

Regenerative agriculture refers to organic farming that uses natural resources exclusively. It is a sustainable farming method that involves growing healthy plants and restoring soil fertility. This creates healthier soils that are less sensitive to current. Regenerative agriculture technologies reduce drought and flooding, improves soil structure and fertility, increases water retention and crop yields, and carbon sequestration in the soil (*Dougherty et al., 2019; Li et al., 2024; Sapkota et al., 2015*).

Given that there is in a period when the water crisis and the effects of climate change are the most important risks, electric or solar-powered machines are increasingly used.

With a contribution of more than 20% of global greenhouse gas emissions, 42% of methane and 75% of nitrogen oxides (NOx), the agriculture and forestry sector are primarily responsible for these emissions. In addition, emissions at farm gates are anticipated to increase over the next few years. Most of these pollutants come from tillage and intensive animal husbandry, but much of it also comes from internal combustion engines (ICE), which are the most common sources of energy in the agricultural and forestry industry.

Various prototypes of electric tractors have been debated in the literature (*Matache et al., 2020; Engström et al., 2018; Ueka et al., 2013; Melo et al., 2019; Rossi et al., 2021; Yes et al., 2019*) from tractors with only electric motors, fully electric tractors, to unmanned hybrid electric tractors (*Gonzales-de-Santos et al., 2016; Beligoj et al., 2022*), but only few of them have ended up being launched on the market.

Farmers are willing to pay more for a safe vehicle rather than a cleaner or more efficient vehicle because reliability is the most important. The main benefits of hybrid technology and electric vehicles, such as fuel economy and reduced exhaust emissions, are not the main reasons influencing purchasing decisions. But eventually, due to the lack of fossil fuels and the spread of agriculture, electric tractors will become the dominant technology in the agricultural industry in the long term (*Scolaro et al., 2021*).

The success of any tillage operation lies in the use of modern agricultural plows, conservation techniques and alternative seeding systems. Finding an innovative and unique solution for modifying the construction and operation of the agricultural plough in order to maintain performance and, in particular, to significantly reduce fuel consumption and therefore CO_2 emissions is a priority. That is why the innovative vibration system for ploughs is also a method of soil conservation. The vibration system for ploughs with bodies in operation and production consists of a new electromagnetic vibration solution and innovative electronic control elements. It reduces the traction force of agricultural ploughs depending on soil conditions, rainfall level and thermal regime (*Croitoru et al., 2016; Croitoru et al., 2017; Ungureanu et al., 2015*).

Innovative strategies to increase soil fertility

To contribute to soil biodiversity and serve as a food source for soil fauna, soil organic matter serves as a reservoir of nutrients such as nitrogen, phosphorus, and sulfur. To facilitate the penetration of roots into the soil, organic carbon in the soil improves the physical environment and supports soil structure. As part of soil organic matter, organic carbon is essential for all processes that take place in soil. The earth's ability to bind water and handle large amounts of rainfall is also crucial for adapting to climate change. The annual rate of organic matter loss varies considerably depending on a variety of factors, including, but not limited to, cultivation methods, type of plant or crop cover, soil drainage status, and weather conditions.

In arid and sandy natural soils, organic matter serves as an "oxygen balloon" for vegetation, absorbing about six times its weight. Soils with organic matter have more complex structures, which improves water infiltration and reduces the likelihood of water compacting, eroding, deserting, and sliding off the ground (*Manea et al., 2023; Rumpel et al., 2020*).

Recent land use and climate change have led to a loss of soil organic carbon, accounting for 10% of Europe's fossil fuel emissions. Therefore, one of the most important strategies for increasing soil fertility is *carbon capture* (*Lorenz et al., 2014; Cooper, et al. 2021*).

Another strategy is *the use of cover crops*. During periods when there are no cash crops, cover crops are commonly grown between the main crops to cover them and keep the plants alive on the ground. This can be done either by planting cover crops after harvest or by sowing too many profit crops, usually cereals, with perennial crops that will develop to maintain soil cover after harvest the following season (*Wagg et al., 2021*).

It is assumed that the use of cover crops with multiple species, including legumes, improve various ecosystem functions. These functions include microbial diversity, biological nitrogen fixation, compaction reduction, beneficial insect attraction, weeds suppression, soil temperature regulation, and water infiltration increase. In addition to improving soil fertility, cover cropping helps to sequester carbon. The widespread adoption of these practices could reduce greenhouse gas emissions from agriculture by 10%. This compares to using no-till cultivation or other cultivation methods (*Kaye et al., 2017; Chahal et al., 2020*).

A current strategy for increasing soil fertility is the use of digitized techniques. By providing improved management systems, digitalization can help farmers increase soil fertility and reduce pollution. For example, "precision agriculture" uses satellite guidance systems to create permanent pathways for machinery to move, while "traffic-controlled agriculture" uses digital crop monitoring to apply the ideal quantity of pesticides and nutrients to crops at the right time. Therefore, agricultural traffic cannot reach cultivated land. Water and air circulation in the soil is improved and the top layer of soil is less compacted, leading to more stable yields during periods of drought or heavy rainfall (*Manea et al., 2023*).

- ✓ ***Bioremediation solutions***

Microbial solutions for improving the quality of agricultural soils

Soil biodiversity encompasses a wide variety of living organisms, including microbes and meso-, macro- and megafauna. Due to the complex interactions they have, biodiversity plays an important role in the functioning of the ecosystem. Regenerative agriculture practices focus on improving the capacity of soil microbes. This helps to recover the fertility of the affected soil, which is 70% of the world, to create healthier and more nutritious food and to fight climate change. The soil microbiota is essential for nutrient cycling, soil fertilization, and the breakdown of organic materials. Microbes in the soil also play an important role in growing healthy soil. An excellent indicator of how well an ecosystem works across the globe is soil strength. Soils with higher microbial diversity are more resistant to disturbance and more resilient than soils with lower microbial biodiversity (*Wagg et al., 2014; Wagg et al., 2019*).

The application of microbial populations and isolation to remediate heavy metal ions in the environment was a particular point of interest, as they have the ability to effectively highlight pollution problems. Microbial populations, mainly bacteria and fungi, have acquired various heavy metal retention mechanisms, making

them good candidates for bioremediation (*Tirri et al., 2017*). It has been pointed out that there are numerous bacterial species that support plants in soil remediation, such as: *Pseudomonas*, *Bacillus*, *Variovorax*, *Klebsiella*, *Sinorhizobium*, *Enterobacter*, *Rhodococcus*, *Flavobacterium*, *Ensifer* and *Kocuria* (*Asad et al., 2019; Zhu et al., 2023; Guo et al., 2020; Wang et al., 2024*) or fungi such as: *Rhizophagus*, *Trichoderma, Beauveria bassiana,* Glomus *versiforme* (*Yang et al., 2021; Arriagada et al., 2009; Gola et al., 2021*).

A new model of soil fertility based on biology is the soil food web. It is a better model because it costs less, does not cause disease, does not pollute and uses fewer chemicals. Microorganisms are the intermediaries between water, plants and nutrients. Plants control the soil's viable food web and exudates through the consumption of carbohydrates and proteins. In addition, they attract certain bacteria and fungi. At the bottom of the soil food web are bacteria and fungi that consume root exudates. Even in the rhizosphere, bacteria and fungi are consumed by larger microbes, nematodes, and protozoa and are excreted as nutrients. Arthropods eat protozoa and nematodes. Arthropods can be eaten by other arthropods, or they can be eaten by snakes, birds, moles, and other animals. Worms, insect larvae, and moles move through the ground in search of food, building paths that allow water and air to enter.

To help create soil structure, components of the soil's food web bind soil particles together, creating tunnels for air and water. The soil food web is a natural design and has seven major advantages. These include preventing disease, retaining nutrients, increasing the availability of mineral nutrients to plants, improving soil structure, breaking down toxic chemicals, growing production plants, and improving crop quality. Root growth hormones are released by microorganisms and other members of the food web in the soil. These growth hormones help plants cope with the current or a flood and help them produce more (*Lowenfels et al., 2010*).

✓***Phytoremediation strategy for the management of contaminated soils***

The sustainable phytoremediation method uses plants to improve polluted environments, such as agroecosystems. New approaches have been reported that use the plant microbiome in remedial processes. Plants can more effectively sequester, degrade, or stabilize contaminants by using this microbial assistance to remediate soils contaminated with heavy metals such as As, Pb, Cd, Hg, and Cr. Some plant species are notable for their hyper-accumulative properties, which work well with their microbial partners and can mitigate heavy metal pollutants. This sustainable biotechnology based on plant-microbe associations improves biodiversity, improves soil structure, and promotes plant growth and health, making it a promising solution to the problem of agricultural pollution globally (*Zhu et al., 2023; Manoj et al., 2020*).

To remove organic and inorganic chemicals from polluted areas, there are a variety of phytoremediation technologies, including phytoextraction, phyto-stabilization, phytodegradation, phytovolatilization, rhizo-filtration, and rhizo-degradation. Different phytoremediation methods depend on the level of cleaning, the type of pollutant, the types of plants and the condition of the site (*Iacov et al., 2018*). Several species with well-developed root systems have the ability to absorb large amounts of pollutants, especially HM, and then transfer them to the leaves and shoots using a sweat pump powered by solar energy. Thus, toxic substances close and are deposited in metabolically inactive cell spaces, such as the vacuole, cell membrane, and cell wall, of the aerial parts, without causing damage to the body as a whole. About 700 species of trees, herbs and shrubs mainly from the *Brassicaceae* family, but also others such as *Euphorbiaceae, Asteraceae, Lamiaceae, Poaceae Scophulariaceae, P. vittata, Thlaspi caerulescens, B. napus, A. bertolonii, S. alfredii and P. American*: *Brassica napus, Brassica juncea, Cannabis sativa, Sinapis, Nicotiana tabacum, Miscanthus spp., Sorghum bicolor, Lemna minor,* etc. are recognized as hyper accumulative plants (*Pruteanu et al., 2018; Pruteanu et al., 2019; Pruteanu et al., 2020; Meers et al., 2005; Brunetti et al., 2011; Barbosa et al., 2015; Nsanganwimana et al., 2014; Xiao et al., 2021; Tăbărașu et al., 2023; Osman et al., 2023*).

- **Renewable energies and technologies that optimize resource consumption in agriculture**

Nowadays, different industries frequently use renewable resources to meet their energy needs. Renewable energy can be used in agriculture for various activities. It can shed light on many problems that have arisen as a result of our dependence on fossil fuels, such as the reduction of fossil fuel reserves, increased spending, harmful effects on the environment, and so on. In the long term, the use of renewable energy in agriculture will help overcome these problems, leading to higher profits and more independence. Energy from these renewable sources can be used for a longer period of time without depleting natural resources. Solar, biomass, wind, and geothermal energy are all renewable energy sources available in agriculture (*Yaqoob et al.2023, Voicea et. al. 2024*).

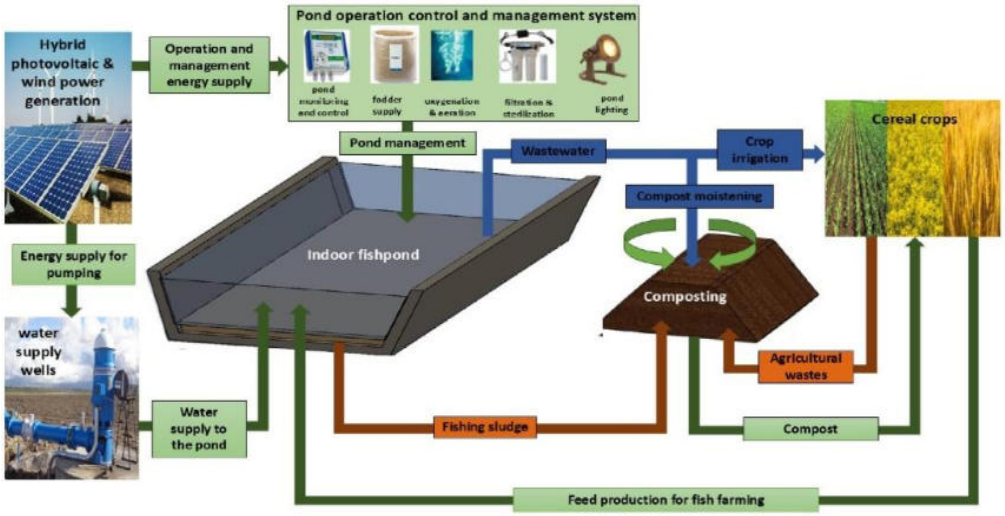


Fig. 5 - Self-Sufficiency Approach within a Sustainable Integrated Pisciculture Farming System (*Voicea et. al., 2024*)

Agricultural activities traditionally rely heavily on fossil fuels, making the transition to renewable sources essential for reducing greenhouse gas emissions and ensuring long-term environmental sustainability. Solar energy systems, such as photovoltaic panels, are increasingly deployed to power irrigation pumps, greenhouse heating, and farm machinery, offering clean and cost-effective alternatives (*Hoogwijk, 2004*). Similarly, wind energy is utilized on farms both for local electricity consumption and for contributing with the surplus energy to the grid. Biogas production from livestock manure and crop residues not only provides a renewable energy source, but also addresses waste management and nutrient recycling challenges (*Hasan et al., 2019a, 2019b*). Hybrid systems that combine solar, wind, and biogas technologies enhance the reliability of energy supply by making use of multiple renewable resources. On-site renewable energy generation improves the energy self-sufficiency of farms and supports the adoption of modern technologies such as precision agriculture tools, automated systems, and environmental monitoring devices *(Baidya Roy and Traiteur, 2010*). Moreover, investments in renewable energy systems can create additional economic opportunities through the sale of excess electricity and the generation of carbon credits (*Armstrong et al., 2014*). Energy-efficient designs and the integration of renewable sources help reduce production costs while maintaining or improving productivity.

Overall, the adoption of renewable energy systems in agriculture supports a transition towards more resilient, economically viable, and environmentally responsible food production systems (*Harris et al., 2014; Sanz et al., 2017; Aschilean et al., 2018*).

CONCLUSION

Global warming affects soil in a number of ways, including soil damage, loss of organic matter, soil compaction and salinization, drought, and flooding. The principles of conservation agriculture can benefit the soil. The structure of the soil depends primarily on cultivation, especially ploughing, which breaks up the soil and destroys earthworm tunnels, which are essential for drainage and water retention. Direct drilling has been shown to increase transit capacity, reduce long-term soil compaction, reduce wind and water erosion, reduce water evaporation, and increase water availability in the soil. Also, due to its low energy consumption, direct drilling reduces investment in machinery and improves planting and harvesting time. Crop residues reduce the use of herbicides, as they suppress weed growth.

Recent literature highlights several critical steps to accelerate the global and local adoption of climate-smart agriculture (CSA). These include developing comprehensive climate-alert strategies, integrating climate change risks into national policy agendas, and empowering farmers through targeted education and training programs. A particularly effective strategy for implementing CSA is the adoption of precision agriculture, leveraging advanced tools such as information technology, geographic information systems (GIS), and remote sensing. These technologies enhance the efficiency of agricultural inputs while providing valuable, high-resolution data on crops, soils, and climatic conditions. Such data-driven insights enable informed decision-making and the selection of optimal cropping strategies that mitigate the adverse impacts of climate change. Ultimately, a coordinated approach combining policy, education, and technology is essential to build resilient agricultural systems and ensure sustainable food production in the face of a changing climate.

Studies shown that implementing various soil health measures (such as maintaining permanent or increased soil cover, minimizing soil disturbance through reduced or no ploughing, and adopting conservation tillage practices like no-till or strip-till), represents a cornerstone of sustainable agriculture. When combined with the strategic use of cover crops and diverse crop rotations, these practices deliver multiple agronomic, ecological, and economic benefits. Improved soil structure and enhanced organic matter content contribute to greater water infiltration and retention, thereby increasing drought resilience and buffering crops against extreme weather events. Conservation practices also promote soil biodiversity, foster nutrient cycling, and reduce erosion, which collectively sustain or even improve long-term agricultural productivity. Furthermore, by reducing soil carbon losses and enhancing sequestration, these approaches lower greenhouse gas emissions and improve the overall environmental footprint of farming systems. Integrating these scientifically proven soil health strategies into mainstream agricultural management is critical for building resilient agroecosystems capable of meeting the growing global demand for food while safeguarding natural resources and mitigating the impacts of climate change.

The studies found that farmers should regularly incorporate organic matter, such as compost or green manure, alongside biochar into their soils to enhance fertility, structure, and moisture retention over time. This combined approach not only improves nutrient availability and microbial activity, but also promotes long-term carbon sequestration, contributing to more resilient and sustainable soil health. Consistent application, tailored to specific soil conditions and crop needs, will maximize these benefits.

The primary limitation of this study lies in the considerable diversity of methodologies, experimental conditions, and assessment metrics reported across the reviewed studies, which complicates direct quantitative comparisons between the evaluated technologies.

Long-term studies of soilless tillage are needed to see how they affect soil compaction, carbon sequestration, soil erosion, soil temperature due to mulch cover, water infiltration and their impact on global warming.

ACKNOWLEDGEMENT

This work was funded by the Ministry of Agriculture and Rural Development – Romania - MADR through the Sectoral Project ADER 18.1.1 *"Developing solutions for restoring soil health while maintaining environmental sustainability by capitalizing on the fertilizer potential of organic fertilizers*" and by the Ministry of Research, Innovation and Digitalization, within the NUCLEU Program, through Project 9N/ 23 04 02 01, „Innovative technology for the production of biofertilizers to restore soil biodiversity and reduce the effects of drought on agricultural land".

REFERENCES

[1] Alfizar and Nasution S.S. (2024). The explosion of pests and diseases due to climate change, IOP Conf. *Ser.: Earth Environ.* Sci. 1297 012072, DOI: https://doi.org/10.1088/1755-1315/1297/1/012072.

[2] Agbehadji, I.E., Schütte, S., Masinde, M., Botai, J., & Mabhaudhi, T (2023). Climate risks resilience development: a bibliometric analysis of climate-related early warning systems in Southern Africa. *Climate,* 12(1). DOI: https://doi.org/10.3390/cli12010003.

[3] Ajala, O.O., Akinnawo, S.O., Bamisaye, A., Adedipe, D.T., Adesina, M.O., Okon-Akan, O.A., Adebusuyi, T.A., Ojedokun, A.T., Adegoke, K.A., and Bello, O.S. (2023). Adsorptive removal of antibiotic pollutants from wastewater using biomass/biochar-based adsorbents, *RSC Advances*, *7*, 4678–4647 DOI: https://doi.org/10. 1039/d2ra06436g.

[4] Akinnawo, S.O., Ayadi, P.O., Oluwalope, M.T. (2023). Chemical coagulation and biological techniques for wastewater treatment. Ovidius *UniversityAnnals of Chemistry, 34 (1)*, pp. *14-21*. DOI: https://doi.org/10.2478/auoc-2023-0003.

[5] Ali, A., Erenstein, O. (2017). Assessing farmer use of climate change adaptation practices and impacts on food security and poverty in Pakistan Clim. *Risk Manag., 16, pp. 183-194,* DOI: *https://doi.org/10.1016/j.crm.2016.12.001*.

[6] Alvar-Beltrán, J., Elbaroudi, I., Gialletti, A., Heureux, A., Neretin, L. Soldan, R. (2021). Climate Resilient Practices: typology and guiding material for climate risk screening. Rome*, FAO,* https://openknowledge.fao.org/handle/20.500.14283/cb3991en.

[7] Annie, M.; Pal, R.K.; Gawai, A.S.; Sharma, A. (2023*).* Assessing the impact of climate change on agricultural production using crop simulation model. int. j. approximately. *Clim. Change, 13*, 538–550. DOI: https://doi.org/10.9734/ijecc/2023/v13i71906.

[8] Antal, M.J., Grönli, M. (2003). The art, science, and technology of charcoal production. *Industrial & Engineering Chemistry Research, Vol; 42*, pp. *1619-1640*. DOI: https://doi.org/10.1021/IE0207919.

[9] Anton-Herrero, R, Garciadelgado, C, Alonsoizquierdo, M, Garciarodriguez, G, Cuevas J, Eymar E. (2018). Comparative adsorption of tetracyclines on biochars and stevensite: search for the most effective adsorbent. *Appl Clay Sci 160:162–172*. DOI: https://doi.org/10.1016/j.clay.2017.12.023.

[10] Archanjo B.S., Mendoza, M.E., Albu, M., Mitchell, D.R.G.,Hagemann,N. Mayrhofer, C., Thi Lan Anh Mai, Zhe Weng, Kappler, A. , Behrens, S., Munroe, P., Achete, C.A., Donne, S. Araujo, J.R., van Zwieten, L., Horvat, J. Enders, Joseph, A. (2017). Nanoscale analyses of surface structure and biocharacter composition extracted from field studies or after cocomposting using advanced analytical electron microscopy, *Geoderma* 294, 70-79. DOI: https://doi.org/10.1016/j.geoderma.2017.01.037.

[11] Armstrong, A., Waldron, S., Whitaker, J., Ostle, N.J. (2014). Wind farm and solar park effects on plant–soil carbon cycling: uncertain impacts of changes in ground-level microclimate. *Global Change Biol.,* 20 (6). DOI: https://doi.org/10.1111/gcb.12437.

[12] Arriagada, C.; Aranda, E.; Sampedro, I.; Garcia-Romera, I.; Ocampo, J.A. (2009). Contribution of the saprobic fungi Trametes versicolor and Trichoderma harzianum and the arbuscular mycorrhizal fungi Glomus deserticola and G. claroideum to arsenic tolerance of Eucalyptus globulus. *Bioresour. Technol. 100, 6250–6257*. DOI: https://doi.org/10.1016/j.biortech.2009.07.010.

[13] Asad, S.A.; Farooq, M.; Afzal, A. (2019). West, H. Integrated phytobial heavy metal remediation strategies for a sustainable clean environment - A review. *Chemosphere, 217, 925–941*. DOI: https://doi.org/10.1016/j.chemosphere.2018.11.021.

[14] Aschilean, I.; Rasoi, G.; Raboaca, M.S.; Filote, C.; Culcer, M. (2018). Design and Concept of an Energy System Based on Renewable Sources for Greenhouse Sustainable Agriculture. *Energies 11, 1201*. DOI: https://doi.org/10.3390/en11051201.

[15] Ashraf, A., Bano, A., Ali, S.A. (2019). Characterisation of Plant Growth-Promoting Rhizobacteria from Rhizosphere Soil of Heat-Stressed and Unstressed Wheat and Their Use as Bio-Inoculant. *Biol plant.;* 21:762–769. DOI: https://doi.org/10.1111/plb.12972.

[16] Bai, N., Zhang, H., Zhou, S., Sun, H., Zhao, Y., Zheng, X., Li, S., Zhang, J., Lv, W. (2020). Long-term effects of straw return and modification of straw-derived biological charcoal on bacterial communities in soil aggregates. *Sci. Rep. 10, 7891*. DOI: https://doi.org/10.1038/ S41598-020-64857-W.

[17] Barbosa, B.; Boléo, S.; Sidella, S.; Costa, J.; Duarte, M.P.; Mendes, B.; Cosentino, S.L.; Fernando, A.N. (2015). Phytoremediation of heavy metal-contaminated soils using the perennial energy crops Miscanthus spp. and Arundo donax L. *Bioenerg*. Res. 8, 1500–1511. DOI: https://doi.org/10.1007/s12155-015-9688-9.

[18] Barskov, S., Zappi, M., Buchireddy, P., Dufreche, S., Guillory, J., Gang, D., Hernandez, R., Bajpai, R., Baudier, J., Cooper, R., Sharp, R. (2019). Torrefaction of biomass: A review of production methods for biocoal from cultured and waste lignocellulosic feedstocks. *Renew. Energy. 142,* 624–642. DOI: https://doi.org/10.1016/j.renene.2019.04.068.

[19] Barzman, M., Bàrberi, P., Birch, A.N.E., Boonekamp, P., Dachbrodt-Saaydeh, S., Graf, B., Hommel, b., Jensen, J. E., Kiss,J., Kudsk,P., Lamichhane, J.L., Messéan, A., Moonen, A. C., Ratnadass, A., Ricci, P., Sarah J.L., Sattin M. (2015). Eight principles of integrated pest management. *Agron. Sustain. Dev. 35, 1199–1215*. DOI: https://doi.org/10.1007/s13593-015-0327-9.

[20] Beligoj M., Scolaro E., Alberti L., Renzi M., Mattetti M. (2022). Feasibility evaluation of hybrid electric agricultural tractors based on life cycle cost analysis, *in IEEE Access, vol. 10*, pp. 28853-28867 DOI: https://doi.org/10. 1109/ACCESS.2022.3157635.

[21] Benedetti, V., Patuzzi, F., Baratieri, M. (2018). Characterization of char from biomass gasification and its similarities with activated carbon in adsorption applications. *Appl. Energ. 227, 92–99*. DOI: https://doi.org/10.1016/j.apenergy.2017.08.076.

[22] Bilias, F., Kalderis, D., Richardson, C., Barbayiannis, N., Gasparatos, D. (2023). The application of biochar as a soil potassium management strategy: A review. *Sci. Total Environment. 858*. DOI: https://doi.org/10.1016/j.scitotenv.2022.159782.

[23] Biriș, S. S., Constantin, A.-M., Anghelache, D., Gageanu, I., Cujbescu, D., Nenciu, F., Voicea, I., Matei, G., Popa, D., & Duțu, M. F. (2021). Considerations regarding the vibrations transmitted to the operator by an axial flow harvester combine. *INMATEH - Agricultural Engineering*, 68(3). DOI: https://doi.org/10.35633/inmateh-68-74.

[24] Bogdan, C., Ranta, O., Ghețe, A.B., Marian, O., Andraș, I.G.C. (2024). A Romanian standpoint on minimum tillage soil system and prospects for an sustainable agriculture: A review. *In: Lorencowicz, E., Huyghebaert, B., Uziak, J. (eds) Farm Machinery and Processes Management in Sustainable Agriculture. FMPMSA 2024. Lecture Notes in Civil Engineering, vol 609. Springer, Cham*. DOI: https://doi.org/10.1007/978-3-031-70955-5_9.

[25] Bousdra, T., Papadimou, S.G., Goliath, E.E. (2023). The use of biochar in the remediation of soils contaminated with Pb, Cd and Cu. *The impact of raw materials and conditions for the preparation of biological charcoal on its remediation capacity. Land 12.* DOI: https://doi.org/10.3390/ Earth 12020383.

[26] Brunetti, G.; Farrag, K.; Soler-Rovira, P.; Nigro, F.; Senesi, N. (2011). Greenhouse and field studies on Cr, Cu, Pb and Zn phytoextraction by Brassica napus from contaminated soils in the apulia region, southern Italy. *Geoderma 160,* 517–523. DOI: https://doi.org/10.1016/j.geoderma.2010.10.023.

[27] Bularda M., Vişinescu I, Ghiorghe A., Vlăduţ V., Cujbescu D. (2020). The effect of conservative agricultural works on soil and field plants and optimized mechanization technologies, I*NMATEH – AGRICULTURAL ENGINEERING* 61(2), pp. 323-338, DOI: https://doi.org/10.35633/inmateh-61-35.

[28] Calcan, S.I.; Pârvulescu, O.C.; Ion, V.A.; Răducanu, C.E.; Bădulescu, L.; Madjar, R.; Dobre, T.; Egri, D.; Moț, A.; Iliescu, L.M. (2022). Effects of biochar on soil properties and tomato growth. *Agronomy, 12, 1824*. DOI: https://doi.org/10.3390/agronomy12081824.

[29] Cârdei, P., Nenciu, F., Ungureanu, N., Pruteanu, M. A., Vlăduț, V., Cujbescu, D., Găgeanu, I., & Cristea, O. D. (2021a). Using statistical modeling for assessing lettuce crops contaminated with Zn, correlating plants growth characteristics with the soil contamination levels. *APPLIED SCIENCES* 11(17), DOI: https://doi.org/10.3390/app11178261.

[30] Cârdei, P., Tudora, C., Vlăduț, V., Pruteanu, A., Găgeanu, I., Cujbescu, D., Bordean, D., Ungureanu, N., Cristea, O. (2021b). Mathematical model to simulate the transfer of heavy metals from soil to plant, *SUSTAINABILITY* 13(11), 6157, DOI: https://doi.org/*10.3390/su13116157*

[31] Carreiras J., Cruz-Silva A., Fonseca B., Carvalho R.C., Cunha J.P., Proença Pereira J., Paiva-Silva C., Santos S.A., Janeiro Sequeira R., Mateos-Naranjo E., Rodríguez-Llorente, I.D., Pajuelo, E., Redondo-Gomèz, S., Matos, A.R., Mesa-Marin, J., Figueiredo, A., Duarte, R. (2023). Improving grapevine heat stress resilience with marine plant growth-promoting rhizobacteria consortia. *Microorganisms; 11:856.* DOI: https://doi.org/10.3390/microorganisms11040856.

[32] Chahal, I.; Vyn, R.J.; Mayers, D.; Van Eerd, L.L. (2020). Cumulative impact of cover crops on soil carbon sequestration and profitability in a temperate humid climate. *Sci. Rep., 10,* 13381. DOI: https://doi.org/10.1038/s41598-020-70224-6.

[33] Chaín J.M., Tubert E., Graciano C., Castango, N. L., Recchi, M., Pieckenstain, F. L., Estrella, M. J., Gudesblat, G., Amodeo, G., Baroli, I. (2020). Growth promotion and protection from drought in Eucalyptus grandis seedlings inoculated with beneficial bacteria embedded in a superabsorbent polymer. *Sci Rep, 10*, p. *18221*. DOI: https://doi.org/10.1038/s41598-020-75212-4.

[34] Choi, J.H., Kim, S.S., Ly, H.V., Kim, J., Woo, H.C. (2017). Effects of water-washing Saccharina japonica on fast pyrolysis in a bubbling fluidized-bed reactor. *Biomass Bioenergy 98,* 112–123. DOI: https://doi.org/10.1016/j.biombioe.2017.01.006

[35] Ciobotaru, I. E., Nenciu, F., & Vaireanu, D. I. (2013). The electrochemical generation of ozone using an autonomous photovoltaic system. *Revista de Chimie,* 64(11).

[36] Cooper, H.V.; Sjögersten, S.; Lark, R.M.; Girkin, N.T.; Vane, C.H.; Calonego, J.C.; Rosolem, C.; Mooney, S.J. (2021). Long-term zero-tillage en-hances the protection of soil carbon in tropical agriculture. *Eur. J. Soil Sci., 72*, pp. 2477–2492. DOI: https://doi.org/10.1111/ejss.1311.

[37] Cordovil, C. M.d.S., Bittman, S., Brito, L.M., Gross, M.J., Hunt, D., Serra, J., Gourley, C., Aranos, S., Skiba,U., Amon, B., Vale, M.J., Cruz, S., Reis, R., Dalgaard, T., Hutchings, N. (2020). Climate-resilient and smart agricultural management tools to cope with climate change-induced soil quality decline, *Climate Change and Soil Interactions, Elsevier*, Pages 613-662. DOI: https://doi.org/10.1016/B978-0-12-818032-7.00022-9.

[38] Croitoru, Şt., Vlăduţ, V., Marin, E., Matache, M., Dumitru, I. (2016). Determination of subsoiler's traction force influenced by different working depth and velocity, *15th International Scientific Conference "ENGINEERING FOR RURAL DEVELOPMENT" Proceedings,* vol. 15, pp. 817-825, Jelgava, Latvia.

[39] Croitoru, Şt., Vlăduţ, V., Voicea, I., Gheorghe, Gh., Marin, E., Vlăduţoiu, L., Moise, V., Boruz, S., Pruteanu, A., Andrei, S., Păunescu, D. (2017). Structural and kinematic analysis of the mechanism for arable deep soil loosening, *PROCEEDINGS OF THE 45 INTERNATIONAL SYMPOSIUM ON*

AGRICULTURAL ENGINEERING "Actual Tasks on Agricultural Engineering", pp. 207-216, Opatija – Croaţia

[40] Cujbescu, D., Nenciu, F., Persu, C., Găgeanu, I., Gabriel, G., Vlăduţ, N.-V., Matache, M., Voicea, I., Pruteanu, A., Bularda, M., Paraschiv, G., & Boruz, S. P. (2023). Evaluation of an optical sorter effectiveness in separating maize seeds intended for sowing. *Applied Sciences,* 13(15). DOI: https://doi.org/10.3390/app13158892.

[41] Das, A., Jain, Y., Agrewale, M. R. B., Bhateshvar, Y. K., Vora, K. (2019). Designing a mini electric tractor concept, in *Proc. IEEE Transp. Electrif. Conf.* (ITEC-India), pp. 1–7. DOI: https://doi.org/10.1109/ITEC-India48457.2019.ITECINDIA2019-134.

[42] Dastogeer K.M.G., Li H., Sivasithamparam K., Jones M.G.K., Wylie S.J (2018). Fungal endophytes and a virus confer drought tolerance to Nicotiana benthamiana plants through modulating osmolytes, antioxidant enzymes and expression of host drought responsive genes. *Environmental and Experimental Botany, 149*, pp. *95-108*. DOI: https://doi.org/10.1016/j.envexpbot.2018.02.009.

[43] Deng, H., He, H., Li, W., Abbas, T., Liu, Z (2022). Characterization of amphoteric bentonite-charged magnetic biochar and its adsorption properties for Cu (2+) and tetracycline. *PeerJ 10, e13030*. DOI: https://doi.org/10.7717/peerj.13030.

[44] Diatta, A.A.; Fike, J.H.; Battaglia, M.L.; Galbraith, J.M.; Baig, M.B. (2020). Effects of biochar on soil fertility and crop productivity in arid regions: A review. *Arab. J. Geosci*. 13, 595. DOI: https://doi.org/10.1007/s12517-020-05586-2.

[45] Dougherty B. (2019). Regenerative Agriculture: The path to healing agroecosystems and feeding the world in the 21st Century. *Nuffield International* Project No. 1801.

[46] Duarte, B., Carreiras, J.A., Cruz-Silva, A., Mateos-Naranjo, E., Rodríguez-Llorente, I.D., Pajuelo, E., Redondo-Gómez, S., Mesa-Marín, J., Figueiredo, A (2024). Marine Plant Growth Promoting Bacteria (PGPB) Inoculation Technology: Testing the Effectiveness of Different Application Methods to Improve Tomato Plants Tolerance against Acute Heat Wave Stress. *Plant Stress.;11:100434.* DOI: https://doi.org/10.1016/j.stress.2024.100434.

[47] Dutta, SK, Sarma, HH, Saud, RK, Konwar, MJ, Gogoi, B, Mahanta, S, Pathak, K. (2024). Impact of organic and natural farming practices on growth, yield attributes, and yield of Joha rice. *Journal of Scientific Research and Reports.* 30(6):302-309. Available: DOI: https://doi.org/10.9734/JSRR/202.

[48] Eekhout, J.P.C.; De Vente, J. (2022). Global impact of climate change on soil erosion and potential for adaptation through soil conservation. *Earth-Sci. Rev., 226,* 103921. DOI: https://doi.org/10.1016/j.earscirev.2022.103921.

[49] Enaime, G., Bacaoui, A., Yaacoubi, A., Lübken, M. (2020). Biochar for wastewater treatment—conversion technologies and applications Appl. *Sci.,* 10. DOI: https://doi.org/10.3390/app10103492.

[50] Engström J., O. Lagnelöv O (2018). An autonomous electric tractor - Simulation of all operations on a Swedish dairy farm, J. *Agricult. Sci. Technol. A,* vol. 8, no. 3, pp. 1–6â. DOI: https://doi.org/10.17265/2161-6256/2018.03.006.

[51] Kong, F., SUN H., Jiankun, LI J., Liu, B., YiI, L., Lan, Y., Han, X., Geng D., Gao Q (2024). Establishment and application of soil fertilization prescription chart, *INMATEH - Agricultural Engineering, Vol. 72, No. 1,* pp *11-21*. DOI: https://doi.org/10.35633/inmateh-72-01.

[52] Fanai, A., Bohia, B., Lalremruati, F., Lalhriatpuii, N., Lalrokimi, Lalmuanpuii R., Singh P.K., Zothanpuia. (2024). Plant growth promoting bacteria (PGPB)-induced plant adaptations to stresses: an updated review. PeerJ Aug 20; 12: E17882. DOI: https://doi.org/10.7717/peerj.17882.

[53] Ferreira, C. S. S., Seifollahi-Aghmiuni, S., Destouni, G., Ghajarnia, N., & Kalantari, Z. (2022). *Soil degradation in the European Mediterranean region: Processes, status and consequences. Science of The Total Environment, 805, 150106.* DOI: https://doi.org/10.1016/j.scitotenv.2021.150106.

[54] Foste, X., Vaneeckhaute, C. (2021). Modifying the resin type of hybrid anion exchange nanotechnology (HAIX-Nano) to improve its regeneration and phosphate recovery efficiency. *NPJ Clean Water, 4 (53*), pp. *1-8*. DOI: https://doi.org/10.1038/s41545-021-00142-1.

[55] Gholizadeh, M., Hu, X. (2021). Removal of heavy metals from soil with biochar composite: a critical review of the mechanism. *J. Environment. Chem. Ing. 9.* DOI: https://doi.org/10.1016/j.jece.2021.105830.

[56] Gola, D.; Tyagi, P.K.; Chauhan, N.; Malik, A.; Srivastava, S.K. (2021). Beauveria bassiana assisted remediation of chromium and indanthane blue. *J. Environ. Chem. Eng. 9, 105552*. DOI: https://doi.org/10.1016/j.jece.2021.105552.

[57] Golia, E.E., Aslanidis, P.S.C., Papadimou, S.G., Kantzou, O.D., Chartodiplomenou, M.A., Lakiotis, K., Androudi, M., Tsiropoulos, N.G (2022). Evaluation of the remediation of soils, moderately contaminated with potentially toxic metals, using different forms of carbon (charcoal, biochar, activated carbon). *Impact on contamination, metal availability and soil indices. Support. Chem. Pharm. 28* DOI: https://doi.org/10.1016/j. Reference.2022.100724.

[58] Gonzalez-de-Soto, M., Emmi L., Benavides, C., Garcia I., Gonzalez-de-Santos, P. (2016). Reducing air pollution with hybrid robotic tractors for precision farming, Biosyst. *Eng., vol. 143,* pp. 79–94. DOI: https://doi.org/10.1016/j.biosystemseng.2016.01.008.

[59] González-Pernas, F.M.; Grajera-Antolín, C.; García-Cámara, O.; González-Lucas, M.; Martín, M.T.; González-Egido, S.; Aguirre, J.L. (2022). Effects of biochar on biointensive horticultural crops and its economic viability in the Mediterranean climate. *Energy*, 15, 3407. DOI: https://doi.org/10.3390/en15093407.

[60] Gornall, J., Betts, R., Burke, E., Clark, R., Camp, J., Willett, K, Wiltshire, A., (2010). Implications of climate change for agricultural productivity in the early twenty-first century. *Philos Trans R Soc Lond B Biol Sci* Sep 27; 365(1554):2973-89. DOI: https://doi.org/10.1098/rstb.2010.0158*. PMID: 20713397; PMCID: PMC2935125*.

[61] Guo, J.; Muhammad, H.; Lv, X.; Wei, T.; Ren, X.; Jia, H.; Atif, S.; Hua, L (2020). Prospects and applications of plant growth promoting rhizobacteria to mitigate soil metal contamination: A review. *Chemosphere 246, 125823*. DOI: https://doi.org/10.1016/j.chemosphere.2020.125823.

[62] Guo, L.; Yu, H.; Kharbach, M.; Zhang, W.; Wang, J.; Niu, W. (2021). Biochar improves soil-tomato plant, tomato production, and economic benefits under reduced nitrogen application in northwestern China. *Plants*, *10, 759*. DOI: https://doi.org/10.3390/plants10040759.

[63] Guzman, A., Chase, M., & Kremen, C. (2019). On-farm diversification in an agriculturally-dominated landscape positively influences specialist pollinators*. Frontiers in Sustainable Food Systems, 3, 87*. DOI: https://doi.org/10.3389/fsufs.2019.00087.

[64] Harris, R.A., Zhoun L., Xia G (2014). Satellite observations of wind farm impacts on nocturnal land surface temperature in Iowa *Remote Sens*. 6 (12). DOI: https://doi.org/10.3390/rs61212234.

[65] Hasan, M., Shang, Y., Akhter ,G., Jin, W. (2019a.), Application of VES and ERT for delineation of fresh-saline interface in alluvial aquifers of Lower Bari Doab*, PakistanJ. Appl. Geophys*., 164 pp. 200-213. DOI: https://doi.org/10.1016/j.jappgeo.2019.03.013.

[66] Hasan, M.U., Malik, A.U., Ali, S., Imtiaz, A., Munir, A., Amjad, W., Anwar, R. (2019b). Modern drying techniques in fruits and vegetables to overcome postharvest losses: A review *J. Food Process. Preserv.,* 43 (12). DOI: https://doi.org/10.1111/jfpp.14280.

[67] He, J. (2024). Enhancing productivity and improving nutritional quality of subtropical and temperate leafy vegetables in tropical greenhouses and indoor farming systems. *Horticulturae, 10(3), 306*. DOI: https://doi.org/10.3390/horticulturae10030306.

[68] Hernandez-Charpak, Y.D., Mozrall, A.M., Williams, N.J., Trabold, T.A., Diaz, C.A. (2024). Biochar as a sustainable alternative to carbon black in agricultural mulch films, *Environmental Research*, Volume 246, 1, 117916. DOI: https://doi.org/10.1016/j.envres.2023.117916.

[69] Heuskin, S.; Verheggen, F.J.; Haubruge, E.; Wathelet, J.P.; Lognay, G. (2011). The use of semiochemical slow-release devices in integrated pest management strategies. *Biotechnology. Agron. Soc. Environ. 15,* 459–470.

[70] Hoogwijk M.M (2004). *On the global and regional potential of renewable energy sources*; - MSc Thesis, Utrecht University Repository, Netherlands. np-net. *pbworks.com*.

[71] Hunter, M.C., Kemanian, A.R., Mortensen D.A. (2021). Cover crop effects on maize drought stress and yield Agric*. Ecosyst. Environ., 311, Article* 107294, DOI: https://doi.org/10.1016/j.agee.2020.107294.

[72] Hussein, F., Alaa Hasan, F. (2024). Biochar Enhanced Chemical and Biological Properties of Contaminated Soils with Lead, IOP Conf. *Series: Earth and Environmental Science*, 1259. DOI: https://doi.org/10.1088/1755-1315/1259/1/012024.

[73] Hwang, S-J. (2020). Eutrophication and the ecological health risk Int. *J. Environ. Res. Public Health,* 17 (6332). DOI: https://doi.org/10.3390/ijerph17176332.

[74] Isticioaia, S.-F., Leonte, A., Gheorghe, M., Popa, L.-D., Carabulea, V., Pintilie, P.-L., Enea, A., Pintilie, A.-S., Vladut, V., & Nenciu, F. (2024). The economic efficiency of some cereals under the influence of climate changes in the central area of Moldova, Romania*. Scientific Papers - Series Management, Economic Engineering in Agriculture and Rural Development,* 24(1).

[75] Jacob, J.M.; Karthik, C.; Saratale, R.G.; Kumar, S.S.; Prabakar, D.; Kadirvelu, K.; Pugazhendhi, A. (2018). Biological approaches to tackle heavy metal pollution: A survey of literature. *J. Environ. Manag. 217,* 56–70.

[76] Jager, H.I., Efroymson, R.A. (2018). Can upstream biofuel production increase the flow of downstream ecosystem goods and services? *Biomass and Bioenergy, 114*, pp. 125-131, DOI: https://doi.org/10.1016/j.biombioe.2017.08.027.

[77] Jager, H.I., Parish, E.S., Langholtz, M.H., King, A.W. (2020). Perennials in Flood-Prone Areas of Agricultural Landscapes: A Climate Adaptation Strategy. *Bioscience*, 70, pp. *278-280,* DOI: https://doi.org/10.1093/biosci/biaa006.

[78] Jawhar, S. A., ÇAM, M. A., Habibi, E., & Yilmaz, Ö, F. (2024). Effects of climate change on animal production. *Journal of Natural Science Review,* 2(2). DOI: https://doi.org/10.62810/jnsrv2i2.30.

[79] Ji, M., Wang, X., Usman, M., Liu, F., Dan, Y., Zhou, L., Campanaro, S., Luo, G., Sang, W. (2022). The effects of different biochar-based raw materials on soil remediation: a review. *Environment. Pollute*. 294, 118655 DOI: https://doi.org/10.1016/j.envpol.2021.118655;

[80] Kan, Y., Mu, X.R., Gao, J., Lin, H.X., Lin, Y. (2023). The Molecular Basis of Heat Stress Responses in Plants. *Mol. Planta; 16 :*1612–1634. DOI: https://doi.org/10.1016/j.molp.2023.09.013.

[81] Kaye, J.P.; Quemada, M. (2017). Using cover crops to mitigate and adapt to climate change. A review. *Agron. Sustain. Dev., 37, 4*. DOI: https://doi.org/10.1007/s13593-016-0410-x.

[82] Khan, A.N., Hassan, M.N., Keyani, R., Amir, Z., Raish, M., Singh, R., Yasmin, H. (2024). Potential of Lactobacillus agilis, Lactobacillus plantarum, and Lactobacillus acidophilus to Enhance Wheat Growth under Drought and Heat Stress. *J. King Saud Univ. Sci. 103334.* DOI: https://doi.org/10.1016/j.jksus.2024.103334.

[83] Lal, R. (2010). Managing soils and ecosystems for mitigating anthropogenic carbon emissions and advancing global food security. *BioScience,* 60(9). DOI: https://doi.org/10.1016/S0065-2113(01)74033-3.

[84] Lamichhane, J.R.; Barzman, M.; Booij, K.; Boonekamp, P.; Desneux, N.; Huber, L.; Kudsk, P.; Langrell, S.R.H.; Ratnadass, A.; Ricci, P., Sarah, J-L., Messèan, A. (2015). Robust cropping systems to tackle pests under climate change. *A review. Agron. Sustain. Dev. 35,* 443–459. DOI: https://doi.org/10.1007/s13593-014-0275-9.

[85] Leng, L., Huang, H., Li, H, Li, J., Zhou, W. ,2019, Biochar stability assessment methods: A review, *Science of The Total Environment*, ISSN: 0048-9697, Vol: 647, Page: 210-222. DOI: https://doi.org/10.1016/j.scitotenv.2018.07.402.

[86] Li, J. M., Cao, L. R., Yuan, Y., Wang, R. P., Wen, Y. Z., Man, J. Y. (2018). Comparative study for microcystine-LR sorption on biochars produced from different plant and animal waste at different pyrolysis themes: influencing mechanisms of biochar properties. *Bio-sour Technol 247:*794–803. DOI: 10.1016/j.biortech.2017.09.120.

[87] Li Y. Y., Xue C. X., Chai C. Q/, Li W., Yao S. B. (2024). Can conservation tillage machinery drive the spatial spillover of the net carbon sink of conservation tillage? Based on the perspective of cross-zone service of agricultural machinery[J]. *Chinese Journal of Eco-Agriculture* 32(2): 283−296. DOI: https://doi.org/10.12357/cjea.20230375.

[88] Lin, H., Wang, Z., Liu, C., Dong, Y. (2022). Technologies for removing heavy metals from contaminated soils on farmland: a review. *Chemosphere 305, 135457*. DOI: https://doi.org/10.1016/j.chemosphere.2022.135457.

[89] Llonch, P., Haskell, M. J., Dewhurst, R. J., & Turner, S. P. (2017). Current available strategies to mitigate greenhouse gas emissions in livestock systems: an animal welfare perspective. *Animal,* 11(2). DOI: https://doi.org/10.1017/S1751731116001440.

[90] Long, E. Y., & Krupke, C. H. (2016). *N*on-cultivated plants present a season-long route of pesticide exposure for honey bees. *Nature communications*, 7(1). DOI: https://doi.org/10.1038/ncomms11629.

[91] Lorenz, K.; Lal, R. (2014). Biochar application to soil for climate change mitigation by soil organic carbon sequestration. *J. Plant Nutr. Soil Ski., 177,* pp.651–670. DOI: https://doi.org/10.1002/jpln.201400058.

[92] Lowenfels, J., & Lewis, W. (2010). Teaming with microbes: the organic gardener's guide to the soil food web. *Rev. ed. Portland, Or., Timber Press*. ISBN-13: 978-0-88192-777-1.

[93] Lundin, O., Rundlöf, M., Jonsson, M., Bommarco, R., & Williams, N. M. (2021). Integrated pest and pollinator management–expanding the concept. *Frontiers in Ecology and the Environment,*19(5). DOI: https://doi.org/10.1002/fee.2325.

[94] Malyan, S.K.; Kumar, S.S.; Fagodiya, R.K.; Ghosh, P.; Kumar, A.; Singh, R.; Singh, L. (2021). Biochar for environmental sustainability in the energy-water-agroecosystem nexus. *Renew. Sust. Energy. Rev*., 149, 111379. DOI: https://doi.org/10.1016/j.rser.2021.111379.

[95] Manea D., Marin E., Bălțatu C., Cismaru E.M., Mateescu M. (2023). Soil health policies in the European Union, *International Symposium Isb_Inma_Teh 2023*, pp. 310-19.

[96] Manoj, S.R.; Karthik, C.; Kadirvelu, K.; Arulselvi, P.I., Shanmugasundaram, T.*; Bruno, B.; Rajkumar, M.* (2020). Understanding the molecular mechanisms for the enhanced phytoremediation of heavy metals through plant growth promoting rhizobacteria: A review*. J. Environ. Manag. 254,* 109779. DOI: https://doi.org/10.1016/j.jenvman.2019.109779.

[97] Mandal, A., Sarkar, B., Mandal, S., Vithanage, M., Patra, A. K., Manna, M. C. (2020). Agrochemicals Detection, Treatment and Remediation Chapter 7- Impact of agrochemicals on soil health, Pesticides and Chemical Fertilizers. pp.161-187, DOI: https://doi.org/10.1016/B978-0-08-103017-2.00007-6.

[98] Marin, E., Cârdei, P., Vlăduţ, V., Biriş, S-Șt., Ungureanu, N., Bungescu, S.T., Voicea, I., Cujbescu, D., Găgeanu, I., Popa, L-D., Isitcioaia, S., Matei, Gh., Boruz, S., Teliban, G., Radu C., Kabas O., Caba I., Maciej J. (2024). Research on the influence of the main vibration-generating components in grain harvesters on the operator's comfort, *INMATEH – Agricultural Engineering* 74 (3), pp. 800-815, DOI: *https://doi.org/10.35633/inmateh-74-85.*

[99] Matache, M.G., Cristea, M., Găgeanu, I., Zapciu, A., Tudor, E., Carpus, E., Popa, L.D. (2020). Small power electric tractor performance during ploughing works, *INMATEH Agricultural Engineering,* vol 60, no. 1/ pp 123-128. DOI: https://doi.org/10.35633/inmateh-60-14.

[100] Mateescu, M., Marin, E., Manea, D., Gheorghe, G.V. Bălțatu, C., Dumitru, D. N., Preda, D. M., Duran, B O. Manoli-Preda, O. D., Ceaușu, D. B. (2023). Research on the development of an innovative energy-independent system for irrigation of agricultural crops, *International Symposium ISB_INMA_TEH 2023*, pp. *326-333*.

[101] McCarthy, N., Kilic, T., Brubaker, J., Murray, S. De La Fuente, A. (2021). Droughts and floods in Malawi: Impacts on crop production and the performance of sustainable land management practices under weather extremes Environ. *Dev. Econ., 26,* pp. 432-449. DOI: https://doi.org/10.1017/S1355770X20000455.

[102] Meers, E.; Ruttens, A.; Hopgood, M.; Lesage, E.; Tack, F.M. (2005). Potential of Brassica rapa, Cannabis sativa, Helianthus annuus and Zea mays for phytoextraction of heavy metals from calcareous dredged sediment derived soils. *Chemosphere 61,* 561–572. DOI: https://doi.org/10.1016/j.chemosphere.2005.02.026

[103] Melo, R. R., Antunes, F. L. M., Daher, S., Vogt, H. H., Albiero, D. Tofoli F. L. (2019). Designing an electric propulsion system for a 9-kW electric tractor suitable for family farming. *IET Electric Power Appl. vol. 13, no. 12,* pp. 1993–2004. DOI: https://doi.org/10.1049/iet-epa.2019.0353.

[104] Minoli, S., Jägermeyr, J., Asseng, S., Urfels, A., Müller, C., (2022). Global crop yields can be lifted by timely adaptation of growing periods to climate change. *Nat Commun 13*, 7079. DOI: https://doi.org/10.1038/s41467-022-34411-5.

[105] Mircea, C., Nenciu, F., Vladut, V., Voicu, G., Gageanu, I., Cujbescu, D. (2020). Increasing the performance of cylindrical separators for cereal cleaning, by using an inner helical coil. *INMATEH - Agricultural Engineering,* 62(3). DOI: https://doi.org/10.35633/inmateh-62-26.

[106] Mohawesh, O.; Albalasmeh, A.; Gharaibeh, M.; Deb, S.; Simpson, C.; Singh, S.; Al-Soub, B.; Hanandeh, A.E. (2021). Potential use of biochar as an amendment to improve soil fertility and tomato and bell pepper growth performance under arid conditions. *J. Soil Sci. Plant Nutr., 21, 2946–2956*. DOI: https://doi.org/10.1007/s42729-021-00580-3.

[107] Moore C.E., Meacham-Hensold K., Lemonnierm P., Slattery, Benjamin C., Bernacchi C.J., Lawson T., Cavanagh A.P. (2021). The effect of increasing temperature on crop photosynthesis: from enzymes to ecosystems, *Journal of Experimental Botany, Volume 72, Issue 8*, 2 April 2021, pp. 2822–2844. DOI: https://doi.org/10.1093/jxb/erab090.

[108] Mukhtar, T., Ali, F., Rafique, M., Ali, J., Afridi M.S., Smith D.L., Mehmood S., Amna, Souleimanov A., Jellani G., Sultan, T., Munis, F.H., Chaudhary, H. J. (2023). Biochemical Characterization and Potential of Bacillus safensis Strain SCAL1 to Mitigate Heat Stress in Solanum lycopersicum L. *J. Plant Growth Regul.; 42:523–538.* DOI: https://doi.org/10.1007/s00344-021-10571-4.

[109] Soumya, N.P. Banerjee R., Banerjee M., Sukanta M., Babu R.L., Hoque M, Reddy I.J., Nandi S., Gupta P.S.P., Agarwal P.K. (2022). Chapter Six - Climate change impact on livestock production, Climate

Smart Livestock Production. *Academic Press*, pp. 109-148. DOI: https://doi.org/10.1016/B978-0-12-822265-2.00010-7.

[110] Nadeem, M.; Li, J.; Wang, M.; Shah, L.; Lu, S.; Wang, X.; Ma, C. (2018). Unraveling Field Crops Sensitivity to Heat Stress: Mechanisms, Approaches, and Future Prospects. *Agronomy 2018, 8, 128*. DOI: https://doi.org/10.3390/agronomy8070128.

[111] Nenciu, F., & Vaireanu, D. I. (2014). A comparative study for assessing the effectiveness of solar trackers used in conjunction with photovoltaic power autonomous systems. *Journal of Optoelectronics and Advanced Materials,* 16 (1–2). pp.102-109.

[112] Nenciu, F., & Vaireanu, D. I. (2014). A versatile system for indoor monitoring of some volatile organic compounds. *Journal of Chemistry,* 65(5).

[113] Nenciu, F., Fatu, V., Arsenoaia, V., Persu, C., Voicea, I., Vladut, N.-V., Matache, M. G., Gageanu, I., Marin, E., Biris, S.-S., & Ungureanu, N. (2023). Bioactive Compounds Extraction Using a Hybrid Ultrasound and High-Pressure Technology for Sustainable Farming Systems. *Agriculture*, *13*(4), 899. DOI: https://doi.org/10.3390/agriculture13040899.

[114] Nenciu, F., Mircea, C., Vladut, V., Belc, N., Berca, L. M. (2021). Design of rotating cylindrical sieve, equipped with customizable homogenization coil. *In Engineering for Rural Development: Proceedings of the 20th International Scientific Conference (pp. 1478–1483). Latvia University of Life Sciences and Technologies.* DOI: https://doi.org/10.22616/ERDev.2021.20.TF316.

[115] Nenciu, F., Oprescu, M. R., Biris, S.-S. (2022). Improve the constructive design of a furrow diking rotor aimed at increasing water consumption efficiency in sunflower farming systems. *Agriculture,* 12(6). 846. DOI: https://doi.org/10.3390/agriculture12060846.

[116] Nenciu, F., Paraschiv, M., Kuncser, R., Stan, C., Cocarta, D., & Vlăduț, V. N. (2022). High-grade chemicals and biofuels produced from marginal lands using an integrated approach of alcoholic fermentation and pyrolysis of sweet sorghum biomass residues. *Sustainability*, 14(1). https://doi.org/DOI:10.3390/su14010402.

[117] Nenciu, F., Stanciulescu, I., Vlad, H., Gabur, A., Turcu, O. L., Apostol, T., Vladut, V. N., Cocarta, D. M., Stan, C. (2022). Decentralized processing performance of fruit and vegetable waste discarded from retail, using an automated thermophilic composting technology. *Sustainability,* 14(5). https://doi.org/DOI:10.3390/su14052835.

[118] Nenciu, F., Vladut, V. ((2021). Studies on the perspectives of replacing the classic energy plants with Jerusalem artichoke and sweet sorghum, analyzing the impact on the conservation of ecosystems. *In IOP Conference Series: Earth and Environmental Science (Vol. 635, Article 012002).* IOP Publishing. DOI: https://doi.org/10.1088/1755-1315/635/1/012002.

[119] Nenciu, F., Voicea, I., Cocarta, D. M., Vladut, V. N., Matache, M. G., Arsenoaia, V.-N. (2022). *"*Zero-waste" food production system supporting the synergic interaction between aquaculture and horticulture. *Sustainability,* 14(20). 13396. DOI: https://doi.org/10.3390/su142013396.

[120] Nenciu, F., Voicea, I., Stefan, V., Nae, G., Matache, M., Milian, G., & Arsenoaia, V.-N. (2020). Experimental research on a feed pelletizing equipment designed for small and medium-sized fish farms. *INMATEH - Agricultural Engineering,* 67(2). DOI: https://doi.org/10.35633/inmateh-67-38

[121] Nihal, R (2020). Global Climate change and its impact on integrated pest management. *Agro Econ. Int. J. 7,* pp.133–137.

[122] Nkoh, J.N., Baquy, M.A.A., Mia, S., Shi, R., Kamran, M.A., Mehmood, K., Xu, R. (2021). A critical-systematic review of biochar interactions with soils and observable results. *Sustainability 13*. DOI: https://doi.org/10.3390/su132413726.

[123] Nsanganwimana, F.; Pourrut, B.; Mench, M.; Douay, F. (2014). Suitability of Miscanthus species for managing inorganic and organic contaminated land and restoring ecosystem services. *A review. J. Environ. Manag. 143,* pp.123–134. DOI: https://doi.org/10.1016/j.jenvman.2014.04.027.

[124] Nunes, F. C., Alvarez, L. J., Nolasco de Carvalho C. C., Gross, E., Soares, T. M., Prasad M. N. V. (2020). Chapter 9 - Soil as a complex ecological system for meeting food and nutritional security. In: Prasad, M. N. V., Pietrzykowski, M. (Eds.) *Climate Change and Soil Interactions. Elsevier.* DOI: https://doi.org/10.1016/B978-0-12-818032-7.00009-6.

[125] Oncescu, T.-A., Persu, I. C., Bostina, S., Biris, S. S., Vilceleanu, M.-V., Nenciu, F., Matache, M.-G., Tarnita, D. (2025). Comparative Analysis of Vibration Impact on Operator Safety for Diesel and Electric Agricultural Tractors. *AgriEngineering,* 7(2). DOI: https://doi.org/10.3390/agriengineering7020040.

[126] Oprescu, M. R., Biris, S.-S., Nenciu, F. (2023). Novel furrow diking equipment-design aimed at increasing water consumption efficiency in vineyards. *Sustainability,* 15(4). 2861. DOI: https://doi.org/10.3390/su15042861

[127] Ortiz-Bobea, A., Ault, T.R., Carrillo, C.M., Chambers, R.G., & Lobell, D.B. (2021). Anthropogenic climate change has slowed global agricultural productivity growth. *Nature Climate Change,* 11(4). DOI: https://doi.org/10.1038/s41558-021-01000-1.

[128] Osman, A.I., Farghali, M., Dong, Y., Kong, J., Yousry, M., Rashwan, A. K., Chen, Z., Al- Fatesh, A., Yap, P. S. (2024). Reducing the carbon footprint of buildings using biochar-based bricks and insulating materials: a review. *Environ Chem Lett 22*, pp. 71–104. DOI: https://doi.org/10.1007/s10311-023-01662-7.

[129] Osman, H.E.; Fadhlallah, R.S.; Alamoudi, W.M.; Eid, E.M.; Abdelhafez, A. A. (2023). Phytoremediation potential of Sorghum as a bioenergy crop in Pb-amendment soil. *Sustainability 15, 2178*. DOI: https://doi.org/10.3390/su15032178.

[130] Patel, A., Singh, P., Dushyant, S. (2018). Farm machinery for conservation agriculture, https://biotecharticles. *com/Agriculture-Article/Farm-Machinery-for-Conservation-Agriculture-4462.html*.

[131] Patwardhan S.B., Pandit, S., Gupta P. K., Jha, N. K., Rawat, J., Josi, H. C., Priya, K., Gupta, M., Lahiri, D., Nag, M., Thakur, V. K., Kesari, K. K. (2022). Recent advances in the application of biochar in microbial electrochemical cells, *Fuel, Volume 311, 122501*, ISSN00162361, DOI: https://doi.org/10.1016/j.fuel.2021.122501.

[132] Paul, A, Sarma, H. H., Kakoti, M., Talukdar, N, Dutta, S.K., Hazarika, P., Goswami A. (2024). Irrigating with intelligence: Sensor-based strategies for efficient agriculture—A review. *Ecology, Environment and Conservation; 338-343.* DOI: https://doi.org/10.53550/EEC.202 4.v30i03s.058.

[133] Popa, L.-D., Isticioaia, S.-F., Vladut, N.-V., Matei, G., Leonte, A., Gageanu, I., Nenciu, F., Pintilie, P.-L., Pintilie, A.-S., & Milea, O. (2023). The multiple applications of industrial hemp (cannabis sativa l.) in the context of sustainable development. *INMATEH - Agricultural Engineering,*75(1). DOI: https://doi.org/DOI:10.35633/inmateh-75-88.

[134] Popescu, E., Nenciu, F., Vladut, V. N (2022a). Reducing the Effects of Drought and Degradation of Agricultural Soils, in the Context of Climate Change, through the Application of Regenerative Ecological Technologies', in M. *Eyvaz et al. (eds.), Drought - Impacts and Management, IntechOpen, London.* DOI: https://doi.org/10.5772/intechopen.104446.

[135] Popescu E., Nenciu F., Vlădut V. (2022b). A new strategic approach used for the regeneration of soil fertility, in order to improve the productivity in ecological systems, *Scientific Papers. Series E. Land Reclamation, Earth Observation & Surveying, Environmental Engineering*. Vol. XI, 2022, pp. 277-284.

[136] Priya, R.S. et al. (2024). Effects of Climate Change on Plant Diseases. In: Abd-Elsalam, K.A., Abdel-Momen, S.M. (eds) *Plant Quarantine Challenges under Climate Change Anxiety*. Springer, Cham. DOI: https://doi.org/10.1007/978-3-031-56011-8_7.

[137] Pruteanu, A., Bordean, D. M., Voicea, I., Vlăduţ, V., Găgeanu, I. (2018). Experimental Research on Heavy Metal Contamination (Cu, Zn, Pb) in Leafy Vegetables, 18th *International Multidisciplinary Scientific GeoConference SGEM 2-8 July 2018, Volume 18, Ecology, Economics, Education and Legislation*, Issue: 5.1, Albena, Bulgaria, pp. 385-392, DOI: https://doi.org/10.5593/sgem2018/5.1.

[138] Pruteanu, A., Bordean, D-M., Vlăduţ, V. (2019). Accumulation of heavy metals in vegetables grown on contaminated soils, P*ROCEEDINGS OF THE 47 INTERNATIONAL SYMPOSIUM ON AGRICULTURAL ENGINEERING "Actual Tasks on Agricultural Engineering",* pp. 135-146, Opatija – Croaţia

[139] Pruteanu, A., Vladut, V., Cardei, P., Bordean, D. (2020). General tendencies of the behaviour of vegetables developed in a soil contaminated with heavy metals, *Journal of Chemistry,* Volume 71, no. 2, pp. 85-90. DOI: https://doi.org/*10.37358/RC.20.2.7897*.

[140] Rahman, M. H. U., Ahmad, A., Wang, X., Wajid, A., Nasim, W., Hussain, M., Ahmad, B., Ahmad, I., ali, Z., Awais, M., Shelia, V., Ahmad, S., Fahd, S., Alam, M., Ullah, H., Hoogenboom, G. (2018). Multi-model projections of future climate and climate change impacts uncertainty assessment for cotton production in Pakistan. *Agric. Forest Meteorol. 253, 94–113.* DOI: https://doi.org/10.1016/j.agrformet.2018.02.008.

[141] Rojas-Downing, M. M., Nejadhashemi, A. P., Harrigan, T., & Woznicki, S. A. (2017). Climate change and livestock: Impacts, adaptation, and mitigation. *Climate risk management,* 16, pp 145-163. DOI: https://doi.org/10.1016/j.crm.2017.02.001.

[142] Rosmawati W., Syah M., Ramadhan F. (2023). Seed bomb innovation as a solution to improve the green economy in Indonesia, *Midyear International Conference*, pp 25-33.
[143] Rossi, C., Pontara, D., Falcomer, C., Bertoldi, M., Mandrioli, R. (2021). A hybrid-electric transmission for agricultural tractors based on a power-sharing e-CVT transmission*, Energies, 14(21), 6912.* DOI: https://doi.org/10.3390/en14216912.
[144] Rugege, D., Vermeulen, S. (2017). Investing in on-farm and post-harvest resilience to climate change in smallholder value chains: Lessons from Rwanda. CCAFS Working Paper no. 193. *Copenhagen, Denmark: CGIAR Research Program on Climate Change, Agriculture and Food Security (CCAFS).* https://hdl.handle.net/10568/80178.
[145] Rumpel, C.; Amiraslani, F.; Chenu, C.; García Cárdenas, M.; Kaonga, M.; Koutika, L.S.; Ladha, J.; Madari, B.; Shirato, Y.; Smith, P., Soudi, B., Soussana, J. F., Whitehead, D., Wollenberg, E. (2020). The 4p1000 initiative: Opportunities, limitations and challenges for implementing soil organic carbon sequestration as a sustainable development strategy. *Ambio.* 49, pp.350–360. DOI: https://doi.org/10.1007/s13280-019-01165-2.
[146] Sachdeva, S., Kumar, R., Sahoo, P. K., Nadda, A. K. (2023). Recent Progress in Biochar Amendments for Immobilization of Heavy Metals in an Agricultural Ecosystem: A Systematic Review. *Environment. Pollute. 319*. DOI: https://doi.org/10.1016/j.envpol.2022.120937
[147] Safarian, S., Rydén, M., Janssen, M. (2022). Development and comparison of thermodynamic equilibrium and kinetic approaches for biomass pyrolysis modeling. *Energies*, 15 (11), 3999. DOI: https://doi.org/10.3390/en15113999.
[148] Sanz Rodrigo, J., Chávez Arroyo, R.A., Moriarty, P., Churchfield, M., Kosović, B., Réthoré, P.E., Hansen, K.S., Hahmann A., Mirocha, J.D., Rife, D. (2017). Mesoscale to microscale wind farm flow modeling and evaluation Wiley Interdiscip. *Rev. Energy Environ.,* 6 (2). DOI: https://doi.org/10.1002/wene.214.
[149] Sapkota, T.B.; Jat, M.L.; Aryal, J.P.; Jat, R.K.; Khatri-Chhetri, A. (2015). Climate change adaptation, greenhouse gas mitigation and economic profitability of conservation agriculture: Some examples from cereal systems of Indo-Gangetic Plains. *J. Integr. Agric., 14,* pp. 1524–1533. DOI: https://doi.org/10.1016/S2095-3119(15)61093-0
[150] Sarma, H.H., Paul, A., Kakoti, M., Goswami, A, Talukdar, N., Borkotoky, B., Dutta, S.K., Hazarika, P. (2024). The aerial genesis: Seed bombing for nurturing earth and ecosystem renaissance—A review. *The Pharma Innovation Journal.* 12(9).
[151] Sarma, H. H., Santanu K. B., Niharika D., Nazmin S., Hrishikesh N., Bikash C. D. (2024). Innovative Approaches for Climate-Resilient Farming: Strategies Against Environmental Shifts and Climate Change. *International Journal of Environment and Climate Change*, 14 (9). DOI: https://doi.org/10.9734/ijecc/2024/v14i94407.
[152] Schilling, K.E., Wilke, K., Pierce, C.L., Kult, K., Kenny, A. (2019). Multipurpose Oxbows as a Nitrate Export Reduction Practice in the Agricultural Midwest Agric. *Approx. Lett., 4,* Article 190035, DOI: https://doi.org/10.2134/ael2019.09.0035.
[153] Scolaro, E., Beligoj ,M., Perez Estevez, M.A., Alberti, L., Renzi, M., Mattetti M. (2021). Electrification of agricultural machinery a review, IEEE Access, vol. *9,* pp. 164520-164541. DOI: https://doi.org/10.1109/ACCESS.2021.3135037.
[154] Setter, C., Silva, F.T.M., Assis, M.R., Ataíde, C.H., Trugilho, P.F., Oliveira, T.J.P. (2020). Slow pyrolysis of coffee husk briquettes: characterization of the solid and liquid fractions. *Fuel 261,* 116420. DOI: https://doi.org/10.1016/j.fuel.2019.116420
[155] Shamim, S., Abdullah, M., Shair, H., Ahmad, J., Farooq, M.O., Ajmal, S. (2024). Evaluation for impact of climate change on wheat (*Triticum aestivum L.*) grain quality and yield traits. *Biol. Clin. Sci. Res. J., 842.* DOI: https://doi.org/10.54112/bcsrj.v2024i1.841.
[156] Sharan, S. P., Sarma, H. H., Khan, T. M. S., Venkatesh, C. (2024). Intelligent sensors and systems: A novel approach to climate smart agriculture. *In Sustainable Farming Systems for Climate Resilience and Improved Human Health. Ninetales Publishing.;* 1:134-144.
[157] Shrestha, S. (2019). Effects of climate change in agricultural insect pest. *Acta Sci. Agric 3:74–80*. DOI: https://doi.org/10.31080/ASAG.2019.03.0727.
[158] Sidhu, C. S., & Joshi, N. K. (2016). Establishing wildflower pollinator habitats in agricultural farmland to provide multiple ecosystem services. *Frontiers in plant science, 7, 363*. DOI: https://doi.org/10.3389/fpls.2016.00363.

[159] Simkin, A.J., Faralli, M., Ramamoorthy, S., Lawson, T. (2020). Photosynthesis in non-foliar tissues: implications for yield. *The Plant Journal 101,* 1001–1015. DOI: https://doi.org/10.1111/tpj.14633.
[160] Singh, H., Northup, B.K.,Rice, C.W., Prasad, P.V.V. (2022). Biochar applications influence soil physical and chemical properties, microbial diversity, and crop productivity: A meta-analysis. *Biochar* 4 (1):3 DOI: https://doi.org/10.1007/s42773-022-00138-1.
[161] Sossidou, E. N., Tsiplakou, E., Zervas, G. (2014). Options for managing livestock production systems to adapt to climate change. *Journal of Earth Science and Engineering,* 4(1).
[162] Stan C., Nenciu, F., Muscalu, A., Vlăduț, V. N., Burnichi, F., Popescu, C., Gatea, F., Boiu-Sicuia, O. A., & Israel-Roming, F. (2022). Chemical composition, antioxidant and antimicrobial effects of essential oils extracted from two new Ocimum basilicum L. varieties. *Diversity,* 14(12). DOI: https://doi.org/10.3390/d14121048.
[163] Stan, C., Nenciu, F., Vlăduțoiu, L., Voicea, I., & Oprescu, M.-R. (2024). Novel Approach for Enhancing Challenging Terrains Using an Integrated Pyrolysis and Furrow-Diking Technology. *Applied Sciences,* 14(24). DOI: https://doi.org/10.3390/app142411815.
[164] Tarniţă D., Oncescu A., Dumitru I., Boştină Şt., Geonea I.D., Vlăduţ N-V., Tarniţă D-N. (2025). Evaluation of vibrations and comfort of an electric tractor driver by modal and experimental analysis, *SUSTAINABLE DEVELOPMENT* 2, pp. 464-473, DOI: https://doi.org/10.1007/978-3-031-91179-8_48.
[165] Tăbărașu, A.-M., Anghelache, D.-N., Găgeanu, I., Biriș, S.-Ș., & Vlăduț, N.-V. (2023). Considerations on the Use of Active Compounds Obtained from Lavender. *Sustainability*, *15*(11), 8879. DOI: https://doi.org/10.3390/su15118879.
[166] Tăbărașu, A.-M.; Nenciu, F.; Anghelache, D.-N.; Vlăduț, V.-N.; Găgeanu, I. (2024a). Hybrid Percolation–Ultrasound Method for Extracting Bioactive Compounds from Urtica dioica and Salvia officinalis. *Agriculture 14, 1561*. DOI: https://doi.org/10.3390/agriculture14091561.
[167] Tăbăraşu, A. M., Găgeanu, I., Vlăduţ, N. V., Matache, M. G., & Anghelache, D. N. (2024b). Experimental research on the extraction of polyphenols from Nettle, Lavender and Sage Using the Percolation Method. *INMATEH-Agricultural Engineering*, *73*(2). DOI: https://doi.org/10.35633/inmateh-73-58.
[168] Talukdar N, Paul A, Sarma H.H., Kakoti M. (2023). Agronomic practices for soil conservation. In Frontiers in agriculture sustainability. *Integrated Publications TM. 1:*159- 172.
[169] Tan, Z., Lin, C.S., Ji, X., Rainey, T.J. (2017). Returning biochar to fields: A review. *Appl. Soil Ecol*., 116, 1–11. DOI: https://doi.org/10.1016/j.apsoil.2017.03.017.
[170] Teiba, I.I., El-Bilawy, E.H., Elsheery, N.I., Rastogi, A. (2024). Microbial Allies in Agriculture: Harnessing Plant Growth-Promoting Microorganisms as Guardians against Biotic and Abiotic Stress. *Horticulturae. 2024; 10:12.* DOI: https://doi.org/10.3390/horticulturae10010012.
[171] Teliban G-C., Burducea M., Mihalache G., Zheljazkov V.D., Dincheva I., Badjakov I., Popa, L-D., Bodale I., Vlădut N-V., Cojocaru Al., Munteanu N., Stan T., Caruso G., Stoleru V. (2022). Morphological, Physiological and Quality Performances of Basil Cultivars under Farming Management, *AGRONOMY* 12(12), 3219, Ipp. 1-18, DOI: https://doi.org/10.3390/agronomy12123219.
[172] Tienda, S., Vida, C., Villar-Moreno, R., de Vicente, A., Cazorla, F.M. (2024). Development of a Pseudomonas-Based Biocontrol Consortium with Effective Root Colonization and Extended Beneficial Side Effects for Plants under High-Temperature Stress. *Microbiol.285:127761,* DOI: https://doi.org/10.1016/j.micres.2024.127761.
[173] Tudora, C., Muscalu, A., Burnichi, F., Popescu, C., Gatea, F., Sicuia, O-A., Vlăduţ, V., Roming-Israel, F. (2022). Evaluation of essential oil and hydrolate from a new hyssop variety (Hyssopus officinalis L.), *NOTULAE BOTANICAE HORTI AGROBOTANICI CLUJ NAPOCA* 50(2). pp.1-17, DOI: https://doi.org/10.15835/nbha50212639
[174] Tudora, C., Nenciu, F., Muscalu, A., Burnichi, F., Gatea, F., Boiu-Sicuia, O. A., & Israel-Roming, F. (2024a). Pesticidal potential of essential oil obtained from a new variety of marigold (*Tagetes patula L*., fam. *Asteraceae*). *Applied Sciences,*14(8). 3159. DOI: https://doi.org/10.3390/app14083159.
[175] Tudora, C., Muscalu, A., Burnichi, F., Gradilă, M., Jaloba, D., Vlăduţ, V.N. (2024b). Allelopathic effect of the essential oil obtained from hyssop (Hyssopus Officinalis L., Fam. Lamiaceae), *SCIENTIFIC PAPERS-SERIES B-HORTICULTURE* 68(1), pp. 923-933
[176] Tudora, C., Cârdei P., Boiu-Sicuia O., Muscalu A., Vlăduţ N-V. (2025). Statistical analysis of the antifungal activity of four essential oils against botrytis cinerea, *AGROLIFE SCIENTIFIC JOURNAL* 14(1), pp. 191-202.

[177] Ueka Y., JYamashita J., K. Sato K., Doi Y. (2013). Study on the development of the electric tractor: specifications and the performance of movement and processing of an electric tractor prototype. Eng. *Agricol., Env- iron. Food, vol. 6, no. 4,* pp. 160–164. DOI: https://doi.org/10.1016/S1881-8366(13)80003-1.

[178] Ungureanu, N., Croitoru, Şt., Biriş, S., Voicu, Gh., Vlăduţ, V., Selvi, K.Ç., Boruz, S., Marin, E., Matache, M., Manea, D., Constantin, G., Ionescu, M. (2015). Agricultural soil compaction under the action of agricultural machinery, *PROCEEDINGS OF THE 43 INTERNATIONAL SYMPOSIUM ON AGRICULTURAL ENGINEERING "Actual Tasks on Agricultural Engineering"*, pp. 31-42, Opatija – Croaţia.

[179] Vílchez, J.I., Niehaus, K., Dowling, D.N., González-López, J., Manzanera, M. (2018). Protection of Pepper Plants from Drought by Microbacterium sp. *3J1 by* Modulation of the Plant's Glutamine and α-ketoglutarate Content: A Comparative Metabolomics Approach Front. *Microbiol., 9,* p. 284, DOI: https://doi.org/10.3389/fmicb.2018.00284.

[180] Vlăduţ, D.I., Vlăduţ, V., Grigore, I., Biriş, S. (2017). Experimental research in qualitative indices of work for equipment for seedbed preparation in conservative system, *16th International Scientific Conference "ENGINEERING FOR RURAL DEVELOPMENT"*, pp. 1174-1179, Jelgava, Latvia.

[181] Vlăduţ, D.I., Biriş, S., Vlăduţ, V., Cujbescu, D., Ungureanu, N., Găgeanu I. (2018). Experimental researches on the working process of a seedbed preparation equipment for heavy soils, *INMATEH – AGRICULTURAL ENGINEERING* 55(2), pp. 27-34.

[182] Vlăduţ, V., Biriş, S.Şt., Bungescu, T., Herişanu, N. (2013). The influence of vibrations on the operator in the grain harvesters*, Applied Mechanics and Materials*, Vol. 430, pp. 290-296, DOI: https://doi.org/10.4028/www.scientific.net/AMM.430.290

[183] Vlăduţ, N.-V., Biris, S.St., Cârdei, P., Găgeanu, I., Cujbescu, D., Ungureanu, N., Popa L.-D., Perişoară, L., Matei, G., Teliban, G.-C. (2022). *C*ontributions to the Mathematical Modeling of the Threshing and Separation Process in An Axial Flow Combine, *AGRICULTURE* 12(10), 1520, DOI: *https://doi.org/10.3390/agriculture12101520*;

[184] Vlăduţ, N-V., Biriş, S.Şt., Paraschiv, G., Ungureanu, N., Bungescu, S-T., Voicea, I., Cujbescu, D., Găgeanu, I., Laza, E., Popa, L-D., Matei, Gh., Atanasov At. (2023a), Considerations regarding the effects of shock and vibration on operators of self-propelled agricultural equipment, *INMATEH – Agricultural Engineering* 71 (3), pp. 823-836, DOI : https://doi.org/10.35633/inmateh-71-74.

[185] Vlăduţ, N.-V., Ungureanu, N., Biriş, S.-Ş., Voicea, I., Nenciu, F., Găgeanu, I., Cujbescu, D., Popa, L.-D., Boruz, S., Matei, G., Ekielski, A., & Teliban, G.-C. (2023b). Research on the identification of some optimal threshing and separation regimes in the axial flow apparatus. *Agriculture,* 13(4). DOI: https://doi.org/10.3390/agriculture13040838.

[186] Vlăduţ, N.-V., Atanasov, A., Ungureanu, N., Ivascu, L.-V., Cioca, L.-I., Popa, L.-D., Matei, G., Boruz, S., Cerempei, V., Titei, V., Nenciu, F., Milea, O.-E., Dumitru, S., & Caba, I. (2024). Trends in the development of conservation/ecological agriculture in the context of current climate change - A review. *INMATEH - Agricultural Engineering,* 74(3). DOI: https://doi.org/10.35633/inmateh-74-86.

[187] Vladutoiu, L.C., Cristea, M., Nenciu, F., Vladut, V.; Olan, M., Grigore, I., Sorica, C., Vanghele, N., Cristea, O.D. (2025). Innovative pyrolysis reactor design for enhanced performance and superior biochar quality, *INMATEH-AGRICULTURAL ENGINEERING, Volume75*, Issue 1, Page 414-422, DOI: https://doi.org/10. 35633/inmateh-75-35.

[188] Vogel, E., Donat, M. G., Alexander, L., Meinshausen, M., Ray, D., Karoly, D. J., Meinshausen, N., Frieler, K. (2019). The effects of climate extremes on global agricultural yields, Environ. *Res. Lett. 14* 054010. DOI: https://doi.org/10.1088/1748-9326/AB154B.

[189] Voicea, I., Cârdei, P., Arsenoaia, V.-N., Ungureanu, N., Nenciu, F., & Vanghele, N. (2021). Using statistical analysis to assess the effects of feeding pellets on fish dietary preferences in an intensive polyculture system. *INMATEH - Agricultural Engineering,*71(3). DOI: https://doi.org/10.35633/inmateh-71-70.

[190] Voicea, I., Fatu, V., Nenciu, F., Persu, C., & Oprescu, R. (2022). Experimental research on bioinsecticide activity obtained by using an oleic extract from dwarf silver fir on some vegetable crops. Scientific Papers *- Series B: Horticulture,* 66(1).

[191] Voicea, I., Nenciu, F., Vlăduţ, N.-V., Matache, M.-G., Persu, C., & Cujbescu, D. (2024). Exploring a Self-Sufficiency Approach within a Sustainable Integrated Pisciculture Farming System. *Sustainability*, *16*(18), 8055. DOI: https://doi.org/10.3390/su16188055.

[192] Wagg, C.; Bender, S.F.; Widmer, F.; van der Heijden, M.G.A. (2014). Soil biodiversity and soil community composition determine ecosystem multifunctionality. *Proc. Natl. Acad. Sci. USA, 111,* pp. 5266–5270. DOI: https://doi.org/10.1073/pnas.1320054111.

[193] Wagg, C.; Schlaeppi, K.; Banerjee, S.; Kuramae, E.E.; Van Der Heijden, M.G.A. (2019). Fungal-bacterial diversity and microbiome complexity predict ecosystem functioning. *Nat. Commun.* 10, 4841. DOI: https://doi.org/10.1038/s41467-019-12798-y

[194] Wagg, C.; van Erk, A.; Fava, E.; Comeau, L.-P.; Mitterboeck, T.F.; Goyer, C.; Were.; McKenzie-Gopsill, A.; Mills, A. (2021). Full-season cover crops and their traits that promote agroecosystem services. *Agriculture, 11, 830*. DOI: https://doi.org/10.3390/agriculture11090830.

[195] Wang D., Jiang P., Zhang H., Yuan W. (2020). Biochar production and applications in agro and forestry systems: A review. *Science of The Total Environment, (), 137775–.* DOI: https://doi.org/10.1016/j.scitotenv.2020.1377.

[196] Wang Y., Zhu Y., Wang K., Tan Y., Bing X., Jiang., Feng W., Feng w., Chen L., Liao H. (2024). Principles and research progress of physical prevention and control technologies for algae in eutrophic water, *iScience Volume 27*, Issue 6109990. DOI: https://doi.org/10.1016/j.isci.2024.109990

[197] Wang, H.; Liu, H.; Su, R.; Chen, Y. (2024). Phytostabilization of Heavy Metals and Fungal Community Response in Manganese Slag under the Mediation of Soil Amendments and Plants. *Toxics 12, 333*. DOI: https://doi.org/10.3390/toxics12050333.

[198] Wang, L., Barta-Rajnai, E., Skreiberg, Ø., Khalil, R., Czégény, Z., Jakab, E., Barta, Z., Grønli, M. (2017). Impact of torrefaction on woody biomass properties. *Energy Procedia 105,* 1149–1154. DOI: https://doi.org/10.1016/j.egypro.2017.03.486.

[199] Xiao, D., Liu, D., Wang, L., Feng, P., Bai, H., and Tang, J. (2020). Climate change impact on yields and water use of wheat and maize in the North China Plain under future climate change scenarios. *Agric. Water Manage.*, 238 (106238). DOI: https://doi.org/10.1016/j.agwat.2020.106238.

[200] Xiao, M.Z., Sun, Q., Hong, S., Chen, W.J., Pang, B., Du, Z.Y., Yang, W.B., Sun, Z., Yuan, T.Q. (2021). Sweet sorghum for phytoremediation and bioethanol production. *J. Leather Sci. Eng. 3,* 32–55. DOI: https://doi.org/10.1186/s42825-021-00074-z.

[201] Yang D., Peng S., Wang F. (2020). Response of photosynthesis to high growth temperature was not related to leaf anatomy plasticity in rice (Oryza sativa L.*). Frontiers in Plant Science 11, 1*. DOI: https://doi.org/10.3389/fpls.2020.00026.

[202] Yang, Q.-L.; Du, T.; Li, N.; Liang, J.; Javed, T.; Wang, H.; Guo, J.; Liu, Y. (2023). Bibliometric Analysis on the Impact of Climate Change on Crop Pest and Disease. *Agronomy, 13, 920*. DOI: https://doi.org/10.3390/agronomy13030920.

[203] Yang, X., Qin, J., Li, J., Lai, Z., Li, H. (2021). Upland rice intercropping with Solanum nigrum inoculated with arbuscular mycorrhizal fungi reduces grain Cd while promoting phytoremediation of Cd-contaminated soil. *J. Hazard. Mater. 406,* 124325. DOI: https://doi.org/10.1016/j.jhazmat.2020.124325.

[204] Majeed, Y., Khan, M. U. K., Waseem, M., Zahid, U., Mahmood, F., Majeed, F., Sultan, M., Raza, A. (2023). Renewable energy as an alternative source for energy management in agriculture, *Energy Reports, Volume 10*, pp.344-359, ISSN 2352-4847, DOI: https://doi.org/10.1016/j.egyr.2023.06.032.

[205] Yoon, P.R., & Choi, J.Y. (2020). Effects of shift in growing season due to climate change on rice yield and crop water requirements. *Paddy and Water Environment, 18,* 291-307. DOI: https://doi.org/10.1007/s10333-019-00782-7.

[206] Yuan P., Wang J. Q., Pan and J., Shen B. X., Wu C. F. (2019). Review of biochar for the management of contaminated soil: Preparation, application and prospect. *Sci total approximately. 659:* 473–490. DOI: https://doi.org/10.1016/j.scitotenv.2018.12.400.

[207] Zaman, C.Z., Pal, K., Yehye, W.A., Sagadevan, S., Shah, S.T., Adesibi, G.A., Marliana, E., Rafique, R. F., Johan, R.B. (2017), Pyrolysis A Sustainable Way to Generate energy from waste, *Pyrolylisis*, ISBN 978-953-51-3312-4. Chapter metrics overview, DOI: https://doi.org/10.5772/intechopen.69036.

[208] Zeba, N., Berry, T.D., Panke-Buisse, K., Whitman, T. (2022). Effects of physical, chemical, and biological ageing on the mineralization of pine wood biochar by a Streptomyces isolate. *Edited by Omeid Rahmani. PLoS ONE 17*, e0265663. DOI: https://doi.org/10.1371/journal.pone.0265663.

[209] Zhang, M., Riaz, M., Liu, B., Xia, H., El-Desouki, Z., Jiang, C. (2020). Two-year study of biochar: Achieving excellent capability of potassium supply via alter clay mineral composition and potassium-dissolving bacteria activity Sci. *Total Environ., 717, Article 137286,* DOI: https://doi.org/10.1016/j.scitotenv.2020.137286.

[210] Zhu, Y., Wang, Y., He, X., Li, B., Du, S. (2023). Plant growth-promoting rhizobacteria: A good companion for heavy metal phytoremediation. *Chemosphere 338,* 139475. DOI: https://doi.org/10.1016/j.chemosphere.2023.139475.
[211] Zilli, M., Scarabello, M., Soterroni, A. C., Valin, H., Mosnier, A., Leclere, D., et al. (2020). The impact of climate change on Brazil's agriculture. Sci. Total Approximately. 740*, 139384.* DOI: https://doi.org/10.1016/j.scitotenv.2020.139384.
[212] ***Soil biodiversity and soil erosion. (2018). *Joint Research Centre, European Soil Data Centre (ESDAC)*.

DESIGN AND EXPERIMENT OF A CLAW-CHAIN GARLIC CLOVE METERING DEVICE

/

爪链式大蒜播种机取种装置设计与试验

Caiqi HU*[1,2], Peng DENG[1,2], Junhao LI[1,2], Pengyu LIU[1,2], Yichen LI[1,2], Siyuan ZHENG [1,2]

[1)] College of Mechanical and Electrical Engineering, Qingdao Agricultural University, Qingdao (266109), China

[2)] Shandong Provincial Key Laboratory of Smart Agricultural Equipment for Protected Horticulture, Qingdao (266109), China

Tel: +86-13616397874; E-mail: hucaiqi@163.com

Corresponding author: Caiqi Hu

DOI: https://doi.org/10.35633/inmateh-76-113

Keywords: *garlic planter; single-seed picking; claw-chain type; EDEM*

ABSTRACT

To solve the problems of multiple picking and missed picking in garlic planter, single-seed picking has become a critical technology that urgently needs improvement. In response, a claw-chain mechanism for single garlic seed picking was developed. Based on theoretical analysis of the clove picking claw's motion, the feasible ranges of claw speed (v), minimum clove-holding length (S_2), and sprocket inclination angle (θ) were determined. Using the EDEM simulation platform, the single-seed picking rate and missed picking rate under different parameter combinations were obtained. A Box–Behnken central composite design was used to conduct a three-factor, three-level quadratic regression experiment involving claw speed, minimum clove-holding length, and sprocket inclination angle. Design-Expert software was employed to establish a response surface model and optimize the key parameters affecting the single-seed picking rate. The optimal parameter combination was a claw speed of 0.05 m/s, a minimum clove-holding length of 32.4 mm, and a sprocket inclination angle of 5.6°. Under these conditions, the single-seed picking rate reached 91.7%, and the missed picking rate was 4.4%, meeting the technical requirements for garlic single-seed planting.

摘要

为解决大蒜种植过程中存在多取漏取问题，单粒取种成为了亟需解决的关键技术。针对此问题，设计了一种爪链式单粒取种装置。通过对取种爪运动状态进行理论分析，确定取种爪速度（v）、取种爪最小容种长度（S_2）及两链轮倾角（θ）的取值范围。利用 EDEM 仿真平台得到单粒取种率、漏取率的相应指标值。运用 Box-Benhnken 中心组合试验方法对取种爪速度、取种爪最小容种长度、两链轮倾角进行三因素三水平二次回归试验设计，采用 Design-expert 软件建立响应面数学模型，对影响单粒取种率的关键参数进行了综合优化，得到最优工作参数组合为取种爪速度为 0.05m/s，取种爪最小容种长度为 32.4mm，两链轮倾角为 5.6°，在此条件下进行试验得到单粒取种率为 91.7%，漏取为 4.4%，满足大蒜种植的单粒取种率要求。

INTRODUCTION

Garlic is a major economic crop with extensive applications in culinary, medicinal, and health-related fields. China has long maintained the largest garlic cultivation area worldwide, stabilized at approximately 11 million mu (≈ 733.000 ha), mainly in Shandong, Henan, and Jiangsu provinces *(Yang et al., 2019; Qin et al., 2019; Zhang et al., 2022)*. Annual exports reach approximately 2.8 million tons, covering over 160 countries and regions. With ongoing agricultural modernization, garlic sowing now demands greater efficiency and precision. However, sowing in China still relies heavily on manual labor, leading to high labor intensity, low efficiency, and issues such as uneven distribution and poor clove placement *(Chen et al., 2021; Wei et al., 2022)*. These challenges raise production costs and reduce crop yield. Garlic planters can enhance sowing quality and efficiency, reduce labor, and support large-scale farming. Yet, current machines often suffer from multiple pickups and missed cloves, compromising sowing performance. Therefore, developing a high-efficiency, high-precision single-seed metering device is of great practical significance and urgent necessity *(Zhang et al., 2022; Furuhata et al., 2015; Manjunatha et al., 2014)*.

[1] *Caiqi Hu, Prof. Ph.D.;Peng Deng, master degree.; Junhao Li, master degree; Pengyu Liu, master degree; Yichen Li, master degree; Siyuan Zheng, master degree;*

Currently, common garlic clove picking methods include socket type, spoon-clip type, and claw-chain type *(Xie et al., 2022; Xue et al., 2024; Suryakant et al., 2024; Smita et al., 2019)*. The socket type utilizes holes on a rotating disc to pick cloves but suffers from low efficiency. The spoon-clip type uses a clove plate to drive the picking spoon, but it often damages cloves. The claw-chain type uses claws installed on a chain to achieve continuous picking and has a relatively simple structure *(Im et al., 2023; Kim et al., 2020; Lee et al., 2023; Gyoung et al., 2018)*. However, due to the large variation in garlic clove shape and size, these methods still frequently result in missed or multiple clove placement, failing to meet agronomic requirements, and a significant gap remains in achieving high-efficiency and high-precision single-seed picking. Therefore, it is necessary to optimize and improve the structural parameters of the picking device to increase accuracy and operation quality *(Yang et al., 2015; Lai et al., 2022; Elwakeel et al., 2025; Marey et al., 2011)*.

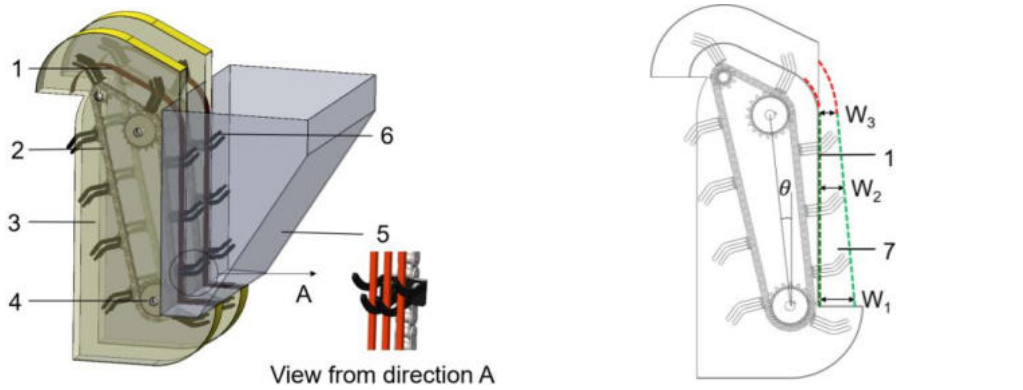
To address the low single-seed picking rate of existing garlic clove picking devices, this study investigates the structural design and working principle of the picking mechanism. A simulation model of the picking process is developed using EDEM software to analyze the interaction between the device and garlic cloves. Key factors influencing the single-seed picking rate and seed-missing rate are identified. A Box–Behnken experimental design is employed to conduct multi-factor optimization trials, from which the optimal parameter combination is determined. Finally, field experiments are performed to validate the accuracy and reliability of the simulation results. The findings provide a theoretical foundation and technical reference for optimizing the structure and enhancing the performance of single-seed picking devices in garlic planters.

MATERIALS AND METHODS

Structure of the Clove Metering Device

The claw-chain clove picking device is shown in Fig. 1. It consists of clove picking claws, chain, sprockets, clove box, guide plate, and outer shell. The claws are fixed on the chain. The sprockets rotate to drive the claws on the chain.

As shown in Fig. 1(b), the two sprockets are installed at an angle. The claws and the guide plate form a clove holding space. As the claws move upward, the internal clove holding space gradually decreases, following the trend shown by the green dashed line. The space relationship is W1 > W2 > W3. When the claw reaches the point where the green slant line meets the red arc, the clove holding space inside the claw remains unchanged.



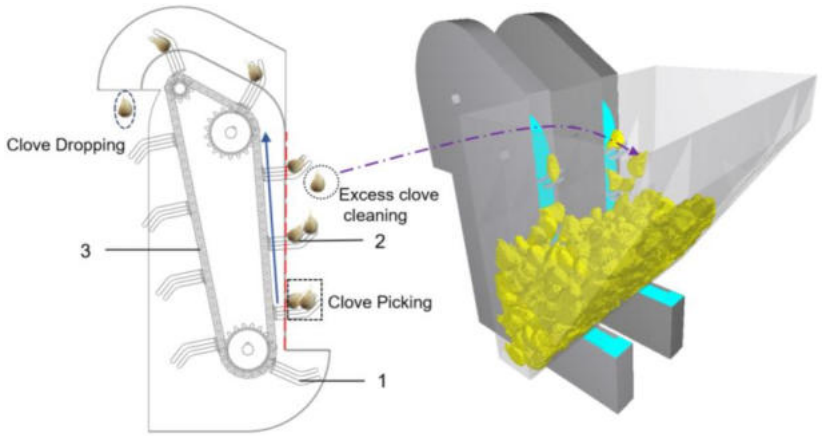
(a) Clove metering device (b) Structure of the clove metering mechanism

Fig. 1 - Structural schematic diagram of the clove picking device

1. Guide plate; 2. Clove picking chain; 3. Housing; 4. Clove picking sprocket; 5. Clove box; 6. Clove picking claw; 7. Clove holding chamber.

Working Principle of the Clove Metering Device

As shown in Fig. 2, the clove picking process includes three stages: picking, cleaning, and dropping. First, garlic cloves are added into the clove box. The chain drives the claws to move upward along the guide plate from the bottom of the box, grabbing several cloves during the ascent. As the claws rise, the internal holding space W gradually decreases. When the clove center of gravity exceeds the claw edge, excess cloves fall off by gravity, completing the cleaning. Since the space reduces to W_3 and remains unchanged, only one clove stays in the claw. Finally, the claw completes clove dropping at the end of its stroke. Throughout the motion, the claw maintains a tilt angle with the horizontal, promoting clove fallback and reducing missed picking.



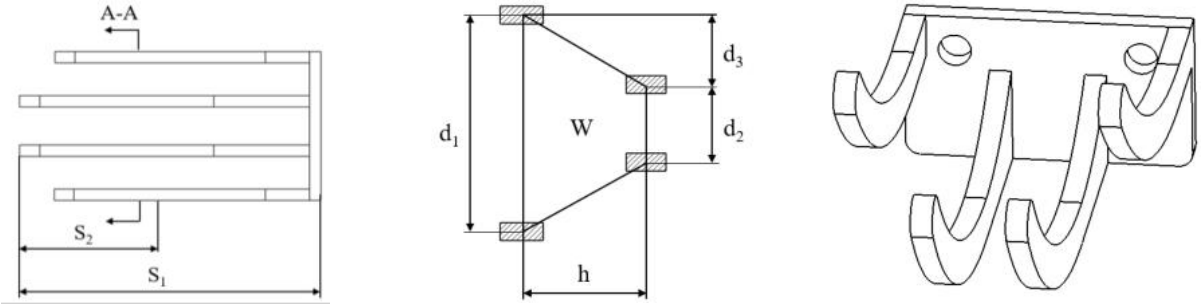
(a) 2D schematic of the clove-picking device (b) 3D diagram of the clove-picking process

Fig. 2 - Working Principle Diagram of the Clove Picking Device

1. Clove picking sprocket; 2. Garlic clove; 3. Clove picking chain; The blue arrow indicates the movement direction of the clove-picking claw; The red dashed line represents the guide plate; The purple dashed line illustrates the excess-clove cleaning process.

Design of Key Components of the Clove Picking Claw

The clove picking claw is the core component for achieving single-seed picking. Its geometry directly affects the performance of the clove picking device. The design must meet several key conditions: firstly, there must be spacing between claws to prevent garlic cloves from falling and to fit with the guide plate; secondly, the internal space must hold at least one garlic clove; thirdly, the shape should closely match the garlic clove to keep it stable inside the claw. To meet these requirements, a four-claw clove picking claw was designed, as shown in Fig. 3. The claws are installed alternately at two high and two low positions.



(a) Top view (b) Section view A-A (c) Axonometric View

Fig. 3 Structure of the clove picking claw

S1 represents the length of the clove picking claw; S2 is the minimum clove holding length; h denotes the height of the claw; d1 and d2 refer to the spacing between the upper and lower clove picking claws respectively; d3 is the spacing between the upper and lower claws; W indicates the cross-sectional area of the clove picking claw.

To ensure a high single-seed picking rate, the claw size must be reasonable. The minimum clove holding length S_2 mainly determines the minimum clove space W_3. Garlic cloves lie horizontally, vertically, inclined, or upright in the clove box. The design is based on the common horizontal position. The claw width should be larger than the maximum clove length and less than twice the minimum clove width. The claw height should be more than half the maximum clove width and less than half the minimum clove length. The claw length should be between twice the maximum clove width and twice the minimum clove length. In the cleaning stage, the minimum clove holding length must be greater than the maximum clove length and less than twice the minimum clove width. Also, the claw's minimum clove holding length should be less than the minimum clove width.

$$\begin{cases} L_{max} \leq \mathrm{d_1} \leq 2B_{min} \\ \frac{B_{max}}{2} \leq h \leq \frac{L_{min}}{2} \\ 2B_{max} \leq S_1 \leq 2L_{min} \\ L_{min} \leq S_2 \leq 2B_{min} \end{cases} \quad (1)$$

where: L_{max} is the Maximum length of garlic; L_{min} is the Minimum length of garlic; B_{max} is the Maximum width of garlic; B_{min} is the Minimum width of garlic.

According to Equation (1), the clove picking claw width is set at the midpoint of the parameter range, 33.3 mm. The claw height is chosen as the median value, 13.8 mm. The maximum clove holding space S_1 ranges from 53 mm to 57.8 mm, and the minimum clove holding space S_2 ranges from 28.64 mm to 34 mm.

Maximum Inclination Angle Between the Two Sprockets

During the cleaning stage, garlic cloves are confined within a narrowing space between the clove picking claw and the guide plate. This causes cloves to contact or be squeezed by the guide plate. If the tilt angle θ is set improperly, the resistance on the cloves during lifting will increase, which may cause clove damage. To prevent this, the compression force on the cloves during the entire lifting process must be less than their minimum crushing force. The force analysis is illustrated in Fig. 4.

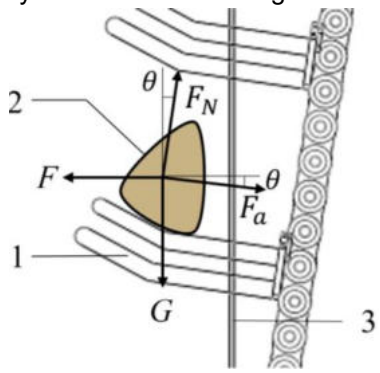


Fig. 4 - Force analysis of garlic cloves during cleaning process
1. Clove picking claw; 2. Garlic clove; 3. Guide plate

$$\begin{cases} F = F_a \cos\theta + F_N \sin\theta \\ G + F_a \sin\theta = F_N \cos\theta \\ F_a = \mu F_N \end{cases} \quad (2)$$

where: F is the thrust, (N); F_N is the support force, (N); F_a is the friction force, (N); G is the Weight of the garlic clove, (N); μ is the friction coefficient between the clove-picking claw and garlic clove; θ is the Inclination Angle Between the Two Sprockets.

From Equation (2), we obtain:

$$\theta = \arctan\left(\frac{F - \mu G}{\mu F - G}\right) \quad (3)$$

The clove picking claw is made of metal, and the coefficient of friction between the garlic clove and the metal material is 0.33. Moreover, the thrust force F must be less than the minimum destructive force of the garlic clove. Substituting into equation (3) yields θ is less than or equal to 18.22°.

Speed of the Clove Picking Claw

When the clove picking claw moves to the circular section of its path, the centrifugal force on the garlic cloves inside reaches its maximum. If this force is too large, the cloves may fly out of the claw, affecting picking performance. Therefore, a force analysis is needed to determine the claw's maximum speed and prevent clove ejection caused by excessive centrifugal force. The force analysis diagram is shown in Fig. 5.

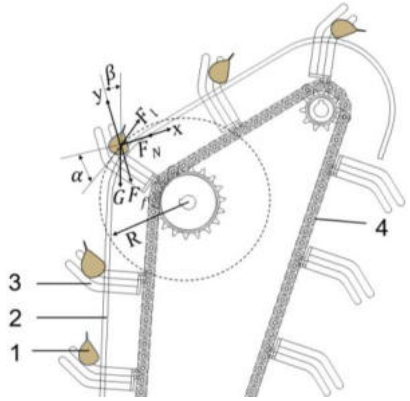


Fig. 5 - Force Analysis Diagram of Garlic Clove
1. Garlic clove; 2. Guide plate; 3. Clove picking claw; 4. Clove picking chain;

Taking the center of gravity of the garlic clove as the origin, the direction opposite to friction force as the y-axis, and the direction of support force as the x-axis, a force analysis of the clove inside the claw is conducted. The equilibrium equation is shown in Equation (4).

$$\begin{cases} F_l \cos\alpha + F_N = G\sin\beta \\ G\cos\beta + F_f = F_l \sin\alpha \\ F_f = \mu F_N \\ F_{l=} \dfrac{mv^2}{R\times 10^{-3}} \end{cases} \quad (4)$$

where: F_l is the Centrifugal force on the garlic clove, (N); G is the Weight of the garlic clove, (N); F_N is the Support force from the clove picking claw, (N); F_f is the Friction force from the clove picking claw, (N); α is the Angle between centrifugal force and the x-axis, (°); β is the Angle between gravity and the y-axis, (°); v is the Movement speed of the clove picking claw, (m/s); R is the distance between the sprocket center and the center of mass of the garlic clove.

According to equation (4), garlic cloves in the clove spoon will slide out along the tangential direction, resulting in clove leakage, when the component of gravity is less than the centrifugal force. Through calculation, the critical velocity *v* is less than or equal to 1.274 m/s.

Clove Picking Process EDEM Virtual Simulation and Analysis

Due to the irregular shape of garlic, 3D scanning technology was used to obtain its model. The model was then optimized using Geomagic Wrap to refine the garlic clove contour, as shown in Fig. 6. The model was saved in STL format. Finally, the 3D models of the clove picking device and garlic clove were imported into EDEM.



(a) Garlic scanning image (b) Garlic EDEM model (c) Clove picking device EDEM model

Fig. 6 - Simulation Models of Garlic Particles and Clove Picking Device

Model Parameters

Based on the materials used for the clove picking device, the clove picking claw, clove box, and clove guide plate are all made of medium carbon steel, Grade 45 (Chinese standard). The main simulation parameters are shown in Table 1.

Table 1

Garlic Clove Picking Simulation Parameters

Parameters	45 Steel	Garlic Clove
Density(kg/m³)	7850	1033
Poisson's Ratio	0.26	0.23
Elastic Modulus (MPa)	2.06×10^5	26.27
Coefficient of Restitution (with particles)	0.511	0.487
Static Friction Coefficient (with particles)	0.473	0.503
Dynamic Friction Coefficient (with particles)	0.117	0.102

A total mass of 10 kg of garlic cloves was generated per group in the particle factory at a rate of 3 kg/s. The cloves were initialized with a downward velocity of 2 m/s and zero angular velocity. To reflect realistic geometric variability, clove orientations were randomized, and a random distribution was used for generation. The size distribution coefficient was set between 0.95 and 1.08 times the measured clove dimensions to simulate actual screening effects.

Simulation Analysis

As shown in Fig. 7, to facilitate performance statistics of the clove picking device, a Grid Bin Group was set at the end of the picking area using EDEM post-processing to monitor cloves picked by the claw. Based on the results, and referring to GB/T 6973-2005 “Test Methods for Single-Seed (Precision) Seeders” and NY/T 503-2015 “Operation Quality of Single-Seed (Precision) Seeders”, the single picking rate Y_1, multiple picking rate Y_2, and missed picking rate Y_3 are calculated by the formulas in Equation (5).

$$\begin{cases} Y_1 = \dfrac{n_1}{N} \times 100\% \\ Y_2 = \dfrac{n_2}{N} \times 100\% \\ Y_3 = \dfrac{n_3}{N} \times 100\% \end{cases} \quad (5)$$

where: n_1 is the number of single garlic cloves picked; n_2 is the number of two or more cloves picked together; n_3 is the number of missed picks; N is the total number of picking attempts.

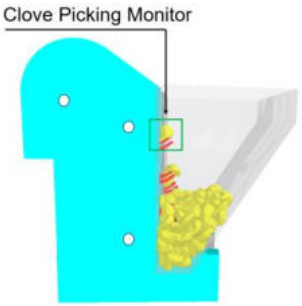


Fig. 7 - Clove Filling Monitor

RESULTS

Effect of Clove-Holding Length of Picking Claw on Filling Performance

Under the conditions of a picking claw speed of 0.05 m/s and a sprocket inclination angle of 7°, the picking claw length (S_1) was set to 53, 54, 55, 56, and 57 mm, and the minimum clove-holding length (S_2) was set to 29, 30, 31, 32, 33, and 34 mm. For each parameter combination, 50 picking operations were conducted, and the test was repeated five times, with the average value taken as the final result. The results, shown in Fig. 8, indicate that when S_1 is kept constant, a smaller S_2 (29~30 mm) results in insufficient clove-holding space after the cleaning stage, causing larger garlic cloves to be removed during cleaning and thus increasing the missed-picking rate. When S_2 is increased to 31–33 mm, the clove-holding space after cleaning is sufficient to accommodate garlic cloves of different sizes, leading to a higher single-seed picking rate. However, when S_2 exceeds 33 mm, the excessive clove-holding space after cleaning tends to retain two smaller cloves simultaneously, increasing the multiple-picking rate and reducing the single-seed picking rate. This demonstrates that S_2 is a key factor affecting clove-filling performance. In contrast, variations in S_1 have little influence on the single-seed picking rate when S_2 is fixed. Therefore, an S_1 of 53 mm within the feasible range and an S_2 of 31–33 mm can achieve optimal single-seed picking performance.

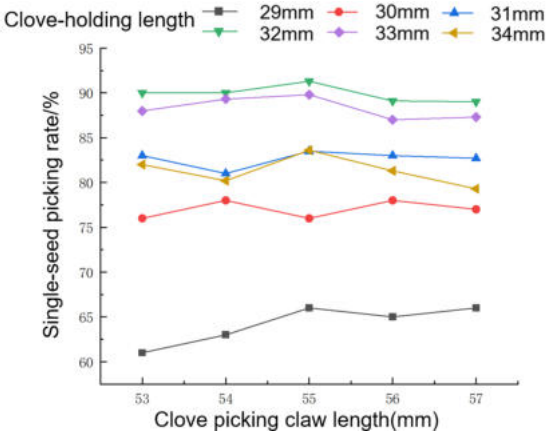


Fig. 8 - Effect of Clove Claw Cavity Length on Clove Filling Performance

Effect of dual sprocket tilt angle on clove filling performance.

The picking claw speed was set to 0.05 m/s, with a minimum clove-holding length of 32 mm. Simulations were run at sprocket angles of 4°, 6°, 8°, and 10°, with 50 picks per trial, repeated five times, resulting in a total of 250 picks for each angle. Statistical analysis was conducted using one-way ANOVA, and differences between sprocket angles were found to be statistically significant ($p < 0.05$). Results are shown in Fig. 9. At small angles, clove space changes little, causing poor cleaning, high multiple picking, and low single-seed picking rate. As the angle increases, cleaning improves and multiple picking decreases. When the angle exceeds 8°, the clove space is too large, causing cloves to be fully cleared and miss rate to rise. Overall, the best filling performance occurs between 5° and 7°, showing sprocket angle affects filling performance.

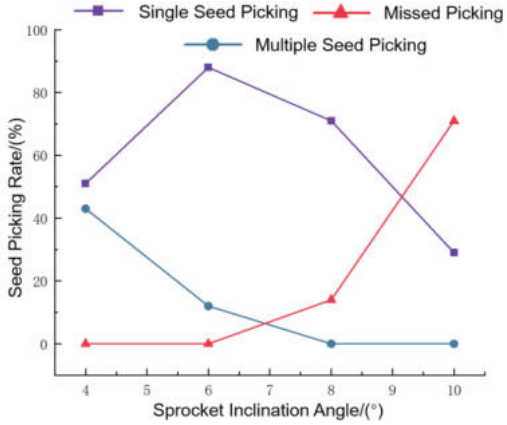
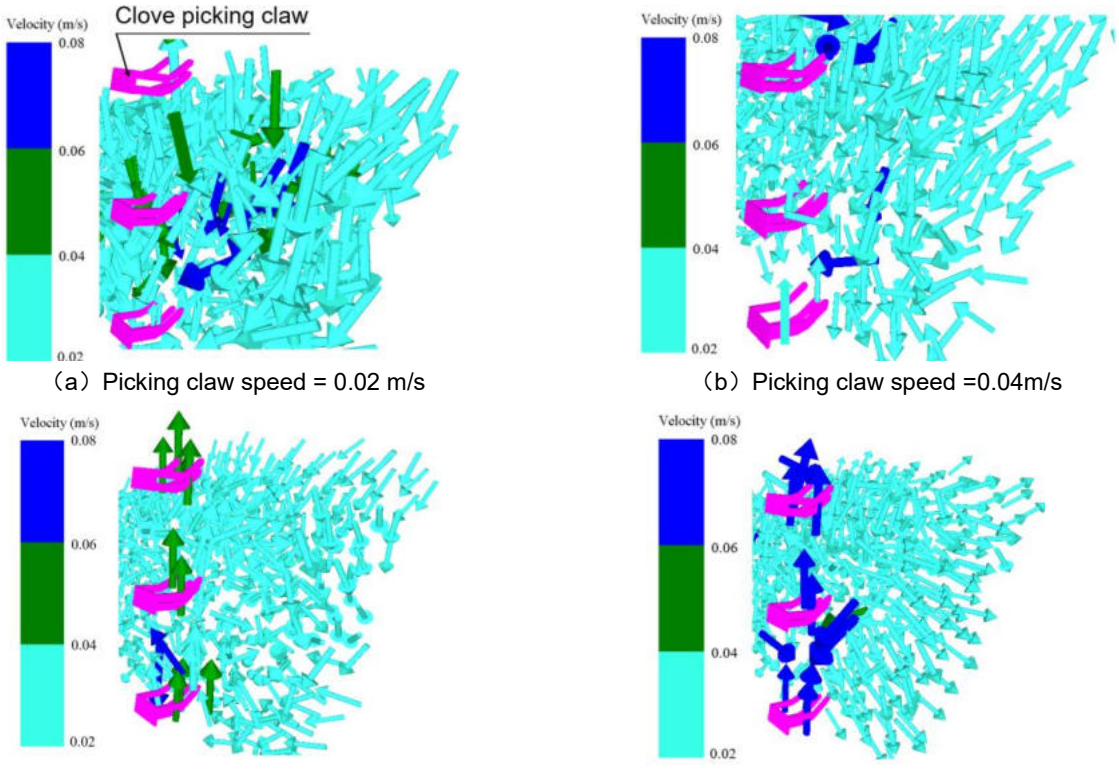


Fig. 9 - Effect of Sprocket Inclination Angle on Filling Performance

Effect of picking claw speed on clove filling performance

With the minimum clove-holding length of the picking claw set to 32 mm and the sprocket angle at 7°, simulation tests were conducted at claw speeds of 0.02, 0.04, 0.06, and 0.08 m/s. Each speed condition involved 50 picking cycles, repeated five times, and the average was taken as the final result. Fig. 11 shows the garlic clove velocity vector diagrams at different speeds, with the arrow indicating the direction of clove movement.



（a）Picking claw speed = 0.02 m/s （b）Picking claw speed =0.04m/s

（c）Picking claw speed =0.06m/s （d）Picking claw speed =0.08m/s

Fig. 10 - Velocity Vector Diagram of the Clove Picking Process

Different colored vector arrows indicate garlic clove velocity direction and magnitude; arrows in the claw show claw velocity, others show clove velocity in the clove box.

When the picking claw moves slowly (Fig. 10a, 10b), its speed is less than or equal to the garlic clove refill speed, resulting in longer contact time and fewer collisions, which leads to a higher multiple picking rate. As speed increases (Fig. 10c, 10d), the claw speed exceeds the refill speed, contact time shortens, collisions increase, and the claw has less time to pick cloves, causing a lower multiple picking rate and higher miss rate. Fig. 11 shows the effect of speed on filling performance. Considering both performance and efficiency, the optimal claw speed is 0.05~0.07 m/s.

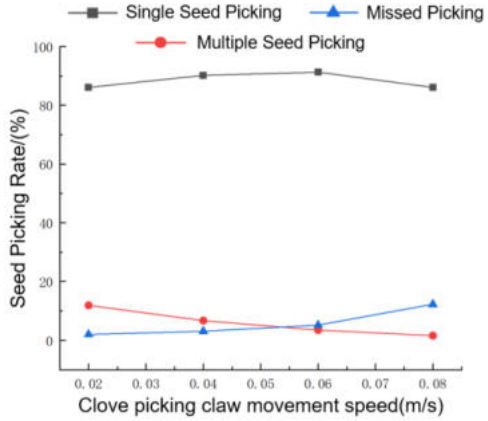


Fig. 11 - Effect of Clove Picking Claw Speed on Filling Performance

Analysis of three-factor, three-level orthogonal experiment

To find the optimal values of the three factors, the Box-Behnken design was used for testing. Based on single-factor tests, the picking claw speed range was set to 0.05~0.07 m/s, minimum clove-holding length to 31~33 mm, and sprocket angle to 5°~7°. The factors and levels for the clove picking device are shown in Table 2, where X_1, X_2 and X_3 are the factor code values of the Picking Claw Speed, Minimum Clove-Holding Length of Picking Claw and Angle Between Two Sprockets.

Table 2

Experimental Factors and Levels

Level	X_1 (m/s)	X_2 (mm)	X_3 (°)
-1	0.05	31	5
0	0.06	32	6
1	0.07	33	7

Experimental Results

Based on the Box-Behnken design, a three-factor, three-level experiment was conducted for the clove picking device. The experience plan and response values are shown in Table 3, where X_1, X_2, and X_3 represent the coded values of each factor.

Table 3

Experimental Design and Results

No.	Influencing Factors			Response Values	
	X_1/(m/s)	X_2/(mm)	X_3/(°)	Y_1/%	Y_2/%
1	-1	-1	0	75.30	12.90
2	1	-1	0	86.30	7.70
3	-1	1	0	78.10	11.80
4	1	1	0	90.10	5.40
5	-1	0	-1	75.80	13.40
6	1	0	-1	85.80	7.80
7	-1	0	1	75.80	13.40
8	1	0	1	92.10	5.70
9	0	-1	-1	80.20	10.90
10	0	1	-1	85.90	8.10
11	0	-1	1	90.20	6.40
12	0	1	1	91.00	5.80
13	0	0	0	87.90	6.90
14	0	0	0	85.70	8.80
15	0	0	0	85.80	8.80
16	0	0	0	85.70	8.80
17	0	0	0	85.70	8.80

Regression Equation and Significance Test

Based on Table 3, a multiple regression fitting analysis was performed using Design-Expert software to establish a quadratic polynomial response surface model of the single-seed picking rate with respect to picking claw speed, minimum clove-holding length, and the angle of the two sprockets, as shown in equations (6) and (7), These are dimensionless coded values and response variables.

$$Y_1 = 91.62 - 1.16x_1 + 6.98x_2 + 0.7875x_3 + 0.85x_1x_2 + 0.825x_1x_3 + 0.25x_2x_3 - 4.72{x_1}^2 - 8.45{x_2}^2 - 3.42{x_3}^2 \quad (6)$$

$$Y_2 = 7.24 + 2.26x_1 - 2.98x_2 + 2.83x_3 + 0.9025x_1x_2 - 0.415x_1x_3 + 0.6825x_2x_3 + 0.13{x_1}^2 + 4.1{x_2}^2 + 1.56{x_3}^2 \quad (7)$$

According to the analysis of variance for the regression equation shown in Table 4, the models for the single seed picking rate(Y_1) and missing picking rate(Y_2) are both highly significant (p<0.01), indicating that the regression models for single seed picking rate and missing picking rate are highly significant. The lack-of-fit tests for both models show p-values greater than 0.05, suggesting the models fit the data well. Based on the p-values, it can be concluded that in the single seed picking rate model, the regression terms X_2, X_1^2, X_2^2 and X_3^2 have extremely significant effects on the model, and the regression terms X_1, X_3, X_1X_2, X_1X_3 have significant effects. The order of influence of factors on the single seed picking rate is: minimum clove-holding length of the picking claw, picking claw speed, and the angle of the two sprockets. In the missing picking rate model, X_1, X_2, X_3 and X_2^2 have extremely significant effects on the model, while X_1X_2 and X_3^2 have significant effects. The order of influence of factors on the missing picking rate is: minimum clove-holding length of the picking claw, angle of the two sprockets, and picking claw speed.

By removing the insignificant influencing factors, the regression equations are optimized as shown in Equations (8) and (9), These are dimensionless coded values and response variables.

$$Y_1 = 91.62 - 1.16x_1 + 6.98x_2 + 0.7875x_3 + 0.85x_1x_2 + 0.825x_1x_3 - 4.72{x_1}^2 - 8.45{x_2}^2 - 3.42{x_3}^2 \quad (8)$$

$$Y_2 = 7.24 + 2.26x_1 - 2.98x_2 + 2.83x_3 + 0.9025x_1x_2 + 4.1{x_2}^2 + 1.56{x_3}^2 \quad (9)$$

Table 4

Variance Analysis of Regression Equations

Source	Single seed picking rate				Missed seed rate			
	Sum of squares	Degrees of Freedom	F-Value	P-Value	Sum of squares	Degrees of Freedom	F-Value	P-Value
Model	897.12	9	231.39	<0.0001***	266.67	9	54.63	<0.0001***
X_1	10.81	1	25.10	0.0015***	40.91	1	75.42	<0.0001***
X_2	389.21	1	903.48	<0.0001***	70.92	1	130.77	<0.0001***
X_3	4.96	1	11.52	0.0115***	64.01	1	118.03	<0.0001***
X_1X_2	2.89	1	6.71	0.0359**	3.26	1	6.01	0.0440**
X_1X_3	2.72	1	6.32	0.0402**	0.6889	1	1.27	0.2969
X_2X_3	0.2500	1	0.5803	0.4711	1.86	1	3.44	0.1062
X_1^2	93.90	1	217.98	<0.0001***	0.0712	1	0.1312	0.7279
X_2^2	300.46	1	697.48	<0.0001***	70.87	1	130.66	<0.0001***
X_3^2	49.32	1	114.49	<0.0001***	10.25	1	18.89	0.0034**
Residual	3.02	7			3.80	7		
Lack of Fit	1.03	3	0.6891	0.6044	1.45	3	0.8205	0.5465
Error	1.99	4			2.35	4		
Sum total	900.14	16			270.47	16		
	R=0.9966 ;Adjusted R²=0.9923; Adeq Precision=44.0164				R=0.9860 ;Adjusted R²=0.9670 ; Adeq Precision=25.8506			

Note: *** indicates $P < 0.001$ (extremely significant), ** indicates $P < 0.01$ (highly significant).

Effect of Interaction Terms Among Factors on the Single Seed Picking Rate

Fig. 12(a) shows the effect of interaction between clove picking claw speed and minimum clove-holding length on the single seed picking rate when the sprocket angle is at the medium level. As the claw speed increases, the single seed picking rate increases first and then decreases. Fig. 12(b) shows the effect of claw speed and sprocket angle when the clove-holding length is at its medium level. When the claw speed is fixed, the picking rate gradually increases with increasing angle. When the claw speed increases to 0.06 m/s, the upward trend due to the larger angle weakens.

Fig. 12(c) shows the interaction between clove-holding length and sprocket angle when the claw speed is at its medium level. When the sprocket angle is fixed, the picking rate first increases and then decreases as the clove-holding length increases.

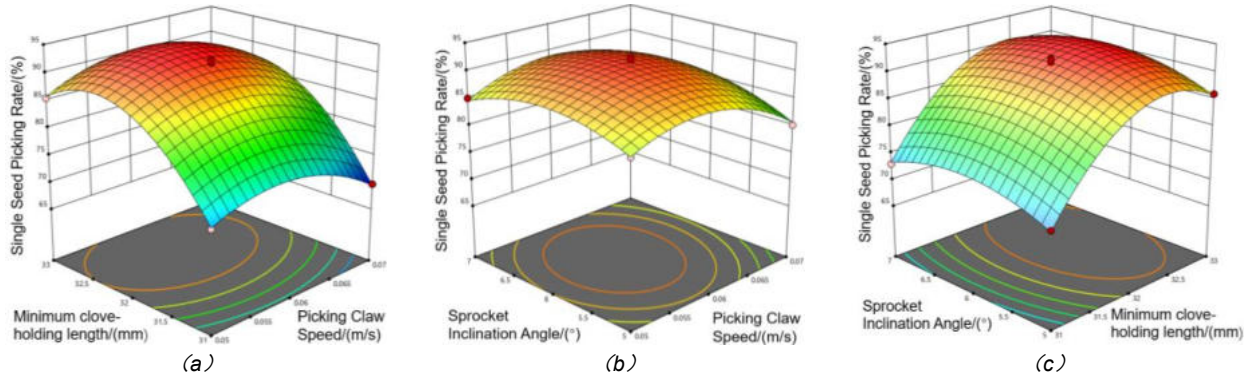


Fig. 12 - Effects of Picking Claw Speed, Minimum Clove-Holding Length, and Sprocket Inclination Angle on Single-Seed Picking Rate

(a)$Y_1(X_1,X_2,6)$;(b)$Y_1(X_1,32,X_3)$;(c)$Y_1(0.06,X_2,X_3)$

The interaction effects of factors on missed picking rate

Fig. 13(a) shows the interaction effect of picking claw speed and minimum clove-holding length on the missed picking rate when the sprocket angle is at its medium level. When the minimum clove-holding length is fixed, the missed picking rate increases with claw speed. When the claw speed is fixed, the missed picking rate decreases as the minimum clove-holding length increases. Fig. 13(b) shows the interaction between claw speed and sprocket angle on the missed picking rate when the minimum clove-holding length is at its medium level. When the claw speed is fixed, the missed picking rate increases with sprocket angle. When the sprocket angle is fixed, the missed picking rate also increases with claw speed. Fig. 13(c) shows the interaction between minimum clove-holding length and sprocket angle on the missed picking rate when the claw speed is at its medium level. When the sprocket angle is fixed, the missed picking rate decreases as the minimum clove-holding length increases. When the minimum clove-holding length is fixed, the missed picking rate increases with sprocket angle.

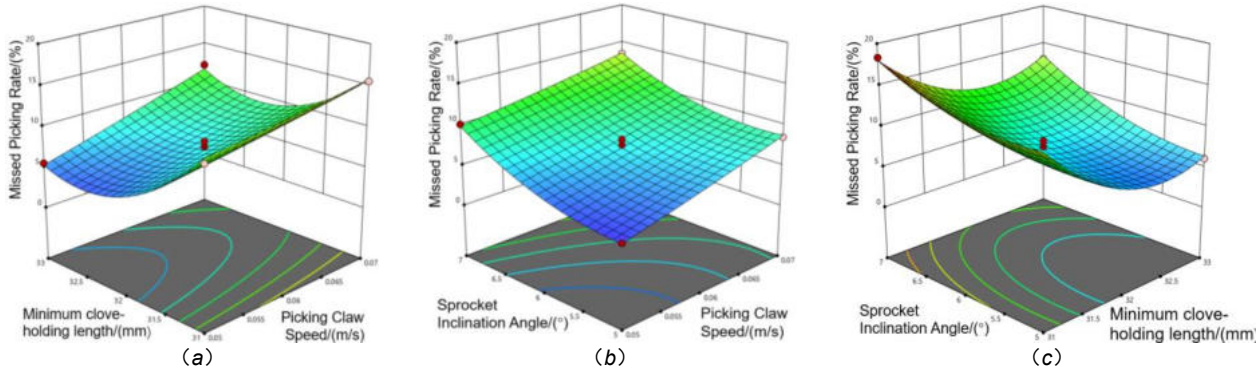


Fig. 13 - Effects of Picking Claw Speed, Minimum Clove-Holding Length, and Sprocket Inclination Angle on Missed Picking Rate

(a)$Y_2(X_1,X_2,6)$;(b)$Y_2(X_1,32,X_3)$;(c)$Y_2(0.06,X_2,X_3)$

Parameter Optimization

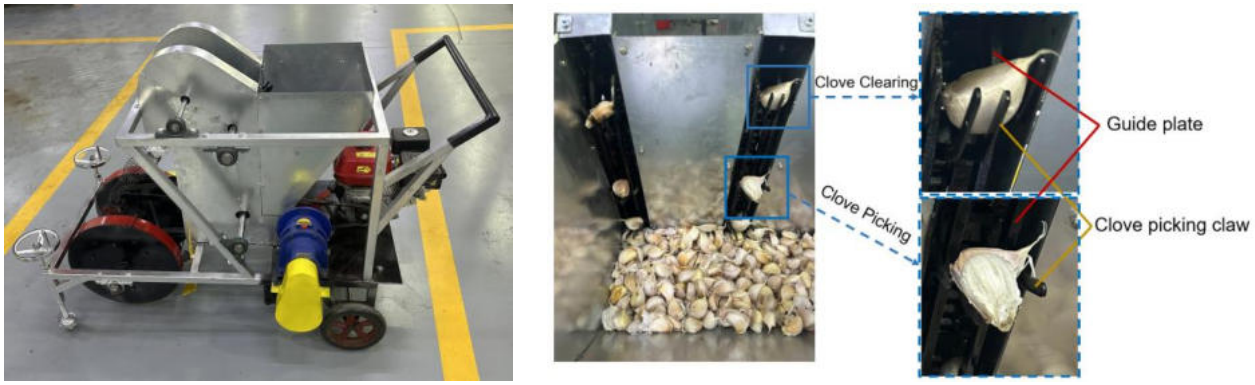
Use Design Expert software to optimize single seed picking rate and missed picking rate. The optimization goal is shown in equation (10):

$$\begin{cases} maxY_1(x_1,x_2,x_3) \\ minY_2(x_1,x_2,x_3) \\ 0.05m/s \le x_1 \le 0.07m/s \\ 31\text{mm} \le x_2 \le 33\text{mm} \\ 5° \le x_3 \le 7° \\ 0 < Y_i < 1, i = 1,2,3 \end{cases} \quad (10)$$

From equation (10), the optimal clove picking claw speed is 0.052 m/s, the optimal minimum clove-holding length is 32.413 mm, and the optimal angle between the two sprockets is 5.597°. At this point, the single seed picking rate is 92.342%, and the missed picking rate is 4.2%.

Experimental Process and Results

To verify the consistency between the single-seed picking rate of the clove picking device and the simulation results, and to evaluate the actual operational performance, the experimental procedure is shown in Fig 14. The test subject was Cangshan garlic, with clove sizes consistent with those used in the simulation. The experiment was conducted in a test field at Qingdao Agricultural University, where the plot surface was flat and the soil type was loam. The experiment was carried out under conditions of a picking claw speed of 0.05 m/s, a minimum clove-holding length of 32.4 mm, and a sprocket inclination angle of 5.6°. Five repeated trials were conducted, each involving 200 picking actions, during which the number of single seeds picked and the number of missed picks were recorded.



（a）Overall view of the garlic planter （b）Experiment process

Fig. 14 - Overall view and experimental process

Table 5

Experimental Results

N0.	Number of single seed Picks/Time	Number of Missed Picks/Time	Single Seed Picking Rate/(%)	Missed Picking Rate/(%)
1	184	9	92	4.5
2	185	8	92.5	4
3	183	9	91.5	4.5
4	180	9	90	4.5
5	185	9	92.5	4.5

The experimental results are shown in Table 5. The average single-seed picking rate measured in the tests was 91.7%, with a standard deviation of 1.04%, while the average missed picking rate was 4.4%, with a standard deviation of 0.22%. The average relative errors between the actual test values and the optimized values for the single-seed picking rate and missed picking rate were 0.70% and 4.8%, respectively, with maximum relative errors of 1.8% and 7.14%. These results indicate that the model is feasible and further validate the accuracy and reliability of the simulation data.

CONCLUSIONS

(1) To address the low single seed picking rate of garlic planter, a claw-chain type single seed picking device was designed. During clove picking process, the device initially picks multiple garlic cloves. As the picking claw rises, its internal volume decreases until only one clove is held.

(2) Based on garlic's geometric features, the structure and size of the picking claw were designed: claw width is set to 33.3 mm, height 13.8 mm, maximum clove holding length between 53 mm and 57.8 mm, and minimum clove holding length between 28.64 mm and 34 mm. The claw's moving speed and the angle between the two sprockets were also calculated theoretically.

(3) Single-factor simulation tests were performed using EDEM software, identifying picking claw speed, minimum clove holding length, and sprocket angle as key factors affecting the single seed picking rate. The preliminary ranges were: claw speed 0.4 m/s to 0.6 m/s, minimum clove holding length 31 mm to 33 mm, sprocket angle 5° to 7°. Then, a three-factor three-level orthogonal test was conducted. Using Design Expert software, the optimal parameters were found: claw speed 0.052 m/s, minimum clove holding length 32.413 mm, sprocket angle 5.597°.

(4) Field tests verified the optimal parameter combination. At claw speed 0.05 m/s, minimum clove holding length 32.4 mm, and sprocket angle 5.6°, the single seed picking rate reached 91.7%, and the missed picking rate was 4.4%, close to the simulation results. This proves the device performs well and meets the agronomic requirements for garlic clove picking.

ACKNOWLEDGEMENT

This research was funded by the National Natural Science Foundation of China (No:31971801), the Natural Science Foundation of Shandong Province of China (No: ZR2020ME252, ZR2020ME250) and Qingdao Science and Technology Benefit-the-People Demonstration Project (25-1-5-xdny-33-nsh).

REFERENCES

[1] Chen, Y., Liu, X., Han, B., Cui, Z., Yang, Y., Guan, C., & Gao, Q., (2021). Development report of China vegetable production mechanization in 2020 (2020 年中国蔬菜生产机械化发展报告). *Journal of Chinese Agricultural Mechanization*, Vol. 6, pp. 1-9, Jiangsu/China.

[2] Elwakeel, A. E., Elbeltagi, A., Dewidar, A., Salem, A., & Abdeen, M., (2025). Development and laboratory evaluation of a novel IoT-based electric-driven metering systemfor high precision garlic planter. *PloS one*, Vol. 20, Egypt.

[3] Furuhata, M., Chosa, T., Shioya, Y., Tsukamoto, T., Seki, M., Hosokawa, H., (2015). Developing Direct Seeding Cultivation Using an Air-Assisted Strip Seeder. *Japan Agricultural Research Quarterly*, Vol. 49, pp. 227-233, Japan.

[4] Gyoung, K., Hee, L., Goo, K., Keun, K., Yong, C., Soo, C., Suk, K., Je, M., (2018). A factor analysis of garlic metering device for development of a garlic planter. *Journal of Agriculture & Life Science*, Vol. 52, pp. 143-151, Korea.

[5] Im, D., Lee, H., Kim, J., Moon, D., Moon, T., Yu, S., & Park, Y., (2023). Bucket Size Optimization for Metering Device in Garlic Planter Using Discrete Element Method. *Agriculture*, Vol. 13, Korea.

[6] Kim, J., Han, H., Oh, J., Chung, W., Cho, S., & Park, Y., (2020). Structural Design of Garlic Plants Footplate Considering Physical Characteristics of Elderly Women. *Journal of Biosystems Engineering*, Vol. 45, pp. 16-23, Korea.

[7] Lai, Q., Jia, G., Su, W., Zhao, L., Qiu, X., & Lv, Q., (2022). Design and Test of Chain-spoon Type Precision Seed-metering Device for Ginseng Based on DEM-MBD Coupling (基于 DEM-MBD 耦合的链勺式人参精密排种器研究). *Transactions of the Chinese Society for Agricultural Machinery*, Vol. 3, pp.91-104, Yunnan/China.

[8] Lee, M., Kang, Y., Cheon, C., & Park, S., (2023). Development and Performance Verification of Line Sowing Type Garlic Planter. *Journal of the Korea Academia-Industrial cooperation Society*, Vol. 24, pp. 598-604, Korea.

[9] Manjunatha, M., Samuel, D., Anurag, K., & Gaikwad, N., (2014). Development and performance evaluation of a garlic peeler. *Journal of food science and technology*, Vol. 11, pp. 3083-93, India.

[10] Marey, S., (2011). Effect of forward speed and tuber characteristics on tuber spacing uniformity for a cup-belt potato planter. *Middle-East Journal of Scientific Research*, Vol. 8, pp. 753-758, Egypt.

[11] Qin, T., Wang, C., Lv, B., Kuang, J., Zhang, Q., Zhang, Q., & Hu, C., (2019). Performance Analysis for the Garlic Seeder with Multilayer Correction Institution (多层矫正式大蒜播种机矫正机构性能分析). *Journal of Agricultural Mechanization Research*, Vol. 5, pp. 81-85, Shandong/China.

[12] Smita, N., Solanki, S., Thakare, H., & Ramteke, R., (2019). Garlic Planting Machineries. *International Journal of Agricultural Engineering*, Vol. 12, pp. 162-169, India.

[13] Suryakant, S., Victor, V., & Naik, R., (2024). Development and Performance Evaluation of GarlicPlanter.*Journal of Experimental Agriculture International*, Vol. 46, pp. 479-485, India.

[14] Wei, H., Wang, X., & Chen, J., (2022). Discussion on the present situation and development of mechanized garlic production in China (中国大蒜机械化生产现状与发展思路探讨). *Journal of Chinese Agricultural Mechanization*, Vol. 4, pp. 175-182, Zhejiang/China.

[15] Xie, Y., Wang, J., Gao, X., Chen, F., Liu, H., & Hu, C., (2022). Design of Garlic Seed-belt Seeder with Maintainability (可保持式大蒜种带播种机的设计). *Agricultural Equipment & Vehicle Engineering*, Vol. 6, pp. 28-31, Shandong/China.

[16] Xue, J., Cai, Z., Zhang, H., Li, X., Lang, T., & Wang, W., (2024). Design and test of seed dispenser of spoon chain potato planter (勺链式马铃薯播种机排种器设计与试验). *Agricultural Engineering*, Vol. 11, pp. 74-82, Yunnan/China.

[17] Yang, B., Zong, Y., & Zhao, B., (2019). Measurement of the International Competitiveness of China's Garlic Industry and Its Influencing Factors (中国大蒜产业国际竞争力测算及影响因素分析). *Agricultural Outlook*, Vol. 10, pp. 113-117, Hebei/China.

[18] Yang, J, Sun, H & Zhang, Z. (2015). A Review on Fundamentals of Distinct Element Method and Its Applications in Agricultural Engineering Realm (离散元法及其在农业工程中的应用综述). *Modern Food*, Vol. 15, pp. 28-33, Zhengzhou/China.

[19] Zhang, J., Song, W., Cao, Y., Wang, C., Guo, H., Zhu, L., & Yang, F., (2022). Design and Experimental Study on Key Components of Garlic Seeder (大蒜播种机关键部件设计及试验研究). *Journal of Agricultural Mechanization Research*, Vol. 8, pp. 129-136, Shanxi/China.

[20] Zhang, X., Yi, S., Tao, G., Zhang, D., & Chong, J., (2022). Design and Experimental Study of Spoon-Clamping Type Garlic Precision Seeding Device. *Wireless Communications and Mobile Computing*, Vol. 2022, China.

WRITING INSTRUCTIONS

Article Types

Three types of manuscripts may be submitted:

1. **Regular articles:** should describe new and carefully confirmed findings, and experimental procedures should be given in sufficient detail for others to verify the work. The length of a full paper should be the minimum required to describe and interpret the work clearly (recommended max.10 pages);
2. **Reviews:** must contain at least three basic elements: an introduction or background information section; the body of the review containing the discussion of sources; and, finally, a conclusion and/or recommendations section to end the paper. The length of a full paper should be the max. 20 pages (if the number of references is 80-100) and max. 45 pages (if the number of references is over 300).

Manuscripts should be written in English (American or British usage is accepted, but not a mixture of these) and submitted directly on the journal website. The 2nd, 3rd and the next versions can be sent by e-mail, ***inmatehjournal@gmail.com*** mentioning the registration number (N…).
Please be sure to include your full affiliation and e-mail address (see Sample manuscript)
The authors are responsible for the accuracy of the whole paper and references.
There are allowed 2 papers by each first author.
The text layout should be in single-column format. To avoid unnecessary errors it is strongly advised to use the "spell-check" and "grammar check" functions of your word processor.

Review Process

All manuscripts are reviewed by 2 members of the Scientifically Review Office. Decisions will be made as rapidly as possible and the journal strives to return reviewers' comments to authors in approx.3 weeks.
The editorial board will re-review manuscripts that are accepted pending revision.

NOTE:

Submission of a manuscript implies: that the work described has not been published before (excepting as an abstract or as part of a published lecture or thesis) that it is not under consideration for publication elsewhere.

1. REGULAR ARTICLES

- Manuscripts should be concise, in ***1.15 line spacing***, and should have 2 cm all over margins. The font should be ***Arial 10 pt.*** Ensure that each new paragraph is clearly indicated, using **TAB at 1 cm**.
- Title will be ***Arial 12 pt***. and explicit figures will be ***Arial 9 pt***.
- Text will be written in English.
- Chapters' titles are written by ***Arial 10 pt, Bold, Uppercase*** (e.g. **INTRODUCTION, MATERIALS AND METHODS**), between chapters is left a space for 10 pt. At the beginning of each paragraph, TAB of 1 cm.
- The paper body will be written in ***Arial 10 pt., Justify alignment***.

TITLE ***Arial 12 pt., Uppercase, Bold, Center*** *(in English language)* and ***Bold Italic*** *(in native language)*.
Should be a brief phrase describing the contents of the paper. Avoid long titles; a running title of no more than 100 characters is encouraged (without spaces).

AUTHORS ***ARIAL 9, Bold, Centre alignment***
Under the paper's title, after a space (enter) 9 pt., write ***authors' names*** and ***affiliations (Arial 8 pt.-Regular)***
When the paper has more than one author, their name will be followed by a mark (Arabic numeral) as superscript if their affiliation is different. Less than 6 authors.
Corresponding author's name (next row), ***(Arial 8 pt.)***. Should be added also: phone, fax and e-mail information, for the paper corresponding author (***font: 8 pt., Italic***).

KEYWORDS ***(In English)*** about 4 to 7 words that will provide indexing references should be listed (title: ***Arial 10pt, bold italic,*** text ***Arial 10 pt., italic***).
A list of non-standard *Abbreviations* should be added. In general, non-standard abbreviations should be used only when the full term is very long and used often. Each abbreviation should be spelled out and introduced in parentheses the first time it is used in the text. Standard abbreviations (such as ATP and DNA) need not to be defined.

ABSTRACT ***(in English and Native language, Arial 10 pt.)***, the title *bold*; the text of abstract: *italic*) should be informative and completely self-explanatory, briefly present the topic, state the scope of the experiments, indicate significant data, and point out major findings and conclusions. The Abstract should be max.250 words. Complete sentences, active verbs, and the third person should be used, and the abstract should be written in the past tense. Standard nomenclature should be used and abbreviations should be avoided. No literature should be cited.

INTRODUCTION (***Arial 10 pt.***) should provide a clear statement of the problem, the relevant literature on the subject, and the proposed approach or solution. It should be understandable to colleagues from a broad range of scientific subjects. We should refer to the current stage of researches performed in the field of the paper to be published, by quoting up-to-date specialty studies, preferably published after 2006, excepting certain referential specialty books/studies, especially papers issued in magazines/journals/conferences/ISI quoted symposia or in other international data bases, which are well known and available.

MATERIALS AND METHODS (***Arial 10 pt.***) should be complete enough to allow experiments to be reproduced. However, only truly new procedures should be described in detail; previously published procedures should be cited, and important modifications of published procedures should be mentioned briefly. Methods in general use need not be described in detail.

RESULTS (***Arial 10 pt.***) should be clarity presented. The results should be written in the past tense when describing findings in the authors' experiments. Results should be explained, but largely, without referring to the literature. Discussion, speculation and detailed interpretation of data should not be included in the Results, but should be put into the Conclusions section.

CONCLUSIONS (***Arial 10 pt.***) The main conclusions drawn from results should be presented in a short Conclusions section. Do not include citations in this section.

Formulae, symbols and abbreviations: Formulae will be typeset in Italics (preferable with the Equation Editor of Microsoft Office 2003) and should be written or marked as such in the manuscript, unless they require a different styling. They should be referred to in the text as Equation (4) or e.g. (4). The formulae should be numbered on the right side, between brackets ***(Arial 10 pt.)***:

$$P = F \cdot v \tag{1}$$

Terms of the equation and the unit measure should be explained, e.g.

P is the power, [W];
F – force, [N];
v – speed, [m/s]

SI units must be used throughout.

Tables should be self-explanatory without reference to the text. The details of the methods used in the experiments should preferably be described in the legend instead of in the text. The same data should not be presented both in table and graph form or repeated in the text.
Table's title will be typed ***Arial 9 pt, Bold, Centered***
In the table, each row will be written Arial 9 pt, single-spaced throughout, including headings and footnotes.
The table should be numbered on the right side, ***Arial 10 pt.***

Figures ***(Arial 9 pt., Bold, Center)***should be typed in numerical order (Arabic numerals). Graphics should be high resolution (e.g.JPEG).Figure number is followed by what represent the figure or graph e.g.:

Fig.1 – Test stand

Legend: ***Arial 8 pt, Italic, Center,*** e.g.:
1 - plansifter compartments; 2- break rolls; 3 – semolina machines; 4 – reduction rolls; 5 – flour

ACKNOWLEDGMENTS (***Arial 10 pt.***) of people, grants, funds etc should be brief (*if necessarily*).

REFERENCES (***Arial 10 pt.***)
(In alphabetical order, in English and in the original publication language).
Minimum 10 references, last 10 years, minimum 3 references from the last 2 years

It can be used "*References*" tool from the *Word Editor*. **APA Style (American Psychological Association)**
https://apastyle.apa.org/style-grammar-guidelines/references/examples

All references must be provided in English

Authors are fully responsible for the accuracy of the references.

References should be **alphabetically**, with complete details, as follows:

Examples:

Books: https://apastyle.apa.org/style-grammar-guidelines/references/examples/book-references

Jackson, L. M. (2019). *The psychology of prejudice: From attitudes to social action* (2nd ed.). American Psychological Association. https://doi.org/10.1037/0000168-000

Kesharwani, P. (2020). *Nanotechnology based approaches for tuberculosis treatment*. Academic Press.

Sapolsky, R. M. (2017). *Behave: The biology of humans at our best and worst*. Penguin Books.

Torino, G. C., Rivera, D. P., Capodilupo, C. M., Nadal, K. L., & Sue, D. W. (2019). *Microaggression theory: Influence and implications*. John Wiley & Sons. https://doi.org/10.1002/9781119466642

In text:

- ***Parenthetical citations***: (Jackson, 2019; Sapolsky, 2017)
- ***Narrative citations***: Jackson (2019) and Sapolsky (2017)

Journal Article:
https://apastyle.apa.org/style-grammar-guidelines/references/examples/journal-article-references

Grady, J. S., Her, M., Moreno, G., Perez, C., & Yelinek, J. (2019). Emotions in storybooks: A comparison of storybooks that represent ethnic and racial groups in the United States. *Psychology of Popular Media Culture*, *8*(3), 207–217. https://doi.org/10.1037/ppm0000185

In text:

- ***Parenthetical citation***: (Grady et al., 2019)
- ***Narrative citation***: Grady et al. (2019)

Conference or Symposium:
https://apastyle.apa.org/style-grammar-guidelines/references/examples/conference-proceeding-references

Duckworth, A. L., Quirk, A., Gallop, R., Hoyle, R. H., Kelly, D. R., & Matthews, M. D. (2019). Cognitive and noncognitive predictors of success. *Proceedings of the National Academy of Sciences*, *USA*, *116*(47), 23499–23504. https://doi.org/10.1073/pnas.1910510116

In text:

- ***Parenthetical citation***: (Duckworth et al., 2019)
- ***Narrative citation***: Duckworth et al. (2019)

Dissertation / Thesis:
https://apastyle.apa.org/style-grammar-guidelines/references/examples/published-dissertation-references

Zambrano-Vazquez, L. (2016). *The interaction of state and trait worry on response monitoring in those with worry and obsessive-compulsive symptoms* [Doctoral dissertation, University of Arizona]. UA Campus Repository. https://repository.arizona.edu/handle/10150/620615

In text:

- ***Parenthetical citations***: (Kabir, 2016; Miranda, 2019; Zambrano-Vazquez, 2016)
- ***Narrative citations***: Kabir (2016), Miranda (2019), and Zambrano-Vazquez (2016)

https://apastyle.apa.org/style-grammar-guidelines/references/examples/unpublished-dissertation-references

Harris, L. (2014). *Instructional leadership perceptions and practices of elementary school leaders* [Unpublished doctoral dissertation]. University of Virginia.

In text:

- ***Parenthetical citation***: (Harris, 2014)
- ***Narrative citation***: Harris (2014)

Patents: Names and initials of authors, year (between brackets), patent title (Italic), patent number,country:
Grant, P. (1989). *Device for Elementary Analyses*. Patent. No.123456. USA.

Legal regulations and laws, organizations:
https://apastyle.apa.org/style-grammar-guidelines/references/examples/iso-standard-references

International Organization for Standardization. (2018). *Occupational health and safety management systems—Requirements with guidance for use* (ISO Standard No. 45001:2018). https://www.iso.org/standard/63787.html

Occupational Safety and Health Administration. (1970). *Occupational safety and health standards: Occupational health and environmental control: Occupational noise exposure* (OSHA Standard No. 1910.95). United States Department of Labor. https://www.osha.gov/laws-regs/regulations/standardnumber/1910/1910.95

In text:

- ***Parenthetical citations***: (International Organization for Standardization, 2018; Occupational Safety and Health Administration, 1970)
- ***Narrative citations***: International Organization for Standardization (2018) and Occupational Safety and Health Administration (1970)

Web references: The full URL should be given in text as a citation, if no other data are known. If the authors, year, and title of the documents are known and the reference is taken from a website, the URL address has to be mentioned after these data.

Citation in text

Please ensure that every reference cited in the text is also present in the reference list (and vice versa).

Do not cite references in the Abstract and Conclusions !.

Unpublished results, personal communications as well as URL addresses are not recommended in the references list.

Making personal quotations (one, at most) should not be allowed, unless the paper proposed to be published is a sequel of the cited paper. Articles in preparation or articles submitted for publication, unpublished, personal communications etc. should not be included in the references list.

Citations style

Text: All citations in the text may be made directly (or parenthetically) as bellow.

- ***single author:*** the author's name (without initials, unless there is ambiguity) and the year of publication:
  "as previously demonstrated *(Brown, 2010)*".
- ***two authors:*** both authors' names and the year of publication: *(Adam and Brown, 2008; Smith and Hansel, 2006; Stern and Lars, 2009)*
- ***three or more authors:*** first author's name followed by "et al." and the year of publication: "As has recently been shown *(Werner et al., 2005; Kramer et al., 2000)* have recently shown ...."

Citations of groups of references should be listed first alphabetically, then chronologically.

Units, Abbreviations, Acronyms

- Units should be metric, generally SI, and expressed in standard abbreviated form.
- Acronyms may be acceptable, but must be defined at first usage.

2. REVIEWS

Reviews and perspectives covering topics of current interest in the field, are encouraged and accepted for publication. A review must have at least 80 references. It might give a new interpretation of old material or combine new with old interpretations. Or it might trace the intellectual progression of the field, including major debates. And depending on the situation, the literature review may evaluate the sources and advise the reader on the most pertinent or relevant.

Literature reviews must contain at least three basic elements: an introduction or background information section; the body of the review containing the discussion of sources; and, finally, a conclusion and/or recommendations section to end the paper.

The following provides a brief description of the content of each: Introduction: Gives a quick idea of the topic of the literature review, such as the central theme or organizational pattern. Body: Contains your discussion of sources and is organized either chronologically, thematically, or methodologically. Conclusions / Recommendations: Discuss what you have drawn from reviewing literature so far.

Edited by: INMA Bucharest
6, Ion Ionescu de la Brad Blvd., sect. 1, Bucharest, ROMANIA
Tel: +4021.269.32.60; Fax: +4021.269.32.73
https:// inmateh.eu
e-mail: ***inmatehjournal@gmail.com***